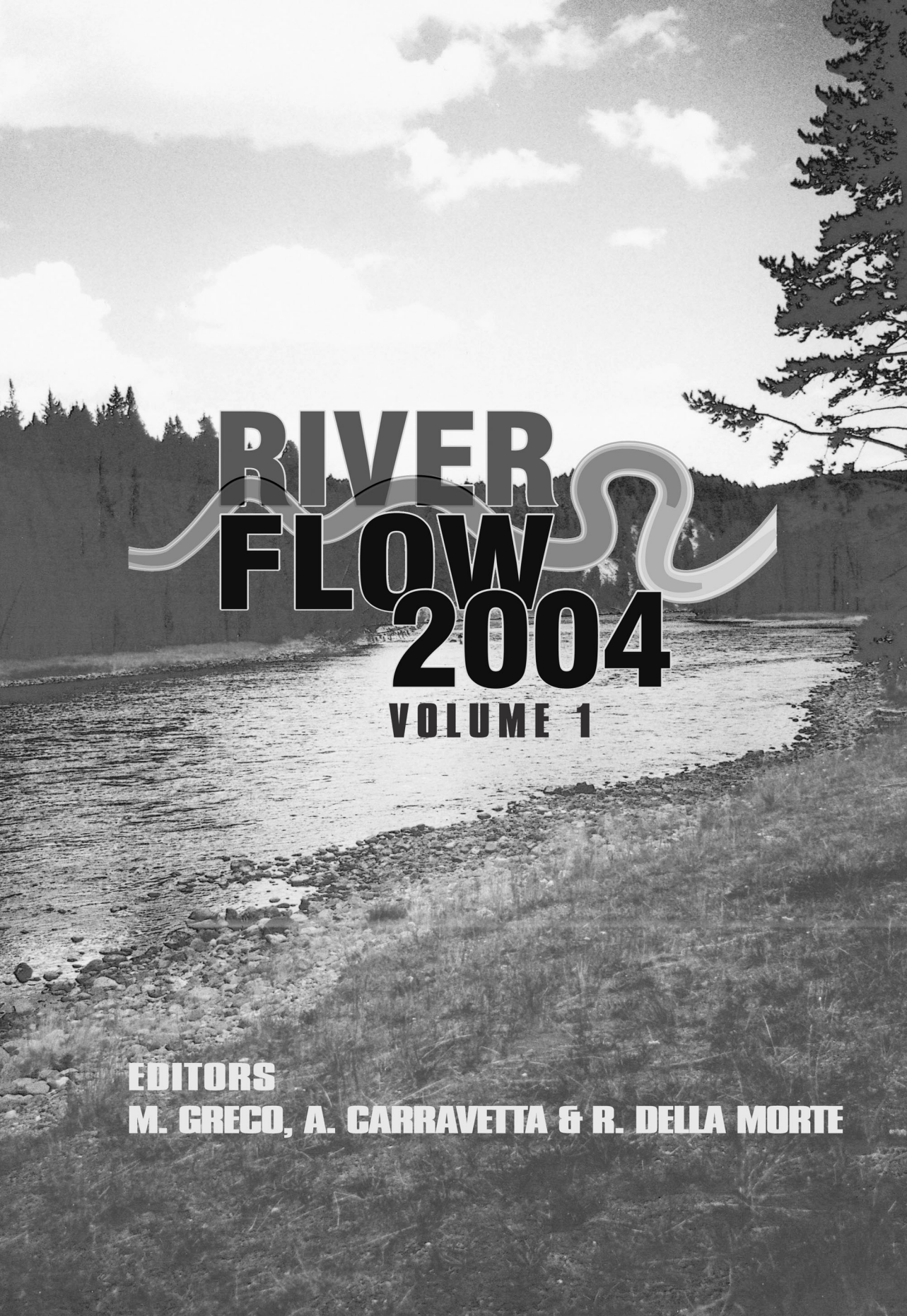

RIVER FLOW 2004
VOLUME 1
EDITORS
M. GRECO, A. CARRAVETTA & R. DELLA MORTE

RIVER FLOW 2004

This page intentionally left blank

PROCEEDINGS OF THE SECOND INTERNATIONAL CONFERENCE ON FLUVIAL HYDRAULICS,
23–25 JUNE 2004, NAPOLI, ITALY

River Flow 2004

Edited by

Massimo Greco, Armando Carravetta & Renata Della Morte
Federico II University of Napoli, Italy

VOLUME 1



A.A. BALKEMA PUBLISHERS Leiden / London / New York / Philadelphia / Singapore

CRC Press
Taylor & Francis Group
6000 Broken Sound Parkway NW, Suite 300
Boca Raton, FL 33487-2742

© 2004 by Taylor & Francis Group, LLC
CRC Press is an imprint of Taylor & Francis Group, an Informa business

No claim to original U.S. Government works
Version Date: 20140513

International Standard Book Number-13: 978-1-4822-9834-5 (eBook - PDF)

This book contains information obtained from authentic and highly regarded sources. Reasonable efforts have been made to publish reliable data and information, but the author and publisher cannot assume responsibility for the validity of all materials or the consequences of their use. The authors and publishers have attempted to trace the copyright holders of all material reproduced in this publication and apologize to copyright holders if permission to publish in this form has not been obtained. If any copyright material has not been acknowledged please write and let us know so we may rectify in any future reprint.

Except as permitted under U.S. Copyright Law, no part of this book may be reprinted, reproduced, transmitted, or utilized in any form by any electronic, mechanical, or other means, now known or hereafter invented, including photocopying, microfilming, and recording, or in any information storage or retrieval system, without written permission from the publishers.

For permission to photocopy or use material electronically from this work, please access www.copyright.com (http://www.copyright.com/) or contact the Copyright Clearance Center, Inc. (CCC), 222 Rosewood Drive, Danvers, MA 01923, 978-750-8400. CCC is a not-for-profit organization that provides licenses and registration for a variety of users. For organizations that have been granted a photocopy license by the CCC, a separate system of payment has been arranged.

Trademark Notice: Product or corporate names may be trademarks or registered trademarks, and are used only for identification and explanation without intent to infringe.

Visit the Taylor & Francis Web site at
http://www.taylorandfrancis.com

and the CRC Press Web site at
http://www.crcpress.com

River Flow 2004 – Greco, Carravetta & Della Morte (eds.)
© 2004 Taylor & Francis Group, London, ISBN 90 5809 658 0

Table of Contents

Preface XV

Organization XVII

Volume 1

Keynote speeches

Recent advances in scour hydraulics 3
W.H. Hager, G. Oliveto, S. Pagliara & J. Unger

Mixing and dispersion in rivers 13
G.H. Jirka

Debris flows and their modeling 29
T. Takahashi

A. Fluvial processes
A.1. Morphology and morphodynamics

The morphology, 3D flow structure and sediment dynamics of a large river confluence: the Rio Paraná and Rio Paraguay, NE Argentina 43
D.R. Parsons, J.L. Best, S.N. Lane, R.J. Hardy, O. Orfeo & R. Kostaschuk

Flow structures in meander bends with recirculation zones: implications for bend movements 49
D.R. Parsons, R.I. Ferguson, S.N. Lane & R.J. Hardy

Influence of geometrical constraints on the evolution of meandering rivers 59
P. Perona & C. Camporeale

Behaviour of small perturbations in 1D mobile-bed models 67
G. Rosatti, L. Fraccarollo & A. Armanini

A new method for the assessment of river network fractal dimensions: introduction, computation and comparison 75
S.G. De Bartolo, R. Gaudio, L. Primavera, S. Gabriele & M. Veltri

2D sediment transport study on Elbe River – Czech Republic 83
P. Jirinec & J. Spatka

Simulation and prediction of river morphologic changes using RubarBE 89
K. El Kadi Abderrezzak & A. Paquier

Gravel river widening by bank erosion in a straight stretch of river – investigations on a numerical model 99
M. Schmautz

Flow in meandering bends 109
D. Termini

On the validity of analytical approach to river regime 119
B. Mengoni, E. Paris & R. Bettess

Mobile-bed experiments on the exchange of sediment between main channel and groyne fields 127
M.F.M. Yossef & H.J. de Vriend

Impact of hydropower schemes at bedload regime and channel morphology of the Danube River 135
K. Holubová, Z. Capeková & J. Szolgay

Investigation of Lithuanian river-channels classification 143
Z. Rimkus

3D numerical modelling of morphological bed changes in the Danube River 151
T. Fischer-Antze, D. Gutknecht & N.R.B. Olsen

Using a 1D steady flow model to compare field determination methods of bank-full stage 155
O. Navratil, M.-B. Albert, C. Boudard & J.-M. Grésillon

Large scale tests for gravel-bed river widening 163
M. Aufleger & A. Niedermayr

Influence of local scouring on natural step pool geometry 173
F. Comiti, A. Andreoli & M.A. Lenzi

Assaying historical maps and relict channel forms for the analysis of channel processes (on example of the Spree River in Germany) 181
N. Nikolaevich, A. Sukhodolov & C. Engelhardt

Monte Carlo method applied to a two-dimensional morphodynamic model 191
J.J.P. Lambeek, H.R.A. Jagers & H. van der Klis

Behavior of a finite disturbance in a mobile bed stream 197
M. Iervolino & A. Leopardi

Bar height formulas to predict the maximum scour depth at riverbanks 205
G. Del Giudice, G. Rasulo & E. Viparelli

Use of sheet-piling submerged vanes 217
R. Guercio, R. Magini & M. Rotondi

A.2. Bed forms and flow resistance

Double-averaged flow field over static armor layers 225
J. Aberle & K. Koll

The numerical simulation of time dependent flow structures over water worked gravel 235
R.J. Hardy & S.N. Lane

Numerical simulation on development process of dunes and flow resistance 245
S. Onda & T. Hosoda

Experimental study of bed-load grain size sorting near incipient motion on steep slopes 253
A. Recking, V. Boucinha & P. Frey

An improved flow resistance formula 259
G. Smart

Large-eddy simulation of flow over rough channel beds 265
T. Stoesser, W. Rodi & G.H. Jirka

Flow over dunes with super-imposed smaller dunes. Turbulent coherent structures and wall similarity hypothesis 273
M.T. Mattar

Effect of bed-load concentration on friction factor in narrow channels 279
F. Calomino, R. Gaudio & A. Miglio

Influence of macro-roughness arrangement on flow resistance 287
F. Canovaro, E. Paris & L. Solari

The effect of bed roughness on velocity profile in open channels 295
A. Mahdavi & M.H. Omid

3D turbulent flow over irregular bed surfaces 301
W. Czernuszenko & A. Rylov

Negative eddy viscosity in river bends 307
R. Booij

Turbulent flow over mobile and molded bedforms: a comparative field study 317
A. Sukhodolov, J. Fedele & B.L. Rhoads

A.3. Over-bank flow and vegetation

Depth-averaged modelling of overbank flow in meandering channels 329
P. Rameshwaran & K. Shiono

Influence of a mobile bed on the boundary shear in a compound channel 337
S. Atabay, D.W. Knight & G. Seckin

Interaction processes in a straight compound channel with rigid and flexible emergent floodplain vegetation 347
I. Schnauder

Numerical evaluation of secondary flow effects on lateral momentum transfer in overbank flows 353
A. Tominaga & D.W. Knight

Effect of lateral variation of roughness on flow conveyance within a trapezoidal channel cross-section 363
H.I. Mohamed

Boundary conditions between panels in depth-averaged flow models revisited 371
D.W. Knight, M. Omran & J.B. Abril

Effect of vegetation on boundary layer with turbulent free stream 381
P. Gualtieri, G. Pulci Doria & L. Taglialatela

Response of velocity to a sudden change of bed roughness in sub critical open channel flow 389
A. Carravetta & R. Della Morte

Velocity distribution in a V-shaped channel 395
M. Mohammadi

River roughness – the integration of diverse knowledge 405
C. McGahey & P.G. Samuels

Improving 1-D modelling of open channel flow in compound channels 415
J.P. Martín-Vide, S. López-Querol & P.M. Moreta

Coherent flow structures in a converging compound channel 423
D. Bousmar, B. Denis & Y. Zech

Variations and correlation of roughness indices of non-vertical non-rigid fully submerged vegetation in open channels 431
A.M. Negm

Recirculating flow behind groynes for compound-channel geometries 437
N. Rivière, S. Proust & A. Paquier

Local velocity at bridge abutments on plain rivers 443
B. Gjunsburgs & R. Neilands

Performance of lateral velocity distribution models for compound channel sections 449
J.F. Weber & A.N. Menéndez

The conveyance capacity of compound channels with large scale floodplain roughness 459
A.R. Heanen, W.R.C. Myers & J.F. Lyness

A study of turbulent flow structure in a partly vegetated river reach 469
T. Sukhodolova, A. Sukhodolov & C. Engelhardt

Open channel turbulent data modeling using fractal geometry 479
A.N. Ziaei, A.R. Keshavarzi & H. Emdad

Expeditive methodology for river water discharge evaluation 487
M. Greco & D. Mirauda

Integrated approaches for modeling sediment transport 495
J.-M. Hervouet & C. Villaret

A.4. Interaction with structures

Riprap failure of bridge piers 503
J. Unger & W.H. Hager

Scour prediction using the Movability Number criteria for incipient motion 511
N. Armitage & C. McGahey

Scouring and flow structure around an attracting groin 521
T. Ishigaki, T. Ueno, M.M. Rahman & A.T.M. Khaleduzzaman

2-D Numerical analysis for flow around an oblique weir in compound open channels 527
M. Iwai, Y. Shimizu & Y. Kawahara

Study of sediment motion in a local scour hole through an image processing technique 535
S. Malavasi, A. Radice & F. Ballio

Computations of 3D turbulent flow structures around submerged spur dikes under various hydraulic conditions 543
I. Kimura, T. Hosoda, S. Onda & A. Tominaga

Numerical simulation of flow instabilities in steep, stepped channels 555
G. Premstaller, P. Rutschmann & M. Oberhuber

Activation of scour around bridge abutment 563
D. Capuano, A. Carravetta & U.M. Golia

Seepage and exit gradient under impervious structures with two sheetpiles on layer of infinite depth 569
G. De Martino, M. Giugni & N. Fontana

The effect of migrating bedforms on local scour around bridge piers 575
M. Bolla Pittaluga, M. Maffei & G. Seminara

Experimental study of the scour hole downstream of bed sills 585
M. Ben Meftah & M. Mossa

Influence of laterally placed side weirs on bed-load transport in a prismatic channel 593
B. Rosier, J.L. Boillat & A. Schleiss

PIV investigation of flow around submerged river bridge deck 601
S. Malavasi, S. Franzetti & G. Blois

Reduction of local scour around bridge abutments with collars 609
Ş.Y. Kayatürk, M.A. Kökpinar & M. Göğüş

Numerical and experimental investigation of local scour downstream of a sill 615
C. Adduce, G. Sciortino & M. Morganti

Flow patterns in local scour holes downstream of a sill caused by turbulent water jets 623
C. Adduce, M. La Rocca & P. Mele

Flow separation at 45 to 90 degree water intakes 631
A. Keshavarzi, L. Habibi & M.J.K. Parsi

Study on structure-induced flow and turbulence considering bed morphology 637
S. Giri, Y. Shimizu & B. Surajate

Observations concerning erosion in model of a mobile river bed 647
L. Ciaravino

A.5. Sediment supply, entrainment and transport

Interaction between particles and water in near-wall region of particle-laden open-channel flows 657
I. Nezu & R. Azuma

Development of a new Marker-in-Cell hydraulic and sediment transport model for braided river flow 667
R.E. Thomas, S.N. Lane & J.L. Best

A finite volume model of flow and sediment transport in the lagoon of Grado-Marano 677
S. Bosa & M. Petti

Field investigation on macro-roughness characterization in mountain rivers 689
F. Canovaro & M. Catella

Pressure fluctuations within subsurface gravel bed caused by turbulent open-channel flow 695
M. Detert, G.H. Jirka, M. Jehle, M. Klar, B. Jähne, H.-J. Köhler & T. Wenka

Simultaneous 3-D PTV and micro-pressure sensor equipment for flow analysis in a subsurface gravel layer 703
M. Klar, M. Jehle, B. Jähne, M. Detert, G.H. Jirka, H.-J. Köhler & T. Wenka

Bed load transport on arbitrarily sloping bed at low Shields stress: preliminary experimental observations 713
S. Francalanci, E. Paris & L. Solari

Particle-fluid interactions in a free surface turbulent flow 721
M. Righetti, G.P. Romano & A. Cenedese

Studies of sedimentation in a large-scale reservoir for power generation 731
T. Shinjo & Y. Fujita

Experimental study of sediment laden flow in a hydraulic jump 739
M.H. Omid & H. Nozari

Can an internal hydraulic jump be inferred from the depositional record of a turbidity current? 745
S. Kostic & G. Parker

Grain size analysis for coarse river beds using digital imagery processing 753
R. Weichert, M. Wickenhäuser, G.R. Bezzola & H.-E. Minor

Development of discrete subaqueous bed forms 761
H. Friedrich, S.E. Coleman, B.W. Melville & T.M. Clunie

Transport dynamics and morphology of a high mountain stream during the peak flow season: the Ürümqi River (Chinese Tian Shan) 769
F. Métivier, P. Meunier, M. Moreira, A. Crave, C. Chaduteau, B. Ye & G. Liu

Study of navigation problems in Nile River reach at Elbogdady 777
A.M. Negm, M.M. Elfiky, M.I. Attia & M.H. Nassar

A computational distributed gravel budget for the lower Fraser River, British Columbia 787
S. Li & R.G. Millar

The influence of drainage network formation and characteristics on a catchment's sediment yield 793
E. Lykoudi & D. Zarris

Flow structure and bedload distribution at alluvial diversions 801
A. de Heer & E. Mosselman

Three dimensional modeling of sediment transport in a channel bend 807
N. Ruether & N.R.B. Olsen

Study on the channel development in a wide reservoir 811
C.J. Sloff, H.R.A. Jagers & Y. Kitamura

Measuring the flow structures that initiate stone movement 821
B. Hofland & R. Booij

Volume 2

B. River hazards
B.1. Dam break and fast transients

Two dimensional modeling of rapidly varying flows by finite volume schemes 837
F. Aureli, A. Maranzoni & P. Mignosa

Experimental modeling of rapidly varying flows on wet bed and in presence of submersible obstacles 849
F. Aureli, A. Maranzoni & P. Mignosa

Velocity measurements in dam-break flow using imaging system 859
A.H.N. Chegini, G. Pender, A. Slaouti & S.J. Tait

1D model of surface waves generated by a reservoir's bank landslide: a case study 869
P. García-Navarro, G. Pérez, P. Brufau & M.E. Vázquez-Cendón

Numerical simulation for destruction process of rubble stones dam 877
E. Harada, T. Hosoda & H. Gotoh

Effects of gradient pressure on resistance law in roll waves and effects of tension surface 885
S. Longo

Mathematical simulation of the effects of bridges and structures on flood waves propagation 895
L. Natale, G. Petaccia & F. Savi

Soil/water interaction during the breaching process of overtopped embankments 903
G. Pickert, G.H. Jirka, A. Bieberstein & J. Brauns

Experiments of dam-break flow in the presence of obstacles 911
S. Soares Frazão, B. Noël & Y. Zech

Sph simulation of dam-break flow in shallow water approximation 919
M. Gallati & D. Sturla

Simulation of flooding caused by an embankment breaking by means of a 2D finite volume numerical model 929
F. Aureli, A. Maranzoni & P. Mignosa

Dike-break induced flow: validation of numerical simulations and case study 937
M. Harms, S. Briechle, J. Köngeter & D. Schwanenberg

Surge wave front in a moving reference system 945
A. Bornschein

Roll waves evolution in channels 951
G. de Freitas Maciel

Physical model tests for dike-break induced, two-dimensional flood wave propagation 959
S. Briechle, A. Joeppen & J. Köngeter

Dispersive effects on linear instability of the Saint Venant flow model 967
C. Di Cristo & A. Vacca

B.2. Bank failure

Non-intrusive imaging measurements of the morphological evolution of a channel during a dam-break flow 977
N. le Grelle, B. Spinewine, S. Soares Frazão & Y. Zech

Experimental investigation of the breach growth process in sand dikes 983
B. Spinewine, A. Delobbe, L. Elslander & Y. Zech

Monitoring and modelling river bank processes: a new methodological approach 993
L. Rossi Romanelli, M. Rinaldi, S.E. Darby, L. Luppi & L. Nardi

Two-dimensional fluvial channel model with bank erosion on triangular grid 999
D. Farshi & H.-E. Minor

B.3. Flood propagation

Influencing factors of flow instabilities in steep and stepped channels 1007
T.F. Ganz & F. Schöberl

3D calculation of curved open channel flow using physical curvilinear coordinates 1013
M.-L. Zhu, Y. Shimizu, M. Nakata, K. Hayashida, K. Ezaki & H. Mizutani

Application of a 2D semi-lagrangian model to unsteady shallow water flow over dry bed 1023
J. Murillo & P. García-Navarro

How a 2-D code can simulate urban flood situations 1031
E. Mignot, A. Paquier & N. Rivière

Detailed validation of CFD for flows in straight channels 1041
N.G. Wright, A.J. Crossley, H.P. Morvan & T. Stoesser

Synthetic hydrographs as a design tool for flood routing evaluation 1049
F. Aureli, A. Maranzoni, P. Mignosa & U. Maione

Surface water modeling of the Biebrza River network 1057
R. Verhoeven, R. Banasiak, D. Swiątek, J. Chormański & T. Okruszko

An improved, robust implicit solution for the two dimensional shallow water equations on unstructured grids 1065
S. Komaei & W. Bechteler

Supercritical flow in channel intersections 1073
N. Riviére & R.J. Perkins

Factors on flood problems in Ubon Ratchathani province, Thailand 1079
C. Chinnarasri, U. Israngkura & S. Jarukamol

Urban fluvial flood modeling using a two-dimensional diffusion wave treatment 1085
D. Yu & S.N. Lane

B.4. Hyper-concentrated flows

Morphology of alluvial fans formed by hyperconcentrated tributaries 1095
S.C. Chen, S.H. Peng & H. Capart

Transient hyper-concentrated flows: limits of some hypotheses in mathematical modelling 1103
D. Berzi & E. Larcan

Numerical simulation of hyper-concentrated flows 1111
D. Komatina & D. Đorđević

Probabilistic estimation of debris-flow discharge by Monte Carlo simulation method 1121
J.C. Chen, C.D. Jan & M.H. Lee

Concentrated mud suspensions flowing in open channels 1125
G. de Freitas Maciel & F.L. dos Santos

Numerical simulation and field observation of debris roll waves in the Illgraben torrent, Switzerland 1133
B. Zanuttigh & B.W. McArdell

B.5. Water pollution and contaminant transport

Some features of distribution of turbulence parameters of a jet flow in the river mouth 1143
R. Khanbilvardi, B. Shteinman, V. Khazin & O. Ozkurt

An integrated system for prevention of pollution due to sewage and waste waters into rivers 1149
F. Boccia, D. Postiglione, A. Fusco & L. Mancusi

A random walk approach for investigating near- and far-field transport phenomena in rivers with groin fields 1157
V. Weitbrecht, W. Uijttewaal & G.H. Jirka

Turbulence of vertical round buoyant jets in a cross flow 1167
M. Ben Meftah, A. Petrillo, P.A. Davies, D. Malcangio & M. Mossa

Shallowness and longitudinal dispersion in rivers 1175
R. Booij

Pollution transport in the lagoon of Grado and Marano: a two dimensional modelling approach 1183
M. Petti & S. Bosa

Numerical simulation of transport processes in not uniform turbulent streams 1193
I. Cotto & R. Revelli

Estimation of longitudinal dispersion and storage zone parameters 1201
P.M. Rowiński, T. Dysarz & J.J. Napiórkowski

Impact of riverine and CSO inputs on coastal water quality under different environmental conditions 1211
S.M. Kashefipour, B. Lin & R.A. Falconer

River model calibration: a genetic algorithm with evolutionary bottlenecking 1217
J.R. Manson & S.G. Wallis

Gas-transfer coefficient in a smooth channel. A preliminary assessment of dimensional analysis-based equation 1223
C. Gualtieri & G. Pulci Doria

A methodological approach for surface water vulnerability assessment 1231
M. Giugni, G. Pappalardo, G. Lombardi & N. Fontana

Longitudinal dispersion in an extreme meander channel, with changes in shape 1237
J.B. Boxall & I. Guymer

Evaluation of longitudinal dispersion coefficients for over-bank flow 1245
S.G. Wallis & J.R. Manson

Evaluation of transverse dispersion coefficient under transient concentration condition 1251
I.W. Seo, K.O. Baek & S.J. Jeong

C. Hydraulics for river management
C.1. River training and restoration

Numerical simulation of bed change under compound channels flow in two-way main channel 1263
H. Yokoyama, Y. Watanabe & Y. Suzuki

River meandering restoration – case study and laboratory experiments 1273
R. Banasiak, R. Verhoeven, L. De Vos & S. Verfaille

Small river re-naturalization and cultural heritage 1281
G. Müller, G. Himmelsbach, C. von Carmer & P. Fröhle

Stability of reinforced block ramp 1291
S. Pagliara & P. Chiavaccini

Three dimensional hydrodynamics of pool-riffle sequences for urban stream restoration 1297
J.F. Rodríguez, M.H. García, F.M. López & C.M. García

Morphological rehabilitation and flood protection by controlled river dynamics – a physical model 1305
U. Stephan & M. Hengl

Destruction of herbaceous vegetation by flood flow on a floodplain in a recovery process 1315
S. Sugio & K. Watanabe

A new bed for the river Inde: a case study with special view on the risk of depth erosion 1325
P. Kamrath, C. Schweim, S. Briechle & J. Köngeter

The complex flow in groyne fields: numerical modelling compared with experiments 1331
W.S.J. Uijttewaal & S.A.H. van Schijndel

Groyne optimisation and river hydrodynamics 1339
G.J. Akkerman, M.A. van Heereveld, M. van der Wal & J.M.T. Stam

C.2. Habitat management and maintenance flows

The environmental impact of dams and weirs: technical issues related to the minimum vital flow release 1347
C. Comoglio

Calculation and visualization of fish movement in the flow with artificial structures 1353
H. Ohashi & Y. Shimizu

An experimental study of velocity fields and flow patterns in aligned deep slot fishways 1359
L. Pena, L. Cea, J. Puertas & T. Teijeiro

Estimating effect of navigation on fish habitats in inland waterways 1365
C. Engelhardt, A. Sukhodolov & C. Wolter

C.3. Flood management and control

River flow forecast by means of selected black box models 1375
A. Piotrowski, P.M. Rowiński & J.J. Napiórkowski

Merging of river training and restoration in river basin management 1383
N. Tamai

Floods managment in Uruguay. The case study of Tacuarembó city 1389
A. Capeluto, L. Teixeira & G. López

New trends in flood risk analysis: working with 2D flow models, laser DEM and a GIS environment 1395
P. Archambeau, B. Dewals, S. Erpicum, S. Detrembleur & M. Pirotton

Floods control in Argentina: learning from the experience 1403
R.A. Lopardo & R. Seoane

Flood management and control in an urban environment – Diakoniaris case study 1411
E.I. Daniil, S. Michas, G. Bouklis, P.L. Lazaridou & L.S. Lazarides

Flood mitigation planning related to land use 1421
Y. Takeuchi & M. Takezawa

Modeling floodplain flow on lower Deer Creek, CA 1429
M.L. MacWilliams, Jr., R.L. Street & P.K. Kitanidis

C.4. Integration of telemetry and GIS

Estimating hydraulic parameters and geometric characteristics of a river from remote sensing data using optimisation methods 1443
H. Roux & D. Dartus

River Flow 2004 – Greco, Carravetta & Della Morte (eds.)
© 2004 Taylor & Francis Group, London, ISBN 90 5809 658 0

Preface

River Flow 2004 is the second International Conference on fluvial hydraulics and has established the periodicity of the series. Organized as specialty conferences under the auspices of the International Association of Hydraulic Engineering and Research (IAHR) with its Fluvial Hydraulics and Eco Hydraulics Sections, River Flow conferences seem to be an important moment of aggregation for many researchers involved in river modelling and observation.

The intense land use of the last century and the lack of adequate sustainable development policies are probably the most important reasons of river hazards. For the importance of water as a resource in the human well-being we need a better comprehension of river processes and an adequate management of fluvial areas.

Scientists are aware of this necessity and largely contribute with their researches toward this aim. This clearly appears in the number of papers presented at River Flow 2004 (174) and from the number of country represented (43). Papers in this volume are related to the following topics:

- **Fluvial processes** (Morphology and morphodynamics; Bed forms and flow resistance; Over-bank flow and vegetation; Interaction with structures; Sediment supply, entrainment and transport);
- **River hazards** (Dam break and fast transients; Bank failure; Flood propagation; Hyper-concentrated flows; Water pollution and contaminant transport);
- **Hydraulics for river management** (River training and restoration; Habitat management and maintenance flows; Flood management and control; Integration of telemetry and GIS).

As the editors of the Conference proceedings we acknowledge the members of the International Scientific Committee for the in-depth reviewing of the manuscripts. The 70% of the accepted papers have been selected for oral presentation (123), while the 30% have been evaluated as more appropriately presented in the poster session (49). All the accepted papers have been included in this volume.

A grateful acknowledgment is deserved to all the members of the Local Organizing Committee for the intense work related to Conference preparation. Finally we acknowledge the Federico II University of Naples that was strongly involved in the success of River Flow 2004 for hosting the Conference, and the various sponsors for their financial support.

Massimo Greco
Armando Carravetta
Renata Della Morte

G. Ippolito Department of Hydraulic and Environmental Engineering, Federico II University of Napoli

This page intentionally left blank

River Flow 2004 – Greco, Carravetta & Della Morte (eds.)
© 2004 Taylor & Francis Group, London, ISBN 90 5809 658 0

Organization

International Scientific Committee

M. Altinakar, University of Mississippi, USA
A. Armanini, University of Trento, Italy
A.M. da Silva, Queens University, Canada
P. Garcia Navarro, University of Zaragoza, Spain
W.H. Graf, EPFL Lausanne, Switzerland
W.H. Hager, ETHZ Zurich, Switzerland
W. Hamza, United Arab Emirates University, UAE
J.M. Hervouet, EDF Chatou, France
F. Holly, IIHR University of Iowa, USA
G.H. Jirka, University of Karlsruhe, Germany
G. Klaassen, IHE, The Netherlands
M. Leclerc, Université de Québec, Canada
D. Lyn, Purdue University, USA
C. Montuori, University of Napoli, Italy
G. Parker, University of Minnesota, USA
N. Tamai, University of Tokyo, Japan
Z.Y. Wang, IRTCES Beijing, China
S. Yalin, Queens University, Canada
Y. Zech, UCL, Belgium

Local Organizing Committee

Massimo Greco, Chairman
Armando Carravetta, Secretary
Giuseppe Del Giudice
Renata Della Morte
Maurizio Giugni
Paola Gualtieri
Domenico Pianese

University of Napoli Federico II

This page intentionally left blank

Keynote speeches

This page intentionally left blank

River Flow 2004 – Greco, Carravetta & Della Morte (eds.)
© 2004 Taylor & Francis Group, London, ISBN 90 5809 658 0

Recent advances in scour hydraulics

W.H. Hager
VAW, ETH-Zentrum, Zurich, Switzerland

G. Oliveto
DIFA, Università della Basilicata, Potenza, Italy

S. Pagliara
Dipartimento di Ingegneria Civile, Università di Pisa, Pisa, Italy

J. Unger
VAW, ETH-Zentrum, Zurich, Switzerland

ABSTRACT: Failure of hydraulic structures by scour is a recent research topic in hydraulics, following spectacular losses of hydraulic structures mainly during floods. The research addressed in this paper refers to two types of scour, namely plunge pool scour and scour related to bridge structures. Based on recent research, the main results are presented along with descriptions on the reasons for scour progress and the basic concepts in which the scour features are hydraulically described. All results were collected from systematic model observations given that numerical predictions are complicated by a highly three-dimensional two-phase flow in bridge scour, and even a three-phase flow in plunge pool scour. The current observations may aid to define the missing items needed for numerical scour analysis in the future. It is also stated that both experimental and numerical approaches will be required in the future to deal with complex problems of scour in general.

1 INTRODUCTION

What is scour? According to an Internet notice: 'Scour is the removal of sediment (soil and rock) from streambeds and streambanks caused by moving water. Although scour may occur at any time, it is usually more significant during high flows, when the water is swift and deep. Swiftly moving water has more energy to lift and transport sediment than slowly moving water'. Is this really correct? We do not think so because an important point related to scour is the *local* erosion of sediments. Sediment transport, in contrast is more extended where sediment is dislocated and possibly deposited again. The difference between (more gradual) erosion and (concentrated local) scour of sediment in fluvial hydraulics may be the principal reason for complication with scour descriptions.

Scour has not been a research topic in hydraulic engineering until the 1930s. Some isolated tests were then conducted because of the failure of various structures and the damages caused. Even in the 1950s small attention was paid to local erosion because hydraulic engineers felt that their structures would withstand all impacts by water flow. This attitude changed only after significant troubles had been observed, such as with plunging jets related to trajectory spillways. Kariba dam on the Zambezi River was a typical example where the scour set a limit to designers, and this site has until now been under significant control and maintenance. Other problems occurred with bridges of which both the piers and the abutments were often a matter of concern. Most of these damages were attributed to unexpected floods and their malicious pattern that results in flow conditions not accounted for in the bridge design. Few damages are known from steep and narrow rivers, whereas most bridge failures occurred in flood plains with relatively small sediment particles where the river usually looks peaceful but where extraordinary forces may be mobilized during floods.

In recent years, scour analysis has become a specialty of fluvial hydraulics, with various books published on this topic. Mention may be made of Breusers and Raudkivi (1991), Hoffmans and Verheij (1997), Melville and Coleman (2000), May et al (2002), and Schleiss and Bollaert (2002). When going through the actual literature, one may observe an almost exponential increase of papers related to scour. This may have several reasons, among which can be stated: (1) Scour

has for a long time not been physically understood, whereas the basic concepts have been formulated within the past decades, (2) Scour experiments are relatively easy to conduct, and many may profit from this ease, (3) Scour can at this time hardly be modeled numerically, or only based on detailed laboratory observations, (4) Instrumentation has been refined and allows actually detailed insight into the hydrodynamic structure of scour, and (5) Scour is still a concern for sites which do not follow the standard arrangement, such as bridges in curves or in braided river reaches, where the direction of the main flow may be subject to significant changes during a flood. This last item was mentioned at this place because the authors do not think that actual failures are the real reason for the increased research activity in scour. Research items undergo also a fashion, and one of the topics of the day is obviously scour related.

The following intends to summarize recent findings of the authors. These include work related to bridge piers and abutments, to groynes both for steady and unsteady flow conditions, and to steady plunge pool scour. In all these cases essentially cohesionless sediment will be considered which can be described as a granular material. Scour is by far more complex, and may relate to almost all fields of hydraulic engineering where sediment is involved. Mention might be made here to problems in estuaries and tidal river reaches, to shore erosion in river curves, to drop structures in smaller river reaches or to oil platforms in the oceans. Accordingly, the present paper covers only a limited number of problems related to the local erosion process.



Figure 1. Trajectory spillway at *Serre-Ponçon* dam, France (La Houille Blanche 2 1993, p. 224).

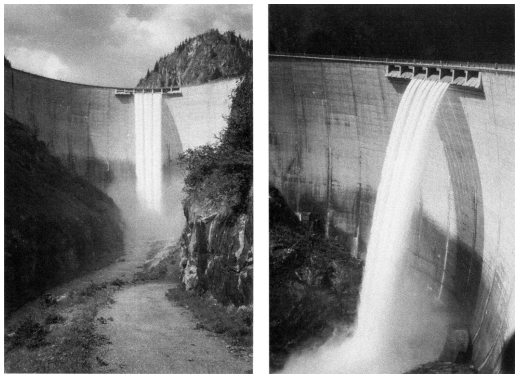


Figure 2. Free jet from crest overflow, general view (left), and side view (right).

2 PLUNGE POOL SCOURING

Scour resulting from plunging jets can be a significant concern both for structural foundation and backwater due to the ridge formation, where the scour material is deposited. Figure 1 shows a trajectory spillway in the French Alps that produces an air-water mixture flow in the atmosphere eventually impacting the downstream valley. Scour may be relatively small in such circumstances because the density of the impinging jet is relatively small, given the immense dispersion of the water flow and the production of spray. This may not be true for an almost vertically falling jet issued at the overfall crest shown in Figure 2, as compared to Figure 1, where the jet develops on a chute.

One reason that plunge pool scour by trajectory jets has received only limited attention until today is the complex experimental arrangement. In the past, thousands of plunge pools have been modeled yet the observations were practically all site related. Accordingly, limited information is presently available on the scour resulting from these jets (Canepa and Hager 2003). VAW has initiated a new research initiative some years ago, which was based on a simplified experimental arrangement: Instead of modeling the entire spillway with an overflow structure or a bottom outlet, the ski-jump structure and the entire trajectory reach, a pressurized jet configuration has been analyzed. Figure 3 shows the test scheme in which the main components are contained.

An air-water mixture jet composed of discharge Q_a and Q_w was supplied to a circular pipe of diameter D that varied between 0.040 and 0.10 m. The ratio of air to water discharges was denoted as $\beta = Q_a/Q_w \geq 0$. For some cases a base flow Q_m was added upstream from the pipe to investigate its effect on the scour. The pipe had an angle α relative to the originally horizontal sediment surface composed of grains with a median diameter d_{50} and a non-uniformity of $\sigma = (d_{84}/d_{16})^{1/2}$ of up to 2.67. The pipe could be submerged below the water surface of which the original flow depth was h_o, or discharge the mixture flow onto the water body. In the following, only the latter configuration will be considered.

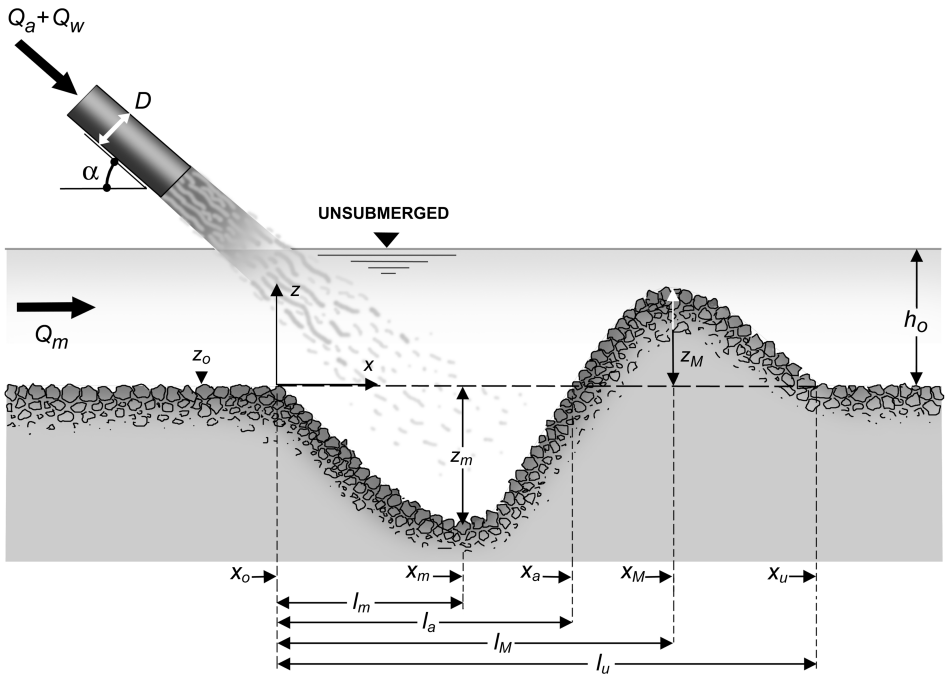


Figure 3. Test arrangement for laboratory investigation in plunge pool scour (Pagliara et al 2004b).

The scour hole resulting from the previous jet arrangement may be described with the maximum scour depth z_m, the maximum elevation of the ridge z_M and various streamwise distances that allow the full description of the scour geometry $z(x)$. It should be noted that there is a significant difference between the so called static and the dynamic scour. The latter occurs under water flow, whereas the static scour results when water flow has stopped. Static scour is usually much smaller than dynamic scour, depending mainly on the jet impact angle.

For incohesive sediment and relatively large jet velocity and jet diameter, it was demonstrated that the Froude similitude applies. Accordingly, because the flow in the vicinity of the scour hole has an almost horizontal surface, the densimetric Froude number $F_{d90} = V/(g' d_{90})^{1/2}$ had the main effect on all scour parameters, with $V = Q_w/(\pi D^2/4)$ as water velocity, $g' = [(\rho_s \rho)/\rho]g$ as reduced gravitational acceleration where ρ_s and ρ are the densities of sediment and fluid, respectively, and d_{90} corresponds to approximately the largest members of the granulate mixture. In prototypes, one may admit typically a $d_{90} = 0.20$ m for a fully developed scour hole in rock.

Based on more than 500 experimental tests, the main features of plunge pool scour have been determined experimentally for an almost two-dimensional arrangement (Canepa and Hager 2003, Pagliara et al 2004a, 2004b). In all the research, the relative maximum scour depth $Z_m = z_m/D$ was of particular interest. The results relating to Z_m may be summarized as follows:

(1) The densimetric particle Froude number F_d is linearly related to Z_m
(2) The effect of the jet impact angle α is small for $45° < \alpha < 90°$ and Z_m for $\alpha = 30°$ is about 80% of the absolute maximum
(3) The more air the jet contains, the less becomes the scour depth (Minor et al 2002)
(4) The tailwater effect as expressed with $T = h_o/D$ is relatively large; scour depths are deeper for small T than for large, because of the jet diffusion in the water body
(5) Sediment non-uniformity σ has no effect when the densimetric particle Froude number F_{d50} is considered using the median grain size d_{50}
(6) The upstream discharge Q_m may be accounted for by the Froude number $F_u = V_u/(gh_o)^{1/2}$ where V_u is upstream average velocity and h_o stillwater depth; Increasing F_u may significantly deepen the scour hole because the suspended material is deposited on the ridge
(7) The jet shape has no significant effect on the scour depth and scour geometry, an important justification for the test arrangement adopted in this research

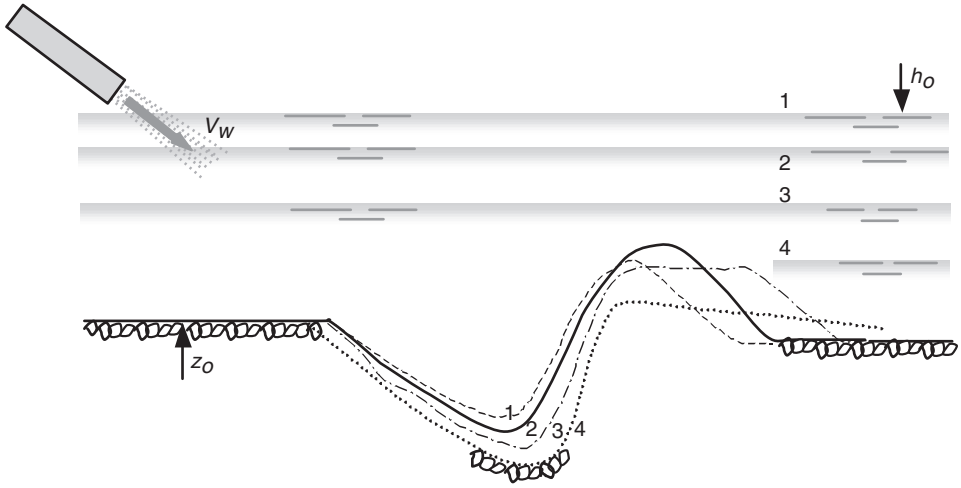


Figure 4. Effect of relative tailwater elevation T on scour geometry (Pagliara et al 2004b).

(8) A number of additional limitation govern the computational model, relating to minimum sediment size, minimum densimetric particle Froude number and the two materials sand and water involved to exclude scale effects.

Figure 4 shows a scheme where the tailwater effect is explained. For a large value of $T = h_o/D$ the scour hole is almost point-symmetrically distributed about the central point with $z = 0$ (case 1). As T decreases (case 2) both the scour depth and the deposition ridge increase. However, if T is further reduced the ridge reduces in height because its overflow has such a strong velocity that ridge erosion is initiated (case 3). By further reducing the relative tailwater to case 4 an even larger scour hole results, whereas the ridge may be completely eroded. This description points to the complexity of scour hole experimentation. This research pointed mainly to the definitions of both maximum scour depth and the scour profile, whereas the ridge characteristics were not fully explored, because of the combined scour and erosion involved by high velocities.

An equation for the maximum scour depth Z_m was presented in terms of the densimetric particle Froude number F_{d50}, the jet air content β, the relative tailwater depth T, the jet angle α relative to the horizontal, and the upstream Froude number F_u (Pagliara et al 2004b). The correlation with the present data was $R^2 = 0.94$. The authors were unable to locate other data series in which all the parameters are specified.

Figure 5 shows a photograph of the test arrangement used for this research. It must be stated that this problem would have hardly been solved without the experimental simplifications introduced as regards the air-water jet arrangement.

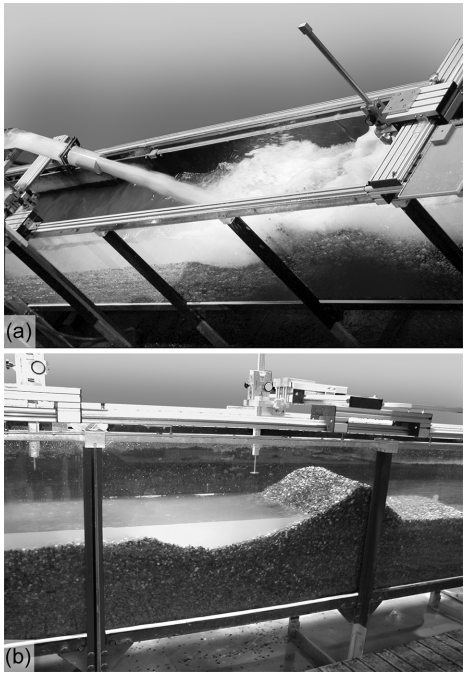


Figure 5. (a) Air-water jet approach flow to test channel, and (b) final scour hole after test.

3 BRIDGE HYDRAULICS

3.1 *Introduction*

Bridges constitute a main infrastructure; their loss may have significant consequences particularly during

floods by cutting off adjacent transportation lines. From modern logistic considerations, the value of a bridge is thus high. Concerns for bridge structures became only a problem after the loss of some important structures. Today, not only the ways of how bridges may be protected against scour are of interest but also the causes of scour. Given that each obstacle placed in fluid flow results in a complex spatial and often highly-turbulent response by the fluid flow, the observation of bridge scour was for a long time obscure, although the main agent was attributed to the development of the horse-shoe vortex. The vortex structure as developed by a bridge pier, for example, is much more complicated as we presently regard the horse-shoe vortex. Due to the deflection of flow along the disturbing element, a strong vertical flow component is generated that may directly attack the sediment surface close to it. Novel instrumentation allows the visualization of these fascinating vortices, and these will be understood when the results are correctly analyzed.

Figure 6 relates to a typical plane velocity distribution upstream of a bridge pier. The flow is characterized by a densimetric particle Froude number $F_{d50} = 2.16$, the approach flow depth is $h_o = 0.13$ m, the approach velocity is $V_o = 0.62$ m/s, the sediment size is $d_{50} = 5.0$ mm, with a sediment non-uniformity parameter $\sigma = 2.13$ for a pier diameter $D = 0.26$ m. The (PIV) velocity field was taken once at the beginning of the experiment (Figure 6a), and after one day (Figure 6b).

Figure 6a shows the axial velocity distribution after 60s from initiation of the test, corresponding to the incipient entrainment of sediment. The approach flow is practically undisturbed up to close to the cylindrical pier and then deflected to either side of it. Note the relatively small surface recirculation zone and scour hole as compared to Figure 6b. The latter plot shows an advanced scour profile in the streamwise direction of some 0.09 m depth in front of the cylinder and a front wave height of some 0.02 m, corresponding to the approach velocity head $V_o^2/2g$. The velocity distribution in the approach region is almost uniform except for the bottom boundary layer and then slightly reduces when approaching the cylinder. More importantly is the deflection of flow, close to the free surface to form the surface recirculation zone, and at the lower flow portion to generate the bottom recirculation that creates the horse shoe vortex. The plot shows various distinct bottom recirculation zones that may be described with two essential vortices, and a small sediment rim between the two. The rim is a usual feature of pier scour, as also shown in Figures 7(a) and 8.

Figure 7 shows views of pier scour in fine sediment under a relatively small and large hydraulic load, including interesting structures of sediment deposition previously mentioned. For larger scour material the wavy deposition structure of the sediment disappears.

The following aims to describe both the overall effects of scour related to bridge structures, and more detailed results that were obtained by using modern instrumentation in scale models. It should be noted that numerical modeling of scour around bridge structures, or even in a general arrangement, is hardly possible these days, given the complex interactions between the fluid and the solid phases combined with a highly turbulent flow field. In contrast to a believe expressed some decades ago, most two- or even three-phase problems of the future will this involve a *combined* experimental and numerical approach. Figure 8 shows the complex scour surface at the end of an experiment, indicating a two-vortex structure close to the sediment surface.

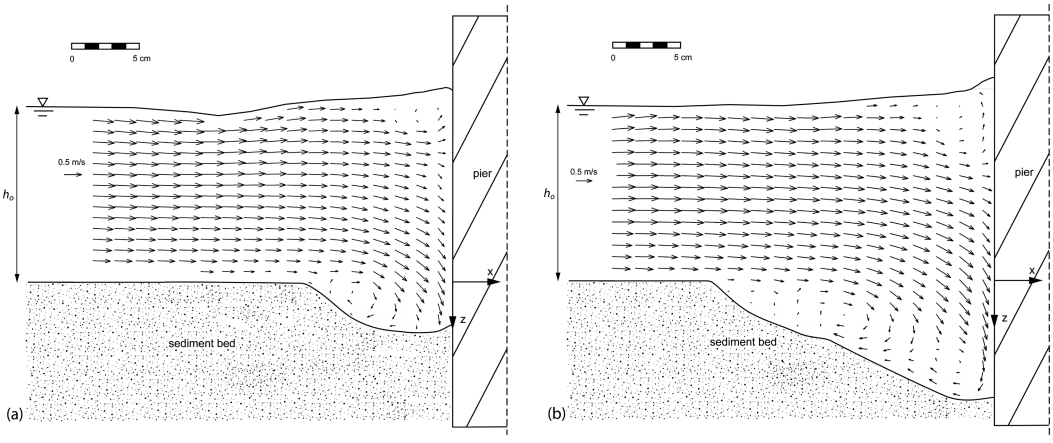


Figure 6. Plane velocity distribution in pier axis upstream of a bridge pier (a) shortly after the beginning of test and (b) after one day.

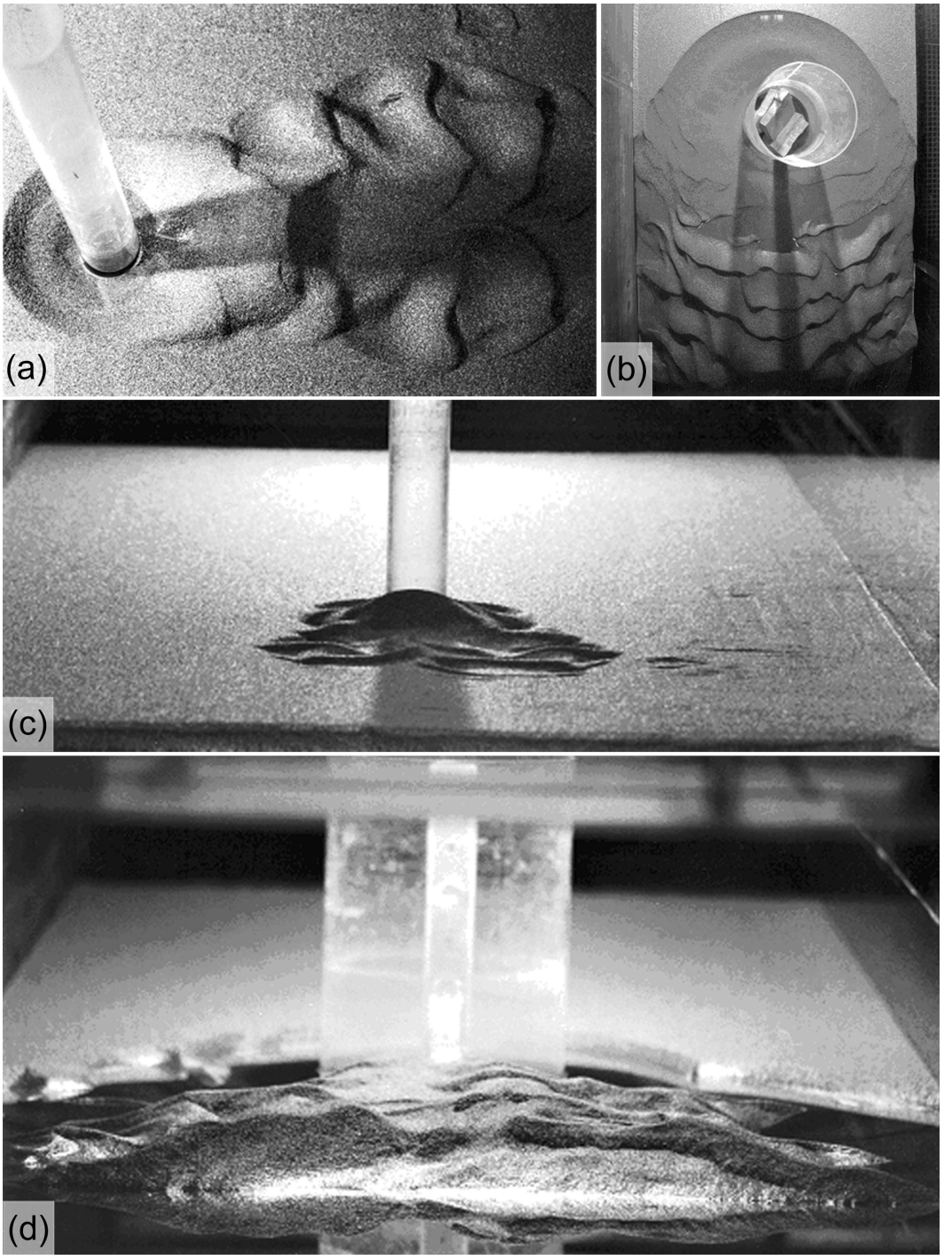


Figure 7. Pier scour (a–b) in plan and (c–d) downstream view (a and c) for small and (b and d) large hydraulic loads.

3.2 *General bridge scour equation*

Consider again cohesionless sediment that is subjected by turbulent fluid flow. As discussed by Oliveto and Hager (2002), the force F opposed by the element of surface A vertical to the direction of flow can be expressed simply by Newton's approach $F = \rho C_d A \bullet V_o^2/(2g)$ where ρ is fluid density, C_d drag coefficient and V_o the approach velocity. In engineering applications, the drag coefficient is often independent of viscous effects and varies exclusively with the element geometry. The extent of the scour hole and particularly the maximum (subscript M) scour depth z_M are assumed to depend directly on the force F, provided viscous effects are absent. Because the scour depth is a length, its determining length scale z_R is made up of relevant lengths that describe the problem. It was found that these are $z_R = (D^2 h_o)^{1/3}$ for a circular-shaped pier, and $(b^2 h_o)^{1/3}$ for a rectangular abutment, respectively. Here, D is the pier diameter, b the abutment width and h_o the approach flow depth (Figure 9).

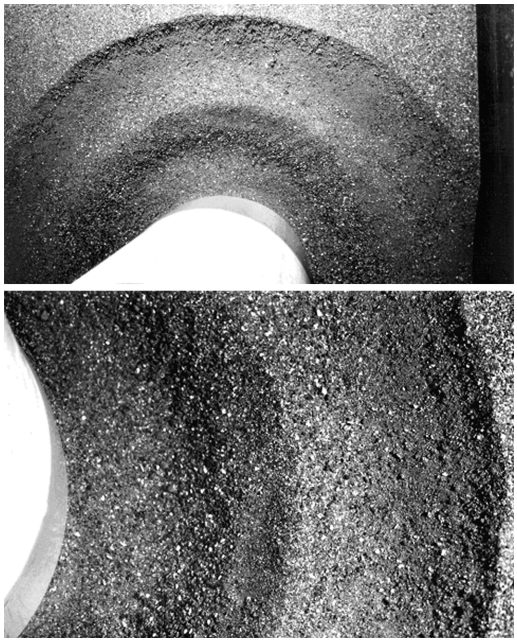


Figure 8. Structure of pier scour after scour hole was drained.

Following the above approach the dimensionless scour depth $Z_M = z_M/z_R$ may thus be represented by a dimensionless velocity head times a function of time to account for scour progress. For flows with an almost horizontal surface across the element, i.e. for strongly subcritical flow, the so-called densimetric particle Froude number $F_d = V_o/(g' d)^{1/2}$ becomes relevant, because the approach Froude number $F_o = V_o/(g h_o)^{1/2}$ is practically zero. The scaling velocity $V_R = (g' d)^{1/2}$ replaces thus the shallow water celerity $(g h_o)^{1/2}$, where d is the relevant sediment size and $g' = [(\rho_s - \rho)/\rho]g$ is the reduced gravitational acceleration with subscript s relating to sediment.

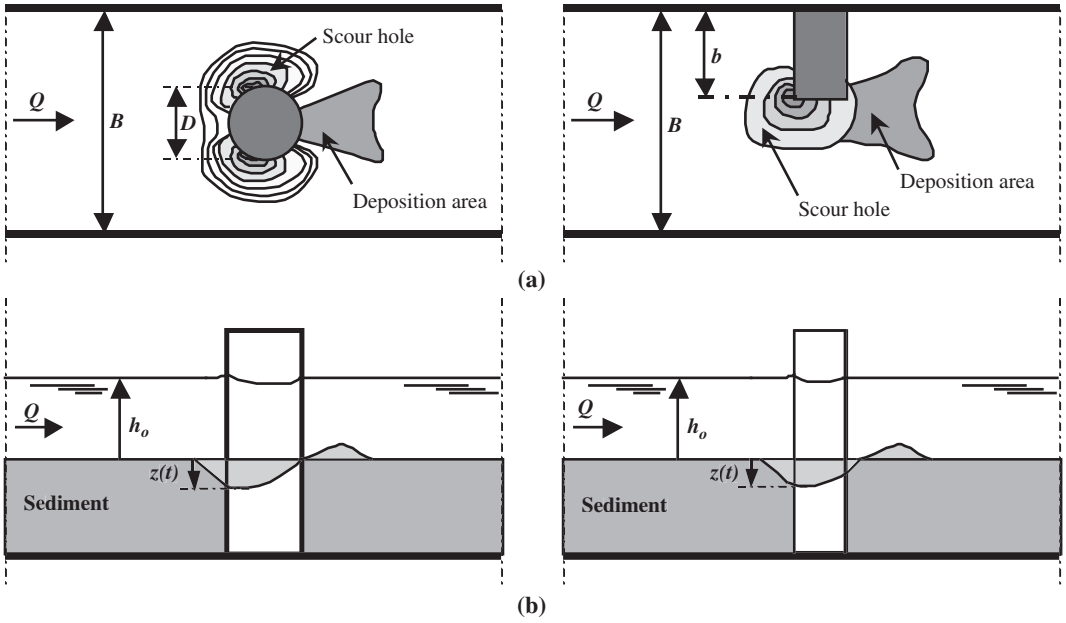


Figure 9. Definition plot for bridge pier (left) and bridge abutment (right), (a) plan, (b) section.

The previous considerations also allow the definition of the time scale, because $t_R = z_R/V_R$ such that the dimensionless time is $T = t/t_R$ simply. As an example, the reference time for bridge piers thus amounts to $t_R = (D^2 h_o)^{1/3}/(g'd)^{1/2}$ and involves parameters that are normally not considered with such processes, such as the relative density between the two phases considered.

The general form of the equation for maximum scour depth thus may be expressed, based on these considerations and detailed experimental observations as (Oliveto and Hager 2002)

$$Z_M = C \cdot N \cdot \sigma^{-1/2} \cdot F_d^{1.5} \cdot \log T \qquad (1)$$

Here, C is a constant, N is a coefficient in analogy to the drag coefficient, thus essentially variable with the scour element geometry, with $N = 1$ for circular-shaped piers and $N = 1.25$ for bluff abutments, and $\sigma = (d_{84}/d_{16})^{1/2}$ is the sediment non-uniformity parameter. The constant was found to be $C = 0.068$. Figure 10 shows scour around a rectangular-shaped abutment.

3.3 Extension of results

Oliveto and Hager (2004) considered additional scour elements, i.e. sloping abutments and spur dikes. The maximum scour depth resulting from these involve also (1). Figure 11 is a definition plot for the sloping abutment with b'' as its width at the original sediment surface and b' its width at the water depth h_o. Abutment angles $30° \le \alpha \le 60°$ were considered. Based on an extensive experimental approach, it was found that (1) may be applied provided the determining width of the element is $b = (b' + b'')/2$ and $N = 1$. The reduction of N from 1.25 to 1.00 is associated with the reduced resistance offered by the sloping as compared to the vertical abutment.

Spur dikes were then also investigated, based on the previous approach. Figure 12 shows an isolated spur whose length perpendicular to the flow direction is b_{eff} and whose average height is $s = (s' + s'')/2$. Note that it is assumed that the spur is fully submerged, i.e. $s < h_o$. Then, (1) may be assumed again provided the reference length is logically set to $z_R = (b_{eff}^2 s)^{1/3}$. Angles of α_s between 45° and 135° were considered, and reasonable agreement between (1) and observations was found, providing a spur factor $N_s = [\cos(\alpha_s/2)]^{1/3}$ was accounted for.

The typical spur effect, namely the flow concentration to the river axis associated with a generation of recirculation zones between two spurs may only be obtained with a series of spur elements. Oliveto and Hager (2004) thus investigated a sequence of three spur dikes and verified (1). It was found that the maximum scour depth is often located upstream of the first spur

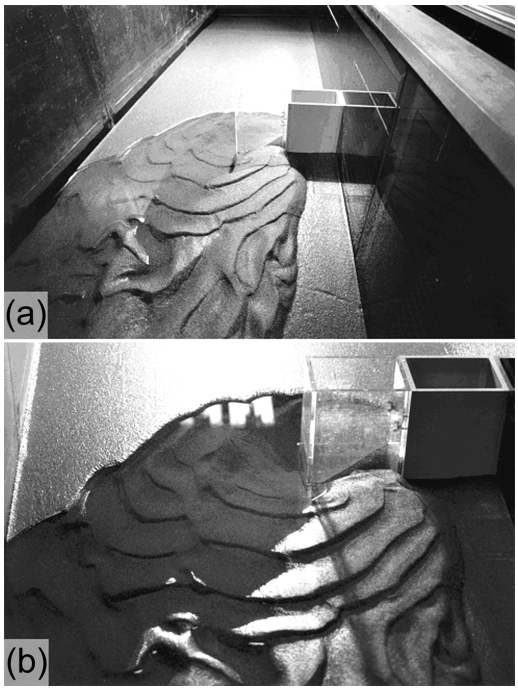


Figure 10. Scour around (a) relatively narrow and (b) wide abutments.

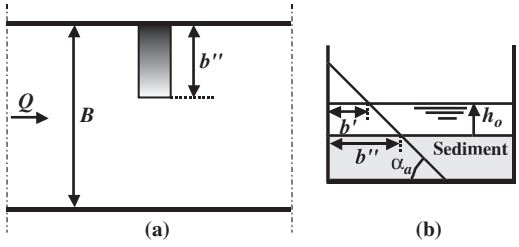


Figure 11. Sloping bridge abutment (a) plan, (b) section.

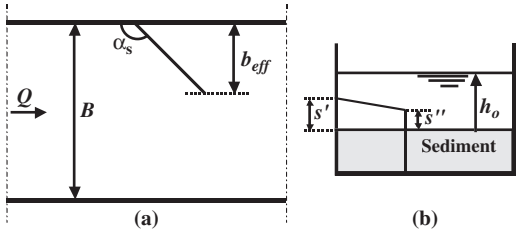


Figure 12. Isolated spur (a) plan, (b) section.

which may be described with the basic scour equation provided adequate coefficients are attributed to the various spur geometries. Until today, observations have not yet proceeded to a final equation involving

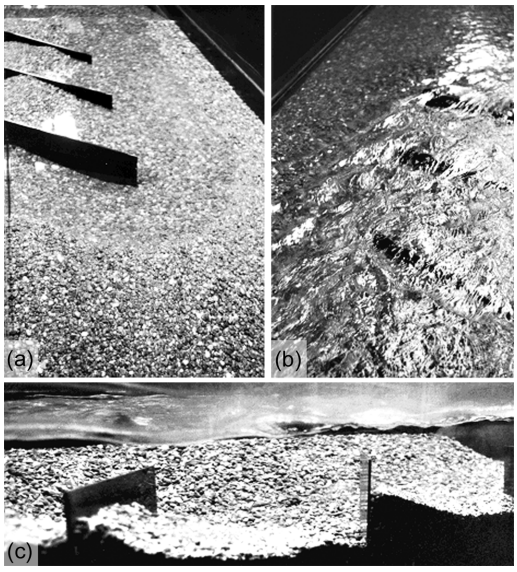


Figure 13. Spur experiments (a) at the end (view in flow direction) and (b) during water flow (view against flow direction); (c) side view.

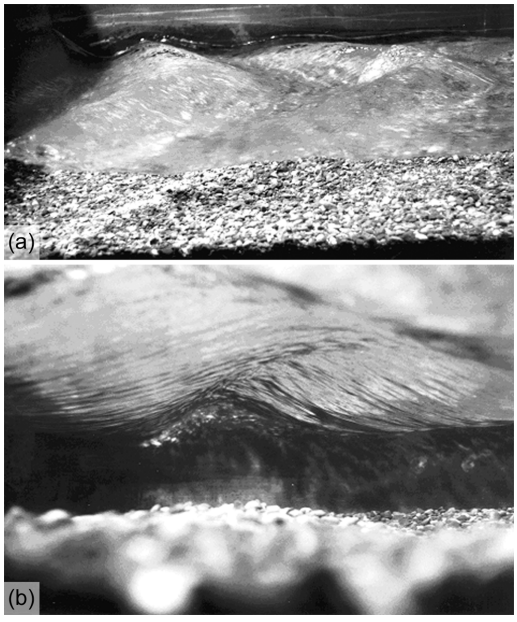


Figure 14. Scour below wave formation, (a) general arrangement and (b) detail of wave flow.

the spur angle α_s, the spur spacing and the spur slope. Figure 13 shows typical photos of spur experiments.

Figure 14 relates to scour below waves that were generated by removing the flow straightener at the channel inflow. Such poor flow conditions must be expected when the approach flow region is not correctly modeled. Here we show this flow because of its interest with the present discussion.

4 CONCLUSIONS

Scour related to hydraulic structures in rivers has many facets, involving the basic development of maximum scour depth and scour extension with time to the complex scour surface associated with the instantaneous velocity field that generates bottom currents responsible for scour advance. The present research intends to show some of the most striking features of scour in relation to plunge pools and to bridge structures. Both problems are characterized by a large number of parameters. Preliminary results were produced by suitably introducing simplifications that allow a straightforward approach to the problem.

For the plunge pool scour problem, the effective spillway was replaced with a pipe in which an arbitrary air-water mixture approach flow was generated. It was demonstrated that the shape of the approach flow on the scour advance has a negligible effect and that the substitute experimental setup suites for experimental observations. The effect of the main parameters mainly on the maximum scour depth was investigated. Results include in addition a generalized scour profile.

For bridge elements, and equation based on the resistance problem was employed and it was demonstrated that the data for various hydraulic elements such as piers or abutments, and spur dykes may be described with such a basic formula, provided the scaling parameters are carefully selected. In both and other research, the densimetric particle Froude number has the main effect on the scour characteristics, provided the sediment involved is sufficiently large that it may be considered incohesive, and the flow is in the turbulent rough regime such that viscosity effects remain insignificant. Problems to be considered in the future relate to both small hydraulic load and small sediment scale, where the viscous effects may not be negligible.

REFERENCES

Breusers, H.N.C., Raudkivi, A.J. (1991). Scouring. IAHR Hydraulic Structures Design Manual 2. Balkema: Rotterdam.

Canepa, S., Hager, W.H. (2003). Effect of air jet content on plunge pool scour. Journal of Hydraulic Engineering 129(5): 358–365.

Hoffmans, G.J.C.M., Verheij, H.J. (1997). Scour manual. Balkema: Rotterdam.

May, R.W.P., Ackers, J.C., Kirby, A.M. (2002). Manual on scour at bridges and other hydraulic structures. CIRIA Publication C551: London.

Melville, B.W., Coleman, S.E. (2000). Bridge scour. Water Resources Publications: Highlands Ranch CO.

Minor, H.-E., Hager, W.H., Canepa, S. (2002). Does an aerated water jet reduce plunge pool scour? Rock scour due to falling high-velocity jets: 117–124, A.J. Schleiss & E. Bollaert, eds. Balkema: Rotterdam.

Oliveto, G., Hager, W.H. (2002). Temporal evolution of clear-water pier and abutment scour. Journal of Hydraulic Engineering 128(9): 811–820.

Oliveto, G., Hager, W.H. (2004). Further results to time-dependent local scour at bridge elements. Journal of Hydraulic Engineering, accepted for publication.

Pagliara, S., Hager, W.H., Minor, H.-E. (2004a). Hydraulics of plunge pool scour. Journal of Hydraulic Engineering submitted.

Pagliara, S., Hager, W.H., Minor, H.-E. (2004b). Plunge pool scour in prototype and laboratory. Intl. Conf. Hydraulics of dams and river structures Tehran, accepted for publication.

Schleiss, A.J., Bollaert, E. (2002). Rock scour. Balkema: Rotterdam.

River Flow 2004 – Greco, Carravetta & Della Morte (eds.)
© 2004 Taylor & Francis Group, London, ISBN 90 5809 658 0

Mixing and dispersion in rivers

Gerhard H. Jirka
Institute for Hydromechanics, University of Karlsruhe, Karlsruhe, Germany

ABSTRACT: Water quality in rivers results from the physical, chemical and biological processes that take place due to multiple pollutant loadings along a river stretch. A sound understanding and description of these processes – usually encapsulated into predictive models – is needed so that design engineers and water authorities can develop appropriate discharge solutions and control strategies that meet applicable water quality laws and objectives. Continuous discharges from municipal, industrial or agricultural sources are subject to a permitting process by water authorities. The "combined approach" in the new EC-Water Framework Directive (WFD, 2000) consisting of environmental quality standards in addition to emission limit values promises improvements in the quality characteristics of surface waters. However, the specification of where in the water body the environmental quality standards do apply is missing in the WFD. This omission will limit its administrative implementation. A clear mixing zone regulation is needed so that the quality objectives of the WFD are not jeopardized. Instantaneous or accidental pollutant releases are another source of pollution loadings on rivers. Water authorities rely increasingly on "river alarm models" that predict the downriver propagation and dispersion of the pollutant mass as well as biochemical decay or adsorption processes. Currently, these models are fraught with considerable parameter uncertainties and an improved understanding of the transport mechanics in river systems with strong morphological variability is needed to minimize these. This is demonstrated for the case of rivers with a long sequence of groin fields that alternately retain and release the pollutant mass, greatly increasing the longitudinal dispersion.

1 INTRODUCTION

Rivers have always been the recipients of liquid water discharges from human activities, be it domestic sources, industrial or agricultural effluents, or mining process waters. Over the last two centuries, since the age of industrialization, the massive increase of industrial production accompanied by the growth of large urban populations has led to severe water pollution problems on many rivers, turning some of them into essentially open cloacae. In many of the developed countries, this adverse situation has fortunately been mitigated since stringent water quality protection laws were instituted in the period between the 1960s and 1980s so that modern pollution control schemes were implemented. Nevertheless, undesirable water quality conditions may persist and further improvements are needed even in these countries. Sadly, however, a rapidly worsening water situation takes place in many of the lesser developed countries, some of the urban megalopolises with unbridled population growth and uncontrolled industrial development being the worst examples.

Riverine water quality, with its spatial and temperoral distribution attributes, is the result of various physical, chemical and biological processes that occur due to the multiple pollutant loadings in a river stretch. A sound understanding and description of these processes – usually encapsulated into predictive models – is needed so that design engineers and water authorities can develop appropriate discharge solutions and control strategies that meet applicable water quality laws and objectives.

It is useful to distinguish two types of pollutant discharge problems as these have different physical response characteristics as well as different pollution control strategies that are used by water authorities. These are continuous discharge problems on one hand and instantaneous release problems on the other.

Continuous discharge problems are given by the more or less steady discharge of pollutants from "point sources" (e.g. effluents from treatment plants, from industries or from mining sources) and from "diffuse sources" (or "non-point sources", e.g. runoff from agricultural land or from urban drainage areas). These discharges occur continuously – even though they may undergo diurnal or seasonal variations – are somewhat controllable – especially so for the "point sources" – and are subject to water quality regulations. For the countries of the European Union the new EC-Water

Framework Directive (WFD, 2000) has the objective of an integrated catchment-oriented water quality protection for all European waters with the purpose of attaining a good quality status by the year 2015. The water quality evaluation for surface waters shall rely predominantly on biological parameters (such as flora and fauna) – however, aided by hydromorphological (such as flow and substrate conditions) and physico-chemical quality components (such as temperature, oxygen or nutrient conditions) – and on specific pollutants (such as metals or synthetic organic compounds). A good chemical quality status is provided when the environment quality standards (specified as concentration values) are met for all pollutants or pollutant groups.

Instantaneous release problems are given by the more or less sudden release of a pollutants mass into a river or adjacent to a river. These are mostly accidental releases or "spills", e.g. from industrial accidents, navigation mishaps, or failure of chemical holding tanks or ponds. The released pollutant mass propagates downstream in the river while gradually being dispersed and partially retained, due to various heterogeneities in the river channel. In order to plan short-term response measures for such accidental spills water authorities increasingly demand the establishment of co-called "river alarm models" that predict the propagation and dispersion of the pollutant mass in the river.

This article reviews the major physical, i.e. hydrodynamic, mechanisms that control these two types of pollutant discharge problems. It points out a major deficiency within the new WFD regulations, i.e. the absence of a clear "mixing zone" definition for continuous point sources, that is likely to limit its effectiveness in improving riverine water quality (see also Jirka et al., 2004). The article also indicates outstanding research needs in this area.

2 CONTINUOUS POINT SOURCE DISCHARGES IN RIVERS

2.1 *Regulatory mechanisms for water quality control*

The WFD defines new strategies against water pollution as a consequence of releases from point or diffuse sources. A new aspect of the EC water policy is the "combined approach", i.e. both limitations on pollutant releases at the source due to promulgation of emission limit values as well as the establishment of environmental quality standards. Releases of pollutants – especially from point sources – must meet both requirements. For most European member countries this new policy means a considerable deviation from current water quality management practice by which the releases of pollutants has been controlled by either one of these two control mechanisms, but usually not their combination.

Ragas et al. (1997) have reviewed the advantages and disadvantages of different control mechanisms in the permitting processes of releases into surface water. *Emission limit values* (ELV) present a direct and effective method for the limitation of pollutant loadings by restricting the concentration for the mass flux of specific pollutants. ELVs are preferred from an administrative perspective because they are easy to prescribe and to monitor (end-of-pipe sampling). From an ecological perspective, however, a quality control that is based on ELVs alone appears illogical and limited, since it does not consider directly the quality response of the water body itself and therefore does not hold the individual discharger responsible for the water body. To illustrate that point consider a large point source on a small water body or several sources that may all individually meet the ELVs but would accumulatively cause an excessive pollutant loading. *Environmental quality standards* (EQS), set as concentration values for pollutions or pollutant groups, that may not be exceeded in the water body itself (WFD, 2000) have the advantage that they consider directly the physical, chemical and biological response characteristics due to the discharge and therefore they put a direct responsibility on the discharger. But a water quality practice that would be based solely on EQSs could lead to a situation in which a discharger would fully utilize the assimilative capacity of water body up to the concentration values provided by the EQSs. Furthermore, the water quality authorities would be faced with additional burdens because of a more difficult monitoring – where in the water body and how often should be measured? – in the case of existing discharges or due to the increased need for a prediction modeling in case of new discharges. The "combined approach" in the WFD combines the advantages of both of these quality water control mechanisms while largely avoiding their disadvantages.

In the future practical implementation of the "combined approach" of the WFD two important questions will have to be addresses by the regulatory authorities: (1) *Where in the water body relative to the discharge point do the EQS-values apply*? Since the WFD provides no specific guidance on that question two extreme interpretations might be applied. First, the EQS-values apply immediately after the discharge with the idea that the whole water body would then be in a state of a good chemical status at every location at every time as indicated by the EQS-values. In that case, however, the EQS-values would be synonymous with the ELV-values! Secondly, the EQS-values apply after complete mixing for river discharges. Since the actual physical mixing processes in rivers are gradually leading to a "discharge plume, considerable areas in the water body would be affected by

concentrations above the EQS-values and would have to be considered as "sacrificial regions", in which a good chemical status would no longer be provided. It is obvious that a compromise, in form of a clear mixing zone regulation, is necessary. (2) *Which procedures shall be used during the permitting process to demonstrate that the discharge will in fact meet the relevant EQS-values in addition to the ELVs*? Not only for existing, but especially also for future, discharges does it seem necessary that different types of predictive models that describe the physical mixing and transport as well as chemical and biological transformation processes be applied so that the water authorities can in fact administer the "combined approach". These models allow to consider different hydrological situations and various scenarios of pollution loadings or central strategies.

2.2 *Mixing processes for continuous point sources in rivers*

When performing design work and predictive studies on effluent discharge problems, it is important to clearly distinguish between the physical aspects of hydrodynamic mixing processes that determine the fate and distribution of the effluent from the discharge location, and the administrative formulation of mixing zone regulations that intend to prevent any harmful impact of the effluent on the aquatic environment and associated uses.

The hydrodynamics of an effluent continuously discharging into a receiving water body can be conceptualized as a mixing process occurring in two separate regions. In the first region, the initial jet characteristics of momentum flux, buoyancy flux (due to density differences), and outfall geometry influence the effluent trajectory and degree of mixing. This region, the "near-field", encompasses the buoyant jet flow and any surface, bottom or terminal layer interaction. In this near-field region, outfall designers can usually affect the initial mixing characteristics through appropriate manipulation of design variables. As the turbulent plume travels further away from the source, the source characteristics become less important and the far-field is attained. In this region ambient environmental conditions will control trajectory and dilution of the turbulent plume through buoyant spreading motions, passive diffusion due to ambient turbulence, and advection by the ambient, often time-varying, velocity field in the river.

For river discharges the problem can be reduced in first order to so-called "passive" sources for which the input momentum and buoyancy effects are of lesser importance and mixing is controlled by the advective and diffusive properties of the ambient flow regime with a resulting discharge plume that follows the prevailing current. Thus, the problem is considered

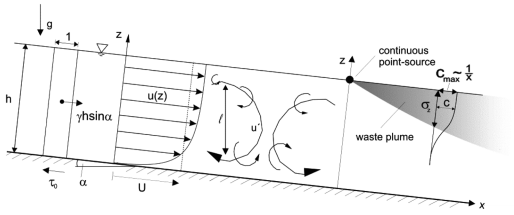


Figure 1. Longitudinal section along an inclined river flow with turbulent flow structure and assumed continuous point source at the water surface.

as a "far-field" effect with passive source characteristics. Research during the last 40 years has led to a solid understanding of the mixing dynamics in rivers as summarized in several textbooks or manuals (e.g., Fischer et al., 1979; Holley and Jirka, 1986; Rutherford, 1994).

The flow in rivers is characterized by turbulence, i.e. more or less large scale eddy motions are superposed on the average flow. The spreading and mixing of mass sources is then controlled by the eddy activities and can be described in analogy to the molecular mixing by an effective turbulent diffusivity E as the product of the velocity u′ and size ℓ of the dominant eddies, $E \sim u'\ell$.

A river with a wide aspect ratio, $B \gg h$, where B is the width and h the average depth, is a simple equilibrium flow in which the bottom shear stress τ_o is counteracting the weight component acting in the flow direction (see Fig. 1), $\tau_o = \gamma hS$ where $\gamma = \rho g$ = specific weight of the water, ρ = water density, g = gravitational acceleration, and S = bottom slope = $\sin\alpha$. The friction velocity $u_* = \sqrt{\tau_o/\rho}$, is obtained on dimensional grounds, so that $u_* = \sqrt{ghS}$. u_* is therefore the major quantity characterizing the fluctuating eddy velocities u′ in channel flows, $u' \sim u_*$, as has been confirmed by many measurements (Nezu and Nakagawa, 1993). It is related to the average velocity U by the frictional properties (roughness) of the bottom and is typically about 5 to 10% of U, $u_* = (0.05 \text{ to } 0.10)U$, with higher values for rough beds.

The large eddies that correspond to the depth of the base flow, $\ell \sim h$, are most effective for the mixing. Moreover, the eddy structure is characterized by a certain spatial anisotropy, their extent in the vertical direction z is more strongly limited than that in the horizontal direction y that lies transversely to the flow direction x. In summary, the following expressions for the turbulence diffusivities result from the above: The vertical eddy diffusivity E_z is

$$E_z = \alpha_z u_* h \qquad (1)$$

where $\alpha_z = 0.07 \pm 50\%$ (Rutherford, 1994) and the horizontal diffusivity E_y

$$E_y = \alpha_y u_* h \tag{2}$$

where $\alpha_y = 0.5 \pm 50\%$ (Fischer et al., 1979) for rivers with moderate variability, thus without strong meanders and without lateral dead water zones.

If a continuous point source is considered at the water surface a mass plume will evolve as is shown in vertical section in Fig. 1 and in plan view in Fig. 2. The pollutant plume spreads both vertically and transverse. Characteristic for such diffusion processes is the approximately Gaussian concentration distribution in the mass plume with the maximum value c_{max} at the water surface and at the river bank. The standard deviation σ describes here a local value $c = e^{-1/2} c_{max} = 0,61 c_{max}$ and is a practical indicator for plume width.

The distance L_{mv} to the location of complete vertical mixing of the plume is often defined as being to the point when the concentration at the bed becomes 90% of the surface concentration and this can be determined by the method of images (Fischer et al., 1979)

$$L_{mv} = 0.4 \frac{Uh^2}{E_z} \tag{3}$$

Using Eq. 1 ($\alpha = 0.07$) and strong roughness, $u_* = 0.10U$, the distance to the location of complete vertical mixing is given by

$$L_{mv} \approx 50h \tag{4}$$

The transverse spreading of a continuous point source located at the bank in a wide river flow ($B \gg h$) is outlined in Fig. 2. The longitudinal coordinate follows in this case any river curvature and a constant rectangular cross-section is assumed. The distance L_{mh} to the location where complete horizontal mixing over the river cross-section takes place is

$$L_{mh} = 0.4 \frac{UB^2}{E_y} \tag{5}$$

With $\alpha_y = 0.5$ and for strong roughness one obtains

$$L_{mh} \approx 8 \left(\frac{B}{h} \right) B \tag{6}$$

It should be noted that these simple equations for the estimation of complete mixing, Eqs 4 and 6, respectively, are (a) independent of the river velocity and (b) primarily governed by the river morphology. The first is because the turbulent mixing coefficients E_y and E_z scale directly with the mean velocity U! Comparison of the two formulas shows that in a wide river ($B \gg h$), the length for complete vertical mixing is always rather small as has been indicated in Fig. 2. Furthermore, in the initially three-dimensional mixing process (until the location where complete vertical mixing takes place) the drop-off of the maximum mass concentration is relatively fast, $c_{max} \sim x^{-1}$ (Fig. 1), while it occurs more gradually in the vertically mixed, thus two-dimensional, mixing phase, $c_{max} \sim x^{-1/2}$ (Fig. 2).

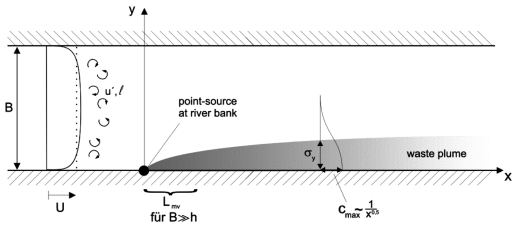


Figure 2. Transversal spreading for a continuous point-source located at the bank of a wide river flow ($B \gg h$), plan view.

Table 1. Examples for the complete mixing of a passive point source located at water surface and at bank of a river.

		Distance to complete mixing	
Example	B/h	Vertical L_{mv}	Horizontal L_{mh}
(i) Large river $B = 250$ m, $h = 3$ m	≈80	150 m	160 000 m
(ii) Small river $B = 5$ m, $h = 0,5$ m	10	25 m	400 m

Two examples are used for the practical illustration of the mixing dynamics of point sources in rivers: (i) Large river (approximately River Rhine near Karlsruhe, Germany, at average discharge), $B = 250$ m, $h = 3$ m, and (ii) small river, $B = 5$ m, $h = 0.5$ m. The calculations given in Table 1 show that complete vertical mixing occurs reasonably fast (150 m and 25 m, respectively), while complete lateral mixing requires considerably larger distances (160 km and 0.4 km, respectively)!

Several comments are in order: (1) The distance to complete vertical mixing will be somewhat reduced if the finite dimensions of the discharge opening are considered or if the source location is varied within the water column, e.g. located at mid-depth. Thus, the discharge design can play a certain role in this initial region. (2) The design features play a lesser role regarding the passive lateral spreading in the far-field. Only the lateral position of the discharge point is a potential factor: e.g. if the source is located in the center of the

river the distances for complete mixing are reduced by a factor 4 (since B/2 is used instead of B in Eq. 5 as the controlling lateral dimension). Beyond that, only the flow conditions in the river are decisive: For uniform flow conditions the estimation according to Eq. 6 would be somewhat low, while for strongly heterogeneous conditions – e.g. strong river meanders, or lateral constrictions that induce secondary flows – the actual distance might be somewhat shorter. (3) Both vertical and lateral complete mixing can be influenced by active mixing processes in the near-field of the discharge. Active mixing by momentum jets – especially in case of multiple diffuser discharges in rivers (e.g. Schmid and Jirka, 1999) – and buoyancy effects due to density differences lead, in general, to a reduction of the length for complete mixing. Models for the classification and prediction of these mixing complexities are available (e.g. Jirka et al., 1996).

Regardless of potential amplifications and complexities, the following rules of thumb apply for the mixing properties of point sources in rivers: (1) Complete vertical mixing is a rapid process with maximal dimensions of a few decades of the water depth. (2) Complete lateral mixing requires large distances. For typical river morphology (B/h = 10 to 100) the complete mixing will require from 100 to 1000 river widths (see also Endrizzi et al., 2002).

These analytical predictions for the delayed lateral mixing that are based on the description of the turbulent river flow properties have been confirmed through numerous field observations, in particular aerial photographs of "visible" plumes, taken from a period before recent source reductions were imposed, as shown in Fig. 3.



Figure 3. Aerial photograph (ca. 1960) of an industrial discharge located near the middle of the regulated River Rhine upstream of Lake Constance (Bodensee). The gradual lateral plume growth of the pollutant is typical for mixing processes in rivers. (Photograph courtesy of D. Vischer, Zurich).

2.3 *Consequences of the "combined approach": need for mixing zone regulations*

The mixing processes due to discharges into water bodies occur according to well understood physical principles, as has been shown above for the case of rivers, and lead to a spatial and temporal configuration of the mass plume and the associated concentration distribution. To what degree do the water quality control measures of the new EC-WFD, in particular its "combined approach" consisting of emission limit values (ELV) and environmental quality standards (EQS), correspond to these physical facts?

The relevant values for ELV and EQS for various pollutants and pollutant groups can be found in different directives of the EC (see e.g. Appendix IX of the WFD) or of the national authorities. By way of example for further analysis, Table 2 contains the values for two chemical pollutants (cadmium and triochlorethane). The ratio ELV/EQS is 10 for triochlorethane and 500 for cadmium. The range of 5 to 1000 is typical for most chemical as well as physical parameters, such as heat (temperature). This ratio describes the impact of the pollutants on the ecosystem, since the ELV is considered to protect against acute (lethal) effects on organisms, while the EQS is supposed to prevent long-time chronic influences. The ratio also expresses the necessary dilution that must be attained through physical mixing or – to

Table 2. Examples for emission limit values (ELV) and environmental quality standards (EQS) for two selected pollutants.

Pollutant example	Emission limit values ELV	Environmental quality standards EQS	ELV / EQS
Cadmium	0.5 mg/ℓ (83/513/EEC)	1 µg/ℓ (76/464/EEC)	500
Trichlorethane	0.1 mg/ℓ (AbwV, Germany, 2000)	10 µg/ℓ (76/464/EEC)	10

some extent – through biological decay and chemical transformation processes.

There can be other ways of prescribing ELV-values, namely through the specification of a "best available technology (BAT)". For example, for sewage outfalls this may be described as some form of treatment, at least primary, or enhanced (e.g. chemically) primary, or a secondary biological treatment stage for nitrogen removal, or a tertiary stage for phosphorus removal. The requirement may be set by national authorities depending on type of water body and its use (fisheries or recreation) or on sensitive ecological zones. In general, such BAT requirements assure a certain degree of nutrient removal. Other indicator parameters, such as bacteria or viruses, are also reduced in the treatment process. For example, while the typical total coliform count for raw sewage ranges from 10^6 to 10^8/100 ml it gets reduced by a factor 100 to 1000 during secondary and by 1000 to 10,000 during tertiary treatment (Larsen, 2000). Assuming an average factor of 1000 the effluent values for total coliform would then be 10^3 to 10^5/100 ml. Existing EC regulations provide some EQS-values for total coliform, e.g. the 500/100 ml given by the EC Bathing Water Directive. Thus, ELV/EQS ratios between 2 to 200 can be obtained from the above estimates. This compares to the "traditional" dilution requirement of about 50 to 100 that has been used for many years for outfall design in the coastal waters of several European countries (Larsen, 2000).

Both measures, concentration values and removal degrees are useful to reduce and control water pollution, but where do these values apply? The "end-of-pipe" specification for the ELV is clear and unequivocal in Art. 2 (40) of the WFD:

"*The emission limit values for substances shall normally apply at the point where the emissions leave the installation, dilution being disregarded when determining them*".

Surprisingly, and quite illogical from the viewpoint of the physical features of the mixing processes, the WFD does not provide any information on the spatial application of the EQS-values. It also does not oblige the national authorities to establish such specification. Therefore, it must be expected that considerable uncertainties and highly variable interpretations or monitoring methods will occur in the practice of water authorities, both as regards the continuing approval of existing discharges as well as the permitting of new ones. The "combined approach" that appears sensible for an integrated ecological water pollution control is in danger of being by-passed or undermined in its practical implementation.

From discussions with personnel from regional water authorities the authors know of two extreme interpretations regarding this omission in the WFD: (1) The EQS-value shall be applied "as near as possible" to the discharge point in order to obtain a good chemical status in an area as large as possible. This highly restrictive interpretation negates the fact that the physical mixing process cannot be reduced to extremely small areas (in the limit this approaches an "end-of-pipe" demand for EQS!), but requires a certain space – in particular for imposed high ELV/EQS ratios. It undermines the balanced objectives of the "combined approach". (2) In case of rivers, the EQS-value applies after "complete mixing in the water body". However, as was shown in the preceding section the longitudinal extent of the pollutant plume until full lateral mixing is attained can be considerable, even in small rivers. This highly generous interpretation could therefore lead to a condition that large regions within a pollutant plume of the point source would be exposed to concentration values above the EQS and would, therefore, represent "sacrificial stretches". A similar evaluation can be found in a recent German strategy report on water research (DFG-KOWA, 2003): "The occasional assumption that environmental quality standards apply only after complete mixing leads in most water body types to intolerably large distances since mixing processes usually occur gradually…".

Thus, the new "combined approach" concept of the WFD is lacking a clear and factually correct mixing zone regulation that preserves the water quality objectives of the "combined approach" and accounts for the physical aspects of the mixing processes. Therefore, a future amendment of the EC-WFD and national regulations for its implementation, respectively, should contain the following approximate wording:

"*The environmental quality standards apply in the case of point sources outside and at the edge of the mixing zone. The mixing zone is a spatially restricted region around the point source whose dimensions shall be specified either according to water body type and use or on an ad-hoc basis.*"

The mixing zone defined in the above statement is a regulatory formulation with the following general attributes: (1) The term "mixing zone" signifies explicitly that mixing processes require a certain space. (2) The term "spatially restricted" should guarantee that the mixing zone shall be minimized by the regulatory authority for the purpose of attaining the environmental quality goals. (3) While the mixing zone includes a portion – namely the initial one – of the actual physical mixing processes, these processes will continue beyond the mixing zone where they lead to further concentration drop-offs in the pollutant plume below the EQS-values. (4) The definition is restricted to "point sources" since diffuse sources usually do not contain clearly distinct mixing processes.

The regulatory concept of mixing zones can also be found in the water quality regulations of other countries. As an example, the U.S. Environmental protection Agency defines in its Water

Quality Handbook:

"*… the concept of a mixing zone as a limited area or volume of water where initial dilution of a discharge takes place*" (USEPA, 1994). A number of supplementary restrictions further define this water quality control principle such as "*… the area or volume of an individual mixing zone … be limited to an area or volume as small as practicable that will not interfere with the designated uses or with the established community of aquatic life in the segment for which the uses are designated*," and the mixing zone shape be "*… a simple configuration that is easy to locate in the body of water and avoids impingement on biologically important areas.*"

Once the principle of a mixing zone has been adopted and defined in the EC-WFD and/or national regulations it is also necessary that national water authorities provide clear guidance for the actual specification of mixing zone dimensions. Two major possibilities exist here:

(a) Specification of numeric mixing zone dimensions according to water body type and biological characteristics:

In the case of *discharges into a river* (see Fig. 4), the width of the mixing zone B_{MZ} can be restricted to a fraction of the river width, e.g. $B_{MZ} = n_B\ B$, with the goal that the majority of the river cross-section provides for unhindered passage of river fauna (fish), or the length of the mixing zone L_{MZ} can be described, e.g. $L_{MZ} = n_L\ B$, with the goal that high concentrations along the river banks are constrained, or both prescriptions may apply jointly. The multiples n_B and n_L – with typical ranges $n_B = 0.1$ to 0.5 and $n_L = 1$ to 5 – may be set by the water authorities based on regional considerations taking into account water body type, water use and biological characteristics.

For the case of *coastal discharges* Jirka et al. (2004) have given analogous recommendations for mixing zone around submerged diffuser outfall structures.

(b) Specification of mixing zone dimensions in an ad-hoc manner:

After prior ecological evaluations or predictions the discharger can request the authority for a mixing zone with a certain dimension with the claim that this would guarantee an integrated water quality protection. Based on its own examinations the authority can agree with that proposal or else demand further restrictions.

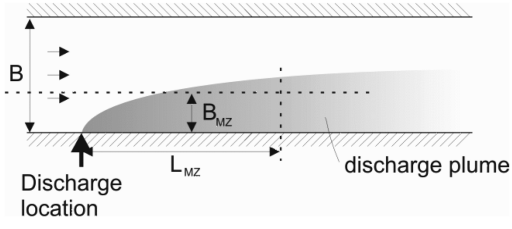


Figure 4. Example of regulatory mixing zone specifications for discharges into rivers: Width of mixing zone B_{MZ}, and/or length of mixing zone L_{MZ}, both defined relative to the river width B.

2.4 *Increased application of modeling techniques for mixing processes*

As another consequence of the "combined approach" of the new WFD values it appears that both dischargers as well as water authorities must increase the application of quantitative predictions of substance distributions in water bodies (water quality parameters in general, mixing processes in particular). This holds for both existing discharges (diagnosis) as well as planned future discharges (prediction).

There are several diagnostic and predictive methodologies for examining the mixing from point sources and showing compliance with EQS-values:

(1) *Field measurements or tracer tests* can be used for existing discharges in order to verify whether EQS-values are indeed met. Field measurements are costly, often difficult to perform, and usually limited to certain ambient conditions. Frequently, they must be supported through mathematical model predictions, on one hand, to establish a clear linkage to the considered discharge (especially if more than one discharge exists), and on the other hand, to synthesize conditions allowing for variabilities in the hydrological or oceanographic conditions or in the effluent rates.

(2) *Hydraulic model studies* replicate the mixing process at small scale in the laboratory. They are supported by similarity laws and are quite reliable if certain conditions on minimum scales are met as has been demonstrated in the past. But just like field tests, they are also costly to perform and inefficient for examining a range of possible ambient/discharge interaction conditions.

(3) *Simple analytical equations or nomograms* (e.g. Rutherford, 1994; Holley and Jirka, 1986) are often satisfactory to predict reliably the mixing behavior of a pollutant plume. For example, the maximum pollutant concentration c_{max} as a function of distance x along the flow for a passive point source at the bank of a river (see Fig. 2) is given by

$$c_{max} = \frac{2 Q_{co}}{h\sqrt{4\pi E_y U x}} \qquad (7)$$

where Q_{co} is the pollutant mass flux of the source (mass/time) and E_y is the lateral turbulent diffusivity from Eq. 2. The factor 2 on the right hand side signifies the reflection effect of the impermeable river bank. In many river applications with relatively uniform cross-sections Eq. 7 would be satisfactory for a conservative

prediction, possibly combined with parameter sensitivity studies (see coefficient α_y in Eq. 2) in order to predict the maximum pollutant concentration along the bank and to demonstrate compliance with the EQS-values. Simple amplifications of Eq. 7 in the form of a stream tube method (see Fischer et al., 1979) are available for strongly meandering and non-uniform river sections.

(4) *Mixing zone models* are simple versions of more general water quality models. They describe with good resolution the details of physical mixing processes (mass advection and diffusion), but are limited to relatively simple pollutant kinetics by assuming either conservative substances or linear decay kinetics. This is acceptable for most applications, since residence times in the spatial limited mixing zones (see previously mentioned specifications) are typically short so that chemical or biological mass transformations are usually unimportant. As for all computer-based models that are concerned with environmental problems – here with water quality as a common good! – the scientific transparency of the predictive models is essential. That means not only that the governing equations and all relevant assumptions must be clearly published but also the actual calculation module must be available as public domain software and thus scientifically verifiable. User interfaces as well as pre- and post-processing modules can, of course, be added, developed and distributed in a for-profit manner in an open market. Undoubtedly, the main problem in the application of mixing zone models is the estimation of its applicability by the user. In particular, simple model types are often limited to certain flow situations. Model assumptions and limitations must be clearly stated by the model developer. But even then it may be difficult for the user with limited experience in these complex processes of fluid mechanics to judge whether a model is applicable for a specific situation. The application of expert systems seems advisable for that problem. An expert system can lead the user in sequential steps through data acquisition, it performs the selection of a specific sub-model or predictive equation depending on the physical situation, it provides the graphical display and interpretation of the predictive values with regard to the compliance with EQS-values and mixing zone regulations, and finally it may provide recommendations regarding additional sensitivity studies or design changes for the optimization of the mixing process. Ragas (2000) provides a comparison of different mixing zone models. The mixing zone model CORMIX (Doneker and Jirka, 1991; Jirka et al., 1996), in particular, is characterized by its wide applicability to many water body types (rivers, lakes, estuaries, coastal waters) and has been successfully used for water quality management under different regulatory frameworks.

(5) *General water quality models* may be required in more complex situations. In simple water bodies, such rivers, coastal regions or estuaries with well defined uni-directional current regimes or with simple reversals, and with moderate pollutant loadings, the use of mixing zone models alone may suffice to arrive at, or to evaluate, a design of a point source discharge that meets regulations. However, in coastal regions with multiple current regimes (inertial, tidal, wind- or buoyancy driven) and in rivers and coastal regions with large pollutant loadings, especially where several sources may interact and additional diffuse sources may exist, mixing zone models must be supplemented by larger-scale (far-field) transport and water quality models. The latter are capable of prediction over greater distances in the water body the concentration distributions for different pollutants, but also for nutrients and other bio-chemical parameters with due consideration of mass transformation and exchange processes. They do not, however, have the high spatial resolution that is required to predict mixing processes and the compliance with EQS-values in a limited mixing zone. An effective and sensible approach for strongly loaded water body reaches is therefore the prior application of general water quality models in order to predict background concentrations in the vicinity of the considered point source. Superimposed on these background considerations are then the additional concentrations within the pollutant plume as predicted by the mixing zone model. For rivers, the model AVG of the German ATV-DVWK, the model QUAL-2 of the U.S. EPA, and the model RWQM1 of the International Water Association are all examples of general water quality models. Such models also form the basis of management procedures for attaining a good quality status in the case of multiple sources, i.e. by following the principle of a distributed waste load allocation for individual water users.

The ultimate goal of European water quality policy as promulgated in the Water Framework Directive of 2000 is the attainment of a good quality status by the year 2015. Therefore, a future amendment of the WFD and of corresponding national implementation procedures must contain a clear and unequivocal mixing zone regulation in order to not jeopardize that goal. Increased usage of several types of water quality models by both dischargers and regulatory authorities will be another key mechanism for reaching that goal.

3 INSTANTANEOUS RELEASE PROBLEMS IN RIVERS

3.1 *River alarm models*

Accidents happen, as the adage says. While the water quality impact of continuous discharges can be

controlled and reduced by water authorities through the aforementioned permitting process, there exist limited control options for accidental pollutant releases or spills. Of course, increased safety regulations and/or redundant design requirements are important for minimizing industrial, mining or navigational accidents that cause short-time chemical pollutant releases in or along rivers. Yet despite such measures accidental spills are bound to occur, albeit with decreased likelihood and frequency.

The major option for water authorities lies in enabling a rapid emergency response to warn downstream users and to mitigate secondary damages, e.g. by shutting down of water intakes during passage of the pollutant mass or limiting recreational uses. The key element for response planning are so-called "river alarm models (RAM)" that allow the on-line operational tracking and prediction of the released pollutant mass by forecasting its movement and dispersion along the river channel. The first such RAM was instituted by the Commission on the Hydrology of the River Rhine in cooperation with the International Commission for the Protection of the River Rhine (ICPR) in the wake of the dioxin spill from the Sandoz plant, Basel, Switzerland, in 1986 that heavily damaged flora and fauna along the entire river. Other recent spill disasters of major proportions have been along the Dnjepr, Russia (1970s), the Guadalquivir, Spain (1998), and the Tisza, Rumania (2001), all of these resulting from the failure of retention dikes for chemical or mixing process waters.

Alarm models are currently being implemented by different European river basin authorities, and presumably around the world. Common for these RAMs is a one-dimensional formulation in order to facilitate the on-line installation on PCs within the water authorities and operation with a minimum of hydrological information on initial and boundary conditions. To a great degree these RAMs are highly empirical as the parameters describing the transport and dispersive characteristics of the pollutant mass in the one-dimensional formulation are subject to large uncertainty, particularly so in river channels with major heterogeneities. These include rivers with highly variable natural morphology, side arms and dead zones as well as regulated river with groins or spur-dikes and secondary floodways. Because of this predictive uncertainty it is necessary to conduct dye dispersion tests in the river in order to deduce the required model parameters. These tests are very time-consuming and expensive and are always limited to the given hydrologic regime (low, average or high flow). A thorough mechanistic understanding of the generic role of channel heterogeneities on mass transport and dispersion is needed to improve the predictive capabilities of existing RAMs and help in the formulation of new ones for other rivers.

3.2 *Dispersion processes for instantaneous mass releases in rivers*

Turbulent flow and transport in a river is, of course, a three-dimensional process. Hence, the concentration c(x, y, z, t) following an instantaneous release of pollutant mass M in a given steady-state velocity field $\vec{q} = (x, y, z)$ is given by the three-dimensional advection diffusion equation (Fischer et al., 1979) in which the turbulent diffusivities E_x, E_y, E_z (each a function of x, y, z) describe the turbulent spreading process (Reynolds-averaged over the time scale of fluctuations). x is the longitudinal coordinate following the river channel, y the lateral and z the vertical coordinate. Under the assumption of uniform unidirectional mean flow – either a straight river channel or in a natural coordinate system following a mildly curving channel – the mean velocity field $\vec{q} = (u, v, w)$ simplifies to u(y, z), $v = 0$, $w = 0$ and diffusivities are functions of y, z only. In principle, the three-dimensional advection–diffusion equation – for general or simplified uniform geometry – can be solved by numerical computational techniques subject to some closure approach on the turbulent diffusivities.

In the practice of RAMs – as for many other water quality or hydraulic problems – the general three-dimensional solution is not feasible for operational reasons or often not necessary. In that case simpler solutions by spatially averaging over one or two transverse dimensions can be obtained. For RAMs the averaging over the entire channel cross-section A, thus integrating over y and z, is typical practice. The one-dimensional mass conservation equation that results from this averaging process reads for a conservative pollutant

$$\frac{\partial C}{\partial t} + U\frac{\partial C}{\partial x} + \frac{\partial}{\partial x}\widetilde{u''c''} = \widetilde{E_x \frac{\partial^2 c}{\partial x^2}} \qquad (8)$$

in which C(x, t) is the cross-sectionally averaged (mean) concentration, U the mean velocity and ~ denotes cross-sectional averaging. The term on the right-hand side specifies the turbulent diffusion (i.e. the role of time-averaged fluctuations) in the longitudinal direction. The crucial term, however, is the so-called "small-scale advective" flux $\widetilde{u''c''}$ which represents the spatial correlation of the deviations of velocity $u''(y, z) = u - U$ and concentration $c''(y, z) = c - C$ from its mean values.

The result of the "small-scale advection" process is shown schematically in Fig. 5 for a uniform channel flow with an internally shear and velocity profile u(y, z). For short times, the concentration distribution strongly resembles the shape of the velocity profile while additional turbulent diffusion causes spreading in all directions, especially also in the transverse direction. For long times, the interaction between the

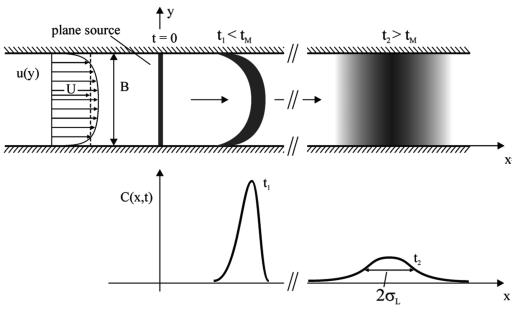


Figure 5. Schematics of longitudinal dispersion process in uniform river. For short times the cross-sectional profile C(x, t) is strongly skewed, for long times it assumes a Gaussian distribution.

longitudinal stretching mechanism due to shear flow and the transverse mixing mechanism due to turbulent diffusion is pronounced and enters an asymptotic state that is called the "longitudinal dispersion" mechanism. In this stage the cross-sectional concentration distribution is essentially homogeneous and is Gaussian in shape in the longitudinal direction. Furthermore, the standard deviation σ_L of this distribution grows $\sigma_L \sim \sqrt{t}$, all attributes that resemble a Fickian diffusion process, i.e. mass diffusion as an ensemble result of many individual independent random processes. In his ground-breaking papers, Taylor (1953, 1954) showed that this dispersion process can be represented by an equivalent advection–dispersion equation

$$\frac{\partial C}{\partial t} + U\frac{\partial C}{\partial x} = E_L \frac{\partial^2 C}{\partial x^2} \tag{9}$$

in which the longitudinal turbulent diffusion term in Eq. 8 has been neglected as being much smaller than the dispersion term. E_L is the coefficient of longitudinal (or shear flow) dispersion.

Taylor has also shown – in his case for axisymmetric pipe flow – that the value of E_L can be computed directly from the distribution of the shear flow u(y, z) and the transverse diffusivities $E_y(y, z)$ and $E_z(y, z)$ through triple integration. For the case of a purely vertically sheared two-dimensional uniform channel flow, u(z) and $E_z(z)$ only, this triple integration reads

$$E_L = -\frac{1}{h}\int_o^h u'' \int_o^z \frac{1}{E_z}\int_o^z u'' dz dz dz \tag{10}$$

in which h is the water depth.

Eq. 10 was first evaluated by Elder (1959) for the turbulent logarithmic velocity profile and associated diffusivities to yield

$$E_L = 5.9 u_* h \tag{11}$$

in which u_* is the shear velocity as the major factor characterizing turbulent eddy velocities.

In another seminal contribution, Fischer (1967) dealt with dispersion processes in natural river channels, that are typically wide and shallow, $B/h \gg 1$, in which B is the river width. He showed that while the velocity profile is doubly sheared u(y, z) the vertical shearing effect u(z) (i.e. Elder's approach) is of lesser importance while the lateral shear $\bar{u}(y)$ becomes dominant as it operates over a much larger scale (B). Here $\bar{u}(y)$ is the vertically averaged velocity profile that has been sketched in Fig. 5. Fischer represented Taylor's integral in depth-averaged form

$$E_L = -\frac{1}{A}\int_o^B (\bar{u} - U) h \int_o^y \frac{1}{E_y h}\int_o^y (\bar{u} - U) h\, dy\, dy\, dy \tag{12}$$

in which $E_y(y)$ is the depth-averaged lateral diffusivity (see Eq. 2). The evaluation of Eq. 12 with measured lateral velocity profile from either laboratory or field experiments showed generally very satisfactory agreement with the dispersion coefficient that has been measured from corresponding dye tracer tests through growth of the variance σ_L^2,

$$E_L = \frac{1}{2}\frac{d\sigma_L^2}{dt} \tag{13}$$

where $t = x/U$ corresponds to the travel time between subsequent measurement stations.

As stated above, the advection–dispersion equation, Eq. 9, the associated values of E_L, and finally its solution

$$C(x,t) = \frac{M}{A\sqrt{4\pi E_L t}}\left\{\exp\left[-\frac{(x - Ut)^2}{4E_L t}\right]\right\} \tag{14}$$

are only valid in the final dispersive stage of the mixing process. The duration of the initial or convective stage is given by the transverse mixing time t_M. For the case of river channels, t_M is given by (Fischer, 1967; Fischer et al., 1979)

$$t_M = 0.4\frac{B^2}{E_y} \tag{15}$$

which corresponds, $t_M U = L_{mh}$, to the associated mixing distance L_{mh} given in Eq. 5. During the convective stage, $t > t_M$, the mean concentration distribution is strongly skewed (see Fig. 5). The behavior of the pollutant mass ("cloud") furthermore depends on the discharge details, whether more or less uniform across the river or whether a release in mid-river or near a bank.

3.3 *The role of channel heterogeneities: influence of groin fields*

It has long been recognized that the dispersion process in natural river channels may be greatly enhanced

beyond the simple shear flow effects in a uniform channel as described in the preceding. Higher order influences, such as dead-zones or retarded flow zones caused by overbank flows, meanders, side arms, partially vegetated areas, and groin fields cause additional flow non-uniformities which result in increased stretching of the pollutant cloud, i.e. increased dispersion once a new asymptotic stage has been reached, as well as a reduction (retardation) of the effective transport velocity c below the cross-sectional mean velocity U, $c < U$.

No consistent, mechanistically justifiable approaches to this problem of channel heterogeneities have been developed to date. A high degree of empiricism prevails on that issue in current practice, e.g. on RAM implementation and operation. Since heterogeneities in channel morphology are irregularly distributed along river distance, one approach has been to accept an unavoidable degree of uncertainties in the value of E_L. A number of empirical equations – or empirical adjustments of theoretical equations as given above – can be found in the literature reflecting this state of affairs. For example, Fischer et al. (1979) give

$$E_L = \alpha \frac{U^2 B^2}{u_* h} \qquad \text{with } \alpha = 0.011 \tag{16}$$

based on an evaluation of Eq. 12 for "typical" lateral velocity profiles and irregularities. They cite that data comparisons show inaccuracies by a factor of ±4 or larger. Mazijk (1996) reports yet larger deviations (factor of 10) with dye tracer data for different stretches of the River Rhine. This is hardly acceptable as predicted maximum concentration values as well as cloud widths are proportional to $\sqrt{E_L}$ (see Eq. 14) leading to substantial operational decision-making uncertainty.

A further consequence of variable channel heterogeneity is the apparent extension of the convective stage of mixing. Since the morphology is constantly changing an asymptotic dispersive state is never reached. This is exemplified by the tracer test results for the River Rhine (Fig. 6) where at distances greatly exceeding a mixing distance t_M (estimated as about 50 km for the release station) a strong skewness persists. (It is worth noting, however, that by virtue of Eq. 15 a curve C(t) at a given station will always be slightly skewed; only curves C(x) at a given time become truly symmetric!) For that reason the RAM (see Mazijk, 1996) contains an empirical adjustment of Eq. 15 in the form

$$C(x,t) = \frac{M}{\frac{Q}{c}\sqrt{4\pi E_L t}} \left\{ \exp\left[-\frac{(x-ct)^2}{4E_L t} \right] \right\} \left\{ 1 + \frac{1}{6} H_3\left(\frac{x-ct}{\sqrt{2E_L t}} \right) \right\} \tag{17}$$

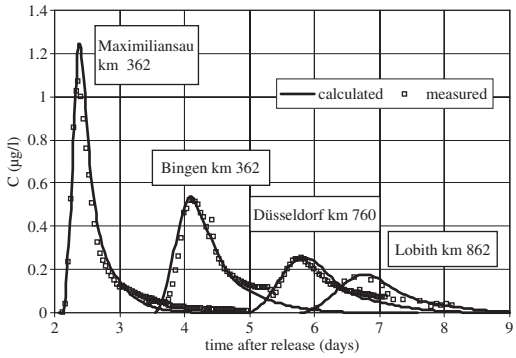


Figure 6. Concentration curves from dye tracer test on River Rhine. Tracer release near Basel (km 170) (after Mazijk, 1996).

in which $H_3(\tau) = \tau^3 - 3\tau$ is the Hermite polynominal of third order to impose a certain skewness. Q is the river discharge and c is the transport velocity, related to the mean velocity U

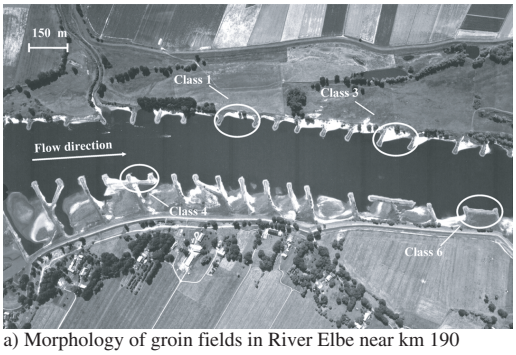
$$c = \frac{U}{1+\beta} \tag{18}$$

where β is nominally the ratio of active stream cross-sectional area A_s to the dead-zone cross-sectional area A_D, $\beta = A_s/A_D$, but in practice is used as best-fit parameter. Fischer's Eq. 16 is used for E_L, with α being another best-fit parameter.

A best-fit model calibration is certainly possible whenever high quality tracer test data sets covering different stretches and hydrologic regimes are available. This is the case for the River Rhine so that the existing Rhine-RAM constitutes a reasonably reliable pollution routing and forecasting tool. It is not satisfactory, however, from a fundamental mechanistic viewpoint and is a severe drawback for the establishment of new RAMs for other major rivers for which tracer data is limited and new extensive tests would be a costly and time-consuming undertaking in each instance.

A research study has been undertaken at the Institute for Hydromechanics (IfH) with the ultimate purpose of reducing the existing uncertainty in specifying transport parameters for RAMs and, thus, improving their prognostic abilities avoiding elaborate calibration effects. An initial focus of the study has been the systematic effect on mass dispersion of a system of groin fields that are arranged regularly along the river bank. This morphological situation is frequently found in regulated European rivers as shown in Fig. 7.

Weitbrecht (2004) (see also Weitbrecht et al., 2004) studied the effect of an infinite series of groin fields on asymptotic mass dispersion in two steps: first, a detailed fluid mechanical understanding of the exchange dynamics at the edge of an individual groin



a) Morphology of groin fields in River Elbe near km 190

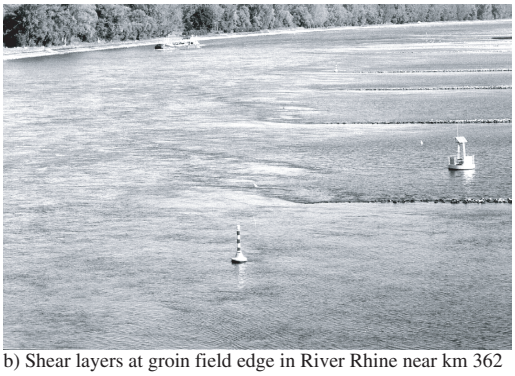

b) Shear layers at groin field edge in River Rhine near km 362

Figure 7. Groin fields on rivers.

field, and second the integrative effect of a sequence of many groin fields.

(a) *Exchange mechanisms between main channel and groin fields*: Groin fields form – depending on their geometry – more or less "dead-zones", i.e. the mean field-averaged forward convective velocity is zero. However, there is an effective shear zone (see Fig. 7b) at the groin field boundary to the mean channel: these causes both a net circulatory mechanism as well as intermittent turbulent exchange between the main river and the groin field. When a pollutant cloud propagates in the main channel a fraction of the cloud mass gets advected into the groin field, is temporarily retained and finally gradually returned into the main river. Thus, understanding the intensity of the exchange mechanism as a function of groin field morphology is key to quantifying the aggregate effect of groin field sequences on dispersion.

Figure 8 shows the tilting laboratory flume at the IfH with 20 m length and 1.82 m width that was used in a series of tests to study groin field flow dynamics. Typical flow velocities were $U = 0.16$ m/s and flow depths $h = 0.046$ m, giving a channel Reynolds number of about 7500, thus well into the Reynolds

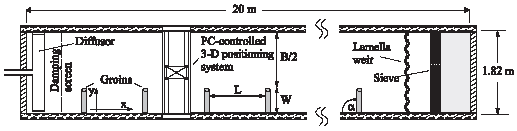


Figure 8. Schematic top view of the laboratory flume tests at IfH for groin field dynamic.

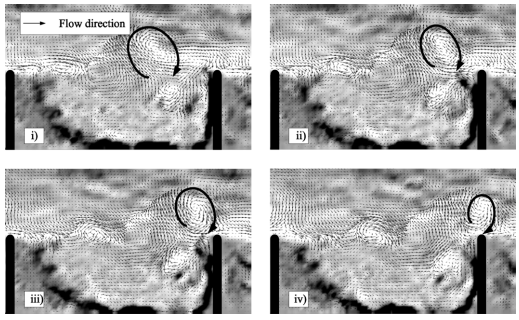


Figure 9. Sequence of instantaneous velocity vectors and vorticity fields (light shading negative vorticity, dark positive) for experiment with groin field aspect ratio $W/L = 0.4$. Time interval between PIV images is 1s.

invariant regime so that the results seem transferable to prototype conditions. Different groin field geometries, $W/L = 0.17$ to 3.3, in which W = groin length and L = spacing length between groins (see Fig. 8), variable inclination lengths and variable depth h_D in the groin field, less than the main channel depth h_s were studied schematically.

The major experimental techniques for deducing the exchange dynamics were surface particle-image-velocimetry (PIV) as described by Weitbrecht et al. (2002) and a planar-concentration-analysis (PCA) of an instantaneous volumetric dye injection within the groin field (see Kurzke et al., 2002). Figure 9 shows a sequence of PIV-generated images with instantaneous velocity and vorticity field. The generation of large coherent structures within the shear layer at the groin field boundary is evident leading to mean and turbulent transport in and out of the groin field. The structure of the mean gyres for groin field with different aspect rating can be seen in Fig. 10. A number of statistical analyses can be performed with these data. A key element is the definition of the exchange velocity E from the instantaneous lateral velocity values v_B at the groin field boundary, i.e. the line of length L connecting the groin heads,

$$E = \frac{1}{2L}\int_{o}^{L} |v_B| \, dx \qquad (19)$$

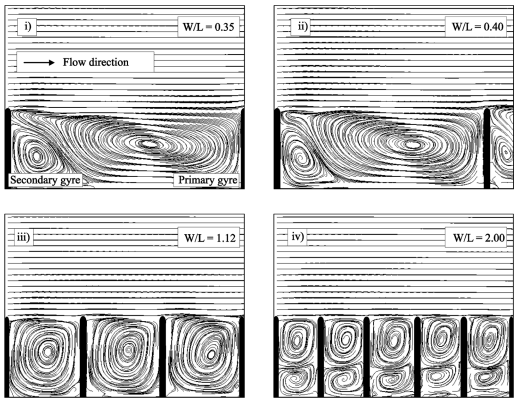


Figure 10. Time averaged surface streamline patterns for different groin field aspect ratios W/L.

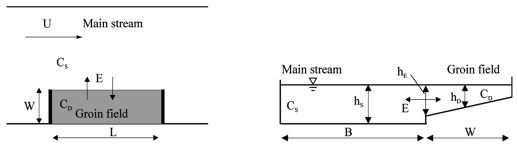


Figure 11. Plan view and cross-section of groin field processes represented as a dead-zone model.

Normalization with the mean stream velocity U gives the dimensionless exchange coefficient

$$k = \frac{E}{U} \tag{20a}$$

As an alternative and independent method for deducing the exchange coefficient the whole groin field volume was injected instantaneously with a volumetric dye source. This was done with a special injection box connected to some 800 injection needles in a 3 cm × 3 cm array. These produced small turbulent dye clouds that rapidly merged forming a uniform volume source. The loss of total dye mass was monitored with the calibrated PCA system and followed fairly well an exponential loss curve with a time constant T_D. Using a dead-zone model (see Fig. 11) as a simple parameterization T_D can be related to a dimensionless exchange coefficient k

$$k = \frac{W}{T_D U}\frac{h_E}{h_D} \tag{20b}$$

Both independent results, Eqs. 19 and 20a,b, were found to be in excellent agreement with each other.

A groin field morphometric parameter was defined by Weitbrecht (2004)

$$\frac{R_D}{h_s} = \frac{WL}{(W+L)h_s} \tag{21}$$

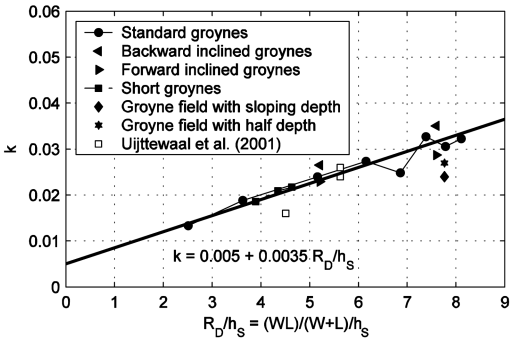


Figure 12. Dimensionless exchange coefficient k at groin field boundary as a function of groin field morphometric parameter R_D/h_S.

where R_D represent a sort of "hydraulic radius" for the groin field. The measured exchange values correlate well with this parameter as shown in Fig. 12, covering a wide range of groin field types and shapes, including data by Uijttewal et al. (2001). The data are well presented by the linear relation

$$k = 0.005 + 0.0035\frac{R_D}{h_s} \tag{22}$$

which can be used as the basis for further predictive work. The observed range of k agrees well with the range 0.01 to 0.03 reported by Valentine and Wood (1979) from the analysis of field data. These authors, however, did not report any morphometric dependence.

(b) *Integrating the effect of a groin field sequence on river dispersion*: Once k (Eq. 22) is given as the boundary information at the edge of the main river channel the advection–diffusion equation can, in principle, be solved to yield the value of the dispersion coefficient in the composite system (main river plus groin field sequence). Valentine and Wood (1977) have proposed a Dead-Zone Model as two coupled differential equations for that purpose. Unfortunately, no analytical solutions are known and numerical methods would take very long to converge to the dispersive regime, being fraught by numerical dispersion in the process.

Weitbrecht (2004) formulated a Lagrangian particle tracking model (LPTM) as an alternative method for obtaining values for the asymptotic regime. A mass of many discrete particles is released initially and uniformly over the system cross-section. The model performs for each time step and for each particle a forward convective step according to the local velocity value u(y) and a random transverse diffusive step proportional to the square root of the local diffusivity $E_y(y)$. A special adjustment is made on the latter step to prevent a "noise-induced" drift component due to gradients $\partial E_y/\partial y$. The lateral boundary condition at a solid

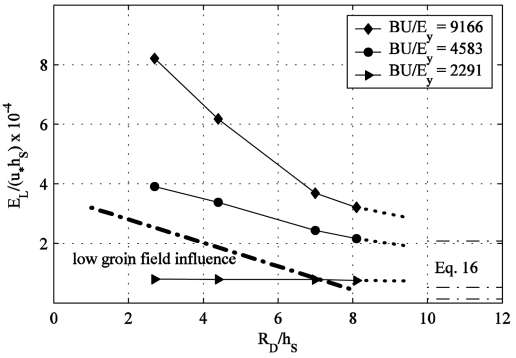


Figure 13. Effective asymptotic dispersion coefficients, normalized as $E_L/(u_* h_s)$, for composite river/groin field system as a function of groin field morphometry R_D/h_S and main river Peclet number $Pe = UB/E_y$. Results from LPTM simulations. Fischer's estimates (Eq. 16) for rivers without groin fields are shown as dash-dotted lines for the three cases of Pe.

side wall (bank) is a reflection condition, while at the groin field boundary a retention condition is imposed, i.e. particles are held for the average retention time T_D before they are released back into the flow.

The LPTM is a useful and convenient method that can be used efficiently on a PC to produce stable statistics on concentration distributions, including lengths of convective period and skewness distributions (for examples, see Weitbrecht et al., 2004). It has been run with the normalized velocity and diffusivity distributions corresponding to the experimental conditions given above.

Some of the LPTM results are summarized in Fig. 13 which displays the asymptotic normalized dispersion coefficient, $E_L/(u_* h_s)$, as a function of two parameters: a main channel Peclet number $Pe = UB/D_y$ and the groin field morphometry parameter R_D/h_s.

Several observations can be made from these qualitative simulations:

- The transverse mixing Peclet number Pe measures the role of forward advection relative to transverse diffusion. Increasing Pe (e.g. by decreasing E_y) also increases the asymptotic dispersion coefficient, consistent with the form of the triple integral (see Eq. 12).
- Decreasing the groin field morphometry factor R_D/h_s means decreasing k and increasing the retention time T_D and causes generally an increase in the value of E_L.
- There appears to be, however, a regime of low Pe and low R_D/h_s (region on lower left in Fig. 13) in which the groin field retention effect is no longer important. In this regime the advection in the main channel is so weak (slow) that the strong exchange effect acts by rapidly absorbing and returning pollutant mass so that the retention effect is no longer visible. The limit line is given by a ratio of transverse mixing time to retention time, $t_M/T_D \approx 10$.
- The orders of magnitude of the normalized coefficients $E_L/(u_* h_s)$ are 0 (10^4). These are quite plausible and agree with some reported field data for many natural channels, e.g. see surveys in Fischer et al. (1979) or Rutherford (1994). For comparison, Fischer's estimates (Eq. 16) for rivers without groin fields are plotted in the right margin of Fig. 13. The drastic enhancement of longitudinal dispersion due to groin fields is evident from these comparisons.

In summary, the study has shown that a systematic description of groin field flow dynamics can lead to an improved quantitative prognosis of the flow and transport parameters in reasonably complex riverine systems. Hopefully, these results and further parametric studies will lead to improvements in the formulation of future river alarm models.

4 CONCLUDING REMARKS

The quantitative understanding of mixing and dispersion processes in rivers is a key element in successful strategies for water quality control and management. Despite great advances that have been made over the last half century there remain a number of challenging research questions that need to be resolved.

For continuous discharges, that are usually subject to a routine permitting process by water authorities, the specification of transverse mixing is most important for meeting given mixing zone regulations. Secondary current and coherent eddy structures, especially in curved or meandering channels, e.g. in the wake of structures or islands, will influence mixing processes.

Many more open research questions concern the longitudinal dispersion process due to instantaneous or accidental pollutant releases in river systems with complex morphology. In order to decrease the present parameter uncertainty systematic studies are needed on the effect of river heterogeneities, such as meandering, overbank floodways and side arms, partly vegetated flow zones, and groin fields, all with variable hydrological conditions, such as water levels.

Finally, the interaction of these physical processes with the chemical and biological transformations that govern the fate of particular chemicals need to be addressed. This includes pollutant sorption processes with fine organic or inorganic suspended or bottom sediments and with biota.

ACKNOWLEDGEMENTS

Work funded by the German National Science foundation (DFG Grant No. Ji 18/4-1,2) and the German

Federal Ministry for Education and Research (BMBF Grant No. 02 WT 9934/9). The assistance of Volker Weitbrecht in the preparation of the manuscript is gratefully acknowledged.

REFERENCES

DFG-KOWA (Deutsche Forschungsgemeinschaft – Senatskommission für Wasserforschung) (2003), Wasserforschung im Spannungsfeld zwischen Gegenwartsbewältigung und Zukunftssicherung, Denkschrift, Bonn

Doneker, R.L. and Jirka, G.H. (1991), Expert Systems for Design and Mixing Zone Analysis of Aqueous Pollutant Discharges, J. Water Resources Planning and Management, 117, No. 6, 679–697

Elder, J. (1959), The dispersion of marked fluid in turbulent shear flow. J. Fluid Mech. 5

Endrizzi, S., Tubino, M., and Zolezzi, G. (2002), Lateral Mixing in meandering channels: a theoretical approach, Proceedings River Flow 2002, International Conference on Fluvial Hydraulics, D. Bousmar and Y. Zech, Eds., Louvain-La-Neuve, Belgium

Fischer, H.B. (1967), The mechanics of dispersion in natural streams, J. Hydraulic Div., Proc. ASCE, 93, 187–216

Fischer, H.B., List, E.J., Kohl, R.C.Y., Imberger, J. & Brooks, N.H. (1979), Mixing in Inland and Coastal Waters, Academic Press, New York

Holley, E.R. and Jirka, G.H. (1986), Mixing and Solute Transport in Rivers, Field Manual, U.S. Army Corps of Engineers, Waterways Experiment Station, Tech. Report E-86-11

Jirka, G.H., Doneker, R.L. and Hinton, S.W. (1996), User's Manual for CORMIX: A Hydrodynamic Mixing Zone Model and Decision Support System for Pollutant Discharges into Surface Waters, U.S. Environmental Protection Agency, Tech. Rep., Environmental Research Lab, Athens, Georgia, USA

Jirka, G.H., Bleninger, T., Burrows, R., Larsen, T. (2004), Environmental Quality Standards in the EC-Water Framework Directive: Consequences for Water Pollution Control for Point Sources, European Water Management European Water Association (EWA)

Kurzke, M., Weitbrecht, V. and Jirka, G.H. (2002), Laboratory concentration measurements for determination of mass exchange between groin fields and main stream. In D. Bousmar and Y. Zech (Eds.), River Flow 2002, Louvain-la-Neuve, Belgium, 369–376

Mazijk, A. van (1996), One-dimensional approach of transport phenomena of dissolved matters in rivers, Ph.D. thesis, Delft University of Technology

Nezu, I. und Nakagawa, H. (1993), Turbulence in Open-Channel Flows, A.A. Balkema, Rotterdam

Ragas, A.M.J., Hams, J.L.M., and Leuven, R.S.E.W. (1997), Selecting water quality models for discharge permitting, European Water Pollution Control, 7(5), 59–67

Ragas, A.M.J. (2000), Uncertainty in Environmental Quality Standards, Doctoral dissertation, University of Nijmegen, The Netherlands

Rutherford, J.C. (1994), River Mixing, John Wiley, Chichester

Schmid, B.H. and Jirka, G.H. (1999), Der Kühlwasserdiffusor des Dampfkraftwerks Donaustadt: expertensystemgestützte Planung und Ausbreitungsberechnung, Wasserwirtschaft, 89, 238–242

Taylor, G.I. (1953), Dispersion of soluble matter in solvent slowly flowing through a tube. Proc. Royal Soc., London, Vol. 219, 186–203

Taylor, G.I., (1954), The dispersion of matter in turbulent flow through a pipe, Proc. Royal Soc., London, Vol. 233, pp 446–468

Uijttewaal, W., Lehmann, D., Mazijk van A. (2001), Exchange processes between a river and its groin fields: model experiments, Journal of Hydraulic Engineering, Vol. 127, No. 11, pp 928

USEPA (U.S. Environmental Protection Agency) (1994), Water Quality Standards Handbook: Second Edition, EPA 823-B-94-005a, Washington, DC, USA

Valentine, E.M. & Wood, I.R. (1977), Longitudinal dispersion with dead zones, J. Hydraulics Division, (HY9), pp 975

Valentine, E.M. & Wood, I.R. (1979), Experiments in longitudinal Dispersion with dead zones, J. Hydraulics Division, (HY8), pp 999

Weitbrecht, V. (2004), Influence of dead-water zones on the dispersive transport in rivers, Doct. Dissertation, University of Karlsruhe

Weitbrecht, V., Kühn, G. and Jirka, G.H. (2002), Large-scale PIV measurements at the surface of shallow water flows, Flow Measurement and Instrumentation, 13, 237–245

Weitbrecht, V., Uijttewal, W. and Jirka, G.H. (2004), A random walk approach for investigating near- and far-field transport phenomena in rivers with groin fields, Proc. River Flow 2004 (this issue)

WFD (Water Framework Directive) (2000), Official Publication of the European Community, L327, Brussels

This page intentionally left blank

River Flow 2004 – Greco, Carravetta & Della Morte (eds.)
© 2004 Taylor & Francis Group, London, ISBN 90 5809 658 0

Debris flows and their modeling

T. Takahashi
Kyoto University, Kyoto, Japan

ABSTRACT: This paper reviews the existing models of debris flow categorizing into the single-phase flow model and the two-phase flow model. Classic single-phase models such as the viscoplastic fluid model and the dilatant fluid model are simple and still give powerful tools in predicting the average behaviors of flow as long as the parameter values included in respective models are properly determined. But, they are often difficult to determine on the a priori arguments of materials and topographical conditions. The behaviors of debris flows are diversified depending on the properties of solid material, solid concentration, flow magnitude, river channel conditions, etc., and they often change their sediment transporting modes while in motion. The two-phase models that consider the debris flow is comprised of the mixture of two continuum media of fluid phase and solid phase are able to classify debris flows and able to analyze the physics of respective flows. As examples of those models, author's theories for inertial debris flow and viscous debris flow are introduced.

1 MODELS FOR MULTI-PHASE FLOW

Many simulation models for granular flow with the negligible effects of interstitial fluid (in a vacuum or in the atmosphere) have been given (single-phase model). They can be categorized into the continuum media model and the discrete particle model. The former model describes the granular assembly as a continuum media and its characteristics are analyzed by the Eulerian forms of the continuity and momentum equations. The discrete characteristics of particle motion are necessarily neglected. The latter model, on the other hand, traces the motion of each particle by the Lagrangian equation.

In the continuum media model, the characteristics of flow as a granular assembly are intrinsic in the stress terms in the Eulerian momentum equation. These terms are obtained from the relationship between the stress and the strain of the continuum that is called the constitutive equation. Although the general constitutive equation under the arbitrary conditions of particle density, particle size distribution, and particle interactions is difficult to obtain, if an appropriate form of it under a particular flow condition is given, the continuum media model can be an operative method to explain the flow characteristics en masse under that condition.

The discrete particle model describes every particle's motion in flow by the Newton's second law equation under the effects of contact forces between the neighboring particles. Two kinds of approach for treating the contact have been adopted: the hard-contact technique and the soft-contact technique.

In the hard-contact technique, particles are considered as rigid bodies, and the contact arises only between the two adjacent particles in an instantaneous moment (Campbell and Brennenn 1985, Straub 2001). This technique has shortcoming on the handling of the simultaneous collision of multiple bodies.

The soft-contact technique is free from the shortcomings in the hard-contact technique (Campbell 2001). At the moment of soft-contact, particles deform a little and forces proportional to the stiffness of particles act at the contact points. The interaction between particles at a contact point is modeled by the deformation of interface instrument that is composed of spring and dashpot connected in parallel. Two sets of such an instrument are mounted normally and tangentially on each contact point. To handle non-cohesive particle, a joint that is nonresistant to tension in normal direction and a slipping joint that is effective under a tangential force beyond a threshold should be connected to the respective sets of instrument (Gotoh & Sakai 1997). Thus, many parameter values must be given beforehand, and if particle number becomes large, load on computer becomes enormous. The implementation of simulation makes clear the motion of individual particles that may be difficult to observe in the physical model tests. But, the quantitative characteristics of average flow such as depth and velocity can be obtained only after the completion of simulation.

In the case of debris flow, the interstitial liquid is water or slurry, so the relative density of particles in flow is small, and therefore, the effects of interstitial fluid often play important roles. Then, the flow should be considered as composed of two phases. Liquid phase is naturally described by the Eulerian flow equation, but as mentioned above, the solid phase may be described as a continuum media or as an assembly of discrete particles.

If solid phase is considered as a continuum media and described by the Eulerian equations, mathematically the model becomes Euler-Euler coupling model. In this model, two momentum equations each for liquid and solid phases are given. These are as following (Iverson 1997):

$$\sigma C\left(\partial \mathbf{v}_s / \partial t + \mathbf{v}_s \cdot \nabla \mathbf{v}_s\right) = \nabla \cdot \mathbf{T}_s + \sigma C \mathbf{g} + \mathbf{F} \tag{1}$$

$$\rho(1-C)\left(\partial \mathbf{v}_f / \partial t + \mathbf{v}_f \cdot \nabla \mathbf{v}_f\right) = \nabla \cdot \mathbf{T}_f + \rho(1-C)\mathbf{g} - \mathbf{F} \tag{2}$$

where $\mathbf{v}_s$ = velocity of solid; $\mathbf{v}_f$ = velocity of fluid; C = solid volume concentration in flow; σ = density of particle; ρ = density of fluid; $\mathbf{g}$ = acceleration due to gravity; $\mathbf{T}_s$ = solid phase stress tensor; $\mathbf{T}_f$ = fluid phase stress tensor; and $\mathbf{F}$ = interaction force per unit volume that results from momentum exchange between the solid and fluid constituents.

Addition of these two equations yields a momentum conservation equation applicable to the bulk mixture. This procedure eliminates the assessment of complicated interactions between fluid and solid phase. If nearly steady uniform flow is considered and the relative velocity between solid and fluid is neglected in Cartesian coordinate system, following two equations are finally obtained (Takahashi 1991):

$$P_{ds} + P_f = (\sigma - \rho) g \cos\theta \int_z^h C dz \tag{3}$$

$$T_{ds} + T_f = g \sin\theta \int_z^h \rho_T dz \tag{4}$$

where P_{ds} = pressure in solid phase; P_f = pressure in fluid phase in excess over hydro-static one; T_{ds} = shear stress in solid phase; T_f = shear stress in fluid phase; ρ_T $\{=(\sigma-\rho)C+\rho\}$ = apparent density of debris flow material; θ = slope of flow surface; h = flow depth; and z = height measured from the bottom of flow.

These equations are fundamental equations in the two-phase fluid model describing the stress balance in the flow of mixture. The essential problem in this two-phase mixture theory is how the left-hand sides of Equations 3 and 4 are described.

If solid phase is considered as an assembly of discrete particles, flow should be analyzed by Euler-Lagrange coupling model, in which individual particle motion is solved by the discrete element method earlier described taking the interaction between particles and fluid into account. Some investigations on bed load transport have been done by this method (Gotoh et al. 1994), but debris flow has not been treated by this method.

2 SINGLE-PHASE CONTINUUM MODELS

In the single-phase continuum models, the mixture of particles and fluid is considered as a kind of continuum fluid whose constitutive relation between stress and rate of strain is to be found empirically by the laboratory tests of samples collected from flow or by the deduction from the back analysis of the model applied to the flow in field.

2.1 *Viscoplastic fluid model*

Debris flow commences from the gradual or the abrupt motions of debris block due to the effects of water, and after the motion of considerable distance, it comes out to flat area and stops. Therefore, if one considers the material itself has strength intrinsically, one can explain the starting of motion attributing to the operations of a stress more than that (yielding) strength, and flow stops if the stress in flow becomes smaller than the strength. Debris flow modeling as a kind of viscous fluid having strength is called 'viscoplastic fluid model', and it assumes the relation between the stress and the strain rate as following:

$$\tau = \tau_y + K(du/dz)^n \tag{5}$$

where τ = shearing stress; τ_y = yielding strength; u = velocity at height z; and K and n = positive parameters.

The simplest in the viscoplastic fluid models is the one setting $n = 1$, that is called 'Bingham fluid model'. This model was first proposed independently by Yano & Daido (1965) and Johnson (1965). Later, Johnson (1970) modified his model to the following 'Coulomb-viscous model':

$$\tau = c + \sigma_n \tan\phi + \mu(du/dz) \tag{6}$$

where c = cohesive strength; σ_n = internal normal stress; ϕ = internal friction angle; and μ = Bingham viscosity.

Viscoplastic fluid models, including the Herschel-Bulkley fluid model that sets $n < 1$ (Coussot 1995) and the polynomial models that add the term $(du/dz)^2$ to Bingham fluid model (Julien & O'Brien 1997) or add $(du/dz)^\eta$ to Equation 6 (Chen 1988), are still frequently used especially for the cases of viscous type debris flow.

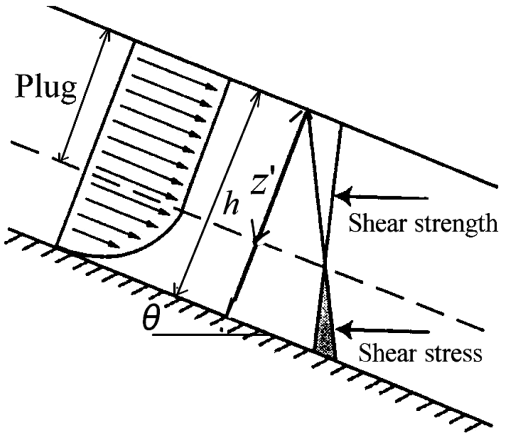


Figure 1. Velocity distribution in Bingham fluid flow.

For example, the stress balance equation for steady uniform Bingham fluid flow is given by

$$\tau_y + \mu(du/dz) = \rho_T g(h-z)\sin\theta \tag{7}$$

The integration of Equation 7 under the boundary condition; $u = 0$ at $z = 0$ gives the velocity distribution throughout the depth as shown in Figure 1 in which z' $(= \tau_y/\rho_T g \sin\theta)$ is the thickness of plug that behaves like a rigid body.

The serious shortcoming of viscoplastic models is the difficulty in determining the crucial parameter values such as τ_y, μ, etc. Those values obtained by laboratory tests and by field observations are usually much different, and they cannot account for the parameter value changes due to the addition or subtraction of water or sediment during in motion. According to the author's observation, the typical viscous type debris flow in the Jiangjia ravine in China lacks the plug that should exist in a viscoplastic fluid flow.

2.2 *Dilatant fluid model*

Debris flow whose main solid components are coarse grains larger than gravel size can often reach to an area flatter than about 4° keeping its high mobility and competence to freight big boulders. Takahashi (1978) inferred such small resistance to flow was caused by the dispersion of grains separated with one another, and the inter-particle collision gave rise to the dispersion of heavier grains than the ambient fluid.

Bagnold (1954) was the first to discover the significance of inter-particle collision as the cause of particle dispersion. His experiments and simple binary grain collision analysis gave the stress-strain relationships in inertial and viscous regimes. In inertial regime, those relationships were given as following:

$$p = a_i \cos\alpha \cdot \sigma\lambda^2 {d_p}^2 (du/dz)^2 \tag{8}$$

$$\tau = p \cdot \tan\alpha = a_i \sin\alpha \cdot \sigma\lambda^2 {d_p}^2 (du/dz)^2 \tag{9}$$

where p = dispersive pressure in flow; a_i = numerical constant; α = collision angle; d_p = grain diameter; λ = linear concentration of grains defined by $\lambda \equiv \{(C_*/C)^{1/3} - 1\}^{-1}$; and C_* = maximum grain concentration when $\lambda = \infty$. He directly measured the excess pressure with grains in flow over that with the plain fluid, so that p in Equation 8 was equivalent to P_{ds} in Equation 3. The grain drag; T_{ds}, corresponding to P_{ds} could not be measured directly but it was deducted from the measured periphery drug that was the total of drugs shared by fluid and grain constituents. Therefore, τ in Equation 9 is equivalent to T_{ds} in Equation 4.

Bagnold used neutrally buoyant solid spheres immersed in a Newtonian fluid in his experiments, but Takahashi (1978) exploited his results to the open channel flow with hyper-concentrated heavy grains assuming uniform distribution of grains throughout depth; the stress balance equations for normal and parallel directions to the bed were given, respectively:

$$\begin{aligned} &a_i \cos\alpha \cdot \sigma\lambda^2 {d_p}^2 (du/dz)^2 \\ &= C(\sigma-\rho)g(h-z)\cos\theta \end{aligned} \tag{10}$$

$$\begin{aligned} &a_i \sin\alpha \cdot \sigma\lambda^2 {d_p}^2 (du/dz)^2 \\ &= \{C(\sigma-\rho)+\rho\}g(h-z)\sin\theta \end{aligned} \tag{11}$$

Referring to the discussion above, this model is an equivalent model to the two-phase model in which the dynamic fluid effects are negligible. But, as far as Equation 11 is concerned, shearing stress in the flow of mixture is described by an expression assuming a single-phase continuum fluid. A kind of fluid having the relationship; $\tau \sim (du/dz)^n$, $n > 1$, is called 'dilatant fluid', so Takahashi's model is called the dilatant fluid model.

Equations 10 and 11 can be easily integrated under the boundary condition; $u = 0$ at $z = 0$, and one can obtain the flow velocity at height z. The result of integration of Equation 11 is given as

$$u = \frac{2}{3d_p}\left(\frac{g\sin\theta}{a_i\sin\alpha}\frac{\rho_T}{\sigma}\right)^{1/2}\frac{1}{\lambda}\left\{h^{3/2} - (h-z)^{3/2}\right\} \tag{12}$$

Mathematically, the velocity distribution function obtained from Equation 10 has not the same expression with the one obtained from Equation 11. Those two

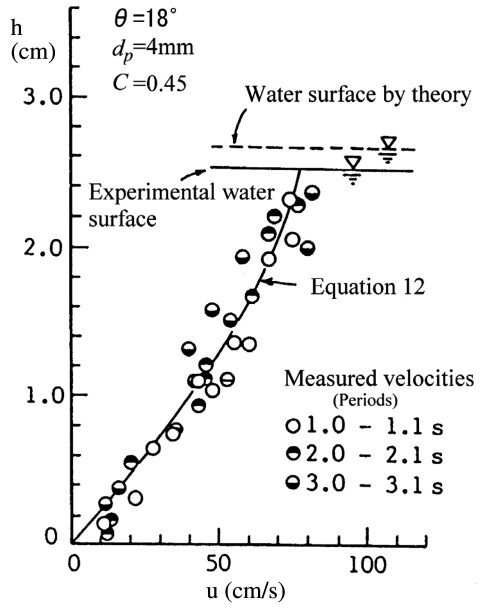


Figure 2. Velocity distribution on rigid bed.

functions become physically equivalent only when the following formula is satisfied:

$$C = \frac{\rho \tan\theta}{(\sigma - \rho)(\tan\alpha - \tan\theta)} \tag{13}$$

For example, if one substitutes $\sigma = 2.65\,\mathrm{gcm}^{-3}$, $\rho = 1.0\,\mathrm{gcm}^{-3}$, $\tan\alpha = 0.75$ and $\theta = 18°$ into Equation 13, one obtains $C = 0.46$. Then, if one puts the mixture of water and grains whose grain diameter is 4 mm and the volume concentration is 0.45, into a rigid bed flume of 18° slope, one observes velocity distribution that fits very well to Equation 12 by giving $a_i = 0.04$ as shown in Figure 2. As another example, if one supplies water onto an erodible bed saturated by water whose slope is steeper than 15°, debris flow develops downstream and approaches an equilibrium state as illustrated in Figure 3. Experiment reveals that in the equilibrium steady flow region grain concentration is given by Equation 13. Thus, the dilatant fluid model can well explain the debris flow in which interparticle collision plays the dominant role, moreover different from viscoplastic fluid model, it can account for the change in solid concentration during in motion (Takahashi 1991).

The assumption of uniform grain distribution throughout depth is, however at least theoretically, too much simplification, and this causes the contradiction that there exists two independent formulae 10 and 11 for one unknown velocity (Iverson & Denlinger

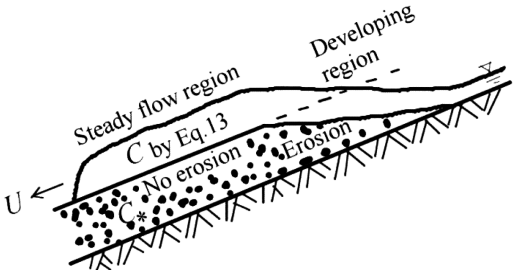


Figure 3. Development of debris flow on erodible bed.

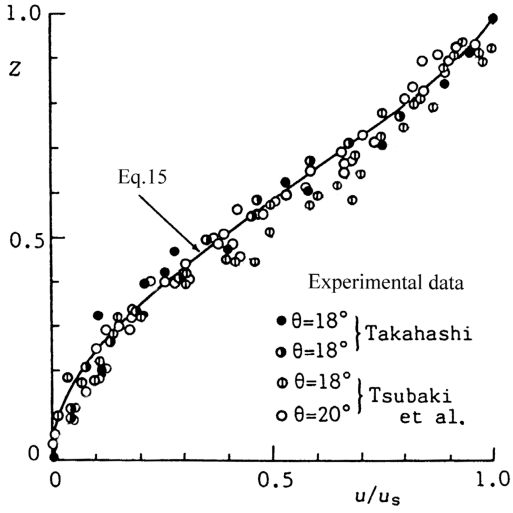


Figure 4. Theoretical velocity distribution and the experimental data.

1987). To dissolve this contradiction, Takahashi (1991) assumed the following formula:

$$\tan\alpha = (C_* / C)^{1/3} \tan\phi \tag{14}$$

Substitution of this formula into Equations 8 and 9 results in rather well fitting to Bagnold's experiment, and also the substitution of this formula into Equations 10 and 11 gives two independent formulae necessary and sufficient to obtain u and C at height z. The results of analysis using these two equations can well explain the vertical grain concentration and velocity distributions on sediment bed. The velocity distribution form is given by

$$\frac{u}{u_s} = 1 - \frac{1}{2}(1 - Z)^{3/2}(2 + 3Z) \tag{15}$$

where u_s = flow surface velocity; and $Z = z/h$. Equation 15 is compared with the experimental data in Figure 4. The vertical velocity distribution on erodible sediment bed (Figure 4) has a peculiar form with

two inflection points; one near the bed and the other near the surface of flow, whereas that on rigid bed, especially when flow contains slightly thinner concentration than equilibrium, has simple concave form (Figure 2) as is explained by the first approximation under the assumption of uniform concentration distribution.

3 TWO-PHASE FLUID FLOW MODEL (MIXTURE THEORY)

As mentioned earlier, how one considers the left-hand side terms in Equations 3 and 4 can be the origin of diverse debris flow theories. The particle dispersive pressure due to inter-particle collision; p_c, and the static skeletal pressure due to enduring contact between particles; p_s, would be the candidates of $P_{ds} \cdot P_f$ exists if the sediment mass contracts volumetrically or if there is a net flux of sediment toward the bed (Iverson 1997). Herein, only quasi-steady flow is considered, so $P_f = 0$. The shear stress due to inter-particle collision; τ_c, the shear stress due to enduring contact between particles; τ_s, and the streaming stress due to migration of particles in one layer to other layer; τ_k, would be the candidates of T_{ds}. The deformation stress within interstitial fluid; τ_μ, and the turbulent mixing stress; τ_t, would be the candidates of T_f. All such candidates cannot prevail simultaneously, but some among others prevail in a particular regime. Therefore, through the discussion of dominant stresses, debris flows can be classified.

3.1 *Coulomb mixture theory (Quasi-static flow)*

Iverson & Denlinger (2001) claims that the Coulomb friction term; τ_s, is almost always larger than the particle collision term; τ_c, stating that the Savage number, defined by Equation 16, in various field examples and the large scale experiment by USGS is smaller than 0.1 as the evidence, and they develop a Coulomb mixture theory as the one only suitable to debris flow.

$$N_{Sav} = \frac{\sigma (du/dz)^2 d_p^{\ 2}}{(\sigma - \rho) gh} \tag{16}$$

The numerator of Formula 16 is, as is clear from Equation 8, the term representing the particle collision effects, and the denominator is the term representing effective pressure at the bottom of flow due to weight of granular mass. They say the denominator is the gravitational grain contact stress that produces Coulomb friction, but it must be noted that the static gravitational contact stress can be transferred from the flow surface to the bottom only when a skeletal structure due to the enduring contact of grains extends throughout the depth. To furnish this necessity, the local solid fractions everywhere should exceed a threshold level C_3. According to Bagnold (1966), C_3 value for natural beach sand is about 0.51. It is true that the denominator represents the effective pressure at the bottom of flow, but it is not necessarily transferred as the static gravitational contact stress. It is transferred as the collision stress when grain concentration is smaller than C_3. If $C \tan\theta$ is multiplied to the denominator, the term represents the effective pressure at the bottom precisely, but the term multiplied by $C \tan\theta$ to the numerator does not represent the magnitude of collision stress. It is $a_i \cos\alpha\lambda^2$ that is to be multiplied as is evident in Equation 8, and Equation 10 is nothing but to show the collision stress balances with effective pressure. Therefore, their Coulomb mixture theory is considered as a model that is suitable for very densely concentrated quasi-static flow.

Herein, we do not dwell on the details of Coulomb mixture theory.

3.2 *Classification of dynamic debris flows*

Dynamic debris flow in this section is defined as the one except for the quasi-static debris flow, in which dynamic stresses predominate in governing the behaviors of debris flow. The total shear stress $\tau (= T_{ds} + T_f)$ in a grain and water mixture is, as mentioned earlier, described as

$$\tau = \tau_c + \tau_k + \tau_s + \tau_\mu + \tau_t \tag{17}$$

If C is larger than about 0.2, τ_k becomes smaller than τ_c and the difference between the two stresses tends to become drastically large as C becomes larger (Takahashi & Tsujimoto 1997). If C is smaller than 0.5, τ_s is almost equal to zero (Bagnold 1966). Therefore, in a dynamic debris flow whose average concentration of coarse grains (except for the constituent making up interstitial slurry) is between 0.2 and 0.5, and if τ_t/τ_c and τ_μ/τ_c are small, $\tau_c/\tau \approx 1$ is satisfied. Debris flow in which the stress due to the collision of particles dominates among others is called 'stony debris flow'. On the other hand, debris flow in which $\tau_t/\tau \approx 1$ is satisfied is called 'turbulent muddy debris flow', and the one in which $\tau_\mu/\tau \approx 1$ is satisfied is called 'viscous debris flow'.

Equation 9 and the other previous theoretical considerations on the constitutive relations of granular flows confirm (Campbell 1990)

$$\tau_c = \sigma d_p^{\ 2} f_1(C)(du/dz)^2 \tag{18}$$

and fluid mechanics give the following forms:

$$\tau_\mu = \mu f_2(C)(du/dz) \tag{19}$$

$$\tau_t = \rho_T l^2 (du/dz)^2 \tag{20}$$

where $f_1(C)$ and $f_2(C)$ = functions of C; μ = viscosity of interstitial fluid; and l = mixing length. From these Equations, one obtains the following formulae:

$$\frac{\tau_t}{\tau_c} \sim \left(\frac{\rho_T}{\sigma}\right)\left(\frac{h}{d_p}\right)^2 \frac{1}{f_1(C)} \tag{21}$$

$$\frac{\tau_\mu}{\tau_c} = \frac{\lambda^{1/2}}{B_a}\frac{f_2(C)}{f_1(C)} \tag{22}$$

$$\frac{\tau_t}{\tau_\mu} \sim R_e \frac{1}{f_2(C)} \tag{23}$$

where $B_a\,(\equiv \sigma\lambda^{1/2}d_p^2(du/dz)/\mu)$ is called Bagnold number and $R_e\,(\equiv \rho_T Uh/\mu)$ is Reynolds number, in which $l \approx h$ and $l(du/dz) \approx U$ are assumed and U = cross-sectional mean velocity.

Summarizing the above discussions, one will come to a conclusion that dynamic debris flows occur in the domain within the ternary diagram as shown in Figure 5, where the three axes represent relative depth, Bagnold number and Reynolds number, respectively. The region where Bagnold number is large and the relative depth is small is that for stony debris flow occurrence. In the region where Bagnold number and Reynolds number are small, viscous debris flow occurs, and in the region where the relative depth and Reynolds number are large, turbulent muddy debris flow occurs. Thus, the areas close to the three apices are occupied by the existence areas of stony, viscous and muddy debris flows, respectively, and the rest of the area in the triangle should be the area of 'hybrid debris flows'.

Previous experiments show that if large particle's transport concentration (Herein, the large particle is defined as the one not being suspended by turbulence, and the transport concentration is defined as the ratio of large particle discharge to the total discharge of large particles plus fluid phase including suspended sediment.) is smaller than about 0.2, large particles cannot disperse in the entire depth of flow. Large particle's mixture layer appears only in the lower area of flow and the upper area is the one of plain water flow layer, small particle's suspension flow layer or slurry flow layer. This type flow can be called 'immature debris flow' in contrast to '(mature) debris flows' in which large particles are dispersed in the entire depth.

Thus, sediment transport phenomena can be categorized by the transport concentrations as plain liquid flow, individual particle transport (bed load and suspended load; $0 < C \leq 0.02$), immature debris flow ($0.02 < C \leq 0.2$), debris flow ($0.2 < C \leq 0.5$), quasi-static debris flow ($0.5 < C \leq 0.6$), and sliding of rigid earth body ($0.6 < C$). The boundary C values indicated are for reference, they should depend on properties of particles such as cohesion, grain shape and the distributions of grain sizes.

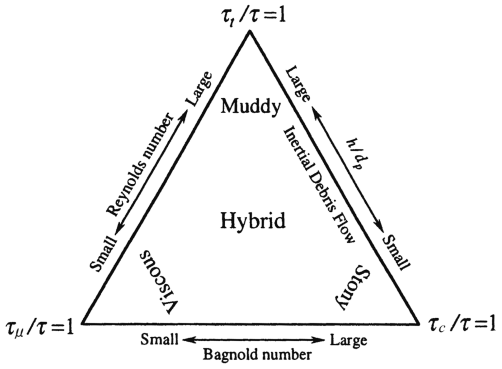


Figure 5. The domain of existence of various type debris flows.

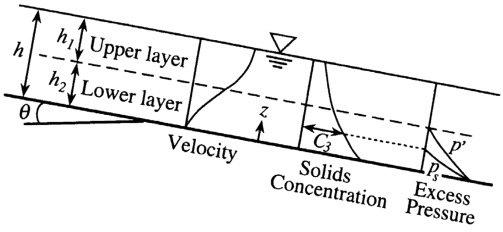


Figure 6. The structure model of an inertial debris flow.

3.3 *Generalized theory for inertial debris flow*

Debris flows that occur in the domain adjacent to the axis representing relative depth in Figure 5 are sometimes called 'inertial debris flow', because the inertial terms; τ_c or τ_t, dominate in flow. The hybrid flow in the inertial debris flow consists of the lower particle collision layer and the upper turbulent suspension layer as illustrated in Figure 6. The ratio of these two layers in flow depends on the relative depth; h/d_p, and the concentration. If relative depth is small and the particle collision layer occupies the entire flow, it is a stony debris flow. If relative depth is large and the turbulent suspension layer occupies almost entire depth, it is a turbulent muddy debris flow. Herein, the theory of Takahashi & Satofuka (2002) is introduced.

Consider an inertial debris flow as illustrated in Figure 6, because τ_μ can be neglected, the balance of force equations in the lower layer in the direction of main flow and perpendicular to it are written as

$$\tau_c + \tau_k + \tau_s + \tau_t = g\sin\theta \int_z^h \{(\sigma-\rho)C + \rho\}dz \tag{24}$$

$$p_c + p_s = g\cos\theta \int_z^{h_2} (\sigma-\rho)Cdz \equiv p' \tag{25}$$

where p' = effective pressure transmitted directly particle to particle; and h_2 = thickness of lower layer. The

upper limit of integration of Equation 25 is h_2, because the particle load in the upper layer is supported by turbulence and it is transmitted to the lower layer as hydro-static pressure.

If solids concentration at the bottom of flow is C_*, the dynamic pressure; p_c, at the bottom must be zero because no flow can exist at such a high concentration as C_*. Therefore, at the bottom all the effective pressure; p', should be borne by the static pressure; p_s. If solid concentration decreases upward, at the height where C becomes equal to C_3, p_s becomes zero. The vertical distribution function of p_s is not yet known, but following function is assumed:

$$p_s = \begin{cases} \dfrac{C - C_3}{C_* - C_3} p' & ; \quad C > C_3 \\ 0 & ; \quad C \le C_3 \end{cases} \tag{26}$$

The relation between p_s and τ_s is assumed as the following Coulomb's equation:

$$\tau_s = p_s \tan\phi \tag{27}$$

The balance of force equation in the upper layer is given as following:

$$\tau_c + \tau_t = \int_z^h \rho_T g \sin\theta dz \tag{28}$$

Takahashi & Tsujimoto (1997) gave the following constitutive equations for dry granular flow:

$$\tau_c = \frac{4}{5}\sqrt{\frac{1}{15\pi}}\frac{1+e}{\sqrt{1-e}} C^2 (1+\lambda)\sigma {d_p}^2 \left(\frac{du}{dz}\right)^2 \tag{29}$$

$$\tau_k = \frac{1}{3(1+\lambda)}\sqrt{\frac{1}{15\pi(1-e)}}\sigma {d_p}^2 \left(\frac{du}{dz}\right)^2 \tag{30}$$

$$p_c = \frac{2}{15} C^2 (1+\lambda)\frac{1+e}{1-e}\sigma {d_p}^2 \left(\frac{du}{dz}\right)^2 \tag{31}$$

where e = restitution coefficient of particles.

Turbulent mixing stress; τ_t, is given by Equation 20, where the mixing length is assumed as $l = \kappa z$, in which κ is Karman constant. Question may arise that in the densely concentrated lower layer, mixing length would have the scale of void between particles. Previously, Takahashi (2000) developed a theory adopting such a concept; $l = d_p/\lambda$ in the lower particle mixing layer and $l = \kappa z$ in the upper turbulent layer. But, interstitial fluid is widespread as a continuum fluid in the entire depth, and so the mixing length may have larger scale than the void between particles. No matter which mixing length is adopted, in the lower layer, τ_t is far smaller than τ_c and τ_s, and it little affects the velocity and the solid concentration there. However, considering the intensity of turbulence, ρ_T in the lower layer is regarded as the density of interstitial fluid, whereas in the upper layer, it is regarded as that of the mixture.

Substitution of these constitutive relations and Equation 26 into Equations 24 and 25 gives the velocity and the solid concentration distributions in the lower layer.

In the upper layer, the substitution of Equations 20 and 29 into Equation 28 gives the velocity distribution. The distribution of solid concentration can be obtained assuming that particles are dispersed by turbulence obeying the similar diffusion equation applicable to normal suspended load analysis.

The criteria whether the upper layer exists and how high the boundary between the upper and the lower layers from the bottom of flow are as following:

1. $w_s/u_* < 1$, where $w_s =$ settling velocity of particles; and $u_* = \sqrt{gh\sin\theta}$. If this criterion is not satisfied particles are not suspended, and in this case, $h_2 = h$.
2. The minimum solid concentration in the lower layer appears at the upper boundary of the lower layer, above that height τ_c is no more larger than τ_t. The experiments for immature debris flow show that the minimum solid concentration; $C_{\lim}$, performed by inter-particle collision is about $0.5C_*$ (Takahashi 1991). Therefore, although it is somewhat expedient, the boundary height is set where the solid concentration calculated in the lower layer, from lower to upper direction, at first becomes equal to $0.5C_*$.

If calculated solid concentration is larger than $C_{\lim}$ in the entire depth, even the criterion (1) is satisfied, there is no upper layer, and $h_2 = h$. If, at certain height, calculated solid concentration becomes smaller than $C_{\lim}$, but the criterion (1) is not satisfied, it is immature debris flow.

Theoretical solid concentration and velocity distributions were obtained corresponding to the conditions; $\sigma = 2.65\ \mathrm{gcm^{-3}}$, $\rho = 1.0\ \mathrm{gcm^{-3}}$, $\tan\phi = 0.7$, $e = 0.3$, $\kappa = 0.3$, $C_* = 0.65$, and $C_3 = 0.5$. Figure 7 shows the examples of the results of calculation, where flow depth is held constant at 2 cm.When particle diameter is 7 mm, even for a steep channel slope of 18°, the condition for particle suspension is not satisfied but particles are dispersed in the entire depth due to the action of inter-particle collision, and the velocity is small. It is stony debris flow. For the same size particles, when channel slope is 6°, particles cannot be dispersed in the entire depth, and it is immature debris flow. When particle diameter is 1mm, even the channel slope is as flat as 6°, the condition for particle suspension is satisfied, and there exists the upper layer in which particles are in suspension. It is hybrid type debris flow.

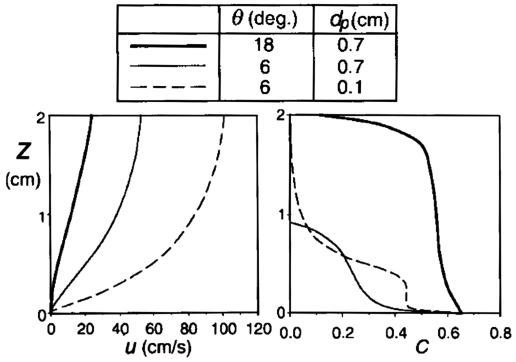


Figure 7. Velocity and particle concentration distributions by the theory.

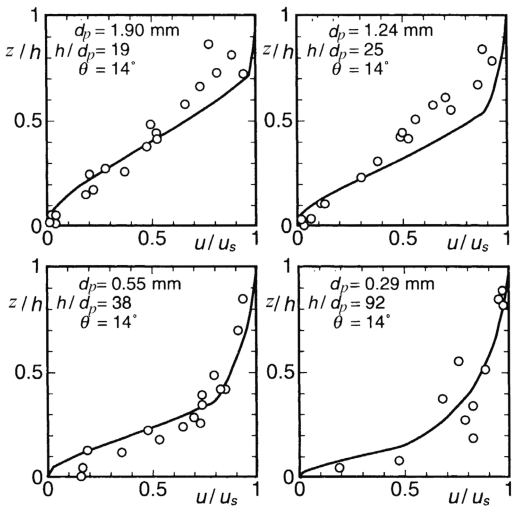


Figure 8. Theoretical and experimental velocity distributions.

Figure 8 compares the theoretically obtained velocity distributions with the experimental data of Hirano et al. (1992), where the velocity is normalized by the surface velocity; u_s. Debris flows in the experiments were generated by supplying water from upstream onto the water saturated erodible bed flume 20 cm in width and 7 m in length. Bed slope was held constant at 14°. The relative depth; h/d_p, was changed by changing both the supplying water discharge and the particle size. The theoretical as well as experimental velocity distribution curves have a tendency to lower the height of boundary between the upper and the lower layers (breakpoint on the curve) and to increase the degree of concavity as the relative depth increases. Moreover, the theoretical curves well fit to the experimental results.

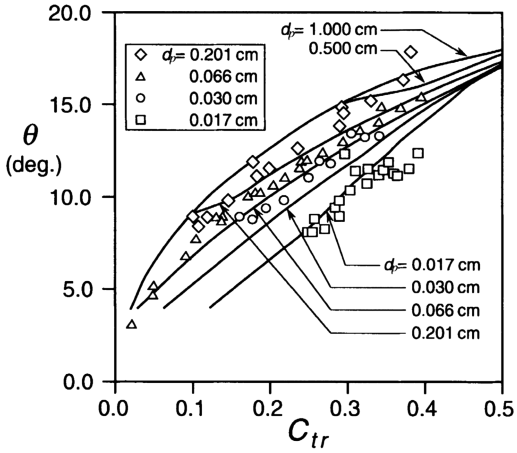


Figure 9. Theoretical and experimental equilibrium transport concentrations.

Figure 9 is a comparison of the theoretical equilibrium transport concentrations; C_{tr}, with author's experimental results. In the experiments debris flows were generated by abruptly supplying water from upstream onto the water saturated erodible bed in a flume 9.9 cm in width and 10 m in length. Bed slope was changed, and the discharge of sediment plus water; Q_T, was held constant at 531 cm^3s^{-1} by trial and error. Four kinds of materials 0.201, 0.066, 0.030 and 0.017 cm in the median diameters, with densities between 2.64 and 2.66 gcm^{-3} and internal friction angles between 38.5° and 39°, were used for the erodible bed. The debris flow samples were collected with a bucket at the outlet of the flume to measure Q_T and C_{tr}. As shown in Figure 9, the theory can well explain the tendency that the smaller the particle diameter, the larger the equilibrium transport concentration becomes under a certain channel slope. This figure further shows that, in comparison with the previous discussion (Takahashi 2000), the revision of mixing length formula improves the goodness of fit to the experiments in the views of boundary plane height between upper and lower layer and solid concentration in upper layer.

In Figure 9, other than those corresponding to the experiments, the theoretical curves for $d_p = 1$ cm and 0.5 cm are also drawn. Under the experimental conditions discussed herein, particles larger than 1 cm in diameter cannot be suspended by turbulence even for the steep channel of 15°. The reason for branching of curves corresponding to $d_p = 0.5$ cm and 0.2 cm from the curve for $d_p = 1$ cm is due to the beginning of suspension from the respective branching points. The theoretical curve for $d_p = 1$ cm almost coincides with the concentration calculated by substituting $\tan\phi = 0.8$ into Takahashi's previous

equilibrium concentration formulae (Takahashi 1991); i.e., for stony debris flow

$$C_\infty = \frac{\rho \tan\theta}{(\sigma - \rho)(\tan\phi - \tan\theta)} \tag{32}$$

and for immature debris flow

$$C_{tr} = 6.7 C_\infty{}^2 \tag{33}$$

Equation 33 is valid only when C_{tr} calculated by this equation is smaller than C_∞ calculated by Equation 32.

It must be noted here that $\tan\phi$ is set equal to 0.8 in the calculation of Equations 32 and 33, but in the calculation of theoretical curves, $\tan\phi$ is set equal to 0.7 (see Equation 27 and parameter values used in the calculation). Why such a different value should be used will become clear by the following explanation.

If particle diameter is large ($d_p > 1$ cm), the settling velocity of particle is given by Newton's equation, and the criterion 1) for particle suspension is written as

$$\frac{h}{d_p} > \frac{\sin\theta}{3.31(\sigma/\rho - 1)} \tag{34}$$

If $\theta = 10°$ and $(\sigma/\rho - 1) = 1.65$ are substituted into this equation, $h/d_p > 32$ is obtained. This means that if the relative depth in an inertial debris flow is smaller than about 30, it is stony debris flow. From the condition 34 and Equation 29, Equation 21 is rewritten as the following formula:

$$\frac{\tau_t}{\tau_c} < \frac{\rho}{\sigma}\left\{\frac{\sin\theta}{3.31(\sigma/\rho - 1)}\right\}^2 \frac{5\sqrt{15\pi(1-e)}}{4(1+e)C^2(1+\lambda)} \tag{35}$$

The largest range value of the right hand side of this formula is obtained by the substitution of $C = 0.2$, $e = 0.3, \theta = 15°. \sigma/\rho = 2.65$, and $C_* = 0.65$. The result is $\tau_t/\tau_c < 0.05$. Namely, in stony debris flow, the turbulent mixing stress is at most 5% of the particle collision stress. This is the reason for a wide applicability of single-phase dilatant fluid model in which fluid stress is neglected. Effective fluid friction being negligible, energy dissipation in stony debris flow is almost solely accomplished (because τ_k is negligibly small) by the solid interfacial friction occurring intermittently during the instant of collision. The effective friction angle α (the angle of encounter between two particles) for densely ($C \approx 0.5$) concentrated flow should be approximately equal to ϕ (Bagnold 1966). If solid concentration decreases as small as about 0.2 in stony debris flow, the angle of encounter between two particles becomes larger than ϕ due to enlarged free distance between particles. Thus, referring to Equation 14, if $\tan\phi$ is 0.7, the average value of $\tan\alpha$ for stony debris flow whose grain concentration is between 0.5 and 0.2 should be about 0.8. Therefore, the equilibrium particle concentration formulae; Equations 13 and 32, are practically identical if average $\tan\alpha$ value is used as $\tan\phi$ in Equation 37.

3.4 *Newtonian fluid model for viscous debris flow*

Quasi-steady debris flows that occur in the domain adjacent to the axis representing Bagnold number in Figure 5 would flow in an orderly manner in which the coarse particles move nearly parallel to the bed keeping tracks within their embedded layer.

Experiments (Bagnold 1954) revealed that the transition from inertia to viscous conditions occupied the range from 450 to 40 in terms of Bagnold number. In the transition range, the total shear stress would be given by

$$\tau = \tau_c + \tau_k + \tau_\mu \tag{36}$$

and as the Bagnold number increases, grain elements; $\tau_c + \tau_k$, becomes surpassed the fluid element; τ_μ, so it approaches stony debris flow. Contrary if Bagnold number becomes small, the dynamic grain elements diminish gradually approaching viscous debris flow. But, in viscous range, according to Bagnold's discussion, although the grain collision stress and grain streaming stress are negligibly small, the effect of grain existence remains to increase the apparent viscosity of mixture. Therefore, the total shear stress in viscous debris flow is a mixed shear stress due to the effect of fluid viscosity as modified by the presence of grains, and cannot be split into grain and fluid elements. Thus, the following formula is given:

$$\tau = \tau_{\mu_a} \tag{37}$$

where $\tau_{\mu_a} =$ viscous fluid stress due to the apparent viscosity μ_a.

The issues in viscous debris flow are why coarse grains heavier than the ambient fluid can be dispersed in laminar viscous flow without collisional effect, and how the apparent viscosity of mixture is estimated. Takahashi et al. (2000) proposed a new Newtonian flow model extending an investigation for neutrally buoyant particles in viscous fluid (Phillips et al. 1992).

The theory considers that the particles experience encounters between adjacent shearing surface and they cause the particle flux; $\mathbf{N_c}$, perpendicular to the main flow direction as following:

$$\mathbf{N_c} = -K_c d_p{}^2 (C^2 \nabla\gamma + C\gamma\nabla C) \tag{38}$$

where $\gamma = du/dz$; and $K_c =$ numerical constant. The term encounter herein does not necessarily mean the interfacial contact, only an approach can cause a

squeezing flow in the interstitial fluid that moves the particle perpendicular to the main flow, because viscosity of fluid is large.

If coarse particles are distributed anisotropically, the apparent viscosity varies spatially. Because the apparent viscosity is larger in the higher concentration region than in the smaller concentration region, the resistance to particle migration into the higher concentration region is larger than into the thinner concentration region. This mechanism gives rise to the particle flux; $\mathbf{N}\mu_a$, as following:

$$\mathbf{N}_{\mu_a} = -K_{\mu_a}\gamma C^2 \frac{d_p^{\,2}}{\mu_a}\frac{d\mu_a}{dC}\nabla C \tag{39}$$

where $K_{\mu_a} =$ numerical constant.

The coarse particles tend to deposit due to gravity, and the flux is given as following:

$$\mathbf{N_s} = -\frac{2}{9}C\frac{d_p^{\,2}(\sigma-\rho)g\cos\theta}{\mu}G(C) \tag{40}$$

where $G(C) =$ hindrance function to account for highly concentrated group settling. Here,

$$G(C) = \frac{1-C}{\eta} \tag{41}$$

is assumed, where $\eta =$ specific viscosity. According to Krieger (1972), it is given as

$$\eta = \frac{\mu_a}{\mu} = \left(1-\frac{C}{C_*}\right)^{-1.82} \tag{42}$$

In a steady state, these three fluxes should balance so as to perform null particle flux perpendicular to the main flow direction. This condition is given by

$$K_c\left(C^2\frac{d\gamma}{dz}+C\gamma\frac{dC}{dz}\right)+K_{\mu_a}\gamma C^2\frac{d\mu_a}{dC}\frac{dC}{dz} + \frac{2}{9}C\frac{(\sigma-\rho)g\cos\theta}{\mu}G(C)=0 \tag{43}$$

The balance of force equation in such a steady uniform flow is given by

$$\tau = \mu_a\gamma = \rho g h\sin\theta\left\{\left(1-\frac{z}{h}\right)+\frac{\varepsilon}{h}\int_z^h C dz\right\} \tag{44}$$

where $\varepsilon = (\sigma-\rho)/\rho$.

Substitution of Equation 44 into Equation 43 yields the particle concentration distribution function;

$$\frac{dC}{dZ} = \frac{F_1}{F_2F_3} \tag{45}$$

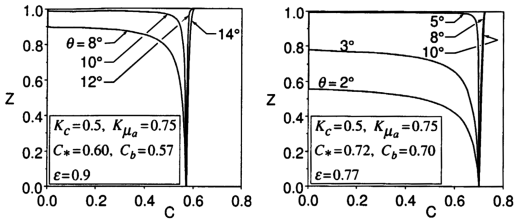


Figure 10. The theoretical distribution of the coarse particle concentrations.

where $F_1 = -(2/9)\varepsilon(1-C)/(K_c\tan\theta)+C(1+\varepsilon C)$; $F_2 = 1+1.82\{(K_{\mu_a}/K_c)-1\}C/C_*(1-C/C_*)^{-1}$; and $F_3 = 1-Z+\varepsilon\int_Z^1 CdZ$.

Figure 10 shows two examples of solid concentration distribution calculated under the combinations of parameters; $C_* = 0.6$, $C_b = 0.7$, $\rho = 1.38\,\mathrm{gcm}^{-3}$ ($\varepsilon \approx 0.9$), and $C_* = 0.72$, $C_b = 0.70$, $\varepsilon = 0.77$. The respective combinations of parameters correspond to the conditions in our laboratory experiment and in the Jiangjia Gully in China. For both cases $K_c = 0.5$ and $K_{\mu_a} = 0.75$ are adopted from the experimental results obtained by Phillips et al. (1992). The concentration at the bottom of flow; C_b, is assumed a little smaller value than C_*, because substitution of $C = C_*$ into Equation 45 cannot make sense. As is clear in Figure 10, when the channel slope is steep, very high solid concentration is maintained up to the surface of flow, and for the relatively mild slope channel, the high concentration abruptly decreases in the upper region. This is the case of immature viscous debris flow.

The coarse particle concentration in a certain slope channel becomes large and uniform as ε becomes small. Namely, the denser the interstitial fluid, the flatter the area the debris flow of a certain solids concentration will reach.

The equilibrium coarse particle concentration for a given channel slope can be obtained by integrating Equation 45. The results corresponding to the conditions used in obtaining Figure 10 are shown in Figure 11. The respective curves show the solid concentration can easily be saturated beyond a certain channel slope, and the value of saturation is, as is clear in Figure 10, approximately equal to C_b. This fact suggests that, as long as flow rate is sufficient, once a saturated flow is formed in an upstream steep channel, it runs down the gradually flattening channel keeping its constant concentration until the slope becomes flatter than a critical one on which the equilibrium concentration is smaller than the saturated value and deposition commences.

The velocity distribution can be obtained by solving Equation 44 under the boundary condition; at $Z = 0$, $u' = 0$, where $u' = u/u_*$. The solution cannot be obtained analytically, but provided the viscosity is approximated as constant from bottom to a height

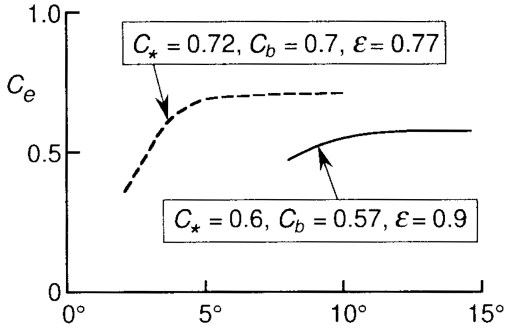


Figure 11. Equilibrium coarse particle concentrations versus channel slopes.

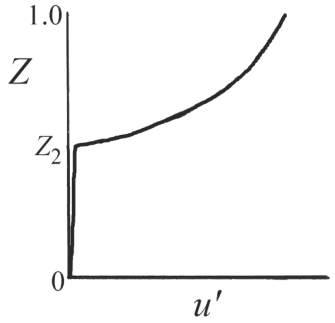


Figure 12. Schematic velocity distribution in an immature viscous debris flow.

$(Z = Z_2)$, it has the tendency like shown in Figure 12. It is given by the following equation:

$$u' = \begin{cases} \dfrac{\rho u_* h}{\mu_a}(1+\varepsilon\overline{C})(Z - \dfrac{1}{2}Z^2) & ; 0 \le Z \le Z_2 \\ \dfrac{\rho u_* h}{\mu}\left\{Z - \dfrac{1}{2}Z^2 + X(Z_2 - \dfrac{1}{2}Z_2{}^2)\right\} & ; Z_2 < Z \le 1 \end{cases} \quad (46)$$

where $X = (1+\varepsilon\overline{C})\mu/\mu_a - 1$; and $\overline{C} =$ mean particle concentration below Z_2.

Well mixed debris flow material in the Jiangjia Gully except for the component larger than 10 mm was imitated by mixing silica sand and kaolin. This material was mixed with water to make the constant solids concentration of $0.56 \sim 0.57$, and it was supplied onto upstream end of experimental flume from a hopper.

The velocity distributions given by Equation 46 are compared with the experimental data in Figure 13, in which $Z_2 = 1$ and $\mu_a = 8.1$ Pa s obtained from the theory explained above, are used. Figure 13(1) is the case of flow on the deposit formed by a previous debris flow surge, and Figure 13(2) is the case of flow on rigid bed. This figure shows that not only the velocity distribution

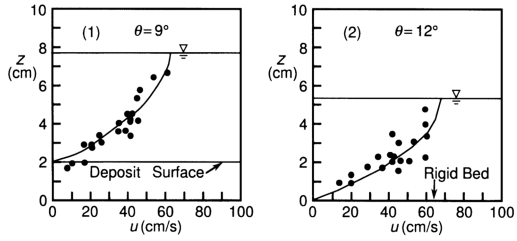


Figure 13. Calculated and experimental velocity distributions.

obeys the Newtonian laminar flow equation equally well on erodible and rigid beds, but also the absolute velocity values are well explained by this theory.

Recently, Armanini et al. (2003) did the similar theoretical and experimental discussion that took the yield strength of interstitial fluid into account.

4 CONCLUSION

In this paper, various concepts for modeling debris flows are reviewed. Under the present state of the art, the mixture model that considers the debris flow material is a mixture of two continua; one is the interstitial fluid and the other is a kind of continuum media comprised of granular assembly, is influential. By the adoption of appropriate constitutive relations, the mixture model is not only able to classify diverse debris flows based on fundamental mechanics but also the behaviors of respective debris flows are explained. Although not being discussed in this paper, application of this model can handle practically important problems such as the predictions of occurrence magnitude and hazardous area.

However, many themes requiring further investigations remain. The examples of those problems are: the effects of wide range distribution of particles on the dynamic behaviors of various debris flows, the determination of the critical size of fine particle that behaves as a coherent whole with interstitial water and the estimation of the physical properties of such a coherent body, the value of solid concentration that determines the transition from quasi-static debris flow to dynamic debris flow in the case that the material is composed of very wide range distribution, the clear-cut definition of transitions between viscous debris flow and stony debris flow, and between viscous debris flow and turbulent muddy debris flow in the ternary diagram, and the mechanics of hybrid debris flows.

REFERENCES

Armanini, A., Dalri, C., Fraccarolo, L., Larcher, M. & Zorzin, E. 2003. Experimental analysis of the general features of uniform mud-flow. In Rickenmann & Chen

(ed.),*Debris flow hazards mitigation: Mechanics, prediction, and assessment; Proc. intern. conf., Davos,* 423–434. Rotterdam: Millpress.

Bagnold, R.A. 1954. Experiments on a gravity-free dispersion of large solid spheres in a Newtonian fluid under shear. *Proc. R. Soc. London, Ser A* 225: 49–63.

Bagnold, R.A. 1966. The shearing and dilatation of dry sand and 'singing' mechanism. *Proc. R. Soc. London, Ser A* 295: 219–232.

Campbell, C.S. 1990. Rapid granular flows. *Annu. Rev. Fluid Mech.* 22: 57–92.

Campbell, C.S. 2001. Granular flows in the elastic limit. *Spec. Publs. Int. Ass. Sediment* 31: 83–89.

Campbell, C.S. & Brennen, C.E. 1985. Computer simulation of granular shear flows. *J. Fluid Mech.* 151: 167–188.

Chen, C.L. 1988. Generalized viscoplastic debris flow. *J. Hydraulic Engrg*. 114(3): 237–258.

Coussot, P. 1995. Structural similarity and transition from Newtonian to non-Newtonian behavior for clay-water suspensions. *Phys. Rev. Lett.* 74: 3971–3974.

Gotoh, H. & Sakai, T. 1997. Numerical simulation of sheet-flow as granular materials. *J. Waterway, Port, Coastal and Ocean Engrg. ASCE* 123(6): 329–336.

Gotoh, H., Tsujimoto, T. & Nakagawa, H. 1994. Numerical model of interface momentum transfer and inter-particle collision in bed-load layer. *Proc., APD-IAHR*: 565–572.

Hirano, M., Hashimoto, H., Fukutomi, K. Taguma, K. & Pallu, M.S. 1992. Nondimensional parameters governing hyperconcentrated flow in an open channel. *Proc. Hydraulic Eng.* 36: 221–226 (in Japanese).

Iverson, R.M. 1997. The physics of debris flows. *Reviews of geophysics* 35(3): 245–296.

Iverson, R.M. & Denlinger, R.P. 1987. The physics of debris flows-A conceptual assessment. In Beschesta et al.(ed) *Erosion and sedimentation in the Pacific rim. IAHS Publ.* 165: 155–165.

Iverson, R.M. & Denlinger, R.P. 2001. Flow of variably fluidized granular masses across three-dimensional terrain. *J. Geophysical Res.* 106(B1): 537–552.

Johnson, A.M. 1965. *A model for debris flow*. Ph.D. dissertation Pa. State Univ.: State College.

Johnson, A.M. 1970. *Physical processes in geology.* New York: Freeman.

Julien, P.Y. & O'Brien, J.S. 1997. On the importance of mud and debris flow rheology in structural design. *Proc. 1st Intern. Conf. on Debris-Flow Hazards Mitigation: Mechanics, Prediction, and Assessment.* 350–359, New York: ASCE.

Krieger, J.S. 1972. Rheology of monodisperse lattices. *Advance of Colloid Interface Science* 3: 111–136.

Phillips, R.J., Armstrong, R.C., Brown, R.A., Graham, A.L. & Abbott, J.R. 1992. A constitutive equation for concentrated suspensions that accounts for shear-induced particle migration, *Phys. Fluids* A4(1): .30–40.

Straub, S. 2001. Bagnold revisited: implications for the rapid motion of high-concentration sediment flows. *Spec. Publs. Int. Ass. Sediment* 31: 91–109.

Takahashi, T. 1978. Mechanical characteristics of debris flow. *J. Hydraulic Div. ASCE* 104: 1153–1169.

Takahashi, T. 1991. *Debris flow.* Rotterdam: Balkema.

Takahashi, T. 2000. Initiation and flow of various types of debris-flow. In Wieczorek & Naeser(ed.) *Debris-flow hazards mitigation: Mechanics, prediction, and assessment, Proc. intern. Conf. Taipei* 15–25. Rotterdam: Balkema.

Takahashi, T. & Satofuka, Y. 2002. Generalized theory of stony and turbulent muddy debris-flow and its practical model. *J. Japan Soc. Erosion Control Eng.* 55(3): 33–42 (in Japanese).

Takahashi, T. & Tsujimoto, H. 1997. Mechanics of granular flow in inclied chute. *J. Hydraulic, Coastal and Environmental Eng., JSCE* 565: 57–71 (in Japanese).

Takahashi, T., Nakagawa, H. & Satofuka, Y. 2000. Newtonian fluid model for viscous debris-flow, In Wieczorek & Naeser(ed.) *Debris flow hazards mitigation: Mechanics, prediction, and assessment, Proc. intern. Conf. Taipei* 255–262. Rotterdam: Balkema.

Yano, K. & Daido, A. 1965. Fundamental study on mud-flow. *Bull. Disaster Orev. Res. Inst. Kyoto Univ.* 14: 69–83.

A. Fluvial processes
A.1. Morphology and morphodynamics

This page intentionally left blank

River Flow 2004 – Greco, Carravetta & Della Morte (eds.)
© 2004 Taylor & Francis Group, London, ISBN 90 5809 658 0

The morphology, 3D flow structure and sediment dynamics of a large river confluence: the Rio Paraná and Rio Paraguay, NE Argentina

D.R. Parsons & J.L. Best
School of Earth Sciences, University of Leeds, Leeds, UK

S.N. Lane & R.J. Hardy
School of Geography, University of Leeds, Leeds, UK

O. Orfeo
CECOAL, Canada Corrientes, Argentina

R. Kostaschuk
Department of Geography, University of Guelph, Canada

ABSTRACT: River channel confluences are ubiquitous features of all fluvial networks and represent sites of complex, three-dimensional flow and sediment dynamics. Current understanding of these sites is based largely on laboratory experiments and study of small-scale natural junctions. These have identified the nature of coherent flow structures at junctions and their controls. This paper reports the initial findings of a study of one of the Worlds' largest river channel confluences: the Rio Paraná and Rio Paraguay in NE Argentina. This study reports and examines the results obtained, including the detailed morphology of the confluence, 3D flow structures in the confluence zone and the sediment dynamics of the region. The results allows us to determine the extent to which conclusions reached from smaller scale studies can be extended to larger spatial scales, and therefore permits an investigation into how this complex scaling impinges upon the processes at river channel confluences.

1 INTRODUCTION

River channel confluences form key nodes within all fluvial networks and are sites at which rapid and large changes occur in channel hydraulic geometry (Richards, 1980; Roy and Roy, 1988), discharge (Richards, 1980; Best, 1988), and fluid mixing (Best, 1987, 1988; Best and Roy, 1991; Gaudet and Roy, 1995). Such sites are thus vital when predicting the flux of sediment and water through channel networks, in assessing the dispersal of sediment and pollutants (Gaudet and Roy, 1995), in considerations of channel habitat and fluvial, in predicting large-scale scour relevant both to the construction of bridges and embankments (Klaassen and Vermeer, 1988; Bradbrook et al., 2001) and in recognising the importance of scour in ancient alluvial sediments (Bristow et al., 1993; Best and Ashworth, 1997).

Flow, sediment transport and bed morphology at open channel junctions is inherently three-dimensional and unsteady and progress in understanding has come from three complementary approaches: laboratory modelling, field quantification and numerical modelling. Early physical modelling produced key advances in understanding the principal controls on confluence morphology and flow dynamics (Mosley, 1976; Best, 1987, 1988) and yielded conceptual models (Best, 1987, 1988) that have been tested at field sites (Roy and Bergeron, 1988; Biron et al., 1993; Rhoads and Kenworthy, 1996, 1998; De Serres et al., 1999). More recent experimental work has also begun to better document the exact nature of flow and distribution of turbulent kinetic energy within 90° junctions (Weerakoon et al., 1991; McLelland et al., 1996; Hsu et al., 1998; Weber et al., 2001) and has confirmed the validity of earlier flume-based conceptual models of confluence flow dynamics. Application of these conceptual models to field cases has identified the role of bed discordance between tributaries (Best and Roy, 1991; Biron et al., 1996a,b; Bradbroook et al., 2001), confluence angle (Mosley, 1976; Best, 1988) and confluence planform curvature (Rhoads and Kenworthy, 1995, 1998; Rhodes and Sukhodolov, 2001). Numerical modelling has proven to be a powerful and

complimentary methodology for yielding significant advances in understanding of the influence of the interactions variables (Bradbrook et al., 2000a, 2001; Lane et al., 1999a,b; 2000), through providing a higher temporal and spatial resolution (Lane et al., 2000), key hydrodynamic information (e.g. water surface and dynamic pressure estimates, Bradbrook et al., 2000a, 2001) and has also excitingly begun to predict the periodic nature of turbulent flow at channel junctions (Bradbrook et al., 2000b). However, two central issues remain. First, there is still debate concerning many key aspects of confluence flow and sediment dynamics, including the origin and nature of secondary flows at channel junctions (Rhodes and Kenworthy, 1996, 1998; Bradbrook et al., 1998; Lane et al., 1999b, 2000), the effects of junction planform (Best, 1987; Rhoads and Kenworthy, 1995, 1998; Bradbrook et al., 2001) and topographic discordance (e.g. Biron et al., 1996; De Serres et al., 1998).

Second, we know very little about the extent to which these small-scale studies can be extrapolated and scaled with larger, potentially more important, junctions (Bristow and Best, 1993; Best and Ashworth, 1997). Although excellent progress has been made in examining the fluid dynamics of large-scale braid bars and distributaries (e.g. Richardson et al., 1996; Richardson and Thorne, 1998; McLelland et al., 1999), this has not been achieved for confluences in dendritic drainage networks and has not detailed the key hydrodynamic variables. Although physical and numerical modelling have become increasingly sophisticated in allowing investigation and explanation of some of the key controlling variables, this has not been matched by detailed, fully three-dimensional studies of flow, sediment transport and bed morphology at open channel junctions that are several orders of magnitude larger. It is reasonable to assume that these models may need further development because of the large number of variables that do not scale linearly and in proportion to the observed flow characteristics. For example, although dunes are often assumed to scale with flow depth (Yalin, 1992), it is not know how such bedforms respond to rapid changes in flow conditions (e.g. depth) within junctions scours.

This paper reports on a survey of one of the world's largest alluvial channel confluences: the junction of the Rio Paraguay and Rio Paraná in NE Argentina.

Therefore this paper addresses this shortfall by reporting on a study into one of the Worlds' largest river channel confluences. The confluence morphology is revealed, along with the dune orientation and scale that indicates the sediment pathways through the confluence region. The 3D flow structure through the confluence is also detailed. The paper also addresses the linkages and feedbacks between the morphology and flow structure, and discusses the implications for geomorphological and sedimentological applications.



Figure 1. Location of the Paraná – Paraguay confluence.



Figure 2. Aerial photograph looking downstream at the junction, illustrating the large scale Kelvin-Helmholtz instabilities along the shear layer that are highlighted by the suspended sediment contrast.

2 STUDY AREA

The study area is located at the confluence of the Rio Paraná and Rio Paraguay, 16 km north of the city of Corrientes (Figs. 1, 2) in Argentina. The Paraná River basin is a 2,600,000 km^2 fluvial system, most of which is in Southern Brazil and Argentina. The mean annual

discharge is about 17,000 $m^3 s^{-1}$. The basin of the Rio Paraguay covers about 38% of the total Paraná basin (Orfeo and Stevaux, 2002). At the confluence, the annual discharge of the Paraná increases by a third and the suspended sediment discharge increases from 5.1×10^6 to 118.7×10^6 (Orfeo and Stevaux, 2002). At the junction the Parana is approximately 2 km wide and the Paraguay is about 800 m wide.

3 METHODS

The fieldwork was completed in May 2003 and involved use of (i) a dual frequency Single Beam Echo Sounder (SBES), (ii) a RESON® INC Multi-Beam Echo Sounder (MBES) to obtain the 3D bed morphology and (iii) an Acoustic Doppler Current Profiler (ADCP) to quantify the 3D structure of flow and suspended sediment movement throughout the confluence.

These instruments were all tied together in terms of position using a Differential Global Positioning System (DGPS). Measurements were made at a total of 67 transects, beginning 2 km upstream in both tributaries and ending 3 km in the main channel downstream of the confluence junction. A detailed mesh of transects (~100) and at-a-point measurements were made in the immediate area of the confluence.

4 RESULTS: MORPHOLOGY

High-resolution, quantitative results depicting the detailed bed morphology from the SBES and MBES have permitted quantification of the nature and geometry of the Paraná – Paraguay confluence, including determination of both the position and scale of a deep scour hole (~32 meters deep) within the mid-section of the confluence (Fig. 3). At this site the tributary channel (the Paraguay) forms the deeper channel entering the confluence and the Rio Paraná thus forms a morphological step at the junction.

Figure 4 shows a cross section view of the large scour hole and also indicates the changes in the dune amplitude through the confluence zone.

The results from the MBES have also enabled us to map the distribution and morphology of bedforms within the junction, and the amplitudes and orientations of dune crests (Fig. 4) have permitted us to examine the principal pathways of sediment through the junction, and critically, in and around the scour hole. Rather than scaling with depth as the channel deepens into the scour hole, dune amplitude seems to initially decline as the pathways of sediment are driven around the edge of the scour hole sides. At the distal end of the scour hole dune amplitude seems to increase as dunes move up and out of the scour (Fig. 4).

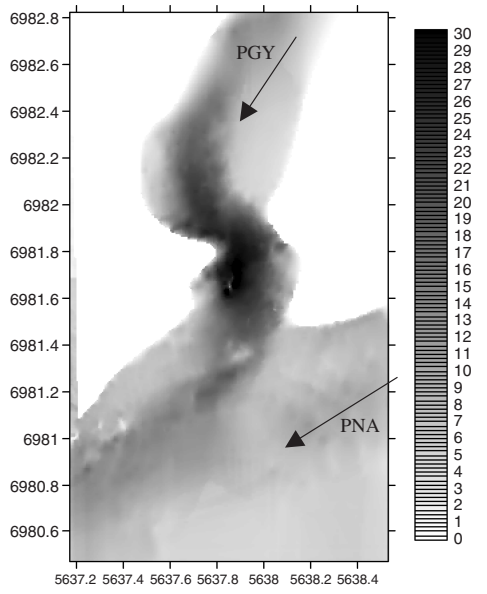


Figure 3. Morphology of the confluence of the Rio Paraná (PNA) and Rio Paraguay (PGY). Arrows indicate general flow direction. Contour units are in meters below water surface, *x* and *y* axis are in kilometers.

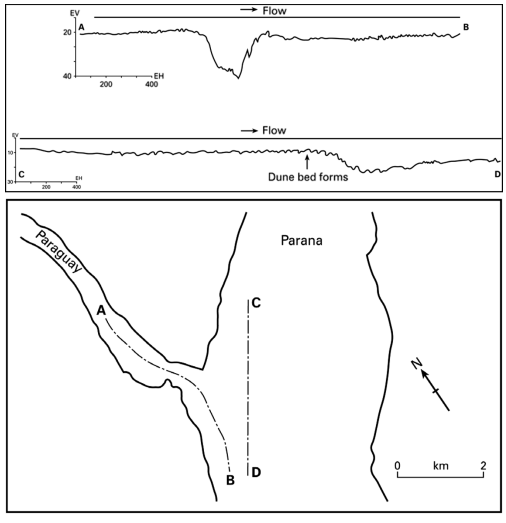


Figure 4. Profile of bed morphology surveyed along the Paraná and Paraguay, illustrating the large dunes present (~3 m high) that migrate through and around the scour hole (*top*). Locations of the two profiles (*bottom*).

5 RESULTS: 3D FLOW

Results from the ADCP have also permitted mapping the mean three-dimensional flow structure upstream,

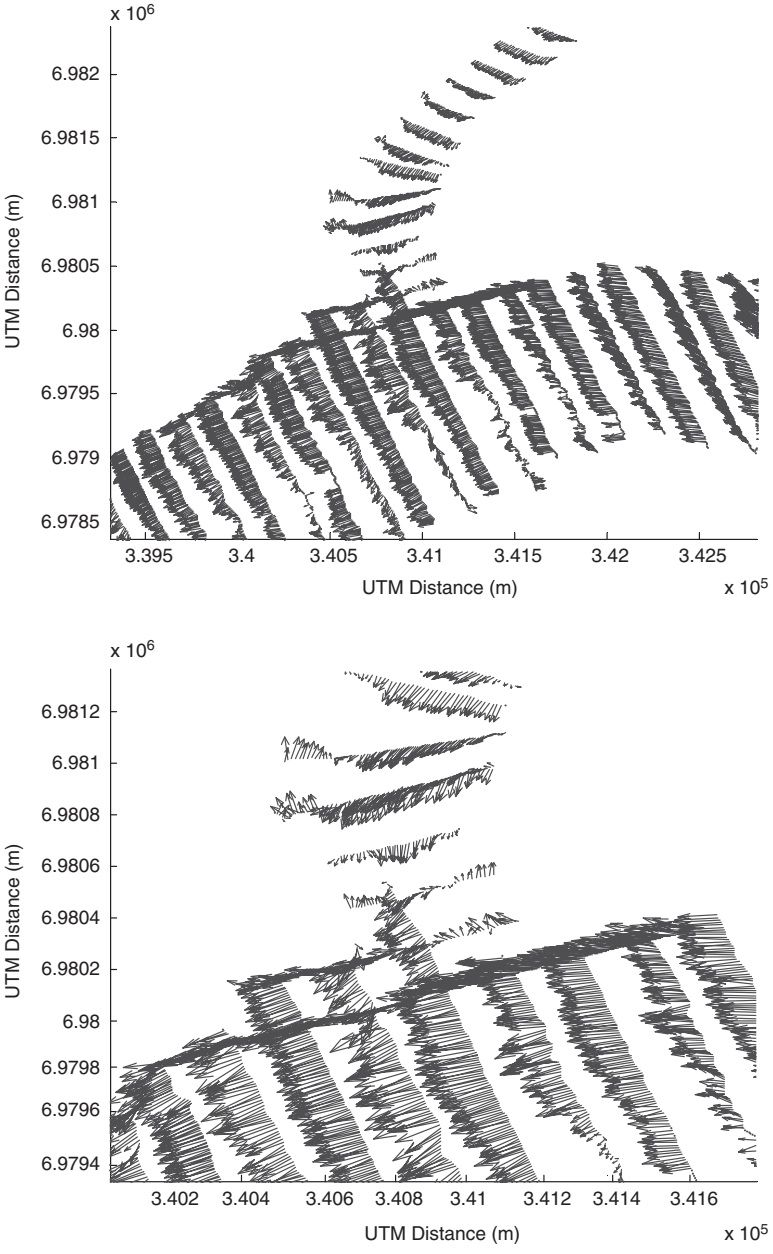


Figure 5. Near surface flow vectors at the confluence junction.

through and downstream of the confluence junction, and allowed examination how this is related to the detailed three-dimensional bed morphology. Initial results suggest distinct areas of flow stagnation, combination and acceleration, separation and recirculation within the confluence (Fig. 5). For example, there is a deceleration of the surface flow in the Paraguay as the confluence is approached. Moreover, within the confluence zone there are significant regions of stagnation and flow separation at both the upstream

junction corner and at the true right bank of the Paraguay (Fig. 5).

6 CONCLUSIONS

This paper has detailed the morphology of one of the Worlds' largest confluence junctions. There are some significant findings, primarily the identification of a large and deep scour hole at the confluence junction, slightly upstream in the Paraguay (the tributary channel) forming a deeper channel entering the confluence and forming a morphological step at the junction which wraps into the main channel close to the true right bank. The 3D velocities illustrate turbulent nature of the combination of the two flows with significant regions of flow stagnation and separation. This paper has identified many similarities in the processes occurring in this junction with smaller channel junctions, although the position of the scour hole within the tributary and the movement of the dunes around the scour hole are major differences.

ACKNOWLEDGEMENTS

We would like to thank the UK Natural Environment Research Council for funding under grant NER/A/S/2001/00445 that allowed this research to be conducted. We are also grateful to Reson Offshore UK Ltd, and in particular John Fraser, for their outstanding collaboration regarding the use of the Multi-Beam Echo Sunder used in this study.

REFERENCES

Best, J.L. 1987. Flow dynamics at river channel confluences: implications for sediment transport & bed morphology. In: Etheridge, F.G., Flores, R.M. & Harvey, M.D (eds.), *Recent Developments in Fluvial Sedimentology, SEPM Special Publication* 39: 27–35.

Best, J.L. 1988. Sediment transport & bed morphology at river channel confluences. *Sedimentology* 35: 481–498.

Best, J.L. & Ashworth, P.J. 1998. Scour in large braided rivers & the recognition of sequence stratigraphic boundaries. *Nature* 387: 275–277.

Best, J.L. & Reid, I. 1984. Separation zone at open channel junctions. *Proc Amer. Soc. Civ. Engnrs. J. Hydraulic Engineering* 110: 1588–1594.

Best, J.L. & Roy, A.G. 1991. Mixing layer distortion at the confluence of channels of different depth. *Nature* 350: 411–413.

Biron, P.M., DeSerres, B., Best, J.L. & Roy, A.G. 1993. Shear layer turbulence at an unequal depth channel confluence. In: Clifford, N., French, J.R. & Hardisty, J. (eds.) *Turbulence: perspectives on flow & sediment transport.* Wiley & Sons.

Biron, P., Best, J.L. & Roy, A.G. 1996a. Effects of bed discordance on flow dynamics at open channel confluences. *Journal of Hydraulic Engineering* 122: 676–682.

Biron, P., Roy, A.G. & Best, J.L. 1996b. Turbulent flow structure at concordant & discordant open-channel confluences. *Experiments in Fluids* 21: 437–446.

Bradbrook, K.F., Biron, P., Lane, S.N., Richards, K.S. & Roy, A.G. 1998. Investigation of controls on secondary circulation & mixing processes in a simple confluence geometry using a three-dimensional numerical model. *Hydrological Processes* 12: 1371–1396.

Bradbrook, K.F., Lane, S.N. & Richards, K.S. 2000a. Numerical simulation of time-averaged flow structure at river channel confluences. *Water Resources Research* 36: 2731–2746.

Bradbrook, K.F., Lane, S.N., Richards, K.S., Biron, P.M. & Roy, A.G. 2000b. Large Eddy Simulation of periodic flow characteristics at river channel confluences. *J. Hyd Res*. 38: 207–216.

Bradbrook, K.F., Lane, S.N., Richards, K.S., Biron, P.M. & Roy, A.G. 2001. Role of bed discordance at asymmetrical river confluences. *Journal of Hydraulic Engineering* 127: 351–368.

Bristow, C.S. & Best, J.L. 1993. Braided Rivers: perspectives & problems. In: Best, J.L. & Bristow (eds), C.S. *Braided Rivers. Spec. Publ. Geol. Soc. Lond.* 75.

Bristow, C.S., Best, J.L. & Roy, A.G. 1993. Morphology & facies models of channel confluences. In: Puidefabregas, C. & Marzo (eds.) *Alluvial Sedimentation, Spec. Publ. Int. Ass. Sediment*. 17.

De Serres, B., Roy, A.G. Biron, P.M. & Best, J.L. 1999. Three-dimensional flow structure at a river channel confluence with discordant beds. *Geomorphology* 26: 313–335.

Gaudet, J. & Roy, A.G. 1995. Effect of bed morphology on flow mixing length at river confluences. *Nature* 373: 138–139.

Hsu, C., Lee, W.J. & Chang, C.H. 1998. Subcritical open-channel junction flow. *Journal of Hydraulic Engineering* 124: 847–855.

Klaassen, G.J. & Vermeer, K. 1988. Confluence scour in a large braided river with fine bed material. *Proc. Int. Conf. on Fluvial Hydraul*., Budapest: Hungary.

Lane, S.N., Biron, P.M., Bradbrook, K.F., Butler, J.B., Chandler, J.H., Crowell, M.D., McLelland, S.J., Richards, K.S. & Roy, A.G. 1998. Integrated three-dimensional measurement of river channel topography & flow processes using acoustic Doppler velocimetry. *Earth Surface Processes & Landforms* 23: 1247–1267.

Lane, S.N., Bradbrook, K.F., Richards, K.S., Biron, P.M. & Roy, A.G. 1999a. The application of computational fluid dynamics to natural river channels: 3D versus 2D approaches. *Geomorphology* 29: 1–20.

Lane, S.N., Bradbrook, K.F., Richards, K.S., Biron, P.M. & Roy, A.G. 1999b. Time-averaged flow structure in the central region of a stream confluence: A discussion. *Earth Surf Pros & Land* 24: 361–367.

Lane, S.N., Bradbrook, K.F., Richards, K.S., Biron, P.M. & Roy, A.G. 2000. Secondary circulation in river channel confluences: measurement myth or coherent flow structure?. *Hydrol Proc* 14: 2047–2071.

McLelland, S.J., Ashworth, P.J. & Best, J.L. 1996. The origin & downstream development of coherent flow structures at channel junctions, In: Ashworth, P.J., Bennett,

S.J., Best, J.L. & McLelland, S.J. (eds.) *Coherent flow structures in open channels.* Wiley & Sons.

McLelland, S.J., Ashworth, P.J., Best, J.L., Roden, J. & Klaassen, G.J. 1999. Flow structure & spatial distribution of suspended sediment around an evolving braid bar, Jamuna River, Bangladesh. In: Smith, N.D. & Rogers, J. (eds.) *Fluvial Sedimentology VI Special Publication of International Association of Sedimentologists*. Blackwells.

Mosley, M.P. 1976. An experimental study of channel confluences, *J. Geology* 84: 535–561.

Orfeo, O. & Stevaux, J. 2002. Huydraulic and morphological characteristics of middle and upper reaches of the Parana River. *Geomorhology* 44: 309–322.

Richardson, W.R.R. & Thorne, C.R. 1998. Secondary currents around braid bar in Brahmaputra River, Bangladesh. *J. Hydraul. Eng*. 124: 325–328.

Richardson, W.R.R., Thorne, C.R. & Mahmood, S. 1996. Secondary flow & channel changes around a bar in the Brahmaputra River, Bangladesh. In: Ashworth, P.J., Bennett, S.J., Best, J.L. & McLelland, S.J. (eds.) *Coherent flow structures in open channels.* Wiley & Sons.

Rhodes, B.L. & Kenworthy, S.T. 1995. Flow structure at an asymmetrical stream confluence. *Geomorphology* 11: 273–293.

Rhodes, B.L. & Kenworthy, S.T. 1998. Time-averaged flow structure in the central region of a stream confluence. *Earth Surface Proceses & Landforms* 23: 171–191.

Rhoads, B.L. & Sukhodolov, A.N. 2001. Field investigation of three-dimensional flow structure at stream confluences: 1. Thermal mixing and time-averaged velocities. *Water Resources Research* 37: 2393–2410.

Richards, K.S. 1980. A note on change in geometry at tributary junctions. *Water Resources Research* 16: 241–244.

Roy, A.G. & Roy, R. 1988. Changes in channel size at river confluences with coarse bed material, *Earth Surface Proceses & Landforms* 13: 77–84.

Roy, A.G., Roy, R. & Bergeron, N. 1988. Hydraulic geometry & changes in flow velocity at a river confluence with coarse bed material, *Earth Surface Proceses & Landforms* 13: 583–598.

Weber, L.J., Schumate, E.D. & Mawer, N. 2001. Experiments on flow at a 90° open-channel junction, *Journal of Hydraulic Engineering* 127: 340–350.

Yalin, M.S. 1992. *River Mechanics.* Pergamon Press: Oxford. Best J.L. 1988. Sediment transport and bed morphology at river channel confluences. *Sedimentology* 35: 481–498.

River Flow 2004 – Greco, Carravetta & Della Morte (eds.)
© 2004 Taylor & Francis Group, London, ISBN 90 5809 658 0

Flow structures in meander bends with recirculation zones: implications for bend movements

D.R. Parsons
School of Earth Sciences, University of Leeds, Leeds, UK

R.I. Ferguson
Department of Geography, University of Sheffield, Sheffield, UK

S.N. Lane & R.J. Hardy
School of Geography, University of Leeds, Leeds, UK

ABSTRACT: This paper details the use of field informed numerical modelling (computational fluid dynamics (CFD)) to investigate the time-averaged three-dimensional flow structures in natural meander bends with zones of recirculating flow. Three bends of a small meandering river with predominantly gravel bed and pool-riffle topography were examined. Two of the bends have inner-bank recirculation eddies (one small, one large), and the third has a large outer-bank eddy. The model is verified and validated using acoustic Doppler velocimeter (ADV) flow measurements taken at an intermediate flow discharge and bankfull discharge conditions are also simulated in one bend. The geomorphological and sedimentological changes in the bends over a three-year period are documented using repeat surveys and the construction of digital elevation models (DEM) of difference. This investigative strategy has permitted an initial inspection of the links between flow processes and form in these complicated meander bends.

1 INTRODUCTION

The dominant flow structure through a meander bend is a helix, which is produced by a difference in flow force balance at the surface and bed. Faster near-surface flow moves towards the outer bank as the centrifugal acceleration acting on it exceeds the centripetal acceleration due to the associated superelevation. The opposite holds for slower-moving near-bed flow, which therefore moves towards the inner bank. Although this simple structure dominates the flow in bends of moderate curvature and symmetric cross section, in many situations it can be complicated by a significant additional process. This factor is flow separation and recirculation with the associated development of 'dead zones' with very low or negative downstream velocities. Flow separation is often associated with bends of high curvature (e.g. Leeder and Bridges, 1975; Hickin and Nanson, 1975) and can occur through reverse eddying and slowly recirculating flow at either the outer bank before the bend apex (Carey, 1969; Hickin, 1977; 1978, 1979; Woodyer et al., 1979; Andrle, 1994) or at the inner bank after the apex (Bagnold, 1960; Ippen and Drinker, 1962; Leeder and Bridges, 1975). Some bends have also been noted as having separation at both banks (e.g. Markham and Thorne, 1992; Andrle, 1994).

Zones of recirculating fluid in rivers are known to be important for a number of reasons. In the shorter term, they are imperfectly mixed with the main flow and act as traps for nutrients, phytoplankton, and pollutants (e.g. Page and Nanson, 1982; Tipping et al., 1993). They also delaying solute mixing and dispersion through the reach (e.g. Guymer, 1998), form foci of deposition of fine sediment, and create distinctive ecological habitats that can act as refugia sites during higher flows (e.g. Reynolds, 2000). In the longer term, the presence of a recirculating eddy can significantly alter the patterns, directions and rates of bend movement (e.g. Hickin and Nanson, 1975; Reid, 1983; Andrle, 1994). Moreover, the development of fine sediment bars/benches and their subsequent aggradation, colonisation and incorporation into the floodplain can have a significant influence on valley floor stratigraphy (Woodyer et al., 1979; Burge and Smith, 1999), contributing to the formation of large swaths of the total floodplain (Page and Nanson, 1982; Hickin, 1986; Burge and Smith, 1999).

Although a few studies have addressed aspects of the flow structure in bends with recirculation

(e.g. Leeder and Bridges, 1975; Andrle (1994), Hodskinson and Ferguson (1998)), there have been no attempts at any description of the detailed 3D flow structure. This paper therefore aims to detail and explain the 3D flow structure though a bends with recirculation zones. The paper also aims to address questions over the similarities and differences between bends with and without recirculation and ascertain whether bends with outer bank recirculation have similar flow structures to those identified in bends with inner bank recirculation. The paper also examines the changes in these bends over a 3-year period and attempts to relate the geomorphological changes.

2 STUDY SITE AND FIELD MEASUREMENTS

The natural meander bends investigated in this paper are situated on the actively meandering River Dean, which flows north-westwards off the Pennine Hills and across the glacial sediments of the Cheshire Plain, Northern England. Its bed and banks consist mainly of gravel but with sand on parts of point bars and in recirculation zones. The Dean has a well-developed pool-riffle morphology and a number of sharp bends along its course, which often exhibit both inner and outer bank separation. Bankfull discharge in the study reach is estimated at between 2.5 and 3.5 $m^3 s^{-1}$. Bankfull width in the reach is typically 4–5 m but varies from 3 to 10 m in places.

Along accessible reaches, 441 meander bends were surveyed in order to assess the frequency of flow separation (see Parsons, 2003, for full details). Of the 441 meander bends identified, 48% had a flow recirculation eddy which extended across the channel to at least an eighth of the bend apex width, 21% of had flow separation extending at least a quarter of the way across, and 9% had a recirculation eddy occupying more than half the width. Separation was slightly more common at the outer bank than the inner (33% against 28%) and a few bends had separation on both sides (13%).

Three of these bends were chosen for detailed study, bend 17 which has a small inner-bank separation; bend 37 which has a large inner-bank separation; and bend 25 which has a large outer-bank separation.

2.1 *Field measurements*

Measurements in bend 37 were made in August 1995 at a time of fairly low and almost steady discharge. The field methods are described by Hodskinson and Ferguson (1998). In brief, the topography was quantified by surveying 12 cross sections, more closely spaced in the sharpest part of the bend. Streamwise and lateral velocity components were measured at the inflow and selected other sections using an electromagnetic current meter. To help specify roughness, a bed-surface grain size distribution was measured by pebble count near the inflow. The topographic, roughness, and inflow data are used below to set up a new CFD model. However, the flow validation data are discarded because they are only 2-D and of coarser spatial and temporal resolution than we subsequently obtained in bend 17.

Bend 17 and Bend 25 were investigated in Summer 2000, again at intermediate to low and almost steady discharge. Its topography was surveyed by total station using breaks of slope to define primary features and spot heights to add detail. These data were used to construct digital elevation models (DEM). The water surface elevation at many points within the submerged area was obtained by recording the vertical angle to the intersection of the reflector rod with the water surface. The edge of the recirculation eddy was also surveyed. Size counts of 100 surface pebbles were made in 1-m^2 quadrats at several locations in the bend to help specify bed roughness. Velocity measurements were made to obtain inflow boundary conditions and spatially-distributed validation data. The measurements were made using a Sontek™ acoustic Doppler velocity meter (ADV) mounted on a specially-made wading rod. This had an attached spirit bubble to ensure the rod was vertical, and a pair of reflectors on a crossbar which were surveyed from the total station to fix the location and orientation of the ADV probe in the same coordinate system as the DEM and CFD model (see Lane et al., 1998, for details). The ADV measures three orthogonal components of velocity at 25 Hz in a sensing volume of <1 cm^3 about 5 cm below the probe. Inflow measurements were made for 120 s at each of several heights every 0.25 m across the channel. These data were used to calculate stream discharge and interpolate the inflow velocity distribution as a boundary condition for the CFD models. Spatially-distributed test data were collected by fixing the ADV at a height and recording for 60 s at each of a number of locations 1–2 m apart throughout the bends, then doing the same with the ADV set at other set heights. This procedure does not generate vertical or lateral velocity profiles of the kind commonly used to test simulations of laboratory flows, but for our field sites and equipment it was quicker than profiling and thus allowed the collection of more data before there was a significant change in water stage (which fell by only 4 mm during the flow measurement period in bend 17). For all velocity measurements, the signal-to-noise ratio and correlation coefficient were used to check the quality of the velocity measurements. Mean velocities were computed and the series were subject to a low-pass Gaussian filter before turbulent kinetic energy (TKE) was calculated.

Repeat morphological surveys were conducted in each bend throughout the study period to investigate the nature of the changes occurring within these complex bends.

2.2 *Bend morphologies*

Bend 17 (Fig. 1a) is a fairly sharp bend which turns 80° to the right over a centreline distance of 10 m. The channel has a bankfull width of 5–6 m so the mean ratio of radius of curvature (R) to width (W) is about 1.4. Total relief from the left-bank floodplain to the deepest part of the pool (near the centreline and past the apex) is 1.4 m. The left, outer bank is 0.9 m high and eroding over its full length. The right, inner bank is less steep and is vegetated down to the low-flow waterline. Neither bank is uniformly curved in plan. The inner bank follows the common pattern of being sharpest at the apex, and the outer bank has a slight reverse curve opposite the apex separating two zones of fairly high curvature. Flow enters over a gravel riffle. This is highest in midstream so there are two talwegs, that on the left being deeper. The mean flow depth varied considerably around the bend, from a maximum of 0.34 m at the inflow to 0.76 m in the pool and 0.51 m at outflow from the bend. The central and outer parts of the bed are gravel throughout, with D_{84} ranging from 69 mm on the riffle to 54 mm in the pool, but most of the small point bar at and beyond the apex of the inner bank is sand.

Bend 37 is a sharp right-hand bend with a deep pool towards the outer bank and a small submerged point bar (Fig. 1b). It follows a long, almost straight, riffle and leads immediately into a left-hand bend. The pool and its eroding outer bank consist of gravel but the point bar is sand-covered. The inner bank is grassed down to the normal waterline. The outer bank is capped by overbank fines with a grass root layer. When surveyed in 1995 bend 37 turned 130° to the right over a distance of 15 m along the outer bank and 7 m along the inner bank. These figures together with the mean channel width of 5.5 m give mean R/W ratios of 1.2 and 0.6 at the outer and inner banks. At the time the fieldwork was done the high curvature led to inner-bank separation which extended most of the way to the outer bank.

Bend 25 (Fig. 1c) is a sharp right-hand bend which turns ∼100° in 10 m immediately after a left-hand bend. This bend was chosen as a well-developed and representative-looking example of a bend with a large outer-bank recirculation. Within the large recirculation zone a large sandy concave-bank bench has formed. The left-hand bend immediately upstream is fairly sharp, causing the talweg at the entrance to the bend to be under the true right-hand (inner) bank, which is undercut right to the apex of the bend. Around the inner bank apex, the bank begins to shallow and becomes a point bar towards the exit of the bend. To the left of the talweg in the entrance to the bend there is a high gravel bar with sand drapes and grass. Bankfull width at the bend entrance is ∼8 m but flow is normally restricted to a width of only 2–3 m in the right-bank talweg. Downstream from the entrance, the whole bend widens

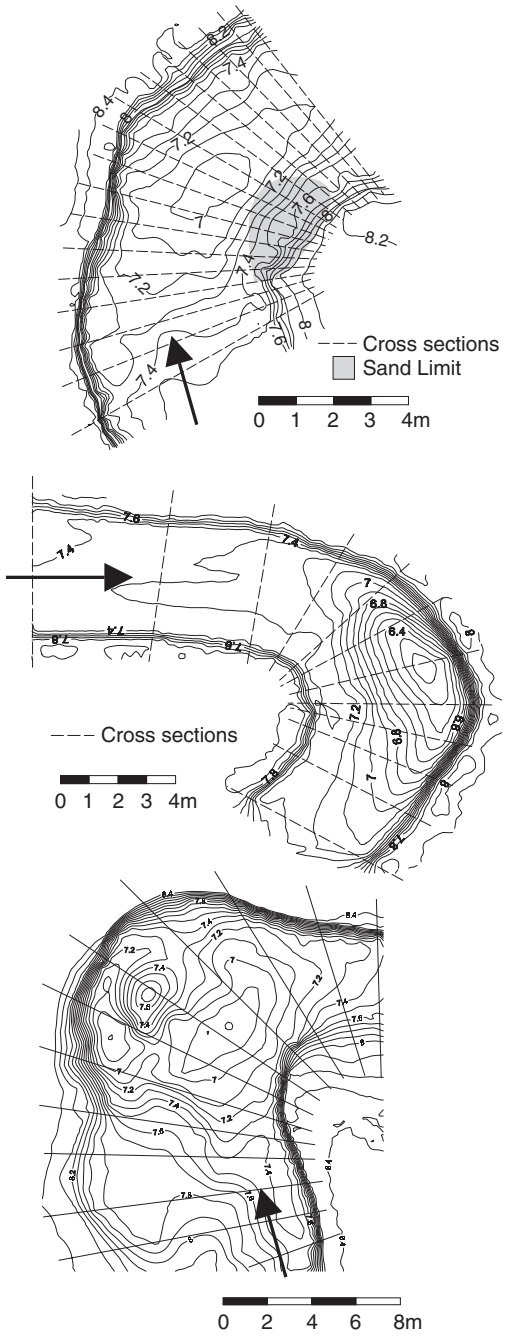


Figure 1. Topography of the study bends as determined by field survey and regular grid kriging. From the *top* Bend 17, Bend 37 and Bend 25. The cross-sections used to interpolate boundary-fitted CFD grids are also shown. Cartesian coordinate system for verification and validation has x positive rightwards along first cross-section in each case. The superimposed arrows indicate the bend inflow direction.

rapidly (~10 m) with the left (outer) bank opening into a fairly elevated backwater area. The right hand side of the channel deepens rapidly into a central pool (~0.9 m deep at the flow stage investigated and ~1.5 m deep at bankfull) which extends past the bend apex, after which the channel becomes shallower and narrower, with an exit width ~4 m normally, but upwards of 6 m at bankfull flow when the point bar is submerged. The outer bank is relatively high (~1.1 m), quite uniformly curved and composed of gravel with a thin capping of fine floodplain sediments. From the outer bank apex onwards it is actively eroding with undercutting of the grassy floodplain. The fastest flow in the bend follows the inner bank and the entire central and outer part of the pool is a recirculation zone. Bend average D_{84} is 34 mm, although this varies considerably, from a D_{84} of 55 mm on the upstream riffle and 78 mm in the pool to a D_{84} of 0.4 mm on the concave bank bench and 0.3 mm in the elevated backwater area. The variation in both width (W) and bank radius of curvature (R_c) around the bend makes it difficult to define an overall R_c/W ratio. However, R_c of the inner bank near the apex is <4 m and that of the outer bank right round the pool is no more than 6 m. Since the channel is ~10 m wide here, the bend R_c/W value is of order 1, which is extremely low.

3 FLOW MODELLING, VERIFICATION AND VALIDATION

The CFD modeling was done using version 3.4 of the PHOENICS™ code, which solves the full 3-D Navier-Stokes equations discretized over a finite-volume grid. Following Lane et al. (1999) we used a hybrid-upwind numerical interpolation scheme. This takes central differences between cells where diffusion dominates but upwind differences where convection is high (Peclet number >2), so is strictly only first-order accurate, but it is more stable than higher-order schemes which can introduce spurious oscillations into solutions. As solution accuracy controls sensitivity to grid design, we undertook a rigorous grid independence tests. The pressure and momentum equations are coupled though the SIMPLEST algorithm (Pantankar and Spalding, 1972). The solution was deemed to have converged when mass and momentum flux residuals were less than 0.1% of the inlet flux and spot values in a critical part of the domain were changing by less than 0.01%.

Direct solution of the Reynolds stress terms in the Navier-Stokes equations cannot be accomplished for natural channel flows with currently-available computer power. Here we use Reynolds averaging, and specifically the two-equation k-ε model modified by renormalization group theory (Yakhot et al., 1992), which has been the choice in most recent open-channel CFD applications (Hodskinson and Ferguson, 1998; Lane et al., 1999; Nicholas and Smith, 1999; Bradbrook et al., 2000), because of its enhanced performance in areas with high rates of strain.

3.1 *Computational grid*

A separate boundary-fitted curvilinear grid was fitted to the irregular topography of each bend by specifying a series of cross-section planes, then interpolating more planes to define a grid with specified numbers of cells in the streamwise, transverse and vertical directions. The surveyed cross-sections were used for bend 37. For bend 17 and 25, we extracted a series of cross sections from the DEM, which gave greater freedom in the position of each cross section. Rapid changes in cell aspect ratio or orientation were avoided in the interests of numerical stability.

The bend 17 model used for the results and analysis had 96 cells longitudinally, 42 across, and 10 vertically. This implies average cell dimensions of $\sim 12 \times \sim 12 \times \sim 6$ cm at the outer bank. The bend-37 model had $80 \times 30 \times 10$ cells, with mean dimensions of $\sim 28 \times 18 \times 5$ cm at the outer bank and the bend 25 model had 110 cells longitudinally, 56 across, and 10 vertically, which translates to $\sim 28 \times 22 \times 6$ cm at the outer bank apex. In all cases mean cell length decreases across the channel towards the inner bank, and cell height varies according to the local flow depth.

To obtain numerical convergence, slight modifications to each grid had to be made. This included placing vertical banks of 0.05 m near the point bars, on the upstream riffle and around the elevated bed region in bend 25, to avoid vanishing cell heights. The abruptness of the curvature of the inner bank in bend 17 and outer bank in bend 25 also had to be reduced slightly.

These grids and cell dimensions were used for validation and flow structure analysis once grid resolution verification checks had been performed, the results of which are detailed below.

3.2 *Boundary conditions*

For each model the necessary boundary conditions relate to inflow, outflow, wall treatment, and water surface. Distributions of velocity across the inflow plane were interpolated from the field measurements described above, using linear interpolation laterally and the law of the wall vertically. A hydrostatic pressure distribution was applied to cells at the outlet plane. Pressure values within the domain are calculated relative to this, so the outlet planes need to be clear of the effects of negative dynamic pressure in areas of reverse flow. Bed and bank roughness was parameterised using Launder and Spalding's (1974) non-equilibrium version of the law of the wall in the layers of cells touching the rough boundaries. Shear further from the boundaries is modeled explicitly. A uniform roughness

height was adopted for each model, estimated from the riffle bed grain size distribution using $k_s = 3.5D_{84}$. This exaggerates the skin roughness of the sandy parts of the bed, but the sand was rippled which adds some form resistance that is not represented in the model grid geometry. The free water surface was represented by the method described in Bradbrook et al. (2000). This allows for variable porosities in the surface layer of cells so that mass continuity is maintained without distorting the streamwise velocity.

3.3 *Model assessment*

Model assessment initially involved model verification followed by model validation.

Verification of the models in terms of the spatial discretization applied was performed using a grid-convergence-index (GCI) analysis (Roache, 1997; Hardy et al., 2002). Two further simulations were performed with a doubling and halving of the grid resolution, permitting estimation of confidence intervals for simulations at each resolution by comparison with simulations at other resolutions. Verification of the model solutions were performed by comparing the field ADV measurements with the predicted time-average flow velocities (Ucrt, Vcrt, and Wcrt) in the DEM Cartesian directions (x, y, and z). Approximate 95% confidence intervals for flow properties on the medium grid, calculated by Roache's method, are mostly around ±10% (and narrower for Ucrt in bend 25 and 37), but wider for vertical velocity Wcrt and in bend 17 and bend 25. Nevertheless, for each model the results show that the original medium-resolution results were close to being grid-independent, and we therefore use them below for validation and then to describe and illustrate the flow structures.

For both bend 17 and bend 25 validation of the model solutions were performed by comparing the field ADV measurements with the predicted time-average flow velocities (Ucrt, Vcrt, and Wcrt), the resultant velocity magnitude (VelMag) and the turbulent kinetic energy (Tke). The simulated values were taken from the nearest cell face in the CFD results, reflecting the fact that in each case the grid cell size is much larger than the ADV sampling volume. Thus, due to this scale difference the locations of point comparisons can differ by ~0.1 m in places, which can have an un quantifiable effect on the quality of the results of the validation exercise. The older 2-D field measurements made in bend 37 were regarded as less reliable for this purpose, though Hodskinson and Ferguson (1998) found reasonable agreement with their fixed-lid CFD simulation of that bend.

In both bend 17 and 25 the horizontal velocity component field measurements and the resultant velocity magnitude were in close agreement with modeled (Table 1). Agreement was less good for the vertical velocity component Wcrt and the Tke. Nevertheless, the prediction of Wcrt direction was generally very good.

Table 1. Agreement between simulated (CFD) and measured (ADV) values in both bend 17 and bend 25 of the five flow variables: velocity magnitude (VelM), its horizontal components Ucrt, Vcrt in the x and y directions of the DEM, its vertical component Wcrt, and the turbulent kinetic energy (Tke).

	Regression slope		
Variable	CFD on ADV	ADV on CFD	Correlation
Bend 17 (n = 62)			
VelM (m s^{-1})	0.82	1.01	0.82
Ucrt (m s^{-1})	0.83	1.08	0.90
Vcrt (m s^{-1})	0.91	0.99	0.89
Wcrt (m s^{-1})	0.37	1.19	0.44
Tke (m^2s^2)	0.40	1.06	0.43
Bend 25 (n = 40)			
VelM (m s^{-1})	1.22	0.78	0.98
Ucrt (m s^{-1})	1.18	0.80	0.97
Vcrt (m s^{-1})	1.21	0.70	0.92
Wcrt (m s^{-1})	0.59	0.46	0.52
Tke (m^2s^2)	0.18	3.63	0.81

Although the CFD predictions do not always match perfectly with the measured velocity and turbulence values the agreement is generally good, and comparable to what has been regarded as acceptable by researchers modeling flume data (Bradbrook et al., 1998; Huang et al., 2002). In view of the additional uncertainties of field data collection we therefore regard the models as adequately validated for use in discussing the flow structures present in the three bends.

The validated simulations provided spatially rich information with which to identify and illustrate the flow structures present in the three bends and to investigate how the flow altered with discharge.

4 RESULTS: FLOW STRUCTURES

Flow in these bends differs from standard descriptions of curvature-induced helical circulation occupying most or all of the wetted width (e.g. Dietrich, 1987). Fast downstream flow with a helical circulation is present in all three bends, but it is restricted to a freestream occupying less than half the channel width, near the opposite bank to the one with flow separation. Both velocity magnitude and strength of helical circulation decrease along this freestream, and the secondary circulation disappears before the exit of the bend. This is in contrast to the usual situation in which

the helix from one bend can extend through a straight section into the next bend. In the bends with inner-bank separation the fastest flow is progressively below the water surface, becoming close to the bed in the bend with the large recirculation eddy. The locations of maximum attack on the banks imply different patterns of bank erosion and bend migration than in ordinary meanders without flow separation.

Inner-bank separation occurs near the point of maximum curvature of the bankline (Fig. 2), with reattachment within a downstream distance of one channel width. Outer-bank separation occurs where an inflow near the inner bank crosses the channel at a sharp bend and impinges near-orthogonally on the outer bank (Fig. 2). In both cases the recirculation eddy is similar to what occurs in a sudden expansion. It has a near-vertical axis and the strongest reverse flow is close to the bank. Recirculation extends further across the channel at the surface than the bed, because of the different orientations of near-surface and near-bed velocity in the freestream of downstream flow. The bankfull simulation showed only a small reduction in size of the recirculation eddy despite a doubling of mean velocity, and the reverse flow was stronger.

The presence of these large separation zones has a number of significant implications, including controls on the nature and dynamics of fine sediment movement through the river reaches and the residence times and progression of pollutants within and through the system. Moreover, large separation zones also have the potential to alter expected bend movements and future migration patterns. The model results demonstrated that several aspects of the flow structure differed substantially to the flow structure found in more classical meander bends: as the downstream flow is steered around the inner bank recirculation zone, the streamwise helix is confined to the outer bank region and is only present in the upstream part of the bend. This is dissipated through vortex stretching as the flow expands beyond the downstream limit of separation. The maximum near bank velocities were found at the outer bank upstream of the bend apex and the region of reverse flow extended further across the channel at the surface than the bed.

It was also discovered that secondary circulation exists within the inner bank recirculation eddy, linked with the freestream outer bank flow through a double-hairpin loop motion. This was constructed by flow moving inwards and downwards distally into the recirculation but outwards and upwards proximally where flow is re-entrained into the freestream helical motion. But there is also strong shear between the downstream flow and recirculation eddy, and our field observations showed that Kelvin-Helmholz vortices are shed from the shear layer. These may also constitute a main part of the mixing mechanism in reality.

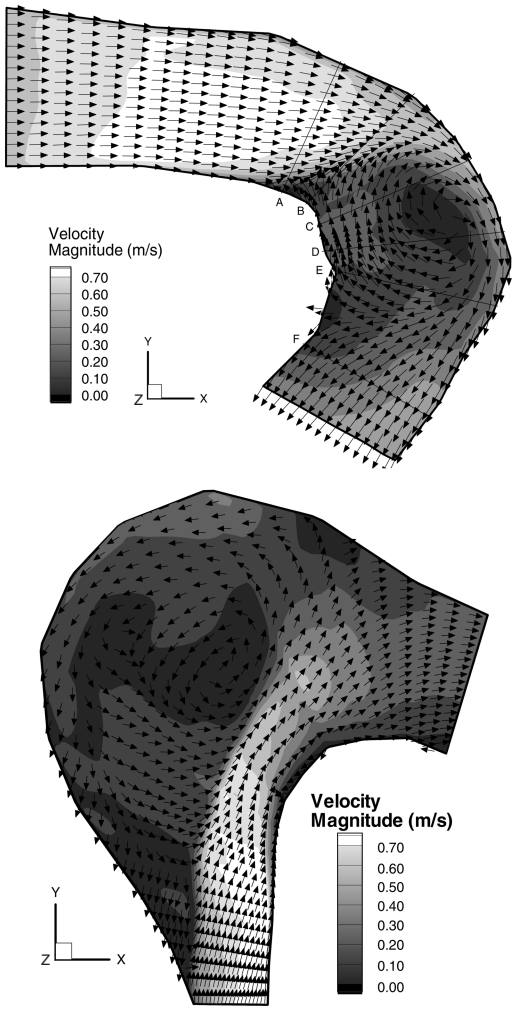


Figure 2. Simulated surface flow velocity magnitude (contours) with direction (unit sizes vectors). For bend 17 (top) and bed 25 (bottom).

5 RESULTS: BEND MOVEMENTS

During the study period both bend 17 and bend 37 have significantly eroded their outer banks (Fig. 3), whilst maintaining the inner bank separation. This bank erosion has been particularly concentrated before the bend apex, resulting in a movement migrating across the floodplain. This is slightly different to what is expected in more classical bends where rates are generally a little lower and the main point of attack on the bank is after the bend apex.

Morphological change in bend 25 has also been significant (Fig. 4). A large part of the inner bank has been eroded, as has the outer bank well downstream of the

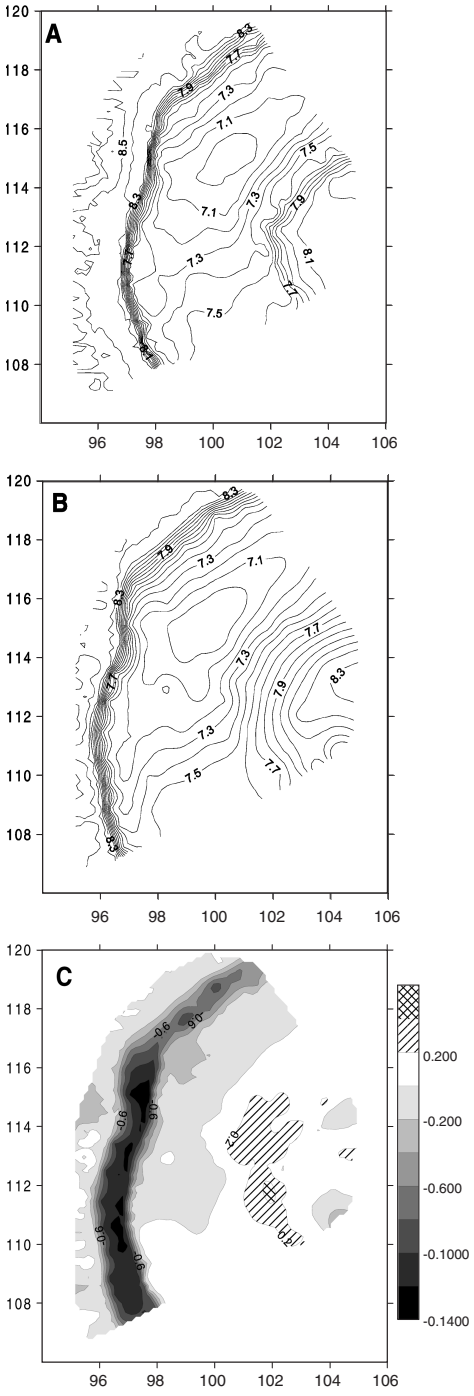


Figure 3. Digital elevation models of Bend 17 (A) July 2000, (B) September 2002, and (C) Identified difference (negative indicates erosion). All unit and contours in meters.

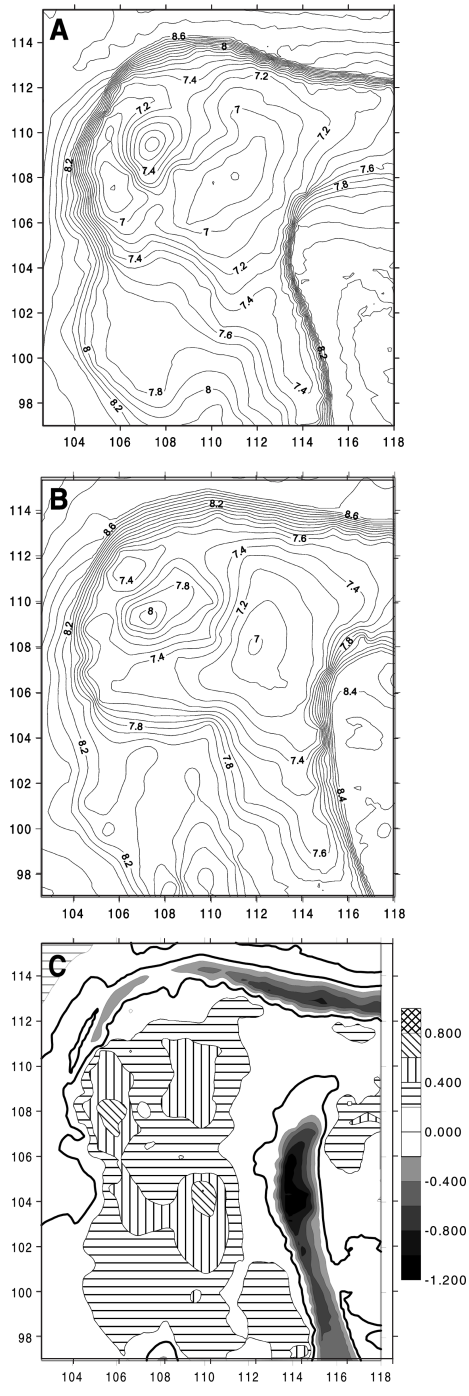


Figure 4. Digital elevation models of Bend 25 (A) August 2000, (B) February 2002, and (C) Identified difference (negative indicates erosion). All unit and contours in meters.

outer bank apex. This has resulted in the opposite to what generally thought to occur in more classical type meander bends. The concave bank bench has grown both in spatial extent and in altitude. These changes suggest a movement away from, and the slow abandonment, of the bank bench. Nevertheless, the high curvature of the inner bankline has remained, and the large separation zone has remained present.

6 CONCLUSIONS

This paper has demonstrated that the flow structures in bends with recirculation zones are significantly different from those traditionally found in more classical, lower curvature, meanders. Bends with separation zones are dominated by the effects of the recirculation and the acceleration of the helical motion in the freestream flow, which in turn produces a zone of high shear between the freestream and the recirculating fluid. This flow structure has a number of implications including altering the rates and directions of bend movements. In the bends investigated in this paper, bends with inner-bank separation have rapidly eroded their outer bank before the apex while the bend with an outer bank separation has significantly eroded its inner bank.

ACKNOWLEDGEMENTS

D.R. Parsons was in receipt of a UK Natural Environment Research Council studentship, which was tied to grant GR3/9715 awarded to S.N Lane and R.I Ferguson. We also thank the local farmer (Mr Williams) for access to the field site; Richard Smith and Simon Tait of the Department of Civil Engineering, Sheffield University, for assistance in constructing the ADV wading rod; Ben Surridge, Louise Sime, Barry Hankin, and David Mould for assistance with fieldwork.

REFERENCES

Andrle, R., 1994. Flow Structure and Development of Circular Meander Pools. *Geomorphology* 9(4): 261–270.

Bagnold, R.A., 1960. Some aspects of the shape of river meanders. *USGS Professional Paper* 282E.

Bradbrook, K.F., Biron, P.M., Lane, S.N., Richards, K.S. & Roy, A.G., 1998. Investigation of controls on secondary circulation in a simple confluence geometry using a three-dimensional numerical model. *Hydrological Processes* 12(8): 1371–1396.

Bradbrook, K.F., Lane, S.N. & Richards, K.S., 2000. Numerical simulation of three-dimensional, time-averaged flow structure at river channel confluences. *Water Resources Research* 36(9): 2731–2746.

Burge, L.M. & Smith, D.G., 1999. Confined meandering river eddy accretions: sedimentology, channel geometry and depositional processes. *Special Publication of the International Association of Sedimentologists* 28: 113–130.

Carey, W.C., 1969. Formation of flood plain lands. *Journal of the Hydraulics Division, ASCE* 95: 981–994.

Dietrich, W.E., 1987. Mechanics of flow and sediment transport in river bends. In: K.S. Richards (ed.), *River channels: environment and process*. Blackwell: Oxford.

Guymer, I., 1998. Longitudinal dispersion in sinuous channels with changes in shape. *Journal of Hydraulic Engineering-ASCE*: 35: 113–130.

Hardy, R., Lane, S.N., Ferguson, R. & Parsons, D.R., in press. Assessing the credibility of a series of computational fluid dynamic simulations of open channel flow. *Hydrological Processes*.

Hickin, E.J., 1977. Hydraulic factors controlling channel migration. In: R. Davidson-Arnott & W. Nickling (eds.) *Research in fluvial systems, Proceedings of the 5th Guelph geomorphology symposium*. Geobooks: Norwich.

Hickin, E.J., 1978. Mean flow structure in meanders of the Squamish River, British Columbia. *Canadian Journal of Earth Sciences* 15: 1833–1849.

Hickin, E.J., 1979. Concave bank benches on the Squamish River, British Columbia. *Canadian Journal of Earth Sciences* 16: 200–203.

Hickin, E.J., 1986. Concave bank benches in the flood plains of the Muskwa and Fort Nelson Rivers, British Columbia. *The Canadian Geographer* 30: 111–122.

Hickin, E.J. & Nanson, G.C., 1975. The character of channel migration on the Beatton River, North-east British Columbia, Canada. *Geological Society of America Bulletin* 86: 487–494.

Hodskinson, A. & Ferguson, R.I., 1998. Numerical modelling of separated flow in river bends: Model testing and experimental investigation of geometric controls on the extent of flow separation at the concave bank. *Hydrological Processes* 12(8): 1323–1338.

Huang, J., Weber, L.J. & Lai, Y.G., 2002. Three-dimensional numerical study of flows in open-channel junctions. *Journal of Hydraulic Engineering-ASCE* 128: 268–280.

Ippen, A.T. & Drinker, P.A., 1962. Boundary shear stress in curved trapezoidal channels. *Journal of the Hydraulics Division-ASCE* 88: 143–179.

Lane, S.N. et al., 1998. Three-dimensional measurement of river channel flow processes using acoustic Doppler velocimetry. *Earth Surface Processes and Landforms* 23(13): 1247–1267.

Lane, S.N., Bradbrook, K.F., Richards, K.S., Biron, P.A. & Roy, A.G., 1999. The application of computational fluid dynamics to natural river channels: three-dimensional versus two-dimensional approaches. *Geomorphology* 29 (1–2): 1–20.

Launder, B.E. & Spalding, D.B., 1974. The numerical computation of turbulent flows. *Computer Methods in Applied Mechanics and Engineering* 3: 269–289.

Leeder, M.R. & Bridges, P.H., 1975. Flow separation in meander bends. *Nature* 253: 338–339.

Markham, A.J. & Thorne, C.R., 1992. Geomorphology of gravel-bed river bends. In: P. Billi, R.D. Hey, C.R. Thorne & P. Tacconi (eds.), *Dynamics of Gravel-bed rivers*. Wiley: Chichester.

Nicholas, A.P. & Smith, G.H.S., 1999. Numerical simulation of three-dimensional flow hydraulics in a braided channel. *Hydrological Processes* 13(6): 913–929.

Page, K.J. & Nanson, G.C., 1982. Concave-bank benches and associated floodplain formation. *Earth Surface Processes and Landforms* 7: 529–543.

Pantankar, S.V. & Spalding, D.B., 1972. A calculation procedure for heat, mass and momentum transport in three-dimensional parabolic flows. *International Journal of Heat and Mass Transfer* 15: 1782–1799.

Parsons, D.R., 2003. *Flow separation in meander bends.* PhD thesis, Sheffield University.

Reid, J.B., 1984. Artificially induced concave bank deposition as a means of floodplain erosion control. In: C.M. Elliott (ed.), *River Meandering: Proceedings of the Conference Rivers '83*. American Society of Civil Engineers: New York.

Reynolds, C.S., 2000. Hydroecology of river plankton: the role of variability in channel flow. *Hydrological Processes* 14(16): 3119–3132.

Roache, P.J., 1997. Quantification on uncertainty in computational fluid dynamics. *Annual Review of Fluid Mechanics* 29: 123–160.

Tipping, E., Woof, C. & Clarke, K., 1993. Deposition and Resuspension of Fine Particles in a Riverine Dead Zone. *Hydrological Processes* 7(3): 263–277.

Woodyer, K.D., Taylor, G. & Crook, K.A.W., 1979. Depositional processes along a very low-gradient, suspended-load stream: the Bawrwon River, New South Wales. *Sedimentary Geology* 22: 97–120.

Yakhot, V., Orszag, S.A., Thangham, S., Gatshi, T.B. & Speziale, C.G., 1992. Development of a turbulence model for shear flow by a double expansion technique. *Physics and Fluids A* 4: 1510–1520.

This page intentionally left blank

River Flow 2004 – Greco, Carravetta & Della Morte (eds.)
© 2004 Taylor & Francis Group, London, ISBN 90 5809 658 0

Influence of geometrical constraints on the evolution of meandering rivers

Paolo Perona
Institute of Hydromechanics and Water Resources Management, ETH – Hönggerberg, Zurich, Switzerland

Carlo Camporeale
Dipartimento di Idraulica, Trasporti ed Infrastrutture Civili, Politecnico di Torino, Torino, Italy

ABSTRACT: The effects of geometrical constraints on downstream river evolution are numerically investigated focusing on the *Ikeda et al. (1981)* model in this work. Despite its simplicity, this model takes spatial memory effects into account, thus allowing for the description of some basic mechanisms typical of real meander, appropriately. Moreover, the whole dynamics can be reduced to the study of three governing parameters: the Parker number Pa, the decay length D and the basic time scale T. The results obtained by spanning a reasonable range of the parameters D, and Pa, and the relative investigation of bounded river reaches of different shapes and length, lead to some interesting observations and first conclusions. These regard the possibility of understanding and potentially quantifying the future changes that occur downstream of the bounded reach as well as providing some useful suggestions on how to control them.

1 INTRODUCTION

Meandering rivers are natural systems in continuous evolution and have long been studied from both an observational and theoretical point of view (e.g. Leopold & Wolman 1960, Allen 1965, Engelund & Skovgaard 1973, Callander 1978, Ikeda et al. 1981, Blondeaux & Seminara 1985, Johannesson & Parker 1989, Lewin 1992, Anderson et al. 1996, Sun et al. 1996, Zolezzi & Seminara 2001, Lancaster & Bras 2003). Important studies in the past, both geomorphological (e.g., Friedkin 1945, Nanson & Hickin 1983, Furbish 1988, Church 1992, Lewin 1992, Whiting & Dietrich 1993) and fluid mechanical (see, for example Ikeda et al. 1981, Blondeaux & Seminara 1985, Johannesson & Parker 1989) have explained the fundamental dynamics of the phenomenon. Such studies thus furnished the basic understanding for other significant theoretical and numerical steps ahead more recently achieved in the description of either short or the long-term behaviour (Liverpool & Edwards 1995, Sun et al. 1996, Zolezzi & Seminara 2001, Edwards & Smith 2002). The picture that arose is that the dynamics of such rivers is intrinsically unstable and complex. Whether at one hand such characteristics attract more speculative studies, on the other hand the way the planimetric evolution of such river occurs is an interesting issue also for engineering purposes (Henriquez et al. 1990, Swanson 1993). For instance, the hydraulic studies can be motivated from the need to investigate the influence of riparian vegetation on bank stability (Millar 2000) or to understand the effects of anthropic modifications. This is the case of meandering rivers whose planimetric evolution may cause erosion of zones where infrastructures are present. Protection of such areas may require the construction of embankments that constrain even long reaches of river and thus limit its morphodynamic evolution. It has been proved, to this regard (see, for example Ikeda et al. 1981, Johannesson & Parker 1989, Zolezzi & Seminara 2001), that planimetric evolution is influenced by both local and neighbour river geometries. In particular, upstream geometry acts on local river dynamics as a fading spatial memory. Rather interesting and relevant to our purposes is, therefore, to show the way the evolution of upstream geometries can influence that of points located downstream. Similarly, the question can also be addressed to understand how these memory effects propagate downstream and eventually whether they can be controlled by geometrically conditioning a given reach of river.

The effects of geometrical constraints on downstream river evolution are therefore numerically investigated in this work using the model proposed by Ikeda et al. (1981). Even if at present these results are mainly qualitatively discussed, they allow to infer some interesting considerations related to the possible effects induced by the construction of river

embankments on the evolution of the reach located downstream of the bound. In particular, these considerations regard the influence of the constraint length and shape, as well as the importance that the spatial memory assumes, depending on the hydraulics and pedological characteristics.

2 MODELLING

All the theoretical studies made up to explain the meandering dynamics start by assuming as generally valid two results that were obtained from the observations made by geomorphologists in the past. These are: (i) the width of the channel tends to remain constant in time thanks to a balancing mechanism of both erosion at the outer bank and simultaneous deposition at the inner bank; (ii) the erosion at the bank is proportional to the exceeding (with respect to the mean velocity of the uniform flow U_0) bank velocity u_{sb} by a characteristic coefficient of bank erosion E. Among the most important models of meandering (see, Ikeda et al. 1981, Johannesson & Parker 1989, Zolezzi & Seminara 2001), the pioneering model proposed by Ikeda et al. (1981) has been used. In the next subsection it will therefore be recalled and, in light of some recent developments (Edwards & Smith 2002), also discussed.

2.1 *The Ikeda-Parker-Sawaj model*

This model employs the de Saint Venant equations for a shallow steady incompressible turbulent flow in a sinuous channel. In this model the effects of secondary currents on bedload transport are considered assuming a semi-theoretical relationship between the bed topography and the local river curvature. The exceeding bank velocity u_{sb} can be readily obtained from a linearized form of the shallow water equations. At constant time, the u_{sb} satisfies the following differential equation (see also Sun et al. 1996):

$$\frac{du_{sb}}{ds}+2C_f\frac{U_0}{H}=bU_0\left(\frac{F^2+A'+A_s-1}{H}C_fk-\frac{dk}{ds}\right), \qquad (1)$$

where s is the intrinsic downstream coordinate along the river axes (Figure 1), b is the half-width of the channel, C_f is a dimensionless friction factor, H the water depth of the uniform flow, k the local curvature of the river centreline, F the Froude number and the constants A' and A_s account for the erosion on a bed slope (erosion factor) and for the convective transport of downstream momentum, respectively (see also Johannesson & Parker 1989). The erosion factor A' is a positive constant and literature has provided evidence that it can vary in the range 2–10 (see, for example Engelund 1974, Hooke 1965, Suga 1963). More recently Edwards & Smith (2002) showed that Equation 1 can be rewritten in a more useful form by introducing the following three parameters:

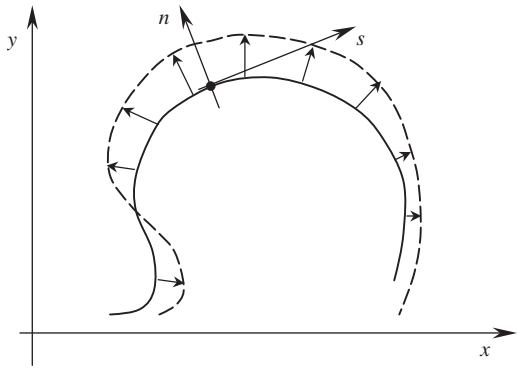


Figure 1. Sketch of the numerical procedure used here to simulate the evolution of meandering patterns. (—) Current pattern; (- -) one temporal step later.

$$D=\frac{H}{2C_f} \qquad T=\frac{D^2}{bEU_0}, \qquad Pa=\frac{F^2+A'+A_s-1}{2},$$

so that it reads

$$\frac{dv}{ds}+\frac{v}{D}=\frac{D^2}{T}\left(\frac{k\,Pa}{D}-\frac{dk}{ds}\right), \qquad (2)$$

where $v=Eu_{sb}$ is the equation assumed for the bank erosion. In this way, the abovementioned quantities D, T and Pa appear to be the effective scaling factors that summarize the hydraulic characteristics of the river provided the current river sinuosity is used to continuously update the hydraulics motion conditions. The decay length D is related to the basic scale of the meander wavelength and corresponds to the distance between the inflection points of the channel and the points where the migration rate vanishes (meander nodes). The Parker number Pa is a dimensionless quantity which measures the strength of secondary flow relative to the shear in downstream velocity due to the outward hydrostatic head gradient (i.e., the Bernoulli shear). The time T accounts for local soil properties and motion conditions. T and D therefore describe the natural sinuosity-dependent time and length scales of the process, respectively. For a given configuration of meandering river, the contribution of Pa can be considered being roughly constant in time, thus reducing the controlling parameters of the process to only D and T (Edwards & Smith 2002). Equation 2 can be easily integrated to obtain, at a sufficient distance

downstream the origin (see, also Sun et al. 1996),

$$v = -\frac{kD^2}{T} + \frac{D}{T} Pa \int_0^s e^{-s'/D} \, k(s-s') \, ds'. \qquad (3)$$

This equation shows that erosion velocity at a point depends on the local geometry and on another term that accounts for the geometry upstream. Therefore, despite its simplicity, the Ikeda et al. model takes spatial memory effects into account and this allows (see, Ikeda et al. 1981, Sun et al. 1996, Edwards & Smith 2002) to appropriately reproducing some basic mechanisms typical of real meanders (e.g. wavelength selection, downstream migration, meander fattening and upstream skewing).

2.2 *Numerical implementation*

The numerical model has been implemented assuming the river behaves as a planar curve that moves onto a sloping plane $\{x, y\}$ by a normal-to-the-curvature driven instability (see, for example Perona et al. 2002). This latter is obtained by integrating the Ikeda et al. (1981) model over the current river shape. This furnishes the value of the exceeding bank velocity for all the points of the river and, then, once it is multiplied for spatial soil erodibility E, the corresponding erosion velocity. Being the simulations mainly devoted to investigate the short-term behaviour of a given reach downstream of the constraint, it is reasonable to assume that the local soil erodibility is both temporally and spatially constant. In particular, the parameters of the sedimentary environment, i.e. the valley length and width (10000 m and 6000 m, respectively) and the coefficient of erodibility E ($1.85 \cdot 10^{-8}$) have been chosen equally for all the simulations presented in this work. The numerical scheme that has been adopted here (see Figure 1) is similar to that already proposed by Sun et al. (1996) (see also Howard 1996), except for the fact that, at each temporal step and according to the current river sinuosity, we update both the bed slope and the steady hydraulics quantities. The points of the river centreline are sampled at a distance equal to $b/2$ and moves at temporal steps of 5 days. Each point, in particular, is then moved in two times, i.e. following a procedure that allows to consider the variations that will occur in the exceeding bank velocity u_{sb} while the curve is moving between the current and the next configuration. Moreover, at each temporal step, the whole curve is re-sampled at the abovementioned spatial interval in order to reduce as much as possible numerical instabilities. This allows avoiding the presence of points where the local curvature would increase too much. An example is that of cutoff events. These are always rather delicate to consider and there is the risk that numerical instabilities can occur. To our purposes this problem is not relevant here, however it has equally been dealt with by applying a suitable numerical procedure, the details of which will be reported elsewhere (Camporeale et al. 2004).

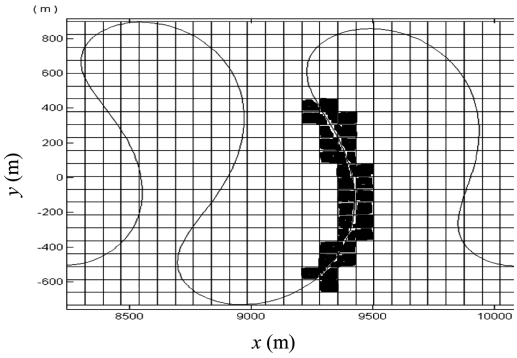


Figure 2. Example of constrained reach. The bound has been simulated by imposing zero erodibility to the cells along the river centreline.

2.3 *Schemes of constraints*

In order to simulate a suitable constraint scheme we overlapped a grid of square cells (size, 25 m × 25 m) to the river. Each of them account for possible variations in the spatial erodibility; in this way, the presence of a constraint has been described by simply setting to zero the erodibility value of the corresponding cells located along the river centreline. It must be said here that little adjustments of the point of the river usually occur during the re-sampling process. This fact, therefore, can induce those points of the river that lie close to the corners of a bounding cell to shift toward a nearer cell, thus becoming actually unbounded. This risk was avoided at occurrence by extending the value of zero erodibility also to some other adjacent cells (see, for example the sketch shown in Figure 2).

Several simulations were done on different schemes of constraint in order to perform the following analysis. First of all, the effects of the constraint length as well as of the geometrical form of the bounded reach were studied. Then an investigation of the influence of the decay length D (i.e. of the hydraulics parameters such, for example, the friction factor, the base flow, etc.) and of the Parker number Pa was also carried out for a fixed constraint scheme.

3 RESULTS AND DISCUSSIONS

In order to quantify at a given time of evolution the actual differences among the free and the constrained configurations, the maximum shifting of both the x and y coordinate was measured (Figure 3). After N years of evolution these quantities are a measure of the effects caused by constraints.

The validity of the results obtained from such measurements, however, is not easy to generalize because of the presence of the convolution integral of Equation 3, i.e. of the fading memory resulting from the shape of the river. To our purposes, however, the afore-mentioned quantities provided at least a global picture that allows for formulating some qualitative considerations below explained.

3.1 *Influence of the constraints shape*

Figure 4 show the effect of the shape of the constrained reach for equal hydraulics simulation conditions ($Q = 325\,\mathrm{m^3/s}$; $C_f = 0.0036$; $b = 35\,\mathrm{m}$; bed slope $= 0.002$; $A' = 10$). In both cases, the length of the constraint was chosen to be equal to 1400 m, approximately. The main difference between the two adopted configurations is that for the case of Figure 4b the constraint has been imaged to limit a river that does not contain any significant straight reaches. The case of Figure 4a, on the contrary, shows a relatively long rectilinear reach just before the bend where the constraint ends. Being that the spatial memory is calculated as in Equation 3, it is therefore expected that the geometry of the river of Figure 4b will give rise to significant differences in the future planimetric developments if compared to those of Figure 4a. The simulation indeed predicts an evolution of the reaches downstream the constraint that is strongly different. For the first case (Figure 4a), in particular, the river with the constraint does not present significant deviation of its evolution when compared with that of the unbounded river. To this regard, it can be noted that the cutoff event showed in Figure 4a occurred nearly at both the same point and time. This result contrasts quite evidently with that obtained in the case of Figure 4b and the difference is mainly due to the relatively less influent effect of the spatial memory, when calculated over reaches that contain long straight reaches.

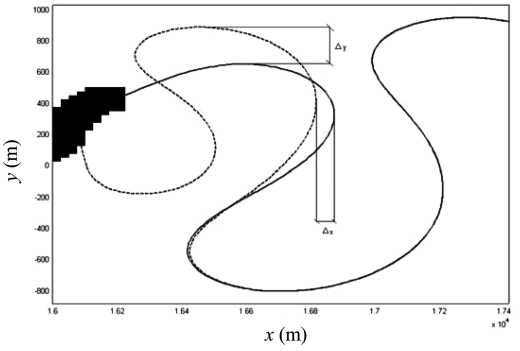


Figure 3. Shifting in cartesian coordinates Δx and Δy among the free (--) and the bounded (—) configurations.

3.2 *Influence of the constraint length*

Along with the results presented in the previous paragraph, it is now expected that the length of the constraint can itself influencing the river evolution. This has been investigated by doing 14 simulations over a river that does not show evident straight reaches. The constraint length was gradually augmented in the range 0–1400 m, after each simulation. All the hydraulics parameters were maintained constantly equal to those mentioned in paragraph 3.1. Results are summarized in Figure 5 that show the magnitude of the shifting measured along the x and the y coordinates between the

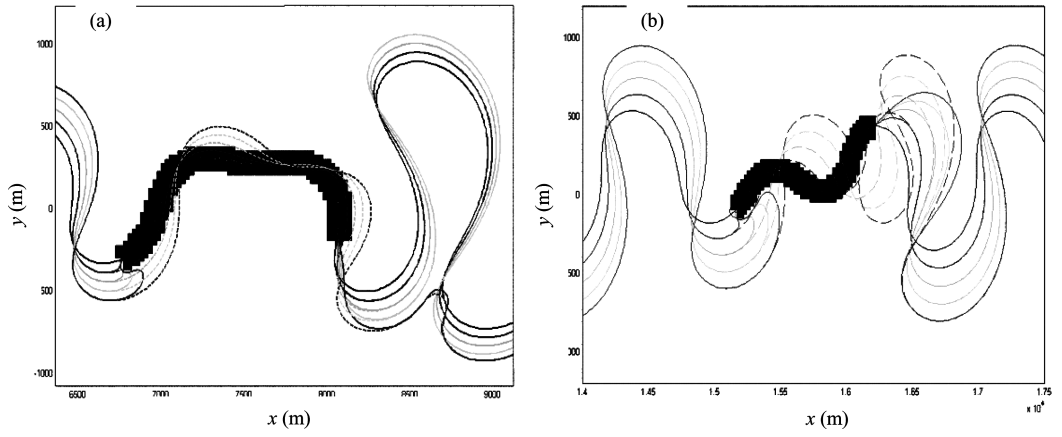


Figure 4. Influence of the shape of the constrained reach. (a) Embankments built along a river that include a rectilinear reach do not seem to produce substantial differences in planimetric evolution of the constrained reach (—) when compared to that (--) of the free configuration. The contrary is evident in (b), where after the same period of evolution (400 ys), the two configurations look significantly different.

free and the constrained river at several years of simulation. Within the evolution time of 400 years, a general asymptotic behaviour with respect to the length of the constraint can be noted for both the coordinate x and y. In particular, over a constraint length of about 400 m, the simulation gave rise to approximately the same difference in the pattern downstream. As the length of the constraint increased, a general increase in the longitudinal migration velocity and a corresponding reduction of the transversal one of the point located downstream the bound was also observed.

3.3 *Influence of decay length and Parker number*

Given a river of assigned geometry (e.g., width b) and pedological characteristics (e.g., erodibility E), then Equation 3 shows that the evolution should depend on two parameters that are the decay length D and the Parker number Pa. However, since the contribution of the convolution integral also depends on the river shape, the two above-mentioned quantities are not sufficient to generalize the results for all possible river configurations. Notwithstanding this, some clues on the role of the two aforementioned parameters D and Pa can be given once a fluvial geometry has been fixed. For the case studied here and shown in Figure 6, the decay length D was varied within the three values 140, 220, 350 m which correspond to the approximate distances downstream 430, 580, 1050 m. These values are related either to the distance downstream after which the influence of the bound is negligible within the observation period, or to the length of the upstream geometry beyond which the convolution integral does not show significant variations. Figure 6, in particular, shows the result of a simulation obtained with a value $D = 430$ m. The corresponding maximum shifting downstream between the free and the bounded configuration is represented in Figure 7. From these diagrams it is interesting to note that within the investigated range of D the river behaviour may even change completely, thus indicating the important significance attributed to such a parameter.

The influence of the Parker number was evaluated by varying it in such a way that the decay length remained constant. This was possible, in particular, by varying the term A' among the values 2, 4, 10, i.e. within the reasonable range that has also been recognized in literature. At constant hydraulics conditions of motion ($F = 0.75$; $H = 1.6$ m; $U_0 = 3$ m/s), this allowed to obtain a reasonable variation of the Parker number among the values 1.8, 2.4, 5.4, respectively. As shown in Figure 8, the effect of the Parker number appears to condition more the shifting of the y

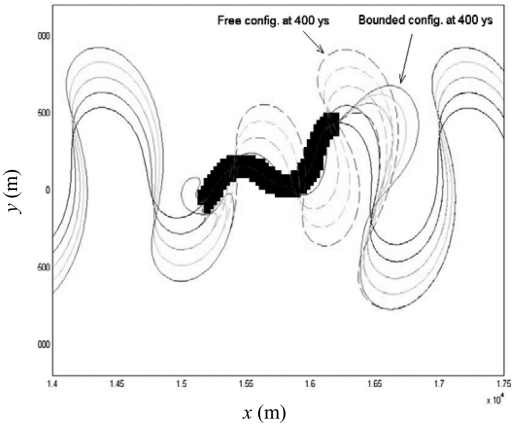


Figure 6. Case study to investigate the influence of the decay length and the Parker number. The constraint length is 1400 m.

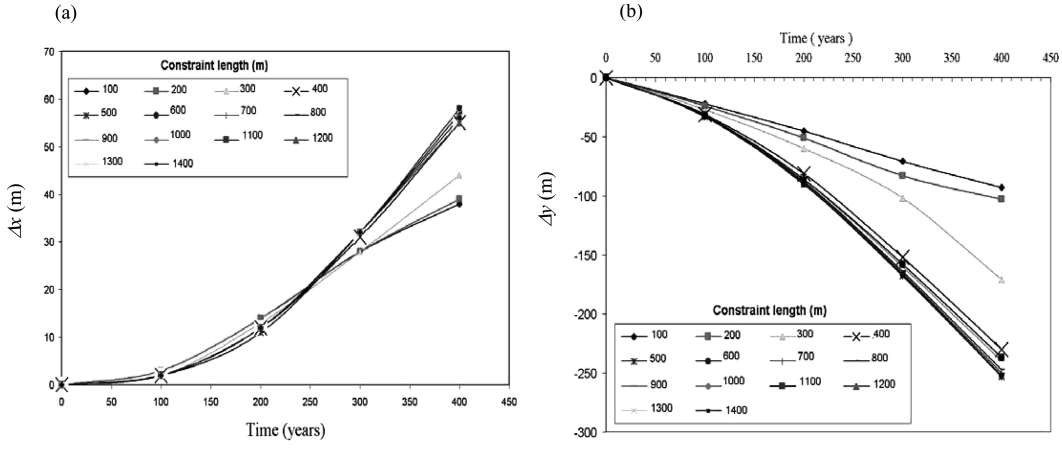


Figure 5. Shifting of the point of the river along the (a) x and (b) y coordinates for different constraint length and at several years of simulation.

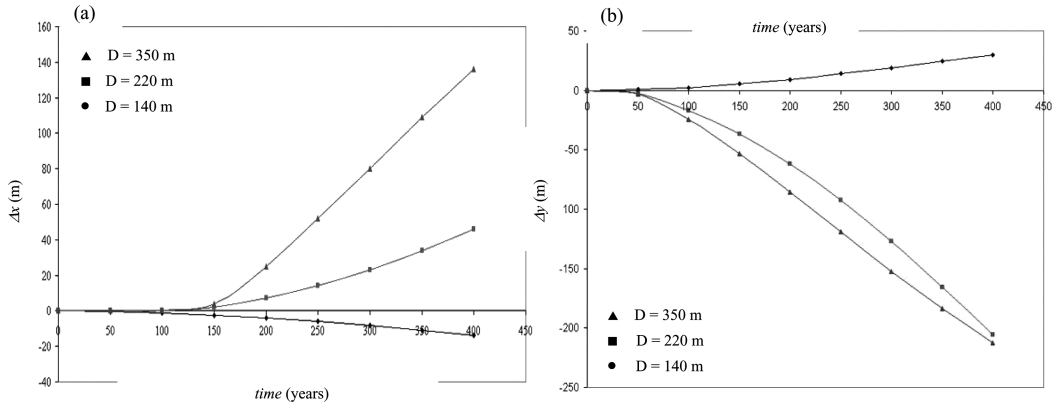


Figure 7. Effect of the decay length on the planimetric developments of the river constrained by the configuration scheme of Figure 6; maximum shifting of (a) the *x* and (b) the *y* coordinates, relative to those of the free configuration.

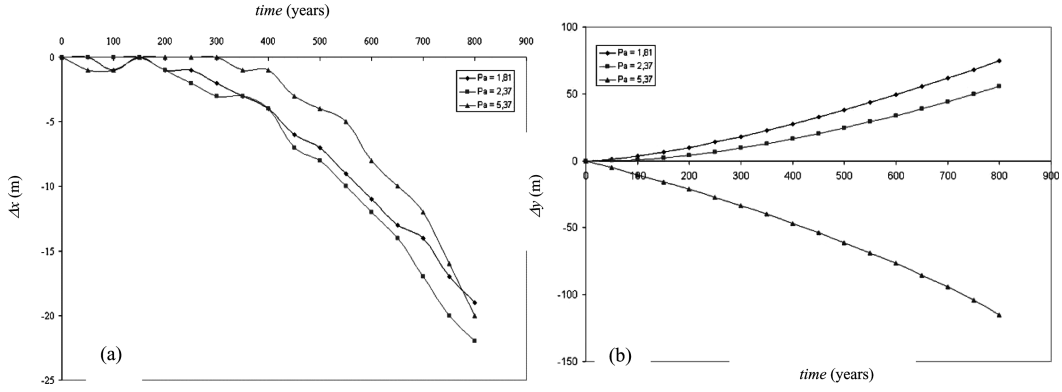


Figure 8. Effect of the Parker number on the planimetric developments of the river constrained by the configuration scheme of Figure 6; maximum shifting of (a) the *x* and (b) the *y* coordinates, relative to those of the free configuration.

coordinate than that of the *x* one. Further analyses that are currently under investigation would seem to associate the reason for such an effect with a contrasting behaviour shown by the transversal and longitudinal migration velocities.

The results so far presented show that changes in the constructive aspect of fluvial embankments might produce even marked differences in the downstream river behaviour. This aspect underlines the importance of considering such infrastructures as useful under multiple points of view that could go beyond the local protection of a given reach of river. An interesting applicative example, for instance, can be that of employing an adequate constrain design to actually either anticipate or postpone those cutoff events whose natural occurrence might compromise important benefits deriving from fluvial utilization (e.g. navigation, irrigation, etc). Given the general character of the present investigation, all the aforementioned aspects are furthermore emphasized. They can be useful in fact to further motivate studies on river re-naturalization and vegetation dynamics, the importance of which ranges from purely speculative interests up to a better understanding of the role and importance of the riparian vegetation for the whole hydraulics ecosystem.

4 CONCLUSIONS

A note concerning the numerical investigation on the effects related to the presence of embankments on river evolution has been discussed in this work. The meandering process has been simulated by means of the basic model of Ikeda et al. (1981) that proven to be useful to both focus and explain some basic mechanisms. A first conclusion is that whenever the construction of an embankment is required, then even significant

changes in the future planimetric developments of the bounded river can occur if the evolution is compared with that obtained without constraints. This is expected, in particular, for those cases where the constraint is built along a portion of river mostly sinuous and lacking of rectilinear reaches. Secondly, for equal geometrical river configurations and hydraulics conditions, the differences in future behaviour depend on the length of the constraint. These results, therefore, underline the importance of a correct definition of such anthropic infrastructures. Furthermore, the influence of the decay length, together with that of the Parker number, improves the knowledge on the role of the effective variables that are involved in the study and provides thus, an interesting starting points for future investigations and further refinements. An example is the possibility of controlling the meandering process either by adopting a suitable constraint scheme or by changing the hydraulics parameters of the interested reaches.

ACKNOWLEDGEMENTS

We wish to thank L. Ridolfi for the interesting discussions and suggestions and R. Coni for having run the simulations.

REFERENCES

Allen, J.R.L. 1965. A review of the origin and characteristic of recent alluvial sediments. *Sedimentology* 5: 89–191.

Anderson, M.G., Walling, D.E. & Bates, P.D. (eds) 1996. *Floodplain processes.* Chichester: John Wiley & Sons.

Blondeaux, P. & Seminara, G. 1985. A unified bar-bend theory of river meanders. *J. Fluid Mech.* 157: 449–470.

Callander, R.A. 1978. River meandering. *Ann. Rev. Fluid Mech.* 10: 129–158.

Camporeale, C., Perona P., Porporato, A. & Ridolfi, L. 2004. To be submitted.

Church, M. 1992. Channel morphology and typology. In P. Calow & G. E. Petts (eds), *The river handbook*, Vol 1: 126–143.

Edwards, B. & Smith, D. 2002. River meandering dynamics. *Phys. Rev. E* 65, 046303.

Engelund, F. & Skovgaard, O. 1973. On the origin of meandering and braiding in alluvial streams. *J. Fluid Mech.* 57(part 2): 289–302.

Engelund, F. 1974. Flow and bed topography in channel bends. *J. Hydr. Div. Am. Soc. Civ. Eng.*, 100, 1631–1648.

Friedkin, J.F. 1945. *A laboratory study of the meandering of alluvial rivers.* US Waterways Exp. Stn. Vicksburg: Mississipi River Commission.

Furbish, D.J. 1988. River-bed curvature and migration: how are they related? *Geology* 16: 752–755.

Henriquez, A., Tyler, K.J. & Hurst, A. 1990. Characterization of fluivial sedimentology for reservoir simulation modelling. *SPE Form. Eval.*, Sept.: 211–216.

Hooke, R.D. 1975. Distribution of sediment transport and shear stress in a meander bend. *Journal of Geology*, 83: 543–565.

Howard, A.D. 1996. Modelling channel evolution and floodplain morphology. In Malcom G. Anderson, Des E. Walling & Paul D. Bates (eds), *Floodplain processes* 1996. Chichester: John Wiley & Sons.

Ikeda, S., Parker, G. & Sawai, K. 1981. Bend theory of river meanders. Part 1. Linear development. *J. Fluid Mech*. 112: 363–377.

Johannesson, H. & Parker, G. 1989. Linear theory of river meanders. In S. Ikeda & G. Parker (eds), *Water Resour. Monogr.* 12: 181–213.

Lancaster, S.T. & Bras, R.L. 2003. A simple model of river meandering and its comparison to natural channels. *Hydrological Processes*, 16: 1–26.

Leopold, L.B. & Wolman, M.G. 1960. River meanders. *Bulletin Geol. Soc. Am.* 71: 769–794.

Lewin, J. 1992. Floodplain construction and erosion. In P. Calow & G. E. Petts (eds), *The river handbook*, Vol 1: 144–161.

Liverpool, T.B. & Edwards, S.F. 1995. Dynamics of a meandering river. *Phys. Rev. Letters* 75(16): 3016–3019.

Millar, R.G. 2000. Influence of bank vegetation on alluvial channel patterns. *Water Resour. Res.* 36(4): 1109–1118.

Nanson, G.C. & Hickin, E.J. 1983. Channel migration and incision on the Beatton river. *J. Hydraulics Div. ASCE* 109: 327–337.

Perona, P., Porporato, A. & Ridolfi, L. 2002. River dynamics after cutoff: a discussion of different approaches. *River Flow 2002 Eds. Bousmar & Zech*, Vol 2: 715–721.

Suga, K. 1963. On local scour at river bends. *Tech. Memo Public, Work Res. Inst., Min. of Const. Japan.*, Vol 5, no. 4 (in Japaneese).

Sun, T., Meakin, P. & Jøssang, T. 1996. A simulation model for meandering rivers. *Water Resour. Res.* 32(9): 2937–2954.

Swanson, D.C. 1993. The importance of fluvial processes and related reservoir deposits. *JPT J. Petr. Technol.* April: 368–377.

Whiting, P.J. & Dietrich, W.E. 1993. Experimental studies of bed topography and flow patterns in large-amplitude meanders 1: Observations. *Water Resour. Res.* 29(11): 3605–3614.

Zolezzi, G. & Seminara, G. 2001. Downstream and upstream influence in river meandering. Part 1. General theory and application to overdeepening. *J. Fluid Mech.* 438: 183–211.

This page intentionally left blank

River Flow 2004 – Greco, Carravetta & Della Morte (eds.)
© 2004 Taylor & Francis Group, London, ISBN 90 5809 658 0

Behaviour of small perturbations in 1D mobile-bed models

G. Rosatti, L. Fraccarollo & A. Armanini
CUDAM - Center for Advanced Studies on Hydrological Risk in Mountain Areas Dipartimento di Ingegneria Civile ed Ambientale, Trento

ABSTRACT: The problem of evolution of a single perturbation in a 1D free-surface flow over mobile-bed is studied theoretically. The proposed method, based essentially on the integration of the canonical form of the primitive variable system, has been tested against numerical solutions. Moreover, it has been exploited to gain insight in the mechanism of small perturbation generation.

1 INTRODUCTION

The analysis of the evolution of a small perturbation in a 1D mobile-bed model is a topic that can help to go into several physical, mathematical and numerical aspects. In particular, this analysis allows to substantiate the use of simplifications or manipulations of the mathematical models, in order to make it easier to find out possible solutions. Furthermore, in numerical models it helps to understand which are the most convenient boundary-conditions to be assigned.

The definition of the problem is very simple: what happen in a channel if the surface elevation, for instance, is locally perturbed? Despite its simplicity the solution is not trivial at all. In fact, this question hides many other ones: how many waves will be generated and which are their speeds of propagation? Do the different physical quantities show an in-phase perturbations or not, and which is the ratio among their amplitudes? Which information actually travels along each wave and how it depends on Froude number?

In this paper we propose a general, simplified approach to obtain the number, the speeds, the signs and the integral amplitudes of the perturbations that are generated by a given initial point-perturbation of the physical variables. This method is essentially based on the integration, along approximated linear wave paths, of the *canonical forms* of the system of equations. In such a way a linearized solution of the problem is looked for, which, nonetheless, keeps fully the hyperbolic features of the evolving phenomenon. Compared to the traditional perturbation method, the present scheme is definitely more simple and more evident as far as the physical interpretation concerns.

In section 2 it is presented the outline of the method which leads to a system of equations for the amplitudes of the perturbations. In section 3 the proposed methodology has been applied to a rather complete 1D system of equations that have been obtained applying the conservation of mass and momentum for a two phases fluid. In section 4 analytical results have been compared with the ones obtained by a highly accurate numerical model. In section 5 the analytical result of a classical simplified 1D model has been compared with the corresponding ones coming out from the complete model. Conclusions are presented in section 6.

2 OUTLINE OF THE METHOD

The quasi-linear system of equations of a generic 1D mobile-bed model can be written, in compact form, in the following way:

$$\mathbb{B}(\mathbf{W})\frac{\partial \mathbf{W}}{\partial t} + \mathbb{A}(\mathbf{W})\frac{\partial \mathbf{W}}{\partial x} = \mathbf{S}(\mathbf{W}) \tag{1}$$

where $\mathbf{W}$ is the vector of primitive variables, $\mathbb{B}(\mathbf{W})$, $\mathbb{A}(\mathbf{W})$ are the Jacobian matrixes of the model equations and $\mathbf{S}(\mathbf{W})$ is the source term vector. In order to make the notation easier, from now on the dependence on $\mathbf{W}$ will not be indicated. The system of equations here considered is strictly hyperbolic, therefore it has real and distinct eigenvalues which can be arranged in descending order:

$$\lambda_1 > \lambda_2 > \lambda_3 > ...\lambda_n \tag{2}$$

where the integer n represents the number of equations in the model.

To catch up the goal of this work, it is necessary to make some hypotheses, which help to clarify

and understand the dynamics of the flow after an appearing disturbance. It is assumed that there is a uniform basic flow $W = \underline{W}$. The initial perturbation consists of a *small* (limited in amplitude and extension) perturbation of any of the primitive variables. This initial perturbation provokes n propagating waves which involve all the physical quantities of interest. Moreover we assume that the path of any generated wave in the (x, t) domain is represented by a single straight line.

The method can be summarized in the following steps:

1. analysis of the eigenvalues of the system (1);
2. rewriting of system (1) in *canonical form*;
3. integration of the canonical form equations along the characteristic paths;
4. calculation of the wave amplitudes.

In the following paragraphs the details of these steps are presented.

2.1 *Canonical form of the equations system*

The eigenvalues λ_i of the system are determined by the roots of the characteristic polynomial that can be obtained from the following equation:

$$\left|\mathbb{A} - \lambda\mathbb{B}\right| = 0 \tag{3}$$

where $|\cdot|$ denotes the determinant of a matrix and $\mathbb{A}, \mathbb{B}$ are the matrices of eq. (1). The canonical form (Toro 1999) can be obtained by means of the left eigenvectors $\mathbf{T}^i$ (corresponding to λ_i), that are defined by the following equations:

$$\mathbf{T}^i\mathbb{A} = \lambda_i\mathbf{T}^i\mathbb{B}, \quad i = 1,\ldots,n \tag{4}$$

Multiplying eq. (1) for each eigenvector it is possible to obtain the normal form of the system:

$$\mathbf{T}^i\mathbb{B}\frac{\partial\mathbf{W}}{\partial t} + \mathbf{T}^i\mathbb{A}\frac{\partial\mathbf{W}}{\partial x} = \mathbf{T}^i\mathbf{S}, \quad i = 1,\ldots,n \tag{5}$$

Then, it is possible to manipulate the equations in order to obtain a new form in which the physical meaning becomes more evident. Using eq. (4), the system (5) can be rewritten as:

$$\mathbf{T}^i\mathbb{B}\frac{\partial\mathbf{W}}{\partial t} + \lambda_i\mathbf{T}^i\mathbb{B}\frac{\partial\mathbf{W}}{\partial x} = \mathbf{T}^i\mathbf{S}, \quad i = 1,\ldots,n \tag{6}$$

which can be cast in the following form:

$$\mathbf{T}^i\mathbb{B}\left.\frac{d\mathbf{W}}{dt}\right|_i = \mathbf{T}^i\mathbf{S}, \quad i = 1,\ldots,n \tag{7}$$

where

$$\left.\frac{d\mathbf{W}}{dt}\right|_i = \frac{\partial\mathbf{W}}{\partial t} + \lambda_i\frac{\partial\mathbf{W}}{\partial x}, \quad i = 1,\ldots,n \tag{8}$$

If the terms

$$\mathbf{T}^i\mathbb{B} = \left[(TB)^i_1, (TB)^i_2, \ldots, (TB)^i_n\right] \tag{9}$$

are considered constant, each equation is a weighted sum of rates of change of the primitive variables along different paths in the space-time domain (*characteristic curves*) defined by the equations

$$\frac{dx}{dt} = \lambda_i \tag{10}$$

and this sum balances the source term. Under the previous assumptions, the characteristic curves are families of straights lines along which information travels: given a generic point $P(x, t)$, it is possible to draw the outgoing characteristics along which information regarding the point propagate forward in time and space (*domain of dependence*, Fig. 1). Along each characteristics λ_i, variations of all the primitive variables occur, but their relative magnitude is essentially determined by the weight $(TB)^i_k$. It may comes out that one of them is much larger than the others: in that case the relevant physical quantity is dominant along the i-th characteristic line.

On the other hand, it is possible to draw also the characteristics that reach point $P(x, t)$: variables here depend on the informations travelling along these lines, which fold the *domain of influence* (Fig. 1).

2.2 *The system of equations for the amplitudes*

The system of equations for the amplitude of the perturbations can be obtained integrating equations (7)

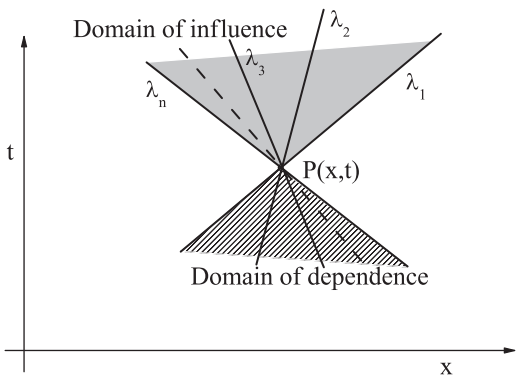


Figure 1. Domain of influence and range of dependence for a generic point $P(x, t)$.

along the characteristic lines. Let's assume, without loosing in generality, that our problem presents three characteristic lines: in a space-time plane, with origin in the place and time where the perturbation is applied, it is possible to draw three straight lines, starting from the origin point and with slope equal to $1/\lambda_i$: these represent the space-time paths of the three waves that the initial perturbation generates (Fig. 2).

If we chose a generic time t_1, the intersections of the line $t = t_1$ with the three characteristic lines give the positions of the waves at that time. Focusing the attention, for example, on the intersection with λ_3, it is possible to integrate along the λ_3 characteristic, the respective equation of system (7) between $t = 0$ and $t = t_1$:

$$\int_0^{t_1} \mathbf{T}^3 \mathbb{B} \left.\frac{d\mathbf{W}}{dt}\right|_3 dt = \int_0^{t_1} \mathbf{T}^3 \mathbf{S} dt \quad \text{along} \frac{dx}{dt} = \lambda_3 \tag{11}$$

Under the assumptions above described, this becomes:

$$(TB)_1^3 \int_{\underline{W}_1+\Delta_1}^{\underline{W}_1+\delta_1} dW_1 + (TB)_2^{\lambda_3} \int_{\underline{W}_2+\Delta_2}^{\underline{W}_2+\delta_2} dW_2 + (TB)_n^3 \int_{\underline{W}_n+\Delta_n}^{\underline{W}_n+\delta_n} dW_n = \mathbf{T}^3 \mathbf{S} \int_0^{t_1} dt \tag{12}$$

where $W_k + \Delta_k$ is the value of the k-th variable in the origin point, i.e. the constant value plus the initial perturbation, and $\underline{W}_k + \delta_k$ is the value of the k-th variable in the point P_3, i.e. the constant value plus the perturbed situation at time t_1. Integration leads to:

$$(TB)_1^3 (\delta_1 - \Delta_1) + (TB)_2^3 (\delta_2 - \Delta_2) + (TB)_3^3 (\delta_3 - \Delta_3) = \mathbf{T}^3 \mathbf{S} \int_0^{t_1} dt \tag{13}$$

Now, it is possible to write two more equations, similar to equation (13) considering the other characteristic lines (belonging to the λ_1, λ_2 families) that arrives in P_3 (Fig. 3):

$$\begin{aligned} (TB)_1^1 \delta_1 + (TB)_2^1 \delta_2 + (TB)_3^1 \delta_3 &= \mathbf{T}^1 \mathbf{S} \int_0^{t_1} dt \\ (TB)_1^2 \delta_1 + (TB)_2^2 \delta_2 + (TB)_3^2 \delta_3 &= \mathbf{T}^2 \mathbf{S} \int_0^{t_1} dt \end{aligned} \tag{14}$$

It is reminded that $\underline{\mathbf{W}}$ is the basic uniform flow.

Equations (13–14) form a linear system that gives the values of the perturbed variables in position the P_3 (Fig. 3). The same procedure can be applied to obtain the values of the wave amplitudes at points P_1 and P_2. If the source term $\mathbf{S}$ in eq. (1) is null or negligible, the system of equations gives a solution that is time-independent.

3 APPLICATION TO A FULLY-COUPLED 1D MOBILE-BED MATHEMATICAL MODEL

The proposed method has been applied to the 1D mobile-bed model described in the following. The model is characterized by a two-phase approach with no slip between the velocities of sediments and water. It is defined by the equations of conservation of liquid mass, solid mass and momentum

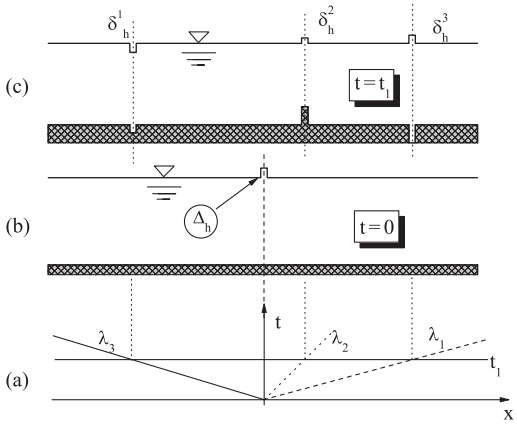


Figure 2. (a) Paths, in the space-time plane, of the waves generated by an initial perturbation of the water level as represented in (b); (c) position, in the physical plane, of the perturbations at time $t = t_1$.

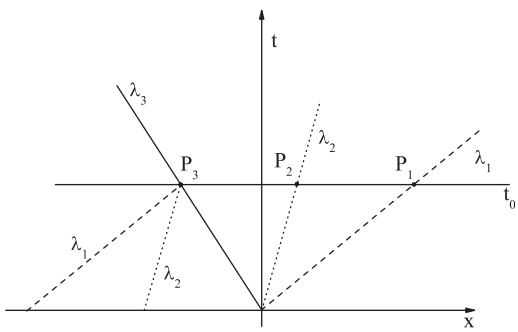


Figure 3. Integration paths, in the space-time plane, used to obtain the amplitude relations valid along λ_3.

(Fraccarollo & Capart, 2002):

$$\begin{aligned}
&\frac{\partial}{\partial t}(h+z_b)+\frac{\partial}{\partial x}(uh)=0\\
&\frac{\partial}{\partial t}(ch+c_b z_b)+\frac{\partial}{\partial x}(cuh)=0\\
&\frac{\partial}{\partial t}[(c\Delta+1)uh]+\frac{\partial}{\partial x}\left[(c\Delta+1)u^2h+\right.\\
&\left.(c\Delta+1)\frac{gh^2}{2}\right]+(c\Delta+1)gh\frac{\partial z_b}{\partial x}=-\frac{\tau}{\rho}
\end{aligned} \tag{15}$$

where h is the water depth, u is the depth-averaged velocity, z_b is the bed surface elevation, c is the depth-average concentration of sediments, c_b is the concentration of sediments in the bed, β is a transport parameter, $\Delta=(\rho_s-\rho)/\rho$ is the relative density of sediments and τ is the bottom stress. The concentration c can be related to u and h by any sediment transport formula. In the following, a simplified power law formula has been adopted:

$$c=\beta c_b u^2/(gh) \tag{16}$$

3.1 *Application of the method in case of plane bed and inviscid fluid*

In order to simplify the calculation, the proposed method has been applied to a specific case of plane bed and inviscid fluid. With these hypotheses, the source term **S** is null and the integration along the characteristics easier. Nevertheless, as shown previously, these assumption are not necessary to obtain the amplitude relations.

In compact form, the Jacobian matrixes of system (15) are:

$$\mathbf{W}=\begin{bmatrix}h\\u\\z_b\end{bmatrix};\mathbf{S}=\begin{bmatrix}0\\0\\0\end{bmatrix} \tag{17}$$

$$\mathbb{B}=\begin{bmatrix}1 & 0 & 1\\ 0 & 2\beta c_b u & c_b\\ u & 3\kappa+h & 0\end{bmatrix} \tag{18}$$

$$\mathbb{A}=\begin{bmatrix}u & h & 0\\ 0 & 3u^2\beta c_b & 0\\ gh+u^2\omega & u(4\kappa+2h\omega) & g(h+\kappa)\end{bmatrix} \tag{19}$$

where $\omega=0.5\ \beta c_b\Delta g+1, \kappa=\beta c_b\Delta u^2$.

The characteristic polynomial (eq. 3) for the present case can be written as:

$$a_0+a_1\lambda+a_2\lambda^2+a_3\lambda^3=0 \tag{20}$$

where the coefficients are functions of the physical variables. Explicit expressions for them can be found in Rosatti & Fraccarollo (2002). It is well known that eq. (20) presents two positive and one negative solutions for each value of the Froude number (Morris & Williams 1996) i.e.:

$$\lambda_1>\lambda_2>0;\quad \lambda_3<0 \tag{21}$$

It is possible to obtain the eigenvalues of the problem as a function of the actual value of λ_i:

$$\begin{aligned}
T_1^i&=-\left(\frac{1}{2}\Omega+1\right)u^2+u\lambda_i-gh\\
T_2^i&=\frac{u(u-\lambda_i)(\Omega u+\lambda_i)+u(gh+\frac{1}{2}\Omega\lambda_i u)}{\lambda_i c_b}\\
T_3^i&=u-\lambda_i
\end{aligned} \tag{22}$$

where $\Omega=\kappa/u^2$.

Inserting eq. (22) in (13–14) one can obtain in explicit form the values of the amplitude as a function of the eigenvalues λ_i and the flow parameters u, h, β, c_b, Δ. Their detailed expression is omitted for shortness.

Actual values of the amplitude of the perturbations can be easily evaluated once the flow parameters have been fixed. Setting $\beta=8.16\times10^{-4}$, $\Delta=1.65$ and $c_b=0.65$, representative values for sand and gravel-bed rivers, the plot of the dimensionless amplitudes as a function of Froude number is the one shown in Figure 4.

It can be noticed that the sum of the dimensionless amplitude of the three water-depth waves (δ_h^i/Δ) is always 1, i.e. is equal to the initial value. As the Froude number change, the distribution of the initial amplitude along the three waves changes: for $Fr\to0$, it is almost equally divided along two waves corresponding to those of the rigid-bed case. For high Froude numbers, the amplitudes along the negative wave λ_3 become negligible while the initial perturbation affects mainly the slower wave λ_2. As far as the bottom perturbation concerns, the sum of the three amplitudes does not give the initial value (i.e. zero) but it shows a maximum for Froude number slightly smaller than 1 (Fig. 5). This means that the initial water depth perturbation causes essentially a deposition wave on the bottom, the amount of which depends on the Froude number. Moreover, the amplitude of the bottom wave, travelling with the faster wave λ_1, change its sign for high Froude number, while in the other two cases the sign remains constant. The maximum deposit travels backward while the maximum scour travels forward with λ_2.

These considerations confirm, for high Froude numbers, the result of de Vries (1995) i.e. that it is possible to associate the hydrodynamic perturbation

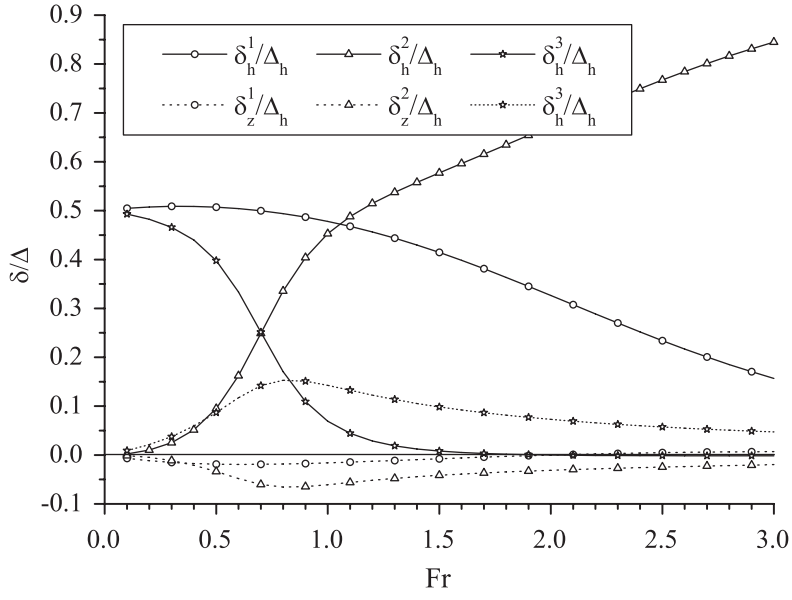


Figure 4. Dimensionless amplitude of water depth h and bottom elevation z versus Froude number of the unperturbed condition along each wave; flow parameters are $\beta = 8.16 \times 10^{-4}$, $\Delta = 1.65$ and $c_b = 0.65$. Apexes refer to the three points P of Figure 3.

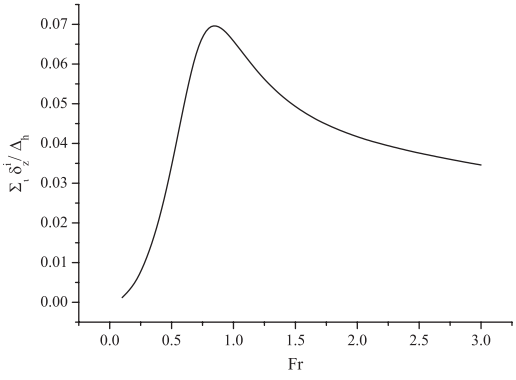


Figure 5. Algebraic sum of bottom dimensionless amplitudes versus Froude number.

to the positive waves λ_1, λ_2 while the bottom variation is essentially associated with the negative wave λ_3. For low Froude numbers, comparison with de Vries's results is not so straightforward because of the assumption of horizontal bed that we have assumed. De Vries obtained this result by means of consideration on the order of magnitude of the terms in the expression for λ_i, but he did not achieve anything about the sign of the perturbations. The proposed approach, instead, extends those results and explains them in term of amplitudes of perturbations.

4 COMPARISON WITH A HIGH RESOLUTION NUMERICAL MODEL

In order to verify the reliability of the proposed method, despite the simplifications, we have compared the theoretical results with the ones obtained with an highly accurate numerical model whose details can be found in Fraccarollo et al. (in prep.). The numerical model is able to solve system (15a–c) without the simplifying hypothesis assumed in the analytical model and therefore we expect that, from an initial perturbation, waves with finite wavelength would take place. Since the analytical model assume that each wave has small amplitude and wavelength, we expect that analytical results may approximate the integral of the amplitude over the wavelength and not the actual maximum amplitude.

The numerical model was applied under the same conditions above described for the theoretical study, i.e. flat, horizontal bed and no bottom stress. The initial perturbation was placed in the origin of the physical plane, regarded only the water depth and spanned over a single computational cell of length Δx. Its non-dimensional amplitude was assigned to be:

$$\frac{\Delta_h}{\underline{h}} = 0.1 \tag{23}$$

In Figures 6 and 7 the results obtained in a subcritical ($Fr = 0.65$) and in a supercritical ($Fr = 1.42$) case

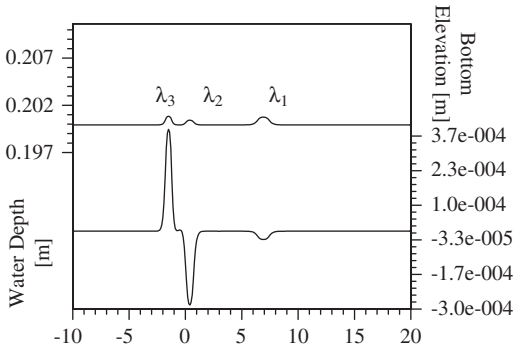


Figure 6. Water depth and bed elevation generated by an initial perturbation of the water depth in the origin; Froude number of the unperturbed condition is 0.65.

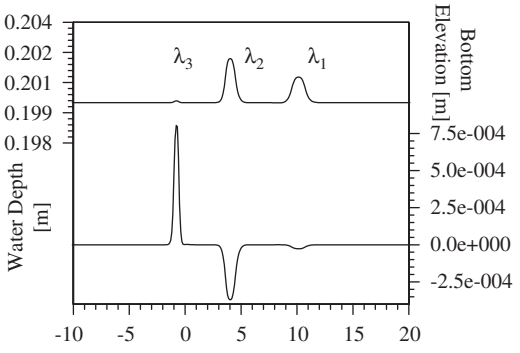


Figure 7. Water depth and bed elevation generated by an initial perturbation of the water depth in the origin. Froude number of the unperturbed flow is 1.42.

respectively are shown. For the case with $Fr = 0.65$, Table 1 shows the comparison between the analytical amplitudes and the integral value of the numerical amplitudes, evaluated by means of:

$$\frac{\delta_h^k}{\Delta_h} = \frac{1}{\Delta_h \Delta x}\int_{L_k}\left(h(x)-\underline{h}\right)dx$$
$$\frac{\delta_z^k}{\Delta_h} = \frac{1}{\Delta_h \Delta x}\int_{L_k}\left(z(x)-\underline{z}\right)dx \qquad (24)$$

where L_k is the wavelength of the k-th perturbation. Analogous result has been obtained for the supercritical case.

Comparison shows a good agreement and this means that, despite the simplifications, the analytical model is able to catch the main features of the complete nonlinear phenomenon. In particular the proposed model is able to give the correct sign of the perturbation amplitudes and gives an useful insight on

Table 1. Analytical and numerical values of the total amplitude in the case of $Fr = 0.64$.

	Analytical	Numerical
δ_h^1	0.502	0.504
δ_h^2	0.197	0.196
δ_h^3	0.299	0.301
δ_z^1	-1.915×10^{-2}	-1.914×10^{-2}
δ_z^2	-0.109	-0.108
δ_z^3	0.127	0.127

the relative importance of the primitive variables along each perturbations in different flow situations.

5 APPLICATION TO A 1D SIMPLIFIED MODEL

The proposed method has been applied to the classical 1D model that can be obtained adding the Exner equation to the equations for the water in order to verify to what extent this simplified model is able to show the features of a more complete one.

In compact form, the system of equation can be written as follows:

$$\frac{\partial}{\partial t}\mathbf{W} + \mathbb{A}\frac{\partial}{\partial x}\mathbf{W} = \mathbf{S} \qquad (25)$$

where

$$\mathbf{W} = \begin{bmatrix} h \\ u \\ z_b \end{bmatrix}; \mathbf{S} = \begin{bmatrix} 0 \\ -\frac{\tau}{\rho} \\ 0 \end{bmatrix}; \mathbb{A} = \begin{bmatrix} u & h & 0 \\ g & u & g \\ uq_h & hq_u & 0 \end{bmatrix} \qquad (26)$$

and

$$q_u = \frac{1}{c_b h}\frac{\partial q_s}{\partial u}$$
$$q_h = \frac{1}{c_b u}\frac{\partial q_s}{\partial h} \qquad (27)$$
$$q_s \propto u^3$$

The normal form of the equations, in the case of horizontal flat bed, can be written as (Armanini 1999):

$$\frac{\lambda_i}{\lambda_i - u}\frac{dh}{dt} + \frac{\lambda_i}{g}\frac{du}{dt} + \frac{dz}{dt} = 0 \qquad (28)$$

and the equations for the amplitudes can be obtained straightforwardly following the proposed method. In particular, the equations for the λ_1 wave amplitudes

becomes:

$$\begin{cases} \dfrac{\delta_h}{\Delta_h} = \Upsilon_1 \dfrac{(\lambda_3 - u)(\lambda_2 - u)}{u} \\ \dfrac{\delta_U}{\Delta_h} = g\Upsilon_1 \\ \dfrac{\delta_z}{\Delta_h} = -\dfrac{\lambda_3\lambda_2}{u}\Upsilon_1 \end{cases} \tag{29}$$

where:

$$\Upsilon_1 = \frac{\lambda_1}{(\lambda_2 - \lambda_1)(-\lambda_1 + \lambda_3)} \tag{30}$$

It is easy to verify that, for $Fr < 2$,

$$\frac{\delta_h}{\Delta_h} > 0;\ \frac{\delta_z}{\Delta_h} > 0 \tag{31}$$

i.e. the bottom perturbation changes the sign if compared to what obtained by the more complete model (see in Fig. 4).

This result informs that the use of simplified models sometimes may lead not only to approximated results in wave speed and amplitude but also, in the worst case, to a thorough different description of the physical solution.

6 CONCLUSION

In this paper an analytical approach able to describe the evolution of an initial point-perturbation in a 1D, mobile-bed free-surface flow, is presented. Results of this approach has been validated against numerical simulations obtained with an high resolution model: analytical amplitudes represent very well the integral amplitudes of the real waves. Furthermore, with this methodology it has been possible to gain a deep insight in the mechanisms that leads a single perturbation to generate several others with different characteristics. It must be stressed that the practical examples presented in this paper cannot be generalized because the equations for the amplitudes depend on the type of initial perturbation as well as the bottom stress and the bottom slope. Nevertheless, the proposed procedure is absolutely general an can be applied to more general cases. In particular this approach will be used, in a forthcoming paper, to impose proper boundary condition in numerical models.

REFERENCES

Armanini, A. 1999. *Principi di idraulica fluviale*. Cosenza: Editoriale Bios.

Fraccarollo, L & Capart, H. 2002. Riemann wave description of erosional dam-break flows, *Journal of Fluid Mechanics*, 461, 183–228.

Fraccarollo, L., Rosatti, G. & Giuliani, M. 2004. A computational method for floods in erosional torrents with applicability from clear water to debris flows. *in prep.*

Morris, P.H. & Williams, D.J. 1996. Relative celerities of mobile bed flows with finite solids concentration, J. of Hydr. Engrg., ASCE, Vol. 122, 6.

Rosatti, G. & Fraccarollo, L. 2002. Metodo di calcolo di moto vario planimetrico con erosione intensa della superficie di fondo. In *28° convegno di Idraulica e Costruzioni Idrauliche, Potenza, 16–19 settembre 2002*. Cosenza: Editoriale Bios.

Toro, E.F. 1999. Riemann Solvers and Numerical Methods for Fluid Dynamics. Springer.

de Vries, M. 1965. Considerations about non-steady bed-load transport in open channels. *Proc. XI IAHR Congr., Vol.3, pap. 3.8*, Leningrad: USSR.

This page intentionally left blank

River Flow 2004 – Greco, Carravetta & Della Morte (eds.)
© 2004 Taylor & Francis Group, London, ISBN 90 5809 658 0

A new method for the assessment of river network fractal dimensions: introduction, computation and comparison

S.G. De Bartolo
Dipartimento di Difesa del Suolo, Università della Calabria, Rende (CS), Italy

R. Gaudio
CNR-IRPI – Sezione di Cosenza, Rende (CS), Italy

L. Primavera
Dipartimento di Fisica, Università della Calabria, Rende (CS), Italy

S. Gabriele
CNR-IRPI – Sezione di Cosenza, Rende (CS), Italy

M. Veltri
Dipartimento di Difesa del Suolo, Università della Calabria, Rende (CS), Italy

ABSTRACT: A new method for the assessment of the fractal dimensions of river networks at given hierarchical orders is presented. It is based on the analogy between river networks and DLA processes. Starting from the outlet section of each drainage area, two tangents to the river network tips can be drawn, forming an internal angle. A supplementary angle is then defined, from which the fractal dimension of a river network is easily computed. An analogous procedure can be followed considering the tangents to the drainage divide. The 'supplementary angle method' (SAM) has been tested on the Corace river network and basin (Calabria, Italy). An empirical relation linking the fractal dimensions computed on river networks and on basin areas has been obtained. A comparison of results from the SAM and the standard box-counting method has been performed, showing an increasing agreement for higher hierarchical orders.

1 INTRODUCTION

The multifractal theory was introduced by Mandelbrot (1972, 1974) and developed by Frisch & Parisi (1985) for the study of turbulent dissipative phenomena and by Halsey et al. (1986) for the analysis of strange attractors in the theory of dynamic systems. In the last few years, several applications have been performed in different fields, including Diffusion Limited Aggregation (DLA) processes (Witten & Sander 1981; Vicsek et al. 1990).

In Hydrology, particular interest was devoted to the study of river basins and networks. In addition to the description of contributing drainage areas of given hierarchical order, slopes, dissipation energy, channel initiation function and width function (Ijjasz-Vasquez et al. 1992; Rinaldo et al. 1992; Rinaldo et al. 1993; Rigon et al. 1993; Rodriguez-Iturbe & Rinaldo 1997), recent results show the possibility of obtaining the multifractal spectrum, $f(\alpha)$, also for negative moment orders (De Bartolo et al. 2004), and a fractal instantaneous unit hydrograph (De Bartolo et al. 2003b).

Due to the fact that a multifractal is a union of monofractal sets, the idea has arisen of decomposing the multifractal spectrum into its constituent monofractal parts (De Bartolo et al. 1995; De Bartolo et al. 2003a). Therefore, the present work deals with the study of sub-basins and relative network portions of a natural basin.

The analysis of the sub-sets has been performed through a new method, derived from the analogy between river networks and DLA processes. The proposed method, applied graphically, has given the fractal dimensions of the Hortonian sub-structures at different hierarchical orders.

Results have been compared to the fractal dimensions obtained with the standard box-counting algorithm, showing an increasing agreement for higher hierarchical orders.

2 ANALOGY BETWEEN RIVER NETWORKS AND DLA PROCESSES

The quantitative description of river networks is due to Horton (1932, 1945), who proposed the well-known hierarchical stream classification criterion, then developed and modified by Strahler (1952, 1964).

In particular, Horton investigated the angular properties of river networks. He proposed a junction angle model (Fig. 1), in which the angle T, measured in the horizontal plane, can be assessed as follows:

$$T = \arccos\left(S_M / S_T\right) \tag{1}$$

S_M and S_T being the gradients (slope tangents) of the main and tributary streams, respectively.

Lubowe (1964) verified that Equation (1) does not give good predictions for streams of the same order, ω. According to Horton (1945) and Lubowe (1964), Howard (1971) noticed that the Hortonian model is not able to predict the junction between two streams of equal declivity, giving Equation (1) zero as result. Therefore, he introduced a new junction angle model (Fig. 2), in which the junction angle, T, is equal to the sum of the entrance angles, E_1 and E_2:

$$E_1 = \arccos\left(S_3 / S_1\right) \tag{2}$$

$$E_2 = \arccos\left(S_3 / S_2\right) \tag{3}$$

S_1, S_2 and S_3 being the gradients of the smaller and larger tributaries and the receiving stream, respectively.

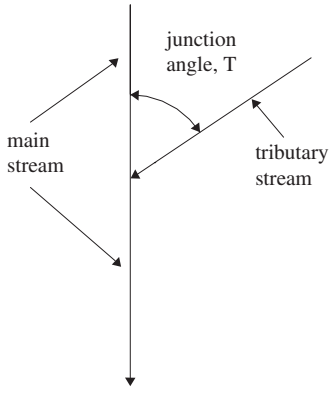


Figure 1. Horton's junction angle model.

A strong analogy subsists between the macroscopic river networks and the microscopic clusters studied in DLA processes. In fact, similar procedures can be used to reconstruct the multifractal spectra in both fields of application. In particular, the angular properties of an aggregate are investigated through the geometry of the cone-angle model (Turkevich & Sher 1985) (Fig. 3), where θ is the cone angle.

In a DLA cluster containing n particles, the maximal probability, $p_{\max}$, that an incoming random walker from infinity can hit a particle is linked to the minimum Lipschitz-Hölder exponent, $\alpha_{\min}$, of the $f(\alpha)$ spectrum. Following the Turkevich & Scher (1985) conjecture, the fractal dimension, D, can be computed as follows:

$$D = 1 + \alpha_{\min} \tag{4}$$

The authors assumed that the outermost tip of the cluster is associated with $p_{\max}$. Therefore, Equation (4) can be rewritten:

$$D = 1 + \alpha_{tip} \tag{5}$$

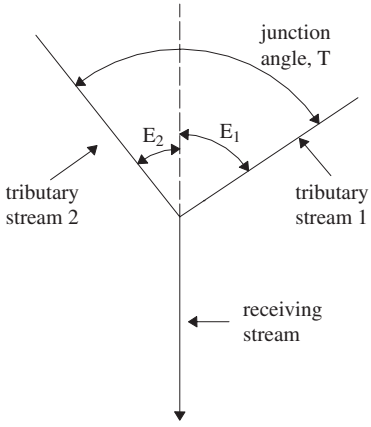


Figure 2. Howard's junction angle model.

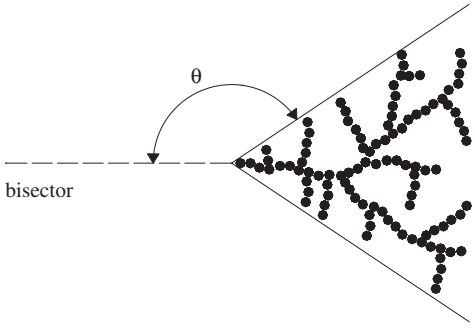


Figure 3. Schematic of the cone-angle model.

where, considering the cone-angle, θ (Fig. 3), the following relation holds (Turkevich & Scher 1985):

$$\alpha_{tip} = \frac{\pi}{2\theta} \tag{6}$$

3 THE SUPPLEMENTARY ANGLE METHOD

A strong analogy appears with the river networks and drainage areas at given hierarchical orders, ω. With reference to Figure 4, let us consider a generic sub-basin of order ω and area A_ω. Starting from the outlet, it is possible to draw the tangents, t_1 and t_2, to the river network tips. Thus the internal angle, $\beta_{\omega,n}$ is identified. Drawing the bisector, the angle $\beta_{\omega,n}/2$ and the supplementary angle $\theta_{\omega,n}$ are obtained. The last one is analogous to the cone angle, θ. Therefore, Equations (6) and (5) become respectively:

$$\alpha_{\omega,n} = \frac{\pi}{2\theta_{\omega,n}} \tag{7}$$

$$D_{\omega,n} = 1 + \alpha_{\omega,n} \tag{8}$$

for $\omega = 1, 2, \ldots, \Omega$, where Ω is the basin order. Equation (7) expresses a Lipschitz-Hölder exponent at the order ω, and Equation (8) the relative fractal dimension.

Due to the fact that it is simpler to identify the drainage divide than the river network, the same graphic method can be adopted for the drainage area (Fig. 5), obtaining the internal angle, $\theta_{\omega,A}$, and the following exponent and fractal dimension:

$$\alpha_{\omega,A} = \frac{\pi}{2\theta_{\omega,A}} \tag{9}$$

$$D_{\omega,A} = 1 + \alpha_{\omega,A} \tag{10}$$

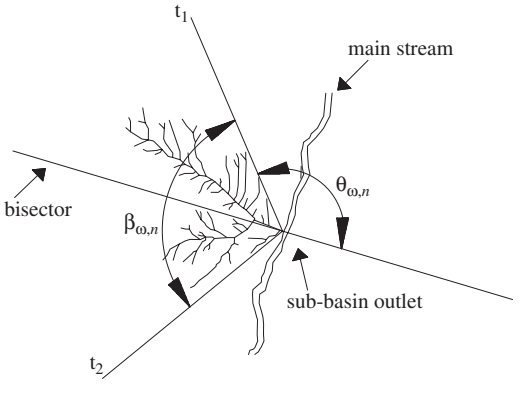


Figure 4. Schematic of the SAM for the river network.

4 APPLICATION

The SAM has been applied to the Corace river basin (Calabria, Southern Italy). The topographic area is $A_\Omega = 294\ \text{km}^2$ and the shape is elongated.

The upper reaches of the basin, with elevations ranging from 700 to 1000 m a.s.l., are made up of conglomerate rocks. The gravels are constituted of metamorphic rock fragments and are highly permeable and resistant to erosion processes. In the lower reaches the source rock lithology changes to silt clays interbedded with silty and sandy marine deposits. The Corace river-mouth is constituted of sediments varying in the texture from granules to cobbles.

The annual average rainfall depth is about 1500 mm.

In Table 1 the number of investigated areas and relative river networks at different hierarchical orders is presented. The basin order is $\Omega = 6$.

Figures 6–7 show the Corace river basin and the sub-areas and networks for $\omega = 2$ to 5, extracted from 1:25,000 scale topographic maps.

The SAM has been applied to all the river networks and drainage areas for $\omega = 2$ to 6, by computing the supplementary angles $\theta_{\omega,n}$ and $\theta_{\omega,A}$.

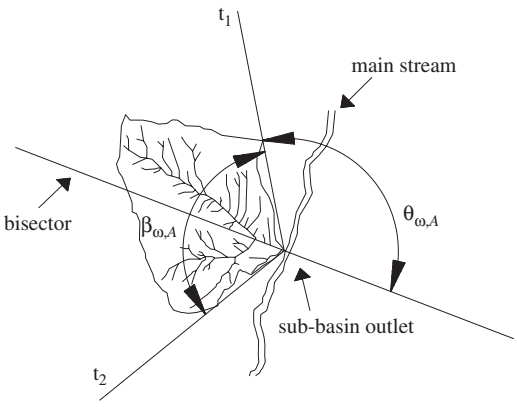


Figure 5. Schematic of the SAM for the drainage area.

Table 1. Number of sub-structures of the Corace river basin at different hierarchical orders.

Order, ω	Number of sub-structures, N_ω
1	3277
2	804
3	178
4	39
5	7
6	1

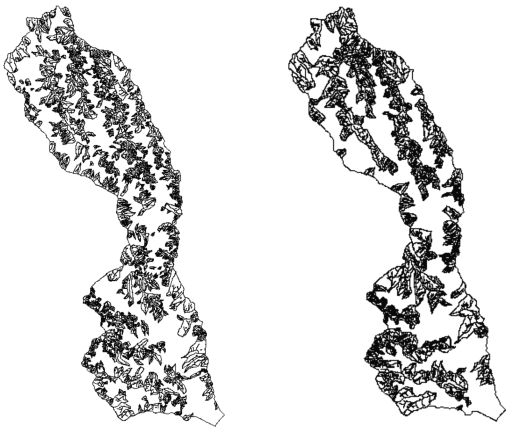


Figure 6. Sub-structures of the Corace river basin for $\omega = 2$ and $\omega = 3$.



Figure 7. Sub-structures of the Corace river basin for $\omega = 4$ and $\omega = 5$.

Results are presented in Table 2. As expected, $\theta_{\omega,n} > \theta_{\omega,A}$. Figures 8–9 show the supplementary angles $\theta_{\omega,n}$ and $\theta_{\omega,A}$, respectively, versus the second order drainage areas, $A_\omega = 2$. Analogous graphs have been obtained for $\omega = 3$ to 6.

For each supplementary angle, the corresponding α_ω and D_ω have been evaluated from Equations (7) to (10). The fractal dimensions for $\omega = 2$ are shown in Figures 10–11, with the power law curves and the regression coefficient, R^2, very close to 1. Analogous graphs have been obtained for $\omega = 3$ to 6. In the case of drainage divide presenting concavities, the SAM may produce unreliable results, as in the case of the fractal dimension greater than 2 in Figure 11.

Table 2. Supplementary angles of the Corace river basin sub-structures at different hierarchical orders, ω.

Order, ω	$\theta_{\omega,n}$ (rad)			$\theta_{\omega,A}$ (rad)		
	min	average	max	min	average	max
2	1.986	2.843	3.123	1.453	2.475	2.953
3	1.787	2.575	2.955	1.666	2.309	2.784
4	1.937	2.474	2.852	1.734	2.279	2.709
5	2.176	2.299	2.538	1.893	2.136	2.436
6	2.443	2.443	2.443	2.339	2.339	2.339

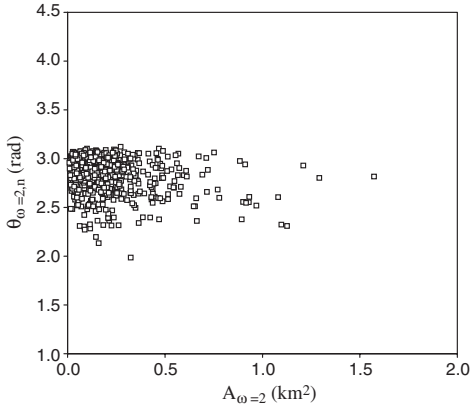


Figure 8. Supplementary angles of the river networks versus the drainage areas for $\omega = 2$ (Corace river basin).

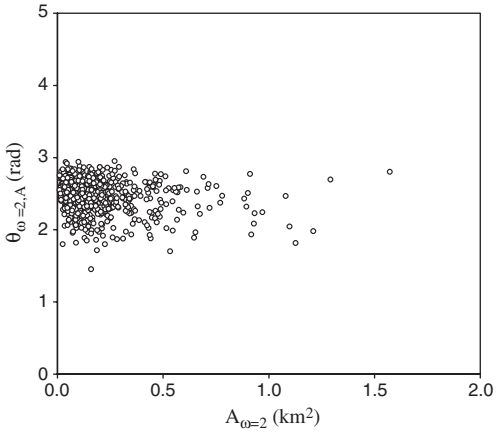


Figure 9. Supplementary angles of the sub-areas versus the drainage areas for $\omega = 2$ (Corace river basin).

The ratio between the fractal dimensions has been plotted versus the ratio of the supplementary angles. Figures 12–13 show the results for $\omega = 2$ and for $\omega = 2$ to 5, respectively, with the power law curves and the regression coefficient, R^2, very close to 1.

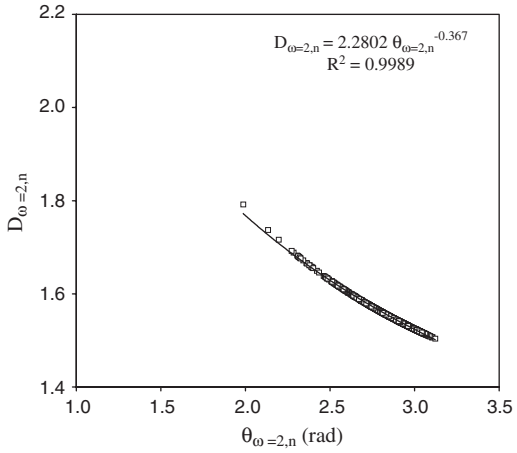


Figure 10. Fractal dimensions versus supplementary angles for the second order river networks (Corace river basin).

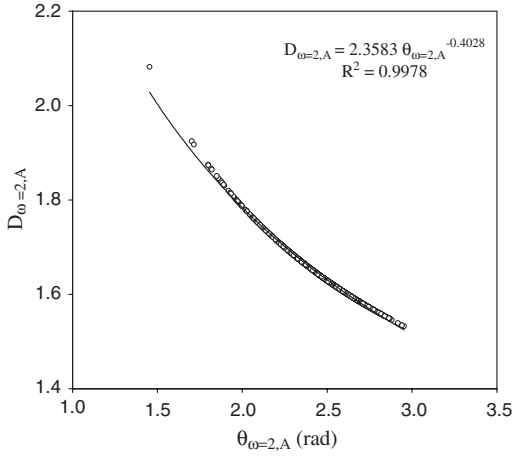


Figure 11. Fractal dimensions versus supplementary angles for the second order drainage areas (Corace river basin).

The following relation has been obtained, valid for hierarchical orders from 2 to 5 in the Corace river basin:

$$\frac{D_{\omega,n}}{D_{\omega,A}} = a\left(\frac{\theta_{\omega,n}}{\theta_{\omega,A}}\right)^{-b} \tag{11}$$

where $a = 1.002$ and $b = 0.397$, with regression coefficient $R^2 = 0.99$.

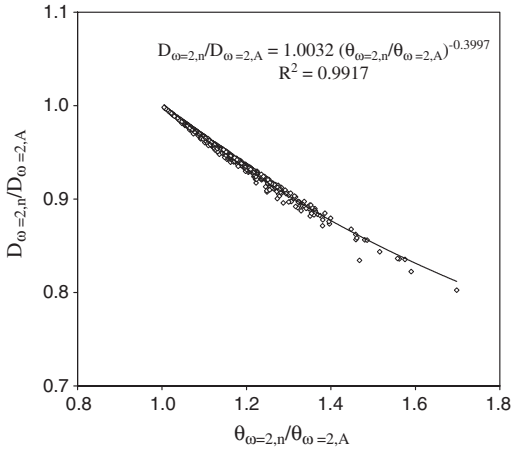


Figure 12. Ratio of fractal dimensions versus ratio of supplementary angles for $\omega = 2$ (Corace river basin).

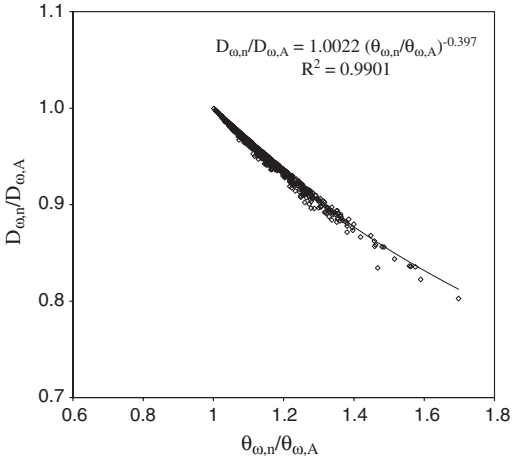


Figure 13. Ratio of fractal dimensions versus ratio of supplementary angles for $\omega = 2$ to 5 (Corace river basin).

5 DISCUSSION

The SAM permits an easy assessment of fractal dimensions of river basin sub-structures (networks and drainage areas) at given hierarchical orders.

As a comparison, the fractal dimensions have been also computed through a standard box-counting algorithm (see, for example, Feder 1988), as follows:

$$D_{\omega}^{bc} = \lim_{\delta \to 0} \frac{\log N(\delta)}{\log (1/\delta)} \tag{12}$$

where δ is the cell side size and $N(\delta)$ the number of covering cells at resolution δ.

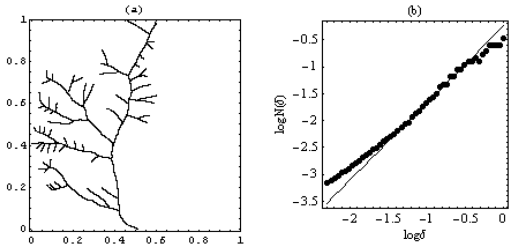


Figure 14. (a) Digitized portion of the Corace river network and (b) scaling curve obtained with the standard box-counting method.

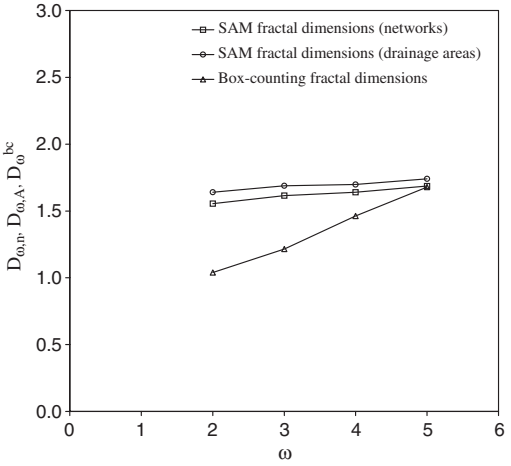


Figure 15. Comparison between the average values of the fractal dimensions for each order, ω, obtained with the SAM and the standard box-counting method (Corace river network).

Figure 14 shows a digitized portion of the Corace river network and the relative scaling curve, from which the fractal dimension has been computed between the cut-off lengths, δ_{min} and δ_{max}, by maximizing the correlation coefficient of the least squares linear regression (De Bartolo et al. 2000).

The average values for each order, ω, of the fractal dimensions obtained with the SAM and the standard box-counting method are compared in Table 3 and shown in Figure 15. Table 3 presents also the average relative errors, computed as follows:

$$\Delta D_{\omega, A-n} = \frac{1}{N_\omega} \sum_{i=1}^{N_\omega} \frac{(D_{\omega,A})_i - (D_{\omega,n})_i}{(D_{\omega,n})_i} \quad (13)$$

$$\Delta D_{\omega, bc-n} = \frac{1}{N_\omega} \sum_{i=1}^{N_\omega} \frac{(D_\omega^{bc})_i - (D_{\omega,n})_i}{(D_{\omega,n})_i} \quad (14)$$

Table 3. Average values of the fractal dimensions and relative errors at different hierarchical orders (Corace river basin).

Order, ω	$D_{\omega,n}$	$D_{\omega,A}$	D_ω^{bc}	$\Delta D_{\omega,A-n}$ (%)	$\Delta D_{\omega,bc-n}$ (%)
2	1.555	1.641	1.040	5.5	−33.1
3	1.616	1.688	1.216	4.5	−24.7
4	1.641	1.697	1.462	3.4	−10.9
5	1.686	1.741	1.679	3.3	−0.4

where N_ω is the number of sub-structures analyzed at the order ω (Table 1).

Results show that the SAM applied to drainage areas overestimates $D_{\omega,n}$, with average relative errors not greater than 5.5 % and decreasing for higher orders. Inversely, the standard box-counting method underestimates $D_{\omega,n}$, with average relative errors that are quite high at the lower orders, but very low at the fifth order.

Being generally easier to identify the drainage divide than the river network tips, the assessment of the river network fractal dimension might be performed just applying the SAM to the drainage area.

6 CONCLUSIONS

The supplementary angle method (SAM) has been presented. The SAM is based on the analogy between river network and DLA processes, in particular on the Turkevich & Scher conjecture, expressed by Equation (4).

The SAM permits an easy computation of fractal dimensions of river basin sub-structures (networks and drainage areas) at given hierarchical orders.

The first application to the Corace river network and basin (Calabria, Italy), extracted from 1:25,000 scale maps, has produced an empirical relation linking the fractal dimensions computed on river networks and on basin areas. Finally, it has been shown that the SAM and the standard box-counting method lead to closer results as the hierarchical order of sub-structures increases.

ACKNOWLEDGEMENTS

The authors are grateful to Eng. Mario Vaccaro for the elaborations of some material presented here, Eng. Tommaso Caloiero for help in preparing some figures and Mr. Manlio Renzelli for assistance in bibliographic research.

REFERENCES

De Bartolo, S.G., Gabriele, S. & Gaudio, R. 2000. Multifractal behaviour of river networks. *Hydrology and Earth System Sciences* 4 (1): 105–112.

De Bartolo, S.G., Maiolo, M., Veltri, M. & Veltri, P. 1995. Sulla caratterizzazione multifrattale delle reti fluviali (in Italian). *Idrotecnica* 6: 329–340.

De Bartolo, S.G., Veltri, M. & Primavera, L. 2003a. Indagine con tecniche a taglia fissa sulla struttura multifrattale delle reti fluviali (in Italian). *L'Acqua* 6: 9–15.

De Bartolo, S.G., Ambrosio, L., Primavera, L. & Veltri, M. 2003b. Descrittori frattali e caratteri morfometrici nella risposta idrologica (in Italian). Atti del Convegno *La difesa idraulica del territorio 2003*, Trieste, Italy, September 10th–12th, in press.

De Bartolo, S.G., Gaudio, R. & Gabriele, S. 2004. Multifractal analysis of river networks: sand-box approach. *Water Resources Research* 40 (2): W02201, doi:10.1029/2003WR00 2760.

Feder, J. 1988. *Fractals*. New York: Plenum.

Frisch, U. & Parisi, G. 1985. On the singularity structure of fully developed turbulence. Appendix to U. Frisch, Fully developed turbulence and intermittency, in *Turbulence and Predictability in Geophysical Fluid Dynamics and Climate Dynamics, Proc. Int. Sch. Phys.*, "Enrico Fermi" Course LXXXVIII: 84–88. Amsterdam: North Holland.

Halsey, T.C., Jensen, M.H., Kadanoff, L.P., Procaccia, I. & Shraiman, B.I. 1986. Fractal measures and their singularities: the characterization of strange sets. *Physical Review A* 33 (2): 1141–1151.

Horton, R.E. 1932. Drainage basin characteristics. *Eos Transactions of the AGU* 13: 350–361.

Horton, R.E. 1945. Erosional development of streams and their drainage basins; hydrophysical approach to quantitative geomorphology. *Geological Society of American Bulletin* 56: 275–370.

Howard, A.D. 1971. Optimal angles of stream junction: geometric, stability to capture and minimum power criteria. *Water Resources Research* 7: 863–873.

Ijjasz-Vasquez, E.J., Rodriguez-Iturbe, I. & Bras, R.L. 1990. On the Multifractal Characterization of River Basins. *Geomorphology* 5: 297–310.

Lubowe, J.K. 1964. Stream junction angles in dendritic drainage pattern. *American Journal of Science* 262: 325–339.

Mandelbrot, B.B. 1972. Possible refinement of the lognormal hypothesis concerning the distribution of energy dissipation in intermittent turbulence. In M. Rosenblatt & C. Van Atta (eds), *Statistical Models and Turbulence, Lecture Notes in Physics* 12: 333–351. New York: Springer.

Mandelbrot, B.B. 1974. Intermittent turbulence in self-similar cascades: divergence of high moments and dimension of the carrier. *Journal of Fluid Mechanics* 62: 331–358.

Rigon, R., Rinaldo, A., Rodriguez-Iturbe, I., Bras, R.L. & Ijjasz-Vasquez, E.J. 1993. Optimal channel networks: a framework for the study of river basin morphology. *Water Resources Research* 29 (6): 1635–1646.

Rinaldo, A., Rodriguez-Iturbe, I., Rigon, R., Bras, R.L., Ijjasz-Vasquez, E.J. & Marani, A. 1992. Minimum energy and fractal structures of drainage networks. *Water Resources Research* 28 (9): 2183–2195.

Rinaldo, A., Rodriguez-Iturbe, I., Rigon, R., Ijjasz-Vasquez, E.J. & Bras, R.L. 1993. Self-organized fractal river networks. *Physical Review Letters* 70 (6): 822–825.

Rodriguez-Iturbe, I. & Rinaldo, A. 1997. *Fractal river basins. Change and self-organization*. Cambridge: Cambridge University Press.

Strahler, A.N. 1952. Hypsometric (area-altitude) analysis of erosional topography. *Geological Society of American Bulletin* 63: 1117–1142.

Strahler, A.N. 1964. Quantitative geomorphology of drainage basins and channel networks. In V.T. Chow, *Handbook of Applied Hydrology*, Sec. 4. New York: McGraw-Hill.

Turkevich, L.A. & Scher, H. 1985. Occupancy-probability scaling in diffusion-limited aggregation. *Physical Review Letters* 55 (9): 1026–1031.

Vicsek, T., Family, F. & Meakin, P. 1990. Multifractal geometry of diffusion-limited aggregates. *Europhysical Letter* 12 (3): 217–222.

Witten, T.A. & Sander, L.M. 1981. Diffusion limited aggregation: a kinetic critical phenomena. *Physical Review Letters* 47: 1400–1403.

This page intentionally left blank

River Flow 2004 – Greco, Carravetta & Della Morte (eds.)
© 2004 Taylor & Francis Group, London, ISBN 90 5809 658 0

2D sediment transport study on Elbe River – Czech Republic

P. Jirinec & J. Spatka
DHI Hydroinform a.s., Prague, Czech Republic

ABSTRACT: The method of two-dimensional mathematical modeling was used for study "Improvement of Navigation Conditions in Elbe River Reach Strekov – CR/FRG border". Hydraulic characteristics, which are important for navigation safety, were determined by the model for situation after construction of two new designed barrages. Sediment transport and morphology changes were simulated in the whole 40 km long Elbe reach under flood condition. Simulations of unsteady flow were applied for period of 6.5 days under real catastrophic flood situation from August 2002 and also for two theoretical floods Q_{20} and Q_5.

Geometry of Elbe river channel, embankment and floodplains were changed based on proposed plan on construction of Male Brezno and Prostredni Zleb barrages including proposed river bed dredging. Mathematical model has defined reaches of difficult navigation conditions and has found reaches where ships could be shifted from their course by transversal flow velocities. The model has also described future sediment transport regime of lower Elbe reach down Strekov after construction of designed barrages and has demarcated areas for necessary fairway dredging.

1 INTRODUCTION

For a long time the navigational conditions on the lower reaches of the Czech section of the Elbe have needed improving. The main obstacle to navigation is the corridor's relatively large longitudinal slope, which means that in a normal hydrological year the water depth is insufficient for navigation for most days of the year. Studies carried out before have shown that a sufficiently raised depth in a section roughly 40 km long from Usti nad Labem (km 70.0) to the state border with Germany (km 110.0) cannot be effectively ensured merely through regulatory measures, or by releases from various parts of the watershed. The only viable solution is to construct two navigation steps in combination with regulatory measures (dredging the navigation deep cut in the river bottom or by concentration structures).

For the proposed conceptual framework of making it navigable it is necessary to verify to what extent the water level will be affected by constructing the barrages and whether the required navigational depths will be attained during low discharges. Likewise it is necessary to map in detail the vector values of speeds in the navigation channel and deal with the flow's effects on vessels (to ensure shipping safety). Finally it is necessary to evaluate the future regime of sediment transport after constructing both planned barrages and above all after realising the essential corridor dredging, which will have a significant impact on the Elbe's sediment regime. Studies carried out previously and newly taken samples of materials from the river bottom including grain-size analyses have demonstrated that the finer fraction material gathers about ten centimetres below the bed pavement. When dredging the bed pavement will be completely removed in many sections and the newly exposed finer bottom material will subsequently be open to the current's effects. The finer the material the more spontaneous the sediment flow that can be expected. The "navigability" conceptual framework assumes dredging will be carried out in three sections with a total length of 25 km.

From the standpoint of the current's hydraulic characteristics the deciding factors for initiating sediment movement are water depth and the energy curve's slope. Therefore during flooding there is a far more significant sediment transport as the water depth is at a maximum. As the flood wave passes by the energy curve's slope changes (as a rule it is at its greatest during the wave's onslaught), therefore it is necessary to study the sediment movement and morphological changes to the channel during unsteady flow. The sediment regime during three flood waves was simulated by a mathematical model:

- the actual flood wave from August 2002 – as the greatest trustworthily recorded flood in this section of the Elbe
- a theoretical flood wave with a peak flow of Q_{20}
- a theoretical flood wave with a peak flow of Q_5.

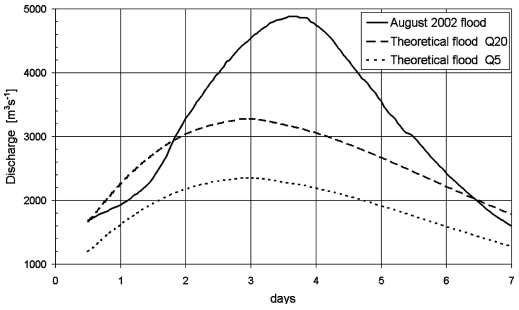


Figure 1. Hydrograms in Usti nad Labem gauging station – upper boundary.

All of the calculations were made for an identical time period of flooding lasting 6.5 days (156 hours). The hydrograms of the actual flood wave from August 2002 in the Czech Hydrometeorological Institute (CHMI) gauging station in Usti nad Labem and the theoretical flood waves Q_5 and Q_{20} are depicted in figure 1.

2 METHODS AND MATHEMATICAL MODEL

For simulation of the sediment transport the 2D mathematical model MIKE 21C (including the module "ST" – Sediment transport) was used, developed by the firm DHI Water & Environment, Hørsholm (Denmark). The entire length of the interest area was described by computational grid of 2670 × 125 points for time consuming calculation of the unsteady flow. The computational grid is denser around structures (bridges, the proposed barrages) at 6–10 points per meter (both lengthwise and crosswise), whilst in several places with a relatively flat flood plain the distance between points is 12 to 20 m. For the study's needs – predicting sediment movement and morphological changes – the level of the interest area's schematisation is sufficient. Houses and blocks of houses were modelled with the aid of a considerably raised terrain (insurmountable barriers); fences and other obstacles of a similar character were simulated by lines of increased roughness. The hydraulic roughness and local increases in flow resistance are assigned to every point of the computational grid.

The model enables either a mere monitoring of the channel proclivity to scouring, or forming sediment deposits in the given hydrological regime or a full-scale prediction of the morphological changes in real time, during which the bottom's relief is modified by the calculated changes (+loads, −scours). In all the calculations made in this study the perpetual updating of the bottom's relief was considered.

The creation of local depositions and scouring is, to a great degree, influenced by the current's transversal circulation. The MIKE 21C model computes the transversal circulation's intensity in the relationship:

$$i_S = u\,\frac{h}{R_S} \tag{1}$$

where i_S = intensity of flow's transversal circulation; u = mean vertical velocity; h = water depth; R_S = streamline curvature radius.

The mathematical model enables a choice of equations for calculating the flow of the bottom sediments from the following authors:

- Meyer-Peter & Müller
- van Rijn
- Engelund & Hansen
- Engelund & Fredsøe

In our case we always used the Meyer-Peter & Müller equation:

$$q_b = 8\sqrt{(s-1)gd^3}\,\left(\Theta' - \Theta_c\right)^{\frac{3}{2}} \tag{2}$$

where q_b = actual sediment transport rate; s = relative density of bed sediment; d = grain diameter; Θ', Θ_c = Shields parameters, as it best fits the conditions in the lower reaches of Czech rivers.

The grain diameter of the bed material was set on the basis of the results of a detailed geological study of the Elbe's bottom. Together 19 samples of bottom material were taken from pre-selected profiles in the section Strekov (km 70.0)–Dolni Zleb (km 105.0). Each sample represented a column of bottom material with a diameter of 355 mm, taken to a depth of 2 m. The cores were documented and subjected to a detailed granulometric analysis, such that each sample had two grain size analyses made – the first characterising the overlying bed pavement, the second being made on the material lying underneath this bed pavement (figure 2). The grain-size analyses were carried out on a standard set of sieves and by measuring the characteristic dimensions of the grains for the screenings. The results are granularity curves, establishing the effective grain size d_e and the characteristic grain size d_{90} (IGHG. 2003).

From the established values of the sampled materials' effective grain size d_e a control file "bed granularity map" for calculation of morphological changes was created. Sections, which won't be affected by dredging the Elbe's bottom, are characterised in this granularity map by the pertinent d_e values of the bed pavement. The sections to be dredged were projected in detail onto a plan of the river channel (their longitudinal and latitudinal extent) and they are characterised by the

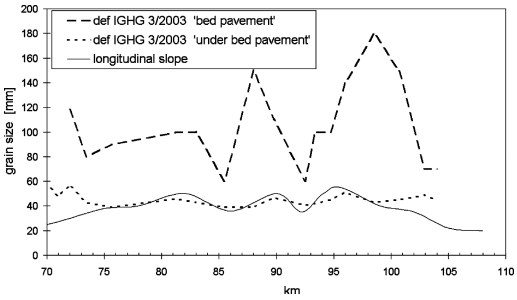


Figure 2. Longitudinal profile of bed grain size.

effective grain size values of the material taken from below the bed pavement.

When modelling sediment transport (especially if there is continuous sediment transport in the monitored section) the simulation result can be influenced by the choice of boundary conditions – sediment flow in the upper profiles or the model's lower boundary conditions. Therefore in our study we compared the influence of two limiting values of boundary conditions on the sediment flow:

– "zero sediment flow"
– "balanced sediment flow" (the model itself generates such a supply/withdrawal of bottom sediments for the input/output so that there are no morphological changes in the cross section of the boundary condition).

for developing morphological changes in the broader vicinity of the boundary conditions.

3 RESULTS

3.1 *Effect of boundary condition*

The effect of the differentially assigned upper boundary condition (sediment flow) on the sediment regime was studied during the onslaught of the August 2002 floods – i.e. during a flood with the highest peak flow from all modelled flood waves.

With sediment flow set at zero local morphological changes were found (erosion in the bed line areas, a deepened navigation deep cut, on the contrary in the centre of the navigation deep cut souring deposits were formed) having an effect up to 400 m away from the upper boundary condition. This was followed by a 1.5 km long section of the Elbe that had no morphological changes whatsoever. When comparing the state of the balanced sediment flow the character of the morphological changes was more or less in agreement – however deposition continued up to a distance of 550 m from the upper boundary conditions.

From comparing results it is possible to state that the value of the assigned sediment flow on the input to the model (from zero up to a balanced saturation of the flow with sediment) has no effect on the sediment regime over the entire 40 km section.

3.2 *The August 2002 flood*

The proposed barrages Male Brezno (km 81.7) and Prostredni Zleb (km 99.0) divide the 40 km interest area (km 70.0 up to km 110.0) into three river reaches. In the lower, roughly 11 km long reach from Prostredni Zleb barrage up to Hrensko there has hardly been any sediment transport nor, therefore, morphological changes in the channel (valid for all 3 simulated flood waves), in spite of this dredging has been proposed from Prostrední Zleb up to km 105.4.

Likewise above Prostredni Zleb to beyond Boletice (km 90.5) no sediment transport was calculated (undredged section). From here against the flow direction up to Male Brezno barrage there is a section of numerous local scourings (as a rule they occur by concave banks behind the elbow's peak) and local depositions (the majority concentrated along convex banks). The most intensive morphological changes were simulated in the section Techlovice – Jakuby (km 85.0–87.0), where the scours were up to 1 m deep on the overall width of the navigation course and the loads regularly attained heights of 0.7–1 m, exceptionally as much as 2.0 m (figure 3). These remarkable morphological changes are linked to the corridor sections proposed for dredging and likewise are connected with high values of vertical velocities and also with the transverse velocity values (figure 4), which were ascertained in previous research in this locality.

Above Male Brezno up to Strekov there are two sections where multiple morphological changes have been calculated. As a rule these scours and loads have a small extent – at most 100 m long and a typical width of probably a third of the navigation course. It is a matter of the section around the municipality Male Brezno (about 1.7 km long), where scours attain a depth of 1.0 m and the loads a height up to 1.5 m. In the second about 3.7 km long reach the scours generally attain a depth of 0.3–0.7 m and the loads a height of 0.3–0.7 m. In the section above the central dock in Usti nad Labem no morphological changes have been ascertained. The deposition formed at 70.0 km cannot be taken to be indicative – it occurs in the direct vicinity of the model's upper boundary conditions.

When assessing the corridor's morphological changes induced by the flood wave from August 2002 the morphological changes that arose during the drop in the flood wave were specially processed. The aim of this was to ascertain whether during the floods the same morphological processes occur in all localities (varying only in intensity) or whether in some localities with the increase of the flood there

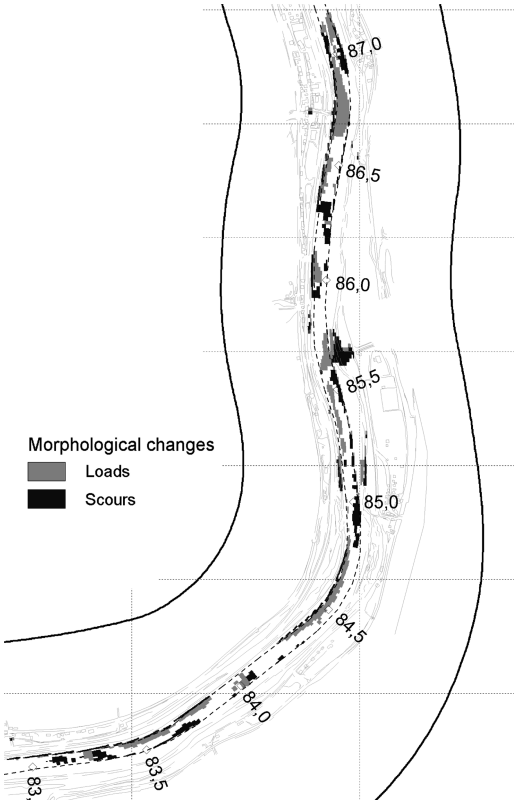


Figure 3. Simulated morphological changes in river section Techlovice – Jakuby; the August 2002 flood.

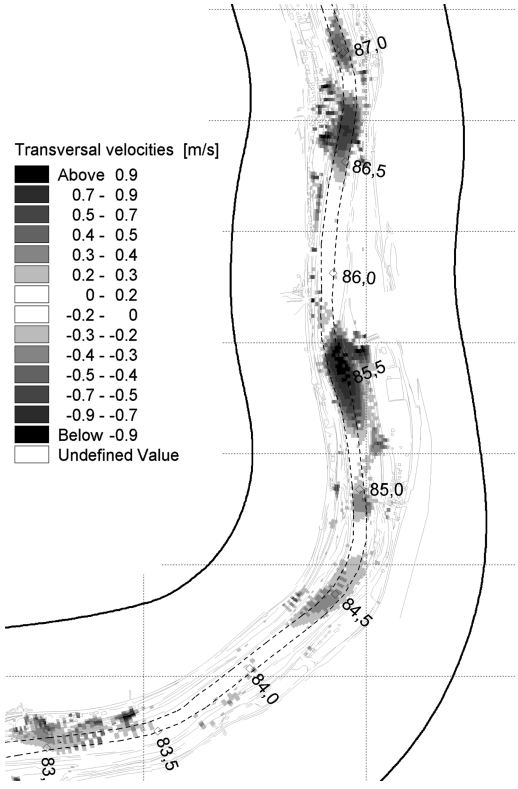


Figure 4. Simulated transversal velocities in river section Techlovice – Jakuby; the August 2002 flood.

was erosion followed by deposition as the floodwater receded. By comparing the detailed "maps of level changes in the river bed" (morphological changes as a consequence of the entire flood wave's passage on one hand and the morphological changes due merely to the drop in the flood wave on the other), it was ascertained that the character of the morphological processes during the flood in the section Strekov–Hrensko is unchanged and is bound to the hydraulic characteristics of the current flow and the river bed material in the given location. As the flood wave recedes the process continues with a considerably lower intensity.

3.3 *Theoretical floods*

The morphological changes to the channel, as a result of simulating the theoretical flood wave Q_{20}, had a similar character to the morphological changes invoked by the August 2002 flood. The occurrence and extent of sections of the morphological changes were practically the same. However the morphological changes took place with a lesser intensity – the scours reached about 80% of the depth of the scours during the flood from August 2002, the loads only 70% of the height of those from the flood of August 2002.

With the passage of the Q_5 flood morphological changes were only ascertained in two relatively short sections. The most significant occurred again in the section Techlovice – Jakuby, where scours 0.70 m deep were formed and the deposits generally attained a height of 0.3–0.6 m, exceptionally up to 1.5 m. The character of these morphological changes was also analogous to the passage of the flood wave of August 2002. In the section above Male Brezno barrage up to Strekov we only calculated morphological changes around the Male Brezno municipality where the scours reached a depth of 0.5 m and deposits a height of 0.6 m.

4 CONCLUSIONS

In the lower reach of the Elbe in Bohemia, Strekov – to the German border, sediment transport and morphological development in the river channel with the advent of a flood wave was modelled on a two

dimensional mathematical model. The calculation was made for the actual flood wave of August 2002 and for two theoretical waves at Q_{20} and Q_5. All of the simulated waves had the same time period of 6.5 days (156 hours).

The morphological changes were simulated for the proposed state of the river channel i.e. after construction of two low navigation steps including proposed dredging of the water course. The MIKE 21C model was used to simulate the flow. The granularity of the river bed material was described in detail by a grain-size map (including removing the river pavement in the dredged areas of the channel), which stemmed from sampling the bed sediments and their granulometric analyses. The study results are a detailed mapping of the channel's morphological changes (mainly in the fairway), which can be expected with the advent of a flood.

The most important conclusions from the study's results are:

– With the advent of Q_5, Q_{20} floods or that of August 2002 an associated movement of bed sediment in the monitored section of the Elbe didn't arise. Only local morphological changes were ascertained these being connected to areas with lower grain-size (as a consequence of removing the bed pavement during dredging).
– As the floodwaters rose and receded in the monitored section of the Elbe there were corresponding morphological processes i.e. some sections (zones) of the corridor are permanently eroded, in others there are permanent deposits. The natural helical flow in the elbows has a conspicuous effect upon these processes. In several relatively short sections of the channel (hundreds of metres up to individual kilometres long) scours were formed with the subsequent nearby deposition. The bed sediment was never carried away for a longer distance.
– The simulated flow of sediments for the model's inputs (from nought up to a flow evenly saturated with sediment) has no effect on the regime for the entire 40 km long section.
– The largest morphological changes were obtained in an approximately 2 km long section below the proposed Male Brezno barrage, where the scours are from 0.2 to 0.7 m (Q_5) or 1 m deep during the August 2002 flooding in the places where the proposed dredging will remove the bed pavement. In this section deposits are also formed (often across the entire width of the fairway) generally from 0.3–0.6 m high (Q_5), or as high as 1 m after the August 2002 floods; however extremes attained heights of over 2 m.
– After constructing the both barrages and dredging the corridor it is necessary to count on removing local deposits from the fairway after the advent of a flood greater than Q_5.

REFERENCES

DHI Hydroinform. 2002. Flood Flow Model of Elbe River. DHI Hydroinform, Prague, December 2002

DHI Hydroinform. 2003. Improvement of Navigation Conditions in Elbe River Reach Strekov – CR/FRG border. DHI Hydroinform, Prague, June 2003

Hydroprojekt CZ. 1998. Design and Complex Assessment of Improvement of Navigation Conditions in Elbe River from Strekov to CR/FRG border. Chapter 3. Morphological Development of Regulated Channel. Hydroprojekt CZ, VRV, VUV T.G.M., March 1998

Hydroprojekt CZ. 1999. Improvement of Navigation Conditions in Elbe River from Strekov to CR/FRG border – Design of 1999 year. Hydroprojekt CZ, Prague, June 1999

IGHG. 2003. Improvement of Navigation Conditions in Elbe River from Strekov to CR/FRG border. Sample Collection from the River Bed in the Fairway. Civil Engineering Geology – IGHG, March 2003

This page intentionally left blank

River Flow 2004 – Greco, Carravetta & Della Morte (eds.)
© 2004 Taylor & Francis Group, London, ISBN 90 5809 658 0

Simulation and prediction of river morphologic changes using RubarBE

K. El Kadi Abderrezzak & A. Paquier
Hydrology and Hydraulics Research Unit, Cemagref, Lyon, France

ABSTRACT: RubarBE is a one-dimensional model for routing water and sediment transport through fixed or movable bed channels. The code simulates and predicts changes in bed composition, channel profile and cross-sectional geometry. This paper provides a general description of the concepts, approaches and hypothesis used in this model. A series of numerical simulations of sediment transport is described in this paper, with the objective of testing the performance and the potential application of RubarBE. The results of the simulations are analysed and discussed. Cross-comparison of different parameters of the model (deposition and scour rate, sediment transport, bed and water profiles …) allows some validation of the system of equations and hypothesis of our modelling system and provides some keys and ideas for further development of the code.

1 INTRODUCTION

Sediment transport and river morphology studies have gained increasing importance in recent years due to environmental concerns and the need to develop engineering and management strategies for sustainable use of water resources and associated infrastructures (Yang 2000). Evaluating the transport, erosion and deposition of sediments is a key element for describing and understanding the behaviour of rivers. Given that, considerable research effort has been put into the simulation of sediment transport and morphology change in rivers. A lot of computer programs have been developed in the last decades. These models provide numerical solutions for complicated situations that include movable bed and sediment transport. Most of the codes that were developed in the past decades, like HEC6 (Thomas & Prashum 1977), IALLUVIAL (Karim & Kennedy 1982) and SEDICOUP (Holly & Rahuel 1990), were built on a one-dimensional approach.

RubarBE described here is a one-dimensional flow and sediment transport model that has been developed by Cemagref in order to solve as simply as possible the requirements of engineers about river problems.

This paper is organised as follows. First, a general description of the concepts and approaches used in RubarBE is provided. Then, several applications of the model are presented to illustrate its capabilities and range of applications. First, the model is tested on problems with theoretical solutions and on laboratory experiments, and then applied to field problems. The results of the numerical simulations are analysed and discussed.

2 DESCRIPTION OF RUBARBE

One-dimensional sediment transport models tend to be easier to parameterise and require fewer assumptions about sediment transport processes than two- and three-dimensional models (Candfield et al. 2002). The Hydrology and Hydraulics Research Unit of Cemagref has developed a 1-D model, RubarBE, for predicting variation of longitudinal bed profile along rivers and changes in the cross-sectional geometry. This computer model has two components: a component to simulate the flow and a component to characterise the changes in river morphology due to erosion or deposition of sediment.

Classical one-dimensional models that represent sediments only by a mean diameter D_{50} clearly do not fully describe the processes that occur in many channels such as armouring. Therefore, RubarBE represents sediments by a mean diameter D_{50} and a complementary parameter, the standard deviation σ. The standard deviation is assessed as the square root of the ratio between D_{84} and D_{16}($\sqrt{D_{84}/D_{16}}$). It was selected as it appears convenient to describe grain size distribution in a river for which sediments are homogeneous (Shih & Komar 1990).

RubarBE includes features such as:

- Computing unsteady flow in open channels with both fixed and movable bed and dealing with sub critical and super critical flow regimes.
- Taking in account the space lag effects by introducing a specific equation.
- Introducing various empirical relationships for calculating the sediment transport capacity in order

to adapt the modelling to the characteristics of the application.
- Incorporating empirical relations to describe the mixtures of sediments that occur during the various calculation steps.
- Computing the distribution of boundary shear stress in a cross-section by using the Merged Perpendicular Method (Khodashenas 1998, Khodashenas & Paquier 1999).
- Computing the distribution of boundary critical shear stress in a cross-section by a relation from (Ikeda 1982).
- Simulating both the changes of riverbed composition and of cross-sectional geometry using the previous components of the code.

Data requirements for this model are modest, involving only a few parameters. Thus, the model is relatively easy to calibrate and to implement.

2.1 *Mathematical basic model*

RubarBE model relies on:
De Saint Venant equations for water.

Continuity equation for sediments written as follows:

$$(1-p)\frac{\partial A_s}{\partial t}+\frac{\partial Q_s}{\partial x}=q_s \qquad (1)$$

where A_s is bed-material area (m^2), Q_s is sediment discharge (m^3/s), q_s is lateral sediment flow per unit of length (m^2/s) and p porosity.

These equations are completed by a **sediment transport capacity formula**; for instance, the (Meyer-Peter & Müller 1948) formula for bedload has been used for the applications here below:

$$C_S=\frac{8La\sqrt{g}}{(\rho_s-\rho)\sqrt{\rho}}\left(\rho JR-\theta_C D_{50}(\rho_s-\rho)\right)^{3/2} \qquad (2)$$

where C_s is sediment transport capacity (m^3/s), θ_c is dimensionless critical stress, D_{50} is median diameter of sediment (m), J is friction slope, L_a is the active width (m) i.e. the width in which sediment transport is effective, ρ_s is density of sediment (kg/m^3), ρ is density of water (kg/m^3).

Finally, a **space lag equation** can be added to introduce a difference between the sediment transport capacity and the actual transport rate that may differ if geometry is not uniform. In RubarBE, the actual sediment transport rate Q_s is linked to the sediment transport capacity C_s through the following relation:

$$\frac{\partial Q_s}{\partial x}=\frac{C_s-Q_s}{D_{char}} \qquad (3)$$

where D_{char} is the lag distance (m).

De Saint Venant equations are solved by a second-order Godunov-type explicit scheme (Paquier 1995). If the parameters in the sediment transport function for a cross-section can be assumed to remain constant during a time step, we can suppose that there is a little variation of the cross-sectional geometry (Yang & Simoes 1998). Thereby, sediment routing (equation 1) can be uncoupled from the water surface profile computations. In practice, this condition can be met by using a small enough time step.

Sediment routing is accomplished by a similar finite difference method. Changes in bottom level are performed at every time step. Solving the equation (1) means estimating at every time step, the input and output of sediments for one cell and spreading the erosion or deposition volume across the cell. Values of the cross-sectional flow area A and flow discharge Q are computed at the middle of a cell between two cross-sections. Thus, it is simpler to compute Q_s also in this middle and to identify it with respectively input and output of sediments if the sediment cell is shifted by half a space step (Balayn 2001).

2.2 *Sediment modelling system*

Inside one cell, a sedimentary compartment corresponds to a set of sediments that have a coherent behaviour. We distinguish four compartments:

- A compartment M_{am} of input sediments and a compartment M_{av} of output sediments.
- A compartment A of the active layer: it contains all the sediments that have moved inside one cell during one time step. Sediment particles are continuously exchanged between flow and the active layer.
- A compartment B of one or several substrate layers: it reflects historical deposition of sediments on the riverbed or undisturbed subsurface.

Sediment particles of each compartment are characterised by the mass M, the mean diameter D and the standard deviation σ. Thus, in a cell, the sediment transfers are schematised as in Figure 1 (Balayn 2001).

When sediment particles pass across a cell, they either reach the downstream of the cell, or settle on the active layer. Entrainment of sediment particles from the active layer and its exchanging with flow causes particles travelling from upstream to be mixed with those from the active layer.

τ_{fm} is the shear stress below which transported sediment particles begin to deposit. τ_{mm} is the shear stress above which sediment particles begin to move.

The mass of the active layer depends on the sediment discharge, the sediment velocities and the dimension of the cell. The model assumes that this mass is defined by $Cs*\Delta x/U$, where Cs is the sediment transport capacity, Δx is the space step and U the mean water velocity.

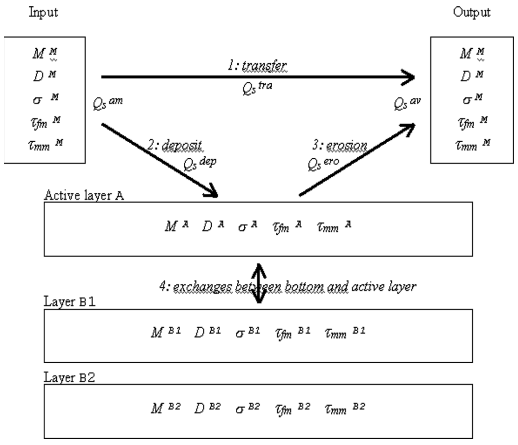


Figure 1. Representation of the sharing of sediments inside one cell (Balayn 2001).

The characteristics of the sediments resulting from the mixing or the sharing of two compartments are defined in the model by empirical relations (Balayn 2001).

2.3 *Computation of cross-section deformation*

RubarBE computes the deformation of cross-sections is computed with the assumption that scour and deposition are directly related to shear stress. The distribution of boundary shear stress around the wetted perimeter of an open channel is governed by cross-sectional geometry, roughness distribution and the existence of secondary flows. Precise computation of shear stress distribution is extremely difficult in one-dimensional models. Thus, empirical methods constitute a good alternative.

RubarBE can calculate the boundary shear distribution τ_j in a cross-section in two ways: either from the uniform equation using water volumetric density ρ, gravity acceleration g, hydraulic radius R and energy slope J ($\tau_j = \rho g R J$, R is computed on the base of the total area and perimeter of the flow) or from the Merged Perpendicular Method. The first method assumes that the boundary shear stress is constant around the wetted perimeter. The second one is a geometrical method that assumes that the energy gradient is the same in all the sub areas. More precisely, it shares the wetted area in small sub areas using the lines perpendicular to the bottom following a complex procedure described in (Khodashenas 1998, Khodashenas & Paquier 1999).

RubarBE can calculate the boundary critical shear distribution τ_{ci} in a cross-section by a relation from (Ikeda 1982):

$$\tau_{cj} = K\tau_{cj}^{*} \tag{4}$$

$$K = \frac{-\alpha Tan^2\Phi Cos\beta_j + \left(Tan^2\Phi Cos^2\beta_j + \alpha^2 Tan^2\Phi Sin^2\beta_j - Sin^2\beta_j\right)^{0.5}}{(1-\alpha Tan\Phi)Tan\Phi} \tag{5}$$

where τ_{cj} critical shear stress in point j of the cross-section with slope β_j, τ_{cj}^{*} critical shear stress in point j for horizontal bottom ($\beta_j = 0°$) (which may vary from one point to an other one, considering, for instance, the riverbed material), β_j local side slope of cross-section in point j, $\alpha = F_L/F_D$, F_L and F_D are respectively dimensionless lift and drag forces, ϕ angle of internal friction of sediment. For the tests here below, the following value is selected $\alpha = 0.85$; τ_{cj}^{*} is calculated by the Shields curve.

The mass of sediment eroded or deposited in one cross-section obtained by the computation is distributed along the section. RubarBE incorporates various empirical relationships between deformation and shear stress. In the case of erosion, the deformation ΔZ_j of an erodible point j of one cross-section is assumed to be proportional to $(\tau_j - \tau_{cj})^{1.5}$. In the case of sedimentation, deposited sediment in one cross-section can be distributed in three ways:

- The cross-section is adjusted in horizontal layers.
- The entire wetted cross-section is moved uniformly up.
- The deformation ΔZ_j of a "deposit" point j is assumed to be proportional to $(1/\tau_j)$.

3 APPLICATION CASES AND RESULTS

3.1 *Theoretical cases*

3.1.1 *Knickpoint migration*

Knickpoint are points of sudden change or inflection in the longitudinal profile of a stream. In general knickpoint may migrate upstream along the channel and have undesirable effects, such as causing banks collapse and undermining bridge piers. Thus, knickpoint development and propagation is a very interesting phenomenon to study.

The simulated channel has a rectangular section, 300 m long × 10 m wide by 4 m deep. The knickpoint is represented by a backward-facing step in the bed with a slope of 0.01 m/m. The upstream and downstream reaches have a slope of 0.001 m/m. The bed material and sediment feed are composed of the same coarse sand and channel width is constant. Table 1 shows the main characteristics of the simulation.

The flow discharge is maintained constant. The sediment feed rate Q_s is specified as the sediment transport capacity of the upstream and downstream reaches. On the downstream side, it is assumed that the flow acted like uniform outflow.

The porosity p of the bed material is assumed to equal to 40%, the sediment density ρ_s to equal

Table 1. Characteristics of the simulation.

Water discharge Q (m^3/s)	Manning coefficient K ($m^{1/3}/s$)	Sediment Diameter D_{50} (mm)	Standard deviation σ	Sediment feed rate Q_s (kg/s)
20	30	1	2.3	17.6

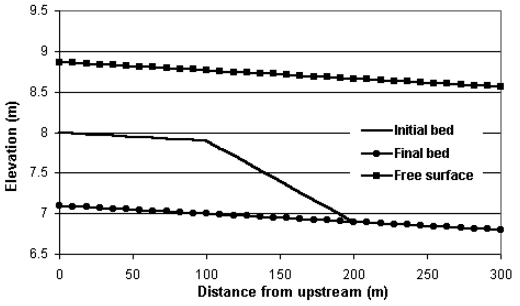


Figure 2. Initial bed, computed equilibrium bed and water surface.

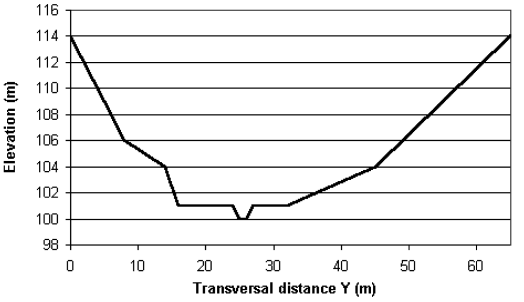


Figure 3. Channel cross-section.

Table 2. Characteristics of the simulation.

Water discharge Q (m^3/s)	Manning coefficient K ($m^{1/3}/s$)	Sediment Diameter D_{50} (mm)	Standard deviation σ	Sediment feed rate Q_s (kg/s)
300	45	1	2.3	29

to 2600 kg/m^3 and the angle of internal friction of sediment φ to equal to 35°.

The central riverbed will suffer from degradation. Theoretically, in dynamic equilibrium, the slopes of the three parts of the channel are expected to equal to 0.001 m/m.

The simulation is accomplished with a uniformly spaced mesh, using cross-sections spaced 10 m apart. The lag distance D_{char} is assumed to equal to 1 m. The initial condition for sediment transport is $Q_s = 17.6$ kg/s. The distribution of the boundary shear stress is calculated by $\tau = \rho g R J$. The dimensionless shear tress θ_c is assumed to equal to 0.047.

Figure 2 shows the initial bed with the equilibrium bed and the water surface profile. The channel is in dynamic equilibrium 280 hours after the start of the simulation. RubarBE was able to predict well the scour depths and the final equilibrium slope (0.001 m/m). There is an overall close agreement between the theoretical solution (a constant riverbed slope of 0.001 m/m) and the result of the simulation.

3.1.2 *Irregular straight open channel*

Usually, natural channels are characterised by an irregular cross-section. An irregular straight open channel of uniform cross section (Fig. 3) is selected to validate the performance of the code. The simulated channel is 1000 m long and the channel bed slope is 0.0001 m/m.

The bed material and sediment feed are composed of the same coarse sand. Table 2 shows the main characteristics of the simulation.

The flow discharge is maintained constant. The sediment feed rate Q_s corresponds to the sediment transport capacity of the simulated channel. The downstream water level is fixed at a constant value of 108.066 m.

The porosity p of the bed material is assumed to equal to 40%, the sediment density ρ_s to equal to 2600 kg/m^3 and the angle of internal friction of sediment φ to equal to 35°.

For this application, a constant space step Δx of 100 m is used. The lag distance D_{char} is assumed to equal to 50 m. The initial condition for sediment transport is $Q_s = 14.5$ kg/s. The distribution of the boundary shear stress is by the Merged Perpendicular Method. The dimensionless shear tress θ_c is assumed to equal to 0.047. The deformation ΔZ_j of a "deposit" point j is assumed to be proportional to $(1/\tau_j)$.

Figure 4 shows the initial bed as well as the channel bed profiles at different times. The channel is in dynamic equilibrium 200 days after the start of the simulation. RubarBE is able to predict both the deposition heights and the advance of the deposition front. However, the numerical results show an "inflection" in the longitudinal profile located at $x = 910.9$ m. This slight change in the bed profile could be due to the influence of the downstream boundary condition and the distribution of sheer stress at $x = 910.9$ m. The channel bed slope upstream from the "inflection point" is about 0.000175 m/m.

Figure 5 shows the evolution of the cross-section at $x = 1000$ m. In a concave angle of a cross-section, computed shear stress by the Merged Perpendicular Method is lower than in a convex angle. Thus high deposition is observed in the concave angles of the channel.

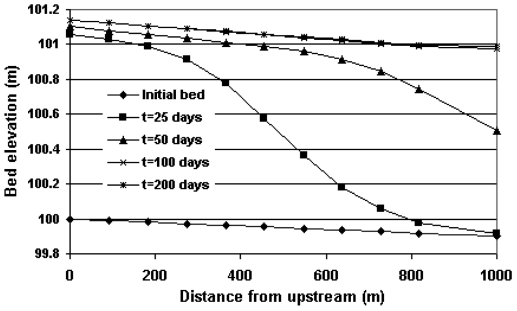


Figure 4. Initial bed and computed channel bed profiles at different times.

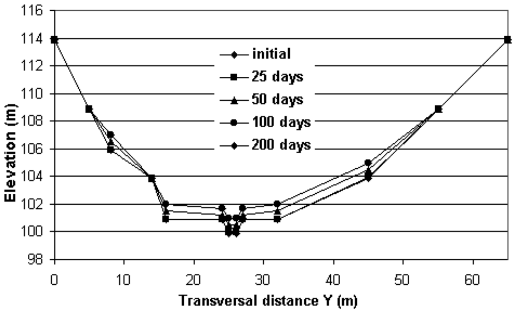


Figure 5. Cross-section deformation: $x = 1000$ m.

The evolution of the riverbed profile and the cross-sectional geometry is affected by the methods used to compute the boundary shear stress. A numerical simulation is performed with the assumptions that the shear stress distribution is calculated by $\tau = \rho gRJ$ and the boundary critical shear distribution computed from the Shields curve (the (Ikeda 1982) relation is not used).

SIM-1 refers to the simulation with the Merged Perpendicular Method and (Ikeda 1982) relation; SIM-2 refers to the simulation with $\tau = \rho gRJ$ and *critical* shear distribution from the Shields curve. Figure 6 shows the dynamic equilibrium beds resulting from the simulation SIM-1 and SIM-2. SIM-2 shows less deposition in the channel bed; the difference between SIM-1 and SIM-2 is about 0.15 m. The equilibrium bed profile computed by SIM-2 is not affected by the boundary condition: a constant slope of 0.000175 m/m is obtained.

3.2 *Laboratory experiment*

While theoretical cases deal with long-term behaviour, the selected test case provides testing of very unsteady flow during a short period.

This test case concerns an experimental small-scale laboratory dam-break waves over movable beds. The experiment was performed by (Spinewine & Zech

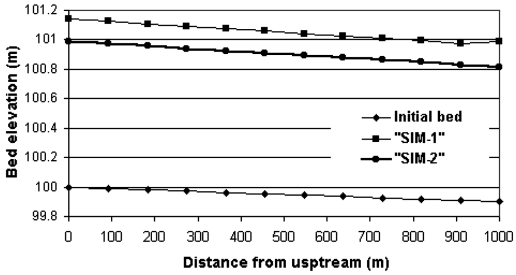


Figure 6. Initial bed, computed equilibrium bed.

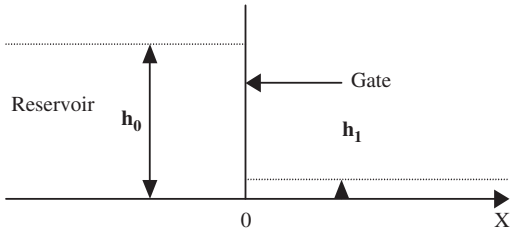


Figure 7. Idealized dam-break problem, h_0 and h_1 are the initial depths upstream and downstream of the dam before failure.

2002) in the framework of the EC-funded IMPACT project at the Department of Civil and Environmental Engineering, Université Catholique de Louvain, Belgium. The objective is to investigate the geomorphic impacts induced by very rapid and transient floods such as those resulting from dam-breaks.

A horizontal flume of rectangular cross-sectional geometry is used. The flume has the following dimensions: length = 2.5 m, width = 0.10 m and sidewall height = 0.35 m. The reservoir is assumed to be long and has the following dimensions: length = 10 m, width = 0.10 m and sidewall height = 0.35 m. The origin of the horizontal axis is located at the gate position. The initial water depths for this case are $h_0 = 0.10$ m if $x < 0$ and $h_1 = 0$ m if $x \geq 0$, where x is the distance along the flume (Fig. 7).

Particles composing the bed are uniform in size: $D_{50} = 3.5$ mm and $\sigma = 1$. The porosity p of the bed material is assumed to 36%, the sediment density ρ_s to 1540 kg/m^3 and the angle of internal friction of sediment φ to 25°.

The Strickler coefficient K was derived from the particle diameter through the classical Meyer-Peter and Müller formula: $K = (21.1/D^{1/6}) = 54$ (m$^{1/3}$/s).

Tests consisted in the sudden opening of a vertical gate that separated the initial water and sediments levels upstream and downstream of the gate. Due to highly unsteady nature of dam break flood propagation; the flume and the reservoir were described through a dense grid of cross-sections. Two constant space steps are

used: $\Delta x = 5$ cm and $\Delta x = 20$ cm. A smaller space step allows obtaining the arrival of the flood wave in a more accurate way. A larger space step allows describing the transition between super and sub critical flow (hydraulic jump) more conveniently.

The initial condition for sediment transport is $Q_s = 0$ kg/s. On the upstream side ($x = -10$ m), a constant depth of water $h = 0.10$ m is imposed. On the downstream side ($x = 2.5$ m), it is assumed that the flow acted like critical outflow. The upstream sediment condition is $Q_s = 0$ kg/s. The time step is variable, but it is chosen so that the maximum Courant number of every cell does not exceed a limited value imposed by the model. The simulations were run for two values of maximum Courant numbers (noted *CFL*): 0.5 and 0.1. The total time of the simulation is 2 second.

For this test case, the distribution of the boundary shear stress is calculated by $\tau = \rho g R J$; the dimensionless shear tress θ_c is calculated by the Shields curve.

For all the runs, the results show that in the near field, rapid and intense erosion accompanies the development of the dam-break wave. In the far field, the solid transport remains intense but the dynamic role of the sediments decreases (Figs 8–9). The flow loses its capacity, the transported material is deposited.

Instabilities of calculations were observed during the numerical tests. Results of simulations depend on the grid spacing, the *CFL* (Figs 8–9) and D_{char} values (Fig. 10). Instabilities are more marked in the case of $CFL = 0.1$. The difference of accuracy between the numerical results increases in the far field (Fig. 11).

The numerical simulations take in account only the bedload transport. This assumption may be restrictive in the modelling of flood or dam break events, where suspended load is important. Added numerical tests were carried out, in which the dimensionless critical shear stress θ_c was supposed nil. Similar behaviour is obtained with non-nil critical shear stress (Fig. 12).

Experimental data are compared to the numerical results. CEM-1 refers to the simulation with a space step of 20 cm, $D_{char} = 1$ m and $CFL = 0.5$; CEM-2 to the simulation with a space step of 20 cm, $D_{char} = 1$ cm and $CFL = 0.5$ and CEM-3 to the simulation with a space step of 5 cm, $D_{char} = 1$ m and $CFL = 0.5$.

Figure 13 shows the comparison concerning the front characteristics: the time of front wave arrival is smaller with the RubarBE model. This behaviour can be explained by influence of the hypothesis and approaches used by RubarBE (average velocity, hydrostatic pressure …) (El Kadi & Paquier 2003, Spinewine & Zech 2003).

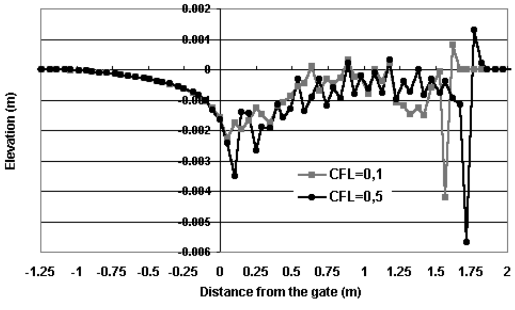


Figure 8. Bottom level: $\Delta x = 5$ cm, $D_{char} = 1$ m, $t = 2$s.

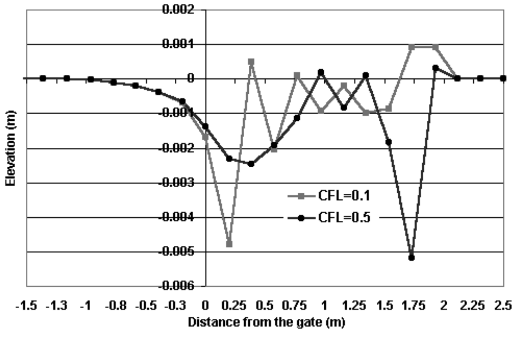


Figure 9. Bottom level: $\Delta x = 20$ cm, $D_{char} = 1$ m, $t = 2$s.

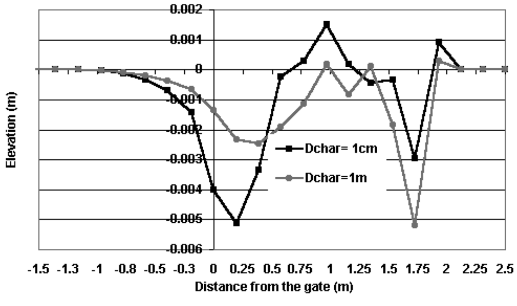


Figure 10. Bottom level evolution with spatial lag D_{char}: $\Delta x = 20$ cm, $CFL = 0.5$, $t = 2$s.

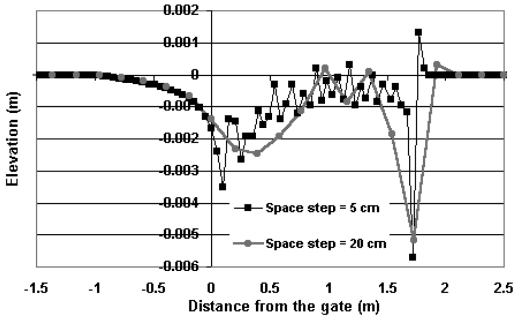


Figure 11. Bottom level evolution: $D_{char} = 1$m, $CFL = 0.5$, $t = 2$s.

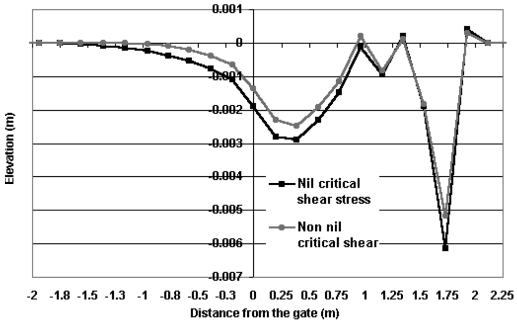


Figure 12. Bottom level evolution with nil or non nil critical shear stress: $\Delta x = 20$ cm, $D_{char} = 1$ m, $CFL = 0.5$, $t = 2$s.

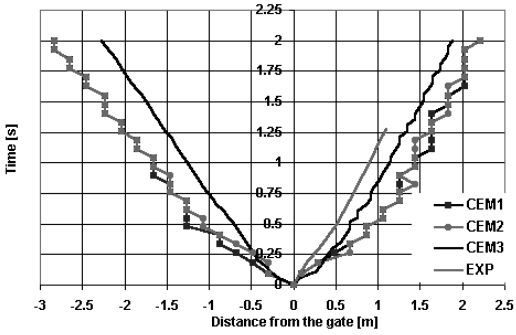


Figure 13. Front characteristics.

However, it must be noticed that the closest approximations to the experimental data seem to be for the numerical CEM-3, i.e. space step of 5 cm, $D_{char} = 1$ m and $CFL = 0.5$. At the same cross-section the difference between the arrival times is around 0.15 s. The shape of the experimental wave front is quite similar to the numerical profiles and small grid space step provides better estimate of arrival time of the flood wave.

The channel friction could affect significantly the propagation of the front wave. A Manning friction coefficient of $0.0185\ m^{1/3}/s$, derived from the diameter of the riverbed material, was selected. The influence of the wall friction was neglected. Then, a sensitivity analysis was carried out. Two different Manning coefficients are tested with the simulation CEM-3. Figure 14 shows that the celerity is quite dependent on the friction coefficient introduced in the numerical model. The agreement between experimental data and RubarBE simulation (CEM-3) is quite improved with a roughness of $0.02\ m^{1/3}/s$ instead of $0.0185\ m^{1/3}/s$ in the previous simulations.

Figures 15a, b, c show the water levels evolution at three cross-sections: $x = -0.25$ m, $x = 0.00$ m and $x = 0.25$ m. Computed water levels agree with experimental data except slight differences observed upstream from the gate. In the reservoir, the closest

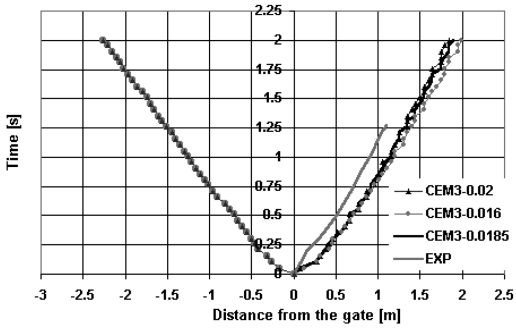


Figure 14. CEM3: front characteristics with different values of roughness.

approximations to the experimental data seem to be for the numerical simulation CEM-3. The simulation CEM-1 provides accurate approximations to the experimental data upstream from the gate. At gate location, the water levels evolution is underestimated. Flow is critical at the gate; decoupled model is inherently less stable than the coupled model in the case of Froude numbers vary close to unity, and they may need a special treatment of time step (Cui et al. 1996).

Beyond the high concentrations of sediment that invalidate the hypothesis of one single phase (see here below), the differences between calculation and experimental results are due to the highly 3-D nature of the dam-break wave for which some of the St. Venant hypothesis (small bottom slopes and curvatures, hydrostatic pressure and uniform velocity distribution in the cross section) are certainly not verified.

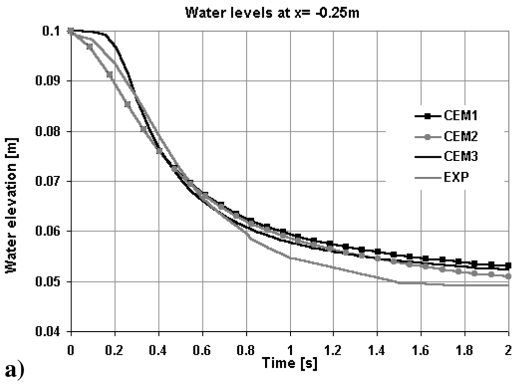
Figures 16a, b, c show the bottom position at three cross-sections: $x = -0.25$ m, $x = 0.00$ m and $x = 0.25$ m. Significant discrepancies between numerical and experimental results are observed through the reservoir and the channel.

The use of the Exner equation and of a maximum sediment transport capacity does not integrate the presence of a mixture of water and sediments in high concentration. This assumption but may be restrictive in the modelling of flood or dam break events. The use of another method for calculating the sediment transport seems to be necessary to take into account high concentration transport.

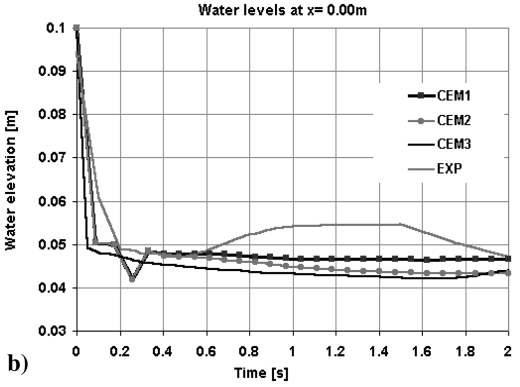
3.2.1 *Field application: Miribel channel*

This field application consists of sediment transport and morphologic changes in the Miribel channel. This channel is located north from Lyon in France. A geomorphologic survey was carried out in the Miribel channel by Malavoi 2000.

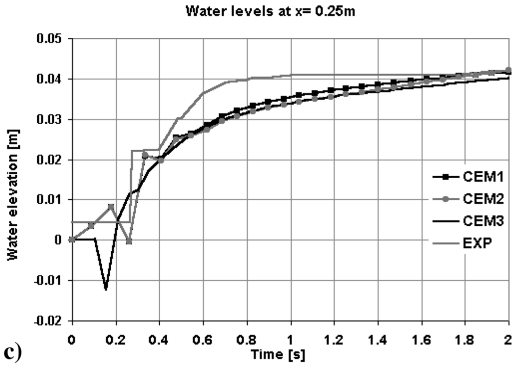
This case schematises the sediment transport in the channel after closing a former excavation in 1990. This pitch of about $400\,000\ m^3$ is located in the upstream



a)

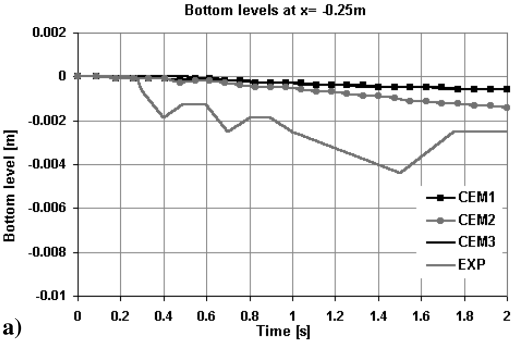


b)

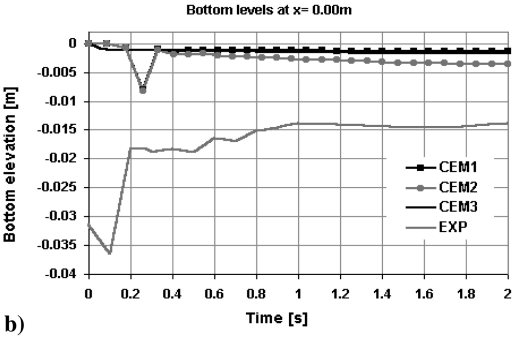


c)

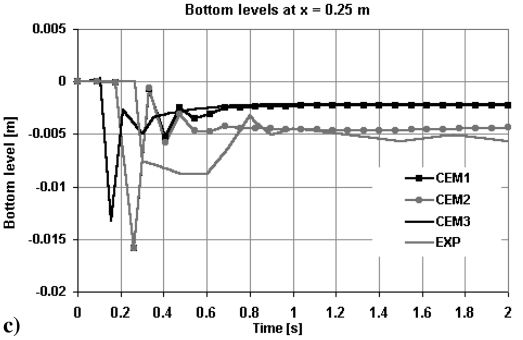
Figure 15. Water levels evolution: a) $x = -0.25$ m, b) $x = 0.00$ m, c) $x = 0.25$ m.



a)



b)



c)

Figure 16. Bottom levels changes: a) $x = -0.25$ m, b) $x = 0.00$ m, c) $x = 0.25$ m.

Table 3. Characteristics of the simulation.

Water discharge Q (m^3/s)	Manning coefficient K ($m^{1/3}/s$)	Sediment Diameter D_{50} (mm)	Standard deviation σ	Sediment feed rate Q_s (kg/s)
850	26	25	2.3	144.7

reach of the channel near the "Thil" village. Since sediments are trapped in this pitch, materials cannot be carried away from the upstream reach to the downstream one. As a consequence, important erosion was observed in the surrounding reaches.

The Miribel channel has a nearly rectangular section, is 16 km long and 85 m wide. The pitch is approximately 2 km long and the channel slope is about 0.00065 m/m. The bed material and sediment feed are composed of the same material. Table 3 shows the main characteristics of the simulation.

The flow discharge Q is maintained constant for a period of 20 days. The sediment feed rate Q_s is

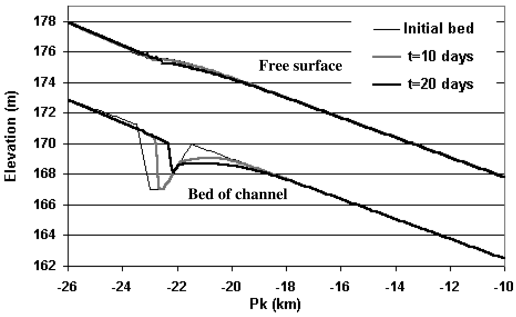


Figure 17. Miribel channel: initial bed, computed equilibrium bed and water surface.

specified as the sediment transport capacity of the upstream and downstream reaches. On the downstream side, it was assumed that the flow acted like uniform outflow.

The porosity p of the bed material is assumed to equal to 30%, the sediment density ρ_s to equal to 2650 kg/m^3 and the angle of internal friction of sediment φ to be 35°.

The channel is described through a grid of cross-sections: a constant grid spacing $\Delta x = 100$ m is used. The lag distance D_{char} is assumed to equal to 1 m. The initial condition for sediment transport is $Q_s = 144.7$ kg/s. The distribution of the boundary shear stress is calculated by $\tau = \rho g R J$. The dimensionless shear stress θ_c is assumed to 0.047. In the case of sedimentation, deposited sediment in one cross-section is distributed in horizontal layers across the channel width.

Figure 17 shows the evolution of the bed profile and free surface with time. The model predicts the progression of scour as well as deposition in the excavation. The evolution of the Miribel bed is controlled by the deposition of sediments in the pitch. The natural passage of sediments through the channel is interrupted by the pitch: sediments are washed into the excavation causing the bed upstream to erode. Downstream of the excavation the bed is lowered as the flow picks up energy on leaving the hole. At the end of the simulation, the deposition rate in the pitch is about 3 m.

4 CONCLUSIONS

RubarBE is designed to simulate single flood event and long-term scour and/or deposition. RubarBE assumes that equilibrium conditions are not necessary reached within each time step; the influence of unsteady conditions during flood events is taken in account through a loading equation.

This paper shows some examples of applications. The model can be used for applications to engineering problems, such as knickpoint migration. In the case of dam-break waves, the use of the Exner equation and of a maximum sediment transport capacity does not integrate the presence of a mixture of water and sediments in high concentration. This assumption is valid for long-term simulations of bed aggradation or degradation, but may be restrictive in the modelling of flood or dam break events. The use of other methods for calculating the sediment transport seems to be necessary to take into account high concentration transport.

RubarBE is in stage of continuous development and improvement. A decisive step was to integrate the calculation of the distribution of the shear stress in the transversal direction and various relationships between deformation and shear stress (Paquier & Khodashenas 2002). Next step should be the validation of the modelling of graded sediment. However, there is still no provision for simulating the development of meanders and the effect of bed forms.

ACKNOWLEDGEMENTS

The authors wish to acknowledge the financial support offered by the European Commission for the IMPACT project under the fifth framework programme (1998–2002), Environment and Sustainable Development thematic programme.

REFERENCES

Balayn, P. 2001. *Contribution à la modélisation numérique de l'évolution morphologique des cours d'eau aménagés lors de crues*. PhD Thesis. Lyon: Université Claude Bernard Lyon 1.

Candfield, H.F., Wilson, C.J., Reneau, S.L., Thomas, W.A., Lane, L.J., Wetherbee, G.A. & Crowell, K.J. 2002. Calibration of a one-dimensional sediment transport model on a two-dimensional scour problem. Meeting. Groundwater and Surface Water Hydrology (*Posters*). The Geological Society of America, 98th Annual Meeting; Corvallis, 13–15 May.

Cui, Y., Parker, G. & Paola, C. 1996. Numerical simulation of aggradation and downstream fining. *Journal of Hydraulic Research*, Vol. 34, No. 2: 185–204.

El Kadi, K. & Paquier, A. 2003. IMPACT Projet: Dam-break wave on movable beds. 3rd IMPACT Workshop (EU-funded research project on Investigation of Extreme Flood Proceeses and Uncertainty), Louvain-la-Neuve, Belgium: CD-Rom Proceedings, in press.

Engelund, F. & Hansen, E. 1967. A Monograph on Sediment Transport in Alluvial Streams. *Teknish Forlag, Technical Press*.

Holly, F.M. & Rahuel, J.L., 1990. New numerical/Physical framework for mobile-bed modeling, Part 1: numerical and physical principals. *Journal of Hydraulic Research*, Vol. 28, No. 4: 401–416.

Karim, M.F. & Kennedy, J.F. 1982. *IALLUVIAL: a computer based flow and sediment routing for alluvial streams and*

its application to the Missouri River. Iowa: Iowa Institute of Hydraulic Research, Report No. 343.

Khodashenas, S.R. 1998. *Modification de la topographie d'une rivière due au transport des sédiments*. PhD Thesis, Lyon: Ecole Centrale de Lyon.

Khodashenas, S.R. & Paquier, A. 1999. A geometrical method for computing the distribution of boundary shear stress across irregular straight open channels. *Journal of Hydraulic Research*, Vol. 37, No. 3: 381–388.

Ikeda, S. 1982. Incipient motion of sand particles on sans slopes. *Journal of Hydraulic Division*, Vol. 108, No. HY1: 95–114.

Malavoi, J.R. 2000. *Etude géomorphologique du canal de Miribel*. Lyon: Hydratec-Voies naviguables de France.

Meyer-Peter, E. & Müller, R. 1948. Formulas for bed-load transport. *Report on second meeting of IARH. IAHR*, Stockholm: 39–64.

Paquier, A. 1995. *Modélisation et simulation de la propagation de l'onde de rupture de barrage*. PhD Thesis, Saint-Etienne: Université Jean Monnet.

Paquier, A. & Khodashenas, S.R. 2002. River bed deformation calculated from boundary shear stress. *Journal of Hydraulic Research*, 40(5): 603–609.

Shih, S.-M. & Komar, P.D. 1990. Hydraulic controls of grain-size distributions of bedload gravels in Oak Creek, Oregon, USA. *Sedimentology*, 37: 367–376.

Spinewine, B. & Zech, Y. 2002. Dam-break waves over movable beds: a "flat bed" test case. 2nd IMPACT Workshop (EU-funded research project on Investigation of Extreme Flood Proceeses and Uncertainty), Mo-i-Rana, Norway: CD-Rom Proceedings.

Spinewine, B. & Zech, Y. 2003. Dam-break wave on movable bed: experimental results and modelling exercise debriefing. 3rd IMPACT Workshop (EU-funded research project on Investigation of Extreme Flood Proceeses and Uncertainty), Louvain-la-Neuve, Belgium: CD-Rom Proceedings, in press.

Thomas, W.A. & Prashum, A.I. 1977. Mathematical model of scour and deposition. *Journal of Hydraulic Division*, Vol. 110, No. 11: 1613–1641.

Yang, C.T. 2000. Sedimentation and River Morphology Studies in the Bureau of Reclamation. *4th International Conference on Hydro-Science and engineering (ICHE)*. Seoul.

Yang. C.T. & Simos, J.M. 1998. *Sediment transport and river morphologic changes*. Denver: U.S. Bureau of Reclamation, Technical Service Center, Sedimentation and River Hydraulics Group.

River Flow 2004 – Greco, Carravetta & Della Morte (eds.)
© 2004 Taylor & Francis Group, London, ISBN 90 5809 658 0

Gravel river widening by bank erosion in a straight stretch of river – investigations on a numerical model

M. Schmautz
SKI GmbH + Co. KG Consulting Engineers, Munich, Germany

ABSTRACT: Removing existing bank protection works allows a lateral erosion and thus widening of a regulated stretch of river. Based on an extensive parameter study, a method was developed to estimate the maximum river width which has to be expected during the widening process – which is the main question while planning a measure of river widening. The controlling parameters and boundary conditions have been identified and the structural evolution of the process was investigated. The research work focuses on straight rivers with cohesionless bed and bank material which play a major role in the alpine region.

1 INTRODUCTION

Nowadays, numerous European rivers are in the stage of erosion with the well known consequences of decreasing water and groundwater levels. One alternative (taken into consideration at several Alpine rivers) for an ecological and hydraulic engineering feasible solution of these problems is to allow a lateral erosion of the river by removing existing bank-protection works. The widening of the river would decrease the bed load transport capacity; the eroded bank material would serve as an additional sediment influx. Existing knowledge about the processes and planning tools for such measures are partially insufficient.

At the Laboratory of Hydraulic and Water Resources Engineering of the Technische Universität München in Obernach fundamental model tests have been carried out by order of the Bavarian State Ministry for Regional Development and Environmental Affairs (fully mobile bed, model length up to 100 m) since the year 2000 to prepare extensive measures of river engineering at the lower courses of the Alpine rivers Iller and Isar which are tributaries of the Danube. The focus of the research is especially on the interaction between degradation, lateral erosion and the hydraulic influence of weirs or ramps which stabilise the river bed in well-defined distances. The conception of the study and the results of several model runs were illustrated in Schmautz & Aufleger (2002) and Aufleger et al. (2003).

The numerical modelling of the processes of bank erosion was subject to an additional research project which was financed by the Deutsche Forschungsgemeinschaft.

Herein, a method was developed to estimate the maximum river width which has to be expected during the widening process – which is the main question while planning a measure of river widening. The controlling parameters and boundary conditions have been identified and the structural evolution of the process was investigated. The research work focused on straight rivers with cohesionless bed and bank material which play a major role in the alpine region.

The investigations were carried out on a hydrodynamic numerical model which had to be extended by appropriate equations to reproduce the main sedimentologic processes during river widening. The development and verification of the numerical model were presented in Schmautz & Aufleger (2002) and in Schmautz (2003). Chapter 2 summarises the main features of the model.

In this paper, the widening process and the developed method to estimate the maximum river width will be illustrated.

2 NUMERICAL MODEL

2.1 *General*

In principle, the procedure of the numerical simulation of gravel river widening is illustrated in Figure 1. For any time step n the computations of the hydrodynamic, morphological and bank stability modules result in a new bed topography which is the basis for the computations in the next time step $n + 1$.

For calculating the bed load transport capacity q_{B*}, a threshold formulation according to the Meyer-Peter/

Müller formula is used:

$$q_{B*} = \rho_S \sqrt{\rho' g d_m^3}\, k_1 (k_2 \theta - \theta_{crit})^{3/2} \quad (1)$$

where $\rho' = (\rho_S - \rho)/\rho$; ρ_S = mass density of bed particle; ρ = mass density of water; g = gravitational acceleration; d_m = mean diameter of grain; k_1, k_2 = constants to be determined by calibration; $\theta = \tau/(\rho_S - \rho)gd$ = dimensionless shear stress (Shields-parameter); and θ_{crit} = critical Shields-parameter.

2.2 *Development works and verification*

In addition to typical numerical 'bed load models', special attention is to be paid to the challenges in the bank regions which are the distribution of the flow and the shear stress as well as the beginning and the direction of the bed load transport.

The hydraulic verification of the applied depth-integrated 2D hydrodynamic model has shown that the main flow processes concerning the lateral erosion and thus the bed shear stresses can be reproduced adequately after calibrating the parameters of the turbulence model.

Before extending the morphological module to simulate the erosion process at the banks, extensive theoretical preparatory work had to be done. The inception and the direction of the bed load transport on an arbitrarily inclined geometry which are affected by fluid and gravitational forces simultaneously were investigated.

Bank stability and bank failure are included by a functional approach based on the angle of repose. The research work focused on bankfull or nearly bankfull discharge where the erosion by the flow is dominant. Bank failure is of inferior importance.

The enhanced model was verified and calibrated by 'recalculating' several physical model tests and comparing the results of the numerical simulation with the measurements. At this, the fundamental large scale model tests (carried out at the Laboratory of Hydraulic and Water Resources Engineering of the Technische Universität München) served as an essential data basis. The results of the numerical simulation are in very good agreement with the experiments concerning the evolution over time as well as the spatial development and the formation of the profiles. Among the parameters, only the formulation for the direction of the bed load transport was subject to the calibration. The other parameters could be defined by means of preliminary investigations.

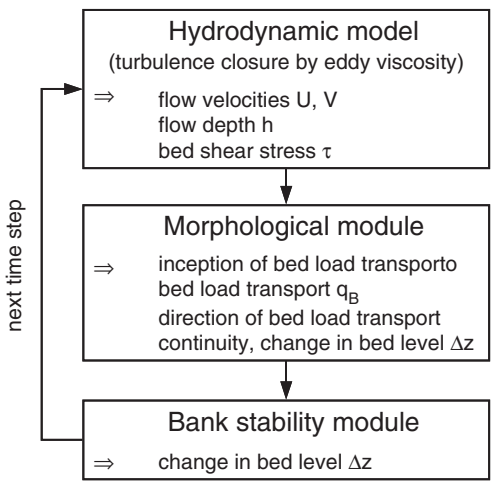


Figure 1. Flow chart for simulating gravel river widening.

3 EVOLUTION OF THE WIDENING PROCESS – RESULTS OF THE PROCESS STUDY

3.1 *General*

The process study aimed at improving the understanding of the widening process (evolution over time and spatial development) and systemising the influence of a few relevant parameters. To this end, simulation runs with well defined parameters were carried out which show the interaction between the changes of the bed level and the river width as well as the development of the water levels, the energy line and the bed load transport in idealised stretches of rivers (Schmautz, 2003).

Figure 2 illustrates the basic possibilities to weave a stretch of river with removed bank protection works into the up- and downstream river reaches. In the case of coinciding parameters, (a) and (b) just differ in the downstream hydraulic boundary condition.

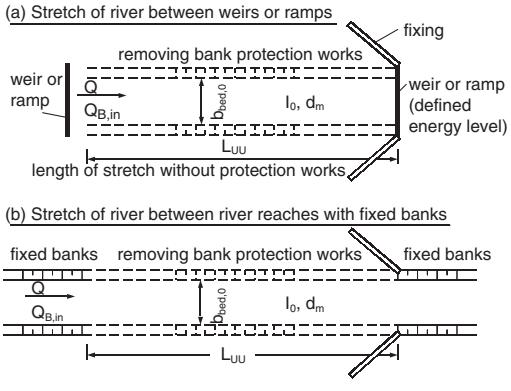


Figure 2. Ways of weaving a stretch of river with removed protection works into the up- and downstream river reaches.

3.2 *Definition of the river width and the median bed level*

To evaluate the simulation runs, characteristic geometric parameters had to be defined. As is shown in Figure 3, parameters that are geometrically well-defined and hydraulically significant, are determined independently of the initial geometry.

To evaluate the widening, two measures are used. The width b_m characterises a hydraulically relevant parameter which depends on the actual discharge among other things. The width $b_{b/2}$ is hydraulically irrelevant but of the advantage that it is independent of the discharge and the bed level.

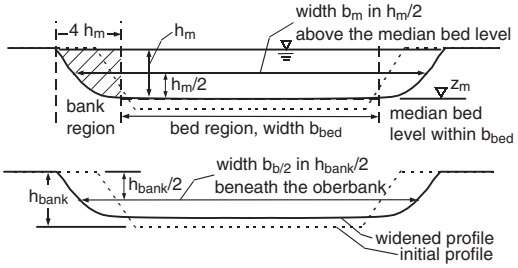


Figure 3. Definition of river width and median bed level (strongly inflated plot).

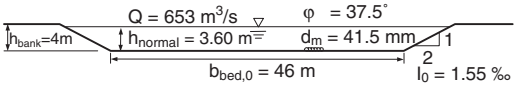


Figure 4. Initial geometry and parameters of the river (I_0 = constant = initial slope).

3.3 *Used parameters and boundary conditions*

Herein, the process study is shown exemplary at two river reaches (reach A and reach B) with an initial geometry and defined parameters depicted in Figure 4. The flow Q is constant and nearly bankfull in the beginning. As a hydraulic boundary condition, a constant downstream water level was defined so that the flow depth at the downstream end corresponds with the flow depth h_{normal} in the initial state.

The reaches A and B only differ in the length L_{UU} which is 832 m in the 'short' reach A and 4000 m in the 'long' reach B. In both reaches the bed load influx varies between 0 kg/s and 42 kg/s. The transport capacity in the initial geometry is about 120 kg/s. Consequently, the rivers suffer from an influx deficit. In the Figures 6, 7 and 9 percent numbers are given in brackets behind the influx rates. The meaning of these numbers is explained in chapter 4.4.2.

In this paper, only the evolution of the river width and the bed level are illustrated.

3.4 *Process and state of equilibrium in river reach A*

3.4.1 *Development without bed load influx (Figure 5)*

In the first two days, a degradation of the bed can be observed in the upstream part of the reach. In the downstream part, the bed aggradates due to the influx from

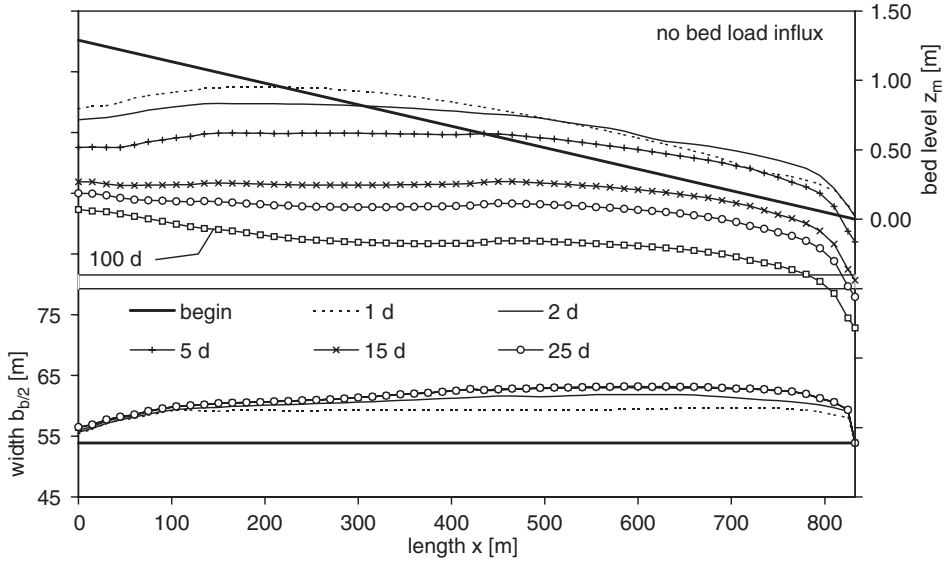


Figure 5. River reach A, evolution of river width and bed level, bed load influx = 0 kg/s.

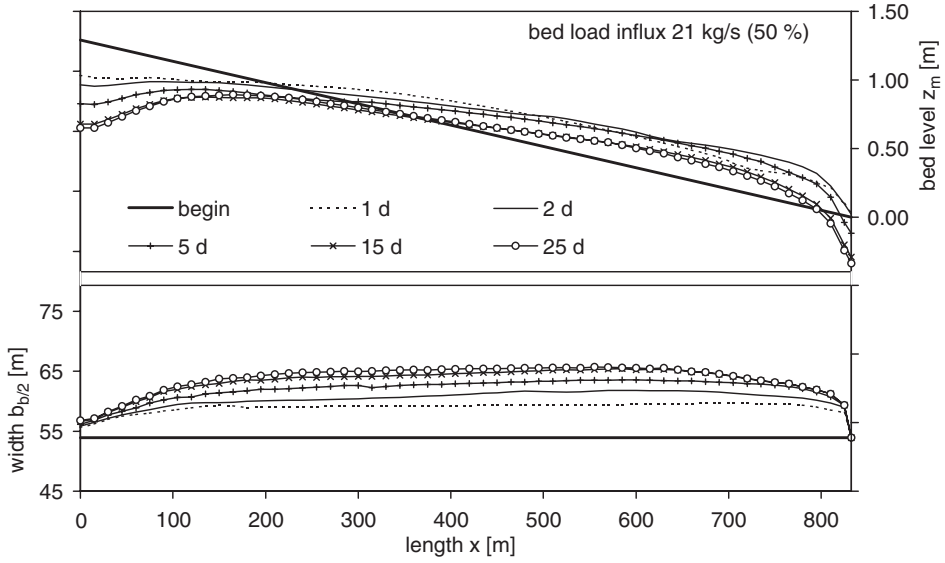


Figure 6. River reach A, evolution of river width and bed level, bed load influx = 21 kg/s.

the eroding stretch and the simultaneous widening. Following, the bed load deficit affects the entire reach and the bed is eroding nearly parallel. The erosion proceeds until the bed load transport comes to rest in the whole stretch of river (after 100 days).

Within the first days, the widening takes place evenly within the bigger part of the reach. Already after 5 days, the widening has finished. The widening process is controlled by the strong erosion of the bed and the resulting reduction of the energy slope and the shear stress which prevents further erosion in the banks. The process between 5 and 25 days can be characterised by a stable bank line (driving shear stress below critical shear stress) and simultaneous bed load transport in the bed.

3.4.2 *Development with bed load influx = 21 kg/s (Figure 6)*

In the upstream third of the reach, an erosion of the bed can be observed, in the downstream part a durable aggradation. After 25 days, the bed has reached a stable final state which has a higher level and higher slope compared to the case without bed load influx.

The widening process lasts considerably longer than in the case without bed load influx and ceases after 25 days. The greater duration of the widening process and the greater maximum widening are due to the higher and stable bed level which prevents a rapid descent of the bed shear stress in the bank region (like in the first case).

Thus, the bed load influx exerts strong influence on the widening process as well as the resulting maximum width. The bed level and the river width after 25 days describe a stable final state of the evolution. The fed bed load moves through the reach without de- or aggradation.

3.4.3 *Comparison after 25 days depending on the bed load influx (Figure 7)*

A direct comparison of four simulations runs shows again clearly the influence of the bed load influx. After 25 days a stable state concerning the river width and the bed level is reached in all rivers (except the bed level in the river without bed load influx). The bed level as well as the maximum river width and the maximum widening are significantly affected by the bed load influx.

3.5 *Process and state of equilibrium in river reach B*

3.5.1 *Development without bed load influx (Figure 8)*

In the entire presented time frame, the reach B degradates in the upper part of the stretch due to the bed load deficit; in the downstream part the river aggradates due to the influx from the eroding stretch and the simultaneous widening. The erosion front is proceeding continuously downstream but does not reach the last third of the stretch during the widening process. The erosion of the bed is not yet finished after the presented 35 days.

During the first 5 days, the river widens completely evenly while the bed level rises largely parallel to the

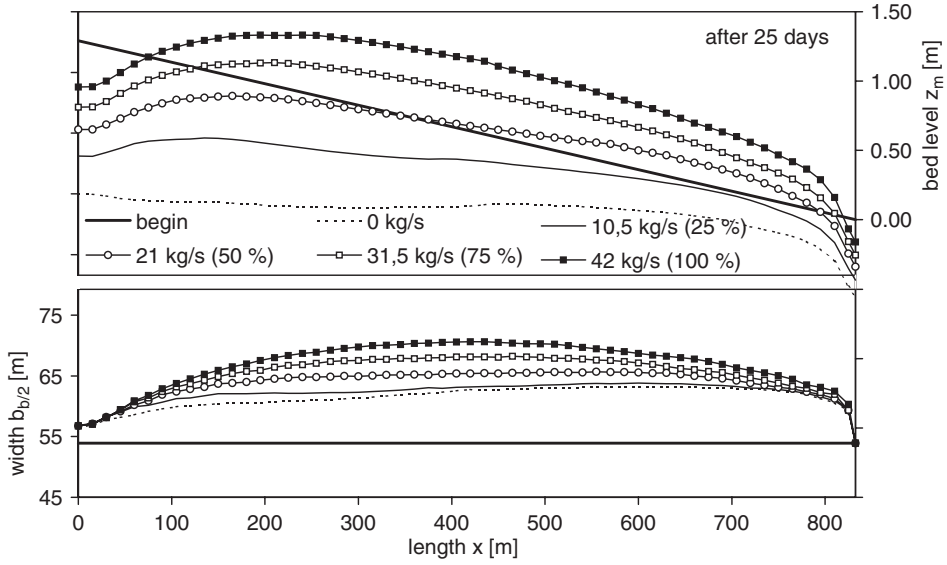


Figure 7. River reach A, river width and bed level after 25 days depending on the bed load influx.

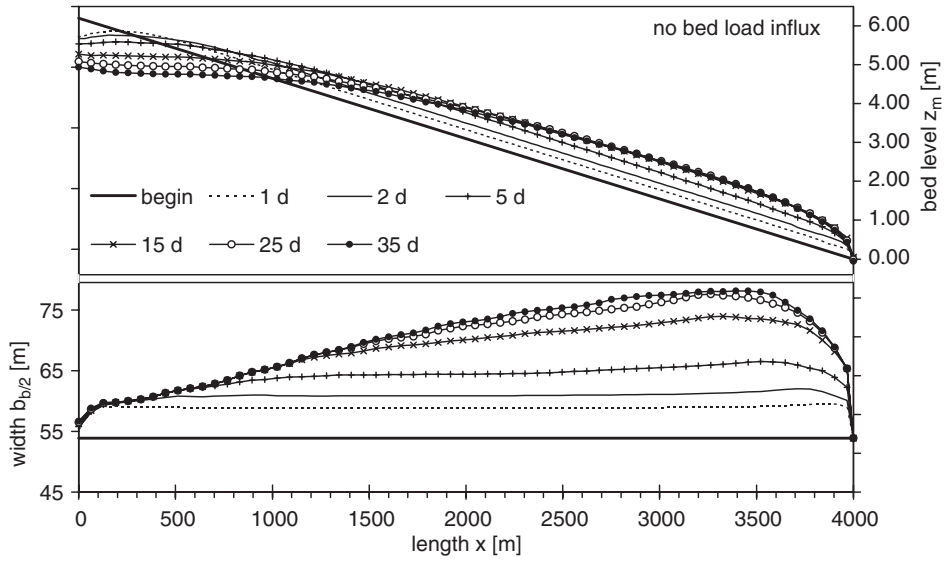


Figure 8. River reach B, evolution of river width and bed level, bed load influx = 0 kg/s.

initial bed level. At the end of the reach, a marginal greater widening can be determined which is due to a higher energy slope as a result of the fixed downstream boundary condition.

Following, the river width increases until a maximum widening after 35 days is attained. Between 3000 m and 3500 m the widening reaches a constant value which exceeds the maximum value in river reach A clearly. The longer duration of the widening of 35 days compared to 25 days in reach A also originates from the greater maximum widening.

3.5.2 *Comparison after 35 days depending on the bed load influx (Figure 9)*

A direct confrontation of the final state in dependence on the influx rates reveals the small influence of the

bed load influx on the process compared to the 'short' river reach A.

After reaching the final state (after 35 days), differences in the bed level and the river width are evident in more than half of the stretch of river. Higher bed load influx leads to higher bed level and river width. In the last third of the reach however, only negligible deviations can be determined. Apparently, the stretch of river with a length of 4000 m is long enough to saturate the bed load transport capacity in the downstream third during the relevant period of widening. Thus, an erosion of the bed is prevented independent of the bed load influx.

3.5.3 *Evolution of the profile at x = 3200 m (Figure 10)*

At the station x = 3200 m, the widening and the deformation of the profile proceed approximately under saturation of the bed load transport capacity. The advancing widening comes along with a progressing raising of the bed level. The transfer of the bank material to the bed region takes place under conservation of mass during the first days. The final state can be characterised by a stable bank line (driving shear stress below critical shear stress, vanishing bed load transport) and simultaneous bed load transport in the bed region.

3.6 *Main conclusions*

The summarised conclusions go beyond the illustrations herein and include the findings made in Schmautz (2003). The parameters 'bed load influx', 'length of the stretch' and 'downstream boundary condition' affect the widening process and thus also the final conditions significantly. Among other things, the following fundamental findings can be formulated:

- The resulting maximum river width is increasing with the length of the stretch until a maximum possible value is reached.
- With rising bed load influx, higher bed and water levels as well as greater river width result. For a sufficient length of the stretch, the maximum final width is independent of the given influx.
- If the water level at the end of the stretch is raised by a tailback from the downstream reach or by a weir or ramp, higher bed levels result compared with the case without tail-back. The maximum final width is smaller.
- During the widening process and also in a possible state of equilibrium, the water levels can lie significantly above those in the initial situation.

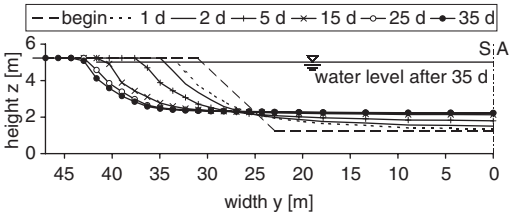


Figure 10. River reach B, evolution of the profile at x = 3200 m, bed load influx = 21 kg/s (plot inflated by factor 2).

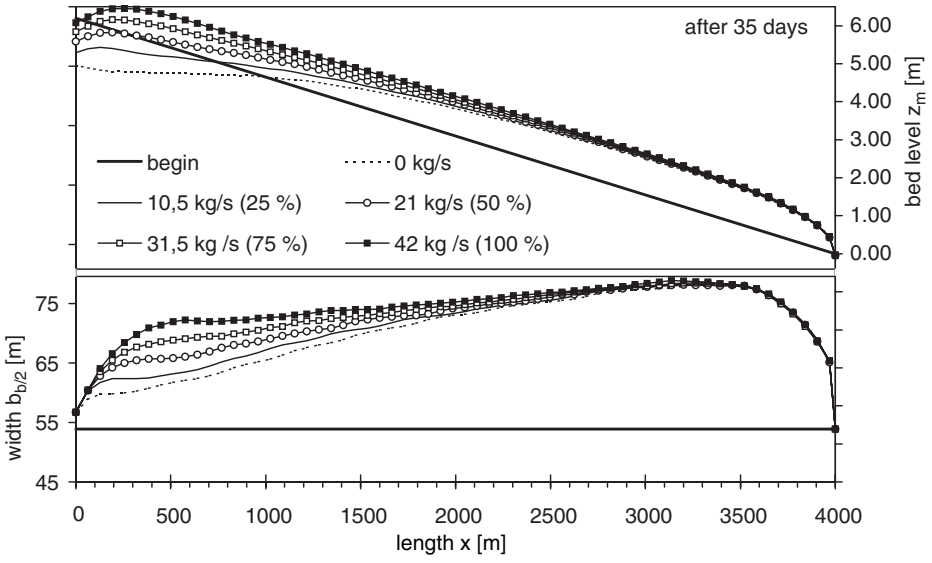


Figure 9. River reach B, river width and bed level after 35 days depending on the bed load influx.

4 PARAMETER STUDY – METHOD TO ESTIMATE THE MAXIMUM RIVER WIDTH

4.1 *General*

4.1.1 *Overview*

On the basis of the qualitative insights into the widening process and the influence of relevant parameters summarised in chapter 3, a method was developed to quantify the maximum river width that has to be expected in a river reach during the widening process.

The basic idea and the scheme of the method are illustrated in Figure 11. The calculation is based exclusively on well known geometric, hydraulic and morphologic input variables and is executed in three steps. In the first two steps, the 'regime width' and the 'regime length' – two characteristic reference values – are computed from the initial geometry, a constant, dominant discharge and a median grain diameter. In the third step, the actual width which is reached in a stretch of river can be determined with the aid of dimensionless diagrams depending on further parameters (length of the stretch, bed load influx and downstream hydraulic conditions).

4.1.2 *Premises for the applicability of the method*

The method is limited to rivers without distinctive morphological structures (bars or braiding). The bed load influx may not exceed the transport capacity in a river with regime conditions. The impact of river bends is not taken into account. The hydrology has to be idealised by a constant dominant discharge.

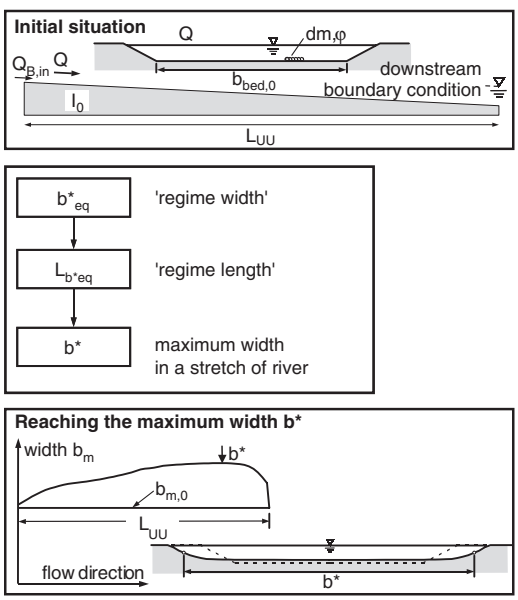


Figure 11. Flow chart to determine the maximum river width.

4.1.3 *Underlying parameters*

The following ranges of the parameters form the basis of the parameter study:

– initial slope	I_0	0,5‰ to 2,0‰
– initial bed width	$b_{bed,0}$	12 m to 80 m
– initial bank height	h_{bank}	1 m to 4 m
– med. grain diameter	d_m	12 mm to 63 mm

4.2 *Regime width b^*_{eq}*

By definition, b^*_{eq} names the width b_m (for the definition of b_m see Figure 3) that is reached in a 'very long' river reach (so called 'equilibrium stretch'). Thereby, 'very long' means that the development in the observed part of the reach is not affected by the up- and downstream boundary conditions. By dimensional analysis and analytic derivations (Schmautz, 2003), the following dependency of b^*_{eq} on the parameters could be found:

$$b^*_{eq} \approx \frac{1{,}04 \cdot Q\, I_0^{7/6}}{k_{Str}\, \rho'^{5/3}\, d_m^{5/3}\, \theta_{m,U}^{5/3}} \qquad (2)$$

where Q = discharge; I_0 = initial bed slope; k_{Str} = Strickler-value; $\rho' = (\rho_S - \rho)/\rho$; ρ_S = mass density of bed particle; ρ = mass density of water; and d_m = mean diameter of grain.

As a new parameter, $\theta_{m,U}$ has been introduced and identified, which characterises the end of the widening process in the 'equilibrium stretch'. The final stable state can be characterised by a stable bank line (driving shear stress below critical shear stress, vanishing bed load transport) and simultaneous bed load transport in the bed region. For this stable state, $\theta_{m,U}$ is evaluated as the median Shields-parameter in the bed region. Figure 12 shows the parameters and their evaluation at the example of the geometry used in chapter 3 (see Figure 4).

f_U defines a further parameter which describes the relation of $\theta_{m,U}$ and the critical Shields-parameter:

$$\theta_{m,U} = f_U \frac{\theta_{crit}}{k_2} = \frac{\theta'_{m,U}}{k_2} \qquad (3)$$

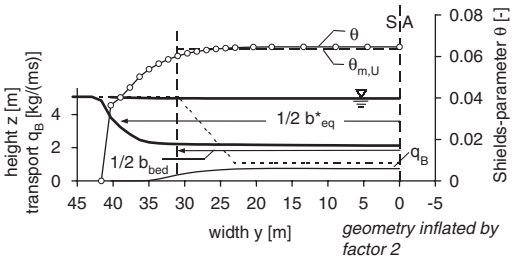


Figure 12. Determination of $\theta_{m,U}$ at an example.

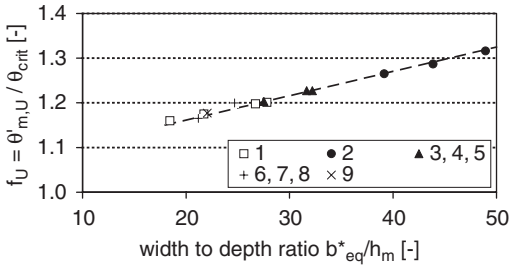


Figure 13. Parameter f_U in dependence of the width to depth ratio (1 to 9: numbers of the rivers in the parameter study).

where k_2 = constant in Meyer-Peter/Müller formula; and θ_{crit} = critical Shields-parameter.

The realised parameter study has shown f_U to be mainly a function of the width to depth ratio b^*_{eq}/h_m as is depicted in Figure 13. The dependence on the angle of repose is negligible.

The determination of the regime width b^*_{eq} by the equations (2) and (3) and by Figure 13 requires an iterative computation.

The so called 'regime bed load transport' $Q_{B,b*eq}$ in the 'equilibrium stretch' can be computed e.g. with the aid of the Meyer-Peter/Müller formula:

$$Q_{B,b^*eq} \approx b_{bed}\ \rho_S \sqrt{\rho' g d_m^3}\ k_1 \left(k_2 \theta_{m,U} - \theta_{crit}\right)^{3/2} \qquad (4)$$

where $b_{bed} \approx b^*_{eq} - 6h_m$.

4.3 *Regime length L_{b^*eq}*

In the process study, a relevant influence of the length L_{UU} on the resulting river width has been identified. With L_{b^*eq}, a characteristic length of the widening process is introduced.

The determination of the regime length L_{b^*eq} is illustrated exemplary in Figure 14 again on basis of the geometry, morphology and hydrology used in the process study (see Figure 4). The ordinate describes the ratio of the maximum widening $(b' - b_0)$ to the widening to the regime width $(b^*_{eq} - b_0)$. An ordinate value of 1.0 means a resulting width of b^*_{eq}. Every point in Figure 14 represents a simulation run for a river reach with a defined length and without bed load influx. Greater length leads to greater river width until a maximum value above b^*_{eq} is reached. The widening to a value greater than b^*_{eq} is due to a higher energy slope as a result of the fixed downstream boundary condition (constant downstream water level so that in the beginning, the flow depth at the downstream end corresponds with the flow depth h_{normal}). For the

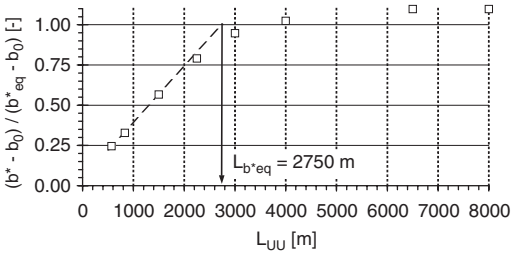


Figure 14. Determination of the regime length, exemplary.

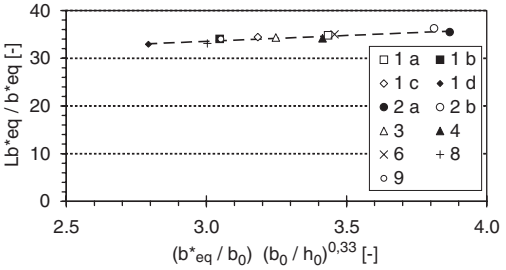


Figure 15. Dependence of the regime length L_{b^*eq} on the parameters (1 to 9: numbers of the rivers in the parameter study), $h_0 = h_m$ in the initial profile and $b_0 = b_{m,0} + 0,3h_0$.

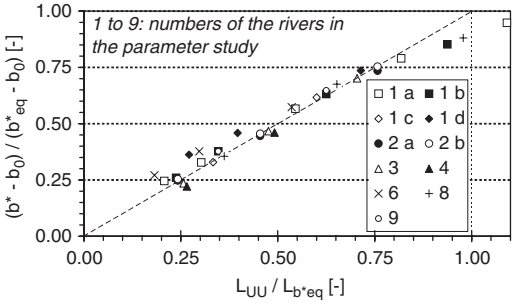


Figure 16. Maximum widening of the river depending on the length of the river reach.

definition of L_{b^*eq}, the region of the linear increase is utilised.

Within the parameter study, the dependence of the regime length on the parameters could be identified and depicted in a dimensionless diagram (Figure 15).

4.4 *Width b**

With the regime width b^*_{eq} and the regime length L_{b^*eq}, characteristic parameters of a river reach have been defined and determined. It remains to quantify the actual maximum width b^* which results during the widening process depending on the reach length and the bed load influx. The effect of the downstream

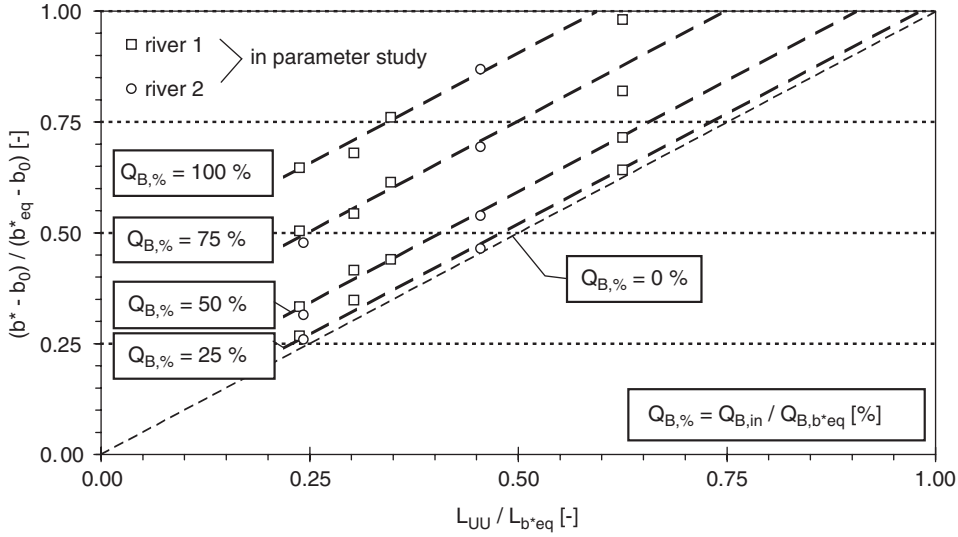


Figure 17. Maximum widening of the river depending on the length and the bed load influx.

hydraulic boundary conditions is not illustrated herein. The downstream water level is constant so that in the beginning, the flow depth at the downstream end corresponds with the flow depth h_{normal}.

4.4.1 *Width b* without bed load influx*

The maximum width b′ which results in a river reach without bed load influx was already used to determine the regime length. The results of all simulation runs are illustrated in Figure 16 in dimensionless form. The ordinate represents the ratio of the maximum widening $(b^* - b_0)$ to the widening to the regime width $(b^*_{eq} - b_0)$. On the abscissa, the length L_{UU} is scaled by the regime length L_{b^*eq}.

The interrelationship can be approximated by a straight line running from (0/0) to (1/1) (except $L_{UU}/L_{b^*eq} > 0,75$).

4.4.2 *Width b* with bed load influx*

Besides the reach length, also the bed load influx influences the maximum widening relevantly (see chapter 3). To formulate a relationship between the reach length, the bed load influx and the widening, the influx rates have to be made comparable. As a reference value, the regime bed load transport Q_{B,b^*eq} is dedicated analog to the regime width and the regime length. The bed load influx can thus be expressed in dimensionless form and in percent $Q_{B,in}/Q_{B,b^*eq}$, respectively.

Within the parameter study, influx rates of 25%, 50%, 75% and 100% were investigated. The results are plotted in Figure 17, again in the well-known way. The regression lines run parallel to the line of no influx. The widening increases with increasing bed load influx.

The bed load influx is limited to the value of the regime bed load transport Q_{B,b^*eq}. Higher influx rated can lead to higher bed slope which can be linked to the formation of morphological structures (bars or braiding). Hereby, the limits of the numerical model would be exceeded.

5 CONCLUSIONS

On a numerical model, the process of gravel river widening in a straight stretch of river has been investigated. The controlling parameters and boundary conditions have been identified and a method was developed to estimate the maximum river width which has to be expected during the widening process.

Current research activities at the institute of Hydraulic and Water Resources Engineering of the Technische Universität München aim at extending the findings to rivers with bends.

REFERENCES

Aufleger, M., Niedermayr, A. & Strobl, T. 2003: Widening of Gravel Bed Rivers – Physical Model Tests in Large Scale. XXX IAHR Congress, Thessaloniki, Greece.

Schmautz, M. & Aufleger, M. 2002: Gravel River Widening by Bank Erosion – Theory and Results of Physical and Numerical Modelling. Proceedings, River Flow 2002 – International Conference on Fluvial Hydraulics, Louvain-la-Neuve, Belgium, Vol. 1.

Schmautz, M. 2003: Eigendynamische Aufweitung in einer geraden Gewässerstrecke. Berichte des Lehrstuhls und der Versuchsanstalt für Wasserbau und Wasserwirtschaft der Technischen Universität München, Heft 96.

This page intentionally left blank

River Flow 2004 – Greco, Carravetta & Della Morte (eds.)
© 2004 Taylor & Francis Group, London, ISBN 90 5809 658 0

Flow in meandering bends

D. Termini
Dipartimento di Idraulica ed Applicazioni Ambientali, Università di Palermo, Palermo, Italy

ABSTRACT: The analysis of flow in bends may be considered as one of the key problems in studying river morphology. In this paper the first results of an experimental investigation of flow around a meandering bend have been reported. The experiments have been carried out in a laboratory meandering channel of large amplitude, both over an immobile flat bed and over an erodible bed. The analysis of the collected data confirm that when the aspect ratio is small the cross-circulation assumes a great importance. In particular, in the case of deformed bed, it seems that a second counter rotating secondary flow cell appears along the bend near the outer bank. When the aspect ratio is large the convective acceleration terms associated with downstream changing channel curvature cannot be neglected in the force balance equation. The stream-wise acceleration of the downstream velocity component is important throughout the bend assuming greater significance when the radius of curvature decreases.

1 INTRODUCTION

Accurate specification of the spatial distribution of bottom stress and flow velocity is of crucial importance in calculation of erosion and deposition zones along the channel. Erosion and deposition, in fact, depend on the divergence of sediment flux (Nelson and Smith, 1989), that is, in turn, related to the characteristics of the flow which erodes the channel itself (Schumm, 1963; Schumm et al., 1972; Hooke, 1975; Jackson, 1975; Chang, 1988; Renz and Jun, 1989). A natural meandering stream represents one of the most complex flow situations: not only it is turbulent and strongly three dimensional, but its irregular topography is continuously changing as results of erosion and deposition processes. In studying such a complex problem, it is necessary to identify the aspects that mainly affect the characteristics of flow and to focus the attention only to their analysis.

Meandering channels are characterized by a downstream changing curvature that strongly affects the hydrodynamic processes along the channel itself. When the flow enters in the bend, a secondary motion is produced by the interaction of the forces associated with centrifugal acceleration, transverse water surface slope and shear stress (Yen 1972). In accordance with Yalin (1992), in a sinuous channel the secondary motion can be considered as the combination of two motions: the elicoidal motion, that consists in a parallel longitudinal motion upon which cross-circulation is superimposed, and the so-called convective acceleration. The first component, to which corresponds a zero specific cross-flow rate, is inducted by the channel curvature; the second component is indeed due to the stream-wise changing curvature. Thus, because of the variable curvature of the channel, the distribution of velocity vectors on the bed is not uniform and convective accelerations occur. Clearly the channel plane shape affects significantly the magnitude of the aforementioned components.

A large amount of research on flow in bends has been performed. In most of the experimental investigations a fixed rectangular cross-section with flat bed has been considered and, thus, different hydraulic conditions from the flow over a deformed bed have been analyzed. Furthermore, constant curved channels have often been used for the experiments (Rozovski, 1965; de Vriend, 1979; Odgaard and Bergs, 1988) and only fully developed channel regions have been examined. On the basis of the experimental observations, some authors (Yen, 1972; Engelund, 1974; Kikkawa et al., 1976; Francis and Asfari, 1978; Zimmerman and Kennedy, 1978) have emphasized the effect of cross-circulation on bed deformation, neglecting the convective accelerations associated to the channel changing curvature.

Other experimental works carried out in meandering channels (Hooke, 1975; Whiting and Dietrich, 1991; Whiting and Dietrich, 1993 a, b), apart from field observations (Lewin, 1972; Jackson, 1975; Bridge and Jarvis, 1976; Thompson, 1986), have highlighted the effect of the flow convective accelerations due to the downstream changing topography and the contribution to the total force balance for a meandering stream.

Recently, Blanckaert and Graf (2001) performed a series of experiments in a constant curved channel with

small aspect ratio (B/h = 3.6, where B = channel width and h = water depth). The authors analysed the interaction between the stream-wise flow velocity and the secondary flow and established that the cross-sectional motion is composed by two cells of circulation: a center-region cell (related to the classical elicoidal motion) and a second counter-rotating cell appearing near the outer bank. The counter-rotating cell acts as a stabilising region between the center region and the outer bank.

On the other hand, some results previously obtained by the author of the present work (Termini, 1999 a, b), in a large amplitude meandering channel, have highlighted that, for large values of the aspect ratio, the convective accelerations due only to changing channel curvature (over flat bed), play the most important rule on the force balance. Thus, in this case, the changing channel curvature is considered the key effect in order to predict the localization of erosion and deposition zones along the channel itself.

In this work the attention is focused to evaluate the importance of cross-circulation and convective flow acceleration on bed deformation and channel migration, for different aspect ratios. The paper gives a description of some recent experiments conducted, in order to analyze the hydrodynamic characteristics of the flow along the bend, in the laboratory meandering channel constructed at D.I.I.A. (Dipartimento di Ingegneria Idraulica ed Applicazioni Ambientali) of Palermo's University (Italy).

Intensive study has been devoted to the erosion zone that develops along the outer bank of the meandering bend. Here, in fact, multiple pools, that can be associated with features called "shingle bars" (Lewin, 1972; Whiting and Dietrich, 1993 a, b), have been observed. These features migrate downstream into the straight reaches connecting the meandering bends. Some authors (Parker and Joanneson, 1989) interpreted them as member of a family of alternating periodic responses to the impulsive forcing by the change in curvature at the bend entrance.

In order to isolate the effect of the channel changing curvature from the effect of the bed topography on flow pattern, the experiments have been conducted both over a flat bed and over an erodible bed. In both cases, the local flow velocity components have been measured along the meandering bend, in order to evaluate the cross-circulation significance and the forcing effect of the bed topography.

2 EXPERIMENTAL INSTALLATION

The experiments were performed in a meandering laboratory channel that follows the sine-generated curve with a deflection angle of 110°. The channel cross section was rectangular with width, B, of 0.50 m. The channel axis was 23,46 m long and the channel banks were of clear 0.2 cm thick plexiglas strips. The bed of the channel was of quarts sand ($D_{50} = 0.65$ mm, $D_{16} = 0.55$ mm and $D_{84} = 0.90$ mm), with longitudinal bed slope of channel axis equal to S = 0.371%.

The plan view of the meandering laboratory channel is reported in Figure 1. Water entered the channel by the return pipe C connecting the pumping tank A to the head divergent D. Then, the water flowed in the straight channel (inflow channel) until to reach the meandering channel reach. In the erodible bed experiments, both the water and the sediment were recycled. They were discharged from the channel into the pumping tank A.

Two runs, called Run 1 and Run 2, characterized respectively by a "small" aspect ratio (B/h = 9.6 < 10) and a large aspect ratio (B/h = 16.6 > 10), have been carried out both over the flat immobile bed and over the erodible bed.

For the flat bed runs, the sand on the bed was impregnated with spray paint which preserved the grain roughness and did not allowed the bed deformation. Table 1 presents the hydraulic conditions for each run: Q indicates the flow rate, h is the water depth, Re∗ is the roughness Reynolds number, Fr is the Froude number.

During each run, the flow velocity components and the water depths were measured. Intensive study was made especially along the channel reach between section 7 and section 31 (see Figure 1); some other sections ("control sections" 37, 43) have also been

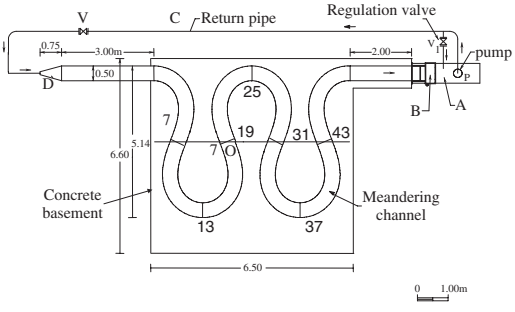


Figure 1. Planview of the experimental apparatus.

Table 1. Hydraulic conditions.

Run	D_{50} (mm)	h (m)	Q (m^3/s)	S (%)	B/h	Re∗	Fr
1	0.65	0.05	0.012	0.371	9.6	83.4	0.42
2	0.65	0.03	0.050	0.371	16.1	66.8	0.33
3	0.65	0.03	0.065	0.371	16.1	43.0	0.73

analyzed in order to check the periodicity both of the water depth and of the flow velocity. The local flow velocities were measured in nine verticals of the measurement sections both by using a 2D side-looking probe Acoustic Doppler Velocimeter (ADV) and by using an Ultrasonic Doppler Velocimeter (DOP2000), that allows to measure instantaneous flow velocity profiles. The DOP2000 was especially used for deformed bed runs, where very small water depths occurred along the inner bank of the curved reaches and the ADV did not provide accurate measured data.

Furthermore, both the flow velocity components and the bed topography measured during previous experiments carried out in the same meandering laboratory channel (Termini, 1999 a, b, c) have also been used in this work (Run 3 of Table 1); the local flow velocity components were measured along the channel reach between section 19 and section 31, by using a propeller.

During each experiment, the water depth was also measured by using a point gage, opportunely attached to a portable carriage that traversed the channel.

3 ANALYSIS OF MEASURED DATA

3.1 *Flat bed experiments*

Flat bed experiments have been carried out in order to isolate the effect of the downstream changing channel curvature and, thus, to analyze how it influences the kinematic characteristics of the flow.

The velocity measurements were made in 17 sections (measurement sections), distant each either 50 cm or so, along the channel reach between section 7 and section 31 (Figure 1). The data have been analyzed assuming a local reference system with longitudinal axis (s) pointing downstream, transverse axis (r) pointing to the inner bank and vertical axis (z) pointing upward.

The analyses of the vertical profiles of the measured longitudinal velocity components (v_s) highlights that when the aspect ratio B/h is less than 10 (Run 1), v_s assumes the maximum value at a water level $z = \delta < \mathrm{h}$; when $\mathrm{B/h} > 10$ (Run 2), v_s has the maximum occurring at a water level $z = \mathrm{h}$. This is in accordance with Blanckaert and Graf's (2001) findings ($\mathrm{B/h} < 10$), where the maximum of longitudinal flow velocity was found close to the outer bank and below the water surface.

As an example, in Figures 2a–2b the vertical profiles of the longitudinal velocity component measured near the channel axis, during Run 1, respectively at the inflection section (section 19) and at the apex section (section 25), are reported. Analogously, in Figures 2c–2d the corresponding vertical profiles measured during Run 2 are also shown.

The measured data of the longitudinal flow velocity component have been interpolated with the logarithmic velocity distribution law:

$$\frac{v_s}{v_*} = \frac{1}{\kappa}\ln\left(\frac{z\,v_*}{\nu}\right) + \Phi\left(\frac{v_*\,k_s}{\nu}\right) \tag{1}$$

where v_* is the shear flow velocity, κ is the Von Karman's constant, ν is the water viscosity, k_s is the representative roughness height and Φ is a function

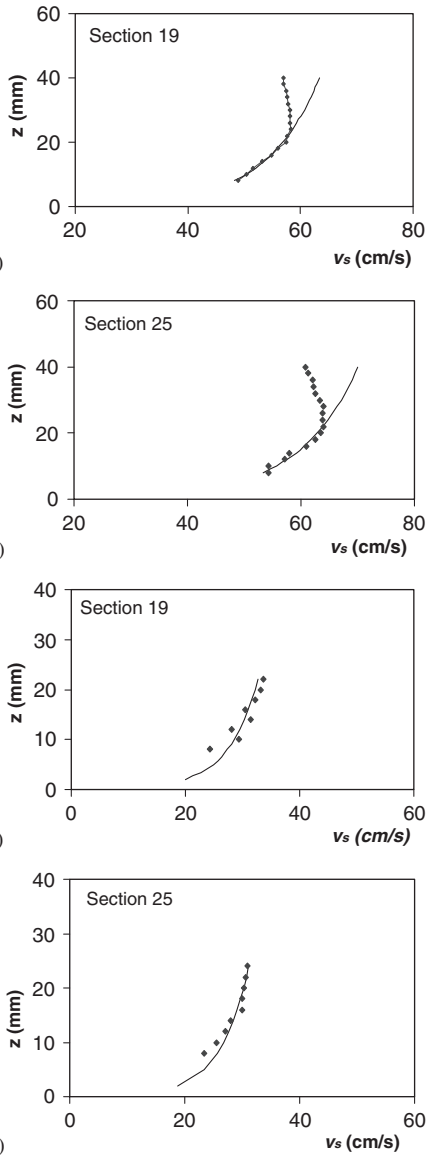


Figure 2. Longitudinal velocity profiles.

that for smooth wall is equal to 5.5 and for absolutely rough wall is estimated as:

$$\Phi = 8.48 - \frac{1}{\kappa}\ln\left(\frac{v_* k_s}{\nu}\right) \qquad (2)$$

The value of the local shear velocity, that is a parameter of the logarithm laws (1), has been estimated by data-fitting.

Figures 2a–2d clearly show that in the case of B/h < 10 (Run 1), the logarithmic law can be fitted to data measured in the range $0 < z < \delta$; in the case of B/h > 10 (Run 2), the logarithmic law can be applied over the entire flow depth.

Furthermore, Figures 3a–3b present the spatial distributions of the velocity vectors measured, during Run 1, along the channel reach between section 19 and section 31, respectively near the bed ($z = 0.8$ cm) and near the free surface ($z = 4.0$ cm); Figures 3c–3d present the corresponding distributions measured, during Run 2, respectively at $z = 0.8$ cm (near the bed) and at $z = 2.0$ cm (near the free surface).

The plane distributions of the measured velocity vectors highlight that in both cases (Run 1 and Run 2), the maximum of flow velocity lies, at the bend entrance, at the inner bank. Along the bend, it crosses the channel and, at the downstream inflection section, it is at the outer bank. At the apex of the bend the plane distribution of flow velocity is almost uniform.

Previous experiments carried out by Leschziner and Rodi (1979) in a constant strongly curved channel (R/B = 1, where R is the radius of curvature of the channel centerline) have shown that the maximum of longitudinal velocity, v_s, occurred always near the inner bank. Blanckaert and Graf (2001) observed, in a constant curved channel with R/B = 5, the maximum velocity component v_s occurring close to the outer bank and in the lower part of the flow depth.

The meandering channel considered in the present work is characterized by a variable ratio R/B passing from a very large value at the inflection section to a small value at the apex section. The spatial distribution of the flow velocity vectors highlights an intermediate behavior: the maximum is found near the inner bank where the ratio R/B is large; then, decreasing the ratio R/B, it moves toward the outer bank, that is reached at the inflection section downstream, where the ratio R/B is large but with negative sign. In the inflection section one wave-length distant, the maximum of flow velocity is found again at the inner bank.

The described pattern of flow velocity vectors highlights the convective behavior of the flow. The flow, in fact, passing from section 19 to section 31 (Figures 3a–3d) accelerates at the outer bank and decelerates at the inner bank. Thus, it can be concluded that because of the acceleration in the upstream bend, flow enters in the reach starting from section 31 with highest velocity near the outer bank.

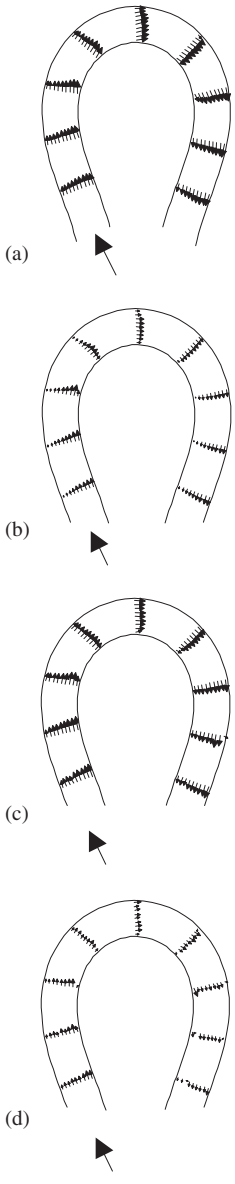


Figure 3. Plane distribution of velocity vectors.

Moreover, Figures 3a–3b show that, when B/h < 10, the cross-circulation is significant: the velocity vectors near the free surface are oriented in the opposite direction (outward) to the velocity vectors near the bed, that are oriented inward. When B/h > 10 (Figure 3c–3d) the velocity vectors near the bed and those near the free surface are almost oriented in the same direction.

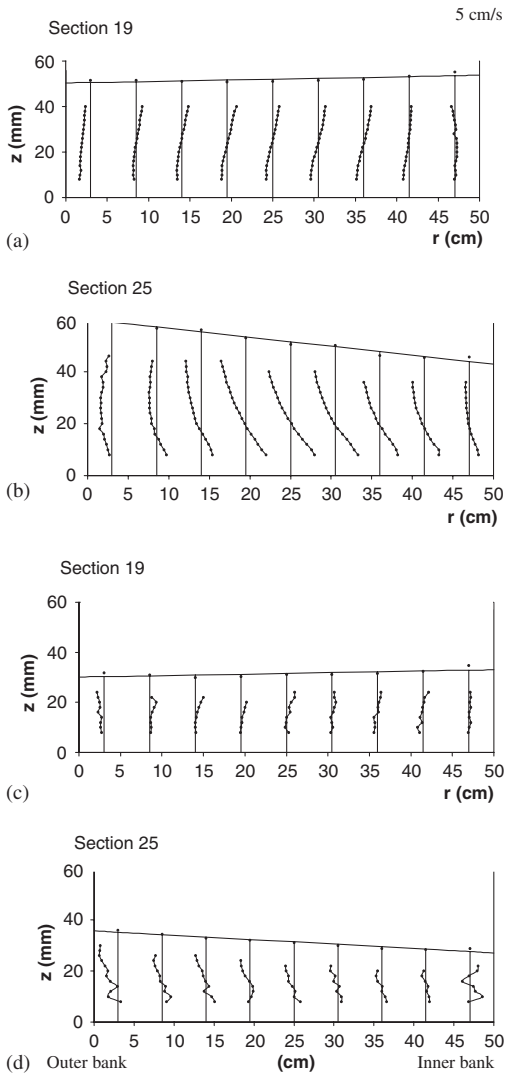


Figure 4. Measured vertical transverse distributions.

The magnitude of the cross-circulation has been also observed by the vertical profiles of the measured transverse flow velocity components (v_r). As an example, Figures 4a–4d present the vertical profiles of v_r measured, both during Run 1 (Figures 4a–4b) and during Run 2 (Figures 4c–4d), at section 25 (apex section) and at section 19 (inflection section). As it is shown, when B/h < 10 (Run 1), the vertical distributions of the transverse velocity component show a change of sign passing from the bed to the free surface and the cross-circulation is significant. Anyway, because of the convective component is not null, the transverse velocity distributions cannot be approximated by theoretical laws (Rozovski, 1965) estimated in fully developed regions, where the convective terms have been neglected. When B/h > 10 (Run 2), the vertical distributions of the transverse velocity component (Figures 4c–4d) do not show a clear change of sign passing from the bed to the free surface. The cross-circulation is very small and the convective velocity component becomes significant.

3.2 *Deformed bed experiments*

During the deformed bed experiments, the bed surface, visible by the clear Plexiglas walls, was intermittently monitored at the outer bank and at the inner bank of the channel by tracing the bed surface on the clear channel walls.

Furthermore, the evolution of the bed deformation in time and the variation of the bed surface at the banks were filmed during the experiment.

The flow velocity measurements were carried out only after the equilibrium bed configuration was reached. It was reached when, as described in previous works (Termini, 1999 a, b, c), both the water-surface slope and the gross bed geometry did not change in time. Along the curved reach, the stable average bed topography presented a front of deposit near the inner bank and a global erosion zone near the outer bank. Furthermore, a series of pools (distant each either almost 1 m) appeared at the outer bank. Each pool is considered as part of a bed-form that is similar to the bar unit developing in straight channels, but with front of deposition occurring always at the inner bank of the bend. These bars, superimposed on the average pattern of the bed, migrated along the bend and the bed levels at the outer bank varied continuously in time. Details of the stable bed topography estimated at the end of Run3 can be found in previous works (Termini, 1999a; Franco et al., 1997).

In deformed bed experiments, the local flow velocity components have been measured only during Run 1. The measurements have been carried out by using DOP2000, because very small flow depths appeared at the inner bank, where the global front of deposition occurred. The same measurement sections selected for the flat bed experiments were considered. For the analysis of data collected in deformed bed experiment, particular attention has been focused to the half cross-section near the outer bank (erosion zone), where the series of pools appeared.

In Figure 5 the vertical distributions of the transverse velocity components measured at the transverse abscissas $r = 8.5$ cm, $r = 14$ cm and $r = 25$ cm of section 25 are reported. In Figure 6 the vertical distributions of the vertical velocity components measured at the same transverse abscissas are also reported. As Figure 5 shows, the vertical distributions of the transverse velocity confirm the formation of a significant

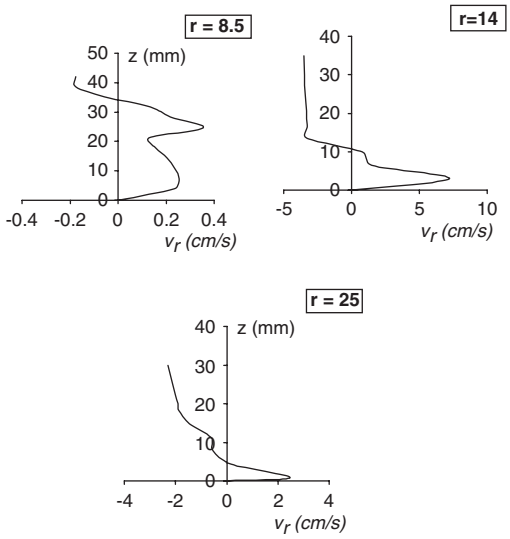


Figure 5. Section 25: measured transverse velocity component.

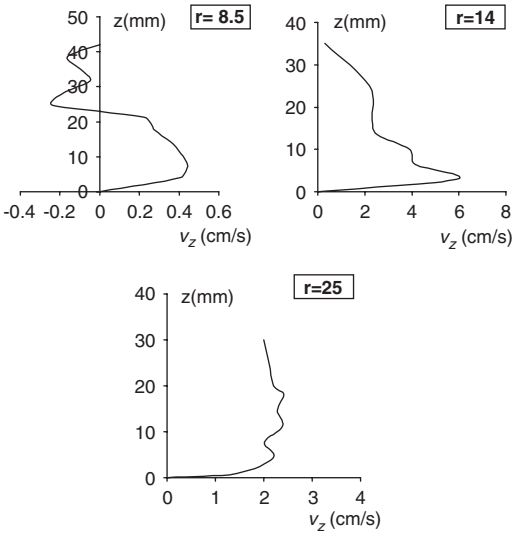


Figure 6. Section 25: measured vertical velocity component.

cross-circulation velocity component, that is of the same order of magnitude as that measured over the flat bed. Thus, the characteristics and the size of the transverse velocity component, given by the combination of the cross-circulation and of the convective velocity component, are essentially produced by the streamwise changing channel curvature and, then, exalted by the evolving bed topography.

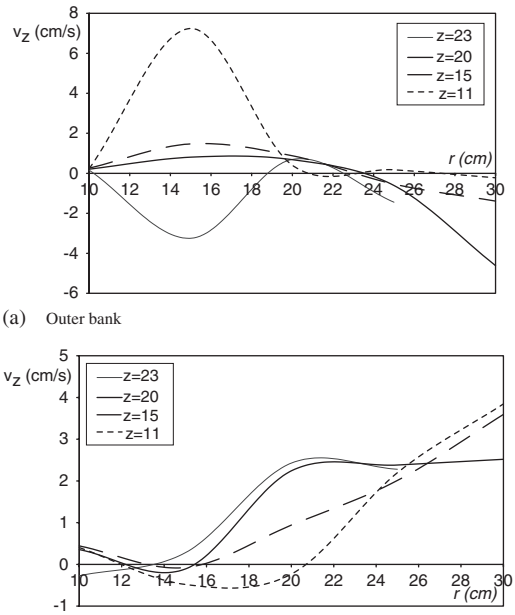


Figure 7. Horizontal profiles at different water depths of the time averaged velocity components: (a) transverse component; (b) vertical component.

Furthermore, the distributions of the vertical velocity component, showed in Figure 6, highlight that at the transverse abscissa $r = 8.5$, i.e. near the outer bank, the vertical velocity has a negative sign in the higher part of the cross-section. This could reveal the existence of a counter-rotating secondary flow cell, in accordance with previous findings (de Vriend, 1981; Blanckert and Graf, 2001; Booij, 2002) obtained in constant strongly curved channels. Blanckert and Graf (2001) attached a great importance to the counter-rotating formation that exerts a protective effect on the bank and reduces the level of the flow turbulent activity.

The aforementioned second flow circulation cell can be also examined in Figures 7a–7b, where the horizontal profiles of the transverse velocity component and of the vertical velocity component are reported, respectively. Both the negative values (vector pointing to the outer bank) of the transverse velocity component, v_s, and the negative values of the vertical velocity component, v_r, appearing near the free surface and at the outside part of the cross-section could confirm the existence of the second counter-rotating circulation flow cell (the first is the cross-circulation, related to the classical elicodal motion), that develops near the outer bank.

Figures 8 and 9, where the isocontours of the transverse velocity component and of the vertical velocity component are reported respectively, show clearly the

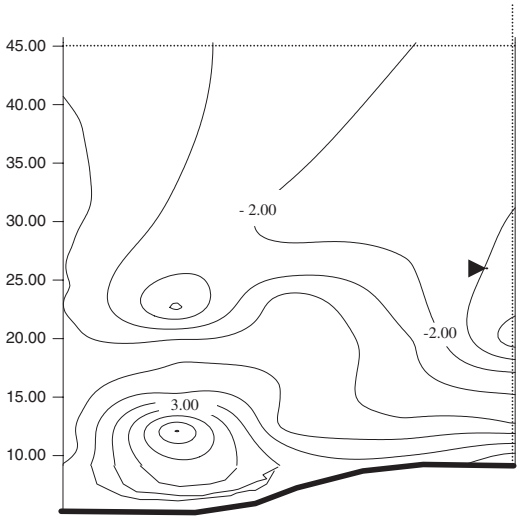


Figure 8. Sez. 25: contour lines of the transverse velocity components.

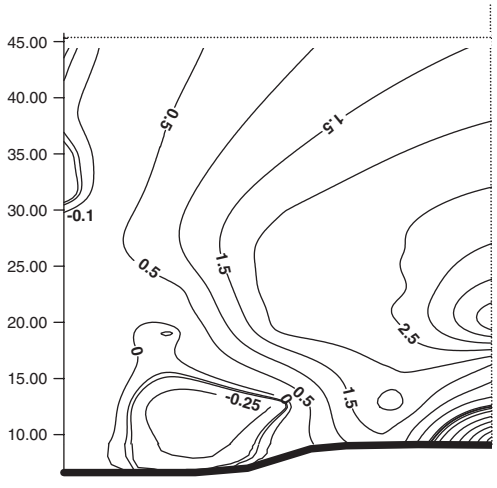


Figure 9. Sez. 25: contour lines of the vertical velocity components.

aforementioned trend and the presence of a rotating cell at the upper outside riverbank.

In Figure 10 the isocontours of the transverse velocity component measured over the flat bed have also been reported. The comparison between Figure 8 (over deformed bed) and Figure 10 (over flat bed) highlights that the second flow circulation cell, forming at the outer bank (erosion zone along the channel), is produced as result of the bed deformation: it does not appear when the bed is flat. In this last case, in fact, Figure 10 suggests that an unique cell of circulating secondary flow develops along the bend: the contour

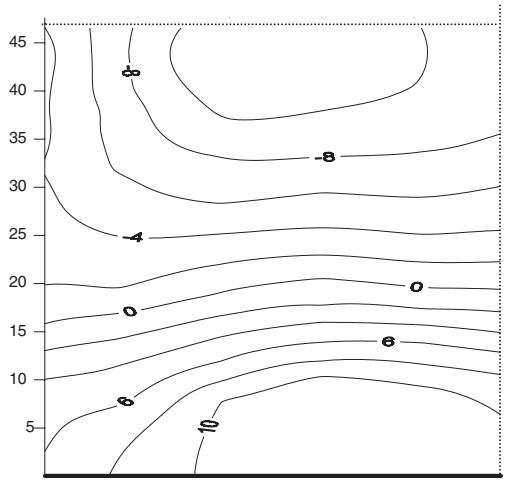


Figure 10. Sez. 25: contour lines of the transverse velocity components (flat bed).

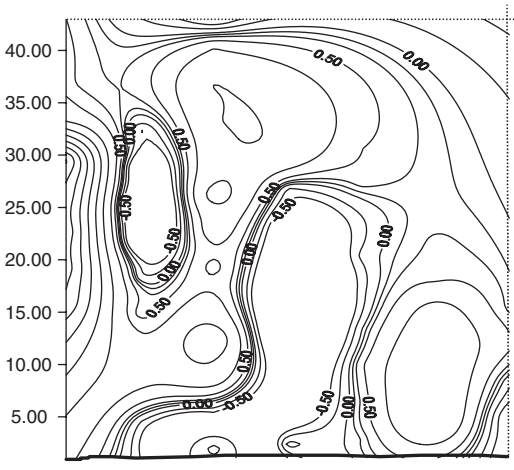


Figure 11. Section 31: contour lines of the transverse velocity component.

lines are regular and no element of separation appears in the cross-section.

Furthermore, Figures 8 and 9 highlight the presence of a third isolate circulation cell, that forms near the bed, where the pools occur.

Figures 11 and 12 show the isocontours of the transverse velocity component measured at the inflection section (section 31), respectively over the deformed bed and over the flat bed; the isocontours of the vertical velocity component measured at the same section with deformed bed are reported in Figure 13. It can be observed that also at the inflection section the bed topography affects the transverse velocity distribution producing a circulating zone at the outer bank, both

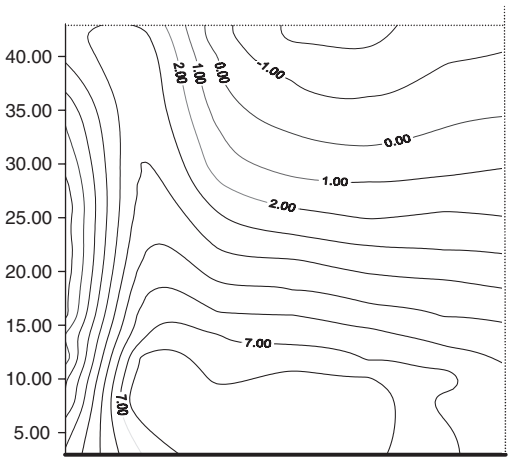


Figure 12. Section 31: contour lines of the transverse velocity component (flat bed).

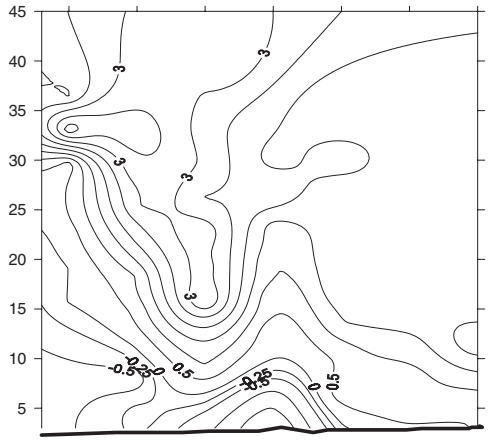


Figure 13. Section 31: contour lines of the vertical velocity component.

near the bed and near the free surface. This circulation is less evident than that produced at the apex section.

4 CONCLUSION

Experimental investigations in a meandering laboratory channel of large amplitude have been carried out in order to analyse the secondary motion characteristics. The experiments conducted with flat bed have mainly shown that: (1) when the aspect ratio B/h is less than 10 (Run 1) the maximum value of the longitudinal flow velocity component occurs at a water level $z = \delta < h$. Furthermore, the maximum flow velocity lies, at the bend entrance, near the inner bank; then, along the bend, it crosses the channel and, at downstream inflection section, it is found at the outer bank. An unique significant large secondary circulation cell, covering the cross-section, develops along the bend; the convective acceleration component is small but it is not null; (2) when the aspect ratio B/h is greater that 10, the cross-circulation can be neglected and the convective acceleration becomes significant.

The experiments conducted with deformed bed ($B/h > 10$) have highlighted that it seems to appear a second counter-rotating secondary flow cell at the upper part of the outer bank, in accordance with previous findings.

The comparison between the flow velocity components measured with flat bed and those measured with deformed bed showed that the transverse velocity component, given by the combination of the cross-circulation and of the convective acceleration component, is essentially produced by the stream-wise channel curvature and, then, exalted by the evolving bed topography.

REFERENCES

Blanckaert K. & W.H. Graf. (2001). Mean Flow and Turbulence in Open-channel, *Bend. Journal of Hydraulic Engineering*, vol. 127, n. 10, pp. 835–847.

Bridge J. & J. Jarvis. (1976). Flow and Sedimentary Processes in The Meandering River South Eskglenclova, Scotland, *Earth surface processes*, 1, pp. 303–336.

Booij R. (2002). Modelling of the secondary flow structure in river bends. International congress River Flow 2002, Belgium 4–6 September.

Chang H.H. (1988). *Fluvial Processes in River Engineering*, Wiley-Interscience publication – John Wily and Sons.

De Vriend H.J. (1981). Velocity redistribution in curved rectangular channels. J. Fluid Mech. 07, pp. 423–439.

Engelund F. (1974). Flow and Bed Topography in Channel Bends, *Journal of Hydraulics Division*, ASCE, 100(11), pp. 1631–1648.

Francis J.R.D. & A.F. Asfari. (1978). Longitudinal Velocity Distributions in Wide Curved Open-Channel Flows. *Journal of Hydraulic Research*, vol. 9, n. 1.

Franco V., M. Lo Brutto & D. Termini. (1997). La Fotogrammetria Digitale per il Rilievo del fondo Deformato di un Modello Fluviale, *L'Acqua*, **2**, pp. 49–56.

Hooke, R. (1975). Distribution of Sediment Transport and Shear stress in a Meander Bend, *The Journal of Geology*, vol. 83, pp. 543–565.

Jackson R.G. (1975). Velocity-Bed-Form-Texture Patterns of Meander Bends in the Lower Wabash River of Illinois and Indiana, *Geological Society of America Bullettin*, 86, pp. 1511–1522.

Kikkawa H., S. Ikeda & A. Kitagawa. (1976). Flow and Bed Topography in Curved Open Channels, *Journal of the Hydraulics Division* – ASCE, 102(9).

Leschziner M.A. & W. Rodi. (1979). Calculation of Strongly Curved Open-Channel Flow. *Journal of the Hydraulics Division* – ASCE, vol. 105, n. Hy10.

Lewin J. (1972). Late stage meander growth. *Nature*, 240, 116.

Nelson J.M. & D. Smith. (1989). Flow in Meandering Channels with Natural Topography, *American geophysical union*, pp. 321–376.

Odgaard A.J. & M.A. Bergs. (1988). Flow Processes in a Curved Alluvial Channel, *Water Resources Research*, 24(1), pp. 45–56.

Ren Z. & G. Jun. (1989). Experimental Study on the Cause of Formation of Alluvial River Patterns, Fourth Int. Symp. on River Sedimentation, June 5–9, China.

Rozovski, I.L. (1965). Flow of water in bends of open channels. The Academy of Sciences of the Ukrainian SSR, Israel Program for Scientific Translations, Jerusalem.

Schumm, S.A. (1963). Sinuosity of alluvial rivers on the great plain. *Geological Society of American Bulletin*, 74, pp. 1089–1100.

Schumm S.A. & H.R. Kkhan. (1972). Experimental Study of Channel Patterns, *Geological Society of American Bullettin*, vol. 83, pp. 1755–1770.

Smith J.D. & S.R. McLean. (1984). A model for Flow in Meandering Streams, *Water Resources Research*, 20(9), pp. 1301–1315.

Termini D. (1999a). Experimental study in a meandering channel: 1. Analysis of bed topography, *I.A.H.R. Symposium on River, Coastal and Estuarine Morphodynamics*; Genova, Settembre 6–10.

Termini D. (1999b). Experimental study in a meandering channel: 1. Analysis of bed topography, *I.A.H.R. Symposium on River, Coastal and Estuarine Morphodynamics*; Genova, Settembre 6–10.

Termini D. (1999c). Boundary Shear Stress Distribution and Convective Accelerations: a forecast methodology of planimetric evolution of meandering channels, *International Water Resources Engineering Conference* ASCE conference, Seattle, 8–12 August.

Thompson A. (1986). Secondary flows and the pool-riffle unit, a case study of the process of meander development. *Earth Surface Processes Landforms*, 11, 631–641.

Whiting P.J. & W.E. Dietrich. (1991). Convective Accelerations and Boundary Shear Stress over a Channel Bar, *Water Resources Research*, 27(5), pp. 783–786.

Whiting P.J. & W.E. Dietrich. (1993a). Experimental Studies of Bed Topography and Flow Patterns in Large-Amplitude Meanders, 1. Observations, *Water Resources Research*, 29(11), pp. 3605–3614.

Whiting P.J. & W.E. Dietrich. (1993b). Experimental Studies of Bed pography and Flow Patterns in Large-Amplitude Meanders, 2. Mechanism, *Water Resources Research*, 29(11), pp. 3615–3622.

Yalin M.S. (1992). *River Mechanics*. Pregamon Press. London.

Yen B.C. (1972). *Spiral Motion of Developed Flow in Wide Curved Open Channel Bend*; Sedimentation (Einstein) – Shen editor.

Zimmerman C. & J.F. kennedy. (1978). Transverse Bed Slopes in Curved Alluvial Streams, *Journal of Hydraulic Division*, vol. 104 Hy1, Proceeding paper 13482, pp. 33–48.

This page intentionally left blank

River Flow 2004 – Greco, Carravetta & Della Morte (eds.)
© 2004 Taylor & Francis Group, London, ISBN 90 5809 658 0

On the validity of analytical approach to river regime

B. Mengoni & E. Paris
Department of Civil Engineering, University of Firenze, Italy

R. Bettess
HR Wallingford, Howbery Park, Wallingford, Oxfordshire, UK

ABSTRACT: The analytical approach to river regime of White et al. (1982) has been analyzed and the validity of the extremal hypothesis has been verified. A modified version of the original method is here proposed in order to improve prediction capability. To this aim, the original trapezoidal cross section has been changed, employing the analytical geometry for stable channel proposed by Cao & Knight (1998). The modified method appears to be still coherent with the extremal hypothesis, and provides better agreement if compared with field and laboratory tests on stable non cohesive straight channels.

1 INTRODUCTION

The shape and the dimension of the cross section of a self formed channel is the result of the complex interaction between flowing water and mobile particles that compose bed and banks.

Despite numerous contributes, the prediction of the stable channel configuration is still an active field of research, where yet no clear agreement about the methods is achieved.

Firstly, simple empirical methods were developed using data from field and laboratory observations, obtaining regime equations (Lindley 1919, Simon & Albertson 1963, Blench 1969) that have been used for long time. However, the typical shortcomings of the empirical methods, have induced many researchers to investigate the processes involved and formulate new approaches.

A more rational approach, known as *tractive force method* was developed on the assumption that in a stable configuration all the particles were in incipient motion condition (Glover & Florey 1951, Lane 1955). Nevertheless, experiments on straight stable channel with coarse non cohesive sediments (Wolman & Brush 1961), have showed that the concept of static equilibrium is not realistic and instead is possible the existence of a dynamic equilibrium, for which the sediments are actively transported in the central bed region and bed load vanished in sidebank regions.

Later, more physically based approaches were proposed by several Authors in an attempt to describe the regime conditions using the basic equations for water and sediment transport.

In particular, the extremal hypothesis combined the friction factor equation and sediment transport equation with an extra one, based on the maximization or minimization of a certain parameter (Chang 1980, Yang et al. 1981, White et al. 1982, Yang 1992, Millar & Quick 1997, Cao & Knight 1997, Millar & Quick 1998). Even if the predictions based on this approach are generally in agreement with large range of observations, the theoretical justifications for such hypotheses are still not clear, and suggests a further investigation.

More recently, approaches based on the employment of basic laws of mechanics have been proposed.

Parker (1978b) noticed that the *tractive force* theory could not be able to describe the case of an active-bed gravel river; in fact, as long as bed load exists in the central region some grains on the banks must also be in motion causing bank erosion and indefinitely widening of the cross section. Parker termed this the "stable-channel paradox" and solved the problem introducing lateral momentum transfer due to the turbulence, obtaining in this way, a lateral redistribution of bed shear stresses. Parker (1978a) introduced also the case of straight sand river, where sediments are actively transported as bed load and as suspended load, considering a balance of lateral bedload and lateral diffusive transport of suspended sediments.

Ikeda et al. (1988) introduced the effects of heterogeneous bed material on gravel river, Ikeda & Izumi (1991) formulated a more rigorous approach for sand rivers, Diplas & Vigilar (1992) reformulated the problem of threshold channel where the shape of the banks is not assumed but become part of the solution;

Cao & Knight (1998) considered the contribution of the secondary currents.

Other contributions considered the time evolution of an initially trapezoidal channel toward a steady stead configuration: experimental data for uniform sediments were collected by Ikeda (1981) and Diplas (1990), for heterogeneous material by Ikeda & Izumi (1991), for bankfull and overbank flow by Valentine et al. (2001) and Valentine & Ershadi (2003).

Straight channel time evolution has been formulated in analytical and numerical way: Pizzuto (1990) presented a numerical method for gravel channel in case of bed load transport. He predicted the shear stress distribution employing the modified area method of Lundgren & Jonsson (1964), then calculated the evolution of bed topography and the bank failure in case of side slope steeper than repose angle. Schippa (1991) presented an analogous numerical model considering suspended load and lateral flux of sediment coming from collapsed banks. Kovacs & Parker (1994) developed a fully mechanistic mathematical model to simulate the evolution process due to bank erosion in case of bedload only.

In this paper, a review of the validity of the extremal hypothesis is carried out by analyzing the White et al. (1982) method. A modified version of the method is proposed by adopting a new cross section geometry. Comparisons of predicted values with experimental results (Valentine et al. 2001) and with field data of non-cohesive gravel and sand streams (Parker 1978b, Parker 1995) have been performed.

2 FORMULATION OF THE PROPOSED METHOD

In the approach of White et al. (1982), in the following cited as WBP method, the determination of the stable cross section was achieved analytically by employing the flow and sediment transport equations, and assuming the minimization of the slope. The calculations were performed considering a rectangular shape, then adjusted to a trapezoidal one of the same cross-sectional area. The bed and bank material have been assumed uniform and homogeneous.

However, several experimental observations (Ikeda 1981, Ikeda et al. 1988, Diplas 1990, Valentine et al. 2001) and numerical simulations (Kovacs & Parker 1994) have demonstrated that the trapezoidal configuration is not stable and always evolves toward a smoother shape. Moreover Valentine et al. (2001), obtained laboratory cross section clearly wider and shallower than that predicted by the WBP method, even if characterized by the same hydraulic area. For this reason, the cross section geometry of the WBP method has been modified, employing a new shape more similar to the one observed in laboratory test.

According to different theories, several shape of bank zones have been proposed in the last years: a cosine curve profile was obtained by Parker (1978a,b), Ikeda et al. (1988) and Pizzuto (1990); an exponential function was obtained from the regression on the experimental data by Ikeda (1981) and by Diplas (1990); a fifth-degree polynomial came from the numerical approach of Diplas & Vigilar (1992); a parabolic profile has been also proposed by several researchers (Chow 1959, Cao & Knight 1998a,b).

Cao & Knight (1998) obtained an analytical expression of the cross section profile on the basis of entropy maximization principle. This geometry has been chosen to modify the WBP method and it is characterized by the following equations (Fig. 1):

$$L = \frac{2Y_c}{\mu} \tag{1}$$

$$\Omega = \frac{8}{3}\frac{Y_c^2}{\mu} + bY_c \tag{2}$$

$$P = \frac{2Y_c}{\mu^2}\left[\mu\sqrt{\left(1+\mu^2\right)} + \ln\left(\mu + \sqrt{1+\mu^2}\right)\right] \tag{3}$$

where L = bank zone width; b = central bed width; W = total surface width; Y_c = central channel depth; Ω = flow area; P = wet perimeter; ϕ = repose angle; μ = tang ϕ coefficient of static friction.

The regime cross section corresponding to a set of given values of water discharge Q, sediment concentration X and sediment size Ds, is obtained by combining the above expressions of geometry (1, 2, 3) and the following flow resistance formula (White et al. 1980) and sediment transport formula (Ackers & White 1973):

$$\frac{F_{gr} - A}{F_{fg} - A} = 1 - 0.76\left[1 - \frac{1}{\exp(\log D_{gr})^{1.7}}\right] \tag{4}$$

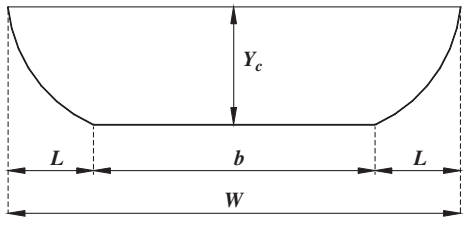


Figure 1. New employed geometry characterized by flat central region and parabolic banks (proposed by Cao & Knight 1998).

$$X = \frac{cS_g D}{Y_c}\left[\frac{F_{gr}}{A} - 1\right]^m \left[\frac{U}{U_*}\right]^n \tag{5}$$

where A, c, n, m = parameters of Ackers & White formula (1973); S_g = specific gravity; ν = kinematic viscosity of the fluid; g = gravity acceleration; U^* = shear velocity; U = mean flow velocity; F_{gr} = particle mobility; F_{fg} = particle mobility of fine grains; D_{gr} = dimensionless grain size, defined as follow:

$$F_{gr} = \frac{U_*^n}{\sqrt{g(S_g - 1)D_s}}\left[\frac{U}{\sqrt{32}\log\frac{10Y_c}{D_s}}\right]^{1-n} \tag{6}$$

$$F_{fg} = \frac{U_*}{\sqrt{g(S_g - 1)D_s}} \tag{7}$$

$$D_{gr} = D_s\left[\frac{g(S_g - 1)}{\nu^2}\right]^{1/3} \tag{8}$$

$$\begin{aligned} &1 \le D_{gr} \le 60 \\ &n = 1.0 - 0.56\log D_{gr} \\ &m = \frac{9.66}{D_{gr}} + 1.34 \\ &\log c = 2.86\ \log D_{gr} - \log^2 D_{gr} - 3.53 \\ &A = \frac{0.23}{\sqrt{D_{gr}}} + 0.14 \end{aligned} \tag{9}$$

$$\begin{aligned} &D_{gr} \ge 60 \\ &n = 1.0 - 0.56\log D_{gr} \\ &m = 0.1 \\ &c = 0.025 \\ &A = 0.17 \end{aligned} \tag{10}$$

2.1 *Analysis of the proposed method*

Results of several numerical runs using the new geometry still confirm the existence of a minimum of the slope. A comparison between data obtained employing the original WBP method and the method modified with the Cao & Knight (1998) geometry (in the following cited as WBP-M method) has been carried out for different sets of Q, X, D.

The comparison is presented in terms of the dimensionless variables defined as follow:

$$W_{\dim} = \frac{W}{D_s} \tag{11}$$

$$Y_{\dim} = \frac{Y_c}{D_s} \tag{12}$$

$$Q_{\dim} = \frac{Q}{\sqrt{gD_s^{\,5}}} \tag{13}$$

As shown in Figure 2, the WBP-M cross sections are constantly wider than the predicted by the original WBP method, while depth values (Fig. 3) do not seem to change significantly.

A further investigation on the variability of the hydraulic parameters in the vicinity of the stable configuration has been carried out to explore the presence of extremal values other than the minimum of slope. A range of width-surface variation within the 60% of the regime value has been considered. Figures 4 and 5 show the hydraulic variables (made dimensionless with the corresponding regime values) for a set of given data ($Q = 200\ \mathrm{m^3/s}$, $X = 100$ p.p.m., $D = 0.4$ mm). It can be observed that, except the slope, no other variable presents an extreme value: all the functions are monotonous respect to width variation. Only the Chezy coefficient C seems to have a roughly constant value for any cross section (Fig. 5).

The coherence of the modified method has been also tested analyzing the condition of vanishing sediment transport. In this case the cross section cannot self adjust and therefore no minimum value of slope is not expected. In Figure 6, the hydraulic variables Y_c,

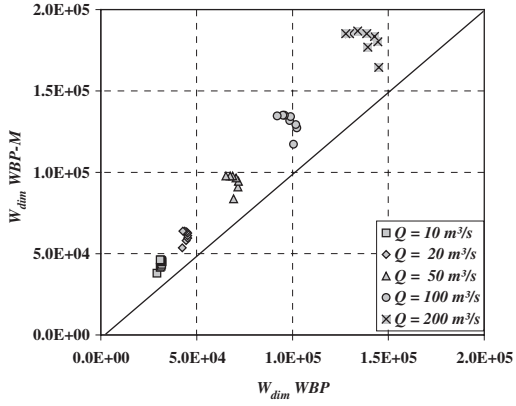


Figure 2. Comparison of dimensionless regime surface width obtained with original WBP method and WBP-M method: different set of Q, X have been considered ($\phi = 29°$, $D = 0.4$ mm).

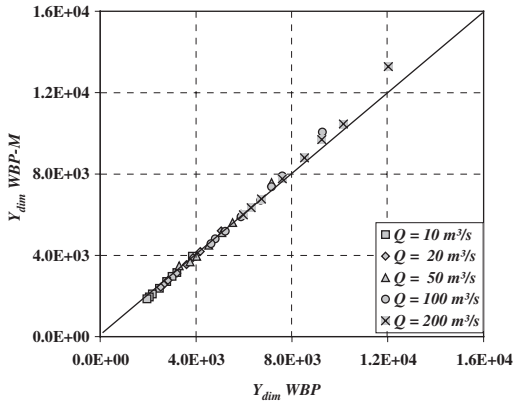


Figure 3. Comparison of dimensionless regime depth obtained with original WBP method and WBP-M method: different set of Q, X have been considered ($\phi = 29°$, $D = 0.4$ mm).

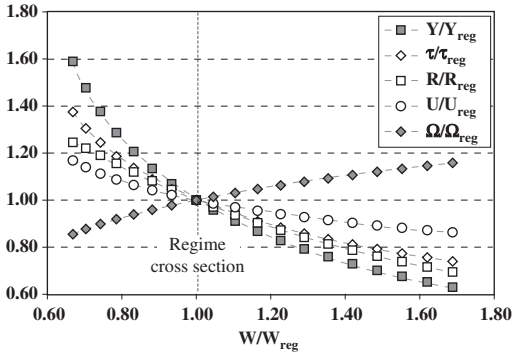


Figure 4. Dimensionless variables for a set of cross sections ($Q = 200$ m^3/s, $X = 100$ p.p.m., $D = 0.4$ mm, $\phi = 29°$).

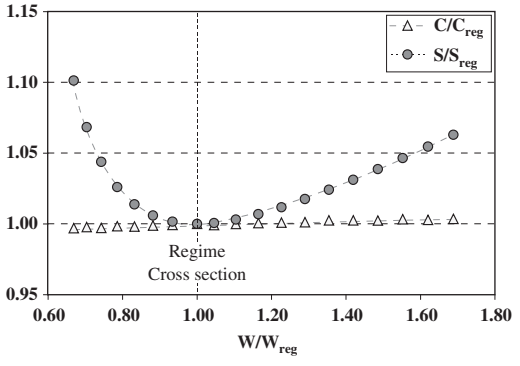


Figure 5. Slope and Chezy coefficient for a set of cross sections ($Q = 200$ m^3/s, $X = 100$ p.p.m., $D = 0.4$ mm, $\phi = 29°$).

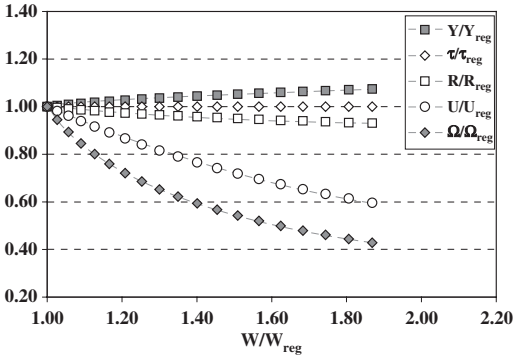


Figure 6. Dimensionless variables for a set of cross sections ($Q = 200$ m^3/s, $X = 0$, $D = 0.4$ mm, $\phi = 29°$).

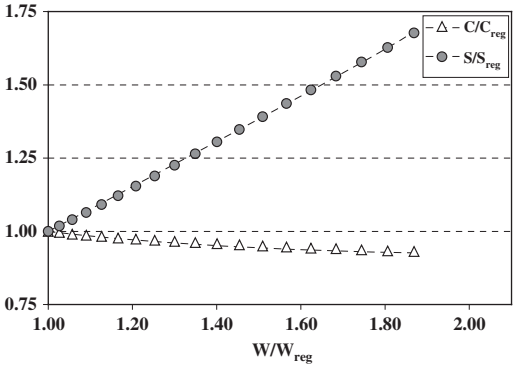


Figure 7. Slope and Chezy coefficient for a set of cross sections ($Q = 200$ m^3/s, $X = 0$ p.p.m., $D = 0.4$ mm, $\phi = 29°$).

R, U, Ω, τ have been shown for the case of $X = 0$, $Q = 200$ m^3/s, and $D = 0.4$ mm. It is still present a monotonous pattern of the hydraulic variables, including slope (Fig. 7).

The above analysis refers to the hydraulic parameters in terms of the cross section averaged values. A further investigation has been carried out in terms of local depth averaged values using a numerical model based on the depth-integration of the Reynolds-averaged Navier-Stokes equations in the form proposed by Shiono & Knight (1989):

$$\rho g d \frac{dH}{dx} - \beta \tau_b + \frac{\partial}{\partial y}\left(H \overline{\tau}_{yx}\right) = \frac{\partial}{\partial y}\left[d\left(\rho \overline{UV}\right)_d\right] \qquad (14)$$

where ρ = fluid density; H = local depth normal to the bed; h = water level; x = streamwise direction; y = transversal direction; U = streamwise velocity; V = lateral velocity; τ_b = bed shear stress; τ_{xy} = Reynolds stress; β = coefficient for the influence of lateral bedslope on bed shear stress.

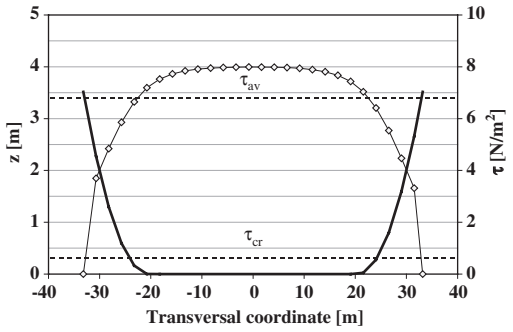


Figure 8. Shear stress distribution of regime cross section ($Q = 200\,\mathrm{m^3/s}$, $X = 100$ p.p.m., $D = 0.4$ mm, $\phi = 29°$). Critical shear stress τ_{cr} and cross section averaged value τ_{av} are also shown.

All terms of (14) are developed as function of unit flow rate q, in order to obtain a second order, nonlinear, non homogeneous, elliptic, partial differential equation that is solved employing a numerical technique based on a finite element method (Defra et al. 2003).

The numerical model, for a given geometry, slope and water depth, provides the corresponding depth averaged hydraulic variables along the transversal coordinate. As example, referring to the regime cross section corresponding to the set of data $Q = 200\,\mathrm{m^3/s}$, $X = 100$ p.p.m, $D = 0.4$ mm, the results of the numerical model in terms of bed shear stress distribution are shown in Figure 8.

It can be observed that the local shear stresses are higher than the critical value in the major part of the bank zone. This disagrees with the Cao and Knight stable cross section hypothesis, according to which the banks should be everywhere in threshold conditions with active sediment transport only in the central bed zone.

2.2 *Comparison with laboratory and field data*

The WBP-M approach has been tested using both field (Parker 1978b, Parker 1995) and experimental data (Valentine et al. 2001).

Valentine et al. (2001) performed experiments in a large laboratory-scale straight non cohesive channel, observing that cross sections predicted with the original WBP approach were too narrow and deep if compared with laboratory results.

Using the WBP-M method, prediction reliability has been improved: stable sections have become wider and shallower and thus in better agreement with experimental data. In Table 1 and 2 are summarized the two considered runs by Valentine et al. (2001) together with the results of the proposed method where the input data for WBP-M method were assumed Q, D_{35}, S, ϕ.

Table 1. Laboratory data (Run 300695, Valentine et al. 2001) and WBP-M results.

		Experimental	WBP-M
Q	[l/s]	25.0	25.0
D_{35}	[mm]	0.74	0.74
S	[‰]	1.83	1.83
Φ	[°]	11.5	11.5
W	[m]	1.76	1.39
d	[m]	0.045	0.07
L/W	[%]	15	49
U	[m/s]	–	0.39
X	[ppm]	–	49.9
τ	[N/m^2]	–	0.84
τ_{cr}	[N/m^2]	0.46	0.46

Table 2. Laboratory data (Run 110595, Valentine et al. 2001) and WBP-M results.

		Experimental	WBP-M
Q	[l/s]	45.0	45.0
D_{35}	[mm]	0.74	0.74
S	[‰]	1.83	1.83
Φ	[°]	11.5	11.5
W	[m]	1.96	1.85
d	[m]	0.068	0.084
L/W	[%]	15	49
U	[m/s]	–	0.41
X	[ppm]	–	85.4
τ	[N/m^2]	–	1.06
τ_{cr}	[N/m^2]	0.456	0.46

The results are satisfactory, even if for Test 1 the geometry still remains slightly deeper and narrower, and bank zone is too large if compared with surface width ($L/W = 49\%$ instead of 15%).

Field data coming from English and American non-cohesive gravel and sand river (Parker 1978, Parker 1995), cover a wide range of discharges, sediment sizes and sediment concentrations.

The WBP-M has been used to predict stable cross section geometry using Q, S and D_{50} as input data.

In Figures 9–12 comparisons between predicted and observed values are presented for both field and laboratory data in term of dimensionless quantities.

In particular, Figure 9 and 10 show good agreement in terms of depth and width predicted values even if width cross section appears slightly under estimate. Moreover Figure 11 and 12 show dimensionless width and depth as a function of dimensionless discharge Q_{dim}.

General agreement of the WBP-M predicted values can be noted either for width and depth data. Finally, data appear to be quite distinct in two groups: one refers to gravel rivers data, for $Q_{\mathrm{dim}} < 10^7$ and one

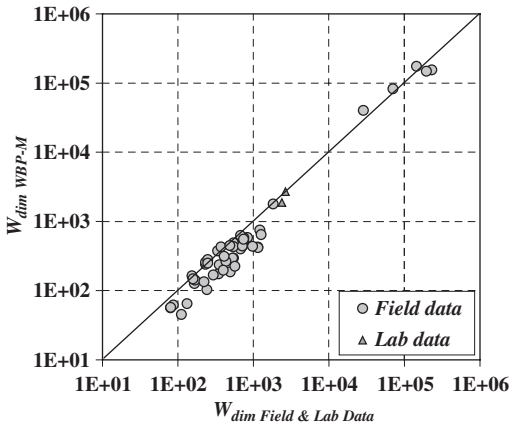


Figure 9. Stable cross section width: comparison between predicted and observed values.

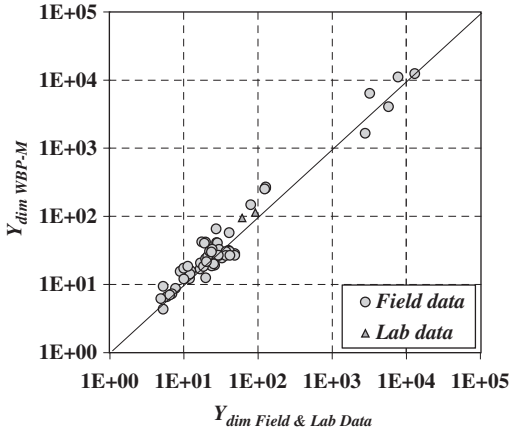


Figure 10. Stable cross section depth: comparison between predicted and observed values.

refers to sand rivers streams data for $Q_{\dim} > 10^9$. This behavior were already observed by Parker (1995).

3 CONCLUSIONS

Several recent experiments and numerical simulations have demonstrated that the trapezoidal shape, as used in the White et al. (1982), appears to be not a stable configuration.

A WBP-M modified method of the WBP analytical approach to river regime is here proposed.

To this aim the trapezoidal cross section geometry has been modified, employing a new shape more similar to the one observed in laboratory tests.

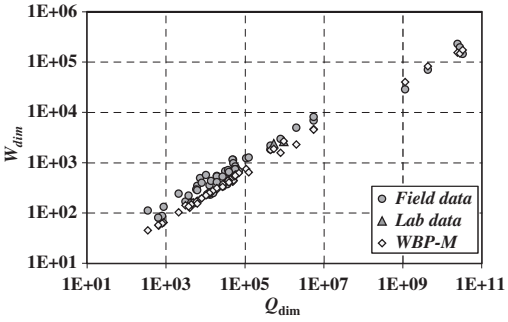


Figure 11. W_{dim} as function of Q_{dim}: comparison between predicted and observed values.

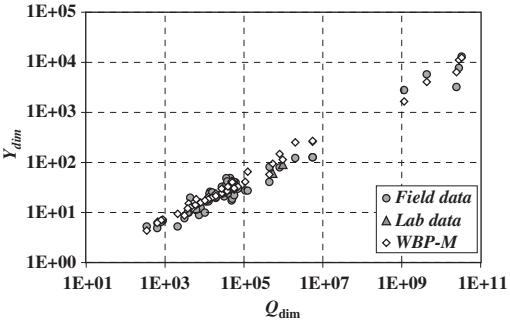


Figure 12. Y_{dim} as function of Q_{dim}: comparison between predicted and observed values.

Particularly the Cao & Knight (1998) geometry has been assumed as the new stable cross section shape in the WBP-M proposed method.

Firstly, the coherence of the extremal hypothesis, which the original method was based on, has been verified: the WBP-M method confirms the existence of a minimum of the slope where river geometry is assumed to be in stable condition.

However WBP-M method provides wider cross sections than those predicted by the WBP method, while depth values are roughly the same. On the other hand, a further investigation reveals that the other hydraulic variables show a monotonous behavior in the proximity of the river regime condition.

Moreover in the case of vanishing sediment transport river cross section cannot adjust its geometry and therefore no minimum value of slope is found.

By using a two-dimensional numerical model the analysis of local depth-averaged hydraulic variables of the stable cross section shows non coherent results with hypothesis formulated by other authors. Particularly the shear stresses distribution along the section does not reveal any critical value in the proximity of the

bank zone, as vice versa postulated by Parker (1978b) and Cao and Knight (1998).

The validity of the WBP-M method has been tested employing both large scale experimental data of Valentine et al. (2001) and field data coming from sand and gravel non cohesive streams (Parker 1978b, Parker 1995).

The proposed method shows significantly improvement of the WBP method in terms of width and depth cross section geometry even if an underestimation in width values is still present.

ACKNOWLEDGMENTS

This work has been developed within the framework of the National project cofunded by the Italian Ministry of University and of the Scientific and Technological Research and by the University of Firenze (COFIN 2001).

NOTATION

A = parameters of Ackers & White formula;
b = central bed width;
C = parameters of Ackers & White formula;
D_s = sediment size;
Y_c = central channel depth;
F_{fg} = particle mobility of fine grains;
F_{gr} = particle mobility;
D_{gr} = dimensionless grain size;
g = gravity acceleration;
H = local depth normal to the bed;
L = bank zone width;
M = parameters of Ackers & White formula;
n = parameters of Ackers & White formula;
P = wet perimeter;
Q = water discharge;
U = streamwise velocity;
U^* = shear velocity;
S_g = specific gravity;
U = streamwise velocity;
V = lateral velocity;
W = total surface width;
x = streamwise direction;
y = transversal direction;
β = coefficient for influence of lateral bed slope on bed shear stress;
ϕ = repose angle;
μ = coefficient of static friction;
ν = kinematic viscosity of the fluid;
ρ = fluid density;
Ω = flow area;
τ = shear stress;
τ_{cr} = critical shear stress;
τ_{xy} = Reynolds stress.

REFERENCES

Ackers, P. & White, W.R. 1973. Sediment transport in open channels: Ackers and White update. *J. Hydr. Engrg., ASCE*, 99(HY4): 1–37.

ASCE Task Committee on Hydraulics, Banks Mechanics and Modeling of River Width Adjustment. 1998. River Width Adjustment I: Process and Mechanism. *J. Hydr. Engrg., ASCE*, 124(9): 881–902.

ASCE Task Committee on Hydraulics, Banks Mechanics and Modeling of River Width Adjustment. 1998. River Width Adjustment II: Modeling. *J. Hydr. Engrg., ASCE*, 124(9): 903–917.

Cao, S. & Knight, D.W. 1997. Entropy based design approach of threshold alluvial channels. *J. Hydr. Res.*, 35(4): 505–524.

Cao, S. & Knight, D.W. 1998. Design for hydraulic geometry of alluvial channels. *J. Hydr. Engrg., ASCE*, 124(5): 484–492.

Chang, H.H. 1980. Geometry of gravel streams. *J. Hydr. Engrg., ASCE*, 106(9): 1443–1456.

Diplas, P. 1990. Characteristics of self formed straight channels. *J. Hydr. Engrg., ASCE*, 116(5): 707–728.

Diplas, P. & Vigilar, G.G. (1992). Hydraulic geometry of threshold channels. *J. Hydr. Engrg.*, *ASCE*, 118(4): 597–614.

DEFRA/Environmental Agency. Flood and Coastal Defence R&D Programme. 2003. Reducing Uncertainty in River Flood Conveyance. Interim report 2: Review of methods for estimating conveyance. *Project W5A-057*.

Glover, R.E. & Florey, Q.L. 1951. Stable channel profiles. *US Bureau of Reclamation* 235.

Kovacs, A. & Parker, G. 1994. A new vectorial bedload formulation and its application to the time evolution of straight river channel. *J. Fluid. Mech*., 267: 153–183.

Ikeda, S. 1981. Self formed straight channels in sandy bends. *J. Hydr. Div., ASCE*, 108(1): 389–406.

Ikeda, S. & Izumi, I. 1991. Stable channel cross section of straight sand rivers. *Water Resour. Res*., 27(9): 2429–2438.

Ikeda, S., Parker, G. & Kimura, Y. (1988). Stable width and depth of straight gravel river with heterogeneous bed materials. *Water Resour. Res*., 24(5): 713–722.

Lindley, E.S. 1919. Regime channels. *Proc., Punjab Enrg. Congr.*, 7.

Lundgren, H. & Jonsson, I.G. 1964. Shear and velocity distribution in shallow channels. *J. Hydr. Div., ASCE*, 90(1): 1–21.

Millar, R.G. & Quick, M.C. 1997. Discussion of 'Development and testing of a riverbank-stability analysis' by S.E. Darby & C.R. Thorne. *J. Hydr. Engrg., ASCE*, 123(11): 1051.

Parker, G. 1978a. Self-formed straight rivers with equilibrium banks and mobile bed. Part 1: the sand-silt river. *J. Fluid. Mech*., 89(1): 109–125.

Parker, G. 1978b. Self-formed straight rivers with equilibrium banks and mobile bed. Part 2: the gravel river. *J. Fluid. Mech*., 89(1): 127–146.

Parker, G. 1995. Gary Parker's river data compendium. http://www.ce.umn.edu/~parker/

Simons, D.B. & Albertson, M. 1963. Uniform water conveyance channels in alluvial material. *Trans. ASCE*, 128(1): 65–167.

Valentine, E.M., Benson, A.I., Nalluri, C. & Bathrust, J.C. 2001. Regime theory and the stability of straight channel with bankfull and overbank flow. *J. Hydr. Resear*., 39(3): 259–268.

Valentine, E.M. & Ershadi, C., 2003. A laboratory study of alluvial channel with unsteady flow. *Proc. Of XXX IAHR Congress,* Thessaloniki, GREECE, Theme C, Vol. 1: 41–48.

Vigilar, G.G. & Diplas, P. 1997. Stable channel with mobile bed: formulation and numerical solution. *J. Hydr. Engrg., ASCE*, 123(3): 188–199.

White, W.R., Paris, E. & Bettess, R. 1980. The frictional characteristics of alluvial streams: a new approach. *Proc., Inst. Of Civ. Engrs.*, 69(2): 737–750.

White, W.R., Bettess, R. & Paris, E. 1982. Analytical approach to river regime . *J. Hydr. Div., ASCE*, 108(10): 1179–1193.

Yang, C.T. 1992. Force, energy, entropy and energy dissipation rate. *V.P. Singh and M.J. Fiorention* (eds), *Entropy and energy dissipation in water resources*: 63–89. The Netherlands: Kluwer Academic Publisher.

Yang, C.T., Song, C.C.S. & Woldenberg, M.J. 1981. Hydraulic geometry and minimum rate of energy dissipation. *Water Resour. Res.*, 17(4): 1014–1018.

River Flow 2004 – Greco, Carravetta & Della Morte (eds.)
© 2004 Taylor & Francis Group, London, ISBN 90 5809 658 0

Mobile-bed experiments on the exchange of sediment between main channel and groyne fields

Mohamed F.M. Yossef & Huib J. de Vriend
Faculty of Civil Engineering and Geosciences, Delft University of Technology, Delft, Netherlands

ABSTRACT: The estimates of the sediment balance for the Rhine branches in the Netherlands during the last three decades and particularly during the high water period of 1995 shows that erosion/sedimentation in the groyne fields plays a major role in the total sediment balance of the river (ten Brinke et al., 2001). In the present modelling practice, this role is not included in morphological predictions. To include the contribution of the groyne fields in the total sediment balance of the river, we need to further understand the sediment exchange process between the main channel and the groyne fields. For this reason, experiments have been conducted in a mobile-bed flume. The flume represents half the width of a schematised river reach with groynes at the left side. The geometrical scale is 1:100, based on typical dimensions of the River Waal. The bed material was scaled to have bed load as well as suspended sediment transport. The flow conditions covered one situation with emerged groynes and three with submerged groynes. Bed level changes, suspended sediment concentrations, and flow velocities were measured. The results show that there is sediment deposition in the groyne fields under emerged as well as submerged conditions. Furthermore, the results demonstrate the differences between the erosion and deposition patterns in the groyne fields for the different flow conditions.

1 INTRODUCTION

1.1 *Background*

Groyne fields are a central element in the river Waal and other Dutch branches of the river Rhine. They form a zone of sediment storage with a significant contribution to the overall sediment budget. Moreover, erosion of the groyne fields may affect the stability of the groynes. Finally, groyne fields provide the sand for the natural formation of wind-blown dunes on the floodplains that are a valuable habitat for riverine flora and fauna.

From the analysis of the findings of ten Brinke et al. (2001) see Table 1, one can conclude that during high water conditions sedimentation in the groyne fields plays a major role in the total sediment balance of the river. However, in the long run there is no net erosion or deposition from/to the groyne fields. Thus, the amount of sediment that is deposited during floods must be released during normal and low flow conditions. The release of sediment from the groyne fields is probably due to the navigation-induced sediment transport. This result emphasises the role that groyne fields play in the total sediment balance of the river.

It is therefore surprising that the existing routine modelling practices ignore the morphological interaction between the main channel and the groyne fields. This is due to a gap in our knowledge concerning the sediment exchange mechanisms. With the present modelling capabilities, even the smallscale sedimentation/erosion in the groyne fields is not reproduced adequately. Recent attempts to reproduce these morphological processes have revealed important shortcomings in the present process knowledge and modelling capabilities (Yossef & Klaassen, 2002). This was the reason of carrying out the present experiments.

Table 1. Sediment balance for the main channel of the Waal River during the last three decades (after ten Brinke et al. 2001).

	Volume × 1000 (m^3/year)		
Sediment source/sink	1970–1990	1990–2000	Year 1995
Input sediment from upstream	+682	+507	+250
Output sediment to downstream	−761	−578	−270
Bed degradation	+489	+264	+573
Groyne fields erosion/deposition	–	–	−373
Floodplain deposition	−53	−53	−180
Dredging	−357	−140	0

± signs refer to gains and losses of sediment transported in the main channel.

1.2 *Objective of the experiments*

The aim of the experiments is to gain insight into the mechanism governing the sediment exchange process between the main channel and the groyne fields mainly under different flow conditions. The experiment described below is expected to fill in part of our knowledge gap.

2 LABORATORY EXPERIMENTS

2.1 *Dimensions*

The experiments were carried out in a specially built facility in the Laboratory for Fluid Mechanics of Delft University of Technology. The dimensions of the model were based on those of the River Waal and the space available in the laboratory. Figure 1 presents a schematic drawing of the model.

The model consisted of a schematised straight river reach, with a geometrically undistorted scale of 1:100 with respect to the Waal River. The working length of the model was 26.85 m, and the width 2 m. In the lateral direction, the model represents half of the river width. The model included nine identical groynes. The first groyne was placed at 4.0 m from the model entrance following three wooden pseudo groynes that were installed to let the inflow of water and sand adjust before reaching the first groyne. The groynes were equally spaced at $S = 2.0$ m, they had a crest length $L = 0.65$ m and a crest height $H_g = 0.25$ m, measured from the concrete bottom. The side slopes were 1:3 in all directions. The dimensions of the model are summarised in Table 2.

2.2 *Experimental conditions*

Uniform quartz sand was used in all test cases. The sand had a median grain size $D_{50} = 0.164$ mm, and a geometric standard deviation $\sigma_g = 1.23$ (σ_g is defined in Eq. 1).

$$\sigma_g = \sqrt{\frac{D_{84}}{D_{16}}} \tag{1}$$

The thickness of the sand layer was varied from 0.125 m (case G1) to 0.175 m (case G3) to simulate a relative lowering of the groyne's crest height. However, in this paper we will present only one of the tested groynes geometries (case G1).

For all test cases the Shields parameter θ (defined in Eq. 2), was set at a value of 0.23, and the suspension

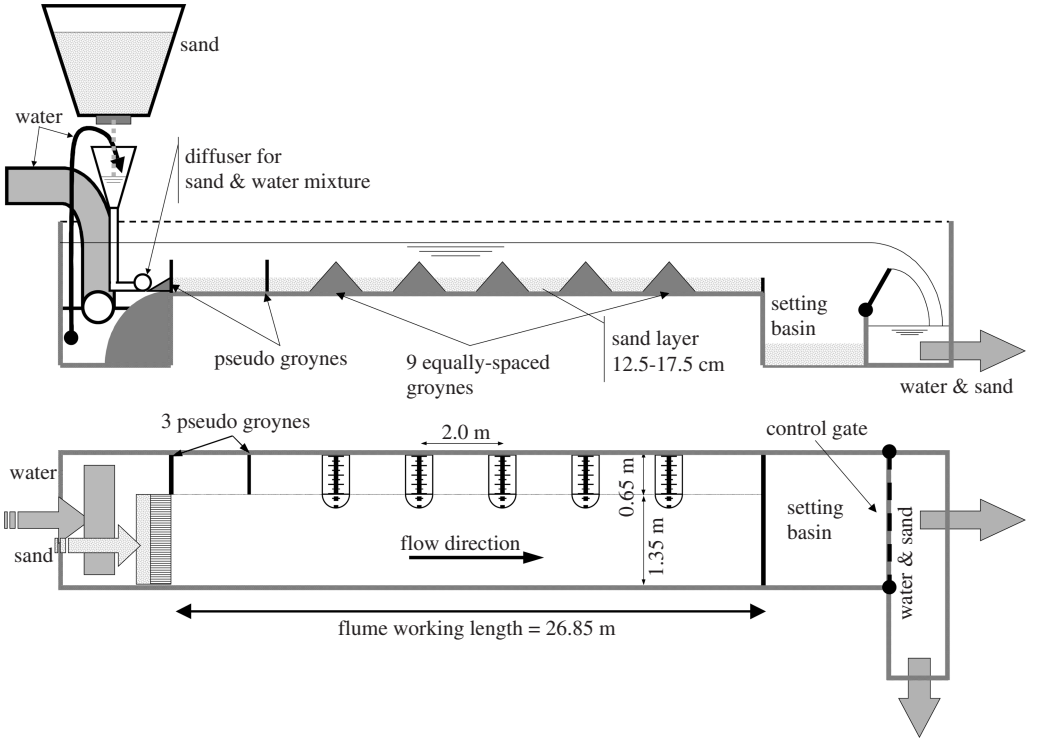


Figure 1. Experimental set-up; schematic drawing not to scale.

number Z (defined in Eq. 3), was set at 1.87, so as to guarantee a suspended sediment profile over the whole water column (van Rijn, 1984).

$$\theta = \frac{u^2}{C^2 \Delta D_{50}} \tag{2}$$

$$Z = \frac{w_s}{\beta \kappa u_*} \tag{3}$$

where C = Chézy coefficient; Δ = sediment specific weight; w_s = particle fall velocity; for D_{50} = median grain diameter, κ = von Karman constant and β is a constant ≥ 1.0. Here we have $D_{50} = 0.164$ mm, $\kappa = 0.4$; and $\beta = 1$.

The hydraulic conditions were chosen to fulfil the sediment transport requirements i.e. constant mobility and suspension in all test cases. Furthermore, for all the test cases Froude number (F_r) small enough (maximum = 0.28), and the Reynolds number (R_e) high enough to ensure subcritical fully-developed turbulent flow in both the main channel ($R_e \cong 1.8 \times 10^4$) and the groyne fields ($R_e \cong 0.5 \times 10^4$).

Table 2. Summary of the model dimensions.

Parameter	Dimension	notes
Model length	26.85 [m]	
Model width	2.00 [m]	
Groyne height (h_g)	0.25 [m]	measured from the bottom of the flume and could be varied using sand
Groyne length (L_g)	0.65 [m]	crest length
Groynes spacing (S)	2.00 [m]	measured from crest level
Spacing to length ratio (S/L_g)	3.08 [–]	for sand layer thickness of 0.125 m
Spacing to height ratio (S/h_g)	16.0 [–]	for sand layer thickness of 0.125 m

$h_g = H_g$ – thickness of sand layer.

Table 3. Summary of the hydraulic conditions of case G1.

Test	h_g (m)	H/h_g	H (m)	$\bar{u}_{mc}$ (m/s)	Q (m^3/s)	R_e	F_r
G1i	0.125	1	0.125	0.277	0.058	11 250	0.27
G1a		1.4	0.175	0.298	0.088	15 626	0.23
G1b		1.7	0.213	0.310	0.111	19 737	0.21
G1c		2.0	0.250	0.320	0.134	23 970	0.20

where: h_g = the groynes height, H = flow depth, $\bar{u}_{mc}$ = mean flow velocity in the channel region, and Q = total discharge, R_e = Reynolds number, and F_r = Froude number.

2.3 *Measurements and data acquisition system*

Several parameters were measured during every test; namely: bed profiles, suspended sediment concentration, flow-velocity, water level, and bed-form movement via video recording. Table 4 provides an overview of the measurements and equipment used during the experiment. In this paper, we will focus on results obtained from the bed profilers.

The bed level development was measured by means of three bed profile followers mounted on a movable carriage. The carriage could move on two rails to scan the area between groynes 5 and 8 i.e. a length of 6.0 m. The speed of the carriage was always set at its minimum value of 0.0315 m/s to obtain the highest spatial resolution of bed measurements. The sampling rate was 10 Hz. This means that the spatial resolution of the bed readings in the longitudinal direction was 3.15×10^{-3} m.

The measured longitudinal profiles were spaced at 0.05 m, starting from 0.20 m from the model's sidewall, and ending at 0.20 m from the other wall, i.e. covering a total model width of 1.60 m. An initial reading was always taken before the start of every test, and measurements were taken after 10, 20, 30, and 40 hours. All the experiments started from an initially flat bed.

3 FLOW PATTERN

3.1 *Emerged groynes*

During the first few hours of the test, the observed flow pattern did not differ much from what was previously

Table 4. Summary measurements and equipment used during the experiment.

		Number of		
Measurement type	Measuring equipment	Instruments	Locations	Times
Bed profile	electronic bed followers	3	between gr. 5 & 8	4 @ 10, 20, 30 and 40 hrs
Suspended sediment	transverse suction system (TSS)	4	2 sections	1 @ 10 hrs
Velocity	electromagnetic flow meters (EMF)	2	2 sections	1 @ 10 hrs
Water level	wave gauges & static devices	2 + 2	4 points	variable
Video imaging	video camera	1	between gr. 5 & 6	continuous

reported by e.g. Uijttewaal et al. (2001) and Yossef & Uijttewaal (2003).

When the groynes are not submerged, the flow inside the groyne fields shows an unsteady circulation behaviour as shown in Figure 2 and characterised by:

- a primary circulation cell that forms in the downstream part of the groyne field and covers nearly two thirds of its spacing, the velocity of which is normally about 30 to 40% of the main channel mean velocity.
- a secondary circulation cell driven by the primary one with an opposite rotating direction and much smaller flow velocity.
- a dynamic eddy that frequently sheds from the tip of the upstream groyne. This eddy migrates in downstream direction and merges with the primary one, which in return changes in size due to the interaction with the migrating eddy. After this eddy has disappeared, another eddy has room to form.

The whole circulation is driven by the main stream via exchange of momentum through the interfacial mixing layer.

Along with the morphological development, the flow pattern changes. With the development of the scour hole, the intensity of the dynamic eddy decreases while stretching in the vertical direction following the newly formed scour hole. After the development of the deposition region, the interaction between the groyne fields and the main channel is hindered and the primary eddy gets slower, which ultimately leads to the disappearance of the secondary circulation cell.

3.2 *Submerged groynes*

If the groynes are submerged, the flow in the groyne fields does not show the circulation pattern as observed in the emerged condition. Yet, the groyne fields can be characterised as slow velocity region. The momentum transfer by the water flowing over the groynes is sufficient to balance the momentum transfer through the mixing layer. The mixing layer in this situation has a constant width. The total turbulence intensity across the mixing layer decreases with the increase level of submergence.

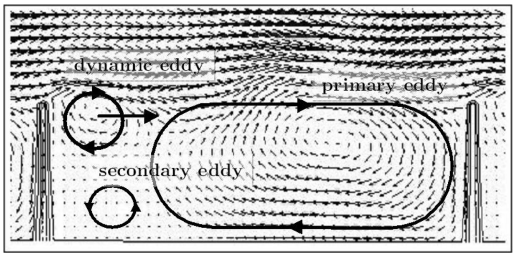


Figure 2. Flow pattern in a groyne field during emerged condition.

In the case of very shallow submergence (case G1a), the flow pattern showed some of the characteristics of the flow in the emerged situation. However, It should be noted, however that the flow over the groynes hinders the horizontal recirculation, ultimately causing it to disappear when reaching a high enough submergence level (cases G1b & G1c).

Generally speaking, the flow in the submerged state shows an alternate accelerating and decelerating pattern between flow over and around the groynes; also see Yossef & Uijttewaal (2003).

Another significant feature for the flow pattern in the case of submerged groynes is the secondary flow structure. This secondary flow occurs along the interfacial line connecting the tips of the groynes and is strongest near the groynes. The flow is directed towards the groyne fields near the bed and towards the main channel near the water surface; also see Peng et al. (1997) and Krebs et al. (1999).

Except for a decrease in turbulence intensity near the tip of the groynes, no significant changes in the flow pattern were observed in response to the bed changes.

4 MORPHOLOGICAL DEVELOPMENT

For all the tested cases, two typical features were observed. The first was the development of a scour hole near the tip of each groyne; the second was the sediment deposition inside the groyne fields. The morphological time-scale for the development of the scour holes was rather short compared to the total running time of the experiment. For each of the tested cases, both scour and deposition patterns looked similar near all groynes except near the first and the last ones.

Nevertheless, there were significant differences between the emerged and submerged cases. In the following two sections, we will describe the results from in further details.

4.1 *Emerged situation*

During the emerged situation, the footprint of the flow pattern was clearly visible in the morphology, as shown in Figure 3. Both the scour hole and the deposition pattern follow the flow pattern as described in Section 3.1.

The scour hole alignment follows the direction of the dynamic eddy. It is oblique to the flow direction and makes an angle of about 30° with the normal line (the imaginary line that connects the tips of the groynes). In a later stage, the scour causes a feedback to the flow by elongating the dynamic eddy in its direction.

The sediment deposition inside the groyne fields takes place through its downstream part (Figure 3). The sediment is transported from the main channel towards the groyne field following the direction of the primary

circulation cell. Along with the drop of the velocity, the sediment settles. The asymmetry of the ripples near the wall deep inside the groyne field is opposite to the main flow direction, but complies with the flow direction inside the groyne fields. This indicates that the effect of the primary circulation cell is extending through the width of the groyne field. The area in the middle of the groyne field, which coincides with the centre of the circulation cell, is free from any bedforms.

Subtracting the final bed level from the initial bed level yields the erosion/deposition pattern at the end of the test. The result is shown in Figure 4, where we can see that the pattern is recurring in all three groyne fields.

4.2 *Submerged situation*

During the submerged situation, the effect of the flow pattern is not explicitly visible on the morphology. The sediment deposition inside the groyne fields takes place across the normal line, see Figure 5. The sediment is transported from the main channel towards the groyne through the mixing layer. From the dye visualisation, we were able to observe the effect of the secondary circulation. As described in Section 3.2, near the bed the flow in the mixing layer is towards the groyne field, transporting the sediment from the main channel into the groyne field. Moreover, due to the high turbulence intensity, the sediment concentration in the mixing layer is kept at a high value (compared to the concentration in the main channel). Consequently, significant sediment transfer took place though the mixing layer.

The volume of sand deposited in the groyne fields decreased with the increase of the water level (Figure 7). Moreover, the location of the deposition moved further inside the groyne fields as the water level increased (Figure 7a, b & c, lower panels).

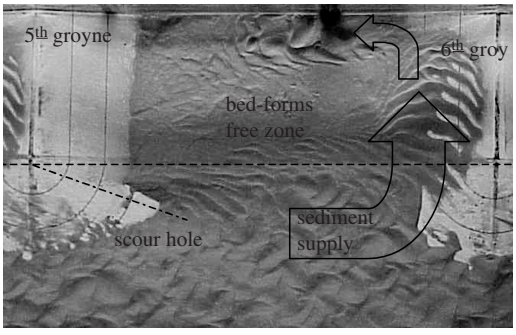


Figure 3. Morphological features for emerged groynes – case G1i; flow from left to right. Picture taken after the end of the test.

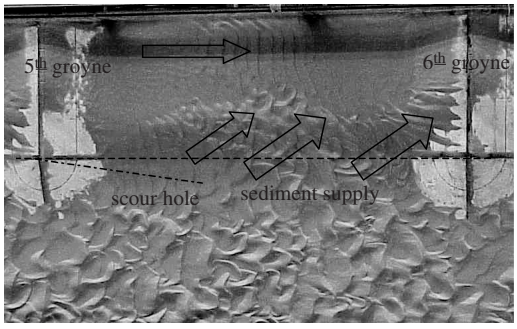


Figure 5. Morphological features for submerged groynes – case G1c. Picture taken after the end of the test.

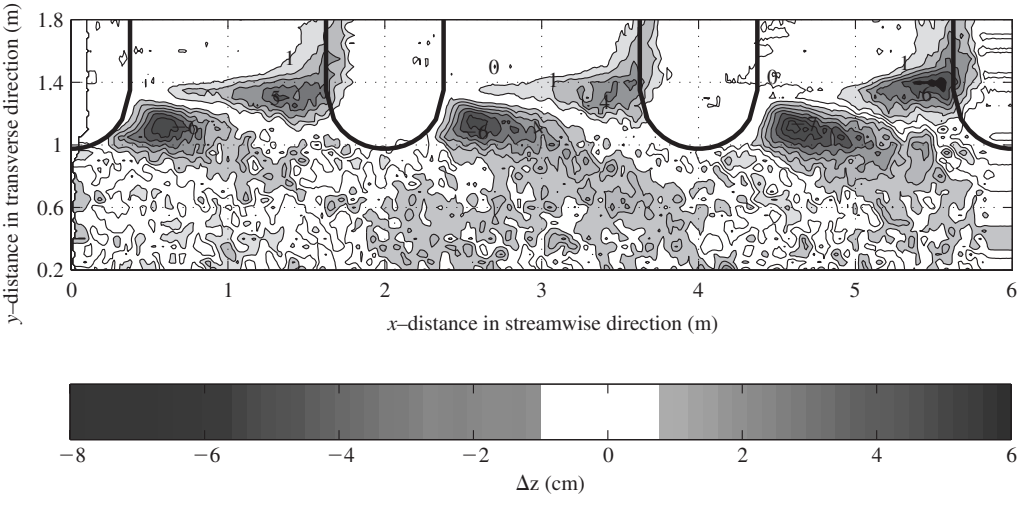


Figure 4. Deposition/erosion pattern after 40 hours for case G1i, $\Delta z =$ bed level after 40 hours – initial bed level.

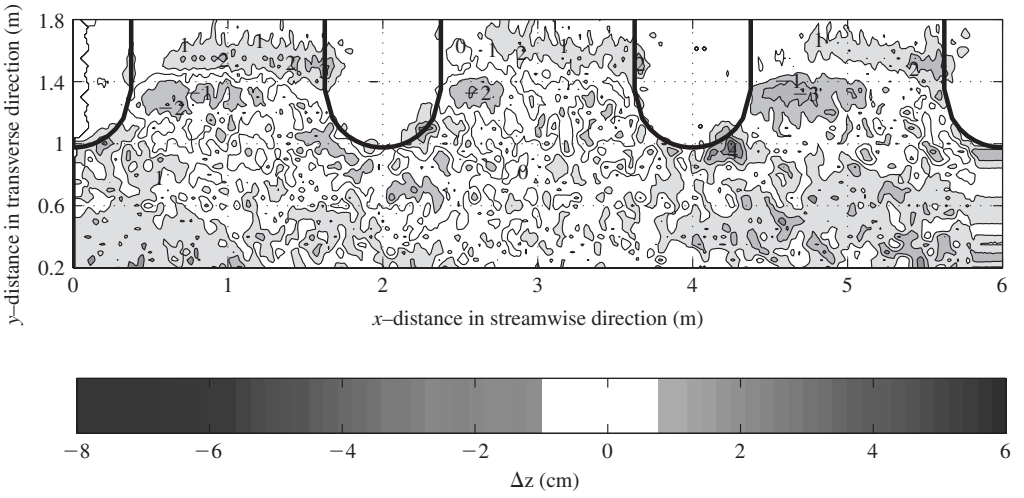


Figure 6. Deposition/erosion pattern after 40 hours for case G1b, Δz = bed level after 40 hours – initial bed level.

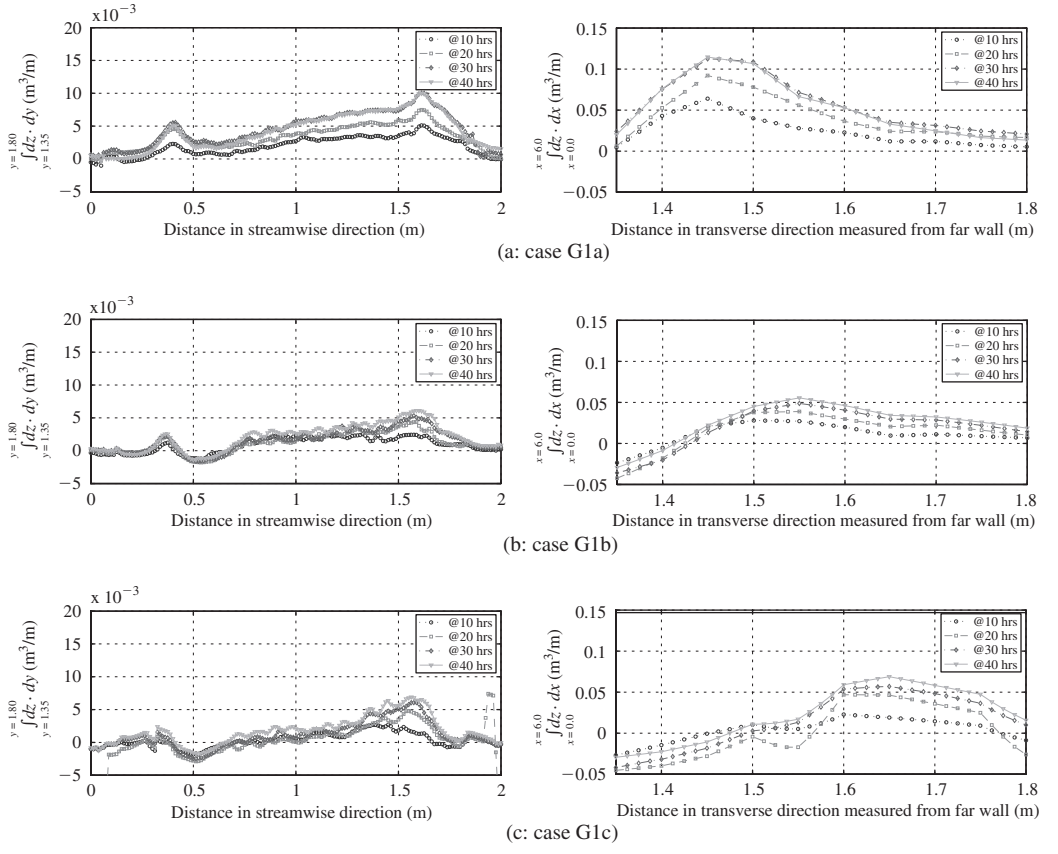


Figure 7. Deposition volume inside the groyne fields for cases G1a, G1b, and G1c; upper panel of every plot is the deposition volume per unit width, lower panel per unit length.

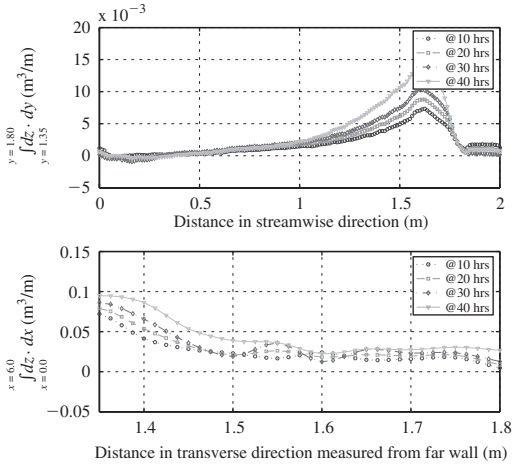


Figure 8. Deposition volume inside groyne fields for case G1i; upper panel per unit width, lower panel per unit length.

Both the depth and the alignment of the scour hole depended on the water level. The scour depth decreased with the increase of the water level, and in all submerged cases the depth of the scour depth was less than in the emerged situation. The alignment of the scour hole also changed with the water level. The scour hole moved towards the groyne fields as the submergence level increased (see, for example, Figure 6).

5 CONCLUSIONS

The mechanism of sediment transport into the groyne fields differs according to the flow situation. In the emerged situation, the sediment is mainly advected towards the groyne fields by the primary circulation cell. In the submerged situation, the sediment is transported to the groyne fields across the whole length of the normal line. The mechanism in this case is a mixture of advection by the secondary circulation and diffusion through the mixing layer.

The results from these experiments showed a decrease in the total deposition volume inside groyne fields as the submergence level increases; compare Figure 8, Figure 7 a, b & c (upper panels). Nevertheless, the experiments were conducted for constant sediment mobility θ for all cases; this condition is violated in the prototype. The lower flow stages in the prototype have lower sediment mobility and vice versa.

ACKNOWLEDGEMENTS

This study is carried out within the framework of theme 1.3 (Intermediate-scale morphological developments in rivers due to human interventions) of the TU Delft research programme DIOC Water, and theme 3 (Coasts and Rivers) of the Delft Cluster joint research programme.

The authors would like to thank the staff members of the Laboratory for Fluid Mechanics of the Delft University of Technology for facilitating the experiment in all its stages, and to thank Ken Thiemann for conducting the experiments.

The authors would also like to thank Messrs. G.J. Klaassen and M. van der Wal, and Drs. E. Mosselman, C.J. Sloff, and W.S.J. Uijttewaal for their constructive comments and discussions during the different stages of the experiment.

REFERENCES

ten Brinke, W. B. M., Bolwidt, L. J., Snippen, E., and van Hal, L. W. J. (2001). "Sedimentbalans Rijntakken 2000" *2001.043*, Riza, Arnhem.

Krebs, M., Zanke, U., and Mewis, P. (1999). "Hydro-Morphodynamic modelling of groin fields" *In: Proc. 28th IAHR Congress*, Graz, Austria.

Peng, J., Kawahara, Y., and Tamai, N. (1997). "Numerical analysis of three-dimensional turbulent flows around submerged groynes" *In: Proc. 27th IAHR Congress*, San Francisco, USA.

van Rijn, L. C. (1984). "Sediment Transport, Part II: Suspended Load Transport" *Journal of Hydraulic Engineering, ASCE*, 110(11), pp. 1613–1641.

Uijttewaal, W. S. J., Lehmann, D., and van Mazijk, A. (2001). "Exchange process between a river and its groyne fields – Model experiments" *Journal of Hydraulic Engineering, ASCE*, 127(11), pp. 928–936.

Yossef, M. F. M., and Klaassen, G. J. (2002). "Reproduction of groynes-induced river bed morphology using LES in a 2-D morphological model" *In: River Flow 2002 – Proc. of the Int. Conf. on Fluvial Hydraulics*, Louvain-la-Neuve, Belgium, 1099–1108.

Yossef, M. F. M., and Uijttewaal, W. S. J. (2003). "On the dynamics of the flow near groynes in the context of morphological modelling" *In: XXX IAHR Congress*, Thessaloniki, Greece, 361–368.

This page intentionally left blank

River Flow 2004 – Greco, Carravetta & Della Morte (eds.)
© 2004 Taylor & Francis Group, London, ISBN 90 5809 658 0

Impact of hydropower schemes at bedload regime and channel morphology of the Danube River

K. Holubová, Z. Capeková & J. Szolgay
Water Research Institute, Bratislava, Slovakia

ABSTRACT: Construction and operation of hydropower plants (HPP) including engineering works to maintain navigation conditions at the Danube River essentially changed flow dynamics and transport capacity of the river. As a consequence significant changes of the river bed morphology have occurred creating reaches with aggradation upstream and degradation downstream of the structures. The results of broad research programme (1996–2002) focused at the changes of bedload transport regime and the river bed morphology of the Danube affected by operation of hydropower schemes Gabcikovo constructed downstream of Bratislava and Freudenau situated in Vienna, are presented. Bedload rating curves based on bedload measurements were developed for two river sections: the Slovak–Austrian Danube upstream of Bratislava and Slovak–Hungarian Danube downstream of Gabcikovo HPP. Increased bedload transport capacity is documented by the results of bedload measurements realised during the period 1997–2002 and supported by analyses of the bed material composition, development of the river bed morphology at both river sections. Bedload transport equations frequently applied in engineering practice (Meyer-Peter & Müller, Ackers & White, Schoklitsch, etc.) to estimate transport rates are compared with the relations developed on the basis of bedload measurements at the Danube. The main attention concentrates at the river section downstream of Gabcikovo HPP, which indicates the most significant morphology changes induced by unsteady flow conditions, deficit in sediment supply and engineering maintenance of the river channel for navigation purposes.

1 INTRODUCTION

Since nineteenth century the Danube River has been influenced by engineering maintenance of the river channel mainly for navigation purposes. After World War II a series of hydropower schemes designed for electricity production and also for improving navigation conditions were constructed upstream of Vienna. During the recent years the last two hydropower plants were put into operation – in Vienna (Freudenau, 1997) and downstream of Bratislava (Gabcikovo, 1992). Some years ago plans were made to construct a power plant at Hainburg, which was supposed to fill the gap between Vienna and Bratislava but national and international protests finally prevented this scheme being realised and forests in the remnant floodplain were protected (Jeaggi, 1992).

Operation of both hydropower plants Freudenau and Gabcikovo including increased degree of the Danube regulation to maintain navigation conditions (dredging, groynes, deflectors) induced higher dynamics of morphology changes. Problems of intensive river bed erosion have occurred downstream of Freudenau and Gabcikovo and more intense deposition influenced Slovak–Austrian Danube upstream of Gabcikovo impoundment. Present morphological changes of the Danube caused evident decrease of low flow water levels in the sections with river bed degradation.

Analyses of morphological development of the Danube river at the section that flows through the Slovak territory arise from a consideration of various opposite tendencies in the river bed development, which is important for understanding of the present river processes. Alternation of longer periods of aggradation and degradation always dominantly affected surface and ground water level regime in this territory. Since 1960s natural aggradation of the river bed that prevailed at the Danube downstream of Devin (km 1880) over a long period, was replaced by successive degradation. Commercial dredging of excessive amounts of gravel induced dramatic changes of the river bed resulting in a progressive fall of water levels upstream and downstream of Bratislava. Water levels decreased by two meters in Bratislava and elsewhere they dropped by one meter during period 1957–1992 (Holubova et al. 1998). Process of river bed aggradation has been re-established again since the Danube was dammed downstream of Bratislava.



Figure 1. Bedload measurements at the Danube (1997–2002).

Dynamic equilibrium between local transport capacity and sediment supply was seriously affected and significant changes of flow dynamics and sediment regime connected with the operation of hydropower schemes linked to this dramatically eroded river bed.

The impact of hydropower schemes at river processes along the Slovak–Austrian and Slovak–Hungarian Danube was analysed in the frame of the bedload research programme that consisted of two main parts. The first one: *Sediment transport at the Danube river under the changed flow conditions in the reach of the Slovak capital* (1996–1998) and the second one: *Changes in sediment transport regime in the Danube, downstream of Gabcikovo HPP* (1999–2002). Both parts of the research programme were based on a broad range of bedload measurements (Fig. 1) to identify changes in bedload transport regime and connected changes of river bed morphology, bed material composition and water level changes. The most important results completed by actualised morphological development and water level changes of low flow ($Q \sim 1000\,m^3 \cdot s^{-1}$), are presented.

2 THE SLOVAK–AUSTRIAN DANUBE

The Danube River between Vienna and Devín (km 1880) is one of the last free-flowing river sections in Austria. Since hydropower plant Freudenau was put into operation (1997) this river section that includes ecologically very rare forest area has been affected by higher morphological dynamics that resulted in the river bed erosion and problems of navigation maintenance during the low flow. Therefore a strong emphasis has been given to the development of strategies for improvement and management of this stretch, which is declared as an Alluvial Zone National Park (Schiemer et al. 2003).

In order to decrease deficit of sediment supply downstream of Freudenau an artificial supply of coarsely sorted sediments ($300{,}000\,t \cdot year^{-1}$) were designed to stabilise the river bed (Zottl 1998). After a few years large amounts of sediments were reduced ($160{,}000\,t \cdot year^{-1}$) but the expected effect – development of river bed armouring – has not been fully achieved yet. Monitoring results of Austrian engineers indicated successive degradation of the river bed (1 cm/year) downstream of Vienna (Kordina et al. 2003). This trend was also proved by practical experience. Unstable conditions downstream of Vienna that induced increased sediment supply also influenced the Danube section upstream of Bratislava. Higher intensity of the riverbed aggradation occurred at the Slovak–Austrian Danube above the edge of impoundment particularly during the recent years. Therefore the main objectives of the first part of research programme (Holubova et al. 1998) were focused at identification of bedload transport regime and morphological changes of the river bed in the section upstream of Bratislava.

2.1 *Changes in bedload regime at the Slovak–Austrian Danube*

Broad research of bedload regime was realised during 60's at Slovak section of the Danube (Szolgay 1960). Bedload measurements at the Slovak–Austrian Danube (km 1870) were re-established in 1997 after 40 years under the changed flow conditions. Twenty-three complete bedload discharge measurements were carried out at km 1878.15. Discharges ranged from $1050\,m^3 \cdot s^{-1}$ to $4350\,m^3 \cdot s^{-1}$ during field works (1997–1998). Complete cross section measurements in five verticals realised by basket sampler (Fig. 1) included continual flow velocity measurements to analyse flow conditions (Holubová 2000). The results were used for evaluation of the bedload rating curve that is given by following regression type of relationship:

$$G_s = 5.7215 \cdot 10^{-6} \cdot Q^{1.903} \quad (1)$$

where G_s = bedload discharge; Q = water discharge.

Figure 2 shows bedload rating curves developed on the basis of field measurements for periods 1997–1998 and 1954–1957. Comparison of both curves indicates that larger amounts of bedload are transported during higher water discharges under the present conditions.

Recent experience showed that the beginning of bedload movement is connected with lower discharges ($880\,m^3 \cdot s^{-1}$) compared with situation in the past ($2000\,m^3 \cdot s^{-1}$). Bedload regime also indicates further changes in characteristics of movement due to unsteady flow conditions and engineering measures mentioned above.

2.2 *Bedload equations appropriate for Slovak–Austrian Danube*

Sediment discharge equations of Meyer-Peter & Müller, Ackers & White, Jaeggi & Smart and Schoklitsch were tested using the field Danube data.

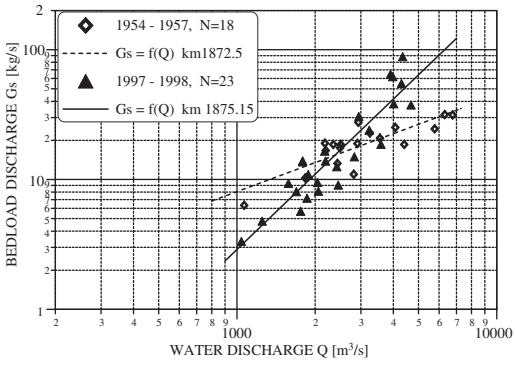


Figure 2. Bedload rating curves for the Slovak–Austrian Danube obtained for periods 1954–1957 and 1997–1998.

Table 1. The results of the bedload equations testing.

Bedload equation (Danube upstream of HPP)	*MNE* (%)
Schoklitsch*	53
Jaeggi & Smart (τ_{cr} = MPM)	60
Jaeggi & Smart ($\tau_{cr} = 0.047$)	61
Schoklitsch	73
Ackers & White	202
Ackers & White*	377
Meyer Peter & Müller*	670

* with fractions.

For each equation the mean normalised error (*MNE*) was estimated (Holubova 2000). The best results were achieved by Schoklitsch equation (with fractions). At the next level Jaeggi & Smart and original form of Schoklitsch equation have comparable errors – both overestimated the results. Meyer-Peter & Müller (with fractions) and Ackers & White (with fractions) equations significantly overestimate calculated values of bedload discharge (Table 1).

Good results were obtained by Meyer-Peter & Müller equation with modified values of constants $A' = 0.039$ and $B' = 0.39$ that were obtained on the basis of bedload measurements at the Danube (km 1878.15). This modified equation enables to spread the range of its applicability for higher discharges compared with equation (1) that should be used for limited discharge range ($1050\ m^3 \cdot s^{-1}$–$4350\ m^3 \cdot s^{-1}$).

2.3 *Morphology development of the river bed*

Aggradation of the Danube river bed was expected in the reach of impounded water levels and predicted by numerical models. Prediction of morphology development could not match the actual situation as the model calibration did not include the effects of an artificial interference into a bedload regime (artificial

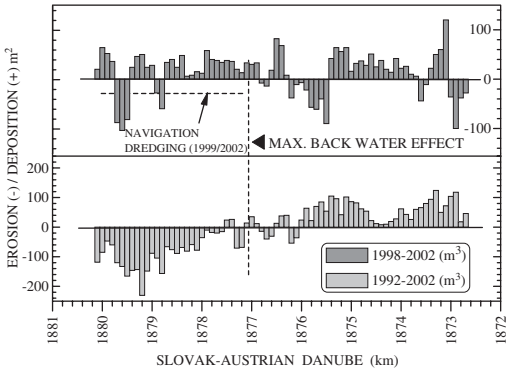


Figure 3. Development of morphological changes of the river bed at the Slovak–Austrian Danube during 1992–2002.

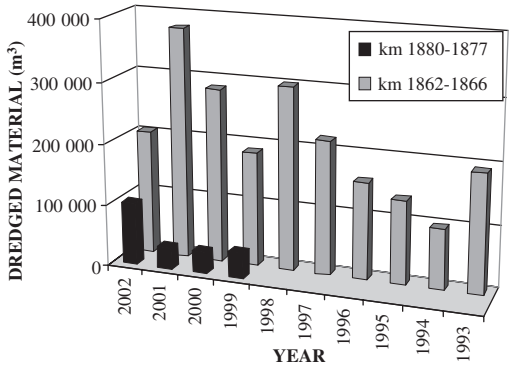


Figure 4. Bed material dredging in the Danube at the sections between km 1880 to km 1877 and km 1862 to km 1864.

sediment supply) and further engineering measures recently implemented in the river channel (groynes modification and construction of new ones, dredging, restoration measures, etc).

The results of morphology analyses at common Slovak–Austrian Danube proved previous assumptions of a more intense process of deposition that has occurred downstream of km 1877 (Fig. 3), which is influenced particularly by backwater effect. Increased transport capacity of the river and higher amounts of bedload transported from Austrian Danube also support aggradation process.

Tendency of river bed aggradation is observed during the recent years also at the section upstream of backwater effect (km 1880–1877) even if over the longer period (1992–2002) erosion prevailed at this section. Since 1998 a navigation dredging is required to maintain navigation conditions. Extracted amounts of a bed material have increased successively (Fig. 4) as more intense deposition has caused navigation problems. Bed material extractions had to be spread upstream of impounded section where

navigation dredging was never required before. Even if total amount of dredging is comparable with bedload transport capacity, the river bed aggradation can be observed particularly during the recent years.

Analyses of a bed material composition indicate changes of physical characteristics that reflect actual river processes.

Larger part of bed material samples that were taken in 1997 proved a higher percentage of coarser fractions compared with situation in the past, while smaller fractions did not exhibit any considerable differences. Grain size distribution of the bed material samples taken from the river channel in the section between km 1880 to km 1866 during 2003 (57 samples) indicates that bed material coarsening evident in 1997 can not be observed yet. Higher volumes of coarser fractions in the samples observed in 1997 (115 samples) upstream of Gabcikovo impoundment could be caused by erosion prevailed at this locality in the past.

At present the bed material composition is almost identical as it was in 1950s (Fig. 5) particularly in the central part of the river channel. Specific flow conditions resulting in local scouring around a head of groynes induced higher sorting of bed material. Therefore coarser gravel is observed at localities close to left and right river banks at the sections with groynes. Reversal trend of bed material composition could be caused by increased volume of bedload from Austrian Danube and deposition re-established at this river section during the recent years (Fig. 3). Downstream of km 1874 only slight increase of finer grains in bed material composition has occurred due to backwater effect.

Conditions for an occurrence of armour layer on the riverbed were assessed by Raudkivi (1981) armouring criteria:

$$\left(\frac{D_{84}}{D_{16}}\right) \geq 2.5 \quad \text{or} \quad \left(\frac{D_{90}}{D_{10}}\right) \geq 5 \qquad (2)$$

where D_{84} = grain diameter (84% finer by weight).

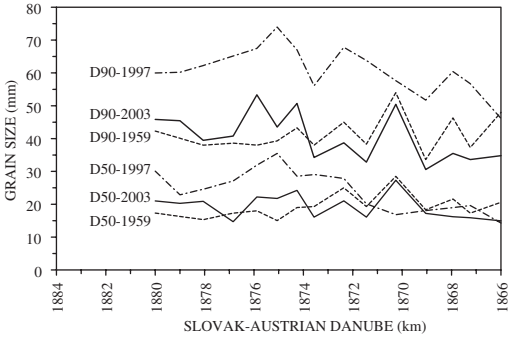


Figure 5. Changes in grain size distribution of the bed material at the Danube upstream of Bratislava.

While in 1997 conditions for bed armouring occurred only very rarely, at present they are identified almost at whole Slovak–Austrian Danube even if practical experience during field measurements did not prove creation of a compact armour layer.

Analyses of bedload and bed material properties indicate that grain size of both is comparable. Bedload grain size characterised by D_{50} ranged from 25 mm to 30 mm and bed material D_{50} from 15 mm to 36 mm (average value 20 mm). Lower amount of finer fractions in bedload samples was caused by coarser mesh (3 mm) of bedload sampler, which did not enable to retain fine gravel and sand in the basket sampler.

3 DANUBE DOWNSTREAM OF GABCIKOVO HYDROPOWER PLANT

Gabcikovo hydropower plant that is built on bypass canal dominantly influenced flow conditions and sediment regime along the common Slovak–Hungarian Danube. Deficit in sediment supply and changed flow dynamics has caused significant degradation of the river bed downstream the old Danube and tailrace canal confluence. Original version of the common Slovak–Hungarian project included construction of lower HPP- Nagymaros (km 1694.6) that would have provided protection of the river bed by created impoundment. As the completion of hydropower plant in Nagymaros was stopped due to protests of public and ecologists in Hungary the river bed is exposed to a strong erosion.

Evaluation of river bed development is rather complicated with regard to high variability of flow dynamics downstream of the old Danube and tailrace canal confluence. Therefore the second part of the research programme (Holubova et al. 2002) was focused at the problems of sediment transport and morphology changes downstream of Gabcikovo. Project included field measurements of bedload discharges, analyses of morphology development, water levels changes and analyses of the river bed composition.

3.1 *Impact of Gabcikovo HPP at river bed morphology and low flow water levels*

Two important phases of the river bed development since Gabcikovo was put into operation are documented at Figure 6. The most intensive degradation of river bed downstream of the old Danube and tailrace canal confluence occurred during the first two years of Gabcikovo operation. During this period the river bed incision reached maximum values in shorter reach (km 1811–1810.5). During next years the maximum value of the river bed incision was slightly reduced but degradation still propagates downstream getting through the bridge Medvedov profile that was stable

over long period. Large amounts of eroded material are transported downstream and deposited at lower reaches. Present situation indicates that dynamic equilibrium has not been achieved yet and process of the river bed erosion still continues (Fig. 6) with negative impacts at water levels (Fig. 7).

Changes of low flow water levels reflect morphological development of the river bed downstream of Gabcikovo. Maximum decrease of a minimum navigation water level ($Q \sim 1010\,m^3 \cdot s^{-1}$) reached value 71 cm during the first years of HPP operation (1992–1996) just downstream of the old Danube and tailrace canal confluence. Decrease of water occurred at shorter reach during this period but successive degradation of the river bed induced further decrease of water level that propagates downstream. At present a maximum decrease of low flow water level reached 1.29 m (km 1811) compared with pre-dam conditions (Fig. 7). Evident decrease of low flow water level was spread downstream.

Significant change of the river bed slope occurs close to Zlatna na Ostrove (Fig. 7). Here the Danube is changing its character from submontane to lowland river.

The river slope is changing from i = 0.232% (km 1811–km 1794) to i = 0.04% (km 1794–km 1766). Bed material eroded and transported from the steeper parts of the Danube is deposited at the reaches with lower gradient causing problems with maintenance of navigation conditions.

Analyses of 57 bed material samples along investigated section (km 1811–km 1792) involved samples from central part and also from left and right parts of the river channel. The main characteristics of bedload samples and bed material samples are very similar. Bedload grain size characterised by D_{50} ranged from 7 mm to 10 mm at locality of field measurements (km 1795.58) and bed material size also given by D_{50} ranged from 8 mm to 14 mm (average value 10 mm).

Composition of the river bed material is rather uniform (Fig. 8) along the whole investigated river section. Bed material characteristics D_{35}, D_{50}, D_{80} showed changes only at lower part of the Danube.

Higher volume of coarser fractions in bed material occurred only locally close to groynes heads and also at the left and right side of the channel influenced by dredging (downstream of km 1794). Possibilities for creation of armour layer evaluated by Raudkivi criteria (2) did not indicate conditions for creation of river bed armouring. Investigation of the river bed topography by ATLAS ultrasonic equipment proved creation of bed forms – mostly dunes with variable size (dune length $L_d = 0.2$ m–0.6 m; dune height $H_d = 0.6$ m–2 m).

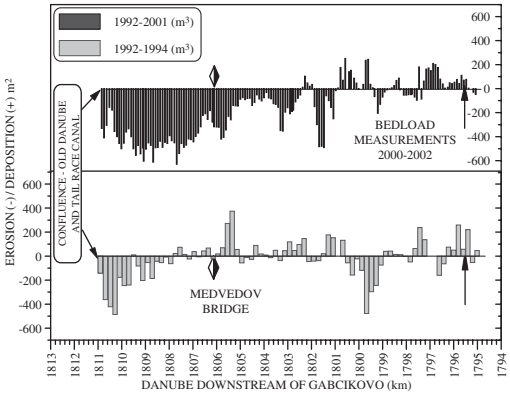


Figure 6. Degradation of the Danube river bed downstream of Gabcikovo hydropower plant during period 1991–2002.

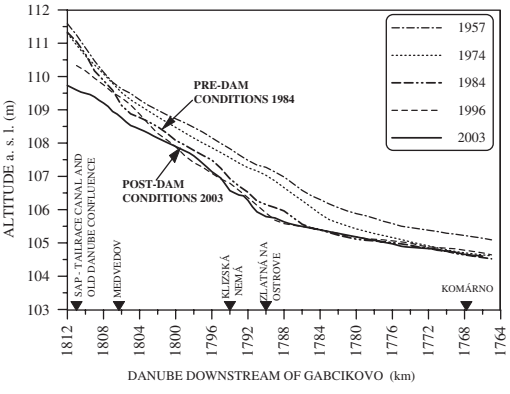


Figure 7. Low flow water levels ($Q \sim 1010\,m^3 \cdot s^{-1}$; min. navigation water level) under the pre-dam and post-dam conditions.

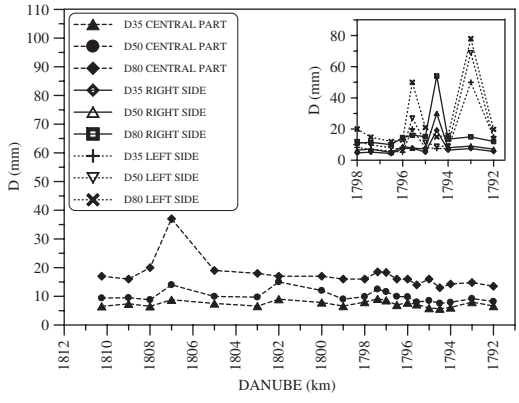


Figure 8. Grain size distribution of the bed material along the Danube section downstream of Gabcikovo.

3.2 *Bedload regime downstream of Gabcikovo*

In order to define bedload regime at present conditions and quantify volumes of bedload transported through the reach, series of field measurements were realised at the locality just above significant change of the river bed slope. This locality (km 1795.58) was selected not only with regard to the significant change of the river bed slope but also with the aim to avoid further impacts that could locally influence bedload regime. During the period 2000–2002 broad series of bedload measurements were done under the discharge conditions reaching from 972 $m^3 \cdot s^{-1}$ to 4745 $m^3 \cdot s^{-1}$. Complete seventy-one bedload measurements in six verticals were realised in cross section by the same method and technical equipment as it was done at Slovak–Austrian Danube. Fluctuation in bedload movement was considered by 10 times repeated measurements at each of verticals (time of each measurement varied from 2 to 5 minutes depending on intensity of bedload movement) and final value in the vertical was obtained as average value. Extent of field works that also included measurements of velocity distribution realised continually with bedload measurements, permanent recording of water level fluctuations, sampling of bedload and bed material, represent data, which are unique at the Danube.

On the basis of bedload measurements realised in the section of the Slovak–Hungarian Danube downstream of Gabcikovo the following regression type of relationship was developed:

$$Gs = 3.224 \cdot 10^{-6} \cdot Q^{1.976} \tag{3}$$

This relationship (3) represents bedload rating curve for the Slovak–Hungarian Danube downstream of Gabcikovo (Fig. 9) recommended for given discharge range. Total amount of bedload transported through the investigated section of the Danube for an average year is about 252,000 m^3. The total amounts of bedload estimated for period 1992–2000 varied from 165,000 m^3 (1998) to maximum value 412,000 m^3 (1999).

Intensity of bedload movement is comparable with the Slovak–Austrian Danube (i = 0.342%) even if the river bed slope at the Slovak–Hungarian Danube is lower (i = 0.232%).

Deficit in sediment supply, higher flow dynamics and bed material that consists of fine gravel, support transport of large amounts of bed material. Increased dynamics of bedload regime influenced topography changes along the investigated section. Changes of channel geometry in the cross section varied in the range from a few centimetres to one meter during two years of field measurements.

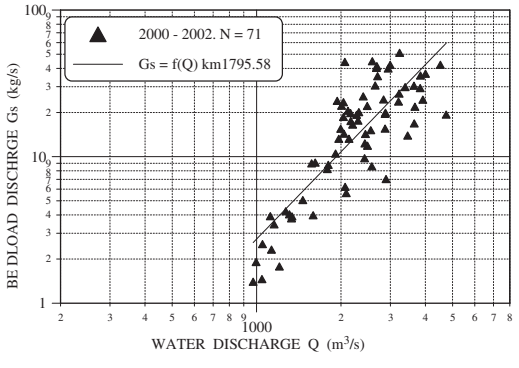


Figure 9. Bedload rating curve based on field measurements at the Danube downstream of Gabcikovo (km 1795.58).

3.3 *Bedload equations for the Danube downstream of Gabcikovo HPP*

Some bedload equations were tested also for the Slovak–Hungarian Danube at the section downstream of Gabcikovo. The same method of testing was used for bedload equations mentioned above except of Jaeggi & Smart equations that were replaced by Rottner ones. Equation of Meyer Peter & Müller was tested with modified values of constants, which were estimated on the basis of bedload measurements as follows: A′ = 0.0378 and B′ = 0.1552.

Similarly as it was for the Slovak–Austrian Danube relatively good results were achieved by Schoklitsch equation but in this case, the form with constant sediment size provided better results.

Comparable results were obtained by Meyer Peter & Müller equation with constants derived from field measurements, Ackers & White equation with constant size of D_{35} and Schoklitsch equation (with fractions). Extremely high values of mean normalised error (*MNE*) for both versions of Rottner equations indicate that these equations are inappropriate for the Danube conditions. Ackers & White equation with fractions provides rather high deviation from measured values.

Table 2. The results of the bedload equations testing.

Bedload equation (Danube downstream of HPP)	*MNE* (%)
Schoklitsch	73
Meyer Peter & Müller (modified A′, B′)	89
Ackers & White	97
Schoklitsch*	106
Rottner	562
Rottner*	980
Ackers & White*	166

* with fractions.

Flow dynamics influenced by operation at Gabcikovo HPP and engineering works implemented in the river channel at the Slovak–Hungarian Danube downstream of Gabcikovo create complicated conditions for bedload regime and quantification of bedload discharges. The results of bedload equation tests proved that these equations frequently used in an engineering practice and also in numerical models would not provide reliable prediction of morphology development at the Danube. Bedload rating curves (1), (2), developed for considered river sections and specific flow conditions of the Danube created necessary background for reliable and physically correct predictions of morphology development.

4 CONCLUSIONS

River processes at the Slovak–Austrian and Slovak–Hungarian Danube are significantly influenced by operation of hydropower schemes Gabcikovo and Freudenau.

Sediment regime at upper part of Slovak–Austrian Danube is affected by increased sediment supply as a result of engineering works and protective measures implemented downstream of Freudenau HPP (artificial bedload supply, restoration measures, navigation dredging, etc). Bedload rating curve based on the results of bedload measurements (1997–1998) proved higher intensity of bedload movement. Total amounts of bedload for average year increased under the present conditions by about 30% compared with situation in 1950s. Higher volumes of sediment supply induced river bed aggradation at the section that is not influenced by backwater effect causing navigation problems. Successive deposition of the river channel would also reduce flood capacity with negative impacts at flood protection in the vicinity of Bratislava.

Present knowledge of bedload regime and morphology development at the Slovak–Austrian Danube indicates the need to formulate common Slovak–Austrian project that should include analyses of the whole Danube section between both hydropower schemes Freudenau and Gabcikovo. This approach would enable the application of all relevant research results, knowledge and experiences achieved in both countries to solve the present problems including stabilisation of the river bed downstream of Freudanau more effectively.

Gabcikovo HPP significantly influenced dynamic equilibrium between sediment supply to the reach and transport capacity through the reach causing intensive degradation of the river bed downstream of hydropower scheme. Morphology development of the river bed proved that bed erosion still continues with negative impact at low flow water levels. Incision of the river bed caused rather dramatic fall of minimum navigation water level that is evident at long section of the Danube. Transported amounts of bedload are deposited downstream of degraded river bed causing navigation problems.

Channel stability (dynamic equilibrium between transport capacity and sediment supply) is necessary condition to provide the main river functions, such as navigation, power generation, flood control, etc. Many problems of river management arise from the inadequate prediction of bedload transport rate. Therefore a new knowledge about bedload regime of the Danube based on field measurements creates unique data for further analyses and application of numerical models. Correct understanding of present river processes at the Danube river enable to propose effective measures to reduce negative impacts of hydropower schemes.

REFERENCES

Holubová, K., Kl'účovská, J. & Szolgay, J. 1998. Environmental Impact of Hydroelectric Power Generation on an Anastomosing Reach of the River Danube. In Peter C. Klingeman et al. (ed.), *Gravel-Bed Rivers in the Environment, Water Resources Publications,* USA, Colorado: Water Resources Publication, LLC. Chapter 14, pp. 293–309.

Holubová, K. 2000. Some Aspects of the Bedload Transport Changes in the Slovak Section of the Danube River. XXth Conference of the Danubian Countries on Hydrological forecasting and Hydrological bases of water management. Bratislava.

Jaeggi, M.N.R. 1992. Effect of Engineering Solutions on Sediment Transport. Dynamics of Gravel-Bed Rivers, in chapter: Impact of Engineering works. John Wiley & Sons, Chichester, UK, pp. 593–606.

Kordina, H. et al. 2003. Comprehensive water management project of river training at the Danube eastern from Vienna. Report of environmental impacts assessment. Wasserstra-ßendirektion (WSD), Bundesministerium für Verkehr, Innovation und Technologie (BMVIT), Vienna.

Schiemer, F. et al. 2003. Restoration concept for large rivers – Experience from the Danube Restoration Project. Lowland River Rehabilitation 2003, Wageningen, the Netherlands, pp. 58.

Szolgay, J. 1964. Suspended load and Bedload Regime in Relation to Present Regulation of the Danube river. Final report, VUVH Bratislava.

Zottl, H. 1998. Granulometrische Sohlverbesserung Eine zukunftsweisende Methode zur Erhohung der Sohlstabilität. Osterreichisches Donau-Symposium, Wien.

This page intentionally left blank

River Flow 2004 – Greco, Carravetta & Della Morte (eds.)
© 2004 Taylor & Francis Group, London, ISBN 90 5809 658 0

Investigation of Lithuanian river-channels classification

Z. Rimkus
Lithuanian University of Agriculture, Kaunas-Akademija, Lithuania

ABSTRACT: The paper reviews the development of river-channels classification (river-channel processes type). A description of the degree of investigation of this point is presented. The importance of river-channels classification to the investigation of subsequent theoretical river bed processes and practical purposes of hydraulic engineering is emphasized.

According to the research of river-channel stability criterion / Grishanin invariant channels of Lithuanian rivers are suggested to be classified into straight channels with alternating bars, adapted type and highly meandering channels. It has been proved that the most important parameters of different type river-channels – mean depth, width and yield – have different interdependencies. The type helps to evaluate river-channel stability and trend of deformations: highly meandering channels have the highest transporting capacity, straight channels with alternating bars – the lowest one.

1 INTRODUCTION

Various river channel forming factors, their complex interrelation, geographical environment of the river, different genetic zones of river basin geomorphological formations create preconditions for the diversity of river channel and floodplain morphological development. Attempts have been made to work out a certain system in this natural diversity i.e. to classify river channels to separate types based on variety and peculiarities of river bed processes. River channel (their macroforms) classification to separate types of their development is useful to designers and builders of hydrotechnical constructions. This makes easier development and application of hydraulic project standards, helps to avoid mistakes in selecting construction site, to evaluate objectively impact on the environment, contributes to efficient application of river channeling devices. Grouping of river bed macroforms enables prognosis of river bed processes, e.g. course of river bed deformation (trend, volume, rate). River-channels classification is necessary for the development of generalized theory of river bed processes (Stream 1998). In this respect many issues are related to the evaluation of the impact on the environment. Recently, evaluation of the impact of hydraulic engineering on the environment has been regulated by the Environmental Impact Estimation law and supplementing normative documents. Environmental impact evaluation is indispensable for the implementation of any hydraulic project. Objective establishment of essential changes in river bed process indices is the basis for correcting the project or providing special environmental measures, related to hydraulic engineering of inland water bodies.

Aim of this work – on the basis of river-channel stability criterion/Grishanin invariant research to propose a river-channel classification methodics, to reason its scientific and practical use.

2 BACKGROUND OF THE PROBLEM AND OBJECT OF THE RESEARCH

2.1 *Short history of river-channel classification*

The first classification of river-channels was suggested by Russian scientists K.I. Rosinskij & I.A. Kuzmin (1947). Their idea was to classify rivers into three types: of direct, meandering and branched out channels. Lack of quantitative connections among different types did not derogate the importance of this classification. In the world practice three types of channels are known as the main ones. After ten years L. Leopold & M. Wolman (1957) divide river-channels into the same types – direct, meandering and branched out.

Later this classification was improved by a number of scientists, working in different regions of the world: N.I. Makkavejev, N.A. Rzanycin, N.E. Kondratjev, I.V. Popov, S. Chitale, D. Saimons, I.F. Karasiov, R.S. Tshalov and others (Makkavajev 1955, Rzanycin 1961, Chitale 1970, Shen 1971, Karasiov 1975, Tshalov 1979, Chanson 2001). Types of river-channels strongly depend on the particular conditions of river formation and physical–geographical conditions in the river

region. Practical hydraulic engineering highly valuates those methodics of channel classification, which are based on quantitative indices of morphological elements of river-channel macroforms. Usually these indices are not complex and do not require expensive initial investigations. One example of such methodics is the method, suggested by B.F. Sniscenko (1980) where river-channels are classifies according to the criterion:

$$A = I_o B_o / IB \quad (1)$$

where I_0 = mean slope of the bottomland; B_0 = mean width of the bottomland; I = mean stream slope; and B = mean width of the channel at the level of water overflow.

All parameters can be easily determined by using cartographic maps of the scale 1 : 1000 – 1 : 25,000. B.F. Sniscenko proposed distribution of river-channels into six types: highly meandering, unfinished meandering, flat branching out, limited meandering, straight channels with alternating bars and channels with islands (braided channel).

Research of the Lithuanian river-channel classification is poor. The final disappearance of glaciers in Europe should be considered the last phase of the Lithuanian river valley and river-channel network formation. River-channels of present shape were formed by the glacier melting or the so called fluvioglacial water. In the post-glacial period rivers in west Lithuania did not cut into their valleys significantly, while in east Lithuania this cut reached 3–5 meters. After the process of cutting into the rivers started formation of bottomlands. The post-glacial period is characterized by strong warming of climate and significant increase in precipitation, which contributed to the formation of modern river-channels (Lietuvos 1958).

In 1960 a Russian scientist S.N. Pinkovskij classified river-channels of Lithuanian and other Euroasian rivers on the basis of big scale map and analysis of geomorphological, geological and hydrological material of North-West part of the former USSR (Pinkovskij 1960). Here river-channels of the main Lithuanian rivers were divided into two groups: highly meandering and not meandering (straight lined and one-branched). The presented scheme is laconic, the classification is relatively old and includes only big Lithuanian rivers, therefore, it is of no significant theoretical and practical importance.

At the same time M. Beconis emphasises that according to the forms of their manifestation the run-of-river processes are geomorphological; morphological formations are distinctly expressed in river-channels and their bottomlands, these processes result in formation of valleys (Beconis 1960). River valley, i.e. the river-channel formation environment, is important to the formation, therefore, successful investigations of run-of-river processes requires knowledge of the regularities of this environment formation. According to M. Beconis side-erosion is very important for river-channel development processes. Under the influence of this erosion high banks of some rivers are destroyed and annual move is 10–20 cm. Slope of the valley is also influenced by mechanical suffusion (wash out of rocks, fine particles and soluble materials through water filtration) and landslip processes. They are often observed in river-channels of South-East Lithuania basin. Recently interesting and useful investigations of run-of-river processes are being carried out by the scientists of Vilnius University and Lithuanian Institute of Geography: A. Cesnulevicius, A. Baubiniene, T. Kovera, M. Paukste, D. Veteikis, J. Volungevicius, etc. They have distinguished and described genetical and dynamical segments of the big Lithuanian rivers, analyzed state of the banks, established the accumulated and eroded sections (Baubiniene 1999, Cesnulevicius et al. 1999, Cesnulevicius 2000).

Author of this paper on the basis of B.F. Siniscenko methodics suggests to divide river-channels of the Nemunas basin in Lithuanian territory into straight channels with alterating bars, forced meandering, limited meandering and high meandering (Rimkus 1988). In comparison with the described methodics of B.F. Sniscenko, here a new type of rivers has been distinguished – forced meandering, while no river-channels of unfinished meandering and flat branching out types have been found in Lithuania. Values of A criterion and their average standard deviations have been established for each class of river-channels. Although the suggested classification of river-channels seemed to be not only of theoretical importance but important in practical engineering it has not become widely used in Lithuania. The lack of motivation of hydraulic engineering specialists concerning the importance of river-channel type determination is considered to be the main reason. Changes of run-of-river processes under the influence of waterworks or negative influence of these processes on the constructions are observed only after a certain period of time. They are not inert and cause no problems in the case of superficial evaluation of this process. Run-of-river processes have not been evaluated because of the following reasons: the traditions existing in the environment of hydraulic engineering specialists, gaps in education of engineers, relatively small rivers in Lithuania (the dominating opinion states that small rivers have no problems), small number of scientists, lack of coordination and financing of their activity, etc.

Political and economical orientation to the European Union, increasing attention to ecological problems and rational use of natural resources, development of science encourage searching for attractive ways to deal with the described problem. Effective

use of natural resources requires good understanding of the regularities of natural phenomena, finding the most effective criteria that are closely related with fundamental essence of the phenomenon and ability to evaluate the impact of economical activity on the environment.

2.2 *Object of the research*

Small streamlets (3–10 km length) dominate in Lithuania by number and total length. Their number reaches 3.6 thousand and they make 50% of the total length of all rivers that are longer than 3 km. The number of medium (10.1–100 km) rivers is 755 and their total length makes 41.5% and the number of big rivers (longer than 100 km) – 17 and total length makes 8.4% of the total length of all measured rivers (37.6 thousand km). The longest and biggest rivers the Nemunas, the Neris, the Sesupe, etc. do not fit the Lithuanian territory or go along the border (Fig. 1 & Tab. 1).

Average density of river network in the country is 1.18 km/km^2. River-channels of most rivers, especially smaller ones, have undergone channelization; according to the length the regulated river-channels make 82.6%, natural ones – only 17.4% (Gailiusis et al. 2001).

3 METHODICS

The criterion of rivers, canals and other natural and artificial waterways channels stability M that has been used in this work is described in literature sources and is also called Grishanin's invariant (Grishanin 1990):

$$M = R(g\chi)^{0.25} / Q^{0.5} = \text{const}, \quad (2)$$

where R = hydraulic radius of the canal; g = acceleration due to gravity; χ = wetted perimeter of the canal; and Q = discharge.

According to K.V. Grishanin the medium M value for the sections of river-channels with fine bed load/sediments is close to the constant M value $M = 0.92 \pm 0.12$, for the gravelled and stony river-channels $M = 0.5 \div 0.6$. Some data shows that invariant M remains constant only for the river-channels of certain type. According to V.I. Antropovskij (1972) $M = 0.9 \div 1.1$ for the channels of unfinished meandering, and $M = 0.4 \div 0.5$ for the channels with

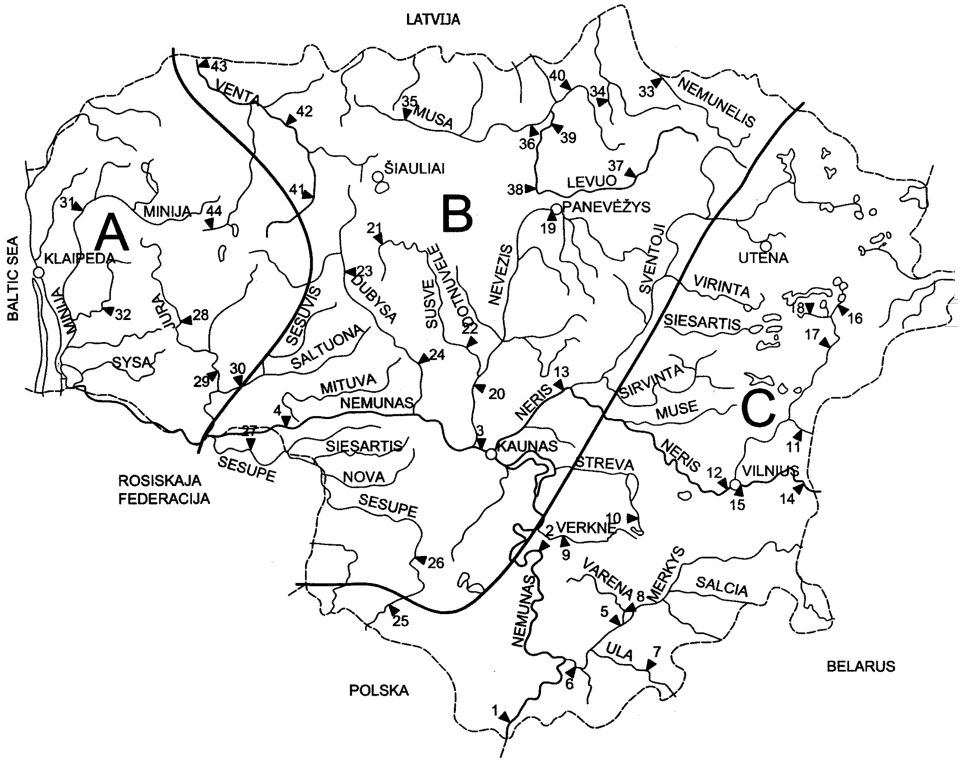


Figure 1. Scheme, hydrological zones and location of water observation stations on the main Lithuanian rivers: A – West Lithuania: B – Middle Lithuania: C – East Lithuania: ▼ – water observation stations.

Table 1. Results of investigation of river-channels stability criterion/Grishanin invariant.

River-water observation station	Grishanin invariant *M*	Empirical deviation *S*	Sniscenko criteria *A*	Type of channel	
				According to previous classification (Rimkus 1988)	Suggested in this work
Group of major rivers					
1. Nemunas–Druskininkai	0.87 (0.77 ÷ 0.97)	0.04	2.51	Str	Str
2. Nemunas–Nemajunai	0.89 (0.76 ÷ 1.13)	0.06	2.05	Str	Str
3. Nemunas Lampedziai	0.76 (0.62 ÷ 0.92)	0.05	2.81	Str	Str
4. Nemunas–Smalininkai	1.07 (0.79 ÷ 1.07)	0.07	2.89	Str	Str
11. Neris–Buivydziai	0.99 (0.71 ÷ 1.19)	0.09	2.46	Str	Str
12. Neris–Vilnius	1.02 (0.88 ÷ 1.23)	0.03	2.02	Str	Str
13. Neris–Jonava	0.74 (0.68 ÷ 0.90)	0.02	1.48	Str	Str
District of Eastern Lithuania					
5. Merkys–Varena	1.22 (0.99 ÷ 1.39)	0.09	25.41	Fr.m	Fr.m
6. Merkys–Puvociai	0.94 (0.86 ÷ 1.05)	0.04	3.05	For.m	Adap
7. Ula–Zervynos	1.05 (0.98 ÷ 1.22)	0.05	3.38	For.m	Adap
8. Varene–Varena	0.97 (0.74 ÷ 1.20)	0.08	8.31	Lim.m	Adap
9. Verkne–Verbiliskes	1.28 (1.14 ÷ 1.55)	0.07	20.32	Fr.m	Fr.m
10. Streva–Semeliskes	0.94 (0.78 ÷ 1.11)	0.08	8.71	Lim.m	Adap
14. Vilnia–Santakai	1.02 (0.75 ÷ 1.25)	0.11	7.85	Lim.m	Adap
15. Vilnia–Vilnius	0.85 (0.56 ÷ 1.52)	0.18	2.35	Str	Str
16. Zeimena–Kaltanenai	1.17 (0.92 ÷ 1.32)	0.07	30.43	Fr.m	Fr.m
17. Zeimena–Pabrade	0.98 (0.78 ÷ 1.18)	0.09	8.19	Lim.m	Adap
18. Lakaja–Lakajai	1.19 (0.97 ÷ 1.23)	0.05	19.38	Fr.m	Fr.m
25. Sesupe–Kalvarija	1.20 (0.99 ÷ 1.49)	0.09	31.01	Fr.m	Fr.m
District of Middle Lithuania					
19. Nevezis–Panevezys	1.00 (0.82 ÷ 1.22)	0.07	8.77	Lim.m	Adap
20. Nevezis–Dasiunai	1.40 (1.19 ÷ 1.79)	0.09	20.62	Fr.m	Fr.m
21. Susve–Siaulenai	1.28 (1.17 ÷ 1.37)	0.05	31.68	Fr.m	Fr.m
22. Susve–Josvainiai	0.92 (0.76 ÷ 1.17)	0.06	9.61	Lim.m	Adap
23. Dubysa–Lyduvenai	1.19 (1.07 ÷ 1.32)	0.05	44.09	Fr.m	Fr.m
24. Dubysa–Padubysis	1.07 (0.80 ÷ 1.32)	0.07	2.31	Str	Str
26. Sesupe - Marijampole	0.88 (0.78 ÷ 0.97)	0.05	2.91	Str	Str
27. Sesupe–Dolgoje	1.23 (1.05 ÷ 1.43)	0.07	3.58	For.m	Adap
33. Nemunelis–Rimsiai	1.09 (0.78 ÷ 1.43)	0.11	9.69	Lim.m	Adap
34. Agluona–Dirvonakiai	1.23 (1.11 ÷ 1.35)	0.08	23.40	Fr.m	Fr.m
35. Musa–Miciunai	0.86 (0.64 ÷ 1.30)	0.11	3.09	Str	Str
36. Musa–Ustukiai	1.05 (0.93 ÷ 1.36)	0.10	9.10	Lim.m	Adap
37. Levuo–Kupiskis	1.72 (1.05 ÷ 2.12)	0.26	32.43	Fr.m	Fr.m
38. Levuo–Bernatoniai	1.18 (1.02 ÷ 1.33)	0.08	18.64	Fr.m	Fr.m
39. Levuo–Pasvalis	0.95 (0.52 ÷ 1.57)	0.25	8.60	Lim.m	Adap
41. Venta–Ramuciai	1.39 (1.23 ÷ 1.64)	0.10	28.36	Fr.m	Fr.m
42. Venta–Papile	1.04 (0.79 ÷ 1.87)	0.20	9.32	Lim.m	Adap
43. Venta–Kuodziai	0.90 (0.68 ÷ 1.35)	0.12	2.40	Str	Str
District of Western Lithuania					
28. Jura–Pajuris	0.97 (0.83 ÷ 1.11)	0.04	4.55	For.m	Adap
29. Jura–Taurage	1.09 (0.81 ÷ 1.29)	0.08	4.14	For.m	Adap
30. Sesuvis–Skirgailiai	1.73 (1.29 ÷ 2.29)	0.15	21.9	Fr.m	Fr.m
31. Minija–Kartena	1.31 (1.07 ÷ 1.63)	0.05	22.79	Fr.m	Fr.m
32. Veivirzas–Mikuiziai	1.81 (1.74 ÷ 2.20)	0.04	20.15	Fr.m	Fr.m
44. Resketa–Gudeliai	0.90 (0.66 ÷ 1.44)	0.12	3.83	Str	Str

Note: Str – straight channels with alternating bars; For.m – forced meandering channels; Lim.m – limited meandering channels; Fr.m – highly meandering channels; Adap – adapted channels

islands. A.N. Lepin & N.K. Aleksandrova (1980) have established that invariant of highly meandering channels is $M = 1.2 \div 1.3$. Other works also present some useful knowledge on this issue (Zelezniakov 1976, Kondratjev et al. 1982, Muchamedov et al. 1970).

As river-channels are relatively wide so having accepted that $R \approx h$ and $\chi \approx B$ the Grishanin invariant obtains the following expression:

$$M = h(gB)^{0.25} / Q^{0.5} = \text{const} \quad (3)$$

where h = medium depth of flow in the channel; B = medium width of flow.

The Grishanin invariant has been calculated in 44 Lithuanian rivers for the cross-sections at which hydrological stations are located and stream velocity, water discharges and main parameters of the channel – depths and widths – are measured at different time (Fig. 1 & Tab. 1). To reduce the influence of antropogenetics on the investigation results hydrometrical, hydrological and hydraulic data of earlier years (not later than 1960) is used. Water discharges and corresponding water depths are selected for the period the most intensive run-of-river processes: $0.75Q_f < . Q_{cal} < 1.25Q_f$ (Q_{cal} – calculated water discharge, Q_f – formative water discharge). Formative discharges are calculated according to the empirical expressions proposed by the author of this paper (Rimkus & Darbutas 1999):

(a) Rivers in hydrological regions of Middle and West Lithuania

$$Q_f = -0.056Q_a^2 + 6.6Q - 1.8 \quad (4)$$

$$Q_a = 0{,}0057F + 1.24 \quad (5)$$

(b) Hydrological region of East Lithuania and bigger rivers – the Nemunas and the Neris

$$Q_f = 0.001Q_a^2 + 0.52Q_a + 4.26 \quad (6)$$

$$Q_a = 0.0065F + 1.16 \quad (7)$$

where Q_a = average water discharge of the river of many years; F = area of the basin km^2.

Types of river-channels and corresponding Sniscenko criteria A have been selected on the basis of earlier investigations (Rimkus 1988).

For the analysis of the dependency of the main channel parameters – depth, width and water discharge – on the type of river-channel three rivers of different channel type have been selected at random; the Neris at Vilnius (No 11, straight channel with alternating bars), the Merkys at Puvociai (No 6, adapted type) and the Sesupe at Kalvarija (No 25, highly meandering).

4 RESULTS

In order to the Grishanin invariant for the classification of Lithuanian river-channels the mean values of invariants, the biggest values of their deviation and empirical averages (S) of the deviation module have been calculated for the rivers presented in the Table 1. The mean values of the invariant vary within 0.85–1.81. Empirical averages of deviation module for most of mean values of invariants are below 0.1, and only highly urbanized rivers have value of this coefficient above 0.1. The highest empirical coefficient of deviation module is 0.26. Wider variation of the invariant can be determined by channel deformations, local flow backups, sudden increase of the channel width, bigger tributaries, etc. (Grishanin 1990).

Generally, different mean values of the invariants, calculated for different river-channels or their sections, and slight absolute values of average empiric values of deviation module corroborate the statement that Grishanin channel stability criterion is quasiconstant (equations 2 and 3) only for certain sections of rivers and can be used as river-channel classification index.

Dependency analysis (Fig. 2) and results of investigations (Channel type = f(A)) earlier conducted by the author of this paper (Rimkus 1988) show that the following three types of river-channels can be distinguished from the whole of points on the basis of identity of mean values of Grishanin invariant: (1) straight channels with alternating bars; (2) forced and limited meandering; (3) highly meandering. Thus, according to Grishanin invariant and considering development of river-channel types classification in other regions (Tshalov et al. 1998) the earlier proposed types of channels – forced and limited meandering – are attributed to one type of river-channels and are called

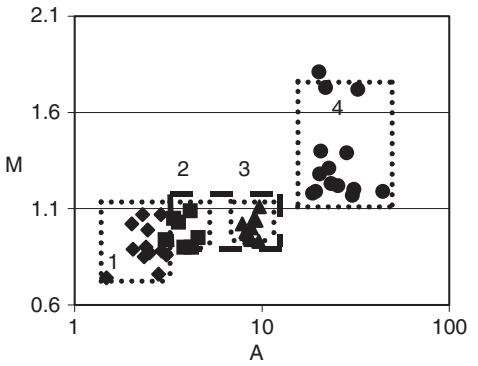


Figure 2. Dependences of river-channel types on Sniscenko criteria A and Grisanin's criteria M: 1 – straight channels with alternating bars; 2 and 3 – adapted meandering channels ((according to former classification (Rimkus 1988); 2 – forced meandering channels and 3 – limited meandering channels)); 4 – highly meandering channels.

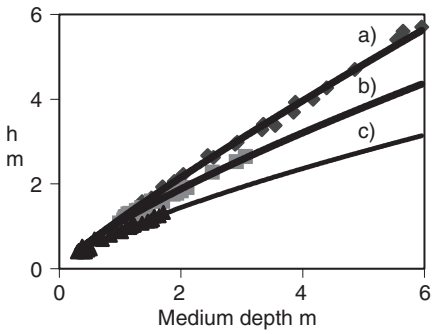


Figure 3. Interrelation of the parameters of the river-channels in different types of beds: (a) the Neris at Vilnius, straight channel with alternating bars; (b) the Merkys at Puvociai, adapted channel & (c) the Sesupe at Kalvarija, highly meandering channel.

channels of adapted type. Calculations show that straight channels with alternating bars have the mean value of the invariant $M = 0.91$ ($0.74 < M < 1.07$), empiric average of deviation module of mean values of Grishanin invariant $S = 0.09$, the corresponding values of adapted type channels are $M = 0.99$ ($0.9 < M < 1.09$), $S = 0.06$; of highly meandering channels – $M = 1.36$ ($1.17 < M < 1.81$), $S = 0.18$.

Graphic interpretation of Grishanin invariant (Fig. 3) illustrates regular interrelation of the main parameters of river-bed – depth, width and water discharge. The invariant equation (3) is expressed with respect to depth:

$$h = MQ^{0.5}/(gB)^{0.25} \equiv h_{med} \tag{8}$$

where h_{med} = medium depth of flow in the channel according to Grishanin invariant.

After that calculations, graphical and statistical analysis are performed according to randomly selected hydrometrical data of different type river-channels.

The analysed relation is relatively close in the rivers of the same type of channel, while comparison shows significant differences. Figure 3 shows the relations, expressed by the following equations:

(a) the Neris at Vilnius (straight channel with alternating bars)

$$h_{med} = 1.17[MQ^{0.25}/(gB)^{0.25}]^{0.88} \tag{9}$$
$$R^2 = 0.99$$

(b) the Merkys at Puvociai (adapted channel)

$$h_{med} = 1.10[MQ^{0.25}/(gB)^{0.25}]^{0.77} \tag{10}$$
$$R^2 = 0.98$$

(c) the Sesupe at Kalvarija (highly meandering channel)

$$h_{med} = 0.88[MQ^{0.25}/(gB)^{0.25}]^{0.71} \tag{11}$$
$$R^2 = 0.96.$$

Different interrelations of the main parameters of the channel are characteristic the river-channels of different type. This should particularly be taken into consideration in the case of reforming of sections of river-channels, e.g. construction of bridges and waterworks, reforming river-channels in lower steps of waterworks, other regulation or renaturalization of river-channels. Tendency to deformations can be determined on the basis of Grishanin criterion and type of river-channel. According to K.V. Grishanin if $M > 1.05$ (channels with tendency to meandering), the river flow does not have full transporting capacity and mud silting of the channel is probable. On the contrary, if $M < 0.90$, the river-channel has an increased transporting capacity and deepening is probable. Thus value of the index M helps to determine not only type of the channel, interrelation of the main parameters, but also channel stability and tendencies to deformations: the lowest transporting capacity is characteristic to highly meandering channels, the highest one – to straight channels with alternating bars (relatively straight channels). This conception is confirmed by famous supporter of hydromorphology theory – B.F. Sniscenko, who states that "...transition from highly meandering channels to straight channels with alternating bars can be related with gradually growing amount of bed and suspended load, and increase of total amount of stream sediments and transporting capacity" (Kondratjev et al. 1982, p.88).

5 CONCLUSIONS

1. Analysis of river-channel classification shows the lack of attention to this problem in Lithuania. Theoretical and practical necessity of river-channel distribution to types is reasoned.
2. Distribution of Lithuanian river-channels to straight channels with alternating bars, adapted channels and highly meandering channels is suggested on the basis of the analysis of river-bed stability criterion/ Grishanin invariant.
3. The interdependancy of the most important parameters of different type river-channels – mean depth, width and discharge – is based on the regularities, characteristic to separate types of channels. Type of the river-channel determines the channel stability and tendencies to deformations: the lowest transporting capacity is characteristic to highly meandering channels, the highest one – to straight channels with alternating bars (relatively straight channels).

REFERENCES

Antropovskij, V.I. 1972. Uravnenija regresii mezdu charakteristikai rusla i potoka pri nezaversennom meandrirovanij, ruslovoj i poimennoj mnogorukavnosti. *Trudy GGI vyp. 195*: 4–19.

Baubiniene, A. 1999. Geografiniai kai kuriu upiu salu pasiskirstymo ypatumai. *Geografijos metrastis 32 t.*: 87–92.

Beconis, M. 1960. Lietuvos TSR upiu salpu isplitimas ir ju tipai. *Geografijos metrastis, III t.*: 163–175.

Chanson, H. 2001. The hidraulics of Open Channel Flow // *www.bh.comcompanions*.

Chitale, S. 1970. River channel patterns. *J.H.D. Pro. ASCE, vol. 96, HY-1*: 201–221.

Cebotariovas, A. 1975. Bendroji hidrologija. Leningradas. *A. Bariso ir K. Kilkaus vertimas į lietuviu kalba*, 1983. Vilnius.

Cesnulevicius, A., Baubiniene, A., Paukste, M., Veteikis, D. & Volungevicius, J. 1999. Rytu Lietuvos upiu krantu bukle. *Geografijos metrastis 32 t.*: 178–193.

Cesnulevicius, A. 2000. Didziuju Lietuvos upiu krantu bukles sasaja su sleniu morfogenine aplinka. *Geografijos metrastis 33 t.*: 267–278.

Gailiusis, B., Kovalenkoviene, M. & Rimaviciute, E. 2000. Tvenkiniu poveikis Lietuvos upiu nuotėkio rezimui. *Geografijos metrastis 33 t.*: 97–107.

Grishanin, K.V. 1979. Dinamika ruslovych potokov. Leningrad: Gidrometeoizdat.

Grishanin, K.V. 1990. Osnovy dinamiki ruslovych potokov. Moskva: Transport.

Karasev, I.F. 1975. Ruslovyje processy pri perebroske stoka. Leningrad: Gidrometeoizdat.

Kondratjev, N.E., Popov, I.V. & Sniscenko, B.F. 1982. Osnovy gidromorfologiceskoj teorij ruslovogo processa. Leningrad: Gidrometeoizdat.

Leopold, E. & Wolman, M. 1957. River channel patterns: braided, meandering and straight. *U. S. Geol. Survey Pap.,* N 282-B.

Lepin, V.M. & Aleksandrova, N.K. 1980. Rasciot glubinnych deformacij estestvennych rusel. *Trudy GGI, vyp. 236*: 23–59.

Lietuvos TSR fizine geografija, 1958. I dalis. Vilnius.

Makkaveev, N.I. 1955. Ruslo reki i erozija v ee baseine. Moskva: AN SSSR.

Muchamedov, A.M., Ismagilov, Ch.A. & Zurajev, T.Z. 1970. O kinematiko-morfologiceskoj zavisimosti r. Amudar'i. *Trudy SANIIRI, vyp.124*: 55–61.

Pinkovskij, S.N. 1960. Karta osnovnych tipov rusel ravnynych rek SSSR. *Trudy III Vsesojuzn. gidrolog. s'jezda, t.5*: 361–366.

Rimkus, Z. 1988. Tipizacija ruslovogo processa rek Litovskoj SSR. *Mokslo darbu rink.: Melioracijos sistemu hidrotechniniu statiniu patikimumo didinimas. LZUA*: 34–43.

Rimkus, Z. & Darbutas, A. 1999. Formative Water Discharges in Lithuanian Riverbeds. *Vandens ukio inzinerija. Mokslo darbai. 8(30)*: 56–65.

Rossinskij, K.I. & Kuzmin, I.A. 1947. Nekotoryje voprosy prikladnoj teorij formirovanija recnych rusel. *V kn.: Problemy regulirovanija recnogo stoka. Moskva*: 88–130.

Rzanycin, N.A. 1961. Morfologiceskije i gidrologiceskije zakonomernosti strojenija recnoj seti. Leningrad: Gidrometeoizdat.

Shen, H.U. (ed.) 1971. River mechanics. Vol. 1. Colorado.

Sniscenko, B.F. 1980. Tipy ruslovogo processa i ich voznichnovenije. *Trudy GGI, No 2636*: 4–40.

Stream Corridor Restoration. Principles, practices, and processes, 1998. *http://www.usda.gov/stream restoration/ newtofc.htm.*

Tshalov, R.S. 1979. Geograficeskoje issledovanije ruslovych processov. Moskva: MGU.

Tshalov, R.S., Alaben, A.M., Ivanov, V.V., Lodina, R.V. & Panin, A.V. 1998. Morfodinamika rusel ravninych rek. Moskva: GEOS.

Zeleznekov, G.V. 1976. Teorija gidrometrij. Leningrad: Gidro-meteoizdat.

This page intentionally left blank

River Flow 2004 – Greco, Carravetta & Della Morte (eds.)
© 2004 Taylor & Francis Group, London, ISBN 90 5809 658 0

3D numerical modelling of morphological bed changes in the Danube River

T. Fischer-Antze & D. Gutknecht
Institute of Hydraulics, Hydrology and Water Resources Management, Vienna University of Technology, Austria

N.R.B. Olsen
Department of Hydraulic and Environmental Engineering, The Norwegian University of Science and Technology, Norway

ABSTRACT: This paper describes numerical modelling of morphological bed changes in the Danube River. The reach modelled in this study has a length of 4 km and is located between Vienna and the Austrian-Slovakian border. The Danube River in this reach is characterised by a great width-to-depth ratio leading to an alternate bar configuration. The August 2002 flood event with a peak of 10,000 m^3/s was modelled. The numerical code is based on a finite volume approach solving the Navier-Stokes equations to obtain the water velocity and the bed shear stress, and the sediment transport is computed by an empirical formula. In the present study, the model was modified by introducing a new sediment transport formula by Wu et al. (2000). Results show a fairly good agreement between measured and calculated bed changes.

1 INTRODUCTION

The Danube River reach between Vienna and the Austrian-Slovakian border has a length of 40 km and is one of two remaining free flowing reaches in Austria. At the upstream end, a hydropower station acts as a barrier to the sediment transport which disturbs the natural sediment dynamics. The reach is significantly influenced by river engineering works in particular by groynes and fixed banks. In regions of minor engineering influence, the development of alternate bars can be observed.

As a consequence of significant manmade encroachments, the reach is in a stage of erosion with an average erosion rate of approximately 2 cm per year; the lack of sediments held back from the upstream dam require compensation by the operator of the hydropower station.

In August 2002, a 100 years flood with a peak discharge of 10,000 m^3 passed the Danube and caused significant bed changes. In this study the bed changes were modelled using the three dimensional model SSIIM on a chosen reach of 4 km. The quality of the results is assessed by comparing measured with calculated bed changes.

2 RIVER MORPHOLOGY

In nature, rivers are exposed to morphological bed changes caused by interaction between flow and sediment transport. Depending on the flow situation and geometrical features of the river, different bed structures can emerge. The Danube River reach in this study is characterised by a width-to-depth ratio of approximately 60 and a depth-to-grain-size ratio of 200. According to literature, the before mentioned values should lead to a dominant alternate bar configuration (Yalin & da Silva, 2001). With a mean grain diameter d_m of 26 mm, ($d_{16} = 6$ mm, $d_{84} = 48$ mm, $d_{90} = 58$ mm) (Zottl & Erber, 1987) the Danube in this reach is classified as a gravel bed river with a wide sieve curve.

3 DATA ANALYSIS

On behalf of the Austrian Waterway Authority bi-annual bed level measurements from a boat are performed to monitor the development of the river bed. The boat position was measured by a differential GPS technology, and the bed levels were determined using single beam echo sounder in combination with water levelling. The system measured the bed levels on pre determined cross-sectional profiles to enable comparisons of different measurement campaigns. The data used for this study have a longitudinal spacing and a cross-sectional distance of 100 m and approximately 0.5 m, respectively.

Pre and post flood surveys performed in spring and autumn 2002 are used in this study. The measured cross-sectional data was processed with

an interpolation software. The river beds from the two surveys were rastered onto a grid with a mesh size of 10 m in both directions. The grid positions for both surveys were kept identical for enabling the creation of differential plots. This methodology allowed to detect the spatial distribution of erosion and deposition patterns which evolved during the period between the two surveys.

Additionally, approximately 30 bed samples dug from the river bed using a grab dredger with a volume of 0.3 m^3 evenly distributed over the whole study reach were taken to achieve a mean grain size distribution of the river bed. The modelled reach was chosen because it was not influenced by engineering work during the measurement interval and because it was within the alternate bar reach.

4 SEDIMENT TRANSPORT

The sediment transport in this study was computed by incorporating a sediment formula for bed load by Wu et al. (2000) to the three-dimensional numerical model. A correction factor accounts for hiding and exposure mechanisms assuming to be a function of the hidden and exposed probabilities, which are stochastically related to the size and gradation of the bed material. The probability of particles d_j staying in the front of particles d_i can be assumed to be the percentage of particles d_j in the bed material, p_{bj}. Therefore, the probabilities of particles d_i hidden and exposed by particles d_j can be obtained as:

$$p_{hi} = \sum_{j=1}^{N} p_{bj} \frac{d_j}{d_i + d_j} \tag{1}$$

$$p_{ei} = \sum_{j=1}^{N} p_{bj} \frac{d_i}{d_i + d_j} \tag{2}$$

$$\eta_i = \left(\frac{p_{ei}}{p_{hi}} \right)^m \tag{3}$$

where N is the total number of particle size fractions of nonuniform sediment mixtures, p_{bi} and d_i are the percentage and the diameter of the ith fraction, respectively, η_i is the correction factor and m is a constant determined to be -0.6.

The hiding and exposure factor is then used to modify the criterion for sediment incipient motion for each fraction,

$$\frac{\tau_{ci}}{(\gamma_s - \gamma) d_i} = \theta_c \cdot \eta_i \tag{4}$$

where τ_{ci} is the critical shear stress for particle d_i in nonuniform sediment mixtures, γ_s and γ are the specific weights of sediment and water, respectively and θ_c is a constant determined to be 0.03.

The non-dimensional fractional bed-load transport rate ϕ_{bi} is defined as

$$\phi_{bi} = \frac{q_{bi}}{p_{bi} \sqrt{(\gamma_s - \gamma) g d_i^3}} \tag{5}$$

where q_{bi} is the transport rate of the ith fraction of bed-load per unit width.

Laboratory and field data was used to establish the formula for the fractional bed-load transport rate. By a regression analysis using least square curve fitting, the following relationship is obtained,

$$\phi_{bi} = 0.0053 \left[\left(\frac{n'}{n} \right)^{1.5} \frac{\tau_b}{\tau_{ci}} - 1 \right]^{2.2} \tag{6}$$

where n' is Manning's coefficient corresponding to grain roughness, here calculated with $n' = d_{50}^{1/6}/20$, n is Manning's coefficient for channel bed which was calibrated here and τ_b is the bed shear stress.

5 NUMERICAL MODELLING OF SEDIMENT TRANSPORT

To compute bed changes over time the semi-implicit numerical model SSIIM (Olsen, 2002) was applied. A finite volume method with a non-orthogonal, structured, and adaptive grid in the vertical direction was used for spatial discretisation. The model solved the Reynolds averaged Navier-Stokes equations in the three directions. The k-ε turbulence closure scheme (Rodi, 1980) computed the stress term and the SIMPLE method (Patankar, 1980) the pressure term.

In SSIIM there are several options to calculate sediment transport. The most tested approach is represented by the formulas of van Rijn (1984, a, b, c). Due to the fact that this formula has a limited range of applicability – it was tested for grain diameters up to 2 mm – the recently published transport formula presented by Wu et al. was incorporated into the model for this study. The two-dimensional distribution of the shear stress is computed from the turbulence model. The vertical bed changes in the centre of a cell in the bed geometry are calculated from the Exner equation where the difference between sediment inflow and outflow in one cell is multiplied with the time step and the result is divided by the area of the cell seen from above. The average bed movement in each cell must be transferred to the corners of the cell, where the vertical levels of the bed are defined (Olsen, 2000). A two

layer concept with an active upper layer and a lower inactive layer enables to model armouring processes.

In this study, sediment transport computations were performed on the 4 km reach. In order to compute the flow with a maximum precision in this reach, a pre test with a length of 8 km was chosen to serve as an input for the initial flow field and to assure a developed flow field at the inflow boundary of the smaller study reach.

The discharge and the water surface elevation in this study were kept constant at the level of the 100 year's flood assuming that most of the transport and bed changes between the two surveys happened during the peak.

6 RESULTS

In figure 1, the 4 km long reach of the Danube River is shown. Figure 1a displays water depths below a predefined fixed low water level. The water is flowing from the left to the right, the numbers along the reach indicate the stream-km decreasing in flow direction towards the Black Sea. Typical morphological features of a natural river in a bend with a mobile bed can be observed being a bar formation in the inner bend and scour at the outer bend. The studied river reach is situated in an environment of alternate bars. Illustrated in figure 1a, one bar ends at the upstream end and another bar is formed at the downstream end of the reach.

Figure 1b shows a differential plot of the pre and post flood bed topography survey. The plot was generated by subtracting the interpolated grid of the pre flood measurement from the post flood grid. This processing allows detection of areas with erosion and deposition together with the amount of bed changes during this period. Several morphological processes can be derived from this figure. The local bed changes remained mostly in the range of ± 1 m. An area of deposition can be observed at the upstream bar, which indicates a bar movement. Furthermore, the point bar dynamics are characterised by an increase of bar height and an erosion of the scour in the outer bend. In a distance of 300 m from the downstream end, a deep hole-like area occurred in the bed levels of spring 2002, which was filled by sediment due to the flood event.

Figure 1c represents the bed changes computed by the numerical model. The above mentioned characteristic features of the bed changes can be reproduced by the model with a fairly good quality. The height of modelled local bed changes coincides well with the measured bed changes. Regions of strong bed changes as the deposition of the upstream bar, the deposition at the second part of the point bar and the deposition due to the filled up hole near the downstream boundary are represented well by the model. Results show, that

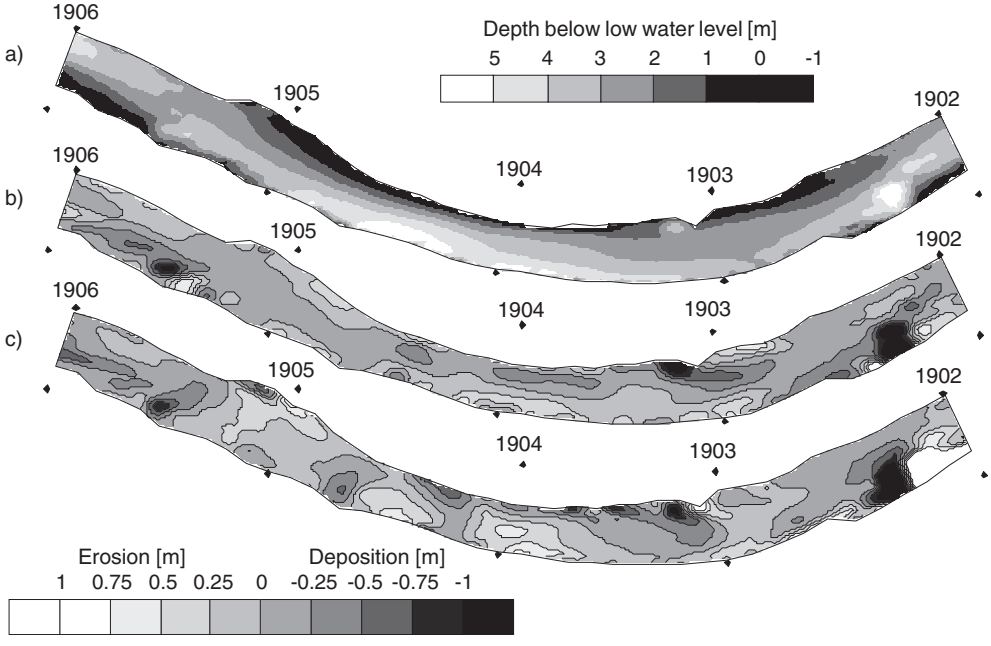


Figure 1. a) Water depths of the Danube River in spring 2002, b) measured bed changes between spring and autumn 2002, c) computed bed changes.

both the position and the amount of bed changes are predicted correctly.

The band of erosion in the scour region and the deposition area in the bar region are modelled with less accuracy. The bed changes in the bend show the correct tendency of erosion and deposition patterns, though the locations and amounts of changes show some deviations. The scour near the outflow of the reach is over predicted by the model.

Generally, the numerical model is capable to predict bed changes caused by a storm water event, both the deposition and erosion patterns and the amounts of changes are predicted reasonably correct for the overall reach.

The deviations from the natural development may be caused by some simplifications in the model which were necessary due to a lack of dense spatial information. For simplification, a constant initial sediment distribution at the bed was assumed, so that pre-existing armouring and sorting processes were not accounted for. The water leaving the main channel into the floodplains was neglected, since slow flow velocities in the shallow areas are assumed to be of minor importance for bed changes. The assumption of a constant discharge will probably be a source of less accurate results. Furthermore, the sediment input into the model had to be estimated, since for such extraordinary floods reliable bed-load measurements are not practicable.

7 CONCLUSIONS

The aim of the present study was to modify an existing three-dimensional numerical code with a new sediment transport formula and test it on the Danube River. The Wu et al. formula was incorporated, which enabled to compute nonuniform sediment transport by accounting for exposure and hiding effects.

The model was tested for a 4 km long reach of the Danube River and was compared against bed level measurements. This study was a first step towards three dimensional modelling of the Danube river. The preliminary results indicate that the model can represent both the amount of local bed changes and the erosion and deposition patterns with a fairly good agreement.

Further testing of the modified model, especially the capability to model sorting processes at alternate bar configurations will be included in future research. Longer reaches with varied discharges will be the next steps.

ACKNOWLEDGEMENT

The first author gratefully thanks Prof. Nils Olsen for providing the opportunity to stay at the NTNU, Trondheim for a guest research period, where this study was performed. Furthermore, the Austrian Waterway Authority is acknowledged for providing the bed topography data.

REFERENCES

Olsen, N.R.B. 2000. *CFD algorithms for hydraulic engineering*. Department of Hydraulic and Environmental Engineering, The Norwegian University of Science and Technology, Norway.

Olsen, N.R.B. 2002. *A three-dimensional numerical model for simulation of sediment movements in water intakes with multiblock option*, User's Manual. Department of Hydraulic and Environmental Engineering, The Norwegian University of Science and Technology, Norway.

Patankar, S. 1980. *Numerical Heat Transfer and Fluid Flow.* Taylor and Francis Publishers.

Rodi, W. 1980. *Turbulence models and their application in hydraulics*. IAHR. State-of-the-art publication.

van Rijn, L. 1984a. *Sediment transport, Part I: Bed load transport*. J. Hydr. Engineering 110 (10): 1431–1456.

van Rijn, L. 1984b. *Sediment transport, Part II: Suspended load transport*. J. Hydr. Engineering 110 (11): 1613–1641.

van Rijn, L. 1984c. *Sediment transport, Part III: Bed forms and alluvial roughness*. J. Hydr. Engineering 110 (12): 1733–1754.

Wu, W. et al. 2000. *Nonuniform sediment transport in alluvial rivers*. J. Hydr. Research 38 (6): 427-434.

Yalin, M., da Silva, A. 2001. *Fluvial Processes*. Delft: IAHR.

Zottl, H., Erber, H. 1987. *Untersuchung der Sohlstabilität im Zusammenhang mit der Staustufe Wien*. Wien, Auftraggeber MA 45.

River Flow 2004 – Greco, Carravetta & Della Morte (eds.)
© 2004 Taylor & Francis Group, London, ISBN 90 5809 658 0

Using a 1D steady flow model to compare field determination methods of bank-full stage

O. Navratil, M.-B. Albert, C. Boudard & J.-M. Grésillon
Cemagref, Lyon, France

ABSTRACT: Existing methods to determine bank-full stage and then bank-full discharge from field measurements give very diverging results. With the aim of clarifying this question, we use a 1D steady flow hydraulic model as reference in order to compare the main existing methods, applied on height case studies. We present here our methodology for one of these cases, the Ardour River at Folles, in the Loire river basin, France. Consistency of bank-full definitions is tested with the help of the hydraulic model. Thus, the evolution of flooded area with discharge at river reach scale allows us to define the hydraulic significance of the different elevations and discuss the validity of each method on the basis of hydraulic definition.

1 INTRODUCTION

Bank-full discharge is an interesting parameter to summarize channel morphology at reach scale and to study morphology – hydrology relationships. But identifying bank-full flow conditions for natural rivers is a heavy challenge. The indepth comparative analysis published by Williams (1978) evidenced that existing methods generally used lead to very diverging results. He wrote that "ideally, the various methods should all be compared with the 'true' bank-full discharge for each station. However, the chances of being present to measure a flow just at bank-full, however defined, are extremely small, and the true bank-full discharges are unknown for the stations of this study. So the different methods are simply compared with one another". Other works aimed to compare different estimations of bank-full discharge (e.g. Radecki-Pawlik 2002). Therefore, we try to follow up these studies, using hydraulic model results, in order to define the hydraulic significance of each stage definition.

2 STUDIED RIVER REACH

Ardour River at Folles is situated in the Loire river basin, France.

The stream reach surveyed is an alluvial river with perennial flow (figure 1). No significant upstream regulation or diversion occurs. Its associated river basin is a 131 km^2 drainage area underlying by a granitic bed rock. The studied reach is 230 meters long, i.e., about 25 times the mean bank-full channel width (Wb = 9 m), with a mean slope of about 0.0047.



Figure 1. Upstream view of the Ardour river reach with main channel and floodplain.

The channel has low sinuosity (1.03) with a well developed floodplain. It is a C3 channel type, according to Rosgen classification (Rosgen 1994). The reach includes a gauging station with 30 years of records and a well-known stage-discharge relationship available from the Regional Environmental Department. A bridge situated at the middle of the river reach does not constrain the main channel flow. Water surface profile starts to be disturbed only for discharge greatly above bank-full conditions (discharge exceeding 20 m^3/s).

3 TOPOGRAPHIC MEASUREMENTS

Topographic measurements were practiced in the stream channel and adjacent floodplain (figure 2) and linked to staff gage elevation using an electronic, digital, total-station theodolite. Nineteen cross-sections were surveyed to describe the main morphological variations and water surface profile at the reach scale.

Along the river reach, eleven morphological features were systematically surveyed at each cross-section to describe the main breaks in the cross section



Figure 2. Topographic measurement in the main channel of Ardour River at Folles.

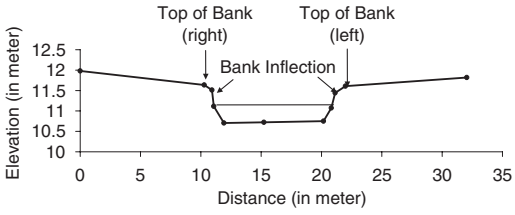


Figure 3. Used reference levels at a channel cross-section (not to scale).

geometry (figure 3): five features on each side of the channel in addition to the thalweg elevation.

The intersection between water surface and channel banks on the left and right sides are also surveyed, to characterize the hydraulic conditions at the time of survey. These measurements have been led at two different flow conditions.

Topographic measurements will be used 1/ to define bank-full elevation all along the river reach on the basis of different definitions and 2/ to build an hydraulic model.

4 BANK-FULL STAGE DEFINITIONS

Two different ways exist to define bank-full stage based on morphological criteria (Williams 1978):

1. On site estimations of the elevation of incipient flooding at different cross-sections, all along the stream survey, using morphological breaks as fields indicators (Leopold et al. 1994, Osterkamp & Hedman 1982).
2. Geometric criteria requiring measured cross-sections (Wolman 1955, Riley 1972, Pickup 1976, Williams 1978, Harrelson et al. 1994).

4.1 *Geomorphic definitions*

Topographic measurements provide two geomorphic indicators at cross-section scale to characterize the transitional area between main channel and floodplain surface: the Bank Inflection and Top of Bank elevations (figure 3).

The Bank Inflection feature corresponds to the upper limit of the main channel. It is the end of the near vertical channel bank. Many authors used to detect this feature on field. Leopold and Wolman define this break as the active floodplain elevation for near straight channel or river reaches that have a low sinuosity (Leopold et al. 1994). It also corresponds to the limit of the active channel (Osterkamp & Hedman 1982).

The Top of Bank feature corresponds to the elevation of the Valley Flat (Williams 1978; Leopold et al., 1994), the flood stage (Emmett 1972) or the predominant bench (Kilpatrick & Barnes 1964). It can be defined as the end of the transitional area between main channel and floodplain, and in this way, the beginning of a near flat surface (figure 3). This morphological feature has been already used for an other study on this river reach (Navratil 2002).

At each cross-section, we retain the mean elevation between left and right side. These geomorphic definitions of bank-full stage are therefore highly dependent on operator expertise and channel difficulties to detect such features (Wahl 1976). However, these measurements provide, rather than a single elevation, a range of bank-full elevation all along the river reach.

4.2 *Geometric definitions*

Using topographic measurements available at cross-sections, we applied three classical methods analyzed by Williams (1978).

Wolman's definition is the elevation corresponding to the minimum in the width to mean depth ratio function of the elevation. It was first introduced by Wolman (Wolman 1955) and used by many authors (Harvey 1969, Pickup & Warner 1976, Richards 1982, Carling 1988, Radecki-Pawlik 2002). Figure 4 shows an example of such a relationship at one cross-section.

Riley's definition is the stage corresponding to the first maximum of the bench index (Riley 1972). This index characterizes the evolution of bank slope versus elevation (from upper to lower elevation). Figure 5 shows such relationship and the bank-full stage defined at a cross section. Different maxima appear, corresponding to other break in bank slope (Radecki-Pawlik 2002).

Williams's definition (Williams 1978) is the elevation corresponding to a change in the relation between wetted area to top width (figure 6).

As evidence in figure 7, the three methods lead to different bank-full elevation values. Williams and

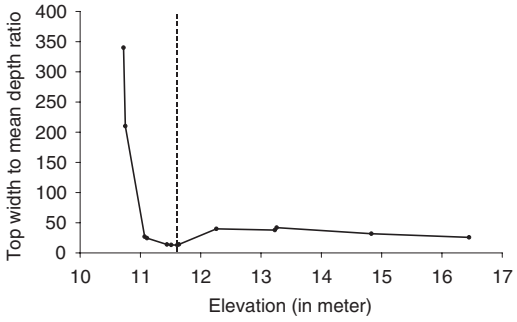


Figure 4. Minimum in the width to mean depth ratio.

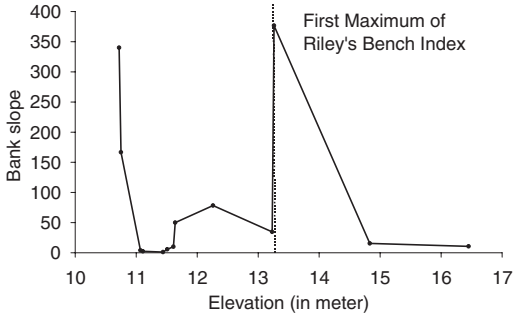


Figure 5. Riley's Bench Index versus elevation.

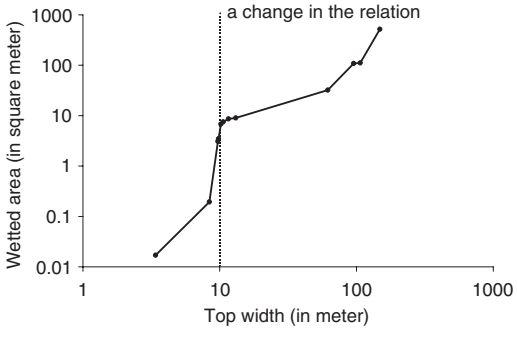


Figure 6. Evolution of the wetted area versus elevation.

Wolman's definition corresponds to the limit of the main channel. Riley's definition corresponds to a higher level.

We obtain three sets of elevation values estimated at each cross-section along the reach and corresponding to three different ways for determining bank-full elevation (example of William's definition at figure 8). For the five definitions, bridge sections are omitted in order to keep cross-sections that are free to adjust their form to actual flow regime.

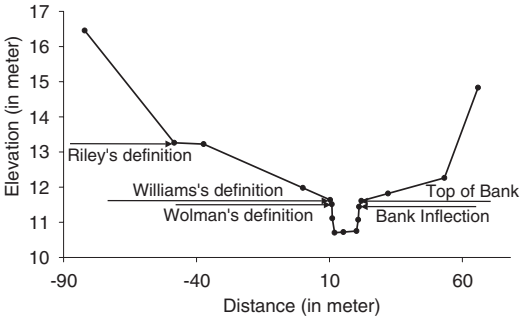


Figure 7. Different bank-full elevations at a cross-section for each definition.

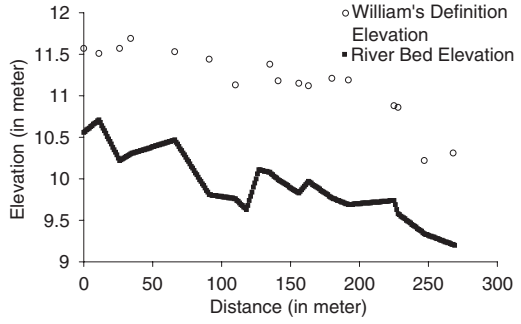


Figure 8. Williams's definition elevations all along the studied reach.

5 HYDRAULIC MODEL

The hydraulic model can be used as a standard of comparison under the condition it provides an accurate estimation of water level at each cross-section for in-bank and over-bank discharges. Other hydraulic parameters as width, wetted perimeter, mean water depth, wetted area and maximum water depth can be derived from this computed elevation.

A one dimensional code of simulation for steady and sub-critical flow is used (Baume & Poirson 1984). The water surface profile is calculated with good accuracy with the equations used into this code (Nicollet & Uan 1979). But, basics hypothesis have first to be verified. The sinuosity of the station being low (see study area), the one dimensional hypothesis is admitted. As we characterize the morphology of the main channel in term of capacity, the steady flow is then justified. As the mean slope is very small for all the station studied, the flow is subcritical. Afterwards, the good accuracy of the river modeling depends on quality of the topographical model, calibration data and method used.

In addition to longitudinal variability of the current cross sections, the topographic measurements

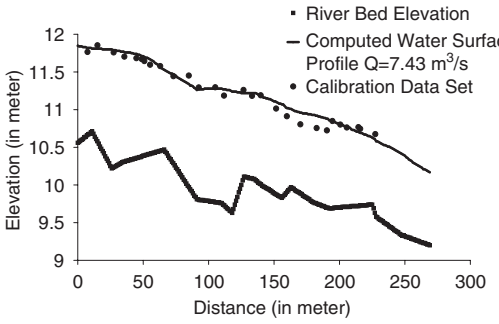


Figure 9. Hydraulic model calibration with a single Manning's "n" value for the entire reach.

included the description of possible hydraulic controls (bridges, weirs). A relationship between water level and discharge at the downstream cross-section was developed using a uniform flow model, in accordance with on field measurements at two different flows.

To calibrate our model, we used water surface profiles measured for two different discharges, one at low flow ($Q = 2.26\ m^3/s$), the other one at near bank-full flow ($Q = 7.43\ m^3/s$). A rating curve is also available by the Regional Environmental Department, with its range of validity. We fitted our model by using the Single Channel Method (Lyness et al. 1997), i.e., a single roughness coefficient for the main channel and the floodplain. A single Manning's "n" value for the entire reach is accepted with a mean error of 5 cm. Figure 9 shows an example of calibration for $Q = 7.43\ m^3/s$. Then, it allows us to calibrate our model for other discharges with the rating curve available at one cross-section and to extrapolate these results for the entire reach. Such a calibration provides a good estimation of water profile for in-bank and over-bank flows within the range of validity of the rating curve.

6 A SYNTHETIC REPRESENTATION OF OVERFLOWING DEVELOPMENT

For the purpose of this study, bank-full stage was defined according to morphological indicators. We consider that bank-full flow occurs at a break in slope, above which small increases in depth are accompanied by disproportionately large increases in width.

To characterize the hydraulic meaning of bank-full definition, we use the hydraulic model to estimate the evolution of flooded area for a large range of flows, at the reach scale. Figures 10a–c shows the flooded area, calculated with the hydraulic model at three different discharges: (a) in-bank flow ($Q = 3.5\ m^3/s$), (b) intermediate flow ($Q = 7\ m^3/s$) and (c) over-bank flow ($Q = 14\ m^3/s$).

For $Q = 3.5\ m^3/s$, the flow is contained in the main channel. For $Q = 7\ m^3/s$, local area are flooded, due

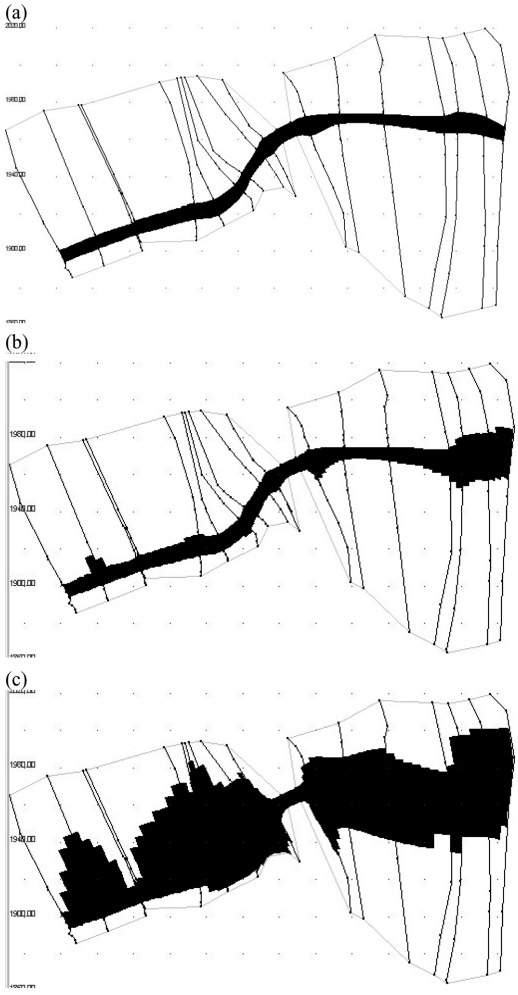


Figure 10a–c. Over view of the flooded area at the reach scale for tree discharges from upstream (right side) to downstream (left side): $Q = 3.5\ m^3/s$; $Q = 7\ m^3/s$; $Q = 14\ m^3/s$.

to vegetation interact with bank morphology and local sedimentation. For $Q = 14\ m^3/s$, the flow is well developed in the floodplain. For this flow conditions, the flooded area is relatively homogeneous, excepted a local area corresponding to bridge's embanked cross-sections at the middle of the reach and a downstream morphological singularity.

With the aim to study overflowing increase at reach scale and to compare different definitions of bank-full elevations, we use the relationship between the flooded area versus discharge (figure 11).

From low flow to about $15\ m^3/s$, the flooded area is significant at the reach scale. For upper flow, variability increases largely.

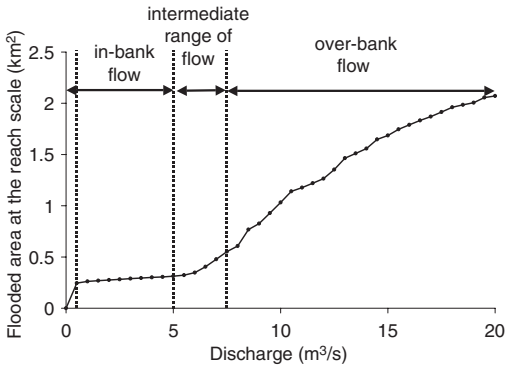


Figure 11. Evolution of the mean flooded area versus discharge (solid line).

At low flow, flooded area increases rapidly for a little rise of discharge (flows of about 0 to 0.5 m^3/s). Next, different ranges of discharge can be characterized when studying the relative increase of flooded area with a constant step of discharge (figure 11):

1. A smooth evolution of the flooded area with a constant rise of discharge: flows from 0.5 to 5 m^3/s.
2. The intermediate range of discharge where local over-bank areas occur, can be associated to the transition between main channel and floodplain flows: flows from 5 to 7.5 m^3/s. Its low bound is characterized by a sudden rise in flooded area.
3. The third range of discharge called the over-bank flow describes the floodplain evolution flow: from 7.5 to about 15–20 m^3/s. Its low bound corresponds to the beginning of a relatively constant increase of flooded area and ended at the limit of the floodplain.

At upper discharge, a smooth evolution of the flooded area versus discharge can be detected, corresponding to valley margin (flows upper than 15–20 m^3/s). Such a relationship will help us to find the hydraulic significance of each of the five bank-full definitions (see bank-full stage definitions).

7 CONSISTENCY OF BANK-FULL DEFINITIONS AT RIVER REACH SCALE

Bank-full stage has been computed at each cross-section all along the site survey, for each definition (table 1). The range of bank-full discharge can be up to a factor 4, showing the great variability for each definition. Bank-full discharge can't be considered at a single cross-section, but rather at a reach scale. These results demonstrate and complete further analysis that concept of bank-full discharge has no significance at a single cross-section (Riley 1972, Williams 1978).

Assumption that bank-full discharge concept is significant at a larger scale, i.e., that water surface profiles corresponds, on the average, to morphological features all along a stream reach, for characteristic discharges is now tested. Water surface profiles are computed for different discharges. The least square method is used to determine the discharge that minimizes, at the reach scale, the mean absolute difference between water surface levels modeled and morphological levels previously defined. For example, figure 12 shows the Williams's bank-full elevation and the adjusted water surface profile for $Q = 7.2\ m^3/s$ (table 1). Table 1 gives the main results of this test for other bank-full definitions. It allows us to appreciate the consistency, at reach scale, of these different bank-full elevations.

For all definitions retained, bank-full elevations are normally distributed around water surface profiles with a 95% confidence interval. The mean difference is less than 0.002 m for each definition. All definitions are then consistent at river reach scale. Characteristic discharges corresponding to morphological features have physical significant at this scale (table 1).

Table 1. Bank-full discharge computed (1) at each cross section and (2) at the reach scale with its mean absolute difference.

	At the cross-section scale	At the reach scale	
Bank-full Definitions	Range of discharge (m^3/s)	Discharge (m^3/s)	Mean absolute difference (m)
Top of Bank	5.7–21.6	8.1	0.17
Bank Inflection	3.2–9.9	5.1	0.12
Wolman's definition	3.8–13.5	6.8	0.15
Williams's definition	4.8–13.5	7.2	0.18
Riley's definition	8–25	15	0.26

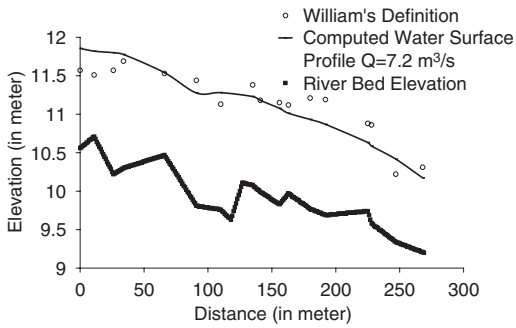


Figure 12. Example of adjustment of water surface profile ($Q = 7.2\ m^3/s$) with William's definition of bank-full stage.

However, each definition of bank-full is more or less consistent all along the site. Mean differences between Top of Bank or the Bank Inflection elevations with water profiles are respectively 0.17 and 0.12 m. Wolman's and Williams's definitions are consistent too but with a mean error a little bit greater than geomorphic definitions (0.15 and 0.18 m). Riley's definition seems to be less consistent than others, with a mean difference of about 0.26 meter. The calibration uncertainty of water level modeled can explain about 20% of variability between water level and morphological features (calibration uncertainties are about 0.05 m). Then we can assess that Wolman and Williams's definition, Top of Bank and Bank Inflection are consistent all along the reach. The Riley's Bench Index seems to be a poor definition of bank-full condition for this site survey.

Bank-full discharge expressed at a cross-section has no significance, but, on the opposite, this metric well describes the main channel morphology averaged at the reach scale. A test of robustness of bank-full discharge value with the length of the survey shows that this length must be about 20 times bank-full width to converge to bank-full discharge estimated using the all studied reach (test lead with the Bank Inflection elevation with an accepted error less than 5%). This test is in accordance with literature recommendations (Harrelson et al. 1994, Leopold et al. 1994).

8 HYDRAULIC SIGNIFICANCE OF BANK-FULL DEFINITIONS AND CONCLUSIONS

Bank-full discharge estimated with the hydraulic model for each definition (table 1) are now associated with its corresponding flooded area (figure 11). We can locate these values on the flooding evolution curve to determine their hydraulic significance (figure 13).

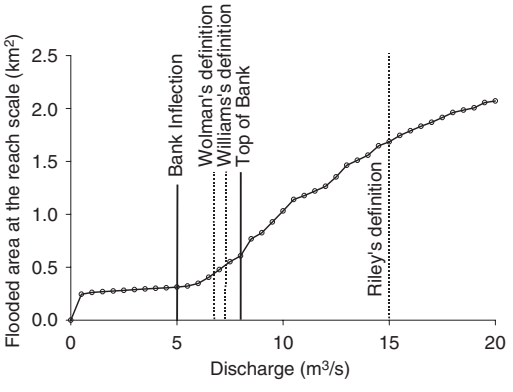


Figure 13. Evolution of the flooded area at the reach scale and bank-full discharges corresponding to different definitions: geomorphic and geometric definitions.

It allows us to compare objectively results provided by the three different studied methods, the geomorphic methods and the incipient flooding at river reach scale.

Wolman's definition corresponds to incipient flooding (figure 13). William's definition corresponds to the same range of flow, i.e., when flood begins to occur at particular cross-section along the reach. Riley's Bench index definition does not correspond to a bank-full elevation. It corresponds to a greater flow in the floodplain. It is certainly due to the first index criteria (Riley 1972) that is inaccurate when considering the all section (Radecki-Pawlik 2002). Top of Bank definition corresponds to the beginning of flow into the floodplain usually called the flood stage. Bank Inflection definition is located at the upper limit of the "in-bank flow" range of discharge. It can be defined as the end of the main channel, just before over-bank flow occurs.

9 PERSPECTIVES

The methodology described above will be applied to seven other river reaches. Expected results of this study are to give objective judgment on the different ways for determining bank-full stage and bank-full discharge and also possibility to gather together sets of bank-full discharge data estimated with different methods, when verified they lead to the same parameter definition. In this way, useful recommendations to improve operational procedures for determining bank-full stage on the field and then bank-full discharge will be provided.

REFERENCES

Baume, J. & Poirson M. 1984. Modélisation numérique d'un écoulement permanent dans un réseau hydraulique maillé à surface libre, en régime fluvial. *La Houille Blanche* 1/2: 95–100.

Carling, P. 1988. The concept of dominant discharge applied to two gravel-bed streams in relation to channel stability thresholds. *Earth surface processes and landforms* 13: 355–367.

Emmett, W. W. 1972. The hydraulic geometry of some Alaskan streams south of the Yukon River, open file report. *US Geological Survey*: 102 p.

Harrelson, C. C. & Rawlins, C. L. et al. 1994. Stream channel reference sites: en illustrated guide to field technique. *G. T. R. R.-F. Collins*, US Fish and Wildlife Service: 61.

Harvey, A. M. 1969. Channel capacity and adjustment of streams to hydrologic regime. *J. of Hydrology* 9: 82–98.

Kilpatrick, F. A. & Barnes H. H. 1964. Channel geometry of Piedmont streams as related to frequency of floods. *US Geological Survey, Professional Paper* 422 E: 10 p.

Leopold, L. B. et al. *Fluvial processes in geomorphology*. New York: Dover Publication.

Lyness, J. F. & W. R. C. Myers et al. 1997. The use of different conveyance calculations for modeling flows in a compound channel. *Journal of the Chartered Institution of Water and Environmental Management* 11(5): 335–340.

Nicollet, G. & Uan M. 1979. Continuous free surface flow over composite beds. *La Houille Blanche* 1: 21–30.

Navratil, O. & M. B. Albert et al. 2002. Water level time series analysis for bank-full flow studies in river. *River Flow. Proc. Intern. Conf. On Alluvial Hydaulics., Louvain-la-Neuve, Belgium, 4–6 September 2002*. Rotterdam: Balkema.

Osterkamp, W. R. & Hedman E. R. 1982. Perennial-streamflow characteristics related to channel geometry and sediment in Missouri river basin. *US Geological Survey* 1242: 37.

Pickup, G. & Warner R. F. 1976. Effects of hydrologic regime on magnitude and frequency of dominant discharge. *J. of Hydrology* 29: 51–75.

Radecki-Pawlik, A. 2002. Bankfull discharge in mountain streams: Theory and practice. *Earth Surface Processes and Landforms* 27(2): 115–123.

Richards, K. S. (ed.) 1982. *Rivers. Form and process in alluvial channels*. New York: Methuen and Co.

Riley, S. J. 1972. Comparison of morphometric measures of bank-full. *J. of Hydrol.* 17(1–2): 23–31.

Wahl, K. L. 1976. Accuracy of channel measurements and the implications in estimating streamflow characteristics. *Modern development in hydrometry*: 311–319.

Williams, G. P. 1978. Bank-full discharge of rivers. *Water Resources Research* 14(6): 1141–1154.

Wolman, M. G. 1955. The natural channel of Brandywine Creek, Pennsylvania. *U.S. Geol. Surv. Prof. Pap*. 271: 56 pp.

This page intentionally left blank

River Flow 2004 – Greco, Carravetta & Della Morte (eds.)
© 2004 Taylor & Francis Group, London, ISBN 90 5809 658 0

Large scale tests for gravel-bed river widening

M. Aufleger & A. Niedermayr
Institute for Hydraulic and Water Resources Engineering, Technische Universität München, Germany

ABSTRACT: Numerous gravel-bed rivers are affected by unceasing degradation problems, mostly caused or increased by technical measures upstream. In Germany removing the bank fixations is regarded as a concept to dissolve the problem. By allowing lateral erosion and in consequence river widening the bed load transport capacity will be decreased. Additionally the eroded bank material will serve as an auxiliary sediment influx. To determine this process of gravel river widening and estimate the possible changes in river morphology, large scale tests are carried out at the Technische Universität München since 1999. In addition to a straight model flume, with a total width of 8 m and a length of 100 m, a double curved model flume with a total width of 10 m and a length of 90 m was constructed to investigate the erosion effects in meandering channels.

1 INTRODUCTION

Incising gravel-bed rivers are one of the main concerns in German river engineering. For the sake of flood protection, energy production with hydropower, land gain for agriculture or improved shipment of rivers, many rivers were changed fundamentally. Like the Bavarian alpine rivers Iller and Isar, which are tributaries of Danube, they were regulated, their width was restricted and the banks fixated. Thus, the bottom shear stress and erosivity increased. As a consequence of the continuing degradation, the water level and thereby the ground water level decreased causing severe harms to the river ecosystem and floodplain, as well as endangering the stability of hydraulic structures.

2 REMOVAL OF BANK FIXATIONS

2.1 *General*

Actually, the removal of the bank fixations is taken into account allowing lateral erosion. Thus, the river will be able to adjust its width, bed elevation and profile to the given constraints. The river bed widening leads to a reduction of the shear stresses and consequently to a reduction of the degradation tendency. In addition, the eroded bank material will serve as an additional sediment influx and will prevent bed level from erosion in the meantime. Though there exist much research work about river regime and stable channel design (e.g. Ackers & White (1973), Bray (1980), Chang (1980), White & Bettess & Paris (1982)), convenient experiences about the process of river widening and the final geometry of a river for given constraints are missing, especially if there is no sediment input from an upstream reach and the free adjustable reach length is restricted.

Considering this lack of suitable research work the improvement of planning tools for river rehabilitation measures basing on the removal of bank fixations was necessary.

Preliminary test were carried out in small model flumes (Schmautz & Aufleger (2002)) and simultaneous extensive analytical investigations were undertaken (Schmautz (2003) and Schmautz (2004)). To minimise the influence of model effects or necessary simplifications, it was necessary of using large model tests.

2.2 *The structure of investigations*

Simultaneous to the physical investigations, a numerical model has been developed to investigate gravel river widening by bank erosion in a straight stretch of river. The physical model hence serves additionally as a perfect method to calibrate and verificate the numerical model (Figure 1). In return the calibrated model simulates a multiplicity of model runs in short time and aids to interpret the test results.

3 FUNDAMENTALS

3.1 *Scale*

The choice of the geometrical scale is essential for the transferability of model test results in prototype data.

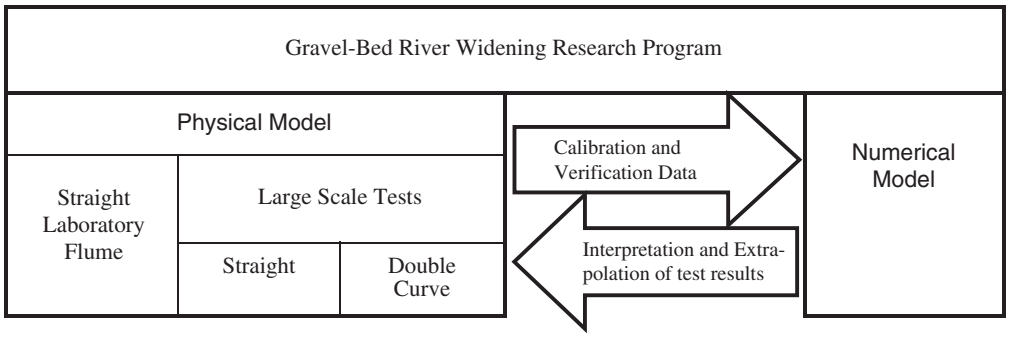


Figure 1. Organisation of the gravel-bed river widening research program.

Regarding bed load transport investigations, for the sake of a good reproduction the model has to be large, which is usually in contradiction to economical aspects and feasibility. In our case, the scale was chosen as large as possible, to reduce side effects on transport in consequence of viscosity.

3.2 *Simplifications*

The model tests are mainly carried out for the sake of investigating the fundamentals in morphological processes, e.g. interaction between river bed widening and bed level erosion or lateral erosion mechanisms. Thus, the intention of the model tests can't be to reproduce the nature in every possible aspect. Adequate simplifications must be chosen for economic reasons and terms of feasibility:

- The influence of vegetation on lateral erosion mechanisms is neglected.
- Identical model sand material is used for the construction of the river banks and the river bed. In nature, the river banks consist of finer gravel than the river bed, but a construction in layers would be much more difficult and the whole model sand should be exchanged due to mixing after each model run.
- The initial state is approximated by an trapezoidal cross-section and either an absolutely straight channel (4.1) or an ideal double curved river reach (4.2).

4 THE TEST CHANNELS

4.1 *The straight channel*

The main focus of the first model tests was to concentrate on the basic principles of the widening process and the interaction between bank erosion and degradation resp. aggradation. Therefore side-effects caused by meandering flow were disregarded, mainly because the regarded Bavarian alpine river Iller is only slightly meandering.



Figure 2. Straight test channel (M = 1:20).

The straight test channel was constructed in 1999 and consists of a 100 m long and 8 m wide flume, supplying sufficient place for lateral erosion. The tests were mainly carried out in the geometrical scale M = 1:20.

Since 2000 a total number of eight model series, some of them consisting of several model runs, were performed regarding different boundary conditions like upstream sediment influx, model sand diameter, initial channel width or the initial longitudinal slope. The results of one model series concerning the river Iller are described in Aufleger & Niedermayr & Strobl (2003).

4.2 *The double curve*

In addition to the straight model flume a double curved model flume with a total width of 10 m and a length of 90 m was constructed in 2002 to investigate the erosion effects in meandering channels. This model test is required by the need for an investigation of the Bavarian alpine river Isar, which is contrary to the river Iller distinctly meandering.



Figure 3. Double curved test channel (M = 1:20).

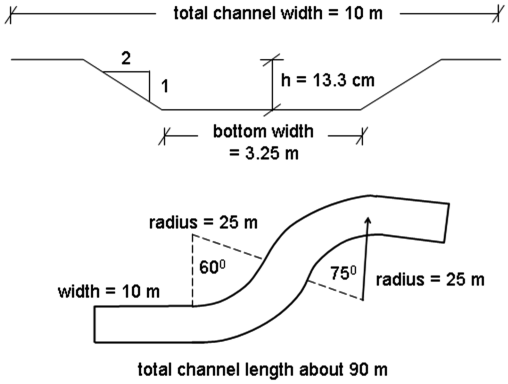


Figure 4. Model dimensions of the double curved test channel.

The construction of the whole model test was conducted in one year, including the development of an adequate measurement device, the build-up of the necessary roofing to protect the cohesionless river bed against rain, the preparation of the initial trapezoidal river bed and the performance of the first model run. A second model run could be performed in 2003.

4.2.1 *General about the hydraulic in river bends*
There exist much research work about the hydraulic in river bends, especially about the degree of the transversal water slope, the cross-sectional motions, i.e. the helical motion resp. secondary flow, and the occurring shear stresses. Measurements were either achieved in natural rivers (e.g. Bathurst & Thorne & Hey (1979)) or rectangular model flumes (e.g. de Vriend (1981) or Blanckaert & Graf (2001)).

General, in river curves secondary flow occurs resulting in motion towards the outside curve near the water surface and towards the inner curve near the bottom. This helical motion increases the shear stress on the outer river bend and causes besides the centrifugal force a transversal bottom slope.

Our model tests concentrate on morphology changes. To minimise the necessary work, in particular concerning the measurement, we abandon expensive and detaily flow velocity measurements. Such highly accurate measurements are intended for the next year. For that matter only general statements concerning the influence of the secondary flow could be made within this paper.

4.2.2 *Test conditions of the double curved model*
The model dimensions are designed appropriate to the situation at the river Isar near the estuary to Danube. The initial profile is approximated to be trapezoidal and two curves representing the meandering river. Radius and angles are corresponding to one river section intended for the realisation of the removal of bank fixations.

The model tests were conducted under the following test conditions:

- geometrical scale M = 1:20
- initial longitudinal slope J = 0.85‰
- model dimensions according to Figure 4
- Parameters R/B = 7.7; R/H = 188, B/H = 24.4 with R: radius of the curves, B: initial river width and H: initial river depth
- model sand diameter $d_m = 1.2$ mm, identical material for bank region and river bottom
- bankfull discharge about $Q = 435\ m^3/s$ which is corresponding to a return period of two till five years
- constant downstream water level corresponding to normal water depth in a downstream straight channel with bank fixations
- Total model run of 50 days in nature, divided into several time steps to record river changes
- in case of the first model test in 2002 no sediment feeding
- in case of the second model test in 2003 sediment feeding about 50% of the transport rate of the upstream initial channel. The transport rate of the initial channel at the given discharge is about $Q_{S,Nature} = 42.4$ kg/s resp. $Q_{S,Model} = 23.7$ g/s, thus the performed sediment feed amounts $Q_{S,Nature} = 21.1$ kg/s resp. $Q_{S,Model} = 11.85$ g/s.

In the river Isar, especially at the location corresponding to the investigated double curve, there is a general lack of sediment feed from upstream. By feeding 50% of the transport rate in the model, two different situations in nature could be investigated. First of all, as a technical measure, sediment is deposited upstream hence the transport capacity is saturated partially. Secondly, an equivalent curve situation downstream, where an adequate bed load influx from upstream occurs, could be reproduced.

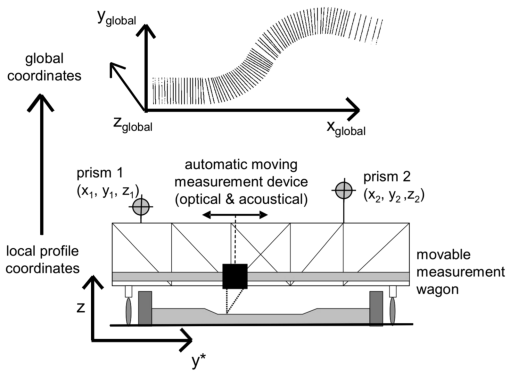


Figure 5. Measurement device and coordinates transformation.

4.2.3 *Measuring and evaluation technology*

The quality of a large model test of such dimensions is definitively affected by the utilised measurement device and furthermore the accuracy of the acquired model data.

The used measurement system mounted on a manually movable measurement wagon is driving automatically transversal to the channel at the rate of 1 m/s. Measurements were achieved either by an optical laser sensor in case of sand level or an ultrasonic sensor in case of water level. The actual position of the measurement wagon is registered by the use of a theodolite and two prisms fixed to the measurement wagon. Afterwards via the use of a geographical information system (GIS), a digital terrain model is created and any section of the model can be evaluated, mainly cross-sections and longitudinal profiles.

4.2.4 *Comment*

Two model test runs in the double curved test channel were performed and are compared within this paper. Their test conditions are only differing in the amount of sediment feed. General the structural and chronological development of the model tests is interesting. Within the scope of this paper only the structural development of the two different model tests after 50 days of model run at bankfull discharge ($Q = 435\ m^3/s$) will be compared in the results. At the end there will be also some conclusions about the time-dependent development.

5 RESULTS

5.1 *General structural development*

After 50 days of model run at bankfull discharge ($Q = 435\ m^3/s$), the river morphology changes relative to the initial state fundamentally (compare Figure 9).

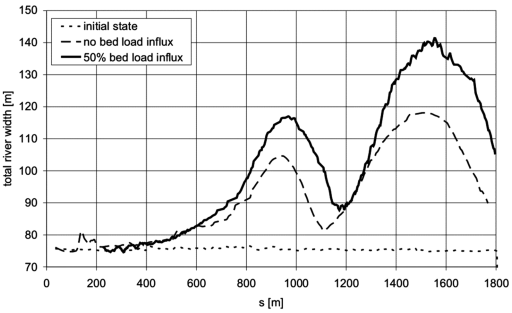


Figure 6. Total river width after 50 days of model run at bankfull discharge ($Q = 435\ m^3/s$).

Both the river width in the first and the second curve augments, while the second curve gets much wider than the first one. In the inner part of the curves material is deposited, particularly decreasing the flow velocity in the inner part of the curves. Explicitly the formation of a Talweg took place, resulting in conjunction with the widening tendency in a rearrangement of the flow towards the outside curves.

5.2 *Widening of the double curve*

In preliminary tests investigating the river Isar in the straight model channel under the same test conditions except that meandering was not displayed, only a slight widening tendency of few meters could be recorded, according to the relative small shear stress value in bank region in case of a straight river reach.

Of course, in a curved flow the stress on the outside banks increases due to the influence of secondary flow and the necessary flow deflection in the bends. In case of removing the bank fixations, the widening will clearly exceed the value of a corresponding straight reach.

Identically in both model runs, the width of the second curve in flow direction exceeds distinctly the first one (Figure 6). Towards the first curve, the incoming flow is affected by the upstream straight reach, therefore the flow smoothly slides along the outside river bank. In contrast, the much steeper angle of flow approach into the second curve causes severe stress on the outside bank and hence increases river widening. In region of the crossover point from the first into the second curve the river width minimises.

River width of the second model run (50% sediment feed) tops in both curves the particular width of the first model run (no sediment feed). This is based upon the sediment feed, which results in less degradation and a higher longitudinal slope (see 5.3). In case of the second curve based on the initial state the width almost doubled.

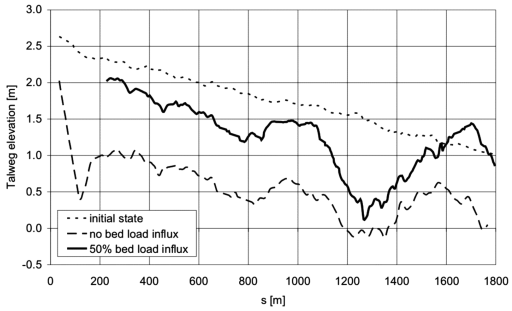


Figure 7. Talweg elevation after 50 days of model run at bankfull discharge ($Q = 435\ m^3/s$).

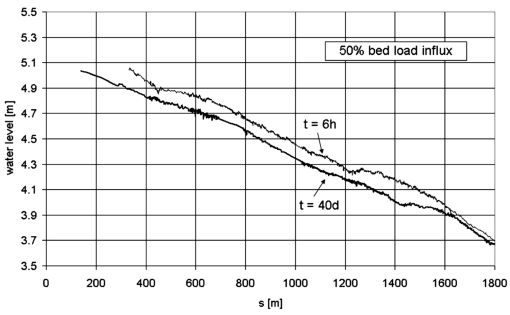


Figure 8. Water level in the second model at bankfull discharge ($Q = 435\ m^3/s$).

Thus, widening is mainly depending on the angle of approach flow, the degree of transport capacity saturation and secondary flow. Furthermore, the flow is concentrated over the deeper outer part of the river sections, resulting in an increasing boundary shear stress outside (compare 5.4).

Concerning the time-dependent development of the two model runs (not displayed), in both cases mainly the second curve is still not getting a dynamically stable state, i.e. for the given discharge and sediment influx the width still increases. Contrary to the model tests in the straight channel, where such a stable state occurs after a few days of model run (Aufleger & Niedermayr & Strobl (2003)), the width development still does not end after 50 days of model run at bankfull discharge, although the widening tendency declines. An explanation for this persistent widening tendency will be shown in 5.4.

5.3 *Bed level*

As the flow area resp. the flow depth and the longitudinal slope affect directly the shear stress and thus the tendency to erode resp. deposit material, an investigation of the actual-state of bed level is fundamental for an evaluation of the morphological development. Within this paper, the Talweg elevation (Figure 7) is investigated.

In both model tests, the Talweg erodes. In the first model test, erosion is about one meter und much more than in the second model test, where sediment feed prevents bed level from erosion and hence causes only few decimeters of erosion.

5.4 *Water level*

Water level decreases about 10 cm during the model run (Figure 8). At the end, the medium water level slope in the second model test is about 0.85‰.

In the first curve almost no transversal slope occurs, contrary to the second curve where water level augments in the outer part of the curve.

5.5 *Cross-sectional development*

The cross-sectional development (Figure 10) displays perfectly the morphological changes in flow direction. In the region of the maximum river width in the first curve ($s = 900$ m) lateral erosion of the outer bank occurs in combination with a development of the Talweg. Together with the deposition of bed load in the inner curve due to secondary flow effects and the influence of the centrifugal force a rearrangement of the flow towards the outer curve results. The same tendency can be noticed in the second curve ($s = 1200$ m).

As the second model run gets wider than the first model test, also the location of the Talweg moves farther to the outer curve. But in addition, the deposition of material in the inner curve is more pronounced. Thus, the effective flow area in both model tests is almost similar.

Velocity measurements confirm that in the inner part of the curves, mainly above the deposited material, almost no flow takes place. The main flow is restricted to the outer part of the curve (Blanckaert & Graf (2001)). The flow velocities resp. shear stresses do not change in the same way as the river widens and as a result the widening tendency declines only in small steps. This fact is a wide difference to the results of the straight channel, where river widening leads to an increase of the flow area and fast to a reduction of flow velocities and thus to decreasing shear stresses.

5.6 *Volume transport*

From the measured cross-sections resp. the generated surface model volume changes based on the initial state can be evaluated. The volume change is defined as being positive in case of eroded material, thus the volume discharge exceeds the bed load influx (Figure 11).

In case of the first model test, where no bed load influx was performed, the volume change corresponds

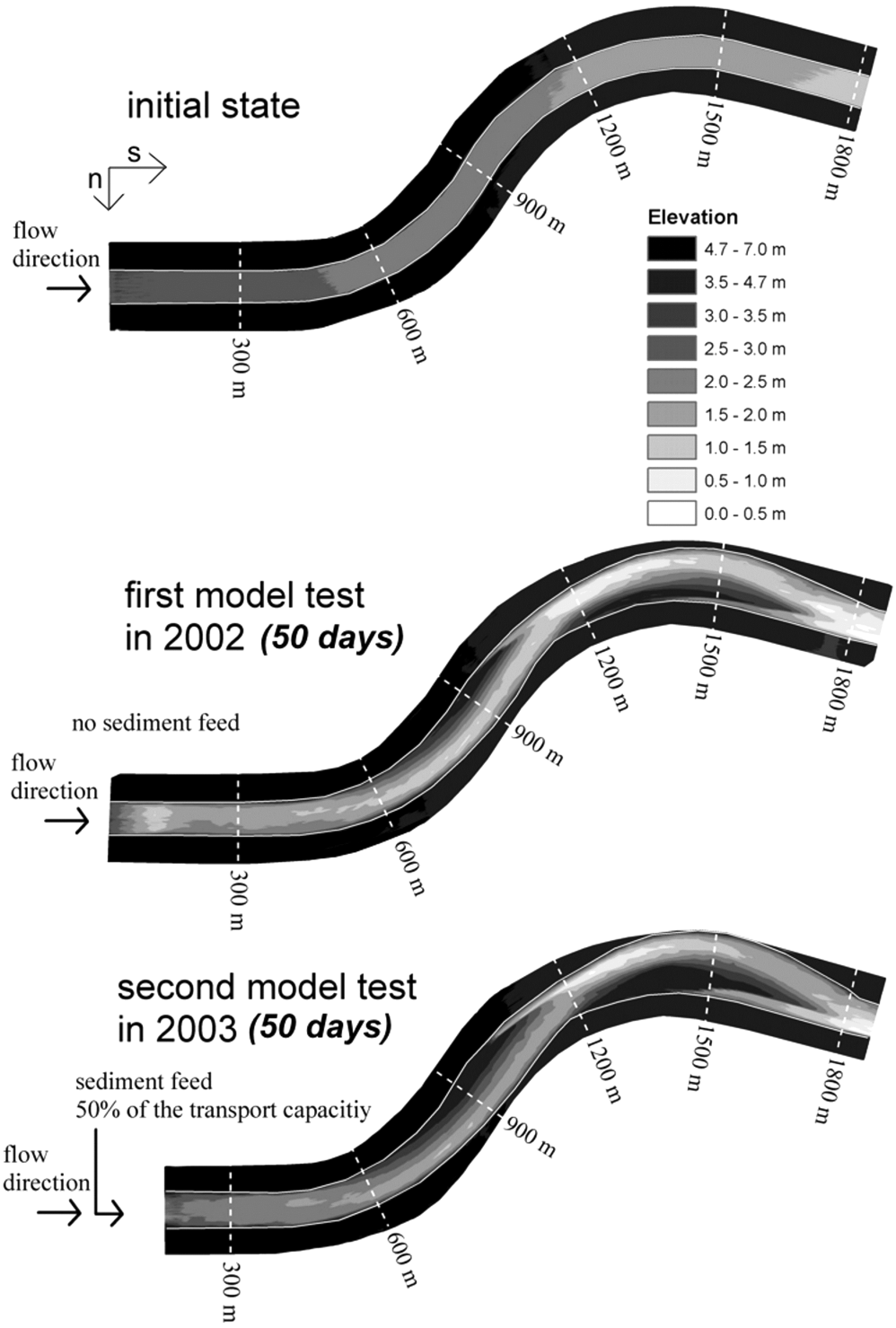


Figure 9. Meandering development after removing existing bank fixations (50 days of bankfull discharge, $Q = 435\ m^3/s$).

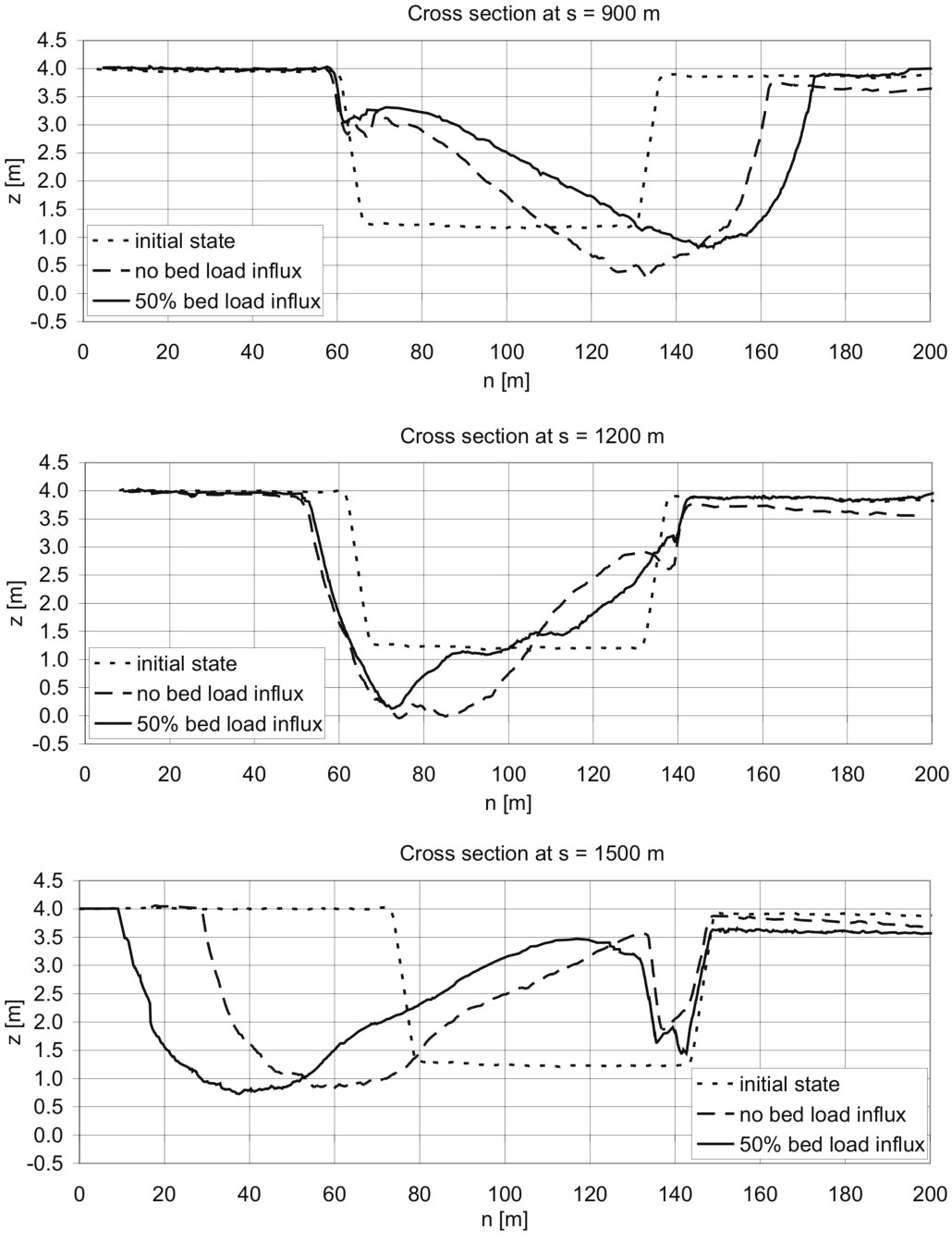


Figure 10. Comparison of cross sections after 50 days of model run at bankfull discharge ($Q = 435\ m^3/s$).

to the volume discharge. In case of the second model test with 50% bed load influx, the volume discharge can be calculated out of the volume change and the totally feed of bed load which is about 50.000 m^3.

The total volume change of the first model run after 50 days of model run is approximately about 60.000 m^3, in case of the second model test only about 35.000 m^3 which means circa 40% less eroded

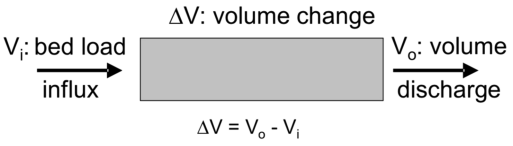


Figure 11. Definition sketch.

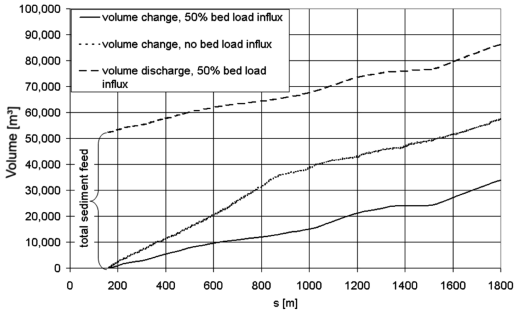


Figure 12. Volume change and volume discharge after 50 days of model run at bankfull discharge ($Q = 435\ m^3/s$).

material. In contrast, the total volume discharge of the second model run is approximately 85.000 m^3, about 40% more transport than in case of no sediment feed.

In the first model run where no bed load influxwas provided, transport capacity is decreasing due to the morphological changes, mainly reduction of the longitudinal slope. The second model test behaves different, sediment feeding prevents river bottom from erosion and the transport capacity remains at a high level.

6 CONCLUSIONS

6.1 *Interaction between sediment feed, bed level and bank erosion*

Responsible for any mass transport thus erosion is the shear stress value. If the local shear stress $\tau(n)$ exceeds the critical value τ_{crit} then mass transport will occur (see Figure 13). As the local shear stress $\tau(n)$ is depending on the position in the river profile and on the flow, bed erosion may appear even if there is no lateral erosion (in deed bank material could slide due to local stability failure).

Due to lateral erosion and sediment influx from upstream or sediment feed (Figure 14), the total amount of incoming sediment can exceed the actual transport capacity and will provoke deposition of the surplus amount of sediment. If there occurs lateral erosion, bank material will move due to the gravity force towards the channel center, hence eroded bank material will be transported at the river bottom and will prevent temporary river bed from erosion. River morphology is influenced by the interaction between

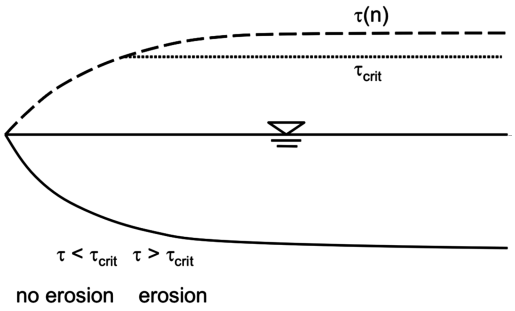


Figure 13. Schematic shear stress distribution.

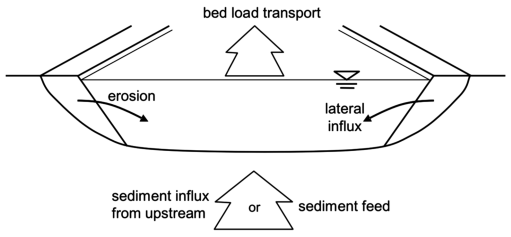


Figure 14. Influence of sediment influx from upstream resp. lateral influx.

lateral influx caused by bank erosion, sediment feed resp. bed load provided by upstream reaches and river bed erosion resp. deposition.

6.2 *Morphology in river bends*

The hydraulic in river curves affects directly the morphology and in return morphological changes influence the hydraulic in bends. The hydraulic is characterised by the centrifugal force, resulting in a transversal water slope and secondary flow.

The development of the channel width in river bends is absolutely contrary to comparable straight river reaches, both concerning structural and time-dependent development of river morphology:

- River width in curves exceeds considerably the value in identical straight channels. In the case of the observed river bends a width of more than 140 m, i.e. a doubling of the initial width, has to be expected.
- The river width is depending on the amount of sediment feed. With increasing sediment feed bed level augments resulting in higher longitudinal slope. This directly forces the widening process.
- Additionally any geometrical change in the approach flow as the shifting of the upstream river bend affects the widening process.
- The whole erosion and deposition process in the river bend is connected directly to the secondary flow.

– As a consequence, the widening occurs not only at the start of the morphology changes, as it could be observed in the straight model channel (Aufleger & Niedermayr & Strobl (2003)). In deed, the influence of the affecting parameters lasts much longer on the widening process and furthermore changes of these parameters could tend to an local increased bank erosion.

REFERENCES

Ackers, P. & White, W.R. (1973): "Sediment Transport: New Approach and Analysis", Journal of the Hydraulics Division, ASCE, Vol. 99, No. HY11, Nov., pp. 2041–2060.

Aufleger, M. & Niedermayr, A. & Strobl, T. (2003): "Widening of Gravel Bed Rivers – Physical Model Tests in Large Scale", Proceedings, XXX IAHR Congress, Thessaloniki, Greece, Vol. 1.

Bathurst, J.C. & Thorne, C.R. & Hey, R.D. (1979): "Secondary Flow and Shear Stress at River Bends", Journal of the Hydraulics Division, ASCE, Vol. 105, No. HY10, Oct., pp. 1277–1294.

Blanckaert, K. & Graf, W.H. (2001): "Mean Flow and Turbulence in Open-Channel Bend", Journal of Hydraulic Engineering, ASCE, Vol. 127, No. 10, Oct., pp. 835–847.

Bray, D.I. (1980): "Regime Equations for Gravel Bed Rivers", Proceedings of the International Workshop on Engineering Problems in the Management of Gravel Bed Rivers, Newton, Powys, United Kingdom, June, 1980.

Chan, H.H. (1980): "Stable Alluvial Canal Design", Journal of the Hydraulics Division, ASCE, Vol. 106, No. HY5, May, 1980, pp. 873–891.

de Vriend, H.J. (1981): "Steady Flow in Shallow Channel bends", Rep. No. 81–3, Comm. on Hydraulics, Dept. Civ. Eng., Delft Univ. Techn., Delft.

Schmautz, M. & Aufleger, M. (2002): "Gravel River Widening by Bank Erosion – Theory and Results of Physical and Numerical Modelling", Proceedings, River Flow 2002 – International Conference on Fluvial Hydraulics, Louvain-la-Neuve, Belgium, Vol. 1.

Schmautz, M. (2003): "Eigendynamische Aufweitung in einer geraden Gewässerstrecke", Berichte des Lehrstuhls und der Versuchsanstalt für Wasserbau und Wasserwirtschaft der Technischen Universität München, Heft 96.

Schmautz, M. (2004): "Gravel river widening by bank erosion in a straight stretch of river – investigations on a numerical model", Proceedings, River Flow 2004 – International Conference on Fluvial Hydraulics, Napoli, Italy.

White, W.R. & Bettess, R. & Paris, E. "Analytical Approach to River Regime", Journal of the Hydraulics Division, ASCE, Vol. 108, No. HY 10, Oct., 1982, pp. 1179–1193.

This page intentionally left blank

River Flow 2004 – Greco, Carravetta & Della Morte (eds.)
© 2004 Taylor & Francis Group, London, ISBN 90 5809 658 0

Influence of local scouring on natural step pool geometry

F. Comiti, A. Andreoli & M.A. Lenzi
Dept. Land and Agroforest Environments, University of Padova, Italy

ABSTRACT: Step pool morphology characterizes many high-gradient streams in a variety of natural settings, but its formative processes and evolutionary dynamics are still poorly understood. In this paper step pool geometry is investigated from the perspective of a comparison with steep alluvial channels where grade-control structures such as check-dams and bed sills make the stream profile resemble a natural stepped stream. Along these channels, local scouring phenomena due to falling jets form plunge pools under each structure, as natural steps determine the formation of pools. In order to test the hypothesis that natural pools and pools formed below grade-control works present analogies with respect to their dimensions, shape and formative dynamics, 37 natural pools and 79 artificial pools have been surveyed in 11 mountain streams of the Eastern Italian Alps. Pools below grade-control works featured a transition between the scour hole and the downstream sloping bed marked by depositional berms. When geometric features such as maximum pool depth, length and step/berm distances are normalized to the jet virtual energy, almost no statistically significant differences have been detected between natural and artificial systems. These results lend support to an upstream-forced cascade model for step pool formation, where falling jets energy controls the geometry of the system, hence representing the most important scaling independent variable.

1 INTRODUCTION

Step pool torrents have been under active research for two decades now, both for their apparent geometric regularity which stimulates hypothesis about its origin, and for the peculiar tumbling flow pattern (Peterson & Mohanty, 1960) they present, which leads to dissipate energy in a different and more effective manner compared to that accounted for by traditional flow resistance formula (Lee & Ferguson, 2002).

An analogy can be found in the sequences of grade-control structures such as check-dams and bed sills placed in alluvial mountain rivers in order to stabilize these channels by preventing bed incision and by reducing their longitudinal slope. The river beds of such trained channels show a stair-like profile, but for lower gradients a positive bed slope – a downward sloping tread – called either ultimate, compensation or equilibrium slope is usually achieved between two drops, because their spacing is large enough to allow the flow to establish a sort of "uniform" regime downstream of the scour pool. However, for steep streams, short spacings are usually assigned, so that the next drop structure locates just at the end of the upstream pool, thus making the profile very similar to a natural step pool sequence.

What gives step pool systems its peculiarity is the hydraulic regime which is featured, that is the above mentioned tumbling flow. It alternates gravity-driven jets just below steps and jet diffusion in pools, in a more or less rhythmic way with critical flow conditions occurring somewhere before the step lips. The passage between supercritical ($Fr > 1$) falling nappes and subcritical ($Fr < 1$) pools is made through a hydraulic jump, where the jet diffuses generating a great deal of turbulence. Therefore flow resistance in step pool systems is dominated by turbulent mixing energy dissipation analogous to that of hydraulic jumps more than by grain or form drag, even though the latter may be significant if steps are very rough (Knighton, 1998). However, if a positive bed slope downstream of the pools is present, also "continuous" energy expenditures take place, but given the macroroughness characteristics of steep boulder beds no supercritical flow is generally established along this span even if it might be present for very short distances (Jarrett, 1984, Grant, 1997, Tinkler, 1997). Therefore at the next downstream step the flow can achieve again critical ($Fr \approx 1$) conditions, thus allowing to treat each step and its related pool identically from a hydraulic standpoint notwithstanding different upstream bed slopes, albeit this procedure might neglect the effect of

different jet issuance angles and different degrees of jet turbulence.

A scour hole – the pool – will be shaped by the diffusing jet if bed material can be entrained and removed by the flow. It is obvious that a pool due its existence to the upstream step, less straightforward is how the variables of the system are interrelated and how they determine the ultimate system geometry. In particular, it is still poorly understood the relative importance between downstream versus upstream boundary conditions, between sediment properties and jet characteristics, and finally what are the physical processes involved in the origin and disruption of natural step pool sequences.

Since the earliest investigations on step pool, a negative correlation between step spacing and channel slope has been identified (Judd & Peterson, 1969; Hayward, 1980; Whittaker, 1987; Grant et al., 1990; Chin, 1999; Chartrand & Whiting, 2000; Weichert et al., 2003) but the parameters of the best-fit power law equation differ considerably among the authors.

All the other possible correlations among dimensional geometrical variables, i.e. step wavelength and height, and external factors as discharge, slope and sediment size have been examined and can be found in Wohl et al. (1997), Chin (1999) and Chartrand & Whiting (2000). However, a marked improvement towards the understanding of variations in step pool geometry has been achieved by the adoption of a non-dimensional approach focusing on the so-called steepness H/L – analogous to a relative wave amplitude – and its normalization by the channel slope, to give the relative steepness factor (Abrahams et al., 1995). It is notable to point out that the ratio height-to-spacing H/L resembles a loss of head per unit of channel length, thus bearing energetic implications (Knighton, 1998). The innovative yet controversial experimental work by Abrahams et al. (1995) demonstrated by flume tests that maximum flow resistance occurs with evenly-spaced steps and within the range:

$$1 < \frac{H/L}{S} < 2 \qquad (1)$$

Such conditions were found by the same authors to describe rather well real step pool streams, where on average was $c = 1.5$. Geometrically, this result shows the lack of significant down-sloping streambed lengths in a step pool reach, i.e. downstream of pools – where bed slope is reversed – only a short, roughly flat zone is generally present before the next step. From an energetic perspective this means that the elevation loss due to steps approximates the total elevation loss along a reach, confirming the role of step-induced spill resistance on the overall energy budget in step pool channels.

Subsequent field investigations (Wohl et al., 1997; Chartrand & Whiting, 2000; Zimmermann & Church, 2001) has somewhat narrowed the extent to which Abrahams et al.'s slope-normalized geometry is valid in real streams, because they have observed for channel slopes below 5–7% ratios c usually larger than 2, and a negative correlation with channel slope. In addition, data from step pool channels in the Italian Alps (Lenzi & D'Agostino, 2000; Lenzi, 2001) confirm its suitability only for streams which have experienced several "ordinary" floods after the step-forming one, otherwise the ratio c tends to be below the unity. Therefore they argued that Eq. 1 might represent a geometrical equilibrium condition requiring processes of bed armoring and localized erosion to occur, in order to scour fine sediment from pools and thus attain a reverse bed-slope between steps. In fact, following an extraordinary flood with unlimited sediment supply, the steepness factor can suddenly decrease as a result of sediment trapped in the pools and a lengthening of step spacing.

To date, morphological studies on step pool streams have all neglected to shed light on scouring process leading to pool formation, apart from the early work by Whittaker (1987) and the more recent one Zimmermann & Church (2001). This paper aims at testing the hypothesis that natural step pool geometry is mostly determined by local scouring phenomena due to jet diffusion, by comparing dimensions of pools found below natural steps and grade-control structures.

2 FIELD SITES AND METHODS

73 scour holes downstream of grade-control structures and 37 pools below natural steps were surveyed in 11 mountain rivers of the Eastern Italian Alps (Fig. 1). Mean longitudinal gradients of the channels range between 0.02 and 0.16.

All the streams are perennial and present a typical Alpine hydrologic regime, with two periods of high stages: in autumn (rainfall floods) and spring (snowmelt runoff). Six streams – whose watersheds are geologically different and very complex – provided data on "artificial" step pools (Fig. 2). For a detailed description of these rivers, see Comiti (2003) or Lenzi et al. (2003), where several analysis of scour pools' dimensions below check-dams and bed sills are presented in detail.

Five channels were selected for the survey of "natural" pools' dimensions (Fig. 3); all but one (Biois River) drain rather small catchments (<20 km^2) and represent typical natural step pool sequences. Natural pools in the Biois were measured in a trained reach between two check-dams. Geologically, the basins lie in the Dolomitical area and present very complex alternations of sedimentary and igneous rocks. An





Figure 1. Examples of natural (above, Rio Cordon creek, Dolomites, Italy) and artificial (below, Biois River, Dolomites, Italy) steps.

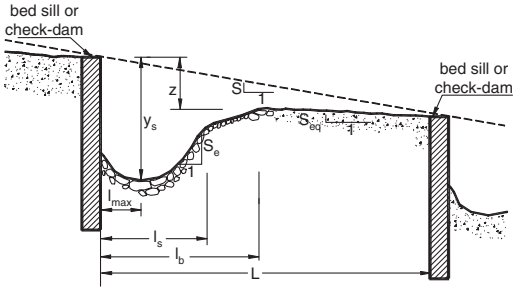


Figure 2. Definition sketch of the geometric variables surveyed below artificial steps.

exception is the Digon catchment, which features a prevalent metamorphic substrate (Andreoli, 2002).

In natural systems, bankfull width at steps, at pools and, most importantly, bankfull flow depth at steps

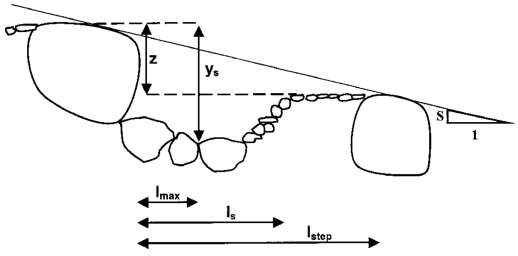


Figure 3. Definition sketch of the geometric variables surveyed below natural steps.

were also surveyed. The latter is hypothesized to correspond to the critical (i.e. Froude number of the flow ≈ 1) flow depth h_c in order to allow a comparison with pools below artificial steps because discharge data in natural channels are available only for the Rio Cordon creek, where a recording station for flow and sediment rates is located just downstream of the surveyed reach (Lenzi, 2001). Therefore initial jet thickness h_c for natural step pools – in contrast to the case of grade-control structures where it was evaluated from flood discharge data – is more roughly estimated from bankfull marks at steps, which of course present several difficulties as to their interpretation. However, Rio Cordon discharge data furnished a means to test this methodology, and proved its validity.

Scour length l_s and berm distance l_b characterize the longitudinal extension of artificial pools, with the latter representing the downstream border of the pool region, because just after the berm the bed typically shows a positive slope. For natural step pools, instead, the longitudinal dimension l_{step} is the distance to next step downstream, since no similar berms were found in natural systems between the scour length location and the next step, and a positive bed slope was generally absent. More details about the field measurements can be found in Comiti (2003).

3 RESULTS

The same dimensionless parameters have been used to analyze both scour holes below artificial steps (i.e. grade-control structures) and natural pool dimensions. Figure 4 shows the relationship between maximum scour depth normalized to critical flow depth and the drop ratio z/h_c, as done in Lenzi et al. (2003) for artificial pools only. Natural and artificial pools are displayed together: their points delineate a similar linear trend, overlying considerably in the range having more measurements, i.e. for $z/h_c < 4$. For larger drop ratios, natural pool data are totally lacking, whereas the two high check-dams points seem to follow the same trend. It is remarkable that such an accordance

is achieved with one parameter only, and no sediment properties are taken into account.

The parameter z/L is now introduced to analyze scour dimensions. It indicates the potential energy lost by the falling jet in the span length between two fixed points, i.e. represents a sort of local gradient relevant to each pool. If berm distance l_b for artificial pools and step spacing l_{step} for natural ones are used, with the ratio y_s/z – analogous to the relative steepness factor c (eq. 1) – considered as the dependent variable, the graph in Figure 5 turns out.

If the parameter in abscissa is regarded as a slope and the y-axis as the relative steepness factor, both referring to berms in the case of artificial pools, Figure 5 becomes analogous to a graph where the steepness factor c is plotted versus channel slope, as in Zimmermann & Church (2001), and a similar decreasing trend is shown. Compared to that graph where the mean channel slope is the independent variable, here the "slope" values are much higher because they derive from local measurements of drop heights and step/berm distances. However, the tendency towards a c or y_s/z of approximately 1.5 is exhibited in both figures, as well as the "rise" up to values around 4 for the lower gradients.

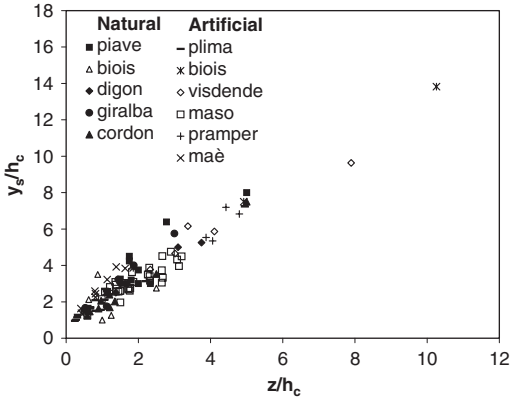


Figure 4. Dimensionless plot of maximum scour depth versus the drop ratio for both grade-control structures' pools (i.e. artificial) and natural step pool.

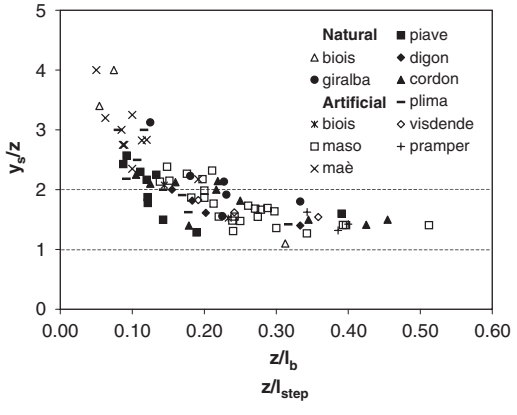


Figure 5. Dimensionless plot of maximum scour depth versus the "local gradient" factor; for artificial pools the berm distance l_b is the reference L, whereas l_{step} is used for natural pools. The range $1 < c < 2$ for the steepness factor proposed by Abrahams et al. (1995) is marked too.

Figures 4 and 5 suggest strong similarities between natural pools and scour holes below grade-control structures; furthermore, a strong link seems to exists between natural steps and depositional berms found downstream of artificial pools. A statistical evaluation of these analogies is then needed. Jet virtual energy at the impingement $E = z + H_s$ (with $H_s = 1.5h_c$) appears to be the physical variable which best normalizes pool dimensions in artificial systems (Comiti, 2003; Lenzi et al., 2003) in the sense that it narrows the variability range of the dependent geometrical variables, leaving only a certain amount of variance due to the system geometry. Therefore if some analogies exist between natural and artificial pools, these are best sought comparing the geometrical variables scaled to this jet energy. The problem is to test statistically whether two independent groups, in this case natural (N) and artificial (A) pools, are significantly similar with respect to some of their features – namely maximum depth and its longitudinal location, length, berm distance/step spacing – when these are made non-dimensional through the jet energy E. The underlying assumption is that similarities in shape reflect similarities in the formative process, even though this might not be always the case, as pointed out by Knighton (1998, p. 225) for meanders.

Given the fairly large sample size available, the commonly-used Student's t-test could be performed. However, this test requires the variances of the two groups to be similar, since their difference may alter test's significance. Here, it was chosen first to verify if variance homogeneity was respected by applying the standard Fischer's F test and the more powerful Levene's test too (Statsoft, 2002). In the case it was not, non-parametric statistics were adopted instead of the t-test in order to decide whether to reject the null hypothesis H_0 "the two sample (groups) belong to the same population". The non-parametric tests analogous to Student's t performed for this analysis are the Mann-Whitney U, the Kolmogorov-Smirnov and the Wald-Wolfowitz. All the calculations were carried out using the software "Statistica 6.1" (Statsoft, 2002).

Maximum scour depth y_s and residual depth $s\,(=y_s - z)$ are the main vertical dimensional characteristics of pools. Their normalization by the jet energy E led to the box-and-whisker graphs reported

in Figures 6a and 6b respectively, where the median value is shown along with the 25–75 percentile range and the overall variation range. The median value is used instead of the mean value because the Student's t test was not reliable for the non-homogeneity of groups' variance, thus non-parametric tests – which refer to the median value – were needed. All the three tests (Table 1) did not allow to reject the null hypothesis of extraction from the same population, being $p \gg 0.10$. The t-test would give the same result too (not shown in the table). These results indicate that the vertical extent of natural pool does not significantly differ from that characterizing pools created by grade-control strutures, when the forcing – i.e. upstream – energy conditions are taken into account.

The normalization through the nominal jet energy for scour length produced l_s/E frequency distributions which turned out to be non significantly different between natural and artificial pools, both using the t-test – but with non-homogenous variance – and the three non-parametric tests (see Table 1). In Figure 7 the graphical comparison is shown, where it can be seen a fairly wider range for the 25–75 percentile region occurring for natural pools, as well as for the overall variation range.

As regards the berm distance and downstream step distance, they were made non-dimensional in the same way, and the two distributions of l_b/E for artificial pools and l_{step}/E for natural pools were obtained. Their statistical comparison gave as result the non-rejection of the null hypothesis by two tests out of three, in fact the Wald-Wolfowitz's led to $p < 0.05$ (Table 1). Looking at their median points (Fig. 8) it

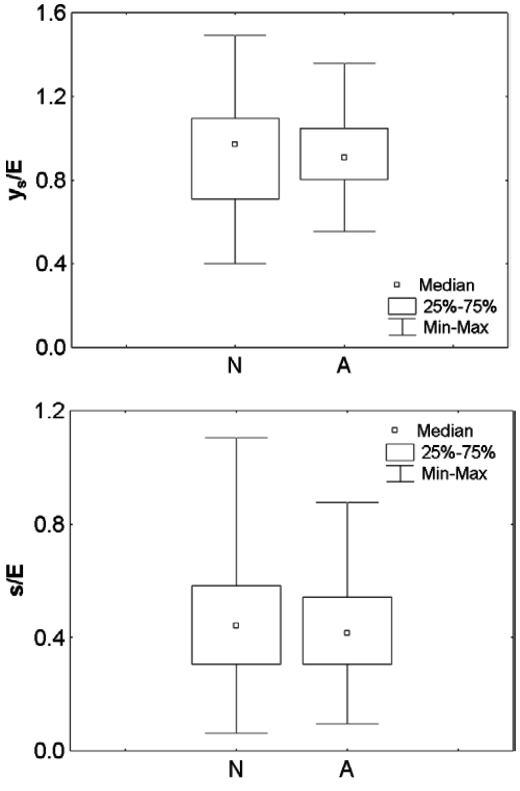


Figure 6. Pool maximum scour depth y_s (a, above) and residual depth s (b, below) normalized to jet energy E, below natural steps (N) and grade-control structures (A).

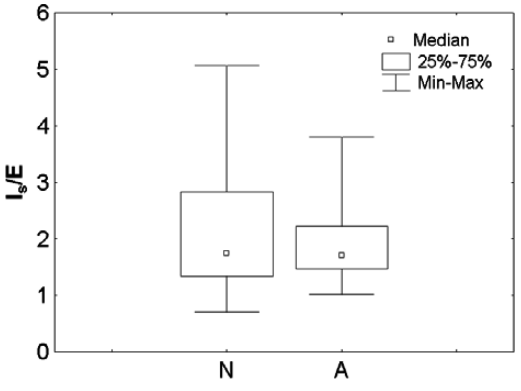


Figure 7. Scour length normalized to jet energy E below natural steps (N) and grade-control structures (A).

Table 1. Pool dimensions normalized to jet energy: descriptive statistics and significance level p for the three non-parametric tests used to compare natural (N) and artificial (A) pools. p-values smaller than 0.05 are highlighted, indicating a probable difference between the two groups.

	Mean		Stand. Dev.		Mann-Whitney	Wald-Wolfowitz	Kolmogorov-Smirnov
	N	A	N	A	p	p	p
y_s/E	0.95	0.92	0.27	0.18	>0.10	>0.10	>0.10
s/E	0.47	0.43	0.22	0.16	>0.10	>0.10	>0.10
l_s/E	2.11	1.88	1.05	0.63	>0.10	>0.10	>0.10
l_b/E	3.00	2.90	1.37	0.78	>0.10	<0.05	>0.10
l_{step}/E							

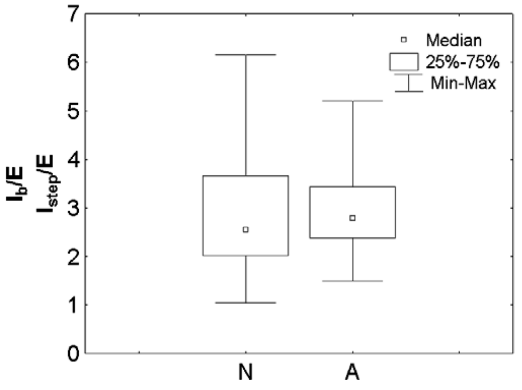


Figure 8. Step and berm distance normalized to jet energy E below natural steps (N) and grade-control structures (A), respectively.

is apparent why their similarity – yet significant on the whole – is less strong than that found for the previous geometrical variables. The fact that normalized berm and step distances on the whole probably belong to the same population prompts to theorize a similar formative process. Finally, pools' geometric ratios such as $l_b/y_s - l_{step}/y_s$ show significant similarities (Comiti, 2003), thus confirming the results from the energy-based approach reported above.

4 DISCUSSION AND CONCLUSIONS

The results of the statistical comparison between pools at grade-control structure and below natural steps lends support to an upstream-forced cascade model, i.e. where falling jet characteristics – virtual energy E given by the specific critical flow energy H_s plus the potential drop energy z – control the geometry of the system, hence representing the most important scaling independent variable. Berms formed at the end of the pools downstream of grade-control structures have been found to be probably analogous both geometrically and sedimentologically (Comiti, 2003) to steps in natural systems.

Field data (Tab. 1) indicate that step spacing L_{step} and berm distance l_b are multiples of the jet energy E, with on average:

$$l_{step}, l_b \cong 3E \cong 3(z + H_s) \quad (2)$$

The present model for step pool formation is valid for all flows which energy E is large enough to cause pool erosion and berm (step) deposition. In steep boulder-bed streams, the availability of a wide range of large clasts – relative to flow depths – allows the existence of different sizes of steps, as described by Hayward (1980) and Chin (1998), having different permanence times.

An extreme event with very low-recurrence interval will be able to form high steps ("major steps") by scouring and depositing downstream the largest mobile boulders present in the stream bed, with a spacing in accordance to the flood energy E. More frequent flood events but still with enough competence to mobilize large clasts will build-up other – less stable – step pool sequences featuring smaller step heights and shorter spacings ("minor steps"), each superimposed on previous – more stable – patterns determined by major steps. Therefore for a given mean channel slope, more than one step wavelength can be encountered depending on the channel's floods history.

To complicate even further the bed configuration, sediment transport occurring as propagating waves filling pools may alter local flow condition altering the regularity of the formative process, as well as non-hydraulic factors such as bank and/or bed obstacles. Hence it is not surprising that many investigators argued that a single, averaged step wavelength poorly represent step pool morphology in the field and even in the laboratory with live-bed conditions (Crowe, 2002).

ACKNOWLEDGEMENTS

This research was funded by the University of Padova, project "Valutazione della pericolosità connessa a colate detritiche sui conoidi alpini", and by the EU Project PL510739 "Epic force" (Evidence-based policy for integrated control of forested river catchments in extreme rainfall and snowmelt).

REFERENCES

Abrahams, A.D., Li, G., and Atkinson, J.F., 1995. Step-pool streams: Adjustment to maximum flow resistance. *Water Resourc. Res*., 31(10), 2593–2602.

Andreoli, A., 2002. Analisi sperimentale sull'influenza dell'erosione localizzata nella dinamica dei torrenti montani. *MSc thesis*, University of Padova, pp. 153 (in Italian).

Chartrand, S.M., and Whiting, P.J., 2000. Alluvial architecture in headwater streams with special emphasis on step-pool topography. *Earth Surf. Process. Landforms*, 25, 583–600.

Chin, A., 1998. On the stability of step-pool mountain stream, *Journal of Geology*, 106, 59–69.

Chin, A., 1999. The morphologic structure of step-pools in mountain streams. *Geomorphology*, 27, 191-204.

Comiti, F., 2003. Local scouring in natural and artificial step pool systems. *PhD dissertation*, University of Padova, Italy, 211 pp.

Crowe, J.C., 2002. An experimental study of the step pool bed form. *PhD dissertation*, The Johns Hopkins University, Baltimore, USA, 147 pp.

Grant, G.E., 1997. Critical flow constrains flow hydraulics in mobile-bed streams: a new hypothesis, *Water Resourc. Res.*, 33(2), 349–358.

Grant, G.E., Swanson, F.J., and Wolman, M.G., 1990. Pattern and origin of stepped-bed morphology in high-gradient streams, Western Cascades, Oregon. *Geol. Soc. America Bull*., 102, 340–352.

Hayward, J.A., Hydrology and stream sediments from Torlesse stream catchment, *Spec. Publ. 17*, Tussock Grassland and Mountain Lands Inst, Lincoln College, New Zealand, 236 pp.

Jarrett, R.D., 1984. Hydraulics of high-gradient streams. *J. Hydr. Engrg.*, ASCE, 110(11), 1519–1539.

Judd, H.E., and Peterson, D.F., 1969. Hydraulics of large bed element channels. *Report PRWG 17-6*, Utah Water Research Laboratory, 85 pp.

Knighton, D., 1998. Fluvial forms and processes: a new perspective, Arnold, London, 383 pp.

Lee, A.J., and Ferguson, R.I., 2002. Velocity and flow resistance in step-pool streams. G*eomorphology*, 46(1–2), 59–71.

Lenzi, MA., 2001. Step-pool evolution in the Rio Cordon, Northeastern Italy, *Earth Surf. Process. Landforms*, 26, 991–1008.

Lenzi, M.A., and D'Agostino, V., 2000. Pattern, origin and dynamics of step pool structures of alpine torrents, *Excerpta*, 14, 21–53, Ed. CUEN, Italy.

Lenzi, M.A., Marion, A., and Comiti, F., 2003. Local scouring at grade-control structures in mountain rivers, *Water Resourc. Res.*, 39(7), 1176–1188.

Peterson, D.F., and Mohanty, P.K., 1960. Flume studies of flow in steep, rough channels*, J. Hydr. Div*, 86, *ASCE,* 55–76.

StatSoft Italia srl, 2002. STATISTICA, version 6, www.statsoft.it.

Tinkler, K.J., 1997. Critical flow in rockbed streams with estimated values for Manning's *n*, *Geomorphology*, 20, 147–164.

Weichert, R., Bezzola, G.R., and Minor, H.E., 2003. Bed morphology, flow resistance and stability of mountain torrents. *Proc. XXX IAHR Congress*, Thessaloniki, Greece, 24–29 August, 159–166.

Whittaker, J.G., 1987. Sediment transport in step-pool streams. In: *Sediment Transport in Gravel Bed Rivers,* Thorne CR, Bathurst JC, Hey RD (eds.). Wiley & Sons; 545–570.

Wohl, E.E., 2000. Mountain Rivers. *Water Resources Monograph* 14, Washington DC, USA., p. 320.

Wohl, E.E., Madsen, S., and MacDonald, L., 1997. Characteristics of log and clast bed-steps in step pool streams of northwestern Montana, USA. *Geomorphology*, 20, 1–10.

Zimmermann, A., and Church, M., 2001. Channel morphology, gradient profiles and bed stresses during flood in a step-pool channel, *Geomorphology*, 40(3–4), 311–327.

This page intentionally left blank

River Flow 2004 – Greco, Carravetta & Della Morte (eds.)
© 2004 Taylor & Francis Group, London, ISBN 90 5809 658 0

Assaying historical maps and relict channel forms for the analysis of channel processes (on example of the Spree River in Germany)

N. Nikolaevich, A. Sukhodolov & C. Engelhardt
Department of Ecohydrology, Institute of Freshwater Ecology and Inland Fisheries, Berlin, Germany

ABSTRACT: Comparative analysis of physical factors for the contemporary and preindustrial states of the riverine ecosystems is a valuable approach in the development of river restoration projects. The present study explores the applicability of advanced methods of hydromorphological analysis to extract detailed information on channel processes from historical maps. Coupled with the modern techniques of infrared aerial photography and field investigations of relict channel forms, these methods allow the determination of characteristic dimensions for preindustrial and paleo-channels. In this study the reliability of a XVIII century map was examined by performing the analysis of contemporary maps and field observations. Sinuous pattern of the river course from historical maps was then processed in the frame of modified sine-generated approach and validated against theoretical relationships. Possibilities for gathering valuable parameters of the channel cross-section from empirical relationships, analysis of infrared and usual aerial photographs and field methods are also illustrated and discussed.

1 INTRODUCTION

In the last three decades, intensive environmental research on rivers had led ecologists, river engineers, and practitioners to recognize the valuable role that physical characteristics of the environment, particularly river flow and channel processes play in the sustainability of riverine ecosystems (Vannote et al. 1980, Cushing & Allan 2001). Valleys, floodplains, and river channels are the elements of landscape comprising the physical component of a riverine ecosystem. Degradation of natural landscapes for intensive land use, urbanization, industrialization, and exploration of natural resources therefore implicitly reflect the decreasing of the ecosystem's sustainability and biodiversity. Recognition for the necessity of reduction and improvements of landscape degradation already inspired many renaturalization projects (Brookes & Shields 1996). However, the efficiency of designing of such projects is presently precluded by the lack of solid theoretical and experimental knowledge on complex relationships between components of a landscape and functioning of the ecosystem.

Most dramatic changes in the landscape of riverine ecosystems appeared in the period of industrialization – a period of the last 250–300 years. The duration of the industrial period is relatively short compared to the characteristic scales of the global climate change, for instance to the past 11000 years of Holocene, or even to the smaller-scale time shifts in the climate as the "little ice age" between XII–XVII centuries (Mauquoy et al. 2002). Therefore preindustrial riverine landscapes were developed gradually in the natural conditions of dynamical equilibrium over long period of time and represented the products of self-organizing system "flow-sediment load-river channel" (Grishanin 1993). The late preindustrial state of river channels was also extensively documented in maps, geological profiles, and hydrological records as transition to the industrial stage required extended planning. These peculiarities of the latepreindustrial period make it a convenient template designed by nature and reflecting the fine balances between water runoff, solid transport, and local limiting factors (Kondratiev et al. 1982).

Although historical maps provide valuable information on the "momentary" pattern of the river channel and therefore can be used as the source of information for advanced methods of channel process analysis, their quality is always of great concern. For example, on a historical map of XVIII century from the Berliner Hauptarchiv one can find channel patterns that look artificial (Fig. 1), especially taking into account the archaic style of the map. Since the channel of the river was straightened, the runoff regulated with in-channel reservoirs, and the solid transport completely transformed by weirs, there remained very few places that can be directly compared to evaluate the quality of the maps. This fact increases the value of indirect methods

of evaluation and, above all, comparison with available theoretical approaches.

Our present study is thus aimed at: (1) critical assessment of historical maps and their suitability for quantitative characterization of channel processes; (2) extraction of quantitative information describing characteristics of the channel forms from maps and comparison of the obtained values with the theoretical models; and (3) accomplishing the data set with the characteristics of the channel cross-section from the complex analysis of aerial photographs performed in normal and infrared lights as well as field drilling. The results reveal that the shape of individual meanders can be accurately described by the sinegenerated curve of Langbein & Leopold (1966) modified to account for asymmetry of natural meanders (Kondratiev et al. 1982). Scaling parameters for meanders can be computed from theoretical relationships developed from sine-generated approach (Zamishlyaev 1982, Yalin 1992).

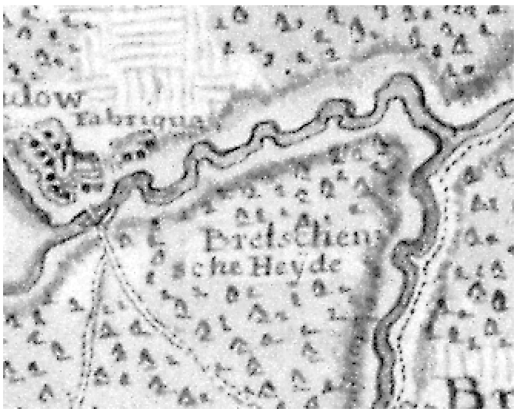


Figure 1. Example of the Spree River channel between Alt Schadow and Kossenblatt from the map dated 1769.

2 ANALYSIS OF CARTOGRAPHIC MATERIALS

2.1 *Direct comparative analysis*

A set of historical documents provided by the Berliner Hauptarchiv served as the factual basis for the present study. It consisted of a map "Lauf des Spree Strohms von Cossenblad über Beeskow und Fürstenwalde, und von Wusterhausen bis Berlin" dated 1769 (Fig. 2), 1 Inch : 500 Ruthen that corresponds to the scale of 1 : 69174, and of longitudinal profile "Nivellements Plan des Spree Strohms von Beeskow bis Fürstenwalde" dated 1791, 1Inch : 60 Ruthen or 1 : 13345.

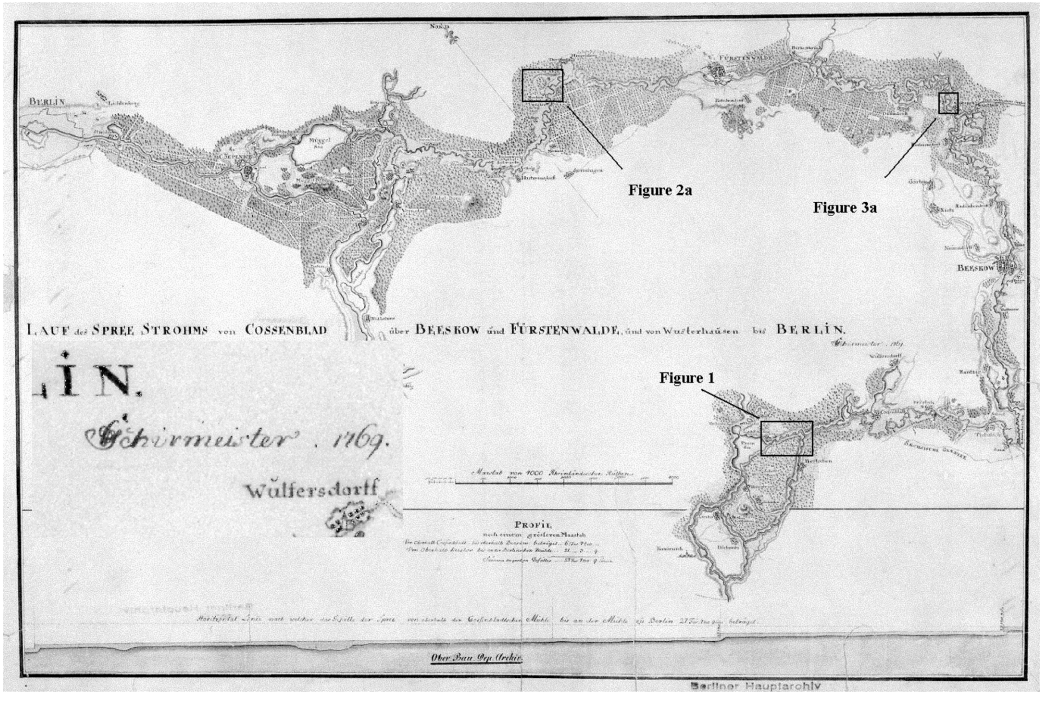


Figure 2. Historical map of the Spree River, 1769.

The set also included contemporary topographical maps of scale 1 : 10000 and 1 : 50000 dated 1985.

Although the preindustrial channel portrayed in the 1769 map was completely transformed in the last century, there are still some distinctive elements of the landscape that can be directly compared to those displayed by the contemporary maps. Because the runoff of river Spree after the Ice Age but long before Holocene was many times greater than 1000 years ago, the valley of the river preserves its history in the form of fully filled with sediments oxbow lakes of huge size: many times larger than present day oxbow lakes. Such relict forms are clearly depicted in the present-day maps and also in the historical maps (Fig. 2). An example of large-scale oxbow lake is shown in Figure 3. Figure 3a displays the enlarged oxbow lake from the historical map (Fig. 2) and Figure 3b shows the corresponding piece of a contemporary map. The centerlines of the oxbow lakes were digitized and scaled for comparison and the resulting curves are presented in Figure 3b. A line of a small canal visible on both maps was used as the alignment line for digitized curves. A close correspondence for these two lines at the downstream part of the channel is evident, but the upstream parts indicate significant deviations. A possible reason for this deviation is the difference in contours of the agricultural land-use that served for determination of oxbow lake margins. Apart from the accuracy problem of this comparison we can conclude that large-scale structures can be measured from the historical map more or less reliably.

Fortunately, close examination of cartographic materials, field trips, and field measurements provided the possibility for a direct comparison of the channel form of the smaller scale pertaining undoubtedly to the preindustrial period (Fig. 4). The banks of two successive meander paths with adjacent flood planes located downstream from the village of Neubrück were armored and preserved in the same form as in the beginning of the last century. Field observations indicate the presence of remnant channels in the downstream parts of flood planes that are so clearly depicted in the historical map (Fig. 4a). The results of field measurements completed in April 2003 are shown in Figure 4b, and a corresponding piece of the contemporary map is presented in Figure 4c. The centerlines of all three channels were digitized, scaled and aligned for comparison. The locations of remnant channels on the flood planes served as the benchmarks for alignment. Comparison of the obtained centerlines is shown in Figure 5. Close correspondence between the contemporary map and the topographic plan (Fig. 4b) outlines an ideal case of comparative analysis. The preindustrial channel deviates systematically all over its path from the present-day centerline. The trend in the deviations of the historical centerline is quite real because it displays natural expansion of the meander. At the same

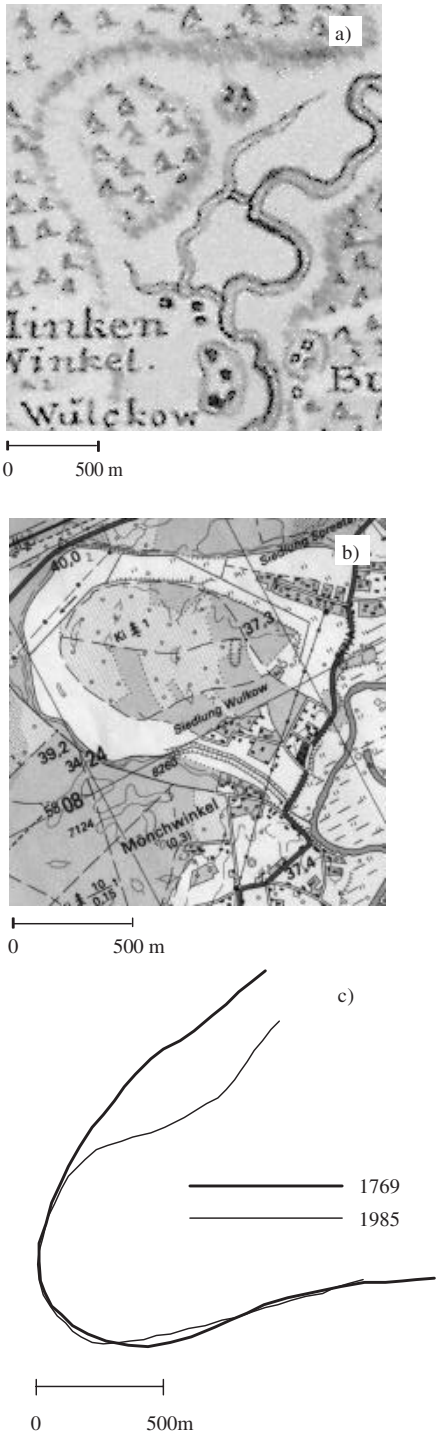


Figure 3. Relict oxbow lake in the valley of the Spree River near the village of Mönchwinkel.

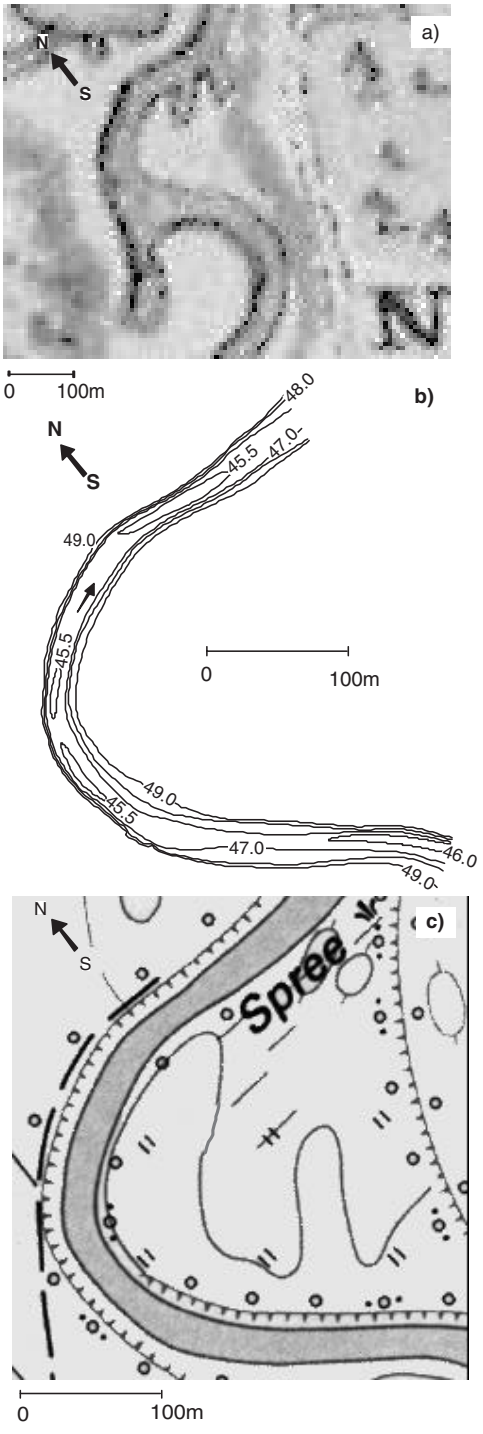


Figure 4. Meander path of the Spree River near the village of Neubrück.

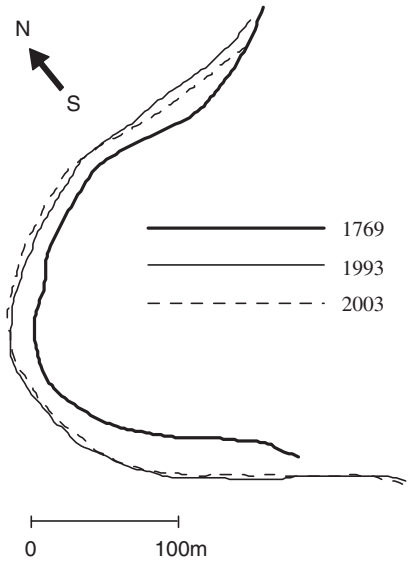


Figure 5. Centerlines of the meandering path downstream of the village of Neubrück.

time, in the downstream part both lines converge owing to the limitations of plane erosion by the valley side (Fig. 4c). Thus, the completed comparison indicates a correspondence between these channel forms.

2.2 *Analysis of meander plane geometry*

Although comparative analysis completed in the preceding section revealed reliability for the particular characteristic form of river channel portrayed in the historical map, the overall pattern of the river channel requires closer examination. To accomplish this goal we provided quantitative characteristics for the plane form of all detectable menders presented in the historical map (Fig. 2), and compared those characteristics to the theoretical description provided by the sine-generated channel pattern and its modifications.

The plane geometry of the individual meander path can be described with the use of some simple geometric quantities. Langbein & Leopold (1966) introduced a concept of minimum variance preceding the development of the principle of self-organization for fluvial systems (Grishanin 1974). Von Schelling (1951) applied the concept of minimum variance and has shown that the most probable path of a meandering stream satisfying the principle is sine-generated curve

$$\theta = \theta_0 \sin \frac{2\pi s}{S_m}, \qquad (1)$$

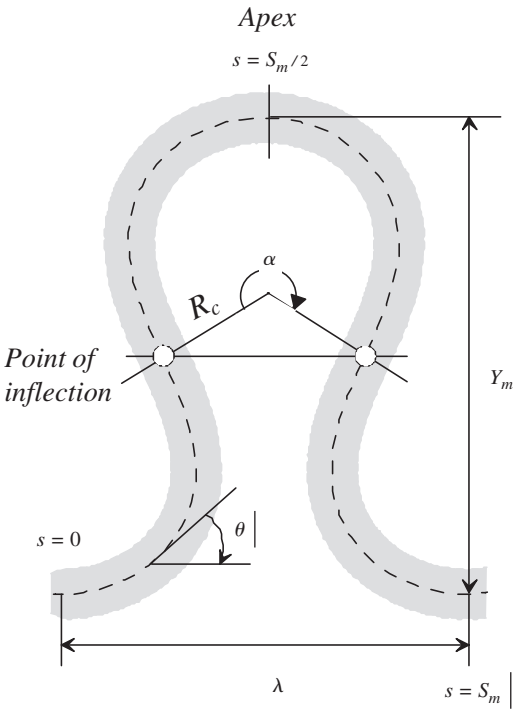


Figure 6. Definition of the meander geometry.

where θ = the angle between the direction measured at a given point along the curve and the mean downstream direction, θ_0 = maximum angle of deviation such as $2\theta_0 = \alpha$ = arc angle (Fig. 6), s = current distance along the path, S_m = total path length. The quantities describing the meander path are shown in Figure 6.

Sine-generated curve is a very useful tool for the quantitative assessment of river meandering pattern because the relationships between principal variables of a meander path can be deduced theoretically. Yalin (1992) presents an extended illustration of the theoretical solution for sine-generated curve that gives ratio Sm/λ- a sinuosity of the meander path

$$\frac{S_m}{\lambda} = \frac{1}{J_0(\theta_0)}, \tag{2}$$

where $J_0(\theta_0)$ = Bessel function of the first kind and zero-th order, and λ = meander wavelength. Zamishlyaev (1982) presented some other quantitative relationships for sine-generated curve

$$\frac{Y_m}{\lambda} = \frac{H_0(\theta_0)}{2J_0(\theta_0)}, \tag{3}$$

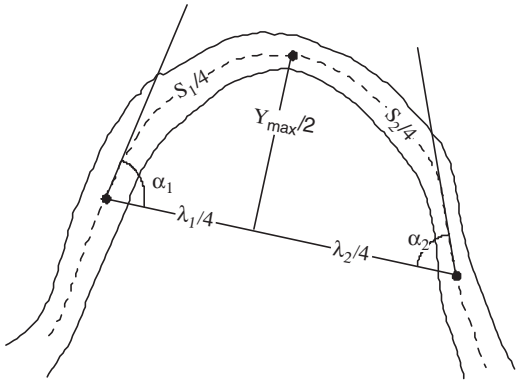


Figure 7. Meander approximation with two adjacent meander bends, the Spree River near the village of Neubrück (the same as in Figure 4).

$$\frac{\overline{R}_c}{\lambda} = \frac{1}{2\theta_0 J_0(\theta_0)}, \tag{4}$$

where Ym = meander amplitude, $\overline{R}_c$ = mean radius of curvature, $H_0(\theta_0)$ = Struve function of the first kind and zero-th order.

Although sine-generated curve represents the symmetric meander bend, the natural meanders of river channels are asymmetric (Fig. 4). To account for asymmetry, it was proposed to describe the meander arc as the combination of two quarters of symmetrical meanders with different parameters (Kondratiev et al. 1982). Their approach is illustrated in Figure 7. Using the hybrid scheme of two sine-generated curves Zamishyaev (1982) developed the following relationships for asymmetric meanders.

$$\frac{S_m}{\lambda} = \exp(\alpha/4)^2, \tag{5}$$

$$\frac{Y_m}{\lambda} = \frac{H_0(\alpha/2)}{2}\exp(\alpha/2)^2, \tag{6}$$

$$\frac{\overline{R}_c}{\lambda} = \frac{\exp(\alpha/2)^2}{\alpha}. \tag{7}$$

The approach was successfully tested on a large data set comprised of rivers from different regions in Russia (Kondratiev et al. 1982) as well as subsequently in Moldova (Nikora 1992) and is therefore recommended as an advanced tool for the analysis of meandering river channel patterns (Nikora 1992, Arnaut 1995).

The historical map (Fig. 2) was manually processed with a compass and protractor to obtain the quantitative characteristics for 44 recognizable meanders in the frame of the approach by Kondratiev et al.

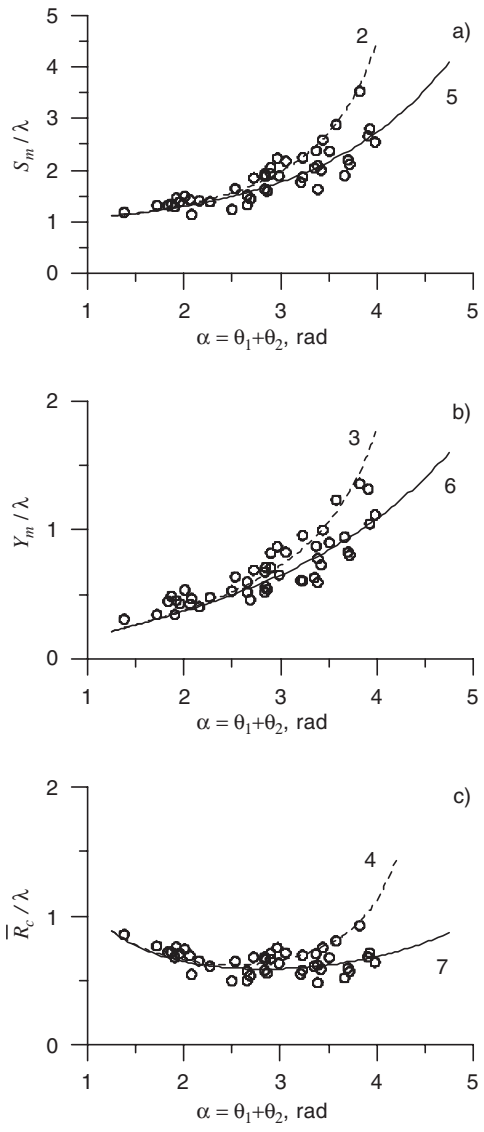


Figure 8. Characteristics of meanders of the Spree River channel and the comparison with theoretical relationships 2–7.

(1982). The obtained results and their comparison with relationships 2–7 are shown in Figure 8.

It can be seen from Figure 8 that geometrical quantities of meanders obtained from the historical map agree with correspondent theoretical relationships. Moreover, scatter in the values and the character of deviation is practically the same as for geometrical quantities measured on contemporary cartographic materials (Arnaut 1995). This particular result confirms the reliability of channel patterns presented by the historical map.

Besides characterization of the plane form of a channel, complete geomorphological description of the river channel should include quantitative description of the channel cross-section. Such characteristics as the bank-full width and depth of the channel are very important for the assessment of hydraulic characteristics and fluxes of water and dissolved substances. Unfortunately the historical maps could provide only little information regarding the channel cross-sections because relief was not measured at that time with sufficient details and the maps as a rule do not provide elevations. To complete the geomorphological description, the analysis of relict channel forms is required, and therefore the next sections describe the assessment of relict channel forms with methods of aerial photography in ordinary and infrared lights.

3 ANALYSIS OF RELICT CHANNEL FORMS

3.1 *Processing aerial photographs*

Many studies show that meandering is quite a general phenomenon observed in different physical systems: studies of oceanic currents (Robinson et al. 1989) revealed a meandering Gulf Stream, meandering of supra-glacial channels was reported in glacial studies, and space-photographs of Mars indicated meandering patterns of relief. A notable feature of meandering flows is a certain relationship between channel width and the meander wavelength. Leopold & Wolman (1957) have obtained an empirical relationship

$$\lambda = 10.9\, B_0^{\,1.01}, \tag{8}$$

where B_0 = width of the channel at bank-full discharge. Relationship 8 and empirical data reported in different studies are shown in Figure 9. Although relationship 8 is purely empirical, it captures most of the fundamental properties of the phenomenon and displays universality over an extremely wide range of scales. Therefore this property can be used for reconstruction of channel cross-section of relict channels. In the industrial period the channels of many rivers were straightened and canalized – a common practice for land use of flood planes and prevention of disastrous flooding. It is usual in river training to fill the meanders of pre-canalized channels with excavated material of a new channel. Therefore relict meanders of the preindustrial period are scarce, but not completely impossible to find. Because the valley of the Spree River was not heavily used for agriculture or industrial purposes, many preindustrial-channel meanders were not buried during river-training works and can be directly assessed with the use of contemporary

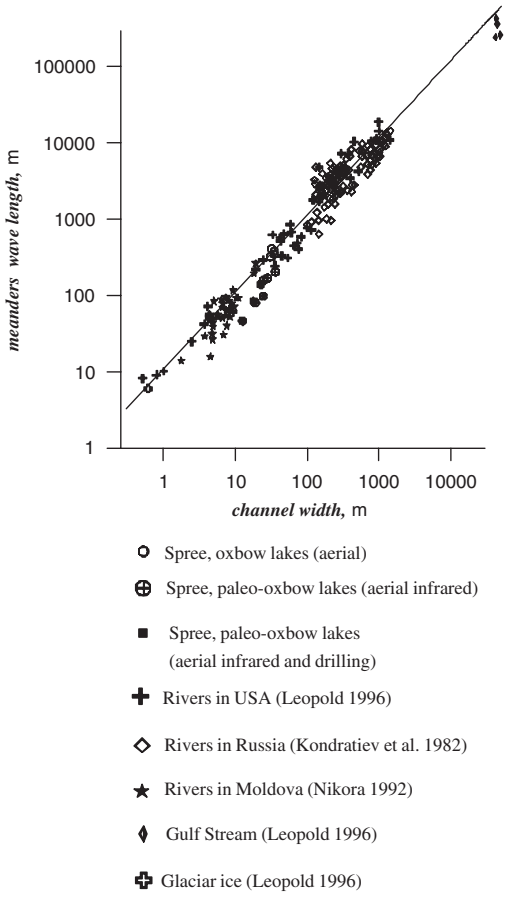


Figure 9. Relationship between channel width and meander wavelength.

methods of aerial photography for direct evaluation of relationship 8 in our case study.

An example of an aerial photograph of an oxbow lake – relict form of the preindustrial channel of the Spree River located near village of Freienbrink is shown in Figure 10. Field observations to verify that bank-full width of relict channels can be accurately measured from the aerial photographs. The bank lines of the channel were contoured by the vegetation on its margins and the channel was segmented over equal distance intervals and the channel width was de-determined at wedges of segments (Fig. 10). The average width of the channel was computed from the data sets. In all, four well-preserved oxbow lakes were identified from aerial observations and processed. The measured channel widths were plotted versus meander wavelength (Fig. 10). Comparison with relationship 8 (presented by line in Fig. 10) reveals applicability and high performance for the relationship.

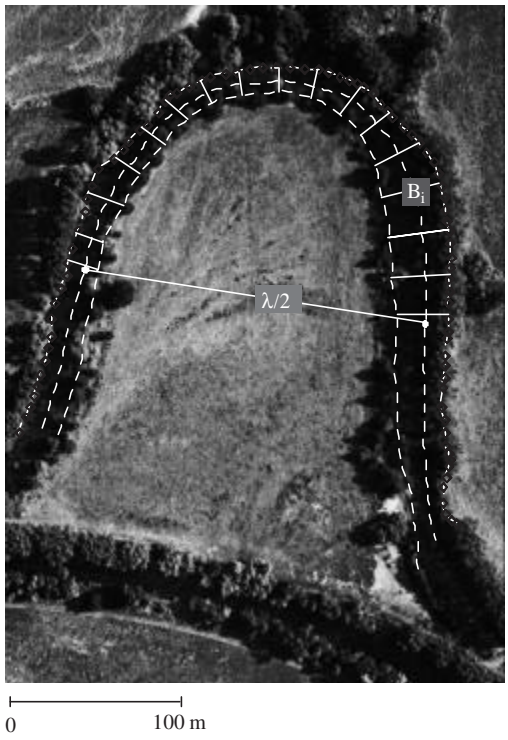


Figure 10. Example of an aerial photograph of relict meander of the Spree River near Freienbrink.

Besides modern methods of aerial photography providing assessment of apparently visible oxbow lakes, the infrared aerial photography also enable visualizing completely filled with sediments paleooxbow lakes. Differences in soil composition and consequently differences in vegetation produces pronounced patterns on infrared aerial photographs (Fig. 11). Paleo-oxbow lakes and other distinct elements of the relief such as paleo-meander scroll bars are clearly depicted and can be measured with the use of the same methodic as described above. Five paleo-oxbow lakes were identified for the investigated channel reach and the corresponding average values of their bank-full width and meander wavelength were plotted in Figure 9. Although the deviation of these data from the relationship 8 was not greater than scatter in the data presented in Figure 9, the data indicate systematic deviation into the region of larger values for channel width. A possible explanation for this observation is the diffusion of boundaries of paleo-oxbow lakes because of denudation, erosion, and agricultural land use. Confirmation or rejection of this hypothesis required direct field investigations. Spatial distributions of alluvium and soil from drilling in the oxbows obtained from those investigations are described in the next section.



Figure 11. Example of aerial photography of the Spree River valley in infrared light.

3.2 *Drilling in paleo-oxbow lakes*

Four paleo-oxbow lakes unambiguously determined with infrared aerial photography were subjected to detailed field measurements. Drilling was performed in representative cross-sections of the lakes (Fig. 12a). An example of spatial distributions of soil in a cross-section of paleo-oxbow lake is presented in Figure 12b. The distribution of peat in drills contours the paleo-channel of the oxbow. It also shows that peat was covered with sand and that the width of the peat area is sufficiently shorter than the width detected from infrared aerial pictures. These measurements support the hypothesis on diffusion of fine sand can explain the deviations of points in Figure 9. The values for the width of paleo-oxbow lakes were corrected according to measurements taken from drillings and were presented in Figure 9. The corrected values indicate a better correspondence with relationship 8.

4 CONCLUSIONS

The present study examined the reliability of a historical map of the preindustrial channel of the Spree River in Germany by direct comparison of the remnant meanders of the river and by applying modern methods of hydromorphological analysis. It is shown that despite their archaic style the historic maps represent a valuable source of reliable information. Major elements of the landscape of the river valley meander

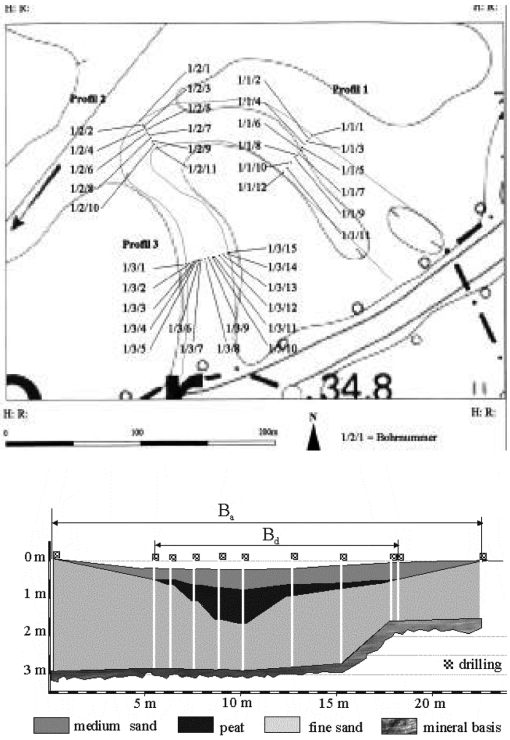


Figure 12. a) Contours of a paleo-oxbow lake and locations of drillings, valley of the Spree River near Mönchwinkel, b) spatial distributions of soil in the drillings, *Ba* and *Bd* are paleo-channel width detected by aerial and drilling respectively.

bends of different sizes – are presented with sufficient details and their quantitative characteristics can be determined with an accuracy comparable with that of the modern cartographic material. The historical map and the quantitative characteristics it contains can be used in river channel restoration projects.

The relationship between planform of meanders of the preindustrial period and width of the channel cross-section was revealed by the comparison of data collected from aerial photographs and field investigations. Diffusion of the banks of paleo-oxbow lakes because of erosion and agricultural use significantly affects the accuracy of determined parameters.

ACKNOWLEDGEMENTS

The authors wish to express their acknowledgements to Randi Carls for the assistance with the analysis of infrared photographs and for providing the results of drilling. The study was supported by the Berlin Senat, Department of Urban Development.

REFERENCES

Arnaut, N.A. 1995. *Factors of Small River Channels Formation, their Classification and Morphometric Relationships (on Example of Small Rivers of Moldova).* Ph.D. thesis, Odessa.

Brookes, A., & Shields, F.D. 1996. Perspectives on river channel restoration. In A. Brookes & F.D. Shields (eds), *River Channel Restoration*: 1–19. Chichester: Wiley.

Cushing, C.E., & Allan, D. 2001. *Streams. Their Ecology and Life.* San Diego: Academic Press.

Grishanin, K.V. 1974. *Stability of Channels in Rivers and Canals.* Leningrad: Hydrometeoizdat.

Kondratiev, N.E., Popov, I.V., & Snishenko, B.F. 1982. *Foundations of Hydromorphological Theory in River Bed Processes.* Leningrad: Hydrometeoizdat.

Langbein, W.B., & Leopold, L.B. 1966. *River Meanders-Theory of Minimum Variance.* USGS Prof. Paper 422-H.

Leopold, L.B., & Wolman, M.C. 1957. *River Channel patterns: braided, meandering, and Straight.* USGS Geol. Surv. Prof. Paper 282B.

Mauquoy, D., van Geel, B., Blaauw, M., & van der Plicht, J. 2002. Evidence from northwest European bogs shows "Little Ice Age" climatic changes driven by variations in solar activity. *The Holocene* 12(1):1–6.

Nikora, V.I. 1992. *Channel Processes and Hydraulics of Small Rivers.* Kishinev: Shtiinca.

Robinson, A.R., Michael, A.S., Leonard, J.W., & Wayne, G.L. 1989. Data assimilation and dynamical interpolation in GULFCAST experiments. *Dyn. of Atmosph. and Oceans* 13:301–316.

Vannote, R.L., Minshall, G.W., Cummins, K.W., Sedell, J.R., & Cushing, C.E. 1980. The river continuum concept. *Canadian J. of Fish. & Aquatic Sc.* 37:130–137.

von Schelling, H. 1951. Most frequent particle paths in a plane. *Am. Geophys. Union Trans.* 32:222–226.

Yalin, M.S. 1992. *River Mechanics.* New York: Pergamon Press.

Zamishlyaev, V.I. 1982. Analytic backgrounds for morphometric relationships. In: *Problems of Hydrology.* Leningrad: Hydrometeoizdat.

This page intentionally left blank

River Flow 2004 – Greco, Carravetta & Della Morte (eds.)
© 2004 Taylor & Francis Group, London, ISBN 90 5809 658 0

Monte Carlo method applied to a two-dimensional morphodynamic model

J.J.P. Lambeek, H.R.A. Jagers & H. van der Klis
WL|Delft Hydraulics, Delft, Netherlands

ABSTRACT: Two main issues in river management in The Netherlands are safety against flooding and navigability. During the recent year a lot of research has been carried out with the objective to increase the capacity of the Dutch Rhine branches with respect to discharge capacity and navigability. The enlargement of the capacity of the rivers by measures within the floodplain appears to be a promising intervention that combines nature restoration and possibilities to guarantee safety against flooding. The investigations concerning the impact of measures to increase the river capacity have been limited, so far, to the hydraulic impact. Little attention has been given to the impact of these measures on the morphodynamic behavior of the river bed and its relation with navigability and safety against flooding.

An improved approach has been developed to investigate the morphodynamic behavior of the river bed under changing discharge conditions. This improved method comprises a Monte Carlo simulation with a two-dimensional morphological Delft3D model that includes the main channel and floodplains. The results of the Monte Carlo simulation have been used to determine the specific locations that are sensitive to changing discharge conditions and where the morphodynamic behavior has impact on the navigability. The present investigation has been limited to the situation without structural interventions. The procedure presented in this paper is considered to be a promising method to obtain insight in the impact of structural floodplain measures on the morphodynamic behavior of the river bed and its relation with navigability and safety against flooding.

1 INTRODUCTION

1.1 *Context*

Recent river management studies in the Netherlands have focused on three topics: safety against flooding, navigability and environmental issues. During the recent year a lot of research has been carried out with the objective to increase the capacity of the Dutch Rhine branches (Silva et al., 2001; WL|Delft Hydraulics & RIZA, 2002, 2003). The enlargement of the discharge capacity by removing narrow sections in the floodplain appears to be a promising measure to combine nature restoration in the floodplains with possibilities to guarantee safety against flooding. Furthermore, the same studies intend to solve navigability problems that are faced at some locations.

For a reach of the river Rhine at the Dutch-German border a two-dimensional morphodynamic model has been applied in order to investigate the morphological impact of possible measures (such as dredging, construction of non-erodible layers, and floodplain widening) on the navigability in this reach (WL|Delft Hydraulics, 2003). The investigation has been based on a single representative hydrograph that was repeated for several years in order to investigate the long-term morphological impact of structural interventions. That approach with a single representative hydrograph is already much better than using a single representative discharge. However, the approach is still deterministic, since it is based on only a single simulation with one repeated hydrograph. Therefore, the approach does not provide you with information on the uncertainty in the impact of the interventions since the natural variability of the hydrograph is not taken into account. Different hydrographs may cause a significantly larger or smaller effect than the hydrograph selected for the single simulation. The objective of the present research is to investigate the impact of uncertainties in the discharge values on the morphodynamic behavior of the river bed.

1.2 *Uncertainty of discharge fluctuations*

Van der Klis (2003) analyzed the uncertainty of discharge fluctuations and the impact on the river bed development. She examined the applicability of Monte Carlo Simulations to quantify the uncertainty in the results of a one-dimensional morphological numerical model. Her conclusion was that the Monte Carlo method is the best method to quantify the impact of

uncertainties in the river discharge on the development of the river bed morphology. The Monte Carlo method makes it possible to analyze the morphological and hydraulic output of the simulations with normal statistical methods.

The objective of the present research is to investigate whether the application of this Monte Carlo method to a two-dimensional morphodynamic model would provide additional useful information that is consistent with prototype observations. For this reason, the number of simulations has been limited to only ten. Later on it is aimed to define a statistical parameter that can be used to determine how many simulations are required for actual statistical analyses of the morphodynamic behavior. It is also aimed to apply this method to study the morphodynamic impact of structural interventions like floodplain lowering.

1.3 *Improved knowledge of morphological behavior*

The knowledge about this morphodynamic behavior of the summer bed is only limitedly used in the management and planning of the Dutch rivers. The results of the present research show that the application of the Monte Carlo method to two-dimensional morphodynamic models is a very promising non-deterministic approach that includes the uncertainty of the discharge and by which the morphodynamic behavior of the riverbed can be studies with standard statistical procedures.

This paper will present the case study that has been used in the investigation in Chapter 2. This is followed in Chapter 3 with an explanation of the Monte Carlo method as it has been applied in the present investigation. Chapter 4 presents the results of the Monte Carlo simulations. Conclusions and recommendations will be presented in Chapter 5.

2 CASE STUDY

2.1 *Two-dimensional morphological Delft3D model*

In the investigation a detailed two-dimensional morphological Delft3D model (Fig. 1) has been used that was earlier developed to study the impact of structural interventions that were planned to solve local navigability problems (Baur et al., 2002). Baur et al. used the model to define combinations of engineering measures which guarantee the required dimensions of the shipping lane, minimize the degradation of the river bed and that do not increase the design water levels for extreme flood conditions. These engineering measures consisted of the use of non-erodible layers, the adaptation of the groynes in length and height and the

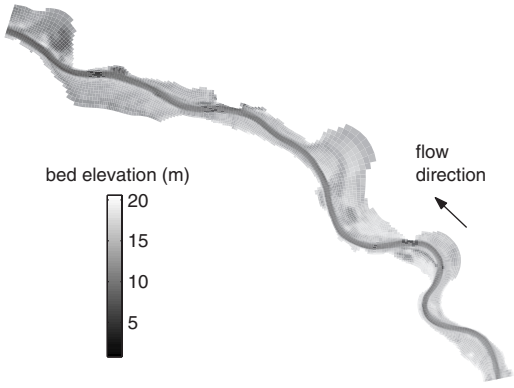


Figure 1. Morphological Delft3D model.

relocation of the embankment at a specific location as well as lowering of the floodplains.

2.2 *Model schematization*

The model schematization includes the main channel (summer bed) and floodplains (winter bed) so that discharge exchange between the summer and winter bed during high discharges is represented by the model. The model area has a length of 42 km. The model topography is schematized in a curvilinear computational grid. The average cell length and width in the summer bed are 150 m and 35 m, respectively. The groyne fields are schematized by two cell rows at the right and left side of the summer bed. The model topography in the areas between the groynes is schematized with the appropriate elevation of the summer bed. The groynes are represented by 2D-weirs of the same heights as the groyne crests. The weirs are oriented perpendicular to the flow direction.

The summer bed roughness and the grain size vary in longitudinal, not in transverse direction. The Chézy-values in the summer bed vary between 52.5 $m^{1/2}/s$ and 56.5 $m^{1/2}/s$ for medium flow and flood conditions and are reduced by 2.5 $m^{1/2}/s$ for low flow conditions. The median grain size is 10 mm.

The hydraulic calibration was performed for the topography of 1995. Computed and measured water levels at four steady-state flow conditions were compared. Deviations of more than 15 cm occur only at two locations for the highest flood conditions; the differences were generally less than 5 cm at low/medium discharge and less than 10 cm at high discharge. The simulation of the 1995 discharge hydrograph provided a verification of the calibration with good results.

For the morphological calibration of the model, a constant discharge simulation was applied. The location and extension of point bars and deep outer bend are well represented. The validated against the morphodynamic development during the period 1995–2000.

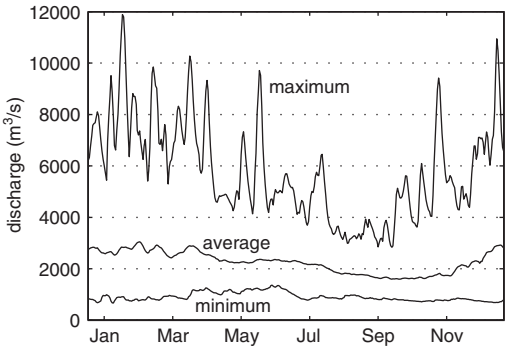


Figure 2. Maximum, average and minimum measured historical Rhine discharge at Lobith.

2.3 *Boundary conditions*

The boundary conditions for the model simulations consisted of the water level at the downstream model boundary and the discharge distribution over the grid cells of the upstream boundary.

In case of a Monte Carlo simulation this implies that for every discharge value to be used in the simulation a separate set of water level and discharge distribution values is required. For only 10 discharge hydrographs of 3 years each approximately 1000 boundary condition sets are required. Normally, the number of hydrographs simulated in a Monte Carlo simulation is even higher. In the present investigation it has therefore been decided to limit the boundary data-set to a limited amount.

The historical data have been converted to see which set of discrete discharge values would have similar characteristics as the historical dataset and still would be workable as input for the Delft3D simulations. As the present research is only first approach, later on the number of discrete discharge values for which boundary conditions are made available can be extended. For now, it was concluded that discretization with steps of 500 m^3/s would represent the actual discharge values well enough for a first approach.

The river bed in the model represented a river bed survey that was carried out in the year 2000. Other prototype data were historical discharge data at the Lobith gauging station (Fig. 2) at the downstream end of the model reach.

3 MONTE CARLO APPROACH

3.1 *Large amount of deterministic simulation*

The principle of Monte Carlo simulation is to run a deterministic model many times. Each model run is driven by a different realization of the input time series (synthesized on the basis of randomly generated parameters). The set of outputs resulting from all model runs is used to determine the statistical properties of the resulting bed levels, like the expected bed level position, its variance and the percentile values. In case of non-linear systems, the statistical mean of the possible morphological responses is not equal to the morphological prediction based on the 'mean' value of each model input (Gardner & O'Neil, 1983).

The random discharge generator is based on a method derived by Duits (1997). The seasonal dependency and the correlation between successive river discharges are considered in this method. The basic data represents 55 years of daily measured Waal discharges at the location Lobith. A statistical description has been derived in five steps:

- Each year is split into 36 periods of 10 days each.
- The measured daily discharges are averaged over these 10-day periods.
- For corresponding 10-day periods through the years, a shifted lognormal distribution function is estimated.
- The correlation between discharges in successive periods is estimated. Duits shows that the discharge in 10-day period i depends on that in the two preceding 10-day periods, $i-1$ and $i-2$.
- Construction of a multivariate lognormal distribution function per 10-day period.

The correlation between the discharges within successive time intervals has been taken into account. This method has been previously applied to the same data by Van Vuren et al. (2002) and Van der Klis (2003). With this statistical model discharge hydrographs have been synthesized by random sampling from these multivariate lognormal distribution functions. The set of results from these simulations is used to determine the statistical properties of the predictions.

The averaging process used in the Monte Carlo sampling includes a method that adjusts the discharge values in such a way that the sediment transport generated by the averaged discharge data for the period of 10 days is equal to the sediment transport generated by the daily average discharge data.

3.2 *Comparison historical and sampled discharges*

Figure 3 presents the maximum, average and minimum historical discharge values of Figure 1 that have been averaged over 10-day periods. The maximum values in Figure 3 are somewhat lower than in Figure 1. This is caused by the fact that very high discharge values usually last shorter than the 10 days over which the values are averaged. The maximum, average and minimum discharge values of the synthesized discharge hydrographs used in the simulations are presented in Figure 4. The overall characteristics of Figures 3 and

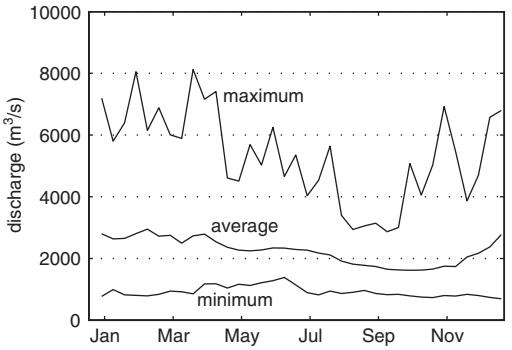


Figure 3. Maximum, average and minimum measured historical Rhine discharge data averaged over 10-day periods.

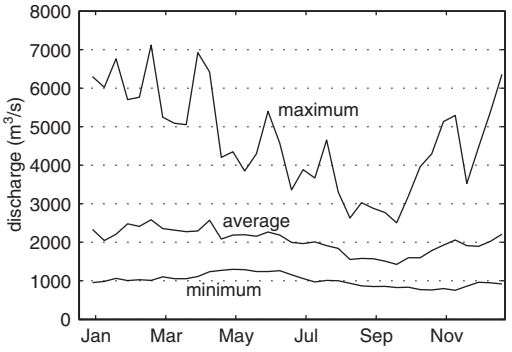


Figure 4. Maximum, average and minimum values of 30 discharge hydrographs synthesized by random sampling from the multivariate lognormal distribution functions.

4 are the same. It can, therefore, be concluded that the sampling method described above has led to discharge hydrographs that give a good representation of the main statistical properties of the prototype discharge distribution.

A few hundred number of simulations may be required for a good statistical analysis of the morphodynamic behavior of the river bed (Van der Klis, 2003). However, the objective of the present research is not to carry out a complete statistical analyses. The results presented here, are only intended as an initial test to see the applicability of a Monte Carlo simulation with a two-dimensional morphological model. Therefore the number of simulations is limited to 10 simulations with a duration of 3 years (i.e. 30 independent hydrographs).

3.3 *Simulations*

A procedure has been developed to run a Monte Carlo simulation with the two-dimensional morphological Delft3D model. This procedure controls the execution of the different model simulations and the exchange of input and output data with a database. During the morphological simulation the hydraulic and morphological output is stored with time steps of five days. Two types of analyses can be carried out with the output data of the simulations. The first analysis considers the impact of discharge fluctuations on the *morphodynamic behavior* of the river bed. This can be done by directly statistically analyzing the output of the bed elevation data that have been stored in the output database.

The second analysis considers the impact of discharge fluctuations on the *navigability*. To guarantee navigability towards Germany, a shipping lane of 170 m wide and 2.8 m deep (under OLR-conditions) is maintained in the considered reach. The abbreviation OLR represents a standardized low water level (in Dutch: overeengekomen laagste rivierstand) which is associated with a characteristic discharge: during 5% of the year a lower discharge occurs. To check whether the dimensions of the shipping lane were satisfied during the simulations, steady state hydrodynamic simulation of OLR-conditions were carried out after each period of 5 days of the morphodynamic simulations. For each model grid the fulfillment of the OLR-criteria (water depth of 2.8 m channel width of 170 m) can be analyzed statistically to investigate the impact of the morphological development under varying discharge conditions on the navigability.

So far, these analyses have focused on the morphodynamics of the navigation channel and on the fulfillment of the OLR-criteria for the present situation only. Structural interventions in the floodplain, like floodplain lowering and other changes to the cross-sectional area of the river, have not yet been considered. The procedure has been successfully tested with 10 discharge hydrographs for a period of three years each. The statistical analyses carried out on the output of the simulations are described in the following chapter.

4 RESULTS

The morphological sensitivity to discharge fluctuations for the present situation has been analyzed with figures of the maximum bed level difference (maximum bed level minus the minimum bed level) and with the standard deviation of the bed elevation during the Monte Carlo simulation. As stated earlier, these data have been determined from the 10 simulations of 3 years with output every 5 days. For each grid cell, therefore, the statistical output for each of the presented parameters is based on 2190 values.

The magnitude of the morphodynamic variations under varying discharge conditions is presented in the Figures 5 and 6. Figure 5 presents the absolute maximum bed level differences for a certain model reach.

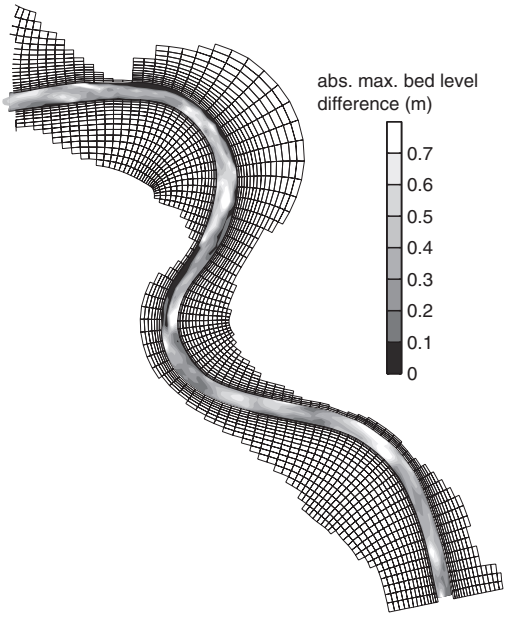


Figure 5. Absolute maximum bed level difference during the Monte Carlo simulation.

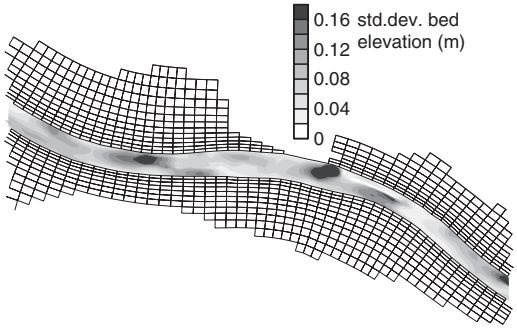


Figure 6. Standard deviation of the bed elevation.

Figure 6 presents the standard deviation of the bed elevation of another model reach. In case the parameters presented in Figure 5 as well as in Figure 6 have high values this implies that the local river bed (elevation) is highly sensitive to discharge fluctuations.

The impact of the morphodynamic behavior on the navigability has been analyzed in two ways. The first method focused on the navigation channel depth, the second on the navigation channel width. Figure 7 presents the frequency that the water depth during OLR-conditions is smaller than the OLR-criteria of 2.8 m. High values of this parameter represent locations where the OLR-criteria for the navigation depth is frequently not fulfilled. This is especially true in the floodplain, but also some locations can be identified

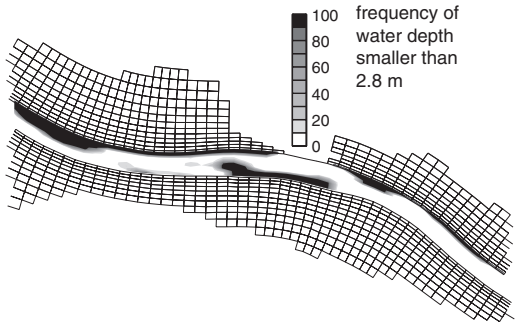


Figure 7. Frequency that the water depth during OLR-conditions is smaller than the OLR-criteria of 2.8 m.

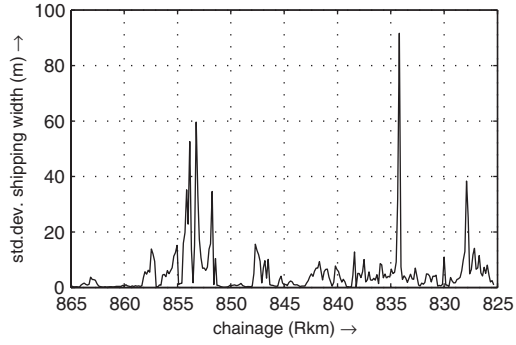


Figure 8. Standard deviation shipping width based on a minimum water depth of 2.8 m during OLR-conditions.

within the navigation channel where the OLR-criteria for navigation depth are frequently not fulfilled.

Figure 8 presents the standard deviation of the channel width in which the water depth is more than the OLR-criteria of 2.8 m. In this figure a high value of the standard deviation means that in this reach the navigation channel width is highly sensitive to discharge fluctuations. In case this is combined with a small absolute values of the navigation channel width this implies that the navigation in this reach could face difficulties during certain discharge conditions.

Figure 9 presents the maximum and minimum value of the navigation channel. In case large differences occur in these two parameters, the navigation channel width is highly sensitive to discharge fluctuations. At some locations the values of the minimum shipping width and even of the maximum shipping width fall below the OLR-criteria of 170 m. The navigability in these reaches clearly faces difficulties.

Based on the statistical data obtained from the Monte Carlo, it is possible to determine the likelihood that the OLR-criteria will not be fulfilled and that the navigability in a certain reach may not be

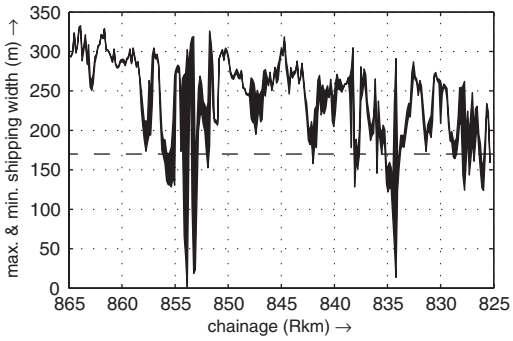


Figure 9. Range of the shipping width (filled area between maximum and minimum values) of the navigation channel width based on a minimum water depth of 2.8 m during OLR-conditions.

guaranteed without additional measures. This information could be used to make a decision whether, where and when dredging should be carried out to guarantee navigability.

The results of the Monte Carlo simulation are consistent with prototype observations. The reaches where navigability problems occur in prototype are clearly represented in the results of the Monte Carlo simulation.

5 CONCLUSIONS AND RECOMMENDATIONS

The application of a Monte Carlo simulation to a two-dimensional morphological model is considered to be a promising method to obtain insight in the morphodynamic behavior of the river bed.

The results of this non-deterministic modeling approach clearly provides insight into the impact of discharge fluctuations on the morphodynamic behavior of the river bed. This additional information is considered valuable when insight is required about the impact of the morphodynamic behavior on other functions of the river.

The impact of discharge variations on the morphodynamic behavior is clearly visible in the results of the Monte Carlo simulation. The results appear to be consistent with prototype observations.

Further research is required to define a statistical parameter that provides insight in the amount of simulations that are required for statistical analyses of the morphodynamic behavior and their certainty. Furthermore, it would be useful to test the Monte Carlo approach with structural measures to the river (floodplain lowering, changes to groyne dimensions, positions of embankments, etc.) and to see the impact of these measures on the morphodynamic behavior. Finally, it would be interesting to apply the Monte Carlo and to study the impact of the morphodynamic behavior under varying discharge conditions and the relation with safety against flooding.

REFERENCES

Baur, T., Havinga, H. & Abel, D. 2002. Internationale Zusammenarbeit bei der Planung von Regulierungsmaßnahmen am Niederrhein: Durchführung flussmorphologischer Simulationen, HANSA International Maritime Journal, 10/2002, pp. 51–56 (in German).

Duits, M. 1997. *Baggeroptimalisatie in rivierbochten*. MSc Thesis, Delft University of Technology (in Dutch).

Gardner, R.H. & O'Neill, R.V. 1983. Parameter uncertainty and model predictions: a review of Monte Carlo results. In: Beck, M.B. & Straten, G. van 1983. *Uncertainty and forecasting of water quality*. Springer-Verslag, Berlin.

Silva, W., Klijn, F. & Dijkman, J. 2001. *Room for the Rhine Branches in The Netherlands. What the research has taught us*. Directorate-General for Public Works and Water Management, Institute for Inland Water Management and Water Treatment, RIZA end WL|Delft Hydraulics.

Van der Klis, H. 2003. *Uncertainty analysis applied to numerical models of river bed morphology*. PhD Thesis, Delft University of Technology.

Van Vuren, S., Van der Klis, H. & De Vriend, H.J. 2002. Large-scale floodplain lowering along the river Waal: a stochastic prediction of morphological impacts. In: Proceedings of River Flow 2002.

WL|Delft Hydraulics 2003. *Grensproject Bovenrijn/Grenzproject Niederrhein. Report no. 3, Investigation of individual engineering measures with 2D morphological model (part 2)*. WL|Delft Hydraulics Project Q2496 (in Dutch).

WL|Delft Hydraulics & RIZA 2002. *Spankrachtstudie. Deelrapport 1–11*. WL|Delft Hydraulics Project Q2975 (in Dutch).

WL|Delft Hydraulics & RIZA 2003. *PKB-studie. Deelrapport A–E*. WL|Delft Hydraulics Project Q3244 (in Dutch).

River Flow 2004 – Greco, Carravetta & Della Morte (eds.)
© 2004 Taylor & Francis Group, London, ISBN 90 5809 658 0

Behavior of a finite disturbance in a mobile bed stream

Michele Iervolino
Dipartimento di Ingegneria Idraulica e Ambientale "Girolamo Ippolito", Università degli Studi di Napoli "Federico II", Napoli, Italy

Angelo Leopardi
Dipartimento di Meccanica, Strutture, Ambiente e Territorio, Università degli Studi di Cassino, Cassino (FR), Italy

ABSTRACT: The commonly adopted approach for modelling unsteady river morphological processes is to couple the Saint Venant equations, for unsteady flow routing, with the Exner equation, for sediment mass conservation. Despite this model is widely adopted, some of its properties do not match physical behavior.

Recently, a new class of morphodynamical models has been proposed, in which the sediment dynamics is somewhat reproduced (four-equations models).

The object of present note is to better exploit the response of a four-equations model to a small bed perturbation through a mixed analytical–numerical procedure in a quasi-linear approximation.

1 INTRODUCTION

Modelling unsteady river morphological processes is a complex, fascinating and still open task. In present work only bed load transport will be considered.

Many Authors (e.g. *Correia et al., 1992, Graf, 1998*) have proposed morphodynamical models using different approaches. However, a common feature of most of them, is to couple hydrodynamics and morphodynamics equations. While the former are well assessed (for a river reach 1D or 2D depth-integrated equations can be applied), many proposals exist about the latter.

The most classical form of morphodynamical models can be obtained coupling sediment continuity equation (the so-called Exner equation) to hydrodynamics equations. This approach (Three-equations model) implies the choice of a bed load transport formula. Because this formula is usually a uniform flow formula (e.g. *Meyer-Peter and Muller, 1948*), the implicit hypothesis of instantaneous adaptation of bed load transport to variations in flow conditions is made (*de Vries, 1965*).

Many examples exist of physical processes that cannot be modelled through this approach. For instance, the earth-dam break test by *Benoist (1983, 1989)* used as a reference by many Authors (e.g. *Leopardi et al., 2003*). This can be explained because in a three-equations model an accelerating stream implies scouring while a decelerating one always causes deposition.

In order to overcome above cited limitations, recently, a new class of morphodynamical models has been proposed: the so-called four-equations models (*Nakagawa & Tsujimoto, 1980, Armanini & Di Silvio, 1988, Phillips & Sutherland, 1989, Di Cristo et al., 2002, Fraccarollo & Capart, 2002*). Encouraging results have been obtained using four-equations models both from theoretical and modelling point of views.

In particular, a behavior of notable relevance in natural streams, i.e. the development of bed forms, cannot be addressed by three-equations model (*Cui & Parker, 1997*), but only considering the flow in vertical direction (*Kennedy, 1963, Engelund, 1970, Raudkiwi & Witte, 1990, Coleman & Melville, 1994, 1996*). It has been interpreted better by referencing to four-equations model. In more detail, linear stability analysis of a four-equations model showed an unstable behavior in regions where bed forms appear *(Vacca et al., 2003)*, so the stability region in mobile bed conditions is considerable smaller than the one of a fixed-bed model.

From the modelling point of view, *Leopardi et al. (2003)* reproduced satisfactorily the Benoist test using a four-equations model.

In order to better understand the behavior of this four-equations model, in the present work the flow over a mobile bed with an initial condition in which a small and smooth disturbance (bump) is superposed to an initially flat bed is solved. The scheme considered, thus, is similar to that used by *Lyn & Altinakar*

(2002) for the classical three-equations model. In their approach the equations were integrated by means of the Riemann Invariants computation, in the hypothesis of balance between friction and slope terms, and linearizing the equations.

One of the main results highlighted in *Lyn & Altinakar (2002)* is that the evolution of the bump is strongly influenced by the flow regime (subcritical, supercritical, transcritical).

In facts, in the hypocritical case, two perturbations originate from the bump, one positive (deposition) travelling downstream, and one negative (scour) travelling upstream, whose celerities are given by two of the characteristics slopes. In hypercritical flow, the same behaviour is observed, the only difference being the kind of perturbations: scouring downstream and deposition upstream. Finally, in the transcritical flow the bump is first eroded, than a nearly symmetric scour appears giving rise to a hole whose length increases with time. Direct numerical simulation of the full problem by the Authors did confirm such general behavior.

It can be seen that the eigenstructure of the model analysed strongly influences the way the bumps travel. This despite the fact that for the three-equations model, no critical state can be defined based upon the criterion of a vanishing celerity (*Liggett, 1993*). Such a behavior is not shared by *Di Cristo et al. (2002)* model, as it is shown in *Iervolino et al. (2003)*.

The object of the present note is to investigate more in depth the response of the four-equations model by *Di Cristo et al. (2002)* to an initially perturbed bed, via a mixed analytical–numerical procedure. In this approach the integration of the nonlinear system is performed by the characteristic method, with the mere linearisation the characteristic curves only.

2 MORPHODYNAMICAL MODEL

In what follows, the model proposed by *Di Cristo et al. (2002)* will be considered. This four-equations model can be written as:

$$\frac{\partial \mathbf{U}}{\partial t} + \mathbf{A}\frac{\partial \mathbf{U}}{\partial x} = \mathbf{S}$$

$$\mathbf{U} = \begin{bmatrix} h \\ u \\ z \\ u_p \end{bmatrix}; \mathbf{A} = \begin{bmatrix} u & h & 0 & 0 \\ g & u & g & 0 \\ 0 & 0 & 0 & \dfrac{G}{(1-p)} \\ 0 & 0 & a & u_p \end{bmatrix}; \mathbf{S} = \begin{bmatrix} 0 \\ -gS_f \\ 0 \\ S_4 \end{bmatrix} \qquad (1)$$

in which:
t: time;
x: space coordinate;
$h = h(t,x)$: depth;
$u = u(t,x)$: mean velocity;
$z = z(t,x)$: bottom elevation;
$u_p = u_p(t,x)$: average particle velocity in the bed-load transport layer;
g: gravity;
p: bed porosity;
$q_s = q_s(u_p)$: bed load volumetric discharge per unit width, where, according to the Authors, q_s may be considered a function of u_p only;

$$G = \frac{\partial q_s}{\partial u_p};$$

$a = g\Delta/(\Delta+1)$, where $\Delta = (\rho_s - \rho)/\rho$;
ρ: water density;
ρ_s: sediment density;
S_f: bottom friction term;
S_4: source term in sediment dynamical equation (see *Di Cristo et al., 2002*, for more details).

The following change of variables is introduced:

$$\zeta = z - z_0(x) \qquad (2)$$

The variable ζ represents the bed elevation respect to the original level z_0 pertaining to each abscissa. For an initially flat bed profile of slope S_b, it is obviously:

$$z_0(x) = -S_b x \qquad (3)$$

2.1 *Mathematical background*

System eigenstructure has been derived by *Iervolino et al. (2003)*. We recall that the four eigenvalues are:

$$\lambda_{1,2} = u \mp \sqrt{gh};$$

$$\lambda_{3,4} = \frac{u_p \mp \sqrt{u_p^2 + \dfrac{4aG}{(1-p)}}}{2}$$

Resulting left eigenvectors, $\mathbf{v_i}$, i = 1, 4, are:

$$\mathbf{v_1} = \begin{pmatrix} 1 \\ -\dfrac{\sqrt{gh}}{g} \\ \dfrac{-(u_p - \lambda_1)\sqrt{gh}}{\dfrac{Ga}{1-p} + \lambda_1(\lambda_2 + 2u + u_p)} \\ \dfrac{\dfrac{G}{1-p}\sqrt{gh}}{\dfrac{Ga}{1-p} + \lambda_1(\lambda_2 + 2u + u_p)} \end{pmatrix}$$

$$\mathbf{v_2} = \begin{pmatrix} \dfrac{1}{\sqrt{gh}} \\ \dfrac{}{g} \\ \dfrac{(u_p - \lambda_2)\sqrt{gh}}{\dfrac{Ga}{1-p} + \lambda_2(\lambda_1 - 2u + u_p)} \\ -\dfrac{G}{1-p}\sqrt{gh} \\ \dfrac{}{\dfrac{Ga}{1-p} + \lambda_2(\lambda_1 - 2u + u_p)} \end{pmatrix}$$

$$\mathbf{v_3} = \begin{pmatrix} 0 \\ 0 \\ 1 \\ \dfrac{\lambda_3}{a} \end{pmatrix}; \quad \mathbf{v_4} = \begin{pmatrix} 0 \\ 0 \\ 1 \\ \dfrac{\lambda_4}{a} \end{pmatrix}$$

Finally, it is possible to compute Riemann Invariants. Multiplying system (1) by left eigenvectors one can obtain:

$$\mathbf{v_i}\frac{\partial \mathbf{U}}{\partial t} + \lambda_i \mathbf{v_i}\frac{\partial \mathbf{U}}{\partial x} = \mathbf{v_i A^{-1} S} \qquad (4)$$
$$i = 1,..,4$$

Riemann invariants are scalar functions $Q_i(\mathbf{U})$ characterized by $\partial Q_i/\partial \mathbf{U} = \mathbf{v_i}$; so they can be computed integrating eigenvectors components respect to system variables.

System (4) can be rewritten in terms of Riemann Invariants so:

$$\frac{dQ_i}{dt} = SV_i \qquad (5)$$
$$i = 1,..,4$$

in which:

$$\frac{d}{dt} = \frac{\partial}{\partial t} + \lambda_i \frac{\partial}{\partial x}$$
$$SV_i = v_i A^{-1} S$$

$$Q_1 = h - \sqrt{\frac{h}{g}}u - \frac{(u_p - \lambda_1)\sqrt{gh}\zeta}{\dfrac{aG}{1-p} + \lambda_1(u_p - \lambda_1)} \qquad (6)$$

$$+ \frac{G\sqrt{gh}\ln\left|aG + \lambda_1(u_p + \lambda_2 + 2u)(1-p)\right|}{\lambda_1(1-p)} \qquad (7)$$

$$Q_2 = h + \sqrt{\frac{h}{g}}u + \frac{(u_p - \lambda_2)\sqrt{gh}\zeta}{\dfrac{aG}{1-p} + \lambda_2(u_p - \lambda_2)} \qquad (8)$$

$$+ \frac{G\sqrt{gh}\ln\left|aG + \lambda_2(u_p + \lambda_1 - 2u)(1-p)\right|}{\lambda_2(1-p)} \qquad (9)$$

$$Q_3 = \zeta + \frac{u_p}{2a}\lambda_3 + \frac{\ln(2(1-p)\lambda_4)G}{1-p}$$

$$Q_4 = \zeta + \frac{u_p}{2a}\lambda_4 - \frac{\ln(2(1-p)\lambda_4)G}{1-p}$$

$$SV_{1,2} = \sqrt{gh}(S_b - S_f) + \frac{\lambda_3}{a}(S_4 - aS_b) \qquad (10)$$

$$SV_{3,4} = \frac{\lambda_3}{a}(S_4 - aS_b) \qquad (11)$$

2.2 *Integration technique*

Integration of system (5) can be performed in the following way.

An uniform, equilibrium flow is assumed as initial condition. Let us note that, according to the given definitions, such a configuration is characterised by constant values of the four variables (u, h, u_p, ζ).

The initial disturbance is then expressed in the form:

$$\zeta(x) = \delta \exp\left(-\frac{x}{L}\right)^2 \qquad (12)$$

where δ is the perturbation amplitude and $L = h_0$, the mean water depth, is the longitudinal scale of the bump.

Initial condition is computed in steady state, neglecting the friction term, and evaluating particle velocity through an equilibrium relation, according to the procedure shown in *Di Cristo et al. (2002)*.

The most important assumption is that changes in the characteristics slopes are negligible for all the integration, so that the characteristic curves are approximated by the straight lines of equations,

$$x = \lambda_i^0 t \qquad i = 1..4 \qquad (13)$$

where λ_i^0 is the i-th celerity valued at the initial state.

Being the characteristic paths known a priori, for a given time t_* it is possible to individuate the extension of the domain in which the perturbation affects the solution (Figure 1). Let us divide this domain into $N - 1$ intervals, bounded by N points. For each point, we can trace back the four characteristic curve to the $t = 0$ axis, thus individuating four intersections.

Along each characteristic curve, the equation (5) is written in the form:

$$Q_i^{t_*} = Q_i^0 + \int_0^{t_*} SV_i dt \tag{14}$$

To solve this equation, an estimation of the integral term is required. Here, the following predictor-corrector technique is used:
the equation is first solved assuming:

$$\int_0^{t_*} SV_i dt \cong SV_i^0 t_* \tag{15}$$

being:

$$SV_i^0 = SV_i\left(Q_i^0\right) = SV_i\left(u^0, h^0, u_p{}^0, \zeta_i^0\right) \tag{16}$$
$$i = 1..4$$

ζ_i^0 is computed where the i-th characteristic line intersects the $t = 0$ axis.

This permits to obtain an estimate of the solution at time t_*, as:

$$Q_i^+ = Q_i^0 + SV_i^0 t_* \tag{14a}$$

Which is used to compute again the source term in (14)

$$SV_i^+ = SV_i\left(Q_i^+\right) = SV_i\left(u^+, h^+, u_p{}^+, \zeta^+\right) \tag{17}$$
$$i = 1..4$$

$$Q_i^{++} = Q_i^0 + SV_i^+ t_* \tag{14b}$$

Both (14a) and (14b) represent, for $i = 1, \ldots, 4$, a system of non-linear algebraic equations respectively in the four unknowns (u^+, h^+, u_p^+, ζ^+) and (u^{++}, h^{++}, u_p^{++}, ζ^{++}).

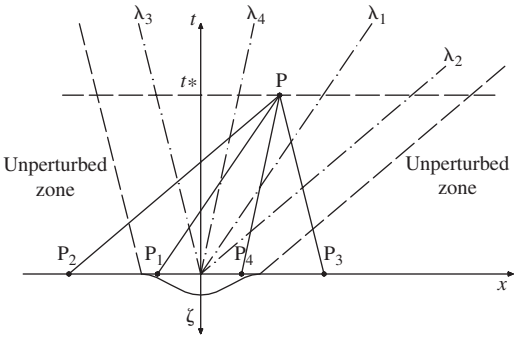


Figure 1. Conceptual sketch (hypercritical flow).

The commercial software Maple™was used to solve numerically the two systems.

Finally, the variables at time $t = t_*$ are computed as:

$$\begin{aligned} u^{t_*} &= \frac{u^+ + u^{++}}{2} \\ h^{t_*} &= \frac{h^+ + h^{++}}{2} \\ u_p{}^{t_*} &= \frac{u_p{}^+ + u_p{}^{++}}{2} \\ \zeta^{t_*} &= \frac{\zeta^+ + \zeta^{++}}{2} \end{aligned} \tag{18}$$

If the solution is known at a sufficiently high number of points, a numerical integration of the bed profile can be performed. Because the initial flow is in equilibrium, the sediment mass in the perturbed region should remain constant. This procedure has been used as a check of the accuracy of the solution technique here presented. With a sufficiently high spatial resolution, the error in sediment mass has been maintained below 1% respect to the initial mass for all the computations. This residual error seems to be imputable to the hypothesis of constant characteristics slopes for $t > 0$.

3 RESULTS

In *Iervolino et al. (2003)* system characteristics were computed. It has been shown that for Froude number less than one, two positive and two negative slopes exist, while for hypercritical conditions three downstream-directed celerities and one upstream-directed characteristic celerity (which is the situation depicted in Figure 1) are found. More in detail, the Table 1 reports data relative to the cases examinated.

Results are plotted in non dimensional form; the length and time scale for normalization are assumed to be L and L/λ_4, respectively, while the ζ values are scaled respect to the initial bump height, δ.

The first case (Figure 2) corresponds strictly to the example discussed in *Lyn & Altinakar (2002)*. In that reference, a linearised model was considered, with the further assumption of balance between friction and slope terms (the so-called quasi-uniform hypothesis).

Table 1.

Case number	δ/h_0	F_r
1	10^{-5}	0.98
2	10^{-4}	0.98
3	10^{-3}	0.98
4	10^{-5}	1.02
5	10^{-5}	1.10

The computation reproduced here was made through a finer approximation, because the friction and slope terms are taken account separately and only the linearization of characteristic slopes is used. Results here obtained are similar from a quantitative and qualitative point of view, to those by Lyn and Altinakar, so their assumption seems to catch the main features of the phenomenon. Of course a major conceptual difference between the two computations exists, due to the different transport models applied.

Two bed waves are found: a deposition wave, moving downstream with the celerity λ_4, and a scouring wave moving upstream with celerity λ_3.

In order to better understand the influence of the quasi-linear approximation here adopted, we repeated the computation increasing the ratio of the bump height to the undisturbed water depth.

In Figures 3 and 4 results are shown, for a ratio δ/h_0 of 10^{-4} and 10^{-3}, respectively. In both cases, the qualitative feature of the evolution does not change, and a growing bump propagating downstream is observed.

The bump growth rate, defined as the ratio of the bump non dimensional height at two different non dimensional times (2 and 3) to the time gap between them, seems to depend on the initial bump height itself. In fact, in Figure 5 it is shown that, for a Froude number of 0.84, it exists a bump height to which corresponds a maximum in the non dimensional growth rate. It can be conjectured that a particular bump height exists, corresponding to a vanishing growth rate, giving a stable, even if moving, perturbation.

Two additional tests were made for hypercritical conditions. The first (Figure 6) corresponds again to an example discussed in *Lyn & Altinakar (2002)*. In our computations, from the original bump, two perturbations arise: one of scour and one of deposition, just like the results by Lyn and Altinakar. However, both waves travel downstream, while the two previous Authors found the deposition wave to travel upstream. It is interesting to note that this latter wave moves with

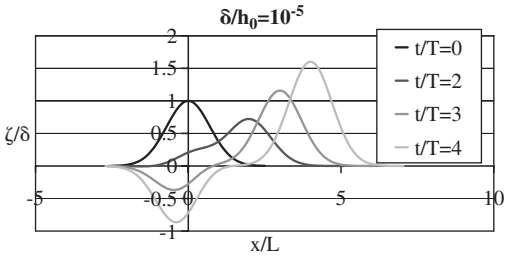


Figure 2. Hypocritical test of Lyn & Altinakar (case 1).

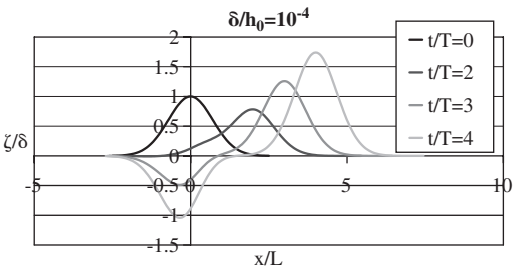


Figure 3. Hypocritical test (case 2).

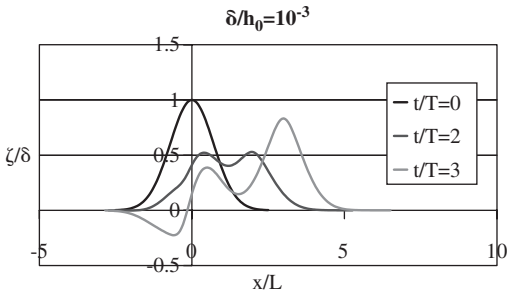


Figure 4. Hypocritical test (case 3).

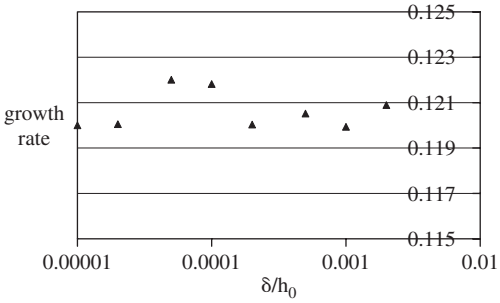


Figure 5. Growth rate between $t/T = 2$ and $t/T = 3$ as a function of the initial bump height ($Fr = 0.84$).

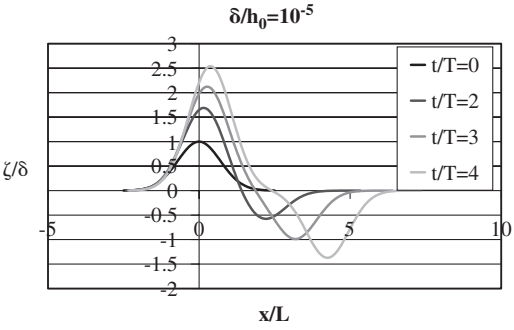


Figure 6. Hypercritical test (case 4).

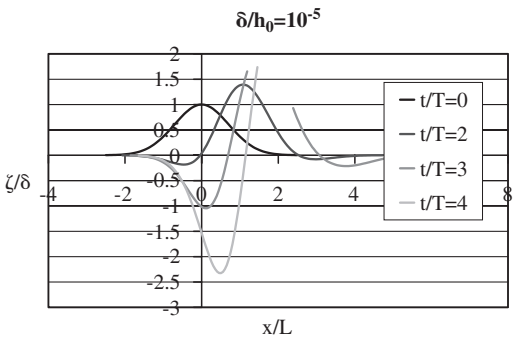


Figure 7. Hypercritical test (case 5).

a celerity corresponding to $\lambda_1 = u - \sqrt{gh}$, and, while directed downstream, lays behind the erosion wave as in Lyn and Altinakar work.

The same behavior (Figure 7) is observed for a greater Froude number. The difference in propagation direction could be explained through the different eigenstructure between the two models.

For this latter example, the solution has not been plotter where the corresponding celerities differed of more than 1% respect to the values at $t = 0$.

Indeed, useful information can be inferred from the results here presented. It has been shown that none of the four celerities can be definitely associated with only bed or water surface propagation, at least as soon as finite amplitude perturbations are considered. As a way of principle, all the the four celerities could carry information, triggered by a bed perturbation, relative to the bed evolution, even the ones which have the same expression of the fixed-bed model celerities.

It seems that in the range of Froude number and bump height here considered, initial bed disturbance affects the bed evolution only downstream in hypercritical streams, both downstream and upstream in hypocritical flows.

4 CONCLUSIONS

In the present note the behavior of a small, but finite, bed perturbation was analyzed.

Starting from an initial flat bed with a small and smooth perturbation (bump), integration of a morphodynamical four-equations model was performed through a linearized method of characteristics.

When dealing with hypocritical flows, two bed waves are found, one which is a deposition wave, moving downstream with the celerity λ_4, and a scouring wave moving upstream with celerity λ_3.

Both perturbations grows in magnitude with time, and the bump growth rate seems to depend on the initial bump height itself. So, it may be conjectured that a particular height corresponds to a vanishing growth rate, giving a stable, even if moving, perturbation.

In our computations in hypercritical flow, from the original bump, two perturbations arise: one of scour and one of deposition, just like the results by *Lyn and Altinakar (2002)*. However, both waves travel downstream, while the two previous Authors found the deposition wave to travel upstream.

So, it seems that in the range of Froude number and bump height here considered, initial bed disturbance affects the bed evolution only downstream in hypercritical streams, both downstream and upstream in hypocritical flows.

Even though the direct practical implications of the above analysis are likely limited (only under well-controlled laboratory conditions, uncertainties in mobile-bed measurements are sufficiently large that the small bed perturbations required for the linear theory to hold cannot be adequately followed), results permit to better understand the way by which the analysed four-equations model conveys information related to a disturbance.

ACKNOWLEDGMENTS

The writers would like to thank prof. Massimo Greco (University of Napoli "Federico II") and Dr. Andrea Vacca (Second University of Napoli) for their interesting suggestions which permitted to improve quality of present work.

REFERENCES

Armanini, A. & Di Silvio, G. (1988) – *A one-dimensional model for the transport of a sediment mixture in non-equilibrium conditions.* Journal of Hydraulic Research, IAHR, vol. 26, n. 3.

Benoist, G. (1983) – *Calcul del'érosion d'une digue par surverse.* EDF Internal report HE 43/83–31.

Benoist, G. (1989) – *Les ètudes d'ondes de submersion des grand barrages d'EDF.* La Houille Blanche, n. 1, pp. 43–54.

Coleman, S.E. & Melville, B.W. (1994) – *Bed-form development.* Journal of Hydraulic Engineering, ASCE, vol. 120, n. 5, pp. 544–560.

Coleman, S.E. & Melville, B.W. (1996) – *Initiation of Bed Forms on a Flat Sand Bed.* Journal of Hydraulic Engineering, ASCE, vol. 122, n. 6, pp. 301–310.

Correia, L.R.P., Krishnappan, B.G. & Graf, W.H. (1992) – *Fully coupled unsteady mobile boundary flow model.* Journal of Hydraulic Engineering, ASCE, vol. 118, n. 3, pp. 476–494.

Cui, Y. & Parker, G. (1997) – *Linear analysis of coupled equations for sediment transport*. Proceedings of the XXVII IAHR Congress, San Francisco, USA, 1256–1261.

de Vries, M. (1965) – *Considerations about non steady bed load transport in open channels.* Proceedings of the 11th IAHR Congress, Leningrad, URSS.

Di Cristo, C., Leopardi, A. & Greco, M. (2002) – *A bed load transport model for non-uniform flows.* Proceedings of Int. Conference "River Flow 2002", Louvain-la-Neuve, Belgium, 3–6 September 2002, Balkema, Rotterdam.

Engelund, F. (1970) – *Instability of erodible beds*. Journal of Fluid Mechanics, vol. 42, part 2, pp. 225–244.

Fraccarollo, L. & Capart, H. (2002) *Riemann wave description of erosional dam-break flows.* Journal of Fluid Mechanics, vol. 461, pp. 183–228.

Graf, W.H. (1998) – *Fluvial Hydraulics*, Wiley.

Iervolino, M., Leopardi, A. & Vacca, A. (2003) – *Some remarks on a morphodynamical model for gravel bed streams.* Proceedings of XXX IAHR Congress, Thessaloniki, 24–29 August 2003.

Kennedy, J.F. (1963) – *The mechanics of dunes and antidunes in erodible-bed channels*. Journal of Fluid Mechanics, vol. 16, part 4 pp. 521–544.

Leopardi, A., Oliveri, E. & Greco, M. (2003) – *Numerical simulation of gradual earth-dam failure.* L'Acqua, n. 2, pp. 47–54.

Liggett, J.A. (1993) – *Critical depth, velocity profiles, and averaging.* Journal of Irrigation and Drainage Engineering, ASCE, 119(2), pp. 416–422.

Lyn, D.A. & Altinakar, M. (2002) – *St. Venant-Exner equations for near-critical and transcritical flows.* Journal of Hydraulic Engineering, ASCE, vol. 128, n. 6, pp. 579–587.

Meyer-Peter, E. & Muller, R. (1948) – *Formulas for Bed-Load-Transport.* Proceedings of 2nd IAHR Congress, Stockolm, 1948.

Nakagawa, H. & Tsujimoto, T. (1980) – *Sand Bed Instability due to Bed Load Motion.* Journal of Hydraulic Division, ASCE, vol. 106, n. HY12, pp. 2029–2051.

Phillips, B.C. & Sutherland, A.J. (1989) – *Spatial lag effect in bed load sediment transport.* Journal of Hydraulic Research, IAHR, vol. 27, n. 1, pp. 115–133.

Raudkivi, A.J. & Witte, H.H. (1990) – *Development of bed features.* Journal of Hydraulic Engineering, ASCE, vol. 116, n. 9, pp. 1063–1079.

Vacca, A., Iervolino, M., Leopardi, A. & Greco, M. (2003) – *Linear Analysis of 1D Flow on Movable Bed*. Proceedings of RCEM 2003, 3rd IAHR Simposium on River, Coastal and Estuarine Morphology, Barcelona 1–5 Settembre 2003.

This page intentionally left blank

River Flow 2004 – Greco, Carravetta & Della Morte (eds.)
© 2004 Taylor & Francis Group, London, ISBN 90 5809 658 0

Bar height formulas to predict the maximum scour depth at riverbanks

G. Del Giudice, G. Rasulo & E. Viparelli
Department of Hydraulic and Environmental Engineering G. Ippolito,
University of Naples Federico II Naples, Italy

ABSTRACT: Floods in alluvial rivers are characterized by channels incision in the alluvial bed during the rising stage and their filling up in the falling stage; this phenomenon is well known and called scour and fill. In this work scour and fill during floods will be described as bar migration in the alluvial bed; when bar trough reaches the riverbank protection, the undermining of longitudinal protection structures may occur if the river bed level is lower than the bank foundation structure. Scour or trough depths below the average riverbed level can be predicted with formulas calibrated using flume data or derived theoretically. In this paper four different formulas for alternate bars will be discussed and their applicability to field data is tested. A simple criterion for riverbank foundation depth estimate is proposed and its applicability to braided rivers is derived by using a correction factor.

1 INTRODUCTION

During flood rising stages velocity and shear stress on the bed increase and the channel bed tends to scour; during falling stages the shear stress decreases and the bed fills. Channel scour and fill are words used to define bed cutting and sedimentation during relatively short periods of time, whereas the terms degradation and aggradation apply to similar processes that occur over a longer period of time. Scour and fill involve times measured in minutes, hours, days, perhaps even a season, whereas aggradation and degradation apply to persistent mean changes over periods of time measured in years (Leopold et al., 1964).

Major scour can be locally caused by transverse structures built in the middle of the alluvial bed or jutting out into it and by the presence of huge boulders in the bed or near the banks. Therefore in alluvial riverbeds each obstacle, which causes whirling motion and alters the sediment exchange between stream and bed, causes rapid local scours or fills, owing to the continuous variations of discharges and stream direction (Viparelli, 1972).

In technical literature many indications are given to predict local scour depths (Raudkivi, 1998) but it is difficult to estimate the scour that a flood causes in alluvial channels without transverse obstacles. In this work scour and fill during a flood will be described as bar movement in the alluvial bed: scour occurs on bar troughs and fill on the crests.

Bars can be classified relative to their position in the bed and their orientation towards the stream direction. Alternate bars are typical of streams flowing in a single channel: these bedforms grow near the banks so the stream flows assuming a pseudomeandering thalweg. In braided rivers the stream flows in two or more channels in the valley and the bars can grow both near the banks and in the middle of the bed, causing the flow to split. They are differently named depending on their orientation towards the stream direction (central, diagonal, transverse, midchannel…) (Leopold & Wolman, 1957; Raudkivi, 1998).



Figure 1. Riverbank protections undermined along Basento river in southern Italy.

During floods bars are in movement in the alluvial bed and their troughs can reach riverbank protection toes causing undermining, if the trough depth below the average bed level is lower than the foundation depth (Fig. 1).

In this paper four formulas to predict trough depths will be briefly described and then estimated and measured scour depths will be compared by means of field data.

2 DESCRIPTION OF FORMULAS

All the considered formulas described in this paper predict the trough depth below the average bed level for rivers with alternate bars.

Three of them use laboratory experiments (Kishi, 1980; Jaeggi, 1984; Ikeda, 1984); the other, on the contrary, results of a mathematical model describing the development of a finite-amplitude alternate bar in a straight channel with erodible bottom (Colombini et al., 1987; Seminara & Tubino, 2003).

In all the flume experiments both the banks and the bottom of the channels were modelled; therefore, these formulas describe alluvial rivers with alternate bars. On the contrary, Seminara's formula, based on the hypothesis of fixed banks, describes alternate bars in reaches where the bottom is much more erodible than the banks.

Maximum trough depths below the average bed level (S) are considered as a fraction of the bar height defined as the elevation difference between the highest and the lowest point in a bar unit (H_{BM}) or in a cross section (H_B). The difference between H_{BM} and H_B is defined in Figure 2.

Kishi and Kuroki

Bar heights and scour depth are maximum along the side walls of a channel and minimum along the centre line (Kishi, 1980). The bar height along the channel wall can be estimated with

$$H_{BM} = B/20 \tag{1}$$

where B is the channel width (Fig. 2).

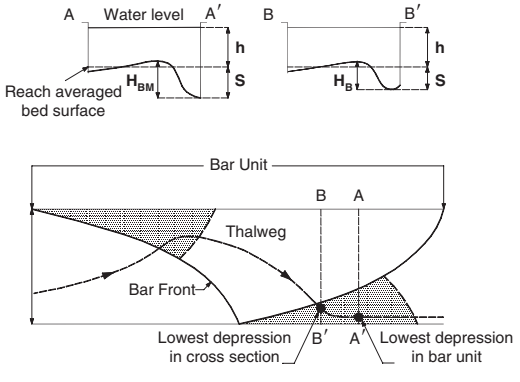


Figure 2. Definition sketch of alternate bars; hatching and broken line indicate pools and thalweg, respectively.

Following Jaeggi to be discussed below, the scour depth can be estimated with

$$S = 0.76\ H_{BM} \tag{2}$$

Jaeggi

From laboratory experiments in a 30 cm wide flume Jaeggi found that the total bar height (H_{BM}) is much higher for alternate bars than for others bedforms, including central bars (Jaeggi, 1984).

He also underlined that H_{BM} is almost independent of discharge and slope and that the ratio of maximum scour depth (S) to the total height seems to be fairly constant and equal to 0.76 for all experiments.

His results are described as

$$S = 0.76\ H_{BM} = B/(6Z_B^{0.15}) \tag{3}$$

where $Z_B = B/d_{50}$, B is the channel width and d_{50} is the median diameter of the particle size distribution of the material used.

Ikeda

In examining his laboratory tests Ikeda found a linear relationship between S and H_B as

$$S = 0.75\ H_B \tag{4}$$

$$H_B = h \cdot (B/d_{84})^{-0.45} \cdot \psi(B/h) \tag{5}$$

Here h is the mean depth of flow and the function $\psi(B/h)$ (Fig. 3) is defined for $B/h \leq 70$, considering $B/h = 70$ as the upper limit of the alternate bar formation region.

For $B/h > 70$–100 alternate bars disappear and multiple bars develop, which characterise the braided river pattern (Ikeda, 1984).

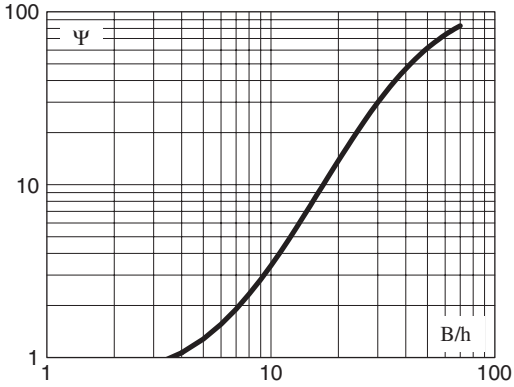


Figure 3. Function Ψ(B/h) (Ikeda, 1984).

The maximum scour depth below the average bed level is considered as a fraction of the total bar height

$$S = 0.57\ H_{BM} \tag{6}$$

$$H_{BM} = h \cdot \{b_1 \cdot [(\beta - \beta_c)/\beta_c]^{0.5} + b_2 \cdot [(\beta - \beta_c)/\beta_c]\} \tag{7}$$

Here $\beta = B/(2h)$ and b_1, b_2, and β_c are functions of the ratio d/h and the Shield's parameter (θ); these functions are defined for $0.001 \leq d/h \leq 0.05$ and $0.05 \leq \theta \leq 0.5$. Therefore, H_{BM} can be considered as a function of channel width B, average stream depth for the uniform unperturbed flow h, average slope i and diameter of sediment modelled as unigrains d. This formula can be applied for $\beta \leq 2\beta_c$.

3 FIELD DATA

The described formulas have been tested with flume data; predicted scour depths have to be compared with measured scours along natural rivers to investigate these formulas applicability for designing.

Field data available in technical literature are unfortunately scarce and can be classified in three groups: Scour depth measured with scour-chains, Scour depth measured with load-cell sensors and Scour depth measured at the United State Geological Survey (USGS) gaging stations.

Measuring stations equipped with scour-chains were installed along Quatal Creek (Foley, 1975) and Redwood Creek (Madej, 1995) in California. These are two small rivers with coarse riverbed material.

Measurements with load-cell sensors were performed on Torrente Serrapotamo in Southern Italy (Penta et al., 1977a and 1977b; Penta et al., 1980). Load-cell sensors give more information than scour-chains because of their ability in showing the cross section evolution during a flood while the chains only measure the maximum scour depth.

Scour measurements at the USGS gaging stations were performed on the Redwood Creek and they describe the cross section evolution during floods. Gaging stations are usually characterized by restricted laterally flows, causing deeper vertical scour than in unconfined sections.

Other field measurements available in technical literature are bar heights (H_{BM}); these can be considered as a fourth class of measures to test the previously described formulas. Bar heights were measured in Washington State along Jenkins, May and Swamp Creek (Konrad et al., 2002). Field data are reported in Appendix.

4 SCOUR INTERPRETATION

As previously mentioned, this paper aims to compare predicted with measured scour depths along alluvial rivers. All the described formulas predict the maximum trough depth below the average bed level as a bar height fraction.

Field data, on the contrary, give the maximum measured scour depth in a cross section. It may happen that in a cross section the maximum scour depth occurs far from the sensor (scour-chain, load cell…); therefore, in cross sections with a significant number of sensors (nine on Torrente Serrapotamo) measured scour depths can be considered as maximum, while in other sections with less sensors only a rough approximation of the maximum value may be made.

It is well known that the bar migration celerity in alluvial beds is much smaller than the flood wave celerity. Considering that all the measuring stations refer to small basins, floods should persist for only few hours and bar troughs can not cross the measuring section. Therefore, the recorded scour depths could be smaller than the maximum trough depths below the average bed level. It is logical to expect that scour depth prediction should be larger than recorded field data.

5 INTERPRETATION OF FORMULAS

All the experimental formulas mentioned have been tested with flume yet indications for their applicability to natural rivers are hardly mentioned.

Jaeggi pointed to the good agreement between scour depth predictions and measurements by replacing the channel width B with $B'' = B\text{-}2nS$, where 1/n is the bank slope and S is the scour depth. His formula can be rewritten as

$$S = 0.76\ H_{BM} = B''/(6Z'^{0.15}_{B}) \tag{3'}$$

where $Z'_B = B''/d_{50}$ and the scour depth (S) has to be found by iteration.

Ikeda illustrated the applicability of his formula to natural rivers comparing predicted and measured bar heights along the Naka River, Japan. The calculated bar height is 7.20 m while the measured value is 5.68 m.

Applying the described formulas to natural rivers is not as easy as it seems. Each river is different, therefore it is fairly impossible to classify them in a rigorous way. Moreover several parameters, as defined in the laboratory and by theoretical models cannot be easily estimated.

For this reason, it seems necessary to underline how the experimental parameters will be considered in this work, how rivers can be distinguished between alternate bars and braided forms and how formulas for alternate bars will be applied to predict scour depths along braided rivers.

Riverbed material

In natural alluvial rivers the particle size distribution is characterized by a coarser and a finer fraction. It is necessary to describe the riverbed material movement referring to a coarser fraction diameter in order to consider the armouring effect.

In this work the riverbed material will be described by d_{90} of the particle size distribution; only along Redwood Creek the median diameter d_{50} of the particle size distribution will be considered because of lack of d_{90} value.

Active riverbed width

All the experimental formulas consider the scour depth as a function of channel width B. In this work B is considered as the active riverbed width.

In narrow reaches the active riverbed coincides with the valley; on the contrary, in reaches where even during rare floods the stream only flows in a part of the valley (large reaches), the active riverbed width has to be determined.

All the reaches, considered in this work, are not very large: during high flow the active floodplain coincides with the whole valley. Therefore, the active bed will be considered as wide as the whole valley.

Gaging stations are characterised by restricted lateral flows, therefore the active floodplain is narrower than the valley; in this work the restricted width will be considered as B in the experimental formulas.

Water depth

It is important to underline that the field data do not always give the average water depth, a parameter necessary to apply Ikeda and Seminara formulas. In this work the average water depth will be estimated with the Gauckler and Strickler formula, hypothesising a rectangular cross section and a friction factor equal to 35 $m^{1/3}/s$.

Braided rivers

In this work rivers are distinguished between "rivers with alternate bars" and "braided rivers" (Kishi, 1980) using Kishi and Kuroki's bed form chart (Fig. 4). In this chart the transition region and the existence regions of alternate bars and braided rivers are plotted as functions of the ratio of shear velocity and its critical value (u^*/u_c^*) and the parameter Bi/h, where B is considered as the active bed width, i is the average riverbed slope and h is the average water depth.

This classification is quite simple and shows whether the described formulas can be applied or not. It is not possible to state how many channels characterise braided rivers.

The number of channels that the stream incises in the alluvial bed of braided rivers is an important parameter to extend formulas for alternate bars to braided rivers.

Alternate bar heights depend mainly on the channel width (B) (Kishi, 1980), a parameter that is here interpreted as the active bed width along natural rivers. Braided rivers are characterised by two or more channels and the active bed width is, in general, larger than that of alternate bar streams while the scour depth is smaller (Jaeggi, 1984). In this paper experimental formulas to predict scour depths will be applied along braided rivers considering the active bed width of each channel $B' = B/m$, where m is the number of channels (Rossi & Silvagni, 1983).

6 COMPARISON BETWEEN PREDICTED AND MEASURED SCOUR DEPTHS

In this paragraph river patterns will be predicted using Kishi and Kuroki's diagram (Fig. 5), then estimated and measured scour depths will be compared. Finally all the formulas will be applied along Torrente Serrapotamo to discuss the extension of formulas for alternate bars to braided rivers.

Kishi and Kuroki's bed form chart shows that all field data along American rivers are in the alternate bars and in the transition regions. Considering that in the transition region alternate bars can develop and that the authors describe bars in their works, all the American rivers will be considered with alternate bars.

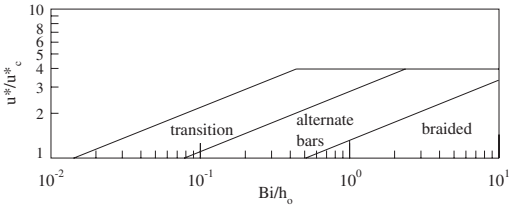


Figure 4. Kishi and Kuroki's bed form chart (Kishi, 1980).

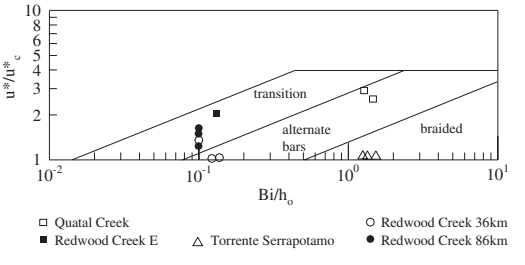


Figure 5. Field data in Kishi and Kuroki's bed form chart.

Kishi and Kuroki

The maximum scour depth was predicted along all the rivers where measurements were performed, because of all the field data report the active bed width (Fig. 6 and Table 1).

Bar heights, measured along Jenkins, May and Swamp Creek, have been multiplied by 0.76 to transform them in scour depths.

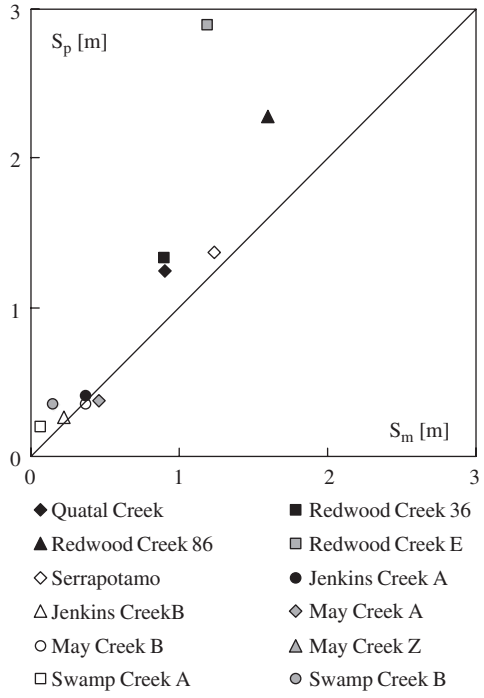


Figure 6. Comparison between measured and predicted scour depths according to Kishi and Kuroki's formula.

Table 1. Comparison between measured (S_m) and predicted (S_p) scour depths according to Kishi and Kuroki's formula.

River	S_m [m]	S_p [m]	$(S_p - S_m)/S_m$ [%]
Quatal Creek	0.90	1.25	38
Redwood Creek 36	0.90	1.33	48
Redwood Creek 86	1.60	2.28	43
Redwood Creek E	1.20	2.90	141
Torrente Serrapotamo	1.24	1.37	10
Jenkins Creek A	0.38	0.40	5
Jenkins Creek B	0.23	0.27	17
May Creek A	0.46	0.38	−17
May Creek B	0.38	0.34	−10
May Creek Z	0.15	0.34	125
Swamp Creek A	0.08	0.19	150
Swamp Creek B	0.15	0.34	125

Kishi and Kuroki's formula tends to underestimate the scour depth only along May Creek, a very narrow stream with a steep slope. In the other three sections of rivers with very narrow banks and high slopes the formula tend to overestimate the scour depth (May and Swamp Creek). Because the bar height depends only on the active bed width, this formula cannot predict the bar height with sufficient accuracy in very narrow reaches.

In section E of the Redwood Creek this formula overestimates again the scour depth; this section was equipped with 3 or 5 scour chains and is about 76 m wide from one bank to the other. The measured scour depth cannot be considered as the maximum in the section because of very few sensors used to monitor the riverbed evolution. Moreover, it is possible that the stream does not flow in a single channel in this reach because the average slope is higher than in the up and downstream reaches. If this hypothesis is true, the scour depth should have been estimated for a braided river.

In all the other sections the difference between the measured and predicted scour depths do not seem very appreciable considering that the authors give this formula to roughly estimate the bar height: the percent error is smaller than 50%.

Jaeggi

This formula predicts the maximum scour depth as a function of the active bed width and the characteristic diameter of the riverbed material.

As said before, defining the characteristic diameter of the riverbed material is not easy, therefore the formula has been applied twice, once using the median diameter of the particle size distribution (Fig. 7 and Table 2) and then referring to d_{90} of the same distribution (Fig. 8 and Table 3).

As done for the Kishi and Kuroki's formula, bar heights were multiplied by 0.76 to transform them in scour depths.

Jaeggi's formula tends to overestimate the scour depth if d_{90} is used to describe the riverbed material instead of d_{50}: the percent errors are all larger than 50% and they show that this formula tends to overestimate scour depth.

Significant differences between predicted and recorded scour depths occur in the same sections as observed using Kishi and Kuroki's formula; while in the other sections this formula tends to overestimate the scour depth more than the Kishi and Kuroki's relation.

Ikeda

The maximum scour depth is considered as a function of the active bed width, the diameter of riverbed

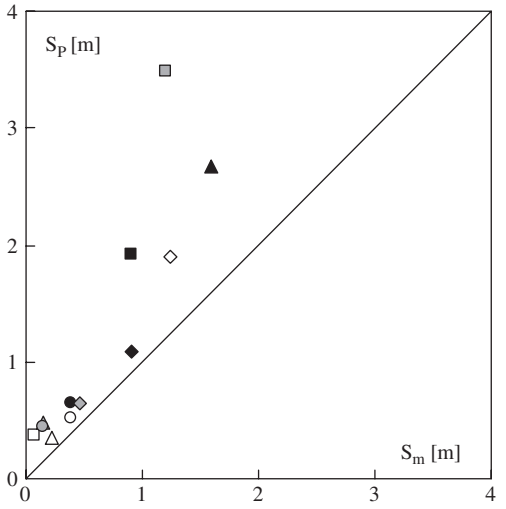


Figure 7. Comparison between measured and predicted scour depths according to Jaeggi's formula for $d = d_{50}$. Symbols as in Figure 6.

Table 2. Comparison between measured and predicted scour depths according to Jaeggi's formula for $d = d_{50}$.

River	S_m [m]	S_p [m]	$(S_p - S_m)/S_m$ [%]
Quatal Creek	0.90	1.08	21
Redwood Creek 36	0.90	1.92	114
Redwood Creek 86	1.60	2.68	67
Redwood Creek E	1.20	3.48	190
Torrente Serrapotamo	1.24	1.90	53
Jenkins Creek A	0.38	0.65	70
Jenkins Creek B	0.23	0.35	55
May Creek A	0.46	0.65	43
May Creek B	0.38	0.51	35
May Creek Z	0.15	0.48	216
Swamp Creek A	0.08	0.38	396
Swamp Creek B	0.15	0.45	193

material coarser fraction and the average water depth (h). Therefore in the measuring stations, where several flood discharges were reported, it has been possible to predict different scour depths. In this work only the maximum and the minimum estimates are considered to define a range variation for scour depth prediction (Fig. 9 and Table 4).

This formula cannot predict scour depth along Jenkins, May and Swamp Creek, because of lack of flood discharge and average water depth measurements in the reference article.

The formula was applied even for $B/h > 70$ extrapolating the function ψ (Quatal Creek, where $B/H = 95$, and Torrente Serrapotamo, where $B/h = 106$–118).

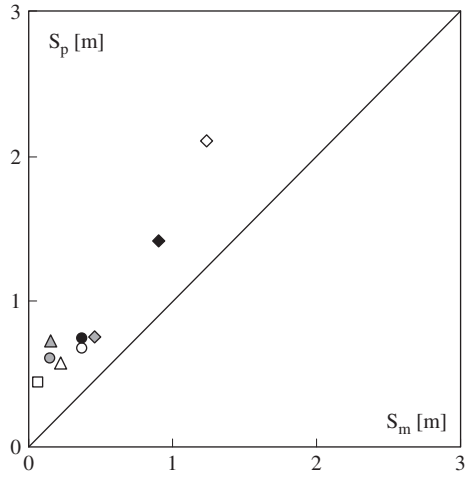


Figure 8. Comparison between measured and predicted scour depths according to Jaeggi's formula for $d = d_{90}$. Symbols as in Figure 6.

Table 3. Comparison between measured and predicted scour depths according to Jaeggi's formula for $d = d_{90}$.

River	S_m [m]	S_p [m]	$(S_p - S_m)/S_m$ [%]
Quatal Creek	0.90	1.42	58
Torrente Serrapotamo	1.24	2.10	69
Jenkins Creek A	0.38	0.74	95
Jenkins Creek B	0.23	0.57	152
May Creek A	0.46	0.75	65
May Creek B	0.38	0.68	79
May Creek Z	0.15	0.73	381
Swamp Creek A	0.08	0.44	485
Swamp Creek B	0.15	0.61	300

In Quatal Creek, Ikeda's formula underestimates the scour depth; it is important to underline that this reach is steep and that the formula was used for $B/h > 70$. In all the other sections the formula tends to overestimate the scour depth without differences with the previously described formulas.

Seminara

The maximum scour depth is considered as a function of the active bed width, the characteristic diameter of the riverbed material, the average water depth and the average slope through the function b_1, b_2, and β_c.

A range variation of scour depth prediction was applied because the formula depends on the average water depth. The scour depth along Jenkins, May and Swamp Creeks was not calculated because of

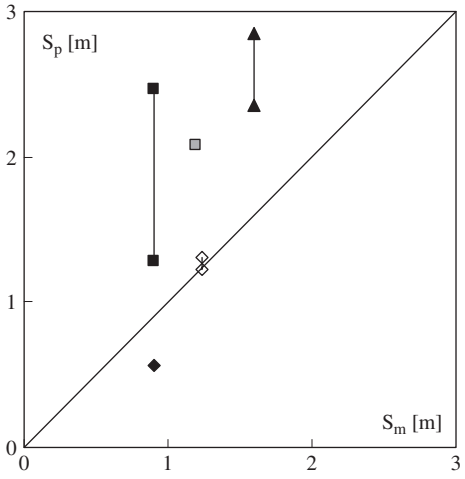


Figure 9. Comparison between measured and predicted scour depths according to Ikeda's formula; points connected by lines are the minimum and the maximum scour depths predicted along a river, where several discharges were recorded. Symbols as in Figure 6.

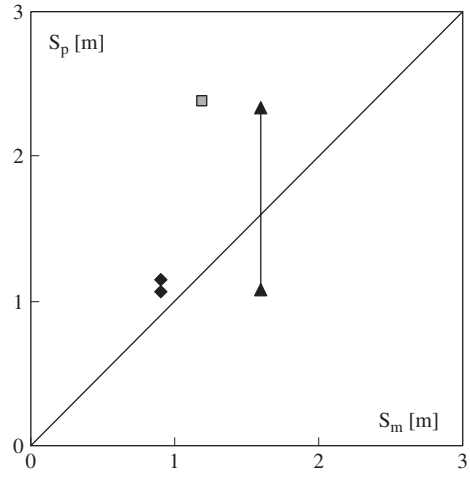


Figure 10. Comparison between measured and predicted scour depths according to Seminara's formula; points connected by lines are the minimum and the maximum scour depth predicted along a river, where several discharges were recorded. Symbols as in Figure 6.

Table 4. Comparison between measured and predicted scour depths according to Ikeda's formula.

River	S_m [m]	S_p [m]	$(S_p - S_m)/S_m$ [%]
Quatal Creek	0.90	0.56	−38
Redwood Creek 36	0.90	1.28 2.47	42 174
Redwood Creek 86	1.60	2.35 2.85	47 78
Redwood Creek E	1.20	2.07	73
Torrente Serrapotamo	1.24	1.22 1.31	−2 6

Table 5. Comparison between measured and predicted scour depths according to Seminara's formula.

River	S_m [m]	S_p [m]	$(S_p - S_m)/S_m$ [%]
Quatal Creek	0.90	1.06 1.15	18 28
Redwood Creek 86	1.60	1.08 2.33	−33 46
Redwood Creek E	1.20	2.37	98

lack of field data. Furthermore along the Torrente Serrapotamo and at the USGS gaging station at the 36th kilometre from the Redwood Creek head either, the inapplicability of formula was stated because of functions b_1, b_2, and β_c being not defined for those reaches characteristics (Fig. 10 and Table 5).

The percent difference between the predicted and the measured scour depths are comparable with the other formulas but this relation was not applied along several rivers considered here because of lack of field data and a restricted range variability of its parameters.

6.1 *Scour depth prediction along braided rivers: Torrente Serrapotamo*

In this paper four formulas to predict the maximum scour depth below the average bed level are tested by comparing measured and estimated scour depths along natural rivers. All the experimental formulas predict the maximum scour depth in rivers with alternate bars; field measurements, on the contrary, were also performed along braided rivers.

Considering that few field data are available in technical literature and that riverbank protections are also built along alluvial rivers, it seems important to test the described formulas along braided reaches.

Scour depths in braided rivers are, in general, smaller than in alternate bar streams depending on a smaller bed-load transport capacity being the discharge split in two or more channels.

Scour depth predictions along Torrente Serrapotamo were performed with the stream flows in two channels divided by a central bar (Fig. 11); therefore the active bed width (B) was substituted by $B' = B/2$. These predictions show that there is not a significant difference between measured and estimated scour depths along that river. It is important to underline that Ikeda's formula, defined for B/h smaller than 70, predicts the scour depth with a small error of 6%, even if it has been used for $B/h > 70$.

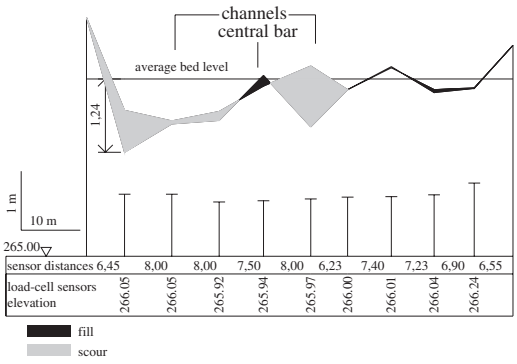


Figure 11. Cross section evolution along Torrente Serrapotamo. It is possible to identify two channels incised in the alluvial bed.

Table 6. Comparison between predicted scour depths along Torrente Serrapotamo, where $S_{measured} = 1.24$ m.

Formula	S (B) [m]	S (B′ = B/2) [m]
Kishi and Kuroki	2.74	1.37
Jaeggi d_{90}	3.33	2.10
Jaeggi d_{50}	2.92	1.90
Ikeda	Not applicable	1.22 1.31
Seminara	Not applicable	Not applicable

The suggested correction on the active riverbed width, used to extend the formulas to braided rivers, should be tested comparing the measured scour depths with predictions made with the whole active bed width (Table 6).

Scour depths predictions reported in Table 6 indicate that the extension of formulas for alternate bars to braided rivers seems to be possible if the active riverbed B is replaced by B′ = B/m, where m is the number of channels. This extension, like the practical use of described formulas, ought to be tested with other field data to deeply investigate their applicability to natural rivers.

7 CONCLUSIONS

A design criterion to estimate the riverbank foundation depth in alluvial rivers is derived assuming that the scour at the toe of riverbank corresponds to the trough depth of migrating bars.

The four considered formulas were tested with flume data but few indications are available for their applicability to natural river. Moreover, these formulas predict the scour depth along rivers with alternate bars but the authors do not give suggestions about scour depth estimation along braided rivers, where scour depths are smaller.

The comparison between predicted and measured scour depths underline that all the described formulas overestimate the scour depths with comparable errors.

Because of difficulty in defining natural river patterns and parameters, it seems logical to refer to a simple design criterion to estimate the maximum scour depth. Such a requirement is well satisfied by adopting, in rivers with alternate bars, the simple formula 0.76B/20, where B is the active riverbed width. Moreover, for braided rivers, formulas for alternate bars can be used considering the active riverbed width B′ = B/m, where m is the number of channels.

The estimated maximum scour depth should be finally multiplied with a safety factor to state the riverbank foundation depth.

ACKNOWLEDGEMENT

The authors would like to thank the reviewers for their useful comments and suggestions.

APPENDIX: FIELD DATA

A *Quatal Creek*

Quatal Creek is an ephemeral stream in the northwestern Ventura County, California. Its upper reach is on the western side of Cerro Noroeste (2526 m) and it is an eastern tributary of Cuyama River. Field data are summarized in Tables A1, A2.

Scour measurements were performed during the 1973–75 winters (Foley, 1975). In this period two important floods occurred (January and December 1974): the scour-chains measured scours of depths 0.4 and 0.9 m. Riverbed material has defined as coarse sand, of median diameter 1.99 mm and of standard deviation 6.15 mm; hypothesizing a Gaussian distribution for the bed material $d_{90} = 1$ cm.

B *Redwood Creek*

Redwood Creek is an alluvial river in northern California. It drains a 725 km^2 basin and is approximately 108 km long (Madej, 1995). Field data are summarized in Tables B1–B6. In Madej's work two approaches were used to estimate the depth of scour during winter floods: scour-chains were installed at seven cross sections (3 to 5 chains per section) and the USGS discharge measurement notes were used to state gaging stations evolution during floods.

Sections equipped with scour chains will be identified with letters A through G, gaging stations with their distance from the riverhead.

Table A1. Quatal Creek data.

A [km^2]	B* [m]	B [m]	i [%]	d_{50} [mm]	d_{90} [mm]
111	65	32.8	2.29	1.99	10

B* is the valley width and B is the active flood plain width.

Table A2. Measured flood data on Quatal Creek.

January 1974		December 1974	
h [m]	S [m]	h [m]	S [m]
0.229	0.4	0.344	0.9

Table B1a. Redwood Creek data at the USGS gaging station at 36 km.

A [km^2]	B* [m]	B [m]	i [%]	d_{50} [mm]	S [m]
175	45.7	35	0.5	45	0.9

Table B2a. Redwood Creek data at the USGS gaging station at 86 km.

A [km^2]	B* [m]	B [m]	i [%]	d_{50} [mm]	S [m]
523	82.3	60	0.2	22	1.6

Table B1b and B2b. Scour depths and discharges measured at the USGS gaging stations in the years 1974 to 1983, in bold maximum scour depth.

Gaging station at 36 km			Gaging station at 86 km		
Date	Q [m^3/s]	Scour depth [m]	Date	Q [m^3/s]	Scour depth [m]
19/02/75	180	0.6	**1/04/74**	**379**	**1.6**
26/02/76	78	0.3	26/02/76	207	0.8
26/02/76	65	0.3	26/02/76	200	0.8
28/02/79	40	0.3	14/12/77	456	1.0
13/01/80	59	0.2	15/12/77	259	0.6
14/01/80	77	0.3	19/01/78	136	0.6
22/12/81	32	0.5	28/02/79	140	0.4
26/01/83	**158**	**0.9**	14/01/80	231	0.8
			14/01/80	259	0.5
			10/02/82	270	0.6
			16/02/82	213	0.3

C *Torrente Serrapotamo*

Torrente Serrapotamo is an ephemeral stream that drains a 164 km^2 basin in carbonated formations; it is a left tributary of Sinni River in Basilicata, Italy

Table B3. Redwood Creek data at the scour-chain cross sections A and B.

A [km^2]	B [m]	i [%]	τ_o [t/m^2]	d_{50} [mm]	S [m]
454	39.6	0.4	0.00599	32	>0.6

Table B4. Redwood Creek data at the scour-chain cross sections C and D.

A [km^2]	B [m]	i [%]	τ_o [t/m^2]	d_{50} [mm]	S [m]
458	57.9	0.32	0.00671	32	>1.2

Table B5. Redwood Creek data at the scour-chain cross section E.

A [km^2]	B [m]	i [%]	τ_o [t/m^2]	d_{50} [mm]	S [m]
468	76.2	0.66	0.01183	32	1.2

Table B6. Redwood Creek data at the scour-chain cross section F and G.

A [km^2]	B [m]	i [%]	τ_o [t/m^2]	d_{50} [mm]	S [m]
729	140	0.12	0.0029	22	>1.8

Table C1a. Torrente Serrapotamo data at the load-cell sensors equipped cross section.

A [km^2]	B [m]	i [%]	d_{50} [mm]	d_{90} [mm]
164	72	1.2	15	33

(Penta et al., 1977a and 1977b; Penta et al., 1980). Field data are summarized in Tables C1a, C1b. The measuring station was equipped with nine load cell sensors to measure total (σ) and pore pressures (u) during floods. Knowing the specific weight of saturated riverbed material ($\gamma_{sat} = 2.35$ t/m^3) it was possible to draw the cross section:

$$\sigma = u + \sigma' = \gamma_w \cdot h + (\gamma_{sat} - \gamma_w) \cdot z_b,$$

where h and z_b are, respectively, the water and the bottom height above the sensor;

$$z_b = (\sigma - u) / (\gamma_{sat} - \gamma_w)$$

Table C1b. Measured discharges and scour depths at the loadcell sensors equipped cross section, in bold maximum scour depth.

Date	Q [m^3/s]	Scour depth [m]
02/11/77	36	0.96
07/12/77	27	0.83
03/04/78	42	0.93
20/10/78	28	1.13
31/10/78	30	1.17
05/01/79	37	1.20
12/01/79	43	0.81
15/02/79	20	1.09
04/11/79	33	1.03
16/11/79	31	1.08
12/01/80	**38**	**1.24**

Table D1. Jenkins Creek data at bar A.

B [m]	d_{90} [mm]	d_{50} [mm]	i [%]	H_{BM} [m]
10.5	68	30	0.1	0.5

Table D2. Jenkins Creek data at bar B.

B [m]	d_{90} [mm]	d_{50} [mm]	i [%]	H_{BM} [m]
7	111	48	0.6	0.3

The measuring station was 1.3 km upstream the stream mouth, the basin average height is 697 m. Torrente Serrapotamo in the monitored reach is braided with two channels.

D *Jenkins Creek*

Jenkins Creek drains a 37 km^2 basin on a glacial outwash plain in the Puget Lowland, Washington State. The mean discharge during the years 1989–1998 was 1.1 m^3/s at the King County station near the mouth. Flood recession is gradual and base flows are high relative to the other streams in the region (Konrad et al., 2002). Bar material is in general well sorted and the median diameter varies between 30 and 48 mm. Field data are summarized in Tables D1, D2. Two gravel bars were observed in the monitored reach: bar A is a midchannel bar in a straight reach and bar B is transverse and coarser than A.

E *May Creek*

May Creek drains a 32 km^2 basin with steep headwaters and extensive glacial till deposits in the Puget Lowland, Washington State. The mean discharge during the years 1989–1998 was 0.7 m^3/s at King County station near the mouth. Floods are characterised by relatively high peaks and rapid recession rates (Konrad et al., 2002) and base flows are low. Field data are summarized in Tables E1–E3.

Table E1. May Creek data at bar A.

B [m]	d_{90} [mm]	d_{50} [mm]	i [%]	H_{BM} [m]
10	95	40	1.1	0.6

Table E2. May Creek data at bar B.

B [m]	d_{90} [mm]	d_{50} [mm]	i [%]	H_{BM} [m]
9	88	31	1.6	0.5

Table E3. May Creek data at bar Z.

B [m]	d_{90} [mm]	d_{50} [mm]	i [%]	H_{BM} [m]
9	135	50	1.1	0.2

Bar material is poorly sorted gravel with a large fraction of sand and finer material and the median diameter varies between 31 and 50 mm. Three bars were monitored: Bar A is a transverse gravel bar with the upstream end in a plane bed reach and the downstream part very steep; Bar B is a transverse bar 200 m downstream from bar A and Bar Z is a transverse bar too, in a relatively straight pool-riffle reach.

F *Swamp Creek*

Swamp Creek drains a 59 km^2 basin comprising a glacial till plateau in the Pudget Lowland, Washington State. The mean discharge in the water years 1980–1989 was 1.0 m^3/s at the USGS station near the mouth. The hydrologic regime falls between those of Jenkins and May Creek: floods have intermediate peaks and mediate recession rates (Konrad et al., 2002). Field data are summarized in Tables F1, F2.

In the upper reach bar material is poorly sorted with very large cobbles lying beneath the gravel surface layer; the lower reach has low gradients and lower capacity to transport sediment, therefore the material is finer. Median diameters vary between 19 and 48 mm. Two gravel bars were monitored: bar A is a midchannel bar in a straight reach with uniform width and a nearly plane bed; bar B is a midchannel bar located in a lower gradient pool-riffle reach.

Table F1. Swamp Creek data at bar A.

B [m]	d_{90} [mm]	d_{50} [mm]	i [%]	H_{BM} [m]
5	130	48	1.2	0.1

Table F2. Swamp Creek data at the bar B.

B [m]	d_{90} [mm]	d_{50} [mm]	i [%]	H_{BM} [m]
9	45	19	0.7	0.2

REFERENCES

Colombini, M., Seminara, G. & Tubino, M. 1987. Finite-amplitude alternate bars. *J. Fluid Mech.,* 181, 213–232.

Foley, M.G. 1975. *Scour and fill in ephemeral streams*. W.M. Keck Laboratory of Hydraulics and Water Resources Division of Engineering and Applied Science. California Institute of Technology, Pasadena, California 91125, Report No. KH-R-33.

Ikeda, S. 1984. Prediction of alternate bar wavelength and height. *Journal of Hydraulic Engineering*, 10 (4), 371–385.

Jaeggi, M. 1984. Formation and effects of alternate bars. *Journal of Hydraulic Engineering,* 110 (2), 1103–1122.

Kishi, T. 1980. *Bed forms and hydraulic relations for alluvial stream*. In Application of Stochastic Processes in Sediment Transport, H.W. Shen and H. Kikkawa (eds.), Cap. 5, 1–31. Water Resources Publication, Fort Collins.

Konrad, C.P., Booth, D.B., Burges, S.J. & Montgomery, D.R. 2002. Partial entrainment of gravel bars during floods, *Water Resources Research*, 38(7,10), 9-1; 9–16.

Leopold, L.B. & Wolman, M.G. 1957. *River channel patterns: braided, meandering and straight.* Physiographic and Hydraulic Studies of Rivers, U.S. Geological Survey Prof. Paper 282-B, Washington.

Leopold, L.B., Wolman, M.G. & Miller, J.P. 1964. *Fluvial processes in geomorphology* W.H. Freeman and Company, San Francisco and London.

Madej, M.A. 1995. *Changes in channel-stored sediment, Redwood Creek, Northwestern California, 1947–1980*. Chapter O in U.S. Geological Survey, Prof. Paper 1454. Geomorphic Processes and Aquatic Habitat in the Redwood Creek Basin, Northwestern California. K.M. Nolan, H.M. Kelsey and D.C. Marron (eds.).

Penta, A., Rasulo, G. & Rossi, F. 1977a. *Fenomeni di erosione e di deposito durante una piena nei torrenti con alvei a fondo mobile e molto larghi. Descrizione di una stazione di misura* Convegno C.N.R., Portici.

Penta, A., Rasulo, G. & Rossi, F. 1977b. *Fenomeni di erosione e di deposito durante una piena nei torrenti con alvei a fondo mobile e molto larghi. Primi risultati di una ricerca in sito* Convegno C.N.R., Firenze.

Penta, A., Rasulo, G., Rossi, F. & Silvani, G. 1980. *Un sistema automatico di misura dei fenomeni transitori di modellamento in alvei alluvionati a regime torrentizio* 27° Convegno di Idraulica e Costruzioni Idrauliche, Palermo 27–29 October.

Raudkivi, A.J. 1998. *Loose boundary hydraulics.* Rotterdam, Balkema.

Rossi, F. & Silvani, G. 1983. *Modellamento degli alvei e criteri di sistemazione dei corsi d'acqua con letti in ghiaia* Giornata di studio su 'Corsi d'acqua con letti di materiale grossolano ed incoerente', Napoli, 213–233.

Seminara, G. & Tubino, M. 2003. *Trasporto solido fluviale* Manuale di Ingegneria Civile Cremonese, ESAC, Roma, 380–409.

Viparelli, C. 1972. *Corsi d'acqua naturali e leggi che ne regolano il modellamento.* Quaderno No. 4, Istituto di Idraulica e Costruzioni Idrauliche, Napoli.

This page intentionally left blank

River Flow 2004 – Greco, Carravetta & Della Morte (eds.)
© 2004 Taylor & Francis Group, London, ISBN 90 5809 658 0

Use of sheet-piling submerged vanes

R. Guercio, R. Magini & M. Rotondi
Department of Hydraulics, Transportation & Roads, University of Rome "La Sapienza", Rome, Italy

ABSTRACT: Submerged vanes have found a large number of applications in river hydraulic to control river bed morphology in different conditions and with different aims. Here an experimental and numerical study, describing the efficiency of vanes built using steel sheet-piling, is described. The employment of steel sheet-piling vanes should simplify the construction of these structures, reducing their costs as well. In particular both in the experimental and numerical experiences the performances of steel sheet-piling vanes have been compared with those of the more usual thin vanes. Both for steel sheet-piling vanes and thin vanes the peculiar features of the hydrodynamic field have been also enhanced through numerical simulations.

1 INTRODUCTION

1.1 *Vanes description*

Submerged vanes are structures installed on river bed at angles of attack between 15° and 20°. They are characterized by a thin thickness or a hydrodynamic profile. Their height is generally equal to 0.2–0.5 times the river mean flow depth, their length is equal to 2–3 times their heights. The presence of these structures generates the formation of secondary flow which modify the intensity and the direction of the shear stresses on the river bed, altering the natural processes of sediment erosion and deposition.

Although the literature indicates that obstacles with characteristics similar to the submerged vanes already had been used in the past for rivers and channels control (Potapov & Pyshkin 1947, Chabert et al. 1961, Jansen et al. 1979), only with the studies lead at the Iowa Institute of Hydraulic Research (IIHR), starting from the '80s, a systematic experimentation on these structures was begun. For this reason in literature it is often spoken of Iowa vanes.

Submerged vanes have been used to control spiral flow and bank-erosion in bends and to deflect sediment in straight channels. A variety of experimental studies (Odgaard & Kennedy 1983, Odgaard & Lee 1984, Odgaard & Mosconi 1987) have yielded a detailed guidance in the design of these types of vanes. Moreover submerged vanes can find also application in many other fields of river hydraulics, namely: maintenance of the optimal depth of a river bed; deepening of the river bed in order to improve or to allow navigability; bridge piers protection; avoiding the obstruction of bridges, water derivations for hydroelectric plants, irrigation channels, braided or wandering rivers control with consequent removal of sand bars; creation of suitable habitats for aquatic fauna; etc. The main advantages of these obstacles are mainly low costs and low environmental impact. Actually it must be emphasized the difficulties of production and installation of structures having, according to the theory, very low thickness or hydrodynamic shape.

1.2 *Straight channel theory*

The most significant feature of the flow formed when a two dimensional boundary layer developing over a flat surface encounters a surface mounted protrusion is the appearance of three complex vortical systems: the horseshoe vortex, the wake vortex and the tip vortex. The first one is generated by adverse pressure gradient upstream of the obstacle and it is characterized by horizontal axis and two counter-rotating legs that wrap the obstacle toe. The wake vortices, characterized by vertical axis, is due to boundary layer separation on the obstacle surface. Finally the tip vortex, typical of submerged obstacles, is generated by pressure gradients between the different sides of the protrusion.

In particular a submerged vane induces a horizontal circulation in the flow downstream. The pressure difference between the pressure side and the suction side of the vane causes the flow on the pressure side to get an upward component and the flow on the suction side a downward component. As a result a tip vortex, springing from a position near the top of the vane, is formed. This vortex travels downstream with the flow where generates an helical motion of the flow and related changes in bed shear stress and bed

topography (Odgaard & Wang 1993). In particular the river bed aggrades in one portion of the channel cross section and degrades in another. The induced transversal velocity can be described by the following equation (Odgaard & Spoljaric 1986):

$$v = 2v_s\left(z/h - 1/2\right) \tag{1}$$

where v = time-averaged velocity component in the y direction; v_s = transverse velocity component at water surface; z = coordinate in vertical direction; h = dept of the flow.

The variation of v_s along the y direction is given by:

$$v_s = v_{sc}\cos\left(\pi\frac{y}{h}\right) \qquad -h/2 < y < h/2 \tag{2}$$

where v_{sc} is v_s at the channel-center line and:

$$V_{sc} = \exp\left(-2kx/\left(1/k + \sqrt{8/f}\right)\right) \tag{3}$$

where $V_{sc} = v_{sc}/v_{so}$; $v_{so} = v_s$ at (x, y) = (0, 0); k = Von Karman's constant; f = Darcy-Weisbach friction factor.

The induced transverse velocity component v gives rise to a transverse bed-shear stress which generates changes in the channel bed. The depth distribution is given by:

$$\frac{\Delta h}{h} = \frac{\Psi}{\pi}\operatorname{sen}\left(\pi\frac{y}{h}\right) \tag{4}$$

where $\Delta h = h - h^*$; h^* = average flow depth; Ψ is function of v_{sc}.

Other analytical theories have been developed (Odgaard & Wang 1991) validating the effects of vane in sediment management.

1.3 *Vane material and shape*

Since the first experiments different materials and shapes have been used in vanes installations. They have been constructed from planks supported by h-piles, round wood poles, rows of dumped rock and reinforced concrete. In recent installations were used patented Iowa vanes having a hydrodynamic design, the vanes were shaped as a double-curved foil with a twisted rear edge and a rounded nose. It has to be underlined that vanes designs are functional as long as their thickness is small compared to their length and height. This is due to flow separation at the leading edges of the vane that generates local scour undermining the stability of the obstacle. To reduce all the problems that occur when constructing, installing and piling thin thickness vanes in this work experimental and numerical tests have been conduced to validate the use of steel sheet-piling vanes. This type of vane simplifies many of the problems related to the installations, reducing the costs as well.

2 EXPERIMENTAL TESTS

2.1 *Details of the experiments*

Laboratory experiments were conducted to evaluate the effectiveness of submerged vanes in controlling sediment redistribution, to validate the foregoing theory and to compare the induced effects on bed channel of sheet-piling vane and thin thickness vane.

Tests were focused on finding the possible loss in efficiency of the sheet-piling vane due to the non-hydrodynamic shape, that could cause greater flow separation at the leading edge of the obstacle. The evaluation of the efficiency was based on verifying the changes on bed morphology due to the two different kind of vane and observing local scour around the obstacle. Many tests were carried on changing angles of attack (from 10° to 20°), geometry and flow conditions. In this paper only the most significant is presented. A 12 m long and 0.4 m wide channel was used for all experiences. Flow rate was 0.018 m^3/s with a corresponding mean velocity, u = 0.3 m/s and an average flow depth, h = 0.15 m. The bed consisted of a 0.1 m thick of sand having a median diameter of 0.5 mm and a density of 2650 kg/m^3. The thin vane was made of aluminum sheet having length L = 17 cm, thickness S = 0.5 cm and height H = 5 cm. The sheet-piling vane presented the same dimensions of the thin one and was a scaled steel sheet-piling Larssen L603K (Fig. 4). The angle of attack was set equal to 20°. Both vanes were installed 6 m downstream of channel inflow; the origin of the axes was placed in the middle of the vane as shown in Figure 4. The choice of the flow conditions and of the dimensions of the vanes resulted from Odgaard's theory and from the available experimental apparatus.

2.2 *Results and analysis*

According to Odgaard & Spoljaric studies, the effects of vanes on downstream bed morphology are significant only until 15/30 times their height, for this reason changes of the bed were measured only for a distance of 24 H downstream of the vane.

As soon as the experiments had run it was observed the rise of a sand ridge just downstream the vane. During the test the ridge grew up and the channel was ideally divided in two regions: in the first one sedimentation occurred, in the second one scour took place. Each test lasted 3 h 30′, time at which quasi-steady condition were reached.

Excluding cross-wise sections at the leading edge of the obstacle, where local scour due to the horseshoe vortex occurs, maximum changes in bed morphology were localized between 40 and 70 cm downstream of the vane. In Figures 1–3 bed profile measures from experimental tests performed with thin and L603K vane at different downstream distances are presented. In the same figures are also reported bed profiles predicted by equation 4.

These results show that the theoretical curve fairly well describes experimental data. But, it can be noticed that it underestimates bed changes for the thin vane, on the contrary it overestimates the effects of L603K vane.

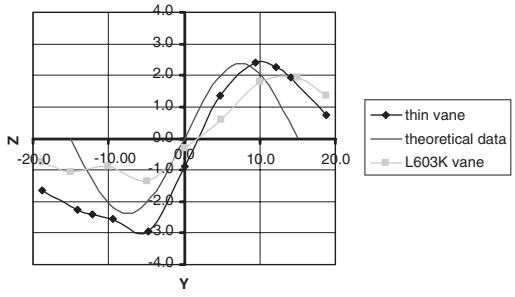


Figure 1. Experimental and theoretical data for x = 40 cm.

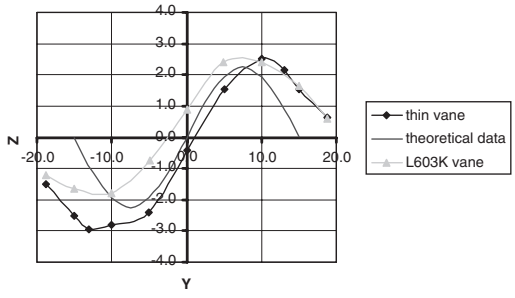


Figure 2. Experimental and theoretical data for x = 55 cm.

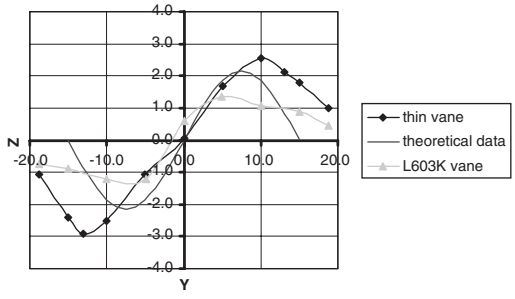


Figure 3. Experimental and theoretical data for x = 70 cm.

It was observed, in fact, that this kind of vane induced less significant modifications in bed morphology.

On the other hand experiments enhanced lower values of local scour for L603K vane, namely for this kind of structure local scour was reduced of about 30% with respect to the thin vane.

3 NUMERICAL EXPERIMENTS

3.1 *Numerical models*

The CFD code used for the numerical simulations was FLOW-3D, which solves the Navier-Stokes equation by the finite difference method. The Volume of Fluid (VOF) method is used for computing free surface motion and the FAVOR method to model complex geometric regions.

Three models were considered to investigate vortical structures, induced velocity fields and bed shear stress fields. The first two simulations were carried on to study the rising and the evolution of tip vortex for both kind of vanes, while the third simulation to obtain a better visualization of the complex vortical fields near the sheet-piling vane.

The first two models had a mesh characterized by the following dimensions: length of 180 cm, wideness of 40 cm and height of 21 cm. The total numbers of cells were 250,000 and 480,000. The vane and the origin of the axes were placed 60 cm away from the fluid entrance.

For the third simulation (Fig. 4) it needed a greater number of cells to visualize correctly the hydrodynamic field. The model was characterized by a length and a wideness of 30 cm and an height of 17 cm for a total number of cells equal to 780,000. The turbulence model used for all the simulations was the RNG (renormalized group). A "specified velocity"

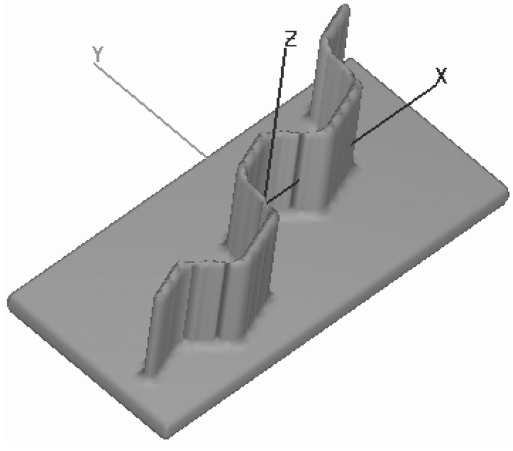


Figure 4. Numerical model of L603K vane.

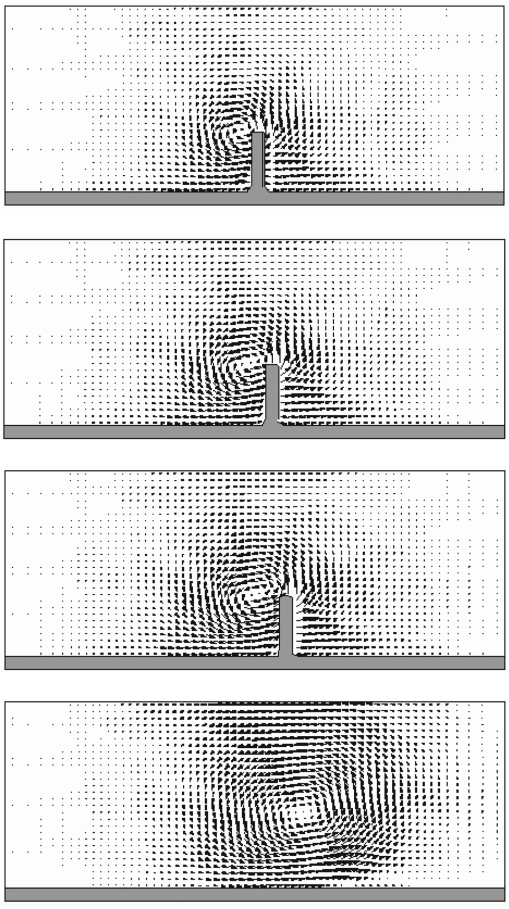


Figure 5. Thin vane. Evolution of tip vortex: cross-wise section y–z; t = 100 s; x = −0.75; 3.75; 6.75; 100 cm.

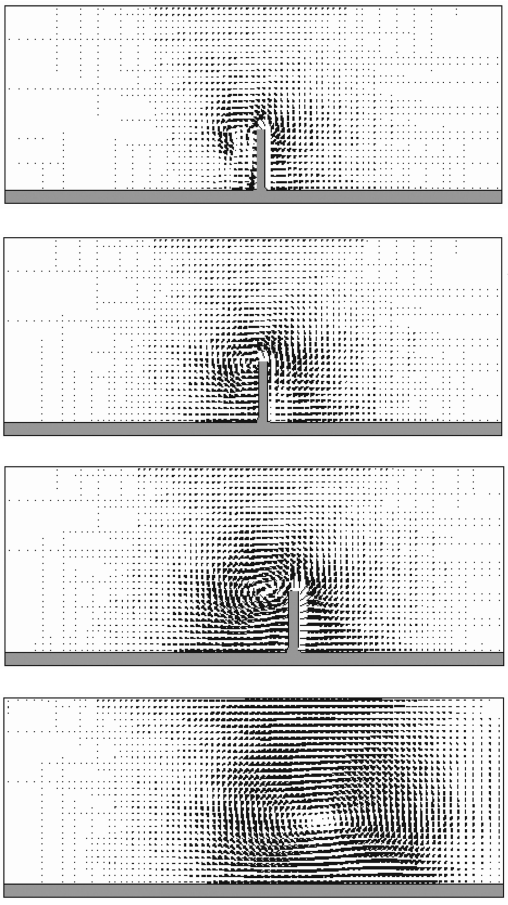


Figure 6. L603K vane. Evolution of tip vortex: cross-wise section y–z; t = 100 s; x = −0.75; 3.75; 6.75; 100 cm.

boundary condition was given for the fluid entering the computational domain, while a "continuative" type for the fluid flowing out.

Vanes dimensions and hydraulic conditions were the same of the ones used in the laboratory experiments. Thin thickness vane was generated by the means of Flow-3D geometry panel, while L603K vane importing a STL file created with Autocad2000. The channel bed had an equivalent surface roughness equal to 0.05 cm.

3.2 *Results*

The running time of the three simulations was t = 100 s, after about 70 s the flow became quasi-steady. The evolution of tip vortex was obtained for both vanes (Figs 5–6). It can be noticed that, excluding the very first cross-wise sections close to the leading edge of the obstacle, no substantial differences between vortices and induced transverse velocity generated by thin and L603K vane are present.

The fluid approaching the vanes gave rise to a secondary flow, that 70 cm away from the obstacles occupies almost the whole cross-wise section.

It is possible to note that for the L603K vane the vortical structure at this distance shows an elliptical shape, while the thin vane generated a circular-shaped vortical structure. The bed transverse velocity intensity and direction in both simulations are similar, namely for the L603K the maximum velocity is about 0.77 of thin vane one.

The third model was created for a better description of velocity field around the sheet-piling vane.

In Figure 7 it can be noticed the mechanism generating the tip vortex at the leading edge of the vane as described previously in paragraph 1.2.

Figure 8 shows the presence of the tip vortex near the top of the structure, but also of another

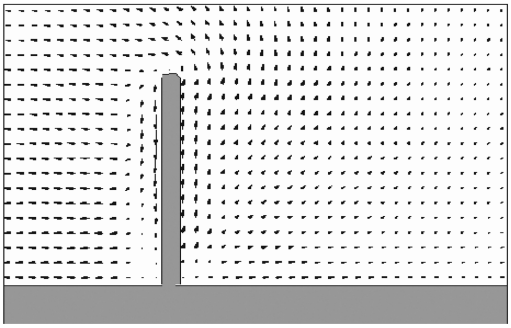


Figure 7. L603K vane. Downward and upward component of velocity at low and high pressure side (plane y–z at $x = -5$ cm).

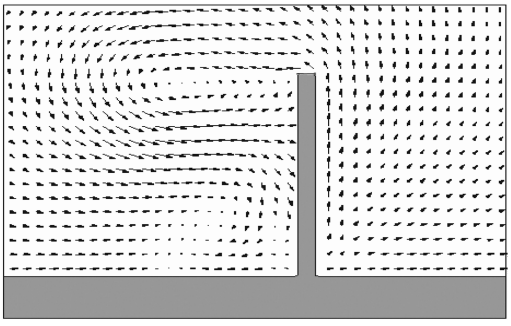


Figure 8. L603K vane. Tip vortex and a leg of horseshoe vortex (plane y–z at $x = 1.5$).

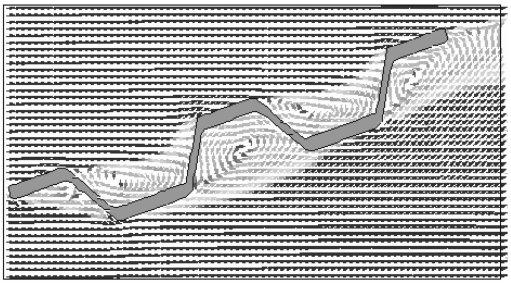


Figure 9. L603K vane. Vortices visualization plane (x–y at $z = 2.5$).

counter-rotating horizontal vortical structure near the bed. Plausibly it is one of the legs of the horseshoe vortex system.

Moreover, according to observations performed during the laboratory tests the presence of vortices with vertical axes had also been enhanced by this numerical simulation.

These vortices are generated by boundary layer separation on L603K vane surface. They looks like to be entrapped in between the indentations on the vane.

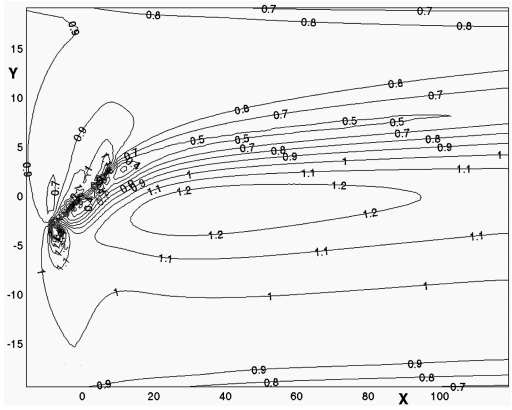


Figure 10. Thin vane. Normalized bed shear stresses at $z = 0$.

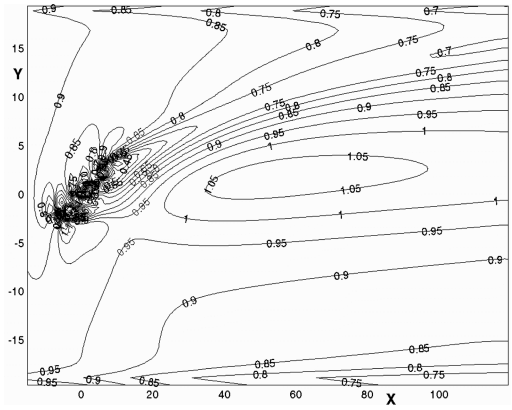


Figure 11. L603K vane. Normalized bed shear stresses at $z = 0$.

Their presence is plausibly responsible for the local scour reduction around the structure. They dissipate, in fact, part of flow energy limiting its scouring capability.

Figures 10, 11 show normalized bed shear stresses for both kind of tested vane. In both simulations it can be noticed the presence of two regions, where respectively sedimentation and erosion occur. The maximum values of bed shear stresses for the thin vane are about 30% higher than those of L603K vane.

This result justify the lower efficiency of L603K vane as described by experimental tests.

3.3 *Validation of theory for thin vane*

Results from the numerical simulation of the thin vane were compared with theoretical data resulting from equations 1–3, already illustrated in paragraph 1.2.

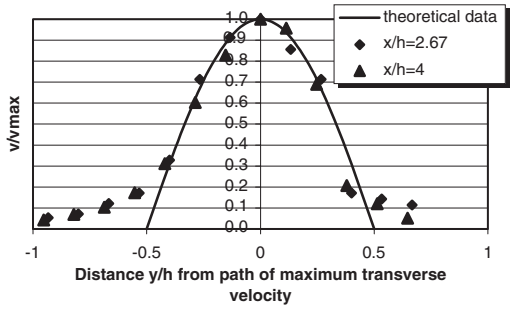


Figure 12. Numerical and predicted values of near-bed transverse velocity.

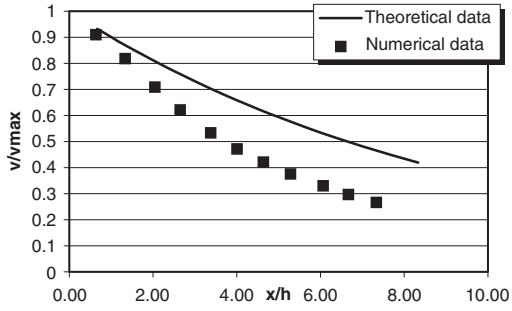


Figure 13. Measured and predicted downstream variation of maximum transverse velocity.

In Figure 12 data of induced transverse velocity are reported, it can be seen that equation 2, for values ranging between −0.5 and 0.5, is a realistic predictor for the transverse velocity.

Figure 13 shows a faster decay of the numerical values of the downstream transverse near-bed velocity than the predicted ones. This behavior had already been verified by the same Odgaard by the comparison between laboratory and theoretical data.

4 CONCLUSIONS

This study was conducted to understand the behavior of sheet-piling vanes and to verify their efficiency in straight channels. Experimental and numerical tests have shown the similarity of the performances of thin and L603K vane. The visualizations of the tip vortex have confirmed the same features for both kind of obstacle. On the other hand the laboratory experiments have shown a minor efficiency of L603K vane in sediment control.

Though sheet-piling vanes induce less changes in bed morphology than thin thickness vanes, they could be considered a realistic alternative to them. Sheet-piling vanes, in fact, are characterized by low costs and sensibly reduce problems related with piling and installation. Moreover steel sheet-piling vanes have also shown lower scour depths around them.

REFERENCES

Barkdoll, B. 1999. Discussion of analysis of flow past submerged vanes, *J. of Hydraulic Engineering* 125(8): 896–899.

DeWitt, R.J. & Odgaard, A.J. 1991. Submerged vane projects for bank stabilization and sedimentation management, *Hydr. Eng. Proc. of the 1991 National Conference*.

Fukuoka, S. & Watanabe, A. 1989. New Bank protection methods against erosion in the river, *Proc. of the Japan-China Joint Seminar on Natural Hazard Mitigation*: 439–448. Kyoto, Japan.

Fukuoka, S. & Watanabe, A. 1993. Analysis of flow and bed profile in a curved channel with vane array, *Proc. of 25th, IAHR Congress*: 2: 445–452. Tokyo, Japan.

Hirt, C.W. 2002. FLOW-3D Manual, Flow Science Inc.

Hoyt, J.W. 2002. Visualization of flow & vortex patterns around high attack-angle vanes, *River Flow 2002, Proceedings of the International Conference on Fluvial Hydraulics, Louvain-la-Neuve, 4–6 September 2002.* Rotterdam: Balkema.

Odgaard, A.J. & Kennedy, J.F. 1983. River-bend protection by submerged vanes, *J. of Hydraulics Engineering* 109(8): 1161–1173.

Odgaard, A.J. & Spoljaric, A. 1986. Sediment control by submerged vanes, *J. of Hydraulics Engineering* 112(12): 1164–1181.

Odgaard, A.J. & Mosconi, C.E. 1987. Streambank protection by submerged vanes, *J. of Hydraulics Engineering* 113(4): 520–536.

Odgaard, A.J. & Spoljaric, A. 1991. Sediment control by submerged vanes. Design basis, *River meandering*, *Water Resources Monograph N.12, American geophysical Union*: 127–151. S.Ikeda & G.Parkers eds.

Odgaard, A.J. & Wang, Y. 1991. Sediment management with submerged vanes. I: Theory, *J. of Hydraulics Engineering* 117(3): 267–283.

Odgaard, A.J. & Wang, Y. 1991. Sediment management with submerged vanes. II: Applications, *J. of Hydraulics Engineering* 117(3): 284–302.

Odgaard, A.J. & Wang, Y. 1993. Flow control with vorticity, *J. of Hydraulic Research* 31(4): 549–562.

Potapov, M.V. & Pyshkin, B.A. 1947. Metod poperechnoy tsirkulyatsii I ego primenenie v gidrotekhnike. *Izd. Ak. Nayk*. SSSR, Moscow (in Russian).

Sinha, S.K. & Marelius, F. 1998. Experimental investigations of flow past submerged vanes, *J. of Hydraulics Engineering* 124(5): 542–545.

Sinha, S.K. & Marelius, F. 2000. Analysis of flow past submerged vanes, *J. of Hydraulic Research* 38(1): 65–71.

Sinha, S.K., Sotiropoulos, F. & Odgaard, A.J. 1998. Three-dimensional numerical model for flow through natural rivers, *J. of Hydraulics Engineering* 124(1): 13–24.

A.2. Bed forms and flow resistance

This page intentionally left blank

River Flow 2004 – Greco, Carravetta & Della Morte (eds.)
© 2004 Taylor & Francis Group, London, ISBN 90 5809 658 0

Double-averaged flow field over static armor layers

J. Aberle & K. Koll
Leichtweiss-Institute for Hydraulic Engineering, Braunschweig Technical University, Germany

ABSTRACT: In a novel approach to investigating the interaction between grain-size distribution, surface geometry, and flow field of open-channel flows, the double-averaged (in temporal and spatial domains) momentum equations are applied to rough-bed open-channel flow. Preliminary results of a laboratory study carried out in the hydraulic laboratory of the Leichtweiss-Institute for Hydraulic Engineering, University of Braunschweig, Germany are presented. The bed layer consisting of a gravel-mixture with $d_{50} = 5$ mm had an initial height of 20 cm. By a step-wise increase of the discharge, armor layers with different stages of stability were developed successively until the maximum bed stability was obtained. After an intermediate armor layer was fully developed, i.e. when sediment transport rate was negligible for an intermediate discharge step, velocity profiles were measured using a 3D-Acoustic-Doppler Velocimeter (ADV). A high resolution Digital Elevation Model (DEM) of the armor layer topography was obtained from a laser scan of the bed. This detailed knowledge of topography is a prerequisite for the applicability of the double-averaged momentum equations in the roughness layer, i.e. the flow region between just above the roughness crests and troughs of the gravel bed. The relationships for the double-averaged velocity distribution and hydraulic resistance are derived and compared with these data.

1 INTRODUCTION

The structure of flows over hydraulically rough beds is important for the understanding of natural rivers. An abundance of studies have been carried out to explore theoretical aspects of turbulent structures of these flows (e.g. Nezu & Nakagawa 1993, Kironoto & Graf 1994, Song & Graf 1994, Nikora et al. 2001). In these studies, progress was achieved in understanding the turbulence structure for high relative submergence and the flow field at distances from the bed sufficiently greater than the roughness height. Recent investigations concerning the nearbed flow structure in flows over irregular rough beds (for both, large and shallow water depths) resulted in improved approaches for the description of the flow field (Dittrich & Koll 1997, Koll 2002, Nikora et al. 2001, 2003). However, these approaches still require parameterization and validation.

In general the turbulent flow field ($Re > 2500$) over rough surfaces can be subdivided into three main layers and a subsurface layer (figure 1). The outer layer is composed of the free surface region and an intermediate region. In the free surface region the turbulent structure is controlled by outer variables, with length and velocity scales specified as the flow depth h and the maximum mainstream velocity u_{max}. The intermediate region ($(z - z_t)/h \leq 0.6$) is not strongly influenced by wall properties or the free surface. In both regions viscous effects are negligible (Nezu & Nakagawa 1993).

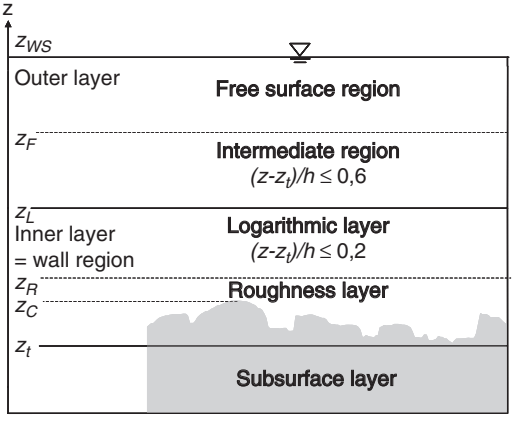


Figure 1. Turbulent flow field over rough beds after Koll (2002), modified; z_t = elevation of roughness troughs, z_c = elevation of roughness crests, z_R = elevation of upper boundary of the roughness layer, z_L = elevation of upper boundary of the logarithmic layer, z_F = elevation of boundary of free surface region, and z_{WS} = elevation of water surface.

In the 'inner layer' or the wall region, which can be subdivided into a logarithmic ($z_R < z < z_L$, figure 1) and a roughness layer ($z_t < z < z_R$), viscous effects are

negligible, too. However, the characteristic scales of the inner layer are different from those of the outer layer. These scales are the shear velocity u_*, the distance from the bed and characteristic scales of the bed topography. The logarithmic layer ranges up to $(z_L - z_t) \leq 0.2\,h$ (Nezu & Nakagawa, 1993).

The roughness layer is influenced by individual roughness elements and occupies the region between 'just above' the roughness crests and roughness troughs. Flow in this region is highly 3D and spatially heterogeneous for the case of natural, irregular beds. The main characteristic scales of the roughness layer are the shear velocity u_* and characteristic lengths of bed topography.

The subsurface layer occupies pores between granular particles. The characteristic scales of the subsurface layer are the shear velocity u_* and pore characteristic lengths.

An abundance of investigations of the flow structure in the near bed region has been based on the Reynolds equations which were used for both modelling and interpretation of experimental data. However, due to the spatial heterogeneity of the flow in this region, time averaged-momentum equations are inconvenient and impractible. Giménez-Curto & Corniero Lera (1996) and Nikora et al. (2001) concluded that 2D approximations based on the Reynolds equations as well as similarity considerations for time-averaged variables are not possible for the near-bed region. To overcome this shortcoming, the Reynolds equations should be supplemented by spatial area (or volume) averaging in planes parallel to the bed for theoretical considerations. The spatially and temporally averaged Navier-Stokes equations were first introduced by Wilson & Shaw (1977) and further developed by Raupach & Shaw (1982), Finnigan (1985), Raupach et al. (1991), and Giménez-Curto & Corniera Lera (1996). In hydraulics, the idea of spatial flow averaging was first introduced by Smith & McLean (1977) and was recently adopted by various researchers (e.g. Nikora et al. 2001, 2002a, 2002b, 2003, Lopez & Garcia 2001, Righetti & Armanini 2002).

In this paper we present preliminary results from a research project carried out for the parameterization of the spatially averaged momentum equations in the near bed flow region. The experimental setup is described and the relationships for the double-averaged velocity distribution are derived and compared with hydraulic and topographic data.

2 DOUBLE-AVERAGING METHODOLOGY

2.1 *Governing equations and spatially averaging*

The turbulent flow of an incompressible fluid can be expressed by the general conservation of mass and the Reynolds equations as:

$$\frac{\partial \overline{u}_j}{\partial x_j} = 0 \tag{1}$$

$$\frac{\partial \overline{u}_i}{\partial t} + \overline{u}_j \frac{\partial \overline{u}_i}{\partial x_j} = g_i - \frac{1}{\rho}\frac{\partial \overline{p}}{\partial x_i} - \frac{\partial \overline{u_i' u_j'}}{\partial x_j} + \nu \frac{\partial^2 \overline{u}_i}{\partial x_j^2} \tag{2}$$

where we adopt the summation convention for repeated index. Here u_i and x_i represent the ith cartesian component of the instantanteneous velocity and position vector with the usual convention $u_i \equiv (u, v, w)$, t is time, p is pressure, g_i is the ith component of the gravity acceleration, ρ is the fluid density, and ν is kinematic viscosity. The overbar denotes ensemble averaging and u_i' denotes the fluctuating part of the velocity component u_i according to the decomposition $u_i = \overline{u}_i + u_i'$.

A similar decomposition is used for the spatially averaging procedure. Velocity and pressure are decomposed into an overall mean $\langle \overline{u}_i \rangle$ and $\langle \overline{p} \rangle$ and a boundary disturbance according to $\overline{u}_i = \langle \overline{u}_i \rangle + \tilde{u}_i$ and $\overline{p} = \langle \overline{p} \rangle + \tilde{p}$. The wavy overbar denotes the disturbance in the flow variables similar to the Reynolds decomposition with $\langle \tilde{u}_i \rangle = \langle \tilde{p} \rangle = 0$. Hence instantaneous velocities and pressure are defined as $u_i = \langle \overline{u}_i \rangle + \tilde{u}_i + u_i'$ and $p = \langle \overline{p} \rangle + \tilde{p} + p'$.

The spatially averaging procedure for the flow region above the roughness crests follows the Reynolds procedure and does not present any difficulties. However, the averaging procedure for the flow region below the roughness crests is not trivial. The averaging region is intersected by roughness elements and, for this case, the spatially averaging operation does not commute with spatial differentiation. Detailed mathematical derivations of the spatial averaged equations are presented in Raupach & Shaw (1982), Finnigan (1985) and Giménez-Curto & Corniera Lera (1996). Here we present the equations from Nikora et al. (2001) which are based on the derivation of the spatially averaged momentum equations by Giménez-Curto & Corniera Lera (1996). The spatially averaged equations for flow above the roughness crests can be expressed as:

$$\frac{\partial \langle \overline{u}_i \rangle}{\partial t} + \langle \overline{u}_j \rangle \frac{\partial \langle \overline{u}_i \rangle}{\partial x_j} = g_i - \frac{1}{\rho}\frac{\partial \langle \overline{p} \rangle}{\partial x_i} - \frac{\partial \langle \overline{u_i' u_j'} \rangle}{\partial x_j} - \frac{\partial \langle \widetilde{u_i} \widetilde{u_j} \rangle}{\partial x_j} + \nu \frac{\partial^2 \langle \overline{u}_i \rangle}{\partial x_j^2} \tag{3}$$

$$\frac{\partial \langle \overline{u}_j \rangle}{\partial x_j} = 0 \tag{4}$$

and for flow below the roughness crests as:

$$\frac{\partial\langle\overline{u}_i\rangle}{\partial t}+\langle\overline{u}_j\rangle\frac{\partial\langle\overline{u}_i\rangle}{\partial x_j}=g_i-\frac{1}{\rho}\frac{\partial\langle\overline{p}\rangle}{\partial x_i}-\frac{1}{A}\frac{\partial A\langle\overline{u_i'u_j'}\rangle}{\partial x_j}$$
$$-\frac{1}{A}\frac{\partial A\langle\widetilde{u}_i\widetilde{u}_j\rangle}{\partial x_j}+\nu\frac{\partial^2\langle\overline{u}_i\rangle}{\partial x_j^2}+\nu\left\langle\frac{\partial^2\widetilde{u}_i}{\partial x_j^2}\right\rangle-\frac{1}{\rho}\frac{\partial\langle\tilde{p}\rangle}{\partial x_i} \qquad (5)$$

$$\frac{\partial A\langle\overline{u}_j\rangle}{\partial x_j}=0 \qquad (6)$$

with $A=A_f/A_0$, where A_f denotes the area occupied by fluid within a fixed region in the x,y-plane at level z within the total area A_0.

The comparison of (3) and (5) with (2) shows that additional terms appear in both equations which are due to form-induced stresses, form drag and viscous drag on the bed. The form induced stresses $\langle\tilde{u}_i\tilde{u}_j\rangle$ appear in both (3) and (5) as a consequence of the spatial averaging like turbulent stresses appear in the Reynolds equations, i.e. form induced stresses $\langle\tilde{u}_i\tilde{u}_j\rangle$ are due to spatial disturbances in time averaged flow. The form drag $1/\rho\langle\partial\tilde{p}/\partial x_i\rangle$ and the viscous drag $\nu\langle\partial^2\widetilde{u}_i/\partial x_j^2\rangle$ appear only in the flow region below the roughness crests. This flow region is highly dependent on roughness geometry as demonstrated by the parameter $A=A_f/A_0$ in (5) and (6). A is important if the roughness elements change their density and cross-sections with coordinates, it disappears if they do not (Nikora et al. 2001).

The spatially averaged Reynolds-equations (3)–(6) may be simplified for the case of turbulent two dimensional, steady, uniform flow over a rough bed with a flat water surface. For a stable, static bed for which the roughness geometry function depends only the vertical coordinate z (3) reduces to:

$$gS_b-\frac{\partial\langle\overline{u'w'}\rangle}{\partial z}-\frac{\partial\langle\tilde{u}\tilde{w}\rangle}{\partial z}+\nu\frac{\partial^2\langle\overline{u}\rangle}{\partial z^2}=0 \qquad (7a)$$

$$g\cos\alpha+\frac{1}{\rho}\frac{\partial\langle\overline{p}\rangle}{\partial z}+\frac{\partial\langle\overline{w'^2}\rangle}{\partial z}+\frac{\partial\langle\tilde{w}^2\rangle}{\partial z}=0 \qquad (7b)$$

and (5) reduces to:

$$gS_b-\frac{1}{\rho}\left\langle\frac{\partial\tilde{p}}{\partial x}\right\rangle-\frac{1}{A}\frac{\partial A\langle\overline{u'w'}\rangle}{\partial z}-\frac{1}{A}\frac{\partial A\langle\tilde{u}\tilde{w}\rangle}{\partial z}$$
$$+\frac{\nu}{A}\frac{\partial^2 A\langle\overline{u}\rangle}{\partial z^2}-\frac{2\nu}{A}\frac{\partial\langle\overline{u}\rangle}{\partial z}\frac{\partial A}{\partial z}-\frac{\nu\langle\overline{u}\rangle}{A}\frac{\partial^2 A}{\partial z^2}+\nu\left\langle\frac{\partial^2\tilde{u}}{\partial x_j^2}\right\rangle=0 \qquad (8a)$$

$$g\cos\alpha+\frac{1}{\rho}\frac{\partial\langle\overline{p}\rangle}{\partial z}+\frac{1}{\rho}\left\langle\frac{\partial\tilde{p}}{\partial z}\right\rangle+\frac{1}{A}\frac{\partial A\langle\overline{w'^2}\rangle}{\partial z}$$
$$+\frac{1}{A}\frac{\partial A\langle\tilde{w}^2\rangle}{\partial z}-\nu\left\langle\frac{\partial^2\tilde{w}}{\partial x_j^2}\right\rangle=0 \qquad (8b)$$

In the above equations $S_b\approx\sin\alpha$ ($\alpha=$ slope angle) is the slope of the averaged bed which is equal to the water surface slope (uniform flow). Equations (7a) and (8a) are for the longitudinal velocity component while (8b) and (9b) are for the vertical one. Due to 2D-flow conditions, equations for the transverse velocity component disappear. The derivation of the vertical distribution of the spatially averaged pressure and the spatially averaged stress distribution are found in Nikora et al. (2001).

2.2 *Roughness geometry function* A

The foregoing derivation of the spatially averaged momentum equations shows the importance of the roughness geometry function A. From the definition $A=A_f/A_0$ it follows that $A=1$ for the region above the roughness crests ($A_f=A_0$). On the other hand, for an impermeable bed $A\to 0$ ($A_f\to 0$) for $z\to z_t$. These two values bound the roughness geometry function, i.e. $0<A(z)\le 1$.

For a rough permeable bed the function A corresponds to the porosity coefficient of the granular material in the subsurface layer with $\partial A/\partial z=0$ ($z<z_t$). For $z_t<z\le z_c$, A is strongly dependent on bed topography, i.e. grain-size distribution of the surface material and surface geometry are important factors. Further properties of the roughness geometry function are discussed in detail by Nikora et al. (2001).

2.3 *Velocity distribution*

Based on (7a)–(8b), Nikora et al. (2001, 2003) derived velocity distributions for spatially averaged flows. Here we focus on equations for the velocity distribution over rough permeable beds. For such beds the position of the reference bed (or zero-plane) is of fundamental importance and the displaced vertical coordinate $Z=z-d_p$ instead of z should be considered (for a review of d_p see Koll 2002 and Nikora et al. 2002). For rough impermeable beds, the reference level may be defined at z_t where $\langle\tilde{u}\rangle=0$ and $\tau=\tau_0$. However, in general $A(z_t)$ is nonzero for permeable beds and the position of the reference bed may be higher (Nikora et al. 2001). Formulations for velocity distributions based on (7a)–(8b) dependent on the relative submergence and the flow regime are described in detail in Nikora et al. (2001, 2003). For flows with large relative submergence Nikora et al.

(2001) described a simple layer model similar to the layer model described in the introduction. The model includes an outer layer, a logarithmic layer and a roughness layer with linear velocity distribution. Linear flow velocity distributions for small relative submergence have been observed by O'Loughlin & Annambhotla (1969), Nakagawa et al. (1988), Dittrich et al. (1996), Nikora et al. (2001) and Koll (2002). Further possible velocity distributions in the roughness layer are discussed by Nikora et al. (2003). We note that analytical or numerical solutions of (7a)–(8b) require parameterization of the spatially averaged turbulent stresses $-\langle\overline{u'w'}\rangle$, form-induced stresses $-\langle\tilde{u}\tilde{w}\rangle$ and the form drag $1/\rho\langle\partial\tilde{p}/\partial x\rangle$. Such data is not yet available and our experiments described in section 3 are specially designed to develop physically based parameters.

3 EXPERIMENTAL METHOD

In this paper we present preliminary data from experiments carried out in a 20 m long, 0.90 wide and 0.60 m high tilting flume in the laboratory of the Leichtweiss-Institute for hydraulic engineering, Braunschweig Technical University. The experiments were carried out with a constant flume slope of $S = 0.0027$. The discharge Q was adjusted by a valve and measured by an inductive flow meter. Eight piezometers were installed in the flume ($\Delta x = 1.00$ m) and the water surface slope was calculated from linear regression.

A coarse sediment mixture ($0.63\text{ mm} < d < 64\text{ mm}$, $d_{50} = 5$ mm, see figure 12 for grain-size distribution) was used as movable bed material for the development of water worked roughness structures. At the first step of an experiment, the well mixed sediment was placed in the flume over a length of 13.40 m and flattened to a thickness of 0.20 m to ensure that the bed slope is parallel to the flume slope. The distance from the flow straightener to the sediment bed was 1.00 m and the gap between was bridged with bricks to avoid extensive scouring at the inlet. At the downstream end the sediment body was stabilized by a 20 cm high sill. The sill was constructed of perforated metal to enable flow in the subsurface layer.

The surface was allowed to armor and a degree of bed stability was established for a given discharge Q_1. When the transport rate was negligible the discharge was reduced to zero and photographs of the armor layer were taken and analyzed by applying a line by number method. The correction method of Fehr (1987) was used to enable a comparison of the results with volumetric samples.

The bed topography was measured along the 1.00 m long and 0.72 m wide test section with a laser displacement meter. The test section was located 8 m from the transition bricks-sediment. The width of the test section was smaller than the total flume width to reduce side wall effects on the measurements. Longitudinal bed profiles were recorded with a sampling interval of $\Delta x = 1.0$ mm and a lateral spacing of $\Delta y = 4$ mm. In total 180 longitudinal profiles were recorded. The precision of the laser probe was 0.06 mm in the z-direction and 0.05 mm in the x-direction. An additional survey was carried out by levelling the bed along its total length in the centerline with increments of $\Delta x = 10$ cm. These measurements were used to estimate bed-slope. Figure 2 shows the flume and the bed structure after a discharge of $Q = 180$ l/s.



Figure 2. Flume and bed structure after an applied discharge of Q = 180 l/s.

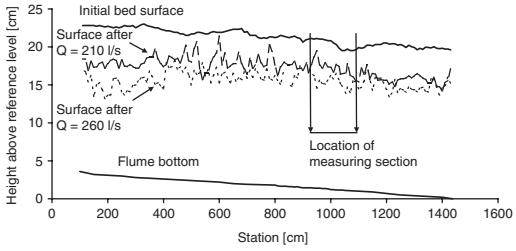


Figure 3a. Development of bed level for discharges of 210 l/s and 260 l/s.

After surveying the bed topography the bed forming discharge Q_1 was increased for the next step to a value Q_2 ($>Q_1$), so that the existing armor layer was destroyed and a new one developed. The above measurements were repeated and the procedure continued as long as the stream could stabilize itself without a considerable loss of slope or the sediment was eroded to the flume-bottom.

The development of bed level during an experiment is shown in figure 3a for two discharges of $Q = 210$ l/s and $Q = 260$ l/s. Note that $Q = 260$ l/s corresponds to the discharge, for which the maximum bed stability was obtained. Figure 3a shows

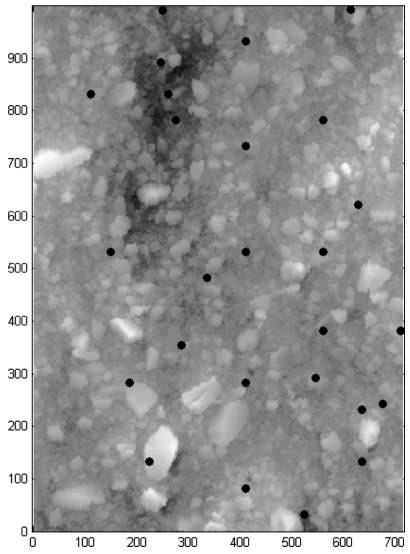


Figure 3b. Location of the positions of the randomly distributed ADV-velocity profiles (indicated by black dots) over the surface in the test section. Surface topography was recorded with a Laser-displacement meter.

that the scour at the upstream end of the sediment body and the sill at the downstream end of the sediment body have no influence on the morphology in the test section. The bed slope remains approximately constant and parallel to the flume slope during the course of the experiment. In the test section, a large number of velocity profiles are recorded to ensure the applicability of the double averaged equations.

Acoustic Doppler Velocimeter (ADV) measurements were carried out at a discharge of 180 l/s. ADV measurements provide instantaneous 3D velocities that makes it possible to obtain various turbulence parameters (Nikora & Goring 1998a, Voulgaris and Trowbridge 1998). Twenty-six randomly distributed velocity profiles were recorded in the test section with a sampling frequency of 25 Hz and with a vertical resolution of $\Delta z = 1$ cm. The ADV measurements were analyzed using WinADV (Wahl 2000). All profiles are referenced to the coordinate system of the 3D-traverse system, i.e. positions of the vertical profiles in the (x, y)-plane are referenced to topography data (figure 3b). Please note that ADV measurements were performed in planes parallel to the flume slope to simplify the spatial averaging procedure. Spatial data from the laser scan have been used for determination of the height of the roughness crests z_c (highest measured elevation) and the elevation of the roughness troughs z_t (lowest measured elevation) with $z_c - z_t = 5.3$ cm.

4 DATA ANALYSIS

ADV measurements are used to discuss differences between time-averaged velocity profiles and turbulence properties with their spatially averaged counterpart. For our analysis we use the transformed vertical coordinate $Z = z - z_t$ which allows the definition of an arbitrary reference level for z (e.g. vertical traverse coordinate).

4.1 *Velocity distribution*

Figure 4 shows the time averaged velocity distributions $\bar{u}(z)$ (solid lines) and the double averaged profile (open circles).

In the region far from the bed surface, the difference between the time averaged velocities $\bar{u}$ and the spatially averaged velocity is small ($\pm 10\%$). This difference increases in the region close to the bed surface due to irregularities of the rough surface (figure 4) and is responsible for the form induced stresses. Figure 5, in which the ratio of the standard deviation of $\langle\bar{u}\rangle$ and the double averaged velocity $\langle\bar{u}\rangle$ is plotted over depth Z demonstrates the spatial variability of $\bar{u}$ in the region close to the surface (note that the standard deviation of $\langle\bar{u}\rangle$ is calculated from the velocity measurements in the corresponding averaging plane). Thus figure 5 may be used to identify the transition between the roughness layer and the logarithmic layer. In figure 5 the identification of this separation point is straightforward at $Z = 6.1$ cm. However, this methodology cannot be applied to identify the separation point for single, solely time-averaged velocity profiles. For such profiles, the separation point must be identified from data-fitting (logarithmic function), turbulence intensities $\overline{u'^2}$, or from Reynolds-stress distribution $-\overline{u'w'}$ (see section 4.2). However, as discussed above, each time-averaged profile depends on local boundary conditions and the heterogeneity of the near bed flow field, hence the obtained result may not be representative.

Based on figure 5, the spatially averaged flow field can be subdivided in different layers (figure 6). In the roughness layer the velocity distribution can be approximated by a linear distribution followed by a logarithmic layer with increase in Z. For the logarithmic region a squared regression coefficient $R^2 \approx 1$ is obtained when fitting the data to a log-function. The same applies to the linear region, although the maximum R^2 value is found for the three points below the roughness crests. Thus it can be concluded that the real value of $z_R - d$ is located between 5.1 and 6.1 cm. However, this issue cannot be resolved due to the spatial resolution of the ADV measurements (9 mm high sampling volume). The logarithmic distribution can be used to describe the flow field up to $0.2\,h$ (figure 1). The velocity distribution in the outer layer is similar

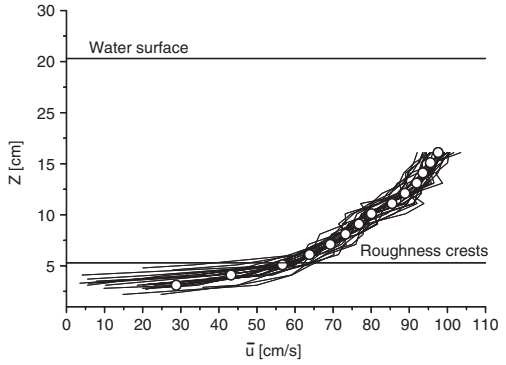


Figure 4. Vertical velocity profiles (lines) and double averaged velocity profile (open circles) for the discharge of $Q = 180$ l/s.

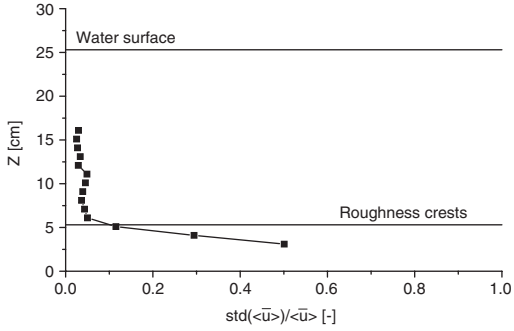


Figure 5. The ratio of the standard deviation of the spatially averaged velocities and the doubled averaged velocity in each averaging layer.

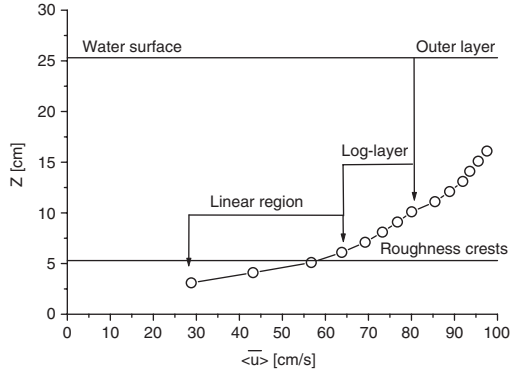


Figure 6. The spatially averaged velocity profile $\langle \bar{u} \rangle$ for $Q = 180$ l/s.

to that for flows over hydraulically smooth beds and is not considered here.

Using the methodology outlined by Koll (2002) and Nikora et al. (2002) for parameterization of the

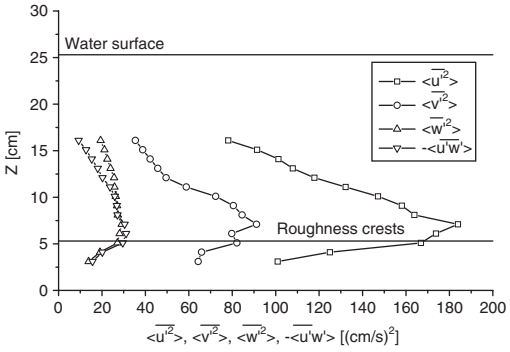


Figure 7. Vertical distribution turbulence intensities $\langle \overline{u'^2} \rangle$ (squares), $\langle \overline{v'^2} \rangle$ (circles), $\langle \overline{w'^2} \rangle$ (up triangles) and Reynolds-stress $-\langle \overline{u'w'} \rangle$ (down triangles).

velocity distribution, the hydrodynamic origin for the logarithmic layer is located 2.63 cm above the roughness troughs. With this displacement height the shear velocity can be calculated with $u_* = \sqrt{ghS}$ (with $h = z_{WS} - d$) to $u_* = 7.8$ cm/s.

4.2 *Turbulence characteristics*

The methodology based on spatially averaged flow variables should also be used in characterizing turbulence properties near rough beds. Figure 7 shows the vertical distribution of time- and spatially averaged turbulence intensities $\langle \overline{u'^2} \rangle$, $\langle \overline{v'^2} \rangle$, $\langle \overline{w'^2} \rangle$, and $-\langle \overline{u'w'} \rangle$. The mean values of $\langle \overline{u'^2} \rangle$, $\langle \overline{v'^2} \rangle$, $\langle \overline{w'^2} \rangle$ and $-\langle \overline{u'w'} \rangle$, are largest close to the roughness crests, i.e. approximately at the transition between roughness layer and logarithmic layer ($6.1\,\text{cm} \leq Z \leq 7.1\,\text{cm}$) and reduce below the roughness crests. However, investigating the deviations of the time averaged values from their spatially averaged counterpart reveals that the deviations increase with decrease in Z and that the maximum deviation is obtained below the roughness crests. This is demonstrated in figure 8, in which the vertical distribution of the standard deviation of $\langle \overline{u'^2} \rangle$, $\langle \overline{v'^2} \rangle$, $\langle \overline{w'^2} \rangle$ and $-\langle \overline{u'w'} \rangle$ in each averaging layer are shown. The increase of the deviations can be interpreted as form induced influences due to effects of local conditions. As an example, the spatial variability of $-\overline{u'w'}$ is shown in figure 9 at $Z = 6.1$ cm. The horizontal line in figure 9 indicates the spatially averaged value $-\langle \overline{u'w'} \rangle$, the squares indicate the obtained Reynolds-stress for each profile. Similar results are obtained for $\overline{u'^2}$, $\overline{v'^2}$, and $\overline{w'^2}$.

The form-induced intensities and form-induced Reynolds-stresses can be evaluated using the same procedure as in figure 7 by plotting the vertical distribution of $\langle \tilde{u}^2 \rangle$, $\langle \tilde{v}^2 \rangle$, $\langle \tilde{w}^2 \rangle$ and $-\langle \tilde{u}\tilde{w} \rangle$ (figure 10). As expected, the form induced intensities attain maximum values below the roughness crests and then reduce with

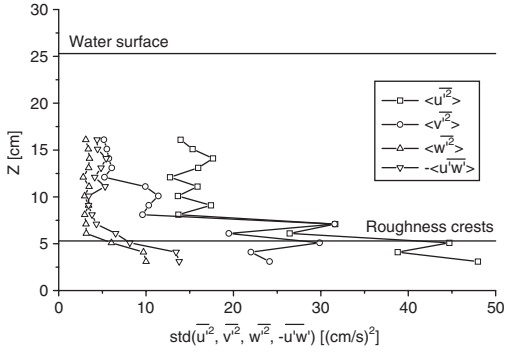


Figure 8. Vertical distribution of standard deviation of turbulence intensities $\langle\overline{u'^2}\rangle$ (squares), $\langle\overline{v'^2}\rangle$ (circles), $\langle\overline{w'^2}\rangle$ (up triangles) and Reynolds-stress $-\langle\overline{u'w'}\rangle$ (down triangles).

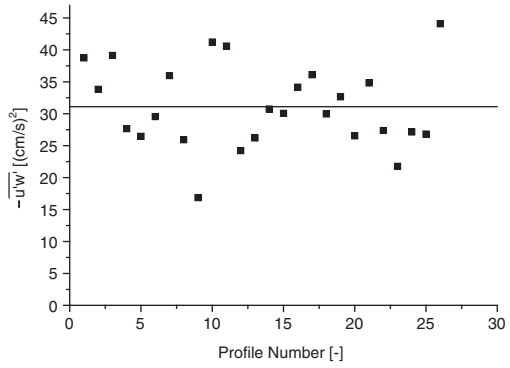


Figure 9. The Reynolds stresses $-\overline{u'w'}$ at the transition between roughness sublayer and logarithmic layer at $Z = 6.1$ cm for each time-averaged profile. The solid line indicates the spatially averaged value $-\langle\overline{u'w'}\rangle$.

increase in Z. For large values of Z the form-induced intensities become negligible compared to their turbulent counterparts. However, below the roughness crests their influence is significant as demonstrated by $\langle\tilde{u}^2\rangle$ (figure 10). Large values of $\langle\tilde{u}^2\rangle$ may be explained as follows. If some points are measured directly above the solid boundary, i.e. when the no slip condition is valid ($\bar{u} \approx 0$) and all other measuring points are above the solid boundary so that $\bar{u} > 0$, the difference $\langle\bar{u}\rangle - \bar{u}$ is large for points at the boundary. The squared difference amplifies this discrepancy (figure 10).

The form induced stress $-\langle\tilde{u}\tilde{w}\rangle$ becomes negligible above the roughness crests and becomes comparable (though less) with $-\langle\overline{u'w'}\rangle$ in the roughness layer (figures 7 and 10). Similar results have been reported by Nikora et al. (2001) for near-bed flow structure for regular spherical segment type of roughness. Further turbulence properties for the flow over artificial beds using the spatial averaging methodology are found in Pokrajac et al. (2003).

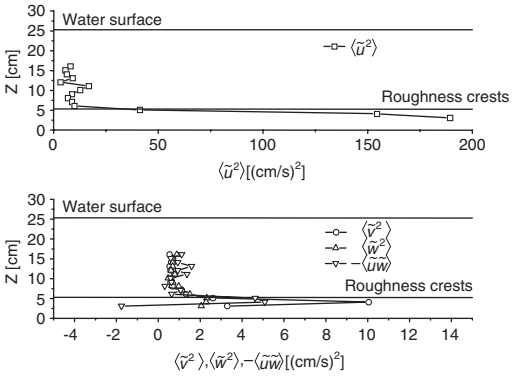


Figure 10. Vertical distribution of form induced intensities $\langle\tilde{u}^2\rangle$ (upper graph, squares), $\langle\tilde{v}^2\rangle$ (lower graph, circles), $\langle\tilde{w}^2\rangle$ (lower graph, up triangles) and $-\langle\tilde{u}\tilde{w}\rangle$ (lower graph, down triangles).

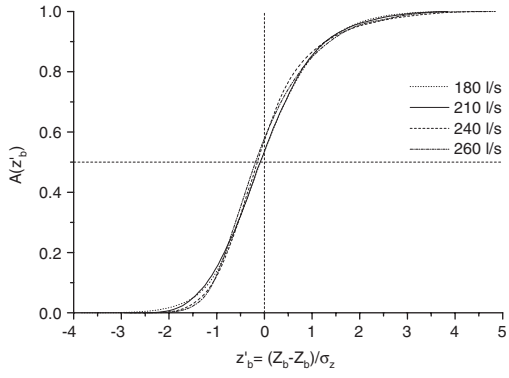


Figure 11. Roughness Geometry function $A(z)$ for water-worked beds after 180, 210, 240, and 260 l/s. Average functions $A(z)$ are presented, Z_b is bed elevation, $\bar{Z}_b$ is average bed elevation, and σ_z is standard deviation of bed elevations.

4.3 *Roughness geometry function A(z)*

The topography data can be used for the determination of the roughness geometry function A which is an essential parameter for the parameterization of (8a) and (8b). Figure 11 shows examples for A for water-worked beds at discharges of 180, 210, 240 and 260 l/s. The estimated averaged functions are comparable to roughness geometry functions shown in Nikora et al. (2001). Figure 11 shows that estimated values of A range from $0 < A(z) \leq 1$. We note that $A = 0$ corresponds to impermeable beds and the laser scan of the surface does not include measurements of the pore volume nor potential free space below large stones lying on the bed. Hence $A = 0$ is the result for laser data although we estimated $A_{min} = 0.28$ for the bed material (porosity). This discrepancy shows that a correction

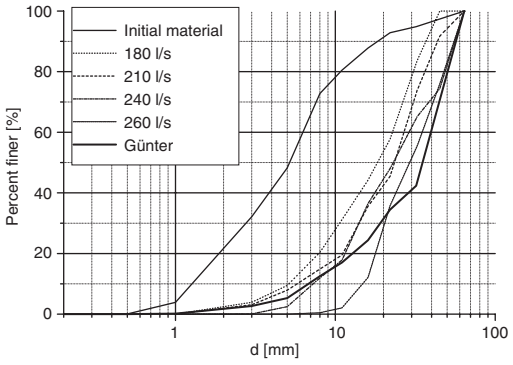


Figure 12. Development of the grain-size distribution of the armor layer. The grain-size distribution for the layer showing maximum bed stability according to the approach of Günter (1971) is indicated.

method for the calculation of the roughness geometry function has to be developed.

The roughness geometry function itself depends on surface geometry and grain size distribution of the armor layer and subsurface layer. Figure 12 shows the development of the grain-size distribution of the armor layer for discharges of 180, 210, 240, and 260 l/s and the grain-size distribution of the armor layer showing maximum bed stability according to the method of Günter (1971). The grain-size distribution for the layer with maximum bed stability according to Günter (1971) is similar to the estimated grain-size distribution after $Q = 260$ l/s. We note that after a further increase of discharge to $Q = 290$ l/s the bed could not stabilize itself, indicating the applicability of Günter's (1971) approach. Investigating armor layer development according to our experimental setup (step-wise increase of discharge) will provide further insight into relevant processes. Furthermore, linking statistical parameters obtained from topography data (e.g. Nikora et al. 1998b, Aberle 2000 and Aberle & Smart 2003) with grainsize distribution will enhance our understanding of water worked roughness structures and their effect on the flow field based on the spatially averaged equations.

5 CONCLUSION

In this paper we suggested that the double-averaged momentum equations should be used for the description of the flow field over rough surfaces. The difference between the Reynolds-equations and the doubled averaged equations were shown using ADV data. The main advantages of the double averaging methodology (temporal- and spatially averaging of the Navier-Stokes equations) are that the flow field near the boundary is directly linked with roughness geometry and that a form drag term and form induced- stresses appear in the momentum equations. Properties of the roughness geometry function have been discussed and the necessity for a correction method for rough permeable beds has been shown if the roughness geometry function is calculated from spatial data.

Further measurements are planned with the described experimental setup, except that ADV measurements will be replaced by 3D-Laser Doppler Anemometer (LDA) measurements. We will use submerged LDA-probes to measure 3D-flow velocities in the near bed region (i.e. below the roughness crests). The LDA velocity data together with the high resolution topography data will enable parameterization of the double-averaged momentum equations. Furthermore, such data will provide insight in the interaction between grain-size distribution, surface geometry, and hydraulic parameters.

ACKNOWLEDGEMENTS

The research was conducted under contract DI-651/4-1 from DFG (Deutsche Forschungsgemeinschaft). A. Dittrich provided helpful advice and generous support to this project. U. Ecklebe provided technical support. The authors are grateful to G. Beyer and T. Schoneboom for assistance with measurements.

REFERENCES

Aberle, J. 2000. Untersuchung der Rauheitsstruktur zur Bestimmung des Fließwiderstandes in Gebirgsbächen unter Klarwasserabfluß. [online], Karlsruhe, Univ., Fak. f. Bauingenieur- und Vermessungswesen, Diss. v. 13.7.2000, http://www.ubka.uni-karlsruhe.de/cgibin/psview?document=2000/bau-verm/5

Aberle, J. & Smart, G.M. 2003. The influence of roughness structure on flow resistance in mountain streams. *J. Hydraul. Res.* 41(3): 259–269.

Dittrich, A., Nestmann, F., & Ergenzinger, P. 1996. Ratio of lift and shear forces over rough surfaces. Coherent Flow Structures in Open Channels. Eds. P.J. Ashworth, S. Bennett, J.L. Best & S.J. McLelland. John Wiley & Sons Ltd., Chichester, U.K.: 125–146.

Dittrich, A. & Koll, K. 1997. Velocity field and resistance of flow over rough surface with large and small relative submergence. *Int. J. Sediment Res.* 12(3), 21–33.

Fehr, R. 1987. Geschiebeanalysen in Gebirgsflüssen. Mitt. der Versuchsanstalt für Wasserbau, Hydrologie und Glaziologie, ETH Zürich, Nr. 92.

Finnigan, J.J. 1985. Turbulent transport in flexible plant canopies. The Forest-Atmosphere Interaction, B.A. Hutchinson and B.B. Hicks, eds., D. Reidel Publishing Co., Dordrecht, The Netherlands, pp. 443–480.

Giménez-Curto, L.A. & Corniero Lera, M.A. 1996. Oscillating turbulent flow over very rough surfaces. *J. Geoph. Res.* 101(C9): 20,745–20,758.

Günter, A. 1971. Die kritische mittlere Sohlenschubspannung bei Geschiebemischungen unter Berücksichtigung der Deckschichtbildung und der turbulenzbedingten Sohlenschubspannungsschwankungen. Diss. Nr. 4649, ETH Zürich, Switzerland.

Kironoto, B.A. & Graf, W.H. 1994. Turbulence characteristics in rough uniform open-channel flow. *Proc. Instn. Civ. Engrg. Water, Maritime, and Energy* 106: 333–344.

Koll, K. 2002. Feststofftransport und Geschwindigkeitsverteilung in Raugerinnen. [online], Karlsruhe, Univ., Fak. f. Bauingenieur- und Vermessungswesen, Diss. v. 12.07.2002, http://www.ubka.uni-karlsruhe.de/cgibin/psview?document=2002/bau-verm/12.

Lopez, F. & Garcia, M.H. 2001. Mean flow and turbulence structure of open-channel flow through emergent vegetation. *J. Hydraul. Eng.* 127(5): 392–402.

Nakagawa, H., Tsujimoto, T. & Shimizu, Y. 1988. Velocity profile of flow over rough permeable bed. 6th IAHR Congress, Kyoto, Japan: 449–456.

Nezu, I. & Nakagawa, H. 1993. Turbulence in open-channel flows, Balkema, Rotterdam, The Netherlands.

Nikora, V.I. & Goring, D.G. 1998a. ADV turbulence measurements: can we improve their interpretation? *J. Hydaul. Eng.* 124(6): 630–634.

Nikora, V., Goring, D. & Biggs, B.J.F. 1998b. On gravel-bed roughness characterization. *Water Resour. Res.* 34(3): 517–527.

Nikora, V., Goring, D., McEwan, I. & Griffiths, G. 2001. Spatially averaged open-channel flow over rough bed. *J. Hydraul. Eng.* 127(2): 123–133.

Nikora, V., Goring, D. & Biggs, B. 2002a. Some observations of the effects of micro-organisms growing on the bed of an open channel on the turbulence properties. *J. Fluid Mech.* 250, 317–341.

Nikora, V., Koll, K., McLean, S., Dittrich, A. & Aberle, J. 2002b. Zero-plane displacement for rough-bed open-channel flows. *Proc. of the Int. Symp. on Fluvial Hydraulics "RiverFlow2002"*, Louvain-la-Neuve, Belgium, pp. 83–92.

Nikora, V., Koll, K., McEwan, I., McLean, S. & Dittrich, A. 2003. Velocity distribution in the roughness layer of rough-bed flows. Submitted paper to *J. Hydraul. Eng.*

O'Loughlin, E.M. & Annambhotla, V.S.S. 1969. Flow phenomena near rough boundaries. *J. Hydraul. Res.* 7(2): 231–250.

Pokrajac, D., Campbell, L.J., Manes, C., Nikora, V.I. & McEwan, I.K. 2003. Spatially-averaged flow over ribbed roughness: Á new application of Quadrant Analysis. Proc. XXX IAHR Congress, Thessaloniki, Greece. Vol. CI: 103–110.

Raupach, M.R. & Shaw, R.H. 1982. Averaging procedures for flow within vegetation canopies. *Bound.-Layer Meteorol.*, 22: 79–90.

Raupach, M.R., Antonia, R.A. & Rajagopalan, S. 1991. Rough-wall turbulent boundary layers. *Appl. Mech. Rev.*, 44(1): 1–25.

Righetti, M. & Armanini, A. 2002. Flow resistance in open channel flows with sparsely distributed bushes. *J. Hydrol.* 269: 55–64.

Smith, J.D. & McLean, S.R. 1977. Spatially averaged flow field over a wavy surface. *J. Geophys. Res.* 83(12): 1735–1746.

Song, T. & Graf, W.H. 1994. Nonuniform open-channel flow over a rough bed. *J. Hydrosci. and Hydr. Engrg.* 12(1): 1–25.

Voulgaris, G. & Trowbridge, J.H. 1998. Evaluation of the Acoustic Doppler Velocimeter (ADV) for turbulence measurements. *Journal of Atmospheric and Oceanic Technology* 15: 272–289.

Wahl, T.L. 2000. Analyzing ADV data using WinADV. 2000 Joint Conference on Water Resources Engineering and Water Resources Planning & Management, Minneapolis, USA.

Wilson, N.R. & Shaw, R.H. 1977. A higher order closure model for canopy flow. *J. Appl. Meteorol.* 16: 1197–1205.

This page intentionally left blank

River Flow 2004 – Greco, Carravetta & Della Morte (eds.)
© 2004 Taylor & Francis Group, London, ISBN 90 5809 658 0

The numerical simulation of time dependent flow structures over water worked gravel

R.J. Hardy & S.N. Lane
School of Geography, University of Leeds, Leeds, UK

ABSTRACT: Our ability to numerically predict the interaction between time dependent fluid flow structures and complex topography has yet to be fully developed. This is largely the result of the problems of designing numerically stable meshes for use with complex topographies and that Reynolds averaged turbulence schemes are typically applied. This paper deals with the numerical simulation of time dependent flows over a water worked gravel. This is achieved by the development of a porosity algorithm for representing complex surface topography in a Cartesian framework and the application of Large Eddy Simulation. The numerical simulations reported in this paper show that there are two distinct scales of boundary influence upon the shallow flow and emphasizes that the measured flow variability at any one point in a natural river will contain both locally derived and upstream inherited flow structures, according to the range of scales of topography present.

1 INTRODUCTION

Research undertaken over the last few years has demonstrated the importance of the structure of gravel river beds for understanding the interaction between fluid flow and sediment transport processes. This includes the observation of periodic high-speed fluid wedges interconnected by low-speed flow regions. These, potentially, have a considerable effect on the shear stress acting on the bed which may initiate sediment transport. Our understanding of these flows has been enhanced significantly through a series of laboratory experiments and supported by field observations. However, the potential of high resolution three-dimensional Computational Fluid Dynamics (CFD) modelling has yet to be fully developed. Although, there has been an increased applications of three-dimensional computational fluid dynamic (CFD) codes to study natural gravel bed river channels, they have normally been applied at the spatial resolution of a single geomorphological unit, such as river confluences (Bradbrook *et al.*, 1998, 2000a,b, 2001; Lane *et al.*, 1999, 2000) or a meander bend (Hodskinson & Ferguson, 1998; Ferguson *et al.*, 2003). To date, no study has considered flow over a gravel bed surface where flow around each individual gravel particle is modelled. This is largely the result of the problem of designing a numerically stable mesh for use with such complex topographies.

Furthermore, for the majority of CFD applications, turbulence closure is generally achieved by applying a Reynolds averaged turbulence scheme. This by definition provides a time averaged solution and thus prevents the numerical simulation of the dynamic fluid wedges discussed above. In order to gain further insight into the dynamics of the fluid wedges, one potential research avenue is the application of Large Eddy Simulation (LES). LES provides an intermediate case between Direct Numerical Simulation (DNS) and Reynolds averaging (RANS) approaches. While DNS deals with all eddies larger than the smallest (dissipation) scale and RANS methods deal with the mean flow characteristics, LES provides an intermediate solution where the properties of all eddies larger than the grid size are calculated and those smaller than this scale modelled by a sub-grid scale (SGS) turbulence transport model. Thus, LES attempts to compute the large scale motion, which is thought to contain most of the variation and momentum (Rogallo & Moin, 1984).

In this paper we present a methodology that is; (i) able to represent complex heterogeneous gravel surfaces in a Cartesian mesh and (ii) provides a numerical framework for the application of LES simulation over complex surfaces. First, we discuss the numerical framework that allows the topography to be included in Cartesian space. This is followed by the validation of the porosity algorithm over a water worked gravel surface for a Reynolds averaged scheme. Finally we demonstrate the potential of this scheme for LES and the numerical prediction of coherent flow structures over gravel surfaces.

2 REPRESENTATION OF TOPOGRAPHY IN 3D CFD SCHEMES

The incorporation of complex topographies within a CFD scheme has been problematic to date as the representation of the large scale topographic features has required the application of boundary fitted co-ordinates (BFC's), which involve mesh deformation in the Cartesian space (if not in the computational space) (Figure 1).

Mesh deformation may change the magnitude of numerical diffusion in the model and lead to uncertainties as to whether observed changes in process representation are due to topographic effects or grid adjustment effects. Secondly, the sub-grid scale topography (e.g. grain surface morphology, grain interactions) within the CFD scheme has to be represented using a roughness parameter (e.g. Hodskinson & Ferguson, 1998; Nicholas & Smith, 1999; Lane *et al.*, 1999) which represents the frictional retardation of the flow at the bed. Thus, the effects of sub-grid scale topography are represented as frictional retardation of the flow at the bed. This is normally based upon a standard 'law of the wall':

$$\frac{u}{u_*} = \frac{1}{k} In\left(\frac{z}{z_o}\right) \tag{1}$$

where u_* is the shear velocity $= \sqrt{\tau_b/\rho}$, κ is the Von Karman constant ($= 0.4$), τ_b is the bed shear stress, ρ is the fluid density and z_o is the height of zero velocity, which depends on the bed roughness. Bed roughness may be defined from the following:

$$z_o = \frac{v}{9u_*}, \text{ for smooth boundaries} \tag{2a}$$

$$z_o = \frac{1}{30}k_s, \text{ for rough boundaries} \tag{2b}$$

where v is the kinematic viscosity and k_s is the equivalent sand roughness following Nikuradse (1933).

Whilst there are significant concerns over turbulence parameterization in these near wall treatments, research has demonstrated that, in natural river channels with gravelly beds, much greater uncertainty is introduced into predictions of the three-dimensional velocity field due to poor knowledge and treatment of topographic variability than is introduced by uncertainty over turbulence treatments at the wall (Lane *et al.*, 1999). The basic principle adopted for representing topographic variability involves the multiplication upwards of the equivalent sand grain roughness (k_s). In a 3D modelling framework, this assumes that the topographic variability that is not included in the model geometry is represented as a sub-grid scale

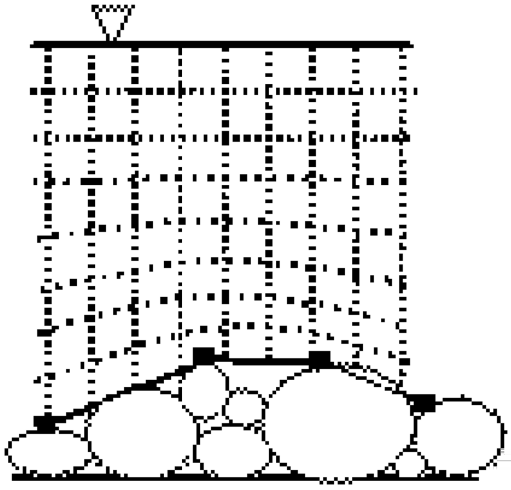


Figure 1. The application of boundary fitted co-ordinates to complex topography.

effect through upscaling. Much of this uncertainty relates to debate over which grain parameter to upscale and by how much. For instance, field investigations suggest that z_o should, including upscaling, take a value of approximately $0.1D_{84}$ (Whiting & Dietrich, 1990; Wiberg & Smith, 1991). Others, specifying it as k_s (noting $k_s = 30z_o$), have suggested approximately $3.5D_{84}$ or $6.8D_{50}$ (Hey, 1979; Bray, 1982). Clifford *et al.*, (1992) show that multiplication of roughness length represents a measure of total flow resistance that incorporates contributions from both individual grains and larger bed forms.

These uncertainties aside, the z_o approach is associated with a number of problems. These include; (i) a wide range of grain percentiles have been adopted. Whilst there is a general preference for the D_{84} (e.g. Whiting & Dietrich, 1990; Wiberg & Smith, 1991) the most appropriate percentile may depend upon the size and sorting of the gravel mix; (ii) the multiplier of roughness length will need to be spatially variable and scale dependent, in relation to both mesh resolution and the topographic content of the data set used to describe the surface; (iii) some studies have noted problems in terms of numerical stability and solution accuracy for flows characterized by high relative roughness (e.g. Nicholas & Smith, 1999) with these difficulties resulting from the existence of an upper limit of k_s for a given near-bed cell thickness (Nicholas, 2001) and (iv) there is the basic problem of setting the reference height of the bed in a numerical mesh: normally, it is assumed implicitly that the effective bed surface in mass conservation terms is the same as the bed surface sampled during field survey.

3 LARGE EDDY SIMULATION TURBULENCE CLOSURE

As discussed above LES can be viewed as a compromise between DNS and RANS approaches. The fundamentally important aspect of LES is that it calculates the properties of all eddies larger than the grid size and models those smaller than this scale by a sub-grid scale (SGS) turbulence transport model. A cut-off point must be drawn in the spectrum of turbulent scales, and in the Smagorinsky sub-grid scale (SGS) model used in this research, it is based on the average local grid spacing. Thus, eddies capable of being resolved by the computational grid are allowed to evolve according to the Navier Stokes equations and a turbulence model (Smagorinsky, 1963) is only employed to represent the effects of turbulence at sub-grid scales (SGS). The mixing length, l, is the characteristic length of the unresolved eddies, defined as: l-min(C_sh,κ.d_{wall}) where C_s is the Smagorinsky constant (0.17), κ is the von Karman constant (0.41) d_{wall} is the normal distance to the nearest wall and h is the representative mesh interval:

$$h = \sqrt{\frac{\partial x^2 + \partial y^2 + \partial z^2}{3}} \tag{3}$$

where ∂x, ∂y, ∂z are the local mesh dimensions in the three co-ordinate directions. Therefore, grid resolution should be sufficient that the scales of interest. Obviously with this formulation, an anistropic mesh will cause the ambiguity in the definition of the SGS length scales, and therefore the mesh shown in Figure 1 will not provide a satisfactory spatial discretization for a LES closure.

Therefore, a development is required where Cartesian meshes can be used where complex topography can be represented both for fast and efficient numerical solution which are numerically stable both for RANS and LES closure turbulence schemes. An approach which fulfils this criteria is outlined below.

4 NUMERICAL SCHEME AND EXPERIMENTAL DESIGN

The numerical scheme involves a finite volume solution of the full three-dimensional Navier-Stokes equations in a Cartesian co-ordinate system. The initial simulations use a Renormalised Group theory (RNG) κ-ε turbulence models. These results are used as initial conditions for the LES simulations where a standard Smagorinsky sub-grid model was applied. The LES simulations are run at a frequency of 10 Hz for 102.4 seconds.

4.1 *Porosity treatment and modification of drag terms*

Recent research (Lane & Hardy, 2002; Lane *et al.*, 2002; Lane *et al.*, 2004; Hardy *et al., in review*) has developed a method for incorporating complex river-bed topographies into regular structured meshes, without the need to use boundary fitted co-ordinates. It uses a porosity based method based upon that identified by Olsen & Stokseth (1995). This involves the use of regular structured grids, in which all control volumes are orthogonal, in both computational and Cartesian space, with the bed topography specified using cell porosities (P); $P = 1$ for cells that are all water; $P = 0$ for cells that are all bed; and $0 < P < 1$ for partly blocked cells. Hardy *et al.* (*in review*) have developed the Olsen & Stokseth method to address issues that were not resolved in the original Olsen & Stokseth study, notably through the inclusion of relevant drag terms (e.g. Wen *et al.*, 1998) in the momentum equations in combination with the porosity treatment. The only modification to the momentum equations is a scaling of the drag term derived from the law-of-the-wall to represent the effective exposed area of the surface. With a first approximation of flow direction, the drag exerted by a given cell is augmented according to the change in porosity in the flow direction, and is achieved by the up-scaling of z_o. The scaling is based upon the effective (equivalent) surface area and all drag is assumed to be exerted along the base of cells, other than for the side walls of the channel. A surface is then fitted to the 3 × 3 matrix of elevations centered on cell for the four surrounding cells into which the flow is entering. The scaling factor (s_{ij}) is then applied to the roughness height in the wall function using. This approach has been successfully validated upon digital particle image velocimetry (DPIV) as applied to a complex but regular, cuboidal surface and (Hardy *et al., in review*) and for the case of flow over rough gravel beds (Lane *et al.*, 2004). The flow over rough gravel bed is reviewed later. The development of this method has allowed an understanding of the way in which a complex gravel-bed surface interacts with the associated flow field and provides the opportunity for understanding the interaction between gravel-bed topography and the associated 3D flow field. The second advantage of this scheme is that it maintains a constant filter length throughout the domain and allows LES simulations to be undertaken.

4.2 *Boundary conditions*

Boundary conditions were specified at the upstream inlet and downstream outlet, at the side walls and at the free surface. The upstream inlet is specified from experimental data (see below) and the downstream outlet is specified as a fully developed flow profile with the hydrostatic pressure set at the surface at the

downstream outlet. At the free surface, the method applied by Bradbrook *et al.* (2000) has been adopted, which uses a symmetry plane at the surface across which all normal resolutes are set to zero. The bed was represented by the porosity algorithm while no-slip conditions were specified at the walls. The standard RNG theory k-ε turbulence model is not modified at the side-walls or the bed and the equilibrium wall function is used. The time averaged simulations are used for the initial conditions for the LES simulation. In this application we use the standard Smagorinski sub-grid scale model.

4.3 *Numerical solution*

The numerical scheme solves the full three-dimensional Navier-Stokes equations discretised using a finite-volume method. The interpolation scheme used is hybrid-upwind, where upwind differences are used in high convection areas (Peclet number >2) and central differences are used where diffusion dominates (Peclet number <2). Although this scheme can suffer from numerical diffusion, it is very stable. The pressure and momentum equations are coupled by applying SIMPLEST, a variation on the SIMPLE algorithm of Patankar & Spalding (1972). This convergence can proceed either smoothly or with damped oscillations to the final solution. To achieve relaxation either: (i) realistic maximum and minimum values may be imposed on the solution; or (ii) relaxation may be used to limit the amount of change allowed in any variable at a given iteration. Weak linear relaxation was used for the pressure correction, while weak false time step relaxation was used for the other variables. The convergence criterion was set such that the residuals of mass and momentum flux were reduced to 0.1% of the inlet flux.

4.4 *Experimental design: laboratory*

The experimental geometry used for model development and validation is based on water worked gravels. A bulk sample of sediment from the River Affric, Scotland was placed in the flume and water worked until a stable bed (no sediment transport) with a realistic structure (Butler *et al*., 2001) was obtained. Table 1 described the hydraulic conditions.

Once the gravels had been water worked, the surface morphology was measured using two media digital photogrammetry (see Butler *et al.* (2002) for full explanation). The experimental set-up allowed generation of DEMs at a spacing of 0.001 m. These DEMs have been subject to intensive data quality tests, in terms of point precision and accuracy and surface precision and accuracy (e.g. Butler *et al.*, 1998, 2001, 2002). For the topography had a mean surface error was 0.0008 m and the standard deviation of error was $\pm$0.0017 m. For the computational experiment a domain was constructed which was regular in the x, y and z directions, with a grid resolution of 0.002 m. The topographic data was transformed into porosity data.

An Acoustic Doppler Velocimeter (ADV) measuring 0.01 m intervals above the bed was used to set the inlet conditions and to obtain validation data. Data were collected at 25 Hz for 120 s and subject to basic screening following Lane *et al*., (1998).

4.5 *Model geometry and boundary conditions*

For the purpose of these experiments, a 0.7 m long and 0.2 m wide section of river gravel was used to define the bed geometry. The computational domain was regular in the x, y and z directions, with a grid resolution of 0.002 m. In the z direction, to allow inclusion of topography data using the porosity treatment, the maximum extent of the domain was set at 0.24 m. Thus, the computational grid was sized at $350 \times 110 \times 120$ (4 620 000 grid cells). Although validation data did not exist two other domains were constructed identical to the 24 cm domain except that the height of the domain was decreased to 12 cm and 6 cm. This was undertaken in order to asses the effect of flow depth of flow structure generation. The inlet boundary conditions were scaled appropriately.

4.6 *Model validation*

Model validation used an automated correspondence algorithm to match ADV measurement locations to corresponding grid cell locations. The size of the model grid cells was 0.002 m by 0.002 m by 0.002 m. The ADV measures in a 0.08 m diameter cylindrical sampling volume, with a height of 0.010 m. Thus, it determines a spatially-averaged velocity that corresponds approximately to 5 by 5 by 4 grid cells. In the presence of strong shear in the flow, this opens up the possibility of high velocity variability in model predictions that will not be captured in the ADV measurements. Thus, the average, standard deviation and range of model predictions corresponding to each ADV measurement location were determined.

Table 1. Basic hydraulic data for the flume experiment.

Parameter	Experimental value
Average flow depth (m)	0.225
Max. flow depth (m)	0.240
Width (m)	0.300
Discharge ($m^3 s^{-1}$)	0.0216
Flow Reynold's Number	2.88×10^4
Froude Number	0.215
Sediment D_{50} (m)	0.020
Sediment D_{84} (m)	0.069

5 RESULTS

5.1 *Validation of the porosity scheme against flume data*

Figure 2 shows a comparison of vertical variation of the downstream variation of velocity above the bed for a velocity profiles taken from an ADV location within the computational domain. The results are extremely encouraging. First, and most importantly as compared with previous experiments (e.g. Nicholas, 2001), the model is especially effective at predicting strong shear, generally between 0.1 and 0.2 z/h above the bed. Although this study differs from Nicholas (2001) in that we do not ensemble model predictions and field data, but consider velocity profiles at specific locations, Nicholas (2001) found that a wall function approach failed to reproduce the shear because: (1) the necessary roughness height required excessively coarse mesh sizes at the bed, reducing resolution of the variation of velocity with elevation above the bed; and (2) the wall function does not represent the larger clasts that protrude into the flow. The porosity approach deals with both of these problems in that it allows application of the wall function to be restricted to grain-scale roughness, permitting much finer grid cells at the bed. When coupled to the specification of the bed using high resolution digital photogrammetry, it also allows representation of the influence of downstream variation in elevation associated with protruding clasts, and hence reproduces both situations where high velocities extend to the bed at the top of protruding clasts and where there is flow separation, both upstream and downstream of large particles. Comparison of model predictions with the experimental velocity are in general are very good with correlation values of 0.91 for flow magnitude, 0.91 for downstream velocity and 0.51 vertical velocity. These compare well with comparison of CFD with smooth bed experiments (c.f. Bradbrook *et al*., 1998).

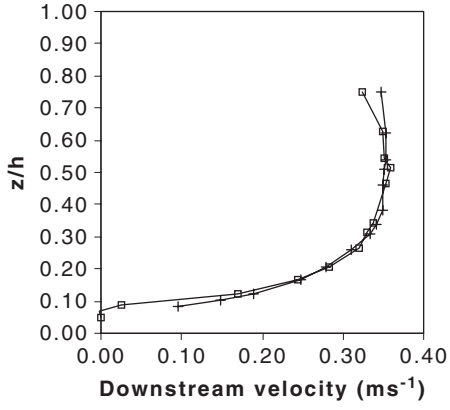


Figure 2. Comparison of predicted downstream velocity profiles with those measured using the ADV. Crossed markers are predicted velocities.

5.2 *Time dependent flow fields over gravel surfaces*

The results presented below have been simulated a frequency of 10 Hz for 102.4 seconds. The only boundary conditions difference to the RNG simulations is that cyclic boundary conditions are used.

Figure 3 shows a series of w-component velocity plots for the centre line for the 0.12 m simulation. Each image is spaced 1 second apart, with the lighter colour representing positive upwards and darker regions representing the negative downwards velocity. In Figure 3a–d positive upward flow can be observed as the flow interacts with the first large clast ($x/l = 0.27$) and shows similarities to classic junction vortex flow. However, after this object the periodic nature of the flow is observed with both positive and negative flow

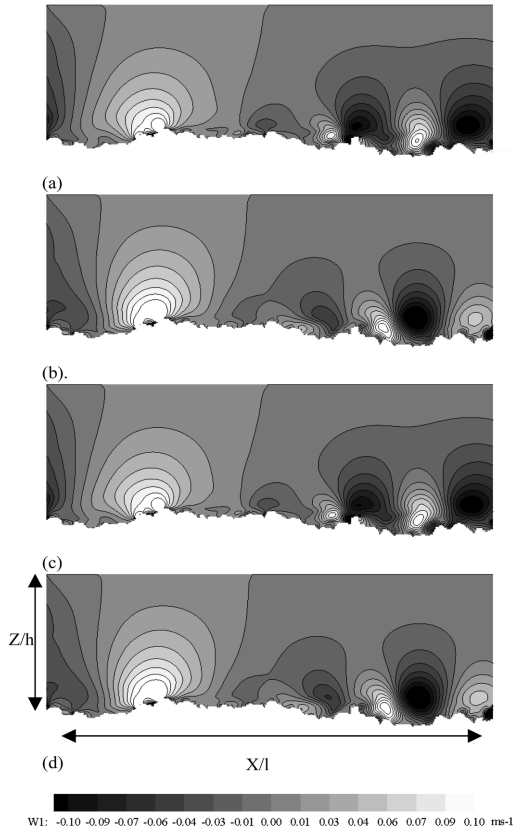


Figure 3. A series of w-component plots down the centre line of the 0.12 m simulation. Each image is separated by 1 second.

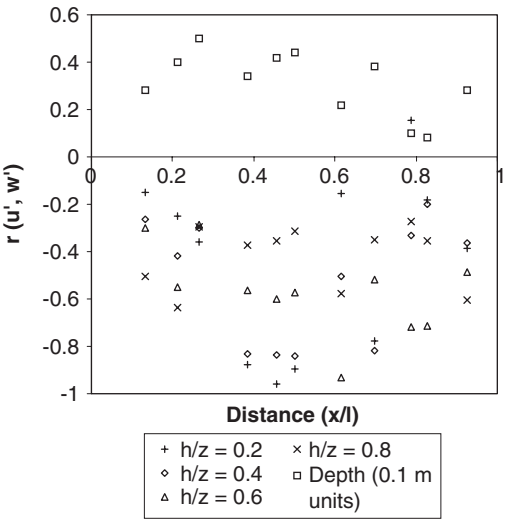


Figure 4. Correlation plots between downstream (u') and vertical (w') velocity deviations against dimensionless distance down the centre line of the model simulations for four dimensionless elevations above the bed.

oscillating over high topographic features. For example in the deepening section of the flow ($x/l = 0.8$) a periodicity between positive and negative flow can be observed at a region of potential uplift. In this type of environment, and would be predicted by a RANS closure model, would be a region of uplift. However, the application of LES enables the prediction of these time dependent structures which appear to be very similar to the fluid wedges which have previously been observed in gravel bed rivers. Although this is qualitative visual validation, the initial results are encouraging in that we are simulating naturally occurring flow structures.

Figure 4 plots the correlation between downstream (u') and vertical (w') velocity deviations against dimensionless distance down the centre line of the model simulations for four dimensionless elevations above the bed. This has a notable pattern: up to $x/l = 0.21$, the strength of correlation increases with elevation above the bed. At $x/l = 0.27$, the correlations have similar values, in the range -0.28 to -0.36. Between $x/l = 0.27$ and $x/l = 0.61$, the patterns are reversed, with very strong negative correlations near the bed, and much weaker correlations higher in the flow. This pattern reverses at $x/l = 0.61$, with the exception of data at $x/l = 0.70$. Figure 3 also shows how these changes are related to large-scale bed elevation. The first three locations (to $x/l = 0.27$) are in a zone of flow shallowing, with stronger correlations higher in the flow. The three locations that follow (up to and including $x/l = 0.50$) have stronger correlations at the bed and correspond to a zone of generally shallow flow. The flow then deepens and the highest correlations are found higher in the flow. The exceptional point ($x/l = 0.70$) is associated with a single clast high point within this deepening zone and, again, this local flow shallowing produces highest correlations close to the bed. This implies that in the shallow flow studied here, the nature of the flow structure is strongly forced by flow shallowing and flow deepening. This leads to the detection on coherent flow structures in the deeper regions.

Figure 5 shows how these correlations are linked to changes in the percentage of events found in each quadrant. We have used the standard definition of quadrants: i.e. quadrant one = outward motions; quadrant two = ejection; quadrant three = inward motions; and quadrant four = sweeps. As expected in a turbulent boundary layer, quadrant two (ejection) and quadrant four (sweep) events. Close to the bed ($h/z = 0.2$, Figure 5a) up until $x/l = 0.27$, the distribution of events is relatively similar, with quadrant two (ejection) and four (sweep) events weakly dominant. From $x/l = 0.21$, the percentage of quadrant two (ejection) and four (sweep) events increases, with them strongly dominant from $x/l = 0.46$, initially in quadrant 2 (ejection), and later in quadrant 4 (sweeps). As with the correlation, there is a switch back at $x/l = 0.61$, with the exception of data at $x/l = 0.70$. This is mirrored, but to a lesser degree, at $h/z = 0.4$ (Figure 4b). Higher in the flow (at $h/z = 0.6$ and $h/z = 0.8$, Figures 5c and 5d) the percentage of events in each quadrant is, in relative terms, more constant, with quadrant two (ejection) and four (sweep) weakly events dominant throughout. Thus the correlation patterns shown in Figure 4 are related to a near-bed strengthening in the contribution of sweeps and ejections in shallowing flows: as the flow shallows, ejection events become dominant at the bed. Once the shallowest parts of the flow are reached, there is a transition from ejection events to sweep events becoming dominant. As the flow deepens the dominance of ejections and sweeps is reduced, except for localized points where individual clasts are found, and where ejections and sweeps are more dominant at the bed.

Figure 6 shows example time-series for a 5 second period for a zone of flow shallowing (Figure 6a) and a zone of flow deepening (Figure 6b). From $x/l = 0.21$ to $x/l = 0.27$, the flow shallows, and the result is a reduction in the magnitude of vertical velocity fluctuations, coupled to stretching of the cyclicity in those fluctuations. At $x/l = 0.21$ (Figure 5a), flows closer to the surface ($h/z = 0.8$) lead flows at the bed. By $x/l = 0.27$, this lead is diminished, and the fluctuations are more synchronous as well as being of smaller magnitude. This probably reflects the growing influence of the bed as the flow shallows, with resistance having a greater effect closer to the bed, and fluctuations in velocity from upstream travelling slower

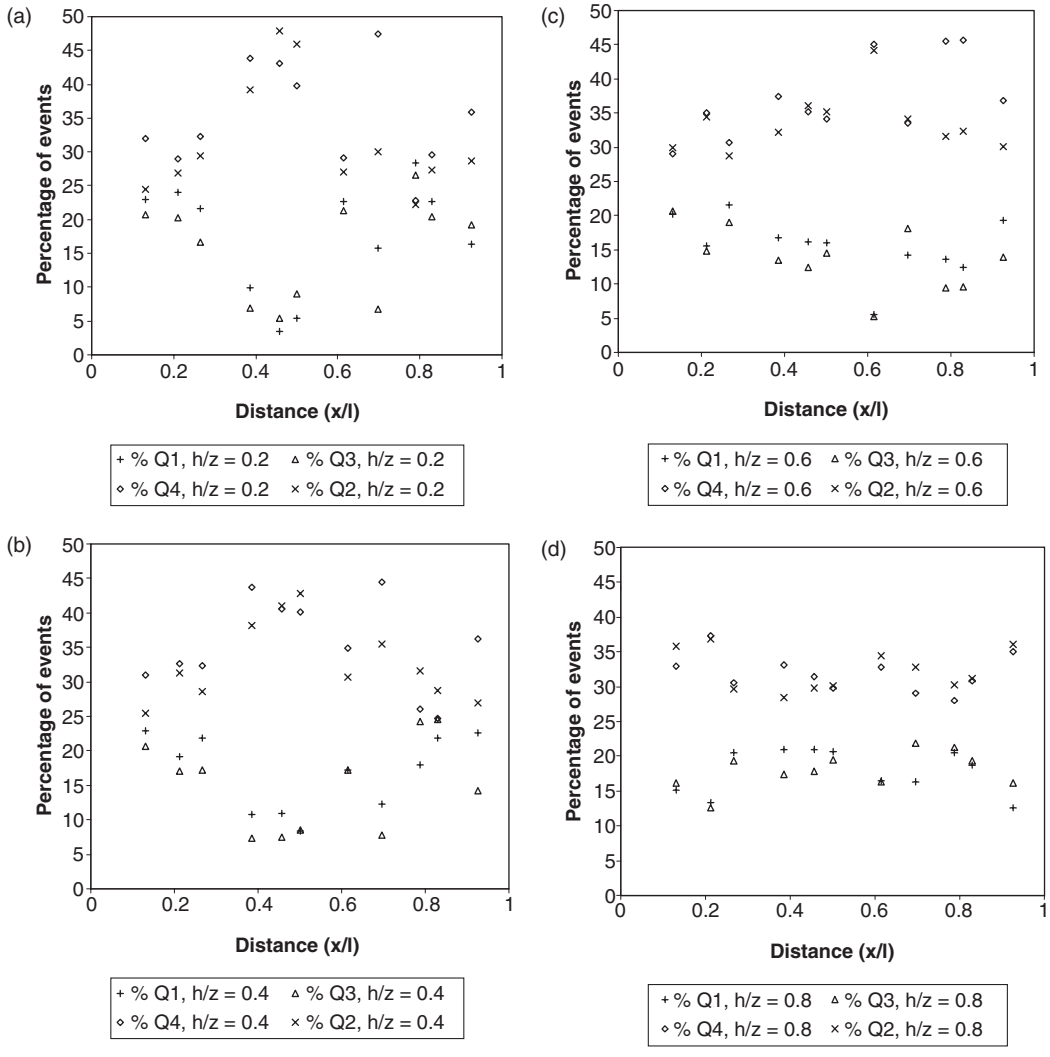


Figure 5. The percentage of events found in each quadrant downstream.

at the bed. As the bed shallows, the effects of resistance are more strongly felt throughout the flow, and the fluctuations are more synchronous, and reduced in magnitude. As the flow deepens (Figure 6b), the fluctuations are more variable in terms of magnitude and time-scale and, as a result, less organized.

The level of organization is greater as the flow starts to deepen ($x/l = 0.50$) than when it becomes deeper ($x/l = 0.61$), with flow at the bed weakly leading flow at the surface. As the flow enters the deeper zone, the reverse of flow shallowing occurs, with the magnitude of fluctuations increasing and their time (and length-scales) decreasing. However, these changes are considerably less coherent than in the flow shallowing zone and this is associated with large-scale separation downstream from the region of very shallow flow (i.e. high bed elevations) such that flow re-circulation effects (including eddy shedding) are superimposed upon the effects of bed resistance upon flow structures. At elevations $h/z = 0.4$ and $h/z = 0.6$, the increase in magnitude of fluctuations can be greater and the compression can be greater. This is probably the zone of maximum influence from the eddy shedding process, and this results in highly irregular, variable magnitude and quite complex flow. In time-averaged measurements or models, this would correspond to the zone of maximum turbulent stresses where the main flow connects with the separation zone.

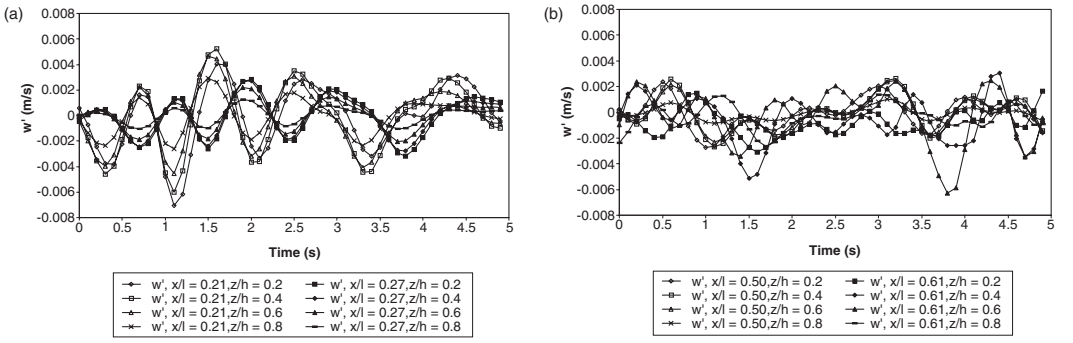


Figure 6. Time series of instantaneous w velocities (w') for $x/l = 0.21$ and $x/l = 0.27$ (Figure 6a) and for $x/l = 0.50$ and $x/l = 0.61$ (Figure 6b).

6 DISCUSSION

This paper has presented a new methodology which enables the inclusion of complex topography within a Cartesian framework. Furthermore, the numerical algorithm provides the framework for the application of LES over these gravel surfaces. In substantive terms, the numerical simulations reported in this paper show that there are two distinct scales of boundary influence upon the shallow flow studied here. The first is the large-scale, associated with clusters of particles, that cause undulations in the bed surface. This leads to water depth variation which, in turn results in changes in the time (and length-scales) and magnitudes of the associated turbulence. In particular, shallowing leads to a reduction in time (and length-scales), but more coherent patterns throughout the flow depth. Deepening is much more complex, as the reducing boundary influence can also lead to near bed flow separation, which is superimposed upon the flow structures inherited from upstream. The second scale relates to processes associated with especially large or isolated clasts which result in similar processes, but over a smaller length-scale. This emphasises that the measured flow variability at any one point in a natural river will contain both locally derived plus upstream inherited flow structures, according to the range of scales of topography present. This will have significant implications for local derivations of bed shear stress. However, the modelling method developed herein opens up exciting possibilities for exploring this effect and using it to develop new methods for parameterising shear stress in sediment transport models.

ACKNOWLEDGEMENTS

RJH was funded on NERC grants GR9/5059, GR3/9715 and NERC fellowship NER/J/S /2002/00663.

REFERENCES

Bradbrook, K.F., Biron, P., Lane, S.N., Richards, K.S. & Roy, A.G. 1998. Investigation of controls on Secondary circulation and mixing processes in a simple confluence geometry using a three-dimensional numerical model. *Hydrological Processes* 12: 1371–96.

Bradbrook, K.F., Lane, S.N., Richards, K.S., Biron, P.M. & Roy, A.G. 2000. Large Eddy Simulation of periodic flow characteristics at river channel confluences. *Journal of Hydraulic Research* 38: 207–16.

Bradbrook, K.F., Lane, S.N. & Richards, K.S. 2000. Numerical simulation of time-averaged flow structure at river channel confluences. *Water Resources Research* 36: 2731–46.

Bradbrook, K.F., Lane, S.N., Richards, K.S., Biron, P.M. & Roy, A.G. 2001. Flow structures and mixing at an asymmetrical open-channel confluence: a numerical study. *ASCE Journal of Hydraulic Engineering* 127: 351–68.

Bray, D.I. 1982. Flow resistance in gravel-bed rivers. In R.D. Hey, J.C. Bathurst, and C.R. Thorne. (eds), *Gravel-bed Rivers*: 109–33. Wiley, Chichester.

Butler, J.B., Lane, S.N. & Chandler, J.H. 1998. Assessment of DEM quality for characterising surface roughness using close range digital photogrammetry. *Photogrammetric Record* 16: 271–91.

Butler, J.B. Lane, S.N. Chandler, J.H. 2001. Application of two-dimensional fractal analysis to the characterisation of gravel-bed river surface structure. *Mathematical Geology* 33: 301–30.

Butler, J.B., Lane, S.N., Chandler, J.H. & Porfiri, K. 2002. Through-water close-range digital photogrammetry in flume and field environments. *Photogrammetric Record* 17(99): 419–39.

Clifford, N.J., Robert, A. & Richards, K.S. 1992. Estimation of flow resistance in gravel-bedded rivers: a physical explanation of the multiplier of roughness length. *Earth Surface Processes and Landforms* 17: 111–26.

Ferguson, R.I., Parsons, D.R., Lane, S.N. & Hardy, R.J. 2004. Flow in meander bends with recirculation at the inner bank. *Water Resources Research*, 39(11) 10.1029 /2003 WR001965. ESG2-1, 13.

Hardy, R.J., Lane, S.N., Lawless, M.R., Elliot, L. Ingham, D.B. & Best, J.L. in review. Development and

testing of numerical code for treatment of complex river channel topography in three-dimensional CFD models with structured grids. *Journal of Hydraulic Research*.

Hodskinson, A. & Ferguson, R.I. 1998. Numerical modelling of separated flows in river bends: Model testing and experimental investigation of geometrical controls on the extent of flow separation at the concave bank. *Hydrological Processes* 11: 1323–38.

Hey, R.D. 1979. Flow resistance in gravel-bed rivers. *ASCE Journal of the Hydraulics Division*: 105: 365–79.

Lane, S.N., Biron, P.M., Bradbrook, K.F., Butler, J.B., Chandler, J.H., Crowell, M.D., McLelland, S.J., Richards, K.S. & Roy, A.G. 1998. Integrated three-dimensional measurement of river channel topography and flow processes using acoustic doppler velocimetry. *Earth Surface Processes and Landforms* 23: 1247–67.

Lane, S.N., Bradbrook, K.F., Richards, K.S., Biron, P.M. & Roy, A.G. 1999. The application of computational fluid dynamics to natural river channels: three-dimensional versus two-dimensional approaches. *Geomorphology* 29: 1–20.

Lane, S.N., Bradbrook, K.F., Richards, K.S., Biron, P.M. & Roy, A.G. 2000. Secondary circulation in river channel confluences: measurement myth or coherent flow structure? Special Edition of *Hydrological Processes*, 14: 2047–71.

Lane, S.N. & Hardy, R.J. 2002. Porous rivers: a new way of conceptualising river a floodplain flows? In: D.B. Ingham & I. Pop. (eds) *Transport Phenomena in Porous Media (II)*. p. 425–49. Pergamon.

Lane, S.N., Hardy, R.J., Elliot, L. & Ingham, D.B. 2002. High resolution numerical modelling of three dimensional flows over complex river bed topography, *Hydrological Processes*, 16: 2261–72.

Lane, S.N., Hardy, R.J., Elliot, L. & Ingham, D.B. 2004. Numerical modelling of flow processes over gravelly-surfaces using structured grids and a numerical porosity treatment. *Water Resources Research*, 40, W01302 10.1029/2002/WR 001934. W01302.

Nicholas A.P. 2001. Computational fluid dynamics modelling of boundary roughness in gravel-bed rivers: An investigation of the effects of random variability in bed elevation. *Earth Surface Processes and Landforms*, 26: 345–62.

Nicholas, A.P. & Smith, G.H. 1999. Numerical simulation of three-dimensional flow hydraulics in a braided channel. *Hydrological Processes*, 13: 913–29.

Olsen, N.R.B. & Stokseth, S. 1995. Three-dimensional numerical modelling of water flow in a river with large bed roughness. *Journal of Hydraulic Research*, 33: 571–81.

Patankar, S.V. & Spalding, D.B., 1972. A calculation procedure for heat, mass and momentum transport in three-dimensional parabolic flows. *International Journal of Heat and Mass Transfer*, 15: 1787–806.

Rogallo, R.S. & Moin, P. 1984. Numerical simulation of turbulent flows. *Annual Review of Fluid Mechanics*, 16: 99–137.

Smagorinsky, J. 1963. General circulation experiments with the primitive equations. Part I: The basic experiment. *Monthly Weather Review*, 91: 99–167.

Wen, X, Ingham, D.B, Dombrowski, N. & Foument, E.A. 1998. The generation of an orthognal grid by the use of a boundary integral technique. *Engineering Analysis with Boundary Elements* 21: 197–205.

Whiting, P.J. & Dietrich, W.E. 1990. Boundary shear stress and roughness of mobile alluvial beds. *ASCE Journal of Hydraulic Engineering*, 116: 1495–511.

Wiberg, P.L. & Smith, J.D. 1991. Velocity distribution and bed roughness in high gradient streams. *Water Resources Research*, 27: 825–38.

This page intentionally left blank

River Flow 2004 – Greco, Carravetta & Della Morte (eds.)
© 2004 Taylor & Francis Group, London, ISBN 90 5809 658 0

Numerical simulation on development process of dunes and flow resistance

S. Onda
Graduate School of Civil Engineering, Kyoto University, Kyoto, Japan

T. Hosoda
Dept. of Urban Management, Kyoto University, Kyoto, Japan

ABSTRACT: Flow resistance in rivers changes with development or attenuation of sand waves. Therefore, it is necessary to know how the flow resistance varies with transformation of sand bed in order to predict the water surface profiles. In this study, the numerical model to reproduce the formation processes of dunes and flow resistance was developed. A depth averaged flow model considering the effects of vertical acceleration and a non-equilibrium sediment transport model are combined. The calculated results on the temporal development processes of dunes, the shape characteristics and flow resistance are compared with previous experimental and theoretical studies.

1 INTRODUCTION

Over erodible bed, various sand waves are formed in response to hydraulic conditions and flow resistance changes with their development or attenuation. Prediction of resistance law is important in river engineering and it is necessary to know how the flow resistance varies with transformation of dunes. So far, a number of experimental and theoretical studies on the formation processes of dunes and flow resistance have been carried out.

As one of the experimental studies on development processes of dunes, Nakagawa & Tsujimoto (1976, 1983) investigated the temporal variations of sand wave spectrum. It was pointed out that in evolution processes of dunes the spectrum peak formed in the generation process moves to lower wave number side with sand waves developed and that in equilibrium state the sand wave spectrum can be expressed as -3 power law.

Engelund (1952) introduced the similarity assumption of the friction and explained that the grain shear stress is a function of the total bed shear stress in flows with same bed configurations. Comparing with other experiments, he derived the relationship between the grain and the total bed shear stress. Kishi & Kuroki (1972) showed that the grain shear stress is a function of the relative depth as well as the total bed shear stress and derived the resistance law for different bed configurations by modifying Engelund's theory.

On the other hand, Hosoda et al. (2002) developed the numerical model to reproduce the formation processes of dunes, incorporating the depth averaged flow model considering the effects of vertical acceleration and the non-equilibrium sediment transport model. However, flow resistance such as increase of the depth in development processes of dunes could not be reproduced.

In this paper, the numerical model, which can also evaluate the flow resistance, is developed, applying the depth averaged flow model by Hosoda et al. The depth averaged flow model has advantages of simulating flows over the sand waves from a practical point of view. The formation processes of micro-scale sand waves such as dunes and antidunes are simulated and the calculated results on the temporal development processes of dunes, shape characteristics and flow resistance are compared with previous experimental and theoretical studies.

2 BASIC EQUATIONS

A depth averaged flow model considering the effects of vertical acceleration is applied to calculate the flow fields. The coordinate system and the hydraulic variables are illustrated in Figure 1.

$$\frac{d}{dx}\left(\frac{q^2}{h}\right)+\frac{d}{dx}\left(\frac{gh^2}{2}\cos\theta\right)-\frac{d}{dx}\left\{\frac{q^2}{3h}\left(\frac{dh}{dx}\right)^2\right\}$$

$$+\frac{d}{dx}\left(\frac{q^2}{3}\frac{d^2h}{dx^2}\right)-\frac{d}{dx}\left(\frac{q^2}{2h}\frac{dh}{dx}\frac{dy_b}{dx}\right)+\frac{d}{dx}\left(\frac{q^2}{2}\frac{d^2y_b}{dx^2}\right)$$

$$+\frac{dy_b}{dx}\left\{gh\cos\theta-\frac{U^2}{2}\left(\frac{dh}{dx}\right)^2-U^2\frac{dh}{dx}\frac{dy_b}{dx}+\frac{U^2h}{2}\frac{d^2h}{dx^2}\right.$$

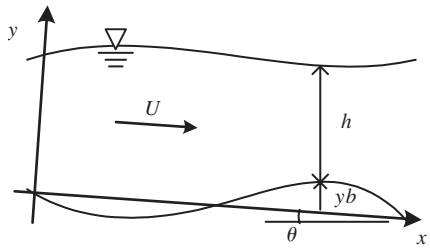


Figure 1. Explanation of symbols.

$$+U^2 h\frac{d^2 y_b}{dx^2}\Bigg\} = gh\sin\theta - \frac{\tau_{bx}}{\rho} + \frac{d}{dx}\left(\alpha h^2 U\frac{dU}{dx}\right) \tag{1}$$

where x: spatial coordinate, h: depth, y_b: bed elevation from x-axis, q: flow discharge per unit width, U: depth averaged velocity, τ_{bx}: x component of bottom shear stress, g: gravity acceleration, θ: bed slope, ρ: density of water and α: coefficient of eddy viscosity (=0.05).

Equation (2) is used to evaluate the bottom shear stress correctly in which the local velocity distribution obtained by potential flow analysis and the accelerating/decelerating effect near a bed are included (Hosoda el al. 1997).

$$\frac{\tau_{bx}}{\rho} = fu_b^2\left(1-\Gamma\frac{dh}{dx}+\Delta\frac{dy_b}{dx}\right), \Gamma = 2, \Delta = 1 \tag{2}$$

$$u_b = \frac{q}{h}+\frac{q}{3h}\left(\frac{dh}{dx}\right)^2+\frac{q}{h}\frac{dh}{dx}\frac{dy_b}{dx}-\frac{q}{6}\frac{d^2h}{dx^2}-\frac{q}{2}\frac{d^2y_b}{dx^2}$$

As the bed variation model, the non-equilibrium sediment transport model is applied.

$$\frac{\partial y_b}{\partial t} = \frac{1}{1-\lambda}\frac{A_3}{A_2}d\left(p_d - p_s\right) \tag{3}$$

where p_s: pick-up rate, p_d: deposit rate, d: sand diameter, λ: porosity of sand bed and A_2, A_3: shape coefficients of sand grain for two and three dimensional geometrical properties, respectively ($=\pi/4, \pi/6$).

The pick-up rate p_s is evaluated by equation (4) proposed by Nakagawa & Tsujimoto (1980) and the deposit rate p_d is calculated combining the pick-up rate and the probability density distribution function of step length.

$$p_s\sqrt{d/(\sigma/\rho-1)g} = 0.03\tau_*(1-0.035/\tau_*)^3 \tag{4}$$

$$f_s(s) = \frac{1}{\Lambda}\exp\left(-\frac{s}{\Lambda}\right) \tag{5}$$

where σ: density of sand, τ_*: non-dimensional tractive force, Λ: step length, s: distance from a point where a sand particle is picked up.

3 NUMERICAL METHOD

The numerical method Hosoda et al. (1994, 2002) used for simulating the undular bore and the flows over dunes is applied to calculate the water surface profiles. However, the flow resistance cannot be reproduced in their numerical results since the pressure distribution is assumed to be hydrostatics in case the depth gradient is greater than a standard value. To refine this aspect, the vertical acceleration terms of the basic equation are multiplied by the attenuation function locally in case the depth gradient is greater than the standard value.

The procedures for calculating the water surface profiles are described as follows.

(i) Each derivative term of the basic equations is descritized using the finite deference forms.

$$\frac{dh}{dx} = \frac{h_{i+1}-h_{i-1}}{2\Delta x}, \frac{d^2h}{dx^2} = \frac{h_{i+1}-2h_i+h_{i-1}}{\Delta x^2}, \cdots$$

(ii) The depths h_i^k at k-th step are supposed to be known. Substituting the depths h_i^k into the finite difference forms of Equation (1), the numerical errors er_i^k at each grid point are obtained. Using this numerical error and the following equations, the depths h_i^{k+1} at next step $k+1$ are calculated.

$$h_i^{k+1} = h_i^k + sig(k)\cdot\omega\cdot\left|er_i^k\right|, \omega = 0.02$$

$$sig(k) = -1\cdot sig(k-1)\ for\ \left|er_i^k\right| \geq \left|er_i^{k-1}\right|$$

$$sig(k) = 1\cdot sig(k-1)\ for\ \left|er_i^k\right| < \left|er_i^{k-1}\right|$$

(iii) The procedure (ii) is iterated until the total error becomes small.

(iv) The bed variation is calculated for 2s ($\Delta t = 0.1$s), using equations (3)–(5).

Then, the iterative procedure for calculating the water surface profiles is performed.

4 HYDRAULIC CONDITIONS

The model flume is shown in Figure 2 and the hydraulic conditions are listed in Table 1. While the flow discharge per unit width q and friction factor f is fixed as 200 (cm^3/s/cm) and 0.01 respectively, the bed slope and the diameter of sand particles are varied as shown in Table 1. Since three boundary conditions on the depth h and gradient dh/dx are required for calculation of the water surface profiles, the following conditions are used.

(1) The depth gradient $dh/dx = 0$ at upstream end.
(2) The depth gradient $dh/dx = 0$ at downstream end.

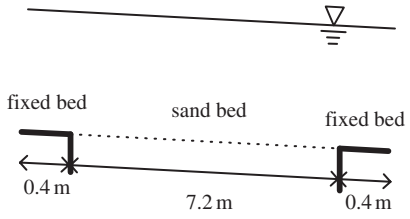


Figure 2. Schematic diagram of model flume.

Table 1. Hydraulic conditions.

Run	Sand diameter d (cm)	Bed slope
D1	0.030	1/500
D2	0.040	1/500
D3	0.045	1/500
D4	0.050	1/500
D5	0.040	1/750
D6	0.045	1/750
D7	0.030	1/1000
D8	0.040	1/1000
D9	0.045	1/1000
D10	0.050	1/1000
A1	0.030	1/40
A2	0.040	1/40
A3	0.045	1/40
A4	0.030	1/50
A5	0.040	1/50
A6	0.045	1/50
A7	0.050	1/50

(3) The depth h = the normal depth at downstream end in case of subcritical flow or the normal depth at upstream end in case of supercritical flow.

In calculation of the bed variations, sediment discharge is supplied from upstream fixed bed not to change the bed elevation sharply between the fixed bed and the movable bed. The bed elevations of the fixed bed are made zero after calculating the bed variations.

5 RESULTS AND DISCUSSION

As the example of the numerical results, the temporal variations of the water surface profiles and the bed elevations in RunD3 are shown in Figure 3. It can be seen that the small disturbance generated from upstream of the sand bed amplifies and propagates to the downstream with the wave height developed and increase of flow resistance is observed.

5.1 *Formation processes of dunes*

To discuss the formation processes of dunes in detail, the temporal variations of the sand wave spectrum in evolution processes of dunes are compared with

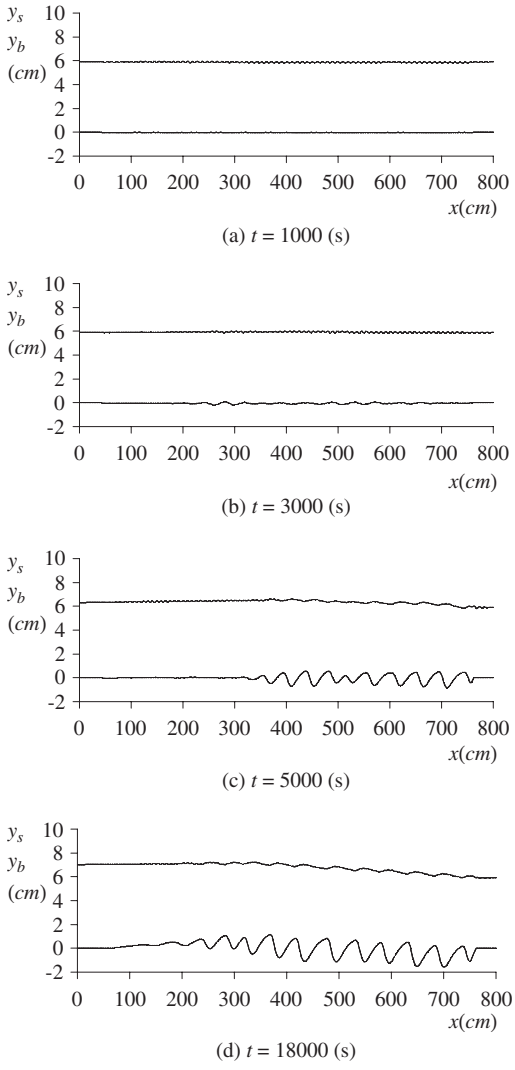


Figure 3. Numerical results in RunD3.

the previous experimental and theoretical studies. The experimental parameters by Nakagawa & Tsujimoto (1976, 1983) are presented in Tables 2 and 3. Figures 4 and 5 show the temporal variations of sand wave spectrum in case of RunD3 and D8. Equation (6) proposed by Hino (1986) is also shown (Figs. 4(d), 5(d)), which is derived based on dimensional consideration.

$$S(k) = \alpha k^{-3}, \ (\alpha = \text{constant}) \tag{6}$$

The enlargement of the bed elevations and the temporal variations of the wave length L, the wave height H and the wave gradient H/L in case of RunD3 are presented in Figures 6 and 7.

Table 2. Summary of experimental parameters by Nakagawa & Tsujimoto (1976).

Sand diameter d_{50} (cm)	Discharge Q (cm^3/s ($\times 10^3$))	Depth h (cm)	Bed slope
0.065	6.33	5.57	1/500
0.065	8.53	6.65	1/500
0.065	9.02	6.47	1/500
0.065	10.01	7.11	1/500
0.065	12.93	8.20	1/500
0.065	18.31	10.00	1/500
0.065	8.04	5.80	1/300
0.065	18.41	8.00	1/200
0.140	15.95	9.25	1/500
0.140	14.46	7.70	1/200
0.140	21.07	9.50	1/200
0.096	12.89	7.80	1/300
0.096	11.29	7.20	1/200
0.096	16.34	8.50	1/200
0.019	7.31	7.00	1/500
0.019	4.97	5.00	1/500

Flume width = 33 cm

Table 3. Summary of experimental parameters by Nakagawa & Tsujimoto (1983).

Sand diameter d (cm)	Average velocity U (cm/s)	Depth h (cm)	Bed slope
0.042	26.81	5.55	1/500
0.042	32.75	8.76	1/500
0.042	36.01	4.74	1/300
0.042	39.33	7.32	1/300
0.042	43.40	9.50	1.300
0.050	35.81	4.97	1/500
0.050	42.05	5.88	1/500
0.050	50.29	10.50	1/500
0.070	39.6	7.0	1/500
0.070	46.4	10.0	1/500
0.070	51.5	11.5	1/800
0.070	50.1	7.0	1/800
0.070	51.7	12.5	1/300

As mentioned above, Nakagawa & Tsujimoto (1976, 1983) pointed out that the sharp spectrum peak is observed in initial stage and that the peak moves to the lower wave number side gradually in formation processes and in equilibrium state sand wave spectrum can be expressed as -3 power law. In the initial stage of the numerical results (Figs. 4(a), 5(a)), the spectrum peak is seen remarkably near the wave number $k = 0.1(\mathrm{cm}^{-1})$. It is thought that these waves are equivalent to the sand waves with short wave length (=10 cm) (Fig. 6 (a)) and corresponding to the sand waves, which fulfill the resonance relation between the water surface and the bed variation (the Airy relation).

In the middle of the development processes (Figs. 4(b)–(c), 5(b)–(c)), the spectrum in low wave number

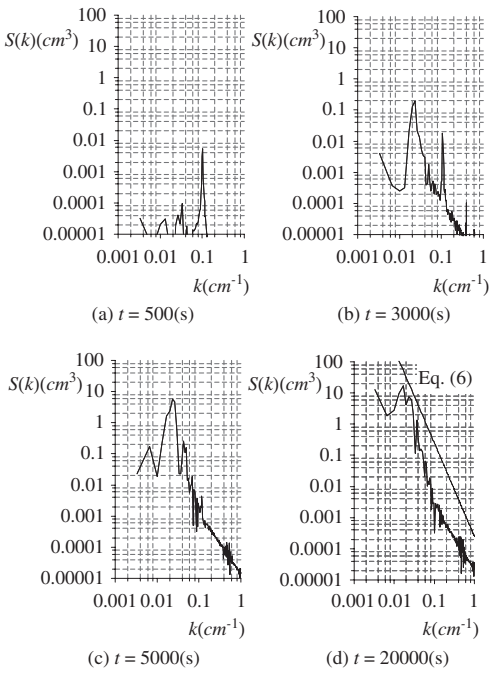


Figure 4. Temporal variations of sand wave spectrum in RunD3.

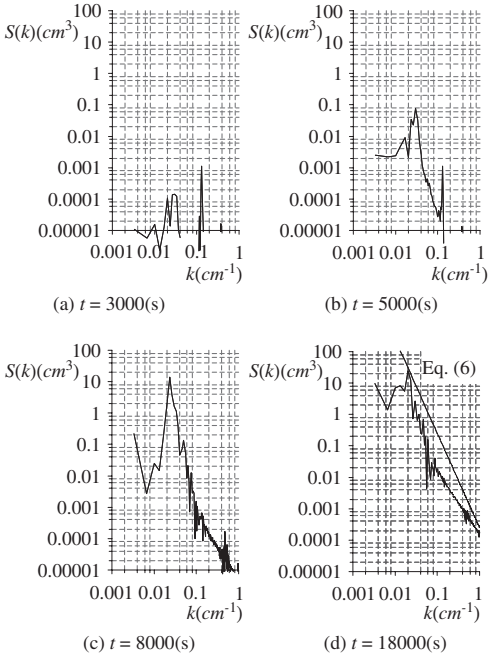


Figure 5. Temporal variations of sand wave spectrum in RunD8.

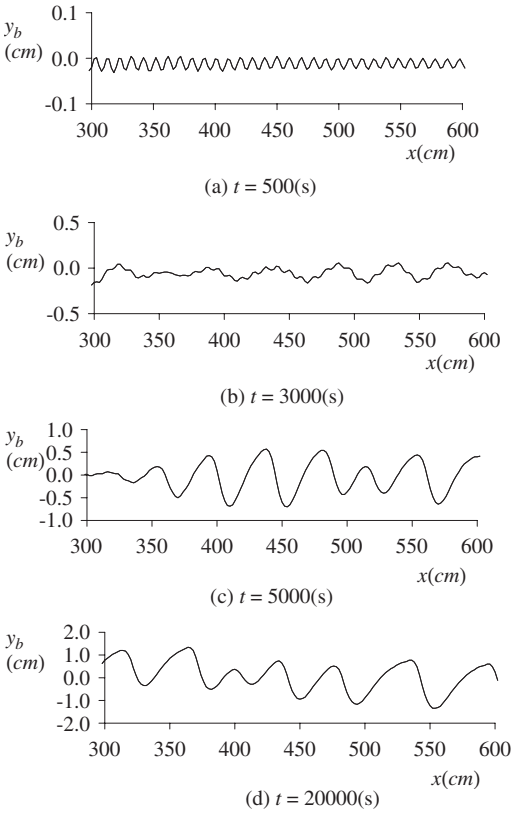


Figure 6. Enlargement of bed elevations in RunD3.

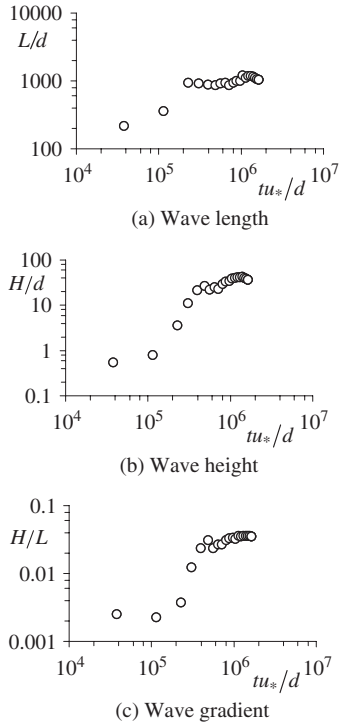


Figure 7. Temporal variation of wave length, wave height and wave gradient.

range grows larger and the spectrum peak is generated. This peak is equivalent to the waves with the wave length ($L = 40$–50 cm) (Fig. 6 (c)). After that it becomes blunt, as the spectrum in low wave number range gets bigger. On development time scale of dunes, Nakagawa & Tsujimoto (1976) reported that evolution of the wave length and wave height is proportional to the square root of non-dimensional time. In the calculated results (Fig. 7), it is found that the wave length is developed sharply from the initial stage to the development processes, although the wave height is developed gradually. This is due to difference of development time scale in dunes formed in the initial stage and the formation processes.

In the equilibrium state (Figs. 4(d), 5(d)), the spectrum in the high wave number range can be expressed as -3 power law as pointed out by Nakagawa, Tsujimoto & Hino.

As for the time scale for fully developed sand waves, the numerical results are compared with the equation (7) proposed by Nakagawa & Tsujimoto (1981) (Fig. 8). Real time scale T_D of the numerical results is obtained from the time that the wave gradient is almost equilibrium.

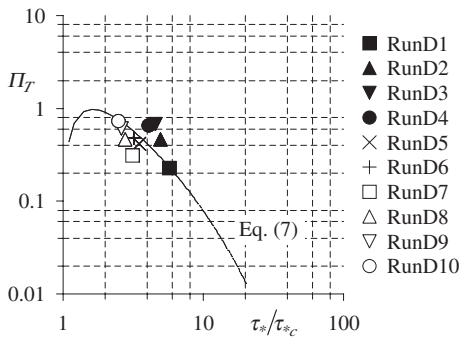


Figure 8. Time scale for fully developed sand waves.

$$\Pi_T \equiv \left\{\frac{T_D\sqrt{(\sigma/\rho-1)gd}}{h}\right\}\left(\frac{d}{h}\right)(\tau_{*c})^{3/2}$$

$$= \frac{1-\rho_0}{2f_s(\alpha)}k_T k_L^2 \frac{\delta}{10\tau_*(\tau_*/\tau_{*c})^{1.5}} \qquad (7)$$

where T_D: real time scale of development, $1-\rho_0 = 0.6$, $f_s(\alpha) = 0.08$, $k_L = 5.0$, $k_T = 2.0$ and δ is wave gradient

Table 4. Numerical results on averaged depth and averaged wave length.

Run	Averaged depth h (cm)	Averaged wave length L (cm)
D1	7.4	42.3
D2	7.1	50.0
D3	6.7	47.0
D4	6.2	58.8
D5	7.4	37.4
D6	7.1	48.0
D7	8.0	32.2
D8	7.8	52.0
D9	7.7	54.4
D10	7.6	46.7

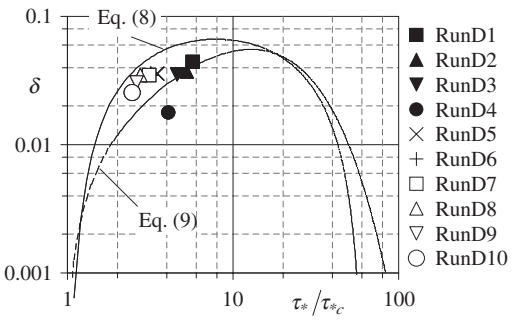


Figure 9. Relation between τ_* and wave gradient.

expressed by equation (9). The numerical results are in good agreement with equation (7).

5.2 *Shape characteristics of dunes*

Table 4 shows the averaged wave length and the averaged depth, which is obtained by using the numerical results from $x = 3.0$ to 6.0 m. Since the wave length of dunes is said to be five times of the depth in previous works, the calculated results are almost reproduced.

Figure 9 shows the relation between the wave gradient ($\delta = H/L$) and the non-dimensional tractive force. It can be seen that the numerical results agree with equation (8) proposed by Fredsoe (1975) and equation (9) by Yalin & Karahan (1979).

[Fredsoe]

$$\delta = \frac{H}{L} = \frac{1}{8.4}\left(1 - \frac{\tau_{*c}}{\tau_*} - 0.4\tau_*\right)^2 \qquad (8)$$

[Yalin & Karahan]

$$\delta = \frac{H}{L} = \delta_{\max}\frac{\eta - 1}{\bar{\eta} - 1}\exp\left(\frac{\bar{\eta} - \eta}{\bar{\eta} - 1}\right)$$

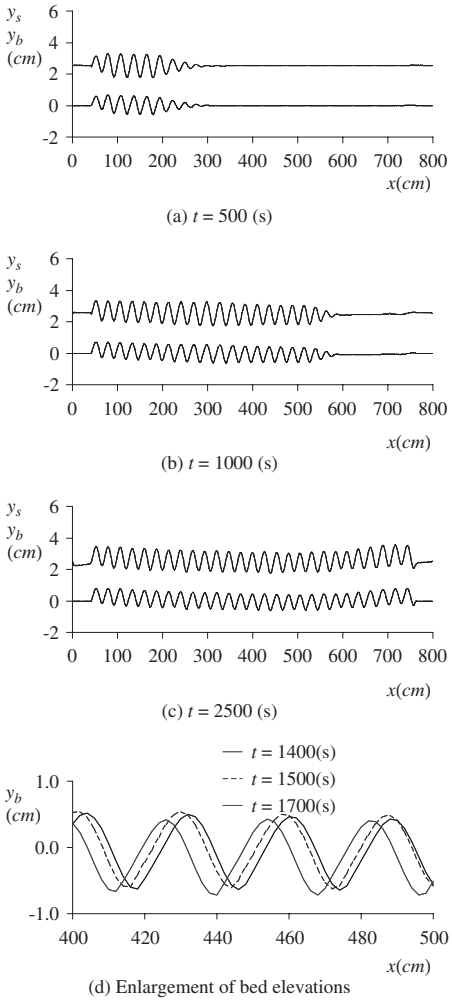


Figure 10. Numerical results in RunA2.

$$\delta_{\max} = 0.0047(\bar{\eta} - 1), \eta = \tau_*/\tau_{*c}$$

$$\bar{\eta} = 12.84\, for 100 \le h/d \le 1.04 \times 10^5 \qquad (9)$$

5.3 *Antidunes*

As the results of antidunes, the temporal variations of the water surface and the bed elevations are presented in Figure 10. It is found that the water surface profiles are out of phase with the bed elevations. Figure 10(d) presents the enlargement of bed elevations from $x = 4.0$ to 5.0 m and it is observed that antidunes propagate upstream.

The temporal variations of the wave number spectrum in case of RunA2 are shown in Figure 11. The spectrum in antidunes is different from the one in

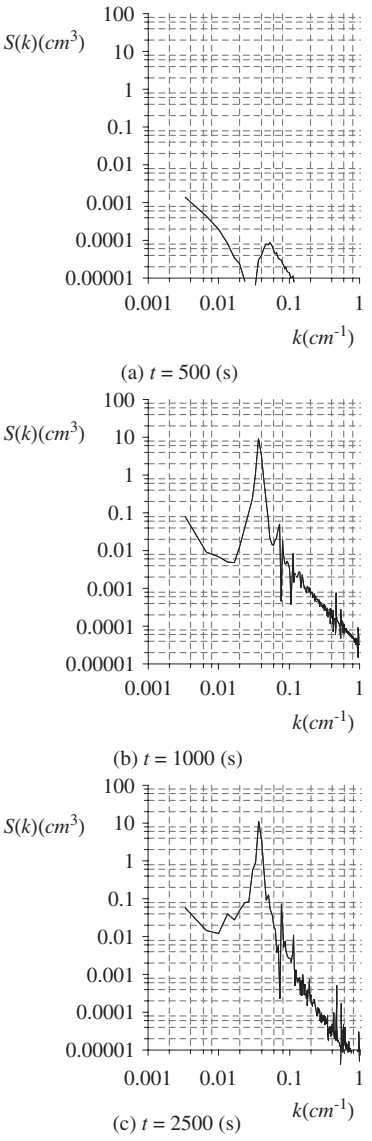


Figure 11. Temporal variation of sand wave spectrum in RunA2.

dunes and the peak is generated in some wave number. Therefore, it turns out that the sand waves are formed regularly.

5.4 *Comparison of regions for formation of different bed configurations*

Figure 12 shows comparison of regions for the formations of different bed configurations. The reference curves (Fig. 12) show the relationship between Froude number (*Fr*) and non-dimensional wave number (*kh*). These curves are expressed by equations (10) and (11) which indicate the minimum Froude number for antidunes and maximum for dunes (10) and the maximum possible Froude number for long-crested features (11), respectively (Kennedy, 1963).

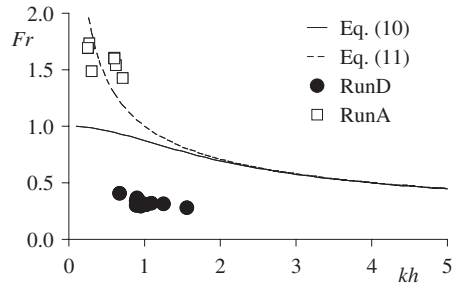


Figure 12. Regions for formation of different bed configurations.

$$Fr^2 = \frac{\tanh kh}{kh} \tag{10}$$

$$Fr^2 = \frac{1}{kh} \tag{11}$$

The calculated results are in good agreement with the regions described by equations (10) and (11).

5.5 *Flow resistance*

Kishi & Kuroki (1972) developed Engelund's theory and derived the resistance law for different bed configurations by arranging a large number of the experimental data. The resistance law (relationship between friction factor and non-dimensional tractive force) for different bed configurations is described as follows:

[Dunes I]

$$\varphi = 2.4(h/d)^{1/6}\,\tau_*^{-1/3} \tag{12}$$

[Dunes II]

$$\varphi = 8.9 \tag{13}$$

[Transition]

$$\varphi = 1.1\times10^{6}(h/d)^{-3/2}\,\tau_*^{3} \tag{14}$$

[Flat bed]

$$\varphi = 6.9(\kappa_0/\kappa)^{1/2}(h/d)^{1/6} \tag{15}$$

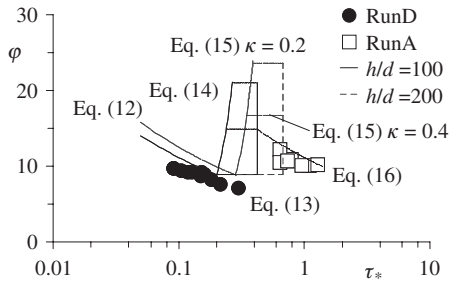


Figure 13. Comparison of friction factor.

[Antidunes]

$$\varphi = 2.8(h/d)^{3/10}\tau_*^{-1/3} \tag{16}$$

where κ_0 & κ: Karman constant in flows only ($= 0.4$) and flows with sediment transport, respectively.

The numerical results are compared with equations (13)–(16) in Figure 13. As the relative depth h/d in equations (13)–(16), 100 and 200 is used. Since it is observed that the calculated results agree with the resistance law, the numerical model in this study can evaluate resistance law. In case of transition and flat bed, further investigations are needed.

6 CONCLUSIONS

In this study the numerical model to predict the formation process of dunes and flow resistance was developed, using the depth averaged flow model considering the effect of vertical acceleration and the non-equilibrium sediment transport model. The numerical results were compared with the previous experimental and theoretical studies and it was indicated that this numerical model can reproduce the formation process of dunes, the shape characteristics and flow resistance.

REFERENCES

Engelund, F. 1952. Closure to "Hydraulic Division", *ASCE*, 117: Paper No. 2528.

Fredsoe, J. 1975. The friction factor and height–length relation in flow over a dune-covered bed, Progressive Report 37, Institute of Hydrodynamics, Technical Univ. of Denmark.

Hino, M. 1986. Equilibrium-range spectra of sand waves formed by flowing water, *J. Fluid Mech*., 34, Part 3: 565–576

Hosoda, T. and Tada, A. 1994. Free surface profile analysis on open channel flows by means of 1-D basic equations with effect of vertical acceleration. *Annual J. of Hydraulic Engrg*., JSCE, 38: 457–462. (in Japanese)

Hosoda, T., Muramoto, Y. and Miyamoto, M. 1997. Bottom shear stresses of flows over a wavy bed by using depth averaged flow equations. *J. of Hydraulic, Coastal and Environmental Eng*., JSCE, 558/II-38: 81–89. (in Japanese)

Hosoda, T., Kato, T. and Onda, S. 2002. Numerical simulations on development processes of dunes. *Proc. of* 13th IAHR-APD Congress, I: 405–410.

Kennedy, J. F. 1963. The mechanics of dunes and antidunes in eridible channels. *J. Fluid Mech*., 16, Part 4: 521–554.

Kishi, T. and Kuroki, M. 1972. Bed forms and resistance to flow in erodible-bed channels (I) – Hydraulic relations for flow and sand waves –, Bulletin of the Faculty of Eng., Hokkaido Univ.: 1–23. (in Japanese)

Nakagawa, H. and Tsujimoto, T. 1976. Experimental study on evolution of sand waves from an initially flattened bed. *Annuals. Disas. Prev. Res. Inst*., Kyoto Univ., 19, B-2: 289–309. (in Japanese)

Nakagawa, H. and Tsujimoto, T. 1980. Sand bed instability due to bed load motion. *Proc*. ASCE, 106, HY12: 2029–2051.

Nakagawa, H. and Tsujimoto, T. 1981. Time-lag resistance of unsteady flow over lower regime sand bed. *Proc*. of 25th *Japanese conference on hydraulics*, JSCE: 1–7. (in Japanese)

Nakagawa, H. and Tsujimoto, T. 1983. Study on formation of sand wave spectrum. *Proc. of JSCE*, 335: 107–115. (in Japanese)

Yalin, M.S. and Karahan, E. 1979. Steepness of sedimentary dunes. *Proc*. ASCE, 105, HY4: 381–392.

River Flow 2004 – Greco, Carravetta & Della Morte (eds.)
© 2004 Taylor & Francis Group, London, ISBN 90 5809 658 0

Experimental study of bed-load grain size sorting near incipient motion on steep slopes

A. Recking
Cemagref, Hydrology and Hydraulic Research unit, Lyon, France

V. Boucinha
INSA-LMFA, Lyon, France

P. Frey
Cemagref, Erosion, Torrent, Snow and Avalanches Research Unit, Grenoble, France

ABSTRACT: Flume experiments of bed-load transport on steep slopes were carried out using image analysis. Many sets of experiments were performed, first with uniform materials, and secondly with mixtures of these uniform materials, in order to assess the grain size sorting effects on bed-load. In each case, bedforms were observed. Although input of water and sediments was stationary, large fluctuations of solid discharge were observed for the non uniform material, associated with a varying slope around the equilibrium value.

1 INTRODUCTION

Research on bed-load solid transport and especially on grain size sorting effects associated with bedforms still remains an open and challenging issue. Experimental research on this topic makes full use of mobile bed tilting flumes with mixtures of water and natural sand-gravel material similar to those encountered in rivers or torrents. In the work presented hereafter, the toilsome and time-consuming manual sieving method is replaced by a new technique called GDS using image analysis for measuring the grain size distribution and the solid discharge downstream of the experimental flume (Bigillon et al. 1999, Frey et al. 2003). Various sets of experiments were performed on an equilibrium slope of 9% to assess the grain size sorting effect on bed-load. A first set of experiment was performed using uniform materials and results are compared to non-uniform materials data obtained by mixture of the previous ones. In both cases observed fluctuations of the grain size distribution and the total solid discharge are presented and discussed.

2 EXPERIMENTAL SETUP

2.1 *Description of the GDS system*

The GDS (figure 1) allows to record images of grains flowing over a back-lighted transparent ramp located at the outlet of the flume. Images were recorded with a frequency of 15 images/sec. From this series of 2D images as input, an algorithm using specific image analysis methods (with the help of WIMA software, Ducottet 1994) allowed to segment the particles, and permitted to calculate their axes dimensions. Considering the average grain velocity, the solid discharge and the grain size distribution were calculated each 3 second. The entire device was successfully validated with an error generally less than 3% on grain size curve parameters and less than 7% on solid discharge (Frey et al. 2003).

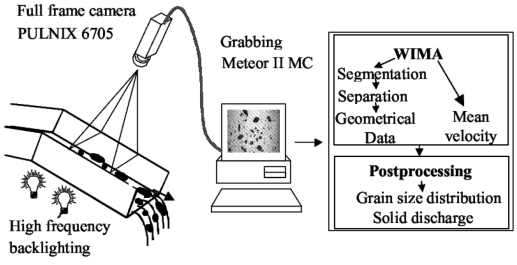


Figure 1. The image processing chain.

2.2 *Materials and experimental flume*

Three uniform materials were selected by sieving natural sand-gravel materials with round meshes. Uniform

Table 1. Three uniform material selected for the experiments.

Diameter	mm	2–3 mm	5–6 mm	8–10 mm
Corresponding sieving with square meshes	<2	13%		
	2–3.15	85%		
	3.15–4	2%		
	4–5		86%	
	6.3–8		14%	59%
	8–10			41%
	>10			
Average weight of a grain (g)		0.015	0.2	1.3

materials will be named in the following relatively to these round meshes diameters (i.e. 2–3, 4–5 and 8–10 mm). Correspondences with square meshes are reported in table 1.

The first aim of the study was to characterize the behaviour of these uniform sediments close to the incipient motion flow. This implied to work at low liquid and solid discharges. As 2D bedforms such as bar formations were excluded from this study, it was also necessary to have a low width to ensure that the supercritical flow occurred over the entire width with only one-dimensional bedforms. The 9% steep flume used for the experiment was 2.3 m long and 5 cm wide. The flow rate at the inlet was regulated and measured by an electromagnetic flow-meter. For each run, liquid and solid discharge were maintained constant. There was no recirculation neither solid nor liquid.

The solid feeding system was specifically developed using a feeding tank and a conveyor belt whose velocity allowed to control the solid discharge. This device was tested with the GDS and ensured a reasonable stable solid discharge even for very low values. In this case, the accuracy is plus or minus the order of magnitude of the grain average size. For example, working at 8 g/s with the 8–10 mm gravel which average particle weight is 1.3 g means an accuracy of ±15%, but becoming better with finer sediments (±5% for the 2–3 mm at 8 g/s). This device was also tested with a mixture of the 2–3/5–6/8–10 mm materials. Results are good and indicate that no sorting effects occur inside the tank, the average solid discharge for each classes remaining constant (figure 2). For this test at 11 g/s, quite large but very short in time fluctuations were observed mainly depending of the 8–10 mm average grain weight (since the average 8–10 mm solid discharge corresponds to 3 g/s).

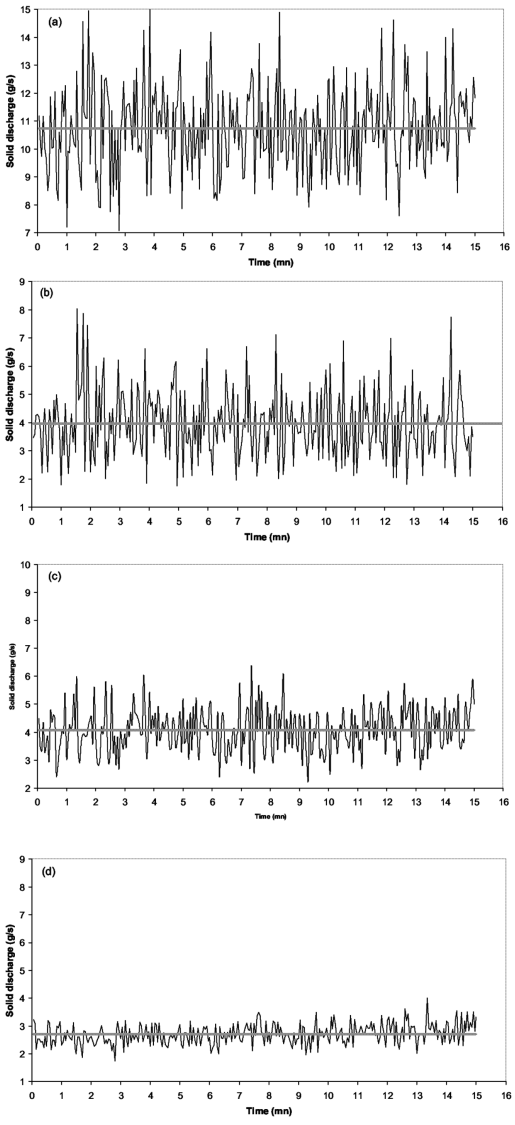


Figure 2. Test of the feeding system with a mixture of 2–3/5–6/8–10 mm uniform materials.
(a) total solid discharge Qs.
(b) Contribution of the 8–10 mm fraction to Qs.
(c) Contribution of the 5–6 mm fraction to Qs.
(d) Contribution of the 2–3 mm fraction to Qs.

2.3 *Experimental conditions*

At the beginning of each run, a 4 cm thick layer of sediment material was uniformly placed at the bottom of the flume to allow aggradation or degradation.

Each run was performed at equilibrium state, meaning that, during the experiment, the changes in the bed elevation and the depth of the flow were small. The main hydraulic parameters for all runs are reported in table 2, Q_{cr} being the assessed incipient motion discharge, Q the liquid discharge, Qs the solid discharge obtained to stabilize a 9% equilibrium slope and H the estimated water depth.

Table 2. Hydraulic parameters and observations for all the experiments (Y = Yes, N = No, BF = bedforms).

mm	Q_{cr} (l/s)	Q (l/s)	Qs (g/s)	H (cm)	BF
2–3	0.07	0.11	8.3	0.7	Y
		0.12	9.5	0.7	(Y)
		0.15	12.1	0.8	N
5–6	0.22	0.26	10	1.2	Y
		0.32	15.8	1.3	Y
		0.39	21.2	1.5	(Y)
		0.48	33.4	1.7	N
8–10	0.52	0.70	14.75	2–2.5	Y
		1.15	67	3–3.5	N
2–3/5–6	0.13	0.17	10.93	0.8	Y
23/56/810	0.24	0.32	11.3	1–1.5	Y

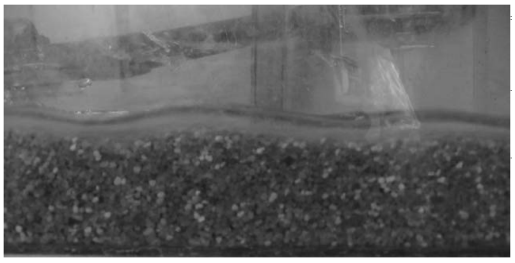


Figure 3. Bedforms in the 2–3 mm.

3 MAIN RESULTS AND OBSERVATIONS

3.1 *Bedforms and stable equilibrium slope with uniform materials*

For each uniform material, antidune-like bedforms were well observed close to the incipient motion liquid discharge (figures 3 to 5). These bedforms always occurred on a constant equilibrium slope. When increasing liquid and solid discharges with the same equilibrium slope, the bedforms became more unstable, almost disappearing at about twice the incipient motion discharge.

Upstream moving of these bedforms was clearly observed. Some characteristics measured through the transparent wall of the flume are given in table 3.

Moreover a cyclic-like pattern seemed to occur similarly for the three uniform materials when observing the bed evolution near the outlet as described on figure 6. At this stage of the experimental development, observations are only qualitative. In a further work analysis of images from the side of the flume should allow to improve our knowledge of bedform processes.

Figures 7 to 9 shows that solid discharges measured with the GDS at the outlet only slightly fluctuate around a constant average value. This is consistent with a perfectly constant equilibrium slope. These fluctuations combine a noise (the entrance signal fluctuation and the measurement device accuracy) with what really happened inside the flume and is therefore not easy to analysed. More data are needed to perform spectral analyses of output solid discharge. Nevertheless a short analysis of the 8–10 mm output signal with bedforms conditions reveals the 40 s period which was measured confirming the cyclic pattern described on figure 6.



Figure 4. Bedforms in the 5–6 mm.



Figure 5. Bedforms in the 8–10 mm.

Table 3. Order of magnitude of the observed bedforms.

Material (mm)	Period T (s)	Wave length λ (cm)	Migration velocity U (cm/s)
2–3	4	8	1.7/2
5–6	10	10–15	1/1.5
8–10	40	40	1

3.2 *Bedforms and unstable equilibrium slope with the non-uniform materials*

Two experiments were performed with two non-uniform materials, mixtures of the previous uniform materials (table 4).

Hydraulic conditions of these runs are given in table 2. For both experiments the measured incipient motion discharge appeared to be nearly the average of incipient motion discharges relative to the constitutive uniform materials of the mixture.

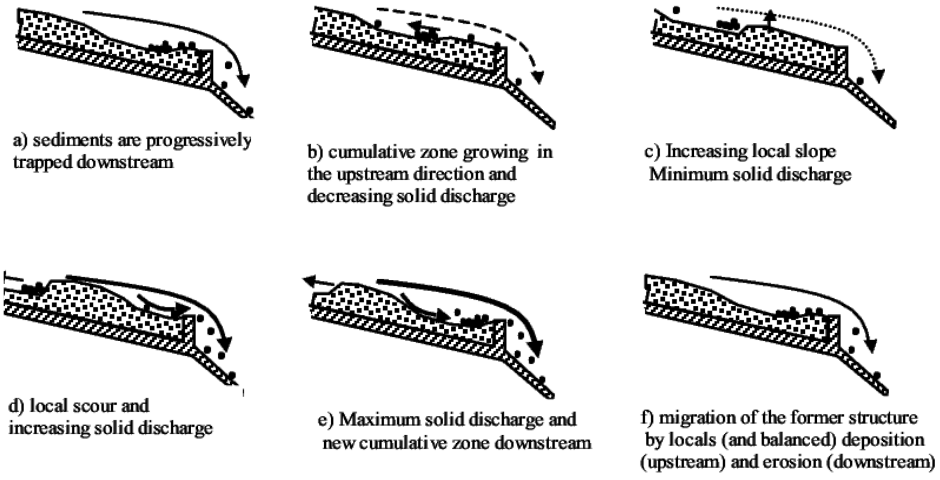


Figure 6. Cyclic like pattern occurring downstream from the flume.

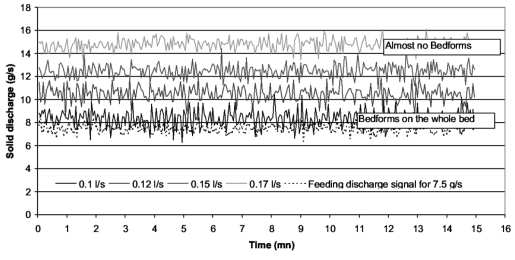


Figure 7. Outlet solid discharge measured with the uniform 2–3 mm material.

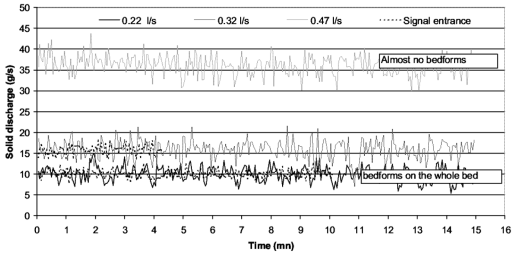


Figure 8. Outlet solid discharge measured with the uniform 5–6 mm material.

Bedforms occurred for both experiments (figure 10) but in a completely different manner compared to what occurred with uniform materials. Many preliminary runs not presented here were performed under different hydraulic and sediment conditions but none permitted to obtain a stable equilibrium slope. Instead, a periodic-like fluctuation around the average equilibrium slope was observed, alternating periods of bed aggradation and degradation.

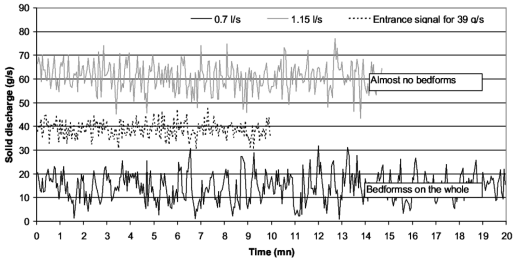


Figure 9. Outlet solid discharge measured with the uniform 8–10 mm material.

Table 4. Non uniform material used in the experiments.

	2–3 mm	5–6 mm	8–10 mm
Run 1%	50	50	none
Run 2%	33	33	33

Aggradation was associated with bedforms and vertical and longitudinal sorting of the sediment with coarser grains progressively covering finer sediments.

Observed wavelengths varied periodically with time and slope:

(a) near the equilibrium slope, bedload is composed of a mixture of all grain sizes and bedforms are unstable. The order of magnitude of the wavelength corresponds to the coarser material.
(b) when the slope increases, bedload is essentially composed of coarser grains, the finer being progressively buried. Bedforms are very similar to those observed with the corresponding coarser uniform material.



Figure 10. Bedforms in the 5–6/8–10 material.

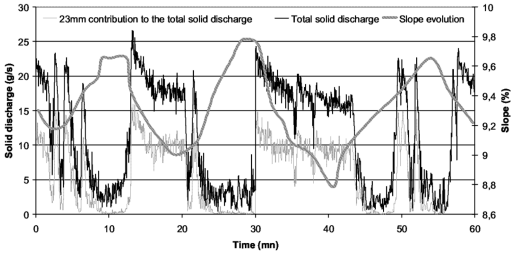


Figure 11. Outlet solid discharge and slope for the non uniform material 2–3/5–6 mm figuring the 2–3 mm material contribution to the total solid discharge.

(c) when the slope is maximum quasi-stationary bedforms are observed. The bed is entirely armoured and the output solid discharge becomes negligible.
(d) the bed suddenly becomes unstable with armouring being destroyed. A large amount of sediment stored in the bed is washed downstream of the flume leading to a very high solid discharge at the outlet.
(e) The erosion process leads to a rapid bed degradation down to a minimum slope inferior to the equilibrium value. During this period, the bed is flat with no bedforms.
(f) When reaching the minimum slope, short-life bedforms appear with a wavelength similar to that observed with uniform finer materials.
(g) These short bedforms quickly disappear by trapping the coarser material. Erosion is replaced by an aggradation process, and the cycle described before starts again with larger bedforms.

This cycle appears very clearly when considering the solid discharge (GDS measurements) at the outlet of the flume for the non-uniform 2–3/5–6 mm and 2–3/5–6/8–10 mm materials (figures 11 to 15).

A quasi-binary signal is observed reflecting the alternating phases of armouring and hyperconcentrated bed-load flow. Both experiments show a low frequency component corresponding to coarser sediments and high frequencies relative to the finer

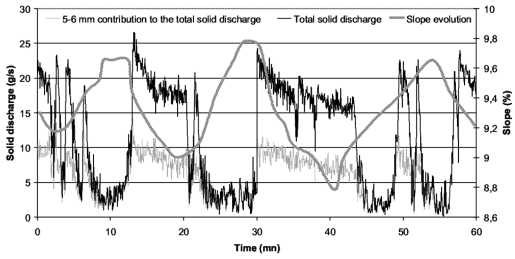


Figure 12. Outlet solid discharge and slope for the non uniform material 2–3/5–6 mm figuring the 5–6 mm material contribution to the total solid discharge.

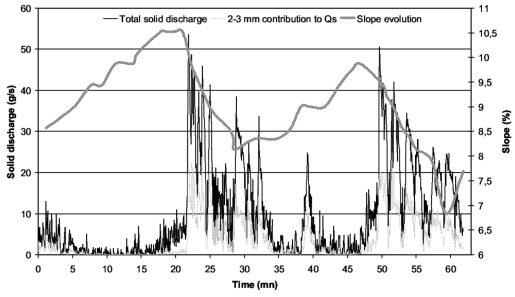


Figure 13. Outlet solid discharge and slope for the non uniform material 2–3/5–6/8–10 mm figuring the 2–3 mm material contribution to the total solid discharge.

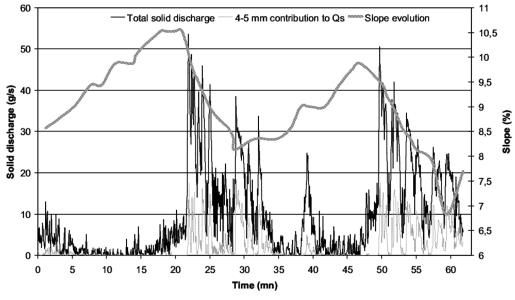


Figure 14. Outlet solid discharge and slope for the non uniform material 2–3/5–6/8–10 mm figuring the 5–6 mm material contribution to the total solid discharge.

material. In both cases, the 2–3 mm contribution to the total solid discharge is equal to zero during the armouring process. For the 2–3/5–6/8–10 mm experiment, only the 8–10 mm participates to bed-load during that phase.

Such phenomena of large fluctuations of solid discharge and slope have already been observed with natural sand-gravel material (Mizuyama 1977, Kuhnle et al. 1988, Suzuki et al. 1998, Frey et al. 2003). In the meantime, no clear explanation is proposed

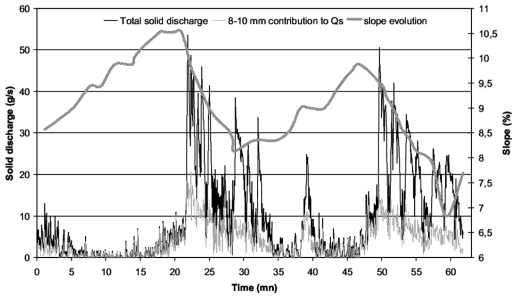


Figure 15. Outlet solid discharge and slope for the non uniform material 2–3/5–6/8–10 mm figuring the 8–10 mm material contribution to the total solid discharge.

which would permit to model the phenomenon, but, a systematic study using different uniform materials, and a second image processing device grabbing from the side of the flume will hopefully allow a better understanding.

4 CONCLUSION

With the help on an original image analysis device (GDS), contrasting results were obtained whether using uniform or non-uniform materials.

In the uniform case, bedforms occurred very close to the incipient motion discharge while disappearing at about twice that discharge. Solid discharges measured with the GDS at the outlet only slightly fluctuated around a constant average value, which was consistent with a perfectly constant equilibrium slope.

In the non-uniform case, using mixtures of the previous uniform materials, no stable equilibrium slope could be observed. Instead, the bed slope fluctuated around a mean equilibrium value, alternating periods of bed aggradation with armouring and degradation. Aggradation was associated with different types of bedforms while the bed was flat during degradation. A quasi-binary output solid discharge signal was measured reflecting the alternating phases of armouring and degradation.

For the time being, no clear explanation is proposed which would permit to model the phenomenon, but a systematic study using different uniform and non-uniform materials and a varying slope is planned. A second image processing device grabbing from the side of the flume will be operated allowing hopefully a better understanding of the dynamics of bedforms.

REFERENCES

Bigillon, F., Frey, P., Ducottet, C., Vierin, N., Ancey, C., Richard, D. and Lanier, J. 1999. Développement d'une technique d'analyse d'images pour la caractérisation du transport solide par charriage. FLUVISU 99, 1–4 June 1999, Toulouse, France, 275–280.

Ducottet, C. 1994. Application of wavelet transforms to the processing of tomographic and holographic images of fluid flows. PhD dissertation, University of Saint Etienne, France.

Frey, P., Ronco, P. and Recking, A. 2002. Fluctuations of bed load solid discharge and grain size distribution on steep slope. Proceedings of RCEM conference, Barcelona, Spain.

Frey, P., Ducottet, C. and Jay, J. 2003. Fluctuations of bed load solid discharge and grain size distribution on steep slopes with image analysis Exp. Fluids DOI: 10.1007/s00348-003-0707-9.

Kuhnle, R.A. and Southard, J.B. 1988. Bed load transport fluctuations in a gravel bed laboratory channel. Water Resources Research 24(2): 247–260.

Suzuki, K., Yamamoto, H. and Kadota, A. 1998. Mechanism of bedload fluctuations of sand-gravel mixture in a steep slope channel proc. of the 11th congress of APD IAHR, Yogyakarta, pp.679–688.

Mizuyama, T. 1977. Bedload transport in steep channel. PhD dissertation, Kyoto University, Japan.

River Flow 2004 – Greco, Carravetta & Della Morte (eds.)
© 2004 Taylor & Francis Group, London, ISBN 90 5809 658 0

An improved flow resistance formula

G. Smart
Nat. Inst. of Water & Atmospheric Research, Christchurch, New Zealand

ABSTRACT: Conventional flow resistance equations are applicable to particular ranges of relative roughness (d/R). At many New Zealand river-gauging sites a marked increase in Manning's n is evident as flow decreases. It is suggested that the increase in n is partly caused by "out of range" application of the Manning equation rather than changes in channel boundary roughness. A full form of the log law, using Z_o for boundary roughness, applicable to a wide range of d/R, is solved to give Z_o values for flows measured at 78 sites on New Zealand rivers. This log law, with constant Z_o for each of the sites, gives better velocity estimates over the range of measured flows than Manning's equation with a constant n. The influences of factors such as grain size, flow depth and shear stress on n and Z_o are investigated.

1 INTRODUCTION

In a dynamic two-dimensional numerical model of a river floodplain, a resistance equation can be evaluated many millions of times to cover the range of depths that occur at each of the different computational nodes of the model. Flow resistance equations are also used for applications as diverse as converting flood marks into flows and aquatic habitat studies. In all such circumstances it is clearly advantageous to have a resistance equation that is applicable at both high and low flow depths.

A study of the roughness characteristics for 78 New Zealand rivers (Hicks & Mason, 1998) reveals that for at least half of the sites, the measured Manning's n coefficient increases by more than 50% over the range from highest to lowest measured stream flows. Thus, errors of more than 50% could be introduced if a constant Manning's n were used to predict flow at these sites. Examples of this phenomenon are shown in Figure 1 for a small and large stream. Such behavior is also reported by Griffiths (1981), Cao (1985), Jarrett (1984, 1990), and many others who have found that hydraulic resistance increases with a decrease in the ratio of hydraulic depth (R) to particle size (d).

Smart *et al* (2002) show that common resistance formulae are applicable only to particular ranges of relative roughness (d/R). In the case of power law equations where U is depth averaged velocity, $U^* = \sqrt{(gRS)}$, K is a constant and S is the energy gradient), the exponent m of $(U/U^*) = K(d/R)^{-m}$ increases from around 0.17 for low (d/R) ratios to $m = 0.5$ or more at high (d/R) ratios. Consequently, poor results will be obtained if an inappropriate power law is used.

It is postulated that the reported changes in Manning's n coefficients may be needed to compensate for the inadequacy of Manning's equation, when used over a wide depth range, rather than reflecting actual changes in hydraulic resistance. The proposition is investigated by seeking an equation with a roughness coefficient

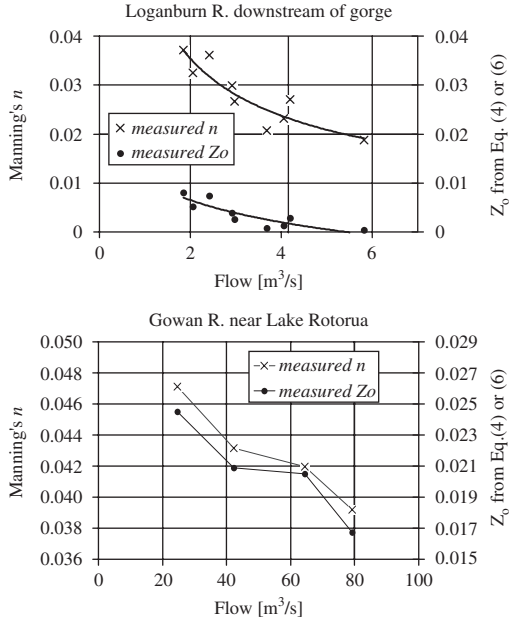


Figure 1. Variation in Manning's n and Z_o with flow at New Zealand river gauging stations.

that is more stable than Manning's n as depth changes at a given site.

Assuming that roughness elements are fully covered by the flow, that the origin of a logarithmic velocity profile is a distance R below the surface and the profile extends to the surface, integrating over the flow depth (from height $z = z_o$ to $z = R$) gives:

$$U = \frac{U*}{\kappa}\left(\left(\frac{1}{1-(z_o/R)}\right)\ln\left(\frac{R}{z_o}\right) - 1\right) \quad (1)$$

where κ is von Karman's constant ($\cong$0.4), and z_o describes the hydraulic roughness of the boundary (the height above the z datum where the log profile velocity = 0).

In situations where $z_o \ll R$, Equation 1 simplifies to more common forms of the log law such as Equation 2, Nikuradse (1933) type equations (2a) or Keulegan (1938) type equations (2b)

$$\frac{U}{U*} = 2.5\ \ln\left(\frac{0.368\ R}{z_o}\right) \qquad z_o << R \quad (2)$$

$$= 5.75\ \log_{10}\left(\frac{12.2\ R}{33.1\ z_o}\right) \qquad z_o << R \quad (2a)$$

$$= 5.75\ \log_{10}\left(\frac{R}{33.1\ z_o}\right) + 6.25 \qquad z_o << R \quad (2b)$$

The equivalent sand grain diameter k_s or a measured grain statistic such as d_{50} is also used in place of z_o with compensating changes in the equation coefficients. An advantage of using z_o is that it is a parameter of the velocity distribution rather than a description of the boundary material. Hence z_o gives hydraulic roughness, as seen by the flow, rather than relying on a boundary characteristic such as bed material grain size. Once z_o is established it can be investigated in terms of physical characteristics of the boundary.

For a smooth boundary, where ν is the kinematic viscosity of water, z_o is independent of bed roughness:

$$z_o = \frac{0.135\ \nu}{U*} \qquad \text{smooth bed} \quad (3)$$

For rough boundaries z_o can be established by precise measurements of the velocity profile or by solving Equation 1 using measured values of R, U and $U*$. The ratio $U/U*$ of Equation 1 diverges from simplified equations of type (2) by more than 1% when $(U/U*) < 10$ or $(z_o/R) > 0.007$.

Equations of type (2) are suitable for low relative roughness situations and are readily inverted to allow calculation of z_o from measured values of U, R and $U^* = \sqrt{(gRS)}$.

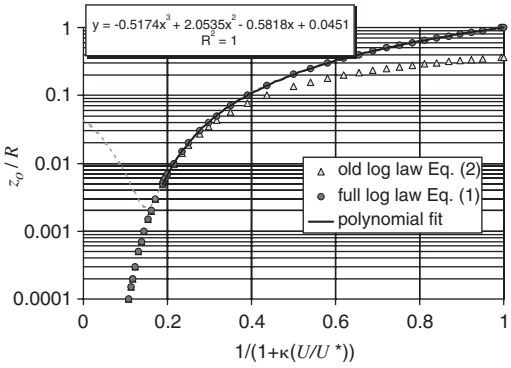


Figure 2. Polynomial representation of z_o/R equivalent to Equation 4.

$$z_o / R = e^{-(1+\kappa\ U/U*)} \quad \text{rough bed, } z_o/R<.007 \quad (4)$$

However, inverting Equation 1 gives:

$$\frac{1-(z_o/R)}{\ln(R/z_o)} = (1+\kappa\ U/U*)^{-1} \quad \text{rough, } 0< z_o/R <1 \quad (5)$$

which is not readily solvable for z_o.

2 METHOD

As shown in Figure 2, Equation 5 can be accurately represented in polynomial form over much of its range. The dashed line in Figure 3 shows that the polynomial approximation is not applicable for $z_o/R <$ 0.005 but Equation 4 is suitable for this range. The polynomial is:

$$z_o/R = -0.5174x^3 + 2.0535x^2 - 0.5818x + 0.0451$$
$$x = (1+\kappa U/U*)^{-1} \qquad \text{use for } x > 0.19 \quad (6)$$

Thus, given R, U and $U*$, z_o can be calculated for all $R > z_o$, using (4) or (6). As z_o is not known *a priori*, in such calculations $x = (1+\kappa U/U*)^{-1}$ gives a better criteria than z_o/R for switching from Equation 4 to Equation 6. For $x < 0.19$ use Equation 4 and for $x \geq 0.19$ use Equation 6. This log law resistance equation is now compared with Manning's Equation.

3 APPLICATION

The above approach was used to calculate Z_o for 566 gauging measurements made at 78 sites on

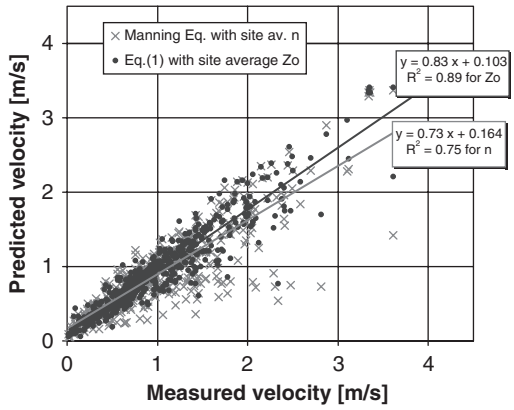


Figure 3. Comparison of equation (1) and Manning equation using site constant resistance coefficients.

Table 1. Prediction errors in velocity (m/s), when using Equation (1) and Manning's equation, each with site constant flow resistance coefficients.

Method	Mean error	Min. error	Max. error	Std. dev.
Const. n	0.108	−0.461	2.190	0.316
Const. Z_o	0.066	−0.419	1.567	0.215

New Zealand rivers. The sites and data are based on the raw measurements used in the New Zealand Manning's n handbook (Hicks & Mason, 1998). A full description of the sites and measuring techniques is given in the handbook. All basic parameters are used as described in the book. At this point it is important to note that some of the assumptions in the log law theory are not necessarily applicable when cross-section averaged values of R and U are used to calculate z_o. To preserve this distinction, an uppercase symbol is now used and Z_o becomes a bulk roughness coefficient similar to Manning's n, which includes bed form and bank vegetation effects if they are present at a river section. This cross-section approach is also implicit in the Keulegan (1938) equation when it is applied to river reaches.

Z_o values calculated as described above are also shown on Figure 1 along with Manning's n. At first glance n and Z_o appear to show a similar variation over the range of flows measured at each of these sites. However, while velocity varies in inverse (linear) proportion to n in the Manning equation, the log law (Equation 2) shows that velocity varies as the inverse logarithm of Z_o over much of the Z_o/R range. In other words, velocity predictions are less sensitive to errors in Z_o (with Equation 1) than to similar errors in n (when using Manning's equation). Using Equation 1 with constant Z_o may give better

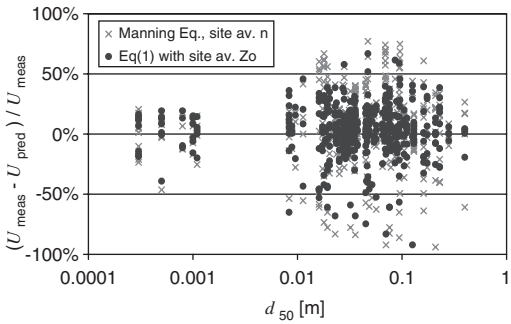


Figure 4. Relative errors in velocity prediction are smaller for silt and sand bed rivers ($d_{50} < 2$ mm). Nine outlying errors (as large as −400%) that are due to external effects, are not shown.

predictions of velocity for a site than the conventional practice of using Manning's equation with a constant n value.

This was tested by investigating errors in predicted velocities when using Equation 1 with constant Z_o and Manning's Equation with constant n values at each of the 78 New Zealand reference sites. The resistance coefficients used were the mean of the values measured at each site (e.g. for the Loganburn site, shown in Figure 1 at the top, values of $n = .028$ and $Z_o = .0036$ were used).

Figure 3 shows measured velocities in comparison with the velocities predicted using the average site resistance coefficient. Statistics on the errors are given in Table 1.

It is apparent that using a site mean n or Z_o results in many velocities being underpredicted. The outcome is especially pronounced when Manning's equation is used. Equation 1 with constant Z_o performs better than Manning's equation with constant n.

Relative errors are given in Figure 4. It is clear that, for this New Zealand data set, velocity prediction with a constant resistance coefficient causes appreciable errors, especially in rivers with median bed material coarser than sand sizes. Excluding the outliers described in the caption of Figure 4, the mean magnitude of the relative error using Manning's equation with a site average n is 20%. Using Equation 1 with a site average Z_o the equivalent mean error is 16%.

4 DISCUSSION

Many factors can change flow resistance at a site. These include overbank effects, bank vegetation, bedforms, sediment loading, seasonal changes, backwater profiles and weed growth. Nevertheless, the above results show that if a constant resistance coefficient is to be used at a particular site, Equation 1 gives

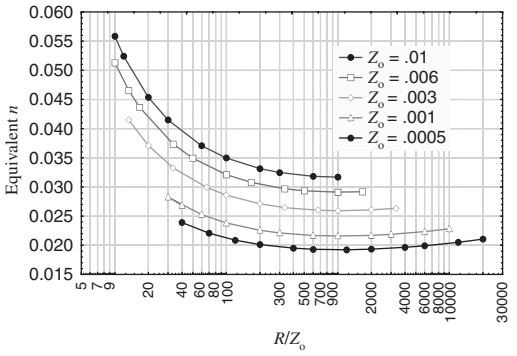


Figure 5. The relationship between Manning's n and Z_o depends on relative roughness Z_o/R.

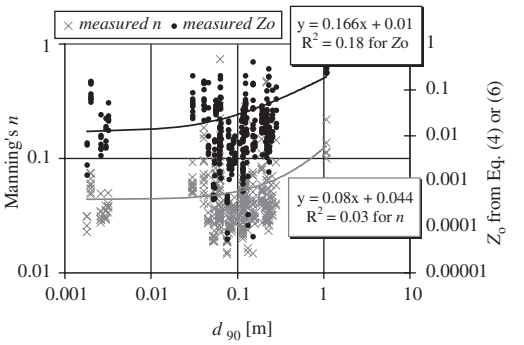


Figure 6. No significant relationship is evident between n and grain size of the river bed. A weak relationship exists between Z_o and d_{90}.

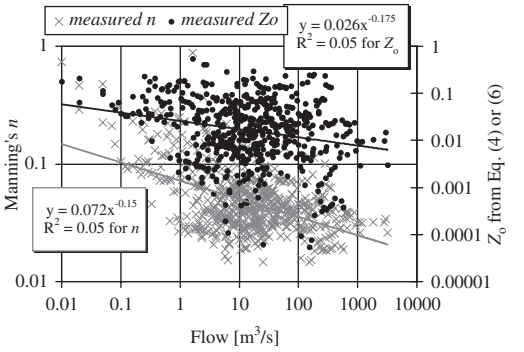


Figure 7. A stronger relationship is evident between Manning's n and flow than between Z_o and flow.

better overall estimates of velocity than the Manning equation, especially in gravel, cobble and boulder bed channels. A problem with applying Equation 1 is that little information is available on Z_o values for use in field situations.

Jacobs & Wang (2003) suggest Z_o for floodplains can be adopted from atmospheric velocity profile measurements. While there is some information on atmospheric Z_o for field crops it would be more straightforward if Z_o could be calculated from boundary properties such as grain size or related to the better known Manning's n values.

Eliminating U from the Manning equation using Equation 1 and $U^* = \sqrt{(gRS)}$ gives a relation between Manning's n and Z_o:

$$n = \frac{\kappa R^{1/6}}{\sqrt{g}} \frac{\left(1-\frac{Z_o}{R}\right)}{\left(\frac{Z_o}{R} - \ln\left(\frac{Z_o}{R}\right) - 1\right)} \qquad (7)$$

This relation is shown graphically in Figure 5.

While it is straightforward to calculate n values from Z_o and R using Equation 7, it is not obvious how to calculate Z_o from n and R except by way of iteration or a chart such as Figure 5.

A second possibility is that Z_o can be calculated from channel properties such as grain size. To make this study, measured n and Z_o values are used (not site averages) and logarithmic graph axes are shown to display the wide range in the variables. Regression lines and statistics refer to the raw (non-logarithmic) data.

Figure 6 shows that there is a weak relation between Z_o and d_{90} grain size ($R^2 = 18\%$). The relationship becomes progressively weaker if d_{84} or d_{50} is used. No significant relationship between n and d_{90} or $d_{90}^{1/6}$ was evident (as implied by the Strickler equation).

Conversely, when flow is used as the predictor, there is a power law relation between n and flow ($R^2 = 26\%$) but little dependence of Z_o on flow ($R^2 = 5\%$). While there is weak power law dependence of n on $R^{-0.25}$ ($R^2 = 10\%$) there is no dependence of Z_o on R. Both n and Z_o depend on energy graident ($n = 0.19\,S^{0.22}$, $R^2 = 25\%$ and $Z_o = 0.29\,S^{0.46}$, $R^2 = 17\%$).

From the above parameters, R, flow and S, are most likely to vary at a given site. An ideal flow resistance coefficient should not vary with these parameters. The above statistics show that Z_o has less variance depending on these parameters than does n.

5 CONCLUSIONS

Many applications require a single equation with constant resistance coefficient to be used for flow resistance calculations at a given location. For the range of New Zealand river sites, power laws of (d/R) and Manning's equation do not satisfy these requirements.

It is suggested that measured changes in Manning's n coefficient at a given site may be needed to compensate for the inadequacy of Manning's equation when used over a wide depth range, rather than reflecting actual changes in hydraulic resistance. An improved flow resistance formula (Equation 1) which is based on log law theory, gives better predictions of measured velocity when used with a constant Z_o than can be given by Manning's equation with a constant n value.

While the new formula performs better than the Manning equation for New Zealand river sites, guidelines on Z_o values are not readily available and further work is required to either provide selection criteria for Z_o values, to allow conversion of n values into Z_o values or to make improvements to the Manning equation.

ACKNOWLEDGEMENTS

This study was funded by contract CO1X0218 from the Foundation for Research Science and Technology (New Zealand).

NOTATION

d	measure of bed particle size
d_{50}	median particle size
d_{90}	particle size for which 90% of bed material is finer
g	gravitational force per unit mass
K	coefficient used in power law equations
m	exponent of power law equations
n	Manning's roughness coefficient
R	hydraulic depth
R^2	squared correlation coefficient
S	energy gradient
U	depth averaged velocity
U^*	shear velocity $= \sqrt{(gRS)}$
x	variable used on horizontal axis of graph
y	variable used on vertical axis of graph
z_o	local hydraulic roughness of channel boundary (the height above the z datum where the log profile velocity $= 0$)
Z_o	cross-section hydraulic roughness
κ	von Karman's constant
ν	kinematic viscosity of water

REFERENCES

Cao, H.H. 1985. Resistance hydraulique d'un lit de gravier mobile a pent raide, etude experimental. *PhD Thesis, Ecole Polytechnique Federal de Lausanne*.

Griffiths, G.A. 1981. Flow resistance in coarse gravel bed rivers. *Journal of Hydraulics Division Proceedings ASCE, 107, HY7*: 899–918.

Hicks, D.M. & Mason, P.D. 1998. Roughness characteristics of New Zealand rivers. *Water Resources Publications, LLC, National Institute of Water & Atmospheric Research Ltd, New Zealand*.

Jacobs, J. & Wang, M. 2003. Atmospheric momentum roughness applied to stage-discharge relationships in flood plains, *Journal of Hydrologic Engineering, 8(2)*.

Jarrett, R.D. 1984. Hydraulics of high gradient streams. *Journal of Hydraulic Engineering, ASCE, 110(11)*: 1519–1539.

Jarrett, R.D. 1990. Hydrologic and hydraulic research in mountain rivers. *Water Reasouces Bulletin. 26(3)*: 419–429.

Keulegan, G.H. 1938. Laws of turbulent flow in open channels. *Journal of the National Bureau of Standards, USA, Research Paper 1151, 21*: 707–741.

Nikuradse, J. 1933. "Stroemumgsgesetze in raughen Roehren", Forshungs Geg. des Ingenieurwesens, Heft 361. *Translated from German as NACA Tech. Memo., 1292*, 62 pp.

Smart, G.M., Duncan, M.J. & Walsh, J. 2002 "Relatively rough flow resistance equations". *Journal of Hydraulic Engineering, ASCE*, 128(6) 568–578.

This page intentionally left blank

River Flow 2004 – Greco, Carravetta & Della Morte (eds.)
© 2004 Taylor & Francis Group, London, ISBN 90 5809 658 0

Large-eddy simulation of flow over rough channel beds

T. Stoesser, W. Rodi & G.H. Jirka
Institute for Hydromechanics (IfH), University of Karlsruhe, Germany

ABSTRACT: In this paper we present the results of several large eddy simulations (LES) of the flow over rough channel beds. The wall roughness is introduced via artificial 2-dimensional square bars, positioned along the channel at varying spacing. The spacing is chosen such that the three roughness types, isolated roughness, wake interference roughness, and quasi-smooth-wall roughness are represented. The vertical velocity profiles exhibit the well known feature of turbulent flows over rough wall flows i.e. a shift of the logprofile above the roughness crests. However, the increment of the shift depends strongly on the arrangement of the artificial roughness elements. In addition, turbulent fluctuations and Reynolds stresses show a dependency on the type of the roughness. Similar to previous experimental and numerical investigations the occurrence of flow into and out of the cavities is shown and vortices are shed into the outer flow. These vortices are associated with the occurrence of low and high speed streaks, a feature that is also found in smooth wall flows. However, the shape and length of these streaks depend strongly on the roughness type.

1 INTRODUCTION

Turbulent boundary layers over roughness elements have considerable engineering interest. Especially in the field of hydraulic engineering, nearly all practical flows are hydraulically rough, i.e. the roughness Reynolds number $\mathrm{Re}* = (u_\tau \cdot d)/\nu$ (where u_τ is the friction velocity, d is a characteristic roughness height and ν is the dynamic viscosity) exceeds a certain value ($\mathrm{Re}* > 70$) and the roughness affects the flow outside the roughness sublayer. This results in a mean velocity profile that differs considerably from the velocity profile over a smooth bed (e.g. Patel, 1998), since surface drag is significantly larger in comparison to a turbulent flow field over a smooth surface. As a consequence, the resulting turbulence characteristics should also reflect the nature of the surface.

According to Raupach (1981) the boundary layer over a rough surface is characterized by a surface layer that can be divided into an inertial or logarithmic layer and a roughness sublayer. Within the inertial layer (IS) the vertical variation of the shear stress can be neglected and the vertical distribution of the flow velocity can be described by a logarithmic law (e.g. Perry et al., 1969). The region of the flow beneath the inertial layer is known as the roughness sublayer (RS) within which the flow is strongly influenced by the individual roughness elements and is therefore spatially inhomogeneous.

The effect of roughness however is not restricted to the mean flow properties. Flow visualizations and measurements (e.g. Grass, 1971, Grass et al., 1991, Djenidi et al., 1999 and many others) as well as recent DNS calculations over rough-walls (Leonardi et al., 2003, Miyake et al., 2002) indicate significant structural changes not only near the rough surface, but everywhere within the boundary layer. It was found that over rough walls the bursting phenomenon seems to be more intense than over smooth walls. Measurements over a series of roughness types reported by Antonia (1994), indicated that the Reynolds stresses are increased relative to a smooth wall. Leonardi et al. (2003) showed that due to surface roughness the size and shape of coherent streaks change drastically as a result of enhanced momentum exchange between the near wall region and the outer flow.

Following the definition of Morris (1955) the effect of roughness is mainly due to the formation of wakes behind the roughness elements resulting in the production of turbulence and the dissipation of energy. According to Morris the longitudinal spacing w is of paramount importance in rough wall channel flow, classifying the roughness into three basic types (Figure 1): isolated roughness flow (k-type), wake interference flow (transitional) and quasi-smooth flow (d-type). However, the overall picture of the effect the roughness has on the near wall structure is far from complete and systematic studies on different types of roughness are rare.

In this paper we show the results of several large eddy simulations (LES) calculations of an openchannel flow over an artificially roughened bed for the

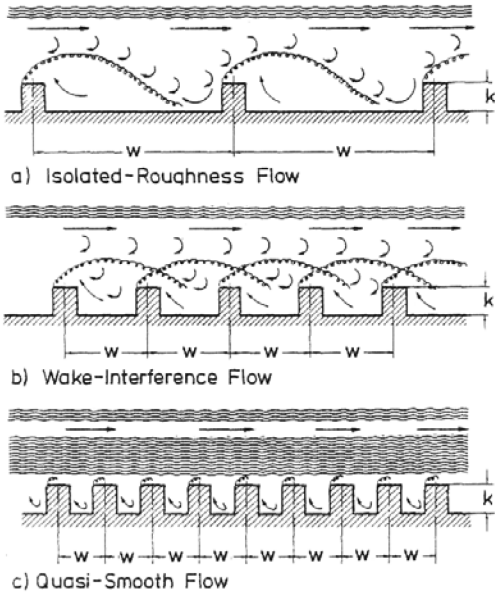


Figure 1. Roughness types in rough wall channel flow according to Morris (1955).

above mentioned three roughness types. The main purpose of this study is to provide further insight into the turbulent flow over rough boundaries and to enhance the understanding of the effect of surface roughness geometry on the mean and instantaneous flow. Spatial and temporal averaging is used to quantify the effects of the three roughness types with regard to flow velocities, turbulent fluctuations and Reynolds stresses. Furthermore, we investigate the occurrence of coherent flow structures in dependence on the nature of the roughness and compare them to the equivalent structures on a smooth wall.

2 NUMERICAL METHOD

The LES code LESOCC developed at the Institute for Hydromechanics (Breuer and Rodi, 1996) is used to perform the LES simulations. The code solves the filtered Navier-Stokes equations on a curvilinear, block-structured grid discretised with the finite volume method. A non-staggered grid with Cartesian velocity components is used. Both convective and diffusive fluxes are approximated with central differences of second order accuracy. The SIMPLE algorithm is employed in order to conserve mass and to couple the pressure to the velocity field. Time advancement is achieved by a second order, explicit Runge-Kutta method. LESOCC is highly vectorised and parallelisation is accomplished by domain decomposition and explicit message passing via MPI. The subgrid stresses of the filtered Navier Stokes equations are computed using the dynamic approach of Germano et al. (1991). The linear noslip ($u^+ = y^+$) boundary condition is used for the walls and on the roughness elements, since the first grid point is placed in the viscous sub-layer ($y^+ \approx 7$).

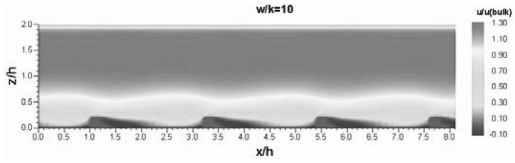
3 FLOW CONFIGURATIONS

Three configurations with ratios of $w/k = 10$ (isolated flow), $w/k = 7$ (wake interference flow) and $w/k = 3$ (quasi smooth flow) are selected in order to simulate the three roughness types according to Figure 1. The boundary conditions and the Re number of 4200, based on half channel depth and bulk velocity, are chosen analogous to recent DNS calculations performed by Leonardi et al. (2003). This allows us to additionally perform a comparison LES – DNS and verify the mathematical model. The roughness Reynolds number Re$*$ is approximately 400 based on the shear velocity u_τ and the roughness height k. The ratio of roughness height to water depths is $k/h = 0.2$. The computational domain spans $8h$ in streamwise, πh in spanwise and $2h$ in vertical directions, respectively. Several simulations with different grid resolutions were carried out. In this paper we will only present the results from the finest grid consisting of $261 \times 61 \times 120$ grid points in streamwise, spanwise and vertical directions, respectively. Periodic boundary conditions were applied in the spanwise and vertical directions. No-slip boundaries were applied on and between the roughness elements, representing the rough lower wall, and on the smooth upper wall.

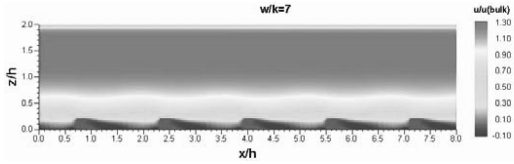
4 RESULTS AND DISCUSSIONS

4.1 *Time averaged flow field*

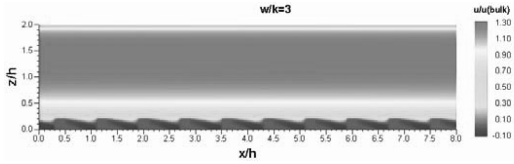
Figure 2 shows the time-averaged flow field above the three roughness types. The flow develops strong separation zones near the roughness elements causing a shear layer of different extent and a strong disturbance of the flow field in the vicinity of the elements. Whereas for the isolated and transitional roughness the flow reattaches in the groove, the separation zone for the quasi-smooth flow fully occupies the cavity that is formed by the roughness elements. The groove is filled completely with a stable eddy creating a pseudo-wall. As a consequence, the average flow field takes a more or less wavy form above the roughness elements for transitional and isolated roughness. Perry et al. (1969) attributed this roughness-induced streamwise distortion to standing waves, forming just above the roughness elements. A more homogenous flow field above the crests (similar to a flow field above a smooth



a) isolated roughness



b) transitional roughness



c) quasi-smooth roughness

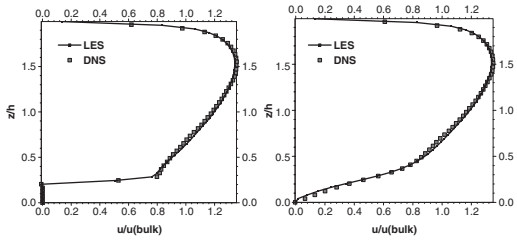
Figure 2. Average flow field for the three configurations (a–c).

wall) appears for the quasi-smooth flow. These features agree fairly well with the sketches from Figure 1.

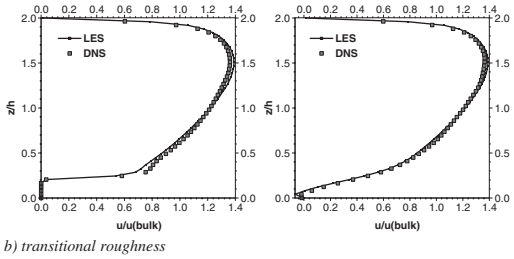
Figure 3 shows the comparison of LES and DNS results for the three types at the top of the bar (left) and in the center of the groove (right side) for the three configurations. A fairly good match could be achieved and the differences can be regarded as insignificant for the further evaluation of the results.

Figure 4 shows the spatially (in streamwise and spanwise directions) averaged distribution of the streamwise velocity. It is apparent for all three roughness types that the maximum of the velocity is shifted from the centre of the channel towards the upper, smooth wall. However, the shift is largest for the isolated roughness and smallest for the quasismooth roughness. This is in accordance with the averaged mean velocity distribution.

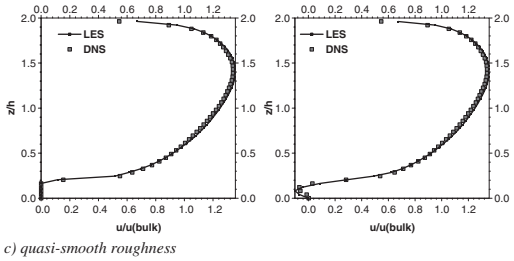
A comparison of the second order statistics i.e. the *rms* values of the streamwise velocity fluctuations, at the top of the bar and in the centre of the groove with the direct numerical simulation (Figure 5) shows a good match in the vicinity of both walls. There, the peak of the turbulent fluctuations is reproduced to a very satisfying degree. For the quasismooth wall the magnitude of $u'u'$ is in a similar range in comparison to the smooth upper wall. As w/k increases the strength of the turbulent fluctuations increases and the intensities are approximately 50% higher near the rough wall. However, in the centre of the channel the fluctuations are generally underestimated. This reflects the rather



a) isolated roughness



b) transitional roughness



c) quasi-smooth roughness

Figure 3. Comparison of LES and DNS results for the mean streamwise velocity component U above the bars (left) and in the centre of the groove (right) for the three configurations (ac).

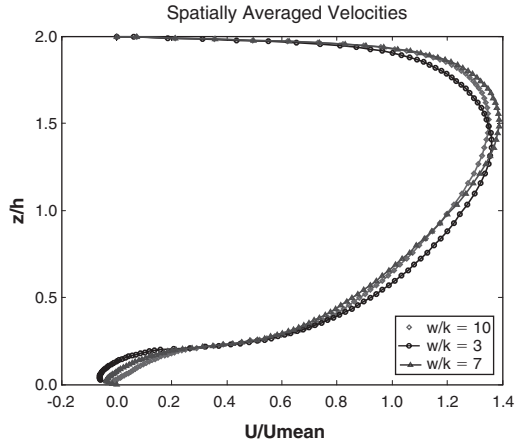
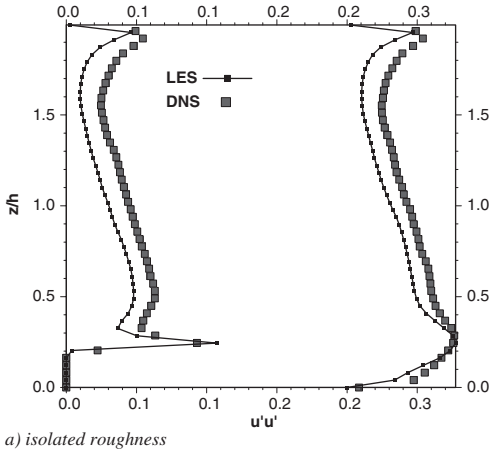
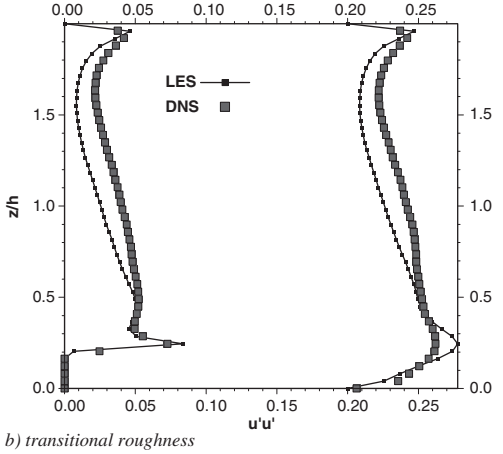


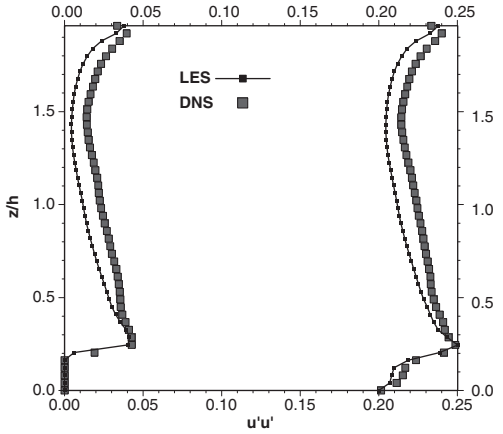
Figure 4. Spatially averaged mean streamwise velocities for the three roughness types.



a) isolated roughness



b) transitional roughness



c) quasi-smooth roughness

Figure 5. Comparison of LES and DNS results for the streamwise turbulent fluctuations u′u′ above the bars (left) and in the centre of the groove (right) for the three configurations (a–c).

coarse resolution (the grid is stretched towards the walls) in this area, since only large scale fluctuations are represented within a LES. Hence, a finer grid, especially in the centre of the channel, is desirable. However, the general features of rough wall channel flow, i.e. a fairly thick boundary layer and, as a consequence, a relatively large shift of the logarithmic region away from the wall is reproduced. Figure 6 furthermore clearly demonstrates that even for the quasismooth roughness the influence of the roughness elements seems to prevail up to approximately 2/3rd of the channel depth.

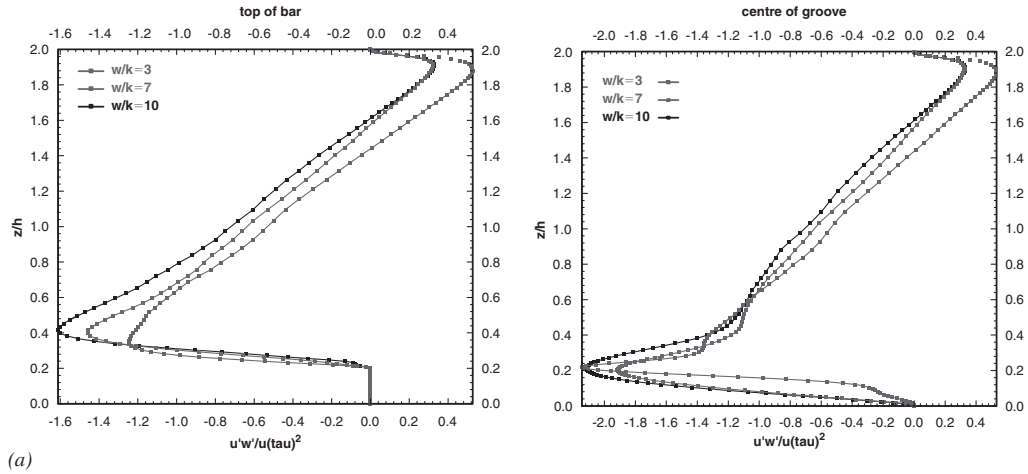
The above mentioned standing waves also affect significantly the turbulence intensity distributions in the vicinity of the rough wall. Figure 6 shows the distribution of turbulent fluctuations u', w' and $u'w'$ normalized by the mean shear velocity at the top of the bar and in the centre of the groove.

There is a significant increase in the Reynolds stresses in the groove compared to the top of the bars. The strength of the intensities again depends on the roughness type, being strongest for the isolated roughness and weakest for the quasi smooth flow. The influence of the rough wall can be seen in the magnitude of each stress component compared to the value of its smooth counterpart. While the difference for u' is rather small, the difference for both $u'w'$ and w' is in the order of up to 4 times the value of the smooth wall. Also notable are the distortions of the stresses especially in the centre of the grooves. Furthermore, the strong distortion of the streamwise fluctuation u' at the top of the bar for both transitional and isolated roughness is apparent. This indicates a superposition of standing waves and suggests that a value of $w/k = 10$ might not be large enough to represent the fully isolated roughness regime.

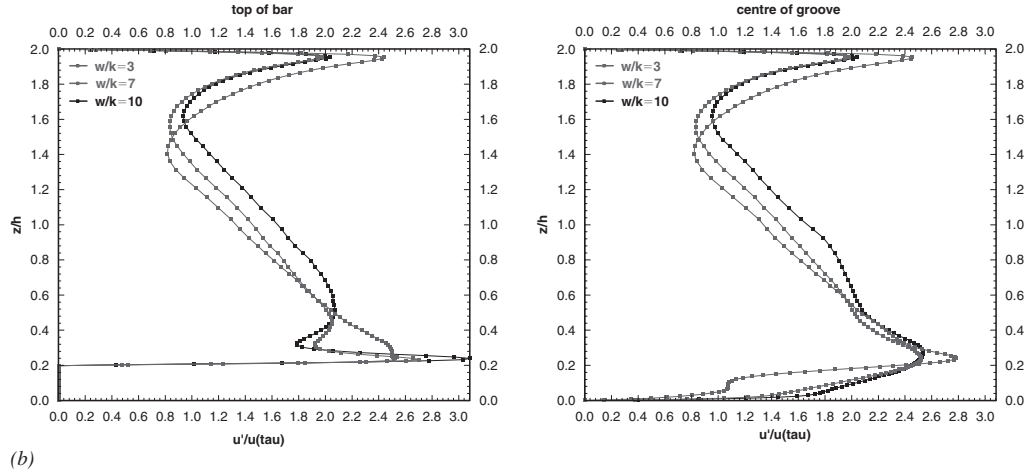
4.2 *Instantaneous flowfield*

Figure 7 shows instantaneous velocity distributions of the perturbation in streamwise direction i.e. u', together with the perturbation velocity vectors ($u'-w'$) in an x–z plane. It illustrates the presence of vortical motion, especially near the elements. It also shows that for the wake interference and the isolated roughness types the perturbation is much stronger than for the quasi-smooth flow, resulting in a more frequent and a stronger shedding of eddies into the flow. The Figure is an obvious reflection of the above mentioned distribution of mean velocities, turbulent fluctuations and Reynolds stresses.

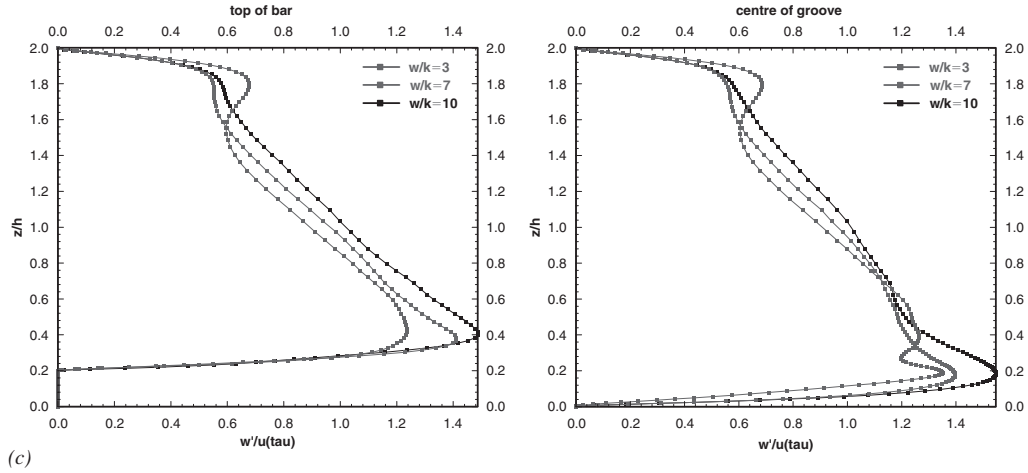
The turbulent boundary layer over a smooth wall is characterized by alternating high and low speed streaks, which lift up and break down during a burst cycle (see e.g. Kline et al., 1967, Robinson, 1991). For the rough wall cases streaky structures are also present just above the roughness elements as was



(a)

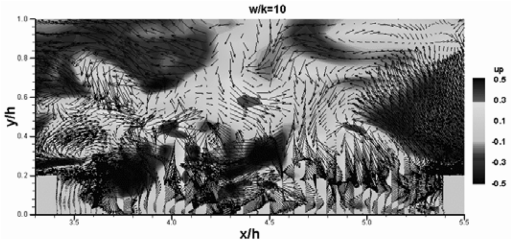


(b)

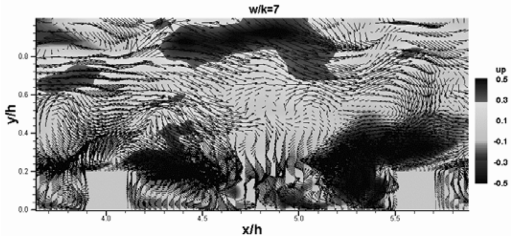


(c)

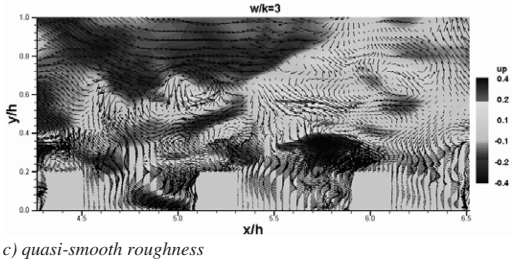
Figure 6. Distributions of u'/u_τ (a), w'/u_τ (b), and $u'w'/u_\tau^2$ (c) for the three configurations at the top of the bar and in the centre of the groove.



a) isolated roughness



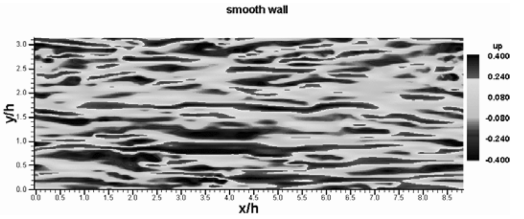
b) transitional roughness



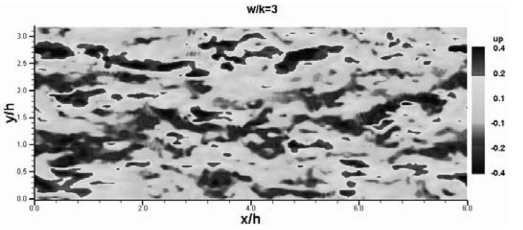
c) quasi-smooth roughness

Figure 7. Distribution of streamwise perturbation (coloured) together with perturbation vectors (u', w') for the three configurations (a–c).

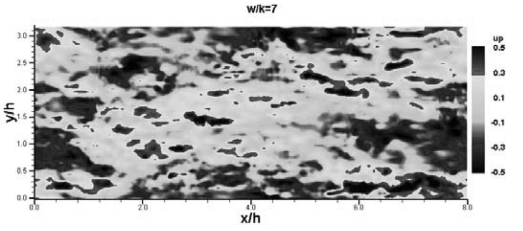
shown by Djenidi et al. (1999) in a laboratory experiment with the help of dye. Figure 8 shows instantaneous distributions of u' in a x–y plane just above the roughness bars for the three roughness configurations and, for a comparison, near the smooth wall. Here, the presence of coherent high (indicated by the red colour) and low speed (blue colour) streaks alternating in the spanwise direction are visible. By increasing the spacing between the bars the strength of these streaks increases, which is due to increased momentum exchange with the outer layer. This is in accordance with observations from a quadrant analysis by Krogstadt and Antonia (1994). Furthermore, with an increase in the ratio of w/k the form of these streaks changes. While near the smooth and quasi-smooth walls the streaks are elongated, they are shorter and wider for the isolated and transitional roughness. However, the streak spacing seems to be constant irrespective of roughness type.



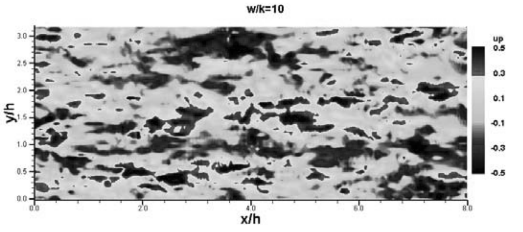
a) smooth wall



b) quasi-smooth roughness



c) transitional roughness



d) isolated roughness

Figure 8. High and low speed streaks for the smooth upper wall (a) and the three roughness configurations (b–d).

5 CONCLUSIONS

In this paper we have presented the results of large eddy simulations of open channel flow over artificially roughened channel bed for the three roughness types: isolated, wake interference, quasismooth roughness. A strong-form-roughness induced shear layer develops above the elements such that instantaneous and mean velocities differ significantly from the velocity distribution over smooth beds. Outflow from and inflow into the cavities are shown to occur for all roughness types. The shedding of vortices into the outer flow plays an

important role in producing/maintaining the boundary layer. This is confirmed by the increase of turbulent fluctuations and Reynolds stresses above the rough wall in contrast to a smooth wall. An important role plays the nature of the roughness, being responsible for the magnitude of the stresses and the distribution of all turbulent quantities in the entire flow. This supports the statement of Djenidi et al. (1999) who underline the inadequacy of a roughness classification scheme based solely on the effect that the roughness has on the mean velocity profile. The present study showed that the type of the roughness is of significance especially in the formation of near wall coherent structures. Although streaks form above all types of roughness, their size and shape are different for each roughness regime.

ACKNOWLEDGEMENTS

This work is part of the research project funded by the German Research Foundation (DFG) under project number JI 18/10-1. The authors would like to thank Dr. Stefano Leonardi for the provision of the DNS data.

REFERENCES

Antonia, R.A. 1994. The Effect of Different Types of Surface Conditions on a Turbulent Boundary Layer. 1st Intern. Conference on Flow Interaction. Ed. N.W.M. Ko & B.H.K. Lee. pp 64–97.

Breuer, M., Rodi, W. 1996. Large Eddy Simulation of Complex Turbulent Flows Of Practical Interest. In: Notes On Numerical Fluid Mech., Flow Simulations With High Performance Computers II. Ed.: Hirschel, E. H. Vieweg & Braunschweig. pp 258–274.

Djenidi, L., Elavarasan, R., Antonia, R.A. 1999. The turbulent boundary layer over Transverse Square Cavities. J. Fluid Mech. Vol. 395. pp 271–294.

Germano, M., Piomelli, U., Moin, P., Cabot, W.H. 1991. A Dynamic Subgrid-Scale Eddy Viscosity Model. Physics Fluids. Vol. 3. pp 1760–1765.

Grass, A.J. 1971. Structural Features of Turbulent Flow Over Smooth And Rough Boundaries. J. Fluid Mech. No. 50(2). pp 233–255.

Grass, A.J., Stuart, R.J., Mansour-Tehrani, M. 1991. Vortical Structures And Coherent Motion In Turbulent Flow Over Smooth And Rough Boundaries. Philosophical Transactions Royal Society Of London A. Vol. 336. pp 35–65.

Kline, S.J., Reynolds, W.C., Schraub, F.A., Rundstadler, P.W. (1967). The Structure Of Turbulent Boundary Layers. J. Fluid Mech. No. 30. pp 741–773.

Krogstadt, P.A., Antonia, R.A. 1994. Structure of Turbulent Boundary Layers on Smooth and Rough Walls. J. Fluid Mechanics. Vol. 245. pp 599–617.

Leonardi, S., Orlandi, P., Djenidi, L., Antonia, A. 2003. Structure of Turbulent Channel Flow with Square Bars on One Wall. Proceedings TSFP-3. Sendai, Japan, 24–27 June 2003.

Miyake, Y., Tsujimoto, K., Nagai, N. 2002. Numerical Simulation Of Channel Flow With A Rib-roughened Wall. J. of Turbulence. Vol. 3. pp 1–17.

Morris, H.M. 1955. Flow in rough conduits. ASCE Transactions, Vol. 120, Paper No. 2745, 373–410.

Patel, V.C. 1998. Perspective Flow at High Reynolds Number and Over Rough Surfaces – Achilles Heel Of CFD. ASME J. Fluids Engineering. Vol. 120. pp 434–444.

Perry, A.E., Schofield, W.H., Joubert, P. N. 1969. Rough wall turbulent boundary layers. J. Fluid Mech. Vol. 37, pp 383–413.

Raupach, M.R. 1981. Conditional Statistics Of Reynolds Stress In Rough-Wall And Smooth-Wall Turbulent Boundary Layers. J. Fluid Mech. Vol. 108. pp 363–382.

Robinson, K. 1991. Coherent Motions in the Turbulent Boundary Layer, Ann. Rev. Fluid Mech. Vol. 23. pp 601–639.

This page intentionally left blank

River Flow 2004 – Greco, Carravetta & Della Morte (eds.)
© 2004 Taylor & Francis Group, London, ISBN 90 5809 658 0

Flow over dunes with super-imposed smaller dunes. Turbulent coherent structures and wall similarity hypothesis

M.T. Mattar
Water Resources Institute of the National University of Santiago del Estero, Argentina

ABSTRACT: This paper shows the results of an experimental work carried out on a glass wall flume with dimensions 67 m × 1.5 m × 1.0 m (length × width × height) installed in the hydraulics laboratory of the Litoral National University, Argentina. The bed of the flume was covered by a train of triangular bedforms, resembling the typical dunes present on the bed of Parana river. The point velocity measurements, aimed to estimate the three components of the velocity vector, were performed by means of an acoustic Doppler velocimeter (ADV). The obtained values were processed and a study was carried out in order to compare the turbulent characteristics of the flow over dunes with the flow over a bed composed by small dunes superimposed over large dunes. The features analyzed were the reattachment length, coherent events, characteristic spatial scales and, finally, it was appraised the wall similarity hypothesis, by means of a comparison between both bed conditions.

1 INTRODUCTION

Most of the flow which are present in nature are turbulent flows and so its mechanics has relevance in the associated transport phenomenon.

In mobile bed when of the critic shear stress is overcome processes of sediment transport take place, generating new shapes when the stress is increased. These turbulent transport processes are greatly influenced by the characteristics and by scale of the turbulent coherent structure. These structures (phenomenon also called bursting) are manifested through periodic events of ejection and sweeps (Nezu, I and H. Nakagawa, 1993).

Nowadays there are many research works intended to evaluate how much the coherent events contribute to the Reynolds stresses though measures in open channels with rough-bed and smooth-bed as well as over totally developed form bed.

A less common bed is that which is formed by dunes with super-imposed smaller dunes (little dunes) like the one in the Parana River, near Villa Urquiza, Entre Rios State, Argentina (Amsler, M and M. Scheider, 1992). Nowadays, there is not a complete comprehension over the mechanics and the evolution of these little dunes. With the purpose of clarifying over some of these aspects, in the present work the influence of the turbulent coherent structures over Reynolds stresses, the characteristics scales and wall similarity hypothesis are evaluated comparatively between a bed with a dunes train and another whit dunes with super-imposed smaller dunes.

2 EXPERIMENTAL PROCEDURE

The measurements tasks of this work were carried out on a glass wall flume in the installed Hydraulics Laboratory of the Litoral National University, Santa Fe State, Argentina. This flume has the following dimensions: 1.50 m width, 1.00 m height and 67.00 m length. A bed's piece is formed by 16 bed forms, with a wavelength of 2.30 m and the bed form height of 0.05 m.

Among the 16 dunes, 9 have super-imposed smaller dunes, called little dunes. These little dunes have 0.12 m length and 0.005 m height. To measure the velocity, an Acoustic Doppler Velocimeter (ADV) was used for laboratories Sontek brand. This is an easy-to-use, versatile instrument which can simultaneously measure the three components of the velocity at a measuring with sampling frequencies up to 25 Hz. This instruments averages a sampling volume of approximately 0.006 m width and changeable height: 0.0012 m, 0.0036 m and 0.005 m. The height of the sampling volume may be specified in the configuration file. In the present work a sampling volume height of 0.0036 m was used to carry out velocity measurements in a permanent uniform flow with a mean flow depth of 0.275 m. The velocity signal was recorded during a sampling time of 180 s (Mattar, M et al., 1999) using a sampling frequency of 25 Hz. The measurements were divided into two parts: *Med1*, the measurements were carried out over a uniform train of dunes, while in *Med2* the measurements were carried out over dunes with super-imposed little dunes.

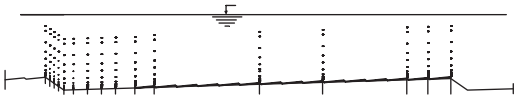


Figure 1. *Med1* and *Med2* scheme.

The measurements were carried out over 16 vertical profiles, each one with 14 points of velocity measurements. The height in meters of the measurements point were the following: 0.002, 0.004, 0.006, 0.008, 0.01, 0.015, 0.02, 0.03, 0.05, 0.08, 0.11, 0.15, and 0.20, measured from the dune's profile. The profile number one was located over a crest of the dune (progressive 0) the profile 16 was fixed in the next crest in downstream direction (progressive 230). In order to obtain a better description of the dynamics of the flow, the vertical profiles for the measurement of velocity were more closely spaced in the separation zone downstream of the dunes. The Figure 1, shows the measurement scheme.

3 COHERENT STRUCTURES

In order to determine the ejection and sweeps the Analysis Quadrant Technique (Lu, S.S and W.W. Willmarth, 1973; Nakagawa, H and I. Nezu, 1977a) was used in the present work. This technique distinguishes the turbulent events according to the signs of fluctuation of the velocities (u' and v') what gives origin to four quadrant. This technical assigns the outward interactions (ascendent movements of high velocity) to the first quadrant ($u' > 0$ and $v' > 0$), the inward interactions (descendent movements of slow velocity) were assigned to the third quadrant ($u' < 0$ and $v' < 0$) the ejections characterized by the transport of the fluid mass from the wall generating a decrease of the shear stress were assigned to the second quadrant and the sweeps events are assigned to the fourth quadrant ($u' > 0$ and $v' < 0$) which involve the flow transport to the wall increasing the shear stress. This is shown in Figure 2.

At any point in stationary flow, the contribution to the total Reynolds stress from quadrant *i*, excluding a hyperbolic hole region of size H, is:

$$\langle u',v'\rangle_{i,H} = \frac{li}{T\to 0}\frac{1}{T}\int_0^T u',v'(t)I_{i,H}(t,H)dt \qquad (1)$$

where $\langle u', v'\rangle_{i,H}$ = contribution from quadrant *i* for a certain threshold value H; $I_{i,H}(t,H)$ = function that registers the event and takes the following values:

1 If (u', v') is inside the quadrant *i*, and if $|u', v'| \le H\,|\overline{u', v'}|$

0 otherwise

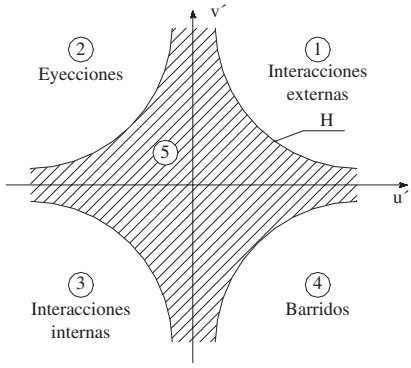


Figure 2. Sketch of region in the $u'v'$ plane.

The stress fraction transported by the contribution defined is:

$$Q_{i,H} = \frac{\langle u',v'\rangle_{i,H}}{\overline{u',v'}} \qquad (2)$$

And the time fraction during which this contribution is being made is:

$$T_{i,H} = \overline{I_{i,H}(u',v')} \qquad (3)$$

3.1 *Fractional contribution to the total Reynolds shear stress*

In the Table 1 the obtained values and the fraction of time of contributions for a profile located in the separation zone, to a height from the bed equal 0.05 m to *Med1* is shown as an example.

In the Table 1 it is shown that for a value of $H = 8$, while the second quadrant contributes 33.72% in a 2.7% of time, the contribution from the 4th quadrant is very little.

In Figure 3 the contribution of the ejection for $H = 2$ and 4 ($Q_{2,2}$ and $Q_{2,4}$) in the whole wavelength ($\lambda = 2.30$ m) is shown, giving a wider vision of the transport dynamics of stress from the second quadrant. In Figure 4 the sweeps contributions are shown. Generally it can be said that when H increases the fourth quadrant contributions decrease more rapidly, while the ejection events continue generating stresses and the contribution fraction of time, $T_{4,H}$ and $T_{2,H}$, from $H = 4$ become insignificant. This demonstrates that the process of transport is highly intermittent in the sense that it occurs during periods of great turbulent activity, what occupies a small fraction of time (Raupach, M.R., 1981).

In Figures 5 and 6 the contributions of the ejection and sweeps respectively for the case of the bed with super-imposed little dunes can be observed (*Med2*).

Table 1. Contributions and time fraction of the contribution to the Reynolds stress from the four quadrants.

H	T_1	T_2	T_3	T_4	Q_1	Q_2	Q_3	Q_4
0	0.1717	0.2825	0.1748	0.3710	−0.1588	0.7839	−0.1454	0.5203
1	0.0517	0.1591	0.0438	0.1724	−0.1208	0.7383	−0.0989	0.4423
2	0.0234	0.1067	0.0175	0.0937	−0.0801	0.6623	−0.0631	0.3270
3	0.0099	0.0804	0.0085	0.0526	−0.0473	0.5963	−0.0413	0.2277
4	0.0052	0.0620	0.0049	0.0258	−0.0316	0.5330	−0.0292	0.1350
5	0.0029	0.0499	0.0027	0.0112	−0.0219	0.4792	−0.0193	0.0699
6	0.0016	0.0407	0.0016	0.0045	−0.0146	0.4290	−0.0133	0.0336
7	0.0013	0.0330	0.0013	0.0022	−0.0132	0.3795	−0.0119	0.0193
8	0.0007	0.0274	0.0009	0.0013	−0.0080	**0.3372**	−0.0085	**0.0127**
9	0.0007	0.0220	0.0004	0.0007	−0.0080	0.2911	−0.0047	0.0068
10	0.0004	0.0169	0.0002	0.0004	−0.0058	0.2421	−0.0026	0.0048

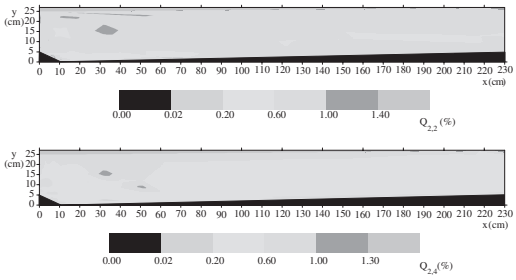


Figure 3. Map of fractional contribution $Q_{2,2}$ and $Q_{2,4}$ in *Med1*.

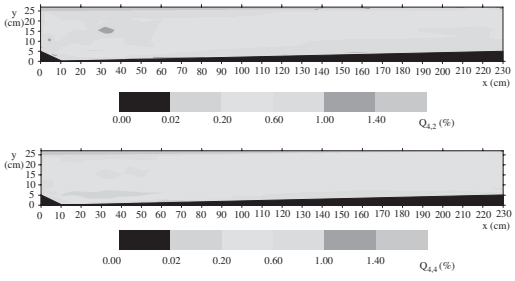


Figure 4. Map of fractional contribution $Q_{4,2}$ and $Q_{4,4}$ in *Med1*.

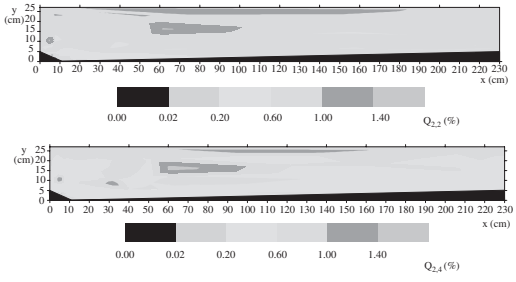


Figure 5. Map of fractional contribution $Q_{2,2}$ and $Q_{2,4}$ in *Med2*.

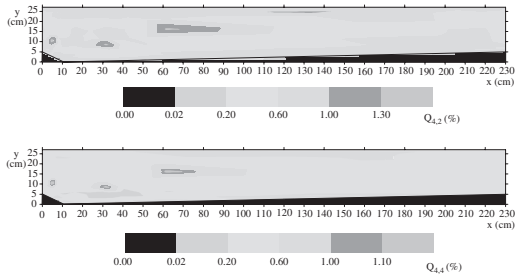


Figure 6. Map of fractional contribution $Q_{4,2}$ and $Q_{4,4}$ in *Med2*.

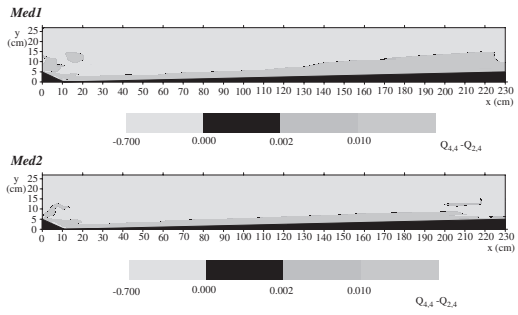


Figure 7. Map of the variation of ΔQ_4 in the whole wavelength.

In Figure 7 the obtained values for the two bed conditions are compared, from the difference among the sweep and ejection contributions for $H = 4$ (ΔQ_4).

4 EDDY SCALES

4.1 *Macroscale L*x

The biggest eddies that occur in the turbulent flow are responsible for the mayor transport of quantity movements for which the macroscale Lx is relevant in the

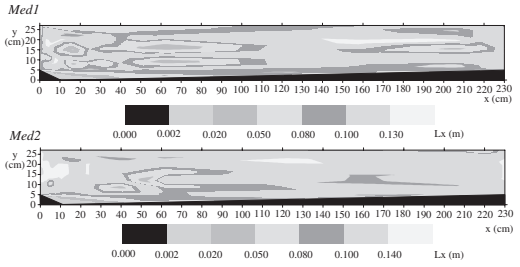


Figure 8. Variation of the macroscale in the whole wavelength.

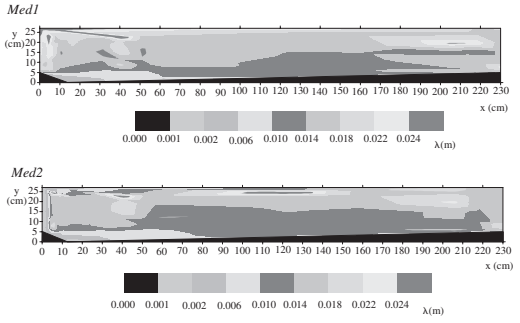


Figure 9. Map of the variation of Taylor's microscale in the whole dune's length.

analysis of the interaction of the turbulence with the mean flow.

The theoretical curve of the dimensionless spatial macroscale, was determined according to the Nezu, I and H. Nakagawa (1993).

The experimental values found in *Med1* and *Med2* are below the theoretical values. In Figure 8 the variation of the macroscale in the two bed conditions are observed.

4.2 *Taylor's microscale* λ

At Every point of each profile the value of Taylor's microscale was calculated according to the Nezu, I and H. Nakagawa (1993). The experimental data are over the theoretical curve but they still keep a trajectory almost parallel to it. In Figure 9 the found experimental are shown.

4.3 *Kolmogoroff's Microscale* η

The Kolmogoroff length microscale is the smallest one manifested in the turbulence, this one decreases when the dissipation increases.

This microscale is defined in function of the inward variables ν and ε (Friedlander, F and L. Topper, 1962).

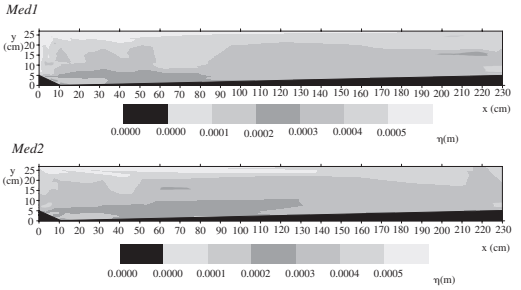


Figure 10. Map of variation microscale in the whole dune's length.

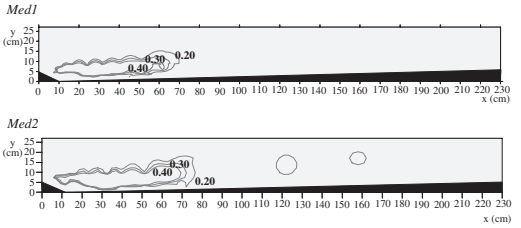


Figure 11. Curves of $Ftke/U*^3 = 0.20$; 0.30 and 0.40 for the two bed conditions.

5 WALL SIMILITUDE

According to the wall similitude hypothesis, there exists a transport of Turbulent Kinetic Energy in dynamic equilibrium state towards the free surface verifying a constant value of *Ftke* in the intermediate zone ($0.15 < y/h_p < 0.70$). For high Reynold's numbers, the dimensionless Kinetic Energy flow with the cubic shear velocity, is a constant value equal 0.30 (López and García, 1999).

In the Figure 11 the experimentally found values were drawn.

6 CONCLUSIONS

(a) The stele formed by the sweeps (fourth quadrant) in the zone of reestablished flow in *Med1*, has a thickness bigger than in *Med2*, whichshows that, apparently, the presence of the little dunes would increase the contribution are from the second quadrant (ejection) near the bed and specially near the crest. The predominance of the sweep events over the ejection ones in the bed proximity and consequently the total shear stress increase could influence in the resuspension elements and sediment transport in the mentioned zone.

(b) In *Med1* as well as in *Med2*, the values of L*x* are below those previous studies of flow in open channels (Nezu, I., 1977a; Raichlen, F., 1967).

(c) The data of Taylor's microscale obtained in this work are minor in a 50% than the ones found in previous studies about flow in open channels for high Reynold's numbers and smooth bed (Nezu, I., 1977; Laufer, J., 1954; Raichlen, F., 1967) and low Reynold's numbers and rough-bed (Nezu, I., 1977a; McQuivey et al., 1969).
(d) With regard to the wall similitude hypothesis, not in any of the two conditions of flow studies in the equilibrium area has been detected where, the production of Kinetic Energy is balanced with the local dissipation rate. Apparently in the case of a dune's train a dunes with super-imposed little dunes we would be in presence of an intermediate area vulnerable to the interactions between the internal and external area.

NOTATION

$Ftke$ = Kinetic Energy vertical flow.
H = threshold used in quadrant analysis.
y = height in meters of the point measurements from the dune's profile.
h_p = flow depth (0.275 m).
Lx = macroscale spatial.
$U*$ = friction velocity.
u', v' = velocity fluctuations.
ε = dissipation of flow energy.

REFERENCES

Amsler, M.L. and Schreider, M.I. 1992. "Aspectos Hidráulicos de la superposición de formas de fondo en el Rio Paraná". Memorias de XV Congreso Latinoamericano de Hidráulica. Sociedad Colombiana de Ingenieros, IAHR, Cartagena, Colombia Vol.3 39–48.

Friedlander, F. and Topper, L. 1962. " Turbulence: Classical papers on statistical theory. Interscience, New York.

Laufer, J. 1954. "The structure of turbulence in fully developed pipe flow". NACA. Tech. Report 1174.

López, F. and García, M. 1999. "Wall Similarity in Turbulent Open-Channel Flow". J. Engrg. Mech., Vol.125 (7).

Lu, S.S. and Willmarth, W.W. 1973. "Measurements of the structure of the Reynolds stress in a turbulent boundary layer. J. Fluid Mech., 60:481–511.

Mattar, M.T., Tevez, A., Toniolo, H., Fernández, R. and López, F. 1999. "Mean flow and turbulence structure over dunes with superimposed smaller bedforms". Anales del 28th Congreso Internacional de la IAHR, Gaz, Austria.

McQuivey, R.S. and Richardson, E.V. 1969 "Some turbulence measurements in open-channel flow". J. Hydraulics Div., ASCE, 95: HY-1:209–223.

Nakagawa, H. and Nezu, I. 1977a. "Prediction of the contributions to the Reynolds stress from the bursting events in open-channel flows". J. Fluid Mech., 80: 99–128.

Nezu, I. and Nakagawa, H. 1993. "Turbulence in open-channel flows". Monograph Series. IAHR.

Raichlen, F. 1967. "Some turbulence measurements in water". J. Eng. Mech., Div, ASCE, 93: EM-2:73–97.

Raupach, M.R. 1981. "Conditional statistics of Reynolds stress in rough-wall and smooth-wall turbulent boundary layers". J Fluid Mech., Vol.108, pp

This page intentionally left blank

River Flow 2004 – Greco, Carravetta & Della Morte (eds.)
© 2004 Taylor & Francis Group, London, ISBN 90 5809 658 0

Effect of bed-load concentration on friction factor in narrow channels

F. Calomino
Dipartimento di Difesa del Suolo, Università della Calabria, Rende (CS), Italy

R. Gaudio
CNR-IRPI – Sezione di Cosenza, Rende (CS), Italy

A. Miglio
Dipartimento di Difesa del Suolo, Università della Calabria, Rende (CS), Italy

ABSTRACT: Many studies concern the influence of bed-load on flow resistance in wide open channels and flumes. In this work the effect of bed-load concentration on the friction factor was investigated experimentally in a narrow channel. Tests were performed both in clear water and sediment transport conditions, using a roughened fixed bed. The present approach revises the Einstein side-wall correction procedure for the decomposition of flow resistance between the bed and the walls, which are of different material and, consequently, different roughness. From the velocity profiles, measured through micro-propellers, it was possible to obtain the bed shear velocities and, then, the mean bed and wall friction factors. An equivalent friction factor was finally obtained. The effects of the sediment concentration on velocities and resistance was analyzed. Also the influence of the walls on the velocity distributions was observed and commented on.

1 INTRODUCTION

Many studies can be found in the literature about the influence of bed-load on flow resistance in wide open channels and flumes.

It is well-known that sediment transport requires an energy expenditure from the flow, thus increasing resistance and reducing velocities.

In the case of narrow channels, the influence of the walls is exerted on the velocity distributions, and in a different way in clear water conditions or in the presence of bed-load.

In the following sections a quick review about the friction factor is presented in both situations.

Revising the Einstein (1942) side-wall correction procedure, in order to take into account the different roughness of bed and walls, an equivalent friction factor is introduced.

1.1 *Clear water friction factor*

In steady, uniform turbulent open-channel flows on a fixed bed, the velocity distribution law may be expressed as follows:

$$\frac{\bar{u}}{u_*} = \frac{1}{\kappa}\ln\frac{z}{z_0} \tag{1}$$

where $\bar{u}$ is the time mean velocity in streamwise direction, u_* the shear velocity, $\kappa = 0.4$ the von Kármán constant, z the height above bed, z_0 the turbulent length, which «describes the characteristic "hydraulic" friction length (or roughness) for the boundary» (Smart 1999).

The shear velocity is a function of the shear stress, τ_0:

$$u_* = \sqrt{\frac{\tau_0}{\rho}} = \sqrt{gRS_0} \tag{2}$$

where ρ is the water density, g the gravity acceleration, R the hydraulic radius and S_0 the longitudinal energy slope, equal to the channel slope in uniform flow conditions.

Introducing the friction factor in clear water conditions, f_0, in the well-known Darcy-Weisbach form:

$$f_0 = \frac{8gRS_0}{U^2} \tag{3}$$

U being the cross-sectional mean velocity, the following expression is obtained:

$$\sqrt{\frac{f_0}{8}} = \frac{u_*}{U} \tag{4}$$

In the case of narrow channels, i.e. for $B/h < 3.5$, where B is the top width and h the water depth (Song et al. 1998), the border effects influence the velocity distribution, which therefore does not present the maximum value at the water surface, but below it. In addition, the shear stress distribution is not constant over the bed (see, for example, Knight & Sterling 2000). Hence, the friction factor in narrow channels is not expressible with Equation (3), where the hydraulic radius is referred to the whole cross-section. In fact, the shear stress assumes different values not only at the bed and the side walls, but also across the bed itself. Following the side-wall correction procedure first proposed by Einstein (1942), for the correct computation of the friction factor in narrow channels it is necessary to subdivide the cross-section into three portions, one relative to the bed and two relative to the side walls: the central portion will be characterized by an average hydraulic radius $\overline{R_b}$ and an average friction factor $\overline{f_{0,b}}$, whilst the lateral portions by $\overline{R_w}$ and $\overline{f_{0,w}}$ (Fig. 1).

In the present work a laboratory test is presented, aimed at the determination of an equivalent friction factor, $f_{0,eq}$:

$$f_{0,eq} = \frac{\overline{f_{0,b}} P_b + \overline{f_{0,w}} P_w}{P} \tag{5}$$

where P_b and P_w are the wetted perimeter of the bed and the walls, respectively; $P = P_b + P_w$ is the total wetted perimeter. Analogously, $\overline{f_{0,b}}$ and $\overline{f_{0,w}}$ are the friction factors relative to the bed and walls, respectively:

$$\overline{f_{0,b}} = \frac{8g\overline{R_b}S_0}{U^2} \tag{6}$$

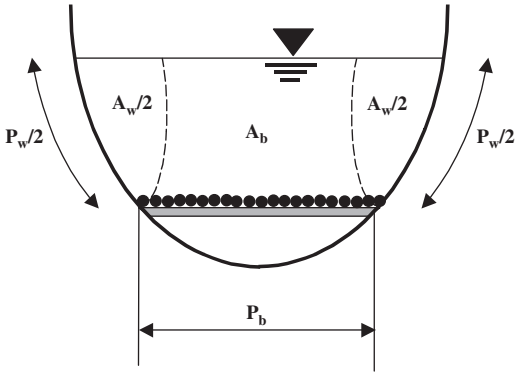


Figure 1. Ovoid section of composite roughness. The wetted areas and perimeters relative to bed and walls are indicated with A_b, P_b and A_w, P_w, respectively. The fixed bed is made of a gravel layer glued on a PVC strip, as explained in Section 2.

$$\overline{f_{0,w}} = \frac{8g\overline{R_w}S_0}{U^2} \tag{7}$$

1.2 *Friction factor in the presence of bed-load*

In the presence of bed-load, an increment of resistance occurs (May 1982; Mayerle et al. 1991; Song et al. 1998; Gaudio & Miglio 2003; etc.).

In this case, the friction factor, f_s, may be expressed as follows:

$$f_s = \varphi\left(f_0, C_V, \frac{d_{50}}{R}\right) \tag{8}$$

where C_V is the volumetric sediment concentration and d_{50} the median grain diameter.

In the following sections, some laboratory tests are presented, aimed to the determination of an equivalent friction factor, $f_{s,eq}$:

$$f_{s,eq} = \frac{\overline{f_{s,b}} P_b + \overline{f_{s,w}} P_w}{P} \tag{9}$$

where $\overline{f_{s,b}}$ and $\overline{f_{s,w}}$ are the friction factors relative to the bed and the walls, respectively.

2 EXPERIMENTAL INSTALLATION

Experiments were carried out at the Laboratory of Hydraulic Models of the Department of Soil Defense, University of Calabria, Italy.

The facility was an 11.0 m-long semi-ovoid perspex channel (250 mm × 375 mm ovoid cross-section), bolted to a tilting truss with longitudinal slope variable from 0.00 to 5.00%.

The channel bottom was made of a 140 mm-wide and 4.0 mm-thick PVC strip, set at the distance of 40 mm from the channel invert (Fig. 2).

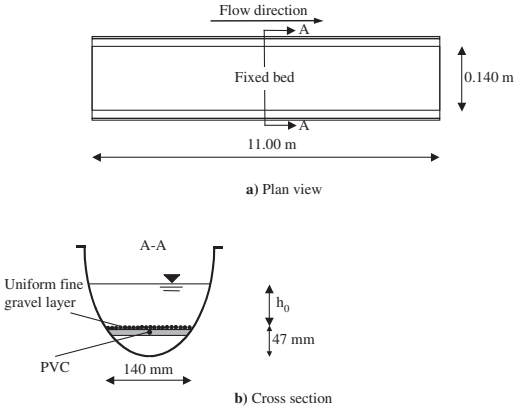


Figure 2. Schematic diagram of the experimental channel. The uniform flow depth is indicated with h_0.

The sediment used in the tests was a uniform fine gravel, with a median diameter $d_{50} = 3.0$ mm and a specific weight $\gamma_s = 26.5$ kN/m^3.

Along the whole channel, a layer of sediment was glued on the PVC strip.

The channel was fed through a 100 mm diameter pipe. The water flowed into a tank at the upstream end of the channel; a grid was inserted to minimize flow disturbances at the channel inlet. The discharge was measured with an ultrasonic flowmeter mounted on the feeding pipe.

A restitution channel, with a Thomson weir for calibration, receives the water flowing from the downstream end of the experimental channel.

Water depths were measured with a digital point gauge with an accuracy of ± 0.01 mm, whereas local velocities with a micro-propeller. These instruments were mounted on a gantry manually moving on rails placed above the side walls of the channel.

Sediments were introduced into the channel through an Archimedes's screw fed from a 70 dm^3 hopper, with a chute attached. The screw is driven by a potentiometer, which permits setting a constant value of the screw rotation velocity; therefore, a uniform volumetric sediment discharge can be injected. The potentiometer was accurately calibrated versus solid discharge. The solid discharge is a linear function of the potentiometer frequency.

The maximum value of solid discharge was 1211 g/min.

The sediment transported by the flow was collected in a basket at the experimental channel outlet, properly dried and weighed, in order to verify that the solid discharge at the outlet was equal to the injected one.

3 TESTS

Six tests were performed in October 2003.

Test 0 was carried out in clear water conditions, tests 1 to 5 in the presence of sediment feeding.

Table 1 presents the hydraulic characteristics of tests, h_0 being the uniform flow depth. The ratio B/h_0 was always less than 3.5, confirming that the channel can be considered as narrow. The solid discharge, G_s, and the volumetric concentration, C_V, are also shown.

Table 1. Hydraulic conditions of tests.

Test	S_0 (%)	Q (l/s)	h_0 (mm)	B (mm)	B/h_0	G_s (g/min)	C_V
0	0.010	11.4	67.7	213	3.15	0	0
1	0.010	11.4	67.7	213	3.15	404	$2.2 \cdot 10^{-4}$
2	0.010	11.4	67.8	214	3.15	605	$3.3 \cdot 10^{-4}$
3	0.010	11.4	68.3	214	3.13	807	$4.4 \cdot 10^{-4}$
4	0.010	11.4	68.6	214	3.12	1009	$5.5 \cdot 10^{-4}$
5	0.010	11.4	69.2	214	3.10	1211	$6.6 \cdot 10^{-4}$

No test presented deposit on the channel bed, also for the maximum value of bed-load (test 5).

It is to be noted that the normal depth, h_0, slightly increased in the presence of bed-load. In tests 3 to 5 a mobile layer much thicker than d_{50} was observed (thickness about 8 mm). According to Sumer et al. (1996), it can be said that a sheet flow layer occurred. The presence of the layer justifies the water depth increment.

For the measure of water depth and local velocities, the middle section, located 5.5 m downstream of the inlet, was selected. In fact, this section was distant enough from the end sections to permit the uniform flow conditions to be established, as verified through the acquisition of the water surface profile.

In particular, for each test, the velocity profiles were acquired along three verticals, as shown in Figure 3. The left and right verticals were chosen symmetric respect to the centerline. Along each vertical, the first value was measured at the height of 10 mm above the gravel bed; the successive 5 measurements were acquired with a step of 2 mm, and the remaining measurements with a step of 5 mm (Fig. 3). At each position, the time mean velocity in streamwise direction, $\overline{u}$, was acquired over a 30 s interval.

4 RESULTS

Figures 4 and 5 show the experimental velocity distributions respectively at the centerline and the lateral verticals, where similar results were obtained, as expected in the present symmetric case.

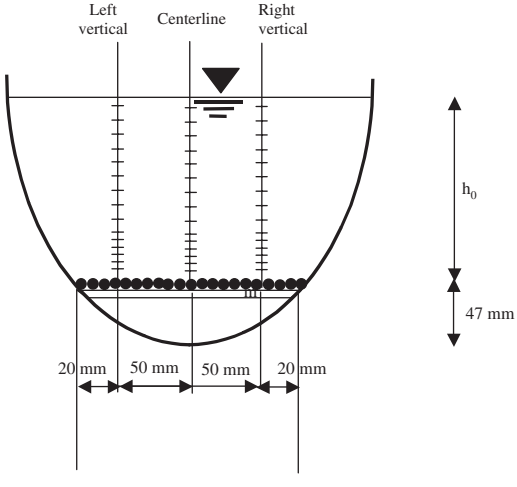


Figure 3. Measuring section. Local velocities were measured at the positions indicated along the three verticals for a 30 s time interval.

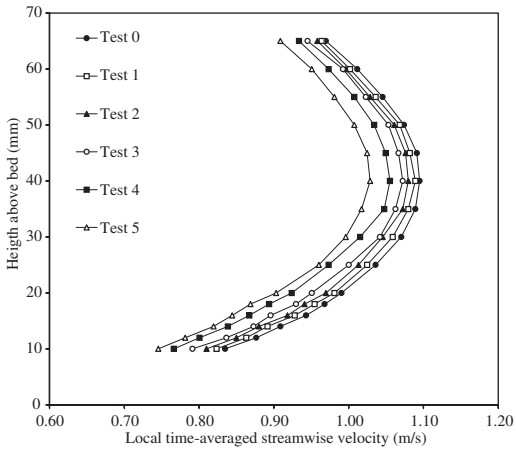


Figure 4. Local time mean velocity distributions (centerline).

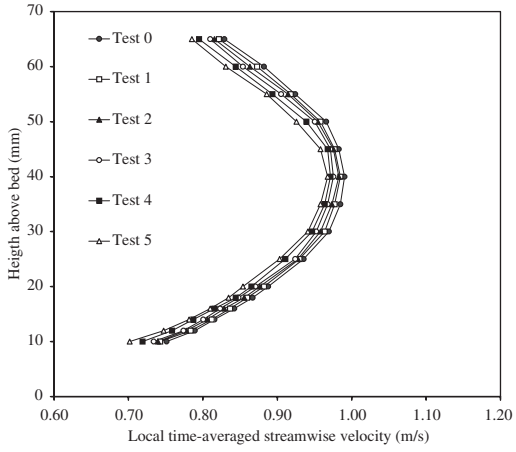


Figure 5. Local time mean velocity distributions (lateral verticals).

It is observed that the local velocities decrease as the volumetric sediment concentration increases.

In addition, the C_V increment produces greater velocity gradients near the bed, as also observed by Omid et al. (2003).

The influence of the walls in the narrow channel is evidenced in the following findings:

1. the maximum local velocity is measured below the water surface;
2. the velocities measured along the lateral verticals are less than the velocities measured along the centerline at the corresponding distances from the bed.

Figures 6 and 7 show the local time-averaged streamwise velocities, $\overline{u}$, versus ln z, respectively at

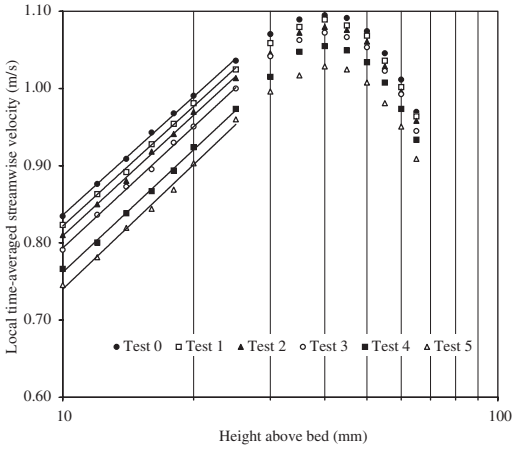


Figure 6. Linear regression straight lines for the determination of the shear velocities from the experimental velocity profiles (centerline).

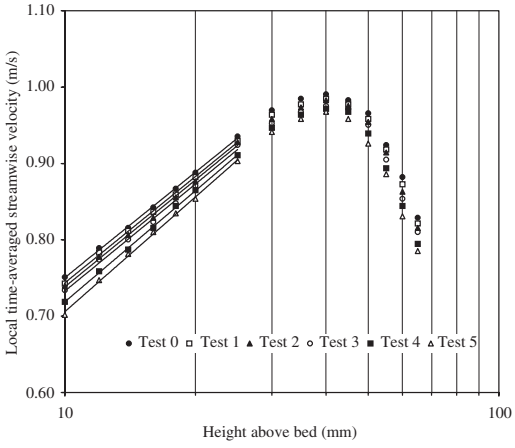


Figure 7. Linear regression straight lines for the determination of the shear velocities from the experimental velocity profiles (lateral verticals).

the centerline and the lateral verticals. It is observed the linear regression straight lines relative to the first seven points. The slopes of the straight lines were used for the determination of the bed shear velocities.

The interpolated points fall in both the inner region ($z/h_0 \leq 0.2$; Graf & Altinakar 1998) and the overlapping region (Smart 1999; Yen 2002). In fact, the relation expressed by Equation (1), which is rigorously valid only for the inner region, can be extended also to the overlapping region, where the velocity distribution is still logarithmic (Graf & Altinakar 1998; Smart 1999; Yen 2002).

The bed shear velocities at the centerline, $u_{*,bc}$, and at the lateral verticals, $u_{*,bl}$, were obtained. Then the

Table 2. Wetted areas and perimeters; top width.

Test	$A(h_0)$ (m^2)	A_b (m^2)	A_w (m^2)	P (m)	P_b (m)	P_w (m)	$B(h_0)$ (m)
0	0.0123	0.0101	0.0022	0.295	0.140	0.155	0.213
1	0.0123	0.0103	0.0020	0.295	0.140	0.155	0.214
2	0.0123	0.0104	0.0019	0.295	0.140	0.155	0.214
3	0.0124	0.0106	0.0018	0.296	0.140	0.156	0.214
4	0.0125	0.0110	0.0015	0.297	0.140	0.157	0.214
5	0.0126	0.0115	0.0011	0.298	0.140	0.158	0.214

following average value was computed:

$$\overline{u_{*,b}} = \frac{u_{*,bc} + 2u_{*,bl}}{3} \tag{10}$$

The average bed hydraulic radius is determined as follows:

$$\overline{R_b} = \frac{\left(\overline{u_{*,b}}\right)^2}{gS_0} \tag{11}$$

The mean bed and wall friction factors, $\overline{f_b}$ and $\overline{f_w}$ respectively, are obtained from Equations (6) and (7) for clear water conditions and analogously in the presence of bed-load.

In particular, the average wall hydraulic radius is determined as follows:

$$\overline{R_w} = \frac{A_w}{P_w(h_0)} \tag{12}$$

where the wall wetted area, A_w, is the difference between the total wetted area, A (expressed as a function of the normal flow depth, h_0), and the bed wetted area, $A_b = \overline{R_b} \cdot P_b$ (Fig. 1):

$$A_w = A(h_0) - A_b \tag{13}$$

Eventually, the equivalent friction factor, f_{eq}, is obtained from Equation (5) for clear water conditions and analogously in the presence of bed-load.

Results are presented in Tables 2 to 4. In particular, Table 4 reports the bed and the wall Reynolds number, Re_b and Re_w respectively, the grain Reynolds number, Re_*, and the Froude number, Fr, computed as follows:

$$\mathrm{Re}_b = \frac{R_b U}{\nu} \tag{14}$$

$$\mathrm{Re}_w = \frac{R_w U}{\nu} \tag{15}$$

$$\mathrm{Re}_* = \frac{\overline{u_{*,b}} d_{50}}{\nu} \tag{16}$$

Table 3. Bed shear velocities, cross-sectional mean velocity and hydraulic radii.

Test	$u_{*,bc}$ (m/s)	$u_{*,bl}$ (m/s)	$\overline{u_{*,b}}$ (m/s)	U (m/s)	$\overline{R_b}$ (m)	$\overline{R_w}$ (m)
0	0.089	0.080	0.084	0.93	0.072	0.014
1	0.089	0.080	0.085	0.93	0.074	0.013
2	0.090	0.081	0.086	0.93	0.075	0.012
3	0.091	0.082	0.086	0.92	0.076	0.012
4	0.092	0.084	0.088	0.92	0.079	0.010
5	0.093	0.087	0.090	0.91	0.083	0.007

Table 4. Friction factors; Reynolds and Froude numbers.

Test	$\overline{f_b}$	$\overline{f_w}$	f_{eq}	Re_b	Re_w	Re_*	Fr
0	0.0655	0.0130	0.0378	67244	13315	253	1.24
1	0.0669	0.0121	0.0380	68312	12337	255	1.24
2	0.0680	0.0114	0.0382	69160	11559	257	1.23
3	0.0702	0.0109	0.0389	69843	10887	259	1.22
4	0.0736	0.0090	0.0394	72084	8851	264	1.21
5	0.0787	0.0067	0.0405	74831	6358	270	1.19

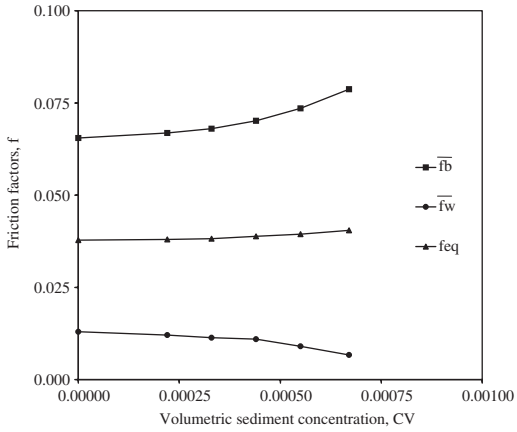


Figure 8. Friction factors.

$$Fr = \frac{U}{\sqrt{g\frac{A}{B}}} \tag{17}$$

where $\nu = 10^{-6}$ m^2/s is the water kinematic viscosity.

The flow was fully turbulent and supercritical, as confirmed by the values of the Reynolds and Froude numbers, respectively: $Re_b > 2000$, $Re_w > 2000$, $Re_* > 200$ (see Graf & Altinakar 1998; Armanini 1999) and $Fr > 1$.

Figure 8 shows the mean bed and wall friction factors and f_{eq} versus the volumetric sediment concentration, C_V. It is observed that the mean bed friction

factor increases with C_V up to about 20%, whereas the mean wall friction factor decreases down to about 48%. The equivalent friction factor, being a weighted average value (with very similar values of the bed and wall perimeters), is almost constant and presents a light increment (about 7%) at the highest concentrations.

Figures 9 and 10 show the normalized velocity differences, σ_{ij}, between the time mean velocities measured in the presence of bed-load (tests 1 to 5) and the corresponding velocities measured in clear water conditions (test 0) at the same height above bed:

$$\sigma_{ij} = \frac{\bar{u}_{ij} - \bar{u}_{0j}}{\bar{u}_{0j}} \tag{18}$$

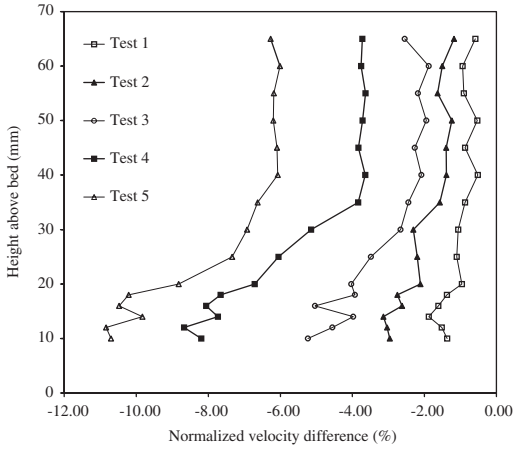


Figure 9. Normalized velocity differences (centerline).

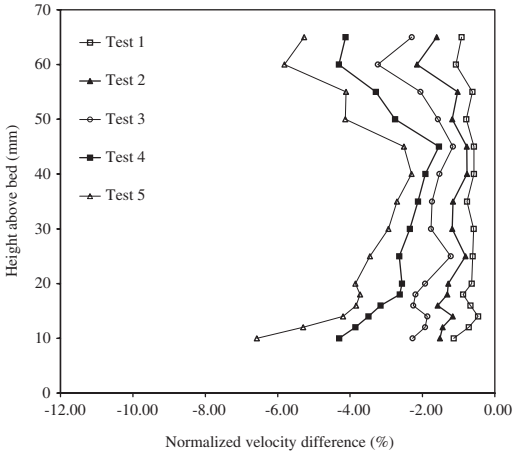


Figure 10. Normalized velocity differences (lateral verticals).

where $i = 1, 2, \ldots, 5$ indicates the tests with presence of bed-load and $j = 1, 2, \ldots, 15$ the measuring points along a given vertical.

At the centerline, it is observed that the percentage differences from the values obtained in clear water conditions increase with C_V (Fig. 9); for high concentration values the differences are greater in the proximity of the bed than close to the water surface.

Also at the lateral verticals the differences increase with C_V (Fig. 10), but less than at the centerline; besides, for a given C_V the values are similar in proximity to the bed and close to the water surface.

5 CONCLUSIONS

The effect of bed-load concentration on friction factor was investigated experimentally in a narrow ovoid perspex channel with a flat fixed 3 mm gravel bed. Tests were performed both in clear water and sediment transport conditions.

The present approach revises the Einstein side-wall correction procedure for the decomposition of flow resistance between the bed and the walls. From the velocity profiles, measured through micro-propellers, it was possible to obtain the shear velocities and, then, the mean bed and wall friction factors. An equivalent friction factor was finally obtained.

It was observed that the mean bed friction factor increases with C_V up to about 20%, whereas the mean wall friction factor decreases down to about 48%. The equivalent friction factor, being a weighted average value (with very similar values of the bed and wall perimeters), is almost constant and presents a light increment (about 7%) at the highest concentration.

At the centerline, it is observed that the percentage differences from the values obtained in clear water conditions increase with C_V; for high concentration values the differences are greater in the proximity of the bed than close to the water surface.

Also at the lateral verticals the differences increase with C_V, but less than at the centerline; besides, they are similar in the proximity of the bed and close to the water surface.

Further investigation is needed with different sediments, discharges and slopes.

REFERENCES

Armanini, A. 1999. *Principi di Idraulica fluviale* (in Italian). Cosenza: Bios.

Einstein, H.A. 1942. Formulas for the transportation of bed load. *Transactions ASCE* 107 (2140): 561–573.

Gaudio, R. & Miglio, A. 2003. Critical Deposit Velocity in Internally Corrugated Pipes. 18th European Junior Scientist Workshop *Sewer Processes and Networks*. Almograve, Portugal, 8–11 November.

Graf, W.H. & Altinakar, M.S. 1998. *Fluvial Hydraulics. Flow and transport processes in channels of simple geometry*. Chichester: Wiley.

Knight, D.W. & Sterling, M. 2000. Boundary shear in circular pipes running partially full. *Journal of Hydraulic Engineering* 126 (4): 263–275.

May, R.W.P. 1982. Sediment Transport in Sewers. Report IT 222. HR Wallingford Ltd., Wallingford, UK.

Mayerle, R., Nalluri, C. & Novak, P. 1991. Sediment Transport in Rigid Bed Conveyances. *Journal of Hydraulic research* 29 (4): 475–495.

Omid, M., Mandavi, A. & Narayanan, R. 2003. Effect of bed load transport on flow resistance in rigid boundary channels. XXX IAHR Congress *Water engineering and research in a learning society: modern developments and traditional concepts*. Thessaloniki, Greece , 24–29 August.

Smart, G.M. 1999. Turbulent velocity profiles and boundary shear in gravel bed rivers. *Journal of Hydraulic Engineering* 125 (2): 106–116.

Song, T., Chiew, Y.M. & Chin, C.O. 1998. Effect of bed-load movement on flow friction factor. *Journal of Hydraulic Engineering* 124 (2): 165–175.

Sumer, B.M., Kozakiewicz, A., Fredsøe, J. & Deigaard, R. 1996. Velocity and concentration profiles in sheet-flow layer of movable bed. *Journal of Hydraulic Engineering* 122 (10): 549–558.

Yen, B.C. 2002. Open channel flow resistance. *Journal of Hydraulic Engineering* 128 (1): 20–39.

This page intentionally left blank

River Flow 2004 – Greco, Carravetta & Della Morte (eds.)
© 2004 Taylor & Francis Group, London, ISBN 90 5809 658 0

Influence of macro-roughness arrangement on flow resistance

F. Canovaro, E. Paris & L. Solari
Department of Civil Engineering, University of Firenze, Italy

ABSTRACT: Experimental data on regular spaced strip arrangement of macro-roughness element are herein analysed by means of a two-layer model, in order to evaluate flow resistance and drag shear stress. Seventytwo experimental runs have been carried out in a glass walled tilting flume. Discharge was varied from 7.3 l/s to 13.5 l/s and slope was varied from 1.0% to 2.5%. Three different pebble sizes with a median axis from 4.3 cm to 8 cm were used as macro-roughness elements. Pebbles were placed on a granular plane bed to achieve a bottom geometry configuration of transverse regularly spaced strips. Results underline a non-linear behaviour of Chezy coefficient as a function of strip wavelength to height ratio, showing a minimum of conductance. Analogously, form induced shear stress presents a maximum, around 80% of total bed shear stress. Even if the reproduced pattern appears to be not wholly representative of natural conditions, comparison of results with other field and laboratory data seems to indicate that a similar dissipative behaviour is recognisable in natural bed forms such as step and pools or dunes.

1 INTRODUCTION

Flow over macroscale roughness may occur in various situations, such as in mountain streams and vegetated channels. In the case of mountain streams, due to the presence of large rocks and boulders protruding from the channel bed and large bed slope, the flow depth is typically comparable with the size of the roughness. In these conditions the longitudinal velocity profile is known to deviate from the classical log law and the classical expression of flow resistance formulae elaborated in the case of lowland rivers are no longer valid (Bathurst 1987).

In particular various Authors (Bathurst 1981, 1985, Baiamonte et al. 1995, Ferro 1999) suggest that flow resistance is a function not only of the relative submergence (defined as mean flow depth to characteristic sediment diameter ratio) but also of further additional parameters related to the "roughness geometry", such as spatial density and arrangement of macro-roughness elements. In particular Baiamonte et al. (1995) suggest, in case of absence of vegetation, the following functional relationship for Chezy coefficient:

$$C = f(Re, Fr, k, \Gamma, P_1, P_2, \tau_*); \quad (1)$$

where Re and Fr are flow Reynolds and Froude numbers, k is relative submergence, Γ is spatial density, P_1 and P_2 are two parameters related to the planimetric layout of macro-roughness elements (hereafter referred as *pattern*) and $\tau*$ is the Shields parameter.

The influence on flow resistance played by *Re, Fr, k*, and $\tau*$ in the case of mountain streams, has been widely investigated by several Authors (Baiamonte 1995, Bathurst 1981, Colosimo et al. 1988, Ferro 1999, Graf 1984); while the role played by macro-roughness spatial density and *pattern*, is not completely clarified.

Rouse (1965) indicates, in the case of a regular *pattern*, that there exists an optimum value of spatial density, ranging between 0.15–0.20, which produce the maximum of flow resistance. As pointed out by Morris (1971) for flow in closed conduits, Rouse findings may be explained in terms of a different behaviour of flow motion in relation to the spatial density of macro-scale roughness. For low values of density, when macro-roughness are "isolated", motion might be regarded as a "non wake interfering" like, while for high values of density, wakes impact together and dissipation decreases.

In order to study the effects of bedforms on flow resistance, a special type of *pattern*, formed by macro-roughness elements arranged according to regularly spaced strips placed perpendicular to flow direction, has been investigated. In particular Davies (1980) and Wohl & Ikeda (1998), suggest that maximum of flow resistance occur when the spacing between the strips is about 10 times the height of macro-roughness elements.

In the present analysis, we investigate flow resistance in the case macro-roughness elements placed according to regularly spaced strips across the plane

bed of a flume. The results obtained are discussed and compared with those proposed by other authors (Egashira & Ashida 1989, Aberle & Smart 2003) interpreting flow resistance in natural bedforms such as step & pool or sand dunes. Results indicates the presence of a maximum in flow resistance when the ratio strip wavelength to height is close to the values commonly observed in natural bedforms, such as step & pool bed forms.

2 THEORETICAL FRAMEWORK

Flow resistance is herein investigated by means of an analytical model, extended from Canovaro et al. (2003), according to which flow region, whose depth is indicated by Y, is divided in two layers.

A bottom layer, laying on the bed, containing part of macro-roughness elements, in which the flow is dominated by the loss of momentum due to the drag around the obstacles. In such layer of thickness d the flow velocity V_b is relatively low and approximately constant.

An upper layer of height Y-d, where the mean flow velocity U is relatively high.

This velocity profile is defined by four variables: U, V_b, Y and d. U and Y are obtained via experiments, d and V_b are unknowns determined by solving flow continuity and streamwise momentum balance equations. Steady flow and spatially averaged uniform conditions are here taken into account. In these conditions, governing equations read as follows:

$$F_g = F_d + F_s \,, \tag{2}$$

$$\frac{Q}{B} = (Y-d)U + \psi d V_b \,. \tag{3}$$

Notations are given at the end of the paper.

In the streamwise momentum balance equation (eq. 2) there are three components: the total water weight along the streamwise direction F_g, the resistance associated to the drag around macro-roughness elements F_d and the resistance due to the surface friction of both granular and boulder surface F_s. These components read as follows:

$$F_g = \rho g Y S \left(1 - \frac{2D_s\Gamma}{3Y}\right) A_C \,, \tag{4}$$

$$F_d = \frac{1}{2}\rho C_D N A_f' V_b^2 \,, \tag{5}$$

$$F_s = \left[\rho\frac{U^2}{C_G^2}(1-\Gamma) + \rho\frac{U^2}{C_P^2}\Gamma\right] A_C \,. \tag{6}$$

In the continuity equation (eq. 3), ψ denotes a reduction coefficient (always < 1) of flow velocity into the bottom layer to take into account the effective area occupied by the flow; therefore ψV_b denotes the mean (apparent) velocity in the lower layer. For regular spaced strips the reduction factor has been defined as the ratio strip length (D_l) to strip wavelength and reads as follows:

$$\psi = \frac{D_m D_l N}{LB} \,, \tag{7}$$

Chezy coefficient is obtained from the following:

$$C = \frac{\overline{U}}{\sqrt{\tau_g/\rho}} \,, \tag{8}$$

where:

$$\overline{U} = \frac{(Y-d)BU^2 + dBV_b^2}{Q} \tag{9}$$

3 EXPERIMENTAL APPARATUS

The experiments are carried out in a 10 m long, 36.5 cm wide and 50 cm deep glass-walled recirculating tilting flume. The measuring reach is 4 meter long with a bed covered by a layer of granular uniform material having a medium size of 7 mm.

Over this granular layer (Fig. 1) the macroroughness elements (represented by pebbles) are disposed in order to roughly simulate natural macroroughness arrangement, such as bed forms or random distributions.

In order to dissipate flow disturbances, before the beginning of the measuring reach a transition reach composed by little quarry rubbles is positioned (Fig. 2).

In the experiments three different sets of pebbles are used, characterized by different medium axis values according to the Wentworth sedimentological scale Φ, as presented in Table 1.

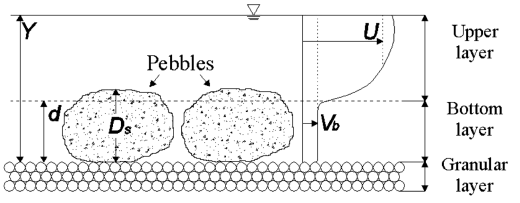


Figure 1. Streamwise section of the velocity profile.

The pattern here investigated is represented by "transverse rows" (Fig. 4) and it refers to a stream-wise sequence of strips. Each strip is made by pebbles, placed over the granular layer with the long axis in flow direction and the short axis perpendicular to the bottom of the flume.

For each set of pebbles the "wave length" λ, i.e. the spacing between two following strips, is varied from 15 to 80 cm. Experiments have been carried out with different discharges from 7.3 to 13.5 l/s, and slope is varied at 1.0 and 2.5 percent.

For each run both total water depth Y and mean flow velocity U are measured. Several time-averaged values of water depth and flow velocity are taken for each run along the measuring reach.

Water surface elevation is measured by means of a set of 19 piezometers, placed below the granular layer, according to the sketch in figure 3; by averaging these 19 values, one space-time averaged water depth value is obtained for each run.

Flow velocity is taken in 33 different points along a wavelength across the middle strip, by means of a micro propeller meter (Fig. 5). Each value is the result of a 400 velocity time-averaging readings, corresponding to a measurement time of 10 seconds. As for the water depth measurement, one space-time averaged velocity value is obtained for each run.

At the end of the experimental activity we have collected 47 runs divided in 5 experiments, each experiment is characterized by different strip height, slope or discharge. A summary of the performed experiments is reported in Table 2.

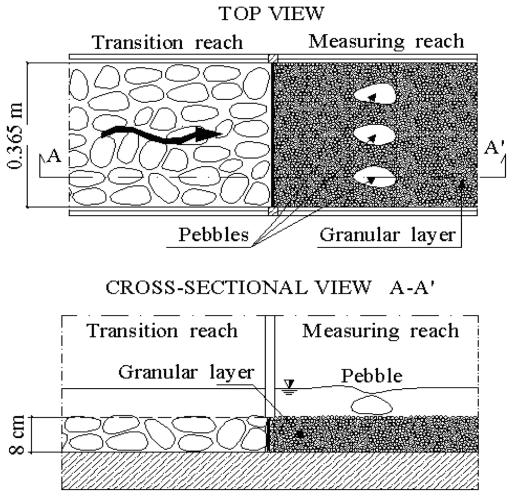


Figure 2. Sketch of the experimental arrangement.

Table 1. Mean geometrical properties of the pebbles employed.

Set of pebbles	Φ	D_s (cm)	D_m (cm)	D_l (cm)	V (cm^3)
1	−5.25	2.6	3.8	5.5	29
2	−5.75	4.3	5.4	8.0	96
3	−6.25	5.7	7.6	9.8	223

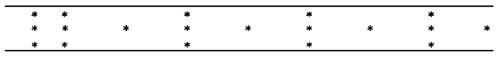


Figure 3. Sketch of the piezometers inlets installed on the channel bottom.

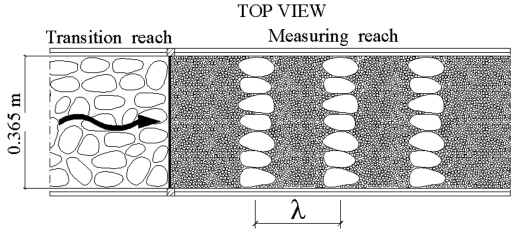


Figure 4. Arrangement of the "transverse rows" pattern.

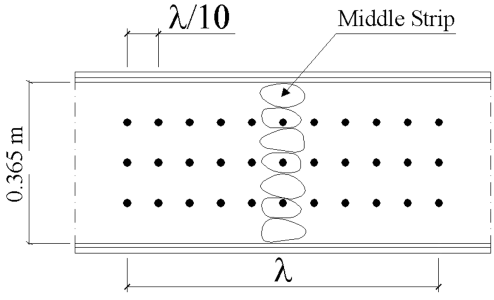


Figure 5. Sketch of velocity measuring points disposition.

Table 2. Summary of performed experiments.

Experiment	Φ	Runs (#)	S (%)	Q (l/s)	λ (cm)
1	−5.25	10	2.5	13.5	10–60
2	−5.75	9	1.0	7.3	15–80
3	−5.75	8	1.0	13.5	15–80
4	−5.75	11	2.5	7.3	10–80
5	−6.25	9	1.0	13.5	15–80

4 RESULTS

Results concerning drag shear stress, dimensionless Chezy coefficient and equivalent roughness are here presented and compared with experimental findings proposed by other authors, on both geometric strip patterns and laboratory step-pool bed forms.

In Figure 6 the ratio between drag induced shear stress and total bed shear stress, τ_d/τ_g, as a function of the λ/D_s ratio is presented.

τ_d/τ_g ratio presents two asymptotic values: ~0.15 when $\lambda/D_s \rightarrow 1$ (maximum packing) and 0 when $\lambda/D_s \rightarrow \infty$ (no macro-roughness). Far from these two asymptotic values, it appears that the drag component fraction is always over the 50% of the total bed shear stress, reaching a maximum of about 80% when λ/D_s ratio is around 10. This value of λ/D_s corresponds to a pebble areal concentration ranging around 0.20.

A comparison between present results and the ones obtained from Canovaro et al. (2003) in case of "random" pattern is presented in Figure 7. It appears that for a similar value of pebble concentration, even the "random" pattern exhibits a maximum, of relatively minor intensity, of τ_d/τ_g.

This result may indicate that regular strips have a deeper influence on flow dissipative mechanism than random elements. From equation (2):

$$1 = \frac{\tau_d}{\tau_g} + \frac{\tau_s}{\tau_g}; \qquad (10)$$

it appears that the surface shear stress τ_s is a small fraction of total bed shear stress τ_g, being τ_s/τ_g ranging around (0.20–0.40), when λ/D_s ratio is around 10.

In Figure 8 is a plot of Chezy coefficient behaviour as a function of λ/D_s ratio. Analogously to τ_d/τ_g ratio also Chezy coefficient behaviour is not monotonic, showing a minimum at the same λ/D_s value at which the relative drag shear stress reaches a maximum. Chezy coefficient is also affected by discharge and slope, increasing as Q increases and S decreases.

The presence of a maximum in flow resistance in case of regular spaced strips has been demonstrated by several Authors.

Wohl & Ikeda (1998) through an extensive experimental activity employing regular spaced strips, obtained a Chezy coefficient behaviour in agreement with the results herein presented, as shown in Figure 9. In particular it can be noted that Chezy coefficient is minimum when λ/D_s is around 10.

Such behaviour is also confirmed by a comparison with results obtained by Johnson & LeRoux (1946) regarding the relative roughness, in the case of geometric strips (Fig. 10). The comparison shows a maximum when $\lambda/D_s \approx 10$, again in agreement with results herein presented.

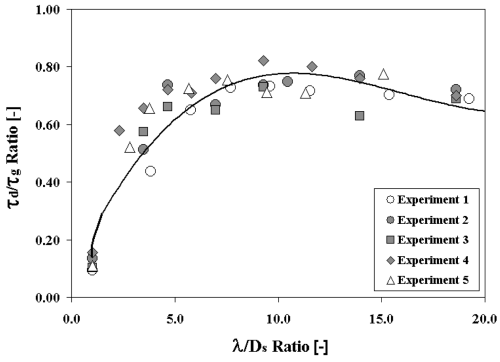


Figure 6. Ratio of drag induced shear stress τ_d to total bed shear stress τ_g as a function of ratio of wavelength λ to strips height D_s.

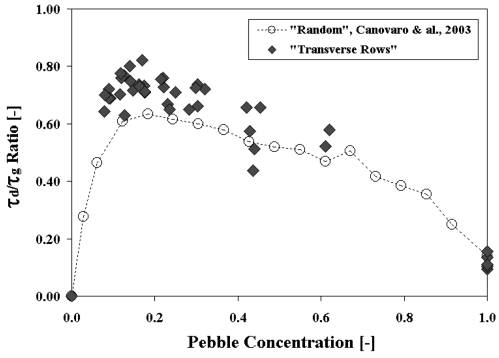


Figure 7. Ratio of drag induced shear stress τ_d to total bed shear stress τ_g as a function of pebble concentration, as from present experiments and experiments from Canovaro et al. (2003) in the case of "random" pattern.

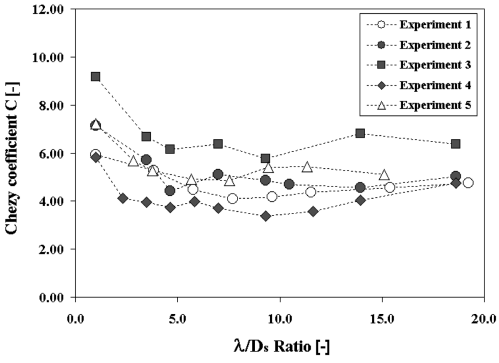


Figure 8. Dimensionless Chezy coefficient as a function of ratio of wavelength λ to strips height D_s.

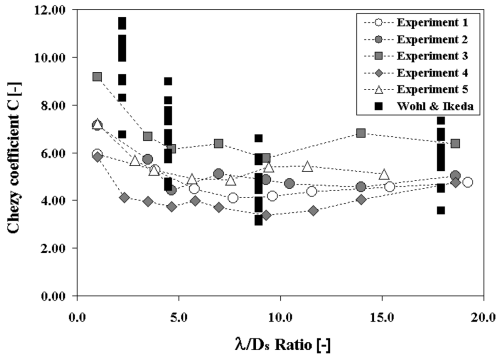


Figure 9. Comparison with Wohl & Ikeda (1998) experiments.

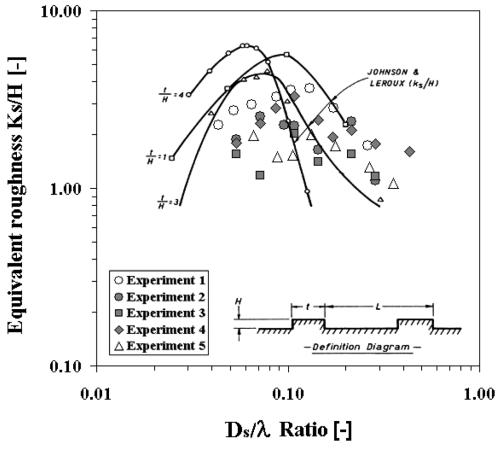


Figure 10. Comparision with Johnson & LeRoux (1946) experiments. In our case the t/H ratio is around 2, with t corresponding to D_l and H corresponding to D_s.

Even if "transversal rows" pattern is only a geometrical schematisation of natural situations, it seems reasonable to consider some general analogy between flow resistance in natural streams and in laboratory flumes.

In particular other Authors (Abrahams et al. 1995, Chin 1999) have observed that λ/D_s attains values around 10 in the case of natural streams with slope ranging between (0.01–0.025). The latter result may indicate that step-pool streams evolve toward an arrangement of steps that maximizes resistance to flow, increasing the form resistance despite of the surface resistance, in the way to reach a stable arrangement (Abrahams et al. 1995).

In the light of the above findings, it seems reasonable to assume that the "transverse rows" pattern is able to reproduce the fundamental dissipative mechanisms

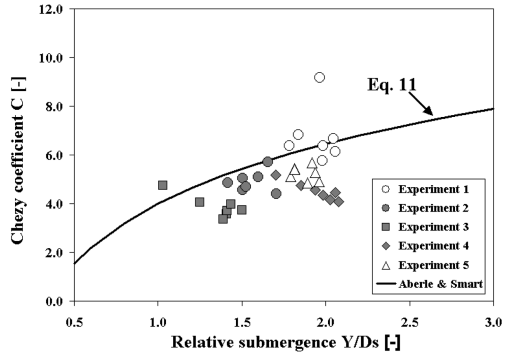


Figure 11. Comparison with Aberle & Smart (2003) formula.

occurring in natural streams with a step-pool morphology. The validity of such assumption is discussed in the following.

Aberle & Smart (2003) derived an empirical formula for the flow resistance in a step-pool morphology from experimental data obtained by Koll (2002) and Rosport (1997). The experiments were carried out in a tilting flume with slopes of 2, 4, 8 and 9.8%, employing two different coarse sediment mixtures, in the way to obtain real step-pool structures. The empirical formula in terms of Chezy coefficient reads as follows:

$$C = 3.54 \ln\left(\frac{Y}{D_{84}}\right) + 4.41 \qquad (11)$$

In Figure 11 equation (11) is shown and compared with the present results. It appears a good agreement even if Aberle & Smart formula tends to slightly overestimates the Chezy coefficient. This behaviour is probably due to the fact that Aberle & Smart have employed a mixture of sediments obtaining a rather smooth step-pool profile.

Finally, the formula proposed by Egashira & Ashida (1989) to evaluate flow resistance in presence of step-pool bed forms, has been compared in Figure 12. The formula reads as follows:

$$C = \left[\frac{0.6 D_s^2}{Y\lambda} + \left(1 - \frac{2.5 D_s}{\lambda}\right) \frac{1}{(6 + 2.5 \ln(Y/k_s))^2}\right]^{-1/2} \qquad (12)$$

The comparison shows a good agreement of experimental data with equation (12), especially for λ/D_s values around greater than 6–7. This behaviour is probably due to the fact that below this value the wavelength of the strips is too small to be interpreted by Egashira & Ashida formula.

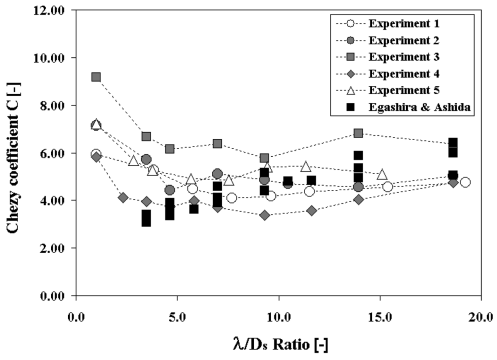


Figure 12. Comparison with Egashira & Ashida (1989) formula.

5 CONCLUSIONS

An extensive laboratory experimental activity has been carried out in order to investigate the influence on flow resistance of a regular spaced pebble strips arrangement, in the case of various flow conditions and strip wavelengths.

Experimental measurements are analysed by means of an interpretative extended model, derived from a previous paper (Canovaro et al. 2003). The model allows to investigate the behaviours of Chezy coefficient and relative drag shear stress as a function of the strip wavelength.

Results suggest that when dimensionless strip wavelength (λ/D_s) is around 10, Chezy coefficient and relative drag shear stress (τ_d/τ_g) present a minimum and a maximum, respectively. In particular the minimum of Chezy coefficient is substantially smaller (about 60%) than in the case of a bed completely covered by macro-roughness elements; at the same time drag shear stress is around 80% of total bed shear stress.

A comparison between present results and the ones obtained from Canovaro et al. (2003) in the case of "random" pattern suggests that, even if both patterns displays similar behaviors, "transverse rows" pattern have a deeper influence on flow dissipative mechanism than random elements.

The presence of a minimum of Chezy coefficient, when λ/D_s is around 10 has been also pointed out by other Authors (Wohl & Ikeda 1998; Johnson & LeRoux 1946); moreover an overall good agreement with present and latter Authors results is displayed.

An analogy between flow resistance in natural streams and in laboratory flumes has been discussed; in particular it seems that "transverse rows" pattern is able to reproduce the dissipative mechanisms occurring in a natural step-pool morphology.

In particular observations of other Authors (Egashira & Ashida 1989; Abrahams et al. 1995; Chin 1999; Aberle & Smart 2003) show both that λ/D_s attains values around 10 in the case of natural streams with slope ranging between (0.01–0.025), and that Chezy coefficient behaviour associated to natural step-pool configurations is in agreement with results herein presented.

The above findings may indicate that step-pool streams evolve toward an arrangement of steps that maximizes resistance to flow, increasing the form resistance despite of the surface resistance, in the way to reach a stable arrangement (Abrahams et al. 1995).

ACKNOWLEDGEMENTS

This work has been developed within the framework of the National project cofunded by the Italian Ministry of University and of the Scientific and Technological Research and by the University of Firenze (COFIN 2001).

NOTATIONS

The following symbols are used in this paper:

A_c = measuring reach surface;
$A_{f'}$ = frontal pebble reduced surface;
B = flume width;
C = Chezy coefficient;
C_d = drag coefficient;
C_G = Chezy coefficient of granular layer surface;
C_P = Chezy coefficient of pebbles surface;
d = displacement;
D_l = long pebble diameter;
D_m = medium pebble diameter;
D_s = short pebble diameter;
D_{84} = the sieve size for which 84% of particle size are smaller;
f = friction factor;
F_d = drag-induced resistance;
F_g = total water weight;
F_s = surface-induced resistance;
k_s = equivalent roughness;
L = measuring reach length;
N = number of pebbles;
Q = discharge;
U = mean flow velocity in the upper layer;
V_b = effective flow velocity in the lower layer;
Y = total water depth;
Γ = spatial density;
λ = strips wavelength;
ϕ = reduction factor;
ρ = water density;
τ_d = drag induced shear stress, $\tau_d = F_d/A_c$;
τ_g = total bed shear stress, $\tau_g = F_g/A_c$;
τ_s = surface shear stress, $\tau_s = F_s/A_c$;

REFERENCES

Aberle, J. & Smart, G. M. 2003. The influence of roughness structure on flow resistance on steep slopes. *Journal of Hydraulic Research*, *IAHR*, 41 (3): 259–269.

Abrahams, A. D., Gang, Li. & Atkinson, J. F. 1995. Step-pool stream: Adjustment to maximum flow resistance. *Water Resources Research*, 31 (10): 2593–2602.

Baiamonte, G., Giordano, G. & Ferro, V. 1995. Advances on velocity profile and flow resistance law in gravel bed rivers. *Excerpta*, 9: 41–89.

Bathurst, J. C., Li, R. M. & Simons, D. B. 1981. Resistance equation for large-scale roughness. *Journal of the Hydraulic Division*, *ASCE*, 107 (12): 1593–1613.

Bathurst, J. C. 1985. Flow resistance estimation in mountain rivers. *Journal of Hydraulic Engineering*, *ASCE*, 111 (4): 625–643.

Bathurst, J. C. 1987. Closure 'Flow resistance estimation in mountain rivers'. *Journal of Hydraulic Engineering*, *ASCE*, 113 (6): 822–824.

Canovaro, F., Paris, E. & Solari, L. 2003. Analysis of resistance of flow over macro-scale roughness: first results. *Proc. of XXX IAHR Congress*, Thessaloniki, GREECE, Theme C, vol. 2: 1–8.

Chin, A. 1999. The morphologic structure of step-pools in mountain streams. *Geomorphology*, *ELSEVIER*, 27: 191–204.

Colosimo, V., Copertino, A. & Veltri, M. 1988. Friction factor evaluation in gravel-bed rivers. *Journal of Hydraulic Engineering*, *ASCE*, 114 (8).

Davies, T. R. H. 1980. Bedform spacing and flow resistance. *Journal of the Hydraulic Division*, *ASCE*, 106 (3): 423–433.

Egashira, S. & Ashida, K. 1989. Flow resistance and sediment transportation in streams with step-pool bed morphology. *Proc. of International Workshop on Fluvial Hydraulics of Mountain Regions.* Trento, ITALY: A31–A44.

Ferro, V. 1999. Friction factor for gravel-bed channel with high boulder concentration. *Journal of Hydraulic Engineering*, *ASCE*, 125 (7).

Graf, W. H. 1984. Flow resistance for steep, mobile channels, *Proc. of Workshop on 'Idraulica del territorio montano'*, *Bressanone*.

Johnson, J. W. & LeRoux, E. A. 1946. Discussion of Powell R.W. 'Flow in a channel of definite roughness'. *Transactions*, *ASCE*, 111: 531–566.

Koll, K. 2002. Feststofftransport und Geschwindigkeitsverteilung in Raugerinnen. *Diss., Univ. Karlsruhe, Fak. F. Bauingenieur und Vermessungswesen.* (in German).

Morris, H. M. & Wiggert, J. M. 1971. Applied hydraulics in engineering. In *John Wiley & Sons*, *Inc*., New York, USA.

Rosport, M. 1997. Fließwiderstand und Sohlstabilität steiler Fließwässer unter Berücksichtigung gebirgsbachtypischer Sohlstrukturen. *Mitt. Des Institut für Wasserwirtschaft und Kulturtechnik, Univ. Karlsruhe*, Heft 196. (in German).

Rouse, H. 1965. Critical analysis of open channel resistance. *Journal of the Hydraulic Division*, *ASCE*, 91 (4): 1–25.

Wohl, E. E. & Ikeda, H. 1998. The effect of roughness configuration on velocity profiles in an artificial channel. *Earth Surface Processes and Landforms*, 23: 159–169.

This page intentionally left blank

River Flow 2004 – Greco, Carravetta & Della Morte (eds.)
© 2004 Taylor & Francis Group, London, ISBN 90 5809 658 0

The effect of bed roughness on velocity profile in open channels

A. Mahdavi & M.H. Omid
Dept. of Irrigation and Reclamation Eng., Tehran University, Tehran, Iran

ABSTRACT: The effect of bed roughness and bed load movement on flow velocity profile in an open channel with uniform flat-bed is experimentally investigated. Experiments were performed in a tilting channel of glass sides and smooth bed made of Perspex, and of rectangular cross-section 250 mm wide and 12.5 m long. Two different grain sizes with diameter of 0.5 and 2.84 mm were used for the roughening of the bed and sediment injection. Sediment injection was performed with the same size of particles used for roughening the bed. Point velocities were measured by a 10 mm propeller current meter. The results indicate that the logarithmic law for velocity profile is valid for different bed conditions and bed load concentrations. However, lower part of the profile is influenced by the bed roughness resulting steeper slope of the profile in logarithmic region. Since the slope of this profile increases, shear stress and consequently friction factor increases, affecting the bulk of flow to reduce the mean flow velocity.

1 INTRODUCTION

The velocity profile is closely related to the friction factor and boundary roughness, though the connection had received relatively little attention until 1980. Because the friction factor can be estimated from the bulk measurements without having to obtain the velocity profile, earlier works until 1980 had tended to consider the two separately, in many cases ignoring the velocity profile altogether since the friction factor is often of more direct engineering interest. The renewal of interest in the characterization of velocity profiles due to work of Itakura and Kishi (1980) and particularly Coleman (1981, 1986) had led to further debate concerning the friction factor.

In open-channel flow the velocity is not uniformly distributed. In this research, only vertical velocity profile is studied. In case of gravel bed and turbulent flow the vertical velocity profile is often assumed to be logarithmically distributed (e.g. Chow, 1959; French, 1986; Graf 1998 and Ferro, 1999). Logarithmic velocity profile can be shown by:

$$u = \frac{u_*}{\kappa} \ln\left(\frac{y}{y_0}\right) \tag{1}$$

where u = velocity [m/s] in distance y [m] from the bed; u_* = the shear velocity [m/s]; κ = Von Karman constant; and y_0 = the integral constant.

The flow can be hydraulically either smooth or rough. Hydraulically smooth flow occurs when the surface irregularities are so small that all roughness elements are entirely submerged in the laminar sub layer (Chow, 1959). Therefore, the bed roughness will not affect the velocity distribution. According to Graf (1998) and Schlichting and Gersten (2000) the flow is smooth if:

$$0 < \frac{u_* k_s}{\nu} < 5 \tag{2}$$

where ν = kinematic viscosity [m^2/s]; and k is the roughness height [mm]. Substituting y_0 for smooth channel in equation 1, one gets:

$$\frac{u}{u_*} = 5.75 \log\left(\frac{u_* y}{\nu}\right) + 5.5 \tag{3}$$

The flow is rough when bed roughness is so large that it produces eddies close to the bottom (Liu, 2001). There is no viscose sub layer and the velocity distribution is affected only by bed roughness. According to Graf (1998) and Schlichting and Gersten (2000) the flow is hydraulically rough if:

$$\frac{u_* k_s}{\nu} > 70 \tag{4}$$

Substituting y_0 for rough channel in equation 1, it follows:

$$\frac{u}{u_*} = 5.75 \log\left(\frac{y}{k_s}\right) + 8.5 \tag{5}$$

In this equation the roughness element k_s, may be considered as the sum of the skin roughness, and sediment transport roughness (suspended load and the bed load transport).

In studies of flow with suspended sediment, two concerns often raised are the effects of suspension on both velocity distribution and flow resistance. Based on the experimental results of Vanoni (1946), Einstein and Chein (1955) and Elata and Ippen (1961), as the sediment concentration increases, the Von Karman constant becomes progressively smaller than that of the clear water value of 0.4. However, this view is not universally endorsed. Imamoto, et al. (1977) found that κ increases with sediment concentration in their experiments while Fukuoka (1980) and Itakura and Kishi (1980) suggested that the value of κ does not change.

Coleman (1981) analyzed his own data and reexamined the data from earlier experiments to show that the change in κ, which was found in the earlier works, were due to incorrect application of logarithmic velocity distribution to the outer flow region where the logarithmic law is really not valid. By applying the logarithmic law only to the region close to the bottom boundary, Coleman found that the presence of suspended sediment has no effect on the value of κ. The value of κ was found to conform to the law of the wake which was introduced by Coles (1956) for boundary layer flows. It appears that Coleman (1981) has presented the most convincing argument to date on the effects of suspended sediments on the velocity distribution in open channels. The general velocity profile given by the logarithmic law plus a wake function seems to be valid for all of the flow depth outside of viscose sub layer.

In comparison to suspended load transport, a few studies were found in the literature regarding the effects of bed load movement on flow resistance and velocity distribution. The generally accepted view is that bed load extracts momentum from the flow which causes a reduction of flow velocity and increase of apparent roughness length (Ryckoczi, 1967; Kennedy, 1969; Wang & Chien, 1985; Mclean, 1992; Song et al., 1998; Begeron et al., 1999). But some researchers believe that bed load movement has no effect on flow resistance (Einstein & Barbarosa, 1952; Vanoni & Nomicos, 1960; Yang & Hirano, 1995).

In this research, the effects of skin roughness and bed load movement with different concentrations on flow resistance and velocity profile are experimentally investigated.

2 EXPERIMENTAL SET UP AND PROCEDURE

Experiments were performed in a tilting channel of glass sides and smooth bed made of Perspex, and of rectangular cross-section 250 mm wide and 14 m long. The downstream end of the channel is provided with a sediment trap with a collecting basket and the weight of sediments collected in the basket is continuously measured by a digital weighing scale. Downstream of the sediment trap is a tailgate consisting of a set of horizontal rotating flaps to provide various degrees of opening for the water to flow through. The tailgate is used to adjust the depth of water in the channel without causing undue backwater effects into the channel. In each of the experiments clear water is supplied at a steady rate from an overhead constant head tank. For experiments with the rough bed, a single layer of uniform sand was glued onto the Perspex bed. The same size of sand was injected to the flow using a screw feeder system to produce bed load at the beginning of the flume. Two different grain sizes $d = 0.5$ 2.84 mm were used in the experiments. Point flow velocities were measured by a 10 mm propeller current meter.

The experiments were carried out with (i) clear water over smooth and rough beds, and (ii) sediment laden flows over smooth and rough beds. In the first series, a number of preliminary experiments were carried out to determine the friction factor f, for smooth and rough rigid beds. Various slopes of the channel and velocities of flow were considered in these experiments. This information was then used to set the depth of flow before injecting sediment at the upstream end in the main experiments.

Prior to the experiments with sediment-laden flow, for a given slope of the channel and discharge of water, a uniform flow without sediments was first obtained by adjusting the tailgate to attain a prescribed depth. Different concentrations of sediments were then injected into the flow at constant rate at the upstream end of the flume. The rate of sediment supply was kept constant by adjusting the feeder and keeping the sand level coinciding with the top level of the container. Flow measurements were made for various injection rates less than the rate at which initiation of sediment deposition on the bed was observed. Bed load particles were collected in the sediment trap provided at the downstream end of the flume to be removed periodically. For each injection rate I expressed in terms of mass rate, the corresponding volumetric concentration of sediment C is simply

$$C = \frac{I}{QS_s} \tag{6}$$

where $Q =$ the water discharge and $S_s =$ the sediment density, is taken to be 2650 kg/m^3. The experimental conditions are summarized as follows:

- sediment diameters used: 0.5 and 2.84 mm
- sediment concentration: 0.0025–0.0075
- water depth: 25–250 mm
- mean velocity: 0.35–1.2 m/s
- bed slopes used: 1:1000, 2.5:1000, 3:1000

For each sediment concentration, two or three flow velocity profiles were measured along the vertical centerline of the cross-section of flow at a position located 8.0 m downstream from the location where sand particles were injected into the flow. Starting from 10 mm above the bed, which was dictated by the size of the current meter, velocities were measured at vertical intervals of 5 mm up to 20% of water depth and then at 10 mm intervals up to the water surface. The measured velocity profiles were then averaged to obtain the mean velocity profile corresponding to a particular sediment concentration. The mean bulk velocity U of each averaged profile was then obtained by integrating the profile over the whole flow depth. The shear velocity $u*$ and the friction factor f were then calculated from the averaged velocity profile using the equations for velocity profile in rough turbulent flow and shear velocity.

3 RESULTS

Figure 1 shows the velocity profiles in normal and semi-log scales for clear water condition. These profiles are presented to show how the experimental results fit the logarithmic law given by equation 2.

3.1 *Effects of bed roughness on velocity distribution*

Two sets of velocity distributions related to the same discharge and bed slope are shown in Figure 2a and 2b to show how bed roughness changes the velocity distributions.

Figure 2a shows velocity distributions for discharge of 30 lit/s on smooth and rough bed. It can be seen that with the same slope, as the bed roughness increases, the velocity decreases especially in lower part of the velocity profile. In other word, the amount of decrease in the lower part of the profile is more than the upper part. The velocities related to the bed roughness of 2.84 mm are higher because the slope of these experiments is more than the others. The amount of this increase in the upper part is more than the lower part. We can also see these results in Figure 2b that is due to discharge of 40 lit/s.

As it can be seen from the figures, changes in discharge and bed slope affect the upper part of flow region while when the bed roughness is changed, the lower part is more affected. This makes the logarithmic part of velocity distribution steeper resulting higher shear velocity. So we expect more friction factor in rough beds. This is shown in Figure 3. This figure shows the logarithmic part of velocity profiles presented in Figure 2 in a semi-logarithmic scale (a is line slope).

As shown in Figure 3, when the bed roughness increases, a and u_* are increased. This increase together with a reduction in mean velocity will increase the friction factor f, according to equation 7.

$$f = 8\left(\frac{u_*}{U}\right)^2 \tag{7}$$

in which $U =$ mean flow velocity.

3.2 *Effects of bed load roughness in velocity profile*

Figure 4a and 4b show the effect of size and concentration of injected sediments on flow velocity distributions.

Figure 4a shows the velocity distributions related to smooth bed (clear water and rough bed with diameter

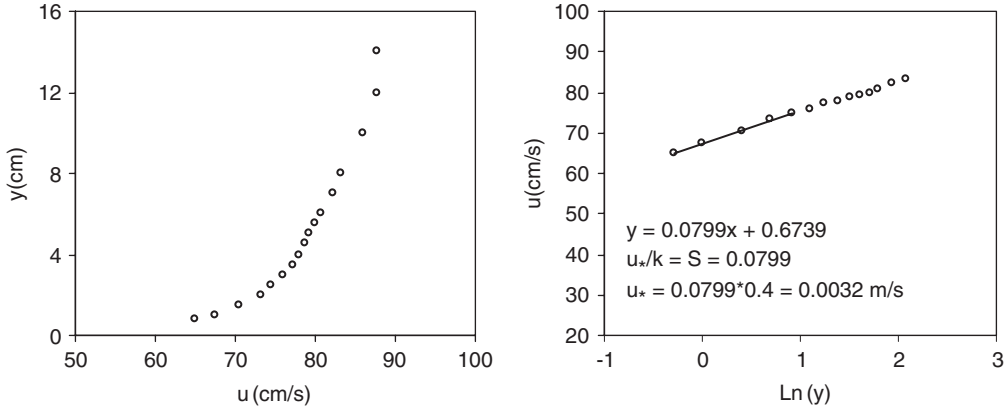


Figure 1. Velocity profile related to clear water on smooth bed.

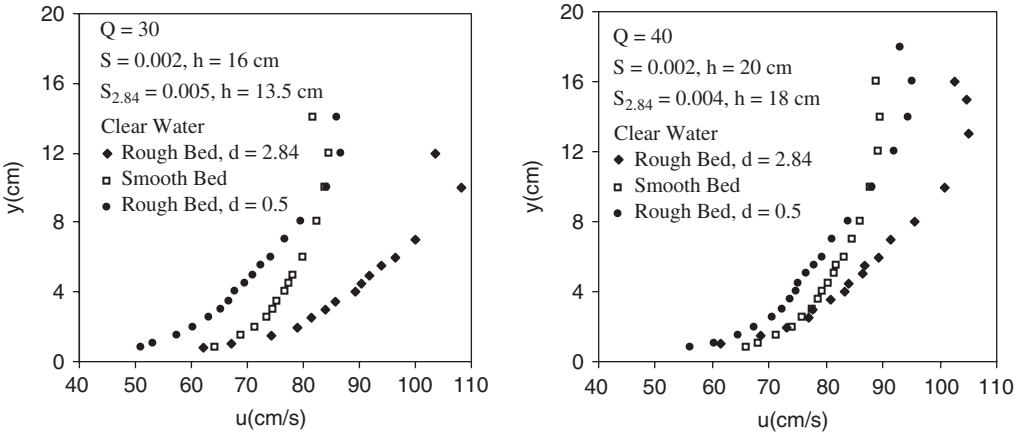


Figure 2. Velocity profiles on smooth and rough bed with different roughness.

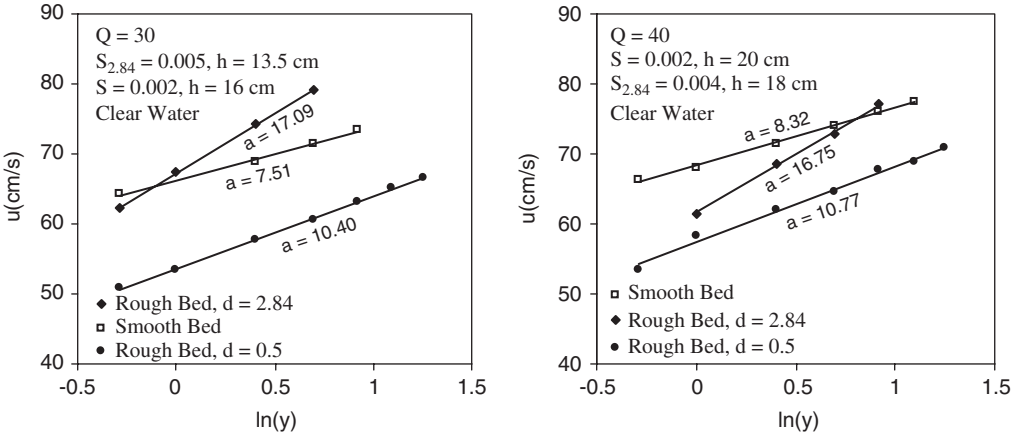


Figure 3. Velocity distribution with semi-log scales for logarithmic part of profiles in Figure 2.

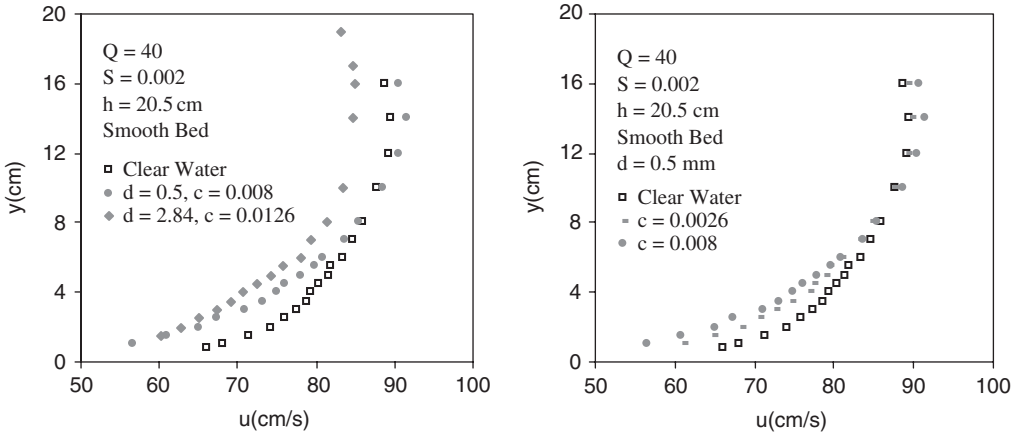


Figure 4. Effect of sediment injection with different diameter and concentration on flow velocity in smooth bed.

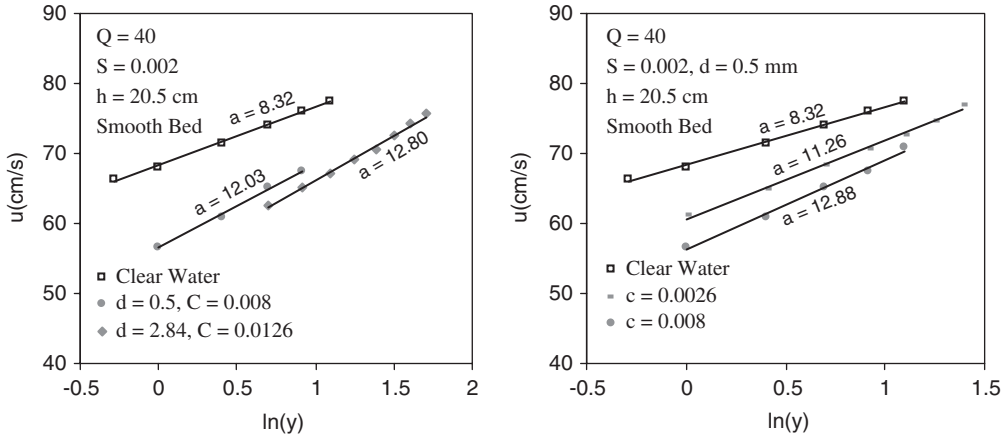


Figure 5. Mean velocity against ln (y) for logarithmic part of velocity profiles in Figure 4.

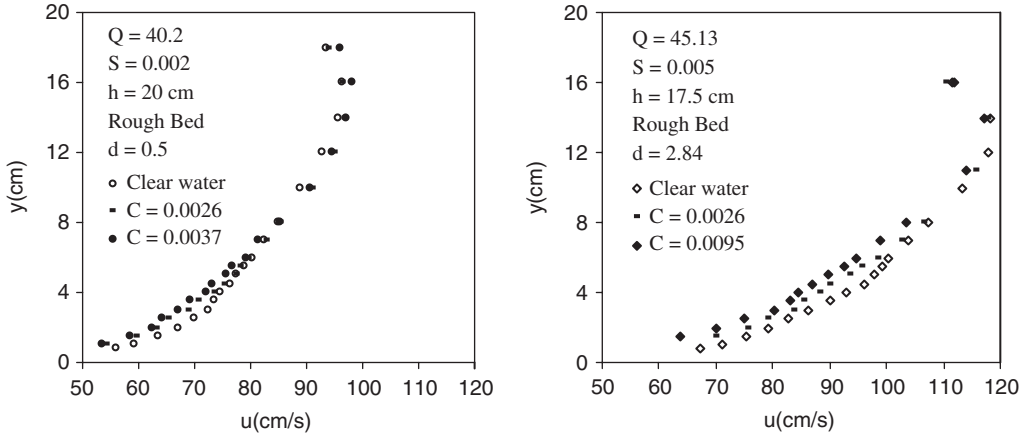


Figure 6. Effect of sediment injection with different concentration on flow velocity in smooth bed.

of 0.5 and 2.84 mm). It shows that the increase of diameter and concentration causes a reduction in flow velocity.

Figure 4b shows the velocity distribution related to smooth bed (clear water and sediment injection ($d = 0.5$ mm) with two sediment concentration. It is clear that sediment injection causes a reduction in velocity especially in lower part of velocity profile. It also shows that increasing sediment concentration causes more reduction of velocity in lower part of velocity distribution profile.

The logarithmic parts of the velocity profiles of Figure 4 are plotted in semi-logarithmic scales in Figure 5 to show the effect of sediment injection on the lower part of the velocity profile. It shows that sediment injection caused an increase in slope of logarithmic part of velocity distribution and shear velocity. Further, this shows increase of concentration also causes more increase in shear velocity.

Figure 6 show the effect of different concentrations on velocity distribution related to rough bed. Figure 6a shows velocity distributions related to rough beds with $d = 0.5$ mm (clear water and two different concentrations of sediment injection with $d = 0.5$ mm). It can be seen that, first, sediment injection causes a reduction in velocity, especially in lower part of profile. Second, increase of concentration has increased this effect. This is also shown in Figure 4b which is due to sediment size $d = 2.84$ mm.

The velocity profile of Figure 6 is also plotted in a semi-logarithmic scale in Figure 7 to see the effect of sediment injection with different concentrations on shear velocity. It can be seen that the sediment injection increase the shear velocity.

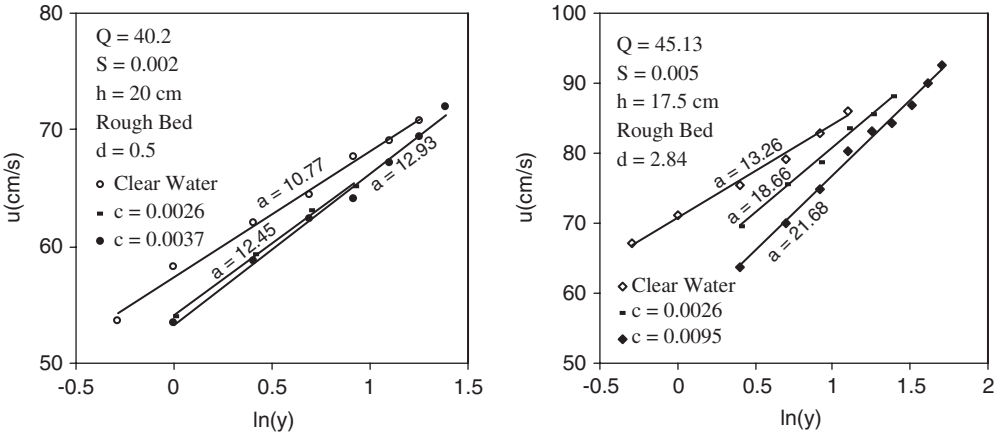


Figure 7. Mean velocity against ln(y) for logarithmic part of velocity profiles in Figure 6.

4 CONCLUSION

The effect of bed roughness and bed load movement on flow velocity profile in an open channel is experimentally investigated. Following are the conclusions:

- experimental results of smooth and rough bed fit the logarithmic law of flow velocity distribution profile,
- changes in discharge and bed slope influence the upper part of velocity profile,
- increase in roughness elements (skin roughness and bed load roughness) affect the lower part of profile making the logarithmic part of velocity profile steeper. Since the slope of this profile increases, shear stress and consequently friction factor increases, affecting the bulk of flow to reduce the mean flow velocity.

REFERENCES

Bergeron, N. E. & Carbnneau, P. 1999. The Effect of Sediment Concentration on Bed Load roughness. J. Hydrological Processes 13(16): 2583–25892.

Colman, N. L. 1981. Velocity profiles with suspended sediment. J. Hydraulic Research 19(3): 211–229.

Colman, N. L. 1986. Effects of suspended sediment on the open channel velocity distribution. Water Resources Research 22(10): 1377–1384.

Itakura, T. & Kishi, T. 1980. Open channel flow with suspended sediments. J. Hydraulic Engineering, ASCE 106(8): 1325–1343.

Khullar, N. K., Kothyari, U. C. & Ranga Raju, K. G. 2002. The effect of suspended sediment on flow resistance. 5th International conference on hydro-science and engineering, September, 18–21, Warsaw, Poland.

Lau, Y. L. 1983. Suspended sediment effect on flow resistance. J. Hydraulic Engineering, ASCE 109(5): 757–763.

Lyn, D. A. 1991. Resistance in Flat-Bed Sediment-Laden Flows. J. Hydraulic Engineering 117(1): 94–114.

Mclean, S. R. 1992. On the calculation of suspended load for non cohesive sediments. J. Geophysics Research 97(C4): 5759–5770.

Pullaiah, V. 1978. Transport of fine suspended sediment in smooth bed channels. PhD thesis, University of Roorkee, Roorkee.

Ryckoczi, L. 1967. Experiment study of flume bed roughness. Symp. Pf 2nd Int. Assn. for Hydr. Res. Vol. 1, Fort Collins, Colo.: 181–186.

Song, T., Chiew, Y. M. and Chin, C. O. 1998. Effect of bed load movement on friction factor. J. Hydraulic Engineering 124(2): 165–167.

Vanoni, V. A. & Nomicos, G. N. 1960. Resistance properties of sediment-laden streams. Transactions of ASCE, 125: 1140–1175.

Vanoni. V. A & Nomecos, G. N. 1960. Resistance properties of sediment laden streams. Transactions of ASCE, 1140–1175.

Yang, Y. & Hirano, M. 1995. A discussion on uniform flow in open channel with moveable gravel bed. J. Hydraulic Research 33(6): 877–879.

River Flow 2004 – Greco, Carravetta & Della Morte (eds.)
© 2004 Taylor & Francis Group, London, ISBN 90 5809 658 0

3D turbulent flow over irregular bed surfaces

W. Czernuszenko
Institute of Geophysics PAS, Warsaw, Poland

A. Rylov
Institute for Water and Environmental Problems, Barnaul, Russia

ABSTRACT: Features of 3D velocity field in an open channel with smooth and regular rough bed are sufficiently known and understood by civil engineers, whereas flows over irregular bed surfaces are still not fully known. The paper deals with 3D rough turbulent flows in straight open channel with irregular bed roughness. The bed of the channel is characterized by roughness elements which can be uniform or non-uniform in sizes, and which can form regular or irregular surfaces of channel bed. It is assumed that the turbulence structure above the viscous sublayer, over regular and non-regular bed roughness is the same and the logarithmic law (Log-Law) describes this structure. This structure is scaled with height (distance from bed), friction velocity, the absolute size of the elements forming the bed roughness and the coefficient designated by letter "B". An open channel turbulent flow is described by the Reynolds equations with simple turbulent model, which is based on the assumption of isotropic but not homogeneous eddy viscosity at a cross-section. The eddy viscosity is described by an enhanced mixing length hypothesis. The model also takes into account the non-isotropic character of normal turbulent stresses at the channel cross-section. The Reynolds equations with the continuity equation for steady, parabolic 3D turbulent flow in open channel are solved for irregular and different height of rough elements forming the channel bed. It is shown how to define the boundary conditions for this bed and how to estimate the parameters defining the turbulence structure over this bed. The numerical simulations show the disturbances in velocity distribution due to the boundary irregularities. To smooth these disturbances the spatial average operation is applied to get the equivalent Log-Law velocity profile, i.e. the equivalent shear velocity, the equivalent size of roughness elements and equivalent coefficient B. It is shown that the boundary conditions defined by this equivalent velocity give reasonable good prime velocity distribution as well as the secondary flow pattern.

1 BASIC HYDRODYNAMIC EQUATIONS

Three-dimensional, steady turbulent flow in an open channel is governed by the Reynolds-averaged Navier-Stokes equations. The continuity and momentum equations for incompressible turbulent flows may be written in the Cartesian tensor notation in the forms:

continuity equation:

$$\frac{\partial U_i}{\partial x_i} = 0, \tag{1}$$

momentum equation:

$$U_j \frac{\partial U_i}{\partial x_j} = -\frac{1}{\rho}\frac{\partial p}{\partial x_i} + F_i - \frac{\partial}{\partial x_j}\left(\overline{u_i u_j} - \nu \frac{\partial U_i}{\partial x_j}\right) \tag{2}$$

where U_i is i-th component of the time average velocity ($i = 1, 2, 3$), p is the pressure, ρ is density and $F = (g \sin\alpha, g \cos\alpha, 0)$. A notation of x for horizontal (longitudinal), y for vertical (downwards) and z for lateral coordinates as well as U, V, W for corresponding velocity components will be used also in the paper.

1.1 *Turbulence model*

An applied turbulence model is simplified version of models presented by Czernuszenko & Rylov (2000) and Czernuszenko & Rylov (2003). The model describes the turbulence structure in the case of anisotropic normal turbulent stresses and the isotropic shear stresses in the form:

$$-\rho\,\overline{u_i u_j} = \begin{cases} -\rho\,\overline{u_i^2} & \text{for} \quad i = j \\ \rho\, l^2 D_{ij}\, S & \text{for} \quad i \neq j \end{cases} \tag{3}$$

where u_i is the ith component of turbulent velocity vector, l is the mixing length, D_{ij} is the deformation rate tensor and quantity S is defined by formula (Czernuszenko & Rylov 2000)

$$S = \sum_{i,k} \left| \frac{\partial U_i}{\partial x_k} \right| \tag{4}$$

For the open channel flows the right-hand sum in Eq. 4 may be reduced to two terms containing derivatives of streamwise velocities in lateral and vertical directions, respectively. The other terms in the sum above containing the lateral and vertical components of the mean velocity vector do not exceed 1–2% of the streamwise component. To solve Eqns. 1 and 2 the total turbulent stress tensor must be known, i.e. the normal and shear turbulence stresses at any point of the cross-section should be prescribed. The normal turbulent stresses and the shear turbulent stresses are defined according to Czernuszenko & Rylov (2003).

1.2 *Hydrodynamic model*

Consider the tilted open channel with bed slope defined by an angle Θ. The flow is steady with average velocity components (U, V, W) directed in x, y and z directions, respectively. Turbulent transport of momentum in x-direction is assumed to be negligible. Therefore, the terms involving second derivatives with respect to x may be omitted. This kind of flow is usually called parabolic in longitudinal direction. The basic equations describing the 3D-velocity field in open channel flows are the continuity 1 and momentum equations 2. Substituting Eq. 3 into Eq. 2 and neglecting higher order terms produces the momentum equations in the form:

$$\frac{\partial U^2}{\partial x} + \frac{\partial VU}{\partial y} + \frac{\partial WU}{\partial z} + \frac{1}{\rho}\frac{\partial p}{\partial x} =$$

$$= g \sin\theta + \frac{\partial}{\partial y}\left(l^2 S \frac{\partial U}{\partial y} \right) + \frac{\partial}{\partial z}\left(l^2 S \frac{\partial U}{\partial z} \right) \tag{5}$$

$$\frac{\partial UV}{\partial x} + \frac{\partial V^2}{\partial y} + \frac{\partial WV}{\partial z} + \frac{1}{\rho}\frac{\partial p}{\partial y} = g\cos\theta + \frac{\partial}{\partial y}\left(-\overline{v^2} \right)$$

$$+ \frac{\partial}{\partial y}\left(2 S l^2 \frac{\partial V}{\partial y} \right) + \frac{\partial}{\partial z}\left(S l^2 \left(\frac{\partial V}{\partial z} + \frac{\partial W}{\partial y} \right) \right) \tag{6}$$

$$\frac{\partial UW}{\partial x} + \frac{\partial VW}{\partial y} + \frac{\partial W^2}{\partial z} + \frac{1}{\rho}\frac{\partial p}{\partial z} = \frac{\partial}{\partial z}\left(-\overline{w^2} \right)$$

$$+ \frac{\partial}{\partial y}\left(S l^2 \left(\frac{\partial V}{\partial z} + \frac{\partial W}{\partial y} \right) \right) + \frac{\partial}{\partial z}\left(2 S l_z^2 \frac{\partial W}{\partial z} \right) \tag{7}$$

where p is the pressure, S is defined by Eq.4. Details on the enhanced mixing length model can be found in Czernuszenko & Rylov (2003).

Boundary conditions which accompany previous equations (Eqns. 5–7) need to be specified along solid boundaries, water surface and up-stream cross-section bounding the calculation domain. Since parabolic flows are considered, boundary conditions do not need to be given at the downstream end of the calculation domain. It is assumed that the flow is uniform with constant width and depth (rigid lid approximation, Rastogi & Rodi 1978). The conditions at the solid boundaries were specified using wall functions technique proposed by Launder & Spalding (1974), i.e., the conditions are specified at a point near a wall which lies outside the laminar sublayer and satisfy the logarithmic portion of the universal law of the wall

$$\frac{U}{U_*} = \frac{1}{\kappa} \ln \frac{y}{k_*} + B, \tag{8}$$

where (a) for smooth channels $k_* = \nu/U_*$, $B \equiv B_s = 5.5$, (b) for rough channels $k_* = k_s$, $B \equiv B_r = 8.5$; U_* friction velocity, y distance from the wall, ν molecular viscosity, B coefficient and k_s the equivalent sand roughness.

Normal velocity components at the solid boundaries and free surface are set to zero. The free surface boundary conditions were specified following the approach of Rastogi & Rodi (1978), which considers free surface acting as a plane of symmetry. Therefore, the gradients of U and V in y-direction are zeros. The condition at the initial cross section $x = 0$ for longitudinal velocity U was taken along with logarithmic distribution. Components V and W were set equal to zero. The essential problem with the boundary conditions is in specifying the logarithmic velocity profile, which in the case of rough, irregular bed surface is not clear.

2 VELOCITY PROFILE OVER REGULAR (SAND) BED SURFACES

Uniform, turbulent flow in the vicinity of a smooth and regular rough (sand) bed is to be considered. If the geometry of the bed roughness is specified, then the flow can be completely defined by the physical properties ρ and μ of the fluid, by the mechanical state of the fluid motion (which is completely determined by the shear velocity U_*), and by the absolute size (height) k of the elements forming the bed roughness.

The velocity profile Eq. 8 is defined for y in the range: $y_{min} < y \ll h$, where y_{min} is either equal to the thickness of the viscous sublayer or to the height of the roughness, whichever is larger. Coefficients k∗

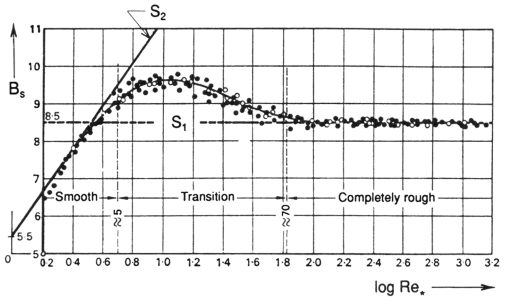


Figure 1. Relation between Bs and Re (after Schlichting, 1968).

and B depend on the regime of turbulent flow, which is defined by non-dimensional number ($U_* k_s/\nu$), so that

1. For ($U_* k_s/\nu$) $< \approx 5$ the regime is called hydraulically smooth flow. Velocity distribution does not depend on the size and nature of the roughness, $k_* = \nu/U_*$ and B is the universal constant equal to 5.5 (see Yalin 1977) (Nezu & Rodi (1986) suggest B = 5.29).
2. For ($U_* k_s / \nu$) $> \approx 70$ the regime is called rough turbulent flow. Velocity distribution does not depend on the viscosity for this type of flow, $k_* = k_s$ and B is the universal constant equal to 8.5 (see Yalin 1977).
3. If the non-dimensional parameter ($U_* k_s/\nu$) is in the range from 5 till 70, approximately the flow is in the transitional regime. In this regime velocity distribution depends on roughness and the value of B which must be estimated from experimental data, Figure 1, Nikuradse's graph (see Yalin 1977) where, index "s" stands for sand roughness.

Two straight lines displayed in Figure 1, namely S_1 and S_2 lines are received from the non-dimensional analysis (see Yalin 1977). Their validity limits are established from measurements carried out for roughness formed by equal size and grains tightly glued on the bed. The problem is how to establish the Nikuradse relation between the Reynolds's number ($U_* k_s/\nu$) and coefficient B in the regime of rough turbulent flows over irregular bed roughness.

3 FLOWS OVER IRREGULAR BED SURFACE

In the case of roughness having the average height k and geometry that is different from the geometry of the sand roughness, the curve B will differ from the curve B_s (Fig.1). However, this difference will mainly be in respect to absolute values and not in "the character" (overall shape) of the curve. It is obvious that the straight line S_2 that does not depend on the nature of roughness must be common for any roughness, which means that all B-curve must "sooner or later" merge into the same straight line S_2 and the constant B = 5.5 must be valid for any geometry roughness. Also, it is clear that curve B may become parallel to the abscissa starting from some "large" Re_*. This threshold value may be different than the one for the curve B_s ($U_* k/\nu = 70$). Its value might be different than 8.5.

Let's consider now a rough turbulent flow over irregular surface gravel bed defined by the granulometric curve (cumulative size distribution) of the bed material. The flow is steady with a unit discharge q and it can be treated as two-dimensional (x–y space). As it was assumed, the velocity distribution along any vertical in the flow is assumed to be logarithmic one but with various friction velocity and parameters, k and B. The question arises, whether it is possible to create "equivalent" velocity profile for an open channel with regular surface bed which gives the same unit discharge q. If the answer is positive, then the velocity profile exists with parameters $U_{*,e}$, k_e and B_e and these parameters are coupled by Eq. 8. Integrating Eq. 8 over the vertical and introducing the unit discharge (mean velocity), one can easily get the following relationship

$$\frac{U_{mean}}{U_{*,e}} = \frac{1}{\kappa} \ln\left(\frac{h}{k_e} \exp\left(B_e\, \kappa - 1\right)\right) \qquad (9)$$

where $U_{*,e}$ is the equivalent friction velocity for considered open channel, that can be different from local friction velocity over irregular bed. The relationship is only valid for the flows in rough turbulent regime, i.e. for Reynolds numbers ($U_* k/\nu$) $> Re_{*,cr}$.

It is plausible to assume that the equivalent velocity profile can be created by averaging of velocity profiles over the suitable area in the plane (x, y = const, z). As a result one could get the averaged velocity profile that matches the logarithmic law with equivalent parameters $U_{*,e}$, k_e and B_e in any range of y. The process of space averaging of velocity profiles over fixed area needs a new theoretical formulation of the problem, which is the objective of the next section.

3.1 *Theoretical formulation*

The tensor of momentum flux density for turbulent flows can be written (see Landau, Lifshitz 1986)

$$\overline{\Pi_{ij}} = \rho \overline{u_i}\,\overline{u_j} + \rho\, \overline{u_{t,i} u_{t,j}} + p\delta_{ij} - \mu \frac{\partial \overline{u_i}}{\partial x_j} \qquad (10)$$

where ρ is the density, u_i the component of velocity vector, p the pressure and μ the viscosity coefficient. The overbar denotes ensemble (time) average and subscript t denotes departure from the average; usually called the turbulent fluctuation.

$$u_i = \overline{u_i} + u_{t,i} \quad , \quad \overline{u_{t,i}} = 0 \qquad (11)$$

It is clear that ensemble averaged flow, at least in the close neighborhood of irregular rough boundary, is strongly spatially heterogeneous. Boundary irregularities originate perturbations in ensemble average flow which we call "boundary disturbances" and which have been already detected experimentally in the steady flow as well (see Raupach et al. 1991). The velocity profiles are essentially determined by the effects of these disturbances. In order to define the boundary disturbances of flow and to smooth out the flow irregularities, a special, spatial averaging operation denoted by the symbol <> is introduced.

$$\langle \overline{u_i} \rangle (y) = \frac{1}{A_w} \iint_{D(x,y,z)} \overline{u_i(x', y = \text{const}, z')}\, dx'dz' \qquad (12)$$

where u_i overbar represents the ensemble averaged velocity and the domain D(x, y, z) is the part occupied by fluid of a fixed region of the plain y = const (assumed parallel to mean bed) centered at the point (x, y, z) and which has an area A_w. The area is large in comparison with the characteristic wavelength of the disturbances $u_i - \overline{u_i}$. Using the spatial averaging Eq. 12, the ensemble average velocity can be split up into an overall mean and a boundary disturbance (subscript b) according to

$$\overline{u_i}(x, y, z) = U_i(y) + u_{b,i}(x, y, z), \quad \langle u_{b,i} \rangle = 0 \qquad (13)$$

After space averaging of Eq. 10 the tensor of momentum flux density takes the form (see for details Gimenez-Curo and Lera (1996):

$$\langle \Pi_{ij} \rangle = \rho U_i U_j + p\delta_{ij} + \rho \langle u_{b,i} u_{b,j} \rangle + \rho \langle \overline{u_{t,i} u_{t,j}} \rangle - \mu \frac{\partial U_i}{\partial x_j} \qquad (14)$$

3.2 *Nature of shear stresses*

Fluid flows in the vicinity of smooth, impermeable, plane surface are usually classified as laminar or turbulent flows. In laminar flows the shear stress arises exclusively from direct action of molecular viscosity. In turbulent flows the shear stress is essentially due to ensemble mean (or time mean) momentum flux of random turbulent fluctuation, also called Reynolds stress. In this kind of flow a very thin layer of fluid adjacent to the wall exists, in which viscous stress predominates since turbulence goes to zero at the boundary.

Let us restrict ourselves to 2D, horizontal and uniform (space averaged) mean motion over an irregular surface. The mean velocity has a component only in the x direction , then U = U(y), V = W = 0, where now y is measured vertically upward from an arbitrary datum. It is assumed that an area integration domain D(x, y, z) is very large in comparison with the characteristic wavelength of the disturbances in order to guarantee that the resulting averaged value varies over length scales large enough as compared with those of the disturbances. The spatially averaged shear stress equation can be directly and easily obtained from Eq.14 for the region of fluid over the crests of roughness as

$$\tau_{xz} = \mu \frac{\partial U}{\partial z} - \rho \langle \overline{u_t w_t} \rangle - \rho \langle u_b w_b \rangle \qquad (15)$$

When comparing with the corresponding equation for flow over a smooth surface, we observe that Eq.15 introduces one extra term, which we call "form-induced stress" or simply "form stress". If the fluid flows over an irregular surface, the form stress (τ_f), added to the mean viscous (τ_v) and mean Reynolds (τ_t) stresses creates a total shear stress. The maximum bed shear stress has therefore three components τ_{ov}, τ_{ot}, and τ_{of} and it appears at the roughness height. Gimenez-Curo & Lera (1996) show that the form stress is fundamental and both other stresses are negligibly small comparing to it, therefore the friction velocity is much larger in the case of the form stress occurring in the turbulent flow.

3.3 *Log-Law for rough flow over irregular bed surfaces*

The problem of reconstruction of the Nikuradse graph for flows over irregular gravel river bed can be reduced to establishing the equivalent Log-Law parameters, i.e., $U_{*,e}$, k_e and B_e. These parameters represent the equivalent velocity profile that can be received by space averaging all of profiles belonging to the domain of averaging. In the considered case, this area is equal to W × L, where W is the width of channel and L is the range of calculation. It is reasonable to assume, that the space averaged velocity profile has the same turbulence structure as the profile over sand roughness. It means, we can assume that for some distances from the bed and at some large Reynolds numbers the logarithmic portion of Log-Law distribution exists. We must define only those distances at which Log-Law is valid, the equivalent friction velocity, the roughness height and the coefficient B.

The distance from the wall at which the Log-Law is valid depends on the geometry of roughness elements and is difficult to be estimated. Experiments of Kirkgöz (1989) show that for uniform, rough surfaces with $d_{90} = 2.36$, 5, 10 and 20 mm the Log-Law starting at the distance from the wall defined by inequality: $U_* y/\nu \geq 40$–50. The equivalent friction velocity can be estimated when the general flow parameters like the depth and the energy slope are known. For uniform

flows the relationship holds

$$U_* = \sqrt{g\,h\,i} \tag{16}$$

The remaining two parameters can be established only based on some field data (measurements) or special numerical simulations. Below there is a proposition such numerical calculations.

4 NUMERICAL SIMULATIONS

The hydrodynamic model (Eqns. 1, 5–7) was applied to simulate the 3D mean stream velocity distribution in turbulent flow in a rectangular channel. To solve the above set of equations the numerical parabolic procedure known as Patankar-Spalding algorithm is used. It solves the set of above equations for three components of velocity U, V, W and pressure P, at each forward step in longitudinal direction. The continuity equation (Eq. 1) is solved for the pressure using the well known Patankar-Spalding (1972) algorithm. The scheme has HYBRID pattern approximation of convective terms (Leschziner 1980). However, due to insignificant secondary velocities it has actually the second order of accuracy. A series of numerical simulations have been performed in order to verify the possibility for finding values of parameters which define this velocity distribution near the bottom as well as within the whole flow. These parameters occur in the Log-Law (8), namely, U_*, k and B.

In order to get a sample of real-life distribution of parameters k and U_* across the bottom in a bed form with irregular roughness, a series of random values for k was generated. This parameter is responsible for roughness modeling across the channel bed when rough turbulent regimes take place as it was discussed before. An example of the distribution of k across the channel bed is depicted in Figure 2.

Knowing the distribution of roughness the local friction velocity has been computed from Eq.9 using the assumption that discharge is uniformly distributed across the channel width and B = 8.5 (the same as for regular roughness).

Table 1 contains the other flow data which pertain to the case of a flow over the bed with irregular roughness (case 1). Computed streamwise velocity distribution as well as secondary currents pattern are shown in Figures 3 and 4.

Streamwise velocity profile of fully developed turbulent flow allows to re-assess parameters k, B incorporated into the Log-Law formula (8). Having velocity profile near the bottom, we are able to find the values of those parameters using least squares method for several verticals close to the channel centerline. Velocity profile at one of them is shown in Figure 5.

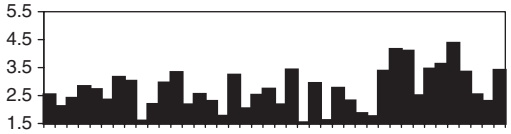


Figure 2. Distribution of roughness (mm) over the channel bed.

Table 1. Data for numerical calculations.

Case	1 – Irregular bed	2 – regular bed
Slope	0.001	0.001
U_*, m/s	0.029–0.034	0.038
k, m	See Figure 2	0.002
U_{mean}, m/s	0.47	0.47
U(0.005), m/s	0.3–0.327	0.337

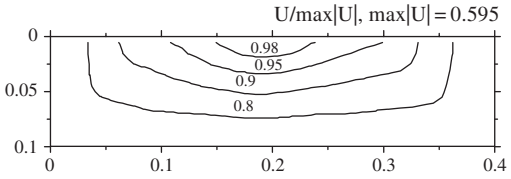


Figure 3. Primary velocity distribution in the channel cross section.

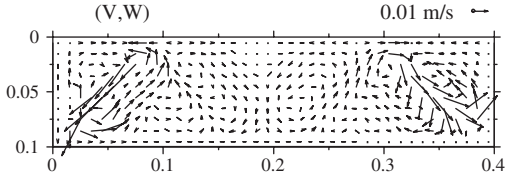


Figure 4. Secondary velocity field in the channel cross section.

Averaging these k and B values gives equivalent values 2 mm, 6.3 for the Log-Law parameters k and B, respectively. In order to verify the effect of so found k_e, B_e upon flow image the next simulation with these k_e, B_e was performed. It may be interpreted as turbulent flow with equivalent regular roughness across the channel. The principal parameters for this run are given in Table 1 (case 2).

The primary velocity distribution as well as secondary currents pattern look similarly to those for the previous case of irregular roughness in the channel. As an example of such coincidence, a picture of velocity profile at the channel centerline is shown in Figure 6.

It follows the same picture for the case 1 quite tightly. Therefore, simulation in channels with irregular roughness elements may be successfully replaced

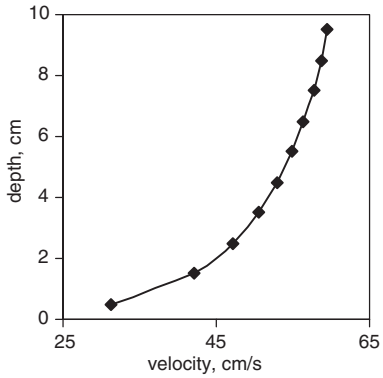


Figure 5. Velocity profile at the channel centerline for irregular roughness.

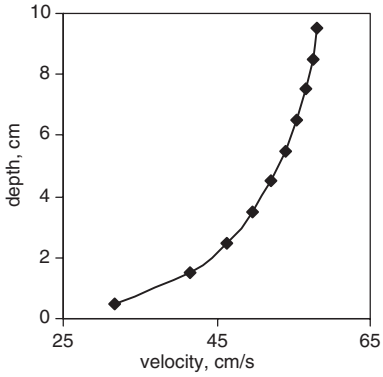


Figure 6. Velocity profile at the centerline for regular roughness with equivalent $k_e = 0.002$, $B_e = 8.3$.

by the same simulation using equivalent regular roughness parameters.

5 SUMMARY AND CONCLUSIONS

1. The logarithmic law is valid also for the rough turbulent flow over irregular distribution of roughness elements but with the coefficient B that is different (usually less) from 8.5 (the case of regular size of roughness).
2. For any turbulent flow over irregular roughness elements the equivalent velocity profile can be found with parameters $U_{*,e}$, k_e and B_e. The equivalent profile represents flow over regular bed roughness and gives the same discharge as the considered flow over irregular roughness.
3. The equivalent velocity profile can be treated as the result of space averaging of all profiles over area which is large in comparison with the characteristic wavelength of the disturbances. The area can be taken as a whole domain of numerical simulations.
4. The procedure for finding the equivalent parameters is as follows:
   (a) Knowing the cumulative size distribution (sieve curve) of bed materials, calculate the lateral distribution of roughness sizes. This calculation can be performed by using random distribution of size of roughness.
   (b) Calculate the local friction velocities from Eq.9 assuming constant mean velocity, depth and coefficient $B = 8.5$ (rough turbulent flow), which are needed for the boundary condition.
   (c) Calculate the boundary condition from the logarithmic law and perform the numerical simulation for given data.
   (d) Choose some calculated velocity profiles for chosen cross-section and for global friction velocity (calculated from Eq. 16) estimate parameters k and B.
   (e) The equivalent parameters for roughness size and coefficient B can be obtained by averaging the calculated parameters.

REFERENCES

Czernuszenko W. & Rylov A. A. (2000). A generalisation of Prandtl's model for 3D open channel flows. *Journal of Hydraulic Research*, **38**, No. 2, 133–139.

Czernuszenko W. & Rylov A. A. (2003). A modeling of shear and normal turbulent stresses in open channel flows. XXX Congress IAHR Thessaloniki, Greece. Proceedings Theme C, **1**, 135–142.

Gimenez-Curo L.A. & Lera A.C. (1996). Oscilating turbulent flow over very rough surfaces. *Journal of Geophysical Research*, **101**, No. C9, 20 745–20 758.

Kirkgöz M.S. (1989). Turbulent velocity profiles for smooth and rough open channel flow. *Journal of Hydraulic Engineering*, ASCE, **15**, No. 11, 1543–1561.

Landau L.D. & Lifshitz E.M. (1986). Fluid Mechanics. Pergamon Press, Oxford.

Launder, B.E. & Spalding, D. B. (1974). The numerical computation of turbulent flows. *Computer Methods in Applied Mechanics and Engineering*, **3**, 269.

Leschziner, M. A. (1980). Practical evaluation of three finite difference schemes for the computation of steady-state recirculation flows. *Computer Methods in Applied Mechanics and Engineering*, **23**, 293–312.

Nezu, I. & Rodi, W. 1986. Open-channel flow measurements with a laser doppler anemometer. *Journal of Hydraulic Engineering*, **112**, No. 5, 335–355.

Patankar S.V. & Spalding D.B. (1972). A calculation procedure for heat, mass and momentum transfer in three-dimensional parabolic flows. *Journal of Heat Mass Transfer*, **15**, 1787–1806.

Rastogi A.K. & Rodi W. (1978). Predictions of Heat and Mass Transfer in Open channels. *Journal of the Hydraulics Division*, **104**, No. HY3, 397–420.

Raupach M.R., Antonia R.A. & Rajagopalan S. (1991). Rough-wall turbulent boundary layers. Appl. Mech. Rev., **44** No. 1, 1–25.

Yalin M.S. (1977). Mechanics of sediment transport. Pergamon Press. Oxford.

River Flow 2004 – Greco, Carravetta & Della Morte (eds.)
© 2004 Taylor & Francis Group, London, ISBN 90 5809 658 0

Negative eddy viscosity in river bends

R. Booij
Faculty of Civil Engineering and Geosciences, Delft University of Technology, the Netherlands

ABSTRACT: Flows in river bends are very shallow and mildly curved free surface flows. The shallowness and the curvature of the flow lead to a few specific flow features that are difficult to reproduce with numerical models. An example is the second counter-rotating secondary flow cell that is observed along steep outer banks in river bends. This second cell has important consequences for the undermining of the outer bank. Another feature is the sign of the shear stress component that transports main flow across the channel. If this shear stress is expressed as a gradient type of momentum transport, then a negative eddy viscosity appears. The negative eddy viscosity can be understood by looking at the mechanism that creates the shear stresses, in this case parcels of water that move upwards and downwards over the flow retaining a substantial part of their original momentum. This can be described with a kind of vertical mixing length model. In contradistinction to gradient type turbulence models, large eddy simulation (LES) reproduces both features correctly.

1 INTRODUCTION

Flows in river bends are shallow turbulent free surface flows. In these flows the important horizontal length scales of the flow are one or more orders of magnitude larger than the flow depth. River bends have large aspect ratios $\{W/h \geq \mathrm{O}(50)\}$ and curvature ratios $\{R/h \geq \mathrm{O}(50)\}$ generally, where h, W and R are the depth, width and radius of curvature respectively. In laboratory models these large ratios are not feasible in most cases. Often the models used are hardly shallow (e.g. models of meandering rivers with aspect ratios of 2 to 4). This leads to a defective modelling of the shallow flow and/or a very restricted insight in the physical processes in shallow flow (Booij, 2003a).

An important aspect of the flow in river bends is the secondary flow. Because of this the largest flow velocities in mildly curved shallow free surface flow are found at the outside of the curved flow, e.g. the outer bend in curved river flow. The mechanism that makes the flow velocity at the outside of the curvature increase at the expense of the velocity at the inside is differential advection, which can be understood as follows. In mildly curved shallow flow the main flow velocity profile over the vertical is almost logarithmic. Hence the centrifugal force due to the curvature of the flow is larger in the upper part of the flow than near the bottom.

On the average this centrifugal force is compensated by the pressure gradient due to a surface slope towards the outer bend. The resulting force is directed to the outward side in the upper part of the flow and to the inward side near the bottom and hence leads to a secondary flow to the outside in the upper part and to the inside near the bottom (see Figure 1). The main flow and the secondary flow together form the helical flow observed in curved shallow flow. In mildly curved shallow flow the amount of water flowing outward is more or less equal to the amount of water flowing inward. However the main flow velocity is larger in the upper part of the flow than in the lower part, hence more main flow momentum is transported outwards in the upper part of the flow than inwards in the lower part. This leads to a net transport of main flow momentum in outward direction and consequently to higher flow velocities at the outer bend.

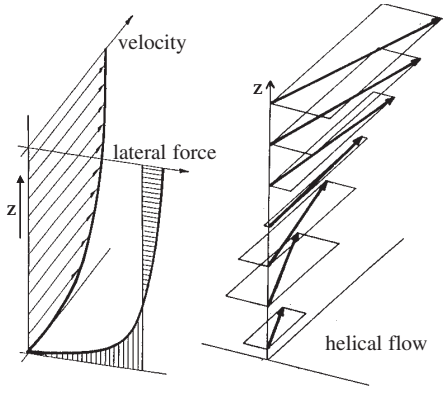


Figure 1. Mechanism of differential advection.

In view of the shallowness of rivers and tidal channels the preference for 2-D horizontal numerical models is understandable. However, the momentum transport by differential advection (i.e. from the region of low velocity at the inside bend to the region with high velocity near the outside bend) requires the implementation of a negative eddy viscosity, which will lead to stability problems. In 3-D computations the secondary flow is computed and hence its advection effects are included, without the necessity of a negative eddy viscosity.

Extensive measurements of the main flow and of the turbulent stresses in a model of a curved shallow free surface flow (Booij and Tukker, 1996) showed another negative eddy viscosity phenomenon. If the shear stress component that transports main flow momentum across the channel is expressed as a gradient type of momentum transport, then again a negative eddy viscosity appears. This negative eddy viscosity and the mechanism of momentum transport that explains this negative eddy viscosity form the main subject of this paper. The apparent negative eddy viscosity means that 3-D computations with gradient type turbulence models (e.g. eddy viscosity or k-ε models) can never yield such a stress component with the correct sign.

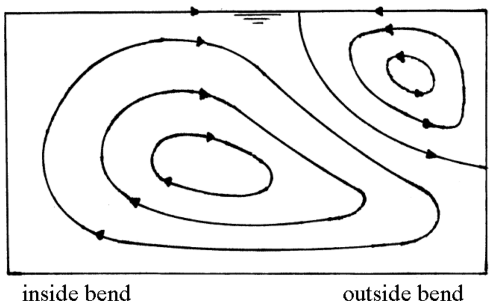


Figure 2. Sketch of two cell system of the secondary flow in a river bend with steep outside bank.

Another feature of the shallow curved river bend flow that is difficult to reproduce is the second, counter-rotating, secondary flow cell observed in river bends with steep sides, see Figure 2 (Vriend, 1981). For relatively deep laboratory model flows this second cell is easy to reproduce with Reynolds average numerical simulations (RANS), but not for real shallow flow conditions (Booij, 2003b).

2 EXPERIMENTAL SETUP

The measurements discussed in this paper were obtained in the curved flume of the Laboratory for Fluid Mechanics of Delft University of Technology (DUT) (see Figure 3). The flume is a compromise

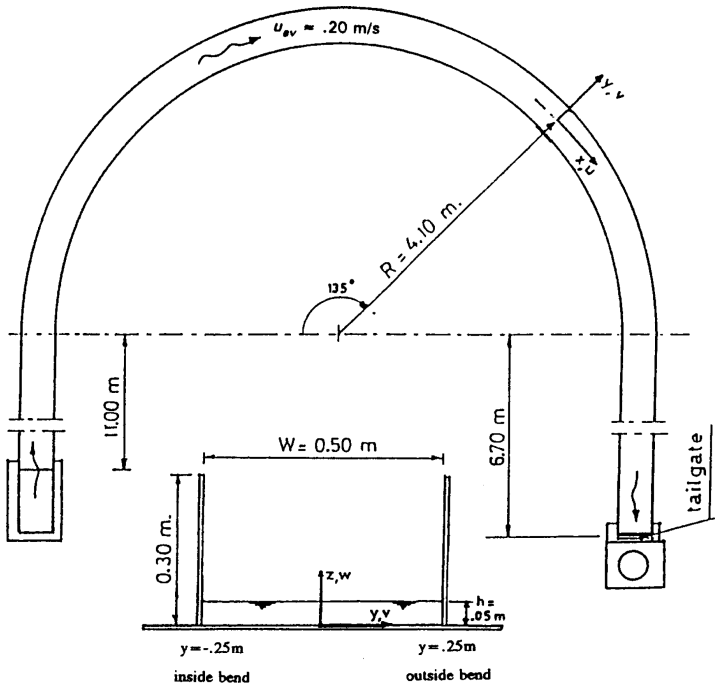


Figure 3. The curved flume of Delft University of Technology (Top view and cross-section).

between real river bends and the possibilities in a laboratory. The cross-section of the flume is rectangular and the measures of the flume are $h = 52$ mm, $W = .50$ m and $R = 4.10$ m. Hence the flume is a model of a relatively shallow ($W/h \approx 10$) and mildly curved ($R/h \approx 80$) river bend. An advantage of this layout is that the flow becomes almost uniform in the second part of the bend (>90°), which makes the flow more appropriate for theoretical investigation and validation of numerical models. A flow of about 5.2 l/s was used, corresponding to an average velocity of about 0.2 m/s over the cross-section.

All measurements discussed here were executed in the nearly uniform flow region at the cross-section of 135° with a 3D laser Doppler velocity meter (LDV) system, measuring through the glass bottom of the flume. The measurements were executed with a DANTEC 3-colour fibre optics system with a 4-Watt Coherent Ar-ion laser and DANTEC BSA processors. The optical system used was a combination of a 2-dimensional probe and a 1-dimensional probe, see Figure 4. The velocity components measured with the 2-D probe (directions 2 and 1 in Figure 4) are the velocity component in transverse direction v and a combination of tangential and vertical velocity components u and w. Combination of the last one with the velocity component (direction 3 in Figure 4) measured with the 1-D probe yields u and w. The relatively large angle (60°) between directions 1 and 3 allows for a relatively precise determination of w with this beam configuration. Identity of the measured particles is assured by requiring arrival time coincidence.

To simplify aligning of the many laser beams a water-filled prism, with sides perpendicular to the optical axes of the two probes, was attached under the measuring cross-section, see Figure 4. The refraction by the glass-plates forming the bottom of the flume and the top of the prism, which were at an angle to the optical axis, complicated the creation of overlapping measuring volumes for the different beam pairs. This refraction effect of the glass plates could be effectively compensated for by a small air-filled slit between them. The measuring system can be traversed in y- and z-direction and the two probes independently in the x-direction (see Figure 3). This combination of 4 movements is required to be able to execute measurements over the cross-section without having to align the beams between measurements. A small measuring volume of the order of .1 mm in all three directions was realized. The measuring time in each point was 6 minutes.

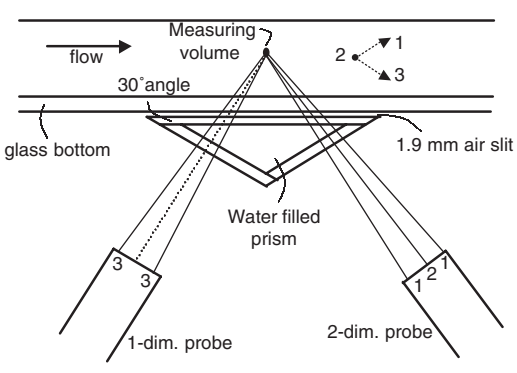


Figure 4. The 3-dimensional LDV beam configuration.

3 SECOND COUNTER-ROTATING SECONDARY FLOW CELL

The measurements clearly showed the existence of a counter-rotating secondary flow cell along the outer bank (see Figure 5), which was earlier mainly reported from measurements in relatively deep and sharply curved flumes (Blanckaert and Graf, 2001).

Standard RANS models can reproduce the main characteristics of the main flow and of the secondary flow patterns. However, the reproduction of the second, counter-rotating cell depends on the sharpness of the bend. In sharp river bends (R/h < 20) it is relatively easy to compute this second cell with several RANS models. However for more realistic gentle bends (R/h > 50) the second cell is not reproduced (see Booij, 2003a). In Figure 6a the result of a computation of the flow in the DUT-flume with a k-ε model is shown. The counter-rotating cell is not reproduced. A 3-D large eddy simulation (LES) did succeed in reproducing the second cell (see Figure 6b) in spite of the for LES unfavourable aspect ratio W/h ≈ 10 of the flume, leading to very unequal sides of the computational cells (Booij, 2002). However, 3-D LES is not yet applicable for the computation of more realistic river layouts.

Blanckaert & Graf (2001) indicate a protecting effect by the second cell. They reason that the second cell displaces the maximum main flow velocity away from the vertical outside wall. In case of more realistic less steep banks the second cell may displace the maximum main flow velocity in the direction of the underside of the outside bank, leading to enhanced undermining. It is clear that a correct computation of the secondary flow pattern is important for the prediction of the morphological development of a river bend.

4 NEGATIVE EDDY VISCOSITY

In Figures 7 and 8 the measured time-averaged velocity profiles and shear stress profiles in the cross-section are plotted. Remarkable is the positive value of the shear stress $\tau_{xy} = \rho\overline{u'v'}$ over the lower half of the vertical in the centre part of the flume. This shear stress transports main flow momentum across the flume.

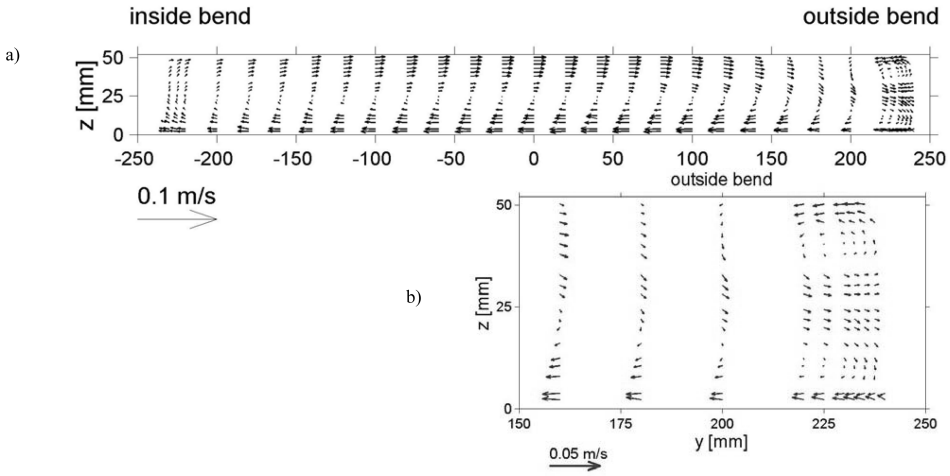
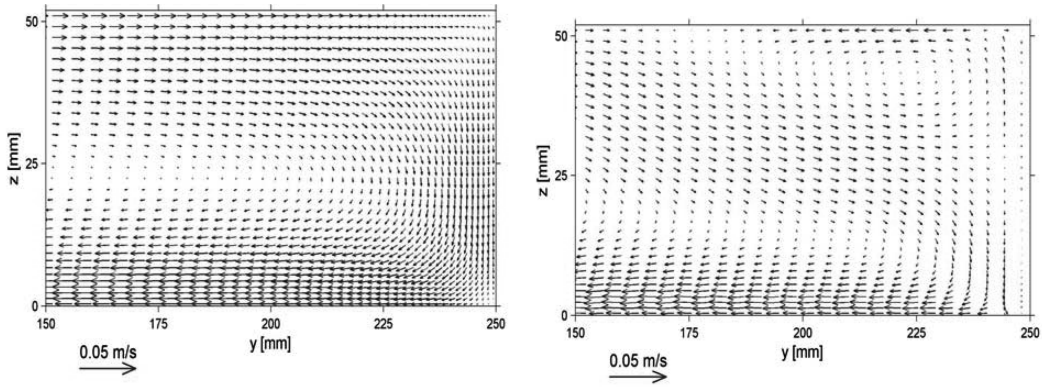


Figure 5. Measured secondary flow field, showing a counter-rotating cell along the upper outside wall. a) the complete cross-section, b) the outside part (blown up for clarity).



a) k-ε model b) LES

Figure 6. The computed secondary flow field in the outside part of the cross-section at 135°. a) k-ε model; b) LES computation, showing the counter-rotating cell along the upper outside wall.

If gradient-type momentum transport is assumed for the different shear stresses, values for the related eddy viscosities can be obtained using the following relations:

$$\frac{\tau_{xz}}{\rho} = \overline{u'w'} = -\nu_{xz}\left(\frac{\partial U}{\partial z} + \frac{\partial W}{\partial x}\right) = -\nu_{xz}\frac{\partial U}{\partial z}$$

$$\frac{\tau_{xy}}{\rho} = \overline{u'v'} = -\nu_{xy}\left(\frac{\partial U}{\partial y} + \frac{\partial V}{\partial x}\right) = -\nu_{xy}\left(\frac{\partial U}{\partial y} - \frac{U}{R}\right)$$

$$\frac{\tau_{yz}}{\rho} = \overline{v'w'} = -\nu_{yz}\left(\frac{\partial V}{\partial z} + \frac{\partial W}{\partial y}\right) = -\nu_{yz}\frac{\partial V}{\partial z}$$

where the used approximations are allowed (but not too close to the sidewalls) because of the uniform flow in this section of the flume. The obtained values for the eddy viscosities in the centre of the cross-section are plotted in Figure 9. Related to the positive value of τ_{xy} is the negative value of the corresponding eddy viscosity ν_{xy}. This negative eddy viscosity applies for a large part of the cross-section (see Figure 10). For comparison the theoretical parabolic eddy viscosity profile for wide straight uniform flow

$$\nu_{xz} = \kappa u_* z(1 - z/h) \text{ with } \kappa = 0.4$$

(corresponding to a logarithmic velocity profile) is included in the plot of Figure 9. As curvature is assumed to suppress this vertical momentum exchange, another profile with lower κ ($= 0.3$) is

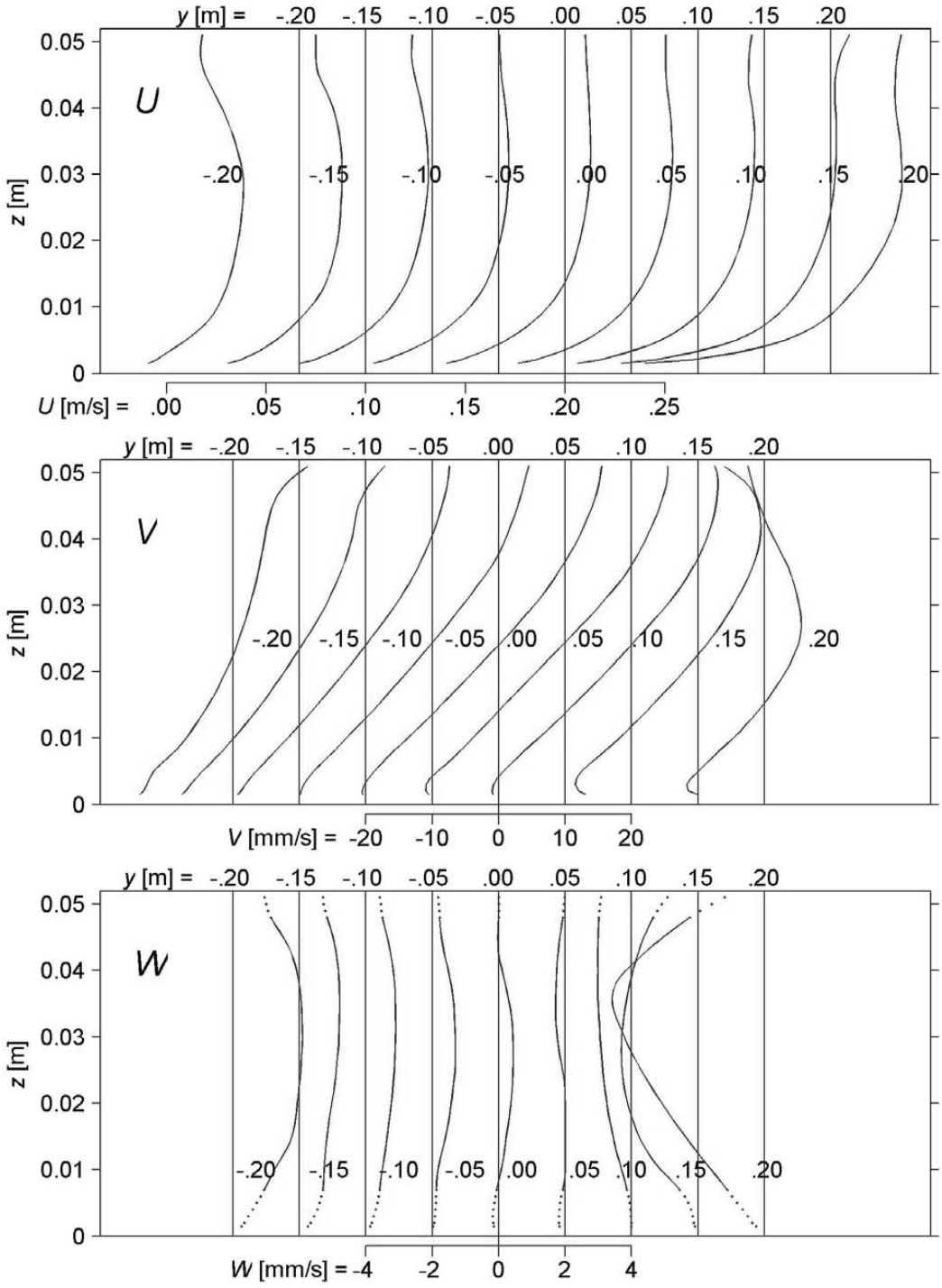


Figure 7. Vertical profiles of the measured time averaged velocity components. (The velocity scale for the middle of the cross-section, y = 0, is given at the bottom. The scales for the other verticals are displaced, see the top of each plot. The vertical lines indicate $U = 0.2$ m/s, $V = 0.0$ m/s and $W = 0.0$ m/s. …….. = approximate and/or extrapolated part of the profile.)

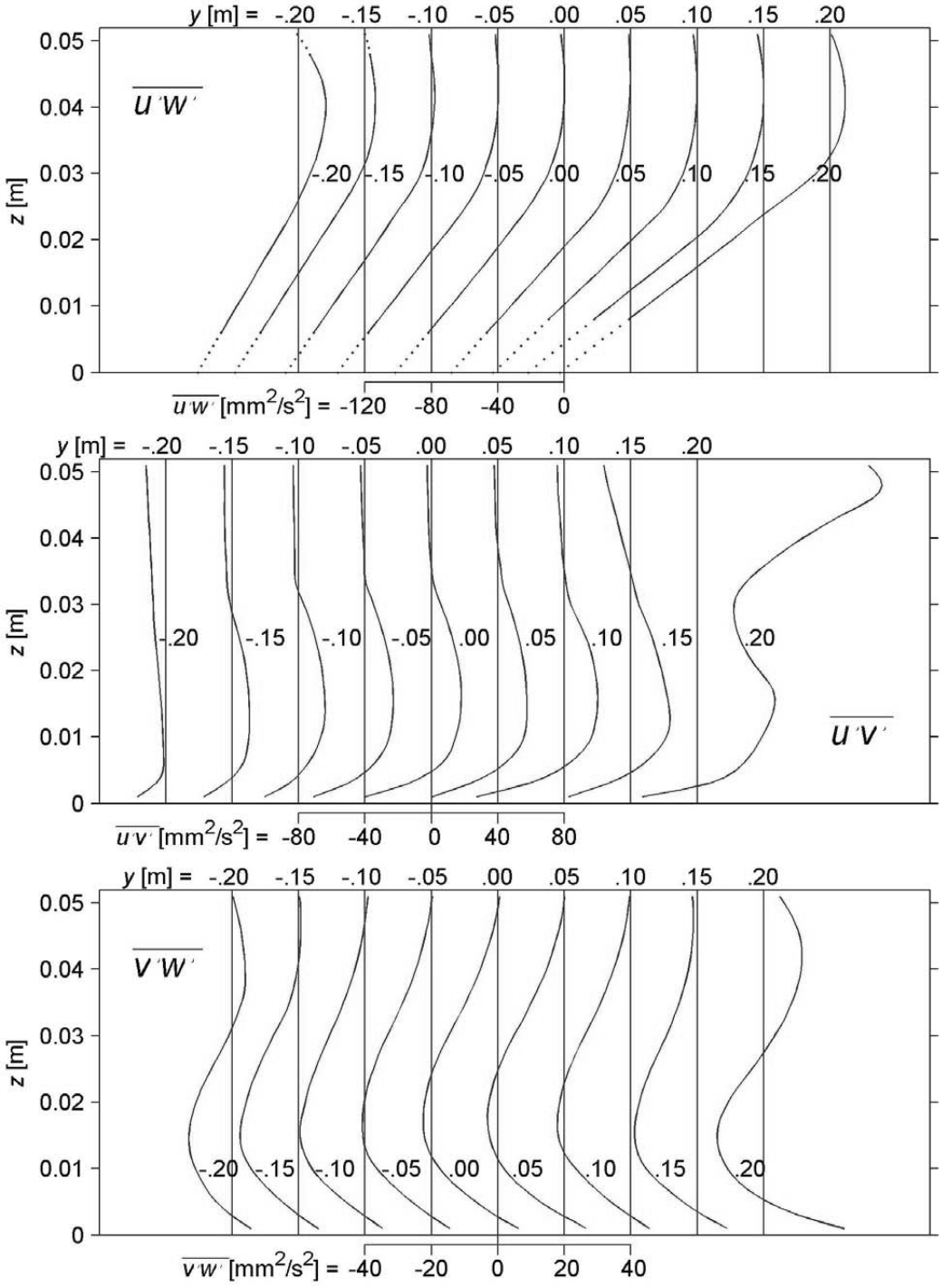


Figure 8. Vertical profiles of the measured shear stresses. (The shear stress scale for the middle of the cross-section, y = 0, is given at the bottom. The scales for the other verticals are displaced, see the top of each plot. The vertical lines indicate zero values. …….. = approximate and/or extrapolated part of the profile.)

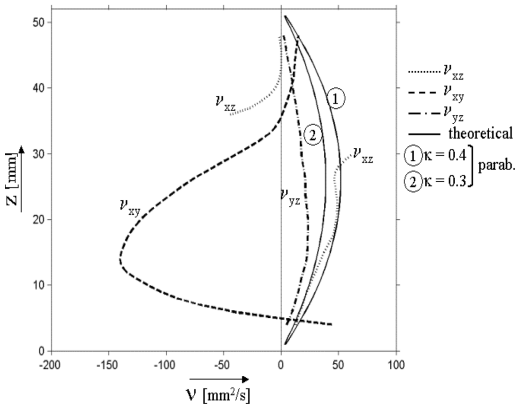


Figure 9. Eddy viscosity profiles corresponding to the three shear stresses τ_{xz}, τ_{xy} and τ_{yz} compared to theoretical parabolic profiles.

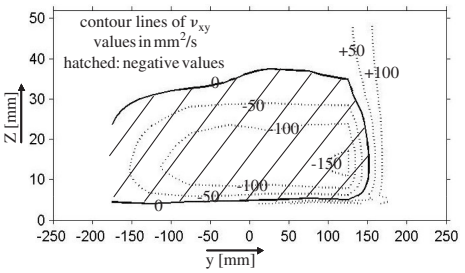


Figure 10. Part of the cross-section with negative ν_{xy} values.

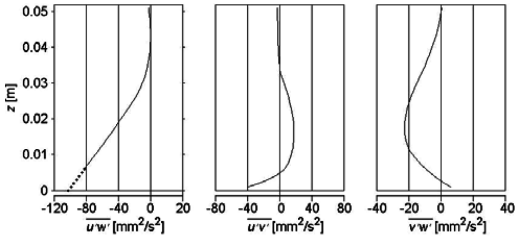


Figure 11. Vertical profiles of the measured shear stresses (. . . . = approximate and/or extrapolated part of the profile).

added. Because gradient type momentum transport models require positive eddy viscosities, the negative value obtained from the measurements explains the inability of this kind of models to reproduce correct shear stresses. This in contra-distinction to LES computations where the velocity and hence also the velocity fluctuation is computed directly.

The plotted results are henceforth restricted to the vertical in the middle of the cross-section. In Figure 11 the measured shear stresses (From Figure 8) for this vertical are given. In Figure 12 the computed shear

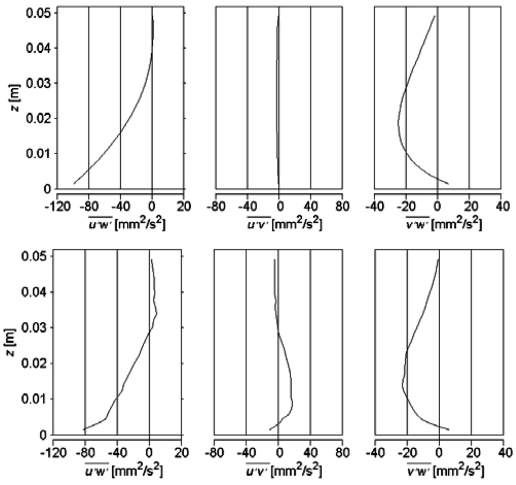


Figure 12. Computed shear stress profiles. Top: k-ε model; bottom: LES computation.

stress profiles are plotted, respectively the results of a k-ε model (top) and the result of a LES computation. The k-ε model does indeed not succeed in computing a correct shear stress τ_{xy}, in contradistinction to LES. For the shear stress results obtained by LES over the complete cross-section see Booij (2003b).

5 EXTENDED MIXING LENGTH CONCEPT

The sign of the shear stresses can be understood if a totally different mechanism is assumed to be responsible for the turbulent velocities in this part of the flow. Parcels of water that move upward from near the bottom arrive at a higher level in the fluid with a positive value of w and relatively low values of u and v, implying a positive $w\prime$ and negative u' and v'. Downward moving parcels have analogously a negative w' and positive u' and v'. Both kind of parcels give a negative contribution to $\overline{u'w'}$ and $\overline{v'w'}$ but a positive contribution to $\overline{u'v'}$. The positive value of $\overline{u'v'}$ has then evidently nothing to do with a gradient of u across the flume as is basic in the gradient type transport theory.

This idea can be worked out using an extension of the mixing length theory of Prandtl. Turbulent parcels of water that move upward through a certain level are assumed to originate from an average distance, l_m, the mixing length, below this level. They have consequently a slightly different velocity, fitting to the level of origin of the parcel, which deviation can be estimated by $u' = -l_m \partial U/\partial z$ and $v' = -l_m \partial V/\partial z$. The vertical velocity component w' is positive and is generally assumed to have roughly the same magnitude as u' so $w' = l_m|\partial U/\partial z|$. A parcel going downward has correspondingly $u' = l_m \partial U/\partial z$, $v' = l_m \partial V/\partial z$ and

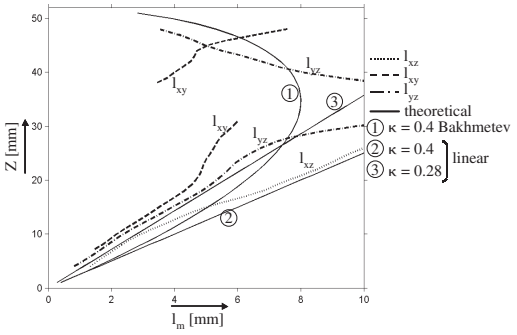


Figure 13. Mixing lengths corresponding to the three measured shear stresses in the center of the flume.

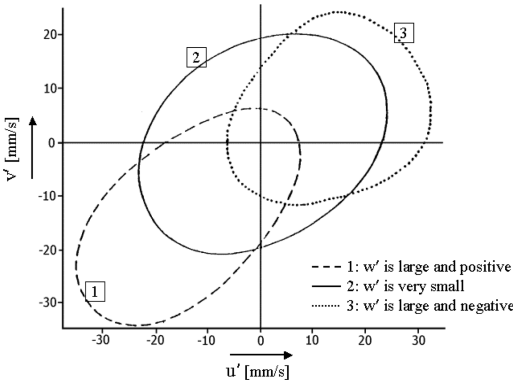


Figure 14. 3-Dimensional correlation of the measured turbulent velocity components. The majority of the measurements falls within the concerning curve.

$w' = -l_m|\partial U/\partial z|$. Averaging over all particles in this model yields consequently

$$\frac{\tau_{xz}}{\rho} = \overline{u'w'} = -l_m^2 \left|\frac{\partial U}{\partial z}\right| \frac{\partial U}{\partial z}$$

$$\frac{\tau_{xy}}{\rho} = \overline{u'v'} = +l_m^2 \frac{\partial U}{\partial z} \frac{\partial V}{\partial z}$$

$$\frac{\tau_{yz}}{\rho} = \overline{v'w'} = -l_m^2 \left|\frac{\partial U}{\partial z}\right| \frac{\partial V}{\partial z}$$

This concept can be evaluated by inspection of the values of l_m obtained from the three measured shear stresses and the gradients of the time-averaged velocity components, see Figure 13. Here the mixing length obtained from the measured shear stress τ_{xz} is notated l_{xz}, etc. The three mixing lengths are compared in Figure 13 with the theoretical Bakhmetev distribution $l_m = \kappa z\sqrt{(1 - z/h)}$, which applies for a straight, wide and uniform free surface flow when a logarithmic velocity profile (with $\kappa = 0.4$) and a linear shear stress distribution are assumed. In the upper part of the flow the time-averaged velocity and the shear stresses deviate strongly from those in a straight flume because of the curvature of the flow. Moreover the velocity gradients and shear stresses are small in that region. Therefore the mixing lengths in the upper half of the flow can hardly be determined. In the lower half the three mixing lengths are all of the same order of magnitude. Moreover they compare well to the Bakhmetev distribution, or the linear distribution expected in the near wall region (see Figure 13), especially if again a slightly lower value of κ (= 0.28 is optimal) because of the suppression of the turbulence due to the curvature is assumed.

The agreement between the different mixing lengths for the three shear stresses obtained from the measurements corroborates the extended mixing length concept. It may be a promising tool for other flows with large velocity gradients over the depth and a strongly depth-depending flow direction. In LES computations the movement of fluid parcels itself is computed, which explains the good result of the LES computation for all three shear stresses.

6 CORRELATION OF VELOCITY FLUCTUATIONS

The concept of the vertical movement of water parcels, which transport horizontal momentum of both directions, can be checked by means of the 3-dimensional correlations of the turbulent velocity components. Here it is used that only LDV-measurements in which all three velocity components could be measured simultaneously were allowed. In Figure 14 three different groups of those measurements are distinguished.

- Measurements showing a large value of w', which means a measurement in a parcel of water that moves relatively fast upwards.
- Measurements showing a large but negative value of w', which means a measurement in a parcel of water that moves relatively fast downwards.
- Measurements showing a small value of w', which means a measurement in a parcel of water that hardly moves in vertical direction.

The curves in Figure 14 indicate where most of the measurements of the horizontal velocity fluctuations can be found. For the positive value of w' most measurement fall within the dashed curve, corresponding to negative values of u' and v'.

For a negative value of w' most measurement fall within the dotted curve, corresponding to positive values of u' and v'. This confirms the assumed mechanism on which the extended mixing length theory was based.

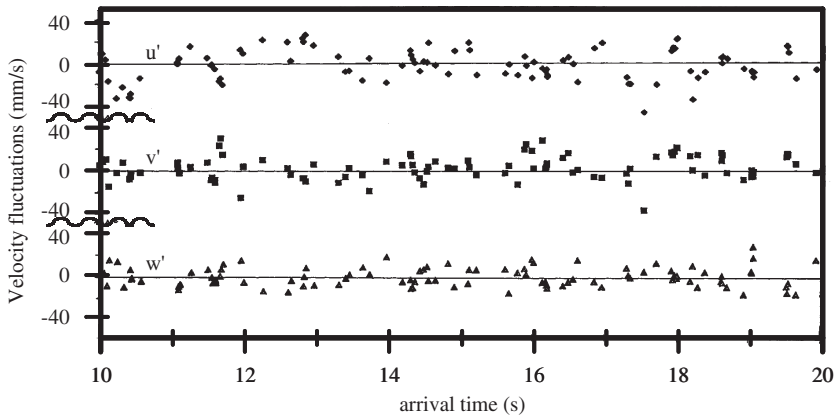


Figure 15. Simultaneously measured turbulent velocity components during a short time interval of 10 s.

These correlations are not easy to observe directly in plots of the instantaneous velocity components, see Figure 15.

7 CONCLUSIONS

- The shallow curved free surface flows in tidal channels and river bends show certain flow features that are difficult to model numerically.
- RANS (e.g. k-ε model) computations can reproduce the main characteristics of the main flow and the secondary flow in a river bend.
- However they fail to give satisfactory reproductions of the complicated secondary flow field in a mildly curved river bend with a steep outside bank: e.g. the second counter-rotating secondary flow cell and shear stresses of the proper sign.
- 3-D LES correctly reproduces the shear stresses and other flow aspects, but is not yet applicable for the computation of more realistic river layouts.
- An extended vertical mixing length model appears to be promising for flows with a depth-dependent flow direction as above the bed in tidal channel and river bends.
- 3-Dimensional correlations of the velocity fluctuations corroborate the assumed mixing length model.

ACKNOWLEDGEMENTS

The author thanks J. Tukker for the accurate execution of the measurements and B.J. Boersma of the Faculty of Mechanical Engineering and Maritime Technology of Delft University of Technology for his help with the LES programme.

REFERENCES

Blanckaert, K. & Graf, W.H. 2001. Mean flow and turbulence in open-channel bend. *J. of Hydr. Engrg* 127 (10): 835–847.

Booij, R. 2002. Modelling of the secondary flow structure in river bends. *Proc. Int. Conf. on Fluvial Hydraulics* I: 127–133. Louvain-la Neuve, Belgium.

Booij, R. 2003a. Laboratory experiments of shallow free surface flows, *Proc. Int. Symp. on Shallow Flows* I: 101–108. Delft, the Netherlands.

Booij, R. 2003b. Measurements and large eddy simulation of flows in some curved flumes. *Journal of Turbulence (J.O.T.)* 4, 008.

Booij, R. & Tukker, J. 1996. 3-Dimensional laser Doppler measurements in a curved flume. *Developments in Laser Techniques and Applications to Fluid Mechanics:* 98–114. Springer: Berlin.

Vriend, H.J. de. 1981. Velocity redistribution in curved rectangular channels. *J. Fluid Mech* 107: 423–439.

This page intentionally left blank

River Flow 2004 – Greco, Carravetta & Della Morte (eds.)
© 2004 Taylor & Francis Group, London, ISBN 90 5809 658 0

Turbulent flow over mobile and molded bedforms: a comparative field study

A. Sukhodolov
Department of Ecohydrology, Institute of Freshwater Ecology and Inland Fisheries, Berlin, Germany

J. Fedele
Department of Geology and Geophysics, University of Minnesota, Minneapolis, USA

B.L. Rhoads
Geography Department, University of Illinois at Urbana-Champaign, Urbana, USA

ABSTRACT: The paper presents some results of a field study designed to examine flow structure over bedforms. It also quantitatively compares these results to previous laboratory investigations of flow over fixed bedforms. In this study measurements of turbulence were obtained in a small river in Illinois, USA over a fine spatial grid of sampling points above a mobile sand wave and a molded replica. Flow remained attached to the riverbed within the troughs for both bedforms, but pattern of stacked wakes, similar to that observed in laboratory studies, was clearly evident in the vertical profiles of turbulence statistics. The spatially non-uniform flow over the mobile bedform appeared to approximate more closely turbulence equilibrium than the flow over the fixed bedform. In as much as propagation velocity of bedforms is an index of transport rates of bed material, results of field and laboratory studies should be compared only for similar bed-material transport rates.

1 INTRODUCTION

The development of mobile bedforms in natural rivers complicates accurate predictions of sediment transport, channel erosion and deposition and flow resistance. Many laboratory and theoretical studies have been conducted in a search for essential mechanisms of bedform development, propagation and interaction with overlying turbulent flow. Because field studies have proven laborious (Korchokha 1968; McLean & Smith 1979; Grinvald & Nikora 1988; Kostaschuk & Villard 1996) and complex (Carling et al. 2000), they are limited both in number and in the level of measurement detail. For the most part, laboratory investigations and theoretical analyses have served as the primary means of studying the problem of bedform-flow interaction. To evaluate the relevance of results of such studies for bedform dynamics in rivers and streams, a need exists for comparisons of findings of field studies with results of laboratory investigations and theoretical analyses.

Laboratory studies often focus only on the structure of turbulent flow over fixed bedforms that replicate the equilibrium forms (Nelson et al. 1993; Lyn 1993; Bennett & Best 1996) that develop on an erodible bed under the same bulk-flow conditions (Guy et al. 1966). In particular, separation and reattachment of flow over bedforms was revealed to be a peculiar property with important dynamic implications for such flows, and recent theoretical efforts have concentrated mainly in incorporating these aspects in the formulation of more advanced models (McLean & Smith 1986, Nelson & Smith 1989). Although presumed as essential mechanism, flow separation is paradoxically a rare phenomenon observed in natural streams (Kostachuk & Villard 1996) with minor effects, as reported in several field studies (Carling et al. 2000).

Various reasons have been proposed for the discrepancy between laboratory and field observations; however, to date, none has been rigorously evaluated. To a great extent the lack of comparative analyses can be attributed to technical limitations. Hot-wire, hot-film anemometers, and laser doppler velocimeters have been used in laboratory studies for about four decades, whereas analogous devices suitable for field studies (acoustic doppler velocimeters or ADV) only became commercially available a decade ago (Kraus et al. 1994). In the field, the need to simultaneously monitor the evolution of mobile bedforms while performing flow measurements has been an additional problem.

Recent developments in echosounding technology (Nikora et al. 1997) and progress in application of ADV measurements to studies of river turbulence (Sukhodolov et al. 1998; Sukhodolov & Rhoads 2001) have opened new possibilities for coupled field studies of flow-bedform dynamics. In this study we take advantage of ADV and echo-sounding technology to: (1) explore simultaneously flow structure over bedforms and the morphological characteristics of bedforms in a mobile-bed natural stream and (2) compare flow structure over mobile bedforms to that over an artificial fixed bedform with a shape derived from the characteristic form of mobile prototypes. This paper presents some preliminary results of the study and qualitatively compares these results to laboratory observations of flow over bedforms. The results contribute to the understanding of basic mechanisms governing flow-bedform interactions in alluvial channels.

2 FIELD MEASUREMENTS

2.1 *River reach*

The study is based on measurements conducted in the Embarras River, 15 km south of Urbana-Champaign in the east central Illinois. The stream is contained within the bottom of a trapezoidal drainage ditch. During the period of measurements (June 5–7, 1998) the bulk characteristics of the flow were: discharge $Q = 0.783\ m^3/s$, mean velocity $U = 0.44$ m/s, river width $B = 5.2$ m, average depth $h = 0.35$ m, water slope $S = 0.00132$, corresponding shear velocity $U_* = 6.7$ cm/s, Froude number $Fr = 0.24$, and $Re = 1.4 \times 10^5$.

2.2 *Measuring systems and equipment*

Measurements of riverbed elevations were performed with a multi-channel microsounder system SH-1M (Nikora et al. 1997). The system consists of six sensors ported at a processing block interfaced to a portable computer and operated either in manual or automatic mode. The system permits synchronous measurements at a sampling rate up to 2 Hz with a spatial resolution of about 2 cm and an accuracy of 1–2 mm for a depth range of 6 to 100 cm.

Records of instantaneous 3-D velocity components were collected using an acoustic doppler velocimeter manufactured by Sontek, Inc. This instrument consists of an ADVLab probe mounted to submersible field electronics. The sampling volume of the probe is located 5 cm from the sensors and is $<0.25\ cm^3$ in size. The resolution of the ADVLab is 0.1 mm/s with a noise level of 1% of the velocity range at a sampling frequency of 25 Hz.

A special measuring platform was constructed to enable precise positioning and traversing of the sensors (Fig. 1). The platform consists of a square 3×3 m



Figure 1. The measuring platform in the Embarras River.

wooden frame mounted on metal uprights. A wooden traversing bar containing a metal mount for the ADV sensor was placed on the wooden frame. Wires were stretched beneath the platform, and parallel to the main direction of current, to support a light aluminum frame oriented in the cross-current direction and housing six echosounding probes placed 10 (1–2), 15 (2–3), 20 (3–4), 25 (4–5), and 30 cm (5–6) apart. A system of tapes stretched along the frame allowed for precise positioning of the traversing bar within the dimensions of the 3×3 m wooden frame. The ADV probe was mounted on a tip of 1.5 m long metal rod aligned with the principal axis of the probe. The vertical alignment of the rod was controlled by a bubble level on the metal ADV mount and by geodetic instruments.

2.3 *Measurements and data processing*

The experimental program for the study comprised:

(1) measurements of riverbed morphology and kinematics of mobile bedforms;
(2) measurements of velocity and turbulence characteristics over natural mobile sand waves, and elevations of the riverbed; and
(3) measurements of velocity and turbulence characteristics over an artificial concrete bedform created from a mold representative of natural bedform characteristics.

The characteristic spatial structure of bedforms within the study reach was determined by moving the array of echosounding probes along several parallel 30 m-long traverses in the streamwise direction and collecting depth readings every 5 cm. To estimate characteristics of bedform propagation the sensors were positioned at a closely spaced series of fixed locations in the streamwise direction and depth readings were collected at a sampling interval of 10 s over a sampling period of 16 hours. In site processing of the spatial riverbed measurements allowed portraying a

typical bedform. A mold corresponding to the dimensions of that form was manufactured – and filled with the concrete, and sand extracted from the riverbed was used to create the bedform surface exposed to the flow. The concrete was left to set while other measurements were performed.

Velocity measurements in the flow over the mobile bedform were obtained at four vertical profiles. Each profile consisted of 15–17 measurements spaced about 2 cm apart. The sampling duration at each measurement location was 200 s at sampling rate 25 Hz. Prior to collecting the velocity data for a specific vertical profile, riverbed elevations were monitored by traversing the array of echosounding probes within the experimental frame (3 m) and recording depths at 5 cm spatial intervals.

The artificial bedform was then exposed to the flow at the same location where a moveable bed form was observed before. Velocity measurements were taken at three verticals along the length of the bedform and topographic profiling of the riverbed profiling was performed once prior to velocity measurements.

Monitoring of water levels was performed on two gauges located 10 m up- and downstream of the frame. Levels were recorded every hour and the variation was less than 0.7 cm for the whole period of measurements.

The software package ExploreV 1.5 (Nortek USA) was used to process the ADV data. Prior to computations of the statistical characteristics of turbulence, each record was inspected visually to identify possible problems, such as spikes, trends or abrupt discontinuities in the time series. Post-processing of the data involved removal of the defective portions of the time series using the data clipping capabilities of the software, spikes detection with a set of criteria implemented in ExploreV and replacement of extreme values produced by interruption of the acoustic beam by floating debris with linearly interpolated values.

3 RESULTS

A coordinate system with a streamwise x direction, a transverse y direction, and a vertical direction z, originating at riverbed and directed toward the free surface is adopted herein. The corresponding velocity fluctuations are u', v' and w', respectively; the mean streamwise velocity is denoted $\overline{U}$.

3.1 *Spatial-temporal characteristics of bedforms*

The longitudinal profile of bed topography along the flow centerline obtained from the echosounding device illustrates the morphology and abundance of sand waves on the channel bed (Fig. 2a). Averaging of a total of six separate longitudinal profiles resulted in a characteristic form 2 m long and 8 cm high with a lee-side angle of 12° and a stoss-side angle of 5°. Comparison

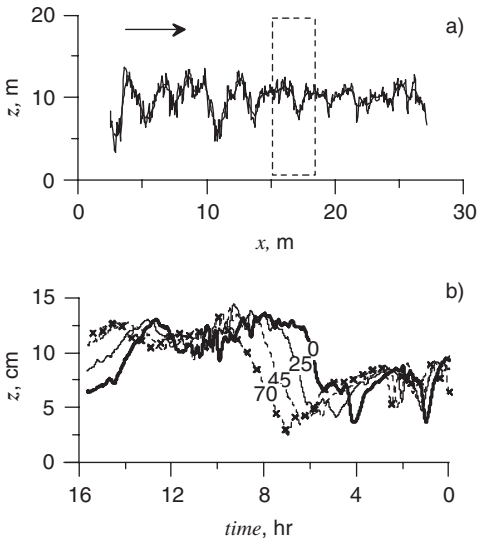


Figure 2. a) Example of a longitudinal profile of bed elevations along the flow centerline (dashed box indicates the position of the measurement platform), and b) temporal change in bedform profile at fixed verticals within the measurement frame (numbers indicate spatial lags in cm).

of the longitudinal profiles at different locations across the stream indicated that bedforms were approximately two-dimensional in the central part of the stream and did not change substantially in shape over transverse distances on the order of two times the depth of flow.

Successive temporal records of riverbed elevation at fixed locations provide insight into kinematics of bedforms (Fig. 2b). From these records, it is possible to estimate the propagation velocity C for a typical bedform as the distance of movement of the lee side of the bedform divided by the time of movement, yielding a mean value for propagation velocity C of 6.5×10^{-5}m/s.

3.2 *Individual bedforms*

When measuring velocity and turbulence profiles over an individual mobile bedform, prior to the start of each vertical profile the riverbed was surveyed with the echosounding device. This scheme allowed precise determinations of the position of each vertical and of the locations of individual sampling volumes relative to the instantaneous morphology of the channel bed (Fig. 3). Successive measurements of a propagating bedform indicated that its shape and dimensions generally remained constant. However, small-scale secondary forms (length of 25–50 cm and height 3–5 cm) superimposed on the large sand wave developed, propagated and disappeared on an irregular basis (Fig. 3a, d). Successive bed profiles

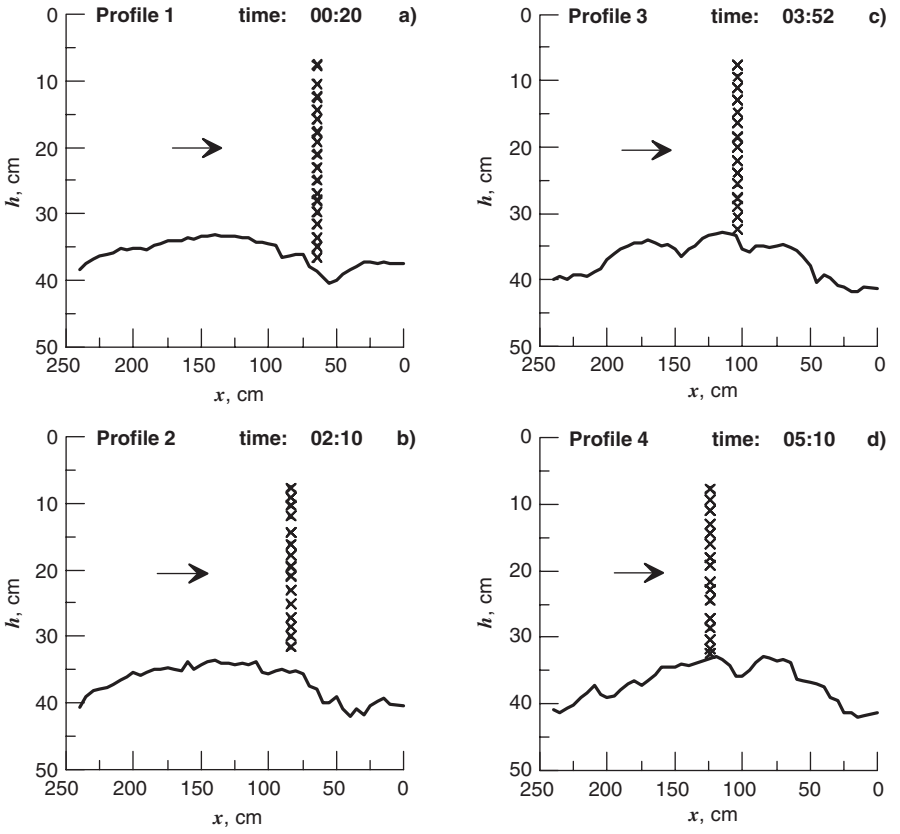


Figure 3. Instantaneous riverbed profiles and locations of ADV's sampling volume during velocity and turbulence measurements (arrows indicate the direction of flow).

were spatially averaged to account for temporal lags associated with bedform motion. The spatial-temporal averaging yielded a characteristic time-averaged shape of the individual mobile bedform (Fig. 4a) and allowed the velocity profiles and ADV sampling locations to be determined precisely relative to the phase-shifted motion of the bedform.

Subsequently, the molded replica of the characteristic bed form (Fig. 2a), was carefully placed in the channel by removing bed material and manually constructing smooth transitions between the artificial bed form and its natural surroundings. The resulting riverbed topography was then surveyed and a longitudinal bed profile that included the artificial bed form was obtained (Fig. 4b).

There is a difference in the shape of the spatially temporally averaged bed form (Fig. 4a) and the artificial bedform (Fig. 4b). The difference is explained inasmuch as the artificial bed form was copied from the instantaneous pictures of the bed forms (Fig. 2a, Fig. 3) that looked steeper than their averaged patterns, which incorporate the secondary small-scale structures.

3.3 *Mean velocity profiles*

The time-averaged values of the streamwise velocity components over the mobile and artificial bedforms show that velocities gradually increase toward the surface in a log-law-like pattern (Fig. 5) No flow separation could be detected within the troughs of either bedform. The main differences between the two velocity profiles are the relatively steep slope of the profile for the artificial bedform and the deviation of two near-bed points from the shape of the profile over the stoss side of the artificial bedform.

3.4 *Turbulent stresses*

Distributions of the primary components of the turbulent stresses $-\overline{u'w'}$ presented in Figure 6. A typical pattern of flow development along bedforms

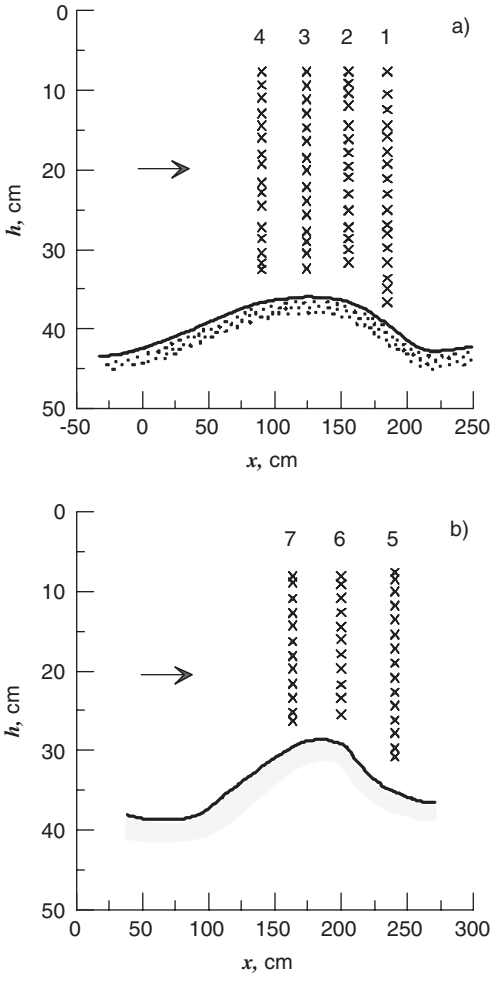


Figure 4. Positions of ADV's sampling volume locations (crosses) over spatially-temporally averaged bedform (a) and its artificial replica (b).

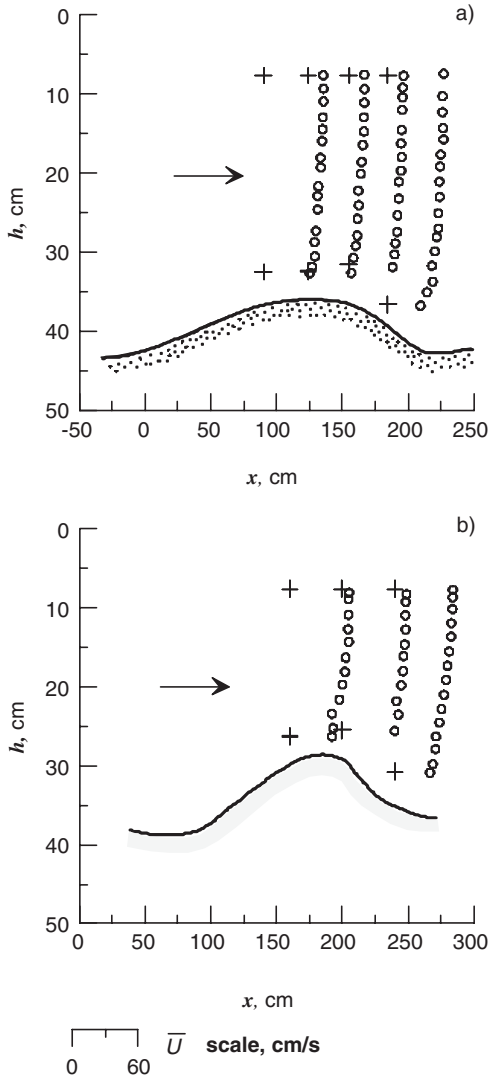


Figure 5. Mean streamwise velocity (circles) distributed over moveable (a) and fixed (b) bedforms, crosses indicate locations of the profiles and zero values of velocity.

(McLean & Smith 1986), including the effect of upstream bedforms, can be observed from the distribution of Reynolds stresses (Fig. 6). The distributions exhibit distinct segmentation marked by abrupt discontinuities in vertical trends of shear stress. These discontinuities occur consistently among all verticals and can be traced from one shear-stress profile to the next over the bedform. The dashed lines shown in Figure 6 depict the segmented configurations of a flow over bedforms. A notable characteristic of the stress profiles for both the mobile and fixed bedforms is the highly irregular pattern of shear stresses over the trough compared to the pattern of near-bed shear stresses over the crest and stoss side of the bedform.

3.5 *Turbulence kinetic energy*

Turbulence kinetic energy $k = 0.5(\overline{u'^2} + \overline{v'^2} + \overline{w'^2})$ represents the integral characteristic of diagonal components of the stresses tensor. The spatial distribution of k can be used to identify zones of high turbulence kinetic energy, which often represent zones of turbulence production (Rhoads & Sukhodolov 2001). Distributions of k suggest that production is greatest over the trough of mobile and fixed bedforms (Fig. 7).

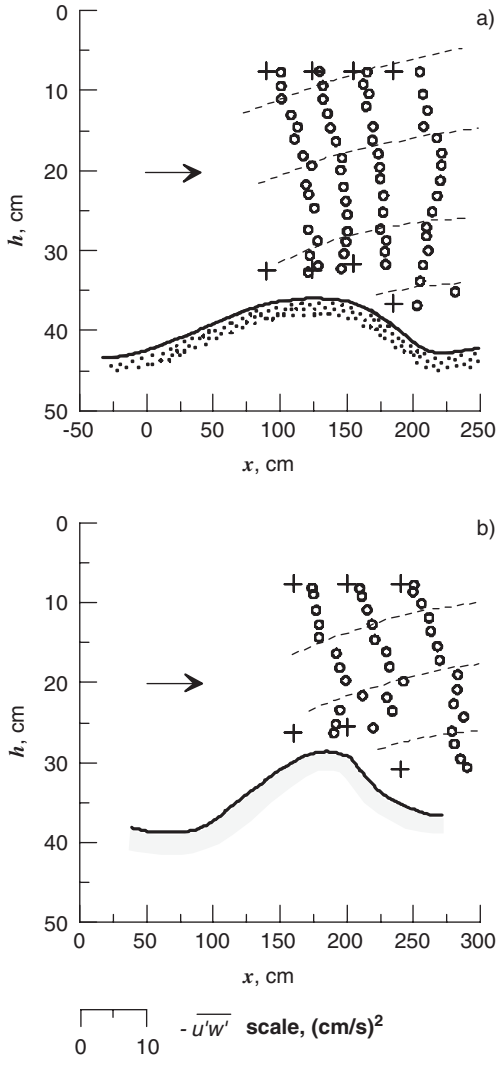


Figure 6. Distributions of the turbulence stresses (circles) in the flow over moveable (a) and fixed (b) bedforms, dashed lines depict the boundaries of layers and crosses indicate locations of the profiles and zero values of stress.

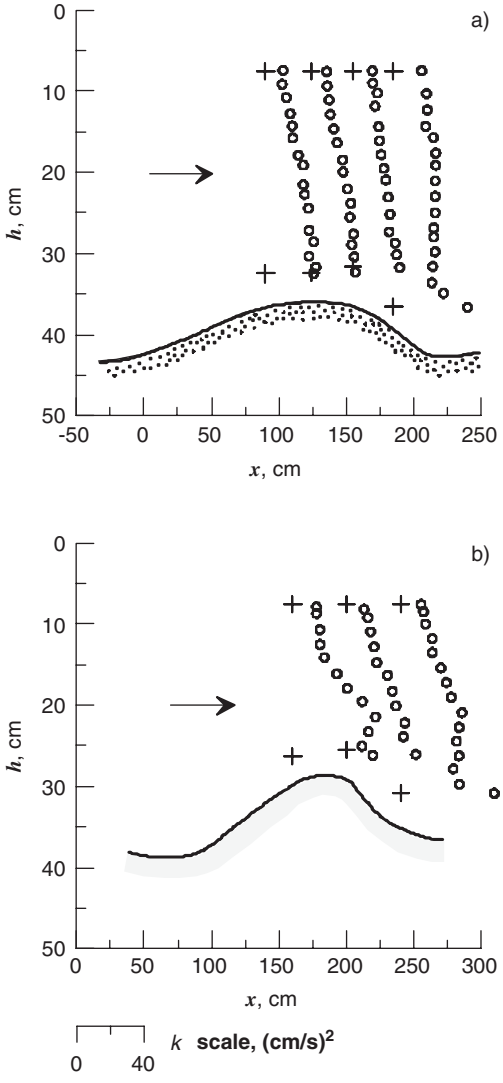


Figure 7. Turbulence kinetic energy (circles) distributions in the flow over moveable (a) and fixed (b) bedforms, crosses indicate locations of the profiles and zero values of energy.

The high values of k over the troughs are indicative of a shear layer marking the upper boundary of an internal boundary upper boundary of an internal boundary layer within the trough. Turbulence kinetic energy is distributed fairly uniformly over the gently rounded crest of the mobile bedform (Fig. 7a). In contrast, the layer of high k is more clearly developed and extends farther upstream over the fixed bedform, suggesting that its high roughness and steep stoss and lee slopes enhances internal shearing of the flow as it moves over this artificial bedform (Fig. 7b).

3.6 *Dissipation rates*

Values of dissipation rate ε were calculated from power spectra of the velocity fluctuations (Fig. 8) using Kolmogorov's –5/3 law

$$S(f) = 0.48\left(\overline{U}/2\pi\right)^{2/3}\varepsilon^{2/3} f^{-5/3} \quad (1)$$

where S = spectral density; and f = frequency. Equation 1 was applied to the inertial subranges – the

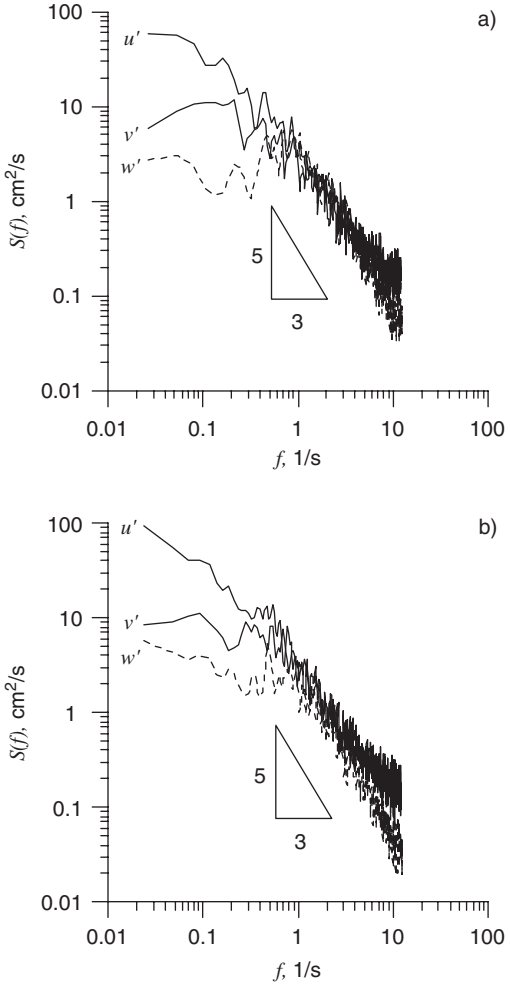


Figure 8. Examples of turbulence spectra measured over trough of the moveable (a) and fixed (b) bedforms.

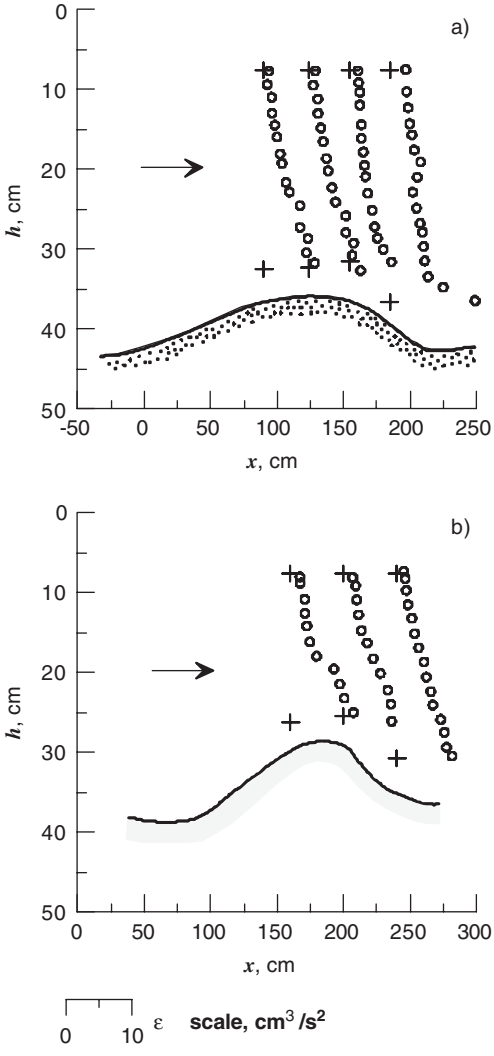


Figure 9. Dissipation rate (circles) distributions in the flow over moveable (a) and fixed (b) bedforms, crosses indicate locations of the profiles and zero values of dissipation rates.

existence of which was defined by relationship

$$S_v = S_w = 4/3 S_u . \quad (2)$$

The patterns of dissipation rate measured over the mobile bedform (Fig. 9a) are similar to the distributions of turbulence kinetic energy (Fig. 7a), indicating that local equilibrium of turbulence energy may be approximated in at least some portions of the flow over bedforms. Upper portions of profiles of k and ε exhibit the greatest similarity. Near the surface of the bedform, vertical patterns of k and ε begin to diverge, especially for the fixed bedform. Thus, flow in this near-bed region departs substantially from equilibrium. Overall, however, rates of dissipation are highest over the lee side of the bedform where values of k also are highest.

4 DISCUSSION AND CONCLUSIONS

Field studies of turbulent flow structure over mobile bedforms have inherent limitations that are difficult if not impossible to accommodate completely. Point measurements of turbulence characteristics require relatively long periods of record to ensure accuracy of high-order statistical moments. To resolve structural properties of the flow at specific locations along the entire length of bedforms, data should be collected over a fine grid involving a large number of

measurement points. At the same time, the total duration for the set of measurement should not exceed the time scale over which the bedform substantially changes shape or position. Refinement of field studies can be achieved through predictions of the total time required for measurements of turbulence relative to the time scale of bedform propagation.

The propagation speed of bedforms depends on their length, with small secondary bedforms moving rapidly over large slower-moving primary forms. The propagation speed C of bedforms recently has been characterized in the semi-empirical formulae (Nikora et al. 1997)

$$C = 0.66\overline{U}\,Fr^{2.9}\left(g\lambda/\overline{U}^2\right)^{-1}. \quad (3)$$

Applying bulk parameters of the flow measured in the Embarras River (Section 2.1) to the equation (3), and using average bedform length $l = 2.0$ m (Section 3.1) yields $C = 4.5 \times 10^{-5}$ m/s. This predicted value matches the measured value of 6.5×10^{-5} m/s (Section 3.1) with an accuracy within 30%. Thus equation (3) can be recommended for planning of bedform measurement programs.

Flow separation on the lee side of bedforms, a characteristic phenomenon almost always reported in laboratory studies, usually is recognized by a significant reduction or even reversal of mean downstream velocity. This effect, however, was not pronounced in the mean downstream velocity distributions reported in this study (Fig. 5). For both the mobile and fixed bedforms, flow remains attached to the riverbed within the trough. Observed bedforms were characterized by lee-side slope angles not exceeding 12°-relatively gentle slopes compared to laboratory bedforms with angles of approximately 30° (Nelson & Smith 1989), values close to angle of repose for sandy material. The lack of flow separation raises some important questions: Why were the bedforms observed in the Embarras River not highly asymmetrical in shape? Given the differences in bedform morphology in field and laboratory studies, to what extent are the results of these two types of investigations comparable?

Obviously, since the motion of bedforms reflects sequential erosion and deposition, and the angle of repose controls the accumulation of the riverbed material at the crests of bedforms, the asymmetric shape with lee-side angles of 30° is characteristic of bedforms with high transport rates. Inasmuch as propagation velocity of bedforms is an index of transport rates of bed material, the results of laboratory and field studies of bedforms should be compared only for similar bed-material transport rates. Simple computations using equation (3) and the data by Nelson & Smith (1989) give an estimate of propagation velocity of 6.3×10^{-4} m/s, a value one order of magnitude larger than the rate observed in the Embarras River.

In formulating their theory of flow over bedforms McLean & Smith (1986) proposed a model of stacked wakes within the flow over the internal boundary layer that develops over the trough on the stoss side of a sand wave. These wakes originate at bedforms upstream of a particular form and can be approximated by the Schlicting far-field wake theory. The patterns of turbulence stresses in this study clearly reveal a staked wake structure over the natural and artificial bedforms (Fig. 6). This effect is most evident in the flow over the artificial bedform (Fig. 6b) than over the mobile bedform (Fig. 6a). In the case of the mobile bedform, the stacked wake structure apparently was disrupted by secondary forms, which of course were absent on the artificial bedform.

The study also reveals some notable differences between flow structures measured over mobile and fixed bedforms. In particular, the spatially nonuniform flow over the mobile bedform appeared to more closely approximate turbulence equilibrium than flow over the fixed bedform. This difference implies that in the absence of secondary bedforms the primary bedform has greater roughness than the mobile bedform for the same flow conditions. Similar effects, for example reduction of drag over the bodies of sharks because of riblets on their skin, are described in literature.

Although the results of this field study partly conform to, yet differ in detail from results of laboratory studies of flow over bedforms, any conclusions must be offered cautiously since a single case study cannot represent the diverse range of condition that exist in nature. The results presented here are preliminary and further analysis is required to gain insight into subtle details of the flow structure. Future work should focus on scaling of turbulence characteristics and the extent to which turbulence characteristics measured in the field can be predicted by contemporary models of flow over bedforms.

ACKNOWLEDGMENTS

Michael Thiele assisted in the collection of the field data. Kelly Frothingham kindly assisted in organizing the logistics of the field campaign, and Steven Graves provided essential tools and friendly encouragement. Funding for this research was provided by the National Science Foundation (SBR 9710068) and the University of Illinois Research Board.

REFERENCES

Bennett, S.J. & Best, J.L. 1996. Mean flow and turbulence structure over fixed ripples and the ripple-dune transition. In Philip J. Ashworth, Sean J. Bennett, James L. Best & Stuart J. MCLelland (eds.), *Coherent Flow Structures in Open Channels; Proc. intern. conf., Leeds, 10–12 April 1995.* Chichester: John Wiley & Sons.

Carling, P.A., Williams, J.J., Gölz, E. & Kelsey, A.D. 2000. The morphodynamics of fluvial sand dunes in the River Rhine, near Mainz, Germany. II. Hydrodynamics and sediment transport. *Sedimentology* 47: 253–278.

Grinvald, D.I. & Nikora, V.I. 1986. *River Turbulence*. Leningrad: Hydrometeoizdat.

Guy, H.P., Simons, D.B. & Richardson, E.V. 1966. *Summary of Alluvial Channel Data from Flume Experiments, 1956–1961*. US Geological Survey Professional Paper: 462-I:1–96.

Korchokha, G.M. 1968. A study of dynamics of sand dunes in the Plomet river. *Transactions of State Hydrological Institute,* 161: 98–119.

Kostaschuk, R. & Villard, P. 1996. Flow and sediment transport over large subaqueous dunes: Fraser River, Canada. *Sedimentology,* 43: 849–863.

Kraus, N.C., Lohrmann, A. & Cabrera, R. 1994. New acoustic meter for measuring 3D laboratory flows. *J. Hydraul. Eng.,* 120(3): 406–411.

Lyn, D.A. 1993. Turbulence measurements in open channel flows over artificial bed forms. *J. Hydraul. Eng.,* 119(3): 306–326.

McLean, S.R. & Smith, J.D. 1979. Turbulence measurements in the boundary layer over a sand wave field. *J. Geophys. Res.* 84(C12): 7791–7808.

McLean, S.R. & Smith, J.D. 1986. A model for flow over two-dimensional bed forms. *J. Hydraul. Eng.,* 112: 300–317.

Nelson, J. & Smith, J.D. 1989. Mechanics of flow over ripples and dunes. *J. Geophys. Res.* 94(C6): 8146–8162.

Nelson, J. McLean, S.R. & Wolfe, S.R. 1993. Mean flow and turbulence fields over two-dimensional bed forms. *Water Resour. Res.,* 29(12): 3935–3953.

Nikora, V.I., Sukhodolov, A.N. & Rowinski, P.M. 1997. Statistical sand waves dynamics in the one-directional water flows. *J. Fluid Mech.,* 351: 17–39.

Rhoads, B. & Sukhodolov, A. 2001. Field investigation of three-dimensional flow structure at stream confluences: I. Thermal mixing and time-averaged velocities. *Water Resour. Res.,* 37(9): 2393–2410.

Sukhodolov, A., Thiele, M. & Bungartz, H. 1998. Turbulence structure in a river reach with sand bed. *Water Resour. Res.,* 34(5): 1317–1334.

This page intentionally left blank

A.3. Over-bank flow and vegetation

This page intentionally left blank

River Flow 2004 – Greco, Carravetta & Della Morte (eds.)
© 2004 Taylor & Francis Group, London, ISBN 90 5809 658 0

Depth-averaged modelling of overbank flow in meandering channels

P. Rameshwaran
Centre for Ecology & Hydrology, Wallingford, Oxfordshire, UK

K. Shiono
Department of Civil and Building Engineering, Loughborough University, Leicestershire, UK

ABSTRACT: A quasi two-dimensional model for calculating depth-averaged velocity and boundary shear stress in meandering channels for overbank flow is developed for a complex cross-section. The model numerically solves the depth-averaged equation for the streamwise motion of flow in a curvilinear coordinate system. The input model coefficients – friction factor, eddy viscosity and advection term – are calculated from the experimental data obtained from the UK Flood Channel Facility. The predictive ability of the model is assessed against experimental data and results from two and three dimensional numerical models with regard to distributions of depth-averaged velocity and boundary shear stress. The results show that the quasi two-dimensional model produces a reasonable simulation of the flow field when appropriate input coefficients are used.

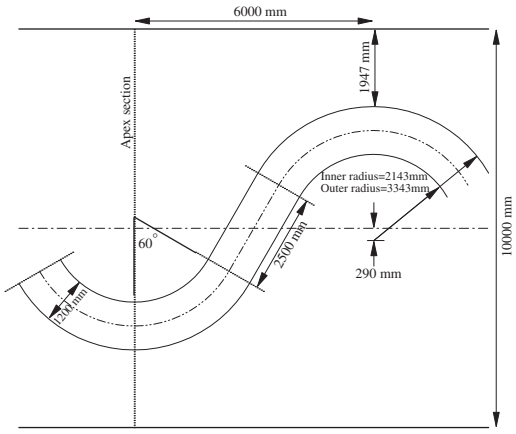
1 INTRODUCTION

Accurate prediction of flow and boundary shear stress for overbank flow in a meandering channel is required by engineers and scientists in order to understand bank erosion, sediment transport behaviour and river ecosystems. There are a number of methods predicting inbank velocity and boundary shear stress in meandering rivers in the literature (e.g. Chang, 1988), but it is difficult to apply such methods to overbank flow since the flow structure is very different to that for inbank flow (Shiono and Muto, 1998). Recently, Rameshwaran and Shiono (2002, 2003) and Rameshwaran and Naden (2003) used two-dimensional (2D) and three-dimensional (3D) numerical models to predict velocity and boundary shear stress in a meandering channel for overbank flow; however, these models take a long time to reach a solution even with the computer power available today. There are one equation depth-averaged 2D models which are much simpler and quicker to solve. Two of these are based on the model developed by Shiono and Knight (1991) for a straight compound channel. They are proposed by Ervine *et al*. (2000) and Spooner and Shiono (2003) for a meandering channel. Ervine *et al*. (2000) simply use the straight channel equation without considering the radius of curvature and the model developed by Spooner and Shiono (2003) model is only applicable to flat bed cases.

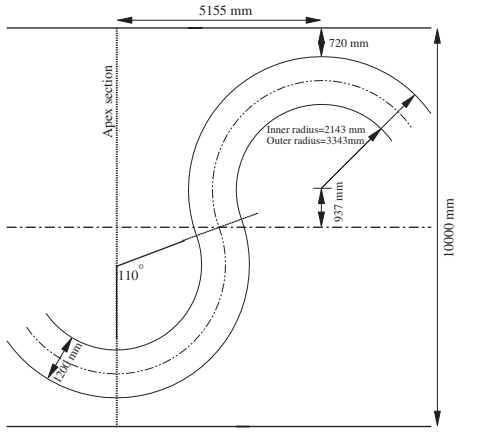
The main objective of this paper, therefore, is to investigate the feasibility of simulating overbank flow in a two-stage meandering channel with a complex cross-section using the one equation 2D model (i.e. quasi 2D model). A model for calculating depth-averaged velocity and boundary shear stress in meandering channels for overbank flow is developed for a complex cross-section. The model equation is solved numerically. In order to solve the equation, friction factor, eddy viscosity and advection terms are required. These are obtained from the experimental data obtained from the UK Flood Channel Facility (UK-FCF). The performance of the quasi 2D model is evaluated by a comparison with the detailed experiment data obtained from the UK-FCF together with results from 2D and 3D numerical models (Rameshwaran and Shiono, 2002 & 2003 and Rameshwaran and Naden, 2003).

2 EXPERIMENTAL DATA

A brief description of the experimental set up for the UK-Flood Channel Facility (UK-FCF) programme is given here. The detail of the programme has been described by Ervine *et al*. (1993) and Lorena (1992). The UK-FCF flume is 60 m long and 10 m wide, with a maximum discharge of 1.1 m^3s^{-1}. Experiments were performed in two-stage meandering channels consisting of flat floodplains with straight floodplain walls and a sinuous main channel, as shown in Figure 1. The top width of the main channel was 1.2 m and the bank slopes were 45° with a bank-full depth of



(a) Sinuosity =1.374



(b) Sinuosity =2.043

Figure 1. Plan details of UK-FCF channel geometries.

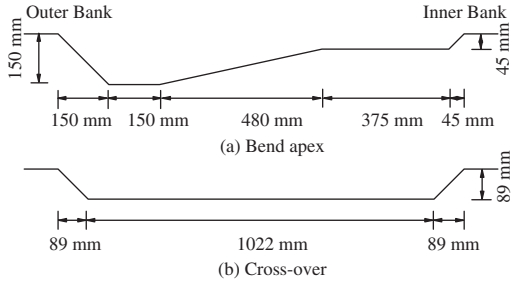


Figure 2. Natural cross-sections.

150 mm. The shape of the meandering channel cross-section was either trapezoidal or 'natural'. The 'natural' channel cross-section (Figure 2) was modelled from seventeen natural river bends and the detail of the

Table 1. Flow conditions.

Case	Sinuosity	Main channel	h_{max} (mm)	Q (m^3s^{-1})
A	1.374	Natural	165	0.0580
B	1.374	Natural	200	0.2250
C	1.374	Trapezoidal	200	0.2500
D	2.043	Natural	200	0.1790

channel design was given by Lorena (1992). The lower sinuosity (1.374) channel, was used with both the trapezoidal and natural channel cross-section, but only the 'natural' channel cross-section was employed for the higher sinuosity (2.043) channel. The channel slope was 0.996×10^{-3} for the lower sinuosity channel and 1.021×10^{-3} for higher sinuosity channel. Detailed measurements of horizontal velocity and bed shear stress were made under steady uniform flow conditions for all four cases considered in this study (Table 1). The flow angle was recorded by a vane connected to a rotary potentiometer and the horizontal velocity was measured using a miniature propeller meter. The shear stress was measured by a Preston tube on the bed.

3 MODEL EQUATION

The equation for the streamwise component of momentum on a fluid element combined with the continuity equation for steady uniform flow using curvilinear coordinates is:

$$\rho\left[\frac{r_{in}}{r_{in}+y_{mc}}\frac{\partial\left(\overline{U}^2\right)}{\partial x}+\frac{\partial\left(\overline{UV}\right)}{\partial y}+\frac{\partial\left(\overline{UW}\right)}{\partial z}+\frac{2\overline{UV}}{r_{in}+y_{mc}}\right]$$

$$=\frac{r_{in}}{r_{in}+y_{mc}}\rho g S_0+\frac{r_{in}}{r_{in}+y_{mc}}\frac{\partial\tau_{xx}}{\partial x}$$

$$+\frac{\partial\tau_{xy}}{\partial y}+\frac{\partial\tau_{xz}}{\partial z}+\frac{2\tau_{xy}}{r_{in}+y_{mc}} \qquad (1)$$

where x, y and z are the streamwise, transverse and vertical directions respectively, $\overline{U}$, $\overline{V}$ and $\overline{W}$ are the temporal mean velocity components corresponding to x, y and z coordinate directions respectively, ρ is the density of water, g is the gravitational acceleration, S_0 is the bed slope gradient, τ is the Reynolds stress in the respective planes, r_{in} is the radius of curvature of the meandering channel inner bank and y_{mc} is the distance across the meandering channel from the inner bank.

The depth-averaged momentum equation can be obtained by integrating equation (1) over the water

depth, H, provided $\overline{W}(H)=\overline{W}(0)=0$ (Shiono and Knight, 1991):

$$\rho\left[\frac{r_{in}}{r_{in}+y_{mc}}\frac{\partial H\left(\overline{U}_d^2\right)}{\partial x}+\frac{\partial H\left(\overline{UV}\right)_d}{\partial y}+\frac{2H\left(\overline{UV}\right)_d}{r_{in}+y_{mc}}\right]$$
$$=\frac{r_{in}}{r_{in}+y_{mc}}\rho gHS_0+\frac{r_{in}}{r_{in}+y_{mc}}\frac{\partial H\left(\tau_{xx}\right)_d}{\partial x}$$
$$+\frac{\partial H\left(\tau_{xy}\right)_d}{\partial y}-\tau_b\sqrt{1+\frac{1}{s^2}}+\frac{2H\left(\tau_{xy}\right)_d}{r_{in}+y_{mc}} \qquad (2)$$

where subscript d indicates a depth-averaged value, τ_b is the bed shear stress and s is the bank slope (1:s – vertical : horizontal). At the apex cross section, assuming $\partial H(\overline{U}_d^2)/\partial x \ll 1$ and $\partial H(\tau_{xx})_d/\partial x \ll 1$ because streamwise velocity is dominant, equation (2) can be written with some manipulation as:

$$\rho\left[\frac{r_{in}+y_{mc}}{r_{in}}\frac{\partial H\left(\overline{UV}\right)_d}{\partial y}+\frac{2H\left(\overline{UV}\right)_d}{r_{in}}\right]$$
$$=\rho gHS_0+\frac{r_{in}+y_{mc}}{r_{in}}\frac{\partial}{\partial y}\left(\rho\lambda H^2\sqrt{\frac{f}{8}}\frac{1}{2}\frac{\partial\overline{U}_d^2}{\partial y}\right)$$
$$-\frac{r_{in}+y_{mc}}{r_{in}}\rho\frac{f}{8}\overline{U}_d^2\sqrt{1+\frac{1}{s^2}}$$
$$+\frac{2}{r_{in}}\left(\rho\lambda H^2\sqrt{\frac{f}{8}}\frac{1}{2}\frac{\partial\overline{U}_d^2}{\partial y}\right) \qquad (3)$$

and $\overline{U}_d=\frac{1}{H}\int_0^H\overline{U}dz$; $\tau_b=\rho\left(\frac{f}{8}\right)\overline{U}_d^2$;

$$\left(\tau_{xy}\right)_d=\rho\left(\varepsilon_{xy}\right)_d\frac{\partial\overline{U}_d}{\partial y};\quad \left(\varepsilon_{xy}\right)_d=\lambda U_*H$$

$$U_*=\sqrt{\frac{f}{8}}\overline{U}_d$$

where $\overline{U}_d$ is the depth-averaged velocity, f is the Darcy-Weisbach friction factor, $(\varepsilon_{xy})_d$ is the depth-averaged eddy viscosity, U_* is the local shear velocity and λ is the dimensionless eddy viscosity.

When $r_{in}\to\infty$ (i.e. straight channel), equation (3) takes the same form as the Shiono and Knight (1991) equation when expressed in a Cartesian co-ordinate system:

$$\rho\frac{\partial H\left(\overline{UV}\right)_d}{\partial y}=\rho gHS_0+\frac{\partial}{\partial y}\left(\rho\lambda H^2\sqrt{\frac{f}{8}}\frac{1}{2}\frac{\partial\overline{U}_d^2}{\partial y}\right)$$
$$-\rho\frac{f}{8}\overline{U}_d^2\sqrt{1+\frac{1}{s^2}} \qquad (4)$$

Shiono and Knight (1991) defined the secondary flow term as Γ and found constant values of Γ in the main channel and on the floodplain using the experimental data from the FCF straight compound channel experiments. The secondary flow term Γ can be written as:

$$\Gamma=\rho\left[\frac{r_{in}+y_{mc}}{r_{in}}\frac{\partial H\left(\overline{UV}\right)_d}{\partial y}+\frac{2H\left(\overline{UV}\right)_d}{r_{in}}\right] \qquad (5)$$

Ervine *et al*. (2000) assumed that the secondary flow term $(\overline{U}\,\overline{V})_d$ could be expressed by the stream-wise depth-averaged velocity squared. Using this assumption regarding the secondary flow term:

$$\left(\overline{UV}\right)_d=K\overline{U}_d^2 \qquad (6)$$

where K is a function which depends on channel geometry and bed roughness values, equation (5) becomes:

$$\Gamma=\rho\left[\frac{r_{in}+y_{mc}}{r_{in}}\frac{\partial HK\overline{U}_d^2}{\partial y}+\frac{2HK\overline{U}_d^2}{r_{in}}\right] \qquad (7)$$

Equation (3) with either of equation (5) or (7) can be solved numerically. In this study, a finite difference discretisation is used. The discretised equations are solved with a Gaussian elimination method. When using equation (5), the value of Γ needs to be defined and when using equation (7), the value of K needs to be defined. In this paper, the value of Γ is used.

4 INPUT MODEL COEFFICIENTS

In order to solve equation (3) with equation (5) for the depth-averaged velocity $\overline{U}_d$, the model coefficients of local friction factor f, dimensionless eddy viscosity λ and secondary flow term Γ across the apex cross-section are required as input data. These model coefficients are estimated as follows.

4.1 *Friction factor*

The formulation for estimating the friction factor across the channel is given below using the roughness height, k_s, or skin friction of the channel surface. The channel surfaces in all the experiments

were composed of smooth cement mortar. The skin friction of the channel surface was measured in a calibration exercise using a straight wide trapezoidal channel and gave a Manning coefficient n of 0.01 (Ackers, 1991). The equivalent sand grain roughness height, k_s, is 0.3 mm, which was calculated from the relationship $n = k_s^{1/6}/(8.25\sqrt{g})$ (Ackers, 1991). Using $k_s = 0.3$ mm, the Colebrook-White equation (C-W equation) can be used to calculate a local friction factor f at any location in a cross-section with depth of water H:

$$\frac{1}{\sqrt{f}} = -2\log\left(\frac{3.02}{\mathrm{Re}\sqrt{f}} + \frac{k_s}{12.3H}\right) \tag{8}$$

where Re is the local Reynolds number defined as:

$$\mathrm{Re} = \frac{4\overline{U}_d H}{\nu} \tag{9}$$

Using $U_* = \sqrt{gHS_0}$ and $f = 8U_*^2/\overline{U}_d^2$, equation (8) can be re-arranged as:

$$f = \frac{1}{\left[-2\log\left(\dfrac{3.02\nu}{\sqrt{128gH^3S_0}} + \dfrac{k_s}{12.3H}\right)\right]^2} \tag{10}$$

This equation can be used to estimate the friction factor f. The validity of this equation was assessed by comparison with the experimental data. The experimentally calculated values of local friction factor, $f(=8\tau_b/(\rho\overline{U}_d^2))$, based on the measured bed shear stress and depth-averaged velocity, and the predicted values using equation (10) are shown in Figure 3 for cases A, B, C and D. The figure shows that the friction factor calculated with equation (10) agrees reasonably well with the experimental data for the cases A, B and C despite the complex flow structure in the main channel. However, the friction factor is under predicted for the large sinuosity case D for most of the cross-section. The discrepancies in the large sinuosity case are largely caused by secondary flow which generates a complex flow structure in the main channel and distorts the vertical profile of velocity from the 2D logarithmic profile assumed in the C-W equation.

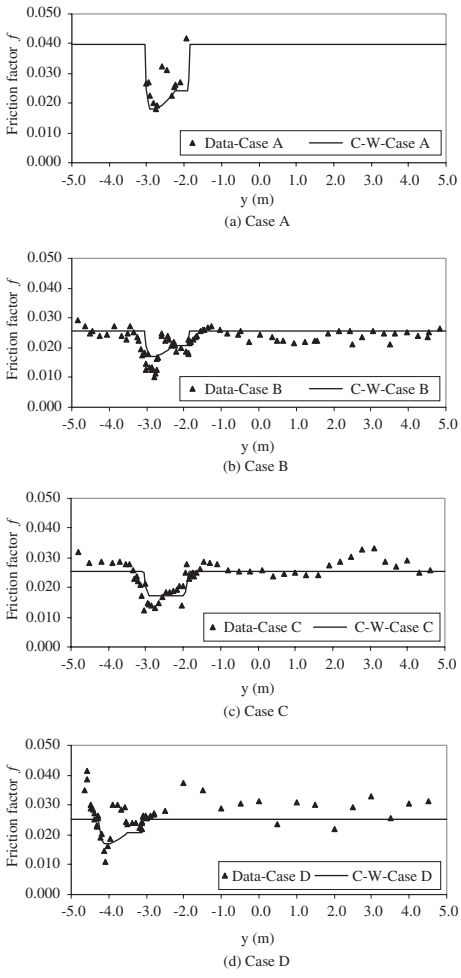


Figure 3. Friction factor f across the apex section.

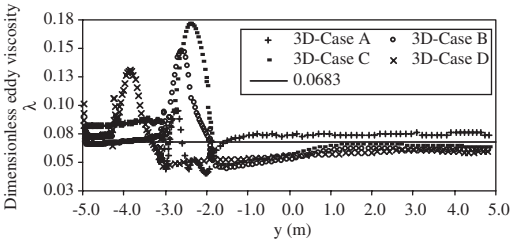


Figure 4. Dimensionless eddy viscosity λ across the apex section.

4.2 *Dimensionless eddy viscosity*

Figure 4 shows the dimensionless eddy viscosity values $\lambda(=(\varepsilon_{xy})_d/(\sqrt{\tau_b/\rho}H))$, obtained from the results of the 3D model study by Rameshwaran and Naden (2003) and the standard depth-averaged value for two-dimensional open channel flow (i.e. $\lambda = \kappa/6 = 0.0683$, where κ is the von Karman constant). In all cases the modelled dimensionless eddy viscosity values on the floodplain are close to the standard value but, in the main channel, the modelled values are much higher than the standard value. Although the dimensionless

eddy viscosity varies across the main channel, initial runs of the quasi 2D model using the non-dimensional eddy viscosity as modelled by the 3D model showed little effect on the solution. The 2D model study carried out by Rameshwaran and Shiono (2003) also showed only a slight effect of the eddy viscosity on the solution for the cases considered here, while Spooner and Shiono (2003) also demonstrated this using experimentally determined eddy viscosity. However, for flow in a straight compound channel, this eddy viscosity could be significant as demonstrated by Shiono and Knight (1991). For a meandering compound channel case, the model is insensitive to the value of dimensionless eddy viscosity used. Thus the standard value of 0.0683 was used for the whole cross-section.

4.3 *Advection term (Secondary flow)*

Spooner and Shiono (2003) demonstrated that the value of Γ for equation (5) varies across the main channel with a constant water depth (i.e. flat bed). In this study, the channel bed level varies, and the equation for Γ obtained by Spooner and Shiono (2003) may not be applicable to the cases considered here. An investigation of Γ was carried out using the measured data. With the measured bed shear stress and velocity distributions across the channel and with the assumed non-dimensional eddy viscosity of 0.0683, Γ was estimated using equation (3). The following geometrical and roughness non-dimensional parameters, while not unique, are sufficient to describe the secondary flow function Γ in non-dimensional form in the main channel at the apex cross-section:

$$\frac{\Gamma}{\rho g h_{mc} S_0} = C\left(\frac{k_{mc}}{k_{fp}}\right)^a r^b \left(\frac{MBW}{FW}\right)^c \left(\frac{y_{mc}}{y_{bf}}\right)^d \left(\frac{h_{mc}}{h_{\max}}\right)^e \quad (11)$$

where C is a constant, a to e are unknown exponents, k_{mc} and k_{fp} are the equivalent sand grain roughness heights in the main channel and on the floodplain respectively, r is the sinuosity, MBW is the meander belt width, FW is the floodplain width, y_{bf} is the main channel at bankfull level, h_{mc} is the local main channel flow depth and $h_{\max}$ is the maximum main channel flow depth.

The constant C and exponents a to e have to be determined empirically. The available limited data have been used to define equation (11). As $k_{mc}/k_{fp} = 1$ for all cases considered here, the following equation was obtained:

$$\frac{\Gamma}{\rho g h_{mc} S_0} = 0.6768 r^{0.7346}\left(\frac{MBW}{FW}\right)^{0.0205} \times \left(\frac{y_{mc}}{y_{bf}}\right)^{0.0542}\left(\frac{h_{mc}}{h_{\max}}\right)^{0.9955} \quad (12)$$

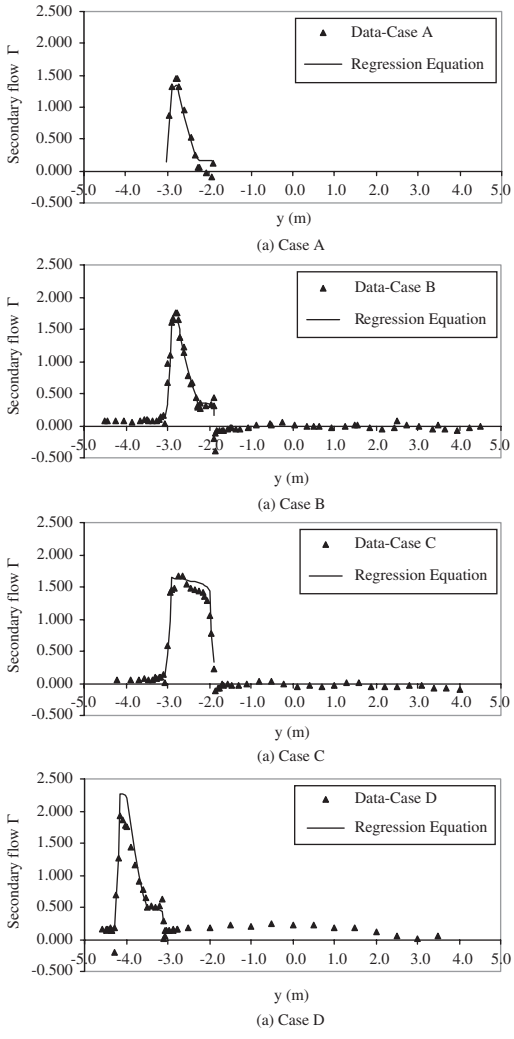


Figure 5. Secondary flow term Γ across the apex section.

The solid lines in the Figure 5 are the Γ distributions obtained from equation (12). Figure 5 also shows that the secondary flow distributions in the main channel are very similar in shape except for case C which has a different bed configuration from the others.

5 RESULTS AND DISCUSSIONS

The depth-averaged velocity and boundary shear stress were simulated at the apex cross-section using equations (3) and (5) with equation (10) for the friction factor, a constant non-dimensional eddy viscosity of 0.0683, equation (12) for the advection term in the main channel and appropriate constant values from

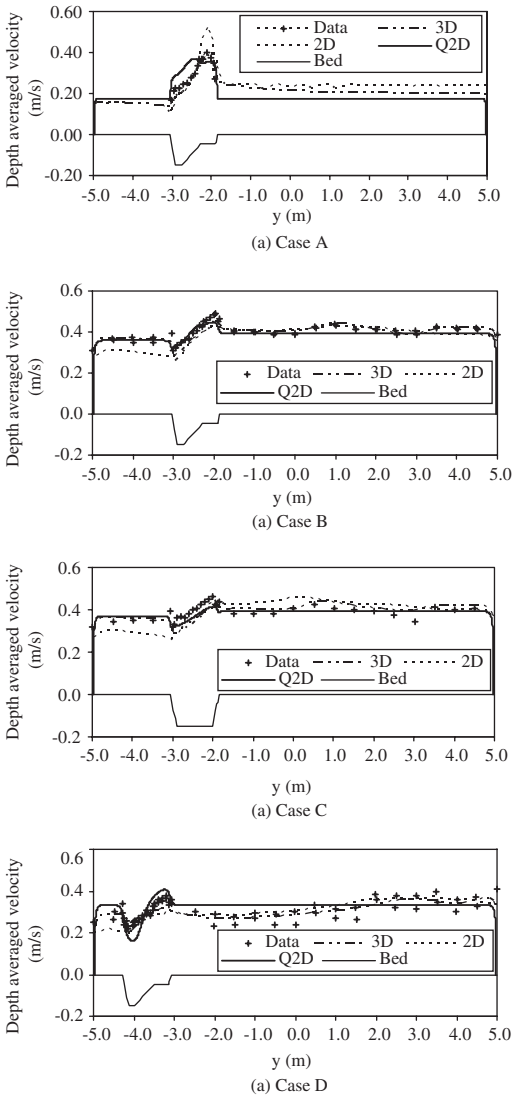


Figure 6. Depth-averaged velocity $\overline{U}_d$ across the apex section.

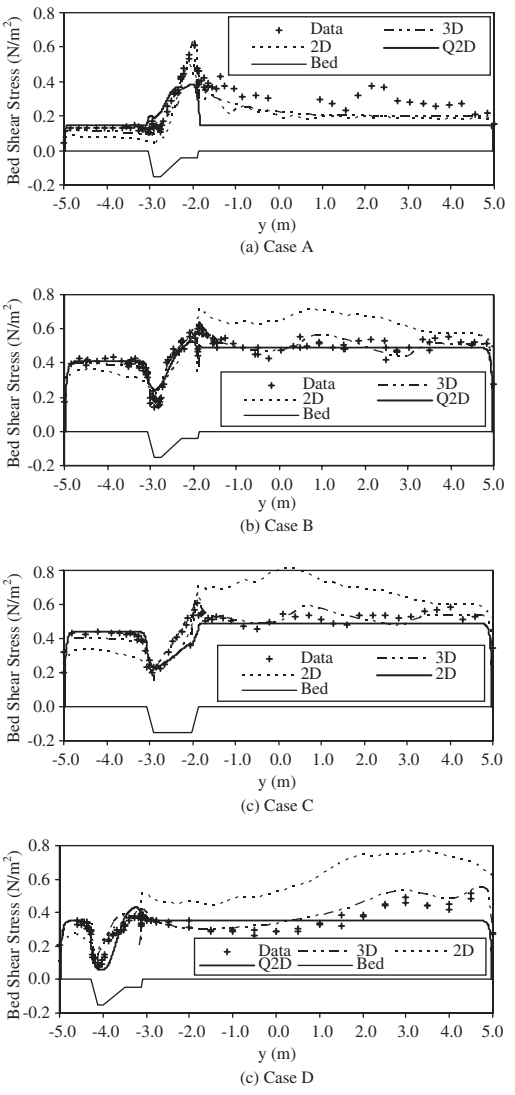


Figure 7. Bed shear stress τ_b across the apex section.

data for the advection term on the floodplain. The profiles of the measured and simulated depth-averaged velocity and bed shear stress at the apex section for cases A, B, C and D are shown in Figures 6 and 7 respectively. In the figures, 3D represents the 3D model results obtained using the 3D Phoenics code by Rameshwaran and Naden (2003), 2D represents the 2D model results obtained using the Telemac-2D code by Rameshwaran and Shiono (2002, 2003) and Q2D represents the present quasi 2D model. The depth-averaged velocity data on the floodplain for case A was not measured.

It can be seen from Figures 6 and 7 that the 3D model predicts the depth-averaged velocity and bed shear stress reasonably well with the exception of the shallower flow case A where the bed shear stress is under predicted.

For the 2D model results, Figures 6 and 7 show that the depth-averaged velocity and bed shear stress are predicted reasonably well in the main channel with the exception of the shallower flow case A where the depth-averaged velocity is over-predicted. On the floodplain, the depth-averaged velocity is under-predicted on the left floodplain and reasonably well predicted on the right floodplain. The bed shear stress

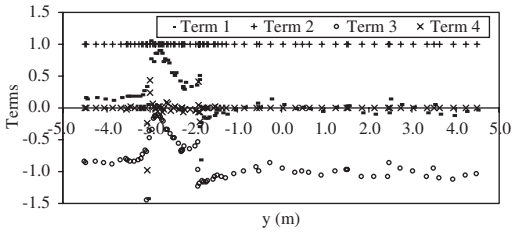


Figure 8. Normalised terms in equation (3) for the case B.

is under predicted on the floodplain for the shallower flow case A. For the deeper flows in cases B, C and D, it is under predicted on the left floodplain and over predicted on the right floodplain. By comparison, the Q2D results show a good prediction in the main channel and a reasonable prediction on the floodplain.

A sensitivity analysis was carried out by normalising equation (3) by $\rho g H S_0$. Figure 8 shows the separate terms in equation (3) for case B. Term 1 is the Γ term, Term 2 is the gravity term, Term 3 is the bed stress term and Term 4 represents the transverse shear stress terms. It was found that the magnitude of the transverse shear stress was negligibly small as found by Spooner and Shiono (2003). It can also be seen from Figure 8 that the bed stress term at the deepest point in the main channel is relatively small but the advection term Γ is significantly larger and almost the same magnitude as the gravity term. This indicates that the determination of Γ is very important.

The data available in this study were very limited in the range of geometrical and roughness parameters covered and equation (12) is essentially for demonstration purposes only. The main flow mechanism contributing to the advection term is the secondary flow. The basic principles behind the generation of secondary flow for overbank has been reported by Shiono and Muto (1998) and Shiono *et al*. (2001). The main factors involved are the angle of the floodplain flow to the main channel flow and the ratio of the main channel water depth to the floodplain water depth. These are represented in equation (12) by the sinuosity and water depth ratio respectively. The values of the exponents in equation (12) confirm that these are the dominant factors. However, the general validity equation (12) will be dependent on additional data. When a larger set of field and experimental data becomes available it will, therefore, be important to re-examine the equation for the advection term in the main channel and to develop a similar equation for the floodplain advection term. When using equation (7) to solve with equation (3), the value of K may be similarly expressed by dimensionless groups and determined by experimental and field data.

6 CONCLUSIONS

A quasi two-dimensional model for calculating depth-averaged velocity and bed shear stress for overbank flow in meandering channels has been developed. The model numerically solves the depth-averaged equation for the streamwise motion of flow in a curvilinear coordinate system. The results show that the model produces a reasonable prediction of the flow field when appropriate input coefficients are used. Overall this research shows that, for practical engineering purposes, reasonable depth-averaged velocity and bed shear stress distributions can be obtained very quickly using this approach.

REFERENCES

Ackers, P. (1991) Hydraulic design of straight compound channels. *Report* SR281, 2 volumes., HR Wallingford Ltd, 131 and 75 pp.

Chang, H.H. (1988) *Fluvial processes in river engineering.* John Wiley & Sons, New York, 456 pp.

Ervine, D.A., Babaeyan-Koopaei, K. and Sellin, R.H.J. (2000) Two-dimensional solution for straight and meandering overbank flow. *J. Hydraul. Engrg*., 126, 653–669.

Ervine, D.A., Willetts, B.B., Sellin, R.H.J. and Lorena, M. (1993) Factors affecting conveyance in meandering compound flows. *J. Hydraul. Engrg*., 119, 1383–1399.

Lorena, M. (1992) *Meandering compound flow*. PhD Thesis, University of Glasgow, UK, 577 pp.

Rameshwaran, P. and Shiono, K. (2002) Predictions of velocity and boundary shear stress in compound meandering channel. *River Flow 2002*, *International Conference on Fluvial Hydraulics*, September 4–6, 2002, Louvain-la-Neuve, Belgium, Edited by D. Bousmar & Y. Zech, Volume 1, 223–231.

Rameshwaran, P. and Shiono, K. (2003) Application of Telemac-2D to two-Stage meandering channel flows. *Proc. Instn. Civ. Engrs Wat., Marit. & Energy*, (In press).

Rameshwaran, P. and Naden, P.S. (Submitted) Modelling of Turbulent Free-Surface Flow in Two-Stage Meandering Channels. *J. Instn. Civ. Engrs Wat., Marit. & Energy*.

Shiono, K. and Muto, Y. (1998) Complex flow mechanisms in compound meandering channels with overbank flow. *J. Fluid Mech*., 376, 221–261.

Shiono, K. and Knight, D.W. (1991) Turbulent open-channel flows with variable depth across the channel. *J. Fluid Mech*., 222, 617–646.

Shiono, K., Rameshwaran, P., Chan, T., Spooner, J. and Chandler, C.H. (2001) Flow mechanisms for the reduction of sediment transport rates in meandering channels at an early stage of overbank flow. *Proceedings of the 2001 International Symposium on Environmental Hydraulics*, 5–8 December 2001, Tempe, Arizona, USA. Paper 46.

Spooner, J. and Shiono, K. (2003) Modelling of meandering channels for overbank flow, *Proc. Instn. Civ. Engrs Wat., Marit. & Energy*, 225–233.

This page intentionally left blank

River Flow 2004 – Greco, Carravetta & Della Morte (eds.)
© 2004 Taylor & Francis Group, London, ISBN 90 5809 658 0

Influence of a mobile bed on the boundary shear in a compound channel

S. Atabay
JBA Consulting Engineers & Scientists, Atherstone, UK

D.W. Knight
Department of Civil Engineering, The University of Birmingham, UK

G. Seckin
The University of Cukurova, Turkey & Honorary Research Fellow at the University of Birmingham, UK

ABSTRACT: Experimental results are presented concerning boundary shear stress and force distributions in a compound rectangular channel comprising one main river channel and one or two symmetrically disposed smooth floodplains. A comparison is made between the boundary shear stresses on the main channel bed for channels having either rigid or mobile beds of the same geometry. The influence of the main channel mobile bed on the momentum transfer between the main channel and the floodplains, and on the boundary shear stresses and forces acting on different elements of the compound channels are investigated. The mobile main channel bed causes the boundary shear stress values on the main channel bed to increase once overbank flow takes place for a given flow depth, and all values are always greater than those in an equivalent rectangular channel i.e. the isolated floodplain case. The rigid main channel bed case shows the opposite trend to the mobile bed case, in that the boundary shear stresses decrease once overbank flow occurs.

1 INTRODUCTION

The flow structure in an open channel is directly related to the distribution of boundary shear stress around the wetted perimeter of the channel. Many investigations have been made into boundary shear in open channel flow, and it has been established that many factors, such as the shape of the cross section, the variation in surface roughness in both longitudinal and lateral directions, the longitudinal variation in planform geometry and sediment concentration, all influence the boundary shear stress distribution (e.g. Christensen & Fredsoe, 1998; Kartha & Leutheusser, 1970; Khodashenas & Paquier, 1999; Knight, Yuen & Alhamid, 1994; Lundgren & Jonsson, 1964; Yang & Lim, 1997; Zheng & Jin, 1998).

Many investigators have especially studied boundary shear stress distributions in compound channels or ducts, since these types of channel are useful for flood conveyance and also feature in river restoration projects (e.g. Lai, 1987; Myers and Elsawy 1975; Myers 1978; Rhodes, 1991; Shiono & Knight 1991; Knight & Shiono 1996; Sear et al., 2000).

Boundary shear is particularly important for two reasons. Firstly, the resistance to flow is directly related to the global boundary shear stress, τ_o, and secondly, the mean bed shear stress τ_b (or bed shear velocity, $u*$ is generally required in many sediment transport equations. Thus being able to predict the boundary shear stress distribution is an essential element in morphological studies and in designing sustainable river channels (Abril & Knight, 2002 & 2004a&b; Atabay, 2001; Knight, 2001). In flood conditions, in which overbank flow occurs the channel becomes a 'compound one, and both the effects of a mobile channel bed on the boundary shear stress distributions, and on the momentum transfer between main channel and floodplain, have to be understood. This paper describes an experimental study in which measurements were made of the boundary shear stress in two compound channels, of the same geometry, but with either rigid or mobile beds in the main channel section.

2 EXPERIMENTAL PROCEDURE

The experiments were undertaken at the University of Birmingham in a non-tilting 22 m long flume with a compound working section length of 18 m. The flume was 1213 mm wide, 400 mm deep and configured into a two stage channel with a 398 mm wide rectangular mobile main channel and two 407.3 mm

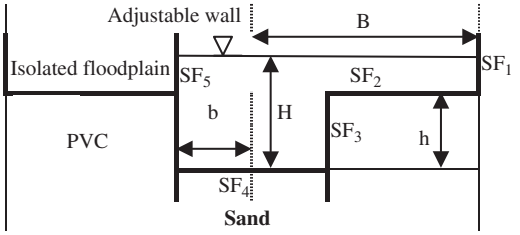


Figure 1. Cross section of 18 m flume.

wide smooth floodplains at an elevation h = 50 mm above the mobile bed, as shown schematically in Figure 1. The sand bed of the main channel was covered with a smooth PVC sheet when rigid bed experiments were to be undertaken, with the height of the floodplain, h, kept at the same value of 50 mm as in the mobile bed experiments.

At the end of the flume a series of three adjustable tailgates were located to produce uniform flow conditions in the 18 m test length. Water surface profiles were measured directly using pointer gauges. The tailgates were calibrated so that the mean water surface slope and the mean longitudinal bed slope could be set equal to the valley slope of the floodplains, fixed at 2.204×10^{-3} for any required test discharge.

Velocity measurements were made at 0.4 of the local depth using a Novar Nixon miniature propeller current meter with a propeller diameter of 13 mm. Local boundary shear stress measurements were made using a Preston tube (Preston, 1954) with an outer diameter of 4.77 mm. This indirect technique (Winter, 1977) was developed originally for smooth boundaries and is essentially based on a Pitot tube in direct contact with the boundary. The Preston tube thus consists of a static tube, closed to the flow that records pressure due to the static head, and a dynamic tube that is placed within the boundary layer facing into the flow that records the total pressure head. The pressure difference between the static and dynamic tubes, Δp, may be converted into boundary shear stress using Patel's calibration equations for smooth boundaries (Patel, 1965). In order to measure the low pressure differences, an inclined manometer with an angle of 13.7° was used. Further details of the apparatus and experimental procedures may be found in Atabay, 2001.

3 EXPERIMENTAL RESULTS

3.1 *Boundary shear stress distributions*

Experiments were carried out for the three test configurations: inbank flow with the side walls, overbank flow with an asymmetric cross-section and overbank flow with a symmetric cross-section. Inbank and overbank flow experiments were carried out in

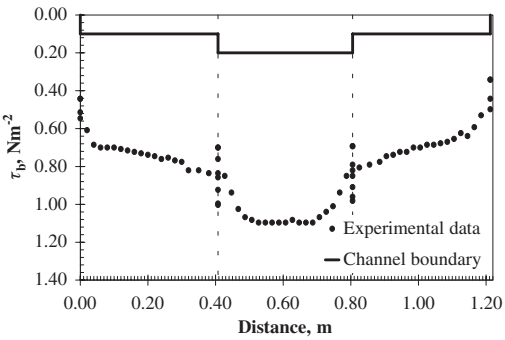


Figure 2. Typical boundary shear stress distribution in a rigid symmetric compound channel.

channels with both mobile and rigid main channel beds in order to make direct comparisons between them. This paper focuses on the effect of the mobile main channel beds on the boundary shear stress data and on the momentum transfer between various zones within the cross section. Results concerning stage-discharge relationships, velocity and boundary shear stress distributions, resistance, bed forms and sediment transport rates are presented elsewhere (Atabay, 2001; Atabay & Knight, 1999 & 2002; Tang & Knight, 2001).

A typical boundary shear stress distribution for the symmetric rigid compound channel is shown in Figure 2. Data on all other channel configurations and depths are given in Atabay (2001). Figure 2 shows a remarkably symmetric data set, with the floodplain values decreasing continuously towards the outer edges due to the relatively large depth and narrow floodplain width in this particular experiment. The main channel values are more uniform in the central region, with evidence of only weak secondary flow cells being present. Given the spatial resolution of the data it was possible, by integration of appropriate values, to obtain high quality mean boundary shear stress and force values for the individual wall elements 1–5, shown in Figure 1.

The average errors in the overall shear stress between the mean integrated experimental value and the theoretical value ($\tau_o = \rho gRS$) were within −2% and +1.0% for all the rigid compound channel tests. The measured data were all corrected by these small amounts in order to standardise all data to what was regarded as the 'correct' energy slope value. The velocity data were likewise compared with the mean value obtained from direct measurement by a Venturi meter, and any small differences used to adjust the individual measurements accordingly.

For the mobile compound channel tests, unlike the measured velocity data, the measured boundary shear stresses data were only obtained on smooth boundary

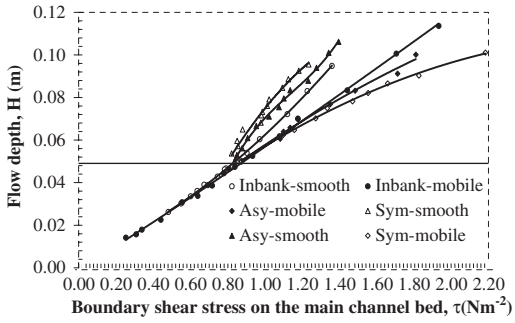


Figure 3. Comparison of mean boundary shear on main channel bed for rigid and mobile bed cases.

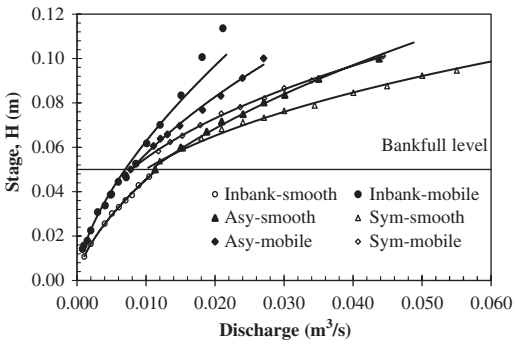


Figure 4. Comparison of stage-discharge curves.

surfaces, as time did not permit bed freezing to take place for all experiments. Bed freezing would have enabled boundary shear to be measured over many dune formations in order to determine a mean value for the main channel bed. Instead, the local boundary shear stress measurements were accepted as measured, without any correction, because of the absence of data on the bed of the main channel. Given the small errors cited earlier for the rigid bed cases, this was not thought likely to introduce any serious error.

3.2 *Boundary shear data*

The effects of the mobile main channel bed on the boundary shear stress can easily be explored by comparing all the main channel bed data together, as shown in Figure 3.

This Figure clearly shows that for a given flow depth the boundary shear stress on the mobile main channel bed is always greater than that on the rigid main channel bed. For a given flow depth the total shear force ($=\rho g A_{total} S_f$) in the mobile and rigid compound channels of same geometry will be the same. It therefore follows that if the shear force in the main channel is increased, due to the mobile bed, the shear force on the floodplain must consequently be reduced. These data need to be read in conjunction with the corresponding stage-discharge data, shown in Figure 4, and the resistance data shown in Figures 5 to 7.

As can be seen from Figure 3, for a given flow depth the boundary shear stress values on the rigid main channel bed decrease once overbank flow takes place, and are always less than those in an equivalent rectangular channel, i.e. the isolated floodplain case. It should also be noted that the boundary shear stress values for the rigid symmetric compound channel case are less than those for the rigid asymmetric compound channel case for a given flow depth. Furthermore, Figure 3 shows that the boundary shear stresses on the mobile main channel bed show the opposite trend to the data from the rigid bed case. With a mobile bed,

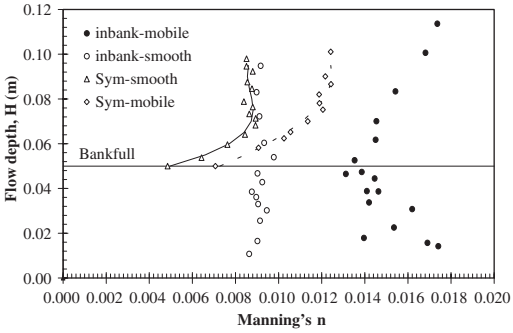


Figure 5. Variation of global Manning's n with depth, H, for symmetric compound channels.

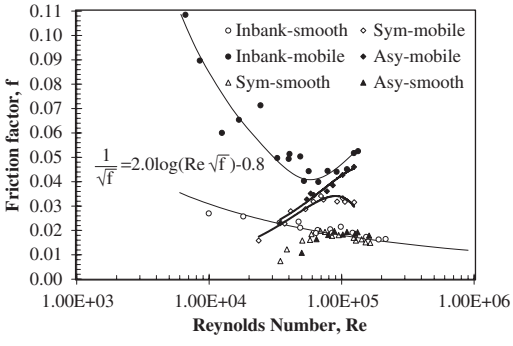


Figure 6. Variation of global Darcy-Weisbach f with Reynolds number, Re.

for a given flow depth, the boundary shear stress values on the main channel bed increase once overbank flow takes place, and are always greater than those in an equivalent rectangular channel, i.e. the isolated floodplain case.

3.3 *Resistance coefficients*

Figure 5 shows the variation of global Manning's n values for the two symmetric compound channels.

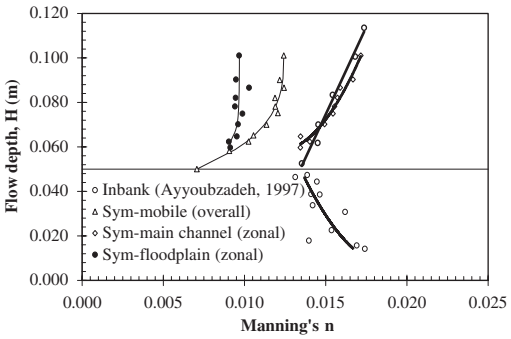


Figure 7. Variation of zonal Manning's n with depth, H, for main channel and floodplain in symmetric compound channels.

For inbank flows ($H < 0.05$ m) and a rigid-bed, Manning's n values are more or less constant at around 0.0091, consistent with values at these Reynolds numbers for the smooth PVC sheets. The corresponding inbank mobile-bed values are much higher, beginning at around 0.018, decreasing with depth to 0.013 at bankfull ($H = 0.05$ m). The higher roughness at very low depths is attributed to higher viscous shear close to the boundary. For high inbank flows ($H > 0.05$ m), n increases with flow depth, as the height of the bed forms increase.

At the bankfull stage ($H = 0.05$ m), Figure 5 shows the apparent reduction in global n values due to the sudden decrease in hydraulic radius. The estimated global Manning's n values at the bankfull level have also been added to Figure 5, assuming that for flow just above bankfull level, the floodplain perimeter is included in the calculation of the section perimeter, but the floodplain area is not included in the section area, thus influencing values of R, and hence n & f as follows:

$$n_{overbank}/n_{bankfull} = (R_{overbank}/R_{bankfull})^{2/3} \quad (1a)$$

$$f_{overbank}/f_{bankfull} = (R_{overbank}/R_{bankfull}) \quad (1b)$$

Values of hydraulic radius, R, were calculated as 0.040 m at bankfull level and 0.022 m (asymmetric) & 0.015 m (symmetric) for the level just above bankfull, giving apparent reductions in n of 33% and 48% due to the reductions in hydraulic radius of 45% and 62% respectively. Thus for the symmetric mobile-bed compound channel, Manning's n drops from a value of 0.0134 just below bankfull to a value of 0.0070 just above bankfull, a reduction of 48%. Likewise the friction factor, f, drops from 0.0410 to 0.0158, a reduction of 62%.

For overbank flows, global n values increase further, and Figure 5 indicates that at high depths n becomes more or less constant, at around 0.0091 (sym-smooth) and 0.0124 (sym-mobile). The first value indicates that at high depths the compound channel starts behaving again like a single channel, whereas the second value indicates that the smooth floodplains have become a greater proportion of the overall channel wetted perimeter, even compensating for the increased roughness in the main channel with a mobile bed.

Figure 6 shows the corresponding global fRe (Darcy-Weisbach-Reynolds number) relationships, along with the smooth law of Prandtl. For inbank flows in smooth rigid-bed channels, as the flow (or Re) increases, f decreases and follows Prandtl's smooth law until the bankfull stage. At this stage, both f and Re are discontinuous, with f values dropping suddenly when the flow is just out of bank. The f values thereafter start increasing again, eventually following the same trend as the smooth law of Prandtl. The mobile-bed cases show a somewhat similar trend, with f initially decreasing until the bankfull stage, thereafter increasing with Re. Similar relationships, obtained from large-scale experimental work, are shown in Shiono & Knight (1991), Knight et al. (1999), Myers et al. (1999) and Knight & Brown (2001).

Figure 7 shows the 'zonal' n values for the symmetric mobile-bed channel, with SCM 'global' values added from Figure 5 for comparison. The zonal values were calculated from integrated velocity measurements in each zone, using imaginary vertical division lines at the main channel and floodplain interface, excluded from the calculation of wetted perimeter for each zone. Inter-facial shear forces, due to lateral momentum transfer, were likewise not taken into account. The zonal main channel n values vary between 0.013–0.018, whereas the floodplain values are more or less constant at a value of around 0.0096. These zonal values are important, since they are frequently required in divided channel methods to calculate the correct discharge in each sub area (Knight et al., 1989).

Figure 7 shows that the main channel zonal n values, calculated by a divided channel method (DCM) are larger than the n values calculated by the single section method (SCM), whereas the floodplain values are smaller than the SCM values. Since these experimentally determined zonal n values include the effects of any momentum transfer arising from lateral shear and vortex behaviour at the main channel/floodplain interface, it follows that if the global n value had been used in any DCM instead, it would lead to a significant over-estimate of discharge in the main channel. Furthermore, since the main channel carries the bulk of the flow at low floodplain depths, this indicates why the DCM overestimates the conveyance of compound channels.

Similar relationships to those in Figure 3 have also been found in the experimental results from the UK Flood Channel Facility (FCF), a large

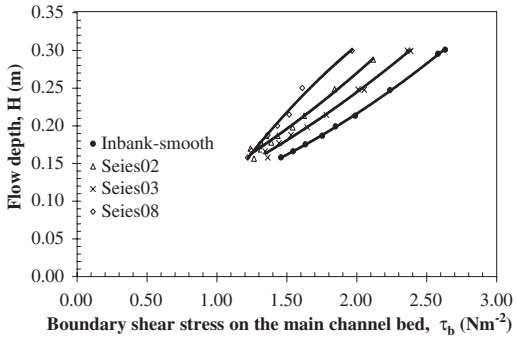


Figure 8. Mean boundary shear on main channel bed for rigid bed channels (FCF data).

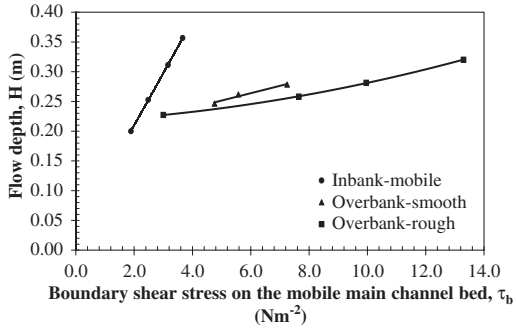


Figure 9. Mean boundary shear on main channel bed for mobile bed channels (FCF data).

scale-experimental compound channel. Figures 8 & 9 show some boundary shear stress data for two compound channels of slightly different geometry, having either rigid or mobile main channel beds, taken from Phase A & Phase C studies of the FCF programme respectively. See Knight & Sellin (1987), Knight & Shiono (1990), Shiono & Knight (1991), Knight (1992), Knight & Brown (2001) and Brown (1997) for further details. The differences in boundary shear stress on the main channel bed are much greater for the FCF than for the Birmingham University flume, due to the much larger scale and bedform dimensions in the FCF. Figures 8 & 9 clearly emphasize the effect of the mobile main channel bed on the shear stresses. Once again it is noted that the boundary shear stress values for the three rigid symmetric compound channel cases in Figure 8 are all less than the corresponding inbank results for the same depth, whereas Figure 9 shows that for the mobile bed cases they are greater.

The measured mean shear stress on each rigid boundary element was multiplied by the appropriate wetted perimeter to give the mean shear force,

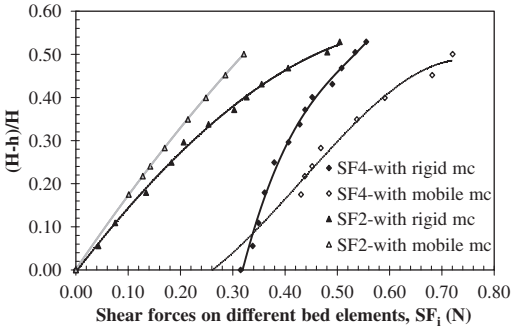


Figure 10. Shear forces acting on elements 2 & 4 for an asymmetric compound channel with a rigid or a mobile main channel bed.

SF, acting on that element. In order to calculate this shear force, the wetted perimeter of the compound channel was divided into various boundary elements as shown in Figure 1. The mean shear force on the main channel bed for the asymmetric and symmetric mobile compound channel was then calculated from the appropriate force balance equation, Equations (2a) & (2b) respectively:

$$SF_4 = \rho g A_{total} S_w - (SF_1 + SF_2 + SF_3 + SF_5) \quad (2a)$$

$$SF_4 = \rho g A_{total} S_w - 2*(SF_1 + SF_2 + SF_3) \quad (2b)$$

3.4 *Apparent shear forces*

Due to the geometry of the cross section, the majority of the total shear force was carried by the main channel bed and floodplain bed elements. The shear forces carried by these boundary elements are shown plotted versus the relative depth in Figure 10 for the asymmetric compound channel case. This Figure shows that the shear forces carried by these elements increase as the relative depth increases. The same data are expressed as percentages of the total shear of the channel in Figure 11. As the flow depth increases, the percentage shear force on the main channel bed, SF_4, decreases, while that on the floodplain bed, SF_2, increases. Figure 11 also shows that for the rigid asymmetric compound channel case the percentage shear forces on the main channel and floodplain bed became equal when the relative depth is around 0.58. This Figure also helps to explain the effect of the mobile main channel bed on the boundary shear forces. Similar relationships between shear forces and relative depth were also found for the symmetric channel cases (see Atabay, 2001).

The apparent shear forces, (ASF), acting on the vertical, and horizontal interfaces were calculated for all channel configurations since these forces are of interest when using any divided channel method for

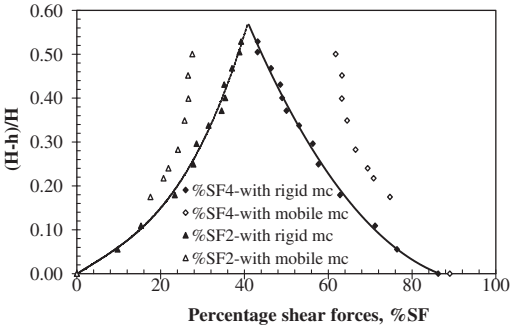


Figure 11. Percentage of total shear force acting on elements 2 & 4 for an asymmetric compound channel with a rigid or a mobile main channel bed.

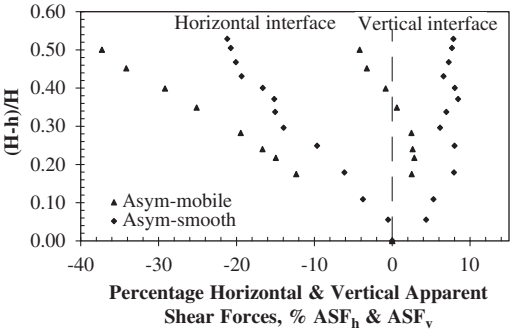


Figure 12. Apparent shear forces on horizontal and vertical interfaces for asymmetric compound channels with smooth floodplains.

conveyance estimation. For example, the apparent shear force on any vertical interface, ASF_v, in a depth-averaged model may be obtained by considering the balance of forces on different elements of the cross-section. Typically a river channel cross-section may be divided into any number of vertical slices in the transverse direction, y, and the flow assumed to be in the streamwise direction, x. The ASF acting on any vertical interface within the cross-section is then defined as the difference between the weight force of those elements resolved in the streamwise direction, up to that particular lateral position, y, minus the integrated boundary shear forces around the wetted perimeter up to the same lateral position. The ASF then accounts for any momentum transfer effects across that vertical slice, arising from turbulent shear, secondary flows and planform vorticity. See Shiono and Knight (1991). A similar procedure applies to where the channel cross-section is divided into horizontal slices.

The vertical interface was taken to be at the main channel/floodplain interface, and the horizontal interface was taken to be at the bankfull level. In order to aid comparison, these forces were normalised by expressing them as a percentage of the total channel shear force, $\%ASF_v$ and $\%ASF_h$ respectively. The data for the asymmetric compound channel are shown in Figure 12. It should be noted that the similar relationships were obtained for the symmetric compound channels.

Figure 12 shows that the percentage apparent shear force on the vertical interface for the rigid compound channel is always positive and greater than that for the mobile compound channel for a given relative depth. This is explained by the fact that in the rigid compound channels at low floodplain flow depths the lateral momentum transfer is greater, due to dissimilar velocities in sub- areas, with the slower floodplain flow retarding the faster main channel flow. In the mobile compound channels, however, the velocities in these sub-areas become more similar, because the mobile main channel bed reduces the flow velocity in the main channel sub-area, due to bedforms and the increased resistance.

At high relative depths (around $(H\text{-}h)/H > 0.35$), the main channel flow actually retards the floodplain flow, indicated by the negative $\%ASF_v$ for these mobile compound channels with smooth floodplains.

In Figure 12, the negative $\%ASF_h$ values on the horizontal interface (at bankfull level) between lower and upper main channel sub-areas, indicate that the upper region of flow is accelerating the flow in the lower main channel. The $\%ASF_h$ for the channel having a mobile main channel bed is always greater than that for the channel having a rigid and smooth main channel bed. This indicates again that the effect of a mobile bed on the flow is obviously more than the effect of a rigid smooth bed, as might be expected from the increase in roughness due to bedforms.

Simple empirical equations between the percentage shear forces carried by each boundary element and the relative depth were obtained for all channel configurations by Atabay (2001). These equations will be useful for further analysis of the resistance coefficients and the sediment transport rate for these particular symmetric and asymmetric compound channels.

4 DISCUSSION OF RESULTS

In order to understand the effect of the mobile bed on the boundary shear in a compound channel, the shear forces carried by the main channel bed and the floodplain have been compared for different channel configurations having rigid and mobile main channel beds. Since the width of the main channel bed was fixed for all channel configurations, the shear forces correspond directly to the main channel bed shear stress, τ_b.

The data collected from the 18 m Birmingham University flume, shown in Figure 3 for both asymmetric and symmetric compound channels, together with the data collected from the large-scale FCF, shown in Figures 8 & 9 for a symmetric compound channel, all point to the same conclusion. It appears that the boundary shear stress values for compound channels with a rigid main channel bed show a decrease once overbank flow takes place, and that the values are always less than those in an equivalent rectangular channel at the same depth. For compound channels with a mobile bed and the same geometry, the opposite appears to be true, in that the boundary shear stresses on the main channel bed increase once overbank flow takes place.

In compound channels with a mobile main channel bed the boundary shear stresses increase significantly with flow depth, in contrast to the rigid bed case. This is due to the greater friction factor for a mobile bed compared with that for a rigid smooth bed. The behaviour of global resistance coefficients for compound channels with either rigid or mobile beds is shown in Figures 5 & 6 to be more complex than for simple channels. Care thus needs to be exercised in assigning global values in any single section method (SCM), especially when the flow changes from being inbank to one in which the flow is overbank with a shallow floodplain depth. The pattern of the global $f\,Re$ relationship shown in Figure 6 is similar to that found in natural rivers, as indicated by Knight et al. (1989).

The global and zonal resistance coefficients shown in Figure 7 indicate the importance of taking into account momentum transfer at the main channel/floodplain interface due to lateral shear and vorticity. Methods for estimating conveyance capacity that ignore these effects, based on simple DCM approaches, are therefore bound to be unreliable. However, some improvements to the divided channel approach have been made, notably by Ackers (1993), who proposed the 'coherence' method (COHM), and by Lambert & Myers (1998), who proposed the weighted divided channel method (WDCM). Both methods are reviewed in detail elsewhere by Atabay & Knight (2004). The COHM and WDCM are shown to give reasonable predictions of conveyance and division of flow between the main channel and the floodplains for homogeneously roughened compound channels, but the WDCM cannot deal with boundary shear and the COHM gives relatively poor predictions of mean boundary shear stress in different sub-areas. Since simple DCM approaches are not capable of predicting boundary shear stress accurately, recourse is usually made to methods based on the depth-averaged form of the Reynolds Averaged Navier-Stokes (RANS) equations.

In such methods, the bed friction, lateral shear and vorticity effects are modelled separately, and good predictions may be obtained, not only for conveyance and division of flow, but also for the lateral distribution of boundary shear. See Abril & Knight (2004a), Knight & Abril (1996), Knight & Shiono (1996) and Shiono & Knight (1991) for application of the Shiono & Knight method (SKM) to various rivers and laboratory flumes. A numerical evaluation of the effects of secondary flow on lateral momentum transfer in overbank flow is given by Tominaga & Knight (2004).

The apparent shear force data shown in Figure 12 indicate that ASF_v for a mobile bed compound channel is different from the rigid bed case, in that it may become positive at high relative depths. Thus in extreme flood events with high depths, the main river channel resistance may become so large that the direction of the momentum transfer is reversed from the more common one in which the floodplain flows retard the main channel flow. However, this should not be taken as a general rule, since the bed regime may change further at even larger discharges, possibly into upper regime flow type, leading to negative values again at even larger depths. Thus the lateral momentum transfer depends significantly on bed shear in the main channel and its use in predicting lower or upper regime bed forms and the corresponding resistance.

It is hoped that these unusual data from some experiments with a mobile bed compound channel will be of value to modellers attempting to simulate sediment motion in compound channels with overbank flow.

5 CONCLUSIONS

The following conclusions may be drawn from this study:

1. Main channel bed shear stresses for compound channels with a rigid main channel bed show a decrease once overbank flow takes place, and are always less than those in an equivalent rectangular channel at the same depth.
2. Main channel bed shear stresses for compound channels with a mobile main channel bed show the opposite trend to the rigid bed case.
3. In compound channels that have a mobile main channel bed, the boundary shear stress increases more with flow depth compared to the rigid bed case. This is due to the greater resistance of the mobile bed than the smooth rigid main channel bed.
4. Particular care needs to be exercised in assigning global resistance values when estimating conveyance capacity by the single section method, especially when the flow changes from being inbank to one in which the flow is just overbank.
5. Zonal resistance coefficients indicate the importance of taking into account momentum transfer at the main channel/floodplain interface when estimating conveyance capacity by any of the divided channel methods.

6. Similar relationships were obtained from the experimental data using both large and small facilities, the FCF and the Birmingham University flumes.
7. It is recommended that divided channel methods be replaced by methods based on the depth-averaged form of the Reynolds Averaged Navier-Stokes (RANS) equations when accurate estimates are required of boundary shear in compound channels.

REFERENCES

Abril, J.B. and Knight, D.W., 2002. Sediment transport simulation of the Paute river using a depth-averaged flow model. *River Flow 2002, Proc. Int. Conf. on Fluvial Hydraulics*, Louvain-la-Neuve, Belgium, Sept., Vol. 2, 895–901, Balkema.

Abril, J.B. and Knight, D.W., 2004a. Stage-discharge prediction for rivers in flood applying a depth-averaged model. *Journal of Hydraulic Research, IAHR*, 41, No. 6, 1–14 (in press).

Abril, J.B. and Knight, D.W., 2004b. Stabilising the Paute river in Ecuador. *Civil Engineering*, 157, November, *Paper 12704*, 171–177, Instn. of Civil Engineers, London.

Ackers, P., 1993. Flow formulae for straight two-stage channels. *Journal of Hydraulic Research*, Vol. 31, No. 4, 509–531.

Atabay, S., 2001. Stage-discharge, resistance, and sediment transport relationships for flow in straight compound channels. *PhD Thesis*, The University of Birmingham, UK.

Atabay, S. and Knight, D.W., 1999. Stage discharge and resistance relationships for laboratory alluvial channels with overbank flow. In River Sedimentation [Eds A.W. Jayawardena, J.H.W. Lee & Z.Y Wang], *Proc. Seventh International Symposium on River Sedimentation, Hong Kong, December 1998*, 223–229.

Atabay, S.A. and Knight, D.W., 2002. The influence of floodplain width on the stage-discharge relationship for compound channels. *River Flow 2002, Proc. Int. Conf. on Fluvial Hydraulics,* Louvain-la-Neuve, Belgium, Sept., Vol. 1, 197–204, Balkema.

Atabay, S.A. and Knight, D.W., 2004. 1-D modelling of conveyance, boundary shear and sediment transport in overbank flow. *Journal of Hydraulic Research, IAHR*, (submitted for publication).

Brown, F.A., 1997. Sediment transport in river channels at high stage. *PhD Thesis*, The University of Birmingham, UK.

Christensen, B. and Fredsoe, J., 1998. Bed shear stress distribution in straight channels with arbitrary cross section. *Progress Report No. 77*, Department of Hydrodynamics and Water Resources, Technical University of Denmark, Lynby.

Kartha, V.C. and Leutheusser, H.J., 1970. Distribution of tractive force in open channels. *Journal of Hydraulic Engineering*, ASCE, Vol. 96, No. 7, 1469–1483.

Khodashenas, S.R. and Paquier, A., 1999. A geometrical method for computing the distribution of boundary shear stress across irregular straight open channels. *Journal of Hydraulic Research, IAHR*, 37, No. 3, 381–388.

Knight, D.W., 1992. SERC Flood Channel Facility experimental data - Phase A, Vols. 1–15, *School of Civil Engineering*, The University of Birmingham, May, (available from HR Wallingford, Oxon, OX10 8BA, UK).

Knight, D.W., 2001. Flow and sediment transport in two-stage channels. *Proc. 2nd IAHR Symposium on River, Coastal and Estuarine Morphodynamics*, September, Obihiro, Japan, 1–20.

Knight, D.W. and Abril, B., 1996., Refined calibration of a depth-averaged model for turbulent flow in a compound channel, *Proc. Instn. of Civil Engineers, Water, Maritime and Energy Division*, London, Vol.118, Issue 3, Sept., Paper No. 11017, 151–159.

Knight, D.W. and Brown, F.A., 2001. Resistance studies of overbank flow in rivers with sediment using the Flood Channel Facility. *Journal of Hydraulic Research*, IAHR, Vol. 39, No. 3, 283–301.

Knight, D.W. and Sellin, R.H.J., 1987. The SERC Flood Channel Facility, *Journal of the Institution of Water and Environmental Management*, Vol. 1, No. 2, October, 198–204.

Knight, D.W. and Shiono, K., 1990. Turbulence measurements in a shear layer region of a compound channel, *Journal of Hydraulic Research*, IAHR, Vol. 28, No. 2, pp 175–196, (Discussion in IAHR Journal, 1991, Vol. 29, No. 2, 259–276.

Knight, D.W. and Shiono, K., 1996. River channel and floodplain hydraulics, in *Floodplain Processes*, (Eds Anderson, Walling & Bates), Chapter 5, J Wiley, 139–181.

Knight, D.W., Shiono, K. and Pirt, J., 1989. Prediction of depth mean velocity and discharge in natural rivers with overbank flow. *Proc. Int. Conf. on Hydraulic and Environmental Modelling of Coastal, Estuarine and River Waters*, (Ed. R.A. Falconer, P. Goodwin, R.G.S. Matthew), Gower Technical, University of Bradford, September, Paper 38, 419–428.

Knight, D.W., Yuen, K.W.H. and Alhamid, A.A.I., 1994. Boundary shear stress distributions in open channel flow. in *Physical Mechanisms of Mixing and Transport in the Environment,* (Eds K. Beven, P. Chatwin & J. Millbank), J. Wiley, Chapter 4, 51–87.

Lai, 1987. Flow resistance, discharge capacity and momentum transfer in smooth compound closed ducts, *PhD thesis*, The University of Birmingham.

Lambert, M.F. and Myers, W.R.C., 1998. Estimating the discharge capacity in straight compound channels. *Proc. Instn Civil Engineers, Maritime & Energy*, Vol. 130, Paper 11530, June, 84–94.

Myers, W.R.C., Knight, D.W., Lyness, J.F., Cassells, J. & Brown, F.A., 1999. Resistance coefficients for inbank and overbank flows. *Proc. Instn. of Civil Engineers, Water, Maritime and Energy Division*, London, Vol. 138, Issue 2, June, 105–115.

Lundgren, H. and Jonsson, I.G., 1964. Shear and velocity distribution in shallow channels. *Journal of Hydraulics Division*, ASCE, Vol. 90, No. 1, 1–21.

Myers, W.R.C. and Elsawy, E.M., 1975. Boundary shear in channel with floodplain. *Journal of Hyd. Division*, Proc. ASCE., vol. 101, No. HY7, 933–946, July.

Myers, W.R.C., 1978. Momentum transfer in a compound channel. *Journal of Hydraulic Research*, IAHR, Vol. 16, No. 2, 139–150.

Patel, V.C., 1965. Calibration of the Preston tube and limitations on its use in pressure gradients. *Journal of Fluid Mechanics*, Vol. 23, Part 1, 185–208.

Preston, J.H., 1954. The determination of turbulent skin friction by means of Pitot tubes. *Journal Roy. Aero. Soc*. Vol. 58, 109–121.

Rhodes, 1991. An experimental investigation of the mean flow structure in wide ducts of simple rectangular and compound trapezoidal cross section, examining in particular zones of high lateral shear, *PhD thesis*, The University of Birmingham.

Sear, D., Wilcock, D., Robinson, M. and Fisher, K., 2000. River channel modification in the UK. In *The Hydrology of the UK* [Ed. M.Acreman], Chapter 3, Routledge, 55–81.

Shiono, K. and Knight, D.W., 1990. Mathematical models of flow in two or multi stage straight channels, *Proc. Int. Conf. on River Flood Hydraulics*, (Ed. W.R. White), Wallingford, September, J. Wiley & Sons, Paper G1, 229–238.

Shiono, K. and Knight, D.W., 1991. Turbulent open channel flows with variable depth across the channel, *Journal of Fluid Mechanics*, Vol. 222, 617–646 (and Vol. 231, October, p 693).

Tang, X. and Knight, D.W., 2001. Experimental study of stage-discharge relationships and sediment transport rates in a compound channel. *Proc. 29th IAHR Congress*, September, Beijing, China, 69–76.

Tominaga, A. and Knight, D.W., 2004. Numerical evaluation of secondary flow effects on lateral momentum transfer in overbank flows. *River Flow 2004, Proc. Int. Conf. on Fluvial Hydraulics*, Naples, Italy, June, (in press).

Winter, K.G., 1977. An outline of the techniques available for the measuring of skin friction in turbulent boundary layers. *Proc. of the Aerospace Science*, Vol. 18, 1–57.

Yang, S.Q. and Lim, S.Y., 1997. Mechanism of energy transportation and turbulent flow in a 3D channel. *Journal of Hydraulic Engineering*, ASCE, Vol. 123, No. 8, 684–692.

Zheng, Y. and Jin, Y.C., 1998. Boundary shear in rectangular ducts and channels. *Journal of Hydraulic Engineering*, ASCE, Vol. 124, No. 1, 86–89.

This page intentionally left blank

River Flow 2004 – Greco, Carravetta & Della Morte (eds.)
© 2004 Taylor & Francis Group, London, ISBN 90 5809 658 0

Interaction processes in a straight compound channel with rigid and flexible emergent floodplain vegetation

I. Schnauder
Institute for Water Resources Management, Hydraulic and Rural Engineering, Universität Karlsruhe (TH), Germany

ABSTRACT: This paper examines the interaction processes between main channel and vegetated floodplain flow zones in an experimental study at the Theodor-Rehbock Hydraulic Laboratory in Karlsruhe. The physical model was composed of a compound channel section in a 20 m long and 1 m wide flume. The floodplain was roughened using both rigid and flexible idealised floodplain vegetation in the form of cylinders. They were arranged at two different densities using a regular staggered configuration. Uniform flow experiments were conducted for different discharges and specifically for high relative flow depths to model extreme flood events. Instantaneous velocities in the longitudinal and cross-streamwise directions were measured using a two component LDV with a high spatial resolution measurement grid at different cross-sections in the longitudinal direction.

1 INTRODUCTION

Compound channels are characterized by a change of roughness and water depth across the channel section resulting in strong lateral gradients of the mean flow velocity. The low velocity floodplain flows are dominated by the large roughness generated by the vegetation. Between these two sections a region with strong momentum exchange and production of coherent turbulent structures occurs, where the velocities are decelerated in the main channel and accelerated on the floodplain. This region is known from literature as interaction zone or apparent shear layer. Many researchers have investigated the interaction phenomena see for example Naot et al. (1996). First, Zheleznyakov (1965) and Sellin (1964) visualized horizontal vortices with vertical axes along the shear layer as the basic mechanism of transfer of momentum. The dimensionless relative water depth h/H, where h is the water depth on the floodplain and H in the main channel, was found as dictating the degree of the momentum exchange. Identical structures were found in compound channels with cylindrical floodplain vegetation in the experiments of Pasche & Rouve (1985). Arnold et al. (1989) continued with the latter researchers and suggested that the interaction mechanism induces helical secondary currents with longitudinal axis. Experiments of Tominaga et al. (1989), Onitsuka et al. (1999) showed that for a rectangular compound cross section without vegetation on the floodplains, that for higher water depths ($h/H > 0.625$) the influence of the horizontal vortices decreases and secondary currents and a strong 3D-vorticity dominate the exchange of momentum.

The important role of floodplain vegetation for river restoration and the increased occurrence of extreme flood events demand a better understanding of the associated hydrodynamic processes. The recent study examines the flow processes in a laboratory model of compound channel flow with vegetated floodplains giving special regard to high relative depths and comparing rigid and flexible vegetation.

2 EXPERIMENTS

2.1 *Experimental equipment: flume and LDV*

A 1 : 100 scale physical model of a half-trapezoidal compound channel was constructed at the laboratory facility. The rectangular flume employed for the experiments was 1.0 m wide, 20.0 m long and set at a fixed bed slope of 0.001. The main channel and floodplain were $B = 52$ cm and $b = 48$ cm wide, the floodplain elevation was $\Delta z = 2.3$ cm. The main channel bank slope was set at 1 : 1. The main channel as well as the floodplain were roughened homogenously with PVC granules of 3 mm diameter ($k_S = 3.6$ mm). The LDV (LASER Doppler Velocimeter) measurements were carried out with an Aerometrics 300 mW Argon-Ion fibre-optical LASER system operating in backward scattering mode. The system in its downward looking

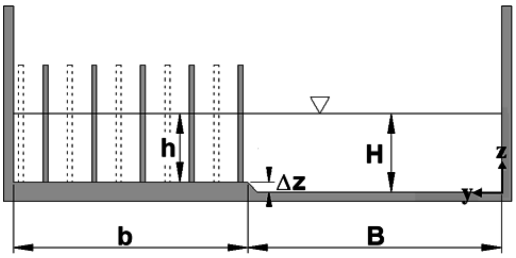


Figure 1. Schematic view of the flume cross section.

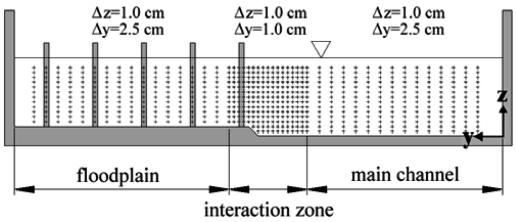


Figure 2. Schematic view of the measurement grid for the different sections.

mode measured the longitudinal and cross-streamwise velocity component. Feeding material (TiO2) was added to the flow to obtain valid sample rates within time steps of 60 seconds at each location. The probe head was mounted on a computer controlled rail carriage equipped with a two-axis traversing system to allow precise control in three directions. The LDV measurements were carried out in a way that separated the cross sections into three regions: main channel, interaction zone and floodplain.

The grid of measurement points was densest in the interaction zone ($0.4\,\text{m} < y < 0.56\,\text{m}$) with lateral and vertical distances of $\Delta y = \Delta z = 1$ cm increments (see Fig. 2). In the main channel ($0\,\text{m} < y < 0.4\,\text{m}$) and floodplain ($0.56\,\text{m} < y < 1.0\,\text{m}$) a higher increment of $\Delta y = 2.5$ cm and $\Delta z = 1$ cm was chosen. Furthermore, several cross sections in longitudinal direction (2 within the main channel and the floodplain, 4–6 in the interaction zone) were measured to analyze the longitudinal change in the velocities at different longitudinal positions relative to the cylindrical floodplain vegetation and hence attempt to examine the heterogeneous flow structure.

2.2 *Floodplain vegetation and density*

Two different types of cylinders were used in two different densities. The first setup (s1) used rigid PVC cylinders of $d_S = 1.0$ cm diameter in a staggered pattern, in which each cylinder covered a projected area of 100 cm^2 ($\Delta x = 10$ cm, $\Delta y = 10$ cm). For the second setup (s2), the rigid cylinders were replaced by flexible ones fabricated of foam rubber with sealed, air-filled pores that kept the cylinders emergent for all tests and allowed streamwise bending and lateral waving motions. The same rigid and flexible cylinders were used in setup (s3) and (s4) but for a higher density in which each element covered a projected area of 50 cm^2 ($\Delta x = 5$ cm, $\Delta y = 10$ cm).

3 EXPERIMENTAL RESULTS AND ANALYSIS

3.1 *Longitudinally averaged mean velocities*

Figure 3 shows contour plots of longitudinally and time averaged longitudinal velocities. The plots refer to a discharge of 20 l/s to point out the influence of vegetation density and flexibility for a similar relative depth ratio ($h/H = 0.83 \div 0.85$).

Generally, the cross section can be subdivided into three different zones according to the predominant hydromechanical process.

First, in the main channel about $y = -0.05$ cm away from the right channel wall is a zone of free open channel flow ($-0.2 < y < -0.05$), where the vertical velocity profiles can be well described by the logarithmic velocity law.

Secondly, the floodplain regime between the left channel wall and the cylinder at the edge to the main channel ($-1 < y < -0.53$), where the wakes generated by the cylinders dominate the flow by their additional production of drag forces and turbulent energy. In this zone the vertical velocity profiles are almost constant over the water depth, but vary in magnitude depending on the relative lateral and longitudinal distance from the cylinders. Only the first row of cylinders ($y = -0.53$ m) contributes to the exchange of momentum and deceleration of main channel velocities. From this point on the vertical floodplain profiles remain periodic in magnitude in the lateral direction. Due to their waving motions and bending, the floodplain contours in Figure 3 are less sharp for the flexible setups (s2 and s4) than for rigid (s1 and s3).

Thirdly, the interaction zone which is characterized by a strong lateral exchange of momentum between the main channel and the floodplain ($-0.53 < y < -0.2$) and the presence of coherent vortices and secondary currents. The strong impact of the momentum exchange on the longitudinal velocities is clearly visible (see Fig. 3). Independent from the floodplain vegetation, all graphs show a near-bed intrusion of higher velocity components from the main channel towards the floodplain and vice versa in the upper regions of the flow. The strongest deformations occurred for the setups with flexible cylinders (s2 and s4) and increased with increasing relative depth ratios. Furthermore, the velocity maximum in the main channel was higher and laterally shifted towards the

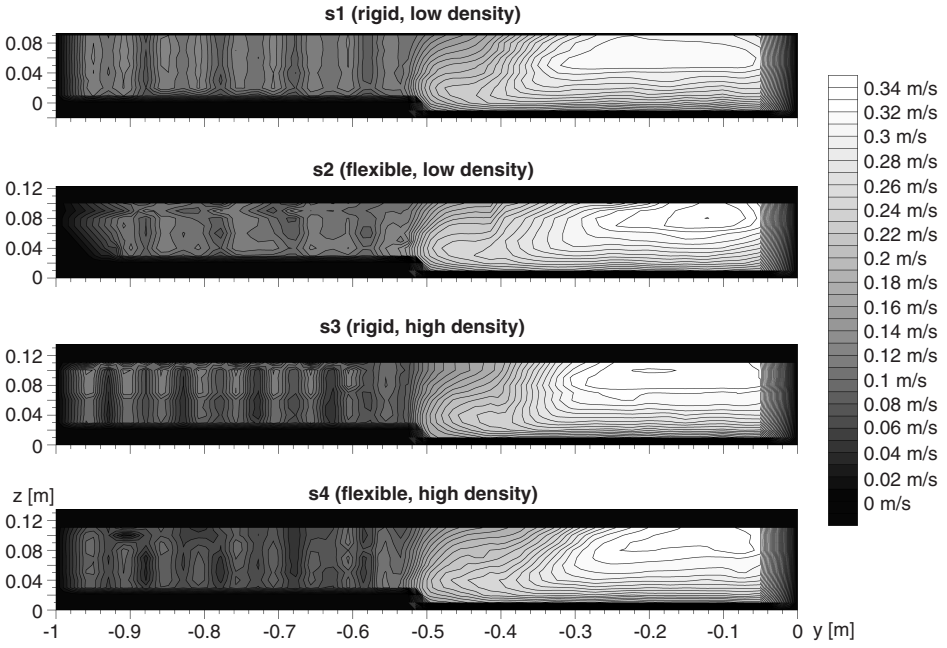


Figure 3. Measured isovelocity contours of temporally and longitudinally averaged velocities for a discharge of $Q = 20$ l/s.

right wall. This suggests that the influence of secondary currents in the present compound channel is remarkably high.

3.2 *Longitudinal change of velocities*

Measurements of 4–6 different cross sections in the interaction zone were used to analyze the longitudinal change of velocities influenced by the position relative to the cylinders. Figure 4 shows six measured profiles exemplarily for setup s2q30 (flexible, sparse, highest discharge $Q = 30$ l/s, $h/H = 0.87$). The longitudinal contours show good homogeneity in the main channel. For the region close to the cylinders ($-0.52\,\text{m} < y < -0.55\,\text{m}$) peaks occur which result from the wake structures and their local deceleration and acceleration effects. Figure 4c refers to a position $\Delta x = 5$ cm in the wake behind a flexible cylinder and shows the lowest velocities of $\bar{u} = 0.035$ m/s in the interaction zone. However it should be noted, that the cylinders were bent streamwise for about $\Delta x = 4.5$ cm (at water level). Hence the contours are not exactly vertical over the water depth.

The vector plots of transverse velocities $\bar{v}$[m/s] in Figure 4 prove the presence of secondary currents. To compensate for nonalignment errors of the LDV, a correction procedure was applied, see Wilson (2003). Assuming no net transfer of momentum in each vertical, correction angles of the LDV head were determined and the transverse and longitudinal velocities recalculated from the measured data. This affected mainly the transverse component, whereas the longitudinal component resulted in changes of less than 0.5%.

The transverse velocities show a near-bed flow from the main channel towards the floodplain ($z < 0.08$ m) and a counter-directed flow from the floodplain towards the main channel close to the water surface ($z > 0.06$ m). This secondary flow is evident in all cross sections and reaches maximum velocities of about $\bar{v} = \pm 0.03$ m/s (respectively 8% of $<\bar{u}>_{max}$). The influence of the wake is also clearly visible in the vector plots of transverse velocities $\bar{v}$[m/s] in Figure 4c which refers to a position $\Delta x = 0.033$ m behind a cylinder. Due to the bending, the transverse flow is directed away from the cylinder (outer wake region) at lower water depths and inwards close to the water surface (inner wake region).

3.3 *Standard deviation of longitudinal change*

In Figure 5 the standard deviations of time averaged velocities were calculated as a measure of their longitudinal change along the channel (using data of 4 cross sections in case s3 and s4, and 6 in s1 and s2). Depth-averaging was carried out because the influence of the water depth was found to have only a minor influence.

The standard deviation is about three times higher for the longitudinal component and shows a stronger

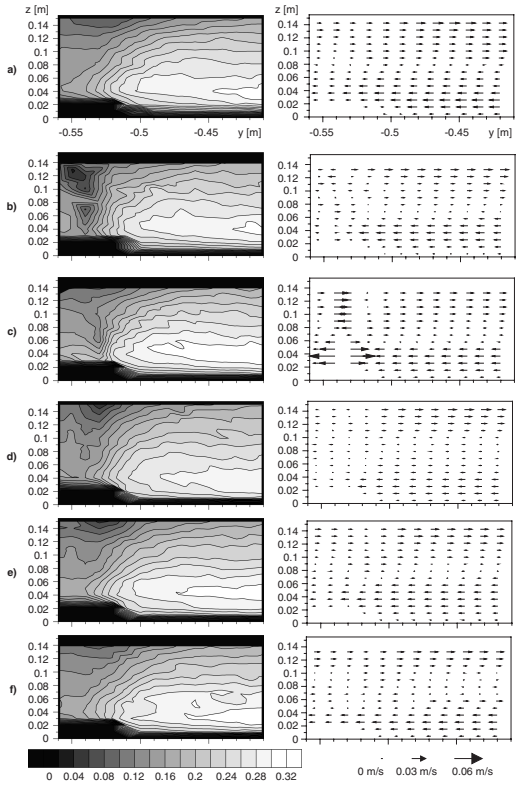


Figure 4a–f. Measured temporally averaged isovelocity contours of longitudinal velocity $\bar{u}$ [m/s] (left) and vector plots of transverse velocities $\bar{v}$ [m/s] (right) for setup s2q30 (flexible, sparse, highest discharge, $< \bar{u} >_{max} = 0.374$ m/s). The six diagrams refer to different longitudinal positions from besides a cylinder (Fig. 4a, topmost) to right in front of the following one (Fig. 4f, bottom). The distance between each sheet was $\Delta x = 1.661$ cm.

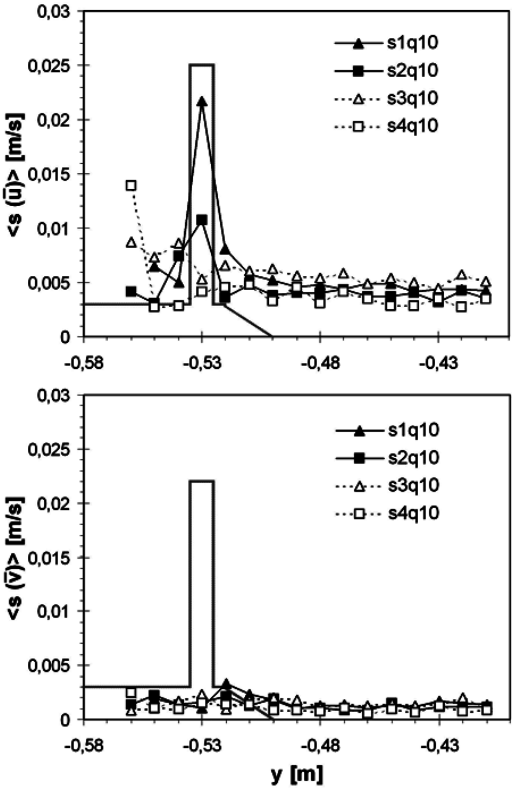


Figure 5. Depth-averaged standard deviations of longitudinal change of longitudinal $<s(\bar{u})>$ [m/s] and transverse $<s(\bar{v})>$ [m/s] time-averaged velocity components for all floodplain vegetation setups and a discharge of $Q = 10$ l/s. The gray line indicates the location of the floodplain boundary position and the first row of cylinders at $y = -0.53$ m.

impact of the cylinder wake where the maximum values were obtained. The sparser configurations s1 and s2 show higher longitudinal variation than the denser setups s3 and s4. Furthermore, the flexibility of the cylinders has a damping effect and decreases the longitudinal standard deviation (see for cases s2 and s4). Away from the floodplain, the standard deviation remains almost constant in the main channel for all setups. The transverse component is distributed very uniformly along the channel and shows no peaks respectively no significant influence of the wake zones of the cylinders.

Generally, with increasing discharges the longitudinal peak values remained constant in the wake zone whereas both components increased in magnitude in the main channel (about 50% for $Q = 20$ l/s and 100% for $Q = 30$ l/s).

3.4 *Turbulent kinetic energy*

The longitudinally and time averaged turbulent kinetic energies in Figure 6 were calculated from the longitudinal and transverse turbulence intensities u_{rms} [m/s] and v_{rms} [m/s] using: $k = ½(u_{rms}^2 + v_{rms}^2)^{0.5}$ and afterwards averaged longitudinally to obtain $<\bar{k}>$ [m^2/s^2]. Figure 6 shows for each setup four different zones of local energy peaks. First, a near-bed zone in the main channel generated by the bed shear stresses. Secondly, above the floodplains the generation of turbulent kinetic energy induced by the cylinders. The third zone marks the vertical boundary shear layer between the floodplain and the main channel in the interaction zone (-0.4 m $< y < -0.3$ m). The fourth local maximum is located within the main channel (at about $y = -0.35$ m) and close to the water surface. This again is related to the impact of secondary currents that shift energy from the floodplain boundary layer into the main channel interior. For the flexible

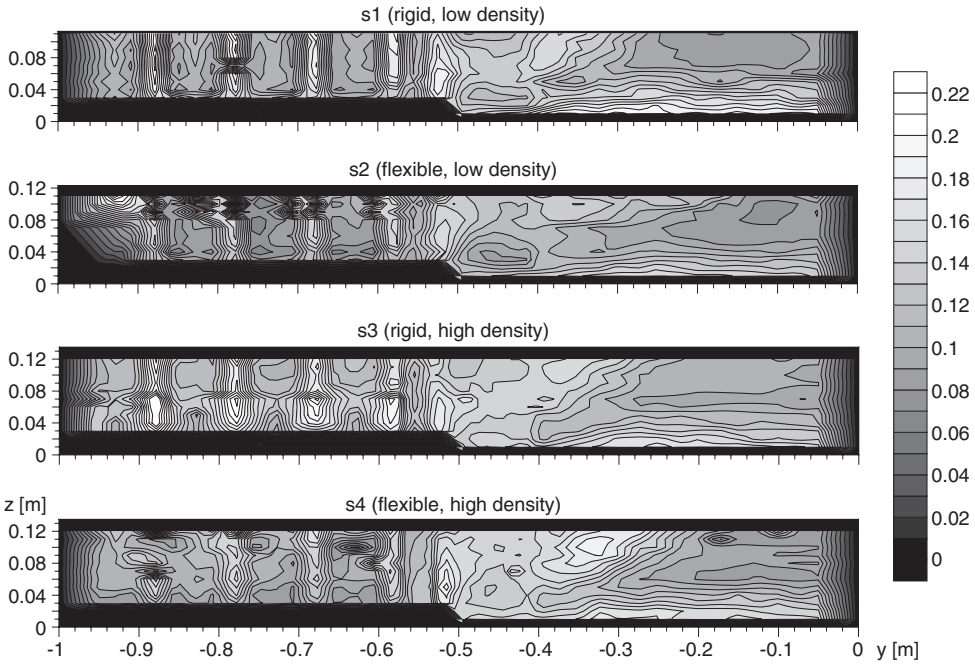


Figure 6. Contour plots of longitudinally and temporally averaged dimensionless turbulent kinetic energy $<k>/(<\bar{u}>_{max})^2$ [−] for a discharge of $Q = 20$ l/s.

cylinders (s2 and s4) the trace of the energy shift is more upward directed and close to the water surface, whereas for the rigid cylinders (s1 and s3) a stronger sideward shift around the vertical level of about half the water depth H occurred.

The magnitude of turbulent kinetic energy at the vegetation boundary layer increased with increasing discharges and relative depth ratios. Compared with the bed shear generated energy, it was lower for the lowest discharge ($Q = 10$ l/s) and higher in case of the highest discharge ($Q = 30$ l/s). This points out that the relative depth ratio as well as vegetation properties are dominant parameter for the boundary shear layer between vegetation and open main channel flow.

4 CONCLUSIONS

The aim of the present study was to characterize the flow field and momentum exchange processes in a compound open channel with vegetated floodplain introducing pseudo-natural properties of vegetation and high relative depth ratios.

It was found that secondary currents are the primary mechanism for momentum exchange. Near the junction a strong intrusion of high longitudinal main channel velocities into the floodplain was found at lower regions of the flow. Whereas slower mean velocities from the floodplain were dispersed far into the main channel at the upper regions of the flow. The analysis of longitudinal change of velocities proved that this effect is non-local and has a high longitudinal heterogeneity along the channel.

The magnitude of the secondary currents increased with increasing water depth and caused significant deflections of the lateral and vertical velocity profiles. Furthermore, the maximum longitudinal velocities in the main channel were shifted away from the vegetation. This effect was amplified by the bending and lateral waving motion of the flexible cylinders.

The distribution of turbulent kinetic energy within the channel confirmed the results. Energy generated at the shear layer between floodplain and main channel was shifted upwards and away from the vegetation corresponding to the measurements of the transverse currents. The magnitude of the boundary turbulent kinetic energy between the vegetation and the main channel was found to be a function of both the relative depth and the floodplain vegetation properties. The highest turbulent kinetic energy was measured for flexible vegetation arrangements compared to the rigid. This was observed at the two highest flow discharges. In fact the lower density flexible vegetation produces higher turbulent kinetic energy than the denser rigid setup. This suggests that the vegetation flexibility has

a stronger influence on turbulent kinetic energy field than the vegetation density.

The experiments herein are a first step towards the physical understanding of interaction processes in compound channels of rigid and flexible vegetation properties. They show that plant properties like waving motions, deflection and compression have an important impact on velocities and exchange processes and have to be taken into account in future research.

ACKNOWLEDGEMENTS

The author acknowledges the financial support of the European Commission, that funded the experiments within the framework of the "RipFor" project (QLRT-1999-1229). Furthermore, the author would like to gratefully acknowledge the DAAD, Bonn, Germany for funding the visit to Dr. C. A. M. E. Wilson at the University of Cardiff, School of Engineering, UK.

REFERENCES

Arnold, U., Höttges, J., Rouve, G. 1989. Turbulence and mixing mechanisms in compound open channel flow. Ottawa. *Proceedings of the XXIII International Congress of the IAHR*, Technical Session A: Turbulence in Hydraulics.

Sellin, R.H.J. 1964. A laboratory investigation into the interaction between the flow in the channel of a river and that over ist floodplain. *La Houille Blanche* 7: 793–802.

Tominaga, A., Nezu, I., Ezaki, K. 1989. Experimental study on secondary currents in compound open-channel flows. Ottawa. *Proceedings of the XXIII International Congress of the IAHR*, Technical Session A: Turbulence in Hydraulics: 15–22.

Naot, D., Nezu, I., Nakagawa, H. 1996. Hydrodynamic behaviour of partly vegetated open channels. Coherent horizontal vortices in compound open-channel flows. *Journal of Hydraulic Engineering, ASCE*, Vol. 122: 625–633.

Onitsuka, K., Nezu, I., Fujita, M. 1999. Coherent horizontal vortices in compound open-channel flows. Hydraulic Modeling (ed. V.P. Singh, et al.), *Water Resources Publications*, Colorado: 17–32.

Pasche, E., Rouve, G. 1985. Overbank flow with vegetatively roughened flood Plains. *Journal of Hydraulic Engineering, ASCE*, Vol. 11: 1262–1278.

Wilson, C.A.M.E., Boxall, J.B., Guymer, I., Olsen, N.R.B. 2003. Validation of a three-dimensional numerical code in the simulation of pseudo-natural meandering flows. *Journal of Hydraulic Engineering, ASCE*, Vol. 129: 758–768.

Zheleznyakov, G.V. 1965. Relative deficit of mean velocity of instable river flow, kinematic effect in river beds with floodplains. Leningrad: *Proceedings of the Eleventh International Conference of the IAHR*.

River Flow 2004 – Greco, Carravetta & Della Morte (eds.)
© 2004 Taylor & Francis Group, London, ISBN 90 5809 658 0

Numerical evaluation of secondary flow effects on lateral momentum transfer in overbank flows

A. Tominaga
Nagoya Institute of Technology, Nagoya, Japan

D.W. Knight
The University of Birmingham, Birmingham, United Kingdom

ABSTRACT: In compound open channel flows, the momentum transfer from the main channel to the flood plain is a strong characteristic and the contribution of the secondary flow is known to be very large. In this study, numerical simulation is conducted to understand the secondary flow effect on the lateral momentum transfer with a standard k-ε model linked artificially with a given secondary flow. This simulation reproduces the typical linear distribution of the momentum transfer term. The simulated secondary flow can decrease the bed shear stress in the main channel. In cases of large relative depth, the secondary flow explains the bed shear stress increase on the flood plain reasonably well, but an unrealistically large secondary flow is required to reproduce the experimental apparent shear stress in cases of small relative depth. Hence another mechanism, like large-scale planform vortices, is needed to explain the characteristic increase of bed shear stress on the flood plain.

1 INTRODUCTION

When rivers flow overbank, significant momentum exchange occurs laterally, causing deceleration in the main channel and acceleration on the flood plains. This noticeable feature of overbank flow was clearly shown by the SERC-FCF measurements (Knight & Sellin (1987)). It is postulated that large-scale planform vortices, rotating about a vertical axis, and streamwise secondary flows are the reason for the momentum transfer from the main channel to the flood plain. The lateral momentum transfer is represented as an apparent shear stress, which is calculated from the balance in a depth-averaged momentum equation. Shiono and Knight (1991) indicated lateral distributions of the apparent shear stress on the Flood Channel Facility (FCF) data. They also measured the Reynolds shear stress and extracted the secondary-flow dispersion term. As a result, the contribution of the secondary flow to the lateral momentum transfer is known to be very large. This secondary flow term plays an important role in the prediction of the bed shear stress and the depth-averaged velocity in compound open channel flows. However, the secondary flow structures that cause such a significant momentum transfer are still not fully understood. An accurate measurement of the secondary flow is very difficult, especially on shallow flood plains. In this study, 3-D numerical calculations were conducted with synthetically generated secondary flows. The patterns of secondary flows were generated according to the typical experimental results of Tominaga & Nezu (1991) and Tominaga et al. (1988). The strength of secondary flows was selected to reproduce the estimated distributions by Shiono & Knight and the effects of secondary flow structure and strength were investigated.

2 DEPTH-AVERAGED MOMENTUM ANALYSIS

The depth-averaged momentum equation is obtained by integrating the streamwise component of the Reynolds averaged Navier-Stokes (RANS) equation over the flow depth (e.g. Shiono & Knight (1991)). The bed shear stress is expressed as follows:

$$\tau_b = \left\{ \rho g d S_0 + \frac{\partial}{\partial y}\left(d\tau_{yx}\right) - \frac{\partial d\,(\rho UV)_d}{\partial y} \right\} \left(1 + \frac{1}{s^2}\right)^{-1/2} \quad (1)$$

where y is the lateral direction, τ_b is the bed shear stress, d is the water depth, S_0 is the bed slope, τ_{yx} is the depth-averaged lateral Reynolds shear stress, $-(\rho UV)_d$ is the shear stress due to the secondary flow, s is the lateral bed slope, ρ is the density of water and

g is the gravitational acceleration. From equation (1), the shift of bed shear stress from the two-dimensional value $\rho g d S_0$ is produced by the second and third terms on the right-hand side. The second term expresses the turbulent diffusion of momentum. The third term accounts for lateral momentum transfer due to the secondary flow and has been measured for only a few cases. This term is defined as Γ by Shiono & Knight (1991).

$$\Gamma \equiv \frac{\partial d(\rho UV)_d}{\partial y} = \rho g d S_0 - \tau_b \left(1+\frac{1}{s^2}\right)^{1/2} + \frac{\partial}{\partial y}\left(d\rho\varepsilon_{yx}\frac{\partial U_d}{\partial y}\right) \quad (2)$$

where the lateral Reynolds shear stress is expressed by an eddy viscosity model, ε_{yx} is the depth-averaged eddy viscosity, and U_d is the depth-averaged velocity. The FCF data show that the actual bed shear stress exceeds the two-dimensional value even in the region of $\partial U_d/\partial y = 0$ on the flood plain (Knight & Shiono, 1996). In this region, the secondary flow term is the only explicable reason for the increase of bed shear stress, as follows:

$$\tau_b - \rho g d S_0 = -\frac{\partial(d\rho UV)_d}{\partial y} \equiv -\Gamma \quad (\partial U_d / \partial y = 0) \quad (3)$$

Shiono & Knight back-calculated the value of Γ from the experimental results of depth-averaged velocity, bed shear stress and the lateral Reynolds shear stress. They also indicated that the lateral distribution of $-(\rho UV)_d$ is almost linear in the main channel and flood plains, respectively. Shiono & Knight (1991), Knight & Shiono (1996), Knight & Abril (1996) and Abril & Knight (2003) solved equation 1 analytically and numerically by adopting respective constant values of Γ for the main channel and flood plain, and got good agreement with the experimental data. However, the secondary flow effects on lateral momentum transfer were estimated indirectly and definite evidence has not been obtained because of the difficulty in measuring the secondary flow sufficiently accurately. It is thus very important to clarify the inner structure of this secondary flow term, Γ.

Many researchers calculated the secondary flow in compound open channels, trying to reproduce the experimental data of Tominaga & Nezu (1991). Naot et al. (1993) used an algebraic stress model and Thomas & Williams (1995) calculated by using Large Eddy Simulation (LES). Their calculations were successful for reproducing secondary flows. However, their geometric conditions were limited to high relative depth and a narrow open channel. The channel was an asymmetric rectangular compound channel with a relative depth $Dr = (H - h)/H = 0.5$ and a width ratio $B/b = 2.0$, where H is the main channel depth, h is the flood plain height, B is the channel width and b is the main channel width. Thomas & Williams (1996) simulated FCF experimental data by using LES. This calculation was undertaken for a symmetric trapezoidal compound channel with $Dr = 0.25$ and $B/b = 2.2$. In this case, the calculated secondary flow pattern was very different from the rectangular case and $Dr = 0.5$. The characteristic inclined upflow from the junction between main channel and flood plain does not appear. But the experimental data used in the comparison was not accurately measured. Moreover, this case has smaller side slope of the main channel ($s = 2$) and a narrow flood plain. The calculated bed shear stress agrees well with the experimental one.

The prediction of secondary flow by high order turbulence models is still an uncompleted task in such a shallow compound open channel flows. Therefore, a standard k-ε turbulence model is used herein for calculating the primary velocity; subject to given or pre-selected secondary flows.

3 NUMERICAL SIMULATION METHOD

The streamwise component of the Reynolds equation and continuity equation were solved numerically by using the k-ε turbulence model. Transport equations of turbulent kinetic energy k and dissipation rate ε were solved with standard model constants. The equations are discretized by a finite volume method with hybrid scheme and solved by the SIMPLE algorithm. A block masking method for a rectangular coordinate system was used to express the cross-sectional shape of the channel. As to the boundary conditions, the near-wall velocity is assumed to comply with the log-law that covers the rough boundary, as follows:

$$\frac{u}{u_*} = \frac{1}{\kappa}\ln\left(\frac{z}{k_s}\right) + B$$

$$B = \left(-3.24 + \frac{1}{\kappa}\ln\left(\frac{U_* k_s}{\nu}\right)\right)\exp\left(-0.08\frac{U_* k_s}{\nu}\right) + 8.5 \quad (4)$$

where k_s is the equivalent roughness height, U_* is the friction velocity, ν is the viscosity and κ is the Karman constant ($\kappa = 0.41$). Equation 6 is the approximation for the Nikuradse's experimental curve for roughness function B. In all FCF cases, $k_s = 0.0004$ m is adopted. The free surface is treated as a rigid lid and all the gradients normal to the water surface are zero.

A standard isotropic k-ε model is known not to reproduce the turbulence-induced secondary flow, and is inadequate in predicting separating or impinging flows. In this study, however, this simple turbulence model has sufficient ability to predict the primary velocity field affected by secondary flows, because the secondary flows are artificially modelled and the channel is prismatic.

Secondary flows are given for each cell by using stream functions in accordance with the experimental results, as follows:

$$\Psi_i = A_i \sin(\pi \hat{y}_i^{B_i}) \sin(\pi \hat{z}_i^{C_i}) \tag{5}$$

$$\hat{y}_i = (y - y_{i1})/(y_{i2} - y_{i1}) \quad \hat{z}_i = (z - z_{i1})/(z_{i2} - z_{i1})$$

$$V = \partial\Psi/\partial z, \; W = -\partial\Psi/\partial y \tag{6}$$

where i is the number of the secondary flow cell, y_{i1}, y_{i2} are the left and right limits of the secondary flow cell, z_{i1}, z_{i2} are the bottom and top limits of the cell, A_i is a constant for the secondary flow strength, and B_i & C_i are constants for eccentricity of the secondary flow. The V and W equations are not solved but the velocity correction by pressure gradient is applied to satisfy the mass conservation. The values of constants were adjusted to reproduce the bed shear stress due to secondary flow obtained by the FCF measurements.

4 SIMULATION RESULTS

4.1 *Secondary flow parameters*

Typical secondary flow patterns that were used in the simulations are shown in Fig.1. This structure of secondary flow is based on the experimental results of Tominaga & Nezu (1991), but it is somewhat modified for simplicity. The flood plain cell is projected into the main channel to achieve effective momentum transfer from the main channel to the flood plain. The secondary flows near the sidewall on the flood plain were not considered in this study. The lower pattern of the case 0308 is almost similar to that measured by Tominaga & Nezu (1991), but the upper pattern has not verified because there is no detailed measurements. Shiono & Knight (1991) measured the secondary flow in the FCF cases of $Dr < 0.24$. Unfortunately, there are few measuring points on the flood plain because of experimental difficulties. Therefore, the secondary flow structures on the flood plain are not clarified yet. As to the main channel, the lower cell of the secondary flow is observed and the maximum velocity is about 0.02 m/s. The upper cell is not clear. On the other hand, from the calculation of Thomas & Williams (1996), the calculated maximum secondary velocity is $0.81U_*$ and maximum value of $-(UV)_d$ is almost $-2.0U_*^2$, where U_* is the friction velocity. The simulated secondary flow is rather large but its structure is similar to the observed one, except for the upper cell.

The strength and shape parameters, A_i, B_i and C_i of the given secondary flows were adjusted for each cell respectively, to reproduce the observed shear stress due to secondary flow. The calculated results of primary velocity, and the momentum transfer due to secondary flow, were then depth-averaged. Fig.2 shows the lateral distribution of $-(\rho UV)_d$ with different values for the strength parameter A for the flood plain cell. The profiles of $-(\rho UV)_d$ show the linearly descending feature that is quite similar to the experimental results calculated from equation 1 by Shiono & Knight (1991), but the magnitude is smaller. Since a much larger secondary flow is required to get the same magnitude as

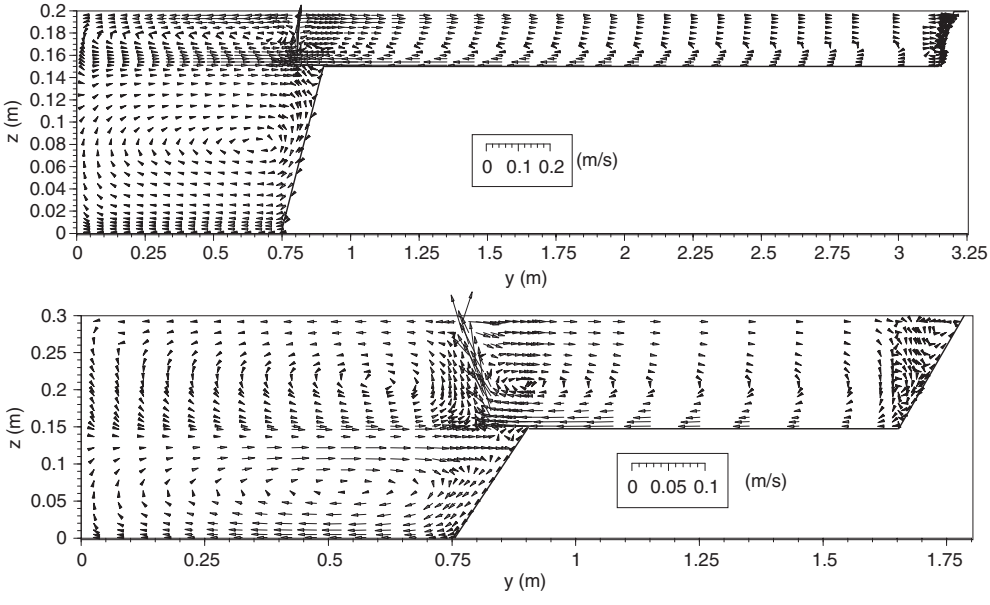


Figure 1. Modelled secondary flow vectors given into calculation (Upper: FCF 0205, Lower: FCF 0308).

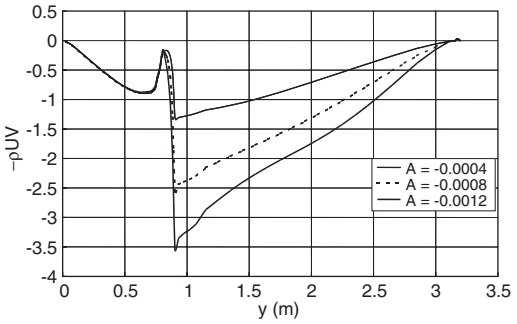


Figure 2. Lateral distribution of the momentum transfer due to secondary flow (calculated).

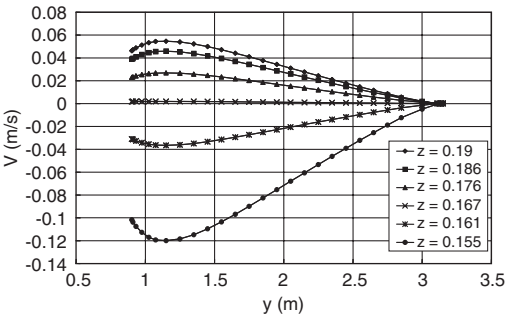


Figure 4. Lateral distributions of lateral velocity on the flood plain (FCF 0205).

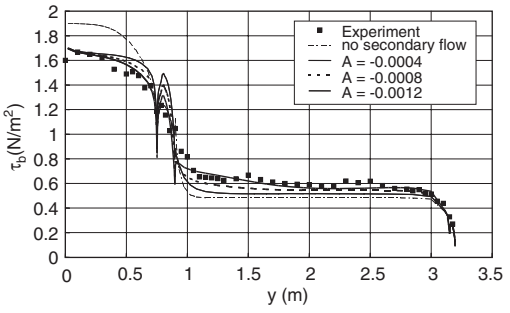


Figure 3. Comparison of lateral distribution of bed shear stress (FCF 0205).

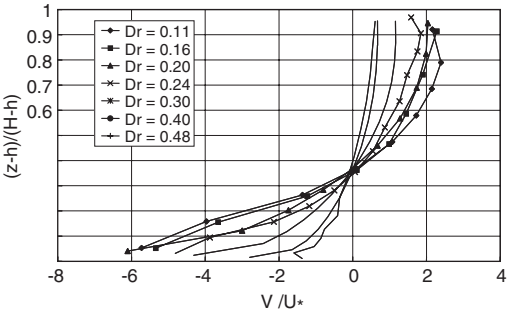


Figure 5. Vertical distributions of lateral velocity on the flood plain (at $y = 1.025$ m).

the experimental $-(\rho UV)_d$, only these three cases are shown.

Fig.3 shows the lateral distributions of experimental and calculated bed shear stress with secondary flow of different strengths. The calculated bed shear stress with secondary flow is in fairly good agreement with the experiment when $A_{fp} = -0.0012$ and it clearly illustrates the effects of secondary flow in comparison with the 'no secondary flow' case. The increase of the bed shear stress on the flood plain corresponds well with the lateral gradient of $-(\rho UV)_d$. On the other hand, the depth-averaged velocity did not increase but somewhat decreased on the flood plain in low relative depth cases, in contrast with the result of the depth-averaged analysis. In high relative depth cases, the velocity on the flood plain also increased to agree with the experiments.

To establish the typical distribution of $-(\rho UV)_d$ on the flood plain, the eccentricity coefficients, B and C, are known to be important. In this case, $B = 0.35$ and $C = 0.6$ were adopted. The coefficient B determines the gradient of $-(\rho UV)_d$, whereas C provides efficiency in lateral momentum transport. Typical lateral distributions of that on the flood plain are shown in Fig.4. Those distributions descending toward the sidewall can establish the linear distribution of $-(\rho UV)_d$. Fig.5 shows the typical vertical distributions of the lateral mean velocity V adjusted for cases of FCF 02-series at the nearly peak position on the flood plain. The values are normalized by the averaged friction velocity. These skewed distributions are similar to those in curved open channels (Tominaga & Nagao (2000)). It is verified that this type of secondary flow profile can most effectively transfer the momentum. However, the required secondary velocity is much larger than that observed in many previous experiments. The maximum secondary flow velocity is almost the order of U_* in most measurements and calculations. With an increase of the flood-plain depth, the required velocity becomes smaller to approach a realistic value, but it is still large, especially near the bed. On the other hand, the maximum lateral velocities for the main-channel lower and upper cells are reasonably less than the order of U_* in the main channel. The bed shear stress in the main channel is well decreased by the given secondary flow structures.

The lateral distributions of the momentum transfer resulting from these secondary flow parameters are

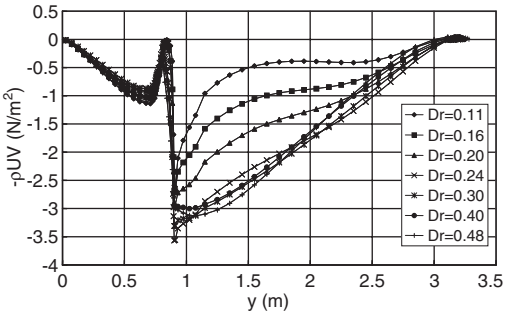


Figure 6. Lateral distributions of the momentum transfer due to secondary flow (FCF 02-series).

shown in Fig.6 for cases of FCF 02-series. The lateral distributions become fairly linear for the cases of $Dr > 0.24$, where Dr is the relative depth defined as $Dr = (H - h)/H$. However, it was difficult to realize the linear distribution for the cases $Dr \leq 0.2$. Although it may be possible to make those more similar to the experimental results by adjusting the parameters, it was not investigated further in this study. The secondary flow structures in a shallow flood-plain depth may be different from the adopted pattern that was observed in cases of deep flood-plain depth. Fig.7 shows the calculated lateral distribution of the bed shear stress in comparison with the experimental data in the case of $Dr = 0.16$ and $Dr = 0.5$. In the case of shallow depth (0203), the calculation agrees reasonably with the experiment even though the momentum transfer term is different from the experimental one. The steep gradient of $-(\rho UV)_d$ near the interface on the flood plain sustains the increase of the bed shear stress. However, the turbulent momentum transfer should make a large contribution to the increase of the bed shear stress in this interfacial region with a large lateral velocity gradient. The increase of the bed shear stress is under-estimated in the region of no lateral velocity gradient. For the case of large relative depth (0308), the bed shear stress is increased over the whole flood plain, but is underestimated near the sidewall. This is because the secondary flow pattern is not properly considered near the sidewall of the flood plain in this simulation.

The lateral momentum transfer due to the secondary flow is also affected by the vertical distribution of the primary velocity. Fig.8 shows the semi-logarithmic plot of the primary velocity at $y = 1.0$ m on the flood plain. The solid line indicates the log law distribution, as follows:

$$\frac{U}{U_*} = \frac{1}{\kappa}\ln\left(\frac{U_* z}{\nu}\right) + A_s \qquad (7)$$

The constant $A_s = 4.8$ is taken from the figure. The value of A_s changes with the lateral position but the

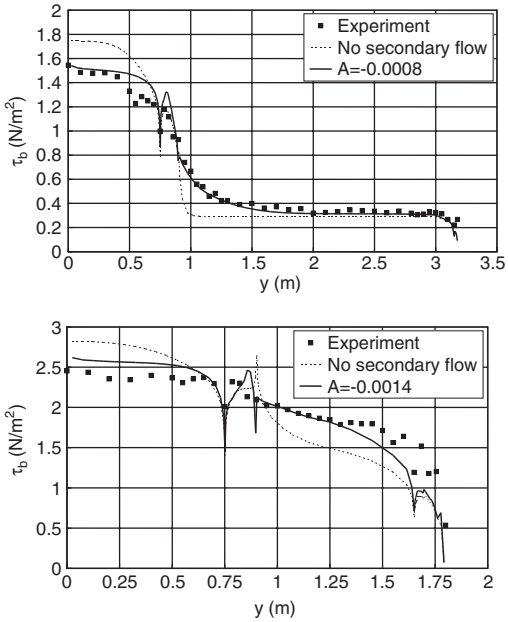


Figure 7. Calculated lateral distribution of bed shear stress (Upper: FCF 0203, $Dr = 0.16$, Lower: FCF 0308, $Dr = 0.5$).

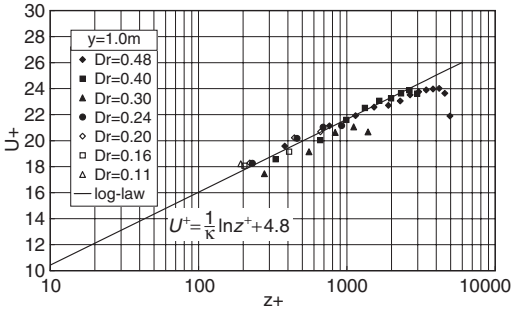


Figure 8. Vertical distributions of primary velocity on the flood plain ($U^+ = U/U_*$, $z^+ = U_* z/\nu$).

gradient is almost constant in all cases. So, it is considered that the primary velocity complies with the log law. It was recognized that the simulated primary velocity also obeys the log-law distribution, approximately.

4.2 *Effects of secondary flow on primary velocity*

Fig.9 shows the calculated lateral distribution of depth-averaged velocity corresponding to the cases in Fig.7. In the case of shallow depth, introducing the secondary flow does not increase the velocity on the flood plain near the interfacial region but rather decrease near

the interfacial region. This is probably caused by too strong an inward velocity near the flood plain bed. In the deeper case, the calculated depth-averaged velocity shows good agreement with the experimental one.

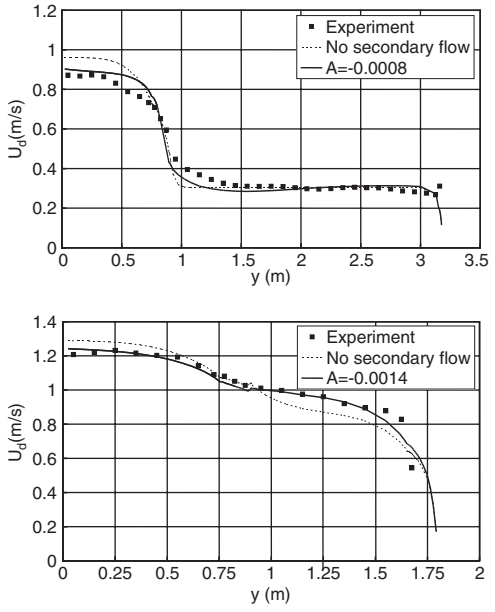


Figure 9. Calculated lateral distribution of depth-averaged velocity (Upper: FCF 0203, $Dr = 0.16$, Lower: FCF 0308, $Dr = 0.5$).

In this case, the secondary flow effects reasonably explain the flow characteristics.

Fig.10 shows the calculated primary velocity contours with and without the given secondary flow in Fig.1. In the case of 0205, the velocity in the main channel is noticeably decreased by the secondary flow effect, whereas that on the flood plain is not changed so much, as seen in Fig.9. Fig.11 shows the measured contours of primary velocity. The calculated result approaches the experimental one by incorporating the artificially generated secondary flow. The total discharge is decreased as a result of the additional energy loss due to the secondary flow. In the case of 0308, the effects of secondary flow work well and calculated contours are very similar to the experimental ones except very near the free surface and the sidewall of the flood plain. Particularly, the flow structure in the interfacial region is well reproduced.

4.3 *Effects of secondary flow on turbulence*

The calculated turbulent kinetic energy k and vertical Reynolds stress $-\rho\overline{uw}$ are shown in Figs.12 and 13, respectively, with and without the secondary flow for the case of 0205. The turbulent kinetic energy is considerably increased around the interfacial region by the effects of secondary flow, whereas that near the bed of the main channel is decreased. The Reynolds stress with the secondary flow indicates minus value below the interface bisector because of the minus gradient of $\partial U/\partial z$. More significantly, it becomes much larger just above the bisector. The secondary flow changes

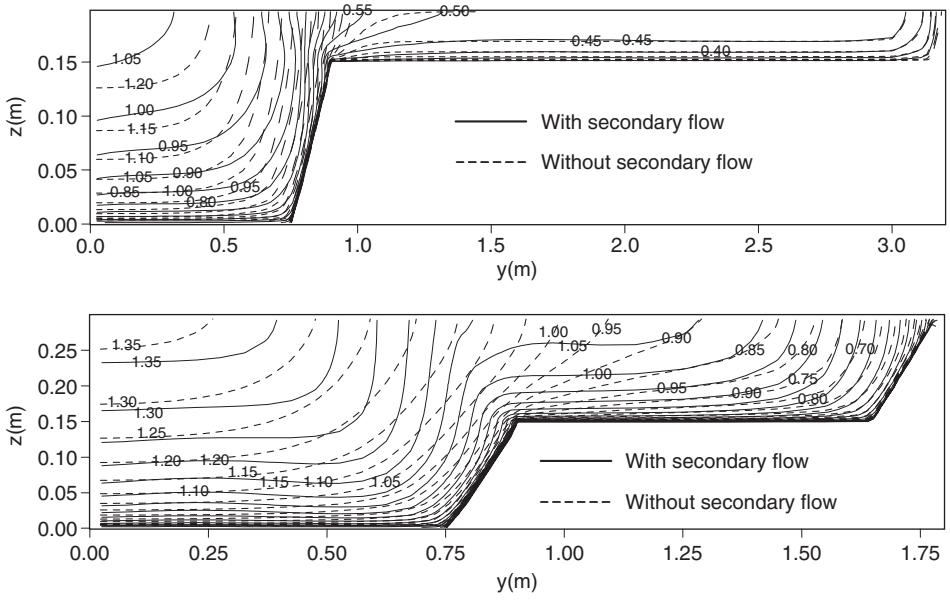


Figure 10. Calculated primary velocity contours (Upper: FCF 0205, Lower: FCF 0308).

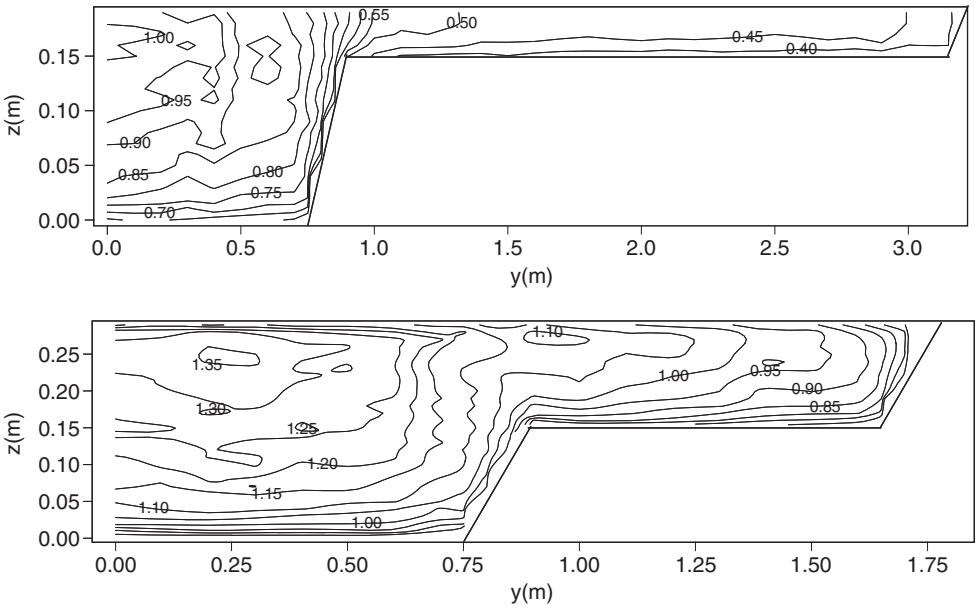


Figure 11. Measured primary velocity contours (Upper: FCF 0205, Lower: FCF 0308).

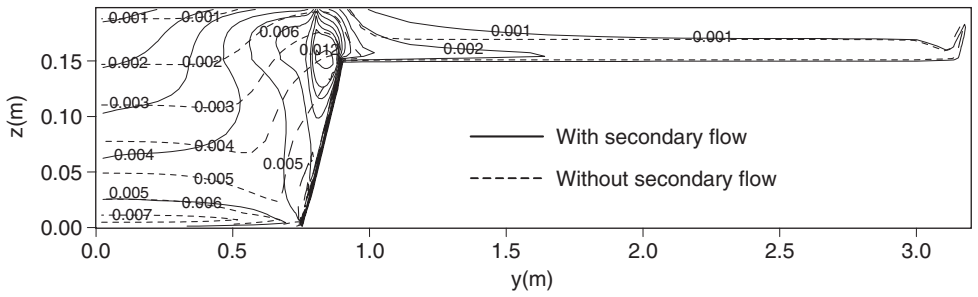


Figure 12. Calculated contours of turbulent kinetic energy k (FCF 0205).

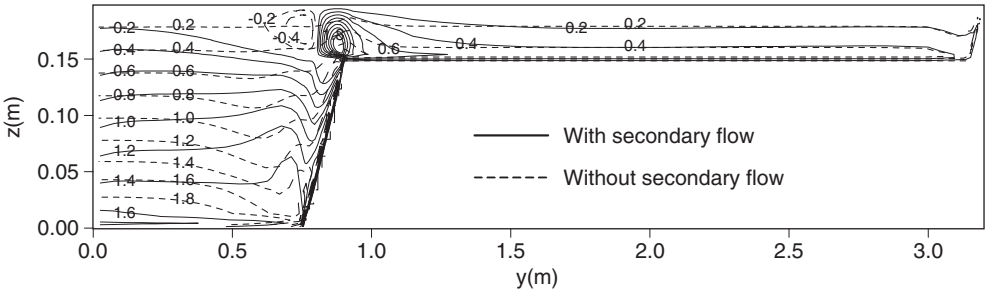


Figure 13. Calculated contours of Reynolds stress $-\overline{\rho uw}$ (FCF 0205).

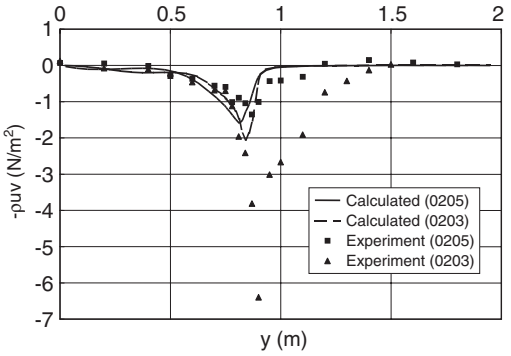


Figure 14. Lateral distribution of Reynolds stress $-\rho\overline{uv}$ ($Dr = 0.24$: at $z = 0.17$ m, $Dr = 0.16$: at $z = 0.16$ m).

the primary velocity gradient and then this increases the generation rate of the turbulent energy. Thus, the secondary flow can cause the drastic increase of the turbulent energy in the interfacial region. It is also considered that the advective energy transfer contributes to this phenomenon.

The lateral Reynolds stress $-\rho\overline{uv}$ is more important because it is directly related to the lateral momentum transfer. Fig.14 shows the lateral distribution of the Reynolds stress $-\rho\overline{uv}$ with the experimental data shown by Shiono & Knight (1991) for the cases of FCF 0205 and 0203. In the case of $Dr = 0.24$, the calculated value is almost similar to the experimental one, though the peak position is shifted toward the main-channel side. With a decrease of the floodplain depth, in the case of 0203, the calculated Reynolds stress increases slightly but the experimental one increases significantly. As a result, the present turbulence model cannot predict the Reynolds stress $-\rho\overline{uv}$ well for shallow compound open channels. This underestimation of the Reynolds stress in the interfacial region is caused by the fact that the present model cannot reproduce the large-scale vortices inherently.

It is well known that large-scale coherent planform vortices, rotating about vertical axes, are generated in compound open channel flows. These large-scale planform vortices cause significant fluctuations in both the longitudinal and lateral velocities, as shown by Knight & Shiono (1990). A time-dependent numerical model is necessary for accounting for such large-scale planform vortices. Accounting for this difference, the given secondary flow is excessive in this interfacial region in this shallow depth case. The turbulent momentum transfer concerns an increase of the eddy viscosity in the depth-averaged analysis using equation 1 but does not contribute to the increase of the bed shear stress in the region of no velocity gradient. In this region, the momentum transfer due to secondary flow is still important.

5 DISCUSSION

In this study, it was shown that the synthetically given secondary flow could reproduce the presumed momentum transfer term in the lateral momentum equation 1. However, it remains to explain why such a large secondary flow is required to simulate the experimentally determined momentum transfer. In the case of low relative depth, the maximum secondary velocity that gave the best fit was around 10–15% of the maximum primary velocity U_{max}, whereas it is known that the measured secondary velocity is generally of the order of 4% (Tominaga & Nezu (1991)). This implies that the increase of the bed shear stress on the flood plain, that is, the value of Γ in equation 2 cannot be explained by only secondary flow effects.

As another mechanism, a uniform open channel flow with planform vortices is considered. Planform vortices are moving with certain celerity and they cause periodic perturbation of all the variables in Eulerian observation. Ikeda et al. (1995) shows the distinctive pictures of the planform vortices. Bousmar & Zech (2002) obtained the celerity and the wave period by experiment and stability analysis. To consider the periodic large-scale motion, a concept of the Unsteady Reynolds Averaged Navier-Stokes (URANS) model is useful. However, the mean velocity dispersion and the Reynolds stress based upon short-time averages are reduced to the usual long-time averaged expression. The planform vortices inevitably interact with the streamwise secondary flow. The secondary flow structure is then a result of time averaging of the complicated three-dimensional flow, including the effects of these planform vortices. The momentum transfer due to the large-scale perturbation should be captured as Reynolds stresses, and then, the secondary flow and the Reynolds stress only remain. In order to clarify this point, it is still necessary to perform careful experiments and time-dependent numerical calculations with a movable free-surface condition.

6 CONCLUSIONS

Numerical simulation is conducted to understand the secondary flow effect on the lateral momentum transfer. The turbulence model used is a standard k-ε model linked with an artificially given secondary flow. This simulation revealed the inner structure of the secondary flow term of the depth-averaged lateral momentum equation. In cases of large relative depth and in the main channel, the secondary flow reasonably explains the bed shear stress increase or decrease. When the relative depth is small, however, an unrealistic strength of secondary flow is required to explain the increase of the flood-plain bed shear stress. This fact implies that another mechanism must be accounted for in the lateral momentum transfer.

Since the momentum transfer due to these vortices are included in the Reynolds stress term in RANS model through the long-time averaging process, the reason for the increase of the flood-plain bed shear stress in cases of small relative depth is still in question. Further experiments and 3-D unsteady numerical simulation are necessary to improve our understanding.

REFERENCES

Abril, J.B. and Knight, D.W. (2003), "Stage-discharge prediction for rivers in flood applying a depth-averaged model", *Journal of Hydraulic Research, IAHR*, 41, No. 6, 1–14. (in press).

Bousmar, D. and Zech, Y. (2002), "Periodical turbulent structures in compound channels", *River Flow 2002*, 177–185.

Ikeda, S., Murayama, N. and Kuga, T. (1995), "Stability of horizontal vortices in compound open channel flow and their 3-D structure", *Journal of Hydraulic, Coastal and Environmental Engineering*, No. 509/II-30, 131–142 (in Japanese).

Knight, D.W. and Sellin, R.H.J. (1987), "The SERC Flood Channel Facility", *Journal of the Institution of Water & Environmental Management*, 1(2), 198–204.

Knight, D.W. and Shiono, K. (1990), "Turbulence measurements in a shear layer region of a compound channel", *Journal of Hydraulic Research*, 28(2), 175–196.

Knight, D.W. and Abril, B. (1996), "Refined calibration of a depth averaged model for turbulent flow in a compound channel", *Proc. Instn. of Civil Engineers, Water, Maritime and Energy*, 118, 151–159.

Knight, D.W. and Shiono, K. (1996), "River channel and floodplain hydraulics", in *Floodplain Processes*, (Eds Anderson, Walling & Bates), Chapter 5, J Wiley, pp 139–181.

Naot, D., Nezu, I. and Nakagawa, H. (1993), "Hydrodynamic behaviour of compound rectangular open channels", *Journal of Hydraulic Engineering*, ASCE, 119(3), 390–408.

Shiono, K. and Knight, D.W. (1991), "Turbulent open channel flows with variable depth across the channel", *Journal of Fluid Mechanics*, 222, 617–646.

Thomas, T.G. and Williams J.J.R. (1995), "Large eddy simulation of turbulent flow in an asymmetric compound open channel", *Journal of Hydraulic Research*, 33(1), 27–41.

Thomas, T.G. and Williams J.J.R. (1996), "Large eddy simulation of symmetric trapezoidal chanel at a Reynolds number of 430,000", *Journal of Hydraulic Research*, 33(6), 825–842.

Tominaga, A. and Nezu, I. (1991), "Turbulent structure in compound open channel flows", *Journal of Hydraulic Engineering*, ASCE, 117(1), 21–41.

Tominaga, A., Ezaki, K. and Nezu, I. (1988), "Turbulent structure in compound open channel flows in rectangular and trapezoidal main channel", *Proc. 3rd Int. Symp. Refined Flow Modelling and Turbulence Measurements*, 601–609.

Tominaga, A. and Nagao, M. (2000), "Secondary Flow Structures in Bends of Narrow Open Channels with Various Cross Sections", *Proc. of 4th International Conference on Hydroscience and Engineering*, in CD-ROM.

This page intentionally left blank

River Flow 2004 – Greco, Carravetta & Della Morte (eds.)
© 2004 Taylor & Francis Group, London, ISBN 90 5809 658 0

Effect of lateral variation of roughness on flow conveyance within a trapezoidal channel cross-section

H.I. Mohamed
Lecturer, Civil Eng. Department, Assiut University, Assiut-Egypt

ABSTRACT: The hydraulic computations involved in design of open channel are (generally) based on the uniform flow formula of Manning. The Manning roughness coefficient (n) in this approach is usually assumed to be constant and not to vary with the flow depth or roughness. It has been known for many years, however, that this assumption is erroneous. An important feature of most rivers and canals is the variation in roughness between channel bed and side banks due to non-homogeneity in excavated soil, bank revetment, and/or vegetations grow. In these channels, flow conditions lead to a complex flow situation with intensive mass and momentum exchange between main channel and banks. Therefore the flow structures that occur in these channels are extremely complex. A method for predicting the total conveyance of trapezoidal channel cross-section with varying roughness in perimeter is developed. Where, a numerical hydraulic model is coupled with a physically based flow-resistance equation. The resulting model is capable of simulating the total conveyance of trapezoidal channels with varying roughness along bed and side banks. To make the model results more amenable to the practicing engineer, design equations and plots were developed. These can be used as an alternative solution for channel designs; relieving the practitioner of the need to run the numerical program. A comparison between the present method and traditional divided channel approach proved that the model is superior on the other methods.

1 INTRODUCTION

Situations where channels sections have roughness varying laterally along the wetted perimeter are often encountered in design problems and laboratory experiments. Canals and tunnels partly lined with different construction materials in bottom and sides, highly vegetated sides with smooth channel bed, and overbanks with varying land use and treatment under high stages are the typical instances. Also, in alluvial channels, a marked difference in roughness has been known to exist across the channel bed and sides, Ahmed and Bakry (1997), El-Attar (1980). Many of irrigation channels are excavated in non-homogenous soil (the roughness of the bed is varied than that of banks or banks itself have varying roughness with depth). If such types of channels are designed by the traditional methods (averaged cross-sectional parameters), this will expose these channels to expensive and environmentally damaging. In all such problems, computations of equivalent roughness for the whole section are sometimes necessary. Various formulas to compute this equivalent or composite roughness can be found in the literature, Chow (1959), French (1996), U.S. Army Corps of Engineers (1994), Armanini and Righetti (1998) and Garbrecht and Brown (1991).

Recent researches have shown that the use of channel with varying roughness as a single unit will underestimate the values of discharge be obtained, Ali and Mohamed (1991), Myers et al. (1999), Dolgopolova (2001). This because the method used ignores the turbulent shear interaction and momentum transfer between the bed and side banks. The turbulent shear (forming vortices) that transfer momentum away from the bed to the banks has been thoroughly investigated by Rabkova and Garanina (2001). Where they measured the three-dimensional components of velocity in trapezoidal cross-section and confirmed kinetic energy exchange between adjacent layers. They concluded that this process controls the formation of longitudinal velocities in the water column. It is common knowledge that characteristic features of the turbulent flow are velocity fluctuations and the vortex motion, which results in the formation of three-dimensional vortices. The displacement of these vortices brings about redistribution of kinetic energy between elements of the liquid. This process is especially active in the zones, where local velocities vary

because of variations in the depth or bed roughness. Under the effect of transverse circulation, the accelerated liquid intrudes into the near bottom layers and vice versa. The result is the general levelling of three-dimensional flow velocity both in the vertical and transverse direction.

To this date, however, very little has been done to evaluate unique model using numerical and mathematical base. As shown from the mentioned above, there are clear needs for physically based methods of predicting the impacts of varying roughness on flow resistance and flow capacity. In the following, a numerical hydraulic model will be coupled with flow resistance equation for computing flow in channels with varying roughness.

2 THEORETICAL CONSIDERATION

As, it is showed above, the division lines used in divided channel method are not shear free boundaries in the case of variation in the roughness through the wetted perimeter due to the turbulent interaction between the fluid streams. Observation of depth average velocity distributions, such as those shown in Rabkova and Garanina (2001), illustrates that there is a transition between the main channel and banks velocities that can not be dealt with by applying an apparent shear stress at a single interface. Rather, there is a variation of the apparent lateral shear stress (τ_{xy}) across the channel. To better model this variation of the apparent shear stress, Lambert and Sellin (1996); Darby and Thorne (1996), (which is a representation of the turbulent momentum exchange $\rho.u.v$) the channel can be subdivided into a finite number of vertical elements as shown in Fig. (1). The vertical element is examined in more detail, using the control volume as in Fig. (1-b). For uniform flow, it can be show that;

$$gSz - B_* \frac{\tau_b}{\rho} + \frac{1}{\rho}\frac{\partial(z\tau_{xy})}{\partial y} = 0 \qquad (1)$$

where S is the longitudinal channel slope and τ_b is the bed shear stress. The coefficient (B_*) associated with the bed shear stress is used to account for the increased area of contact with the channel bed due to the lateral inclination of the channel bed at a cross-section (S_y) and is equal to $\sqrt{1+S_y^2}$. A factor similar to (B_*) was first introduced by Rodi (1980) and by both Lambert and Sellin (1996); Darby and Thorne (1996). This approach to the derivation of Eq. (1) was chosen because of its ease and accessibility. The solution of Eq. (1) and in particular the evaluation of the apparent lateral shear stress (τ_{xy}) and the bed shear stress (τ_b) are detailed below.

In Eq. (1), the downstream component of the weight of a unit value of water (term 1) is assumed to be balanced by frictional bed shear (term 2) and lateral shear (term 3) only. The value of bed shear stress (τ_b) can be expressed by:

$$\tau_b = \frac{f}{8}.\rho.u^2 = \frac{f}{8}.\rho.\frac{q^2}{z^2} \qquad (2)$$

where q = discharge per unit width, f = Darcy-Weisbach friction factor, u = mean velocity through the element and ρ = water density.

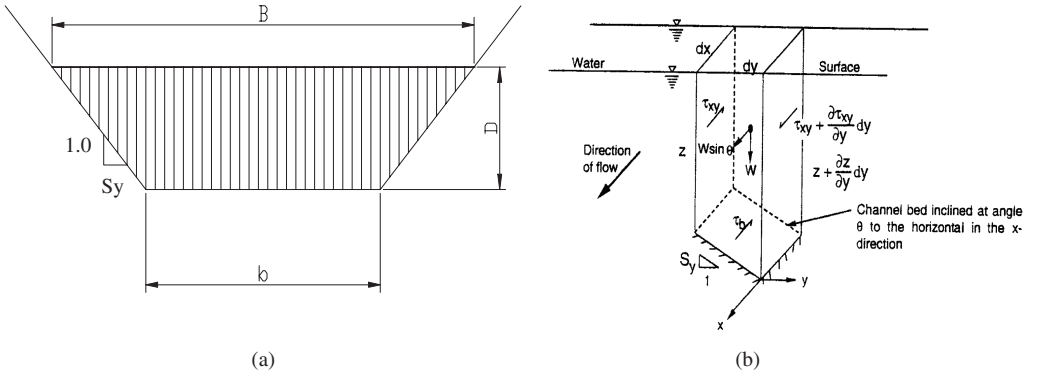
The value of the lateral shear stress (τ_{xy}) (term 3) can be expressed by:

$$\tau_{xy} = \mu.\frac{\partial u}{\partial y} \qquad (3)$$

where μ = absolute viscosity.

Then (term 3) in equation (1) can be formulated as follow

$$\frac{1}{\rho}\cdot\frac{\partial(z.\tau_{xy})}{\partial y} = \frac{1}{\rho}\cdot\frac{\partial(z.\mu.\frac{\partial u}{\partial y})}{\partial y} = \frac{1}{\rho}\cdot\frac{\partial(\mu.\frac{\partial q}{\partial y})}{\partial y} = \frac{\partial}{\partial y}\left[\varepsilon.\frac{\partial q}{\partial y}\right] \qquad (4)$$



(a) (b)

Figure 1. A schematic sketch of a channel division into a finite number of small vertical elements.

where ε = eddy viscosity and the other parameters as defined before.

Now by substituting Eqs. (2) and (4) into Eq. (1) the following expression for describing the unit discharge distribution across the channel is obtained.

$$g.S.z - B_{*}.\frac{f}{8}.\frac{q^2}{z^2} + \frac{\partial}{\partial y}(\varepsilon.\frac{\partial q}{\partial y}) = 0.0 \quad (5)$$

A solution of this equation is possible with the addition of non-slip boundary conditions (q = 0) at the outer boundaries of the channels. The numerical solution of Eq. (5) is obtained using a finite difference approximation and the solution of the resulting system of non-linear equations is performed using the Newton-Raphson method. In Eq. (5) all the terms except the Darcy-Weisbach friction factor (f) and the eddy viscosity coefficient (ε) can be evaluated.

A simple but reliable eddy viscosity model is used in (5).

$$\varepsilon = NEV.u_{*}.z \quad (6)$$

where $u_* = \sqrt{g.z.S}$ = local shear velocity (m/s); and NEV = user-specified non-dimensional eddy viscosity coefficient, usually taken as approximately 0.16, Darby and Thorne (1996) assumed uniform value across the channel.

To apply the flow model for predicting the distribution of the unit discharge for a specified water-surface elevation, it is necessary to estimate local Darcy-Weisbach friction factor at each computational node across the wetted perimeter, accounting for sediment roughness elements. A procedure developed by Masterman and Thorne (1992) is used herein to do this. Their method is based on the physically based Colebrook-White equation.

$$\frac{1}{\sqrt{f}} = a + c.\log\frac{z}{k} \quad (7)$$

where k = local roughness height (m); c = coefficient assumed to take the value of von karman coefficient (0.4); and a = coefficient that is a function of the cross-sectional shape of the channel.

For rough bed, Masterman and Thorne (1992) suggest that Hey's (1979) calibration of Eq. (7) offers reasonable predictive ability, so that

$$\frac{1}{\sqrt{f}} = 2.03\log\frac{a_s z}{3.5k} \quad (8)$$

where z = local flow depth; k = local roughness height; and a_s = shape-correction factor given by Hey (1979), and

$$a_s = 11.1(R/D)^{-0..314} \quad (9)$$

where R = hydraulic radius and D = the maximum water depth.

Eqs. (5)–(8) have been implemented in a computer program that provides estimates of unit discharge of a channel of a specified cross-section geometry and gradient, bed material size for the channel bed and side banks. The cross-section is divided into a number of computational nodes as a precursor to the numerical solution of (5). Two hundred computational nodes are used to ensure satisfactory numerical performance, Darby and Thorne (1996).

3 MODEL APPLICATIONS

To study the effect of variation of wetted perimeter roughness, a number of numerical experiments were performed where the roughness of the bank was increased three times higher than the bed roughness, the side bank slope was changed three times, the ratio of channel bed width to water depth ratio was changed two times and the roughness of the bed also was increased three times than the roughness of banks. Table (1) shows the different variables used in

Table 1. Variables used in the computations.

Run no.	d_b (m)	d_s (m)	S_y	b/D
1	0.002	0.004	1	5
2	0.002	0.002	1	5
3	0.002	0.006	1	5
4	0.002	0.008	1	5
5	0.002	0.002	1.5	5
6	0.002	0.004	1.5	5
7	0.002	0.006	1.5	5
8	0.002	0.008	1.5	5
9	0.002	0.002	2	5
10	0.002	0.004	2	5
11	0.002	0.006	2	5
12	0.002	0.008	2	5
13	0.002	0.002	1	10
14	0.002	0.004	1	10
15	0.002	0.006	1	10
16	0.002	0.008	1	10
17	0.002	0.002	1.5	10
18	0.002	0.004	1.5	10
19	0.002	0.006	1.5	10
20	0.002	0.008	1.5	10
21	0.002	0.002	2	10
22	0.002	0.004	2	10
23	0.002	0.006	2	10
24	0.002	0.008	2	10
25	0.004	0.002	1	5
26	0.006	0.002	1	5
27	0.008	0.002	1	5
28	0.004	0.002	1.5	5
29	0.006	0.002	1.5	5
30	0.008	0.002	1.5	5
31	0.004	0.002	2	5
32	0.006	0.002	2	5
33	0.008	0.002	2	5

this study where the longitudinal bed slope and water depth were kept constants at 0.0001 and 2.0 m height respectively.

Figure (2) shows the unit discharge for different values of ds/db ratio larger than 1.0 at b/D value equal to 5.0 for side bank slope equal to 1.0, where d_s = the mean particles size for side banks materials; d_b = the mean particles size for bed channel materials; b = the bed channel width and D = the maximum water depth. From this Fig., it is noticeable that the variation in bank roughness affects the distribution of the unit discharge where the unit discharge decreases by increasing the side bank roughness and this effect is not only restricted to the bank but also extends along the main channel.

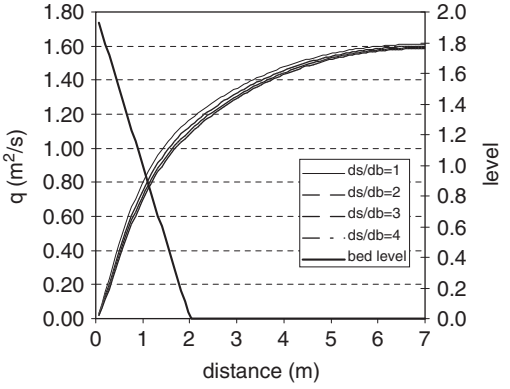


Figure 2. Lateral variation in discharge for different ratio of bank roughness to bed roughness at b/D = 5 and $d_s > d_b$ for side bank slope equal to 1.0.

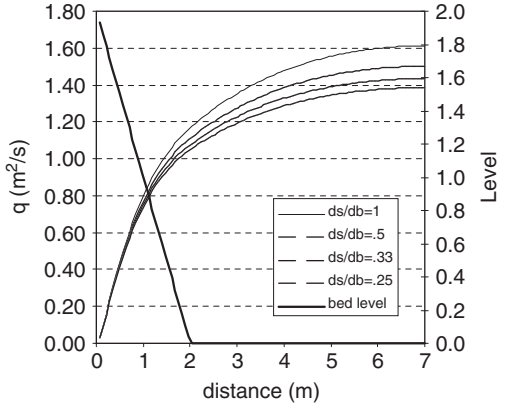


Figure 3. Lateral variation in discharge for different ratio of bank roughness to bed roughness at b/D = 5 and $d_b > d_s$ for side bank slope equal to 1.0.

Also, Fig. (3) shows the unit discharge distribution for different values of d_s/d_b smaller than 1.0 where the bank roughness was kept constant and the bed roughness was increased. From this Fig., it is noticeable that the variation in the bed roughness affects the distribution of the unit discharge and this effect is high at mid of channel and decreases in the direction of channel banks.

Figure (4) shows the ratio of flow capacity of non-uniform channel roughness to the flow capacity of uniform channel roughness versus the ratio of bank to bed roughness for different side bank slope at ratio of channel bed width to depth ratio equal to 5. It is apparent from that Figure, that the channel total flow capacity decreases by increasing of the bank roughness and this decreasing increases by increasing of the channel bank slope. In the same way, in Fig. (5)

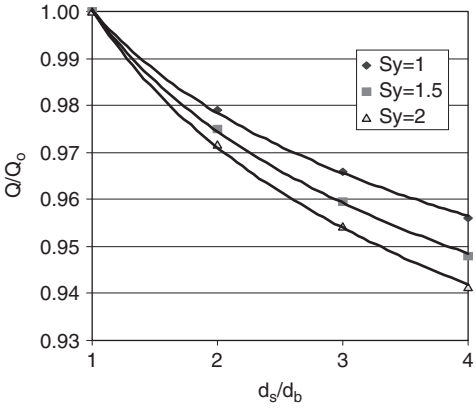


Figure 4. Values of Q/Q_0 versus d_s/d_b for different side bank slopes at b/D = 5 and $d_s > d_b$.

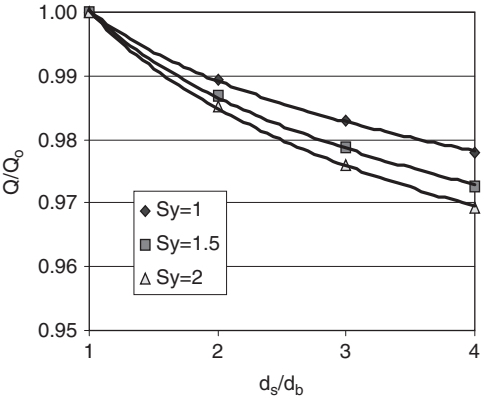


Figure 5. Values of Q/Q_0 versus d_s/d_b for different side bank slopes at b/D = 10 and $d_s > d_b$.

the same relation was drawn for ratio of channel bed width to depth equal to 10. With comparison between Fig. (4) and Fig. (5), it can be observed that the rate of decrease in flow capacity reduces by increasing of channel bed width to depth ratio.

To show the effect the ratio of increasing the channel bed roughness, Fig. (6) shows the relation of the dimensionless discharge versus the ratio of bank roughness to bed roughness for different bank slope values at ratio of channel bed width to depth equal to 5.0. From that Fig., it is noticeable that the reduction may be arrive to about 0.88% in the flow capacity at value of d_s/d_b equal to 0.25 and this reduction decreases by increasing of the side bank slope but the effect of side bank slope is not so high such as that the result from the variation in roughness.

In Fig. (7), values of the equivalent Manning roughness coefficient to the uniform cross-section roughness ratio (n_e/n_o) were drawn versus d_s/d_b ratio for the different side bank slopes at b/D equal to 5 and d_s/d_b greater than 1.0. The data for each value of side bank slope (S_y) clustered around a curve, which may be expressed in the form;

$$\frac{n_e}{n_o} = a.\ln(\frac{d_s}{d_b}) + 1.0 \qquad (10)$$

where a is a coefficient depending on the side bank slope (S_y).

The correlation between a and S_y may be given in the form;

$$a = 0.0177 + 0.0141.(S_y) \qquad (11)$$

By the same way, in Fig. (8), the numerical results on between n_e/n_o and d_s/d_b was drawn for b/D ratio equal to 10. It can be shown that the relation follow the same previous logarithmic formula (Eq. (10)) and the correlation between a and S_y may be given in the form;

$$a = -0.0098.S_y^{\,2} + 0.03377.(S_y) - 0.008 \qquad (12)$$

Finally, in Fig. (9) values of n_e/n_o ratio were plotted versus d_s/d_b at the case of bed roughness higher than the bank roughness for the different values of side bank slope and b/D equal to 5. It can be shown from this Fig., that the same logarithmic relation (Eq. 10) still applied and the constant a can follow the following relation.

$$a = 0.0072.S_y^{\,2} - 0.0292.(S_y) + 0.1212 \qquad (13)$$

In the future, we will try to generalize this relation for a wider range of channel width to depth ratios and will be validated by experimental results.

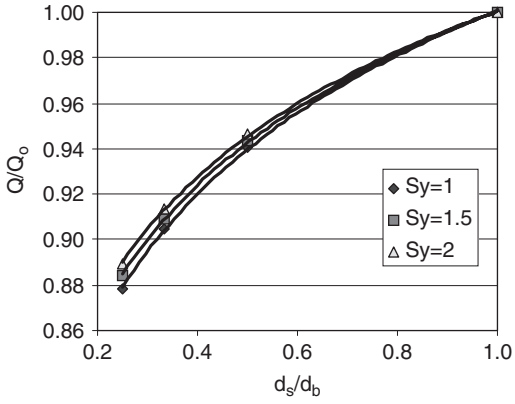


Figure 6. Values of Q/Q_0 versus d_s/d_b for different side bank slopes at $b/D = 5$ and $d_b > d_s$.

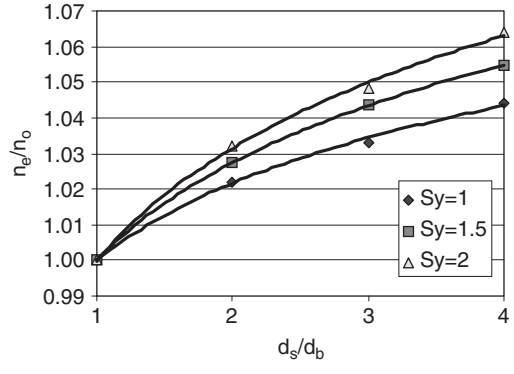


Figure 7. Values of n_e/n_o versus d_s/d_b for different values of side bank slope at $b/D = 5$ & $d_s/d_b > 1.0$.

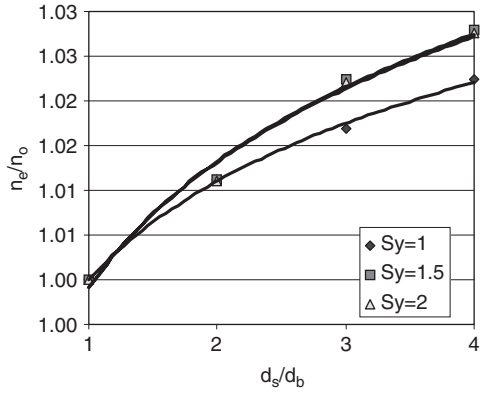


Figure 8. Values of n_e/n_o versus d_s/d_b for different values of side bank slope at $b/D = 10$ & $d_s/d_b > 1.0$.

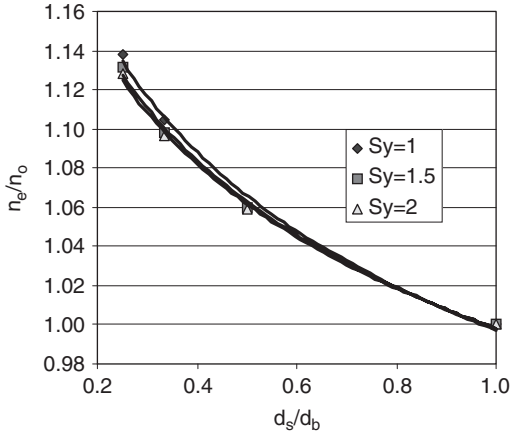


Figure 9. Values of n_e/n_o versus d_s/d_b for different values of side bank slope at $b/D = 5$ & $d_s/d_b < 1.0$.

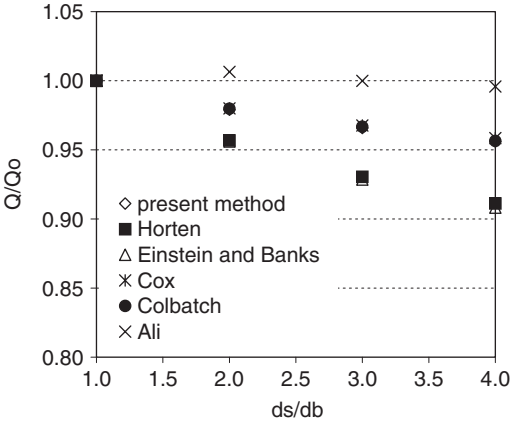


Figure 10. A comparison between the present method and other methods.

4 COMPARISON BETWEEN THE PRESENT METHOD AND AVAILABLE METHODS

Figure (10) shows a comparison between the present method and other methods found in literatures. More details about these methods can be found in Ali and Abdelrahem (2001), Chow (19590, French (1996) and U.S. Army Corps of Engineers (1994). Where in these methods, the flow area is divided into number of parts each with an associated wetted perimeter and roughness coefficient. There are a well agreement between the present method and both Cox and Colbatch method, however Horten and Einstein & Banks methods give values for the total discharge less than the present method. This attributes to that Horton assumed that each of subdivisions of the flow area has an average velocity equals to the mean velocity of the total area and Einstein & Banks assumed that the total force-resisting motion equal to the sum of the subsection resisting forces. In contrary to this, Ali's method gives values higher than the present method.

5 CONCLUSIONS

To minimize the discrepancy in total conveyance value for flow in channel with variation in roughness through the wetted perimeter, a new subdivision method take into account the momentum transfer and lateral shear stress distribution between the elements was introduced. A numerical model that predicts the flow capacity of a channel with varying roughness through perimeter has been developed. This model significantly differs from previous subdivision methods in that it consistently accounts for the momentum transfer through the inner and outer region of the channel.

To assess the model's predictive ability, results generated by the model were compared with available methods. To provide the design engineer with a practical means of generating the model results without having to run the numerical model, equations and plots based on model were developed for the equivalent Manning roughness coefficient.

REFERENCES

Ahmed, A. I., and Bakry, M. F., (1997), "Roughness Characteristics of Lined Canals", Al-AZHAR Eng. Fifth Int. Conference, Cairo, Egypt.

Ali, N. A., and Mohamed, A. A., (1991), "Computation of Flow Capacity in Compound Channel with Varying Roughness", Engineering Research Bulletin, University of Helwan, Faculty of Eng. & Tech., Mataria, Cairo, Egypt. Vol. 3.

Ali, N. A., and Abdelrahem, G. A., (2001), "Lectures notes in open channel hydraulics and hydraulic machines", Assiut University, Assiut, Egypt.

Armanini, A., and Righetti, M., (1998), "Flow Resistance in compound Vegetated Channel", ICHE conference.

Chow, V. T., (1959), "Open channel hydraulics", McGRAW-HILL Book.

Darby, S. E., and Thorne, C. R., (1996), "Predicting Stage-Discharge Curves in Channels with Bank Vegetation", Jour. of Hydraulic Eng., Vol. 122, No. 10, pp. 583–586.

Dolgopolova, E., (2001), "Plane river resistance", IAHR conference, Beijing, China.

El-Attar, S. T., (1980), "Design of open channels", Ph. D. Thesis, Faculty of Eng., Assiut University, Assiut, Egypt.

French, R. H., (1996), "Open–Channel Hydraulics", McGRAW HILL Book.

Garbrecht, J., and Brown, G. O., (1991), "Calculation of Total Conveyance in Natural Channels", Jour. of Hydraulic Eng., Vol. 117, No. 6, pp. 788–798.

Hey, R. D., (1979), "Flow resistance in gravel–bed rivers", Jour. Hydr. Div., ASCE, 105 (4), 365–379.

Lambert, M. F., and Sellin, R. H. J., (1996), “Discharge Prediction in Straight Compound Channels Using the Mixing Length Concept”, Jour. of Hydraulic Research, Vol. 34, No. 3, pp. 381–395.

Masterman, R., and Thorne, C. R., (1992), “Predicting influence of bank vegetation on channel capacity”, Jour. Hydr. Engrg., 118(7), 1052–1058.

Myers, W. R. C., Lyness, J. F., and Cassells, J. B. (1999), “Estimation of Roughness Coefficient for Compound Channels”, IAHR Conference, Graz, Austria.

Rabkova, E. K., and Garanina, E. V., (2001), “Distribution of Averaged Local Velocities in an Open Turbulent Flow”, Water Resources, Vol. 28, No. 5, 2001, pp. 577–580.

Rodi, W., (1980), “Turbulence Models and Their Application in Hydraulics- A State of the Art Review”, IAHR book publications, Delft.

U.S. Army Corps of Engineers, (1994), “Methods for Predicting n values for Manning Equation”, EM 1110-2-1601.

This page intentionally left blank

River Flow 2004 – Greco, Carravetta & Della Morte (eds.)
© 2004 Taylor & Francis Group, London, ISBN 90 5809 658 0

Boundary conditions between panels in depth-averaged flow models revisited

D.W. Knight & M. Omran
The University of Birmingham, Birmingham, UK

J.B. Abril
Consultant in River Engineering & Honorary Research Fellow at the University of Birmingham, UK

ABSTRACT: This paper revisits the issue of the boundary conditions between panels or domains in depth-averaged flow models. The Shiono and Knight Method (SKM) is used to illustrate a potential problem in such models, since sometimes the boundary conditions are misapplied, leading to invalid results in some cases, despite giving reasonably good results in other cases under certain circumstances. Experimental results and numerical studies are used to illustrate the problem and a suggestion is made as to how one of the most commonly used boundary conditions should be applied. Algebraic expressions within the analytical solutions of SKM were modified to illustrate the importance of using correct inter-panel boundary conditions.

1 INTRODUCTION

A two-stage, or compound channel, consists essentially of two major parts, the main river channel and the flood plains. In natural rivers, the flow is confined within the main channel for the majority of the time. However, during flood events the flow spills over onto the adjacent floodplains, which themselves form part of the 'overall' river system. Since compound channels are frequently used in flood alleviation schemes, it is important to be able to predict the conveyance capacity, velocity distribution, and boundary shear stress distribution for a given flood event. The velocity and boundary shear stress are also required when establishing the stage-discharge relationship, a relationship that is important in flood studies, since it is often extrapolated to estimate water levels for discharges higher than those that have actually been observed. The same parameters of depth-averaged velocity and boundary shear stress also feature in many engineering design studies concerning river morphology, sediment transport, bank protection, vegetation and habitats.

The determination of these parameters is a difficult and challenging task for river engineers, due to the strong shear layers that develop at the main channel-floodplain interface when the water level is above the bank full stage. Due to the difference in velocity between the faster moving water in the main channel and the slower moving water in the flood plain, a lateral transfer of momentum takes place, which significantly affects the conveyance capacity, the velocity and boundary shear stress distributions in such channels (Knight & Shiono, 1996). Lateral distribution methods (LDM) have been shown to give promising results in modelling compound channels, and one such method, an analytical one, is known as the Shiono and Knight Method (SKM).

2 THEORETICAL BACKGROUND

SKM is based on a depth-averaged form of the streamwise Reynolds Averaged Navier-Stokes (RANS) equations, expressed for steady uniform flow by Shiono and Knight (1990 & 1991) as:

$$\rho g H S_0 - \frac{1}{8}\rho f U_d^2\left(1+\frac{1}{s^2}\right)^{1/2} + \frac{\partial}{\partial y}\left[\rho\lambda H^2\left(\frac{f}{8}\right)^{1/2} U_d \frac{\partial U_d}{\partial y}\right] = \frac{\partial}{\partial y}\left[H\left(\rho\overline{(UV)}_d\right)\right] \quad (1)$$

in which S_o = channel bed slope, s = channel side slope (1:s, vertical:horizontal), H = depth, U_d = depth-averaged streamwise velocity, λ = dimensionless eddy viscosity f = local Darcy-Weisbach friction factor, U = velocity component in the x, streamwise, direction, V = velocity component in the y, lateral, direction and y = lateral co-ordinate.

Equation (1) depends on depth-averaged parameters of velocity, Reynolds stresses and secondary flow, which in turn are governed by three calibration coefficients f, λ, Γ, concerned with local bed friction, lateral shear, and secondary flow respectively. These coefficients are defined by:

$$\tau_b = \frac{f}{8}\rho U_d{}^2;\ \lambda = \frac{\bar{\varepsilon}_{yx}}{U_* H};\ \Gamma = \frac{\partial}{\partial y}\left[H\left(\rho \overline{UV} \right)_d \right] \quad (2)$$

in which τ_b = local bed shear stress, U_* = shear velocity and $\bar{\varepsilon}_{yx}$ = depth-averaged eddy viscosity.

Analytical solutions to equation (1) are given by Shiono and Knight (1988) and Knight & Shiono (1996), distinguishing between constant and variable depth domains. Once the values of f, λ, Γ are specified for each domain or panel, and boundary conditions applied, then analytical expressions for U_d and τ_b, may be obtained. Knowing U_d and H across the channel, lateral integration of the product will give the discharge, and repeated use gives the stage-discharge relationship.

Shiono and Knight (1988, 1990) originally proposed two boundary conditions at each domain junction for the sloping wall case as follows:

- Continuity of the depth-averaged velocity

$$(U_d)_i = (U_d)_{i+1} \quad (3)$$

- Continuity of the lateral gradient of the depth-averaged velocity

$$\left(\frac{\partial U_d}{\partial y} \right)_i = \left(\frac{\partial U_d}{\partial y} \right)_{i+1} \quad (4)$$

These have continued to be used by themselves under certain circumstances and by other authors, e.g. Ervine et al. (2000), without their limitations always being either fully explained or appreciated. The purpose of this paper is therefore to highlight this issue, especially where there are significant changes in depth or parameters between panels.

3 BOUNDARY CONDITIONS BETWEEN PANELS

Many researchers have conducted experimental investigations into the flow structures at the junction between rivers and their floodplains. Data sets from the large scale studies in the Flood Channel Facility (FCF) (see Knight, 1992; Knight & Sellin, 1987), and from studies in wind tunnels by Lai (1987) and Rhodes (1991), are used herein to illustrate the lateral variation in depth-averaged parameters.

Lai (1987) and Rhodes (1991) performed experiments in compound air ducts, to study the mean flow structure and in particular the boundary shear stress and velocity distributions. These data are used to check the variation of depth-averaged velocity, U_d, lateral gradient of the depth-averaged velocity, dU_d/dy, local water depth, H, unit discharge, q, lateral gradient of the unit discharge, dq/dy, and the apparent shear force (ASF) across the floodplain/main channel interface. Experiments have been selected from these data to illustrate the effects of main channel side slope, by distinguishing between channels with vertical walls and channels with sloping walls. It should be noted that the data of Lai and Rhodes were obtained with a very fine lateral spacing interval, Δy, in the vicinity of the main channel/floodplain interface, in some cases as small as 1 mm. Furthermore, the vertical interval Δz was such that the U_d values were obtained from the average of between 6 and 17 local streamwise values, depending on the geometry of the cross section.

These very high quality sets can therefore be used to illustrate the boundary conditions between panels in depth-averaged flow models.

Figure 1 shows results from Experiment 14 (Rhodes, 1991), in which a large compound duct with a vertical side wall element was used, giving a step in the bed elevation of approximately 20 mm, as shown in Figures 1(a) & 1(b). The experimental results in Figures 1(c)–1(f) show that only the unit discharge q is continuous at the main channel/floodplain, interface, as would be expected from Samuels (1989), whereas U_d, dU_d/dy, H and dq/dy are not. Although q is continuous, there is a relatively large change at the interface position.

Thus the boundary conditions between panels are:

$$(U_d)_i \neq (U_d)_{i+1};\quad (q)_i = (q)_{i+1};$$

$$\left(\frac{dU_d}{dy} \right)_i \neq \left(\frac{dU_d}{dy} \right)_{i+1};\ \left(\frac{dq}{dy} \right)_i \neq \left(\frac{dq}{dy} \right)_{i+1} \quad (5)$$

Equation (5) indicates that the boundary conditions suggested in equations (3) and (4) are invalid for cross sections with any vertical side wall elements, as might be expected.

Figure 2 shows results from Experiment 20 (Rhodes, 1991) in which the same duct had one sloping side wall installed. Figures 2(c)–(f) show that U_d, H and q are continuous at the main channel/floodplain interface, whereas dU_d/dy and dq/dy are not. Consequently, the boundary conditions can be summarised as follows:

$$(U_d)_i = (U_d)_{i+1};\qquad (q)_i = (q)_{i+1};$$

$$\left(\frac{dU_d}{dy} \right)_i \neq \left(\frac{dU_d}{dy} \right)_{i+1};\ \left(\frac{dq}{dy} \right)_i \neq \left(\frac{dq}{dy} \right)_{i+1} \quad (6)$$

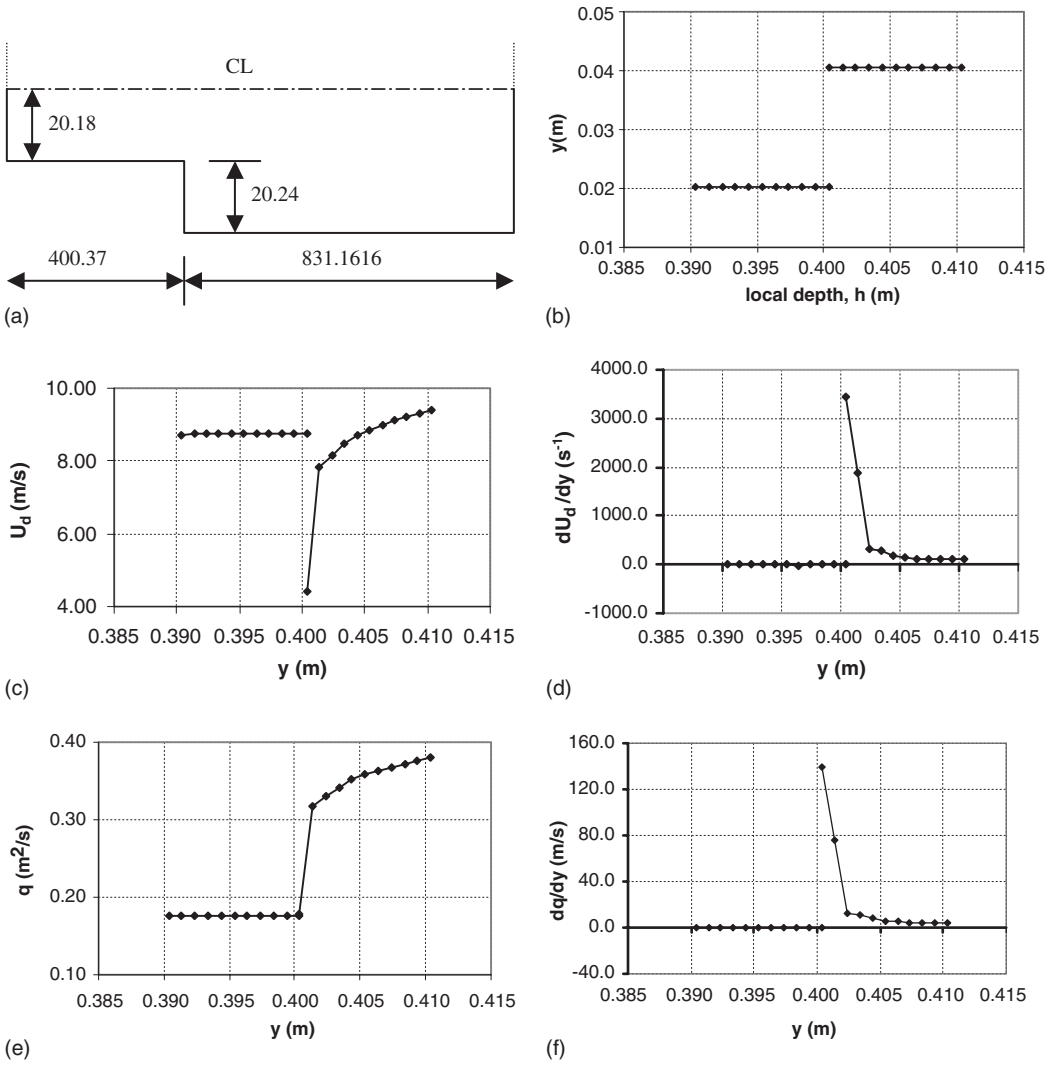


Figure 1. Results for Exp. 14 (Rhodes, 1991) (a) Geometry of duct cross section (mm), (b) Water depth variation, H versus y, (c) Velocity distribution, U_d versus y, (d) Velocity gradient distribution, (e) Unit discharge distribution, (f) Unit discharge gradient distribution.

Equation (6) shows that for a channel with a sloping side wall only the boundary condition in equation (3) is valid. The second boundary condition, in equation (4), is seen to be invalid for this particular experimental case. For sloping side walls, because H is always continuous the first two statements in (6) are equivalent as an inter-panel boundary condition.

Figure 3 shows some bed shear and apparent shear force data from Experiment 75 of Lai (1987), in which a small compound rectangular duct was used.

Figures 3(b) & (c) show the lateral distributions of bed shear stress on elements B1 and B2, although measurements were also made of wall shear stresses on elements W1 and W2 as well.

The distribution of the apparent shear force (*ASF*), shown in Figure 3(d), is demonstrably discontinuous over the vertical interface. Figure 3(e) shows that the discontinuity is equal to the value of the shear force measured on the vertical wall, as expected.

The apparent shear force may be determined for any vertical slice in a depth-averaged model by considering the balance of forces acting on a particular element of the cross-section. For example, in a typical depth-averaged flow model for a river, the channel

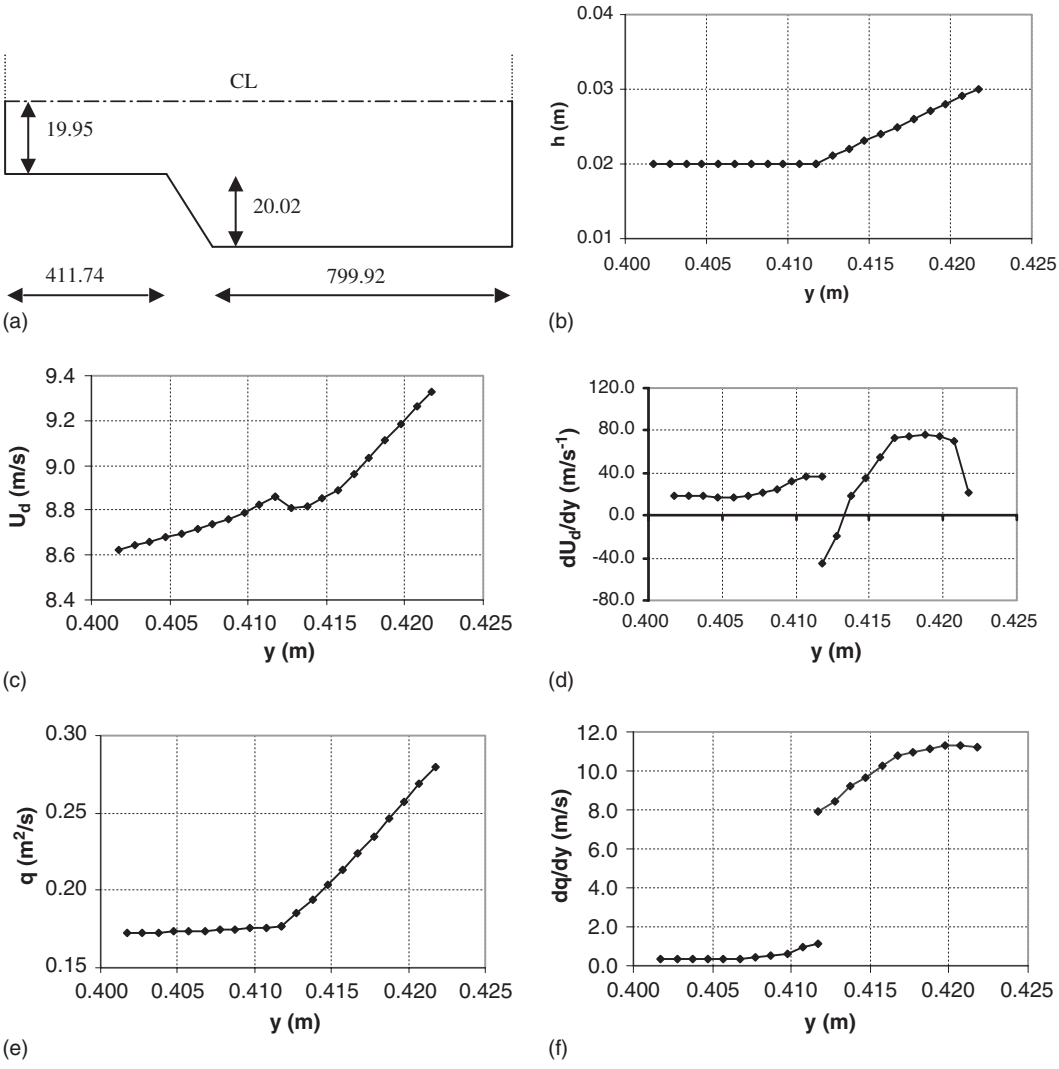


Figure 2. Results for Experiment 20 (Rhodes, 1991) (a) Geometry of cross section (mm), (b) Water depth variation, (c) Velocity distribution, (d) Velocity gradient distribution, (e) Unit discharge distribution, (f) Unit discharge gradient distribution.

cross-section is divided into any number of vertical slices in the transverse direction, y, and the flow assumed to be predominately in the streamwise direction, x, given by equation (1). The apparent shear force (ASF) acting on any vertical slice within the cross-section is then defined as the difference between the weight force of those elements, resolved in the streamwise direction up to that particular lateral position, y, minus the integrated boundary shear forces around the wetted perimeter up to the same lateral position. The ASF thus accounts for any momentum transfer effects across that vertical slice, arising from turbulent shear, secondary flow and planform vorticity.

Shiono & Knight (1991) have shown that the depth-averaged apparent shear stress (ASS) acting on any vertical interface within the cross-section, $\bar{\tau}_a$, may be calculated by integrating equation (1) to give

$$\bar{\tau}_a = -\frac{1}{H}\int_0^y \left[\rho g H S_0 - \tau_b\left(1+\frac{1}{s^2}\right)^{1/2}\right] dy \qquad (7a)$$

The apparent shear force (ASF) per unit streamwise distance is then given by $\bar{\tau}_a H$. If the apparent shear force at the interface from the floodplain side is denoted by ASF_1 and the apparent shear force from the

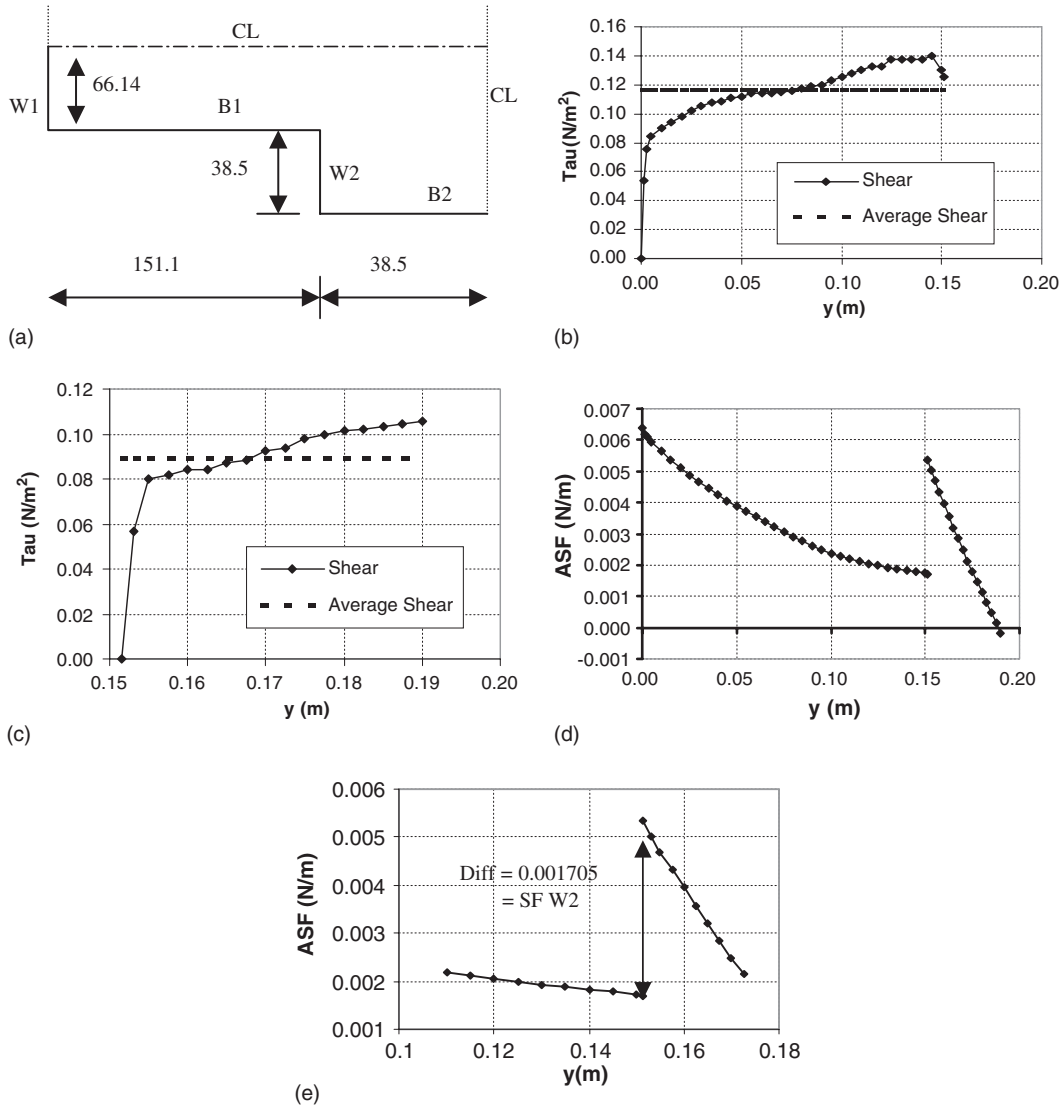


Figure 3. Results for Experiment 75 (Lai, 1987) (a) Geometry of cross section (mm), (b) Shear stress and average shear stress for bed 1, (c) Shear stress and average shear stress for bed 2, (d) Apparent shear force distribution, (e) Apparent shear force distribution at interface.

main channel side is denoted by ASF_2, then one can write:

$$ASF_1 = \rho g A_{FP} S_f - SF_{FP} \tag{7b}$$

$$ASF_2 = \rho g A_{FP} S_f - SF_{FP} - SF_{wall} \tag{7c}$$

where A_{FP} = area of the floodplain, SF_{FP} = shear force on the floodplain and SF_{wall} = shear force on the vertical wall.

From Figures 1 to 3, it is clear that the boundary conditions in equations (3) and (4) need to be applied with care. The first condition, given as equation (3), is clearly only valid for sloping side walls, as a step change in H introduces a corresponding step change in U_d. The second condition, given as equation (4), is not generally true, regardless of whether or not there is a vertical or sloping side wall. However, as Fig. 2(c) shows, there are circumstances where it might appear to be valid, either where insufficient

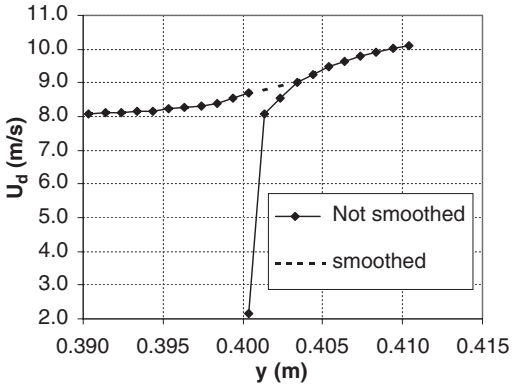


Figure 4. Experiment 17 of Rhodes (1991).

care is taken over acquiring data or where the data is 'smoothed' too much in any subsequent processing stage. This is illustrated better in Figure 4, in which depth-averaged velocity data from Experiment 17 of Rhodes (1991) is used, obtained from the larger compound rectangular duct. If the velocity in the main channel is depth-averaged at the vertical wall, then measured at increments of 1 mm from the junction, the 'Not smoothed' distribution is obtained.

However, if the first measurement of the velocity distribution had started at a point just 3 mm away from the main channel/floodplain junction, the 'Smoothed' curve would have been obtained. This indicates that particular care needs to be taken over measurements near the main channel/floodplain junction, as any omission or subsequent smoothing of the data can lead to inaccurate conclusions.

4 MATHEMATICAL ANALYSIS OF BOUNDARY CONDITIONS

In order to demonstrate these matters further, Abril (2003) performed mathematical analysis of the boundary conditions between panels in compound channels distinguishing between cases with continuous and discontinuous parameters f, λ, Γ and H using the SKM in comparison with the RFMFEM finite element model by Abril (1997). Two types of channel were considered, a compound rectangular channel, i.e. one with a vertical side wall, and a compound trapezoidal channel, i.e. one with a sloping side wall.

4.1 *Compound trapezoidal channel*

As a result of this analysis, for a compound trapezoidal channel, from a physical point of view the continuity between panels should satisfy equation (8):

$$U_d^{(1)} = U_d^{(2)} \tag{8a}$$

$$H^{(1)}\tau_{yx}^{(1)} = H^{(2)}\tau_{yx}^{(2)} \tag{8b}$$

Equation (8a) states that U_d should be continuous at the main channel/floodplain junction, and equation (8b) states that there is continuity of the unit force, $(H\tau_{yx})$, where τ_{yx} is the depth-averaged Reynolds shear stress, given by $\tau_{yx} = \rho\lambda H\sqrt{\frac{f}{8}}U_d\frac{\partial U_d}{\partial y}$. From equation (8b) one can write:

$$\left[\rho\lambda H^2\sqrt{\frac{f}{8}}U_d\frac{\partial U_d}{\partial y}\right]^{(1)} = \left[\rho\lambda H^2\sqrt{\frac{f}{8}}U_d\frac{\partial U_d}{\partial y}\right]^{(2)} \tag{9}$$

Provided that H is continuous and the velocity U_d is continuous at the junction, as they would be in a compound trapezoidal channel, equation (9) may be simplified to give:

$$\left[\lambda\sqrt{\frac{f}{8}}\frac{\partial U_d}{\partial y}\right]^{(1)} = \left[\lambda\sqrt{\frac{f}{8}}\frac{\partial U_d}{\partial y}\right]^{(2)} \tag{10}$$

Equation (10) can then be written as:

$$\mu^{(1)}\frac{\partial U_d^{(1)}}{\partial y} = \mu^{(2)}\frac{\partial U_d^{(2)}}{\partial y} \tag{11}$$

where

$$\mu = \lambda\sqrt{\frac{f}{8}} \tag{12}$$

Equations (8a) and (11) explain the results obtained in graphs 2(c) and 2(d), in which the depth-averaged velocity is continuous over the main channel/floodplain junction, while the lateral gradient of this velocity is not. However, as already pointed out, there are some circumstances where the boundary condition given in equation (4) might appear to be valid, firstly when local flow conditions might actually produce it and secondly when insufficient care is taken over acquiring and processing data. From the mathematical viewpoint equation (11) is equal to equation (4) only if f, λ and H are continuous across the compound section, thus the value of μ will be equal for adjacent panels, resulting in $(\partial U_d/\partial y)_i = (\partial U_d/\partial y)_{i+1}$. The latter has already been illustrated in Figure 4, using smoothed data.

4.2 *Compound rectangular channel*

A similar analysis was performed by Abril (2003) for a compound rectangular channel, where the boundary conditions between panels were assumed to be:

$$\left(\frac{q}{H}\right)^{(1)} = \left(\frac{q}{H}\right)^{(2)} \text{ or } \left(U_d\right)^{(1)} = \left(U_d\right)^{(2)} \tag{13a}$$

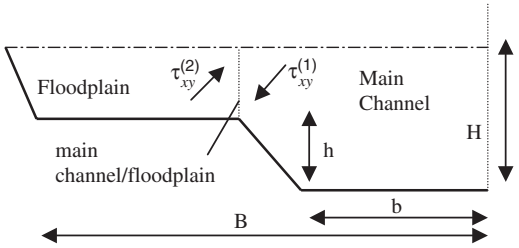


Figure 5. Compound trapezoidal channel.

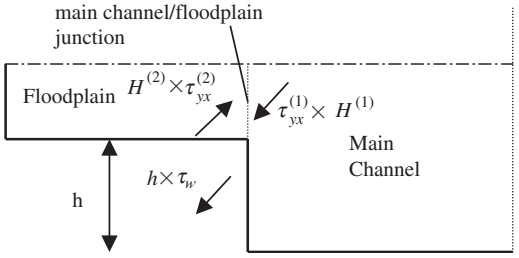


Figure 6. Compound rectangular channel.

$$H^{(1)}\tau_{yx}^{(1)} = H^{(2)}\tau_{yx}^{(2)} - h\tau_w \tag{13b}$$

However, Equation (13a) could be replaced by:

$$q^{(1)} = q^{(2)} \text{ or } \left(HU_d\right)^{(1)} = \left(HU_d\right)^{(2)} \tag{13c}$$

Equation (13c) has been illustrated in Figure 1(e), which shows that the unit discharge, $q = H \times U_d$, is continuous across a rectangular compound channel. Equation (13b) has been illustrated in Figure 3(e), which shows that the ASF is discontinuous over the vertical wall and the discontinuity is equal to the shear force on this wall. This is further illustrated in Figures 5 & 6, where the force equilibrium at the main channel/floodplain interface is shown for both types of channel.

Equation (13b) can be rearranged as:

$$\Psi^{(1)}U_d^{(1)}\frac{\partial U_d^{(1)}}{\partial y} = \Psi^{(2)}U_d^{(2)}\frac{\partial U_d^{(2)}}{\partial y} - h\tau_w \tag{14}$$

where

$$\Psi = \rho\lambda H^2\sqrt{\frac{f}{8}} \tag{15}$$

Equation (14) shows that the force on the vertical wall element has to be known, or supplied, before applying this particular boundary condition. This can be inconvenient from an analytical point of view, when determining the flow in a compound rectangular channel as an iterative procedure has to be employed to obtain the lateral distribution of U_d, prior to calculating the total discharge.

4.3 *Large scale vortex motions*

It should be noted that the use of the depth-averaged Reynolds stress in equations (8b) & (13b), rather than the apparent shear stress at any interface, appears to preclude any direct contribution from large scale vortex motions. However, these contributions are already simulated within the SKM by the Γ parameter (Shiono & Knight, 1991), and standard values were used herein, ensuring compatibility across groups of panels. Functional relationships for the ratio of Γ values between the main river channel and the floodplains, and its dependence upon depth, have been proposed (Knight & Abril, 1996; Abril & Knight, 2004b). Particular Γ values need therefore to be applied over several panels (positive in the river and negative on the floodplain) in order to mimic these large flow structures. The precise Γ values that should be used in all types of flow is as yet unknown, but experience in applying the SKM to both steep mountain rivers and mild slope valley rivers has proved to be reasonably successful (Abril & Knight, 2004b). The inclusion of the effects of planform vorticity into RANS based models is itself known to be problematic (Tominaga & Knight, 2004).

5 IMPLICATIONS OF USING DIFFERENT BOUNDARY CONDITIONS

The analytical solution of the SKM was used to investigate the impact of the boundary conditions in (11) and (14). Since no *a priori* analytical expression for the shear force on any vertical wall element in a compound channel has yet been obtained, the examples that follow will only cover the case of sloping side walls, using one FCF result from series 02 and one from a hypothetical channel.

Figure 7 shows the effect of different boundary conditions on the lateral distribution of depth-averaged velocity, U_d, for FCF experiment 020601 with $H = 0.21355$ m. The FCF series 02 relates to a symmetrical compound trapezoidal channel with $b = 0.75$ m, $B = 3.15$ m, $h = 0.15$ m and $s = 1.0$ for the geometrical parameters shown in Figure 5.

Because of the symmetry, only 4 panels are needed in SKM for each half of the cross section (main channel bed, main channel side slope region, floodplain bed, floodplain side slope region). The parameter values that gave the best fit were found to be: $f = 0.018$,

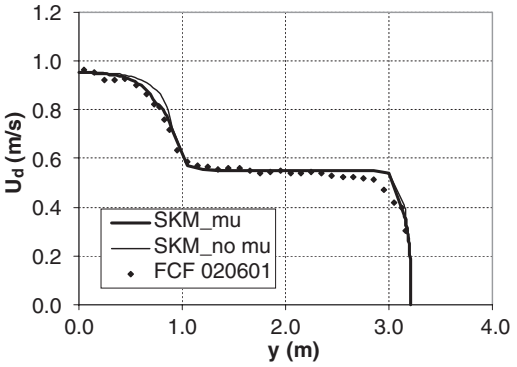


Figure 7. Lateral distributions of U_d (Example 1).

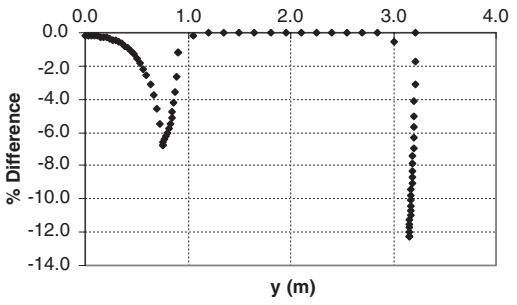


Figure 8. Differences in local U_d (Example 1).

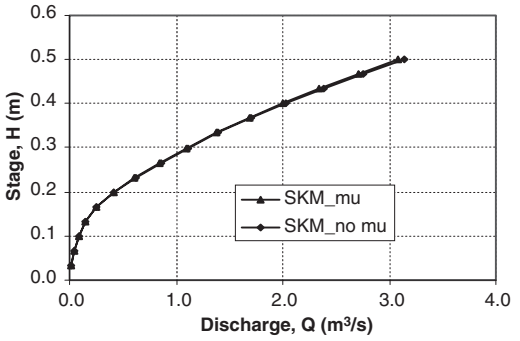


Figure 9. Stage-discharge relationships (Example 1).

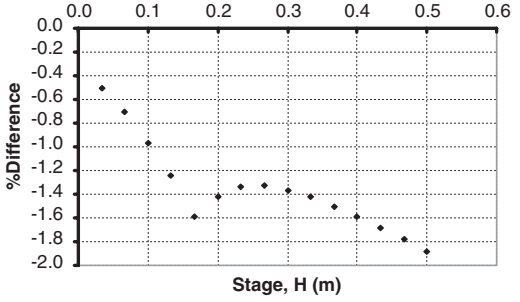


Figure 10. Differences in discharge (Example 1).

0.015, 0.022, 0.070; $\lambda = 0.07$, 0.20, 0.10, 0.10; and $\Gamma = 0.15$, 0.15, -0.20, -0.20 for the 4 panels respectively, with panels 1 & 2 being on the floodplain and panels 3 & 4 in the main channel. The boundary condition given by equation (11) was then tested with the same values of f, λ and Γ for two cases: $\mu^{(1)} = \mu^{(2)}$ and $\mu^{(1)} \neq \mu^{(2)}$ with μ being prescribed by equation (12) for each panel. The latter condition gave values of $\mu = 0.0093$, 0.0245, 0.0148 & 0.0265 respectively for the 4 panels. It should be noted that the values of f, λ and Γ were calibrated to fit the FCF data since the purpose of this paper is to show the effect of the new boundary conditions on SKM and not to discuss the calibration philosophy. It can be seen from Figure 8 that the introduction of the μ factor reduces the velocity over the side slope regions, with local errors in U_d of as much as 7%.

However, because the side slope region is relatively small, the total discharge only changes from $0.4842\,\mathrm{m^3 s^{-1}}$ to $0.4908\,\mathrm{m^3 s^{-1}}$, i.e. a change of -1.35%. At larger depths, the differences are still less than 2%. A comparison of the stage-discharge curves for this example is shown in Figure 9, and the differences are shown in Figure 10. These Figures indicate, that using the correct boundary condition, based on equation (11) with appropriate μ factors, the discharge is reduced compared to setting $\mu^{(1)} = \mu^{(2)}$.

Figure 11 shows the results for a hypothetical 9 node flood channel, divided into 8 panels each with a different side slope, roughness, eddy viscosity and secondary flow strength. Each panel was further divided into 10 sub-areas to improve computational accuracy. The panel (1-8) f values were varied from 0.02 by an increment of 0.01 per panel to 0.09, λ values were varied from 0.07 by an increment of 0.07 per panel to 0.56 and Γ values were taken as 0.15 (panels 1 & 2), 0.30 (panels 3 & 4), 0.45 (panels 5 & 6) and 0.60 (panels 7 & 8). The geometrical parameters were chosen to represent a small river with floodplains rougher than the main river channel. The computed stage-discharge relationships in Figure 11 again indicate that the introduction of the μ factor reduces the discharge.

Figure 12 shows that for a depth of 3.0 m the difference in discharge is as much as 15% ($45.437\,\mathrm{m^3 s^{-1}}$ to $39.676\,\mathrm{m^3 s^{-1}}$), thus warranting the inclusion of the correct boundary condition. Further examples of how the SKM may be used to make stage-discharge predictions are shown in Knight, Shiono & Pirt (1989) and Abril & Knight (2003b). An example of the use of

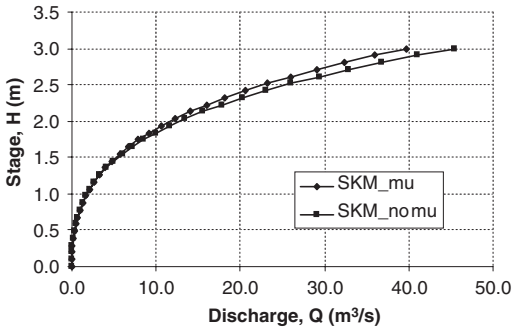


Figure 11. Stage discharge relationships (Example 2).

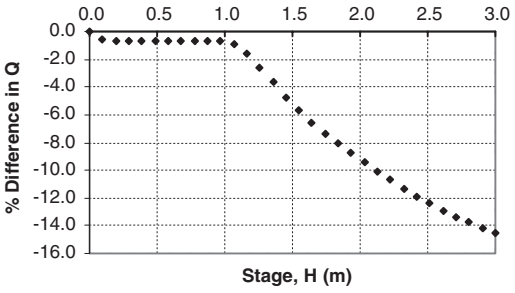


Figure 12. Differences in discharge (Example 2).

the SKM in simulating sediment transport is shown in Abril & Knight (2002 & 2003a).

6 CONCLUSIONS

The boundary conditions between panels in depth-averaged models have been shown to be important when either analysing experimental data or formulating a numerical model. Using a simple velocity gradient law at each panel junction in channels is appropriate where f & λ are the same across panel interfaces, regardless of differences in Γ. Where f & λ differ across panel interfaces, then it has been shown that the assumption of a simple gradient law is inappropriate, and can lead to possible overestimates of velocity and hence discharge. Although differences in total discharge may be small in certain cases, the differences in local values of depth-averaged velocity may be significant when the inter panel μ ratios are set equal to unity. Where f, λ and Γ vary significantly between panels, then physical and numerical studies have illustrated the need to introduce the correct boundary condition, based on equation (11) for channels with side slopes, and equation (14) for channels with any vertical wall elements or discontinuities in bed elevation. Particular care needs to be taken in experimental measurements in the interface region between the main channel and the floodplain, or in smoothing data, as poor spatial resolution may lead to false conclusions being made.

ACKNOWLEDGEMENTS

The authors acknowledge the support of the Engineering & Physical Sciences Research Council (EPSRC) which enabled Professor Abril to visit Birmingham under the terms of a Visiting Fellowship, GR/R54880/01.

REFERENCES

Abril, J.B., 1997. Numerical river modelling of turbulent flow, sediment tranport and flood routing using the finite element method, Thesis submitted for the degree of Doctor of Philosoply – PhD, The University of Birmingham, UK.

Abril, J.B., 2003. Benchmark comparisons of the analytical and finite element solutions of the SKM. *Internal Report, School of Civil Engineering*, August: University of Birmingham, UK.

Abril, J.B. and Knight, D.W., 2002. Sediment transport simulation of the Paute river using a depth-averaged flow model. *River Flow 2002, Proc. Int. Conf. on Fluvial Hydraulics,* Louvain-la-Neuve, Belgium, September, Vol. 2, 895–901, Balkema.

Abril, J.B. and Knight, D.W., 2004a. Stabilising the Paute river in Ecuador. *Civil Engineering*,*Paper 12704,* Instn. of Civil Engineers, London, Vol. 157, February, 32–38.

Abril, J.B. and Knight, D.W., 2004b. Stage-discharge prediction for rivers in flood applying a depth-averaged model. *Journal of Hydraulic Research, IAHR*, 41, No. 6, 1–14. (in press).

Ervine, D.A., Babaeyan-Koopaei, K. and Sellin, R.H.J., 2000. Two-dimensional solution for straight and meandering overbank flows. *Journal of Hydraulic Engineering*, ASCE, Vol. 126, No. 9, September 653–669.

Ervine, D.A., Babaeyan-Koopaei, K. and Sellin H.J.R., 2000. Two-dimensional solution for straight and meandering overbank flow. *Journal of Hydraulic Engineering*, Vol. 126, No. 9.

Knight, D.W., 1992. SERC Flood Channel Facility experimental data – Phase A, Vols. 1–15, *School of Civil Engineering*, The University of Birmingham, May, (available from HR Wallingford, Oxon, OX10 8BA, UK).

Knight, D.W. and Abril, B., 1996., Refined calibration of a depth-averaged model for turbulent flow in a compound channel, *Proc. Instn. of Civil Engineers, Water, Maritime and Energy Division*, London, Vol. 118, Issue 3, September, Paper No. 11017, 151–159.

Knight, D.W. and Sellin, R.H.J., 1987. The SERC Flood Channel Facility, *Journal of the Institution of Water and Environmental Management,* Vol. 1, No. 2, October, 198–204.

Knight, D.W. and Shiono, K., 1996. River channel and floodplain hydraulics, in *Floodplain Processes*, (Eds Anderson, Walling & Bates), Chapter 5, J Wiley, 139–181.

Knight, D.W., Shiono, K. and Pirt, J., 1989. Prediction of depth mean velocity and discharge in natural rivers with overbank flow. *Proc. Int. Conf. on Hydraulic and Environmental Modelling of Coastal, Estuarine and River Waters*, (Ed. R.A. Falconer, P. Goodwin, R.G.S. Matthew), Gower Technical, University of Bradford, September, Paper 38, 419–428.

Lai, 1987. Flow resistance, discharge capacity and momentum transfer in smooth compound closed ducts, *PhD thesis*, The University of Birmingham.

Rhodes 1991. An experimental investigation of the mean flow structure in wide ducts of simple rectangular and compound trapezoidal cross section, examining in particular zones of high lateral shear, *PhD thesis*, The University of Birmingham.

Samuels, P.G., 1989. Some analytical aspects of depth averaged flow models, *Proc. Int. Conf. on Hydraulic and Environmental Modelling of Coastal, Estuarine and River Waters*, (Ed. R.A. Falconer, P. Goodwin, R.G.S. Matthew), Gower Technical, University of Bradford, September, Paper 37, pp 411–418.

Shiono, K. and Knight, D.W., 1988. Two-dimensional analytical solution for a compound channel, *Proc. 3rd Int. Symposium on Refined Flow Modelling and Turbulence Measurements,* Tokyo, Japan, July, 503–510.

Shiono, K. and Knight, D.W., 1990. Mathematical models of flow in two or multi stage straight channels, *Proc. Int. Conf. on River Flood Hydraulics*, (Ed. W.R. White), Wallingford, September, J. Wiley & Sons, Paper G1, 229–238.

Shiono, K. and Knight, D.W., 1991. Turbulent open channel flows with variable depth across the channel, *Journal of Fluid Mechanics*, Vol. 222, 617–646 (and Vol. 231, October, p 693).

Tominaga, A. and Knight, D.W., 2004. Numerical evaluation of secondary flow effects on lateral momentum transfer in overbank flows, *Proc. River Flow 2004*, Naples, Italy, June.

River Flow 2004 – Greco, Carravetta & Della Morte (eds.)
© 2004 Taylor & Francis Group, London, ISBN 90 5809 658 0

Effect of vegetation on boundary layer with turbulent free stream

P. Gualtieri, G. Pulci Doria & L. Taglialatela
Hydraulic and Environmental Engineering Department Girolamo Ippolito, University of Naples Federico II, Napoli (Italy)

ABSTRACT: Effects of vegetation on flow hydraulic characteristics as flow resistance, conveyance capacity, turbulence characteristics, represent a very studied research topic, mostly in relation to uniform flow condition. In this paper effect of vegetation on velocity distributions in a boundary layer are experimentally investigated. Vegetation is modelled through regular array of vertical brass cylinders of two different heights. Local mean velocity distributions were detected through an LDA system. The presence of vegetation produces an evident change in velocities profiles and a meaningful increase of boundary layer thickness. But in any case the equilibrium boundary layer characteristics are preserved with vegetation too.

1 INTRODUCTION

1.1 *Vegetated surfaces problems*

In the past, vegetation on river beds has been considered just as a source of flow resistance, and for this reason it has been usually eliminated in order to improve the water conveyance.

Now, vegetation is no longer regarded merely as an obstruction to the movement of the water, but rather as a mean for providing stabilization for banks and channels, habitat and food for animals, and pleasing landscapes for recreational use. Therefore the preservation of vegetation is of great relevance for the ecology of natural and artificial systems.

For this reason, the study of the effects of vegetation on the hydrodynamic behaviour of the rivers represents one of the most basic knowledge required by hydraulic engineers.

Vegetation may be regarded as a kind of surface roughness whose effects depend mainly on height, density, distribution and type of vegetation.

Mean flow and turbulence characteristics of open channel flows over a submerged vegetated boundary has been studied by either laboratory measurements or numerical computations through proper turbulence models.

In particular, referring to the mean velocity profile above submerged vegetation, it is known that it depends on several factors.

Numerous investigations have been made about the velocity profile above either rigid or flexible submerged vegetation.

Rigid vegetation was modelled through wooden or metallic cylinders, flexible vegetation was modelled through plastic strips or through grass or other vegetation types (Bettess 2003, Fisher-Antze et al. 2001, Kouwen et al. 1969, Kouwen et al. 1973, Kouwen et al. 1981, Lopez et al. 2001, Stone et al. 2002, Sung-Uk 2001, Tsuijimoto et al. 1990, Tsuijimoto 1999).

1.2 *Boundary layer problems*

On another hand, the hydrodynamic behaviour of boundary layer is one of the most important topics of fluid mechanics. The classical boundary layer is born when a uniform potential current, without any turbulence, strikes against a flat plate parallel to the current direction. In this situation, an almost entirely turbulent flow is born near the plate, and its thickness grows in the direction of the flow itself.

This turbulent flow is called a boundary layer one, whereas the yet potential current superimposed to it is called external layer flow. The hydrodynamic laws which rule the boundary layer are now reasonably well known, also if they need yet further research. In particular, in the aforementioned hydrodynamic condition, the value of the pressure gradient along the flat plate is the most important parameter which fixes the local mean velocity distribution along the direction orthogonal to the plate. For instance, one of the first researchers who established for this distribution in case of smooth plate a law more advanced than the simpler logarithmic one was (Coles 1956): his law is called the "wake law".

This "wake law" supposes that the simple logarithmic law must be corrected with the addition of a further term formed through the product of a universal law and a parameter (called Π) depending on

the non dimensional value of the pressure gradient along the plate. This "wake law" is valid only if this non dimensional value of pressure gradient is constant along the plate itself: in this case the boundary layer is called an "equilibrium boundary layer" and the non dimensional velocity distribution is the same in all its different sections.

A more sophisticated type of boundary layer flow is that which is born when a turbulent current strikes against the flat plate parallel to the current direction.

This is obviously an important type of boundary layer, because the presence of turbulence in streams is a very frequent condition. At the present time, the impact of free stream turbulence on fully turbulent boundary layer has been investigated in several experimental, analytical and computational studies.

Many of these studies deal with the effects of free stream turbulence on the main statistical turbulence quantities and in particular with the mean local velocity distribution laws (Bandypadhyay 1992, Blair 1983a, b, Castro 1984, Charnay et al. 1971, 1976, Evans 1985, Evans & Horlock 1974, Hancock & Bradshaw 1983, Hancock & Bradshaw 1989, Hoffmann & Mohammady 1991, Huffman et al. 1972, Kline 1960, Mc Donald & Kreskowsky 1974, Meier & Kreplin 1980, Robertson & Holt 1972).

Coming back to the previous example, Coles believed that his "wake law" could represent also this type of boundary layer, because he assumed that the presence of turbulence in free stream would have the same consequences on velocity distribution than an adverse pressure gradient.

Two of the writers too worked in previous years in the boundary layer with free stream turbulence research field (Gualtieri & Pulci Doria 1997, 1998a, b, 1999, 2001, 2003, Pulci Doria 1991), performing their experimental tests in a water boundary layer instead of air boundary layer as usual. The produced papers dealt with the influence of free stream turbulence on boundary layer thickness and the main statistical turbulent quantities, on the possibility of conceiving a particular boundary layer model, and some of them (Gualtieri & Pulci Doria 1998b, Pulci Doria 1991) dealt in particular with the inside mean velocities distribution problem. The investigated boundary layers were always equilibrium ones with zero value of piezometric head (condition that for water is equivalent to the zero value of pressure gradient in air).

2 AIM OF PRESENT PAPER

In the growing literature about vegetated streams the effects of vegetation on boundary layer characteristics has been not yet considered, at least in relation to authors' knowledge. A new research line recently opened by the authors therefore regards, in relation to boundary layers with free stream turbulence, the possibility of discovering how wall vegetation can affect their dynamic development, the values of their thickness at different distances from the leading edge, and the mean velocities distribution inside. This type of research has clearly a basic theoretical meaning, but also can aid to clear applied problems, as for instance to detect the rapidity of changes of a current behaviour after abrupt changes of the nature of the vegetated walls.

The aim of the present paper is to give first contributions to this new research line through comparisons between the behaviour of a boundary layer with free stream turbulence on a flat plate and of a boundary layer with the same free stream turbulence but developing on differently vegetated plates.

In particular our objective is to examine the interconnection between vegetation and mean velocity distribution in a turbulent boundary layer developing in a water channel. Towards this end, the vegetation has been modelled through regular array of vertical brass cylinders, having two different heights, whose values are comparable with the boundary layer thickness.

3 EXPERIMENTAL PLANT

3.1 *Fundamental plant*

For the sake of carrying out suitable experimental surveys, the plant represented in Figures 1, 2 has been used.

The main device of the experimental plant is a variable slope channel 4 m long and 15 cm large, with plexiglass walls and bottom, coming out from a feeding tank supplied by a circulation pump. This tank feeds the channel through an adjustable rectangular sluice gate. The inlet towards the sluice gate is modelled through a suitable plexiglass device so shaped to avoid any possible trouble to the incoming current.

In this plant, it is possible to measure the water height in the tank, the height of the sluice gate, the slope of the channel, and the water heights in all cross sections of the channel itself.

In the first sections of this channel a boundary layer flow is generated on the bottom. This boundary layer grows in the following sections, until its thickness attains the same value of the circulating flow height at a distance from the inlet of the channel (boundary layer leading edge) depending on the dynamic characteristics of the flow itself, but which is in any case of the order of 1 m or something less. In a true boundary layer the external layer flow thickness should be very high (theoretically infinitely high) and the current should be very large (theoretically infinitely large): consequently the described channel flow could not be considered a true boundary layer flow. Nevertheless, in hydraulic literature this way of generating a

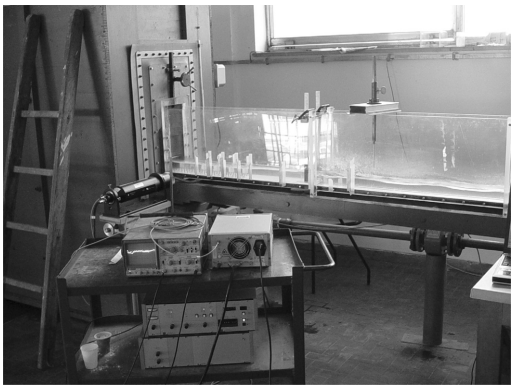


Figure 1. Photo of the experimental channel.

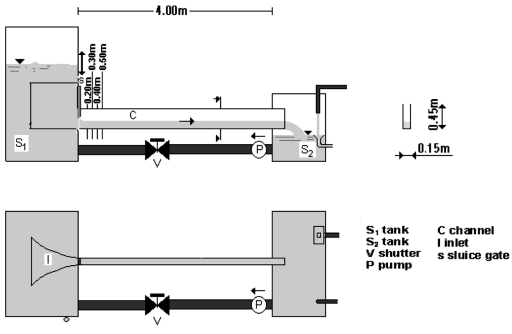


Figure 2. Layout of the experimental channel.

boundary layer is very common. The authors too used this type of plant other times, in their already remembered papers, and in these papers they stressed that the statistical quantities distributions (as mean velocities and velocities momentums, length scales and so on ….) were in accordance with the literature ones for boundary layers: in particular, for instance, mean velocities distributions were in accordance with Coles' wake law, except in the upper part of the boundary layer (till velocities attained the 97% values of the external layer velocities), where Coles law cannot fit perfectly experimental data, also if the Π parameter is suitably varied. Moreover, very recently, the same authors of this paper prove definitively in a new paper (Gualtieri et al. 2004) through systematic experimental surveys conceived deliberately for this sake, that the aforementioned current can be wholly considered a boundary layer flow, at least until the thickness of the boundary layer doesn't attain almost the thickness of the current (that is to say practically till a little more than $50 \div 60$ cm from the inlet).

The instantaneous velocity measurements have been carried out through LDA technique. A new generation compact LDA device has been used. The beam was of a frequency out of visible band (not visible ray). The optical system worked in backscatter, with Bragg cell and frequency shifter.

The data sampling system consisted of a simple and classic frequency tracker, which performed also the mean of the data (with mean times that could be freely chosen) in order to obtain in real time the values of local mean velocities. Each value of local mean velocity was in fact obtained through a mean time of 200 s, that had been considered sufficient to eliminate at least the main part of turbulent velocity fluctuations.

Finally an electromagnetic device, which is not shown in Figure 2, was disposable along the pipe which supplies the tank, in order to measure the flow-rate in condition of permanent motion.

3.2 *Vegetation modelling*

The experimental surveys have been performed with the superimposition of a further removable plate on the bottom of the channel. This additional plate was 1,20 m long, 15 cm large, and 1 cm thick. The plate was as large as to be exactly introduced in the channel between the two lateral walls. The first 20 cm of the length of the plate were disposed before the sluice gate, laid on the plexiglass suitable shaped device. The first 10 cm of the length of the plate were blunted from 0 to the 1 cm plate thickness, so to let the water enter the channel without disturbances even in presence of this plate.

The plate filled the channel till a section 1 m far from the sluice gate section. This length was sufficient to let the boundary layer fully develop till the section where its thickness attained the current height. After the plate the current came down a 1 cm step and consequently became irregular, but this circumstance did not matter as the current itself was a supercritical one.

Three types of additional removable plate were prepared in order to represent different types of vegetated currents. The first plate was a simple flat plate, and it produced a comparison classical boundary layer flow. The second and the third plate were vegetated ones.

In particular, in order to represent vegetation on these plates, it has been chosen to drive into them many cylindrical little brass vertical sticks, whose diameter was of 4 mm. They have been arranged in an array like that of Figure 3. Eleven rows of six sticks everyone have been prepared, with sticks 2,5 cm far each another and 1,25 cm far from the lateral walls. Each row followed the previous one at a distance of 5,0 cm, and the first row was placed 2,5 cm from the inlet of the channel (sluice gate section). The meshes of the array were therefore rectangular ones 5,0*2,5 cm^2 wide. Two sticks arrays have been proved, the first one with 5 mm high sticks, and the second one with 10 mm high sticks. The second and third plates therefore one another in the sticks height.

In this way, in each plate, the whole arrangement was symmetric, the centreline of the channel bottom

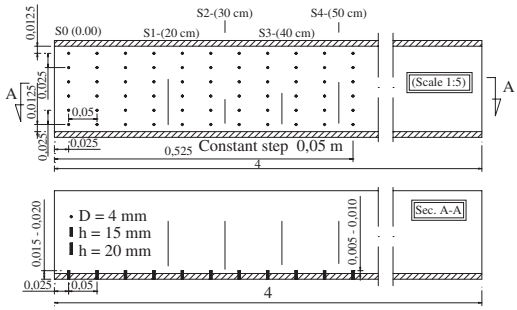


Figure 3. Modifications of the experimental channel.

was free from sticks and it was possible carry out velocity distribution (from the bottom to the free surface) measurements on this centreline. In particular four test sections have been chosen 20 cm, 30 cm, 40 cm, 50 cm respectively far from the channel inlet. These test sections were all placed exactly between two following rows, so that the measurement verticals lied in any case exactly in the centre of a rectangular mesh.

4 EXPERIMENTAL SURVEYS CARRIED OUT AND RELATIVE RESULTS

Three different conditions of boundary layer flow have been experimentally considered. The first condition was a flow along the flat plate without sticks; the second one was a flow along the plate with 5 mm high sticks; the third one was a flow along the plate with 10 mm high sticks. Comparisons have been performed among these three conditions. In order to let the comparisons be meaningful, in all conditions, some fundamental hydraulic parameters have been kept constant.

The height of the sluice gate has been always of 7.49 cm. Consequently the height in the vena contracta was of 4.61 cm.

The head of the tank above the vena contracta was always of 10,34 cm. Consequently the velocity in the vena contracta was of 1,424 m/s. The flow-rate was of 9.85 l/s.

In each condition, attention was paid to maintain a substantially horizontal free surface (at least in the first 50 cm of the flow where measurements had to be carried out), in order to cause the boundary layer to be always an equilibrium one with zero piezometric head gradient (as a liquid flow was dealt with, it was necessary to keep constant the piezometric head and no more the simple pressure as it happens in gas flows). In order to obtain this condition the slope of the channel had to be changed in each different condition because of the different bottom friction losses without sticks, with 5 mm sticks and with 10 mm sticks. In particular,

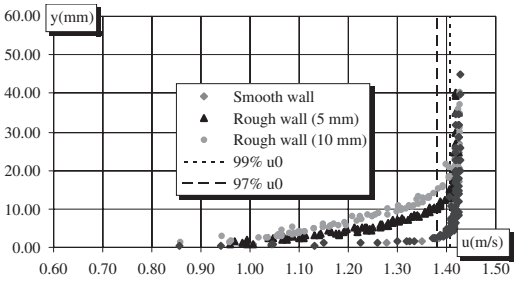


Figure 4. Velocity profile in section 1.

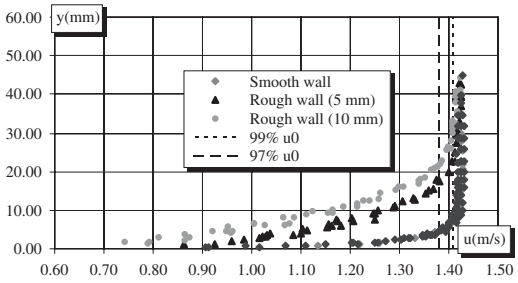


Figure 5. Velocity profile in section 2.

0,25%, 1,13%, 1,45% slopes were established in the three conditions respectively. It is evident that with presence of sticks, and mostly with 10 mm sticks, the slope increases because of the increased bottom resistances. In such a manner, the hydraulic head was constant and equal to 10,34 cm also along the whole current in each flow condition; and the velocity in the external layer was 1,424 m/s always and everywhere.

Finally, the flow condition without sticks and with smooth bottom are just alike to one of those experimented in (Gualtieri et al. 2004) on the same experimental plant.

In that paper it was stressed that the feeding device of the channel couldn't generate a perfect potential flow in the external layer, and that on the contrary this external layer presented a turbulence level characterized by the ratio u'/u* (between the r.m.s. value of turbulence fluctuations u' and the friction velocity on the bottom u*) nearly equal to 1,5. Therefore the examined current was to be considered, in every flow condition, a current with not negligible free stream turbulence.

In each of these three flow conditions, local mean velocity distributions have been measured in the four aforementioned test sections. The results of these measurements are referred in Figures 4, 5, 6, 7. Each Figure corresponds to one test section, and contains the experimental velocity distributions relative to without sticks, 5 mm sticks and 10 mm sticks flow conditions.

Some first qualitative results are immediately evident. The vegetation presence affects widely velocity

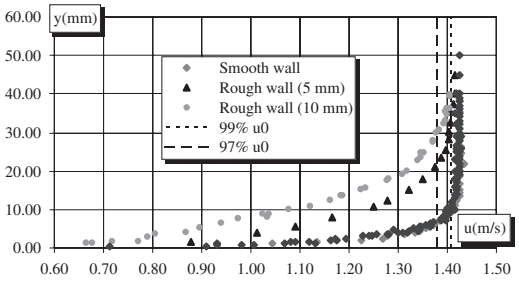


Figure 6. Velocity profile in section 3.

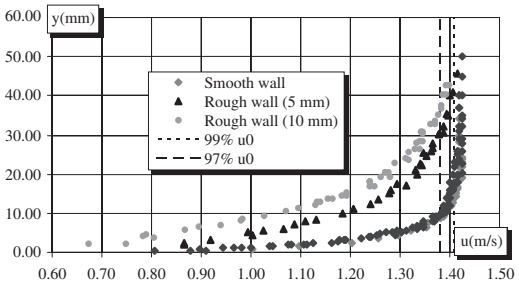


Figure 7. Velocity profile in section 4.

distributions in boundary layers. In particular, with presence of vegetation, the boundary layer thickness grows and the velocities inside the boundary layer decrease. The total flow-rate of the current, which doesn't vary in the different conditions, is secured, also with smaller velocities, by the increase of the slope and consequent increase of the cross sections. The momentum of the current, on the contrary, decreases with vegetation presence because of the increased bottom resistances. At last it is very meaningful to notice that, at least at first sight, no evidence appears of possible irregularities of the velocity distributions at the height of the sticks.

At a deeper insight, it would be possible to observe, in the section 20 cm far from the sluice gate, a little irregularity in velocity distributions either in 5 mm sticks plate or and more in 10 mm sticks plate. In this paper this irregularity will be not considered.

In Table 1 the values of the different 99% thickness in the different test sections and the different flow conditions are reported. These values have been evaluated through a special procedure. In fact it is difficult to read directly on the diagrams the 99% thickness. On the contrary it is much easier to read the 97% thickness. Therefore the first step was to read on the diagrams the 97% thickness values. The second step was to read as best as possible also the 99% values. For each diagram and each condition the ratio between the 99% and the 97% thickness values was performed. If the boundary layer is in each flow condition an equilibrium one, the

Table 1. Boundary layer thickness.

	Smooth (0 mm)	Rough (5 mm)	Rough (10 mm)
δ_{S1} (mm)	3.8	15.0	19.6
δ_{S2} (mm)	7.1	26.4	30.8
δ_{S3} (mm)	10.9	33.0	41.4
δ_{S4} (mm)	13.5	43.5	50.4

aforementioned ratio must be equal in each condition for the four test sections, and the possible differences of measured values must be imputed to reading errors, mainly of 99% values, which are more difficult to be correctly read. In this hypothesis it was possible to compute the means among the four values of each flow condition in order to obtain the best estimate of the ratio for every flow condition. Consequently these means were computed in relation to each condition (three mean values of the ratio were obtained, and in particular, the values 1,65, 1,50, 1,40 respectively with smooth, or 5 cm sticks, or 10 cm sticks bottom). Finally the 99% boundary layer thickness was computed, in each test section and each flow condition, as the product of the 97% thickness of the considered velocity distribution among the twelve experimentally obtained, and the aforementioned mean relative to the suitable flow condition. Later in this paper we shall come back on the hypothesis of equilibrium boundary layer.

The final values of Table 1 corroborate the previous qualitative remarks. Moreover this table can be read in alternative ways, making some simple interpolation of data. Let's consider the sections where the boundary layer thickness in condition of smooth bottom equals the heights of the sticks (23,6 cm from the leading edge for 5 mm sticks, and 37,6 cm from the leading edge for 10 mm sticks); in these sections the thickness of boundary layer was the following ones: in the section at 23,6 cm from the leading edge the thickness of boundary layer flow with 5 mm sticks was of 19,1 mm; in the section at 37,6 cm from the leading edge the thickness of boundary layer flow with 10 mm sticks was of 38,9 mm. The increase of boundary layer thickness has been of 3,82 in the first case and of 3,89 in the second case. Yet alternatively, the same boundary layer thickness is attained in 6,67 cm in the first case and in 10,20 cm in the second case; that is to say that the distance from the leading edge necessary to attain the boundary layer thickness equal to the sticks height is 3,54 times less in the first case and 3,68 times less in the second case. It is possible to say that, taking into account a thickness of boundary layer of the same value as the sticks height, the presence of stick-modelled vegetation on the bottom of the channel makes adaptation processes in river flow behaviours in any case about 3,7 times faster.

5 NON DIMENSIONAL VELOCITY DISTRIBUTIONS

All the twelve velocity distributions reported in Figures 4, 5, 6, 7 can be transformed in non dimensional ones through the V_0 velocity in the external layer and the 95% δ thickness of the boundary layer.

In Figures 8, 9, 10 the non dimensional velocity distributions respectively in condition of smooth bottom, 5 mm sticks and 10 mm sticks are reported: the ordinates of the diagrams have been cut at the 2 value.

It is evident in each figure that the four velocity distributions relative to the four test sections are clearly superimposed one another: that is to say that non dimensional velocity distributions are alike in each flow condition.

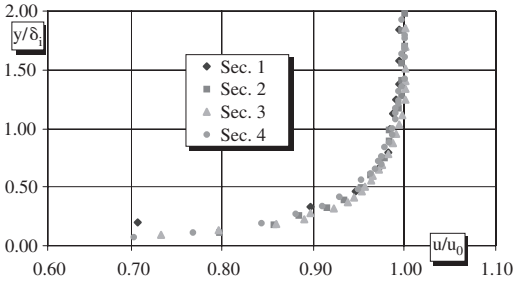


Figure 8. Velocity profiles in all sections with a smooth bed.

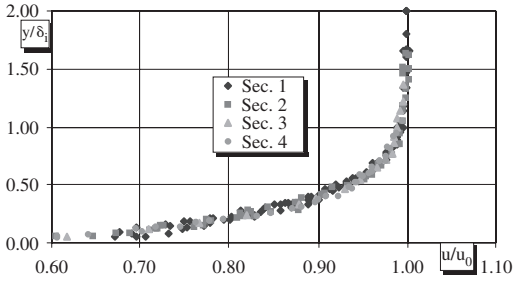


Figure 9. Velocity profiles in all sections with a rough bed (5 mm).

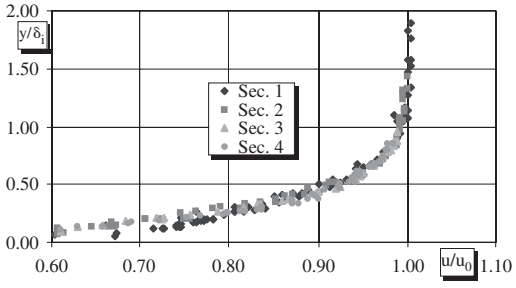


Figure 10. Velocity profiles in all sections with rough bed (10 mm).

This behaviour of velocity distribution, on the ground of a reasoning that will be immediately performed, is the clear marker of the equilibrium state of the three considered flows, not only in case of smooth bottom (obviously), but also in case of vegetated surfaces: and this circumstance represents a completely new phenomenon.

On this matter, it is suitable to remember that, according to the rule, a boundary layer on a flat plate is called an equilibrium one when in external layer pressures (or piezometric heads for liquids) have a streamwise zero gradient, and consequently velocity distributions, once they have been made non dimensional in the shape of velocity defect laws, appear to superimpose one another.

In the case we are dealing with, it is very hard also only to try to represent velocity distributions in the shape of velocity defect laws, because, in order to obtain such a representation, it is necessary to refer to friction velocity. Now, in the considered vegetated flows, the friction velocities are variable from a point to another one also in the same section (as it happens to velocity distributions too) because of the presence of the sticks. Therefore, in this paper and unless further information should be given in future work, the possibility to refer to friction velocity has been discarded.

Furthermore the distances of test sections from the inlet (from 20 cm to 50 cm), are of the same order, and in this condition in the classic boundary layer the friction velocities differ very little one another. Consequently the superposition of velocities distributions in the shape of velocity defect laws implies with good approximation also superposition of simply made non dimensional diagrams and vice-versa. This conclusion is fully confirmed by the diagrams of Figure 8. They certainly should be superimposed in the shape of velocity defect law, as they refer to a surely equilibrium boundary layer, and they appear to be superimposed also in diagrams simply made non dimensional. As a result of this reasoning, the condition of equilibrium flow can be assessed, also in the flows over vegetated bottom considered in this paper, directly through the superposition of simply non dimensional velocity distributions, as it has been done at the beginning of this paragraph.

The circumstance that the flows over vegetated surfaces appear to be equilibrium flows, is a very important and intriguing result.

In fact, in each of the two sticks conditions, the sticks height is a constant value in all the four test sections. Consequently, this height, if made non dimensional with respect to the local boundary layer thickness, assumes a different value in the four test sections. This notwithstanding, the velocity distributions

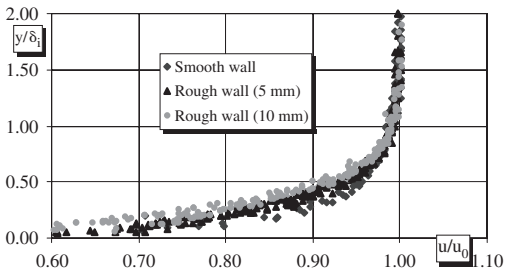


Figure 11. Dimensionless velocity profiles for all section in any roughness conditions (0, 5, 10 mm).

is not affected by this circumstance. That is to say that the sticks presence affects the whole behaviour of the boundary layer, not affecting, at least at the accuracy level we can attain, the velocity distribution at the exact height of sticks (as it had been already qualitatively noticed).

It is important here to stress that the equilibrium state implies equality of non dimensional velocity distribution along the whole boundary layer thickness (as it clearly happens), so that equilibrium state is truly existing and it would not be possible to attribute this equality to the methodology employed for the evaluation of the boundary layer thickness, which involved only two values of velocity.

In Figure 11 the three non dimensional velocity distributions of previous diagrams are reported all together. It is sufficiently clear in this new diagram that the three considered distributions don't superimpose one another. That is to say that the presence of vegetation affects the velocity distributions not only in dimensional shape but also in non dimensional shape referred to external layer velocity and 99% boundary layer thickness. The equilibrium states relative to the three flow conditions are not the same.

6 CONCLUSIONS

In last years much attention has been paid to the problem of the behaviour of free stream currents with vegetated surfaces in relation to atmospheric or river flow problems. Most of these researches, or perhaps all these researches, deal respectively with wind problems or uniform river flow problems. The study of the influence of vegetated walls on the growth of turbulent boundary layer can let us understand some further behaviours of the currents.

The analysis of boundary layer data in flows with smooth walls and vegetated walls shows that in the former case the behaviour of fluid mechanics processes in relation to boundary layer thickness equal to vegetation height adapt itself more rapidly, and that this greater rapidity can be computed in about 37%.

From the point of view of basic fluid mechanics, the most important conclusion coming from the collected data is that, also in case of regular stick-shaped vegetated wall, the boundary layer flow, if the free surface is kept constant, behaves as an equilibrium boundary layer. This behaviour in any case belongs to velocity distributions relative to verticals placed in the centres of the sticks meshes.

It must be however remembered the little irregularity found in velocity distributions of 20 cm test section which certainly will request a deepening of experimental survey and consequent data interpretation.

At last, the non dimensional velocity distributions relative to flow conditions on smooth bottom or on stick vegetated walls are not alike, showing that the condition of equilibrium is different in the flows without sticks, or with sticks of different heights.

REFERENCES

Bandypadhyay, P.R. 1992 Reynolds Number Dependence of the Freestream Turbulence Effects on Turbulent Boundary layers *AIAA Journal* 30 (7) 1910–1912

Bettess, R. 2003 On the hydraulic roughness of vegetation in channels XXX *I.A.H.R., Congress Tessaloniki (Greece)* Theme C 25–30

Blair, M.F. 1983a Influence of Free-Stream Turbulence on Turbulent Boundary Layer Heat Transfer and Mean Profile Development. Part I Experimental Data *Transactions of the ASME Journal of Heat and Mass Transfer* 105 (feb) 33–40

Blair, M.F. 1983b Influence of Free-Stream Turbulence on Turbulent Boundary Layer Heat Transfer and Mean Profile Development. Part II Analysis of results *Transactions of the ASME Journal of Heat and Mass Transfer* 105 (sep) 41–47

Castro, I.P. 1984 Effects of Free Stream Turbulence on Low Reynolds Number Boundary Layers *Transactions of ASME Journal of Fluid Engineering* 106 (sep) 298–306

Charney, G., Comte-Bellot, G. & Mathieu, J. 1971 Development of a turbulent boundary layer on a flat plate in an external turbulent flow *AGRD CCP 93–71* 27.1–27.10

Charnay, G., Mathieu, J. & Comte-Bellot, G. 1976 Response of a turbulent boundary layer to random fluctations in an external stream *The Physics of Fluids* 19 (9) 1261–1272

Coles, D. 1956 The Law of the Wake in the turbulent Boundary layer *Journal of Fluid Mechanics* (1) 191–226

Evans, R.L. 1985 Freestream Turbulence Effects on Turbulent Boundary Layers in an Adverse Pressure Gradient *AIAA Journal* 23 (11) 1814–1816

Evans, R.L. & Horlock, J.K. 1974 Calculation of the Development of Turbulent Boundary Layers With a Turbulent Freestream *Transactions of the ASME Journal of Fluid Engineering* 1974 (dec) 348–352

Gualtieri, P. & Pulci Doria, G. 1997 Non dimensional distribution of longitudinal integral length scales in a turbulent boundary layer *FLUCOME '97 Congress Hayama Japan* 161/166

Gualtieri, P. & Pulci Doria, G. 1998a Skewness, Kurtosis and Length Scales experimental distributions laws based on a three bands model in a turbulent boundary layer *Excerpta of Italian contributions to the field of hydraulic engineering* 12 155/194

Gualtieri, P. & Pulci Doria, G. 1998b A proposal of a physically based thickness definition and of a new mean velocities distribution law in a turbulent boundary-layer on the ground of LDA measurements *13th Australasian Fluid Mechanics Conference Melbourne*

Gualtieri, P. & Pulci Doria, G. 1999 Boundary Layer Intermittency Model *Int. IUTAM Symp. on Geometry and Statistics of Turbulence Hayama Japan* 379/384

Gualtieri, P. & Pulci Doria, G. 2001 A Correct Model of Variance, Skewness, Kurtosis in Boundary Layer with Turbulent External Layer 14th *Australasian Fluid Mechanics Conference Melbourne* 259/262

Gualtieri, P. & Pulci Doria, G. 2003 A correct model of longitudinal integral length scales in boundary layer with turbulent external layer 2nd *International Conference on Heat Transfer, Fluid Mechanics, and Thermodynamics H.E.F.A.T., Victoria Falls Zambia*

Gualtieri, P., Pulci Doria, G. & Taglialatela, L. 2004 Experimental validation of turbulent boundary layers in channels 3rd *International Conference on Heat Transfer, Fluid Mechanics, and Thermodynamics H.E.F.A.T., Cape Town South Africa, June*

Hancock, P.E. & Bradshaw, P. 1983 Influence of Free-Stream Turbulence on Turbulent Boundary Layers *Transactions of the ASME Journal of Fluids Engineering* 105 (sep) 284–289

Hancock, P.E. & Bradshaw, P. 1989 Turbulent structure of a boundary layer beneath a turbulent free stream *Journal of Fluid Mechanics* 205 45–76

Hoffmann, J.A. & Mohammady, K. 1991 Velocity Profiles for Turbulent Boundary Layers Under Freestream Turbulence *Transactions of the ASME Journal of Fluid Engineering* 113 (sep) 399–404

Huffman, G.D., Zimmerman, D.R. & Bennett, W.A. 1972 The effect of Free-stream turbulence leel on turbulent boundary layer behaviour *AGARDograph 164 Paper I-5* 91–115

Kline, S.J., Lisin, A.V. & Waitman, B.A. (1960) Preliminary experimental inestigation of effect of free-stream turulence on turbulent boundary-layer growth *N.A.C.A. TN D-368* 1–60

Kouwen, N., Unny, T.E. & Hill, H.M. 1969 Flow retardance in vegetated channels *Journal Hydraulic Division ASCE* 95(2) 329–342

Kouwen, N. & Unny, T.E. 1973 Flexible roughness in open channels *Journal Hydraulic Division ASCE* 99(5) 684–698

Kouwen, N. & Unny, T.E. 1981 Flow resistance in vegetated waterways *Trans. ASEE* 24(3) 684–698

Lopez, F. & Garcia, M.H. 2001 Mean Flow and Turbulence Structure of Open-Channel Flow Through Non-Emergent Vegetation *Journal of Hydraulic Engineering* 2001 (may) 392–402

Mc Donald, H. & Kreskowsky, J.P. 1974 Effects of free stream turbulence on the turbulent boundary layer *International Journal of Heat and Mass Transfer* 17 705–716

Meier, H.U. & Kreplin, H.P. 1980 Influence of Freestream Turbulence on Boundary-Layer Development *AIAA Journal* 18(1) 11–15

Naot, D., Nezu, I. & Nakagara, H. 1996 Hydrodynamic Behavior in partly vegetated open channels *Journal of Hydraulic Engineering* 1996 (november) 625–633

Nezu, I. & Onitsura, K. 2002 Turbulent structures in partly vegetated open-channels flows with LDA and PIV measurements *Journal of Hydraulic Research* 2001 6(39) 629–642

Pulci Doria, G. 1991 Statistical quantities distributions and the use of the entropy concept *Int. Conf. on Entropy and Energy Dissipation on Water Resources, Maratea* 541–586

Robertson, J.M. & Holt, C. 1972 Stream turbulence effects on turbulent boundary layer *Journal of Hydraulic Division Proceedings of the American Society of Civil Engineers* 98 (HY6) 1095–1099

Stone, B.M. & Shen, H.T. 2002 Hydraulic Resistance of Flow in Channels with Cylindrical Roughness *Journal of Hydraulic Engineering* 2002 (may) 500–506

Tsuijimoto, T.& Kitamur, T. 1990 Velocity profile of flow in vegetated-bed channels *KHL Progressive Report n.1 Kanazawa University Japan*

Tsuijimoto, T. 1999 Fluvial processes in stream with vegetation *Journal of Hydraulic Research* 37(6) 789–803

River Flow 2004 – Greco, Carravetta & Della Morte (eds.)
© 2004 Taylor & Francis Group, London, ISBN 90 5809 658 0

Response of velocity to a sudden change of bed roughness in sub critical open channel flow

A. Carravetta & R. Della Morte
Department of Hydraulic and Environmental Engineering, University of Naples Federico II

ABSTRACT: Large variations in the flow field and bottom stress may be determined by an abrupt change of the channel bed from smooth to rough. The variation in the mean local velocities propagates in the current by a gradual increase in thickness of an internal boundary layer. Instead, the presence of a sudden peak in shear velocity downstream the bed change may be observed, the so-called *overshooting*. The entity of the peak is related to several factors, including the entity of the roughness change, the size of the bed elements and emergence of the rough part of the bed with respect to the smooth one, the reduction in the current cross section due to water level depression and bed elevation and the entity of the pressure gradient. A large number of experiments appears necessary in order to investigate all these interactions: the writers are currently carrying out such experimental work.

The results of a part of these experiments are discussed in this paper. An abrupt change in bed roughness from smooth to rough was brought about by positioning a single layer of stones on the smooth bed of a flume. Emersion of the rough part of the bed with respect to the smooth one, flow rate, water levels were systematically varied. Experiments confirmed that the spatial distribution of bottom shear stresses down the roughness change is related both to flow characteristics and bottom geometry.

1 INTRODUCTION

The effect on open channel flows of sudden changes in bed roughness is an interesting problem of river hydraulics. The main goal of many Authors dealing with such a topic has been to find out the spatial distribution of shear stresses across the change. In many cases the presence of a sudden increase in shear velocity immediately downstream the roughness change was observed, and indicated as the overshooting property of shear velocities. The presence of this property was stated by some authors (Nezu & Tominaga, 1994). On the other side, Chen & Chiew (2003) observed the absence of overshooting. The real presence of overshooting could cause local scours in rivers with problems regarding the stability of waterworks.

Starting from the channel section where bed configuration changes from smooth to rough, an internal boundary layer of increasing thickness develops near the bottom. Within the boundary layer the velocity profile is deformed by the change in bed resistance and by an increment in velocity which verify in the upper part of the current.

The problem of the response of an internal boundary layer to a step change in the boundary conditions was largely studied in the past, but mainly concerning aeronautical and environmental science (Smits & Wood, 1985). In river hydraulics the problem can assume a higher complexity because a change in channel geometry necessarily occurs together with a pressure gradient induced by the free surface variation.

The writers have recently carried out experiments where a smooth to rough change was investigated (Carravetta & Della Morte, 2002, 2004). The dimensions of the rough bed grains were 1.9 and 6.0 mm. The velocity profiles along channel axis were well interpreted by using a defect log-law along the whole vertical, in absence of any velocity dip. Shear velocity distribution along the bed was determined and overshooting was observed. The maximum value of shear velocity, representing the overshooting peak, was found to be related to the parameter:

$$K_{d*} = \frac{u_{*1} d_a}{\nu}$$

with u_{*1} the shear velocity of the approaching current and d_a the difference between the levels of the bottom before and after the roughness change. This dimensionless parameter will be called in the following *emersion Reynolds number*. Overshooting was of a higher entity for larger K_{d*} values, i.e. for bed roughness increasingly emerging over the upstream bed and/or for increasing shear velocity of the approaching



Figure 1. View of the experimental channel.

current. In order to confirm this interpretation a new set of experiments has been performed with a larger size of bed particles.

2 LABORATORY SET-UP

A perspex channel 8.0 m long, 0.76 m wide and 0.76 m deep, having a fixed slope $i = 0.001$, was used for the experiments. Large scale disturbances at the channel inlet were avoided by inserting a metallic sieve. Different water levels were obtained along the channel by inserting a step in the downstream section. Two different steps were used: the first (step I) 0.025 m height and 0.15 m length, the second (step II) 0.15 m height and 0.15 m length.

At $x_o = 5.0$ m from the inlet of the channel a single layer of stones was positioned on the bottom, for a longitudinal length of 9.5 m, Figure 1. Average diameter of the stones was $k_{rou} = 30.0$ mm (Fig. 2). The roughness change is represented in Figure 3. Two values of emersion d_a of the rough bed were obtained by elevating the smooth up-stream floor with mobile elements: $d_a = k_{rou}$ (bed configuration C); $d_a = 0.5k_{rou}$ (bed configuration D).

On each configuration of the channel bed, several steady state tests were performed with different flow rates or upstream water levels, h_1, measured at the section $x - x_0 = -0.40$. A summary of the experimental conditions is reported in Table 1. Experiments were performed in the intermediate and small scale roughness range (Bathurst, 1985), with h_1/k_{rou} variable between 8.06 and 3.07.



Figure 2. Plain view of the roughness elements.

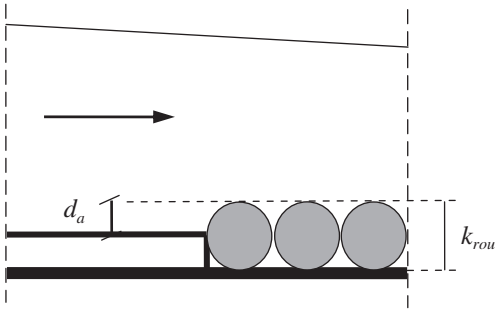


Figure 3. Side view of the roughness change.

Table 1. Summary of tests.

Case	d_a (mm)	Q (m^3/s)	h_1 (m)	Fr	$Re \cdot 10^5$
CI-1	30.0	0.020	0.116	0.21	0.80
CI-2	30.0	0.040	0.147	0.30	1.51
CI-3	30.0	0.055	0.157	0.36	2.04
CI-4	30.0	0.070	0.186	0.37	2.47
CII-1	30.0	0.040	0.239	0.14	1.29
CII-2	30.0	0.055	0.261	0.17	1.71
DI-1	15.0	0.020	0.101	0.26	0.83
DI-2	15.0	0.040	0.124	0.38	1.58
DI-3	15.0	0.055	0.144	0.42	2.09
DI-4	15.0	0.070	0.166	0.43	2.56
DII-1	15.0	0.040	0.212	0.17	1.35
DII-2	15.0	0.055	0.240	0.20	1.77

An acoustic profiler, Signal Processing DOP2000, was used to acquire the vertical distribution of local velocities along channel axis at the distances $x - x_0 = -0.40; -0.30; -0.20; -0, 10; -0.05; 0.00; 0.05; 0.10; 0.40; 0.80; 1.20; 1.60; 2.0; 2.4$ m. The origin of the vertical axis y on the rough part of the bed was fixed at $0.5k_{rou}$ below the particle crest. Water levels along channel axis were measured by using a point gauge with a vernier scale.

3 RESULTS

As an example of test results, the vertical profiles of local velocity are represented in Figure 4, for test CI-2, and Figure 5 for test DI-2. In the same figures the profiles of computed turbulence intensity are also plotted, along with the corresponding water levels.

The results of a previous test, performed with the same flow rate, but with a different choice of bed geometry – $k_{rou} = 6.0$ mm and $d_a = k_{rou}$ – are plotted in Figure 6 (Carravetta & Della Morte, 2002; 2004 test B3). Two regions in the velocity profile can be observed: a *bed region*, where an internal boundary layer of increasing thickness develops, and a *core region* in the upper part of the current. In each of the two regions a different response to bed roughness change is evident. In the core region, the velocity profile exhibits a rigid translation, due to flow acceleration induced both by the water depth depression and by the velocity reduction in the bed region. In the bed region, the velocity profile is deformed by the change in bed resistance and the increment in velocity in the core region. Also the vertical distribution of turbulence intensities undergoes a modification in the bed region. Within the internal boundary layer, larger values of turbulent intensity were observed when compared to the ones at equal y on the smooth part of the channel. The same kind of modification was present on Chen & Chiew's and Nezu & Tominaga's measured Reynolds stresses.

The evolution of the velocity profiles in the present tests with larger roughness size was slightly different, as observed in Figure 4. In particular, the velocity profiles undergo a larger deformation that can be better observed in the plot of Figure 7, where the velocity profiles, measured at different abscissa, are superimposed.

Immediately downstream the bed change, the profile deformation is similar to the one observed in the case of small bed elements, but larger because of the stronger variation of the current cross section. An acceleration in the upper part of the current and high velocity gradients at the bottom are present.

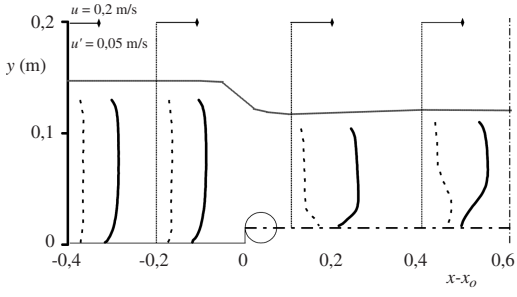


Figure 4. Streamwise mean local velocity, turbulence intensity, water level for case CI-2 (stone in figure is undistorted).

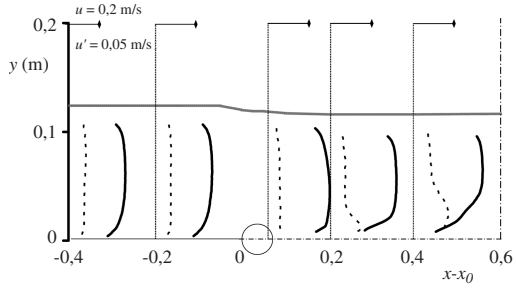


Figure 5. Streamwise mean local velocity, turbulence intensity, water level for case DI-2 (stone in figure is undistorted).

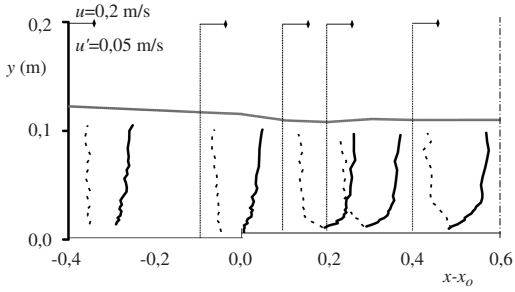


Figure 6. Streamwise mean local velocity, turbulence intensity, water level for $k_{rou} = 6.0$ mm and $d_a = k_{rou}$.

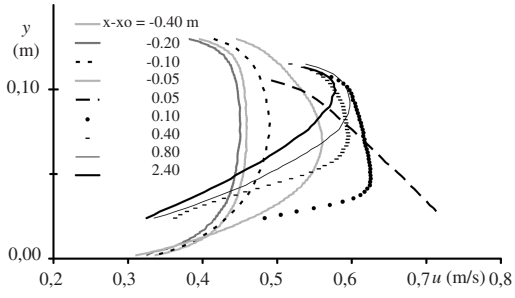


Figure 7. Streamwise mean local velocities for case CI-2.

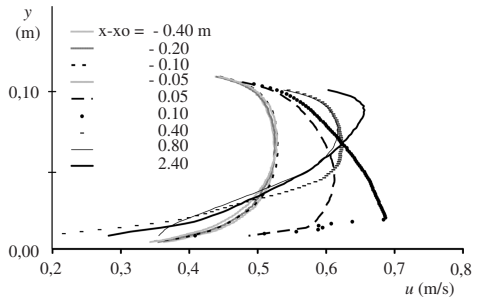


Figure 8. Streamwise mean local velocities for case DI-2.

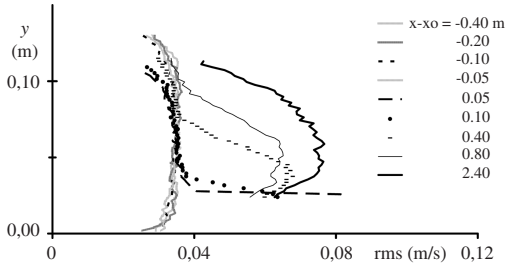


Figure 9. Turbulence intensities for case CI-2.

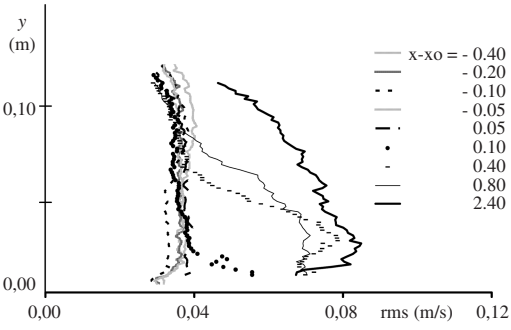


Figure 10. Turbulence intensities for case DI-2.

For large $x - x_0$ values, the change in the local velocity profile is characterized mainly by the presence of a progressive transition to the S-shaped form that is peculiar to gravel bed streams (Baiamonte et al., 1995; Nikora & Smart, 1997). In this phase a water level recovery is present.

In test DI-2 (Figs. 5, 8), where the contraction of the cross section was lower, for the presence of a smaller emersion of the rough bed with respect to the smooth part, the velocity profiles undergo a smaller deformation.

The vertical distribution of turbulence intensity exhibits a more gradual modification (Figs. 9, 10). Turbulence intensity increases in the internal boundary layer. The increase in thickness of this layer with the distance from the roughness change is evident.

In conclusion, experimental evidence shows that, for given flow rate, upstream water level h_1 and emersion d_a of the rough bed are relevant quantities for the entity of the current cross section and, then, of the deformation of the velocity profile immediately downstream the roughness change. The value of k_{rou} seems relevant in the spatial variation of the boundary layer at larger distances from the roughness change.

4 DISCUSSION

The writers in previous studies, referring to $k_{rou} = 1.9 \div 6.0$ mm (Fig. 6), argued the validity along the whole vertical of a double-log law written in the form:

$$\frac{u_s - u}{u_*} = \frac{1}{k} \ln\left(\frac{s}{y}\right) \tag{1}$$

with s thickness of the internal boundary layer and u_s velocity value at the distance s from the bed. On the rough bed two different values of shear velocities, u_*, were used in equation (1). For the core region, u_* was assumed as constant and equal to the upstream value u_{*1} at $x - x_o = -0.40$. For the bed region u_* was found by optimization. Least square method was applied to all measured data along the vertical.

With reference to the present data, the velocity distributions (Figs. 7, 8) cannot be interpreted by a law as simple as equation (1), because of the large size of the roughness elements. Nevertheless, eq. (1) was still used but with reference to the only part $(yu_*/\nu) \geq 30$ and $(y/s) < 0.2$ of each vertical. Equation (1) is consistent with the final velocity distribution: in fact, log-law was found to be valid for $(y/h) < 0.2$ even in the intermediate roughness scale (Baiamonte et al., 1995).

Therefore, equation (1) was written in the form:

$$\frac{u_{y=0.2\,s} - u}{u_*} = \frac{1}{k} \ln\left(\frac{0.2\,s}{y}\right) \tag{1'}$$

The thickness s of the boundary layer was assumed as the height of the part of the current where larger values of turbulent intensity were observed when compared to the ones at equal y on the smooth part of the channel. The value of velocity at $y = 0.2s$ was taken from measures. The least square method on the measured data was used to obtain u_* values. Schofield (1976) suggested a trial and error procedure for the assessment of the origin of the velocity profile and of the shear stress value. As in the case of Islam & Logan (1976), the recommended procedure has not been attempted because of the fewness of data near the wall. The origin of the vertical profiles in the

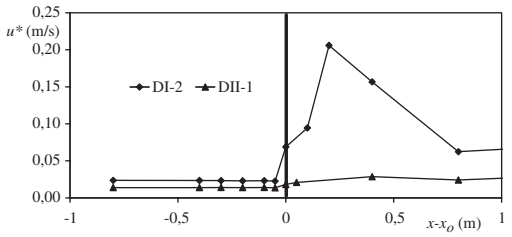


Figure 11. Space distribution of u_* in test DI-2 and DII-1.

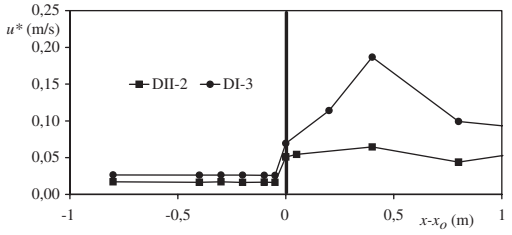


Figure 12. Space distribution of u_* in test DI-3 and DII-2.

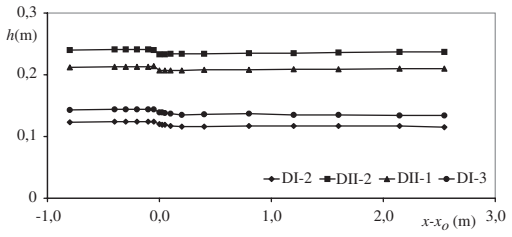


Figure 13. Water levels in test DI-2, DI-3, DII-1 and DII-2.

y direction was fixed at ¼ of the equivalent roughness height below the particle crest, corresponding to $0.5\,k_{rou}$ (Robertson, 1971; Bayazit, 1983).

In Figure 11 (cases DI-2 and DII-1) and Figure 12 (cases DI-3 and DII-2) the space distributions of shear velocities u_* are plotted. Tests refer to $k_{rou} = 30.0$ mm and $d_a = 0.5k_{rou}$ with the same flow rate, but different water levels, as observed in Figure 13. Overshooting is present only in the tests with smaller water levels (DI-2 and DI-3). The peak in shear velocity is limited to a short portion of the channel bed.

In Figures 14, 15 the space distribution of u_* values is plotted for test having the same flow rate -0.02 and $0.04\,m^3/s$ respectively, but different dimension of roughness elements and emersion d_a of the rough bed. Shear velocity exhibits a different behaviour depending on the geometry of the bed: the level of overshooting increases for increasing emersion d_a of the roughness elements, but the higher is the level of overshooting the faster the shear velocity after the peak reaches its downstream values. This

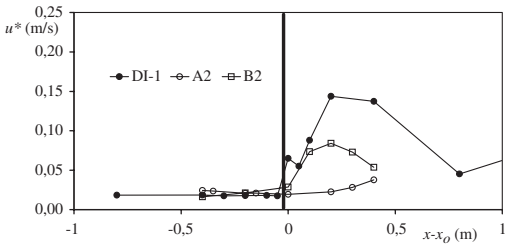


Figure 14. Space distribution of u_* in test DI-1 ($k_{rou} = 30.0$ mm, $d_a = 0.5k_{rou}$), A2 ($k_{rou} = 1.9$ mm, $d_a = k_{rou}$) and B2 ($k_{rou} = 6.0$ mm, $d_a = k_{rou}$), $Q = 0.02\,m^3/s$.

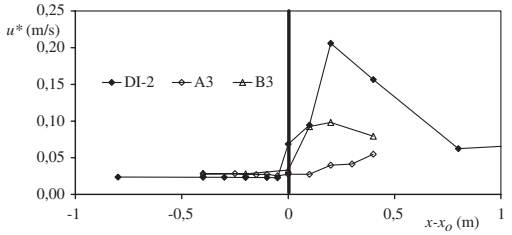


Figure 15. Space distribution of u_* in test DI-2 ($k_{rou} = 30.0$ mm, $d_a = 0.5k_{rou}$), A3 ($k_{rou} = 1.9$ mm, $d_a = k_{rou}$) and B3 ($k_{rou} = 6.0$ mm, $d_a = k_{rou}$), $Q = 0.04\,m^3/s$.

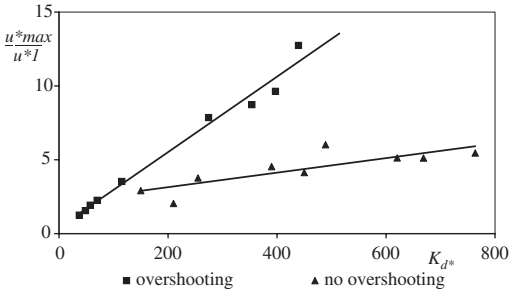


Figure 16. $u_{*\max}/u_{*1}$ versus K_{d*}.

finding could explain the reason why overshooting was not found at all in the experiments with $k_{rou} = 30.0$ mm and $d_a = k_{rou}$. In these experiments rough bed values of shear velocity were already observed at $x - x_o = 0.05$ m, where just the queue values of an eventual peak in shear velocity were probably evaluated from velocity data.

In Figure 16, u_{*max}/u_{*1} values for each test are plotted versus the corresponding emersion Reynolds number K_{d*}. Data confirm the influence of K_{d*} on the overshooting property. Two trends appear in the figure: the first is related to tests where overshooting was observed, the second to tests where u_* reaches directly the rough bed values without overshooting. In the range of writers' experiments the product $h_1 \cdot d_a$ was

effective to assess the presence of overshooting. Overshooting was present only in experiments with $h_1 \cdot d_a$ smaller than 0.0032. This finding is in agreement with the results of Nezu & Nakagawa (1991).

5 CONCLUSIONS

The results of several tests on the transition from smooth to rough bed in open channel flow have been presented. Each steady state experiment was different for bed geometry and approaching flow conditions.

Velocity and turbulence intensity profiles revealed strong modifications along the rough bed downstream the bed change. The space evolution of an internal boundary layer was observed.

Streamwise velocities in the boundary layer were interpreted with the defect log-law and shear velocity were calculated by least square method.

Tests show that the real presence and the entity of the overshooting property, namely the presence of a peak in the shear velocity distribution along the rough part of the bed, were related both to bed geometry and flow conditions. In particular, the product between upstream water level, h_1, and rough bed emersion, d_a, seems to be relevant for assessing the real presence of overshooting.

The entity of overshooting was related to the value of shear velocity on the smooth bed, and to the emersion of the rough bed with respect to the smooth one.

SYMBOLS

B	channel width
d_a	grain emersion
Fr	Froude number
h	flow depth
h_1	flow depth at section $x - x_o = -0.4$
k	von Karman constant
K_{d*}	emersion Reynolds number
k_{rou}	roughness height
Q	flow rate
Re	Reynolds number
s	thickness of the internal boundary layer
u	streamwise mean local velocity
u'	RMS of streamwise local velocity
u_s	streamwise mean local velocity at $y = s$
u_*	shear velocity
u_{*1}	shear velocity at section $x - x_o = -0.4$
$u_{*\max}$	maximum shear velocity at overshooting
x	streamwise coordinate
x_o	coordinate of bed roughness change
y	vertical coordinate
ν	kinematic viscosity

REFERENCES

Baiamonte G., Giordano, G., Ferro, V. (1995), "Advances on velocity profile and flow resistance law in gravel bed rivers", Excerpta, IX: 41–89.

Bathurst, J. C. (1985), "Flow resistance estimation in mountain rivers", Proc. ASCE, HY12(104).

Bayazit, M. (1983), "Flow structure and sediment transport mechanics in steep channels", Proc. Euromech 156: Mech. of sediment transport, Balkema, Rotterdam: 197–206.

Carravetta, A., Della Morte, R. (2002), "Caratteristiche cinematiche di una corrente in un canale con variazione di scabrezza al fondo", Proc. 28th Italian Congress of Hydraulic and Waterworks, Potenza, III: 35–42 (in Italian).

Carravetta, A., Della Morte, R. (2004), Discussion on Chen, X., Chiew, Y. M. (2003) "Response of velocity and turbulence to sudden change of bed roughness in open-channel flow", *Journal of Hydraulic Engineering*, accepted for publication.

Chen, X., Chiew, Y. M. (2003), "Response of velocity and turbulence to sudden change of bed roughness in open channel flow", *Journal of Hydraulic Engineering*, 129(1): 34–43.

Nezu, I., Nakagawa, H. (1991), "Response of velocity and shear stress to abrupt irregularity of bed roughness in streams", Proc. 24th Congress of IAHR, Madrid, A: 235–242.

Nezu, I., Tominaga, A. (1994), "Response of velocity and turbulence to abrupt changes from smooth to rough beds in open-channel flow", Proc. Symposium on Fundamentals and Advancements in Hydraulic Measurements and Experimentation, Buffalo, N.Y., 195–204.

Nikora, V. I., Smart, G. M. (1997), "Turbulent characteristics of New Zealand gravel bed rivers", *Journal of Hydraulic Engineering*, 123(9): 764–773.

Robertson, J. M. (1971), Discussion on Antonia A. R., Luxton R. E. (1971) "Response of a turbulent boundary layer to an upstanding step change in surface roughness", *Journal of Basic Engineering*, 93(1): 32–34.

Smits, A. J., Wood, D. H. (1985), "The response of turbulent boundary layers to sudden perturbations", *Ann. Rev. Fluid Mech.*, 17: 321–358.

River Flow 2004 – Greco, Carravetta & Della Morte (eds.)
© 2004 Taylor & Francis Group, London, ISBN 90 5809 658 0

Velocity distribution in a V-shaped channel

M. Mohammadi
Dept. of Civil Eng., Faculty of Eng., Urmia University & Faculty of Eng., Khoy Azad University, Khoy, Iran

ABSTRACT: To explore the hydraulic characteristics of a V-shaped channel, several series of experiments were conducted for measuring *point velocity* and *boundary shear stress*. Low & high-speed velocity propellers were used for measuring point velocities. In order to show the effect of cross sectional shape on the distribution of depth-averaged velocity in the experimental channel, some measurements of point velocities were undertaken for different flow cases. The contour plots of 2D isovels were drawn interpolating among averaged depths and velocities at a given position, obtained from superposing the various profile sections. It can be seen that the isovels are parallel to the channel boundary in a region close to the bed, and almost symmetric about the centerline, but not completely. A strong surface phenomenon is observable throughout the isovels plots. The variation of point velocities in each slice considered along spanwise direction in order to study the depthwise velocity profile distributions are plotted. Integrating the local velocities, u, over the flow depth, h, gives the depth-averaged velocity, U_d. The lateral variations of depth-averaged velocities are plotted. The results illustrate that the distributions are almost symmetrical about the cross sectional centerline, but they deviate for some flow cases; despite the flow condition was uniform for all cases. It may be found that the widely used log-law for vertical profile of velocity is not accurate and it is not applicable for any channel shape. At large flow depths the maximum velocity occurs at the centerline and reduces continuously towards the sidewalls indicating that the sidewalls exert a large influence on flow behavior. This leads to the view that the secondary current cells affect the flow behavior.

1 INTRODUCTION

When a fluid passes over a solid boundary, the boundary exerts a force on the fluid which is magnified by a reduction in the fluid viscosity. The reduction in velocity becomes less apparent as the distance from surface increases. The region varying flow velocity next to the solid boundary is referred to as a *boundary layer*. For a smooth surface the boundary layer can be divided into three regions, namely *laminar, transitional* and *turbulent*. Figure 1 illustrates these regions and logarithmic velocity profile for a rough boundary together with the turbulent mixing-length, by considering a hypothetical flat plate, immersed in flowing fluid. A full details on this subject may be found in some hydraulics textbooks and Mohammadi (1998).

Herein, for every set of flows both point velocities in cross section and dynamic pressures in contact with channel boundary were measured for the same flow condition. For both velocity and boundary shear stress, the data are analyzed from a variety of different perspectives, and the results from each analysis are used to interpret the mechanics occurring in the flow. The findings from each perspective complement each other and highlight the consistency of the experimental data. This paper also deals with the presentation of all experimental data, together with the analysis of results obtained so far.

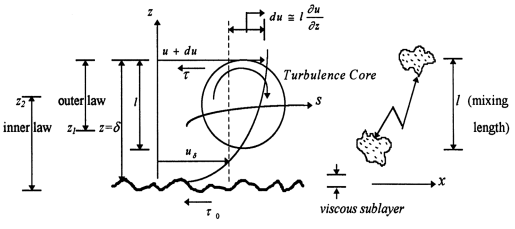


Figure 1. Regions of boundary layer Inner and Outer laws, and logarithmic velocity profile for a rough boundary with turbulent mixing-length (after Mohammadi, 1998).

2 BACKGROUND THEORY

Nezu & Rodi (1985) found, based on accurate laser Doppler anemometer measurements of secondary currents in open-channel flows, that the flow is strongly

dependent on the aspect ratio $\alpha \equiv b/h$ where b is the channel width and h is the flow depth). Depending on this ratio, a channel can be classified as narrow or wide, as indicated below.

(a) Narrow channel ($\alpha \leq \alpha_c \approx 5$). Secondary currents due to sidewall effects result in a "dip" in the velocity distribution near the surface such that the maximum velocity is below the water surface.
(b) Wide channel ($\alpha > \alpha_c$). The strength of the secondary currents due to sidewall effects is reduced in the central zone of the channel within a band of width equal to $b - \alpha_c h$. As a result, two-dimensional (2D) flow properties are present in this region in the long-term structures averaged over turbulence, as long as the wide span variation of the bed-shear stress is a periodic.

The vertical distribution of stream wise velocity in turbulent open-channel flows is very complex. Three regions (see Fig. 1) have been identified in the vertical flow field for steady uniform flow in smooth, wide, open channels: (a) the wall region [$y/h \leq 0.15$ to 0.2, y is the distance above the boundary], referred to as the inner layer in boundary-layer theory, where the length and velocity scales are ν/u_*, and u_*, respectively, where ν is the kinematic viscosity of the fluid, u_* is the boundary shear velocity defined as $u_* = (\tau_b/\rho)^{1/2}$, τ_b is the boundary shear stress, and ρ is the fluid density; (b) the free-surface region [$0.6 \leq y/h \leq 1$], where the length and velocity scales are the flow depth h and the maximum velocity u_{max}; and (c) the intermediate region 0.15 to $0.2 < y/h < 6$, that is not strongly affected by either the wall properties or the free surface properties and where turbulent energy production and dissipation are approximately equal. Within the wall region in wide channels with a smooth bed, the velocity distribution in the viscous sublayer, i.e., $yu_*/\nu << B$ is described as

$$u^+ = y^+ \tag{1}$$

where $u^+ = u/u_*$, $y^+ = y\ u_*/\nu$ and $B \approx 26$ (Nezu and Rodi, 1986), whereas in the region $B << y^+\ h\ 0.2u_*/\nu$ the velocity distribution can be described by the logarithmic law

$$u^+ = \frac{1}{\kappa} \ln y^+ + A \tag{2}$$

where κ is the von Karman constant (equal to 0.41), and A is a constant. In the case of rough channels, the length scale is represented by Nikuradse's equivalent sand roughness k_s, which accounts for the effect of the roughness elements. In general, k_s is a function of the shape, height, and width of the roughness elements, as well as their spatial distribution on the channel surface. Experimental observations suggest that the more uniform and evenly distributed the roughness elements on the channel bed are, the closer is k_s to the actual height of the protrusions (Schlichting, 1979). Depending on the ratio of roughness and viscous length scales (often referred to as non dimensional roughness parameter or roughness Reynolds number), $ks^+ = u_*\ k_s/\nu$, the turbulent flow regime in wide open channels can be classified as hydraulically smooth, transitionally rough, or fully rough. The flow regime is considered hydraulically smooth for $k_s^+ < 5$, fully rough for $k_s^+ > 70$, and transitionally rough for the range in between. In general, for the range between hydraulically smooth and completely rough flows, the logarithmic-law distribution is applicable whenever k_s is used as the length scaling factor; that is

$$\frac{u}{u_*} = \frac{1}{\kappa} \ln\left(\frac{y}{k_s}\right) + A_r \tag{3}$$

where $Ar = f(k_s^+)$. According to Nikuradse's measurements, for a turbulent flow in completely rough regime $Ar = 8.5$ (Schlichting, 1979) and, thus, Equation (3) can be reduced to

$$\frac{u}{u_*} = \frac{1}{\kappa} \ln\left(\frac{30y}{k_s}\right) + A_r \tag{4}$$

Nezu and Nakagawa (1993, pp. 16–17) discuss that the logarithmic law is inherently valid only in the wall region and that deviations of the velocity distribution from this law should be accounted for by considering a wake function such as that proposed by Coles (1956). However, in practical applications it is still commonly assumed that the logarithmic law describes the velocity distribution over the entire depth of uniform, steady open-channel flows. The power law is an alternative model to represent the vertical distribution of the streamwise velocity in open-channel flows. Chen (1991) presented a generalized power-law model for velocity distribution in open channels and analyzed the ranges of applicability of different powers. In general, the power-law model is expressed as

$$\frac{u}{u_*} = a\left(\frac{y}{y'}\right)^m \tag{5}$$

where y' is defined as the physical location in the boundary layer at which $u = 0$, and a and m are a coefficient and an exponent, respectively. Based on theoretical considerations, Chen (1991) shows that for perfect agreement between the power law and the logarithmic law, the product of κ, m, a, and e, (where e is the base of natural logarithms) should be equal to 1. From this condition, upon substitution of the values of e and κ, the expression $m.a = 0.92$ is obtained.

This indicates that the exponent m is inversely proportional to the coefficient a. However, this is only a particular case that corresponds to a unique point in the domain of the logarithmic law. For fully rough flows, a relation between y' and k_s can be obtained from the logarithmic law as $y' = k_s/e^{\kappa A_r}$ g or approximately $k_s/30$ (Chen, 1991). For this case, best-estimate values for a and m in the power law that for a certain range of u/u_* or (y/y') satisfy the logarithmic law within a given tolerance in a least-squares sense can be obtained based on nonlinear regression analysis. This part of the Chen analysis demonstrates that both parameters in the power law m and a vary with global relative roughness for fully rough flows due to incomplete similarity.

Several methods are available to estimate u_* (see e.g. Nezu and Nakagawa, 1993, pp. 48–49). The simplest one, derived for steady uniform flow in wide channels, estimates $u_* = \sqrt{ghS_0}$, in which g is the gravitational acceleration, and S_0 is the slope of the channel bed (for uniform flow the slope of the channel bed, the friction slope, and the water surface slope are all equal). In the case of steady non uniform flow, the energy slope S replaces S_0. Accurate assessment of the representative bed slope in the vicinity of the measured section is difficult; therefore, u_* must be estimated with other methods. These methods, however, are only applicable when accurate measurements of either velocity fluctuations or wall shear stress are available, such as in the case of carefully performed laboratory experiments. An alternative method frequently applied to determine u_* is based on the best fit of the measured mean velocity distribution to the logarithmic law.

3 EXPERIMENTAL APPARATUS AND PROCEDURE

To investigate the hydraulic characteristics of a V-shaped bottom channel (see Fig. 2 for cross-section and notation), several series of experiments were conducted for measuring *point velocity* and *boundary shear stress*. The described experimental channel, was built inside the existing 15 m long tilting flume. Low and high speeds velocity propellers were used for measuring point velocities, and a Preston tube was used for measuring dynamic pressures to evaluate boundary shear stress.

For a certain channel bed slope, a discharge was introduced and uniform flow was established using stage-discharge results and discharge-tailgate relationships. To avoid the effects of upstream entrance and drawdown at the downstream end a section of 2 m from the tailgate was chosen as a measuring section. This section was the same as that chosen for normal depth and boundary shear stress measurements.

Several series of experiments were conducted for measuring primary point velocity in a V-shaped bottom

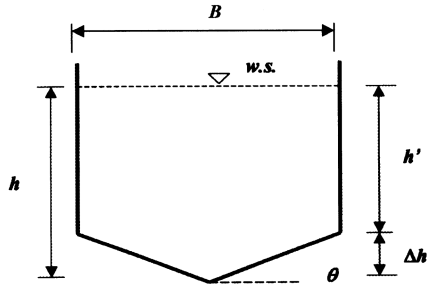


Figure 2. V-shaped bottom channel cross-section.

channel. Low & high speeds velocity propellers were used for measuring point velocities. For a certain channel bed slope, a discharge was introduced and uniform flow was established using stage-discharge results and discharge-tailgate relationships. The flume was supported by two hydraulic jacks and rotated about a hinge joint beneath the middle of the channel. The flume also had a motorized slope control system with a mechanical visual read out on a ruler at the upstream end of the flume used for determining the precise channel bed slope. The maximum slope obtainable was $S_0 = 2\%$. The experimental channels, with a V-shaped bottom cross section built by using PVC panels to make a 14.5 m long channel having 50 mm crossfall, were built along the inside centerline of the existing flume.

Water was supplied to the channel by an overhead tank through a 101.6 mm pipeline for discharges up to $30\,\mathrm{ls}^{-1}$ and a 355.6 mm pipeline for discharges higher than $30\,\mathrm{ls}^{-1}$. To reduce large-scale disturbances, and in order to ensure that the flow was uniformly distributed, a system of honeycombing was placed at the upstream end of the channel where the entrance tank and bell-mouth shaped inlet transition section were located. However for the case of supercritical flow i.e. $\mathrm{Fr} > 1$ the honeycomb was not very useful. Individual bell-mouth shaped transition sections were designed and made for each channel types and served to reduce separation and improve the development of the mean flow into the channels. Discharge measurements (up to $30\,\mathrm{ls}^{-1}$) were made by means of a Venturi meter connected to mercury and air/water manometers at the head of the flume. An electromagnetic flow meter was also installed in the supply line after the Venturi and was used to check discharges. For the case of higher discharges a dall-tube connected to an air/water manometer was used in the 355.6 mm diameter supply line.

The flume had a very rigid bottom designed for high loads, and therefore it was not necessary to do any deflection tests. A slatted tailgate weir was installed in the downstream end of the channel in order to minimize upstream disturbance of the flow, and hence allowed a greater reach of the channel to be employed for experimental measurement in subcritical flows.

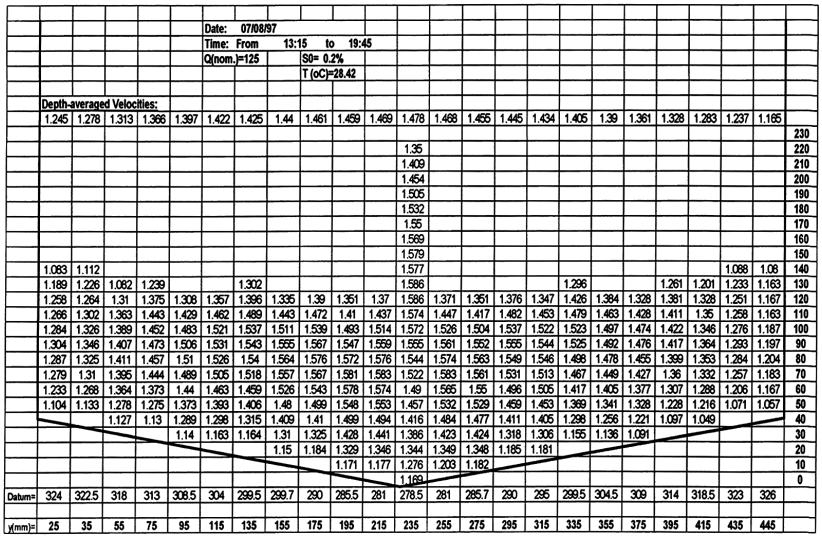


Figure 3. The averaged point velocities measured in V-shaped channel: $Q = 125.89\,\mathrm{ls}^{-1}$ & $S_0 = 0.2\%$.

The test section consisted 12 m long zone, commencing at a distance of 1.25 m from the channel entrance and 1.85 m from the flume entrance. However, for supercritical flows, because of the S2 profiles, the test length was reduced to about 7 m. A trolley was mounted on rails running along the flume with a depth probe, having an electrical contact to the water surface level (accurate to 0.1 mm) and hence the channel bed slope was obtained. It has also been possible to do lateral measurements using the same trolley. The depth was measured at one meter and sometimes half a meter intervals in the test length by means of a centerline pointer probe moved down from the instrument carriage.

The present research work deals with the velocities measured different positions inside of the channel cross-section and velocity distributions. Local velocity measurements were carried out by using the propeller technique with two Nixon 14 mm low and high speed propellers, namely type 403 serial No 1976 Low Speed, and type 404 serial No 1981 High Speed. The related calibration equations are

$$u = 0.0063N - 0.0112 \tag{6}$$

(for low speed probe type 403/1976)

$$u = 0.0194N - 0.0394 \tag{7}$$

(for high speed probe type 404/1981)

The probe was mounted on a carriage and aligned vertically inside water flow and normal to the bed. It was placed on the channel every 10 mm intervals on the vertical lines and every 20 mm intervals in spanwise direction. The velocity numbers (N) were recorded by connecting the propeller to a simple indicator. The reading numbers were applied to assess the primary velocities using equations 6 & 7.

4 VELOCITY MEASUREMENTS RESULTS, ANALYSIS AND DISCUSSION

4.1 *Primary velocities*

In order to explore the distribution of depth-averaged velocity in a V-shaped channel, some measurements of point velocities were undertaken for different flow discharges. As an example, the positions of velocity measurements within the channel cross-section is shown plotted in Figure 3, for the condition of $Q = 125.89\,\mathrm{ls}^{-1}$ & $S_0 = 0.2\%$. A propeller indicator was set on 10 seconds and at least five numbers were recorded. Those five numbers were then averaged to obtain for evaluating the primary point velocities.

Applying a corresponding calibration equation for any propeller, the point velocities were obtained. Point velocities were measured at a number of vertical sections normal to the bed along the spanwise direction to cover as much of the cross section as possible at 20 mm and sometimes 10 mm intervals. For flow discharges up to $30\,\mathrm{ls}^{-1}$ an em flow meter was used, and for flows higher than $30\,\mathrm{ls}^{-1}$ a Dall tube was used for discharge measurement.

The local point velocities were multiplied by the surrounding subareas, and integrated slice by slice, from which the integrated discharge, $Q_{int.}$, was obtained. The *electro-magnetic flow meter* discharge, $Q_{em.}$, and

Dall tube discharge, $Q_{dall.}$, were then compared with the integrated discharges obtained from velocity measurements. The percentage error values of discharges were expressed as

$$\%\,Q_{err} = \frac{Q_{\text{int}} - Q_{em/dall}}{Q_{em/dall}} \times 100 \qquad (8)$$

Depth-averaged velocities were then adjusted to the em/Dall mean values, so that when integrated they gave $Q_{int.} = Q_{em/dall}$. The discharge errors calculated via eq. 6. were very small in the case of large flow depths, typically less than 2% but increased for low flow depths slightly. Overall, the percentage error values are reasonably satisfactory.

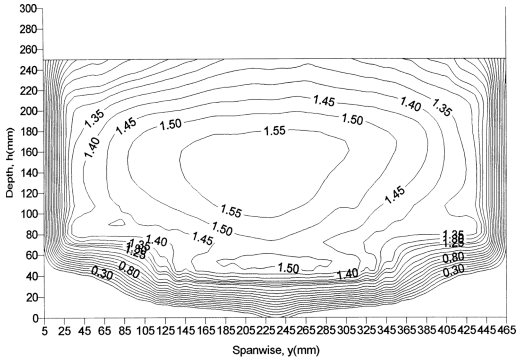


Figure 4. Isovel plot for V-shaped channel: $Q = 125.89\ \text{ls}^{-1}$ & $S_0 = 0.2\%$.

4.2 *2D Isovels diagrams*

In order to transform the point velocities to 2D isovel diagrams, a commercial software package known as "SURFER-6.04" was used. The contour plots were drawn interpolating among averaged depths and velocities at a given position, obtained from superposing the various profile sections. The errors due to the averaging velocities and depths at a given point or section were not significantly different from any extreme value for that point or section. However one of the drawbacks with this software is that the calculations and diagrams are undertaken assuming a computational square mesh i.e. a rectangular channel cross section. This can provoke problems when the geometry of channel is not easily represented by this approach. Nevertheless, this does not affect the overall accuracy of the interpolation, but it produces a non smooth boundary when the results are viewed graphically. It also implies that the isovels near the channel boundary only represent the actual distributions approximately. However from a quantitative point of view, the software is adequate. To solve this problem, a series of data was produced representing the channel boundary at small intervals along the wetted perimeter, and they were replaced as a channel boundary having zero velocities. The channel boundary is therefore viewed reasonably well. One of the representative 2D isovel patterns for different flow conditions is shown in Figure 4.

The primary point velocities were normalized by the section mean velocity, U, and plotted in a similar manner. A complete set of the results is presented by Mohammadi (1998). All the isovel plots illustrate the presence of steep velocity gradients close to the channel boundary, a feature that is characteristic of turbulent boundary layer flow. As can be seen from these Figures, the isovels are parallel to the channel boundary in a region close to the bed, and almost symmetric about the centerline, but not completely. The plotted Figures likewise Figure 4, however indicate that as the flow depth increases, and the channel gets steeper, the isovel patterns become more distorted and the position at which maximum isovel value occurs is depressed below the water surface. From the sediment transport point of view, this phenomenon causes more lift and erosion on the bed particles, and hence more sediment movement.

The distortion of the isovels and the location of maximum velocity are strong evidence of secondary currents being present in this V-shaped bottom channel. The discontinuity between the V-shaped bottom part of the channel and the vertical walls is responsible for those distortions producing anisotropic turbulence. In some cases related to the steeper channels, the isovels are compressed towards the corner regions. This may suggest that momentum is being transported towards the corners. This phenomenon can be seen in the data and isovel contours given by Powell & Posey (1959 and 1961) for triangular 90° channels, and in Wasley (1961) for the vertical walled shallow triangular channels. No explanation was attempted by them. It has also been noted by Tominaga et al (1989) for trapezoidal channels. They however proposed that this may be related to the bed generated vortex, and the free surface flow.

A strong surface phenomenon is also observable throughout the isovel plots. It can be seen that the distortions increase as the flow depth increases and the slope gets steeper. This effect likely to be linked to the number of secondary flow cells. If the secondary flow patterns could be drawn accurately from direct measurements of V & W precise conditions could be drawn.

4.3 *Vertical distribution of local velocities and prediction of friction velocities*

The variation of point velocities in each slice considered along span wise direction in order to study the depth wise velocity profile distributions is

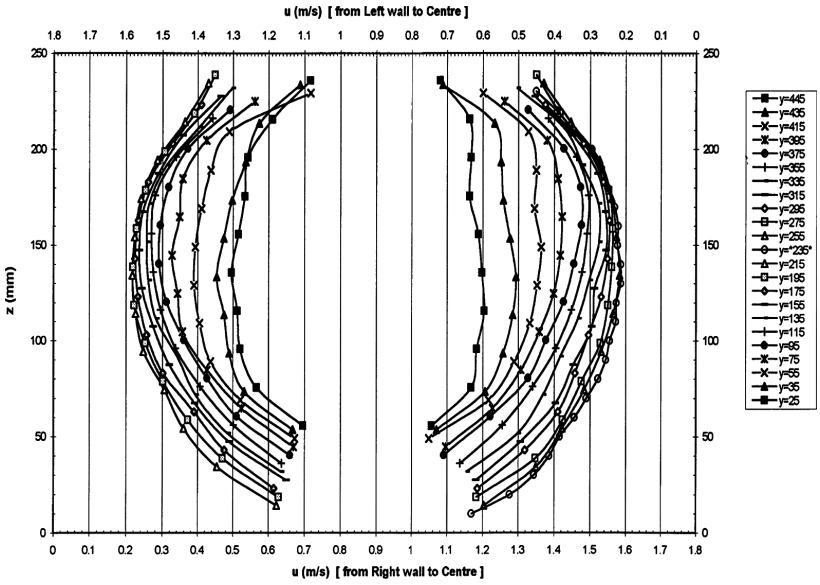


Figure 5. Velocity profiles over the depth, z, at different spanwise positions, y, in a V-shaped channel: $Q = 125.89\,\mathrm{ls}^{-1}$ & $S_0 = 0.2\%$.

shown plotted in Figure 5. Figure 5 is in fact the sectional drawings for the 2D isovel contours explained in the previous section. The profiles are plotted from the wall towards the channel centerline. As can be seen from Figures likewise Figure 5, when profiles are going close to the flow surface, they tend towards the centerline part of the channel cross section. This again indicates the strong presence of secondary currents.

It is customary to compare velocity profiles with the universal logarithmic velocity law. In order to do this, the local velocity, u_i, must be normalized by the subsection friction velocity, u_{*i}, i.e. by u_{*w}, for the velocities normal to the walls and by u_{*b} for velocities normal to the bed, to give value of u^+, where $u^+ = u/u_{*i}$. The depth levels, z, at which velocities were measured must also be normalized, as $u_{*i}z/v$ for velocities over smooth surfaces, and as $z^+ = z/k_s$ for velocities over rough boundaries. The local shear velocity, u_{*l}, can be calculated by using a semi-logarithmic relationship between the local velocities and related depths. For this purpose the following equation may be applied

$$u_{*l} = \frac{M_s \kappa}{2.303} \tag{9}$$

where M_s is the regression coefficient, and κ is the Karman constant taken in this study as $\kappa = 0.41$ suggested by Nezu & Rodi (1986). Then the local shear stress is estimated by

$$\tau_l = \rho u_{*l}^2 \tag{10}$$

However it was not possible to apply this approach, because the above mentioned relationship in equation (9) did not give a reasonable value for M_s with which to evaluate the local friction velocities. Instead the boundary shear stress results were used to estimate the local friction velocities, where the flow conditions for boundary shear stress were the same as for the velocity measurements used were also measured. For the V-shaped bottom channel, this process was carried out and the results were used for log-law examination.

Using the local boundary shear stress measurements the adjusted values of shear velocity $u_{*l} = \sqrt{\tau_l/\rho}$ were tabulated and used to compare the experimental relating data with the universal velocity law. The variation of normalized point velocities, $u^+ = u/u_{*l}$ at $y = 75$, 155, 235, 315, & 395 mm along spanwise direction are shown plotted versus ln (z^+) in Figure 6. The universal logarithmic velocity law, used by Nezu & Rodi (1986) coefficients are: $A = 2.427$ & $B = 5.29$.

It is clear that experimental results are not consistent with the universal logarithmic velocity law, as might be expected. As can be seen from the Figures likewise Figure 6, the universal log-law only matches some parts of velocity profiles in some flow conditions. For example, it lies on centerline profile at $Q = 25.03\,\mathrm{ls}^{-1}$ & $S_0 = 0.9\%$, and for the case of $Q = 50.931\,\mathrm{ls}^{-1}$ & $S_0 = 0.4\%$ it matches a little with profiles at $y = 155$ & 355 mm positions. However in some cases of flows, the universal law is far from

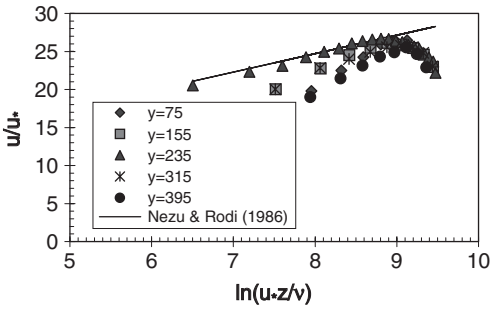


Figure 6. u/u_* versus $\ln(u_* z/v)$ at different span wise positions, y: $Q = 125.89$ l/s & $S_0 = 0.2\%$.

agreement with the experimental data (see Mohammadi, 1998). As expected, the strong effects of cross sectional shape and secondary currents on the flow behavior in this particular channel shape cause the relating distributions to deviate from their simple 2D distribution law.

4.4 *Lateral distribution of depth-averaged velocities*

Integrating the local velocities, u, over the flow depth, h, gives the depth-averaged velocity, U_d. As an example, Figure 7a shows the lateral variations of depth-averaged velocities and also their normalized distributions for different flow discharge and slope settings. The section mean velocities are also shown as solid lines related to every flow test on the same Figures. It can be seen from these Figures that the distributions are almost symmetrical about the cross sectional centerline, but they deviate for some flow cases, despite the flow condition was uniform for all cases. At large flow depths the maximum velocity occurs at the centerline and reduces continuously towards the sidewalls indicating that the sidewalls exert a large influence on flow behavior. These data would be useful for validating various computational models, such as the 2D depth-averaged model given by Shiono & Knight (1991). The measured depth-mean velocities were also normalized by section mean velocity, U_d/U and plotted versus spanwise direction, y, for some selected flow tests, as shown in Figures likewise Figure 7b. It can be seen from this Figure that some deviations are observable. This leads to the view that the secondary current cells affect the flow behavior.

4.5 *Location of maximum point velocity and its relation with section mean velocity, U*

In open channel flows, the maximum velocity, u_{max}, and its location in a channel cross section as well as the mean velocity, U ($= Q/A$), is a valuable parameter. In

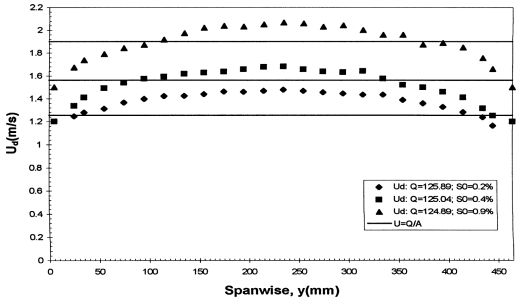


Figure 7a. Lateral distribution of depth-averaged velocity in a V-shaped channel: $Q = 125$ ls^{-1}.

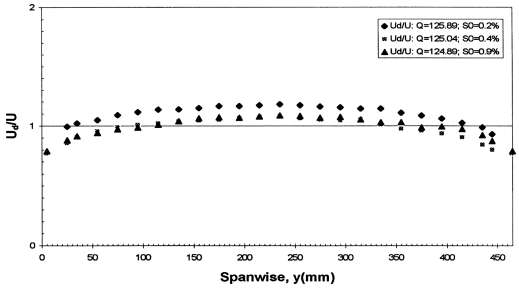


Figure 7b. Dimensionless lateral distribution of depth-averaged velocity in a V-shaped channel: $Q = 125$ ls^{-1}.

contrast with U, it is mentioned very little. The location of the maximum velocity in a channel cross section depends upon the shape of the channel cross section, and consequently it depends upon the resultant effects of the secondary currents. The relation between U and u_{max} for pipe flows in most textbooks is referred to as

$$\frac{U}{u_{\max}} = c \tag{11}$$

where c is a constant and is equal to 0.8167 (Streeter & Wylie, 1979). This relationship can be achieved by using the Prandtl (1/7th) velocity distribution law in a circular pipe as:

$$\frac{u}{u_{\max}} = \left(\frac{z}{r_0}\right)^{1/7} \tag{12}$$

in which u is the point velocity at a depthwise distance, z, from the pipe wall, and r_0 is the pipe radius. Chiu (1988 & 1989), Chiu & Murray (1992), Chiu et al (1993), and Chiu & Said (1994 & 1995) have studied the velocity distribution in either pipe flows or open channel flows, and by applying the entropy concept

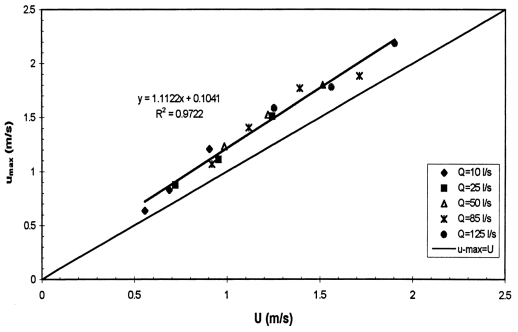


Figure 8. Variation of maximum velocity values in a V-shaped channel at different flows.

they have given the following equation to describe the ratio c:

$$\frac{U}{u_{\max}} = \frac{e^M}{e^M - 1} \cong \frac{1}{M} = c \qquad (13)$$

where M is the dimensionless entropy parameter ($M = 1/c = 1.2244$ for pipe flows and does not satisfy the approximate equality very well). According to Chiu & Said (1994 & 1995) the measurable maximum velocity can be considered as a 'single' value, from which one can know the range of the velocity in a channel cross section and furthermore obtain useful information about the type of open channel flow. The above relationships between U and u_{max} was examined by Xia (1997) for a natural river i.e. Mississippi river and by Sterling (1997) for a part-full pipe channel. They found that there is a linear relationship between u_{max} and U. It may be concluded that for natural rivers and man-made channels, the maximum velocity might play a useful role, but not as important as U. For open channel flows of different cross sectional shapes, not only does the constant number c or M vary, but also the location of the maximum velocity does alter. This makes the use of u_{max} somewhat problematic.

In order to determine the location of the maximum velocity and its relationship with section mean velocity, U, for different flow conditions, Figure 8 was constructed. Figure 8 illustrates that there is a good linear relationship between u_{max} and U, given by

$$u_{\max} = 1.1122U + 0.1041 \quad (R^2 = 97.22\%) \qquad (14)$$

Employing a least square analysis on the data and imposing the condition that the trend line set to zero i.e. when $U = 0$, then $u_{max} = 0$, and one gives

$$u_{\max} = 1.1934U \qquad (R^2 = 97\%) \qquad (15)$$

A comparison of equations (13) and (15) gives constant parameter values as: $c = 0.8379$ and $M = 1.1934$. This result confirms that for a V-shaped bottom channel the value of dimensionless entropy parameter, M, is lower than that of the standard value for circular pipe flows.

The position of maximum velocity in the spanwise direction, was produced. It was seen from this Figure that the majority of the data lie on the central slice of the cross section at $y = 230$ mm, with only a few data positioned in two neighbouring slices.

5 SUMMARY AND CONCLUSIONS

The primary velocity and boundary shear stress measurements have been undertaken in the uniform flow condition for five target flow discharges of 10, 25, 50, 85 & 125 ls^{-1} at four different channel bed slopes of 0.1%, 0.2%, 0.4% & 0.9% (see Mohammadi, 1998). In addition 16 different flow conditions were examined for velocity and the same 16 for boundary shear stress, in a V-shaped bottom channel. Therefore a considerable amount of data has been collected and the associated parameters have been analyzed. On the basis of results already presented in previous sections, the main findings are:

1. Experimental velocity isovels and transverse velocity distributions have been presented for uniform flow conditions.
2. The isovel plots (see Fig. 4) are generally symmetric, except in the central region where a local maximum occurs. However, it seems that the generally symmetrical distributions of primary flow are sometimes unstable, so that an alternative pattern of asymmetry may form. Such an alternating pattern is random for different flow conditions, being affected by secondary flow cells which make the flow 3D.
3. The depth wise velocity profiles tend towards the centerline of the channel near the water surface (see Fig. 5). This finding is one of the strong evidence for the presence of secondary currents. It is more apparent for the higher Froude numbers.
4. The logarithmic velocity law developed for wide open channel flows, has been shown to be largely ineffective for the current channel shape (see Fig. 6).
5. The distributions of depth-averaged velocity show that they are fairly flat for low Froude numbers (see Figs. 7a & b). This is not the case for higher Froude numbers.
6. There is a good linear relationship between the maximum velocity, u_{max}, and section mean velocity, U, and is given by equations 11 & 12 (see Fig. 8).
7. The depth wise position of maximum velocity is shown to be at near the surface for low Froude numbers. The filament of maximum velocity is depressed below the free surface as the Froude number increases.
8. For the V-shaped bottom channel, the dimensionless entropy parameter, M, introduced by Chiu is greater than that of given for the full pipe flows.

9. The random or stochastic nature of a fundamental instability of the flow field, was also seen in the data of Powell & Posey (1959 & 1961) and Wasley (1961). No explanation for the observed asymmetry was attempted. However, Tominaga et al (1989) proposed that this may be related to the bed generated vortex, and the free surface vortex.
10. There is a strong evidence of cross sectional shape effects on the distribution of velocity.
11. The effect of multiple pairs of secondary flow cells was evident in the perturbations of the depth-averaged velocities for both subcritical and supercritical flows. Although at low flow depths where the Froude number is not so high i.e. greater aspect ratios the presence of secondary currents was not immediately apparent in the primary velocity distributions as measured by the propellers.
12. The number of perturbations, and hence the number of secondary flow cells, has been shown to be dependent on the flow depth and discharge i.e. the aspect ratio. Up to three pairs of flow cells can be detected at a large discharge in a steep channel with a V-shaped bottom.
13. The information in this chapter may prove useful to any computational modelers dealing with channels with a similar shape. The work may also be valuable to river engineers trying to solve stable channel problems as well as sediment transport in channels with side slopes, similar to channels with a V-shaped bottom.

REFERENCES

Chen, C.L. 1991. Unified theory on power laws for flow resistance. *J. of Hydraulic Eng.,* ASCE, Vol. 117, No. 3, March: pp. 371–389.

Chiu, C.-L. 1988. Entropy and 2-D velocity distribution in open channels, *J. of Hydraulic Eng.*, ASCE, Vol. 114, No. 7, July.

Chiu, C.-L. 1989. Velocity distribution in open channel flow, *J. of Hydraulic Eng.*, ASCE, Vol. 115, No. 5, May.

Chiu, C.-L. & Abidin Said, C.A. 1994. Modelling of maximum velocity in open-channel flow, Proc. Hydraulic Div. Conf., Vol. 1, New York: pp. 381–385.

Chiu, C.-L. & Abidin Said, C.A. 1995. Maximum and mean velocities and entropy in open-channel flow, *J. of Hydraulic Eng.*, ASCE, Vol. 121, No. 1, January.

Chiu, C.-L. Lin, G.-F. & Lu, J.-M. 1993. Application of probability and entropy concept in pipe flow study, *J. of Hydraulic Eng.*, ASCE, Vol. 119, No. 6, June: pp. 742–756.

Chiu, C-L. & Murray, D.W. 1992. Variation of velocity distribution in along non uniform open channel flow", *J. of Hydraulic Eng.*, ASCE, Vol. 118, No. 7, July: pp. 989–1001.

Coles, D. 1956. The law of the wake in the turbulent boundary layer, *J. of Fluid Mechanics*, Vol. 1, No. 2: pp. 191–226.

Mohammadi, M. 1998. Resistance to flow and the influence of boundary shear stress on sediment transport in smooth rigid boundary channels. *PhD Thesis*, School of Civil Engineering, The University of Birmingham, England.

Nezu, I. & Nakagawa, H. 1993. Turbulence in Open-Channel Flows. Balkema Publishers, Rotterdam, The Netherlands.

Nezu, I. & Rodi, W. 1985. Experimental study on secondary currents in open channel flow. Proc., 21st Congress of IAHR, Melbourne, Australia, Vol. 2, 1985: pp. 115–119.

Nezu, I. & Rodi, W. 1986. Open-channel flow measurements with a Laser Doppler anemometer. *J. of Hydraulic Eng,* ASCE, Vol. 112 No. 5 May: pp. 335–355.

Schlichting, H. 1979. Boundary Layer Theory, Seventh ed., McGraw-Hill Classic Text Book Series, New York.

Shiono, K & Knight D.W. 1991. Turbulent open channel flows with variable depth across the channel. *J. Fluid Mechanics*, Vol. 222: pp. 617–646.

Sterling, M. 1997. The distribution of boundary shear stress in an open channel circular conduit running part-full, *PhD Thesis*, University of Birmingham, Birmingham, England.

Tominaga, A. Nezu, I. Ezaki, K. & Nakagawa, H. 1989. Three-dimensional turbulent structure in straight open channels", *J. of Hydraulic Eng.*, ASCE, Vol. 27, No. 1, August.

Xia, R. 1997. Relation between mean and maximum velocities in a natural river", *J. Hydraulic Eng.*, ASCE, Vol. 123, No. 8, August.

Posey, C.J. & Powell, R.W. 1961. Water surface profiles and velocity distributions for flow in a long uniform channel. Rocky Mountain Hydraulic Laboratory Report, No. 26, April.

Powell, R.W. & Posey, C.J. 1959. Resistance experiments in a triangular channel. *J. Hydraulic Div.*, ASCE, Vol. 185, No. HY5, May.

Wasley, R.J. 1961. Uniform flow in a shallow triangular open channel. *J. Hydraulics Div.*, ASCE, Vol. 87, No. HY5, September.

This page intentionally left blank

River Flow 2004 – Greco, Carravetta & Della Morte (eds.)
© 2004 Taylor & Francis Group, London, ISBN 90 5809 658 0

River roughness – the integration of diverse knowledge

C. McGahey & P.G. Samuels
Water Management Department, HR Wallingford, Howbery Park, Benson Lane, Wallingford, Oxon, UK

ABSTRACT: In 2000, the Environment Agency of England and Wales identified the need to reduce the uncertainty associated with flood level prediction through using recent research advances on river and flood plain conveyance (Samuels et al, 2002). This has led to the development of the Conveyance Estimation System (CES), involving a partnership between researchers and experts in hydraulics, aquatic vegetation and software development and with close consultation with typical users. A key component of this development was taking knowledge on river resistance from a diverse set of sources, covering different types of vegetation in the river and on the flood plain and, different channel dimensions and bed material type. The calculation methods are documented elsewhere (McGahey & Samuels, 2003) and are based on the Darcy friction factor to represent local river bed stresses coupled with other fluid dynamic processes. Most data sets on flow resistance provide average values of Manning's *n* for whole river sections and include the influence of bed material, vegetation and larger scale topographic variation. A key requirement of the CES project was to produce a roughness advisor to allow the user to access this information in a structured manner and construct information for the CES conveyance calculation. The field data also needed further interpretation to assess the local resistance properties to include in the calculations. This paper describes the integration of this information on flow resistance into the conveyance calculations in the CES software including an approach for the estimation of friction factors when the flow depth is comparable to the effective roughness length scale.

1 INTRODUCTION

Over the past two decades there has been an improvement in knowledge and understanding related to estimating the conveyance capacity of natural channels. Research into the exact nature of the flow processes such as local friction, turbulence due to lateral shearing and the presence of secondary flows, together with an ever increasing database of observed flow parameters such as the managed programme of research on the Flood Channel Facility (FCF) at HR Wallingford, provides the facility for testing and validating these new approaches. Significant contributions include those of Chang (1983), Ervine & Ellis (1987), Shiono & Knight (1989), Ackers (1993), Bousmar & Zech (1999) and Ervine et al (2000). Historically, most one-dimensional hydrodynamic software packages are based on the Manning equation, first published in 1891 (Manning, 1891). This empirically derived equation is not based in rigorous physics and provides meaningless results for sudden changes in area or wetted perimeter with depth, where shape effects are ignored.

In 2000, the Environment Agency commissioned a Scoping Study into reducing the uncertainty related to flood level predictions. The key outcome was a Targeted Programme of research to be undertaken by a multidisciplinary team of experts and led by HR Wallingford, which would deliver a Conveyance Estimation System (CES). This stand-alone software would comprise three core components: the Roughness Advisor for assistance in the estimation of local roughness, the Conveyance Generator for the improved calculation of conveyance and the Uncertainty Estimator which provides some measure of uncertainty for the predicted water level. The CES would be available as open code for inclusion in any one-dimensional hydrodynamic modelling software.

The conveyance methodology to be incorporated in the CES (McGahey & Samuels, 2003) is based on the depth integration of the Reynolds Averaged Navier-Stokes Equations (HR Wallingford, 2003).

$$gHS_o - \frac{f\beta q^2}{8H^2} + \frac{\partial}{\partial y}\left[\lambda H\left(\frac{f}{8}\right)^{1/2} q \frac{\partial}{\partial y}\left(\frac{q}{H}\right)\right] = \alpha\Gamma + (1-\alpha)C_{uv}\frac{\partial}{\partial y}\left[\frac{q^2}{H}\right] \quad (1)$$

where:

g = gravitational acceleration (m/s^2)
q = streamwise unit flow rate (m^2/s)
H = local depth normal to the channel bed (m)
S_o = reach-averaged longitudinal bedslope
y = lateral distance across the channel (m)
β = coefficient to account for influence of local bedslope on the bed shear stress
α = function of the reach-averaged sinuosity

The total flow rate Q (m^3/s) is calculated from integrating this lateral unit flow distribution across the channel section, and hence the total cross-section conveyance K (m^3/s) is determined from,

$$K = \frac{Q}{S_f^{1/2}} \approx \frac{\int q\,dy}{S_o^{1/2}} \tag{2}$$

where the reach-averaged longitudinal friction slope S_f is approximated by the reach-averaged longitudinal bedslope S_o.

Equation (1) has four calibration coefficients: the local friction factor f, the dimensionless eddy viscosity λ, the secondary flow parameter Γ and the coefficient of meandering C_{uv}. The intention of this paper is to describe the approach adopted for determining the lateral variation of f for a given depth of flow. The conversion of a unit roughness 'n' to an equivalent resistance f is described, with particular consideration given to the evaluation of f where the roughness height is large relative to the local water depth.

2 LATERAL DISTRIBUTION OF f FOR A GIVEN DEPTH

Previous approaches for determining the lateral distribution of f for a given depth include:

1. Diagrams for pipe resistance such as the Moody Diagram, where the pipe diameter can be replaced by four times the hydraulic radius R (m) for open channel flow.
2. The Blasius equation which is applicable for smooth turbulent flows where the flow conditions are dominated by the viscous forces, typically used for experimental flumes ($4000 < Re < 10^5$). This formula is based on pipe flow.
3. The Kármán-Prandtl equation which is used at higher Reynolds Numbers, where the Blasius equation under-predicts f.
4. The Hazen-Williams equation, which is derived for pipe flow.
5. The 'Power Law' approach, which relates the ratio of the Darcy-Weisbach resistance coefficient on the floodplain f_{fp} and main channel f_{mc} respectively, to the relative depth by a power of 3/7 (Shiono & Knight, 1991; Rhodes & Knight, 1994).
6. Calibrated relationships that relate the main channel resistance f_{mc} to the floodplain resistance f_{fp} by an empirically derived factor R_f (Knight & Abril, 1996; Abril, 1997).
7. The Chezy (1768) equation with an additional conversion to relate the Chezy coefficient C (m$^{0.5}$.s^{-1}) to f as a function of the hydraulic radius. The Chezy equation is based on balancing the resistive force due to the wetted perimeter and the square of the average velocity with the driving force due to the longitudinal bedslope and the cross-sectional area. It is therefore applicable where rough turbulent flow dominates as a result of the boundary friction represented by C.
8. The Manning equation with an additional conversion to relate Manning's n to f as a ratio of the local depth to the power 1/3. This equation is independent of the Reynolds number and the friction factor depends only on the hydraulic radius. Manning's equation is therefore only recommended for fully rough turbulent flow conditions. The units of n are s.m$^{-1/3}$, although some authors believe that the roughness is not related to time and that it includes a gravitational term $g^{0.5}$, giving the actual units of n as m$^{1/6}$ and thus relating n to the hydraulic radius $R^{1/6}$. Based on the approximations in deriving the Manning equation and the uncertainty in the value of n, it seems unjustifiable to carry the numerical constant to more than three significant figures (Chow, 1959).
9. The full Colebrook-White (1937) equation i.e. inclusive of the smooth and rough turbulent laws. White identified two types of surface: those that give a constant f at sufficiently high Reynolds Numbers i.e. where f is dependent on the relative roughness only (rough law) and those for which f continues to decrease as the Reynolds Number increases (smooth law). In general, the values of f appear to be larger for pipes at the same Reynolds Number and relative roughness. Kirshmer (1949) attributed the differences to the secondary flows that are not present in pipe flow. The transition from smooth to fully rough flow is further dependent on the form and spacing of the roughness elements (Henderson, 1966; US Task Force, 1963).

These approaches are not applicable to channels whose beds are in motion. It is assumed throughout that the bed topography is fixed.

The lateral distribution of f in the Conveyance Generator is based on a form of the Colebrook-White equation, with coefficients suitably adapted for open channels.

$$\frac{1}{\sqrt{f}} = -2.03\log\left[\frac{k_s}{12.27H} + \frac{3.09\nu}{4q\sqrt{f}}\right] \tag{3}$$

This equation was selected over the Chezy and Manning equations, as (i) it covers smooth turbulent,

transitional and rough turbulent flows; (ii) it has a strong physical basis as it is derived from the logarithmic velocity profile together with the channel geometry; and (iii) it incorporates the variation of roughness with depth. Data measurements from the Mississippi, Tennessee and Irrawaddy Rivers (Chow, 1959) clearly illustrate this variation of the cross-section roughness n with depth, and in particular, the rapid increase of n at low flows. Ackers (1958) published a thorough study of channel flow and concluded that the Colebrook-White formula is the best available. He noted that k_s should be increased by 20% over the value for the same material in pipes, to correct for the different cross-sectional shape.

In equation (3), the coefficient '2.03' is from taking von Kármán's universal constant as 0.4 (assumes clear water). The coefficients '12.27' and '3.09' are based on this coefficient together with the channel cross-section shape and the nature of the roughness elements. Previous research (Henderson, 1966; Keulegan, 1938; Rouse, 1938; Zegzhda, 1938) has provided advice on the coefficients for a variety of channel types, ranging from smooth rectangular shapes to fully rough, wide, natural channels. The coefficients in equation (3) are based in part on this advice. However, since the application of the Colebrook-White is to local element 'slices' rather than the entire cross-section for which the equation was derived, these predictions of f are further compared to the f-values back-calculated from bed shear stress measurements. The EPSRC FCF managed programme of research provided high quality flow, velocity and shear stress data for straight, skewed and meandering trapezoidal compound channels, situated in a 56 m long, 10 m wide and 0.4 m deep laboratory flume. Velocity measurements were taken with a vane attached to a rotary potentiometer at regular spacing across the sections, for a number of depths within each vertical column. This enables calculation of the local depth averaged velocity profile U_d (m/s), and together with the measured (using a Preston tube) bed shear stresses τ_b (N/m^2), the local resistance f can be determined,

$$f = \frac{8\tau_b}{U_d^2 \rho} \tag{4}$$

where ρ (kg/m^3) is the fluid density. Comparison of the Conveyance Generator predicted f-values to the FCF Phase A data (Figure 1) confirms the applicability of the selected coefficients in equation (3) for smooth channels over a range of depths, including both inbank and out-of-bank flow.

3 NEW APPROACH TO MANNING'S n-VALUE

Historically, the Manning n-value (Chow, 1959) has been widely used for describing resistance due to vegetation, substrate and other anticipated energy losses in the channel and floodplain system. This n-value is defined here as an engineering n_e-value, as it incorporates energy losses due to local bed friction, turbulence generated from the main channel – floodplain interaction and helical secondary flows that result from the planform channel sinuosity. This Manning n_e is thus all-encompassing.

Due to the widespread use of this Manning n_e-value, most resistance advice, photographs and summation approaches in the literature (Barnes, 1967; Chow, 1959; Cowan, 1956; Hicks & Mason, 1998) are expressed in terms of 'n_e'. The Roughness Advisor (RA) in the CES is thus based on an n rather than an f resistance value to maintain user familiarity and confidence. This was a critical decision from the Project User Consultative Group to receive wider user acceptance. The fundamental difference is that this advice is based on a local n_l value, which is the equivalent 'Manning' n_e-value due to the local bed friction only. This includes boundary losses due to three *components*: surface material (e.g. sand, clay, bedrock), vegetation (e.g. grass, reeds, water lillies) and irregularites (e.g. groynes, urban trash, pools and riffles). All the remaining energy losses are incorporated through the other calibration parameters λ (lateral shear), Γ (secondary flows in straight channels) and C_{uv} (secondary flows in meandering channels) in equation (1).

The roughness advice provided by the RA is based on an extensive literature review of over 700 references covering existing methods and data for estimating roughness (HR Wallingford, 2003). Many of the approaches have been developed for a particular aspect of the river channel e.g. vegetation, boulders or large-scale roughness elements. The measured data is generally given in terms of a combined roughness value for the section i.e. inclusive of the three roughness *components* as well as shape effects. The process of disaggregating the data into unit components due to the different features was a difficult task. Since Chow, which forms the basis of the RA, there have been more studies providing insight into the roughness of different features, especially vegetation.

The RA provides advice through descriptions that are where possible, accompanied by photographs. In the absence of any survey data or channel description, the RA provides advice using the national data set obtained through the national survey of river habitats (River Habitat Survey, Raven et al., 1998). This survey was based on a 10 by 10 km square grid and 25 items were assessed at each river cross-section, spaced at 50 m intervals, in 500 m long river segments. This enables the user to enter the UK grid reference of the study reach and receive advice on expected in-channel and bank-side aquatic vegetation.

For a channel reach, three roughness *types* have been established in the RA: bed, bank and floodplain.

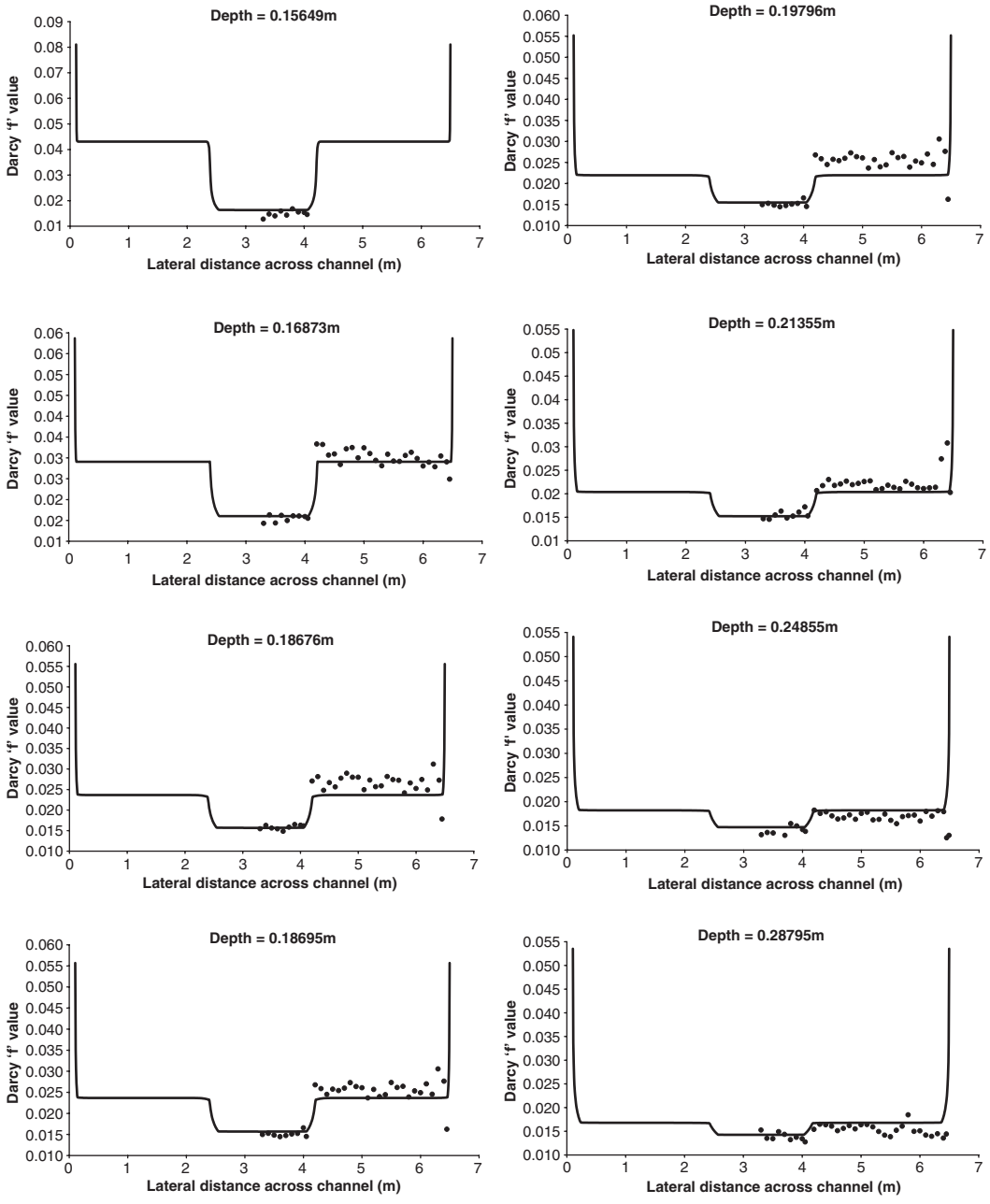


Figure 1. Lateral distribution of resistance f with depth.

Within each of these types, the roughness can be composed of up to three *components*: surface material, vegetation and irregularities. All roughness components include a minimum, maximum and expected n_l-value and for the vegetation, the seasonal variation of n_l is provided. The surface materials include natural [e.g. bedrock, cobbles, gravel, sand, silt, clay, peat, earth, firm soil, bare ploughed soil] and man-made [e.g. sheet piling, stone block, hazel hurdles, gabion, concrete, rip-rap, wood piling] roughness values. The

Table 1. Unit roughness n_l for twelve vegetation morphotypes.

Aquatic vegetation by RHS vegetation type	Unit roughness n_l min	mean	max
1. None If none visible check predictions from RHS data set			
2. Free-floating plants typically algae or duckweeds, medium deep drainage channel [depth = 1.1 to 2.5 m, velocity = 0.1 to 0.6 m/s]	0.010	0.030	0.040
3. Filamentous algae attached shallow nutrient rich waters [depth = 0.05 to 0.5 m, low velocities]	0.000	0.015	0.050
4. Mosses attached to bed or banks [depth ≈ 1 m]	0.000		0.030
5. Trailing bank-side plants [depth = 0.5 to 3 + m]	0.000	0.050	0.100
6. Emergent reeds, rushes, flag and large grasses	0.020	0.150	0.200
7. Floating-leaved typically water lillies in deeper slower waters	0.030	0.100	0.140
8. Emergent broad-leaved rooted plants, water cress or water parsnip	0.050	0.150	0.50+
9. Submerged broad-leaved, pondweeds [depth = 0.06 to 1.2 m, velocity 0.2 to 0.9 m/s]	0.020	0.100	0.200
10. Submerged fine-leaved, shallow rivers, chalk streams, water crowfoot, pondweeds [depth = 0.2 to 0.6 m, velocity = 0.2 to 0.7 m/s]	0.020	0.300	0.45+
11. Submerged fine-leaved, medium depth rivers, regular management [depth = 0.6 to 1.2 m, velocity = 0.3 to 0.8 m/s]	0.021	0.100	0.249
12. Submerged fine-leaved, medium to deep rivers, some management [depth > 1.2 m, velocity = 0.3 to 1.0 m/s]	0.010	0.080	0.120

natural vegetation includes 12 morphotypes (Table 1) based in part on the RHS data as well as categories due to human intervention such as grass, hedges, trees, shrubs and crops e.g. wheat, sorghum, corn, cotton, soybeans and sunflower. Irregularites include urban trash, groynes, exposed boulders, pools and riffles, ridges on ploughed fields, undulations on the floodplain and obstructions such as debris deposits, exposed roots, stumps, logs, piers and isolated boulders.

For solution of equation (1), the lateral variation of f is required, and hence the lateral distribution of this local boundary roughness n_l. Since the local roughness at a point in the section can comprise up to three roughness *components*, these can be combined to get the total unit roughness at a point through,

$$n_l = \sqrt{n_{veg}^2 + n_{sur}^2 + n_{irr}^2} \tag{5}$$

where n_{veg}, n_{sur} and n_{irr} are the local roughness values due to vegetation, surface material and irregularity respectively. These are associated with a depth of 1m, selected as a representative depth of flow for UK rivers. The reason for adopting the "root sum of the squares" approach is twofold: it highlights the contribution of the largest roughness component; and the roughness is squared before being combined since the energy loss is related to the square of the local velocity. The assumption is that the roughness mechanisms are mutually independent and hence the total resistance can be expressed as the sum of the individual resistances.

Previous work (Einstein & Banks, 1950) employed a similar approach whereby the measured bed shear stress relative to the square of the velocity (τ/v^2) was compared to the addition of this term for the independent resistance components. This is similar to equation (5) with both sides squared. The local roughness contributions from flow over (i) flat blocks, (ii) an offset and (iii) pegs were measured. These were combined and compared to the total measured roughness due to all three components, and the measured total resistance values were found to correlate well with the combined data. It was concluded that the separate resistances should be expected to have an additive property provided the roughness types do not exhibit excessive mutual interference.

4 CONVERSION OF LOCAL MANNING n_l TO AN EQUIVALENT ROUGHNESS k_s

Solution of equation (3) requires the conversion of the local roughness 'n_l' to an equivalent length scale 'k_s'. Although the roughness height k_s is traditionally defined in terms of the sand grain dimension (Nikuradse, 1933), the vegetation k_s can be interpreted as an equivalent turbulence length scale i.e. a measure of the turbulent eddy size. This length scale may be greater than the water depth, e.g. willow trees, boulders etc., as it represents the horizontal mixing action, whereby eddies may be larger in plan than the local water depth. The equivalent k_s value can be determined from (variation of Strickler, 1923; Ackers, 1958),

$$n_l = 0.038 k_s^{1/6} \tag{6}$$

This equation is only applicable where the depth H is in the range of 7–140 times the roughness size. For the flow conditions under which the equation was derived,

this was found to be suitable, as it was applied to the whole cross-section or three regions: i.e. the main channel and two floodplains. For application within the Conveyance Generator, two issues arise:

1. In equation (1), the solution is required for each lateral division across the section and hence for a given section the local roughness height may be equivalent to a large fraction of the depth or in some cases, exceed it e.g. tall grass on the floodplain. This typically occurs at low inbank and low overbank flows.
2. Large typically-used Manning n-values result in highly inflated k_s values. E.g. should the bed material be characterised by large boulders, with an equivalent Manning n-value of 0.5, this would produce a k_s value over 5,000 km, which is meaningless in terms of the channel depth anywhere in the cross-section or entire river reach (Table 2).

An alternative approach is to use the rough turbulent law, i.e. the first term in equation (3),

$$\frac{1}{\sqrt{f}} = -2.03\log\left[\frac{k_s}{12.27H}\right] \tag{7}$$

where f is given by,

$$f = \frac{8gn_l^2}{H^{1/3}} \tag{8}$$

Hence at a depth of 1 m, k_s is given by,

$$k_s = 12.27H10^{\left[\frac{H^{1/6}}{\sqrt{8g}n_l(-2.03)}\right]} = 12.27\times 10^{\left[\frac{1}{\sqrt{8g}n_l(-2.03)}\right]} \tag{9}$$

This relationship and equation (6) can be viewed in Figure 2 and Table 2 for a typical range of n_l values. As n_l approaches infinity, the bracketed term approaches zero, and k_s asymptotes to 12.27, the coefficient in the Colebrook-White law. In the Acker's approach, k_s approaches infinity, and hence equation (9) is preferable. For the region $0.01 < n_l < 0.025$, both laws predict a similar relationship. These approaches are not suitable for experimental flumes where the smooth turbulent law dominates e.g. in Table 2 the values of k_s for $n_l \leq 0.01$ decrease rapidly. The assumption is that the unit roughness k_s is constant with depth, although this has been shown otherwise for whole cross-section k_s-values in tidal reaches. Knight (1981) considered the variation of n, f and k_s with stage in the 1.2 km long tidal reach of the Conwy Estuary and found that all three parameters varied significantly with depth. In particular, the Nikuradse roughness

Table 2. Comparison of k_s predictions based on the calculation approach of Ackers and the simplified Colebrook-White Law.

n_l (s.m$^{-1/3}$)	Equivalent k_s (Colebrook-White Rough Law) (m)	Equivalent k_s (Ackers, 1958) (m)
0.0010	3.0373E − 55	3.3212E − 10
0.0050	9.2805E − 11	5.1894E − 06
0.0100	3.3745E − 05	3.3212E − 04
0.0500	9.4780E − 01	5.1894E + 00
0.1000	3.4102E + 00	3.3212E + 02
0.5000	9.4980E + 00	5.1894E + 06
0.8000	1.0455E + 01	8.7064E + 07
1.0000	1.0795E + 01	3.3212E + 08
100000	1.2270E + 01	3.3212E + 38

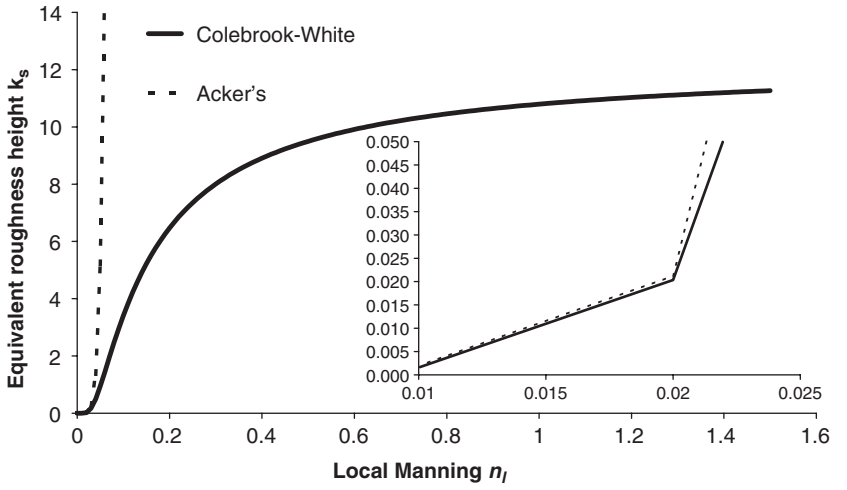


Figure 2. Conversion or n_l to k_s for a typical range of n_l values.

height k_s was found to vary significantly with stage, increasing from 0.2 m at high water to a value (2.5 m) comparable with the water depth at low water.

5 CONVERSION OF EQUIVALENT ROUGHNESS k_s TO LOCAL FRICTION FACTOR f

Once k_s has been determined, the full Colebrook-White equation (3) can be used for the solution of f at a given depth. This approach is not universally applicable, and it can provide unrealistically large values of f. Consider the term in brackets in equation (3). Should the flow be characteristic of a natural river, with a large k_s/H ratio, the viscous forces and hence the smooth law contribution become negligible. As k_s/H approaches 12.27, the bracketed term approaches one, and the logarithm tends to zero. The result is that,

$$\frac{1}{\sqrt{f}} = \textit{very small positive number} \tag{10}$$

and the inverse of this small number squared provides an unrealistically large f-value (Table 3). This f is meaningless and thus at high k_s/H ratios, a Power Law is introduced.

$$\frac{8}{f} \propto a_2\left(\frac{k_s}{H}\right)^{a_3} \quad \text{for } H < a_4 k_s \tag{11}$$

The mathematical formulation of the velocity distribution in the overlap region of the boundary layer (i.e. between regions dominated by either viscous or inertia forces) must be either of the logarithmic or the Power Law form. The logarithmic form (i.e. basis for the Colebrook-White Law) is generally favoured as it covers a wider range of Reynolds Numbers, whereas the Power Law must change with Reynolds Number and also with roughness. In the literature, the Power Law generally relates f to $R^{1/3}$. For simplicity, it is assumed in equation (11) that $a_3 = 1$ (Samuels, 1985). The coefficients a_2 and a_4 can hence be derived through ensuring equations (6) and (10) are continuous in f and that the derivative of f with respect to depth, df/dH, is continuos at the cross-over point between these two laws i.e. at $H = a_4 k_s$. Expressing equation (11) at the upper limit of its range of applicability,

$$f = \frac{8}{a_2}\frac{k_s}{H} = \frac{8}{a_2}\frac{1}{a_4} \tag{12}$$

and taking the derivative with respect to depth gives,

$$\frac{\partial f}{\partial H} = -\frac{8}{a_2}\frac{k_s}{H}\frac{1}{H} = -\frac{8}{a_2 a_4 H} \tag{13}$$

Rearranging equation (7) in terms of f and setting $a_1 = 8 \times 2.03^2[\log_{10} e]^2 = 6.218$ yields,

$$f = \frac{8}{a_1}\left[\ln\left(\frac{12.27H}{k_s}\right)\right]^{-2} \tag{14}$$

and df/dH is given by,

$$\frac{\partial f}{\partial H} = \frac{-16}{a_1 H}\left[\ln\left(\frac{12.27H}{k_s}\right)\right]^{-3} \tag{15}$$

Equating the expressions for f and df/dH from equations (12) to (15) gives $a_2 = 41.3015$ and $a_4 = 1/1.6606$. Thus for a k_s/H ratio greater than 1.66, the Power Law is used to solve for f, where

$$f = \frac{8}{41.3015}\frac{k_s}{H} \tag{16}$$

To prevent unrealistically large predictions of f, the upper limit is set at a ratio of $k_s/H = 10$, which corresponds to an f-value of 1.937. This restricts f from approaching infinity as H approaches zero for shallow flows. The maximum measured resistance in Nikuradse's (1933) experiments is approximately 0.125 in the laminar region, and the entire turbulent region falls well below an f-value of 0.1. Essentially this large f-value would occur in regions with extremely shallow water relative to the roughness elements that are expected to have a virtually negligible contribution to the overall cross-section conveyance. Thus the exact value of f is of little significance.

For $k_s/H < 1.66$, equation (7) is employed, and the smooth law component is only introduced for experimental channels.

Figure 3 illustrates how, for a given n_l value ($n_l = 0.05$), these friction laws are selected depending on the k_s/H ratio. For this case, the Colebrook-White equation increases rapidly below a stage of 0.5 m,

Table 3. Calculated resistance f values for an increasing absolute roughness over depth relationship.

Roughness ratio k_s/H	Equivalent resistance f
0.5	0.13
1	0.20
1.66	0.32
2	0.39
8	7.03
10	30.74
12	2598.70
12.26	1935416.14
12.27	∞

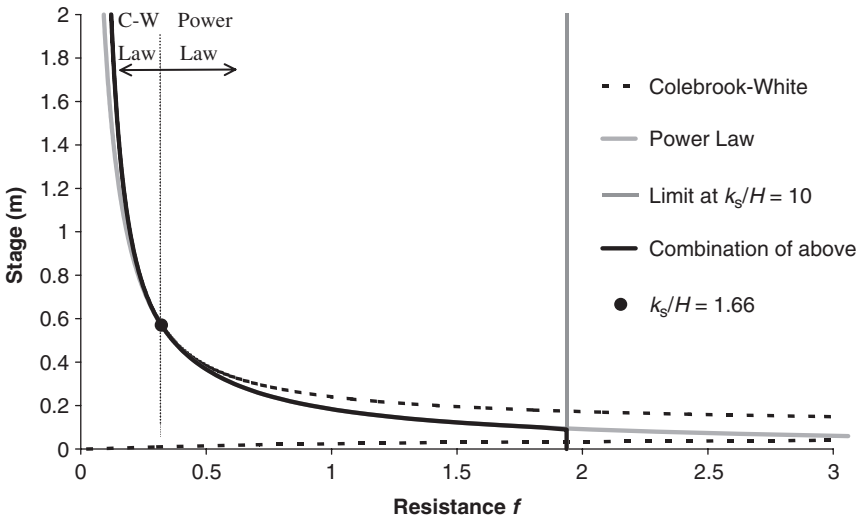


Figure 3. Graphical representation of the combined Friction Laws.

i.e. the region where the k_s/H ratio approaches 12.27. The Power Law replaces the Colebrook-White Law in this region and is restricted at $k_s/H = 10$.

For smooth turbulent flow e.g. experimental flow conditions, a lower limit on k_s is set i.e. $k_s = 0.1$ mm. This corresponds to an n_l value of 0.0109. The distribution for f is determined from the full Colebrook-White equation (3). Since the rough term will have a virtually insignificant contribution, the distribution of f will be based on the viscous effects and can be solved iteratively. The Blasius Law would be a suitable alternative.

The complete approach for estimating the lateral distribution of f for a given depth of flow, from the local n_l values provided by the RA, is illustrated in Figure 4.

6 CONCLUSIONS

An extensive literature review of roughness methods and data has provided a source of interdisciplinary knowledge and advice on river roughness. This roughness information is presented within the Roughness Advisor (RA), a core component of the Conveyance Estimation System. The RA provides unit roughness values for the three component roughnesses: surface material, vegetation and irregularities. This roughness is based on skin friction only, and does not incorporate form losses or shape effects, the latter of which is considered in the conveyance calculation. The unit roughness values are combined to form the total unit roughness at a point within the channel section, and hence converted to an equivalent k_s value that is constant with depth. The resistance f for a given depth of flow is determined from this k_s value. Consideration has been given to the extrapolation of the existing friction laws for flow conditions that they were not specifically derived for.

7 RECOMMENDATIONS

The RA may be extended to provide more advice on representation of urban floodplains, changes in roughness with velocity and/or relative depth [e.g. grass bending at high flows] and form losses between consecutive cross-sections. The roughness calculation within the Conveyance Generator may be updated to include a function that accounts for the additional resistance due to bedforms.

ACKNOWLEDGEMENTS

This paper draws upon the Targeted Programme of research commissioned by the Environment Agency as project W5A-057 under the joint DEFRA/Agency Flood and Coastal Defence R&D Programme. We wish to thank Dr Mervyn Bramley, the Agency Project Manager for his encouragement and support. The contributions of all team members, in particular those of Dr Hugh Dawson and Karen Fisher, and the academic expert advisory panel are also gratefully acknowledged. The views expressed in this paper are, however, personal and the publication does not imply

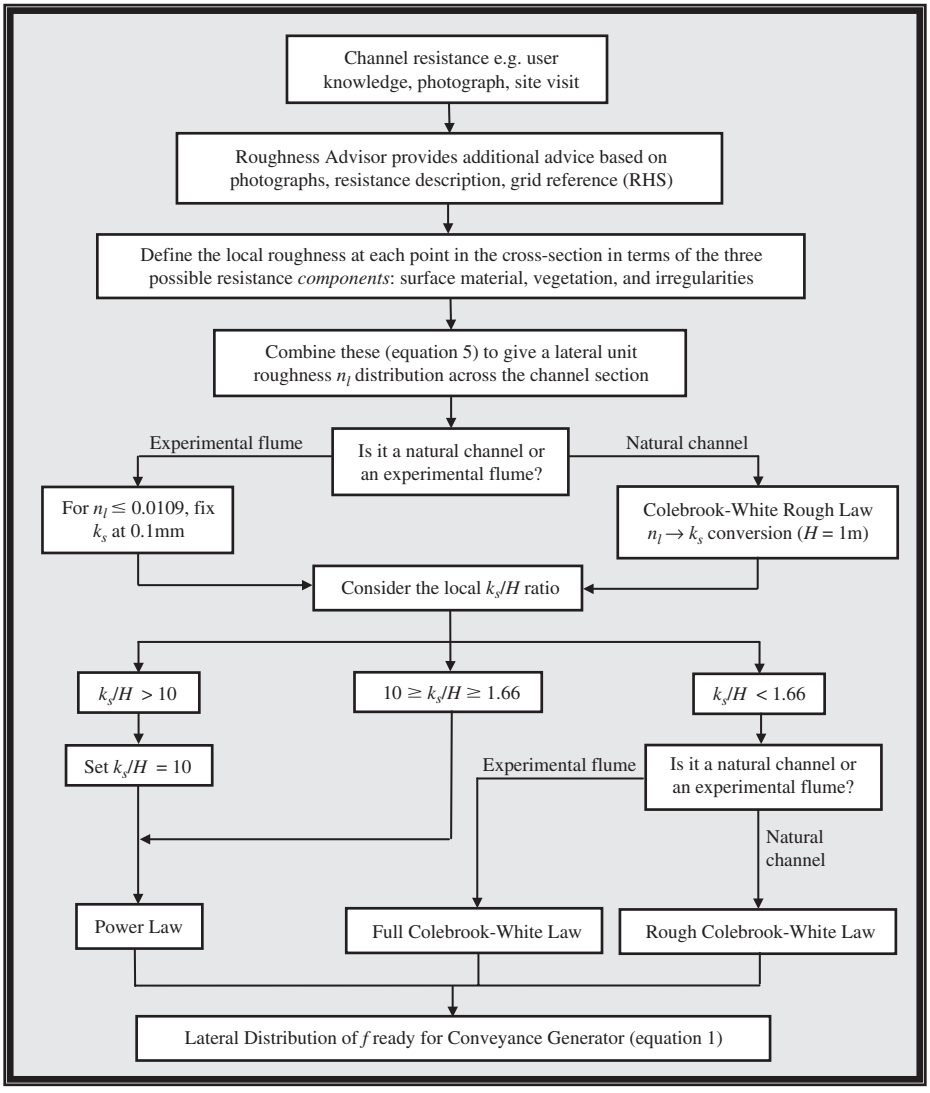


Figure 4. Complete calculation process for the resistance f from the Roughness Advisor n_l-values.

endorsement by either the Environment Agency or the Department for Environment, Food and Rural Affairs (DEFRA).

REFERENCES

Ackers, P. 1958. Resistance of Fluids Flowing in Channels and Pipes, *Hydraulics Research Paper No. 1*, HMSO, London.

Ackers, P. 1993. Flow Formulae for Straight Two-Stage Channels, *Journal of Hydraulic Research, IAHR*, Vol. 31, No. 4, pp. 509–531.

Abril, J.B. 1997. Numerical River Modelling of Turbulent Flow, Sediment *Transport and Flood Routing using the Finite Element Method*, PhD Thesis, January, School of Engineering, The University of Birmingham, England, UK.

Barnes, H.H. 1967. Roughness Characteristics of Natural Channels, US Geological Survey, *Water-Supply Paper No. 1849*, pp 214, Washington DC.

Bousmar, D. & Zech, Y. 1999. Momentum Transfer for Practical Flow Computation in Compound Channels, *Jnl. of Hydr. Eng.*, ASCE, Vol. 125, No. 7, July, pp 696–706.

Chang, H.H. 1983. Energy Expenditure in Curved Open Channels, *Journal of Hydraulic Engineering*, Vol. 109, No. 7, pp 1012–1022.

Chezy, A. 1768. In: On the Origin of the Chezy Formula by C. Herschel, *Journal Association of Engineering Societies*, Vol. 18, pp 363–368.

Chow, V.T. 1959. *Open Channel Hydraulics*, McGraw-Hill Book Company, US.

Colebrook, C.F. & White, C.M. 1937. Experiments with Fluid Friction in Roughened Pipes, *Proc. of the Royal Society*, A161, pp 367–379.

Cowan, W.L. 1956. Estimating Hydraulic Roughness Coefficients, *Agricultural Engineering*, Vol. 37, pp 473–475.

Einstein, H.A. & Banks, R.B. 1950, Fluid Resistance of Composite Roughness, *Transactions of the American Geophysical Union*, Volume 31, No. 4, pp 603–610.

Ervine, D.A. & Ellis, J. 1987. Experimental and Computational Aspects of Overbank Floodplain Flow, *Trans. Royal Society of Edinburgh: Earth Sciences*, Vol. 78, pp 315–475.

Ervine, D.A., Babaeyan-Koopaei, K. & Sellin, H.J. 2000. Two-dimensional Solution for Straight and Meandering Overbank Flows*, Journal of Hydraulic Engineering*, ASCE, Vol. 126, No. 9, September, pp 653–669.

Henderson, F.M. 1966. *Open Channel Flow*, The Macmillan Co., New York.

Hicks, D.M. & Mason, P.D. 1998. *Roughness Characteristics of New Zealand Rivers*, NIWA, Christchurch, pp 329.

HR Wallingford, 2003. Reducing Uncertainty in River Flood Conveyance: Interim Report 2 Roughness Review, Project W5A- 057, *HR Wallingford Ltd*., United Kingdom.

HR Wallingford, 2003. Reducing Uncertainty in River Flood Conveyance: Interim Report 3 Review of Methods for Estimating Conveyance, Project W5A- 057, *HR Wallingford Ltd*., United Kingdom.

Keulegan, G.H. 1938. Laws of Turbulent Flow in Open Channels, *Journal of Nat. Bureau of Standards*, Research Paper 1151, Vol. 21, pp 707–741.

Kirschmer, O. 1949. Reibungsverluste in Rohren und Kanalen, *Die Wasserwirtschaft*, Vol. 39, No. 7, pp 8.

Knight, D.W. 1981. Some field measurements concerned with the behaviour of resistance coefficients in a tidal channel, *Estuarine, Coastal and Shelf Science*, Vol. 12, pp 303–322.

Knight, D.W. & Abril, B.J. 1996. Refined Calibration of a Depth-Averaged Model for Turbulent Flow in a Compound Channel, *Proc. Inst. of Civil Engineers Water, Maritime and Energy*, Paper 11017, Vol. 118, Sept., pp 151–159.

Manning, R. 1891. On the Flow of Water in Open Channels and Pipes, *Transactions of the Institute of Civil Engineers of Ireland*, Vol. 20, pp 161–207.

McGahey, C. & Samuels, P.G. 2003. Methodology for conveyance estimation in two-stage straight, skewed and meandering channels, XXX IAHR Congress, Thessaloniki, *Volume C1 of Proceedings published by IAHR*.

Nikuradse, J. 1933. Translates to: Laws of Flow in Rough Pipes, *Verein deutscher Ingenieure, Forschubgsheft*, No. 361, Berlin.

Raven, P.J., Holmes, H.T.H., Dawson, F.H., Fox, P.J.A., Everard, M., Fozzard, I. & Rouen K.J. 1998. River Habitat Quality The Physical Character of Rivers and Streams in the UK and the Isle of Man, River Habitat Report No. 2, *Environment Agency*, pp 90.

Rhodes, D.G. & Knight, D.W. 1994. Velocity and boundary shear in a wide compound duct. *Journal Hydr. Res*., IAHR, Vol 32(5), 743–764.

Rouse, H. 1938. *Fluid Mechanics for Hydraulic Engineers*, McGraw-Hill Book Co., New York.

Samuels, P.G. 1985. Modelling of River and Flood Plain Flow using the Finite Element Method, PhD Thesis, Department of Mathematics, *University of Reading*, Hydraulics Research Report no. SR61, November.

Samuels, P.G., Bramley, M.E. & Evans, E.P. 2002. Reducing Uncertainty in Conveyance Estimation*, Paper presented at River Flow 2002*, Université Catholique Louvain, September 2002, Papers published by Balkema & Sons.

Shiono, K. & Knight, D.W. 1989. Two-Dimensional Analytical Solution for Compound Channel, *Proc. 3rd Intl. Symposium on Refined Flow Modelling and Turbulence Measurements*, Universal Academy Press, pp 591–599.

Shiono, K. & Knight, D.W. 1991. Turbulent Open-channel flows with Variable Depth across the Section, *Journal of Fluid Mechanics*, Vol. 222, pp 617–646.

Strickler, A. 1923. Translates to: Some Contributions to the Problem of the Velocity Formula and Roughness Factors for Rivers, Canals and Closed Conduits, *Mitteilungen des Eidgenossischen Amtes fur Wasserwirtschaft*, Bern Switzerland, No. 16.

US Task Force on Friction Factors in Open Channels 1963. Friction Factors in Open Channels*, Journal of the Hydraulics Division*, Proc. ASCE, Vol. 89, No. HY2, pp 97–141.

Zegzhda, A.P. 1938. *Teoriia Podobiia I Metodika Rascheta Gidrotekhnicheskikh Modelei* (Translates as: Theory of Similarity and Methods of Design of Models for Hydraulic Engineering), Gosstroiizdat, Leningrad.

River Flow 2004 – Greco, Carravetta & Della Morte (eds.)
© 2004 Taylor & Francis Group, London, ISBN 90 5809 658 0

Improving 1-D modelling of open channel flow in compound channels

Martín-Vide, J.P.
Technical University of Catalunya, Barcelona, Spain

López-Querol, S.
University of Castilla-la Mancha, Av.C.J. Cela, Spain

Martín-Moreta, P.
Civil Engineer, IAHR member, San Gerardo, Madrid, Spain

ABSTRACT: The paper is intended to discuss how well or badly the common 1-D numerical models of open channel flow are behaving in terms of flow distribution across any section in a compound channel. Comparison is made with new experiments in a physical model of a reach of the Besòs river Restoration Project close to Barcelona. The case in focus involves thick vegetated floodplains (wetlands in prototype), a low-flow meandering channel and high water depths over the main channel and floodplains. 1-D models fail to predict the velocities in the main channel (which are exaggerated) and floodplains (which are underestimated). The paper describes an improvement of the 1-D computation based on the consideration of the shear stress at the main channel-floodplain interface on the one hand, and the influence of upstream velocity distribution with the help of 2-D numerical models on the other hand.

1 INTRODUCTION

Water-profile computation in open channel flow is customarily done by means of 1-D numerical models based on the energy equation. In the case of compound channels (those made of a main channel and a pair of floodplains) a great effort has been made in the last decades to take into account the complex mechanisms in the main channel-floodplain interfaces. Bousmar & Zech (1999) presented a summary of the single channel method, the divided channel method corrected empirically by Ackers (1992), and the lateral distribution method. They also proposed an exchange discharge model aimed at improving the 1-D practical computation, consisting of a term standing for the turbulent momentum flux through the interfaces plus a term for the change of geometry in floodplains, either increasing or decreasing in width.

Similarly, the research in this paper aims to discuss some very simple refinements in the 1-D models that can cope with such complexities in a straightforward way. The research focuses on the prediction of the flow distribution across the channel. While the free surface profile seems to be more easily simulated by 1-D numerical models, the same does not hold for the velocities unless the appropriate term at the interface is used. The correction preferred here is the use of lateral momentum transfer as well as a force on the interfaces, as was done before by Wormleaton & Merrett (1990). Moreover, attention is paid to the results given by widely used 2-D models which give some hints on how to improve 1-D numerical modelling. The numerical models are compared with new experiments, which involve two rough vegetated floodplains.

2 EXPERIMENTS

Several physical models were built in the context of a restoration program for the River Besòs in the urban area of Barcelona (Martín-Vide, 2001). The model of a river consisting of a low-flow meandering channel and two floodplains was used in the experiments. Figure 1a is a photograph of the model.

The bed in the main channel and floodplains was filled with gravel 20 mm in size. Flexible plastic strips were selected so as to simulate the roughness characteristics of *Phragmites australis* (a spontaneous weed in the area, which was the main specimen in the restoration plan). These plastic plants completely covered both floodplains with a density of 1 plant every 10×10 cm.

The flow rate was measured by a V-notch weir. Two tests were run with each discharge: one without plants



Figure 1a. River Besòs model. See the meandering low flow channel and the plastic strips on the floodplains. In the tests, the simulated vegetation completely covered the floodplains.



Figure 1b. Test on the roughness of plastic plants in the straight flume.

(i.e. with gravel everywhere) and the other with plants. Only the latter are dealt with here. Discharges amounting 96.3 and 171.3 l/s were chosen, so that the plants were always completely submerged. Figure 2 shows in plan view the central part of the domain, which is the part to be used in the 1-D and 2-D numerical modelling. It includes one complete low-flow channel wavelength. Measurements in the physical model were made on 11 cross sections, a sub-set of the sections drawn in Figure 2. Water surface profiles were measured with point gauges at three points across each section, one over the centre of the main channel and the other two close to the walls. Extensive velocity measurements were performed with a 2D electromagnetic

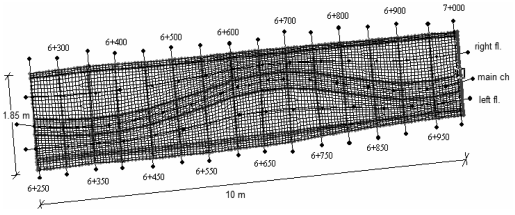


Figure 2. Plan view in the experimental set-up (sections named like prototype distances).

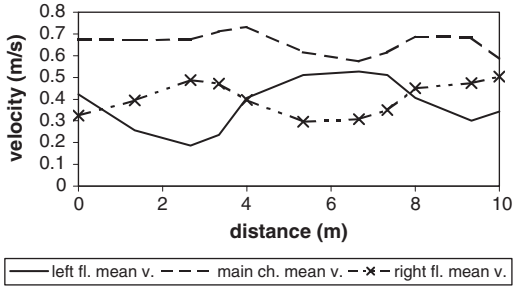


Figure 3. Mean velocities measured in the prototype, on the left floodplain, main channel and right floodplain, for the discharge of 171.3 l/s.

probe. The probe was placed at any vertical in such a way that the measurement point was always at a distance from the bed equal to the 40% of the local water depth (an approximation for the mean velocity). Three measurement verticals were located in the main channel, one at its centre and the other two 15 cm to the centre's right and left; two more verticals were located in both floodplains 5 cm from the main channel verges. Finally, verticals 5, 20, 35 and 65 cm from each wall were used if they fitted. The main flow velocity components (v_x) are the only ones dealt with here. As an example, Figure 3 shows the main channel and floodplain velocities along the model. As the main channel wanders from side to side, so the floodplain velocities increase or decrease.

Tests on the roughness characteristics of the gravel and plants were run on a 0.97 m wide, 10 m long flume in uniform flow on the same slope and with the same unit discharges as in the main experiments (Fig. 1b). The Manning coefficient of the gravel was $n = 0.025$. The one for the plastic plants implanted on the same gravel was dependant on the flow rate, as expected, varying from $n = 0.062$ (minimum flow rate) to $n = 0.049$ (maximum flow rate in the experiments).

3 1-D MODELLING PERFORMANCE

1D models based on the energy equation or Bernoulli equation will be compared here with the experimental

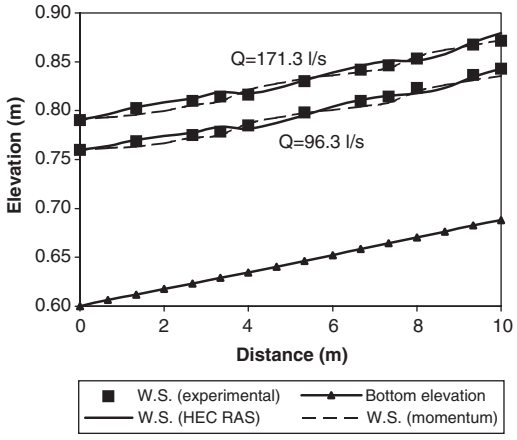


Figure 4. Experimental and computed water surface profiles (W.S.) by using Hec-Ras and momentum equation for discharges of 96.3 and 171.3 l/s.

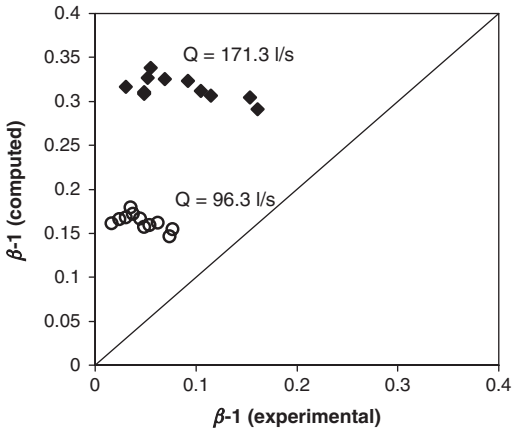


Figure 5. Experimental and computed (Hec-Ras or momentum) Boussinesq coefficients.

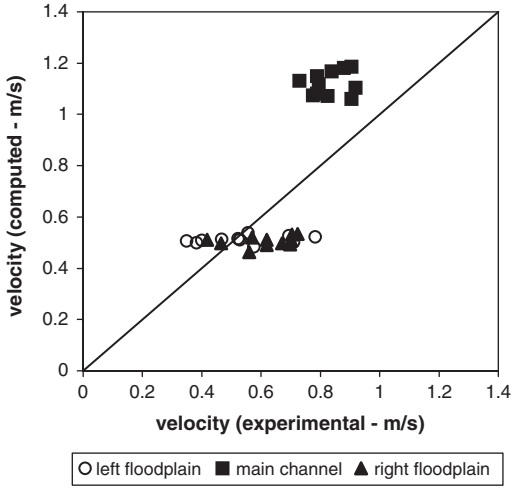


Figure 6. Experimental and computed velocities (momentum equation) in floodplains and main channel for the discharge of 171.3 l/s.

results in terms of water surface profile and velocity distributions. The well-known Hec-Ras model is used, as well as a second 1D model that "duplicated" Hec-Ras but allowed some refinements to be introduced. One refinement is the use of the momentum equation for the whole calculation. In a step by step procedure, the equation to be solved states that:

$$\beta_1 \frac{v_{m1}^2 A_{tot1}}{g} + z_{tot1} \cdot A_{tot1} = \beta_2 \frac{v_{m2}^2 A_{tot2}}{g} + z_{tot2} \cdot A_{tot2} - \frac{d}{2} \cdot (I_1 \cdot A_{tot1} + I_2 \cdot A_{tot2}) + \frac{d}{2} (A_{tot1} + A_{tot2}) \cdot s \quad (1)$$

where the subscripts 1 and 2 stand for the downstream and upstream sections respectively, m and tot stand for mean and total, β is the Boussinesq coefficient, A is flow area, v is flow velocity, g is gravitational acceleration, d is the distance between two consecutive sections, z is the depth of centroid, I is friction slope and s is the angle of the bed slope. Only one friction slope (I) is used for the whole section. As usual in 1-D models, the conveyance in each zone (main channel and floodplains) is given by:

$$K_k = \frac{A_k}{n_k} Rh_k^{2/3} \quad (2)$$

where k stands for the zone, n is the Manning coefficient and Rh is the hydraulic radius.

The friction slope is given by:

$$I = \left(\frac{Q}{K_{tot}} \right)^2 \text{ where } K_{tot} = \Sigma K_k \quad (3)$$

Figure 4 shows how well both Hec-Ras and the second model (using momentum equation) compare with the experimental water surface profiles for the two discharges. However, the computed flow distribution in a case like this, with thick vegetated floodplains, departs considerably from the experimental one. The computed velocities on the main channel are considerably higher than the experimental ones but they are considerably lower on the floodplains. This is shown by the comparison between experimental and numerical β coefficients in Figure 5 (in terms of $\beta - 1$). The velocities are much more uniformly distributed in reality than in 1-D modelling, since their experimental β coefficients are much lower. The same is shown in Figure 6, in which computed and experimental velocities are

compared for 171.3 l/s. The fact that arises from this comparison is that 1-D models based on either energy or momentum equation fail to simulate flow distribution even though they simulate water levels well. It should be kept in mind that the case in the experiments is characterized by very different roughnesses in main channel and floodplains and by high water depths.

4 WHAT CAN BE LEARNED FROM 2-D MODELLING

The FESWMS 2-D model has been applied to the computational domain in Figure 2. The model solves the depth-averaged Navier-Stokes equations. Two boundary conditions apply: a known water depth downstream and a known velocity distribution upstream (both known from the experiments). The computational mesh is made of rectangular elements with one node at its centre, one node at each corner and one node at the centre of each side (so that there is a total of 9 nodes in each element).

The way the total energy losses are shared by bed friction (through a roughness coefficient) and the turbulence (through a dissipation coefficient) was analysed against the experiments. The experimental results are best simulated if the roughness coefficient measured in the laboratory (Fig. 1b) is reduced to 60% of its initial value in the main channel (gravel) and to 80% of its initial value in the floodplains (vegetation). These percentages are close to the ones obtained by Vionnet et al. (in press) in a previous work with the same data but with the Telemac-2D model and the Lateral Distribution Model.

Figure 7 shows an example of the comparison between experiments and 2-D computation with FESWMS regarding water surface elevation and flow energy at one particular section. The section is located at an inflection point (section 6+500 in Fig. 2). The agreement is not bad, but more importantly, notice that the maximum flow velocities (i.e. the maximum $v^2/2g$ terms, which go from the surface line to the energy line) are not occurring inside the main channel, but on its right bank. The same feature is observed in the velocity plot in plan view (Fig. 8). The line of maximum velocity does not follow the main channel axis but goes straighter. This is due to the obstruction caused by the vegetation upstream. Upstream of the inflection point there is a mass of plants obstructing the flow through the left floodplain, whereas the flow through the right floodplain is eased by the presence of the main channel itself.

5 IMPROVEMENT IN 1-D MODELS

One alternative to the usual 1-D modelling in order to improve the prediction of mean velocities is discussed

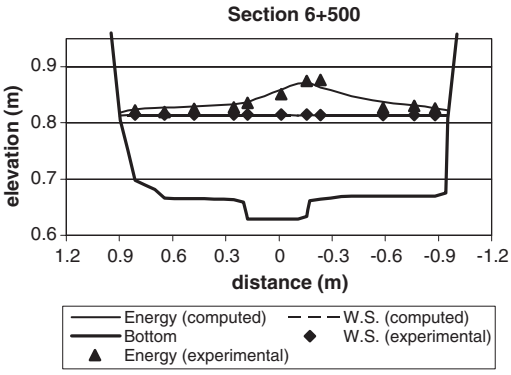


Figure 7. Experimental and computed water surface (W.S.) and energy elevations in one cross section (named as in prototype), for a discharge of 171.3 l/s.

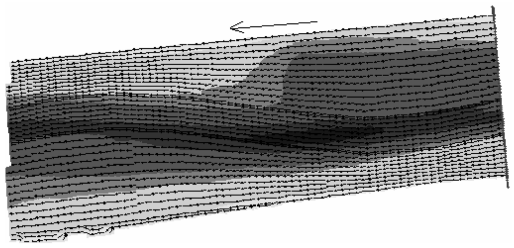


Figure 8. Plan view of velocity results between sections 6+600 and 7+000 (named like in prototype), for the discharge of 171.3 l/s. (the darker the faster).

in this paragraph. The shear stress at the main channel-floodplain interface by using the Boussinesq hypothesis is $\tau_{xy} \sim (\partial v_x/\partial y + \partial v_y/\partial x)$. This shows the need to take into account in 1-D modelling a term standing for the turbulent friction (the first partial derivative in τ_{xy}) plus a term standing for the lateral momentum transfer (the second partial derivative in τ_{xy}). Since the floodway walls are parallel, it is assumed that the v_y components are negligible everywhere. However, since the main channel wanders across the left and right floodplains, there is a large lateral momentum transfer due to the change in floodplain size. This term plus one standing for the turbulent friction are included in the model, closely following the lines of Bousmar & Zech (1999). The obstruction due to the mass of vegetation upstream of a section, which is the main lesson learned from 2-D modelling, is also taken into account, as will be shown.

The first step in this improved 1-D model is the assumption that the water profile is already known with enough accuracy through the solution of Eq. (1) (with one boundary condition downstream in subcritical flow) and that it will not change significantly despite the adjustments in flow distribution across

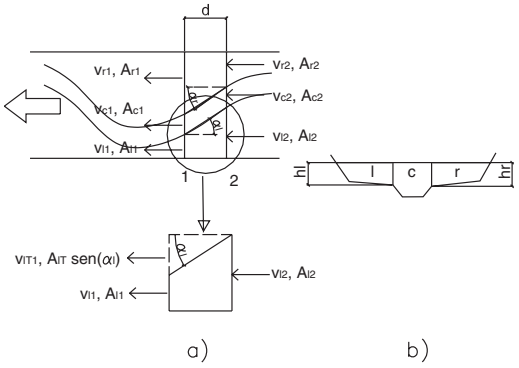


Figure 9. Sketch in plan (a) and cross section (b) for the development of Eqs (4)–(6).

the section. Therefore, every geometrical parameter is known; at any section j the flow areas A_{lj}, A_{cj}, A_{rj} and the conveyances K_{lj}, K_{cj}, K_{rj} for the three zones (main channel and floodplains) are known. Thus, the mean friction slope I_j and the mean velocity v_{mj} are known. Equation (1) can be applied to each zone as follows (see Fig. 9a):

$$\frac{v_{l1}^2 A_{l1}}{g} + z_{l1}\cdot A_{l1} + \frac{v_{lT}^2 A_{lT}\sin(\alpha_l)}{g} + z_{rT}\cdot A_{lT}\cdot\sin(\alpha_l) = \frac{v_{l2}^2 A_{l2}}{g} + z_{l2}\cdot A_{l2} - \frac{d}{2}\cdot(I_1\cdot A_{l1} + I_2\cdot A_{l2}) + \frac{d}{2}(A_{l1}+A_{l2})\cdot s + F1 \quad (4)$$

$$\frac{v_{r1}^2 A_{r1}}{g} + z_{r1}\cdot A_{r1} + \frac{v_{rT}^2 A_{rT}\sin(\alpha_r)}{g} + z_{rT}\cdot A_{rT}\cdot\sin(\alpha_r) = \frac{v_{r2}^2 A_{r2}}{g} + z_{r2}\cdot A_{r2} - \frac{d}{2}\cdot(I_1\cdot A_{r1} + I_2\cdot A_{r2}) + \frac{d}{2}(A_{r1}+A_{r2})\cdot s + F3 \quad (5)$$

$$\frac{v_{c1}^2 A_{c1}}{g} + z_{c1}\cdot A_{c1} - \frac{v_{lT}^2 A_{lT}\sin(\alpha_l)}{g} - z_{rT}\cdot A_{lT}\cdot\sin(\alpha_l) - \frac{v_{rT}^2 A_{rT}\sin(\alpha_r)}{g} - z_{rT}\cdot A_{rT}\cdot\sin(\alpha_r) = \frac{v_{c2}^2 A_{c2}}{g} + z_{c2}\cdot A_{c2} - \frac{d}{2}\cdot(I_1\cdot A_{c1} + I_2\cdot A_{c2}) + \frac{d}{2}(A_{c1}+A_{c2})\cdot s + F2 \quad (6)$$

The new terms with respect to Eq. (1) are the momentum transfer through the meandering interface (Fig. 9a) and the turbulent friction force per unit weight F (F1 for the left floodplain, F3 for the right floodplain and F2 for the main channel). v_{lT}, y, v_{rT} are the velocities going in or out between the main channel and the floodplains. These velocities are assumed to have only v_x components. They are determined by the continuity equation (see Fig. 9a). A_{lT}, y, A_{rT} are the interface flow areas, computed by averaging water depths between two consecutive cross sections, a distance d apart (Fig. 9b):

$$A_{lT} = \frac{1}{2}\frac{d}{\cos(\alpha_l)}(h_{l1} + h_{l2}) \quad (7)$$

$$A_{rT} = \frac{1}{2}\frac{d}{\cos(\alpha_r)}(h_{r1} + h_{r2}) \quad (8)$$

The sign of the angles α_l and α_τ of the interface (left and right) with respect to the floodway walls is positive if flow goes out of one zone and negative if flow goes into one zone. For example, in Figure 9a, α_l is positive and α_τ is negative. This sign convention is consistent with Eqs (4), (5) and (6), where $\sin(\alpha)$ keeps the sign of α and conveys its sign to the lateral momentum transfer term. Note that the sum of Eqs (4), (5) and (6) is just Eq. (1) because:

- $\frac{v_{l1}^2 A_{l1}}{g} + \frac{v_{c1}^2 A_{c1}}{g} + \frac{v_{r1}^2 A_{r1}}{g} = \beta_1\frac{v_{m1}^2 A_{tot1}}{g}$

(definition of coefficient β)

- $\frac{v_{l2}^2 A_{l2}}{g} + \frac{v_{c2}^2 A_{c2}}{g} + \frac{v_{r2}^2 A_{r2}}{g} = \beta_2\frac{v_{m2}^2 A_{tot2}}{g}$

(idem)

- $z_{l1}\cdot A_{l1} + z_{c1}\cdot A_{c1} + z_{r1}\cdot A_{r1} = z_{tot1}\cdot A_{tot1}$

(definition of centroid)

- $z_{l2}\cdot A_{l2} + z_{c2}\cdot A_{c2} + z_{r2}\cdot A_{r2} = z_{tot2}\cdot A_{tot2}$

(idem)

- $\frac{d}{2}\cdot(I_1\cdot A_{l1} + I_2\cdot A_{l2}) + \frac{d}{2}\cdot(I_1\cdot A_{c1} + I_2\cdot A_{c2}) + \frac{d}{2}\cdot(I_1\cdot A_{r1} + I_2\cdot A_{r2}) = \frac{d}{2}\cdot(I_1\cdot A_{tot1} + I_2\cdot A_{tot2})$

- $\frac{d}{2}(A_{l1}+A_{l2})\cdot s + \frac{d}{2}(A_{c1}+A_{c2})\cdot s + \frac{d}{2}(A_{r1}+A_{r2})\cdot s = \frac{d}{2}(A_{tot1}+A_{tot2})\cdot s$

- The lateral momentum transfer terms are cancelled.
- F2 = −F1 − F3 (Newton's third law) (Fig. 10).

Prior to the numerical solution of Eqs (4)–(6), they have been used to test the magnitude of the new terms. This is done by substituting any variable in Eq. (5) by its experimental value (depths, areas, velocities …). Fig. 11 is a graph of the magnitude of the lateral momentum transfer term on the one hand, and the magnitude of it plus the turbulent friction force per

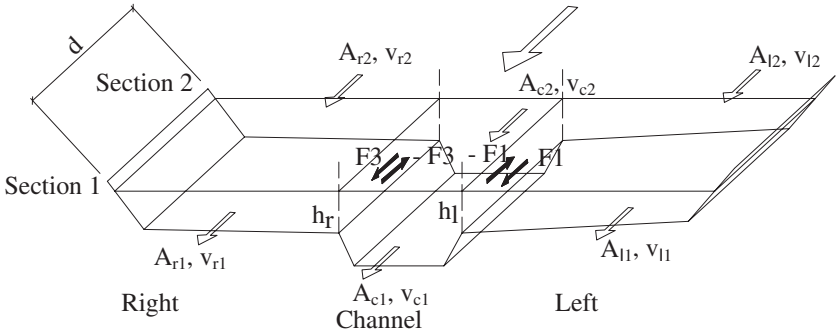


Figure 10. Sketch of turbulent friction force per unit weight for floodplains and main channel. Newton's third law.

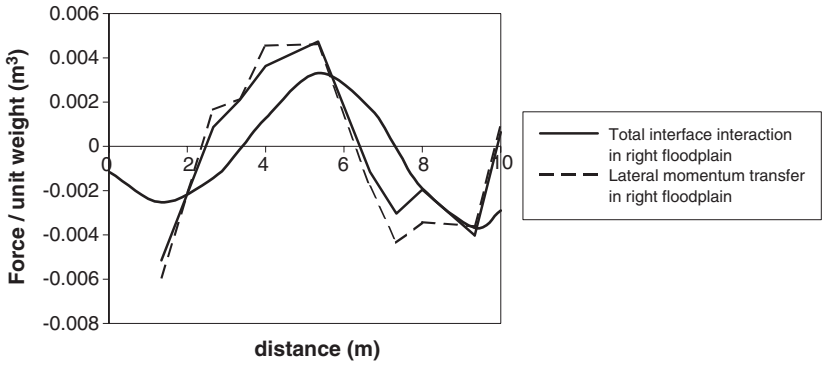


Figure 11. Computation of interaction between main channel and right floodplain only with the experimental data. The low flow meandering channel is drawn in full line for comparison.

unit weight F on the other. Both magnitudes are plotted along the channel coordinate. The main point in Figure 11 is that the friction force is much less (almost negligible) than the lateral momentum transfer.

Coming back to the numerical computation, Eqs (4)–(6) are applied from upstream to downstream. An upstream boundary condition is given in terms of measured flow velocities. The calculation between two consecutive cross sections gives the flow velocities in the 3 zones at the downstream section. The unknowns are v_{l1}, v_{c1}, v_{r1}, v_{lT} and v_{rT}. As shown above, Eqs (1), (4), (5) and (6) are not independent: only 3 of them are actually independent since (1) = (4)+(5)+(6). Moreover, Eq. (1) has already been used to get the water profile, so only 2 equations are left. The 3 equations still needed to solve the 5 unknowns are:

- Continuity at the section:

$$Q = v_{l1} \cdot A_{l1} + v_{c1} \cdot A_{c1} + v_{r1} \cdot A_{r1} \quad (9)$$

where Q is known,

- Continuity at each control volume between two consecutive cross sections and the interface, with the assumptions stated above (Fig. 7a):

$$v_{l2} \cdot A_{l2} = v_{l1} \cdot A_{l1} + v_{lT} \cdot A_{lT} \cdot \mathrm{sen}(\alpha_l) \quad (10)$$

$$v_{r2} \cdot A_{r2} = v_{r1} \cdot A_{r1} + v_{rT} \cdot A_{rt} \cdot \mathrm{sen}(\alpha_r) \quad (11)$$

Furthermore, the forces F1 and F3 are assumed to be proportional to the velocity difference between main channel and floodplain, by averaging between two consecutive cross sections, as well:

$$F1 = \frac{1}{2} C \cdot d \cdot (h_{l2} \cdot (v_{c2} - v_{l2}) + h_{l1} \cdot (v_{c1} - v_{l1})) \quad (12)$$

$$F3 = \frac{1}{2} C \cdot d \cdot (h_{r2} \cdot (v_{c2} - v_{r2}) + h_{r1} \cdot (v_{c1} - v_{r1})) \quad (13)$$

where C is a coefficient. Calibration of C with the experimental tests, by getting the best agreement in velocity distribution, has given C = 0.0012 for 171.3 l/s and C = 0.0030 for 96.3 l/s.

By substituting v_{lT}, v_{rT}, F1 and F3 in Eqs (4) and (5), which are quadratic equations, two solutions for v_{l1} and v_{r1} are obtained. The criterion for selection of one of them is based on the degree of obstruction

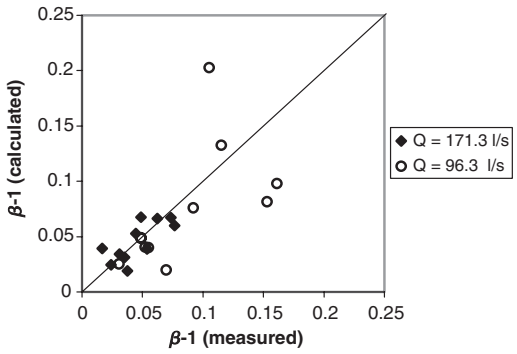


Figure 12. Experimental and computed (improved 1-D momentum model) Boussinesq coefficients.

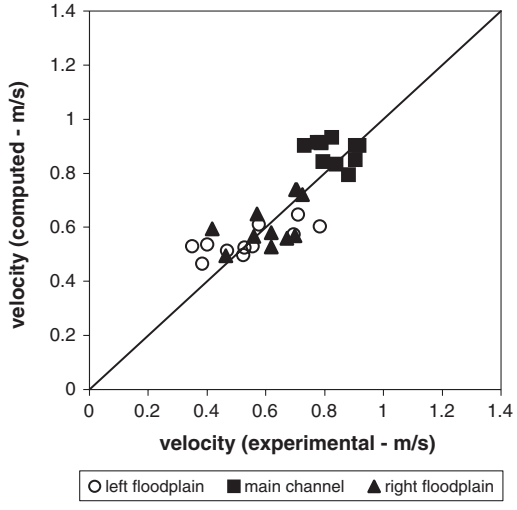


Figure 13. Experimental and computed velocities (improved 1-D momentum model) in floodplains and main channel for the discharge of 171.3 l/s.

upstream. The derivative of the floodplain conveyance along the coordinate $\partial K/\partial x$ is taken as a surrogate of the degree of obstruction (because the floodplains are fully covered with vegetation). If a length of one quarter of the meandering low flow channel wavelength upstream is used to compute this derivative, the agreement between computation and experiments is the best. Then, if $\partial K/\partial x > 0$ the solution selected is the maximum of the two possible ones; otherwise the minimum is selected. This criterion is related to the relative importance of the momentum output through cross-section 1 and the momentum transfer through the interface (see Fig. 9a). There are also some computations in which no real solution of quadratic Eqs (4)–(5) exists. This is thought to be related to having neglected a v_y component, especially in the velocities v_{lT} and v_{rT}. It should be pointed out, finally, that this method is successful because it involves what happens (in terms of obstruction to the flow) in the next 1/4 of the wavelength upstream in the computation of the flow distribution at a section.

Figures 12 and 13 summarize the results of this improved 1-D model. They must be compared with Figures 5 and 6 respectively, which are their counterparts, by using the common 1-D model (like Hec-Ras). Figures 12 and 5 in terms of $(\beta - 1)$ show a great improvement for both flow rates. The same can be said of Figures 13 and 6 in terms of velocities themselves. While the experimental β coefficients are not higher than about 1.16, the computed β coefficients with the use of common 1-D model in case of vegetated floodplains are extremely high, which is corrected in the improved 1-D model. Notice also how the main channel velocity was exaggerated with common 1-D model but comes to be close to the experimental velocities with this improved 1-D model.

6 CONCLUSIONS

This paper tries to draw attention to the fact that 1-D conventional numerical modelling of free-surface flow (like the model Hec-Ras) fails to reproduce the flow distribution across the section in compound channels, i.e. it fails to predict the main or low-flow channel velocity and the floodplain velocities (left and right). This is proven at least in the case of thick vegetated floodplains, high water depths and meandering low-flow channels, as in the experiments.

Secondly, it shows two main reasons for this failure, which are also the ways for improvement:

1. The lack of any shear stress at the interface between main channel and the floodplain (a very well-known fact), in which one must distinguish two different sources of shear stress: lateral momentum transfer and turbulent friction,
2. The lack of any influence of the flow distribution upstream. This has been proven to be important with the help of a 2-D numerical model.

The paper shows a simple improvement of the 1-D equations, which include two new terms to take into account the first drawback and a procedure to take into account the second one.

NOTATION

Symbols:

α = angle between the interface and the main flow direction, in plan view.
β = Boussinesq coefficient
τ = shear stress

A = flow area
C = coefficient
d = distance between two consecutive sections
F = turbulent friction force per unit weight
g = gravitational acceleration
I = friction slope
K = conveyance
n = Manning coefficient
Q = discharge
Rh = hydraulic radius
s = angle of the bed slope
v = flow velocity
z = depth of centroid

Subscripts:

1 = downstream section
2 = upstream section
c = main channel
l = left floodplain
j = section number j
k = zone number k in a section
m = mean
r = right floodplain
tot = total
T = transversal
x = main flow direction
y = horizontal direction perpendicular to main flow direction

REFERENCES

Ackers, P. 1992. Hydraulic design of two-stage channels. *Proceeding Inst. of Civil Engineers, Water, Maritime and Energy*: 96, 4, 247–257.

Bousmar, D., Zech, Y. 1999. Momentum transfer for practical flow computation in compound channels. *Journal of Hydraulic Engineering ASCE*, 125, 7, 696–706.

Martín-Vide, J.P. 2001. Restoration of an urban river in Barcelona, Spain. *Environmental Engineering and Policy*, *Springer-Verlag*, 2, 2000, 030/1–030/7.

Vionnet, C., Tassi, P., Martín-Vide, J.P. Estimates of flow resistance and eddy-viscosity coefficients for 2D modelling on vegetated floodplains. *Hydrological processes*. In press.

Wormleaton, P.R., Merrett, D.J. 1990. An improved method of the calculation for steady uniform flow in prismatic main channel/flood plain sections. *Journal of Hydraulic Research*, 28, 2, 157–174.

River Flow 2004 – Greco, Carravetta & Della Morte (eds.)
© 2004 Taylor & Francis Group, London, ISBN 90 5809 658 0

Coherent flow structures in a converging compound channel

D. Bousmar
Fond National de la Recherche Scientifique and Civil and Environmental Engineering, Université catholique de Louvain, Belgium

B. Denis & Y. Zech
Civil and Environmental Engineering, Université catholique de Louvain, Belgium

ABSTRACT: This paper investigates the possible coexistence of the two kinds of momentum transfer observed in compound channels, that cause significant conveyance decrease, namely: (1) the turbulent interaction that develops in the shear layer between main channel and floodplains in a prismatic channel; and (2) the geometrical transfer due to cross-sectional changes in a non-prismatic channel. Experiments are performed in a symmetrically narrowing compound channel and focus on the behaviour of the shear layer along the transition between the prismatic and the non-prismatic reaches. A digital imaging technique enables to clearly identify horizontal turbulent structures in the upstream prismatic reach and to follow those structures when entering the converging reach. It is observed that the horizontal vortices are stretched as they are translated in the main channel and then quickly split into smaller scale structures that do not affect any more the conveyance.

1 INTRODUCTION

The flow in a compound channel is characterised by significant momentum transfers between the main channel and the floodplain. In a prismatic compound channel, a shear layer develops at the interface between both subsections due to flow velocity difference. Large-scale horizontal vortices grow in this shear layer and govern the observed momentum transfer. In a non-prismatic compound channel, a mass transfer and a corresponding momentum transfer between subsections are due to geometrical non-uniformity. These effects result in an overall channel conveyance decrease that has to be modelled when simulating flood propagation or mapping flooded areas.

Several one-dimensional methods were proposed to face these compound-channel modelling requirements. Most of them are dedicated either to prismatic (e.g. Shiono & Knight 1991, Ackers 1992) or to non-prismatic geometries (e.g. Greenhill & Sellin 1993, Ervine et al. 2000) and address only one specific momentum transfer source. Only few methods, like the Exchange Discharge Model – EDM (Bousmar & Zech 1999, Bousmar 2002) attempt to encompass both situations.

Experimental data is also lacking on the transition between prismatic and non-prismatic reaches, in order to investigate the possible coexistence of both momentum transfer processes. Available data sets are usually focused either on prismatic compound channels (e.g. Knight 1992) or on non-prismatic ones (e.g. Sellin et al. 1993, Bousmar et al. 2004).

This paper therefore investigates experimentally the behaviour of the shear layer along the transition between a prismatic and a non-prismatic reach. Additional measurements are performed in the symmetrically narrowing compound channel used by Bousmar et al. (2004). The possible stretching, splitting or vanishing of the horizontal vortices in the narrowing reach is explored using digital imaging, to determine whether some turbulent momentum transfer remains in the non-prismatic reach, in addition to the geometrical transfer.

2 EXPERIMENTAL SETUP

Experiments are performed in a 10 m long and 1.20 m wide compound-channel flume at the Université catholique de Louvain, Belgium. The upstream part of the flume is shaped with a symmetrical cross-section made of coated plywood that presents one main-channel 400 mm wide and 50 mm deep, flanked by two floodplains 400 mm wide. The floodplains width then reduces symmetrically, resulting in a single main-channel cross section at the downstream end of the flume (Fig. 1). For the Cv6 series, the new measurements are performed with only a part of the converging

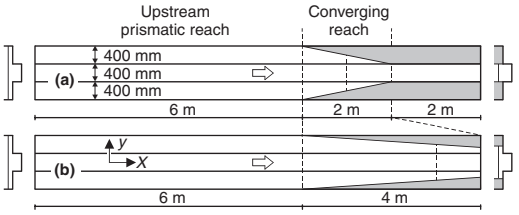


Figure 1. Plan view and typical cross-sections of test geometries. (a) Cv2: 2 m long narrowing floodplains; and (b) Cv6: 6 m long narrowing floodplains (partially, limited by flume end).

Table 1. Experiments: geometries and flow conditions.

Run	Cv2/02/10	Cv2/03/10	Cv6/02/10
Convergence length [m]	2	2	6(4)
Converging angle [°]	11.3	11.3	3.8
Flow depth at mid-convergence [mm]	62.5	71.4	62.5
Relative flow depth [−]	0.2	0.3	0.2
Discharge [l/s]	10	10	10

reach modelled, to keep a prismatic reach long enough to enable the full development of the shear layer.

Each subsection is supplied independently, enabling adjustment of upstream discharge distribution, and tailwater is controlled with an adjustable weir. Total discharge is measured by an electromagnetic flowmeter, and water levels and velocities are recorded by an automatic point gauge and a Pitot tube, respectively (Bousmar et al. 2004). Table 1 summarises the geometries and flow conditions investigated in the present paper.

In addition to classical flow-depth and velocity-distribution measurements, the flow structures are investigated by surface velocimetry using a Particle-Tracking Velocimetry (PTV) system (Capart et al. 2002). The flow free-surface is seeded with expanded-polystyrene pearls of 4–6 mm diameter. The successive positions of these floating tracers are recorded using a digital camera, at a frame rate of 10 Hz during 60 s, and with an image size equal to 1024 × 380 pixels, covering a 2.40 m length of the flume. Area of interest along the flume length are covered with two or three successive stations of the camera. Post-processing of the recorded images enabled the identification of the tracers, the reconstruction of their trajectories, the filtering of these trajectories, and the estimation of the tracer velocities. More than 20,000 distinct tracers are usually detected in each image sequence. In addition to the velocities calculated at the tracer positions, instantaneous velocity fields are also interpolated on a regular grid for further analysis purpose.

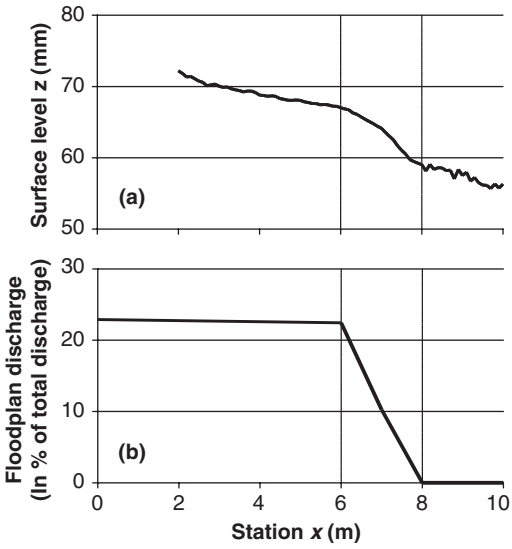


Figure 2. Cv2/02/10 case: (a) free-surface profile; and (b) ratio between floodplain and total discharge.

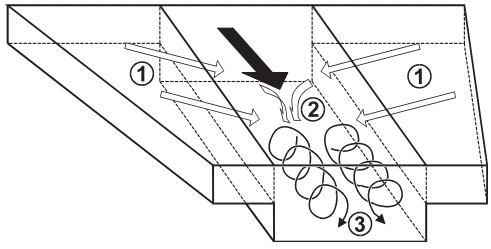


Figure 3. Schematic view of the flow structure in a compound channel with narrowing floodplains.

3 GENERAL FLOW DESCRIPTION

A description of the main flow features was previously obtained using classical measurements (Bousmar 2002, Bousmar et al. 2004). Only some conclusions are presented here. A typical free-surface profile is given in Figure 2a for the run Cv2/02/10. Due to the channel constriction, the flow is accelerated and the flow depth decreases accordingly. As the floodplain width reduces, the floodplain discharge is also forced in the main channel (Fig. 2b), resulting in a significant mass transfer.

The observations on the flow structure are synthesised in Figure 3: (1) a transverse current is generated from floodplains to main channel due to the channel constriction; (2) these currents enter the main channel, then plunge towards the channel bottom, due to symmetry; and (3) helical flow results in the inbank part of the main channel, with two counter-rotating cells.

These secondary currents can be found somewhat similar to those of meandering channels as described e.g. by Sellin et al. (1993): both are located in the inbank area and are generated by floodplain flow crossing or entering the main-channel. However, the present flow structure is less complex: it is symmetrical and no flow is ejected from the main channel to the floodplains.

The total head loss were estimated for several cases and compared with the friction losses, estimated from experiments in a prismatic channel with the same cross section. A significant additional loss was highlighted in the non-prismatic geometries due to the momentum transfer associated with the observed mass transfer. The momentum transfer and additional loss increase with converging angle, flow depth, and total discharge.

4 COHERENT STRUCTURES IN THE UPSTREAM PRISMATIC REACH

4.1 *Time-averaged analysis*

The coherent turbulent structures that develop in the shear layer at the interface between main channel and floodplain are first characterised in the upstream prismatic reach, before investigating their behaviour in the converging reach. Similar analysis previously performed in an asymmetric compound channel indicated that a minimum flume length of 5 m is necessary to obtain a full development of the shear layer (Bousmar & Zech 2003). The upstream part of the converging reach was therefore located at $x = 6$ m, resulting in a partial setting for the Cv6 geometries (Fig. 1) compared to the initial experiments by Bousmar et al. (2004).

In a first stage, the time-averaged surface velocity distribution is computed from the instantaneous surface velocity field in the upstream prismatic reach ($3.6 < x < 6.0$ m) for case Cv2/02/10 (Fig. 4). The distribution of the longitudinal velocity component U confirms previous measurements: higher velocities are found in the main channel and a smooth transition is observed through the interface with the floodplain due to the shear-layer development. The transverse velocity V distribution presents two particular features: (1) there is a surface flow towards the main channel axis in the area $-0.35 < y < 0.35$ m and towards the outer banks in the outer areas; and (2) the standard-deviation of V reaches a peak values near the interfaces (at $y \approx -0.25$ and 0.25 m).

The transverse surface flow towards the channel axis can be first supposed to correspond to geometrical transfers already taking place upstream of the converging reach. The pattern of surface streamlines, plotted from the time-averaged velocity field, indicates however that another phenomena occur (Fig. 5): the floodplain streamlines do not converge towards main channel as would be observed in the case of a converging reach, but tend to diverge from the interface area. This surface divergence is due the secondary helical currents observed in the main-channel. These currents indeed exist in the converging reach as quoted above, but also in a prismatic reach as highlighted by Tominaga & Nezu (1991). They generate upward flows in the interface area and downward flows near the channel axis.

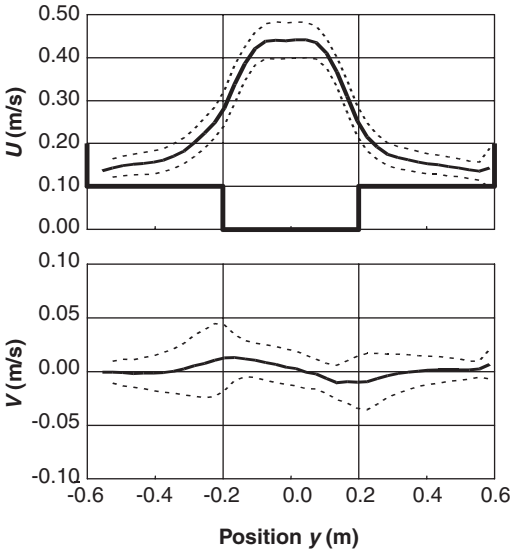


Figure 4. Time-averaged surface velocity distribution, Cv2/02/10 case, upstream prismatic reach. Dotted lines indicate a one standard-deviation interval around the measured velocity. Positive transverse velocity V flows towards increasing y.

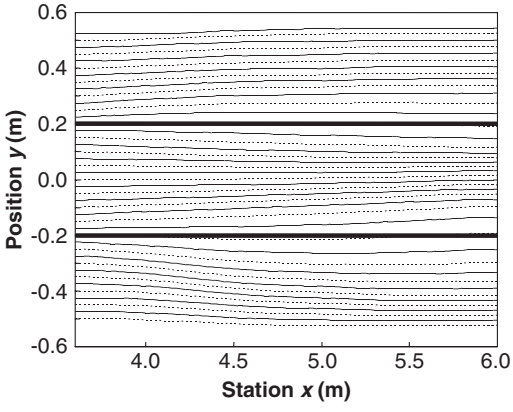


Figure 5. Surface streamlines, computed from time-averaged velocity field, Cv2/02/10 case, upstream prismatic reach.

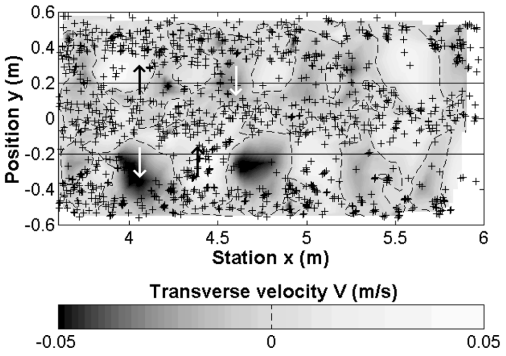


Figure 6. Instantaneous tracers distribution and transverse velocity field, Cv2/02/10 case, image 110, upstream prismatic reach.

Additionally, Nezu & Nakayama (1997) showed that these upward flows are intermittent and closely related to the development of the large horizontal vortices observed in the shear layer. This effect is not visible on the time-averaged plot in Figure 5, but can easily be identified when plotting instantaneous tracers distribution together with the transverse velocity field (Fig. 6). The transverse velocity presents alternate positive and negative values, indicating the existence of large horizontal structures. The tracer density is uneven: higher concentrations are found in areas were surface water flows towards main channel, corresponding to vortex edges; while lower concentrations correspond to vortex centres and intermittent upwards-flow areas.

4.2 *Periodical structures analysis*

The observed peaks of the standard-deviation of V in the interface area (Fig. 4) can now be explained by the presence of the horizontal vortices that developed in the shear layer. The periodicity of these turbulent structures is highlighted by the analysis of a time series of V values at a given interface point, or more accurately by the analysis of the time series along the whole interface, as plotted on Figure 7, following Bousmar & Zech (2002, 2003). The periodical alternation of positive and negative velocities is again clearly depicted. The variation frequencies are extracted using a Fourier analysis of these series (Fig. 8). A clear peak is obtained at the period $T = 2.75$ s for $x < 5$ m, and at $T = 3.75\ s$ for $x > 5$ m, indicating that the structures are possibly still growing in this area.

The transverse velocities vary with time at a given station, but also with space at a given time (Fig. 6). This indicates the presence of a row of vortices in the shear layer. The displacement of these structures is depicted by the pattern of diagonals shown by positive and negative velocities on Figure 7. The vortex celerity

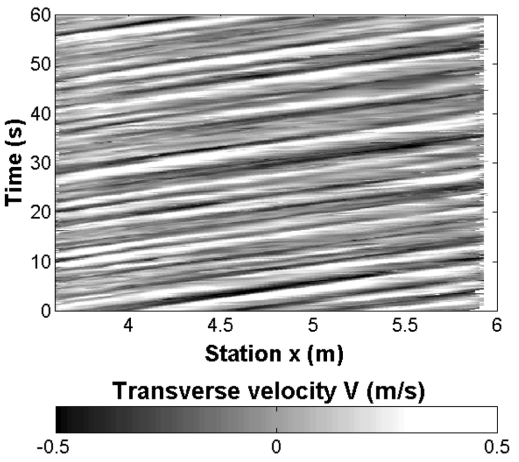


Figure 7. Transverse velocity V, Cv2/02/10 case, upstream prismatic reach: variation with time along interface ($y = 0.25$ m).

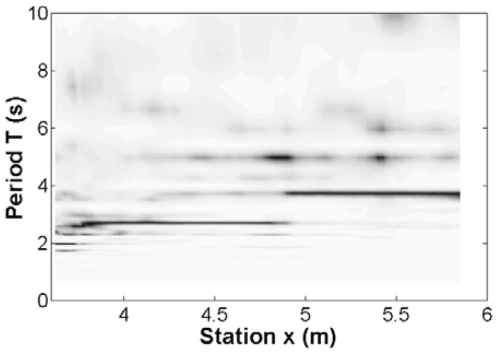


Figure 8. Transverse velocity V, Cv2/02/10 case, upstream prismatic reach: spectral analysis ($y = 0.25$ m). Dark areas correspond to high energy density.

c is estimated from the slope of such a diagonal:

$$c = \frac{\Delta x}{\Delta t} \approx \frac{2.40 \text{ m}}{12.4 \text{ s}} = 0.194 \text{ m/s} \qquad (1)$$

This celerity is lower than the longitudinal velocity U at the interface $y = 0.20$ m (Fig. 4), indicating that (1) the vortices move at the floodplain velocity; and (2) their centres are located on the floodplain and not on the interface. From vortex celerity c and vortex period T, the vortex wave length obtains

$$\lambda = T\,c \approx 0.53 \text{ .. } 0.73 \text{ m} \qquad (2)$$

The Lagrangian single particle trajectories are then plotted in a frame moving at celerity c, clearly depicting the vortex structures (Fig. 9). As inferred from

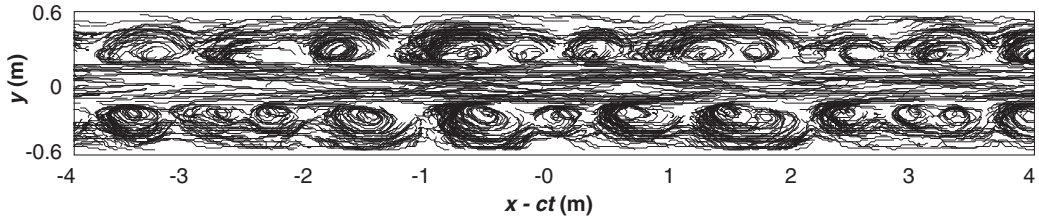


Figure 9. Particle trajectories in a frame moving at vortex celerity ($c = 0.194$ m/s), Cv2/02/10 case, upstream prismatic reach. Abscissa values correspond to the moving frame and not to actual station.

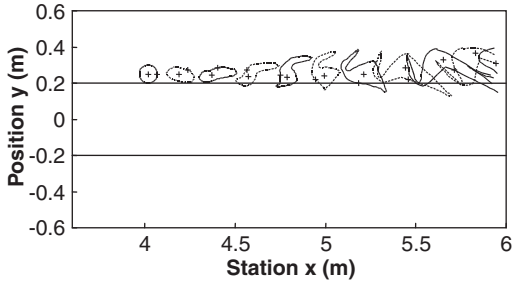


Figure 10. Vortex deformation: displacement of virtual particles in the actual instantaneous velocity field, Cv2/02/10 case, upstream prismatic reach. Separate plots correspond to $\Delta t = 1$ s intervals.

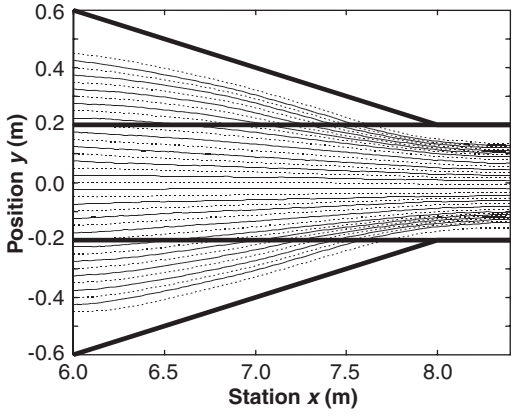


Figure 11. Surface streamlines, computed from time-averaged velocity field, Cv2/02/10 case, converging reach.

celerity values, the vortex centres are located on the floodplains. The vortex wave length $\lambda \approx 0.72$ m is also assessed from the trajectories plot. It can be noted that some merging structures are still observed, e.g. at $(x - ct) \approx 1.5$ m. No clear synchronisation is found between the periodical structures in the two shear layers. This indicates that they present independent instability behaviour, due to the lateral distance between both interfaces (Bousmar & Zech 2001).

Lastly, the behaviour of a single vortex can be investigated by computing the displacement of selected virtual tracers in the instantaneous velocity field. Such tracers are seeded on an idealised circular streamline located around a vortex centre (Fig. 10). The tracers are found to rotate around the circle centre. Secondary structures then grow and deform the initial circular streamline, due to smaller scale turbulence. The area enclosed by the streamline also increases when moving downstream: upwards flow in the vortex-centre zone leads to streamline divergence at the free surface, where the tracers are observed.

5 COHERENT STRUCTURES IN THE CONVERGING REACH

5.1 *Cv2/02/10 case analysis*

Similar analysis are performed in the non-prismatic part of the flume for case Cv2/02/10. Surface streamlines and time-averaged velocity distributions at selected stations are given on Figures 11–12. Transverse velocities V are found to increase along channel length, due to the mass transfer occurring in the convergence. A maximum value is observed near $x = 7$ m, where an inflexion point was found in the free-surface profile (Fig. 2).

The longitudinal surface velocity U has also a local maximum near this station $x = 7$ m, while the depth-averaged value was continuously increasing along the converging reach (Bousmar et al. 2004). The decrease of the surface velocity is probably due to the transverse currents generated by the convergence that mainly affect the upper layer of the main channel (Fig. 3). This confirms the significance of the momentum transfer effects due to geometrical changes of the channel.

The analysis of the transverse velocity V variation with space and time is now performed along a streamline originating near the interface, and no more along the interface itself, in an attempt to follow the vortices displacement with the averaged flow. Transverse velocities and spectral analysis are plotted on Figures 13–14. Variations of the transverse velocities V are still observed but flow from main channel towards floodplain almost disappears after $x = 7$ m. Also the

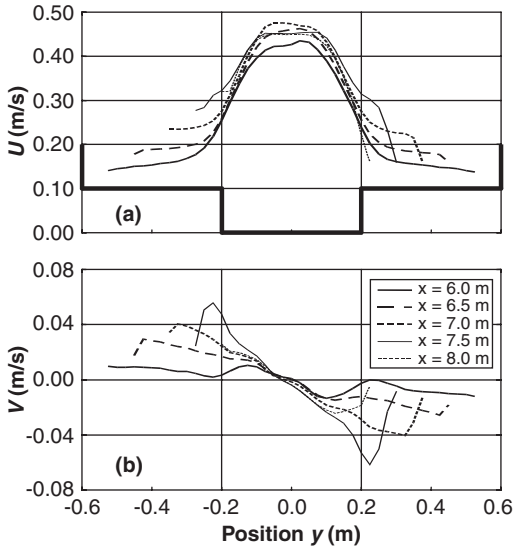


Figure 12. Time-averaged surface velocity distribution, Cv2/02/10 case, converging reach. Positive transverse velocity V flows towards increasing y.

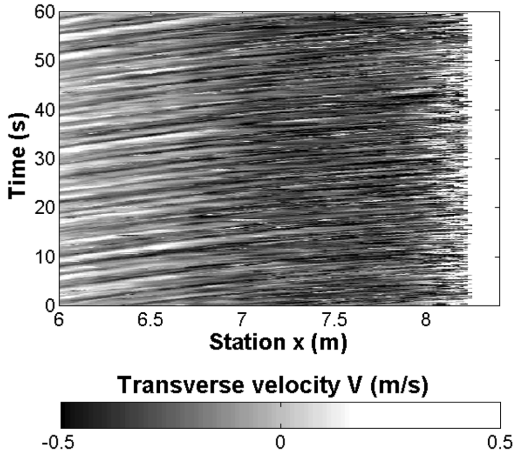


Figure 13. Transverse velocity V, Cv2/02/10 case, converging reach: variation with time along a streamline (originating at $y = 0.25$ m).

celerity of the coherent structures tends to increase from $c = 0.205$ m/s at $x = 6.00$ m to $c = 0.421$ m/s at $x = 8.00$ m, due to the flow acceleration.

A clear frequency peak is again found in the upstream part of the convergence ($x < 7$ m) at $T = 3.75$ s (Fig. 14), corresponding to a wave length $\lambda = 0.77$ m. In the downstream part, no defined period can be identified. The spectral density seems located in lower period values than upstream, indicating the splitting of the horizontal vortices in smaller structures.

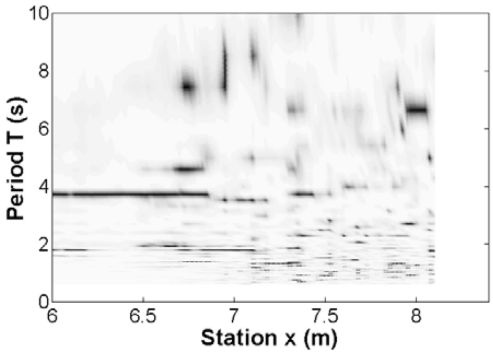


Figure 14. Transverse velocity V, Cv2/02/10 case, converging reach: spectral analysis ($y = 0.25$ m). Dark areas correspond to higher energy density.

The tracers trajectories are again plotted in a moving frame. Now the transverse positions y are distorted by stretching the streamlines shown on Figure 11 to a regular grid, again in an attempt to follow the vortices displacement. Figure 15 shows that some horizontal structures can still be found in the first part of the convergence ($6.00 < x < 7.00$ m), but then no more coherent structures appear. This confirms that the horizontal vortices have split into smaller scale, probably tri-dimensional, structures.

This vanishing of large horizontal vortices is further evidenced by computing the displacement of virtual tracers in the instantaneous velocity fields (Fig. 16). The initial structure is stretched when entering the main channel, due to the velocity gradient. After $x = 7$ m, the whole structure is located in the main channel. Its width to length ratio is such that it can no more subsist as a single vortex. It will breaks into smaller vortices whose wave lengths are in the range of the flow depth, resulting thus in 3D structures.

5.2 *Other cases analysis*

The analysis of case Cv2/03/10 almost leads to similar results. Vortices are weaker in the upstream prismatic reach, due to a lower velocity gradient between subsections. They tend therefore to disappear faster when entering the convergence.

As a conclusion for the two cases investigated in the Cv2 series, it seems that the horizontal coherent structures vanish rapidly in the non-prismatic reach. The structures still observed in the upstream part of the convergence in Cv2/02/10 case are probably vestiges of the structures developed in the prismatic reach and the shear layer plays a weaker role in the non-prismatic reach in terms of momentum transfer.

In Cv6/02/10 case, periodical structures are observed along the whole converging reach modelled ($6.00 < x < 10.00$ m). This is probably due to the lower

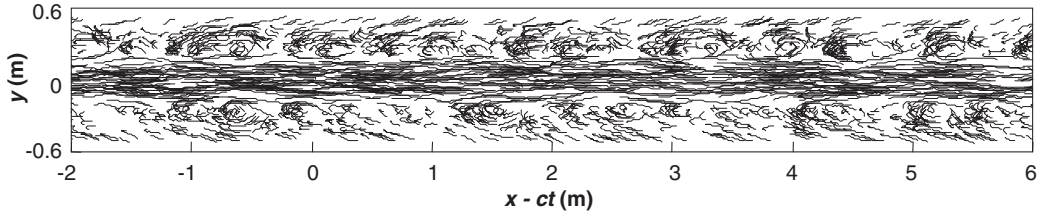


Figure 15. Particle trajectories in a frame moving at vortex celerity ($c = 0.205$ m/s) and distorted according to streamlines pattern, Cv2/02/10 case, converging reach. Abscissa values correspond to the moving frame and not to actual station. Ordinate values correspond to the origin of streamlines.

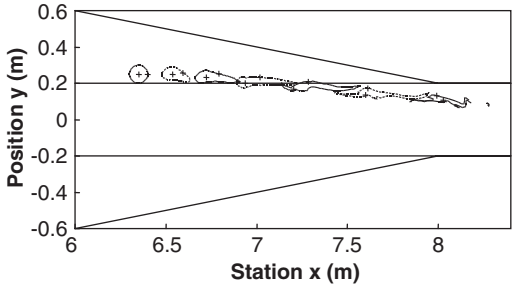


Figure 16. Vortex deformation: displacement of virtual particles in the actual instantaneous velocity field, Cv2/02/10 case, converging reach. Separate plots correspond to $\Delta t = 1$ s intervals.

converging angle, that generates less mass transfer. Nevertheless, as the end of the convergence is not reproduced in the experimental setup, the floodplains do not completely vanish downstream, resulting also in a different flow behaviour. No definitive conclusion could therefore be obtained for this case.

6 CONCLUSIONS

The coherent turbulent structures have been investigated in a symmetrically narrowing compound channel, using digital imaging techniques, in addition of previous measurement campaigns.

In the upstream prismatic reach, large-scale horizontal vortices were observed in the shear layer that develops at the interface between subsections. Interactions have been evidenced between the helical secondary currents existing in the main channel and those horizontal vortices, in the form of intermittent upwards flows in the interface area, that led to a divergence of surface streamlines. The shear layer and the associated vortices were the main source of momentum transfer between main channel and floodplains in this reach.

In the converging reach, the horizontal vortices were rapidly forced into the main channel due to the transverse currents generated by the floodplain narrowing. The vortices were there stretched and split into smaller 3D structures. The few horizontal vortices actually observed were thus mainly vestiges of the upstream structures and the momentum transfer was mostly due to the mass transfer associated with the geometrical changes.

ACKNOWLEDGEMENT

The authors are grateful to Benoît Spinewine, Civil and Environmental Engineering, Université catholique de Louvain, Belgium, for its valuable help with the digital imaging technique.

REFERENCES

Ackers, P. 1992. "Hydraulic design of two-stage channels", *Proc. Institution of Civil Engineers, Water, Maritime and Energy*, 96(4): 247–257.

Bousmar, D. 2002. *Flow modelling in compound channels. Momentum transfer between main channel and prismatic or non-prismatic floodplains*, PhD Thesis, Université catholique de Louvain, Louvain-la-Neuve, Belgium.

Bousmar, D. & Zech, Y. 1999. "Momentum transfer for practical flow computation in compound channels", *Journal of Hydraulic Engineering, ASCE*, 125(7): 696–706.

Bousmar, D. & Zech, Y. 2001. "Periodic turbulent structures modelling in a symmetric compound channel", *Proc. 29th Congress of IAHR, Beijing*, Tsinghua University Press, Beijing, D1: 244–249.

Bousmar, D. & Zech, Y. 2002. "Periodical turbulent structures in compound channels", *River Flow 2002, Proc. Int. Conf. on Fluvial Hydraulics, Louvain-la-Neuve, Belgium, September 2002*, Swets & Zeitlinger, The Netherlands, 1: 177–185.

Bousmar, D. & Zech, Y. 2003. "Large-scale coherent structures in compound channels", *Proc. Int. Symp. on Shallow Flows*, Delft, The Netherlands, I: 173–180.

Bousmar, D., Wilkin, N., Jacquemart, J.-H. & Zech, Y. 2004. "Overbank flow in symmetrically narrowing floodplains", *Journal of Hydraulic Engineering, ASCE*, 130(4), in press.

Capart, H., Young, D.L. & Zech, Y. 2002. "Voronoï imaging methods for the measurement of granular flows", *Experiments in Fluid*, 32: 121–135.

Ervine D.A., Babaeyan-Koopaei K. & Sellin, R.H.J. 2000. "Two-dimensional solution for straight and meandering

overbank flows", *Journal of Hydraulic Engineering, ASCE*, 126(9): 653–669.

Greenhill, R.K. & Sellin, R.H.J. 1993. "Development of a simple method to predict discharges in compound meandering channels", *Proc. Institution of Civil Engineers, Water Maritime and Energy*, 101(1): 37–44.

Knight, D.W. (Ed.) 1992. *SERC Flood Channel Facility Experimental Data-Phase A*, Report SR314, HR Wallingford, UK.

Nezu, I. & Nakayama, T. 1997. "Space-time correlation structures of horizontal coherent vortices in compound open-channel flows by using particle-tracking velocimetry", *Journal of Hydraulic Research, IAHR*, 35(2): 191–208.

Sellin, R.H.J., Ervine, D.A. & Willetts, B.B. 1993. "Behaviour of meandering two-stage channels", *Proc. Institution of Civil Engineers, Water, Maritime and Energy*, 101: 99–111.

Shiono, K. & Knight, D.W. 1991. "Turbulent open channel flows with variable depth across the channel", *Journal of Fluid Mechanics*, 222: 617–646.

Tominaga, A. & Nezu, I. 1991. "Turbulent structure in compound open channel flow", *Journal of Hydraulic Engineering, ASCE*, 117(1): 21–41.

River Flow 2004 – Greco, Carravetta & Della Morte (eds.)
© 2004 Taylor & Francis Group, London, ISBN 90 5809 658 0

Variations and correlation of roughness indices of non-vertical non-rigid fully submerged vegetation in open channels

A.M. Negm
Professor of Hydraulics, Civil Engg. Dept., College of Engg., Garyouns University, Benghazi, Libya

ABSTRACT: This study presents the results of an experimental investigation on the effect of fully submerged non-vertical non-rigid cylindrical vegetation on the roughness indices in open channels. The considered roughness indices are the friction factor f, the Chezy's roughness coefficient C, and the Manning's roughness coefficient n. Six model were tested using three different channel bottom slopes. The vegetation elements were distributed in staggered way in four of them and in parallel way in the other two. It was found that the trend of variation of the roughness indices with the Froude number are similar regardless of the distribution pattern. The values of the roughness indices were found to be a function of Froude number F_n, the channel bottom slope S, and the roughness density I. Statistical prediction models were developed to estimate the roughness indices in terms F_n, S and I using the multiple linear regression analysis. Good agreement were obtained between predictions of the developed models and the measured values.

1 INTRODUCTION

Management of rivers and canals flows necessitates sufficient information on the type of vegetation, its density, degree of submergence and degree of resistance to the flow. Such information may be obtained through different kinds of studies either by various methods of simulation and modeling techniques like those done by Shimizu et al. (1992a, b), Shimizu & Tsujimoto (1994), Kutija & Hong (1996), Nezu & Onitsuka (1999), Choi & Kang (2000) and Fischer-Antze et al. (2001), or through field measurements carried out by Bakry et al. (1992) and Dolgopolova (1998), or achieved by experimental tests of roughness elements simulating the vegetation either in rigid state, such as those accomplished by Shimizu et al. (1991) and Tsujimoto et al. (1992), or for flexible case, such as that done by Kouwen and Unny (1973), Christensen (1985), EL-Hakim & Salama (1992) and El-Samman & Attia (1999) or for non-flexible no-rigid state which was covered by Fahti-Maghadam and Kouwen (1997) and Wu et al. (1999).

The resistance of vegetation to the flow may be measured by one of the roughness indices as the friction factor (f), the Chezy's roughness coefficient (C), Manning's roughness coefficient (n) or the so-called retardance coefficient (N).

Recently, Negm (2003) investigated the effect of partially submerged vegetation on the variation of the roughness indices in rectangular open channel. The vegetation elements were non-vertical rigid cylinders of diameter 0.735 cm with a height of 5 cm. Three vegetation densities were used (I = 0.6%, 1.2% and 2.1%) and three slopes (S = 0.377%, 0.754% and 1.1307%) with a range of Fr = 0.25 to 0.72. He obtained the following prediction equation for the roughness indices f, C and n.

$$f_r = 8.373(F_r)^{-1.936}(S)^{1.067}(I)^{0.148} \quad (1)$$

hence,

$$f = 0.223R^{-0.25} + 8.373(F_r)^{-1.936}(S)^{1.067}(I)^{0.148} \quad (2a)$$

or alternatively,

$$f = 5.836(F_r)^{-1.704}(S)^{0.929}(I)^{0.147} \quad (2b)$$

Also,

$$C = 3.667(F_r)^{0.852}(S)^{-0.464}(I)^{-0.074} \quad (3)$$

and

$$n = 0.166(F_r)^{-1.1626}(S)^{0.537}(I)^{-0.083} \quad (4)$$

The coefficients of determination of the equations 1, 2b, 3 and 4 are 0.997, 0.994, 0.994 and 0.996 respectively while the standard error of estimate for the same equations are 0.017, 0.02, 0.01 and 0.009 respectively.

This paper presents the results of an experimental study on the effect of using non-rigid cylindrical roughness simulating vegetation under the effect of fully submerged flow conditions using various bottom slopes and various densities arranged in staggered manners. The results were presented in terms of the roughness indices f, C and n. Statistical prediction models were developed to predict the values of roughness indices for this type of vegetation.

2 THEORETICAL BACKGROUND

Using the dimensional analysis, the roughness indices could be proved to be function of the relative roughness height K/R (K is the height of roughness and R is the hydraulic radius), the Froude number, F_n, the bottom slope, S, the roughness intensity, I, and the method of distribution of vegetation, ϕ (staggered or parallel) as follows:

$$f \text{ or } C \text{ or } n = \phi_1\left(\frac{K}{R}, F_n, S, I, \phi\right) \quad (5)$$

in which F_n ($F_n = V/(gy)^{0.5}$, V is the average velocity, y is the average depth of flow, g as the gravitational acceleration. Normally it is difficult to obtain precise values of K/R in open channels and hence it will be dropped from Eq.(5). Thus Eq.(5) becomes:

$$f \text{ or } C \text{ or } n = \phi_2\left(F_n, S, I, \phi\right) \quad (6)$$

Also, ϕ is neglected because one distribution type is used.

The function ϕ_2 is an arbitrary function to be determined by using the multiple regression analysis based on the experimental data.

3 EXPERIMENTAL WORK

The experiments of the present study were conducted on a glass sided tilting flume of 9 m long working section. The flume is 30.5 cm wide and 30 cm deep. The water depths were measured by means of point gauges (of ± 0.1 mm accuracy) mounted on instrument carriages. The discharge was measured by a pre-calibrated V-notch installed in a measuring tank. The measuring tank is located below the outlet of the flume at its downstream end and is connected directly to underground sump tank. The flume is equipped with a tailgate to control the tailwater depth. A centrifugal pump lifts the water from the underground sump to the flume inlet. The water runs through the flume working section then returns back to the sump tank via the measuring tank.

Plastic cylinders tubes of diameter equals 7.35 mm and height of 50 mm was used to simulate the vegetation in the channel bed. The plastic tube is normally flexible when its length and the affecting force are sufficient. However, a length of 50 mm from such tubes is being non-vertical but the flow forces are not capable to move any portion of the fixed cylinders and therefore they are termed non-vertical rigid vegetation. The elements were fixed in the flume bed through holes of equal diameters in a wooden plate 354.735 cm long. The model was fixed at 300.05 cm from the flume entry. Each tested model consisted of many elements arranged either in staggered or parallel to form one of the tested models. A total of six models were tested under submerged flow conditions. Out of the six tested models, the elements in 4 models were arranged in staggered way with intensities of 0.6%, 2.1%, 2.327% and 8.8%. The elements of the other two models were arranged in parallel way with intensities of 1.2% and 4.654%. The roughness intensity was calculated by multiplying the cross section of one element by the number of element in the model divided by the product of the roughened length and the width of the flume. A typical staggered model with intensity of 0.6% consisted of 148 cylinders with 59 rows having transverse spacing of 6 cm and longitudinal spacing between roughness elements of 10 cm. The tests were conducted under uniform flow conditions when no roughness elements were used but with roughness elements the flow through the test section varies due to the increasing head loss from upstream to downstream side of the model. The bottom slope was varied three times for each tested model as 0.3765%, 0.7538% and 1.1307%. The depths of flow were measured at four locations. The first depth measurement was taken at 5 cm upstream the model. The other three depth measurements were taken at equal spacing from the first one, each one is 100 cm apart from the other one, such that the fourth reading is at 65 cm away from the end of the model.

4 RESULTS AND DISCUSSIONS

The friction factor was computed from the measured quantities using the equation $f = (8gRS)/V^2$ in which V is the average values of the velocity at the three locations over the length covered by vegetation, R is the average hydraulic radius, S is the bottom slope and g is the acceleration due to gravity. The computed values of f were used in Coolebroke resistance equation, to compute the relative roughness height K/R by trials and error procedure. The values of friction factors for non-vegetated channel, f_s, was calculated using Blasius equation, $f_s = 0.223R_n^{-0.25}$ in which R_n is the Reynolds

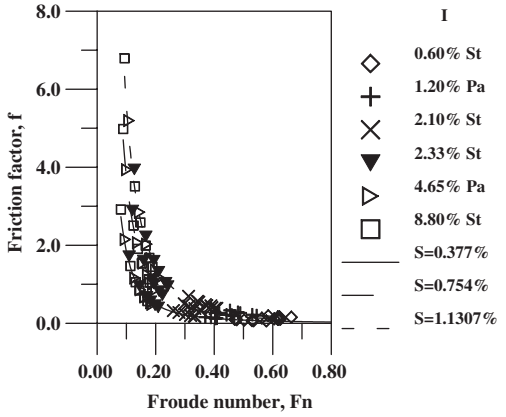


Figure 1. Relationship between f and F_n for different vegetation intensities and slopes.

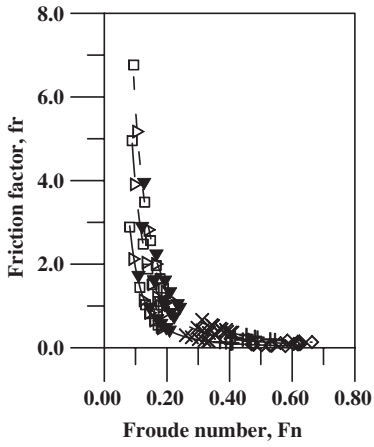


Figure 2. Relationship between f_r and F_n for different vegetation intensities and slopes.

number. The friction factor for the vegetated bed was obtained by subtracting f_s from f. The Chezy roughness coefficient was computed using $C = (8g/f)^{0.5}$ while Manning n was computed using $n = R^{1/6}/C$.

The variations of total friction factor f with F_n for different tested vegetation intensities, I, different patterns, and channel bottom slope, S are given in Figure (1). It is observed that the friction factor is very small for non-vegetated channel compared to vegetated one. The trend of variation of f with F_n is nonlinear with higher values at lower Froude number and vice versa. Steeper bottom slopes produces higher values of the friction factor which match with the fact that the friction increases with the increase of the energy slope as more energy is dissipated when the resistance to the flow is large. The friction factors for larger vegetation density is greater than for those having smaller vegetation density. Larger vegetation densities produce higher friction factors at smaller Froude number because the velocity is reduced when the flow suffers from high vegetation or roughness resistance. It should be mentioned that the friction factor due to vegetation only, f_r, (Fig. 2) follows the same trend of variation because the total friction factor is the sum of the friction factor due to non-vegetated and vegetated channel beds.

The variation of Manning Roughness n with F_n shown in Figure (3) shows similar trend as f with F_n because n is inversely proportional with the velocity and directly proportional with the slope. Also, at low values of F_n and larger values of I, the friction factor is higher. Manning's n decreases with the increase of F_n at constant slope since small values of n means little resistance to the flow and hence high velocity values that yield larger F_n. Low density of vegetation offer relatively smaller resistance to the flow and hence it produces smaller values of n.

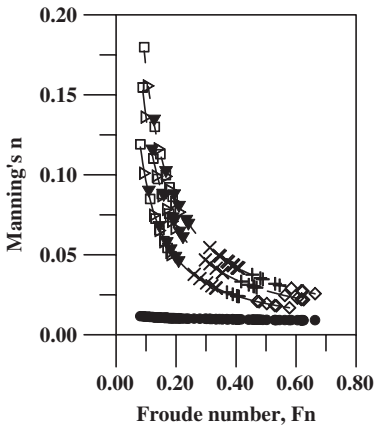


Figure 3. Relationship between n and F_n for different vegetation intensities and slopes.

Inversely to f and n, the variations of C with F_n as shown in Figure (4) follows a linear increasing trend assuming constant slope with smaller values of C at low F_n and high I. The values of C is higher for larger slopes. The values of C for non-vegetated bed is very high compared to those of vegetated channels. Vegetation with higher densities offers more resistance to the flow and hence the coefficient C will be smaller yielding smaller velocity value at constant slope.

It is interestingly to observe that the plot of the equivalent roughness height, K/R with F_n indicated in Figure (5) follow similar trend to those of f with F_n and n with F_n because larger values of K/R normally produce higher roughness indices f and n at lower values of F_n.

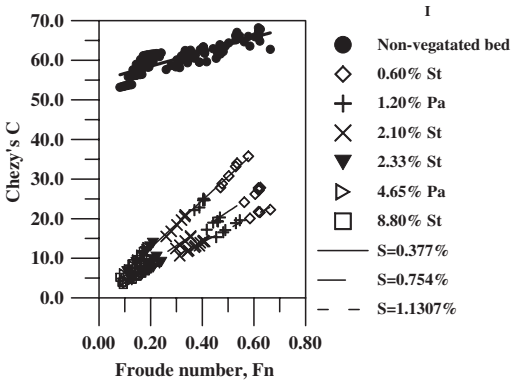


Figure 4. Relationship between C and F_n for different vegetation intensities and slopes.

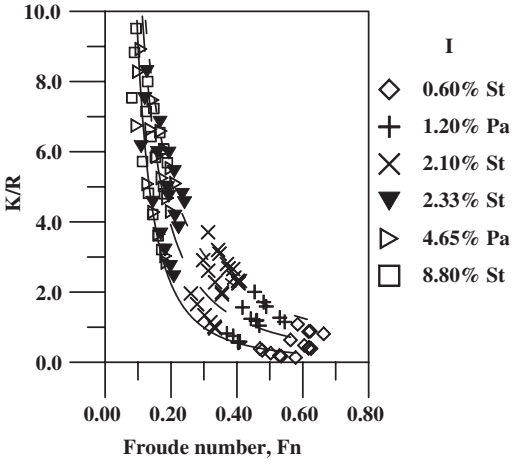


Figure 5. Relationship between K/R and F_n for different vegetation intensities and slopes.

5 PREDICTION OF ROUGHNESS INDICES OF VEGETATED BED

Using the collected data for the three roughness patterns and the three bottom slopes, the multiple linear and non-linear regression were used to test numerous proposed model to correlate the parameters of Eq.(6). The following set of equations were found to be well representative for the data with both coefficient of determination and standard error of estimate as given below.

$$f_r = 7.526(F_r)^{-2.088}(S)^{1.100}(I)^{-0.048} \quad (7)$$

hence

$$f = 0.223R_n^{-0.25} + 7.526(F_r)^{-2.088}(S)^{1.100}(I)^{-0.048} \quad (8a)$$

or alternatively,

$$f = 6.549(F_r)^{-2.022}(S)^{1.035}(I)^{-0.076} \quad (8b)$$

Also,

$$C = 3.462(F_r)^{1.011}(S)^{-0.518}(I)^{0.038} \quad (9)$$

and

$$n = 0.164(F_r)^{-1.009}(S)^{0.507}(I)^{-0.016} \quad (10)$$

The coefficients of determination of the equations 7, 8b, 9 and 10 are 0.997, 0.997, 0.994 and 0.999 respectively while the standard error of estimate for the same equations are 0.025, 0.031, 0.013 and 0.004 respectively.

Figures 6a, b, c, d show the comparison of the measured values of the roughness indices and the predicted values using Eqs.(7), (8b), (9) and (10). It is observed that good agreement was achieved between measured values and predicted ones using the developed equations.

Combining the data of the previously developed models for partially submerged vegetations with the present data for fully submerged vegetations, the following equations were obtained.

$$f_r = 7.898(F_r)^{-2.014}(S)^{1.086}(I)^{-0.028} \quad (11)$$

hence,

$$f = 0.223R_n^{-0.25} + 7.898(F_r)^{-2.014}(S)^{1.086}(I)^{-0.028} \quad (12a)$$

or alternatively,

$$f = 6.561(F_r)^{-1.944}(S)^{1.009}(I)^{-0.061} \quad (12b)$$

Also,

$$C = 3.459(F_r)^{0.972}(S)^{-0.505}(I)^{0.030} \quad (13)$$

and,

$$n = 0.163(F_r)^{-1.021}(S)^{0.509}(I)^{-0.02} \quad (14)$$

The coefficients of determination of the equations 11, 12b, 13 and 14 are 0.992, 0.993, 0.992 and 0.999 respectively while the standard error of estimate for the same equations are 0.042, 0.044, 0.021 and 0.007 respectively.

Figures 7a, b, c, d show the comparison of the measured values of the roughness indices and the predicted values using Eqs.(11), (12b), (13), (14). It is observed that good agreement was achieved between measured values and predicted ones using the developed equations for both partially and fully submerged vegetations.

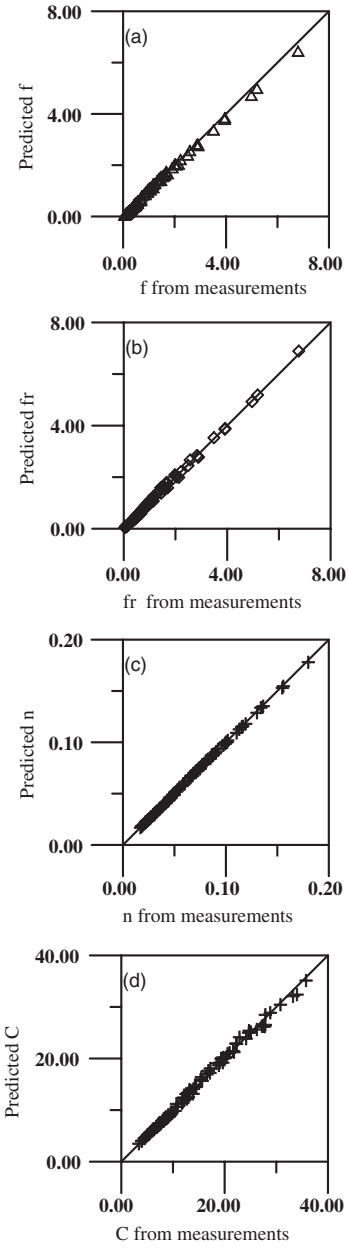


Figure 6. Measured values for roughness indices versus predicted ones (a) f using eq.(8b), (b) f_r using eq.(7), (c) n using eq.(9), and (d) C using eq. (10).

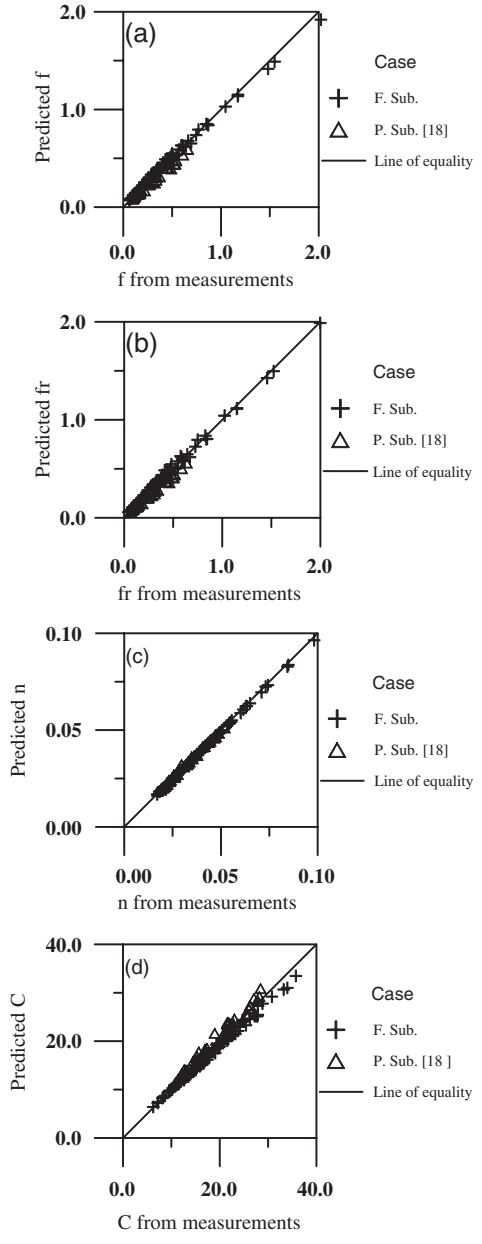


Figure 7. Measured values for roughness indices versus predicted ones (a) f using eq.(12b), (b) f_r using eq.(11), (c) n using eq.(13), and (d) C using eq. (14).

6 CONCLUSIONS

The results of an experimental investigation on the effect of Froude number, F_n, channel bottom slope, S, and vegetation intensity, I on the roughness indices of fully submerged cylindrical non-rigid non-vertical vegetation were presented. The total friction factor, f, the friction factor due to vegetation only, f_r, the Manning roughness coefficient, n, and the Chezy roughness coefficient, C, were all used in the analysis. The trend of variation of f, f_r and n with F_n were all similar and having decreasing trend with the increase of F_n while C is increasing with the increase of F_n.

The values of the roughness indices are higher for steeper slopes and for larger vegetation intensity. Prediction models (Eqs. 7, 8, 9 and 10) were developed using the statistical methods to predict the roughness indices. Comparison of predicted values with those obtained from measurements indicated good agreement. Also, general models (Eqs. 11, 12, 13 and 14) for both partially and fully submerged vegetations were developed by combining the present data with the previously published ones for partially submerged vegetation.

REFERENCES

Bakry, M.F., Gates, T.K. and Khattab, A.F. 1992. Field measured hydraulic resistance characteristics in vegetation-invested canals. *Journal of Irrigation and Drainage Engineering*, ASCE, Vol. 118, No. 2: 256–274.

Choi, S.U. and Kang, H.S. 2000. Non-isotropic turbulent modeling of vegetated open channel flows, *Proc. of abstracts and Papers (on CD ROM) of the 3rd Int. Conf. On Hydro-Science and Engineering*, Vol. IV, Souel, Korea.

Christensen, B.A. 1985. Open channel and sheet flow over flexible roughness. *Proc. 24th IAHR Congress, Melbourne, Australia*, No. 1: 462–467.

Dolgopolova, E.N. 1998. Investigation of friction factor for nature streams. *Proc. of the 3rd Int. Conf. On Hydro-Science and Engineering, ICHE'98*, Published on CD ROM and Booklet of Abstracts, Vol. III, Cottbus/Berlin, Germany.

El-Hakim, O. and Salama, M.M. 1992. Velocity distribution in branched flexible roughness. *Journal of Irrigation and Drainage Eng.*, ASCE, Vol. 118, No. IR6: 914–927.

El-Samman, T.A. and Attia, K.M. 1999. Branched flexible roughness effects on velocity distribution. *Proc. 3rd Int. Conf. On Civil & Arch. Eng.*, ICCAE, Millitary Technical College, Egypt, March 9–11, Paper No. HW3.

Fahti-Maghadam, M. and Kouwen, N. 1997. Non-rigid non-submerged vegetative roughness on floodplains. *Journal of Hydraulic Engineering*, ASCE, Vol. 123, No. 1: 51–57.

Fischer-Antze, T., Stoesser, T., Bates, P. and Olsen, N.R.B, 2001. 3D numerical modelling of open channel flow with submerged vegetation. *Journal of Hydraulic Research*, IAHR, Vol. 39, No. 3: 303–310.

Kouwen, N. and Unny, T.E. 1973. Flexible roughness in open channels. *Journal of Hydraulics Division*, ASCE, Vol. 99, No. HY5: 713–728.

Kutija, V. and Hong, H.T.M. 1996. A numerical model for assessing the additional resistance to flow introduced by flexible vegetation. *Journal of Hydraulic Research*, Vol. 34, No. 1: 99–114.

Negm, A.M. 2003. Variations and correlation Of roughness indices of non-vertical non-rigid partially submerged vegetation in open channels. *Proc. of ICCES1, Assuit University, Faculty of Engineering, Civil Engineering Dept.*, Oct. 7–9, 2003, Vol. 1.

Nezu, I. and Onitsuka, K. 1999. 3-D turbulent structures in partly vegetated open-channel flows. *Proc. Envron. Hydr., ed. By Lee, Jayawaedena and Wang*, Balkema, Rotterdam, The Netherlands: 305–310.

Shimizu, Y., Tsujimoto, T. and Nakagawa, H. 1992a. Numerical study on turbulent flow over rigid vegetation-covered bed in open channels. *Proc. JSCE, JSCE*, No. 447: 35–44.

Shimizu, Y., Tsujimoto, T. and Nakagawa, H. 1992b. Numerical study of fully-developed turbulent flow in vegetated and non-vegetated zones in a cross section of open channel, *Proc. Hydr. Eng., JSCE*, No. l36: 265–272.

Shimizu, Y. and Tsujimoto, T. 1994. Numerical analysis of turbulent open channel flow over a vegetation layer using a k-ε turbulence model. *Journal of Hydro-Science and Hydraulic Engineering*, Vol. 11, No. 2: 57–67.

Shimizu, Y., Tsujimoto, T, Nakagawa, H. and Kitamura, T. 1991. Experimental study on flow over rigid vegetation simulated by cylinders with equi-spacing. *Proc. JSCE*, No. 438/II-17: 31–40.

Tsujimoto, T., Shimizu, Y., Kitamura, T. and Okada, T. 1992. Turbulent Open channel flow over bed covered by rigid vegetation. *Journal of Hydro-Science and Hydraulic Engineering*, JSCE, Vol. 10, No. 2: 13–25.

Wu, F-C., Shen, H.W. and C., Y-J. 1999. Variation of roughness coefficients for unsubmerged and submerged vegetation. *Journal of Hydraulic Engineering*, ASCE, Vol. 125, No. 9: 934–942.

River Flow 2004 – Greco, Carravetta & Della Morte (eds.)
© 2004 Taylor & Francis Group, London, ISBN 90 5809 658 0

Recirculating flow behind groynes for compound-channel geometries

N. Rivière
LMFA, Lyon, France

S. Proust & A. Paquier
CEMAGREF Lyon, Lyon, France

ABSTRACT: Overbanks flows in a straight geometry are quite uncommon in the field. They usually cross transition reaches where the flow width can significantly varies. The extreme case is met when important obstacles, such as bridge-abutments, are present on the floodplain. They locally promote a rapid variation of the hydraulic parameters of the flow. Indeed, they first act like a groyne in a single-bed channel and so create downstream a slack-flow where silting can occur, while they promote local scour near their corner. Then, in the particular case of compound channels, they also partially block off the flow in the flood plain and promote a huge discharge transfer to the main channel. Available results on abrupt expansions in single-bed channel show that the flow in the vicinity of the obstacle obeys to two asymptotic regimes: deep or shallow water flows (Babarutsi et al., 1989) defined by a bed friction number. First, they have to be extended to the case of groynes and secondly to the case of compound channel geometries where the overspeed in the main channel affects the recirculation zone. Experiments are conducted both in single and compound channels. They confirm the validity of the expansion observations in the case of groynes, but under some corrections. They also put in evidence the crucial influence of another parameter in compound channels: the relative water depth in the floodplain.

1 INTRODUCTION

Flood flows are classically divided in two parts: a deep and rapid flow in the main channel and a more shallow and slower flow in the flood plain. The flood plain is usually occupied by vegetation, by small relieves or by small buildings that act on the uniform discharge distribution through an increase of its roughness. More important obstacles, such as bridge-abutments, can locally promote a rapid variation of the hydraulic parameters. First, they act like a groyne in a single-bed channel. They thus create a recirculation flow where silting can occur, but a more dangerous effect exists as they also induce local scour near their corner. Second, in compound channels geometries, they partially block-off the flow in the flood plain and give birth to a huge discharge and momentum transfer towards the main channel, generating secondary-current cells (Proust et al., 2002). Such behaviour is similar to the one observed in the main channel of skewed compound channels (Elliot & Sellin, 1990) so as in meandering compound channels (Shiono & Muto, 1998). From an engineering point of view, it seems necessary to characterise the mutual influence of the groyne and of the compound channel. Sturm and Janjua (1994) point out that the overspeed in the low bed must be taken into account to correct the correlations giving the scouring at the abutment corner. Conversely, the nature of the recirculation area downward obstacles seems to affect the ability to redistribute the discharge towards the flood plain and to recover the uniform flow discharge distribution (Proust et al., 2002).

Studies concerning the flow around an obstacle are available mainly in single, prismatic, channels, where the length of the recirculation zone varies with flow conditions. Babarutsi et al. (1989) work on sudden enlargements that can be assimilated to groynes of infinite thickness. They put in evidence two asymptotic regimes: shallow and deep water flows. The distinction is related to a bed friction number $S = f.d/(8h)$ where d is the enlargement width and where f, the Darcy-Weisbach friction coefficient, and h, the water depth, are defined in the expansion cross-section. In the shallow regime ($S > 0.1$), the recirculation length does not depend on the enlargement width:

$$L \approx (4.8h/f) \qquad (1\text{-a})$$

In the deep flow regime ($S < 0.05$), it depends only on the enlargement width:

$$L \approx 8d \qquad (1\text{-b})$$

Babarutsi et al. (1996) explain the difference between the two regimes by two distinct turbulence productions. The bed friction produces small eddies – with a horizontal axis- and is dominant in the shallow regime; the transverse velocity shear produces larger eddies – with a vertical axis- and is dominant in the deep flow regime.

The case of groynes attached to one bank is more complex. First, the flow has to skirt the obstacle. A strong contraction is then created, resulting in an important flow acceleration, notably close to the bed (Molinas et al., 1998). In the groyne section, the flow is no more homogeneous, as it was in the case of enlargements. Both the water depth and the velocity intensity increase from the obstacle corner to the opposite wall; the velocity is also deviated towards this wall. This influences the recirculation zone length: values reported in the literature vary from $12.5d$ (Tingsanchali and Maehswaran, 1990) to $11d$ (Ouillon and Dartus, 1998). They concern, to the authors' knowledge, exclusively the deep flow regime, but are clearly higher than the $8d$ observed with enlargements. As the shallow regime is most common in the flood plains, it is necessary to improve the knowledge of the groyne working in this regime.

Francis et al. (1968) show that in a rectangular duct, the influence of a inclined obstacle is the same as its projection perpendicularly to the main stream direction, seeing that its inclination from the bank is in the range 60°–150°. Thus, in the sequel, only obstacles perpendicular to the flood plain bank and to the flow are considered. Molinas and Hafez (2000) indicate that the abutment thickness has a straightening effect past the upstream corner: the recirculation zone is more pronounced downward the groynes that are thicker. Hence, the study is focused on infinite thickness obstacles (enlargements) and, on the other hand, on negligible thickness obstacles (metal plates). Otherwise, several obstacle widths are considered, as Francis et al. (1968) underline the influence of the distance to the wall opposite to the groyne corner.

First, the experimental set-up and the measuring techniques are described. Then, the experimental results are exposed, for enlargements and after for groynes, both in single and in compound channels. The observed behaviours and the possibility to model the different regimes are finally discussed.

2 EXPERIMENTAL SET-UP AND MEASURING TECHNIQUES

Experiments are performed in a compound channel flume of useful length $L = 8\,\text{m}$, of total width $B = 1.2\,\text{m}$ (Fig. 1), with a bed slope $S_0 = 1.8 \times 10^{-3}$. The main-channel bank is vertical and 5 cm high, while its width is $B_{mc} = 0.4\,\text{m}$. The flood plain width is

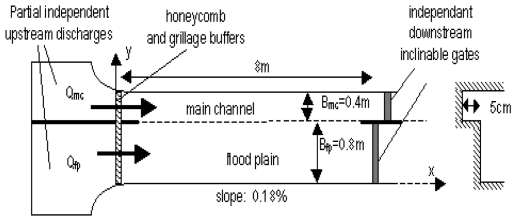


Figure 1. Experimental set-up.

$B_{fp} = 0.8\,\text{m}$. The bed is made of PVC. The upstream stilling basin is separated in two chambers that allow to adjust independently the partial discharges: Q_{mc} in the main channel and Q_{fp} in the flood plain.

When a single-bed channel is needed, only the flood plain is used; it is separated from the main-channel by plywood plates. They are covered by plastic rubber on their submerged part, ensuring a roughness equivalent to the one of PVC.

A centrifugal pump provides water to the flume, distributed between the two channels, from an underground sump. For each channel, the water enters the stilling basin through a perforated cylinder, and then crosses honeycombs and grillage buffers. Q_{mc} and Q_{fp} are measured by two electromagnetic flow meters installed on each supply pipe. Indeed, during experiments in compound channels, the ratio Q_{mc}/Q_{fp} is adjust to match the one of a uniform flow defined by the relative water-depth $H_r = h_{fp}/h_{mc}$, where h_{fp} is the water depth in the floodplain and h_{mc} in the main channel. This avoids flow-development problems due to the relatively small length to width ratio $B/L \approx 6.7$ (Bousmar et al., 2003). Last, two independent adjustable gates, one at the downstream end of each bed, allow a constant water depth in the whole channel.

The water levels are measured thanks to a moveable point gauge, with a reading accuracy of ± 0.1 mm. Velocities are acquired by a miniature propeller (1.5 cm of diameter). Their alignment with the x-direction is checked using a homemade miniature vane, with an accuracy of about $\pm 2°$. Depth-averaged velocities are obtained from 4 measurements on each vertical in the main channel, and then integrated to give Q_{mc}. In the high bed, the mean velocity is deduced from the evaluation of the cross section of the flowing part and the substraction of Q_{mc} from the whole discharge.

The bed friction has to be characterised in the flood plain. Due to the range of Reynolds numbers encountered, the friction coefficient varies with the local velocity. Considering the Darcy-Weisbach coefficient f, and a small h/B ratio, it writes (Graf, 2000):

$$\frac{1}{\sqrt{f}} = -2\log_{10}\left(\frac{k_s}{12R_h} + \frac{3.4}{\sqrt{\lambda}\,\text{Re}}\right) \qquad (2)$$

This relation is valid for a hydrodynamically smooth bed. First, this requires a Reynolds number $Re = 4R_hU/\nu > 2000$, where R_h is the hydraulic radius and U the average velocity. Considering a section of width B and depth h, the two latter write respectively $R_h = 4hB/(2h+B)$ and $U = Q/(hB)$. Secondly, the smooth assumption was checked for every flow thanks to a Moody diagram, considering $k_s < 0.05$ mm (PVC sheets). The two conditions were always fulfilled in the flood plain in the experiments.

Two techniques of flow visualisation are used to locate the stagnation point and thus the reattachment length L. First, milk is injected into the flow, approximately at middepth. Second, photographs give the trajectories of sawdust particles spread on the free surface, with 8s time of exposure. The stagnation point is adopted from an average of 6 to 10 photographs. The first technique is far less accurate as vertical vortices are produced at the enlargement (or obstacle) angle; they grow as they are advected towards the recirculation end. Depending on the flow depth, their typical size can reach there the order of the reattachment length. Thus, the random passage of vortices – frequency O(0.1 Hz)- strongly affects the motion of the injected milk, and so the location of the stagnation points (Figs 2-a and 2-b).

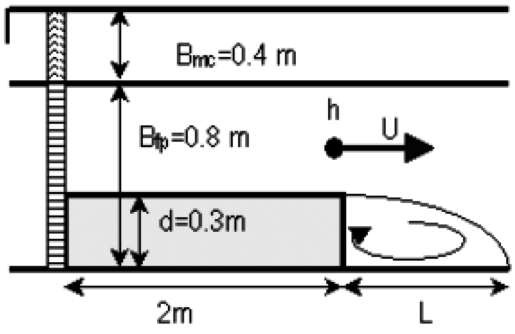


Figure 2-a. Lateral expansion configuration.

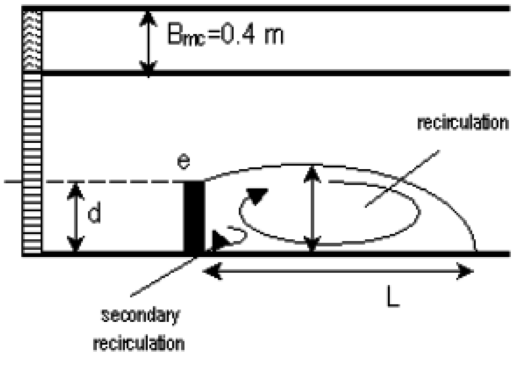


Figure 2-b. Groyne configuration.

3 EXPERIMENTAL RESULTS

3.1 *Lateral expansion*

A wooden case, 2 m long, partly blocks off the flow entering the channel (Fig. 2-a) and forms a lateral expansion of width $d = 0.3$ m ($d/B_{fp} = 0.375$). The flow velocity and depth are almost uniform just upstream the expansion.

First, Figure 3 shows the overestimation of L/d measured by milk injection due to the presence of the advected vertical vortices mentioned above.

In the isolated flood plain, the results are in agreement with the experiments of Babarutsi et al.(1989), and obey to two asymptotic regimes corresponding to high (>0.06 rather than 0.1) or small (<0.05) values of the bed friction number S. As the main objective was the groyne, only two measurements are performed in a compound channel: they seem to put in evidence another parameter, the relative water-depth H_r. It must be notice that the H_r value refers to the one of uniform flow corresponding to the inlet ratio Q_{mc}/Q_f. For $H_r = 0.2$, the expansion acts like in a single bed. For $H_r = 0.4$, the behaviour is really different. However, too few points were acquired to propose a definite conclusion on the role of H_r, as the main purpose was groynes, which are studied in next section. First, it must be shown if obstacles of negligible thickness follow the same behaviour as obstacles of infinite thickness, i.e. expansions. Second, more numerous measurements have to be performed to examine the role of H_r.

3.2 *Groynes*

Four obstacles (brass plates of negligible relative thickness e/d) of width $d = 10$, 15.6, 30 and 40 cm are used (Fig. 2-b). The corresponding rati d/B_{fp} are respectively 0.125, 0.2, 0.375 and 0.5. The velocity shear is stronger at the groyne corner than in the case of the expansion. Consequently, bigger vertical vortices are produced and advected towards the stagnation point, causing a higher dispersion in the length L measurements.

3.2.1 *Single bed geometry*

The first results concern the single bed flows. Again, S is derived with the flow parameters of the obstacle section. Figure 4 clearly shows the existence of two asymptotic regimes: deep and shallow, also in the case of obstacles, but with somewhat different features.

A first one is the underestimation of L/d by relations (1-a) and (1-b). This is mainly due to the flow contraction that does not exist in the case of abrupt expansions. This is valid for both regimes. In the deep flow limit, the values are conform to the one reported in the literature, about $L/d = 10$–12 instead of 8. When the flow is dominated by friction, the slope of L/d as a function of S is similar to the one observed with

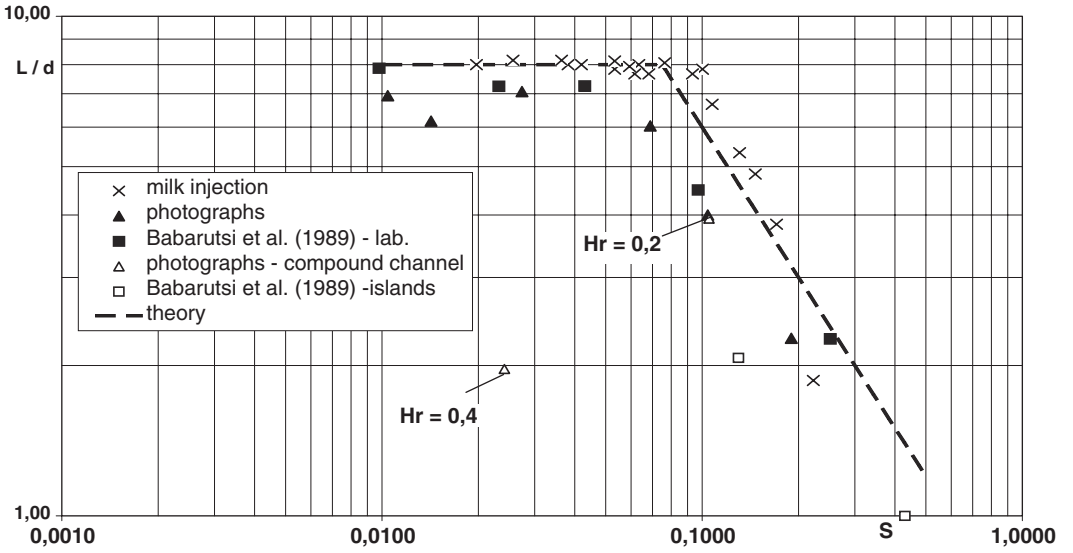


Figure 3. Reattachment length over obstacle width ratio, downstream a sudden enlargement in single and compound channels (sawdust photographs and milk injection).

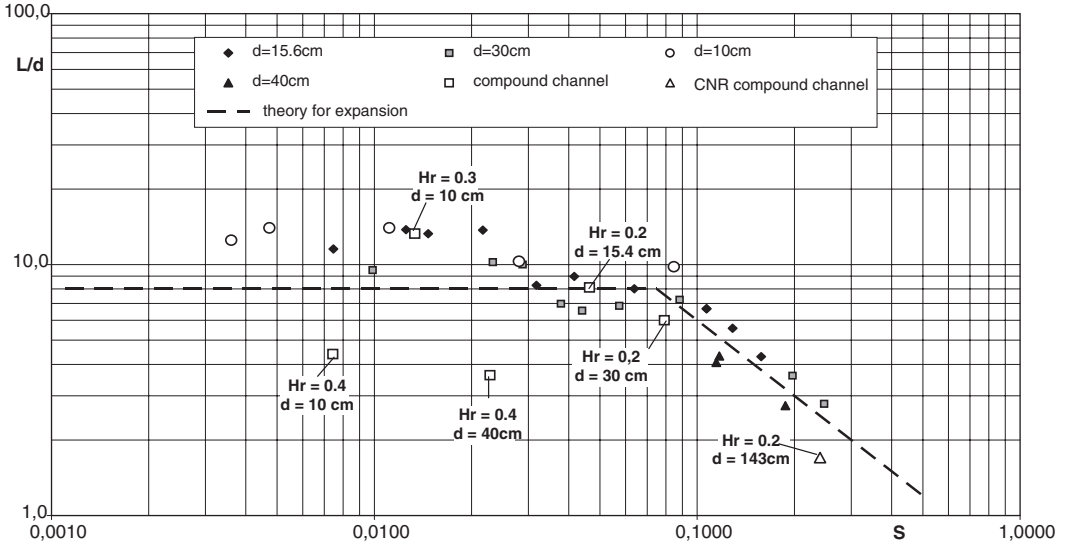


Figure 4. Reattachment length over obstacle width ratio, downstream groynes in single and compound channels (sawdust photographs only).

enlargements, but with an upward shift for d < 0.3 m. For higher d, another parameter must be accounted for: the ratio d/B_{fp}, as proposed in the literature (Francis et al., 1968), but only for a deep flow regime. Indeed, the more the wall opposite to the groyne is close to the corner (strong d/B_{fp}), the more the reattachment length is reduced. The upward shift between the data obtained for $d/B_{fp} = 0.12$ and 0.375 illustrates this effect in the deep limit, so as the downward shift for $d/B_{fp} = 0.5$ in the shallow limit.

3.2.2 *Compound channel*

A clear feature that confirms the experiments performed on an expansion is observed. With $H_r = 0.2$, the water depth in the flood plain is small and S is high for $d = 0.154$ and 0.3 m: the behaviour is like

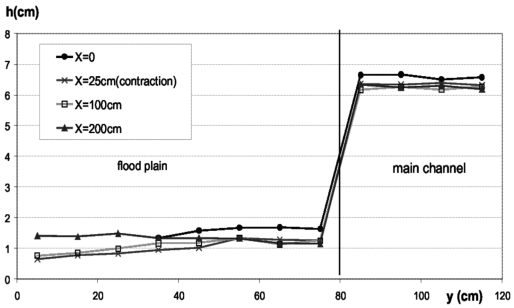


Figure 5-a. Water depth profiles $H_r = 0.2$; $d = 0.375$ B_{fp}; $L = 6$d.

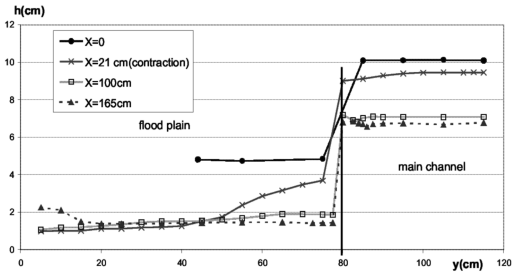


Figure 5-b. Water depth profiles $H_r = 0.4$; $d = 0.5$ B_{fp}; $L = 4.2$d.

a shallow water flow in a single bed. With $H_r = 0.3$ and $d = 0.1$ m, the regime becomes "deep-water", and again the behaviour is similar to the one observed in single beds. On the other hand, the $H_r = 0.4$ configurations correspond again to values of L/d really smaller than the theory prediction, and this both for small or high d/B_{fp} values. Additional experimental values, obtained previously in a concrete compound channel flume (total length = 13 m, total width = 3 m, $B_{fp} = 2.2$ m), at the Compagnie Nationale du Rhone, are given in Figure 4 (CNR compound channel). The obstacle was either 143 cm or 77 cm large, and the relative water depth H_r for uniform flows was either 0.2 or 0.33.

They confirm the preceding results but with a rougher bed as the Manning roughness was $n = 0.013\ \mathrm{m}^{-1/3}\cdot\mathrm{s}$ -resp. $0.011\ \mathrm{m}^{-1/3}\cdot\mathrm{s}$ – in the flood plain -resp. in the main channel-. Experimental details can be found elsewhere (Proust et al., 2002).

The evolution of the water depth h downstream the obstacle is sketched on Figure 5-a and Figure 5-b. In this figures, measuring the depth from the bottom of each bed causes a huge discontinuity for $y = 80$ cm but allows gauging the relative evolution of the flow depth in each bed. Four transverse profiles are acquired: a first one in the obstacle section, the second in the maximum contraction section, a third one at the end of the recirculation area and a fourth one between the two latter.

For the configuration ($H_r = 0.2$, $d = 0.375B_{fp}$), the water depth variation on the flood plain are about 30%. On the opposite, for ($H_r = 0.4$, $d = 0.5B_{fp}$), the water depth sharply decreases downstream the obstacle: the reduction reaches a factor 5. This should result in strong longitudinal variations of h, U, f and finally of S. To check this point, velocity profiles are acquired simultaneously with the water depths.

Then, f and S are calculated from the averaged depth and axial velocity in a section. The results are sketched on Figure 6, where the evolution of S is plotted as a function of x/L, both for groynes and expansions. For $H_r = 0.2$ or 0.3, the variations of S are small on the whole recirculation length, and S reaches a constant value. Conversely, S varies steadily on the whole reattachment length for $H_r = 0.4$, both for the expansion and the $d/B_{fp} = 0.5$ groyne. For the latter, S is multiplied by 4, that should cause an evolution from deep regime to the transition zone described by Babarutsi. Regarding CNR data, by sake of clarity, the S evolution for Hr = 0.2 and d = 143 cm, which varies between too high values, namely 0.2 and 0.8 is not plotted on Figure 6. Nevertheless, from $x/L = 0.3$, the S value is almost constant around 0.8. For the other configuration, the good position of experimental point in Figure 4, is in agreement with the absence of regime modification on Figure 6.

In Figures 3 and 4, the odd position of the $H_r = 0.4$ measurements is thus due the fact that the value of S, computed in the obstacle section, cannot be representative of the different S values until the reattachment. The upstream value of S is so unable to account for the competition between the different turbulence production sources that finally condition the size of the recirculation zone.

4 DISCUSSION

Experiments were performed to examine if the asymptotic regimes identified by Babarutsi et al. (1989), observed for abrupt expansions in single bed flow, can be extended to other flow cases. First, sharp obstacles were used instead of an enlargement. Very similar trends are observed, but another parameter has to be taken into account: the relative distance between the groyne corner and the opposite wall. It is interesting to notice that the local increase of the friction coefficient f due to modifications of the vertical velocity profiles, as suggested by Molinas et al. (1998), does not prevent from using the S criteria that is estimated through a global friction coefficient f. Second, experiments were conducted in a compound channel instead of a single bed. In this case, as long as H_r is small enough, the reattachment length behaves like in single channel. When H_r reaches higher values (0.4 in the

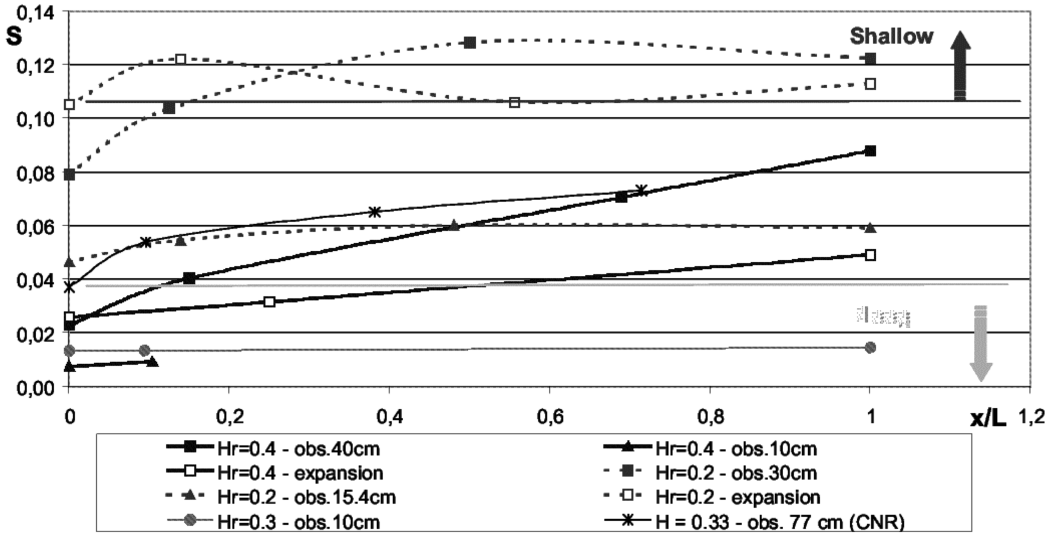


Figure 6. Longitudinal variations of S downstream the expansion and the groynes.

present experiments), the reattachment length can considerably decrease both for abrupt expansions and obstacles. The longitudinal gradient of the water depth from the main channel to the flood plain are able to cause important variations of the bed friction number. The possibility to define a mean value of *S* is still to develop.

Thus, future work has to be devoted to complete the data set with a measuring technique giving access to a more precise location of the reattachment point so as to turbulent variables. The experimental set-up is well adapted to this scope, through its transparent section allowing optical measurements.

ACKNOWLEDGEMENTS

Authors are thankful to A. Bergez, L. Pontal and F. Vion for their experimental participation on the project. Experiments were funded in the framework of the project "2-D modelling of a flood plain – Representation of obstacles" from PNRH (French National Program of Hydrological Research) and of the project "Modelling of hydrodynamic processes with free surface in case of singularities" from the ACI (Concerted Action) "Prevention of natural catastrophes" funded by the French Ministry of Research.

REFERENCES

Bousmar, D., Rivière, N., Proust, S., Paquier, A., Morel, R., Zech, Y. (2003). Upstream discharge distribution in compound-channel flumes, submitted to *Journal of Hydraulic Engineering.*

Ackers, P. (1992). "Hydraulic design of two-stage channels", *Proc., I.C.E., Water, Maritime and energy*, Thomas Telford, London, 96(4), 247–257.

Babarutsi, S., Ganoulis, J., Chu, V.H. (1989). "Experimental investigation of shallow recirculating flows". *Journal of Hydraulic Engineering*, 115(7), 906–924.

Babarutsi, S., Nassiri, M., Chu, V.H. (1996). "Computation of shallow recirculating flow dominated by friction". *Journal of Hydraulic Engineering*, 122(7), 367–372.

Bousmar, D. & Zech,Y. (1999). Momentum transfer for practical flow computation in compound channels, *Journal of Hydraulic Engineering*, 125(7), 696–706.

Elliot, S.C.A. & Sellin, R.H.J. (1990). "SERC Flood channel facility: skewed flow experiments", J. Hydr. Reas., 28(2), 197–214.

Graf, W.H. (2000). "Hydraulique Fluviale: écoulements et phénomènes de transport dans les canaux de géométrie simple", Presses Polytechniques et Universitaires Romandes, Lausanne.

Molinas, A. & Hafez, Y. (2000). "Finite element surface model for flow around vertical wall abutments". *Journal of Fluids and Structures*, 14(5), 711–733.

Nicollet, G. & Uan, M. (1979), "Ecoulements permanents à surface libre en lit composés", *La Houille Blanche*, 1, 21–30.

Proust, S., Rivière, N., Bousmar, D., Paquier, A., Morel, R. (2002). "Velocity measurements in a concrete experimental channel representing a floodplain", Hydraulic Measurements and Experimental Methods, EWRI-ASCE, july 28- august 2, Estes Park, Colorado, USA.

Shiono, K. & Muto, Y. (1998). "Complex flow mechanisms in compound meandering channels with overbank flow". *J. Fluid Mech.*, 376, 221–226.

Sturm, T.W. & Janjua, N.S. (1994). "Clear-water scour around abutments in floodplains". *Journal of Hydraulic Engineering*, 120(8), 956–972.

Sturm, T.W. & Sadiq, A. (1996). "Water surface profiles in compound channels with multiple critical depths", *Journal of Hydraulic Engineering*, 122(12): 703–709.

River Flow 2004 – Greco, Carravetta & Della Morte (eds.)
© 2004 Taylor & Francis Group, London, ISBN 90 5809 658 0

Local velocity at bridge abutments on plain rivers

B. Gjunsburgs & R. Neilands
Riga Technical University, Riga, Latvia

ABSTRACT: Scour phenomena at bridge abutments on plain rivers in flood were studied. A differential equation for the bed sediment movement for clear water was used, and a new method for computing the development of scour depth with time at the abutments in flood was elaborated. The method was confirmed by experimental data. Laboratory tests were made in flumes with fixed and sand beds. The tests showed the streamline concentration, a sharp drop in water level, and a rapid increase in velocity at the corner of the abutment. The local velocity with a vortex structure, which formed a scour hole at the abutments, depended on the open flow parameters, magnitude of backwater, contraction rate of bridge crossings, scour depth, and flood parameters. A formula for the local velocity was derived. It was found that the flow structure at the abutments differed from that near the piers: there was no runflow and downflow. Whether the equilibrium stage of scour can or cannot be reached depended on the characteristics of flood and river bed. It was also found that tests in the conditions of a steady flow did not reflect the changes in real flow and scour during the flood.

1 INTRODUCTION

Bridge failure during the flood as a result of scour at piers and abutments can lead to considerable environmental damages and losses. Although the problem is of great importance, scour at bridge abutments on plain rivers has not been studied much.

An analysis of the literature shows that there is no common opinion concerning the velocity that forms scour holes and no unified methods for calculating the local (maximum) velocity at the abutments.

Methods and formulas for calculating the depth of scour at the abutments employing the mean velocity of open flow, the Froude number with this velocity, or the mean velocity of the flow near the abutments were used by Laursen & Toch (1956), Froelich (1989), Richardson et al. (1990), Melville (1997), Melville & Coleman (2000), Kothyari & Ranga Raju (2001), and Radice et al. (2002). The existence of the maximum (local) velocity near the abutments has been confirmed in laboratory tests by Latishenko (1960).

Some authors consider that the flow pattern and scour at the piers are of the same structure as near the abutments – Laursen (1963), Kothyari et al. (1992), Melville (1997), Kothyari & Ranga Raju (2001), and that downflows at the piers and the abutments are identical – Kwan (1984, 1988).

In the majority of methods and formulas, the equilibrium scour depth at bridge abutments has been calculated; however, Radice et al. (2002) failed to reach the equilibrium stage of scour in long-term tests.

In the present study, a differential equation of equilibrium of the bed sediment movement for clear water is used and a new method for calculating the scour development with time at the abutments during the flood is elaborated. The method is confirmed by experimental data.

In our tests, the concentration of streamlines, a sharp drop in water level, a local increase in the velocity, and scour hole are observed at the corner of the abutment. It is found that, due to the vortex system, the movement of sediments starts at a lower velocity.

The flow pattern at the abutments is not the same as that near piers. There is no runflow and downflow, since on the plain rivers the streamlines go around the abutment.

Whether the equilibrium stage of scour can or cannot be reached depends on the flood and river-bed parameters. Tests in the conditions of a steady flow do not reflect changes in the real flow during the flood.

The local velocity depends on the characteristics of the flow, magnitude of backwater, contraction of the flow, scour depth, and flood parameters. A formula for the local velocity is proposed.

2 EXPERIMENTAL SETUP

Tests were carried out at the Transport Research Institute (Russia) in flumes 3.5 m wide and 21 m long

Table 1. Experimental data for open flow conditions in flumes.

Test	L (cm)	h_f (cm)	V (cm/s)	Q (l/s)	Fr	Re_c	Re_f
L1	350	7	6.47	16.60	0.0780	7500	4390
L2	350	7	8.58	22.70	0.0103	10010	6060
L3	350	7	10.3	23.60	0.1243	12280	7190
L4	350	7	8.16	20.81	0.0984	10270	5590/5660
L5	350	7	9.07	23.48	0.1094	11280	6140/6410
L6	350	7	11.1	28.13	0.1339	13800	7550/7840
L7	350	13	7.51	35.48	0.0665	13700	9740
L8	350	13	8.74	41.38	0.0756	16010	11395
L9	350	13	9.90	47.10	0.0876	14300	14300
S1	134.5	5	6.30	4.24	0.0890	7110	3000
S2	134.5	5	9.52	6.50	0.1360	10400	4450
S3	134.5	5	10.58	7.30	0.1510	12090	5000

and at the Budapest Technical University (Hungary) in flumes 1.35 m wide and 9.0 long.

Experimental data for the open-flow conditions were presented in Table 1.

The tests with a fixed (cemented) bed were performed for different flow contractions, in order to investigate the velocity and the water level changes in the vicinity of the embankment, along it, and near a modelled abutment. The aim of tests with a sand bed was to study the scour processes, the changes in the velocity with time, the effect of hydraulic parameters and the contraction rate of the flow, grain size of the bed material, and the scour development in time. The openings of the bridge model were 50, 80, 120, and 200 cm in the first flume and 44.5, 57.5, 77.5, and 97.5 cm in the second one. The contraction rate of the flow Q/Q_b (where Q was the discharge of the flow and Q_b was the discharge of the flow in a bridge opening in open-flow conditions) varied from 1.25 to 5.69 at a depth of floodplain of 5, 7, and 13 cm, and the Froude numbers varied from 0.078 to 0.151. The slope was 0.0012 and 0.0015 for the first and second flumes, respectively.

The tests with a sand bed were carried out in the conditions of clear water. The sand was placed 1 m up and down the contraction of the flumes. The mean size of grains was 0.24 and 0.67 mm in the first flume and 0.5 and 1.0 mm in the second one with a standard deviation. The condition that $\mathrm{Fr}_R = \mathrm{Fr}_f$ was fulfilled, where Fr_R and Fr_f were the Froude numbers for the plain river and for the flume, respectively. The tests in the flumes lasted for 7 hours, the vertical scale was 50 and the time scale was 7. With respect to the real conditions, the test time was equal to 2 days. This was the mean duration of time steps, into which the flood hydrograph was divided.

The development of scour was examined with different flow parameters in time intervals within one 7 hours step and within two steps of hydrograph, 7 hours each.

3 METHOD

The differential equation of equilibrium for the bed sediment movement in the conditions of clear water has the form:

$$\frac{dw}{dt} = Q_s \,. \tag{1}$$

According to laboratory tests, $w = 1/6\pi m^2 h_s^3$, where t is the time and Q_s is the sediment discharge out of the scour hole.

The left-hand part of Eq. (1) can be written as

$$\frac{dw}{dt} = \frac{1}{2}\pi m^2 h_s^2 \frac{dh_s}{dt} = a h_s^2 \frac{dh_s}{dt} \,, \tag{2}$$

where h_s is the scour depth and m is the steepness of the scour hole. The sediment discharge was determined by the Levi (1969) formula:

$$Q_s = AB \cdot V_l^4 \,, \tag{3}$$

where $B = mh_s$ is the width of a scour hole, V_l is the local velocity at the abutment, and A is a parameter in the Levi (1969) formula:

$$A = \frac{5.62}{\gamma}\left(1 - \frac{\beta V_o}{V_l}\right)\frac{1}{d^{0.25} h_f^{0.25}} \,. \tag{4}$$

Here, γ is the specific weight of sediments, β is the coefficient of reduction in velocity V_o due to the vortex system, V_o is the velocity required to start the movement of sediments, d is the size of grains of the bed material, and h_f is the depth of water in the floodplain.

The sediment discharge upon development of the scour is

$$Q_s = A\, mh_s \cdot V_l^4 = b \frac{h_s}{k\left(1 + \dfrac{h_s}{2h_f}\right)^4} \,, \tag{5}$$

where $b = Am \cdot V_l^4$; k is the coefficient of changes in the discharge due to the scour. The hydraulic characteristics, the contraction rate of flow, the velocities V_o and V_l, the grain size in different layers of the bed, the sediment discharge, the depth, and the width of the scour hole varied during the flood.

Upon development of the scour, we have

$$A = \frac{5.62}{\gamma} \cdot \left[1 - \frac{\beta V_o}{V_l} \left(1 + \frac{h_s}{2h_f} \right)^{1.25} \right] \cdot \frac{1}{d^{0.25} \cdot h_f^{0.25} \left(1 + \frac{h_s}{2h_f} \right)^{0.25}} \quad (6)$$

Taking into account formulas (2) and (5), differential equation (1) can be presented as

$$ah_s^2 \frac{dh_s}{dt} = b \frac{h_s}{k \left(1 + \frac{h_s}{2h_f} \right)^4}$$

or

$$D_i \cdot h_s \left(1 + \frac{h_s}{2h_f} \right)^4 dh_s = dt . \quad (7)$$

After integration, we have

$$t = D_i \int_{x_1}^{x_2} h_s \left(1 + \frac{h_s}{2h_f} \right)^4 dh_s .$$

According to the method presented, the hydrograph was divided in time steps, and each step in turn was divided into small time intervals (Fig. 1). It was assumed that D was constant inside the time interval.

After integration with new variables, $x = 1 + h_s / 2h_f$, $h_s = 2h_f(x - 1)$ and $dh_s = 2h_f dx$ we obtain

$$N_i = \frac{t_i}{4D_i h_f^2} + N_{i-1}, \quad (8)$$

where $N_i = 1/6x_i^6 - 1/5x_i^5$ and t_i is time interval.

Using the graph $N = f(x)$ or the data of Table 2 for the calculated N_i, we find x_i and the depth of the scour at the end of time interval:

$$h_s = 2h_f(x - 1) . \quad (9)$$

To determine the scour depth development during the flood, the hydrograph was divided into time steps with duration of 1 or 2 days, and each time step was divided into time intervals up to several hours. In laboratory tests, the time steps were divided into 20 time intervals. For each time step, the following parameters must be determined: h_f – depth of water in the floodplain, Q/Q_b – contraction rate of the flow, Δh – maximum backwater, d – grain size, H – thickness of the bed layer with d, and γ – specific weight of the bed material. As a result, we have V_l, V_o, A, D, N_i, N_{i-1}, and h_s at the end of time intervals and finally at the end of the time step. For the next time step, the flow parameters changed because of the flood and the scour developed during the previous time step.

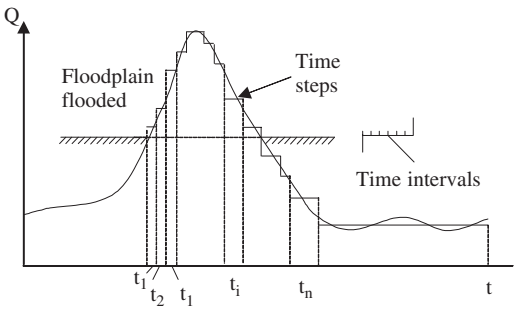


Figure 1. Hydrograph divided in time steps and time intervals.

Table 2. The value of N_i as a function of x_i.

x_i	1	1.2	1.4	1.6	1.8
Ni	−0.033	0.0002	0.18	0.70	1.90
xi	2	2.2	2.4	2.6	2.8
Ni	4.29	8.62	15.98	27.2	46.07

4 RESULTS

When approaching the contraction of the bridge, the streamlines were bended by the embankment, and then the flow went parallel to it. The velocities along the extreme streamline dropped down almost to the minimum and then gradually increased (Fig. 2), and a spiral vortex system developed. At the corner of the abutment, the concentration of streamlines, a sharp drop in water level, and a rapid increase in the velocity were found (Fig. 3). A horizontal vortex developed, which reduced the opening of the bridge. As was found in the tests, the local velocities near the abutments existed at any contraction of the flow.

To calculate the local velocity, we used the Bernulli equation for two cross sections of a unit streamline. Then the formula for the local velocity near the abutment was

$$V_2 = V_l = \varphi \sqrt{2g\Delta Z} , \quad (10)$$

where φ was the velocity coefficient and ΔZ was the difference in water levels at the corner of the abutment.

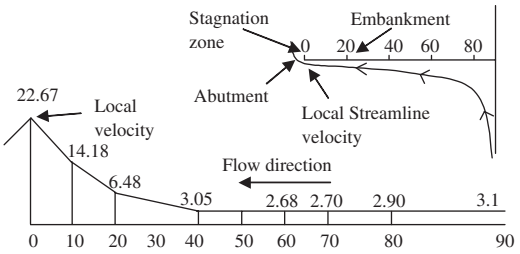


Figure 2. Velocity distribution in the vicinity of an abutment. Test SS1.

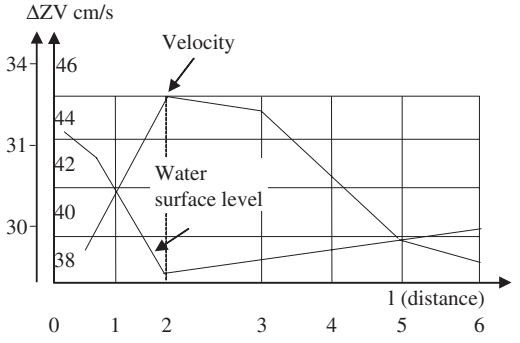


Figure 3. Changes in the velocity and water level near the abutment. Test FL6.

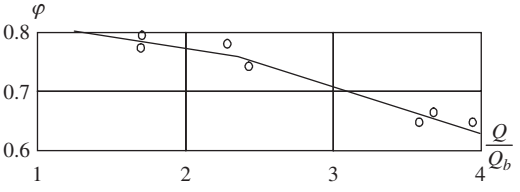


Figure 4. Coefficient ϕ versus the contraction of the flow.

It was found in the tests that the water level difference ΔZ was equal to the maximum backwater Δh. We checked it for different values of the opening width, discharge, flow depth, and Froude numbers. The maximum backwater was determined by using the Rotenburg (1969) formula.

The velocity coefficient in Eq. (10) depended on the rate of contraction of the flow (Fig. 4).

Table 3 presented a comparison between the experimental and calculated data for local velocities at the abutments.

The discharge across the width of a scour hole before and after the scour was as follows: $Q_f = k \cdot Q_{sc}$, where Q_f was the discharge across the width of the scour hole with a plain bed and Q_{sc} was the discharge across the width of the scour with a depth h_s.

$$mh_s \cdot h_f V_l = k(mh_s h_f + \frac{mh_s}{2} \cdot h_s) \cdot V_{lt} \,. \tag{11}$$

The local velocity at any depth of the scour hole can be determined from formula (11):

$$V_{lt} = \frac{V_l}{k\left(1+\frac{h_s}{2h_f}\right)} = \frac{\varphi\sqrt{2g\Delta h}}{k\left(1+\frac{h_s}{2h_f}\right)} \,. \tag{12}$$

According to the experimental data, the coefficient k depended on the contraction of the flow (Fig. 5).

Using formulas (10) and (12) we can find the local velocities at any depth of scour around the abutment and for any step of the hydrograph.

Table 4 presented a comparison between the experimental data and computed scour depth with the use of local velocity.

The flow parameters varying with each step of the hydrograph affected considerably the depth of

Table 3. Comparison between the experimental data and the calculated local velocity at the abutments.

Test	L_b (cm)	Δh (cm)	ΔZ (cm)	$\frac{\Delta h}{\Delta Z}$	$\frac{Q}{Q_b}$	$V_{l\,calc.}$ (cm/s)	$V_{l\,exp.}$ (cm/s)	$\frac{V_{l\,calc.}}{V_{lexp.}}$
FL1	50	2.10	2.40	0.87	5.27	36.81	39.3	0.94
FL2	50	3.70	3.90	0.95	5.69	43.20	43.4	0.99
FL3	50	4.07	4.40	0.92	5.55	46.61	50.3	0.92
FL4	80	1.25	1.36	0.92	3.66	33.04	36.0	0.92
FL5	80	1.75	1.70	1.03	3.87	39.76	39.0	1.02
FL6	80	2.50	2.40	1.04	3.78	45.85	45.2	1.05
FL7	120	0.50	0.58	0.90	2.60	25.85	25.1	0.92
FL8	120	1.05	1.01	1.08	2.69	34.05	33.8	1.01
FL9	120	1.38	1.45	0.95	2.65	38.77	39.4	0.98
FL10	120	0.35	0.32	1.09	1.56	22.08	21.6	1.02
FL11	200	0.40	0.43	0.93	1.66	23.97	23.1	1.04
FL12	200	0.51	0.55	0.93	1.67	26.01	27.3	0.95

the scour. For example, in test SL4 at $Q = 16.6$ l/s, $h_f = 7$ cm, $Q/Q_b = 3.66$, $d = 0.24$ mm, and $\Delta h = 1.19$ cm, the scour depth was 10.1 cm after 7 hours. In test SL 19 at $Q = 35.48$ l/s, $h_f = 13$ cm, $Q/Q_b = 4.05$, $d = 0.24$ mm, and $\Delta h = 1.42$ cm scour depth was 13.6 cm after 7 hours.

In test TL1, we modelled two (SL4 and SL19) steps of the hydrograph. The scour depth after 14 hours of test TL1 was 14.3 cm, which was not equal to the sum of the values obtained in two separate tests, namely 23.7 cm.

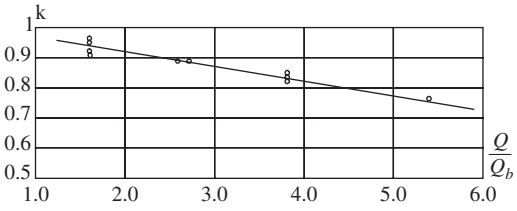


Figure 5. Coefficient k versus the contraction of the flow.

The scour development with time was studied in tests SS and SL for a steady flow, as a step of hydrograph, and in tests TL for an unsteady flow.

Figures 6–7 showed a comparison between the experimental data and the computed depth of scour development with time under steady and unsteady flow conditions.

5 CONCLUSIONS

It was found that, as a result of the streamline concentration, vortex structure, sharp drop in water level, and

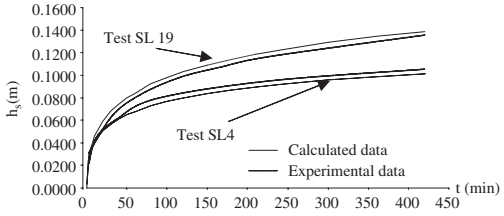


Figure 6. Scour development in time under steady flow conditions.

Table 4. Comparison between the experimental data and the calculated depth of scour at the abutments.

Test	Q (l/s)	$\frac{Q}{Q_b}$	h (cm)	l_b (cm)	Δh (cm)	d (mm)	V_l (cm/s)	t (hours)	$h_{s\,\mathrm{exp.}}$ (cm)	$h_{s\,calc.}$ (cm)	$\frac{h_{s\,\mathrm{exp.}}}{h_{s\,calc.}}$
SS1	4.24	2.5	5	44.5	0.457	0.50	23.45	7	2.37	2.26	1.05
SS2	7.30	2.5	5	44.5	0.953	0.50	33.87	7	6.34	6.21	1.02
SS3	6.50	2.5	5	44.5	0.816	0.50	31.34	7	5.07	5.32	0.95
SS4	6.50	2.0	5	57.0	0.569	0.50	26.73	7	3.58	3.45	1.04
SS5	4.24	2.0	5	57.0	0.323	0.50	20.14	7	0.70	0.73	0.96
SS6	7.30	2.0	5	57.0	0.665	0.50	28.89	7	4.10	4.27	0.96
SS7	7.30	1.5	5	77.5	0.444	0.50	23.90	7	2.03	2.07	0.98
SS11	7.30	1.25	5	97.5	0.330	0.50	20.73	7	0.71	0.67	1.06
SL1	16.6	5.27	7	50.0	2.200	0.24	36.81	7	13.30	12.91	1.03
SL4	16.6	3.66	7	80.0	1.190	0.24	33.04	7	10.1	9.79	1.03
SL5	22.7	3.87	7	80.0	1.790	0.24	39.76	7	12.80	13.03	0.98
SL9	23.6	2.65	7	120	1.280	0.24	38.77	7	5.70	5.51	1.03
SL10	16.6	1.56	7	200	0.380	0.24	22.08	7	2.97	3.08	0.96
SL11	22.7	1.66	7	200	0.450	0.24	23.97	7	4.11	4.16	0.99
SL12	23.6	1.67	7	200	0.530	0.24	26.01	7	5.09	5.16	0.98
SL16	16.6	3.66	7	80.0	1.190	0.67	33.17	7	3.30	7.98	1.04
SL17	22.7	3.87	7	80.0	1.790	0.67	39.76	7	9.6	10.00	0.96
SL18	23.6	3.78	7	80.0	2.350	0.67	45.85	7	12.53	12.32	1.02
TL1	16.66	3.66	7	80.0	1.19	0.24	33.04	14	14.3	14.50	0.99
	35.48	4.05	13	80.0	1.42	0.24	34.65				
TL2	22.7	3.87	7	80.0	1.80	0.24	39.76	14	19.0	17.76	1.07
	41.38	3.99	13	80.0	1.80	0.24	39.26				
TL3	23.6	3.77	7	80.0	2.35	0.24	45.85	14	24.2	23.14	1.05
	47.1	4.05	13	80.0	2.70	0.24	49.15				
TL4	16.6	3.66	7	80.0	1.19	0.67	33.04	14	9.37	9.87	0.98
	35.48	4.05	13	80.0	1.42	0.67	34.65				
TL5	22.7	3.87	7	80.0	1.80	0.67	39.76	14	12.8	13.09	0.98
	41.38	3.99	13	80.0	1.80	0.67	39.26				
TL6	23.6	3.78	7	80.0	2.35	0.67	45.85	14	19.3	18.45	1.045
	47.1	4.05	13	80.0	2.70	0.67	49.15				

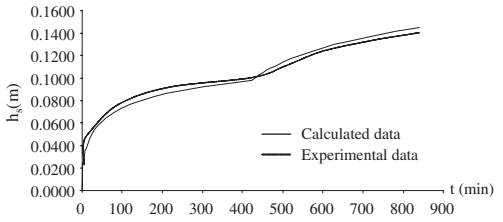


Figure 7. Scour development in time under unsteady flow conditions.

local increase in the velocity the depth of scour around the bridge abutments on plain rivers was higher than in opening of the bridge.

The flow structure at the abutments was not the same as that near the piers. The streamlines flew around the abutments, and there was no runflow and downflow as in the case at the piers.

The local velocity with a vortex structure formed scour holes and depended on the characteristics of the flow, magnitude of backwater, contraction rate of the bridge crossings, and the depth of scour. A formula for the local velocity was derived. The local velocity reduced in time because of the scour and changed with the flood.

According to this method, the equilibrium stage of scour can or cannot be reached, depending on the flood and river bed parameters. The tests in the steady flow conditions did not reflect the changes in the real flow and scour during the flood.

A differential equation for the bed sediment movement for clear water was used and a new method for computing the scour depth development in time at the abutments during the flood was elaborated. The method was confirmed by experimental data.

REFERENCES

Floelich, D. C. 1989. Abutment scour prediction. *Presentation. Transport Research Board.* Washington, DC.

Kandasamy, J. K. 1989. Abutment scour. *Report 458. School of Engineering.* The University of Auckland, Auckland. New Zealand.

Kothyari, U. C. & Ranga Raju, K. G. 2001. Scour around spur dikes and bridge abutments. *Journal of hydraulic research* 39 (4): 367–374.

Kwan, T. F. 1984. Study of abutment scour. *Report 328. School of Engineering*. The University of Auckland, Auckland. New Zealand.

Kwan, T. F. 1988. Study of abutment scour. *Report 451. School of Engineering*. The University of Auckland, Auckland. New Zealand.

Латышенков, А. М. 1960. Вопросы гидравлики искусственно сжатых русел. Стройиздат, Москва.

Леви И. И. 1969. Динамика русловых потоков. Гидрометеоиздат, Москва.

Laursen, E. M. & Toch, A. 1956. Scour around bridge piers and abutments. Bulletin 4. Jowa Institute of Hydraulic Research, Jowa, USA.

Melville, B. W. 1997. Pier and abutments scour: integrated approach. *Journal of hydraulic engineering* 123 (2): 125–136.

Melville, B. W. & Coleman, S. E. 2000. Bridge scour. *Water resources publication, LCC*, Highland Ranch, Colorado, USA.

Neilands, R. & Gjunsburgs, B. 2001. Scour development in time near abutments. *Architecture and construction science. Scientific proceedings of Riga Technichal University. Riga* 2 (2): 123–129.

Radice, A., Franzetti, S. & Ballio, F. 2002. Local scour at bridge abutments. *Proceedings of the International Conference on Fluvial Hydraulics, River Flow 2002, Louvian – La – Neuve 2*: 1059–1068.

Richardson, E. V., Simons, D. B. & Julien, P. Y. 1990. *Highways in the river environment. FHWA – H* 190 – 016, Federal Highway administration, U.S. Department of Transportation, Washington, DC.

Ротенбург, И. С. & Вольнов, В. С. 1969. Примеры проектрования мостовых переходов. Высшая школа, Москва.

River Flow 2004 – Greco, Carravetta & Della Morte (eds.)
© 2004 Taylor & Francis Group, London, ISBN 90 5809 658 0

Performance of lateral velocity distribution models for compound channel sections

J.F. Weber
Universidad Nacional de Córdoba and Universidad Tecnológica Nacional, Córdoba, Argentina

A.N. Menéndez
INA (National Institute for Water) and Universidad de Buenos Aires, Buenos Aires, Argentina

ABSTRACT: In this paper, the scope of 2D-Horizontal and 1D-Lateral models for lateral velocity distribution is addressed, and their relative and absolute performances are tested by making comparisons between their predictions, on the one side, and experimental and field velocity data, on the other side. The models considered are: the Divided Channel Method (DCM), the Lateral Distribution Method (LDM) and a 2D Horizontal hydrodynamic finite-element model (RMA2).

1 INTRODUCTION

Hydraulic engineering studies related to floods usually require the lateral distribution of flow velocity across the compound channel section, constituted by the main channel and the floodplain. 2D-Horizontal numerical models (such as the public domain software RMA2 of USACE) are now broadly accepted as an appropriate theoretical model to solve this problem. However, as in the majority of applications the longitudinal scale of flow variation is much larger than the lateral scale of variation (given by the flow width), the longitudinal and lateral flow variations can be accounted for separately (Menéndez 2003); the first one, through well-established 1D-Longitudinal models based on de Saint Venant equations (Cunge et al. 1980), while the second one, using 1D-Lateral models.

1D-Lateral models, which solve the lateral distribution of the longitudinal depth-averaged flow velocity, have become the subject of analysis and application in recent years. They run between simple and relatively old empirical and heuristic formulations – such as the methods of Lotter (1933), or Divided Channel Method (DCM, used in software HEC-RAS, 2001), Horton (1933), and Pavlovski (1931) – to physically-based equations, like the Lateral Distribution Method (LDM) proposed by Wark et al. (1990).

2 MODEL DESCRIPTIONS

In the following paragraphs, the three models used in the present work are briefly described: the DCM; the analytical solution proposed by Shiono & Knight (1988, 1991) to the LDM, and the RMA2-WES 2D-Horizontal hydrodynamic finite-element model (Donnell et al. 2001).

2.1 *DCM model*

Lotter (1933), and later Einstein & Banks (1950) divided the cross section into subsections, and assumed that the energy grade slope was the same for any subsection, and that the interfaces between them behaved as impermeable boundaries, i.e., that there was no diffusion of lateral momentum (leaving the friction as the only energy loss), to calculate the partial discharge Q_i for any such subsection:

$$Q_i = K_i S_0^{1/2} \tag{1}$$

where $S_0 =$ longitudinal slope; and $K_i =$ hydraulic conveyance, given by

$$K_i = \frac{A_i R_i^{2/3}}{n_i} \tag{2}$$

where $A_i =$ flow area, $R_i =$ hydraulic radius, and $n_i =$ Manning's roughness coefficient for subsection i.

The lateral velocity distribution, V_i, can then be obtained as

$$V_i = \frac{Q_i}{A_i} \tag{3}$$

This is the method implemented in software HEC-RAS (HEC 2001) as *Flow Distribution Option*.

2.2 *LDM model*

The LDM (Wark et al. 1988) is based on the steady-state continuity and momentum depth-averaged equations of motion. Combining both equations, and neglecting longitudinal derivatives, the following expression is obtained

$$\rho g S_0 Y - \frac{f}{8}\rho V^2\sqrt{1+\frac{1}{s^2}} + \frac{d}{dy}\left[\rho\lambda\sqrt{\frac{f}{8}}Y^2 V\frac{\partial V}{\partial y}\right] = 0 \quad (4)$$

where $\rho =$ density of water; $g =$ gravitational acceleration; $Y =$ local flow depth; $f =$ Darcy's friction coefficient; $V =$ depth-mean velocity; $s =$ lateral bed slope; $y =$ lateral coordinate; and $\lambda =$ non-dimensional Boussinesq eddy viscosity.

Equation 4 takes into account the effects of friction and diffusion as dissipative terms. The source term represents the effect of water weight.

Shiono & Knight (1988) obtained the analytical solutions of Equation 4 across subsections where the depth (Y) is constant or a linear function of the lateral coordinate. These solutions are given in equations 5 (for constant depth) and 6 (for linear depth). In these expressions, η, ψ, and ω are constants given by equations 7–9. Coefficients a and b in equations 5–6 must be calculated solving a linear system of equations. This system is obtained by imposing the matching conditions expressed in equations 10–11 at the interface between subsections. For a section composed by N subsections, $2N-2$ equations result from applying 10–11.

Although Abril (2003) showed that the boundary condition given by Equation 11 is not strictly true, it will be consider as correct for the present work.

$$V_{(y)} = \sqrt{a_1 e^{\eta y} + b_1 e^{-\eta y} + \frac{8gS_0 Y}{f}} \quad (5)$$

$$V_{(y)} = \sqrt{a_2 Y^{\psi} + b_2 Y^{-\psi-1} + \omega Y} \quad (6)$$

$$\eta = \sqrt{\frac{2}{\lambda}}\sqrt{\frac{f}{8}}\frac{1}{Y} \quad (7)$$

$$\psi = \frac{1}{2}\sqrt{1+\frac{s\sqrt{1+s^2}}{\lambda}\sqrt{8f}} - \frac{1}{2} \quad (8)$$

$$\omega = \frac{gS_0}{\frac{\sqrt{1+s^2}}{s}\frac{f}{8} - \frac{\lambda}{s^2}\sqrt{\frac{f}{8}}} \quad (9)$$

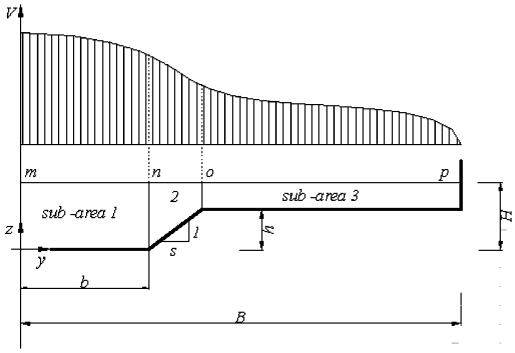


Figure 1. Scheme of a simplified compound channel section.

$$V_1^{\,n} = V_2^{\,n} \quad (10)$$

$$\frac{\partial V_1^{\,n}}{\partial y} = \frac{\partial V_2^{\,n}}{\partial y} \quad (11)$$

The remaining two equations arise from the boundary conditions at the two extremes. For example, in the case of a cross section as shown in Figure 1, the two boundary conditions correspond to the no-slip condition at point p and zero derivative in point m (symmetric section).

2.3 *2D model*

The RMA2 model (Donnell et al. 2001) is a 2D depth-averaged finite-element hydrodynamic numerical model. It was originally developed by Norton, King and Orlob (1973) and actually supported by WES-USACE. It solves the shallow water equations, i.e. (neglecting wind shear stress and Coriolis acceleration):

$$Y\frac{\partial u}{\partial t} + Yu\frac{\partial u}{\partial x} + Yv\frac{\partial u}{\partial y} - Y\varepsilon\left(\frac{\partial^2 u}{\partial x^2}+\frac{\partial^2 u}{\partial y^2}\right) + \\ + gY\left(\frac{\partial z_b}{\partial x}+\frac{\partial Y}{\partial x}\right) + \frac{gun^2}{Y^{1/3}}\sqrt{u^2+v^2} = 0 \quad (12)$$

$$Y\frac{\partial v}{\partial t} + Yu\frac{\partial v}{\partial x} + Yv\frac{\partial v}{\partial y} - Y\varepsilon\left(\frac{\partial^2 v}{\partial x^2}+\frac{\partial^2 v}{\partial y^2}\right) + \\ + gY\left(\frac{\partial z_b}{\partial y}+\frac{\partial Y}{\partial y}\right) + \frac{gvn^2}{Y^{1/3}}\sqrt{u^2+v^2} = 0 \quad (13)$$

$$\frac{\partial Y}{\partial t} + Y\left(\frac{\partial u}{\partial x}+\frac{\partial v}{\partial y}\right) + u\frac{\partial Y}{\partial x} + v\frac{\partial Y}{\partial y} = 0 \quad (14)$$

where u and v are the x and y components of the velocity vector, respectively, and ε is the horizontal eddy-viscosity, calculated as:

$$\varepsilon = \lambda Y V_* = \lambda \sqrt{g S_0} Y^{3/2} \quad (15)$$

The numerical solution of equations 12–14 is implemented through the finite-element method. The program uses both quadrilateral and triangular elements. The weighted-residuals Galerkin method is used for spatial integration. An explicit finite-difference scheme is used for time integration.

3 EXPERIMENTAL DATA

Two sources of experimental data were used for validation: those from the SERC Flood Channel Facility experimental flume (Shiono & Knight 1988, 1991), and measurements from river Severn at Montford, UK (Knight et al 1989).

3.1 *Laboratory data*

The SERC Flood Channel Facility is a laboratory flume 56 m long and 10 m wide, with discharges up to a maximum of 1.1 m^3/s. Velocities were measured by means of mini propeller current meters (Shiono & Knight 1991).

For the present work, eight experiments, distributed in two groups according to floodplain width, are considered. Taking as a reference Figure 1, the total half-width B is 3.15 m for Group A and 1.65 m for Group B; the main channel half-width is the same for both groups, and equal to 0.75 m; the longitudinal slope is fixed in 0.001027; the main channel depth relative to floodplains (h) is 0.15 m. The total depth H and the discharge Q vary for each case, as shown in Tables 1 and 2. These tables also present the non-dimensional geometric parameter D_r, defined as:

$$D_r = \frac{H - h}{H} \quad (16)$$

Manning's roughness coefficient n was used instead of Darcy's coefficient f to characterize channel roughness. Coefficient n was assumed constant and equal to 0.0104. It was verified (Weber 2003) that results are relatively insensitive to which of the coefficients is considered as a constant.

The relation between parameters n and f is the following:

$$f = \frac{8gn^2}{\sqrt[3]{Y}} \quad (17)$$

Table 1. Hydraulic parameters for experimental data. Group A.

	Case 1	Case 2	Case 3	Case 4	Case 5
H (m)	0.1690	0.1780	0.1870	0.1980	0.2879
Q (m^3/s)	0.2483	0.2821	0.3237	0.3830	1.1142
Dr	0.111	0.157	0.197	0.242	0.479

Table 2. Hydraulic parameters for experimental data. Group B.

	Case 6	Case 7	Case 8
H (m)	0.1667	0.1987	0.3000
Q (m^3/s)	0.2421	0.3325	0.8349
Dr	0.100	0.245	0.500

Table 3. Hydraulic parameters for River Severn, UK.

	Discharge (m^3/s)	Depth (m)
Case 1	330.8	7.81
Case 2	220.6	6.92
Case 3	188.8	6.15

Table 4. Roughness coefficients for River Severn, UK.

			Manning's coefficient n		
Point	y (m)	f	Case 1	Case 2	Case 3
1	0.00	0.038	0.0212		
2	8.00	0.038	0.0230	0.019	0.0193
3	71.00	0.5	0.1037	0.1002	0.0981
4	79.00	0.04	0.0318	0.0312	0.0308
5	96.00	0.5	0.1037	0.1002	0.0981
6	105.00	0.1	0.0373	0.0309	0.0312
7	128.00	0.1	0.0345		

3.2 *Field data*

Field data used for the present work consists of three velocity profiles measured at a cross section in river Severn at Montford, UK (Knight et al. 1989). This is the longest river of England. Its mean discharge is 43 m^3/s. The longitudinal slope at the surveyed location is 0.0002. Table 3 shows the discharge and depth associated to the three cases considered.

Roughness coefficients were taken as reported in the original work (Knight el al. 1989). For the application of DCM and RMA2 models, the corresponding values of Manning's n were obtained. Table 4 shows all these values.

4 MODELS APPLICATION

Applications of the three models to the two sets of experimental data are described in the following.

4.1 *DCM model*

The DCM model was applied through software HEC-RAS (HEC 2001). This soft, aimed at solving gradually varied flow with a 1D-Longitudinal model, has a feature called *Flow Distribution*, which calculates (using the DCM) the lateral velocity distribution in specified cross sections. Users can control the points where they want to obtain the results, through the specification of a Δy value.

For the application of HEC-RAS, a rectilinear prismatic channel, with the known flow depth imposed as downstream boundary condition, was considered. The lengths of the 1D models were 56 m for the laboratory flume experiments and 10,000 m for River Severn. The results for middle-located stations were used for comparison with experimental data, in order to avoid influence from the boundary conditions.

In order to investigate the influence of lateral discretization on the accuracy of the predictions, different discretization steps were tested. Figures 2–3 show the lateral velocity profiles predicted for two cases in the laboratory flume (Case 1 with $H = 0.169$ m and Case 5 with $H = 0.288$ m). Figures 4–5 are the velocity profiles computed for two cases in River Severn (Case 1 with $H = 7.81$ m and Case 3 with $H = 6.15$ m). It is observed that a finer discretization does not necessarily means higher precision for the DCM.

4.2 *LDM model*

The analytical solution of LDM was applied using a specially-developed software, named "Lateral" (Weber & Menéndez 2003). This soft proceeds through the following steps:

- It calculates the characteristic constants η, ψ, and ω (Equations 7–9) for each subsection.
- It calculates the coefficients matrix and the independent-term vector.
- It solves the algebraic system of equations.
- It calculates the mean-depth lateral profile of the longitudinal velocity for a specified Δy.

In case of natural streams with no vertical walls, the non-slip condition leads to the trivial solution,

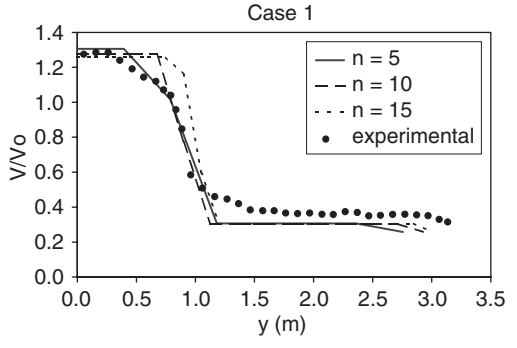


Figure 2. Lateral velocity distribution for Case 1 of SERC channel as predicted by DCM.

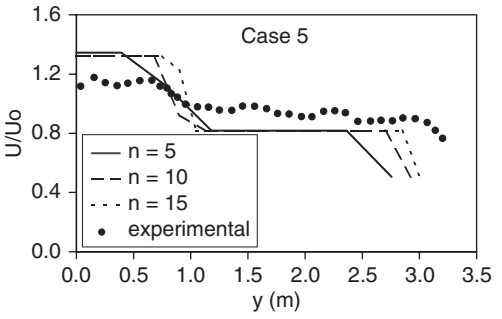


Figure 3. Lateral velocity distribution for Case 5 of SERC channel as predicted by DCM.

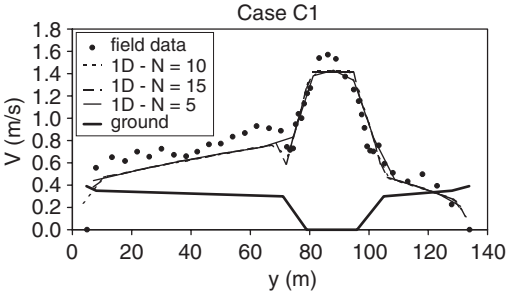


Figure 4. Lateral velocity distribution for Case 1 of river Severn as predicted by DCM.

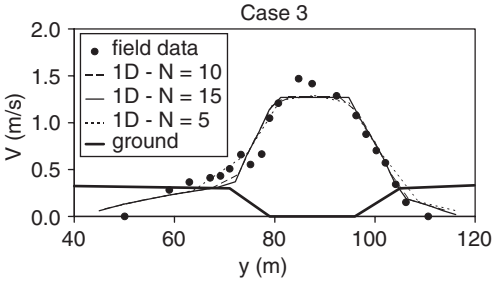


Figure 5. Lateral velocity distribution for Case 3 of River Severn as predicted by DCM.

because $Y = 0$. Then, this condition was slightly modified to:

$$V_{(\delta y)} = \delta V \tag{17}$$

where $\delta Y =$ minimum imposed depth considered in calculations, and $\delta V =$ minimum imposed velocity corresponding to depth δY. Although δY and δV appear as new parameters, experience shows that they have only a local influence. Values of 0,001 m and 0,1 m were used for δY in laboratory flume and in River Severn, respectively. The minimum velocity δV was taken as 0,1 m/s for both cases.

Instead of working with $V(y)$, function $V^2(y)$ was used, which allows to deal with a linear system of algebraic equations. Solution to this system were obtained through Gauss Elimination Method.

Figures 6–9 show the results of the application of LDM to the same cases as Figures 2–5. These figures correspond to similar results reported in Shiono & Knight (1988) and Knight et al. (1989).

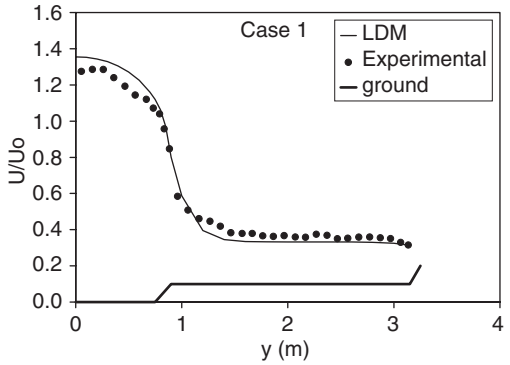


Figure 6. Lateral velocity distribution for Case 1 of SERC channel as predicted by LDM.

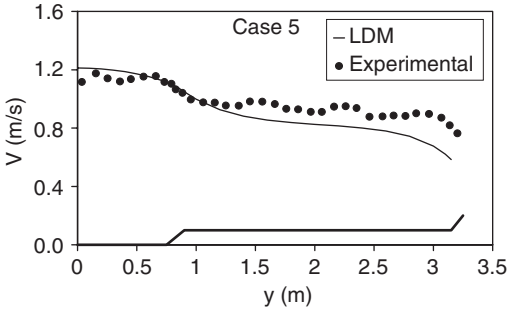


Figure 7. Lateral velocity distribution for Case 1 of SERC channel as predicted by LDM.

4.3 *2D model*

The 2D model RMA2 was used to predict the lateral velocity distribution for the same cases as the previous models. A prismatic geometry was developed using an *ad-hoc* software called GEO. It constructs a structured rectangular finite-element mesh, as shown in Figure 10.

The length of the channel was taken as the minimum one necessary to achieve a stabilized solution. It resulted lengths of 10 m for the laboratory cases and 600 m for River Severn. The Δx step was assumed fixed at 0.1 m for laboratory cases and 4 m for River Severn.

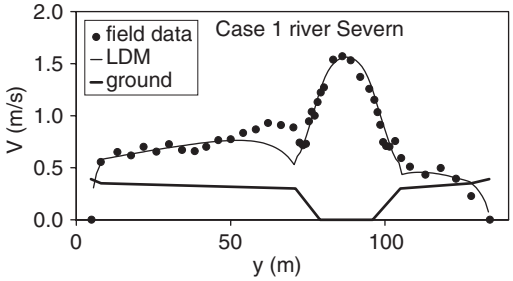


Figure 8. Lateral velocity distribution for Case 1 of River Severn as predicted by LDM.

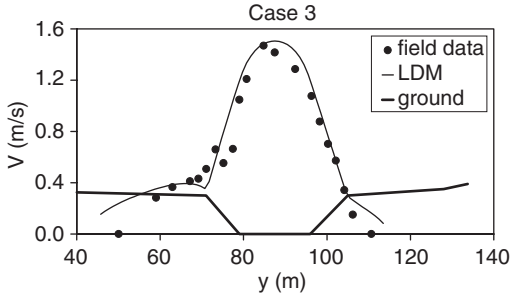


Figure 9. Lateral velocity distribution for Case 3 of River Severn as predicted by LDM.

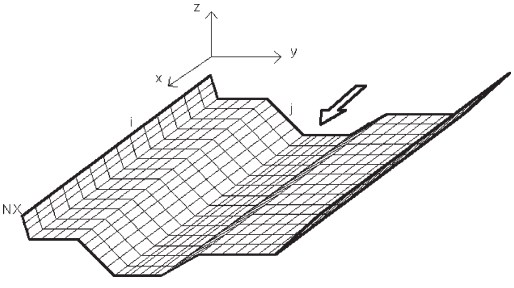


Figure 10. Finite-element mesh generated by software GEO.

Table 5. Mesh dimensions for SERC channel.

	No. of elements	No. of nodes
Group no. 1	4998	15317
Group no. 2	3213	9932

Table 6. Mesh dimensions for River Severn.

	No. of elements	No. of nodes
Case 1	5550	17025
Case 2	5550	17025
Case 3	4500	13861

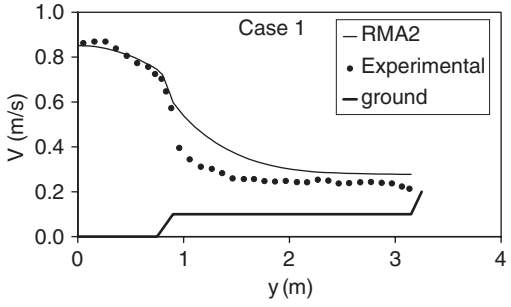


Figure 11. Lateral velocity distribution for Case 1 of SERC channel as predicted by 2D model.

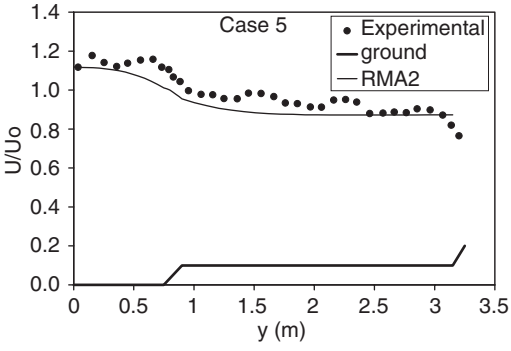


Figure 12. Lateral velocity distribution for Case 5 of SERC channel as predicted by 2D model.

The Δy step was different for the main channel, the banks and the floodplains. For the laboratory cases, Δy was 0.05 m for the main channel, 0.025 m for the banks and 0.1 m for the floodplains; whereas for River Severn cases, Δy was taken as 1.50 m for the main channel, 2 m the for banks and 4 m for the floodplains. With these selections, the resulting mesh dimensions are as shown in Tables 5–6.

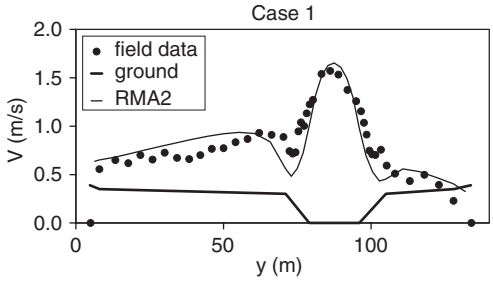


Figure 13. Lateral velocity distribution for Case 1 of River Severn as predicted by 2D model.

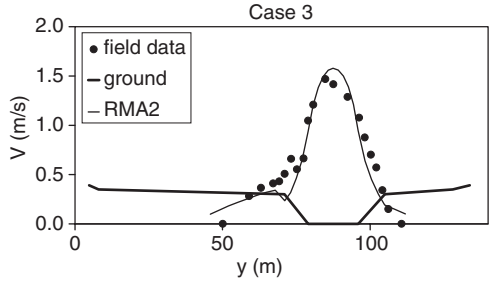


Figure 14. Lateral velocity distribution for Case 3 of River Severn as predicted by 2D model.

The turbulence parameter $E = \rho\varepsilon$ was correlated with parameter λ used in LDM model through Equation 15. For the laboratory cases, artificially high values of E were taken, in order to assure numerical stability. Values between 14.2 to 114.4 Pa · s were used for field data and 3 to 20 Pa · s for laboratory data. The known water level was imposed as the downstream boundary condition. Figures 11–14 show the lateral velocity distribution as calculated by RMA2.

5 MODELS PERFORMANCE

Absolute and relative performances of the used models are discussed next.

5.1 *DCM model*

The Divided Channel Method main limitation is associated to the absence of lateral momentum diffusion. As a consequence, the lateral velocity profile tends to copy the channel bottom form (see Figures 4–5). This limitation is particularly significant for skewed V-shaped sections, where diffusion plays an important role.

Another consequence of this lack of diffusion is that the lateral velocity distribution depends strongly on the discretization step. Specifically, it is better to minimize

the number of subsections considered, as recommended in HEC-RAS user's manual (HEC 2001), which constitutes a way of artificially smoothing out the profile.

For laboratory cases, the DCM model tends to overestimate main channel velocities and underestimate floodplain velocities. This anomaly increases as floodplain flow depth increases (see Figures 2–3).

5.2 *LDM model*

As was presented in early works (Shiono & Knight 1988, 1991), the LDM model adequately predicts the lateral velocity distribution, particularly for laboratory cases. Dispersion in the prediction of velocity profiles for natural rivers is a frequent feature, although there are some examples of very satisfactory applications of LDM model to natural streams (Weber & Tarrab 2003).

Additionally, LDM model results an adequate predictor of stage-discharge relation, as can be seen in Figure 15, related to Group A of laboratory cases. Weber (in press) shows an example of application of the LDM model to predict the stage-discharge relation for a natural stream.

Predictions are relatively insensitive to non-dimensional eddy viscosity values for the floodplains over a relatively large range (Weber & Del Prete 2003). On the contrary, main channel λ values are decisive to perform a good prediction.

5.3 *2D model*

RMA2 model shows limitations to predict the lateral velocity distribution for laboratory cases, due to excessive artificial eddy viscosity necessary to guarantee numerical stability, thus producing excessively smoothed-out profiles. This effect is more significant as floodplain depth decreases (see Figures 11–12).

This is not the case for field data comparisons (River Severn). Instead, the limitations are associated to assuming constant E values.

In contrast to the LDM model, RMA2 model is not a handy tool to predict stage-discharge relations in compound channels, due to the relatively large amount of time-machine necessary to perform the calculations.

5.4 *Relative performance of models*

Figures 16 and 17 show the lateral velocity distribution predicted by the three models considered in this paper, together with the experimental data, for Cases 4 and 7, respectively, of SERC channel. For common parameters, the same or equivalent values are assumed. It can be clearly noted the absence of diffusive effects in the DCM prediction, and, on the contrary, the excess of diffusion showed by the 2D model.

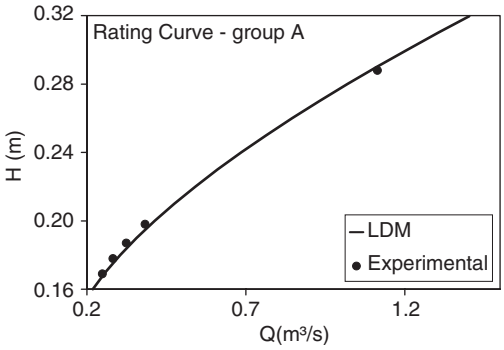


Figure 15. Rating curve for SERC channel. Group A cases.

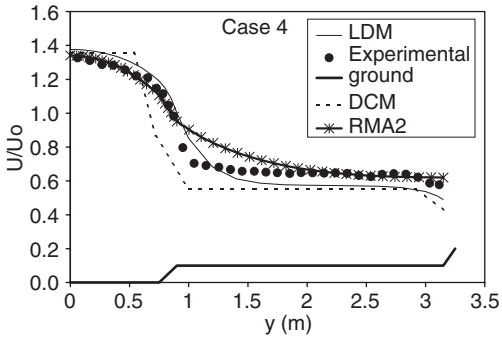


Figure 16. Comparison among DCM, LDM and 2D models predictions for Case 4 of SERC channel.

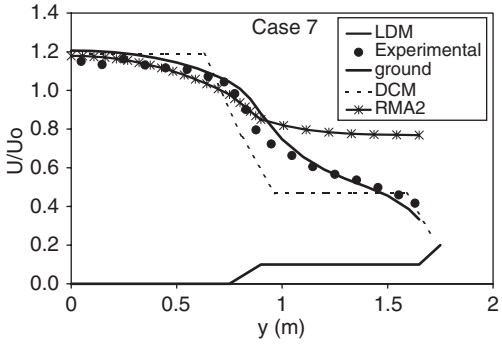


Figure 17. Comparisons among DCM, LDM and 2D models predictions for Case 7 of SERC channel.

With the DCM model, the velocities in the floodplain are usually better represented than in the main channel, where the models tend to give a more uniform profile. The calculation gets poorer as the water depth in the floodplain increases, and its use is not recommended for relative depths over about 0.4.

The LDM model has the possibility of considering the energy loss due to the vertical-axis eddies which develop in the shear layer between the main channel and the floodplain.

Additionally, LDM model can include a sink term to account for the longitudinal-axis eddies, known as secondary currents, which take place at the toe of the main channel bank, acting as an apparent shear stress at the main channel-floodplain interface (Wormleaton & Merrett 1990) and, hence, producing an additional and significant momentum transfer from the main channel to the floodplain. As a consequence, the LDM can provide a much better agreement, if properly tuned.

Regarding 2D-Horizontal models performance, it is shown that it is better for natural than for laboratory channels. In the last case, the difficulty lies in the fact that the artificial viscosity necessary to attain numerical stability (at least for RMA2) is usually higher than the physical eddy viscosity; hence, velocity gradients are smoothed out.

The agreement of this solution improves for higher floodplain water heights, and gets acceptable for relative depths over about 0.4, thus complementing with the DCM model. On the other hand, for natural channels the agreement is relatively satisfactory for the whole range of water depths.

In any case, 2D-Horizontal model could not match the LDM performance, and this is due to the fact that there is no formulation yet to account automatically for the effects of secondary currents at the toe of the main channel (RMA2 already includes an implementation of a parametric formulations to represent the effects of secondary currents in curved flow).

6 CONCLUSIONS

The main conclusions from the present work are the following:

- The DCM model (through software HEC-RAS), in spite of its simplicity, gives a reasonable prediction of the lateral velocity distribution from the engineering point of view.
- The main limitation of DCM model is associated to the absence of momentum lateral diffusion, which lowers precision specially in the calculated main channel velocity values.
- The LDM model adequately represents both the lateral velocity distribution and stage-discharge relation.
- 2D-Horizontal models performs better for natural than for laboratory channels. In the last case, the difficulty lies in the fact that the artificial viscosity necessary to attain numerical stability (at least for software RMA2) is usually much higher than the physical eddy viscosity; hence, velocity gradients are smoothed out
- For laboratory cases, the calculation with DCM gets poorer as the water depth in the floodplain increases, and its use is not recommended for relative depths over about 0.4. On the other hand, RMA2 results improve for higher floodplain water heights, and gets acceptable for relative depths over about 0.4, thus complementing with the DCM model.

ACKNOWLEDGMENTS

Authors would like to thank to Prof. Koji Shiono for providing his experimental data set. First author also acknowledges Science & Technology Secretary, University of Cordoba (Argentina), for support through its High Education Scholarship Program.

REFERENCES

Abril, B. 2003. *Benchmark comparisons of the analytical and finite element solutions of the SKM*. Technical Report EPSRC Research Grant – GR/R54880/01. University of Birmingham, UK.

Cunge, J., Holly, F. & Verwey, A. 1980. *Practical Aspects of Computational River Hydraulics*. Boston: Pitman.

Donnell, B. P. (ed.) 1996. *User's Guide to RMA2 WES version 4.3*, U.S. Army Corps of Engineers, Waterways Experiment Station, Hydraulic Laboratory.

Einstein, H. A. & Banks, R. B. 1950. Fluid resistance of composite roughness. *Transactions, American Geophysical Union* 31(4): 603–610.

HEC 2001. *HEC – RAS Hydraulic Reference Manual*, U.S. Army Corps of Engineers, Davis, CA.

Horton, R. E. 1933. Separate roughness coefficients for channel bottom and sides. *Engineering News Record* 111(22): 652–653.

Knight D. W., Shiono, K. & Pirt, J. 1989. Prediction of depth mean velocity and discharge in natural rivers with overbank flow. *Proceedings of the International Conference on Hydraulic and Environmental Modellling of Coastal, Estuarine and River Waters*: 419–428. Bradford.

Lotter, G. K. 1933. Soobrazheniia k gidravlicheskomu raschetu rusel s razlichnoi sherokhovatostiiu stenok (Considerations on hydraulic design of channels with different roughness of walls). *Izvestiia Vsesoiuznogo NuachnoIssledovatel'skogo Instituta Gidrotekhniki (Transactions, All-Union Scientific Research Institute of Hydraulic Engineering)* 9: 238–241. Leningrad.

Menéndez, A. 2003. Selection of optima mathematical models for fluvial problems. *Proceedings of 3rd IAHR Symposium on River, Coastal and Estuarine Morphodynamics.* Barcelona, Spain.

Pavlovskii, N. N. 1931. K voprosu o raschetnoi formule dlia ravnomernogo dvizheniia v vodotokahk s neodnorodnymi stenkami (On a design formula for uniform movement in channels with nonhomogeneous walls). *Izvestiia Vsesoiuznogo NuachnoIssledovatel'skogo Instituta Gidrotekhniki (Transactions, All-Union Scientific Research Institute of Hydraulic Engineering)*. 3: 157–164. Leningrad.

Shiono, K. & Knight, D. W. 1988. Two-dimensional analytical solution for a compound channel. In Y. Iwasa, N. Tamai & A. Wada (eds.), *Proceedings of 3rd International Symposium on Refined Flow Modeling and Turbulence Measurements:* 503–510. Tokyo, Japan.

Shiono, K. & Knight, D. W. 1991. Turbulent open-channel flows with variable depth across the channel. *Journal of Fluid Mechanics* 222: 617–646. Great Britain.

Wark, J. B., Samuels, P. G. & Ervine, D. A. 1990. A practical method of estimating velocity and discharge in a compound channel. In White, W. R. (ed.), *River flood hydraulics*: 163–172. Chichester, UK: John Wiley & Sons.

Weber, J. F. & Del Prete, P. 2003. Calibration and uncertainty analysis of parameters of analytical model for floodplain flow distribution. *Mecánica Computacional* 22. Bahía Blanca, Argentina: AMCA. In Spanish

Weber, J. F. & Menéndez, A. N. 2003. LATERAL model to predict lateral velocity distribution in natural streams. *Mecánica Computacional* 22. Bahía Blanca, Argentina: AMCA. In Spanish

Weber, J. F. & Tarrab, L. 2003. Modeling lateral velocity distribution in natural streams: case Parana river. *Mecánica Computacional* 22. Bahía Blanca, Argentina: AMCA. In Spanish

Weber, J. F. 2003. *1D–2D integrated modeling of floodplain flows*. M Sc thesis, University of Cordoba, Argentina. In Spanish.

This page intentionally left blank

River Flow 2004 – Greco, Carravetta & Della Morte (eds.)
© 2004 Taylor & Francis Group, London, ISBN 90 5809 658 0

The conveyance capacity of compound channels with large scale floodplain roughness

A.R. Heanen, W.R.C. Myers & J.F. Lyness
University of Ulster at Jordanstown, Belfast, UK

ABSTRACT: Accurate prediction of river conveyance during over-bank flow especially in the urban environment is a topic which is of increasing significance in today's society and is of interest to insurers and home owners alike. The problem has been investigated experimentally by means of a straight compound channel with large scale block roughness which simulates urban development on the floodplains. Asymmetric compound and simple channel geometries have also been investigated. Stage discharge relationships have been determined, together with 2D velocity distributions using a Nortek two dimensional Acoustic Doppler Velocimeter, for several roughness cases. The data has been analysed to yield zonal discharges and flow resistance characteristics as well as transverse velocity profiles. The research highlights the effects of large scale vorticity, previously unrecognised in floodplain research and goes on to review the suitability of using 1D roughness coefficients and draws conclusions as to the limitations of such methods in light of the present findings.

1 INTRODUCTION

Rivers represent one of mans most important assets, this being the case towns and cities have historically tended to develop on the banks of rivers. Much of this development has taken place within the confines of the rivers floodplains, leaving a legacy of what are often prime buildings liable to severe flooding. Often there is no viable way of preventing this flooding and engineers are left with the task of predicting the magnitude of the flood and the extremities of the area that will be affected in order to be able provide reliable advice to those occupying the affected buildings. This process of flood estimation is a very complex problem, with variables such as rainfall runoff rates requiring accurate prediction, in order to have a value of the discharge a river may have to accommodate.

Once the amount of water going into the river system has been calculated, a stage discharge relationship for the channel must be estimated in order that the level the water is going to rise to can be predicted. It is the estimation of such stage discharge relationships that this paper is primarily concerned with.

In the mid 1960s, first Sellin (1964) and then Zhelezenyakov (1965, 1971) reported the difficulties involved with discharge estimation in compound channels. Since then a wide range of methods have been suggested to estimate stage discharge relationships for rivers that have over-topped their main channel banks, inundating their floodplains. These range from one dimensional models, such as those suggested by Ackers (1991), Lambert and Myers (1998) to complex two and three Dimensional models, a summary of which has been given by Wright (2001). Due to the complexity of 2D and 3D models, the majority of river engineers still prefer to use the more simplistic 1D models.

Thanks to the large amount of empirical data relating to such models it is possible to generate accurate estimates for the majority of cases.

A large amount of empirical data relating to such models has been made available through the work that was undertaken at the UK Flood Channel Facility, HR Wallingford, England, the conception and nature of which are described by Knight and Sellin (1987). Wark et al (1994) present the data from phases A and B of this program in the form of a design guide for river engineers.

There is however a lack of empirical data relating to cases where urban development has taken place on the floodplain. Due to the large amount of urbanisation that has taken place on the banks of many rivers, it is obvious that this is an area that needs attention.

This paper presents data forming part of a large body of research that has been conducted at the University of Ulster with the aim of addressing this issue.

2 EXPERIMENTAL PROCEDURE

The Experiments were carried out in the Hydraulics Laboratory at the University of Ulster, Northern

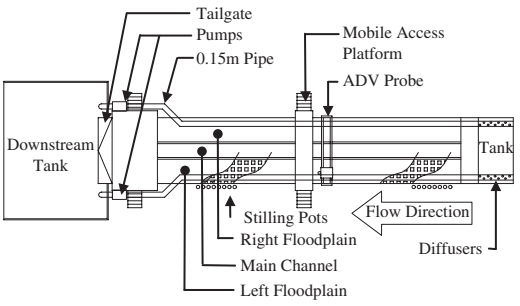


Figure 1. Schematic plan of the compound channel. NB: simple channel had same basic layout.

Ireland. Two main channel geometries were used:

1. An 18 m long compound channel: The basic channel geometry (Fig. 1) consisted of a straight main channel with symmetric floodplains. The trapezoidal main channel had a top width of 500 mm a bankfull depth of 50 mm and side slopes of 45°. The floodplains were each 700 mm wide; giving a total compound channel width of 1900 mm. Tapping points were located on the side slopes of the main channel at 1 m centers.
2. A 10 m long rectangular channel designed as a 1:1 scale of one of the compound channels floodplains. This provided a means of comparing the compound channel floodplain data with data from a floodplain not subject to interaction forces from the main channel flow. The geometry consisted of a 700 mm wide rectangular channel, with tapping points located in the centre of the channel at 1 m centers.

During the experiments discharge was measured using two electromagnetic flow meters. The channel bed slope (So) was 0.00185 in all cases. Uniform flow was ensured in all test series through control by a hinged weir across the full width of the channel. A minimum of three water surface profiles were measured for each discharge, two of which where of a lesser slope than the bed slope and one of which was of a greater slope than the bed slope. The correct tailgate setting was then found by plotting these slopes against the tailgate setting and casting a polynomial curve through them. The correct tailgate setting was then established from this curve. Water surface profiles were measured with pointer gauges in stilling pots connected to each of the tapping points. Flow velocities where measured using a two-dimensional side facing Nortek Acoustic Doppler Velocimeter (ADV). Flow patterns where investigated using dye injection and time lapse photography

Table 1 defines the channel geometries and roughness configurations investigated.

The roughness elements used were surface penetrating, 95 mm by 95 mm square blocks, 150 mm in height. They were placed square to the flow, 100 mm apart in both directions, as shown in Figure 2.

Table 1. List of series.

Series	Channel type	Schematic of roughness case
C1	Compound channel	
C2	Compound channel	
C3	Compound channel	
C4	Compound channel	
C5	Compound channel	
C6	Asymmetric compound channel	
C7	Asymmetric compound channel	
S1	Simple channel	
S2	Simple channel	
S3	Simple channel	
S4	Simple channel	
S5	Simple channel	

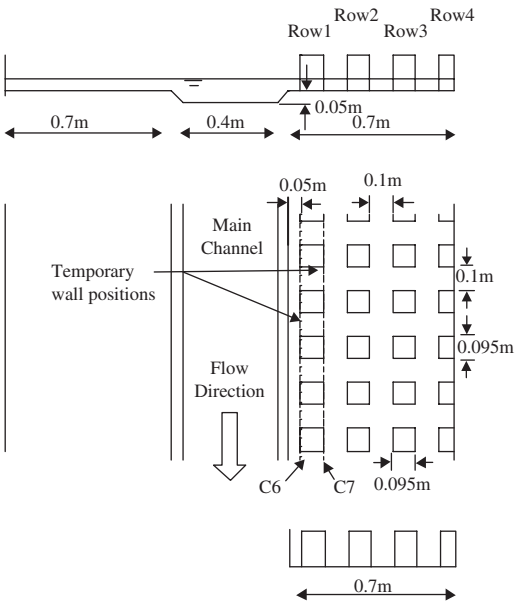


Figure 2. Channel geometry.

3 INTERPRETATION OF RESULTS

3.1 *Stage discharge analysis*

Table 2, summarises the discharge equations of the form $Q = C.D^E$ for each of the test series here presented. R^2 values have also been given for each of the test series. It can be seen that all R^2 values are better

Table 2. Values of discharge equation coefficients.

Series	C	E	R^2
C1	48.289	2.806	0.995
C2	6.4036	2.11	0.9968
C3	6.4248	2.103	0.9934
C4	7.2996	2.1111	0.9993
C5	11.982	2.3192	0.999
C6	10.012	2.2526	0.9965
C7	11.995	2.3345	0.997
S1	5.6419	1.8519	0.9948
S2	1.2865	1.5316	0.9949
S3	0.4368	1.3243	0.9993
S4	0.1892	1.2512	0.9988
S5	0.1708	1.3387	0.9984

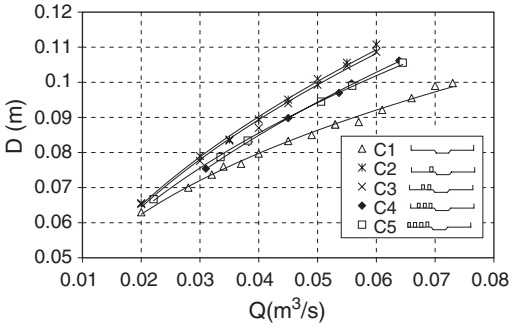


Figure 3. Influence of varying left floodplain roughness.

than 0.99, indicating the reliability of the results is quite high.

3.1.1 *Compound channel*

Figure 3 illustrates the influence of varying roughness on the left floodplain on the compound channel stage discharge relationship.

Comparing the discharge relationships for the smooth compound channel (Series C1) with that for the compound channel with a single row of roughness elements set 50 mm back from the main channel edge (Series C2), it can be seen that a significant reduction in discharge capacity is experienced. This is what would be expected from the presence of large scale roughness in this vicinity of the channel, as when placed here the roughness elements cause turbulence in the area most significant to the total compound channel discharge (i.e. the main channel) This turbulence acts to significantly reduce the mean downstream velocity (as can be seen in Fig. 10). When the second row roughness elements is added (Series C3) there is little variation in the stage discharge relationship, however, there does appear to be a slight increase in discharge capacity. This is not as expected, as the blockage area has been increased by the presence of the second row of roughness elements and the area affected by turbulence has also been increased by its presence.

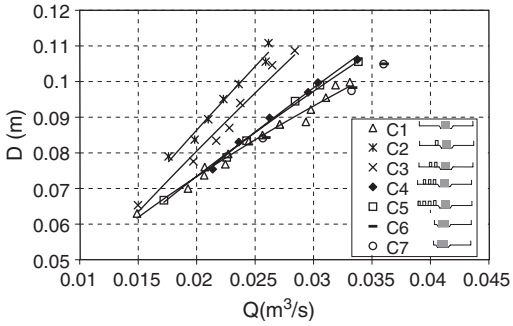


Figure 4. Main channel stage discharge diagram.

When the third row of roughness elements are added (Series C4) the discharge capacity can again be seen to increase and this time the increase is quite significant. This is unexpected as both the blockage area and the area of the floodplain subject to high turbulence levels have been increased. Obviously the compound channel is not behaving as expected. The increase in the compound channel discharge capacity would appear to be attributed to the un-roughened portion of the channel becoming more hydraulically efficient as roughness is added behind the initial row of roughness elements. Consideration will now be given to the elemental stage discharge diagrams in order to confirm this.

3.1.2 *Zonal stage discharges: main channel*

Figure 4 above shows the stage discharge relationships for the main channel. The trend noted in the whole channel results, of a reduction in capacity when the first row of roughness elements is added followed by incremental increases in capacity as rows of roughness elements are added behind the initial row can be seen to be repeated here, however the increases are more pronounced. This would point to the fact that increases in the discharge capacity of the main channel plays quite a significant role in the whole channels discharge capacity increasing.

The increase in discharge capacity which occurs between series C2 and C5 can be seen to result in the main channel being almost as efficient as for the smooth channel case.

It is clear from these results that as the number of rows behind the initial row of roughness elements is increased the main channel is becoming more efficient. The proposed reason for this is that a reduction in turbulence is caused by the presence of the additional rows of roughness elements behind the initial row. Section 4 below considers the cause of this.

In series C6 and C7 the left floodplain is blocked. Series C6 approximately conforms to the discharge

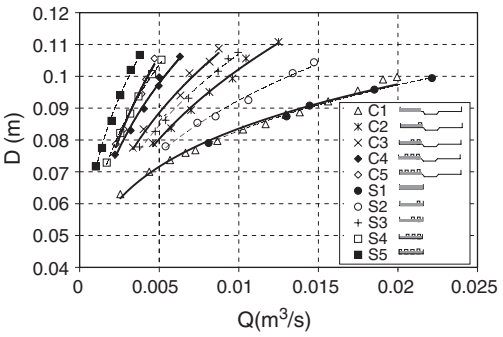


Figure 5. Left hand floodplain stage discharge diagram.

data for the smooth case. This is as would be expected, as a smooth wall set at the main channel face of the roughness elements is used to block flow down the left hand floodplain, no turbulence would then be caused to slow down the main channel flow.

Series C7 also appears to conform to the discharge data for series C6 but this is not what was expected as the wall baffling the left hand floodplain has this time set behind row 1 of roughness elements, leaving row 1 exposed to the flow. It would therefore have been expected that the main channel discharge would have been reduced slightly by turbulence caused by the presence of the roughness elements. This is not the case however as can be seen from Figure 4, although at first this result seems slightly ambiguous, it can be explained by considering secondary flow structures discussed below in Section 4.

3.1.3 *Zonal stage discharges: left (roughened) floodplain*

Figure 5 presents stage discharge relationships for the roughened, left hand, floodplain. Also shown are measurements taken in the 700 mm wide simple channel indicated by dashed lines l. The simple channel results have the purpose of providing data for a non interacting floodplain, in order to determine the effect, main channel/floodplain interaction has on the discharge characteristics of the floodplain.

Considering the interacting roughened floodplain it can be seen that, as expected the discharge capacity is reduced as the number of roughness elements is increased. The most pronounced reduction being that which takes place when the first row of roughness elements is added, It can also be seen that the stage discharge relationship for series C2 has a greater gradient than that of series C1. This is due to the increase in turbulence as the water depth increases.

Comparing the stage discharge relationships obtained in series C1–C5 it can be seen that the reduction between series C2 and C3 is of approximately equal magnitude to the reduction between series C3 and C4. When the half row of roughness elements is added (Series C5) the magnitude of the reduction is approximately a half of the previous reductions when rows of full roughness elements were added.

Considering the simple channel results it can be seen as expected, that the discharge capacity of the channel is reduced as the number of rows of roughness elements is increased. In this case however the reduction in capacity is quite regular from the addition of the first row, whereas in the interacting floodplain case the first row of roughness elements caused a much more pronounced reduction in discharge capacity.

Figure 5 shows that as expected the interacting and non-interacting smooth channel stage discharge relationships lie approximately on top of one another. This helps to clarify the accuracy of the results and illustrates that the two channels are directly comparable.

Figure 5 also shows that the interacting floodplain is significantly less efficient than the non interacting floodplain, Indeed for any given discharge the increase in stage experienced in the interacting floodplain would appear to be almost twice that experienced in the non-interacting floodplain.

When the second row of roughness elements is added however the reduction in the discharge capacity of the non-interacting floodplain is larger than that of the interacting floodplain. While this is true, it is still seen however that the non interacting floodplain is more efficient than the interacting floodplain.

When the third row of roughness elements is added again a larger reduction occurs in the non interacting floodplain than occurs in the interacting floodplain. The larger reduction in the non interacting floodplain this time results in its becoming less efficient than the interacting floodplain with the same roughness present.

When the row of half roughness elements is added to the two channels (Series C4 and S4) the reduction in the capacity of the non interacting floodplain is greater than the reduction experienced in the interacting floodplain.

The difference in the way the interacting and the non-interacting floodplains react to the presence of rows of roughness is something which is significant. It is obvious that interaction with the main channel remains greatly significant even at maximum floodplain roughness This contradicts the intuition that as roughness increased the interaction effects would become less apparent.

3.1.4 *Zonal stage discharges: right (un-roughened) floodplain*

Figure 6 illustrates how variations in the roughness on the left floodplain affect the discharge capacity of the right floodplain, which has not undergone any variation in roughness. The variations apparent on Figure 6 are therefore due to momentum transfer. It would be expected that the stage discharge relationships would

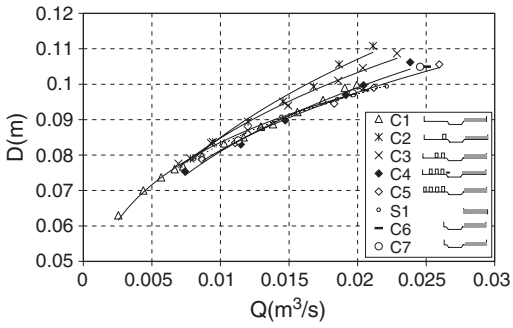


Figure 6. Right hand floodplain stage discharge diagram.

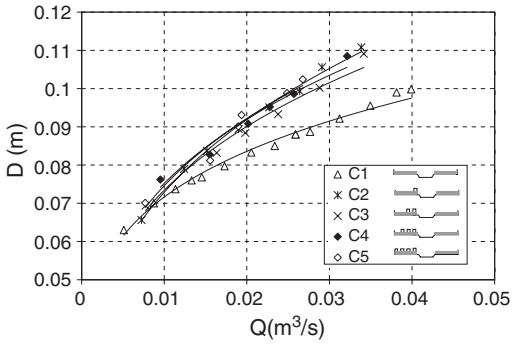


Figure 7. Combined floodplain stage discharge diagram.

act in a similar manner to those found for the main channel Figure 6 shows that when the first row of roughness elements is added (Series C2) the discharge capacity of this floodplain reduces considerably. At low depths this reduction is not so apparent but as the stage increases the reduction in capacity becomes more and more prominent.

When the second row of roughness elements is added the discharge capacity of this floodplain improves marginally, as was the case in main channel. The third row of roughness elements causes another improvement in this channels discharge capacity. Figure 6 shows that the stage discharge relationship recorded for this floodplain when 3 rows of roughness are present on the opposite floodplain is approximately concurrent with that recorded for it when the opposite floodplain was smooth. This is what would be expected, considering the very minor difference in the stage discharge relationships in the main channel.

Considering the stage discharge relationships diagrams obtained for the case where the left floodplain is completely blocked (Series C6 and C7). Figure 6 shows that series C6, which has a smooth wall placed 50 mm back from the main channel approximates the stage discharge relationship of series C1, C4 and C5.

Figure 6 also shows that the stage discharge relationship curve for series C7 lies approximately on top of that relating to series C6, This is as would be expected given the main channel acts in a similar manner .

3.1.5 *Zonal stage discharges: floodplains*

Figure 7 shows the stage discharge analysis for the two floodplains. The discharge capacity can be seen to reduce significantly when the first row of roughness elements is added. The addition of the second row of roughness elements produces an increase in discharge capacity. If we bear in mind that the left hand floodplains discharge capacity reduces when the second row is added (as seen in Fig. 5) it is evident that the discharge increase in the right hand floodplain (noted in Fig. 6) is greater in magnitude than the reduction in the left hand floodplains and actually acts to improve

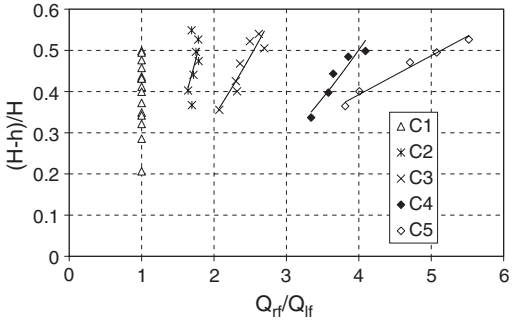


Figure 8. Qrf/Qlf vs. relative depth for the straight compound channel.

the over all discharge capacity. This then shows that overall the discharge capacity of the floodplains is actually improved by the presence of a second row of roughness elements behind an existing row at the main channel edge.

When the third row of roughness elements is added (Series C4) the discharge capacity is seen to reduce somewhat, however the floodplains remain more efficient than was the case in series C2. The addition of the row of half roughness elements (in Series C5) has no discernable impact on the discharge capacity of the floodplains.

3.2 *Roughened/un-roughened floodplain ratios*

Figure 8 illustrates how the contribution of the left and right hand floodplains vary with depth as well as roughness.

As expected Figure 8 shows the Q_{rf}/Q_{lf} ratio increasing as roughness is added and the contribution of the roughened floodplain reduces. Considering the case were just one row of roughness elements is present on the left floodplain, Figure 8 shows that the ratio remains approximately constant with depth.

When the second row of roughness elements is added the ratio increases quite significantly with depth

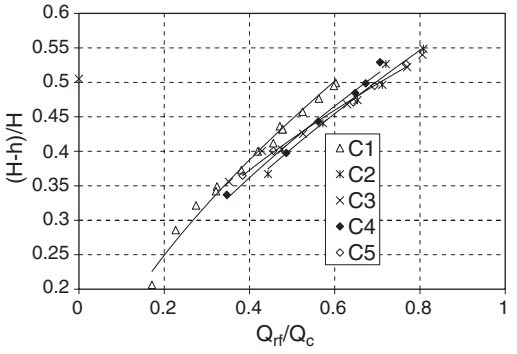


Figure 9. Q_{rf}/Q_c vs. relative depth for the straight compound channel.

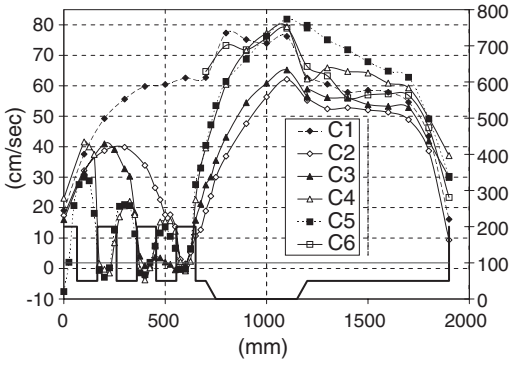


Figure 10. Cross sectional velocity profiles (Water depth = 99 mm).

from around 2 at a relative depth of around 0.35 to around 2.7 at a relative depth of about 0.55. When the third row of roughness elements is added the increased significance of the right hand floodplains contribution is apparent by the quite large increase in the Q_{rf}/Q_{lf} ratio. The addition of the row of half roughness elements can be seen to cause a further increase in the ratio, although lesser in magnitude than the previous.

Figure 9 illustrates how additional roughness affects the ratio of the Q_{rf}/Q_c, ie the ratio of the un-roughened floodplain discharge to the main channel discharge. As expected the floodplain becomes more significant as depth increases. The initial row of roughness elements causes an increase in the Q_{rf}/Q_c ratio, indicating that the right- floodplain's contribution to the total flow in the un-roughened channel is increased when roughness is added to the left hand floodplain. This is as would be expected if we consider what is happening in this portion of the compound channel. The main channel discharge is reduced with the addition of the first row of roughness elements. The right hand floodplain discharge is also reduced indicating that turbulence is carried over to the right hand floodplain from the left hand floodplain. Obviously the turbulence will have been retarded somewhat before it reaches the right hand floodplain and therefore the reduction in the right hand floodplain would be expected to be less than the reduction in the main channel, a fact indicated by the Q_{rf}/Q_c ratio increasing.

When the second row of roughness elements is added it can be seen that the ratio again increases somewhat at high relative depths, with subsequent rows of roughness elements causing little variation in the ratio.

3.3 *Velocity profiles*

3.3.1 *Symmetric compound channel*

Figure 10 presents depth averaged cross sectional velocity profiles obtained at 40% depth for the compound channel. The normal depth is constant at 100 mm for all roughness cases illustrated. In the smooth boundary case the floodplain velocity increasing as it approaches the faster moving main channel. The velocity then steps up as the water depth suddenly changes before stepping down again in a symmetrical fashion at the right hand bank of the main channel.

When a single row of roughness elements is added (Series C2) the velocity in the roughened left hand floodplain does not increase as it approaches the main channel, rather it is reduced, forming a velocity profile between the row of roughness elements and the left hand floodplain wall, rather like that you would expect to find in a simple channel. The velocity in the main channel is reduced significantly in series C2 peaking at around 0.62 m/s, around 20% less than the peak experienced in the series C1. The peak velocity now occurs in the proximity of the main channel edge, the step then experienced between the main channel and the right hand floodplain is much less pronounced than that experienced in the series C1. The velocity profile in the right floodplain runs approximately parallel to the that measured in the smooth channel, but at around 15% less.

Considering the measured velocity profile for the compound channel with two rows of roughness elements (Series C3), Figure 10 shows that the peak velocity experienced in the left floodplain between the floodplain wall and the row of roughness elements is approximately equal to that experienced in the same place when only 1 row of roughness elements was present. The velocity then reduces sharply about 150 mm before the edge of the row of roughness elements.

The sharp reduction in velocity between the peak velocity and the low velocities inline with the roughness elements is notable when it is compared with the increase in velocity in the same area when only one row of roughness elements is present. The increase recorded when two rows of roughness elements are

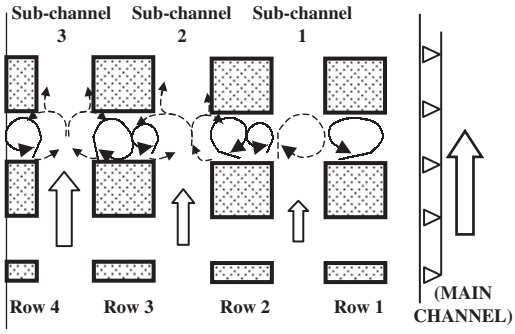


Figure 11. Vortices trapped between the roughness elements.

present is more akin to what would be expected from a smooth boundary.

The velocity in between the two rows of roughness elements can be seen to be very low. The velocities in the main channel and right hand floodplain run parallel with those recorded for the series C2 at around 3 cm/sec faster.

The velocity profile recorded when 3 rows of roughness elements were present (Series C4) appears to indicate that the maximum velocity behind the roughness elements occurs quite rapidly. It appears also that the maximum velocity recorded on the floodplain is again similar in magnitude to that recorded for series C2 and C3. Comparing the peak velocities between rows 1 and 2 and rows 2 and 3 and those behind row 3 there appears to be a stepped increase as distance from the main channel increases.

This phenomenon was not predicted, although it would fit in well with the hypothesis of secondary flow structures being set up between the roughness elements (see Fig. 11).

The velocity in the main channel for series C4 appears to peak at around the vicinity of the main channel right hand bank. The peak velocity on this occasion is seen to be approximately equal to that recorded in the main channel for the smooth floodplain case. The velocity profile goes through a transition stage similar to that experienced in the smooth case as the water depth reduces coming onto the right hand floodplain. The right hand floodplain velocities again run approximately parallel with those recorded for the smooth case (Series C1) but at around 0.7 m/s faster.

When the row of half roughness elements is added (Series C5) at the left hand floodplain wall, it would appear that the secondary flow structures are completely stabilised. The stepped increase in velocities occurring between the rows of roughness elements is again apparent on the left hand floodplain, this time quite a regular increase appears to have occurred.

The maximum velocity in the main channel has been offset to the right bank of the main channel, and as was the case when three rows of roughness elements where present, The maximum velocity occurring is slightly greater than that which occurred in the smooth case. The expected transition in velocity between the main channel and the floodplain does not occur; instead the high velocities carry over into the floodplain, resulting in a velocity profile similar to what would be expected at much deeper flow depths, when the compound channel begins to act as a single channel.

3.3.2 *Asymmetric compound channel*

Figure 10 shows that the velocity profile for the asymmetric channel with a smooth wall baffling the left hand floodplain (Series C6) approximates to that recorded for the symmetric channel when no roughness was present on the left hand floodplain. The same is true for series C6. The velocities occurring in the main channel when 3.5 rows of roughness are present are slightly higher than these. This indicates that not only do the secondary flow structures set up between the roughness elements cause an effective 'hydraulic smoothing' of the row of roughness elements they also appear to cause an acceleration of the flow near the unroughened floodplain edge. This acceleration may be caused by the flow structures somehow acting to linearise the flow paths of the water particles in the main channel or vortices between the roughness elements may act to speed up the water. It must be borne in mind when reading the results that the velocity profile comparison in Fig. 10 is for a relative depth of around 0.5. At lower depths the velocity profile obtained for 3.5 rows of roughness elements does go through a transition stage between the main channel and floodplain.

4 COMMENT

The results presented in the previous section highlight behavior which was not predicted at the outset of the experimental program. When a single row of roughness was added to the compound channel, it significantly reduced the channels discharge capacity. The magnitude of the reduction in capacity was greater than that which was expected.

The elemental stage discharge relationships indicated that the roughness elements not only reduced the capacity of the floodplain they were present on, but actually reduced the capacity of the main channel as well as the un-roughened floodplain.

The cross sectional velocity profile illustrates how the reduction in capacity is spread across the channel. The velocity in the portion of the left hand floodplain which is behind the roughness elements is reduced from what was recorded in that area when the floodplain was smooth. This is what was expected, as

turbulence in the area would be expected to have increased.

When a row of roughness elements is added behind the roughness elements there is a slight increase in discharge capacity overall as can be seen in Figure 3. Figures 4 to 9 show that this increase in discharge capacity is attributable to the main channel and the right hand floodplains discharge capacity increasing. Figure 7 shows that the floodplain on which the roughness elements are actually placed reduces in discharge capacity as would be expected, however the reduction in the capacity of the left hand floodplain when row 2 was added is only about a half of the reduction in the capacity experienced when row 1 was added. The increase in capacity in the main channel and left hand floodplains are greater in magnitude however and overall the result is that the compound channel is more efficient.

When the third row of roughness elements is added the increase in the discharge capacity of the compound channel is much greater. The elemental stage discharge relationships show that the roughened floodplains reduction is similar to that experienced when the second row of roughness elements was added, however the increase in the capacity of the main channel and right hand floodplain is much more significant than that experienced when row 2 was added.

The addition of the half row of roughness elements has little impact on the main channels discharge capacity however it causes a slight increase in the capacity of the right hand floodplain. The left hand floodplains capacity is reduced slightly, as expected.

5 VORTICITY

It would appear from the behavior of the main channel that as rows of roughness elements are added behind the initial row the turbulence in the main channel is reduced. It may be assumed therefore that the presence of rows of roughness behind the initial row causes an effective hydraulic smoothing of the 'surface' of the row of roughness elements. The reason for this 'hydraulic smoothing' may be that eddy structures are developed between the roughness elements, as shown in Figure 11 below

It would be reasonable to assume that the size of the vortex developed either side of the block depends on the velocity differential, ie: if the velocity of the water at side 1 is significantly lower than the velocity of the water on side 2, then the vortex that is developed on side 2 will be much larger than that which is developed on side one. The larger and stronger the vortex developed, the smoother the side will effectively become.

Figure 12 below illustrates a possible mechanism of vortexes, based on the principles highlighted in Figure 11 above. Figure 12 represents the case when 3.5 rows of roughness elements are in place.

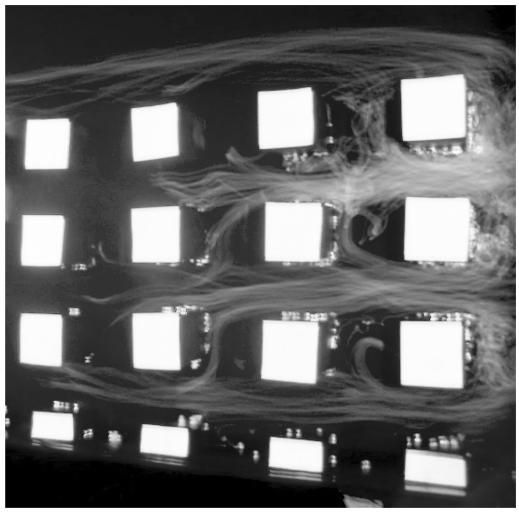


Figure 12. 10 Second exposure of water surface floats traveling downstream between roughness elements.

The arrow size used in the Figure 11 represents the velocity magnitude in each of the sub channels. The fast moving main channel on the right of row 1 causes quite a large, strong vortex to develop between the roughness elements of row 1. This causes the right hand surface to be 'hydraulically smoother' for the water in the main channel, by reducing or preventing water from the main channel being drawn in between the roughness elements, as well as reducing the amount of outflow from the floodplain into the main channel between the roughness elements. This then permits the flow paths of the water particles therein to linearise.

Because the vortex on the right side of row one is so strong, it only permits a small vortex (or perhaps none at all) to develop on the left hand side, meaning that the surface of the roughness elements is 'hydraulically rougher' on the right side of sub-channel 1 (Fig. 11).

Because this is the case, then the vortex developed at the left side of sub-channel 1, is also weak, due to the low velocities caused by the right hand side. Hence the vortex at the left side of row 2 has more chance to develop, resulting in a smoother surface on the left of row 2, allowing the velocity in sub-channel 2 to develop slightly higher. Sub-channel 3 develops to a still higher velocity via a similar process.

Surface floats and dye injection techniques were used to try to capture the above vortex structures. Figrue 12 is an image of luminous floats traveling down the roughened floodplain. The image was captured over a ten second time period. The variation in the velocity of the three sub-channels is apparent in the picture by the variation in the distance traveled downstream in each of the sub channels over the 10 second time period. Some indication of the eddy structures

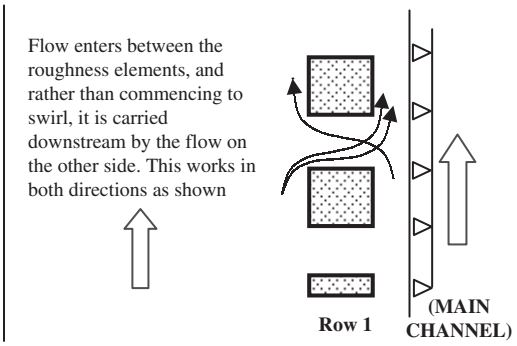


Figure 13. Schematic of flow interaction between main channel and floodplain, when 1 row of roughness elements is in place at the main channel edge.

can also be seen, as well as some interchanging of flow between the sub-channels.

Video was also used to capture the patterns of the floats flow paths. Analysis of these indicates that there are secondary flow patterns within the sub-channels themselves (indicated by the dashed vortices in Fig. 11). These secondary flow patterns would act to stabilize the vortex structures between the roughness elements, preventing the flow in the faster moving main channel from destructing the vortex structures as occurs when a single row of roughness elements is present (see Fig. 13 above).

Flow visualization indicates that there is mass transfer between the roughness elements in both directions when only one row of roughness elements is present on the floodplain, as shown in Figure 13 above, although most transfer seemed to be taking place from the floodplain to the main channel, indicating that the main channel was effectively sucking the slower moving water in the floodplain into itself. This obviously would cause turbulence on both sides of the roughness elements. When only one row of roughness elements was in place irregular, unstable 'gushing' was observed between the roughness elements, also pointing to flow structures such as the above.

6 CONCLUSIONS

1. When a single row of roughness elements is added beside the main channel a significant reduction of around 20% in the capacity of the compound channel is observed.
2. When subsequent rows of roughness elements are added behind the initial row of roughness elements it has a positive effect on the compound channels discharge capacity.
3. The rows of roughness cause significant effects on conveyance in all zones of the compound channel, not just the floodplain upon which they are placed.
4. The discharge capacity of the floodplain which has roughness added to it reduces as the number of rows of roughness increases
5. The discharge capacity of the main channel and the un-roughened floodplain increase when additional rows of roughness are added behind the initial row.
6. The reduction of capacity in the roughened floodplain appears to be approximately equal to the increase in capacity in the un-roughened floodplain when rows of roughness are added behind the initial row of roughness, resulting in the combined floodplain stage discharge diagram showing little variation when rows of roughness are added.
7. A stepped velocity increase with distance from the main channel is observed between the rows of roughness elements.
8. Flow visualization techniques have been employed and suggest the development of vortices between the roughness elements.
9. Conventional 1D discharge estimation methods take no account of the phenomena here reported.
10. An explanation of the behavior of the channel has been suggested which will require further investigation.

NOMENCLATURE

A – Cross sectional area
d – Floodplain depth
D – Total depth
V – Velocity
Q – Total discharge
Q_c – Main channel discharge
Q_{lf} – Left floodplain discharge
Q_{rf} – Right floodplain discharge
Q_f – Combined floodplain discharge

REFERENCES

Ackers P., 1991 Hydraulic design of straight compound channels, Report no. SR281, October, HR Wallingford Ltd.

Knight D.W., Sellin R.H.J., 1987 The SERC Flood Channel Facility, *Journal of the institution of water and environmental management*, London, vol.1, no. 2, pp198–204.

Lambert M.F., Myers W.R.C., 1998 Estimating the discharge capacity in straight compound channels, *Proceedings of the Institution of Civil Engineers: Water, Maritime and Energy,* June, vol. 130, pp 84–94, paper 11530.

Sellin R.H.J., 1964 A laboratory investigation into the interaction between flow in the channel of a river and that over its floodplain. La Houille Blanche, Grenoble, vol. 7, 793–801.

Wark J.B., James C.S., Ackers P., 1994 Design of Straight and Meandering Compound Channels, R & D Report 13, National Rivers Authority Bristol.

Wright N.G., 2001 Conveyance Implications for 2-D and 3-D Modeling. Scoping Study for reducing uncertainty in river flood conveyance, A report Prepared for HR Wallingford and the Environment Agency.

Zhelezenyakov G.V., 1965 Relative Deficit of mean velocity of instable river flow, kinematic effect in river beds with floodplains, Proceedings of the 11th international congress of the association for hydraulic research, Leningrad, USSR.

Zhelezenyakov G.V., 1971 Interaction of channel and floodplain streams, proceedings of the 14th international congress of the association for hydraulic research, Paris, France, August, vol. 5, pp144–148.

River Flow 2004 – Greco, Carravetta & Della Morte (eds.)
© 2004 Taylor & Francis Group, London, ISBN 90 5809 658 0

A study of turbulent flow structure in a partly vegetated river reach

T. Sukhodolova, A. Sukhodolov & C. Engelhardt
Institute of Freshwater Ecology and Inland Fisheries, Berlin, Germany

ABSTRACT: The development of macrophytes in rivers modifies hydrodynamic variables and complicates prediction of retention of particulate organic matter in fluvial systems. The paper presents some results of a field study designed to explore distribution of turbulence characteristics in a cross-section of a low land river partly inhabited by submersed macrophytes. The analysis is focused on applicability of semi-analytical solutions to describe spatial structure of the flow as a combination of simple flow models. Particular, it is shown that flow in macrophyte stands can be described by the mixing-layer model, while between the stands the flow approaches conventional logarithmic law. A comparison with the flow non-affected by vegetation is also presented and the differences quantitatively evaluated.

1 INTRODUCTION

Although freshwater macrophytes colonizing small lowland rivers produce considerable biomass – a source of fine particulate organic material utilized by invertebrates (Cushing & Allan 2001), the role of macrophytes in ecosystems is generally associated with their effect on river flow and habitats of sundry species of the aquatic life (Carpenter & Lodge 1986). A quantitative assessment of the effects of macrophytes represents therefore a challenging task for ecologists, river practitioners, and the community of hydrodynamic scientists (Denny 1988; Nepf 1999; Righetti & Armanini 2002). Numerous difficulties make the field studies scarce and the quantitative methods are mainly developed in laboratory flume studies (Stephan & Gutknecht 2002). Therefore application of methodological approaches always requires verification and adaptation to the conditions of natural streams and is presently precluded by the lack of field data.

Macrophytes form patchy patterns composed of stands variable in dimension and locality, having well defined margins leading to the development of significant gradients in flow velocities. Within the stands the flow is reduced due to the shading by stems and leaves of plants and hence the sedimentary deposition processes are enhanced. Spatially the stands are separated by areas of free flowing water that promote active transport of bedload (Sand-Jensen & Pedersen 1999). The patchiness of spatial patterns and spatial variety in species composition of stands are prominent properties differentiating flows in natural streams from their laboratory surrogates.

Complexity of the spatial patterns results in the subsequent complexity of flow patterns that absorb wakes behind stands, internal boundary layers developing over plant canopies on the general pattern of the open-channel flow (Nezu & Nakagawa 1993). Because the quantitative assessment of those flow patterns (wakes, mixing and boundary layers) requires consideration of turbulence characteristics (Nepf 1999), the field study's design should consider the measurements of turbulence characteristics and turbulent stresses as the most essential variable. Unfortunately available field studies are limited to the measurements taken on some verticals along the stand's length and provide only turbulence fluctuations as the measure of turbulence (Sand-Jensen & Pedersen 1999).

Theoretical basis for assessment of peculiarities of velocity field in geophysical flows is provided by the logarithmic law

$$\frac{\overline{U}(z)}{U_*} = \frac{1}{k}\ln\left(\frac{z}{z_0}\right) \tag{1}$$

where $\overline{U}$, U_* = mean and shear velocity respectively, k = constant, z = vertical coordinate originating at bed, and z_0 = hydrodynamic roughness. For flows over vegetation equation (1) is modified by the introduction of displacement height δ (Figure 1).

$$\frac{\overline{U}(z)}{U_*} = \frac{1}{k}\ln\left(\frac{z+\delta}{z_0}\right) \tag{2}$$

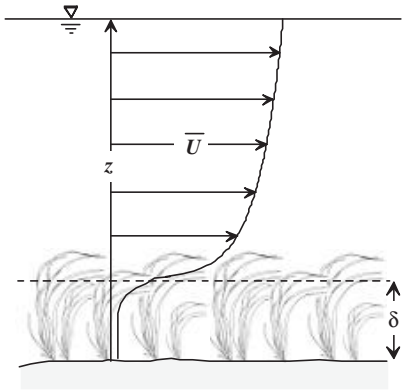


Figure 1. Scheme of the flow over vegetation.

In the laboratory flows the thickness of macrophyte layers is preserved to be small compared to the total flow depth, thus favoring the application of equation (2). However, the height of macrophyte stands in natural streams may reach the values comparable to the local depth of the flow, consequently making (2) insufficient if not inapplicable. Raupach et al. (1996) have suggested using mixing layer analogy for the flow inside and on the upper edge of the vegetation canopy and consequently the mean velocity profile can be described as (Michalke 1965)

$$\frac{\overline{U}(z)}{U_s} = 1 + \tanh\left(\frac{2z}{\delta}\right) \tag{3}$$

where $U_s = \Delta\overline{U}/2$, $\Delta\overline{U}$ = difference in the mean velocities across the mixing layer. Application of equation (2) to the river flow conditions requires knowledge of shear velocity, then hydrodynamic roughness can be evaluated by fitting the measured velocity profile. Local shear velocity value can be estimated only from the measured distribution of turbulence stresses since in the spatial complex flow with vegetation its value is supposed to deviate substantially from the value corresponding to the uniform flow condition

$$U_* = \sqrt{ghS} \tag{4}$$

where g = gravity acceleration, h = mean flow depth, and S = slope of the free surface. Close examination of turbulence characteristics and their comparison with the typical distributions in mixing layers are also required for equation (3) which has not yet been so popular as equation (2) in river flow applications.

Developments in the acoustic methods for measurements of turbulence characteristics (Kraus et al. 1994) and their success in river flow applications (Sukhodolov et al. 1998; Rhoads & Sukhodolov 2001) inspire to perform advanced field studies. This paper represents some results of a study conducted: i) to explore spatial structure of the flow in a partly vegetated channel of lowland river; ii) to verify applicability of the conventional logarithmic law (equation (1)), modified logarithmic law (equation (2)), mixing layer analogy (equation (3)); and iii) to portray the spatial patterns of turbulence characteristics in the cross-section of the river and relate them to the integral characteristics of mixing and hydraulic retention.

2 FIELD MEASUREMENTS

2.1 *River reach*

The study is based on turbulence measurements carried out in the Spree River near the village of Freienbrink, 10 km east of Berlin, Germany. In the study reach the channel is straight with stonearmored banks and with a bed covered by sands of about 1 mm mean diameter. Measurements were performed in July 2000 at water discharge of 3.25 m^3/s that provided following bulk characteristics of the flow: mean velocity 0.19 cm/s, river width 20.6 m, averaged depth 0.83 m, free surface slope 1.18×10^{-4}, Froude number 0.07, Reynolds number 0.2×10^5, shear velocity according to (4) 3 cm/s. The typical macrophytes in the study reach were *Sagittaria Sagittifolia, Potamogeton Crispus, and Ceratophyllum Demersum* (Figure 2).

2.2 *Measuring system and equipment*

Instantaneous velocities were recorded in this study with the acoustic doppler velocimeters (ADV) manufactured by Sontek, Inc. ADV consists of a field probe connected to splash-proofed electronics. The probe has a sampling volume of 0.125 cm^3 located 10 mm from the probe head. The resolution of ADV is 0.1 mm/s with a noise level of 1% of the velocity range at sampling frequency of 25 Hz. The probe was mounted on a special tripod (Figure 3) enabling accurate vertical alignment of the device and preventing the flow-induced vibration. Alignment of the probe, positions of the vertical profiles, and determinations of the water slope were performed with a laser total station.

2.3 *Measurements and data processing*

Velocities were measured at 10 vertical profiles uniformly spaced across the river width. Eight velocity profiles included 5-point measurements over the local depth and two profiles comprised of 12 points each. The time of velocity recording was 3 minutes, providing sufficient accuracy for computing turbulence characteristics (Sukhodolov et al. 1998).

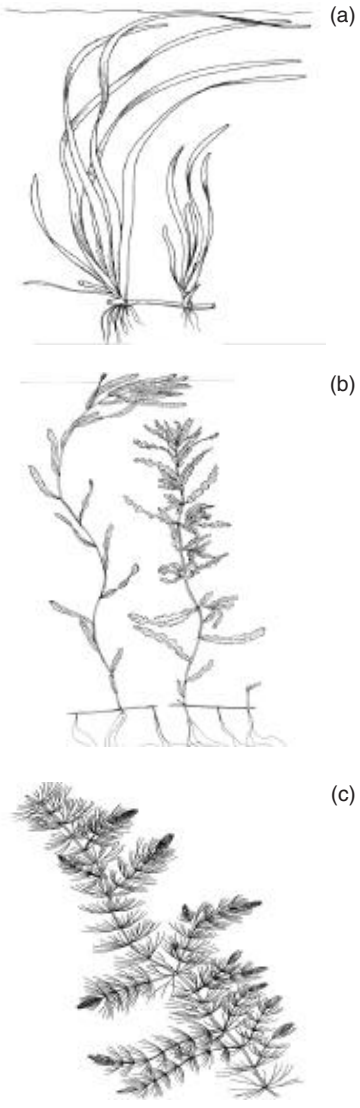


Figure 2. *Sagittaria Sagittifolia* (a), *Potamogeton Crispus* (b), *and Ceratophyllum Demersum* (c).

Time series of velocity measurements were inspected visually during sampling to identify obvious errors, such as systematic acoustic noise caused by leaves of plants on the sampling volume of sensor or the sensor itself. When necessary, the sampling duration was increased to obtain a clean record of data. The effect of doppler noise was evaluated by placing the probe in a bucket of still stream water, obtaining velocity measurements over an appropriate sampling interval (Nikora & Goring 1998). These tests indicated that the variance of acoustic noise for each velocity component is a least 2 orders of magnitude less than the variance of



Figure 3. The ADV probe mounted on the tripod in the vegetated reach of the Spree River.

each measured velocity component. Following the recommendation to perform as little conditioning of the data as necessary, based on its quality (Stull 1988), no lowpass filtering of the data at high frequencies was conducted. Under low noise conditions such filtering can modify the data to a greater extent than the noise (Bath 1974). However, a few of the time series contained spikes caused by the interruption of acoustic beams by leaves. Such spikes typically span 3 to 6 individual velocity readings (at 25 Hz) and have a noticeable influence on high-frequency portion of power spectra (Sukhodolov & Rhoads 2001). A 3-sigma filter, where sigma is the standard deviation of the data, was used to remove spikes from the time series. Application of the filter removed spikes without altering the rest of the time series.

3 RESULTS AND ANALYSIS

A coordinate system with a streamwise x direction, a transverse y direction of positive values toward the right, and a vertical direction z originating at riverbed and directed toward the free surface is adopted herein. The corresponding velocity fluctuations are u', v', and w', respectively.

3.1 *Flow field overview*

The records of velocity time series were processed to obtain mean values and turbulence characteristics. Total turbulence shear stresses were computed as

$$\tau = \rho\sqrt{\overline{u'v'}^2 + \overline{u'w'}^2 + \overline{v'w'}^2}\,, \tag{5}$$

and turbulent kinetic energy in accordance with

$$k = 0.5\left(u'^2 + v'^2 + w'^2\right). \tag{6}$$

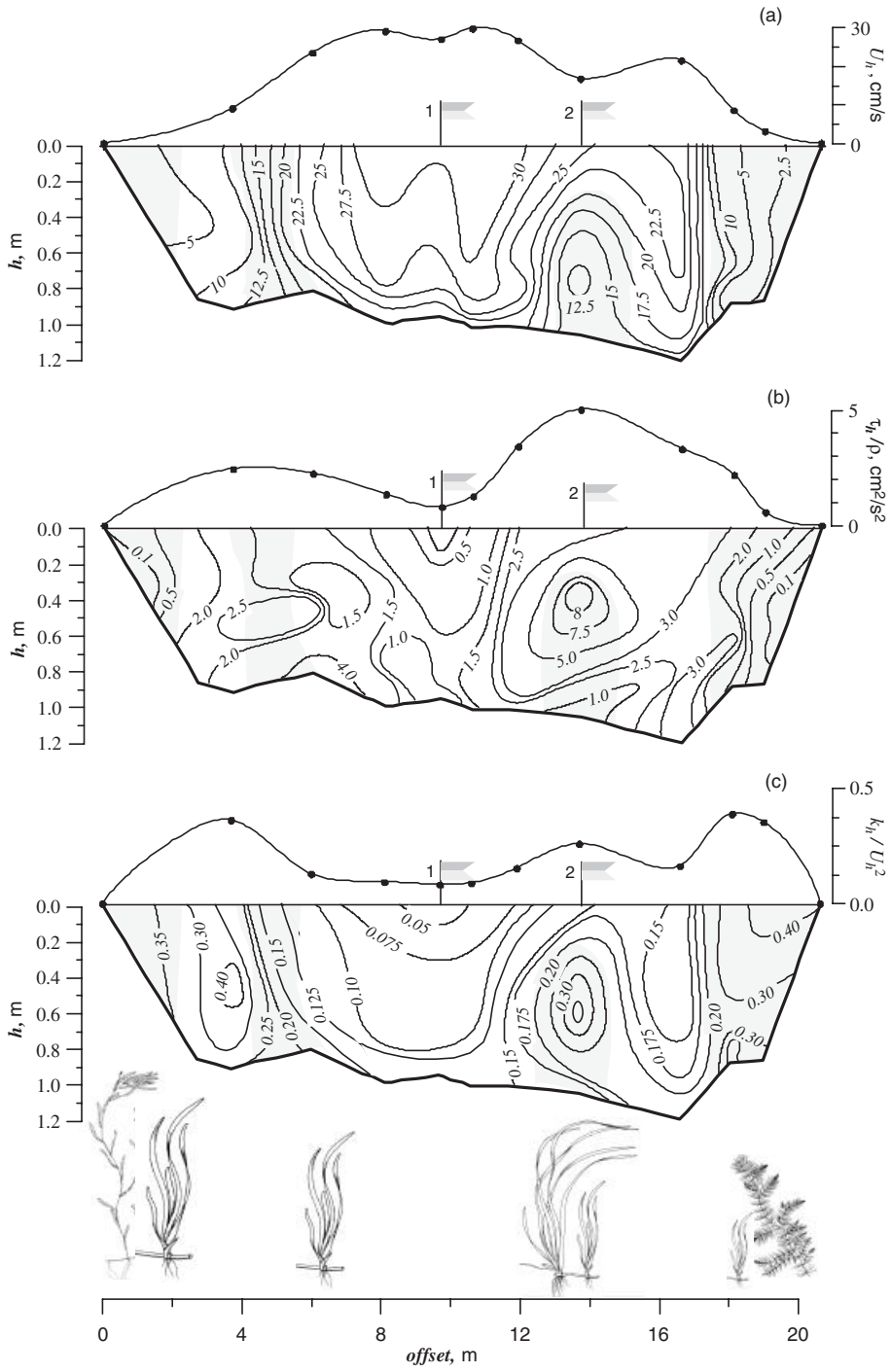


Figure 4. Distributions of mean velocity (a), shear stress (b), and turbulence intensity (c) in a cross-section of the Spree River near the village Freienbrink. Banners indicate the locations of the profiles surveyed with extended resolution. Shaded areas indicate projections of the macrophyte stands. Depth-averaged values are shown on the top of correspondent cross-sectional plots.

Obtained values were used to plot spatial distributions of local mean velocities (Figure 4a), turbulence shear stresses (Figure 4b), and dimensionless values of turbulence kinetic energy $I = k/\overline{U}^2$ often called turbulence intensities. The distributions of plants species, abundance, and depth-averaged flow characteristics are also shown in Figure 4. In the crosssection of the river, the macrophytes formed four well-distinguished stands (Figure 4).

Two stands were attached to the riverbanks; two others were located at offsets 5–6 m and 13–15 m from the left bank respectively. The stands in the central part of the flow were exclusively formed by *Sagittaria Sagittifolia.* Owing to elongated and streamlined leaves, *Sagittaria Sagittifolia* sustains relatively high velocities developed in the central part of the channel. *Potamogeton Crispus* was present in the stand attached to the left bank and exposed to the north. *Ceratophyllum Demersum* was growing in the stand at the right bank, and obviously increased the density of vegetation distribution inside the stand.

Close examination of spatial distributions of the three principal quantities of the mean flow and turbulence characteristics (Figure 4) indicates a notable difference between flow patterns over stands in the central part of the channel and those attached to the banks. The distributions of flow characteristics near the banks are nearly uniform over flow depth and gradually change toward the water's edge. In contrast, the flow patterns over the stands in the central part exhibit variations in both the vertical and transverse directions. Although the depth averaged mean velocity distribution (Figure 4a) displays reduced values for areas with stands, significantly increased values of turbulence stresses are only attributed to the *Sagittaria Sagittifolia* stands in the central part of the cross-section (Figure 4b).

Two vertical profiles of turbulence characteristics were measured with greater spatial and temporal resolutions. The locations of these profiles are shown with banners in Figure 4. Profile 1 was sampled in the area between macrophytes stands, and profile 2 inside the stand located in the central part of the flow. The results and analysis described in the following sections will be dedicated to the examination and comparison of distributions of characteristics for those profiles.

3.2 *Vertical profiles of turbulence characteristics*

Distributions of turbulence primary shear stress over flow depth $-\overline{u'w'} = f(z/h)$ measured at verticals 1 and 2 are shown in Figure 5. The stresses values for the profile 1 were scaled with the local shear velocity $U_* = 1.38$ cm/s; the value determined fitting the linear regression as (Nezu & Nakagawa 1993)

$$-\overline{u'w'} = U_*^2\left(1 - z/h\right). \tag{7}$$

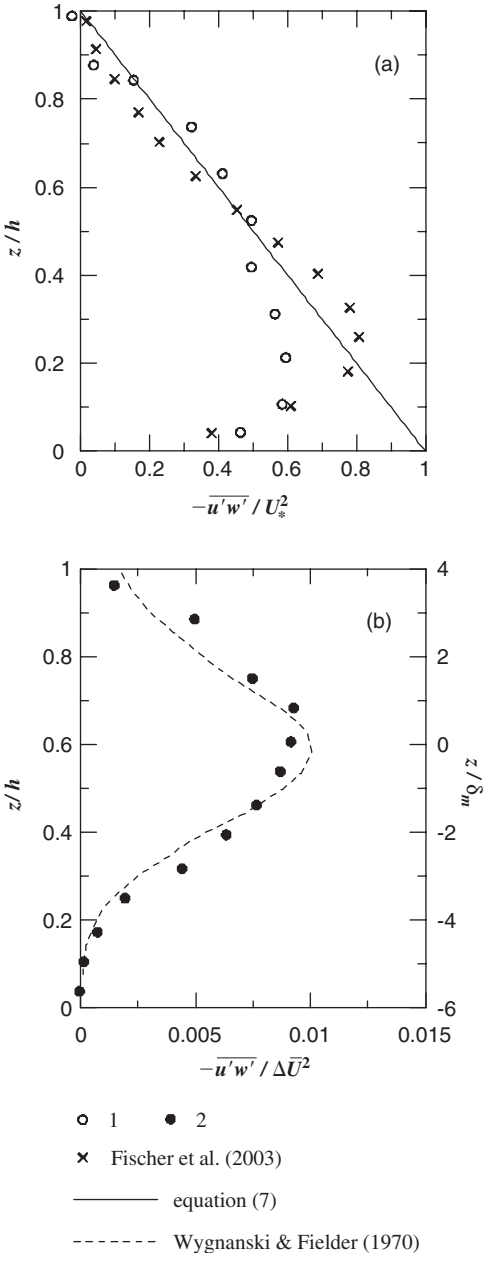


Figure 5. Distributions of turbulence shear stresses over the flow depth (a) in the area between stands, and (b) in the stand of macrophytes.

For the comparison with the conditions of vegetation-free channel in the same river reach, the dimensionless data by Fischer et al. (2003) are also presented in Figure 5.

Stresses measured in the macrophyte stands (profile 2) were scaled with the mean velocity difference across the mixing layer $\Delta\overline{U} = 30$ cm/s to fit the similarity curve by Wygnanski & Fiedler (1970). Momentum thickness of the mixing layer δ_m equaled 11 cm, and its averaged center position was located at $z/h = 0.6$.

Obtained local value of shear velocity was used to scale values of mean velocity for profile 1. Fitting conventional logarithmic law (1) to the dimensionless data, the value of hydrodynamic roughness height $z_0 = 0.013$ cm (von Karman parameter equaled 0.41) was assessed. The mean velocity values measured in macrophyte stands (profile 2) were scaled according to equation (3) using the values $U_s = 15$ cm/s and $\overline{U}_0 = 11$ cm/s. The results of measurements are presented in Figure (6).

Vertical distribution of turbulence kinetic energy in the open-channel flow obeys the semi-theoretical relation proposed by Nezu & Nakagawa (1993)

$$k/U_*^2 = D_k \exp\left(-2C_k\, z/h\right). \qquad (8)$$

where $D_k = 5.72$, and $C_k = 1.0$ – empirical coefficients (Sukhodolov et al. 1998). Measured k values scaled with U_* and $\Delta\overline{U}$, defined from stresses distributions for profiles 1 and 2 respectively, are shown in Figure 7. A dimensionless curve by Wygnanski & Fiedler (1970) is plotted in Figure 7b for comparison.

3.3 *Turbulence spectra and scales*

Turbulence spectra are often used to assess turbulence energy generated by the interaction of mean flow with vegetation. Golovatiuk & Nikora (1984) and Nepf (1999) report existence of two wellseparated, narrow-energy supply regions in turbulence spectra attributed to shear turbulence (lowfrequency) and wake turbulence (high-frequency) because of separation of flow on plant stems (Nikora 2000; Nepf 2000). In addition, the dissipation rate values and, respectively, the internal scales of turbulence (Kolmogorov scale) can be obtained processing the turbulence spectra in the frame of homogeneous isotropic turbulence theory (Monin & Yaglom 1971).

Turbulence spectra were calculated using the autocovariation functions and smoothed with the Tukey's correlation window (Jankins & Watts 1968). Typical turbulence spectra measured in this study are presented in Figure 8.

Owing to relatively low turbulence level, the spectra were affected by acoustic noise at higher frequencies. Averaged noise spectra, obtained in still river water as recommended by Nikora & Goring (1998) are shown in Figure 8. Integrating spectral densities over different frequency bands provided the quantitative estimates of noise impact. It was obtained that on average, noise contributed 1–5% extra energy into the

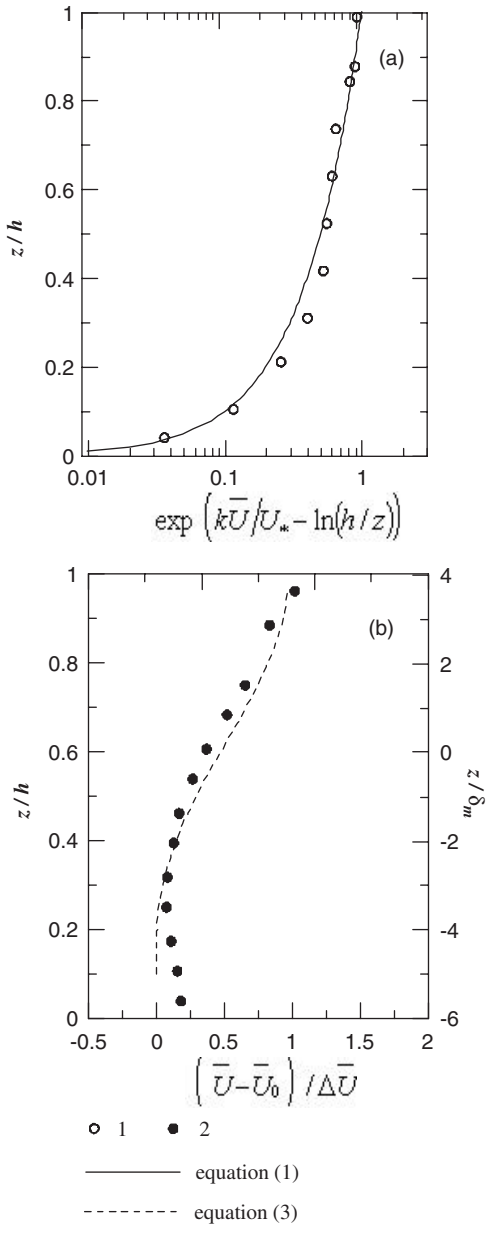


Figure 6. Distributions of mean velocity over the flow depth (a) in the area between stands, and (b) in the stand of macrophytes.

velocity records. Effect of noise was stronger in the areas between stands and closer to the free surface of flow.

The shape of spectra measured in the macrophyte stands had no distinct separation in the high frequencies similar to that reported by Golovatiuk & Nikora

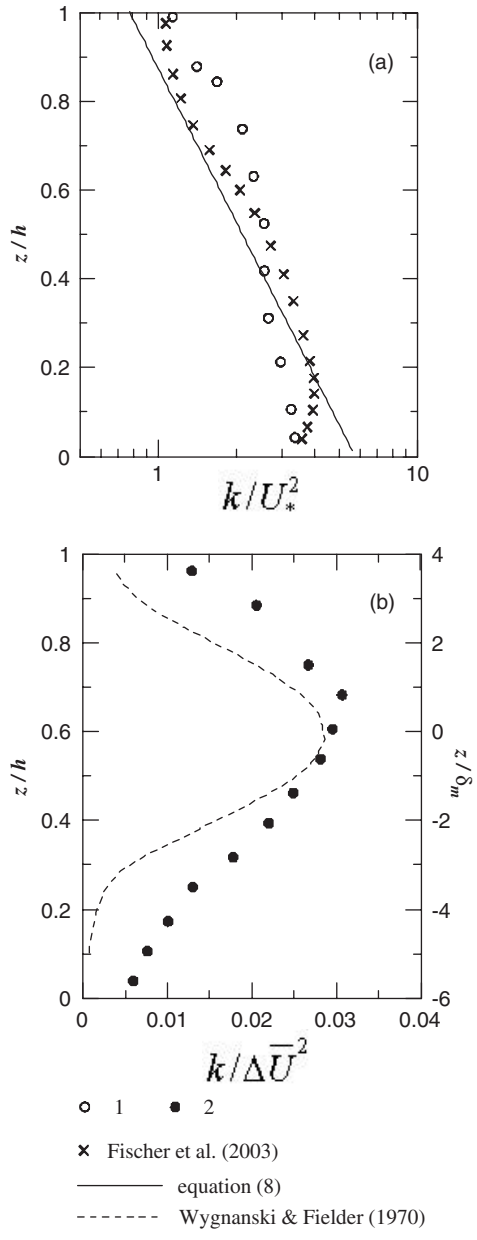


Figure 7. Distributions of turbulence kinetic energy over the flow depth (a) in the area between stands, and (b) in the stand of macrophytes.

(1984) and Nepf (1999). Some distortions in the inertial subrange at higher frequencies were attributed to the noise effect. Most probably that was because of the relatively high background level of shear turbulence, maximum spectral density in the present study being at least 10 times higher than reported by Nepf (2000),

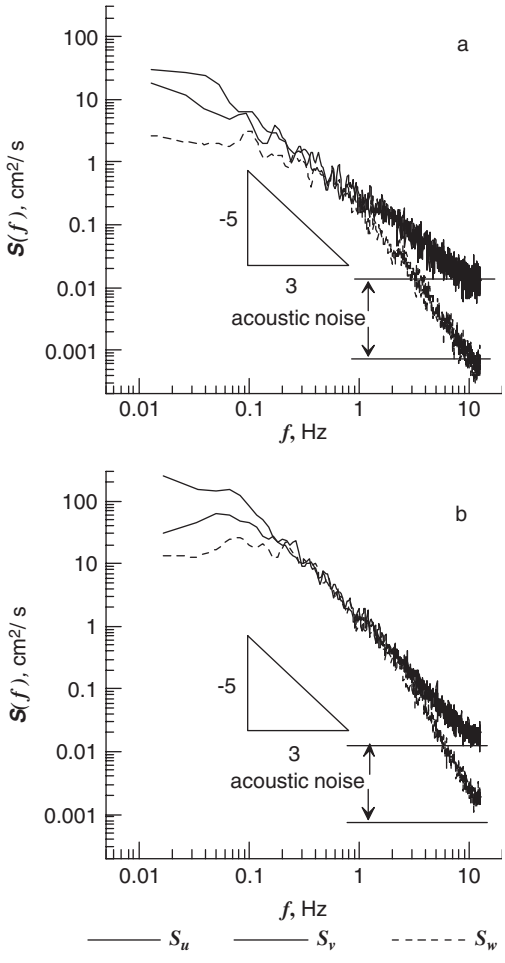


Figure 8. Examples of turbulence spectra measured (a) in the area between stands and (b) in the stand of macrophytes; $z/h = 0.75$.

the impact of wake from stems and leaves of plants was undetectable in the spectra.

Inertial subrange in the spectra was detected applying the relationship between spectral densities of velocity vector components $S_{vv} = S_{ww} = 4/3 S_{uu}$. Dissipation rate ε values were evaluated from the velocity spectra inside the inertial subrange

$$S_u(f) = 0.48\varepsilon^{2/3}\left(\overline{U}(z)/2\pi\right)^{2/3} f^{-5/3}, \quad (9)$$

where f = frequency. Kolmogorov's internal scale of turbulence was calculated as

$$\eta = \left(\nu^3/\varepsilon\right)^{1/4}, \quad (10)$$

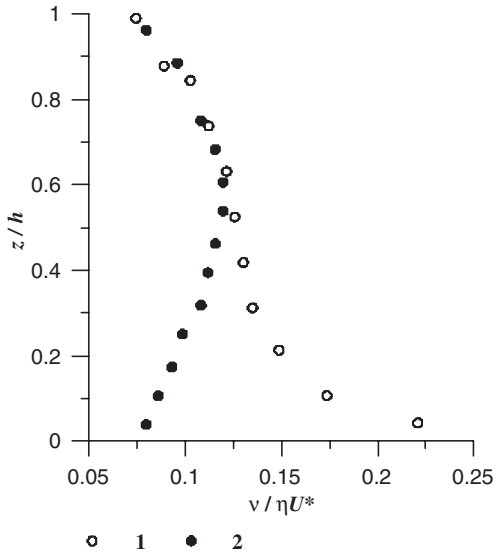


Figure 9. Distributions of dimensionless Kolmogorov's scales over river depth.

where v = kinematic viscosity. Dimensionless distributions of the Kolmogorov's scales are presented in Figure 9.

3.4 *Hydraulic effect of vegetation*

The overall hydraulic effect of in-stream vegetation is generally perceived through the increase of the mean depth, decrease of mean velocity, and, respectively, in the enhanced hydraulic retentivity of the stream as compared to the non-vegetation conditions. For the investigated river reach such a comparison is possible because of availability of a comprehensive set of measurements of water discharge, mean flow velocities, and depth. The observations formed this data set were conducted systematically as one measurement per month during a period of three years. The measurement program was comprised of mean velocity measurements with electromagnetic current meter in 5 points at every vertical. Verticals were located every 2 m across the width of the river. The data and empirical relationships between discharge and bulk flow parameters for nonvegetation conditions are presented in Figure 10. For discharge $Q = 3.25\ \mathrm{m^3/s}$, from the empirical relationships $U = 0.14Q^{0.47}$, the value of mean velocity equals 0.24 m/s, and mean river depth from $H = 0.43Q^{0.42}$ equals 0.71 cm. Thus, velocity was reduced about 27% whereas depth increased 17%.

The low-transit flow areas sometimes called dead zones are recognized for extended hydraulic retentivity and can be described in the frame of the longitudinal model with dead zones (Valentine & Wood 1977,

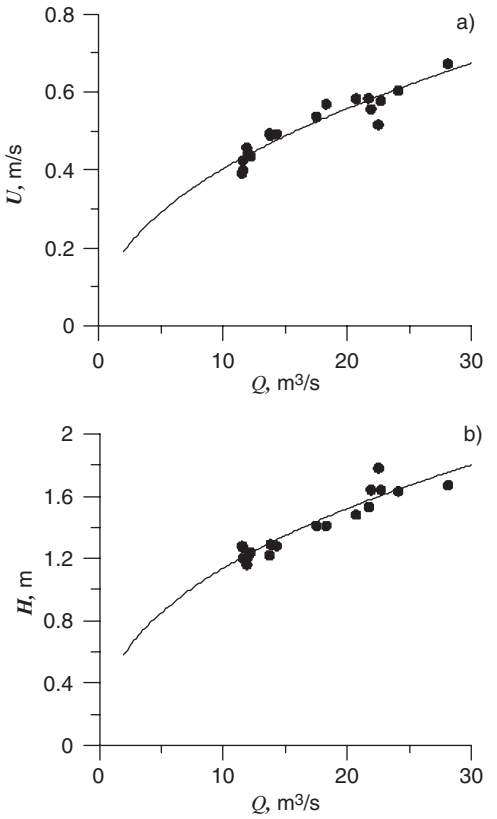


Figure 10. Measured bulk velocity (a) and depth (b) as the functions of discharge for the experimental river reach.

Czernuszenko et al. 1998)

$$\varepsilon = \frac{A_d}{B\,h} \tag{11}$$

where ε = dead zone parameter, A_d = area of dead zone in the cross-section, B = width, and h = mean depth of the flow. Assuming that the projection of macrophyte stands on the cross-sectional area approximate the area of dead zones, it is possible to assess the effect of macrophytes on the hydraulic retention of dissolved matter in the flow using the relationship by Czernuszenko & Rowinski (1997)

$$T = \frac{2D}{U^2} + \frac{x}{U}\left(1 + \varepsilon\right) \tag{12}$$

where T = retention time, D = longitudinal dispersion coefficient, U = mean velocity, and x = distance from the point of release. As the first term in (12) represents the initial size of the contaminant cloud, it can

be neglected for the fixed distance x. With this simplification, the ratio between retention time T_M of the vegetated channel and retention time T of a vegetation-free channel can be represented as

$$\frac{T_M}{T} = (1+\varepsilon)\left(1+\frac{U-U_M}{U}\right) \quad (13)$$

and gives a value of 1.67 for this case study.

4 CONCLUSIONS

The results of this study contribute to the understanding of the three-dimensional spatial and temporal structure of turbulence in partly vegetated sandy bed lowland river. Analysis of cross-sectional patterns of mean velocities and basic turbulence characteristics indicates that submersed macrophyte stands located in the central part of the flow produce flow patterns different from those formed by macrophytes in stands attached to the river banks. Flow pattern and composition of stands were interrelated: plants with streamlined morphology of stems and leaves were dominant in the stands of the central part of the stream, while those attached to banks stands were more diverse and dense. Consequently, the descriptive analysis of flow patterns and their quantitative characterization require different models to serve as the conceptual framework for the analysis.

In this study two approaches were examined: an application of the open-channel plane quasi- uniform flow for the vegetation-free patches between stands and the mixing layer analogy for the flow over macrophyte stands. The analysis is concerned with the distribution of mean velocities, shear stresses and turbulent kinetic energy over the river depth. An agreement between theoretical and experimental results was established, favoring therefore the application of hybrid models for quantitative analysis of complex flow patterns.

The overall hydraulic effect of in-stream vegetation was estimated. Obtained results indicate the significance of the macrophytes' effect on retention processes in natural streams and outline the necessity for complex field investigations comprised of tracer experiments on longitudinal dispersion and investigation of complex spatial patterns of velocity field and turbulence characteristics.

ACKNOWLEDGEMENTS

The authors are thankful to Dr. Sabina Hilt for the help in macrophytes taxonomy, and to Hannes Nützmann for the assistance in field measurements.

REFERENCES

Carpenter, S.R., & Lodge, D.M. 1986. Effects of submersed macrophytes on ecosystem processes. *Aquatic Botany* 26: 341–370.

Cushing, C.E., & Allan, D. 2001. *Streams. Their Ecology and Life.* San Diego: Academic Press.

Czernuszenko W., & Rowinski P. 1997. Properties of the dead-zone model of longitudinal dispersion in rivers. *J. Hydr. Res.* 35(4): 491–504.

Czernuszenko, W., Rowinski, P.M., & Sukhodolov, A.N. 1998. Experimental and numerical validation of the dead-zone model for longitudinal dispersion in rivers. *J. Hydr. Res.,* 36(2): 269–280.

Denny, M.W. 1988. *Biology and the Mechanisms of the Wave-Swept Environment.* Princeton: Princeton University Press.

Fischer H., Sukhodolov A., Wilczek S., & Engelhardt C. 2003. Effects of flow dynamics and sediment movement on microbial activity in a lowland river. *River Research and Applications* 19(5–6): 473–482.

Jenkins, G.M., & Watts, D.G. 1968. *Spectral analysis and its applications.* Merrifield: Holden-Day.

Golovatiuk, A.S., & Nikora, V.I. 1984. Experimental investigation of hydraulic resistance in streams with emergent vegetation. *Dynamics and Thermics of Rivers, Reservoirs and Estuaries* 1: 105–107.

Kraus, N.C., Lohrmann, A., & Cabrera, R. 1994. New acoustic meter for measuring 3D laboratory flows. *J. Hydraulic. Eng.,* 120(3), 406–411.

Michalke, A. 1965. On spatially growing disturbances in an inviscid shear layer. *J. Fluid Mech.* 23: 521–544.

Monin, A.S., & Yaglom, A.M. 1971. *Statistical fluid mechanics.* Vol. 1, *Mechanics of turbulence.*, Cambridge: MIT Press.

Nikora, V.I., & Goring, D. 1998. ADV measurements of turbulence: can we improve their interpretation? *J. Hydraul. Eng.* 124(6): 630–634.

Nikora, V.I. 2000. Comment on "Drag, turbulence, and diffusion in the flow through emergent vegetation" by H.M. Nepf. *Water Res. Research* 36(7): 1985–1986.

Nepf, H.M. 1999. Drag, turbulence, and diffusion in the flow through emergent vegetation. *Water Res. Research* 35(2): 479–489.

Nepf, H.M. 2000. Reply. *Water Res. Research* 36(7): 1987–1988.

Nezu, I., & Nakagawa, H. 1993. *Turbulence in openchannel flows.* Rotterdam: Balkema.

Raupach, M.R., Finnigan, J.J., & Brunet, Y. 1996. Coherent eddies and turbulence in vegetation canopies: the mixing-layer analogy. *Boundary Layer Met.* 78: 351–382.

Rhoads, B.L., & Sukhodolov, A.N. 2001. Field investigation of three-dimensional flow structure at stream confluences: I. Thermal mixing and time-averaged velocities. *Water Resour. Res.*, 37(9), 2393–2410.

Righetti, M., & Armanini, A. 2002. Flow resistance in open channel flows with sparsely distributed bushes. *Journal of Hydrology* 269: 55–64.

Sand-Jensen, K., & Pedersen, O. 1999. Velocity gradients and turbulence around macrophyte stands in streams. *Freshwater Biology* 42: 315–328.

Stephan, U., & Gutknecht, D. 2002. Hydraulic resistance of submerged flexible vegetation. *Journal of Hydrology* 269: 27–43.

Stull, R.B. 1988. *An Introduction to Boundary Layer Meteorology.* Massachusetts: Kluwer.

Bath, M. 1974. *Spectral Analysis in Geophysics.* New York: Elsevier.

Sukhodolov, A.N., Thiele, M., & Bungartz, H. 1998. Turbulence structure in a river reach with sand bed. *Water Resour. Res.*, 34(5), 1317–1334.

Sukhodolov, A.N., & Rhoads, B.L. 2001. Field investigation of three-dimensional flow structure at stream confluences: II. Turbulence. *Water Resour. Res.*, 37(9), 2411–2424.

Wygnanski, I., & Fiedler, H.E. 1970. The twodimensional mixing region. *J. Fluid Mech.* 41: 327–361.

Valentine, E.M., & Wood, I.R. 1977. Longitudinal dispersion with dead zones. *J. Hydr. Div., ASCE*, 103(HY9): 975–990.

River Flow 2004 – Greco, Carravetta & Della Morte (eds.)
© 2004 Taylor & Francis Group, London, ISBN 90 5809 658 0

Open channel turbulent data modeling using fractal geometry

A.N. Ziaei, & A.R. Keshavarzi
Irrigation Department, Shiraz University, Shiraz, Iran

H. Emdad
Mechanical Eng., Department, Shiraz University, Shiraz, Iran

ABSTRACT: Fractals are objects that display self-similarity or self-affinity over a wide range of scales. Fully developed turbulence indeed consists of a hierarchy of eddies, or scales of various disorders. Thus, this can be one type of fractal. Turbulence can be studied in velocity field. Time series of velocity components are very irregular. Modeling of such velocity fluctuations using Euclidean functions is almost impossible, however, fractal interpolation functions (FIF) can be attractive tools to fulfill this desire.

In this study, FIF was used to model more than 200000 time series of velocity fluctuations and Reynolds shear stress in open channel flows. Fractal dimension of velocity fluctuation components and shear stress was calculated using FIF. Fractal dimensions of u′, v′, and u′v′ were found to be 1.615, 1.657, and 1.559, respectively. The relationships of fractal dimension with Froude and Reynolds numbers were also investigated.

1 INTRODUCTION

In the most basic sense, fractals are objects that display self-similarity over a wide range of scales. Analogous to the Euclidean dimension of classical objects, each fractal object, or turbulent eddy, is associated with a characteristic dimension called the fractal dimension. It forms a basis to measure the fragmentation or roughness. Richardson (1922) pointed out that fully developed turbulence indeed consists of a hierarchy of eddies, or scales of various disorders. Turbulent eddies have their corresponding large, little, lesser, and least wiggles-down to where viscosity stops the process. Thus this can be one type of fractal. If we consider these turbulent eddies as fractal objects, then the theory of fractals may be applicable to turbulence (Jaw & Chen, 1999).

Fractal geometry concerns with complicated subset of geometrically simple space such as R^2. In deterministic fractal geometry the focus is on the subset of a space that are generated by simple contractive geometrical transformations of the space into itself. A transformation f: $X \to X$ on a metric space (X, d) is called contractive or contraction mapping if there is a constant $0 \le s < 1$, such that: $d(f(x), f(y)) \le s\, d(x, y) \forall x, y \in X$.

A general affine shear transformation can be defined as:

$$w_n\begin{pmatrix} x \\ y \end{pmatrix} = \begin{pmatrix} a_n & 0 \\ c_n & d_n \end{pmatrix}\begin{pmatrix} x \\ y \end{pmatrix} + \begin{pmatrix} e_n \\ f_n \end{pmatrix} \quad (1)$$

where a_n, c_n, d_n, e_n, and f_n are transformation parameters. This means that on the x–y plane, lines parallel to y-axis are mapped into lines parallel to y-axis. Every contractive mapping on a complete metric space has a fixed point on that metric space. To define a fractal object, it is first necessary to define iterated function systems (IFS).

1.1 *Iterated function systems*

An iterated function system (IFS) consists of a complete metric space (X, d) together with a finite set of contraction mapping W_n: $X \to X$ with respective contractivity factors s_n, for $n = 1, 2, \ldots, N$. The notation for the IFS just announced as $\{X; W_n, n = 1,2, \ldots, N\}$ and its contractivity factors is $S = \max\{s_n, n = 1,2, \ldots, N\}$. Let now $\{X; W_n, n = 1,2, \ldots, N\}$ be an iterated function system with contractivity factors. Then the transformation W: $H(X) \to H(X)$ defined by

$W(B) = \cup W_n$; $n = 1, \ldots, N$ for all $B \in H(X)$ is a contraction mapping on the complete metric space (H(X), h(d)) with contractivity factor S. That is, h(W(B), W(C)) ? S h(B, C) for all B, $C \in H(X)$. Its unique fixed point, $A \in H(X)$ obeys $A = W(A) = \cup W_n(A)$ and is given by $A = \mathrm{Lim}_{n\to\infty}\ W^{on}$ (B) for any $B \in H(X)$. The fixed point $A \in H(X)$ described above is called the attractor of the IFS. The attractor is the fractal object.

In order to show a very irregular and ragged curve of turbulent properties such as temporal variations of velocity fluctuation components and Reynolds shear stress is a fractal object, it should be accurately modeled by a set of self-affine maps. Fractal interpolation function (FIF) is a very powerful tool to modeling of such curves. The graph of an FIF is the attractor of an IFS that passes through the given interpolation points. In other words, FIF also provide a new means for fitting experimental data such as velocity components data. Moreover, one can ensure that the fractal dimension of the graph of FIF agrees with that the data over an a – propriate range of scales.

Let a set of data $\{(x_i, F_i) \in R^2: i = 0, 1, 2, \ldots, N\}$ (interpolation points) be given. The attractor, which is denoted by G, is the graph of a continuous function f: $[x_0, x_N] > R$ which interpolates the data. If an IFS of the form $\{R^2; W_n, n = 1,2, \ldots, N\}$ is considered, where the maps are affine shear transformations, the transformations are constrained by the data according to:

$$W_n\begin{pmatrix} x_0 \\ F_0 \end{pmatrix} = \begin{pmatrix} x_{n-1} \\ F_{n-1} \end{pmatrix} \text{ and } w_n\begin{pmatrix} x_N \\ F_N \end{pmatrix} = \begin{pmatrix} x_n \\ F_n \end{pmatrix}$$

for $n = 1, 2, \ldots, N$. The situation is summarized in Figure 1.

Let d_n be any real number, the above equations can always be solved for a_n, c_n, e_n, and f_n in terms of the data and d_n. i.e.

$$a_n = \frac{x_n - x_{n-1}}{x_N - x_0} \tag{2}$$

$$e_n = \frac{x_N x_{n-1} - x_0 x_n}{x_N - x_0} \tag{3}$$

$$c_n = \frac{F_n - F_{n-1}}{x_N - x_0} - \frac{d_n (F_N - F_0)}{x_N - x_0} \tag{4}$$

$$f_n = \frac{x_N F_{n-1} - x_0 F_n}{x_N - x_0} - \frac{d_n (x_N F_0 - x_0 F_N)}{x_N - x_0} \tag{5}$$

Then the fractal dimension of the FIF can be calculated by:

$$\sum_{n=1}^{N} |d_n| a_n^{D-1} = 1 \quad \text{if} \quad \sum_{n=1}^{N} |d_n| > 1 \tag{6}$$

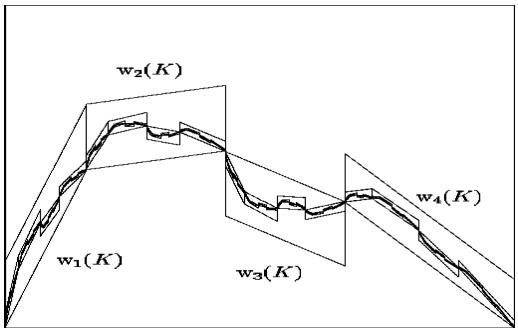


Figure 1. Construction of FIF using IFS of shear transformation (after Barnsley, 1993).

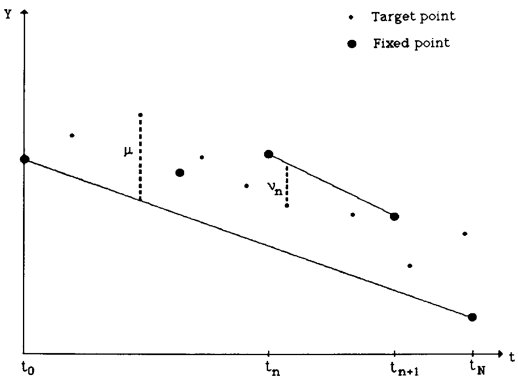


Figure 2. Schematic of fixed points and target points distribution (after Marvasti & Strahle 1995).

where D is the fractal dimension. Up to now it is explained how to calculate a_n, c_n, e_n, and f_n, but two other parameters are unknown; the first one is number of transformations (N) and the second one is d_n, which is afterwards called vertical scaling factor (VSF).

Strahle (1991) presented a simple method to calculate the VSF. It suffers from some shortcomings. Marvasti & Strahle (1995) improved the previous method. Their algorithm also starts by categorizing the data into fixed and target points. But unlike the Strahle's method, the number of target points between each pair of fixed points is declared as a variable. This scheme is shown in Figure 2. The dark solid points are the fixed points and the smaller ones are the target points. What remain to be determined are N and d_n. This scheme doesn't suggest any idea for selection of N, but the vertical scaling factor d_n is obtained by first drawing a line between the first and the last data point (i.e. (x_0, F_0), and (x_N, F_N)). Next the point which has the longest vertical distance to the line is calculated. This is designated as μ in Figure 2 that can be positive (point above the line) or negative (point below the line). A line is then drawn between the fixed points on

the nth interval and the distance of the farthest target point above or below this line is calculated. This is designated as v_n in Figure 2. The vertical scaling factor is then defined as:

$$d_n = \frac{v_n}{\mu} \tag{7}$$

Although this scheme doesn't have some of the previous method's difficulties, but the minimum essential target point to generate accurate model is unspecified.

Mazel & Hayes (1992) presented geometric and analytic methods to calculate the VSF. The geometric method is the same as Marvasti & Strahle method. The analytic method is based on least square optimization. Furthermore, they presented an iterative algorithm for finding both the interpolation points and the VSF for a given arbitrary data set. The algorithm is based on the property that the resulting fractal function is self-affine. By the collage theorem, if the function can be covered with affine transformation of itself, and have the distance between the function and the collage of the function small, the attractor of the IFS will be a close approximation to the function. However, since the algorithm uses exhaustive search, it is too time consuming to be of practical use.

Vines (1993) compared results of different methods for one-dimensional signal modeling. He suggested using local extremums of the data sequence as the fixed points of the maps. The extremum points are obtained by introducing some filters, and selecting those points which have the most deviation. Vines (1993) showed that this method is very efficient and the results are comparable with exhaustive search. In this manner, even without the effect of the IFS, the model roughly follows the original data using a series of straight-line segments. Then the mapped data portion can be used to further increase the accuracy of the model. Due to advantages of the last approach, in this study it is used with few improvements for turbulent data modeling.

In this study, the improved FIF is used to model time series of certain flow properties such as u′, v′, and u′v′ in open channel flow. It is utilized to prove that these properties can be categorized as fractal objects. The reliability of the method for calculating the fractal dimension of data set is also scrutinized. Then it is applied to calculate the fractal dimension of the turbulent data. The relationships between fractal dimension of the flow properties and Reynolds and Froude numbers are also studied.

2 DEVELOPED COMPUTER PROGRAM

The Vines (1993) and Mazel & Hayes (1992) methods were incorporated to obtain the efficient number of interpolation points and suitable vertical scaling factors. The required computer program was developed using Matlab Language. The program consisted of a main body and five subroutines (Figure 3). The program is based upon the flowchart shown in Figure 4.

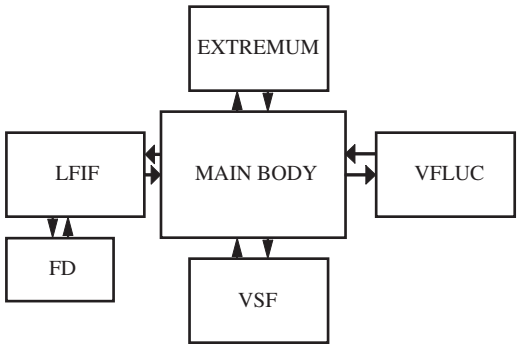


Figure 3. Structure of the developed computer program.

2.1 *Input file*

Input file includes velocity components U and V that were measured during a period of time in a laboratory flume in different distances from the bed. Therefore, every input file consisted of an M × 3 matrix; M is the number of time intervals, in which the measurement was made.

2.2 *Flowchart*

In the main body of the program, after reading the input file, the VFLUC subroutine is called. In this part, velocity fluctuations components (u′, v′) are calculated. Turbulent shear stress (u′v′) is calculated as multiplication of the velocity fluctuation components. Afterwards, t, u′, v′, and u′v′ are stored as column vectors. According to sign of u′ and v′, u′v′ values are divided into four quadrants. i.e.

Quadrant 1: $u' > 0, v' > 0$

Quadrant 2: $u' < 0, v' > 0$

Quadrant 3: $u' < 0, v' < 0$

Quadrant 4: $u' > 0, v' < 0$

u′v′ in different quadrants accompanied with their related time values and they are saved in separated matrices. All of the above matrices (i.e. t, u′, v′, u′v′, Quadrant 1, Quadrant 2, Quadrant 3, Quadrant 4) are stored in a cell array and returned to main body.

Now turbulent data matrices are ready to fractal modeling. The next step is determination of fixed points. In order to determine fixed points (the number of maps), EXTREMUM subroutine is called. In

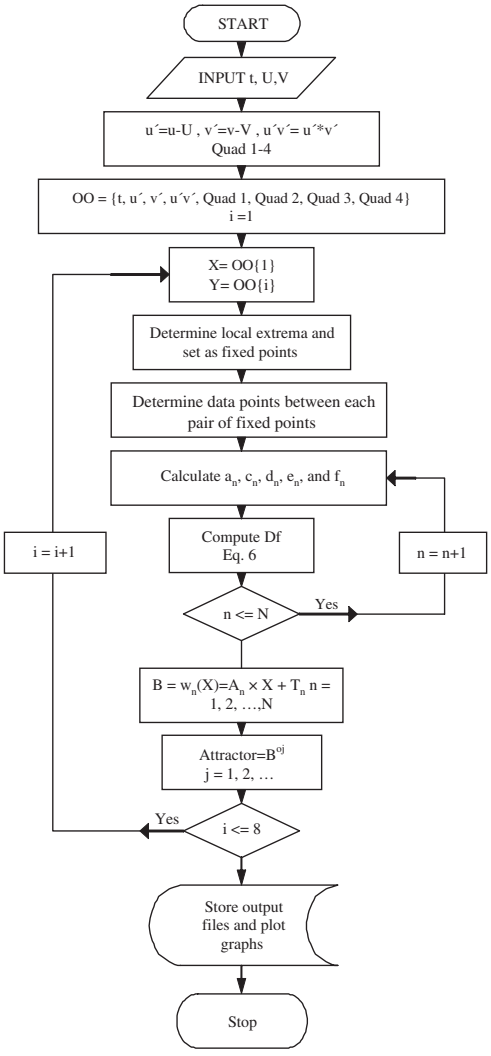


Figure 4. Flowchart of the developed computer program.

this subroutine, the local extremums of data set are specified using a number of filters. They are:

- The extremum is a point on which the sign of numerical derivative changes.
- Each maximum should be followed by a minimum and vise versa.
- Sequential extrema which have a specific trend should be removed i.e. (Figure 5),

The number of maps is equal to the number of sequential pair of fixed points. To calculate the values of a_n, c_n, d_n, e_n, and f_n, after determination of fixed points, the data points between each pair of fixed points are specified in the main body. Every data set is

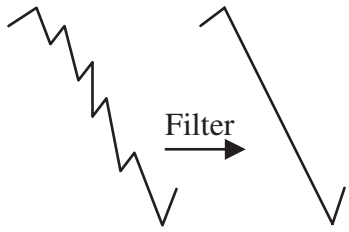


Figure 5. Sequential extrema with a trend.

divided into N section (the number of maps or transformations). Each section as an array is entered into VSF subroutine to compute the largest distance between the line that connect two endpoints of the section and the data points. This value is v_n. The average value of distances is also stored as g_n. These values are returned to the main body. Then d_n is calculated as:

$$d_n = v_n / \mu \qquad \text{if } d_n \le 1$$

$$d_n = g_n / \mu \qquad \text{if } d_n > 1$$

The values of mapping parameters a_n, c_n, e_n, and f_n are calculated in LFIF subroutine according to Equations 2–5. The fractal dimension is obtained by solving Equation 6 numerically in FD subroutine using Newton-Raphson method. Afterwards, since mapping parameters and the number of maps is known, the fractal interpolation function can be constructed.

3 DATA SET DESCRIPTION

In this study the turbulent data, which had been measured by Keshavarzi (1997), were used. The data include time series of velocity components that are measured in experimental flume using 2D electromagnet velocity meter. Data sets comprised of different flow conditions in term of discharge, flow depth, velocity and in sequence, Reynolds and Froude numbers. Uniform and non-uniform flow conditions were stabilized using a gate at the end of the flume. Each test which was specified by a letter, consisted of several time series of velocity components measured in different distances from the flume bed.

4 RESULTS AND DISCUSSIONS

The result of this study can be categorized in two main parts as follow:

- u', v', and $u'v'$ data modeling.
- Fractal dimension of turbulent data.

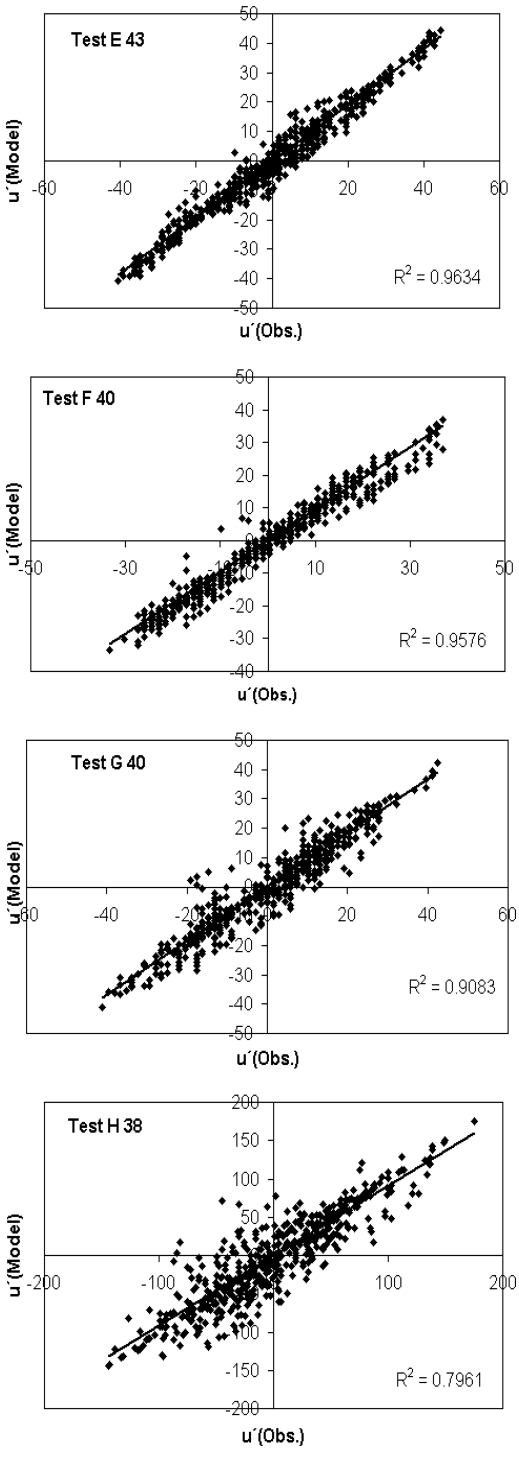


Figure 6. Comparison between observed and computed u′ (first iteration) for some data sets.

4.1 *u′, v′, and u′v′ data modeling*

The model has determined suitable local extremums which roughly follow the original data. Therefore, it was expected that the attractor be close enough to the data. The results of first iteration of the model are compared with measured turbulent data in Figure 6. According to collage theorem, the closer this run of model is to the data, the fractal interpolation function (attractor) closer to the given data set.

The results revealed good agreement between measured and simulated data. In some data set there exist some deviations which are to some extend because of unsuitable local extremums. Using more restricted filters may decrease these discrepancies.

Modeling the whole length of every data set is very time consuming. Thus only a small part of a couple of data sets were modeled. The computed fractal model using five iterations are compared with observed values for some data sets in Figure 7.

4.2 *Fractal dimension of turbulent data*

The strahle (1992) and marvasti and strahle (1995) methods were used to calculate VSF, and in sequence the fractal dimension. However, they required great number of data points to calculate accurate fractal dimension. Furthermore, for some data sets the calculated d_n was greater than unity which was unacceptable.

The results of the extremum method for a number of data sets are presented in Figures 8 and 9. The fractal dimension reached a constant value with about 500 data points. Therefore, the presented model is able to compute accurate fractal dimension with only 500 data points. This method can be a good substitution for the Box-counting method because the latter method has been very unreliable for some turbulent data sets due to the elusiveness of the flat region on the logarithmic plot (Marvasti and Strahle, 1995).

4.2.1 *Fractal dimension of u′, v′, and u′v′ data sets*

The fractal dimension of u′, v′, and u′v′ for all data sets were calculated. All the values were averaged to calculate the mean fractal dimension of turbulence properties. The fractal dimension of u′, v′, and u′v′ were found to be 1.615, 1.657, and 1.559, respectively.

The mean fractal dimension (Df) of each test, averaging from different depths at which velocity measurements were made, and related flow conditions are tabulated in Table 1. These values are plotted versus Reynolds and froude numbers in Figures 10 and 11, respectively.

It seems that Df is independent of Reynolds number. While Df and Froude number are somehow correlated. The results are reasonable because of dominancy of gravity force in open channel flows.

As can be seen in Table 1, Fr greater than 0.6 belongs to uniform conditions. It is obvious that uniform flow

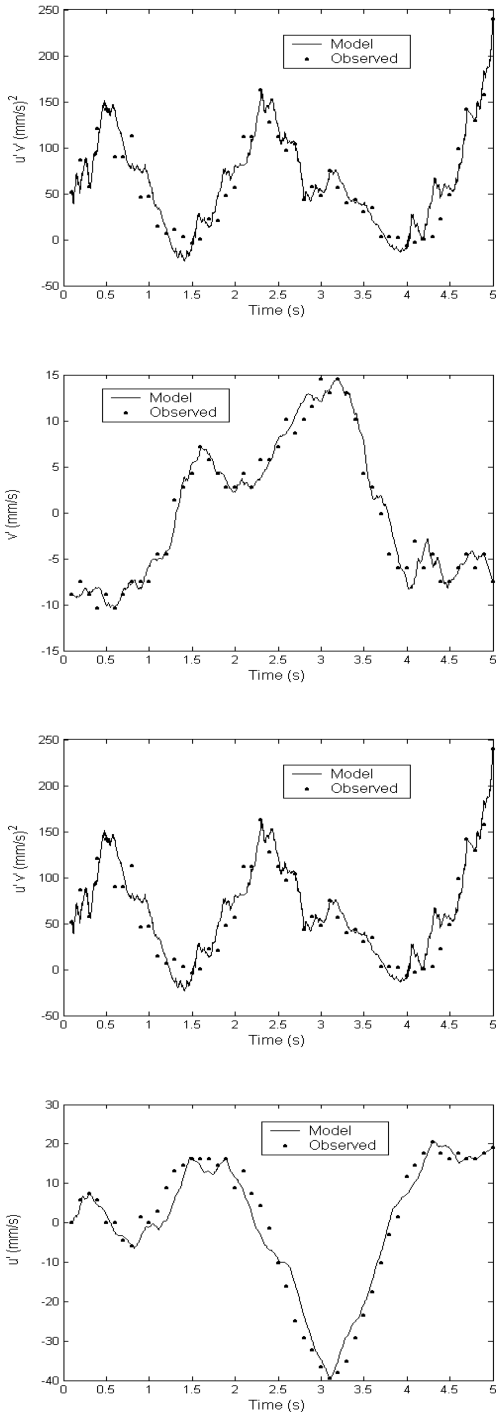


Figure 7. Comparison between observed turbulent data for small parts of some data sets.

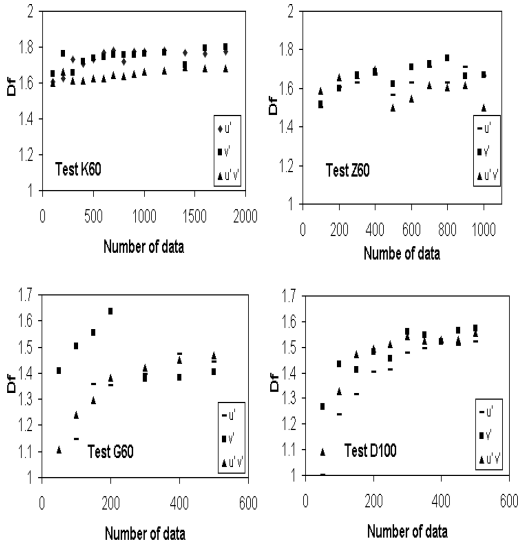


Figure 8. Fractal dimension versus number of data for some data sets.

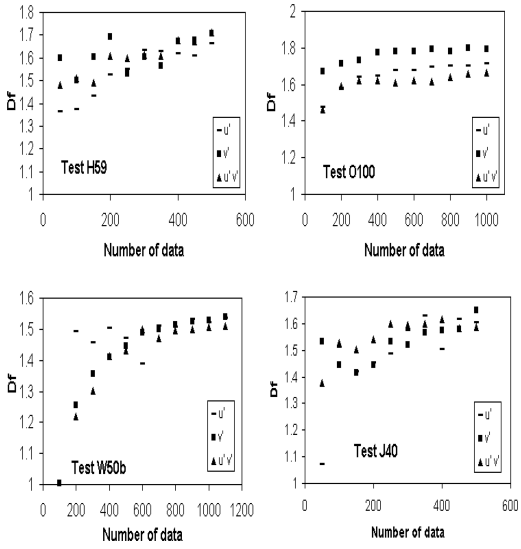


Figure 9. Fractal dimension versus number of data for some data sets.

decreases the turbulence intensity and in consequence the fractal dimension of the velocity component and Reynolds shear stress.

All the above results revealed that fractal dimension can be used to characterize turbulence properties. In other words, all wide range of length and time scales can be reduced to single parameters such as fractal dimension.

Table 1. Df for different flow conditions.

	1	2	3	4	5	6	7	8	9	10
Test	D	E	F	G	H	J	K	L	M	N
Q(l/s)	47	63.7	76.3	52	58	73.6	40.2	61	30.3	22
H(mm)	294	355	154	276	120	145	120	212	154	70
T(Co)	15.5	15	15	15	15.5	14	13.5	13.5	13	12.2
So	0.005	0.005	0.005	0.005	0.005	0.005	0.005	0.005	0.005	0.005
Umean (m/s)	0.26	0.29	0.81	0.31	0.79	0.83	0.55	0.47	0.32	0.52
Fr	0.15	0.16	0.66	0.19	0.73	0.70	0.51	0.33	0.26	0.62
Rate(1/s)	10	10	10	10	10	10	10	10	10	10
Flow condition	S & N	S & N	S & U	S & N	S & U	S & U	S & N	S & N	S & N	S & N
Re	39232	48258	83115	44750	68235	81778	47294	58994	33007	29333
DF(u′)	1.556	1.382	1.402	1.501	1.675	1.584	1.778	1.713	1.745	1.723
DF(v′)	1.638	1.589	1.448	1.536	1.651	1.620	1.747	1.708	1.767	1.765
DF(u′v′)	1.573	1.520	1.418	1.505	1.604	1.582	1.681	1.667	1.648	1.632

	11	12	13	14	15	16	17	18	19	20
Test	O	P	Q	V	W	Wb	X	Y	YY	Z
Q(l/s)	48.5	79.8	97.5	22.7	47.5	47.5	48.5	40.85	40.3	30.5
H(mm)	166	230	265	70	172	100	170	146	143	103
T(Co)	13	13	12.6	24.4	24.4	24.4	18.6	19	19	19
So	0.005	0.005	0.005	0.005	0.005	0.005	0.005	0.005	0.005	0.005
Umean (m/s)	0.48	0.57	0.60	0.53	0.45	0.78	0.47	0.46	0.46	0.49
Fr	0.38	0.38	0.37	0.64	0.35	0.79	0.36	0.38	0.39	0.48
Rate(1/s)	10	10	10	10	10	10	10	10	10	10
Flow condition	S & N	S & N	S & N	S & U	S & N	S & U	S & N	S & N	S & N	S & N
Re	51486	74579	85526	30267	49790	58642	51053	45288	44978	37377
DF(u′)	1.733	1.730	1.737	1.532	1.492	1.474	1.641	1.680	1.672	1.672
DF(v′)	1.773	1.778	1.764	1.558	1.567	1.544	1.704	1.690	1.668	1.692
DF(u′v′)	1.695	1.682	1.674	1.491	1.503	1.488	1.634	1.654	1.634	1.627

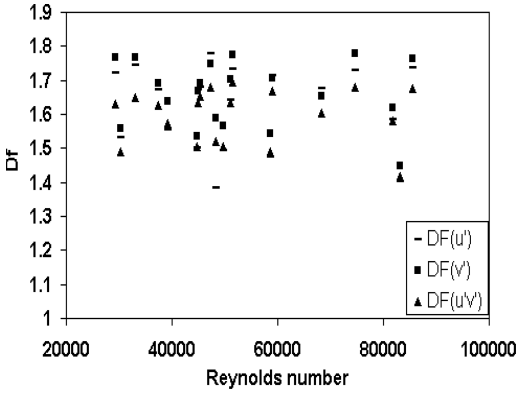


Figure 10. Fractal dimension versus Reynolds number.

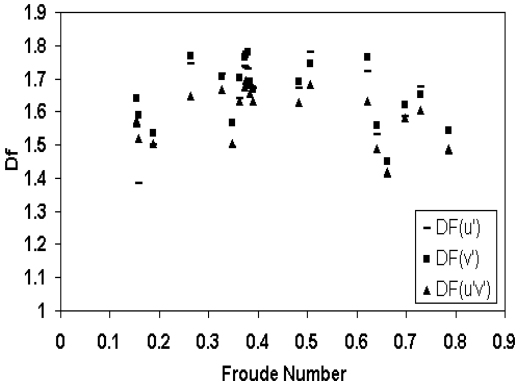


Figure 11. Fractal dimension versus Froude number.

5 CONCLUSIONS

Fractal interpolation functions were successfully used to turbulence properties modeling. Extrema method found to be a good approach to find the desirable number of affine transformations. It was also more efficient than exhaustive search to find the optimum number of transformations. Moreover it was able to calculate accurate fractal dimension of the 1-d fractal curve with using the minimum number of data points (only 500 data points).

Time series of velocity fluctuation components and turbulence shear stress were approximated using fractal interpolation functions. The approximation can be improved by improving the extremum selection filters or even by selecting them manually. There were not a specific relationship between normalized depth and fractal dimension of u' and v' for all data sets. Fractal dimension of u', v' and $u'v'$ were correlated to Froude number and somehow with Reynolds number of the flow and this relationship was different in uniform and non-uniform flows. The fractal dimension of u', v', and $u'v'$ range from 1.4 to 1.8 and the average of them are 1.615, 1.657, and 1.559, respectively. These values can be used for turbulence modeling in open channel flows.

REFERENCES

Barnsley, M. F. 1993. *Fractals Everywhere*. Morgan Kaufmann. San Deigo. 531p.

Jaw, S. Y., and C. J. Chen. 1999. Near wall turbulence modeling using fractal dimensions. *J. Eng. Mech. ASCE*. Vol. (125): 804–811.

Keshavarzi, A. R. 1997. Entrainment of sediment particles from a flat mobile bed with the influence of near-wall turbulence. *Ph.D. Thesis*. University of New South Wales, Australia. 353p.

Marvasti, M. A., and W. C. Strahle. 1995. Fractal geometry analysis of turbulent data. *Signal Processing.* Vol. (41): 191–201.

Mazel, D. S., and M. H. Hayes. 1992. Using iterated function systems to model discrete sequences. *IEEE Trans.* Vol. (40): 1724–1734.

Richardson, L. F. 1922. *Weather Prediction by Numerical Process.* Cambridge University Press, London.

Strahle, W. C. 1990. Turbulent combustion analysis using fractals. *AIAA J.* Vol. (3): 409–417.

Vines, G. 1993. Signal modeling with iterated function systems. *Ph.D. Thesis*. Georgia Institute of Technology, USA. 118p.

River Flow 2004 – Greco, Carravetta & Della Morte (eds.)
© 2004 Taylor & Francis Group, London, ISBN 90 5809 658 0

Expeditive methodology for river water discharge evaluation

M. Greco & D. Mirauda
CIMA-Department of Environmental Engineering and Physics, Basilicata University, Potenza, Italy

ABSTRACT: Recent aims and developments in water resource policies and management have been to achieve a high level of protection in both river systems as well as in the environment by natural hazard prevention and/or reduction. In river water management, the lack of direct field measures resulting from the necessity to dedicate long periods of time and effort represents a weakness in control and forecasting procedures. This paper is in reference to a detailed series of monitoring activities performed on Lucanian Rivers by applying the expeditive methodology for water discharge measurement and assessment, which is capable of maintaining a high quality data and results. Furthermore, this analysis allows us to show the results obtained by adopting the entropy velocity distribution (Chiu 1988) on the data collected using the reduced point method and by performing sensitive analyses on the entropy parameter, thus showing low variation in the estimation of water discharge.

1 INTRODUCTION

The need to design and construct systems of monitoring and control for water resources that are able to produce uniform, trustworthy and comparable data comes from various needs in management, planning and projects developed for the performance of ordinary and extraordinary operations of preservation and conservation for the involved territory as well as for the surrounding environment.

The crucial element of these interventions lies in the availability and reliability of field data. Availability time is especially important in cases of emergency and disaster. The limits of availability are due in part to the heterogeneous area covertures of measuring systems and their partial interconnection and integration and in part to constant conflicts between those organizations responsible for carrying out controls and measures, thus slowing down the information flow. Furthermore, the crucial need to maintain product efficiency in the system of measures is associated to this problem because it requires both innovative technologies (used in order to perform remote data acquisition and to successively transfer the data in real time) as well as continuous and systematic gauge calibration through integrations with ground data.

This need is transversally present for monitoring physical, chemical and environmental parameters and it assumes a primary role in order to perform procedures under conditions of emergency. A prime example of this is the need for flood risks of a constant upgrading of depth/discharge scales in control sections. This upgrading represents a critical element in the chain of warning.

Under this context, field operation efficiency is not a secondary aspect in order to have a correct level of operation for controlling and forecasting procedures which more often than not are considered less important than the performance of upgrades for modeling and measurement techniques.

In the case of water discharge measurement, the difficulties encountered, occurring during the field activities, encourage the development and implementation of models of computation or measuring technologies developed in order to reduce the time of data acquisition and processing without having to sacrifice measurement precision.

In this work, a detailed description of a series of monitoring activities performed on the principal rivers of Basilicata Region has been reported and a comparison between the possible methods of field measurement of liquid discharge has been made. Regarding to normative methods, the reduced point methods (the three-point methods, the one-point method) have been employed maintaining the quality level of the final data product, dramatically reducing acquisition time.

A further help is given applying mathematical models, derived from the application of maximization theories of the informational entropy (Chiu, 1987, 1989, 1991 and 1995), to the data collected in order to evaluate the flow field and compute the water discharge.

The entropy velocity distribution, in fact, requires the assessment of one parameter, M, which can be

obtained through the knowledge of the mean – maximum flow velocities ratio (Chiu, 1987). Moreover, the extension of such law to natural flow allows sufficient reliability also in condition of geometric irregularity and for ordinary flow regime (Greco et al., 2002). The application of the entropic profile to river flow deals interesting results also for practical purposes in order to define the velocity distribution in the cross section and provide an expeditive method to compute the water discharge reducing the time for surveying and computation.

2 FIELD MEASUREMENTS

The results presented and discussed below are in reference to field measurements collected during surveying and calibration activities performed on hydrometrical gauge stations managed by local Authorities for the control of the main rivers of Basilicata Region (Southern-Italy). Several measures were performed at different cross sections of the Basento, Bradano, Cavone, Agri and Sinni Rivers (Fig. 1) for the period between February 2002 and March 2003.

The sections for the Basento River are located both upstream (BA1 station), in the mid-valley zone (BA2 station) and downstream (BA4 station and BA5 station). The sections for the Cavone (CA2 station) and Sinni Rivers (SI1 station) are located in the mid-valley areas close to the delta, while the section for the Bradano River (BR1 station) is located in the mid-valley zone and the section for the Agri River (AG1 station) can be found on the Sauro Torrent, which is the main tributary in hydraulic left bank.

The evaluation of river water discharge can be performed according to the ISO 748/1997, using the velocity-area method which represents an efficient and reliable tool. Operatively, computations require the dividing the section areas into several verticals and a further subdivision of each vertical into discrete points, in order to evaluate the mean velocity of the flow along each vertical.

The velocity measurements were performed by using a current meter, a suitable diameter and a pitch propeller (Fig. 2a). The measurements were performed through wading by using a graduated rod and a mobile trolley system with a single drum winch fitted on it (Figs 2b,c). All field activities were recorded and in field reports, information such as cross section data (measurement code, river name, location name, station name, date and time of measurement, section width, etc.), instrument data (propeller diameter, propeller pitch, measurement duration, calibration lines, etc.) and row measurement data (distance, water level, number of rounds, etc.) were included.

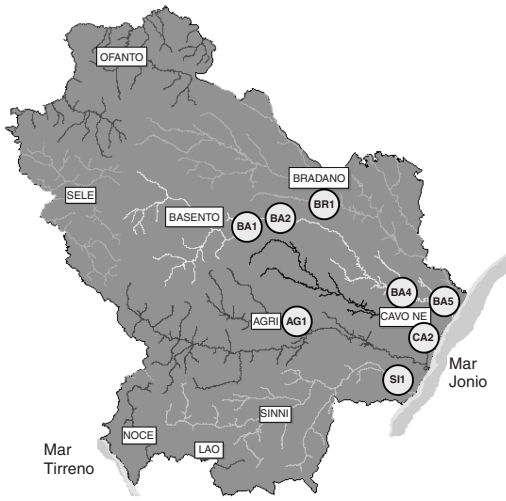


Figure 1. Positioning of measurement stations.

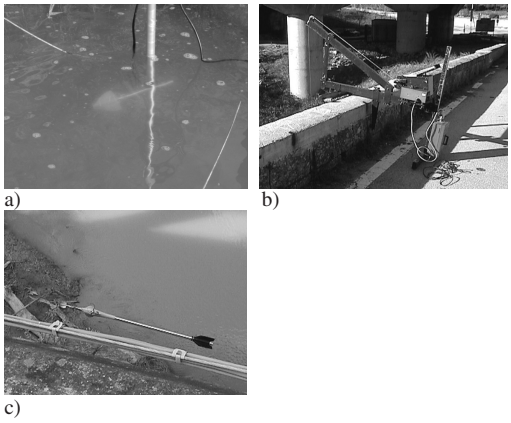


Figure 2. a) Current-meter for wading; b) equipment for performing measurements from bridge; c) sounding weight.

3 NORMATIVE METHODS

The number of verticals and the distribution inside the cross section is chosen case by case based on section width, riverbed geometry and flow regimes and characteristics, while the measurement points are fixed according to the measurement methodology used, that is, by wading or bridge, and to technique.

The main objective was to obtain a correct evaluation of the mean velocity for each vertical and measurement section which is related to a reliable reconstruction of field flow obtained through velocity point measurements in diverse positions of hydraulic sections distributed between the surface and riverbed. The most rigorous approach must strictly follow the criterion that the difference in velocity between two

consecutive points must be less than 20% compared to the higher measured value and that the points found close to the riverbed and to the surface must be fixed according to the dimensions of the instrument used.

Once the velocity for each point along the vertical has been obtained, it should be possible to calculate the velocity distribution by which the mean velocity for the vertical considered can be obtained. In order to carry out a very accurate measure, the method requires a long time and therefore it is not likely to be applied in cases of systematic field measurement. In order to avoid these difficulties, reduced point methods are being used more frequently during field activities because they require short periods of time and they maintain a good level of accuracy as well.

These methods are classified as follows:

(a) two-points method: velocity observations are collected for each vertical by placing the current-meter at 0.2 and 0.8 of the total depth measured below the surface. The average between the two values should be the mean velocity along the vertical:

$$\bar{v} = \frac{v_{0.2} + v_{0.8}}{2} \tag{1}$$

(b) one-point method: velocity observations are collected for each vertical by placing the current-meter at 0.6 of the total depth measured below the surface.
The observed value should be the mean velocity along the vertical:

$$\bar{v} = v_{0.6} \tag{2}$$

Methods much more refined and precise, but requiring long measurement times, propose the use of equations in which velocity measurements are taken at several different depths.

For example, in the six-point method the average velocity is obtained by the following relation:

$$\bar{v} = 0.1\left(v_s + 2v_{0.2} + 2v_{0.4} + 2v_{0.6} + 2v_{0.8} + v_b\right) \tag{3}$$

for the five-point method:

$$\bar{v} = 0.1\left(v_s + 3v_{0.2} + 3v_{0.6} + 2v_{0.8} + v_b\right) \tag{4}$$

for the three-point method:

$$\bar{v} = \frac{\left(v_{0.2} + v_{0.6} + v_{0.8}\right)}{3} \tag{5}$$

where v_s and v_b represent velocity observations near the surface and the riverbed respectively.

Once the mean velocities of each vertical are evaluated, it is possible to compute the water discharge using the mean-section method or mid section method. In the first one, the partial discharge is computed by multiplying the average value of mean velocities of two adjacent verticals times the area included in the respective verticals. The equation of the partial discharge between two verticals 1 and 2, with depth d_1 and d_2, mean velocities v_1 e v_2 and b horizontal distance between the two verticals, is the following:

$$q = \left(\frac{\bar{v}_1 + \bar{v}_2}{2}\right) \cdot \left(\frac{d_1 + d_2}{2}\right) \cdot b \tag{6}$$

The total discharge is obtained by summing the partial discharges calculated.

In the second method the partial discharge between two verticals is obtained as the product of each value of the mean velocity multiplied by the depth d_i and the sum of the semi-distance between the adjacent verticals. The total discharge is obtained by summing these partial discharges in the following way:

$$Q = \sum \bar{v}_i d_i \frac{b_i + b_{i+1}}{2} \tag{7}$$

The latter method was used in the following elaborations in alternative to the mean-section method, because it gives more precise results and reduces computation time.

Table 1 shows the discharges computed by applying the reduced point methods (one and three-point methods) and the six-point method for different rivers and periods.

Particularly, the six-point method was the most ideal for calculating the most precise discharge value, according to the large number of measurements performed in the cross section and for each measuring vertical.

Figures 3, 4, 5 and 6 show the comparison between the area-velocity curves derived using the mean velocity values computed on each vertical, starting from the measurements obtained through different methods. The graphs show the measuring sections of different rivers at various sampling times.

The figures and table show a negligible difference between the discharge computed through the use of different methods and the relative uncertainties.

There are slight deviations between the deviations $SQ_{6/3}$ and $SQ_{1/3}$ computed between the discharge measured through the three-point method, taken as datum discharge, and the discharges measured using the six-point and one-point methods respectively, as well as between the deviations $I_{6/3}$ e $I_{1/3}$ defined as:

$$I_{6/3\max} = \frac{(Q_6 + I_6) - (Q_3 - I_3)}{(Q_3 - I_3)} \quad I_{6/3\min} = \frac{(Q_6 - I_6) - (Q_3 + I_3)}{(Q_3 + I_3)} \tag{8}$$

Table 1. Discharges computed using different methods and relative uncertainties.

Station	Date	Q_{6p} (m^3/s)	Unc.Q_6 (%)	Q_{3p} (m^3/s)	Unc.Q_3 (%)	Q_{1p} (m^3/s)	Unc.Q_1 (%)
BA4	03/03/2003	17,04	±7,3	16,74	±7,5	16,25	±8,1
BA1	28/01/2003	30,75	±6,26	29,77	±6,34	29,85	±6,46
AG1	17/01/2003	–	–	1,98	±4,98	1,98	±4,99
BA2	09/07/2002	–	–	1,28	±6,29	1,29	±6,28
BA5	17/05/2002	–	–	1,68	±5,50	1,74	±5,46
BR1	02/05/2002	–	–	1,79	±6,37	1,75	±6,44
BA5	22/03/2002	–	–	2,35	±4,87	2,42	±4,85
BA2	14/03/2002	–	–	1,93	±5,57	1,95	±5,56
BA4	14/03/2002	4,29	±7,23	4,31	±7,22	4,49	±7,15
BA1	26/02/2002	2,39	±15,52	2,35	±15,54	2,35	±15,57

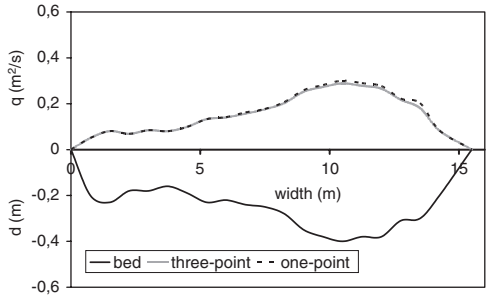


Figure 3. Comparison between discharges for unit width measured using the three-point and one-point methods (Metaponto, Basento 22/03/2002).

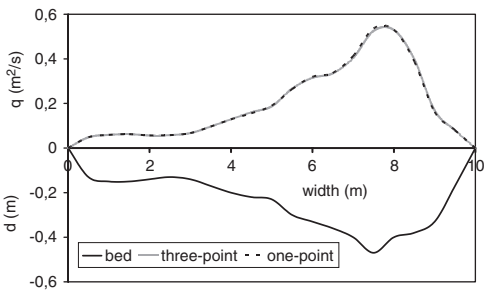


Figure 4. Comparison between discharges for unit width measured using the three-point and one-point methods (Aliano, Agri 17/01/2003).

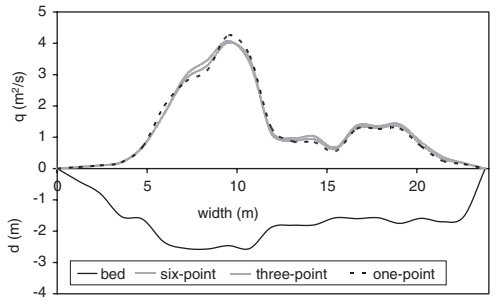


Figure 5. Comparison between the measured discharges for unit width collected by six-point, three-point and one-point methods (Campomaggiore, Basento 28/01/2003).

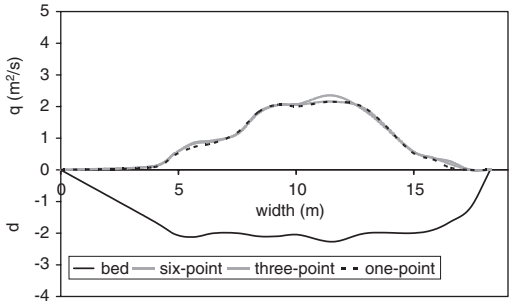


Figure 6. Comparison between the measured discharges for unit width collected by six-point, three-point and one-point methods (Bernalda, Basento 03/03/2003).

$$I_{1/3\max} = \frac{(Q_1 + I_1) - (Q_3 - I_3)}{(Q_3 - I_3)} \quad I_{1/3\min} = \frac{(Q_1 - I_1) - (Q_3 + I_3)}{(Q_3 + I_3)} \qquad (9)$$

Figures 7 and 8 show the comparison between the computed deviation values and summarize the results observed pointing out the excellent equivalence for the analyzed measurements between the three-point and the six-point method underlining the possibility of successfully using the reduced point methods instead of the rigorous one.

Using more detail, from the figures it can be observed how errors committed when using reduced methods (3 or 1 point) are very low for absolute values, this is particularly true regarding the maximum and minimum random and systematic uncertainties suggested by the ISO.

Finally, if a comparison is carried out between the average values of deviations and the average

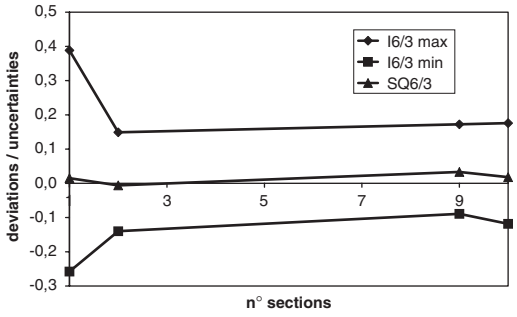


Figure 7. The deviations and uncertainties observed comparing the six-point to the three point methods.

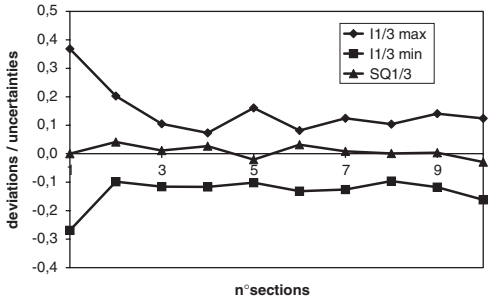


Figure 8. The deviations and uncertainties observed comparing the one-point to the three point methods.

Table 2. Comparison between the average values of minimum and maximum deviations and uncertainties valued with different methods.

$S\bar{Q}_{6/3}$	$\bar{I}_{6/3\,max}$	$\bar{I}_{6/3\,min}$	$S\bar{Q}_{1/3}$	$\bar{I}_{1/3\,max}$	$\bar{I}_{1/3\,min}$
0,015	0,205	0,140	0,008	0,133	0,127

where: $S\bar{Q}_{6/3}$: mean of deviations between the six-point and three point methods; $\bar{I}_{6/3\,max}$: mean of maximum uncertainties between the six-point and three point methods; $\bar{I}_{6/3\,min}$: mean of minimum uncertainties between the six-point and three point methods; $S\bar{Q}_{1/3}$: mean of deviations between the one-point and three point methods; $\bar{I}_{1/3\,max}$: mean of maximum uncertainties between the one-point and three point methods; $\bar{I}_{1/3\,min}$: mean of minimum uncertainties between the one-point and three point methods.

uncertainty values (Table 2), it is seen how the observed deviations, in absolute value, are always lower than the minimum and maximum uncertainty values. Therefore, deviations existing in the different methods applied herein are very moderate compared to systematic and random valuable errors.

4 ENTROPIC MODEL AND ANALYSIS

Based on a probabilistic approach and using the concept of the informational entropy of physics system, Chiu (1988) derived the following relation of the velocity profile on a vertical:

$$\frac{u}{u_{max}} = \frac{1}{M}\ln\left[1+\left(e^{M}-1\right)\frac{\xi-\xi_0}{\xi_{max}-\xi_0}\right] \tag{10}$$

where u is the local velocity, ξ is a dimensionless variable, depending on the reference system adopted, ξ_0 and ξ_{max} are the values to which correspond the minimum of the velocity ($u = 0$) and the maximum ($u = u_{max}$) respectively, while M is the entropy parameter controlling the profile shape.

The following relationship defines the coordinate ξ:

$$\xi = \frac{y}{D-h}\exp\left(1-\frac{y}{D-h}\right) \tag{11}$$

where D is the maximum depth of the flow in the investigated cross section coinciding, in the present study, to the variable h_{max}, h is the depth from the free surface in which the maximum of the velocity is observed and y is the local coordinate perpendicular to the bottom, at which the zero velocity takes place.

In the case of natural and artificial free surface flows, in which the current width is significantly greater than the height (wide cross section), it is commonly supposed that velocity grows monotonically with the height y, passing from zero at the bottom to the maximum at the free surface ($h = 0$), thus, the Equation 11 becomes:

$$\xi = \frac{y}{D} \tag{12}$$

The entropic parameter M has been evaluated according to the classical formulation of Chiu, as a function in the relation between the mean and maximum cross section velocity:

$$\frac{\overline{u}}{u_{max}} = e^{M}\left(e^{M}-1\right)^{-1} - \frac{1}{M} \tag{13}$$

Following the entropy theory, data processing allows us to evaluate the parameter M for each used measuring method: the six-point, the three-point and the one-point methods.

Although the maximum velocity occurred below the free surface for each section, Equation 12 was used to represent the coordinate ξ in order to quicken the computation process of discharge. This assumption, even if it implies having to assume greater approximations in the computation of the final values, is acceptable, especially if it is considered in an operative simplification and automation context for discharge computation

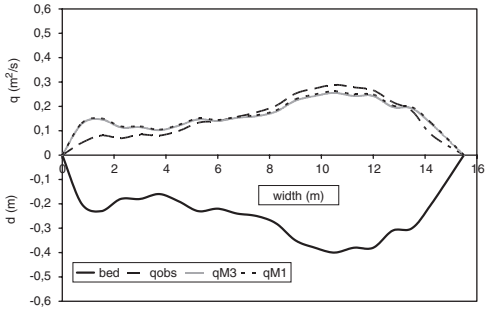


Figure 9. Comparison between discharges for unit width observed and computed using M3, M1 (Metaponto, Basento 22/03/2002).

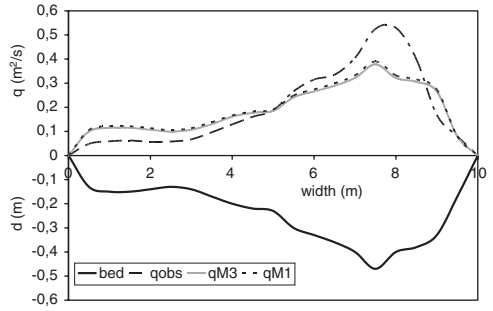


Figure 10. Comparison between discharges for unit width observed and computed using M3, M1 (Aliano, Agri 17/01/2003).

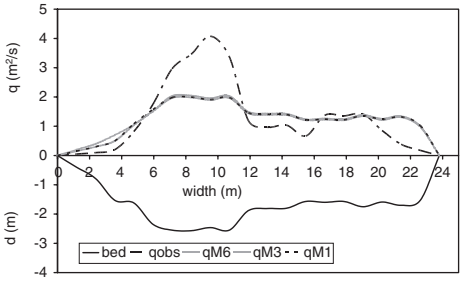


Figure 11. Comparison between discharges for unit width observed and computed using M6, M3, M1 (Campomaggiore, Basento 28/01/2003).

procedures. A higher accuracy in the evaluation of the coordinate ξ, and in particular of the value ξ_{max}, implies a better fitting of computed velocity compared to the observed one applying a very small change in the average velocity value on the vertical and, consequently, not relevant for the purposes of the present work.

Figures 9, 10, 11, 12 and Table 3 show the comparison between the discharge values obtained when using

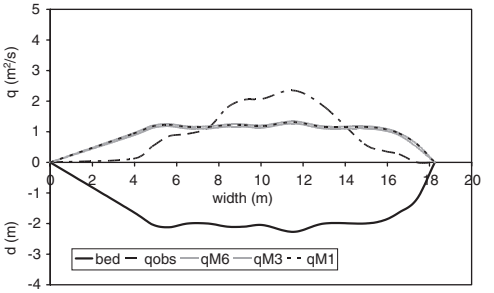


Figure 12. Comparison between discharges for unit width observed and computed using M6, M3, M1 (Bernalda, Basento 03/03/2003).

Table 3. Observed and computed discharges with M_6, M_3 and M_1 for different sections.

Station	Data	Q_{ob} (m^3/s)	Q_{M6} (m^3/s)	Q_{M3} (m^3/s)	Q_{M1} (m^3/s)
BA1	26/02/2002	2,39	1,82	1,86	1,85
BA4	14/03/2002	4,29	3,32	3,35	3,43
BA2	14/03/2002	1,93	–	1,84	1,91
BA5	22/03/2002	2,35	–	2,62	2,69
BR1	02/05/2002	1,79	–	1,49	1,67
BA5	17/05/2002	1,68	–	1,71	1,83
BA2	09/07/2002	1,28	–	1,21	1,23
AG1	17/01/2003	1,98	–	1,84	1,91
BA1	28/01/2003	30,75	28,21	27,48	27,86
BA4	03/03/2003	17,04	16,29	17,35	17,07

the entropic method and the corresponding values derived from systematic field measure processes.

More detailed, the analytic and graphic representations plot the entropic parameter M value computed on the basis of field data acquired when applying the six-point, three-point and one-point methods.

The generic M_i (i = 1, 3, 6) (Figs 9, 10, 11, 12) represents the value computed applying the Chiu model to the mean and maximum velocity values obtained from the sampling with the "i" point method. It is seen that the value Q_{Mi} is the discharge obtained from entropic distribution of measurements acquired through the use of the relative reduced point method. The value Q_{oss} is the discharge observed, when applying normative methods, using the highest number of points acquired during field measurements.

Figures 9, 10, 11 and 12, useful for graphically representing discharges by unit of width, show a typical "behavior" of an entropic model in relation to flow concentration as seen in an irregular geometric section. It is important to note that in Figure 12 the evaluated model averages the specific flows rendering the whole section a contributor to the outflow and cause the energetic information coupled to graphic representation to be lost.

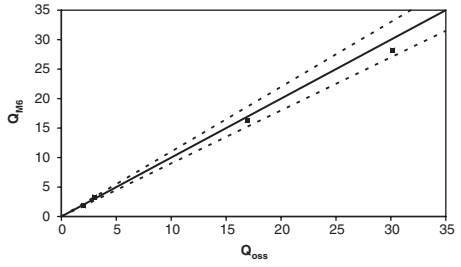


Figure 13. Comparison between observed discharges computed with entropic distribution and with value of M6.

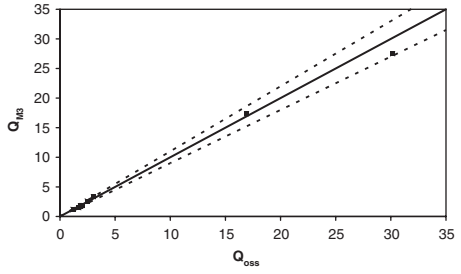


Figure 14. Comparison between observed discharges computed with entropic distribution and with value of M3.

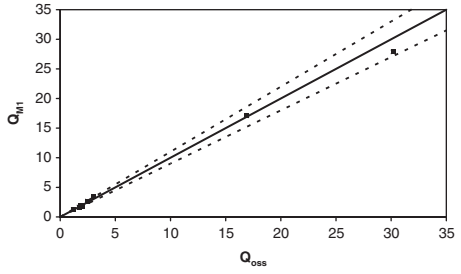


Figure 15. Comparison between observed discharges computed with entropic distribution and with value of M1.

The entropic model response, in fact, is reliable enough to evaluate discharges, in terms of absolute value, indistinctly for M_6, M_3, M_1 estimations, as is observed in the graphs (Figs 13, 14, 15) which show the observed value versus the calculated value and the confidence band at 10%.

The deviations observed, of the order of 7–12%, are generally very negligible considering the approximation coming from the possible errors when measurements were taken. This leads to the uncertainty values included in the ±10% interval.

5 CONCLUSIONS

Procedures for water discharge measurement in a river require acquisition techniques, methods and data processing procedures that are able to reduce both field operation and computation time while maintaining a high quality and reliability levels of the results obtained.

In this paper the possibility of fitting field measurements, obtained from rivers, through the use of conventional methods such as ISO and through the use of the entropic velocity model, has been evaluated.

The results provided underline the possibility of using both reduced point expeditive measurement methods as well as the entropic model for water discharge and flow field evaluation.

REFERENCES

Chiu, C.L. 1987. Entropy and probability concepts in hydraulics. *Journal Hydraulic Engineering ASCE* 113: 583–600.

Chiu, C.L. 1989. Velocity distribution in open channel flow. *Journal Hydraulic Engineering ASCE* 115: 576–594.

Chiu, C.L. 1991. Application of entropy concept in open channel flow. *Journal Hydraulic Engineering ASCE* 117: 615–628.

Chiu, C.L. 1995. Maximum and mean velocity and entropy in open channel flow. *Journal Hydraulic Engineering ASCE* 121: 26–35.

Greco, M. 1998. Distribuzione entropica di velocità in un corso d'acqua naturale. *XXVI Convegno di idraulica e Costruzioni idrauliche* 1:103–112.

Greco, M. 1998. Entropy velocity profile: application in natural river. *International Symposium Environmetal Engineering and Healt Sciences*, Cholula, Mx.

Greco, M. 1999. Entropy velocity distribution in a river. *I.A.H.R. Symposium Environmetal on River Coastal and Estuarine Morphodynamics*, Genova.

Greco, M. & Mirauda, D. 1999. Downward and upward approach for entropy velocity profile. *International Conference Water, Environment, Ecology, Socio-Economics, and Health Engineering*, Seoul, Korea.

Greco, M. & Mirauda, D. 2002. Valutazione globale del parametro entropico di velocità. *L'Acqua* 5:17–23.

ISO 748: 1997, Measurement of liquid flow in open channel – Velocity-area methods.

ISO 3454: 1983, Liquid flow measurement in open channels – Direct depth sounding and suspension equipment.

ISO 1100-1: 1996, Measurement of liquid flow in open channel – Part 1: Establishment and operation of a gauging station.

ISO 1100-2: 1998, Measurement of liquid flow in open channel – Part 2: Determination of the stage-discharge relation.

ISO/TR 7066-1: 1997, Assessment of uncertainty in calibration and use of flow measurement devices – Part 1: Linear calibration relationships.

ISO/TR 7178: 1983, Liquid flow measurement in open channels – Velocity-area methods – Investigation of total error.

Xia, R. 1997. Relation between mean and maximum velocities in a natural river. *Journal Hydraulic Engineering ASCE* 123: 720–723.

This page intentionally left blank

River Flow 2004 – Greco, Carravetta & Della Morte (eds.)
© 2004 Taylor & Francis Group, London, ISBN 90 5809 658 0

Integrated approaches for modeling sediment transport

J.-M. Hervouet & C. Villaret
Laboratoire National d'Hydraulique et Environnement Electricité De France, Research & Development, Chatou, France

ABSTRACT: This paper exemplifies, in the field of sediment transport, the need for an integrated approach coupling all physical phenomena. Three cases are successively dealt with, in the framework of the Telemac hydroinformatic system: coupling of hydrodynamics with bed-load transport, simultaneous treatment of bed-load and suspended sediment transport, and finally integrated computation of hydrodynamics and suspended sediment in 3 dimensions.

1 INTRODUCTION

Sediment transport, be it on a shoreline, in an estuary or in a river, is highly depending on complex interactions between currents, waves and turbulence. In a field where physical laws are mostly empirical and sometimes insufficiently known, expertise will always remain a key asset, but numerical modeling gives more and more relevant information. Recent progresses stem from an integrated approach where all the physical phenomena are concurrently dealt with, either within the same computer program, or by means of coupling techniques.

Numerical simulations show that a correct representation of different physical phenomena is obtained only with a close coupling between computer programs, in order to update currents, waves, and bottom elevation. The framework of the developments described hereafter is the Telemac hydro-informatic system, namely its 2 hydrodynamic modules: Telemac-2D (Shallow water equations in 2 dimensions) and Telemac-3D (3-dimensional Navier-Stokes equations, either with or without hydrostatic pressure assumption, see [1]), as well as its sediment transport module Sisyphe (a co-property of CETMEF, UTC, EDF, and SOGREAH). Sisyphe solves the equation of the bed evolution, using various bed-load transport-rate formulas. This model has been recently updated to deal with suspended sediment transport. In 2 dimensions, a step-by-step coupling between Telemac-2D and Sisyphe has been implemented, with significant improvements, as discussed in paragraph 2.

The influence of waves is also a key parameter in coastal zones, and so far we have treated it by adding forcing terms in the shallow water equations, which is actually only a chaining of programs, namely Telemac-2D and the module Tomawac, the latter computing the generation of waves under the influence of wind. This chaining is classical and will not be detailed here.

The two different kinds of sediment transport are bed-load and suspended load. The first one is treated by means of an empirical transport formula, whereas the latter can be tackled by an advection–diffusion equation. This approach will be detailed in paragraph 3. A concurrent treatment of bed-load and suspended sediment transport enables a more realistic behaviour when dealing with non-equilibrium flows, and this will be exemplified on the example of a trench migration.

In 3 dimensions, the advection–diffusion is fully integrated in the Telemac-3D hydrodynamic module, to take into account suspension, with all its interactions with the flow, due to the modifications of density. We describe in paragraph 4 a validation test-case with an analytical solution based on the Rouse profile, with an improvement to prevent unrealistic solutions near the bottom.

2 COUPLING HYDRODYNAMICS AND BED-LOAD TRANSPORT

2.1 *Chaining and coupling*

The close interaction between bed evolution and currents proves to be so important that it cannot be neglected in many cases.

Before implementing internal coupling we resorted to a simplified approach consisting of a first computation of hydrodynamics with Telemac-2D, without any feedback of bed evolution, followed by a computation of bed-load transport with a rough updating of velocities with respect to bed evolution. As a matter of

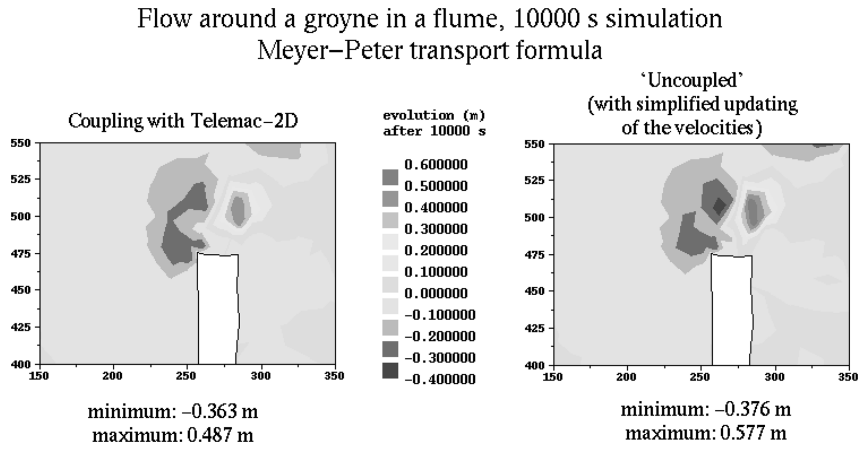


Figure 1. Importance of a coupling of hydrodynamics with bed-load transport.

fact, we assumed that the product of depth and velocity remains locally constant, so that the velocity decreases in erosion zones and increases in deposit zones, which is the required effect.

We compare here this simplified approach, hereafter denoted as 'uncoupled', to the fully coupled solution which consists of exchanging at every time-step the velocities and bottom elevation between the 2 coupled computer programs.

2.2 *Example 1*

We compute the erosion around a groyne in a flume. The flume is 250 m wide and the groyne is 25 m wide and about 125 m long. The average depth is 10 m and the velocity around the groyne about 10 cm/s. The results obtained with a time-step of 2,5 s and after 10000 s of real time are presented on figure 1 (left: 'coupled', right: 'uncoupled'). There is an excess of about 20% of deposits in the 'uncoupled' case. As a matter of fact, the higher velocities above deposits in the coupled case contribute to limit their growth, a phenomenon which is only partly taken into account with our simplified updating approach. This latter technique, though classically used in Sisyphe when run in standalone mode, is thus less efficient than a real coupling.

2.3 *Example 2*

Evolution and filling of a trench (depth: 15 cm and length: 5 m) under the influence of a uniform steady flow. The flow conditions are the following: depth at the entrance 0,5 m and average velocity 1 m/s. The 'coupled' and 'uncoupled' results, all other parameters remaining the same, are presented on figure 2. They show, with coupling, a better numerical stability, and a more realistic physics, even if the evolution of the trench is roughly the same.

3 SIMULTANEOUS TREATMENT OF BED-LOAD AND SUSPENSION

3.1 *A coupling approach*

The Telemac system was originally built to enable an independent treatment of suspended sediment transport (Subief 2D module) and bed-load transport (Sisyphe module).

Subief-2D deals with the transport of fine and generally cohesive sediment: it solves an advection–diffusion equation for the concentration. On the bottom, erosion and deposit laws give the fluxes between the bed and the suspension.

Sisyphe computes the bed-load transport of non-cohesive material, using semi-empirical laws to get the transport rate. It is done under the assumption of a local equilibrium between the turbulent flow and the bed, which is generally the case when there is only bed-load transport, but not as soon as suspended sediment is added. After the recent developments of Sisyphe, we can now compute in a fully consistent and concurrent way the suspended load and the bed-load.

3.2 *Principle of the model*

The water column is divided into:

(1) A thin layer of thickness a $\sim 2D_{50}$, within which the sediment is transported by bed-load, under the assumption of an equilibrium state.
(2) The free water column itself, where the sediment is maintained in suspension by turbulence mixing.

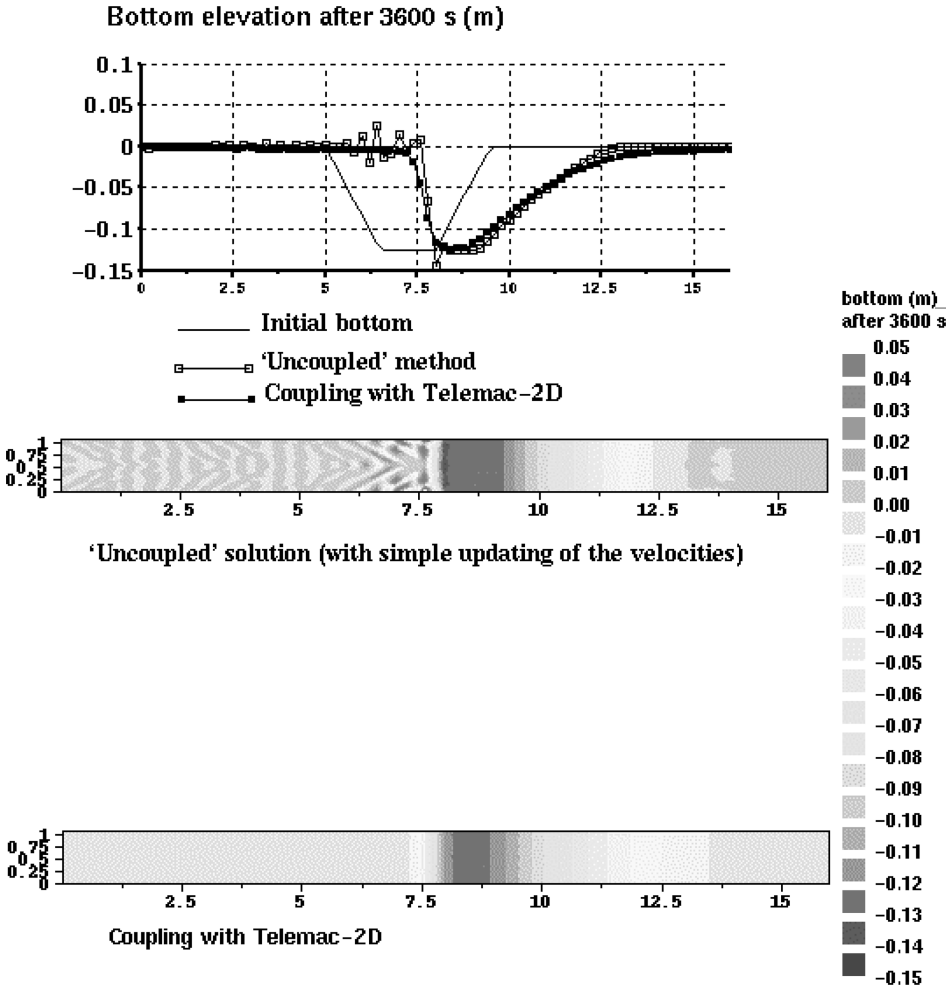


Figure 2. Coupled or 'Uncoupled' bed-load transport – evolution of a trench. Upstream flow conditions : U = 1 m/s, h = 0.5 m. Sediments grain size: $D_{50} = 500\ \mu m$. Computation 1 (standalone Sisyphe) and 2 (Sisyphe coupled with Telemac 2D are done in the same conditions Dt = 0.1 s, Meyer-Peter transport formula, Strickler friction coefficient St = 40).

We assume that the suspended sediment concentration behaves as a passive tracer, which means that it just follows the mean and turbulent flow velocity, with its downward settling velocity. After a depth-integration of the 3-dimensional advection–diffusion equation, between the top of the bed-load layer and the free surface, we get the following equation for the depth-integrated concentration $\overline{C}$:

$$\frac{\partial \overline{C}}{\partial t} + \vec{U}.\nabla(\overline{C}) = div(\nu_t \nabla(\overline{C})) + \frac{(E-D)_{z=a}}{h} \qquad (1)$$

Here E and D are the sediment (erosion–deposition) fluxes at the interface between the bed-load layer and the suspension. z = a stands for the top of the bed-load layer, h is the water depth. ν_t is the sediment diffusivity, considered to be equal to the eddy viscosity coefficient. The bed evolution equation must also take these fluxes into account and reads:

$$(1-n)\frac{\partial Z_f}{\partial t} + div(Q_c) + (E-D)_{z=a} \qquad (2)$$

Z_f is the bottom elevation, n is the bed porosity and Q_c the bed-load transport rate.

3.3 *Flux at the interface*

The net flux at the interface is:

$(E\text{-}D)_{z=a} = W_s\,(C_{eq} - C_a)$

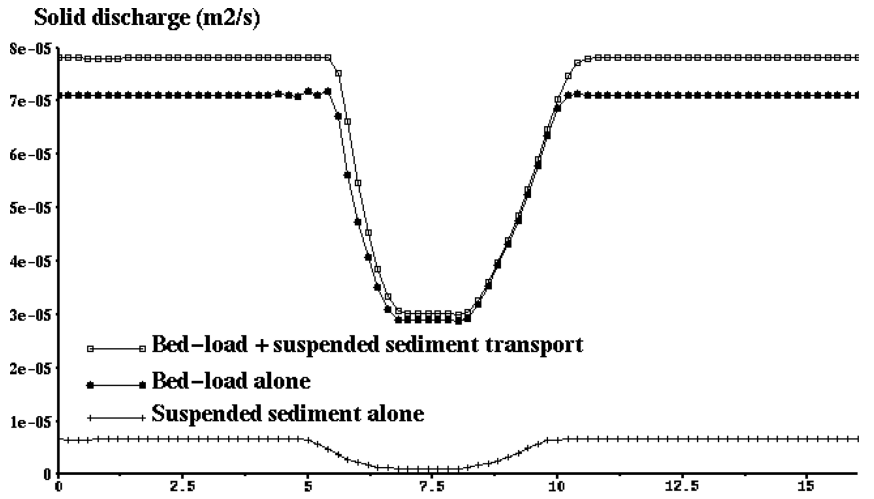


Figure 3. Coupling bed-load and suspended sediment transport. The total transport rate Qt is decomposed into $Q_t = Q_c + Q_s$; Q_c is the bed-load transport and Q_s, the suspended sediment transport ($Q_s = h\ U\ C$). With same parameters than figure 2.

W_s (>0) being the downward settling velocity, C_{eq} the equilibrium concentration and C_a the concentration at $z = a$. When the equilibrium state is reached ($C_a = C_{eq}$), only the bed-load contributes to the bed evolution.

3.4 *Concentration at the equilibrium state*

Several formulas are available in the literature to calculate the equilibrium concentration as a function of the bottom friction. The Zyserman and Fredsoe (see [2]) formula has been programmed in Sisyphe. In the 2-dimensional approach, the depth-averaged concentration must be linked to the concentration on the bottom C_a. We assume here that the concentration follows a Rouse profile along the vertical (equation 9 hereafter), which, combined to the fact that the velocities obey a logarithmic law in the rough turbulent regime, yields the following value of C_a:

$$C_a = \frac{\overline{UC}}{u_*} \times \frac{\kappa}{I}\left[\frac{1-a/h}{a/h}\right]^R \qquad (3)$$

where u_* is the friction velocity, κ the von Karman constant, R is the Rouse number: $W_s/(\kappa\, u_*)$, and I the Einstein integral defined by : $I = I_1\ \mathrm{Log}(30h/k_s) + I_2$, where k_s is the bed roughness, and:

$$I_1 = \int_{a/h}^{1}\left(\frac{1-u}{u}\right)^R du \quad I_2 = \int_{a/h}^{1}\left(\frac{1-u}{u}\right)^R Log(u)\, du \qquad (4)$$

3.5 *Application*

This full numerical model has been applied to the same previously described trench test-case, with the same flow and sediment parameters. Here bed-load transport is dominant, as shown in figure 3, however the effect of suspension is important and tends to speed-up the trench migration (figure 4).

4 HYDRODYNAMICS AND SUSPENSION IN 3 DIMENSIONS

4.1 *Rouse profile*

The hydrodynamic model Telemac-3D is coupled with an advection–diffusion equation for suspended sediment, which reads:

$$\frac{\partial C}{\partial t} + div\left[(\vec{U} + \vec{W}_s)\, C\right] = div(\nu_t\, \overrightarrow{grad}(C)) \qquad (5)$$

where $\vec{W}_s$ is the settling velocity vector, with components $(0, 0, -W_s)$. The solution procedure is fully embedded within the hydrodynamics time loop, along with the turbulence model.

The computations have been validated against an analytical solution, in the case of a uniform flow in a rectangular channel with a constant slope, without lateral friction but with a bottom friction. We choose the following mixing-length turbulence model:

$$\nu_t = {l_m}^2 \frac{\partial u}{\partial z} \text{ with } l_m = \kappa z\left(\sqrt{1-\frac{z}{h}}\right) \qquad (6)$$

which is consistent with a parabolic profile of turbulent viscosity and a logarithmic velocity profile (see [3]):

$$\nu_t = \kappa u_* z\left(1-\frac{z}{h}\right) \qquad (7)$$

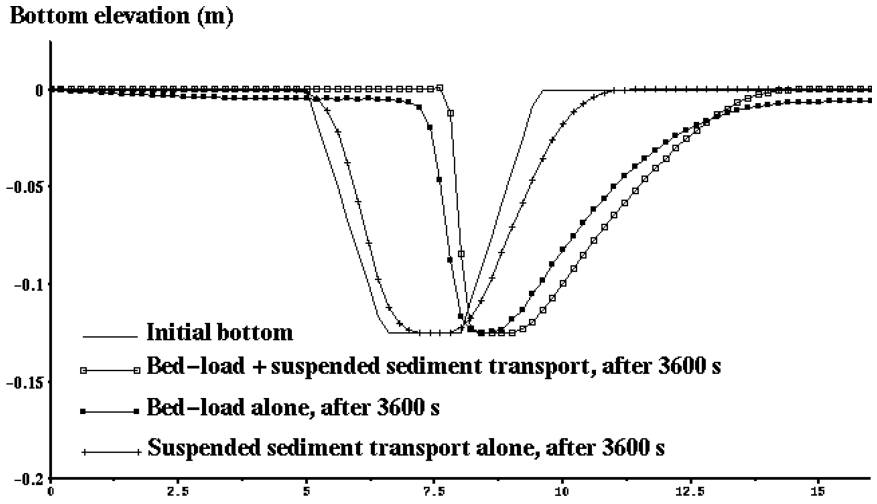


Figure 4. Coupling bed-load and suspended sediment transport – evolution of a trench.

In the case of steady and uniform flows, the advection–diffusion equation simplifies into a balance between the turbulence diffusion and settling terms:

$$\frac{\partial(-W_s C)}{\partial z} = \frac{d}{dz}(\nu_t \frac{dC}{dz}) \tag{8}$$

which after integration gives the well-known Rouse profile of the concentration:

$$C = C_{h/2}\left[\frac{h-z}{z}\right]^R \tag{9}$$

where $C_{h/2}$ is the concentration at mid-depth ($z = h/2$).

The total sediment flux at the entrance of the channel is $Q\,C_0$. By integrating the Rouse profile we can then deduce the value of $C_{h/2}$.

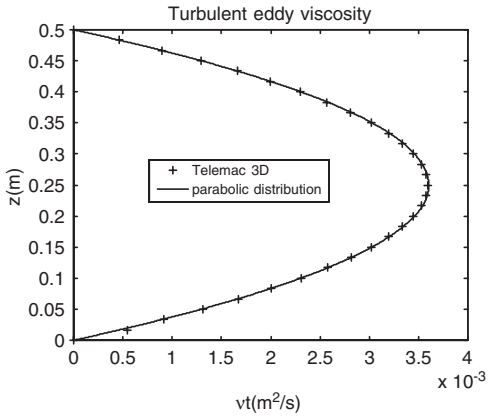


Figure 5. Theoretical and computed turbulent viscosity profile obtained with the Nezu and Nakagawa mixing-length model.

4.2 *Numerical parameters*

The upstream concentration is assumed to be constant, equal to C_0, and we choose $C_0 = 0.02$. The settling velocity W_s is 0.01 m/s.

The channel length is 500 m, its width 100 m, the bed slope is $1.01\,10^{-3}$. The bed roughness is $k_s = 0{,}0162$ m. The flow discharge is $Q = 50\ m^3/s$. The prescribed elevation downstream is 0,5 m.

With those data, the depth in the channel is constant and equals 0.5 m, and the depth-averaged velocity is 1 m/s. The friction velocity u_* is 0.0703 m/s. The maximum diffusivity coefficient, obtained at $z = h/2$, is equal to $3.6\,10^{-3}\ m^2/s$. Telemac-3D computations were performed with a mesh composed of 30 layers of elements on the vertical, and 1000 time steps of 1 s each. Figure 5 compares the theoretical and computed values of the diffusivity coefficient. The discrepancy is less than 1%. Figure 6 compares the theoretical and computed velocity profiles. These results fully validate the hydrodynamics.

The mid-depth concentration is in this case: $C_{h/2} = 1.87\,10^{-2}$. The computed value, in the same conditions as stated above, is $1.88\,10^{-2}$. However discrepancies of concentration near the bottom were observed, and were only explained by the fact that the Rouse profile is not correct in a close vicinity of the bottom, which led us to propose a slightly amended theoretical solution.

4.3 *Modified Rouse profile*

The drawback of the Rouse concentration profile in numerical simulations is that it gives an infinite

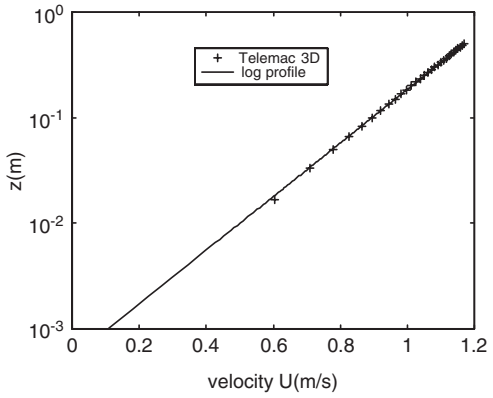


Figure 6. Theoretical and computed velocity profile obtained with the Nezu and Nakagawa mixing-length model.

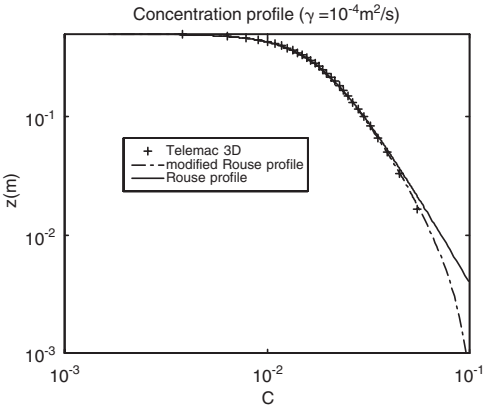


Figure 7. Rouse profile, modified Rouse profile, Telemac-3D results with 30 layers of elements on the vertical (log-log representation).

concentration on the bottom. As a matter of fact, the computations are performed up to $z = 0$, where the turbulent viscosity vanishes. We propose hereafter an analytical solution including the effect of a constant laminar viscosity ν, which is not negligible near the bed. Assuming that the concentration is still 0 at the free surface, we now have to solve:

$$\frac{\partial(-W_s C)}{\partial z} = \frac{\partial}{\partial z}\left[(\nu + \nu_t)\frac{\partial C}{\partial z}\right] \tag{10}$$

which can be integrated to yield:

$$C = C_{h/2}\left[\frac{h - z}{z + \dfrac{\nu}{\kappa u^*}}\right]^R \tag{11}$$

With this new profile the value of $C_{h/2}$ has to be slightly corrected and becomes $1.90\,10^{-2}$. The laminar viscosity precludes an infinite concentration on the bottom. The bed concentration $C_{z=0}$ is however highly sensitive to the prescribed value of the laminar viscosity. For example, we find $C_{z=0} = 0.233$ for $\nu = 10^{-5}$ m^2/s (computed value: 0.106) and $C_{z=0} = 0.106$ for $\nu = 10^{-4}$ m^2/s (computed value: 0.0898). Finding a more accurate value of C at the bottom would require more layers of elements because of the very sharp profile. It is however clear that the computed solution tends to this modified Rouse profile, as shown on figure 7 which corresponds to 30 layers and $\nu = 10^{-4}$ m^2/s.

5 CONCLUSION

We have seen here only a few examples of integrated approaches in the field of sediment transport. Many others could be described, the more so if waves and water quality are involved. As a unique programme dealing with all equations and physical phenomena would raise computer engineering and maintenance problems, a modular solution seems a viable technique. It will certainly develop more and more as long as open architectures are available.

REFERENCES

1. Hervouet J.-M. : Hydrodynamique des écoulements à surface libre, modélisation numérique avec la méthode des éléments finis (in French). Presses des Ponts et Chaussées. ISBN 2-85978-379-2. 2003.
2. Zyserman, J.A., Fredsoe, J. : Data analysis of bed concentration of suspended sediment, J. of Hydraulic Engineering, ASCE, Vol. 120, N°9, pp 1021–1042. 1994.
3. Nezu, I., Nakagawa, H.: *Turbulence in Open-Channel Flows*, IARH, 1993.

This page intentionally left blank

River Flow 2004 – Greco, Carravetta & Della Morte (eds.)
© 2004 Taylor & Francis Group, London, ISBN 90 5809 658 0

Riprap failure of bridge piers

J. Unger & W.H. Hager
VAW ETH-Zentrum, Zurich, Switzerland

ABSTRACT: The entrainment of riprap elements placed around a bridge pier is investigated, using previous research relative to the Shields' entrainment function for turbulent rough flow, and its modification due to the presence of a bridge pier. A novel failure definition is offered first, based on the loss of a riprap element in the immediate surrounding of the pier. Then, the effects of approach flow conditions and pier geometry are separated from the effects of relative riprap size and number of riprap layers placed concentrically around the pier. This concept is verified with preliminary experiments conducted for a sediment mixture to result in a plot in which the individual effects of riprap and sediment diameters, sediments layers, relative bridge pier diameter, density ratio between sediment and fluid phases, and relative approach flow depth are related to the entrainment upstream velocity under which riprap failure occurs. This diagram contains also a division line between the two failure modes observed, namely riprap sliding into the adjacent sediment erosion, and riprap rolling out from the conglomerate. This paper may thus be considered a first step for the definition of a generalized riprap failure equation in relation to bridge piers.

1 INTRODUCTION

Water flow around bridge piers has received significant attention in the past years, because the failure of a bridge normally corresponds to the loss of an important infrastructure. The substructure of bridges is subject to a large variety of geometrical designs, such that these flows depend on a significant number of geometrical parameters, in addition to the most pertinent flow features. In the following, the simplest configuration will be considered, corresponding to a cylindrical pier of diameter D, around which a concentric riprap is placed. The individual elements of the riprap (subscript R) have a diameter d_R and involve n rows, as shown in the definition sketch (Figure 1). The sediment (subscript s) around the riprap has a median diameter d_{50s} and a non-uniformity $\sigma = (d_{84}/d_{16})^{1/2}$; the densities of the fluid and the sediment are ρ and ρ_s, respectively. Further, the upstream (subscript o) approach flow characteristics may be described with the approach velocity V_o and the flow depth h_o. The problem to be attacked thus may be stated as: For a given pier protected with a riprap, what are the hydraulic conditions that result in its failure?

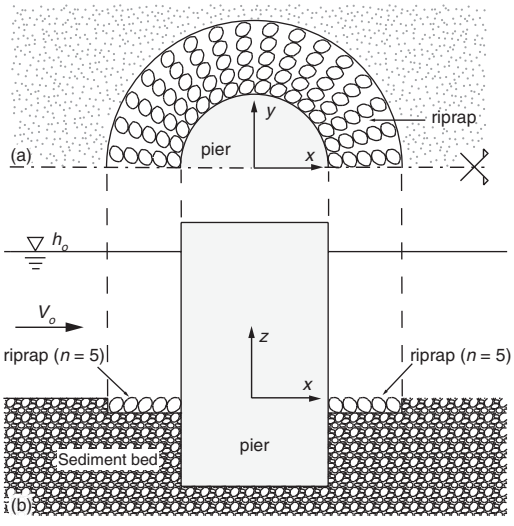


Figure 1. Definition sketch for riprap arrangement around a circular-shaped pier (a) plan, (b) section.

A literature review reveals that this problem has received some attention in the past, given the relevance in river engineering. Hamill (1999) defines a densimetric riprap (subscript R) Froude number $F_R^2 = V_p^2/(g' d_R) = 0.692\,K^2/2$ with $K = 1.5$ for round-nosed piers and $K = 1.7$ for rectangular piers, $g' = [(\rho - \rho_s)/\rho]g$ as reduced gravitational acceleration and V_p as the velocity at the pier which is typically $1.5V_o$. Melville and Coleman (2000) list a total of 12 formulae for the prediction of the required riprap. Based on a riprap densimetric Froude number $F_R^2 = V_{Rc}^2/[g' d_R]$ where V_{Rc} is the critical (subscript c)

velocity for the entrainment of the riprap elements of size d_R, a number of proposals are stated. Either, an upper limit of F_R^2 is indicated as a function of the relative riprap size d_R/h_o or the maximum admissible upstream velocity V_o is expressed in terms of relative riprap size and the bridge pier geometry. All equations listed involve the Froude similitude although it is known that viscous effects may occur for small hydraulic models. The number of riprap layers around the pier has not been accounted for systematically, and the limitations for the various equations are not properly stated.

Hager and Oliveto (2002) considered a simplified version of the Shields diagram. Depending on the relative sediment diameter $D^* = (g'/\nu^2)^{1/3} d_{50}$, where d_{50} is the size of a uniform sediment bed and ν is kinematic viscosity, three relations for the entrainment (subscript i for inception) densimetric Froude number $F_{di} = \sigma^{-1/3} V_{oi}/(g' d_{50})^{1/2}$ were defined. Provided $D^* \geq 150$, this relation simply reads with R_{ho} as the hydraulic radius of the approach flow

$$F_{di} = 1.65 (R_{ho}/d_{50})^{1/6} \tag{1}$$

Equation (1) thus applies for relatively large sediments for which viscous effects are absent.

The results were extended to bridge piers, i.e. (1) was considered as the entrainment condition for a bridge pier of diameter $D \rightarrow 0$. Compared to the arrangement tested by Shields, only the relative pier width $\beta = D/B$ with B = channel width must be considered in addition to all other parameters involved. A coefficient (subscript β for presence of pier) $\Phi_\beta = F_{d\beta}/F_{di} < 1$ was thus introduced. For circular-shaped bridge piers, the experiments indicated that (Hager and Oliveto (2002))

$$\Phi_\beta = 1 - (2/3)\beta^{1/4} \tag{2}$$

The entrainment condition for circular bridge piers of relative diameter β in a flow with a relative hydraulic radius R_{ho}/d_{50} may thus be expressed as

$$\begin{aligned} F_{d\beta} &= \sigma^{-1/3} V_{o\beta}/(g'/d_{50})^{1/2} \\ &= 1.65 (R_{ho}/d_{50})^{1/6} [1 - (2/3)\beta^{1/4}] \end{aligned} \tag{3}$$

The entrainment velocity $V_{o\beta}$ under which scour is initiated for flows in which viscosity has no dominant effect [$D^* = (g'/\nu^2)^{1/3} d_{50} > 150$] at a bridge pier in a uniform sediment surface thus depends on the approach hydraulic radius R_{ho}, sediment size d_{50} and relative pier diameter D/B. It is important to note that (3) degenerates to Shields' entrainment condition for $\beta = 0$. In the following this concept will be extended to piers containing a riprap protection.

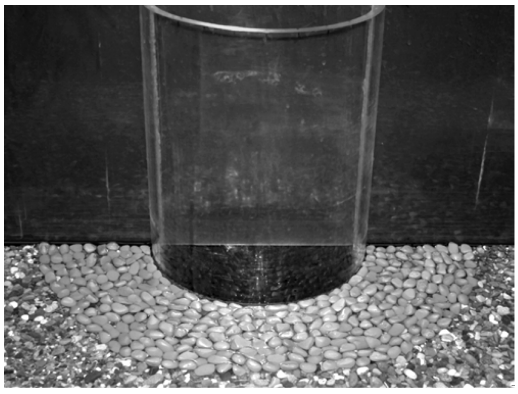


Figure 2. Riprap arrangement about a pier, half-channel setup ($D = 260$ mm, $n = 10$, $d_R = 13$ mm).

2 EXPERIMENTS

2.1 *Experimental setup*

Figure 1 shows a definition plot with the main parameters V_o = approach flow velocity, h_o = approach flow depth, x = streamwise coordinate and y = transverse coordinate, d_R = riprap size and n = numbers of layers concentrically arranged about the pier. Up to now one sediment was employed in the VAW scour channel (Hager et al. 2002). It may be described with $d_{16} = 1.75$ m, $d_{50} = 5.0$ m and $d_{84} = 9.2$ mm, thus $\sigma = 2.29$. Piers were arranged both in the channel axis and along the left channel side wall, in order to simplify experimental observations. It was demonstrated by Hager and Oliveto (2002) that the half-channel and the full channel arrangements are identical, provided that the pier diameter is larger than some 5% of the channel width, to inhibit effects of boundary layer flow along the glass wall. Figure 2 shows a typical experimental arrangement prior to a test, involving 10 riprap rows. Figure 3 shows the complete scour channel used for scour researches at VAW.

Circular-shaped piers and half piers of diameters $D = 110$, 260 and 457 mm were used. The sizes of the riprap elements were $d_R = 12, 13, 19, 30, 50$ mm such that the relative riprap size $\delta = d_R/d_{50s}$ varied between $2.6 < \delta < 10$. Depending on the experimental conditions, $n = 1, 3, 5$ and 10 was normally tested for the number of riprap rows. Discharges varied between 0.042 and 0.11 m^3/s, resulting in failure densimetric particle Froude numbers F_{dR} between 1.5 and 3.3. Table 1 gives an overview of the test conditions of the present research. It is planned to extend similar tests to sediments of other size (d_{50}) and non-uniformity parameter (σ) to check for these additional effects.

The preparation of an experiment involved the following works (for details refer to Hager et al.

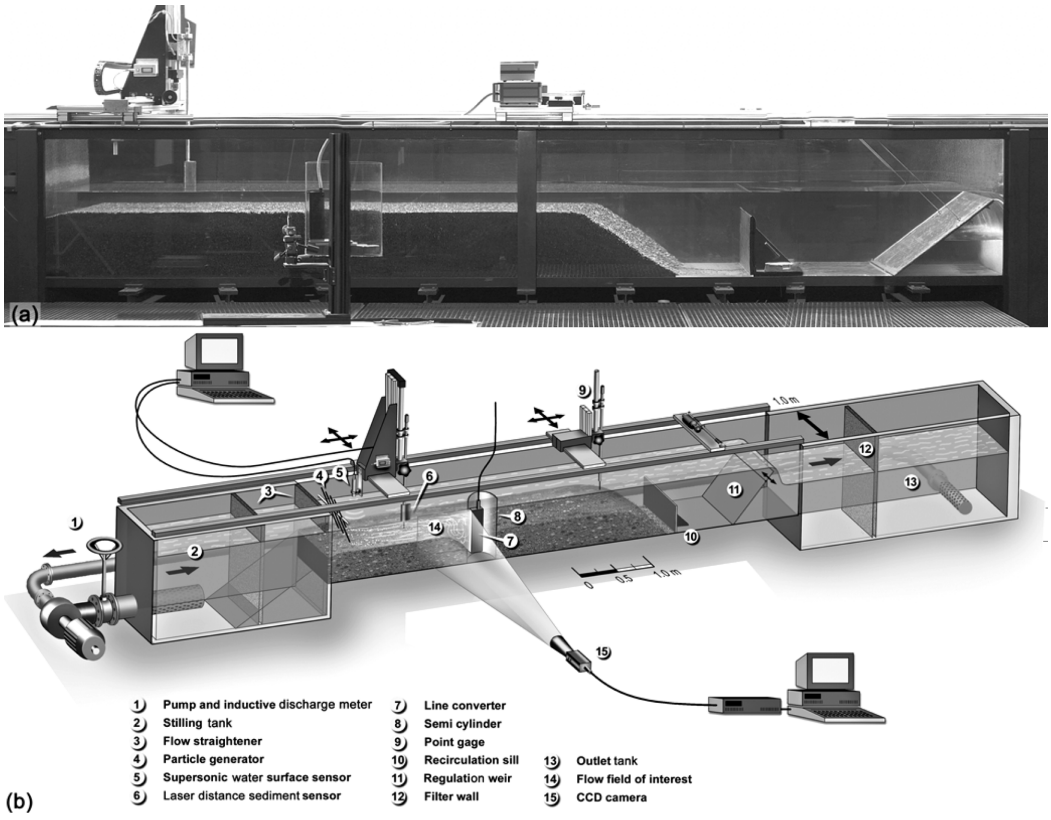


Figure 3. Test channel including PIV apparatus (left), Bridge pier (center left), Travelling mechanism (center right) and Sediment retain and flap gate (right); (b) Schematic experimental setup.

2002): (1) Placement of the cylinder, (2) Placement of the sediment leaving free space for the riprap, (3) Placement of the riprap, (4) Control that the sediment-riprap surface was exactly horizontal, (5) Slow filling of the scour channel with water up to the required flow depth, (6) Start of pumps and slow increase of discharge up to the required discharge, (7) Slight lowering of tailwater depth until conditions without any sediment movement occur, (8) Further lowering to the tailwater depth under which first particles move and setting time to zero, (9) Further slow lowering of tailwater until riprap failure, and (10) After stop of discharge observation of the riprap failure under 'dry' conditions.

The previous procedure was extended from experiences with bridge pier scour as described by Hager et al. (2002). The reproduction of some experiments indicated reasonable accuracy.

2.2 *Riprap failure*

The failure of a riprap may be defined by various methods. In the present research, a simple definition was applied: Riprap failure occurs when the first riprap element along the pier perimeter is dislodged. Accordingly, if riprap elements along the outer riprap perimeter are transported either by sliding or rolling, failure has not yet occurred. Also, because only the failure mechanism was closely investigated, one riprap layer of equal size in depth was considered. Once failure has occurred, the test was stopped. Future research has to investigate the pier scour development protected by a riprap.

Two main failure types were observed for piers extended with a circular riprap plan arrangement: (1) Sliding and (2) Rolling. Sliding typically occurred when the riprap was much larger in size than the surrounding sediment, whereas rolling of a riprap element out of the entire riprap arrangement occurred typically if its size was only slightly larger than the sediment size. However, no riprap failure as previously defined was observed by rolling, because only some riprap elements rolled out without riprap stability problems.

Figure 4 shows the four typical steps resulting in riprap failure by sliding. In Figure 4(a) an initial surface scour may be observed downstream of the pier,

Table 1. Test conditions ($d_{50s} = 5.0$ mm, $\sigma_s = 2.29$ for all runs).

Run (–)	d_{50R} (mm)	n (–)	D (mm)	Q (m^3/s)	Cylinder (–)
1	30.0	1–5	457	0.042	half
2	30.0	1–5	457	0.08	half
3	30.0	1–5	457	0.09	half
4	19.0	1–5	457	0.08	half
5	19.0	1–5	457	0.09	half
6	12.0	1–10	457	0.08	half
7	13.0	1–10	457	0.10	half
8	50.0	1–5	457	0.10	half
9	19.0	1–10	457	0.06	half
2a	30.0	1–5	260	0.08	half
3a	30.0	1–5	260	0.09	half
4a	19.0	1–10	260	0.08	half
5a	19.0	1–10	260	0.09	half
6a	13.0	1–10	260	0.08	half
7a	13.0	1–10	260	0.10	half
8a	50.0	1–5	260	0.10	half
2b	30.0	1	110	0.08	half
4b	19.0	1–3	110	0.08	half
5b	19.0	1–3	110	0.09	half
6b	13.0	1–5	110	0.08	half
7b	13.0	1–5	110	0.10	half
11	19.0	1–5	110	0.08	full
12	19.0	1–10	110	0.10	full
13	13.0	1–10	110	0.10	full

roughly at 120° away from the channel axis. Surface erosion may lead to the loss of a riprap element by sliding into the erosion hole (Fig. 4b). No failure in the previous sense was observed for one row of riprap stones, however, because both erosion and subsequent scour start at an angle of ~75°.

The presence of the elliptical erosion surface reduces the velocity in the immediate tailwater region of the pier such that the erosion surface migrates upstream along the interface between riprap and surrounding sediment, roughly at a location of 75° from the channel axis, if the tailwater level is slightly reduced (Fig. 4c). A further slight reduction leads to sliding of the riprap element located at the interface first, and this process continues towards the pier surface when progressively lowering the tailwater level. Riprap failure in the present sense occurred under a well defined upstream flow depth h_{oi} for a given discharge and pier and riprap arrangement, such that all required information for the systematic riprap failure was available.

Figure 5 is complimentary to Figure 4. In each image, water was drained to the original sediment elevation, and the remaining water in the erosion surface or the scour hole was colored white to improve visibility on the photographs. Figure 5(a) again relates to the surface erosion downstream of the riprap, with a fully intact riprap protection. Some riprap elements are seen dislodged in Figure 5(b) due to a local scour. Reducing the tailwater slightly more results in the relatively abrupt migration of the lateral scour hole to some 75° at the interface between sediment and riprap (Fig. 5c). Reducing tailwater still more leads to the failure of riprap, i.e. a riprap element fails close to 75° away from the channel axis. It is observed from Figure 5(d) that the riprap protection is compact both at the up- and downstream pier regions.

Figure 6 shows typical photos of incipient erosion, and the riprap immediately after failure. Once conditions have developed to the latter state, scour advances extremely fast to reach conditions without any riprap. This development has not yet been investigated, however.

3 PRELIMINARY TEST RESULTS

Based on the previous considerations on the entrainment conditions, an attempt was made to formulate riprap failure as

$$\mathrm{F}_{dR} / [1.65 (R_{ho} / d_{50s})^{1/6} \Phi_R] = f(n, \delta) \qquad (4)$$

The left side of (4) includes the effects of the failure densimetric Froude number $\mathrm{F}_{dR} = \sigma^{-1/3} V_{oR} (\mathrm{g}' d_{50})^{1/2}$ divided by the product of relative approach flow hydraulic radius (R_{ho}/d_{50s}) times a pier extension effect Φ_R similar to Φ_β previously considered for the pier extension. Evidently, Φ_R depends only on $\beta = D/B$ and thus involves the relative pier width. Based on the present observation $\Phi_R = 1 - \beta^{0.4}$ fitted better for $0.055 < \beta < 0.229$ than (2) and was adopted in the following. Because all basic parameters except of the riprap arrangement are included on the left side of (4), its right side must account for the effects of relative riprap diameter $\delta = d_R/d_{50s}$, and the number n of riprap rows around the pier.

Figure 7 shows the preliminary test results for one sediment size, five riprap sizes, and four different row arrangements. It may be noted that the data align almost linearly in a double-logarithmic plot. Also, the curves for various values of n have a common origin at (1;1), such that a relatively simple prediction of data is possible. Obviously, the case $\delta = 1$ corresponds to a limit riprap size $d_R = d_{50s}$ for which the conditions predicted by Hager and Oliveto (2002) are asymptotically obtained. At the present preliminary stage, no equations are yet presented in order to come up with a final design relation that may be applied under well defined experimental limitations. It is noted that the scatter of data is relatively large. Shields' data for the entrainment condition in the basic sediment arrangement involves a scatter of approximately ±10%. The data of Hager and Oliveto (2002) have a scatter of approximately ±15% scatter, given the additional parameter

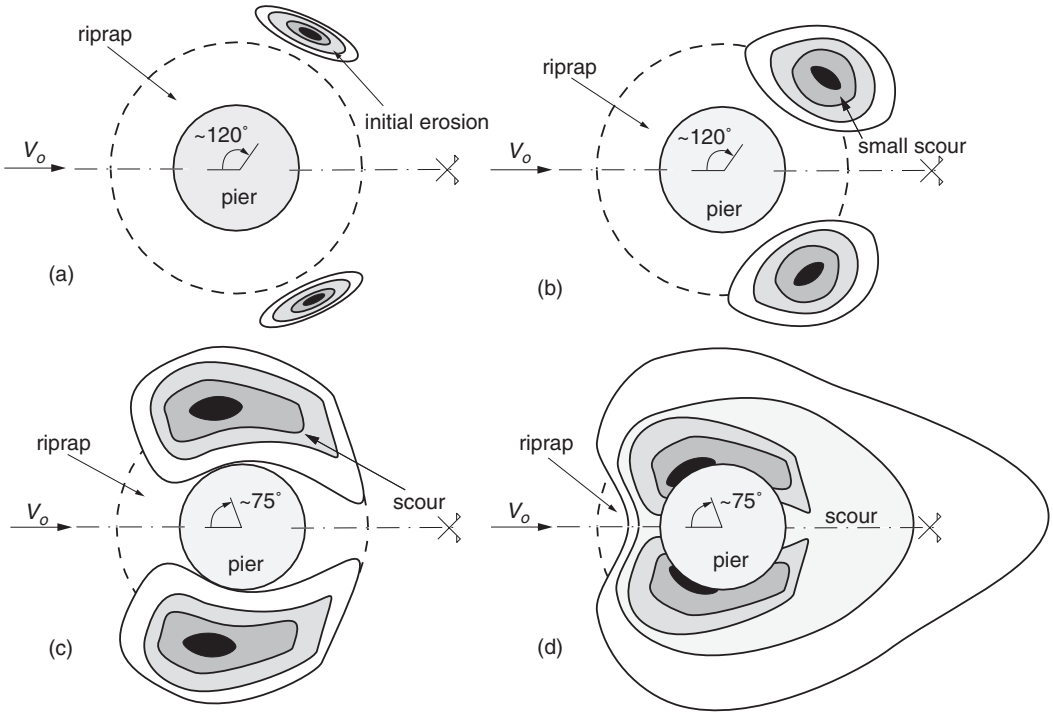


Figure 4. Typical sequence of riprap failure by sliding for $n > 1$ (a) Inception of erosion at ∼120°, (b) Sliding of outer riprap element into erosion hole, (c) Migration of erosion surface to ∼75°, and (d) Riprap failure at ∼75°.

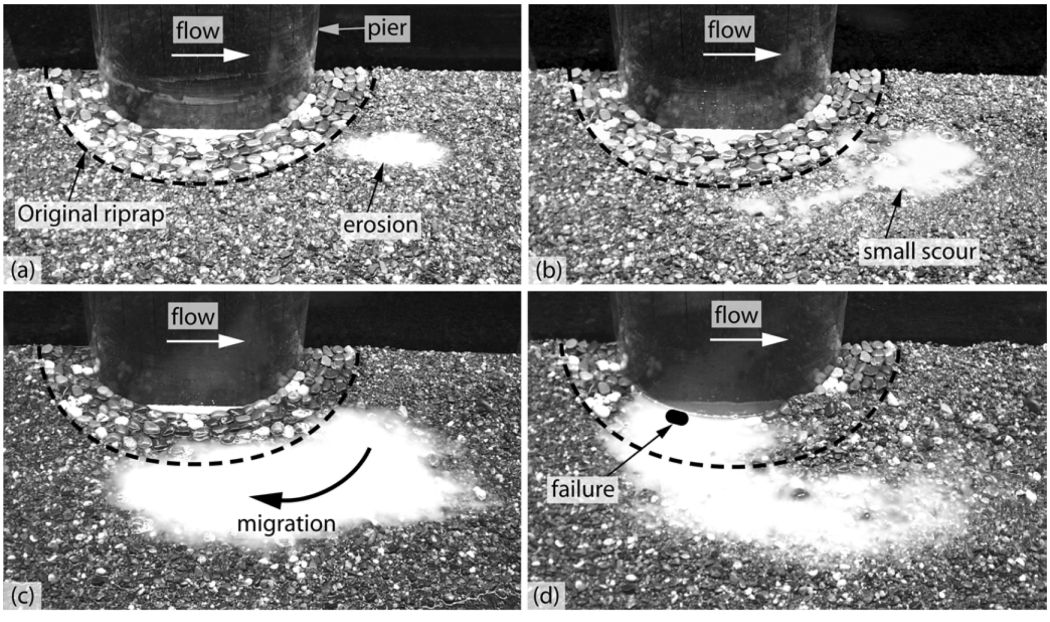


Figure 5. Temporal evolution of scour (a) Initial erosion at ∼120°, (b) Migration of scour hole to ∼90° first riprap row failure at ∼120°, (c) External riprap failure between ∼120° to ∼90°, (d) Riprap failure at ∼75° with development of typical bridge pier scour topography ($Q = 0.08\,\mathrm{m^3/s}$, $\mathrm{F}_{dR} = 1.3 - 2.0$, $D = 457\,\mathrm{mm}$, $d_{50s} = 5\,\mathrm{mm}$, $d_R = 19\,\mathrm{mm}$).

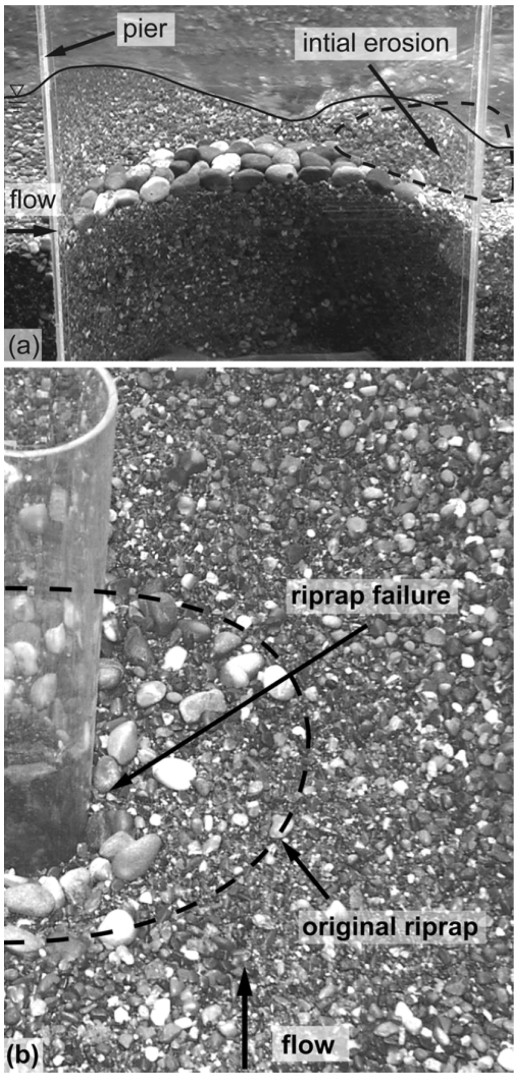


Figure 6. Evolution of riprap failure (a) Side view on initial erosion surface, (b) Riprap failure.

involved. In the present configuration, two additional parameters have to be accounted for, such that a scatter of some ±25% may be expected. This order of magnitude is normal in fluvial hydraulics, when considering for instance sediment transport.

Figure 8 shows the comparison between measurement (subscript *meas*) and the preliminary prediction (subscript *pred*) of the Froude number F_{dR}, of which a reasonable correlation may be observed. The method previously outlined must be tested for other sediments until a generalized design is available, however.

4 SLIDING OR ROLLING?

Entrainment of an uniform sediment surface as considered by Shields always occurs by rolling (or even by saltation) of sediment particles. Rolling of riprap elements may thus asymptotically be regarded as a Shields' process applied to the sediment particles of diameter d_R. According to (3) rolling (subscript r) follows the relation

$$F_{dr} = 1.65(R_{ho}/d_R)^{1/6}[1-(2/3)\beta]^{1/4} \quad (5)$$

provided $F_{dr} = V_{ri}/(g' d_R)^{1/2}$ with $V_{ri} = V_o/(1-\beta)$, thereby accounting for the velocity at the pier side instead of the upstream velocity. Figure 9 compares (5) with observations, resulting in an excellent agreement. It was previously mentioned that none of the riprap failed by rolling, because all riprap stones dislodged *at* the pier by sliding into the adjacent scour hole. Yet, rolling was observed for $n > 1$, normally also at the pier side thus enlarging the scour hole and resulting in the final failure of riprap. The rolling data in Figure 7 show a trend, yet additional experiments will be needed to confirm this approach.

5 IMPACT OF PRESENT RESEARCH

Riprap failure may be considered as a general case of entrainment of sediment transport in fluvial hydraulics. The present design equations for the prediction of riprap failure neglect this framework, and may thus be considered as purely experimental approaches for which the asymptotic conditions are not satisfied. Some recent proposals include the correct non-dimensional quantities and will be tested with the present approach, once the test program is concluded.

It is important to note that this project separates the various effects by using a product arrangement of independent functions, each accounting for a particular effect. For $\delta = 1$, i.e. when the riprap size degenerates to the surrounding sediment size, the final result must tend to Shields' approach. It may be seen from Figure 7 that the failure densimetric Froude number, or the failure approach velocity increases both as δ and n increase, for otherwise identical conditions. Adding more riprap rows thus allows larger upstream velocities, as do larger riprap sizes, compared to a pier without any riprap protection ($\delta = 1$). The present research also indicates that riprap failure occurs never at the leading nor at the wake pier region but at about 75° away from the channel axis. If various riprap sizes are available, the largest elements must thus be placed close to the sides of a pier, whereas smaller elements may be located both at the up- and downstream sides of the pier relative to the approach flow direction.

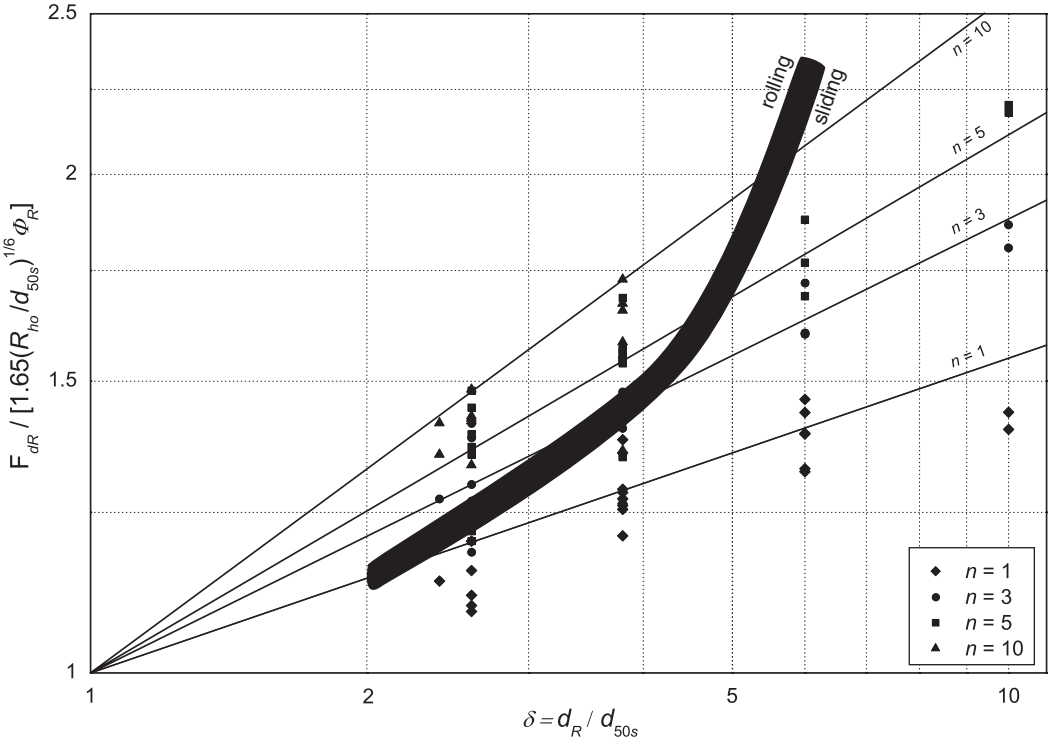


Figure 7. Preliminary test results showing reduced failure densimetric Froude number versus relative riprap size δ for various numbers n of riprap rows. Transition area between sliding and rolling failure mode (in gray).

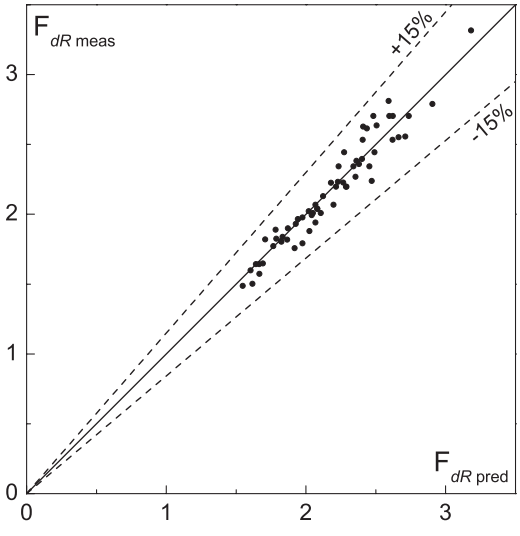


Figure 8. Failure densimetric particle Froude number F_{dR}; Comparison of prediction (line) with observations (symbols) for sediment tested.

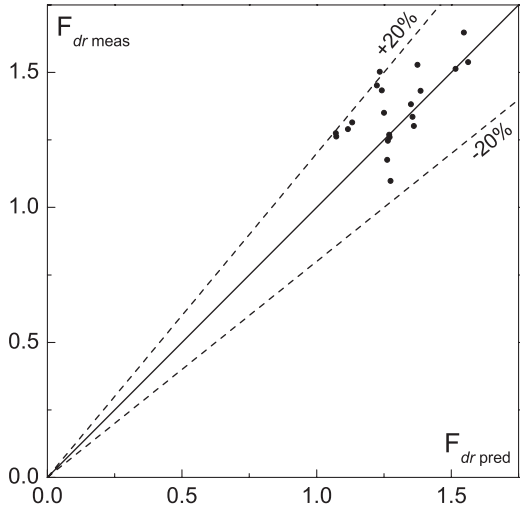


Figure 9. Rolling of singular riprap elements; Comparison of prediction (line) and observations (symbols) for F_{dr} according to (5) and data (in gray) of Figure 7.

6 CONCLUSIONS

The failure of a uniform riprap arranged concentrically about a circular-shaped bridge pier was investigated experimentally, based on previous research on the entrainment condition for bridge piers in the absence of riprap. A systematic approach was introduced that contains all determining elements without the riprap on the left side, and only the riprap parameters on the right side. Based on detailed hydraulic experimentation, a preliminary plot was presented that shows the main features of the expected final result. Accordingly, the entrainment of scour around a bridge pier may be controlled significantly by increasing both the relative riprap size and the number of riprap rows placed around the pier. More research is needed to present a final design equation, along with limitations for application in fluvial engineering.

NOTATION

B river width
d sediment size
D pier diameter
D^* relative sediment size
F Froude number
g gravitational acceleration
g′ reduced gravitational acceleration
h flow depth
n number of riprap rows
R_h hydraulic radius
V velocity
x streamwise coordinate
y transverse coordinate
z vertical coordinate
β relative pier diameter
δ relative riprap size
Φ presence of pier or riprap
ρ density
ν kinematic fluid viscosity
σ sediment non-uniformity parameter

Subscripts

c critical
i entrainment
o upstream
p pier
R riprap
s sediment
β pier

REFERENCES

Hager, W.H. & Oliveto, G. 2002. Shields' entrainment criterion in bridge hydraulics. *Journal of Hydraulic Engineering* 128(5): 538–542.

Hager, W.H., Unger, J. & Oliveto, G. 2002. Entrainment criterion for bridge piers and abutments. *River Flow 2002* 2: 1053–1058, D. Bousmar, Y. Zech, eds. Swets & Zeitlinger, Lisse, the Netherlands.

Hamill, L. 1999. *Bridge hydraulics*. Spon: London.

Melville, B.W. & Coleman, S.E. 2000. *Bridge scour*. Water Resources Publications: Highlands Ranch, CO, USA.

River Flow 2004 – Greco, Carravetta & Della Morte (eds.)
© 2004 Taylor & Francis Group, London, ISBN 90 5809 658 0

Scour prediction using the Movability Number criteria for incipient motion

Neil Armitage
Department of Civil Engineering, University of Cape Town, South Africa

Caroline McGahey
Formerly Department of Civil Engineering, University of Cape Town, now HR Wallingford Ltd., Howbery Park, Wallingford, Oxfordshire, UK

ABSTRACT: Liu (1957) developed the Movability Number (*Mn*) as an alternative to the Shields' (1936) dimensionless mobility factor for predicting the incipient motion of non-cohesive sediment subject to steady unidirectional flow on plane channel beds. Previous work has shown how *Mn* may be used to predict the likelihood of scour over a wide range of boundary conditions including laminar, transitional, and turbulent, as well as sloped in any direction.

In this study, the commercial CFD flow solver CFX, Version 4.3 (1999) was used to simulate open channel flow conditions and predict the scour potential. Contours of predicted scour potential around a vertical weir, an abutment and two piers were generated and compared to the observed equilibrium scour patterns measured in small-scale laboratory models. The results of the numerical computations correlate reasonably well with the experimental data.

1 INTRODUCTION

The estimation of the probable maximum scour profiles around engineering structures situated within open channel flow is an essential parameter in the foundation design of those structures. This is demonstrated by the frequency of bridge failure due to the unexpectedly deep local scour at the supports, i.e. the abutments and piers, during peak flood conditions. Currently, scour prediction is based largely on the use of empirical equations (e.g. Liu et al. 1961; Breusers et al. 1977; Jain & Fischer 1979; Melville 1992; Raudkivi, 1998), or alternatively on the results derived from hydraulic scale models.

This paper investigates the use of the Movability Number criteria for incipient motion, originally developed by Liu (1957) and subsequently extended by the principal author (and others), in conjunction with commercial computational fluid dynamics (CFD) software for the determination of scour potential. CFX Version 4.3 (1999) (CFX-V4.3) was used to solve the conservation equations for fluid motion in the specified domain around selected structures. User defined subroutines were written into the coding to interpret the output in a form suitable for the Movability Number (*Mn*) approach. The software was then used to determine the scour potential upstream of a vertical weir, and around a vertical-wall abutment protruding at 90 degrees from the riverbank and two cylindrical bridge piers. The results of the numerical computations correlate reasonably well with the experimental data.

2 THE MOVABILITY NUMBER CRITERIA FOR INCIPIENT MOTION

Incipient motion, in the context of sediment transport, is that critical point at which sediment particles on the boundary of a fluid (e.g. the bed or banks of a river) begin to move. In concept, if the fluid force is below that required for the motion of a particle, there will not be any movement. If it is greater than that required for motion, there will be movement. The boundary between the two may be described as "incipient" motion – i.e. the particle is starting to move.

Fluid boundaries normally, however, comprise of millions of particles, each with a unique size, shape, electrical charge, density, packing and orientation, and subject to a unique instantaneous flow within the flow field. It is obvious that some particles are more easily moved than others are, in other words, motion occurs with lower fluid forces than the average. On the other hand, it is also obvious that some particles remain stationary even when subjected to

higher than average fluid forces that would move most other particles. Taken as a whole, it is clear that the motion might be of one or two particles only, several particles at a time, or involve general movement of the surface of the bed. Each level of movement is associated with its own particular "critical" conditions. This has been recognised by many researchers over the years, notably Kramer (1935), who defined three intensities of motion ("weak", "medium" and "general" movement) near the critical or threshold condition. More recently, Shvidchenko & Pender (2000a, 2000b) defined I, the intensity of motion (or transport intensity) in terms of m, the number of particle displacements during the time interval t, and N, the total number of surface particles over the sample area, such that

$$I = \frac{m}{Nt} \tag{1}$$

For turbulent boundaries, Shvidchenko & Pender (2000a & 2000b) used $I \approx 10^{-4}$ s^{-1} for their definition of incipient motion and compared it to the Kramer (1935) definition of "weak" motion. Extensive analysis of incipient motion data obtained by many researchers since 1914 (Armitage & McGahey 2003) appear to indicate that motion is generally first observed at approximately $I = 2 \times 10^{-5}$s^{-1}.

The onset of "incipience" can be predicted via several fluid parameters of which the best known involve flow velocity, bed shear stress, or stream power. Most of the published literature uses the dimensionless mobility factor – which is derived from the bed shear stress – as popularized through the work of Shields (1936). A number of researchers, however, have preferred the use of the "Movability Number" parameter introduced by Liu (1957). He came to the conclusion that the local velocity, and hence the various drag coefficients, were all functions of the particle Reynolds Number, $Re*$, defined as

$$Re_* = \frac{u_* d}{\nu} \tag{2}$$

where d is the particle diameter and ν is the kinematic viscosity, whilst the shear velocity, $u*$, is defined as

$$u_* = \sqrt{\frac{\tau_0}{\rho}} \tag{3}$$

where τ_0 is the shear stress at the boundary and ρ is the fluid density. Liu then developed a new dimensionless parameter comprising of the ratio of the shear velocity, $u*$, to the particle settling velocity, v_{ss}, which he termed the "Movability Number", which will hereinafter be abbreviated to *Mn*. He came to the conclusion that for incipient motion, there was a unique relationship between this new parameter *Mn* and $Re*$, i.e.

$$Mn = \frac{u_*}{v_{ss}} = f\left(Re_*\right) \tag{4}$$

A plot of the critical *Mn* value for incipient motion (Mn_c) versus $Re*$ has a similar shape to the better known plot of the critical Shields' parameter θ_c versus $Re*$ (the so-called "Shields' diagram"). However, it has the advantage that sediment parameters such as diameter, shape factor and density – which help to make up θ_c – are effectively replaced by the single parameter of settling velocity. As with the Shields' diagram, the plot does not include the flow velocity, local or average.

Several researchers (e.g. Bagnold 1966, Rooseboom 1975, Van Rijn 1987, Julien 1995, and Raudkivi 1998) have noted relationships between Mn_c and particle motion. Analysis of incipient motion data taken from measurements on natural quartzitic sand particles in water by numerous researchers since 1914 have enabled the senior author to develop the following relationships (Armitage & McGahey 2003)

$$\frac{u_*}{v_{ss}} = \frac{2.2}{Re_*^{1.4}} \quad \text{(Laminar boundaries)} \tag{5}$$

$$\frac{u_*}{v_{ss}} = 0.17 \quad \text{(Turbulent boundaries)} \tag{6}$$

where I was determined to be in the order of 2×10^{-5}s^{-1}. Correction has been made for non-horizontal beds and for relative roughness, d/Y, where Y is the flow depth. The full relationship between *Mn* and I, taking into account the bed slope and the relative roughness (turbulent boundaries only) is given by

$$Mn = \frac{u_*}{v_{ss}} = \psi\left(0.2405 + 0.0066\ln\left(I\right) + 0.204\frac{d}{Y}\right) \tag{7}$$

where ψ is the correction for the bed-slope given by

$$\psi = \sqrt{\cos\beta\left(1 - \frac{\tan\beta}{\tan\phi_r}\right)\cos\gamma\left(1 - \frac{\tan^2\gamma}{\tan^2\phi_r}\right)}^{1/2} \tag{8}$$

Here β is the longitudinal slope (positive if there is a fall in the direction of flow), γ is the transverse slope, and ϕ_r is the angle of repose of the sediment. Figure 1 depicts a plot of *Mn* versus $Re*$ for all the data used to determine Equations 5 and 6. Figure 2 shows what happens when Equation 7 is used to adjust the incipient motion criteria (related to I) for turbulent boundaries with small relative depth.

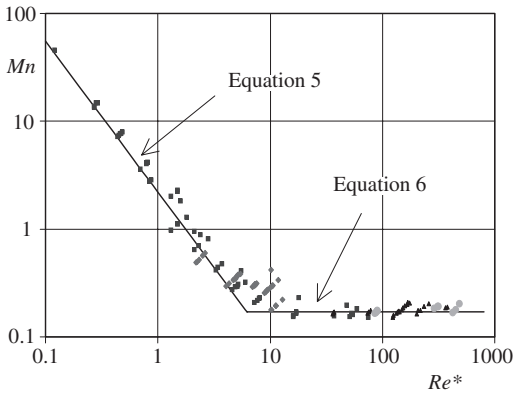


Figure 1. Plot of *Mn* versus *Re*∗ for all data describing "weak" motion ($I \approx 2 \times 10^{-5} s^{-1}$) (Armitage & McGahey, 2003).

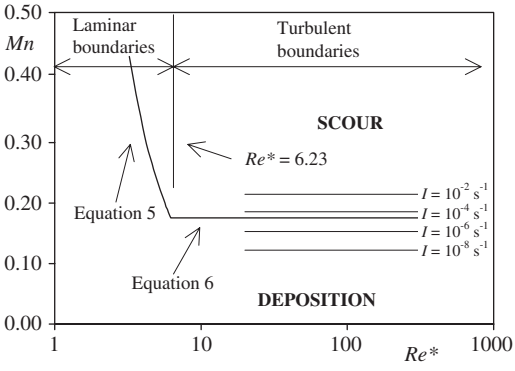


Figure 2. Plot of *Mn* versus *Re*∗ showing the impact of varying *I* (Armitage & McGahey, 2003).

It is apparent that the key issue with incipient motion is not so much the stability of the individual particle, but rather the point below which the rate of scour becomes so slow that it has negligible impact within practicable time scales. For this investigation, this was deemed to be with $I \approx 2 \times 10^{-5}$ giving $Mn \approx 0.17$ over turbulent boundaries.

3 THE NUMERICAL MODEL

The CFD software, CFX-V4.3 a "Finite Volume" package, was utilized to solve the conservation equations for fluid motion, and additional subroutines were written into this software to produce the output in the desired form. Unfortunately Version 4.3, the version available at the time of analysis, did not incorporate an algorithm for modeling free surfaces and had to be adapted to simulate open channel flow. The software was used to predict the scour potential in terms of *Mn* in the vicinity of several simple structures. The adaptation of the CFD software is summarized below. The work is described in greater detail in McGahey (2001).

3.1 *Mesh refinement*

A suitable flow domain in the vicinity of the obstruction was identified and modelled using the geometry description software incorporated into the CFX package. It was then divided into finite volumes using a mesh that was biased to limit the number of cells. A fine mesh was used adjacent to the bed and the region around the shapes representing the structures. Particle movement commences at the bed and *Mn* is at a maximum in the regions with high velocity gradients, which are in the vicinity of the bed and the structures. A coarser mesh was used elsewhere so as to reduce both the CPU time and the size of the data files to be manipulated in the post-processors. The degree of refinement was assisted by means of an initial simulation of steady uniform flow in a long rectangular channel with the same flow rate and cross-section as the test section. The simulation was carried out using a relatively coarse mesh. One of the outputs was the approximate shear stress τ_o at the bed. The shear velocity $u*$ could then be determined from Equation 3. For the scour simulation, the thickness, *y* (mm), of the smallest cells at the channel bed was set at approximately

$$y = \frac{y^+ \nu}{u_*} \tag{9}$$

with the dimensionless depth $y^+ \approx 11.84$ representing the effective boundary between the viscous and turbulent zones in the boundary layer.

3.2 *Boundary conditions*

The upstream boundary condition was assumed to be that of steady uniform flow in a rectangular channel. To reduce the length of the numerical model, a logarithmic function characteristic of the turbulent boundary layer was specified for the inlet velocity distribution. At the outlet face, the gradients of all the transported materials were specified, the pressure was extrapolated from upstream conditions and mass continuity was satisfied. The symmetry condition was used for the side boundaries when modelling a symmetrical structure i.e. piers, thus facilitating a reduction in the number of cells used. Boundaries of the flow domain representing the channel bed were set as walls with the no-slip condition typically used for viscous fluids. The sediment roughness was modelled through an additional user routine that adjusted the logarithmic velocity distribution in the boundary layer. The roughness height was interpreted as the mean sediment diameter.

CFX-V4.3 does not offer a free surface algorithm. Three alternatives were considered for the modelling of the free surface: a symmetry condition, a rigid-lid incorporating an air interface, and a moving wall. The moving wall was chosen as it most accurately predicted the turbulent viscosity distribution with depth. Fortunately, the flow conditions that were being modelled were characterized by approximately flat surfaces, with sub-critical flow and moderate energy losses. The moving wall was given the surface velocity of the water to avoid the generation of spurious shear forces in the surface cells.

3.3 *Shear stress distribution with depth*

In turbulent flow, the shear stresses are determined principally by the velocity gradients. In an infinitely wide, rectangular channel with steady flow, the shear stress τ (Pa) in the direction of flow on a layer with its normal orientated in the direction of increasing depth may be calculated from

$$\tau = \rho g S_0 (D - y) \tag{10}$$

where S_o is the bed slope, D (m) is the total depth and y (m) is the height of the layer above the bed. Despite the specification of a logarithmic velocity distribution at the inlet, Equation 10 was only satisfied a considerable model distance downstream of the inlet. The initial run described in Section 3.1 above was thus also used to determine the distributions of turbulent kinetic energy, k, and rate of viscous dissipation, ε, as shear stress is dependent on these values. These distributions were then programmed as part of the inlet boundary condition in the scour simulation to ensure the correct upstream shear stress distribution.

3.4 *Differencing scheme*

The selection of the differencing scheme was based on the modelling of a benchmark problem with widely published results. The problem selected was that of the lid-driven cavity. This is a two-dimensional problem, where the flow in a cavity is driven by a constant horizontal velocity over the surface, causing the flow to slowly rotate about some horizontal axis. Results of the vertical and horizontal velocity profiles are widely published, the most well known benchmarking results being those produced by Ghia et al. (1982). It was found that the QUICK scheme provided the most accurate approximation, and was thus implemented throughout this investigation for the velocity and pressure terms. In the case of the turbulent kinetic energy and rate of dissipation terms, however, the QUICK differencing scheme gave rise to converged solutions with negative k or ε values when the grid did not adequately resolve the shear layer. These terms were therefore determined using either the upwind or hybrid scheme.

3.5 *Turbulence model*

The selection of the turbulence model was made after comparisons had been made between the velocity and shear stress distributions obtained using the various turbulence options offered by CFX and those measured by Cellino and Graf (2000) over two-dimensional bedforms. Of the available turbulence models in CFX, the k-ε model gave the best results and was used for the two-dimensional problem involving the prediction of the scour upstream of a weir. All the more complex three-dimensional problems, however, had Reynolds numbers in the range 10 000–20 000. The normal k-ε model is known to over-predict both the shear stresses and the turbulence intensities under these circumstances. The Low Reynolds number k-ε model, recommended for Reynolds Numbers in the range 5 000–30 000 (CFX Manual 1999), was therefore used in its place. This model required an extremely fine mesh at the channel bed as no wall functions are incorporated into the algorithm.

The two main parameters required for the turbulence models are the dissipation length scale and the turbulence intensity. A sensitivity analysis of the dissipation length scale and turbulence intensity for the lid-driven cavity benchmark problem showed that values of 0.01 and 0.05 respectively approximated the results of Ghia et al. (1982) most accurately. These were specified as input into the initial course mesh model (see Section 3.1) before being refined for the scour simulation.

3.6 *Pressure correction and solvers*

The default pressure correction in CFX-V4.3 is the SIMPLEC algorithm. This was used throughout except when convergence difficulties were encountered, whereupon the SIMPLE or the PISO algorithms were implemented. The STONE solver was used for the u-, v- and w-velocity components; the ICCG solver was used for the pressure term; and the line solvers were used for the turbulent kinetic energy and rate of viscous dissipation. These solvers were adequate for the two-dimensional problems, however the solutions obtained with these solvers diverged for the three-dimensional abutment and pier models. The BLOCK STONE solver was thus implemented for the u-, v-, and w- velocity components in the case of the abutment and pier examples described in this paper, whilst the AMG solver was introduced for the pressure term. The CFX Manual (1999) recommends this when the pressure-correction is not being adequately treated and the percentage of well-ordered blocks is low, which was the case with these examples.

3.7 *Steady state versus transient flow simulation*

The transient option was investigated. To reduce computational time, the model was initially run using fixed time steps, and then restarted with adaptive time stepping to adjust the time step as the solution converged. The default backward differencing and linear time differencing options were selected. The model output, however, showed no sign of the expected vortex street. This was attributed to the suppression of the free vortices through dampening against the moving wall surface boundary. At the bed, the scour potentials were similar to those for the steady state solution. In view of this, steady state simulation was used throughout.

3.8 *Determination of Movability Number*

CFX-V4.3 is written in Fortran 77. Additional Fortran subroutines were written to access the basic flow variables and determine, inter alia: velocity gradients, shear velocities, and *Mn*.

4 NUMERICAL SCOUR PREDICTION

Four physical model tests were selected for which the extent of the scour was known, and that represented an increasing order of modelling complexity. The numerical model was then used to simulate the physical models and the results compared.

4.1 *Upstream of vertical weir*

Harnett (1998) investigated the scour profiles upstream of a weir for a variety of sediment sizes. Uniform silica sand of three different diameters were separately placed onto the bottom of a 6.38 m long laboratory flume sloped at 1:127.6. The surface of the sand bed was made horizontal with a 50 mm high weir located at the downstream end of the flume. The bed was then subjected to a constant flow of clear water until a stable scour profile was achieved – generally after approximately 35 hours (Figure 3).

One run involving a flow of 3.5 *l*/s over a sand with a median diameter of $d_{50} = 0.86$ mm and a settling velocity of 0.09 m/s, was simulated by the numerical model in both the initial and final conditions. To facilitate the interpretation of the plots, virtual Movability Numbers, Mn', were generated for the whole of the water column using virtual shear velocities computed from Equation (3) after the substitution of τ for τ_0. The critical value for incipient motion with a turbulent boundary, Mn_c, is 0.17 and thus the maximum value of the Mn' contour plot (Figure 4) was set at this value.

In the analysis of the initial, pre-scour condition, the value of the virtual Movability Number reaches values

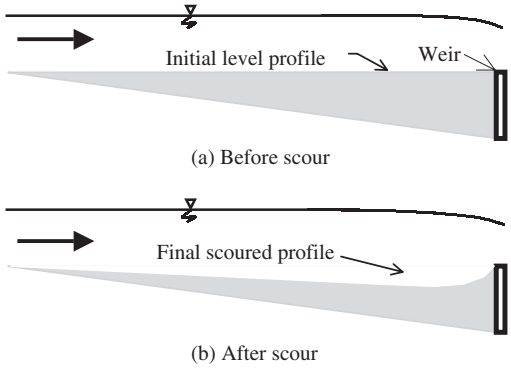


Figure 3. Scour upstream of a weir (Harnett 1998).

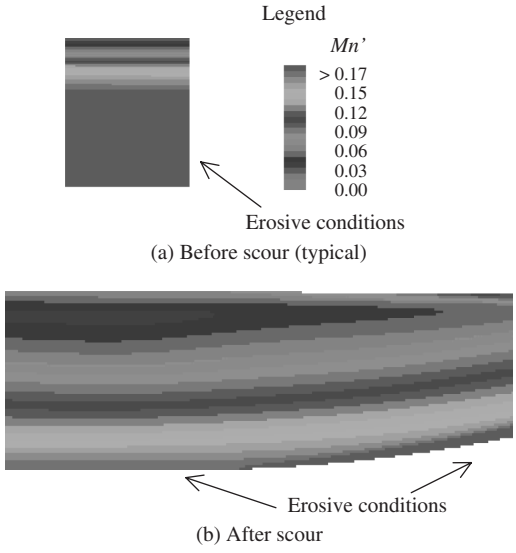


Figure 4. Mn' contour plots for scour upstream of a weir (McGahey 2001).

in excess of 0.17 through more than half the water column above the channel bed, indicating strongly erosive conditions. In the analysis of the final scoured profile, the value of 0.17 is only just attained at the channel bed thus confirming that the scour profile is now approximately in equilibrium with the flow.

4.2 *Determination of erosive conditions around a pier situated within a rectangular channel*

Midgley (2000) examined the scour of thin sediment layers of uniform quartzitic sands of various sizes placed around a 45 mm diameter circular pier centrally located in a 605 mm wide flume and subjected to a steady flow. One run involving a flow of 7.69 *l*/s,

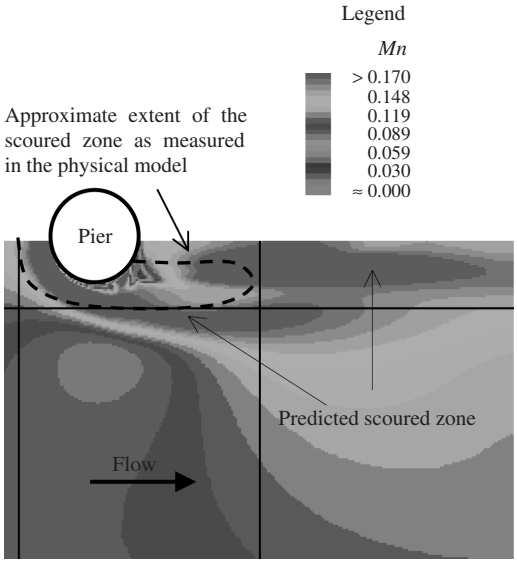


Figure 5. *Mn* contour plots on the bed of a rectangular channel in the vicinity of a pier (McGahey 2001).

depth 74 mm, over a sand with a median diameter of $d_{50} = 0.55$ mm and a measured settling velocity of 0.089 m/s, was simulated by the numerical model. The boundary was determined to be turbulent. The result is depicted in Figure 5. The modelling was simplified by assuming symmetry along the centreline of the pier and channel. The actual scour profile has been superimposed onto the model output for comparison.

The numerical simulation appears to correctly predict the scour zone upstream of the pier, but it suggests that the scour zone should be displaced further away from the centreline downstream of the pier. Furthermore, it predicts scour in the lee of the pier in what is usually a deposition zone. It is quite possible that these anomalous results can be partly explained by the use of a moving, essentially flat, boundary for the free surface. This distorts the flow patterns in the lee of the pier. In this region, the water surface would be expected to drop owing to the acceleration of the flow around the sides of the pier. Keeping the free surface artificially elevated increases the pressure on the bed, which in turn increases the local shear stresses and forces the high-speed separated jet further away from the centreline. This is exactly as observed in the case of the displaced scour zone.

The scour zone identified in the lee of the pier in what is usually a deposition zone is a consequence of the erroneous flow patterns computed in the lee of the pier possibly resulting from the free-surface approximation. The k-ε turbulence model is also known to be subject to error in separated flow zones.

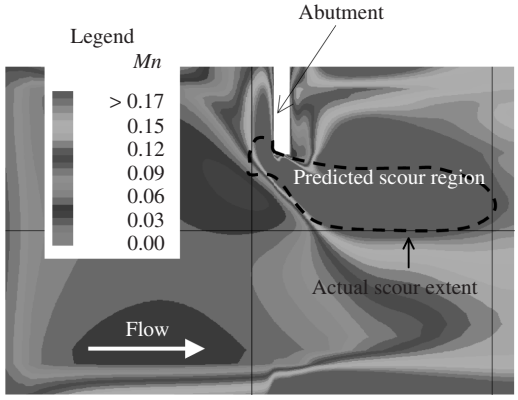


Figure 6. *Mn* contour plot on the bed of a rectangular channel in the vicinity of an abutment (McGahey 2001).

4.3 *Determination of erosive conditions around an abutment situated within a rectangular channel*

Mitchell (2000) examined the scour of thin layers of uniform quartzitic sands of various sizes placed on a level floor around a vertical-wall abutment located in a 820 mm wide rectangular flume and subjected to a steady flow. The abutment had a length of 220 mm, was 35 mm thick, and was set at an angle of 90 degrees to the flow direction. Approximately 1 litre of sediment was sprinkled evenly over the flume bed. The flow was then allowed to scour the material around the structure until equilibrium was reached after about 3 hours.

One run involving a flow of 10.2 *l*/s, depth 100 mm, over a sand with a median diameter of $d_{50} = 0.55$ mm and a measured settling velocity of 0.089 m/s, was simulated by the numerical model. Once again, the boundary was determined to be turbulent giving Mn_c in the order of 0.17 (Figure 6). The scour pattern that was experimentally observed has been superimposed.

In this instance, the predicted scour region is larger than the measured scour region. As with the pier simulation, *Mn* is higher in the region downstream of the abutment than would be expected – particularly in the vicinity of the channel wall. It is likely that this is once again a consequence of the free-surface approximation.

4.4 *Determination of erosive conditions around a pier situated on a mobile bed*

Babaeyan-Koopaei (1996) undertook laboratory investigations into the scour profiles around piers and abutments. A unique feature of his research was that the experiments were carried out in a regime flume, i.e. a self-formed laboratory channel, resulting in the mobility of the entire cross-section. These represented

natural field conditions where channels are generally non-rectangular, with mobile banks and possible overbank flow. The flume was 22 m long, 2.5 m wide and had a depth of 600 mm. The particle mean diameter, d_{50}, was 1 mm.

One of these experiments, test no. 38B (Babaeyan-Koopaei 1996), was modelled numerically in both the initial and final conditions. This experiment investigated the scour profile around a 48 mm diameter cylindrical pier, centrally located in the channel. The flow rate was 2.5 *l*/s and the average water depth was 129.5 mm. The maximum scour depth adjacent to the pier was 55.6 mm. Two conditions were modelled: prior to scour i.e. in the self-formed channel with the pier installed but before introduction of the test flow, and after development of the equilibrium scour profile around the pier. The particle settling velocity was estimated as being approximately 0.129 m/s. The model geometry for the initial case is shown in Figure 7. A three-dimensional user patch was created adjacent to the bed, and this is also depicted.

The incipient motion critical function for sediment on an uneven bed is given by:

$$Mn_{c(\beta,\gamma)} = \left.\frac{u_*}{v_{ss}}\right|_{\beta,\gamma} = \psi \left.\frac{u_*}{v_{ss}}\right|_{0} = \psi Mn_c \qquad (11)$$

where the subscripts indicate a sloped bed (β, γ) and a horizontal bed (0) respectively. The function was computed at a depth of 0.5 mm above the channel bed. The boundary was found to be turbulent. As the geometry for the initial condition was created with a level bed, this critical function should have been approximately equal to 0.17 over most of the channel bed i.e. the value of the Mn_c for incipient motion on a turbulent boundary. This can be seen to be the case when the values are graphed for each cell centre at the boundary in Figure 8. The values that are not equal to 0.17 come from the cells situated adjacent to the pier, where the velocity vectors are not horizontal.

A scour potential, Ω, was defined as the difference between the *Mn* calculated by the program, and $Mn_{c(\beta,\gamma)}$ as

$$\Omega = Mn - Mn_{c(\beta,\gamma)} \qquad (12)$$

The scour potential indicates the extent to which the flow is trying to scour the bed (positive value) or deposit on it (negative value). A zero scour potential indicates that the flow neither wants to scour or deposit i.e. the bed is in equilibrium with the flow at that point.

Figure 9 shows Ω calculated by the program in the vicinity of the pier prior to the commencement of scour. Most of the values fall in the range 0.1 to 0.25 indicating erosive conditions. The values are highest in the vicinity of the pier, indicating the greatest scour

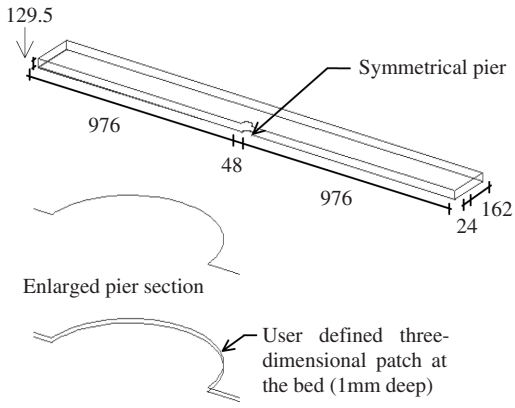


Figure 7. The model geometry for the initial, pre-scour, condition. Dimensions in mm (McGahey 2001).

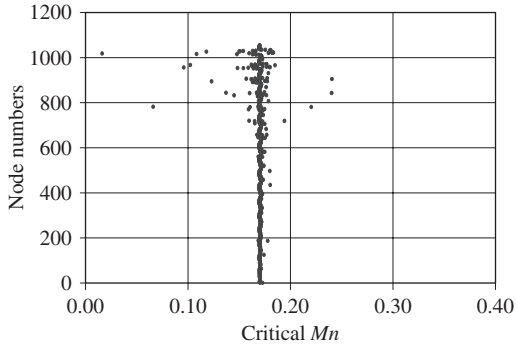


Figure 8. Critical *Mn* for each boundary cell prior to the development of scour (McGahey 2001).

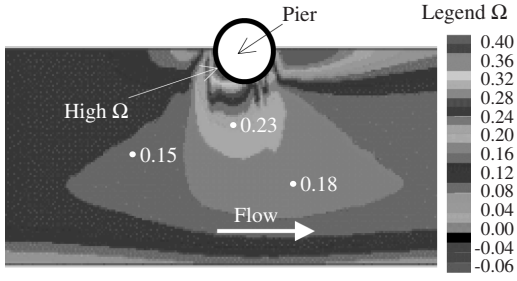


Figure 9. Plot of Ω in the vicinity of the pier prior to the development of scour (McGahey 2001).

potential in this region. The results were plotted using the program IDL (2000).

Ideally, the scour potential should be used to indicate the probable deformation of the boundary. This would be an iterative procedure with the scour potentials being recalculated for each boundary adjustment. The final solution would be obtained once all scour

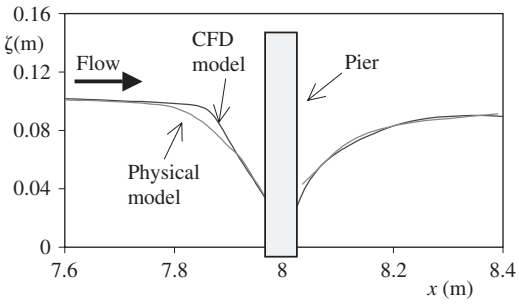


Figure 10. Elevation of bed in the physical model and CFD model on a long-section through the centreline (McGahey 2001).

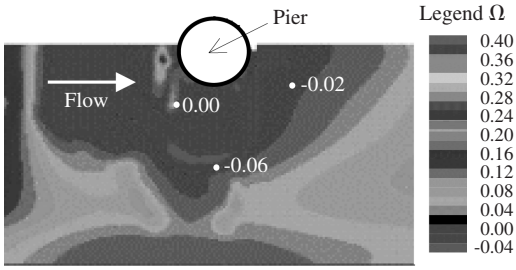


Figure 11. Plot of Ω in the vicinity of the pier after the development of local scour (McGahey 2001).

potentials were close to zero. In CFX-V4.3, however, this cannot be automated. A new geometry has to be determined for each iteration by the operator. In this instance, therefore, the scour potentials were only computed for the initial and final state of the physical model.

Figure 10 depicts the elevation, ζ, of the bed in the physical model and the CFD model on a long-section (x-axis) through the centreline. The profile in the CFD was created through best-fit smooth curves linking spot heights measured in the physical model. Since there is a slight deviation between the two profiles (real and modelled), this introduces a source of unavoidable error.

Figure 11 shows Ω over the scoured boundary. The values fall in the range −0.04 near the scour hole to 0.06 further away. This indicates that the profile is now approximately in equilibrium with the flow. A more accurate rendition of the physical model profile and better modelling of the free surface might possibly have improved the accuracy.

5 CONCLUSIONS

This paper investigates the use of the Movability Number (*Mn*) criteria for incipient motion, originally developed by Liu (1957) and subsequently extended by the author (and others), for the determination of scour potential. This was tested by computing values of *Mn* in a commercial CFD package, CFX Version 4.3 (CFX-V4.3), and comparing the results to measurements taken from physical models.

In CFX-V4.3, the standard k-ε and the Low Reynolds Number k-ε models were found to provide the best predictions of the turbulent shear stresses for the two- and three-dimensional flow-fields respectively. Since CFX-V4.3 does not incorporate a free surface algorithm, the free surface was modelled with a moving wall boundary condition, which suppressed the formation of any vortex streets, as well as artificially raising some local pressures. The QUICK differencing scheme was implemented for the discretisation of the velocity and pressure terms, while the HYBRID scheme was employed for solution of the turbulent quantities.

The scour predictions of the numerical model were compared with scour profiles measured in the laboratory upstream of a weir and around a vertical-wall abutment and two cylindrical piers. Despite the limitations of the software, the results were sufficiently encouraging to suggest that there is potential for the use of this method for scour prediction.

ACKNOWLEDGEMENTS

The information contained in this paper emanates from a project funded by the Water Research Commission of South Africa (WRC) entitled: *An investigation into the critical conditions for the deposition and re-entrainment of natural sediments and litter in rapidly varied flow through hydraulic structures* (WRC Project No. K5/1098). The final report was by Neil Armitage and Caroline McGahey and is entitled: *A unit stream power model for the prediction of local scour in rivers* (WRC Report No. 1098/1/03). The support of the WRC is gratefully acknowledged.

REFERENCES

Armitage, N. & McGahey, C. 2003. *A unit stream power model for the prediction of local scour in rivers*. Pretoria, South Africa: Water Research Commission of South Africa Report No. 1098/1/03.

Babaeyan-Koopaei, K. 1996. *A study of straight channels and their interaction with bridge structures*. University of Newcastle upon Tyne: PhD Thesis.

Bagnold, R.A. 1966. An approach to the sediment transport problem from general physics. *US Geological Survey Professional Paper 422–1*, 37 pages.

Breusers, H.N.C, Nicolet, G. & Shen, H.W. 1977. Local scour around cylindrical piers. *Journal of Hydraulic Research, IAHR*, 15(3): 211–252.

CFD-V4.3 1999. CFD Version 4.3. CFX Software/AEA Technology, Waterloo, Ontario, Canada.

CFX Manual 1999. CFX Version 4.3, CFX Software/AEA Technology, Waterloo, Ontario, Canada.

Cellino, M. & Graf, W.H. 2000. Experiments on suspension flow in open channels with bed forms. *Journal of Hydraulic Research, IAHR*, 38(4): 289–297.

Ghia, U., Ghia, K.N. & Shin, C.T. 1982. High-Resolutions for incompressible flow using the Navier-Stokes equations and a multi-grid. *Journal of Computational Physics*, 48: 387–411.

Harnett, B.R. 1998. *Damming of the River Sabie, South Africa: The sedimentation problem.* University of the Witwatersrand, Centre for Water and the Environment: Internal Report.

IDL 2000. Interactive Data Language, Version 5.2. Research Systems International (UK) Ltd., Crowthorne, Berkshire, UK.

Jain, S.C. & Fischer, E.E. 1979. *Scour around circular bridge piers at high Froude numbers, Report No. FHWA-RD-79-104.* Washington D.C., Federal Highway Administration.

Julien, P.Y. 1995. *Erosion and sedimentation.* Cambridge University Press.

Kramer, H. 1935. Sand mixture and sand movement in fluvial model. *Transactions ASCE*, 100: 798–873.

Liu, Hsin-Kuan 1957. Mechanics of sediment-ripple formulation. *Journal of Hydraulics Division ASCE*, Vol. 83 (HY2) 1–23.

Liu, K.-K., Chang, F.M. & Skinner, M.M. 1961. *CER 60 HKL 22, Effect of bridge construction on scour and backwater.* Colorado State University, Civil Engineering Section.

McGahey, C. 2001. *A computational fluid dynamics model for sediment movement based on the unit stream power approach.* University of Cape Town: MSc(Eng) Thesis.

Melville, B.W. 1992. Local scour at bridge abutments. *Journal of Hydraulic Engineering, ASCE*, 123(2): 615–631.

Midgley, M. 2000. *Sediment movement around piers in open channel flow.* University of Cape Town: BSc(Eng) Thesis.

Mitchell, A. 2000. *Sediment transport around abutments in open channel flow.* University of Cape Town: BSc(Eng) Thesis.

Raudkivi, J.J. 1998. *Loose boundary hydraulics*. Rotterdam, A.A. Balkema.

Rooseboom, A. 1975. *Sediment transport in rivers and reservoirs*. University of Pretoria, South Africa: D.Eng dissertation (in Afrikaans).

Shields, A. 1936. *Application of similarity principles and turbulence research to bed load movement*. Pasadena: California Institute of Technology (translated from German).

Shvidchenko, A.B. & Pender, G. 2000a. Flume study of the effect of relative depth on the incipient motion of coarse uniform sediments. *Water Resources Research*, 36(2): 619–628.

Shvidchenko, A.B. & Pender, G. 2000b. Initial motion of streambeds composed of coarse uniform sediments. *Proceedings of the Institution of Civil Engineers, Water & Maritime Engineering*, 142 (December): 217–227.

Van Rijn, L.C. 1993. *Principles of sediment transport in rivers, estuaries and coastal seas.* Netherlands: Aqua Publications.

This page intentionally left blank

River Flow 2004 – Greco, Carravetta & Della Morte (eds.)
© 2004 Taylor & Francis Group, London, ISBN 90 5809 658 0

Scouring and flow structure around an attracting groin

T. Ishigaki, T. Ueno, M.M. Rahman & A.T.M. Khaleduzzaman
Ujigawa Hydraulics Laboratory, Disaster Prevention Research Institute, Kyoto University, Japan

ABSTRACT: An attracting groin, of which the head is shifted toward downstream, is not typically used in a submerged situation, because a flow over the groin attacks a bank and erodes it. While an attracting groin has this disadvantage, it was used as one of the traditional counter measures for protecting bank erosion about 400 years ago. In order to clarify this contradiction, the hydraulics of the groin is investigated experimentally in this paper. Local scour and flow structure around an attracting groin have been measured in submerged cases. It was found that the scour holes are produced near the head of groin in shallow flow, and the holes are observed near the root of groin in deeper flow. This result means that an attracting groin can be applied for protecting bank erosion in restricted situations.

1 INTRODUCTION

Recently, the environmental design has become one of important factors in planning flood control measures. Hydraulic engineers recognized that some traditional counter measures for flood are good examples of the matter. Floods are not fully controlled by the traditional measures, however, the nature is not fully destroyed by them. By now the engineers have a better opinion of the engineering.

One of the traditional measures is a groin that is discussed in this paper. The attracting groin has been built 400 years ago along the Katsura river in Kameoka city, Kyoto, Japan. An attracting groin involves a head shifted downstream, and the groin is set at the angle of 65 degrees with the normal to bank. According to a legend, the groin was set for protecting bank erosion, but scouring is generally observed near the root of attracting groin, as shown in Figure 1. The figure shows the patterns of scour and deposit around three types of submerged groins. The objective of setting the groin contradicts the hydraulic phenomena observed around it. In order to clarify the contradiction, the hydraulic aspects of this groin are investigated experimentally in this paper.

Many researchers have studied the hydraulics of groins, and three topics have been recently investigated. These are local scour (Kuhnle et al. 1999, Ohmoto & Hirakawa 2000, Elawady et al. 2001, 2002), the flow structure (Tominaga et al. 1997, Uittewaal & Berg 2002), and the mass exchange in the groin fields (Uittewaal et al. 2001, Kurzke et al. 2002). They have dealt with the groins of angle −30 to 30 degrees. Such groins in this paper are out of consideration, thus scour and flow structure around an attracting groin with large angle of 65 degrees is investigated here.

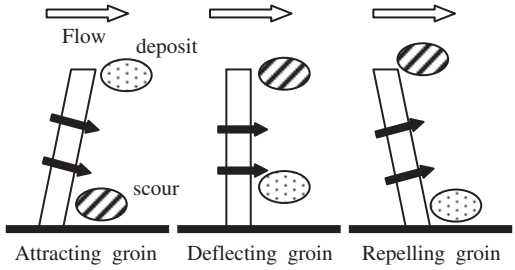


Figure 1. Scour and deposit around the three types of groins.

2 OLD GROINS

The two old groins are still remaining on the righthand side of the Katsura river in Kameoka basin, as shown in Figure 2. Those groins are Kami-Naizen and Shimo-Naizen named after the lord of a clan about 400 years ago. Kami-Naizen is upstream of the Shimo-Naizen groin. Kameoka basin is on the west side of Kyoto and the area is about 40 km^2. The Katsura river runs through the basin from west to east and connects to narrow valley called "Hozu gorge". This gorge works as a constriction during floods and the backwater extends over the basin. The two groins have been used for protecting bank erosion.

The original length of Kami-Naizen was 36.9 m and Shimo-Naizen was 90 m. Both groins were made of

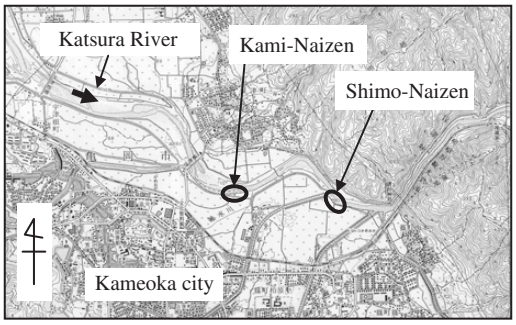


Figure 2. Survey map of old groins in Kameoka.

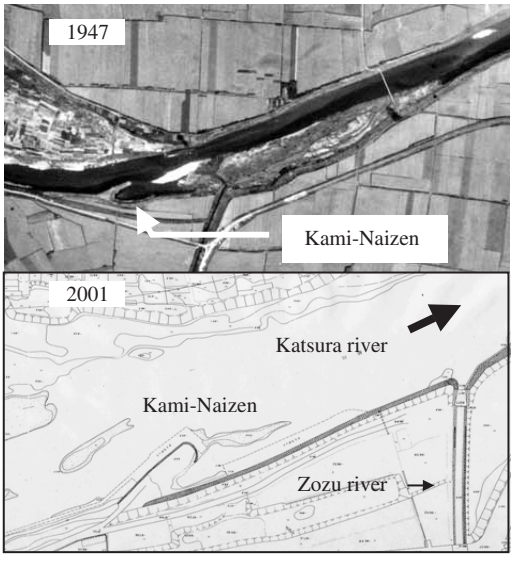


Figure 3. Air photo of Kami-Naizen in Oct. 1947, and the map in Oct. 2001.

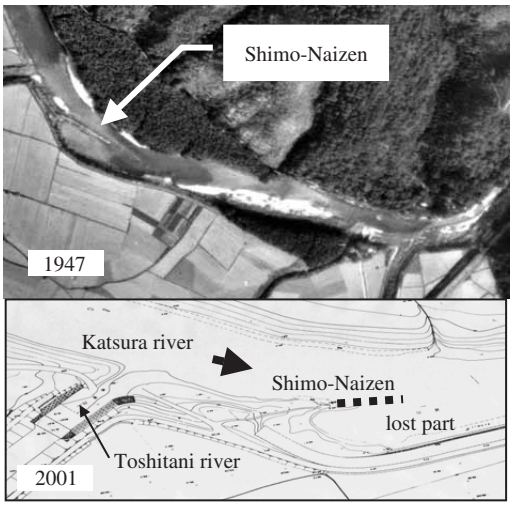


Figure 4. Air photo of Shimo-Naizen in Oct. 1947, and the map in Oct. 2001.

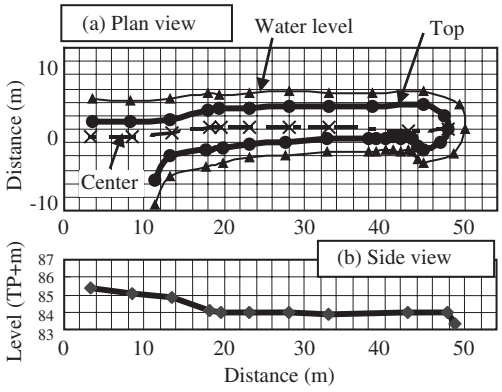


Figure 5. Plan and section of "Kami-Naizen" groin in 2001.

rocks. Figures 3 and 4 are air photos of the two groins in 1947 and maps in 2001. It is found that the length of Kami-Naizen has not changed, whereas Shimo-Naizen has become shorter. Shimo-Naizen had an original length until 1988, then the head part was swept away by a flood and not repaired. Figure 5 shows the present form of Kami-Naizen of which the length is longer than the original length of 36.9 m. Thus, some experiments have been done on Kami-Naizen and the local scour and flow structure around it were investigated by a model of 1/100 scale.

Tradition says that groins deflect the flow and protect the bank from erosion, however, there seems to be an additional function that is to keep the navigation channel and make ponds behind the groins. As logs and goods had been transported through the Katsura river for some ages, these navigation channel and embayment were needed. The ponds behind the groins were used to anchor small boats and rafts.

3 LOCAL SCOUR AND FLOW STRUCTURE

3.1 *Experimental set-up and methods*

Figure 6 is a model of Kami-Naizen groin (scale: 1/100). The model was set at the angle of 65 degrees on the right hand side bank in a straight channel with a flat bed. The channel was 10 m long, 0.9 m wide and 0.3 m deep installed with a discharge control system. The center part of the channel was made of movable bed filled with fine sand of which the mean diameter was 0.26 mm. The movable bed section was 1.8 m long and 0.2 m deep. Bed form, velocity, water level and

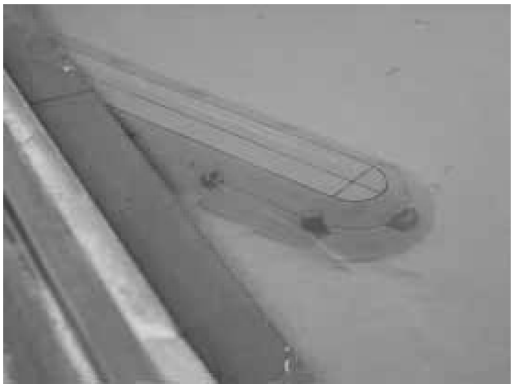


Figure 6. Hydraulic model of "Kami-Naizen" groin, (scale = 1/100).

Table 1. Hydraulic test conditions.

Case	H/h	H (cm)	Q (l/s)	Groin
1	0.82	4.08	7.27	non-submerged
2	1.22	6.06	10.78	submerged
3	1.41	7.00	12.60	submerged
4	1.62	8.00	14.40	submerged
5	1.92	9.48	17.38	submerged

H: depth, h: groin-height = 4.95 cm, Q: discharge, Width = 90 cm, Length = 10 m, Sand, dm = 0.26 mm

flow were measured under clear water scour in five cases of different water depths, which included four submerged conditions and one non-submerged case, as shown in Table 1. H/h is the relative depth, where H is the flow depth and h is the height of groin. The ratio between the friction velocity and the critical friction velocity of the bed material was kept from 0.83 to 0.91 by setting the same velocity in all cases.

A laser level meter, an ultra-sonic level meter and an electro-magnetic velocimeter were the equipments used for the measurements of bed form, water level and velocity, respectively. Flow patterns were observed on the water surface and in a cross section of flow by using normal and submergible video cameras.

3.2 *Bed form and flow structure*

Figure 7 shows flow patterns on the water surface for non-submerged and submerged groins. The flow patterns were visualized by sawdust as a tracer. Approach flow was deflected to the channel center by the groin in the non-submerged case and the dead zone was produced behind the groin. In the submerged case, the approach flow was also deflected, however, some part of the flow ran over the groin and to the bank. It was

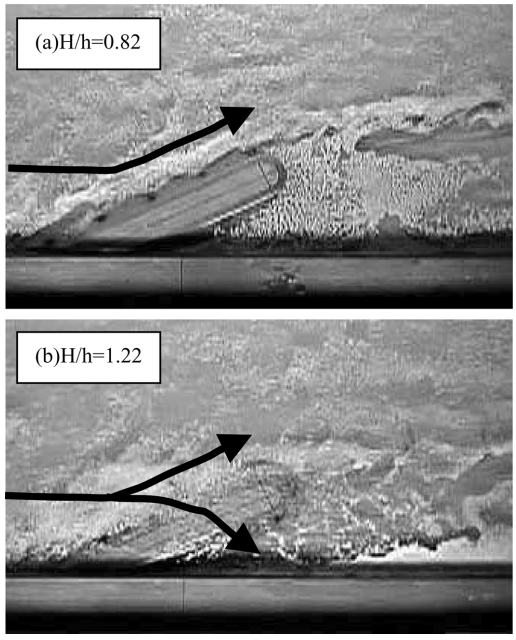


Figure 7. Flow patterns on the water surface in case of (a) non-submerged and (b) submerged groin.

easily anticipated that this overtopping flow causes local scour and bank erosion behind the groin.

Figure 8 shows bed form measurements in the non-submerged and three submerged cases. The friction velocity was almost same in all cases. The measurements were done after one hour in all the cases. Dark color shows scouring parts and bright color shows depositing parts. The depth and height is shown in the difference from the original bed level. In the non-submerged case, a scour hole is produced near the head of groin at first, and then other holes are produced in sequence. Approach flow is deflected by the groin and converges along the groin. This flow produces the first hole and runs up the downstream slope of the hole, and then reattaches the bed and scours the next hole. This mechanism was also observed in all cases.

The second figure is the bed form in the submerged case of H/h = 1.22. As the depth of overtopping flow is shallow and its velocity is slow, the bed form is not so different from the data in the nonsubmerged case. As shown in Figure 7, some part of approach flow runs over the groin, however, local scour is not observed behind the groin. This means that the local scour is not severe while the groin is submerged.

The third figure for H/h = 1.41 shows that scour holes can be observed near the head and root of the groin, and the last figure of H/h = 1.62 indicates that scour holes are produced only near the root of a groin in deeply submerged cases. The longitudinal profiles of

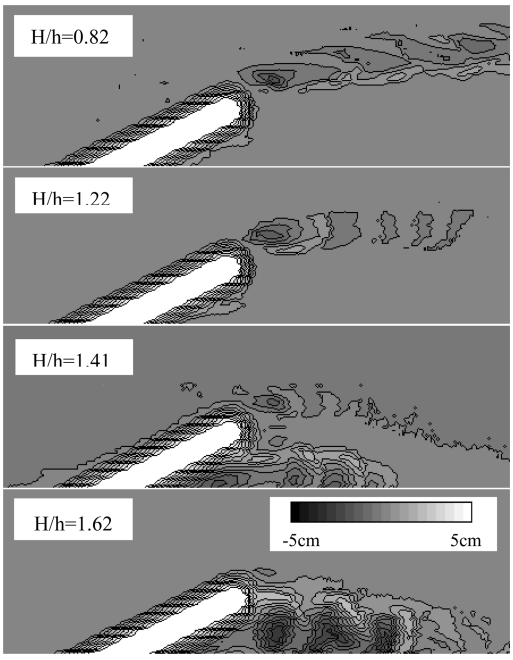


Figure 8. Bed forms around the groin for various groin submergences.

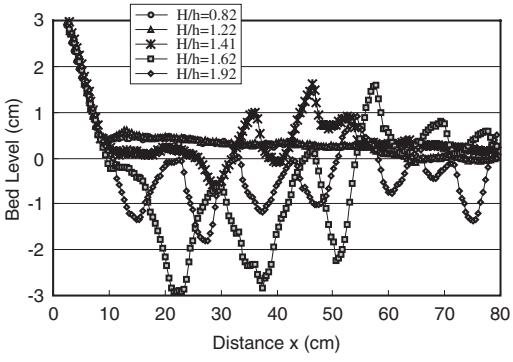


Figure 9. Longitudinal profiles of bed form near the root of groin at y = 6 cm, apart from the bank.

bed form near the root of groin, y = 6 cm apart from the bank, are shown in Figure 9. The origin of the x-axis is the center of groin at the connecting part to the bank. Scour holes can be observed except for the cases of H/h = 0.82 and 1.22. Deepest scour is not in the deepest case of H/h = 1.92, but in H/h = 1.62. From these results, it is found that the position of the scour hole varies with the head to root of groin when the relative depth increases, and that the scour depth depends on the hydraulic condition.

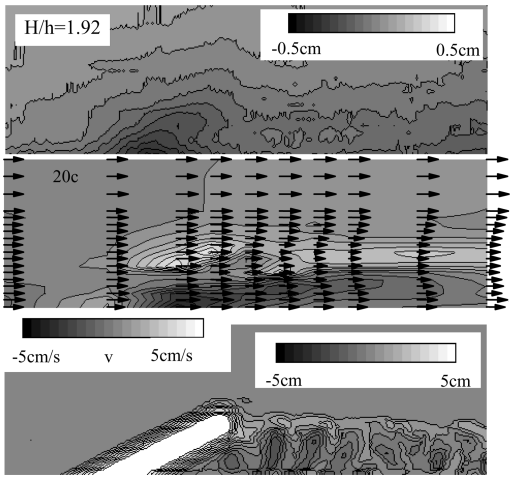


Figure 10. Profile of water-surface (top), velocity (middle) and bed (bottom) for submerged flow.

To investigate the relation between flow structure and bed form around the groin, profiles of water surface, velocity distribution and bed from were measured for H/h = 1.92, as shown in Figure 10. The water level is the difference from the mean flow depth. The two velocity components were measured at 1 cm above the groin top by using an electro-magnetic velocimeter. Arrows in the velocity distribution are the longitudinal component of velocity u, and the contour lines show the distribution of vertical component of velocity, v. The dark color is downwelling part and the bright color is up-welling part. Notation of the bed form is identical as in Figure 8. The water level over the groin is lower than the surrounding. It means that the flow is accelerated there. From the velocity distribution, it is found that the accelerated flow goes downward and intrudes into the wake region of groin, and then scours the bed. The velocity of this intruding flow depends on the hydraulic condition as mentioned before. And the upwelling part near the groin head indicates that some part of the deflected flow by the groin runs over the groin.

4 CONCLUSIONS

Scour and flow structure around an old attracting groin have been investigated by using a groin model of 1/100 scale. The conclusions are as follows:

1. For non-submerged and submerged conditions with shallow flow depth, a scour hole has been observed on the downstream side of groin head, and deep scour holes are produced on the downstream side of the groin root in another cases of submerged conditions. The location of scour hole depends on the

hydraulic condition and a hydraulic condition prevents severe bank erosion. There is a possibility to make an embayment and keep its depth identical as the old groin mentioned in this paper.

2. For the old groin, the flow velocity around the groin becomes slow during floods of large discharge because the floods are dammed up by the narrow gorge in downstream and the flow velocity becomes slow. It is presumed that the groin has been planned with consideration of the results obtained here.
3. Results of velocity measurement and flow visualization show that flow over a groin makes an important role of scouring behind the groin. It shows that the scouring around an attracting groin closely relates to the flow structure.
4. One of the important conclusions of this paper is that a traditional counter measure is useful when hydraulic engineers consider the design with nature for flood control.

REFERENCES

Elawady, E., Michiue, M. & Hinokidani, O. 2001. Characteristics of scour around repelling spur-dikes, *Proc. of 29th Congress of IAHR, Beijing*: Theme D, II, 343–349.

Elawady, E., Michiue, M. & Hinokidani, O. 2002. An investigation of scour around attracting spur-dikes, *Advances in Fluid Modelling and Turbulence Measurements, Proc. of 8th Intr. Symp. on Flow Modelling and Turbulence Measurements, Tokyo*: 111–118, World Scientific.

Kuhnle, R.A., Alonso, C.V. & Shields Jr., F.D. 1999. Geometry of scour holes associated with 90 spur dikes, *Journal of Hydraulic Engineering, ASCE*: 25, (9), 972–978.

Kurzke, M., Weitbrecht, V. & Jirka G.H. 2002. Laboratory concentration measurements for determination of mass exchange between groin field and main stream, *River Flow 2002, Bousmar & Zech (eds.)*: 1, 369–376.

Ohmoto, T & Hirakawa, R. 2000. Secondary current structure in open-channel flow with a series of submerged groyns, *Proc. of 12th Congress of APD-IAHR, Bangkok*: 1, 189–199.

Tominaga, A., Nagao, M. & Nezu, I. 1997. Flow structure and mixing processes around porous and submerged dikes, *Proc. of 27th Congress of IAHR, San Francisco*: Theme B, 1, 251–256.

Uittewaal, W.S.J & Berg, M.H. 2002. Experiments on physical scale models for submerged and non-submerged groynes of various types, *River Flow 2002, Bousmar & Zech (eds.)*: 1, 377–383.

Uittewaal, W.S.J., Lehmann, D. & Mazijk, A. 2001. Exchange processes between a river and its groyn field: model experiments, *Journal of Hydraulic Engineering, ASCE*: 127, (11), 928–936.

This page intentionally left blank

River Flow 2004 – Greco, Carravetta & Della Morte (eds.)
© 2004 Taylor & Francis Group, London, ISBN 90 5809 658 0

2-D Numerical analysis for flow around an oblique weir in compound open channels

M. Iwai & Y. Shimizu
Hokkaido University, Sapporo, Japan

Y. Kawahara
Kagawa University, Takamatsu, Japan

ABSTRACT: Flood flow around the Daijyu weir in Yoshino River is complicated because it includes an oblique weir in compound open channel. To consider the safety for this weir, the analysis of the three-dimensional flow features such as hydraulic jump, eddies, large scale of back flow region and curved flow is necessary. In this study, a two-dimensional numerical model including friction forces from wall and bed is applied and compared with the experiment set up with the same conditions as the Yoshino River. Friction coefficients are locally changed because flow characteristics are different among low, flood channel and high velocity region. CIP method is used to calculate the flow, and shown the basic characteristics of flow. However, two-dimensional model is not sufficient to calculate hydraulic jump phenomena in flood channel. The safety for this weir is examined changing the oblique weir height and its angle.

1 INTRODUCTION

In Japan, the oblique weirs can be found in many places. In Yoshino River, the Daijyu submerged weir is constructed obliquely to the flow direction for the reasons of historical backgrounds. This makes the flows in this river more complicated. Moreover, during flood the combination of floodplain and submerged-oblique weir has a complex interaction contributed to the flows in this river. Figure 1 shows the flood in Yoshino River in September 1974. A detour flow apart from oblique weir occurred at the left floodplain. Hydraulic jump and other complex flow features can possibly be occurred around and behind the weir. These could be roughly concluded that to consider the safety function of the Daijyu weir during flood, the analysis of the three-dimensional flow features is necessary to evaluate the safety of this river. Many researches, however, lack this kind of examples and experiments and have not clarified most of the unclear points.

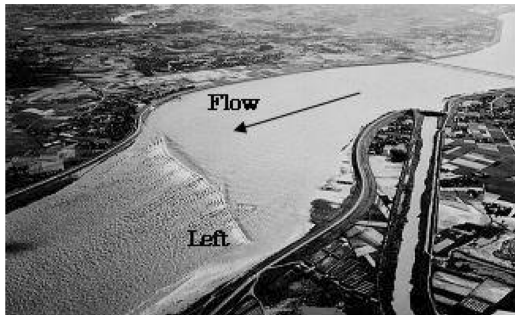


Figure 1. Flood in Yoshino River in September 1974.

The model experiment was performed for the purpose of perceiving the fundamental of flow features around the oblique weir (Matsushita et al., 2003). Detoured flow, back flow region, complex flow features were observed in the experiment. The analysis of the model experiment is significant to consider the safety of functionality of Daijyu weir.

In the experiment, three-dimensional flow is occurred because of effects from presence of flood channel and the oblique weir. At the downstream of the weir, a high-velocity flow, eddies and turbulence are occurred in flood and main channel. To analyze these phenomena, three-dimensional turbulence models have been developed.

The classical approach would be to follow the concepts of Large Eddy Simulation (LES) model for analyzing turbulence flow. Smagorinsky model is a typical LES model. Grid scale eddies are solved directly and sub-grid scale eddies are resolved by modeling Smagorinsky constant.

Horizontal two-dimensional flow is calculated directly by numerical simulation and turbulence, which

scale is not over water height is coupled by modeling. (Nadaoka and Yagi 1993). These models are applied in shallow-water flows included turbulence model and obtained good results. These models need to evaluate some coefficients experientially. However, the process of the numerical simulation is complicated because in these models, the momentum equation contains the energy from eddy effect and finally the accurate calculation results could be obtained.

Because vertical and horizontal flows are co-existed in the flow, then three-dimensional numerical model is theoretically suitable for this analysis of complicated flow features. To simplify this, two-dimensional flow equation is chosen to study. Hydrodynamic force is introduced into two-dimensional momentum equation. This model was applied in the flow around submergible groin. Water-jumps around groins obtained from experiments, could be simulated. Therefore, two-dimensional analysis can be simulated partly some features as taking into account the force which is dominant for flow.

In this study, three-dimensional equation is simplified to be a two-dimensional equation with detailed friction model. The two-dimensional generalized coordinate system was applied in calculation. Friction coefficients in the basic equations were modeled in more details. The safety of the weir and its vicinity are investigated comparing with other weirs having different heights and oblique angles.

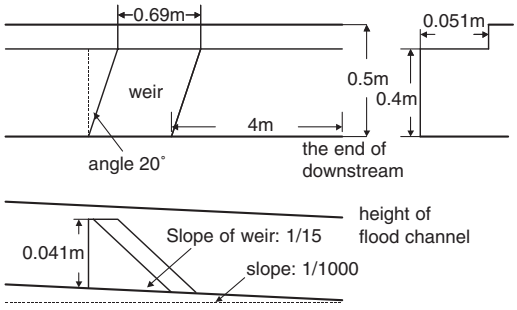


Figure 2. The model channel in experiment.

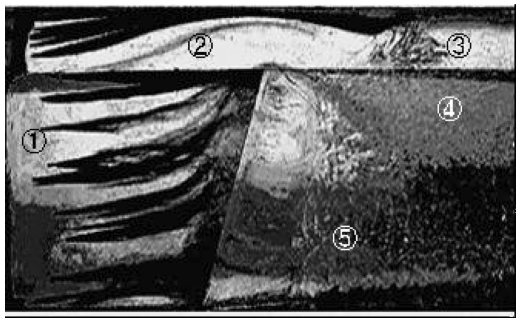


Figure 3. Visualization for streams used colorant injected in bottom at the upstream of the weir.

2 THE SUMMARY OF MODEL EXPERIMENT

Figure 2 shows the model channel in experiment. The height of the submerged-oblique weir is 0.046 m, which is smaller than the height of flood channel. Channel is fixed at grade of one in a thousand, with a total width of 0.5 m. Flood channel is set at left side of this compound channel. Flood channel width is 0.051 m and 0.1 m height. The oblique angle of the weir which grade is one in fifteen is 20 degrees.

Figure 3 is visualization for streams used colorant injected in bottom at the upstream of the weir. The important flows observed from experiment are shown in Fig. 3. ① is represented the lower-layer flows that started from the bottom of main channel and travel along the inner wall of main channel on the left side. ② is the flow started originally on flood channel and also started from main channel in the upper layer, then overflowed to the flood channel. This flow keeps running on the flood channel along left wall because this flow is pushed by hydraulic jump ③ at downstream flood channel and will not flow back to main channel. This can be observed from colored flow from upstream at flood channel will remain on the flood channel. There are various flow patterns in the area of the weir, going straight over the weir, circulating, upward flow, back flow and flow over the weir such as ⑤. Hydraulic jump can be seen behind the weir.

Curved flows at ② go to ④ regions. Back flow region is shown marking ④, velocity distribution of this area has a direction to vertical. Complicated vortex flow is shown at boundary between back flow region at ④ and fair current region at ⑤. Straight high-speed flow is shown in the vicinity of right bank. The paper written by Matushita et al., shows the other detail features of flows.

3 CALCULATION CONDITION OF FLOW

3.1 *Model equations*

The two-dimensional, unsteady, incompressible flow which is conducted in a generalized coordinate system has been calculated using the following continuity and momentum equations.

$$\frac{\partial}{\partial t}\left(\frac{h}{J}\right)+\frac{\partial}{\partial \xi}\left(\frac{hu^{\xi}}{J}\right)+\frac{\partial}{\partial y}\left(\frac{hu^{\eta}}{J}\right)=0 \qquad (1)$$

$$\frac{\partial u^{\xi}}{\partial t} + u^{\xi}\frac{\partial u^{\xi}}{\partial \xi} + u^{\eta}\frac{\partial u^{\xi}}{\partial \eta} + \alpha_1 u^{\xi}u^{\xi} + \alpha_2 u^{\xi}u^{\eta} + \alpha_3 u^{\eta}u^{\eta}$$
$$= -g\left[\left(\xi_x{}^2 + \xi_y{}^2\right)\frac{\partial H}{\partial \xi} + \left(\xi_x\eta_x + \xi_y\eta_y\right)\frac{\partial H}{\partial \eta}\right]$$
$$-\frac{C_b u^{\xi}}{J}\sqrt{\left(\eta_y u^{\xi} - \xi_y u^{\eta}\right)^2 + \left(-\eta_x u^{\xi} + \xi_x u^{\eta}\right)^2} + D^{\xi} \quad (2)$$

$$\frac{\partial u^{\eta}}{\partial t} + u^{\xi}\frac{\partial u^{\eta}}{\partial \xi} + u^{\eta}\frac{\partial u^{\eta}}{\partial \eta} + \alpha_4 u^{\xi}u^{\xi} + \alpha_5 u^{\xi}u^{\eta} + \alpha_6 u^{\eta}u^{\eta}$$
$$= -g\left[\left(\eta_x\xi_x + \eta_y\xi_y\right)\frac{\partial H}{\partial \xi} + \left(\xi_x{}^2 + \xi_y{}^2\right)\frac{\partial H}{\partial \eta}\right]$$
$$-\frac{C_b u^{\eta}}{J}\sqrt{\left(\eta_y u^{\xi} - \xi_y u^{\eta}\right)^2 + \left(-\eta_x u^{\xi} + \xi_x u^{\eta}\right)^2} + D^{\eta} \quad (3)$$

in which, x, y are orthogonal coordinate axis, t is time, ξ, η is plane coordinate axis in generalized coordinate, h is water depth, H is water level, u^{ξ}, u^{η} is contravariant tensor in ξ or η direction, J is Jacobian determinant in coordinate transformation, C_b is bed friction coefficients. Other coefficients and diffusion term show following.

$$\alpha_1 = \xi_x\frac{\partial^2 x}{\partial \xi^2} + \xi_y\frac{\partial^2 y}{\partial \xi^2} \quad (4)$$

$$\alpha_2 = 2\left(\xi_x\frac{\partial^2 x}{\partial \xi \partial \eta} + \xi_y\frac{\partial^2 y}{\partial \xi \partial \eta}\right) \quad (5)$$

$$\alpha_3 = \xi_x\frac{\partial^2 x}{\partial \eta^2} + \xi_y\frac{\partial^2 y}{\partial \eta^2} \quad (6)$$

$$\alpha_4 = \eta_x\frac{\partial^2 x}{\partial \xi^2} + \eta_y\frac{\partial^2 y}{\partial \xi^2} \quad (7)$$

$$\alpha_5 = 2\left(\eta_x\frac{\partial^2 x}{\partial \xi \partial \eta} + \eta_y\frac{\partial^2 y}{\partial \xi \partial \eta}\right) \quad (8)$$

$$\alpha_6 = \eta_x\frac{\partial^2 x}{\partial \eta^2} + \eta_y\frac{\partial^2 y}{\partial \eta^2} \quad (9)$$

$$D^{\xi} = \frac{\partial}{\partial \xi}\left[\frac{\tau_{\xi\xi}}{\rho}\right] + \frac{\partial}{\partial \eta}\left[\frac{\tau_{\eta\xi}}{\rho}\right] \quad (10)$$

$$D^{\eta} = \frac{\partial}{\partial \xi}\left[\frac{\tau_{\xi\eta}}{\rho}\right] + \frac{\partial}{\partial \eta}\left[\frac{\tau_{\eta\eta}}{\rho}\right] \quad (11)$$

in which, τ_{ab} is b-axis component of a shear force that affects the plane which is a vertical to a-axis. ρ is a density of water.

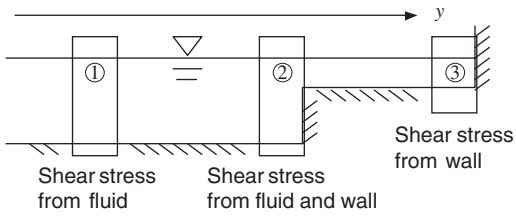


Figure 4. Patterns of shear stress acting on fluid body. (y-direction).

3.2 *Numerical model*

To solve Equations (2)–(11) the CIP scheme is adopted for advection phase. This is proved to be a suitable scheme to maintain hydraulic energy in the case of energy loss flow due to hydraulic jump by a work from Shimizu et al., that CIP method was adopted in the calculation of flow with a series of vertical dropped spillway by and reproduced the hydraulic jumps.

At the upstream of the weir, the viscosity is high because bed and wall of channel are smooth. Friction from wall influences on the flow at flood channel. Friction from the wall of weir influences on the flows that crossover the flood channel because the height of the weir wall is almost equal to the water depth.

The main idea of this study is that the water body has shear forces acting differently on individual location, meaning that the shear stresses have to be modeled locally. To examine the above mentioned idea, shear stresses acting on fluid body are considered and classified into three types as illustrated in Fig. 4. One is that shear stresses only from fluid friction act on both sides of water column ①. Two is that there is only fluid friction acting on left side of water column ②, while the right side is partly wall friction and fluid friction. Three is that take place on the left side, while on the right side shear stress is from wall friction.

When Equation (10) and (11) transform discretization, difference of shear stresses is considered in this research. For example, the shear stress is included in the following equations,

$$\frac{\tau_{xx}}{\rho} = \upsilon_t\left(\frac{\partial u}{\partial x} + \frac{\partial u}{\partial x}\right), \quad \frac{\tau_{yx}}{\rho} = \upsilon_t\left(\frac{\partial u}{\partial y} + \frac{\partial v}{\partial x}\right)$$
$$\frac{\tau_{xy}}{\rho} = \upsilon_t\left(\frac{\partial v}{\partial x} + \frac{\partial u}{\partial y}\right), \quad \frac{\tau_{yy}}{\rho} = \upsilon_t\left(\frac{\partial v}{\partial y} + \frac{\partial v}{\partial y}\right) \quad (12)$$

$$\upsilon_t = \frac{1}{6}\kappa u_* h \quad (13)$$

$$u_*{}^2 = C_b\left(u^2 + v^2\right) \quad (14)$$

in which, υ_t, is eddy viscosity, u^* is shear velocity.

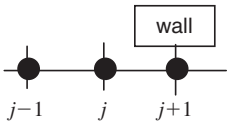


Figure 5. How to deal with shear stress by calculation step.

Shear stress from wall is assumed proportional to velocity square adjacent to the wall. When the fluid on the side wall has water depth higher than the height of side wall, a viscosity term will be prorated between water depth and the height of side wall because viscosity from fluid is considered as well as friction acted by side wall. For that reason, acted ② and ③ is showed Equations (15)–(17).

$$\frac{\tau_{yx}{}^{j}}{\rho} = \upsilon_t \left(\left(\frac{\partial u}{\partial y} \right)^{j} + \left(\frac{\partial v}{\partial x} \right)^{j} \right) \tag{15}$$

$$\frac{\tau_{yx}{}^{j+1}}{\rho} = \frac{h_w}{h} C_w u \sqrt{u^2 + v^2} + \upsilon_t \left(\left(\frac{\partial u}{\partial y} \right)^{j+1} + \left(\frac{\partial v}{\partial x} \right)^{j+1} \right) \frac{h - h_w}{h} \tag{16}$$

$$\frac{\tau_{yx}{}^{j+1}}{\rho} = C_w u \sqrt{u^2 + v^2} \tag{17}$$

in which, superscript j is calculation step shown in Fig. 5, C_w is friction coefficients of wall, h_w is the height of the wall. Equation (16) show ②, Equation (17) show ③. Equations (12)–(17) is transformed to generated coordinate and used in this research.

3.3 *Deal with friction coefficients*

Table 1 shows the calculation condition. Viscosity becomes bigger on the flood channel because Reynolds number is smaller than that in downstream main channel. In this experiment, velocity could not be measured because water depth is not high enough to measure. The flow on the flood channel is considered to be a laminar flow. On the other hand, hydraulic jump high-speed flow is distinguished around the weir. Compared with upstream of the weir, it has high Reynolds number. If friction coefficient values remain the same, calculation result will be different from experiment result, which is not supposed to be.

In this research, various friction coefficients are determined. In order to understand the changes among upstream or downstream regions of the weir, flood channel or main channel and their combinations, calculation results is compared with experiments. Table 2 shows how to give their friction coefficients. Manning roughness is represented a bed friction. The value of Manning roughness in flood channel bottom is given three times bigger than that of downstream main channel bottom. Velocity is amplifying around the area of the weir connected to the flood channel (assumed that 8 cm in upstream direction from the junction of the weir and flood channel) in order to curve flow on main channel into flood channel so that Reynolds' number is high as the velocity is increasing. Manning coefficient is set 2/3 of other places. Manning coefficient at sidewall is constant to prevent calculation from complexity. When Manning coefficient is 0.01–0.03, C_b is then 0.002–0.04 and the C_w value also falls into this range. As a result, the C_w value is appropriate.

Table 1. Calculation condition.

Term	Value
Discharge (m^3/s)	0.0243
Water depth at the end of downstream (m)	0.066
Δx (m)	0.04
Δy (m)	0.02

Table 2. Friction coefficients on the calculation.

Place	Value
Bed in flood channel	$n = 0.03$
Around the weir in flood channel	$n = 0.02$
Bed in the main channel	$n = 0.01$
Side wall	$C_w = 0.02$

4 CALCULATION RESULT

4.1 *Water depth*

Calculation result of water level compared with experimental data is shown in Fig. 6. Calculation time is 150 seconds, while result is averaged from 80–150 seconds for stable period. X is flow direction and y shows distance started from right bank. For convenience of plotting, location of plots from calculation differs from experimental location by 5 mm. This effect could be ignored.

In the region of $x = 140-160$ cm and from flood to main channel, hydraulic jump is observed. Water depth is calculated smaller and smaller after the weir. It is the same to experiment. Hydraulic jump position, however, is differed in main channel. Hydraulic jump in flood channel does not appear. The results are the same when friction coefficients on bed and wall are changed. It seems that basic equations, (1)–(3), did not drive energy conservation.

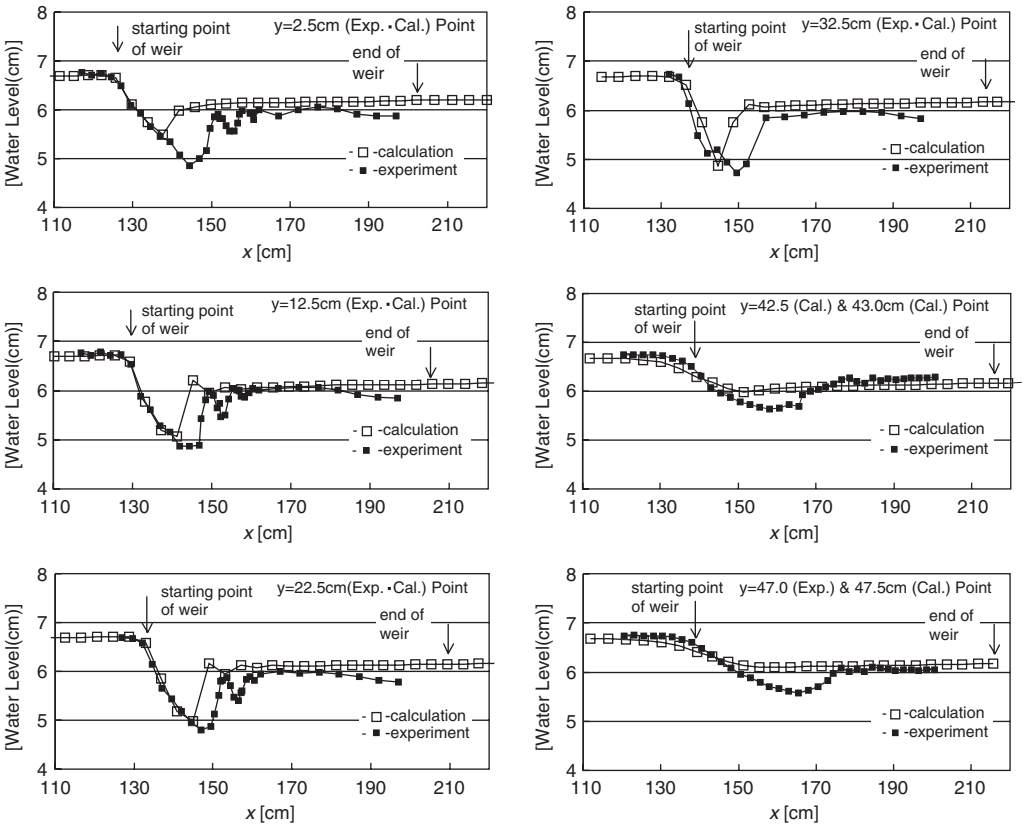


Figure 6. Comparison of water depth between calculation and experiment result.

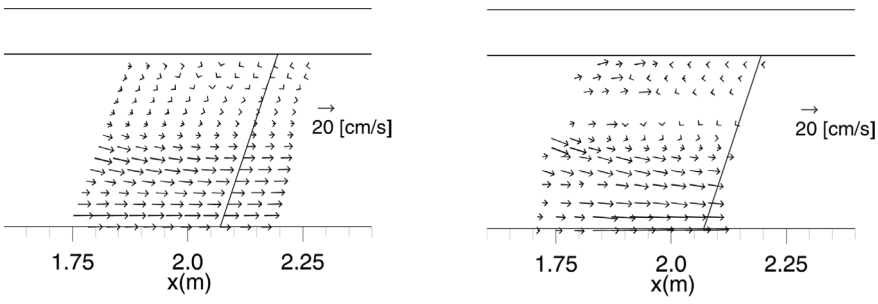


Figure 7. Velocity distribution at downstream of the weir (top: calculation, bottom: experiment).

4.2 *Velocity and friction distribution*

Figure 7 shows velocity vectors after the weir. In experiment, the back flow region can be observed at downstream of the weir and left bank of main channel. In this specific location, three-dimensional flow pattern is strong compared to other places. The velocity distribution has a big change in vertical direction. Velocity distribution of calculation has zero or minus values and indicates that there are "back flow region" or "dead flow region" at left bank of main channel after the weir. At right bank of main channel, calculation flow goes straight along the right wall as in experiment, but velocity is not same in order of magnitude.

Figure 8 shows contour of friction velocity. Figure 9 shows the flow visualized by using oiled-slide method and Fig. 10 shows contour of absolute modulus value

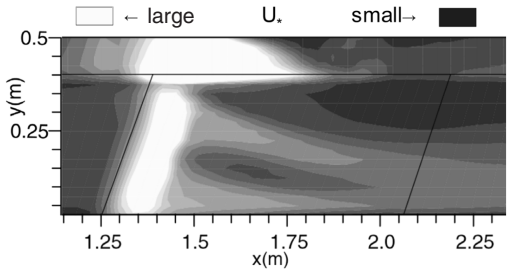


Figure 8. Contour figure of friction velocity.

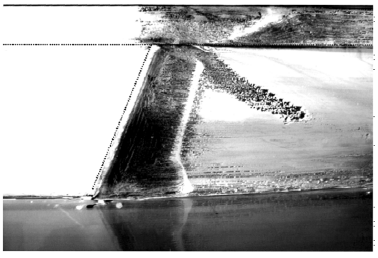


Figure 9. Flow by visualized using oiled-slide method.

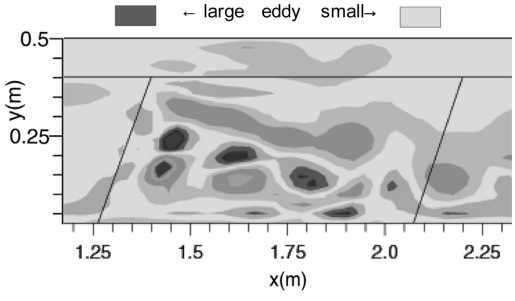


Figure 10. Contour figure of friction velocity.

of vorticity. Oiled-slide method indicates the magnitude of bed friction and directions. Black color shows strong bed friction.

Experiment shows strong bed friction affected on hydraulic jump after the weir. Flow is accelerated upstream of the weir in flood channel, then oblique hydraulic jump occurred.

Before and after oblique hydraulic jump, shear stress is increasing. It is shown that large shear stress leads to vortices in boundary between back flow and following region. Increasing shear stress is calculated after the weir in main channel. However, oblique hydraulic jump is not calculated, so shear stress at downstream in flood channel decreases on the against accelerated flow region at upstream is shown.

Calculation results show large friction at boundary between back and following region, but this scale

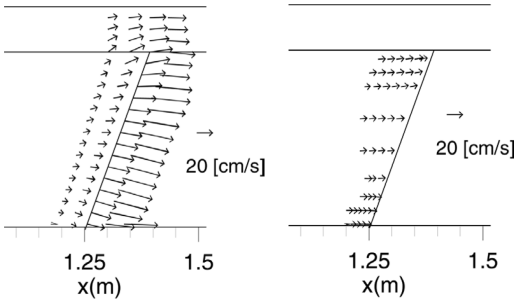


Figure 11. Velocity vector at downstream of the weir (left: calculation, right: experiment).

is smaller than the experiment. At the right of them, strong and small vortices, which is not appeared in the experiment is produced. It must be that downstream main flow of the experiment appears to have weak following vortices or a dead flow region. Large friction region is not appeared in the experiment but is shown in the calculation.

Velocity vector at downstream of the weir is shown in Fig. 11.Three-dimensional flow affected on the weir and flood channel appear at this place. Flow, which is shown velocity vector figure of experiment, is made slower because of effect from the weir and flood channel.

On the other hands, calculation flow is accelerated before the weir. It is difficult to discuss about calculation results because velocity at the same point different from surface to bottom in the experiment and velocity is depth-averaged by two-dimensional plane calculation. Flow running on flood channel is appeared at left bank of main channel.

4.3 *Validity of the result*

Two-dimensional analysis result of model experiment that has been calculated on the channel included oblique weir is conducted a deliberation on, whether this model can be applied in safety assessment. Major obtained conclusions are here.

(1) Curved flow is occurred at junction of weir and flood channel where flow characteristic is strongly three-dimensional. Two-dimensional model that is used in this study can explain gross outline of occurrence of these flow phenomena.
(2) Velocity at bed differs from surface flow velocity at back flow region. Strong back flow in experiment came out as dead and back flow region in the calculation despite three-dimensional flow appeared.
(3) CIP method is described as good energy conservative calculation system. It can give the rough outline of hydraulic jump shown in the experiment using non-conservative equations.

Table 3. The calculation with various shape of the weir.

Case	Changing term	Value after changing
Run-0	–	–
Run-1	Angle of weir	−20 degree
Run-2	Height of weir	90% of experiment

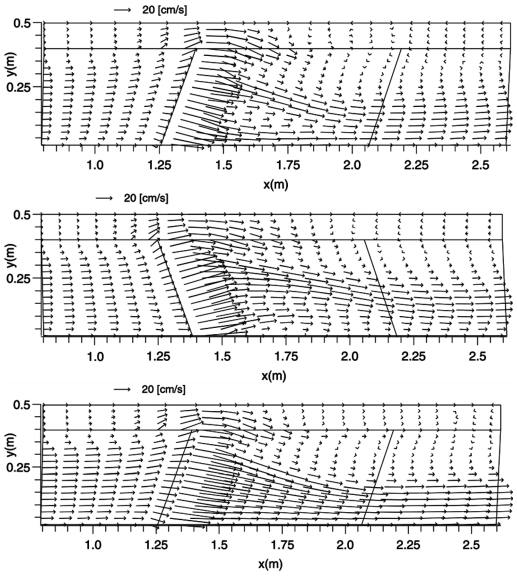


Figure 12. Velocity vector of the calculation.

Consequently, this model is good for explaining the outline of flow but could not replicate the detail of experiment, for example vertical characteristics.

5 SAFETY INVESTIGATION OF THE WEIR

It is considered that damages of river and basin are from the hydraulics jumps and accelerated flows, which is shown in the model experiment represented for the Daijyu weir. Simulations are performed by changing of heights and angles of the weir and the safety by these changes is investigated. The calculation with various shapes of the weir is shown in Table 3. Velocity vector of the calculation is shown in Fig. 12. The condition of Run-0 is the same as existing condition.

In Run-1, characteristics of flow are outlined below. Detour flow originates from flow near flood channel. Flows run to flood channel and concentrate to right of the river. High-speed flow at right bank shown in Run-0 does not appear. Dead flow region is shown in left bank of the main channel at downstream of the weir.

The height of the weir in Run-2 is smaller than Run-0. Velocity is higher in upstream of the weir in main channel. High-speed flow is shown at the same place of Run-0. The flow is directed to the right bank and continues straight with the constant speed. Dead region is shown in downstream at left bank of main channel.

Flood can flow easily at the right of river, but may cause to heavy damages to right bank. In the case of Run-1 and Run-2, flow in flood channel could not be predicted because flow simulation cannot be calculated exactly on Run-0. Especially, flow in main channel meet at flood channel on Run-1, complicated flow may occur. Ignored them, Run-1 is the most safe calculation of all cases because of low velocities at both banks.

6 CONCLUSION

Two-dimensional numerical method shown in this study can show flow of model experiment of the Daijyu weir and safety of the weir is investigated.

Some special flow cannot be produced, for example hydraulic jumps in flood channel. It must be checked that CIP method with non-conservative can be applied flow with energy loss such as hydraulic jumps.

Hydrodynamic forces must be considered in two-dimensional numerical model because this flow includes the structures. This model will be introduced in future.

Three-dimensional model must be considered if more accurate analysis is needed.

REFERENCES

Kawaguchi, H., Watanabe, A. and Fukuoka, S. 2001. 2-D numerical analysis of flow around submersible groin for different groin angle. *Proceeding of Hydraulic Engineering, JSCE,* Vol.45, 385–390 (in Japanese)

Matsushita, K., Kawahara, Y. and Tanaka, Y. 2003. Flood characteristic around oblique weir in compound open channel. *Proc. of Shikoku Chapter of JSCE,* 188–189 (in Japanese)

Nadaoka, K. and Yagi, H. 1993. Horizontal large-eddy computation of river flow with transverse shear by SDS & 2 DH model, *Journal of Hydraulic Coastal and Environmental Engineering., JSCE*, No.473,25–34 (in Japanese)

Shimizu, Y., Fujita, M. and Hirano, M. 1999. Calculation of and bed deformation in compound channel with a series of vertical drop spillways. *Proceeding of Hydraulic Engineering, JSCE,* Vol.43, 683–688 (in Japanese)

Smagorinsky, J. 1963. General circulation experiments with the primitive equations. I. The basic experiment. *Month.Wea. Rev.,* 91, 99–164.

This page intentionally left blank

River Flow 2004 – Greco, Carravetta & Della Morte (eds.)
© 2004 Taylor & Francis Group, London, ISBN 90 5809 658 0

Study of sediment motion in a local scour hole through an image processing technique

S. Malavasi, A. Radice & F. Ballio
Politecnico di Milano, Dept. I.I.A.R., Milan, Italy

ABSTRACT: The kinematics of the grains on the bottom of a local abutment scour hole was filmed during a clear water experiment and analysed by means of an image processing technique. The identification of natural sediments moving on a background of similar ones is complicated, due to the absence of contrast. This complication can be overcome using a technique based on the subtraction between successive frames. The method allowed to identify the temporal and spatial variation of the grain activity, and also to display the paths of the moving particles. The scour characteristics vary as the dimension of the hole increases: the 3D horseshoe vortex structures seem to play a major role only after the initial stage, during which the process is rather dominated by the 2D acceleration due to the abutment blocking effect; in the development stage the process appears to be a succession of transport events and periods of stillness, with increasing irregularity as time proceeds.

1 INTRODUCTION

Local scour phenomena at bridge structures have been studied through experimental works for many years. Since the early 1960s equations have been proposed for the prediction of the scour depth once the control parameters of the incoming flow and of the bridge structure are known. Despite the large amount of experimental data, many aspects of the erosion process remain unclear; the predictive ability of scour equations is, in some cases, inadequate (see for example Radice et al., 2002).

These reasons indicate that phenomenological studies at the sediment scale may be an important complement to the classical "black box" scour experiments. The evolution of the scour hole around piers and abutments is generally believed to be driven by the action of the three-dimensional horseshoe vortex system that develops in the vicinity of the obstacle. In the past, some studies that investigated the nature of the flow field have been published (e.g. Kwan & Melville, 1994; Dey et al., 1995; Mayerle et al., 1995; Molinas et al., 1998; Ahmed & Rajaratnam, 2000; Graf & Istiarto, 2002). To our knowledge, no studies considered the dynamics of the granular bed, even though the fluid–sediment interaction is a key item for the interpretation and modelling of local erosion phenomena. It is important to remark that the usual plane bed inception and transport equations do not necessarily apply to the case of a hole eroded by a three-dimensional and spatially highly variable flow field.

In this study, the kinematics of the grains on the bottom of a local abutment scour hole was filmed during a clear water experiment and subsequently analysed by means of an image processing technique. Image processing (IP) is largely used for the measurement of fluid flow fields; in such cases, the fluid is seeded through very small, neutrally buoyant particles. Less frequently IP has been applied to problems concerning sediments. Image techniques were used in order to extract information on the granulometric distribution of still grains (e.g. Fraccarollo & Marion, 1995; McEwan et al., 2000). Other studies dealt with steady bed load (e.g. Drake et al., 1988; Lee & Hsu, 1994; Niño & Garcia, 1996; Pilotti et al., 1997; Papanicolaou et al., 1999; Strom et al., 2002) or with debris flow (e.g. Capart et al., 2002). The application of IP to local erosion sums up all the complications related to the phenomena mentioned above, and adds some further, due to the complexity of the process. Local scour is a transient phenomenon, which may take long time to develop; the spatial distribution of the moving grains may be extremely variable, ranging from sporadic dispersed movements to high density clouds of sediments at varying distances from the bottom; the geometry of the scour hole is highly three-dimensional, thus complicating the focusing of the bottom; the moving particles lay on a background of similar grains, so that their identification is not straightforward.

In the mentioned literature studies, some of the quoted difficulties were bypassed through the use of synthetic multicoloured sediments; in this work we

developed a technique that is based on image subtraction that can also be applied to natural sediments. The number of particles moving in a certain time interval was assumed as an indicator of the activity of the process. The kinematics of the grains was interpreted also with reference to the particle paths, which were related to the structure of the flow field near the obstacle.

2 EXPERIMENTAL SETUP AND SCOUR TEST

The experiment reported herein was performed in a rectangular channel, 15 m long and 0.6 m wide. The channel was filled with approximately uniform natural sediments of mean diameter $d_{50} = 1.9$ mm. The rectangular abutment model was made in PVC and its dimensions were $b = 20.2$ cm and $L = 10.2$ cm, respectively, in the transverse and in the streamwise directions.

The test parameters were: uniform water depth $h = 9.5$ cm; mean flow velocity $U = 0.47$ m/s; longitudinal slope $S = 0.0012$. These corresponded to nearly incipient condition for the undisturbed bed (Shields parameter $\phi = (h \cdot S)/(\Delta \cdot d_{50}) = 0.03$, in which $\Delta = (\rho_s - \rho)/\rho$ is the specific gravity of the sediments).

Figure 1 shows the temporal evolution of the maximum scour depth d_s with time T for a previous experiment having the same control parameters. Scour depth continuously increases with time, but at a decreasing rate; in the same way, the grain activity is very intense at the beginning of the process, yet becoming weaker as the phenomenon proceeds in time and the scour rate decreases.

The grain movement was filmed with a black and white CCD camera of a frame rate set to 50 fps and a resolution of 576 × 763 pixel, and a PC equipped with a proper frame grabber. The duration of each recording was typically 2 or 4 seconds (100 or 200 images); the position of the films along the test duration is shown in Figure 1. Two time scales will be used in the following: t will indicate time within a film, while T will indicate the scour test time.

The sediment kinematics was filmed from the top; in order to avoid image distortion due to the irregularity of the free surface in the proximity of the obstacle, a wide plexiglass window just touching the water was put on the channel, thus obtaining clear images without disturbing appreciably the flow. Some control scour depth values were measured also during the visualization run, resulting in negligible differences from those plotted in Figure 1. This demonstrated that the plexiglass window did not distort significantly the process.

The film area was rather limited, its dimensions being approximately $11 \times 8\ \text{cm}^2$; thus, the CCD was placed in different positions all around the abutment, in order to investigate the dynamics of the grains

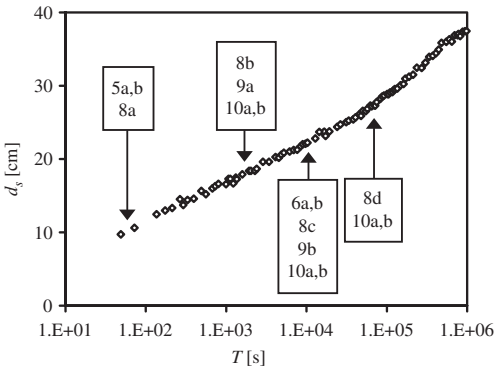


Figure 1. Temporal evolution of scour depth. Labels indicate the Figures in this work where results for the corresponding temporal positions are presented.

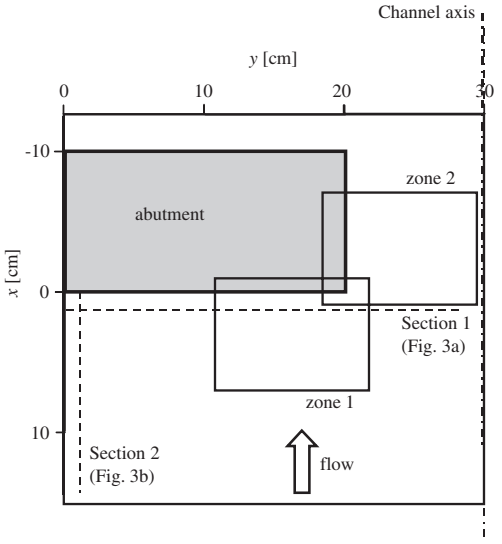


Figure 2. Definition sketch and position of the film zones. The planimetric coordinate system and the measuring sections for scour values are indicated.

at different locations in the scour hole. Results that will be presented herein refer to the zones shown in Figure 2. For comparison between the filming zone and the scour hole, Figure 3 shows the geometry of the latter (d indicates the scour depth at a certain location) as surveyed at times similar to the ones at which the films were taken.

3 IMAGE SUBTRACTION TECHNIQUE

The identification of the moving grains was performed through an image subtraction technique. Grey

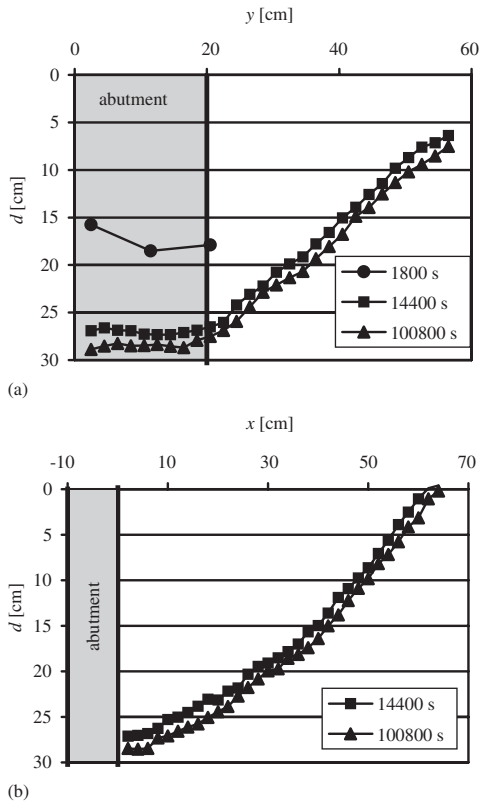


Figure 3. Scour hole bottom profile at instants similar to those in which the grain kinematics was filmed; transversal section 1 (a) and longitudinal section 2 (b). Time T in seconds.

images were used; the intensity value of each pixel lays between 0 (black) and 255 (white). If a particle is moving, its positions in two subsequent frames will be different: these locations are in the following 1 and 2. As a consequence of the particle displacement, a change in the intensity values of the pixels corresponding to positions 1 and 2 will occur in both frames. The difference between the first and the second image (which we computed as second-first) gives a third, which ideally has non-zero values in positions 1 and 2 and zero values elsewhere. The non-zero difference values will be positive in position 2 and negative in position 1 if a bright particle locally moves on a background of darker, and vice versa. The subtraction image, therefore, contains the image of the particle in both positions; this duplication is easily removed by filtering to zero all negative values. In this way the non-zero values give a single representation of the moving particle, corresponding to position 2 if a bright particle moves on a background of darker, to position 1 in the opposite case. Thus, the positive difference image shows the starting position of particles that are darker than their local background and the arrival position of the ones that are brighter than it.

The positive difference image was then thresholded to obtain a binary representation where a unit value was assigned to the pixels corresponding to the particle position and zero was assigned elsewhere. The binary image appeared as uniformly black with a white blob representing the moving particle. In real cases with many grains moving, the binary image was typically affected by noise (i.e. many small blobs were present), which was due to small movement or to little changes in the intensity values of the pixels that did not correspond to real displacements. The little blobs were eliminated through image filtering to obtain a clearer image, containing only the information on non-vanishing movements.

The complete thresholding and filtering procedure involves four parameters: the binning threshold *bin* (which lays between 0 and 255), the pixel connection criterion (based either on 4 or on 8 neighbouring pixels), and two coefficients, named C and $D_{\min}$, for filtering. First, the binary image was computed. Low binning factors and 8-connectivity give few big blobs, when the image of a particle is connected to those of the surrounding moving grains; high binning factors and 4-connectivity give the opposite. All the blobs having a dimension smaller than $D_{\min}$ were eliminated. Finally, the average dimension (in pixel) of the blobs was computed, and all blobs with a dimension smaller than the fraction C of the average value were eliminated from the image. High C values eliminate many blobs and vice versa. The first filter (involving $D_{\min}$) was required because if no appreciable movement takes place, the binary image will have very small blobs, which will not be completely eliminated by the C filter. The chosen parameter combination was: $bin = 77$, 4-connection, $C = 0.5$, $D_{\min} = 30$. This set of parameters was chosen by eye, comparing the result of the computation to the direct superimposition of successive frames. The calibration parameters do not need to be changed as long as the particle characteristics and the lightning are kept constant.

It should be noticed that the processing technique was defined and tuned for a correct and robust identification of the *number* of moving particles, but not of their *dimension*: in particular, the resulting average dimension (in pixel) of the blobs was highly dependent on the value of the calculation parameters, and it may be different than in the original frames.

At the end, the binary image was inverted in order to have white background images with black blobs.

Figure 4 shows an example of application of the described technique: images (a) and (b) are two successive frames; some of the moving grains have been circled. Image (c) is the absolute difference (b) – (a), which has non-zero values in positions 1 and 2 and small noise spots. Image (d) is the positive difference

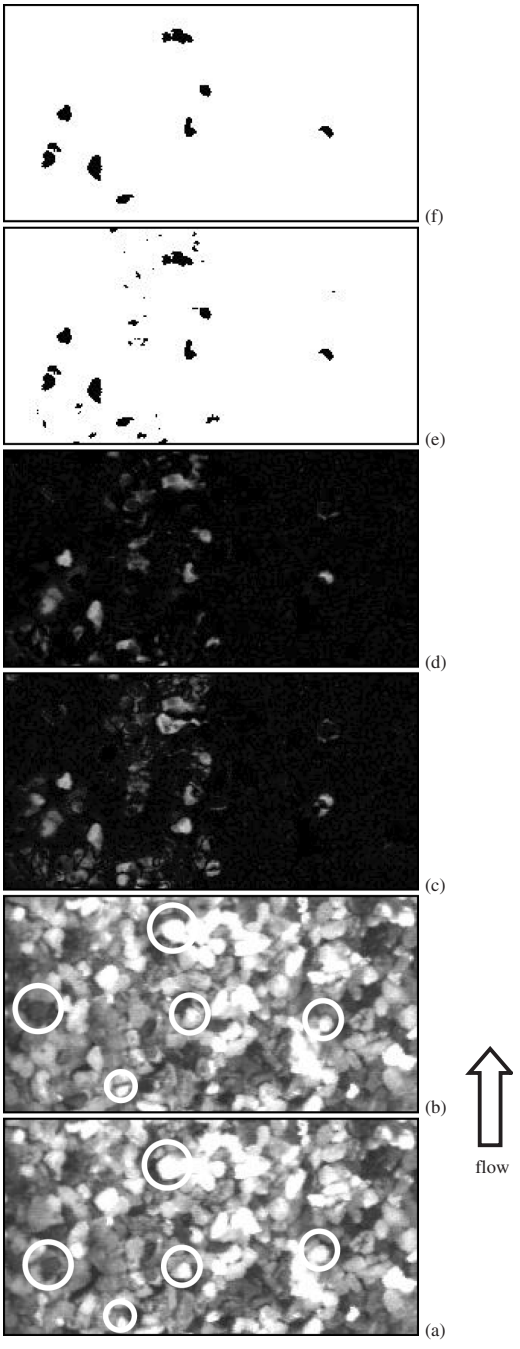


Figure 4. Example of image subtraction technique: upstream image (a), downstream image (b), absolute difference image (c), positive difference image (d), negative of thresholded difference image (e), negative of filtered difference image (f). In the upstream and downstream images some of the moving particles are circled. Flow is from bottom to top.

image, retaining only the positive difference values. Image (e) is the binary difference image after thresholding. Image (f) is the final binary filtered representation.

4 PARTICLE PATHS

The superimposition of successive blob images allows to identify the positions successively occupied by the moving grains, and thus their paths. Figures 5 and 6 show examples of such a visualisation for the scour test.

The grain paths for an initial stage of the process are shown in Figure 5 ($T = 120$ s): the two representations (a) and (b) are the results of two series of ten successive difference images, respectively, corresponding to $t = 0.2 \rightarrow 0.4$ s and $t = 1.2 \rightarrow 1.4$ s within one film. Some of the more evident paths have been highlighted through arrows; the black and white representation

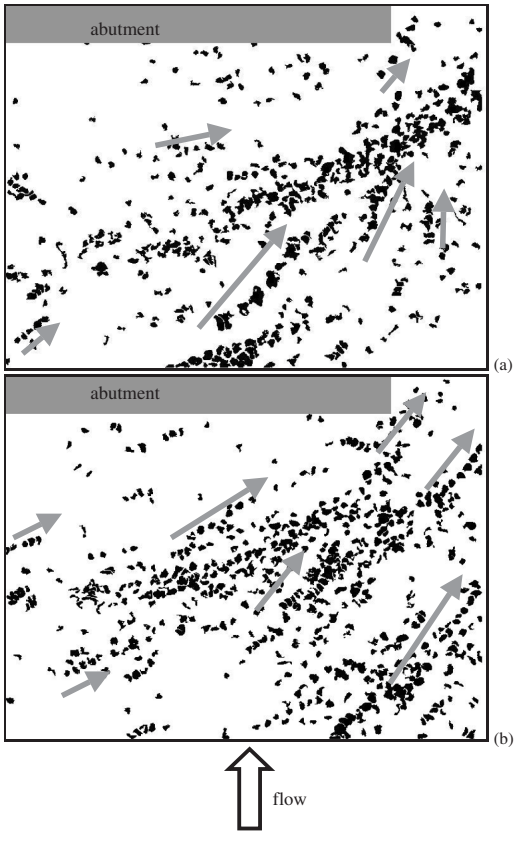


Figure 5. Superimposition of 10 successive difference images for zone 1 and $T = 120$ s. The interval between the two sequences in (a) and (b) was equal to 1 s. In grey is the visible part of the abutment. Some clear paths are highlighted through arrows. Mean flow direction is from bottom to top.

does not allow to identify the successive positions of the grains, while this is evidently possible from the single subtraction images. Figures 5a and 5b clearly indicate the presence of a well structured and temporally stable path field for the grains, which is coherent with a typical 2D flow pattern around an obstacle; this result would indicate the mean acceleration due to the abutment blocking effect as the responsible of the particle motion during the first stage of the erosion process. The 3D effects of the vortex structures in front of the abutment are hardly visible, due to the strong stretching by the outer flow. Further visualisations confirmed this result.

Visualisations of the grain paths for developed stages of the process demonstrated a completely different phenomenology: the movement is not continuous in time and well structured in space, but rather dominated by intermittent events with variable spatial characteristics. Figure 6a ($T = 120$ s, $t = 0.2 \rightarrow 0.4$ s) shows absence of appreciable grain activity. One second later (Figure 6b, $T = 120$ s, $t = 1.2 \rightarrow 1.4$ s) grain paths show the presence of a flow structure sweeping the particles away from the abutment against the main flow direction, and a small corner structure at the side. This indicates that in the development stage of the scour process the main scouring agent is determined by three-dimensional unsteady vortex structures upstream of the abutment; as the scour hole becomes deeper, the vortex stretching by the outer flow is evidently weaker and the flow and grain kinematics becomes more complex.

The characteristics of the sediment activity described for the initial and mature stage of the erosion process are coherent with literature descriptions of the phenomenon (e.g. Kwan & Melville, 1994; Radice et al., 2002); to the best of our knowledge, however, such characteristics had never been documented by measurements and/or visualisations.

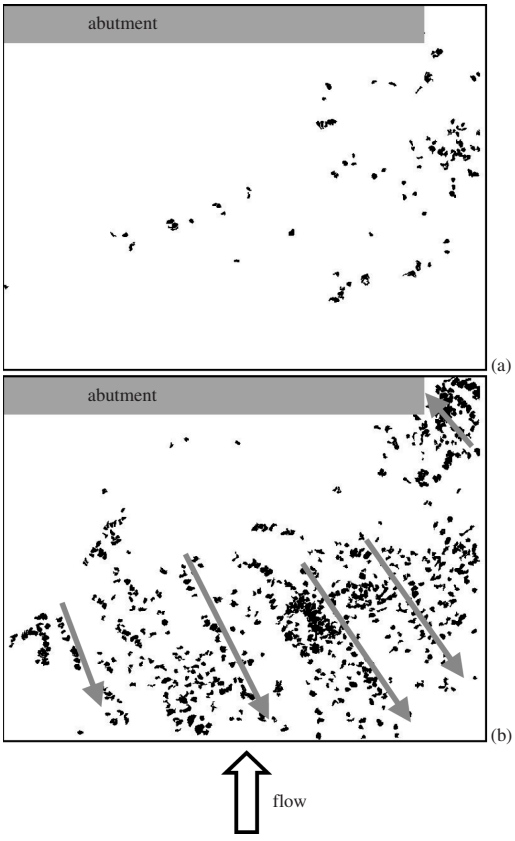


Figure 6. Superimposition of 10 successive difference images for zone 1 and $T = 11100$ s. The interval between the two sequences in (a) and (b) was equal to 1 s. In grey is the visible part of the abutment. Some clear paths are highlighted through arrows. Mean flow direction is from bottom to top.

5 MOVEMENT INTENSITY

Once the moving particles were identified, a percentage index of the intensity of movement (*IM*) can be evaluated as:

$$IM = \frac{N}{N_I}, \tag{1}$$

where N is the number of blobs in the thresholded subtraction image and N_I is the number of particles visible in the frame. To obtain the time evolution of *IM*, the calculation was conducted for each couple of successive frames, so that a film of duration of 2 s (100 frames) gave 99 successive values of *IM*. For the evaluation of N_I, particles at the image borders were visually counted, so that N_I was calculated as the product of the average numbers of particles in the two directions. Any algorithm for particle identification within a single picture (e.g. McEwan et al., 2000) may be also used for an automatic evaluation of N_I.

IM is an average indicator of the grain activity over the measuring zone. To highlight the spatial variability of the movement intensity (demonstrated by visual observation), the measuring zone was divided into windows of inspection, and individual *IM* values were calculated for each zone. Results that will be presented in the following refer to a subdivision of the measuring zone into 9 windows of inspection (Figure 7 shows an example of division for zone 1); the dimension of each window was approximately 2×3 cm^2.

Figure 8 shows the time evolution of *IM* over a duration of 2 s for zone 1, window 9 for increasing run times T. At the beginning of the erosion process (Figure 8a, $T = 120$ s, see also Fig. 5) *IM* values are typically $20 \div 40\%$, indicating that a high percentage

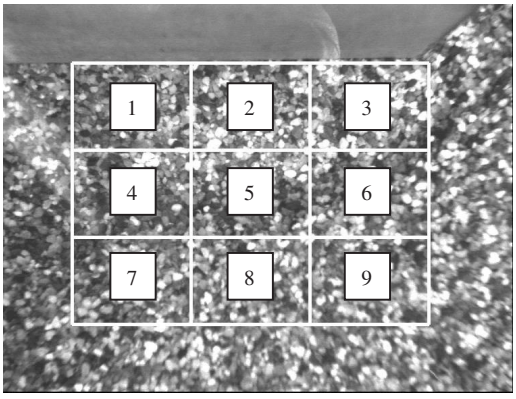


Figure 7. Typical division into inspection windows (numeration indicated) for an image in zone 1. Flow is from bottom to top. The abutment can be seen at the top of the image.

of the particles move. The grain activity progressively decreases as time proceeds, and after one day (Fig. 8d) values of *IM* were reduced by one order of magnitude.

Figure 8a shows fluctuations of *IM*, but no period of rest; a different behaviour can be recognised for longer run times (Figures 8b→8d). This observation is in agreement with those drawn in the precedent paragraph, according to which the grain kinematics was stable only in the initial stage of the scour process, while afterwards it was composed by a succession of transport events and periods of stillness. This again indicates the different temporal stabilities of the flow field along the process, where the decreasing degrees of stretching of the vortex structures by the outer flow make three-dimensional unsteady characteristics of the vortex flow field progressively more evident. Notice that such unsteadiness can not be appreciated by scour depth values (Figure 1) since the characteristic time scales of the scour hole evolution are much larger than those of the flow field and, consequently, of the water–sediment interaction.

Relatively regular successions of transport events can be observed for $T = 1800$ s (Figure 8b); available movies are too short for definitive conclusions about intermittency periods for higher run times (Figures 8c and 8d).

Figure 9 shows the computed values of *IM* for zone 1 at time $T = 1800$ s (a) and for zone 2 at time $T = 11100$ s (b). The spatial variability of the sediment intensity of movement can be observed by the time evolution of *IM* at different locations around the abutment. The spatial distribution of *IM* values is consistent with the visualisations of Figures 5 and 6, in which the density of the blobs in a certain area is proportional to the grains activity at the same location.

Spatial coherence of the grain motions can be inferred from the similarities in temporal trends of

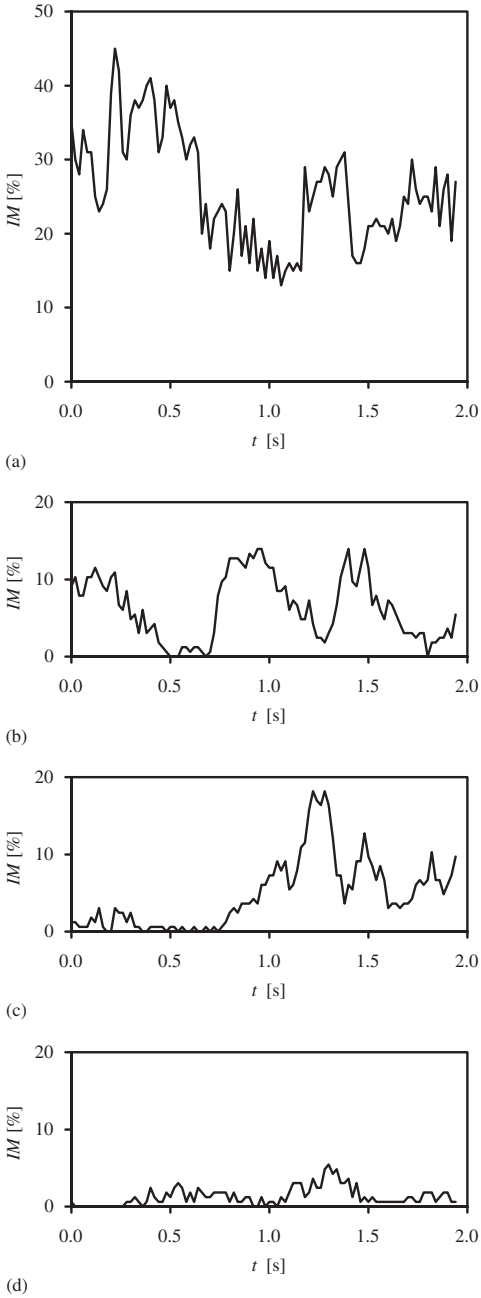


Figure 8. Temporal evolution of *IM* for zone 1, window 9. Time $T = 120$ s (a), 1800 s (b), 11100 s (c), 86400 s (d).

neighbouring windows, for example in windows 7, 8 and 9 in Figure 9a. It is reasonable to interpret such results as the effect of coherent structures in the flow field.

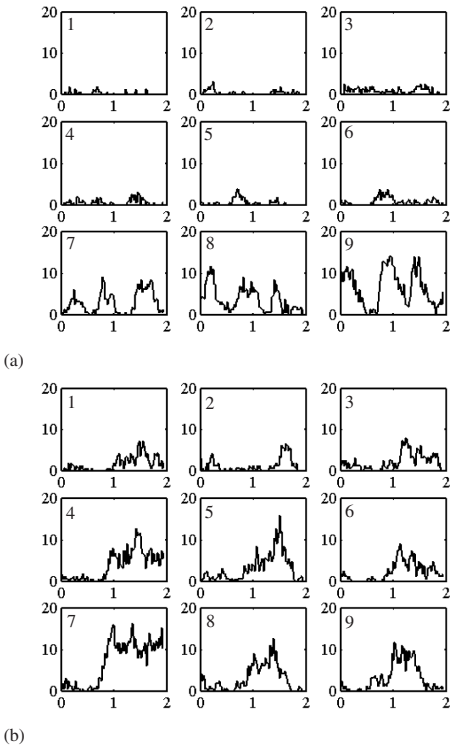


Figure 9. Temporal variation of *IM* for zone 1, $T = 1800$ s (a), and for zone 2, $T = 11100$ s (b). On the x axis: t [s], on the y axis: *IM* [%]. Window numeration in upper left corner.

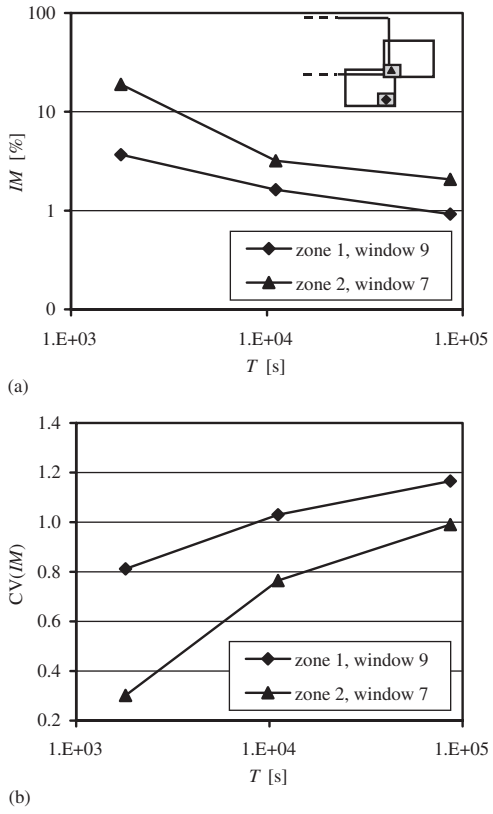


Figure 10. Temporal evolution of mean value *IM* and of its variation coefficient.

The time series of *IM* were averaged to obtain mean indicators of the intensity of movement. Each mean value was computed averaging data obtained from three or four repeated films (thus 297 or 396 *IM* values corresponding to 6 or 8 s). Then, the variation coefficient CV of the same data set was calculated. Figure 10 shows the evolution of *IM* with run time for window 9 in zone 1 and window 7 in zone 2 (corresponding to the most active positions for each zone), and the variation coefficient CV of the intensity index. As erosion proceeds, the mean value of *IM* decreases and its variation coefficient increases. This observation synthesizes all those drawn above: in the initial stage of scour the grain activity is intense and rather stable; with increasing erosion depth, the mean grain activity decreases due to longer and longer periods of stillness while its unsteadiness increases, presumably reflecting a similar behaviour of the flow field.

6 CONCLUSIONS

The grain motion at the bottom of a local abutment scour hole was investigated using an image processing technique. The identification of the moving grains was achieved by computing the difference image between two successive frames.

The movement intensity is variable for different locations around the obstacle. The most active positions are slightly upstream of the abutment nose and adjacent to the abutment side. Activity is rather stable in the initial stage, while it is characterized by a succession of intense transport events and periods of stillness afterwards. The mean grain activity decreases with increasing scour depths, while its unsteadiness increases.

Results for the grain activity can be correlated with expected features of the flow field, and in particular with the spatial and temporal characteristics of the vortex system in front of the abutment.

The indications from present visualisations and measurements may be of importance for conceptual or numerical modelling of erosion processes: any model aiming to achieve a physically sound scour prediction should be able to reproduce and incorporate the complex spatial and temporal variability of the sediment dynamics.

REFERENCES

Ahmed, F. & Rajaratnam, N. 2000. Observations on flow around bridge abutment. *Journal of Engineering Mechanics* 126(1): 51–59.

Capart, H., Young, D.L. & Zech, Y. 2002. Voronoï imaging methods for the measurement of granular flows. *Experiments in Fluids* 32: 121–135.

Dey, S., Bose, S.K. & Sastry G.L.N. 1995. Clear water scour at circular piers: a model. *Journal of Hydraulic Engineering* 121(12): 869–876.

Drake, T.G., Shreve, R.L., Dietrich, W.E., Whiting, P.J. & Leopold, L.B. 1988. Bedload transport of fine gravel observed by motion-picture photography. *Journal of Fluid Mechanics* 192: 193–217.

Fraccarollo, L. & Marion, A. 1995. Statistical approach to bed-material surface sampling. *Journal of Hydraulic Engineering* 121(7): 540–545.

Graf, W.H. & Istiarto I. 2002. Flow pattern in the scour hole around a cylinder. *Journal of Hydraulic Research* 40(1): 13–20.

Kwan, R.T.F. & Melville, B.W. 1994. Local scour and flow measurements at bridge abutments. *Journal of Hydraulic Research* 32(5): 661–673.

Lee, H.Y., & Hsu, L.S. 1994. Investigation of saltating particles motions. *Journal of Hydraulic Engineering* 120(7): 831–845.

Mayerle, R., Toro, F.M. & Wang S.S.Y. 1995. Verification of a three-dimensional numerical model simulation of the flow in the vicinity of spur dikes. *Journal of Hydraulic Research* 33(2): 243–256.

McEwan, I.K., Sheen, T.M., Cunningham, G.J. & Allen, A.R. 2000. Estimating the size composition of sediment surfaces through image analysis. *Proc. Instn Civ. Engrs Water Mar. Engng* 142: 189–195.

Molinas, A., Kheireldin, K. & Wu, B. 1998. Shear stress around vertical wall abutments. *Journal of Hydraulic Engineering* 124(8): 822–830.

Niño, Y. & Garcia, M.H. 1996. Experiments on particle-turbulence interactions in the near-wall region of an open channel flow: implications for sediment transport. *Journal of Fluid Mechanics* 326: 285–319.

Papanicolaou, A.N., Diplas, P., Balakrishnan, M. & Dancey, C.L. 1999. Computer vision technique for tracking bed load movement. *Journal of Computing in Civil Engineering* 13(2): 71–79.

Pilotti, M., Menduni, G. & Castelli, E. 1997. Monitoring the inception of sediment transport by image processing techniques. *Experiments in Fluids* 23(3): 202–208.

Radice, A., Franzetti, S. & Ballio, F. 2002. Local scour at bridge abutments. *River Flow 2002, International Conference on Fluvial Hydraulics, Louvain-la-Neuve, Belgium,* 2: 1059–1068.

Strom, K., Papanicolaou, A.N. & Odeh, M. 2002. Formation of cluster microforms and effects on bedload transport. *River Flow 2002, International Conference on Fluvial Hydraulics, Louvain-la-Neuve, Belgium,* 1: 565–573.

River Flow 2004 – Greco, Carravetta & Della Morte (eds.)
© 2004 Taylor & Francis Group, London, ISBN 90 5809 658 0

Computations of 3D turbulent flow structures around submerged spur dikes under various hydraulic conditions

I. Kimura
Dept. of Civil Engineering, Matsue National College of Technology, Matsue, Japan

T. Hosoda
Dept. of Civil Engineering, Kyoto University, Kyoto, Japan

S. Onda
Graduate School of Civil Engineering, Kyoto University, Kyoto, Japan

A. Tominaga
Dept. of Architecture and Civil Engineering, Nagoya Institute of Technology, Nagoya, Japan

ABSTRACT: This paper describes the numerical study on 3D turbulent flow structures around submerged spur dikes. Effects of three hydraulic parameters, S/L (S: interval length of two spur dikes, L: length of spur dikes), T/h (T: height of spur dikes, h: depth), θ (= inclination angle), are examined through the comparison of numerical results and previous experimental results focusing on both time-mean and time-dependent aspects. A non-liner k-ε model is adopted as a turbulence model to reproduce the vortex shedding from a tip of a spur dike and secondary currents. The numerical results show that the flow near the bed, which is particularly important for sediment transport, is affected by both inclination angle and the ratio of T/h. In the downstream inclined spur dikes, the unsteady vortex shedding is generated from the first spur dike and the period is determined by the feedback effect of impinging shear layer. The frequency jump of the vortex shedding can be seen between S/L = 2 and S/L = 4 in the numerical results.

1 INTRODUCTION

Spur dikes (or groins) are well-used man-made river structures for navigation and protection of riverbanks. Recently, a new aim is added to the construction of spur dikes, that is, spur dikes become to be focused as structures for environmental functions. An embayment formed around spur dikes due to sedimentation, which is called "Wando" in Japan, provides favorable habitat for wide variety of fauna and flora. Figure 1 shows an example of a group of Wandos in Kiso River in Japan. However, the condition and process of formation of the embayment has not elucidated enough. Therefore, it is necessary to clarify the time-mean and unsteady behavior of the 3D flow pattern around spur dikes as well as the mass exchange between the spur dikes zone and main channels, which has a controlling effect on the environment and sedimentation.

The flow field around submerged spur dikes are characterized by a horseshoe vortex formation near the root of a spur dike, recirculations with a vertical axes between two spur dikes and vortex shedding from the tip of a spur dike due to the shear instability. Those flow structures have been captured both experimentally and numerically. Tominaga et al (2001) performed a laboratory test with PIV method and showed that, in time-mean flow field, the flow from the mainstream toward the inner part between two spur dikes is predominant around upstream-inclined spur

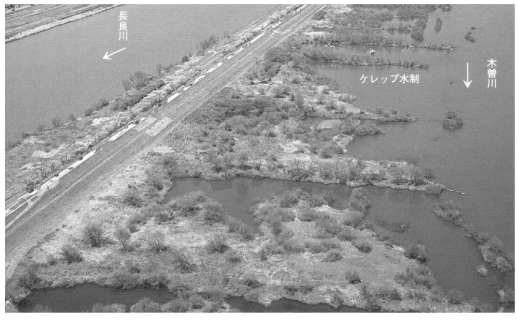


Figure 1. Spur dikes and "Wando" in Kiso River.

dikes, whereas, the flow in the reverse direction is predominant around downstream-inclined spur dikes. The results in the experiment cannot be applied directly to practical purposes because the ratio of the vertical scale against the horizontal scale is much larger than that of real rivers. However, the experiment with such deformed spatial conditions is effective to extract clearly fundamental properties of 3D flow structures. Veitbrecht & Jirka (2001) also performed PIV measurements around inclined un-submerged spur dikes in a shallow open channel flow and examined the flow patterns and mass exchange processes between the groyne area and the mainstream.

Numerical simulations with URANS models have been recognized as powerful and economical tools for prediction of 3D unsteady flow structures around bluff bodies. Kimura et al (2003) performed 3D computations with a well-tuned non-linear k-ε model under the conditions of the laboratory test by Tominaga et al (2001). In the numerical results, both time-mean and time-dependent flow features around upstream/downstream inclined spur dikes were in reasonable agreement with the experimental results. The numerical results also showed that the deviation of the flow by the first spur dike of a group of spur dikes has significant influence on the vortex shedding from the edge of spur dikes. Those results found in previous investigations are helpful for understanding of fundamental flow features. However, more systematic approach is required to obtain a useful data for effective design of spur dikes in practical river works.

In this study, 3D (three dimensional) turbulent flow structures around submerged spur dikes under various hydraulic conditions are examined numerically. Special focus is given to the influence of three hydraulic parameters: (i) the inclination angle between mainstream and spur dikes, (ii) S/L (S: interval length of two spur dikes, L: length of spur dikes) and (iii) T/h (T: height of spur dikes, h: depth). A non-linear k-ε model under the generalized curvilinear coordinate is adopted as a turbulence model considering the balance between accuracy and a computational expense. The numerical results are compared with experimental results and the effects of the parameters on time-mean and time-dependent flow features are discussed.

2 COMPUTATIONAL METHOD

2.1 *Basic equations*

The Reynolds averaged 3D flow equations with contravariant components of velocity vectors on a generalized curvilinear movable coordinate system are used as governing equations in this study. The equations are composed of a continuity equation, momentum equations and k-ε equations as follows.

[Continuity equation]

$$\frac{1}{\sqrt{g}}\frac{\partial V^{\alpha}\sqrt{g}}{\partial \xi^{\alpha}} = 0 \tag{1}$$

[Momentum equation]

$$\frac{\partial V^{i}}{\partial t} + \nabla_j\left[V^i(V^j - W^j)\right] + V^i\nabla_j W^j + V^j\nabla_j W^i = F^i - \frac{1}{\rho}g^{ij}\nabla_j p + \nabla_j\left[-\overline{v^i v^j}\right] + 2\nu\nabla_j e^{ij} \tag{2}$$

[k equations]

$$\frac{\partial k}{\partial t} + \nabla_j\left[k(V^j - W^j)\right] + k\nabla_j W^j = -g_{il}\overline{v^i v^j}\nabla_j V^i - \varepsilon + \nabla_j\left\{\left(\frac{D_t}{\sigma_k} + \nu\right)g^{ij}\nabla_i k\right\} \tag{3}$$

[ε equations]

$$\frac{\partial \varepsilon}{\partial t} + \nabla_j\left[\varepsilon(V^j - W^j)\right] + \varepsilon\nabla_j W^j = -C_{\varepsilon 1}\frac{\varepsilon}{k}g_{il}\overline{v^i v^j}\nabla_j V^i - C_{\varepsilon 2}\frac{\varepsilon^2}{k} + \nabla_j\left\{\left(\frac{D_t}{\sigma_k} + \nu\right)g^{ij}\nabla_i \varepsilon\right\} \tag{4}$$

where ξ^l = generalized curvilinear coordinate (see Figures 2 and 3), t = time, V^i = contravariant component of the velocity vector of flows, W^i = contravariant component of the velocity vector of grid motion, p = pressure, ν = molecular dynamic viscosity, ρ = density of water, k = turbulent energy, ε = turbulent energy dissipation rate, g_{ij} and g^{ij} = covariant and contravariant component of metric tensor, g = det(g_{ij}) and F^i = contravariant component of gravity acceleration. ∇^i indicates a covariant differential, for instance,

$$\nabla_i A^k = \frac{\partial A^k}{\partial \xi^i} + A^j\Gamma_{ij}{}^{k} \tag{5}$$

where Γ^k_{ij} = Christoffel symbol described as

$$\Gamma_{ij}{}^{k} = \left\{\begin{matrix} k \\ i\,j \end{matrix}\right\} = \frac{1}{2}g^{km}\left(\frac{\partial g_{jm}}{\partial \xi^i} + \frac{\partial g_{im}}{\partial \xi^j} - \frac{\partial g_{ij}}{\partial \xi^m}\right) = \frac{\partial \xi^k}{\partial x^p}\frac{\partial^2 x^p}{\partial \xi^i \partial \xi^j} \tag{6}$$

To calculate a complex turbulent flow with separation and vortex shedding, a 2nd-order non-linear k-ε model by Kimura & Hosoda (2003) is adopted as a turbulence model. This model has been applied to various flow fields, such as, a flow around a square cylinder

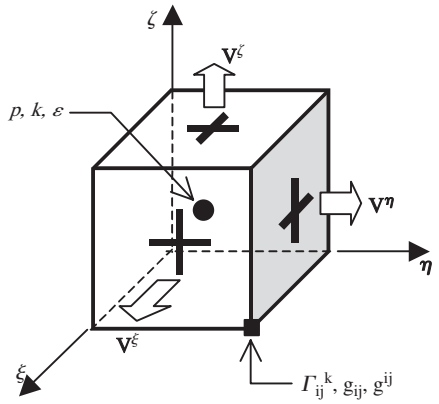


Figure 2. Arrangement of hydraulic variables and metric tensors on full staggered grid.

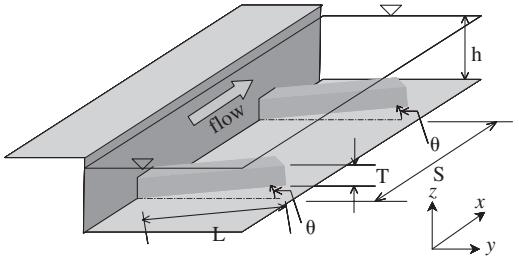


Figure 3. Schematic diagram of the flow field and notations of symbols.

(Kimura & Hosoda 1999), a flow around a surface-mounted cubic obstacle (Kimura & Hosoda 2000) and a compound open channel flow (Kimura et al 2001). The constitutive equations of the model are described as follows.

$$-\overline{v'^i v'^j} = D_t S^{ij} - \frac{2}{3}k\delta^i_s g^{sj} - \frac{k}{\varepsilon}D_t\left[\alpha_1 Q_1 + \alpha_2 Q_2 + \alpha_3 Q_3\right] \quad (7)$$

$$D_t = C_\mu \frac{k^2}{\varepsilon} \quad (8)$$

$$Q_1 = S^{i\alpha}g_{\alpha l}\Omega^{lj} + S^{j\beta}g_{\beta l}\Omega^{li} \quad (9)$$

$$Q_2 = S^{i\alpha}g_{\alpha l}S^{lj} - \frac{1}{3}S^{k\alpha}g_{\alpha m}S^{m\beta}g_{\beta k}\delta^i_l g^{lj} \quad (10)$$

$$Q_3 = \Omega^{i\alpha}g_{\alpha l}\Omega^{lj} - \frac{1}{3}\Omega^{k\alpha}g_{\alpha m}\Omega^{m\beta}g_{\beta k}\delta^i_l g^{lj} \quad (11)$$

$$S^{ij} = g^{j\alpha}\nabla_\alpha V^i + g^{i\alpha}\nabla_\alpha V^j \quad (12)$$

$$\Omega^{ij} = g^{j\alpha}\nabla_\alpha V^i - g^{i\alpha}\nabla_\alpha V^j \quad (13)$$

The model coefficients are not constants but functions of the strain parameter S and the rotation parameter Ω. In this study, all the coefficients are given as functions with one variable M for simplicity as follows (Kimura & Hosoda 2003).

$$\alpha_1 = -0.1325 f_M,\ \alpha_2 = 0.0675 f_M,\ \alpha_3 = -0.0675 f_M \quad (14)$$

$$f_M = \frac{1}{1+0.02M^2},\quad M = \max[S,\Omega] \quad (15)$$

$$C_\mu = \min\left[0.09,\ \frac{0.3}{1+0.09M^2}\right] \quad (16)$$

$$S = \frac{k}{\varepsilon}\sqrt{\frac{1}{2}S^{i\alpha}g_{\alpha j}S^{j\beta}g_{\beta i}} \quad (17a)$$

$$\Omega = \frac{k}{\varepsilon}\sqrt{\frac{1}{2}\Omega^{i\alpha}g_{\alpha j}\Omega^{j\beta}g_{\beta i}} \quad (17b)$$

Equations (14) and (15) were adjusted through the consideration of the distribution of turbulent intensities in a simple shear flow compared with the previous experimental results (Kimura & Hosoda 2000). Equation (16) was tuned to satisfy the realizability in a simple shear flow and singular points in both 2D and 3D flow fields (Hosoda et al 2001).

The standard linear k-ε model is also applied for the comparison of turbulence models. The constitutive equation of the standard model is

$$-\overline{v'^i v'^j} = D_t S^{ij} - \frac{2}{3}k\delta^i_s g^{sj},\quad D_t = C_\mu \frac{k^2}{\varepsilon} \quad (18)$$

where C_μ is 0.09 (=const.).

2.2 *Outline of numerical method*

The differential equations governing the mean-velocities and the turbulence field are solved with the finite volume method on full-staggered grid system. The arrangement of hydraulic variables on a full-staggered grid is shown in Figure 2. The metric tensors and the Cristoffel symbols are defined only at grid points to save computer memory and the values at other positions are interpolated at each computational step.

QUICK scheme is applied to the convection terms and the central differencing is used for the diffusion terms in the momentum equations. The hybrid central upwind scheme is applied to the k and ε equations for the computational stability. Adams-Bashforth scheme with second-order accuracy in time is used for time integration in each equation. The basic equations are discretized as fully explicit forms and are solved successively along the time axis step by step. The pressure field is solved using iterative procedure at each time step using SOLA algorithm by Hirt et al (1975).

2.3 *Boundary conditions*

Since the present turbulence model is a heigh Reynolds number type, the wall function approach is applied as the wall boundary conditions for k and ε. The wall friction is evaluated by the log-law. At the downstream end of the computational domain, the longitudinal gradients of all variables are assumed to be zero. At the boundary inlet, the level of k is chosen to be $(0.02U_0)^2$ (U_0 = averaged velocity). The value of ε at the inlet is determined from the value of k at the inlet and Equation (18) by specifying the ratio $D_t/\nu = 10$ (Bosche & Rodi 1998).

The free surface elevation is solved by the simple relation in Equation (19) since the contravariant components of the velocity vector are used in the basic equations (Takizawa et al 1992).

$$\Delta h = \sqrt{g_{33}} V^3 \Delta t \tag{19}$$

where Δt = time increment and Δh = surface elevation during Δt. To consider the rapid attenuation of turbulent intensities in the depth-wise direction near the free surface, the eddy viscosity is multiplied by the following dumping function (Hosoda 1990).

$$f_s = 1 - \exp\left(-B \frac{(h-y)\varepsilon_s}{k_s^{3/2}} \right) \quad , \quad (B = 10) \tag{20}$$

where sub-s indicates the value at the surface layer. The turbulent dissipation rate ε at the surface layer is evaluated by the following formula proposed by Sugiyama et al (1995) to calculate the secondary currents of 2nd kind.

$$\varepsilon_s = \frac{C_{\mu 0}^{3/4} k_s^{3/2}}{0.4 \Delta y_s} , \ (C_{\mu 0} = 0.09) \tag{21}$$

2.4 *Initial conditions*

At the beginning of the calculation, U (=velocity in the longitudinal direction (x-direction)) = U_0 (=averaged bulk velocity), V (=velocity in the transverse direction (y-direction)) = 0, $k = k_{in}$ and $\varepsilon = \varepsilon_{in}$ (k_{in} and ε_{in} are the values of k and ε at the inlet boundary) are specified over the whole computational domain. In order to avoid the influence of the initial conditions, the numerical results after 50 seconds from the initial conditions are used for the following examinations.

3 COMPUTATIONAL CONDITIONS

3.1 *Hydraulic conditions*

Spur dikes are constructed in a group in usual river works. However, we consider a flow field, in which only two spur dikes with same length, height, angle, etc. are attached to the left bank, for simplicity. Special attention is given to the influence of following three hydraulic parameters.

(i) θ: inclination angle between a spur dike and transverse direction of the main stream
(ii) S/L: S: spatial interval of two spur dikes, L: length of a spur dike
(iii) T/h: T: height of a spur dike, h: water depth

The computations were performed under different hydraulic conditions as shown in Tables 1, 2 and 3. The total number of computational cases becomes 15 and 7 cases of them coincide with the conditions of the laboratory tests by Tominaga et al (2001) or Tominaga et al (2002).

3.2 *Computational domain and numerical grids*

The upstream and downstream ends of the computational domain are set at 3 m distances from spur dikes to avoid the influence of the open boundaries around the spur dikes. The channel width in the laboratory tests by Tominaga et al (2001) and Tominaga et al (2002) is 30 cm, however, the width of 20 cm

Table 1. Hydraulic conditions of computations in Series A.

Run	θ	Direction of inclination	Common parameters
A1*	−30	Upstream	B = 30 cm
A2	−20	inclined	S/L = 2
A3	−10		T/h = 1/2
A4*	0	Right angled	S = 10 cm
A5	10	Downstream	L = 5 cm
A6	20	inclined	h = 8 cm
A7*	30		T = 4 cm
			Q = 4.1 l/s
			Slope = 1/2000
			Fr = 0.19
			Re = 1.37 × 104
			(B: channel width)

* Experiments in the same conditions have been presented by Tominaga et al (2001, 2002) in these Runs.

Table 2. Hydraulic conditions of computations in Series B.

Run	S/L	Common parameters
B1	1	B = 30 cm, θ = 30°, T/h = 1/2
B2*	2	L = 5 cm, h = 8 cm, T = 4 cm
B3*	3	Q = 4.1 l/s, Slope = 1/2000
B4*	4	Fr = 0.19, Re = 1.37 × 104

* Experiments in the same conditions have been presented by Tominaga et al (2001, 2002) in these Runs.

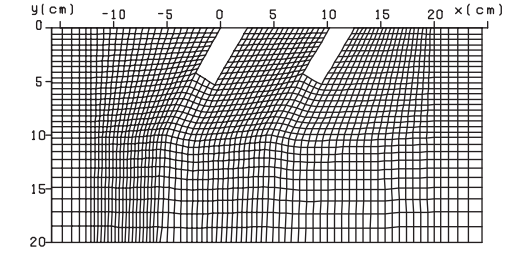
from the left bank is included into the computational domain.

Numerical grids in the x-y plane at the vicinity of spur dikes in Runs A1 and B4 are shown in Figures 4(a) and (b), respectively. These grids are generated with the aid of the graphical grid generator "Rubbnet" developed by Chiba & Takemoto (1999). The grid over the roof of the spur dikes is moved in vertical direction according with the surface elevation calculated by Equation (19) at each time step. The number of grid points at y and z directions in each Run becomes 30 (y-direction) × 8 (z-direction). The grid point in x-direction in Series A and Series C becomes 104 and that in series B is varied from 81 (Run B1) to 108 (Run B4) according with the length of the interval of two spur dikes.

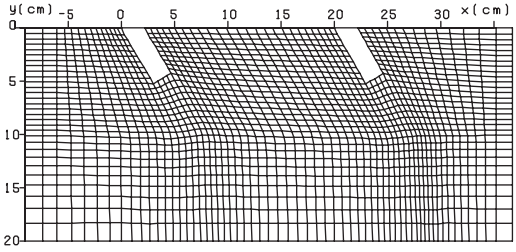
Table 3. Hydraulic conditions of computations in Series C.

Run	T/h	Submerged/ non-submerged	Common parameters
C1	1/4	Submerged	B = 30 cm, $\theta = 30°$
C2*	1/2	Submerged	S/L = 2, L = 5 cm
C3	3/4	Submerged	S = 10 cm, h = 8 cm
C4	1/1	Non-submerged	Q = 4.11/s
			Slope = 1/2000
			Fr = 0.19
			Re = 1.37 × 104

* Experiments in the same conditions have been presented by Tominaga et al (2001, 2002) in these Runs.



(a) Run A1.



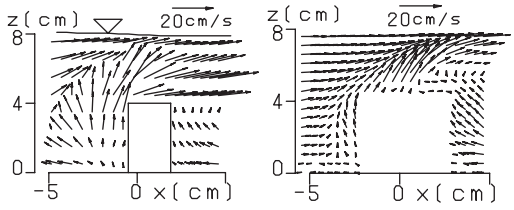
(b) Run B4.

Figure 4. Examples of numerical grids around the spur dikes in the x-y plane.

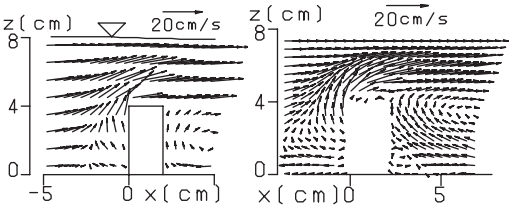
4 RESULTS AND DISCUSSIONS

4.1 *Effects of inclination angle (Series A)*

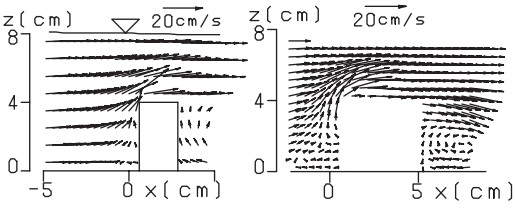
The inclination angle θ between the spur dikes and the transverse direction of the channel (see Figure 3) is varied from −30° to +30° in Runs A1–A7. The most affected part of the flow fields by θ seems to be the upper region of the first (upstream) spur dike. Figure 5 shows the time-averaged velocity vectors in a x-z plane near the right bank (y = 5 mm) in Runs A1, A3 and A7. The experimental results by Tominaga et al (2001) are shown together in Figure 5. Since the experiment was performed by PIV, the flow pattern at the backside of the inclined spur dikes could not be captured. Therefore, the plotted area of the velocity vectors of the experimental result is smaller than that of the numerical result. Both the experimental and numerical results show that a strong upward flow is generated in the upper part of the first spur dike and reverse flow is generated at the upstream region in Run A1. The upward and reverse flows around the first spur dike can be seen in Run A7 though the flows are much weaker than those in Run A1. The flow features in Run A4 seem to be a middle pattern between Runs A1 and A7.



(a) Run A1 (Cal.) (b) Run A1 (Exp.)



(c) Run A4 (Cal.) (d) Run A4 (Exp.)



(e) Run A7 (Cal.) (f) Run A7 (Exp.)

Figure 5. Flow patterns around the first spur dike near the side wall in the series A (x-z plane, y = 5 mm).

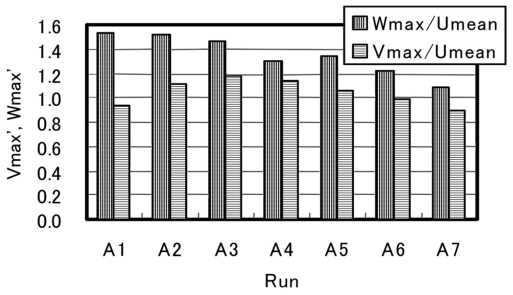


Figure 6. Flow deviation effects in upward and transverse directions in the series A.

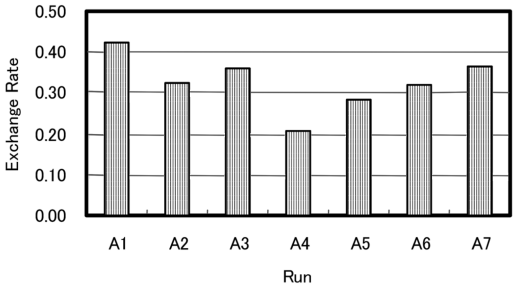


Figure 7. Dimensionless mass-exchange coefficients between the spur dike zone and mainstream in the series A.

It has been pointed out through the previous experimental and numerical studies (Kimura et al (2002) and Tominaga et al (2001)) that the flow pattern near the bed between two spur dikes, which dominates the sediment transport, is closely affected by the inclination angle. Those studies show that the flow from the mainstream toward the inner part between two spur dikes is dominant around upstream inclined spur dikes, while the flow in the opposite direction is dominant around downstream inclined spur dikes. The similar features were observed again in the present numerical results in series A, that is, as θ increases the outflow near the bed becomes stronger (The figures are not shown for the saving of the space.).

The flow deviation effect is one of important roles of spur dikes for the protection of riverbanks. In order to examine the relation between the effect of flow deviation and the inclination angle, the maximum velocities in transverse and upward directions non-dimensionalized by the bulk velocity, V_{max}/U_{mean} and W_{max}/U_{mean} (U_{mean}: bulk velocity (=17.1 cm/s)) in the series A are shown in Figure 6. This figure indicates that the effect of the flow deviation in upward direction becomes larger around upstream inclined spur dikes while the effect in the transverse direction becomes larger around the rightangled spur dikes.

Tominaga et al (2003) defined a "spur dike zone" as a region of river channel walled by two spur dikes. The clarification of the mass transport between the spur dike zone and the mainstream is important for prediction of water quality and river environment around spur dikes. In this study, dimensionless mass exchange coefficient R′ between the spur dike zone and the mainstream is defined as

$$R' = \frac{1}{V_d} \int_A |U_r| da \cdot \frac{S}{U_{mean}} \tag{22}$$

where, V_d: volume of the spur dike zone, U_r: normal velocity at the surface of the spur dike zone, S: interval length of two spur dikes and A: area of the interface between the spur dike zone and the mainstream (total area of x-y and x-z planes). Figure 7 shows the dimensionless mass exchange coefficient R′ in series A. This figure shows that the mass exchange becomes larger as the absolute value of the inclination angle becomes larger and it becomes minimum around right-angled spur dikes.

The unsteady flow features around spur dikes are also important for both river environment and flood control. Kimura et al (2003) pointed out through the comparison of numerical and experimental results that the unsteady motion around the spur dikes is mainly caused by the vortex shedding from the tip of the first spur dike. Figure 8 shows the temporal variation of the velocity in the transverse direction (y-direction) in the series A. The location is the middle point of the tips of two spur dikes (see the diagram in Figure 10) at z = 3.5 cm. Figure 9 shows the experimental results by Tominaga et al (2002) in Runs A1, A4 and A7. Both the experimental and numerical results indicate that the flow oscillation is small in the case of upstream inclined spur dikes and the magnitude of the oscillation becomes larger as θ increases. The oscillation with maximum amplitude can be seen in the case of maximum inclination angle (Run A7).

4.2 *Effects of the interval of two spur dikes (Series B)*

Figures 11, 12 and 13 shows the comparison of the time-averaged velocity vectors in a horizontal plane at z = 5 mm in Runs B2–B4 in both the numerical and experimental results. In the numerical results, the flow from the spur dike zone toward the main channel is dominant regardless of the interval length. The qualitative flow pattern in Run B4 is slightly different from the other Runs because the vortex formed around the downstream part of the first spur dike is significantly stretched in the stream-wise direction. These flow features in the numerical results are in good agreement with the experimental results.

Figure 14 shows the horizontal flow pattern at z = 5 mm in the numerical result of Run B1. The flow

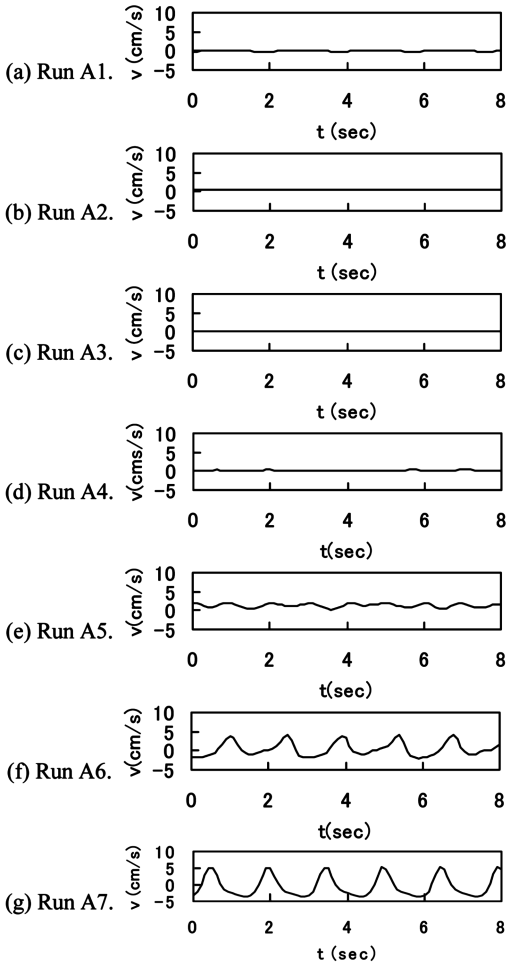


Figure 8. Temporal variations of velocities in the transverse direction (y-direction) at the center part between two spur dikes (see Figure 10) at z = 35 mm (Series A, Cal.).

pattern in this case is very different from the flows in Runs B2–B4, namely, the velocity between the spur dikes is much smaller than those in other 3 cases and the dominant flow direction cannot be clearly detected. These numerical results indicate that the outflow from the spur dike zone is dominant near the bed around downstream inclined spur dikes only if the interval length of two spur dikes is larger than the length of spur dike.

Time dependent features were also closely affected by the interval length. Figure 15 shows temporal variations of velocities in the transverse direction (y-direction) at the center point between the tips of two spur dikes at z = 35 mm. This figure shows that the flow in Run B1 is almost steady and the flows in other 3 Runs yield fluid oscillation. We can see quite

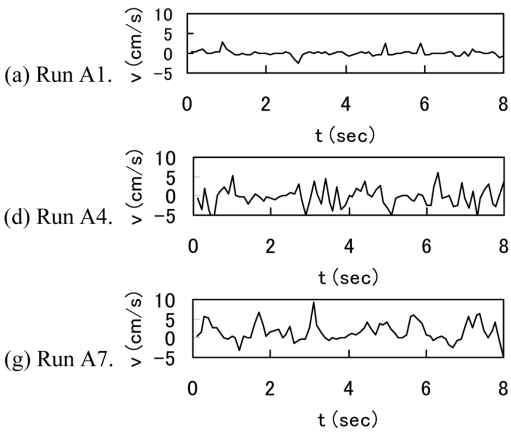


Figure 9. Temporal variations of velocities in the transverse direction (y-direction) at the center part between two spur dikes (see Figure 10) at z = 35 mm. (Series A, Exp. by Tominaga et al (2001)).

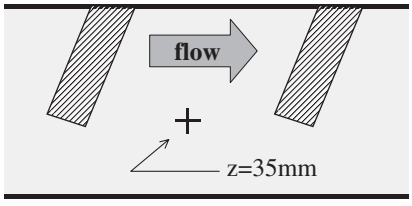
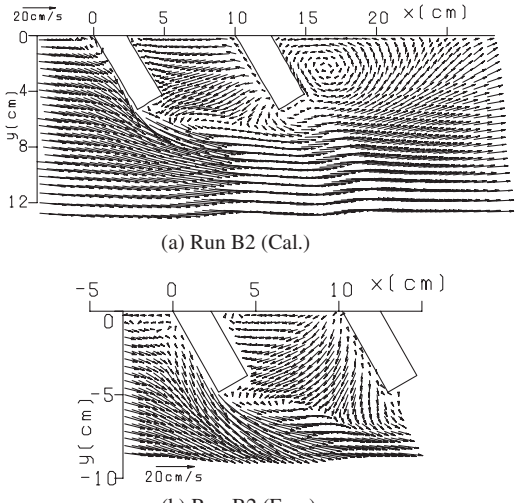


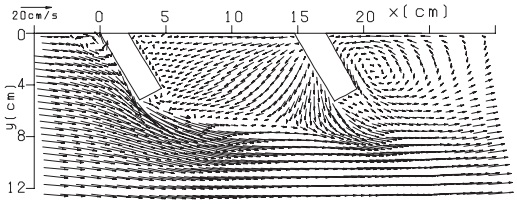
Figure 10. Schematic diagram of the location of measurement point of velocities in a horizontal plane in Figures 8, 9, 15 and 19.



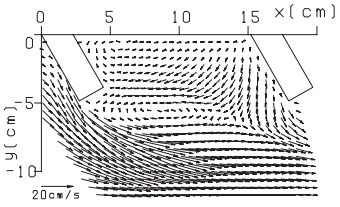
(a) Run B2 (Cal.)

(b) Run B2 (Exp.)

Figure 11. Comparison of time-averaged velocity vectors between the numerical and experimental results in a horizontal plane in Run B2 (x-y plane, z = 5 mm).

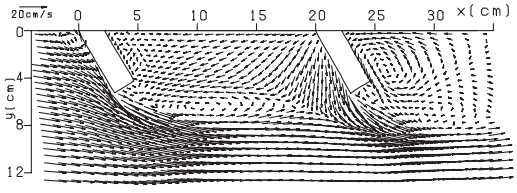


(a) Run B3 (Cal.)

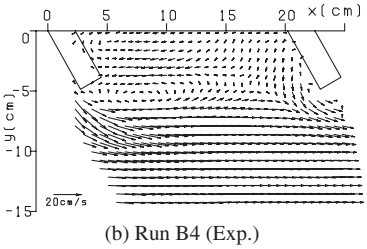


(b) Run B3 (Exp.)

Figure 12. Comparison of time-averaged velocity vectors between the numerical and experimental results in a horizontal plane in Run B3 (x-y plane, z = 5 mm).



(a) Run B4 (Cal.)



(b) Run B4 (Exp.)

Figure 13. Comparison of time-averaged velocity vectors between the numerical and experimental results in a horizontal plane in Run B4 (x-y plane, z = 5 mm).

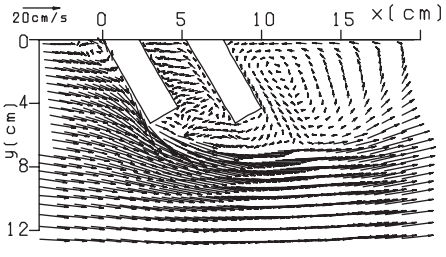


Figure 14. Time-averaged velocity vectors in the numerical result in a horizontal plane in Run B1 (x-y plane, z = 5 mm).

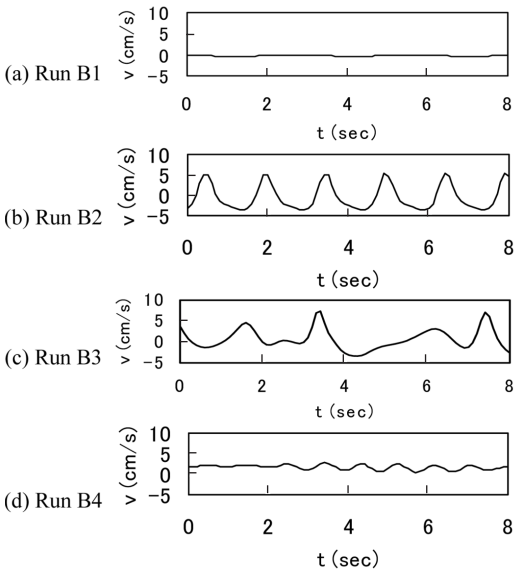


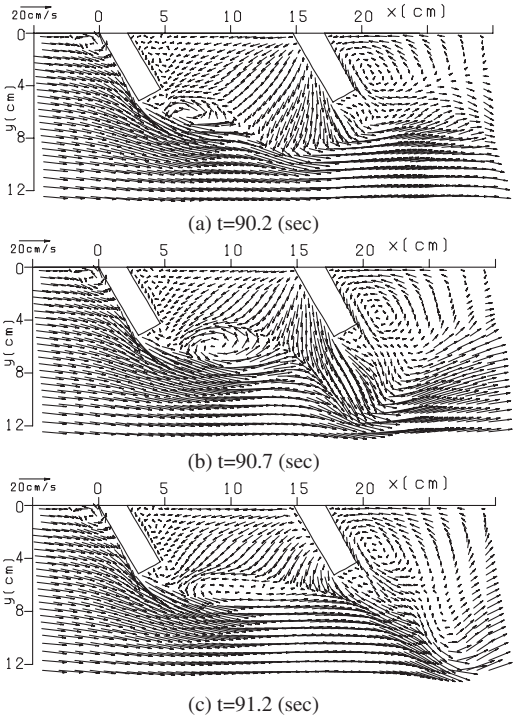
Figure 15. Temporal variations of velocities in the transverse direction (y-direction) at the center between the tips of two spur dikes (see Figure 10) in the computations of series B (z = 35 mm).

periodic oscillations in the results of Run B2 and B4 while the oscillation in Run B3 is chaotic. In order to consider the fluid oscillation, we should notice that the flow around two spur dikes is a typical case of the impinging shear layer with a feedback loop. The formation of the feedback loop is explained as follows: (i) the separated vortex from the first spur dike impinges upon the second one, (ii) the effect of impinging stimulates the upstream sensitive region of initial separation, (iii) the stimulation cases the next vortex shedding, then a feedback loop is formed between two spur dikes and the frequency is rocked. Rockwell & Naudascher (1978) showed the ranges of Strouhal numbers in different feedback modes as

$$St_1 = \frac{fS}{U_0} \approx 0.4 \sim 0.6 \quad \text{(1st mode)} \tag{23a}$$

$$St_2 = \frac{fS}{U_0} \approx 1.0 \sim 1.4 \quad \text{(2nd mode)} \tag{23b}$$

where St_1/St_2: strouhal number of 1st/2nd mode, f: frequency of fluid oscillation, S: interval length of two obstacle and U_0: bulk velocity. The 1st mode indicates the feedback loop which contains only one vortex in a loop, while, the feedback loop of the 2nd mode contains two vortices in it. The numerical results show that the strouhal number in Run B2 is within the range of the 1st mode while the strouhal number in Run B4 is within the range of the 2nd mode. Consequently, it



(a) t=90.2 (sec)

(b) t=90.7 (sec)

(c) t=91.2 (sec)

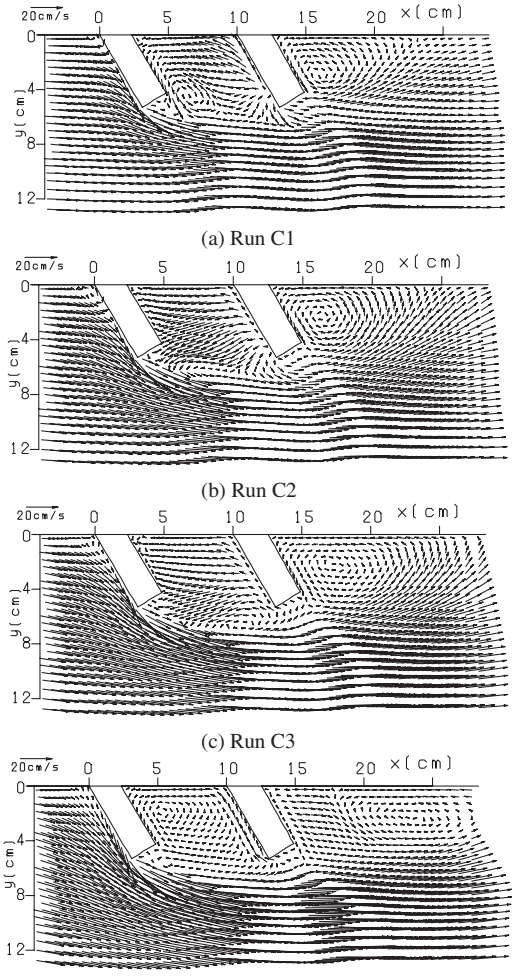
Figure 16. Computational results of vortex shedding from the tip of the first spur dike in Run B3 (x-y plane, z = 5 mm).

is pointed out that the frequency jump from the 1st mode toward the 2nd mode occurs between S/L = 2 and S/L = 4. The irregular oscillation seen in Run B3 is likely to be a transition flow between the 1st and 2nd modes.

Figure 16 shows a pattern of the vortex shedding from the tip of the first spur dike in the computational results of Run B3.The similar unsteady feature can be seen in Runs B2 and B4. Since the vortex disappears near the second spur dike due to the influence of impinging, the affected area of fluid oscillation with large amplitude is limited around the spur dike zone.

4.3 *Effects of relative height (Series C)*

Figure 17 shows the time-averaged flow patterns in a horizontal plane near the bed (z = 5 mm) in the series C. The flow patterns in Runs C2 and C3 are characterized by outflows form the inner part toward the main-stream, which is in compatible with the common flow pattern around downstream inclined spur dikes reported in some previous studies (e.g., Yamashita et al (2001), Tominaga et al (2001) and Kimura et al (2002)). Contrarily, the flow from the main-channel toward the spur dike zone, which has been reported as



(a) Run C1

(b) Run C2

(c) Run C3

(d) Run C4

Figure 17. Time-averaged velocity vectors in a horizontal plane in the computational results of series C (x-y plane, z = 5 mm).

a typical flow pattern around upstream inclined spur dikes, is dominant in Run C1. Therefore, it is pointed out that the flow direction near the bed depends on the relative height of spur dikes as well as the inclination angle. The flow pattern in Run C4, in which a large circulation with a vertical axis can be seen, is also very different from the other 3 cases.

Figure 18 shows the flow patterns in a vertical x-z plane at y = 25 mm in the series C. A vortex in the clockwise direction can be seen between two spur dikes in the results of Runs C1–C3; on the other hand, a vortex in the opposite direction is generated in the result of Run C4. The results in Figure 18

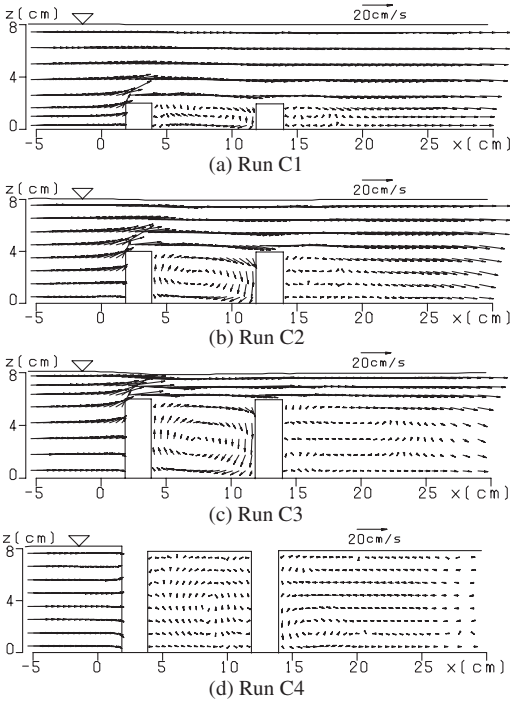


Figure 18. Time-averaged velocity vectors in a vertical plane (x-z plane) in the computational results of the series C (y = 25 mm).

clearly show that the flows around non-submerged spur dikes are qualitatively different from the flows around submerged spur dikes.

Figure 19 shows the temporal variation of velocities in the transverse direction (y-direction) at the center part between the tips of two spur dikes near the bed (z = 35 mm) in the computational results in the series C. The flow pattern in the non-submerged case (Run C4) is almost steady and the other computations with Runs C1–C3 yield unsteady flow patterns. The fluid oscillation around spur dikes is caused by the vortex shedding due to the shear instability. There are two kinds of shear layers around submerged spur dikes: one is a horizontal layer along the roofs of the spur dikes and the other is a vertical layer in an x-z plane along the tips of spur dikes. The comparison of the velocity variations between the submerged and non-submerged cases indicates that the shear layer in the horizontal plane seems to be more important to generate the fluid oscillations. The amplitudes of the oscillations in Runs C1 and C3 are smaller than that in Run C2. The reason seems to be that the development of the shear layer in the x-y plane is suppressed by the bed (Run C1) or the free surface (Run C3).

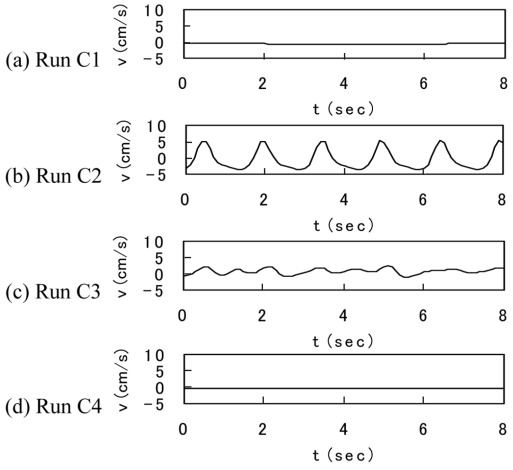


Figure 19. Temporal variations of velocities in the transverse direction (y-direction) at the center part between the tips of two spur dikes (see Figure 10) in the computations of series C (z = 35 mm).

5 CONCLUDING REMARKS

This paper described the numerical study on time-mean and time-dependent 3D turbulent flow structures in open channel flows around submerged spur dikes. A non-linear k-ε model developed by Kimura & Hosoda (2003) in a curvilinear movable coordinate was adopted as a turbulence model and the results were examined through the comparison with the laboratory tests with PIV performed by Tominaga et al (2001, 2002). Special focus was given to the three hydraulic parameters, i.e., the inclination angle, the interval of two spur dikes and the relative depth and the flows under 15 different conditions were considered.

The major findings of our study are listed as follows.

1. The effect of flow deviation in the upward direction becomes larger as the inclination angle in the upstream direction increases, while the flow deviation in the transverse direction becomes maximum around right-angled spur dikes.
2. The mass exchange rate between the spur dike zone and the mainstream becomes larger as the absolute value of the inclination angle becomes larger.
3. The fluid oscillation, which is caused by the vortex shedding from the tip of the first spur dike due to the shear instability, is closely affected by the inclination angle. The amplitude increases as the inclination angle in the downstream direction becomes larger.
4. From the comparison of submerged and non-submerged spur dikes, it is likely that shear layer in a horizontal plane at the height of the spur dikes

is more important for the fluid oscillation than that in a vertical plane along the tips of spur dikes.

5. The dominant direction of the flow near the bed between two spur dikes, which is important for sediment transport, is affected by the relative depth as well as the inclination angle.

REFERENCES

Bosch, G. & Rodi, W., 1998. Simulation of vortex shedding past a square cylinder with different turbulence models. *International Journal for Numerical Methods in Fluids*, 28: 601–616.

Chiba, S. & Takemoto, Y., 1999. A Study of numerical flow simulators of the Ise Bay, the second report – Development of a computer program for generation of two dimensional structural grids, making use of graphical user interface. *Yokkaichi University Journal of Environmental and Information Sciences*, 2(2): 103–126 (in Japanese).

Gatski, T. B. & Speziale, C. G., 1993. On explicit algebraic stress models for complex turbulent flows. *Journal of Fluid Mechanics*, 254: 59–78.

Hirt, C. W., Nichols, B. D. & Romero, N. C., 1975. SOLA – a Numerical solution algorithm for transient fluid flows. *Los Alamos Scientific Report*, LA-5852.

Hosoda, T., 1990. Ph.D. Thesis, Kyoto University (in Japanese).

Hosoda, T., Kimura, I. & Onda, S., 2001. Some necessary conditions for a non-linear k-ε model in classified flow Patterns with a singular point. *Proceedings of 2nd International Symposium on Turbulence and Shear Flow Phenomena*, Stockholm, Sweden, 3: 155–160.

Hosoda, T., Sakurai, T., Kimura, I. & Muramoto, Y., 2000. 3-D computations of compound open channel flows with horizontal vortices and secondary currents by means of non-linear k-ε model. *Journal of Hydroscience and Hydraulic Engineering*, 17(2): 87–96.

Kawaguchi, H. & Fukuoka, S., 2000. Study on hydrodynamic forces on submersible groins in series. *Proceedings of Hydro Informatics, Non-linear Analysis-2*, Iowa City, IA, USA (CD-ROM).

Kimura, I., Kitamura, T., Sumi, T., Takeda, M., Onitsuka, K., Sho, K. and Otsuka, K., 2002. Coorporative research on morphological evolution and environmental functions of embayed topography formed around spur dikes in the tidal area of the Kiso River. Advances in River Engineering, JSCE, Vol.8, 365–370 (in Japanese).

Kimura, I. & Hosoda, T., 1999. 3-D Unsteady flow structures around rectangular column in open channels by means of non-linear k-ε model. *Proceedings of 1st International Symposium on Turbulence and Shear Flow Phenomena*, Santa Barbara, CA, USA, 1001–1006.

Kimura, I. & Hosoda, T., 2000. Numerical simulation of flows around a surface-mounted cube by means of a non-linear k-ε model. *Proceedings of 9th International Symposium on Flow Visualization*, Edinburgh, Scotland, Paper No.388 (CD-ROM).

Kimura, I. & Hosoda, T., 2003. A non-linear k-ε model with realizability for prediction of flows around bluff bodies. *International Journal for Numerical Methods in Fluids*, 42, Wiley, 813–837.

Kimura, I., Hosoda, T. & Onda, S., 2002a. Numerical simulator on full staggered boundary fitted coordinate system for the analysis of 3D turbulent flows in open channels. *Yokkaichi University Journal of Environmental and Information Sciences*, 4(1): 145–170 (in Japanese).

Kimura, I., Hosoda, T. & Onda, S., 2002b. Prediction of 3D flow structures around skewed spur dikes by means of a non-linear k-ε model. In D. Bousmar and Y. Zech (eds), *River Flow 2002*, 1: 65–73. Rotterdam: Balkema.

Kimura, I., Hosoda, T., Onda, S. and Tominaga, A., 2003. 3D numerical analysis of unsteady flow structures around inclined spur dikes by means of a non-linear k-ε model. *Proceedings of the International Symposium on Shallow Flows*, Delft, The Netherlands, Part III, 205–212.

Pope, S. B. 1975. A more general effective viscosity hypothesis. *Journal of Fluid Mechanics*, 72: 331–340.

Rockwell, D. & Naudascher, E., 1978. Review – Self-sustaining oscillations of flow past cavities. *Transaction of the ASME, Journal of Fluid Engineering*, 100: 152–165.

Sugiyama, H., Akiyama, M. & Matsubara, T., 1995. Numerical simulation of compound open channel flow on turbulence with a Reynolds stress model. *Journal of Hydraulic, Coastal and Environmental Engineering*, 515/II-31: 55–65 (in Japanese).

Takizawa, A., Koshizuka, S. & Kondo, S., 1992. Generalization of physical component boundary fitted co-ordinate (PCBFC) method for the analysis of free-surface flow. *International Journal for Numerical Methods in Fluids*, 15: 1213–1237.

Tamoto, N., Tominaga, A. & Ijima, K., 2003. Flow structures in continuous spur dike zone with orientation angle. *Proceedings of the 30th Congress of IAHR*, Greece, pp. 1–6 (CD-ROM), 2003.

Tominaga, A., Ijima, K. & Nakao, Y., 2001. PIV analysis of flow structures around skewed spur dikes. *Annual Journal of Hydraulic Engineering, JSCE*, 45: 379–384 (in Japanese).

Tominaga, A. & Ijima, K., 2002. Effects of interval length on flow structures around submerged spur dikes. *Annual Journal of Hydraulic Engineering, JSCE*, 46, 475–480 (in Japanese).

Weitbrecht, V. & Jirka, H., 2001. Flow patterns in dead zones of rivers and their effect on exchange processes. *Proceedings of 3rd International Symposium on Environmental Hydraulics*, Tempe, AZ, USA, (CD-ROM).

Yamashita, Y., Ito, A., Takeda, M. & Matsuo, N., 2001. *Proceedings of Annual Conference of Civil Engineers*, Chubu Chapter, JSCE, 237–238 (in Japanese).

This page intentionally left blank

River Flow 2004 – Greco, Carravetta & Della Morte (eds.)
© 2004 Taylor & Francis Group, London, ISBN 90 5809 658 0

Numerical simulation of flow instabilities in steep, stepped channels

G. Premstaller, P. Rutschmann & M. Oberhuber
Institute of Hydraulic Engineering, University of Innsbruck, Austria

ABSTRACT: This study deals with flow instabilities in steep, stepped channels. The origin of the research is based on an incident during a twenty-year flood at the river Ruetz in Tyrol, Austria. During this flood event flow instabilities occurred which lead to the overtopping of the riverbanks and the damaging of the revetments. An extensive study on a physical model was carried out. Velocity and water depth measurements in physical models can only be obtained with limited resolution and boundary conditions are hard to control and to modify. In numerical models flow conditions can be determined at each point of the computational mesh and complete control of boundary conditions is possible. In a first step two-dimensional investigations were undertaken in order to verify appearance of flow instabilities for the numerical approach. Three-dimensional runs were performed in order to verify the numerical model. Finally different scenarios were calculated and evidence on the origin of flow instabilities in steep stepped channels was found.

1 INTRODUCTION

In 1991 a rare event of flow instabilities at the river Ruetz was observed. Since then no other occurrences were reported for the Ruetz or other mountainous rivers in Austria.

Herrmann (2003) described a partially comparable event at a cascade-spillway at Sorpe dam near Langscheid, Germany. Cascade waves overtopped the spillway way before design discharge was reached. Due to the scarcity of such events only few literature can be found.

Chanson (1994) basically distinguished two kinds of flows in cascades, namely tumbling and shooting flows. While for tumbling flow a fully developed hydraulic jump develops after each cascade, shooting flow is a special form of open channel flow with macro-roughness. While Chanson (1994) and Boes (2000) investigated cascades with vertical and horizontal steps, Whittaker (1982) investigated step-pools in mountain streams.

Le Fessant (2001) studied macro-roughness in steep channels with triangular and rectangular obstacles. Three different flow regimes were observed at slopes steeper than 3%: wave-trains, wave packets and sinusoids.

Ganz (2001, 2003) investigated the origin and the development of such instabilities using two differently scaled physical models. The influence of channel geometry, discharge, suspended sediments, viscosity, bed roughness and bed erosion were investigated. While bed roughness, suspension concentration, viscosity and scour holes did not influence wave occurrence significantly, bed slope, discharge and geometry had a big influence. For discharge and bed slopes upper and lower limits of wave appearance could be established.

Le Fessant (2003) carried out numerical studies on this subject. The studies focused on the development of roll waves and wave trains and compared results with experimental data. In order to initiate wave development small sinusoidal perturbation were generated at the inflow.

2 NUMERICS

2.1 *Numerical scheme*

The computations in the present paper have been performed using the commercial FLOW3D software developed by the founder of Flow Science Inc., C.W. Hirt from Los Alamos Scientific Lab. The software uses several key features invented by C.W. Hirt for numerical treatment of the Navier-Stokes equations, solutions to free surface flows and meshing of complicated geometries.

The FLOW3D program uses a finite difference or finite volume solution for the Navier-Stokes equations. The two methods coalesce for rectangular cuboid blocks. In order to minimize artificial diffusion for convective processes a fully explicit treatment of the corresponding terms is implemented. It is the philosophy of the vendors that the program automatically

performs all of the possible choices for relaxation and time stepping in order to obtain best results. As can be assumed from the use of the program the momentum and continuity equations must be solved in a decoupled way like in the projection method. i.e. after solution of the momentum equation pressure iteration is performed to satisfy continuity. The convergence criteria for this iterative procedure can be controlled by the user through modification of the default values.

2.2 *Free surface treatment*

The difficulty of solving the Navier-Stokes equations for free-surface flow problems is the unknown position of the interface between air and water. Several options for such flows have been developed, namely:

- The marker and cell (MAC) method of Harlow & Welch, (1965) computes flow on a fixed mesh covering at least the maximum extent of wetted area. For the region covered with fluid the momentum equations are solved. Information on the position of the free surface is obtained indirectly using marker particles released in the water body and convected by the flow. The number of marker particles governs accuracy of the MAC Method. Therefore for a limited number of particles the computational time is acceptable but the free surface is only crudely represented. The opposite applies for a high number of markers.
- The arbitrary Lagrangian Eulerian (ALE) method is often used in conjunction with a finite element approach favourably with space/time elements. The position of the free surface is always represented through a mesh boundary and the corresponding boundary nodes are convected in a fully Lagrangian way. Nodes in the interior of the domain may be arbitrarily shifted from time step to time step in order to ensure mesh quality. Once the quality criteria are violated or element nodes have been twisted a complete re-meshing of interior nodes is necessary. The method is very accurate for representation of the interface however complicated to program due to the frequent re-meshing. Furthermore it fails for flows where the water body is not contiguous.
- The Volume of fluid (VOF) method which is very similar to the level set (LS) method is based on a fixed mesh covering at least the maximum extent of wetted area, (see MAC method). For the wetted areas the momentum equations are solved and additional scalar information is convected with the flow field. The VOF and LS methods distinguish only in the scalar information being convected. For the VOF method the scalar information defines the ratio water/air for each cell, for the LS method the scalar information is the perpendicular distance from cell mid-point to free surface. Both methods have the advantage that they are very robust and fast, however the VOF method may be subject to numerical diffusion depending on the implementation. The LS method is more CPU intensive. However due to the continuous scalar function used the numerical diffusion can be neglected.

The father of the VOF method is C.W. Hirt, see (Nichols, B.D. & Hirt, C.W., (1971) & Hirt, C.W. and Nichols, B.D, (1981)). Hirt and Nichols achieved to modify the MAC method in a way to retain the volume-tracking feature without its large memory and CPU costs.

The FLOW3D software claims that the implemented VOF method is at least as accurate as the piecewise linear interface construction (PLIC) method without specifying details. In the PLIC-VOF method the position of the free surface is determined in two steps: The air/water ration is computed for each cell in a convection step and a reconstruction algorithm serves to position the free surface without stair step effects as a continuous boundary. The boundary is represented by a linear straight line (2D) or a planar surface (3D) intersecting the computational cell. The position of this intersection is determined satisfying the scalar air/water function and considering the corresponding information from neighboring cells for determining the normal direction. This procedure guarantees that the pressure free surface remains a clearly defined and un-smeared interface.

2.3 *Mesh generation*

A very important part of numerical computations is the mesh generation. Numerical schemes are also characterized by the order of accuracy both in space and time. This characterization indicates to what order terms of a Taylor-series expansion are used for the numerical approximation. A scheme with "second order accuracy in space" means that terms up to quadratic terms are considered. However the order of accuracy strictly only applies to uniform cells having equidistant spacing. If this is not the case the order of accuracy decreases and therefore also depends on the mesh used. Having this in mind it seems clear that for complicated geometries complicated meshing algorithms have to be used. In order to preserve complete freedom in meshing of complicated structures an unstructured grid is used as for most finite element codes. FLOW3D however uses a completely different approach to achieve good quality meshing by a structured grid approach namely the fractional area volume obstacle representation (FAVOR) method.

In FLOW3D the computational mesh is always a structured rectangular mesh consisting of only rectangles (2D) or cuboid blocks (3D). However the overall length of the computational mesh in all three coordinate directions can be subdivided into irregularly spaced distances. Therefore in a very simple case a

FLOW3D mesh can be defined by only nine figures, namely by a triple set of information for all coordinate directions indicating the beginning and the end coordinate and the number of cells. Of course with this information it would only be possible to work with a cuboid space representation and it would be impossible to model more complicated geometries. Therefore in FLOW3D the possibility exists to position obstacles in this very simple basic grid. The obstacles can be so called FLOW3D primitives, i.e. very simple geometric bodies such as cubes, cones, spheres etc., or obstacles represented through triangulated surfaces obtained either by scattered x, y, z-data or from a CAD software (STL or IDEAS files). In other software packages such obstacles are often represented then by a stair-step geometry where each sub-region of an obstacle either completely fills or does not occupy a computational cell. The FAVOR method, described by Sicilian (1995), uses the same algorithms as for the representation of the free surface with VOF. Instead of using the scalar information indicated above information on the blocking of a cell through an obstacle is given and this information is transferred into an accurate reproduction of the obstacle using a similar technique like the PLIC method. Therefore each obstacle may intersect cells and will then be represented by a straight line (2D) or a linear plane (3D) having arbitrary normal direction. Such it is possible to correctly represent even complex geometries through a computational mesh, which is from it's origin a structured and even rectangular grid. For complex geometries FLOW3D allows to represent the computational area through a multi-block approach. The meshing technique described above has one big advantage: it decouples computational mesh and topography and therefore allows to change grid resolution with changing only three figures, namely the number of cells in all coordinate directions. This advantage has been used to assure mesh independent solutions as described in the following section.

2.4 *Turbulence model*

For the computations a two-equation turbulence model has been used, the well-known and well-tested k-ε turbulence model, see Harlow and Nakayama (1968) and Jones and Launder (1972), where k denotes the turbulent kinetic energy and ε the turbulent dissipation rate. Both parameters can be described by a non-linear system of PDE's. Constant terms within these equations have been found through experiments conducted mainly for fully turbulent flow in free jets and mixing layers. A careful comparison and state of the art paper by Rodi (1984) shows that for the current application the k-ε turbulence model is a good choice. However a comparison with results from computations without using a turbulence model or a simple Prandtl mixing length model shows no noticeable influence from this choice.

3 RESULTS AND DISCUSSION

Both three-dimensional and two-dimensional simulations were carried out. While three-dimensional simulations were run to calibrate the numerical model, the faster two-dimensional simulations were run to analyse the detailed flow features and the possible origin of wave formation.

3.1 *Numerical model building*

The geometry of the numerical model was a reproduction of the 16 meters long flume used by Ganz (2003). The mesh height was fixed at 0.4 meters, while the cross-section was different for two-dimensional and three-dimensional runs.

The steps were modelled as solid obstacles. The distance between the obstacles was initially 50.5 cm, the crest width was 2.7 cm and the height 7.4 cm, see Figure 1. The mesh had to be locally refined at the steps in order to comply with the geometry of the obstacles.

The intake was modelled as a cuboid box with inflow through a 1.0×0.4 meter bottom hole. The filling of the box was modelled once. For all further simulations the filled box was used as initial condition.

At the intake steady inflow boundary conditions were assumed. Since flow was supercritical at the outflow no "fixed-water-depth" boundary conditions had to be set there.

FLOW3D usually works with explicit time stepping but implicit treatment of specific terms is possible. For this study a purely explicit formulation was used and the program automatically chooses a time step size to satisfy the CFL criterion. Every 0.2 seconds an interpolated output file with the main flow variables like velocities, pressure and water surface height was produced.

For each space-dimension a gravitational acceleration component can be defined independently. This feature was used to simulate bed slope. Only one half of the chute was modelled applying a symmetric boundary condition at the chute centre line in order to CPU time safe.

The surface roughness can be chosen independently for obstacles and mesh. According to the physical simulations described by Ganz (2001) and Clara (2002) the bed roughness was defined as $k = 0.3$ mm to fit the physical model.

3.2 *Three dimensional verifications*

A crucial part of every numerical study is the verification of the numerical model. This usually is done by

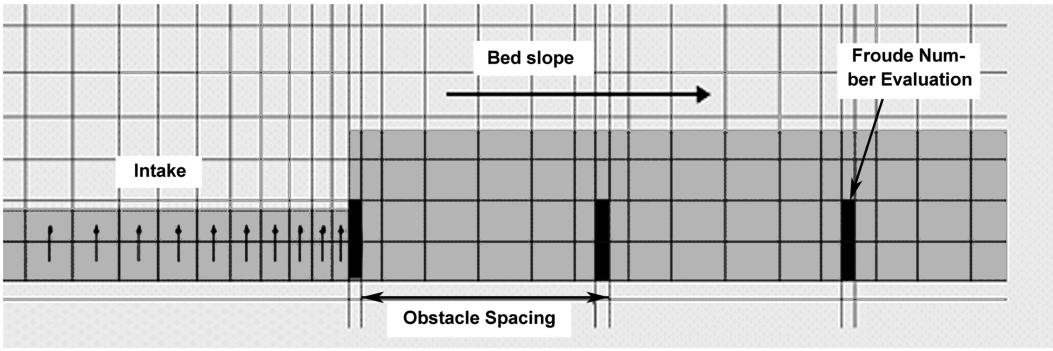


Figure 1. Definition sketch for numerical model building.

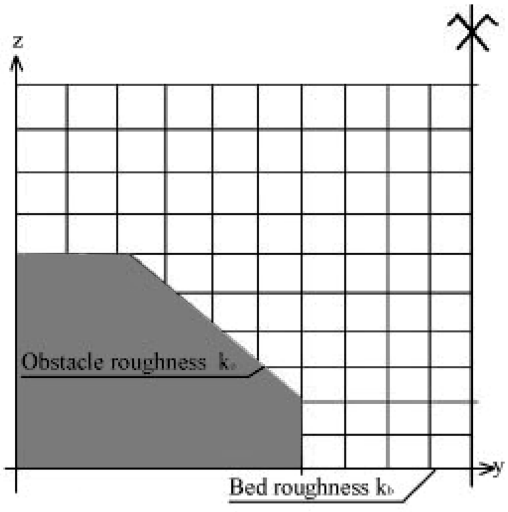


Figure 2. Cross section with mesh and obstacle in the three-dimensional model.

comparing numerical results with measured physical data. Since the two-dimensional grid was not suitable for the representation of the physical model geometry used by Ganz (2003) three-dimensional runs had to be done.

Hence for verification a non-uniform structured mesh with 200 cells in x-direction, 10 cells in y-direction and 10 cells in z-direction was used. The trapezoid channel was modelled using a rough mesh wall boundary condition at the channel bottom and rough obstacles at the channel sides. Mesh and side roughness could be varied independently to allow for the representation of the laboratory conditions.

Several computations were done using different discharges and bed slopes and suspension concentrations according to the measurements done in the physical model. The water depths measured in the physical model and the ones calculated in the numerical model showed reasonably good correspondence, which is evidence, for reliability of the numerical model.

Ganz (2003) found no evidence for effects in the cross-sectional plane causing flow instabilities. The investigations also showed that sediment concentrations did not affect wave formation significantly. In order to save CPU time further investigations were carried out on a two-dimensional numerical model with very high spatial resolution to obtain correct wave formation.

3.3 *Two-dimensional modelling*

Like in the three-dimensional case, the two-dimensional simulations were performed using a 16 meter long and 0.4 meter high mesh. The same bed roughness as in three-dimensions was assumed.

The grid was discretized with 521 cells in x-direction and 40 cells in z-direction while in y-direction a single cell only was assumed.

3.3.1 *Variation of obstacle spacing with fixed bed slope*

Preliminary investigations with the two-dimensional geometry lead to a qualitative assessment at which bed slope optically good sample waves appeared. For 0.505 meters step spacing and a discharge of 0.012 m^3/s this was the case at 7% bed slope. Consequently this slope was chosen for additional runs with differing obstacle intervals. The aim of these tests was to find out whether and how obstacle spacing influences wave development. Additionally a spacing of 1.10 meters, 0.25 meters, 0.1 meters and irregular spacing was investigated. While at small spacings like 0.1 and 0.25 meters no significant waves could be observed for a spacing wider than 0.5 meters instabilities occurred.

At the interval of 1.10 meters a fully developed hydraulic jump developed between the obstacles. In Figure 3 waves propagate from one cascade to the next interfering with the hydraulic jump in the next field.

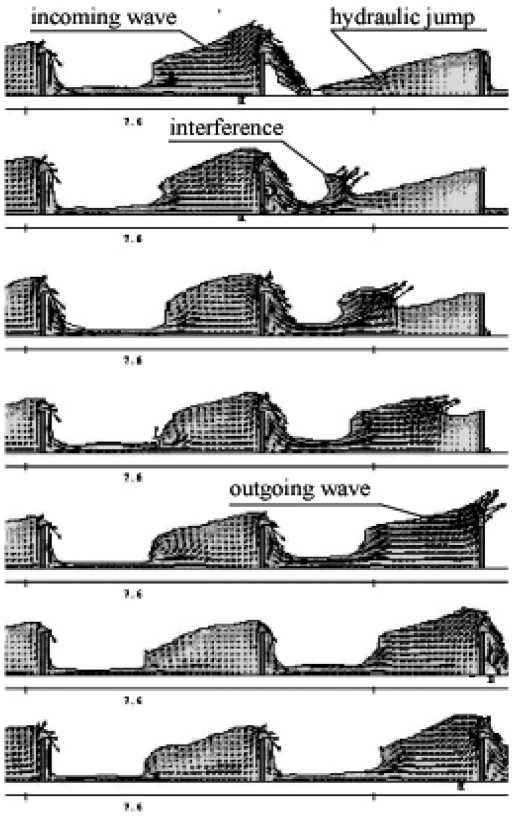


Figure 3. Flow instabilities occurring due to a fully developed hydraulic jump.

The oscillations caused by the hydraulic jump appeared to be the reason of the instabilities in the flow field.

3.3.2 *Variation of discharge and slope with fixed obstacle spacing*

Due to the assumption that hydraulic jumps were causing flow instabilities a single geometry was chosen in order to simulate flows with varying discharges and bed slopes. To check whether hydraulic jumps appeared Froude numbers were calculated at the obstacle crest for each run.

For the set-up described in section 3.3.1 a spacing of 0.25 meters did not show flow instabilities. Therefore this spacing was chosen for further investigations where five different discharges were used and the slope was modified until instabilities occurred.

Consecutively results were checked whether waves appeared. Two different criteria of wave appearance were employed (Figure 5):

– During the calculations FLOW3D allows the observation of the development of state variables like mean-kinetic energy, fluid surface area, volume error, time step size and others. When flow instabilities appeared mean-kinetic energy plots showed oscillations, while a smooth curve could be observed when no waves appeared.
– Post-processing two-dimensional, animated plots were utilized to assess optically whether instabilities occurred or not.

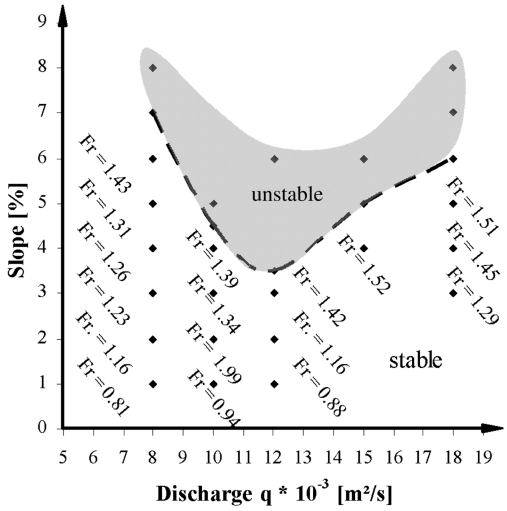


Figure 4. Numerical runs at 0.25 meters obstacle spacing. Discharge and slope are varied and Froude number determined at stable condition.

Each run was assessed using these criteria. For stable flow conditions no wave generation occurred and a single Froude number could be calculated at the obstacle crest. Runs were lead until instable conditions with instability generation occurred. In the case of unsteady flow instabilities the Froude number could not be defined any more. As can be seen in Figure 4 flow instabilities occurred at Froude-numbers near 1.5. This is close to the transition between an ondular and a weak hydraulic jump, which occurs according to literature at a Froude-number of 1.7. The difference between the two figures may be explained by the fact that the flow over the step is accelerated and may therefore reach higher values when hitting the subcritical water body between the steps.

4 CONCLUSIONS

The present paper shows computational results for steep stepped channels where flow instabilities have been observed despite steady inflow conditions. The computations have demonstrated that instabilities can develop not only in prototype and Lab but also in numerical computations. A qualitative comparison

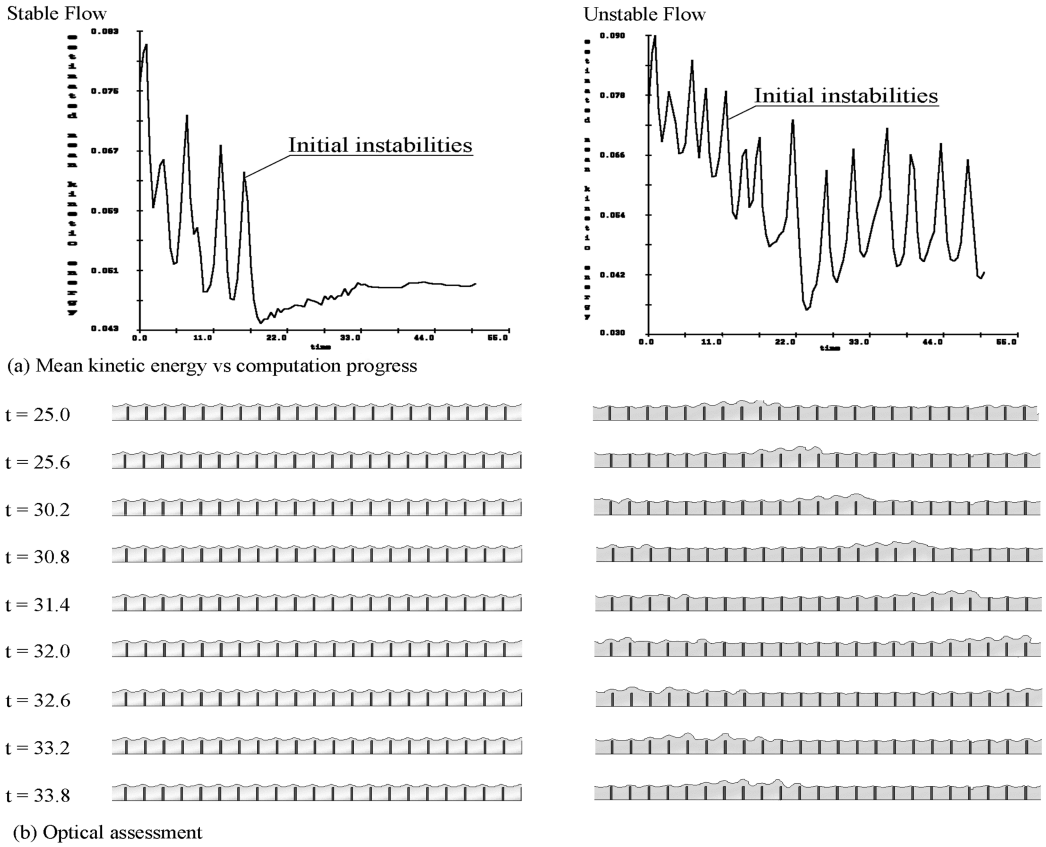


Figure 5. Comparison between stable flow conditions and unstable flow conditions.

between Lab data and numerical results shows reasonable agreement. In order to restrict CPU time with detailed resolution in space most computations have been performed using a two-dimensional approach. A comparison of Lab results in a trapezoidal channel and of the two-dimensional computations is only qualitatively possible due to cross-sectional velocity variations in the Lab flume.

The current work focused on the occurrence of flow instabilities and aimed to resolve the underlying mechanism. Results with fully developed instabilities showed the occurrence of a classical hydraulic jump between neighboring steps. On the other hand no instabilities could be observed for subcritical flow conditions. As can be seen from Lab and numerical investigations the instabilities correspond to a beat indicating the occurrence of two oscillations, which differ only slightly in frequency. We therefore assumed that one of these frequencies could be the unsteady motion attributed to a classical hydraulic jump. Therefore we analyzed the Froude number in the cross-section of the steps.

We investigated a particular geometry where height and spacing of the steps was fixed. Five different discharges where investigated and the slope was modified for a given discharge from flat to steep until instabilities could be detected. We could show that occurrence of instabilities was bounded to a step Froude number larger than about 1.5. We assume that this characteristic Froude number is linked to the occurrence of a week hydraulic jump, which according to literature occurs for a Froude number of approximately 1.7. The difference between the two figures may be explained by the fact that the flow over the step is accelerated and may therefore reach higher values when hitting the subcritical water body between the steps.

Even though a realistic explanation for the mechanism could be found further work has to be performed to assure this assumption. Namely a careful comparison of physical model investigations in a rectangular cross-section where the flow can be regarded as two-dimensional must be performed and the comparison with numerical results must be expanded to a set of varying geometries. Also careful analysis of both

Fourier series from physical and numerical model tests must be carried out.

REFERENCES

Boes, R. 2000. *Zweiphasenströmung und Energieumsetzung an Grpßkaskaden*. Zürich: Mitteilung der Versuchsanstalt für Wasserbau, Hydrologie und Glaziologie.

Chanson, H. 1994. *Hydraulic Design of Stepped Cascades, Channels, Weirs and Spillways*. Oxford: Pergamon.

Clara, G. 2002. *Experimentelle Analyse von Abflussinstabilitäten in steil geneigten Absturztreppen*. Innsbruck: Diplomarbeit – Universität Innsbruck.

Ganz, T.F. 2002. *Abflussinstabilitäten bei Absturztreppen*. München: TU München.

Ganz, T.F. 2003. *Entstehung und Entwicklung von Abflussinstabilitäten bei Absturztreppen. Modellanalyse über den Einfluss von Gerinnegeometrie, Sohlrauheit und Suspensionsgehalt.* Innsbruck: Dissertation- Universität Innsbruck.

Harlow, F.H. & Nakayama, P.I. 1968. *Transport of Turbulence Energy Decay Rate*, Los Alamos Sci. Lab., University of California Report LA-3854.

Harlow, F.H. & Welch, J.E. 1965. *Numerical Calculation of Time-Dependent Viscous Incompressible Flow of Fluid with Free Surface*, The Physical of Fluids, 8(12), pp. 2182–2189.

Herrmann, G. 2003. *Abflussinstabilitäten der Hochwasserentlastung Sorpetalsperre.* Aachen : Rheinisch- Westfälische Technische Hochschule Aachen.

Hirt, C.W. & Nichols, B.D. 1981. *Volume of Fluid (VOF) for the Dynamics of Free Boundaries*, J. Comput. Phys., 39, 201–225.

Jones, W.P. & Launder, B.E. 1972. *The Prediction of Laminarization with a Two-Equation Model of Turbulence*, International Journal of Heat and Mass Transfer, Vol. 15, pp. 301–314.

Le Fessant, A.-L. 2001. *Étude des instabilités d'un écoulement à surface libre – Sur un fond à géométrie périodique.* Toulouse: Institut National Polytechnique de Toulouse.

Nichols, B.D. & Hirt, C.W. 1971. *Calculating Three-Dimensional Free Surface Flows in the Vicinity of Submerged and Exposed Structures*, J. Comp. Phys. 12, 234.

Rodi, W. 1984. *Turbulence Models and Their Application in Hydraulics*, IAHR state-of-the-Art-Paper.

Sicilian, J.M. 1990. "*A FAVOR™ Based Moving Obstacle Treatment for FLOW-3D®*," Flow Science Technical Note #24, April 1990 (FSI-90-TN24).

Whittaker, J. 1982. *Flow and Sediment Movement in Stepped Channels.* Christchurch: University of Canterbury.

This page intentionally left blank

River Flow 2004 – Greco, Carravetta & Della Morte (eds.)
© 2004 Taylor & Francis Group, London, ISBN 90 5809 658 0

Activation of scour around bridge abutment

D. Capuano & A. Carravetta
Department of Hydraulic and Environmental Engineering, University of Naples Federico II

U.M. Golia
Department of Civil Engineering, Second University of Naples

ABSTRACT: Scour evolution around bridge piers and abutments is a master topic in river hydraulics for the relevance of the process on waterworks stability. Clear water experiments are usually employed to obtain the maximum scour depth, for given obstacle geometry and flow conditions. In this paper new experiments under clear water conditions are presented, performed in the transitional flow regime, i.e. with grain Reynolds numbers between 5.3 and 9.0. The Reynolds numbers varied between 12000 and 25000.

Time evolution of the maximum scour depth changed significantly if the same experiment was repeated, even under negligible variation of the flow conditions. Therefore, different sets of repetition of the same experiment were obtained for each flow condition and statistical properties were inferred for each set. Two scour phases were observed during the process, in agreement with the observation of others. Regression lines and confidence intervals for scour depth evolution were found for each of the two phases. An attempt was made to represent scour evolution in dimensionless units.

1 INTRODUCTION

Numerous literature is available on scour activation around a bridge abutment. An exhaustive review can be found by Melville & Coleman (2000) and in several recent papers (Oliveto & Hager 2002, Radice & Franzetti 2002a, b).

Equilibrium depth in clear water conditions is often assumed to be an upper limit for scour depth and thus useful for design purposes. Because of the long duration of scour experiments, the real presence of such an asymptotic value is a still open question. This question is relevant also in the prediction of scour evolution. Many of the available formulas employ the maximum scour depth value as length scale.

Other approaches override the problem of equilibrium scour depth. These methods are based on the existence of two linear trends in the log-lin $d(t)$ representation of the maximum scour depth, represented by two equations, one for the lower and one for the higher level. A particular dimensionless time is defined to evaluate the dimensionless scour depth when log-lin $d(t)$ slope changes.

New experiments are presented here, in order to cover a range of grain Reynolds numbers, $R_* = d_{50}u_*/\nu$, smaller than those usually found in literature for clear water scour experiments.

To stress the importance of covering such conditions it can be observed that the result of experiments on pier scour performed with $R_* < 10$ failed to be modeled in the past (Oliveto & Hager 2002, Franzetti et al. 1994).

The sediment size used in the flume -0.5 mm median diameter- is of the order of that which would be used in the model of a river mouth if length scaling is maintained undistorted.

The present experiments revealed some peculiarities that reflect on the application of both scour depth prediction methods.

Concerning the first method, the presence of an equilibrium scour depth was not clearly stated during the experiments, especially for the largest flow rates. Additionally, abutment scour models based on the first method are not expressly developed and calibrated for the range of parameters of writers' experiments (Oliveto & Hager 2002, Melville 1997).

When dealing with the second method, an evident change in the trend of scour evolution in the log-lin $d(t)$ plot was not always observed. A large dispersion of data was present, as observed also in pier scour at low R_* values (Chabert & Engeldinger 1956), making difficult to estimate the fitting lines of the two level of scour.

2 LABORATORY SET-UP AND RESULTS

A laboratory flume, 0.15 m wide and 4.10 m long was partially filled with sand as a horizontal granular bed.

Table 1. Long duration experiments.

Test	Q (l/s)	h (cm)	Temp. (°C)	V (m/s)	Fr	R	D_*	R_*	$\vartheta \cdot 10^{-2}$	$\frac{\vartheta}{\vartheta_c}$	$\frac{b}{h}$
A1	0.80	2.75	12.0	0.19	0.37	12600	11.2	5.33	2.03	0.64	0.55
A2	0.80	2.70	18.5	0.20	0.38	15000	12.5	6.37	2.07	0.66	0.56
A3	1.00	2.85	14.5	0.23	0.44	16700	11.7	6.75	2.85	0.91	0.53
A4	1.00	2.85	21.0	0.23	0.44	19600	13.0	7.87	2.80	0.90	0.53
A5	1.20	3.15	23.5	0.25	0.46	24200	13.5	8.90	3.19	1.03	0.48
A6	1.20	3.15	23.5	0.25	0.46	24200	13.5	8.90	3.19	1.03	0.48

Table 2. Short duration experiments.

Test	Q (l/s)	h (cm)	Temp. (°C)	V (m/s)	Fr	R	D_*	R_*	$\vartheta \cdot 10^{-2}$	$\frac{\vartheta}{\vartheta_c}$	$\frac{b}{h}$
B1–B5	0.80	2.70	21.0	0.20	0.38	15900	13.0	6.74	2.06	0.66	0.55
B6–B16	1.00	2.85	25.0	0.23	0.44	21500	13.8	8.59	2.78	0.90	0.53
B17–B22	1.20	3.15	24.0	0.25	0.46	24500	13.6	9.00	3.19	1.02	0.48

Sand was of 0.5 mm median grain size, with geometric standard deviation, assuming a log-normal distribution, $\sigma_g = 1.3$ and $\gamma_s = 26.9\,\text{kN/m}^3$. A 1/10 ramp was located at the inlet of the channel to maintain a gradually varied flow. Subcritical clear water flow conditions were adjusted in the flume. A fixed water level was imposed at the downstream end of the channel by inserting a weir in the terminal tank, whose upper level was above the granular bed.

Main data of experiments are summarized in Table 1 and Table 2, with symbols defined in the final nomenclature. In Table 1 the results of long duration experiments (lasted 2–6 days) are reported. Short time repetitions of the same experiments of Table 1 are summarized in Table 2 (duration 1000–3600 seconds). During the long time experiments discharge varied by ±1% and the temperature varied up to 7°C. No significant variations of discharge and temperature were observed during the short time experiments.

When steady state flow conditions were obtained in the channel, corresponding to the imposed discharge, the experiment was started by inserting a glass prism simulating the abutment, of width $b = 0.015\,\text{m}$ and length $L = 0.15\,\text{m}$, as showed in Figure 1. No differences in scour evolution were found by increasing the discharge to the given value with the glass prism already positioned in the flume.

Scour was measured for each test close to the abutment wall (point A in Figure 1), where maximum scour was always found to happen. Digital images were used to determine the scour extension.

In Figure 2 scour evolution is presented as measured during all long duration experiments: maximum scour depth, d_s, is plotted versus $\log(t)$. At the end of the long duration experiments an equilibrium scour depth was apparently reached only for the smaller discharges.

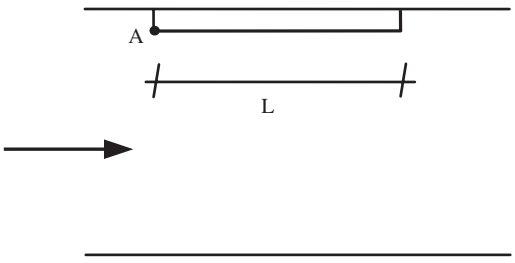


Figure 1. Plane view of the channel with wall abutment.

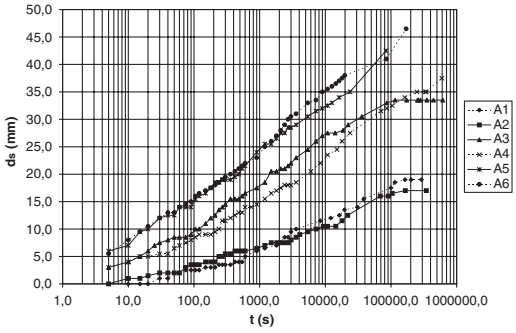


Figure 2. Time evolution of scour depth in test A1–A6.

In Figures 3–5 the results of short duration experiments are reported grouped by discharge. The data

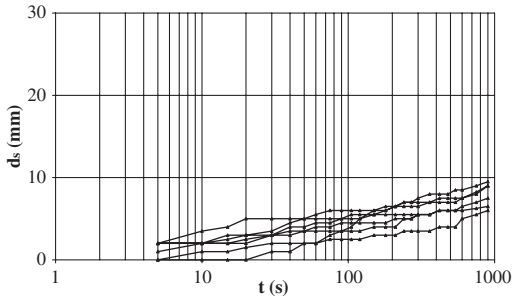


Figure 3. Time evolution of scour depth in test B1–B5.

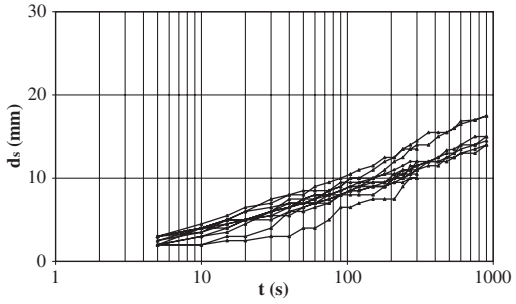


Figure 4. Time evolution of scour depth in test B6–B16.

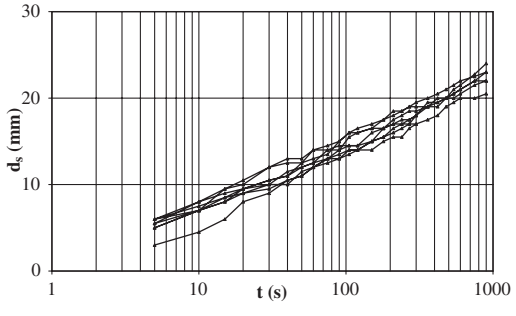


Figure 5. Time evolution of scour depth in test B17–B22.

reveal a large dispersion, but an interesting feature is the presence in each single experiment of a variation in the slope of the $d_s(t)$ data, in agreement with the findings of others (Cardoso & Bettess 1999, Radice & Franzetti 2002a, b). This variation reveal a peculiar time t_c in scour evolution: t_c seems to be smaller for higher flow rate.

3 AVERAGE SCOUR EVOLUTION

The least square method was applied to all data grouped by discharge to find the parameters of the two interpolation lines in the log-lin $d(t)$ plot together with

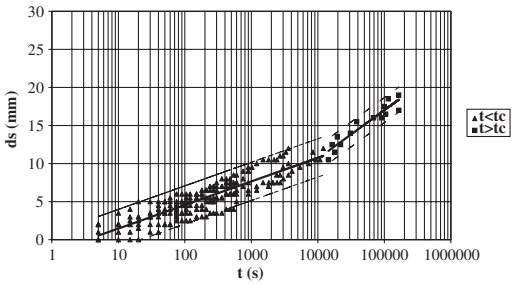


Figure 6. Temporal evolution of scour depth in test A1, A2, B1–B5, interpolar lines and 95% confidence band.

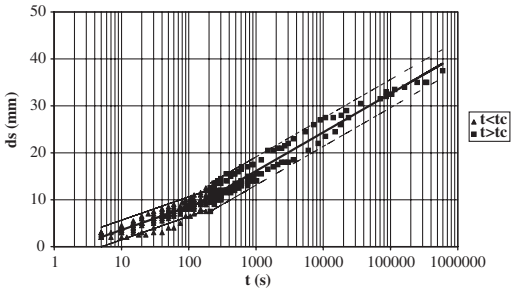


Figure 7. Temporal evolution of scour depth in test A3, A4, B6–B16, interpolar lines and 95% confidence band.

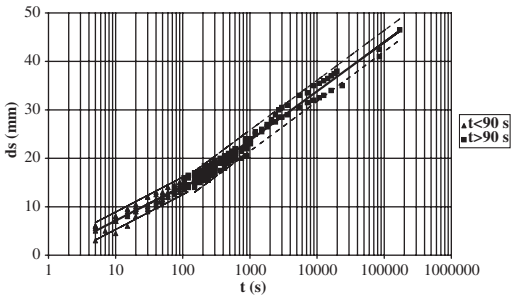


Figure 8. Temporal evolution of scour depth in test A5, A6, B17–B22, interpolar lines and 95% confidence band.

the t_c time. In the regression procedure few values were excluded of test A1, A2 and A3 because an equilibrium scour depth was apparently reached. The results of the regression analysis are presented in Figures 6–8: data for $t < t_c$ and $t > t_c$ are marked with different symbols. Two 95% confidence bands are also plotted in the figures.

Two different mechanisms of scour advance were observed for times smaller or larger than t_c.

For $t < t_c$, an activation phase of the scour mechanism appears to occur. The scour has the pattern shown in Figure 9: the hole did not reach yet the side of the flume.

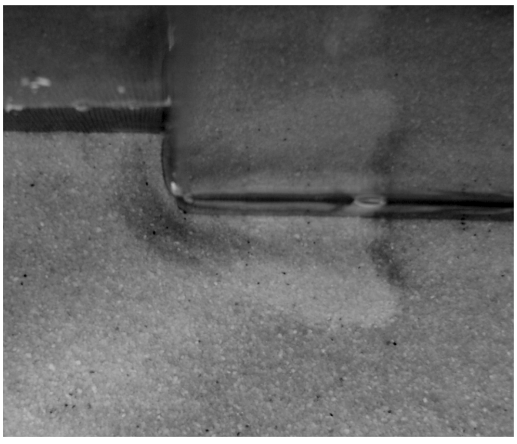


Figure 9. Plan view of the scour hole for $t < t_c$.

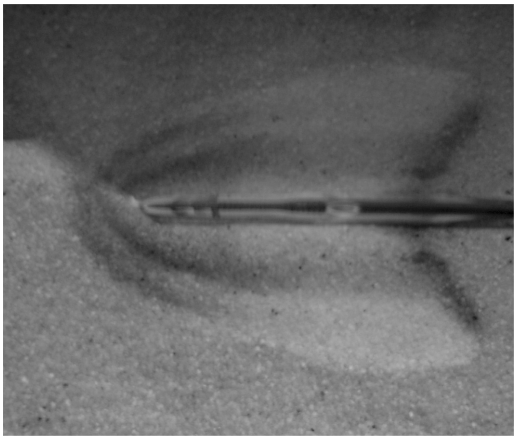


Figure 10. Plan view of the scour hole for $t > t_c$.

For $t > t_c$, a fully activated scour mechanism was present, the corresponding geometry shown in Figure 10 where it can be seen that the scour extends up to the flume wall: in this activated phase the scour bed shape changes, with a discontinuity in the bed slope along the hole. This effect has been linked to the presence of two counter rotating vortices (Kwan & Melville 1994).

Radice & Franzetti (2002a, b) found that all data of scour evolution could collapse in two lines in the log-lin representation if time and scour depth had been divided by proper dimensionless units. On the basis of a large number of literature experiments, the authors determined the characteristic length:

$$a = 2.10\sqrt{bh}\left(\frac{b}{h}\right)^{0.17}\left(\frac{\sqrt{bh}}{d_{50}}\right)^{0.17}\left(\frac{L}{b}\right)^{0.07}\vartheta^{0.63} \qquad (1)$$

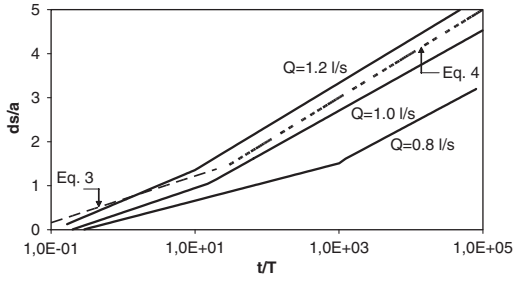


Figure 11. Dimensionless scour evolution.

and time:

$$T = 538.11\frac{\sqrt{bh}}{V}\left(\frac{b}{h}\right)^{0.77}\left(\frac{L}{b}\right)^{-0.46} \qquad (2)$$

They proposed the following relations for the two levels of scour:

$$\frac{d_s}{a} = 0.53\log\left(\frac{t}{T}\right) + 0.69 \qquad \text{for } \frac{t}{T} < 30 \qquad (3)$$

$$\frac{d_s}{a} = 0.53\log\left(\frac{t}{T}\right) \qquad \text{for } \frac{t}{T} \geq 30 \qquad (4)$$

Relations (1) and (2) are plotted with dotted lines in the log-lin d_s/a vs. (t/T) diagram of Figure 11. In the same figure are also plotted the regression lines of writers experimental results: scour depths and times were scaled with a and T values, calculated on the basis of the average parameters for each group of discharge.

The plot of Figure 11 revealed that:

- the relation (3) proposed by Radice & Franzetti (2002a, b) for $t/T < 30$ does not represent well writers experimental results;
- on the contrary, for $t/T \geq 30$, the agreement between equation (4) and writers experiments is much better, for the higher flow rates;
- writers' regression lines for $t > t_c$ have approximately the same unit slope, confirming the good structure of equation (4);
- the change in scour level perform approximately at the same dimensionless depth, $d_{sr}(t_c)/a = 1 \div 1.5$, for all flow rates, but for different values of t_c/T;
- for the lowest flow rate the discrepancy between equation (4) and writers results becomes very large.

4 SCATTER OF RESULTS IN A SINGLE TEST

Considering now that any test in each group of discharge can be considered as a repetition of the same experiment – with the exception of a small difference

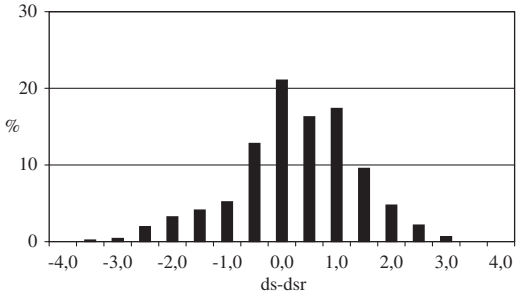


Figure 12. Frequency distribution of scour depth deviations, $t < t_c$.

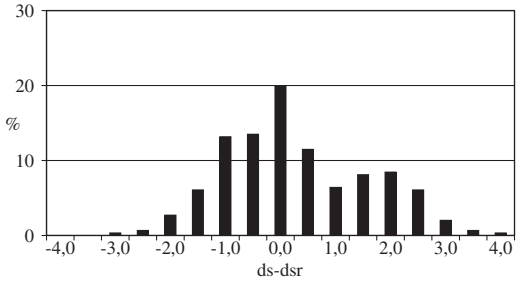


Figure 13. Frequency distribution of scour depth deviations, $t > t_c$.

in water level between test A1 and A2, and of temperature between long duration and short duration test-, then the evolution of scour depth during a single test can be considered as a random variable.

The range of deviations $d_s - d_{sr}$ of all data around the regression lines for $t < t_c$ is plotted in Figure 12. Deviations seem almost normally distributed with differences $d_s - d_{sr}$ as high as ± 2.5 mm.

In the histogram of Figure 13 the range of $d_s - d_{sr}$ values for $t > t_c$ is plotted. Of course, a smaller number of data is available for the long duration experiments and, therefore, the deviations $d_s - d_{sr}$ are less representative of the randomness of scour evolution in the higher level of scour.

Nevertheless, data pattern of long duration test (Fig. 2) suggest a different explanation of the deviations showed in Figure 13: the succession of scour depth in the log-lin $d(t)$ plot, and the position of data respect to the regression line, seem influenced by the depth value $d_s(t_c)$ attained at the end of the activation phase ($t < t_c$). Specifically, a difference in scour depth between two tests observed at the end of the activation phase will be mostly conserved also in the further scour evolution. Therefore, for $t = t_c$, a base deviation, d_b, of the data of each single test from the regression line seems present. This base deviation was set equal to the difference between the scour depth measured at

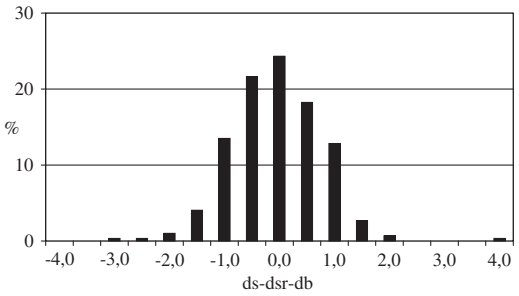


Figure 14. Frequency distribution of residual scour depth deviation, $t > t_c$.

the end of the activation phase, $d_s(t_c)$, and the predicted scour depth at time t_c, $d_{sr}(t_c)$.

Then, new deviations $d_s - d_{sr} - d_b$ for all test in the activated phase ($t > t_c$) were calculated. The range of $d_s - d_{sr} - d_b$ values is plotted in Figure 14.

The deviation of data decreases from a range of ± 3 mm (Fig. 13) to a range ± 1 mm (Fig. 14), not much larger than the measurement resolution expected with sediment particles of 0.5 mm. This finding seems to confirm the previous argument and stress the role of the activation phase of scour on its further scour evolution.

5 CONCLUSIONS

The results of tests performed for small grain Reynolds numbers revealed the following aspects of the scour process:

- the maximum scour depth data, when represented as a function of time in a log-lin plot, spreads along two regression lines, the first valid for $t < t_c$ (activation phase), the second for times larger than t_c (activated phase). Two different mechanisms of erosion seem active for the two level of scour;
- regression lines and confidence interval were found for each level of scour;
- single test repetition exhibit a large spreading of data around the regression line in the first level of scour;
- in the second level of scour the overall dispersion around the regression was not smaller, but data from each test seems to lie on individual patterns;
- scour evolution in the second level of scour was in agreement with the law proposed by Franzetti & Radice (2002a, b), only for the larger discharges.

NOMENCLATURE

a dimensionless length scale
b abutment transverse width

d_{50}	median grain size
D_*	dimensionless sediment size
d	maximum scour depth
d_b	depth correction at $t = t_c$
d_s	measured scour depths
d_{sr}	calculated scour depths
F_r	Froude number
h	approach flow depth
L	abutment longitudinal length
Q	flow rate
R	Reynolds number
R_*	grain Reynolds number
t	time from scour activation
t_c	time of interception of linear regressions
T	time scale
u_*	shear velocity
V	cross-sectional average velocity
γ_s	specific weight of sediment
ϑ	dimensionless shear stress
ϑ_c	dimensionless critical shear stress
σ_g	geometric standard deviation
ν	kinematic viscosity

REFERENCES

Cardoso A.H., Bettess R. 1999. Effects of time and channel geometry on scour at bridge abutments, *Journal of Hydraulic Engineering* 125(4): 388–399.

Franzetti S., Malavasi S., Piccinin C. 1994. Sull'erosione alla base delle pile di ponte in acque chiare, XXIV Convegno di Idraulica e Costruzioni Idrauliche T4: 13–24. Napoli.

Kwan R.T.F., Melville B.W. 1994. Local scour and flow measurements at bridge abutments, *Journal of Hydraulic Research* 32(5): 661–673.

Melville B.W. 1997. Pier and abutment scour: integrated approach, *Journal of Hydraulic Engineering*, 123: 125–136.

Melville B.W., Coleman S.E. 2000. Bridge Scour, Water Resources Publication, Colorado, USA.

Oliveto G., Hager W.H. 2002. Temporal evolution of clear water pier and abutments scour, *Journal of Hydraulic Engineering* 128(9): 811–820.

Radice A., Franzetti S. 2002°. Stima della Profondità dell'Erosione alle Spalle dei Ponti Fluviali, XXVIII Convegno di Idraulica e Costruzioni Idrauliche, Potenza 3: 17–26.

Radice A., Franzetti S. 2002b. Local scour at bridge abutments, River Flow 2002, Bousmar & Zech 2:1059–1068.

River Flow 2004 – Greco, Carravetta & Della Morte (eds.)
© 2004 Taylor & Francis Group, London, ISBN 90 5809 658 0

Seepage and exit gradient under impervious structures with two sheetpiles on layer of infinite depth

G. De Martino & M. Giugni
Dip. di Ing. Idraulica ed Ambientale G. Ippolito, Università di Napoli Federico II, Naples, Italy

N. Fontana
Dipartimento di Ingegneria, Università del Sannio, Benevento, Italy

ABSTRACT: Seepage force represents one of the most common cause of failure of hydraulic structures. Several methods are available in technical literature to provide a good estimate of the factor of safety against seepage erosion. According to Terzaghi, the factor of safety can be determined comparing the exit gradient with the critical gradient. Obviously, the calculation of the critical gradient is very simple, while more complex is the evaluation of the exit gradient. In the present work is presented and discussed the analytical solution of the seepage under a structure with two sheetpiles, resting on the surface of a infinite, homogeneous and isotropic porous medium. A very general solution of the flow has been achieved by means of conformal mapping technique, applying the well-known Schwarz-Christoffel transformation; so, once the size of the structure and of the flow domain have been defined, the exit gradient can be calculated to perform a quick estimate of safety factor.

1 INTRODUCTION

Any hydraulic structure subjected to seepage underneath must be evaluated for stability with due consideration to seepage forces. To this aim various methods are available in the literature; one of the most well known is the method of Bligh and Lane (Lane 1935) which was set up after studying the behaviour of over 200 masonry weirs and dams.

The method is based on the observation that piping may be avoided if the water velocity is such as to prevent the removal of solid material at the structure's downstream toe, which is the section where the hydraulic gradient reaches its maximum value.

A different approach was followed by Terzaghi (Terzaghi & Peck 1967), who showed that the rising of a mass of soil as a result of seepage forces takes place if the average hydraulic gradient downstream of the structure i_{em} exceeds the critical gradient i_c.

The value of i_{em} can be calculated by considering the value of the average hydraulic gradient in the prism adjacent to the toe, of depth s (equal to the length of the sheetpile) and base s/2. The critical gradient instead corresponds to quicksand condition: if we consider all the forces acting on a unit volume of soil through which seepage occurs, it can calculated as $i_c = \gamma'/\gamma$, where γ' indicates the submerged unit weight of soil and γ is the unit weight of water. This makes it possible to define a factor of safety against piping:

$$FS = \frac{i_c}{i_{em}} \tag{1}$$

Obviously the estimate of i_c is not a problem as it is related to the characteristics of the soil; in any case, when information is lacking, it is generally taken as unity. It is a more complex task to determine the value of i_{em}, which is related to the characteristics of the flow domain and, therefore, to the size of the structure and the characteristics of the soil.

By following this procedure, the present paper suggests assessing the stability to seepage forces by comparing the maximum value assumed by the hydraulic gradient (which occurs at the downstream toe of the structure) with the critical gradient i_c. In a recent paper (De Martino et al. 2003) Authors have investigated the exit gradient at the downstream toe of a retaining structure with two sheetpiles resting on a finite depth layer. The present paper instead analyses the seepage established underneath of a retaining structure fitted with two cut-off walls on an isotropic and homogeneous soil of infinite depth (Fig. 1).

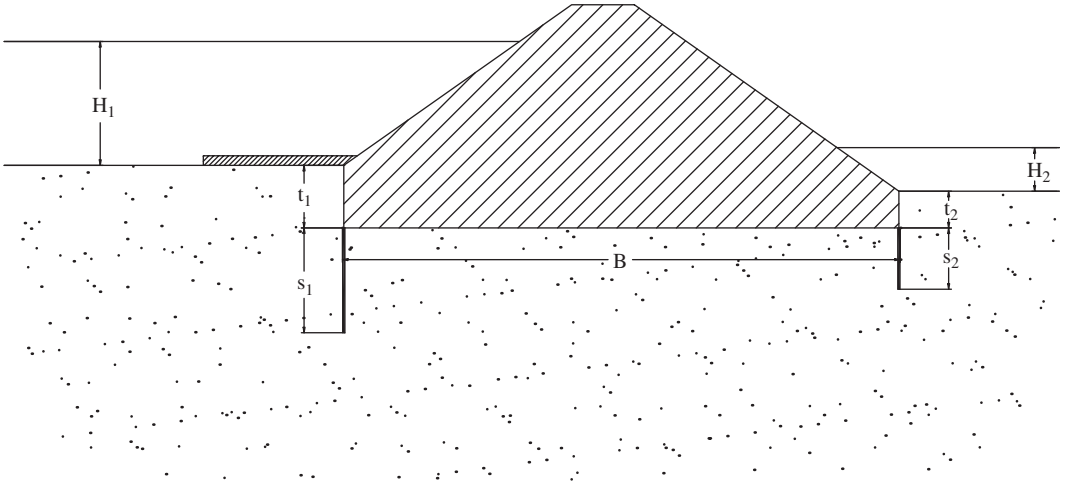


Figure 1. Scheme of the geometric domain.

2 THE ANALYTICAL SOLUTION

The literature contains analytical solutions for seepage underneath hydraulic structures, but only for simple weirs or dams and for soils which are assumed generally isotropic and homogeneous (Polubarinova-Kochina 1962, Harr 1962).

In these papers the technique of conformal mapping is adopted, which makes it possible to derive the solutions of many important classes of groundwater flow problems. In fact, if we define the complex potential as $\omega = \varphi + i\psi$, where φ is the velocity potential function and ψ the stream function, all the desired characteristics of the flow can be obtained once the function ω is known in each point of the flow domain. In order to obtain the functional relationship $\omega(z)$ which defines the complex potential as a function of the complex coordinate $z = x + iy$, Pavlovsky (1956) showed that the problem can be solved by introducing an auxiliary complex variable ζ, called the parametric variable and defined in a complex half-plane. In this way we can map the z and ω planes onto the upper or lower half of the ζ plane and, once the transformation functions $\omega(\zeta)$ and $z(\zeta)$ are known, we can define, by inverting the latter, the relationship $\omega = \omega(z)$.

The functions $z(\zeta)$ and $\omega(\zeta)$ are determined by adopting the conformal mapping method and the Schwarz-Christoffell transformation is used. In fact, for the seepage in question it can be shown that the boundary in the complex potential plane is represented by a polygon. The sides of this polygon are defined by the boundary conditions on the velocity potential and the stream function. Similarly, the boundary of hydraulic structure foundations is generally made up of rectilinear segments, so that the flow domain can also be referred to a polygon. In the following sections, a more detailed description of the mapping procedures used for solving the problem is provided.

2.1 *Mapping the geometric domain*

The scheme considered here is totally general, as it can envisage different lengths for cutoff walls and different depths for the upstream and downstream plane (Fig. 2a). The solution was obtained using the technique of conformal mapping (Nehari 1952) and it makes it possible to determine all the characteristics of the flow field, thus enabling the assessment of the exit gradient i_e at the downstream toe of the structure and the uplift force exerted by the water. For the considered scheme, the mapping of the flow domain into the semi-plane of the auxiliary variable ζ is as follows:

$$z = A \cdot \int \frac{(\zeta - c_2)(\zeta - c_5)}{\sqrt{(\zeta - c_1)(\zeta - c_3)(\zeta - c_4)(\zeta - c_6)}} d\zeta + C \quad (2)$$

In particular, we can assign arbitrarily three conditions; so we assume $c_1 = -c_6 = -1$, while the third condition arises from consideration that $z = \pm\infty$ if $\zeta = \pm\infty$.

After these assumptions Equation 2 becomes:

$$z = A \cdot \int \frac{(\zeta - c_2)(\zeta - c_5)}{\sqrt{(\zeta + 1)(\zeta - c_3)(\zeta - c_4)(\zeta - 1)}} d\zeta + C \quad (2')$$

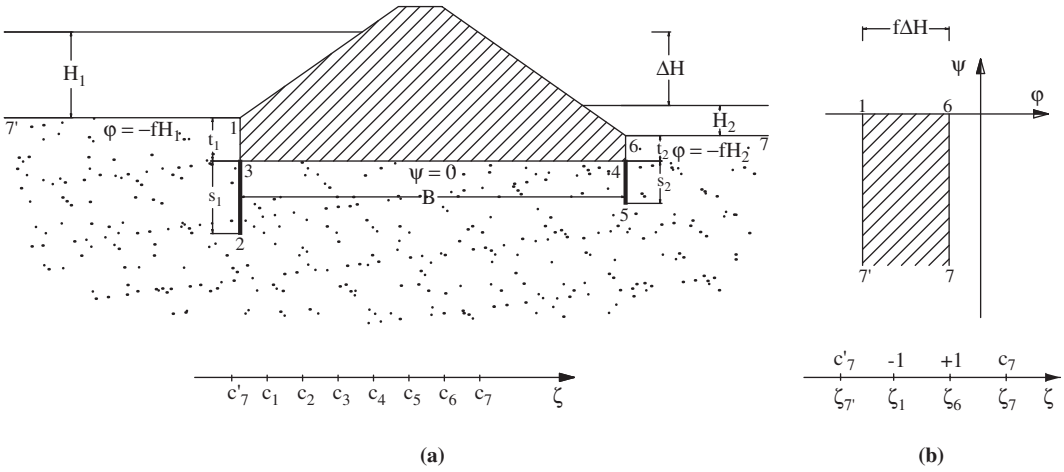


Figure 2. Geometric (a) and complex potential (b) domains.

which can be closed form integrated, giving the following expression for z:

$$z = \frac{A}{\sqrt{\frac{\zeta-1}{\zeta+1}}\sqrt{\zeta-c_4}\sqrt{\zeta-c_3}}\{(c_3-\zeta)(c_4-\zeta) + \frac{1}{\sqrt{\frac{(-1+c_3)(1+\zeta)}{(1+c_3)(\zeta-1)}}}[\sqrt{\frac{(\zeta-c_4)}{(1+c_4)(\zeta-1)}}\sqrt{\frac{\zeta-c_3}{(1+c_3)(\zeta-1)}}\cdot$$

$$(\zeta-1)[(1+c_4)(c_3-1)E-2(-c_2+c_3+(c_2-1)c_5)F$$

$$+2(-2c_2+c_3+c_4-2c_5)\Pi]]\}+C \qquad (3)$$

In Equation 3, $F = F(\varphi, m)$, $E = E(\varphi, m)$, $\Pi = \Pi(n, \varphi, m)$ are, respectively, the elliptic integrals of the first, the second and the third kind (Abramowitz & Stegun 1970). The values of the argument, the module and the parameter are defined as follows:

$$\varphi = \mathrm{ArcSin}\left(\sqrt{\frac{(c_3-1)(1+\zeta)}{(1+c_3)(\zeta-1)}}\right)$$

$$m = \frac{(c_4-1)(c_3+1)}{(c_4+1)(c_3-1)}$$

$$n = \frac{(c_3+1)}{(c_3-1)}$$

The constants $c_2, \ldots, c_5$, A, C can be determined by mapping the points on the real axis of the auxiliary variable's semi-plane onto the points in the geometric domain:

- point 1: $\zeta = -1$; $z = -i \cdot t_1$
- point 2: $\zeta = c_2$; $z = i \cdot s_1$
- point 3: $\zeta = c_3$; $z = 0$
- point 4: $\zeta = c_4$; $z = B$
- point 5: $\zeta = c_5$; $z = B + i \cdot s_2$
- point 6: $\zeta = 1$; $z = B - i \cdot t_2$

This yields a system of 6 equations in the unknowns c_2, c_3, c_4, c_5, A and C. Since the system is strongly non-linear, it was not possible to obtain a direct solution and, therefore, the Newton-Raphson method was adopted.

2.2 *Mapping the complex potential domain*

Figure 2b depicts the complex potential domain in the case of a stratum overlying an impermeable substratum. In particular, $\Delta H = H_1 - H_2$ represents the water level difference upstream and downstream of the structure, while f indicates the coefficient of permeability of the porous layer. In this case the Schwarz-Christoffel transformation is written as follows (Polubarinova-Kochina 1962):

$$\omega = M\int\frac{1}{\sqrt{(\zeta-1)(\zeta+1)}}d\zeta + N$$

which yields, with the corresponding boundary conditions, the following expression of the complex potential:

$$\omega = f\Delta H\left(\frac{\arcsin(\zeta)}{\pi} - \frac{1}{2}\right)$$

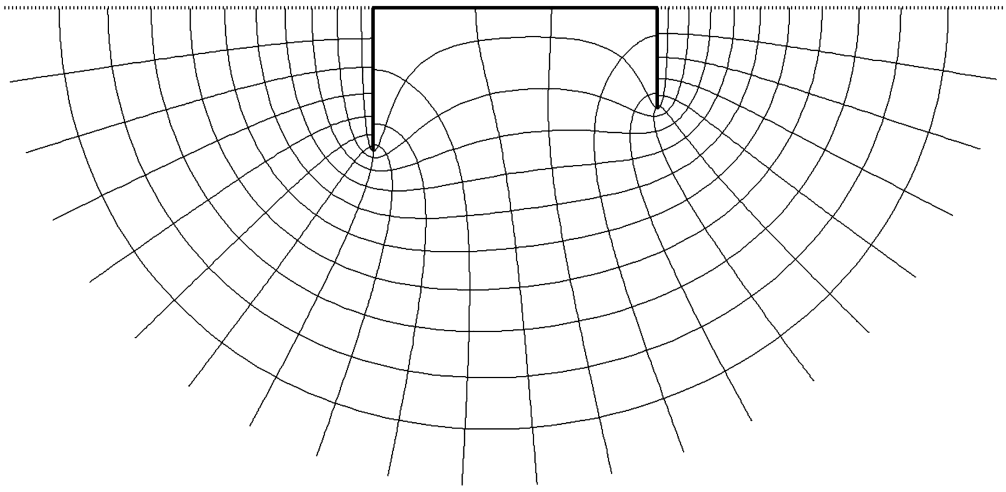


Figure 3. Example of flow net for flat-bottomed structure resting on infinite depth layer.

3 ANALYSIS OF RESULTS

After mapping z and ω onto the half-plane of the auxiliary variable, by eliminating ζ from relationships $z(\zeta)$ and $\omega(\zeta)$, we can derive the expression of $\omega(z)$, which makes it possible to define, for a generic point of the flow domain (with complex coordinate $z = x + iy$), the complex potential $\omega = \varphi + i\psi$. It is thus possible to define the flow net and all the elements of greater interest in the flow field (hydraulic gradient, uplift pressures, etc.). By way of an example, Figure 3 reports the flow net for a structure with two sheetpiles resting on an infinite depth layer, with $s_1/B = 0.5$ and $s_2/B = 0.35$.

In the present paper, analysis is limited to the values of the hydraulic gradient, which is directly connected to the problem of stability to seepage forces in hydraulic structures. With reference to the above mentioned Terzaghi criterion, it is admitted that the estimate of the piping safety coefficient is given by Equation 1, in which the value of i_{em} (average gradient in the prism adjacent to the cutoff wall, of depth s and base s/2) is substituted with the value of the exit gradient i_e, which represents the maximum of the hydraulic gradient values downstream of the structure. If the soil is homogeneous and isotropic, this value reaches its maximum at the downstream toe of the structure and, therefore, at point 6 (cfr. Fig. 2a). The expression of the hydraulic gradient in a generic point is obtained from the relation:

$$i = \frac{1}{f}\frac{d\omega}{dz} = \frac{1}{f}\frac{d\omega}{d\zeta}\frac{d\zeta}{dz}$$

and hence from the ratio between the derivatives of the functions $\omega(\zeta)$ and $z(\zeta)$. Consequently, the expression of i_e is given by:

$$i_e = \frac{\Delta H}{\pi} A \frac{(\zeta - c_2)(\zeta - c_5)}{\sqrt{(\zeta - c_3)(\zeta - c_4)}} \tag{4}$$

Using Equation 4 made it possible to obtain the diagram in Figure 4 which, for a flat-bottomed structure ($t_1 = t_2 = 0$), report the values of i_e as the s_1/B and s_2/B ratios vary. The dashed line indicates the values of i_e corresponding to the condition $s_1 = s_2$ which bounds the field of values generally adopted in technical practice ($s_1 > s_2$).

Analysis of the diagrams allows some interesting considerations to be made:

- the values of i_e obviously tend to decrease as s_1 and s_2 increase. However, this reduction is more marked for a certain field of values, as can be inferred from Figure 4. It therefore follows that, above a fixed value of s_1/B and s_2/B, increasing the length of the cutoff walls is practically ineffective in terms of reducing the values of the exit gradient;
- as pointed out in De Martino et al. (2003), the case of infinite thickness stratum gives the upper limit value of the exit gradient when the B/T ratio decreases (being T the thickness of the porous layer). So the hypothesis of infinite depth supplies the maximum values of i_e, and hence reference can be made to this when working safety conditions are desired or when the depth of the layer is not known.

In fact, in Figure 5 the variation of the exit gradient as the B/T ratio varies is reported for a retaining hydraulic structure. The circle, in particular, represents the exit gradient in the case of infinite depth layer

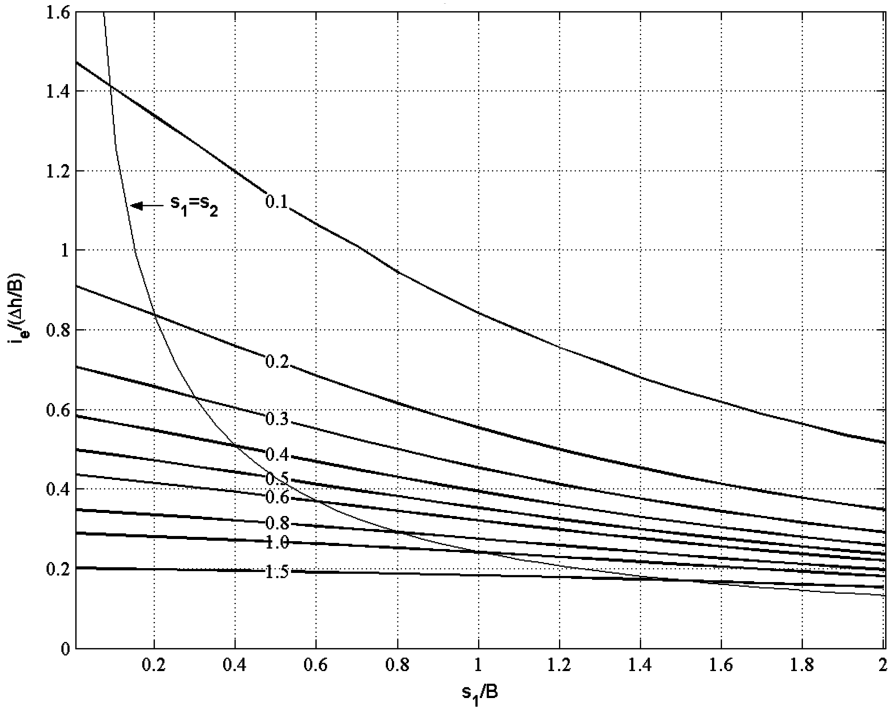


Figure 4. Exit gradient for infinite depth layer.

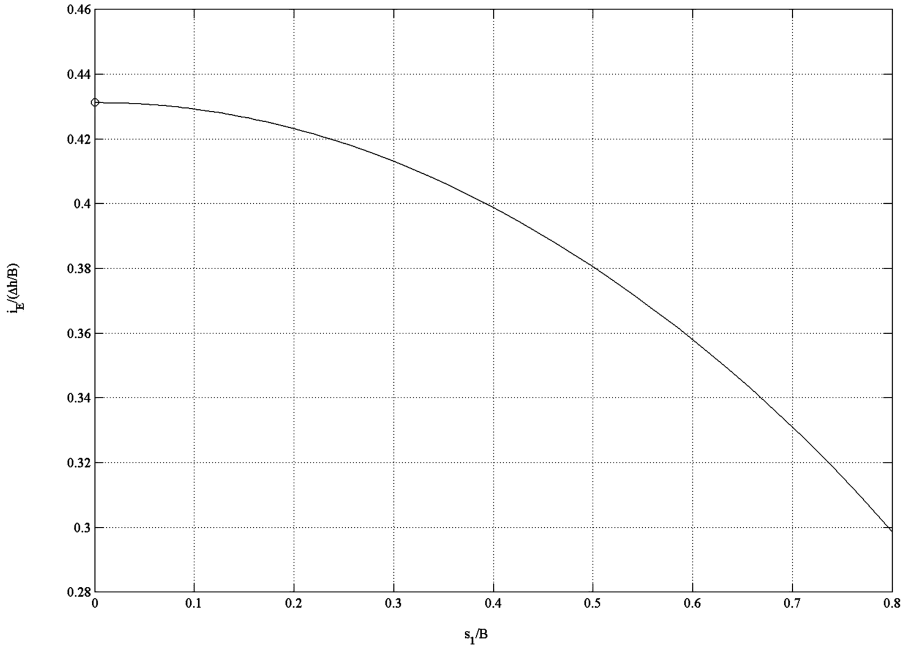


Figure 5. Trend of the exit gradient when the B/T ratios decreases.

and it coincides with the value inferred from the finite depth solution (De Martino et al. 2003) when B/T tends to zero.

4 CONCLUSIVE REMARKS

Seepage analysis for hydraulic structures has been developed by means of conformal mapping technique, applying the well known Schwarz-Christoffel transformation. In particular, the flow field established underneath hydraulic structures fitted with two sheetpiles on a homogeneous and isotropic soil of infinite depth has been analysed and a general closed-form solution has been derived.

The analytical solution allows to compute the maximum value of the hydraulic gradient (which occurs at the downstream toe of the structure) and therefore to assess stability to seepage forces by means of a factor of safety against piping according to Terzaghi. The diagram obtained for flat-bottomed structures (Fig. 4) can supply in this way a strong support in the design phase, especially when working safety conditions are desired or when the depth of the layer is not known.

Obviously, analytical modelling of the seepage can't give complete information on stability of soils subjected to seepage forces. In this view, Authors are currently conducting laboratory experiments at the Dipartimento di Ingegneria Idraulica ed Ambientale *G. Ippolito* of Naples University *Federico II*, in order to analyse experimental values and compare them with the ones derived from the theoretical model.

REFERENCES

Abramowitz, M. & Stegun, I. A. 1970. *Handbook of mathematical functions*. Dover Publications, New York, USA.

De Martino, G., Fontana, N. & Giugni, M. 2003. Seepage and Exit Gradient under Impervious Structures with Two Sheetpiles on Layer of Finite Depth. *International Conference on Water and Environment: Planning, Development, Utilization, Conservation and Management (Integrated Engineering, Scientific, Technological, and Socio-Economic Approaches) (Dec 2003)*, Regional Research Laboratory, Council of Scientific and Industrial Research, Bhopal.

Harr, M. E. 1962. *Groundwater and Seepage*. McGraw-Hill Book Company, New York, USA.

Lane, E. W. 1935. "Security from underseepage: Masonry dam on earth foundation". *Trans. Am. Soc. Civil Engrs*, ASCE, 100.

Nehari, Z. 1952. *Conformal Mapping*. McGraw-Hill Book Company, New York, USA.

Pavlovsky, N. N. 1956. *Collected works*. Akad. Nauk, Leningrad, USSR.

Polubarinova Kochina, P. Ya. 1962. *Theory of Ground Water Movement*. Princeton University Press, Princeton, USA.

Terzaghi, K. & Peck, R. B. 1967. *Soil mechanics in engineering practice.* John Wiley and Sons, New York, USA.

River Flow 2004 – Greco, Carravetta & Della Morte (eds.)
© 2004 Taylor & Francis Group, London, ISBN 90 5809 658 0

The effect of migrating bedforms on local scour around bridge piers

M. Bolla Pittaluga, M. Maffei & G. Seminara
Dipartimento di Ingegneria Ambientale, Università degli Studi di Genova, Italy

ABSTRACT: In the present paper the interaction between the downstream migration of alternate bars and the local scour near bridge piers is investigated through experimental observations performed in the laboratory of the Department of Environmental Engineering of the University of Genova.

If the bridge does not have aprons, it is well known that a local scour is generated around the bridge piers at equilibrium, and its evaluation is usually performed on the basis of empirical relationships (e.g. Breusers et al. 1977), while the water level profile remains almost unaltered by the presence of the obstruction (Marchi 1996). To the authors' knowledge there is scarce information concerning the interaction between water flow and piers when small bedforms (dunes) or large bedforms (alternate bars) migrate through the bridge piers. We then focus our attention on the effect of bedform migration on the intensity of local pier scour.

Experiments are performed on various settings with pier models constraining the cross section of streams flowing on erodible beds where bedforms are initially allowed to develop. Bedform migration and its interaction with bridge piers is carefully monitored by means of a profile indicator placed at the head of the bridge pier and performing periodic surveys of bed topography by means of a laser system.

1 INTRODUCTION

The prediction of the maximum expected scour around bridge piers is, needless to say, of great practical relevance. Underestimation of the scour depth and of its areal distribution results in design of too shallow foundations which can get exposed to the flow creating safety problems in terms of bridge stability. Great difficulties are sometimes experienced in restoring pier foundations which got exposed to the flow. On the other hand, overestimation of the scour depth results in uneconomical design. Several mechanisms are known to be responsible for scouring processes in rivers, such as lateral channel migration, long-term degradation, narrowing of the river cross section, bedform migration, interaction between flow fields and obstructions like bridge piers or abutments, insufficient sediment supply, etc. In the present context our attention is focused on the estimation of the local scour at bridge piers due to the non linear interaction between two of the scour mechanisms mentioned above, namely the local scour due to the horseshoe vortex flow around the piers and bedform migration. It is well known that the system of horseshoe vortex and associated downflow at the pier are the main agents responsible for the local scour at bridge piers. Several contributions can be found in the literature on the detailed study of the latter process, notable among them Laursen and Toch (1956), Baker (1981), Raudkivi & Ettema (1983), Chiew & Melville (1987), Graf & Yulistiyanto (1998).

Similarly, several empirical and semi-empirical relationships have been proposed to estimate the maximum local scour at bridge piers or abutments, see for instance Shen et al. (1969), Melville & Sutherland (1988), Melville (2001), HEC-18 (U.S. Federal Highway Administration, 2001). Some of them also propose approximate criteria to account for the effect of bedform propagation on the maximum local scour.

Actually, the available knowledge on the effect of bedform migration on scour prediction relies heavily on the pioneering work of Shen et al. (1969), where two formulas to evaluate the equilibrium depth of scour were reported: the former by Breusers (1965) linking the scour depth to the pier width, the latter by Larras (1963) basically adding a multiplicative factor to account for the pier shape. In Shen et al.'s experiments the effect of dune migration on the equilibrium depth of scour was investigated leading to the suggestion that adding half the expected height of dunes to the estimated equilibrium scour depth for plane bed is a safe procedure to evaluate the maximum expected depth. In fact, according to the above authors, dunes affect the equilibrium scour depth by a simple additive effect whereby scour is increased as the dune trough crosses the scour hole and viceversa it is decreased as the crest passes through. Note, however,

that laboratory data of Shen et al. (1969) suggest that the latter criterion overestimates the effect of dunes. Due to the lacking of both theoretical and experimental investigations of the effects of bedforms other than dunes, the above recommendation has been extended to the case of different kinds of bedforms like alternate bars (Melville & Coleman, 1999). In spite of the fairly wide knowledge of the main mechanisms responsible for the formation and development of alternate bars (e.g. Colombini et al., 1987, Seminara & Tubino, 1989, Schielen et al., 1993, Repetto et al., 1999, Repetto et al., 2002, Federici & Seminara, 2003), to our knowledge the effect of such bedforms on the scour induced near obstructions like bridge piers or abutments is, surprisingly, completely ignored. The importance of the latter phenomenon (presumably much more relevant in terms of maximum expected scour depths) is ever increasing as river regulation works, widely pursued in the last few decades, have led to an increased presence of large scale migrating bedforms in regulated rivers. Though in the case of dunes experimental observations suggest that the interaction between scour depths are at most additive, one may reasonably wonder whether a similar behaviour is to be expected in the case of different bedforms such as alternate or central bars.

The laboratory experiments we have performed were indeed aimed at reaching some insight on the latter phenomenon and, possibly, suggesting corrections of design recommendations based on the experimental observations. In particular we wished to monitor the effects of the propagation of an alternate bar pattern on the intensity and spatial distribution of the local pier scour, depending on the relative position of the bridge piers in the cross section.

It will be shown in Section 3 that the interaction between the horseshoe vortex, the main agent responsible of local pier scour, and the migration of alternate or central bars through bridge piers may lead to oscillations of the local scour which can be easily linked from a qualitatively point of view to the migration of bar fronts. However, it turns out that the effect of the interaction is non linear, in other words it cannot be simply evaluated using a procedure similar to that suggested by Shen et al. (1969) for the case of dune migration.

The rest of the paper is organized as follows. A brief description of the experimental apparatus and the experimental technique used is given in the next Section. Section 3 reports the experimental results while some discussion and final remarks conclude the paper.

2 EXPERIMENTAL SET UP

2.1 *Experimental apparatus*

Experiments have been conducted in the laboratory of the Department of Environmental Engineering of the University of Genova in a rectangular straight flume with length $L_C = 18\,\text{m}$, width $2B = 0.6\,\text{m}$ and sidewalls consisting of steel frames with plexiglass windows. The flume is filled with nearly uniform sediment characterized by a mean diameter $d_{50} = 1.2\,\text{mm}$ and a density $\rho_s = 2650\,\text{kg/m}^3$. Sediments are initially placed on the bottom of the flume in order to give rise to a uniform bed slope.

The water entering the upstream end of the flume is supplied by a pump connected to an underground water tank and controlled by an electronic valve. A differential manometer is used to measure the flow discharge entering the flume. The stream flow is also fed with a solid discharge in open loop. The sediment load is controlled by a mechanical device such to provide a sediment supply equal to the transport capacity of the uniform flow for given water discharge and bed slope. At the downstream end of the flume the water and sediment mixture are filtered by a sediment trap catching 100% of the sediment passing through. The clear water is then collected in a tank connected to the underground water tank.

2.2 *Methods*

Every experiment consists of two parts. In the first part, starting from a flat bed, bedforms are generated and let develop until they reach a steady condition. Note that by steady conditions we mean that bedforms still migrate along the channel but display a nearly constant spatial envelope in time. During bedform growth, the bottom topography is scanned at different times by means of a laser system. Scanning is performed in a sequence of cross sections distant $0.1 \div 0.2\,\text{m}$ from one another. In each cross section measurements of bottom elevation are performed every 3 mm. The reach of the flume where measurements were taken ranges between $x = 5\,\text{m}$ and $x = 15\,\text{m}$. Note that the origin of the longitudinal axis is located at the outlet cross section and the positive x-direction points upstream. The upstream limit of the measuring reach ($x = 15\,\text{m}$) is determined by the constraint that about 3 meters are required for the supplied sediment to spread all over the entire cross section. Moreover, the choice of the downstream limit of the measuring reach ($x = 0.5\,\text{m}$) is imposed by the size of the moving carriage where the laser system is placed. Once the equilibrium state is obtained, the bottom topography is again measured and the bridge pier(s) is (are) placed into the flume.

In the second part of the experiment the interaction between bedform migration and the local scour at bridge pier is analyzed by monitoring the evolution of bottom elevation at a fixed location by means of a profile indicator. The probe of the latter is placed in a position as close as possible to the head of the bridge pier. In fact, the local scour around bridge piers attains its maximum value just upstream the pier itself. The experiment is usually terminated when at least one

Table 1. Summary of experimental conditions.

EXP.	Q (l/s)	i_f%	Y_0 (mm)	U_0 (m/s)	Q_s (kg/min)	θ	β	β_{CR}
U0520	3.9	0.5	20	0.32	0.026	0.051	14.9	3.5
U0530	7.9	0.5	30	0.42	0.617	0.076	9.9	8.9
U0526	6.2	0.5	26	0.38	0.323	0.066	11.4	6.5

complete bedform has crossed the bridge. Finally, the bottom topography is scanned once again by means of a laser system in order to ascertain whether the presence of the bridge has significantly affected the bedform pattern.

A summary of the experimental conditions is reported in Table 1. Here Q denotes water discharge, i_f is the initial slope of the channel, Y_0 is the average flow depth, U_0 is the cross sectionally averaged flow velocity, Q_s is the total sediment discharge, θ is the average Shields stress acting on the bottom, β is the aspect ratio (more precisely half width over depth) and β_{CR} is its critical value above which alternate bars form (Colombini et al. 1987).

Some preliminary experiments (Table 1) have been performed in order to find the most appropriate conditions for the formation of alternate bars. In the first run (U0520) a mixed alternate-central bar pattern formed at the beginning of the experiment, amplified until bars emerged and eventually stopped migration. This experimental condition was then not suitable to investigate the effect of the interaction of such bedforms with bridge piers. Moreover, as the Shilelds stress was quite close to its threshold value for sediment motion, the time scale of bottom evolution was very large. In the second run (U0530) the aspect ratio of the stream was very close to its critical value for bar formation, hence the bedforms were quite unstable alternating periods of growth with periods of decay. In the third run (U0526) the most appropriate conditions were found: alternate bars formed and reached an equilibrium condition in a time scale of the order of few hours ($3 \div 4$ h).

Three tests have then been conducted under the latter conditions:

- in the first test one bridge pier was placed close to the sidewalls of the flume (U0526_PL)
- in the second test two bridge piers were placed symmetrically with respect to the longitudinal axis of the flume (U0526_PS)
- in the third test one bridge pier was placed along the longitudinal axis of the flume (U0526_PC)

3 EXPERIMENTAL RESULTS

3.1 *The formation of alternate bars*

As mentioned above, the first part of the experiment was devoted to the generation of bedforms until they reached an equilibrium condition. The Figures 1 and 2 show the typical evolution of the bed pattern in the channel at different times, showing the growth and migration of alternate bars in the experiment U0526. Note that the differences between the patterns observed after 4 and 6 hours are relatively small, hence we assumed that the configuration reached after 4 hours was at equilibrium. The distinctive features of free bars are summarized in Table 2, where L_b denotes bar wavelength, H_{BM} is the bar height defined as difference between the maximum and the minimum elevations within a bar unit, c_b is the bar wavespeed estimated by comparison of the longitudinal bed profiles measured at different times and x_b is the longitudinal coordinate of the position of the bar front.

Note the spatially growing character of the bar envelope arising in particular in the pattern of bottom topography after 4 or 6 hours which shows that an equilibrium bar amplitude may have been reached in the downstream part of the flume. Also note that the value of the bar height farthest from the inlet is fairly close to the values predicted by the non linear theory of Colombini et al. (1987) and to the empirical formula given by Ikeda (1984) (Table 3). In Table 3, the values of the dimensionless maximum scour depths measured relative to the average bottom elevation s_M/H_{BM} are also reported and show the asymmetry of the bars over the cross section.

3.2 *Local scour at bridge piers: brief literature survey*

Before discussing the experimental results concerning the interaction between the local scour at bridge piers and bedform migration, it may be worthwhile to give a brief summary of the state of the art. As mentioned in the Introduction, the estimate of bridge scour relies heavily on the work of Shen et al. (1969) in which two formulas to evaluate the equilibrium depth of scour are reported. Breusers (1965) suggested, for cylindrical piers, that:

$$\frac{d_{se}}{b} = 1.4 \tag{1}$$

where d_{se} is the equilibrium scour depth and b is the pier width. A second relationship, which accounts for

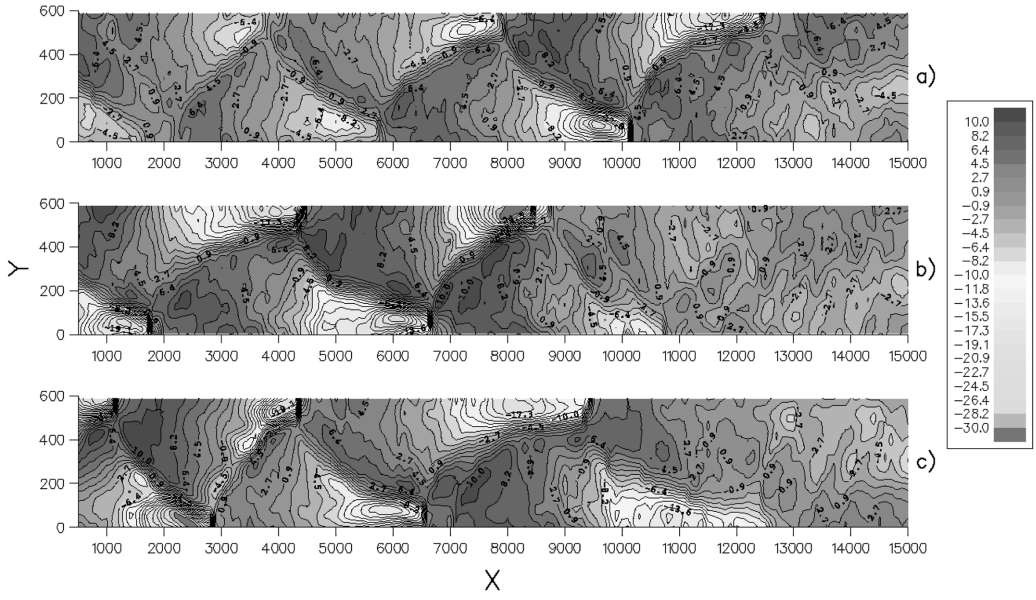


Figure 1. The pattern of bottom topography in the channel at different times, showing the growth and migration of alternate bars. The initial bottom elevation has been filtered out. Scales are in millimeters. Flow is from right to left. (a) t = 2 h; (b) t = 4 h; (c) t = 6 h.

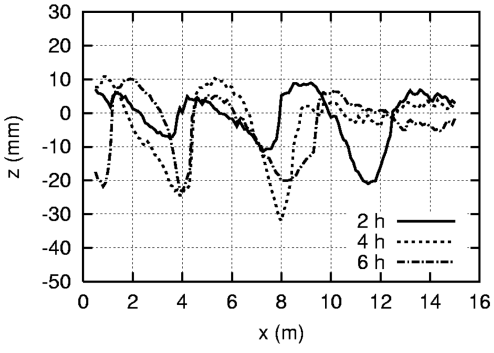


Figure 2. Longitudinal bed profiles (at a distance of 64 mm from the right sidewall) measured at different times, showing the growth and migration of alternate bars. The initial bottom elevation has been filtered out. Scales are in millimeters. Flow is from right to left.

pier shape is due to Larras (1963) and reads:

$$\frac{d_{se}}{b} = 1.42 \cdot K \cdot b^{-0.25} \qquad (2)$$

where the coefficient K depends on the shape of the pier.

The effect of dunes on the equilibrium scour depth was also investigated and led to the recommendation

Table 2. Free bar characteristics.

Time (h)	x_b (m)	L_b (m)	H_{BM} (mm)	c_b (m/h)
2.0	12.6	4.6	36	–
	8.0	4.2	23	–
4.0	12.8	4.1	19	1.95
	8.7	4.3	46	1.80
6.0	9.4	5.0	32	2.15
	4.4	3.2	46	1.60

Table 3. Free bar heights and dimensionless maximum scour depths at equilibrium.

	H_{BM}(mm)	s_M/H_{BM}
Experiment	46	0.71
Colombini et al.	38	0.57
Ikeda (84)	40	0.5

that adding one half of the expected dune height to the equilibrium scour depth leads to a safe estimate of the maximum expected depth.

Other factors affect the scour depth. In particular, Breusers et al. (1977) proposed the following equation:

$$\frac{d_{se}}{b} = 2 \cdot \tanh\left(\frac{Y_0}{b}\right) \cdot f_1 \cdot f_2 \cdot f_3 \qquad (3)$$

where Y_0 is the undisturbed flow depth and the coefficients f_1, f_2 and f_3 depend on the ratio of the undisturbed average flow speed and its critical value for sediment motion, on pier shape and on the angle of attack, respectively.

An integrated approach to estimate the local scour depth at bridge foundations has also been presented by Melville (2001). The approach is based on empirical relations, termed K-factors, that account for the effects on scour depth of flow depth and foundation size, flow intensity, sediment characteristics, foundation type, shape and alignment, geometry of the approach channel. The K-factors are evaluated by fitting envelope curves to existing data. Following Melville (2001), at equilibrium the local scour at a bridge foundation can be evaluated by the following relationship:

$$\frac{d_{se}}{b} = K_{yW} \cdot K_I \cdot K_d \cdot K_s \cdot K_\theta \cdot K_G \cdot \qquad (4)$$

where the various K's are empirical expressions accounting for the effects of various factors on scour depth: K_{yW} (flow depth); K_I (flow intensity); K_d (sediment size); K_s (pier or abutment shape); K_θ (pier or abutment alignment); K_G (channel geometry). This method does not give any direct information concerning the possible influence of bedform migration on scour depth which, however, are likely to be included in the existing data used by Melville to fit his envelope curve (4).

3.3 *Local scour with plane bed*

A rectangular bridge pier, characterized by a width $b = 110$ mm, length of 300 mm and round nose, was aligned with the channel axis.

A first run has then been conducted in order to determine the equilibrium scour depth experienced with plane bed under the same hydraulic conditions (U0526) in which the tests with bedforms were later conducted.

Figure 3 shows a comparison between the experimental value of the equilibrium scour depth ($d_{se} =$ 66 mm) and the predictions of different empirical predictors, namely the equation of Breusers et al. (1977) and the approach of Melville (2001). Using a value for the pier shape coefficient f_2 equal to 1 (round nosed pier) the Breusers et al.'s relation underestimates the maximum scour depth ($d_{se} = 51$ mm) which is highly overestimated by Melville's formula ($d_{se} = 107$ mm).

3.4 *Interaction between bedforms and bridge piers*

Once the pattern of bottom topography has reached a steady condition, the bridge pier(s) is (are) placed into the flume. Three different configurations for the bridge

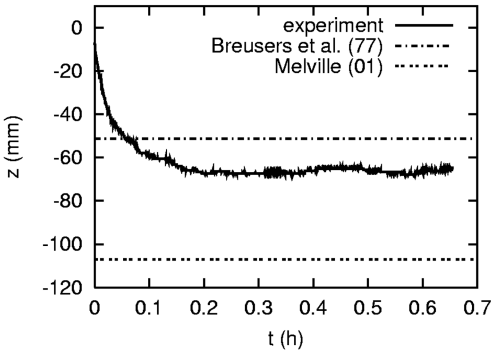


Figure 3. The time evolution of the bottom elevation under plane bed condition is compared with the equilibrium values predicted by Breusers et al.'s (1977) and Melville's (2001) formulas. The origin of the vertical z axis is located at the initial bottom elevation.

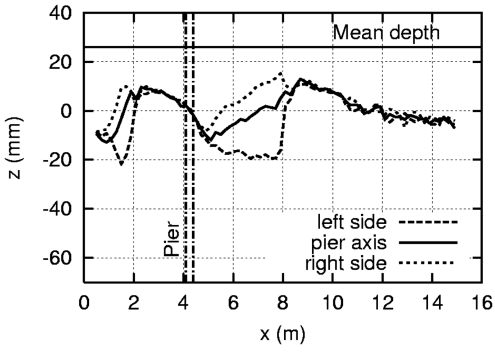


Figure 4. Longitudinal cross sections of the bottom aligned with the axis and with the two sides of the bridge pier just before the latter was placed in the flume (experiment U0526_PL). The origin of the z axis lies on the initial bottom.

piers have been investigated under the same hydraulic conditions.

3.4.1 *Lateral bridge pier (experiment U0526_PL)*

Figure 4 shows three longitudinal cross sections of the bottom observed just before the pier was placed in the flume: the cross sections were aligned with the position of the pier axis and with the two sides of the bridge pier. The axis of the pier was located at a distance of 135 mm from the right sidewall. Note that the pool of the alternate bar approaching the bridge pier is located roughly 3 m upstream the pier and exhibits a relative scour with respect to the mean bottom elevation of 20 mm.

The time evolution of the bottom elevation due to the interaction between the bar migration and the local scour at the pier is shown in Figure 5. The

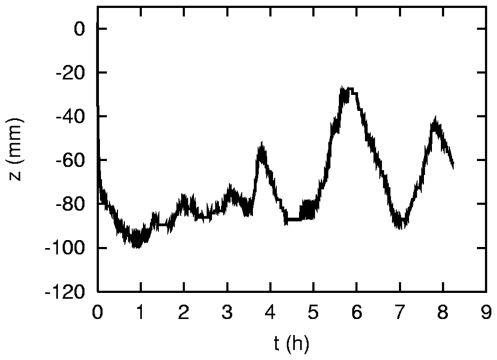


Figure 5. The time evolution of the bottom elevation ahead of the bridge pier in experiment U0526_PL shows the effect of bar migration through the bridge. The origin of the z axis lies on the initial bottom.

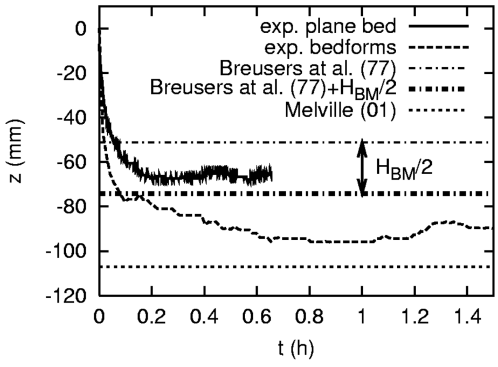


Figure 6. Comparison between the bottom elevation ahead of the bridge pier measured under plane bed conditions and in the presence of bars (U0526_PL) and the values predicted by different empirical formulas. The origin of the vertical z axis lies on the initial bottom.

oscillations due to bar migration are easily detectable when Figure 5 is compared to the case of plane bed (Figure 3). Note that the scour depth is strongly affected by the migration of bedforms and exhibits a peak ($d_{se} = 98$ mm) considerably greater than the one observed in the case of plane bed ($d_{se} = 66$ mm).

A comparison between the values predicted by the above mentioned formulas and the experimental values is reported in Figure 6, which also includes the estimate obtained by adding half the bar height ($H_{BM}/2 = 23$ mm) to the value predicted by Breusers et al. (1977).

This first experiment shows clearly that the interaction between the horseshoe vortex and the migration of alternate bars through the bridge piers leads to oscillations of local scour which reach a peak that cannot be simply evaluated superimposing the two effects.

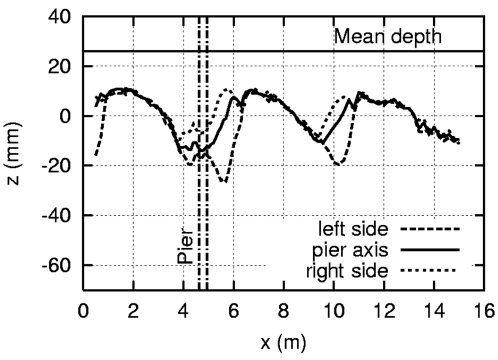


Figure 7. Longitudinal cross sections of the bottom aligned with the axis and with the two sides of the left bridge pier just before the two piers were placed in the flume (experiment U0526_PS) The origin of the z axis lies on the initial bottom.

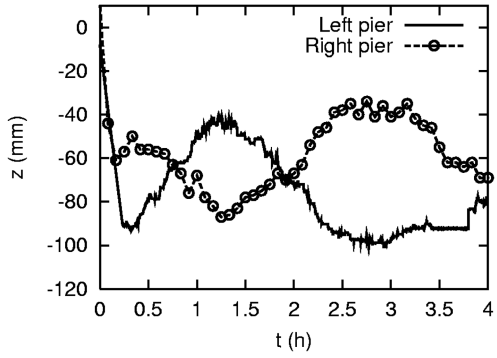


Figure 8. The time evolution of the bottom elevation ahead of each bridge pier in experiment U0526_PS shows the effect of bar migration through the bridge. The origin of the z axis lies on the initial bottom.

3.4.2 *Two symmetric bridge piers (experiment U0526_PS)*

The effect of the migration of alternate bars on local scour at piers is even more detectable in the test in which two bridge piers were located at symmetric positions close to the sidewalls of the flume. The axis of each pier was placed at a distance of 135 mm from the closer sidewall. Figure 7 shows three longitudinal cross sections of the bottom observed just before the pier was placed in the flume: the cross sections were again aligned with the position of the pier axis and with the two sides of the bridge pier. Note that the maximum scour of the alternate bar approaching the left pier is located very close to the pier and reaches a peak of 24 mm relative to the mean bottom elevation.

The feedback of bar migration on local scour is then shown in Figure 8 where the alternance of scour and deposition at the two piers is clearly detected.

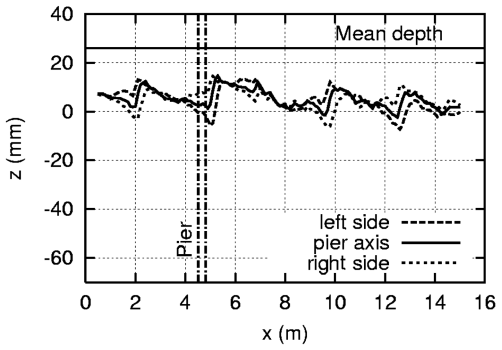


Figure 9. Longitudinal cross sections of the bottom aligned with the axis and with the two sides of the bridge pier just before the latter was placed in the flume (experiment U0526_PC). The origin of the *z* axis lies on the initial bottom.

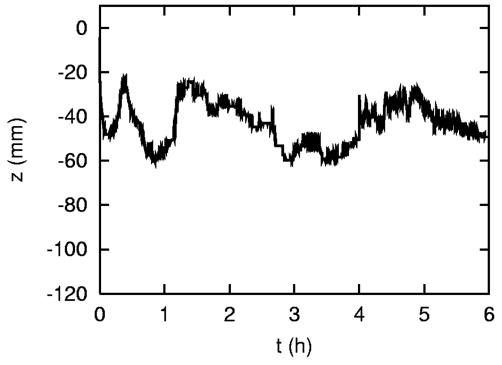


Figure 10. The time evolution of the bottom elevation ahead of each bridge pier in experiment U0526_PC shows the effect of bar migration through the bridge. The origin of the *z* axis lies on the initial bottom.

Also note that comparing Figure 8 with Figure 5 shows that the maximum scour depth is not affected by the number of piers placed in the flume.

3.4.3 *Central bridge pier (experiment U0526_PC)*
In the next experiment the bridge pier was aligned with the channel axis in order to investigate to what extent the relative position of the pier in the cross section affects the scour and deposit driven by the migration of alternate bars. The longitudinal cross sections of the bed aligned with the axis and with the two sides of the bridge pier just before it was placed into the flume are shown in Figure 9. Note that, in this case, the bottom elevation close to the pier exhibits smaller oscillations mostly associated with deposit rather than scour.

As expected, the time evolution of the local scour ahead of the pier (Figure 10) displays oscillations which are characterized by a peak similar to that observed in the case of plane bed and by an amplitude much greater than the amplitude of the approaching alternate bars.

It is also worth pointing out that the pattern of alternate bars was not significantly affected by the presence of the obstruction (Figure 11). In particular, at least in the absence of bridge aprons, the presence of a constriction does not stop bar migration.

4 DISCUSSION AND CONCLUSIONS

The preliminary experimental observations described in Section 3 allow us to draw some tentative conclusions.

(i) The morphodynamic interaction between migrating bars and bridge piers leads to a non linear enhancement of the scour induced by the classical horseshoe mechanism.
(ii) The migration speed of bars as well as the bar pattern are not significantly affected by the presence of the piers.
(iii) The usual design recommendations which suggest to account for the effect of bedforms by simply adding half the bedform height to the estimated scour depth require some warning, at least for cases where the bridge piers are aligned with the pools of migrating bars.

The source of nonlinearity of the morphodynamic interaction is partly due to the strongly asymmetric lateral bed profile typical of migrating bars, which makes the maximum scour s_M associated with the bar larger than half the bar height ($H_{BM}/2$) (Fig. 12).

Moreover and more significantly, Breusers et al's equation (3) suggests that the scour depth is strongly correlated with the undisturbed flow depth Y_0. When a bar pool reaches the pier front, the effective depth to be employed in equation (3) is the sum of the undisturbed stream flow depth plus the maximum bar scour. One readily realizes that this leads to a non linear enhancement of the scour predicted by equation (3). In particular for shallow flows, i.e. for values of Y_0/b sufficiently small, equation (3) predicts that d_{se} is proportional to twice the local flow depth, hence:

$$d_{se} \approx 2(Y_0 + s_M) >> 2Y_0 + H_{BM}/2 \qquad (5)$$

The latter argument is clearly demonstrated in Figure 13, which shows that, applying equation (3) with Y_0 replaced by $(Y_0 + s_M)$ leads to a prediction for the scour depth much closer to the observed value.

The error associated with the additive procedure increases as the flow depth decreases (or the pier width increases) and may become fairly small for very thin piers.

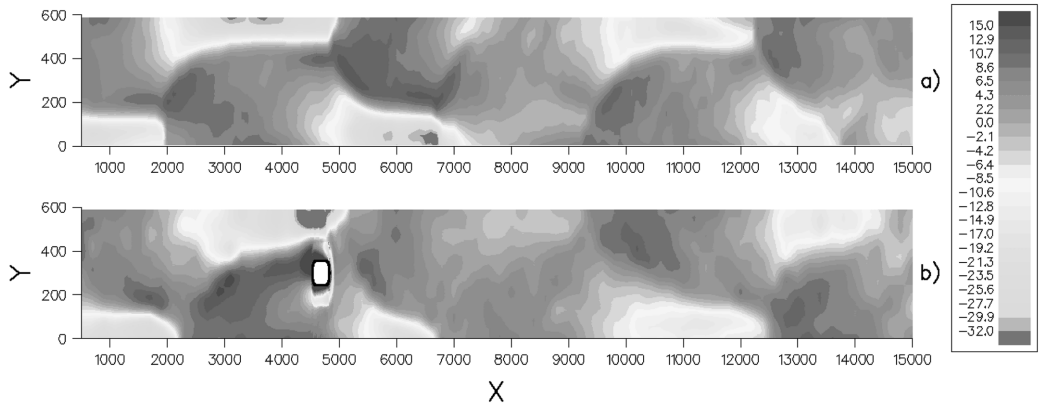


Figure 11. The pattern of bottom topography in the channel at different times, showing that alternate bars are not significantly affected by the presence of the obstruction. The initial bottom elevation has been filtered out. Scales are in millimeters. Flow is from right to left. (a) t = 4 h; (b) t = 8 h.

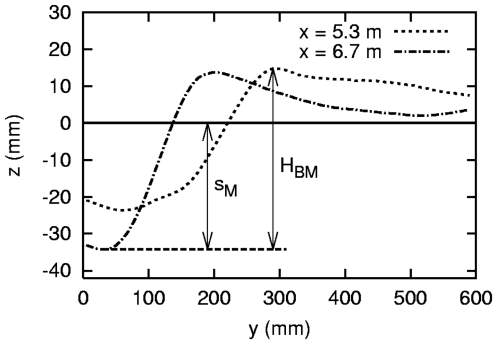


Figure 12. Lateral bed profiles at the bar pool and bar front are plot, showing asymmetry leading to the maximum scour s_M associated with the bar being larger than half the bar height ($H_{BM}/2$) (experiment U0526_PL).

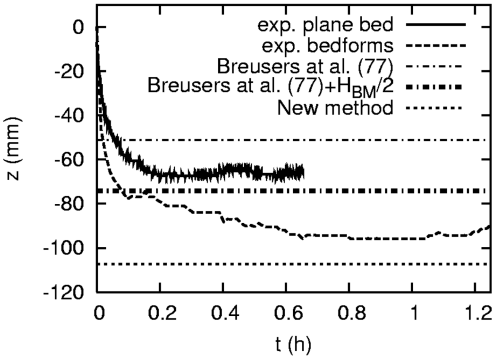


Figure 13. Comparison between the bottom elevation ahead of the bridge pier measured under plane bed conditions and in the presence of bars (U0526_PL) and the values predicted by Breusers et al's (1977) relationship corrected either adding $H_{BM}/2$ or applying equation (3) with Y_0 replaced by $(Y_0 + s_M)$. The origin of the vertical z axis lies on the initial bottom.

Needless to say, the above results will have to be substantiated by a wider experimental investigation, examining the effects of multiple row bars, pier alignment, transport in suspension, etc.

Moreover, the basic idea arising from our results will deserve further thoughts concerning the interaction of bend scour with abutment scour of bridges crossing meander bends.

ACKNOWLEDGMENTS

This work has been funded by the Italian Ministry of University and of the Scientific and Technological Research under the National Projects PRIN 2002/2003 "Safety and control of masonry bridges", "Morphodynamics of fluvial network" and cofunded by the University of Genova. Partial support has also come from Fondazione Cassa di Risparmio di Verona, Vicenza, Belluno ed Ancona under the Project RIMOF.

REFERENCES

Baker, C.J. 1981. New design equation for scour around bridge piers. *Journal of the Hydraulic Division, A.S.C.E.*, Vol. 107, HY-4.

Breusers, H.N.C. 1965. Scour around drilling platforms. *Bulletin, Hydraulic Research 1964 and 1965*, I.A.H.R., Vol. 19, pp. 276.

Breusers, H.N.C., Nicollet, G. & Shen, H.W. 1977. Local scour around cylindrical piers. *Journal of Hydraulic Research*, Vol. 15, 3: 211–252.

Chiew, Y.M. & Melville, B.W. 1987. Local scour around bridge piers. *Journal of Hydraulic Research, I.A.H.R.*, Vol. 25, No.1.

Colombini, M., Seminara, G. & Tubino, M. 1987. Finite-Amplitude Alternate Bars. *J. Fluid Mech.*, 181: 213–232.

Federici, B. & Seminara, G. 2003. On the convective nature of bar instability. *J. Fluid. Mech*., 487, pp. 125–145.

Graf, W.H. & Yulistiyanto, B.M. 1998. Experiment on flow around a cylinder, the velocity and vorticity fields. *Journal of Hydraulic Research, I.A.H.R.*, Vol. 36, No. 4, pp. 637–653.

HEC-18, 2001. Evaluating scour at bridges. *Hydraulic Engineering Circular No. 18, Federal Highway Administration (FHWA)*, USDOT, Washington, D.C.

Ikeda, S. 1984. Prediction of alternate bar wavelength and height. *Journal of Hydraulic Engineering, A.S.C.E.*, Vol. 110, No. 4, pp. 371–385.

Marchi, E. 1996. Interventi per ridurre l'effetto di un restringimento (pile di ponti o altre ostruzioni). Atti del *XXV Convegno di Idraulica e Costruzioni Idrauliche*, Torino.

Melville, B.W. & Sutherland, A.J. 1988. Design method for local scour at bridge piers. *Journal of Hydraulic Engineering, A.S.C.E.*, Vol. 114, No. 10, pp. 1210–1226.

Melville, B.W. & Coleman, S.E. 1999. Bridge scour. *Water Resources Publications, LLC,* 572pp, ISBN 1-887201-18-1.

Melville, B.W. 2001. Pier and abutment scour: an integrated apporach. *Journal of Hydraulic Engineering, A.S.C.E.*, Vol. 123, No. 2, pp. 125–136.

Larras, J. 1963. Profondeurs maximales d'erosion des fonds mobiles autour des piles en riviere, *Annales des ponts et chaussees*, Paris, Vol. 133, No. 4, pp. 411–424.

Laursen, E.M. & Toch, A. 1956. Scour around bridge piers and abutments. Bull. No. 4, *Iowa Highway Research Board*, U.S.A., May.

Raudkivi, A.J. & Ettema, R. 1983. Clear-water scour at cylindrical piers. *Journal of the Hydraulic Division, A.S.C.E.*, Vol. 109, No. 10, pp. 338–350.

Repetto, R., Tubino, M. & Zolezzi, G. 1999. Free bars in rivers *J. Hydr. Res.*, 37(6): 759–775.

Repetto R., Tubino M. & Paola C., 2002. Planimetric instabilities of channels with variables width. *J. Fluid. Mech*., 457, pp. 79–109.

Schielen, R., Doelman, A. & de Swart, H.E. 1993. On the nonlinear dynamics free bars in straight channels. *Journal of Fluid Mechanics*, 252, pp. 325–356.

Seminara, G. & Tubino, M. 1989. Alternate bars and meandering: free, forced and mixed interactions. In *River Meandering*, edited by S. Ikeda and G. Parker, Water Res. Monogr., 12, AGU, Washington, D.C., 267–320.

Shen, H.W, Schnider, V.R. & Karaki, S. 1969. Local scour around bridge piers. *Journal of the Hydraulic Division, A.S.C.E.*, Vol. 95, No. HY6, pp. 1919–1940.

This page intentionally left blank

River Flow 2004 – Greco, Carravetta & Della Morte (eds.)
© 2004 Taylor & Francis Group, London, ISBN 90 5809 658 0

Experimental study of the scour hole downstream of bed sills

M. Ben Meftah
Water Engineering and Chemistry Department, Technical University of Bari, Italy

M. Mossa
Civil and Environmental Engineering Department, Technical University of Bari, Italy

ABSTRACT: An experimental study on long local scouring downstream of bed sills in monogranular sand bed was carried out in the hydraulic laboratory flume at the Mediterranean Agronomic Institute of Bari (Italy). The main objectives of this study are the determination of the scour hole dimensions, with its maximum scour depth, at the equilibrium stage, and the investigation of the influence of sills on the distribution of the three velocity components through the scour hole at the same stage. Four experimental configurations were tested, the main difference between them being the distance between sills. Based on experimental data, the classical dimensional analysis of the variables that influence the development of the scour hole has been carried out in order to obtain two empirical formulas predicting the maximum scour depth and the length of the scour hole at the equilibrium stage. Moreover, it was observed that the distance between sills influences the scour hole dimension and shape. The three velocity components of the flow, measured with an Acoustic Doppler Velocimeter (ADV), show that in the scour hole, at the equilibrium stage, the three-components of the flow turbulence intensities are very high. Near-bed flow vortexes in addition to secondary currents are also observed.

1 INTRODUCTION

The bed in the direct neighborhood of hydraulic structures is generally protected against current and eddies. The length of the bed protection depends on the permissible scour (maximum scour depth and upstream scour slope). When the length of the bed protection is increased, the scour process is less intense due to the decay of turbulence energy and the adaptation of the velocity profile downstream of the hydraulic structure. For a designer, the most important scour parameter is the maximum scour depth in the equilibrium phase, defined as the time when the scour hole and the bed profile spatial characteristics along the flume do not change any longer. Anyway, the extent of the scour hole is strongly dependent on time. Initially, the scour development with time is rapid, then it decreases gradually to reach the equilibrium stage after a long time. The magnitude of the maximum scour depth depends on the bed shear stress, the turbulence condition near the bed, the sediment characteristic (density of the bed material, sediment-size distribution, porosity, cohesive or non-cohesive bed material, etc.).

In gravel bed rivers, bed sills are used to limit bed degradation and to control erosion in the proximity of bridge piers or in channels downstream of stilling basins of dams. There is extensive literature on scour (Borman, 1988; Breusers, 1966; Habib et al., 1994; Hoffmans et al., 1995; Hoffmans and Verheig, 1997; Hoffmans, 1998; Javal and Kenneth, 1985; Kandasany and Melville, 1998; Smith and Strang, 1967; Van der Meulen and Vinje, 1995).

In addition, the bed sill could have a number of impacts upon the flow velocity, and the impacts from the sill can vary spatially. Furthermore, the presence of the bed sill causes a redistribution of the flow velocity. It can decrease or increase the flow turbulence, create vortex phenomenon and/or secondary current velocity.

This study is concerned with an experimental investigation of the scour hole phenomenon due to a current flowing over sills in an erodible bed of sand particles. The variation of the scour hole with time, the equilibrium water and bed profiles, in addition to the three flow velocity components at different sections along the channel were assessed for each configuration. Two different scour hole topologies were observed, depending upon the distance between sills.

2 THEORETICAL BACKGROUND

Local scour hole is typical of non-cohesive bed river, downstream of the bed sills. After a long period of time the scour hole reaches an equilibrium state.

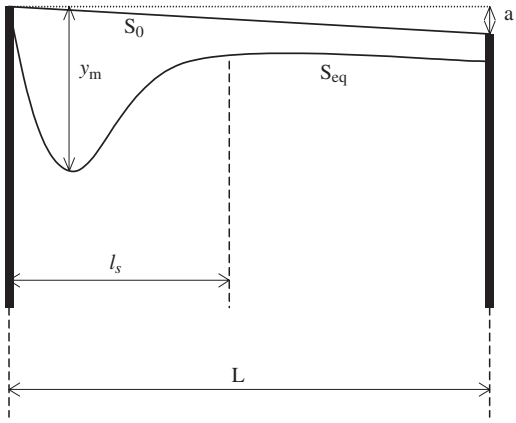


Figure 1. Sketch of the scour hole.

At the equilibrium, the geometry of the system under consideration is shown in Figure 1 (Gaudio et al., 2000).

Based on this geometric shape of the bed profile, the maximum scour depth y_m, or the scour length l_s, can be expressed as:

$$y_m \text{ or } l_s = f(g, \nu, \rho_w, \rho_s, q, h_u, d_{50}, L, a) \quad (1)$$

where g is the gravity acceleration, ν = kinematic water viscosity, ρ_w = water density, ρ_s = sediment density, q = discharge per unit width, h_u = flow depth over the sill, d_{50} = grain size for which 50% of the total weight of the sediment is finer, L = distance between sills, and a = difference between the level of two successive sills, a is calculated as:

$$a = L \cdot S_0 \quad (2)$$

where S_0 is the initial bed slope.

The application of the *Buckingham* Π *theorem* to equations (1) leads to:

$$\frac{y_m}{h_u} \text{ or } \frac{l_s}{h_u} = f\left(\frac{q^2}{gh_u^3\Delta}, \frac{q}{\nu}, \frac{\Delta d_{50}}{h_u}, \frac{L}{h_u}, \frac{\Delta a}{h_u}\right) \quad (3)$$

where:

$$\Delta = \frac{\rho_s - \rho_w}{\rho_w}. \quad (4)$$

The $q^2/gh_u^3\Delta$ ratio is the square of the Froude number Fr, and the q/ν ratio is the Reynolds number. Generally, in open-channels, the flow is almost always fully turbulent. Thus, the dependence upon the Reynolds number could be neglected. Since the parameter a is determined as the product of the distance between sills L and the initial bed slope S_0, the ratio L/h_u can be removed from equations (3). Furthermore, the effect of the channel width is here implicitly neglected by choosing variables per unit width. In addition, in the present study sand grains have an almost constant value of the relative submerged particle density, Δ, equal to about 1.65. Because of this constancy, the effect of Δ is not shown in the present study.

According to these simplifying assumptions, equations (3) can be reduced to:

$$\frac{y_m}{h_u} \text{ or } \frac{l_s}{h_u} = f\left(\frac{q^2}{gh_u^3\Delta}, \frac{\Delta d_{50}}{h_u}, \frac{\Delta L S_0}{h_u}\right) \quad (5)$$

The determination of equations (5) was one of the main objectives of the present paper.

3 EXPERIMENTAL SET-UP

The experimental work was carried out in a horizontal flume in the laboratory of the Mediterranean Agronomic Institute of Bari (Italy). This flume is 7.72 m long, 0.30 m wide, and has a depth of 0.40 m. The floor of the flume is constructed with Plexiglas, while the lateral walls are made of glass, which allows us better side viewing of the flow. Water is fed in from an upstream reservoir with a maximum charge of 54 cm equipped with stilling grid and lateral weir, which maintains a constant head upstream of a movable gate constructed at the upstream end of the flume. This gate is made of Plexiglas and allows the passage of different discharges with different corresponding channel flow depths. The flume is supplied by a pump with maximum discharge of 24 l/s through a steel pipe. To create a smooth flow transition from the upstream reservoir to the flume, a wooden ramp was placed at the inlet of the flume; the wooden ramp is 1.55 m long, 0.15 m thick and has the same width of the channel cross section (Figure 2).

At the downstream end of the flume, water is intercepted by a stilling reservoir, equipped with three vertical grids to stabilize water, and a triangular weir (V-notch sharp crested weir) to measure the flow discharge.

To protect against erosion of the sand bed of the flume, control sills were placed along the channel. Four sets of tests were performed during the experimental work, the difference between them being the distance (L) between sills (Set 1: L = 1 m; Set 2: L = 2 m; Set 3: L = 4 m; Set 4: L = 3 m). The sill level decreases progressively going from the upstream section to the downstream section of the channel, respecting a constant initial slope fixed at the value of 0.0086. The sills used in the experiments consisted of PVC plates 0.30 m wide and 0.01 m thick (Figure 1).



Figure 2. Laboratory flume.

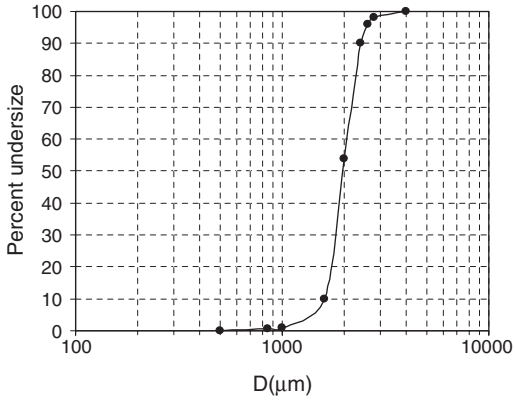


Figure 3. Grain-size distribution curve.

The flume bottom is covered with an erodible bed material layer consisting of sand particles with mean average size (d_{50}) of 1.8 mm and specific density of 2.65 g/cm^3. The grain-size distribution curve of the sand is illustrated in Figure 3. The uniformity coefficient $C_u = d_{60}/d_{10}$ was equal to 1.6, where d_{60} = grain size for which 60% of the total weight of the sediment is finer and d_{10} = grain size for which 10% of the total weight of the sediment is finer. Thus, the sediment can be considered as uniform. Along the channel, the sand layer decreases progressively from the upstream sections to the downstream sections, respecting the initial slope predetermined by the sills.

During the experiments, the bed profile along the channel at various times was marked on the glass sidewalls of the flume by means of different colors. At the equilibrium stage, the water level profile along the centerline was measured using an electrical hydrometer with an accuracy of 1/10 of millimeter. At the same stage, the bed profiles along the centerline and near the two side-walls of the channel were determined using a point gage with an accuracy of 1/10 of millimeter.

Table 1. Main parameters of each test.

No.	Test	Q (m^3/s)	q (m^2/s)	L (m)	t_d (h)	T (°C)
1	T04	0.006	0.021	1	25	13
2	T05	0.010	0.033	1	29	15
3	T06	0.005	0.015	1	25	15
4	T07	0.012	0.039	1	26	16
5	T08	0.008	0.027	1	27	19
6	T09	0.006	0.021	2	27	19
7	T10	0.006	0.027	2	24	20
8	T11	0.010	0.033	2	27	21
9	T12	0.012	0.044	2	27	22
10	T13	0.014	0.046	2	26	23
11	T14	0.006	0.020	4	25	25
12	T15	0.008	0.027	4	25	25
13	T16	0.010	0.033	4	25	26
14	T17	0.005	0.016	4	25	27
15	T18	0.005	0.015	3	25	27
16	T19	0.006	0.021	3	25	27
17	T20	0.008	0.027	3	25	27
18	T21	0.010	0.033	3	25	27
19	T22	0.012	0.040	3	25	27

In order to study the effects of the sill upon the flow velocity at the equilibrium, the measurements of the three-velocity components along the flume at different positions have been recorded during this experimental work, using an Acoustic Doppler Velocimeter (ADV).

The main parameters of the tests are illustrated in Table 1, where, Q = flow discharge through the channel, T = water temperature, and t_d = total duration of each test.

During all the experimental work, the measurement of the flow depth over sills, h_u, the maximum scour depth, y_m, and the length of the scour hole, l_s, were assessed for each test. The flow depth over a sill was measured as the vertical distance between the top of the sill and the water profile. The maximum scour depth was determined as the vertical distance between the initial bed profile and the center of the scour hole at the equilibrium stage. The scour length was determined as the distance between the sill and the point downstream of the scour hole where the slope reaches a constant value. The aforementioned variables are shown in Table 2. For tests T04 to T08, the scour hole occupied all of the space between the sills, and, therefore, l_s was not determined.

4 RESULTS

4.1 *Scour hole progress*

Examining all the tests, it has been shown that the extent of the scour hole is strongly dependent on time.

Table 2. Measured variables.

No.	Test	y_m (m)	h_u (m)	l_s (m)
1	T04	0.039	0.03	(*)
2	T05	0.088	0.054	(*)
3	T06	0.028	0.026	(*)
4	T07	0.105	0.062	(*)
5	T08	0.064	0.043	(*)
6	T09	0.053	0.035	1.2
7	T10	0.057	0.042	1.3
8	T11	0.070	0.054	1.6
9	T12	0.081	0.063	1.8
10	T13	0.090	0.070	2.0
11	T14	0.076	0.032	1.4
12	T15	0.090	0.043	1.7
13	T16	0.112	0.054	2.1
14	T17	0.065	0.027	1.1
15	T18	0.050	0.027	1.0
16	T19	0.061	0.035	1.2
17	T20	0.071	0.043	1.4
18	T21	0.084	0.052	1.7
19	T22	0.094	0.062	2.0

(*)Quasi-parabolic shape of the scour hole.

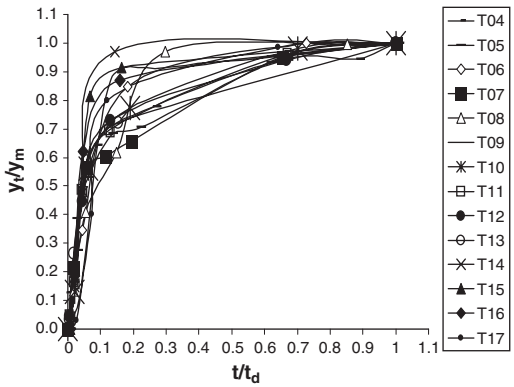


Figure 4. Similarity of scour holes evolution.

So, it was observed that there are three stages of the local scour hole development.

Initially, the scour hole development with time is rapid, and this is due to the high rate of solid transport achieved on the downstream end of each sill. The high rate of the solid transport is a consequence of the high forces of the bed-shear stresses exerted over the sand bed at the initial time. To study the different stages of the development of the scour hole as a function of the time for each test, and their similarity, the values of y_t/y_m have been plotted against t/t_d (where y_t is the scour hole depth at time t, and t_d, as written, is the duration of each experiment, i.e. the time when the scour hole reached the equilibrium phase). Figure 4 shows that the scour development as a function of time

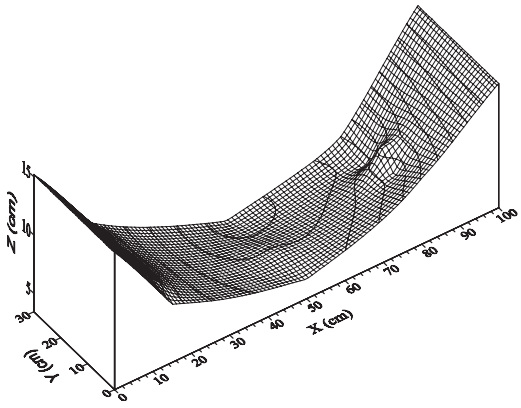


Figure 5. Quasi-parabolic shape.

presents three different phases. Figure 4 shows, as well, that at the initial stage the scour hole depth for each test reaches about 65% of the maximum scour depth during a time less than 10% of the duration after which the equilibrium stage was reached.

A second stage is characterized by an increase scour degree much smaller than the first stage. Figure 4 also shows that during this stage, the depth of the scour hole increases globally with a percentage of 25% of the maximum scour hole through a time estimated of 30% of the duration after which the equilibrium stage was reached. As is well known, the increase degree of y_t/y_m depends on the magnitude of the bed-shear stress. Therefore, it can be said that the shear stress acting over the bed reduces with the increase of the scour hole depth.

A final slow stage is that for which the scour achieves equilibrium after a long period of time. The equilibrium phase was assumed to be reached when no transport of sediment particles is observed along the channel. Figure 4 indicates that the bed deformation or the scour hole evolution is extremely slow during this stage. It can be observed that, during a time more than 60% of the duration after which the equilibrium stage was reached, the scour depth increases only with a value around 10% of the maximum scour depth.

4.2 *Scour hole shape*

According to the experimental results, it was observed that the scour hole shape depends strongly upon the distance between sills. It was seen that during the first set of tests with an interval length equal to 1 m, the scour hole shape is quasi-parabolic. An example (T05) of a three-dimensional scour hole is shown in Figure 5. This configuration is characterized by a scour hole which occupies all of the space between sills. It was also observed that the scour hole dimensions were

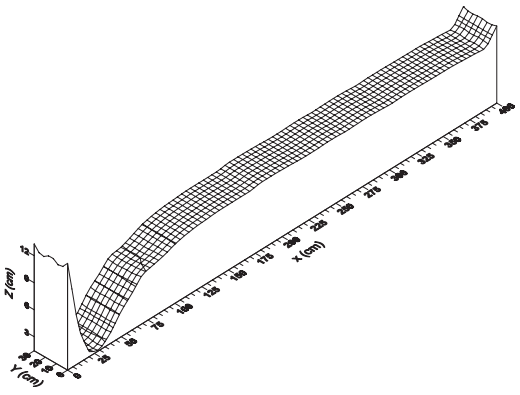


Figure 6. "Spoon" shape.

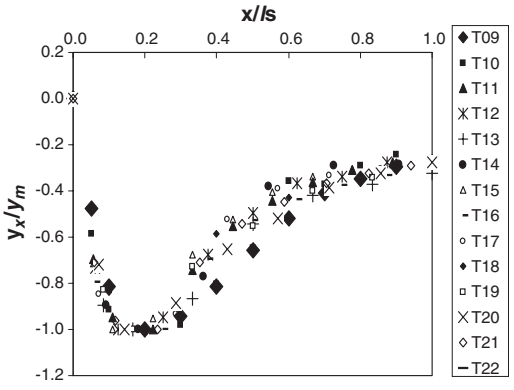


Figure 7. Similarity of the scour profiles.

influenced by the proximity of sills, especially when the flow discharge is elevated.

Furthermore, when the interval length between sills is large such as in the cases of the second, the third and fourth sets of tests, which have an interval of 2 m, 4 m and 3 m, respectively, the scour hole shape is similar to a "spoon" profile. An example (T16) of a three-dimensional scour hole profile is shown in Figure 6.

To study the similarity of the scour profile, the values of y_x/y_m at the equilibrium stage have been plotted against x/l_s, for T04 to T22, as shown in Figure 7 and Figure 8. y_x and y_m are the depth of the scour hole at the longitudinal distance x (x = 0 m at the upstream sill position) and the maximum scour depth at equilibrium phase, respectively.

Figure 7 indicates that the scour profiles for T09 to T22 are similar in nature. This result is in agreement with the findings of other authors for other scouring processes (Chatterjee et al., 1994, Gaudio et al., 2000). Furthermore, and according to the experimental results, it can be noted that the scour hole profiles

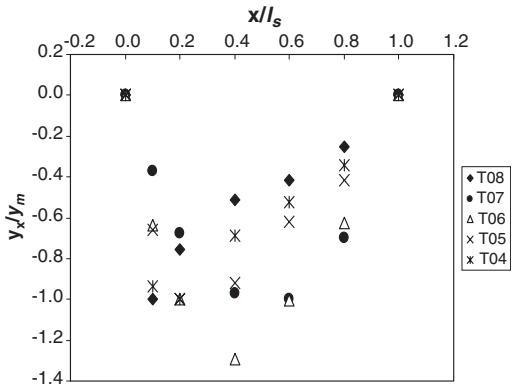


Figure 8. Non-similarity of the scour profiles.

Table 3. Non-dimensional parameters.

No.	Test	y_m/h_u	$q^2/\Delta g h_u^3$	$\Delta LS_o/h_u$	$\Delta d_{50}/h_u$	l_s/h_u
1	T04	1.142	0.676	0.417	0.087	(*)
2	T05	1.627	0.423	0.261	0.055	(*)
3	T06	1.085	0.855	0.556	0.116	(*)
4	T07	1.701	0.403	0.230	0.048	(*)
5	T08	1.481	0.574	0.330	0.069	(*)
6	T09	1.525	0.665	0.822	0.086	22.792
7	T10	1.343	0.586	0.673	0.070	23.862
8	T11	1.295	0.423	0.523	0.055	22.784
9	T12	1.287	0.398	0.453	0.047	22.346
10	T13	1.287	0.375	0.405	0.042	22.173
11	T14	2.386	0.722	1.773	0.093	18.325
12	T15	2.102	0.574	1.320	0.069	18.805
13	T16	2.065	0.421	1.043	0.055	18.683
14	T17	2.453	0.850	2.142	0.112	16.923
15	T18	1.898	0.788	1.606	0.112	19.881
16	T19	1.767	0.668	1.233	0.086	19.672
17	T20	1.663	0.597	0.997	0.070	19.718
18	T21	1.606	0.468	0.814	0.057	20.238
19	T22	1.516	0.407	0.687	0.048	20.957

(*)Quasi-parabolic shape of the scour hole.

for the first set of tests (with a distance between sills of 1 m) are not similar in nature, as shown in Figure 8. This is due to the strong influence of the distance between sills for this configuration. Thus, it should be noted that when the length of the scour hole is comparable to the distance between sills, "the sills interfere" with the development of the scour (Gaudio et al., 2000).

4.3 *Scour hole dimensions at equilibrium stage*

The non-dimensional parameters for the experimental work discussed here have been determined for each test and illustrated in Table 3. Recall that over a sill with a small thickness, the depth of the flowing

Table 4. Values of h_u and h_c.

No.	Test	h_u (m)	h_c (m)	r (%)
1	T04	0.034	0.035	3.23
2	T05	0.054	0.048	6.96
3	T06	0.026	0.029	11.19
4	T07	0.062	0.054	7.46
5	T08	0.043	0.042	1.22
6	T09	0.035	0.036	2.06
7	T10	0.042	0.042	0.82
8	T11	0.054	0.048	8.73
9	T12	0.063	0.054	10.18
10	T13	0.070	0.060	11.48
11	T14	0.032	0.034	2.51
12	T15	0.043	0.042	0.86
13	T16	0.054	0.048	5.53
14	T17	0.027	0.030	4.86
15	T18	0.027	0.029	4.83
16	T19	0.035	0.036	1.86
17	T20	0.043	0.042	0.29
18	T21	0.052	0.048	5.13
19	T22	0.062	0.054	8.21
	Average			5.13

water fluctuates around the critical flow depth. A comparative study between the flow depth over sills, h_u, measured during the experimental work and the critical flow depth, h_c, calculated for each test is presented in Table 4. It can be seen that the maximum rate of variation between the measured and calculated flow depth (indicated by r%) is 11.48% and the minimum is 0.29%. The average variation for all tests is 5.13%, which is considered very small. Thus, the flow depth over sill can be estimated with the formula of the critical flow depth, h_c:

$$h_u \approx h_c = \left(\frac{q^2}{g}\right)^{1/3} \tag{6}$$

According to these simplifying assumptions, equations (5) can be reduced to:

$$\frac{y_m}{h_u} \text{ or } \frac{l_s}{h_u} = f\left(\frac{\Delta LS_0}{h_u}\right) \tag{7}$$

The plot of y_m/h_u versus $\Delta LS_0/h_u$ for the tests of the scour hole which are similar in nature, as shown in Figure 9, indicates that all the points fall approximately on a single line. So, the linear regression of these points leads to the first of equations (7) to become:

$$\frac{y_m}{h_u} = 0.714\,\frac{\Delta LS_0}{h_u} + 0.989\ . \tag{8}$$

This equation is valid for $0.405 \le \Delta LS_0/h_u \le 2.142$, with a correlation coefficient $R^2 = 0.88$.

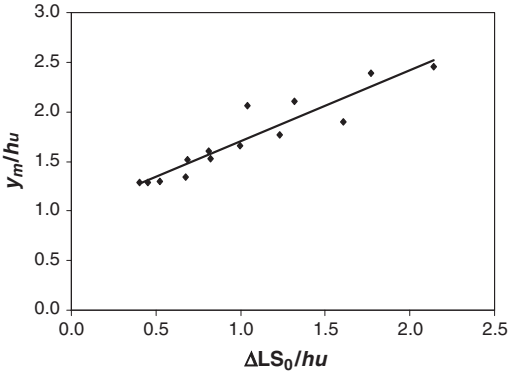


Figure 9. Correlation of the y_m/h_u ratio with $\Delta LS_0/h_u$ ratio.

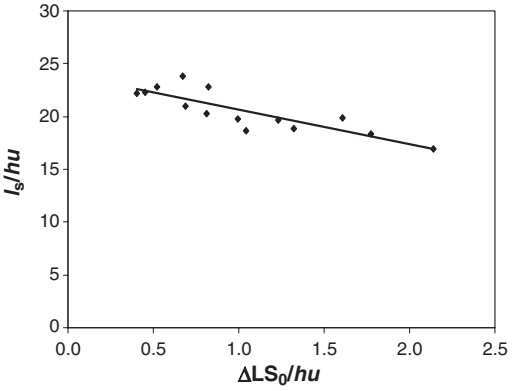


Figure 10. Correlation of the l_s/h_u with $\Delta LS_0/h_u$.

The plot of l_s/h_u against $\Delta LS_0/h_u$ of the same tests, as shown in Figure 10, leads to the following relationship:

$$\frac{l_s}{h_u} = -3.27\,\frac{\Delta LS_0}{h_u} + 23.90\ . \tag{9}$$

This equation is valid for $0.405 \le \Delta LS_0/h_u \le 2.142$, with a correlation coefficient $R^2 = 0.71$.

4.4 *Flow characteristics through the scour hole*

During all the experimental runs, it was observed that, at the equilibrium stage, the sediment particles through the bed scour hole move in a random fashion without leaving it. In order to study the causes of this observation, measurements of the flow velocities along the scour hole were taken. An example (T16) of flow velocity vector field obtained along the centerline of the channel is shown in Figure 11. The velocity vectors are the resulting mean velocities of the vertical and stream-wise velocity components.

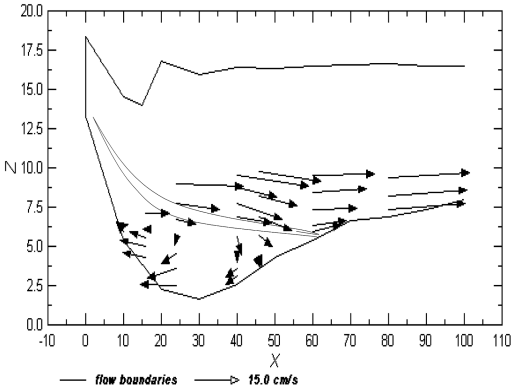


Figure 11. Flow motion along the second scour hole with x in cm and z in cm.

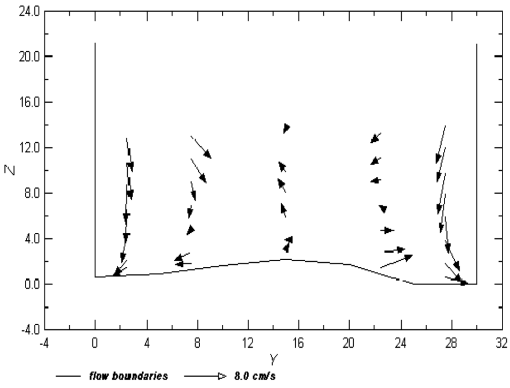


Figure 12. Secondary flow in the cross section at x = 75 cm from the second sill with y in cm and z in cm.

This figure indicates that the stream is very turbulent near the scour hole bed; however, it is smoother and more orderly going toward the free-surface flow and downstream of the equilibrium bed hole. In addition, Figure 11 shows that, near the bed of the scour hole, flow rotationality and vortex trends occurred. Near the free surface the flow is assumed monodirectional due to the dominance of the stream-wise velocity.

4.5 *Secondary currents*

It has long been established in academic literature that flow in alluvial rivers is strongly three-dimensional (Peters and Goldberg, 1989). The secondary currents were originally defined by Prandtl (1952) as currents, which occur in the plane normal to the axis of the primary flow. They originate from interactions between the primary flow and gross channel features.

The measurements of the flow velocity along different cross sections of the channel were determined during this experimental work. An example (T13) of the resulting mean velocities of the span-wise and vertical velocities along the transversal centerline of the scour hole is presented in Figure 12. This figure clearly indicates that there is a development of cells of secondary currents through the central cross-section of the scour hole. These secondary currents consisted of two symmetrical cells of helical rotation located near the sidewalls of the channel. The presence of these secondary currents have a direct influence upon the transversal bed profile of the scour hole, resulting in the development of a sand ribbon in its center.

4.6 *Turbulence intensity*

The three-components of the flow turbulence index are defined as the ratio of the standard deviation of the stream-wise, span-wise and vertical velocity

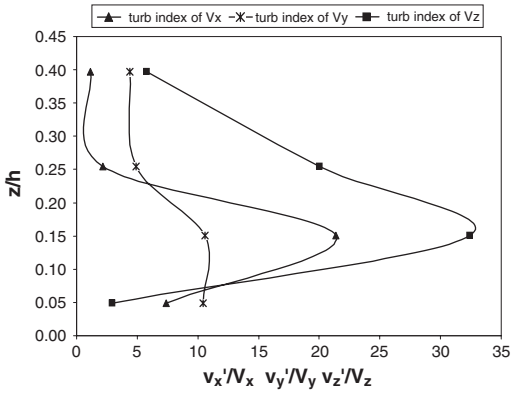


Figure 13. Flow turbulence intensity.

fluctuation v'_x, v'_y, and v'_z, by the relative flow velocity average V_x, V_y, V_z, respectively. The plot of these components against z/h (z is the distance from the channel bottom and h is the flow depth in the section analyzed), an example (T12) is shown in Figure 13, indicates that the flow turbulence, near the bed of the scour hole, is very intensive, as shown in Figure 13, at z/h = 0.05, the turbulence index of the stream-wise and vertical velocity has a value of 7 and 2.5, respectively, increases extensively to reach the value of 20 and 37 for z/h = 0.15, and decreases gradually to reach the value of 1 and 6 for z/h = 0.4. The results of Figures 12 and 13 explain why the motion of the sediment particles is in a random fashion without leaving the scour hole location at the equilibrium stage.

5 CONCLUSIONS

Four sets of tests were conducted in the hydraulic laboratory of the Mediterranean Agronomic Institute of

Bari to predict long term local scour at bed sills. One uniform sediment was used respecting a constant initial bed slop of 0.0086. The experiments show the following results.

The extent of the scour hole is strongly dependent on time. Three stages of the local scour hole development were observed: an initial rapid stage, a progressive stage, and a final decelerated stage.

The scour hole shape depends strongly upon the distance between sills. Two forms of the scour hole were discovered, i.e. a quasi-parabolic shape occurred with a small distance and a shape similar to a "spoon" profile occurred with large distances. The scour profiles are similar in nature for a large distance between sills, but, not similar for a small distance.

Using classical dimensional analysis, the maximum scour depth and the length of the scour hole at the equilibrium stage were articulated as a function of non-dimensional parameters. According to some logical simplifying assumptions, two empirical formulas (8) and (9) were determined to predict the maximum scour depth, y_m, and the length of the scour hole, l_s, respectively. The maximum scour depth and the length of the scour hole depend strongly upon the distance between sills.

The bed sills lead to a redistribution of the flow velocity and a flow rotationality. Intensive flow turbulence and vortex trends occurred in addition to secondary currents in the center of the scour hole.

ACKNOWLEDGEMENTS

The research described and the results presented herein were obtained from an experimental study on long local scouring downstream of bed sills in monogranular sand bed conducted in the hydraulic laboratory of the Mediterranean Agronomic Institute of Bari in 2002.

REFERENCES

Borman, N.E. 1988. Equilibrium Local Scour Depth Downstream of Grade Control Structures. *Ph.D. Dissertation*. Colorado State University. Fort Collins, CO.

Breusers, H.N.C. 1966. Conformity and time scale in two-dimensional local scour. *Proc. Symposium on model and prototype conformity, 1–8.* Hydraulic Research laboratory. Poona (also Delft hydraulics, Delft, Publication 40).

Chatterjee, S.S., Ghosh, S.N. & Chatterjee, M. 1994. Local scour due to submerged horizontal jet. *Journal of hydraulic engineering ASCE* 120(8): 973–991.

Gaudio, R., Marion, A. & Bovolin, V. 2000. Morphological effects of bed sills in degrading rivers. *Journal of hydraulic research* 38(2): 89–96.

Habib, E., Mossa, M. & Petrillo, A. 1994. Scour downstream of hydraulic jump. conference papers. *The international journal on hydropower & dams, modelling, testing & monitoring for hydro. Plants,* Budapest, Hungary: 591–602.

Hoffmans, G.J.C.M. & Krystian, W. Pilarczyk 1995. Local scour downstream of hydraulic structures. *Journal of hydraulic engineering ASCE* 121(4): 326–339.

Hoffmans, G.J.C.M. & Verheij, H.J. 1997. *Scour manual*. A.A. Balkema, Rotterdam, Brookfield.

Hoffmans, G.J.C.M. 1998. Jet scour in equilibrium phase. *Journal of hydraulic engineering ASCE* 124(4): 430–437.

Farhoudi, J. & Smith, K.V.H. 1985. Local scour profiles downstream of hydraulic jump. *Journal of hydraulic research* 23(4): 343–358.

Kandasany, J.K. & Melville, B.W. 1998. Maximum scour depth at bridge piers and abutments. *Journal of hydraulic research* 36(2): 183–197.

Peters, D.D. & Goldberg, A. 1989. Flow data in large alluvial channels. In Maksimovic and Radojkovic (eds). *Computational modeling and experimental methods in hydraulics*. Elsevier, London.

Prandtl, L. 1952. *Essentials of fluid dynamics*. Blackie, London. 452pp.

Smith, C.D. & Strang, D.K. 1967. Scour in stone bed. *Proceedings of the Twelfth Congress of the International Association for Hydraulic Research*. Fort Collins, CO. September 11–14, 1967. Colorado State University. Vol. 3: 65–73.

Van der Meulen, T. & Vinje, J.J. 1995. Three-dimensional local scour in non-cohesive sediments. *Proc. 16th IAHR-congress*. Sao Paulo, Brasil (also Delft Hydraulics, Delft Publication 180).

River Flow 2004 – Greco, Carravetta & Della Morte (eds.)
© 2004 Taylor & Francis Group, London, ISBN 90 5809 658 0

Influence of laterally placed side weirs on bed-load transport in a prismatic channel

B. Rosier, J.L. Boillat & A. Schleiss
Laboratory of Hydraulic Constructions (LCH), Swiss Fed. Inst. of Technology, Lausanne, Switzerland

ABSTRACT: Lateral side weirs on channels are widely used in irrigation and flood regulation. They are installed at the bank along the main-channel with the purpose to divert or spill in a controlled manner water over their crest when the water level in the channel exceeds a certain limit. This lateral loss of water is responsible for the reduction of sediment transport capacity in the main-channel by decreasing the bottom shear stress. This yields to the formation of sediment deposits which raise the bed level locally. As a consequence, the design discharge to be diverted over the side weir is increased. By the help of an experimental setup the physical processes in the main-channel and on the side weir were analyzed systematically. The test series confirm the processes mentioned above. These processes are strongly transient showing a tendency towards an equilibrium state of the river bed.

1 INTRODUCTION

The content of the present paper results from the multidisciplinary flood protection research project *DIFUSE* (**Di**gues **Fu**sibles et **S**ubmersibl**e**s, Fuse plugs and overflow dams at rivers) involving governmental offices,[1] private companies[2] and four research institutes. The task of the research institutes is to establish design criteria for fuse plugs (Ecole d'ingénieurs de Fribourg, *EIF*), to investigate the stability of submerged river dykes including scouring at the toe (Ecole d'ingénieurs du canton Vaud, *EIVD*) and to study the effects of a side overflow on sediment transport in a natural channel. The latter is treated by the *Laboratory of Hydraulic Constructions (LCH)* and topic of this paper.

The particular objectives of the *LCH* contribution to this work is to collect experimental data which can be used to conduct a non-dimensional parameter analysis to predict the hydraulic behaviour of the diverting weir. Combined with a photogrammetrical approach, the purpose is to determine river bed changes and to find empirical relationships. Furthermore, the collected data serves as main-input to generate a 3D numerical model in order to analyze the effects mentioned above in detail and to widen the application range from the simplified conditions of the physical model to more general cases.

A better understanding of the process of sediment transport in a channel with lateral overflow will allow to develop and to provide appropriate design criteria for the engineer. This regards the residual risk and optimized geometric alignment for the side weir guaranteeing a sufficient bed-load transport capacity in the main-channel.

From the total amount of 12 test series performed, the process of data collection, data analysis as well as results are described and discussed in detail for one individual experiment.

2 THEORETICAL CONSIDERATIONS

2.1 *Flow equation for side weirs*

The equation of spatially varied flow for outflow over a weir on a fixed bed is (Borghei et al. 1999 & Singh et al. 1994):

$$\frac{dy}{dx} = \frac{S_0 - S_f - \left(\frac{\alpha Q}{gA^2}\right)\left(\frac{dQ}{dx}\right)}{1 - \left(\frac{\alpha Q^2 B}{gA^2}\right)} \qquad (1)$$

where y = depth of flow in main-channel; x = longitudinal direction; S_0 = bottom slope; S_f = energy slope;

[1] Office Fédéral des Eaux et de la Géologie (OFEG), Berne; Service des Routes et Cours d'Eau du canton du Valais (SRCE), Sion.
[2] Hydronat SA, Vétroz; Etablissement Cantonal d'Assurances des Bâtiments (ECAB), Fribourg.

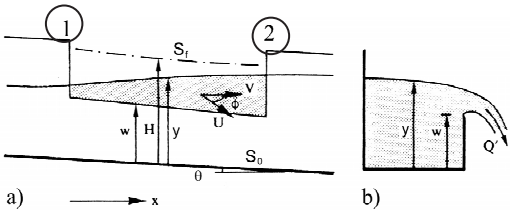


Figure 1. Definition sketch: a) longitudinal section; b) cross section.

α = kinetic energy correction coefficient; A = cross section area of the flow; and B = channel width (Fig. 1).

From the constant specific energy concept ($S_0 - S_F = 0$), and $\alpha = 1$, the general equation of weirs can be written as follows:

$$q = -\left(\frac{dQ}{dx}\right) = C_d \frac{2}{3}\sqrt{2g}\; h^{3/2} \tag{2}$$

and from the specific energy equation, the following equation is obtained:

$$Q = B\, y\sqrt{2g\,(E-y)} \tag{3}$$

where q = discharge per unit length over the weir; C_d = discharge coefficient; g = acceleration due to gravity; h = measured head above the crest; and $E = y + Q^2/2gA^2$ = specific energy. Substituting (2) and (3) in (1), integrating the resultant equation and arranging for C_d, De-Marchi introduced the discharge coefficient as follows (Chow 1973):

$$C_d = \frac{3B}{2L}\left(\phi_2 - \phi_1\right) \tag{4}$$

where L = effective length of the weir crest between sections 1 and 2 (Fig.1); and ϕ = varied flow function, expressed as:

$$\phi = \frac{2E-3w}{E-w}\sqrt{\frac{E-y}{y-w}} - 3\sin^{-1}\sqrt{\frac{E-y}{E-w}} \tag{5}$$

where w = height of the weir. Knowing the flow conditions at sections 1 and 2 and the geometrical configuration of the weir, the discharge coefficient C_d can be obtained.

Further, from dimensional analysis:

$$C_d = f\left(F_1, \frac{w}{y_1}, \frac{L}{y_1}\right) \tag{6}$$

where F_1 = upstream Froude number in the main channel. For the constant specific energy concept, C_d is assumed to be independent of L, hence (6) reduces to:

$$C_d = f\left(F_1, \frac{w}{y_1}\right) \tag{7}$$

The variation of parameters appearing in Equation 7 can be measured experimentally. Several relationships relating C_d to these parameters have been developed (Borghei et al. 1999).

2.2 *Sharp-crested weir*

The sharp-crested side weir is not only a measuring device for open channel flow but also the simplest form of overflow spillway. Using the general equation of weirs (2), the discharge over a sharp-crested weir can be expressed by (Naudascher 1992):

$$Q = C_q\, L\, \frac{2}{3}\sqrt{2g}\; h^{3/2} \tag{8}$$

where C_q = discharge coefficient for sharp-crested weirs.

According to the well-known weir formula of Rehbock, the coefficient C_q in Equation 8 is approximately (Naudascher 1992):

$$C_q = 0.61 + 0.08\frac{h}{w} \tag{9}$$

Measurements by Rouse (1957) indicate that this equation holds up to $h/w = 5$ but can be extended to $h/w = 10$ with fair approximation (Chow 1973).

3 EXPERIMENTAL MEASUREMENTS

3.1 *Experimental setup*

The tests were conducted in a rectangular 2.0 m wide, 30 m long and 1.2 m deep flume existing at the *LCH*. The flume was subdivided longitudinally into two separate channels by a vertical 0.9 m high smooth wall. The first channel, being 1.5 m wide, represents the actual testing facility including the mobile bed and the side weir on the right river bank. The second one, 0.47 m wide, constitutes a lateral channel permitting to evacuate the laterally diverted discharge. A general layout of the experimental setup is shown in Figure 2.

3.2 *Tested parameters and sediment characteristics*

In order to determine the influence of lateral overflow on bed-load transport, the main-channel discharge including flood hydrographs, diverted discharge,

channel slope, length of the lateral weir crest, number of weirs and sill height were considered as test parameters.

Table 1 gives an overview of the whole range of test series. In the present paper, experiment B02 is discussed in detail.

The channel facility originally possesses a horizontal slope. The bottom slope for each experiment is created by adjusting the mobile bed to the requested slope. The mean thickness of the sand layer is 0.24 m. The bed material used in all tests consists of sand having a mean diameter $d_m = 0.75$ mm (Fig. 3).

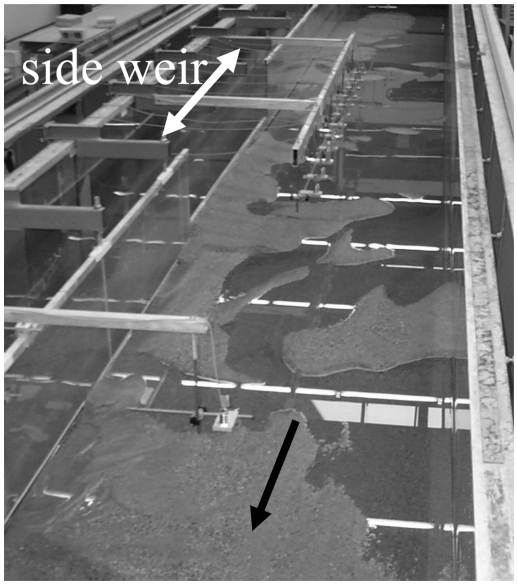


Figure 2. General view of the test facility with the main channel, the lateral side weir, the mobile bed and the excavation channel.

3.3 *Measuring procedure*

Sediment has been fed into the upstream end of the flume via a conveyer belt which has been calibrated before. The quantities to be supplied have been estimated according to the formula of Smart & Jäggi 1983. Sediment fed was adjusted during the test in order to maintain a constant water level for a certain discharge in the uniform flow stretch at the upstream end of the flume.

The upstream discharge was delivered by the use of three pumps feeding one pipe controlled by an electromagnetic flow meter. A steady flow rate could therefore be easily set and maintained accurately throughout the duration of each test. The diverted discharge was measured by a standard sharp-crested weir installed in the excavation channel.

Water depth along the main-channel as well as on the sharp-crested weir in the lateral channel were recorded continuously with a frequency of one measurement per second by the use of an ultrasonic gauge (voltage between 0 and 10V). The voltage was transformed into a distance to a reference level located

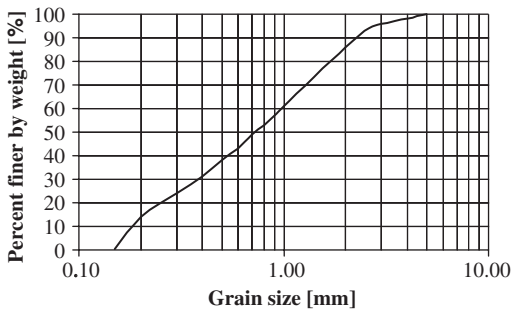


Figure 3. Grain size distribution curve for the bed material used in the tests ($d_m = 0.75$ mm).

Table 1. Overview of the test series and parameters studied.

No of test	No of weirs n_D	Length of weirs crest L [m]	Sill height w [m]	Flume slope S_0 [%]	Discharge Q [l/s]	Test duration t [h]
B01	1	3.0	0.10	0.2	150	2.25
B02	**1**	**3.0**	**0.10**	**0.2**	**210**	**2.0**
B03	1	3.0	0.10	0.4	190	2.0
B04	1	3.0	0.10	0.1	120	2.25
B05	1	3.0	0.10	0.2	180	2.1
B06	1	3.0	0.10	0.3	175	2.25
TdC01	2	2.5	0.09	0.1	117	2.25
TdC02	2	2.5	0.09	0.2	173	2.0
TdC03	2	2.5	0.09	0.3	220	2.0
TdC04	2	2.5	0.09	0.2	126	2.0
TdC05	2	2.5	0.09	0.2	220	2.0
D01	0	0.0	0.00	0.2	180	1.75

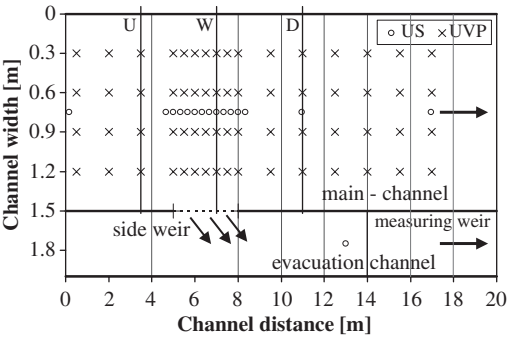


Figure 4. Definition sketch for measurement installation. US – water level recording, UVP – velocity measurement, U – cross section Upstream, W – Weir and D – Downstream respectively.

at the crest of the side weir. The error of the level measurement is less than 1 mm (average $\pm$ 0.5 mm). Altogether 15 ultrasonic gauges were installed longitudinally in the centre line of the channel, one located upstream of the side weir, 12 in the reach of the side weir (every 0.33 m), two downstream of the weir and one upstream of the measuring weir in the excavation channel (Fig. 4).

Velocities were measured with an Ultrasonic Doppler Velocity Profiler (Metflow SA, Model UVP-XW) allowing to obtain instantaneously a 1D-velocity profile over the whole channel depth (Metflow 2000). For each 1D-profile, 128 data points in time were recorded with a spatial resolution of 128 points over flow depth. Eight probes, each inclined by 25°, were mounted on a measuring frame fixed on a traversing beam whereof four probes were orientated in the longitudinal channel direction and four perpendicular to the main-channel axis, thus allowing to constitute a 2D velocity field. The used probes had an emitting frequency of 2 MHz. Velocity profiles were recorded every 30 minutes for 16 cross sections, whereof three were located upstream of the weir, seven in the array of the weir (every 0.5 m) and six in the downstream section of the channel (Fig. 4). The velocity measurements were also used to detect the bed. The surface was obtained from the signal for which the velocity as well as the variance were close to zero (Hersberger 2003).

3.4 *Analysis of the bed topography*

As far as the monitoring of the river bed topography is concerned, a photogrammetrical approach has been applied serving as a three-dimensional surface measurement tool. Digital photogrammetry is based upon automated analysis of digital imagery using the basic principle of the perspective projection. Two images of an object are acquired from two separate locations with known coordinates. If at least five points (photocontrol points) at known object locations are clearly visible on both images, a spatial resection can be carried out to derive the positions and orientations of the images. With the help of automated stereo matching, conjugate points can be identified and elevation coordinates are extracted (Geisler et al. 2003 & Lane et al. 2001).

For the present study five photographs with an overlap of 60% have been taken to cover the whole channel. This has been done for the initial flat bed situation and after each experiment for the final bed situation after controlled emptying of the channel. The camera was mounted at the gantry crane at about 6.5 m above the flume and 18 photocontrol points were distributed along the channel and in the laboratory. The orientation (position and aiming angles), triangulation and the creation of a digital terrain model (DTM) have been performed on the photogrammetric workstation DPW 750 by HelavaLeica running on Unix.

The program system used for the analysing process is called SocetSet. For the creation of the DTM a grid resolution of 2,5 $\times$ 2,5 cm has been chosen. A quality control feature for the automatic terrain extraction may indicate a successful automatic correlation or good measurement as well as the opposite. This tool is called Figure Of Merit (FOM) and gives a numerical value assigned by the terrain extraction process. FOMs are proportional to the average correlation coefficient, so in general the larger the number, the better the measurement. During the determination of the DTM some regions especially the crest of dunes showed a low average correlation coefficient. For this reason data points possessing a lower average correlation coefficient than 54 have been eliminated by the help of a macro written in Excel. The resulting “empty” DTM regions have been filled manually by so called brake lines provided by a geomorphic editor. This treatment leads to the final DTM used for analysis.

4 RESULTS

4.1 *Water level and diverted discharge*

Water level measurements reveal strongly transient processes. In Figure 5 the evolution of the water level for a cross section upstream (U), in the middle of the side weir (W) and downstream (D) (see Fig. 4) as well as for the sharp-crested side weir in the excavation channel are presented (time step 200 sec.). At the beginning of the experiment the water level over the measuring weir in the excavation channel rapidly increases corresponding to an increasing diverted discharge (Equation 8). With elapsing experiment time the level reaches a maximum before tending towards an almost constant value.

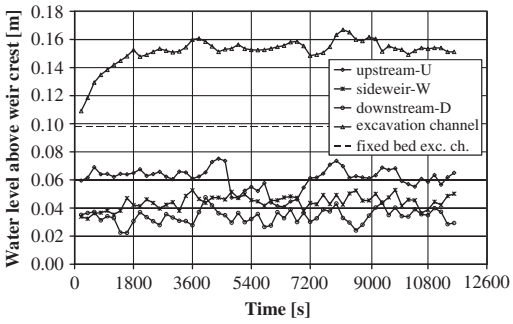


Figure 5. Time evolution of water level for cross-sections (U), (W) and (D). Furthermore the water level over the sharp-crested weir in the lateral channel is presented. The reference level is the side weir crest.

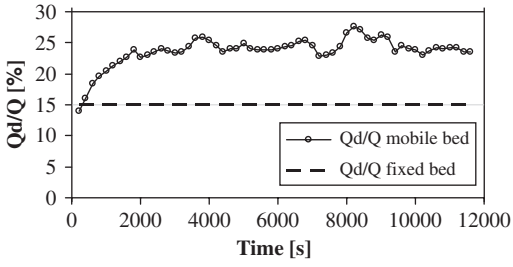


Figure 6. Time evolution of diverted discharge (Q_d) in percentage of total discharge (Q) introduced upstream ($Q = 210$ l/s).

Due to the passage of dunes, the evolution of the diverted discharge turns out to be oscillatory (Fig. 6). The diverted discharge amounts on average to 25% of the total discharge introduced. Compared to the diverted discharge for a fixed bed it can be noticed that the ratio diverted discharge/discharge is about 43% higher with a mobile bed.

4.2 *Velocities*

Qualitative velocity profiles in channel axis and perpendicular to the weir for three typical cross sections are plotted in Figure 7. For each cross section (U, W, D), a profile at the beginning and at the end of the test has been measured at 0.9 m channel width (Fig. 4).

As far as the profiles in flow direction are concerned, at the beginning of the experiment the velocity profile is almost homogenous to become quite disturbed in the weir alignment as well as in the downstream channel section. The distance to the free water surface is nearly equal for all profiles meaning that the water depth is almost similar for the three cross sections. From this, a regular and undisturbed formation of the bed level can be concluded. At the end of the test,

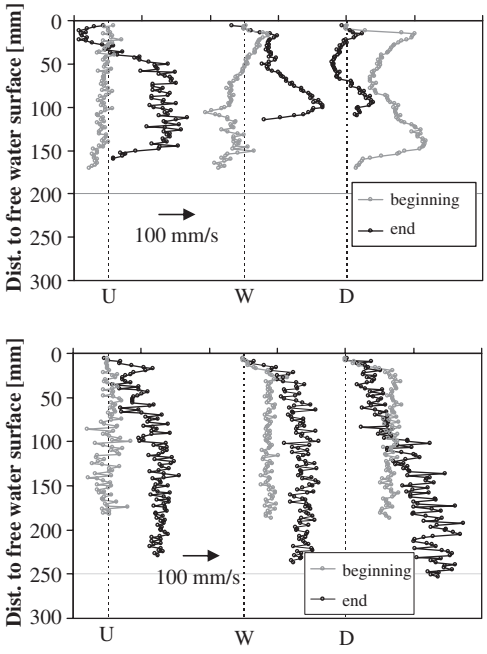


Figure 7. Velocity measurements parallel to channel axis (top) and perpendicular (bottom) for sections U, W and D (from left to right) at the beginning and the end of test run B02. Dashed line: $v = 0$ mm/s.

the velocity distribution is regular for the upstream part whereas further downstream irregularities are encountered. The distance to the free water surface decreases. Assuming a horizontal water surface level, the bed level has therefore increased.

The velocity profiles perpendicular to the weir are nearly constant over flow depth for the beginning of the test run. With elapsing time the velocity component towards the weir increases.

The velocity measurements have also been successfully used for the detection of the bed surface. Therefore the development of the bed over time can be determined, which is not possible with the photogrammetrical treatment since only the final bed situation can be measured. The information about the ground is less dense because only eight points for the eight probes are obtained instead of 1.5 m/0.025 m = 60 points from the photogrammetry. Nevertheless, it helps to get an idea about the development of the bed over time.

4.3 *River bed topography*

After introducing the flow to the prepared initial flat bed by a small discharge, a rapid change of bed roughness due to the formation of dunes appears. Upstream

of the side weir the dunes are of quite uniform character whereas in the reach of the weir and downstream the regular formation is clearly disturbed. In Figure 8 the bed after 2 hours experiment is presented. From the

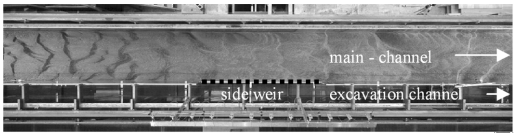


Figure 8. Bed topography after 2 hours test for run B02. The dashed black line shows the position of the side weir.

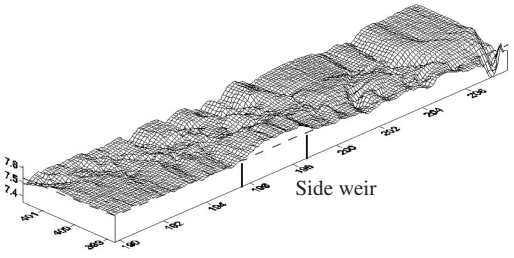


Figure 9. DTM of the final bed situation for the entire flume (flow from left to right). The dashed line indicates the initial bed level.

procedure described in paragraph 3.4, the DTM for the final bed situation has been extracted (Figs 9, 10).

An analysis concerning the level difference between the initial and the final bed clearly illustrates the formation of sediment deposits in particular in the reach of the side weir (Fig. 10). A volumetric balance between cross sections U and D reveals a deposited volume of 0.044 m^3 or 116 kg.

Typical cross-section profiles extracted from the DTM at cross sections U, W and D are shown in Figure 11. This figure indicates that no significant changes could be observed upstream whereas deposition processes have taken place on the right bank in the weir array nearly up to the top of the weir crest. The mean bed level elevation in this cross section amounts to 0.03 m. The initial level difference between the weir crest and the mobile bed of 0.1 m is therefore reduced to 0.07 m representing a reduction of the cross section of about 33%. Due to these deposits, the flow velocity opposite to the weir is increased resulting in an erosion process. This erosion process continues further downstream in an oscillatory manner before attenuating. Figure 11 (top) illustrates this phenomena. Sedimentation reaches on the right bank are followed by eroded reaches on the left bank. In Figure 2 these observations are pointed up in a qualitative way. Outgoing from the weir side, an erosion gutter,

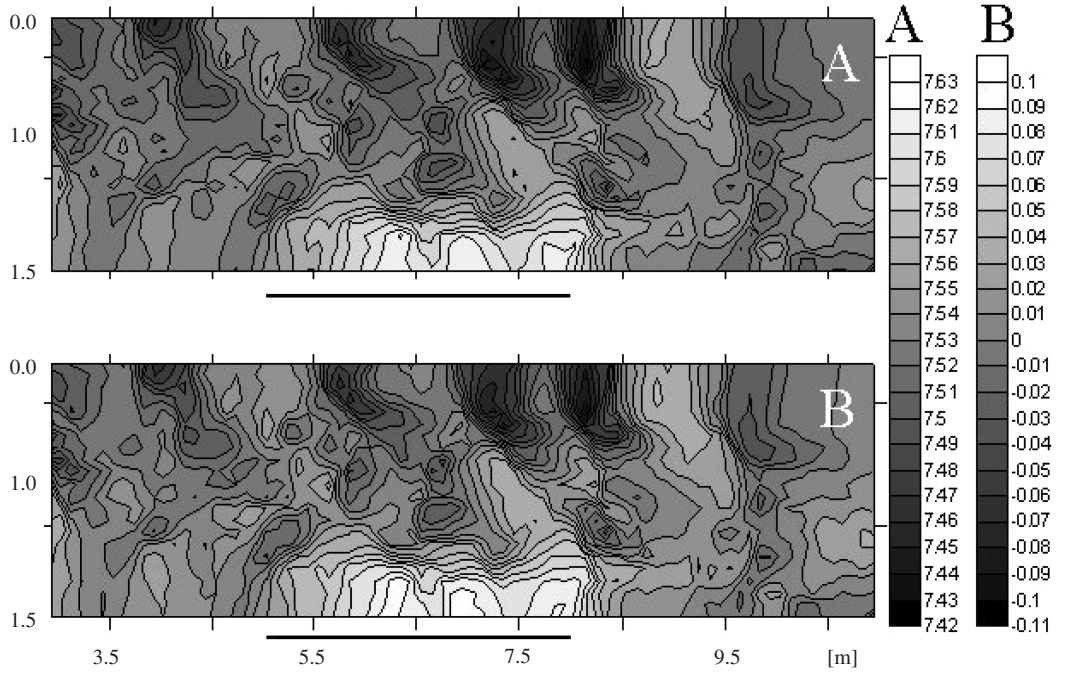


Figure 10. (A) Plan view of the final bed situation (between cross sections U and D); (B) level difference between the initial flat bed and bed topography after 2 hours test for run B02 (between cross sections U and D). The level of the weir crest is 7.62 m, the level of the initial bed in the middle of the weir is 7.52 m.

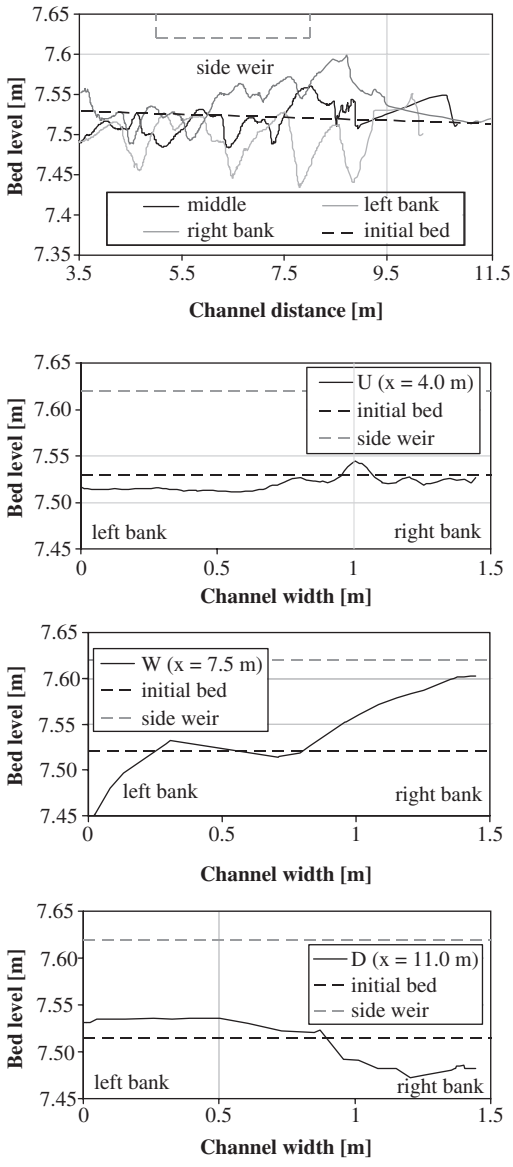


Figure 11. Longitudinal profiles in the middle of the channel, left and right bank and cross-sections U, W and D for the final state of the river bed (from top to bottom).

at the end of the test still filled with water, is running to the right and again to the left. In the downstream section the mobile bed tends to keep almost the same level as the initial bed (see also Fig. 10).

4.4 *Synopsis of results*

The flow is attracted by the lateral side weir leading to a progressive modification of the bed morphology. The diverted discharge induces an elevation of the mobile bed near the weir alignment and erosion processes further downstream on the opposite river bank.

The migration of dunes is manifested by a temporal variation of the water level and diverted discharge. These variations are representative for the interaction between the hydraulic and sedimentary phenomena.

5 CONCLUSION AND PERSPECTIVE

At the actual stage of the research project, great deal of analysis remains to be carried out. However, some preliminary ideas can be expressed.

The analysis of one test series confirms the formation of local deposits of sediments in the reach and downstream of the lateral side weir, particularly on the weir side of the channel. On the one hand these deposits increase the flow velocity opposite to the weir resulting in additional stress to the bank since the cross section is reduced. This aspect is indicated by eroded bed material. On the other hand the bed elevation is combined with an elevation of the water level resulting in an increased diverted discharge over the side weir. This process is strongly transient since at the beginning of the experiment the diverted discharge/mainchannel discharge ratio is low, then rapidly increases to a maximum before reaching almost a constant value.

In this process, a tendency towards an equilibrium state of the river bed is observed which is also indicated by a strongly wavy water surface in the reach of the side weir at the beginning of the test which becomes smoother with elapsing experiment time.

Based on the examination of the first test series, the remaining experiments will be analysed according to the same procedure to finally perform a non-dimensional parameter analysis and to develop empirical relationships for the hydraulic and sedimentary behaviour. The collected data will also serve to calibrate a 3D numerical model in order to analyze the observed effects in detail and to widen the application range.

A better understanding of the interaction between sediment transport and lateral overflow will allow to develop and to provide appropriate design criteria for engineers involved in the design of fuse plugs on rivers in the framework of flood protection projects.

ACKNOWLEDGEMENT

The authors would like to express their gratitude to the *CTI* (Commission pour la Technologie et l'Innovation) for their sustained funding for the research program under grant number 4898.1.

REFERENCES

Borghei, S.M., Jalili, M.R. & Ghodsian, M. 1999. Discharge coefficient for sharp-crested side weir in subcritical flow. *Journal of Hydraulic Engineering, ASCE* 125 (10): 1051–1056.

Chow, V.T. 1973. *Open Channel Hydraulics*. Singapore: McGraw-Hill.

Geisler, T., Breitenstein, S., Hammer, A., Mayr, D. & Klasinc, R. 2003. Hydraulic modelling – Mapping of river bed. In Granulis, J. & Prinos, P. (eds), *Water engineering and research in a learning society: Modern Developments and traditional concepts; Proc. XXX*th *IAHR congress, Thessaloniki, 24–29 August 2003.*

Hersberger, D.S. 2003. Wall roughness effects on flow and scouring in curved channels with gravel bed. In Schleiss, A. (ed.), *Communications du Laboratoire de constructions hydrauliques (LCH)* 14. Lausanne: Ecole PolytechniqueFédérale de Lausanne (EPFL).

Lane, S.N., Chandler, J.H. & Porfiri, K. 2001. Monitoring river channel and flume surfaces with digital photogrammetry. *Journal of Hydraulic Engineering, ASCE* 127 (10): 871–877.

Metflow 2000. UVP Monitor Model UVP-XW User's guide. Metflow SA, Lausanne.

Naudascher, E. 1992. *Hydraulik der Gerinne und Gerinnebauwerke*. Wien New York: Springer Verlag.

Rouse, H. 1954. *Engineering hydraulics*. New York: John Wiley & Sons.

Singh, R., Manivannan, D. & Satyanarayana, T. 1994. Discharge coefficient of rectangular side weirs. *Journal of Irrigation and Drainage Engineering, ASCE* 120 (4): 814–819.

Smart, G.M. & Jäggi, M.N.R. 1983. Sedimenttransport in steilen Gerinnen. In Vischer, D. (ed.), *Mitteilungen der Versuchsanstalt für Wasserbau, Hydrologie und Glaziologie (VAW)* 64. Zürich: Eidgenössische Technische Hochschule Zürich (ETHZ).

River Flow 2004 – Greco, Carravetta & Della Morte (eds.)
© 2004 Taylor & Francis Group, London, ISBN 90 5809 658 0

PIV investigation of flow around submerged river bridge deck

S. Malavasi, S. Franzetti, G. Blois
Politecnico di Milano, Dept. I.I.A.R., Milan, Italy

ABSTRACT: The flow field around a submerged bridge deck has been experimentally investigated here. The deck submersion may be a critical situation for structural stability of river bridges. This problem has been not sufficiently discussed in the past. In order to clarify some aspects of the hydrodynamic loading mechanism, we have kinematically studied the characteristics of the large-scale vortexes in the bridge wake by an original PIV technique. The bridge deck has been modeled by means of a rectangular cylinder. Mean and time-averaged velocity fields have been studied for low submergence ratios of the bridge deck. The work has provided some interesting results. The flow fields around the deck had shown a strong asymmetry and a complex vortex shedding regime, the analysis of which has allowed us to highlight the main differences from symmetrical unbounded case and to associate the considered kinematic behavior to the corresponding dynamic reaction.

1 INTRODUCTION

During a critical river flood event, a bridge may become partially or completely submerged by the flow. This situation may seriously endanger the structure stability, as highlighted by Ballio et al. (1998) in a survey about the vulnerability of many Italian river bridges.

In spite of the actuality of the problem, only few references are present in literature about this subject (Tainsh 1965, Denson 1982, Naudasher & Medlarz 1983, FHWA 1995). Moreover, as highlighted in a recent paper (Malavasi & Guadagnini 2003), usually the studies are referred to specific bridge typologies, consequently the results are hard to generalize. Malavasi & Guadagnini studied the dynamic stress on a bridge deck due to its partial or total submersion. They modeled the structure by means of a cylinder with rectangular cross section. This shape mimics quite well several bridge deck typologies. They studied the dynamic behavior of the model by direct force measurements, for several submergence levels. Their results highlighted significant differences between the considered asymmetrical bounded conditions and the more studied condition of unbounded flow. Moreover, the Authors highlighted that the worst situation for the bridge stability occurs for low water level above the structure, which is a realistic and relatively frequent condition. In this situation the mean force coefficients are significantly higher than those corresponding to the immersion in unbounded flow.

The study of fluid structure interaction between an indefinite rectangular cylinder and an unbounded flow is a basic subject of fluid mechanics, and it keeps a significant interest, as the recent literature confirms (Noda & Nakayama 2003, Hemon & Santi 2002, Shimada & Ishiara 2002, Li & Melbourne 1999, Yu & Kareem 1998, Deniz & Staubli 1997). On the contrary, the situation of the rectangular cylinder immersed in an asymmetrical bounded flow was less considered in the past.

In order to clarify some aspects of the dynamic loading on inundated river bridges, in this work we have investigated the flow field structure around a specific bridge deck. It has been modeled with a rectangular cylinder of aspect ratio $l/s = 3$, where l is the in-flow direction length and s is the thickness of the cylinder cross-section (see Fig. 1).

Instantaneous and time-averaged 2D velocity fields have been experimentally obtained by applying an original Particle Image Velocimetry (PIV) technique. This technique allows to perform long series of instantaneous sequential velocity fields. The temporal evolution and the mean structure of the velocity fields close to a submerged bridge have been here discussed for low submergence conditions. Moreover, considering the direct relation between the hydrodynamic loading and flow structure, we have compared our kinematic results with the frequency analysis of the force components and with mean force coefficients obtained in previous works, in the same hydrodynamic conditions (Malavasi et al. 2002, Malavasi & Guadagnini 2003).

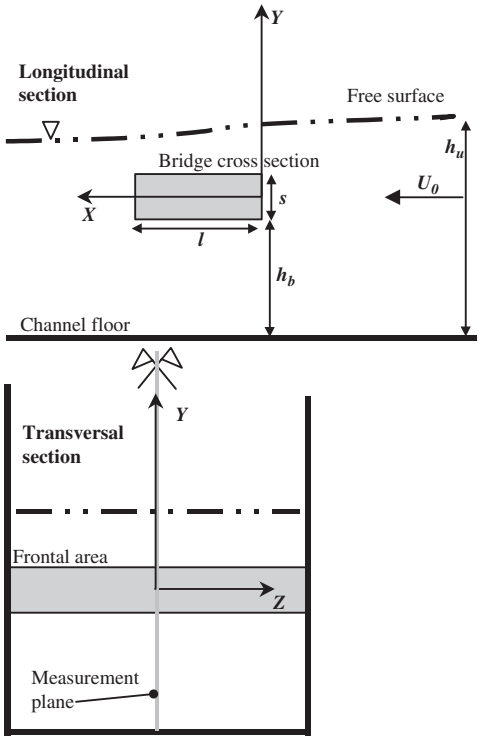


Figure 1. Definition sketch of hydraulic set-up.

2 OVERVIEW OF THE PROBLEM

The immersion of a solid body in a turbulent flow induces a distortion of the incoming flow field. The process is characterized by a strong kinematic and dynamic instability. The interaction is connected with the shear layer separation from the body and with the formation of coherent structures in the obstacle wake. As above mentioned, the fluid dynamic behavior of an indefinite rectangular cylinder submerged by a free surface flow (Fig. 1), is not sufficiently studied in literature. To introduce the main aspects of the phenomenon we refer to the unbounded flow scheme, that can be seen as a limit case of a bounded flow in which the boundary conditions have negligible effects on the flow field.

In the case of a sharp edge elongated rectangular cylinder, the flow detaches on the upstream (primary separation) and downstream corners (secondary separation), and the flow distortion is a function of several parameters. The vortices generated close to the body develop and shed from it creating an unsteady wake. The characteristics of the wake are dependent on the Reynolds number of the obstacle $\mathrm{Re} = U_0 / \nu$ (where U_0 is the mean velocity of the incoming flow and ν is the kinematic viscosity). The vortex shedding mechanism is the main responsible of structural excitation in a stationary flow.

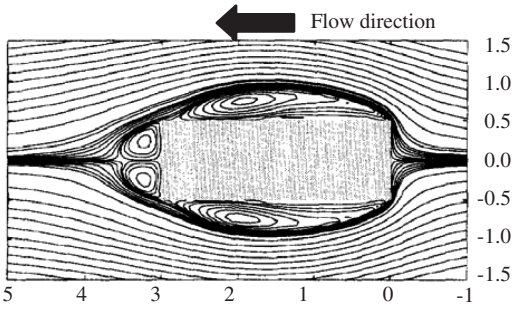


Figure 2. Mean flow field numerically obtained in unbounded flow around a rectangular cylinder, Yu & Kareem 1998; $l/s = 3$, $\mathrm{Re} = 10^5$.

Figure 2 shows the mean flow field around a rectangular cylinder ($l/s = 3$) in unbounded flow, numerically obtained by Yu & Kareem (1998) at $\mathrm{Re} = 10^5$. The primary separation of the shear layer occurs on the leading edge. The separated flow initially diverges from the body with an angle that is function of the separation pressure and then curves toward the cylinder surface. When the reattachment occurs, the flow makes a region of recirculation known as *separation bubble*. In this condition the secondary separation at the downstream edge of the cylinder causes the roll up of the flow in the rear face that generates a secondary vortex, periodically shedding from the body surface. In some cases, when the reattachment of the primary separation is unsteady, the two turbulent structures interact and the vortex shedding becomes more complex.

To simplify the phenomenon description, the main vortex shedding regimes have been defined and classified in literature considering the characteristics of the large vortices. In the case of steady flow condition and of rigid obstacle, we refer to the following classification (Deniz & Staubli 1997):

- LEVS (Leading-edge vortex shedding): the flow separation occurs at the leading-edge with formation of vortices, dominating the near wake of the body;
- TEVS (Trailing-edge vortex shedding): a decisive flow separation at the trailing-edge occurs and vortex-shedding is analogous to the von Kármán street behind circular cylinders;
- ILEV (Impinging leading-edge vortices): a flow separation at the leading-edge and impingement of the leading-edge vortices at the side surfaces and/or edges of the body are present;
- AEVS (Alternate-edge vortex shedding): both the leading-edge and the trailing-edge mechanisms are present.

In unbounded flow the Reynolds number (Re), the cylinder aspect ratio (l/s), the free stream turbulent level $Tu = u'_{rms}/U_0$ (where u'_{rms} is the standard deviation of the inflow velocity on X direction) and the incidence angle α (the angle between the mean inflow direction U_0 and the longitudinal axis of the cylinder X) are the main parameters which affect both the wake structure and the force distribution. They are extensively studied in literature.

For a large range of conditions, several studies show the negligible influence of Reynolds number, when it exceed the value $Re = 10^4$ (Okajima 1982, Deniz & Staubli 1997).

The aspect ratio (l/s) affects significantly the vortex shedding. When $l/s < 2$ only the primary separation occurs because the shear layer, separated at the leading edge, involves the entire side of the cylinder (LEVS); on the contrary, when $l/s > 6$ the flow, separated at the leading edge, reattached permanently; consequently the trailing-edge separation (TEVS) dominates the vortex shedding. For $2 < l/s < 6$ the literature indicates a complex situation of possible unstable reattachment (Shimada & Ishiara 2002, Yu & Kareem 1998, Deniz & Staubli 1997). In this case the presence of mixed structures (ILEV) is function of parameters such as the Reynolds number and the upstream flow turbulence.

Free stream turbulence level (Tu) has received a great attention in literature because it significantly influences the structure and the development of the shear layer separated off the upstream corners (Haan et al. 1998, Li & Melbourne 1999, Saathoff & Melbourne 1997, Noda & Nakayama 2003). Nakamura et al. (1996) experimentally investigated the effects both of turbulence level and scale on pressure distribution along the surface of rectangular cylinders with various aspect ratios. They found that the main effect of Tu is to shift the reattachment point. An increasing of Tu leads to a progressively shorten formation bubble and consequently to a possible strong modification of vortex shedding. Noda and Nakayama (2003) founded that turbulence shakes the shear layer over a distance comparable with turbulence scale. This mechanism intermittently provides the shift of the separated shear layer either towards or far from the body surface.

Of course, also the incidence angle (α) affects the shedding mechanism. When $\alpha \neq 0$ the symmetry of the flow structure is compromised. Consequently, on a side of cylinder prevails the LEVS and on the other the TEVS. When this condition occurs the vortex shedding is characterized by the AEVS regime.

In the case of bounded flow, another significant parameter is the blockage ratio, which, in the case of indefinite rectangular cylinder at zero incidence, can be defined by the ratio $\gamma_b = s/h$, where h is the depth of the upstream bounded flow. For a rectangular cylinder in a symmetric flow field, Okajima et al. (1997), studying the blockage effect on the drag coefficient $C_D = F_D/(0.5 \cdot \rho \cdot U_0^2 \cdot s)$ (where F_D is the mean drag force per unit length of cylinder and ρ is the fluid density) and on the Strouhal number $Sh = f \cdot s/U_0$, (where f is the vortex shedding frequency), showed that both C_D and Sh increases when γ_b increases.

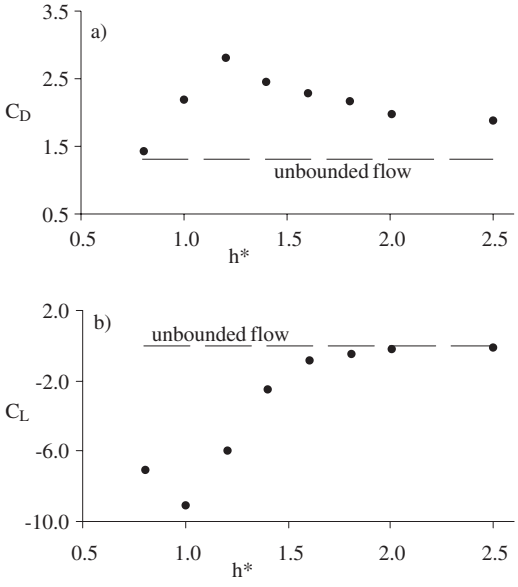


Figure 3. Dependence between mean force coefficients and submergence level h^* for a rectangular bridge deck at $Fr_s = 0.26$. (• Experimental database of Malavasi & Guadagnini 2003; – reference value in unbounded flow condition).

In case of bounded free surface flow, Malavasi et al. (2001, 2002) highlighted how the presence of the free surface may significantly change the mean force coefficients and the Strouhal number (Sh) of the vortex shedding in comparison with the unbounded characteristic values. Moreover, Malavasi & Guadagnini (2003) extended their attention to the cases of partial and low submergence level. In Figures 3a, b, for a deck Froude number $Fr_s = U_0/(gs)^{0.5} = 0.26$, is shown the relation between experimental drag and lift force coefficients (C_D, C_L), and low value of submergence ratio $h^* = (h_u - h_b)/s$ where h_u and h_b are respectively the distances between the free surface and the channel floor and between the bottom bridge deck side and the channel floor (Fig. 1), while the force coefficients are: $C_D = F_D/(0.5 \cdot \rho \cdot U_0^2 \cdot s)$ and $C_L = F_L/(0.5 \cdot \rho \cdot U_0^2 \cdot s)$, where F_L is the mean lift force per unit length of the cylinder. Ther is a significant difference of force coefficients for bounded flow compared with unbounded flow.

3 EXPERIMENTAL APPARATUS AND METHOD

The experimental set-up (Malavasi & Guadagnini 2003) consisted in a not tilted plexiglas open water channel with rectangular cross section, 0.6 m height, 0.5 m width and 5.0 m length. Flow rate and water depth were regulated by an inlet valve and by a downstream grid weir respectively. The sharp edge rectangular cylinder employed as bridge deck model was rigidly fixed to the channel side-walls at a distance of 3.35 m from the inlet section and at a distance of $h_b = 0.14$ m from the channel floor. The cylinder was placed with its generatrix parallel to the channel floor and with the front face normal to the direction of undisturbed flow.

The reference section for the control of boundary conditions was located 0.60 m upstream the leading edge of the cylinder to ensure negligible velocity deviation due to the obstacle presence. A set of three piezometric taps, evenly spaced in spanwise direction, was used to measure the free surface level h_u in the reference section. The flow rate was measured by means of a rectangular sharp-crested weir with an uncertainty of ± 0.001 m^3/s. Mean vertical and spanwise velocity profiles were performed by measuring the instantaneous velocities by an impeller flow-meter (diameter $d = 0.007$ m; uncertainty $u_v = \pm 1\%$). Acquisition time of two minutes ensures the stability of the mean velocity. Free stream turbulence level measured was $Tu = 14\%$.

The flow fields around the bridge deck model were measured using an original PIV (Particle Image Velocimetry) technique expressly developed thinking to hydraulic applications. The 2D velocity fields were obtained measuring the bi-dimensional trajectories of seeding particles in a defined time interval. This is possible by filming the seeding flow on the measurement plane and by using a delayed exposure time. Figure 4 shows an example of acquired frame in which the trajectories of the running particles are well visible. The length of each trajectory, obviously, was due to the corresponding instantaneous local flow velocity and to the shutter time of the video-camera. An exposure time of 0.02 s was used.

The image acquisition rig was composed by an illumination system, a particle dispenser, a progressive scan camera (CCD: Charge Coupled Device) and a personal computer equipped with a frame grabber board for high-speed data transfer. In our arrangement we have been able to grab monochromatic images with a resolution of 763×576 pixel at a frame rate of 50 Hz for a maximum time interval of 16 s. The measurement plane (Fig. 1) was defined by means of a light sheet. It was 7 mm in thickness with a diverging angle of about 0.4 degree and was obtained by a linear halogen lamp (1600 W power) assembled with

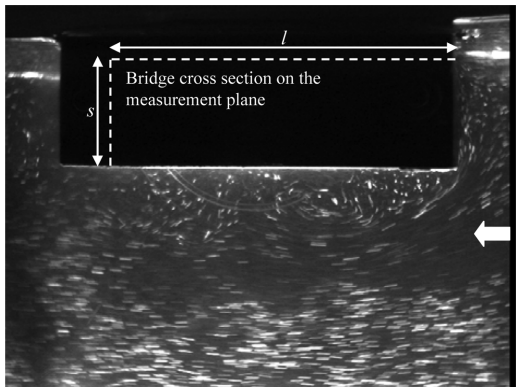


Figure 4. Single image of the seeded flow at the bottom of the bridge deck model (exposure time: 0.02 s; $Fr_s = 0.26$, $h^* = 1$). l and s indicate the dimension of the cylinder in the measurement plane.

two slits system. White spherical polystyrene particles with an average diameter of $\phi = 400\,\mu$m and a density of $\rho_\rho = 1050$ kg/m^3 were used to emphasize the flow trajectories. The polystyrene density, very close to the water one and the particle dimension, ensured the minimization of gravitational and inertial effects on the particles movements.

As the acquisition apparatus, the numerical analysis of the image here used differs from the correlation image method usually employed in PIV analysis. By applying the blob-analysis algorithm on each frame, we measured the geometrical characteristics of each recognized particle trajectory: location, module and orientation. The particle velocity module was obtained dividing the displacement length by the camera exposure time. The direction ambiguity was solved using the velocity information on two consecutive frames. The velocity within the time (Δt) between two consecutive frames can be assumed steady. Starting from a specific position at t_i, in which a data is available, the particle position at time t_{i+1} can be predicted by velocity information on the image t_i. The predicted position can be easily verified by available data (position/velocity) on the image t_{i+1}. By applying the described analysis on an acquired image sequence we obtained a series of instantaneous 2D velocity fields. This analysis provided unstructured data fields, so the data were integrated on a regular grid. A square mesh grid of 1.5 cm, with an overlapping of 50% was used.

4 RESULTS

The main characteristics of the flow field generated by the interaction of the rectangular bridge model with the free surface flow are here discussed starting from streamline representations. The aim is to study

the influence of free surface on evolution of large-scale vortices and to investigate their implication on the structure loading. Since the high submergence of bridges have less practical interest, we have restricted the investigation to low submergence ratios. Low submergences represent the most interesting condition for the relatively high frequency of their occurrence and for the peculiarity of their dynamic behavior (Figs 3a, b).

The instantaneous velocity fields are averaged on different time-windows in order to highlight both the vortex structure evolution and the mean flow configuration. For the former the average–window is determined referring to the dominant vortex shedding frequency calculated by Malavasi et al. (2002) on the basis of force measurements. For the latter we use the whole acquisition interval.

An example of flow field evolution at the bottom side of the bridge is illustrated in Figure 5 by means of nine flow fields for the significant case $\mathrm{Fr_s} = 0.26$, $h^* = 1.4$. The first picture is very similar to the last one, highlighting the periodicity of the phenomenon. Each flow field is calculated averaging the data belonging to 20 consecutive frames, so the time window dimension is $0.02 \times 20 = 0.4$ s. The overlapping time of 50% (10 frames) provides us to obtain one averaged field every 0.2 s. Each field is referred to the center of the corresponding time window. The total period of a sequence constituted by n time averaged fields can be obtained as $0.2 \times (n - 1) = 1.6$ s.

The sequence of images in Figure 5 shows at the bottom of the cylinder the unsteady reattachment of the shear layer separated on the leading edge and the consequent unsteady condition of the separation bubble. The increasing of bubble size appears evident as its longitudinal stretching. The downstream bubble convection is clearly shown by the vortex focus displacement. This behavior involves that reattachment point progressively shifts to the downstream corner (Fig. 5, $0.2\ \mathrm{s} < t < 1.2\ \mathrm{s}$). The evolution leads to a situation of completely separated flow in which the bubble is no longer confined by the shear layer and goes to interact with rear vortices (Fig. 5, $t = 1.4$ s). On the whole, the reattachment condition prevails. When the reattachment disappears we can notice the presence of two vortices with the same rotation sense in the same step (Fig. 5, $t = 0$ s and $t = 1.6$ s). The upstream one refers to generating bubble; the second is the bubble in its final state of development. This evidence confirms the presence of the ILEV mechanism, supposed by Malavasi et al. (2002). Moreover, by considering the time interval between the first (Fig. 5, $t = 0$ s) and the last image (Fig. 5, $t = 1.6$ s) we can roughly estimate the frequency of the vortex evolution that is $f_0 \cong 0.6$ Hz (80 frames, with 0.02 s of shutter time and 50 Hz of frame rate). This value accords with the result of the frequency analysis obtained using

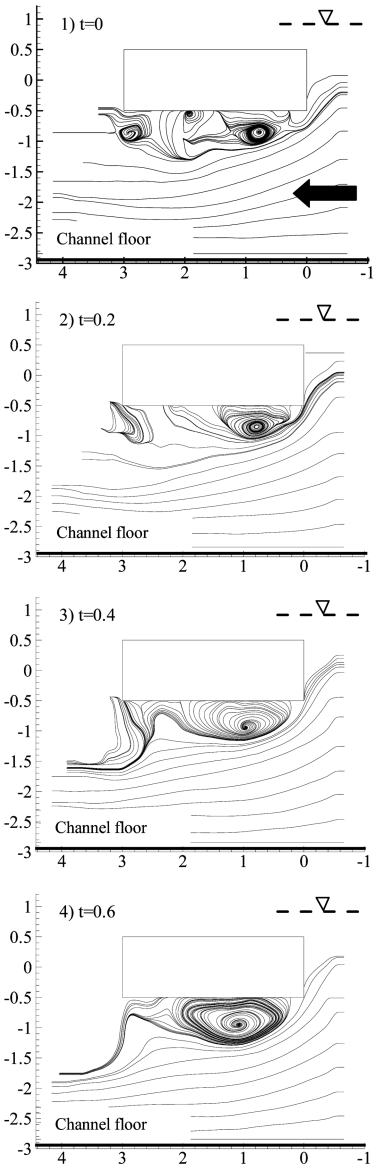


Figure 5. Flow evolution at the bottom of the bridge deck model ($\mathrm{Fr_s} = 0.26$ and $h^* = 1.4$). Streamlines calculated from velocity fields averaged on temporal window of 0.4 s, 50% overlapping.

the lift component of the experimental database of Malavasi & Guadagnini (2003), showed in Figure 6: the frequency analysis of the lift force component on the bridge deck highlights a dominant frequency ($\cong$0.6 Hz) that accords with the developing of separation bubble depicted in Figure 5. The higher dominant

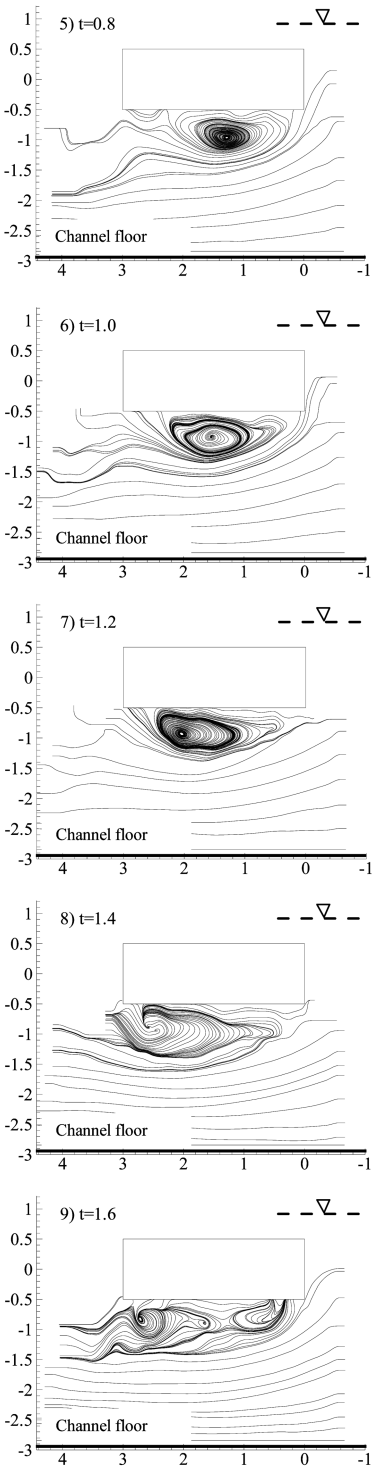


Figure 5. Continued

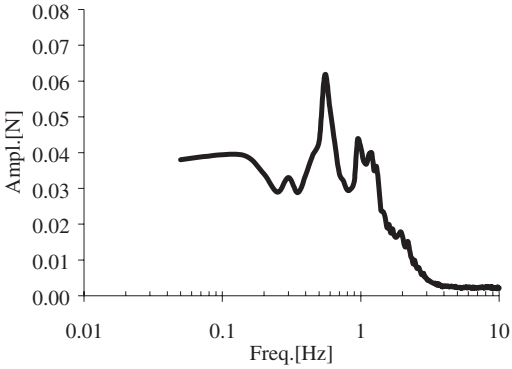


Figure 6. Frequency analysis of the lift force on the bridge deck for $h^* = 1.4$. Experimental database of Malavasi & Guadagnini (2003).

frequency ($\cong$1.0 Hz) accords with the frequency of the vortex shedding downstream the obstacle.

The situation on the upper side of the bridge seems to support the high frequency value, indeed, the presence of the free surface favors the shear layer reattachment and inhibits the bubble formation, so the permanent separation occurs on the down-stream corner only.

The distortion of the flow and the absence of the upper side separation bubble are highlighted by the mean flow field obtained by the time average of several velocity fields acquired with different fields of view. Figures 7, 8 show the streamlines of the 2D mean velocity field around the obstacle at $\mathrm{Fr_s} = 0.26$ and $h^* = 1.4$ and $h^* = 1$ respectively. These results give new information for the phenomenon knowledge, which up to now was based only on the mean force coefficients behavior (Figs 3a, b).

It is well known that the separation bubble generates a low-pressure area on the corresponding side of the obstacle. In symmetrical condition (Fig. 2), the mean separation bubbles at the opposite sides of the obstacle have the same dimension and the resulting lift force is zero ($C_L = 0$). In the asymmetrical case depicted in Figure 7 ($h^* = 1.4$, $\mathrm{Fr_s} = 0.26$), the presence of only one significant separation bubble at the lower side of the bridge deck induces a resulting negative lift force ($C_L = -2.5$). As h^* decreases from 1.4 to 1, the dimension of the mean bubble increases and as a consequence the module of lift increases too. When $h^* = 1$ the bubble reaches its maximum dimension (Fig. 8) and the lift coefficient (Fig. 3b) reaches its minimum value ($C_L = -9.1$).

In literature some comments on the relationship between the C_D and, the mean dimensionless thickness and position of the vortex of the wake are available for unbounded conditions (Igarashi & Mayumi 2001, Bearman & Trueman 1972). Nevertheless our

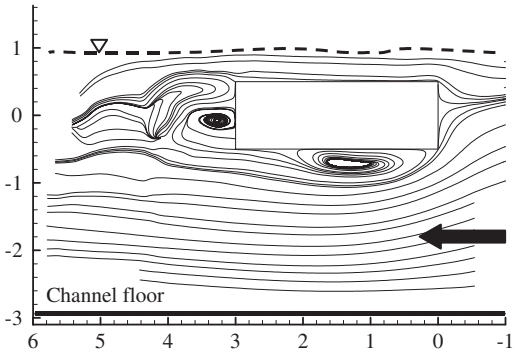


Figure 7. Streamlines of the mean velocity field measured around the bridge deck model ($Fr_s = 0.26$ and $h^* = 1.4$).

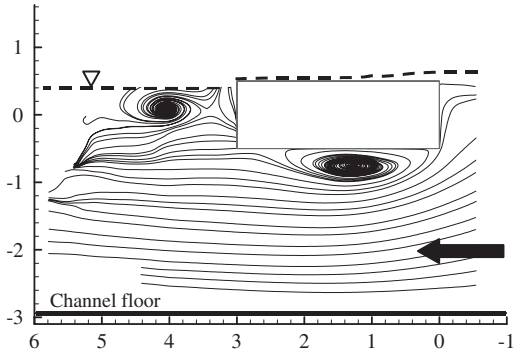


Figure 8. Streamlines of the mean velocity field measured around the bridge deck model ($Fr_s = 0.26$ and $h^* = 1$).

experiments (Figs 7, 8) seem to provide not enough information about the behavior of the C_D with h^*. More experimental evidences are necessary to understand the trend of figure 3a that, in the range here considered, presents a not-monotonic behavior.

5 CONCLUSIONS

The problem of submerged river bridges has been the object of the present study. A kinematic investigation has been conducted on a rectangular bridge deck model. The flow structure around the model has been studied in order to understand some dynamic behaviors highlighted by force analysis in previous works. Time evolutions of 2D flow fields and mean flow fields have been experimentally obtained by applying a PIV technique expressly developed. It has been successfully tested on a hydraulic model of relative large dimension and its applicability to hydraulics is verified. The kinematic analysis of the flow field leads to the following major conclusions:

- At the bottom of the bridge deck is evident the presence of the separation bubble that evolves with the ILEV regime. On the contrary, at the upper side of the bridge, low submergence levels ($h^* = 1$ and 1.4) prevent the separation bubble development. On the rear face of the obstacle, for $h^* = 1.4$, an atypical alternate vortex shedding appears significantly distorted by the flow asymmetry; for $h^* = 1$ it has been not found.
- The analysis of the flow field evolution allows to associate the dominant frequencies of shedding, identified by the frequency force analysis, with their proper shedding regimes. Here we have associated the ILEV regime with the dominant force frequency $f = 0.6$ Hz.
- On the basis of the structure of the mean flow fields around the obstacle we have clarified some interesting aspects of the hydrodynamic loading on the bridge deck. When h^* decreases, the download lift force ($-C_L$) increases due to the increasing of the separation bubble dimension at the bottom side of the deck.

REFERENCES

Ballio, F., Bianchi, A., Franzetti, S., De Falco, F., Mancini, M. 1998. Vulnerabilità idraulica di ponti fluviali. *XXVI Convegno di Idraulica e Costruzioni Idrauliche*, Catania 9–12 September 1998. CUECM, ©1998: 3, 69–79. (in Italian).

Bearman, P.W. & Trueman, D.M. 1972. An Investigation of the Flow Around Rectangular Cylinders. *Aeronautical Quarterly*: 23, 229–235.

Deniz, S. & Staubli, Th. 1997. Oscillating rectangular and octagonal profiles: integration of leading- and trailing-edge vortex formation. *Journal of Fluids and Structures*: 11(1), 3–31.

Denson, K.H. 1982. Steady-state drag, lift, and rolling-moment coefficients for inundated inland bridges, Rep. No. MSHD-RD-82-077, reproduced by National Technical Information Service, Springfield, Virg., 1–23.

Federal Highway Administration (FHWA). 1995. Stream stability at highway structures. Rep. No. FHWA-HI-96-032, FHWA, Washington, DC, 56–59.

Haan, F.L., Kareem, A., Szewezyk, A.A. 1998. The effects of turbulence on the pressure distribution around a rectangular prism. *Journal of Wind Engineering and Industrial Aerodynamics*: 72, 47–60.

Hemon, P. & Santi, F. 2002. On the aeroelastic behavior of rectangular cylinder in cross-flow. *Journal of Fluids and Structures*: 16(7), 855–889.

Igarashi, T. & Mayumi, Y. 2001. Fluid flow and heat transfer around a rectangular cylinder with small inclined angle (the case of a width/height ratio of a section of 5). *International Journal of Heat and Fluid Flow*: 22, 279–286.

Li, Q.S. & Melbourne, W.H. 1999. Turbulence effects on a surface pressures of rectangular cylinder. *Wind and Structure*: 2/4, 253–266.

Malavasi, S., Franzetti, S., Lanfranconi, M. 2002. Effetti dinamici di una corrente a superficie libera su un cilindro rettangolare. *28° Congresso di Idraulica e Costruzioni Idrauliche*, Potenza: vol. 1, 627–634. Editoriale BIOS. (in Italian).

Malavasi, S., Riva, M., Vanali, M., Larcan, E. 2001. Hydrodynamic forces on a submerged bridge. *Fluid Structure Interaction*: 45–54. S.K. Chacrabarti & C.A. Brebbia (eds). Halkidiki, Greece, 26–28 September 2001. WitPRESS.

Malavasi, S. & Guadagnini, A. 2003. Hydrodynamic Load on River Bridge. *Journal of Hydraulic Engineering* (ASCE): Vol. 129, No. 11, November 1. (in press).

Nakamura, Y., Ohia, Y., Ozono, S., Nakayama, R. 1996. Experimental and numerical analysis of vortex shedding from elongated rectangular cylinders at low Reynolds numbers 200–10^3. *Journal of Wind Engineering and Industrial Aerodynamics*: 65, 301–308.

Naudasher, E. & Medlarz, H.-J. 1983. Hydrodynamic loading and backwater effect of partially submerged bridges. *Journal of Hydraulic Research*: 21(3), 213–232.

Noda, H. & Nakayama, A. 2003. Free-stream turbulence effects on the instantaneous pressure and forces on cylinders of rectangular cross section. *Experiments in Fluids*: 34, 332–344.

Okajima, A. 1982. Strouhal numbers of rectangular cylinders. *Journal of Fluids Mechanics*: 123, 379–398.

Okajima, A., Yi, D., Kimura, S., Kiwata, T. 1997. The blockage effects for an oscillating rectangular cylinder at moderate Reynolds number. *Journal of Wind Engineering and Industrial Aerodynamics*: 69–71, 997–1011.

Saathoff, P.J. & Melbourne, W.H. 1997. Effects of free-stream turbulence on surface pressure fluctuations in a separation bubble. *Journal of Fluids Mechanics*: 337, 1–24.

Shimada, K. & Ishiara, T. 2002. Application of modified k-ε model to the prediction of aerodynamic characteristics of rectangular cross section cylinders. *Journal of Fluids and Structures*: 16(4), 465–485.

Tainsh, B.E. 1965. Investigation of forces on submerged bridge beams. University of New South Wales (Library of the water research laboratory) Report n° 108 March 1965.

Yu, D. & Kareem, A. 1998. Parametric study of flow around rectangular prisms using LES. *Journal of wind Engineering and Industrial Aerodynamics*: 77&78, 653–662.

River Flow 2004 – Greco, Carravetta & Della Morte (eds.)
© 2004 Taylor & Francis Group, London, ISBN 90 5809 658 0

Reduction of local scour around bridge abutments with collars

Ş.Y. Kayatürk & M.A. Kökpinar
Hydraulics Lab., State Hydraulic Works, Yücetepe-Ankara, Turkey

M. Göğüş
Hydraulics Lab., Civil Engineering Dept., Middle East Technical University, Eskişehiryolu, Ankara, Turkey

ABSTRACT: Estimation of the depth of scour at bridge foundations is a problem that has perplexed designers for many years. In this study, an investigation on the reduction of scour around bridge abutments using rectangular collars was carried out for clear-water flow over uniform sediment particles. The primary cause of local scour around a bridge abutment is the presence of vortex flow called the principal vortex. The growth of vortex can be arrested by forming a rigid surface around the abutment with a collar plate. The primary objective of this study is to determine the scour reduction of collars of different sizes at different elevations for abutments. Experimental results showed that a collar plate placed on the abutment at the bed level reduces the maximum scour depth by 45% in comparison to an unprotected abutment. However, in the eventuality of lowering or rising the collar with reference to the sand bed, its efficiency depends on the abutment's width and length.

1 INTRODUCTION

Scour of a streambed at bridge piers and abutments during flood events has resulted in more bridge failures than all other causes in recent history. For example, all major bridge failures that occurred in New Zealand during the period 1960-1984 showed that, 29 were attributed to abutment scour of the 108 failures recorded (Melville, 1992). Unfortunately, because of the failure experiences, abutment scour has been the subject of intense research during the last decades. However despite a lot of research on this topic, abutment scour is still a problem of engineering concern and the mechanisms that govern the interaction of the approach flow with the foundation structure, the river bed and the scour are still not entirely understood (Kandasamy and Melville, 1998).

Because the maximum scour depth is insufficient to describe the problem of bridge failures caused by scouring, the protection methods of bridge structures have been searched.

Traditional engineering methods applied to local scour problems are not very sophisticated. There are three basic approaches of providing protection to the bridge foundation: (a) to place the bridge foundations of structures deeply, (b) to enhance the ability of the bed material to resist erosion, (c) to reduce the power of the eroding agents, which is normally achieved by placing an extended base plate or collar at or around the bed level or providing an array of piles in front of the bridge foundations (Chiew, 1992; Singh et al., 1995).

The primary objective of the present study is to investigate the scour reduction of collars with different sizes and at different elevations around bridge abutments.

2 LITERATURE REVIEW

A literature review shows that placing a collar (thin plate) around a bridge pier can reduce the depth of scour. Chiew (1992) conducted experiments in a 0.30 m wide and 8 m long channel having a cohesionless, uniform sand of a median particle size of 0.33 mm. Chiew used a single cylindrical pier of 32 mm-diameter and investigated the effect of a slot, a collar and a combination of both on bridge pier scour. A combination of collar and slot can be an appropriate alternative solution to riprap protection in tackling scour problems at bridge piers.

Kumar et al. (1997) used a 1-m wide, 30 m long flume having a longitudunal slope of 7.73×10^{-4} and uniform sediments of median diameters 0.78 mm, 1.18 mm and 1.54 mm as bed material. The scour reduction efficacy of slots of two different lengths provided along the height of the pier with a constant width of 0.25D was studied, where D is the diameter of

the pier. They also developed a predictive equation for scour reduction by the use of collars of different elevations at or above the bed level. For the experiments on collar efficiency, five collar sizes (1.5D, 2D, 2.5D, 3D, and 4D) were used. They presented an equation for predicting the scour depth with collars and concluded that larger diameter collars at or close to the bed were more effective.

Singh et al. (2001) investigated arresting the growth of the vortex on rigid surface as a collar plate or by confining it within an enclosure like a sleeve skirting around the pier. Uniform sediment with $d_{50} = 0.285$ mm was employed in a 12-m long, 0.6-m wide channel. Model piers of diameters 25 mm and 62 mm were used. The best location was at 0.1D below the average bed level where a collar plate of a diameter twice of the pier gave a performance potential of 91%. In addition, a collar plate equal to twice the diameter of the pier was able to reduce scour by 68% when placed at the bed.

This review demostrates that most of the works toward the understanding of scour evolution were conducted on bridge piers. Therefore, the primary objective of the present study is to determine the scour-reduction efficacy of collars of different sizes and shapes, placed at different elevations of abutments.

3 DIMENSIONAL ANALYSES

For clear-water approach flow conditions, the equilibrium scour depth, $(d_{se})_c$, at an abutment with a collar is a function of:

$$(d_{se})_c = f_1\left\{\begin{matrix} L_a, B_a, B_c, Z_c, T_c, U, y, S, g, \\ \rho_s, \rho, \mu, d_{50}, \sigma_g, t, B \end{matrix}\right\} \quad (1)$$

where, L_a = the lateral dimension of the abutment, B_a = abutment width, B_c = collar width, Z_c = elevation of the collar with respect to the sand level, T_c = collar thickness, U = mean approach flow velocity, y = approach flow depth, S = slope of the channel, g = gravitational acceleration, ρ_s = the density of the sediment, ρ = the density of the fluid, μ = dynamic viscosity of fluid, d_{50} = median particle grain size, $\sigma_g = (d_{84}/d_{16})^{0.5}$ = geometric standard deviation of sediment size distribution, t = scouring time, and B = channel width.

Buchingham's π theorem gives the dimensionless terms:

$$\frac{(d_{se})_c}{y} = f_2\left\{\begin{matrix} \frac{L_a}{y}, \frac{B_a}{y}, \frac{B_c}{y}, \frac{Z_c}{y}, \frac{T_c}{y}, \frac{\rho_s}{\rho}, \\ \frac{U}{\sqrt{gy}}, \frac{B}{y}, \frac{\mu}{Uy\rho}, \frac{Ut}{y}, S, \sigma_g, \frac{d_{50}}{y} \end{matrix}\right\} \quad (2)$$

Considering that the experiments are conducted with one sediment size, constant bed slope, channel width, collar thickness, abutment length, duration of the experiment, and discharge, one can simplify Equation (2) as

$$\frac{(d_{se})_c}{y} = f_3\left(\frac{B_a}{B_c}, \frac{Z_c}{y}\right) \quad (3)$$

the reduction in the scour depth around the bridge abutments as compared to case without collar, d_{se}, is

$$\frac{d_{se} - (d_{se})_c}{d_{se}} = f_4\left(\frac{B_a}{B_c}, \frac{Z_c}{y}\right) \quad (4)$$

or

$$\frac{(d_{se})_c}{d_{se}} = f_5\left(\frac{B_a}{B_c}, \frac{Z_c}{y}\right) \quad (5)$$

4 EXPERIMENTAL PROCEDURE

Experiments were conducted under clear water conditions, $U_*/U_{*c} < 1$, where U_* is the shear velocity of the approach flow and U_{*c} is the value of U_* at the threshold. A rectangular channel with transparent walls, 30 m long and 1.5 m wide was filled with erodable uniform sediment. The general view of the channel is shown in Figure 1.

The flume flow was supplied from a water tank by a pump and measured by a sharp-crested rectangular weir. The depth of flow and the bed profile measurements were conducted by a point gage with a vernier scale to the nearest 0.1 mm.

The mobile bed was made of uniform sand having a median diameter of $d_{50} = 1.48$ mm and a distribution ratio of $\sigma_g = 1.28$. The depth and length of the sand layer in the working reach were 0.50 m and 10 m, respectively.

Figure 2 shows a definition sketch with a typical view of a collar-abutment arrangement used in this study. The abutments used were always rectangular in plan, having widths of $B_a = 0.025$ m, 0.05 m and 0.10 m and lengths are kept constant at $L_a = 0.25$ m. According to Oliveto & Hager (2002) and initial findings of this study, the effect of the streamwise abutment length is small and may be dropped.

The scour hole was obtained by performing a 6-hours continuous run under clear-water conditions and both maximum scour depth and scour formation at the abutment site were investigated.

Four different collar widths $B_c = 0.025$ m, 0.050 m, 0.075 m and 0.10 m were used for all abutment types. As the efficiency of the collar is also a function of

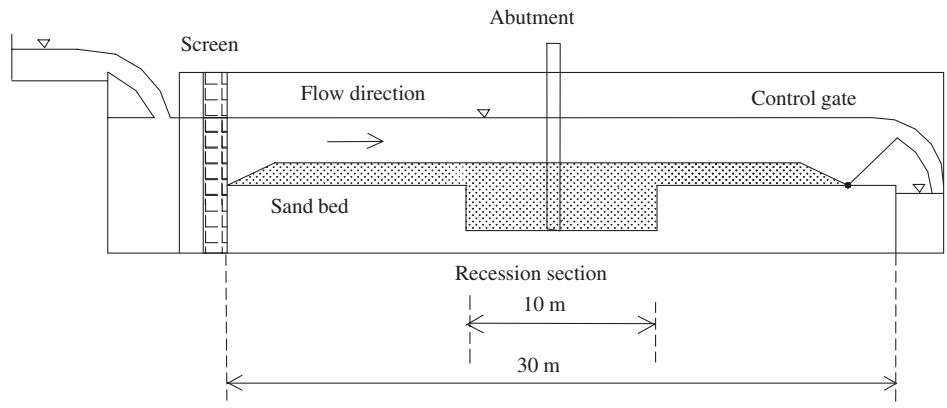


Figure 1. General view of the experimental installation.

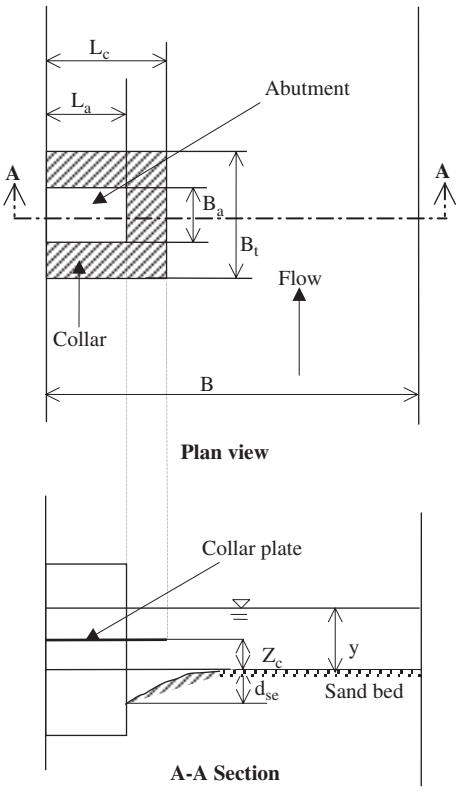


Figure 2. Definition sketch of collar-abutment arrangement.

its vertical location on the abutment, different collar widths were placed at different elevations on the abutments; such as at the bed level, 0.025 m and 0.050 m above the bed level.

5 SCOUR MECHANISM

Local scour around a solid abutment results from the down flow at the upstream face of the abutment and the subsequent development of a horseshoe vortex at its base. Hence, one way of reducing scour is to weaken and possibly prevent the formation of the downflow and the horseshoe vortex.

A collar at any level above the bed divides the flow into two regions; i.e. above and below the collar. For the region above the collar, it acts as an obstacle against the downflow in which the downflow looses its strength an impingement at the bed. For the region below the collar, the downflow and the horseshoe vortex are reduced. However, the efficacy of a collar depends on its size and the location on the abutment with respect to the bed.

6 ANALYSES OF RESULTS

In this study, in order to obtain the maximum reduction in scour depth, various collar and abutment widths were investigated systematically. Figure 3 shows the effect of the various sizes of collar plates on maximum scour depth around abutments. From this figure, it is clearly seen that the maximum reduction in scour depth is observed while the location of the collar plate approaches to the sand bed level ($Z_c/y \rightarrow 0$) for a given abutment width B_a and collar width B_c. Among the tested abutment–collar arrangements, the one having $B_a = 10\,\text{cm}$ and $B_c = 0\,\text{cm}$ for $Z_c/y = 0$ yielded the maximum reduction of 45% in scour depth. Figure 4 shows the efficiency of the collar for the abutments and for the piers together. In this figure, the abutment data was obtained for $B_a = 10\,\text{cm}$ and the pier data were obtained from the previous studies of Tanaka and Yano,

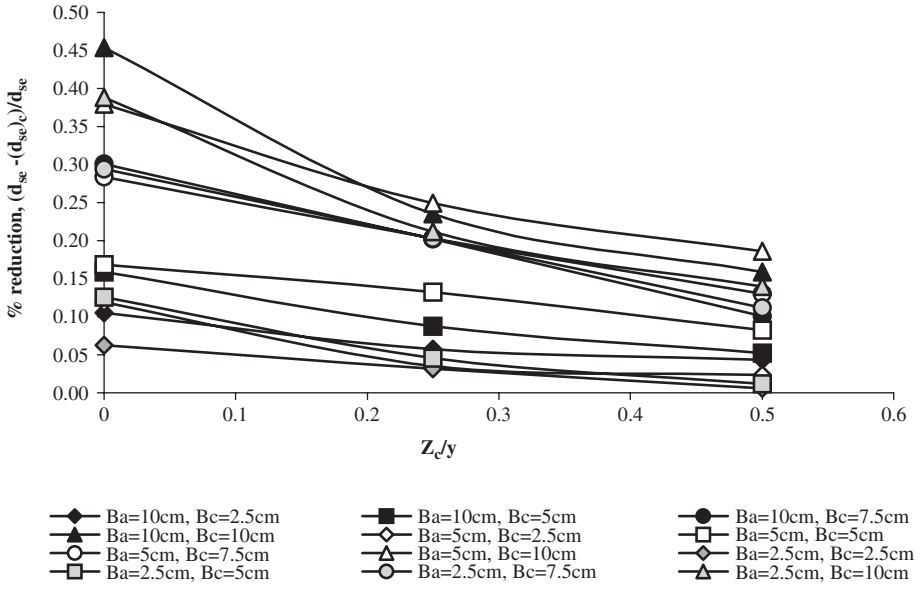


Figure 3. Effect of sizes of collar plates on maximum scour depth around abutment.

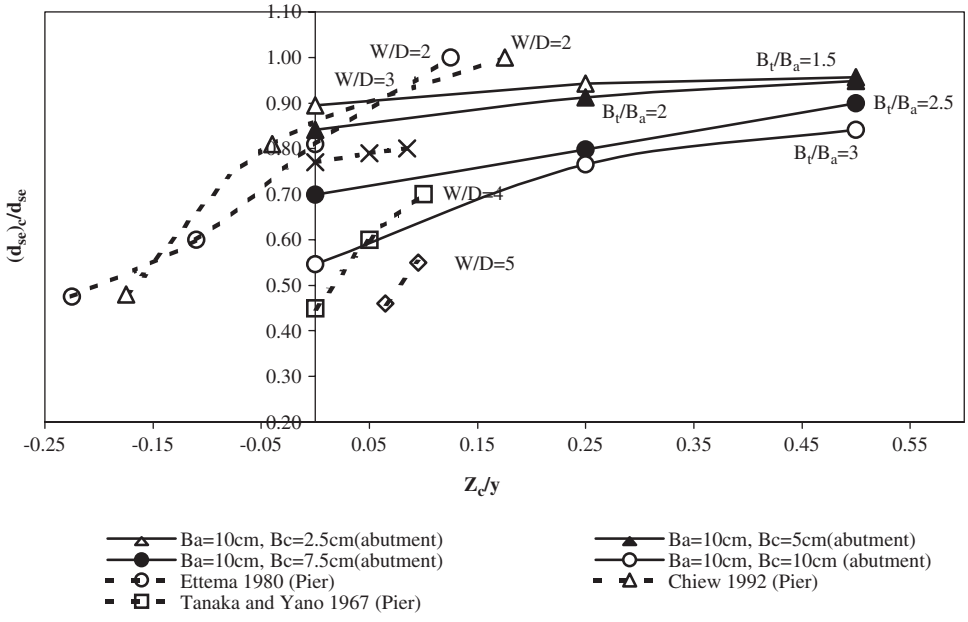
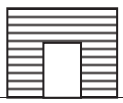
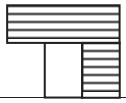
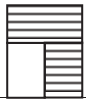
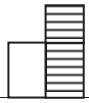


Figure 4. Experimental data on the effect of collar size and position for piers and abutments.

Ettema, and Chiew (Chiew, 1992). The size of the collar with respect to the pier size in circular bridge piers is generally expressed with the ratio W/D (where W is the diameter of the collar and D is the diameter of the pier). In order to compare the pier data with the abutment data, dimensionless term B_a/B_c, was replaced with $(2B_c + B_a)/B_a$ or simply with B_t/B_a. If one assumes that W/D ratio for circular piers is equivalent to the

Table 1. Optimization of collar shape

Parameters of flow and abutment	Q=50l/s, L_a=25cm, B_a=10cm, B_c=10cm, Z_c=0				
Plan views of collar shapes (Flow direction ←)	full	(a)	(b)	(c)	(d)
					
Maximum scour depth, d_{se}, (cm)	18.3	18.3	18.3	19.9	23.2

value of B_t/B_a, the trend lines of constant W/D and B_t/B_a are in agreement. From an extrapolation to be made in Figure 4 it can be concluded that if $B_t/B_a > 3$, reduction of maximum scour depth is higher than 45% ($B_a = 10$ cm).

Table 1 summarizes the experiments, which were conducted to investigate the most economical shape of collars to be used on abutments. Since the maximum scour reduction was observed when the collar was placed at sand bed level, the experiments related with full or partial collar forms were conducted only for $Z_c/y = 0$. For this reason the abutment of $L_a = 25$ cm and $B_a = 10$ cm was selected since it gave the maximum reduction in the scour depth.

In addition to full-collar experiments, those partial-collars given in Table1 were tested under the same flow conditions, at bed level $Z_c = 0$. Results of the experiments showed that partial–collars of shapes (a) and (b) cause a maximum erosion depth of $d_{se} = 18.3$ cm as the full-collar, whereas collar shapes (c) and (d) result in higher scour depths of 19.9 cm and 23.2 cm, respectively.

Therefore, the partial-collar shape (b) can be considered the optimum form from an economical point of view.

7 CONCLUSIONS

A collar prevents the sediment particles from erosion by downflow. Efficacy of a collar plate to prevent scour is a function of its size and its vertical location on the abutment. As the size of collar plate increases the scour depth decreases.

Collar plates of sizes $B_c = 0.25B_a$, $B_c = 0.5B_a$, $B_c = 0.75B_a$, and $B_c = B_a$, for an abutment width of $B_a = 0.10$ m reduce maximum scour depth about by 10%, 17%, 30% and 45%, respectively, at the bed level of unprotected abutment.

The reduction in the scour depth of the abutment of $B_a = 0.10$ m is increased from 20% to 45% by changing the location of the collar on the abutment from 0.5y to bed level.

The effect of the collar on the scour depth around the pier and abutment is similar for clear-water conditions and uniform sediment sizes.

Instead of full-collars, (b) type of partial collars given in Table 1 can be used to provide maximum reduction in scour depth from economical point of view .

LIST OF SYMBOLS

B	channel width
B_a	abutment width
B_c	collar width around abutment
B_t	total width of collar and abutment, $2B_c + B_a$
D	pier diameter
d_{se}	maximum scour depth at the abutment without collar
$(d_{se})_c$	maximum scour depth at the abutment with collar
d_{50}	median size of sediment
g	gravitational accelaration
L_a	projecting length of abutment, perpendicular to the flow
S	channel slope
t	scouring time
T_c	collar thickness
U	approach flow velocity
U_*	shear velocity of the approach velocity
U_{*c}	shear velocity of approach flow at the threshold condition
μ	dynamic viscosity of fluid
W	collar diameter around a pier
y	undisturbed approach flow depth
Z_c	depth of the collar with reference to the bed level
σ_g	standard deviation of particle–size distribution
ρ	fluid density
ρ_s	sediment density

REFERENCES

Chiew, Y. M. 1992. Scour protection at bridge pier. *Journal of Hydraulic Engineering*, 18(9): 1260–1269.

Kandasamy, J. K., and Melville, B. W. 1998. Maximum local scour depth at bridge piers and abutments. *Journal of Hydraulic Research*, 36(2): 183–198.

Kumar, V., Raju, K. G. R., and Vittal, N. 1997. Reduction of local scour around bridge piers using slots and collars. *Journal of Hydraulic Engineering*, 125(12): 1302–1305.

Melville, B. W. 1992. Local scour at bridge abutments. *Journal of Hydraulic Engineering*, 118(4): 615–631.

Oliveto, G., and Hager, W. H. 2002. Temporal Evolution of clear-water pier and abutments scour. *Journal of Hydraulic Engineering*, 128(9): 811–820.

Singh, C. P., Setia, B., and Verma, D. V. S. 2001. Collar-sleeve combination as a scour protection device around a circular pier. *XXIX IAHR Congress Proceedings*, *Beijing, Vol. II*, 202–210.

Singh, K. K., Verma, D. V. S., and Tiwari, N. K. 1995. Scour protection at circular bridge pier. *Sixth International Symposium on River Sedimentation*, *New Delhi, India*: 1057–1068.

River Flow 2004 – Greco, Carravetta & Della Morte (eds.)
© 2004 Taylor & Francis Group, London, ISBN 90 5809 658 0

Numerical and experimental investigation of local scour downstream of a sill

C. Adduce, G. Sciortino & M. Morganti
Dipartimento di Scienze dell'Ingegneria Civile, Università degli Studi di Roma "RomaTRE", Roma

ABSTRACT: This paper presents the results of a laboratory and a numerical study investigating the local scour downstream of a sill followed by a rigid apron. Nine experiments were run in clear water scour conditions, as varying the discharge. A mathematical model simulating the local scour downstream of the sill and using both the experimental velocity fields and the physical and mechanical properties of the sand was developed. The mathematical structure of the model consisted of a second order partial differential parabolic equation whose unknown is the shape of the mobile bed. The numerical integration of this nonlinear equation, with suitable boundary conditions, indicated agreement with the measured scour profiles at the equilibrium condition. Upon comparing the experimental and the numerical data, a similar temporal evolution of the maximum scour depth was observed.

1 INTRODUCTION

Local scour downstream of hydraulic structures is a relevant problem, given its significant practical value. Scour can endanger the stability of structures and cause the risk of failure, if the foundations are not designed taking into account the maximum scour depth.

The study of the local scour process is a complex problem, given the numerous variables related to both the heterogeneity of the eroded soil and the turbulent flow, producing the erosive. Many studies investigated this problem, trying to give a better understanding of this complex phenomena.

Local scour due to a two-dimensional wall jet was investigated by Farhoudi & Smith (1985), who studied the geometrical similarities of the scour profiles in time. Kurniawan et al. (2001) showed the flow pattern of an eroding jet, caused by the flow passing under a gate. Chatterjee et al. (1994) investigated scouring processes downstream a submerged horizontal jet, giving empirical relations for the time to reach the equilibrium stage, location of maximum scour depth and peak of the dune. Ghafar et al. (1995) and Habib et al. (1994) studied local scour caused by hydraulic jumps formed over a rigid apron downstream of a sluice gate with LDA. Karim & Ali (2000) tested a CFD model in order to predict the flow field in local scour holes. Dey & Westrich (2003) and Mazurek et al. (2003) investigated local scour of a cohesive soil produced by submerged horizontal jets.

Rajaratnam (1980) studied the erosion due to circular wall jets. Hogg et al. (1997) modelled the erosion caused by a planar turbulent jet, comparing numerical results with the laboratory experiments by Rajaratnam (1981).

Mossa (1998) and Gaudio & Marion (2003) investigated the temporal evolution of local scour profiles downstream of a grade control structure, Lenzi et al. (2002) studied the scouring process due to the presence of different bed sills. Sills are used to prevent excessive channel-bed degradation, but the erosive action of the flowing water causes downstream local scour, which can endanger the stability of the structure and cause the risk of a failure.

The present paper uses both laboratory and numerical experiments, a local scour downstream of a sill followed by a rigid apron in clear water scour conditions. Nine laboratory experiments were run, varying the discharge in order to investigate the influence of this parameter on the development of the scour hole. A numerical model, simulating the temporal evolution of the scour profile downstream of the sill, was developed. The model, uses the equation of continuity for the local solid discharge, the experimental data about the spatial development of the eroding wall jet and the physical and mechanical properties of the sand. The analysis of the forces acting on the sand particles was performed taking into account the angle of repose of the sand, the instantaneous shape of the mobile bed and a model for the shear stress following an approach similar to that proposed by Hogg et al. (1997). The

mathematical model consisted of a second order partial differential parabolic equation whose unknown is the shape of the mobile bed. Numerical integration of this nonlinear equation, with suitable boundary conditions, namely absence of solid discharge both at the inflow and at the end of the mobile bed agrees with the measured scour profiles. A similar temporal evolution of the maximum scour depth was also observed by comparing the experimental and numerical data.

The paper is organized as follows: the experimental apparatus is described in section 2, the mathematical model and its numerical integration are presented in sections 3 and 4, respectively. The comparison between the laboratory measured and numerical simulated both scoured profiles and time development of the maximum scour depth are discussed in section 5. The conclusions of the work are presented in section 6.

2 EXPERIMENTAL SET UP

The experiments were conducted at the hydraulic laboratory of "RomaTre" University, in a 17 m long, 1 m high and 0.8 m wide tilting flume of a rectangular cross section. Scouring tests were carried out in a 0.3 m high, 0.8 m wide and $L = 3$ m long sediment recess section, positioned 7 m downstream of the inlet of the flume and created raising artificially the flume bed. A uniformly graded sand of mean diameter $d_{50} = 0.72$ mm and $d_{90} = 0.96$ mm, a density $\rho_s = 2650\,kg/m^3$, was used to fill the sediment recess section, in order to have a mobile bed. The same sand was glued both to the upstream and downstream fixed-bed sections, to produce a bed of homogeneous roughness. All tests were conducted under clear water scour conditions.

A sill of height $D_p = 0.15$ m, followed by a $L_p = 0.5$ m long rigid apron, was positioned upstream of the test section, as shown in figure 1. A control gate, positioned at the end of the flume, was used to vary the tailwater conditions.

The water level in the flume is measured using a capacitive point gage of accuracy ± 0.10 mm, mounted on a carriage which moved along the flume. The water discharge at the inlet, controlled by an inlet valve, was measured with an electromagnetic flowmeter.

Before starting the experiments, the level of the mobile sand bed, positioned in the sediment trap, was set to the same height as the fixed bed. To avoid undesirable scour of the sediment bed, the control gate was completely closed and the flume was slowly filled with water pumped from the laboratory water reservoir. The water discharge was then slowly increased and set to the desired experimental value, to avoid any movement of the sand bed. The experiments started when the tailwater depth was set to the desired experimental value, by opening the control gate. The water discharge was maintained constant for

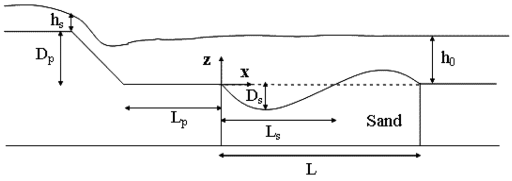


Figure 1. Definition sketch for model tests: plan view.

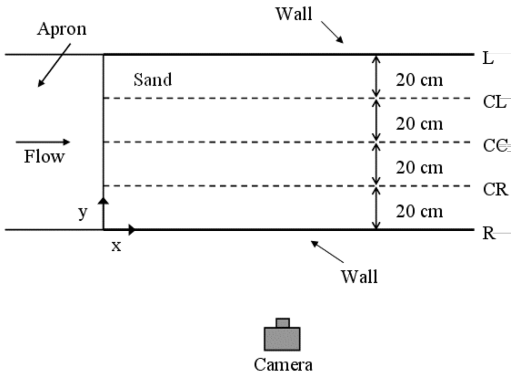


Figure 2. Definition sketch for model tests: top view.

the entire duration of the experiment. The evolution of the scour hole was recorded using a CCD camera connected to a digital videocassette recorder. A detailed study of the temporal evolution of the scour hole was possible using image analysis techniques. At the end of an experiment, when the scouring process had reached an equilibrium state, velocity measurements were performed by an ultrasonic velocity profiler (Signal-Processing DOP2000).

Measurements of the bed profile were made in 5 different longitudinal sections of the flume, using a point gage of accuracy ± 0.10 mm. These 5 longitudinal profiles were called R, CR, CC, CL and L and are positioned at a distance from the right wall of the flume of 0 cm (measure on the right wall), 20 cm, 40 cm, 60 cm, 80 cm (measure on the left wall), respectively as shown in figure 2.

The parameters water discharge (Q), water depth over the sill (h_s), water depth downstream of the sill (h_0) and maximum scour depth (D_{smax}), are presented in Table 1.

3 MATHEMATICAL MODEL

The mathematical model proposed in this paper simulates the local scour downstream of a sill. It uses the equation of continuity for the local solid discharge, the experimental data on the spatial development of the eroding wall jet and the physical and mechanical

Table 1. Experimental parameters.

Test	Q [l/s]	h_s [m]	h_0 [m]	D_{smax} [m]
1	11.0	0.021	0.126	0.042
2	12.3	0.024	0.129	0.044
3	14.2	0.023	0.134	0.050
4	16.2	0.023	0.137	0.061
5	18.4	0.028	0.143	0.067
6	20.5	0.029	0.140	0.069
7	24.8	0.032	0.151	0.077
8	25.8	0.034	0.156	0.082
9	31.2	0.038	0.163	0.107

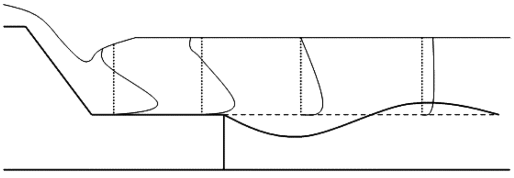


Figure 3. Sketch of the velocity profiles downstream of sill for a rigid bottom (dashed lines).

properties of the sand. The analysis of the forces acting on sand particles is performed taking into account the angle of repose of the sand, the instantaneous shape of the mobile bed and the shear stress obtained with the hypothesis of a wall jet, since this was the case observed experimentally. During the local scouring process the wall jet like profile changes (Hoffmans & Verheij 1997) (figure 3) and the shear stress related to it has been a subject of recent investigations (Dey & Westrich 2003). It is supposed that during the scour process the bed shear stress varies with a Gaussian like characteristics (Hogg et al. 1997).

The condition of transport, for an horizontal bottom, can be written as:

$$\tau_{idr} > \bar{\tau}_{cr} = p_e \phi \tag{1}$$

where

$$\phi = \tan(\varphi) \tag{2}$$

p_e is the weight of a grain, τ_{idr} is the hydrodynamic bed shear stress, $\bar{\tau}_{cr} = \text{const} \cdot (\gamma_s - \gamma) \cdot d_{50}$ (Shields 1936), $\gamma_s = \rho_s g$, g being the acceleration of gravity, $\gamma = \rho g$, ρ being the water density and φ is the angle of repose of a grain. In the following the value of const = 0.047.

If the bottom is not flat and it is described by an equation z = z(x,t), the transport conditions have to be modified, to account for the effect of the bottom slope. In the following description $\mathbf{n_f}$ and $\boldsymbol{\tau_f}$ are the unit vectors, orthogonal and tangent to the bottom, respectively, with $\mathbf{n_f} \cdot \mathbf{k} < 0$, where $\mathbf{k}$ is an upward unit

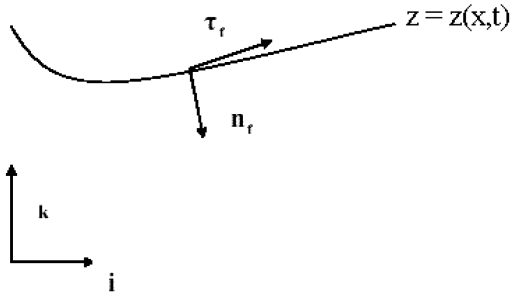


Figure 4. Definition sketch of the unit vectors τ_f and n_f.

vector parallel to the z axis, $\mathbf{i}$ is the unit vector parallel to the x axis and $\boldsymbol{\tau_f}$ has the same direction of the mean flow (figure 4).

Hence

$$\mathbf{n_f} = \frac{\nabla[z(x,t) - z]}{|\nabla(z(x,t) - z)|} = \frac{z_x \mathbf{i} - \mathbf{k}}{\sqrt{1 + z_x^2}} \tag{3}$$

$$\boldsymbol{\tau_f} = \frac{\mathbf{i} + z_x \mathbf{k}}{\sqrt{1 + z_x^2}} \tag{4}$$

z_x is the space derivative of z(x,t). In this case τ_{cr} is given by

$$\tau_{cr} = \mathbf{p_e} \cdot \mathbf{n_f} \phi = (-p_e \mathbf{k}) \cdot \mathbf{n_f} \phi = \frac{p_e \phi}{\sqrt{1 + z_x^2}}. \tag{5}$$

Considering equation (1)

$$\tau_{cr} = \frac{\bar{\tau}_{cr}}{\sqrt{1 + z_x^2}} \tag{6}$$

where $\bar{\tau}_{cr}$ is the critical stress for a flat bottom. The stress acting on a grain is obtained by adding the hydrodynamic bed shear stress and stress due to the gravity, τ_g as

$$\tau = \tau_{idr} + \tau_g = \tau_{idr} + (-p_e \mathbf{k}) \cdot \boldsymbol{\tau_f}. \tag{7}$$

Or

$$\tau = \tau_{idr} - \frac{\bar{\tau}_{cr} z_x}{\phi \sqrt{1 + z_x^2}} \tag{8}$$

The condition of incipient motion is

$$\tau = \tau_{idr} + \tau_g > \tau_{cr} \tag{9}$$

or

$$\tau_{idr} > \tau_{cr} - \tau_g = \frac{\bar{\tau}_{cr}\left(\phi + z_x\right)}{\phi\sqrt{1+z_x^2}} \tag{10}$$

Equation (10) reduces to equation (1) for $z_x \to 0$, i.e. a horizontal bottom.

In order to model the volumetric solid discharge Q_s at the bottom, it is reasonable to suppose, from (10), a functional relation as

$$Q_s = f(\psi), \quad \psi \equiv \tau_{idr} - \frac{\bar{\tau}_{cr}\left(\phi + z_x\right)}{\phi\sqrt{1+z_x^2}} \tag{11}$$

If we suppose that the velocity of the solid particles is locally parallel to the bottom, the continuity equation for the solid material can be written as:

$$\frac{\partial z}{\partial t} + \frac{\partial}{\partial x}\left(Q_s \boldsymbol{\tau}_f \cdot \mathbf{i}\right) = 0 \tag{12}$$

or

$$\frac{\partial z}{\partial t} + \frac{\partial}{\partial x}\left(\frac{Q_s}{\sqrt{1+z_x^2}}\right) = 0 \tag{13}$$

Hence by using (11) the following equation holds

$$\frac{\partial z}{\partial t} + \frac{Q_s'}{\sqrt{1+z_x^2}}\left(\frac{\partial \tau_{idr}}{\partial x} - \frac{\bar{\tau}_{cr}\left(1-\phi z_x\right)}{\phi\left(1+z_x^2\right)^{3/2}}\frac{\partial^2 z}{\partial x^2}\right) +$$

$$- Q_s \frac{\partial z}{\partial x}\frac{\partial^2 z/\partial x^2}{\left(1+z_x^2\right)^{3/2}} = 0 \tag{14}$$

where the prime′ denotes the derivative with respect to the variable ψ. The equation is non-linear and it has a parabolic structure.

The hydrodynamic bed shear stress, at a distance δ from the wall, caused by a turbulent 2D wall jet can be modelled using (Schlichting 1979)

$$\tau_{idr} = \frac{\alpha\rho U_m^2}{U_m^{1/4}\left(\delta/\nu\right)^{1/4}} \tag{15}$$

where $\alpha = 0.0283$ is a numerical coefficient, U_m is the maximum velocity of the jet and ν is the kinematic viscosity of the fluid. In order to estimate the transport action at the moving bottom, δ is chosen as the distance at which the Nikuradse number is $N_i = \delta u_*/\nu \cong 10$, as it occurs in the viscous sublayer. Further we assume that the friction velocity, u_*, is given by $U_m\sqrt{g}/\chi$, valid for a turbulent rough and uniform flow and where $\chi = 2.49\sqrt{g}\log(13.3Rf/d_{50})$. In the previous relation d_{50} is the mean sand diameter, R is the hydraulic radius and f is the shape factor of the flume cross section. Given the above assumptions it follows that $\delta/\nu = N_i/u_* = N_i\chi/(U_m\sqrt{g})$, hence

$$\tau_{idr} = \frac{\alpha\rho U_m^2}{N_i^{1/4}\left(\chi/\sqrt{g}\right)^{1/4}} \tag{16}$$

with the following maximum velocity decaying law (Hogg et al. 1997, Schlichting 1979)

$$U_m = C_1\frac{M}{\nu}\left(\frac{\nu^2}{Mx}\right)^m \tag{17}$$

for $m \cong 0.5$ is

$$U_m = C_1\sqrt{\frac{M}{x}} \tag{18}$$

where C_1 is a constant, $M = \int_z^{h_0} u^2\,dz$, h_0 is the undisturbed water depth over the mobile bed, and u is the local velocity component along the longitudinal direction of the flume. Assuming $h + z = h_0$, as experimentally detected, where h is the instantaneous water depth, and using the approximation $M \cong q^2/(h_0 - z)$, where q is the discharge for unit width, equation (16) where $\beta = (\alpha C_1^2)$ becomes

$$\tau_{idr} = \frac{\rho\beta q^2}{N_i^{1/4}(\chi/\sqrt{g})^{1/4}x(h_0 - z)} \tag{19}$$

This equation reasonably approximate the bed shear stress at a certain distance from the initial profile of the jet (for $x = 0$ it is singular) for the case of a fixed bottom. During the local scouring process the wall-jet like profile changes and the shear stress related to it has been object of recent investigations (Dey & Westrich 2003). Similarly to Hogg et al. (1997), we assume that the shear stress evolves like a law obtained multiplying equation (19) by a Gaussian decay G(x, z) (Hogg et al. 1997). It follows:

$$\tau_{idr} = \frac{\rho\beta q^2}{N_i^{1/4}(\chi/\sqrt{g})^{1/4}x(h_0 - z)}G(x,z) \tag{20}$$

In conclusion the Meyer-Peter and Muller transport formula is used for the solid transport, using as independent variable ψ (instead of $\tau - \bar{\tau}_{cr}$ for a flat bed), given by

$$Q_s(\psi) = \frac{13.3}{\sqrt{\rho(\gamma_s - \gamma)}}\psi^{3/2}\eta(\psi) \tag{21}$$

including the no transport condition $\eta(\psi)$, which is defined by the Heaviside function

$$\eta(\psi) = \begin{cases} 1 & \text{if } \psi \geq 0 \\ 0 & \text{if } \psi < 0 \end{cases} \tag{22}$$

The potential law expressed by (21) is a continuous function together with its derivatives, because the exponent $(3/2) > 1$.

4 NUMERICAL INTEGRATION OF THE MODEL

Numerical integration of the mathematical model was performed adopting a Mac-Cormack-like scheme, applied to the conservative form of equation (14), constituted by equation (13). Two difference operators, denoted respectively by B and F, backward and forward, were defined as

$$Bz_i^n \equiv \frac{z_i^n - z_{i-1}^n}{\Delta x} \tag{23}$$

$$Fz_i^n \equiv \frac{z_{i+1}^n - z_i^n}{\Delta x} \tag{24}$$

where

$$z_i^n \equiv z\big|_{x=i\Delta x,\, t=n\Delta t} \tag{25}$$

$\Delta x = L/M$ is the spatial step of integration, M is the number of interval of discretization and Δt is the temporal step of integration. The following predictor-corrector numerical scheme is defined according to the following integration scheme

$$z_i^P = z_i^n - \Delta t B\left(\frac{Q_s}{\sqrt{1+Fz_i^n}}\right) \tag{26}$$

$$z_i^C = z_i^P - \Delta t F\left(\frac{Q_s}{\sqrt{1+Bz_i^P}}\right) \tag{27}$$

$$z_i^{n+1} = \frac{1}{2}\left(z_i^n + z_i^C\right) \tag{28}$$

where C and P denote the corrector and predictor step, respectively.

This algorithm is completely defined assigning suitable boundary conditions at $x = 0$ and $x = L$. These boundary conditions are the clear water scour condition at the inlet of the mobile bed and the absence of solid transport at the end of it.

Using equation (10) the condition of absence of solid transport at the end of the mobile bed can be written as

$$\frac{\tau_{idr}(z)}{\tau_{eff}(z_x)} = \lambda < 1 \tag{29}$$

where $\tau_{eff} = \tau_{cr} - \tau_g$ and λ is a parameter of the model, whose value has to be suitably chosen.

The condition of clear water scour at the inlet of the mobile bed can be discretized as

$$\frac{\tau_{idr}(z_0^{n+1})}{\tau_{eff}\left(\dfrac{z_1^{n+1} - z_0^{n+1}}{\Delta x}\right)} = \lambda_0 \tag{30}$$

here z_1^{n+1} is a known value, because it is calculated in an internal grid point, so that (30) is an equation in which the only unknown is z_0^{n+1}, which can be numerically solved for the assigned λ_0 values.

The condition of absence of solid transport at the end of the mobile bed can be discretized as

$$\frac{\tau_{idr}(z_M^{n+1})}{\tau_{eff}\left(\dfrac{z_M^{n+1} - z_{M-1}^{n+1}}{\Delta x}\right)} = \lambda_M \tag{31}$$

Equation (31) is numerically solved as equation (30), to find the unknown z_M^{n+1}.

5 RESULTS AND DISCUSSION

In figures 5 and 6 the laboratory measured scour profiles in 5 different longitudinal sections are presented,

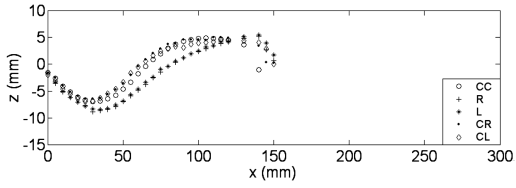


Figure 5. Scour profiles measured in different longitudinal sections for test 6.

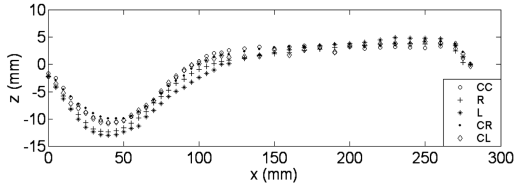


Figure 6. Scour profiles measured in different longitudinal sections for test 9.

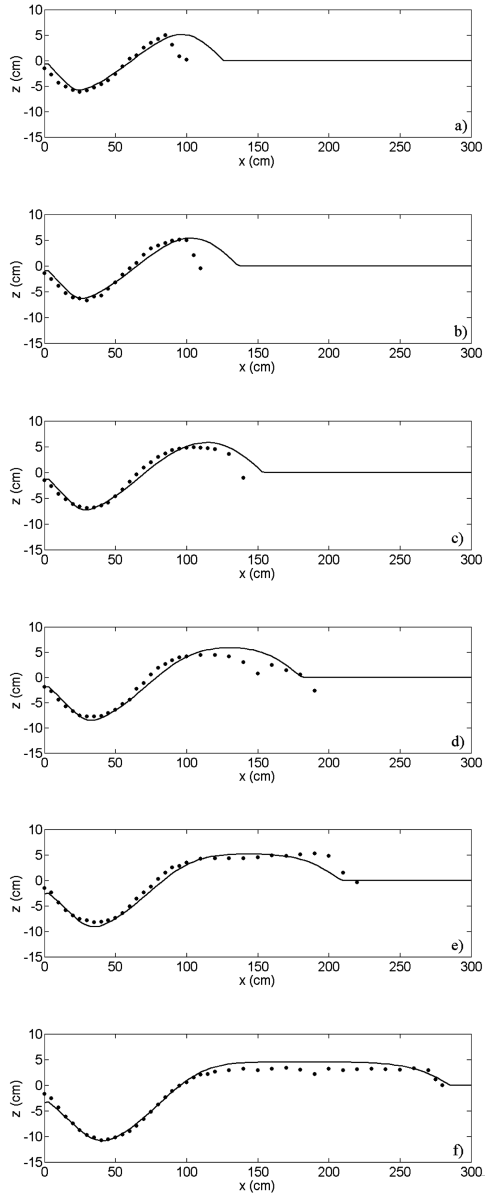


Figure 7a–f. Numerical (line) and laboratory measured (dots) scour profile for test 4, test 5, test 6, test 7, test 8 and test 9, respectively.

for tests 6 and 9 respectively. All the longitudinal profile measurements are made at the equilibrium scour condition.

Following the reference system of figure 2, the five longitudinal profiles are called R, CR, CC, CL, L, corresponding to distances from the right wall of the flume, along the y axis, of 0 cm, 20 cm, 40 cm, 60 cm and 80 cm (left wall) respectively. The eroded bed is always symmetrical respect to the center line of the flume (figures 5 and 6), while it is also quasi-2D for large discharges (figure 6).

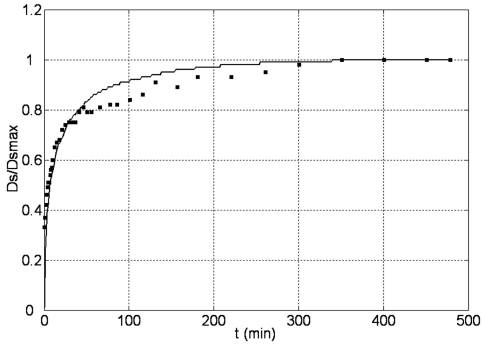


Figure 8. Time evolution of the dimensionless numerical (line) and laboratory measured (dots) maximum scour depths for test 4.

In figures 7a–f the comparison between the measured laboratory bed profiles (dots) and the numerical profiles (lines) is presented. All the bed profile measurements refers to the centre of the flume at the equilibrium scour condition.

Six different tests are simulated: test 4 (figure 7a), test 5 (figure 7b), test 6 (figure 7c), test 7 (figure 7d), test 8 (figure 7e), test 9 (figure 7f). A good agreement between the predicted scour hole and the measured profiles for all the simulated tests. It is to be noted that the mathematical model, as a consequence of the boundary conditions, predicts at any instant a bed profile in which the volume of the scoured bed is strictly equal to the volume of the dune. When the model simulates the dune profile downstream of the scour hole some differences arise. For large discharges (tests 7–9) the dune profiles predicted by the model are similar to the measured, while when the discharges are smaller (tests 4–6), the dunes predicted by the model are always longer than those measured. This behaviour can be explained both by the characteristics of the model described above and because the bottom profile are observed to be quasi 2D when the discharges are large (tests 7–9), while it is symmetrical respect to the center line of the flume but no more quasi 2D for smaller discharges (tests 4–6). Bed profiles measurements in five different longitudinal sections of the flume were made, to study these different behaviours. All the tests performed show that the scour holes are always quasi 2D, while the dunes could be quasi 2D or symmetrical respect to the flume centreline, depending on the discharge value. As the discharge increases, the scour profile becomes more and more 2D.

The maximum scour depth and lengths increase with increasing discharges (see figures 7a–b). For smaller discharges a small dune, with a sharp dune

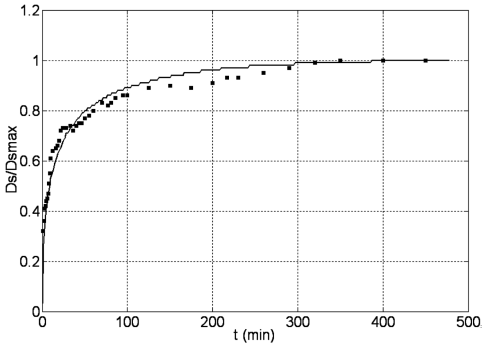


Figure 9. Time evolution of the dimensionless numerical (line) and laboratory measured (dots) maximum scour depths for test 8.

crest, follows the scoured hole. Increasing the discharge the dune crest becomes flatter and longer. For very large discharges some small dunes are observed forming on the dune top.

In figures 8 and 9 the comparison of the temporal evolution of the experimental (squares) maximum scour depth and the numerical is presented. Both the experimental and numerical instantaneous maximum scour depth (Ds) are divided by the maximum scour depth at the end of the run (Dsmax).

The numerical model agrees with the measured time development of the maximum scoured depth. Figure 8 and 9 refer to runs 4 and 8 respectively.

6 CONCLUSIONS

Laboratory and numerical model were presented to study local scour downstream of a sill, followed by a rigid apron in clear water scour conditions. A one-dimensional numerical model, simulating the evolution of the scour hole was developed. Agreement between the measured scour profiles at the equilibrium state and the predictions is observed, together with the temporal evolution of the maximum scour depth. From the bed profiles measured in five different longitudinal sections of the flume, it is possible to observe that the larger the discharge is, the more 2D the scour profile is, the better the performances of the numerical model are. A possible future development of this study is the improvement of the numerical model, starting from experimental measurements of the shear stress inside the scour hole and coupling the continuity equation of solid discharge with the equation of continuity and momentum.

ACKNOWLEDGEMENTS

Laboratory activities were supported by Italian Funding COFIN 2002-2004 “Modellazione di processi idrodinamici in sistemi fluidi stratificati, di correnti a superficie libera e in pressione a celerità variabile.”, section “Modellazione sperimentale di fenomeni erosivi localizzati nelle correnti a superficie libera”.

REFERENCES

Chatterjee, S. S., Ghosh, S. N. & Chatterjee, M. 1994. Local scour due to submerged horizontal jet. *Journal of Hydraulic Engineering* 120(8): 973–992.

Dey, S. & Westrich, B. 2003. Hydraulics of submerged jet subject to change in cohesive bed geometry. *Journal of Hydraulic Engineering* 129(1): 44–53.

Farhoudi, J. & Smith, K. V. H. 1985. Local scour profiles downstream of hydraulic jump. *Journal of Hydraulic Research* 23(4): 343–358.

Gaudio, R. & Marion, A. 2003. Time evolution of scouring downstream of bed sills 41(3): 271–284.

Ghafar, A. A., Mossa, M. & Petrillo, A. 1995. Scour from flow downstream of a sluice gate after a horizontal apron. *Sixth international symposium of river sedimentation; Proc. int. symp. New Delhi, 7-11 November 1995*. New Delhi: Oxford & IBH publishing CO. PVT. LTD: 1069–1088.

Habib, E., Mossa, M. & Petrillo, A. 1994. Indagine sperimentale sull’escavazione in un canale a fondo mobile posto a valle di un risalto idraulico. *Proc. nat. symp. XXIV Convegno di idraulica e costruzioni idrauliche; Napoli* T4: 25–36.

Hoffmans, G. J. C. M. & Verheij, H. J. 1997. *Scour manual.* Rotterdam: Balkema.

Hogg, A. J., Huppert, H. E. & Dade, B. 1997. Erosion by planar turbulent jets. *Journal of Fluid Mechanics* 338: 317–340.

Karim, O. A., Ali, K. H. M. 2001. Prediction of flow patterns in local scour holes caused by turbulent water jets. *Journal of Hydraulic Research* 38(4): 279–287.

Kurniawan, A., Altinakar, M. S. & Graf, W. H. 2001. *Flow pattern of an eroding jet*, Proc. of XXIX IAHR Congress, Beijing, China: 537–544.

Lenzi, M. A., Marion, A., Comiti, F. & Gaudio, R. 2002. Local scouring in low and high gradient streams at bed sills. *Journal of Hydraulic Research* 40(6): 731–739.

Mazurek, K. A., Rajaratnam, N. & Sego, D. C. 2003. Scour of cohesive soil by submerged plane turbulent wall jets. *Journal of Hydraulic Research* 41(2): 195–206.

Mossa, M. 1998. Experimental study on the scour downstream of grade-control structures. *XXVI Convegno di Idraulica e Costruzioni Idrauliche*; Catania, 1998, 3: 581–594.

Rajaratnam, N. 1980. Erosion by circular wall jets in cross flow. *Journal of Hydraulic Division, ASCE.* 106(11): 1867–1883.

Rajaratnam, N. 1981. Erosion by plane turbulent jets. *Journal of Hydraulic Research* 19(4): 339–358.

Schlichting, H. 1979. *Boundary layer theory*. Mc Graw Hill. New York.

Shields, A. 1936. Anwendunk der anlichkeits mechanik und der turbulenzforschung auf die geschiebebewegung. *Mitt. Preuss. Versuchsanst. Wasser Schiffs.* 26.

This page intentionally left blank

River Flow 2004 – Greco, Carravetta & Della Morte (eds.)
© 2004 Taylor & Francis Group, London, ISBN 90 5809 658 0

Flow patterns in local scour holes downstream of a sill caused by turbulent water jets

C. Adduce, M. La Rocca & P. Mele
Dipartimento di Scienze dell'Ingeneria Civile, Università degli Studi di Roma "RomaTRE", Roma

ABSTRACT: The present study investigates local scour downstream of a sill followed by a rigid apron, due to a wall jet and a surface jet, related to the development over the apron of a hydraulic jump and an undular hydraulic jump, respectively. Eight laboratory experiments were run, for variable discharge and downstream water depth. A transition jump, which changes intermittently between a hydraulic jump and an undular hydraulic jump, was observed. The different characteristics of the scouring process due to different kinds of jumps are presented, together with the velocity fields inside the scour hole, due to both the surface jet and the wall jet. A stability analysis of the undular hydraulic jumps shows their intermittent behaviour. Agreement between the mathematical model and the laboratory results was found.

1 INTRODUCTION

Sills are used to prevent excessive channel-bed degradation, but the erosive action of the flowing water causes downstream local scour endangering the stability of the structure itself and causing the risk of failure. Mossa (1998) and Gaudio & Marion (2003) investigated the temporal evolution of local scour downstream of a grade control structure, whereas Lenzi et al. (2002) studied the scouring process due to the presence of different bed sills.

The water flowing over a sill creates different kinds of jet, related to different hydraulic conditions, such as a wall jet, if a hydraulic jump forms downstream of the sill, or a surface jet for an undular hydraulic jump.

Recent investigations considered local scour downstream of jets created by water flowing downstream of different hydraulic structures (sills, gates, spillways). Farhoudi & Smith (1985) investigated local scour due to a two-dimensional wall jet, along with geometrical similarities of the scour profiles in time. Kurniawan et al. (2001) showed the flow pattern of an eroding jet, caused by the flow passing under a gate. Chatterjee et al. (1994) investigated the scouring process downstream of a submerged horizontal jet, with empirical relations for the time to reach the equilibrium state, the location of maximum scour depth and the peak of the dune. Mossa et al. (1995) and Habib et al. (1994) studied a local scour caused by hydraulic jumps formed over a rigid apron downstream of a sluice gate, making velocity measurements with LDA. Dey & Westrich (2003) and Mazurek et al. (2003) investigated local scour of a cohesive soil produced by submerged horizontal jets.

Many of these studies deal with wall jets or hydraulic jumps created downstream of hydraulic structure; for undular hydraulic jump, the local scour evolution can be very different, related to the development of a different kind of velocity field.

An undular hydraulic jump develops in open channel flow when the upstream Froude number is $1 < Fr_u < 1.7$ (Chow 1959). Chanson & Montes (1995) investigated experimentally the undular hydraulic jump, indicating both 5 different types and the formation of lateral shock waves for $Fr_u > 1.2$. Montes & Chanson (1998) measured the velocity field in an undular hydraulic jump, showing its tridimensionality and developed a mathematical model in order to simulate the velocity, pressure and energy distribution in the jump. Ohtsu et al. (1997, 2001) found that the formation of the jump depended not only on the inflow Froude number but also on the boundary-layer development. They showed photographs of the free water surface related to different types of undular hydraulic jumps. Bukreev (2001) studied undular hydraulic jumps in open channel flow over a sill and showed a transition condition between the free surface jet (undular hydraulic jump) and the submerged jet (hydraulic jump). Other recent investigations focused on the determination of the analytical free surface profile in presence of a steady undular hydraulic jump (Grillhofer & Schneider 2003, Steinruck et al. 2003). All these numerical and laboratory studies investigated the undular hydraulic jump, over a rigid flat bottom.

The present study investigates with laboratory experiments local scour due to both submerged and surface jets, i.e. due to hydraulic jumps and undular hydraulic jumps, respectively. Eight tests were run changing both the water discharge and the downstream water depth, in order to develop both undular hydraulic jumps and hydraulic jumps over the apron. A transition jump, which intermittently changes between an undular hydraulic jump and a hydraulic jump, was observed. The velocity fields, measured in the scour hole with an ultrasonic velocity profiler, both in case of an undular hydraulic jump and a hydraulic jump, are presented. A mathematical model, following Montes & Chanson (1998) approach accounting for the scour, was applied to study the stability of the undular hydraulic jump.

The paper is organized as follows: the experimental apparatus is described in section 2, the laboratory measured velocity profiles are presented in section 3, the stability analysis of the undular hydraulic jump with a mobile bed is described in section 4. The conclusions of the work are presented in section 5.

2 EXPERIMENTAL SET-UP

The laboratory experiments were conducted, at the hydraulic laboratory of "RomaTre" University, in a 17 m long, 1 m high and 0.8 m wide tilting flume of rectangular cross section. Scouring tests were carried out in a 0.3 m high, 0.8 m wide and $L = 3$ m long sediment recess section, positioned 7 m downstream of the flume inlet and by raising artificially the flume bed. An uniformly graded sand characterized by $d_{50} = 0.72$ mm, $d_{90} = 0.96$ mm and a density $\rho_s = 2650$ kg/m^3, was used to have a mobile bed. The same sand was glued both to the upstream and downstream fixed-bed sections, to produce a bed of homogeneous roughness. All the tests were conducted in clear water scour conditions.

A sill of height $D_p = 0.15$ m followed by a rigid apron of length $L_p = 0.5$ m was positioned upstream of the test section, as shown in Figure 1. A control gate, positioned at the end of the flume, was used to change the downstream water depth. The water level in the flume was measured using a capacitive point gage of accuracy ± 0.10 mm, mounted on a carriage which moves along the flume. The water discharge at the inlet was controlled by an inlet valve and measured by an electromagnetic flowmeter.

Before starting the experiments, the level of the mobile sand bed, positioned in the sediment trap, was set to the same height of the fixed bed. In order to avoid the undesirable scour of the sediment bed, the control gate was completely closed and the flume slowly filled with the water pumped from the laboratory water reservoir by an auxiliary pumping device. The water discharge was then slowly increased, starting from zero, and set to the desired experimental value, paying attention to avoid any movement of the sand bed. The experiment started when the downstream water depth was set to the desired experimental value by opening the control gate. The water discharge was maintained constant for the entire duration of the experiment. The evolution of the scour hole was recorded using a CCD camera connected to a digital video-cassette recorder. At the end of the experiment, when the scouring process was assumed to have reached an equilibrium state, velocity measurements are performed by an ultrasonic velocity profiler (Signal-Processing DOP2000).

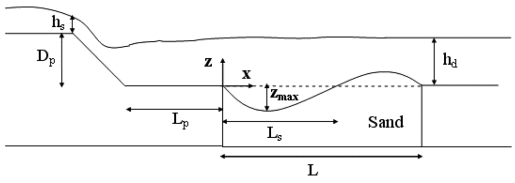


Figure 1. Definition sketch for model tests.

The UVP (Ultrasonic Velocity Profiler) is constituted by a piezoelectric probe, which works both as emitter and receiver of a signal consisting of ultrasonic pulses travelling across the fluid and backscattered by the targets, i.e. small air bubbles or particles, moving with the flow. For a detailed description of the UVP technique, see Takeda (1995, 1999). The size of the measurement volume depends on the characteristics of the probe (emitting frequency and diameter) and increases far from the probe, due to the lateral spreading of the pressure wave. During the present experiments probes with an emitting frequency of 2 MHz and a diameter of 14 mm were used, for a divergence angle equal to 1.83°. The UVP allows a quasi-instantaneous measurement of the velocity in different volumes (gates), positioned along the axis of the probe. The distance between the center of these gates used for the experiments is 3.52 mm. The longitudinal size used for the sampling volume is 2.96 mm, while its lateral size depends on the distance from the transducer. Three probes with the same emitting frequency were used (Longo et al. 2001), for the measurement of the profiles of the horizontal and the vertical velocity components. Velocity profiles of both the horizontal and the vertical component are measured in different points along the centreline of the flume.

The experimental parameters water discharge (Q), water depth over the sill (h_s), water depth downstream of the sill (h_d) and maximum scour depth (z_{max}), are presented in Table 1.

3 EXPERIMENTAL RESULTS

Eight laboratory experiments were run to investigate local scour due to water jets. The discharge and the

Table 1. Experimental parameters.

Test	Q [l/s]	h_s [cm]	h_d[cm]	z_{max} [m]
H1	31.20	3.80	16.19	0.107
H2	36.45	4.10	16.91	0.139
T1	30.00	4.20	18.57	0.040
T2	34.04	4.45	18.86	0.056
T3	38.64	4.80	19.34	0.108
U1	31.01	4.80	19.88	0.051
U2	33.10	5.00	20.36	0.055
U3	37.40	5.20	20.78	0.062

downstream water depth were varied. Three different kinds of water jets were observed: Wall jet, Surface jet and Transition jet, related to the development of a hydraulic jump, an undular hydraulic jump and a transition jump respectively. The transition jet is defined as a jet which changes intermittently between a surface jet and a wall jet, related to the intermittently change of an undular hydraulic jump into a hydraulic jump, respectively. Both the velocity field and the scour hole development related to the different kinds of jet are different.

3.1 *Qualitative results*

A different behaviour, both concerning the development of the scour hole and the measured velocity field, is observed for the different kinds of hydraulic jump.

When a hydraulic jump forms over the rigid apron downstream of the sill, a wall jet with a reverse flow close to the water surface is observed (tests H1 and H2). The scour process develops very fast during the first minutes of the run and becomes slower and slower with time advance. The sand is moved downstream by the wall jet and a dune is formed. The scour hole increases both in depth and length together with the dune, which continues its downstream movement and increases in length and height. At the end of the test the scour hole and the dune were quasi-2D.

When an undular hydraulic jump forms over the rigid apron downstream of the sill, a surface jet with a reverse flow close to the bottom was observed (tests U1, U2 and U3). The sand, positioned close to the rigid apron, was moved upstream over the apron, creating a small dune, which moved towards the sill. The sand which was far from the apron slowly moved downstream by the flow. At the end of the test it was possible to observe the presence of two dunes: a first which covers all the apron and part of the sill and a second positioned downstream over the mobile bed. The dune over the apron is not 2D, together with the scour hole and the dune downstream, which are symmetrical respect to an axis passing through the centreline of the flume.

In tests T1, T2 and T3 a transition jump was observed: a jump which changes in time between a hydraulic jump and an undular hydraulic jump. In these tests the velocity field continues to change in time showing both the presence of a wall jet and a surface jet. When a surface jet was present the sand is partly moved upstream over the apron and partly moved downstream over the mobile bed, as for tests U1, U2 and U3. The sand moving upstream formed a dune over the rigid apron, which increased height and length. Suddenly the undular hydraulic jump developed into a hydraulic jump, with a wall jet velocity distribution, pushing fast the sand present over the apron downstream. The sand created a new dune, which moves over the eroded bed and partly fills the scour hole. The undular hydraulic jump and the hydraulic jump can be present over the apron simultaneously in different horizontal sections of the flume. So it is possible to observe that the sand over the apron at the same time, but in different horizontal sections, is partly moved downstream and partly upstream. The scour hole at the end of the test is 3D, because of the presence of a intermittently and 3D flow field.

3.2 *Measured velocity fields*

The velocity field was measured by an ultrasonic velocity profiler (Signal-Processing DOP2000); the bed and the free surface profiles were both measured along the centreline of the flume. They are shown in Figures 2 and 3 for tests H1 and U1, respectively. The horizontal and vertical distances were made dimensionless by h_s, the water depth over the sill. Due to the instrument configuration, data can not be obtained in regions closer to 5 cm from the water surface.

Figure 2 shows the velocity field inside the scour hole for test H1. Ten velocity profiles, positioned at $x = -5, 5, 15, 25, 35, 45, 55, 65, 75$ and 85 cm, respectively, following the reference system shown in Figure 1, were measured. The first profile at $x = -5$ cm shows a wall jet like vertical velocity distribution, or a hydraulic jump, over the apron downstream of the sill.

It is possible to observe a reverse flow at the top of the first measured profile. The wall jet like vertical velocity distribution develops into free-jet like pattern downstream of the apron, with a mobile bed, as shown by the velocity profiles positioned at $x = 5$ cm and $x = 15$ cm. The top reverse flow is not present in these velocity profiles, for $x = 5$ cm the velocity assumes very small values both at the top and at the bottom of the vertical profile. For $x = 15$ cm a small positive horizontal component is present at the top of the velocity profile, while at the bottom the velocity is close to zero. A small negative horizontal velocity component, close to the bottom, is present for $x = 25$ cm, $x = 35$ cm and $x = 45$ cm. From $x = 55$ cm to $x = 85$ cm, a positive horizontal velocity component both close to the

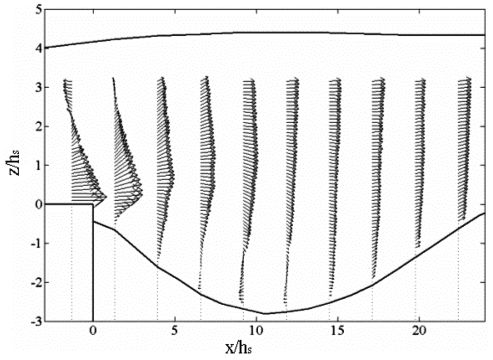


Figure 2. Velocity field for test H1.

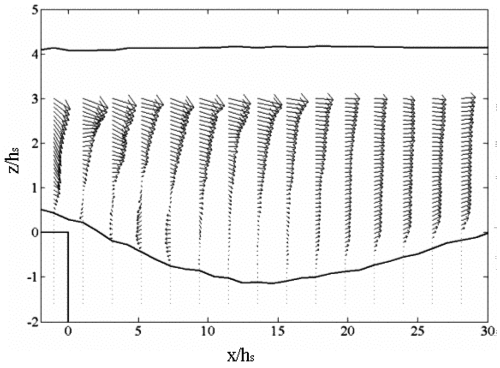


Figure 3. Velocity field for test U1.

top and to the bottom of these velocity profiles was observed.

Figure 3 shows the velocity field inside the scour hole of test U1. Fifteen velocity profiles, positioned at $x = -5$, 5, 15, 25, 35, 45, 55, 65, 75, 85, 95, 105, 115, 125 and 135 cm, respectively, were measured following the reference system shown in Figure 1. In this test an undular hydraulic jump developed over the rigid apron, so a surface jet is present. No reverse flow close the water surface was observed. All the measured profiles show a large positive horizontal velocity component at the top of the flow. A small reverse flow close to the bottom can be observed at $x = 5$ cm, $x = 15$ cm, $x = 25$ cm and $x = 35$ cm. The horizontal velocity component close to the bottom downstream of $x = 45$ cm is first small, then increases in the downstream direction.

4 MATHEMATICAL SIMULATION

4.1 *Stability analysis of undular hydraulic jump on a mobile bed*

The stability analysis consists of the unsteady motion equations considered in the streamline centred s-n

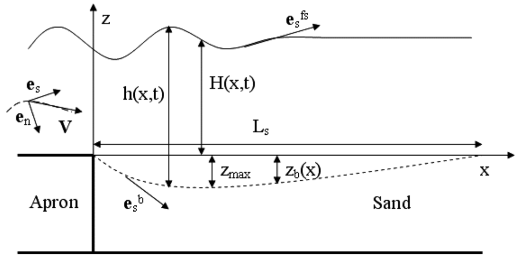


Figure 4. Definition sketch for the mathematical model.

system of reference (Rouse 1938). As a fundamental hypothesis, we assume that the modulus of the velocity vector does not depend on time, while the direction of the velocity does. Such a hypothesis makes sense for steady flow, in which the unsteadiness is due to perturbations of an order of magnitude smaller than that typical for the flow characteristics (discharge, downstream water depth). The quantities required for the description of the phenomenon are defined in Figure 4.

Let $\mathbf{V}$ be the velocity vector, defined as $\mathbf{V} = V(s,n)\,\mathbf{e}_s(s,t)$, being V the modulus, $\mathbf{e}_s$ the unit vector tangent to the instantaneous streamline, s the coordinate on it and n the coordinate along the direction normal to the instantaneous streamline at $s = 0$.

The equations of motion are:

$$V\frac{\partial V}{\partial s} = -\frac{1}{\rho}\frac{\partial p}{\partial s} - g\frac{\partial z}{\partial s} \tag{1}$$

$$\frac{V^2}{R} + V\frac{\partial \mathbf{e}_s}{\partial t}\cdot\mathbf{e}_n = -\frac{1}{\rho}\frac{\partial p}{\partial n} - g\frac{\partial z}{\partial n} \tag{2}$$

where the term $\partial\mathbf{e}_s/\partial t$ accounts for the dependence of the direction of $\mathbf{V}$ on the time and R is the radius of curvature of the instantaneous streamline. The direction of the term $\partial\mathbf{e}_s/\partial t$ is parallel to $\mathbf{e}_n$: that is why it appears in (2). It is important to note that terms accounting for tangential stress have been neglected.

Such a hypothesis is to be considered reasonable only far from boundary layers, i.e. far from the bed and the free surface.

As a consequence, equation (1) gives the Bernoulli equation

$$\frac{V^2}{2} = -g\left(\frac{p}{\rho g} + z\right) + \text{const} \tag{3}$$

Inserting equation (3) in (2), the following equation for the determination of V is obtained

$$\frac{V^2}{R} + V\frac{\partial \mathbf{e}_s}{\partial t}\cdot\mathbf{e}_n = V\frac{\partial V}{\partial n} \tag{4}$$

which is the same obtained by Montes & Chanson (1998), but the term accounting for the unsteadiness of

the perturbations imposed to the base flow. Of course, for such equation is useful, it is necessary to express all the unknown quantities (e.g. R, $\partial \mathbf{e}_s/\partial t$, $\mathbf{e}_s$) appearing in the coefficients. Adopting the geometrical hypothesis of Montes & Chanson (1998), it is possible to express such quantities in terms of the bottom and free surface profiles and their derivatives with respect to x, t.

Here we assume that the bottom profile does not depend on time, while the free surface profile does. Such an assumption makes sense, because it is evident from the experiments that, in condition of quasi-equilibrium scour, the order of magnitude of the time scale of the evolution of the free surface is much smaller of the corresponding time scale of the bottom profile.

If we assume that $\partial V/\partial n = -\cos(\theta)\partial V/\partial z$, θ being the angle formed by the tangent to the instantaneous streamline with the horizontal axis, and if we introduce the non dimensional variable η, defined as:

$$\eta = \frac{z - z_b(x)}{h(x,t)} \tag{5}$$

equation (4) becomes, written in a compact way

$$\frac{\partial V}{\partial \eta} = AV\eta + BV + C\eta \tag{6}$$

in which the coefficients A, B, C are defined as

$$A = \frac{hH''}{1+(H')^2} - \frac{hz_b''}{1+(z_b')^2} \tag{7}$$

$$B = \frac{hz_b''}{1+(z_b')^2} \tag{8}$$

$$C = \frac{h\dot{H}'}{1+(H')^2} \tag{9}$$

where:

$$H'' = \frac{\partial^2 H}{\partial x^2} z_b'' = \frac{d^2 z_b}{dx^2} \tag{10}$$

$$\dot{H}' = \frac{\partial^2 H}{\partial x \partial t} \tag{11}$$

The influence of the unsteadiness due to the perturbations is considered by coefficient C, while A and B account for the curvature effects both concerned with the free surface and the bed.

The solution of equation (6) is the sum of the homogeneous solution

$$V_{om} = c_{om} e^{\frac{A}{2}\eta^2 + B\eta} \tag{12}$$

and of the particular solution, which can be expressed as a power series

$$V_p = \sum_{i=0}^{N} a_i \eta^i \tag{13}$$

whose coefficients are defined by means of a recurrence relation obtained substituting the particular solution in equation (6) and equating terms with the same power of η.

The constant c_{om} is determined by imposing that $(V_p + V_{om})_{\eta=1} = V_{fs}$, V_{fs} being the velocity on the free-surface, and then expressing V_{fs} through the mean velocity U, defined as:

$$U \approx \int_0^1 V d\eta \tag{13b}$$

After some calculations, it is possible to obtain the analytical expression of the horizontal and vertical velocity components as well as the pressure as

$$u \approx V = c_{om} e^{\frac{A}{2}\eta^2 + B\eta} + \sum_{i=0}^{N} a_i \eta^i$$

$$v = V \sin\theta = \left(c_{om} e^{\frac{A}{2}\eta^2 + B\eta} + \sum_{i=0}^{N} a_i \eta^2 \right) \cdot \tag{14}$$

$$\left[(1-\eta) \frac{z_b'}{\sqrt{1+(z_b')^2}} + \eta \frac{H'}{\sqrt{1+(H')^2}} \right] \tag{15}$$

$$p = \int_\eta^1 \left\{ \rho g h + \rho \left[(1-\xi) \frac{z_b''(x,t)}{\left(1+(z_b')^2\right)} + \xi \frac{H''(x,t)}{1+(H'(x,t))^2} \right] hV^2 + \rho h V \xi \frac{H'(x,t)}{1+(H'(x,t))^2} \right\} d\xi \tag{16}$$

Expressions (14), (15) and (16) depend on $z_b(x)$, h(x,t), U(x,t), $H(x,t) = z_b(x) + h(x,t)$ as well as on an undetermined coefficient a_0. An analytical determination of this latter is possible, but is rather complicated. In this work such a coefficient is left undetermined and calibrated on the experimental results. Moreover, it is assumed that $z_b(x)$ is given by interpolations of experimental measurements. At last evolution equations for h(x,t),U(x,t) can be obtained by considering integral forms of the continuity and momentum equation (Montes & Chanson 1998)

$$\frac{\partial h}{\partial t} + \int_0^1 V d\eta = 0 \tag{17}$$

$$\frac{\partial U}{\partial t} + g\frac{\partial}{\partial x}\int_0^1 \left(\frac{V^2}{2g} + h\eta + z_b + \frac{p}{\rho g}\right)d\eta = -\frac{\lambda U|U|}{8\Re} \quad (18)$$

where λ, and $\Re$ are, respectively, the friction factor and the hydraulic radius, defined in the usual way for open channel flow with a mobile bed (Marchi & Rubatta 1980, Garde & Ranga Raju 1977). Equations (17) and (18) are the classic Saint Venant equations for free surface flows, in which curvature effects connected to the free surface and bottom profiles have been accounted. For the last step is to assume the unknown functions h(x,t) and U(x,t) as the sum of a base flow and an unsteady perturbation with a known dependency on time:

$$h(x,t) = h_0(x) + h_1(x)e^{\gamma t} \quad (19)$$

$$U(x,t) = U_0(x) + U_1(x)e^{\gamma t} \quad (20)$$

It is supposed that the perturbations are small quantities with respect to the quantities of the base flow, at least at the early stage. Then, substituting expressions (19) and (20) in equations (17) and (18), it is possible to discard nonlinear terms with respect to the perturbations. Imposing that the expressions (19) and (20) satisfy equations (17) and (18), two different differential systems are obtained. The first can be used to determine the base solution $h_0(x)$, $U_0(x)$, while the second, known the base solution, is useful to determine the evolution of the perturbations flow, characterised by $h_1(x)$, $U_1(x)$. The parameter γ, which can be considered as an eigenvalue of the linear and homogeneous perturbation equations, gives information on the stability of the base solution: if the real part of γ is positive, perturbations imposed on the base solution will tend to destroy the base solution and then this latter is considered unstable. On the contrary, if the real part of γ is negative, perturbations imposed on the base solution will tend to decrease with time and the base solution is considered stable. Of course, such conclusions are considered valid in the framework of a linear stability analysis: i.e. they are valid in the early stage of the perturbations.

4.2 *Computational considerations and analysis*

The differential equations for the determination of the base flow and the perturbations are omitted for the sake of simplicity. However it is important to observe that it is difficult to obtain the solution of the differential equations for the base flow $h_0(x)$, $U_0(x)$, due to their strongly nonlinear nature. On the other hand, the aim of this work is to investigate the stability of a given experimental condition, which represents the base flow: so the base flow is assumed known, interpolating experimental results. More precisely, the free surface profile $H_0(x) = h_0(x) + z_b(x)$ and the bottom profile $z_b(x)$ are measured along the x direction, in correspondence of the centreline of the experimental channel, while the mean velocity $U_0(x)$ is obtained as

$$U_0(x) = \frac{Q}{b h_0(x)} = \frac{Q}{b[H_0(x) - z_b(x)]} \quad (21)$$

Q being the discharge, considered constant with respect to time.

Interpolating expressions for $H_0(x)$, $z_b(x)$ adopted in this work are the following

$$H_0(x) = h_d + \eta \sin\left(\frac{2\pi x}{l_0}\right) \quad (22)$$

$$z_b(x) = z_{b0} + z_{max} \sin\left(\frac{2\pi x}{l_s}\right) \quad (23)$$

where l_0 and η are respectively the measured wavelength and amplitude of the free surface undulations, defined respectively as the distance between the first two crests of the free surface and half the distance between first crest and first throat. L_s and z_{max} are the measured wavelength and the maximum scour depth. z_{b0} is the scour depth in correspondence of the end of the apron, i.e. at $x = 0$. The measured wavelength of the bottom is defined as the wavelength with which the sine expressions (23) and (24) best fit the scour profile. For the sake of simplicity, no decaying phenomena were considered for the free surface undulations.

Six experimental configuration were considered, whose characteristics are shown in Table 2.

Where Fr_d is the Froude number, defined with the characteristics of the flow downstream, far from the undular hydraulic jump, where the motion has become uniform again.

$$Fr_d = \frac{Q}{b H_0 \sqrt{g H_0}} \quad (24)$$

The stability of the experimental configurations can be investigated by solving the linear differential equations for the perturbation flow $h_1(x)$, $U_1(x)$. Such

Table 2. Experimental configurations.

Run	Fr_d	l_0[m]	η[m]	L_s[m]	Stability
T1	0.15	0.12	0.0045	1.5	Unstable
T2	0.17	0.15	0.003	2.4	Unstable
T3	0.18	0.18	0.002	3.0	Unstable
U1	0.14	0.35	0.003	3.0	Stable
U2	0.15	0.25	0.004	3.8	Stable
U3	0.16	0.35	0.0035	4.0	Stable

differential equations, though linear, have coefficients depending on x and an approximate procedure is adopted in order to solve them. Such a procedure consists in assuming a Fourier series development of the perturbation flow, in which the fundamental wavelength of the perturbation flow coincides with the wavelength of the free surface undulations, and in substituting it in the perturbation equations. Imposing a suitable solvability condition, an algebraic equation, whose order depends on the number of modes adopted in the Fourier expansion, is obtained for γ. The real part of this latter gives indications on the stability of the base flow.

Results are shown in the stability diagrams presented in Figure 5 and Figure 6, in which the horizontal axis represents the wavelengths of the undular hydraulic jump, the vertical axis the Froude number, defined with the downstream characteristics of the flow. In Figure 5 the lines (black, grey and dashed lines refer to the experimental conditions in Table 1 by T1, T2 and T3 respectively) separate the unstable from the stable region: the stability region is on the right of the lines. The three unstable experimental configurations are represented in the diagram by a square, a circle and a triangle and are referred to T1, T2 and T3 respectively.

In Figure 6 the lines (black, grey and dashed lines, which refer to the experimental conditions indicated in Table 1 by U1, U2 and U3 respectively) separate the unstable from the stable region: the stability region is on the right of the lines. The three unstable experimental configurations are represented in the diagram by a square, a circle and a triangle and are referred to U1, U2 and U3 respectively.

The horizontal lines limit the area over which it is physically possible to have a hydraulic jump for the experimental conditions considered: i.e. they are obtained imposing that the upstream Froude number is less than for the considered discharges. The stability diagram is divided into three regions: the stable region on the right, the unstable region on the left and the no hydraulic jump region in the lower part.

As a general remark, we observe that undular hydraulic jumps of small wavelength tend to become unstable and then evolve to different forms of hydraulic jumps. At last we observe that the theoretical predictions confirm the experimental observations.

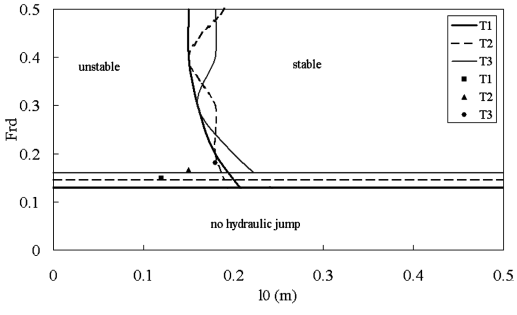


Figure 5. Stability diagrams for tests T1, T2, T3.

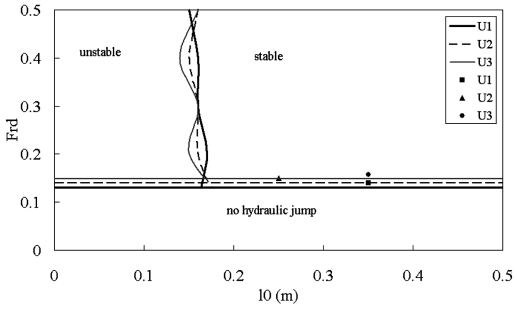


Figure 6. Stability diagrams for tests U1, U2, U3.

CONCLUSIONS

The qualitative description of local scour development, due to three different kinds of jets, a wall jet (hydraulic jump), a surface jet (undular hydraulic jump) and a transition jet (transition between hydraulic and undular hydraulic jump), is presented. The scour hole is observed to be quasi 2D if a hydraulic jump develops over the apron. If the local scour is caused by an undular hydraulic jump or a transition jump, it is 3D. The profiles of the vertical and horizontal velocity component, measured in the scour hole, by an ultrasonic velocity profiler, both in case of a hydraulic jump and an undular hydraulic jump are presented.

The stability analysis of the undular hydraulic jump, performed starting from the unsteady momentum equations, written in the s, n coordinate system, permits to characterise the time evolution of the flow, assumed as the superposition of a base and a perturbation flow. In particular, the stability of the flow is expressed by a coefficient γ which can be considered as the eigenvalue of the perturbation equations. His real part gives information of the stability of the considered experimental conditions. Comparisons between analytical and experimental results are satisfactory.

ACKNOWLEDGEMENTS

Laboratory activities were supported by Italian Funding COFIN 2002–2004 “Modellazione di processi idrodinamici in sistemi fluidi stratificati, di correnti a superficie libera e in pressione a celerità variabile.”, section “Modellazione sperimentale di fenomeni erosivi localizzati nelle correnti a superficie libera”.

REFERENCES

Bukreev, V. I. 2001. Undular jump in open-channel flow over a sill. *J. App. Mech. Tech. Phy.* 42(4):596–602.

Chanson, H. & Montes, J. S. 1995. Characteristics of undular hydraulic jumps: Experimental apparatus and flow patterns. *Journal of Hydraulic Engineering*, ASCE 122(2): 129–144.

Chatterjee, S. S., Ghosh, S. N. & Chatterjee, M. 1994. Local scour due to submerged horizontal jet. *Journal of Hydraulic Engineering*. 120(8): 973–992.

Chow, V. T. 1959. *Open Channel Hydraulics*. New York: Mc Graw Hill.

Dey, S. & Westrich, B. 2003. Hydraulics of submerged jet subject to change in coesive bed geometry. *J. Hydr. Eng*. 129(1): 44–53.

Farhoudi, J. & Smith, K. V. H. 1985. Local scour profiles downstream of hydraulic jump. *Journal of Hydraulic Research*. 23(4): 343–358.

Garde, R. J. & Ranga Raju, K. G. 1977. *Mechanics of sediment transport and alluvial stream problems.* New York: Wiley.

Gaudio, R. & Marion, A. 2003. Time evolution of scouring downstream of bed sills. *J. Hydr. Res.* 41: 271–284.

Grillhofer, W. & Schneider, W. 2003. The undular hydraulic jump in turbulent open channel flow at large Reynolds numbers, *Phys. Fluid.* 15(3): 730–735.

Habib, E., Mossa, M. & Petrillo, A. 1994. Indagine sperimentale sull'escavazione in un canale a fondo mobile posto a valle di un risalto idraulico. *Proc. nat. symp. XXIV Convegno di idraulica e costruzioni idrauliche; Napoli* T4: 25–36.

Kurniawan, A., Altinakar, M. S. & Graf, W. H. 2001. *Flow pattern of an eroding jet*, Proc. of XXIX IAHR Congress, Beijing, China: 537–544.

Lenzi, M. A., Marion, A., Comiti, F. & Gaudio, R. 2002. Local scouring in low and high gradient streams at bed sills. *Journal of Hydraulic Research* 40(6): 731–739.

Longo, S., Losada, I. J., Petti, M., Pasotti, N. & Lara, J. L. 2001. Measurements of breaking waves and bores through a USD velocity profiler. *Technical Report UPR/UCa_01_2001.* University of Parma, E.T.S.I.C.C. y P., Ocean & Coastal Research Group Laboratory, Universidad de Cantabria, Spain, 2001.

Marchi, E. & Rubatta, A. 1980. *Meccanica dei fluidi. Principi e applicazioni idrauliche.* Bologna: UTET.

Mazurek, K. A., Rajaratnam, N. & Sego, D. C. 2003. Scour of cohesive soil by submerged plane turbulent wall jets. *Journal of Hydraulic Research*. 41(2): 195–206.

Montes, J. S. & Chanson, H. 1998. Characteristics of undular hydraulic jumps: Experiments and analysis, *J. Hydr. Eng.* 124(2):192–205.

Mossa, M. et al. 1995. Scour from flow downstream of a sluice gate after a horizontal apron. *Sixth internazional symposium river sedimentation; Proc. intern. symp., New Delhi, 7–11 November 1995*. New Delhi: Oxford & IBH publishing Co. Pvt. Ltd.

Mossa, M. 1998. Experimental study on the scour downstream of grade-control structures. *XXVI Convegno di Idraulica e Costruzioni Idrauliche*; Catania, 1998, 3: 581–594.

Ohtsu, I., Yasuda, Y. & Gotoh, H. 1997. Discussion of characteristics of undular hydraulic jumps: experimental apparatus and fow patterns. *J. Hyd. Eng.* 124(2): 161–162.

Ohtsu, I., Yasuda, Y. & Gotoh, H. 2001. Hydraulic condition for undular-jump formation. *J. Hydr. Res.* 39(2):203–209.

Rouse, H. 1938. *Fluid Mechanics for Hydraulic Engineering*. New York: McGraw Hill.

Steinruck, H., Schneider, W. & Grillhofer, W. 2003. A multiple scale analysis of the undular hydraulic jump in turbulent open channel flow. *Fluid Dyn. Res.* 33: 41–55.

Takeda, Y. 1995. Velocity profile measurements by ultrasonic Doppler method. *Experimental Thermal and Fluid Science*. 10(4): 444–453.

Takeda, Y. 1999. Ultrasonic Doppler method for velocity profile measurements in fluid dynamics. *Experiments in Fluids.* 26(3): 177–178.

River Flow 2004 – Greco, Carravetta & Della Morte (eds.)
© 2004 Taylor & Francis Group, London, ISBN 90 5809 658 0

Flow seperation at 45 to 90 degree water intakes

Keshavarzi, Alireza
Assistant Professor, Irrigation Department, Shiraz University, Shiraz, Iran

L. Habibi
Postgraduate student, Irrigation Department, Shiraz University, Shiraz, Iran

M.J. Kazemzadeh Parsi
Research Assistant, Irrigation Department, Shiraz University, Shiraz, Iran

ABSTRACT: An experimental study was used to understand flow structure at water intake. To find the optimum angle at water intake, the separation zone was compared for five deflection angles from 45 to 90-degrees. The experimental tests were carried out in an experimental flume with rectangular cross section. The velocity of the flow inside each intake was measured in 727 points of fluid in a fine grid. The points of velocity measurements include 243 points at three horizontal layers and 486 points in 6 cross sections. Two components of flow velocity were measured using an electromagnetic disk type velocity meter (PE-30 Type, DELFT). Five types of water intake with 45, 56, 69, 79 and 90-degree were installed at one side of a straight canal. To compare the separation in five types of water intakes, the size of the separation zones inside the lateral was measured at similar flow condition. The water intake with minimum separation was defined as the optimum angle for installation of water intake. It was found that the optimum angle is 55-degree at water intake.

1 INTRODUCTION

The streamlines of the flow at a straight open channel are approximately parallel to the flow direction. When a water intake with an angle is installed at one side of the canal, the streamlines of the flow deflect toward the intake. At this flow condition, a separation zone is produced at one side in the lateral canal. The flow structure at open-channel junction was studied by many researchers; for example, Taylor (1944), Law and Reynolds (1966), Hager (1984), Hsu et al (1998) and Grace and Priest (1958). Taylor (1944) considered the flow depth at upstream and downstream of a canal junction as a parameter of flow condition and produced a theoretical development. Most previous studies were carried out in junction where flow in two channels combines together and flow separation occurs in the main channel. But, at water intake flow diverts from the main channel and flow separation occurs in the lateral. In a study by Neary and Odgaard (1993), the vertical secondary current at water intake with 90-degree diversion was investigated. To study the secondary current, they considered the velocity distribution and separation zone at the bed and water surface of 90-degree diversion. However, little study was carried out to understand the flow structure inside the water intakes with angles different from the 90-degree. In this study, to find the optimum angle, a comprehensive experimental test was carried out in the laboratory and separation size was measured at water intake with five different angles.

2 EXPERIMENTAL SETUP

The experiments were carried out in a non recirculating experimental flume with a lateral. The experimental model was built in hydraulic laboratory of Shiraz University, Shiraz, Iran. Five water intakes were installed at one side of the main channel. The water intakes were installed with 45, 57, 67, 89 and 90-degree to the main channel. The main channel consists of a rectangular cross section with base width of 0.50 m, height 0.40 m and 15.80 m length. The longitudinal slope of the flume was set to 0.003. In order to visualize the flow structure at water intake, one side wall of the flume at the front of water intake was built of glass. The first water intakes were installed at a distance of 6.40 m from the inlet. The lateral diversion channel consists of 0.25 m width, 0.40 m height and zero slope. The Flow separation at 45 to 90-degree water intakes 2 main canal and the lateral were built of smooth

concrete. The flow of the intakes passed downstream through a 7.63 m lateral canal. The flow rate at the end of main and lateral canals was measured using two pre-calibrated right-angle V-notches. To make streamlines parallel to the main canal direction, a series of flow straightener were used at the inlet of the main channel. A schematic diagram of the experimental model is shown in figure 1.

The experimental tests were performed at flow rate equal to 16 liter per second. The depth of flow for all tests was a constant depth (16 cm) using downstream gates. The velocities of the flow in two components were measured using an electromagnetic velocity meter (PE-30 Model, Ellipsoid type, DELFT). The velocity measurement was done at three layers in depth of flow at water intakes. The velocity in the horizontal layers was measured at a regular grid. The grid size for the velocity measurement in horizontal layers was 25 mm in width and 50 mm in the length of the intake. To find the size of separation zone in depth, the velocity of the flow was measured at three depths as: 3 cm from the bed, 6 cm from the bed and 12 cm from the bed. Additionally, a fine measurement was carried out at cross sections of 10, 20, 30, 40, 50 and 60 cm from the inlet of water intakes. The depth increment for velocity measurement in vertical was selected in 2 mm increment. The vertical measurement at cross sections was selected at a grid size of 2 mm by 2.5 mm. Due to the size of electromagnetic velocity meter probe, it was not able to measure the velocity very close to the bed and water surface. The experiments were performed at different flow conditions and they are listed in table 1.

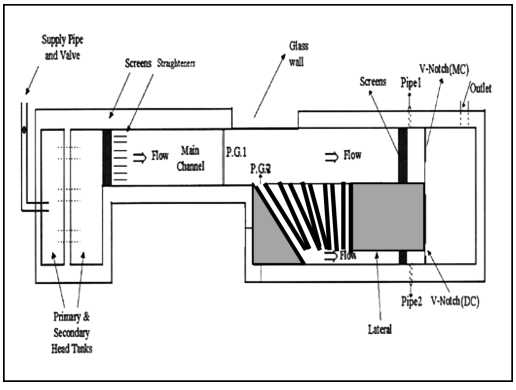


Figure 1. A schematic of experimental setup.

3 RESULTS AND DISCUSSION

To find a relationship between deflection angle of water intake and separation size, the velocity of the flow at two components were measured. The velocities were measured in time for duration of 40 seconds with sampling rate of 0.1 Hz. Therefore, a total number of 400 velocity data at each point of flow was recorded in the computer. The time-averaged velocity in the flow direction ($\overline{U}$) and in transverse direction ($\overline{V}$), at each point were calculated using the following equations:

$$\overline{U} = \frac{1}{n}\sum_{i=1}^{n} u_i$$

$$\overline{V} = \frac{1}{n}\sum_{i=1}^{n} v_i$$

where, u_i and v_i are instantaneous velocities in the flow direction and transverse direction, respectively, and n is the number of sampling. Figures 2 to 15 show the velocity vector and particle trace plots at the depths of 3, 6 and 12 cm from the bed. They are plotted for five different angles. The most feature of the plots is the observation of the separation zone along the water intake. The separation zones are very clear at the upstream or downstream portion of the water intake. The width and length of the separation zone were derived from the plots.

The particle trace plots show the location of the separation zone and deflected streamlines toward the intake. It can be seen that in the separation zone the streamlines are deflected from the wall at upstream of water intake. The size of the separation zone is small near the bed, while it is large near the surface. Neary and Odgaard (1993) pointed out that this occurs because of high velocity near the water surface. Due to the difference in velocity particularly where streamlines are very close, a momentum transfer occurs between the streamlines and produces a series of eddies. The eddies will move downstream of the intake. The eddies dissipate energy along the intake.

Table 1. Experimental flow condition.

Angle (Degree)	Q (L/s)	Flow depth (cm)	Main channel Fr	Intake channel Fr	Main channel Re	Intake channel Re
90	12.03	16.02	0.150	0.299	28697	57394
79	13.15	16.13	0.130	0.259	25107	50213
68	13.68	16.07	0.136	0.271	26131	52263
56	13.57	16.01	0.135	0.271	25923	51846
45	13.50	16.06	0.134	0.268	25790	51580

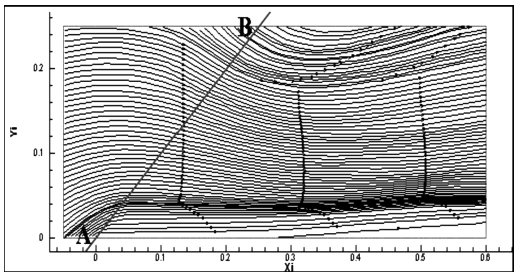


Figure 2a. Streamlines for 45-degree water intake at 3 cm from the bed.

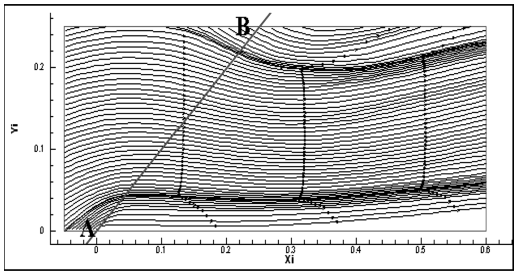


Figure 2b. Streamlines for 45-degree water intake at 6 cm from the bed.

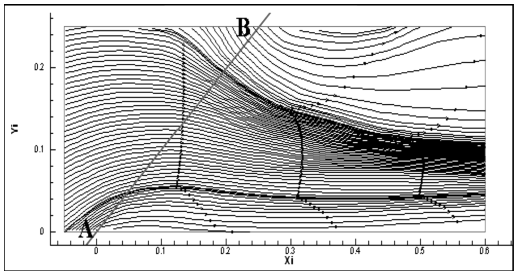


Figure 2c. Streamlines for 45-degree water intake at 12 cm from the bed.

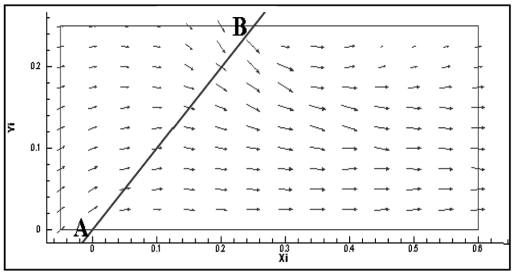


Figure 2d. Velocity vectors for 45-degree water intake at 12 cm from the bed.

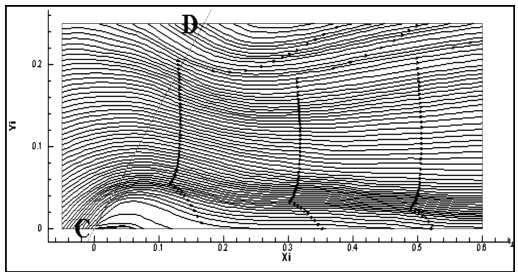


Figure 3a. Streamlines for 56-degree water intake at 3 cm from the bed.

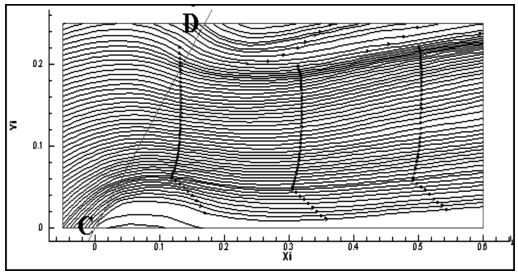


Figure 3b. Streamlines for 56-degree water intake at 6 cm from the bed.

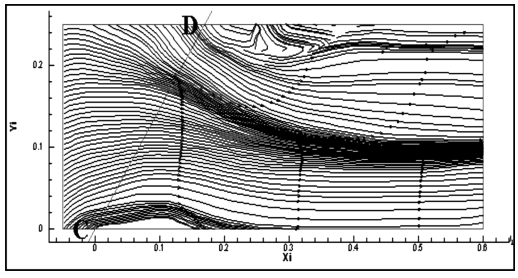


Figure 3c. Streamlines for 56-degree water intake at 12 cm from the bed.

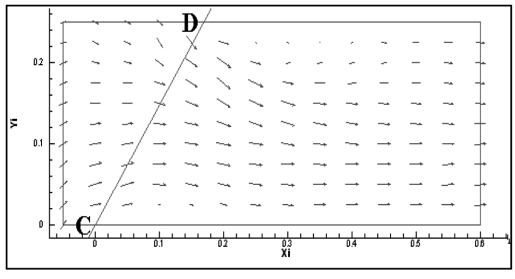


Figure 3d. Velocity vectors for 56-degree water intake at 12 cm from the bed.

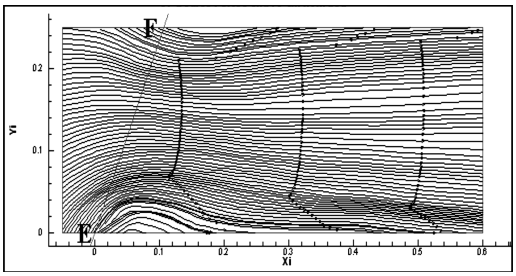


Figure 4a. Streamlines for 67-degree water intake at 3 cm from the bed.

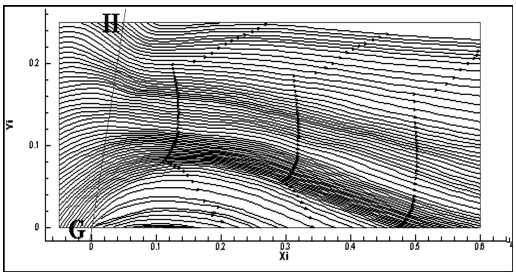


Figure 5a. Streamlines for 79-degree water intake at 3 cm from the bed.

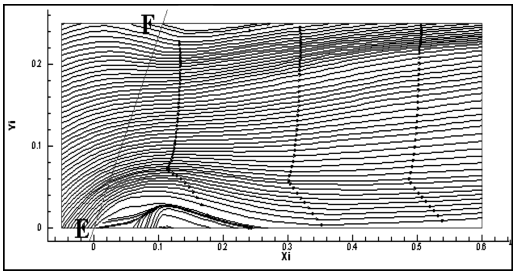


Figure 4b. Streamlines for 67-degree water intake at 6 cm from the bed.

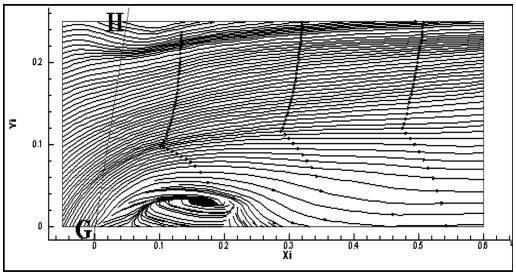


Figure 5b. Streamlines for 79-degree water intake at 6 cm from the bed.

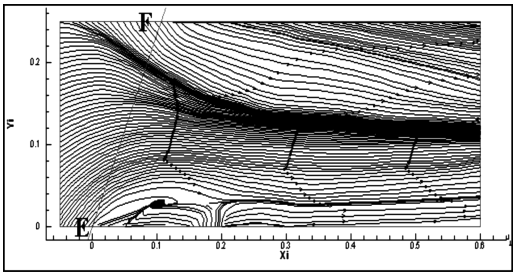


Figure 4c. Streamlines for 67-degree water intake at 12 cm from the bed.

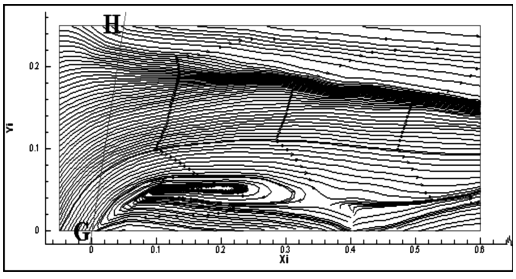


Figure 5c. Streamlines for 79-degree water intake at 12 cm from the bed.

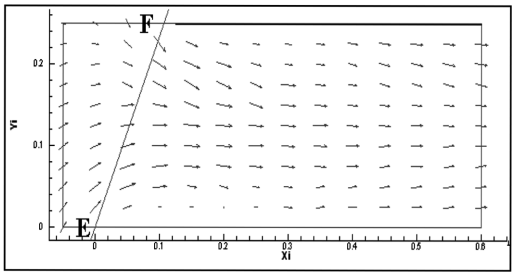


Figure 4d. Velocity vectors for 67-degree water intake at 12 cm from the bed.

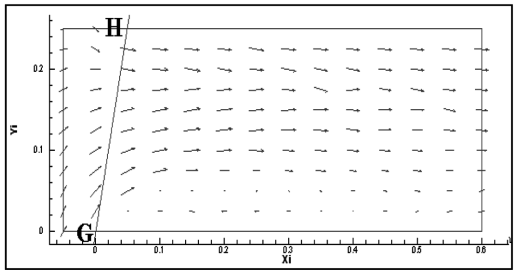


Figure 5d. Velocity vectors for 79-degree water intake at 12 cm from the bed.

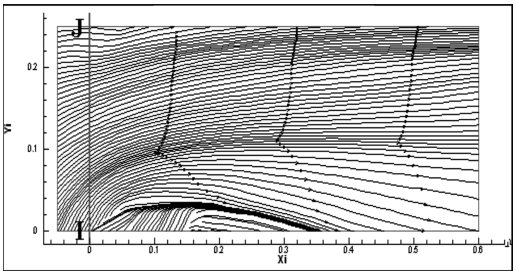


Figure 6a. Streamlines for 90-degree water intake at 3 cm from the bed.

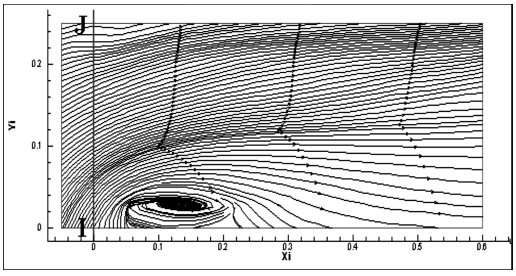


Figure 6b. Streamlines for 90-degree water intake at 6 cm from the bed.

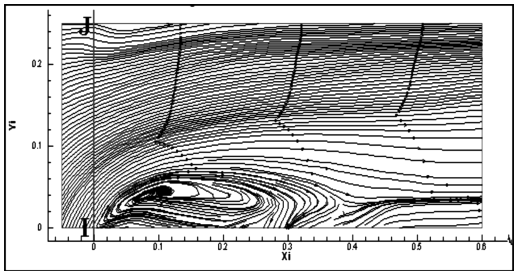


Figure 6c. Streamlines for 90-degree water intake at 12 cm from the bed.

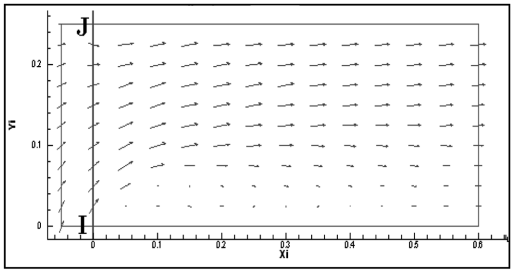


Figure 6d. Velocity vectors for 90-degree water intake at 12 cm from the bed.

The large separation size will cause higher momentum transfer between streamlines and therefore large eddies will form. At this condition a large amount of energy will dissipate along the intake. This will cause less flow rate inside the intake. To minimize the separation zone, and producing less energy dissipation, design of intake with minimum separation size is necessary and it is the major focus of this study.

Figures 2 to 6 show that how the size of separation varies for different angle and at similar flow condition.

Point A at figures 2a, 2b and 2c indicate upstream of the 45-degree water intake and point B in the same figures indicates downstream of the 45-degree water intake. Also the letters C, E, G and I indicate upstream, whereas, the letters D, F, H and J in figures 3 to 6, indicate downstream of 56, 67, 79 and 90-degree at water intakes, respectively. At 90-degree water intake, the separation zone is mostly occurred at the upstream of water intake, while at 45-degree water intake it occurs at the downstream portion. The size of separation is very large at 90-degree angle and it grows to the half of the width of the water intake. Therefore, as the deflection angle decreases from 90 to 45 degrees, the 3 size of separation changes at upstream and downstream of water intake. At 79-degree water intake the size of separation decreases at upstream and a small separation starts to grow at downstream when compares to 90-degree water intake. Again at the angle of 67-degree, the formation of separation occurred both at upstream and downstream of the intake. At intake with the angle 56-degree, there is minimum separation zone was produced at upstream and downstream portions.

As previously mentioned, at intake with the angle of 45-degree, the separation zone is relatively large at downstream, while at the same time, the separation zone is small at upstream. It means that location of the separation zone moves from upstream to downstream when compared the separation zone in 90 and 45-degree intake.

The width and the length of the separation at upstream and downstream were measured for the angles of 45, 56, 67, 89 and 90-degree and they are plotted separately for upstream and downstream locations. The length of the separation is plotted in figure 7 for upstream and downstream, while the width of the separation for upstream and downstream are plotted in figure 8. The intersection of the best-fit equations represents the optimum angle of the water intake. From the above figures, the minimum separation zone was found to occur at 55-degree water intake both at the upstream and downstream. Therefore, the optimum angle for the water intake was found to be 55-degree.

A statistical analysis of the data is shown that there is a relation between the angle of water intake and the size of separation. The following relations were found

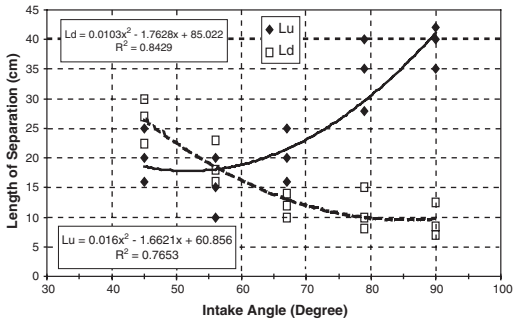


Figure 7. Length of separation at upstream and downstream water intake

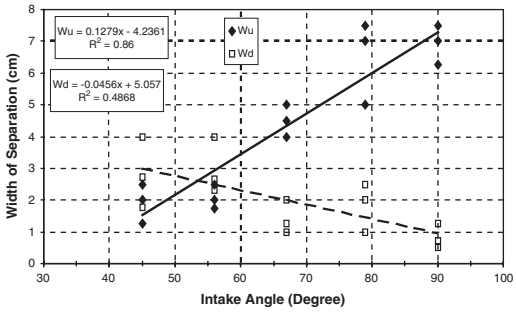


Figure 8. Width of separation at upstream and downstream of water intake.

for the length and the width of the separation.

$$L_d = 0.01\theta^2 - 1.76\theta + 85, \quad R^2 = 0.84 \tag{1}$$

$$L_u = 0.016\theta^2 - 1.66\theta + 61, \; R2 = 0.77 \tag{2}$$

$$Wu = 0.128\,\theta - 4.24, \qquad R2 = 0.86 \tag{3}$$

$$W_d = -0.046\theta + 5.06, \qquad R2 = 0.49 \tag{4}$$

where θ is the angle of water intake and L_d, and L_u, are the length of separation at downstream and upstream of water intake and W_u and W_d are the width of the separation at the upstream and downstream, respectively.

Additionally, it was found that the separation zone moves from upstream to downstream when the angle of water intake changes from 90-degree to 45-degree. The size of separation at 90-degree water intake is very large at upstream when compared to 45-degree deflection angle. Therefore, it was found that the formation of separation zone is very sensitive to the deflection angle at the intakes.

4 CONCLUSION

An experimental study was carried out to study the characteristics of flow structure and separation zone at upstream and downstream of the water intake. The water intakes were varied from 45- to 90-degree angles. The water intakes were diverted from a main channel. The measurement of velocity was done at grid of 25 by 50 mm along the water intakes. The measurements were done at three depth level of 3, 6 and 12 cm from the bed or at 0.2 h, 0.6 h and 0.8 h from the surface. To find the optimum angle for the formation of separation zone between different angles (45- to 90-degree) the width and length of separation zone at upstream and downstream of the water intakes were measured. Some relations were found for width and length at upstream and downstream. It was found that totally the optimum angle for separation is 55-degree. Additionally it was found that the separation moved from upstream to downstream, when the angle changes from 45- to 90-degree.

REFERENCES

Barkdoll, Brain D., Robert Ettema and A. Jacob Odgaard (1999). Sediment control at lateral diversions: Limits and enhancements to vane used. *J. Hyd. Engrg.,* ASCE, 125(8): 862–870.

Hager, W. H. (1984). An approximate treatment of flow in branches and bends. *Proc.,* Inst. of Mech. Engineers, 198C(4): 63–69.

Hsu, C. C., WU, F. S. and Lee, W. J. (1998). Flow at 90° equal-width open-channel junction. *J. Hyd. Engrg.*, ASCE, 124(2): 186–191.

Hsu, C. C. Tang, C. J., Lee, W. J. and Shieh, M. Y. (2002). Subcritical 90 equal-width open channel dividing flow. *J. Hyd. Engrg.*, ASCE, 128(7): 716–720.

Law, S. W. and Reynolds, A. J. (1966). Dividing flow in an open channel. *J. Hyd. Div.*, ASCE, 92(2): 207–231.

Marelius, F. and Sinha, S. K. (1998) Sediment control at water intake along sand-bed river. *J. Hyd. Engrg.*, ASCE, 124(5): 542–546.

Neary, Vincent, S. and Jacob Odgaard, A. (1993). Three dimensional flow structure at open-channel diversions. *J. Hyd. Engrg*., ASCE, 117(11): 1223–1230.

Odgaard, A. J. and Spoljaric, A. (1987). Sediment control by submerged vanes. *J. Hyd. Engrg.*, ASCE, 122(12): 1164–1181.

Taylor, E. H., (1944). Flow characteristics at rectangular open-channel junctions. *Trans.*, ASCE, 109: 893–912.

Wang, Y. A., Jacob Odgaard, A. and Melville, B. W. and Jain, S. C. (1996). Sediment control at water intake. *J. Hyd. Engrg.*, ASCE, 122(6): 353–356.

Weber, Larry J., Eric D. Schumate and Nicola Mawer (2001). Experiments on flow at 90° open-channel junction. *J. Hyd. Engrg*., ASCE, 127(5): 340–350.

River Flow 2004 – Greco, Carravetta & Della Morte (eds.)
© 2004 Taylor & Francis Group, London, ISBN 90 5809 658 0

Study on structure-induced flow and turbulence considering bed morphology

S. Giri, Y. Shimizu & B. Surajate
Hokkaido University, Japan

ABSTRACT: The study reported herein was conducted in a meandering like laboratory flume in order to determine near-bed flow and turbulent characteristics around river training structures with and without scour hole/deposition. Observation was performed near a couple of spurs placed in different part of the bend simultaneously. The purpose of this study is to evaluate near-bed three dimensional flow field, the turbulent stresses and the turbulent kinetic energy distribution around spurs with rough rigid bed as well as with developed bed morphology under similar flow condition. This study has revealed the distinctive characteristics of flow & turbulence quantitatively before and after the development of structure-induced bed morphology. Likewise, distinction in flow and turbulence near spurs placed in different part of the bend simultaneously was also investigated. Furthermore, a simple flow visualization technique was implemented to observe the generation and migration of vortices from the tip of the structure. A preliminary attempt was made to simulate the flow and vorticity field in near-spur region using 2D numerical model and validated with experiment on flow with spurs for rigid bed case as well.

1 INTRODUCTION

The prediction of structure-induced flow and morphology is of great significance from practical engineering point of view. Taking this into consideration, various physical and numerical studies (Shimizu & Nishimoto, 1993) were performed in the past and still being carried out. However, quantitative determination of flow and turbulent characteristics considering structure-induced bed evolution has not received due consideration. To our knowledge, very few have been done in this connection (Melville & Raudkivi, 1977; Graf & Istiarto, 2002). Of most the past studies were carried out on the flow pattern near spur for rigid & smooth bed. Some studies were conducted to analyze the flow around structure using theory of three-dimensional turbulent boundary layers (Rajaratnam & Nwachukwu, 1983; Ferdous & Rajaratnam, 2000) as well as to evaluate the exchange process between spur region and transit flow (Uijttewaal, 2001; Chen & Ikeda, 1997). Study on structure-induced mean flow pattern throughout the bend reach was performed by authors (Giri et al, 2003) that was verified with a numerical model in which flow characteristics in shear layer region was simulated using subgrid scale model (Surajate & Shimizu, 2003; Uittenbogaard, 2001).

It is to be emphasized that the flow field near spur-like structures is completely three-dimensional. It becomes more complicated while consider the bed morphology. Consequently, it is thought to be of importance to determine the turbulent characteristics, viz. turbulent stresses & energy distribution in the vicinity & nearby region before and after the development of scour-holes and deposition so as to assess the distinction in the flow and turbulence before and after the development of river bed morphology. On the other hand, it is necessary to assess, simultaneously, the flow and turbulence near spurs placed in different part of bend in order to quantify their interaction as well as allocation effect.

This study has made a basic attempt to determine the three-dimensional flow field and turbulence induced by spurs and bed morphology. The objective of this study is to achieve an initial insight into the flow and turbulent structure with and without considering bed morphology near spurs placed in different bends. Such kind of studies may be of use to understand the physical mechanism associated with structure-induced bed evolution and mixing process before and after the development of bed morphology assessing simultaneously the effect of change of the bend direction. A three-dimensional ADV was used to measure the instaneous flow field.

A preliminary numerical study was performed using 2D CIP numerical technique. The case of rigid bed experiment on flow with spurs was used to validate this numerical model. Velocity distribution throughout the bend reach was reproduced numerically and

compared with experimental results. Similarly, vortices shedding from the tip of spurs were also simulated using this model.

An attempt was made to visualize the migration of small eddies generated from the tip of the spurs using simple experimental technique.

2 EXPERIMENTAL SET UP

This experiment was carried out in a laboratory flume of Applied Hydrology Laboratory of Hokkaido University. The flume was 28 m long and 1 m wide with a meandering reach of 7.7 m wave length having 3 consecutive bends of 40°, 80° & 40° arc angles respectively. Detail can be found in Giri et al. (2003). The experimental condition has been adopted according to the characteristics of Plane Rivers with mild slope and sub-critical flow. Experiment was performed for clear-water condition. The channel bed was filled up with uniform sand having median grain size of 1.2 mm. A couple of non-submerged spurs were used (h = 15 cm) with the length, namely 1/4 of channel width. Spur 1 & spur 2 were placed in 35° of arc angle in bend 1 and 60° of arc angle in bend 2 (Fig.1). In order to make the near spur region rigid, the cement powder was used that enables the sand particles to be interlinked. A clear water experiment was conducted with 60 hrs of run when scour and deposition was seen to have attained quazi-equilibrium condition so as to perform study for the case with developed bed topography. The temporal development of scour-holes has been depicted in Figure 2. Quazi-equilibrium bed topography for this experimental case can be found in Giri & Shimizu (2004).

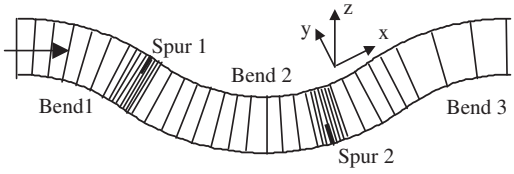


Figure 1. Schematic location of measured sections with 1° to 5° intervals.

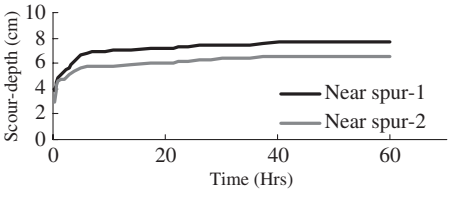


Figure 2. Temporal development of scour-holes.

Table 1. Test condition.

Approach flow depth, h (cm)	10.5
Froude number, Fr	0.18
Flow Reynolds number, Re	19530
Average velocity, U_0 (cm/sec)	18.6
Sediment diameter, d_{50} (mm)	1.20
Flow intensity, U_t/U_{0*}	0.5
Shear velocity, U_* (cm/sec)	1.14

Measurement was performed using a 3D Acoustic Doppler Velocimeter with the frequency of 25 Hz (25 samples/sec) for more than 1 min at each measurement points. Measurement was concentrated on near bed region (about 60% of average flow depth). More than 1500 data points were measured throughout the bend reach. More detail measurements were conducted around both spurs. Raw data were processed and filtered using spike removal algorithm developed by Wahl (2000, 2003). Data processing has included calculation of average velocities, turbulent intensities, Reynolds stresses in all three directions, and aggregated measures of data quality. It is to be noted that some data with low correlation & SNR were removed. See Table 1 for the test condition.

Flow visualization was performed using high-resolution digital video camera. The shadow of eddies was captured throwing the light from halogen lamp to the channel surface in the dark conducting experiment in the night. The migration of small eddies (their shadow) were visible quite clearly.

3 DATA ANALYSIS AND DISCUSSION

Shear velocity was calculated using method described in Giri & Shimizu (2003).

3.1 *Calculation of turbulent characteristics*

The turbulent characteristics (normal stresses, Reynolds stresses & turbulent kinetic energy) were computed using root-mean-square (RMS) of the turbulent velocity fluctuations as well as covariances for all three velocity combinations.

The RMS of turbulence denotes the standard deviation of the samples taken by ADV and equal to the normal stress for respective velocity component, e.g. for downstream velocity component:

$$RMS[V_X'] = \sqrt{\overline{[V_X']^2}} = \sqrt{\frac{\sum V_X^2 - (\sum V_X)^2 / n}{n-1}} \qquad (1)$$

where V_X' – downstream velocity fluctuation; n – number of sample.

Similarly, the transverse and vertical component of normal stresses can be expressed.

For the analysis of Reynolds stresses, the covariance is used that denotes the correlation between two variables and can be expressed as:

$$CovXY = \overline{V_X' V_Y'} = \frac{\sum V_X V_Y}{n-1} - \frac{\sum V_X \sum V_Y}{n(n-1)} \quad (2)$$

$\overline{V_x' V_z'}$ and $\overline{V_y' V_z'}$ can be expressed in similar way.

The turbulent kinetic energy can be defined as:

$$k = 0.5\left(\overline{[V_X']^2} + \overline{[V_Y']^2} + \overline{[V_Z']^2}\right) \quad (3)$$

3.2 *Flow and turbulent analysis*

The mean flow and turbulent analysis was performed throughout the bend reach of channel for a horizontal layer at 40% of the depth from the channel bed. This level is taken as the location where velocity magnitude is equal to its depth-average value for uniform flow (Graf, 1998). It was observed that in this layer longitudinal and transverse velocity profiles are not much varied for both cases. However, in shear layer region, the mixing length for the case with scour-deposition was found to be greater (Fig. 3) apparently due to the effect of deposition in shear layer region. Similarly, with the scour case the flow deflection is greater in upstream-stagnated region but lower in region away from the tip of spurs. The downflow in this layer is found to be significantly greater for scour-deposition case (Fig. 4). Variation of normal and Reynolds stresses as well as kinetic energy in longitudinal direction along the spurs tip in both bends has been depicted in Figure 5 and 6 respectively. It can be seen that normal stresses in all three direction, dominant component of Reynolds stress and turbulent kinetic energy amplify in the vicinity of spur. Turbulent level seems slightly higher near spur 1 region than near spur 2. Similarly, turbulent characteristics are found to be larger in this layer for rigid bed case. Spatial distribution of normalized turbulent intensities, Reynolds stresses and kinetic energy over vertical sections located in front of spurs, along spurs and behind them has been depicted in form of contour plots for 40% of width and about 50%–60% of depth (Fig. 7). Plots have been presented for both cases and bends (Figs 9–13). Some selected sections (5 cm in

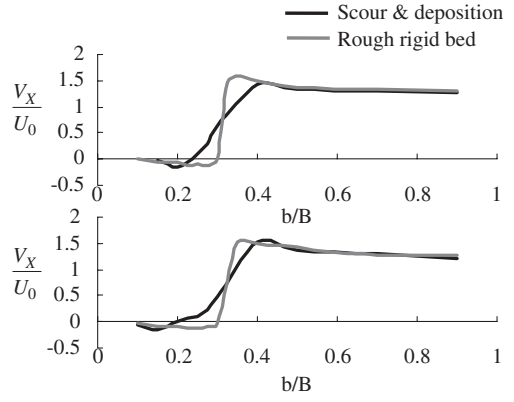


Figure 3. Typical examples of shear-layer profile.

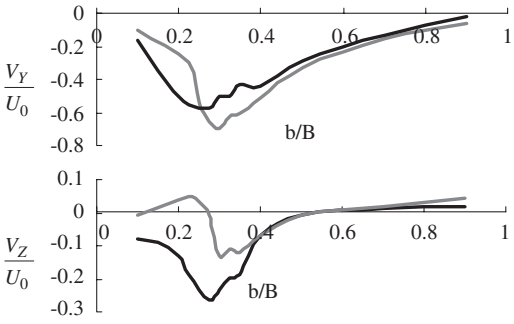


Figure 4. Typical examples of flow deflection and downflow velocity distribution near spur.

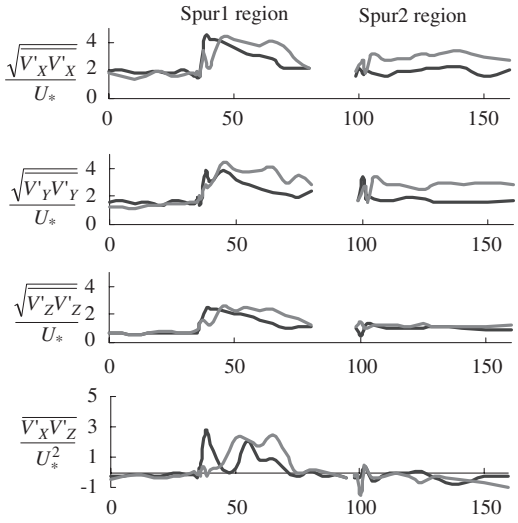


Figure 5. Variation of normal & Reynolds stresses.

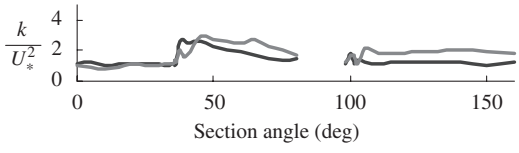


Figure 6. Variation of turbulent kinetic energy along the tip of spurs.

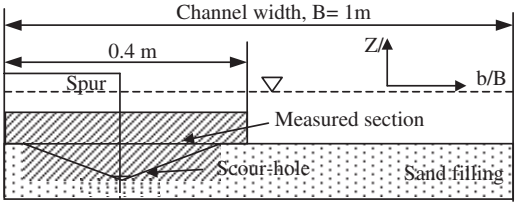


Figure 7. Schematic sketch of measured section.

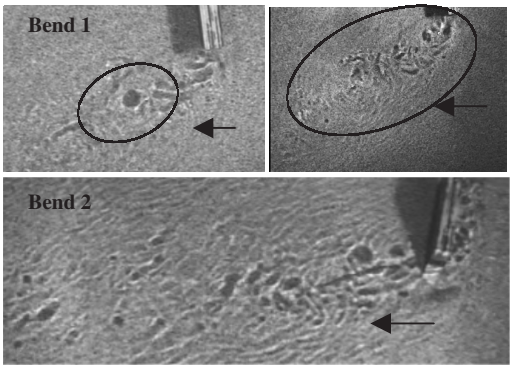


Figure 8. Vortices, shedding from the tip of spurs and in shear layer.

front of spurs, 5 cm behind spurs and along the spurs for both bends) with dominant components have only been illustrated within the scope of this paper.

The nature of normal & Reynolds stresses distribution in near spur region appears to be rather chaotic that was observed by Graf and Istiarto (2002) as well. As it is to be expected, the turbulent characteristics were seen to amplify in the vicinity, particularly in shear layer. In other word, normal and Reynolds stresses were found with high magnitudes behind the spur rather than in front of it. Furthermore, the turbulent stresses appear to be slightly higher near spur 1 region; however in second bend near spur 2 turbulent characteristics were found to possess splash characteristics with chaotic behavior. This evidence indicates the complicated flow structure due to the bend and influence of spur placed in preceding bend that generates the small eddies (see 3.3) and in turn produces effect on flow pattern in successive bend. Nonetheless, the distinction in turbulent characteristics near spurs placed in two different bends is thought to be still not clear and thus subject to further investigation. Turbulent characteristics in layers upper than scour-hole were found to damp after the development of scour-hole.

The flow & turbulence inside the scour is seen to be complicated with some splash behavior beneath the spur. However they possess very local & splashy character that eventually may not have significant impact

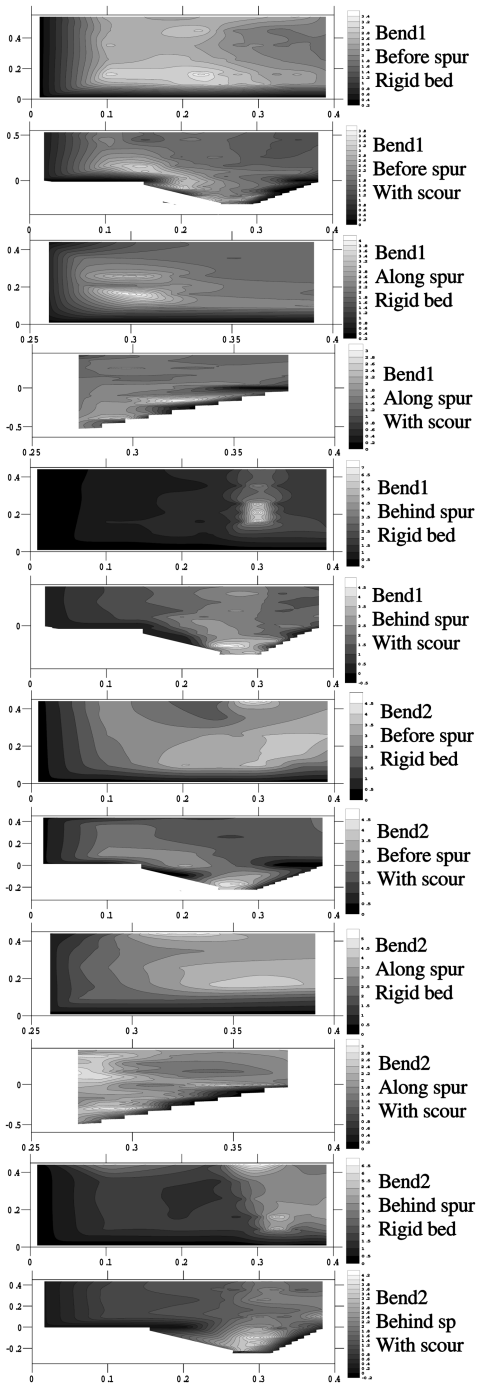


Figure 9. Contour plotting of Normal stress $\sqrt{\overline{V_x' V_x'}}/U*$. *Remarks: Scale has been distorted. Color level alters case by case.*

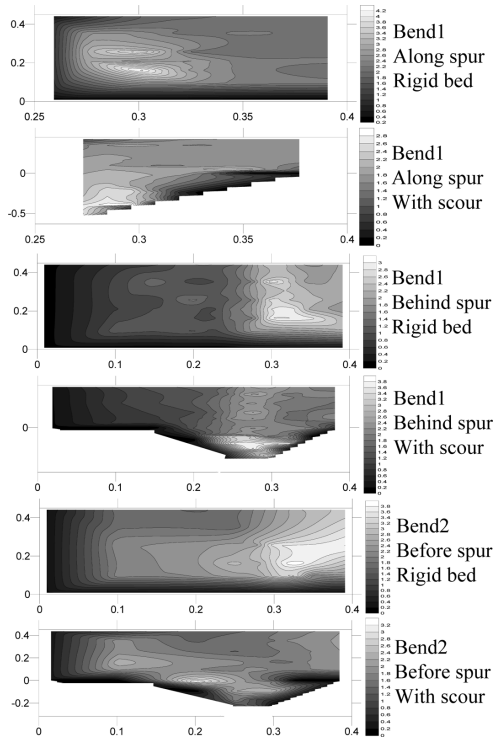


Figure 10. Contour plotting of Normal stress $\sqrt{\overline{V_y' V_y'}}/U*$.

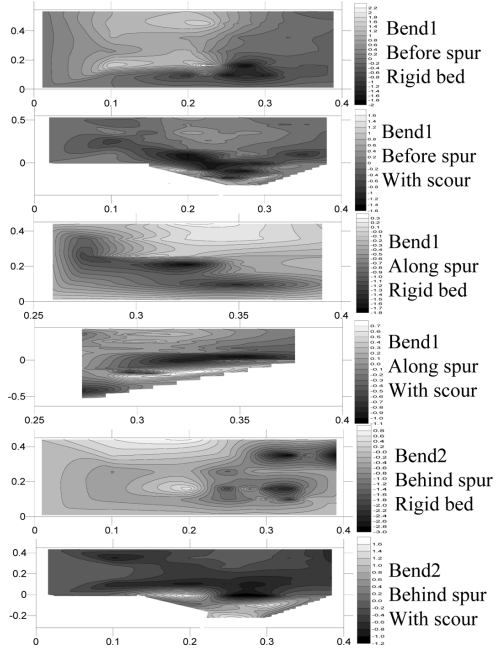


Figure 11. Contour plotting of Reynolds stress $\overline{V_x' V_z'}/U^2*$.

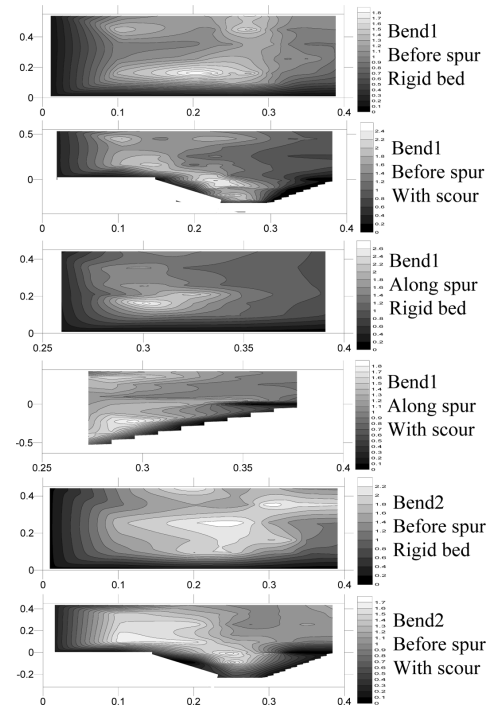


Figure 12. Contour plotting of Normal Stress $\sqrt{\overline{V_z' V_z'}}/U*$.

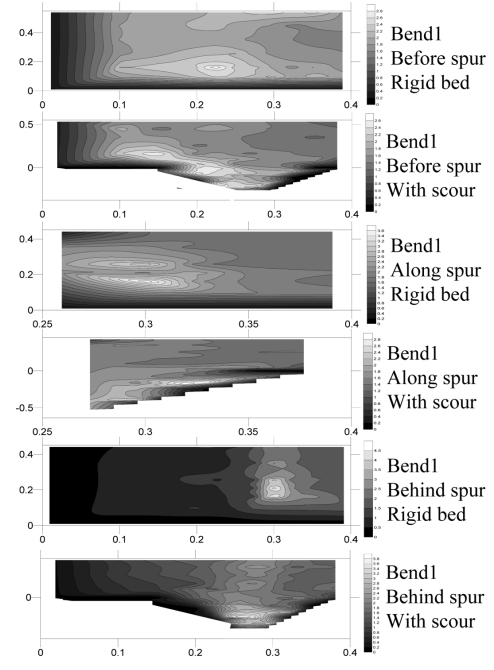


Figure 13. Contour plotting of turbulent kinetic energy K/U_*^2.

on near bed sediment entrainment (except for some sort of sediment motion inside the scour-hole).

It is obvious that the turbulent kinetic energy has similar characteristic. In the vicinity and shear layer, the turbulent kinetic energy appears to possess higher amplitude and becomes uniform in the same region after the development of scour. However, it appears inside the scour hole. Besides, in the dead region in front of and behind spurs, all components of normal stresses & kinetic energy are uniform having low turbulence. It becomes amplified in the vicinity and shear layer, apparently due to the generation of turbulent agents like vortices in this region.

3.3 *Flow visualization*

An attempt was made to visualize the generation of vortices from the tips of the spurs and their migration towards downstream region. Under the light of halogen lamp in the dark, the shadow of these small eddies (Fig. 8) and their migration speed are visible very well. The migration speed of these eddies was observed to be near to average velocity. This observation verifies the prior study (Chen and Ikeda, 1997). Vortices generated from the tip of spur 1 are seen to be migrating towards second bend where spur 2 located and even accumulated in dead region in front of spur 2. Likewise, some of them accumulated in recirculation region near the reattachment point before having diffused. Furthermore, these vortices are more random in case of movable bed (with scour and deposition). Such kind of vortices possesses high turbulent energy and is responsible for scouring & mixing process in down stream.

4 NUMERICAL MODEL

A preliminary attempt was made to calculate average flow (streamwise and transverse velocities) along the channel for the case with rough rigid bed using a simple two dimensional numerical model. Following basic equations were used:

$$\frac{\partial h}{\partial t}+\frac{\partial (hu)}{\partial x}+\frac{\partial (hv)}{\partial y}=0 \tag{4}$$

$$\frac{\partial (hu)}{\partial t}+\frac{\partial (hu^2)}{\partial x}+\frac{\partial (huv)}{\partial y}=-gh\frac{\partial H}{\partial x}$$

$$-C_d u\sqrt{u^2+v^2}+hv_t\left(\frac{\partial^2 u}{\partial x^2}+\frac{\partial^2 u}{\partial y^2}\right) \tag{5}$$

$$\frac{\partial (hv)}{\partial t}+\frac{\partial (huv)}{\partial x}+\frac{\partial (hv^2)}{\partial y}=-gh\frac{\partial H}{\partial y}$$

$$-C_d v\sqrt{u^2+v^2}+hv_t\left(\frac{\partial^2 v}{\partial x^2}+\frac{\partial^2 v}{\partial y^2}\right) \tag{6}$$

where x and y = co-orthogonal coordinates; t = time; u and v = depth-averaged velocity components in x and y directions respectively; h = depth; H = water surface elevation; g = gravitational acceleration; and C_d = bed friction coefficient.

No sub grid model was used for turbulence as no significant effect of the subgrid model for such a small scale simulation was found. Simple eddy viscosity concept was used as follows:

$$\nu_t = \frac{k}{6}u_* h * A \tag{7}$$

where, k = Karman constant; u_* = shear velocity; A = weight coefficient.

Shear velocity was calculated using following expression:

$$u_* = \frac{gn^2(u^2+v^2)}{h^{1/3}} \tag{8}$$

Several value of weight coefficient A was used to evaluate the effect of viscosity in high turbulent region. Not so significant effect was found within the values of 0.1 to 1.

4.1 *Numerical algorithm*

Navier-stokes equations are transformed into non-conservation form and calculated splitting them into non-advection and pure advection phase. Non-advection phase was calculated using CIP (Cubic-interpolated Pseudo-particle) numerical method (Shimizu, 2002; Yabe and Ishikawa, 1990), e.g.:

Non-advection phase 1:

$$\frac{\partial u}{\partial t}+u\frac{\partial u}{\partial x}+v\frac{\partial u}{\partial y}=-g\frac{\partial H}{\partial x}-C_d u\sqrt{u^2+v^2} \tag{9}$$

Non advection phase 2:

$$\frac{\partial u}{\partial t}=\nu_t\left[\frac{\partial^2 u}{\partial^2 x}+\frac{\partial^2 u}{\partial^2 y}\right] \tag{10}$$

Advection phase:

$$\frac{\partial u}{\partial t}+u\frac{\partial u}{\partial x}+v\frac{\partial u}{\partial y}=0 \tag{11}$$

Equations (5), (6) & (7) were transformed to general coordinate system and came to the following

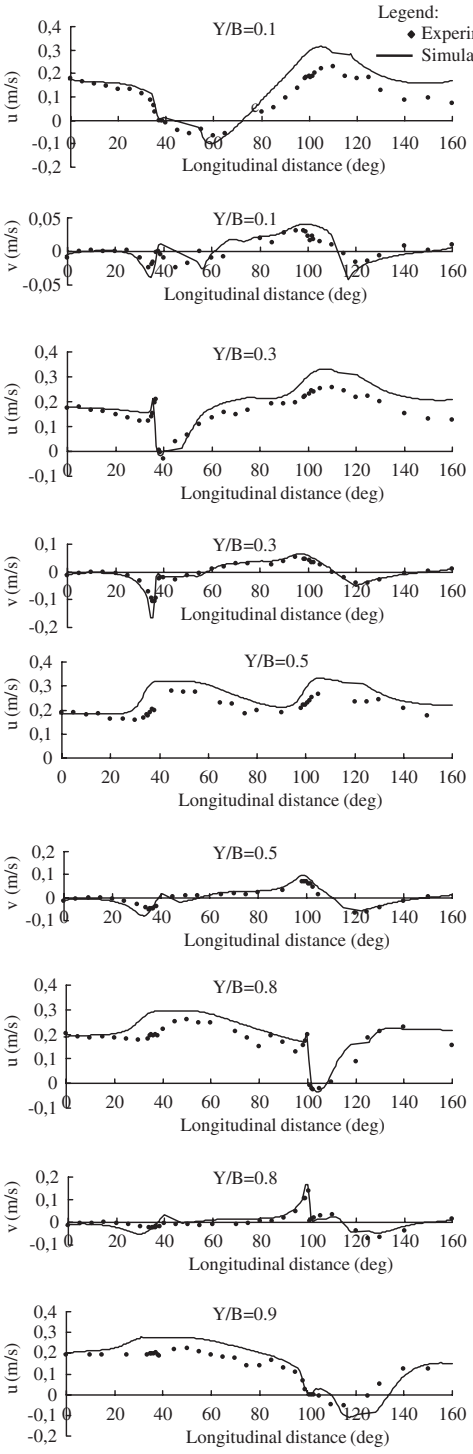


Figure 14. Streamwise and transverse velocity profiles in different longitudinal sections along the channel.

boundary fitted continuity and momentum equations (see Shimizu & Surajate, 2003 for more detail):

$$\frac{\partial}{\partial\tau}\left(\frac{h}{J}\right)+\frac{\partial}{\partial\xi}\left[\left(\xi_t+u^{\xi}\right)\frac{h}{J}\right]+\frac{\partial}{\partial\eta}\left[\left(\eta_t+u^{\eta}\right)\frac{h}{J}\right]=0 \quad (12)$$

$$\frac{\partial u^{\xi}}{\partial\tau}+\left(\xi_t+u^{\xi}\right)\frac{\partial u^{\xi}}{\partial\xi}+\left(\eta_t+u^{\eta}\right)\frac{\partial u^{\eta}}{\partial\eta}$$
$$+\alpha_1 u^{\xi}u^{\xi}+\alpha_2 u^{\xi}u^{\eta}+\alpha_3 u^{\eta}u^{\eta}-D_{\xi}$$
$$=-g\left[\left(\xi_x{}^2+\xi_y{}^2\right)\frac{\partial H}{\partial\xi}\left(\xi_x\eta_x+\xi_y\eta_y\right)\frac{\partial H}{\partial\eta}\right] \quad (13)$$
$$-\frac{C_d u^{\xi}}{hJ}\sqrt{\left(\eta_y u^{\xi}-\xi_y u^{\eta}\right)^2+\left(-\eta_x u^{\xi}-\xi_x u^{\eta}\right)^2}$$

$$\frac{\partial u^{\eta}}{\partial\tau}+\left(\xi_t+u^{\xi}\right)\frac{\partial u^{\eta}}{\partial\xi}+\left(\eta_t+u^{\eta}\right)\frac{\partial u^{\eta}}{\partial\eta}$$
$$+\alpha_4 u^{\xi}u^{\xi}+\alpha_5 u^{\xi}u^{\eta}+\alpha_6 u^{\eta}u^{\eta}-D_{\eta}$$
$$=-g\left[\left(\eta_x{}^2+\eta_y{}^2\right)\frac{\partial H}{\partial\eta}\left(\xi_x\eta_x+\xi_y\eta_y\right)\frac{\partial H}{\partial\xi}\right] \quad (14)$$
$$-\frac{C_d u^{\eta}}{hJ}\sqrt{\left(\eta_y u^{\xi}-\xi_y u^{\eta}\right)^2+\left(-\eta_x u^{\xi}-\xi_x u^{\eta}\right)^2}$$

where ξ and η = spatial coordinates and τ = time; D_ξ and D_η = momentum diffusion term in ξ and η directions (Shimizu & Itakura, 1991).

Furthermore, the vortices in the plane normal to vertical axis (z) are calculated using following well-known equations:

$$\varpi_z=\frac{\partial u}{\partial y}-\frac{\partial v}{\partial x} \quad (15)$$

The average flow-field and the time depended vortices shedding have been successfully simulated using this model. Moreover, the results of the calculation has been depicted quantitatively for average flow property and compared with experimental data. The streamwise and transverse velocity components along the channel are compared and depicted in Figure 14. Likewise, streamwise and transverse velocity profile along shear layer is depicted in Figure 15 that shows agreeable result. Figure 16 shows velocity profiles and contour plotting of the simulation results. Similarly, vorticity field was simulated using this numerical model which has qualitatively shown realistic result. Typical examples of simulation result of vorticity field near spurs for some selected time steps are depicted in Figure 17. Quantitative comparison with experimental results should be made for the further verification of model. It can be said that this simple two dimensional numerical model has been satisfactorily able to simulate the mean flow field of such a complicated case.

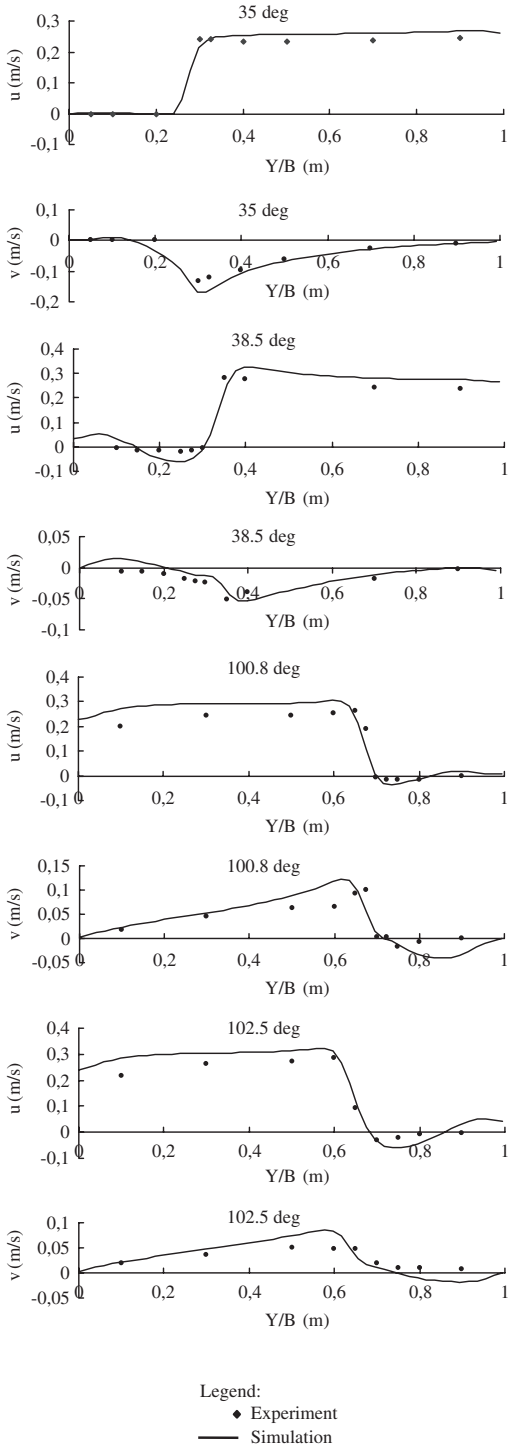


Figure 15. Streamwise and transverse velocity profiles along shear layer.

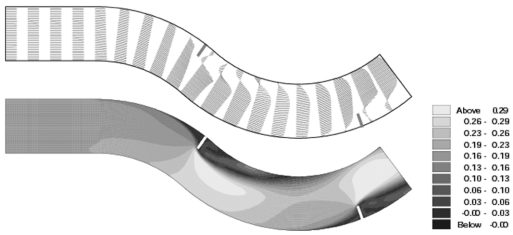


Figure 16. Average velocity field: plotting of simulation result.

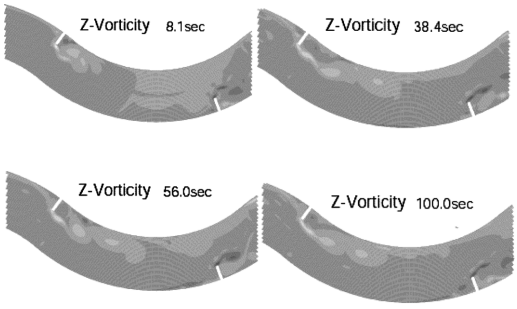


Figure 17. Vorticity field: plotting of simulation results for some selected time steps.

It is obvious that there may still lack in this model and space to bring about an improvement which is in progress. Furthermore, 3D calculation is supposed to be performed so as to improve the results and possibility of the model that enables three dimensional flow structures as well as turbulent characteristics to be simulated properly.

5 CONCLUSION

The turbulent characteristics were found to be very chaotic and high near both spurs. They were seen to have most pronounced in shear layer region rather than in upstream part of the spurs and much chaotic in case of developed morphology, apparently due to the deposition in the wake region. The turbulent intensities, Reynolds stresses and turbulent kinetic energy are considerably higher in near spur region for the rigid bed case. After the development of scour, these characteristics become uniform and even collapsed in upper layer. Inside the scour-hole, turbulent level was seen to be slightly higher, particularly beneath the spur tip; however it seems to possess splash characteristic that does not appear to have significant impact. Besides, turbulent level seems to be higher near spur 1 region rather than near spur 2. Nevertheless, this phenomenon does not seem to be clear enough for any conclusion to

be made and is thought to depend on flow condition as well. The turbulent kinetic energy is much stronger in shear layer region and in the scour-hole near the maximum depth, whereas it was found to be low & uniform over the depth in dead regions in front of and behind the spurs.

A simple two dimensional numerical model has been developed using a novel numerical technique referred to as CIP. The mean flow field for the case of rigid bed as well as vorticity field was simulated using the model satisfactorily with realistic results. In order to simulate 3D flow field and turbulent characteristics in the vicinity of spurs, 3D extension of this model is required to be performed, which is in progress.

It appears to be possible to visualize shedding of turbulent structures like vortices and their migration pattern simply capturing the shadow of these structures. Such visualization seems to be simple to evaluate the shedding of the vortices and their migration towards downstream and can be used to validate numerical simulation as well. Moreover, behavior of such turbulent structures is of importance, since they are responsible for sediment entrainment as well as for mixing process.

Such kind of studies is of significance to add to knowledge on the assessment of the role of turbulence in sediment entrainment and mixing process before and after the bed evolution. Similarly, additional work and more thorough analysis may provide a key to relate the turbulence characteristics with structure-induced sediment entrainment and deposition as well as their temporal evolution. On the other hand, the simultaneous effect of the river training structures on the flow and turbulence and, in turn, on the channel bed and mixing process considering channel plan form is also subject of practical and academic interest.

This experimental data may be of use to further elaboration of numerical model on turbulence around spurs.

REFERENCES

Chen, F. & Ikeda, S. 1997. Horizontal separation flow in shallow open channel with spur dikes, *Journal of Hydroscience & Hydraulic Engineering*, Vol.15, No.2.

Ferdous, A. & Rajaratnam, N. 2000. Observation on flow around bridge abutment, *Journal of Engineering Mechanics*, ASCE, Vol.126, No.1.

Giri, S. & Shimizu, Y. 2004. Observation on bed variation in a meandering like flume with river training structures, *Annual Journal of Hydraulic Engineering*, JSCE, Vol.48.

Giri, S. & Shimizu, Y. 2003. Structure-induced bed-forms & temporal development of local bed in the bend reach of a laboratory flume, *3rd IAHR Symposium on River, Coastal & Estuarine Morphodynamics*, Barcelona.

Giri, S., Shimizu, Y. & Fujita, M. 2003. Flow characteristics in a mildly meandering channel with & without river training structures, *Annual Journal of Hydraulic Engineering*, JSCE, Vol.47.

Graf, W.H. & Istiarto, I. 2002. Flow pattern in the scour hole around a cylinder, *Journal of Hydraulic Research*, IAHR, Vol.40, No.1.

Graf, W.H. & Altinakar, M. 1998. Fluvial Hydraulics, *J. Wiley & Sons ed.*, Chichester, Great Britain.

Melville, B.W. & Raudkivi, A.J. 1977. Flow characteristics in local scour at bridge piers, *Journal of Hydraulic Research*, IAHR, Vol.15.

Rajaratnam, N. & Nwachukwu, B. 1983. Flow near groin-like structures, *Journal of Hydraulic Engineering*, ASCE, Vol.109, No. 3.

Richardson, J. & Panchang, V. 1998. Three-Dimensional Simulation of Scour-Inducing Flow at Bridge Piers, *Journal of Hydraulic Engineering*, ASCE, Vol.124, No.5.

Shimizu, Y. 2001. 2D flow using CIP meth*od, Applied Hydrology Laboratory*, lecture notes.

Shimizu, Y. & Itakura, T. 1991. Calculation of flow and bed deformation with a general non-orthogonal coordinate system. *Proc. of XXIV IAHR Cong.*, Madrid, Spain, Vol.C: 241–248.

Shimizu, Y. & Nishimoto, N. 1993. Numerical analysis of bed variation around spur dikes, *Research report of CERI of Hokkaido Development Bureau.*

Surajate, B. & Shimizu, Y. 2003. Numerical simulation with subgrid model- A case of meandering channel with river training structures, *Proc. of Shallow Flows-2003*, Delft, Netherlands.

Uijttewaal, W.S.J. 2001. Exchange Process between a river and its groyne fields: Model experiment, *Journal of Hydraulic Engineering*, ASCE, Vol.127, No.11.

Uittenbogaard, R. 2001. Summary SGS model for HLES, *Note*, Delft Hydraulics, Netherlands.

Wahl, T. 2003. Discussion of "Despiking Acoustic Doppler Velocimeter data", *Journal of Hydraulic Engineering*, ASCE, Vol.129, No.6.

Wahl, T. 2000. Analyzing ADV data Using WinADV, *Joint Conference on Water Resources Engineering and Water Resources Planning & Management*, ASCE, Minneapolis.

Yabe, T. & Ishikawa, T. 1990. A numerical cubic-interpolated pseudoparticle (CIP) method without time splitting technique for hyperbolic equation, *Journal of PSJ*, Vol.59(7).

This page intentionally left blank

River Flow 2004 – Greco, Carravetta & Della Morte (eds.)
© 2004 Taylor & Francis Group, London, ISBN 90 5809 658 0

Observations concerning erosion in model of a mobile river bed

L. Ciaravino
Department of Hydraulic and Environmental Engineering "G. Ippolito", Naples, Italy

ABSTRACT: This paper reports an analysis of the experimental results regarding localized scour on a mobile bed, caused by a stream with a three-dimensional hydrodynamic pattern. This pattern is affected by the geometry of the cross sections of stream flow and by a marked asymmetry in the supply. The experimental installation is represented by a physical model reproducing a stilling basin and a downstream section of a mobile river bed. The experimental data highlight the influence exerted by the diameter of the granular material, used to reproduce the mobile bed, on scour geometry. The particular and complex hydrodynamic phenomenon causing scour and the obtained results suggested an interesting working hypothesis for the subsequent experimental activities.

1 INTRODUCTION

There are a number of important issues regarding river dynamics, such as the determination of general solid transport and river modelling, but localized scour in mobile river beds is certainly a major concern.

Scour may be induced by particular geometries of the river bed but also and above all by man-made structures.

By interacting with the water flow, these structures modify the stream flow pattern and may lead to critical values of velocity V_c and shear stress τ_c being exceeded along the bed and/or the banks, thus setting the eroded material in motion. (Shield, 1936; Einstein, 1942; Kalinske, 1947).

Generally, the structure may give rise to limited local turbulence, such that the mean kinematic characteristics of the whole cross section of river bed concerned remain practically unaffected (in this case the structure is normally defined as an obstruction), or it may have a more general impact on the river section (in which case it is referred to as a constriction).

With reference to the most common structures, an interesting practical problem lies in the determination of localized scour caused by a stream flow which, with considerable kinetic energy, leaves the layer covering the river bed with rigid material before returning to the uncovered, and hence submitted to erosion, bed.

In general, these localized scour phenomena are studied through simplified (mainly two-dimensional) experimental installations and numerical models with permanent flows (the overall river geometry likewise is permanent) and with no solid material in suspension being transported from upstream (see References in general).

However, in practical cases this phenomenon may present not negligible three-dimensional characteristics and, therefore, the inadequacy of numerical models often means that the phenomenon has to be studied by means of a specific physical model.

The present paper analyses the results of an investigation previously carried out on a physical model, one of whose aims was to study scour downstream of a stilling basin.

These results are essentially qualitative and, despite their specific nature, provide considerations that can be held to be of general interest.

2 CONSIDERATIONS REGARDING PHYSICAL MODELS OF MOBILE RIVER BEDS

Studies on physical models are based on the theory of similarity between a prototype (original river work) and a model (in reduced scale).

The scale S is defined as the ratio between the single model quantity (indicated by the subscript m) and the corresponding prototype quantity (indicated by the subscript p).

Generally speaking, in order to define the mechanical similarity between the prototype and the model, it is necessary to define the relationship between three fundamental dimensional quantities, such as length, time and force (Montuori, 1997).

Studying physical models of free surface flows encounters an intrinsic limitation in the actual choice of scale relationships between the quantities in question, caused by the fact that the prototype phenomena and the modelled phenomena are subjected to the same

acceleration of gravity g and that, in any case, water is used as the experimental fluid.

In this case (stream flows governed by gravity), when the effects of viscosity, elasticity, surface tension and cavitation are negligible then Froude's law of similarity is held to be valid and hence the Froude number:

$$Fr = V/(g \cdot h)^{1/2} \quad (1)$$

is the same for model and prototype (where V is the mean velocity and h is the water depth) that is:

$$Fr_m = Fr_p \quad (2)$$

that provides the scale:

$$S_{Fr} = Fr_m/Fr_p = 1 \quad (3)$$

From which, as is well known, being S_L the length scale, it can be derived:

$$S_V = S_L^{1/2} \quad (4)$$

that is velocity scale;

$$S_Q = S_L^{5/2} \quad (5)$$

that is flow rate scale;

$$S_T = S_L^{1/2} \quad (6)$$

that is time scale.

The above mentioned conditions are sufficient to solve the problem of mechanical similarity when both in prototype and in model the conditions are of fully developed turbulence.

When a model is studied in which a mobile river bed has to be reproduced, it is necessary to identify further criteria (Pezzoli, 1979; Calomino et al., 1997).

In particular, with regard to a study of localized scour in model, the main criterion consists of setting the condition that the densimetric particle Froude number Fr_d is constant (even in critical conditions of incipient sedimentary motion), therefore it can be written:

$$Fr_d^2 = R \cdot J/[d \cdot (\gamma_S/\gamma_W - 1)] = cost \quad (7)$$

in which γ_W and γ_S are the specific weights of water and solid grains of diameter d, respectively, and where R and J are the hydraulic radius and the hydraulic gradient, which is generally made equal to the slope i of river bed.

Therefore, the corresponding scale will be:

$$S_{(Frd^2)} = Fr_{dm}^2 / Fr_{dp}^2 = 1 \quad (8)$$

where Fr_{dm} and Fr_{dp} are model and prototype densimetric particle Froude number respectively.

Consequently, the reduction scale of the solid grain diameters will be:

$$S_d = d_m/d_p = S_L \cdot (\gamma_{Sp} - \gamma_W) / (\gamma_{Sm} - \gamma_W) \quad (9)$$

where γ_{Sp} and γ_{Sm} are the specific weights of solid grains in prototype and in model respectively.

If solid material of the same type as that found in the prototype is used in the model, although smaller than in the prototype according to the length scale, very often a grain size is obtained so small that grains remain in suspension during the experimental tests. The drawbacks related to the reduction scale of the solid mobile material could be overcome by adopting a distorted model.

In this case, if we use S_h to indicate the height scale, which is different from the planimetric length scale S_L, and $D = S_h/S_L$ to indicate the distortion ratio, and once again assuming the densimetric particle Froude number to be constant, it can be written:

$$S_d = D^2 \cdot S_L \cdot (\gamma_{Sp} - \gamma_W) / (\gamma_{Sm} - \gamma_W) \quad (10)$$

Therefore, if a scale S_d is wanted to give solid grains that are lighter and greater in size, a height scale S_h has to be imposed smaller than the planimetric length scale S_L. However, the latter hypothesis could upset the Froude hydraulic similarity as the reduction in the S_h scale generally results in a reduction in the Reynolds number, thus making it fall to values that are incompatible with fully developed turbulent flow conditions.

However, the complicated definition of the parameters characterising the solid mobile material from the real river bed, which are necessary for more accurate modelling (grain-size curve, cohesion and homogeneity of mobile river bed material) may introduce a certain randomness in the results obtained with the experimental tests. For this reason, in technical modelling practice there is a tendency to work on the simplest models which comply with Froude's similarity rather than on distorted models.

Froude type models yield excellent results as regards quantities related to the hydraulic characteristics of the considered flow being studied and, by using suitable methodologies, important although only qualitative results can be obtained for defining erosion phenomena.

A modelling technique that is still held to be valid in determining both scour and granular material to be adopted, is the one suggested by Scimemi (1939), also studied by Veronese (1937) and later adopted by Ghetti & Zanovello (1954) as well.

This technique starts from the considerations made by Schoklitsch (1935) and confirmed by Veronese,

which state that under identical conditions the localized scour site increases as the characteristic diameter d of the mobile material decreases until it assumes a value close to 5 mm, below which value the scour remains constant. Therefore, Scimemi suggests experimenting on a model with decreasing grain sizes until the scour is determined by extrapolation with respect to the material of diameter $d = 0$.

Ghetti (1954), also adopts this technique and claims that, with all other conditions remaining the same and varying the grain size, the scour is geometrically similar; a model can therefore be used to measure the velocity field for comparisons with the critical velocity of the prototype material in order to obtain, with a certain degree of approximation, the actual size of the eroded area in the prototype.

3 ANALYSIS OF THE MODEL AND THE EXPERIMENTAL RESULTS

In the light of the considerations made in the previous sections, the present study analyses experimental scour measurements that had previously been taken using a mechanically similar model complying with Froude's law and reproducing a stilling basin and a brief downstream section of a mobile river bed.

In actual fact the above mentioned model is part of a more complex model that was intended to clarify the hydraulic working of a structure comprising the stilling basin and the outlet devices (two spillways from which water is directed in one open channel and two bottom sluices from which water is directed in two free flow tunnels).

However it was necessary to check the working of the stilling basin in order to reduce the scour in the downstream mobile river bed to tolerable limits (Ciaravino & Ciaravino, 2003).

It should be noted that the hydraulic operation of the basin was characterised by a marked three-dimensional effect which affected the geometry and the entity of the scour in the reproduced mobile bed. This three-dimensional effect is caused by the asymmetry with which the flows from the outlet works are directed into the basin under the various conditions.

The model was built in reduced geometric scale $S_L = 1/50$ from which the scale of reduction for the other hydraulic quantities can be derived, under the hypotheses made and as it was pointed out in the previous section.

The mobile river bed downstream from the stilling basin was reproduced by using a natural granular material of two different sizes d:

- sand graded with a 4×4 mm mesh riddle;
- gravel graded using a 10×10 mm mesh riddle (and which does not pass through the riddle mentioned in the previous point).

That is to say, two sizes were chosen that essentially fall into the two fields ($d < 5$ mm and $d > 5$ mm) identified by Schoklitsch and by Veronese.

The structures reproduced in the model are shown in diagram form in Figures 1 to 4.

These figures also report the results of the mobile bed scour measurements in some of the different operating conditions that were analysed.

In actual fact, several batteries of tests were conducted, each time modifying the stilling basin geometry in order to determine which one resulted in a reduction of scour.

It should be pointed out that, in order to allow conclusions to be drawn from the analysis of the experimental results, the various test batteries are equivalent.

That is to say that it is possible to draw the same general conclusion from all the test batteries conducted with the various geometrical configurations.

Therefore the figures report the results of the tests carried out on a particular basin geometry with two different flow rates.

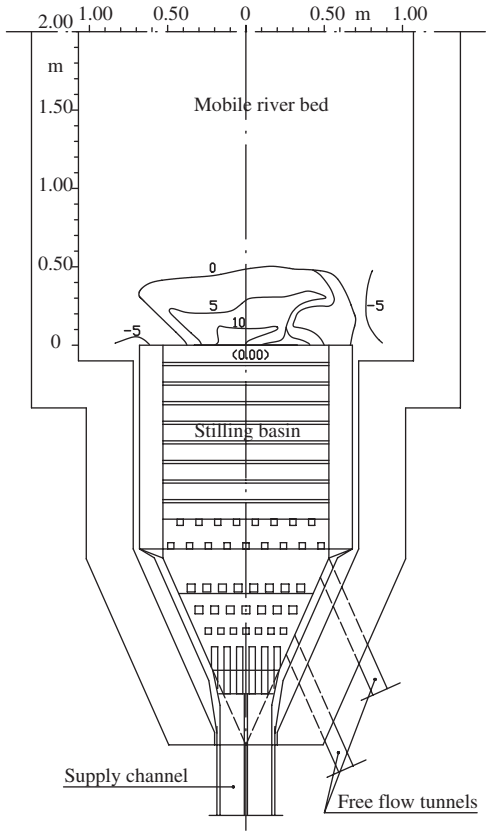


Figure 1. Experimental tests in mobile river bed reproduced with gravel. Flow rate in model: $Q_m = 0.017$ mc/s.

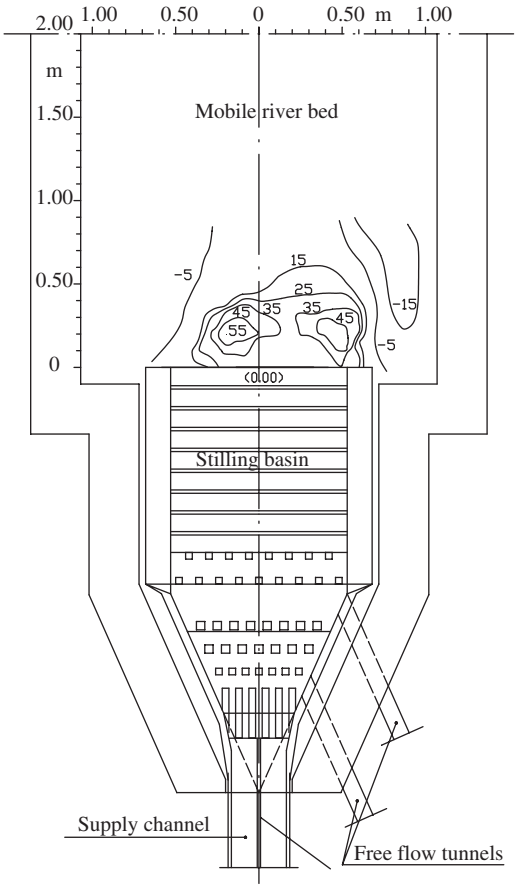


Figure 2. Experimental tests in mobile river bed reproduced with sand. Flow rate in model: $Q_m = 0.017$ mc/s.

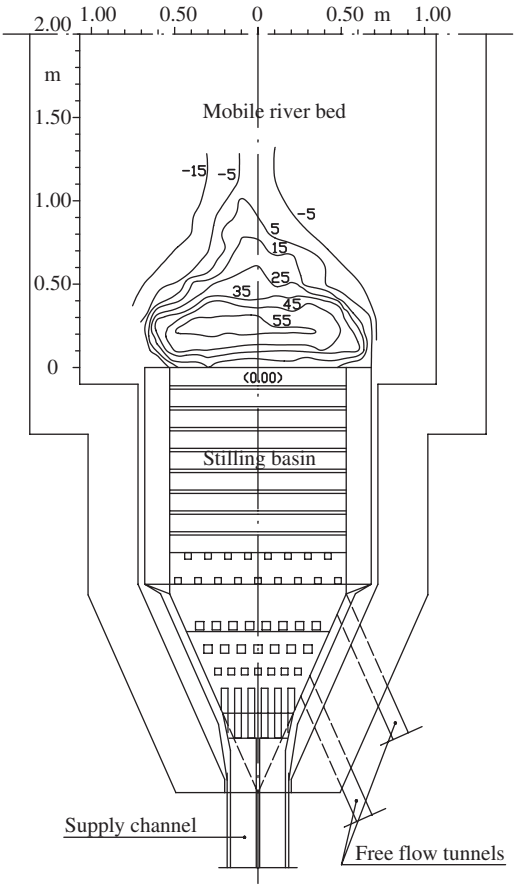


Figure 3. Experimental tests in mobile river bed reproduced with gravel. Flow rate in model: $Q_m = 0.064$ mc/s.

In particular, tests are reported with the maximum flow rate of the stilling basin, equal in the model to $Q_m = 0.064$ mc/s, and with an intermediate flow rate of $Q_m = 0.017$ mc/s.

Tests have been repeated both with a mobile bed reproduced using sand and with one reproduced using gravel.

In order to take into account the evolution over time of the scour and hydrodynamic phenomena and so as to obtain practically stable scour depths even when the mobile bed was reproduced with sand, every single test had a duration of 1.5 hours.

In the figures the scour is measured in millimetres starting from a reference value 0.00 equal to the bed height in the terminal section of the stilling basin.

Starting from this 0.00 reference value, the figures also indicate the scours with positive values and solid material deposits with negative values.

Figure 1 and Figure 2 report experimental scour measurements produced by the model flow rate $Q_m = 0.017$ mc/s when the mobile bed is reproduced with gravel or sand, respectively.

The maximum scours with this flow rate are 10 mm and 55 mm in the two cases.

Figure 3 and Figure 4 report the experimental measurements of scour produced by the model flow rate $Q_m = 0.064$ mc/s when, once again the mobile bed is reproduced with gravel or sand, respectively.

The maximum scours with this flow rate are, in the two cases, 55 mm and 145 mm.

As a first conclusion, we can say that the experimental measurements confirm the increase in scour depth as the granular material diameter decreases in the investigated field (Scimemi, 1937; Chia-Chun Wu et al., 2002).

Moreover it can be noticed that, for both model flow rates, a considerable difference in the resulting scour geometry can be observed, with other conditions remaining the same, when the bed is reproduced with sand and when it is reproduced with gravel.

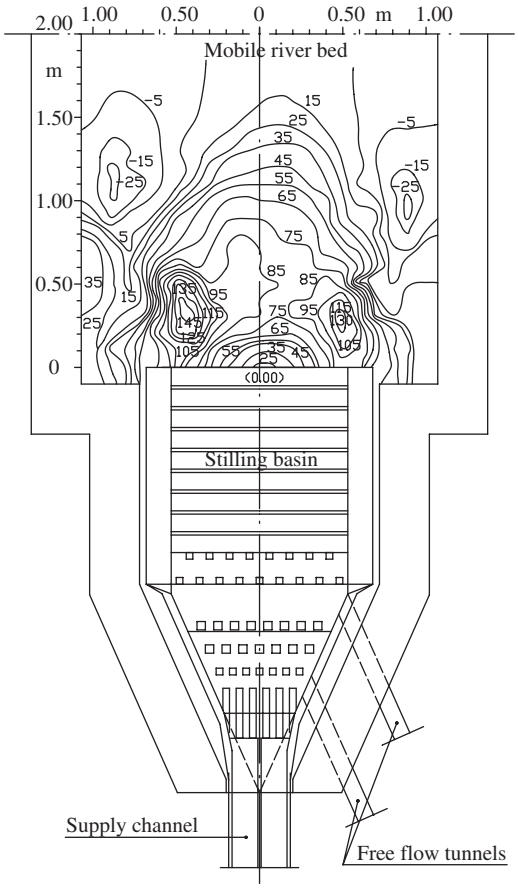


Figure 4. Experimental tests in mobile river bed reproduced with sand. Flow rate in model: $Q_m = 0.064$ mc/s.

In the case of the gravel bed (Fig. 1 and Fig. 3) the scour assumes an axially symmetrical pattern with an appreciable reduction along the sides and downstream, with a somewhat uniform and considerably flattened transverse conformation and with a depositing area that may also reach the axial area downstream, for the higher flow rate.

As a matter of fact the ratio between the longitudinal dimension (parallel to the axis) and the transverse dimension (orthogonal to the axis) of the level curves measured experimentally, is less than 1 and in the area of greatest depth, for the higher flow rate, it assumes a value of about 0.12.

For these tests with gravel as the mobile bed material, the ratio between maximum scour and the flow rate (variable between 0.60 and 0.86) also assumes a value of lower than 1.

When the bed is reproduced with sand (Fig. 2 and Fig. 4) the scour assumes a conformation with a lesser degree of symmetry than in case of gravel (caused, for the smaller flow rate, by a greater possibility for the stream to meander through the stilling basin), characterised by two deep lateral scours. For the higher flow rate, these two lateral scours are of elliptical shape and they are however located symmetrically and downstream of the lateral edges of the stilling basin. This deep scours are practically double size of the scouring produced near the axis.

The measure of the scour in the axial area is, moreover, very close to the size of the maximum scour obtained with sand and the same flow rate.

In the case of experiments conducted with sand the ratio, between the longitudinal and transverse dimensions of the level curves measured experimentally, is also higher than 1 and in the area of greatest depth, for the higher flow rate, it assumes a value equal to about 2.50.

Moreover, for the tests with sand, also the ratio between maximum scour and flow rate assumes a value higher than 1 (more than 2.25).

Therefore, when the size d of the granular material in the model is changed and when there are flow phenomena with highly three-dimensional characteristics, the above mentioned experimental measurements point out a remarkable lack of geometrical similarity.

In actual fact, for the deep scours measured in the experiments, the stream flow was characterised by marked eddies that are thought to be associated to upward forces relative to velocity gradients and turbulent velocity components directed along the normal to the grain lying plane.

Clearly, in this hydrodynamic pattern the sand can be set in motion by these actions, due to the non-uniform distribution of the velocities, before being transported downstream where it is deposited when the velocities fall below the critical value.

In the model, the described sand transport mechanism seems to supply the depositing of granular material both in the most lateral area of the reproduced bed and the axial area which seems to be eroded in a lesser degree than it was expected.

The experimental measurements point out that the dragging action, transmitted from the stream flow by means of eddies, creates an effect and hence a final geometric conformation of the scour that is not independent of the size d of the grains making up the mobile bed.

In other words, as the diameter varies, not only the maximum depth but also the geometry of the scour is modified.

This affects and determines the distribution of the field of velocity vectors and the bed equilibrium profile for the corresponding supply conditions.

In fact it is possible that, for bed shear stress values τ_o close to (but lower than) the critical value τ_c of incipient motion for grains, particular conformations

of the river bed may give rise to particular orientations of the grain layers such as to favour local grain motion conditions and, hence, favour scour (Ghetti, 1979).

The complexity of the observed phenomenon is certainly deserving of further investigation, both experimental and theoretical.

Indeed, considerable interest seems to lie in the determination of the parameters regulating the scour phenomenon in the presence of eddies such as that observed experimentally, both to understand the theory of the phenomenon and to propose an analytical model that could be used to evaluate the entity of the scour phenomenon.

One possible initial simplified approach, taking into account the gradual diffusion of the stream flow which causes eddies (the eddies are not actually caused by an obstacle), is to consider the phenomenon linked to the ratio τ_o/τ_c between the bed shear stress and the critical shear stress as previously defined.

This approach would lead to the possible definition of a relationship like the one proposed in other cases by Laursen (1952):

$$e_{max} / h = f (b/h , \tau_o / \tau_c) \qquad (11)$$

in which the maximum scour e_{max} divided by water depth h is a function both of the ratio b/h and of the above mentioned ratio τ_o/τ_c, where b is equal to the distance between the stream flow axis (where the maximum velocity is found) and the eddies.

This approach encounters an objective difficulty in determining the local values of τ, in the presence of eddies and in the presence of a mobile river bed (Carravetta et al., 1999, 2000).

Moreover, the influence of the time variable on the determination of the considered quantities should not be forgotten.

Remember that, in the case of a fixed river bed and for eddies caused by a narrowing represented by a flat vertical plate laid transversally to the flow, Adami (1970) (Adami & Da Deppo, 1974) determined the distribution of the shear stresses on the bed.

In particular these experimental measurements pointed to shear stress values in the eddy area that are up to four times greater than the shear stress when the obstacle constituted by plate is absent.

This interesting result confirms the need for a systematic investigation of the experimental determination of local stresses τ in the presence of a mobile river bed in order to evaluate scour.

4 CONCLUSIONS

The study reported in the present paper supports the view that localized scour phenomena such as the type examined here, i.e. depending both on three dimensional and asymmetrical hydrodynamic patterns and also on the time variable, cannot be easily solved using numerical models, and normally have to be studied through specific physical models.

The experimental measurements have confirmed the necessity, if we are to obtain a closer to prototype, albeit qualitative, geometrical conformation of the scouring phenomenon, to carry out different batteries of tests with different values for the diameter d of the granular material reproducing the mobile bed studied.

This methodology must be in particular followed, in the modelling practice, if a model of simple Froude similarity is adopted in the experiments.

Moreover, this procedure may mitigate the uncertainty of scour evaluation resulting from the difficulty encountered in adequately modelling the grain size and the consistency of the material making up the actual mobile bed.

Because of the experiment's three-dimensional nature, the experimental measurements point out a lack of geometrical similarity in the scour when, with all other conditions remaining the same, the size of the diameter d of the granular material making up the mobile bed in the model is changed (in particular when passing from diameters of $d < 5$ mm to diameters of $d > 5$ mm).

This result cannot be derived by hydrodynamic patterns simpler than the one considered in the present paper.

Moreover, as the diameter d varies, not only the maximum scour depth but also its geometry is modified.

Consequently, there is a further possibility to modify the field of the velocity vectors, the bed shear stress and the bed equilibrium profile, for the corresponding supply conditions.

The particular geometrical conformation of the scour measured in the experimental installation seems to be related to the formation of eddies appearing in the flow in the areas of maximum scour.

Note that these eddies practically form in such a way that it can be defined as free formation (i.e. without an obstacle) as a result of the expansion of the stream flow which is characterised transversally by differences in water depth.

The interesting observed phenomenon suggests the need for theoretical and experimental investigations in order to gain a more complete definition of the phenomenon and to obtain an analytical model that could be used for evaluating the size of scour.

The working hypothesis to be followed calls for the main parameter to be the ratio τ_o/τ_c between the bed shear stress and the critical shear stress of incipient flow of the material making up the mobile bed.

Finally, the complexity of the phenomenon suggested exploring an experimental working hypothesis

based on the overlapping of effects induced by eddies and longitudinal transport.

An experimental installation is thus being prepared so as to analyse the action of a fixed eddy on a mobile bed, reproduced using different grain sizes, as a preliminary step to the following studying of more complex installations with longitudinal transport.

ACKNOWLEDGMENTS

The development of the present study is inserted in the Research Project of National Interest PRIN 2002 which is co-ordinated by Prof. Guelfo Pulci Doria (Department of Hydraulic and Environmental Engineering "G. Ippolito", Naples, Italy) concerning, among the other subjects, the interaction of turbulence and eddy phenomena with water bodies.

REFERENCES

Abdel-Azim M. Negm, Osama K. Saleh, Gamal M. Abdel-Aal Mohamed F. Sauida 2002. Investigating scour characteristics downstream of abruptly enlarged stilling basins. *River Flow 2002*. Louvain La-Neuve. Belgium. 4–6 settembre 2002.

Adami A. 1970. Esame experimental del moto a pelo libero a valle di una piastra verticale disposta trasversalmente alla corrente. *Atti Istituto Veneto SS.LL.AA.* Tomo CXXVIII.

Adami A. 1971. Uno schema di calcolo per la determinazione della escavazione a valle di traverse. *L'Energia Elettrica*, n.12.

Adami A. 1979. Fenomeni localizzati ed erosione negli alvei. *Moderne vedute sulla meccanica dei fenomeni fluviali*: pp.157–183. Bressanone (Brixen) 8–12 Ottobre.

Adami A. & Da Deppo L. 1974. Esame sperimentale della scia turbolenta a valle di un ostacolo discontinuo verticale, posto normalmente ad un corrente a pelo libero. *XIV Convegno di Idraulica and Costruzioni Idrauliche*. Napoli.

Ade F. & Rajaratnam N. 1998. Generalized study of erosion by circular horizontal turbolent jets. *Journal of Hydr. Research* Vol.36: pp.613–635.

Ali K.H.M. & Lim S.Y. 1986. Local scour caused by submerged wall jets. *Proc.,Instn. Civil Engineers* Part 2, 81: pp.607–645.

Ali K.H.M. & Neyshaboury A.A.S. 1991. Localized scour downstream of a deeply submerged horizontal jet. *Proc., Instn. Civil Engineers* Part 2, 91: pp.1–18.

Breusers H.N., Nicollet G. & Shen H.W. 1977. Local scour around cylindrical piers. *Journal I.A.H.R.* n.3.

Breusers H.N. & A.J. Raudkivi 1991. Scouring. *Hydraulic Structures Design Manual IAHR A.A. Balkema*. Rotterdam.

Calomino F., D'Ippolito A., Gaudio R. & Gironda Verardi M. 1997. Studio su modello idraulico delle opere di protezione dall'erosione del canale di restituzione a valle della diga sul Fiume Esaro a Farneto del Principe. *18° Corso di aggiornamento* Guardia Piemontese Terme (CS). 10–13 settembre 1997.

Carravetta A., Di Cristo C. & Greco M. 1999 Un modello quasi-tridimensionale per alvei mobili. *Giornate di studio "La difesa idraulica del Territorio"*, Trieste, 23–24 settembre 1999.

Carravetta A., Greco M. & Leopardi A. 2000 Un modello quasi-tridimensionale per alvei mobili: effetti indotti dalla presenza di un pennello in un corso d'acqua. *XXVII Convegno Nazionale di Idraulica e Costruzioni Idrauliche*. Genova.

Cartens M.R. 1966. Similarity laws for localized scour, *Proc. ASCE*, HY 3.

Catakli O., Ozal K. & Tandogan R. 1973. A study of scours at the end of stilling basin and use of horizontal beams as energy dissipators. Comm.Int. Grands Barrages. Madrid.

Chia-Chun Wu, Chien-Hsuan Hou, Chiang-No Chen & Chen-Yang Shih 2002. Determination of groundsills interval for stream training. *River Flow 2002*. Louvain La-Neuve. Belgium. 4–6 settembre 2002.

Ciaravino G. & Ciaravino L. 2003. Considerazioni sul proporzionamento ed impatto dei bacini di dissipazione. *Giornate di studio su "La difesa idraulica del territorio 2003".* 10–12 settembre. Trieste.

Einstein A.H. 1942. Formulas for the transportation of bed-load. *Trans ASCE.*

Ghetti A. 1954. Similitude des effouillements du lit des rivières dans les zones de diffusion de veines rapides. *Ass. Int. d'Hydrologie Scintifique* Pubbl. n.38.

Ghetti A. 1979. Forma delle sezioni degli alvei naturali and teoria del regime. *Moderne vedute sulla meccanica dei fenomeni fluviali*: pp.95–127. Bressanone (Brixen) 8–12 Ottobre.

Ghetti A. & Zanoviello A. 1954. Esame delle escavazioni d'alveo a valle della traversa mediante esperienze su modelli in piccole scale. *I Convegno di Costruzioni Idrauliche.* Roma.

Gill M.A. 1972. Erosion of sand beds around spur-dikes. *Proc.ASCE Hy 9 Settembre.*

Graf W.H. & Altinakar M.S. 1998. Fluvial Hydraulics. *J. Wiley and Sons*. London.

Kalinske A.A. 1947. Movement of sediment as bed-load in rivers. *Trans. Amer. Geoph.Union.*

Karim O.A. & Ali K.H.M. 2000. Prediction of flow Patterns in local scour holes caused by turbulent water jets. *Journal of Hidr. Research* Vol.38: pp.279–287.

Kurniawan A., Altinakar M.S. & Graf W.H. 1999. Flow pattern of eroding eroding jet. *Rapporto annuale 1999 Ecole Pol. Fed. de Lausanne.* Lausanne.

Istiarto I., Graf W.H., Altinakar M.S. & Zech Y. 1999. 3D Modeling of flow around a cylinder. *Rapporto annuale 1999 Ecole Pol. Fed. de Lausanne.* Lausanne.

Lacey G.F. 1946. A general theory of flow alluvium. *J. Inst. Civil Engrs.* Vol.27.

Lacey G.F. 1958. Flow in alluvial channels with sandy mobile beds. *Proc. Inst. Civil Engrs.* Vol.9.

Laursen E.M. 1952. Observation on the nature of scour. *V Hydraulic Conference.* Iowa City.

Levi J.J. 1961. Effet dynamique d'un courant a haute turbolence sur des ouvrages hydraliques et sur le lit des rivieres. *IAHR.* Dubrovnik.

Mongiardini V. 1979. Fenomeni idraulici in corrispondenza degli attraversamenti dei corsi d'acqua: fenomeni idrografici ad essi connessi. *Moderne vedute sulla meccanica*

dei fenomeni fluviali: pp.157–183. Bressanone (Brixen) 8–12 Ottobre.
Montuori C. 1997. Complementi di idraulica. *Liguori editore.* Napoli.
Nebbia G. 1938. Sul proporzionamento di traversa a soglia prolungata per dissipatori a risalto. *Acque and Gas* n.3.
Nebbia G. 1938. Sui fenomeni di escavazioni di fondo a valle di luci a battente od a stramazzo. *Acqua and gas* n.4.
Nebbia G. 1940. Sui dissipatori a salto di Bidone, Basi teoriche. *L'Energia Elettrica* n.3.
Nebbia G.1940. Sui dissipatori a salto di Bidone, Ricerca sperimentale. *L'Energia Elettrica* n.6.
Nebbia G. 1941. Sui dissipatori a salto di Bidone, Norme di proporzionamento. *L'Energia Elettrica* n.7–8.
Nola F. & Rasulo G. 1989. Escavazioni a valle di dissipatori a risalto. *Idrotecnica* n.2, Marzo-aprile.
Pezzoli G. 1979. Considerazioni attuali sul trasporto solido and sulla modellazione degli alvei. *Moderne vedute sulla meccanica dei fenomeni fluviali* : pp.157–183. Bressanone (Brixen) 8–12 Ottobre.
Pica M. 1974. Trasporto solido di fondo. *L'Energia elettrica* Vol.51 n.8.
Radice A., Franzetti S. & Ballio F. 2002. Local scour at bridge abutments. *River Flow 2002*. Louvain La-Neuve. Belgium. 4–6 settembre 2002.
Rajaratnam N. & Macdougall R.K. 1983. Erosion by plane wall jets with minimum tailwater. *Journal of Hidr. Eng*. ASCE, Vol.109: pp.1061–1064.
Schoklitsch A. 1935. Stanraum verlandung und Kolkbwehr, *Sprinter.* Wienna.
Scimemi E. 1939. Sulla relazione che intercede fra gli scavi osservati nelle opere idrauliche originali and nei modelli. *L'Energia Elettrica* n.11.
Shen H.W. 1971. River Mechanics. *Vol.II.* Fort Collins USA.
Shields A. 1936. Anwendung der Aenlichkeitsmechanik und der Turbulenzforschung auf die Geschiebebewegung. *Mitteil PVWES.*
Veronese A. 1937. Erosioni di fondo a valle di uno scarico. *Annali dei LL.PP.* n.9.

A.5. Sediment supply, entrainment and transport

This page intentionally left blank

River Flow 2004 – Greco, Carravetta & Della Morte (eds.)
© 2004 Taylor & Francis Group, London, ISBN 90 5809 658 0

Interaction between particles and water in near-wall region of particle-laden open-channel flows

I. Nezu
Professor, Dept. of Civil & Global Environmental Eng., Kyoto University, Japan

R. Azuma
Ph.D. Student, Dept. of Civil & Global Environmental Eng., Kyoto University, Japan

ABSTRACT: The present study focuses on the interaction between solid-particles and fluid in particle-laden open-channel flows. Turbulence measurements of both particles and fluid (water) were conducted by means of a discriminator particle-tracking velocimetry (PTV). The titanium compound polystyrene (specific density = 1.16 to 1.29, diameter = 0.39 to 1.18 mm) was used for solid-particles. In these experiments, the ratio between the particle scale and turbulence-length one was changed systematically. As the results, it was found that the particle velocity is larger than the fluid velocity in the near-wall region of $y^+ \leq 15$, whereas the former is smaller than the latter in the region of $y^+ > 15$. This relative velocity between the particles and fluid increases with an increase of the particle diameter and specific density. The sweeps of particles near the wall become much larger than the ejections of particles as the diameter and specific density are larger. These facts suggest strongly that the particle motions may inrush towards the wall and transport high momentum to fluid.

1 INTRODUCTION

Particle-laden flows have been paid attention by many researchers because it changes the flow resistance law and plays an essential role in sediment transport. The earlier studies of sediment transport have been explained empirically by changes of fluid velocity profiles and an expression of the sediment concentration was derived from diffusion theory, e.g. see Yalin (1972). However, the simultaneous velocity of solid-particles and fluid is needed to estimate the effects of interaction between solid-particles and fluid quantitatively.

Recently, simultaneous measurements of particles and fluid in particle-laden flow have been conducted for the background mentioned above. The changes of velocity profiles were examined when the particle-laden flow was compared with clear-water flow, and consequently the relative velocity between particles and fluid was revealed by some researchers, e.g., Kaftori *et al.* (1995), Best *et al.* (1997) and Muste & Patel (1997). Experiments on particle-laden flows can be classified into two groups, the inner-layer ($y/h \leq 0.2$) and outer-layer ($y/h \leq 0.2$) experiments. As for the experiment on outer-layer flow, Itakura & Kishi (1980) pointed out that the wake-strength parameter Π in the log-wake law was changed by the existence of particles. Cellino & Graf (1999) observed that the value of Π increased with the particle concentration. On the contrary, Valiani (1991) reported that Π decreased and a significant change was observed in the inner layer where the particle concentration is high. It has not yet reached agreement about the value of Π, but the changes of this outer-layer property are considered to be influenced from the inner-layer one.

On the other hand, as for on the inner-layer experiment, Kulick *et al.* (1994) have measured the velocities of fluid and copper particles in a vertical wind duct by a laser Doppler anemometer (LDA). They have discriminated the fluid and powder data by the difference of the amplitude of LDA burst signals in the measurement volume. Kaftori *et al.* (1995) have measured turbulence characteristics in an open-channel flow including polystyrene particles over the smooth bed. They tried to discriminate the particle signals from the fluid-flow signals by making use of the voltage of burst signals. Best *et al.* (1997) have conducted simultaneous measurements of glass beads and fluid by means of phase Doppler anemometer (PDA) in an open-channel flow, in which the same glass particles were attached on the channel bed. Muste & Patel (1997) have measured the velocities of sand-particles and fluid in open-channel flow over the movable-sand bed using

a discriminator LDV that combines LDV (or LDA) with a unit for particle-size discrimination.

Kulick *et al.* (1994) and Kaftori *et al.* (1995) observed no meaningful differences of velocity profiles between the clear-water flow and particle-laden flow. On the contrary, Best *et al.* (1997) and Muste & Patel (1997) observed a downward shift of fluid-velocity profiles in particle-laden flow. The factors of this downward shift in velocities may be due to the bed roughness and the effect of particles. They pointed out that the factor is only the bed roughness, but an interaction between particles and fluid will probably influence fluid-velocity profiles. It is because this interaction has a close relation to the momentum exchange. In this mechanism, particle motions are explained by the bursting motions of fluid in the near-wall region, e.g., Sumer & Deigaard (1981), Rashidi *et al.* (1990) and Nino & Garcia (1996). However, experimental data and knowledge about the interaction between turbulence of the near-wall fluid and the particle motions are not yet sufficient to understand and develop the two-way models in particle-laden flows.

In this study, some experiments were conducted in smooth bed, which was covered by no roughness elements. Particularly, the near-wall region was highlighted, in which the interaction between particles and fluid is most significant. The titanium-compound polystyrene (specific density = 1.16 to 1.29, diameter = 0.39 to 1.18 mm) was used for solid-particles, and the ratio between the particle scale and the turbulence-length one was changed systematically in keeping the latter fixed. Simultaneous measurements of water and these particles have been conducted by means of a discriminator particle-tracking velocimetry (PTV). The particle-data and fluid-data were separated by the discriminator of occupied-area sizes of the particle images. The hydro-dynamic characteristics of both the near-wall and outer layer were investigated intensively.

2 EXPERIMENTAL SETUP AND HYDRAULIC CONDITIONS

2.1 *Experimental equipment*

The experiments were conducted in a 4 m long and 5 cm wide tilting flume, as shown in Figure 1. x, y and z are the streamwise, vertical and spanwise coordinates, respectively. The present PTV/PIV system was the same as used by Nezu & Onitsuka (2001). The instantaneous velocity components and $\tilde{u}(t) \equiv U + u(t)$ and $\tilde{v}(t) \equiv V + v(t)$ were measured by PTV with a discriminator, as mentioned later. In which, the capital letter and the small letter denote the time-averaged value and turbulent fluctuations, respectively. Particles recirculated with water through the flume and the measurements were conducted one hour later from

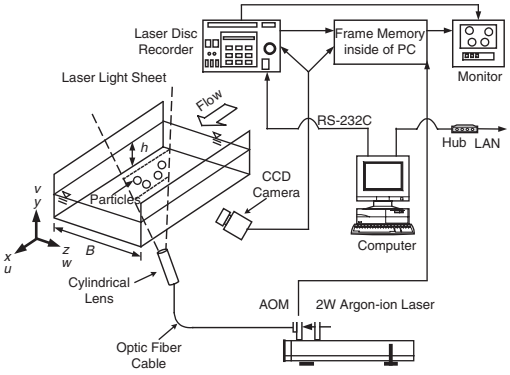


Figure 1. Experimental set-up and PTV arrangement.

the begin of water circulation, at which the flow and particles motions attained an equilibrium state.

A 2W Argon-ion laser beam was guided through an optical fiber cable and illuminated vertically from the channel bottom as a 2 mm thickness laser light sheet (LLS), see Figure 1. LLS can be adjusted by the computer control AOM, in which the emission interval and duration were adjusted as 3–6 ms and 0.5–0.9 ms, respectively, as schematized in Figure 2. Pair of images of particles were taken by a high sensitive CCD camera (SONY), which was placed near the sidewall. Its resolution was 512×480 pixels. The original image consists of the odd and even scanning lines and the time interval is 1/30 s (30 Hz). The images were recorded by a digital laser-disc recorder (SONY).

2.2 *Experimental conditions*

The hydraulic conditions are summarized in Table 1. In which, $d_p(\equiv d)$ is the median diameter of particle, ρ_p is the specific density of particle, U_m is the mean bulk velocity, U_* is the friction velocity (its evaluation method will be discussed later in section 4.3), h is the water depth, $R_* \equiv U_* h/\nu$ is the Reynolds number based on U_*, $Re \equiv U_m h/\nu$ is the Reynolds number based on U_m, $Fr \equiv U_m/\sqrt{gh}$ is the Froude number and $\overline{C}$ is the particle volumetric concentration averaged in the whole flow depth. The case name of PM denotes PMMA/PS (poly-methyl methacrylate/polystyrene), T denotes the titanium compound polystyrene and the figures denote the compound ratio and particle-diameter. The diameter d_p and specific density ρ_p of particles were systematically changed, i.e., $dp = 0.39$ to 1.18 mm and $\rho_p = 1.15$ to 1.29. The case of CW4 is clear-water flow. In this study, two kinds of experiments were conducted in each case, (A) and (B). For one group (A), a size of the measurement region is the whole flow depth, and for the other group (B) the near-wall region from the channel bed up to 20 mm (the close-up pictures). The actual length of 1 pixel

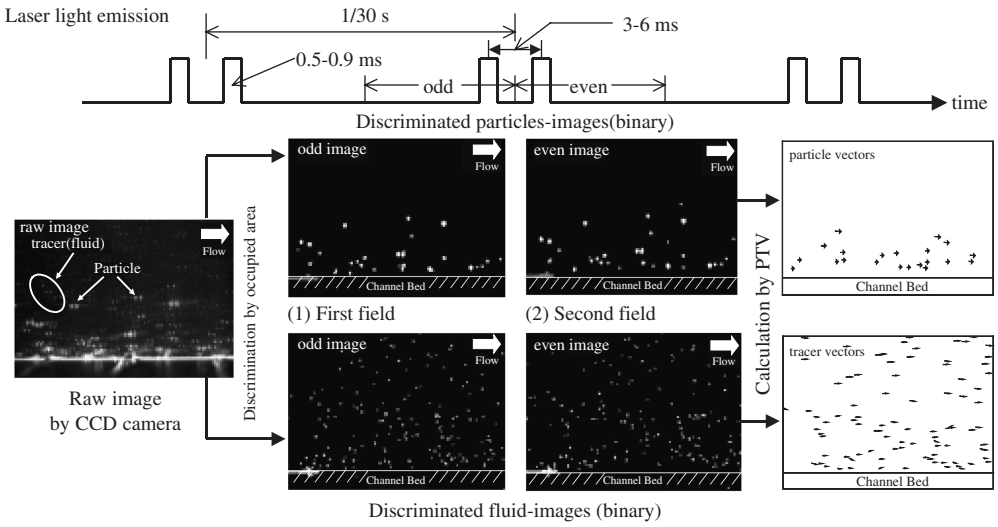


Figure 2. Image processing of solid-particles and fluid tracer.

Table 1. Hydraulic conditions.

Case	d_p (mm)	ρ_p	h (cm)	U_m (cm/s)	U_* (cm/s)	κ	R_*	$Re \times 10^4$	Fr	$\overline{C}$ (%)
CW4	–	–	5.0	43.1	2.12	0.412	999	2.03	0.62	–
PM13	1.00	1.15		42.0	2.15	0.386	1013	1.98	0.60	0.22
T1004	0.39	1.16		42.4	2.13	0.408	1003	2.00	0.61	0.04
T1005	0.46	1.16		43.1	2.13	0.409	1003	2.03	0.62	0.05
T1006	0.55	1.16		43.0	2.16	0.407	1017	2.03	0.61	0.05
T1007	0.65	1.16		42.7	2.14	0.400	1008	2.01	0.61	0.08
T1009	0.85	1.16		42.5	2.15	0.393	1012	2.00	0.60	0.10
T1012	1.18	1.16		42.0	2.16	0.390	1017	1.98	0.62	0.32
T1506	0.55	1.23		43.3	2.18	0.408	1027	2.04	0.62	0.06
T1507	0.65	1.23		43.2	2.19	0.399	1032	2.03	0.61	0.08
T1509	0.85	1.23		43.0	2.16	0.389	1017	2.03	0.61	0.07
T2006	0.55	1.29		43.2	2.16	0.400	1017	2.03	0.62	0.05
T2007	0.65	1.29		42.7	2.16	0.396	1017	2.01	0.61	0.06
T2009	0.85	1.29		42.9	2.16	0.385	1017	2.02	0.61	0.07

corresponded to 0.153 mm for A and 0.0303 mm for B, respectively.

The water discharge Q and the flow depth h were set almost constant throughout all of experiments. Consequently, $h = 50$ mm and $U_m = Q/A = 42.0$ to 43.3 cm/s were obtained. Thus, the turbulence scale, l, of water fluid was the almost same in all experiments, and in contrast the particle scale, d_p, was changed in a wide range. The effect of particle size on particle–fluid interaction will be revealed because the value of d_p/l is a significant factor in turbulence modulation mechanism, as pointed out by Gore & Growe (1989). In the (B) group, the mutual interaction between particles and fluid was investigated in detail as a parameter of the wall unit, i.e., ν/U_*, in which superscript symbol "+" is used here.

In contrast, the diameter and density of seeding particles (Nylon 12) for water fluid are 0.1 mm and 1.02, respectively; we call the fluid tracer. The test section was located 3 m downstream of the channel entrance. The measuring time of PTV was 60 s (1800 frames). These methods are the almost same as used by Nezu & Onitsuka (2001).

3 CALCULATION METHOD OF FLUID AND PARTICLES VELOCITY

3.1 *Discrimination of fluid and particle data*

Any discrimination between particle and fluid on a snapshot image of CCD camera has firstly to be

developed for simultaneous measurements. There are some methods, for example, (1) particle-color discrimination (discriminated by color of particles) and (2) particle-area discrimination (discriminated by the occupied area of particles).

Figure 2 shows an example of the raw image and processing images of solid-particles and fluid tracer. The raw image consists of the odd and even scanning lines. First of all, the brightness of raw image was adjusted most suitably, and separated into the odd and even fields. The separated images were binarized then and discriminated by using a threshold value of the occupied area of particles.

For this occupied-area discrimination, it is important to set a resolution of CCD camera reasonably. In this study, the length of 1 pixel in the CCD image corresponded to 0.102 mm for (A) group and 0.040 mm for (B) group. The occupied area of the minimum diameter 0.39 mm (case T1004) was larger than 15 pixels, while that of fluid tracer was 1 pixel. Therefore, it was easy to discriminate automatically the solid-particles and fluid. This occupied-area discrimination method was applied reasonably to all cases of the present experiments.

3.2 *Calculation algorithm*

Nezu *et al*. (1999) have conducted PTV measurements of sand particles over a gravel bed by making use of the 4-fields-image algorithm, which is one of the most popular methods in PTV. However, it was very difficult to track sand-particle motions near the bed by the earlier PTV algorithm using four consecutive images, because these motions were quite complicated, i.e., the dropping sand particles are sometimes reflected on the channel and lifted upward again. In contrast, Okamoto *et al*. (1995) have developed a 2-fields-image algorithm, based on the pattern matching of the particle cluster between two consecutive images using invisible elastic springs; they called the "spring model".

The spring model PTV is very powerful for flow fields including even the appearing and disappearing particles in images. Nezu *et al*. (2001) have tried to apply the spring model PTV to a sediment-laden open-channel flow and concluded that this model is very reliable even in such an open-channel flow. Therefore, this algorithm was also adopted in this study.

4 RESULTS AND DISCUSSIONS

4.1 *Clear water flow*

Figure 3 shows the mean velocity profiles of clear water flow (CW4), which is almost same hydraulic condition as particle-laden flows (Table 1). The symbols (PTV) and (LDA) in Figure 3 indicate the results by PTV and LDA, respectively. The PTV data are

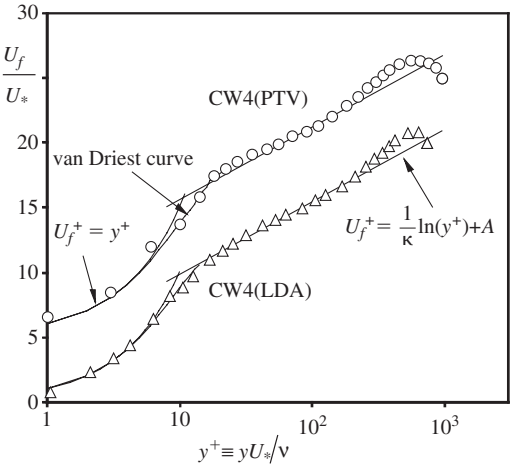


Figure 3. Streamwise velocity profiles of clear-water.

shifted 5 units in the vertical axis to avoid confusions. Three theoretical curves are included in Figure 3.

$$U_f^+ = y^+ \qquad \text{for } y^+ \le 5 \qquad (1)$$

$$\frac{dU_f^+}{dy^+} = \frac{2\left(1 - y^+/R_*\right)}{1+\sqrt{1+4\ell^{+2}\left(1-y^+/R_*\right)}} \qquad \text{for } 5 \le y^+ \le 30 \qquad (2)$$

$$U_f^+ = \frac{1}{\kappa}\ln y^+ + A \qquad \text{for } y^+ \ge 30 \qquad (3)$$

in which, $U^+ \equiv U/U_*$ and $y^+ \equiv yU_*/\nu$ are the inner parameters normalized by the inner variables of the friction velocity, U_*, and the kinetic viscosity, ν. Equation (1) is the theoretical formula in the viscous sublayer of $y^+ \le 5$, whereas (3) is the log-law that is satisfied in the region of $y^+ \ge 30$, in which κ is the von Karman constant and A is the integration constant. No analytical solution is available in the buffer layer of $5 < y^+ < 30$, but a numerical curve is obtained from (2) by using the van Driest damping function; we call the "van Driest curve".

$$\ell^+ = \kappa y^+ \Gamma \quad \text{and} \quad \Gamma = 1 - \exp\left(-y^+/B\right) \qquad (4)$$

in which, ℓ^+ is the normalized mixing length and $R_* \equiv hU_*/\nu$ is the Reynolds number based on the friction velocity. Nezu & Nakagawa (1993) have reviewed that the von Karman constant, κ, is really a universal one of $\kappa = 0.41$ over smooth and rough beds in open-channel flows of clear water.

The maximum velocity is observed at $y/h = 0.6$ and such a velocity-dip occurs due to secondary currents, because the aspect ratio, B/h, is as small as 1 in this experiment, as pointed out by Nezu & Nakagawa (1993). These secondary currents would cause a

downward flow at the center of channel. The reason why such a small aspect ratio of channel was adopted here is the optical limitation in PTV measurements of comparatively dense particle concentration flow, in spite of occurrence of secondary currents. However fortunately, both of LDA and PTV data are in a good agreement with the theoretical curves of (1)–(3) from the viscous sublayer to the log-law layer of $y/h \leq 0.2$. The friction velocity, U_*, was evaluated from the theoretical formula of (1), and then the Karman constant, κ, was calculated from (3). Consequently, $\kappa = 0.41$ was obtained and this result coincides perfectly with that of Nezu & Rodi (1986).

Figure 4 shows the Reynolds stress, $-\overline{uv}/U_*^2$, measured with the present PTV and LDA. The theoretical curves of (5) and (6) are included in Figure 4.

$$\frac{-\overline{u_f v_f}}{U_*^2} = 1 - \frac{y}{h} - \frac{dU_f^+}{dy^+} \quad (5), \text{ and } \quad \frac{-\overline{u_f v_f}}{U_*^2} = 1 - \frac{y}{h} \quad (6)$$

The measured values of $-\overline{uv}$ deviate significantly from (6) in the outer layer of $y/h > 0.2$ and indicate negative values near the free surface. This deviation is caused by secondary currents, as discussed by Nezu & Nakagawa (1993). However, both of LDA and PTV data are in a good agreement with the theoretical curve of (5) in the inner layer of $y/h < 0.2$. Therefore, it is considered that the inner layer does not affected by secondary currents and we can highlight this near-wall region in the present study. It should also be noticed the friction velocity, U_*, evaluated from (1) in the viscous sublayer coincides well with that evaluated from the Reynolds stress distribution of (6).

4.2 *Classification of multiphase flows*

Elgobashi (1994) has classified multiphase flows on the basis of Stokes number St and the volumetric particle concentration, C. The Stokes number is defined as $St \equiv t_p/t_e$, in which $t_p \equiv \rho_p d_p^2/(18\rho_f \nu)$ is the particle relaxation time, $t_e \equiv l/u'$ is the eddy turnover time of fluid and u' is its turbulence intensity. The eddy characteristic length-scale l was approximately identified as a mixing length ℓ and evaluated from (4).

Figure 5 shows the vertical profiles of the volumetric particle concentration, C. The Rouse formula of (7) is indicated in Figure 5.

$$\frac{C}{C_a} = \left\{ \left(\frac{h_p - y}{h_p - a} \right) \left(\frac{a}{y} \right) \right\}^Z \quad , \quad Z = \frac{w_s}{\beta \kappa U_*} \qquad (7)$$

in which, w_s is the settling velocity of particles, h_p is the thickness of suspended layer and C_a is the particle concentration at $y = 0.05h_p$. The value of β was chosen in order that the curve of (7) coincides with the measured present data of C. In all cases, the vertical profiles of C

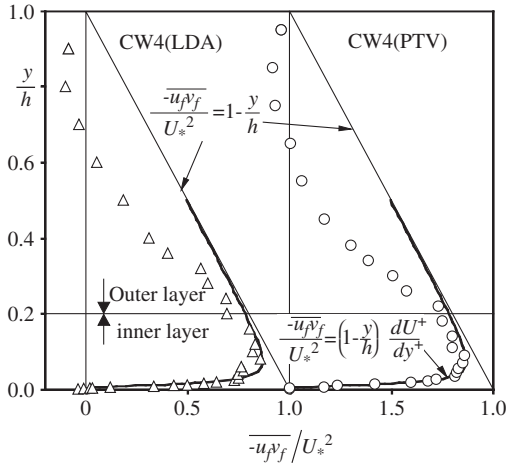


Figure 4. Reynolds stress distributions of clear-water.

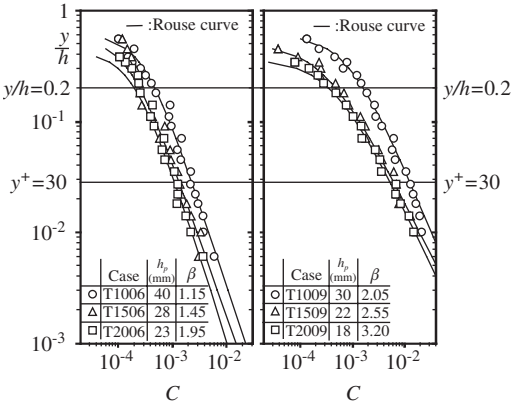


Figure 5. Vertical profiles of particle concentration.

were expressed satisfactorily by the Rouse formula of (7). However, the value of β was much larger than 1.0. Therefore, the particle motions may show the bed-load rather than the suspended ones, because the particle layer, h_p, did not reach the water surface.

According to Elgobashi (1994), a diagram of St vs. C is shown in Figure 6. The turbulence in the region of $St > 1$ is enhanced by solid particles, whereas it is depressed by particles in the region of $St < 1$. The Stokes number St in particle-laden open-channel flow increases with an increase of the particle concentration C and it is larger than the unity near the bed, i.e., $t_p > t_e$. This fact suggests strongly that the turbulence generated by particles is larger than that of clear water flow very near the wall. On the contrary, the turbulence will be depressed due to the existence of particles in the outer layer.

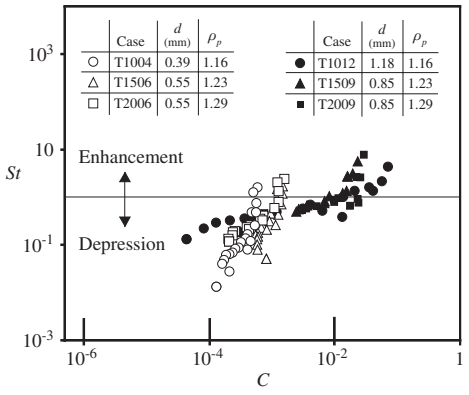


Figure 6. Classification of multiphase flows.

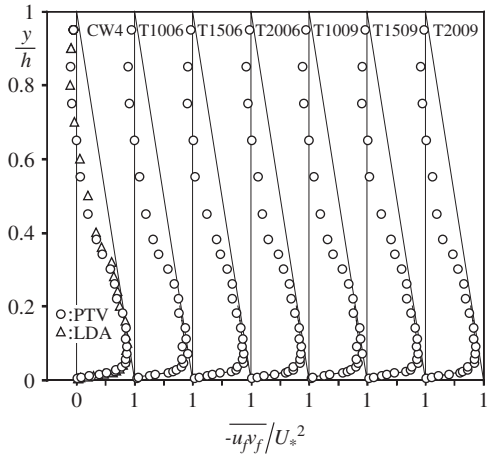


Figure 7. Reynolds stress distributions of fluid in particle-laden open-channel flows.

4.3 *Evaluation of friction velocity*

It is difficult to evaluate the friction velocity, U_*, from the log-law of (3) in particle-laden open-channel flows, because the von Karman constant, κ, in such flows is not perfectly established even now. Guo & Julien (2001) have reviewed previous data of velocity profiles in sediment-laden open-channel flows that were obtained by intrusive (conventional) velocity measurements such as Pitot tubes. They suggested that the von Karman constant κ, decreased with an increase of the sediment concentration, especially in dense suspended sediment-laden flows. In contrast, Muste (2002) has recently reviewed the sources of bias errors in sediment-laden flow data and pointed out that the von Karman constant remains a universal one of $\kappa = 0.41$ even in dilute sediment-laden flows on the basis of non-intrusive measurements such as LDA and PDA.

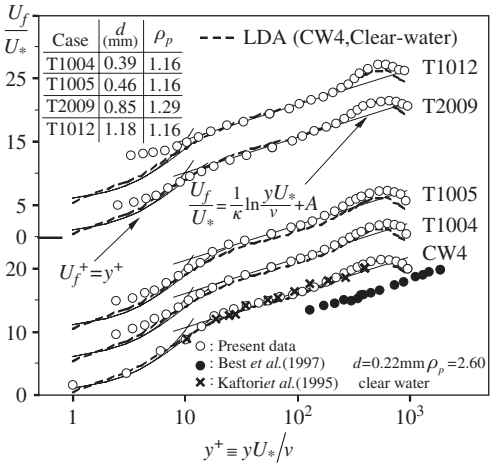


Figure 8. Mean velocity profiles of fluid in two-phase particle-laden open-channel flows.

Figure 7 shows the measured values of Reynolds stress of fluid, $-\overline{u_f v_f}$, in particle-laden open-channel flows. These values coincide well with the theoretical curve of (5) in the inner layer of $y/h < 0.2$. Therefore, in this study, the friction velocity, U_*, was determined by an extrapolation of the measured Reynolds stress, $-\overline{u_f v_f}$, to $y = 0$, i.e., using (6). This evaluation method was also used by Lyn (1991), Kaftori *et al*. (1995), Muste & Patel (1997) and Best *et al*. (1997). The values of U_* evaluated from $-\overline{u_f v_f}$ distributions are indicated in Table 1, together with the values of κ evaluated then from (3) using these values of U_*. The friction velocity increases in the existence of particles and increases with particle diameter and specific density. It is also observed that the von Karman constant decreases slightly with particle diameter, d_p, specific density, ρ_p, and mean concentration, $\overline{C}$.

4.4 *Mean velocity profiles of fluid and particles*

Figure 8 shows the mean velocity profiles of fluid, U_f, in two-phase open channel flows. Each case is shifted by 5 units in the vertical direction. Our LDA data of clear water, LDA data of Kaftori *et al.* (1995) and PDA data of Best *et al.* (1997) are also shown in Figure 8. These profiles of $U_f^+ = U_f/U_*$ agreed well with clear-water LDA data except for the buffer layer of $y^+ < 30$. Best *et al.* (1997) and Muste & Patel (1997) pointed out that the velocity profiles of fluid, U_f^+, in sediment-laden flows showed a downward shift as compared with the clear water flow. However, this downward shift was not observed in this study, because the present flow condition was no roughness elements covered on the bed, as mentioned in Figure 2. Of particular significance is that the velocity of U_f^+ in the

region of $y^+ \leq 10$ for particle-laden flow is larger and flatter than that for clear-water flow.

Figure 9 shows the mean velocity profiles of particles, U_p. The particle velocity, U_p, is slightly smaller than the fluid velocity, U_f, and parallel to the log-law line of fluid in the region of $y^+ > 30$ in all cases. The same results were obtained by Rashidi *et al*. (1990), Kaftori *et al*. (1995) and Nino & Garcia (1996). In contrast, the particle velocity near the wall is larger than the clear-water one, which was also observed by Kaftori *et al.* (1995). These particles will transport the high-momentum to the surrounding fluid and make it high velocity. As a result, the fluid velocity is larger than the clear-water one, and thus the flatter distribution was observed these in this study.

4.5 *Relative velocity*

Differences between fluid and particle velocities are not so clearly recognized in the plots of Figures 8 and 9. Therefore, the relative velocity between the particles and fluid phases, $U_r \equiv U_f - U_p$, is examined in the following ways.

4.5.1 *Effect of particle density*

Figure 10 shows the relative velocity, $U_r \equiv U_f - U_p$, together with the results of Kaftori *et al.* (1995) and Best *et al.* (1997). In this figure, the particle scale (particle diameter, $d \equiv p$) keeps almost constant ($d = 0.8$ and 0.85 mm), and the particle density, ρ_p, was changed from 1.05 to 1.29. The relative velocity, U_r, is positive farther from the wall ($y^+ > 15$), i.e., the fluid velocity, U_f, is larger than the particle velocity, U_p. In the outer layer of $y^+ \leq 200$, the values of U_r are small and constant in all cases. They also coincide well with the data of Best *et al*. (1997) who used the glass particles of $\rho_p = 2.6$ and measured the U_r in the region of $y^+ > 150$. Therefore, the effect of particle density, ρ_p, on the relative velocity is not recognized significantly in the outer layer. This is because that the particle relaxation time t_p is much smaller than the eddy turnover time $t_e (St << 1)$ and thus the particles can follow the fluid sensitively.

In contrast, the relative velocity is negative in the near-wall region of $y^+ \leq 15$, that is, $U_p > U_f$, which coincide well with the data of Kaftori *et al*. (1995). In a comparison of case T2009 ($\rho_p = 1.29$) and PS08 ($\rho_p = 1.05$), the relative velocity increases slightly with an increase of the particle density, ρ_p. The particles moving toward the wall have a grain inertia and high momentum when they inrush into the near-wall region. In contrast, the fluid velocity is depressed by the viscous effect. Consequently, the particle velocity, U_p, is larger than the fluid one, U_f, and the particles will transport some momentum to fluid in the near-wall region. This momentum transfer to fluid increases with the particle density and induces the flatter distributions of fluid velocity, U_f, near the wall.

4.5.2 *Effect of particle diameter*

Figure 11 shows the relative velocity, U_r, in which the particle density, ρ_p, keeps constant ($\rho_p = 1.16$) and the particle diameter, d_p, change from 0.39 mm to 1.18 mm. The particle velocity, U_p, is smaller than the fluid velocity, U_f, in the region of $y^+ \geq 15$, whereas the former is larger than the latter in the near-wall region ($y^+ < 15$). It should be noted that the effect of particle diameter on the relative velocity, U_r, is recognized clearly. That is to say, the value of U_r increases with an increase of particle diameter, d_p. This is because the particle relaxation time, $t_p \propto d_p^2$, becomes much larger as d_p increases. Consequently, the effect of particle

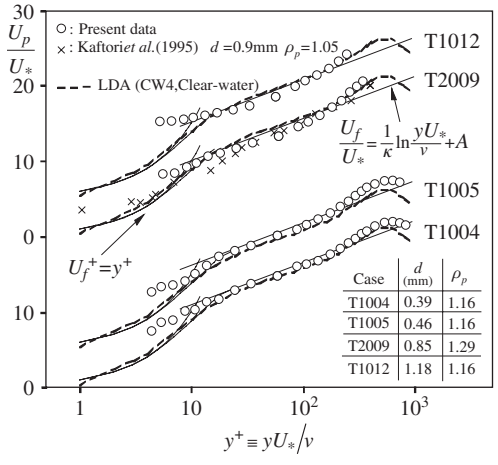


Figure 9. Mean velocity profiles of particles in two-phase open-channel flows.

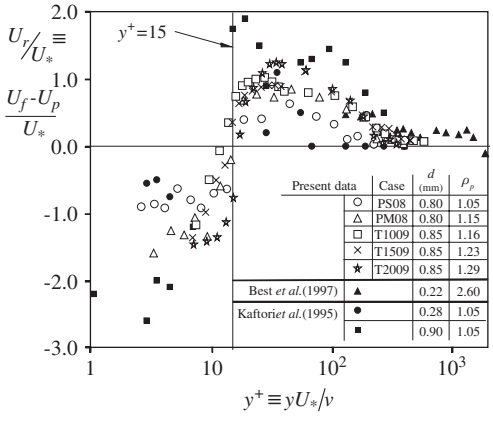


Figure 10. Relative velocity between particles and fluid in open-channel flows (Effect of particle specific-density, ρ_p).

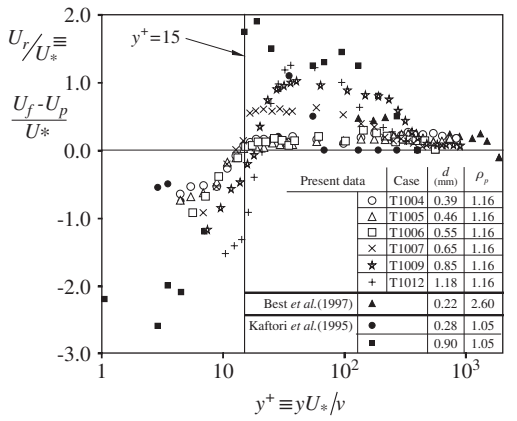


Figure 11. Relative velocity between particles and fluid in open-channel flows (Effect of particle diameter, d_p).

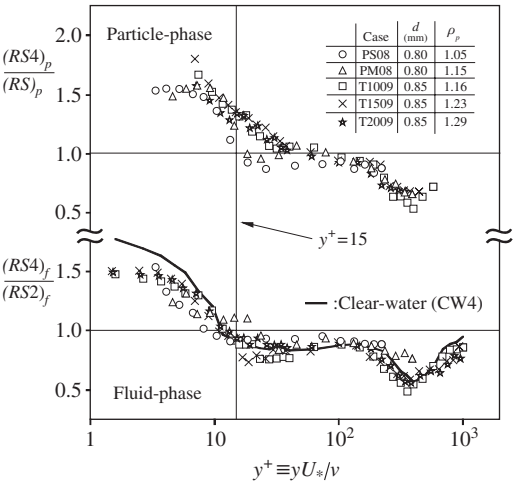


Figure 12. Relation between ejections and sweeps of fluid and particle motions (Effect of particle specific density, ρ_p).

diameter, d_p, on the particle-fluid interaction will be larger rather than the effect of particle density, ρ_p.

4.6 *Quadrant Reynolds stress and bursting motions*

4.6.1 *Quadrant theory*

In the previous section, the particle velocity, U_p, becomes larger than the fluid velocity, U_f, very near the wall due to both the high momentum of particles and the viscous effect of fluid. Momentum transfer of turbulence in smooth-wall boundary layer is identified as bursting motions of fluid. These motions are analyzed successfully by a quadrant theory of the instantaneous Reynolds stress $-u(t)v(t)$, as pointed out by Nakagawa & Nezu (1977). The 1st quadrant motion is the outward interaction ($u > 0, v > 0$), whereas the 3rd quadrant is the inward interaction ($u < 0, v < 0$). The 2nd quadrant ($u < 0, v > 0$) motion transports the low momentum ($\rho u < 0$) to the upward region ($v > 0$) that is called the "ejection", whereas the 4th quadrant ($u > 0, v < 0$) transports the high momentum ($\rho_u > 0$) to the downward region ($v < 0$) that is called the "sweep". It is well known that the ejections and sweeps are significantly contributory to bursting motions. The contributions of ejections $RS2$ and sweeps $RS4$ of fluid motions are defined as follows:

$$(RS2)_f \equiv \left(-\overline{u_f v_f}\right)_2 = \begin{cases} -S(t)u_f(t)v_f(t) & \text{for } u_f < 0, v_f > 0 \\ 0 & \text{otherwise} \end{cases} \quad (8)$$

$$(RS4)_f \equiv \left(-\overline{u_f v_f}\right)_4 = \begin{cases} -S(t)u_f(t)v_f(t) & \text{for } u_f > 0, v_f < 0 \\ 0 & \text{otherwise} \end{cases} \quad (9)$$

in which, the function $S(t)$ is given by

$$S(t) = \begin{cases} 1 & \text{if } \left|u_f(t)v_f(t)\right| > Hu_f'v_f' \\ 0 & \text{otherwise} \end{cases} \quad (10)$$

The threshold value H is usually set as $H = 1$ in order to distinguish the bursting events from non-coherent ejection-like and sweep-like turbulence in clear-water flows. So, this study also chosen $H = 1$.

In the same manner, this quadrant theory is now applied to the particle motions in two-phase flow. The contributions of ejections and sweeps of particle motions are defined as $(RS2)_p$ and $(RS4)_p$, respectively.

4.6.2 *Effect of particle density*

Figure 12 shows the ratio of sweeps to ejections, $RS4/RS2$, for fluid and particle motions, in which only the particle density, ρ_p, was changed. In the case of clear-water, CW4, the value of $RS4/RS2$ is almost constant of 0.8–0.9 in the inner layer of $15 < y^+ < 200$, and these ratios of fluid phase in particle-laden flow are similar to that of clear-water flow. In the region of $y^+ < 10$, the contribution of sweeps is larger than that of ejection, $(RS4)_f > (RS2)_f$, and these ratios of fluid in particle-laden flow were smaller than that of clear-water flow. It may be supposed that the bursting motions of fluid is restrained by an existence of particles.

On the other hand, as for the particle phase in particle-laden flow, the profiles are similar to those of fluid phase and thus the particle motions are controlled by motions of surrounding fluid. In the near-wall region of $y^+ < 50$, $(RS4)_p/(RS2)_p$ is larger than the unity irrespective of particle density. It should be noted that the ratio of sweeps to ejections of particles becomes larger than that of fluid in the region of $10 < y^+ < 100$, in which bursting motions occur most violently, e.g., see Nezu & Nakagawa (1993).

Figure 13 shows the distributions of $(RS4)_p/(RS4)_f$ and $(RS2)_p/(RS2)_f$. In the region of $15 < y^+ < 200$,

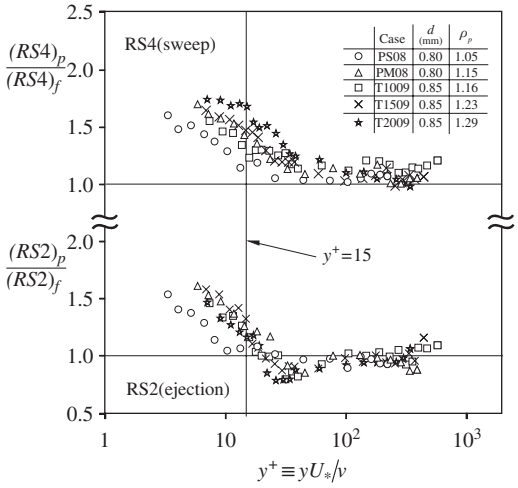


Figure 13. Relation between contributions of particles and fluid (Effect of particle specific density, ρ_p).

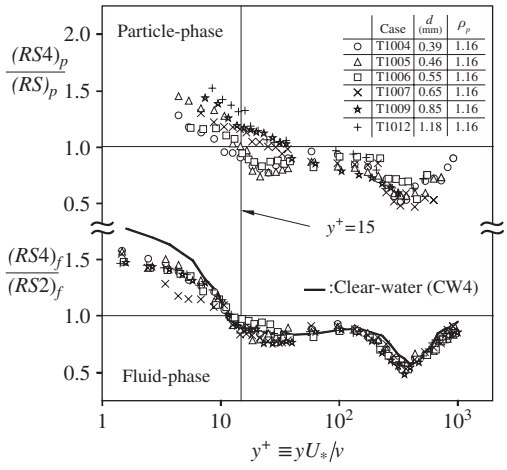


Figure 14. Relation between ejections and sweeps of fluid and particle motions (Effect of particle diameter, d_p).

the ratio $(RS2)_p/(RS2)_f$ of ejections is smaller than the unity and thus the ejection contribution of fluid is larger than that of particles. In contrast, the ratio $(RS4)_p/(RS4)_f$ of sweeps is larger than the unity in all regions, namely the sweep contribution of particles is larger than that of fluid. The difference between the particle and fluid motions are much remarkable in the region of $y^+ < 15$ and especially the sweeps of particle motions is much larger than those of the surrounding fluid. The particles having high momentum rush into the near-wall region and some of these particles may rebound from the wall like ejections. The sweeps of particles become larger as the particle density increases. This is due to the grain inertia effect.

4.6.3 *Effect of particle diameter*

Figure 14 shows the ratio $RS4/RS2$ of fluid and particles, in which only the particle diameter, d_p, was changed widely. The distributions of $(RS4)_f/(RS2)_f$ are in a good agreement with Figure 12, which implies that the fluid motions are not so significantly affected by particle sizes. In contrast, the distributions of $(RS4)_p/(RS2)_p$ changes systematically with the diameter, d_p. The ratio $(RS4)_p/(RS2)_p$ of particles increases with an increase of the particle diameter, i.e., the grain inertia effect. Particles are lifted up by the ejections of fluid and accelerated in the upper region of high velocity. These particles having high-momentum fall down due to gravity into the near-wall region and consequently the contribution of particle sweep motions is most predominant with the particle diameter.

Figure 15 shows the ratio between the contributions of particles and fluid, in which only the particle diameter was changed. The contribution of particle sweeps

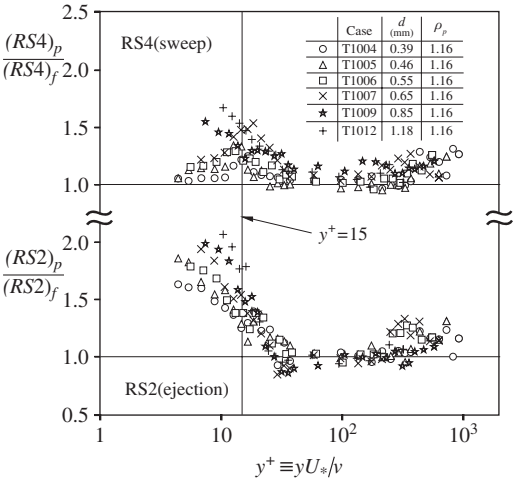


Figure 15. Relation between contributions of particles and fluid (Effect of particle diameter, d_p).

is larger than that of fluid, and this property becomes more significant with an increase of particle diameter.

5 CONCLUSIONS

Simultaneous measurements of both particles and fluid (water) were conducted in particle-laden open-channel flows by means of PTV. Particles and fluid were discriminated by the occupied area size of particle images on CCD camera. The mean velocity and the bursting motions of particles and fluid were examined

by changing the particle diameter and specific-density systematically. The main findings obtained in this study are as follow:

(1) Above the near-wall region of $y^+ > 15$, the particle mean velocity, U_p, is smaller than the fluid mean velocity, U_f, and this relative velocity increases with the particle diameter and specific density. This is because the inertia force increases with the particle diameter and specific density.
(2) In the near-wall region of $y^+ \leq 15$, the particle mean velocity, U_p, is larger than the fluid mean velocity, U_f. This may be because the fluid velocity is decelerated by viscous effect near the wall, while the particles inrush toward the wall with high-momentum.
(3) Interactions between particles and fluid were examined by the quadrant analysis. The difference between particles and fluid interactions was observed in the near-wall region where the contribution of sweeps is larger than that of ejections. This contribution of particles increases with the particle diameter and specific density. The sweeps of particles are much larger than those of fluid, and in turn the particles contribute to a uniformity of velocity gradient near the wall.

The existence of particles has a significant influence on flow field of the near-wall region as well as that of the outer layer. The near-wall region is very important to consider the interaction mechanism between turbulence and particles and this study will offer a meaningful perspective of particle-laden open-channel flows.

ACKNOWLEDGEMENTS

The experimental solid-particles used here, supplied from Mr. Ozaki and Dr. Ohara, Sekisui Plastics Co., Japan, are gratefully acknowledged.

REFERENCES

Best, J., Bennett, S., Bridge, J. & Leeder, M. 1997. Turbulence modulation and particle velocities over flat sand beds at low transport rate. *J. Hydr Eng.*, ASCE, 123: 1118–1127.

Cellino, M. & Graf, W.H. 1997. Sediment-laden flow in open-channels under noncapacity and capacity conditions. *J. Hydr Eng.*, ASCE, 125: 455–462.

Elgobashi, S. 1994. On predicting particle-laden turbulent flows. *Appl.Sci. Res.*, 52: 309–329.

Guo, J. & Julien, P.Y. 2001. Turbulent velocity profiles in sediment-laden flows. *J. Hydraulic Res.*, IAHR, 39: 11–23.

Gore, R.A. & Crowe, C.T. 1989. Effects of particle size on modulating turbulent intensity. *Int. J. Multiphase Flow.*, 15: 279–285.

Itakura, T. & Kishi, T. 1980. Open channel flow with suspended sediments. *Proc. ASCE*, 106, HY8: 1325–1343.

Kaftori, G., Hetsroni, G. & Banerjee, S. 1995. Particle behavior in the turbulent boundary layer. II. Velocity and distribution profiles. *Phys. Fluids*, 7: 1107–1127.

Kulick, J.D., Fessler, J.R. & Eaton, J.K. 1994. Particle response and turbulence modification in fully developed channel flow. *J. Fluid Mech.*, 277: 109–134.

Lyn, D.A. 1991. Resistance in flat-bed sediment-laden flows. *J. Hydr Eng.*, ASCE, 117: 94–114.

Muste, M. 2002. Sources of bias errors in flume experiments on suspended-sediment transport. *J. Hydraulic Res.*, IAHR, 40: 695–708.

Muste, M. & Patel, V.C. 1997. Velocity profiles for particles and liquid in open-channel flow with suspended sediment. *J. Hydr Eng.*, ASCE, 123: 742–751.

Nakagawa, H. & Nezu, I. 1977. Prediction of the contributions to Reynolds stress from bursting events in open-channel flows. *J. Fluid Mech.*, 80: 99–128.

Nezu, I. & Nakagawa, H. 1993. *Turbulence in Open channel Flows*. IAHR Monograph, Balkema, Rotterdam.

Nezu, I., Esaki, K. & Onitsuka, K. 1999. Interaction between turbulent structure and bed-load transport in open-channel flows. *Hydraulic Modeling* (eds. Singh *et al*.). Water Resources Publications. Colorado. USA: 63–76.

Nezu, I. & Onitsuka, K. 2001. Turbulent structures in partly vegetated open-channel flows with LDA and PIV measurement. *J. Hydraulic Res.*, IAHR, 39: 629–642.

Nezu, I., Onitsuka, K. & Azuma, R. 2001. Turbulence measurements of open-channel flows over gravel bed. Proc. of 3rd Int. Symp. on Measurement Techniques for Multiphase Flows. Fukui. Japan: 266–272.

Nezu, I. & Rodi, W. 1986. Open-channel flow measurements with a laser Doppler anemometer, *J. Hydr Eng.*, ASCE, 112: 335–355.

Nino, Y. & Garcia, M.H. 1996. Experiments on particle-turbulence interactions in the near-wall region of an open channel flow: implications for sediment transport. *J. Fluid Mech.*, 326: 285–319.

Okamoto, K., Hassan Y.A. & Schmidl, W.D. 1995. New tracking algorithm for particle image velocimetry. *Experiment in Fluids.*, 19: 342–347.

Rashidi, M., Hetsroni, G. & Banerjee, S. 1990. Particle-turbulence interaction in a boundary layer. *Int. J. Multipahse Flow.*, 16: 935–949.

Sumer, M.B. & Deigaard, R. 1981. Lift forces on moving particles near boundaries. Part 2. *J. Fluid Mech.*, 109: 311–337.

Valiani, A. 1991. The von-Karman coefficient in sediment-laden flow. *J. Hydr Res.*, IAHR, 29: 129–136.

Yalin, M. 1972. *Mechanics of sediment transport*. Pergamon Press.

River Flow 2004 – Greco, Carravetta & Della Morte (eds.)
© 2004 Taylor & Francis Group, London, ISBN 90 5809 658 0

Development of a new Marker-in-Cell hydraulic and sediment transport model for braided river flow

R.E. Thomas
Schools of Geography and Earth Sciences, University of Leeds, Leeds, UK

S.N. Lane
School of Geography, University of Leeds, Leeds, UK

J.L. Best
School of Earth Sciences, University of Leeds, Leeds, UK

ABSTRACT: This paper presents a new Marker-in-Cell hydraulic and sediment transport model. This model simulates fluid flow and sediment transport in the horizontal plane and depth, logarithmic velocity profile and deposits in the vertical plane. Non-uniform total-load sediment transport by size class is simulated by using a non-equilibrium approach, taking into account hiding and exposure effects among different size classes. To represent historical erosion and deposition, the bed is divided into a surface or active layer and a subsurface layer.

The model is being applied to a reach of the braided South Saskatchewan River, Saskatchewan, Canada to examine small-scale spatial and temporal processes. This reach has been affected by the 1967 closure of Gardiner Dam 30 km upstream, which causes the river to be significantly below sediment transport capacity for much of the time. However, analyses suggest minimal channel adjustments downstream of around 13 km of the dam. Bed adjustment must therefore be simulated utilizing a non-equilibrium approach.

1 INTRODUCTION

1.1 *Modeling braided rivers*

Combining the definitions of Lane (1957) and Leopold & Wolman (1957), a braided river is one that "flows in two or more anastomosing channels around alluvial islands" (Leopold & Wolman 1957), forming a pattern resembling "the intertwining effect of a braid when viewed from above" (Lane 1957). On observation, braided rivers appear to exhibit chaotic hydraulic and sedimentologic interactions (but see the work of Foufoula-Georgiou & Sapozhnikov 2001), linked to complex patterns of flow convergence and divergence related to the form-process feedback associated with bar formation and migration. Classically, braiding has been associated with a combination of factors such as high slope, abundant bedload, coarse grain size, and flashy discharge (e.g. Leopold & Wolman 1957, Schumm & Khan 1972, Fredsoe 1978, Schumm et al. 1987). In contrast to these findings, Paola (2001) stated that "Braiding is the fundamental instability of streams flowing in noncohesive material". Channels formed in material of little or no cohesion or vegetative stability (to restrict channel widening) tend to braid. Those with cohesive banks and/or vegetation become progressively more sinuous or anastomosed (Smith & Smith 1980, Nanson & Knighton 1996), especially if there is some base-level control. Within sandy flume channels, meandering is merely a dynamic phase of channel adjustment. Once the thalweg becomes mildly sinuous, the flow cuts across emergent point bars forming incomplete chute cutoffs (e.g. Friedkin 1945, Schumm & Khan 1972, Schumm et al. 1987).

The task of successfully modeling the behavior of braided rivers is therefore a difficult one. Many previous authors have addressed the issue by applying a range of modeling solutions, the dimensionality of which has been controlled largely by the scale at which the model was to be applied. Contingent upon limitations imposed by computing power (Nicholas 2003) and a lack of integrated field and laboratory datasets at a suitable resolution (Lane & Richards 2001), approaches range in complexity in relation to the spatial and temporal scales to which they are applied. For example, at the scale of individual braid bars or confluence units, two-dimensional depth-averaged and fully three-dimensional hydraulic models have been used to simulate flow patterns (e.g. Lane & Richards 1998,

Bradbrook et al. 1999, Lane et al. 1999, Nicholas & Sambrook Smith 1999). At the braidplain scale, one-dimensional models of section-averaged flow and bedload transport (e.g. Paola 1996, Nicholas 2000), simplified two-dimensional cellular automata models (e.g. Murray & Paola 1994, Thomas & Nicholas 2002) and, recently, two-dimensional models have been applied (e.g. McArdell & Faeh 2001, Nicholas 2003). However, despite recent advances, numerical modeling has contributed surprisingly little to our understanding of the hydraulics and sedimentology of braided rivers.

1.2 *The Marker-in-Cell method*

Given the apparent dichotomy between the need for three-dimensional models and the associated computational and data limitations, one novel solution to the problem is the Marker (or Particle)-in-Cell method (Tetzlaff & Harbaugh 1989). This method was originally developed at the Los Alamos laboratory for use in particle physics (e.g. Harlow 1964), but was adapted to fluvial hydraulics during the 1980s by John Harbaugh and his graduate students at Stanford University (e.g. Tetzlaff & Harbaugh 1989). The Marker-in-Cell method can be considered to combine the best aspects of classical Lagrangian and Eulerian methods (Tetzlaff & Harbaugh 1989). Lagrangian units that characterize the properties of the fluid (e.g. velocity and sediment load) are tracked through an Eulerian mesh that characterizes the field variables (e.g. depth and bed elevation). As units accelerate and decelerate due to interactions with each other and topography, erosion and deposition are induced. Table 1 reviews the advantages and disadvantages of the approach.

The Marker-in-Cell method has been utilized in the SEDSIM family of models (e.g. Tetzlaff & Harbaugh 1989, Koltermann & Gorelick 1992, Wendebourg 1994, Chin 1997, Tuttle & Wendebourg 1999, Tetzlaff & Priddy 2001, Griffiths et al. 2001). However, the applicability of early versions of SEDSIM was largely limited by flow and sediment continuity problems. Flow was discretized in time and space using fluid elements of finite mass and volume. The average velocity and flow depth in each grid cell was determined by updating these quantities in accord with fluid elements that traveled through the cell during each time step (Chin 1997). Therefore, at low bed slopes, flow continuity may not have been maintained in an individual grid cell if the cell did not receive new fluid elements before fluid elements previously present in the cell left it, resulting in a discontinuous water surface (Chin 1997). Alternatively, if flow decelerated, fluid elements tended to congest and create a 'water mountain', so that fluid elements moving towards a water mountain were blocked and shunted sideways (Chin 1997). Both these possibilities caused flow directions and sediment transport to become erratic and unpredictable, and the bed topography to change rapidly as sediment was eroded and deposited irregularly.

Table 1. Advantages and disadvantages of the Marker-in-Cell approach as compared to traditional Eulerian and Lagrangian approaches.

Advantages	Disadvantages
Handles flow-field distortion	Computationally demanding
Fluid elements help resolve sub-grid scale features	Within a large region of flow there must be no small region for which detailed resolution is required
Relatively simple to deal with 2+ dimensions (fluid flow in 2-D, plus depth, logarithmic velocity profile and deposits)	It must be not be necessary to know in detail the fluid variables at Eulerian grid boundaries at any given instant of time
Handles material interfaces	

1.2.1 *Overcoming continuity problems*

As recognized by Chin (1997), continuity problems can be overcome by utilizing a mixed Lagrangian-Eulerian flow representation. Instead of fluid elements, flow is represented by momentum tracers that have neither mass nor volume. For each tracer, the momentum equation is solved in its Lagrangian form to reduce numerical dispersion, while the continuity equation is solved in its Eulerian form to achieve improved mass conservation. The accuracy of flow representation is directly related to the number of tracers, with flow velocities averaged within grid cells, yielding velocity components for the downstream and cross-stream directions. In addition, the Lagrangian momentum equations which were initially simplified assuming a uniform vertical velocity, have been modified to utilize the von Kàrmàn-Prandtl logarithmic velocity profile (e.g. van Niekerk et al. 1992) exhibited in natural rivers. It is believed that the use of momentum tracers in this way may permit the simulation of some of the more stochastic features noted in braided rivers (e.g. Paola 1996, Nicholas 2000).

2 EQUATION DERIVATION

The model presented here can be readily separated into a hydraulic sub-model and a sediment transport sub-model.

2.1 *Hydraulic sub-model*

It is possible to obtain two key equation sets for a single fluid unit from Newton's laws of motion: (i) the law of conservation of mass for an incompressible fluid in Eulerian form and (ii) the Navier-Stokes momentum equations for an incompressible fluid (Lane 1998).

2.1.1 *Mass conservation*

In two dimensions, and assuming that the fluid is homogeneous, incompressible and at constant temperature, the continuity or mass conservation equation can be expressed as:

$$\frac{\partial h}{\partial t} + \nabla.(h\mathbf{Q}) = 0 \tag{1}$$

where $h =$ fluid depth; $t =$ time; and $\mathbf{Q} =$ depth- and time-averaged horizontal velocity ($\bar{u}\mathbf{i} + \bar{v}\mathbf{j}$).

2.1.2 *2-D Navier-Stokes momentum equations*

Derivation of the two-dimensional Navier-Stokes momentum equations requires the integration of the full three-dimensional momentum equations in the x and y directions with respect to z. During this process, we assume a hydrostatic pressure distribution with constant density over the fluid depth, and neglect the Coriolis force and water surface wind stress terms (Lane 1998). In this paper, a constant velocity profile, r, is applied in the vertical dimension, where r is the function that satisfies

$$\mathbf{q}_{xy}(x_0, y_0, z) = r\left(\frac{z - z_b}{h}\right)\mathbf{Q}(x_0, y_0) \tag{2}$$

where $\mathbf{q}_{xy} =$ horizontal velocity ($u\mathbf{i} + v\mathbf{j}$); $z =$ an elevation within the flow; $z_b =$ bed elevation; and $h =$ flow depth.

Setting $s = (z - z_b)/h$ and $\int_0^1 r(s)ds = 1$, we obtain (Tetzlaff & Harbaugh 1989):

$$\begin{aligned}
&\frac{\partial \mathbf{Q}}{\partial t} + \frac{\partial (h + z_b)}{\partial t}\frac{\mathbf{Q}}{h}\alpha + (\mathbf{Q}\cdot\nabla)\mathbf{Q}\beta - \frac{\partial (h + z_b)}{\partial t}\mathbf{Q}\chi \\
&- \frac{\mathbf{Q}}{h}(\mathbf{Q}\cdot\nabla)z_b\varepsilon - \frac{\mathbf{Q}}{h}(\mathbf{Q}\cdot\nabla)h\alpha \\
&= -g\nabla(h + z_b) + \frac{\mu}{\rho}\nabla^2\mathbf{Q} \\
&- \frac{\mu}{\rho h}\left((2(\nabla(h\phi))\cdot\nabla)\mathbf{Q} + \mathbf{Q}\nabla^2(h\phi)\right) + \frac{\mu\mathbf{Q}\gamma}{\rho h^2} \\
&- c_f\frac{\mathbf{Q}|\mathbf{Q}|}{h}
\end{aligned} \tag{3}$$

where $\mu =$ molecular viscosity; $\rho =$ fluid density; $c_f =$ Darcy-Weisbach friction coefficient; and

$$\alpha = 1 - \mathrm{r}(1),\ \beta = \int_0^1 r^2(s)\,ds,\ \chi = \mathrm{r}(1)\text{-}\beta,$$

$$\varepsilon = \tfrac{1}{2}\left[r^2(1) - r^2(0)\right],\ \phi = 1 - \frac{1}{h}\left[r(1)(h + z_b) - r(0)z_b\right],$$

and $\gamma = r'(1) - r'(0)$.

2.1.3 *Vertical velocity profile*

Figure 1 illustrates two potential velocity profiles. The first, from Toffaleti (1969 in Vanoni 1975) expresses the horizontal point velocity as the product of the depth- and time-averaged velocity and s raised to a power related to temperature (Vanoni 1975). The second sets r so that within the boundary layer ($0.2 \geq s$), the profile obeys the law-of-the-wall and above this level, the velocity is constant (e.g. Tetzlaff & Harbaugh 1989). Despite the obvious differences between the profiles, the coefficients, α through γ, can be approximated for both profile shapes as: $\alpha \approx 0$, $\beta \approx 1$, $\chi \approx 0$, $\varepsilon \approx -0.5$, $\phi \approx -z_b/h$, and $\gamma \approx -\kappa$ (e.g. Tetzlaff & Harbaugh 1989), where κ is the von Kàrmàn constant which has a value of ≈ 0.33 in suspended sediment-laden flows (Bennett et al. 1998).

Equation 3 therefore reduces to (in Lagrangian form):

$$\begin{aligned}
&\frac{D\mathbf{Q}}{Dt} + \frac{\mathbf{Q}}{2h}(\mathbf{Q}\cdot\nabla)z_b = -g\nabla(h + z_b) + \frac{\mu}{\rho}\nabla^2\mathbf{Q} \\
&+ \frac{\mu}{\rho h}\left((2(\nabla z_b)\cdot\nabla)\mathbf{Q} + \mathbf{Q}\nabla^2 z_b\right) - \frac{\mu\kappa\,\mathbf{Q}}{\rho h^2} - c_f\frac{\mathbf{Q}|\mathbf{Q}|}{h}
\end{aligned} \tag{4}$$

Equations 1 and 4 provide a complete mathematical description of flow for an isotropic Newtonian fluid (Tetzlaff & Harbaugh 1989). The system of equations is solved using the Lax differencing method and the second-order Runge-Kutta method, which maintain second-order accuracy in both space and time (Press et al. 1992).

2.2 *Sediment transport sub-model*

For the determination of sediment transport in a non-uniform sediment mixture, it is convenient to divide

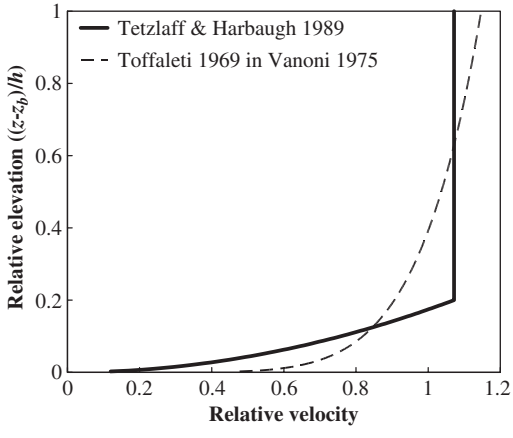


Figure 1. Potential vertical velocity profiles. Relative velocity is such that unit area is bounded by the curves.

the mixture into several size classes. For each size class k, the three-dimensional convection-diffusion equation of sediment transport is:

$$\frac{\partial c_k}{\partial t}+\frac{\partial(uc_k)}{\partial x}+\frac{\partial(vc_k)}{\partial y}+\frac{\partial(wc_k)}{\partial z}-\frac{\partial(\omega c_k)}{\partial z}$$
$$=\frac{\partial}{\partial x}\left(\varepsilon_s\frac{\partial c_k}{\partial x}\right)+\frac{\partial}{\partial y}\left(\varepsilon_s\frac{\partial c_k}{\partial y}\right)+\frac{\partial}{\partial z}\left(\varepsilon_s\frac{\partial c_k}{\partial z}\right)+q_s \qquad (5)$$

where c = concentration; t = time; u, v and w = velocity components in the x-, y- and z- directions, respectively; ω = particle fall velocity; $\varepsilon_s = \nu/\sigma_s$ = eddy diffusivity of sediment (ν = eddy viscosity and σ_s = turbulent Prandtl-Schmidt number); q_s = rate of sediment inflow from surrounding cells and other sources; and the subscript k denotes the kth size class.

The sediment transport sub-model presented here operates in two dimensions, namely, in the direction of the horizontal Lagrangian velocity and vertically through the flow. Therefore, we assume that the mass behavior of the number of tracers present in the flow will represent any cross-stream variations in sediment transport. We can therefore derive the following convection-diffusion equation of total load sediment transport (van Niekerk et al. 1992, Wu et al. 2000a):

$$\frac{\partial(hC_{tk})}{\partial t}+\frac{\partial(\mathbf{Q}hC_{tk})}{\partial ij}-\frac{\partial(\omega hC_{tk})}{\partial z}=\frac{\partial}{\partial ij}\left(\varepsilon_s h\frac{\partial C_{tk}}{\partial ij}\right)$$
$$+\frac{\partial}{\partial z}\left(\varepsilon_s h\frac{\partial C_{tk}}{\partial z}\right)+E_{bk}-D_{bk}+q_s \qquad (6)$$

where C_{tk} = total load sediment concentration of the kth size class, defined as $C_{tk} = c_k + q_{bk}/(\mathbf{Q}h)$; $\mathbf{Q}$ = the Lagrangian velocity; ij = the horizontal plane in the direction of $\mathbf{Q}$; E_b = entrainment rate of particles from the bed; and D_b is deposition rate of particles onto the bed.

2.2.1 *Non-equilibrium total load transport model*

Many early sediment transport models assumed that local equilibrium conditions applied when simulating bedload transport. This sets the actual bedload transport rate to be equal to the sediment transport capacity under equilibrium conditions. However, this may lead to unrealistic predictions of bed deformation, especially in cases where flows are above (e.g. after urbanization, forest exploitation, channelization; Simon 1992, Stott et al. 2001, Trimble 1997) or below (e.g. downstream of a reservoir; Sherrard & Erskine 1991) capacity for much of the time, so that non-equilibrium transport effects should be taken into account.

As the problem of total load sediment transport has been approached utilizing a method that incorporates suspended load fluxes, the bed change relation by size fraction due to bed-material load can be formulated as:

$$(1-\lambda)\frac{\partial Z_k}{\partial t}=\alpha\omega_k(C_{tk}-C_{t^*k}) \qquad (7)$$

where λ = bed porosity; Z = bed deformation; α = non-equilibrium adaptation coefficient; and C_{t*} = the total load transport capacity, defined as $C_{t*} = c_* + q_{b*}/(\mathbf{Q}h)$.

2.2.1.1 Non-equilibrium adaptation length

The non-equilibrium adaptation length can be considered as a time scale representing the adjustment rate of the sediment mass C_t to C_{t*}, the equilibrium sediment mass, which is a function of local, instantaneous flow conditions. Various formulations of α exist in the literature. For particles transported in suspension, Armanini & Di Silvio (1988) suggest:

$$\frac{1}{\alpha}=\frac{a}{h}+\left(1-\frac{a}{h}\right)\exp\left[-1.5\left(\frac{a}{h}\right)^{-1/6}\frac{\omega}{u_*}\right] \qquad (8)$$

where a = thickness of the surface or active layer; and u_* = shear velocity.

Among others, Phillips & Sutherland (1989) and Wu et al. (2000b) have proposed relations for sediment particles transported as bed load. However, although it was not derived for sediment particles transported as bed load, the formulation of Armanini & Di Silvio (1988) is adopted, because for coarse particles it correctly tends to $C_t = C_{t*}$ as $\alpha \ll \Delta x/\mathbf{Q}$, where Δx is the distance step.

2.2.1.2 Sediment transport capacity

Sediment transport capacity is the transported sediment load under equilibrium conditions (i.e. uniform flow and no net erosion or deposition). Sediment transport capacity is determined utilizing a modified version of the SEDTRA module (Garbrecht et al. 1996, Langendoen 2000), which determines the fractional transport capacities of bed load and suspended load, and takes into account hiding and exposure effects among different size classes. The modified version of SEDTRA calculates the total sediment transport by size fraction for fourteen predefined particle size classes (0.004 mm < d < 64 mm) with a suitable transport equation for each size fraction:

- transport as wash load without deposition for sediment particles smaller than 8 μm,
- Laursen (1958) for silts and fine sands (0.008–0.063 mm),
- Yang (1973) for sands (0.063–2.0 mm), and
- Meyer-Peter and Muller (1948) for gravels (2.0–64 mm).

The total sediment transport capacity, C_{t*}, is then defined as:

$$C_{t^*} = \sum_k p_k C_{*k} \tag{9}$$

where p_k = fraction of sediment in the kth size class available for transport; and C_{*k} = sediment transport capacity of the kth size class. The fraction p_k depends on the fractional content by volume of size class k in the surface layer and the fraction of sediment in the kth size class entering the reach from upstream and the streambanks.

2.2.1.3 Accounting for hiding and exposure

For sediments with a widely graded size distribution, the differences in the critical flow strength tend to be significantly reduced (e.g. Wilcock 1993). Widely graded sediment beds tend to increase the critical flow strength for initiation of the sizes finer than the mean size and decrease the critical flow strength of the sizes coarser than the mean size (e.g. Kuhnle 1993). To account for the hiding and exposure effect of non-uniform sediment mixtures, the sediment size used to calculate the critical flow strength for each size class is adjusted by considering the effect of the mixture on the critical flow strength of individual size fractions. SEDTRA defines the critical diameter for initiation of each of the fourteen size fractions as (Wilcock 1993, Kuhnle 1993, Garbrecht et al. 1995, Kuhnle et al. 1996):

$$d_{c,k} = d_k \left(\frac{\bar{d}}{d_k} \right)^x \tag{10}$$

where $\bar{d}$ = mean size of the bed material; and x = a hiding coefficient that ranges from 0 to 1. For $x = 1$, the mean size of the sediment is the critical diameter for all size fractions and all fractions tend to move at the same flow strength. For $x = 0$, each size fraction behaves independently of the others and the d_k for each size fraction is used to calculate flow strength at which motion begins (Kuhnle et al. 1996).

Extensive testing of SEDTRA found it to be applicable to channels with widely graded sediment distributions and to channel networks with variable sediment characteristics (Garbrecht et al. 1996). Garbrecht et al. (1996) tested SEDTRA against Brownlie's (1981) data set. Garbrecht et al. (1996) concluded that for laboratory data, about 80% of the computed sediment transport rates were within a factor of two of the measured values and about 90% were within a factor of three. For field data, about 55% of the computed sediment transport rates were within a factor of three and about 70% were within a factor of 5.

2.2.1.4 Fall velocity

The equations of Laursen (1958), Yang (1973) and Armanini & Di Silvio (1988) all require the fall velocity ω to be determined. This is attained by one of two methods. For well-rounded natural sediment particles, the fall velocities provided by the U.S. Interagency Committee on Water Resources, Subcommittee on Sedimentation (USICWR 1957) are utilised. For particles of irregular shapes, sizes and densities, or when temperature data is lacking, the method of Dietrich (1982) is applied. Dietrich (1982) found good agreement between his predictive equations and data from a number of other researchers. For further details, see Dietrich (1982).

2.2.1.5 Mixing layer algorithm

To represent historical erosion and deposition, the bed can be divided into a surface or active layer and a subsurface layer. These layers constitute the mixing layer (e.g. Hirano 1971). Sediment particles are continuously exchanged between the water column and the surface layer. In contrast, sediment particles only exchange between surface layer and substrate when the bed scours or fills (Fig. 2). Variation in the bed material composition in the surface layer is determined

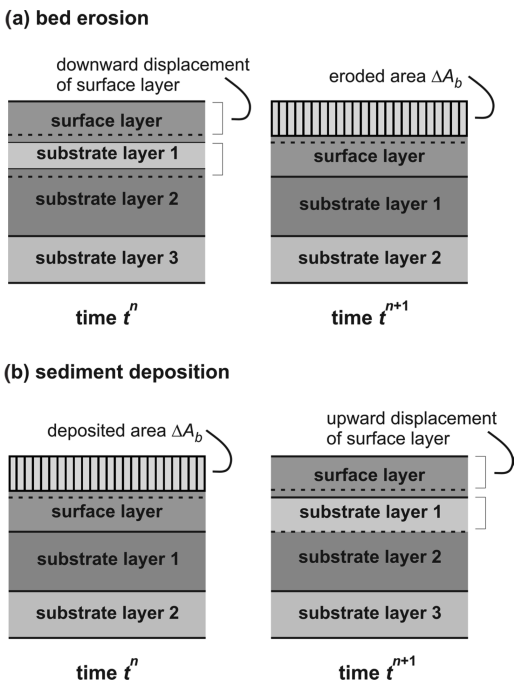


Figure 2. Bed-material sorting within the mixing layer: (a) entrainment of sediment particles from the surface layer displaces the layer downward, causing sediment from the surface layer to mix with substrate layers 1 and 2; and (b) deposition of sediment particles leads to an upward displacement of the surface layer and causes part of the surface layer to become new substrate layer 1 (from Langendoen 2000).

from mass conservation:

$$\frac{\partial\left(\beta_k^s a\right)}{\partial t} = \frac{\partial z_{bk}}{\partial t} + \beta_k^*\left(\frac{\partial a}{\partial t} - \frac{\partial z_b}{\partial t}\right) \tag{11}$$

where β_k^s = bed material composition in the surface layer; a = thickness of the surface layer, which is related to flow and sediment transport conditions as well as bed deformation; $\partial z_b/\partial t$ = total bed deformation rate; $\beta_k^* = \beta_k^s$ when $\partial a/\partial t - \partial z_b/\partial t = 0$; and β_k^* = the bed material composition in the subsurface layer when $\partial a/\partial t - \partial z_b/\partial t = 0$.

The thickness of the surface or active layer is related to the time scale under consideration (van Niekerk et al. 1992, Langendoen 2000). For very small time scales, the surface layer can be considered as a thin layer containing particles susceptible to entrainment into the flow due to a momentary increase in the bed shear stress. If the time scale is of the order of the time it takes for a bed form to traverse its own wavelength, the thickness of the surface layer is approximately the height of the bed form. For very long time scales during which considerable changes in bed level elevation may occur, the surface layer thickness is related to the thickness of the layer of material eroded or deposited. In this paper, we follow van Niekerk et al. (1992) and Takebayashi et al. (2003), who consider the surface layer thickness to be a function of shear stress. The method of Takebayashi et al. (2003) is utilized. The surface layer thickness is expressed as:

$$a = \frac{\overline{d}}{C_t \cos\theta\left(\tan\varphi - \tan\theta\right)}\tau_* \tag{12}$$

where φ = angle of repose; θ = local bed slope; and τ_* = non-dimensional shear stress of the mean bed-material diameter.

3 MODEL APPLICATION

The model is at present being applied to the South Saskatchewan River, Saskatchewan, Canada. At the time of writing, simulations were not complete and so results will not be presented at this stage. Definitive results will be presented at the meeting.

3.1 *Field location description.*

The South Saskatchewan River (Fig. 3) is formed in Southern Alberta by the junction of the Bow and Oldman Rivers, from where it flows eastwards until its confluence with the North Saskatchewan River in central Saskatchewan. Postglacial incision into highly erodible glacial deposits and Cretaceous sediments has acted to localize sediment sources to the lower, steepened sections and immediate sides of the valley (Ashmore 1993). The sediments that make up the valley sides permit mass movements, extensive gullying and the development of badlands (Ashmore & Day 1988a, Ashmore 1992). Indeed, microscale erosion studies of badlands developed in Cretaceous shales of the Red Deer River valley, Alberta, indicate that annual erosion from this small portion of the basin is equivalent to the annual load of the river (Ashmore 1993). Similar localized erosion occurs along other rivers in southern Alberta and Saskatchewan, including the South Saskatchewan, Bow and Oldman rivers (Ashmore 1993).

3.1.1 *Previous studies and implications*

A number of studies have documented sediment loads and concentrations for a reach of the South Saskatchewan River around Outlook, Saskatchewan (e.g. Cant & Walker 1978, Rasid 1979, Ashmore & Day 1988a, Ashmore 1992), as well as bar and channel geometries (e.g. Cant & Walker 1978, Rasid 1979). In this reach, the river flows in a valley about 0.6 km wide, with an average slope of 0.0003. Bar-full discharge (equivalent to the elevation of the 'sand flats' described by Cant & Walker (1978)) is 280 $m^3 s^{-1}$, while bank-full discharge (required to inundate islands and floodplains) is around 1240 $m^3 s^{-1}$. The total drainage area is approximately 158,600 km^2, although the contributing area is only around 85,700 km^2, since the rolling and hummocky topography of the glacially sculpted Prairies cause large areas to be internally drained (Ashmore & Day 1988a).

The hydrological and sedimentological regime of the river has been greatly altered by human activity in the past 100 years. For example, in the South Saskatchewan system upstream of the Alberta-Saskatchewan border, it has been estimated that consumptive water use has reduced natural flows by 15–25% (Prairie Provinces Water Board 1982 in Ashmore & Day 1988b). Of greater significance is the construction and closure in 1967 of Gardiner Dam 30 km upstream of Outlook, which stands 64 m high and 4.8 km wide, impounding about 9.4×10^9 m^3 of water to form Lake Diefenbaker (Rasid 1979). In terms of the hydrological regime, the closure and operation of Gardiner dam resulted in a decrease in the magnitude of high flows, an increase in the magnitude of low flows, and a re-distribution of high flows from the spring and early summer, representing snowmelt runoff, to the winter months (Fig. 4). In addition, consumptive uses of water from Lake Diefenbaker, such as irrigation, municipal and industrial water supply account for about 5% of annual flows and in an average year, evaporation losses from Lake Diefenbaker's surface account for an additional 5% of annual flows.

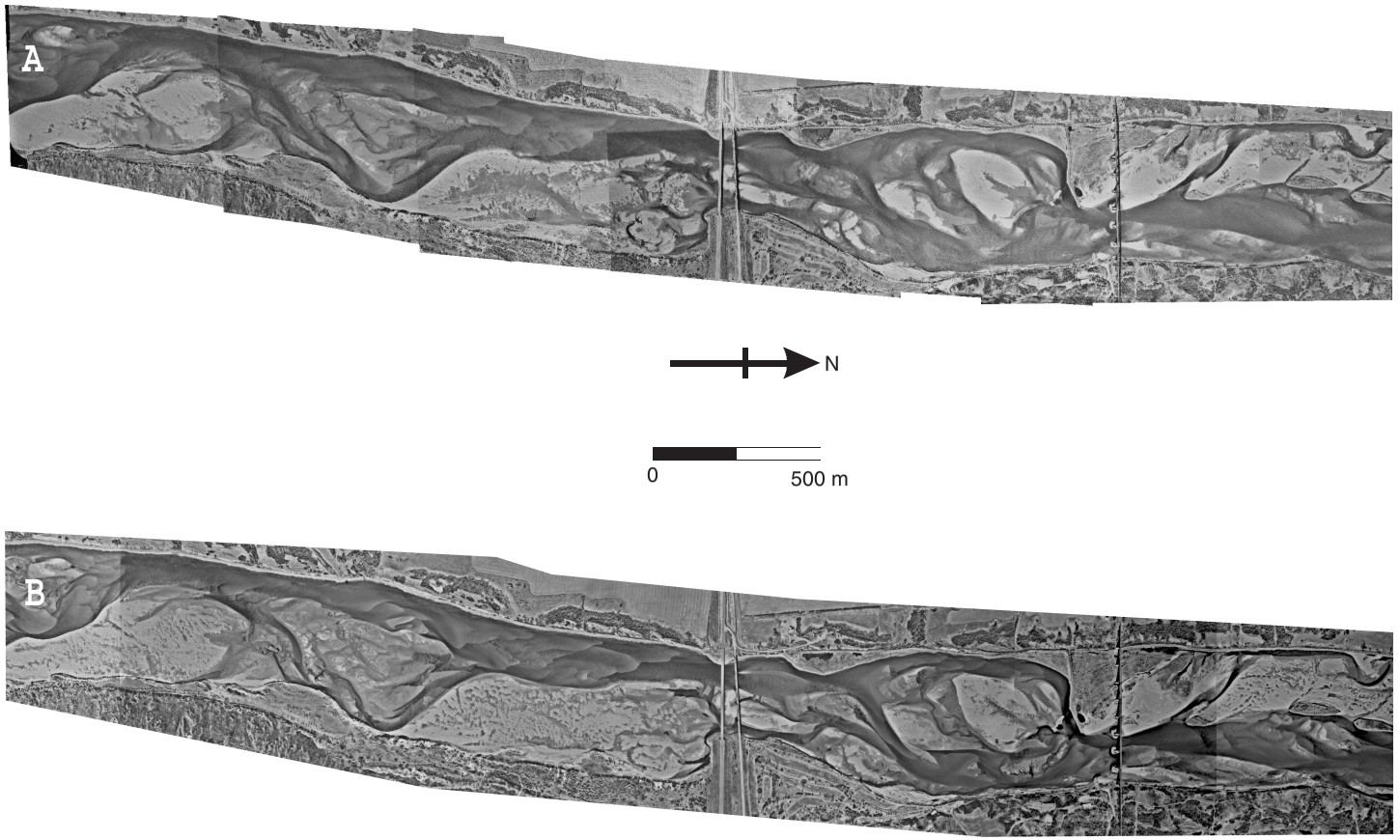


Figure 3. Rectified aerial photo mosaics of the South Saskatchewan River at Outlook, Saskatchewan; note the clarity of the water and hence of the bedforms. These images have been used to create high precision (~ 0.1 m) Digital Elevation Models. Mosaic A was captured on 30th April 2001 and mosaic B was captured on 14th May 2002. The flow direction is approximately due North.

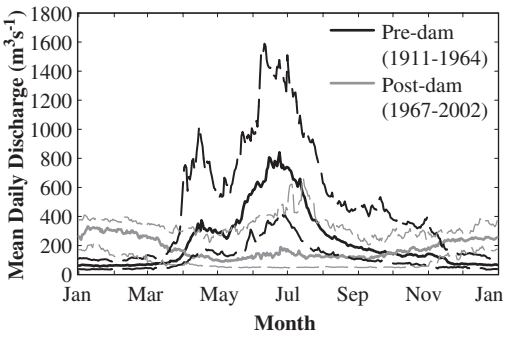


Figure 4. Average annual hydrographs constructed for the Water Survey of Canada gauge 05HG001 South Saskatchewan River at Saskatoon. Dashed lines represent 10th and 90th percentiles, respectively. Note the vast change in the annual flow regime.

In terms of the sedimentological regime, because of its length (225 km) and storage volume, Lake Diefenbaker can be considered to have a 100% sediment trapping efficiency (Yuzyk 1983). Suspended sediment concentrations have hence been substantially reduced (Rasid 1979), with mean concentrations falling from 350 to 30 mg l^{-1} and bankfull concentrations falling from 1400 to 650 mg l^{-1}.

Perhaps surprisingly, however, early post-dam research (Rasid 1979) noted bed lowering over the study reach of only 0.2 m, a figure Cant & Walker (1978) found to be "much less than local fluctuations due to channel shifting" (p. 627). In addition, Cant & Walker (1978) noted that a comparison of aerial photographs obtained before and after the emplacement of the dam shows that the planform of the river, in terms of its braid-bar scale, type and activity, is unchanged. Indeed, more recent research (Phillips 2003) suggests that there has been minimal impact on the mean bed elevation from around 13 km downstream of the dam.

The lack of change in the characteristics of the channel and sediments of the South Saskatchewan River is perhaps surprising, given the significant changes in both the hydrological and sedimentological regimes. This causes the river to be significantly below sediment transport capacity for much of the time. Galay et al. (1985) used the HEC-6 flow-sediment model developed by US Army Corps of Engineers to predict future degradation on the South Saskatchewan River. Results predicted degradation of 4.2 m within 1.6 km of the dam by the year 2000. However, Phillips' (2003) analysis indicates average bed degradation of 0.54 m and thalweg degradation of 2.06 m. Clearly, the model employed by Galay et al. (1985) significantly overestimated degradation. This finding reinforces the desirability of non-equilibrium treatments of sediment transport.

4 CONCLUSIONS

Exploration of the Marker-in-Cell method (Tetzlaff & Harbaugh 1989) was recently advocated by Paola (2001). This paper has presented a new Marker-in-Cell hydraulic and sediment transport model. This model simulates fluid flow and sediment transport in the horizontal plane and depth, logarithmic velocity profile and deposits in the vertical plane. Non-uniform total-load sediment transport is simulated by using a non-equilibrium approach. Sediment transport capacity is determined utilizing a modified version of the SEDTRA module (Garbrecht et al. 1996, Langendoen 2000), which determines the fractional transport capacities of bed load and suspended load, and takes into account hiding and exposure effects among different size classes. To represent historical erosion and deposition, the bed is divided into a surface or active layer and a subsurface layer. Sediment particles are continuously exchanged between the water column and the surface layer. In addition, when the bed scours or fills, sediment particles exchange between surface and subsurface layers.

The model is presently being applied to a reach of the South Saskatchewan River, Saskatchewan, Canada to explicate small-scale spatial and temporal processes. This reach has been affected by the closure of Gardiner Dam 30 km upstream, in 1967. However, comparison of aerial photographs obtained before and after the emplacement of the dam indicates that braid-bar scale, type and activity is relatively unchanged, while cross-section analyses suggest minimal degradation downstream of around 13 km of the dam. This is despite significant changes to both the hydrological and sedimentological regimes, which cause the river to be significantly below sediment transport capacity for much of the time. Modeling of the study reach with an equilibrium total load sediment transport model by Galay et al. (1985) significantly overestimated the amount of degradation observed in the South Saskatchewan River. This over-estimation reinforces the desirability of non-equilibrium treatments of sediment transport. It is hoped that this model will contribute to improving process representation in simulating feedbacks between morphology, flow and sediment transport (Bates & Lane 2000), and hence improving our understanding of braided rivers.

ACKNOWLEDGMENTS

RET was supported by NERC studentship NER/S/A/2002/10484 awarded to the School of Geography, University of Leeds. RET would also like to thank Eddy Langendoen of the CWPRU, USDA-ARS-National Sedimentation Laboratory and Yafei Jia of the National Centre for Computational Hydroscience and

Engineering at the University of Mississippi, Oxford, MS for useful discussions.

REFERENCES

Armanini, A. & Di Silvio, G. 1988. A one-dimensional model for the transport of a sediment mixture in non-equilibrium conditions. *Journal of Hydraulic Research* 26: 275–292.

Ashmore, P.E. & Day, T.J. 1988a. Spatial and temporal patterns of suspended-sediment yield in the Saskatchewan River basin. *Canadian Journal of Earth Sciences* 25: 1450–1463.

Ashmore, P.E. & Day, T.J. 1988b. Effective discharge for suspended sediment transport in streams of the Saskatchewan River Basin. *Water Resources Research* 24: 864–870.

Ashmore, P.E. 1992. Sediment delivery in large prairie river basins, Western Canada. In J. Boden, D.E. Walling & T.J. Day (eds.), *Erosion and sediment transport monitoring programmes in river basins. Proceedings of the International Symposium held at Oslo, Norway, 24–28 August 1992*: 423–432. Wallingford: IAHS.

Ashmore, P.E. 1993. Contemporary erosion of the Canadian landscape. *Progress in Physical Geography* 17: 190–204.

Bates, P.D. & Lane, S.N. (eds.) 2000. *High Resolution Flow Modelling in Hydrology and Geomorphology*. Chichester: Wiley.

Bennett, S.J., Bridge, J.S. & Best, J.L. 1998. The fluid and sediment dynamics of upper-stage plane beds. *Journal of Geophysical Research* 103: 1239–1274.

Bradbrook, K.F., Biron, P.M., Lane, S.N., Richards, K.S. & Roy, A.G. 1999. Investigation of controls on secondary circulation in a simple confluence geometry using a three-dimensional numerical model. *Hydrological Processes* 12: 1371–1396.

Brice, J.C. 1964. Channel patterns and terraces of the Loup Rivers in Nebraska. *USGS Professional Paper* 422-D. Washington: US Government Printing Office.

Brownlie, W.R. 1981. *Compilation of alluvial channel data: laboratory and field. Report No.* KH-R-43B. Pasadena: W.M. Keck Laboratory of Hydraulics and Water Resources, Division of Engineering and Applied Science, California Institute of Technology.

Cant, D.J. & Walker, R.G. 1978. Fluvial processes and facies sequences in the sandy braided South Saskatchewan River, Canada. *Sedimentology* 25: 625–648.

Chin, S. 1997. *A three-dimensional numerical model for simulating flow and sediment transport processes in fluvial and deltaic environments. Unpublished PhD dissertation*. Stanford: Department of Geological and Environmental Sciences, Stanford University.

Dietrich, W.E. 1982. *Settling velocities of natural particles. Water Resources Research* 18: 1615–1626.

Foufoula-Georgiou, E. & Sapozhnikov, V.B. 2001. Scale invariances in the morphology and evolution of braided rivers. *Mathematical Geology* 33: 273–291.

Fredsoe, J. 1978. Meandering and braiding of rivers. *Journal of Fluid Mechanics* 84: 609–624.

Friedkin, J.F. 1945. *A laboratory study of the meandering of alluvial rivers*. Vicksburg: US Waterways Experiment Station.

Galay, V.J., Pentland, R.S. & Halliday, R.A. 1985. Degradation of the South Saskatchewan River below Gardiner Dam. *Canadian Journal of Civil Engineering* 12: 849–862.

Garbrecht, J., Kuhnle, R.A. & Alonso, C.V. 1995. A Sediment transport capacity formulation for application to large channel networks. *Journal of Soil and Water Conservation* 50: 527–529.

Garbrecht, J., Kuhnle, R.A. & Alonso, C.V. 1996. A transport algorithm for variable sediment sizes: Fundamental concepts and equations. *Proceedings of the Sixth Federal Interagency Sedimentation Conference, Las Vegas, Nevada*, VI-8-VI-15. Washington, DC: US Government Printing Office.

Griffiths, C.M., Dyt, C., Paraschivoiu, E. & Liu, K. 2001. SEDSIM in hydrocarbon exploration. In D.F. Merriam & J.C. Davis (eds.), *Geologic modeling and simulation, sedimentary system.* New York: Kluwer Academic/Plenum.

Harlow, F.H. 1964. The particle-in-cell computing method for fluid dynamics. In B. Alder, S. Fernbach & M. Rotenberg (eds.), *Methods in computational physics v.3*: 319–343. London: Academic Press.

Hirano, M. 1971. River bed degradation with armoring. *Proceedings Japan Society of Civil Engineers* 195: 55–65.

Koltermann, C.E. & Gorelick, S.M. 1992. Paleoclimatic signature in terrestrial flood deposits. *Science* 256: 1775–1782.

Kuhnle, R.A. 1993. Incipient motion of sand-gravel sediment mixtures. *ASCE Journal of Hydraulic Engineering* 119: 1400–1415.

Kuhnle, R.A., Garbrecht, J. & Alonso, C.V. 1996. A transport algorithm for variable sediment sizes: application to wide sediment size distributions. *Proceedings of the Sixth Federal Interagency Sedimentation Conference, Las Vegas, Nevada*, VI-1-VI-7. Washington, DC: US Government Printing Office.

Lane, E.W. 1957. A study of the shape of channels formed by natural streams flowing in erodible material. *Missouri River Division Sediment Series* 9. Omaha: U.S. Army Engineer Division, Missouri River.

Lane, S.N. 1998. Hydraulic modelling in hydrology and geomorphology. A review of high resolution approaches. *Hydrological Processes* 12: 1131–1150.

Lane, S.N. & Richards, K.S. 1998. Two-dimensional modelling of flow processes in a multi-thread channel. *Hydrological Processes* 12: 1279–1298.

Lane, S.N. & Richards, K.S. 2001. The 'validation' of hydrodynamic models: some critical perspectives. In M.G. Anderson & P.D. Bates (eds.), *Model validation: perspectives in hydrological science*: 413–439. Chichester: Wiley.

Lane, S.N., Bradbrook, K.F., Richards, K.S., Biron, P.A. & Roy, A.G. 1999. The application of computational fluid dynamics to natural river channels: three-dimensional versus two-dimensional approaches. *Geomorphology* 29: 1–20.

Langendoen, E.J. 2000. CONCEPTS - CONservation Channel Evolution and Pollutant Transport System. *Research Report* 16. Oxford, Mississippi: USDA-ARS-NSL.

Laursen, E.M. 1958. The total sediment load of streams. *ASCE Journal of the Hydraulics Division* 84, 1530-1–1530-36.

Leopold, L.B. & Wolman, M.G. 1957. River channel patterns: braided, meandering and straight. *US Geological*

Survey Professional Paper 282-B. Washington DC: US Government Printing Office.

McArdell, B.W. & Faeh, R. 2001. A computational investigation of river braiding. In M.P. Mosley (ed.), *Gravel-Bed Rivers V*: 73-94. Wellington: New Zealand Hydrological Society, Inc.

Meyer-Peter, E. & Muller, R. 1948. Formulas for bed-load transport. *International Association for Hydraulic Structures Research 2nd Meeting, Stockholm, Sweden, 1948*, 39–64.

Murray, A.B. & Paola, C. 1994. A cellular model of braided rivers. *Nature* 371: 54–57.

Nanson, G.C. & Knighton, A.D. 1996. Anabranching rivers: their cause, character and classification. *Earth Surface Processes and Landforms* 21: 217–239.

Nicholas, A.P. 2000. Modelling bedload yield in braided gravel bed rivers. *Geomorphology* 36: 89–106.

Nicholas, A.P. 2003. Investigation of spatially distributed braided river flows using a two-dimensional hydraulic model. *Earth Surface Processes and Landforms* 28: 655–674.

Nicholas, A.P. & Sambrook Smith, G.H. 1999. Numerical simulation of three-dimensional flow hydraulics in a braided channel. *Hydrological Processes* 13: 913–929.

Paola, C. 1996. Incoherent structure: Turbulence as a metaphor for stream braiding. In P.J. Ashworth, S.J. Bennett, J.L. Best & S.J. McLelland (eds.), Coherent Flow Structures in Open Channel Flows: 705–723. Chichester: Wiley.

Paola, C. 2001. Modelling stream braiding over a range of scales. In M.P. Mosley (ed.), *Gravel-Bed Rivers V*: 11–46. Wellington: New Zealand Hydrological Society, Inc.

Phillips, B.C. & Sutherland, A.J. 1989. Spatial lag effects in bed load sediment transport. *Journal of Hydraulic Research* 27: 115–133.

Phillips, R.T.J. 2003. *Downstream geomorphic impacts of reservoir construction on the sand-bed braided South Saskatchewan River, Saskatchewan. Unpublished BSc (Hons.) Dissertation*. Burnaby: Department of Geography, Simon Fraser University.

Prairie Provinces Water Board. 1982. *Water demand study: Historical and current water uses in the Saskatchewan-Nelson Basin*. Regina: Prairie Provinces Water Board.

Press, W.H., Teukolsky, S., Vetterling, W. & Flannery, B. 1992. *Numerical Recipes in C*. Cambridge, UK: Cambridge University Press.

Rasid, H. 1979. The effects of regime regulation by the Gardiner Dam on downstream geomorphic processes in the South Saskatchewan River. *Canadian Geographer* 23: 140–158.

Schumm, S.A. & Khan, H.R. 1972. Experimental study of channel patterns. *Geological Society of America Bulletin* 83: 1755–1770.

Schumm, S.A., Mosley, M.P. & Weaver, W.E. 1987. *Experimental Fluvial Geomorphology*. New York: Wiley.

Sherrard, J.J. & Erskine, W.D. 1991. Complex response of a sand-bed stream to upstream impoundment. *Regulated Rivers: Research and Management* 6: 53–70.

Simon, A. 1992. Energy, time, and channel evolution in catastrophically disturbed fluvial systems. *Geomorphology* 5: 345–372.

Smith, D.G. & Smith, N.D. 1980. Sedimentation in anastomosed river systems: examples from alluvial valleys near Banff, Alberta. *Journal of Sedimentary Petrology* 50: 157–164.

Stott, T., Leeks, G., Marks, S. & Sawyer, A. 2001. Environmentally sensitive plot-scale timber harvesting: impacts on suspended sediment, bedload and bank erosion dynamics. *Journal of Environmental Management* 63: 3–25.

Takebayashi, H., Egashira, S. & Okabe, T. 2003. Braided streams formed on beds with non-uniform sediment. In A. Sanchez-Arcilla & A. Bateman (eds.), *Proceedings of the 3rd IAHR Symposium on River, Coastal and Estuarine Morphodynamics*: 787–798. Madrid: IAHR.

Tetzlaff, D.M. & Harbaugh, J.W. 1989. *Simulating Clastic Sedimentation.* New York: van Nostrand Reinhold.

Tetzlaff, D.M. & Priddy, G. 2001. Sedimentary process modeling: from academia to industry. In D.F. Merriam & J.C. Davis (eds.), *Geologic modeling and simulation, sedimentary system.* New York: Kluwer Academic/Plenum.

Thomas, R. & Nicholas, A.P. 2002. Simulation of braided river flow using a new cellular routing scheme. *Geomorphology* 43: 179–195.

Toffaleti, F.B. 1969. Definitive computations of sand discharge in rivers. *ASCE Journal of the Hydraulics Division* 95: 225–248.

Trimble, S.W. 1997. Contribution of stream channel erosion to sediment yield from an urbanizing watershed. *Science (Washington)* 278: 1442–1444.

Tuttle, K.J. & Wendebourg, J. 1999. Applying sedimentary process simulation to assess the spatial distribution of hydraulic conductivities. In J.W. Harbaugh, W.L. Watney, E. Rankey, R. Slingerland, R. Goldstein & E. Franseen (eds.), *Numerical Experiments in Stratigraphy: Recent Advances in Stratigraphic and Sedimentologic Computer Simulations*: 323–336. Tulsa: SEPM.

USICWR, 1957. *Some fundamentals of particle size analysis. A study of methods used in measurements and analysis of sediment loads in streams. Report No. 12*. Minneapolis: Sub-committee on Sedimentation, US Interagency Committee on Water Resources.

van Niekerk, A., Vogel, K.R., Slingerland, R. & Bridge, J.S. 1992. Routing of heterogeneous sediments over a movable bed: model development. *Journal of Hydraulic Engineering* 118: 246–262.

Vanoni, V.A. (ed.) 1975. *Sedimentation Engineering*. New York: ASCE.

Wendebourg, J. 1994. *Simulating hydrocarbon migration and stratigraphic traps. Unpublished PhD dissertation*. Stanford: Department of Applied Earth Sciences, Stanford University.

Wilcock, P.R. 1993. Critical shear stress of natural sediments. *Journal of Hydraulic Engineering* 119: 491–505.

Wu, W., Rodi, W. & Wenka, T. 2000a. 3-D numerical modeling of water flow and sediment transport in open channels. *Journal of Hydraulic Engineering* 126: 4–15.

Wu, W., Wang, S.S.Y. & Jia, Y. 2000b. Nonuniform sediment transport in alluvial rivers. *Journal of Hydraulic Research* 38: 427–434.

Yang, C.T. 1973. Incipient motion and sediment transport. *ASCE Journal of the Hydraulics Division* 99: 1679–1704.

Yuzyk, T.R. 1983. *Lake Diefenbaker, Saskatchewan: a case study of reservoir sedimentation*. Ottawa: Sediment Survey Section, Water Survey of Canada, Water Resources Branch, Inland Waters Directorate, Environment Canada.

River Flow 2004 – Greco, Carravetta & Della Morte (eds.)
© 2004 Taylor & Francis Group, London, ISBN 90 5809 658 0

A finite volume model of flow and sediment transport in the lagoon of Grado-Marano

S. Bosa & M. Petti
Dipartimento di Georisorse e Territorio, University of Udine, Italy

ABSTRACT: The Grado-Marano Lagoon in the Northeast of Italy has many problems related to the silting of its navigable channels and hence a study of sediment transport inside the basin is becoming necessary. A finite volume numerical model for simulating solid transport in lagoons is proposed. Of all the different techniques to evaluate the numerical fluxes in the integration scheme, one technique was adopted, that solves a local Riemann problem at each intercell. To choose the most appropriate solver for this kind of problem, a test was developed to simulate the tidal run-up and run-down on a beach. Some results are shown in the paper. The sediment transport was evaluated through the Van Rijn total load formula. Finally the model was used to simulate the oscillations of consecutive tides in the Grado-Marano lagoon and the results are discussed.

1 INTRODUCTION

The Grado-Marano Lagoon is a large basin on the Adriatic coast in the Northeast of Italy and represents one of the most important Italian lagoon systems. It extends about 32 km from east to west and 5 km from north to south (Figs 1, 2).

In the last years a growing deterioration of the environment has occurred on this site causing silting of the navigable channels with sediments. This process happens both in natural and artificial channels and it is becoming a serious problem for the local population, navigation being one of its main sources of income (fishing, tourism, etc).

Nowadays, there is no plan for regulating environmental operations like dredging of navigation channels or construction of lagoon structures to limit the silting of the channels. There are two main reasons: the sediments are polluted and up to the present time no reliable hydraulic model has been used to study sediment transport phenomena inside the lagoon. The presence of polluted sediments requires technical solutions, whose validity can be tested only with a model. The lack of a reliable model for testing possible technical solutions has inspired the present work.

The study of sediment transport in lagoon basins is a complex three-dimensional phenomenon and is controlled by turbulent diffusion, tidal currents and wind, the geometry of the bed. Erosion and sedimentation processes of non-cohesive sediments are mainly controlled by vertical turbulence, while circulation of sediments is due essentially to convective tidal and wind currents; horizontal turbulent diffusion is less important in this process. Hydrodynamic characteristics and particle properties of sediments in the lagoon show that both suspension and bed load transport mechanisms are important.

In the present work a finite volume numerical model for simulating both suspended and bed load sediment transport is proposed. The field of motion of the flow is described by vertically integrated 2-D coupled equations (the classical shallow water equations). For calculating the sediment transport, both Van Rijn (1984a, b) and Ackers & White (1973) formulations are considered.

In the model we use an explicit time-dependent discretization based on a split finite volume method. The classical Godunov approach is used, with the Harten, Lax and van Leer (HLL) Riemann solver (Toro 1999, 2001). The resulting scheme is second-order accurate in space and time and satisfies the Total Variation Diminishing (TVD) condition.

The model implemented is able to represent steep water fronts and fronts with concentration of sediment, and it can be used to determine bed changes near lagoon structures and dredged navigation channels for moderate irregularity of the bottom.

Some hydrodynamic tests used to choose the solver are presented here. Finally some numerical simulations on the Grado-Marano lagoon are presented and it is shown how tidal currents control sediment circulation inside the basin.

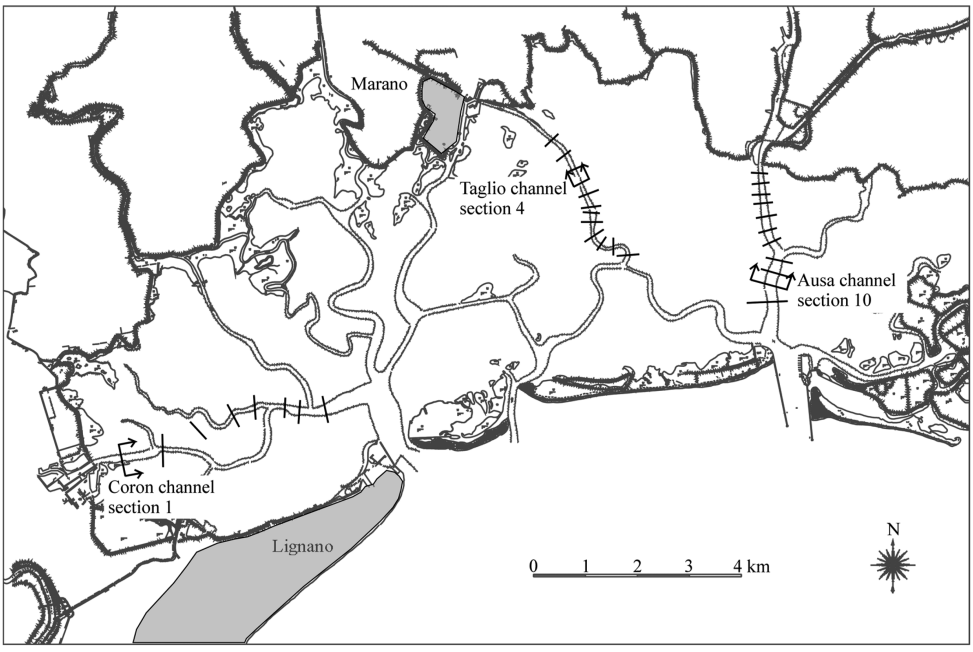


Figure 1. West part of Grado-Marano Lagoon; in bold the cross sections of the channels considered in paragraph 4. The arrows show the cross section depicted in paragraph 4.

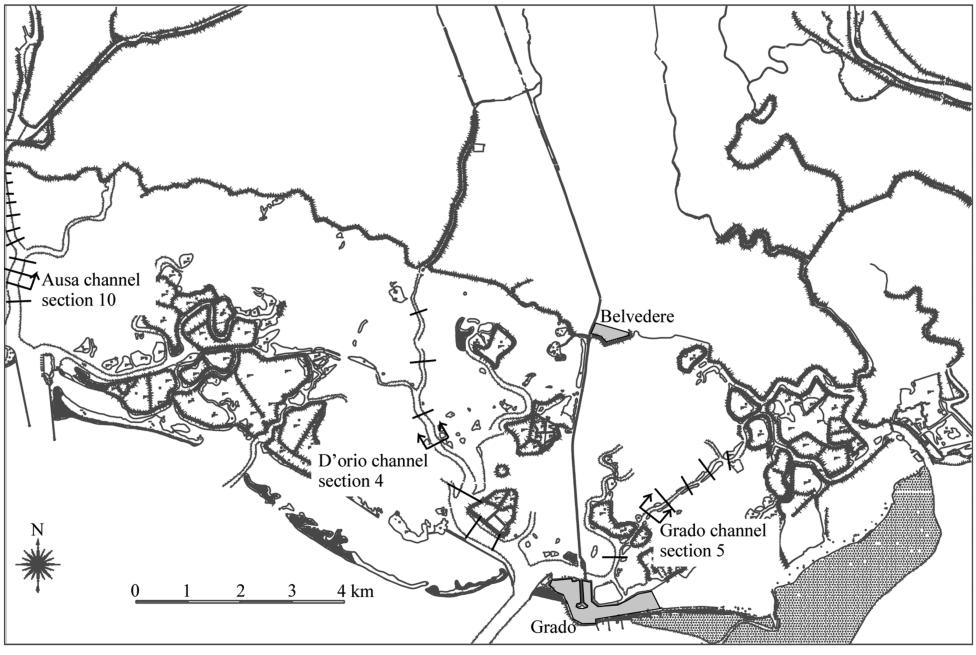


Figure 2. East part of Grado-Marano Lagoon; in bold the cross sections of the channels considered in paragraph 4. The arrows show the cross section depicted in paragraph 4.

2 MORPHODYNAMIC MODEL

The model proposed can be subdivided into two main phases: the first one solves the hydrodynamic problem and the second one calculates the new bed elevation through the Exner equation.

2.1 *Hydrodynamic model*

The equations used to describe the motion are the well-known shallow water equations. The shallow water hypothesis is very close to reality, because water depth is very small compared with the planimetric dimension of the motion field. The equation system (Liggett 1994) is:

$$\frac{\partial \mathbf{U}}{\partial t}+\frac{\partial \mathbf{F}(\mathbf{U})}{\partial x}+\frac{\partial \mathbf{G}(\mathbf{U})}{\partial y}=\mathbf{S}_f(\mathbf{U})+\mathbf{S}_t(\mathbf{U}) \tag{1}$$

with:

$$\mathbf{U}=\begin{bmatrix} h \\ Uh \\ Vh \end{bmatrix} \quad \mathbf{S}_f(\mathbf{U})=\begin{bmatrix} 0 \\ -gh\dfrac{\partial z_f}{\partial x}-g\dfrac{U\sqrt{U^2+V^2}}{K_s{}^2h^{1/3}} \\ -gh\dfrac{\partial z_f}{\partial y}-g\dfrac{V\sqrt{U^2+V^2}}{K_s{}^2h^{1/3}} \end{bmatrix}$$

$$\mathbf{F}(\mathbf{U})=\begin{bmatrix} Uh \\ U^2h+gh^2/2 \\ UVh \end{bmatrix} \quad \mathbf{G}(\mathbf{U})=\begin{bmatrix} Vh \\ UVh \\ V^2h+gh^2/2 \end{bmatrix} \tag{2}$$

$$\mathbf{S}_t(\mathbf{U})=\begin{bmatrix} 0 \\ \dfrac{\partial}{\partial x}\left(\upsilon_t h\dfrac{\partial U}{\partial x}\right)+\dfrac{\partial}{\partial y}\left(\upsilon_t h\dfrac{\partial U}{\partial y}\right) \\ \dfrac{\partial}{\partial x}\left(\upsilon_t h\dfrac{\partial V}{\partial x}\right)+\dfrac{\partial}{\partial y}\left(\upsilon_t h\dfrac{\partial V}{\partial y}\right) \end{bmatrix}$$

where h is the water depth, U and V are the velocities on the horizontal plane $x-y$, g is the gravity acceleration, z_f is the bed elevation, K_s is the Gauckler-Strickler coefficient and υ_t is the turbulent viscosity (assumed isotropic on the horizontal plane). $\mathbf{U}$ is the variables vector, $\mathbf{F}$ and $\mathbf{G}$ are the fluxes vectors in x and y directions, $\mathbf{S}_f$ is the source vector due to the bed slope and flow resistance and $\mathbf{S}_t$ is the source term due to turbulence; in the following the sum of $\mathbf{S}_f$ and $\mathbf{S}_t$ is referred to simply as source term.

The differential system has been discretized using temporal splitting, which is second order accurate (Toro 2001) and that can be summarized by:

$$\mathbf{U}^{n+1}=\mathcal{S}^{(\Delta t/2)}\mathcal{A}^{(\Delta t)}\mathcal{S}^{(\Delta t/2)}(\mathbf{U}^n) \tag{3}$$

where $\mathbf{U}^n$ and $\mathbf{U}^{n+1}$ are the solution vectors at time t and $t+\Delta t$, $\mathcal{A}$ and $\mathcal{S}$ are the convective and the source operators.

To evaluate $\mathbf{S}_t$, it is necessary to quantify the turbulent viscosity coefficient υ_t. A scale analysis shows that υ_t can be expressed as the product of a velocity scale that accounts for turbulent oscillations and a length scale to account for vortex dimensions; in this work the former is assumed to be the friction velocity u_* and the latter the water depth:

$$\upsilon_t=\xi h u_*=\xi h\frac{n\sqrt{g}\sqrt{U^2+V^2}}{h^{1/6}} \tag{4}$$

where ξ is an dimensionless coefficient. The most appropriate values for ξ in literature are extremely variable (between 0.1 and 100), so that often ξ becomes an instrument to calibrate numerical models (Garcia & Kahawita 1986, Maa 1990 and Pedlosky 1987). Some tests on the Grado-Marano lagoon showed that the change of ξ does not substantially modify the results. In this work a value of 10 is assumed for ξ in the following tests.

The most difficult step in Equation 3 is the convective one:

$$\mathbf{U}_{con}=\mathcal{A}^{(\Delta t)}(\mathbf{U}^n), \tag{5}$$

where $\mathbf{U}_{con}$ is the solution of the homogeneous pure convective problem. Equation 5 can be written explicitly as:

$$\begin{cases} \dfrac{\partial \mathbf{U}}{\partial t}+\dfrac{\partial \mathbf{F}(\mathbf{U})}{\partial x}+\dfrac{\partial \mathbf{G}(\mathbf{U})}{\partial y}=0 \\ \mathbf{U}(0,x,y)=\mathbf{U}^n(x,y) \end{cases} \tag{6}$$

To solve the homogeneous problem in Equation 6, the new variable $\mathbf{H}$ is introduced:

$$\mathbf{H}=(\mathbf{F} \quad \mathbf{G}); \tag{7}$$

after which it is possible to integrate the differential equation on a generic control volume $\boldsymbol{\Omega}$ in the horizontal plane:

$$\Omega\frac{\partial \mathbf{U}}{\partial t}+\oint_{\partial\Omega}\mathbf{n}\cdot\mathbf{H}ds=0 \tag{8}$$

where $\mathbf{n}$ is the outward unit normal vector to the control volume boundary.

Using a finite difference method, with time accuracy of first order, we get:

$$\Omega_i\frac{\mathbf{U}_i^{n+1}-\mathbf{U}_i^n}{\Delta t}+\sum_{k=1}^{4}n_{ik}H_{ik}^n\Delta s_{ik}=0 \tag{9}$$

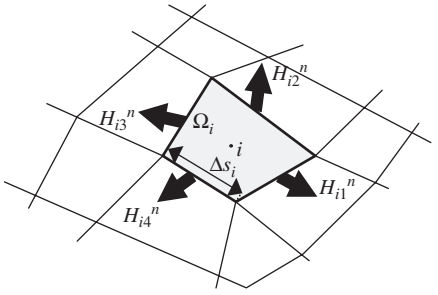


Figure 3. i-th control volume and the fluxes associated to its boundary.

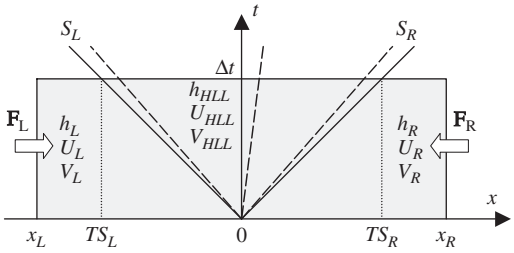


Figure 4. x–t plane used to solve the Riemann problem.

where the meaning of the terms in the summary is depicted in Figure 3.

The evaluation of the fluxes H_{ik}^n is the most important step in the solution of Equation 9. One way to evaluate them is to solve a local Riemann problem between two neighbouring cells. The different techniques that take inspiration from this method are called 'Riemann solvers'. There are exact solvers and approximate solvers. The most used approximate solvers can be subdivided into two classes. In the first class, one computes an approximate solution and then the numerical flux is obtained by evaluating the exact physical flux vector at this approximate state. In the second class one directly obtains an approximation of the flux.

To choose an appropriate solver some preliminary tests were evaluated. Included in these were tests of wave run-up on a beach, these were key to the description of the run-up of the tide on the banks near the sea at the boundary of the lagoon and the phenomenon of periodical emersion and immersion of the sand banks inside the lagoon. In the following the results of these tests are shown.

Some solvers proposed by Toro (1999) (FORCE, centered Godunov and HLL) were tested and the HLL solver gave the best results. For this reason the approximate solver HLL was chosen and is now briefly presented.

The approximate solver family first computes an approximate solution $\mathbf{W}_{ik}(x/t)$ (where $\mathbf{W}_{ik}$ is the vector of the variables h, U and V associated with the k-th side of the i-th cell) to the Riemann problem; then an approximate numerical flux is obtained by evaluating the physical flux

$$\mathbf{F}_{ik} = \mathbf{F}\,(\mathbf{W}_{ik}\,(0)). \tag{10}$$

The HLL solver assumes a constant solution $\mathbf{U}_{HLL}$ in the region between characteristic straight lines (S_L and S_R) representing the left and right perturbation (waves) of a hyperbolic problem. Also the corresponding flux $\mathbf{F}_{HLL}$ is constant. $\mathbf{U}_{HLL}$ can be found by integrating (5) on the control volume $[(x_L - x_R) \times (0 - \Delta t)]$ shown in Figure 4. In this figure the subscript L and R identify two regions, called left and right region, where the left and right wave have not arrived yet; for example h_L, U_L,V_L, $\mathbf{F}_L$, are respectively the water depth, the velocities in x and y directions and the fluxes vector in x direction of the left region. The left and right waves move with wave speed S_L and S_R.

In this way $\mathbf{U}_{HLL}$ is obtained:

$$\mathbf{U}_{HLL} = \frac{\mathbf{U}_R S_R - \mathbf{U}_L S_L + \mathbf{F}_L - \mathbf{F}_R}{S_R - S_L} \tag{11}$$

where $\mathbf{F}_\mathrm{L}$ and $\mathbf{F}_\mathrm{R}$ are the physical fluxes obtained from $\mathbf{U}_\mathrm{L}$ and $\mathbf{U}_\mathrm{R}$.

To evaluate the flux $\mathbf{F}_\mathrm{HLL}$ one can integrate (6), as done to obtain $\mathbf{U}_\mathrm{HLL}$, but on the control volume $[(x_L - 0) \times (0 - \Delta t)]$.

In this way one obtains:

$$\mathbf{F}_{HLL} = \frac{S_R S_L \left(\mathbf{U}_R - \mathbf{U}_L\right) + S_R \mathbf{F}_L - S_L \mathbf{F}_R}{S_R - S_L}. \tag{12}$$

Hence the numerical flux on the intercell is:

$$\mathbf{F}_{ik} = \begin{cases} \mathbf{F}_L & S_L \geq 0 \\ \mathbf{F}_{HLL} & S_L \leq 0 \leq S_R \\ \mathbf{F}_R & S_R \leq 0. \end{cases} \tag{13}$$

The final model is made second order accurate also in space, through the use of 'minmod' limiters, that assume a linear distribution of the variables inside each cell (Hirsch, 1984).

To increase the accuracy of the solution it is also necessary to improve the evaluation of the source term; hence we introduced a technique to calculate the bed slope, consisting in associating to each cell in x and y direction the bed slope of the plane made by the two neighbouring cells in the two different directions, as shown in Figure 5.

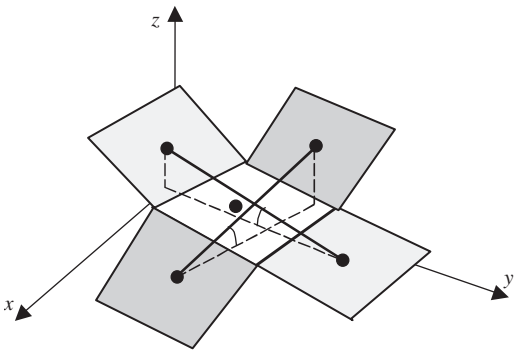


Figure 5. Structure of the bed slope evaluation with a second order accuracy.

2.2 *Solid transport model*

Assuming slowly varied motion and the absence of lateral mass entering the control volume, the bidimensional sediment mass conservation can be written as:

$$\frac{\partial q_{sx}}{\partial x}+\frac{\partial q_{sy}}{\partial y}+\frac{\partial z_f}{\partial t}(1-p)=0 \tag{14}$$

where q_{si} is the total sediment volumetric rate in i direction, and p is the porosity. Equation 14 is known as the Exner equation.

Integrating Equation 14 on a generic control volume and discretizing it with an explicit second order accurate finite volume scheme, one obtains:

$$z_{fi}^{\,n+1}=z_{fi}^{\,n}-\frac{\Delta t}{(1-p)\Omega_i}\sum_{k=1}^{4}n_{ik}q_{sik}^{n+1/2}\Delta s_{ik}\,; \tag{15}$$

where $q_{sik}^{n+1/2}$ is a value between q_{sik}^{n+1} and q_{sik}^{n} (the subscripts i and k mean that q_s is associated with the k-th side of the i-th cell.

2.3 *Solid transport evaluation*

In the Grado-Marano lagoon the hydrodynamic field and the sediment diameters do not allow us to neglect either the bed load or the suspended load transport.

In the development of the present model we used the Van Rijn (1984) and Ackers & White (1973) formulae to evaluate the sediment transport.

The Van Rijn formulation evaluates the bed load and the suspended load separately and their sum gives the total load in x and y directions q_{sx} and q_{sy}. For the volumetric rate of the bed load in x and y directions q_{bx} and q_{by}, he proposed an expression valid for particles in the range 200–2000 μm (Van Rijn, 1984a):

$$q_{bi}=0.053\sqrt{g\left(S_g-1\right)d_{50}{}^3}\,\frac{T_i^{2.1}}{D_*^{0.3}}\qquad i=x,y \tag{16}$$

where g is the gravity acceleration, S_g is the specific gravity, d_{50} is the particle diameter, T_i is the transport stage parameter in i direction and D^* is the dimensionless particle parameter.

To evaluate the suspended solid volumetric rate in x and y directions q_{ssx} and q_{ssy} he proposed (Van Rijn 1984b):

$$\begin{aligned}q_{ssx}&=\frac{\left(\frac{a}{h}\right)^{Z'_x}-\left(\frac{a}{h}\right)^{1.2}}{\left(1-\frac{a}{h}\right)^{Z'_x}\left(1.2-Z'_x\right)}Uhc_{ax}\\ q_{ssy}&=\frac{\left(\frac{a}{h}\right)^{Z'_y}-\left(\frac{a}{h}\right)^{1.2}}{\left(1-\frac{a}{h}\right)^{Z'_y}\left(1.2-Z'_y\right)}Vhc_{ay}\end{aligned} \tag{17}$$

where a is the reference level where the reference concentration in i direction c_{ai} is evaluated, h is the water depth, U is the mean water velocity and Z_i' is the modified suspension number in i direction.

To evaluate the parameters used in Equation 16, one has to calculate first the Shield's parameter in x and y directions θ_x and θ_y:

$$\begin{aligned}\theta_x&=\frac{(Uh)\sqrt{(Uh)^2+(Vh)^2}}{K_s^{\,2}\left(S_g-1\right)d_{50}h^{7/3}}\\ \theta_y&=\frac{(Vh)\sqrt{(Uh)^2+(Vh)^2}}{K_s^{\,2}\left(S_g-1\right)d_{50}h^{7/3}}\end{aligned} \tag{18}$$

then the critical Shield's parameter is needed and here the formulation proposed by Brownlie (1981) is used to evaluate θ_{cr0}, independent from the bed slope:

$$\theta_{cr0}=0.22D_*^{-0.6}+0.06e^{-17.77D_*^{-0.6}}\,; \tag{19}$$

the dimensionless particle parameter is:

$$D_*=d_{50}\left[\frac{\left(S_g-1\right)g}{\upsilon^2}\right]^{1/3}, \tag{20}$$

where υ is water kinematic viscosity coefficient. To consider the bed slope Chiew & Parker (1994) proposed modifying θ_{cr0}, obtaining:

$$\theta_{cri}=\cos\alpha_i\left(1-\frac{\tan\alpha_i}{\tan\varphi}\right)\theta_{cr0}\qquad i=x,y\,, \tag{21}$$

where α_x and α_y are the bed slopes in x and y directions and φ is the angle of repose of the sediment.

After that one can easily calculate the transport stage parameter as:

$$T_i = \frac{\theta_i - \theta_{cri}}{\theta_{cri}} \qquad i = x, y \,. \tag{22}$$

To evaluate the suspended load, it is necessary to calculate first the critical Shield's parameter for suspended sediments by following Van Rijn's works:

$$\begin{aligned} \theta_{crs} &= \frac{0.24}{D_*} && 1 < D_* \le 4 \\ \theta_{crs} &= 0.14 D_*^{-0.64} && 4 < D_* \le 10 \\ \theta_{crs} &= 0.04 D_*^{-0.1} && 10 < D_* \le 20 \\ \theta_{crs} &= 0.013 D_*^{0.29} && 20 < D_* \le 150 \\ \theta_{crs} &= 0.055 && D_* > 150 \end{aligned} \tag{23}$$

The suspended transport stage parameter in i direction T_{si} is then:

$$T_{si} = \frac{\theta_i - \theta_{crs}}{\theta_{crs}} \qquad i = x, y \,. \tag{24}$$

Assuming $a = 0.015h$, the reference concentration can be evaluated as:

$$c_{ai} = 0.015 \frac{d_{50}}{a} \frac{T_{si}^{\ 1.5}}{D_*^{\ 0.3}} \qquad i = x, y \,. \tag{25}$$

Calculating the modified suspension numbers as proposed by Van Rijn (1984b), one can finally obtain the suspended solid volumetric rate from Equation 17.

The Ackers White formulation (1973) directly obtains the total load in x and y directions q_{sx} and q_{sy} as:

$$\begin{aligned} q_{sx} &= G_{grx} d \frac{(Uh)}{h} \left(\frac{U}{u_*} \right)^n \\ q_{sy} &= G_{gry} d \frac{(Vh)}{h} \left(\frac{V}{v_*} \right)^n \end{aligned} \tag{26}$$

where G_{gri} is the general transport parameter in i direction, d is the grain diameter, h the water depth, U and V, u_* and v_* the mean and shear velocities in x and y directions and n is a parameter depending on the dimensionless particle size. The general transport parameter may be calculated as:

$$G_{gri} = C \left(\frac{F_{gri}}{A} - 1 \right)^m \qquad i = x, y \,, \tag{27}$$

where C, A and m are parameters depending on the dimensionless particle size and F_{gri} is:

$$\begin{aligned} F_{grx} &= \left[\frac{u_*^{\ n}}{\sqrt{g(S_g - 1)d}} \right] \left[\frac{U}{\log\left(10.65 \frac{h}{d} \right)} \right]^{1-n} \\ F_{gry} &= \left[\frac{v_*^{\ n}}{\sqrt{g(S_g - 1)d}} \right] \left[\frac{V}{\log\left(10.65 \frac{h}{d} \right)} \right]^{1-n} \end{aligned} \tag{28}$$

It is easy to see that while in Van Rijn's formulation the coefficient responsible for the beginning of grain motion depends both on particle dimension and bed slope, in the Ackers & White one it depends only on sediment dimension.

To choose one of these two formulations a mining trench test was simulated: a trench situated

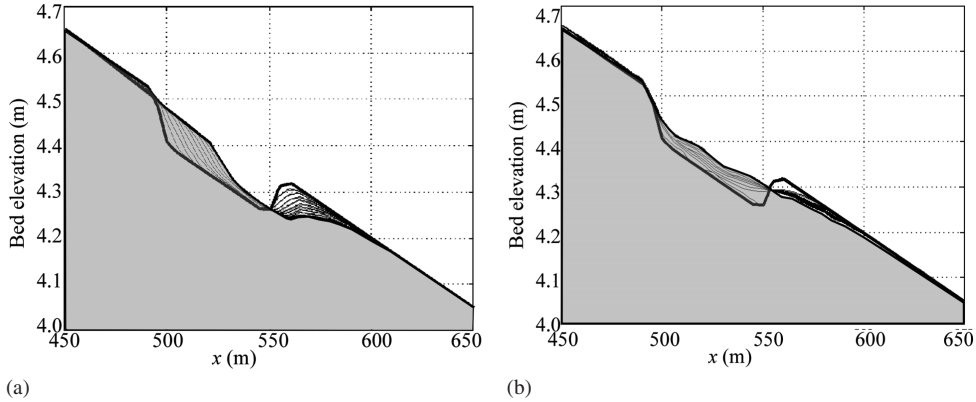


Figure 6. Mining trench test. In (a) Van Rijn's formula is used, while in (b) Ackers & White's formula is used.

transversely on a chute with slope 0.3% was modeled. The bottom of the trench was inerodible. The results of the simulations are shown in Figures 6a (using Van Rijn's formulation) and b (using Ackers & White's formulation).

Table 1. Parameters used for the tidal test.

Channel length (m)	Channel width (m)	Cell length (m)	Slope (%)
50	10	2	5

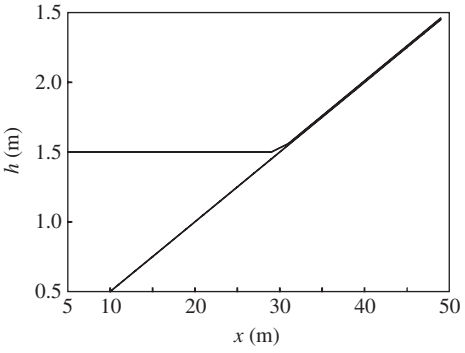


Figure 7. Initial conditions for the tidal test.

The results obtained using Van Rijn's formulation agree with a realistic evolution of the bed elevation (convective and diffusive phase) described by Armanini & Di Silvio (1988), Lee et al. (1993) and Gill (1994). On the other hand the result using the Ackers & White formulation is worse, perhaps because of the omission of the bed slope in calculating the beginning of sediment motion.

On the basis of these considerations in the next simulation only the Van Rijn formula was used.

3 VALIDATION TESTS

In this section the hydrodynamic tests are related, to show the reason why the HLL solver was chosen.

To verify that a solver is able to represent the run-up and run-down of tides on isles and sand banks, a test was carried out to simulate a sinusoidal wave on a sloping beach in a channel. The mesh parameters are summarized in Table 1; the initial conditions were zero velocity and constant water level H_0 (Fig. 7); the sinusoidal wave amplitude was 0.5 m and the period was equal to 560 s (in the following we call this test 'tidal test').

In the test flow resistance was omitted and a Courant number 0.7 used. Different simulations were carried out with different solvers: FORCE, centered Godunov and HLL. The results are shown in Figures 8–10. All

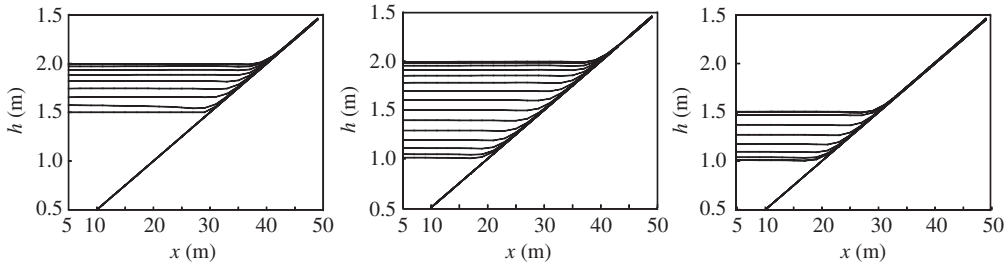


Figure 8. Tidal test: the results with FORCE solver. From the left to the right the first ascending phase of the sinusoid, the descending one and the second ascending one.

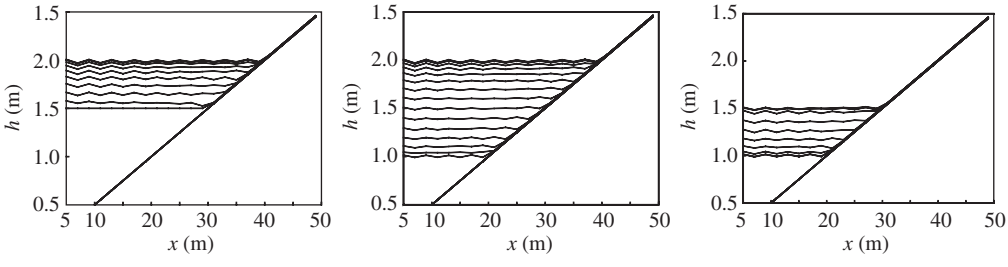


Figure 9. Tidal test: the results with centered Godunov solver. From the left to the right the first ascending phase of the sinusoid, the descending one and the second ascending one.

solvers are able to describe the wave run-up and run-down on the sloping beach, showing that they can all describe the effects of the tide on the isles and sand banks. Nevertheless both FORCE and centered Godunov solvers show some oscillations and for this reason the HLL solver was chosen.

The next attempt to get a better solution was to use the Nujic's technique (Nujic 1995), who proposed moving the pressure term $0.5\ gh^2$ from the flux vectors **F** and **G** to the source term; Nujic's idea was to work with the water level gradient instead of bed slope to avoid instability arising from the irregularity of the bottom, very evident in stationary flow conditions. Applying this method to the previous test, an improvement of the solution in static conditions is observed, but, dynamic tests show worse results (Figs 11–13) than that obtained with the technique illustrated before.

4 APPLICATION ON GRADO-MARANO LAGOON

The present model was applied to the Grado-Marano Lagoon to study erosion and silting of some of its channels in order to check its applicability in planning channel dredging interventions. The usual tide with amplitude of about 0.5 m is not considered to be of great influence from a sediment transport point of view. The most consistent transport phenomena are in correspondence with high tidal oscillations that take place only a few times a year. The model was applied to this kind of event.

To this purpose, we built a grid, made by about 31,000 quadrangular elements with the support of Italian numerical cartography.

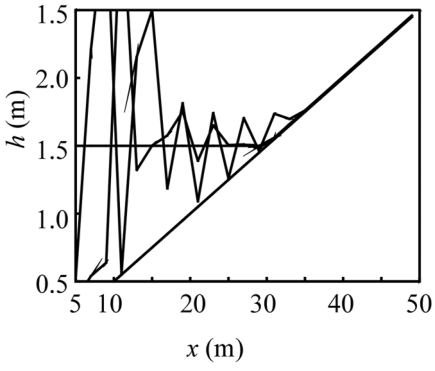


Figure 12. Tidal test: the results with Nujic's technique and centered Godunov solver. Even in the first ascending phase of the sinusoid the solver becomes unstable.

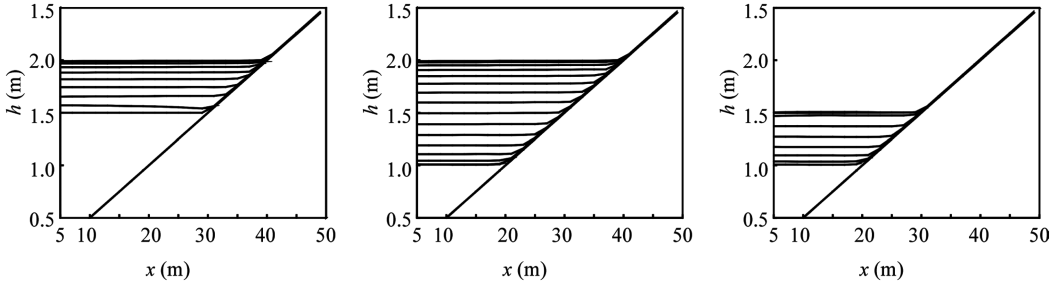


Figure 10. Tidal test: the results with HLL solver. From the left to the right the first ascending phase of the sinusoid, the descending one and the second ascending one.

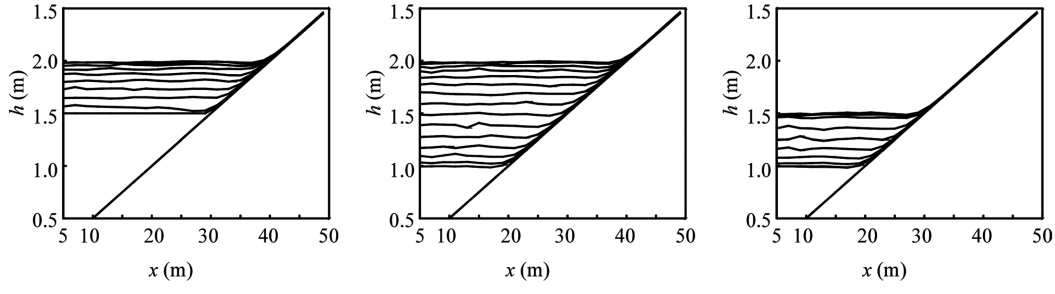


Figure 11. Tidal test: the results with Nujic's technique and FORCE solver. From the left to the right the first ascending phase of the sinusoid, the descending one and the second ascending one.

The model works with almost any kind of quadrangular cells, even if irregular; this allows the modeling of the most critical regions (i.e. the channels) and hence to find more realistic values for the flow characteristics (water depth and velocities). The result is a very coarse grid where the bed elevation is quite regular and a very fine one near the channels.

Initial conditions are quasi-dynamic, that is, at the beginning of the simulations the water depth and velocities of the lagoon are those found after some tidal oscillation. Wall and beach conditions have been imposed on all the lagoon boundary except for the lagoon mouths. The water flow contribution of the lagoon rivers is negligible compared to the water mass that goes in and out from the lagoon mouths.

At the lagoon mouths a tidal oscillation was assigned, which was characterized by wave height of 1.5 m and period of 12 hours. The duration of each simulation was 60 hours.

Only one Manning resistance coefficient was used all over the lagoon. To evaluate it, a calibration was made, which was based on the phase delay of astronomical tides measured by tide-gauges located in Grado and Belvedere (expected in 25 min). A Manning coefficient 0.020 $m^{-1/3}s$ was used, because it gave the best data fit.

Concerning the solid transport, the van Rijn formula was used with a characteristic sediment diameter equal to 0.2×10^{-3} m (Brambati 1970).

To simulate silting and erosion of the channels, 5 channels were studied (Figs 1–2). Figures 14-18 show the development of the bed of one cross section of each channel. It can be observed that in many channels deposition occurred.

The shape of the cross sections analyzed, is quite similar to the convective phase of a mining trench. One explanation for this could be that the oscillatory sediment movements caused by tides are not completely reversible, because of the hydrodynamic field and lagoon morphology. Thus a preferential flow direction is created, causing the moving and the silting of channels. Present computer performance does not

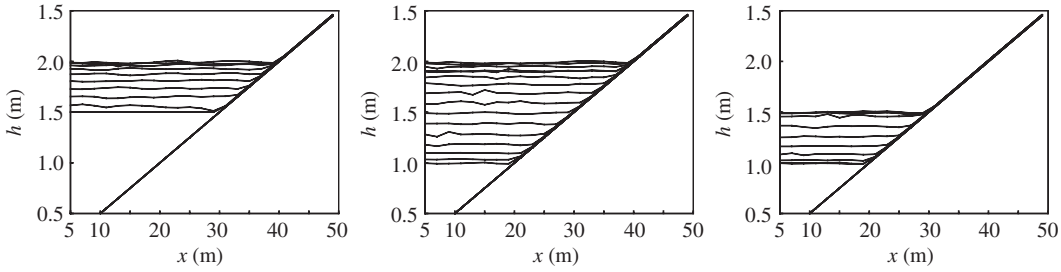


Figure 13. Tidal test: the results with Nujic's technique and HLL solver. From the left to the right the first ascending phase of the sinusoid, the descending one and the second ascending one.

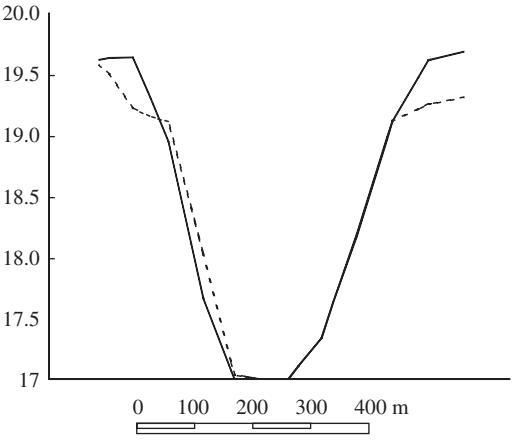


Figure 14. Section n. 1 of Coron channel; the continuous line is the initial cross section, the dotted one is the same section 60 hours later.

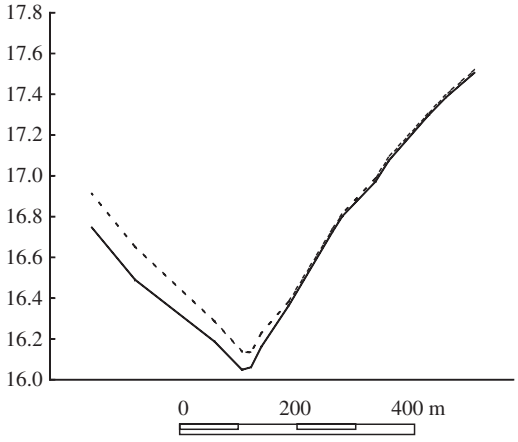


Figure 15. Section n. 4 of Taglio channel: the continuous line is the initial cross section, the dotted one is the same section 60 hours later.

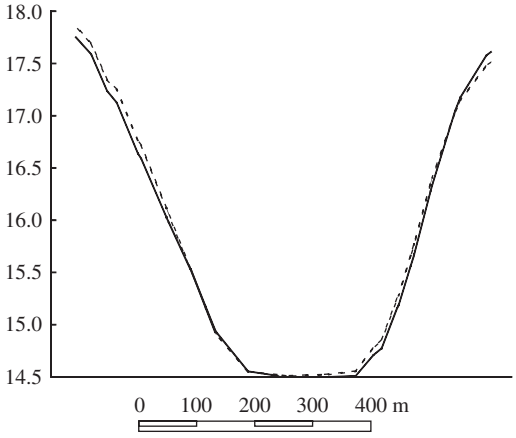


Figure 16. Section n. 10 of Ausa channel: the continuous line is the initial cross section, the dotted one is the same section 60 hours later.

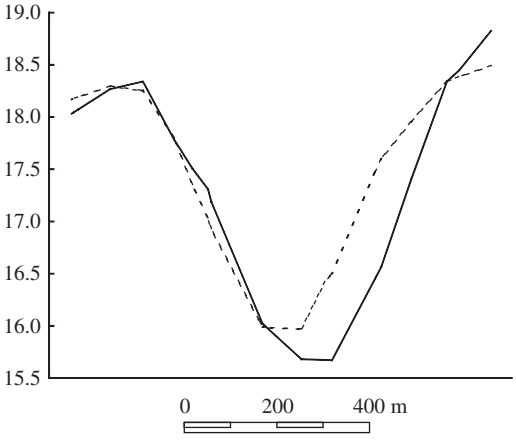


Figure 17. Section n. 4 of D'Orio channel: the continuous line is the initial cross section, the dotted one is the same section 60 hours later.

allow the application of this model on such a large domain with a simulation lasting some years; nevertheless the results obtained could be considered indicative of channel silting phenomena, because associated with medium to high tidal events.

5 CONCLUSIONS

A horizontal bidimensional finite volume numerical model to study sediment transport in lagoon systems is proposed. To evaluate the numerical fluxes on the intercells in the hydrodynamic model a local Riemann problem was solved, using the HLL solver. The choice of this particular solver was based on the result of some

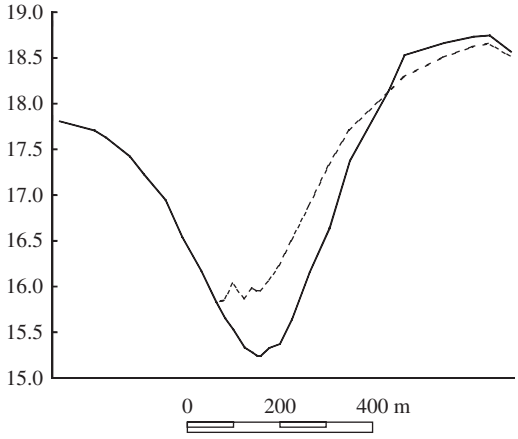


Figure 18. Section n. 5 of Grado channel: the continuous line is the initial cross section, the dotted one is the same section 60 hours later.

preliminary numerical tests, that also have an analytical solution. To evaluate the sediment transport, Van Rijn and Ackers & White formulae were used and the Van Rijn formula was preferred on the basis of the results of some classical solid transport tests.

The application of the sediment transport model on the Grado-Marano lagoon shows that almost all the lagoon basin is subject to continuous bed elevation change. The simulation performed shows that the sediment transport phenomena are not completely reversible, even if the input data comprises a complete oscillation; this behaviour can be ascribed to hydrodynamic characteristics and lagoon morphology.

The results obtained show the efficiency of the model in finding the channel sections that are most disposed to silting phenomenon. It also gives useful information about sediment volumes deposited. Hereafter, coupling the present model with an appropriate statistical tides analysis, it would be possible to use them for planning future channel dredging interventions in the lagoon.

REFERENCES

Ackers P., White W.R., 1973, Sediment transport: new approach and analysis, J. of Hydr. Div., ASCE, Vol. 99, 2041–2060, HY11.

Armanini A., Di Silvio G., 1988, A one-dimensional model for the transport of a sediment misture in non-equilibrium conditions, J. of Hydr. Res., Vol. 26, No. 3, 275–292.

Brambati A., 1970, Provenienza, trasporto ed accumulo dei sedimenti recenti nella laguna di Marano e di Grado e nei litorali tra i fiumi Isonzo e Tagliamento, Memorie della Società Geologica Italiana, Vol. IX, 281–329, Arti Grafiche Pacini Mariotti, Pisa, in Italian.

Brownlie W.R., 1981, Discussion of Total load transport in alluvial channels, J. of Hydr. Div., Proc., ASCE, HY12.
Chiew Y.M., Parker G., 1994, Incipient sediment motion on non-horizontal slopes, J. of Hydr. Res., Vol. 32, No. 5, 649–660.
Garcia R., Kahawita R.A., 1986, Numerical solution of the St. Venant equations with the MacCormack finite-difference scheme, International Journal of Numerical Methods in Fluids, Vol. 6, pp. 259–274.
Gill M.A., 1994, Hydrodynamics of mining pits in erodible bed under steady flow, J. of Hydr. Eng., Vol. 120, No. 11, 1337–1348.
Hirsch C., 1984, Numerical computation of internal and external flows, Vol. 2, John Wiley & Sons, Chichester.
Lee H.Y., Fu D.T. and Song M.H., 1993, Migration of rectangular pit composed of uniform sediments, J. of Hydr. Eng., Vol.119, No. 1, 64–80.
Ligget J.A., 1994, Fluid mechanics, McGraw-Hill, Inc., Singapore.
Maa J.P., 1990, An efficient horizontal two-dimensional hydrodynamic model, Coastal Engineering, Vol. 14, pp. 1–18.
Nujić M., 1995, Efficient implementation of non-oscillatory schemes for computation of free-surface flows, J. of Hydr. Res., Vol. 33, No. 1, 101–111.
Pedlosky J., 1987, Geophysical fluid dynamics, Second edition, Springer-Verlag, New York.
Toro E.F., 1999, Riemann solvers and numerical methods for fluid dynamics, 2nd edition, Springer, New York.
Toro E.F., 2001, Shock-capturing methods for free-surface shallow flows, John Wiley & Sons, Chichester.
Van Rijn L.C., 1984a, Sediment transport Part I, J. of Hydr. Eng., Vol. 110, No. 10, 1431–1456.
Van Rijn L.C., 1984b, Sediment transport Part II, J. of Hydr. Eng., Vol. 110, No. 11, 1613–1640.

This page intentionally left blank

River Flow 2004 – Greco, Carravetta & Della Morte (eds.)
© 2004 Taylor & Francis Group, London, ISBN 90 5809 658 0

Field investigation on macro-roughness characterization in mountain rivers

F. Canovaro & M. Catella
Department of Civil Engineering, University of Firenze, Italy

ABSTRACT: The macro-roughness characteristics obtained by field measurements are herein analyzed for mountain rivers. In this conditions flow resistance is deeply affected by geometrical and spatial characteristics of macro-roughness elements. The roughness geometry complexity makes difficult the evaluation of a representative roughness height. In the present paper a criterion for macro-roughness characterization based on bed surface surveys and photographs is proposed. Experimental data collected during field activities were satisfactory compared to data from laboratory investigations.

1 INTRODUCTION

The flow resistance in mountain rivers is deeply affected by the large-scale roughness mainly related to spatial density, arrangement and size of the sediment particles in the channel (Sayre & Albertson 1963, Barnes 1978, Bathurst et al. 1981).

The empirical relations taking into account only particle-size to estimate flow resistance in gravel or boulder bed channels give normally unreliable results (Bray 1985, Nikora 1998, Baiamonte 2001).

To determine the flow resistance in steep channels the macro-roughness geometry has to be characterized in terms of the cumulative effects of arrangement and spatial density of the coarser sediments protrusions above the stream bed.

The primary objective of this study is to characterize the macro-roughness elements in natural mountain streams.

The effective roughness height, representative of the protrusion distribution, has been defined using the location and the elevation of the highest point and the contact points between all particles exposed along a series of cross sections. In particular the methodology proposed by Gomez (1993) for a laboratory flume has been extended to field conditions.

The field data collected throughout a three months survey has been compared with results obtained by Gomez on a stable armored surface in a laboratory flume showing good agreement.

2 SITES OF FIELD INVESTIGATION

Primarily the detection of suitable stream reaches for the investigation has been conducted. In order to avoid additional effects on flow resistance, the main properties of the studied channel should be: straight reach without sinuosity, spread presence of macro-roughness, absence of macro scale bed morphologies such as bars or step-pool.

The three sites of Navale, Picignana and Resco Creeks located in the mountain region of Tuscany (Italy) have been considered.

The general morphology of the streams under investigation are very much alike. They run in carved channels within the deep straits of the valley with no alluvial plain. They show a plan-form sinuosity values ranging round the unity both in the case of low and high flows. Bed slopes are around 2–3% and sediments feeding is strong, quite sorted and coarse (essentially gravel, cobbles and boulders).

In particular, the Picignana Creek bed surface is randomly spread by isolated boulders without showing any transversal or longitudinal structure (Fig. 1), thus recognizable as a cascade stream morphology (Montgomery & Buffington 1997).

The Navale and Resco Creeks bed surfaces are composed by irregular sequences of small and big boulders transversely placed along the entire cross section (transverse rib morphology). This morphology differs from the step-pool in terms of absence of pools and sediment deposition in the upstream side, minor height of the step and a more regular streambed profile (Lenzi et al. 2000).

The main characteristics of channel reaches geometry and bed surface are listed in Table 1.

3 MACRO-ROUGHNESS MEASUREMENTS

3.1 *Bed topography measurement*

In order to characterize bed surface variations, the stream bottom elevation has been recorded with



Figure 1. Cascade stream bed morphology in the Picignana Creek.



Figure 2. Transverse rib stream bed morphology in the Resco Creek.

Table 1. Main characteristics of channel geometry and bed surface of reaches the reaches under investigation. The Navale, Picignana and Resco Creeks are in the following cited respectively as NA, PC, RS.

Stream code	Length (m)	Width (m)	Slope (%)	D_{50} (mm)	D_{90} (mm)
NA	45	8.2	3.1	79	549
PC	45	7.0	5.5	145	519
RS	30	6.9	2.6	127	467



Figure 3. Bed surface field measurements (Resco Creek).

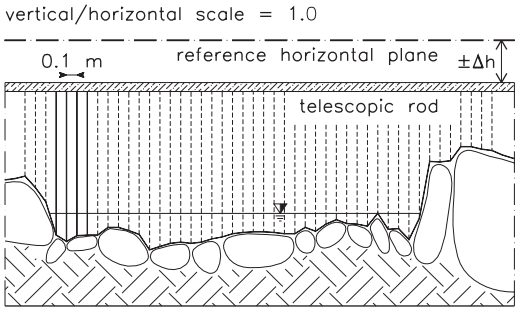


Figure 4. Sketch of the bed surface measurements.

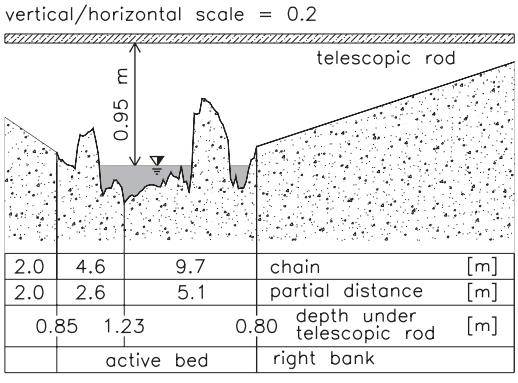


Figure 5. Schematic stream transect profile from bed elevation measurements (Resco Creek – transect 1).

reference to an arbitrary horizontal axis established with an engineering grade level.

The bed surveys for each cross section has been conducted using a needlepoint depth gage mounted on a 9 meters long aluminum telescopic rod fixed horizontal (Figs 3, 4). Measurements have been conducted at 10 centimeters intervals, while average elevations have been determined by fitting lines using linear least squares regression.

An example of a single cross section bed surface profile is reported in Figure 5.

Bed measurements has been repeated for all the cross sections in which the study reaches have been subdivided.



Figure 6. Vertical photographs of bed surface (Resco Creek).

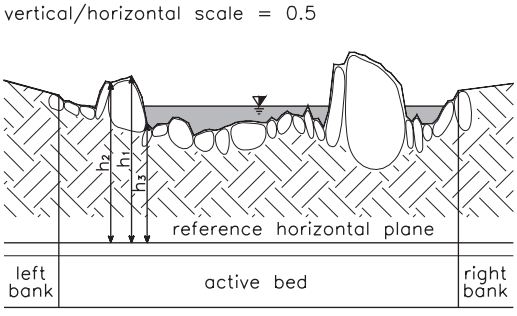


Figure 7. Characterization of bed surface topography (Resco Creek – transect 1). Effective roughness height of the sediment particle $h = h_1 - (h_2 + h_3)/2$.

In particular in the Navale and Picignana Creeks 9 transects have been identified in two 45 meters long reaches, while in the Resco Creek 10 transects in a 30 meters long reach have been defined.

Following Gomez (1993), the location and the elevation of the highest point and the contact points between the sediment particles has been detected along a cross section (Fig. 7). The sediment arrangement on the bed surface has been reconstructed by means of a series of vertical photographs (Fig. 6) taken across each stream transect along the telescopic rod.

The photographs have been taken by a digital camera positioned on the top of a vertical 5-m-long rod, able to reproduce a stream portion 5-m-long and 4-m-wide.

3.2 *Macro-roughness characterization*

In order to characterize the macro-roughness geometry two main aspects need to be considered. First, a criterion to determine the roughness height of each protrusion has to be defined. Second, a roughness height representative of the cumulative effects of protrusion distribution has to be determined.

In the present paper the Gomez methodology has been extended to define the bed surface roughness height of a single particle in field condition.

The effective roughness height h of a single particle has been defined as the difference in elevation between the highest point on the particle itself and the average elevation of the two contact points of the adjacent particles respectively on the right and left side (Fig. 7).

This definition takes the entire bed surface variation into account for the macro-roughness assessment.

The representative roughness height k of the sediment elements constituting the bulk has been determined as the average value of the effective roughness heights for $h \geq h_{95}$ (the height for which 95% of the effective roughness height are smaller). The h_{95} value has been chosen since the sediments with $h \geq h_{95}$ are the most responsible to the macroroughness, assuming that few large particles dominate the flow resistance (Robertson & Wright 1973, Burkham & Dawdy 1976).

The single particle effective roughness heights for $h \geq h_{95}$ for the three reaches under investigations are reported in Table 2.

Table 2. Effective roughness heights, for $h \geq h_{95}$, of single particle on the bed surface. The *b*-axis corresponds to the median particle size (intermediate axis).

NA		PC		RS	
b-axis (mm)	*h* (mm)	*b*-axis (mm)	*h* (mm)	*b*-axis (mm)	*h* (mm)
430	365	670	415	600	405
580	440	690	406	640	611
730	445	910	615	660	360
1170	655	1610	740	920	740

3.3 *Macro-roughness behavior*

The collected field data has been compared with results obtained by Gomez on a stable armored surface in a laboratory flume.

With reference to Figures 8–10, field data representing the effective roughness height have been plotted against the median particle size for each stream, and compared with laboratory data by Gomez.

Note that to make the two sets of results comparable both the roughness height and median particle size are made dimensionless with the D_{90} of the respective surface bed material.

Agreement between field and laboratory bed surface roughness heights appears very good in terms of pattern. In terms of absolute values, field effective

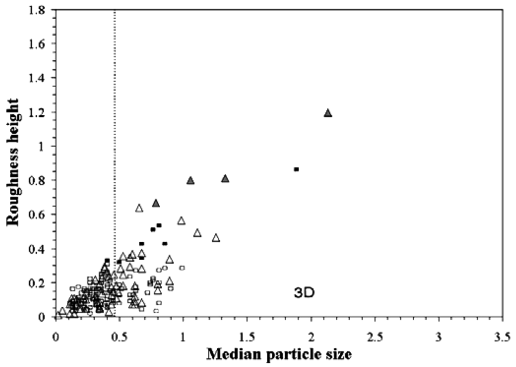


Figure 8. Dimensionless effective roughness height versus dimensionless particle size. Triangle and square represent respectively Navale field results and Gomez laboratory results. Solid symbols indicate effective roughness elements, $\geq h_{95}$ in height.

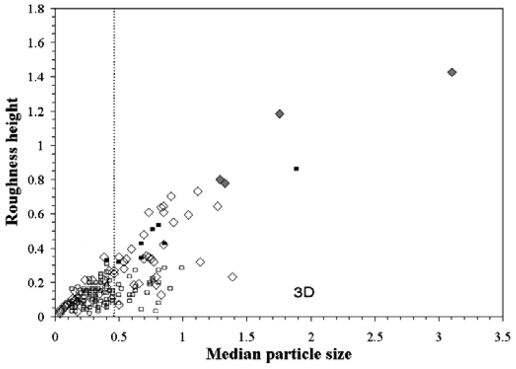


Figure 9. Dimensionless effective roughness height versus dimensionless particle size. Rhombus and square represent respectively Picignana field results and Gomez laboratory results. Solid symbols indicate effective roughness elements, $\geq h_{95}$ in height.

roughness heights for $h \geq h_{95}$ seem to be fairly greater than laboratory values.

In Figure 11 a comparison between all the three field sites under investigation and laboratory results is reported. It emerged that the most contribute to flow resistance is due not to a single particle size, but to all the sediment particles characterized by an intermediate axis grater than D_{90} (except for the first effective roughness element, $\geq h_{95}$ in height, in the Navale Creek reported in Table 2). Thus, in the present study the coarser particles of the bed surface appear to be the only responsible of the representative roughness height. The protrusions above the stream bed are not due to the finer particles because they are not exposed on the stream bottoms as result of the armoring processes.

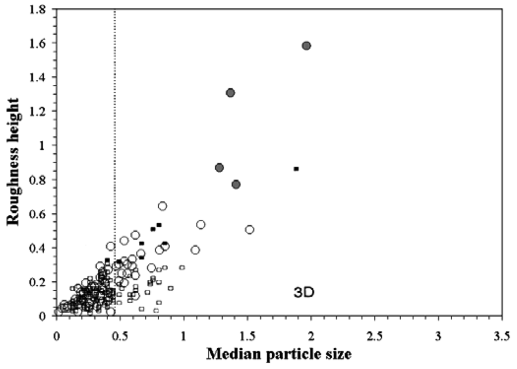


Figure 10. Dimensionless effective roughness height versus dimensionless particle size. Circle and square represent respectively Resco field results and Gomez laboratory results. Solid symbols indicate effective roughness elements, $\geq h_{95}$ in height.

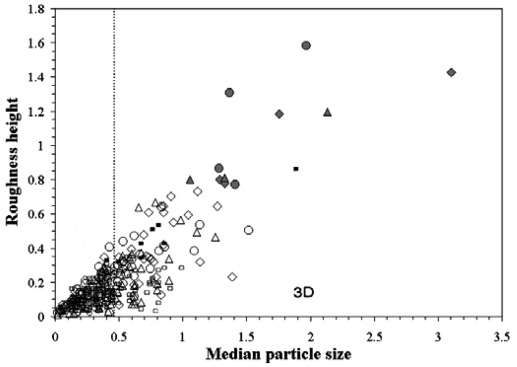


Figure 11. Dimensionless effective roughness height versus dimensionless particle size. Solid symbols indicate effective roughness elements, $\geq h_{95}$ in height.

4 CONCLUSIONS

A criterion for the characterization of the representative roughness height of the protrusion arrangement on the bed surface in a mountain river is proposed. The methodology by Gomez has been extended to natural rivers.

The effective roughness height is not defined using empirical relations based on particle-size distributions, but it involves the height and the distribution of protrusions derived from bed surveys and vertical photographs.

The effective roughness height from field measurements and from Gomez laboratory flume, make dimensionless with D_{90}, show a good agreement in terms of pattern, while in terms of absolute values field data seem to be fairly greater than laboratory values.

The representative roughness height of the bed surface has been determined as the average value of the effective roughness heights for $h \geq h_{95}$, assuming these heights as the most responsible of the flow resistance.

Present results underline that the effective roughness height with $h \geq h_{95}$ are characterized by an intermediate axis grater than D_{90}. Thus, the coarser particles of the bed surface appear to be the only responsible of the representative roughness height.

ACKNOWLEDGMENTS

This research was funded by the Istituto Nazionale per la Ricerca Scientifica e Tecnologica sulla Montagna (INRM) in the framework of the research program "Dinamica e regimazione del trasporto solido in relazione della difesa del territorio montano" 2001.

Moreover, the Authors wish to thank Miss Giulia Gianassi for her important role in carrying out the field measurements.

NOTATIONS

The following symbols are used in this paper:

D_{50} = median diameter of surface bed material;
D_{90} = the sieve size for which 90% of particle size are smaller;
h = effective roughness height of a particle;
k = representative roughness height.

REFERENCES

Baiamonte, G. 2001. Un approccio teorico per la determinazione della legge di resistenza al moto in alvei granulari a fondo fisso. *L'Acqua* 1: 7–18 (in Italian).

Barnes, H.H. 1967. Roughness characteristics of natural channels. *Water Supply Paper 1849*, *United States Geological Survey*, *Washington DC*.

Bathurst, J.C., Li, R.M. & Simons, D.B. 1981. Resistance equation for large-scale roughness. *Journal of the Hydraulic Division*, *ASCE* 107(HY12): 1593–1613.

Basil, G. 1993. Roughness of stable, armored gravel beds. *Water resources research* 19(11): 3631–3642.

Bray, D.I. 1985. Flow resistance in gravel-bed rivers. In R.D. Hey, J.C. Bathurst and C.R. Thorne (eds), *Gravel bed rivers*: 109–132. New York: John Wiley & Sons Ltd.

Bunte, K. & Abt, S.R. 2001. Sampling surface and subsurface particle-size distributions in wadable gravel- and cobblebed streams for analyses in sediment transport, hydraulics, and streambed monitoring. Gen. Tech. Rep. RMRS-GTR-74. Fort Collins, CO: U.S. Department of Agriculture, Forest Service, Rocky Mountain Research Station.

Burkham, D.E. & Dawdy, D.R. 1976. Resistance equation for alluvial-channel flow. *Journal of the Hydraulic Division, ASCE* 102: 1479–1489.

Lenzi, M.A., D'Agostino, V. & Sonda, D. 2000. *Ricostruzione morfologica e recupero ambientale dei torrenti*. Cosenza: Bios (in Italian).

Montgomery, D.R. & Buffington, J.M. 1997. Channel-reach morphology in mountain drainage basins. *GSA Bulletin*, 109(5): 596–611.

Nikora, V.I., Goring, D.G. & Biggs, B.J.F. 1998. On gravelbed roughness characterization. *Water resources research* 34(3): 517–527.

Robertson, J.A. & Wright S.J. 1973. Analysis of flow resistance in channels with gravel beds. *American Society of Civil Engineers*, *Proceedings of the 21st AnnualHydraulic Division Specialty Conference*, New York: 63–72.

Sayre, W.W. & Albertson, M.L. 1963. Roughness spacing in rigid open channels. *Transactions of American Society of Civil Engineers* 128: 343–372.

This page intentionally left blank

River Flow 2004 – Greco, Carravetta & Della Morte (eds.)
© 2004 Taylor & Francis Group, London, ISBN 90 5809 658 0

Pressure fluctuations within subsurface gravel bed caused by turbulent open-channel flow

M. Detert & G.H. Jirka
Institute for Hydromechanics (IfH), University of Karlsruhe, Germany

M. Jehle, M. Klar & B. Jähne
Interdisciplinary Center for Scientific Computing (IWR), University of Heidelberg, Germany

H.-J. Köhler & T. Wenka
Federal Waterways Engineering and Research Institute (BAW), Karlsruhe, Germany

ABSTRACT: Results from an experimental study of the interaction between turbulent open-channel flow and the flow in a porous subsurface gravel layer are presented. Synchronous measurements are carried out with miniature temporally high resolution pressure sensors and with 3D-PTV (particle tracking velocimetry). First data sets are analysed in detail. The ultimate results may help in understanding the processes of erosion and sedimentation, as well as mass exchange processes. The long-term goal of this project is to improve the engineering design of stable beds for waterways.

1 INTRODUCTION

Many problems in hydraulic engineering deal with the morphodynamic changes due to construction of hydraulic structures such as groynes, weirs or mounted embankments. The efficiency of hydraulic constructions depends on the stability of the river bed or the artificial geotechnical armoring layer, respectively. For example, the Iffezheim barrage at the Rhine-river near Karlsruhe needs about 200.000 m^3 of gravel per year additionally to avoid erosion in the downstream river bed.

Over the last 100 years much research work has been done to gain insight into the theoretical background of river bed stability. However up to now no satisfactory, physically founded formula has been established to answer definitely the question of river bed stability. The understanding of the individual processes, the functional chain of cause and effect is not developed far enough to predict destabilization. Hence, the success of a hydraulic construction cannot be guaranteed satisfactorily.

2 BACKGROUND

The stability of a gravel bed in an open-channel flow is usually described by the Shields (1936) parameter, τ^*. It is defined as the ratio of the frictional load on the grain ($\sim \rho_w \, u^{*2} \, d^2$) to the gravitational force on the grain that may resists against movement ($\sim g \, (\rho_s - \rho_w) d^3$). The value of $\tau^* = 0.03$ to 0.06 is often used as the limit for bed protection. This and other correlations, e.g. Meyer-Peter/Müller (1949), yield a good estimation for most practical engineering problems. However, these equations consider uniform flow. They do not reproduce the local unsteady physical processes on the gravel bed due to turbulence.

For a more detailed consideration of stability problems the analysis of the influence of fluctuating forces is important. Fluctuating forces might be caused by turbulence of open-channel flow including the occurrence of coherent structures as well as the involvement of the whole hydrodynamic system which consists of free surface flow, combined with the subsurface gravel layer and eventually the groundwater flow.

The discovery of the so-called bursting phenomenon in turbulent flows by Kline (1967) generated a new interest in studying the structures of boundary layer turbulence. As is described by Grass (1971), fluid near the bottom is thrown upwards during an ejection phase, during a sweep phase fluid is pumped towards the bottom. Burst-cycles occur over both smooth and rough surfaces. They have a strong impact on pressure peaks on the bottom which might cause the erosion of single grains (Drake, 1988; Hoyal, 1985; Gyr et al.,

1996). Emmerling (1973) noticed instantaneous pressure peaks max(p) as high as six times the medium pressure fluctuations rms(p). Raudkivi (1982) as well as Dittrich et al. (1999) correlate rms(p) to shear stress τ_0 as rms(p) = C τ_0, with C varying from 0.5 to 5.0, with an average of 3.0. Referring to Emmerling max(p) must be taken into consideration up to 18 τ_0!

Recent developments in measuring techniques allow new methods for observing the above mentioned processes using piezometric pressure sensors with high resolution in time (Aktiv Sensor, 2003; Hofland et al., 2003) and 3D-PTV, i.e. particle tracking velocimetry (Klar, 2001). Hence a Filter and Erosion Research Club (FERC) was initiated by Dienst Wegen Waterbouwkunde (DWW) Rijkswaterstaat (Netherlands), Kingston University (Great Britain), the Federal Waterways Engineering and Research Institute (BAW), the Interdisciplinary Center for Scientific Computing (IWR) and the Institute for Hydromechanics (IfH) for using a combination of these above mentioned techniques.

The primary motivation of this study is to improve the understanding of the influence of hydrodynamic structures on the behavior of a gravel layer. An additional focus lies on the optimization of a gravel layer as a filter layer for protection for an underlying sand layer.

The long-term goal of this project is to improve the safe design of stable beds for waterways.

3 EXPERIMENTAL SETUP

3.1 *Flume*

The measurements are performed in an open channel flume with length L = 40 m, breadth B = 0.9 m and a maximum flow rate $Q_{max} = 0.275\ m^3/s$. Figure 1 shows a sketch of the experimental setup.

A sand layer of $H_S = 0.5$ m height covered by a porous gravel layer of $H_P = 0.04$ to 0.20 m height is placed in the flume over a length of L = 30 m, optionally with and without hydraulic contact to the sand layer. This is achieved by omitting or inserting a rubber mat, respectively. The measuring-area is located at 15 m; hence influences of inlet and outlet are supposed to be negligible. The grain diameter of the gravel is $d_{50} = \sim 10$ mm, with a degree of non-uniformity $Cc = d_{60}/d_{10} = 1.25$. The mean grain diameter of the uniform sand is about $d_{50} = \sim 1$ mm.

The measurements are made simultaneously by miniature pressure sensors with high temporally resolution and 3D-PTV in three artificial gravel pores. In addition, up to seven more pressure sensors and endoscopic observation of the sand-gravel-boundary can be applied. The measurement program is given in Table 1.

The measuring program is defined for water depth of $H_A/d_{50} = 20$ and $H_B/d_{50} = 40$. Variation in discharge and water depth provides flow conditions up to low mobility transport conditions based on the Shields parameter, τ^*. Supplementary measurements are done with glass spheres, having a $d_{50} = 10$ mm.

Long waves are generated artificially by a wave generator located 9.25 m downstream the measuring-area. Thus, the influence of an oscillating water level will be studied.

The flow rate is measured by a magnetic inductive flowmeter, the water level is detected by an external

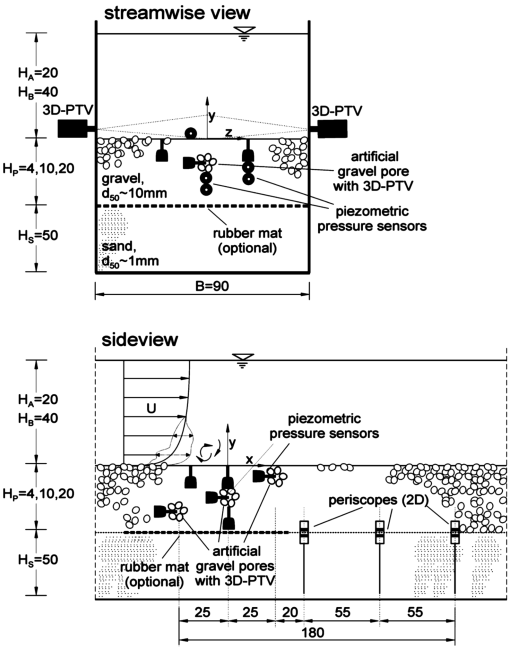


Figure 1. Sketch of experimental setup, dimensions [cm], not scaled.

Table 1. Measuring program, increasing shear stress $\tau_0/\tau_{cr} = 0.1$ to 1.0, $\tau_{cr} = 6.8$ Pa.

flow conditions	τ_0/τ_{cr}	0.1	0.2	0.4	0.6	0.8	1.0
gravel	H_p/d_{50}						
with rubber mat	20	$W_{A,B}$	$H_{A,B}$	$H_{A,B}$	H_A	-	-
	10	$W_{A,B}$	$W_{A,B}$	$W_{A,B}$	H_A	H_A	H_A
	4	$W_{A,B}$	$H_{A,B}$	$H_{A,B}$	H_A	H_A	H_A
gravel	H_p/d_{50}						
without rubber mat	20	-	-	-	-	-	-
	10	$W_{A,B}$	-	$W_{A,B}$	-	-	-
	4	$W_{A,B}$	-	$H_{A,B}$	-	-	-
glass spheres	H_p/d_{50}						
with rubber mat	4	$H_{A,B}$	$H_{A,B}$	$H_{A,B}$	-	-	-
	2	$H_{A,B}$	$H_{A,B}$	$H_{A,B}$	-	-	-

explanation:		
	$H_{A,B}$	gauging at water depth H_A=20cm, H_B=40cm
	$W_{A,B}$	gauging incl. wave generator
	H_p	height of porous granular filter
	d_{50}	mean gravel diameter

ultrasonic probe with hydraulic contact to the flume. Steady flow conditions for each measurement are provided by controlling the gate valve at the inlet and the movable weir at the outlet automatically.

3.2 *Micro-pressure sensors*

The micro-pressure sensors were manufactured in a development cooperation of Aktiv Sensor GmbH (Berlin) and the Institute for Hydromechanics (IfH).

The principle of these in-situ micro-pressure sensors is based on the 'piezoresistive' effect. The initial point is an element of silicium, with implanted resistances in its bending panel. Figure 2 and 3 show photographs of the essential sensor components and three versions of testing sensors.

Figure 4 shows a photograph of the encapsulated head of the pressure pickup and its flexible tube for pressure equalisation as it was used for the measurements.

The differential pressure is measured with reference to atmospheric pressure, here additionally with compensation of temperature. For water resistance, the housings of the sensors are encapsulated with slowly hardening epoxy resin and sealed up with clear varnish. The maximal dimensions of the sensors are as small as $2 \times 1.2 \times 1.2\,cm^3$, with a shape similar to a bigger gravel grain. Due to signal conditioning by the purpose-built amplifier the guaranteed maximum measurable frequencies are 100 Hz. Hence,

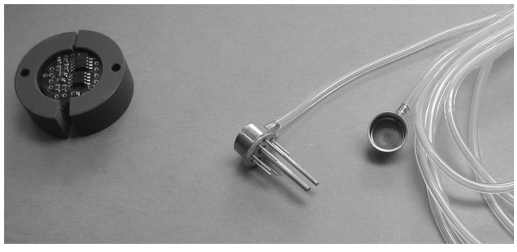


Figure 2. Micro-pressure sensors components, from left to right: amplifying blank (pressure transducer, series AU), piezoelectric pressure pickup (series AT, not encapsulated) and cap (series C) with drilled hole and flexible tube for pressure equalisation.

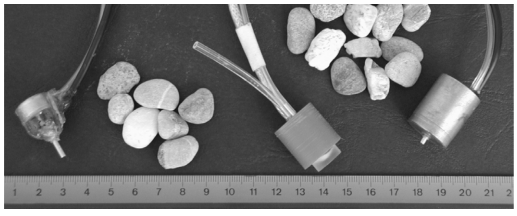


Figure 3. Testing micro-pressure sensors, from left to right: encapsulated with epoxy resin, with plastic and with brass.

measurements of pressure fluctuations up to the estimated Kolmogorov-scale-frequency of 50 Hz (Nezu et al., 1993) is possible. To avoid aliasing effects, the measurements are performed at a rate of 500 Hz.

The sensor elements are deliverable for maximal pressures of 1.6 to 10^7 kPa. 6 kPa were chosen to be appropriate for the provided flow conditions with maximal 60 cmWC within the gravel layer. Thus the absolute range of the pressure sensors is 0 to 6 kPa. Due to the analog-digital-card, the increment of discretisation is 1.5 Pa (0 to 6 kPa) or 0.7 Pa (0 to 3 kPa).

The ready-built sensors were calibrated by Aktiv Sensor GmbH to 0 to 10V according to 0 to 6 kPa at pressure of 3 and 6 kPa with a tolerance in accuracy of less than 1.0% full scale. Within a range of pressure fluctuations of e.g. 150 Pa the accuracy is less then the increment of discretisation.

After a few months in use the sensors showed an offset of up to 1V corresponding to 0 Pa. As tests showed the calibrating factor of 1.67 V/kPa stayed the same. Thus, on the one hand the maximal detectable static pressure is reduced up to 90%, on the other hand the measurement of fluctuations is not affected. To gain the right static pressure the sensors were calibrated before every measurement by comparing the measured signal with the water level detected by an ultrasonic probe.

Tests under flume-conditions showed that extraneous high frequency noise was disturbing the amplified signal, as it can be seen in Figure 5. Therefore, a low-pass filter with RC = 0.33 ms was interposed. Its theoretical damping H(f) can be calculated by

$$H(f) = \frac{1}{\sqrt{1^2 + (2\,\pi\,f\;RC)^2}} \qquad (1)$$

where f = frequency [Hz]; RC = time constant.

Thus, the filter leads to damping of signals e.g. with 50 Hz to 99.5% and signals with 10 kHz to 4.8% which



Figure 4. Head of micro-pressure sensor above gravel $d_{50} = \sim 10$ mm.

is acceptable for the provided flow conditions. The clarifying effect on the signal is shown in Figure 6.

Only a few pressure sensors started drifting without any obvious reason as shown in Figure 7. Figure 8 shows a signal gauged simultaneously under the same flow conditions which is not drifting. Thus, the provided flume conditions must have been constant. Gauged drifting signals like this were simply rejected.

Pressure sensors are located at vertical positions of $y/d_{50} = 1.0$ (above), 0.0 (at top) and at various positions within the gravel layer. Each three sensors are adapted on three artificial gravel pores to gain simultaneously insight in pressure and velocity. Simultaneous measuring was performed additionally by up to seven pressure sensors over two minutes. These sensors are locally fixed on a grid as shown in Figure 9.

Compared with standard mechanical pressure sensors the miniature pressure sensors including an amplified calibrated signal are low-cost sensors.

3.3 *3D-PTV*

Pore flow is measured by tracking tracer particles with two flexible fiber optic endoscopes, integrated into each artificial pore. Synchronized CMOS-cameras are used to acquire stereoscopic image sequences of the tracer particles in real-time with a frame rate of up

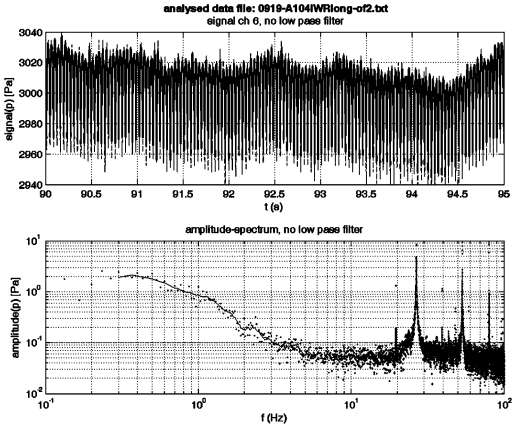


Figure 5. Example signal [Pa] and amplitude-spectrum [Pa] without low-pass filtering, $y/d_{50} = -4.3$, $\tau_0/\tau_{cr} = 0.4$, $\tau_{cr} = 6.8$ Pa, $H_A/d_{50} = \sim 10$, $H_P/d_{50} = \sim 10$, hydraulic contact between gravel and sand layer.

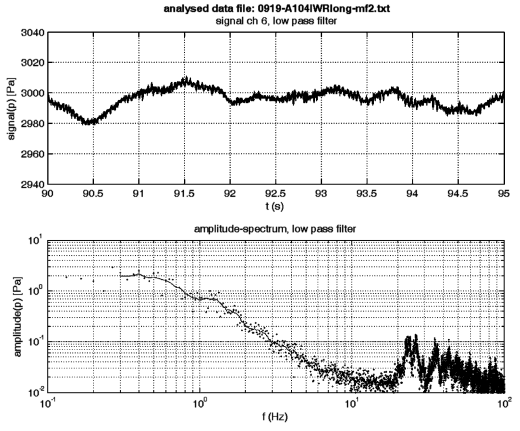


Figure 6. Example signal [Pa] and amplitude-spectrum [Pa] with low-pass filtering, the same flow conditions as in Figure 5.

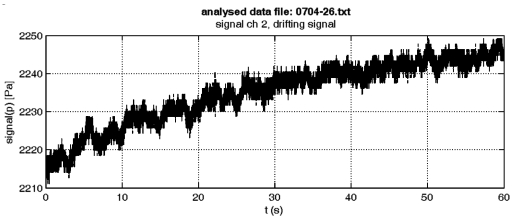


Figure 7. Signal [Pa] with drifting, $\tau_0/\tau_{cr} = 0.1$, $\tau_{cr} = 6.8$ Pa, $H_A/d_{50} = \sim 21$, $H_P/d_{50} = \sim 20$, no hydraulic contact between gravel and sand layer.

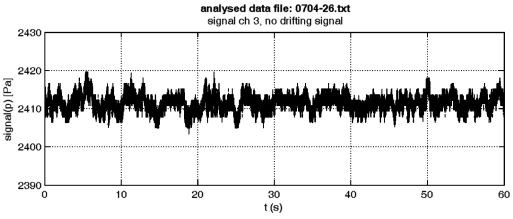


Figure 8. Signal [Pa] without drifting, gauged simultaneously with the example signal in Figure 7.

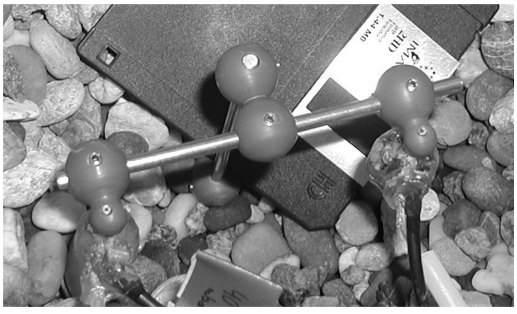


Figure 9. Positioning of two sensors on a lattice (see dimensions of a floppy disc).

to 400 Hz. The 3D Lagrangian flow velocities of the tracer particles along their trajectories can be determined using a three-dimensional particle tracking velocity (3D-PTV) algorithm, which is based on stereo correlation of two-dimensional particle trajectories.

The free surface flow directly above one of the artificial pores is explored by a conventional stereo camera setup applying the developed 3D-PTV algorithms.

Sediment movements are analysed by three rigid endoscopes (periscopes) observing the interface between gravel and subsoil at three different positions. The image sequences are recorded by three standard CCD-cameras. Motion of sand or gravel is detected using techniques developed in digital image processing. The calculation of the optical flow using the structure tensor technique allows to obtain a dense 2D displacement vector field (Jähne et al., 1998). Altogether, 11 cameras are operated simultaneously with a total data thruput of about 125 MB/s. To keep the data amount within reasonable limits, the sequence duration for one measurement is 60 s (approximately 7 GB of image data).

Measurements of the whole 3D-PTV-system and micro-pressure sensors are carried out simultaneously (see also Klar et al., 2004).

3.4 *ADCP*

To gain additional insight into the velocity regime, a 1D-ADCP (Acoustic Doppler Current Profiler), namely a DOP 1000 (Signal Processing, Suisse) is used. The ADCP uses a pulsed ultrasonic echo technique to measure streamwise velocity profiles. The parameters of the ADCP have to be adjusted optimally for each flow condition. Thus, the resolution varies from 1 to 2 mm and 20 to 100 Hz. The maximal velocity U in streamwise direction is 1.2 m/s.

Due to the measuring technique of the ADCP it is only possible to measure probable velocity profiles from $y/d_{50} = 1.0$ to 12.0 above the gravel layer. Profiles with duration of 30 to 45 s were measured at various wall distances to get time averaged isoline U-2D velocity plots. Working with the ADCP in the measuring area is not possible because of spatial limits. Therefore this gauging instrument is located 3.3 m downstream from the measuring area in order not to disturb the pressure sensors and 3D-PTV.

3.5 *Wave gauge*

To detect variation and oscillation of the water level, especially while generating waves with the wave machine, a wave gauge is installed. Its principle is similar to the 'GHM – Dynamic Liquid-Level' (Delft Hydraulics, 2003) while measuring the resistance between two vertical submerged rods of stainless steel. Measurements are recorded at a rate of 500 Hz.

4 PRELIMINARY RESULTS AND DISCUSSION

4.1 *Pressure fluctuations*

Each data set is smoothed with a simple moving average window of $\Delta t = 0.006$ s to eliminate outlying values. Thus, p_m denotes the smoothed values.

Figure 10 shows an example of the pressure fluctuations $\mathrm{rms}(p_m)$ of the averaged pressure signal for increasing shear stress τ_0/τ_{cr} up to low mobility conditions at $\tau_{cr} = 6.8$ Pa. Vertical positions of the piezometric pressure sensors vary from $y/d_{50} = 1.0$ above to -7.5 within the gravel layer. The relative water depth is $H_A/d_{50} = \sim 20$, the relative thickness of the gravel layer is $H_P/d_{50} = \sim 10$. No hydraulic contact to the underlying sand layer is given.

For $\tau_0/\tau_{cr} = 1.0$ and $y/d_{50} = 0.0$ at the top of the gravel layer the $\mathrm{rms}(p_m)$ is about $3.2\,\tau_0$ which confirms Raudkivi (1982) and Dittrich et al. (1999) with C being mostly 3.0.

Furthermore, the damping of the gravel becomes obvious. Whereas the ratio $\mathrm{rms}(p_m)/\tau_0$ at $y/d_{50} = 1.0$ above the gravel can be calculated to $C = 10$, the ratio is about $C = 2.2$ at $y/d_{50} = -1.0$. Deeper down no difference between vertical positions can be detected. The ratio $\mathrm{rms}(p_m)/\tau_0$ is given mostly by $C = 1.8$.

Concentrating on the gradient of $\mathrm{rms}(p_m)$ as a function of τ_0 it can be seen that, to a first approximation, the dependency is linear.

Figure 11 shows the maximal pressure fluctuation of the averaged pressure signal $\max(p_m)$ as a function of shear stress τ_0. The flow conditions are the same as in Figure 10. For $\tau_0/\tau_{cr} = 1.0$ at $y/d_{50} = 1.0$ at the top of the gravel layer $\max(p_m)/\tau_{cr}$ leads to a ratio of $\mathrm{rms}(p_m) = 18\tau_0$ which confirms the results of Emmerling (1973). As Figure 10 and 11 resemble each other, the dependence of $\max(p_m)$ and $\mathrm{rms}(p_m)$ seems to be linear.

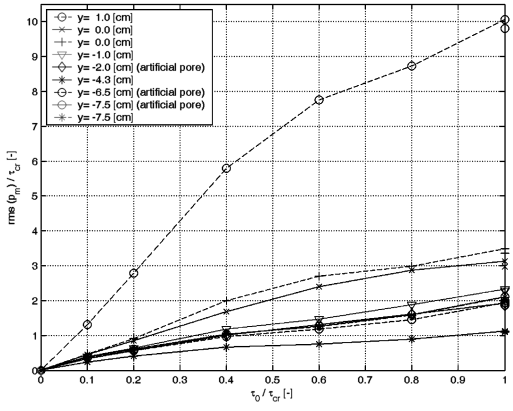


Figure 10. $\mathrm{rms}(p_m)/\tau_0$ [-] for increasing τ_0/τ_{cr}, $\tau_{cr} = 6.8$ Pa, $H_A/d_{50} = \sim 20$, $H_P/d_{50} = \sim 10$, variation in vertical position. No hydraulic contact between gravel and sand layer.

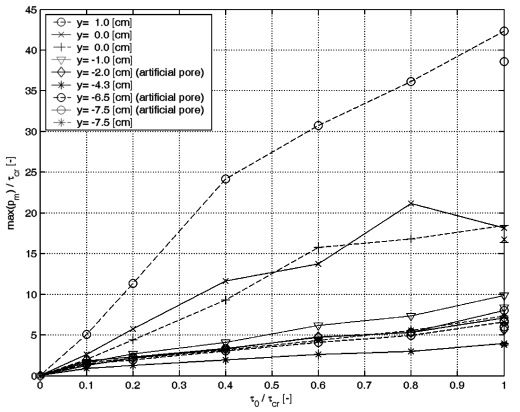


Figure 11. $\max(p_m)/\tau_0$ [-] for increasing τ_0/τ_{cr}, $\tau_{cr} = 6.8$ Pa, $H_A/d_{50} = \sim 20$, $H_P/d_{50} = \sim 10$, variation in vertical position, no hydraulic contact between gravel and sand layer.

In Figure 12 examples of analysed power spectral densities PSD(p_m) [Pa^2/Hz] are shown for the same flow conditions as mentioned before.

For at $y/d_{50} = 1.0$ to 0.0 above and at top of the gravel layer the results agree with Kolmogorov's $k^{-5/3}$ law for the turbulence cascade in open-channel flow (e.g. see Nezu et al., 1993). Within the gravel layer a significant damping between 1 and 3 Hz can be recognized. Below $y/d_{50} = \sim -4.0$ within the gravel layer there is no identifiable difference in damping pressure fluctuations higher than 3 Hz. The pressure fluctuations seem to be dominated by the long wave fluctuating water level. For designing a stable filter thinner than $H_P/d_{50} = 4$ the influence of turbulence of open-channel flow has to be taken into consideration.

4.2 *Other results*

Figure 13 shows an example for analysing data-files from the ADCP. The isoline plot shows the medium velocity u/U in streamwise direction. The influence of the walls becomes obviously. More analysing with respect to fluctuations and statistics still has to be done.

Results regarding both the velocity and fluctuations in the velocity gained by 3D-PTV within the artificial gravel pores and in the free surface flow will be carried out soon. They will be compared with the synchronous pressure measurements. Furthermore possible sediment movements observed by the three endoscopes have to be analysed in detail and have to be correlated to an oscillating water level, respectively.

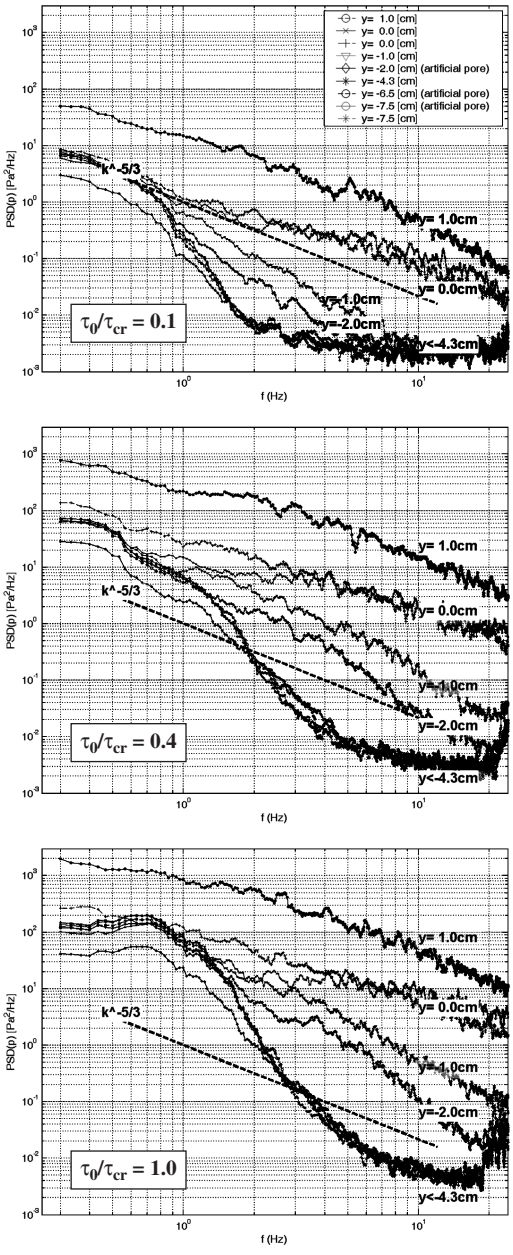


Figure 12. Power spectral density [Pa^2/Hz] for increasing $\tau_0/\tau_{cr} = 0.1$ (above), 0.4 (middle) and 1.0 (below), variation in vertical position, $\tau_{cr} = 6.8$ Pa, $H_A/d_{50} = \sim 20$, $H_P/d_{50} = \sim 10$. No hydraulic contact between gravel and sand layer.

5 CONCLUSIONS

Results from an experimental study of the interaction between turbulent open-channel flow and the hydrodynamic reaction in porous gravel layer are shown.

A new method of measuring pressure fluctuations due to open channel flow both on subsurface and within a gravel layer has proved its functionality. Pressure fluctuations are measured with miniature and

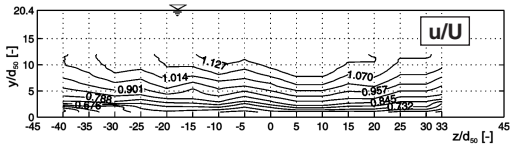


Figure 13. Example for analysing data-files from ADCP, here isolines of u/U [-], view in streamwise direction, $y/H_A = 1.0$ to 12.0 (vertical). $U = 670$ mm/s, $\tau_0/\tau_{cr} = 0.4$, $H_A/d_{50} = \sim 20$, $H_P/d_{50} = \sim 10$. No hydraulic contact between gravel and sand layer.

temporally high resolution piezoelectric sensors which are very flexible in use.

Results for the power spectral density of pressure fluctuations in the water column and at top of the gravel layer agree with Kolmogorov's $k^{-5/3}$ law for the turbulence cascade in open-channel flow. Within the gravel layer an essential damping between 1 and 3 Hz can be recognized. Below $y/d_{50} = \sim -4.0$ within the gravel layer there is no identifiable difference in damping pressure fluctuations higher than 3 Hz. Thus, the pressure fluctuations are dominated by the long wave fluctuating water level. For dimensioning stable filters thinner than four times the gravel diameter the influence of turbulence of open-channel flow has to be taken into consideration.

Furthermore, the experimental setup allows synchronous measurements of pressure and velocity within three artificial pores and in open-channel flow via 3D particle tracking velocimetry. First results are promising.

REFERENCES

Aktiv Sensor GmbH. 2003. www.aktiv-sensor.de/en/f_prod.html. Berlin.

Delft Hydraulics. 2003. http://www.wldelft.nl/inst/prof/ghm/index.html. Delft.

Dittrich, A. 1999. Sohlenstabilität naturnaher Fließgewässer. *Statusbericht 1998/1999 der WBW Fortbildungsgesellschaft*: pp. 42–49, Vol. 5. Heidelberg: WBW.

Drake, T.G., Shreve, R.L., Dietrich, W.E. Whiting, P.J. & Leopold, L.B. 1988. Bedload Transport of Fine Gravel observed by Motion-Picture Photography. *Journal of Fluid Mechanics*: Vol. 192, pp. 193–217. Cambridge.

Emmerling, A. 1973. Die momentane Struktur des Wanddruckes einer turbulenten Grenzschichtströmung. In:*Mitteilungen aus dem Max-Planck-Institut für Strömungsforschung*. Vol. 56. Göttingen: Max.Planck-Institut.

Gyr, A., Müller, A. 1996. The Role of Coherent Structures in Developing Bedforms During sediment Transport. In: *Coherent Flow Structures in Open Channels*. Chichester: John Wiley & Sons Ltd.

Hofland, B. 2003. Entrainment Of Large Particles from Granular Bed Protections under Low-Mobility Transport Conditions. In A. Gyr and W. Kinzelbach (eds), *Sedimentation an Sediment Transport*. Dordrecht: Kluver.

Hoyal, D.C.J.C., Depinto, J.V., Atkinson, J.F. & Taylor, S.W. 1995. The Effect of Turbulence on Sediment Deposition. *Journal of Hydraulic Research*. Vol. 33, No. 3, pp. 349–359.

Jähne, B., Haußecker, H., Scharr, H., Spies, H., Schmundt, D. & Schurr, U. 1998. Study of Dynamical Processes with Tensor-Based Spatiotemporal Image Processing Techniques. In: *ECCV*, pp. 322–336. Heidelberg: Springer.

Klar, M. 2001. 3-D Particle Tracking Velocimetry applied to Turbulent Open-Channel Flow over a Gravel Layer. Diploma Thesis, University of Heidelberg. Available at http://klimt.iwr.uni-heidelberg.de

Klar, M., Jehle, G., Jähne, M., Detert, M., Jirka, B. Köhler, H.-J. & Wenka, T. 2004. Simultaneous 3-D PTV and Micro-Pressure Sensor Measurement as Equipment for Subsurface Gravel Layer Flow Analysis. In: *Proceedings of the Conference RiverFlow2004, Napoli*; Rotterdam: Balkema.

Kline, S.J. 1967. Reynolds, W.C., Schraub, F.A. & Runsatdler, P.W. The Structure of Turbulent Boundary Layers. *Journal of Fluid Mechanics*: Vol. 30, pp. 741–773. Cambridge.

Meyer-Peter, E. & Müller, R. 1949. Eine Formel zur Berechung des Geschiebetriebs. In: *Schweizerische Bauzeitung*: Vol. 67, No. 3, pp. 29–32. Suisse.

Nezu I. & Nakagawa, H. 1993. Turbulence in Open-channel Flows, In: *IAHR/AIRH Monograph Series*. Rotterdam: Balkema.

Shields, A. 1936. Anwendungen der Ähnlichkeitsmechanik und der Turbulenzforschung. *Mitteilungen der Preußischen Versuchsanstalt für Wasserbau und Schiffbau*. Heft 26. Berlin.

This page intentionally left blank

River Flow 2004 – Greco, Carravetta & Della Morte (eds.)
© 2004 Taylor & Francis Group, London, ISBN 90 5809 658 0

Simultaneous 3-D PTV and micro-pressure sensor equipment for flow analysis in a subsurface gravel layer

M. Klar, M. Jehle & B. Jähne
Interdisciplinary Center for Scientific Computing (IWR), University of Heidelberg, Germany

M. Detert & G.H. Jirka
Institute for Hydromechanics (IfH), University of Karlsruhe, Germany

H.-J. Köhler & T. Wenka
Federal Waterways Engineering and Research Institute (BAW), Karlsruhe, Germany

ABSTRACT: An experimental setup for the simultaneous analysis of flow, pressure and sediment movement within and above a gravel layer covering a sand base layer in an open-channel flow is presented. A multi-camera setup is used to acquire digital image sequences from various locations of the flow field. Optical access to the gravel layer is provided by endoscopic imaging. The image sequences are analysed by a 3-D Particle-Tracking Velocimetry algorithm and optical flow techniques to calculate 3-D Lagrangian trajectories of seeding particles resp. 2-D displacement vector fields of sand particles. Special micro-pressure sensors based on the piezoelectric effect have been developed, which can be inserted into the gravel layer at arbitrary locations. The system is used to perform extensive measurements in an experimental flume under a wide range of flow conditions, including surface waves. The goal of the experiments is to gain new insight into the physical flow processes inside the gravel layer and to quantify the influence of turbulent fluctuations on the stability of both the gravel and the sand grains. This paper focuses on the description of the measurement system. A detailed analysis of the results will be given in a later publication.

1 INTRODUCTION

An experimental setup for combined measurements of pressure, flow and sediment transport processes is presented. The physical system under investigation is an open-channel flow above a base layer of fine sand, which is covered by a gravel filter layer. Of particular interest are the hydromechanical processes and flow fields within the gravel layer and at its interfaces with the free surface flow above and the sand layer below are of particular interest, e.g. for the analysis of erosion and sedimentation in the context of river bed stability. We have developed an experimental setup that enables a quantitative study of pressure and flow in such a configuration. The system consists of two major parts:

- a multi-camera arrangement together with endoscopic imaging to record digital image sequences of the flow fields at various locations within and above the gravel layer,
- micro-pressure sensors to measure the pressure at up to 10 arbitrary locations.

Digital image processing techniques are used to extract velocity data from the image sequences, namely a 3-D Particle-Tracking Velocimetry (3-D PTV) algorithm and an optical flow technique.

The paper is organized as follows: section 2 gives a detailed description of the measurement setup. The digital image processing is briefly explained in section 3. In Section 4 some of the first results gained from the test series carried out are presented. Further measurements and final results of the ongoing intensive evaluations and interpretations of the flume test are scheduled to be published in the near future. Conclusions are given in section 5.

2 EXPERIMENTAL SETUP

2.1 *Flume*

The experimental system has been implemented in an open channel flume located at the Federal Waterways Engineering and Research Institute (Bundesanstalt für Wasserbau, BAW). The flume is $L = 40\,m$ long

and $B = 0.9\,m$ wide. The maximum flow rate is $Q_{max} = 0.275\,m^3/s$. A sand layer of height $H_S = 0.5\,m$ covered by a porous gravel layer of height $H_P = 0.04$ to $0.20\,m$ is placed in the flume over a length of $L = 30\,m$, optionally with and without hydraulic contact to the sand layer. This is achieved by omitting or inserting a rubber mat. The measuring-area is located at 15 m, hence influences of inlet and outlet are supposed to be negligible. The grain diameter of the gravel is $d_{50} = \sim 10\,mm$, with a degree of non-uniformity $C_c = d_{60}/d_{10} = 1.25$. The mean grain diameter of the uniform sand is about $d_{50} = \sim 1\,mm$. The measuring program is defined for water depth of $H_A/d_{50} = 20$ and $H_B/d_{50} = 40$.

Figure 1 shows sketches of the experimental setup; the measurement program is given in Table 1. Variation in discharge and water depth provides flow conditions up to low mobility transport conditions based on Shields parameter, τ_*. Supplementary gauges will be made with glass spheres, having a $d_{50} = 10\,mm$.

Long waves are generated artificially by a wave generator located 9.25 m downstream from the measuring-area. Thus, the influence of an oscillating water level can be studied. Figure 2 shows a photograph of the wave generator.

The flow rate is measured by a magnetic inductive flowmeter, the water level is detected by an external ultrasonic probe with hydraulic contact to the flume.

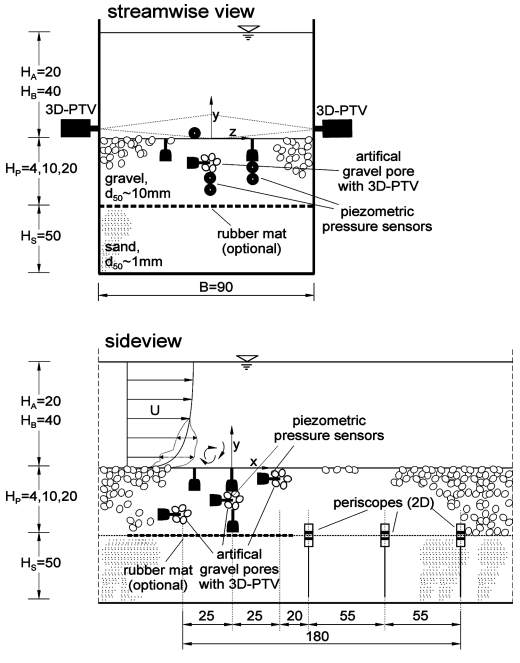


Figure 1. Sketch of experimental setup, dimensions [cm], not to scale.

Steady flow conditions for each measurement are provided by controlling the gate valve at the inlet and the movable weir at the outlet automatically.

At the measurement area, optical access to the flume is given by plexiglass windows inserted into the channel walls over a length of 4 m. Different experimental instrumentation is installed, compare the sketch in Figure 1. In particular, the setup consists of the following parts:

- a stereo camera setup for the investigation of the free surface flow immediately above the gravel layer,
- three endoscopic stereo setups to record the flow fields inside specially prepared artificial gravel pores inside the gravel layer,
- three rigid endoscopes inserted from below the channel to observe the sand-gravel-boundary,

Table 1. Measuring program, increasing shear stress $\tau_0/\tau_{cr} = 0.1$ to 1.0, $\tau_{cr} = 6.8\,Pa$.

flow conditions	τ_0/τ_{cr}	0.1	0.2	0.4	0.6	0.8	1.0
gravel	H_p/d_{50}						
with rubber mat	20	$W_{A,B}$	$H_{A,B}$	$H_{A,B}$	H_A	-	-
	10	$W_{A,B}$	$W_{A,B}$	$W_{A,B}$	H_A	H_A	H_A
	4	$W_{A,B}$	$H_{A,B}$	$H_{A,B}$	H_A	H_A	H_A
gravel	H_p/d_{50}						
without rubber mat	20	-	-	-	-	-	-
	10	$W_{A,B}$	-	$W_{A,B}$	-	-	-
	4	$W_{A,B}$	-	$H_{A,B}$	-	-	-
glass spheres	H_p/d_{50}						
with rubber mat	4	$H_{A,B}$	$H_{A,B}$	$H_{A,B}$	-	-	-
	2	$H_{A,B}$	$H_{A,B}$	$H_{A,B}$	-	-	-

explanation:		
	$H_{A,B}$	gauging at water depth H_A=20cm, H_B=40cm
	$W_{A,B}$	gauging incl. wave generator
	H_p	heigth of porous granular filter
	d_{50}	mean gravel diameter



Figure 2. Wave generator.

– up to ten pressure sensors at arbitrary locations within the gravel layer (three of the sensors are attached to the artificial gravel pores used for the flow measurement).

The data acquisition is carried out simultaneously by all these subsystems, which are described in more detail in the following.

2.2 *3-D PTV: Free surface flow*

In order to acquire stereoscopic image sequences of the free surface flow, two CCD-cameras (Pulnix TM 6701 AN) are mounted on the left and right side of the flume, viewing the center of the channel in upstream direction through the glass windows (Figure 3). The optical axes of the two cameras enclose an angle of about 90 degrees, maximizing the size of the stereo volume (about 5 cm in all directions), which is viewed by both cameras. Two glass prisms filled with water are attached to the channel side windows to make the optical axes of the cameras perpendicular to the air-glass interface. In this way, refraction effects of the optical rays passing the multimedia interfaces are minimized. Three halogen lamps are used to illuminate the stereo volume from above the water surface. Visualization of the flow is provided by small air bubbles suspended in the water.

To enable particle tracking at large flow velocities, the frame rate of the cameras must be high enough to keep the displacements of the particles between successive images within certain limits. For standard video capturing, the Pulnix TM 6701 AN delivers images of 640 by 480 pixels at a frame rate of 60 Hz. However, the camera also offers a partial scan mode, reducing the image size to 640 by 200 pixels, but increasing the frame rate up to 125 Hz. This mode has been used for the measurements.

The acquired image sequences have to be stored in the computer memory before they are written to a harddisk. Thus, the maximum duration of one stereo image sequence of the free surface flow is about $\Delta t = 20\,s$, limited by the PC memory.

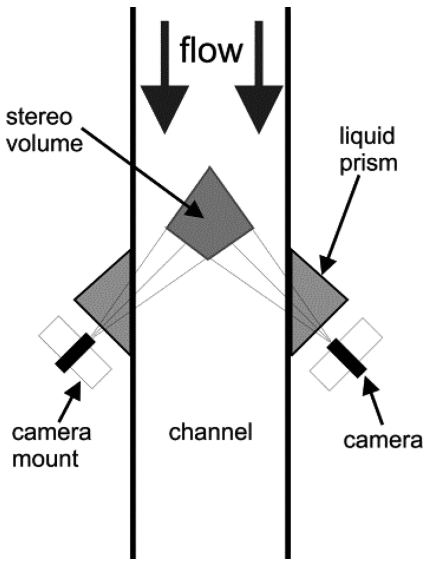


Figure 3. Top view of the stereo camera setup for 3-D PTV above the gravel layer. The cameras view the channel in upstream direction through water-filled glass prisms attached to the channel side walls.

2.3 *3-D PTV: Pore flow*

Flow measurements inside three single pores of the gravel layer are carried out using three miniaturized endoscope stereo setups. The basic principle of these setups is the same as for the free surface flow, namely to acquire stereoscopic image sequences of the flow field inside the pore volume by viewing it from two different directions. Two flexible fiber-optic endoscopes of 2.4 mm diameter are attached to an adapted artificial gravel pore made of grains fixed to each other (Figures 4 and 5).

Illumination of the pore volume is provided by an optical fiber-bundle guiding the light from a halogen cold light source into the pore. The purpose of the artificial pore is to hold the endoscopes and the illumination fiber at a fixed relative position and to keep surrounding grains in the gravel layer from blocking the endoscope view. To perform flow measurements, the three artificial pores are embedded in the gravel layer at different positions (Figure 6). A solution of tracer particles is added to the flow upstream of the pores, and particle image sequences of the two different endoscope views are recorded simultaneously.

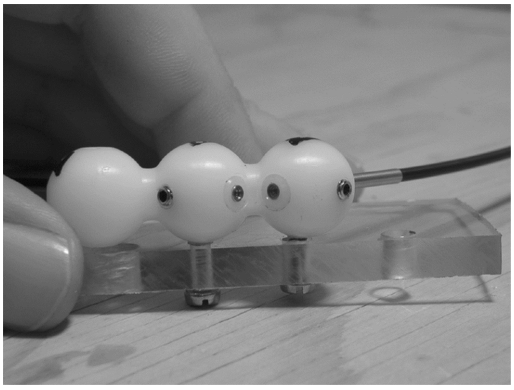


Figure 4. Endoscope stereo setup. For velocity measurements in the gravel layer, this stereo rig is attached to the artificial pores, viewing the pore volume inside.

The size of the observation volume inside the pores is about 5 mm in all directions. Since the tracer particles cover this small volume very rapidly, the cameras must have even higher frame rates than in the case of the free surface flow. Hence, two of the three artificial pores are equipped with high-speed Megapixel-CMOS-cameras (Photonfocus MV-D1024). These cameras allow to read out only a region of interest on the sensor, which has been set to a size of 184 by 184 pixels. Zoom optics are used to fit the endoscope image to this image size on the sensor.

By decreasing the image resolution in this way, a maximum frame rate of 400 Hz can be achieved. The third endoscope setup is working with standard CCD-cameras running at 50 Hz. This setup can only be used in the lowermost position within the gravel layer, where the flow velocities are expected to be lowest.

The image data of all three setups are written to RAID hard-disk arrays in real-time during the acquisition. Thus, the duration of the sequences is only limited by the RAID capacity. For a single measurement, a sequence duration of 60 s has been chosen.

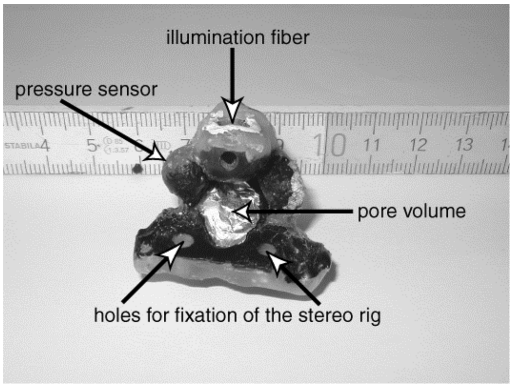


Figure 5. Artificial gravel pore.

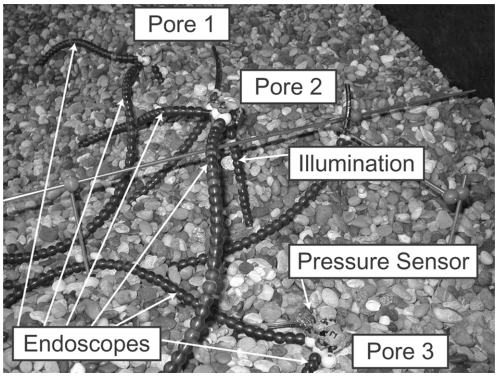


Figure 6. Installation of the three artificial pores in the gravel layer.

2.4 *Sand movement*

Sediment movement is detected by three rigid endoscopes (Figures 7 and 8), inserted into the flume from below. The effects of sediment motion are expected to occur at the gravel-sand interface. Goal is to record a sequence of two-dimensional images, which can be analyzed by optical flow techniques described below. Thus, the requirements of the endoscopic setup are:

– Observation of the process of sediment motion should be as contact-free as possible.



Figure 7. Rigid endoscope for subsoil observation. The endoscope is inserted into a protection tube containing the illumination fibers, which can be seen at the corners of the glass window.



Figure 8. Rigid endoscopes inserted into the flume from below to observe motion of sand grains.

– A large observation area is needed.
– A working distance of a defined distance should be kept.
– Sufficient and homogeneous illumination should be provided.
– The setup has to be reliable in the rough environment of the flume.

In order to meet these demands, special protection heads have been designed (Figure 6). With an aperture angle of 90 degrees and a viewing distance of approximately 7 mm, a circular area of about 12 mm in diameter can be observed.

Standard CCD-cameras (SONY XC-73CE) have been used for image acquisition. Image sequences are acquired at a resolution of 512 by 512 pixels and a frame rate of 25 Hz. Thus a data thruput of approximately 20 MB/s is achieved for all three endoscopes. Image sequences can be written to a RAID system in real-time during the acquisition.

2.5 *Micro-pressure sensors*

The micro pressure sensors were manufactured in a development cooperation of Aktiv Sensor GmbH (Berlin) and the Institute for Hydromechanics (IfH).

The principle of these in-situ micro-pressure sensors is based on the "piezoresistive" effect. The initial point is an element of silicium, with implanted resistances in its bending panel. Figure 9 shows a photograph of the encapsulated head of the pressure pickup and its flexible tube for pressure equalisation.

The differential pressure is measured in reference to atmospheric pressure, here additionally with compensation of temperature. For water resistance, the housings of the sensors are encapsulated with slowly hardening epoxy resin and sealed up with clear varnish. The maximal dimensions of the sensors are as small as $2 \times 1.2 \times 1.2\,cm^3$, with a shape similar to a bigger gravel grain. Due to signal conditioning by the purpose-built amplifier the guaranteed maximum measurable frequencies are 100 Hz. Hence, measurements of pressure fluctuations up to the estimated Kolmogorov-scale-frequency of 50 Hz (Nezu et al. 1993) is possible. To avoid aliasing effects, the measurements are performed at a rate of 500 Hz.

The absolute range of the pressure sensors is 0 to 6 kPa. Due to the analog-digital-card, the increment of discretisation is 1.5 Pa (0 to 6 kPa) or 0.7 Pa (0 to 3 kPa).

The ready-built sensors were calibrated by Aktiv Sensor GmbH to 0 to 10 V according to 0 to 6 kPa at pressure of 3 and 6 kPa with a tolerance in accuracy of less than 1.0% full scale. Figure 10 shows an example of a recorded signal.

Pressure sensors are located at vertical positions of $y/d_{50} = 1.0$ (above), 0.0 (at top) and at various positions within the gravel layer. Each three sensors are adapted on three artificial gravel pores to gain simultaneously insight in pressure and velocity. Simultaneous measuring was performed by up to ten pressure sensors over two minutes. The sensors are locally fixed on a grid as shown in Figure 11.

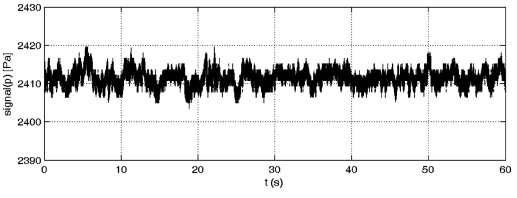


Figure 10. Pressure signal [Pa], $\tau_0/\tau_{cr} = 0.1$, $\tau_{cr} = 6.8$ Pa, $H_A/d_{50} = \sim 21$, $H_P/d_{50} = \sim 20$, no hydraulic contact between gravel and sand layer.

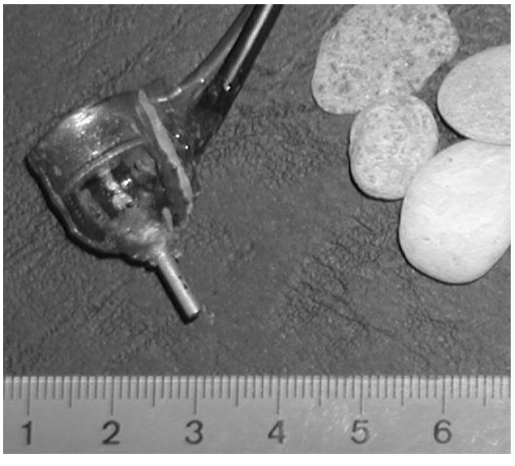


Figure 9. Head of micro pressure sensor outside the flume and above gravel $d_{50} = \sim 10$ mm.

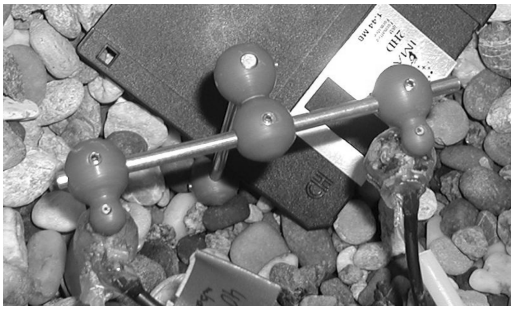


Figure 11. Positioning of two sensors on a lattice (see dimensions of a floppy disc).

3 DIGITAL IMAGE PROCESSING

This section gives a very brief introduction to the digital image processing techniques that are used to extract velocity information from the image sequences. For more information, the reader is referred to the references given below.

3.1 *3-D PTV*

In order to extract 3-D velocity information from the image data, the stereo sequences are processed by a 3-D PTV algorithm. In the first step of the algorithm, individual particle images are identified and tracked from one image to the next throughout both image sequences. The result of this step is a coordinate list of the 2-D particle trajectories in the image planes. In the second step of the algorithm, stereo correlations between the 2-D trajectories are established. Finally, if a unique correspondence of two trajectories in the left resp. right image plane has been found, the 3-D world coordinates of this particle trajectory are calculated by triangulation of the corresponding rays of sight. More details about the image processing are given in (Klar 2001) and (Klar et al. 2002).

In order to establish stereoscopic correspondences between the images and extract metric information, i.e. the 3-D particle coordinates, it is necessary to perform a geometric calibration of the stereo system before the measurements are carried out. A special endoscope calibration setup is used to acquire images of a calibration target defining known 3-D coordinates. To provide the same optical conditions as in the measurements, the calibration images are recorded in a vessel filled with water. The mathematical model for all cameras is a standard pinhole-camera, extended by lens distortion parameters (Zhang 2000). The 3-D accuracy of the calibration has been determined by taking an additional view of the calibration target (not used to estimate the camera parameters) with known position and calculating the 3-D positions of the target points. The results have been compared to the known 3-D positions. The mean errors and their standard deviations are given in Table 2.

The values given in Table 2 provide only a rough estimation of the accuracy, since the latter is influenced by many factors, e.g. accuracy of feature extraction in the image plane, quality of fit result of the camera calibration and 3-D accuracy of the calibration target. A closer inspection of the accuracy will be part of future work.

Table 2. Errors of the 3-D coordinate calculation (endoscopes). X and Y are the lateral, Z is the depth coordinate.

Directions	X	Y	Z
mean error (μm)	8	−9	37
standard deviation (μm)	35	33	15

3.2 *Optical flow*

The main task of the image processing is to estimate the velocity of grain motion. Especially the flow and wave induced grain motion at the sand-gravel-interface is one of the targets of the flume tests in order to investigate the influence of the impounding pressure fluctuations on the underlying sand bed and the actual filter stability at the interface between sand and gravel. If erosion of sand grains were to be induced by turbulent flow conditions, the stability of the anticipated bed protection could be endangered (Davis et al. 2003). Taking the submerged soil under shallow water conditions as an unsaturated pore medium into account, pore pressure fluctuations may easily destabilize protection measures. Especially pressure fluctuations caused by waves may contribute to enhanced sand bed erosion (Schwab et al. 2003).

Towards this end, the apparent motion in the images, the so-called optical flow, is calculated. The structure tensor technique proved to be well-suited for this task. The main idea is the estimation of orientation in a $2+1$ dimensional spatiotemporal brightness distribution, which is composed of the recorded sequence of the two-dimensional images. This method yields good results on highly textured image regions and for velocities of the order of one pixel per frame and below. Both conditions are met by the sediment image sequences. In addition to the velocity, the structure tensor method also provides a confidence measure. From

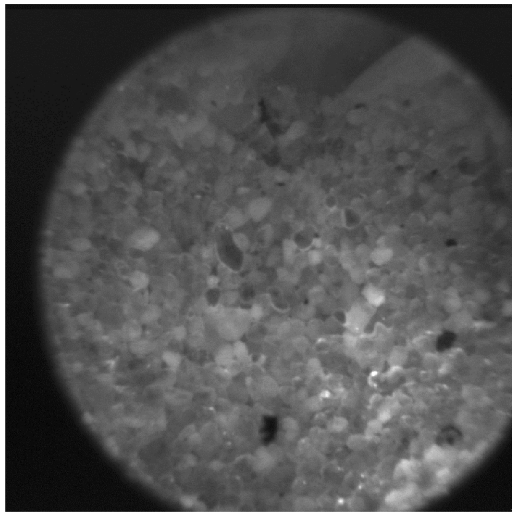


Figure 12. Example of an acquired image.

the 2-D displacement vector field other quantities can be derived, such as divergence and vorticity. Figure 13 shows a snap-shot of the vector field. A summary of the image processing is shown in Figure 14 in terms of a flowchart. A detailed description of each image processing step is given in (Jähne et al. 1998). The application of image processing to the analysis of particle movement is explained in Spies et al. (1999) in detail.

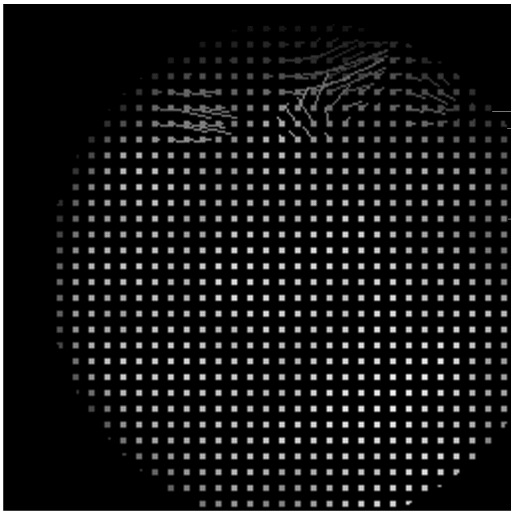


Figure 13. Example of a displacement vector field. Arrows express sediment motion occurring especially at the top of the observed area.

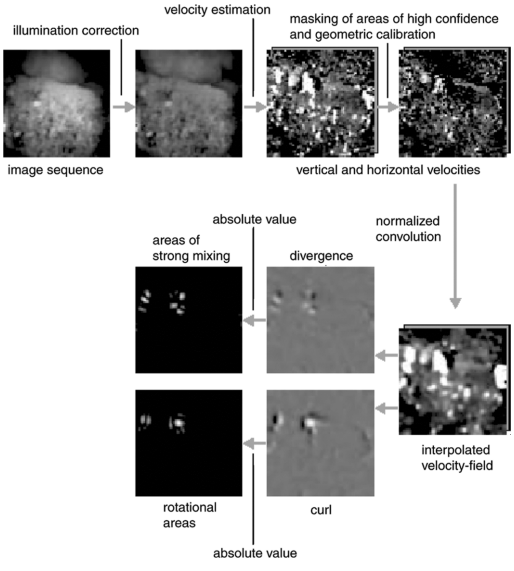


Figure 14. Image processing flowchart.

4 FIRST RESULTS

In this section, some results obtained with the presented setup are discussed. These results are part of an extensive series of measurements (see Detert et al. 2004) which are still in progress. Therefore the results shown here have to be considered as preliminary examples, showing the potential of the measurement techniques. A comprehensive analysis of all results will be given in a later publication.

In the discussion, the following (right-handed) coordinate system will be used:

x: coordinate in streamwise direction, increasing in flow direction
y: vertical coordinate, origin at the gravel-water-interface
z: spanwise coordinate, origin at the centerline of the flume

In all experiments, the spanwise position of the artificial pores is at the centerline of the flume ($z = 0$).

The basis for the further data analysis and reduction consists of three types of data, which are obtained simultanesously with the presented techniques:

– 3-D Lagrangian flow trajectories inside the three artificial pores and in the free-surface flow straight above one of the pores,
– 2-D displacement vector fields in three vertical planes at the gravel-sand interface,
– time series of the pressure at up to eight locations in the gravel layer.

4.1 *Pore flow: 3-D visualization*

Figure 15 shows a 3-D visualization of a reconstructed flow field. The Lagrangian particle trajectories within a time interval of 0.5 s can be seen in the image. The trajectories reveal that the flow field inside the pore

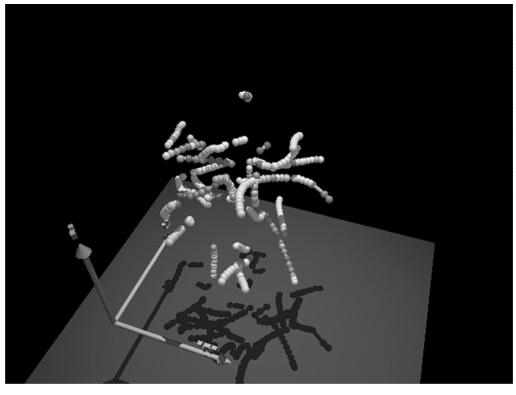


Figure 15. 3-D visualization of the particle trajectories inside the pore volume.

is really three-dimensional, which underlines the need for a three-dimensional measurement technique.

4.2 *Pore flow: Velocity time series*

In this experiment, two of the artificial pores, have been positioned at the uppermost position in the gravel layer at $y = -2$ cm, i.e. 2 cm below the interface towards the free surface flow. The separation between the pores in x-direction was 25 cm. The pore volume of one of the pores was in direct contact with the free surface flow via an opening in vertical direction (this pore is referred to as "open" pore in the following). At the other pore, this opening was covered by a pebble, so there was no direct contact with the free surface flow in vertical direction ("closed" pore in the following). An experiment has been carried out with a flow discharge of $Q = 0.056\ m^3/s$ and a water depth of $H_A/d_{50} = 20$. These values correspond to a mean velocity in the free surface flow of about 0.3 m/s and 10 % of the critical shear stress for (gravel-)bed destabilization. Figures 16 and 17 show the first 30 s of the time series of the streamwise (u) and vertical (v) velocities inside the two pores. The time series have been calculated by spatial averaging of all velocity vectors inside the pore volume. The plots show the damping effect of the pebble covering the "closed" pore: the flow velocities inside this pore are significantly lower than in the "open" pore, in spite of the fact that both pores are located in the same vertical position at the gravel-water interface. The velocity fluctuations in the "closed" pore are also dampened: the standard deviations in the "closed" pore are approximately 50 % smaller than in the "open" pore.

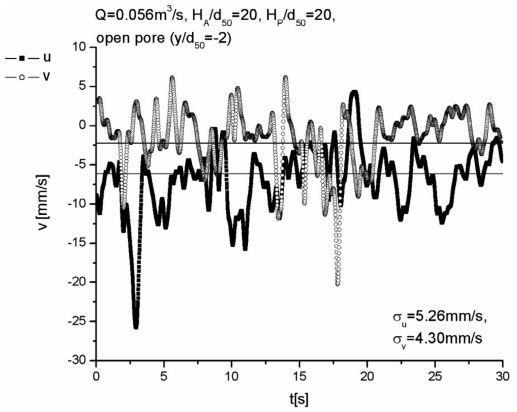


Figure 16. Time series of streamwise (u) and vertical (v) velocity in the "open" pore. The horizontal lines indicate the mean velocities.

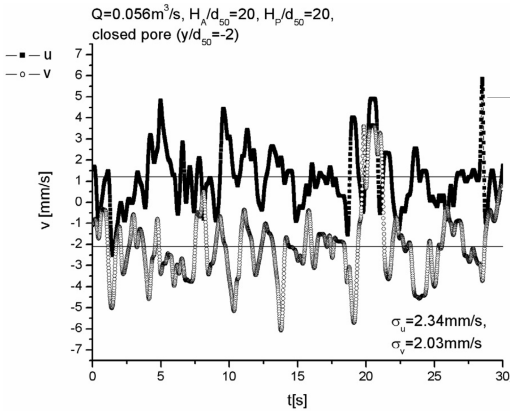


Figure 17. Time series of streamwise and vertical velocity in the "closed" pore. The horizontal lines indicate the mean velocities. Note the change of scale in the ordinate as compared to Figure 16.

4.3 *Pore flow: Power spectra of fluctuations*

In a second experiment, one of the artificial pores has been put in different vertical positions sequentially: $y/d_{50} = -2, -8$ and -16. For each position, an image sequence has been acquired under the same flow conditions as in the experiment in section 4.1. Time series of the absolute value of the 3-D velocity have been calculated, again by spatial averaging of all the vectors inside the pore. Figure 18 shows the power spectra of the three velocity time series. The spectra show that the significant frequencies are in the range of 1 to 5 Hz. Further, at $y/d_{50} = -16$, the amplitudes are roughly two orders of magnitude smaller than at $y/d_{50} = -2$. Fluctuations in the pore flow are dampened with increasing depth in the gravel layer.

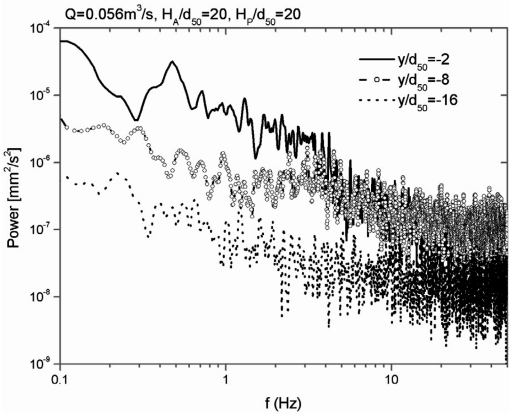


Figure 18. Power spectra of velocity data obtained from different vertical positions in the gravel layer. The damping effect of the gravel layer is evident.

4.4 *Sediment motion: Velocity time series*

These analyses have been carried out with a wave-height (bottom to top) of approximately $W_B/d_{50} = 15$ and a wave-period of approximately 2 s. Wave generation was started 40 s before data was taken. Discharge rate was $Q = 0.026\ m^3/s$, water depth was $H_B/d_{50} = 40$. There was no rubber mat placed in the flume. The height of the granular filter was $H_P/d_{50} = 10$.

From the displacement vector fields a horizontal and a vertical mean velocity can be obtained by averaging the components of the velocity vectors in x- and y-direction. The averaging was performed on regions with a high confidence measure only. In Figure 19 (lower part) the components of the mean velocity are plotted against time. Figure 19 (upper part) shows the corresponding measured wave gauge. Obviously, there is a correlation between wave gauge and mean velocity. The time series of mean velocity consists of a superposition of an undulating periodic part and some outliers. The outliers result from individual sand grains moving especially in the upper part of the recorded images. Evidence for this is given in Figure 20, where the vertical mean velocity in the upper half is compared with the vertical mean velocity in the lower half.

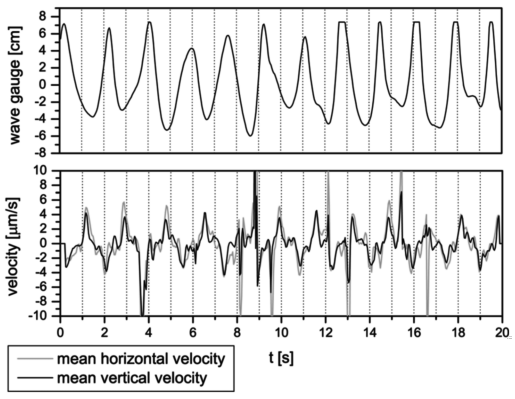


Figure 19. Time series of wave gauge and mean velocity of sand grains.

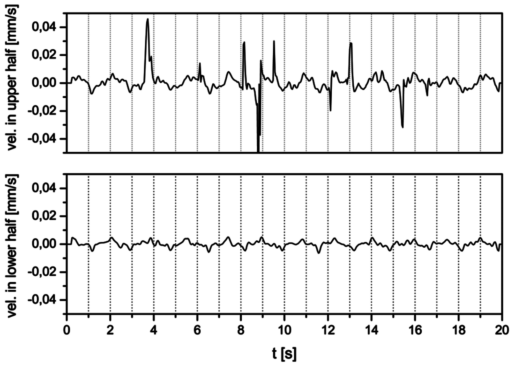


Figure 20. Vertical mean velocities of sand grains in the upper half of the recorded images in comparison with the mean velocities in the lower half.

The presented results demonstrate the correctness and accuracy of the used algorithm, which is confirmed by analyses based on simulated data. We would like to point out, that the analysed image sequence was chosen arbitrarily. A detailed analysis will follow in a later publication.

5 CONCLUSIONS

An experimental setup for simultaneous flow and pressure measurements within and above a gravel layer covering a sand base layer in an open-channel flow has been presented. The flow fields at several positions within and above the gravel layer are analyzed using a multi-camera setup to acquire stereoscopic image sequences of the flow. Endoscopic imaging is applied to get optical access to the gravel layer. Another endoscopic setup is used to detect and quantify motion of sand grains in the base layer. Up to ten micro-pressure sensors based on the piezoresistive effect deliver time series of pressure data. All measurements are carried out simultaneously.

To extract velocity information from the image sequences, digital image processing techniques are applied. A 3-D Particle-Tracking Velocimetry algorithm yields the Lagrangian particle trajectories inside three artificial pores and in the free-surface flow above one of the pores. Displacements of sand grains are calculated using an optical flow technique.

The system is used to perform extensive measurements in an experimental flume under a wide range of flow conditions including surface waves. First results from an experimental study of the interaction between turbulent open-channel flow and the hydrodynamic reaction in the porous subsurface gravel layer have been presented. The damping of velocity fluctuations with increasing depth in the gravel layer is clearly reflected in the results. A spectral analysis shows that the dominant fluctuation frequencies are in the range of 1 to 5 Hz.

Future experimental work includes another series of measurements after the gravel in the measurement area has been replaced by glass beads of 1 cm diameter. Further, the influence of an obstacle on the gravel surface will be studied. The results of these experiments will be compared with LES-simulations (Stoesser et al. 2004) (glass beads) resp. Lattice-Boltzmann-simulations (Davis et al. 2004) (obstacle), which are currently being carried out.

REFERENCES

Davis, M., Köhler, H.-J., Koenders, M. A. & Schwab, R. 2003. Hydraulic Failure and soil structure deformation due to wave and draw down loading. In: *ASCE-Proceedings of the Coastal Structure 2003 Conference*, August 26–29 2003, Oregon, USA.

Davis, M., Köhler, H.-J. & Koenders, M. A. 2004. Unsaturated subsoil erosion protection in turbulent flow conditions. *Submitted (July 2003) to IHR Journal of Hydraulic Research*.

Detert, M., Klar, M., Jehle, M., Jirka, G., Jähne, B., Köhler, H.-J. & Wenka, T. 2004. Pressure Fluctuations on and in Subsurface Gravel Layer Bed caused by Turbulent Open-Channel Flow. In: *Proceedings of the Conference RiverFlow2004, Napoli*; Rotterdam: Balkema.

Jähne, B., Haußecker, H., Scharr, H., Spies, H., Schmundt, D. & Schurr, U. 1998. Study of Dynamical Processes with Tensor-Based Spatiotemporal Image Processing Techniques. In *ECCV*, pp. 322–336. Springer.

Klar, M. 2001. 3-D Particle-Tracking Velocimetry applied to Turbulent Open-Channel Flow over a Gravel Layer. Diploma Thesis, University of Heidelberg. Available at *http://klimt.iwr.uni-heidelberg.de*

Klar, M., Jehle, M., Spies, H. & Jähne, B. 2003. Investigation of structure changes in unsaturated subsoil. In: Jähne, B., (ed.), *Image Sequence Analysis to Investigate Dynamic Processes, Lecture Notes in Computer Science*, Springer, Berlin, in preparation.

Klar, M., Stybalkowski, P., Spies, H. & Jähne, B. 2002. A miniaturised 3-D Particle-Tracking Velocimetry System to measure the Pore Flow within a Gravel Layer. In: *11th International Symposium Applications of Laser Techniques to Fluid Mechanics*, 8–11 July 2002, Lisbon, Portugal.

Schwab, R. & Köhler, H.-J. 2003. Behavior of near-saturated soils under cyclic wave loading. In *Proc. of the 3rd Intern. Symposium on Deformation Characteristics of Geomaterials*, IS Lyon 2003, September 22–23 2003, Lyon, France.

Spies, H., Beringer, O., Gröning, H. & Haußecker, H. 1999. Analyzing Particle Movements at Soil Interfaces. In: Jähne B., Haußecker, H. & Geißler, P., eds., *Handbook on Computer Vision and Applications*, vol 3, pp. 699–718. Academic Press.

Stoesser, T., Rodi, W. & Jirka, G. 2004. Large-Eddy Simulation of Flow over Rough Channel Beds. In: *Proceedings of the Conference RiverFlow2004, Napoli*; Rotterdam: Balkema.

Zhang, Z. 2000. A flexible new technique for camera calibration. In: *IEEE Transactions on Pattern Analysis and Machine Intelligence* 22 (11), pp. 1330–1334.

River Flow 2004 – Greco, Carravetta & Della Morte (eds.)
© 2004 Taylor & Francis Group, London, ISBN 90 5809 658 0

Bed load transport on arbitrarily sloping bed at low Shields stress: preliminary experimental observations

S. Francalanci, E. Paris & L. Solari
Department of Civil Engineering (Florence)

ABSTRACT: Bagnold hypothesis is one of the fundamental assumption of many bed load transport model. However the failure of the Bagnold hypothesis has been recently demonstrated. Based on this result an alternative model has been proposed by Parker et al. (2003) for the evaluation of bed load transport on arbitrarily sloping bed at low Shields stress. In this work an experimental study to investigate the effect of relevant slopes on dynamics of bed load transport, motion characteristics and transport dynamics of bed particles is carried out. Experimental equipment and preliminary observations are presented and discussed in the context of verifying the theoretical findings of Parker, Seminara, Solari (2003).

1 INTRODUCTION

One of the crucial aspect of any morphodynamic model including therefore the complex topography occurring in a gravel bed river, is to evaluate the sediment transport when the bed is characterized by 'steep' slopes, such as near the banks and along the bar fronts.

The problem of evaluating bed load transport in the case of gentle slopes under uniform equilibrium conditions has been widely investigated (see for instance Ashida & Michiue, 1972, Engelund & Fredsoe, 1976, Wiberg & Smith, 1985, Sekine & Kikkawa, 1992, Nino & Garcia, 1994). In the case of steep slopes various authors have proposed equations similar to the ones derived for gentle slopes (Smart, 1984; Damgaard et al., 1987) corrected through the introduction of an empirical function depending on the local bed slope. These analyses provide a deterministic description of bed-load transport through two main steps.

In the first step an estimate of the average speed of saltating particles is provided, either from a saltation model or, more simply, considering an equivalent uniform translatory motion of particles in which the effects of particle rebound are taken into account by means of a bulk dynamic coefficient of Coulomb friction. The latter approach, though it provides a more schematic view of the particle dynamics, is sufficient to give an estimate of the mean particle velocity in reasonable agreement with the experimental observations.

The second step is devoted to the evaluation of the average areal concentration of saltating particles, i.e. the average volume of saltating particles per unit area. Evaluation of this quantity is not an easy task since the number of particles in motion is related to the spatial and temporal frequencies and on the intensity of near wall turbulent events. To overcome this difficulties many models rely on Bagnold assumption, according to which the areal concentration of particles in motion is such that the fluid shear stress at the bed must be reduced to the critical value corresponding to the incipient motion of bed particles.

2 THEORETICAL BACKGROUND

The validity of Bagnold hypothesis has been questioned since the experimental work of Fernandez Luque and van Beek (1976) until the recent theoretical model proposed by Seminara G., Solari L. & Parker G. (2002) in which the failure of Bagnold hypothesis is theoretically demonstrated.

Fernandez Luque & van Beek (1976) performed detailed observations of the dynamics of saltating particles at fairly low Shields stress and discussed the validity of Bagnold hypothesis: for values of the latter stress smaller than about 0.1 the assumption appeared to fail.

Seminara G., Solari L. & Parker G. (2002), by means of a three dimensional generalization of Bagnold assumption, show that, for given particle Reynolds number and local longitudinal slope, Bagnold assumption can only be satisfied provided the local lateral slope does not exceed a threshold value, which depends on the applied Shields stress. As the latter increases, the maximum lateral inclination allowed

for the occurrence of equilibrium bed load transport decreases until to reach values ranging about few degrees, well below the angle of repose. This failure motivates the abandonment of the Bagnold constraint, even for nearly horizontal beds.

Based on the experimental findings of Fernandez Luque & van Beek, an alternative model for evaluating bed load transport on arbitrarily sloping beds has been elaborated by Parker G., Seminara G. & Solari L. (2003). This model, in which a three dimensional formulation of bed load transport is proposed, preserves the overall structures of the Bagnolds formulation according to which the bed load layer is described as a thin finite layer, at the base of which the fluid shear stress is reduced to a value, denoted as residual shear stress due to the transfer of streamwise momentum from the fluid to the saltating grains. The fluid shear stress at the bed drops to the critical value for particle motion only when there is no motion (*static equilibrium*), on the contrary when bed load transport occurs, shear stress at the bed must be above the critical value in order for the flow to be able to entrain grains (*dynamic equilibrium*).

The Bagnold constraint is then replaced with an Einsteins structure for entrainment formulation, according to which equilibrium of bed interface is dynamic rather than static, in that equilibrium is achieved through a balance between an entrained sediment flux and a deposited flux.

The analysis of Parker G., Seminara G. & Solari L. (2003) is here briefly summarized.

The vectorial bed load transport rate $\hat{\boldsymbol{q}}$ made dimensionless with Einstein's scale is given as

$$\hat{\boldsymbol{q}} = \hat{\xi} \cdot \hat{\boldsymbol{V}}_{\boldsymbol{P}} \tag{1}$$

where $\hat{\xi}$ = mean areal concentration of saltating particles made dimensionless with particle size D; $\hat{\boldsymbol{V}}_{\boldsymbol{P}}$ = layer-averaged mean velocity of bed load particles made dimensionless with the quantity $\sqrt{(s-1)gD}$ where g is gravity and s relative density of particle.

The averaged particle velocity vector $\hat{\boldsymbol{V}}_{\boldsymbol{P}}$ is obtained by imposing a vectorial balance between averaged active and resistive forces. The former are represented by drag force and the tangential component along the bed of the submerged particle weight; the latter interprets the effect of interactions of particles with the bed and is estimated through a coefficient of dynamic friction.

The averaged concentration of particles in motion is determined from a generalization of the experimental results of Fernandez Luque & van Beek (1976). In particular $\hat{\xi}$ appears to be in a quasi linear increasing relationship with the excess of residual shear stress. This quantity is represented by the difference between the residual shear stress at the bed and the critical shear stress for the onset of particle motion. The excess of residual shear stress maybe taken as a measure of the residual turbulent activity at the bed which appear to be responsible for the entrainment of particles into the bed load layer. In the following $\tau*$ is the dimensionless applied shear stress, and $\tau*_{co}$ is the critical Shields stress for the onset of sediment motion in the case of vanishing longitudinal and transversal inclination, while the dimensionless excess of residual shear stress is denoted as $\tau*_b - \tau*_{co}$.

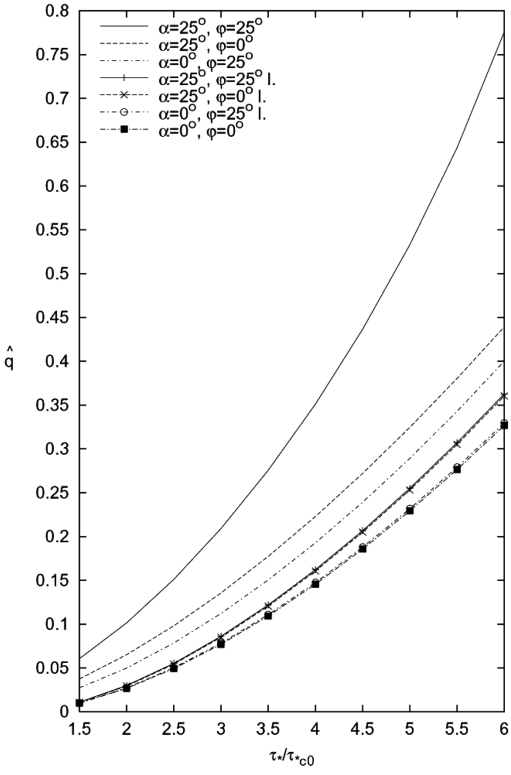


Figure 1. Plot of $\hat{\boldsymbol{q}}$ predicted from the theoretical model Parker, Seminara & Solari (2003) as a function of $\tau*/\tau*_{co}$ for various combinations of streamwise and transverse inclination.

As a summary of the model results, it is shown in figure 1 the dimensionless volume sediment transport rate per unit width for different values of longitudinal and transversal inclination. Moreover the fully nonlinear results of the entrainment formulation for bed load transport on a finite, arbitrary slope, are compared with the linear approximation to which the analysis reduces when the bed inclinations are sufficiently small.

The linear and nonlinear formulations obviously yield the same result for the case of horizontal bed. But on sloping beds the intensity of bed load transport increases with the external applied stress faster than on horizontal beds, the more so as the longitudinal and lateral slopes increase.

3 EXPERIMENTAL ACTIVITY

In the present study it is investigated the bed load transport mechanism when transversal and longitudinal slopes are not negligible and low values of the applied Shields stress occurs. The general aim of such investigation is to provide an experimental verification of the theoretical model proposed by Parker et al. (2003).

The experimental activity is carried out as follows: (i) preliminary set of experiments on a plane, fixed, artificially roughened bed, with no transverse slope; the channel is fed with uniform sediment; (ii) fixed bed experiments with laterally tilted bottom and uniform sediment; the longitudinal inclination is 5°, 10°, 15°, while the transversal inclination is 5°, 10°, 15°, 20°, combined together; (iii) set of experiments (a) repeated with mobile bed.

4 EXPERIMENTAL SET-UP

The experimental set-up is characterized by different layouts in the case of fixed and mobile bed; in this paper experimental results are only presented for the case of fixed bed.

4.1 *Laboratory apparatus*

The motion of saltating bed load particles is investigated in a free surface laboratory flume (figure 2).

The main apparatus consists of a tilting, recirculating flume, 10 m long, 0.365 m wide and 0.45 m deep, equipped for clear water flows up to 28 l/s and slope adjustment up to 5°. In order to obtain higher bed inclinations, a 2 m long 0.23 m wide plane has been built inside the flume with inclination adjustable up to 15°. Due to entrance effects the length of measuring reach is only about 1 m.

The sediment particles are fed at a constant discharge by means of a sediment feeder.

Particle velocity field is studied through PIV (particle image velocimetry), in order to measure the intensity and direction of the averaged velocity vectors.

A schematic representation of the fixed bed experimental setup is shown in figure 3. In particular, the computer controls the digital camera and the illumination system, for the acquisition of particle images, through a timing control device; video images of bed load particles saltating over the bed are taken from the upper side of the flume and acquired by the frame grabber. A collimated light source, located on a side of the flume, illuminates the bed load layer, not interfering with free water surface. The interrogation area has a length of about 0.5 m.

A mono-component laser Doppler anemometer has been employed to measure both sediment particle velocity and flow velocity distribution.

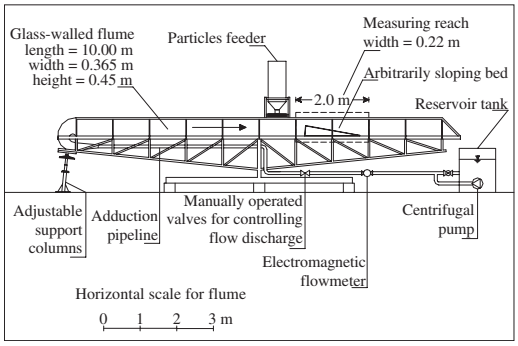


Figure 2. Laboratory flume.

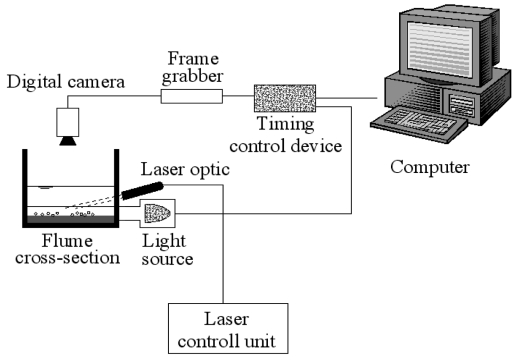


Figure 3. Fixed bed experimental set-up.

4.2 *Particle properties*

The particles must satisfy the following requirements in all the range of investigated of bed slopes: mobility at low Shields stress; ratio water depth to particle size sufficiently high to allow particle saltation, even in the case of high slope; relatively high friction angle thus allowing particles disposition according to a given transversal inclination.

The selected material is represented by steel particles with a density of 7850 kg/m^3, shaped like disks with almost uniform size of 3 mm of diameter and of 0.6 mm of thickness.

4.3 *PIV system*

Measurements of particle motion are obtained through PIV technique, which is based on the following components: seeding, illumination, image recording and image processing.

The seeding is based on particle tracers lightened from pulsating light and visible from digital camera: in the experiments the steel sediment particles act as tracers and their velocity is then measured. In fact, steel material is highly reflecting and so visible to the

camera, while the fixed bed is black dyed to observe the particles moving on it.

The illumination system, with stroboscopic pulsating light, is able to produce couples of lamp light to acquire couples of images. The frequencies range of couple images is of 0.5–5 Hz with a resolution of 0.1 Hz, while the interframing time between two images of a single couple is in the range 1–10 ms with a resolution of 0.1 ms.

The digital camera for the image recording is characterized by high resolution (max resolution 1360×024 pixel), that allows to take images in which single particle consists of a bulk of pixel, and a short interframing rate, that allows to capture two images in which particle tracers cover a relative small distance into the bed plane. Both digital camera and system illumination are controlled and synchronized by a computer. The CCD (Charge Coupled Device) plane is oriented parallel to the sloping bed layer. The particle velocity measured field is the one projected on the bed load saltation layer.

Image processing is carried out through a commercial software for PIV data analysis. In figures 4–5 a couple of analyzed images are presented.

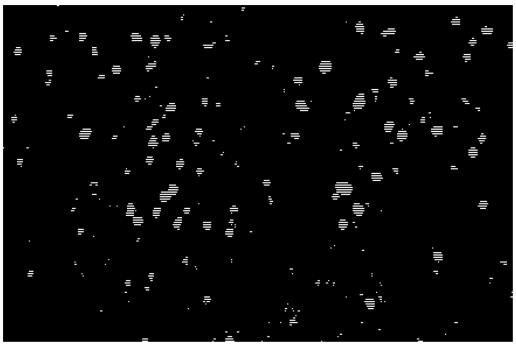


Figure 4. Image of moving particles a.

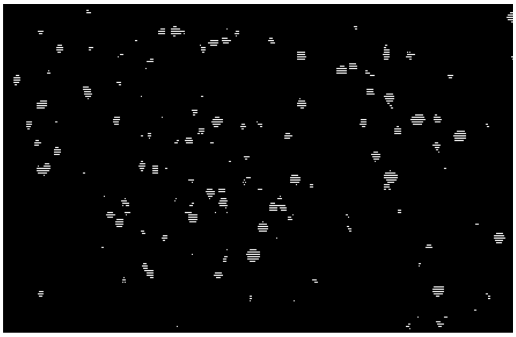


Figure 5. Image of moving particles b.

5 EXPERIMENTAL INVESTIGATIONS

5.1 *Preliminary activity*

Preliminary experiments have been carried out in order to check the behavior of the experimental set-up and to define basic parameters such as equivalent roughness of fixed granular bed and critical Shields stress for the onset of sediment motion.

The equivalent roughness of fixed granular bed has been evaluated in condition of fully turbulent flow and it appears to range around 0.8–1.2 times the particle diameter.

The critical Shields stress $\tau*_{co}$ for the onset of sediment motion in the case of vanishing bed slopes has been experimentally estimated to be about 0.03. Tests on the sediment mobility in the case of a streamwise finite slope have shown a reasonable agreement with the Shields value.

Moreover preliminary tests have been performed on the PIV system. An example of particle velocity field obtained by means of PIV technique is reported in figure 6, in the case of a longitudinal inclination of 5°.

Notwithstanding the experimental variability of the particles velocity field, due to the fact that there are relatively few particles in motion, it appears that on average the particle velocity is in agreement with the measurements obtained in the same condition with laser Doppler anemometer.

5.2 *Experimental data*

Experimental data here discussed have been obtained during the first sets of experiments on a plane, fixed, artificially roughened bed, with no lateral slope. In particular results are referred to three sets of experiments in the case of longitudinal inclinations of 1.7°, 5° and 10° and for various flow conditions.

As regards the liquid phase, measurements of flow discharge and flow velocity have been carried out by means of electro-magnetic flow meter and laser Doppler anemometer. In particular, for a given bed location, vertical velocity profile have been defined

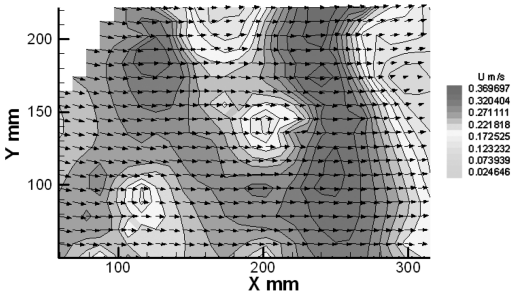


Figure 6. Particle velocity field ($\alpha = 5°$).

Table 1. Velocity flow profile parameters in the experimental conditions.

Longitudinal inclination	Q (l/s)	u* (m/s)	ε/D	$\tau*$
$\alpha = 1.72°$ (S = 3%)	11.8	0.092	0.704	0.048
	13.6	0.106	0.952	0.065
	15.6	0.110	0.849	0.069
	18.0	0.116	0.878	0.077
$\alpha = 5.00°$ (S = 8.7%)	2.68	0.094	0.709	0.051
	3.10	0.099	0.777	0.056
	3.56	0.101	0.929	0.058
	3.95	0.105	0.939	0.064
	5.02	0.118	0.979	0.080
	7.00	0.141	1.615	0.114
	9.00	0.142	0.783	0.115
$\alpha = 10.00°$ (S = 17.4%)	1.61	0.084	0.753	0.041
	2.15	0.095	0.941	0.051
	2.61	0.108	1.103	0.067
	3.10	0.112	1.077	0.072
	3.62	0.118	1.259	0.079
	4.14	0.123	1.159	0.086
	4.60	0.127	1.365	0.093
	5.10	0.128	1.341	0.094
	5.60	0.134	1.277	0.104
	6.10	0.136	1.310	0.107
	7.01	0.147	1.404	0.123

Table 2. Sediment bed load transport and mean particle velocity in the experimental conditions.

Longitudinal inclination	Q (l/s)	Qs (g/s)	V_p (m/s)
$\alpha = 1.72°$ (S = 3%)	11.8	20	0.62
	13.6	29	0.72
	15.6	62	0.73
	18.0	81	0.77
$\alpha = 5.00°$ (S = 8.7%)	2.68	11	0.58
	3.10	30	0.64
	3.56	60	0.64
	3.95	70	0.69
	5.02	114	0.74
	7.00	159	0.86
	9.00	215	1.07
$\alpha = 10.00°$ (S = 17.4%)	1.61	63	0.59
	2.15	122	0.69
	2.61	177	0.78
	3.10	167	0.82
	3.62	214	0.92
	4.14	228	1.02
	4.60	290	1.08
	5.10	322	1.11
	5.60	281	1.02
	6.10	349	1.06
	7.01	403	1.10

through at least 10 points along the flow depth. The friction velocity u* and the bed roughness length ε have been estimated via regression analysis assuming a logarithmic velocity profile in the near bed region. The experimental conditions and the results obtained from the regression analysis are reported in Table 1 for each slope S, together with the dimensionless applied shear stress $\tau*$, estimated from u*.

As regards the solid phase, feeding of sediments into the channel was in dynamic equilibrium with the given flow conditions. Input solid discharge was established to match the maximum rate of particle leaving the downstream end of the measuring reach, without any deposition phenomena. The profile of particle velocity within the saltation transport layer has been measured with laser Doppler anemometer and a layer-averaged value has been evaluated. Measurements of sediment velocities and solid discharges for the flow conditions in Table 1, are reported in Table 2.

6 DATA ANALYSIS

Mean value of sediment velocity, bed load transport rate and mean areal concentration are presented and compared with the theoretical results predicted by Parker et al. (2003) and the experimental findings of other Authors.

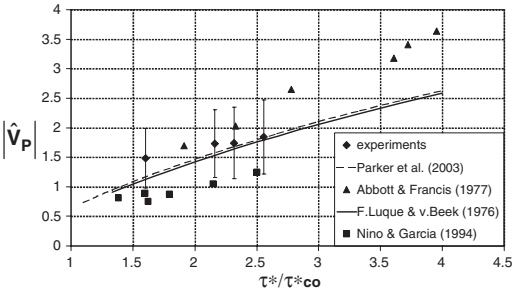


Figure 7. Dimensionless particle velocity ($\alpha = 1.7°$).

The dimensionless mean value of particle velocity $\hat{V}_P$ as a function of the ratio dimensionless applied shear stress $\tau*$ to critical Shield stress $\tau*_{co}$ is reported in figure 7 in the case of longitudinal bed inclination of 1.7°. The data seems to confirm the theoretical findings of the model proposed by Parker et al. (2003) and are in reasonable agreement with the experimental findings by Nino & Garcia (1994), by Abbott & Francis (1977) and the experimental interpretation by Fernandez Luque & van Beek (1976).

The dimensionless bed load discharge is reported as a function of $\tau*/\tau*_{co}$ in figure 8. The measurements are in agreement with the model proposed by Parker et al. (2003).

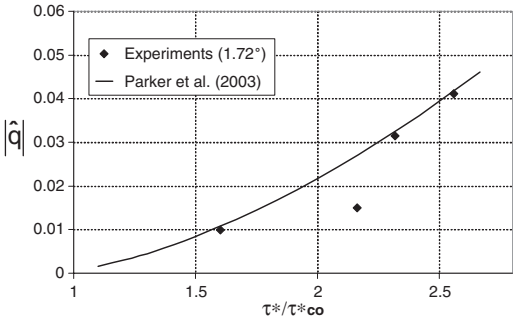


Figure 8. Dimensionless bed load discharge ($\alpha = 1.7°$).

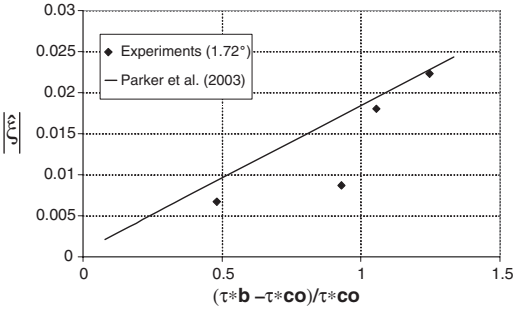


Figure 9. Dimensionless mean areal bed load concentration ($\alpha = 1.7°$).

The dimensionless values of areal concentration of particles in motion, estimated from the measurements of bed load discharge and particle velocity, are reported in figure 9 and compared with the theoretical ones, in terms of ratio excess of residual stress to $\tau*_{co}$.

This first set of data shows good agreement with the theoretical model, and the particles velocity data are in the same range of values observed by other Authors.

Moreover, experimental conditions with streamwise inclination of $\alpha = 5°$ and $\alpha = 10°$, and no transversal slope ($\varphi = 0°$), are here analyzed. The flow conditions were adjusted to obtain values of the $\tau*/\tau*_{co}$ ranging from 1 up to 4.

The measured values of particles velocity are well predicted by the theoretical model, as it can be noted from figure 10.

In figure 11 the measured values of bed load transport rate are compared to the corresponding theoretical ones, for each different slope.

In figure 12 the values of areal concentration of bed load transport, evaluated from the experimental data, are compared with the theoretical ones. The agreement is quite good, and the relation between the areal concentration and the excess of residual stress is close to the linear one.

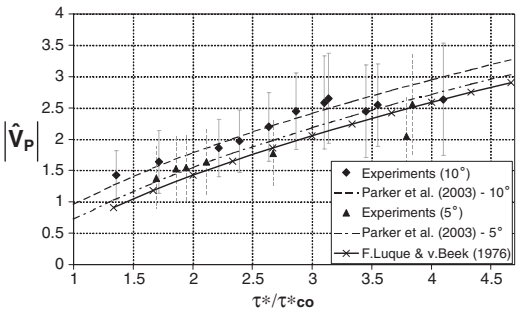


Figure 10. Dimensionless particle velocity ($\alpha = 5°$, $\alpha = 10°$).

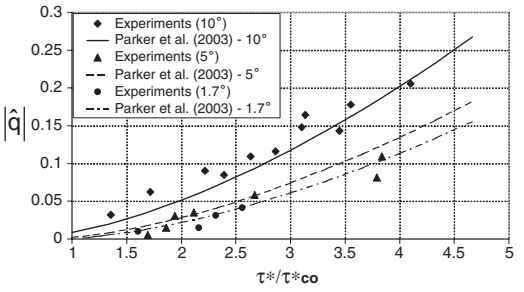


Figure 11. Dimensionless bed load transport.

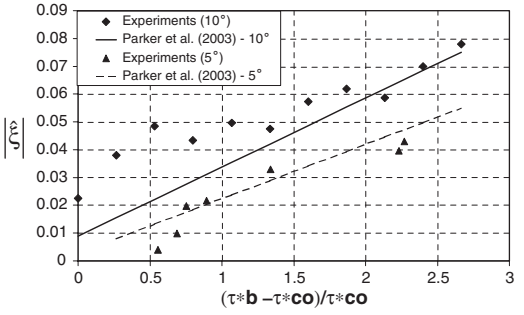


Figure 12. Areal bed load concentration ($\alpha = 5°$, $\alpha = 10°$).

The value of the coefficient of dynamic friction on a nearly horizontal bed has been fitted to different values ranging from 0.3 up to 0.6 to obtain a good agreement of the experimental data. This parameter may be influenced by the flow conditions. Further investigations are needed to clarify this point.

Finally, the fitting of the experimental data with the theoretical line is very good and induces to predict the reasonable validity of the model Parker et al. (2003) for bed load transport on arbitrarily sloping bed.

7 CONCLUSIONS

An experimental activity aimed to study the particle dynamics and bed load transport on arbitrarily sloping bed at low Shields stress has been carried out. The effects of steep bed slope on dynamics of bed load transport are investigated to test the validity of the theoretical model proposed by Parker et al. (2003) and the reliability of available experimental data from other sources (Abbott & Francis (1977), Fernandez Luque & van Beek (1976), Nino & Garcia (1994)).

The experimental set-up, here presented, allows the measurements of sediment transport rate, particle velocity and field particle motion through PIV technique and laser Doppler anemometer. Preliminary activity has been devoted to determine the basic parameter such as critical Shields stress for the onset of sediment motion.

The first set of experiments, with a slope $S = 3\%$, shows good agreement between measured particle velocities and the ones collected by other Authors.

The other sets of experiments, characterized by higher values of slope, seem to confirm the theoretical model proposed by Parker et al. (2003) in terms of prediction of particle velocity, concentration of particles in motion and bed load transport rate.

Further investigation on particle dynamics will be carried out by means of PIV technique.

The case of bed with both longitudinal and transversal inclination, considering also the case of mobile bed, will be carried out in the future experiments.

ACKNOWLEDGEMENTS

This work has been developed within the framework of the National Project cofunded by the Italian Ministry of University and of the Scientific and Technological Research and by the University of Florence (COFIN 2001) "Morphodynamics of fluvial networks". The authors are also grateful to Prof. Lamberti and to Dr. Zanuttigh (DISTAR, Univ. Bologna) for the help with the laboratory instruments. Simone Carotti is gratefully acknowledged for his help during the experimental activity.

REFERENCES

Ashida, J.E. & Michiue, M. 1972. Saltation and suspension trajectories of solid grains in a water stream. *Philos. Trans. R. Soc. London*. Ser. A 284: 225–254.

Bagnold, R.A. 1956. The flow of cohesionless grains in fluids. *Philos. Trans. R. Soc. London*. Ser. A 249: 235–297.

Bagnold, R.A. 1973. The nature of saltation and "bed-load" transport in water. *Proc. R. Soc. London*. Ser. A 332: 473–504.

Bridge, J.S. & Bennett, S.J. 1992. A model for the entrainment and transport of sediment grains of mixed sizes, shapes and densities. *Water Resour. Res.* 28(2): 337–363.

Damgaard, J.S., Whitehouse, R.J.S. & Soulsby, R.L. 1997. Bed-load sediment transport on steep longitudinal slopes. *J. Hydraul. Eng*. 123(12): 1130–1138.

Engelund, F. & Fredsoe, J. 1976. A sediment transport model for straight alluvial channels. *Nord. Hydrol*. 7: 293–306.

Fernandez Luque, R. & van Beek, R. 1976. Erosion and transport of bed load sediment. *J. Hydraul. Res*. 14(2): 127–144.

Kovacs, A. & Parker, G. 1994. A new vectorial bed load formulation and its application to the time evolution of straight river channels. *J. Fluid Mech*. 267: 153–183.

Nino, Y. & Garcia, M. 1994. Gravel saltation, 1, Experiments. *Water Resour. Res*. 30(6): 1907–1914.

Nino, Y. & Garcia, M. 1994. Gravel saltation, 2, Modeling. *Water Resour. Res*. 30(6): 1915–1924.

Parker, G., Seminara, G. & Solari, L. 2003. bed load at low Shields stress on arbitrarily sloping beds: alternative entrainment formulation. *Water Resour. Res*. 39(7), 1183, doi:10.1029/2001WR001253.

Seminara, G., Solari, L. & Parker, G. 2002. Bed load at low Shields stress on arbitrarily sloping beds: Failure of the Bagnold hypothesis. *Water Resour. Res.* 38(11), 1249, doi: 10.1029/2001WR000681.

Sekine, M. & Kikkaua, M. 1992. Mechanics of saltating grains. II. J. Hydraul. Eng. 118(4): 536–558.

Sekine, M. & Parker, G. 1992. bed load transport on transverse slopes. *J. Hydraul. Eng*. 118(4): 513–535.

Smart, G.M. 1984. Sediment transport formula for steep channels. *J. Hydraul. Eng*. 110(3): 267–276.

Wiberg, P.L. & Smith, J.D. 1985. A theoretical model for saltating grains in water. *J. Geophys. Res*. 90(C4): 7341–7354.

Wiberg, P.L. & Smith, J.D. 1989. Model for calculating bed load transport of sediment. *J. Hydraul. Eng*. 115(1): 101–123.

This page intentionally left blank

River Flow 2004 – Greco, Carravetta & Della Morte (eds.)
© 2004 Taylor & Francis Group, London, ISBN 90 5809 658 0

Particle-fluid interactions in a free surface turbulent flow

M. Righetti
CUDAM-Department od Civil and Environm. Engineering – Univ. of Trento, Italy

G.P. Romano
Department of Mechanics and Aeronautics – University of Roma "La Sapienza", Italy

A. Cenedese
DITS – Department of Hydraulics and Transportation – University of Roma "La Sapienza", Italy

ABSTRACT: The work focuses on the interaction between the solid (spherical particles) and the fluid phases in the near-wall region of an open channel flow. In the experiments the velocity field is measured with a Phase Doppler Anemometer. In comparison to the clear-water conditions, in the particle-laden flow the streamwise mean velocity are reduced in the outer layer ($y^+ > 20$), while increased in the viscous sublayer; turbulence intensities of both the streamwise and vertical velocity components are damped in the outer region, while enhanced in the near-wall region. Particles are faster than the fluid at the wall and are slower than the fluid in the outer layer. An original explanation to these findings is proposed, related to the mechanism of particle entrainment and deposition. The damping of turbulence is explained as a conseguence of the momentum exchange between the phases in the buffer region during the burst events. The quadrant analysis of the Reynolds stresses corroborates this hypothesis.

1 INTRODUCTION

Several theoretical, numerical and experimental studies have tried to model two-phase flows, but this is a hard task whenever particle-particle interactions have to be taken also into account (high particle concentrations). This is especially true for the near-wall region of open channel flows, where the particle concentration increases towards the bed. Early investigations, concerning the sediment transport in open channel flows, accounted for particles by empirical changes of the fluid streamwise mean velocity profile (Vanoni 1946; Itakura & Kishi 1980; Coleman 1981), while expressions for the sediment concentration were obtained by diffusive theories (e.g. Yalin 1972). Generally, the particles are assumed as a passive scalar, for which the velocity is assumed substantially equivalent to the fluid velocity, except for the vertical component which is given by the fall velocity. Refined measurements in two-phase flows (Lyn 1986, 1988; Tsuji & Morikawa 1982; Tsuji, Morikawa & Shiomi 1984; Kulick, Fessler & Eaton 1994; Kaftori, Hetsroni & Banerjee 1995; Muste & Patel 1997; Best et al. 1997; Greimann, Muste & Holly 1999), point out the modifications not only of the fluid mean velocity profile, but also of the fluid turbulence intensity profile; it is also noticed a difference between particle and fluid longitudinal velocities (the particle velocity lag).

In particular, for sediment-laden flows, Coleman (1986), Lyn (1988) (in the smooth bed regime) and Best et al. (1997), Muste & Patel (1997) (in the transitional bed roughness regime) have observed a decrease of the whole fluid velocity profile in comparison to clear water conditions. Coleman (1986) tried to explain such a reduction using two mechanisms; one due to "boundary roughness" and the other to "suspended sediments", while Best et al. (1997) and Muste & Patel (1997) ascribed the velocity reduction only to the former. However, in the measurements over a rough wall at low particle concentration (as those by Best et al. (1997) and Muste & Patel (1997), it appears difficult to explain the observed downward shift of the velocity profile only through an enhancement in wall roughness. This suggests the existence of another mechanism of interaction, which could be related to the momentum exchange between the solid and the fluid during the particle settling and suspension.

As far as the effect of particle presence on turbulence characteristics is concerned, the first theoretical attempt of explanation was made by Owen (1969)

who defined the particle relaxation time ($t^* = \rho_p d_p^2/18\,\rho_f \nu_f$, according to the Stokes' law), and suggested that small particles, which have a relaxation time smaller than the characteristic time of energy-containing eddies ($t_e = l/\sigma_u$, where l is the integral length-scale, which is proportional to the distance from the wall and σ_u is the measured turbulence intensity at the same distance), follow the flow with some delay which causes damping of turbulent fluctuations; on the other hand, "large" particles (i.e. having $t^* \gg t_e$) can enhance the turbulent intensity. Even if there is an agreement between the different authors as far as the logarithmic region is concerned, the behaviour for $y^+ < 10$ remains unclear, as also the dependence on the particle concentration and size.

Moreover, the particle dynamics and the mechanisms of entrainment and deposition have been related to the dynamics of the burst-sweep cycle which characterises the near-wall turbulence (Grass 1974; Sumer & Oguz 1978; Sumer & Deigaard 1981; Niño & Garcia 1996; Shen & Lemmin; 1999). The main conclusions of the experiments and numerical simulations concerning the relation between particle lifting and the bursting phenomenon are that the bursting process is effective in entraining particles, giving rise to fluctuations of the local concentration in phase with the burst-sweep cycle, as reported by Shen & Lemmin (1999). However the dynamical interaction (momentum exchange) between the two phases during the burst-sweep cycle and the effect of particle size and concentration must be also investigated and it is one of the aims of the present work.

2 EXPERIMENTAL SETUP

2.1 *The facility*

A closed-circuit rectangular Plexiglas open channel is used with the axes aligned along the streamwise (x), vertical (y) and spanwise (z) directions. The channel dimensions are 3 m along x, 0.1 m along z with a free surface height, h, equal to about 0.02 m (Figure 2). The channel is inclined by a traversing mechanism which allows the channel slope, i_f, to be fixed with an error of $\pm 0.05\%$ (the effective slope measured with the 100 μm and 200 μm particles ranges between 0.70% and 1.5%); this slope was measured at rest by means of water level staffs at four sections along x and at three locations along z in each section. The measurement system consists of a Phase Doppler Anemometer (PDA), which employs the green and blue light of a 2 W Laser scattered from the tracers. The PDA enables one to obtain both the velocity (as an usual Laser Doppler Anemometry (LDA) system) and the size of particles from the phase difference of the Doppler signals between photo-receivers placed at different positions. Experiments were performed both for clear-water and for particle-laden flows; the test section was located at about 2.0 m downstream of the inlet section ($x/h \cong 100$, where x starts at the inlet). Distilled water was used as the carrier phase seeded with polymer particles as tracers (mean diameter 12 μm, density 1.05 g/cm^3), whereas two glass spherical particle sizes (mean diameter 100 μm and 200 μm, density 2.6 g/cm^3) were used as the solid phase. The average volumetric particle concentration (C_{av}) in sediment-laden flow was evaluated by weighing particles and water; it was in the order of 10^{-3}. Profiles of the vertical distribution of the solid particle concentration have been measured for the two size classes (not shown); the experimental data reasonably follow the Rousean distribution and this could be an indication that the suspended particles are in equilibrium conditions (Vanoni 1946).

Table 1. Experimental conditions for the five runs performed.

h (cm)		U_f (cm/s)	u_* (cm/s)	(d_p) (μm)	C_{av}	Re	Fr
2.3	clear water	63	3.10	–	0	14500	1.3
2.3	low conc.	57	3.40	100	1.6	14500	1.18
2.3	high conc.	63	3.59	100	4	15500	1.2
2.0	low conc.	60	4.15	200	1.2	12900	1.37
2.5	high conc.	67	3.78	200	3.8	16750	1.28

2.2 *The experiments*

The experiments were conducted in uniform flow conditions, at Reynolds numbers $Re = U_f h/\nu_f$ (where U_f is the depth-average streamwise flow velocity) ranging from 13000 up to 16500. For each experiment, the flow depth ranges from 2 cm to 2.5 cm about, thus the width to depth ratio is quasi-constant, ranging from 4 to 5. It is important to point out that all the experiments were performed with Froude numbers, Fr, larger than one (supercritical regimes). These conditions were selected after observing that for the sediment-laden experiments when moving from the sub-critical to the super-critical regime the bed forms change from dunes to a plane bed configuration (without bed forms, see e.g. Yalin 1972).

The experimental conditions for the clear-water and sediment-laden conditions acquisitions are summarized in Tables 1 and 2.

For each experiment in sediment-laden conditions, the average volumetric concentration is between $1.2 * 10^{-3}$ and $1.6 * 10^{-3}$; the bed is only partially covered by the solid particles. This fact strengthens the opportunity to compare the sediment-laden flow with the clear water on a smooth rather than on a rough

Table 2. Experimental conditions for the sediment-laden runs.

h (cm)	(d_p) (μm)	C_{av} ($*10^3$)	Re	Fr	w_s/u_*	t^* $s*10^3$	t^*u^{*2}/ν_f
2.3	100	1.6	14500	1.18	0.32	1.6	2.04
2.3	100	4	15500	1.2	0.32	1.6	2.06
2.0	200	1.2	12900	1.37	0.92	6.1	11.3
2.5	200	3.8	16750	1.28	1.01	6.1	8.7

wall; therefore, the origin of the vertical axis is taken exactly at the wall for all the experiments (clear-water and particle-laden experiments).

All the results will be presented in a dimensionless form by using wall variables. The evaluation of the friction velocity (that is the shear at the wall) is one of the crucial problems in near-wall flow measurements. As pointed out by Muste & Patel (1997), small variations of it strongly affect the plot of the mean velocity. Therefore, special care is given to determine this velocity.

The uncertainty in friction velocity depends on the evaluation method used; two possibilities have been considered (the logarithmic law was not used because in a two-phase flow the value of the von Karman constant could be a priori unknown):

– to compute the wall shear from the momentum balance equation

$$\tau_0 = \gamma_f \left[(1 - C_{av}) + \frac{\rho_p}{\rho_f} C_{av} \right] R_h i_f \qquad \textbf{(1)}$$

where $\gamma_f = \rho_f g$ (g is the gravitational acceleration), R_h is the hydraulic radius and i_f is the channel slope;

– in analogy with the method proposed by Harder & Tiederman (1991), to compute the wall shear by the Reynolds stress profile,

$$\tau_0 = -\rho_f \left[(1 - \bar{c}_{(y)}) \overline{u_f v_f}_{(y)} + \frac{\rho_p}{\rho_f} \bar{c}_{(y)} \overline{u_p v_p}_{(y)} \right] / (1 - y/h) \qquad \textbf{(2)}$$

where $\bar{c}_{(y)}$ is the mean volumetric concentration at distance y from the wall (u and v are used for the fluctuating velocity components, while u' and v' for the rms values). In the previous relation, the viscous stress term was not considered because the friction velocity was determined by an extrapolation down to the wall of the total stress measured for $y/h > 0.1$; in this region, the viscous stress is negligible in comparison to the Reynolds stress.

For the clear water conditions, the difference between the two estimates of shear velocity is less than 3%, in agreement with Nezu & Nakagawa (1993). On the other hand, for the experiments with particles (sediment-laden flow), the difference is much higher (up to 15/20%). This difference, especially for high particle concentrations, could depend on extra terms that should be included in eq. (2); they consider the mutual interactions between solid and fluid phases and other contributions (Ishii 1975). Therefore, in sediment-laden flows the measured Reynolds stress profile does not necessarily follows the classical linear trend along the flow depth and the first evaluation was preferred over the second.

3 RESULTS

3.1 *Mean velocity and turbulence*

To assess the reliability of the present measurements, a comparison with results given in the literature for the near-wall region of a single-phase flow has been performed (not shown), the measured data agreed satisfactorily with experimental results obtained by Laufer (1950), Karlsson & Johansson (1986) and Wei & Willmarth (1989), at nearly the same Reynolds number. The clear-water data are acquired with exactly the same set-up used for the two-phase flow but without solid particles in the flow.

In Figures 1, 2 and 3 the experimental values of the mean streamwise velocity profile U^+ are reported and compared with the linear , the "classical" logarithmic laws of the wall and the law of White (White 1974):

$$U^+ = y^+, \qquad U^+ = U/u^* = 1/k \ \ln\left(y^+\right) + B,$$
$$U^+ = \frac{1}{k}\ln\left(y^+\right) + 5.5 - \frac{1}{k}\ln\left(1 + 0.3\, d^+\right) \qquad (3)$$

For the particle-laden flows, the contributions of the solid and fluid phases are separated. The values of $k \approx 0.4$ and $B \approx 5.5$ as proposed by Nikuradse, are assumed, d^+ is the dimensionless particle size. The figures show that the velocity profiles of fluid and solid phases decrease, if compared with the clear-water, similarly to the observations of Coleman (1986), Valiani (1991), Muste & Patel (1997) and Best et al. (1997). In the following the experiments in sediment laden conditions are examined and discussed.

For the fluid phase, the decrease in the logarithmic region is almost independent of the distance from the wall and the von Kármán constant k remains equal to about 0.4. The effect of particles is also to erode the extension of the logarithmic law, from the bottom (i.e. the buffer zone) and from the top (i.e. the wake region). Moreover, the amount of the decrease is smaller than by assuming a wall roughness equivalent to the particle diameter, but, nevertheless, it is proportional to the particle concentration.

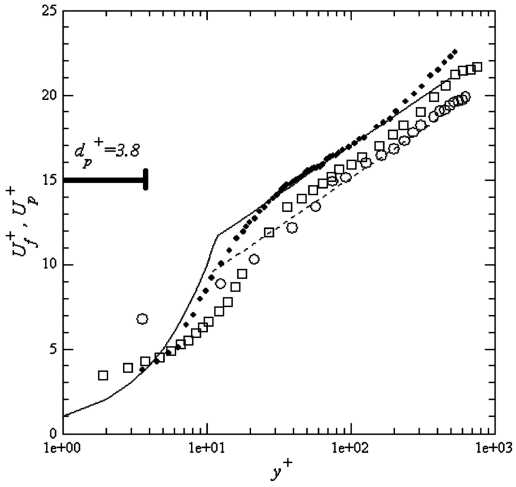


Figure 1. Mean velocity profile for the fluid phase. Clear-water ●; 100 μm particle laden flows at high concentration ◯; 100 μm particle laden flows at low concentration □.

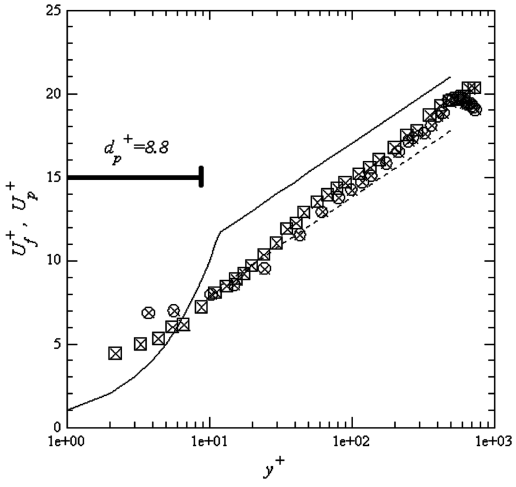


Figure 2. Mean velocity profile for the fluid phase. 200 μm particle laden flows at high concentration ⊗; 200 μm particle laden flows at low concentration ☒.

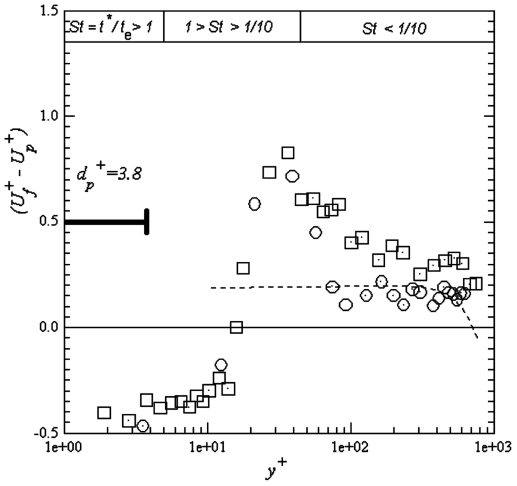


Figure 3. Difference between mean velocity of the fluid and solid phases for the 100 μm particles. High concentration ◯, low concentration □. The regions with different values of the Stokes number are indicated. The dashed lines represent predictions by the model of Greimann, Muste & Holly (1999).

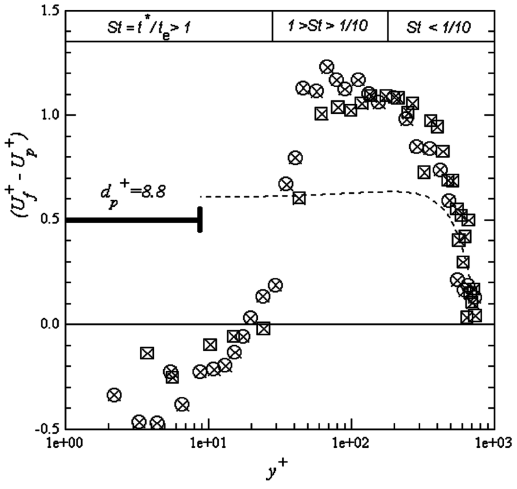


Figure 4. Difference between mean velocity of the fluid and solid phases for the 200 μm particles. High concentration ☒, low concentration ⊗. The regions with different values of the Stokes number are indicated. The dashed lines represent predictions by the model of Greimann, Muste & Holly (1999).

A better insight into the kinematics of heavy particles is achieved by considering Figures 3, 4, where the streamwise velocity difference between fluid and solid is plotted for the two particle sizes.

In the figures, the different values attained by the Stokes number are also indicated; the Stokes number was evaluated roughly estimating the characteristic time of energy containing-eddies by the relation (Tennekes & Lumley 1972).

In a layer close to the wall ($y^+ < 20$), with an extension almost independent of the particle size, the particles are faster than the fluid (the difference between the two velocities is up to 0.4 u_*). This difference is lower for the largest size particles,seems to be slightly dependent on the particle concentrations and is approximately constant when approaching the wall. Across the region $20 < y^+ < 50$ (the amplitude of this interval seems to depend on the Stokes number, i.e. on

the particle size), there is an abrupt change in the sign of the fluid-particle velocity difference and the fluid becomes faster than the particles (the velocity difference is between 0.8 u_* and 1.2 u_*). Here, the maximum velocity differences are achieved; the 100 μm particles show a velocity lag that is about 1.3 ÷ 1.5 times lower than the larger particles. This region is just the one where wall-burst phenomena are stronger. Moving further from the wall, in the region where the Stokes number is smaller than 1/10, the fluid-particle velocity difference decreases to zero.

The previous behaviour could be explained as follows: far from the wall ($y^+ > 200$), the solid particles follow quite accurately and immediately fluctuations of the fluid velocity field, being the time scale for particle modifications (particle relaxation time) much smaller than the characteristic eddy time scale ($St \ll 1$). When moving closer to the wall ($20 < y^+ < 100$), where the velocity fluctuations are larger than far from the wall (see next section), the particles are not longer able to respond promptly to the turbulent fluctuations, thus exhibiting an increasing deviation from the fluid velocity ($St \leq 1$). Such a velocity lag can be explained if the particle motion is associated to the dynamics of the wall vortical structures. As reported in the model by Adrian, Meinhart & Tomkins (2000), flow ejections are related to the velocity field induced by a primary hairpin and represent the dominating part of the near-wall dynamics at these distances from the wall (Lu & Willmarth 1973). In this region, the particles are convected and lifted up by ejections of low momentum fluid from the wall region; due to their inertia ($St \leq 1$), they take memory of such a low momentum, thus exhibiting a velocity lag in comparison to the surrounding fluid. In the very near-wall region ($y^+ < 10$), injections of high momentum fluid dominate the wall dynamics; high momentum particles are carried on the wall by such events. These particles respond very slowly to the local velocity field and, due to their inertia, they retain their velocity which is higher than that of the surrounding fluid ($St > 1$). This fact leads to the non zero longitudinal mean velocity at the wall. This mechanism is similar to that provided by Kulick, Fessler & Eaton (1994) i.e. a transfer of momentum due to the solid particles moving towards the wall from the faster upper layer. The momentum exchange between solid and fluid phase will be investigated in the next.

The dimensionless rms velocity fluctuations along the streamwise and vertical directions are given in Figures 5, 6, 7 and 8 together with the corresponding clear-water profiles. For the streamwise component (Figs. 5, 6), from the outer region down to $y^+ \approx 30$, the fluctuations of both fluid and solid phases in particle-laden conditions are similar to those in clear-water; only a very slight damping is noticed in this region for both the size classes in comparison to the clear-water

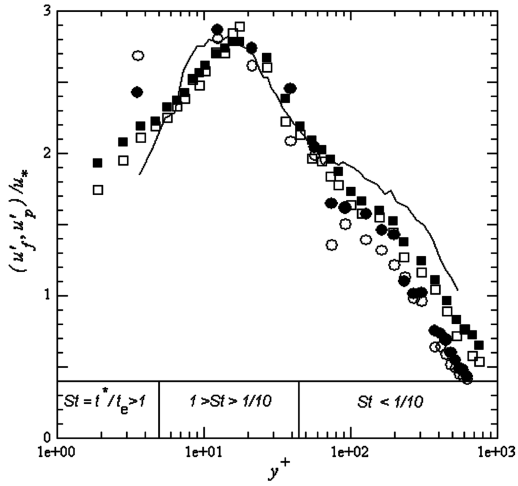


Figure 5. Rms profiles of the streamwise velocity component for the 100 μm particles, compared with clear-water measurements; solid symbols are for the solid phase and open symbols for the fluid phase, circles for high conc. experiments, square boxes for low conc.;—clear-water measurements.

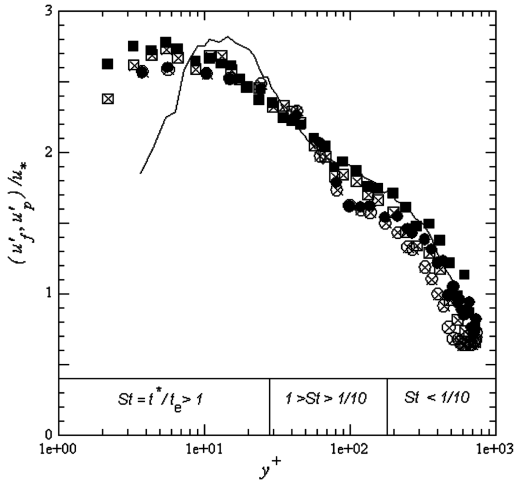


Figure 6. Rms profiles of the streamwise velocity component for the 200 μm particles, compared with clear-water measurements; symbols as in Figure 5.

profile, the damping being enhanced for higher concentrations. Closer to the wall, these fluctuations are firstly damped ($7 < y^+ < 20$) and then enhanced ($y^+ < 7$) in comparison to the clear-water profile by amounts that increase as the particle size and concentration. Accordingly to Owen (1969), the region where substantial modifications of the streamwise

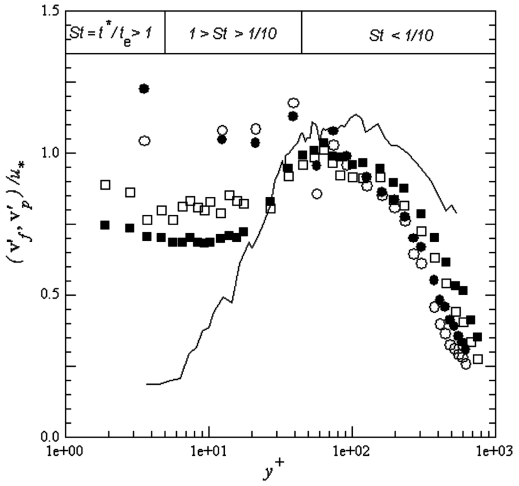


Figure 7. Rms profiles of the vertical velocity component for the 100 μm particles, compared with clear-water measurements; symbols as in Figure 5.

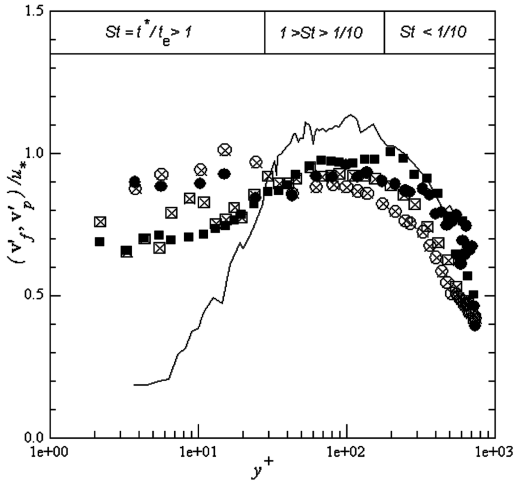


Figure 8. Rms profiles of the vertical velocity component for the 200 mm particles, compared with clear-water measurements; symbols as in Figure 5.

fluctuation profile are observed roughly corresponds to t* > te or $St > 1$ (the intervals for the different values of the ratio $St = t^*/t_e$ are also reported in the figures). It is important to notice that, in the present particle-laden conditions, the streamwise rms velocity of the solid phase is larger than that of the fluid, all along the vertical profile.

For the vertical fluctuations in particle-laden conditions (Figs. 7, 8), down to $y^+ \approx 30$ the damping in comparison to the clear-water profile is stronger than for the streamwise fluctuations (more than 20%) for both size classes. In contrast to the horizontal fluctuations, substantial modifications of the vertical fluctuation profile are observed already for $0.1 < St < 1$. This is not what can be expected for rough walls, where velocity fluctuations in the outer region are enhanced rather than damped (Nezu & Nakagawa 1993; Krogstad & Antonia 1999); therefore, in the outer region the effect of the solid phase cannot be represented merely by an increased wall roughness. For $y^+ < 30$, a strong enhancement of vertical velocity fluctuations (dependent of the particle concentration) is noticed. Moreover, in particle-laden conditions, while in the outer region the fluctuations of the solid phase are larger than those produced by the fluid, in the region $y^+ < 30$ they are smaller.

In order to explain these observations, it is necessary to follow the considerations previously outlined, i.e. that the solid particles are mainly driven by the fluid wall dynamics (mean field, as depicted in Figures 1…4). As a consequence, particles carry momentum and momentum fluctuations from the regions where they are moving from. In this sense, the behaviour of the particles at a given distance from the wall is influenced by that of the fluid at another distance if there is a dynamic connection between the two; as pointed out in the dynamical model by Adrian, Meinhart & Tomkins (2000), this connection is particularly effective for $y^+ < 200$. Therefore, if this point of view is admitted, in order to explain the behaviour of the turbulence intensity (fluctuating field) in the buffer and in the outer region ($y^+ > 20$), the behaviour in the very near-wall region cannot be neglected. Providing that the intense fluid ejections from the inner wall region lift up the solid phase, the differences in time scales between the fluid and the particles ($St \leq 1$) indicate that the latter retain the low momentum and the high velocity fluctuations experienced by the fluid during the bursting events. This circumstance could explain why in the outer region the particle rms fluctuations are systematically larger than those of the fluid, along both longitudinal and vertical directions. Nonetheless, fluctuations are still smaller than in clear-water; this could be due to ejected lumps of fluid which have to spend part of their vertical momentum in order to overcome the gravity force and to lift up the solid particles. The longitudinal particle-fluid velocity differences suggest that, at the same time, a momentum exchange between the two phases in streamwise direction also occurs. The observation that in particle-laden conditions both the streamwise but especially the vertical fluid fluctuations are damped in comparison to the clear-water (in the outer region), suggests that this momentum exchange is more effective along the vertical. Owing to this momentum exchange, part of the turbulent kinetic energy produced during the bursting events is transferred to the particles and it is no more

at disposal of the turbulent diffusion process that takes place in the outer layer.

The previous explanations of the observed results in terms of fluid wall dynamics call for an investigation of wall events using measurements of the Reynolds stress.

3.2 *Reynolds stresses and quadrant analysis*

In order to have a deeper insight onto the mechanisms specifically involved in particle motion close to the wall, the quadrant analysis of the Reynolds stress is performed (Lu & Willmarth 1973). In the following only the results for clear water, 100 μm and 200 μm low concentration experiments are reported, being the results for the other particle laden experiments analogue. At each distance from the wall, the average contribution to the Reynolds stress of the i-th quadrant on the (u, v) plane can be evaluated as

$$\overline{uv}_{i(H)} = \lim_{T\to\infty} \frac{1}{T} \int_0^T uv_{i(t)} S_{i(t,H)} dt \qquad i=(1,2,3,4) \qquad (4)$$

where $uv_{i(t)}$ is the contribution of the Reynolds stress to the i-th quadrant, T is the acquisition time interval and the function S is defined as $S_i(t,H) = 1$ if $|uv|i > Hu'v'$ and $S_i(t,H) = 0$ otherwise (where $|uv|_i$ indicates the absolute value). The sum of contributions from all quadrants must be exactly equal to the total Reynolds stress. The threshold level H (defined in terms of the local rms velocity fluctuations u' and v', which is a crucial parameter for such an analysis, has been changed between 0 and 1. The following results refers to the value $H = 0$.

Another average can be evaluated by computing the intensity of the i-th quadrant, i.e. by weighting the Reynolds stress with the time spent within the quadrant itself (T_i):

$$\langle uv \rangle_{i(H)} = \lim_{T\to\infty} \frac{1}{T_i} \int_0^T uv_{i(t)} S_{i(t,H)} dt = \frac{T}{T_i} \overline{uv}_{i(H)} \quad i=(1,2,3,4) \quad (5)$$

where the sum of all contributions, $\langle uv \rangle$, is now different from the total Reynolds stress; due to the time-weighting. The aim of the quadrant analysis is to achieve a deeper insight into the possible reasons for damping effects acting on the turbulence structure and on the mechanisms of entrainment due to the solid particles; from this point of view, the intensity of Reynolds stress is considered a better indicator than the average contribution.

In Figures 9, 10, 11, the quadrant profiles (obtained using eq. (5)) are shown for the fluid phase of the 100 μm and 200 μm particles at lower concentrations and compared to the result in clear-water conditions.

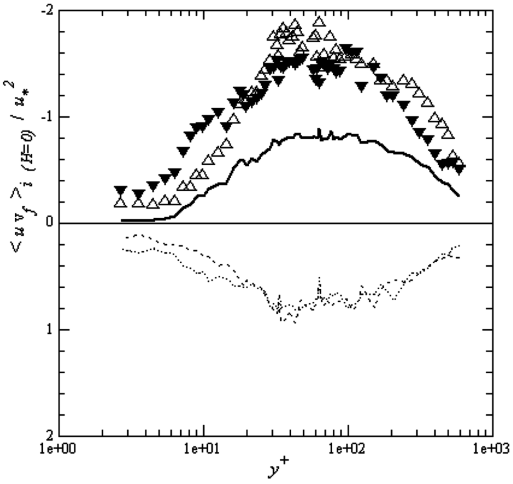


Figure 9. Profiles of intensity of Reynolds stress from each quadrant for clear water ; ·····, quadrant I; △, quadrant II; - - - - -, quadrant III; ▼, quadrant IV; —, whole Reynolds stress.

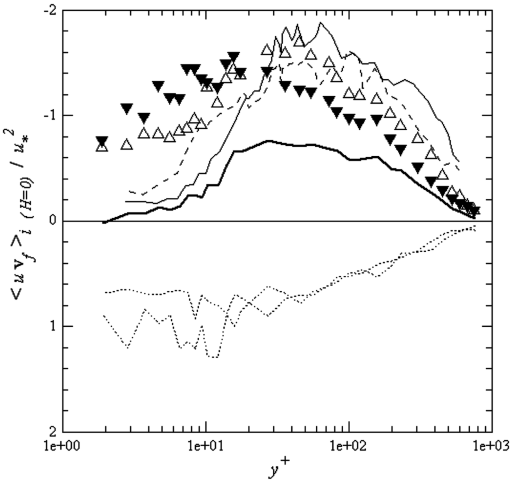


Figure 10. Profiles of intensity of Reynolds stress from each quadrant for the fluid phase of the 100 μm particles and for the clear water. 100 μm particles: △, quadrant II; ....., quadrant I and quadrant III; ▼, quadrant IV; —, whole Reynolds stress. Clear water: —, quadrant II; - - - - - quadrant IV.

The results obtained in clear-water are in agreement with those of Lu & Willmarth (1973) for a smooth bed. The quadrant profiles for clear-water and sediment-laden conditions have a similar behaviour; however, all quadrant intensities in the sediment-laden profiles are enhanced for $y^+ < 20$ (similarly to rms and Reynolds stress profiles). In particular, close to the wall, the second $(u < 0,\ v > 0)$ and fourth $(u > 0,\ v < 0)$ quadrant

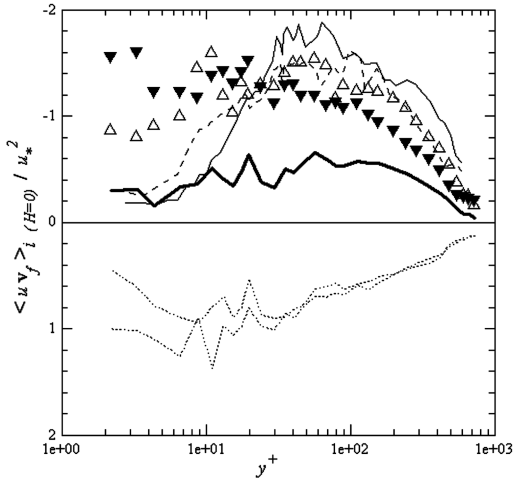


Figure 11. Profiles of intensity of Reynolds stress from each quadrant for the fluid phase of the 200 μm particles and for the clear water. 200 μm particles: △, quadrant II; ....., quadrant I and quadrant III; ▼, quadrant IV; —, whole Reynolds stress. Clear water: —, quadrant II; - - - - - quadrant IV.

events have intensities more than two times larger than in clear-water conditions. As it is well known, a second quadrant event corresponds to an ejection, while a fourth quadrant to a sweep (Lu & Willmarth 1973). The crossover between the second and fourth quadrants and between the first and third quadrants at $y^+ \approx 20$ is almost unaffected by the particles. In the region $20 < y^+ < 200$, there is an overall damping of the quadrant intensities, which is especially appreciable for the second quadrant (at $y^+ \approx 40$ about 30%). The described effects are observed to increase with the particle size and concentration.

As conjectured in the previous sections, the wall dynamics phenomena have a complex interaction with the solid particles; in particular, the flow ejections (second quadrant) are responsible for particle lift up and are supposed to yield a significant part of their momentum to the particles. Thus, as observed, ejections are expected to be damped in sediment-laden conditions, whereas this phenomenon must be less effective for sweeps (fourth quadrant).

For the outer layer the results are similar to those of the logarithmic region.

So, summarizing, in the region $10 < y^+ < 30$ (and on a lesser extent in the region $30 < y^+ < 100$), the whole "coherent" averaged intensity of the fourth but especially of the second quadrant is reduced in comparison to the "incoherent" part; it decreases from 78% to 67% respectively for the clear water and the 200 μm particles (accordingly the "non-coherent" averaged intensity increases from 22% to 33%). This effect is consistent with the previously described phenomenon of a reduction in the intensity of fluctuations and Reynolds stress as a consequence of the fluid momentum loss due to particle lift up.

4 CONCLUSIONS

Experiments were performed to analyse the effect of solid particles on the velocity field in near-wall turbulence. Glass spheres of diameters equal to 100 mm and 200 μm, with a mean volumetric concentration equal to 10^{-3}, were employed. The experiments were performed at Froude numbers larger than one (supercritical regimes) to attain a plane bed configuration (without bed forms); these conditions are different from those encountered in some practical applications where the regime is subcritical.

The experiments were performed at a Reynolds number equal to about 15000 (based on the water height and on the average streamwise velocity), where data from other authors are widely available. The minimum distance from the wall at which measurements were made was equal to about 3 wall units, i.e. well inside the viscous sublayer.

For sediment-laden flow, the mean velocity profile exhibits in the logarithmic and outer regions a noticeable decrease, increasing as the dimensionless particle size d^+ and the particle concentration, that is in agreement with the hypothesis of considering the particles as mostly standing on the wall and acting on the flow similarly to a rough wall. The simultaneous increase of the profile in comparison to clear-water in the inner region ($y^+ < 5$), leads to a velocity gradient normal to the wall for the sediment-laden flow which is smaller than in clear-water and to a non-zero velocity at a distance from the wall equal to about 2 wall units. This is a consequence of the "sliding and rolling" particle motion at the wall which also drives the surrounding fluid.

Considering the differences between the velocity of the fluid and of the particles, it has been measured that this difference is negative (particles faster than fluid) close to the wall ($y^+ < 20$), while it becomes positive (fluid faster than particles) further from the wall ($y^+ > 20$). This change in the relative velocity occurs in the region where the particle relaxation time is of the same order of magnitude of the characteristic time of energy-containing eddies (Stokes number close to one), so that particles slowly respond to changes of the local fluid velocity. Moreover, in the same regions the interaction of particles with the sweep-burst cycle takes place; for $y^+ > 20$, particles are convected and lifted up by intense fluid ejections (bursts) carrying low momentum fluid from the wall region (thus exhibiting a lower velocity in comparison to the surrounding fluid), whereas close to the wall ($y^+ < 20$) fluid injections (sweeps) carry on the wall

high momentum particles (which retain their velocity which is higher than that of the surrounding fluid).

The profiles of the rms fluctuations of the streamwise and vertical velocity components are damped in the outer layer (especially for the vertical component) while enhanced in the inner part in comparison to the clear-water measurements. The results in the outer layer are different from what expected for a rough wall, where the rms fluctuations are observed to increase over the whole layer; therefore, the mechanism of particle-fluid interaction must be different from a simple increased equivalent wall-roughness due to particles. Moreover, in the experiments with particle-laden conditions, the streamwise rms velocity of the solid phase is consistently larger than that of the fluid all along the measured vertical profile. On the other hand, the vertical fluctuations of the solid phase are larger than those produced by the fluid in the outer layer while smaller in the region $y^+ < 30$. The momentum balance along the vertical reveals a significant momentum exchange between the two phases, particularly effective in the buffer region where bursts are intense; the present measurements reveal that this momentum transfer is predominant along the vertical direction. This exchange leads to a reduction of the turbulent energy production in the buffer region that is no more at disposal for the turbulent diffusion processes in the outer layer. This mechanism could, at least in part, explain the turbulent damping observed in the outer layer. These considerations are clarified by considering the dynamics of the near-wall structures which makes a connection between the behaviours in the buffer and outer regions ($y^+ > 20$) and those in the very near-wall region. In particle-laden conditions, for $y^+ > 20$, particles are lifted up by bursts, gain momentum from the fluid phase and carry fluctuations levels which are higher than those of the surrounding fluid (but still lower than in clear-water). For $y^+ < 20$ sweeps carry particles with high rms velocities close to the wall and the observed fluctuations are even larger than in clear-water. In the last condition, the difference between particle and fluid fluctuations also depends on the presence of the wall which bounds the vertical fluctuations of the particles.

The question of particle-flow interaction is lastly addressed by separating the Reynolds stress intensity in "coherent" or "incoherent" events using the quadrant analysis. For "coherent" events, the second quadrant corresponds to ejections, while the fourth to sweeps; first and third quadrant events are referred as "incoherent". The quadrant analysis indicates substantial differences in particle-fluid interactions between the wall ($y^+ < 10$) and the buffer regions. For $y^+ < 10$, the intensity of ejection events (second quadrant) gains importance over sweeps in sediment-laden conditions (in comparison to clear-water). On the other hand, in the buffer region both Reynolds stress coherent intensities decrease when comparing sediment-laden to clear-water conditions, the damping of ejection events being stronger than that of sweeps; this circumstance corroborates the previously mentioned hypothesis of a significant momentum transfer between the two phases.

REFERENCES

Adrian, R.J., Meinhart, P. & Tomkins 2000 Vortex organization in the outer region of the turbulent boundary layer. J. Fluid Mech. 422, 1–54.

Best, J., Bennett, S., Bridge, J. & Leeder, M. 1997 Turbulent modulation and particle velocities over flat sand beds at low transport rates. J. Hydr. Engrg., ASCE 123, 12, 1118–1129.

Coleman, N.L. 1981 Velocity profiles with suspended sediment J. Hydr. Res., IAHR, Delft, The Netherlands 19, 211–229.

Coleman, N.L. 1986 Effect of suspended sediment on the open channel velocity distribution. Water Resources Research 22, 1377–1384.

Grass, A.J. 1974 Transport of fine sand on a flat bed: turbulence and suspension mechanics. In *Proc. Euromech 48*, Inst. Hydrodynamic and Hydraulic Engrg. Tech. Univ. of Denmark, pp. 33–34.

Greimann, B.P., Muste, M. & Holly, F.M. 1999 Two-phase formulation of suspended sediment transport. J. Hydr. Res., IAHR, Delft, The Netherlands 37, 4, 479–500.

Ishii, M. 1975 Thermo-Fluid dynamic theory of two-phase flow, Eyrolles, EDF, Paris.

Itakura, T. & Kishi, T. 1980 Open channel flow with suspended sediments. J. Hydr. Div., ASCE 106, 1325–1343.

Kaftori, D., Hetsroni, G. & Banerjee, S. 1995 Particle behaviour in the turbulent boundary layer II. Velocity and distribution profiles. Phys. of Fluids 7, 5, 1107–1121.

Karlsson, R.J. & Johansson, T.G. 1986 In Selected papers of the 3rd Symposium on Application of Laser Techniques to Fluid Mechanics, Lisbon, Portugal, pp. 273–289.

Krogstad, P.A. & Antonia, R.A. 1999 Surface roughness effects in turbulent boundary layers. Experiments in Fluids 27, 450–460.

Kulick, J.D., Fessler, J.R. & Eaton, J.K. 1994 Particle response and turbulence modification in fully developed channel flow. J. Fluid Mech. 277, 109–134.

Laufer, J. 1950 Investigation of turbulent flow in a two-dimensional channel. NACA Tech. Note TN2123.

Lu, S.S. & Willmarth, W.W. 1973 Measurement of structure of the Reynolds stress in a turbulent boundary layer. J. Fluid Mech. 60, 481–511.

Lumley, J.L. 1978 Two-Phase and Non Newtonian Flows. In Turbulence (edited by P. Bradshaw), Springer-Verlag, Berlin, pp. 289–324.

Lyn, D.A. 1986 Turbulence and turbulent transport in sediment-laden open channel flows. Report KH-R-49, W.M. Keck Lab. of Hydr. and Water Resour. California Inst. of Tech., Pasadena, USA.

Lyn, D.A. 1988 A similarity approach to turbulent sediment-laden flows in open channels. Turbulence and turbulent transport in sediment-laden open channel. J. Fluid Mech. 193, 1–26.

Muste, M. & Patel, V.C. 1997 Velocity profiles for particles and liquid in open channel flow with suspended sediment. J. Hydr. Engrg., ASCE 123, 9, 742–751.
Nezu, I. & Nakagawa, H. 1993 Turbulence in open channel flows. In IAHR Monograph. A. A. Balkema, Rotterdam, The Netherlands.
Niño, Y. & Garcia, M.H. 1996 Experiments on particle-turbulence interactions in the near-wall region of an open channel flow: implications for sediment transport. J. Fluid Mech. 326, 285–319.
Owen, P.R. 1969 Pneumatic transport. J. Fluid Mech. 39, 407–432.
Righetti, M. 1994 Interaction between fluid and suspended sediments in the near-wall region of an open channel flow (in italian). PhD. Thesis, University of Padova, Italy.
Shen, C. & Lemmin, U. 1999 Application of an acoustic particle flux profiler in particle-laden open channel flow. J. Hydr. Res., IAHR, Delft, The Netherlands, 37, 3, 407–419.
Sumer, M.B. & Deigaard, R. 1981 Lift forces on moving particles near boundaries. Part 2. J. Fluid Mech. 109, 311–337.
Sumer, M.B. & Oguz, B. 1978 Particle motions near the bottom in turbulent flow in an open channel. J. Fluid Mech. 86, 109–127.
Tennekes, H. & Lumley, J.L. 1972 A first course in turbulence. MIT Press, Cambridge, USA.
Tsuji, Y. & Morikawa, Y. 1982 LDV measurements of an air-solid two-phase flow in a horizontal pipe. J. Fluid Mech. 120, 385.
Tsuji, Y., Morikawa, Y. & Shiomi, H. 1984 LDV measurements of an air-solid two-phase flow in a vertical pipe. J. Fluid Mech. 139, 417–434.
Valiani, A. 1991 The von-Kàrmàn coefficient in sediment-laden flow. J. Hydr. Res., IAHR, Delft, The Netherlands 29, 1, 129–136.
Vanoni, V.A. 1946 Transportation of suspended sediment by water. Transactions ASCE 111, Paper N°2267, 67–133.
Wei, T. & Willmarth, W.W. 1989 Reynolds-number effects on the structure of a turbulent channel flow. J. Fluid Mech. 204, 57–96.
White, A. 1974 Viscous fluid flow. Mc Graw Hill, N.Y.
Yalin, G. 1972 Mechanics of sediment transport. Pergamon Press.

River Flow 2004 – Greco, Carravetta & Della Morte (eds.)
© 2004 Taylor & Francis Group, London, ISBN 90 5809 658 0

Studies of sedimentation in a large-scale reservoir for power generation

T. Shinjo
Electrical Engineering Dept., Electric Power Development Co., Japan

Y. Fujita
River Basin Research Center, Gifu University, Japan

ABSTRACT: The initial total storage capacity of 327 Mm^3 of Sakuma dam reservoir in 1957 has been reduced to 213 Mm^3 in 2002 due to sedimentation of 114 Mm^3. In order to reduce flood damage in the upstream area caused by the sedimentation, attempts to lower the riverbed is being continued by dredging and flushing with river water. However, riverbed has not been lowered sufficiently, hence more efficient measures are required. So, accumulated reservoir data of flow discharge, cross sectional surveying and grain size distribution were examined to clarify actual state of the sedimentation. Results of the examination show that sediment concentration is decreasing. Another results of sediment movement were compared with those evaluated from 1-D analyses of non-uniform flows, indicating the efficiency of the sediment flushing. Accumulation curves of volumetric changes of cross sections were obtained for individual grain sizes, which can express sediment movement in the reservoir properly.

1 INTRODUCTION

The central part of Japanese archipelago has a large amount of sediment yield and a large scale dam reservoir for power generation, Sakuma Dam, is located there. The Sakuma Dam is constructed at middle reach of The Tenryu River, which flows southward to the Pacific Ocean through the Inadani Valley between the Central and Southern Japan Alps, starts from Lake Suwa located almost center of Japan. It has trunk length is 213 km and drains a catchment area of 5,090 km^2. It also has a large river with a high flow volume. The Tenryu River Basin consists of strata from Paleozoic to Alluvium, and includes visible igneous, sedimentary, and metamorphic rocks. Because of its particularly steep topography accompanied by the fragile geology of the Median Tectonic Line, heavy rains and flood flows erode, discharge, and transport extremely large quantities of sediment. Figure 1 is a map of the Tenryu River Basin .

Dams constructed on the main course of the Tenryu River are, from the upstream end, the Yasuoka Dam and the Hiraoka Dam operated by the Chubu Electric Power Co. and the Sakuma Dam, Akiha Dam, and the Funagira Dam operated by the Electric Power Development Company (EPDC). There are 10 dams on its tributaries including the Miwa Dam and the Koshibu Dam that are operated by the MLIT. The total sedimentation rates (total sedimentation/total storage capacity) of two of these dams, the Ya suoka Dam and the Hiraoka Dam, were 80.1% and 84.9%* respectively in 2002, and because there has been only a slight change in these numbers during the past 20 years**, it has been concluded that almost all of the sediment that flows down the Tenryu River and its tributaries flows into the Sakuma Reservoir.

The Sakuma Dam located near the end of a narrow gorge directly downstream from the Inada Valley and about 70 km from the mouth of the river. A concrete gravity dam that is 293.5 m long and 155.5 m high, and has dam volume of 1.12 Mm^3, it was completed in 1956. The water stored in the reservoir of the Sakuma Dam having initial capacity of 327 Mm^3 is used to generate electric power at the Sakuma Power Station (max. output 350 MW), producing more electric power than any other hydropower plant in Japan (approx. 1.5 TWh/year). Part of the stored water is directly supplied to agricultural and industrial water users and to public water supply systems. Water that has been used to generate electric power at the Sakuma Power Plant is used again by five more downstream power plants (Sakuma No. 2, Akiha No. 1, 2, and 3, and Funagira, total maximum output 1.911 GW) and is also used to maintain the river's normal flow volume that includes water for agricultural users and public water supply systems. The average annual inflow water volume to

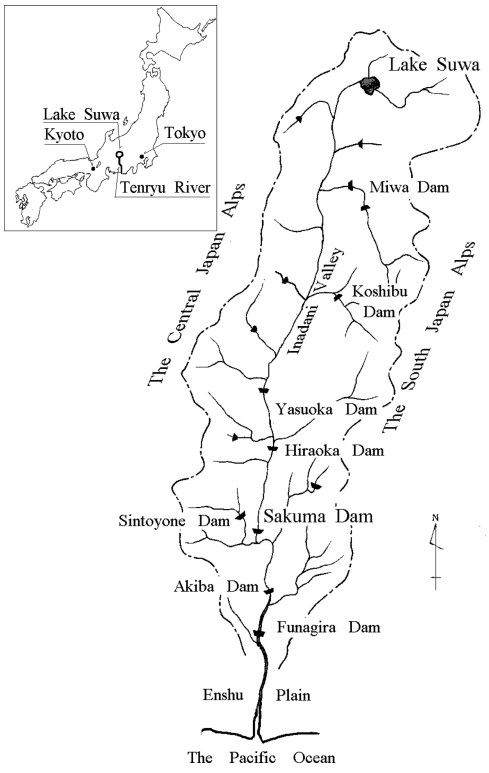


Figure 1. Location of the Tenryu River and a map of its basin.

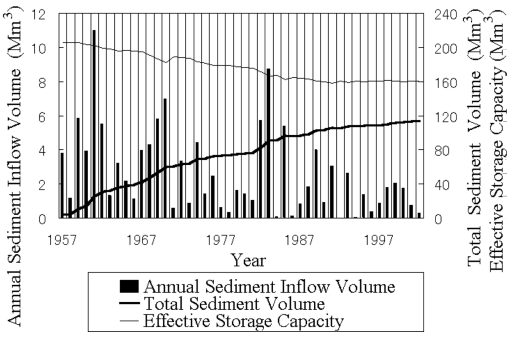


Figure 2. Volumetric changes in annual sedimentation of the Sakuma Reservoir.

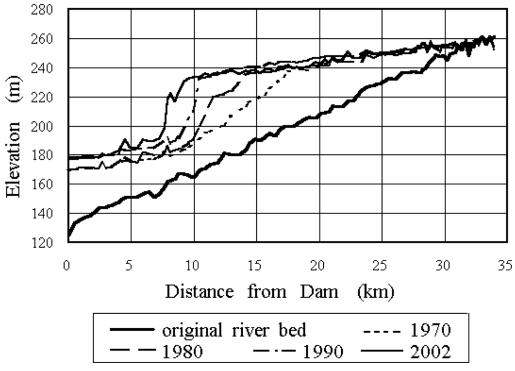


Figure 3. Change of the longitudinal profile of the riverbed in the Sakuma Reservoir.

the Sakuma Dam is extremely high, at 5 Gm^3/year, and because of the river basin conditions described above, this water carries a large quantity of sediment. Therefore the total volume of sediment in 2002 reached 114 Mm^3 that equaled approximately 35% of the total reservoir capacity of 327 Mm^3, and was the highest in Japan.

This paper reports first an outline of the sedimentation in the Sakuma Reservoir and countermeasures taken to deal with this problem, and clarifies sediment behaviors in the reservoir, including the results of a study of the properties of the inflow of sediment and effects of promotion of sediment movement (flushing sediment with flowing water). This study is attempt to use existing data and from the view point of river mechanism towards future development of countermeasures against of reservoir sediment.

2 SEDIMENT PROCESS OF THE SAKUMA RESERVOIR

2.1 *Volumetric changes in annual sedimentation*

Figure 2 shows volumetric changes in annual sedimentation of the Sakuma Reservoir as change over the years of the inflow sediment volume, total accumulative sediment, and effective storage capacity. This figure shows that about 10 years after the dam was completed, large quantities of sediment continued to flow into the reservoir at a rate of 4.2 Mm^3/year, but later, in years such as 1970 and 1983 when large-scale runoff occurred, quantities of sediment greater than 5 Mm^3/year flowed into the reservoir, but the inflow sediment volume has tended to decrease, reaching an average of about 1.2 Mm^3/year during the past decade.

2.2 *Sediment process in the reservoir*

Figure 3 shows change of the longitudinal profile of the riverbed in the Sakuma Reservoir. The high water level of the reservoir is EL. 260 m (dam water level; 40 m), the low water level is EL. 220 m, (reference level of dam water; 0), and the available depth is 40 m.

According to Figure 3, sedimentation has progressed gradually from the upstream end of the reservoir, and in about 1970, the delta shoulder formed near the EL. 236 m point approximately 18 km from the dam (below, distances represent distances from

the dam). During the winter of 1971–1972, the construction of the Shintoyone Pumped Storage Power Station was accompanied by a decline of the water level in the Sakuma Reservoir to below 220 m, flushing the deposited sediment, and by about 1980, the delta shoulder had formed not only near EL. 230 m, but also near EL. 220 at a distance of about 12 km. Since the Shintoyone Pumped Storage Power Station began operating in 1972, the Sakuma Reservoir has almost constantly maintained a water level higher than EL. 230 m. The elevation of the delta shoulder is fixed at approximately EL. 230 m as it was shaped in 1990, and upstream from the delta shoulder, sedimentation advanced forming a gentle sedimentation gradient, but the riverbed is almost unchanged upstream from the 30 km point. And beginning in 1991, as one of the sedimentation countermeasures described below, the reservoir level was lowered to a target level of EL. 232.5 m where it was maintained for about one month in the winter dry period, resulting in the delta shoulder advancing to about the 10 km point by 2002 while maintaining an elevation close to EL. 232.5.

2.3 *Current countermeasures against the sedimentation****

At the Sakuma Dam, the following sedimentation countermeasures were implemented in order to "prevent submergence of the land during flooding in the upstream river basin" because a large quantity of sediment was deposited in the reservoir, raising the upstream riverbed.

(a) Flushing operation with river water
For 35 days from mid February to late March during the dry period, the water level in the reservoir of the Sakuma Dam was reduced, maintaining the water level at a target of EL. 232.5 m in order to form a natural river course inside and upstream from the reservoir, and to use the river water in this area to move deposited sediment below the effective capacity in the downstream part of the reservoir. The results of measurements show that between 1 M to 2 Mm^3/year of sediment was moved.

(b) Artificial transport to the dead capacity of the reservoir
A dredge was used to dredge sediment from the middle part of the reservoir, then the dredged sediment was transported and dumped at or below the effective capacity of the downstream part of the reservoir. The target was approximately 0.4 Mm^3/year.

(c) Artificial removal from the reservoir
Dredged sediment was used by quarry operators as concrete and asphalt aggregate and as sand for golf courses. The target was approximately 0.4 Mm^3/year.

But, of these sediment countermeasures, transport within and removal from the reservoir could only be applied in the middle part of the reservoir because of restrictions on the draft of barges. Because flushing operation is done during the dry season, the scale of runoffs that occur during that period is not large and it is difficult to move large particle size sediment in the river basin, so as shown in Figure 3, in the upstream river, the sediment has not been removed as the riverbed has fallen.

3 CHARACTERISTICS OF SEDIMENT INFLOW TO THE RESERVOIR

Figure 2 shows that extremely small quantities of sediment flowed into the Sakuma Reservoir in the two years following 1961, 1970, and 1983 that were years when the annual sediment inflow was high. This is assumed to be the impact of measurement accuracy, but it is also hypothesized that the deposited sediment in the upstream river is excessively scoured by large scale runoffs that transport it all to the reservoir at one time, with the result that during the next two years, little sediment is carried down the river, lowering the quantity of sediment carried into the reservoir. Figure 4 shows the changes in annual inflow of water and sediment.

The total annual water discharge has ranged from a little more than 3.0 Gm^3/year to a little less than 8.0 Gm^3/year since 1957 when the Sakuma Power Station began operating. The total sediment inflow volume was higher than 5.0 Mm^3/year in 1961, 1970, and 1983, but the total annual water discharge in those years was approximately 5.5, 4.7, and 7.6 Gm^3/year, and except for 1983 when the past maximum annual water discharge was recorded, the average value was not exceeded in 1961 and 1970. Inversely, in 1998 when the second highest annual water discharge of 7.5 Gm^3/year was recorded, the total sediment inflow volume was low at 2 Mm^3.

In this way, the total sediment inflow volume is not necessarily large, just because the annual water discharge is large. And as shown in Figure 5, change over years is indicated by calculating the annual average inflow sediment concentration by dividing the annual sediment inflow volume by the annual water discharge. According to this, in 1961, 1970, and 1983 when the sediment inflow volume was high, the annual average inflow sediment concentration was higher than in was in the previous and following years, but the tendency for the annual average inflow sediment concentration to fall overall is conspicuous. It is, therefore, hypothesized that the sediment inflow volume at the Sakuma Reservoir will either be maintained or fall gradually in the future, as long as a phenomenon that sharply increases the inflow sediment volume does not occur.

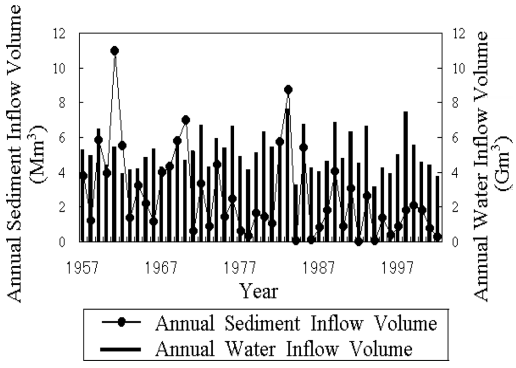


Figure 4. Changes in annual inflow of water and sediment.

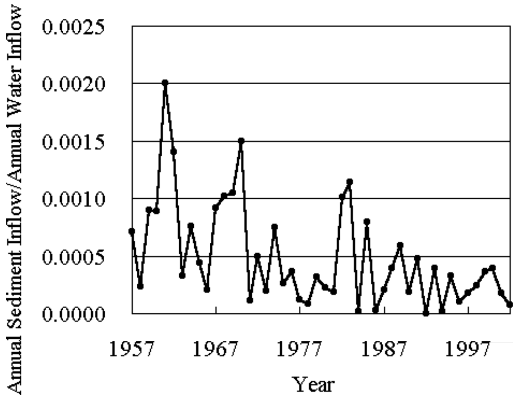


Figure 5. Changes in annual mean of sediment concentration.

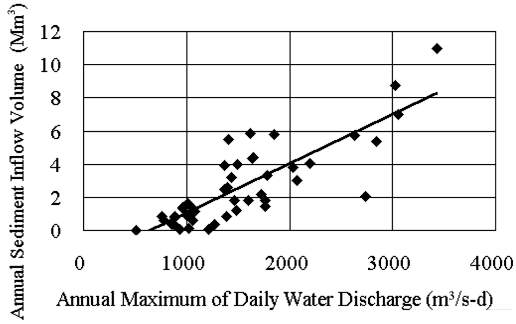


Figure 6. Correlation between annual sediment inflow volume and annual maximum daily water discharge.

Because as shown by Figures 4 and 5, high correlation between the annual sediment inflow volume or the annual average inflow sediment concentration with the annual total water discharge cannot be counted on, correlation analysis of the annual maximum of daily discharge, the annual maximum discharge, and the annual total of the daily average discharge equal to or above a stipulated value was performed. As shown in Figure 6, the results show the clearest correlation between the annual maximum of daily discharge and the annual sediment inflow volume. But as seen in 1999, there are years far from the regression line, so in the future, it will be necessary to carry out a detailed study of the governing flow volume of the sediment inflow volume.

4 CHARACTERISTICS OF SEDIMENT MOVEMENT IN THE RESERVOIR

4.1 *The particle size distribution of the deposited sediment*

As stated above, even though sedimentation countermeasures have been taken in the Sakuma Reservoir, the upstream riverbed has not fallen. To study this point, an attempt was made to clarify the state of movement of the sediment by studying the quantity of change of the particle size distribution and the lateral section of the deposited sediment.

The particle size distribution of the deposited sediment was surveyed in 1979, 1980, 1981, 1983, 1988, 1992, 1995, 1997, 1998, and 1999, but the surveys up to 1995 were primarily carried out to clarify whether or not it is possible to effectively use the deposited soil as aggregate or as clay for ceramics manufacturing by sampling sediment on the surface, but there are details of the sampling locations that are not clear. However, the surveys of 1997, 1998, and 1999 were done by, according to the location, boring holes to a depth of 20 m, taking samples from the holes, and using them to measure particle size distribution by sieve analysis and by precipitation analysis in order to clarify the state of sediment deposition inside the reservoir.

First, the depths involved in sediment movement were hypothesized based on the results of a sedimentation survey of the riverbed section. The results of a comparison of the lateral section shape of the same section in 1997 and 1998 that was made to obtain the deposition thickness or the eroding depth revealed that at locations where the delta shoulder had advanced, a maximum of 10 m of sediment or more was deposited, and that there are sections where encouraging sediment transport had caused scouring of about 8 m. But because the change in almost all the sections was within a range of 5 m, it was judged that the range of the sediment movement is limited to approximately 5 m from the surface, and assuming that the particle size distribution related to sediment movement can be obtained by averaging the data from the surface to the depth of 5 m, these are averaged in a case where samples are taken from multiple locations in a single section. The particle size distribution is shown at

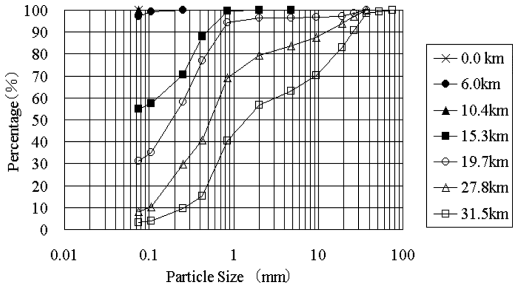


Figure 7. Particle size distribution of sediment (1981, 83).

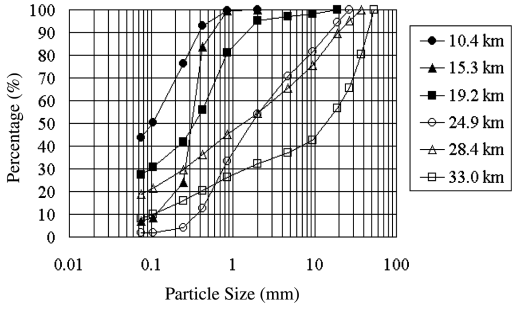


Figure 8. Particle size distribution of sediment (1997, 98, 99).

representative locations for 1981 and 1983 in Figure 7 and for 1997, 1998, and 1999 in Figure 8.

Both figures show that the particle size distribution generally coarsens with the distance upstream, and that the reservoir triggers classification action, but according to Figure 7, at that time, sedimentation in the range from the delta shoulder to the downstream 10 km location consisted of at least 95% silt.

In Figure 8 on the other hand, the range to the 10 km location was not surveyed, so a comparison with the situation in this range is impossible. But while the fine particle near the 15 km point increases more than in it does in Figure 7, upstream from the 20 km location, the fine particle declined coarsening the material. It is hypothesized that this is a result of the movement of the fine particle from the upstream area by flushing operation that began in 1991.

4.2 *Longitudinal changes in particle size distribution and critical particle size of incipient motion*

To clarify the state of sediment movement inside the reservoir by flushing operation, a reservoir level of EL. 233 m and discharge of 150 m^3/s that are the average water level and inflow volume during the period were set to calculate the traction force by a one-dimensional numerical analysis of the river course in 1981 and in

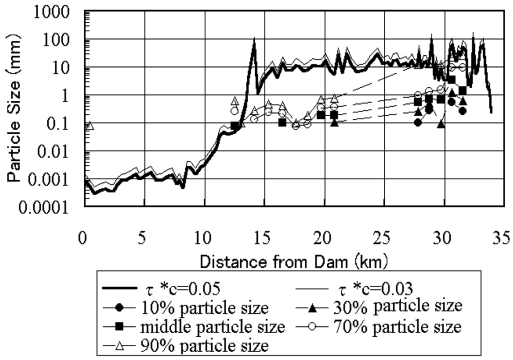


Figure 9. Longitudinal changes in each particle size and critical particle size of incipient motion (1981, 83).

1997. Figure 9 and Figure 10 show the results of longitudinal changes in each size, 10%, 30%, 50%, 70%, 90%, and critical particle size of incipient motion.

According to Figure 9, in part of the river downstream from the 30 km location in 1981 before beginning of flushing operation, sediment that was at least 90% particle size or less could be transported, and upstream from the 30 km point, sediment up to 70% could be transported, suggesting that flushing operation had adequately flushed sediment from the midstream to the upstream parts of the river.

According to Figure 10 on the other hand, the range where sediment of 90% particle size or less could be transported was limited to the river up to the 25 km location, and even further upstream, it appears that sediment of about 70% particle size could not be transported. Although the effectiveness of flushing operation has declined a little from its initial level upstream under the impact of coarsening of the sediment, it can be counted on to continue to be adequately effective in the midstream part of the river.

Therefore, it is assumed that although the traction force is adequate, the riverbed has not fallen upstream from the middle of the reservoir for the last few years, because such conditions have been created by the inflow of a quantity of sediment either higher than or equivalent to the quantity transported. It is also hypothesized that the actual quantity of sediment that is transported has fallen because as a result of rippling of the riverbed, the traction force that was calculated cannot effectively transport all the sediment. To clarify these points, the total quantity transported must be calculated in detail based on a sediment transport by particle size equation, but because this paper cannot discuss that question, it will be left as a challenge for the future.

Turning to the second reason, it is highly likely that riverbed ripples of the lower regime were caused according to The Froude Number or the particle size. But in the case of the Sakuma Reservoir, there are

many sections where the ratio of hydraulic radius to average particle size has reached the 10^4 order, exceeding the range of the existing riverbed ripple data, so a judgement is impossible and we hope to observe and clarify the actual way the riverbed shape was formed as soon as possible.

A comparison of Figure 9 and Figure 10 shows conspicuous coarsening of the sediment between the 10 km and 15 km locations, while inversely the fine particle is higher from the 17 km to the 18 km locations than it is further upstream and downstream. In the latter part, the river flows from a slightly narrow straight part to a wider meandering part, and it is hypothesized that the fall in the flow speed deposits the fine particle and also alters the critical particle size incipient motion. Similarly, according to Figure 10, the percentage of silt and fine sand near the 22 km location rises, but this tendency is not shown by Figure 9. Nearby, a straight slightly narrow part of the river is directly linked to a meandering part that is equally narrow, so it is possible that the weir effect of the flow causes the increase of fine sediment, and it is assumed that this trend is confirmed only by extremely recent data because the flow properties now closely resemble the properties of the flow in a normal river as a result of flushing operation. It is necessary to deal with these matters by conducting a study with the effects of discharge during normal reservoir operation clearly separated from the action of flushing operation.

Among the surveys done in 1981 and 1983 and the surveys done in 1997, 1998, and 1999, there are only four cases where the same section was surveyed, and even in sections surveyed more than once, it is not possible to know if the same location was surveyed. It is, therefore, difficult to state positively that the sediment has been coarsened. And because the number of data are limited, even in a case where multiple locations of a single section are surveyed, regardless of whether the locations are on the inside or the outside of a bend, the results are averaged and this is compared with the results of one-dimensional analysis. But it is necessary to do a detailed study of the effects of flushing operation, and we wish to undertake this challenge in the future.

4.3 *Sediment transport of individual particle size class in the reservoir*

The state of movement of sediment inside the reservoir was evaluated by particle size based on the particle size distribution and the quantity of section change of the deposited sediment in the previous part of this report.

4.3.1 *Sedimentation volume of individual particle size class in the reservoir*

In the Sakuma Reservoir, every year the volume of deposited sediment is measured after the runoff season, and the shape of the lateral section of reservoir and the quantity of sedimentation are reported to the Ministry of Economy, Trade, and Industry and to the Ministry of Land, Infrastructure and Transport. These section measurements are used to calculate the quantity of sediment by particle size for each section. Because in the Sakuma Reservoir, sediment is dealt with by transporting it within the reservoir and removing it from the reservoir as explained above, it is necessary to restore it to its condition before the sediment was processed by correcting the quantity removed from the reservoir and the quantity transported inside the reservoir according to the measurement results. Therefore, the quantity transported within the reservoir and the quantity removed from the reservoir and dredging and disposal location data concerning these movements of sediment are extracted from work documents to calculate the quantity of sediment corrected for each section. But although a local quarry operator transported sediment out of the reservoir in 1981 and 1982, there were no work documents specifying the dredged locations, so it was impossible to compensate for effects. The previous paragraph also applies to the particle size distribution of the sediment used for the analysis.

4.3.2 *Sediment transport of individual particle size class in the reservoir during terms of flushing operation and the other*

Figure 11 shows the longitudinal accumulation curve of sedimentation volume of individual classes that was obtained by accumulating the quantity of sedimentation for each particle size in each section calculated by multiplying the quantity of change of the section in 1981 and 1982 by the percentage of sediment at each particle size. Figure 12 shows the results of the same process for 1997 and 1998.

Because it is assumed that except for extremely fine sediment, no sediment passes through a large dam such as the Sakuma Dam, the curves on these figures represent the quantities of sediment by particle size that have passed through each section during the same period. Because even in the case of fine sediment, it is possible to estimate the quantity that passes through if the turbidity at the dam site is measured, if the curves corresponding only to that quantity move upward in parallel, the quantity that passes through each section is shown.

According to Figure 11, the accumulation curves of sediment volume of all particle sizes move upward to the right, and in 1981, the sediment flowing into the reservoir was deposited sequentially in the upstream direction. The quantity of inflow sediment with particle size less than 0.075 mm was extremely large and it was deposited in almost all parts of the reservoir, but it was conspicuous up to the 13 km location.

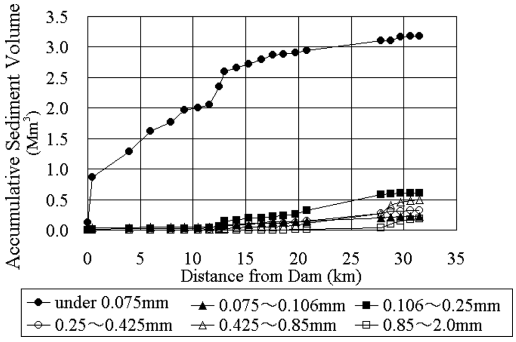


Figure 11. Longitudinal accumulation curve of sedimentation volume of individual classes, expressing their transported volume (1981–82).

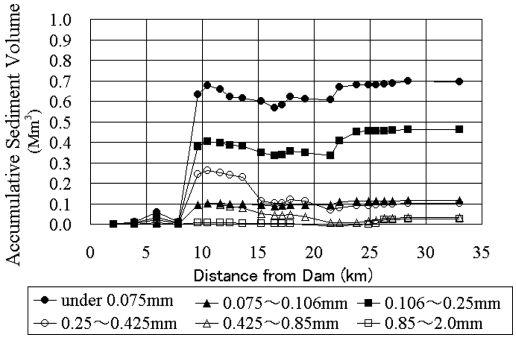


Figure 12. Longitudinal accumulation curve of sedimentation volume of individual classes, expressing their transported volume (1997–98).

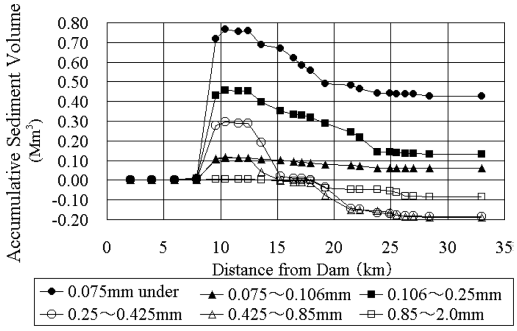


Figure 13. Longitudinal accumulation curve of sedimentation volume of individual classes, expressing their transported volume (Dec. 2000–May 2001).

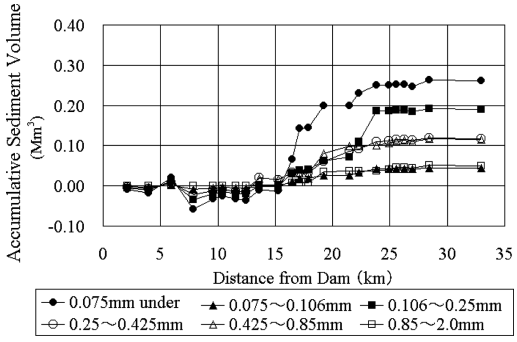


Figure 14. Longitudinal accumulation curve of sedimentation volume of individual classes, expressing their transported volume (Jun. 2001–Nov. 2001).

According to Figure 12 on the other hand, curves that fluctuate vertically match closely, indicating that there are alternating deposition and eroding zones. To take particle size of 0.85 mm or less as an example, the accumulative deposition of this sediment rises abruptly near the 10 km location showing that sedimentation has advanced here, and this tendency is particular clear for the fine sediment. Upstream from that location to near the 20 km location, this quantity falls, revealing eroding, and further upstream, after passing through a short part where sedimentation measures have been taken, there is almost no change in the accumulative quantity in any particle size upstream from the reservoir. This shows that in 1997, the sediment flowing into the reservoir had flowed downstream from the 25 km location without being deposited on the upstream riverbed. But the quantity that passed through clearly fell sharply from 1981. The increase in the quantity of deposition near the 10 km location is a result of the fact that most of it is fine sediment and the flushing operation had flushed out the small particle size sediment. Furthermore, the advanced sedimentation near the 22 km location conforms with a part of the river where the traction force fell as also seen in Figure 10. In this way, a longitudinal accumulation curves of sedimentation volume by particle size class is a useful way to show the process of sedimentation inside the reservoir.

And the great differences between the fluctuation of the curves in Figure 11 and Figure 12 reflects big differences in the quantity flowing in. For example while in 1981 and 1982 there were large runoffs, in 1998 and 1999, there were no large runoffs but the reservoir was operated by flushing operation.

Next, the effect of sediment movement in the reservoir by flushing operation is clarified by the longitudinal accumulation curve of sedimentation volume of individual classes. The sedimentation survey in the Sakuma reservoir is carried out in November and May after flushing operation. Figure 13 shows that from November 2000 to May 2001. Figure 14 shows that from May 2001 to November 2001. It is clear that flushing operation is greatly effective to transport sedimentation. We approached same attempts in other

years, but the efficiency of flushing is invisible in some case. This reason is supposed that intervals of around 200 m of cross section survey masked advanced distance of sediment delta. So, we started to survey more closely sediment delta by sound wave inquiry.

5 CONCLUSIONS

The process of sedimentation in the Sakuma Reservoir was studied based on the results of past surveys. The results have clarified the following points.

- The annual average inflow sediment concentration in the Sakuma Reservoir is tending to fall.
- The annual sediment inflow volume at the Sakuma Reservoir is closely correlated with the annual maximum daily dischrge.
- A comparison of the particle size distribution of the sediment around 1981 and around 1997 has shown that upstream, the coarsening of the sediment is conspicuous, revealing that the effectiveness of flushing operation has fallen to some degree in the upstream river.
- A comparison of the longitudinal accumulation curves of sedimentation volume by particle size class in 1981 ,1997, 2000 and 2001 clearly reveals that the state of deposition of the inflow sediment and the sedimentation inside the reservoir and state of eroding differ sharply between the two periods, clearly showing the effectiveness of the flushing operation.

In the future, horizontal two-dimensional flow analysis will be performed using the dam water level, water discharge and other data to clarify the sediment movement mechanisms that are the background to the sediment movement inside the Sakuma Reservoir that this study has clarified, and the results will be applied to propose and implement more effective sedimentation countermeasures.

ACKNOWLEDGEMENTS

The staff of the Chubu Regional Headquater and the Sakuma Power Administration Office of the Electric Power Development Company (EPDC) provided and organized documents used to prepare this report. Mr. Keisuke Ohashi and Mr. Takano Toshiya, graduate students at Gifu University, and Koyama Tetsuro, an undergraduate student of the same university also helped with the organization of the data. The authors wish to express their deep gratitude to them for their valuable assistance.

REFERENCES

* Ministry of Economy, Trade and Industry. 2003. The state of sedimentation in reservoirs for hydro power in 2002. *Electric Power Civil Engineering* No.307: 150–159

** Ministry of Trade and Industry. 1983. The state of sedimentation in reservoirs for hydro power in 1982. *Electric Power Civil Engineering* No.186: 109–115

*** Kouichiro, Kikuchi & Mineo, Muranaga & Katsukuni Itagusu. 2000. The state and countermeasure for sedimentation in Sakuma reservoir. *Electric Power Civil Engineering* No.291: 41–45

River Flow 2004 – Greco, Carravetta & Della Morte (eds.)
© 2004 Taylor & Francis Group, London, ISBN 90 5809 658 0

Experimental study of sediment laden flow in a hydraulic jump

M.H. Omid
Assistant Professor, Dept. of Irrigation and Reclamation Eng., University of Tehran

H. Nozari
Postgraduate student, Dept. of Irrigation and Reclamation Eng., University of Tehran

ABSTRACT: An experimental investigation was made to study the effects of bedload transport on super critical flow and hydraulic jump in a rectangular channel. Experiments were performed in a stilling basin of rectangular cross-section 500 mm wide and 3 m long. Uniform sands of 1.435, 4.05, and 5.555 mm and non-uniform sand of 0.63 mm with different concentration were used in the experiments for various types of hydraulic jump with Froude number ranging from 3 to 9. The results indicate that the sediment size and sediment concentration makes no changes to the incoming super critical flow conditions and therefore, has no effect on the characteristics of the jump (sequent depth, energy loss and length of jump). However, the incoming sediments are deposited in the sub critical zoon (end of jump) and move downstream as bedload. The motion of the sediment is wave-like with a mild slope at the front followed by a raised bed of nearly uniform thickness terminating into a step. This sand wave performs a control section similar to the end sill in a stilling basin and keeps the hydraulic jump position at the beginning of the basin. The thickness and the position of the front of this sand wave are expressed as a function of upstream Froude number.

1 INTRODUCTION

Bed-load transport is a common occurrence in natural and artificial streams. The transport of sediments along rigid channels is of importance to the design and operation of lined canals in irrigation practice and channels in treatment works. In many engineering applications with respect to sediment motion in rigid channels, bed load is the predominant mode of transport and hence has received the greatest attention. While the rate of sediment particles transported by the flow is depended on the flow characteristics; the present of sediments can also change the structure and characteristics of the flow. Research on this interdependent relationship in both open channel and pipe flows has been well documented by Einstein (1942), Mayer-peter and Muller (1948), Bagnold (1966), Wang and Chien (1985). On the other hand, in open channel flow, the transition between supercritical and sub critical flow is characterised by a sharp rise in the free surface elevation, strong turbulence and splashing. It is an interesting phenomenon that has caught the imagination of many research workers since its first description by Leonardo da Vinci (1452–1519). The Italian engineer Bidon (1818) is credited with the first experimental investigation of this phenomenon. Since then, considerable research effort has gone into the study of this subject. Although the hydraulic jump has been investigated experimentally for nearly two centuries, little information is known of the sediment laden flow in the hydraulic jump.

Turner (1973) induced a turbidity current undergoes a hydraulic jump by a change in bed slope in the contact of a canyon-fan transition. He showed that the conjugated depth of hydraulic jump in a turbidity current may be determined by:

$$\frac{y_2}{y_1} = \frac{1}{2}\left(\sqrt{1+8R_i^{-1}} - 1\right) \tag{1}$$

where R_i is Richardson number defined by:

$$Ri = \frac{g\,R\,C\,h}{U^2} \tag{2}$$

in which y_1 and y_2 are upstream and downstream depth of flow, C is sediment concentration and U is mean velocity.

Marcelo H. Garcia (1993) studied the characteristics of hydraulic jump in sediment driven bottom currents. He produced both the sediment-laden and saline fluid hydraulic jumps. He concluded that the saline and muddy hydraulic jumps have similar characteristics. A clear correlation between thickness of

deposition and grain size of the sediment driving flow was observed. For similar inlet conditions, the currents laden with coarser sediment generated thicker deposits. The most important effect of the change in flow regime was a marked reduction of the bed shear stress downstream of the hydraulic jump. Chanson (1997) developed a complete analogy between vertical plunging jet flows and hydraulic jumps in horizontal channel with partially-developed inflow. His study showed that the relationship between bubble frequency and air concentration differs between hydraulic jump flow and plunging jet flow. In a plunging jet flow, the bubble frequency and air concentration are not related by a unique parabolic shape.

H. Chanson and Brattberg (2000) studied the effect of the air-water shear flow in a hydraulic jump. They concluded that with partially-developed inflow conditions, a hydraulic jump is characterised by two air-water flow region with significantly different properties. In the air-water turbulent shear region, the void fraction distribution follows a solution of the diffusion equation and the bubble frequency profile exhibits a triangular shape with a maximum value. In the recirculation region, the air content increases toward 100% and the bubble frequency profile follow a different trend which is related to a different air-water flow structure and bubble size composition. Bergeron and Carbnneau (1999) considered the effect of sediment concentration on bed load roughness. They concluded that increasing sediment concentration induced a steepening of the near-bed velocity gradient that due to increase of shear stress and a corresponding increase of the roughness scale. Khullar et al (2002), on the basis of experimental study on the effect of suspended sediment on flow resistance have shown that the effect of suspended sediment on flow resistance is not the same in the both rigid and alluvial channel. They showed that in the absence of any noticeable change in bed form size the value of friction factor in alluvial channels is found to decrease with an increase in the suspended sediment concentration. In rigid boundary channels the friction factor value can decrease or increase with an increase in the value of the suspended sediment concentration.

This paper presents the results of flume experiments to investigate the experimental study of the sediment laden flow in a hydraulic jump. The results presented in this paper are expected to be useful in designing the stilling basins in the presence of sediment laden inflow.

2 EXPERIMENTAL SET UP AND PROCEDURE

Experiments were conducted in the hydraulic laboratory at Tehran University. Experiments were performed in a channel of glass sides and smooth bed, and of rectangular cross-section 500 mm wide and 9 m long. The downstream end of the channel is provided with a sediment trap and downstream tailgate to adjust the tail water depth. The supercritical inflow was initiated by a gate opening from an upstream head tank and the sediment was injected to the flow at the back of the gate. One uniform sand of 4.05 mm with different concentration was used in the experiments for various types of hydraulic jump with Froude number ranging from 3 to 9. For each Froude number, four sediment concentrations were produced. For each injection rate I, expressed in terms of mass rate, the corresponding volumetric concentration of sediment C simply is:

$$C = \frac{I}{Q\gamma_s} \tag{3}$$

Where Q is the water discharge and γ_s is the grain specific weight taken as 2650 kg/m^3. The experimental conditions are summarized as follows:

- Uniform sediment diameters used: 1.435, 4.05, 5.555 mm
- Non-uniform sediment diameters used: 0.63 mm
- Froude numbers: 3, 4.5, 6, 7.8 and 9
- Sediment concentration: 0.16, 0.3, 0.4 and 0.5%

3 RESULTS

For considering the effect of the sediment concentration on hydraulic jump, sediment concentration was increased in a number of experiments and the depths of flow before and after the jump was measured. In Figure 1 are shown the experimental results of the variation of y_2/y_1 as a function of initial Froude number Fr_1, for sediment with different size. This figure shows that the sediment laden inflow makes no changes to the ratio of the sequent depth of hydraulic jump.

Effect of sediment concentration on relative energy loss is shown in Figure 2. In this figure is also shown theoretical line of relative loss. This figure also shows the sediment concentration has no change to the loss of energy.

The variation of relative jump length Lj/y_1 as a function of initial Froude number Fr_1, for different sediment concentration is shown in Figure 3. The results show that the sediment laden inflow makes no changes to the length of hydraulic jump.

For considering the effect of the sediment size on hydraulic jump, sediment size was increased in a number of experiments and the characteristic of jump was measured. The result shows that the sediment size has no effect on parameter of hydraulic jump (Figs 4 to 6).

As it was presented in the above figures, sediment transport, sediment size and their concentration in the range of present study in our experiments has no effects

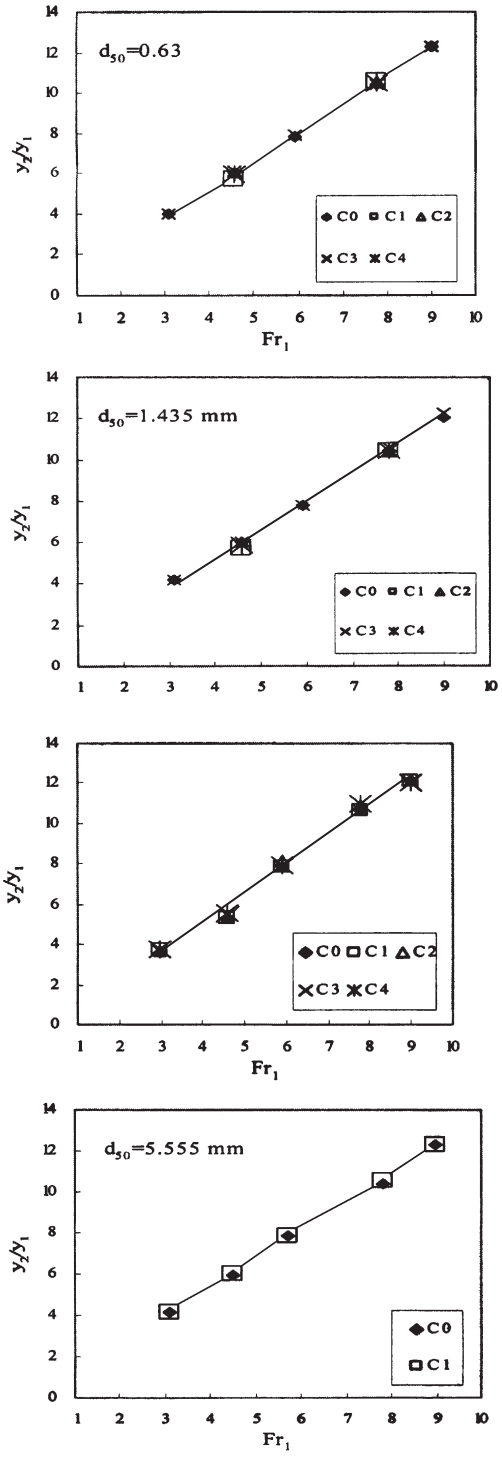


Figure 1. Variations of conjugated depth of jump for different sediment concentration.

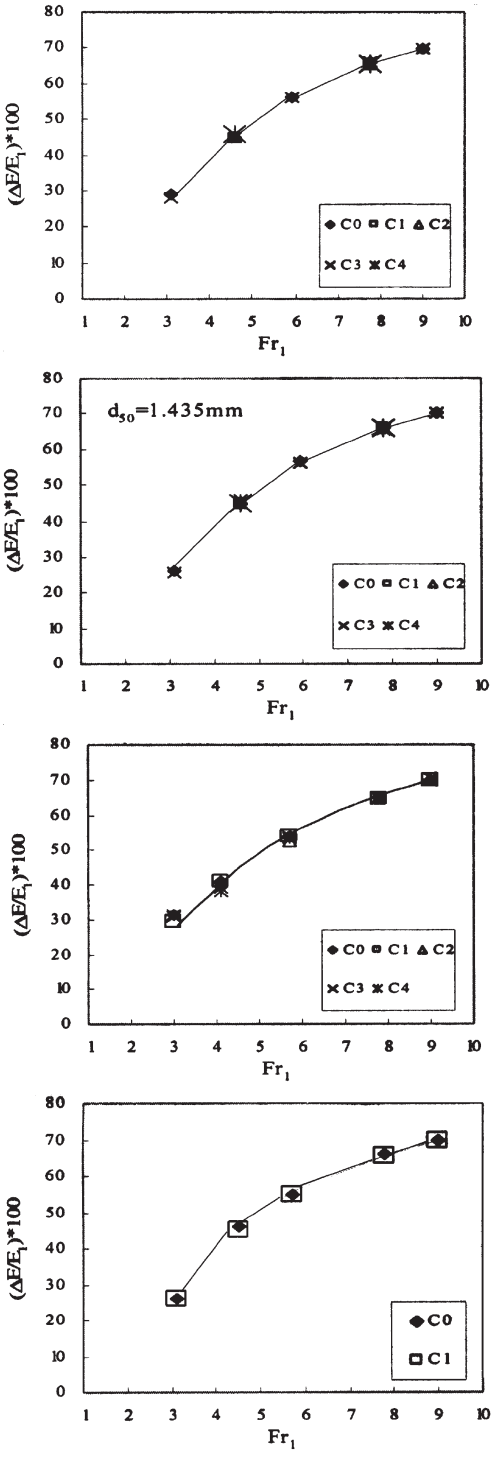


Figure 2. Relative energy loss in a jump for different sediment concentration.

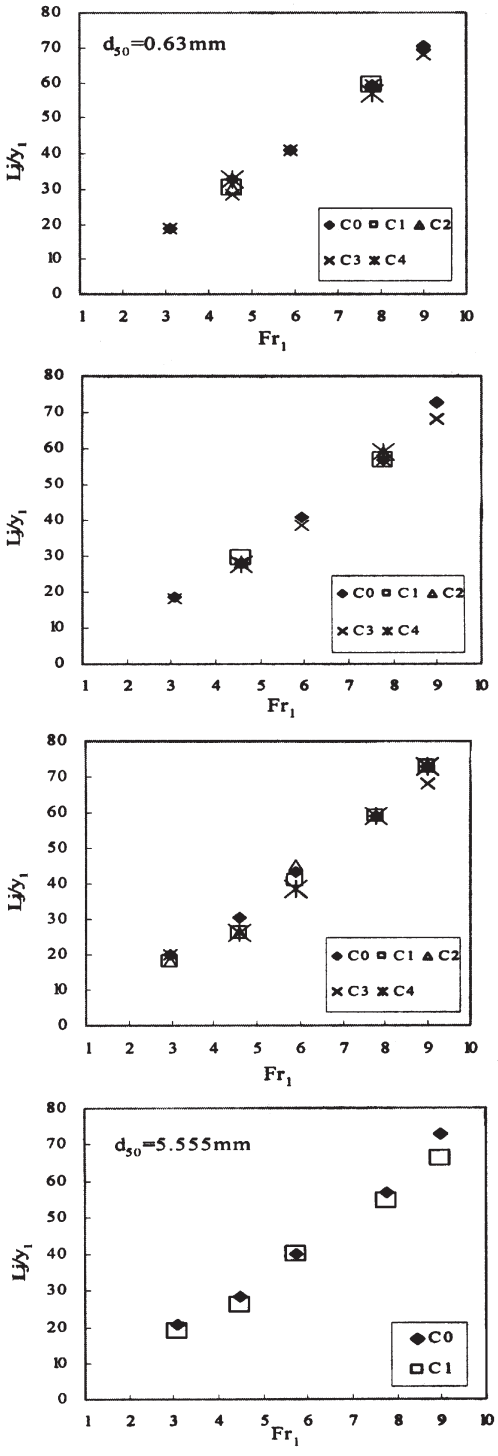


Figure 3. Length of hydraulic jump for different sediment concentration.

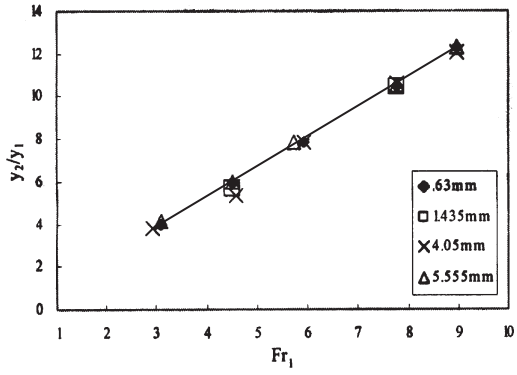


Figure 4. Variations of conjugated depth of jump for different sediment size.

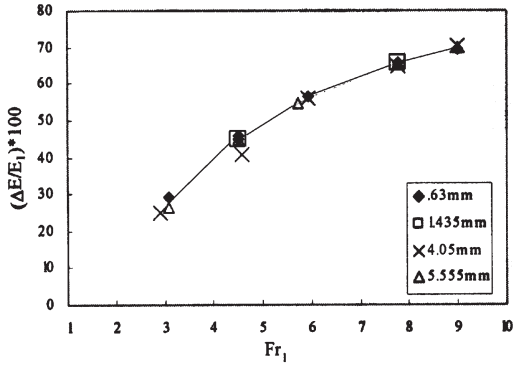


Figure 5. Relative energy loss in a jump for different sediment size.

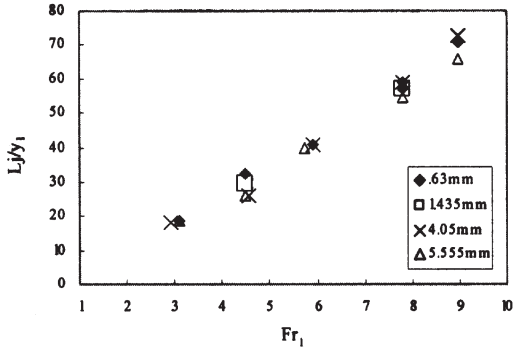


Figure 6. Length of hydraulic jump for different sediment size.

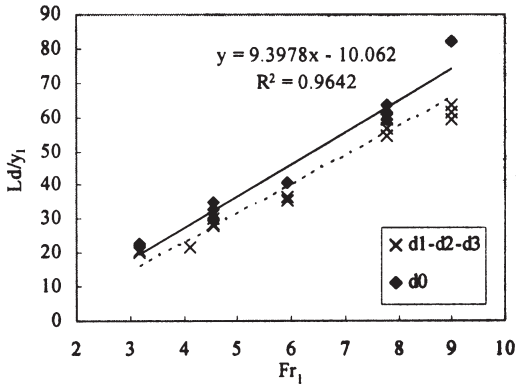


Figure 7. The position of the front of the sand dune wise from the gate.

on the hydraulic jump characteristics. However, the incoming sediments are deposited in the sub critical zoon (downstream of jump) and move downstream as bedload. The motion of sediment is wave-like with a mild slope at the front followed by a raised bed of nearly uniform thickness terminating into a step with an angle equal to the submerged angle of repose of sediment. The position of the front of this dune-wise sand wave is almost unvarying in a certain flow and sediment conditions but the ending step moves downstream making a growing sand wave with a constant speed which is related to the inflow sediment rate. The position of the front of this dune-wise sand wave from the gate is shown in Figure 7.

In this Figure, the length of the jump for clear water and trend line for non-uniform sand are shown as a dotted line and a straight line respectively. The above figure implies that the position of the front of this dune-wise sand wave from of the gate equal to the length of the jump for three uniform sands (1.435, 4.05 and 5.555 mm). But in the non-uniform sand, sediment was finer than the other sands and transported further than the gate and movement to down stream channel like several dune.

This sand wave performs a control section similar to the end sill in a stilling basin and keeps the hydraulic jump position at the beginning of the basin. The thickness of the front of this sand wave is functions of upstream Froude number. In Figure 8 the dimensionless form of the experiment data compared with the theoretical height of the end sill. As it can be seen from the figure, there is a good agreement between the two sets of results.

The main variables that govern the thickness of the erosion wave in an open rigid boundary channel with deposited bed include hydraulic characteristics of flow such as the water depth, the flow velocity or the shear velocity and the bed slope, and the sediment characteristics such as grain size and initial bed

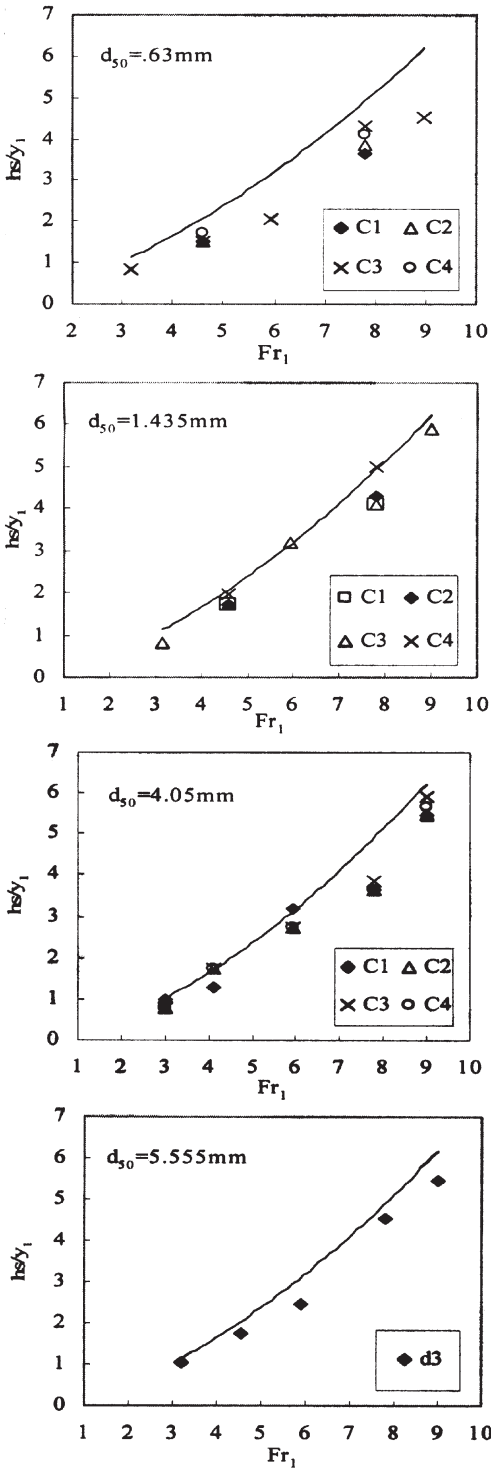


Figure 8. The thickness of the front of the sand dune wise.

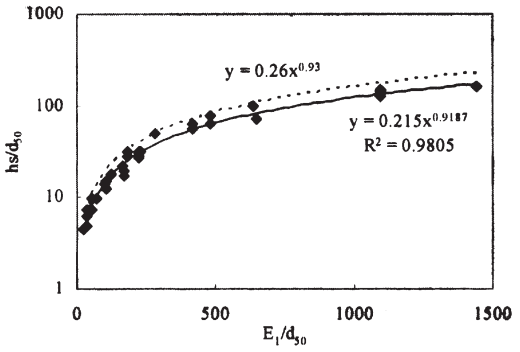


Figure 9. Sand wave height as a function of specific energy.

thickness. Omid et al (2001) introduced a different non-dimensional parameter using upstream specific energy. They showed that the sand wave height is a function of specific energy upstream of the erosion wave for sub critical flow and it determined by:

$$\frac{h_s}{d_{50}} = .26\left(\frac{E_s}{d_{50}}\right)^{0.93} \quad (4)$$

where h_s is the thickness of the sand wave, d_{50} is particle size such that 50% of particles are finer than this size by weight and E_s is the specific energy upstream of the sand wave.

In this present paper, the relationship between the thickness of the sand wave and specific energy upstream the channel is studied for super critical flow and all the experimental data collapsed onto a single carve. The best formula to fit experimental data as shown in Figure 9 was found to be a simple power relationship between the relative thickness of the sand wave and non-dimensional upstream specific energy of the flow as:

In this picture the purpose formula by Omid for sub critical flow and the best trend line for all data of present paper are shown by dotted line and straight line respectively.

4 CONCLUSIONS

The effect of sediment concentration in the hydraulic jump in a rectangular stilling basin has been investigated experimentally for uniform sediment. The following are the conclusions:

- The results indicate that the sediment laden inflow makes no changes to the incoming super critical flow conditions and so has no effect on the hydraulic jump parameters,
- Sediment concentration has no effect on the characteristics of the jump (sequent depth, energy loss and length of jump),
- Sediment size makes no changes to the characteristics of the jump,
- The incoming sediments are deposited downstream of jump and move downstream as bedload. The motion of sediment is wave-like with a mild slope at the front followed by a raised bed of nearly uniform thickness terminating into a step with an angle equal to the submerged angle of repose of sediment,
- The position of the front of this dune-wise sand wave is almost unvarying in a certain flow and sediment conditions,
- Standing sand wave developed at downstream of jump performs a control section similar to the end sill in a stilling basin and keeps the hydraulic jump position at the beginning of the basin. The thickness and the position of the front of this sand wave are functions of upstream Froude number and
- There is a relationship between the relative thickness of the sand wave and upstream specific energy of the flow.

REFERENCES

Bergeron, N.E and Carbnneau, P. 1999. "The Effect of Sediment Concentration on Bed Load roughness", J. Hydrological Processes, Vol. 13(16): 2583–2859.

Chanson, H. 1997. "Air bubble entrainment in open channels: Flow structure and bubble size distributions", Int. J. Multiphase Flow, Vol. 23, No. 1, pp. 193–203.

Chanson, H. and Brattberg, T. 2000. "Experimental study of the air-water shear flow in a hydraulic jump", Int. J. Multiphase Flow, pp. 583–607.

Garcia, Marcelo H. 1993. "Hydraulic jumps in sediment-driven bottom currents", J. Hyd. Eng., Vol. 119, No. 10, pp. 1094–1117.

Lyn, D.A. 1991. "Resistance in Flat-Bed Sediment-Laden Flows", J. Hyd. Eng., Vol. 117, No. 1, January, 94–114.

Khullar, N.K., Kothyari, U.C. and Ranga Raju, K.G. 2002. The effect of suspended sediment on flow resistance, 5th International conference on hydro-science and engineering, September, 18–21, Warsaw, Poland.

Omid, M.H. 2001. Erosion of sediment deposits from rigid rectangular channels, Ph D. Thesis, Department of civil and construction engineering, the University of Manchester institute of science and technology.

River Flow 2004 – Greco, Carravetta & Della Morte (eds.)
© 2004 Taylor & Francis Group, London, ISBN 90 5809 658 0

Can an internal hydraulic jump be inferred from the depositional record of a turbidity current?

S. Kostic & G. Parker
National Center for Earth-surface Dynamics, St. Anthony Falls Laboratory, Minneapolis, Minnesota, USA

ABSTRACT: Turbidity currents emanating from a submarine canyon and debouching onto an associated submarine fan often undergo an internal hydraulic jump near the canyon-fan transition. It is hypothesized here that the sudden decline in bed shear stress due to an internal hydraulic jump leaves a clear signature in the sediment deposit. This hypothesis is studied using the numerical model presented below. The experimental data of Garcia (1993) on turbidity currents near a canyon-fan transition are used to verify the model. Numerical experiments with input parameters similar to those of Garcia (1993) are designed in order to demonstrate that under the right conditions turbidity currents mark the resulting sediment deposit in a submarine canyon-fan system by leaving a detectible depositional signature at the location of the jump. The model is then employed to investigate the characteristics of the depositional signature created by a generic field-scale turbidity current.

1 INTRODUCTION

Turbidity currents are a dominant driving mechanism responsible for the genesis of submarine canyons and associated fans. A typical canyon-fan configuration is illustrated in Figure 1 (Pirmez, 1994). It encompasses (a) a relatively steep-slope, narrow submarine canyon excavated by net erosive underflows and (b) a low-slope, fan-shaped submarine fan or abyssal plain placed by net depositional underflows. Submarine fans are either channelized or unchannelized. Here the case of fans traversed by distinct, well-formed channels is analyzed. The channels act to limit lateral spread of turbidity currents.

Decrease in slope in the downstream direction can cause a turbidity current to undergo an internal hydraulic jump near the canyon-fan transition. A hydraulic jump, internal or otherwise, is a zone of rather sharp transition from a high-velocity supercritical flow upstream to a low-velocity subcritical flow downstream. In open-channel flow, a supercritical regime is described by the standard Froude number greater than a value near unity, while a subcritical regime corresponds to a Froude number less than a value near unity. In turbidity currents, the standard roude number is substituted by the densimetric Froude number.

Generally, supercritical flows exert a relatively high shear stress on the bed, whereas subcritical flows exert a relatively low shear stress on the bed. The sudden decline in bed shear stress due to an internal hydraulic jump might be expected to leave a clear signature in the sediment deposit, e.g. turbidites, created by a turbidity current in the vicinity of a canyon-fan transition.

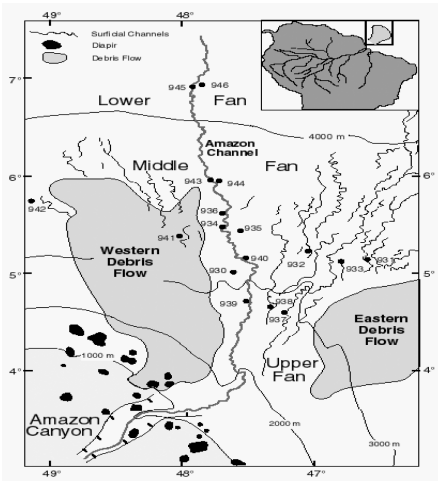


Figure 1. Typical configuration of a submarine canyon-fan system. Amazon Canyon & Fan (from Pirmez, 1994).

The nature of the hydraulic jump and the resultant deposits have been the subject of speculation. Menard (1964) related the development of levees bordering deep-sea channels to the thickening of a turbidity current after a hydraulic jump. Van Andel & Komar (1969) interpreted the characteristics of sediment deposits in

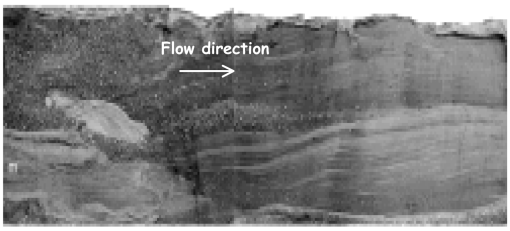


Figure 2. Depositional signature left by a hydraulic jump. The Oak Ridge Moraine, Canada (from Russell & Arnott, 2003).

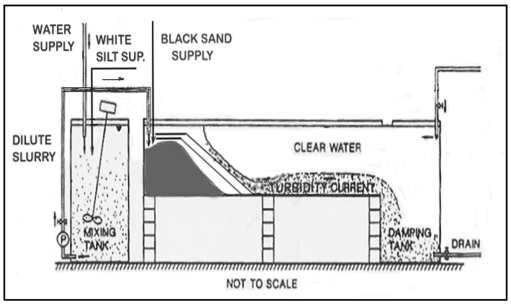


Figure 3. Experimental set-up.

enclosed basins in terms of the hypothesized occurrence of a hydraulic jump. Mutti (1977) suggested that turbidity currents undergoing a change in slope drop excess sand due to a hydraulic jump, thus causing characteristic turbidites just downstream. Recently, Russell & Arnott (2003) provided stratigraphic evidence of hydraulic jump conditions in a subaqueous glaciolacustrine fan succession in the Oak Ridges Moraine, southern Ontario, Canada (Figure 2).

Internal hydraulic jumps in sediment-driven flows remain unobserved in the field. As for observation at experimental scale, only a few studies are available (Garcia, 1989, 1993; Lamb et al., 2004; Toniolo, 2003). Garcia & Parker (1989) and Garcia (1993) induced a hydraulic jump at a sharp change in slope, Lamb et al. (2004) and Toniolo (2003) created a hydraulic jump by ponding the turbidity current downstream.

The goal of the work reported here is to demonstrate how a numerical model can be employed to investigate whether a hydraulic jump can be really inferred from the depositional record. The experimental data of Garcia (1993) are used for calibration and verification of the numerical model. The model is applied to various scenarios of turbidity currents developing along a sloping bed at experimental scale. A field-scale simulation provides insight into the characteristics of a depositional signature resulting from a generic field-scale turbidity current.

2 MODEL FORMULATION

2.1 *Geometric set-up*

The numerical model presented herein is intended to simulate turbidity currents of constant width propagating along the bed of a canyon-fan system. The model allows for a bed of arbitrary geometry. However, in the numerical simulation at experimental and field scale shown bellow the initial bed profile is assumed to consist of an upstream portion with constant, positive slope joining continuously to a downstream portion that is horizontal. This bed configuration is illustrated in Figure 3. The sloping upstream portion represents a loose surrogate for a submarine canyon, and the horizontal downstream portion is a loose surrogate for a submarine fan or abyssal plain.

2.2 *Governing equations*

A dense bottom underflow propagating along a canyon-fan system can be described by the following set of single-layer, layer-averaged equations in dimensionless form:

$$\frac{\partial \hat{h}}{\partial \hat{t}} + \frac{\partial \hat{U}\hat{h}}{\partial \hat{x}} = \frac{0.00153\hat{U}}{0.0204 + \dfrac{1}{Frd_0^2}\dfrac{\hat{C}\hat{h}}{\hat{U}^2}} \tag{1}$$

$$\frac{\partial \hat{U}\hat{h}}{\partial \hat{t}} + \frac{\partial \hat{U}^2\hat{h}}{\partial \hat{x}} = -\frac{1}{2Frd_0^2}\frac{\partial \hat{C}\hat{h}^2}{\partial \hat{x}} - \frac{\hat{C}\hat{h}}{Frd_0^2}\frac{\partial \hat{\eta}}{\partial \hat{x}} - c_D\hat{U}^2 \tag{2}$$

$$\frac{\partial \hat{C}\hat{h}}{\partial \hat{t}} + \frac{\partial \hat{C}\hat{U}\hat{h}}{\partial \hat{x}} = \hat{v}_s\left(\frac{e_s}{C_0} - r_0\hat{C}\right) \tag{3}$$

$$(1-\lambda)\frac{\partial \hat{\eta}}{\partial \hat{t}} = \hat{v}_s\left(r_0 C_0 \hat{C} - e_s\right) \tag{4}$$

where $\hat{t} = tU_0/h_0$, $\hat{x} = x/h_0$, $\hat{v}_s = v_s/U_0$, $\hat{h} = h/h_0$, $\hat{U} = U/U_0$, $\hat{C} = C/C_0$, $\hat{\eta} = \eta/h_0$, t = time, x = bed-attached downslope distance, h = turbidity current thickness, U = layer-averaged current velocity, C = layer-averaged concentration of suspended sediment, and η = elevation of the bed. h_0 and U_0 are respectively the current thickness and velocity at the canyon head.

The formulation contains the following dimensionless parameters: Frd_0 = densimetric Froude number at the canyon head, c_D = bed friction coefficient, r_0 = an order-one multiplicative constant, C_0 = suspended sediment concentration at the canyon head, e_S = sediment entrainment coefficient, $\hat{v}_S$ = fall

velocity of sediment, S_i = initial bed slope, and λ = sediment porosity.

The densimetric Froude number Frd_0 expresses the ratio of inertial to buoyancy force at the canyon head, and is given by

$$Frd_0 = \frac{U_0}{\sqrt{RgC_0h_0}} \tag{5}$$

where g is gravitational acceleration, and R is the submerged specific gravity of the sediment (=1.65 for quartz silt).

The entrainment of sediment into suspension by turbidity currents is here estimated from the model of Kostic & Parker (2003), which accommodates different formulations for numerical simulations at experimental and at field scale. The model is adapted from the relations by Garcia & Parker (1993), and Wright & Parker (in press). That is, the entrainment coefficient e_s takes the form:

$$e_s = k\frac{aZ^5}{1+\frac{a}{0.3}Z^5} \tag{6}$$

where k is an adjustment coefficient, and a is a constant, given as follows:

$$k = \begin{cases} 1, & \text{exp. scale} \\ 0-0.01, & \text{field scale} \end{cases} \tag{7}$$

$$a = \begin{cases} 1.3\cdot10^{-7}, \text{Garcia \& Parker (1993)}, & \text{exp. scale} \\ 7.8\cdot10^{-7}, \text{Wright \& Parker (2003)}, & \text{field scale} \end{cases} \tag{8}$$

The adjustment of k at field scale is not a part of the original relations, but is introduced here to account for limits on the erodibility of the bed over which the turbidity current runs. In addition, Z is a similarity variable, defined as:

$$Z = \alpha_1 \frac{u_*}{v_s} Re_p^{\alpha_2} S_f^{\alpha_3} \tag{9}$$

In the above equation u_* = shear velocity due to skin friction, Re_p = particle Reynolds number, S_f = friction slope, and α_1, α_2, α_3 = parameters, given by:

$$u_* = \sqrt{c_D}\,U \tag{10}$$

$$Re_p = \sqrt{RgD}\,D/\nu \tag{11}$$

$$S_f = c_D Frd^2, \quad Frd = U/\sqrt{RgCh} \tag{12}$$

$$(\alpha_1,\alpha_2) = \begin{cases} (0.586, 1.23), & \mathrm{Re}_p \le 2.36 \\ (1.0\ \ , 0.6\ ), & \mathrm{Re}_p > 2.36 \end{cases} \tag{13}$$

$$\alpha_3 = \begin{cases} 0, & \text{exp. scale} \\ 0.07, & \text{field scale} \end{cases} \tag{14}$$

with D = median grain size of the sediment, ν = kinematic viscosity of water, and Frd = densimetric Froude number.

Finally, the fall velocity v_S is a function of particle Reynolds number. Here it is calculated from the relation of Dietrich (1982).

The details on the dimensionless analysis can be found in Kostic & Parker (in prep.). It is useful to note from Eqs. (1)–(14) that any characteristic parameter Y of the flow field of an underflow emanating from a submarine canyon and debouching onto an associate fan can be expressed as a function of the following dimensionless parameters:

$$Y = f\left(Frd_0, \mathrm{Re}_p, v_s/U_0, u_*/v_s, c_D, r_0, C_0, \lambda, S_i\right) \tag{15}$$

In the work reported here the ratio u_*/v_s is replaced by the bed Shield number τ^* which characterizes the degree to which the flow can mobilize the bed sediment. It is defined as

$$\tau^* = \frac{u_*^2}{gRD} \tag{16}$$

2.3 *Initial and boundary conditions*

Initial and boundary conditions for the numerical model are discussed in detail in Kostic & Parker (in prep.). At $t = 0$ the dependent dimensionless variables h, U and C at all nodal points are set equal to 1. The initial bed elevation for every grid point is determined from a prescribed initial slope S_i. Because of the hyperbolic nature of governing equations, the number and location of physical boundary conditions correspond to the number and location of characteristics that propagate into the flow domain (Kostic & Parker, 2003a).

For the supercritical inflow boundary considered here, which corresponds to a high-velocity flow near the head of a canyon, three boundary conditions needs to be formulated, that is

$$\hat{h}(x=0,t)=1,\ \hat{U}(x=0,t)=1,\ \hat{C}(x=0,t)=1, \tag{17-19}$$

while the outflow BC's take the form

$$\hat{U}(x=s,t)=\frac{ds}{dt},\ \hat{\eta}(x=s,t)=\hat{\eta}_n(s) \tag{20,21}$$

where η_0 is an antecedent bed elevation as yet unmodified by the turbidity current, and s denotes the position of the turbidity current head in a deforming grid.

Once an underflow covers the prescribed length of a computational domain, no physical boundary condition is required for either supercritical or subcritical flow unless a downstream control is imposed there. This is indeed the case in the numerical simulations at experimental scale that follow. In the experiments of Garcia & Parker (1989) and Garcia (1993) the condition of a critical densimetric Froude number at the outflow boundary needs to be imposed to account for a free outfall (Figure 3).

The remaining variables are calculated from the flow domain by means of first-order extrapolation.

2.4 *Numerical scheme*

The governing Eqs. (1–4), together with the initial and boundary conditions, are solved numerically by the explicit ULTIMATE QUICKEST method (Leonard 1979 & 1991), which is third-order in both time and space. The scheme provides a robust, mass-conservative formulation that is capable of dealing with highly advective transport and complex boundary conditions. More comprehensive consideration of the algorithm can be found in Kostic & Parker (2003a).

3 NUMERICAL SIMULATIONS AT EXPERIMENTAL SCALE

3.1 *Validation of the model*

The numerical model is validated using experiments by Garcia (1993) on internal hydraulic jumps in turbidity currents driven by well-sorted sediment. The experimental flume is shown in Figure 3. It was 30 cm wide and 70 cm deep. A submarine canyon was modeled by a 5 m long inclined bed with a slope of 0.08 ($\theta = 4.6°$), followed by a 6.6 m long horizontal bed that represented the associated abyssal plain. A free outfall at the end of the horizontal region acted as a downstream control. The currents were allowed to develop until a quasisteady state continuous flow was reached.

As can be seen from Table 1, the inlet current thickness was kept at 3 cm. The corresponding flow rate per unit width was set at either 25 or 33 cm^2/s, yielding inlet velocities of 8.3 and 11.0 cm/s respectively. The median grain size D of the sediment used to generate the turbidity currents was 4, 9, 30 and 65 μm. However, the underflows driven by 4-μm sediment are not of interest for the work presented here, since they were too fine to produce any noticeable deposit in the canyon-fan system during the designed run time. Inlet Reynolds numbers were always larger than 2700, ensuring turbulent conditions there. Additional input parameters include the estimated bed friction coefficient $c_D = 0.01$ and the estimated sediment porosity $\lambda = 0.5$.

Table 1. Input parameters for the numerical model.

Exp.	h (cm)	U (cm/s)	C x 10^3	D (μm)	Run time (min)
DAPER4	3.0	8.3	2.95	9	33
DAPER7	3.0	8.3	8.60	9	30
GLASSA2	3.0	8.3	3.39	30	30
GLASSA5	3.0	8.3	3.94	30	30
GLASSA7	3.0	11.0	2.66	30	30
GLASSB1	3.0	11.0	3.00	65	38
GLASSB2	3.0	11.0	6.00	65	27
GLASSB3	3.0	11.0	1.50	65	28

Figures 4a, 5a and 6a demonstrate good agreement between measured and simulated streamwise variation in sediment mass deposited per unit bed area by turbidity currents driven by 9, 30 and 65 sediment respectively. Both the observations and calculations pertain to the end of each run. The best fit with experimental observations was attained with $r_0 = 1$ for the runs with 9 and 30 μm. For the runs with 65-μm sediment the best fit was obtained with this multiplicative constant set equal to 2. These choices can be loosely justified by the sediment concentration profiles that appear to be more uniform in vertical in underflows driven by fine-grained sediment.

Figures 4b, 5b and 6b show the numerical predictions of the interface elevation $\eta + h$ for turbidity currents driven by 9, 30 and 65 μm respectively, while the Figures 4c, 6c and 7c illustrate how the corresponding densimetric Froude number F_{rd} varies along the model canyon-fan system. Experimental data for the current interface and densimetric Froude number are not available.

The numerical results support experimental observations by Garcia (1993), that can be summarized as follows:

(a) Currents driven by 9-μm sediment are weakly depositional along the canyon and fan (Figure 4a). They reach the end of the model fan at $x = 11.6$ m. They are supercritical along the canyon, and subcritical on the fan, with a distinct intervening hydraulic jump (Figure 4b,c).
(b) 30- and 65-μm currents are strongly depositional, and create turbidites that display roughly exponential decrease in thickness with distance from the sediment source (Figure 5a, 6a).
(c) 30-μm currents reach the end of model fan, while continuously decelerating and thickening after the slope break (Figure 5b). They do not show evidence of an internal hydraulic jump (Figure 5c).
(d) 65-μm currents rapidly disintegrate before they reach the end of the model fan (Figure 6b,c).

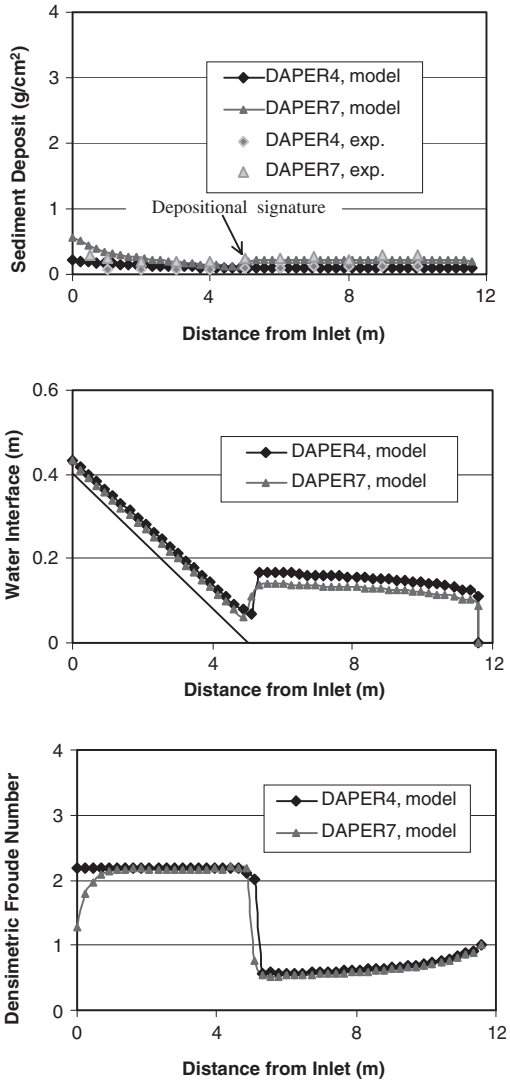


Figure 4. Turbidity current driven by 9-μm sediment: (a) Depositional pattern (b) Underflow interface with an internal hydraulic jump (c) Densimetric Froude number.

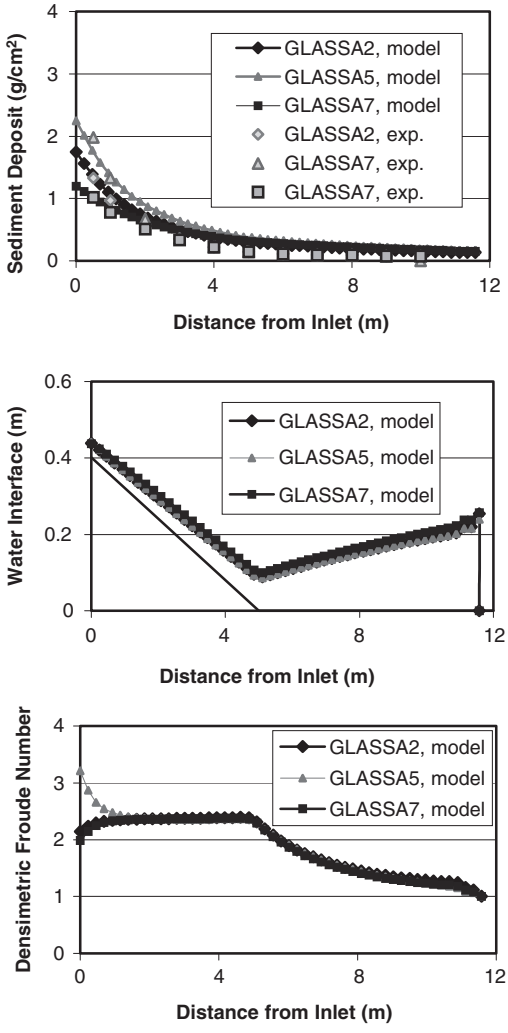


Figure 5. Turbidity current driven by 30-μm sediment: (a) Depositional pattern (b) Water interface with an internal hydraulic jump (c) Densimetric Froude number.

According to the numerical predictions, they die out when the layer-averaged concentration of suspended sediment drops to below 0.1% of the inlet value, e.g. at the distance $x = 5.38$ m for run GLASSB1, $x = 5.37$ m for run GLASSB2 and $x = 5.95$ m for run GLASSB3. These flows deposit too rapidly to display an internal hydraulic jump (Figure 6c), a result confirmed by Choi & Garcia (1995).

For the work presented here the most important observation of Garcia (1993) is that the break in canyon-fan slope does not seem to cause any clear discontinuity in the depositional pattern of those currents which are capable of reaching the downstream end of the fan. This notwithstanding, the present numerical simulations of experiments that involved an internal hydraulic jump reveal a modest but clear depositional signature associated with a drop in shear stress right after the jump. This is manifested in terms of an upstream-facing "step" or thickening of the deposit from the upstream to the downstream side of the jump. For example, in the case of runs DAPER4 and DAPER7 the simulated deposit mass per unit bed area shows an increase of 0.0053 and 0.076 g/cm^2 respectively across zone of the jump.

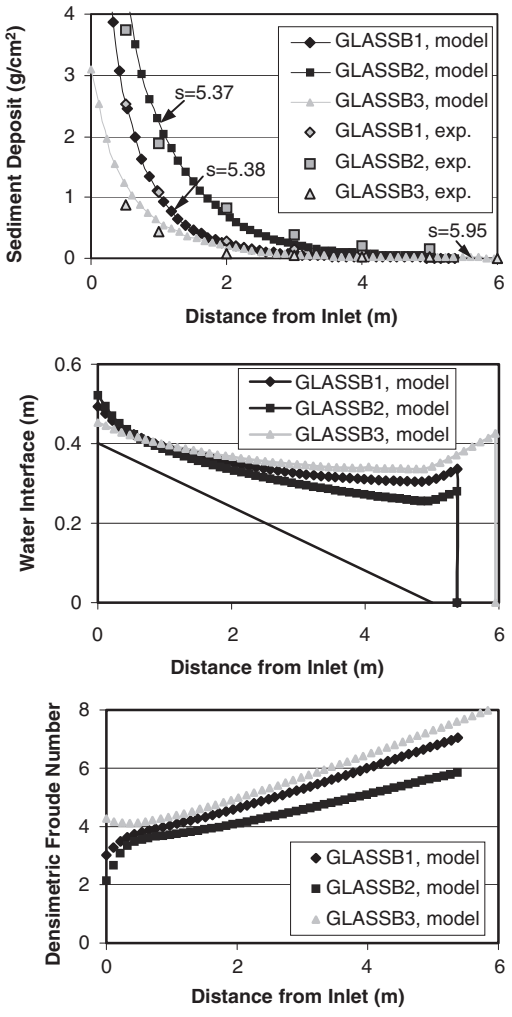


Figure 6. Turbidity current driven by 65-μm sediment: (a) Depositional pattern (b) Water interface with an internal hydraulic jump (c) Densimetric Froude number.

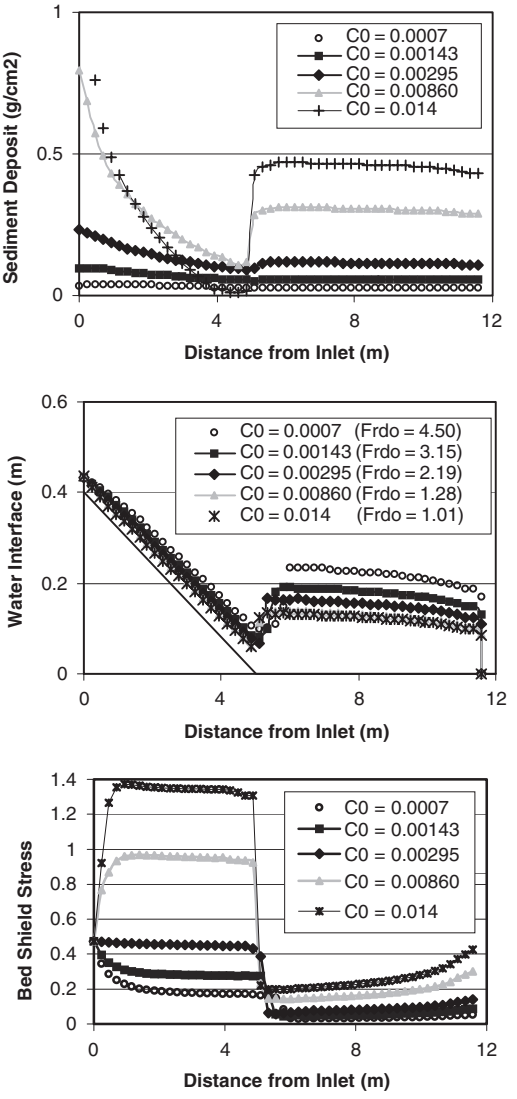


Figure 7. Numerical experiments with 9-μm sediment: (a) Depositional pattern (b) Water interface with an internal hydraulic jump (c) Bed Shield stress.

A close inspection of the experimental data of Figures 4a, 5a and 6a reveals that the measurements of run DAPER7 contains such a depositional signature as well (Figure 4a). The step is near the numerically predicted size. In the case of run DAPER4, the predicted step is sufficiently small that it would not have been clearly seen in the data (Figure 4a). There is no evidence of a depositional signature in the data for the 30- and 65-μm currents, which do not undergo a jump (Figure 5a, 6a). Therefore, the data and numerical results for run DAPER7 provide the first relatively clear hint that under the right conditions a hydraulic jump might leave a depositional signature. This hint is pursued in the numerical experiments below.

3.2 *Numerical experiments at laboratory scale*

Having found that the numerical model can reproduce the features of turbidity currents near the experimental canyon-fan transition reported by Garcia (1993), the model is now extended to a parametric study of hydraulic jumps. The details on this study can be found in Kostic & Parker (in prep.).

Numerical experiments presented here, however, aim to demonstrate how runs using the DAPER material (9 μm) can under certain conditions can leave a noticeable depositional signature. In particular, the

effect of suspended sediment concentration C_0 at the canyon mouth on the formation of an internal hydraulic jump and a corresponding depositional signature is elucidated below.

The model input parameters are: $h_0 = 3$ cm, $U_0 = 8.3$ cm/s, $R = 1.65$, run time $= 40$ min. The inflow volumetric concentration of suspended sediment is varied in the range $0.0007 \leq C_0 \leq 0.014$. The lower limit is intended to simulate a dilute underflow, and the upper limit is selected to describe an underflow with an inflow densimetric Froude number close to the unity.

Figure 7a reveals that denser turbidity currents tend to deposit sediment from their very inception, and are in general more erosive in the supercritical region, and more depositional in the subcritical region. An increasing drop in shear stress associated with the jump (Figure 7c) is responsible for a successively more pronounced depositional signature (Figure 7a). In addition, turbidity currents with lower inflow buoyancy flux are slower and thicker in both their super- and subcritical regions (Figure 7b), with an internal hydraulic jump that forms further downstream of the canyon-fan break.

An increased drop in shear stress and consequently more noticeable depositional step can be also obtained by changing some other dimensionless parameters, such as e.g., by increasing the bed resistance c_D, or the initial canyon slope S_i (see Kostic & Parker (in prep.)).

4 MODEL APPLICATION AT FIELD SCALE

It is useful to demonstrate how the numerical model can be employed to investigate the qualitative and quantitative characteristics of a depositional signature at field scale. Therefore, a generic model reach is designed to be representative of a canyon-fan system in the field.

Froude similarity is used to scale-up the input parameters associated with 9 μm material (DAPER) to field dimensions. That is

$$Frd_f = Frd_e \tag{22}$$

where the subscript "f" denotes "field", and the subscript "e" denotes "experiment". Assuming that R is the same in the experiments and the field, (22) results in

$$\frac{(U)_f}{(U)_e} = (\chi_h \chi_C)^{1/2} \tag{23}$$

with the scale ratios for length and concentration defined as

$$\chi_h = \frac{(h)_f}{(h)_e} \qquad \chi_C = \frac{(C)_f}{(C)_e} \tag{24}$$

Here the length scale ratio is set to 300, and concentration scale ratio to 1. The field model thus has the following input parameters: $h_0 = 9$ m, $U_0 = 1.4$ m/s, $C_0 = 0.003$, $R = 1.65$ and $c_D = 0.0025$. The canyon-fan system is assumed to be 3.48 km long. The initial bed profile of the system has a break at 1.5 km, such that the bed slope upstream and downstream of the break is 4% and 0%, respectively. The grain size of sediment is set to 20 μm.

No downstream control is imposed, so as to allow turbidity currents to propagate freely. Total computation time is 60 days of continuous flow. In the field, this 60 days would be divided into a series of smaller flow durations, e.g. a few hours or days, with long dormant periods in between.

It is value to note here that in the numerical simulations at field scale the adjustment coefficient k of the sediment entrainment model (see Eqs. (6–14)) must be set equal to a value smaller than the unity in order to obtain physically realistic solutions. The adjustment coefficient k may be interpreted as a limitation on the supply of sediment from the bed that is available for entrainment due to e.g. partial consolidation of the bed. In the case when $k = 0$, a purely depositional turbidity current is generated. If however $0.007 < k \leq 1$, a turbidity current accelerates so strongly that the energy constraints of Parker et al. (1986) fail to be satisfied. The end result is a pronounced and unphysical numerical scouring along the entire canyon-fan system.

Therefore, the following values of the adjustment coefficient are set in the calculation: $k = 0.003$, $k = 0.005$ and $k = 0.007$. Figure 8a illustrates that more erosive underflows create far more noticeable depositional signatures at the location of an internal hydraulic jump. Also, the jump is pushed further upstream from the canyon-fan break (Figure 8b). The final bed elevation is presented in Figure 8b for $k = 0.005$. It reveals: a) a clear depositional step associated with the hydraulic jump; b) a change in slope gradient associated with the slope break; and c) a deposit of uniform thickness in the subcritical region.

5 CONCLUSIONS

Results of the numerical model reported here provide clear evidence that turbidity currents can under some circumstances leave a more or less pronounced depositional signature where they go through an internal hydraulic jump driven by declining slope. The depositional signature is created by the sudden drop in bed shear stress generated by the internal hydraulic jump. Therefore, the location of such a depositional signature defines the location of an internal hydraulic jump as well.

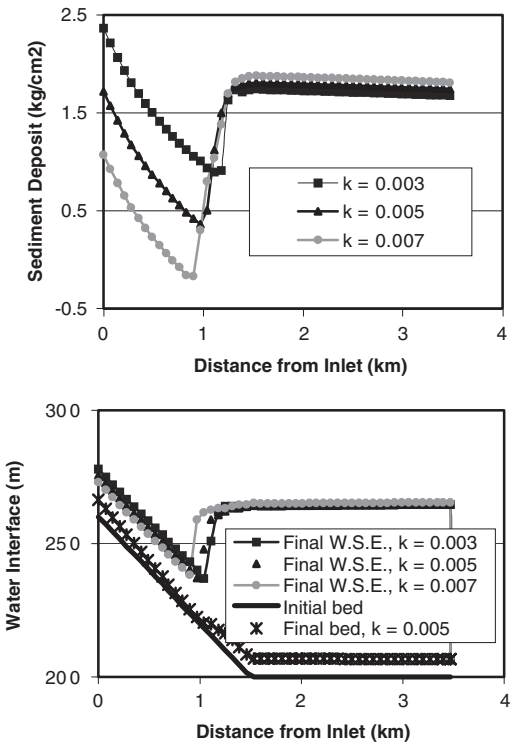


Figure 8. Numerical simulations at field scale: (a) Depositional pattern (b) Current interface and final bed.

The model was successfully verified against the experiments by Garcia (1993) on internal hydraulic jumps in turbidity currents driven by well-sorted sediment. The experimental observations and numerical predictions for Garcia's run DAPER7 provide the first hint that under the right conditions a hydraulic jump might leave a depositional signature. Numerical experiments reveal that a depositional step becomes indeed more noticeable than the one reproduced by the run DAPER7 for higher values of e.g. suspended sediment concentration C_0 at the canyon head, bed resistance c_D or initial canyon slope S_i. Numerical simulations at field scale provide insight into the characteristics of a depositional signature resulting from a generic field-scale turbidity current. It is demonstrated that swifter turbidity currents leave more detectible depositional signatures.

REFERENCES

Dietrich, E.W., 1982, Settling velocity of natural particles, Water Resources Research, 18 (6), 1626–1982.

Choi, S.U. & Garcia, M. 1995, Modeling of one-dimensional turbidity currents with a dissipative – Galerkin finite element method. *J. Hydr. Research*, Vol. 33, 623–647.

Garcia, M. & Parker, G., 1989, Experiments on hydraulic jumps in turbidity currents near a canyon-fan transition, *Science*, 245, 393–396.

Garcia, M., 1993, Hydraulic jumps in sediment-driven bottom currents, *Journal of Hydraulic Engineering*, 1993, 1094–1117.

Garcia, M. & Parker, G. 1993. Experiments on the entrainment of the sediment into suspension by a dense bottom current. *J. Geoph. Research*, 98, 4793–4807.

Kostic, S. & Parker, G., in prep. Internal hydraulic jumps created by turbidity currents at slope break – Formation limits and depositional signature.

Kostic, S. & Parker, G., 2003, Progradational sand-mud deltas in lakes and reservoirs: Part 1. Theory and numerical modeling, *Journal of Hydraulic Research*, 41 (2), 127–140.

Lamb, M.P., Hickson, T., Marr, J.G., Sheets, B., Paola, C. & Parker, G., 2004, Surging versus continuous turbidity currents: flow dynamics and deposits in an experimental intraslope minibasin, *Journal of Sedimentary Research*, 74(1).

Leonard, B.P., 1979, A stable and accurate convection modeling procedure based on quadratic upstream interpolation, *Comp. Methods in Applied Mechanics and Engineering*, 19, 59–98.

Leonard, B.P., 1991, The ULTIMATE conservative difference scheme applied to unsteady one-dimensional advection, *Comp. Methods in Applied Mechanics and Engineering*, 88, 17–77.

Menard, H.W., 1964, *Marine Geology of the Pacific*, McGraw-Hill, New York.

Mutti, E., 1977, Distinctive thin-bedded turbidite facies and related depositional environments in the Eocene Hecho Group (South-central Pyrenees, Spain), *Sedimentology*, 24, 107–131.

Parker, G., Fukushima, Y. & Pantin, M.H., 1986, Selfaccelerating turbidity currents, *Journal of Fluid Mechanics*, 171, 145–181.

Pirmez, C., 1994, *Growth of a Submarine Meandering Channel-levee System on the Amazon Fan*, Ph.D. thesis, Columbia University, New York, USA.

Russell, H.A.J. & Arnott, R.W.C., 2003, Hydraulic-jump and hyperconcentrated-flow deposits of a glacigenic subaqueous fan: Oak Ridges Moraine, southern Ontario, Canada, *Journal of Sedimentary Research*, 73(6).

Toniolo, H., 2003, Debris flow and turbidity current deposition in the deep sea and reservoirs, Ph.D. thesis, University of Minnesota, 233 p.

Van Andel, T.H. & Komar, P.D., 1969, Ponded sediment of the Mid-Atlantic Ridge between 22 and 23 degrees north latitude, *Bulletin of Geological Society of America*, 80, 1163–1190.

Wright, S. & Parker, G., in press, Flow resistance and suspended load in sand-bed rivers: simplify stratification model, *Journal of Hydraulic Engineering*.

River Flow 2004 – Greco, Carravetta & Della Morte (eds.)
© 2004 Taylor & Francis Group, London, ISBN 90 5809 658 0

Grain size analysis for coarse river beds using digital imagery processing

R. Weichert, M. Wickenhäuser, G.R. Bezzola & H.-E. Minor
Laboratory of Hydraulics, Hydrology and Glaciology (VAW), Swiss Federal Institute of Technology Zurich (ETH)

ABSTRACT: The present paper describes a fast, easy and inexpensive method to determine the grain size distribution of the subsurface of coarse river beds digital imagery analyses. The proposed procedure was empirically derived from flume experiments performed at the Laboratory of Hydraulics, Hydrology and Glaciology (VAW) of the Swiss Federal Institute of Technology (ETH) in Zurich and is validated with independent flume and field data for different river types (gravel-bed rivers to torrents).

1 INTRODUCTION

Quantification of the grain size distribution of river beds remains an issue of large importance for a wide range of river engineering problems. The bulk sieve analysis, customary sampling method in sand-bed rivers, is often not practical for rivers with coarser bed material because of the large samples required for representativeness (Mosley & Tindale 1985, Diplas & Fripp 1992). For gravel-bed rivers several surface-orientated sampling procedures have proven their validity (Fehr 1986, Church et al. 1987).

Bulk sieve analyses are volumetric samples of the subsurface material. In gravel-bed rivers the bed surface is often coarser than the underlying material. Thus, to provide equivalence of the surface-orientated sampling methods to the bulk sieve analysis, several important differences with respect to the sampling procedures have to be taken into account. First it has to be distinguished, whether the samples are evaluated by weight or by number. For both, particles of each size collected are assigned to size classes, resulting in number-based or weight-based distributions of the sample. However, the number-based methods are more practical under field conditions because no material has to be removed from the field site.

Secondly, the survey of grain sizes can be carried out as areal, line transect or point sample. An areal sample contains all grains that are exposed to the flow within a selected area, whereas for the transect sampling, all particles lying beneath a line are surveyed. The point analysis is mostly applied by using a regular square grid, where all stones under the grid nodes are part of the sample or by a random walk procedure (Wolman 1954, Leopold 1970, Hey & Thorne 1983).

Kellerhals & Bray (1971) showed on the base of an idealised cube model that these fundamental differences lead to specific weighting factors Θ which are integrated in an appropriate conversion model. The conversion model allows to turn number- or weight-based distributions of the surface into an equivalent volumetric distribution of the subsurface:

$$\Delta p_i = \frac{n_i \cdot d_i^{\Theta}}{\sum_1^n n_i \cdot d_i^{\Theta}} \tag{1}$$

Herein Δp_i represents the weight proportion of a fraction of the subsurface, d_i is the grain size of the fraction i, n_i is the number of grains within the fraction i of the surface sample and n is the total number of grains of the sample.

As the cube model assumes voidless packing, and a homogenously composed mixture, it should be considered as a basis for an adequate conversion model. Consequently, there are modified models in the literature which account for more realistic assumptions with respect to porosity, and particle size and shape (Diplas & Sutherland 1988, Fraccarollo & Marion 1995).

The models mentioned above do not contain an explicit armour layer, and therefore do not account for the missing finer components in the surface layer. Additionally, number-based sampling procedures are limited to coarser material ($d > 8$ mm: (Kellerhals & Bray 1971, Adams 1979, Fraccarollo & Marion 1995). Therefore surface-orientated sampling requires an appropriate conversion model to infer from a coarse armour layer to the grain size distribution of the subsurface. This could be done by combining partial (i.e. truncated) grading curves (Anastasi 1983).

In contrast to the theoretical models, Fehr (1986) derived conversion factors Θ on an experimental base. He performed large scale laboratory tests with coarse

bed material ($d_{max} = 0.20$ m) for channel gradients ranging up to 8%. Fehr based his analysis on well-developed armoured beds without explicit bed features and suggested to account for the neglected finer components by adding a Fuller distribution to the converted sample. He found conversion factors slightly smaller than suggested by Kellerhals & Bray (1971).

Besides the described methods the application of remote sensed procedures has attracted increasing interest. Photographical methods represent an easy and rapid way to obtain grain size information of the surface layer of a river bed. However, analyses by digital imagery processing are basically adaptations to the methods described above, as the images are used to perform number-based samples (areal, transect or point counting) within the photograph (Adams 1979, Church et al. 1987, Rosport 1997, McEwan et al. 2000). The advantage by using the image processing is that no grains have to be removed from the river bed. This is useful in torrents, where large bed elements limit the applicability of the manual methods, or within flume experiments where the removal of surface grains is made impossible by the experimental setup (e.g. Weichert et al. 2003).

The automated extraction of grain size data, rather than performing manual number-based analyses within the image, has become more important with further advances in image processing. Automated approaches to date use imaging laser altimetry to produce high resolution digital elevation models (DEM) (McEwan et al. 2000) or digital photogrammetry (Butler et al. 1998, Butler et al. 2001). A combination of both was tested by Butler et al. (2001), but the advantage of additional information does not improve the results.

However, the most important property of any automatic image-based procedure is that the grain boundaries must be strongly contrasted with other parts of the image. Contrasts in digital photogrammetry are based on differences in brightness and colour intensities. Besides the fact that identical stones with respect to the lithology, possess similar intensities, imbrication and shadowing effects of adjacent grains blur good contrasts. Consequently, several researchers use a variety of edge detection and edge dilatation algorithms to improve the segmentation of the particles (e.g. McEwan et al. 2000).

Grain geometry is generally characterised by its principle axes. The a- and c-axis are assigned to the longest and shortest axis respectively. Following this, the b-axis is defined as the perpendicular axis to the plane spanned by the a- and c-axis. Analyses of plan view images suffer from the principle drawback that additional bias is introduced due to imbrication of the grains either by other grains or by shadowing effects. Even for completely exposed grains (a- and b-axis revealed) the apparent b-axis may be less than the actual b-axis because of tilting of the grain. Therefore, the revealed axis lies somewhere in-between of the b- and c-axis. Thus, on average, measured axes will be smaller than actual axes and additional correction is needed (Adams 1979). Church et al. (1987) noted that the magnitude of the correction is dependent upon the magnitude and angle of imbrication, and thus is specific to the sample site studied.

The determination of the b-axis from an image can be performed in two optional ways. First, it is possible to correct the values of the grain sizes measured in the photograph (e.g. the minimum dimension perpendicular to the longest axis visible in the image) in order to improve the estimates for the true values of the b-axes. Another possibility is to fit ellipses for a fixed a-axis. The b-axis is then determined as that for which the ellipse has the same area as the actual grain (Butler et al. 2001).

Depending on the camera and the photographical procedure, additional distortion may result from optically imperfect lenses, or tilted camera axis. Butler et al. (2001) examined the influence of digital image rectification. They found that the use of rectified images does not significantly improve the result.

The review of existing literature shows that a number of imperfections affects the automated extraction of grain size data from digital imagery. Additionally, the survey of finer fractions is often excluded (e.g. Butler et al. 2001). As some of these deficiencies are difficult to quantify, the procedure described in the present paper is derived on an empirical base, using flume data of experiments performed at the Laboratory of Hydraulics, Hydrology and Glaciology (VAW) of the Swiss Federal Institute of Technology (ETH) in Zurich (Wickenhäuser, unpubl.).

2 METHODOLOGY

The present paper outlines a procedure to extract grain size data from plan view digital imagery. The proposed method can be divided into four stages. The first stage describes the image acquisition in the field, whereas the other stages involve the image processing steps, starting from the photograph and resulting in the grain size distribution of the subsurface material.

2.1 *Field work*

First of all, attention must be given to ensure that the sample site allows for a representative evaluation of the river bed material. Although often stated as a precondition, the consequences of a non representative sample site may be immense (see e.g. Crowder & Diplas 1997).

The photographs should be taken of a dry bed section from an appropriate height (Fig. 1). The "flying



Figure 1. Vertical photograph of the river bed.

height" of the camera should be chosen in order to provide that the image is of the correct scale with respect to the size of grains that are of interest. For the channel beds surveyed, the ratio of image length to maximum grain size varied between 10 and 15.

The scale of the image can be obtained by placing a measuring-tape on the gravel surface at the sample site. The axis of the camera should be held approximately vertical to minimise distortion effects. Additionally, it must be provided that the ambient light is homogeneous within the photographed area. Changing light condition within the image may complicate the detection of grain contours.

2.2 *Preprocessing of the image*

The purpose of image preprocessing is to create a quasi-binary image which is suitable for the following automated extraction of grain size data. This step can be implemented with standard photo-processing software.

First, the photograph is transformed into a greyscale image as shown in Figure 2. The associated histogram points out that the image exhibits the full range of grey levels.

Basically, the following preprocessing step is equivalent to a manual thresholding process. It must be decided which grey tones are assigned to the sample

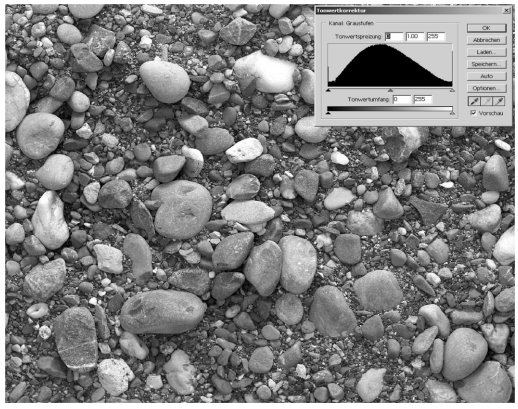


Figure 2. Greyscale image.

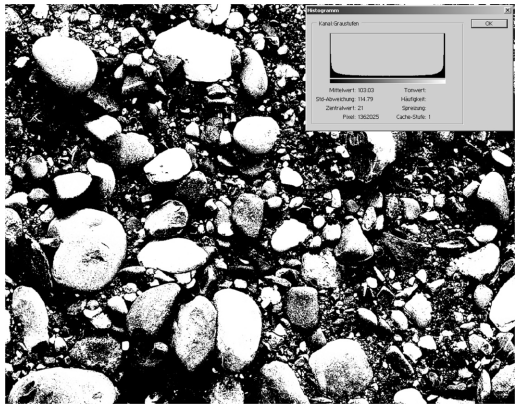


Figure 3. Quasi-binary image.

and which intensity levels are excluded. The resulting image should exhibit reasonable delineations of the particles of interest (Fig. 3). This subjective thresholding process ensures that an adequate portion of the grains is part of the sample.

However, as grey levels in an image of a natural deposit are often in a similar range, a perfect delineation of all grains is rather impossible. For the proposed method, this deficiency is not affecting the results in a major way as long as enough objects are delineated reasonably. The histogram in Figure 3 shows that the preprocessed photograph is a quasi-binary image with just two modes nicely separated by a valley.

2.3 *Extraction of grain size data*

The software Image Tool 3.0 (freeware: http://ddsdx.uthscsa.edu/dig/itdesc.html) is used for the automated extraction of grain size data. As it is shown in

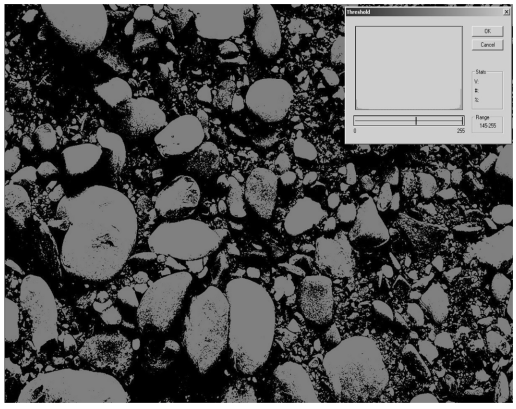


Figure 4. Threshold setting.

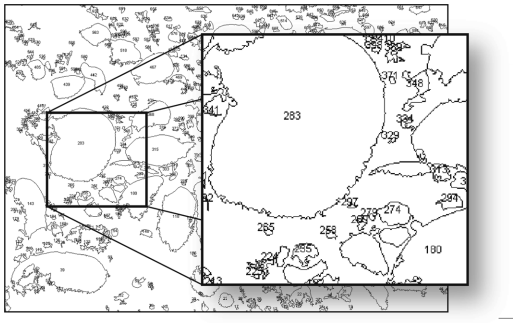


Figure 5. Recognised objects.

Figure 3 the amount of small impurities within sharply contrasted stones is considerably large. As this would result in a large error for the finer fractions, particles smaller than a predetermined value are excluded from the analysis. In the present study the diameter of the smallest particle to be recognised was about $d^*_{min} = 0.14\, d_{max}$.

Thus, for a given maximum grain size, the smallest particle that still is detected reliably can be determined. As the programme carries out pixel-based analyses, the length scale of the image is required to convert d^*_{min} from a unit length into pixel.

As shown in Figure 4, the following manual thresholding process can be carried out easily, because the image is already quasi-binary. Hence, the threshold can be placed in the large gap between the two modes.

Once the threshold has been set, the software scans the image and identifies objects (Fig. 5). In the following step all recognised objects are analysed. Besides other information, the programme measures the longest and shortest axis of the recognised objects. These data are used for the following conversion to determine the volumetric distribution of the subsurface layer.

2.4 *Conversion model*

The described conversion model is mainly an adaptation to the method proposed by Fehr (1986).

The mean of the longest and shortest axes of the recognised objects is assumed to be a measure of the grain b-axis. These lengths are assigned to size classes resulting in a number-based frequency distribution of the surface layer. Basically, the described procedure is something in-between of a point analysis and an areal analysis, depending on the number of recognised objects. The only difference to the customary point analysis is that the random selection is made by the automated object recognition rather than by a grid-based system or a random walk procedure.

With the image scale the pixel-based distances are transformed into unit lengths. Equation 1 is used to convert the number-based distribution of the surface layer into a volumetric distribution of the subsurface. For the flume experiments a weighting factor of $\Theta = 0.8$ gave the best results. As particles smaller than a threshold value are excluded from the analysis, the proportion of the finer material within the sample is underestimated. Thus, the sample has to be corrected and the missing finer components are replaced by a Fuller distribution in the way suggested by Fehr (1986).

The theoretical values for the conversion from a number-based point- or areal-analysis into a volumetric distribution of the subsurface are $\Theta = 0$ and $\Theta = 2$, respectively. As the automated object recognition represents something in-between of these two sampling techniques, the empirically derived weighting factor of $\Theta = 0.8$ fits well to the theoretical values proposed by Kellerhals & Bray (1971).

The flume experiments were performed to simulate steep open channels with very coarse surface layers. Consequently, the empirically derived weighting factor Θ takes into account pronounced armouring effects. Besides the influence of different sampling procedures, Θ additionally includes all other imperfections resulting from the digital imagery processing.

Both, these imperfection and the composition of the surface-layer are dependent on the degree of armouring and thus depend on the river type and the preceding hydraulic loads.

3 CALIBRATION

The proposed procedure was derived on the base of experiments performed in a 5.5 m long and 0.3 m wide tilting flume at slopes of 7.5%, 10.0%, and 12.0% respectively (Fig. 6).

A widely-graded sediment mixture was used, that corresponds to a typical grain size distribution of a torrent. The standard deviation of the grading curve was $\sigma = (d_{84}/d_{16})^{1/2} = 2.9$.



Figure 6. Flume for calibration experiments.

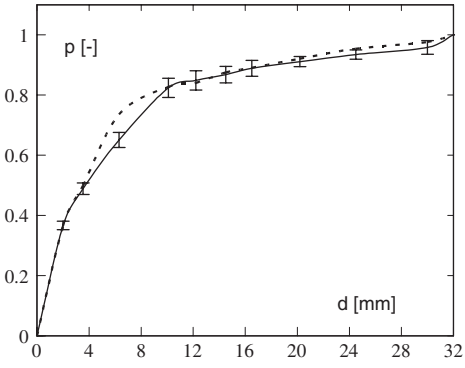


Figure 7. Volumetric distribution of the subsurface obtained by bulk sieve analysis (- - -) and automatic object recognition (—) for the calibration experiments.

For each slope the flume bed was initially built up by a uniform layer of homogeneously mixed sediment. After the saturation of the void volume the discharge was subsequently increased to allow for the formation of a coarse armour layer with distinct bed features. These bed features are commonly addressed as steps and pools. Vertical photographs of the armour layers were the basis for the derivation of the digital imagery processing procedure.

Figure 7 shows the comparison between the volumetric distribution of the subsurface obtained by a bulk sieve analysis (- - -) and the average grading curve of all experiments resulting from the automatic object recognition (—). The error bars represent the standard deviation for all analysed photographs. Thereby, each photograph was analysed several times. The mean standard deviation averaged over all fractions is 2.3%. Thus, the mean standard deviation, basing on 30 processed images, gives a quantity for the sensitivity of the suggested image processing procedure.

In addition to the natural sediment mixture, all experiments were repeated with partially coloured mixtures. For that purpose, all grain sizes of one quarter of the entire mixture were coloured. This resulted in very sharply contrasted particles, giving a good basis for the automated object recognition.

Consequently, painting a specific amount of the total sediment volume represents a useful alternative under laboratory conditions.

4 RESULTS

4.1 *Flume data*

Flume experiments with a similar grain size distribution ($\sigma = 3.1$) as for the calibration series are performed in another flume at slopes of 9.0%. The flume is 13 m long and 0.6 m wide. Starting from an unloaded and homogenously mixed sediment (0 l/s), the discharge is subsequently increased allowing for armouring (2 l/s) and the formation of steps and pools (8 l/s). As shown in Figure 8 the grading curves obtained with the automated object recognition (—) approaches the sieving curve (- - -) with increasing discharge. This points out that the derived weighting factor of $\Theta = 0.8$ correspond to a well developed, coarse armour layer with distinct bed features, typical for steep open channels.

Besides this grain size distribution typical for steep open channels, a second sediment mixture typical for gravel-bed rivers was tested. These experiments are being performed in a 28.5 m long and 3.2 m wide flume at slopes between 1.3% and 2.3%, in order to obtain a braided morphology. As the spatial variation of the bed shear stress is high in braided rivers, special attention was paid to the choice of the sample area. The bed section chosen for the survey showed significant armouring.

As visible in Figure 9, the proposed method is also applicable in gravel-bed rivers, where no explicit formation of bed features could be observed. Nevertheless, the grading curve obtained by automatic object recognition lies somewhat above the distribution of the subsurface material. This observation can be attributed to the fact that the tested river-type differs from the calibration river-type and the derived conversion factor overcompensates the lack of fine material in the surface layer.

4.2 *Field data*

In addition to the flume data, the proposed method has also been tested under field conditions. As bulk sieve

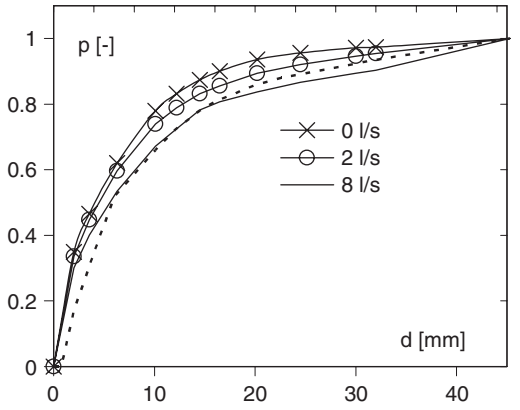


Figure 8. Volumetric distribution of the subsurface obtained by bulk sieve analysis (- - -) and automatic object recognition (—) for a steep open channel tested in a flume experiment for different hydraulic loadings.

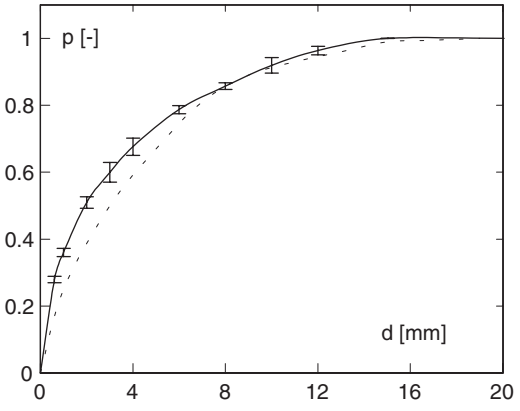


Figure 9. Volumetric distribution of the subsurface obtained by bulk sieve analysis (- - -) and automatic object recognition (—) for a braided gravel-bed river tested in a flume experiment.

analyses would have resulted in large sample quantities, the surface-orientated transect sampling method as suggested by Fehr (1986) was used to obtain reference grading curves. The validity of this method has been proven for gravel-bed rivers. However, in torrent-beds large bed elements limit the application of the transect sampling method.

As a consequence, in a first stage the comparison with field data is carried out for gravel-bed rivers to ensure that the reference grading curve is determined with sufficient accuracy. The first river tested is the Töss River, a midland gravel-bed river, which originates in the northern foothills of the Alps and meets the Rhine River about 20 km southwest of Schaffhausen.

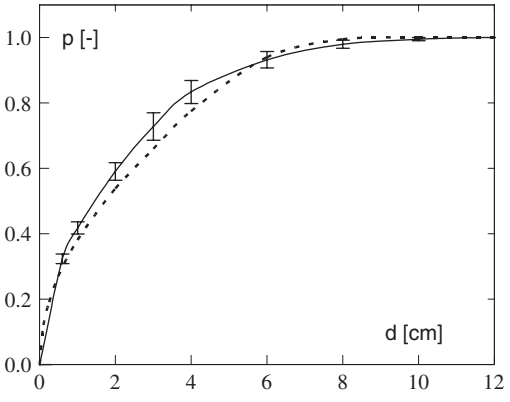


Figure 10. Volumetric distribution of the subsurface obtained by bulk sieve analysis (- - -) and automatic object recognition (—) for the Töss River, Switzerland.

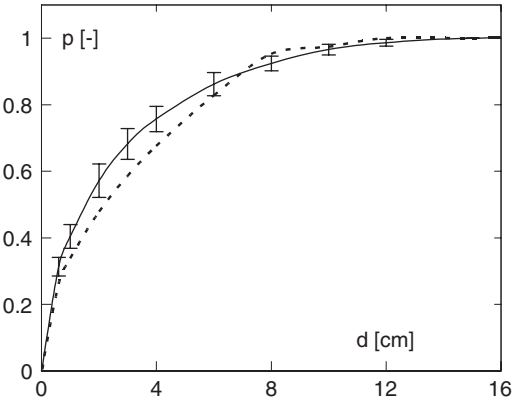


Figure 11. Volumetric distribution of the subsurface obtained by bulk sieve analysis (- - -) and automatic object recognition (—) for the Reuss River, Switzerland.

The Töss River is characterised by relatively fine material ($d_{max} = 0.12$ m). The standard deviation of the grading curve is $\sigma = 3.0$, thus armouring of the river bed is an existent phenomena (Little and Mayer 1972).

Figure 10 shows that the digital imagery processing method provides a good approximation of the subsurface layer. Nevertheless, the implementation of the conversion factor derived for an armour layer that correspond to torrent beds, again leads to a somewhat finer grading curve.

As shown in Figure 11 a similar result is obtained for the lower reach of the Reuss River. The Reuss River, a mountain stream, originates in the Alps near the Gotthard pass and flows towards Lake Lucerne. In the upper Reuss valley the river bed contains very large boulders. In the lower reach the channel gradients decrease and the bed material is considerably finer.

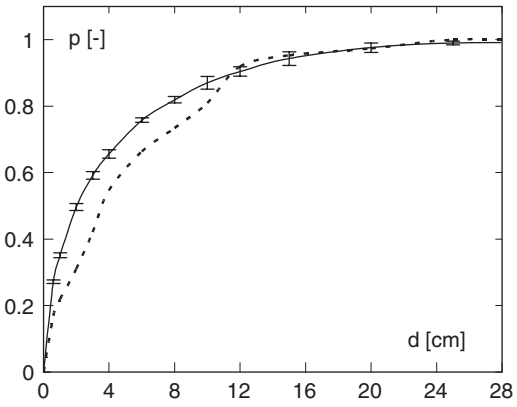


Figure 12. Volumetric distribution of the subsurface obtained by bulk sieve analysis (- - -) and automatic object recognition (—) for the Flaz River, Switzerland.

The sample (Fig. 11) was taken from a river bar, which contained finer and more mobile material. Thus, the present sample does not represent the coarser river bed, which shows a pronounced armour layer. Nevertheless, considering the comparison between the reference grading curve and the grading curve obtained by automated object recognition, the proposed procedure produces good results.

The last river investigated up to date is the Flaz-river in the Engadin valley, a region located in the east of Switzerland. The sample was taken from a river bar, which again was composed of more mobile material. However, the maximum grain size ($d_{max} = 0.25$ m) of the sample is large.

Figure 12 shows that the approximation obtained by the digital imagery processing method is good, but again somewhat too fine.

5 CONCLUSIONS

The present paper describes a method to extract the grain size distribution of the subsurface of coarse river bed material by analysing digital imagery. The main advantage of evaluating digital photographs is that several samples can be taken within short time.

The present paper focuses on the conversion from a surface-orientated sampling method basing on automated object recognition towards the grain size distribution of the subsurface layer. The suggested procedure was derived in flume experiments with a grain size distribution typical for steep open channels. The comparison with independent flume data shows that the proposed method gives reasonable results for torrent beds. For torrents the standard sampling procedures are limited in their applicability, thus the developed method may be an alternative to obtain grain size information of the subsurface layer.

However, as the proposed method bases on vertical pictures of a dry bed section, this method is not applicable in narrow ravines with considerable discharges even under low flow conditions. In contrast to gravel-bed rivers, in torrents the bed material of the surface layer is not necessarily an image of the subsurface layer, but is highly influenced by hillslope processes. Thus, further investigation is needed to determine the limitations of the proposed method for torrent beds under field conditions.

In a first step the method was tested for gravel-bed rivers, resulting in promising approximations to the reference grading curves of the subsurface. The results show that the proposed method is a useful tool to determine the grain size distribution of the subsurface of gravel beds in a fast, easy and inexpensive way. As the results slightly differ between torrents and gravel-bed rivers further improvements of the suggested procedure are required.

The processing procedure was performed several times within the same image. The mean standard deviation averaged over all performed experiments and over all fractions revealed a value of $\sigma_p = 2.3\%$. This value suggests, that the image processing procedure gives reproducible results.

As two different cameras were used for the field and laboratory experiments, it was possible to study the effect of optically imperfect lenses on the method. In accordance with the results obtained by Butler et al. (2001), this additional distortion does not affect the results, as for both, laboratory and field conditions good results were obtained.

6 LIST OF SYMBOLS

d_X: Grain size for which X% of the total sample are smaller.
d_i: Grain size of the fraction i.
d_{max}: Maximum grain size.
d^*_{min}: Smallest particle to be recognised in the automated object recognition.
n: Total number of grains collected within a surface sample.
n_i: Number of grains within the fraction i of a surface sample.
p: Proportion of the total sediment volume.
Δp_i: Proportion of weight of a fraction i of the subsurface layer.
σ: Standard deviation of the grading curve.
σ_P: Standard deviation of p.
Θ: Weighting factor for the conversion model.

REFERENCES

Adams, J. 1979: "Gravel Size Analysis from photographs", *Journal of the Hydraulic Division*, ASCE, Vol. 105, No. HY10, 1247–1255.

Anastasi, G. 1983: “Geschiebeanalysen im Felde unter Berücksichtigung von Grosskomponenten”, *Mitteilungen der Versuchsanstalt für Wasserbau, Hydrologie und Glaziologie*, ETH Zürich, Nr. 70.

Butler, J.B.; Lane, S.N.; Chandler, J.H. 1998: “Assessment of DEM quality for characterizing surface roughness using close range digital photogrammetry”, *Photogrammetric Record*, 16(92): 271–291.

Butler, J.B.; Lane, S.N.; Chandler, J.H. 2001: “Automated extraction of grain-size data from gravel surfaces using digital image processing”, *Journal of Hydraulic Research*, Vol. 39, No. 5, 519–529.

Church, M.A.; McLean, D.G.; Wolcott, J.F. 1987: “River bed gravels: Sampling and analysis”, in “*Sediment Transport in Gravel-bed Rivers*”, ed. Thorne, C.R.; Bathurst, J.C.; Hey, R.D., John Wiley & Sons Ltd., 43–88.

Crowder, D.W.; Diplas, P. 1997: “Sampling heterogeneous deposits in gravel-bed streams”, *Journal of Hydraulic Engineering*, Vol. 123, No. 12, 1106–1117.

Diplas, P.; Sutherland, A.J. 1988: “Sampling techniques for gravel sized sediments”, *Journal of Hydraulic Engineering*, ASCE, Vol. 114, No. 5, 484–501.

Diplas, P.; Fripp, J.B. 1992: “Properties of various sediment sampling procedures”, *Journal of Hydraulic Engineering*, Vol. 118, No. 7, 955–970.

Fehr, R. 1986: “A method for sampling very coarse sediments in order to reduce scale effects in movable bed models”, *IAHR Toronto Symposium ’86 on Scale Effects in Modelling Sediment Transport Phenomena*, Toronto, Ontario, 383–397.

Fraccarollo and Marion 1995: “Statistical approach to bed-material surface sampling”, *Journal of Hydraulic Engineering*, ASCE, Vol. 121, No. 7, 540–545.

Hey, R.D.; Thorne, C.R. 1983: “Accuracy of surface samples from gravel-bed material”, *Journal of Hydraulic Engineering*, ASCE, Vol. 109, No. 6, 842–851.

Kellerhals, R.; Bray, D.I. 1971: “Sampling procedures for coarse fluvial sediments”, *Journal of the Hydraulic Division*, ASCE, Vol. 97, No. HY8, 1165–1180.

Leopold, L.B. (1970): “An improved method for size distribution of stream bed gravel”, *Water Resources Research*, Vol. 6, No. 5, 1357–1366.

Little, W.C.; Mayer, P.G. 1972: “The role of sediment gradation on channel armouring”, Report No. ERC-0672, *Environmental Resource Center*, Georgia Inst. of Technology, Atlanta, Georgia.

McEwan, I.K.; Sheen, T.M.; Cunningham, G.J.; Allen, A.R. 2000: “Estimating the size composition of sediment surfaces through image analysis”, *Proceedings of the Institution of Civil Engineers, Water and Maritime Engineering*, 142, Dec., 189–195.

Mosley, M.P.; Tindale, D.S. 1985: “Sediment variability and bed material sampling in gravel-bed rivers”, *Earth Surface Processes and Landforms*, 10, 465–482.

Rosport, M. 1997: “Fliesswiderstand und Sohlenstabilität steiler Fliessgewässer unter Berücksichtigung gebirgsbachtypischer Sohlstrukturen”, *Mitteilungen des Instituts für Wasserwirtschaft und Kulturtechnik.* Universität Karlsruhe, Heft 196.

Weichert, R.; Bezzola, G.R.; Minor, H.E. 2003: “Bed morphology, flow resistance and stability in mountain torrents”, *Proc. of the XXX IAHR Congress*, Thessaloniki, Greece, Theme C, Vol. II, 159–166.

Wickenhäuser, M. 2003: “Methoden zur Sohlenaufnahme in Wildbächen”, [“Methods for the grain size analysis in torrents”], Diplomarbeit, *Versuchsanstalt für Wasserbau, Hydrologie und Glaziologie*, ETH Zürich (unpublished-diploma thesis).

Wolman, M.G. 1954: “A method of sampling coarse river-bed material”, *Transactions of the American Geophysical Union*, Vol. 35, No. 6.

River Flow 2004 – Greco, Carravetta & Della Morte (eds.)
© 2004 Taylor & Francis Group, London, ISBN 90 5809 658 0

Development of discrete subaqueous bed forms

H. Friedrich, S.E. Coleman, B.W. Melville & T.M. Clunie
The University of Auckland, New Zealand

ABSTRACT: Experimental investigation of subaqueous bed forms has been undertaken and analyzed. Based upon already-existing theories in the area of sediment bed-form initiation and development, 7 experimental runs were carried out in a 440 mm-wide, glass-sided, 12 m-long laboratory flume. For each run, bed profiles were measured at 30 sec intervals. The sediment in use was a fine sand with $d_{50} = 0.2$ mm. The study is the first of a series of studies looking at the phenomenon of submerged sediment bed-form behaviour. The main purpose of the study was to gain information on the relations central to linkages between bed-form propagation speed, sediment-transport rate and predictions of bed development. Relations predicting equilibrium sandform speeds as functions of flow conditions and sediments are available in the literature, although these relations have not been widely tested. More general relations predicting sand-form speeds as functions of flow conditions, sediments, and bed-form magnitudes remain to be determined.

1 INTRODUCTION

1.1 *Bed-form movement and sediment transport*

For any sediment bed form propagating steadily without changing size or shape, sediment continuity considerations readily lead to $q_{SH} = cH$, where q_{SH} = the volume rate of sediment transport over the crest of the bed feature per unit width of channel, c = bedform celerity and H = bed-form height measured crest to subsequent trough (e.g., Coleman and Melville, 1994). Depending on how sediment volume is measured, this can also be expressed as $q_{SH} = cH(1\text{-}p)$ for equilibrium or slowly-growing subaqueous bed forms (Nino et al., 2002), where p is the porosity of the deposited sediments.

A relation, such as that above, between sediment transport and the magnitudes and speeds of propagating discrete bed forms (ripples and dunes) is potentially very useful. If sediment is transported as bed load in the form of bed forms, measurements or predictions of bed-form magnitudes and celerities as these waves develop, facilitate estimation of sediment-transport rates for the developing bed (as well as equilibrium bed-form transport rates). Such estimations increasingly underpredict transport rates as the proportion of transport bypassing bed-form lee faces, e.g. as suspended load, increases for stronger flows. Mohrig and Smith (1996) provide a method for estimating the bypassing fraction (up to 60%), whereby measurements or predictions of bed-form magnitudes and speeds can be used to estimate sediment-transport rates generally, and not just where sediment in motion remains cycling within individual bed forms.

1.2 *Sandwave initiation theories*

Different theories exist about the initiation of sandwave development. Kennedy (1969) led the stability theory approach with his irrotational flow analysis. Coleman and Fenton (2000) showed, however, that the theory of irrotational flow is inadequate for sandwave generation. Coleman and Eling (2000) further showed that bed forms have their genesis in wavelets (small scale sediment waves, which are primarily a function of sediment size and not flow characteristics).

Raudkivi (1983) proposes that sandwave initiation occurs through streamline oscillations within high-shear and constant velocity zones within the flow profile.

Other researchers, among them Nezu and Nagakawa (1993), conclude that grain entrainment and sandwave initiation are caused by the flow's coherent turbulent structure, which interacts with the bed surface.

The range of analyses and conjecture reflects the current lack of understanding of the phenomena controlling sediment-wave generation, such phenomena potentially including grain movements, flow-bed instabilities and bed-wave interactions.

2 SANDWAVES

2.1 *Classification of sandwaves*

ASCE (1966) faced the problem of dividing sandwaves into ripples and dunes. The criteria for the distinction are still controversial, especially when a possible transition from ripples to dunes or viceversa occurs. The

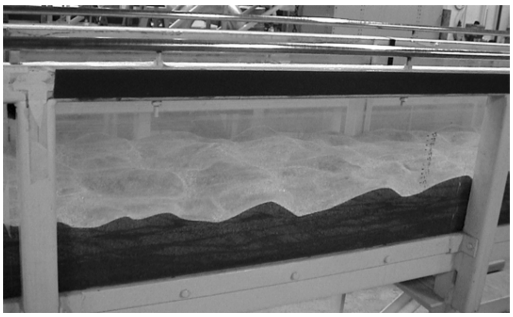


Figure 1. Ripple bed forms during experimental runs conducted at The University of Auckland.

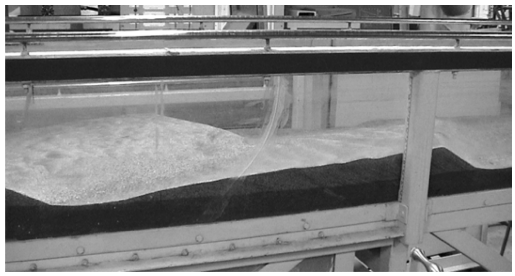


Figure 2. Dune bed forms during experimental runs conducted at The University of Auckland.

cause and behaviour of this transition is of great interest, but up to now the behaviours of, and transitions between, these different kinds of sandwaves remain unclear. Widely-accepted classifications of ripples and dunes, with their associated characteristics, are fundamental for this research and are summarized in the next two sections. One aim of the present research is to further investigate distinctions between ripples and dunes as bed forms.

2.2 *Ripples*

According to ASCE (1966), ripples are small finesediment bed waves, which do not influence the water surface (Fig. 1).

It is widely accepted that ripples are small triangular sandwaves that are usually longer than 0.06 m and shorter than 0.6 m, and are restricted to sands finer than 0.6 mm. McLean (1990) states that ripples display wavelengths of the order of 0.1–0.2 m and heights of 0.01–0.02 m.

Furthermore, the theory was introduced that small-scale ripples may exist on an otherwise flat bed or may be superimposed on the stoss sides of larger bed forms. It remains unclear, however, what makes these superimposed bed forms ripples, and not dunes growing in between larger dunes, especially for sediments of $d_{50} > 0.6$ mm.

In line with the superimposed bed forms being ripples, Raudkivi (1997) observes that rippleforming conditions can occur downstream of the reattachment point of the surface of separation for an upstream dune crest, i.e. where the bed-shear stress is low. Yalin (1992) concludes that ripples are due to the viscous structures at the bed, defining ripples as the bed forms 'imprinted' by the viscous flow structures (undulations) at the bed of a nevertheless turbulent flow.

2.3 *Dunes*

Dunes (Fig. 2) are bed waves that occupy a significant portion of the flow depth, causing the water surface to be disturbed.

Hydrodynamically, they affect the flow with topographic accelerations and decelerations of the flow field extending all the way to the free surface (Maddux (2002)).

Dunes are normally larger and more two-dimensional features when compared to ripples. On beds of coarser uniform-grains (in general it is assumed for sediment grain sizes >0.6 mm) only dunelike features develop. According to Bass (1993), no dunes form with sand finer than 0.15 mm. Dunes are generally restricted to sand-like sediment, but can occasionally also occur with coarser uniform-grained materials. Dunes are irregular sandwaves.

The longitudinal profile is roughly triangular, with a mild and slightly curved upstream surface, where as the downstream slope can be taken to be equal to the dynamic angle of repose ϕ of the sediment.

3 EXPERIMENTAL INVESTIGATION

3.1 *Experimental arrangements*

Seven experiments were carried out, concentrating on sandwave development for different flows. Some of the runs reached equilibrium stages, for others recording was stopped before equilibrium. Table 1 shows an overview of the experimental runs.

The experiments were conducted in a 12 m-long, 0.38 m-deep and 0.44 m-wide glass-sided openchannel flume. Water is recirculated, as well as the sediment. On the rails of the flume, a carriage carries a depth sounding probe. The carriage traveled over a distance of 4–7 m, depending on the characteristics of the runs. For the first experiments, the carriage was moved manually downstream and upstream. For the later experiments, the carriage was motorized, making more efficient use of the equipment and time.

Before each run, the slope of the flume and the temperature of the water were measured and recorded. The velocity profile for each pump setting and equilibrium bed profile were also measured.

Table 1. Overview of conducted runs.

Run	Pump Setting	Run Duration [h:m:s]	Equilibrium	U [m/s]	Fr [−]	Re ($\times 10^3$)	U* [m/s]	θ [−]	Re* [−]
R1	13	2:02:00	no	0.3850	0.2621	1179	0.0302	0.2825	6.1723
D1	21	4:41:59	yes	0.6570	0.4472	2012	0.0673	1.4003	13.7430
RD1	13–21	3:10:45	yes	0.6570	0.4472	2012	0.0673	1.4003	13.7430
R2	10	1:20:41	no	0.2530	0.1722	775	0.0214	0.1409	4.3595
R/D3	18	1:58:43	no	0.5170	0.3519	1583	0.0582	1.0461	11.8783
R4	10	3:12:36	yes	0.2530	0.1722	775	0.0214	0.1409	4.3595
RD2	10-21	6:30:23	yes	0.6570	0.4472	2012	0.0673	1.4003	13.7430

R: Flat Bed → Ripple/D: Flat Bed → Dune/RD: Ripple → Dune/R/D → according van Rijn (1984) transition flow from ripple to dune.
Note: fine to medium sand with $d_{50} = 0.2$ mm and $d_{90} = 0.28$ mm, $v = 0.9798$; $\mu = 0.000001$; $u_c = 0.0115$; $S = 0.001$; $\tau = 21°C$; $s = 2.65$; $h = 0.22$ m; $m = 0.75$ m

Prior to each run, the sediment bed was flattened and the depth-sounding probe was fixed on the carriage. The technique behind the depth-sounding system is based on Coleman (1997), and has since been further improved at The University of Auckland. The depth-sounding system was used to record the profiles of the developing bed. According to Coleman (1997) the accuracy of bed elevation measurement is ±0.4 mm. The distance along the flume was measured using a potentiometer mounted on a 0.199 m diameter wheel running down the outside of the flume side-wall. The streamwise position was recorded at 2.45 mm distance increments, accuracy of measurement being ±1.23 mm.

For each experimental run, measurements were taken at the centreline of the flume. Therefore, only two-dimensional data evaluation can be carried out.

Bed profiles were recorded initially every 30 sec for a run, with profiles in the latter stages of the experiments recorded every 5 to 15 min.

3.2 *Range of experiments*

As seen from Table 1, flows were chosen for the different experimental runs based on the aboveintroduced sandwave theories, where distinctions are made between ripples and dunes. The chosen sediment for all the runs is a fine sand with $d_{50} = 0.2$ mm. This sand was chosen to ensure the development of both ripples and dunes. Therefore, one can study the differences in subaqueous sandwave initiation and development to equilibrium state for the two types of bed forms.

Bed-form development started for five runs from flat bed conditions and for two runs, the transition from ripple to dune beds was studied.

Figure 3 shows the classification of the flows and bed configurations according to van Rijn (1984). For four runs (refer to Table 1) the bed forms reached equilibrium magnitudes.

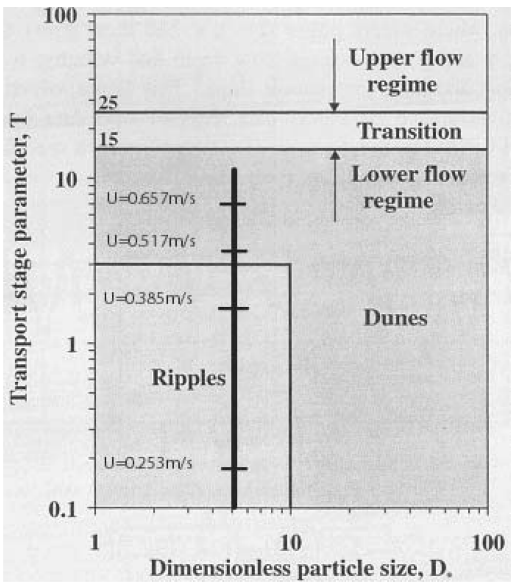


Figure 3. The present flows (see Table 1 for U values) classified in terms of dimensionless flow and sediment parameters.

4 BED-FORM DATA ANALYSIS

4.1 *General remarks*

For each run, the mean (depth-averaged) fluid velocity U, and the bed shear velocity u* were determined from the measured centreline flow velocity profile (see Table 1).

Analysis of the different experimental runs according to Coleman (1996) indicated the bed-form results to be in line with previous research. The writers then focused on a more detailed and explicit analysis of

aspects of bed forms instead of a general and traditional study. A principal goal was to gain enough information to formulate an automatic means of analyzing the development of subaqueous sediment waves. In the past, most of the analysis has been done with a large manual work load and automated analyses were often distorted because of simple determinations of wave height and length, which provide the basis for all submerged sediment wave analyses.

Therefore, this paper will focus on explicit parts of run R/D3, with special attention given to relations central to linkages between bed-form propagation speed, as a function of flow, sediment and bed-form parameters; sediment-transport rate as a function of bed-form speed and bed-form height; and the degree to which bed-form geometry can be taken to be similar. The considerations in the analyses presented here will help to provide means of automating the evaluation of the development of subaqueous sediment waves in the future and will show where there are major inconsistencies in these analyses to date.

4.2 *Bed-form development of run R/D3*

Run R/D3 started from flat bed conditions, with bed profiles recorded for 2 hrs. Bed profiles for the first 10 min are shown in Figure 4.

One can see from Figure 4 that the initiation of bed forms can be a sudden uniform phenomena (see bed forms 10:20:14 AM and 10:20:44 AM in Figure 5). Therefore any role of stochastic turbulence in bed-from generation, as discussed in Section 1.2, must be questioned.

The bed-form unification model as proposed by Raudkivi and Witte (1990) predicts that smaller bed forms run into larger bed forms. This theory has its basis in the assumption that smaller bed forms migrate faster than larger bed forms. Therefore the larger bed forms resulting from coalescence migrate even slower. The question arises, how do new bed forms develop, because as seen from Figure 5, the number of bed forms does not change dramatically once a stable environment is established for a flow.

The speculation arises that new bed forms develop once an original large bed form gets unstable for the existing flow conditions. What then are the characteristics for bed forms to become unstable?

One parameter responsible for the breaking up of bed forms and therefore creation of new bed forms is assumed to be the rate of sediment transport. As introduced earlier, sediment transport can be defined as the product of wave propagation speed and wave height. Some inconsistencies with this assumption will be analyzed herein, the next section focusing on individual developing bed forms in terms of the two main characteristics that sediment-transport rate is dependent on: bed-form height and bed-form speed.

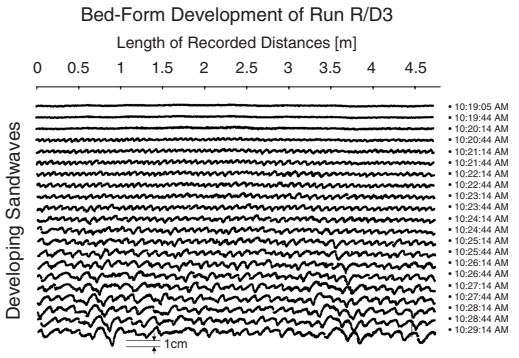


Figure 4. Bed-profile plot for run R/D3 – starting from flat bed conditions – results shown over a time of 10 min.

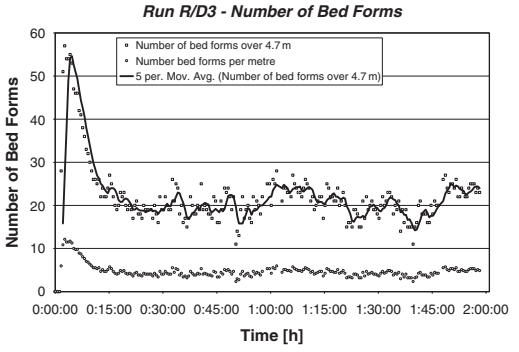


Figure 5. Number of identified bed forms (run R/D3) from development phase to equilibrium phase (2 hrs).

4.3 *Bed-form determination regarding speeds and heights*

In order to make comments about bed-form propagation speed and sediment-transport rate, criteria to define individual bed forms are needed. A common approach is to determine local maxima and minima of the recorded time series of bed forms. Once this is done, the calculation of the bed-form propagation speed is the movement of the crest position of an individual sandwave over the recorded time interval. This approach neglects the aspect of changing bedform shape, as displayed in Figure 6. Changes of bed-form shape can be especially observed during the initial stages of bed-form development.

As Figure 7 shows, as a sandwave migrates, the shape of the sandwave changes and therefore speeds determined by crest movement alone, can distort the assessment of true sandwave speeds.

Development of bed-form height over the whole duration of run R/D3 (determined using the approach

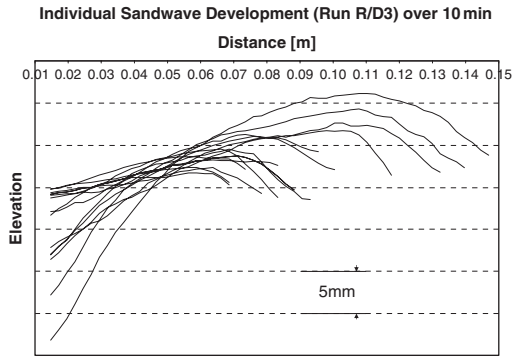


Figure 6. Change of bed-form shape during the development of subaqueous sandwaves (run R/D3 – individual sandwave).

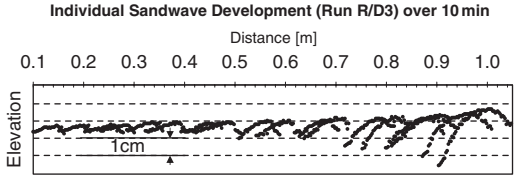


Figure 7. Propagation of an individual sandwave over a period of 10 min (run R/D3).

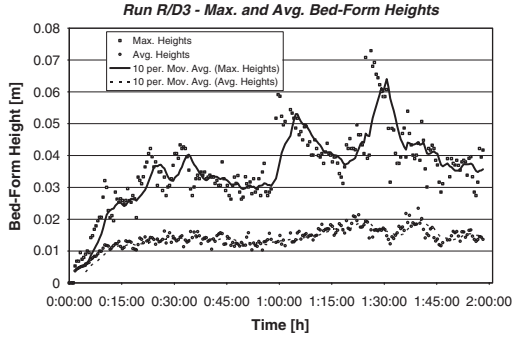


Figure 8. Development of bed-form height for run R/D3.

of locating local maxima/minima) can be seen in Figure 8.

According to the writers' knowledge most studies concentrate on location of crests/troughs through location of local maxima/minima (as indicated above), h or use change of lee-slope steepness values to locate the transition from the crest to the lee slope. In terms of determining bed-form heights, both methods give problems in analysis of the present data. Therefore a selected length of bed forms in the developing phase of Run R/D3 was studied in greater detail, mostly via manual considerations. The main aspects studied

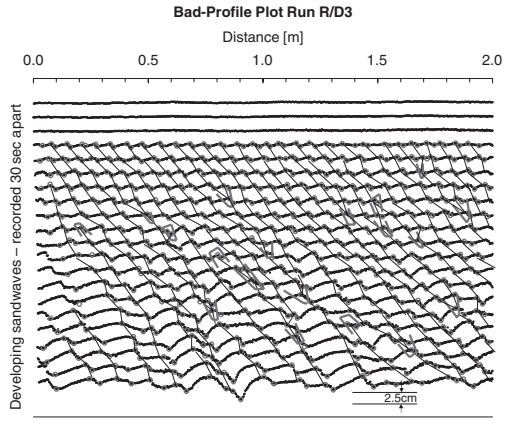


Figure 9. Bed-profile plot highlighting the propagation of bed forms (run R/D3).

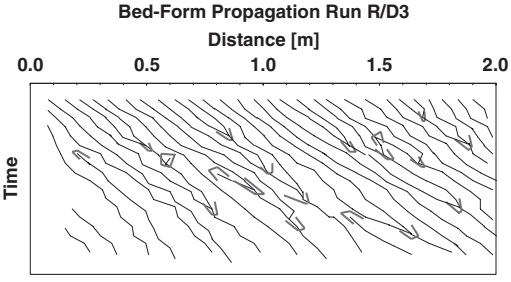


Figure 10. Bed-form coalescence and generation highlighted from Figure 9.

were determination of bedform shape, and based on that information, calculation of bed-form heights and propagation speeds and sediment-transport rate.

4.4 *Bed-form coalescing, generation and life expectancy*

Bed-form propagation speed is not only dependent on bed-form shape, but also the environment of the sandwaves interactions with surrounding bed forms influencing bed-form speeds. As a bed develops for a particular flow, new sandwaves can form and old sandwaves will die. This behaviour of sandwaves emerging and dying is directly related to the sediment-transport rate for the flow. For Run R/D3, Figures 9 and 10 show the initial phase of bed development for a 2 m long section of the flume. Figure 10 highlights the emerging and dying sandwaves over the period of bed development.

In Figure 10, newly generated bed forms typically arise after the merging of existing bed forms,

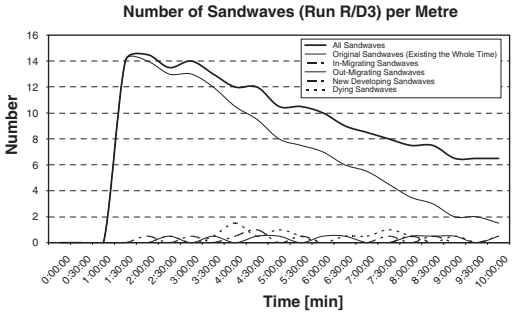


Figure 11. Overview of original and newly-formed sandwaves (run R/D3).

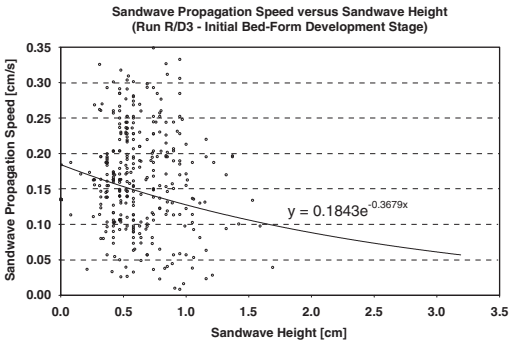


Figure 12. Sandwave propagation speed versus sandwave height for run R/D3; 10 min period.

consistent with the throughpassing mechanism highlighted by Coleman and Melville (1994) and Raudkivi and Witte (1990).

The life expectancy of an individual sandwave during bed development has received little attention to date. Figure 11 gives an overview for Run R/D3 of the distribution of sandwaves, over the 10 min period studied, with each sandwave being evaluated according its origin. Figure 11 shows that after 10 min, only 20% of the overall sandwaves were original sandwaves, these having not been consumed in sandwave coalescence.

A relation for the life expectancy of individual sandwaves can possibly be determined as a function of flow, slope, sediment size and water depth. In order to determine such a relation, further analyses of different flow environments and different sediment sizes must be carried out.

4.5 *Bed-form speed versus height and sediment transport*

Figures 12 and 13 show sediment-transport-rate-related data observed in experimental run R/D3. Because flow and sediment size did not change for this run, the dependency of sandwave propagation speed on sandwave height can be assessed for this run. Once further experimental runs are carried out and analyzed, a comparison with already existing formulas for bed-form speed and sediment transport can be undertaken.

Sandforms propagate downstream by sediment being transported from their stoss sides and deposited on their lee sides (Fig. 13). Based on laboratory data, Coleman and Melville (1994) present a preliminary expression for bed-form speed as a function of flow, sediment and bed-form parameters, that indicates bed-form speed to decrease with increasing bed-form height. Based principally on numerical simulations of bed forms, Nino et al. (2002) similarly conclude

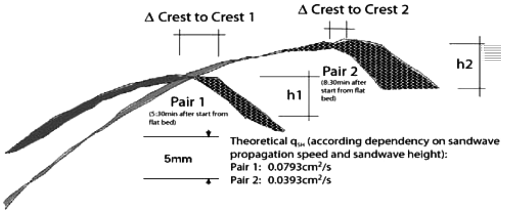


Figure 13. Sediment transport for two individual sandwave pairs as the waves develop (run R/D3).

that bed-form speed is approximately inversely proportional to bed-form height. Prediction of bed-form speed as a function of flow, sediment and bed-form parameters needs further work however.

Figure 12 shows propagation speeds of individual sandwaves versus sandwave height for Run R/D3. As predicted in the literature, sandwave propagation speed generally decreases with increasing sandwave height, although this result is certainly not clear in the data of Figure 12. Any decrease in speed with increasing height is furthermore small in comparison with other available data (e.g. Baas (1993) and Coleman and Melville (1994)). From Figure 12 it would not be expected that the relations between speed and height in the literature would be true for the present results.

Clearly, the relations predicting bed-form speed as a function of bed-form and flow parameters require further work. In this regard, the concept that bed-form migration speed decreases with increasing bed-form height is central to the bed-form unification model of Raudkivi and Witte (1990). This model, based on the motions and interactions of individual bed features and building on the earlier work of Führböter (1983), provides descriptions that are consistent with physical observations of the evolution from 'plane-bed' conditions to equilibrium of subcritical-flow sediment waves (Coleman and Melville, 1994). Predictions of

this model will be improved, however, with improved modeling of bedform speed as a function of flow, sediment and bed-form parameters.

Figure 13 shows why solely considering speed as a function of sandwave height can provide ambiguous results. Displayed are four sandwaves, namely two pairs of waves that were recorded 30 sec apart. The time gap between the two pairs is 4 min. One can clearly see changes in shape for the four individual bed forms. If sediment transport is taken to be dependent on the average height of two successive sandwaves and the propagation speed measured crest to crest, one comes to the result that the sandwave sediment transport of pair 1 (Fig. 13) is of higher intensity than that for pair 2. In contrast, visual inspection indicates that pair 2 transported in 30 sec more sediment load than pair 1. In this regard, the bed-form shape of pair 2 shows an obvious change in the lee-face steepness, which is not accounted for in calculation of the sediment-transport rate as a function of bed-form speed and height. It is therefore proposed that more attention should be given to the change of shape for successive sandforms. These changes should be incorporated in the calculation of sediment-transport rate. In order to do so, more analyses are necessary to show the dependence of sediment transport on bed-form shape. This research is continuing.

5 CONCLUSIONS

For beds developing to equilibrium, relations central to linkages between bed-form propagation, sediment-transport rate and predictions of bed development (e.g. Raudkivi and Witte, 1990) have been investigated herein: principally, the product of bedform speed and bed-form height as bed-forms develop, and the relation of this product to sediment-transport rate; bed-form speed as a function of flow, sediment and bed-form parameters; and the degree to which bed-form geometry can be taken to be similar (including whether steepness can be taken to be constant) as bed forms develop. All these considerations have been analyzed for one main flow, seen as a first major step in a 3 year project. The data and insights of the presented paper will provide the basis of further research in this area.

The next step will be in terms of the last of the above mentioned considerations. In this regard, power-law relations for the growth of sediment-wave lengths and heights with time for steady and changing flows (Coleman and Zhang, 2003) currently indicate that bed-form steepness is essentially invariant during bed-form development, although this inference requires confirmation from focused experimental measurements of developing bed forms. Further insight in the still-debated topic of distinctions between ripples and dunes is also expected.

The present experiments and data analysis will be extended to other open-channel flows. In addition to using the present 440 mm-wide glass-sided laboratory flume, there will be data accessible from 135 mm open-channel flows, and rectangular closed conduit flows, with bed development from plane bed to equilibrium configuration measured for each experimental series for a range of homogenous sediments and ranges of flows.

ACKNOWLEDGEMENTS

The research was partly funded by the Marsden Fund (UOA220) administered by the New Zealand Royal Society. The authors are furthermore grateful to Dr V. Nikora for useful discussions and suggestions.

REFERENCES

ASCE Task Force on Bed Forms in Alluvial Channels of the Committee on Sedimentation. 1966. Nomenclature for bed forms in alluvial channels. *J. Hyd. Div*., 92(3): 51–64

Baas, J.H. 1993. *Dimensional Analysis of Current Ripples in recent and ancient depositional Environments*. Faculteit Aardwetenschappen. Utrecht, Rijksuniversiteit Utrecht: 199.

Coleman, S.E. 1996. *Wave generation and development on a sandy river bed – Discussion*. Issues and Directions in Hydraulics, Rotterdam, The Netherlands, Nakato & Ettema (eds): 145–155

Coleman, S.E. 1997. Ultrasonic Measurement of Sediment Bed Profiles. *27th Congress of the International Association for Hydraulic Research*, San Francisco, California, U.S.A.

Coleman, S.E. & Eling, B. 2000. Sand wavelets in laminar open-channel flows. *Journal of Hydraulic Research*, 38(5).

Coleman, S.E. & Fenton, J.D. 2000. Potential-flow instability theory and alluvial stream bed forms. *Journal of Fluid Mechanics*, 418: 101–118.

Coleman, S.E. & Melville, B.W. 1994. Bed-form development. *Journal of Hydraulic Engineering, ASCE*, 120(4): 544–560.

Coleman, S.E. & Zhang, H. 2003. Sediment-wave development in subcritical water flow. Submitted for rereview to *Journal of Hydraulic Engineering, ASCE*.

Führböter, A. 1983. Zur Bildung von makroskopischen Ordnungsstrukturen (Strömungsriffel und Dünen) aus sehr kleinen Zufallsstörungen. *Mitteilungen des Leichtweiss Instituts, Technical University of Braunschweig*, Braunschweig, Germany, 79: 1–51 (in German).

Kennedy, J.F. 1969. The Formation of Sediment Ripples, Dunes, and Antidunes. *Ann. Rev. Fluid Mech.*, 1: 147–168.

Maddux, T.B. 2002. *Turbulent Open Channel Flow over Fixed Three-Dimensional Dune Shapes*. PhD-Thesis, Mechanical Engineering. Santa Barbara, University of California, California, U.S.A.: 155.

McLean, S.R. 1990. The stability of ripples and dunes. *Earth-Science Reviews*, 29(1-4): 131–144.

Mohrig, D. & Smith, J.D. 1996. Predicting the migration rates of subaqueous dunes. *Water Resources Research*, 32(10): 3,207–3,217.

Nezu, I. & Nagakawa, H. 1993. *Turbulence in open-channel flows*. IAHR AIRH monograph series, Rotterdam, The Netherlands: Balkema.

Niño, Y., Atala, A., Barahona, M. & Aracena, D. 2002. Discrete particle model for analysing bedform development. *Journal of Hydraulic Engineering, ASCE*, 128(4): 381–389.

Raudkivi, A.J. 1983. Thoughts on ripples and dunes. *Journal of Hydraulic Research*, JAHR, 21(4): 315–321.

Raudkivi, A.J. 1997. Ripples On Stream Bed. *Journal of Hydraulic Engineering*, 123(1): 58–64.

Raudkivi, A.J. & Witte, H.H. 1990. Development of bed features. *Journal of Hydraulic Engineering, ASCE*, 116(9): 1063–1079.

van Rijn, L.C. 1984. Sediment transport, Part III: Bed forms and alluvial roughness. *Journal of Hydraulic Engineering, ASCE.* 110(12): 1733–1754.

Yalin, M.S. 1992. *River Mechanics*. New York, U.S.A.: Pergamon Press. Inc. New York.

River Flow 2004 – Greco, Carravetta & Della Morte (eds.)
© 2004 Taylor & Francis Group, London, ISBN 90 5809 658 0

Transport dynamics and morphology of a high mountain stream during the peak flow season: the Ürümqi River (Chinese Tian Shan)

F. Métivier & P. Meunier
Laboratoire de dynamique des systèmes géologiques, Institut de physique du globe de Paris, France

M. Moreira
Laboratoire de Géochimie, Cosmochimie, Institut de physique du globe de Paris, France

A. Crave
Géosciences Rennes, France

C. Chaduteau
Laboratoire de Géochimie, Cosmochimie, Institut de physique du globe de Paris, France

B. Ye
Tian Shan Glaciological station, Chinese Academy of Sciences, P.R. China

G. Liu
Department of Geography, Peking University, Beijing, P.R. China

ABSTRACT: In order to get some insight into the poorly known dynamics of high mountain streams measurements of flow and sediment transport (both solute, suspended and bed load) were conducted at three different alluvial sites along the Ürümqi He (Chinese Tian Shan). The discharge of this high mountain stream (headwaters at 4000 m), is in part controlled by glacial melting. This first survey took place during the high flow season in July 2001. Although of short duration it brings some useful insight into the dynamics of flow and sediment transport by the river during the high flow season. (i) Bed load transport during peak flow can account for more than 80% of the solid flux. (ii) Bed and solute loads together account for more than 90% of the Total load of the river at the range front. (iii) In the glacial valley site, measurements made before and during a nearly bank-full flood event indicate that transport of gravel seems to be more or less a continuous process in riffle or step-pool sections, whereas larger pools, that temporarily store the material delivered by the riffles, are flushed during a flood event. (iv) A strong correlation exists between suspended and bed load. This suggests that movement along the bed is necessary to unhide the smallest particles and put them into suspension.

1 INTRODUCTION

Rivers are by far the main carriers of erosion products (Goudie, 1995). The rate at which and the mechanisms by which a river is able to incise relief and evacuate the eroded masses delivered from the slopes is essential to our understanding of both stream morphology and landscape evolution. It is even more crucial in active mountain ranges where sustained tectonic uplift, orographic precipitations and glacial melting, should maintain significant erosion rates and enhance river dynamics. Despite this datasets on sediment transport and morpho-dynamics of high mountain streams are sparse (Wohl, 2000).

We report hereafter results from a preliminary study on the morpho-dynamics of the Ürümqi He, a high mountain stream of the northern Tian Shan (China). The river headwaters are made by retreating glaciers. The Ürümqi River initiates at 3600 m ASL from the melt of a glacier known as Glacier N° 1. The river flows through two steep sections separated by a flat basin where the town of Hou Xia and the glacial station of the Chinese Academy of science are located. The river length from its headwater to the piedmont

where it enters a semi-desert environment is on order of 60 km.

2 MORPHOLOGY OF THE ÜRÜMQI RIVER AND ITS CATCHMENT

2.1 *Sampling sites description*

2.1.1 *Site 1: glacial valley*

The first sampling site is located in the glacial valley at an elevation of 3300 m approximately 8 km downstream of glacier number 1 which is the source of the Ürümqi River (Fig. 1). The river flows on glacial moraines though a series of cascades and flats (Fig. 1).

The long distance profile of the valley is steep and grain size of surface particles is gravel-like. D_{50} of the surface samples is 21.5 mm and D_{90} is equal to 158 mm. Figure 1 and 7 show the study site. It is located in a confluence zone between to riffles. Upstream the river is divided into two branches flowing around a central bar. Bed is step like with a mean slope of 4.9%. A pool is located at the confluence. The long distance averaged bed slope is steep $S \sim 2.5\%$. Most of the measurements were carried at the downstream end of the pool where the river is the widest (average wetted perimeter P_w varies from 9 to 12 m) and the shallowest (average hydraulic radius between R between 0.2 and 0.4 m). Some measures were taken in the pool ($P_w \sim 7$ m, $R \sim 0.5$ m). Some where also carried in the riffle section upstream.

2.1.2 *Site 2: Hou Xia*

The second sampling site is located at the outlet of the upstream gorge before the town of Hou Xia (literally: after the gorge, Fig. 1). As in the case of the glacial valley, the measurement site is between two riffles or step-pool sections. At the end of the upstream riffle a pool stands as in the case of site 1 although no active confluence exist at present. Bed slope averages 1.5% at the site. The wetted perimeter remained quite stable during measurement days P_w between 22.5 and 23.5 m, more than twice the perimeter of the river upstream near the glaciers. Abandoned terraces can be seen in the valley, the glacial station being built on one of these.

2.1.3 *Site 3: range front*

The third sampling site is located at the range front just outside the downstream gorge of the river. Our measurement, as for the above mentioned, is located before a riffle section where the river splits into three

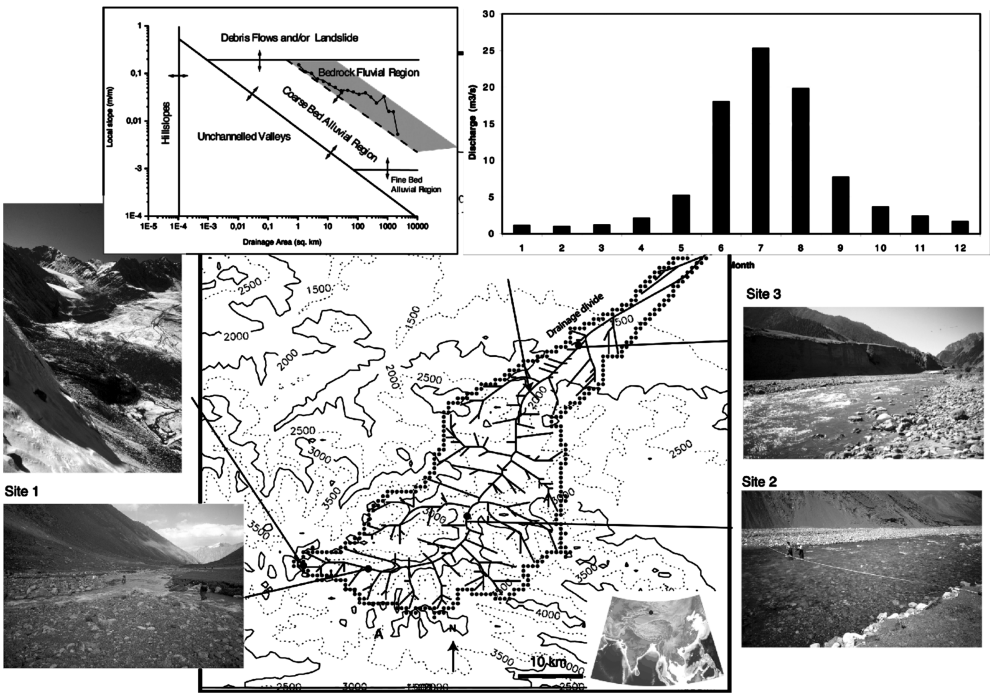


Figure 1. Location map of the Ürümqi He Drainage. Average monthly discharge measurements are made at a gaging station build in gorges a few kilometers south of the range front. Drainage network and slope-area relationship were extracted from the 30-arc second DEM GTOPO30. Most of the streams reported on the map north of the gaging station are not perennial. Upper left, slope area relationship for the Ürümqi He. Upper right, monthly discharge at the downstream station.

main branches. The wetted perimeter was between 21 and 22 m during measurements and the hydraulic radius between 0.5 and 0.6 m. The river is dynamic and measurements where difficult. At the range front the most prominent feature in the landscape is made by large terraces standing almost 100 m above the present day river bed. These terraces which are fill-cut at the range front progressively turn into strath terraces a few kilometers downstream where tertiary red beds are seen to dip southward under a sub horizontal dark gray gravel bed layer marking the ancient river plain, a feature common to all the rivers of northern Tian Shan.

2.2 *Data acquisition*

Discharge was measured at each site using an OTT velocimeter. 295 velocity profiles were measured corresponding to 30 complete gagings of the Ürümqi He (Fig. 2). Velocity profiles were measured regularly across the river (between 1 and 2 m distance depending on the site). Water was sampled 26 times with a USDH 48 depth integrating sampler for suspensions or solute load. The sampler was equipped with a 0.64 mm nozzle. Samples were filtrated to a threshold of 0.2 microns to separate suspensions and solute load and prevent chemical reactions in the bottles after sampling. Suspensions were dried and weighted in the laboratory. Bed load was measured using a 15 cm entrance Helley-Smith sampler. The Helley-Smith was equipped with 250 microns mesh bags. Each bed load section is composed of at least 6 to 10 point measurements regularly spaced along the section. At each point the sampler was left for 60 s (30 s during the highest flows). 95 sections were measured during this survey. Topographic measurements were conducted at site 1 and 2 using a Wild T2000 Total station equipped with a laser distance meter that permits measurements with an accuracy of less than 1 cm. Surface granulometry was established using statistical counting (Wolman, 1954). Minimum size measured was 1 mm.

Solute transport in the Ürümqi river catchment has been discussed at length by Liu et al. (1995), and Williams et al. (1995), on the basis of sampling of the river at places near our sampling sites. We will therefore hereafter concentrate on the solid load.

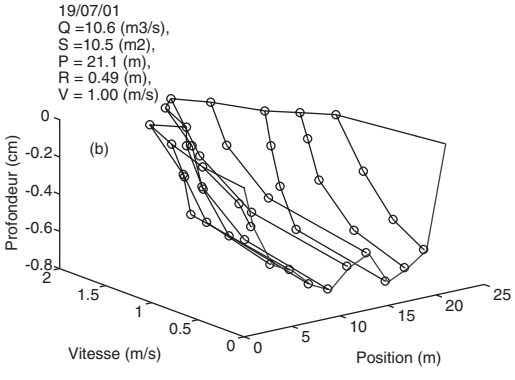


Figure 2. Sample velocity profile at site 2.

3 VELOCITY SCALE IN MOUNTAIN STREAMS

Velocity profiles were leveled regularly at each site of the Ürümqi He. Shear velocity estimates were performed by adjusting a logarithmic profile to the data according to:

$$\frac{u}{u_*} = \frac{1}{\kappa}\ln\left(\frac{z}{k_s}\right)$$

Where u is the velocity of the flow at depth z, u_* is the shear velocity, k_s the bed roughness and $\kappa = 0.4$ the von Karman constant. In gravel bed rivers such as the Ürümqi He, the bed roughness usually scales with the D_{90} of bed material distribution (e.g. Wilckock, 1996). Following Wilcock (1996) another estimate can then be derived using the average velocity but still assuming a logarithmic form of the velocity profile:

$$\frac{U}{u_*} = \frac{1}{\kappa}\ln\left(\frac{h}{ek_s}\right)$$

Here U is the depth averaged velocity, and h the flow depth. The estimates were then compared (Fig. 3). The results clearly show a poor agreement for the Hou Xia site. The two other sampling sites do not

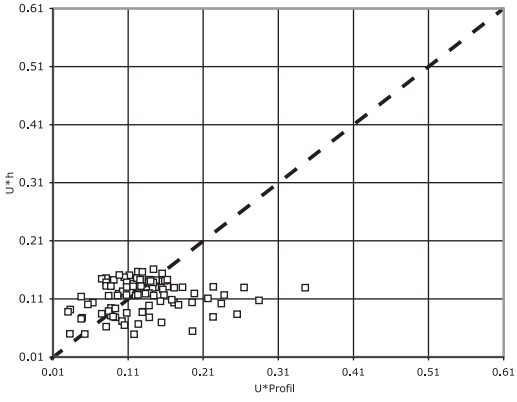


Figure 3. Correlation between estimates of the shear velocity at site 2.

show a convincing correlation. If the velocity distribution was logarithmic throughout the flow depth as often supposed both estimates of the shear velocity should correlate with a 1:1 slope. As this is not the case velocity profiles can not be considered to follow a logarithmic distribution on the timescale of leveling (Wohl, 2000). The average velocity should then be preferred and considered the only relevant velocity scale at the scale of conventional sampling (60 s per measurement). Care should therefore be taken when devising transport equations with shear velocities.

4 SEDIMENT TRANSPORT

4.1 *Importance of the bed load component*

Numerous studies have focused on bed load transport by mountain streams (Wohl, 2000). The reasons for this are that (1) bed load is probably an important component of the total mass transport, and (2) it bears a first order control on the morphology of many mountain streams. Measurements made in the Ürümqi River attest that bed load transport is significant during high flow. Daily averages of bed load show that it represents approximately 64, 20 and 45% of the total daily load at the glacial valley site, Hou Xia and at the range front respectively during the measurement period. These values are high especially in the glacial valley and, perhaps more surprisingly, at the range front 60 km downstream of the headwaters. Only at Hou Xia is suspension the dominant mode of transport of the solid load. One might find two explanations for this. The Hou Xia basin is the place where the river profile is the flattest. Flattening of the along stream profile of the river should therefore logically lead to lower values of bed load transport because of the concurrent reduction in stream power expenditure (Métivier & Meunier, 2003 and references therein). The low value of bed load may also come from the fact that between the glacial valley and Hou Xia, the river cuts relatively deep into the range. There its bed is mostly rock floured. The river, when it enters the Hou Xia plain a few hundreds of meters before site 2, may not be a transport limited stream but a supply limited river. This then could explain why the bed load component of the solid load drops to 20%. These results clearly show that any mass balance or sediment budget conducted in high mountain streams should incorporate bed load measurements.

4.2 *Fractional l transport*

Some samples were kept and dried in the laboratory. Sieving was performed and the bed load was decomposed into Φ-size fractions $\alpha_{l,Di}$. The coarse fractions were then normalized to the corresponding fractions

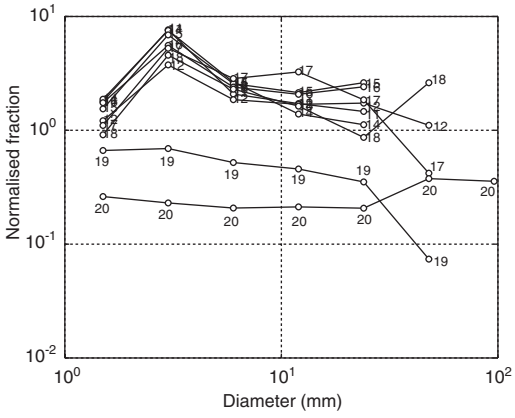


Figure 4. Comparison between the ratio of a given *i*th-size fraction in transport to the same fractions on the bed surface with the median diameter of the *i*th size fraction. Numbers indicate day of measurement.

of the bed surface $\alpha_{b,Di}$. Figure 4 shows the plot of these normalized fractions against grain diameter

$$\frac{\alpha_{l,D_i}}{\alpha_{b,D_i}} = f(D_i)$$

During July 19 and 20 fractional transport seems, to the first order to be independent of grain diameter. Parker et al. (1982) proposed that grains moved in proportion to their presence on the bed surface. This hypothesis was developed in order to explain transport of bed material in paved gravel Bed River and was checked against data from Oak Creek (Oregon). Parker et al. (1982) called this phenomenon equal mobility. It was then argued by others (Wilcock, 1997; Wilcock & McArdell, 1997) that equal mobility was but an end-member of partial transport. Partial transport of matter seemed to be more representative of bed load transport by rivers in which bed material does not move in large proportions.

In the Ürümqi He No true pavement can be defined over large surfaces of the bed. The unstable nature of braided channels is probably the reason for this. In fact the river presents a braiding morphology at several places in the glacial valley (site 1) and everywhere both in Hou Xia (site 2) and at the Range front. Surface granulometry performed at site 2 (Hou Xia plain) shows the local variability of grain size distributions and its relationship with bed structures (Fig. 5).

For example the grain size distribution in a confluence pool has a D_{50} of 1 cm whereas the D_{50} of a mid-bar nearby reaches approximately 4.5 cm. Bed material measurements in Hou Xia, on the braid plain, therefore show that grain size distribution of bed material varies according to flow structures and position on the bed.

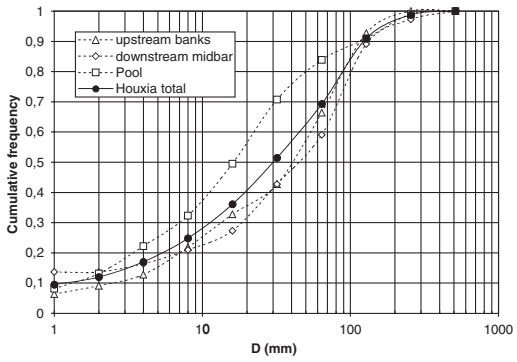


Figure 5. Surface distribution of bed material in the Hou Xia braid plain.

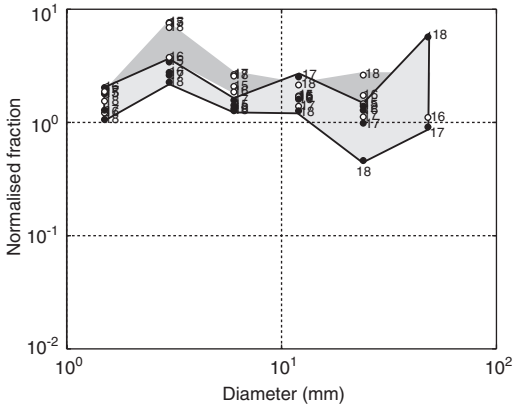


Figure 6. Open circles and dark shade of gray envelope: same as Figure 4 for the Hou Xia sampling site. Dark circles and light shade of gray envelope: normalization is done with the surface granulometry of a pool.

Equal mobility is clearly achieved downstream at the Range Front where transport rates are very high (Fig. 4 profiles 19 and 20). For other days and sites sands in the range 2–4 mm seem to be over represented in the bed load compared both to there respective abundance on the bed and to other grain sizes.

Fractional transport in braided streams should take the bed surface distribution of grains depicted above into account. Indeed in Hou Xia the measurement section was located after a very dynamic pool. As selective surface granulometry was performed at this site, we tested the possible influence of spatial variations in the surface granulometry. Figure 6 shows the result. Although some variability remains due most probably to the small number of samples, the curves (dark circles) are strongly smoothed and approach equal mobility for the fractions with sizes less than 2 cm. The residual variability may possibly come from the subsurface (Parker et al., 1982) as it has been shown that the granulometry of the subsurface is often finer than the granulometry of the surface material.

4.3 *The step/pool-pool transport unit*

One very interesting feature of the Ürümqi He concerns the way bed load is transported. As the material is coarse its characteristic distance of travel is probably quite small. Does such river morphology exhibit some particular spatial scales or pattern that would be indicative of the distance of travel of the grains making up the bed? One striking pattern of the Ürümqi He in the glacial valley is the succession of steep riffles or step-pool sections that alternate with flatter pool sections (Fig. 7). During our survey of the river in the glacial valley we continuously measured bed load both in a step-pool section and after a large confluence pool (Fig. 7). Between July 11 and July 14 when we left for the second site downstream in Hou Xia, a nearly bank full flood wave passed trough the measurement section. In two days the discharge rose by an order of magnitude. Peak discharge occurred on July the 13th and reached more than 6 m^3/s. Figure 8 shows daily averages of bed load in both step-pool and pool sections together with the average daily discharge.

Our measurements indicate that bed load transport in the step-pool section is weakly dependent on discharge. The load remains high before during an after the flood. On the contrary transport in the pool is strongly discharge-dependent. Bed load rises by nearly two orders of magnitude between July 11 and July 13. This variable dependence can probably be explained by the difference in the local h/D_{90} ratios. In the step-pool section this ratio varies little and is on order of 1 because large boulder of diameter similar to the flow depth strongly that regulate the flow like spill gates. In the pool where the water height is always large the bottom shear stress is probably much more dependant on flow conditions and therefore variable.

The mass balance between the flux transported into the pool along the step-pool section and the flux leaving the pool is approximately 2. Thus before and after the flood, bed load is transported to the pool efficiently by turbulence in the step-pool sections. Most of the mass is then stored in the pool. During the flood event the pool is flushed and sediments get delivered to the next step-pool section where they are transported at a seemingly constant rate.

Bed load granulometry clearly is affected by the passage of this wave (Fig. 9). Before the flood the size of the material transported from the step-pool to the pool is largely coarser then the granulometry of the material leaving the pool. Therefore sedimentation takes place and gravels are stored in the pool, in agreement with the mass balance (Fig. 8). During the

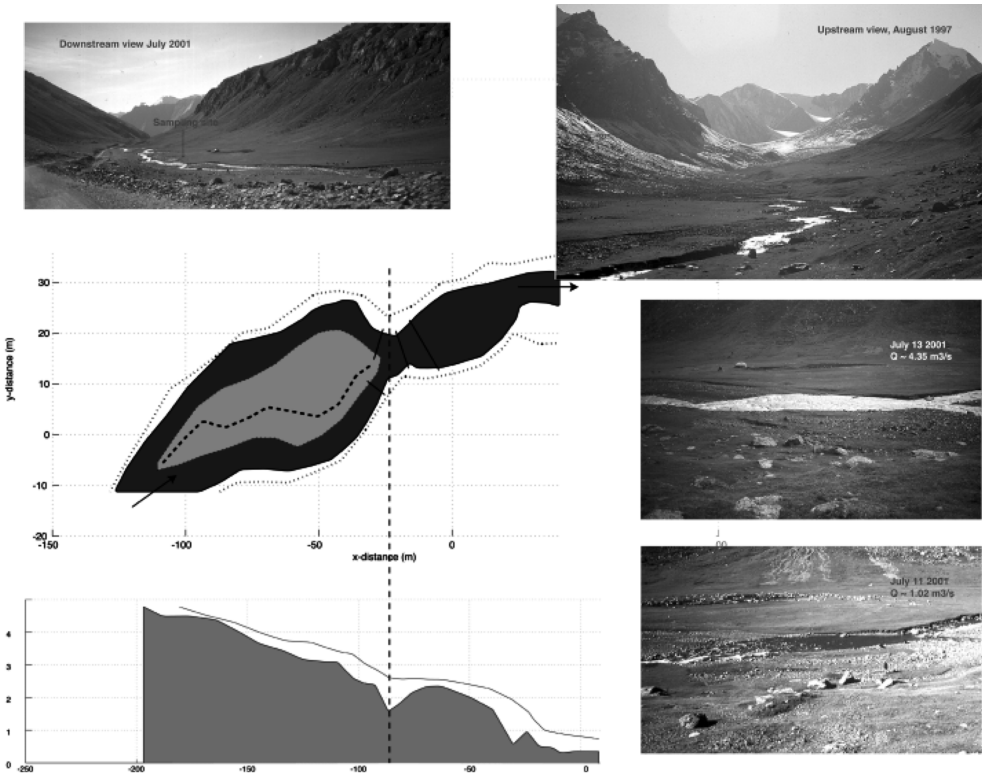


Figure 7. Study site in glacial valley. Upper two photographs: sampling site and glacial valley views with head water glaciers at a distance. On left: pictures of sampling site during and before bank full discharge. Map of sampling site leveled with Wild T2000 theodolite and laser distance-meter.

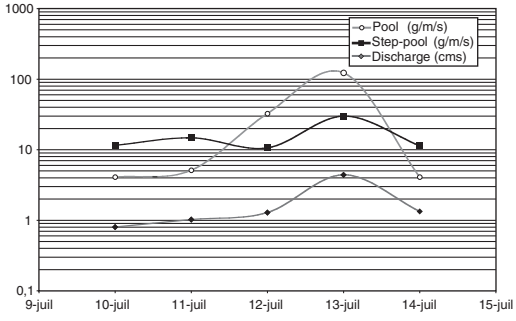


Figure 8. Daily average values of bed load and discharge.

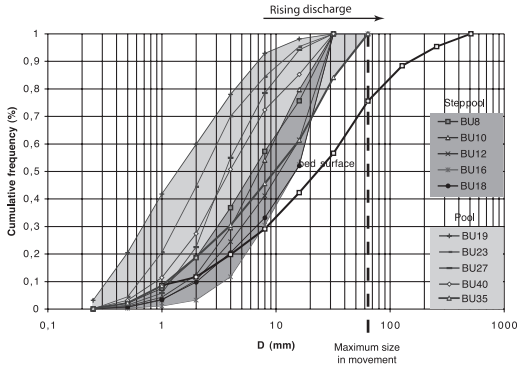


Figure 9. Granulometry of bed samples. Dark grey shades correspond to material transported in the step-pool section. Light grey shades correspond to material transported in pool section.

flood the granulometry of the material leaving the pool rises and becomes of the same order of magnitude as the granulometry of particles fed to the pool from the step-pool section upstream. There again these results are in good agreement with the mass balance indicating that the pool is being flushed. The balance of fluxes into and out of the confluence pool equals approximately 2. This means that the flood wave washed out all the sediments stored during the preceding 3 days and that equilibrium is approximately achieved at the time scale of our survey. Future research will concentrate on trying to establish longer term balance of fluxes at

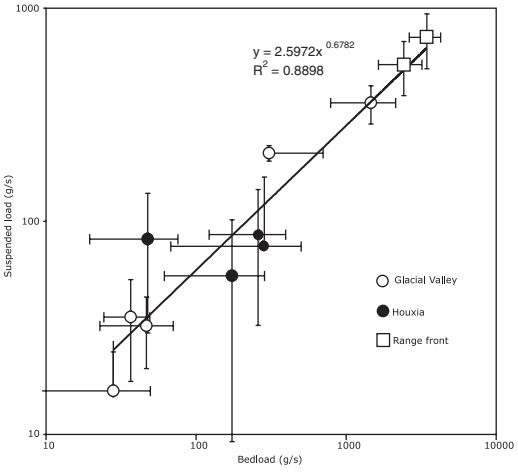


Figure 10. Correlation between average daily suspended and bed load along the Ürümqi He.

the scale of morphologic structures as this balance is important to understand the characteristic lengths of transport of be material and the characteristic velocities at which such structures may evolve (e.g. Wohl, 2000 and references therein).

4.4 *Suspended load*

Suspended load was measured with the use of a USDH 48 depth integrated sampler attached to a wading rod. Between one and three samples were retrieved each day. Daily variations are insignificant with the exception of July 12 and 13 during the passage of a bank full flood wave. As suspension was sampled throughout the flow depth the concentration obtained should be representative of the true flux although depth integrated sampling may bear some uncertainties because of the very transient nature of suspended load near the bed. Sediments transported mainly consist in fine rock flour. Very few silts were sampled. Overlaps between suspended and bed load samples is therefore negligible.

There are clearly two striking features with the suspended load of the Ürümqi He. The first one is that suspended load clearly appears to be the minor mode of transport along the Ürümqi He. During our survey the water was clear except during July the 12th and the 13th when the flood wave passed through. Suspended load accounts for at most 22% of the total load carried by the Ürümqi in the glacial valley. It accounts for less than 10% both in Hou Xia and at the range front.

The second important observation that can be made is the strong correlation that seems to exist between suspended and bed load as shown in Figure 10. Averages of bed and suspended load are well correlated through a power-law relationship.

This strong correlation clearly suggests that most of the suspended sediments come from the alluvial bed and are released by movement of coarse particles, sands, gravels and cobbles. This also implies that sediment feeding from the slopes is negligible. The Ürümqi Drainage lies in an arid environment. Very few precipitations occurred during our journey. When precipitations occur the principal mode of mass transport on the slopes seems to be gravity driven flows. Wash load is clearly not a dominant process and therefore explains why such a nice correlation occurs. This certainly deserves further research for at least two reasons. Understanding such a correlation may help us achieve correct estimates of the mass fluxes transported by mountain rivers without having to measure the bed load component explicitly. The difficulty of sampling bed load in gravel bed rivers has been known for long and estimating bed load movement through the measurement of suspended load clearly is an issue in studies of erosion and sediment transport by rivers. Further more such a relationship existing between bed load and fine particles release from the bed remains unclear and badly documented whereas it may shed light on the dynamics of fine particles movement and temporary storage in gravel bed streams. Rivers like the Ürümqi He may well be ideal places to study such entrainment.

5 SUMMARY

A survey was performed on three reaches of the Ürümqi He, a high mountain stream of northern Tian Shan (China). Our survey shows the close link between the morphology (step-pool to pool) and sediment transport in these step mountain rivers. Equal mobility of the grains seems to be achieved in one of the reaches. At all three sites suspended and bed load are strongly correlated. These results confirm the importance of further researches on bed load transport and the control it exerts on mountain stream morphology. Especially it is suggested that concurrent and systematic measurements of both velocity profiles bed load fluxes and granulometry are needed in order to understand the coupled evolution of river morphology and transport dynamics. Furthermore local mass balance at the scale of morphologic structures such as step-pools and pools shows how grain sorting and temporary storage occurs in mountain streams. At lower flows sands are transported throughout the system whereas gravels only move in step-pool sections and are trapped in pools. Long term mass balance coupled with granulometry of bed material movement and hydraulic measurements should then lead to a better understanding of the timescales and lengthscales of grain movement and of the timescales of morphologic changes in mountain streams.

REFERENCES

Goudie, A. 1995. *The changing earth*. Blackwell Science Publishers.

Liu, F., Williams, M., and Yang, D. 1995. Snow and water chemistry of a headwater alpine basin, Ürümqi River, Tian Shan, PR China. In Williams, M. and Tranter, M., editors, *Biogeochemistry of seasonally snow covered catchments*, IAHS-AIHS Publ. 228.

Parker, G., Dhamotharan, S., and H., S. 1982. Model experiments on mobile, paved gravel bed streams. *Water Resources Research*, 18: 1395–1408.

Wilcock, P. 1996. Estimating local bed shear stress from velocity observations. *Water Resources Research*, 32: 3361–3366.

Wilcock, P. 1997. The components of fractional transport rate. *Water Resources Research*, 33: 247–258.

Wilcock, P. and McArdell, B. 1997. Partial transport of a sand/gravel sediment. *Water Resources Research*, 33: 235–245.

Williams, M., Yang, D., Liu, F., Turk, J., and J.M., M. 1995. Controls on the major ion chemistry of the Ürümqi River, Tian Shan, People's Republic of China. *Journal of Hydrology*, 172: 209–229.

Wohl, E. 2000. *Mountain Rivers*. Water resources monograph 14. AGU.

River Flow 2004 – Greco, Carravetta & Della Morte (eds.)
© 2004 Taylor & Francis Group, London, ISBN 90 5809 658 0

Study of navigation problems in Nile River reach at Elbogdady

A.M. Negm
Professor of Hydraulic Engineering, Faculty of Engineering, Garyounis University, Benghazi, Lybia

M.M. Elfiky & M.I. Attia
Associate Professors, Dept. of Water & Water Structures Eng., Faculty of Engineering, Zagazig University, Zagazig, Egypt

M.H. Nassar
Assistant Lecturer, Dept. of Water & Water Structures Eng., Faculty of Engineering, Zagazig University, Zagazig, Egypt

ABSTRACT: The present paper concerned with investigation of solving natural sediment problems at Elbogdady reach, south Luxor staff gauge, 712.80 km U/S of Roda staff gauge on the Nile River. The main purpose of the paper is to investigate the navigation problems in the considered river reach and to suggest the best location for the required quay or platform. Proper solutions has been suggested and studied for sedimentation problems. Each alternative has been evaluated from both hydrodynamics and sediment transport points of view. The best proposal has been selected from a set of alternative proposals. A 2-D numerical model (SED-2) has been applied for simulating the sediment transport along the river reach.

1 INTRODUCTION

Planning of harbors covers the collection, processing and using of the natural choice of location and orientation of major port components such as access channels, breakwaters, basins, quays and specialized berths. It covers also, the choice of type of structures for preliminary engineering and cost estimates as well as design criteria for the different structures. The conditions affecting the quays planning may be climatic conditions; winds, temperature, rainfall and Humidity. Oceanographic conditions; waves, tides, currents and Sediment transport may have an important effect on the quays planning. Topographic, hydrographic conditions and soil conditions effect on the quay location. The following properties of the navigation channel through navigable streams should be investigated carefully while the design procedure.

- Channel location and orientation,
- Channel width and side slopes,
- Channel minimum water depth, and

Characteristics of the channel bends. The subjects of sediment transport and flow in alluvial streams are gaining it importance with the increasing utilization of water resources. Considerable research had been done in sediment transportation and the problems related alluvial streams in the past four decades by hydraulic engineers, geologists and researchers from other disciplines such as fluid mechanics. The knowledge of the distribution of sediment in the vertical is eventually used to compute the total suspended load carried by the stream. Observations in laboratory flumes and natural streams have shown that the concentration of suspended load in the vertical direction decreases with increase in distance from the bed. The sediment transported past a strip of unit width and thickness will be $(c_* u \, dz)$ c and u are the local sediment concentration and the local velocity respectively. The method of integrating $(c_* u)$ over the depth had been proposed by Einstein H.A. 1942. Also, Bagnold R.A. 1966 introduced an energy balance concept and related.

The suspended load transport to the work done by the fluid. Many authors had studied the simulation of sediment transport with various techniques. A number of attempts have been introduced including the laboratory investigations, the field studies and the numerical models. The numeric attempts have been surveyed. Paintal A.S. 1971 investigated a stochastic model of bed load transport Lung W.S. & O'Conner D.J. 1982 modified a 2-D mass transport equation in estuaries. Lin P. & Shen H.W. 1984 developed a 2-D model by characteristic method. Characteristic method was applied to analyze the two-dimensional unsteady flow

over a bed of fine sediment. Cole P. & Miles G.V. 1983 developed a 2-D model of mud transport. The model studied the transportation of well-mixed cohesive sediments in estuaries and coastal waters. Van Rijn L.C. 1986 investigated the mathematical modeling of suspended sediment in non-uniform flows. Galappatt G. and Vreugdenhil C.B. 1986 introduced a depth-integrated model for the suspended sediment transport. Schoellhamer D.H. 1988 investigated a two dimensional Lagrangian simulation of suspended sediment. Pacheco R. & Ceballos 1989 introduced an analytical solution to enable the prediction of the sediment transport. Wang K.H. & Hu H. 1998 built a two-dimensional mathematical model for calculating suspended sediment transport in open channels. Ahmed Z. et al. 1999 studied a finite difference solution method as a tool for solving the equation of longitudinal dispersion of conservative pollutants in open channels. Verbanck M.A. et al. 2002 applied the classical Rouse-Schmidt procedure to compute the vertical distribution of suspended solids concentrations in open-channel flows.

2 NAVIGATION PROBLEMS

In order to develop more than more water transport facilities, river channels must be improved so that they are suitable for navigation. Several rivers in Europe such as the Danube, the Volga, and the Rhine and such rivers as the Mississippi in U.S.A. and the Yangtze in China have been developed and regulated for inland navigation. Inland navigation is also practised on some of the Indian rivers in the eastern part of the country. This improvement for navigation is effected by one or more of the following processes: canalization, regulation by river training works, providing lateral canals with locks, dredging to deepen the critical sections, and providing storage reservoirs to supplement minimum flow and increase the water depth. Application of these methods requires a deep insight into river hydraulics.

The sedimentation problems in the Nile River become more severe after the construction of the Aswan High Dam because of the sediment free flow has the ability to convey sediment from either the river bed or banks causing a bed degradation and bank erosion. The following section introduces some of previous works in sediment transport branch and some of sedimentation problem, which happen over long reaches at the Nile River. Gasser M.M. 1988 introduced report on the best alignment of the two approach channels of the new navigation look at Naga-Hammadi. Gasser M.M. 1988 introduced final report on study of navigation problems existing on the Nile River at Selwa-Bahary. Ahmed M.A. & Ahmed M. 1997 introduced report on study of scouring problem which existing on the east bank of Nile River at Rashid branch at El-Wardan km. 34.000.

3 DESCRIPTION OF THE PROBLEM

Elbogdady reach is located south Luxor staff gauge, 712.80 km U/S of Roda staff gauge. This area has been studied by the Nile Research Institute (NRI), El-Mottasem M. & Zaki A. 1994. The main target of this investigation was to precise the efficiency of the reach as a quay for cargoes and floated hotels. The safest path of the navigation should be detected as shown in Figure 1. Hydrological data were collected about maximum and minimum discharges through the studied reach. Also, it has included the study of maximum

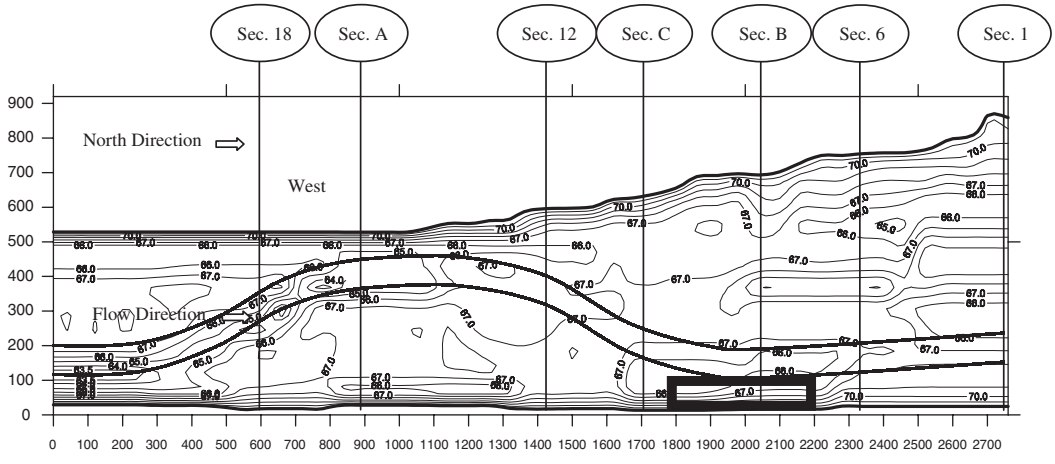


Figure 1. Topographic map of the studied reach at Elbogdady area 1993.

and minimum water levels of the Nile River at the studied reach from 1970 to 1993. The collected data are as follows in Table 1.

4 APPLIED MODELS

The 2-D hydrodynamic model (HYD-2) by Elfiky M.M. et al. 1997 used for simulating the flow field, it was based on the solution of the Reynolds form of Navier-Stokes equations for turbulent flow. The governing equations of (HYD-2) used for simulating the flow field, are the momentum equations in x and y directions in addition to the continuity equation, reading as:

$$\frac{\partial \bar{u}}{\partial t}+\bar{u}\frac{\partial \bar{u}}{\partial x}+\bar{v}\frac{\partial \bar{u}}{\partial y}+g\frac{\partial z_s}{\partial x}+\frac{\tau_{bx}}{\rho h}-\frac{\sum F_x}{\rho h}-\varepsilon_{fx}\nabla^2\bar{u}=0 \quad (1)$$

$$\frac{\partial \bar{u}}{\partial t}+\bar{u}\frac{\partial \bar{u}}{\partial x}+\bar{v}\frac{\partial \bar{u}}{\partial y}+g\frac{\partial z_s}{\partial y}+\frac{\tau_{by}}{\rho h}-\frac{\sum F_y}{\rho h}-\varepsilon_{fy}\nabla^2\bar{v}=0 \quad (2)$$

$$\frac{\partial h}{\partial t}+\frac{\partial h\bar{u}}{\partial x}+\frac{\partial h\bar{u}}{\partial y}=0 \quad (3)$$

The sediment behavior has been simulated using the 2-D sediment transport model (SED-2) Elfiky M.M. et al. 2002 which simulates the sediment transport behavior in rivers. The movement of the suspended sediment in alluvial streams can be governed by the mass balance equation of sediment. Integrating the 3-D convection-diffusion equation of the suspended sediment in vertical direction, yielding

$$\frac{\partial h\bar{c}}{\partial t}+\frac{\partial h\overline{uc}}{\partial x}+\frac{\partial h\overline{vc}}{\partial y}-\varepsilon_{sx}\frac{\partial}{\partial x}h\frac{\partial \bar{c}}{\partial x}-\varepsilon_{sy}\frac{\partial}{\partial y}h\frac{\partial \bar{c}}{\partial y}+\alpha w_s(\bar{c}-c_*)=0 \quad (4)$$

Table 1. The hydrological collected data.

The collected data	In flood case	In emergency case	In winter closure case
Total discharge	245 mm^3/ day	605 mm^3/ day	65 mm^3/ day
Water level	(73.58)	(75.77)	(69.06)

Water slope for Nile River in this reach is assumed to be equals about 4 cm/km.

in which $\bar{u}$ and $\bar{v}$ are the depth-averaged velocity components in x and y directions, respectively, g is the gravitational acceleration, z_s is the elevation of water surface above reference plane, h is the flow depth, ρ is the water density, τ_b is the bottom shear stress, F is the external deriving force, ε_f is the horizontal fluid diffusion coefficient, $\bar{c}$ is the depth averaged sediment concentration, c_* is the sediment carrying capacity, ε_s is sediment horizontal diffusion coefficient, α is the ratio of sediment concentration near the bed to the averaged concentration.

5 REACH INVESTIGATION

5.1 *Hydrographic studies*

The hydrographic survey was done for Elbogdady river reach on 1993 through 18 lateral cross-sections from Km. 710.280 to Km. 712.220, as shown in Figure 1. It can be noticed that the top width of water surface varies between 891 m at Sec. (1) to 581 m at Sec. (18) for the flood season, while it varies between 798 m at Sec. (1) to 466 m at Sec. (18) for winter season. The river cross-section width tends to increase toward the north direction. It can be noticed easily the proposed navigation path, which was suggested by the (NRI). Also, the bed topography of this river reach has been investigated using the old surveys carried out between 1970 to 1993 to predict the history of the bed variations within this area. Figure 2 shows the bed topography of Elbogdady river reach carried out on 1982. Comparing between contour map 1982 and the recent one 1993, it has been found that the river west side between Sec. (12) to Sec. (18) has subjected to a great scouring process. While, the west side has subjected to a silting process between Sec. (1) to Sec. (12). In the east side, no variance can be noticed on the bed levels between Sec. (1) to Sec. (12). As a result of the above notation, (NRI) reported that the best location of the quay may be located at the east side between Sec. (6) to Sec. (12).

5.2 *Hydrodynamic simulation*

The considered river reach has been schematized in a uniform rectangular mesh with $\Delta x = 20.0$ m and $\Delta y = 20.0$ m. The reach was investigated at first, using the 2-D hydrodynamic model (HYD-2) for two flow cases; case of minimum passing discharge and the flood case. The water slope was adjusted to be about 4.2 cm/km for the first case, while it was 4.0 cm/km for the second one. Moreover, a variation in the bed levels, within 0.01 m may be taken place, to simulate the velocities in the field. Velocities in lateral and longitudinal directions and discharge distribution were investigated. It was very important to satisfy

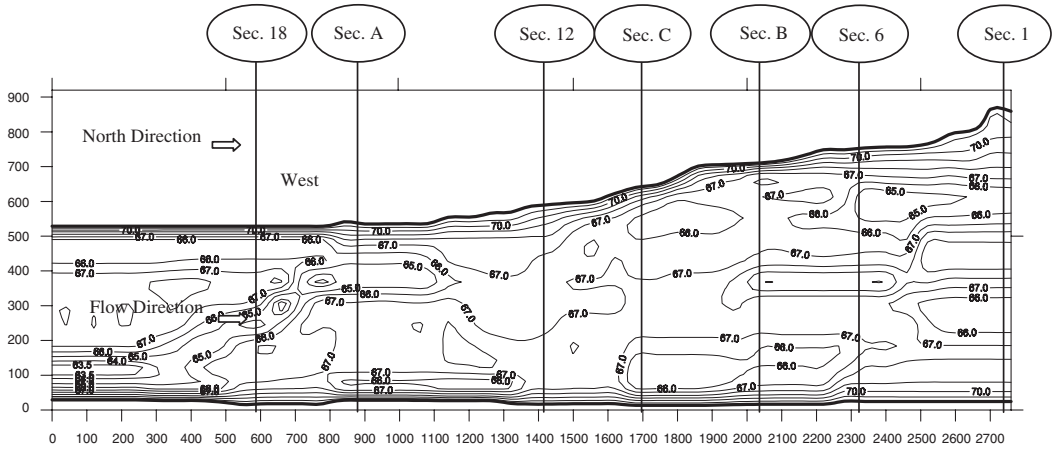


Figure 2. Topographic map of the studied reach at Elbogdady area 1982.

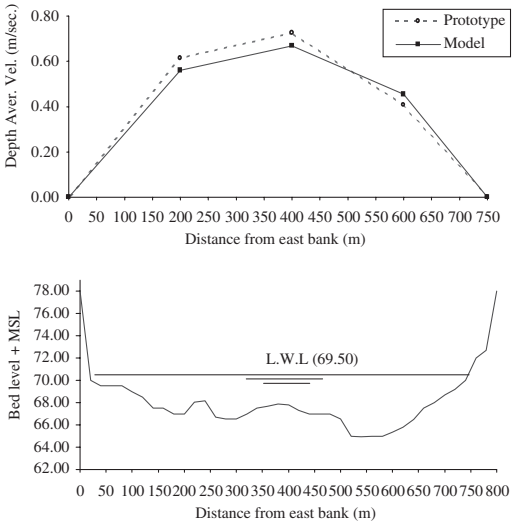


Figure 3. Comparison between prototype and model for Sec (6).

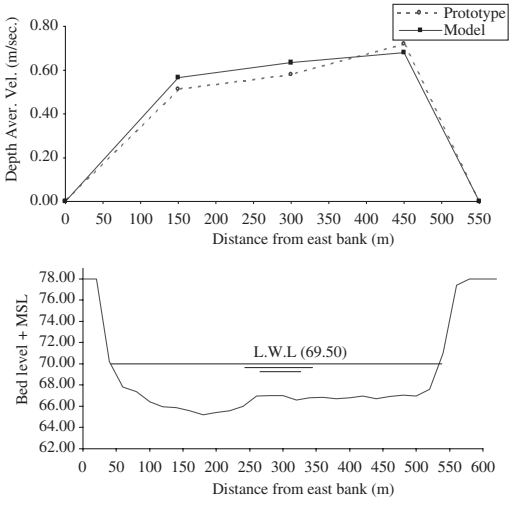


Figure 4. Comparison between prototype and model for Sec (12).

the hydrodynamic model calibration before using its velocity computations in the developed model solving the convection-diffusion equation in two dimensions. Figures 3,4 show the comparison between the velocity field measurements and the HYD-2 model outputs at Sec. Sec (6) and Sec (12), respectively. It can be clearly seen that, there are acceptable agreements between the hydrodynamic model (HYD-2) results and the field measurements. Now, the best site of the quay should be studied and the safest path of the navigation thought Elbogdady reach should be investigated with the help of the developed model SED-2 in addition to the HYD-2 model outputs.

6 PROPOSED SOLUTIONS

The optimal scientific solution for the problem has depended on the investigation of the problem reasons. In addition, it has investigated the problem effects on the Nile River morphology and the necessary steps for the problem elimination. Proper solutions may be suggested and easily studied for the present problem to define the optimum proposal. All proposals, which have been suggested for the navigation path has been, introduced as shown in Figure 5. It can be noticed easily that the first proposal was suggested by the (NRI). There are some dredging areas as shown in the other proposal. These dredging areas were suggested with

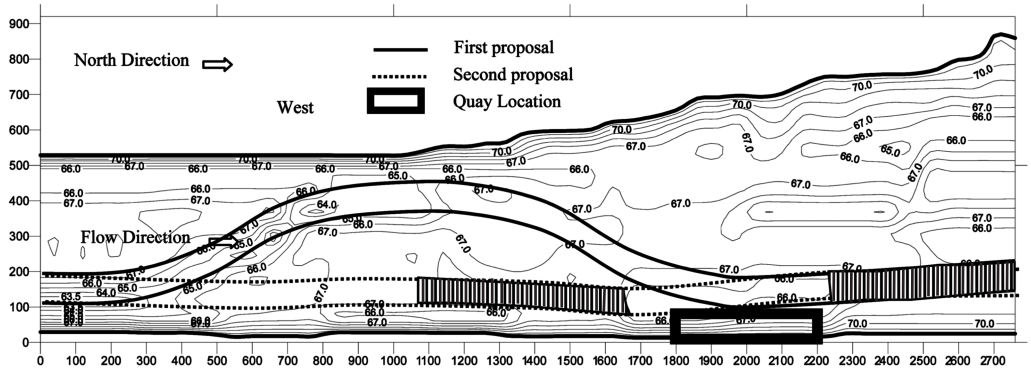


Figure 5. The proposed navigation paths at the studied reach for all proposals.

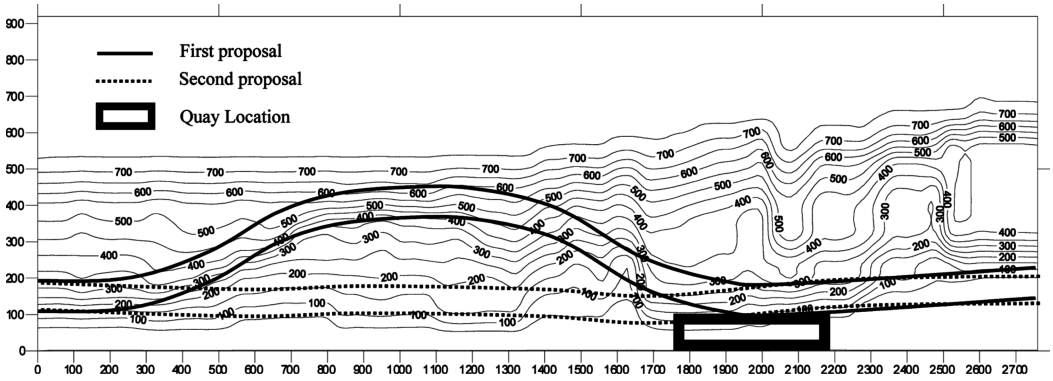


Figure 6. The stream distribution at the studied reach.

bed level (66.00) achieving the necessary conditions for a navigation path.

The suggestion of the two proposals is mainly depend on the stream distribution as shown in Figure 6. The suggestion depends also on the following consideration. The orientation should normally be perpendicular to the deepest contour lines to reduce the dredging materials and dredging costs as well. Moreover, the channel must be straight, if possible and the S-curve orientation is should be carefully designed. The prevailing wind direction must be taken into consideration while planning procedure to reduce the wave forces acting on the sailing ships. The minimum width for a straight navigable channel may be ranged as 3 to 4 times of the maximum vessel width for one lane traffic, and 5 to 6 times of the average vessel width for two-lane traffic. For the side slopes of the navigable channels, the type of deposits, forming the channel bed materials, plays the important role for selection the appropriate and stable side slope.

7 COMPARISON BETWEEN PROPOSALS

Comparison between the proposals depends on the investigating of the historical bed topography, the sediment process, and the cost.

The navigation path should be pass through the deepest points in the studied reach. Investigating the 1993 bed topography, it can be noticed that the deepest point in the studied reach in the east side is located between Sec. (6) to Sec. (8) with bed level (64.53) and the minimum water depth reads 4.97 m. In addition, the deepest point at the west side has been found between Sec. (16) and Sec. (18) with bed level (63.91) and the minimum water depth reads 5.57 m. Achieving the necessary conditions for a navigation path, it is better to suggest the navigation path following the thalwage line which bind between the deepest area along the considered river reach, these consideration support both of the first and third proposals more than the second proposals.

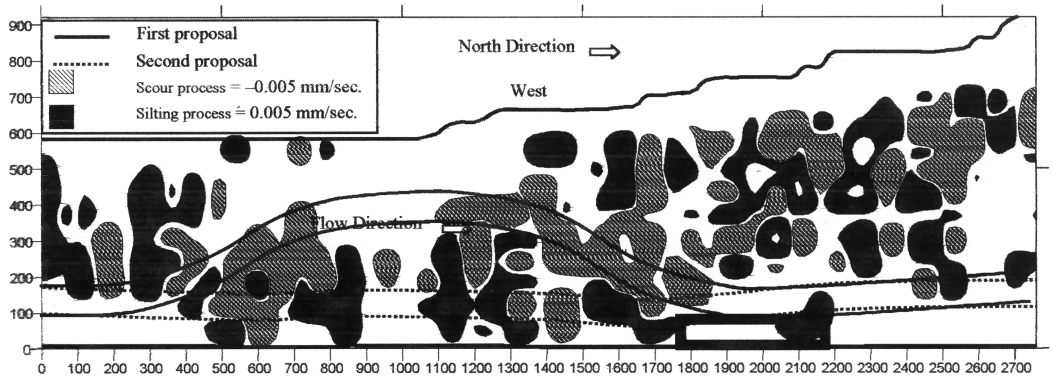


Figure 7. Scour and silting zones for LWL (Bed-1993).

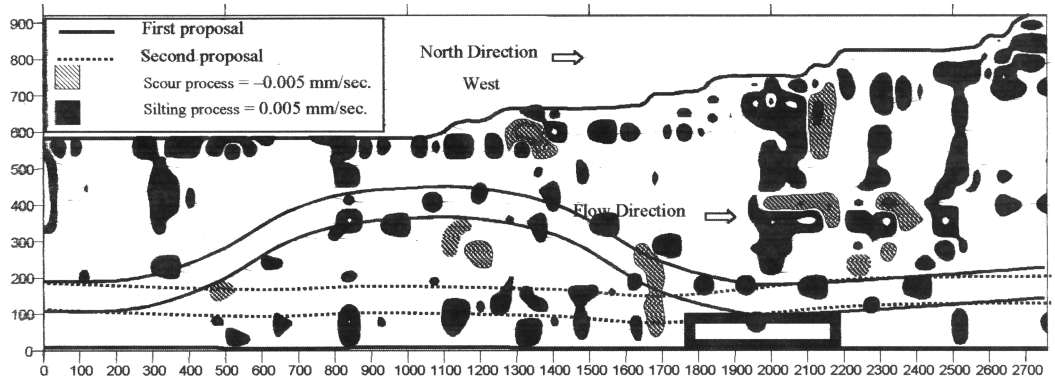


Figure 8. Scour and silting zones for HWL (Bed-1993).

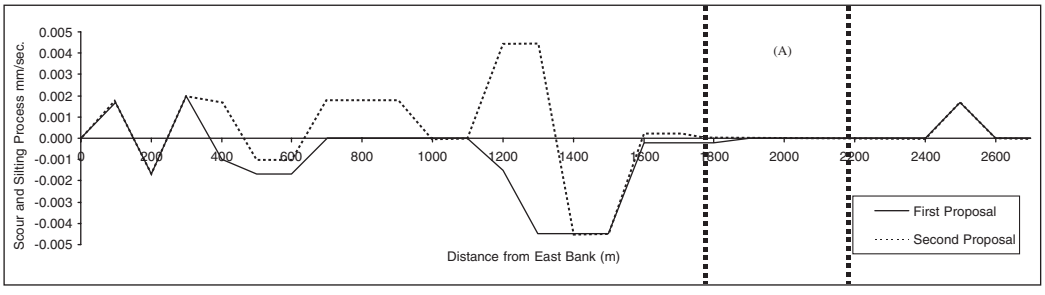


Figure 9. Comparison between the sediment processes at centerline of the navigation paths for the two proposals.

A main decision to accept the suggested navigation path depends on the investigation of the sediment process, which supports the first suggestion as shown in Figures 7,8.

It can be noticed easily in the second proposal for navigation path, there are many locations of scour and silting processes. It can not be acceptable at all, because it may be very danger with respect to the navigation process. But, it can be noticed in the first proposed navigation path for the two extreme flow cases that there are some locations, which may be subjected to scour process and very little zones subjected to silting process.

The sedimentation process at the centerline of the two proposed navigation paths has been shown in Figure 9. It can be noticed that the second proposal should be subjected for the more active sedimentation rates. This notation supports the first proposal. Also, the

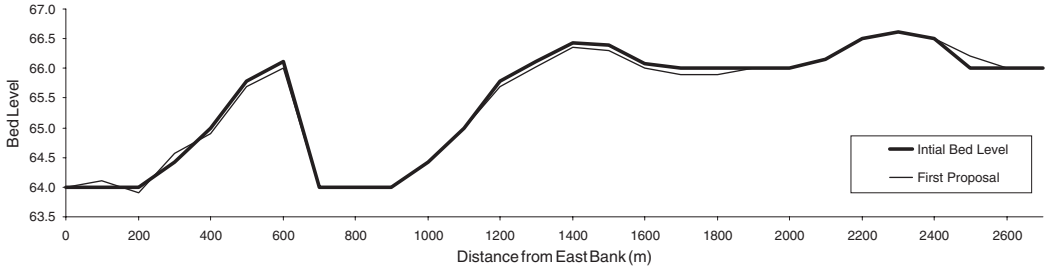


Figure 10. Comparison between bed levels at centerline of navigation path for the first proposal for 30-days prediction.

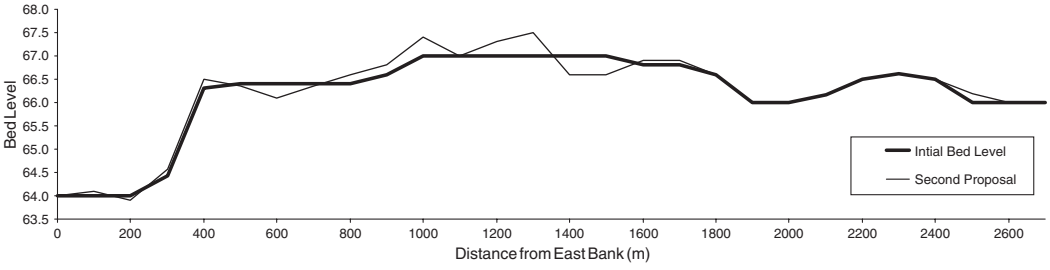


Figure 11. Comparison between bed levels at centerline of navigation path for the second proposal for 30-days prediction.

updated bed along the two proposed navigation paths for 30-days has been detected as seen in Figures 10, 11. The figures define the bed variation along the two proposed navigation paths during 30-day. It clears that the first suggested navigation path should be subjected to scour process only along its centerline and the silting process may not accrue along the suggested navigation path. But, the second navigation path should be subjected for critical sedimentation processes specially starting from Km. 700.

The cost may play an important role in determine the best proposal. The volume of dredging materials and the length of the navigation path may be the important factors, which determine the cost for each proposal. Finally, the comparison between the alternative proposals may be summarized as shown as in Figure 12. The comparison cleared that, the first proposal is the more acceptable one than the other.

Finally, the suggested navigation path for the first proposal may be safe from the hydraulic point of view in addition to the historical bed topography investigations.

8 QUAY SITE INVESTIGATION

The sediment behavior has been simulated using the 2-D models (SED-2) for the two flow cases at LWL and HWL. Also, the river bed topography surveyed on 1982 and 1993 were considered while simulation. The safest location of the quay should be investigated through the studied reach taking into consideration the following factors:

- The orientation should be parallel to and beside the suggested navigation path with enough area,
- The orientation should be parallel to and beside the high way traffic, and
- The silting process should not be accepted as possible.

Generally, the quay site should be located at stable zone. Achieving the above conditions for a quay site, the site location shown in Figure 13 has been proposed. Figure 7 shows the sediment behavior for the studied reach at LWL considering the map 1993. It can be noticed that the studied reach has subjected to scour and silting processes, especially at the west bank. It is clear also that the east bank has subjected to little sediment behavior. Also, the sediment behavior has been studied considering the HWL flow case for the map 1993, as shown in Figure 8. It can be noticed that the suggested quay location is not subject to scour or silting process. As shown in Figure 9, the zone (A) clears the sediment process at the recommended location of the quay. It can be noticed that the sediment process at this location is very small. Also, comparing between the bed variation for the recent contour map 1993 and the predicted on for 30-days at Km. (1800) as shown in Figure 14, it has been found that the river west side has subjected for silting process. But, the east side at the recommended location of the quay, the bed may be subjected for sediment

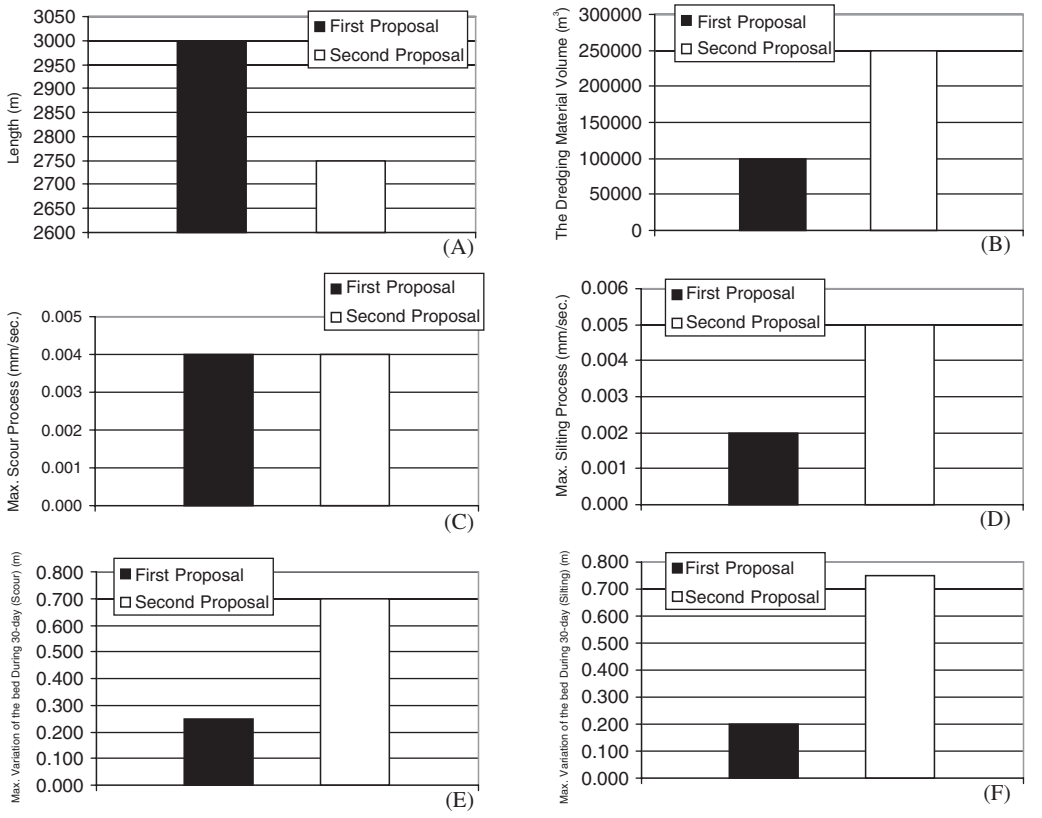


Figure 12. The comparison between alternative proposals.

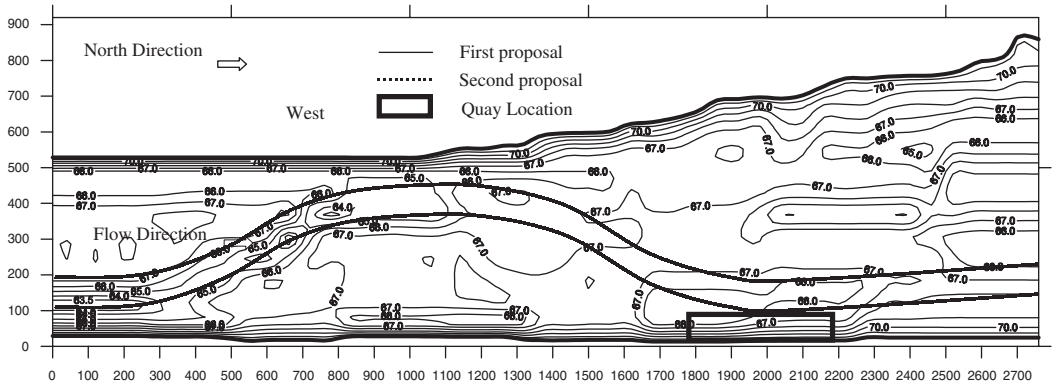


Figure 13. The recommended location of the quay and navigation path.

process, which is mainly scouring process. Hence, it can be concluded that the suggested quay site may be considered as a stable zone. This result matches with the historical investigations during the last three decades.

As a result, the proposed site for the quay was recommended for the following reasons:

– The bed topography history refers that the suggested quay site lies in a stable zone,

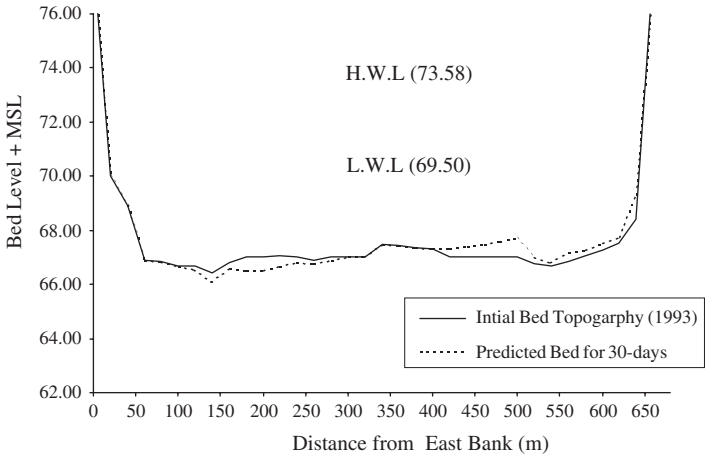


Figure 14. The comparison between the initial bed level and the predicted one for 30-days at the quay.

– The sediment behavior seems to be in equilibrium condition within the proposed site,
– The predicted bed topography after 30-days confirms the above notes also, and
– The proposed site dimensions satisfy the navigation requirements.

9 CONCLUSION

In this paper, The Nile reach at Elbogdady area south Luxor staff gauge has been restudied. The investigation of the reach has cleared that, the reach is suitable for the navigation processes. Proper solution has been suggested. Finally, the first proposal has been supported as the most optimal proposal. Also, the best location of the quay has been studied. It can be noticed easily the best location of the quay is at the east side of the reach. The investigation has been done by the 2-D sediment transport model (SED-2), which can predict the locations of scouring and silting zones along the considered river reach.

ACKNOWLEDGMENT

The authors wish to thank all the engineering staff of Nile Research Institute (NRI), National Water Research Center, Delta Barrages, Egypt for great help and facilitating the necessary field data required for the verification procedure.

REFERENCES

Ahmed M.A. & Ahmed M. 1997. Report on Study of Scouring problem Existing on the East Bank of Nile River at Rashid Branch at El-Wardan km.34.000. HRI, Delta Barrages, NWRC, Egypt.

Ahmed Z. & Kothyari U.C. & Raju K.G. 1999. Finite Difference Scheme for Longitudinal Dispersion in Open Channels. J. Hydraulic Research 65(3): 389–406.

Bagnold R.A. 1966. An Approach to Sediment Transport Problems from General Physics. USGS Professional 1(422): 11–37.

Cole P. & Miles G.V. 1983. Two-Dimensional Model of Mud Transport. J. Hydraulic Engineering. ASCE 109(1): 21–32.

Einstein H.A. 1942. Formulas for Transportation of Bed Load. Transe. J. Hydraulic Research 107(2): 121–132.

Elfiky M.M., Marmoush Y.R. & Abdel-Aal G.M. 1997. A 2-D model simulating the flow patterns in Rivers. The Egyptian Journal for Engineering Sciences and Technology (EJEST), Fac. of Eng., Zagazig Univ., Jan. 1(1): 60–67.

Elfiky M.M., Negm M., Owais T.M. & Nassar M. 2002. A 2-D model simulating the Sediment Transport in Rivers. M.Sc. Thesis) Fac. of Eng., Zagazig Univ.

El-Mottasem M. & Zaki A. 1994. Report on Study of Sediment Problem Existing on Elbogdady Reach. NRI, Delta Barrages, NWRC, Egypt.

Galappatt G. & Vreugdenhil C. B. 1986. Depth-Integrated Model for Suspended Sediment Transport. J. Hydraulic Research 23(4): 345–356.

Gasser M.M. 1988. Final Report on Study of Navigation problems Existing on the Nile River at Selwa-Bahary. HSRI Pub., Delta Barrages, Egypt.

Gasser M.M. 1988. Report on the Best Alignment of the Two Approach Channels of the New Navigation Look at Naga-Hammadi. HSRI Pub., Delta Barrages, Egypt.

Lin P. & Shen H.W. 1984. Two-D Flow with Sediment by Characteristics Method. J. Hydraulic Engineering 110(5): 615–626.

Lung W.S. & O'Conner D.J. 1982. Two Dimensional Mass Transport in Estuaries. J. Hydraulic Engineering 110(10): 1210–1220.

Pacheco R. & Ceballos 1989. Transport of Sediment Analytical Solution. J. Hydraulic Research 27(4): 501–518.

Paintal A.S. 1971. A Stochastic Model of Bed Load Transport. J. Hydraulic Research 9(1): 13–23.
Schoellhamer D.H. 1988. Two Dimensional Lagrngian Simulation of Suspended Sediment. J. Hydraulic Engineering 114(10): 1002–1023.
Van Rijn L.C. 1986. Mathematical Modeling of Suspended Sediment in Non-uniform Flows. J. Hydraulic Engineering 112(6): 589–600.
Verbanck M.A., Laaji A. & Niyonzima A. 2002. Computing River Suspended Load Over Bed Forms in the Lower, Transition and Upper Hydraulic Regime. River Flow 2002, Proceedings of the International Conference on Fluvial Hydraulics.
Wang K.H. & Hu H. 1998. Modeling Suspended Sediment Transport in Open Channels. Department of Civil and Environmental Engineering University of Houston.

River Flow 2004 – Greco, Carravetta & Della Morte (eds.)
© 2004 Taylor & Francis Group, London, ISBN 90 5809 658 0

A computational distributed gravel budget for the lower Fraser River, British Columbia

S. Li & R.G. Millar
Dept. of Civil Engineering, University of British Columbia, Vancouver, B.C., Canada

ABSTRACT: A depth-averaged 2D model is used to compute a distributed sediment budget for a gravel-bed reach of lower Fraser River. The model couples the hydrodynamics and bedload transport of multiple size fractions, and computes bed level changes on a curvilinear grid. Bedload transport, surface coarsening, spatial variation in the size distribution, and morphologic change are calculated, for five steady discharges. For each discharge, longitudinal variation in bedload transporting capacity is determined by integrating transporting capacity across the channel at each 50 m section, defining zones of aggradation and degradation. A bedload transport rating curve is developed at the boundary of each zone, and the mean annual bedload transport across each boundary is obtained. The distributed sediment budget is determined. This yields average annual rates of gravel aggradation and degradation volumes for each zone. The computed sediment budget agrees well with results based on high quality field measurements of gravel transport.

1 INTRODUCTION

The Fraser River is a major river of British Columbia, Canada, that rises in the Rocky Mountains and flows generally SW into the Strait of Georgia at Vancouver, B.C. The so-called "Gravel Reach" is located along the Fraser Valley between Laidlaw and Sumas Mountain (Fig. 1a). The Gravel Reach consists of an anabranching network of gravel-bed channels, which are separated by relatively stable vegetated islands and less stable gravel bars. The Gravel Reach is located on a confined alluvial fan, which has developed downstream of the town of Hope where the Fraser emerges from a steep canyon through the mountains. The reduction in channel gradient downstream of Hope results in deposition of the gravel load, which causes long-term aggradation of the channel bed. There is an abrupt termination of the Gravel Reach at Sumas Mountain (Fig. 1a). Downstream of this point the Fraser is a tidally-influenced sand-bed river.

The morphology of the Gravel Reach is a consequence of the gravel deposition, and it provides exceptionally rich and diverse instream habitat. There are also substantial management issues related to flooding, riverbank erosion and gravel extraction. Flood protection is provided principally by a system of dykes that were constructed several decades ago. A recent revision of the design flood profile (UMA 2000) has found that in places the dykes do not currently provide adequate protection for the design flood. This is due in part to bed aggradation as a consequence of gravel deposition. Annual gravel extraction is recommended as one management option to maintain the flood profile and the integrity of the flood protection system (Church et al. 2001).

Effective gravel management including removal requires a distributed sediment budget that includes estimates of the gravel inflow to the reach, the longitudinal variation in gravel transport rates, and locations of aggrading and degrading zones. Previous work includes gravel transport measurements conducted by Water Survey of Canada near Agassiz (Fig. 2), and longer term morphological estimates of gravel deposition based on repeated bathymetric surveys of the Gravel Reach in 1952, 1984, 1999 and a recently-conducted survey in 2003 (McLean and Church 1999; Church et al. 2001).

In this paper we present the first results obtained by applying a 2D morphological model to the Gravel Reach in order to obtain a distributed sediment budget. We have modified MIKE21C, a curvilinear hydrodynamic-river morphology model developed by DHI Water and Environment (DHI 1999). Modifications are necessary as the original model formulation was developed for sand-bed rivers and does not adequately describe important features of gravel transport and gravel bank stability and erosion. We modify the bedload transport algorithm and use the surface-based transport model developed by Parker (1990). The remaining sections of this paper describe the

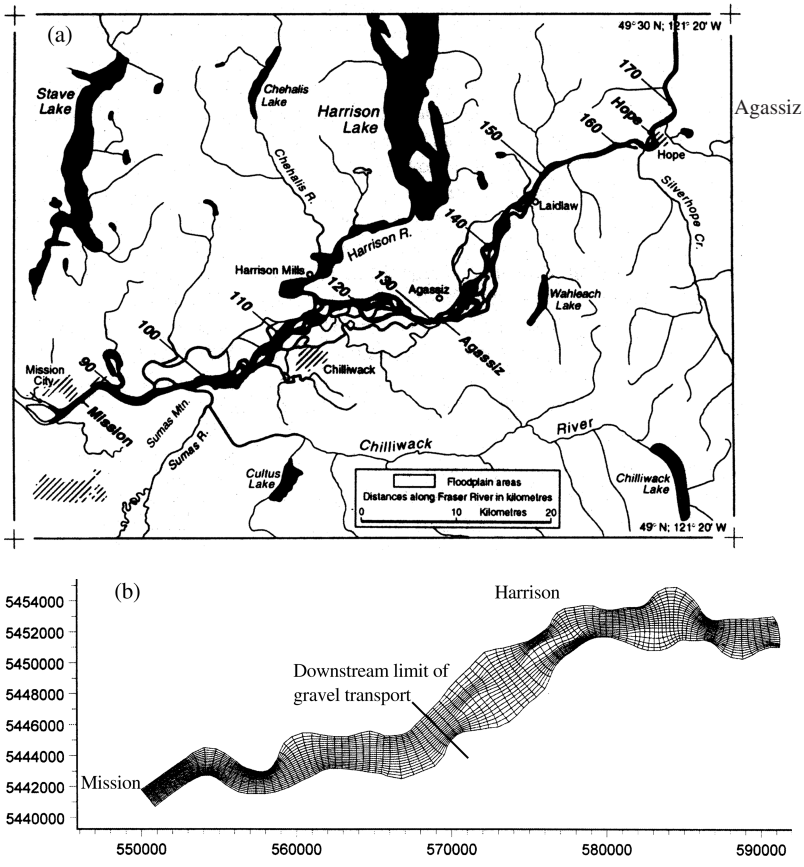


Figure 1. Map of the Lower Fraser area (a), showing river kilometres upstream from Sand Heads (from Church et al. 2001). The gravel reach is between about 95 and 150 km. The area of this study is between Mission and Agassiz (b), covered by a curvilinear grid of 79 rows × 800 columns (plotted every 4th row and 8th column). Typical grid spacing in the along- and cross-channel direction is 50 and 25 m, respectively. The most refined cells are located in the main channel and special care in terms of flow splitting is taken for sub-areas with multiple channels.

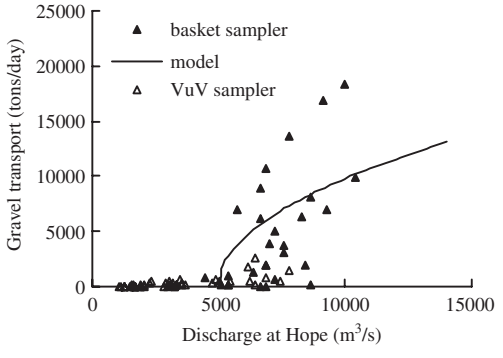


Figure 2. Fraser River gravel transport near Agassiz. Measurements collected by Water Survey of Canada (1967–1986). The solid line represents the computed rating curve from this study for the same location (km 44).

data used, outline the model theory, and present the preliminary results.

2 DATA

We obtained data of bathymetry, discharge and sediment for model input, verification and sediment budget evaluation. The bathymetry data were collected in 1999. A digital elevation model (DEM) developed from this survey by Mr. Darren Ham provides an approximate 25 × 25 m coverage over the entire reach. Initial grain size distributions of the bed material are derived from field measurements of sediment transport (McLean and Church 1999). A flow duration curve and histogram was developed from discharge data measured at Hope (1912–1997) and is used in the sediment budget calculations. Inflows at

the Harrison River were obtained from a hydrologic study conducted by UMA (2001).

3 MODEL

Here we provide a brief outline of the modified model. The surface-based gravel bedload algorithm of Parker (1990) is used because it explicitly accounts for development of surface coarsening, and hiding and exposure of different grain sizes on the bed surface. The subsurface sediment mixture is divided into eight grain size intervals. Mike 21C solves vertically-integrated 2D equations of continuity and momentum conservation (St. Venant equations) to yield velocity field and free surface elevation, from which local bed shear stress is determined. Helical flows, which arise from curving streamlines in a river, around an island or a middle-channel bar and produce flow-direction deviations from the depth-averaged velocity vector, are also computed using schemes suggested by Engelund (1974) and Struiksma et al. (1985). The effects of helical flows on near-bed flow and bed shear stress can be substantial.

Sub-grid motions not explicitly resolved are parameterized through an eddy-viscosity coefficient. It is determined using the scheme by Smagorinsky (1963), which relates the coefficient to the local flow deformation and spatial resolutions. Its value is adjusted solely to maintain numerical stability. The model was implemented on an orthogonal curvilinear grid, covering the Lower Fraser between Mission and Agassiz (Fig. 1b). This curvilinear grid not only realistically resolves riverbanks, islands and gravel bars, but also allows the flexibility of using higher resolutions in dynamically more important regions like the main channel.

On the established grid, the flow field and free surface elevation at each grid point are predicted as functions of imposed upstream (discharge) and downstream (water level) conditions, bottom friction and eddy viscosity. The net sediment flux in or out each local cell is evaluated, and bed level changes are computed using the sediment continuity equation (Exner equation).

Bedload transport simulations were carried out on a sub-grid downstream from Agassiz to the downstream limit of gravel transport (Fig. 1b). There is no established rating curve at the downstream boundary, and therefore the hydrodynamic model is extended downstream to the gauging station at Mission where a rating curve has been developed. We conducted five simulations with steady discharges at Agassiz: 6000, 8000, 10,000, 12,000 and 14,000 m^3/s. The discharge of 5000 m^3/s represents the approximate threshold below which there is negligible gravel transport at Agassiz (Church et al. 2001). Each simulation was run for 48 hours of model time, which takes about 15 hours of CPU (real) time.

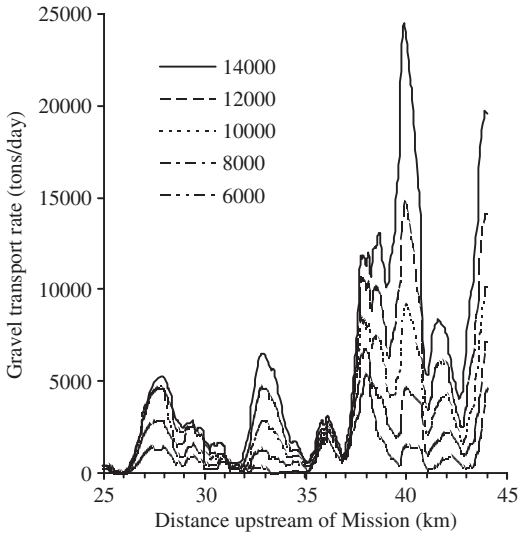


Figure 3. Longitudinal variation in total cross section gravel bedload transport rates for discharges ranging from 6000 to 14,000 m^3/s. Data has been smoothed by averaging with five adjacent cross sections in both the upstream and downstream directions.

4 RESULTS

Calibration of the model was performed by comparing computed water level with data from eight gauging stations located along the gravel reach, which are from the HYDAT database (Water Survey of Canada). Calibration was achieved by adjusting distributed bottom friction coefficient (Strickler number or 1/n). The computed water levels at the gauge locations match the data with differences less than 0.15 m.

For each cell bedload transport rates generally increase to a maximum shortly after the beginning of simulation, and then decrease with time as the bed surface coarsens. An approximate steady state for all size fractions is reached after a period of time (generally 18 hours or more of model time), which represents a condition of equilibrium transport in which all size fractions display near equal mobility (Parker 1990). Examination of the surface grain size distribution along the reach shows that the bed surface coarsens in regions of high flow.

Transport rates are integrated across the channel to provide sectional totals. Longitudinal variation in the sectional total transport rates shows considerable spatial variation (Fig. 3), even after smoothing. Raw model output from Mike 21C has been smoothed by averaging transport rates over five cross-sections immediately upstream and downstream. The smoothing is necessary to make the output appear less noisy, and to define boundaries between aggrading and

Table 1. Summary of gravel budget calculations for aggrading and degrading zones.

Zone	Distance of upstream boundary from Mission (km)	Annual gravel load across upstream boundary (tons/year)	Annual aggradation volume (m^3/year)
1	44.0	340,000	183,000
2	42.8	38,300	−31,500
3	42.0	90,200	29,400
4	41.1	41,600	−87,400
5	40.0	186,000	60,500
6	39.3	86,000	−163,000
7	37.9	355,000	184,000
8	37.0	51,600	−38,500
9	36.1	115,000	61,200
10	35.1	14,000	−13,700
11	33.0	36,700	18,800
12	32.0	5600	−22,100
13	31.0	42,100	11,400
14	30.0	23,300	−25,700
15	29.5	65,700	15,600
16	28.8	40,000	−48,500
17	27.9	120,000	68,800
18	26.2	6550	

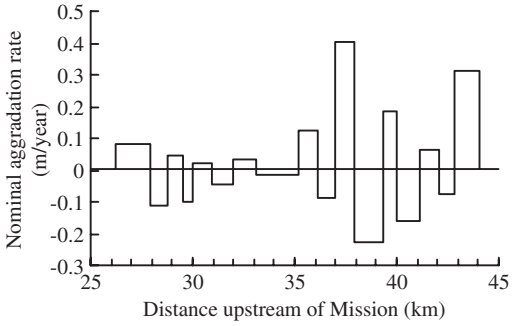


Figure 4. Nominal aggradation rate which is equal to the annual aggradation volume (Table 1) divided by the zone length times a nominal active channel width of 500 m.

degrading zones. Boundaries are identified as peaks or troughs that delineate changes in the longitudinal transport gradient. Positive downstream gradients indicate increasing downstream bedload transporting capacity and zones of degradation, whereas negative downstream gradients reflect decreasing capacity and characterise zones of aggradation.

A gravel bedload rating curve is developed from the model-derived transport rates at each boundary by fitting an equation of the form:

$$G_b = a(Q - 5000)^b \quad (1)$$

where G_b = transport rate (tons/day); Q = discharge (m^3/s); the value 5000 (m^3/s) is the threshold discharge below which little gravel transport occurs (Fig. 2); and coefficients a and b are empirically derived. This rating curve is then integrated with the flow duration histogram to provide an estimate of the average annual transport capacity:

$$G_{bT} = \sum_{i=1}^{n} 365.25 G_{bi} p_i \quad (2)$$

where G_{bT} = average annual load (tons/year); G_{bi} = transport rate (tons/day) from the rating curve (1) corresponding to Q_i from the flow duration histogram; p_i = the proportion of the time the flow is within the range represented by Q_i (where $\Sigma p_i = 1$); and 365.25 is the conversion factor for the number of days in one year. Calculated annual gravel loads across the upper boundary of each zone are given in Table 1.

Average annual aggradation (degradation) volumes for each zone are derived from conservation of mass assuming a bulk density of 1.65 tons/m^3:

$$I - O = \Delta S \quad (3)$$

where I = inflow volume at upstream boundary (m^3/year); O = outflow volume at downstream boundary (m^3/year); and ΔS = change in gravel storage volume (m^3/year) (Table 1). Finally, the nominal aggradation rate (m/year) for each zone is determined assuming a nominal active channel width of 500 m (Fig. 4).

5 DISCUSSION AND CONCLUSIONS

This analysis represents the first attempt at computing a distributed gravel budget for the Fraser River Gravel Reach using a hydrodynamic model. The results appear to compare favourably with previous estimates derived from field measurements. Although there is tremendous scatter, the computed rating curve for Agassiz-Rosedale Bridge (km 44) plots more or less about the middle of the measured gravel transport data collected by Water Survey of Canada at the same location (Fig. 2). Based on this rating curve our analysis returns an average annual gravel load passing the Agassiz-Rosedale Bridge of 340,000 tons/year (206,000 m^3/year), which compares very well-perhaps fortuitously-with the estimate from Church et al. (2001, p. 65) of between 170,000–230,000 m^3/year. None of these values include the sand component.

The current gravel budget analysis is based on the 1999 bathymetric survey, and provides a snapshot of the equilibrium gravel transporting capacity at the time of the survey. It is not possible to directly compare

these results with the previous work of Church et al. (2001) who defined aggrading and degrading cells based on overlays of the 1952, 1984 and 1999 surveys. The Church et al. (2001) results represent averages over the 47-year period. A better test would be to compare our computed gravel budget with locations and rates of aggradation/degradation for the period between 1999 and the recent 2003 survey. These results are not yet available.

Provided further testing supports the analysis presented in this paper, then the computed gravel budget provides useful information for gravel management and development of gravel removal targets within the Fraser River Gravel Reach. Zones of active aggradation are well defined and can be ranked in terms of aggradation rate. Zone boundaries can be used as boundary conditions to define smaller model subdomains that are more amenable to intensive model simulation that includes bed elevation changes, and bank erosion and retreat.

ACKNOWLEDGMENTS

This study is funded by the Natural Sciences and Engineering Research Council of Canada through an NSERC Strategic Grant held by M. Church, E. Hickin and R. Millar. The authors wish to thank Darren Ham for providing the 1999 DEM, and Shafiq Islam for his effort in preparing the model grid. Mike Church provided the grain size data. Finally thanks to DHI Water & Environment especially Bo Christensen, Hans Enggrob and Jesper Kjelds for access to the Mike 21C source code, and for ongoing technical support and advice.

REFERENCES

Church, M., Ham, D. & Weatherly, H. 2001. *Gravel management in lower Fraser River*. *Technical Report*, Dept. of Geography, University of British Columbia, Vancouver, B.C., Canada.

DHI. 1999. *MIKE21C user's guide and scientific documentation*. *Technical Report*, Danish Hydraulic Institute, Hørsholm, Denmark.

Engelund, F. 1974. Flow and bed topography in channel bends. *Journal of Hydraulic Division*, ASCE 100, No. HY11: 1631–1648.

McLean, D.G. & Church, M. 1999. Sediment transport along the lower Fraser River 2. Estimates based on the long-term gravel budget. *Water Resources Research* 35: 2549–2559.

Parker, G. 1990. Surface-based bedload transport relation for gravel rivers. *Journal of Hydraulic Research* 28(4): 417–436.

Smagorinsky, J. 1963. General circulation experiments with the primitive equation. Part I: the basic experiment. *Monthly Weather Review* 91: 99–165.

Struiksma, N., Olesen, K.W., Flokstra, C. & de Vriend, H.J. 1985. Bed deformation in curved alluvial channels. *Journal of Hydraulic Research* 23(1): 57–79.

UMA Engineering Ltd. 2000. *Fraser River gravel reach hydraulic modelling study. Technical report prepared for the City of Chilliwack*. UMA Engineering Ltd., Victoria, B.C., Canada.

UMA Engineering Ltd. 2001. *Fraser and Harrison Rivers: hydrologic and hydraulic investigations, Report prepared for the City of Chilliwack.* UMA Engineering Ltd., Victoria, B.C., Canada.

This page intentionally left blank

River Flow 2004 – Greco, Carravetta & Della Morte (eds.)
© 2004 Taylor & Francis Group, London, ISBN 90 5809 658 0

The influence of drainage network formation and characteristics on a catchment's sediment yield

E. Lykoudi
Department of Geological Sciences, School of Mining Engineering and Metallurgy, National Technical University of Athens, Athens, Greece

D. Zarris
Department of Water Resources, School of Civil Engineering, National Technical University of Athens, Athens, Greece

ABSTRACT: The influence of certain geomorphologic parameters, such as the bifurcation ratio, on a catchment's sediment yield is rarely reported in the literature in contrast to the catchment area, which is assumed as a predominant morphological parameter for quantifying catchment sediment yields. In this paper, the influence of the catchment bifurcation ratio on the sediment yield is examined. Specifically, the mean weighted bifurcation ratio is proposed so as to give more weight to the first order streams of the overall drainage pattern in the context of sediment productivity and delivery. Mean annual sediment yields from four adjacent catchments in Western Greece have been estimated. It is shown that in catchments with higher bifurcation ratios there is an increase in sediment yield estimates, which is mainly accounted for the neo-tectonic activity and the geomorphologic processes in the area.

1 INTRODUCTION

1.1 *Global sediment yield estimates*

At present, sediment yield estimations are achieved mainly from simple empirical models that relate mean annual sediment yield (S_Y in t/km^2) to catchment properties, including drainage area, topography, climate and vegetation characteristics (e.g., Flaxman, 1972, Jansen & Painter 1974, Dendy & Bolton 1976, Walling 1983). In some cases, catchment area (A in km^2) seems to be the only explanatory variable used to predict sediment yield (Dendy & Bolton 1976, Higgit & Lu 1996, Webb & Griffiths 2001, Verstraeten et al. 2003). Catchment sediment yield usually decreases with basin scale, mainly because sediment sinks, such as floodplains, will generally increase, assuming the concept of source–transport–deposition continuum as the ideal fluvial system (Schumm 1977). However, there is a significant variability of sediment yield with catchment area. For two catchments with the same area but contrasting climates and geomorphologic regimes will likely exhibit completely different sediment yields. Indeed, Parker & Osterkamp (1995) compiled mean annual sediment discharges from 24 gauged rivers in the United States. Drainage areas ranged from 1.6×10^3 to 1.8×10^6 km^2. Mean annual sediment yields ranged from less than 5 to more than 1480 t/km^2. Linear and non-linear regression analyses of mean annual sediment yields with drainage area indicate no statistical significant relationships. Furthermore, Avendano Salas et al. (1997) presented a dataset of sediment yield values from 60 catchments based on reservoir sedimentation rates throughout Spain. The relation between S_Y and A for the 60 catchments is:

$$S_Y = 4139A^{-0.43}, R^2 = 0.17 \quad (1)$$

That means that the drainage area explains only the 17% of the observed variability of the sediment yield estimates, even within the same region. On the contrary, Dendy and Bolton (1976) presented data from sediment deposits in reservoirs for 800 catchments throughout the USA. There was a statistically significant relation between mean annual sediment yields and drainage areas of the form of the equation (reprinted from Lane et al. 1997):

$$S_Y = 674A^{-0.16}, R^2 = 0.68 \quad (2)$$

Additionally, data from 37 catchments in northern Arizona show a remarkably good correlation with catchment area (Webb & Griffiths 2001). Sediment

discharge (Q_S in t/yr) exhibits a power function with catchment area of the form:

$$Q_S = 193A^{1.04}, R^2 = 0.86 \quad (3)$$

Lu et al. 2003 reported that from 248 sediment discharge measurement sites within the Upper Yangtze catchment in China, sediment yield exhibits a fairly good correlation with subcatchment drainage area in the form of the equation:

$$S_Y = 849.15A^{-0.0785}, R^2 = 0.7735 \quad (4)$$

Moulder and Syvitski (1996) showed that Q_S is strongly correlated to catchment area and the maximum catchment elevation ($H_{\max}$) as:

$$\log(Q_S) = 0.406\log(A) + 1.279\log(H_{\max}) - 3.679, R^2 = 0.67 \quad (5)$$

It is likely that the increasing trend of sediment discharge with maximum elevation is a surrogate of tectonic activity. Milliman and Syvitski (1992) concluded that the strong correlation between sediment and topographic relief may not indicate that the second is the cause of the first, but rather that both are caused by another factor less susceptible to numerical modeling, namely tectonism. Furthermore, rivers that drain active edges of continental margins (e.g., western South and North America) or collision margins (e.g., southern Europe and southern Asia) are generally much smaller, but collectively they transport similar amounts of sediment as do large passive margin rivers.

Someone might have to consider the random or systematic errors that are associated with such estimates used in the regression equations described above. For instance, if a catchment sediment yield is derived from reservoir sedimentation rates, this estimation is subject to quite a lot of parameters that can induce significant errors, depending on the extend of the reservoir and the available instrumentation. More specifically, errors can be accounted during the hydrographic survey of the reservoir (e.g., GPS selected availability, varied velocity of hydrographic vessel) and during the post-processing of the hydrographic data (e.g., inaccurate Digital Terrain Models (DTMs) for old reservoirs before the dam impoundment, obscure definition of mud–water interface). Moreover, significant errors are connected with estimation of deposits' density, especially if it is not possible to collect undisturbed samples from the reservoir's invert. Moreover, the same applies to sediment yield estimates from sediment discharge rating curves, especially as a design practice in Greece. Simultaneous measurements of river discharge and sediment discharge are mainly conducted only in low-flow periods, thus any extrapolation for wash loads at the time of low frequency – high magnitude flood flows will generally give misleading results.

Conclusively, it is noted that there is not a "universal expression" between sediment yield and catchment area, not only because there are different types of catchment geology, hydrology and topography but also because regional tectonics and geomorphology play an important role on the sediment availability within the catchment.

1.2 *Catchment bifurcation ratio and sediment delivery ratio*

Horton (1945) stated that the decrease in number and increase in lengths of streams with centripetal order is approximately geometric and hypothesized that the increase in mean subcatchment area is also geometric. These statistical relations are known as the "*Horton's laws*" of stream numbers, lengths and areas. Their respective series ratios are designated as the bifurcation, length and area ratios. The bifurcation ratio (R_B) between successive stream orders, according to Strahler's (1964) classification, is then defined as:

$$R_B = \frac{N_U}{N_{U+1}} \quad (6)$$

where $N_U =$ number of streams with order U. The mean bifurcation ratio is the average value of the corresponding ones for the successive stream orders. Typical values of bifurcation ratios between 2 and 4 are typical for most natural fluvial systems. The ideal number of streams for a basin of a given order, according to Horton (1945), is then as follows:

$$N_U = R_B^{(K-U)} \quad (7)$$

The symbol K is defined as the order of the main trunk stream.

It is supposed that, while calculating the mean bifurcation ratio, the streams of higher order have the same weight with the streams of the first and second order. This is obviously not representative; especially from sediment yield oriented considerations. It could be more appropriate to assign more specific weight to the first order streams (according to the proportion of the number of these streams against the total number of streams) than to the streams of the highest order. This could be rational, since the first order streams are pointing towards the sediment source areas of the specific catchment and contribute more to sediment availability. We then use the mean weighted bifurcation

ratio ($R_{B,W}$), which is determined as:

$$R_{B,W} = \frac{\sum_{i=1}^{n}(R_{B:i,i+1}(N_i + N_{i+1}))}{\sum_{i=1}^{n} N_i} \quad (8)$$

The mean weighted bifurcation ratio is not intended to replace the mean bifurcation ratio in Equation 7; this will certainly give wrong results. This ratio intends to give a first estimation on the degree of the catchment's maturity or, in other words, how much the specific catchment has developed all its streams of any order depending on its geomorphologic state.

Bifurcation ratio is by no means involved in any empirical (statistical) regression relations with sediment yield in international literature, according to the authors' knowledge. It is included, however, in statistical relations with catchment sediment delivery ratio, *DR*, (i.e. the proportion of eroded sediment that finally reaches the catchment's outlet). Roehl (1962) using sediment yield data from 15 catchments from the Southeast USA and source erosion estimates derived from the Universal Soil Loss Equation (USLE), stated that (reprinted from McCuen 1998, p. 795):

$$DR = 18620A^{-0.23}\left(\frac{L}{R}\right)^{-0.51} R_B^{-2.79} \quad (9)$$

where L = watershed length; and R = watershed relief (or the elevation difference), all in English units and *DR* expressed as a percentage. The concept of delivery ratio might be valuable in conceptualizing sediment yield processes but is highly uncertain in its application. Indeed, source erosion is at least as difficult to be computed (usually with the USLE) as the sediment yield itself.

It is evident from Equation 9 that the delivery ratio is a decreasing function of bifurcation ratio. It is supposed that higher bifurcation ratios are likely to reveal elongated catchments with long, thin drainage networks that forces sediment to deposit within the stream network, especially if moderate magnitude flood events are prevailing and/or the vegetation cover is dense.

The objective of this paper is to show that, according to our sediment yield data for four adjacent catchments in Western Greece, sediment yield and delivery is generally an increasing function of bifurcation ratio, in contrast to Roehl's (1962) findings. We argue that (a) the mean weighted bifurcation ratio is the most appropriative indication of catchment bifurcation in terms of sediment yield, because it gives more weight to the first order streams that, in turn, point towards the sediment source areas, and (b) local geomorphologic regime and tectonic activity (e.g., orogenic uplift), that support higher bifurcation ratios, together with the high intensity of storms and runoff events are the driving forces for higher sediment production rates, thus for higher sediment yields.

2 RESEARCH FRAMEWORK

2.1 *Study area*

Four adjacent catchments in western Greece are selected for analysis. Acheloos River, Agrafiotis River and Megdovas River are discharging at Kremasta reservoir, whereas Evinos R. is discharging at the Patraikos Gulf (see Figure 1). Kremasta dam was built at exactly the confluence of Agrafiotis and Megdovas Rivers with the main stem river (Acheloos R.) and was firstly operated at 1965. Sediment yield estimates for the three rivers discharging at Kremasta Reservoir were computed as reservoir sedimentation rates after a comprehensive hydrographic survey (Zarris et al. 2002). The DTMs before the dam impoundment (1964) and the period of hydrographic survey (1998–99) have been subtracted to produce the volume

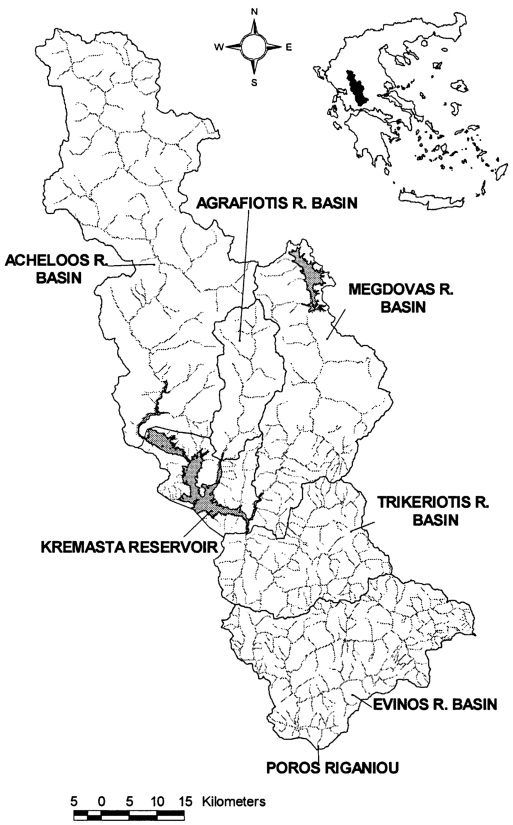


Figure 1. Map of the selected catchments with drainage network (only shown 3rd, 4th, 5th and 6th order streams).

of deposited sediments. The density of the sediments was estimated by the extraction and laboratory analysis of two sedimentary cores from the reservoir's invert. These rivers are discharging separately in the reservoir so as their sediment yield could be estimated independently. Trikeriotis River, actually a subcatchment of Megdovas R, while presented in Figure 1, is computed together with Megdovas R. as one catchment, since their sediment deposits in the reservoir could not be computed independently. Mean annual sediment yield of the Evinos R. at Poros Riganiou measuring discharge station was computed by means of applying the ordinary suspended sediment discharge rating curves to the available sample of mean daily discharges (Nalbantis 1990).

The source erosion of the three basins discharging at the Kremasta reservoir was estimated by applying the USLE on a GIS platform. The sediment delivery ratios were then estimated for all but the Evinos R. catchment.

Mean annual inflow at the Kremasta reservoir is 76.6 m^3/s, a significant portion of which belongs to Acheloos River itself (49.9 m^3/s). The mean annual discharge of Evinos River at Poros Riganiou measuring site is estimated as 24.75 m^3/s. Poros Riganiou is located upstream of the river's delta in the Patraikos Gulf, but the catchment can be considered as an ideal conceptual system of erosion–transport–deposition continuum. All streams are perennial but are subject to severe floods because of the intense storms that are enhanced by the orographic uplifting of the Pindos mountain range. All streams are sixth order catchments (according to Strahler's classification system) except Agrafiotis R., which is a fourth order catchment, due to its relative small area.

Table 1 presents the sediment yields and delivery ratios estimated for the catchments under consideration. The results generally follow the trend of higher sediment yields and delivery ratios with decreasing catchment areas, except the sediment yield from Acheloos catchment. Particularly, Agrafiotis R. sediment yield is in the same order of magnitude even with the majority of Japanese rivers (Oguchi et al. 2001), which are famous for their pronounced sediment yields.

Applying the Equation 9 to the data of Table 1, delivery ratios are calculated equal to 0.13, 0.12 and 0.24 for the Acheloos R., Agrafiotis R. and Megdovas R. catchments respectively. It is shown that Roehl's equation not only gives misleading results for these basins (except for Megdovas R.) but also changes completely the order of the basins with higher delivery ratios. Indeed, Agrafiotis R., which exhibits the highest delivery ratio, according to our estimates from the Kremasta reservoir sedimentation rates, seems to have the least corresponding value according to Roehl's equation. The authors are unaware of any similar work by other researchers on that issue and this paper is dedicated to give some insight on the possible correlation of bifurcation ratio with sediment yield and delivery ratio.

2.2 *Geology of the study area*

The geologic structure of the catchments under consideration has directly affected the formation of the drainage network and the morphology of the relief. The geologic setting of the study area is covered by formations of the "*Gavrovo*" and the "*Pindos*" geotectonic zones, which belong to the external "*Hellenides*", as well as post-alpine formations, ophiolites and igneous rocks. More specifically, the Acheloos River catchment is mainly formed by flysch and thickly bedded limestone of the "*Gavrovo*" zone, and alternations of the flysch with thinly bedded limestone, irestone and clastic sediments of the "*Pindos*" zone, which are intensely folded. The catchments of the rest of the rivers under consideration are consisted of the intensely folded formations of the "*Pindos*" zone. More specifically, an extended part of the northeastern part of the Evinos catchment is formed only by the "*Pindos*" flysch with depth on excess of 1000 m. Figure 2 presents a synoptic view of the geologic formations of the region.

2.3 *Regional tectonics*

The "*Gavrovo*" zone is characterized by a gentle tectonism, with synclines and anticlines, of which the axes follow a NW-SE direction as well as faults with a NW-SE and NE-SW direction. The "*Pindos*" zone is characterized as a gigantic tectonic cover, heavily

Table 1. Characteristic elements of selected catchments.

Catchment	Area (km^2)	S_Y (t/km^2)	*DR*	Mean Bifurcation ratio	Mean weighted bifurcation ratio
Acheloos R.	1733	1184.6	0.17	4.20	4.94
Agrafiotis R.	320	2034.8	0.42	5.62	5.86
Megdovas R.	1239	489.4	0.22	3.89	4.75
Evinos R.	884	734	–	3.86	5.27

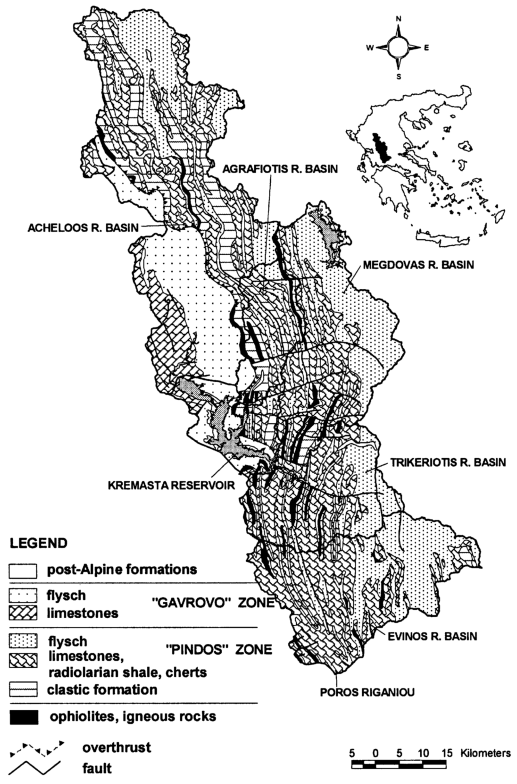


Figure 2. Geo-tectonic map of the study area.

cracked. This tectonism is demonstrated with microplications with axial direction NW-SE, thrusts of the same direction as well as faults, which are contemporary of the alpine structures following the same directions or more recent following a W-E direction.

Generally, the "*Pindos*" zone has been undergone intensified tectonic strain due to the considerable movement of the "*Pindos*" formations over the "*Gavrovo*" zone. Particularly, over the thrusting front (where the whole of the Agrafiotis R. and the eastern part of the Acheloos R. catchments are situated), the tectonic stress is pronounced.

The main faults and thrusts are presented synoptically in Figure 2.

3 DISCUSSION

We consider, like Milliman and Syvitski (1992), that the topographic/tectonic character of a river catchment plays an important role in determining its sediment yield and that catchment area plays only a supplementary role. For instance, both Japan and New Zealand are characterized by high-relief mountains on active margins, coupled by tropical cyclones, which are assumed as the driving forces for the world's highest recorded sediment yields under natural conditions.

3.1 *Mean bifurcation ratio and mean weighted bifurcation ratio*

Bifurcation ratios are normally assigning the values between 2 and 4, whereas 4 should be suggested as the "ideal" value of a catchment's bifurcation (Leopold & Langbein 1962, Costa-Cabral & Burges 1997). Yang (1971) measured 14 basins in the maturity stage in the middle-western USA. The bifurcation ratio of those basins ranges from 3.29 to 4.79, with a mean value of 4.05, which is nearly equal to 4.0. Other researchers (e.g., Eyles 1968, Gustafson 1973) reported less bifurcation ratio values for areas such as Germany (3.98), Australia (3.45) and Israel (3.75). The catchments of Northern Europe and North America were formed in a much older geologic period; therefore their catchments and rivers are stable, so that channel streams consisted mainly of the most probable networks in which the bifurcation ratio is close to a value of 4.0. As noted in Table 1, the mean bifurcation ratios of the examined catchments are quite high, higher than the average value of most catchments in other countries with less tectonic activity. The Agrafiotis R. bifurcation ratio value is even higher than the corresponding value observed even in Japanese catchments. For instance, Shimano (1992) measured the morphometric parameters of 180 catchments all over Japan. The values of bifurcation ratios range from 3.2 and 5.4 while most of them range between 3.6 and 4.8. Agrafiotis R. also exhibits a quite significant sediment yield and sediment delivery ratio, which is one of the highest values ever reported in the literature, particularly for the European region.

There are two basic elements, which are important to be carefully noticed. Firstly, there is a deficit of the first order streams for all the catchments between the observed number of these streams and the supposed number according to the first Horton's law. The arithmetic values are given in Table 2.

Secondly, another interesting point comes from the comparison between the mean bifurcation ratio and the mean weighted one (from Table 1). It is evident that for the Agrafiotis R. the difference between these values is almost infinitesimal, while the same differences for the other catchments are significant. It is implied, however, that these observations are in some way interconnected.

Agrafiotis R., which exhibits the highest bifurcation ratio, has the lowest deficit of the first order streams. In pure numbers, it needs only 5 first order streams in order to reach the ideal state, as described by Horton's scaling law. At the same time, the difference

Table 2. Comparison between observed first order streams against simulated ones as resulted from Horton (1945).

Basin	Observed first order streams	Simulated first order streams (from Horton, 1945)	% Deficit
Acheloos R.	1195	1308	9.45
Agrafiotis R.	172	177	3.20
Megdovas R.	840	888	5.70
Evinos R.	817	854	4.48

between the mean and the weighted mean bifurcation ratio is very small. We argue that these observations are closely related to the high sediment yield of this particular basin. Since Agrafiotis R. has developed almost the total number of the first order streams that it could be possible to develop, then, giving more weight to the first order streams, does not considerably increase the mean weighted bifurcation ratio of the catchment. This is also explained by the high bifurcation between the first and second order streams (4.53) for that particular catchment. It could be concluded that this catchment reaches the state of full maturity; it has developed almost the whole of its drainage network and finally exhibits high sediment yield values.

On the other side, the other catchments need a considerable number of first order streams to reach the ideal state of maturity. Acheloos R. needs 113 first order streams, Megdovas R. 48 streams and Evinos R. 37 streams. For these catchments, the mean weighted ratio gives more substantial differences compared with the simple mean ratio. Based on the local geotectonic regime, the fate of these catchments is to further develop their drainage basins so as to reach the maturity that Agrafiotis R. has already reached. Therefore the sediment yields of these catchments will further increase, especially the Acheloos R. catchment, which has the most considerable hysteresis in terms of its drainage network formation, but it already exhibits a quite impressive sediment yield, constituting a possible exception to the general approved relation of increasing area – decreasing sediment yield.

3.2 *Interrelations of geomorphologic and tectonic elements with sediment yields*

The Agrafiotis R. catchment is situated over the thrusting front of the "Pindos" cover; therefore its formations are heavily cracked. Additionally, all the river catchments are being undergone neo-tectonic movements, particularly orogenic uplift, which is characteristic of their geologic age. Agrafiotis R. catchment is already in an early mature state while the rest of the catchments are in a younger state.

Orogenic movements are also responsible for the high sediment yields, because the equilibrium between the excess available sediment (from rock weathering) and the transport downstream should be reached at all times. Channel incision through tectonic forcing is evident which keeps the catchment in a mature state, while constantly rejuvenated. Channel incision adds more first order streams in the drainage system, increasing the order of the whole catchment and re-arranging the overall drainage network; thus finally conveying new sediment source areas to the catchment outlet. Moreover, the uplift creates steeper stream slopes that, in turn, develop higher stream power of the flow, especially in large infrequent floods, which are typical in Mediterranean environments. Indeed, Snyder et al. (2003) stated that, comparing basins from high uplift zones (uplift rates around 4 mm/yr) to the ones in the low uplift zones (uplift rates approximately 0.5 mm/yr), streams in high uplift zones are about twice as steep for a given drainage area, therefore exhibit an increase of the catchment response to rainfall and sediment. Significant stream power values in V-shaped streams can easily transport sediment downstream (as wash load), increasing sediment delivery to the catchment's outlet. These processes of orogenic uplifting and increasing sediment yield are seem to be probably everlasting leading to continuously changing catchments and drainage patterns.

4 CONCLUSIONS

This paper has introduced the bifurcation ratio concept in the context of sediment yield and delivery ratio processes of a catchment in order to draw useful interconnections between these geomorphologic parameters. Primarily, it was shown that the Roehl's (1962) equation, that assumed the sediment delivery ratio as a decreasing function of the bifurcation ratio does not hold, at least for the four adjacent catchments in Western Greece. On the contrary, it was shown that it is, in fact, an increasing function of the bifurcation ratio and was assumed that the regional neo-tectonic activity coupled with the state of maturity that these basins exhibit, are the influential factors for the relatively high sediment yield.

It was shown that, for active tectonic areas, the increase of the bifurcation ratio entails greater sediment yields because there are more first order streams encouraging the conveyance of detached sediments to reach the drainage network. Additionally, the axial erosion in V-shaped, first order, streams with high stream power–low frequency flood peaks, transports the wash load further downstream, so as the residence times of the sediments within the catchment will be relatively low. This of course is a prerequisite for higher catchment sediment yields.

Finally, it was proposed that the mean weighted bifurcation ratio is a better indicator for qualitatively describing the drainage pattern in terms of sediment production, availability and transport. For catchments, that have fully developed their drainage patterns, according to Horton, the difference between the mean and the mean weighted bifurcation ratio is insignificant. On the contrary, for young catchments, which are still developing their drainage forms, the difference is significant because there is also a considerable deficit of the first order basins relative to the ideal value for the perfect fluvial system.

The observations of this paper, especially the contradicting results with Roehl's equation, could give a motive to the geomorphologists, engineers and other earth scientists to cast their shadows over the real influence of the geomorphologic pattern of the catchment (e.g., drainage network formation, tectonic activity) over the long-term evolution of sediment yield. It is important to notice that there are no equations with global applicability but any approach will be tailored and specified for any particular catchment or region with homogenous geomorphologic characteristics.

ACKNOWLEDGMENTS

This work is a continuation of the research project "Appraisal of river sediment deposits in reservoirs of hydropower dams" funded from the General Secretariat of Research and Technology (GSRT) and the Public Power Corporation (PPC) of Greece. The authors would like to thank Demetris Koutsoyiannis, research coordinator of the project, for his valuable comments and supervision during the research project.

REFERENCES

Avendano Salas, C., Sanz Montero, E., Rayan, C. & Gomez Montana, J.L. 1997. Sediment yield at Spanish reservoirs and its relationship with the drainage area. *Proceedings of the 19th Symposium of Large Dams*, Florence, International Committee on Large Dams, Paris: 863–874.

Costa-Cabral, M.C. & Burges, S.J. 1997. Sensitivity of channel network planform laws and the question of topologic randomness, *Water Resources Research* 33 (9): 2179–2197.

Dendy, F.E. & Bolton, G.C. 1976. Sediment yield-runoff drainage area relationships in the United States. *J. Soil and Water Cons.* 31: 264–266.

Eyles, R.J. 1973. Stream net ratios in West Malaysia. *Geol. Soc. Amer. Bull.* 79: 701–712.

Flaxman, E.M. 1972. Predicting sediment yield in western United States. *J. Hydr. Div. ASCE*, 98 (12): 2073–2085.

Gustafson, G.C. 1973. *Quantitative Investigation of the Morphology of Drainage Basins Using Orthophotography*. Munchener Geographische Abhandlungen: 157p.

Higgit, D.L. & Lu, X.X. 1996. Patterns of sediment yield in the Upper Yangtze Basin, China. In D.E. Walling, B.W. Webb (eds.), *Erosion and Sediment Yield: Global and Regional Perspectives* (proceedings of the Exeter Symposium), IAHS Publ. 236, IAHS: 205–214.

Horton, R.E. 1945. Erosional development of streams and their drainage basins-hydrological approach to quantitative morphology. *Geol. Soc. Amer. Bull.* 56:275–370.

Jansen, J.M.L. & Painter, R.B. 1974. Predicting sediment yield from climate and topography. *Journal of Hydrology.* 21: 371–380.

Lane, L.J., Hernandez, M. & Nichols, M. 1997. Processes controlling sediment yields from watersheds as functions of spatial scale. *Environmental Modeling and Software* 12 (4): 355–369.

Leopold, L.B. & Langbein, W.B. 1962. The concept of entropy in landscape evolution. *USGS Prof. Paper 500-A*: 1:20.

Lu, X.X., Ashmore, P. & Wang, J. 2003. Sediment yield mapping in a large river basin: the Upper Yangtze, China, *Environmental Modeling & Software* 18: 339–353.

Lykoudi, E. 2000. Geomorphologic evolution of the Upper Acheloos River basin, *Ph.D. Thesis*, Department of Mining Engineering and Metallurgy, National Technical University of Athens, pp. 256 (in Greek).

McCuen, R.H. 1989. *Hydrologic Analysis and Design*. Englewood Cliffs. New Jersey: Prentice Hall.

Milliman, J.D. & Syvitski, P.M. 1992. Geomorphic/tectonic control of sediment discharge to the ocean: the importance of small mountainous rivers. *Journal of Geology* 100: 525–544.

Moulder, T. & Syvitski, J.P.M. 1996. Climatic and morphologic relationships of rivers: Implications of sea-level fluctuations on river loads. *Journal of Geology* 104: 509–523.

Nalbantis, J. *Appraisal of existing potential for improving the water supply for Greater Athens, Volume 15: Hydrological Design of Evinos reservoirs.* Research Project, National Technical University of Athens.

Oguchi, T., Saito, K., Kadomura, H. & Grossman, M. 2001. Fluvial geomorphology and paleohydrology in Japan. *Geomorphology* 39: 3–19.

Parker, R.S. & Osterkamp, W.R. 1995. Identifying trends in sediment discharge from alternations in upstream land use. In W.R. Osterkamp (ed.), *Effects of Scale on Interpretation and Management of Sediment and Water Quality*, Proc. of a Boulder Symposium, IAHS Publ. No. 226: 207–213.

Roehl, J.W. 1962. Sediment source areas, delivery ratios and influencing morphological factors. *International Association of Hydrological Sciences Publication no. 59*: 202–213.

Schumm, S.A. 1977. *The Fluvial System*. New York: John Wiley.

Shimano, Y. 1992. Characteristics of the stream network composition of the drainage basin in Japanese islands. *Environ. Geol. Water Sci.* 20 (1): 5–14.

Snyder, N.P., Whipple, K.X., Tucker, G.E. & Merritts, D.J. 2003. Channel response to tectonic forcing: field analysis of stream morphology and hydrology in the Mendocino triple junction region, northern California. *Geomorphology* 33:97–127.

Strahler, A.N. Quantitative geomorphology of drainage basins and channel networks. In V.T. Chow (ed.)

Handbook of Applied Hydrology. Section 4-II. New York: McGraw-Hill.

Verstraeten, G., Poesen, J., deVente, J. & Koninckxx, X. 2003. Sediment yield variability in Spain: a quantitative and semiqualitative analysis using reservoir sedimentation rates. *Geomorphology* 50:327–348.

Walling, D.E. 1983. The sediment delivery problem, *Journal of Hydrology.* 65:209–237.

Webb, R.H. & Griffiths, P.G. 2001. Sediment delivery by ungaged tributaries of the Colorado River in Grand Canyon. USGS Fact Sheet 018–01.

Yang, C.T. 1971. Potential energy and stream morphology, *Water Resources Research* 7 (1):311–322.

Zarris, D., Lykoudi, E. & Koutsoyiannis, D. 2002. Sediment yield estimation from a hydrographic survey: A case study for the Kremasta reservoir basin, Greece, *Proceedings of the 5th International Conference* "*Water Resources Management in the Era of Transition*", Athens, 4–8 September: 338–345 p.

River Flow 2004 – Greco, Carravetta & Della Morte (eds.)
© 2004 Taylor & Francis Group, London, ISBN 90 5809 658 0

Flow structure and bedload distribution at alluvial diversions

Arjan de Heer & Erik Mosselman
Delft University of Technology & WL/Delft Hydraulics, Delft, The Netherlands

ABSTRACT: Bulle (1926) carried out well-documented experiments on the bedload distribution at alluvial diversions. We re-analyzed his results by simulating the experiments numerically using Delft3D. The bifurcation angles and the roundnesses of the angles in the upstream walls of the channel entrances are found to have a strong effect on flow structure and the division of bedload transport rates over the bifurcated channels. Hence they are key ingredients for the nodal point relations that are used to specify the sediment transport distribution at bifurcations in one-dimensional river models. Other key ingredients are found to be the division of discharges over the bifurcated channels, the widths and average depths of water flowing to the left channel and water flowing to the right channel, the widths of the channel entrances and sediment mobility.

1 INTRODUCTION

Bifurcations play a central role in a multitude of problems in river engineering and fluvial sedimentology. They are part of the elementary confluence-diffluence unit in braided rivers. They affect the stability of rivers on alluvial fans and in deltas. They determine the required maintenance in irrigation canals that take off from rivers as well as in secondary channels that are created for the ecological rehabilitation of floodplains. Finally, they are a key element in developing bend cutoffs and avulsions, the latter being important not only in river engineering but also in alluvial stratigraphy for oil reservoir exploration. It is therefore surprising that the fluvial processes in bifurcations have not been studied as much as those in confluences, especially when realizing that the 1-D hydraulic and morphological modelling of confluences is straightforward. The 1-D modelling of bifurcations is more problematic, because it requires additional input in the form of a nodal point relation that specifies how sediment transport rates are divided over the two branches of the bifurcation.

Flokstra (1985) and Wang et al. (1995) demonstrate that the morphological development of the bifurcated channels depends sensitively on the parameters of the nodal point relation. Certain parameter ranges produce a behaviour in which one of the channels is closed inevitably by sedimentation, whereas other parameter ranges produce a behaviour which tends to a stable equilibrium in which both channels remain open.

Nodal point relations are an issue if bedload transport is dominant. Situations with mainly suspended load do not pose great difficulties. The sediment transport rates of vertically homogeneous suspensions are divided simply in proportion to the discharges through the bifurcated channels. Suspensions with vertical concentration gradients can be approximated by analytical concentration profiles. Integration over the vertical leads to depth-averaged concentrations as a function of local flow depth and flow strength at the entrances of the bifurcated channels. Multiplication by discharge yields the sediment transports into the bifurcated channels (Slingerland & Smith, 1998). For bedload-dominated rivers, however, nodal point relations are usually purely empirical. A first step away is the physically-based approach of Bolla Pittaluga et al. (2001, 2003). Our study shows, however, that their approach still leaves room for improvement.

We focus this paper on alluvial *diversions* as a special case of alluvial *bifurcations*. In alluvial diversions, the main channel has the same direction upstream and downstream of the bifurcation, so that only one of the bifurcated channels has a non-zero bifurcation angle.

Bulle (1926) carried out well-documented experiments on the bedload distribution at alluvial diversions. We re-analyzed his results by simulating the experiments numerically using Delft3D. The analysis shows that bifurcation angles strongly affect the division of sediment transport rates over the bifurcated channels. Nodal point relations should hence account for this effect.

2 DATA AND METHOD

2.1 *Bulle's (1926) experiments*

Bulle's experimental set-up consisted of a 0.2 m wide main flume and a 0.2 m wide diversion flume, taking off from the main flume under various angles. Here we consider only the experiments with an angle of 30°. The discharge was 5 l/s. The tailgates were set in such a way that, initially, this discharge was divided equally over the two branches. Experiments were carried out on a fixed bed without sediments, a fixed bed partly covered with sediment and a fully alluvial mobile bed. The sediments consisted of sands with sizes up to 1.2 mm, mainly transported as bedload. Bulle did not report more details on the grain size distribution.

Bulle found that the diversion produced a curved flow pattern that induced a helical motion with outward flow near the water surface and inward flow near the bed. In this way, a disproportionate amount of the bedload was transported into the diversion channel, cf. Figure 1. This has become known as the '*Bulle effect*' among river engineers. Furthermore, Bulle found that the flow separated at the entrance of the diversion channel, producing an eddy along the outer wall. A smaller eddy occurred on the opposite side along the outer wall of the main channel, cf. Figure 2. During the experiments with sediment, the discharge through the diversion channel initially decreased due to sedimentation (after 45 minutes, Figure 3), but later increased back to the original value (after 75 minutes, Figure 4). The size of the eddy could be reduced by making the angle in the upstream wall of the channel entrance rounder.

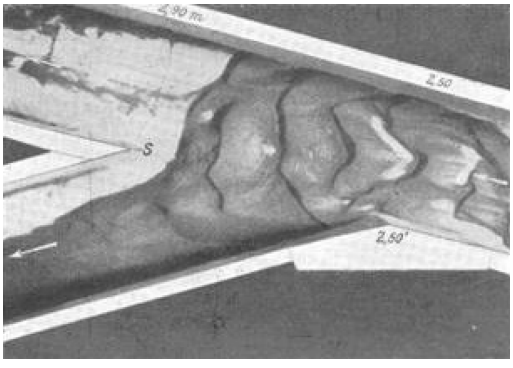


Figure 1. Disproportionate amount of bedload into diversion channel (Bulle, 1926).

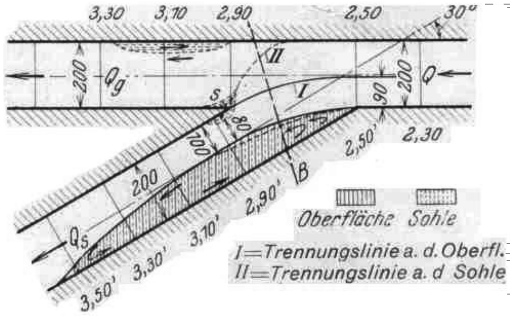


Figure 2. Flow pattern with eddies in diversion channel and main channel (Bulle, 1926).

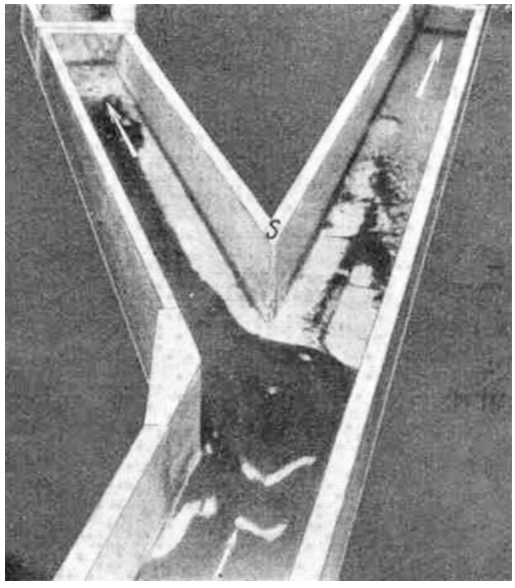


Figure 3. Sediment cover after 45 minutes (Bulle, 1926).

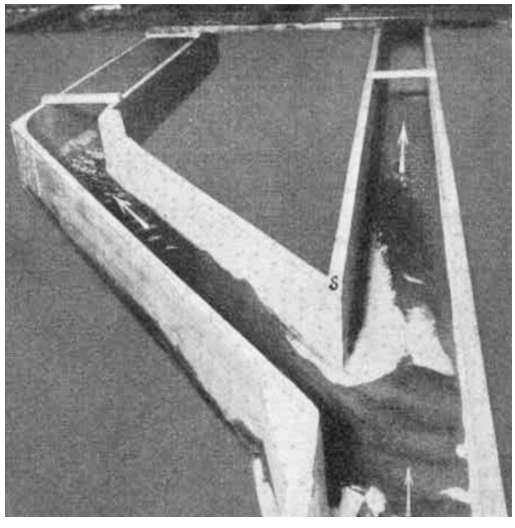


Figure 4. Sediment cover after 75 minutes (Bulle, 1926).

The Bulle effect and the generation of eddies represent two distinct mechanisms by which bifurcation angles affect the division of sediment transport rates over the bifurcated channels.

2.2 *Numerical model*

Bulle's experimental set-up was schematized in the Delft3D modelling system. Figure 5 shows a detail of the computational grid around the bifurcation. The numerical schematization was mirrored with respect to the real configuration to facilitate De Heer's (2003) comparison with similar experiments by Riad (1961), not reported here. We made three-dimensional computations of the flow and two-dimensional depth-averaged computations of sediment transport. Here we focus only on the flow computations. The Chézy coefficient for hydraulic roughness was 36 $m^{1/2}/s$.

3 RESULTS

Figure 6 shows the computed flow pattern. The model reproduces eddies in the main channel and the diversion channel. However, the computed eddy in the main channel is too large and the computed eddy in the diversion channel too small. We find that these results can be influenced by grid resolution, eddy viscosities and wall friction. The main cause of the disagreement seems to be, however, that the numerical grid implies too round an angle in the upstream wall of the channel entrance. This complies with Bulle's experimental finding that the size of the eddy in the diversion channel can be reduced by making this angle rounder. The problem is that a sharper angle in the numerical grid would increase the truncation errors in the discretized equations due to deviations from grid smoothness and grid orthogonality.

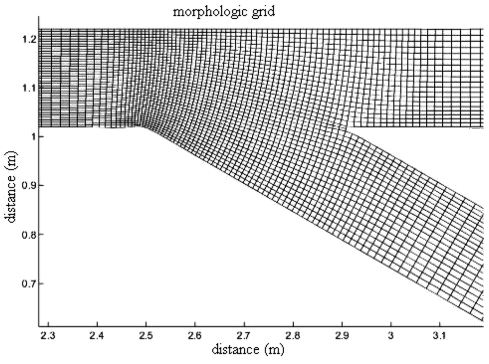


Figure 5. Computational grid around bifurcation.

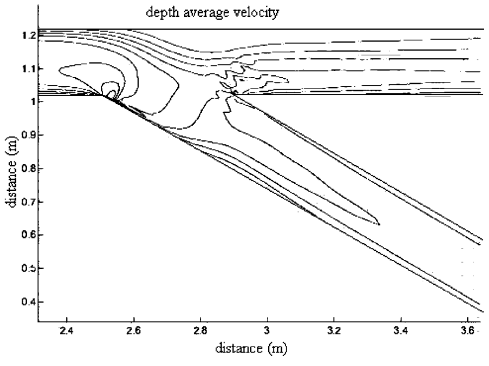


Figure 6. Computed pattern of depth-averaged flow velocities.

4 DISCUSSION

4.1 *Importance of bifurcation angle*

It has been common knowledge since long that channels with a large bifurcation angle tend to experience sedimentation. In the nineteenth century, research in present-day India, Pakistan and Bangladesh was at the frontier of river engineering. Many of the design rules in the handbooks of Joglekar (1956, 1971) and Varma et al. (1989) stem from that period. These handbooks recognize the importance of bifurcation angles in, for instance, their guideline that the alignments of pilot channels for artificial bend cut-offs should be made at a curvature flatter than the dominant curvature of the river itself. Klaassen et al. (1993) and Mosselman et al. (1995) find empirically that larger bifurcation angles increase the probability of channel abandonment in the braided Brahmaputra-Jamuna river.

Traditionally, this importance of bifurcation angles is explained from the Bulle effect. However, the generation of eddies appears to be important as well. That places various earlier empirical findings and engineering design rules in a new light. The typical sedimentation pattern at the entrance of alluvial diversions as shown in Figure 7 may result as much from the trapping of sediments in an eddy as from flow divergence and the Bulle effect.

In the eighteenth century, works to stabilize the Rhine bifurcation at Pannerden ("Pannerdense Kop")

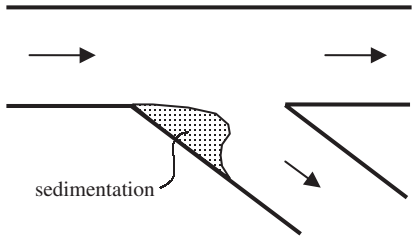


Figure 7. Typical sedimentation pattern at entrance of an alluvial diversion.

by trial and error have been the cradle of Rijkswaterstaat, the executive body of the Ministry of Transport and Public Works in the Netherlands (van de Ven, 1976, 1979). The solution finally arrived at was a slender flow divider between two bifurcating channels with negligible bifurcation angles. Recent two-dimensional morphological computations of the Pannerdense Kop by Sloff et al. (2003) demonstrate that the large width-to-depth ratios of the Rhine branches make the Bulle effect of minor importance. Apparently, the failures of earlier solutions with larger bifurcation angles must be ascribed to sedimentation in areas of flow separation.

Another example is the prescription by Joglekar (1956, 1971) and Varma et al. (1989) that the entrances of pilot channels for artificial bend cut-offs should be made bellmouth. The rationale might be that the resulting wider entrance section prevents eddies from squeezing the flow-conveying part into a narrow zone with a large bifurcation angle.

4.2 *Nodal point relations in 1-D models*

The division of bedload transport over the branches of a bifurcation depends on conditions in the branches, conditions in the local area immediately upstream of the bifurcation and conditions upstream of this local area. These three types of conditions are discussed subsequently below.

4.2.1 *Conditions in the branches*

The conditions in the branches can be divided into downstream water level controls, cross-sections along the branches, hydraulic roughnesses along the branches and eddies close to the bifurcation. The water level controls, cross-sections and hydraulic roughnesses manifest themselves in the division of discharges at the bifurcation. Generally this division can be computed by a 1-D model without further difficulties, applying a backwater calculation for each branch and a water surface closure condition. This part of the conditions in the branches is therefore represented sufficiently by the division of discharges. Joglekar's (1956, 1971) cut-off ratio and the analytical expressions of Klaassen et al. (1989) and Jagers (2003) for the conditions in the branches are covered in this way.

The eddies depend to a large extent on the bifurcation angles and the roundness of the angles in the upstream walls of the channel entrances. It is worth noting that eddies may even affect the division of discharges when one of them squeezes the entrance of a branch so much, that it becomes an obstacle with a local drop of the water level.

4.2.2 *Conditions in local area immediately upstream of the bifurcation*

The conditions in the local area immediately upstream of the bifurcation can be subdivided into parameters characterizing the local primary flow field, parameters characterizing the local secondary flow field, parameters characterizing the local bed topography and parameters characterizing local sediment mobility. The primary flow field is defined as the flow field that has the same depth-averaged flow velocities as the full flow field but equiform flow velocity distributions over the vertical. The secondary flow field is defined as the difference between the full flow field and the primary flow field. It vanishes when averaged over depth.

In the primary flow field, a vertical separation plane can be identified between a body of water flowing to the left branch and a body of water flowing to the right branch. Neglecting spatial variations in hydraulic roughness, the shape of the separation plane depends mainly on the division of discharges, the widths and average depths of the water bodies on either side of the separation plane and the widths of the entrances of the branches. These parameters determine also the cross-sectionally averaged flow velocities in each water body and hence, depending on sediment mobility, the primary supply of sediment to each branch of the bifurcation.

A secondary sediment supply arises because sediments can pass the separation plane of the primary flow by helical water motion and by gravity pull along transversely sloping beds. The helical flow is a form of local secondary flow that depends on the curvature of the horizontal projection of the vertical separation plane. This curvature follows from the shape of the separation plane and hence from the same parameters, mentioned above, that determine this shape. The gravity pull depends on local sediment mobility and the local transverse bed slope. The latter might be represented by the difference between the flow depths in the two water bodies divided by half of the local width.

Summarizing, the conditions immediately upstream of the bifurcation seem to be represented sufficiently by the division of discharges, the widths and average depths of the water bodies on either side of the separation plane, the widths of the entrances of the branches and local sediment mobility. The laboratory experiments of Federici (2003) confirm the importance of sediment mobility. Wang et al. (1995) have shown that the stability of bifurcations depends also on the nonlinearity of the sediment transport formula for the relevant range of flows and hence on sediment mobility.

4.2.3 *Conditions upstream of the local area*

The upstream conditions are responsible for asymmetries in the transverse distributions of flow velocities, sediment transports and bed topography immediately upstream of the bifurcation. Laboratory experiments by Federici (2003) and two-dimensional computations of the Pannerdense Kop by Sloff et al. (2003) confirm

that those asymmetries are important factors. The degree of asymmetry can be represented by the local transverse bed slope, which also figures among the conditions in the local area immediately upstream of the bifurcation. The transverse bed slope can be defined as the difference between the flow depths in the two water bodies on either side of the separation plane divided by half of the local width.

4.2.4 *Towards a physically-based relation*

The key ingredients identified can be seen as building blocks for a physically-based nodal point relation. The transverse bed slope has been included in the nodal point relation of Bolla Pittaluga et al. (2001, 2003), who find that the associated transverse exchange of sediment produces invariably stable bifurcations with both branches open, unless the Shields parameter falls under its critical value for incipient motion. However, their nodal point relation does not account for the effects of upstream asymmetries, local curvature-induced secondary flows or local eddies, that are represented empirically by the parameters of the nodal point relation of Flokstra (1985) and Wang et al. (1995). Figure 7 shows that the sedimentation induced by a bifurcation angle tends to increase this angle. This destabilizing effect is opposite to Bolla Pittaluga's stabilizing effect that the sedimentation induced by a transverse bed slope tends to decrease this slope. We therefore expect that further refinement of the analysis of Bolla Pittaluga et al. by including more effects will reveal that a downstream branch may be closed in conditions above the critical Shields value as well.

A generic physically-based nodal point relation might once be found for river bifurcations with fixed banks. If banks erode, however, bifurcation angles and other parameters of local geometry change. This implies changes in the nodal point relation that can never be predicted using a 1-D model alone. One-dimensional morphological computations of bifurcating river systems can hence be meaningful in a limited number of situations only. In many cases, 2-D or 3-D models will remain a necessity.

5 CONCLUSIONS

Bulle's (1926) experiments reveal two mechanisms by which bifurcation angles affect the division of sediment transport rates over the bifurcated channels. First, flow curvature produces the 'Bulle effect' by which a disproportionately high amount of bedload enters the channel with the largest bifurcation angle. Second, flow separation produces eddies that affect the division of flows and trap sediments. The eddies are larger in channels with larger bifurcation angles and also larger if the upstream angle in the wall is sharper.

The numerical model reproduces the eddies in the main channel and the diversion channel. However, the agreement between computed and observed flows is not good. We ascribe this primarily to the rounder angle in the numerical representation of the upstream wall of the entrance of the diversion channel. The problem is that a sharper angle would increase the truncation errors in the discretized equations due to deviations from grid smoothness and grid orthogonality.

The main ingredients for a physically-based nodal point relation are found to be:

- the division of discharges over the bifurcated channels;
- the bifurcation angles;
- the roundness of the angles in the upstream walls of the channel entrances;
- the widths and average depths on either side of the separation plane between primary flow towards the left branch and primary flow towards the right branch;
- the widths of the channel entrances;
- the mobility of the sediment.

These elementary parameters determine implicitly the compound parameters of flow curvature and transverse bed slope.

ACKNOWLEDGEMENTS

Rijkswaterstaat RIZA commissioned WL|Delft Hydraulics to carry out this study. We thank Dr. Arjan Sieben of Rijkswaterstaat RIZA for his suggestions and support and Prof. Marco Tubino of the University of Trento for his elucidations on the work by Bolla Pittaluga et al. The work by the first author served the partial fulfilment of the requirements for the Masters of Science degree in Civil Engineering at Delft University of Technology.

REFERENCES

Bolla Pittaluga, M., Repetto, R. & Tubino, M. 2001. Channel bifurcation in one-dimensional models: a physically based nodal point condition. *Proc. 2nd IAHR Symp. River, Coastal and Estuarine Morphodynamics*, 10–14 Sept. 2001, Obihiro, Japan, pp. 305–314.

Bolla Pittaluga, M., Repetto, R. & Tubino, M. 2003. Channel bifurcation in braided rivers: Equilibrium configurations and stability. *Water Resources Research*, AGU, Vol. 39, No. 3, 1046.

Bulle, H. 1926. *Untersuchungen über die Geschiebeableitung bei der Spaltung von Wasserläufen*. VDI Verlag, Berlin (in German).

Federici, B. 2003. *Topics on fluvial morphodynamics*. PhD Thesis, University of Genova, Dottorato di ricerca in ingegneria idraulica e modellistica dei sistemi ambientali (in Italian).

Flokstra, C. 1985. *De invloed van knooppuntsrelaties op de bodemligging bij splitsingspunten*. Report R2166, Waterloopkundig Laboratorium (WL|Delft Hydraulics) (in Dutch).

Heer, A.F.M. de 2003. *Sedimentverdeling bij riviersplitsingen; Ontwerp van een splitsingspuntrelatie*. Afstudeerverslag, TU Delft, werkdocumentnummer RIZA 2003.102X, projectnummer WL|Delft Hydraulics Q3336 (in Dutch).

Jagers, H.R.A. 2003. *Modelling planform changes of braided rivers*. PhD thesis, University of Twente.

Joglekar, D.V. (ed) 1956. *Manual on river behaviour, control and training*. Central Board of Irrigation and Power, Publ. No. 60, New Delhi.

Joglekar, D.V. (ed) 1971. *Manual on river behaviour, control and training*. Central Board of Irrigation and Power, Publ. No. 60 (revised), New Delhi.

Klaassen, G.J. & Zanten, B.H.J. van 1989. On cutoff ratios of curved channels. *Proc. 23rd Congress IAHR*, Ottawa (also *Delft Hydraulics Publication*, No. 444).

Klaassen, G.J., Mosselman, E. & Brühl, H. 1993. On the prediction of planform changes in braided sand-bed rivers. In S.S.Y. Wang (ed), *Advances in Hydro-Science and – Engineering*, Publ. Univ. Mississippi, University, Mississippi, pp. 134–146.

Mosselman, E., Huisink, M., Koomen, E. & Seymonsbergen, A.C. 1995. Morphological changes in a large braided sand-bed river. In E.J. Hickin (ed), *River geomorphology*, Wiley, pp. 235–247.

Riad, K. 1961. *Analytical and experimental study of bed load distribution at alluvial diversions*. Dissertation, Delft Univ. Technol., Waltman.

Slingerland, R. & Smith, N.D. 1998. Necessary conditions for a meandering-river avulsion. *Geology*, Vol. 26, No. 5, pp. 435–438.

Sloff, C.J., Bernabè, M. & Baur, T. 2003. On the stability of the Pannerdense Kop river bifurcation. *Proc. IAHR Symp. River, Coastal and Estuarine Morphodynamics*. In A. Sánchez-Arcilla & A. Bateman (eds), Publ. IAHR, Madrid, ISBN 90-805649-6-6, pp. 1001–1011.

Varma, C.V.J., Saxena, K.R. & Rao, M.K. (eds) 1989. *River behaviour, management and training*. Central Board of Irrigation and Power, Publ. No. 204, Vol. I (revision of Publ. No. 60), New Delhi.

Ven, G.P. van de 1976. *Aan de wieg van Rijkswaterstaat; Wordingsgeschiedenis van het Pannerdens Kanaal*. Zutphen (in Dutch).

Ven, G.P. van de 1979. De waterverdeling tussen de Rijntakken in de 17e en 18e eeuw. *De Ingenieur*, Vol. 91, No. 11, pp. 193–199 (in Dutch).

Wang, Z.B., Fokkink, R.J., Vries, M. de & Langerak, A. 1995. Stability of river bifurcations in 1D morphodynamic models. *J. Hydr. Res.*, IAHR, Vol. 33, No. 6, pp. 739–750.

River Flow 2004 – Greco, Carravetta & Della Morte (eds.)
© 2004 Taylor & Francis Group, London, ISBN 90 5809 658 0

Three dimensional modeling of sediment transport in a channel bend

N. Ruether & N.R.B. Olsen
Department of Hydraulic and Environmental Engineering, The Norwegian University of Science and Technology, Trondheim, Norway

ABSTRACT: A three dimensional numerical model is introduced which is able to calculate the sediment transport rate and the according bed changes over time in river bends. The model was tested against data from laboratory experiments. Several detailed studies of the lateral bed load movement on side slopes were investigated to find the appropriate formulas describing the physical phenomena of sediment transport in alluvial channel bends. Considering a stability analysis of a sediment particle on a side slope, and introducing an appropriate algorithm which takes the characteristic movement of sediments in river bends into account, the calculated velocities as well as the bed level changes over time showed a good agreement with the measurements.

1 INTRODUCTION

Sediment transport in river bends is of highest interest in the field of sedimentation engineering. The lateral bed load transport and corresponding lateral migration of rivers is one of the major unknown herein. Many research studies have been carried out to investigate particle movement on side slopes in channel bends. The flow in river bends is dominated by transverse secondary currents. The sediments are eroded by the accelerated flow at the outer part of the bend and transported by the secondary currents to the inner part. Here they tend to deposit due to the reduced velocity and shear stress, forming a so called point bar. Additionally, bed load particles tend to move down slope in response to gravity. This force is acting contrary to the force from the secondary currents, and keeps the river bed in an equilibrium condition.

2 BED LOAD TRANSPORT IN RIVER BENDS

Sediment transport in river bends is mainly influenced by the complex flow structure. To understand morphodynamics in river bends and consequently to derive formulas for sediment transport on side slopes, a number of researchers (van Bendegom 1947; Engelund 1974; Kikkawa et al. 1976; Ikeda et al. 1982 a, b; Olesen 1987; Kovacs & Parker 1994) has done investigations in this field. The main results are the following. The sediment particle on a side slope has a lower critical shear stress compared to those on the flat bed. Furthermore it is observed that the sediment particle being transported on a transversal slope is not following the direction of the near bed velocity as it would on a flat bed. To reproduce the sediment transport in channel bends, it was necessary to find reasonable models from the literature. Investigations on an incipient motion criteria of particles on side slopes leads to a formula calculating a factor K (Eq. 1) which is reducing the critical shear stress of sediments resulting in an effective shear stress for particles on side slopes (Brookes 1963). The factor K is a function of the sediments' friction angle of repose, the transversal slope and the direction of the near bed velocity.

$$K = -\Delta + \sqrt{\left(\frac{\sin\alpha\sin\delta}{\tan\Phi}\right) - \cos^2\Phi\left[1 - \left(\frac{\tan\alpha}{\tan\Phi}\right)^2\right]} \qquad (1)$$

$$\Delta = \frac{\sin\alpha\sin\delta}{\tan\Phi} \qquad (2)$$

where δ = angle between the stream line and the direction of the near bed flow velocity; α = transversal slope of the channel bed; Φ = slope parameter similar to the sediments friction angle of repose.

The characteristic mechanism how the sediments are transported in channel bends is described by an equation derived by Engelund (1981). It is a further development of a formula by Engelund (1974) which was based on a static consideration of the forces acting on a grain on side slopes. The improvements are done by introducing a modified shields parameter which is

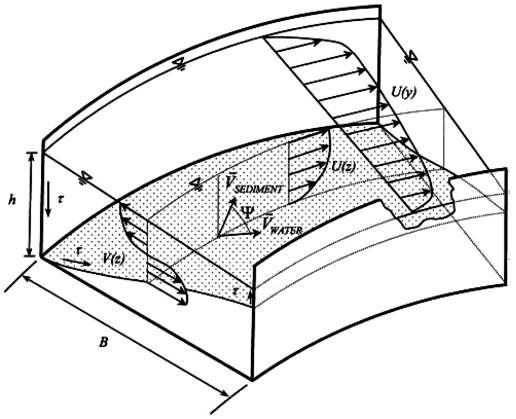


Figure 1. Velocity and sediment directions on a sloping bed in a channel bend.

derived empirically considering the skin frictino of the sediments. The equation reads

$$\tan(\psi) = \frac{0.6}{\sqrt{\Theta'}} \cdot \frac{\partial h}{\partial n} \tag{3}$$

$$\Theta' = 0.4 \cdot \Theta^2 + 0.06 \tag{4}$$

$$\Theta = \frac{\tau_b}{\rho_W g \left(\frac{\rho_S}{\rho_W} - 1 \right) \cdot d_{50}} \tag{5}$$

where $\Psi =$ angle between the sediment transport direction and the main flow direction; $\partial h/dn =$ tan $(\alpha) =$ transversal slope of the channel bed; $\Theta' =$ shields parameter related to the skin friction; $\Theta' =$ shields parameter; $\rho_W =$ density of water; $\rho_S =$ density of sediments; $d_{50} =$ sediments size where 50% is smaller. $\tau_b =$ bed shear stress.

The model leads to an angle of the sediment transport Ψ related to the direction of the near bed velocity, being a function of both the transversal slope $\partial h/\partial n$ and the shields parameter related to the skin friction Θ'. At the initial stage of the scour and deposition process in a channel bend, where the bed is still flat, a bed load particle will move along the same direction as the flow at the bed which is skewed inward due to the effect of the secondary flow. However, as the deformation of the bed develops, the path of the particles does not longer follow the direction of the flow at the bed due to the effect of gravity. Dependent on the side slope of the bed geometry the bed load is transported more in the direction of the outer part of the channel bend. This mechanism is illustrated in Figure 1, explaining the process described previously and the terminology of the parameters used in the model of Engelund.

3 THREE DIMENSIONAL SIMULATION OF SEDIMENT TRANSPORT

The numerical model which is used in the present study is called *SSIIM* and is developed by Olsen (2002). It solves the Reynolds-averaged Navier-Stokes equations in three dimensions to compute the water flow using the finite volume approach (Olsen 2003) as discretization method. The k-ε turbulence closure scheme (Rodi 1980) computed the stress term and the *SIMPLE* method (Patankar 1980) the pressure term. The suspended sediment transport was calculated by solving the transient convection-diffusion equation for sediment concentration. The diffusion coefficent was set equal to the eddy viscosity taken from the k-ε model. To define the boundary conditions for the suspended sediment concentration, van Rijn's (1984b) formula was applied to the cells closed to the bed. Additionally, the bed load transport was calculated using the bed load formula by van Rijn (1984a). The bed level changes were then calculated by solving the continuity equation in order to predict the vertical changes in the bed morphology over time. The direction of the transported material is then equal to the direction of the velocity at the bed. This might be sufficient in cases where no steep gradients in the bed evolution occur and the river course stays mainly straight. In contrast to this, sediment transport in river bends is a complex phenomenon and demands a more advanced model for sediment transport. From literature it is known that the direction of the transported material differs from the direction of the flow velocity near the bed. Therefore a new algorithm is implemented. It follows equation 3 and gives the transported sediments a certain direction, which is mainly depending on the transversal slope of the bed. Further on, a new incipient motion criterion for particles on side slopes is used. The results are compared with those of the default sediment algorithm, in order to see the sensitivity of this process.

4 RESULTS

Kawai and Julien (1996) observed the bed level changes in a 90° bended flume under uniform flow condition. The resulting bed level changes of the physical model study are illustrated in Figure 2. In the 0.2 m wide channel an almost uniform bed material with a mean diameter of $d_s = 0.6$ mm is used to form the initially flat bed with a longitudinal slope of 1/300. Both the water and the sediment discharge were kept constant to a value of Q = 4.0 l/s and $Q_B = 0.00144$ l/s. The observed bed scour at the outer bank has a maximum depth of 0.11 m and is located near the bend angle α; $= 60°$. At bend angles of $10° < \alpha < 40°$, a point bar was formed near the inner bank. During the whole

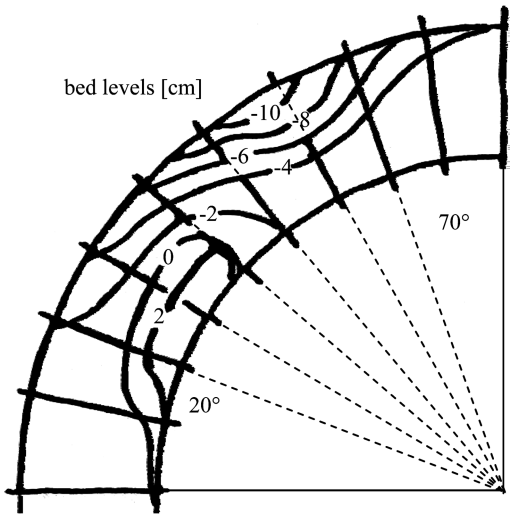


Figure 2. Contour map of the bed level changes from the physical model study.

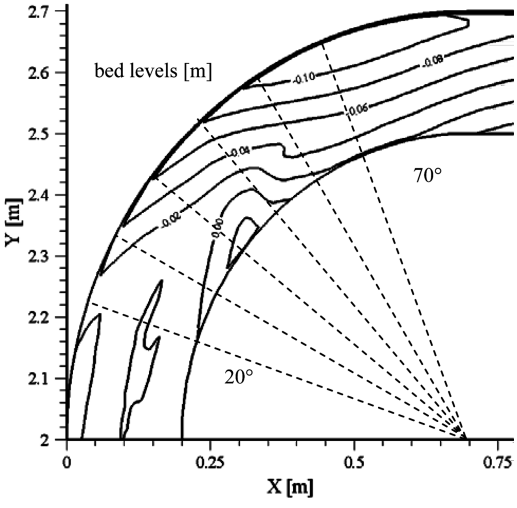


Figure 3. Contour map of the bed level changes from the numerical simulation.

study time of 200 hours no bed forms were observed (Julien 2003).

Figure 3 illustrates the contour map of the bed level changes of the numerical calculations after the full simulation time. The bed changes were calculated with the default sediment transport algorithm. Herein, the sediment transport direction is in accordance with the direction of the near bed flow velocity. Considering Figure 3 one can see that the maximum values of the calculated bed changes are matching the measured ones from the physical model. However the locations

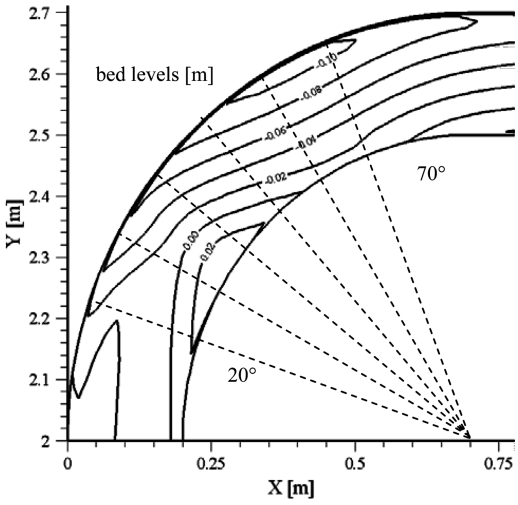
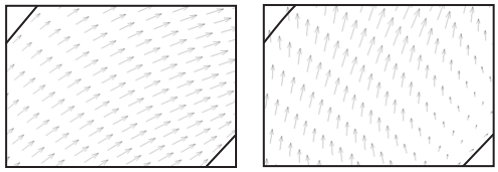


Figure 4. Contour map of the bed level changes from the numerical simulation considering the difference in directions of bed velocity and sediment transport and a modified motion criteria for particles on side slopes.

of the maxima in bed changes are shifted towards the downstream direction of about 10°. The maximum scour and the minimum water depth are at a bend angle of about 70° and 40°, respectively. More over the plane dimensions of the point bar deposit at the inner side of the bend are too small compared to the measured values. These deviations could be interpreted as an over estimation of the sediment transport in longitudinal direction. Most likely this is due to the fact that the lateral sediment transport in this simulation was too small.

Figure 4 shows the contour map of the bed level changes with the zero reference to the initial flat bed, with the modified bed load transport algorithm according to the model after Engelund (Eq. 3).

Looking at the bed changes one can see that these results are much closer to the measurements than that without the enhanced sediment transport algorithm. In this case, both the range of the bed elevation and the location of the maximum values are matching the results from the physical model. The plane dimensions of the scour and deposition are also fitting better the observed values. In the Figures 5a and b, the vectors of the sediment transport direction are illustrated. One can see that in the beginning of the calculation (Fig. 5a) where the bed is still flat, the vectors are slightly skewed towards the inner part of the bend following exactly the direction of the flow. This fact proves that the model is able to predict the secondary flow in channel bends. With the development over time, illustrated in Figure 5b, the bed starts to deform and direction of the sediments to deviate from the direction of the



(a) (b)

Figure 5. Direction of the sediment transport situated at the entrance of the bend during flow calculation: (a) on a flat bed and (b) on a transversal sloped bed. (Flow is from down left to up right).

flow. At the end of the simulation time and the fully developed bed topography, the vectors are pointing mostly to outer part of the bend, in the direction of the transversal slope.

5 CONCLUSION

A three dimensional model is presented which is capable to calculate the flow field and the sediment transport in a channel bend of 90°. The model uses formulas based on a stability analysis for sediment particle on a side slope, and introduces an appropriate algorithm which takes the characteristic movement of sediments in river bends into account. The calculated velocities as well as the bed level changes over time showed good agreement to measurements from a physical model study.

REFERENCES

van Bendegom, L. 1947. Some flow considerations of river morphology and river improvements, *De Ingenieur*, 59(4), B1–B11 (in Dutch; English translation available as Translation 1054, National Research Council of Canada, 1963).

Brookes, H.N. 1963. discussion of, Boundary shear stress in curved trapezoidal channels, by Ippen, A.T. and Drinker, P.A., *Journal of Hydraulic Division, ASCE*, (89), No. HY 3.

Engelund, F. 1974. Flow and bed topography in channel bends, *Journal of Hydraulic Division, ASCE*, (100), No. HY11.

Engelund, F. 1981. The motion of sediment particles on an inclined bed, prog. Rep. 53, *Inst. Hydrodynamic and Hydraulic Engrg., Tech. Univ. Denmark*,

Ikeda, S. 1982a. Incipient motion of sand particles on side slopes, *Journal of Hydraulics Division* (108), No. HY1.

Ikeda, S. 1982b. Lateral bed load transport on side slopes, *Journal of Hydraulics Division* (108) No. HY11.

Julien, P. 2003. Personal communication.

Kawai, S., Julien, P. 1996. Point bar deposit in narrow sharp bends, *Journal of Hydraulic Research*, (34), No. 2.

Kikkawa, H., Ikeda, S., Kitagawa, A. 1976. Flow and bed topography in curved open channel, *Journal of Hydraulics Division*, (102) No. HY9.

Kovacs, A., Parker, G. 1994. A new vectorial bedload formulation and its application to the time evolution of straight river channels, *Journal of Fluid Mechanics,* (267).

Olesen, K.W., 1987. Bed topography in shallow river bends, Doctoral thesis, *Delft Univ. of Technol., Dep. of Civil Engineering*.

Olsen, N.R.B. 2002. A three dimensional numerical model for simulation of sediment movements in water intakes with multiblock option, User's manual.

Olsen, N.R.B. 2003. Hydroinformatics, fluvial hydraulics and limnology, *Department of Hydraulic and Enironmental Engineering, The Norwegian University of Science and Technology, Norway.* (www.bygg.ntnu.no/~nilsol/sib5050/flures5.pdf)

Patankar, S.V. 1980. Numerical Heat transfer and fluid flow, *Taylor and Francis Publishers*.

van Rijn, L.C. 1984a. Sediment Transport Part I: Bed load transport, *Journal of Hydraulic Engineering*, (110), No. 10.

van Rijn, L.C. 1984b. Sediment Transport Part II: Suspended load transport, *Journal of Hydraulic Engineering*, (110), No. 11.

Rodi, W. 1980. Turbulence models and their application in hydraulics, *IAHR, state-of-the-art publication*.

River Flow 2004 – Greco, Carravetta & Della Morte (eds.)
© 2004 Taylor & Francis Group, London, ISBN 90 5809 658 0

Study on the channel development in a wide reservoir

C.J. Sloff
WL | Delft Hydraulics & Delft University of Technology, Delft, The Netherlands

H.R.A. Jagers
WL | Delft Hydraulics

Y. Kitamura
Chigasaki Research Institute, J-POWER (Electric Power Development Co., Ltd.), Chigasaki, Japan

ABSTRACT: In most reservoirs incisive channels are formed within the widening depositional area (the delta). Understanding this phenomenon is important for the development of an efficient sedimentation control strategy that uses these natural erosion processes to remove the deposits. Laboratory experiments in a wide rectangular flume with an initially flat alluvial bed showed that the location of the channel is determined by the initial flow pattern, and by the up- and down-stream conditions that control this pattern. In these experiments the channel formed along the left bank although the outflow was positioned on the right bank. Two to three major horizontal eddies developed which force the flow field to support the observed curved channel. This particular behavior could also be reproduced by a two-dimensional (depth-averaged) morphological model of the experiment using the Delft3D modeling system. The simulations indicate that the observed asymmetry in channel position, and sudden switches in channel location can be explained by the sensitivity of this flow pattern to geometry and boundary conditions. Following this verification of the model-approach, a case-study has been carried out for Senbiri reservoir in the Hokkaido region in Japan which shows the characteristic channel pattern as observed in the flume experiment. Two-dimensional simulations indicate that time-dependent control of outflow gates and modification of bend pattern in upstream river reach can be applied to increase erosion of the deposits.

1 INTRODUCTION

Reservoirs for hydropower, storage or flood control, positioned in an alluvial river are subject to sediment deposition in which sediment deposits are non-uniformly distributed over the reservoir area. Sediments that are transported by the river settle within the active storage of the reservoir, forming an advancing delta of coarse sediments at the head of the reservoir, and forming a more uniform bottom-set bed of fine sediments in the deeper parts of the reservoir (e.g., Graf, 1983, Sloff, 1997). These deposits reduce the capacity and lifetime of the reservoir. To fight these losses and support sustainable management of reservoir capacity, it is necessary to understand and predict the relevant phenomena. Mathematical modeling techniques, especially two- and three-dimensional models, are considered to have most potential for this purpose, as the relevant processes and their interactions can be quantified properly.

One of the phenomena in reservoirs that is not well investigated and theoretically explained is the formation of incisive channels in the depositional area (delta) of the reservoir. It is most pronounced in reservoirs with a seasonal fluctuating water level (as in most hydropower, flood-control and water-supply reservoirs), or in reservoir that are operated with regular water-level draw-down to flush sediments from the delta (e.g., Fan and Morris, 1992). In many reservoirs these channels can be found, e.g. see figure 1, as they are a common feature of deltaic deposition in wide reservoirs.

Nevertheless a full understanding of the development of these incisive channels is required to enable successful sediment-management strategies. Modeling of the channels may help to forecast deposition patterns, and to improve flushing operations using the erosive channel flow. Reliable theory regarding both the dynamic dimensions (width and depth) of these channels, and the varying location of such a channel is not yet available.

The lack of knowledge regarding these phenomena initiated a study to channel formation, applied to sedimentation and channel formation in a small

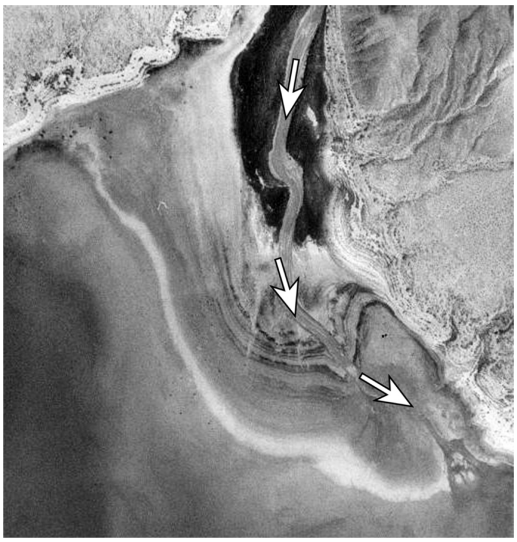


Figure 1. Photograph of a channel (see arrows) in the delta top-set bed in Lake Mead (USGS, aerial photograph 1994).

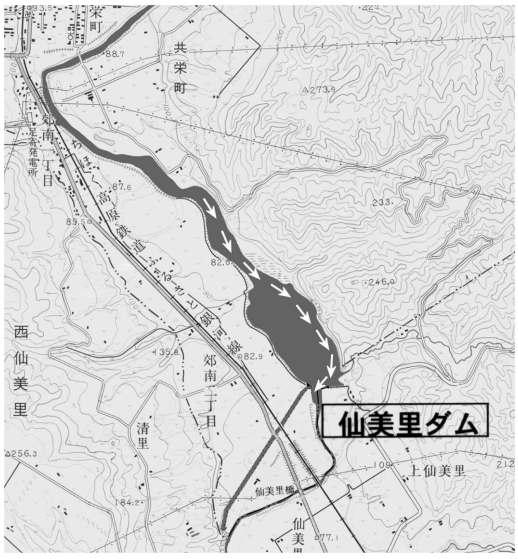


Figure 2. Topographic map of Senbiri reservoir (Hokkaido, Japan) with arrows indicating the location of the channel within the reservoir.

reservoir in Japan. This reservoir is characterized by a pronounced channel formed on the far left side of the reservoir, with a large depositional area next to it on the right (J-POWER, unpublished).

The concerning *Senbiri* Reservoir, with a relatively small storage capacity, is located in the Toshibetsu River (tributary of the Tockachi River) in the Hokkaido area, and has a quite large catchment area. Therefore, during floods, much water and sediment is flushed through the reservoir. Nevertheless the deposits are gradually growing, and clogging up the conveyance. It was found that, despite of the location of dam outlets on the far right side, the channel remained at the left side, such that at the right side a quiescent deposition area is maintained. A similar behavior was for instance reported in flume experiments of flushing operations by Schälchli (1987).

The study aims at investigating the causes of this observed behavior, and find measures to initiate the erosion of deposits from the right side by redirecting the eroding flow during high discharges. Therefore this study has been focused mainly on the location of the channel (rather than its depth and width) and comprises both experiments in a wide laboratory flume, and two-dimensional mathematical modeling using the Delft3D modeling system (WL | Delft Hydraulics, 2003). These modeling approaches allow for a representation of the spatial variations in flow and morphology that are supposed to determine channel development. Application of the numerical modeling approach to prototype conditions of Senbiri reservoir has been worked out afterwards to verify the findings, and for proposing site-specific measures.

In chapter 2 the processes are introduced that cause the formation of channels in reservoirs. The modeling activities and results of wide flume modeling are presented in chapter 3 and 4, while the case study with prototype simulations in Senbiri reservoir is discussed in chapter 5. The results are discussed in chapter 6.

2 MORPHOLOGICAL PROCESSES

The channels in reservoirs that are relevant in relation with this study, are those which develop by an interaction of deltaic deposition during periods of relatively high pool levels, and erosion during periods of low pool levels and/or high discharges (flushing). The processes that shape and position the channel are complex and highly dependent on the flow and sediment-transport conditions.

2.1 *Channel formation during deposition*

The morphological evolution in the backwater reach is of a deltaic type, in which in a narrow reservoir the flow and sediment spread evenly across the pool, while in a wide reservoir the flow enters the pool much as a jet (Vanoni, 1977). Below the jet-flow a submerged ridge develops which subtends a submerged channel which will be built up to the surface and will extend farther into the reservoir, e.g. see figure 1 (ridge development into SE-direction). Fine sediment are carried and deposited to both sides of the channel, by reverse eddies that are generated by the jet flow. A process of building up of channel deposits followed

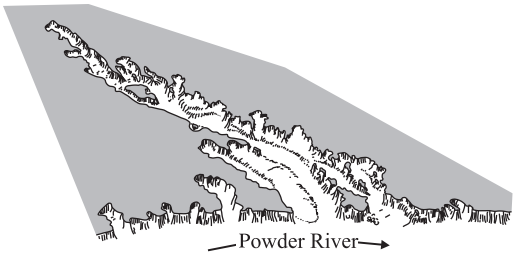


Figure 3. Back cutting of a channel caused by meander cut-offs in the Powder River, USA by Gay et al. (1998). Flow direction is from top to bottom.

by avulsions leads to an unstable process in which even multiple distributary channels may develop. Nevertheless, in situations with periodic floods or with significant draw-down of water levels usually a single main channel can be found.

2.2 *Channel formation during erosion*

The specific channel-erosion processes in reservoirs are controlled primarily by the upstream and downstream conditions, i.e. discharge and sediment supply from upstream, and water level and outflow downstream. For this study two types of channel-erosion processes in reservoirs can be mentioned:

- retrogressive erosion i.e. head ward (upstream) back-cutting into the deposits, see figure 4. These are the processes that occur during draw-down of the *downstream* water levels (using the bottom outlets). The phenomena can be compared to morphological processes due to meander cut-offs, for instance shown in figure 3. The main flow tends to be concentrated in the channel. The channel dimensions are not only determined by transport of particles, but also by erosion of the banks through geotechnical processes such as sliding of the banks after undercutting.
- degradation, growing in downstream direction and caused by highly erosive inflows at the *upstream* inflow boundary, see figure 4. This situation is less common, and caused by an upstream deficit of sediment (e.g., caused by an upstream dam).

2.3 *Channel location*

Flow patterns that are brought about by the river and reservoir geometry (bathymetry), are assumed to control the location of the channel. As soon as conditions give rise to channel formation, the prevailing flow pattern is determining the onset of course of the channel. Often the jet-like inflow from the river is directed by the river-channel upstream and the large supporting horizontal eddy(s) next to this jet in the reservoir. After the channel is formed its location is rather stable, and

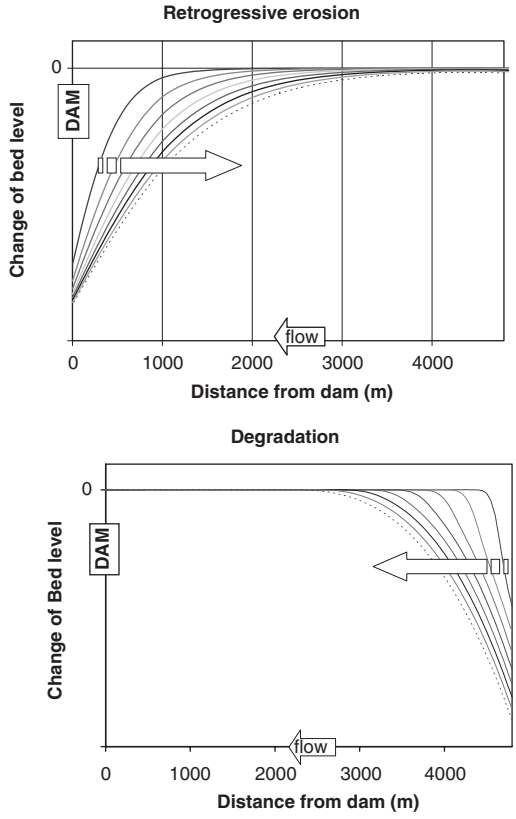


Figure 4. Erosion processes in a reservoir (1D modeling results). Upper figure: retrogressive erosion induced by downstream water level drawdown; Lower figure: degradation induced by reduced sediment inflow from upstream.

difficult to shift as its depth enforces the flow pattern to follow the channel path.

Since the initial flow pattern and initiation processes of channel formation are sensitive to the conditions, the location of the channel is difficult to predict.

In Senbiri reservoir in Japan the channel is formed by a combination of deposition by riverine sediments, and erosion by water-level draw-down during floods. Laboratory experiments, and mathematical model simulations show in the following sections how the flow patterns determine the channel location.

3 WIDE FLUME EXPERIMENTS

3.1 *Laboratory experiments*

Laboratory experiments were set up to examine the phenomena of channel formation as observed in Senbiri reservoir. The experiments were carried out in a wide morphological flume at J-POWER, Chigasaki

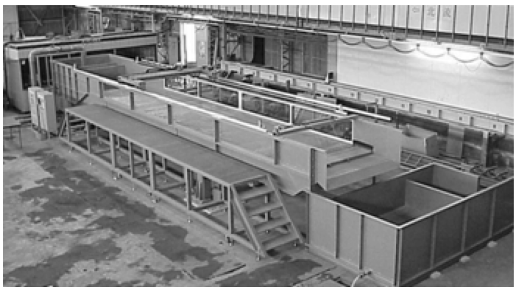


Figure 5. Wide morphological flume at hydraulic laboratory of J-POWER, Chigasaki R&D Centre (flow direction in this picture is from left to right).



Figure 6. Thickness of sediment layer (top view) at the end of flume experiment B-b-1c (arrows indicate inflow and outflow).

R&D Center in Japan, as shown in figure 3. The model section of the flume is 2 m wide and 7 m long. To reproduce schematically the observed channel development, a relatively wide and shallow flow field was generated on a slightly sloping sediment layer (slope 1/600). The flow enters the model at the upstream side through a narrow (40 cm wide) culvert in the middle of the flume, while the outflow was forced through a narrow opening on the *right*-hand side of the lower boundary. A discharge of 0.025 m^3/s was imposed (without sediment), resulting in a flow depth of about 0.15 m.

By the clear-water inflow a channel is eroded in the sediment layer (by means of degradation). Since the sediment layer was initially only five centimeters thick, the fixed bottom of the flume was exposed after erosion. Similar to the observations in Senbiri reservoir, the channel did not develop along the shortest path from inflow to outflow gate, but developed toward the outer left side (opposite of the outflow location). Figures 6, 7 and 8 show the final configuration of the channel after experiment B-b-1c.

One of the proposed measures in Senbiri reservoir for changing the course of the channel, is the partial closure of the existing channel through a sediment dike. To test the effectivity of this measure an experiment was carried out starting from the end-situation of the experiment above. In figure 9 is shown how a small dam was created from bed-material, to partially close the original channel. Sediment for the dam was taken from the right-hand side (dotted line indicates original bank line).

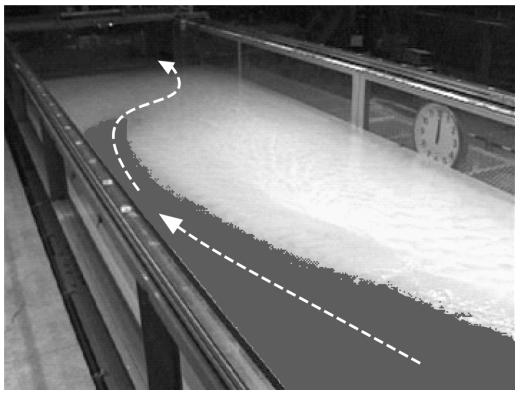


Figure 7. Photograph, looking downstream, of eroded channel (dashed arrows) at end of flume experiment B-b-1c (after 72 h).



Figure 8. Photograph, looking upstream, of eroded channel (dashed arrows) at end of flume experiment B-b-1c (after 72 h).

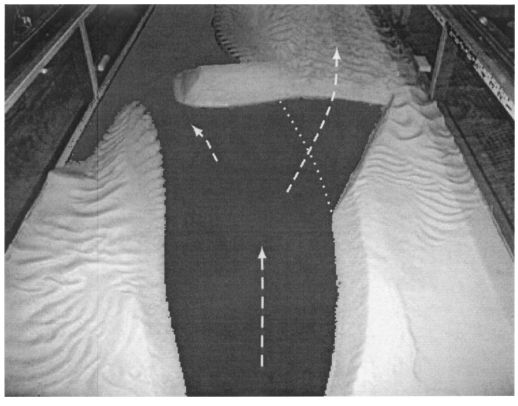


Figure 9. Initial situation for experiment B-b-3c (looking downstream) with position of a small dam to partially close the original channel.

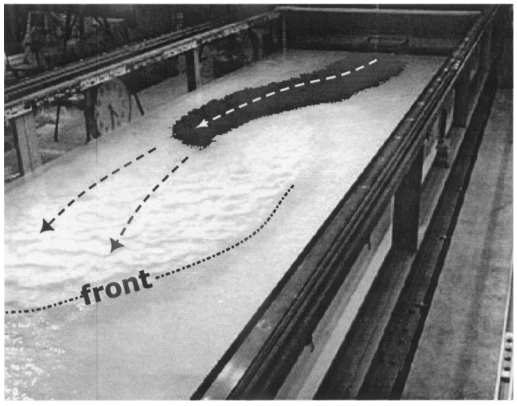


Figure 10. Photograph, looking upstream, of eroded channel and flow pattern (dashed arrows) during flume experiment B-b-3c after about 4 hours.

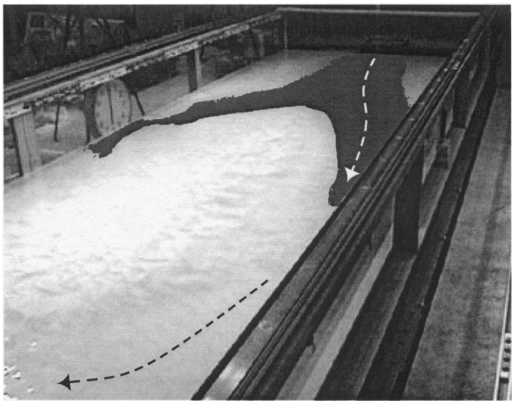


Figure 11. Photograph, looking upstream, of eroded channel (dashed arrows) at end of flume experiment B-b-3c (after 72 h).

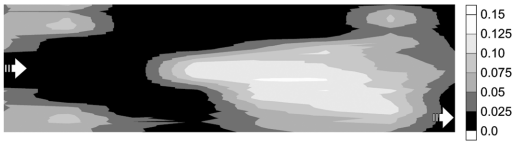


Figure 12. Thickness of sediment layer at the end of flume experiment B-b-3c.

In figure 10 the situation is shown after about 4 hours. Due to the small dam the flow is forced towards the right side of the flume, and starts to erode through the deposits. Eroded sediments are transported downstream forming a wide advancing front over which the flow fans out. Due to the fanning out of the flow it losses its transporting capacity and causes the front to built up to form an underwater-ridge (see figure 10).

After about 4.5 hours the main flow suddenly switches back to left side, and starts to erode the small dam. The flow pattern completely reverses, and again a bed topography similar to the end-situation of the previous experiment (B-b-c1) is obtained at the end. The end state of the experiment is shown in figures 11 and 12.

Analyzing these experiments it is assumed that after 4.5 hours a state developed, due to bed topography (and bed-form roughness), in which the flow-gradient to the left overgrows the gradient towards the right.

The phenomena observed in this last experiment B-b-3c show some analogy to the stability of channel bifurcations (e.g., Sloff et al., 2003), in which the left and right channel are the branches downstream of the bifurcation. The system may maintain a state of an unstable 'quasi-equilibrium' in which only one branch is open. After some period of morphological evolution the system can reach a point in which a transfer to a new state occurs, in which the other branch is open. From theoretical analyses of Wang et al. (1995) it is known that this transition can occur very suddenly.

On basis of mathematical model results the observed phenomena are further analyzed and explained. These analyses are presented in the following chapter.

4 MATHEMATICAL MODELING

4.1 *Delft3D modeling system*

As shown in the previous sections the spatial variations in morphology require an accurate description of the flow patterns within the reservoir. Therefore, to study the channel formation in reservoirs a two-dimensional or three-dimensional mathematical model is most appropriate. For this reason simulations of the flume experiments and of the Senbiri reservoir were carried out using the Delft3D modeling system. To be able to unraffle and analyze the models it is decided to select an approach which includes a simulation of only the most processes which are assumed to drive the channel formation:

- Depth-average shallow water equations are solved with a constant eddy viscosity for horizontal turbulence effects. These horizontal turbulence effects are very relevant for simulating the flow pattern (jets and eddies), and enter the momentum equations for 2D flow by the Reynold's stresses F_ξ and F_η(m/s^2). These forces are expressed by the following Laplace operator for turbulent momentum flux:

$$F_\xi = \nu_{11}\left(\frac{1}{G_{\xi\xi}}\frac{\partial^2 u}{\partial \xi^2}+\frac{1}{G_{\xi\xi}}\frac{\partial^2 u}{\partial \eta^2}\right)$$

$$F_\eta = \nu_{11}\left(\frac{1}{G_{\xi\xi}}\frac{\partial^2 v}{\partial \xi^2}+\frac{1}{G_{\xi\xi}}\frac{\partial^2 v}{\partial \eta^2}\right)$$

with ν_{11} is a constant eddy viscosity (m^2/s), $G_{\xi\xi}$ and $G_{\eta\eta}$ are coefficients to transform curvi-linear to rectangular co-ordinates (m^2), u and v are flow velocities (m/s) in ξ- and η-direction of the curvi-linear grid (reducing to x- and y-direction on a rectangular grid). Near closed boundaries a more complex form is used to account for the shear stresses along these boundaries.

- The bed sediment is assumed to be of a uniform grain size, and the sediment transport rate can be based on total-transport formula. For this purpose a 2D form of the Ashida and Michiue (Egashira et al., 1997) formula is applied, which is expressed by:

$$s_{bi} = 17\gamma\sqrt{\Delta g D_m^3}\,\tau_{*m}^{3/2}\left(1-K_c\frac{\tau_{*cm0}}{\tau_{*mf}}\right)\left(1-\sqrt{K_c\frac{\tau_{*cm0}}{\tau_{*mf}}}\right)$$

  In which D_m is the mean diameter (m), K_c is a correction factor due to the influence of bed slope, γ is a calibration factor, τ_{*cm0} is the non-dimensional critical stress, and τ_{*mf} is the actual non-dimensional Shields value computed on the depth-averaged velocity and the mean grain size.
- The effect of relevant 3D processes such as helical flow in a bend (following from curvature of the flow field by a parameterized model), and the effect of gravity on sediment on a sloping bed, are reproduced by correction of the sediment-transport direction as follows (additional to the effect of coefficient K_c which affects the transport magnitude):

$$\tan(\beta) = \frac{\sin(\alpha) - f(\tau_{*mf},\eta)\dfrac{\partial z_b}{\partial \eta}}{\cos(\alpha) - f(\tau_{*mf},\xi)\dfrac{\partial z_b}{\partial \xi}}$$

  with α is the near-bed flow direction (corrected for helical flow), β is the direction of sediment transport, $\partial z_b/\partial\xi$ and $\partial z_b/\partial\eta$ is the bed level slope, and $f(\tau_{*mf},\xi)$ is a function dependent on the ratio τ_{*cm0}/τ_{*mf}, on bed slope components, and some other flow and sediment related quantities.
- For simulations of the flume experiments a sediment-layer on top of a fixed concrete bed is modeled. Therefore the underlying concrete bed is modeled as a non-erodible layer. The used modeling concept for non-erodible is that of Struiksma (1999).

Since during morphologically relevant conditions the bed is assumed to be submerged over the entire domain, the morphological processes are dominated by scouring and accretion of sediment, also for the steep slopes at the submerged channel banks. Typical geotechnical bank-erosion phenomena (e.g., sliding of banks) seem therefore not relevant for the channel location in the flume, and are therefore not included in the model.

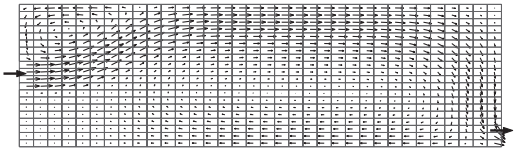


Figure 13. Stationary flow field computed for the observed initial flume conditions (plane bed, constant discharge), and plotted on the numerical grid.

To further reduce the complexity of the system, specific processes, such as sediment sorting and convection-diffusion effects of suspended-sediment concentrations are not included for the moment (although these effects can be simulated with the modeling system).

4.2 *Delft3D simulations for the laboratory experiments*

The flume experiments were repeated using Delft3D in order to study whether the relevant processes can be reproduced mathematically, and what features (e.g., varying roughness, non-erodible layers) are controlling the phenomena.

The model was represented by a simple rectangular grid with grid spacing of about 20 cm in flow direction and 10 cm in transverse direction. A Chézy value of 60 m$^{1/2}$/s was used for bed-roughness, and a roughness height of 0.05 mm was used for wall roughness. A median grain size D_{50} of 0.26 mm was used to represent the bed sediment. And it was assumed that if the sediment layer on the bed becomes less than 2 cm, the influence of the fixed concrete bed enters the transport computation as the troughs of bed forms are assumed to reach the concrete. As the simulations were only mend for qualitative comparison, little effort was spend to calibration.

In figure 13 the simulated stationary flow field is shown that is computed starting from an initial condition of stagnant water with a plane bed. The flow pattern was found to agree with the observations, showing a channel positioned on the left, supported by a large stable eddy on the right hand side, and a small eddy left of the flume entrance. Nevertheless it was also found that this simulated pattern can switch to a reverse pattern with the channel positioned on the right side, and the eddy on the left side. This could be achieved by changing the initial state, or the local geometry. The sensitivity to these conditions is quite strong.

The morphological simulation shows that the initial flow pattern with a jet-type concentrated flow channel, drives the incision of the main channel on the left side. Comparison of simulated results in figures 14 and 15 with the observations in figures 6, 7 and 8 show that there is a striking agreement, despite of the difference

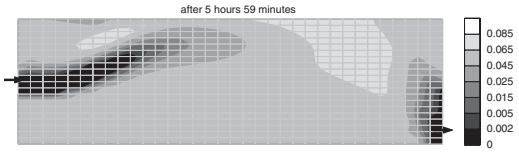


Figure 14. Thickness of sediment layer above concrete flume bed simulated after 6 hours (experiment B-b-1c).

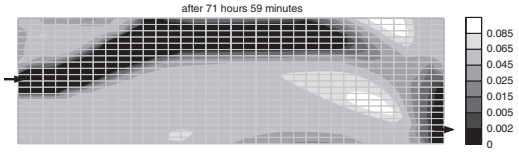


Figure 15. Thickness of sediment layer above concrete flume bed simulated after 72 hours (experiment B-b-1c).

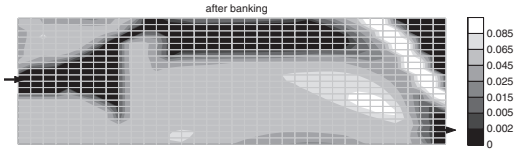


Figure 16. Thickness of sediment layer above concrete flume bed, initial simulation B-b-3c.

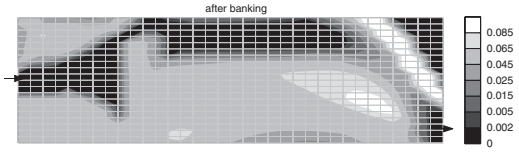


Figure 17. Thickness of sediment layer above concrete flume bed simulated after 4.5 hours (just before switching).

in layer-thickness (due to underestimation of initial sediment-layer thickness in the computation).

Also the experiment B-b-3c has been simulated, in which the final state of experiment B-b-1c is modified as shown in figure 16.

As a consequence of this initial topography simulation shows that the main flow is directed towards the right side due to the obstruction of the left-hand channel, which corresponds to the observations. Sediment-transport and erosion is therefore mainly occurring on the right-hand side, see figure 17.

The observed sudden switch from channel erosion on the right, to channel erosion on the left side (after 4.5 hours) could not be reproduced automatically by the simulation (the flow pattern remained stable). Most likely some small erosion of the small dam and formation of the ridge (see figure 10) are not fully reproduced by the model. This might be a matter of further calibration. Nevertheless, by stopping the simulation,

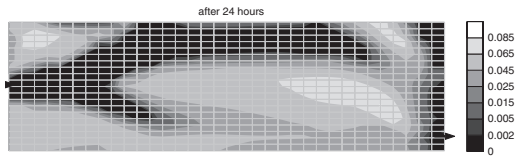


Figure 18. Thickness of sediment layer above concrete flume bed simulated after 24 hours.

generating a new flow pattern with the main flow along the left bank, and restarting the simulation with this flow field, the observed continuation of channel development could be reproduced (see figure 18).

It is concluded from these simulations that notably the small changes in geometry affect the flow pattern in such a way that the main channel can switch from 'equilibrium states' with a left or a right position of the channel. Nevertheless, it is not disproved that in this set-up with an asymmetric position of the outflow gate, the channel tends to develop towards the opposite side (taking the longest path).

Knowing now that the modeling system can be used to reproduce the observed morphological behavior, a model was set-up for Senbiri reservoir. In the following chapter the results are presented, and show what this means in a prototype situation.

5 CASE STUDY: SENBIRI MODEL

In chapter 1 the Senbiri reservoir has been introduced. It is supposed that the morphology of the reservoir is predominantly determined during floods. Main flow is concentrated along the left bank, despite the location of the outflow gates at the right bank (figure 2). On basis of annual sediment balance data of the measured reservoir volume it was found that net sedimentation occurs in years with lower peak discharges, and net erosion occurs in years with high peak discharges (i.e., 1992 and 1998).

The reservoir and part of the upstream Toshibetsu river was schematized in the Delft3D modeling system, using a curvi-linear numerical grid (about 170×18 grid points). The model is shown in figure 19. The length of the model is about 5 km, and the grid size is about 20 to 50 m in longitudinal direction, and 15 to 40 m in transverse direction. The dam is the lower boundary of the model, by which the gates are modeled as open water-level boundaries. Furthermore, the model uses a constant Manning roughness coefficient of $0.035\,\mathrm{m}^{1/3}/\mathrm{s}$, and a grain size varying from $D_{50} =$ 10 mm in upstream reach to 1 mm at the dam. Sediment transport is computed again using the 2D form of the Ashida and Michiue equation, multiplied with a factor of 2 after (rough) calibration and a dimensionless critical shear stress (τ^*_{crit}) of 0.05.

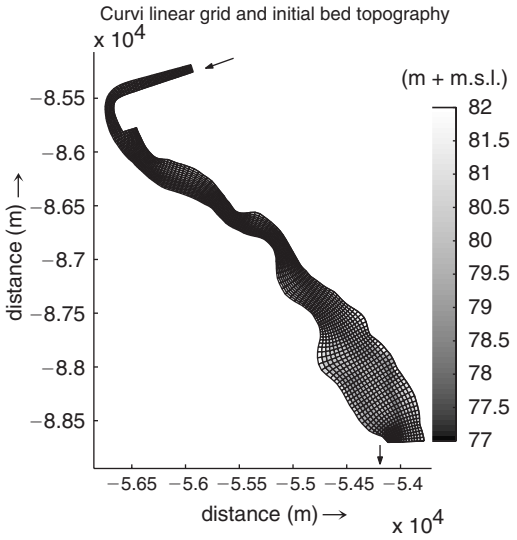


Figure 19. Model of Senbiri reservoir: numerical grid and initial bed topography (taken from a 1988 bathymetric map).

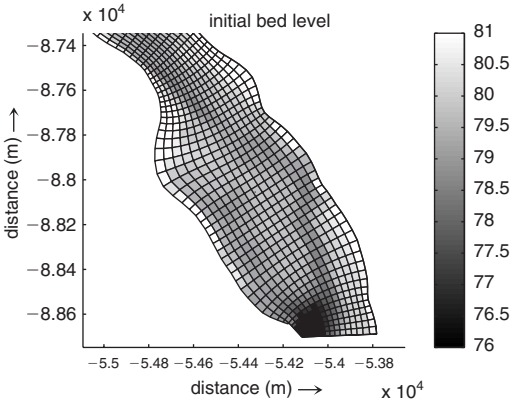


Figure 20. Initial bed topography in reservoir reach.

Several simulations were carried out with different boundary conditions:

- Simulations based on a constant discharge ranging from 200 to 800 m^3/s imposed at the upper boundary. These discharges are characteristic average values of observed flood discharges.
- Simulations based on a varying discharge, using a hydrograph that represents the peak discharges during the years 1994–2000 (up to almost 1000 m^3/s).

In all simulations the channel was found to persistently develop along the left bank, as shown in figures 20 and 21. Only during very high discharges the channel was able to break through the sand bar

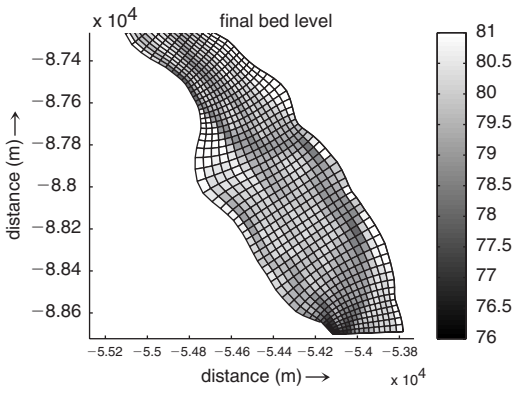


Figure 21. Final bed topography in reservoir reach.

on the right side to form a temporary cut-off channel (bend cut-off). These events explain the observed erosion during high discharges in 1992 and 1998. Nevertheless, these cut-off events can only occur when water levels at the dam are not completely draw down, because then the flow becomes concentrated in the existing deep channel on the left.

The flow field that causes the channel to be oriented to the left may also be influenced by the position of river banks and the onset of a bend towards the left just upstream of the widening part of the reservoir. It might be considered to design upstream measures to modify the channel direction, e.g. modify the meander pattern in such a way (by bank displacement) that the channel is forced to flow to the right instead of to the left. Furthermore it is possible to use floating surface vanes (anchored to the banks) during floods to force the upper sediment-free water towards the right to erode the deposits, and allow the lower sediment-laden water to flow to the left, towards the deep channel.

The simulations also confirmed the important role of boundary conditions in sedimentation and erosion. The computations show that the type and schematization of the upper boundary determines the supply of sediment to the model. At the same time the operation of the gates during the floods has a significant impact on erosion and sedimentation processes within the reservoir area. Any disagreement between modeled and actual sediment in- and out-flow affects the sediment balance.

6 DISCUSSION

Laboratory experiments and numerical simulations for a wide flume show that channel formation in reservoirs is particularly controlled by the flow pattern. It is therefore highly dependent on the boundary conditions, the initial flow conditions and the geometry (and changes in time). Due to the sensitivity of the

flow pattern to these conditions it is difficult to predict the exact location of the channel. On the other hand, the sensitivity of flow patterns creates opportunities to redirect the channel direction by means of small interventions in the flow field (e.g., operation of water-levels at gates, or constructions that redirect the flow within the reservoir).

Although the simulations show that a 2D depth-averaged model can be used to reproduce the observed features in laboratory in field, it is believed that further improvement of the modeling technique can lead to more reliable predictions. For a better approximation of the eddies and jets it is recommended to use a more detailed model for horizontal turbulence. For instance techniques such as HLES (horizontal large eddy simulation) or even fully 3D approaches can be considered. Furthermore, the sediment-transport model can be extended with multiple size fractions (e.g., Sloff et al., 2003) and convection-diffusion processes for suspended sediment. For application to prototype conditions these sediment-transport processes are quite relevant for reservoir morphology (e.g., to distinguish between development of coarse delta deposits and fine bottom set bed). Verification of the models for laboratory experiments with retrogressive erosion and graded-sediment feeding (instead of the presently performed degradation experiment) are thought to be necessary for validation as well.

To effectively apply the channel incision processes for removing deposits, the location of the channel can be changed by modifications of the flow pattern. Before a channel is formed these interventions can be much smaller than after its formation, because the channel attracts the main flow, and stabilizes the flow pattern.

The present study has not yielded new information regarding the dimensions of channels. For flushing sediments it is considered relevant to know the channel width and depth in order to estimate the gain of reservoir capacity, but present knowledge is too narrow. Water-losses due to flushing need to be balanced by the capacity gains. To obtain more knowledge on quantification more profound scientific research is therefore required.

REFERENCES

Egashira, S., Jin H., and K. Ashida K. 1997. Numerical model for river mouth sand-bar flushing and its application to river mouth regulation. *Proc. 27th congress of IAHR in San Francisco*, Theme B, Vol. 1, p. 719–724.

Fan, J. and Morris G.L. 1992. Reservoir Sedimentation. I: Delta and Density Current Deposits. *J. Hydr. Engrg*, ASCE, 118 (3), p. 354–369.

Gay, G.R., Gay H.H., Gay W.H., Martinson H.A., Meade R.H., Moddy J.A. 1998. Evolution of cutoffs across meander necks in Powder River, Montana, USA. *Earth Surface Processes and Landforms* 23 (7), p. 651–662.

Graf, W.H. 1983. The hydraulics of reservoir sedimentation. *Int. Water Power and Dam Construction*. 35 (4), p. 45–52.

Schälchli, U. 1987. Reservoir sedimentation and flushing in a hydraulic model. In: *Topics in Hydr. Modelling*, Proc. 22nd IAHR Congress, Lausanne, Switzerland, p. 240–245.

Sloff, C.J. 1997. S*edimentation in reservoirs*. Ph.D. thesis, Delft University of Technology. Also: Comm. on Hydr. and Geotechn. Engrg, Faculty of Civil Engrg., Delft Univ. of Technology, Report. No. 97–1.

Sloff, C.J., Bernabè M., Baur T. 2003. On the stability of the Pannerdense Kop river bifurcation. In: *Proc. 3rd IAHR Symposium on River, Coastal and Estuarine Morphodynamics*, RCEM 2003, Barcelona, p. 1001–1011.

Struiksma, N. 1999. Mathematical modelling of bedload transport over non-erodible layers. In: *Proc. IAHR Symposium on River, Coastal and Estuarine Morphodynamics*, RCEM 1999, Genova, p. 89–98.

Vanoni, V.A. 1977. *Sediment engineering*. ASCE, New York.

Wang, Z.B., Fokkink R.J., de Vries M., Langerak A. 1995. Stability of river bifurcations in 1D morphodynamic models. *J. Hydr. Research*, IAHR, 33 (6), p. 739.

WL | Delft Hydraulics. 2003. *Delft3D User manuals*, WL | Delft Hydraulics, The Netherlands.

This page intentionally left blank

River Flow 2004 – Greco, Carravetta & Della Morte (eds.)
© 2004 Taylor & Francis Group, London, ISBN 90 5809 658 0

Measuring the flow structures that initiate stone movement

Bas Hofland & Robert Booij
Environmental Fluid Mechanics Section, Faculty of Civil Engineering and Geosciences, Delft University of Technology, Delft, The Netherlands

ABSTRACT: This paper deals with the entrainment of coarse material from a streambed under a uniform turbulent flow with low-mobility transport. The flow field during the actual entrainment of a single stone was measured using the PIV technique. In order to determine the flow structures responsible for this entrainment the flow field was conditionally averaged over many entrainment events. The resulting flow fields show that two flow structures are responsible for the entrainment: the first is a large-scale sweep ($u' > 0$, $v' < 0$), causing increased quasi-steady forces, the second is an embedded small-scale structure with vertical velocity fluctuations, $\sigma(v')$, causing turbulence wall pressure fluctuations (TWP). The increased $\sigma(v')$ is often associated with a single spanwise vortex or a small hairpin-vortex packet. The structures can be present simultaneously in the instantaneous flow fields. It is hypothesised that the vertical fluctuations initiate the motion of the stone and the sweep moves the stone further over its pivot point. This hypothesis is supported by the fact that the intensities of the structures are negatively correlated: if one of the structures is more intense, the other does not have to be as intense. Some intense sweep events show no significant small-scale structure.

1 INTRODUCTION

Bed protections near hydraulic structures are often composed of several layers consisting of loose granular material (riprap). Especially for non-uniform flow, the existing equations for stability of stones in the top layer have limited validity. The transport rate of stones under design conditions is low, with a Shields factor near the "critical" value of 0.055. Low-mobility transport is also important for gravel bed rivers (Andrews & Smith, 1992). The present measurements are therefore aimed at low-mobility transport. This complicates the measurements, as the movement of the stones becomes a rare event, caused by the fluctuating forces created by the turbulence in the flow.

An elaborate measurement set-up was used to capture the flow and pressure field at the moment of entrainment of a stone from a granular bed. The measurements can aid the understanding of damage to granular bed protections and entrainment of sediments from river beds. This paper focuses on the determination of the flow structures that cause entrainment.

2 EXPERIMENTAL SET-UP

The experiments focussed on the movement of a single stone, the target stone. This makes it possible to average the flow field at the moment of entrainment.

A flume of 20 m long and 0.495 m wide was used. The bed material had a nominal diameter, d_{n50}, of 17.8 mm ($d_{n50} = \sqrt[3]{V_{50}}$, where V_{50} is the median stone volume). The flow conditions that can be generated are not sufficient to move the stones. Therefore the target stone was copied with epoxy resin having a density, ρ_s, of 1300 kg/m^3 . It had a d_n of 1.86 mm and a Curry shape factor of 0.62. The position of the target stone and various sensors in the granular bed is depicted in Figure 1. An inductive sensor was used to see if the stone was touching the bed. As the main mode of movement is pivoting (Carling et al. 1992; and our own observations), it was possible to place the stone

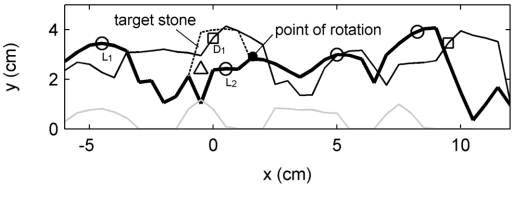


Figure 1. Measured longitudinal sections of the granular bed near the target stone indicating positions of pressure sensors (◯: upward/lift, □: forward/drag, off-centre) and motion sensor (Δ). Dashed line: target stone, thick line: centre of flume, thin line: 40 mm off-centre, grey line: fixed bed. Flow is from left to right. The y-coordinate is different than for the flow results.

on a hinge in such a way that the motion is the same as in the prototype situation. Further, the motion of the stone was obstructed by a little bar after pivoting over roughly 40 degrees. When the stone reaches the bar, the hydrodynamic force on the stone has increased. Therefore the stone remains pushed against the bar until it falls back with the passage of a negative fluctuation. In cases where the stone was allowed to rotate further, it did not fall back, which means that it would have moved from its position without the bar present.

2.1 *Flow parameters*

The Reynolds number was 10^5, based on the water depth h of 0.159 m and the mean bulk velocity U of 0.64 m/s. The turbulence was considered fully developed with the rough bed spanning a length of 66 h upstream to 28 h downstream of the target stone. The width/depth ratio of about 3 implies the presence of some secondary flow. The shear velocity u_* was determined from the water level slope at 0.062 m/s, giving a Shields factor of $\Psi = u_*^2/(\rho_s/\rho - 1)gd_{n50} = 0.073$, and a Particle Reynolds number of $u_* d_{n50}/\nu = 1.2 \cdot 10^3$. The Shields factor is higher than expected. The low movement frequency of the stone ($0.11\ \mathrm{min}^{-1}$) was expected at a lower Ψ. It could be that because of the low stone density the added mass is relatively more important, increasing the critical Shields factor. Because the hinge was placed about 1.5 mm higher than the original point of rotation, the resistance of the stone against pivoting could also have been slightly higher than assumed.

In this paper x and y are the streamwise and upward coordinates respectively and u and v the corresponding velocity components. The time average of u is denoted as $\overline{u}$, the fluctuating part $(u - \overline{u})$ as u', and a spatial average over area a is $<u>_a$.

2.2 *Equipment*

A LaVision PIV system (hardware and software) was used to measure streamwise vertical 2-D velocity fields in the centre of the flume above the target stone. The dedicated *Kodak* ES1.0 camera (1K × 1K pixels) and 50 mJ double-pulsed *New-Wave* YAG laser have a maximum double-frame sampling frequency of up to 15 Hz. The time interval between two images in a pair was 2 ms. The flow was seeded with hollow glass spheres of 10 μm diameter.

The distance between light sheet optics and the measuring area was set to about 1.5 m in order to keep the divergence angle of the sheet width limited.

The rail on which the optics were mounted was placed in line with the flume (Fig. 2). The laser sheet was guided towards the measuring area using two coated mirrors where it was about 1.5 mm thick and 150 mm wide. It entered the water surface undistorted through a streamlined window. In order to diminish the bed reflections of the light sheet, the stones under the light sheet were painted fluorescent red and an optical filter was placed in front of the camera.

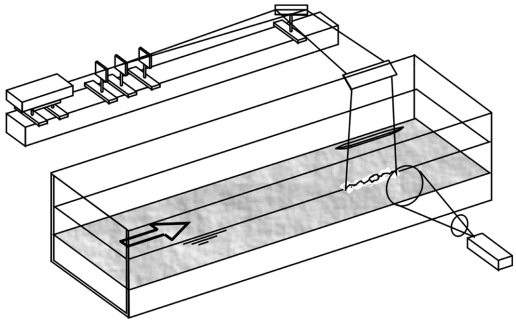


Figure 2. PIV set-up with laser (top left), sheet optics, mirrors, window on water surface and camera (bottom right).

The velocities were determined using a multipass cross-correlation method with discrete window offset, using window sizes of two times 32 × 32 pixels and one time 16 × 16 pixels with a 50% overlap. This gave a vector spacing Δx of 1.2 mm. The final results were checked using a median filter (with the possibility to select the second correlation peak), an absolute vector range, and a minimum ratio of the height of the correlation peak to the highest noise peak of 1.1. The Kolmogorov length scale was not resolved. Therefore the small-scale turbulence (wavelengths smaller than 2.4 mm) will cause noise in the determination of the velocity vectors. Still typically 95% of the vectors were validated. The unresolved fluctuations will not lead to significant forces on the stone and are therefore not of interest.

Miniature, low-range, piezo-resistive pressure transducers (Honeywell, 24PCEFAXX) were used to capture the pressure fluctuations near the target stone.

2.3 *Timing*

We discern two modes of motion of the target stone, rocking and moving. The stone was assumed to have moved (i.e. lifted out of its pocket) if it had reached the obstructing bar. The fact that the stone is sometimes pushed against the bar shows up in the histogram of durations of stone motions in Figure 3. If the stone is pushed against the bar it takes much longer for it to fall down again. This gives the small second maximum around $\Delta T_{up} = 10$ s. The target stone was assumed to have moved when the duration of detachment exceeded the time between the two maxima in the histogram (dashed line). Otherwise the mode of movement was regarded as rocking. The threshold of one second was not strictly dividing both modes of movement, so for determination of the real movements, visual inspection of the recordings was necessary.

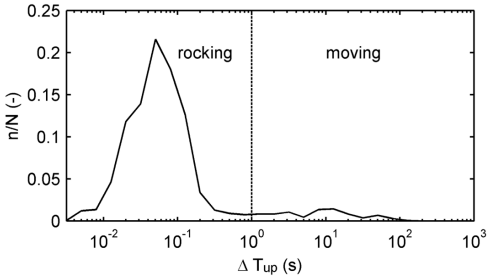


Figure 3. Histogram of the durations that the target stone is detached from the bed.

The stone moved on average once every 526 s, while the PIV apparatus had a limited storage capacity (1 GB of RAM). Therefore the PIV and pressure measurements were only saved when the stone was not in contact with the bed for at least 1 s and was thus regarded to have moved. The recordings were made continuously and stored in a ring buffer, so measurements could still be saved from before to after the entrainment. As the stone fell back to its original position eventually, a new recording started automatically when the prior data were saved and the stone was back in its original position. In principle the time between the detachment of the stone and the first consecutive PIV recording was measured very accurately, which would increase the precision of determination of the position of flow structures that lead to movement of the stone. Due to instrumentation problems, however, we were not able to use this information.

3 PHYSICAL CONCEPTS

In previous work the origin of pressure fluctuations was examined (Hofland, subm. a, b). However, the displacement of a stone does not only depend on the magnitude of the pressure fluctuations, but also on their location and duration. Therefore the actual movement of a stone was used as a trigger to distinguish the velocity fields leading to stone entrainment.

It could be that several types of flow structure are responsible for the entrainment of stones and that they vary in size. We will use some of the knowledge obtained in the previous research to find the flow structure(s) that cause(s) the movement of the stone. We previously identified two force-generating mechanisms. Therefore we will first divide the flow fields for all events into two classes, corresponding to these mechanisms. These are:

- Quasi-steady force fluctuations, caused by large-scale sweeps ($u' > 0, v' < 0$).
- Small-scale turbulence wall pressure fluctuations (TWP), caused by small-scale wall normal fluctuations (v') and vortices.

These two classes should be recognisable in the flow field and can help to distinguish between different flow structures that cause entrainment. Next we will describe how we can distinguish them.

3.1 *Quasi-steady forces*

Most stability formulae that incorporate turbulent fluctuations regard the streamwise velocity near the bed (or $u*$). This is based on the fact that the steady drag and lift force vary according to $|u|u$ and u^2 So a fluctuation of u will lead to quasi-steady fluctuating forces. To quantify the influence of this force generating mechanism we will average the instantaneous u-velocity in the PIV recordings over a relatively large area A above the stone, yielding $<u>_A$, and regard the values of $F_A \propto |<u>_A|<u>_A$ and its fluctuations.

3.2 *Turbulence wall pressures*

A turbulent flow over a bed creates wall pressure fluctuations (TWP) on this bed, even if it is smooth. These pressures are not created by the streamline curvature that is caused by the obstruction of the flow by the stone itself (which is the case for the quasi-steady forces), but are due to the turbulence in the flow. These pressures can also lead to net forces on bed material (Hofland, subm. b).

The origin of turbulent wall pressure fluctuations (TWP) can be small-scale vortices. As only TWP with a length scale of the order of the stone diameter d will give significant forces on a stone, a vortex at 0.5–2 d above the target stone will induce a large (lift) force. The force vector rotates clockwise from a lift to a drag direction as the vortex passes. This lift-drag combination could be efficient in starting the entrainment.

To identify the presence of this force-generating mechanism we will regard the instantaneous standard deviation of v in area B near the target stone, $\sigma(v)_B$. This value becomes large when a vortex is present, and is not very sensitive to the exact position of the vortex. Not only vortices, but a wall normal fluctuation of any kind is linked to TWP as a Reynolds decomposition of the Euler equation shows that pressure gradients are caused by the term:

$$\frac{\partial p'}{\partial x} \approx \ldots - \rho v' \frac{\partial \overline{u}}{\partial y} \tag{1}$$

Due to the 2-D measurements, vortices with axes parallel to the measuring plane cannot be identified as such.

4 DATA PROCESSING

4.1 *Splicing*

In order to regard the large-scale flow structure a hybrid technique was used to merge a sequential

series of PIV recordings, which will be called splicing here, after the technique used for joining pieces of rope by interweaving strands.

To this end first the correlation of the upstream part of the outer u' field of the first image and an equally sized downstream part of the outer u' field of the second image was determined as a function of the overlap length. The overlap at which this function was maximal was taken as the (instantaneous) value of the convection velocity of the total flow structure. Subsequently a new flow field is created by averaging the velocities of the overlapping part of the two images, and adding the remaining parts on both sides. This total image is now used as the first image and the third image from the series as the second. This process is repeated for all recordings during the measurement of a single event.

The resulting image can be seen both as a spatial image or as a temporal image with a direction opposite to the spatial image.

The process is similar to transforming a point measurement into a spatial measurement based on Taylor's hypothesis. Differences are that: the vertical structure is instantaneously measured, each velocity value is averaged over a few measurements. (Here the average is based on roughly three vector fields as the structure moves about 1/3 of the whole field per recording). And the convection velocity is determined for every image.

4.2 *Inspection of vector plots*

It can be difficult to distinguish the structural features of an instantaneous turbulent flow field when large gradients are present in a flow or when the flow structures have a wide range of scales. Both these complicating factors are present in the wall flow that is being examined here. Therefore the flow field is often decomposed in various spatial or temporal scales. Adrian et al. (2000b) give an overview of several possibilities. All techniques give different output, and many are dependent on (arbitrary) parameters.

Even for the 33 cases of stone movement using only a few different methods to regard the flow field will yield too much information to handle. For convenience we inspected the instantaneous plots first using a Reynolds' decomposition, because only one image results from this decomposition. For closer inspection we used the Galilean transform (subtracting a bulk velocity from all vectors) and plots of the swirling strength, λ. The latter is a measure of the intensity of the local rotation in a flow field. It is capable of pinpointing separate vortices accurately. We use a definition where it is positive with a vortex present:

$$\lambda = \max(\omega^2 - \gamma^2, 0) \qquad (2)$$

where ω is vorticity and γ is the strain rate.

5 RESULTS

5.1 *Mean flow*

From the PIV measurements the profiles of the mean ($\overline{u}$) and rms [$\sigma(u)$] velocity can be determined. They are depicted in Figure 4. The relative depth h/k_s (k_s is equivalent sand roughness height) is rather low. Therefore the rms profile does not overlap the semi-empirical profile of Nezu & Nagakawa (1993). Near the bed it does coincide with the measurements by Wang et al. (1993).

The spatial fluctuations of the flow from the horizontal mean are depicted in Figure 5. It can be seen that the flow follows the bed elements, with some 3-D influences. At $y = 15$ mm the direct influence of the bed on the mean flow is considered to be small.

5.2 *Classification*

According to §3, we expect that the indicators F'_A and/or $\sigma(v)_B$ will have high values if the respective

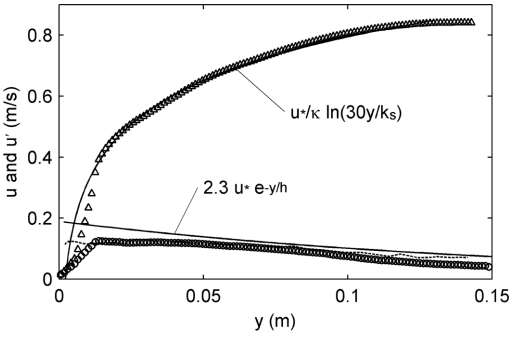


Figure 4. Measured profiles of $\sigma(u)$ (○) and $\overline{u}$ (Δ). The fitted log-law and the Nezu & Nagakawa (1993) rms profile are represented by the solid lines. The dashed line is the data by Wang et al. (1993) for $\sigma(u)$ with $h/k_s = 2.7 \cdot u*$ differed from the one determined from the water surface slope.

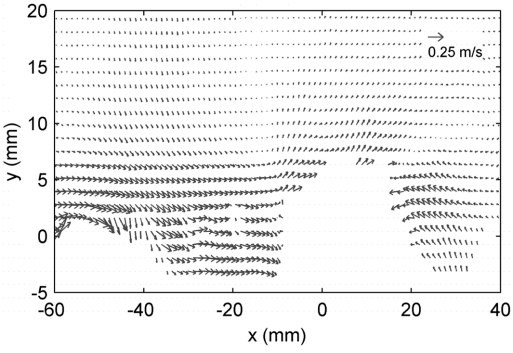


Figure 5. Spatial fluctuations of mean flow. The horizontally-averaged $<\overline{u}>_H$, is subtracted from $\overline{u}$.

quasi-steady forces (sweeps events) or the TWP are important. Therefore we plotted the combination of these indicators for all flow fields just before movement of the stone. Several sizes for the averaging areas A and B were tried, and the ones that caused the most pronounced distinction of extreme values of F'_A and $\sigma(v)_B$ were chosen. The final extents of the areas are depicted in Figure 6. Area B turned out to be larger than area A. This was unexpected, as the quasi-steady flow structure was expected to be larger.

Figure 7 depicts the combinations of F'_A and $\sigma(v)_B$ for the flow fields just before movement and for a measurement with a fixed stone.

It is clear that the values of the indicators for the flow fields just before movement are among the maximum values of the long measurement. This confirms that the force generating mechanisms corresponding to the indicators both play a role in the entrainment process.

The values of F'_A and $\sigma(v)_B$, belonging to the flow fields before entrainment are negatively correlated. No clear groups of data points appear, but we will call values of large F'_A sweep events, and with large $\sigma(v)_B$ TWP events. The dashed lines indicate the arbitrary limits of this classification. We distinguish 14 TWP, 13 sweep and 6 transitional events.

F'_A is positive for almost all events, so the longitudinal velocity is increased during entrainment. This has been shown previously by Nelson et al. (1995).

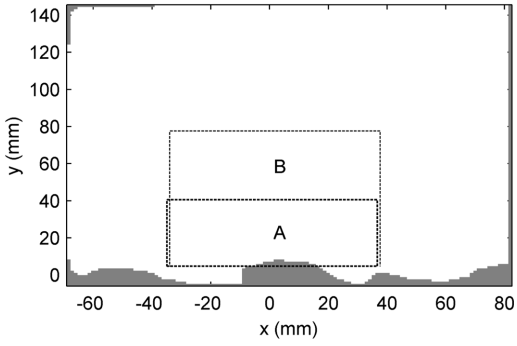


Figure 6. Areas used for averaging. The target stone is located at $(x, y) = (0, 0)$.

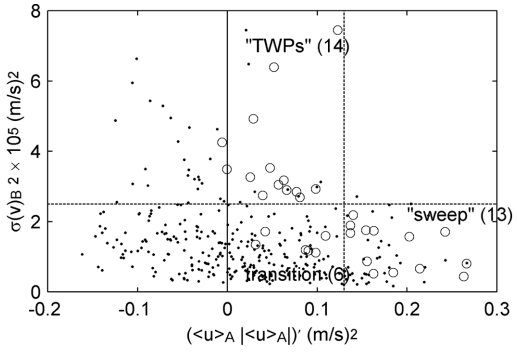


Figure 7. Classification of events. F'_A ($|<u>_A|<u>_A$) and $\sigma(v)_B$ indicate quasi-steady and TWP forces respectively. Dots are the values of a 10 min./0.5 Hz measurement with a fixed stone. The circles are the values just before stone movement. The dashed lines distinguish the sweep and TWP events.

5.3 *Pressures*

The measured pressures, conditionally averaged over all stone movements are depicted in Figure 8.

The pressure on the lift sensor (located on top of a stone) upstream of the target stone decreases when the target stone moves. It is reasonable to conclude that the target stone experiences lift as well.

The pressure under the target stone decreases slightly just before movement. This is probably because the flow through the pore under the target stone increases due to the increased u in the outer flow. When the stone begins to move the pressure increases. This is explained by the increasing exposure of the stone, which leads to a stagnation pressure under the target stone.

The drag pressure sensor (on the upstream side of a stone) 40 mm besides the target stone shows an increased drag around the moment of movement. This is clearly due to the quasi-steady mechanism: an increased longitudinal velocity increases the stagnation pressure upstream of the stone.

The differences between the sweep and TWP events are not very large. A difference is that the lift upstream of the target stone starts to increase earlier for the TWP events. A second difference is that the magnitude of the drag pressure is higher for the sweep events, which agrees with the larger $u|u|$ for which they were selected.

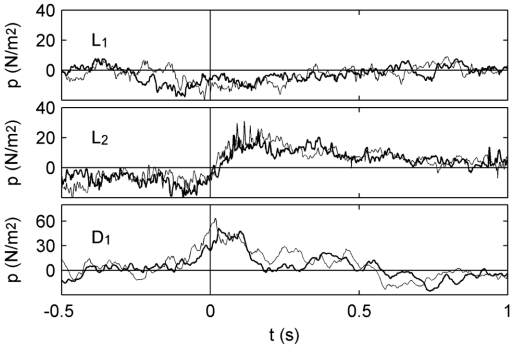


Figure 8. Conditionally averaged pressures near target stone during entrainment at $t = 0$ for sweep (thin line) and TWP (thick line) events. Top: lift sensor upstream of target stone (L_1, Fig. 1). Middle: sensor under target stone (L_2, Fig. 1). Bottom: drag sensor next to target stone (D_1, Fig. 1).

5.4 *Conditional averages*

Before inspecting the instantaneous flow fields, we will inspect the smoother conditionally averaged flow fields. If a certain structure appears we can check afterwards whether the structures present in these fields can be recognised in the instantaneous fields as well.

The conditionally averaged sequences of sweep events (Fig. 9) shows a large-scale ($\approx 4\,h$ in streamwise direction) area of increased longitudinal velocity. The largest part of this area has a downward directed vertical velocity, which indicates that it is indeed a sweep (this was not sure yet, as the sweeps were classified based on u only). In this large-scale sweep a small-scale patch of fluid moving upwards is embedded just upstream of the stone (after first movement), and a small-scale patch of downward moving fluid is embedded just downstream of the stone (before first movement).

The shape and size of the wedge-shape sweep is similar to that identified by Buffin-Bélanger et al. (2000) from measurements in a gravel bed river. The shape can be slightly different due to the fact that we plotted u' instead of $u'/\sigma(u)$. Their largest structures had a duration, T, of more than 5 s, which is about $TU/h \approx 5\,h$. So the size of the present structure is similar.

The conditionally averaged sequence of TWP events (Fig. 10) shows a similar flow structure as the sweep event. Only the large-scale patch with increased u' is smaller and has lower velocities. Conversely, the small-scale patches with up- and down-ward motions are more intense. The number of high λ values for this case around the position of the stone is both higher than for the sweep case and for other positions in the conditionally averaged TWP field. The increased number of high λ values (vortices) becomes more clear if we average the number of points of the lower plot at every longitudinal location, see Figure 11. The sweep events did not exhibit as clear an increase of high λ values around the place/time of movement.

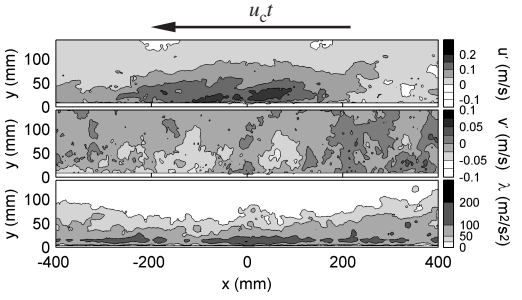


Figure 9. Spliced and conditionally averaged recording for sweep events. Stone moves at $x = 0$. Upper plot: u', middle plot: v', bottom plot: smoothed λ.

5.5 *Small-scale instantaneous flow structure*

We will now investigate the small-scale flow structures with intense v fluctuations around the first movement of the target stone in more detail. The large-scale increased value of $u$was indeed visible for most sweep events. However, inside this large-scale structure u is often locally decreased just before movement. Many TWP-events had a decreased flow velocity just above the stone as well. A decreased u corresponds to a clockwise-rotating span-wise vortex. Not all sweep events exhibited a small-scale structure.

As only vortices at a distance of about the stone size can create considerable forces, only part of the entire flow field was inspected. We saw that 12/14 of the TWP events and 9/13 of the sweep events had intense span-wise vortices near the stone (upstream of the stone on the image before movement and downstream of the stone on the image after movement). Around the point with high λ a rotational flow field is indeed visible if the proper convection velocity is subtracted.

One flow structure that can be discerned is a single vortex rotating in the clockwise direction. This can be responsible for lifting the stone, as it causes

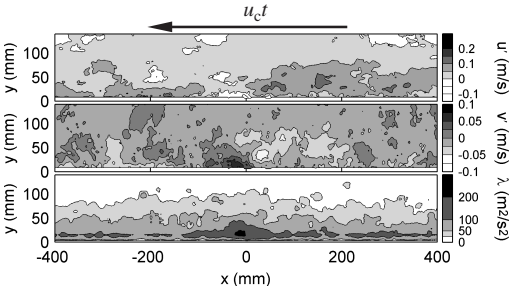


Figure 10. Spliced and conditionally averaged recording for TWP events. Stone moves at $x = 0$. Upper plot: u', middle plot: v', bottom plot: smoothed λ.

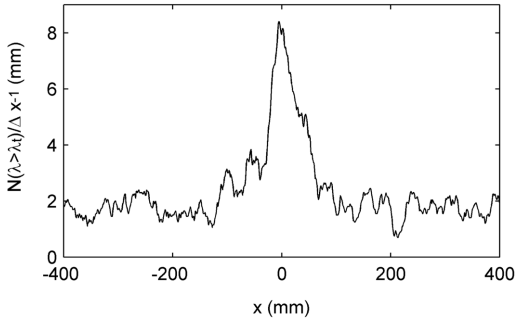


Figure 11. Average number of points where $\lambda > 200\,\mathrm{m^2 s^{-2}}$ during TWP events determined from spliced and conditionally averaged recording. The λ field was smoothed with a filter with a width of $20\Delta x$.

a low-pressure area under its core. This is sometimes accompanied by an ejection (an increased upward flow upstream of and below the vortex), which is an indication that it is part of a horseshoe/hairpin vortex: the induced velocity of the hairpin legs causes the ejection. The two structures together are called a hairpin vortex signature (HVS; Adrian, 2000a). In Figure 12 an example of such a vortex is depicted. Similar flow fields were found at 4/13 of the TWP events and 2/14 of the sweep events, the centre of the vortex typically 20–30 mm above the top of the stone. The value of λ has several maxima, but a "noisy" image can be expected in such a turbulent flow. Upstream of the large vortex six smaller ones are present, arranged as indicated by the dashed line.

Another small-scale flow structure that can be discerned is a hairpin vortex packet (HVP: a series of broad horseshoe/hairpin vortices, with the heads aligned at an angle with respect to the bed, that cover an area of almost uniform low-momentum (Adrian et al., 2000a). A clear HVP was visible at 5/13 of the sweep events and 3/13 of the TWP events. In the HVP the velocity is retarded and directed upward (relative to the ambient large-scale flow, not to the mean flow). An example is depicted on Figure 13. This area has a decreased velocity. The HVP is embedded in a large-scale sweep ($u' > 0, v' < 0$). The increased u follows after the ejection has (slightly) lifted the stone from the ground.

A few velocity fields without a clear cause of entrainment do show a small vortex of low intensity that rotates anti-clockwise. This flow structure could be very efficient in dislodging the stone, as it creates an increased quasi-steady drag and TWP-lift simultaneously.

5.6 *Large-scale spliced flow structure*

Not all large-scale spliced flow fields have been checked as of now. We only took the same events as presented above in detail.

The sweep event in Figure 14 (same as in Figure 13) resembles the conditional average of Figure 9 remarkably. The small-scale upward velocity at $x = 0$, which was seen to belong to a HVP. The length of the sweep is about $4\,h$, equal to the length in the conditional average. The gradients and the maximum value of u are larger in the instantaneous event, which is due to the fact that it was not smoothed by an averaging procedure.

The TWP event in Figure 15 (same as in Figure 12) does have the clear v fluctuation at the moment of entrainment. This is followed by a smaller sweep event. The two structures are not as clearly overlapping as with the sweep event. Over the length of the spliced plot there seem to be three HVPs, one of which includes the strong vortex that moves the stone at $x = 0$ (Fig. 13). These HVPs are indicated in Figure 15 by the inclined dashed lines. At these lines there is a transition from an ejection to a sweep region, and there are many vortices (increased λ) present. The angles of the lines are about 18°, 16° and 22°, which is on the high side of the range 10°–20° as provided by Tomkins (2001).

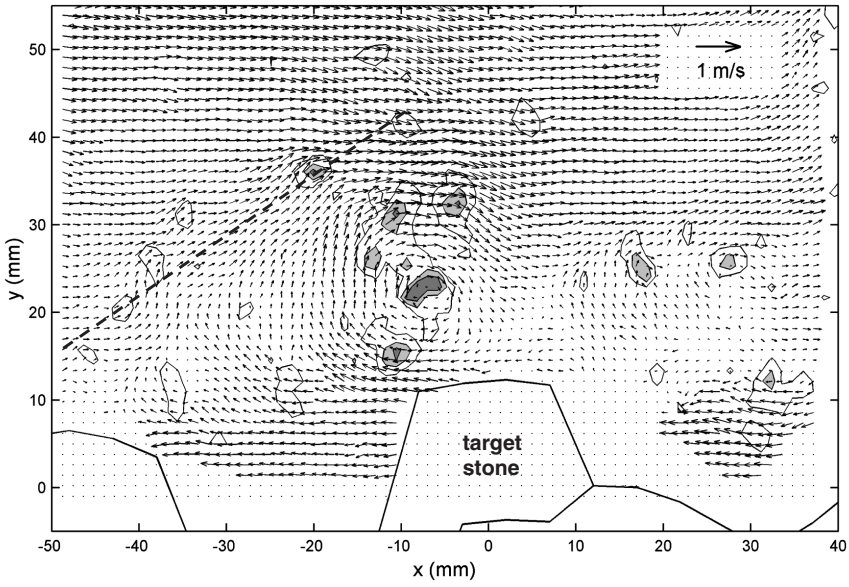


Figure 12. Detail of typical instantaneous flow field with single vortex just before movement of the target stone. u-0.65U. (event 5). Shading: $\lambda > 350/1400/2800\,\mathrm{m^2 s^{-2}}$.

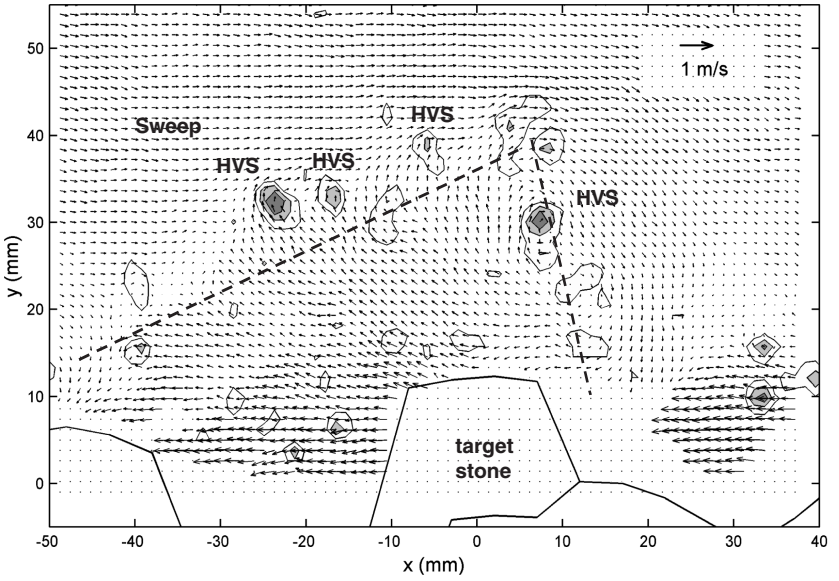


Figure 13. Detail of instantaneous field with small hairpin vortex packet inside a large-scale sweep just before movement of the target stone (event 28), u-1.0U. Shading: $\lambda > 350/1400/2800\,\mathrm{m^2 s^{-2}}$.

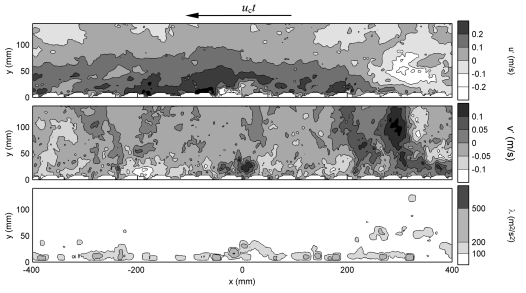


Figure 14. Large-scale spliced flow field of sweep event #28, see also Figure 13. The stone moves at $x = 0$. Top plot: u', middle plot: v', bottom plot: λ (smoothed).

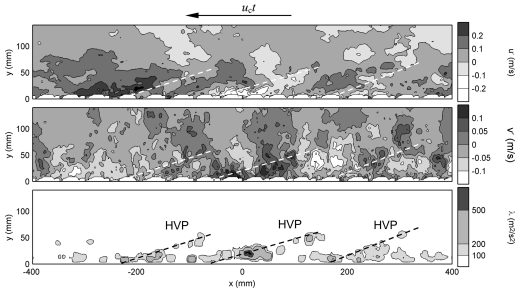


Figure 15. Large-scale spliced flow field of TWP event #5, see also Figure 12. The stone moves at $x = 0$. Top plot: u', middle plot: v', bottom plot: λ (smoothed).

6 DISCUSSION

The combination of a large-scale sweep and a small-scale ejection is optimal for moving material from a bed. A sweep causes an increased drag and lift force due to the enlarged longitudinal velocity. However, the corresponding negative v' decreases the lift. For the first movement of the stone, the lift force is often important as the vertical exposed area of the stone is still small and the torque created by the drag force is not very large yet. Therefore an increased lift force of short duration is necessary to dislodge the stone. Once it is slightly raised, the drag force alone is capable of moving the stone further over its point of rotation.

Adding a convected small-scale ejection to a sweep can result in an outward interaction ($u' > 0, v' > 0$), as depicted in Figure 16. The large-scale sweep has a longer duration than the ejection, so the resulting force vector fluctuates as indicated by the curved arrow. This makes that the force direction follows the angle of repose – which moves in consequence of the moving stone – such that the torque remains large for a longer time.

Which kind of structure will eventually move the stone depends on the shape and position of the stone. The shape of the target stone is typical for bed protection. It has sharp edges, and a normal shape factor. Its smallest axis points upwards. This means that the area on which a lift force can act is usually larger than the vertically exposed area that determines the drag force.

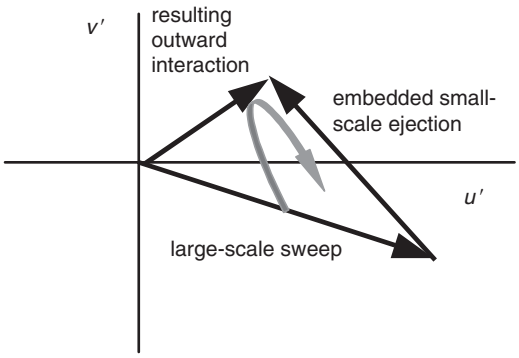


Figure 16. Illustration of a sweep and a convected ejection near a stone create an outward interaction.

When starting an experiment with low mobility transport, the transport is seen to gradually decrease, until it reaches a steady state, caused by the rearrangement of the top particles most susceptible to movement (water-working). The orientation of the top particles often becomes imbricated. The quasi-steady drag force is less effective on these stones. The present stone position is therefore probably illustrative for a water-worked bed. We are quite confident that the mechanisms as described in this paper are important for low-mobility transport on a water-worked bed. In addition, the lower the protrusion or the higher the angle of repose, the more important the TWP events become. Measurements with other stones and surrounding geometries have been done and will be used to check the universality of the present geometry.

In trial experiments we observed that a slight change in position drastically changed the stability of the stone. Moreover we saw that a stone often slightly changes its orientation in its pocket without moving (rocking). These two facts support the hypothesis that a stone moves very slowly to a more unstable position after which it will finally move. Furthermore, as two kinds of structure are necessary at the same time to move a stone, the chance that this occurs is smaller than the chance of the occurrence of one. Both mechanisms introduce a long time scale in the entrainment process, and can explain the measurements of Paintal (1971), who measured transport at Shields factors as low as 0.02.

7 CONCLUSIONS

The conclusions derived here apply to a single stone with its specific position, shape, size, and density. Still the results can be illustrative for the entrainment process of coarse bed material.

The stone was entrained during periods with increased longitudinal velocity. It often gets an initial lift (or rotation) by a fluctuating vertical velocity. This lets the exposed area and angle of repose be such that the stone is moved more easily by the increased u reaching the stone after the v' fluctuation.

The increased longitudinal velocity is part of a large-scale sweep motion (typically 4 h in streamwise and 2/3 h in the vertical direction), and causes quasi-steady forces on the stone. The fluctuating vertical velocity is often caused by single vortices or vortex packets close to the stone (typically 0.5–2 d) which cause turbulence wall pressure fluctuations.

The intensities of the two flow structures are negatively correlated. This can be explained by the fact that if one is more intense, the other can be less intense and vice versa. Strong sweep events without the increased small-scale vertical fluctuations were also observed. But nearly all events had at least a slightly increased longitudinal velocity. The TWP and sweep events can occur sequentially or with the small TWP structure nested inside the larger sweep.

ACKNOWLEDGEMENT

The research has been financially supported by the Road and Hydraulic Engineering Division of the Ministry of Transport, Public Works, and Water Management, (contract DWW-1700) and Delft Cluster, under the theme Coast and River.

REFERENCES

Adrian, R.J., Meinhart, C.D. and Tomkins, C.D. 2000a. Vortex organization in the outer region of the turbulent boundary layer. *J. of Fluid Mechanics* 422: 1–54.

Adrian, R.J., Christensen, K.T., Lui, Z.-C. 2000b. Analysis and interpretation of instantaneous turbulent velocity fields. *Exp. in Fluids* 29: 275–290.

Andrews, E.D. and Smith, J.D. 1992. Theoretical model for calculating marginal bedload transport rates of gravel. In Billi, P., Hey, C.R., Thorne, C.R. and Tacconi, P. (eds), 3rd *int. workshop on dynamics of gravel-bed rivers*, New York: John Wiley & Sons.

Buffin-Bélanger, T., Roy, A.G. and Kirkbride, A.D. 2000. On large-scale flow structures in a gravel-bed river. *Geomorphology* 32: 417–435.

Carling, P.A., Kelsey, A. and Glaister, M.S. 1992. Effect of Bed Roughness, Particle Shape and Orientation on Initial Motion Criteria. In Billi, P., Hey, C.R., Thorne, C.R. and Tacconi, P. (eds), 3rd *int. workshop on dynamics of gravel-bed rivers*, New York: John Wiley & Sons.

Hofland, B., Booij, R., Battjes, J.A. submitted, a. Measurement of fluctuating pressures on coarse bed material. *J. Hydraulic Eng.*

Hofland, B., Battjes, J.A., Booij, R., Fontijn, H.L. submitted, b. Turbulent wall pressures and rough bed stability, theory and measurements. *J. of Fluids and Structures*.

Nelson, J.M., Shreve, R.L., McLean, S.R., Drake, T.G. 1995. Role of near-bed turbulence structure in bed load transport and bed form mechanics. *Water Resources Research* 31(8): 2071–2086.

Nezu, I. and Nagakawa, H. 1993. *Turbulence in open-channel flow*s, Rotterdam: Balkema.

Paintal, A.S. 1971. Concept of critical shear stress in loose boundary open channels. *J. Hydraulic Research* 9(1): 9–113.

Tomkins, C.D. 2001. *The structure of turbulence over smooth and rough boundaries*. University of Illinois at Urbana Champaign, Urbana, Illinois. PhD thesis.

Wang, J., Dong, Z., Chen, C. and Xia, Z. 1993. The effects of bed roughness on the distribution of turbulent intensities in open-channel flow. *J. Hydraulic Research* 31(1): 89–98.

This page intentionally left blank

B. River hazards
B.1. Dam break and fast transients

This page intentionally left blank

River Flow 2004 – Greco, Carravetta & Della Morte (eds.)
© 2004 Taylor & Francis Group, London, ISBN 90 5809 658 0

Two dimensional modeling of rapidly varying flows by finite volume schemes

F. Aureli, A. Maranzoni & P. Mignosa
Dipartimento di Ingegneria Civile, dell'Ambiente, del Territorio & Architettura, Parma, Italy

ABSTRACT: The two dimensional shallow water equations are currently accepted as the mathematical basis for the study of rapidly varying wave propagation phenomena. In the present work, two different TVD second order numerical codes based on a finite volumes discretization of the mentioned system of conservation laws are implemented. The first belongs to the family of MUSCL-Hancock centred slope limiter schemes (SLIC); the second is based on the WAF (Weighted Average Flux) scheme where second order of accuracy is achieved by solving the conventional *piece-wise constant* Riemann problem and averaging it over space and time. Numerical solutions have been validated by comparison with the results of other numerical models for literature test cases and with experimental results obtained by the authors. The comparisons confirm that the models can be reliably used to deal with rapidly varying flows characterized by shocks and by transitions between subcritical and supercritical flow.

1 INTRODUCTION

The time dependent two dimensional shallow water equations are currently accepted as the mathematical basis for the study of rapidly varying wave propagation phenomena such as dam-break flows or levee breakings. For this reason, in the recent years, the efforts of many researchers in the field of hydroinformatics were devoted to the integration of the shallow water equations by means of different kinds of numerical techniques; among these the finite volume approach appear nowadays to be of dominant interest (Toro 1997, Toro 2001, LeVeque 2002).

In the following work, two different TVD second order numerical codes based on a finite volumes discretization of the mentioned system of conservation laws are developed.

The paper is organized as follows. In the next paragraph the 2D shallow water equations are recalled and the details of the two numerical models for solving the homogeneous part of the equations, together with the treatment of the source terms, are exposed. In the third paragraph the results obtained by means of the two numerical codes are compared with the solutions, close to exact ones, for some test cases widely considered as reference. In the fourth paragraph the capabilities of the numerical codes were tested by comparison with experimental results available in the recent literature.

2 NUMERICAL MODELS

The presented numerical schemes are based on a finite volume discretization of the two dimensional shallow water equations written in the integral form

$$\frac{d}{dt}\int_A \mathbf{U}\, dA + \int_C \mathbf{H}\cdot\mathbf{n}\, dC = \int_A \mathbf{S}\, dA \tag{1}$$

where A represents the area of the integration cell, C the cell boundary, $\mathbf{n}$ is the outward unit vector normal to C, while $\mathbf{H} = (\mathbf{F}, \mathbf{G})$ represents the tensor of fluxes. The corresponding conservation differential form of Equation 1 is:

$$\frac{\partial \mathbf{U}}{\partial t} + \frac{\partial \mathbf{F}}{\partial x} + \frac{\partial \mathbf{G}}{\partial y} = \mathbf{S}$$

$$\mathbf{U} = \begin{pmatrix} h \\ uh \\ vh \end{pmatrix}, \quad \mathbf{F} = \begin{pmatrix} uh \\ u^2 h + \frac{1}{2} g h^2 \\ uvh \end{pmatrix}, \tag{2}$$

$$\mathbf{G} = \begin{pmatrix} vh \\ uvh \\ v^2 h + \frac{1}{2} g h^2 \end{pmatrix}, \quad \mathbf{S} = \begin{pmatrix} 0 \\ gh\left(S_{0x} - S_{fx}\right) \\ gh\left(S_{0y} - S_{fy}\right) \end{pmatrix}$$

In Equations 1 and 2, t indicates time and g is the gravitational acceleration, while S_{0x}, S_{0y}, S_{fx}, and S_{fy} are the bottom and frictional slopes along the x and y axes, respectively.

The Manning equation is used to compute the friction terms:

$$S_{fx} = \frac{n^2 uh\sqrt{(uh)^2 + (vh)^2}}{h^{10/3}}; S_{fy} = \frac{n^2 vh\sqrt{(uh)^2 + (vh)^2}}{h^{10/3}} \tag{3}$$

in which n is the Manning roughness coefficient.

Both the numerical schemes are shock capturing second order extensions of the Godunov upwind method and are *unsplit* in the sense that the updating of the solution of the homogeneous part of Equation 1 is obtained in a single step, involving flux contributions from all intercell boundaries. In the special case in which the computational domain is composed of Cartesian cells of area $\Delta x \times \Delta y$, an explicit conservative finite volume scheme reads:

$$\overline{\mathbf{U}}_{i,j}^{n+1} = \mathbf{U}_{i,j}^{n} - \frac{\Delta t}{\Delta x}(\mathbf{f}_{i+\frac{1}{2},j} - \mathbf{f}_{i-\frac{1}{2},j}) - \frac{\Delta t}{\Delta y}(\mathbf{g}_{i,j+\frac{1}{2}} - \mathbf{g}_{i,j-\frac{1}{2}}) \tag{4}$$

In Equation 4 the x and y directions are designated by the subscripts i and j respectively, while the time level is indicated by the superscript n; $\mathbf{f}_{i\pm1/2,j}$ and $\mathbf{g}_{i,j\pm1/2}$ represent the numerical fluxes in the x and y directions respectively.

To avoid unphysical or spurious oscillations in the vicinity of high gradients of the solution a TVD constraint was enforced on the schemes by means of different well-known limiter functions.

2.1 *SLIC numerical model*

The scheme is a second order extension of the first-order centred FORCE scheme and results from replacing the Godunov flux by the Force flux in the MUSCL-Hancock scheme (Toro 1997, Toro 2001). It is called SLIC as an acronym for Centred Slope LImiter; it computes the intercell numerical flux in the following steps. The first step requires the definition of a set of boundary extrapolated variables that for the x co-ordinate can be expressed as (Hirsch 1990):

$$\mathbf{U}_{i+\frac{1}{2},j}^{L} = \mathbf{U}_{i,j}^{n} + \frac{1}{4}(1-k)\mathbf{\Phi}_{i-\frac{1}{2},j}^{+}\left(\mathbf{U}_{i,j}^{n} - \mathbf{U}_{i-1,j}^{n}\right) + \\ + \frac{1}{4}(1+k)\mathbf{\Phi}_{i+\frac{1}{2},j}^{-}\left(\mathbf{U}_{i+1,j}^{n} - \mathbf{U}_{i,j}^{n}\right) \tag{5}$$

and

$$\mathbf{U}_{i+\frac{1}{2},j}^{R} = \mathbf{U}_{i+1,j}^{n} - \frac{1}{4}(1+k)\mathbf{\Phi}_{i+\frac{1}{2},j}^{+}\left(\mathbf{U}_{i+1,j}^{n} - \mathbf{U}_{i,j}^{n}\right) + \\ - \frac{1}{4}(1-k)\mathbf{\Phi}_{i+\frac{3}{2},j}^{-}\left(\mathbf{U}_{i+2,j}^{n} - \mathbf{U}_{i+1,j}^{n}\right) \tag{6}$$

where the superscripts L and R refer to left and right extrapolated variables. In Equations 5 and 6 the parameter k represents the amount of *upwinding* that is maximum for $k = -1$: in this case all the information coming from one of the sides of the considered cell is discarded, being the extrapolation applied on the other side only. Always in Equations 5 $\mathbf{\Phi}_{i-1/2,j}^{+}$ and $\mathbf{\Phi}_{i+1/2,j}^{-}$ represent diagonal *limiter* matrices (3×3) that enforce a TVD constraint in the data reconstruction step in order to limit the slopes of the extrapolating function (Toro 1997, Toro 2001). The kind of bilinear extrapolation performed leads to a second order of accuracy in space. In order to achieve the same accuracy in time, once the boundary extrapolated variables are defined, a new set of boundary variables is obtained evolving on a half of the current Δt the relations 5 and 6 in the following way (Toro 2001):

$$\overline{\mathbf{U}}_{i+\frac{1}{2},j}^{L} = \mathbf{U}_{i+\frac{1}{2},j}^{L} - \frac{\Delta t}{2\Delta x}\left[\mathbf{F}\left(\mathbf{U}_{i+\frac{1}{2},j}^{L}\right) - \mathbf{F}\left(\mathbf{U}_{i-\frac{1}{2},j}^{R}\right)\right] + \\ - \frac{\Delta t}{2\Delta y}\left[\mathbf{G}\left(\mathbf{U}_{ij+\frac{1}{2}}^{L}\right) - \mathbf{G}\left(\mathbf{U}_{ij-\frac{1}{2}}^{R}\right)\right] \tag{7}$$

$$\overline{\mathbf{U}}_{i+\frac{1}{2},j}^{R} = \mathbf{U}_{i+\frac{1}{2},j}^{R} - \frac{\Delta t}{2\Delta x}\left[\mathbf{F}\left(\mathbf{U}_{i+\frac{3}{2},j}^{L}\right) - \mathbf{F}\left(\mathbf{U}_{i+\frac{1}{2},j}^{R}\right)\right] + \\ - \frac{\Delta t}{2\Delta y}\left[\mathbf{G}\left(\mathbf{U}_{i+1,j+\frac{1}{2}}^{L}\right) - \mathbf{G}\left(\mathbf{U}_{i+1,j-\frac{1}{2}}^{R}\right)\right] \tag{8}$$

The flux is then given by:

$$\mathbf{f}_{i+\frac{1}{2},j}^{FORCE} = \mathbf{f}_{i+\frac{1}{2},j}(\overline{\mathbf{U}}_{i+\frac{1}{2},j}^{R}, \overline{\mathbf{U}}_{i+\frac{1}{2},j}^{L}) = \\ = \frac{1}{2}\left[\mathbf{f}_{i+\frac{1}{2},j}^{RI}(\overline{\mathbf{U}}_{i+\frac{1}{2},j}^{R}, \overline{\mathbf{U}}_{i+\frac{1}{2},j}^{L}) + \mathbf{f}_{i+\frac{1}{2},j}^{LF}(\overline{\mathbf{U}}_{i+\frac{1}{2},j}^{R}, \overline{\mathbf{U}}_{i+\frac{1}{2},j}^{L})\right] \tag{9}$$

where the superscripts *LF* and *RI* refer to *Lax-Friedrichs* and *Richtmyer* intercell numerical fluxes respectively (Richtmyer & Morton 1967, Hirsch 1990):

$$\mathbf{f}_{i+\frac{1}{2},j}^{LF} = \mathbf{f}_{i+\frac{1}{2},j}^{LF}\left(\overline{\mathbf{U}}_{i+\frac{1}{2},j}^{L}, \overline{\mathbf{U}}_{i+\frac{1}{2},j}^{R}\right) = \\ = \frac{1}{2}\left[\mathbf{F}\left(\overline{\mathbf{U}}_{i+\frac{1}{2},j}^{L}\right) + \mathbf{F}\left(\overline{\mathbf{U}}_{i+\frac{1}{2},j}^{R}\right)\right] + \frac{1}{4}\frac{\Delta x}{\Delta t}\left(\overline{\mathbf{U}}_{i+\frac{1}{2},j}^{L} - \overline{\mathbf{U}}_{i+\frac{1}{2},j}^{R}\right) \tag{10}$$

$$\mathbf{f}_{i+\frac{1}{2},j}^{RI} = \mathbf{f}_{i+\frac{1}{2},j}^{RI}\left(\overline{\mathbf{U}}_{i+\frac{1}{2},j}^{L}, \overline{\mathbf{U}}_{i+\frac{1}{2},j}^{R}\right) = \mathbf{F}\left(\widetilde{\mathbf{U}}_{i+\frac{1}{2},j}\right)$$

$$\widetilde{\mathbf{U}}_{i+\frac{1}{2},j} = \frac{1}{2}\left(\overline{\mathbf{U}}^{L}_{i+\frac{1}{2},j} + \overline{\mathbf{U}}^{R}_{i+\frac{1}{2},j}\right) + \\ + \frac{1}{2}\frac{\Delta t}{\Delta x}\left[\mathbf{F}\left(\overline{\mathbf{U}}^{L}_{i+\frac{1}{2},j}\right) - \mathbf{F}\left(\overline{\mathbf{U}}^{R}_{i+\frac{1}{2},j}\right)\right] \tag{11}$$

2.2 *WAF numerical model*

The second code developed is based on the WAF (Weighted Average Flux) scheme (Toro 1992, Toro 1997). Its key feature is that the second order of accuracy can be achieved by solving the conventional *piece-wise constant* Riemann problem and averaging it over space and time.

Considering the x-split homogeneous shallow water equations:

$$\frac{\partial \mathbf{U}}{\partial t} + \frac{\partial \mathbf{F}}{\partial x} = 0 \quad \text{where}$$

$$\mathbf{U} = \begin{pmatrix} h \\ uh \\ \varphi h \end{pmatrix}, \qquad \mathbf{F} = \begin{pmatrix} uh \\ u^2 h + \frac{1}{2} g h^2 \\ \varphi uh \end{pmatrix}, \tag{10}$$

it can be observed that the third equation represents a conservation law for φh where φ plays the role of a passive scalar simply advected by the x velocity u. This passive scalar can for example represent the modulus of the velocity vector $\boldsymbol{v}$ whose direction is trivial, being the co-ordinate direction y. By means of the Strang splitting (LeVeque 2002) it is then possible to extend the 1D WAF scheme to two or more space dimensions applying in turn the one-dimensional difference operator to each of the co-ordinate directions. For the general y co-ordinate j the WAF flux is defined via the *integral average*:

$$\mathbf{f}^{WAF}_{i+\frac{1}{2}} = \frac{1}{t_2 - t_1} \cdot \frac{1}{x_2 - x_1} \int_{t_1}^{t_2} \int_{x_1}^{x_2} \mathbf{F}\left(\mathbf{U}^{*}(x,t)\right) \cdot dx \cdot dt \,, \tag{11}$$

where $\mathbf{U}^{*}(x,t)$ is the solution of the Riemann problem with *piece-wise constant* data $\mathbf{U}_i$, $\mathbf{U}_{i+1}$.

Choosing $x_1 = -\Delta x/2$, $x_2 = \Delta x/2$, $t_1 = 0$, $t_2 = \Delta t$ and approximating the time integration by the mid-point rule it's possible to obtain:

$$\mathbf{f}^{WAF}_{i+\frac{1}{2}} = \frac{1}{\Delta x} \int_{-\frac{\Delta x}{2}}^{\frac{\Delta x}{2}} \mathbf{F}\left(\mathbf{U}_{i+\frac{1}{2}}\left(x, \Delta t/2\right)\right) \cdot dx \tag{12}$$

that becomes the summation:

$$\mathbf{f}^{WAF}_{i+\frac{1}{2}} = \sum_{k=1}^{N+1} w_k \, \mathbf{F}^{(k)}_{i+\frac{1}{2}} \tag{13}$$

where N is the number of conservation laws (in this case $N = 3$), w_k are the weights given by:

$$w_k = \tfrac{1}{2}\left(c_k - c_{k-1}\right), \quad c_0 = -1, \quad c_{N+1} = 1 \tag{14}$$

where $c_k = \Delta t \cdot S_k / \Delta x$ and S_k are respectively the Courant number and the speed for wave k.

To compute numerical solutions by Godunov-type methods, as the one adopted, it is possible to use exact or approximate Riemann solvers. For the shallow water equations in particular, the approximate ones proved to be very robust and simple to compute. The Riemann solver adopted is the approximate HLLC solver (Toro 2001), that is based on a modification of the basic HLL scheme (Harten et al. 1983) to account for the influence of intermediate waves. The HLL solver takes in fact into account a simple wave structure in which only the smallest and largest signal velocities are considered. Intermediate waves, such as shear waves and contact discontinuities that arise when extra equations are added to the basic 1D shallow water equations like in Equations 10, are ignored in this approach. In the HLLC approach the complete three wave structure is considered. It is useful to observe that the third flux component in (10), $\mathbf{f}^{(3)}_{i+1/2}$ can be expressed as the product of the first flux component $\mathbf{f}^{(1)}_{i+1/2}$ and the variable φ the latter representing the y velocity v. Then retaining the HLL fluxes for the first two components of the flux and remembering that the exact solution of the Riemann problem in terms of the advected velocity v is:

$$v = \begin{cases} v_i & \text{if } s^* \geq 0 \\ v_{i+1} & \text{if } s^* < 0 \end{cases} \tag{15}$$

s^* being the speed wave in the star region, it is possible to express the numerical flux as:

$$\mathbf{f}^{(m)}_{i+\frac{1}{2}} = \frac{S_{i+1} \cdot \mathbf{F}^{(m)}_{i} - S_i \cdot \mathbf{F}^{(m)}_{i+1} + S_{i+1} \cdot S_i \cdot \left(\mathbf{U}^{(m)}_{i+1} - \mathbf{U}^{(m)}_{i}\right)}{S_{i+1} - S_i} \tag{16}$$

where $m = 1, 2$ is the vector component.

The third component of the numerical flux is then obtained as:

$$\mathbf{f}^{(3)}_{i+\frac{1}{2}} = \begin{cases} \mathbf{f}^{(1)}_{i+\frac{1}{2}} \, v_i & \text{if } s^* \geq 0 \\ \mathbf{f}^{(1)}_{i+\frac{1}{2}} \, v_{i+1} & \text{if } s^* < 0 \end{cases}. \tag{17}$$

Proper estimates of all the three wave speed S_i, s^* and S_{i+1} can be obtained by one of the several methods proposed in literature (Toro 1997, Toro 2001).

2.3 *Treatment of source terms*

In both the numerical schemes the treatment of the source term **S(U)** is accomplished by means of a time-operator splitting technique (Toro 1992). The solution procedure is split into the solution of two sub-problems. First the homogeneous problem of Equation 4 with initial data $\mathbf{U}^n$ is solved to obtain a provisional solution $\bar{\mathbf{U}}^{n+1}$ for the next time level, then the solution $\mathbf{U}^{n+1}$ of the system of ordinary differential equations:

$$\frac{d\mathbf{U}}{dt} = \mathbf{S}(\mathbf{U}) = \mathbf{S}_0(\mathbf{U}) + \mathbf{S}_f(\mathbf{U}), \tag{13}$$

with initial data $\bar{\mathbf{U}}^{n+1}$, is obtained separately for the slope (Equation 14) and friction effects (Equation 15), by means of an implicit trapezoidal method of second order of accuracy:

$$\begin{aligned} \mathbf{U}^*_{i,j} &= \bar{\mathbf{U}}^{n+1}_{i,j} + \frac{\Delta t}{2}\left[\mathbf{S}_0(\bar{\mathbf{U}}^{n+1}_{i,j}) + \mathbf{S}_0(\mathbf{U}^*_{i,j})\right] \\ \mathbf{U}^*_{i,j} &= \bar{\mathbf{U}}^{n+1}_{i,j} + \Delta t\ \mathbf{S}_0(\bar{\mathbf{U}}^{n+1}_{i,j}) \end{aligned} \tag{14}$$

$$\begin{aligned} \mathbf{U}^{n+1}_{i,j} &= \mathbf{U}^*_{i,j} + \frac{\Delta t}{2}\left[\mathbf{S}_f(\mathbf{U}^*_{i,j}) + \mathbf{S}_f(\mathbf{U}^{n+1}_{i,j})\right] \\ \mathbf{U}^{n+1}_{i,j} &= \mathbf{U}^*_{i,j} + \Delta t\left[\mathbf{I} - \frac{\Delta t}{2}\mathbf{Q}_f(\mathbf{U}^*_{i,j})\right]^{-1}\mathbf{S}_f(\mathbf{U}^*_{i,j}) \end{aligned} \tag{15}$$

where **I** is the Identity matrix (3×3) and $\mathbf{Q}_f$ is the Jacobian matrix of $\mathbf{S}_f$.

3 REFERENCE TEST CASES

In this section the results obtained by means of the two numerical models previously described are compared with reference solutions, close to the exact ones, for some test cases widely considered in the recent literature.

3.1 *Circular dam break problem*

This problem was tested by many Authors in the last decade (Glaister 1991, Alcrudo & Garcia Navarro 1993, Liska & Wendroff 1999, Toro 2001, LeVeque 2002).

A cylindrical water column is placed in the centre of a wet, horizontal and frictionless domain. At $t = 0$ the water column initially at rest is suddenly released and the time evolution of depth and velocity fields is calculated.

Following the example reported by Liska & Wendroff a 10 m high water column with radius of 11 m is placed in the centre of a 50×50 m domain wetted with 1 m of water.

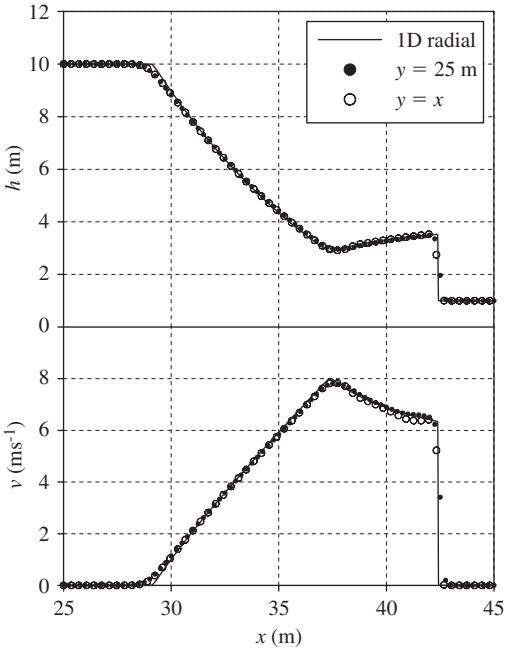


Figure 1. Circular Dam-Break problem. Axial and diagonal results at $t = 0.69$ s obtained by the 2D SLIC model (201×201 cells). Radial solution obtained by the WAF model (2000 cells).

Since the problem has cylindrical symmetry along the radial direction r, the results of the 2D numerical calculations can be compared with the solution obtained by solving the following one dimensional inhomogeneous system (Toro 2001):

$$\frac{\partial \mathbf{U}}{\partial t} + \frac{\partial \mathbf{F}(\mathbf{U})}{\partial r} = \mathbf{S}(\mathbf{U}) \tag{16}$$

with

$$\mathbf{U} = \begin{bmatrix} h \\ uh \end{bmatrix}, \mathbf{F}(\mathbf{U}) = \begin{bmatrix} uh \\ u^2h + \frac{1}{2}gh^2 \end{bmatrix}, \mathbf{S}(\mathbf{U}) = -\frac{1}{r}\begin{bmatrix} uh \\ u^2h \end{bmatrix} \tag{17}$$

where $u = u(r, t)$ represents the radial velocity.

In Figure 1 axial ($y = 25$ m) and diagonal ($y = x$) plots of water depth and velocity at $t = 0.69$ s (the same presented by Liska & Wendroff) calculated by the SLIC model are shown. Figure 2 reports the same plots obtained with the WAF model.

The domain was halved and cut at $x = 45$ m in order to discriminate all the computational points. In both figures the 2D numerical solution is compared with the radial solution obtained by solving Equation 16

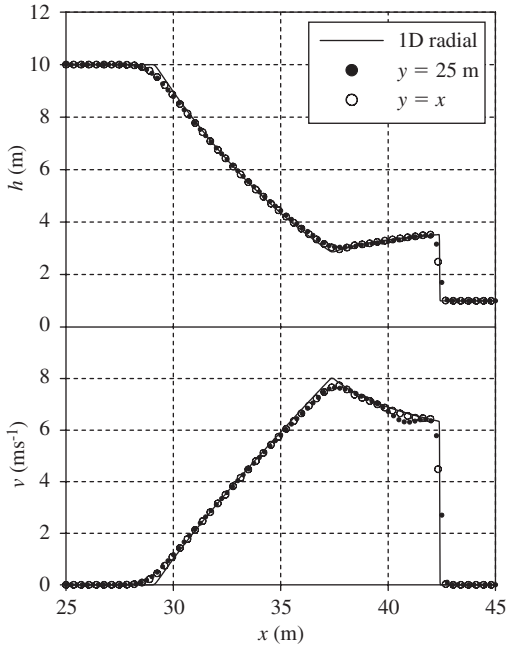


Figure 2. Circular Dam-Break problem. Axial and diagonal results at $t = 0.69$ s obtained by the 2D WAF model (201×201 cells). Radial solution obtained by the WAF model (2000 cells).

with the WAF model (Toro 2001) and with a very fine mesh of 2000 cells on the domain $25 \leq r \leq 50$ m. This solution can be considered a good approximation of the exact one.

The figures demonstrate that the radial symmetry of the water depth is very well preserved by both the numerical schemes. Hardly appreciable asymmetries can be observed in the velocity field, just behind the shock. The shock front is captured in two spatial intervals and the overall results fit well the 1D radial reference solution.

3.2 *Shock focusing problem*

More delicate is the shock focusing problem. This rotational symmetric test, solved on an orthogonal Cartesian mesh, causes a lot of difficulties for any kind of numerical method and many 2D models are not able to resolve it well (Billett 1994, Morel et al. 1996, Liska & Wendroff 1999).

In the centre of a square dimensionless domain $(-1.5, 1.5) \times (-1.5, 1.5)$ is placed an idealized circular wall of radius 0.35. The height is 0.1 inside the wall and 1 outside. Initially the system is at rest. At $t = 0$ the wall is removed, giving origin to a circular

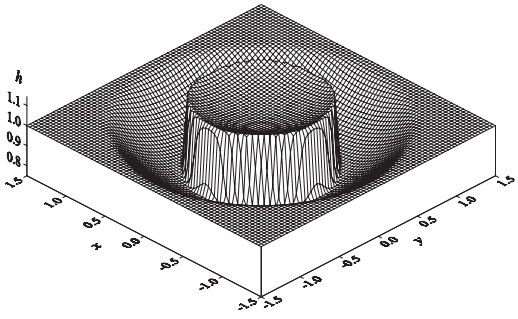


Figure 3. Shock focusing problem. 3D plot of water depth at $t = 1.00$ obtained with the WAF model (161×161 cells).

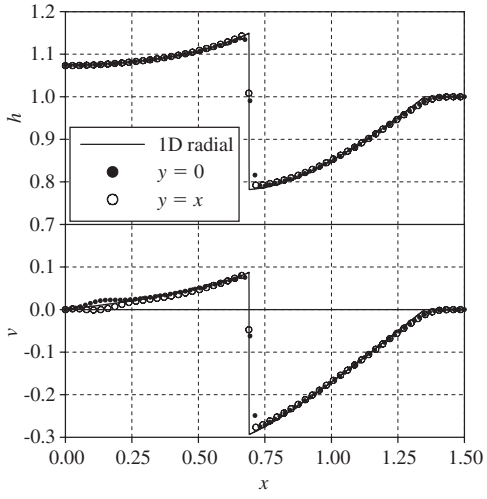


Figure 4. Shock-focusing problem. Axial and diagonal results at $t = 1$ obtained by the 2D SLIC model (161×161 cells). Reference radial solution obtained by the WAF model (5000 cells).

shock that starts to move inward, while a rarefaction wave propagates towards the domain boundaries. The shock progressively concentrates and after passing through the singularity at (0, 0) expands outwards. In the calculations a mesh with 161×161 points and a dimensionless acceleration $g = 1$ were adopted as in Liska & Wendroff (1999).

In Figure 3 the 3D plot of water depths at $t = 1.00$ obtained by the WAF model is shown. At this time the shock has already passed through the focusing point (0, 0) and is expanding outwards.

In Figure 4 axial ($y = 0$) and diagonal ($y = x$) plots of water depth and velocity at $t = 1.00$ calculated by the SLIC model are shown. A Courant number $Cr = 0.5$ and the *van-Leer limiter* were adopted in the

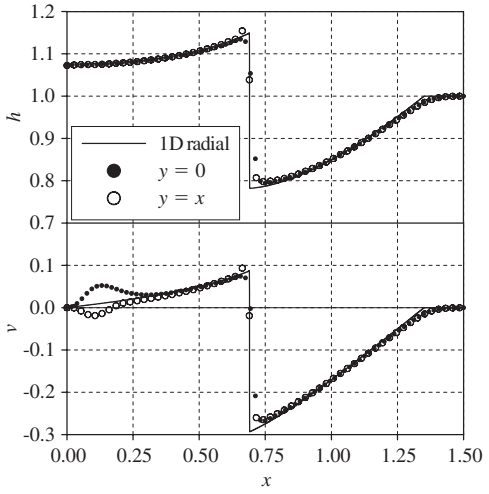


Figure 5. Shock-focusing problem. Axial and diagonal results at $t = 1$ obtained by the 2D WAF model (161×161 cells). Reference radial solution obtained by the WAF model (5000 cells).

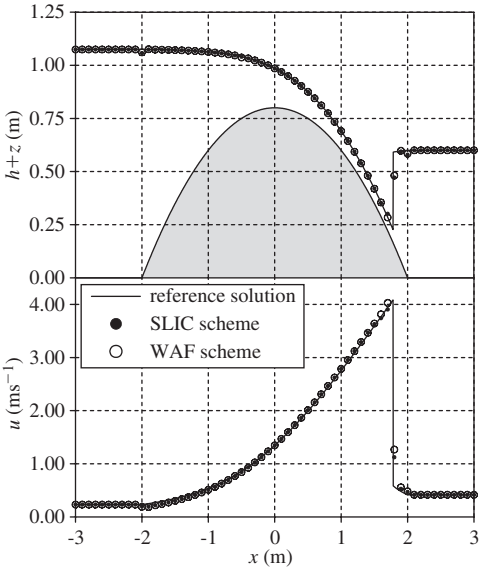


Figure 6. 1D steady flow on a steep bump. Numerical results obtained by the 2D SLIC and WAF models. Reference solution obtained by the application of Bernoulli energy equation and momentum principle through the jump.

calculations. Figure 5 reports the same plots obtained with the WAF model ($Cr = 0.7$ and *van-Leer limiter*). The domain was halved in order to be able to discriminate all the computational points. Note that across the shock there is a change in the sign of the velocity vectors.

Once again both the 2D numerical solutions are compared with the radial solution obtained by solving Equation 16 with the WAF model and with a very fine mesh of 5000 cells on the domain $0 \le r \le 1.5$. This solution can be regarded as the reference one.

From the figures it can be deduced that circular symmetry is preserved very well for the water depth, since the axial and diagonal solutions are almost overlapping. For the total velocity, on the other hand, a large difference between axial and diagonal results can be observed. The difference is more evident in the WAF solution but is still present in the SLIC one. As pointed out by Morel et al. (1996) this loss of symmetry is due to errors produced at the focusing point, since until the shock reaches this point the symmetry is very well preserved. The same authors argued that this behaviour is due to the *limiter* and suggested a strategy to reduce this asymmetry.

3.3 *1D steady flow on a steep bump*

This test is similar to the one reported in Caleffi et al. (2003) except for the height of the bump which was increased from 0.2 to 0.8 m as in Liska & Wendroff (1998). The aim is to verify the correctness of the bottom slope source term treatment in presence of critical transitions (from subcritical to supercritical and vice versa) together with the shock capturing properties of the two numerical codes.

In a $(-10, +10) \times 1$ m rectangular horizontal and frictionless channel a bump in the bottom elevation z_b is described by the following profile:

$$z_b(x, y) = \begin{cases} 0.8 - 0.2 \cdot x^2 & -2 \le x \le 2 \text{ m} \\ 0 & \text{otherwise} \end{cases}. \qquad (18)$$

The domain is discretized with square cells of 0.1 m. At the upstream boundary a constant discharge of 0.250 m^3/s was imposed, whereas downstream a constant water level of 0.60 m was set. These conditions cause a hydraulic jump to locate just upstream the end of the bump. Initial conditions are not important, since they influence only the transition towards the steady state, which was considered reached once the fifth decimal value of the conserved variables (h, uh) no longer changed in time (the third variable vh is always zero). The reference solution is obtained by solving the cubic algebraic equation derived by the Bernoulli theorem with a spatial discretization $\Delta x = 0.005$ m. The jump was located with the same degree of accuracy by the application of the momentum principle.

Figure 6 shows the numerical solutions obtained by means of the SLIC and WAF models, together with the reference solution in the $-3 \le x \le 3$ m sub-domain (outside the values are rigorously constant).

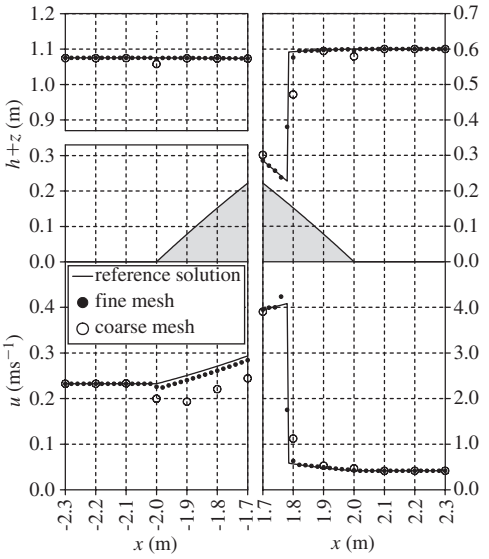


Figure 7. 1D steady flow on a steep bump. Details of water surface elevation and velocity obtained by the SLIC model with two mesh sizes together with the reference solution.

The results obtained by the numerical models are similar, as the same is the treatment of the slope source term in both the codes. Since in this test the source term plays a very important role, the other differences between the two models are masked.

In both the numerical codes, the jump is correctly located and caught in only two spatial intervals. Water surface elevations fit fairly well the reference solution, except for the two grid points located at the beginning and end of the bump, where the profile of the bottom is not smooth. A small dip in water elevation occurs due to the splitting treatment of the source terms that doesn't satisfy the C-property (Bermudez & Vazquez 1994).

The overall velocity profiles computed by the two models compare very well with the reference solution except for some grid points past the beginning of the bump, where the numerical velocity is slightly underestimated.

These differences between computed results and reference solution are strongly highlighted by the height of the bump and by the relatively coarse mesh, and decrease significantly with the mesh size. Figure 7 shows details of the results obtained adopting the SLIC model on a refined mesh ($\Delta x = 0.02$ m), together with those obtained on the coarse mesh ($\Delta x = 0.10$ m) and the reference solution. It can be observed that the dip in the water elevation was reduced to inappreciable size and also the velocity at the beginning of the bump fits better the reference solution.

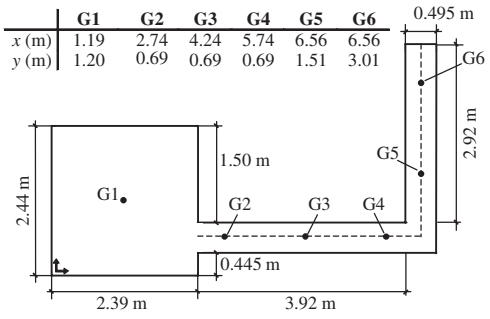


Figure 8. Experimental set-up and gauges location for the CADAM test case on a 90° sharp bend (from Soares Frazão et al. 2001)

4 LITERATURE TEST CASES

At the aim to test the capabilities of the a.m. numerical codes in presence of solid walls, initially dry bottoms and truly 2D flows, their results are compared in this section with two literature experimental tests on rapidly varying flows induced by the removal of a sluice gate.

4.1 *CADAM test case on a 90° sharp bend*

This experimental test was realized in the framework of the CADAM European project in the laboratory of the Civil Engineering Department of the Université catholique de Louvain, Belgium (Soares Frazão & Zech 1999, Soares Frazão et al. 2000, Soares Frazão et al. 2001).

Figure 8 shows the experimental set-up and the location of the six gauges. The bottom of the channel is horizontal. The downstream end of the channel is open. Initially water is at rest in the reservoir with a level of 0.20 m above the bottom of the channel that is initially dry. At $t = 0$ the sudden pull up of the gate separating the reservoir from the channel simulates the dam-break. After about 3 seconds the wetting front reaches the bend, then the reflection at the wall gives origin to a bore which travels upstream, back to the reservoir. Downstream the bend, multiple reflections against the walls occur.

The Manning friction coefficients were estimated by the a.m. authors as $n_b = 0.0095\, s \cdot \mathrm{m}^{-1/3}$ for the bottom and $n_w = 0.0195\, s \cdot \mathrm{m}^{-1/3}$ for the walls.

In the numerical description of the channel the end section was slightly modified in order to reproduce the free fall. At this aim a short high slope slide was introduced, at the end of which a far-field condition was set. At the lateral boundaries reflective (free-slip) conditions were imposed. The latest condition does not consider at all the influence of the walls. In order to take into account this effect, although approximately,

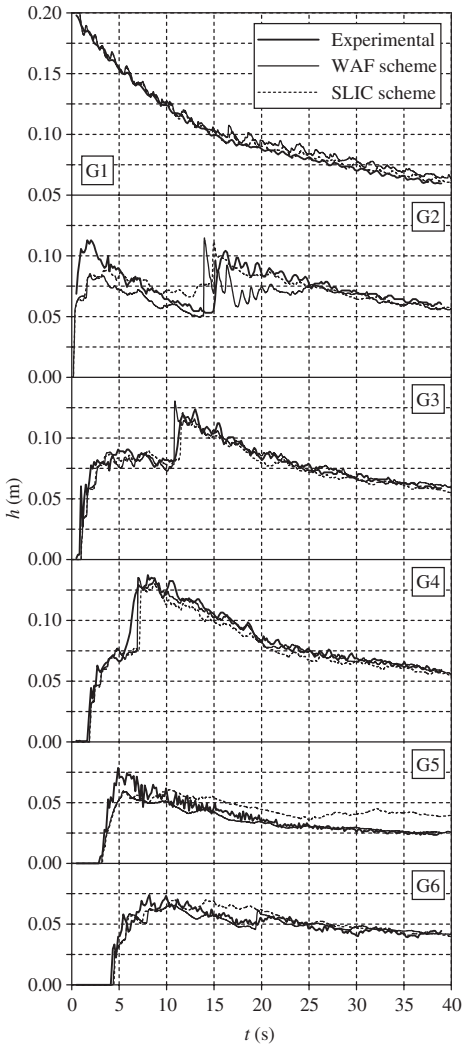


Figure 9. CADAM test case on a 90° sharp bend. Experimental and numerical water depth time series at the gauges locations.

a numerical Manning roughness coefficient was evaluated by means of the formula:

$$\overline{n} = \left(\frac{2 \cdot h \cdot n_w^{3/2} + B \cdot n_b^{3/2}}{B} \right)^{2/3} \tag{19}$$

where B is the channel width. Equation 19 can be derived from the Einstein's formula by suppressing the wall contribution in the wetted perimeter at the denominator.

Figure 9 shows the water level time series at the six gauges locations. On the whole the comparison

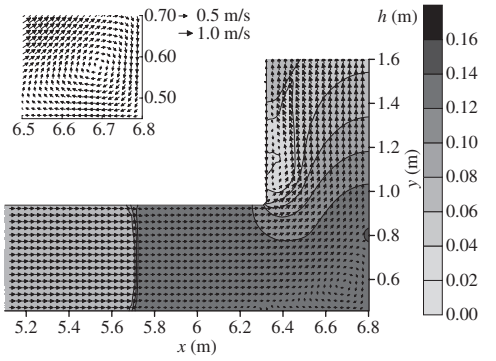


Figure 10. CADAM test case on a 90° sharp bend. Numerical (WAF model) water depth flow field with velocity vectors at $t = 7$ s.

between numerical and experimental results is satisfactory, even if at gauges G2 and G5 some significant differences occur between the two models and with respect to the experimental data. The wetting front and the main shock wave are located in time very well. On the other hand both the models are not able to correctly catch the secondary oscillations in the experimental data, due to the multiple reflections at the boundaries.

Figure 10 shows water depth and velocity fields in the bend at $t = 7$ s computed with the WAF model. The velocity field seems to fit well the measured one, reported in Soares Frazão et al. (2001); the WAF model is also able to outline the re-circulation region observed experimentally at the outer corner of the bend, as highlighted in Figure 10.

The SLIC model is not able to reproduce this behaviour.

4.2 *Parma experimental tests on a lateral breach*

This experimental test was realized in the laboratory of the Civil Engineering Department of the University of Parma, Italy (Aureli & Mignosa 2002).

In a 10 m long laboratory flume (Figure 11) in which is flowing a constant discharge $Q = 0.01$ m^3/s a lateral breach is suddenly opened. This causes the sudden inundation of a planar surface, initially dry.

The perturbations rapidly propagate in the flume towards the upstream and downstream boundaries. After about 2 seconds the water in the plane begins to reach the contour, falling into the gutter. At $t = 5$ s the water has wetted all the upstream and longitudinal boundary of the plane but not the farther downstream one. About at $t = 60$ s the flow is almost steady.

Measurements of water level and velocity histories were accomplished at various places around the breach site by means of ultrasonic distance and velocity meters (for more details see Aureli & Mignosa 2002).

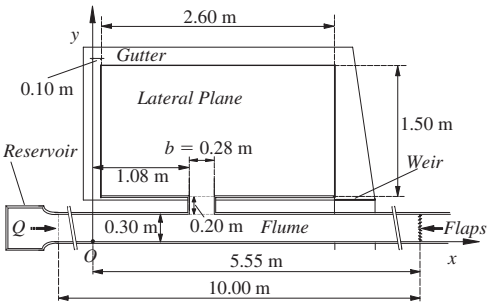


Figure 11. Parma experimental tests on a lateral breach. Picture and dimensions of the experimental set-up.

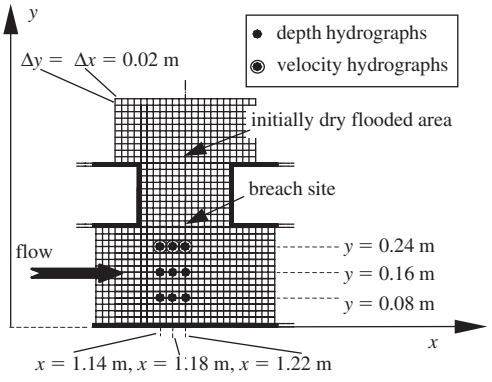


Figure 12. Parma experimental tests on a lateral breach. Particular of the experimental set-up in proximity of the breach zone with reference grid and measurement sites.

In Figure 12 a sketch of the zone of the breach with the reference grid and measurement locations is presented.

The Manning friction coefficient in the flume, experimentally estimated in uniform conditions with different discharge values, was almost the same both for the bottom and the walls and equal to $0.01\ \mathrm{s \cdot m^{-1/3}}$. Nevertheless, to take into account the walls friction, Equation 19 was applied again in the calculations.

The simulation was performed by means of the WAF model with mesh size $\Delta x = \Delta y = 0.02$ m until the final steady-state ($t = 60$ s). A far-field boundary condition was set at the downstream end of the channel.

Numerical and experimental water level time series at some significant locations are reported in Figure 13. In the figure a stretching of the hydrographs was made for the first – and more significant – five seconds.

At $x = 1.14$ m the three numerical hydrographs are close to the experimental ones. At $x = 1.18$ m and $x = 1.22$ m the overall behavior is still fairly good, but much more discrepancies between numerical and experimental values are now present. This is essentially due to the strong surface curvatures

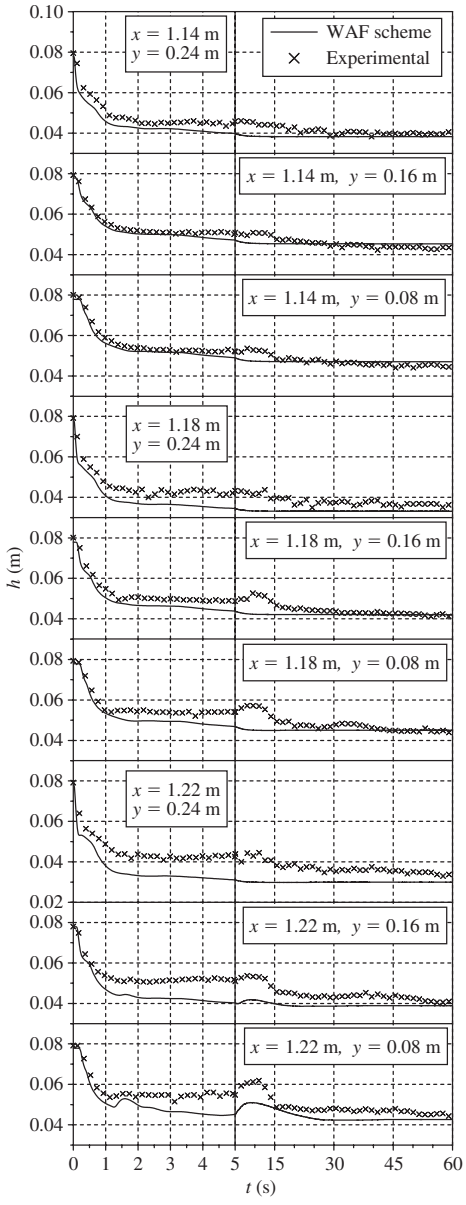


Figure 13. Experimental and numerical results for Parma test cases on a lateral breach.

which make difficult to obtain accurate experimental measurements (the divergence of the ultrasonic beam is about 3.5°) and do not allow to properly interpret the phenomenon – which is essentially 3D – with a 2D depth-averaged numerical model.

In Figure 14 the comparison of three numerical and experimental v_y time series (see Figure 12 for the location inside the flow field) are presented.

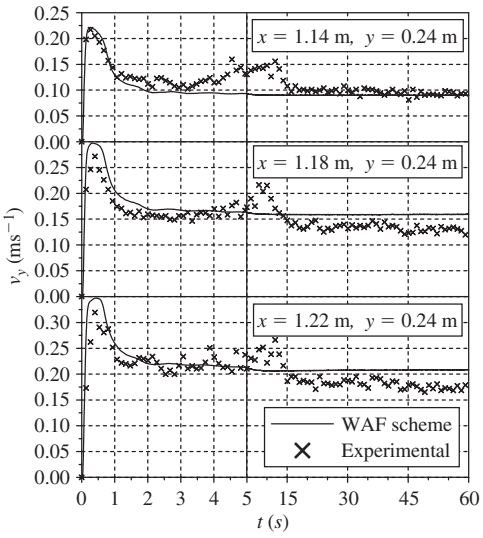


Figure 14. Numerical (WAF model) and experimental velocities (y-component) time series.

The measured velocity profiles were acquired at $z = 0.02$ m. The calculated values agree well with the measured data in the first seconds, when v_y starts to increase and then rapidly decreases. As for the water level hydrographs, oscillations appear in the experimental values in the middle times (4–15 s). They are probably due to wave disturbances originated at the breach location and reflected from the boundaries; these oscillations are not properly caught by the numerical model. Again, final steady-state numerical y velocities agree satisfactorily with observations at $x = 1.14$ m, while at the other points the experimental values are overestimated by the computations.

5 CONCLUSIONS

Two finite volumes schemes for the integration of the 2D shallow water equations were presented. The first belongs to the MUSCL – Hancock centred schemes family; the second is based on the Weighted Average Flux method. In both models the source term is treated by means of a time-operator splitting technique.

Numerical results were firstly computed for reference test cases, for which a solution close to the exact one is available. Both numerical models perform well with all the tests, the only exception being the velocity field of the shock-focusing problem. In this case the numerical results show a lack of radial symmetry, mainly for the WAF model. Also the 1D steady flow on a steep bump is satisfactorily resolved, especially on a fine grid.

Two literature experimental cases were then simulated; the comparisons are more than satisfactory and confirm that the models can be reliably used to deal with rapidly varying flows characterized by shocks, wetting fronts and by transitions between subcritical and supercritical conditions.

For this flows, characterized by a strong variability in space, the evaluation of the capabilities of numerical models could be improved by comparison with high resolution spatial experimental information, instead of local measurements only. At this aim an experimental investigation was presented by the writers in a related paper (Aureli et al. 2004).

REFERENCES

Alcrudo, F. & Garcia Navarro, P. 1993. A high resolution Godunov-type scheme in finite volumes for the 2D shallow water equations. *International Journal for Numerical Methods in fluids* 16: 489–505.

Aureli, F. & Mignosa, P. 2000. Two-dimensional flows due to dam or levee-breaking. *Proceedings Int. Symposium on River Flood Defence*. Kassel: Hercules Verlag.

Aureli, F. & Mignosa, P. 2002. Rapidly varying flows due to levee-breaking, In Bousmar, D. & Zech, Y. (eds.), *River Flow 2002, Proceedings of the First International Conference on Fluvial Hydraulics*, *Louvain La Neuve, Belgium, 4–6 September 2002*. Lisse: Balkema.

Aureli, F., Maranzoni, A. & Mignosa, P. 2004. Experimental Modelling of Rapidly Varying Flows on wet bed and in Presence of Submersible Obstacles, submitted to River Flow 2004.

Bermudez, A. & Vazquez, M.E. 1994. Upwind methods for hyperbolic conservation laws with source terms. *Computers Fluids* 23(8): 1049–1071.

Billett, S.J. 1994. A Class of Upwind Methods for Conservation Laws, PhD Thesis, Cranfield University.

Brufau, P. & Garcia-Navarro, P. 2000. Two-dimensional dam break flow simulation. *International Journal for Numerical Methods in fluids* 33: 35–57.

Caleffi, V., Valiani, A. & Zanni, A. 2003. Finite volume method for simulating extreme flood events in natural channels. *Journal of Hydraulic Research* 41(2): 167–177.

Harten, A., Lax, P.D. & Van Leer, B. 1983. On upstream differencing and Godunov-type schemes for hyperbolic conservation laws. *SIAM Review* 25(1): 35–61.

Hirsch, C. 1988–1990. *Numerical Computation of Internal and External Flows*. Chichester: Wiley & Sons.

Glaister, P. 1991. Shallow water flow with cylindrical symmetry. *Journal of Hydraulic Research* 29(2): 219–227.

Lax, P.D. & Wendroff B. 1960. Systems of conservation laws. *Comm. Pure Applied Mathematics* 13: 217–237.

LeVeque, R.J. 2002. *Finite Volume Methods for Hyperbolic Problems*. Cambridge: Cambridge University Press.

Liska, R. & Wendroff, B. 1998. Composite schemes for conservation laws. *SIAM J. Numer. Anal.* 35(6): 2250–2271.

Liska, R. & Wendroff, B. 1999. Two-dimensional shallow water equations by composite schemes. *International Journal for Numerical Methods in fluids* 30: 461–479.

Morel, A.T., Fey, M. & Maurer, J. 1996. Multidimensional high order method of transport for the shallow water

equations. Report no 96-09. Zurich: Swiss Federal Inst. of Technology.

Richtmyer, R.D. & Morton, K.W. 1967. *Difference methods for initial value problems*. New York: Interscience-Wiley.

Soares Frazão, S. & Zech, Y. 1999. Effects of a sharp bend on Dam-Break flows. *Proceedings of XXVIII IAHR Congress*, *Graz, 22–27 August 1999.* Graz: Technical University.

Soares Frazão, S., Morris M. & Zech, Y. 2000. "Concerted Action on Dambreak Modelling: Objectives, Project Report, Test Cases, Meeting Proceedings" (CD-ROM), UCL, Civ. Eng. Dept., Hydraulic Division, Louvain-la-Neuve.

Soares Frazão, S., Spinewine B. & Zech, Y. 2001. Digital-imaging velocity measurements and numerical modelling of a dam-break flow through a 90° bend. *Proc. of XXIX IAHR Congress*, *Beijing, 16–21 September 2001*. Beijing: Tsinghua University Press.

Toro, E.F. 1992. Riemann problems and the WAF method for solving the two-dimensional shallow water equations. *Phil. Trans. R. Soc. London A* 338: 43–68.

Toro, E.F. 1997. *Riemann Solvers and Numerical Methods for Fluid Dynamics*. Berlin, Springer Verlag.

Toro, E.F. 2001 *Shock–Capturing Methods for Free Surface Shallow Flows*. Chichester: Wiley & Sons.

This page intentionally left blank

River Flow 2004 – Greco, Carravetta & Della Morte (eds.)
© 2004 Taylor & Francis Group, London, ISBN 90 5809 658 0

Experimental modeling of rapidly varying flows on wet bed and in presence of submersible obstacles

F. Aureli, A. Maranzoni & P. Mignosa
Dipartimento di Ingegneria Civile, dell'Ambiente, del Territorio & Architettura, Parma, Italy

ABSTRACT: The results of two experimental tests concerning rapidly varying flows, originated by the sudden removal of a gate, are described. In the first the flow expands on a flat plane initially wet for few seconds, then reflects against solid walls. In the second a submersible obstacle is placed in the flat area in order to simulate an abrupt change in the topography. By adding a colouring agent to the water it was possible to obtain a solution with colour intensity increasing together with water thickness. Quantitative information about water depth distribution in the domain was obtained back lighting the Plexiglas bottom of the experimental facility and taking photographs of the area of interest. The tones of the images acquired were converted into water depths by means of transformation functions derived from a preliminary calibration. The test conditions were then simulated with a 2D numerical finite volumes model presented here briefly.

1 INTRODUCTION

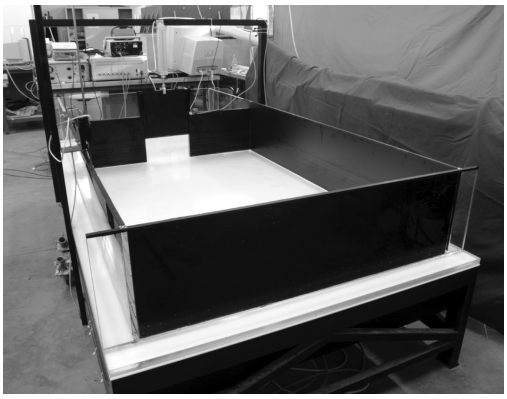
Rapidly varying flows such as those resulting from the sudden collapse of a dam are, apart from the first moments, strongly affected by the topography of the region subject to flooding. Valley contractions, irregular bed slopes and obstacles present in the flow field are key factors that can induce the formation of hydraulic jumps, shocks, wave reflections and other sudden changes in the flow behaviour. In modeling this kind of flows, usually accomplished by solving numerically the 2D shallow water equations, the terms related to resistance and topographical influence are synthesized in the so-called source terms. However the capabilities of the numerical schemes are often verified comparing computed results only with analytical solutions in which the source terms are equal to zero. Since for truly 2D unsteady flows analytical solutions are not available – even for simple geometries and in the absence of the source terms of the equations – it is worthwhile to validate numerical models by comparison with experimental results too (Bechteler et al. 1992, Bellos et al. 1992, Fraccarollo & Toro 1995, Brufau & Garcia-Navarro 2000, CADAM 2000, Soares Frazão et al. 2001).

The paper presents the results of a laboratory investigation having the aim to acquire experimental data of rapidly varying free surface flows induced by the sudden removal of a sluice gate. Two experimental tests are presented here. In the first the flow expands on a flat plane initially wet for few seconds, then reflects against solid walls. In the second an obstacle was placed in the flat area in order to simulate an abrupt change in the topography; the obstacle was chosen thin enough so that it can be submerged by the water but in the meantime enough thick to influence significantly the overall phenomenon. Amongst the available experimental methods to measure water depths, a colorimetric technique applied to the images acquired with a high resolution digital camera was favoured (Braschi et al. 1994). This choice allows to obtain information in the whole area of interest, highlighting the main flow field characteristics, such as shocks and hydraulic jumps, without introducing any disturbance in the flow field.

The results of the experimental investigation were then compared with the numerical results obtained by means of a 2D finite volume numerical code, realised by the authors themselves, whose main features are described here briefly and explained in depth in another paper presented at this Conference (Aureli et al. 2004).

2 EXPERIMENTAL FACILITY AND TEST CONDITIONS

The experimental facility (Figs. 1a, b), set up at the hydraulic laboratory of Parma University, consists of a rectangular tank with a flat bottom made by transparent Plexiglas. The tank is divided by a wall into two portions: the smaller having the function of reservoir



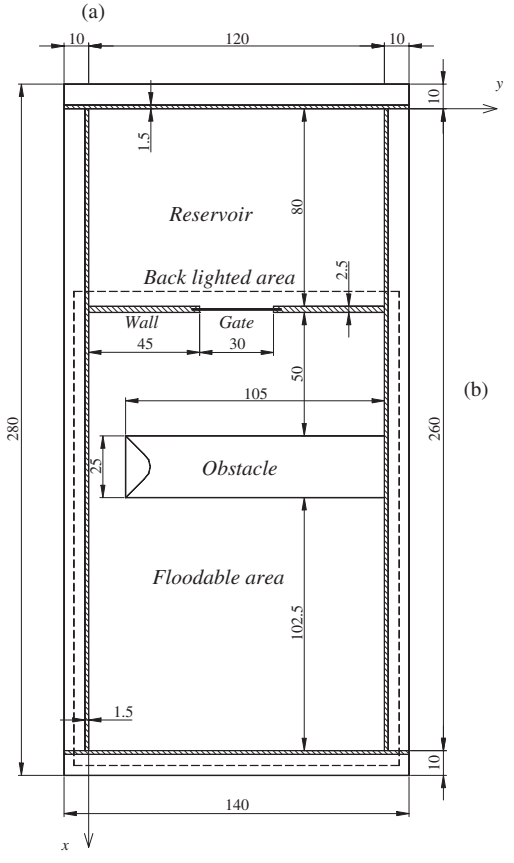


Figure 1. (a) Picture and (b) main dimensions (in cm) of the experimental facility.

and the bigger subject to the flooding consequent to the sudden removal of a gate, placed in the middle portion of the dividing wall. The aluminium gate is seated in a trapezoidal groove for seal reasons and is moved by a pneumatic piston which ensures that the total stroke (0.20 m) is released in about 8/100 s.

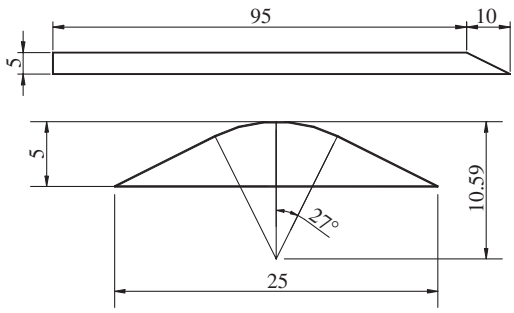


Figure 2. Shape and dimensions (in cm) of the obstacle.

In order to reproduce in a schematic way the effects of an abrupt change in the bottom topography on the flow field, one of the tests was performed placing asymmetrically an obstacle in the floodable area. Likewise the flat bottom, the obstacle itself was realized in a block of Plexiglas so as to be as much transparent as possible. The location and dimensions of the obstacle (Fig. 2) are such that it can be completely submerged by the water flowing from the reservoir after the release of the gate, but in the meantime to significantly influence the overall phenomenon.

At the aim of acquiring water depths in the flooded area via colorimetric techniques, this part of the tank was back lighted with cold fluorescent lamps placed in such a way to obtain a luminance as uniform as possible over the entire investigation area.

Colorimetric information were obtained adding to the water a fixed quantity of a coloring agent (methylene blue) and taking photographs of the back lighted floodable area by means of a reflex digital camera (Canon EOS 10D). The camera is equipped with a 22.7×15.1 mm CMOS sensor and is capable to acquire 9 frames at about 3 Hz with the maximum resolution of 3072×2048 pixels; afterwards the filling of the buffer allows to acquire only one frame every 1.8 seconds about.

The camera was placed on a tribrach in order to put the optical axis as normal as possible with respect to the bottom of the facility and aligned with the center of the floodable area. To time exactly each picture a 0.01 s resolution digital timer was set in a lateral portion of the frame, triggered by the movement of the gate.

The experimental investigation was completed by point measurements of water depth time series accomplished by means of a piezoelectric ultrasonic distance meter. The gauge was located close to the longitudinal wall ($x = 1.627$ m, $y = 0.022$ m in the coordinate system of Figure 1b), to be out from the perspective projection of the back lighted bottom.

In the following the results of two laboratory tests are reported, whose main characteristics are

Table 1. Main features of the experimental tests.

Test No.	Initial upstream water level (m)	Initial downstr. water level (m)	Obstacle
1	0.15	0.01	Absent
2	0.15	0.00	Present

summarized in Table 1. In the first, due to the presence of an initially wet floodable area, a shock is expected to move downstream and, after few seconds, to reflect against the solid walls of the experimental facility. In the second test the floodable area is initially dry, but the presence of the obstacle induces a complex flow field with the formation of hydraulic jumps and reflections. The aim of the experimentation is to track this two dimensional structures and to reproduce them with the mathematical model.

3 MEASURING TECHNIQUE AND CALIBRATION

The adding of a fixed quantity of colouring agent (methylene blue) to the water permits to obtain a solution whose color intensity, increasing with water thickness, can be translated in quantitative information about water depth distribution in the flow field. This technique allows to obtain water depth information in the whole area of interest avoiding in the meantime any kind of disturbances in the flow (Braschi et al. 1994).

The acquired RAW images were firstly converted in TIFF format (8 bit per channel), avoiding any artifact eventually introduced by compression algorithms or sharpness filtering, and then the three RGB layers were merged in 8 bit grey space. Figure 3 shows an example of the photograph taken at $t = 4.77$ s during the Test 2.

Before each test a spatial calibration was performed taking several photographs of the back lighted area submerged with an increasing thickness (from 1 to 15 cm) of water, previously colored, at rest condition. This calibration procedure allows to account for every local disturb that could be caused by a not perfect uniformity of the lighting field, by the light absorption of the Plexiglas block of the obstacle (if present), by the optics vignetting and by all the other external chances.

From the calibration images it was possible to derive for each pixel a transformation function between grey tones, ranging from 0 to 255, and water depths (from 0 to 15 cm) and then to estimate indirectly the water depth. The colouring agent concentration (12.5 g/m^3) and exposure parameters, of course fixed for all the calibration and test photographs, were chosen in such a way to cover a range of grey tones as wide as possible.

Figure 4 shows three examples of the transformation functions *grey scale – water depth* for a central pixel, for a pixel on the edge of the back lighted area and for a pixel belonging to the obstacle. From the graph it can be observed that for thin water depths the precision of the conversion is high (about 55–60 grey tones between 0 and 1 cm), whereas for thick layers of water the precision decreases significantly (about 6 grey tones in the range 13–15 cm). The repeatability error, that is the differences in the grey value for the same pixel in different shots taken at the same conditions, is typically of one or, at most, two grey tones. Then the percentage error in the water depth estimation is almost constant and of about 2%.

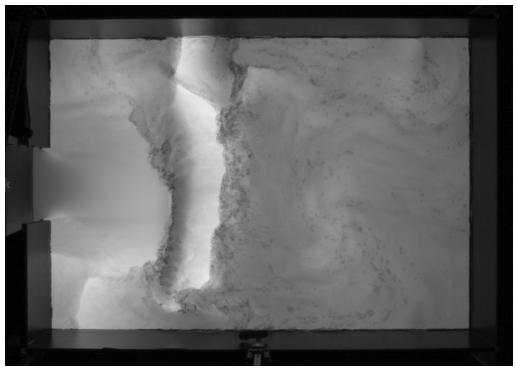


Figure 3. Picture taken during Test 2 at $t = 4.77$ s.

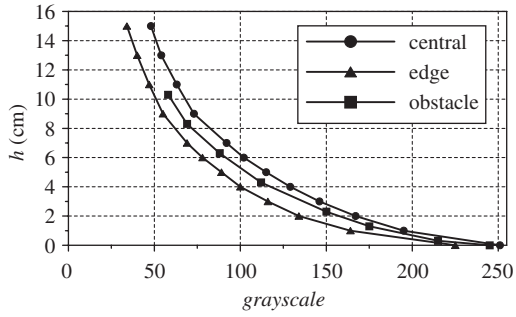


Figure 4. Examples of transformation functions *grey scale-water depth* for a central pixel, for a pixel on the edge of the back lighted area and for a pixel belonging to the obstacle (Test 2).

Other sources of errors are due to anomalous light reflections against the walls and to the entrapment of air bubbles in the water. To get out of the first source, all the walls and the gate itself were internally blackened. For the second source of errors, no general solution was found. Small air bubbles do not affect very much the images indeed, since the pixel dimension (7.4 μm) corresponds to about 1 mm in the real field and then all the smaller irregularities are masked; the bigger bubbles, on the other hand, give rise to anomalous reflections which darken the contours sometimes – but sometimes not – below the minimum grey values

recorded during the calibration procedure. Since during the test execution water depth values higher than the initial one in the reservoir (15 cm) were not expected, it was decided to not extrapolate the transformation function but to discard these data instead.

A post processing routine was set up in order to calibrate the camera and to transform the central projection of each image in a real orthophotograph.

Firstly the inner calibration of the camera and of the lenses was performed, once and for all, by means of a commercial package (PhotoModeler Pro 4.0, 2000). From the calibration the exact focal length (c), the principal point coordinates (ξ_0, η_0) and the radial (k_1, k_2) and decentering (p_1, p_2) lens distortion parameters were derived. To any pixel of the sensor surface, being FC, ξ, η (Fig. 5) the system of image coordinates, the following compensation was applied:

$$\xi_c = \xi + dr_\xi + dp_\xi, \qquad \eta_c = \eta + dr_\eta + dp_\eta, \tag{1}$$

where the radial distortion components are:

$$dr_\xi = (\xi - \xi_0)(1 + dr), \quad dr_\eta = (\eta - \eta_0)(1 + dr), \tag{2}$$

with:

$$dr = k_1 r^2 + k_2 r^4, \; r^2 = (\xi - \xi_0)^2 + (\eta - \eta_0)^2, \tag{3}$$

whereas those for decentering distortion read:

$$\begin{aligned} dp_\xi &= p_1\left[r^2 + 2(\xi - \xi_0)\right]^2 + 2p_2(\xi - \xi_0)(\eta - \eta_0), \\ dp_\eta &= p_2\left[r^2 + 2(\eta - \eta_0)\right]^2 + 2p_1(\xi - \xi_0)(\eta - \eta_0). \end{aligned} \tag{4}$$

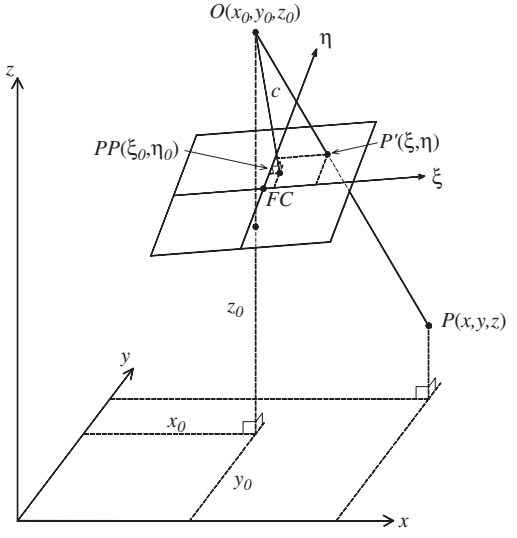


Figure 5. Relation between image and object coordinates (Kraus 1997).

Then the six parameters of the outer orientation, which define the position and attitude of the camera in the object coordinate system (x_0, y_0, z_0 and the angles of rotation ω, ϕ, κ on the primary, secondary and tertiary axis), were derived using three control points with known image and object coordinates. The reconstruction of the orthogonal projection of the water depth field on the object coordinate system, known the water depth z for each pixel and the outer orientation of the camera, was based on the collinearity equations:

$$\begin{aligned} x &= x_0 + (z - z_0)\frac{r_{11}(\xi - \xi_0) + r_{12}(\eta - \eta_0) - r_{13}\,c}{r_{31}(\xi - \xi_0) + r_{32}(\eta - \eta_0) - r_{33}\,c} \\ y &= y_0 + (z - z_0)\frac{r_{21}(\xi - \xi_0) + r_{22}(\eta - \eta_0) - r_{23}\,c}{r_{31}(\xi - \xi_0) + r_{32}(\eta - \eta_0) - r_{33}\,c}, \end{aligned} \tag{5}$$

where the parameters r_{ij} (i, $j = 1, 2, 3$) are the elements of a spatial rotation matrix which describes the attitude in space of the photograph relative to the object coordinate system xyz (Kraus 1997).

Finally, the scatter data obtained in the object coordinate system were interpolated on a Cartesian grid with $\Delta z = \Delta y = 5$ mm perfectly superimposable to that adopted in the mathematical model. The interpolation was based on the following inverse distance relation:

$$\tilde{z} = \sum_{i=1}^{N} \frac{z_i}{d_i^2} \Big/ \sum_{i=1}^{N} \frac{1}{d_i^2} \tag{6}$$

where N are the scatter data searched in a circle with 1 cm radius around the grid point, each of them characterised by the water depth z_i at distance d_i from the grid point. Anyhow, the high number of scatter points make the interpolation procedure substantially unimportant.

The acquiring and correction procedure, although not free from inaccuracies, allows nevertheless a comprehensive reconstruction of the phenomenon and of its characteristics.

4 NUMERICAL SIMULATION

The adopted numerical code is based on a finite-volumes discretization of the 2D shallow water equations written in integral form:

$$\frac{d}{dt}\int_A \mathbf{U}\, dA + \int_C \mathbf{H}\cdot\mathbf{n}\, dC = \int_A \mathbf{S}\, dA, \tag{7}$$

where A represents the area of the integration cell, C the cell boundary, $\mathbf{n}$ is the outward unit vector normal to C and t is the time; $\mathbf{U} = (h, uh, vh)^T$ is the vector

of the conserved variables (water depth and specific discharge in x and y directions); $\mathbf{H} = (\mathbf{F}, \mathbf{G})$ is the tensor of fluxes, being $\mathbf{F} = (uh, u^2h + 0.5gh^2, uvh)^T$ and $\mathbf{G} = (vh, uvh, v^2h + 0.5gh^2)^T$, with g acceleration due to gravity; $\mathbf{S} = (0, gh(S_{0x} - S_{fx}), gh(S_{0y} - S_{fy}))^T$ is the source term,where S_{0x}, S_{0y}, S_{fx} and S_{fy} are, respectively, the bottom and frictional slopes along the x and y axis.

The Manning equation is used to compute the friction terms:

$$S_{fx} = \frac{n^2 uh\sqrt{(uh)^2 + (vh)^2}}{h^{10/3}}, S_{fy} = \frac{n^2 vh\sqrt{(uh)^2 + (vh)^2}}{h^{10/3}} \quad (8)$$

in which n is the Manning roughness coefficient.

The adopted numerical method for the solution of the homogeneous part of (7) belongs to the class of MUSCL-Hancock centred slope limiter schemes, known in literature under the acronym *SLIC* (*Slope LImiter Centred*) (Toro 1997, Toro 2001); it is explicit, shock capturing, high resolution, *TVD*, of second order of accuracy both in time and space and it is based on the *unsplit* formula:

$$\overline{\mathbf{U}}_{i,j}^{n+1} = \mathbf{U}_{i,j}^{n} - \frac{\Delta t}{\Delta x}(\mathbf{f}_{i+\frac{1}{2},j} - \mathbf{f}_{i-\frac{1}{2},j}) - \frac{\Delta t}{\Delta y}(\mathbf{g}_{i,j+\frac{1}{2}} - \mathbf{g}_{i,j-\frac{1}{2}}). \quad (9)$$

In (9) $\mathbf{U}_{i,j}^{n}$ represents the vector of the integral averages of the conserved variables over the element (i, j) at time $t = t^n$, Δt is the time step, Δx and Δy are the mesh sizes, $\mathbf{f}$ and $\mathbf{g}$ are the intercell numerical fluxes in x and y directions, respectively.

Numerical fluxes are based on the *FORCE* (*First-ORder Centred*) (Toro 1997, Toro 2001) method. The source term $\mathbf{S}$ is treated with a *splitting* technique (Toro 1997, Toro 2001).

A more detailed description of the numerical scheme can be found in a related paper presented at this Conference (Aureli et al. 2004).

The computational domain was described by means of a Cartesian *cell – centred* discretization with square cells of 5×5 mm. The computational time step Δt was controlled via the *CFL* stability criterion, with Courant Number $Cr = 0.95$. Reflective, free-slip conditions were imposed on the solid boundaries. The Manning coefficient for the Plexiglas bottom was set at $0.007\ \mathrm{s\,m^{-1/3}}$.

As an example, the complete numerical results for Test 2 at $t = 4.77$ s are shown in Figure 6.

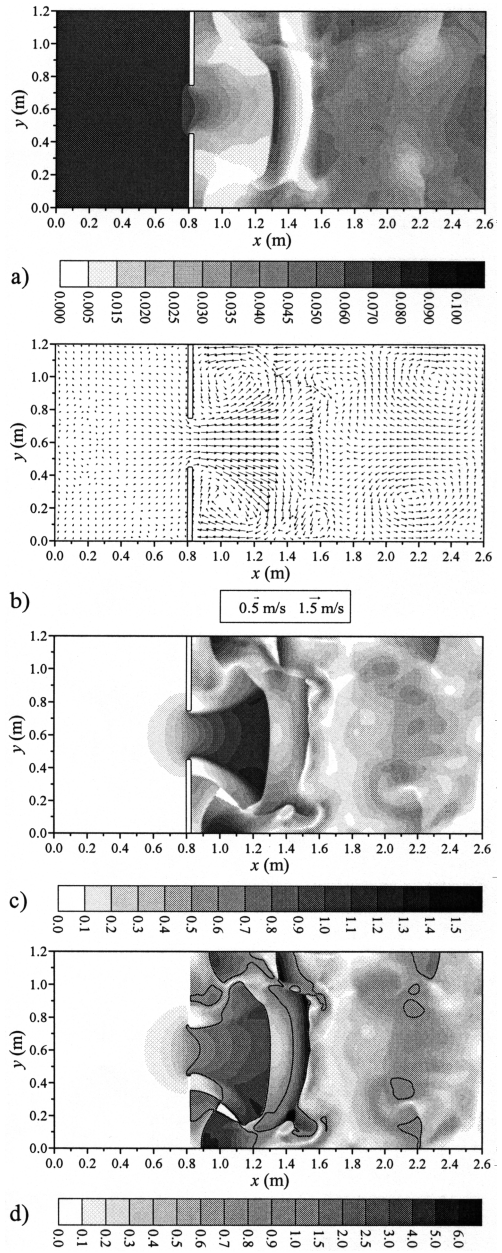


Figure 6. Numerical results for Test 2 at the time $t = 4.77$ s: a) contour map of water depths (m), b) vector map of velocity field c) contour map of velocity norm (m/s), d) contour map of Froude numbers with line at $Fr = 1$ drawn.

5 COMPARISON BETWEEN EXPERIMENTAL AND NUMERICAL RESULTS

Figures 7 to 14 show snapshots of experimental and computed water depths in the floodable area at different times for the two tests presented here.

The areas on the borders of the orthophotographs, where not enough information was available to interpolate a reasonable water depth value, were blacked. They of course increase with the water depth. The

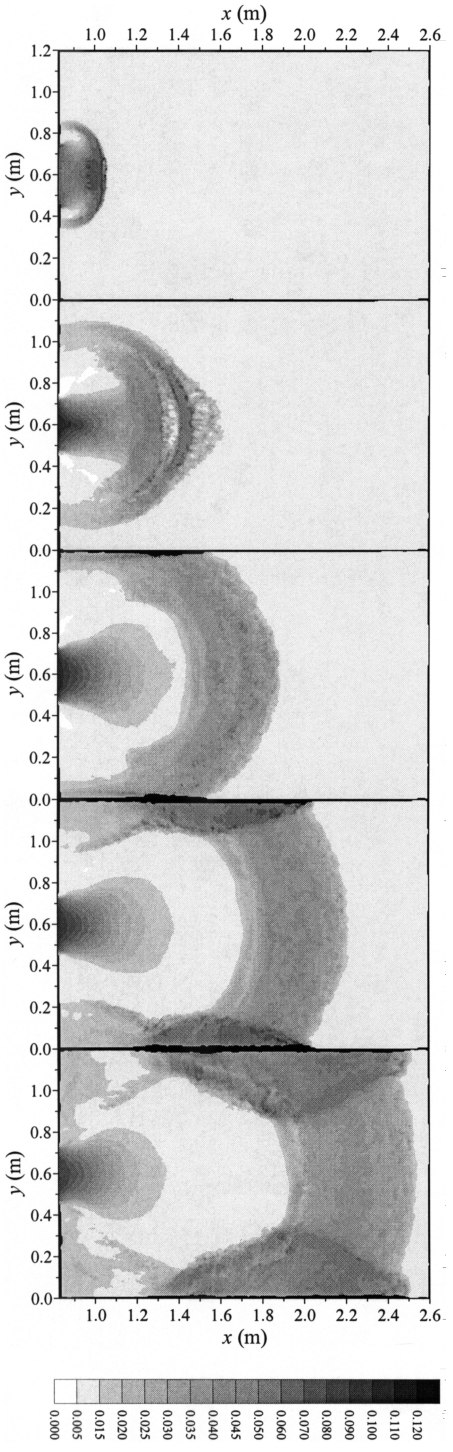


Figure 7. Experimental water depths (m) for Test 1 at $t = 0.24$ s, $t = 0.59$ s, $t = 0.94$ s, $t = 1.29$ s, $t = 1.64$ s.

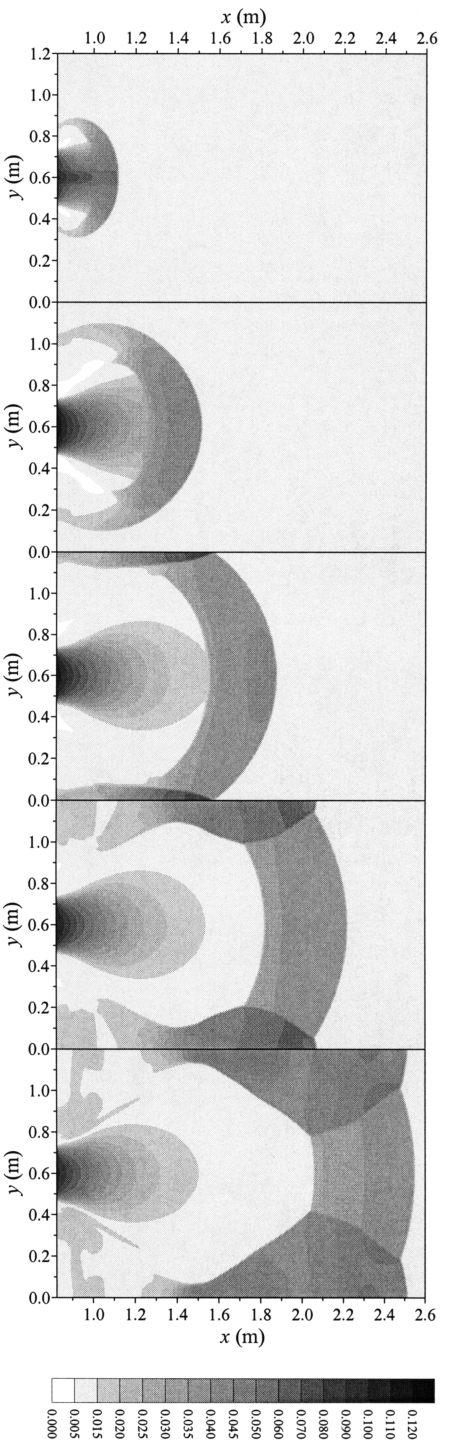


Figure 8. Numerical water depths (m) for Test 1 at $t = 0.24$ s, $t = 0.59$ s, $t = 0.94$ s, $t = 1.29$ s, $t = 1.64$ s.

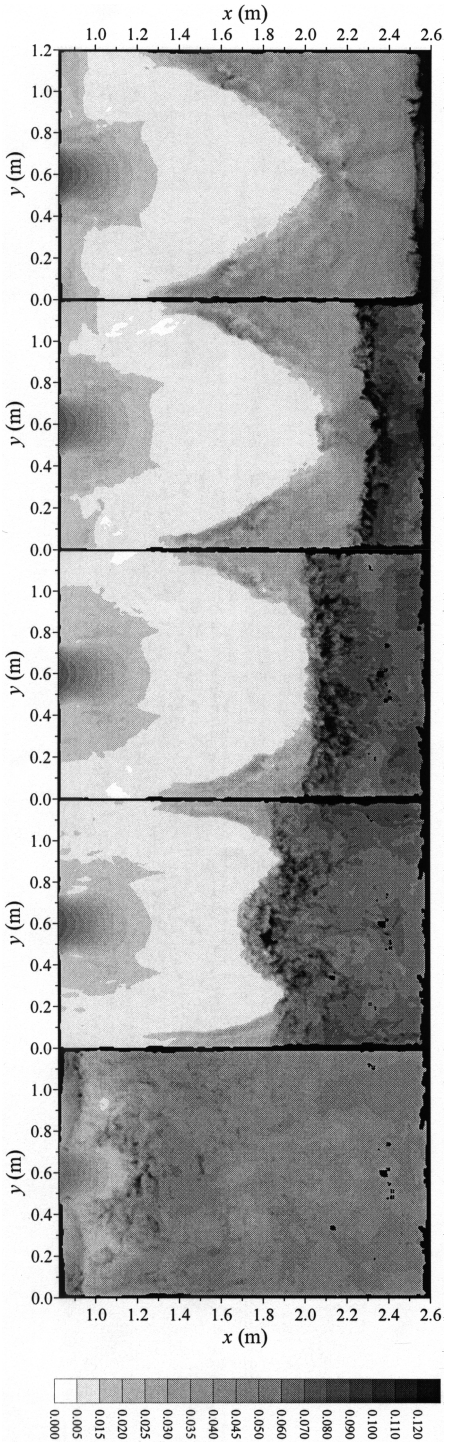


Figure 9. Experimental water depths (m) for Test 1 at $t = 2.00$ s, $t = 2.35$ s, $t = 2.70$ s, $t = 3.05$ s, $t = 4.89$ s.

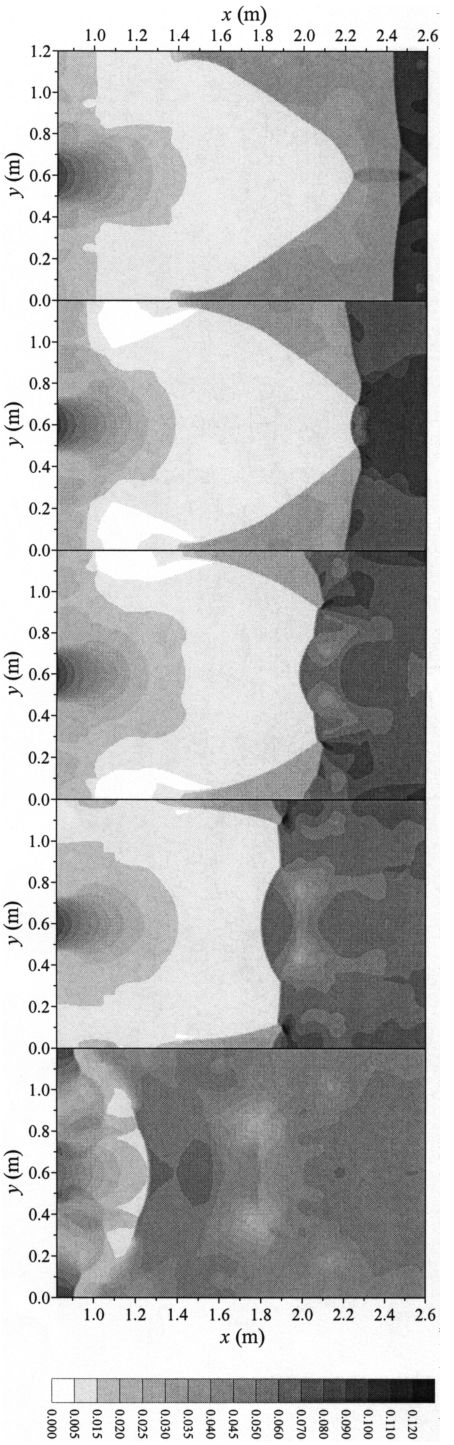


Figure 10. Numerical water depths (m) for Test 1 at $t = 2.00$ s, $t = 2.35$ s, $t = 2.70$ s, $t = 3.05$ s, $t = 4.89$ s.

blacked areas inside the domain are due to the air bubble anomalous reflections previously discussed.

In Test 1, the shock moving downstream on the still water (Figs. 7 and 8), together with those originated on the lateral walls, are caught very well by the numerical model. After the reflection against the downstream wall (Figs. 9 and 10) the position and shape of the moving upstream hydraulic jump is reproduced fairly well, too.

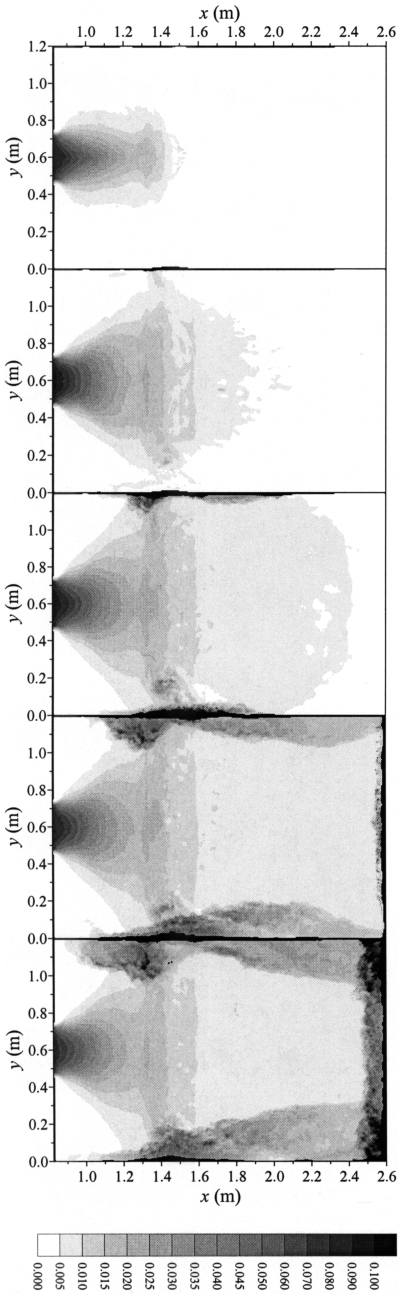


Figure 11. Experimental water depths (m) for Test 2 at $t = 0.46$ s, $t = 0.81$ s, $t = 1.16$ s, $t = 1.51$ s, and $t = 1.86$ s.

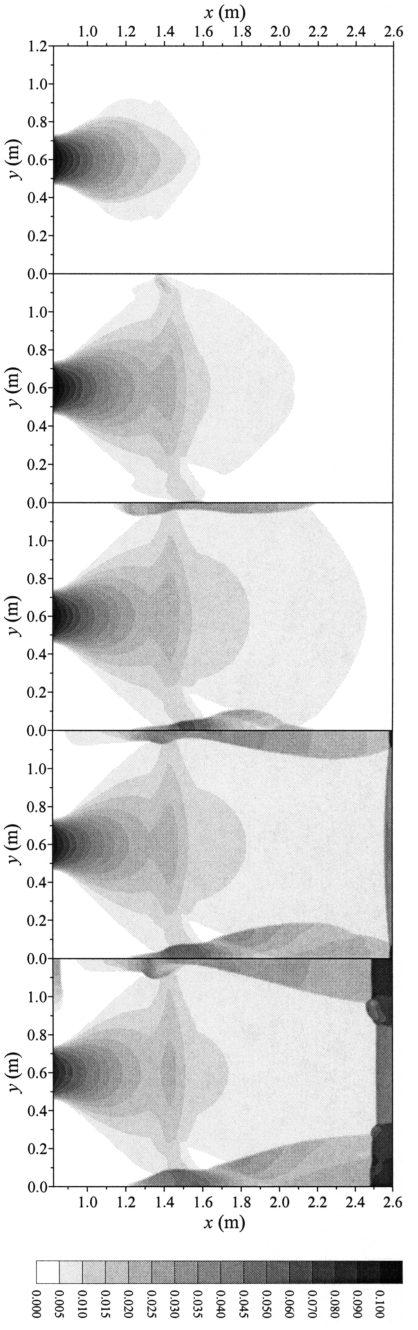


Figure 12. Numerical water depths (m) for Test 2 at $t = 0.46$ s, $t = 0.81$ s, $t = 1.16$ s, $t = 1.51$ s and $t = 1.86$ s.

In Test 2, the water at first overflows the obstacle, which shows a moderate effect on the overall flow field (Figs. 11–12). Then, some complex structures start to develop, mainly upstream the obstacle on the left side (Figs. 13–14). These structures are satisfactorily caught by the numerical model even if during the intermediate times ($t = 1.86 \div 2.93$ s) their dimensions are slightly underestimated.

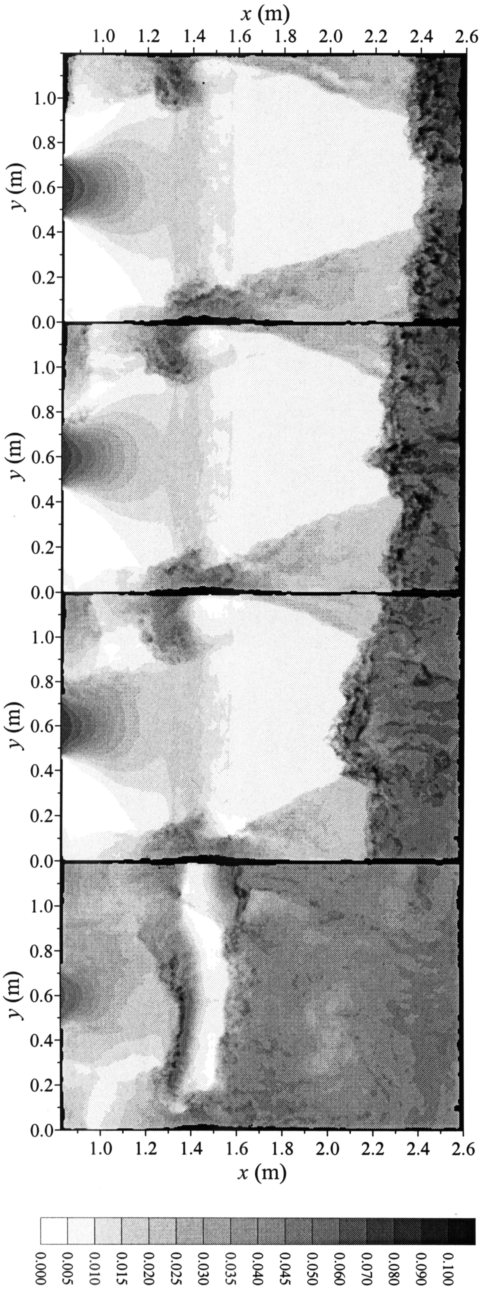


Figure 13. Experimental water depths (m) for Test 2 at $t = 2.21$ s, $t = 2.58$ s, $t = 2.93$ s, $t = 4.77$ s.

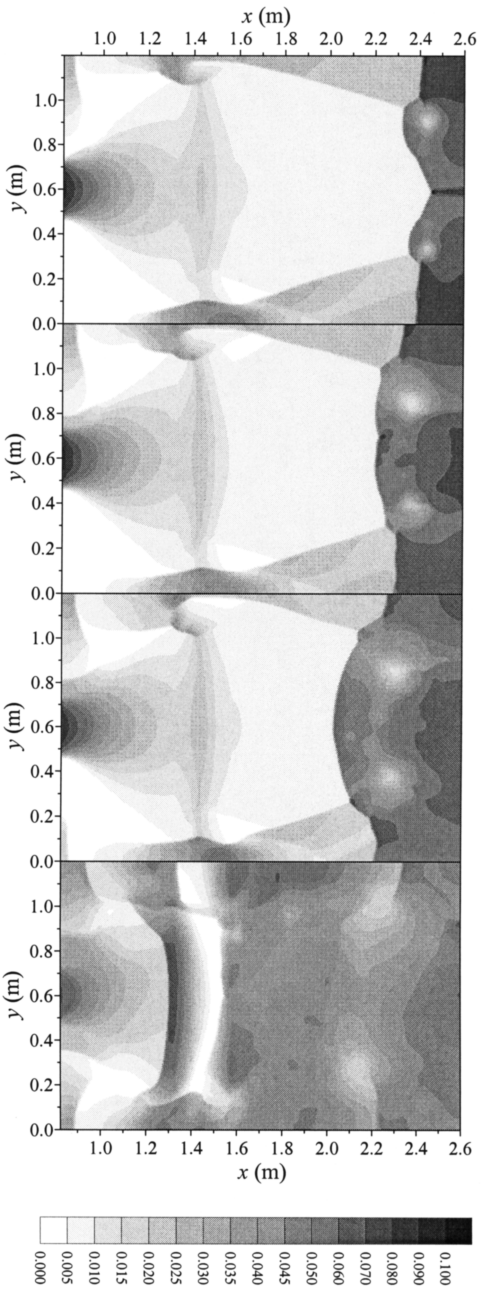


Figure 14. Numerical water depths (m) for Test 2 at $t = 2.21$ s, $t = 2.58$ s, $t = 2.93$ s, $t = 4.77$ s.

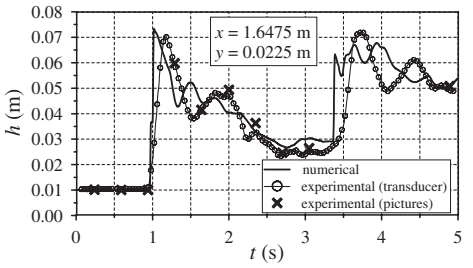


Figure 15. Comparison between experimental and numerical water level time series (Test 1).

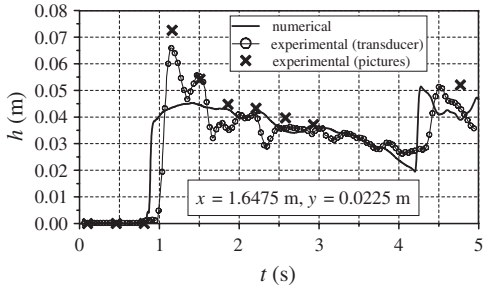


Figure 16. Comparison between experimental and numerical water level time series (Test 2).

At $t = 4.77$ s, on the other hand, the experimental water depth flow field becomes again very well reproduced by the numerical model.

Figures 15 and 16 show the water depth time series derived from the ultrasonic transducer, from the orthophotographs and from the numerical model at the location reported in the graphs (cfr. Fig. 1b).

In Test 1 (Fig. 15) the comparison between the results obtained by means of the two experimental techniques is fairly good. The computed results match well the experimental ones too, especially before the second shock at $t \approx 3.5$ s. The results for Test 2 (Fig. 16) are less satisfactory. The computed water depths show a less peaked value at $t \approx 1.2$ s with respect to those derived with both the experimental techniques; also, the time location of the first shock is slightly anticipated. In the intermediate times, however, the values deduced by the orthophotographs and those computed fit fairly. It must be stressed that the comparison is made at a very bad location, close to the solid wall, in order to avoid the presence of the transducer body on the acquired images.

6 CONCLUSIONS

Experimental results for two rapidly varying flows due to partial dam break were derived using coloured water and taking photographs of the area of interest. The acquired images were then transformed into orthophotographs and the grey tone of each pixel was converted into water depth by means of a previously calibrated transformation function.

The adopted technique allowed to obtain a high resolution spatial information, avoiding in the meantime any kind of disturbances in the flow field. It proved to be advantageous, with respect to few point measurements, in tracking the several moving structures which often occur in this kind of phenomena due to the superimposition of reflected waves.

The comparison between experimental data and numerical results, obtained by means of a 2D finite volume code realized by the authors, showed an overall good agreement, despite some differences at local scale.

The proposed 2D numerical model seems then to be capable to reproduce in a reasonable way the main characteristics of the phenomena under investigation.

REFERENCES

Aureli, F., Maranzoni, A. & Mignosa, P. 2004. Two dimensional modeling of rapidly varying flows by finite volume schemes, submitted to River Flow 2004.

Bechteler, W., Kulisch, H. & Nujic, M. 1992. 2-D Dam-Break Flooding Waves: Comparison between Experimental and Calculated Results. In A.J. Saul (ed.), *Floods and Flood Management.* Dodrecht: Kluwer Academic Publishers.

Bellos, V., Soulis, J.V. & Sakkas, J.G. 1992. Experimental investigations of two dimensional dam-break-induced flows. *Journal of Hydraulic Research*, IAHR 30(1): 47–63.

Braschi, G., Dadone, F. & Gallati, M. 1994. Plain flooding: near field and far field simulations. In Molinaro & Natale (eds.) *Modelling of Flood Propagation over Initially Dry Areas; Proc. intern conf., Milan, 29 June–1 July 1994.* New York: ASCE.

Brufau, P. & Garcia-Navarro, P. 2000. Two-dimensional dam break flow simulation. *International Journal for Numerical Methods in fluids* 33: 35–57.

CADAM, Concerted Action on Dam Break Modelling 2000. Soares Frazão, S., Morris, M. and Zech, Y. eds. Université Catholique de Louvain, Civ. Eng. Depth., Hydraulics Division, Louvain-la-Neuve, Belgium, CD-ROM.

Fraccarollo, L. & Toro, E.F. 1995. Experimental and numerical assessment of the shallow water model for two-dimensional dam-break type problems. *Journal of Hydraulic Research*, IAHR 33(6): 843–864.

Kraus, K. 1997. *Photogrammetry.* Bonn: Dümmler.

PhotoModeler Pro Version 4.0 2000., Vancouver: Eos Systems Inc.

Soares Frazão, S., Spinewine, B. & Zech, Y. 2001. Digital imaging velocity measurements and numerical modelling of a dam-break flow through a 90° bend. *Proc. XXIX IAHR Congress, Beijing, 16–21 September 2001.* Theme C: 240–245. Beijing: Tsinghua University Press.

Toro, E.F. 1997. *Riemann Solvers and Numerical Methods for Fluid Dynamics*. Berlin: Springer Verlag.

Toro, E.F. 2001. *Shock-Capturing Methods for Free-Surface Shallow Flows*. Chichester: John Wiley & Sons.

River Flow 2004 – Greco, Carravetta & Della Morte (eds.)
© 2004 Taylor & Francis Group, London, ISBN 90 5809 658 0

Velocity measurements in dam-break flow using imaging system

A.H.N. Chegini & G. Pender
Department of Civil & Offshore Engineering, University of Heriot-Watt, Edinburgh

A. Slaouti
Department of Engineering & Technology, Manchester Metropolitan University, Manchester

S.J. Tait
Department of Civil & Structural Engineering, University of Sheffield, Sheffield

ABSTRACT: An investigation of dam-break flow with dry and wet beds downstream has been undertaken. An image analysis system based on tracer particles was used in the laboratory to record the instantaneous velocity variations in the area of interest in the downstream channel and visualise the flow structure. The experimental measurements of the flow velocity downstream dry and wet-bed were obtained. Higher values of velocity were obtained for the dry-bed case than for the case with downstream water depths. Measurements from the experimental study were used for comparison with analytical solutions, which demonstrates a good agreement with experimental results.

1 INTRODUCTION

Dam-break flows have been studied for a long time, but the flooding caused by the dam rupture only received focused attention during the Second World War due to bombing. These failures and the associated damage have emphasised the importance of evaluating the safety of existing dams for design and planning purposes.

Predictive mathematical model investigations of the effect of dam-break floods have been carried out by several researchers several decades and some important results have been obtained, see for example Su & Barnes (1970), Fread (1977) and Bellos & Sakkas (1987). Since field data for this flow is very difficult to obtain, it is necessary to collect experimental data to verify the mathematical models. Several experimental investigations of dam-break flow have been reported in the last four decades, see Derssler (1954), Miller & Tschantz (1972), Bell *et al*. (1992) and Lauber & Hager (1998 & 1999).

With the improvement made in computer technology, computational models of flows in dam failures are widely used and have become predictive tools. In addition, physical models are more expensive than a computational equivalent. Examples of computational model studies dam-break flows can be found in Soulis (1992) and Glaster (1993) who compared these with recent experimental data for dam-break flows. On the other hand, a range of novel experimental methods based on signal and image analysis system have been developed for measuring flow velocities which are particularly useful in unsteady flows such as dam-break flow. Such data can be used for the validation of numerical calculations. Traditional velocity measurement methods are laser Doppler anemometry (LDA) and hot-wire anemomerty (HWA) provide single-point measurements (Buchhave, 1989). These methods have high accuracy. Alternative methods are whole field measurement techniques, which should be viewed as complementary measuring tools. In these methods, the flow field is illuminated with a thin light sheet from a powerful source and might be filmed photographically or digitally. Once several particles appear in the illuminated area, then the velocity vectors can be obtained for this area using tracking algorithm techniques based on auto-correlation, cross-correlation or Young's fringe method see Cenedese & Paglialunga (1990), Adrian (1989) and Buchhave (1992).

In this paper, the main objective is to investigate the instantaneous whole-field velocity of the dam-break flows by tracking particles seeded in the flow, after the bore has become established. Previous work concentrated on the initial stages of dam-break flow, theoretically, numerically and experimentally see Stansby, Chegini & Barnes (1998). A measuring system enables individual particles in the flow to be tracked directly. Particle tracking velocimetry (PTV)

and particle streak velocimetry (PSV) methods were applied for a digital system. These methods do not need photographic development and processing time, although spatial resolution can be a problem using standard SVHS video equipment. In this study, PSV was used, measuring streaks to obtain maximum average of the particle movements for all the downstream dry and wet bed cases. The automated PTV method was suited to subcritical flows which was assessed by comparing with PSV measurements. Finally, the experimental velocity measurements were compared with computational calculation.

2 EXPERIMENTAL METHOD

The experimental rig was an open channel flume with a horizontal bed. The test facility consisted of a 15.24 m length of 0.4 m by 0.4 m rectangular cross section flume. Part of the upstream and downstream walls of the dam site were made with clear Perspex to view the flow. The upstream end of the flume was closed but the downstream end was open for the dry case and had different level weirs for the downstream wet-bed conditions. These weirs were utilised to form the downstream wet-bed initial conditions. The dam site was set up at 9.76 m from the upstream end. A thin movable metal plate (3 mm thick) was used to simulate the instantaneous dam-break. This slid in small plastic channels mounted at a section around the flume bed and sides. A rope was attached to the top of the dam plate and loops through a pulley to a 7 kg weight which was released from about 0.8 m above the laboratory floor. The experiments were made with an upstream depth (H) of 0.1 m and downstream depths of dry, 0.1 H, 0.3 H, 0.45 H and 0.55 H. More details of the test facility used to generate the dam-break flows can be found in Chegini (1997).

In this study, an instantaneous whole flow field plane visualisation and velocity measurements of the area of interest were investigated using PTV and PSV techniques. These methods are based on tracer particles which are added to the flow and then illuminated with a powerful light source. The particles were spherical, 80 micron in diameter, solid polystyrene seeding powder with a relative density of 1.0 ± 0.2, which made the particles neutrally buoyant in water and able to follow the flow. The particles were mixed in the flow rig before running each test. The light source for illumination in the field of view was a 4 watt Argon ion laser. The laser beam was transmitted from the laser light source to the light sheet generator by using a 20 m long optical fibre link. The light sheet generator produced a vertical plane light sheet with the width of 1–3 mm along the flume. A JVC TK-1085E colour CCD camera was used to record a 8.4 cm by 6.9 cm picture field. The camera operates with PAL standard for video scanning of 25 images/second. The camera was connected to a VCR, PC and TV screen, allowing instant monitoring of the field of vision and enabling the motion of flow to be recorded for further processing. The schematic arrangement of the laboratory set-up is shown in figure 1. In order to analyse an analogue camera output or a standard video signal, this has to be converted to an array of digital information known as a digital image.

A device known as a 'Frame Grabber' is used to convert the original analogue signal. This device can be fitted internally into one expansion slot of the standard personal computer or can be externally connected to it. All frame grabbers freeze the analogue signal and discretely sample it to provide an image which is a series of discrete digital values that are then stored in a two dimensional array of numbers. This array of individual element numbers (pixels) with an integer color (grey level) is represented as the digital image. Frame grabber boards are equipped with a minimum of two buffers per image but can have many more, each buffer image having 512×512 pixels with 256 (8 bit) grey levels. The digital image can be processed on the board memory or the host computer from the buffer. Each digital data element (pixel) is denoted by a number, which represents the amount of light intensity of a small area of the visual image. The sampled number of each pixel conventionally gives the level of darkness or brightness of the small area. Zero represents black, the maximum value, 256, denotes white and intermediate values designate various shades of grey. This software was written in parallel C for a 3L compiler to control image capture and processing.

3 IMAGE ANALYSIS SYSTEM

The captured images were cleaned-up by filtering and then thresholding. Therefore, the background becomes black (grey level 0) and the foreground particle images become white (grey level 256). At this stage, all seeding particles appear in the frame image sequence as white colour. The images are now suitable for further processing. The technique of applying image analysis to obtain quantitative velocity flow field information from particle movement encompasses a number of different methods. They are differentiated by the form of the captured image and the analysis technique employed. The displacement of individual particles within a field of view over the known short time period yields information about the velocity vector field simultaneously over the whole plane for which the particle image data was gathered. The following section describes two techniques PTV and PSV and concludes with a description of their application to a dam-break flow system.

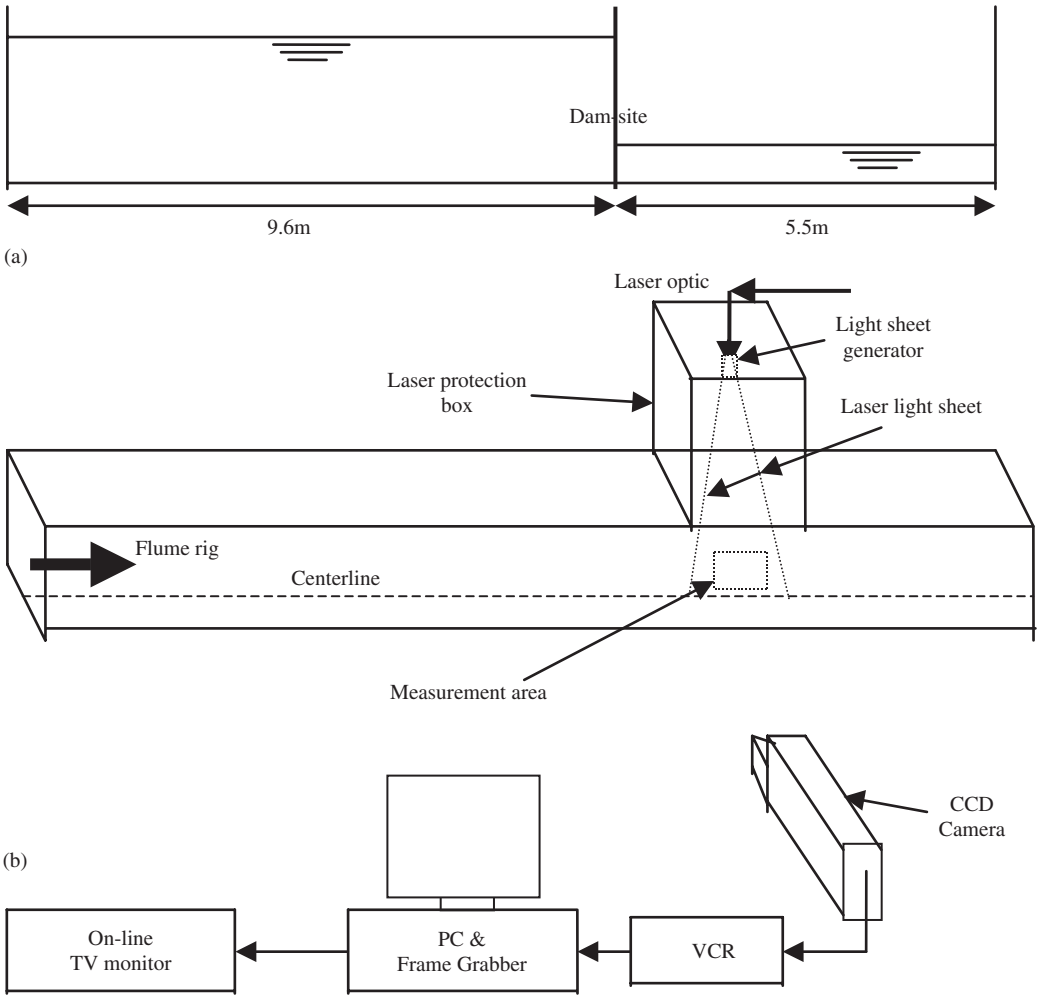


Figure 1. Sketch of experimental facility of dam-break flow (a) side view of the flume; (b) laboratory arrangement.

3.1 *Particle tracking velocimetry*

This method requires individual particles to be located in an image and successive images to be recorded on successive frames. The system analyses pairs of single exposed digital images to produce whole field maps of velocity vectors. Particle images at different times exist on the separate frames. There is no directional ambiguity in the calculated vectors and the direction of particle motion is easily found. There is also no lower limitation on particle motion between frames. The particle tracking technique is used to accurately determine the position of a particle in an image frame and compare it with its location at a known short time interval later (in a successive frame). The distance traveled by an individual particle is then calculated and the velocity found knowing the time interval between images. This process is repeated for all of the particles appearing in the frame sequence.

In this study, the automated particle tracking system was used for subcritical flows. The digitised images were improved by using image processing techniques, and the particles are tracked by means of a localised correlation function. This technique is based on the comparison of a small window around a particle image in one frame with a series of windows around many particles in a later frame. A match is required between the spatial pattern of neighboring particles around each window with a corresponding window in another frame. The window which gives the best correlation can be used to locate each particle pair. Various correlation algorithms have been developed to allow the tracking of particles from frame to frame. Examples

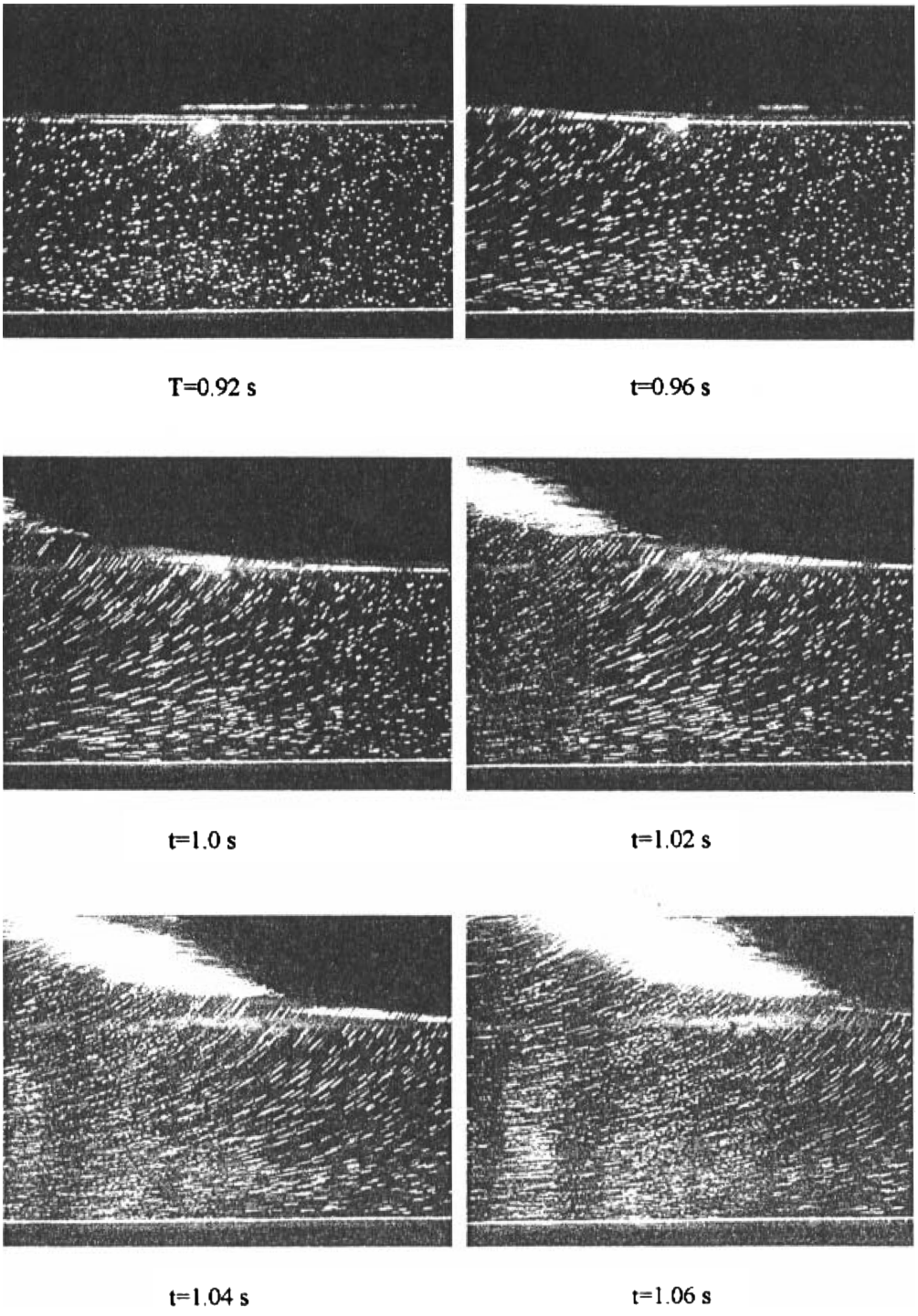


Figure 2. Typical time series of the raw digitised images at downstream of the dam site with initial water depth condition.

of these are Dalziel (1992), Brucker & Althaus (1992), Hassan *et al*. (1992). A number of complex flow situations has been analysed successfully by using PTV. For example, see Nishio *et al*. (1992), Uemura *et al.* (1989).

3.2 *Particle streak velocimetry*

Seeding particles in the fluid medium may be recorded on a single frame of photographic or video film by using a relatively long exposure time. The application of particle streak in fluid mechanics has been used for qualitative flow visualisation as illustrated in Van Dyke (1982). Particle streak images can be digitised for development into the quantitative measuring technique known as particle streak velocimetry (PSV). This method is usually used when the fluid has a seeding particle concentration less than that for PTV. This method does not require individual streak images to be overlapped and distinguished from each other. PSV enables accurate individual streak lengths to be determined and then analysed. As the exposure time is known, it becomes possible to obtain the velocity associated with a particle streak. The processing of the streak images includes filtering the images to eliminate noise and thresholding to separate the streak from the background. The white streaks corresponding to the particles can then be located and measured, see Kobayashi & Saya (1988). The image analysis for locating streak images and measuring their lengths with known exposure time to obtain the velocity field has been demonstrated in a wide variety of flow situations, see Utami & Ueno (1987), Green & Gerrard (1993).

The problem with streak image measurements is that in a real flow situation the particles may enter or leave the plane of interest (i.e. the light sheet) during the exposure time. This means that the actually recorded streak length of the particles will be less than the actual distance moved by the particle. Therefore, this will lead to an incorrect estimate of velocity, which is reported by researchers such as Khalighi & Lee (1989) and Adamczyk & Rimai (1988). According to the sensitivity of the recording medium particle streaks may not be recorded at all if they travel too fast. Some attempts have been made to resolve such problems with a degree of success, see Marko & Rimai (1985).

In this present study, particle images were digitised using equipment that has already been described. A manual method of streak line measurement is used whereby a cursor is carefully moved around the screen to measure the length of streak images. Tests were performed at a variety of initial conditions with different exposure times. These will be described including some results in the following section.

4 RESULTS

The most interesting of the experimental results will be shown here. More details regarding the experimental data can be found in Chegini (1997). In this paper, visualisation and measured velocity fields are presented by analysing images using PTV and PSV methods. The free surface profiles in the initial stages of the dam-break flow from the digitised images have already been published see Stansby *et al.* (1998). Visualisation and velocity field measurement of dam-break flows over obstacle have also been produced by image analysis methods, Chegini (1997). Surface elevations at various longitudinal positions were also measured using resistance probes and essentially confirmed the results from the digitised images. Details of the surface profile plot with the identified area (8.4×6.9 cm) of the recording digitised images at centred 85 cm downstream of the dam-site for the downstream dry-bed and wet-bed initial flow conditions can be found in Chegini (1997). Figure 2 shows typical time series of the raw digitised images at location $x = 85$ cm downstream of the dam-site for different initial flow depth ratios. These raw digitised images of the flow are processed to obtain the time series of the whole flow field. Note that $x = 0$ corresponds to the dam-site. To aid illumination, seeding powder is dropped on the water around the area of interest. The powder is neutrally buoyant in water. The velocity fields are here defined by the tracking of the particle streaks.

The raw digitised flow field images used to obtain the velocity field for the fixed camera position at 85 cm downstream of the dam-site. Some images suggest these regions are in fact a mixture of spray and particles. The results show white long straight and mixed lines with some brighter areas. These are due to high speed and turbulent flow with entrained air. Given the above problems and the fact that the time interval between image is too long the Particle Tracking Velocimetry (PTV) technique cannot match between the two sequence frames. Since the video images were not clear enough as explained, the particle streak velocimetry (PSV) method was applied to obtain the maximum average of velocity. The streak images were measured at several frames on the video play back system whilst the digitising procedure took place. As the relationship between pixels and object distance and exposure time were known the velocity could be determined. Taking the reading of the length of the straight lines, the results can be plotted on a graph, as shown in figure 3, based on streak line measurement technique. This figure shows that the velocity increased quickly at the beginning and then decreased with some variation, to a more or less stable value. This figure also emphasises the bore velocity wave in the front of the flow propagation in the downstream section. The results show that the initial slope of the velocity variation with

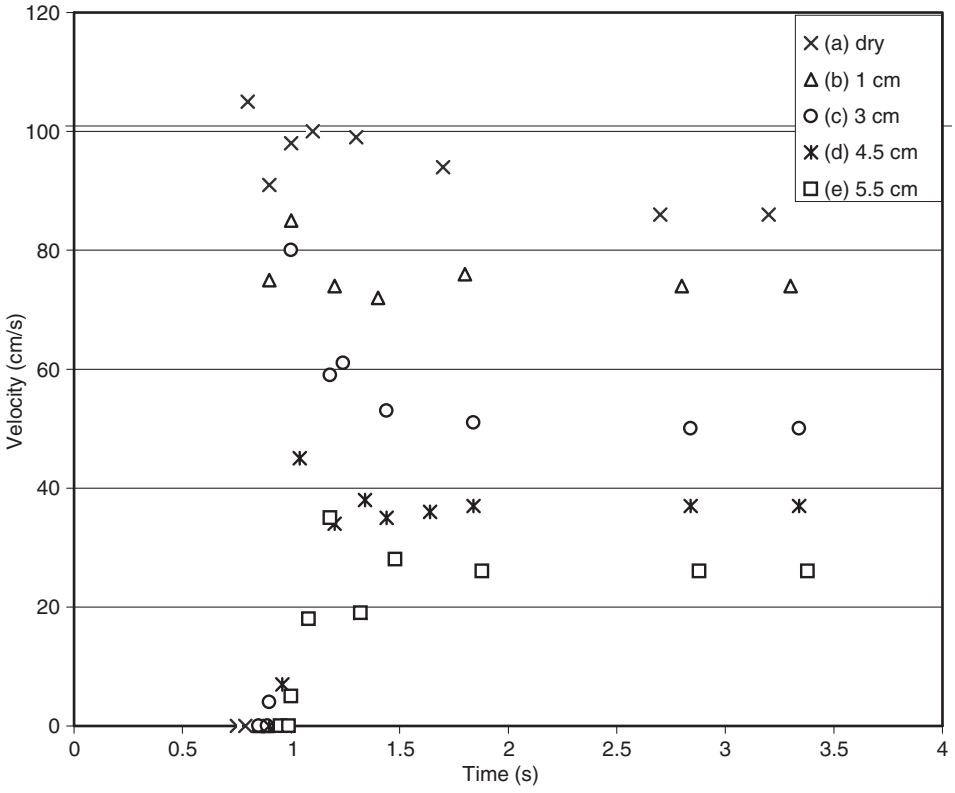


Figure 3. Variation of the streamwise velocity against time obtained by PSV for different initial water depth flow conditions.

time decreases as the downstream initial water depth increases.

Finally, some frames of the digitised flow field images were analysed to obtain the velocity information by the particle tracking technique for a downstream initial depth of 4.5 cm and 5.5 cm which presents the subcritical flows. The typical results are shown in figure 4 as frames progresses. Observation of the results from the particle tracking technique and digitised images emphasises the similarity as expected. The digitised flow field images of the wave propagation in the downstream initial conditions also show clearly that the flow particles in the stationary area had moved before the wave as confirmed by PTV results. A general comparison between the maximum average of the velocity obtained by PSV (Fig. 3) and PTV (Fig. 4), shows reasonable agreement for the cases with the depth ratios of 0.45 and 0.55.

5 COMPARISON OF ANALYTICAL AND EXPERIMENTAL RESULTS

An analytical solution of the homogenous, incompressible, unsteady, one-dimensional flow, considering flow friction forces but neglecting wind and coriolis force effects, was applied. A hydrostatic pressure distribution was assumed throughout the flow field. Readers can find the theory in Stoker (1957) and more details of calculation in Chegini (1997). Figure 5 shows the comparisons between analytical solutions and experimental measurements for the test flume under dry-bed and wet-bed flow conditions. For all depth ratios, the velocity fields eventually became quite stable after the bore develops downstream. The experimental velocity fields show the upper limit of the flow including the air/water mixture as compared with analytical results. In general, these comparisons are considered to be satisfactory for the downstream supercritical and subcritical flow region.

6 CONCLUSIONS

An image analysis system has been applied to the dam-break flow for investigation of the instantaneous whole flow field visualisation and measurement of the velocities. The whole flow field velocity data may be used to assess the ability of a computer model to simulate

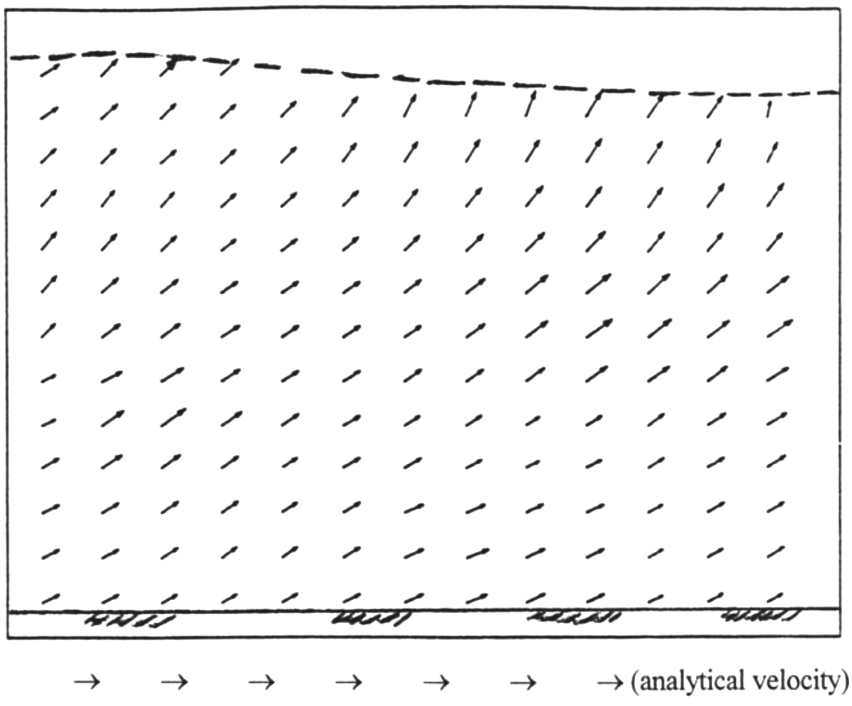


Figure 4. Typical instantaneous interpolated velocity field obtained by PTV at downstream of the dam site for subcritical flow condition.

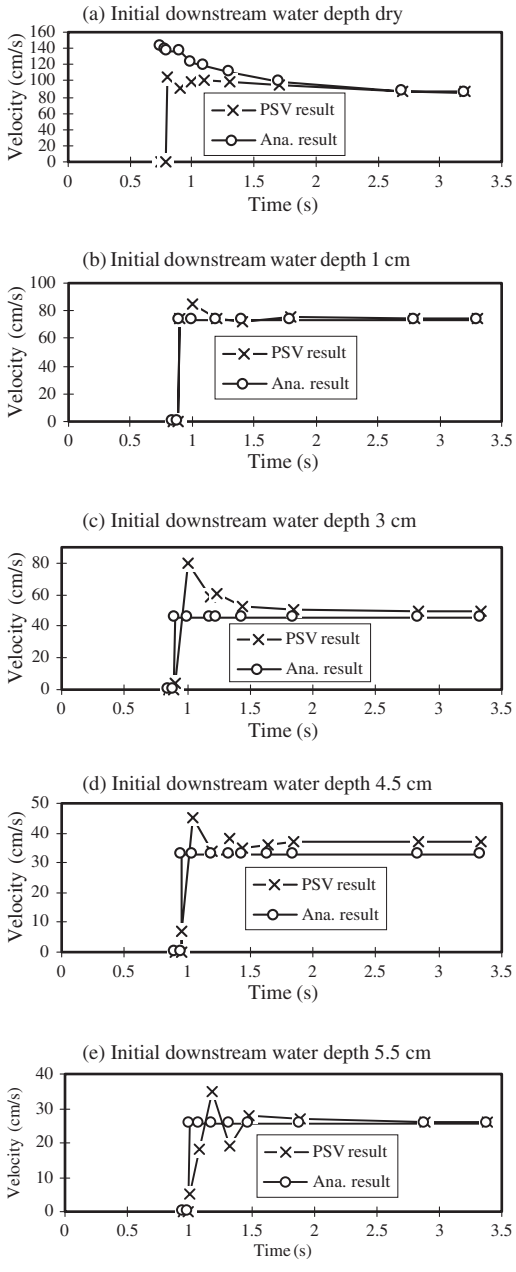


Figure 5. Comparison of the variation of the velocity against time obtained by PSV and analytical calculation.

flow structure. The system has limitations which correspond to the high water speed and turbulent flow with entrained air.

Experimental flow visualisation of the dam-break flow has shown interesting movements of the flow particles in the stationary area before the arrival of the wave. These features are confirmed by PTV results and have not been reported previously. As the experiments show, the front wave interaction with the downstream dry-bed or wet-bed flow conditions produce a complex phenomena, but the velocity profiles become established after a front wave. Experimental velocity results after the front wave is consistent with those obtained from analytical solution.

ACKNOWLEDGEMENT

The help and supervision of Professor P.K. Stansby at UMIST is gratefully acknowledged. The loan of the argon-ion laser from Dr J.T. Turner is also acknowledged.

REFERENCES

Adamczyk, A.A. & Rimai, L. 1988. 2-Dimensional particle tracking velocimetry (PTV), technique and image processing algorithms. *Experiments in fluids* 6: 373–380.

Adrian, R. 1989. Engineering application of Particle Image Velocimeters. *Proceeding of ICALOE'89, Laser Institute of America*: 56–71.

Bell, S.W., Elliot, R.C. & Chaudhry, M.H. 1992. Experimental results of two-dimensional dam-break flows. *Journal of Hydraulics Research* 30 (2).

Bellos, C.V. & Sakkas, J.G. 1987. 1-D dam-break flood wave propagation on dry bed. *Journal of Hydraulics Engineering* 113 (12): 1511–1525.

Brucker, C. & Althaus, W. 1992. Study of vortex breakdown by particle tracking velocimetry (PTV). *Experiments in fluids* 13: 339–349.

Buchhave, P. 1989. Advances in turbulence measurement techniques, *Advance in Turbulence*. George, W.K. & Arndt, R. (eds), Hemisphere Publishing.

Buchhave, P. 1992. Particle image velocimetry-status and trends. *Experimental Thermal and Fluid Science* 5: 586–606.

Cenedese, A. & Paglialunga, A. 1990. Digital direct analysis of a multi-exposed photograph. *Experiments in Fluids* 8: 273–280.

Chegini, A.H.N. 1997. Investigation and analysis of dam-break flows. *PhD dissertation*. University of Manchester.

Dalziel, S.B. 1992. Decay of rotating turbulence, Some particle tracking experiments. *Applied Scientific Research* 49: 217–244.

Derssler, R.F. 1954. Comparison of theories and experiments for the hydraulic dam-break wave. *Assemble general de Rome. Int. Assoc. Hydro* 3 (38): 319–328.

Fread, D.L. 1977. The development and testing of a dam-break flood forecasting model. *Proceeding of dam-break flood modelling workshop*. Washington, D.C. USA Water Resources Council: 164–197.

Glaster, P. 1993. Flux difference splitting for open-channel flows. *Inter. Jour. for Numerical Method in Fluids* 16: 629–654.

Green, R.B. & Gerrard, J.H. 1993. Vorticity measurements in the near wake of a circular cylinder at low Reynolds numbers. *Journal of Fluid Mechanics* 246: 675–691.

Hassan, Y.A., Blanchat, T.K. & Seeley Jr, C.H. 1992. PIV flow visualisation using particle tracking techniques. *Measurement Science and Technology* 3: 633–642.

Imaichi, K. & Ohmi, K. 1983. Numerical processing of flow visualisation pictures measurement of two-dimensional vortex flow. *Journal of Fluid Mechanics* 129: 283–311.

Khalighi, B. & Lee, Y.H. 1989. Particle tracking velocimetry, an automatic image processing algorithm. *Applied Optics* 28 (20): 4328–4332.

Kobayashi, T. & Saya, T. 1988. A real-time velocity measurement algorithm for two-dimensional flow fields. *2nd International Symposium on Fluid-Control, Measurement, Mechanics and Flow visualisation*, Sheffield, UK: 174–178.

Lauber, G. & Hager, W.H. 1998. Experiments to dambreak wave: Horizontal channel. *Journal of Hydraulic Research* 36 (3): 291–307.

Lauber, G. & Hager, W.H. 1999. Experiments to dambreak wave: Sloping channel. *Journal of Hydraulic Research* 36 (5): 761–773.

Marko, K.A. & Rimai, L. 1985. Video recording and quantitative analysis of seed particle track images in unsteady flows. *Applied Optics* 24 (21): 3666–3677.

Miller, W.A. & Tschantz, B.A. 1972. Laboratory investigation of one-dimensional wave motion in open channels. *Paper presented at the National Water Resources Engineering Meetingm, ASCE*, Atlanta-Georgia: 24–28.

Nishio, S., Himeno, Y. & Okuno, T. 1992. Flow measurement around oscillating circular cylinder in uniform flow. *Proceeding of the Workshop on Hull form Design and Flow Phenomena*. Inchon. Korea.

Soulis, J.V. 1992. Computation of two-dimensional dam-break flood flows. *Inter. Jour. for Number. Methods in Fluids* 14: 631–664.

Stansby, P.K., Chegini, A.H.N. & Barnes, T.C.D. 1998. The initial stages of dam-break flow. *Journal of Fluid Mechanics* 374: 407–424.

Stoker, J.J. 1957. Water wave. *Interscience publishers*. Wiley and sons. New York.

Su, S.T. & Barnes, A.H. 1970. Geometric and frictional effects on sudden release. *J. Hyd. Div. ASCE* 96 (11): 2185–2200.

Uemura, T., Yamamoto, F. & Ohmi, K. 1989. A high speed algorithm of image analysis for real time measurement of two-dimensional velocity distribution. *Flow Visualisation FED* 85: 129–133.

Utami, T. & Ueno, T. 1987. Experimental study on the coherent structure of turbulent open -channel flow using visualisation and picture processing. *Journal of Fluid Mechanics* 174: 399–440.

Van Dyke, M. 1982. An album of Fluid Motion. *Parabolic Press*.

This page intentionally left blank

River Flow 2004 – Greco, Carravetta & Della Morte (eds.)
© 2004 Taylor & Francis Group, London, ISBN 90 5809 658 0

1D model of surface waves generated by a reservoir's bank landslide: a case study

P. García-Navarro, G. Pérez & P. Brufau
Fluid Mechanics, CPS, University of Zaragoza, Spain

M.E. Vázquez-Cendón
Applied Mathematics, University of Santiago de Compostela, Spain

ABSTRACT: The work presented is a contribution to the predictive numerical modelling of surface waves generated by bank slides. The study is based on a one dimensional approach assuming that the flow generated is governed by the St, Venant equations. The mechanism triggering the solid slide is out of the scope of the work, therefore the slide properties are set as external parameters. The flow equations are solved with an upwind scheme specially adapted to wetting/drying boundaries.

1 INTRODUCTION

The study of the sliding movement of land volumes is of great complexity. Generally speaking, it can be classified according to several factors such as the time scale associated (from very slow like in glaciers to very fast like in mud or debris flows), the content of water, the slope of the terrain or the characteristics of the involved materials. On the other hand, it can be triggered by another diversity of factors. There is a particular aspect, matter of this study, concerned with the impact of important volumes of sliding materials falling into water volumes, either in movement (rivers) or at rest (lakes, reservoirs). In such events the risk is not precisely associated to the sliding mass but in first instance to the waves generated by the energy transferred to water by collision. A second risk is the possibility of heavy deposition of material in the river bed forming an artificial dam able to accumulate an important volume of water but not for a long time, giving rise to further catastrophic dam failure.

In this work, a one-dimensional mathematical model for water flow and sliding mass movement is presented. The resulting equations are essentially the shallow water equations with time dependent bed level and/or time dependent channel width supplied with an external rule for the time dependencies and a modified friction term. They are solved by means of an upwind scheme based on Roe's method with special care put on the wet/dry or dry/wet interfaces.

The model is applied to the simulation of a real case. The Santa Liestra reservoir is a project on Esera River by Santa Liestra village in the Spanish Pyrenees. The project is intended to regulate 81.9 Hm^3 at the upper part of the river. There is controversy due to the risk associated to potential land slides in the nearby mountains forming the banks of the future reservoir. With the proposed model, the objective was to simulate the consequences of the described potential slides in their interaction with the reservoir. The starting point for this study were previous geological studies of the area and a former study developed by CEDEX (Centro de Estudios y Experimentación de Obras Públicas).

One of the risk areas identified by geologists is placed on the left bank of the river near a narrow section. It involves more than 50 Hm^3 of meteorized and fractured materials. One of the theories describing a possible risk scenario states that the lower part of this solid volume could become saturated when filling the reservoir, leading to instability.

The topology of the area is markedly one-dimensional with the hypothetic falling mass representing a transversal sliding. We have made the hypothesis of rigid sliding, that is, movement of the volume in a block with a falling celerity of 10 m/s, according to previous studies.

The sliding volume was characterized by means of six geological cross sections every 250 m, estimating the average thickness and volume for each of them.

The river channel was modeled by means of trapezoidal cross sections of variable bottom width and side slope. The simulation was performed using 1000 grid nodes along the river and a time step subject to CFL = 0.7 for the transient calculation. The initial

water depth in the reservoir was the less favorable corresponding to full reservoir, that is, water surface level $h_{in} = 642$ m and water at rest (initial conditions). The friction coefficient for the Manning law used was $n_{Manning} = 0.04$. The slide modeling was based on the geometric description of the sliding volume and a special mathematical treatment of transversal sliding described in the main text.

2 GOVERNING EQUATIONS

2.1 *Flow equations*

Flow movement in the longitudinal reservoir considered is assumed to be well described by the 1D shallow water equations. The shallow water equations are an approximation to the three-dimensional reality. The water velocity in a river, for instance, varies from bank to bank and in the vertical direction. However, for many practical applications, these variations may be ignored and the problem be approximated as variable only in the spatial direction along the main flow. In case of continuous solutions the differential form is deduced. In terms of the wetted cross section $A(x, t)$ and the discharge $Q(x, t)$

$$\frac{\partial A}{\partial t} + \frac{\partial Q}{\partial x} = 0 \tag{1}$$

$$\frac{\partial Q}{\partial t} + \frac{\partial}{\partial x}\left(\frac{Q^2}{A} + gI_1\right) = gA(S_0 - S_f) + gI_2 \tag{2}$$

where S_0 and S_f are bed and energy slope terms and I_1 and I_2 are pressure terms, all of them well described elsewhere (). Equations (1), (2) can also be written in compact differential form

$$\frac{\partial \boldsymbol{U}}{\partial t} + \frac{\partial \boldsymbol{F}(x, \boldsymbol{U})}{\partial x} = \boldsymbol{H}(x, \boldsymbol{U}) \tag{3}$$

called the conservative form where

$$\boldsymbol{U} = \begin{pmatrix} A \\ Q \end{pmatrix}, \quad \boldsymbol{F} = \begin{pmatrix} Q \\ \frac{Q^2}{A} + gI_1 \end{pmatrix}, \quad \boldsymbol{H} = \begin{pmatrix} 0 \\ gA(S_o - S_f) + gI_2 \end{pmatrix}$$

A different, non-conservative form can be derived

$$\frac{\partial \boldsymbol{U}}{\partial t} + \boldsymbol{J}\frac{\partial \boldsymbol{U}}{\partial x} = \boldsymbol{H}(x, \boldsymbol{U}) - \frac{\partial \boldsymbol{F}(x, \boldsymbol{U})}{\partial x} = \boldsymbol{H}^*(x, \boldsymbol{U}) \tag{4}$$

where $\boldsymbol{J}$ is the Jacobian matrix

$$\boldsymbol{J} = \frac{\partial \boldsymbol{F}}{\partial \boldsymbol{U}} = \begin{pmatrix} 0 & 1 \\ c^2 - u^2 & 2u \end{pmatrix}$$

with eigenvalues

$$\lambda_1 = u + c$$
$$\lambda_2 = u - c$$

and with eigenvectors

$$\boldsymbol{e}_1 = \begin{pmatrix} 1 \\ u + c \end{pmatrix}, \quad \boldsymbol{e}_2 = \begin{pmatrix} 1 \\ u - c \end{pmatrix}$$

u is the fluid velocity and c is the small water surface waves celerity

$$c = \sqrt{\frac{gA}{\sigma}}$$

Being a hyperbolic system, it admits characteristic formulation and the eigenvalues are equal to the slopes of the characteristic curves in (x, t). This is the property in which Roe's scheme is based.

2.2 *Slide modeling*

The slide movement will be considered solid and compact, formed of the same material as the flow bed or walls, neglecting deformation and infiltration of water into the solid matrix.

The sliding is modeled in the frame of a one-dimensional approach by assuming the sudden motion of either the channel bed or the channel side wall, both conforming the solid–liquid boundary. This involves the assumption of a time and space variable channel geometry. From the mathematical point of view, these effects modify the dynamic equation as time variable source terms inducing transient flow (waves) in the mass of water. When the slide direction is the same as the channel main direction, the model is based on a channel bed movement (longitudinal slide). The channel bed level (z) depends on both position x and time t. The slide size (volume or thickness) and velocity into the fluid are modeled by means of variations in the function $z\ (x, t)$.

Sliding along a direction normal to the channel main direction is referred to as transverse sliding and the modeling is based on channel breadth variations along distance x and time t, $\sigma_f\ (x, t)$. As in the case of bed variation, the adequate definition of the function $\sigma_f\ (x, t)$, characterizes the physical parameters of the sliding mass.

This procedure is useful to model sliding shapes entering the channel as a pulse, parabola, triangle, etc, which can be completely submerged or emerge from the water. The movement followed by the shape function is that of the assumed sliding mass. In the longitudinal sliding, the bed movement induces a pressure excess that pushes also in the longitudinal direction.

Therefore, a wave traveling in the direction of the perturbation is generated.

However, in the case of a transverse sliding, water is pushed by one of the side walls against the opposite side and forced to climb up. The result is that the initial surface level is raised and two front waves traveling both upstream and downstream are generated. All movements follow a unique direction in the longitudinal sliding case, being adequately modelled by a one-dimensional approach. This is not the case for a transverse sliding, since the transmitted waves are normal to the perturbation direction. The water surface level pattern is complex and the fluid behaviour depends on many factors. The actual phenomenon is locally tridimensional. However, we model it with a one-dimensional approach so that it can be plugged into a 1D river or channel model. The main difficulty associated with naively modelling transverse sliding in 1D is that, at a given cross section, the predicted centroid of the fluid cross section is at a different position than that of the real fluid, hence leading to different waves due to the potential energy accumulated. Channel breadth variation is not enough and should be complemented with channel bed variation. A way to introduce this kind of information into the one-dimensional model is required. The strategy used in this work is described in ().

It is customary in shallow water models to use a parametric formulation the energy slope, both in steady and unsteady turbulent cases, either in terms of the Chezy coefficient C_{chezy} or the Manning roughness factor n (*ref*).

$$S_f = \frac{u|u|}{C^2_{Chézy}\left(\frac{D_h}{4}\right)} = \frac{n^2 u|u|}{\left(\frac{D_h}{4}\right)^{4/3}}$$

where D_h represents the hydraulic diameter. This is the accepted friction model for fixed bed problems. When the bed is moving at a celerity $v_d\ (x,t)$, that is, in the zone where a sliding is taking place, the relative velocity between flow and solid bed $u - v_d$ is the key variable in order to introduce a term containing the shear interaction between the solid mass inmovement and the longitudinal flow. Furthermore, and in order to model the presence of new materials in the channel bed, a friction coefficient different from the channel bed roughness (n^*) value must be introduced. In these cases, the following is applied [40] [39] for S_f:

$$S_f = \frac{(u-v_d)|(u-v_d)|}{C^{*2}_{Chézy}\left(\frac{D_h}{4}\right)} = \frac{n^{*2}(u-v_d)|(u-v_d)|}{\left(\frac{D_h}{4}\right)^{4/3}}$$

3 NUMERICAL METHOD

The numerical method used in this work is an upwind finite volume method based on Roe's approximate Riemann solver. This technique has proved efficient for unsteady shallow water problems over fixed bed [21].

The computational domain will be divided into a finite number of uniform cells ($\Delta x = cte$) for the numerical resolution of the equations. The time stepping procedure will be based on a variable time step Δt, always determined by the numerical stability requirements. The criterion used is the Courant-Friedrich-Lewy (CFL), which states that the maximum allowable time step, compatible with stability, in this case is given by

$$\Delta t_{Cr} = \frac{\Delta x}{|u| + c}$$

therefore requiring that the dimensionless CFL number

$$\mathrm{CFL} = \frac{\Delta t}{\Delta t_{Cr}}$$

is always less that unity for stability $\mathrm{CFL} \leq 1$.

The numerical method has been implemented as described in () and () and will not be repeated here.

When modelling landslides and their interaction with water volumes, it is possible and frequent to encounter at the same time wet ($h > 0$) and dry nodes ($h = 0$) in the domain, as pointed before. The limit between a wet node and a dry node will be called a wetting/drying interface and poses a special difficulty from the numerical point of view in the two following situations in which a dry cell is placed next to a wet-dry and has a higher bed level:

$h_{i+1} = 0$ and $z_i + h_i < z_{i+1}$ (Fig. 1)

We need to redefine Δz as $\Delta z = h_i$ instead of $\Delta z = z_{i+1} - z_i$ in order to ensure mass conservation at least in steady state [6].

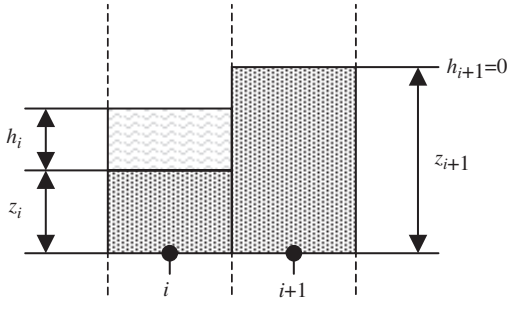


Figure 1. Wet-dry interface (case A).

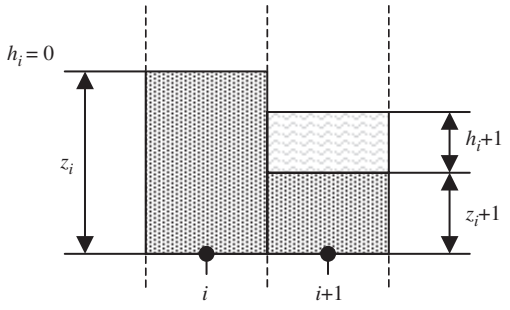


Figure 2. wet-dry interface (case B)

$h_i = 0$ and $z_{i+1} + h_{i+1} < z_i$ (Fig. 2)

We need to redefine Δz as $\Delta z = -h_{i+1}$ instead of $\Delta z = z_{i+1} - z_i$ for the same reason.

4 APPLICATION TO A REAL CASE

After the validation of the model against experimental data for a longitudinal sliding and the calibration of the solutions by means of academic test cases (), the numerical method will be applied to a case of practical interest characterized by irregular cross sections and realistic dimensions. The problem consists of the evaluation of the consequences of the potential catastrophic falling of an important volume of solid material into a reservoir. It is the projected Santa Liestra reservoir, on the Esera river near Santa Liestra village, at the Spanish Pirynees. The construction of a reservoir at that location is intended to regulate 81.9 Hm^3, at the upper part of the river. There is an open controversy linked to the dam building due to the potential landslide risk described by a sector of the scientific community. The starting point for the study has been based on a previous report made by the CEDEX (Centro de Estudios y Experimentación de Obras Públicas), and some useful geological data. The more relevant properties will be next outlined; for more geological details, see the references.

Figure 3 shows a sketch of the topographic situation of the reservoir indicating the maximum envisaged water level of 642 m and the location of the potential sliding area at the left bank of the Esera river. The problem in this area is markedly one-dimensional and the sliding can be modelled by means of a transverse sliding model, as the figure suggests.

The volume of the involved materials is bigger than 50 Hm^3 according to the geological prospections. Besides, the kind of materials and their fractured and meteorized state, and the fact that the low parts would become saturated when filling the reservoir contribute to the possibility of a sudden and catastrophic failure. This work, however, does not focus on the conditions

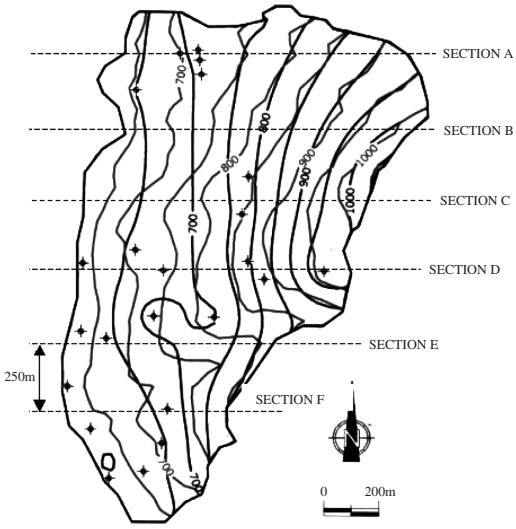


Figure 4. Sliding volume defined by the two bounding surfaces.

Table 1. Sliding volume geometric data.

Section	Location x (m)	Thickness z_0 (m)	Area A_d (m^2)	Celerity v_d (m/s)
A	750	5	1000	10
B	500	25	15000	10
C	250	70	50000	10
D	0	80	56000	10
E		50	30000	10
F		50	24000	10

under which the sliding could be triggered. Our study starts from the hypothesis that the sliding takes place and is motivated by the study of the consequences of the impact over the stored water.

Figure 4 shows a detail of the potential sliding volume, with the red lines representing level isolines at the surface in contact with the air and blue lines level isolines at the discontinuity surface. For simplicity, the sliding was assumed rigid, that is, falling in a single block, and with a celerity of 10 m/s. This is a maximum risk scenario but follows the hypothesis made in previous studies. Six geological sections as shown on Fig. 4 were used to study the geometry of the sliding volume each of them associated to an average thickness $z_0(x)$ and a surface $A_d(x)$. These values are gathered in Table 1. Any other intermediate value is calculated by interpolation from them.

As the table indicates, the simulation model locates the origin of the x axis at section D. The reason for this was the realization after several simulations that, due to the morphological properties, section D was a split

point where the induced water discharge divided into two opposite directions, one heading towards Morillo de Liena and the other to the opposite direction with no interaction between them. Therefore, as we were interested in the modeling of the North heading waves, the South part was neglected.

The river geometry in the domain under study was based on river cross sectional data approximated to trapezoidal shapes. Table 2 shows their location along the river axis as well as other variables of interest.

Figure 5 represents the longitudinal variation of the top water width at initial conditions, that is, with the reservoir at maximum water level (642 m), from the 3500 m considered in the simulation. The reach was extended near the tail of the reservoir to include the villages of Morillo de Liena and Navarri into the study in order to evaluate their risk of flooding.

The simulation was performed using 1000 space intervals and a fixed bed roughness $n_{Manning} = 0.04$. using the geometric slide data and the transversal sliding model described in **. The speed of the solid mass movement is assumed constant considering a balance between resistance forces and inertia forces over the sliding volume. The sliding motion at a computational node is finished when all the volume assigned to that point has fallen into the water. Every node has a solid slice of material assigned and the algorithm evaluates the size of transverse sliding at every time step. The numerical results are sumarized and plotted in Figs. 6 to 9.

Table 2. Geometry of the river.

Location x (m)	Bed level z (m)	Slope θ (rad)	Bottom width σ_{in} (m)
0	615	1.04	20
250	617	1.22	10
500	620	1.30	40
750	622	1.30	20
1000	622	1.34	40
2250	628	1.16	10
3000	650	0	400
3500	660	0	500

From the results shown in Figs. 6 to 9 it can be signaled that in the first seconds after the sliding motion starts, very high discharges are produced since water is displaced at a great velocity by the solid materials fallen into the reservoir. The surface wave generated advances towards Morillo against an adverse slope, hence losing energy and celerity. At about $t = 60$ s, the sliding area remains dry, acting as a solid obstacle and with all the volume of water moving towards the tail of the reservoir. On the other hand, it can be estimated from the numerical results that the wave celerity, when the wave front is nearly 10 m deep, is as high as 14 m/s. The wave is rapidly damped at the end of the reach due mainly to the wide section at that location. When the wave reaches Morillo it is still 3 m deep and advances at a velocity around 6 m/s.

5 CONCLUSIONS

A one-dimensional numerical model has been presented as a tool to simulate landslide movements and their interaction with water volumes. Having been previously proved as adequate for wave propagation problems on rigid bed channels and validated with experimental data, it can also be adapted to situations

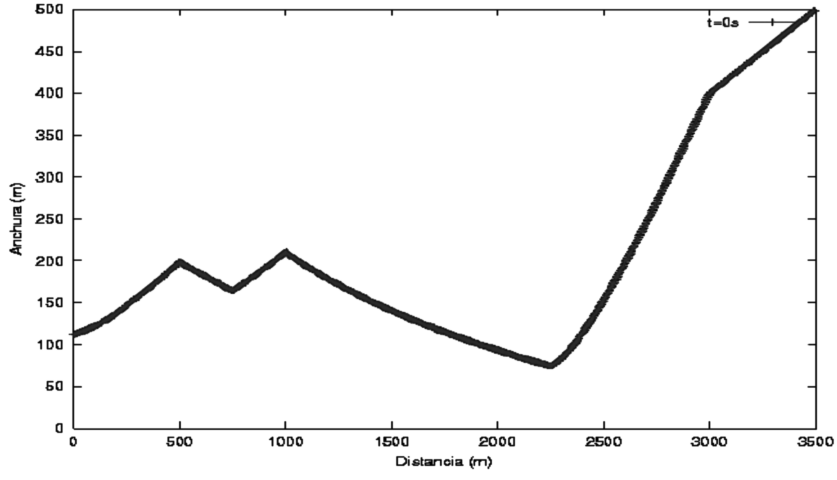


Figure 5. Reservoir top water width at water level 642 m.

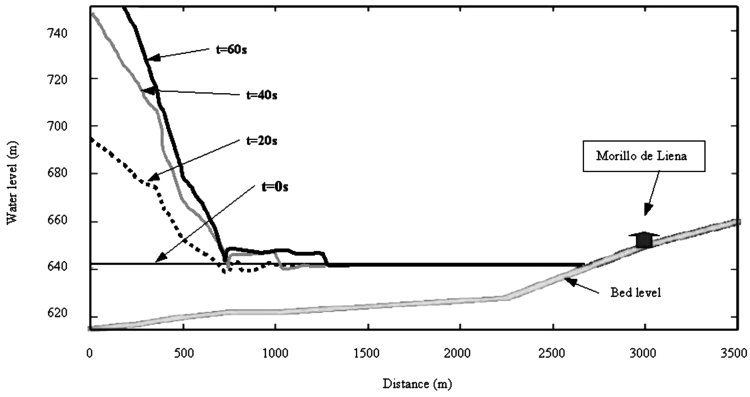


Figure 6. Shock wave propagation towards Morillo de Liena (read arrow at $x = 3000$). Blue line is bottom level at $t = 0$.

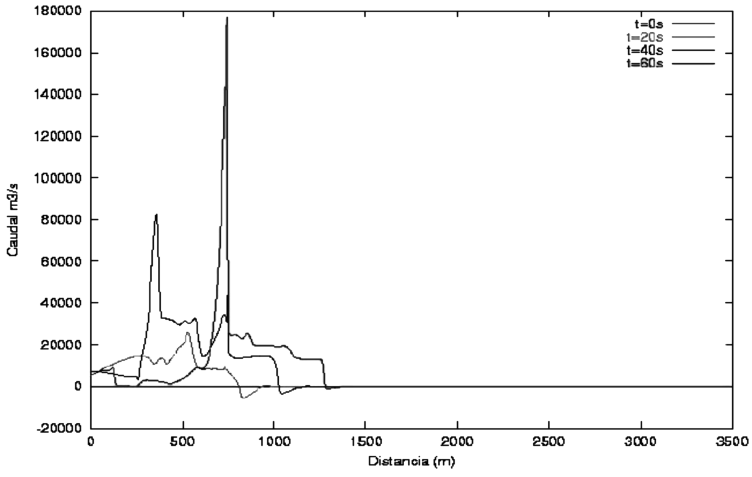


Figure 7. Discharge distribution corresponding to the water depth distributions in Fig. 6.

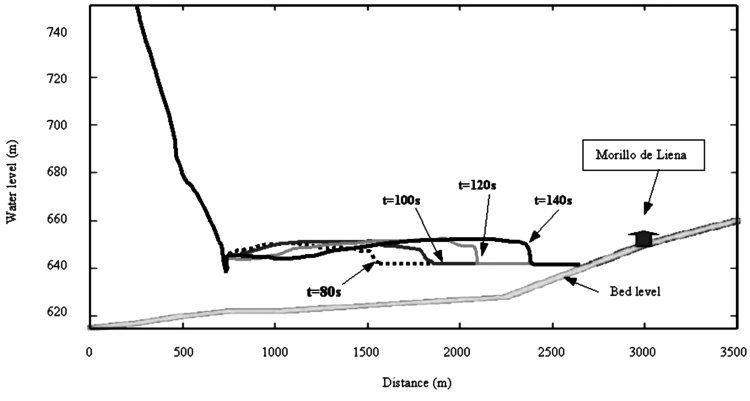


Figure 8. Shock wave water depths (Morillo de Liena at arrow head, $x = 3000$).

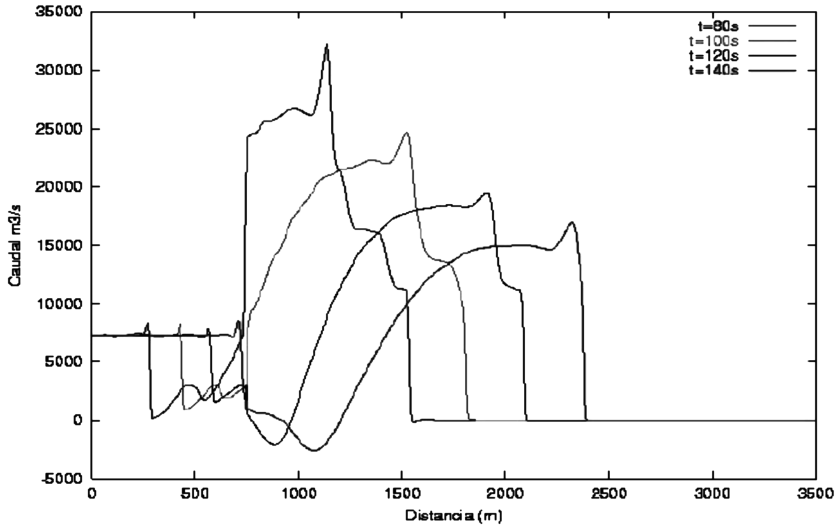


Figure 9. Discharge distributions corresponding to the water levels in Fig. 8.

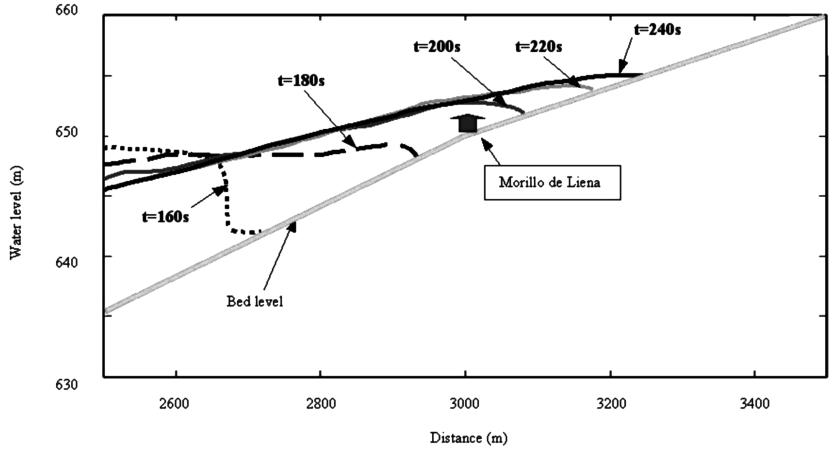


Figure 10. Detail of the water depth evolution near Morillo de Liena.

of channel bed variations in time, allowing for accurate results. The simulation tool developed enables conservative, fast and dynamic calculations of a wide variety of cases including irregular cross sections in presence of different sorts of sliding motions that are characterized depending on their geometry and kinematic properties. From the numerical point of view, it can be concluded that the scheme used, based on the first order explicit Roe's method, is a suitable for this kind of problems.

Longitudinal slides generate both a shock wave traveling in the same sense as the moving solid and a depression wave travelling in the opposite sense. Both the thickness and celerity of the sliding volume are key factors at defining the momentum exchange and hence the wave generated. The particular shape of the solid moving front is less important. Transverse sliding modeling in a one-dimensional approach has to be carefully treated. An algorithm based on the movement of the center mass of the wetted section has been applied to simulate a real case of potential lateral sliding.

The results show the characteristics of the wave generated, magnitude and celerity and the potential risk for the river bank population. This results can be considered the consequence of a preliminary study. It is

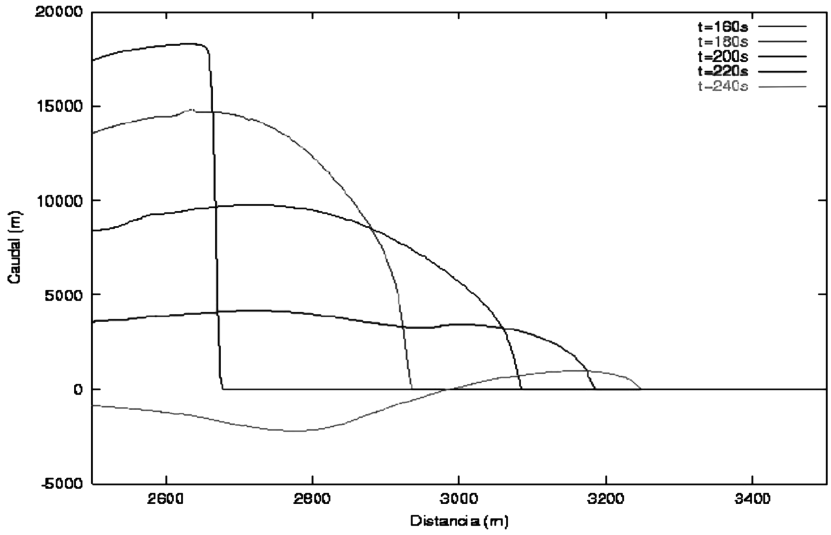


Figure 11. Detail of the discharges near Morillo de Liena.

doubtless necessary to perform more exhaustive and detailed studies of the sliding dynamics, and the river bed geometry since these are the most determinant factors for the wave advance.

REFERENCES

Brufau P., Vázquez-Cendón M.E. & García-Navarro P.A numerical model for the flooding and drying of irregular domains. *International Journal for Numerical Methods in Fluids*, 39, 2002.

Burguete J. & García-Navarro P. Accurate numerical resolution of the shallow water equations using an upwind implicit scheme with large CFL. Technical report, Fluid Mechanics. Universidad de Zaragoza, 2001.

Carracedo J.C., Simon J. Day, Hervé Guillou & Pérez Torrado F.J. Giant Quaternary landslides in the evolution of La Palma and El Hierro, Canary Islands. *Journal of Volcanology and Geothermal Research* 94, May 1999.

Casas Sáinz A.M. Evolución de vertientes y riesgos geológicos en el Ésera medio (tramo Santa Liestra-Morillo de Liena). *Informe técnico. Departamento de Ciencias de la Tierra. Universidad de Zaragoza. Agosto 1997*.

Chow V.T. Open-Channel Hydraulics. *McGraw-Hill*, 1959.

Cunge J.A., Holly F.M. & Verwey A. Practical Aspects of Computational River Hydraulics. *Pitman Publishing*, 1980.

García-Navarro P. & Vazquez-Cendon M.E. On numerical treatment of the source terms in the shallow water equations. *Computers & Fluids* 29, 1999.

Gutiérrez Elorza M. Geomorfología climática. *Ed. OMEGA*, 2001.

Hubbard M.E. & García-Navarro P. Flux Difference Splitting and the Balancing of Source Terms and Flux Gradients. *Journal of Computational Physics*, 165, 2000.

Kiersch George A. Vaiont Reservoir disaster. *Geotimes*, May–June 1965.

Roe PL. Approximate Riemann solvers, parameter vectors and difference schemes. *Journal of Computational Physics*, 43, 1981.

Thomas, M.F. Geomorphology in the tropics. A study of weathering and denudation in low latitudes. *Wiley*, Chichester, 1994.

Vázquez-Cendón M.E. *Numerical solution of the shallow water equations in channels with movable bed. Technical report*, Departamento de Matemática Aplicada de la Universidad de Santiago de Compostela, 2001.

Vila JP. *Étude méthodologique des éffects d'une avalanche de neige dans une retenue d'eau.* Rapport final. CEMAGREF, Division Nivologie. 1985.

River Flow 2004 – Greco, Carravetta & Della Morte (eds.)
© 2004 Taylor & Francis Group, London, ISBN 90 5809 658 0

Numerical simulation for destruction process of rubble stones dam

E. Harada & T. Hosoda
Dept. of Urban Management, Kyoto Univ., Yoshida Honmachi, Sakyo-ku, Kyoto, Japan

H. Gotoh
Dept. of Urban and Environmental Engrg., Kyoto Univ., Yoshida Hnomachi, Sakyo-ku, Kyoto, Japan

ABSTRACT: A rubble stones dam is sometimes destroyed at the time of the big flood. It is important for the effective design of the rubble stones dam to understand the destruction mechanism due to the big flood. Interaction between rubble stones is dominant in the destruction process, so key to the detailed understanding of the destruction mechanism is how to evaluate the each rubble stones motion. And also the evaluation of the interaction between solid phase and liquid phase is key too. In this paper, the solid phase is modeled by using the Distinct Element Method, and the numerical simulation based on the solid-liquid two phase flow modeled by Euler-Lagrange coupling is performed to investigate the detailed mechanism for the destruction process of the rubble stones dam.

1 INTRODUCTION

Porous dam is made of rubble stones in consideration of harmony with the nature. By the way, disasters of the destruction of the rubble stones dam due to a big flood have been reported. Hence, to understand the mechanism of the destruction process of the rubble stones dam is important for the effective design of the rubble stones dam. The destruction process of the rubble stones dam is composed of collision between rubble stones, or solid-solid phase, and interaction between rubble stones and fluid, or solid-liquid phase, these processes are very complex, so it is difficult for the detailed investigation of the destruction process of the rubbles stones dam by the measurement of experiments. And also, needless to say, development of the numerical simulation code, which can express these processes, is an effective tool for detailed analysis of the destruction process of the rubble stones dam. Therefore, the purpose of this paper is investigation of these processes of the rubble stones dam numerically by development of the solid-liquid two phase flow numerical simulation code by the two way method, especially solid phase is modeled by using the Movable Bed Simulator, or MBS, proposed by Gotoh, H. & Sakai, T. (1997), which is based on the Distinct Element Method, or DEM, propsed by Cundall, P.A. & Strack, O.D.L. (1979) which can evaluate the solid-solid interaction. The destruction mechanism of the rubble stones dam is investigated numerically from the driving force acting on the rubble stones. Furthermore, the comparison numerical simulation with experiments is discussed.

2 OUTLINE OF THE SIMULATION MODEL

2.1 *Model of solid phase*

The distinct feature of the destruction process of the rubble stones dam is that the rubble stones shows the transition process from static condition of rubble stones to movement process such as collision and repulsion by the driving force of water flow. So, to evaluate the each rubble stone motion with collision an repulsion, solid phase is calculated by the MBS, or Movable Bed Simulator, proposed by Gotoh, H. & Sakai, T. (1997), which is based on the DEM, or Distinct Element Method proposed by Cundall, P.A. & Strack, O.D.L. (1979). Each particle (= each rubble stone) motion is defined by the following translation and rotational equations:

$$\rho\left(\frac{\sigma}{\rho}+C_M\right)A_3 d^3\frac{d\mathbf{v}_p}{dt} = -A_3 d^3\nabla P+\mathbf{f}_{gr}+\mathbf{f}_{p\,\mathrm{int}}+\mathbf{f}_D \tag{1}$$

$$\frac{\sigma\pi d^5}{60}\frac{\mathrm{d}\boldsymbol{\omega}_p}{\mathrm{d}t}=\mathbf{T} \tag{2}$$

$$\mathbf{f}_{\mathrm{gr}}=-\sigma A_3 d^3\mathbf{g} \tag{3}$$

$$\mathbf{f}_{\mathrm{D}} = \frac{(1-c)}{2}\rho C_{\mathrm{D}} A_2 d^2 \left|\mathbf{u}-\mathbf{v}_{\mathrm{p}}\right|\left(\mathbf{u}-\mathbf{v}_{\mathrm{p}}\right) \tag{4}$$

$$C_{\mathrm{D}} = C_{\mathrm{D}\infty} + \frac{24\nu}{d\cdot\left|\mathbf{u}-\mathbf{v}_{\mathrm{p}}\right|} \tag{5}$$

where ρ = density of fluid ($\rho_{\mathrm{water}} = 1.0$ and $\rho_{\mathrm{air}} = 0.001$); σ = density of particle ($\sigma = 2.65$); C_{M} = added-mass coefficient($C_{\mathrm{M}} = 0.5$); A_2, A_3 = two- and three-dimensional geometrical coefficients of particle ($A_2 = \pi/4$ and $A_3 = \pi/6$); d = diameter of particle ($d = 0.005$ m); $\mathbf{V}_{\mathrm{p}}$ = velocity vector of particle; t = time; P = pressure of water; $\mathbf{f}_{\mathrm{gr}}$ = body force vector; $\mathbf{f}_{\mathrm{p\ int}}$ = particle/particle interacting force vector; $\mathbf{f}_{\mathrm{D}}$ = drag force vector; $\boldsymbol{\omega}_{\mathrm{p}}$ = angular velocity of particle; $\mathbf{T}$ = torque acting on particle; $\mathbf{g}$ = gravity force vector; C_{D} = drag coefficient($C_{\mathrm{D}\infty} = 0.4$); and ν = kinematic viscosity. The contacting condition of each particle is looked for at every renewal of the calculation time step (Δt). The acting force between contacting particles is evaluated by spring and dashpot system shown in Figure 1, which is introduced in both of the normal and tangential direction. And also, in this simulation, particles are non-cohesive, hence the joint, which has no resistance to the tensile force, is assumed in the normal direction. While, in the tangential direction, the friction force(friction coefficient $\mu = 0.577$) works. To describe this characteristics, the joint, which slips at the time limit of the shear stress, is assumed in the tangential direction. The detailed model of interaction between particles is mentioned in the paper (Gotoh, H. & Sakai, T. (1997)). The tuning parameters (spring constants in normal and tangential directions (k_{n}, k_{s}) and damping constants in normal and tangential directions (η_{n}, η_{s})) are determined with following the optimization procedure given by Gotoh et al. (2001). The tuning parameter are as follows: $k_{\mathrm{n\ air}} = 707.52$ N/s; $k_{\mathrm{s\ air}} = 272.12$ N/s; $\eta_{\mathrm{n\ air}} = 0.70$ Ns/m; $\eta_{\mathrm{s\ air}} = 0.43$ Ns/m in the air, $k_{\mathrm{n\ water}} = 840.82$ N/s; $k_{\mathrm{s\ water}} = 323.39$ N/s; $\eta_{\mathrm{n\ water}} = 0.83$ Ns/m; $\eta_{\mathrm{s\ water}} = 0.52$ Ns/m in the water. These parameters are determined to show the good agreement with experiment result. The share of particle concentration (c) and the component of drag force ($\mathbf{f}_{\mathrm{Di}}$) in each calculation domain cell are evaluated from the position of all particles calculated by the governing equations (1) and (2). And then these values are used in the solid-liquid coupling.

2.2 *Model of liquid phase*

Continuity and momentum equations to the local averaged flow of incompressible fluid are described as follows:

$$\frac{\partial(1-c)}{\partial t} + \frac{\partial}{\partial x_{\mathrm{j}}}(1-c)u_{\mathrm{j}} = 0 \tag{6}$$

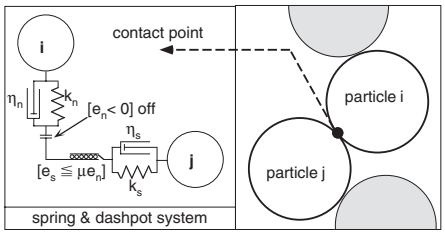


Figure 1. Spring and dashpot system between contacting particles.

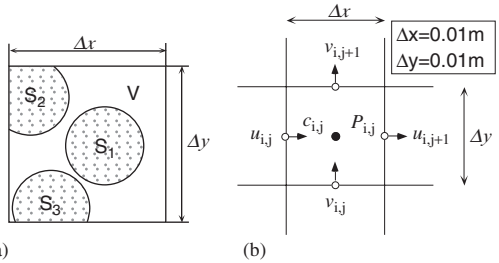


Figure 2. (a) share of the particles in the cell; (b) fluid-variable layout.

$$\frac{\partial}{\partial t}\left\{\rho(1-c)u_{\mathrm{i}}\right\} + \frac{\partial}{\partial x_{\mathrm{j}}}\left\{\rho(1-c)u_{\mathrm{i}}u_{\mathrm{j}}\right\} =$$
$$\rho(1-c)\mathrm{g}_{\mathrm{i}} - (1-c)\frac{\partial P}{\partial x_{\mathrm{i}}} + \frac{\partial(1-c)\tau_{\mathrm{ij}}}{\partial x_{\mathrm{j}}} - F_{\mathrm{Di}} \tag{7}$$

$$c = \beta \sum_{\mathrm{k}} \frac{A_2 d^2 s_{\mathrm{k}}}{V} \tag{8}$$

$$F_{\mathrm{Di}} = \frac{1}{V}\sum_{\mathrm{k}} f_{\mathrm{Di}}\, s_{\mathrm{k}} \tag{9}$$

$$\tau_{ij} = \rho\left(\nu + \nu_t\right)\left(\frac{\partial u_i}{\partial x_j} + \frac{\partial u_j}{\partial x_i}\right) \tag{10}$$

where β = correction factor for three-dimensional effect ($\beta = 0.67$); x_{i} = Cartesian components x, y; $\mathbf{u}_{\mathrm{i}}$; averaged fluid velocity in Cartesian components u, v; $\mathbf{f}_{\mathrm{Di}}$ = component of drag force of each particle; V = the cell area; S_{k} = share of k-th particle in the cell (shown in Figure 2); τ_{ij} = component of stress tensor; and ν_{t} = kinematic eddy viscosity. And also, interaction force at interface between solid phase and liquid phase is evaluated by drag force.

2.3 *Model of turbulent flow*

In this paper, turbulent flow is modeled by standard k-ε turbulent model of second closure model based on the isotropic eddy viscosity. k and ε equations including the existence of particles can be written as follows:

$$\frac{\partial(1-c)k}{\partial t}+\frac{\partial(1-c)ku_j}{\partial x_j}= (1-c)P_k-(1-c)\varepsilon+D_k-G_k \tag{11}$$

$$\frac{\partial(1-c)\varepsilon}{\partial t}+\frac{\partial(1-c)\varepsilon u_j}{\partial x_j}= \frac{(1-c)\varepsilon}{k}\left(C_{\varepsilon 1}P_k-C_{\varepsilon 2}\varepsilon\right)+D_\varepsilon-G_\varepsilon \tag{12}$$

$$P_k=-\overline{u_i'u_j'}\frac{\partial u_i}{\partial x_j} \tag{13}$$

$$\overline{u_i'u_j'}=\frac{2}{3}k\delta_{ij}-\nu_t\left(\frac{\partial u_i}{\partial x_j}+\frac{\partial u_j}{\partial x_i}\right);\ \nu_t=C_\mu\frac{k^2}{\varepsilon} \tag{14}$$

$$D_k=\frac{\partial}{\partial x_j}\left\{(1-c)\left(\frac{\nu_t}{\sigma_k}+\nu\right)\frac{\partial k}{\partial x_j}\right\} \tag{15}$$

$$D_\varepsilon=\frac{\partial}{\partial x_j}\left\{(1-c)\left(\frac{\nu_t}{\sigma_\varepsilon}+\nu\right)\frac{\partial \varepsilon}{\partial x_j}\right\} \tag{16}$$

where $k=$ turbulent energy; $\varepsilon=$ energy dissipation; $Pr=$ production of turbulent energy due to shear stress; and G_k, $G_\varepsilon=$ term in consideration of components the turbulent fluctuating caused by the existence of sand particle. The recommend values by Launder, B.E. & Spalding, D.B.(1974) for the constants in the k-ε turbulent model are as follows: $C_\mu=0.09$; $\sigma_k=1.0$; $\sigma_\varepsilon=1.3$; $C_{\varepsilon 1}=1.44$; $C_{\varepsilon 2}=1.92$. The evaluation of the G_k and G_ε are neglected for the simplification.

2.4 *Outline of computing method*

The coupling between solid phase and liquid phase is calculated by repeating calculation of liquid phase and solid phase alternately. The marching procedure of calculation from the time $n\Delta t_f$ to the time $(n+1)\Delta t_f$ is as follows. For the first step, the prediction value of velocity ($\mathbf{u}^*$)

$$\mathbf{u}^*=\mathbf{u}^n-\frac{\Delta t_f}{\rho(1-c)}\left\{\rho\nabla\cdot(1-c)\mathbf{u}^n\mathbf{u}^n+\rho\mathbf{u}^n\left(\nabla\cdot c\mathbf{v}_p\right)-\rho(1-c)\mathbf{g}+(1-c)\nabla P^n-\nabla\cdot(1-c)\boldsymbol{\tau}^n+\mathbf{F}_D{}^n\right\} \tag{17}$$

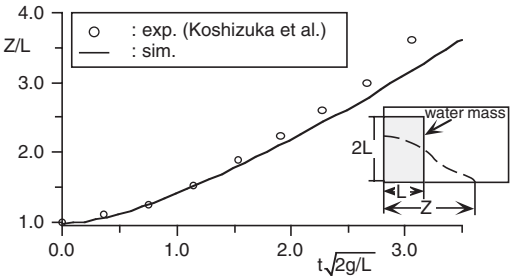


Figure 3. Motion of tip of the broken water.

which is obtained by discretization of equation (7) transformed into the conservative form, is given by using the velocity($\mathbf{u}^n$) and the pressure(P^n) at the time $n\Delta t_f$ where $\Delta t_f=$ time step of the liquid phase ($\Delta t_f=0.00025$ s); $n=$ marching time step; and $\tau=$ stress tensor. The second step, the iterative calculation, which corrects the velocity and the pressure, is performed by the Highly Simplified Marker and Cell method, or HSMAC, proposed by Hirt, C.W. & Cook, J.L. (1972) until the prediction value of velocity ($\mathbf{u}^*$) satisfies the continuity equation for the multi phase flow,

$$\nabla\cdot\left\{(1-c)\mathbf{u}^*+c\mathbf{v}_p{}^n\right\}=0 \tag{18}$$

which is derived from sum of each continuity equation of the liquid phase and solid phase, and then the velocity ($\mathbf{u}^{n+1}$) and the pressure (P^{n+1}) at the time $(n+1)$ Δt_f is computed. Next, the particle positions are evaluated from the MBS with using that renewed flow field ($\mathbf{u}^{n+1}$, P^{n+1}). And the drag force and the share of solid phase in each cell of the flow field are computed, and these are used to the next time step of the liquid phase. This series of processes are iterated till the designated calculation time. And also, the governing equations are discretized by the finite volume method, or FVM, on the staggered grid, and also upwind difference scheme is used in the advection term.

2.5 *Boundary conditions and initial conditions*

The upper side of Figure 4 shows the calculated domain. The destruction and the flowing process of the mound (rubble stones dam) is simulated. The mound is formed by arranging the uniform diameter particles in the plover-shaped. To visualize the fluid motion, the Lagrangian massless marker particles are arranged in the fluid mass. The wall boundary conditions of k and ε are given by the wall function, and the velocity profile in the log-law region is given by presuming turbulent flow on the smooth bed.

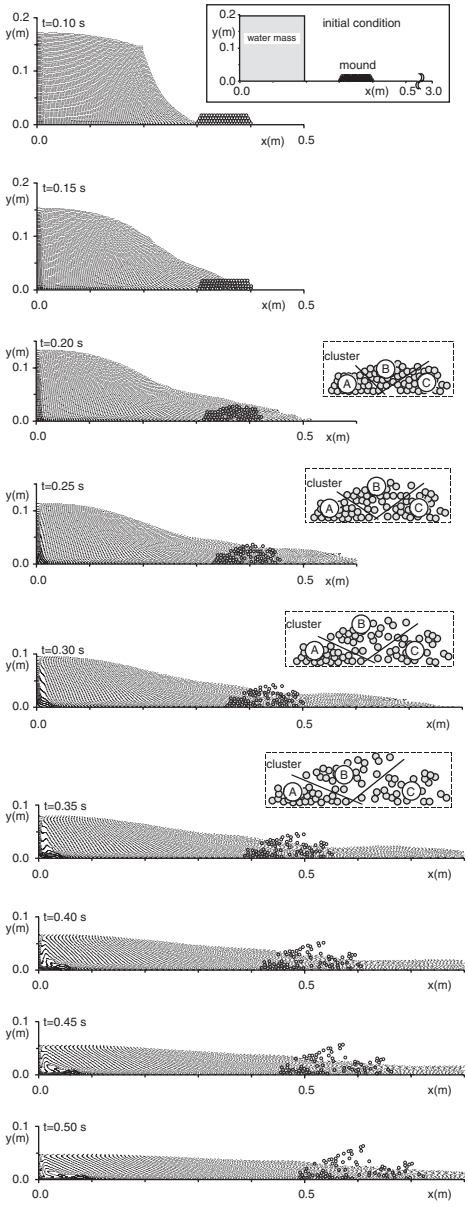


Figure 4. Snapshots of destruction process of the rubble stones dam.

3 SIMULATION

3.1 *Destruction process of rubble stones dam*

The motion of the tip of the water mass running on the bottom wall is shown in Figure 3 to verify the liquid phase of present simulation code. Simulation result shows the good agreement compared with the experiment by Koshizuka et al. 1995. Figure 4 shows the snapshots of the destruction process of the rubble stones dam. The tip of the water mass reaches the toe of the mound (left side of the mound) around the time $t = 0.1$ s, and then infiltration of water to the pore of the mound occurs. Increase of the water surface level due to the resistance of the mound is shown around the mound at the time $t = 0.15$ s. And also, the mound slides with deflection at its center part by the drag force acting on the mound due to the relative velocity between mound and water mass at the time $t = 0.20$–0.25 s. Furthermore, zooming in the deformation of the mound at this stage in detail, two tensile deformation lines occurs inside the mound and separation to three clusters are confirmed. After the time $t = 0.30$ s, flow mode of the mound particles are classified by cluster-A, cluster-B and cluster-C. The particles of cluster-B are transported with pushing out into the air, and most of the particles of cluster-C are transported with swelling in the water. While, the particles of cluster-A are transported with slight deformation in comparison with other clusters.

3.2 *Mechanism of destruction*

The driving force concerned in the present simulation code consists of pressure gradient force, inter-particle force and drag force. Under these driving forces, the velocity vector of particles in the early destruction process of the rubble stones dam is shown in Figure 5. The accelerating process of the particles is shown clearly from the velocity vector of particles. The acceleration rate of the cluster-A is smaller than that of the cluster-C, the tendency to the dispersion of the particles between the cluster-A and the cluster-C shown in Figure 4 is reconfirmed. Next, the transport process of the particles due to the pressure gradient force is examined.

Figure 6 shows the time series of the pressure distribution, and also, gauge pressure is used in pressure indication. A high pressure part around the toe of the mound due to the collision with broken water mass at the time $t = 0.15$ s gradually permeates inside the mound, and influences the transformation of the mound. Furthermore, a high pressure part from center to back inside the mound is found at the time $t = 0.20$–0.28 s, which might be a helpful to generate the cluster of mound. And also, this high pressure part inside the mound might push the particles of the cluster B out of the air.

The transport of the particles due to the drag force acting on the particles and the inter-particle force at the mound is discussed. Figure 7 shows the time series of mean inter-particle force, mean drag force and the total number of the contact points between particles. The mean inter-particle force classified in two

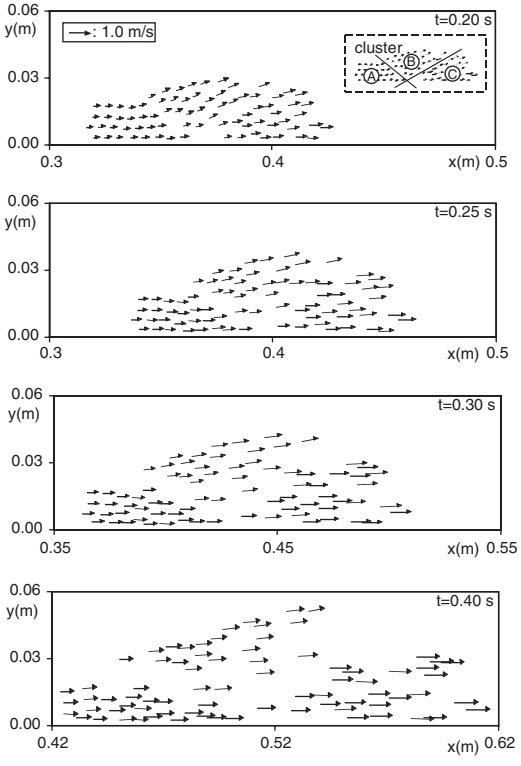


Figure 5. Velocity vector of the rubble stones dam.

blocks of increase section (block-1) and occasional occurrence section (block-2). The abrupt increase of interaction force between particles due to the collision with the collapsing water in the block-1 lead to the destruction of the mound inner structure, and also the energy, which make the mound disperse, would be concentrated. While, in the block-2, the dispersed particles mix with the broken water and transport under the solid-liquid two phase flow. And also, the inter-particle force in this block-2 only occurs occasionally, hence the drag force and pressure gradient force dominates to the destruction of the mound. The abrupt increase number of contact points between particles are also shown from the time series of the total number of the contact points between particles, and it is confirmed that the dominant force to the dispersion of the mound particles is the inter-particle force. In the transport process of the block-2, the slight change of the contact points between particles is found, therefore, the driving force by the inter-particle force is comparatively smaller than other factors of driving force. And also, although the number of the contact points between particles show the slight fluctuation, the inter-particle force and the drag force are not shown

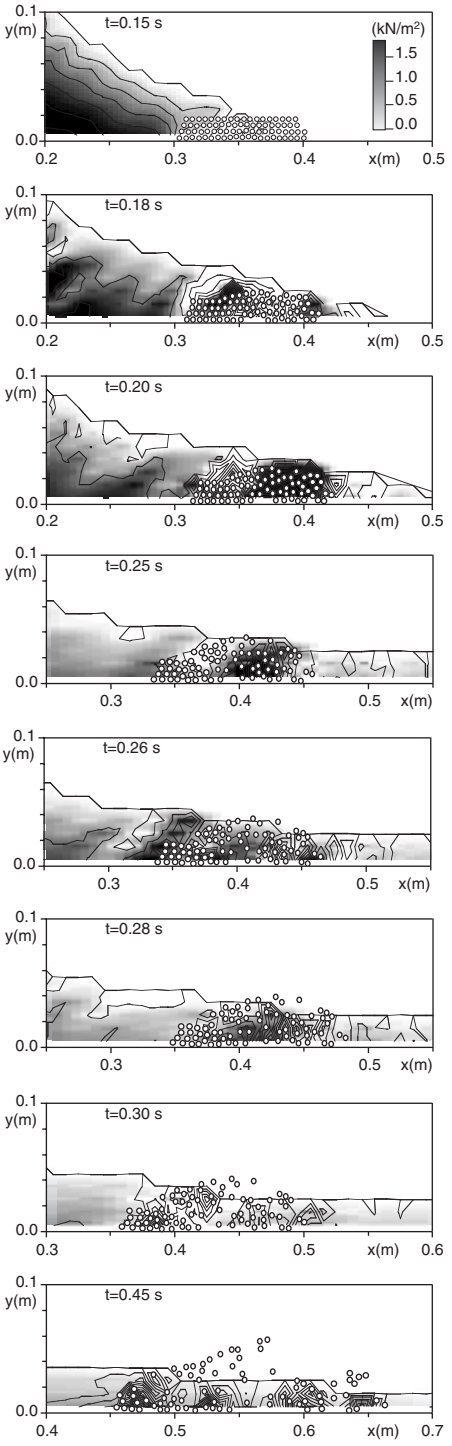


Figure 6. Pressure distribution around collapsing rubble stones dam.

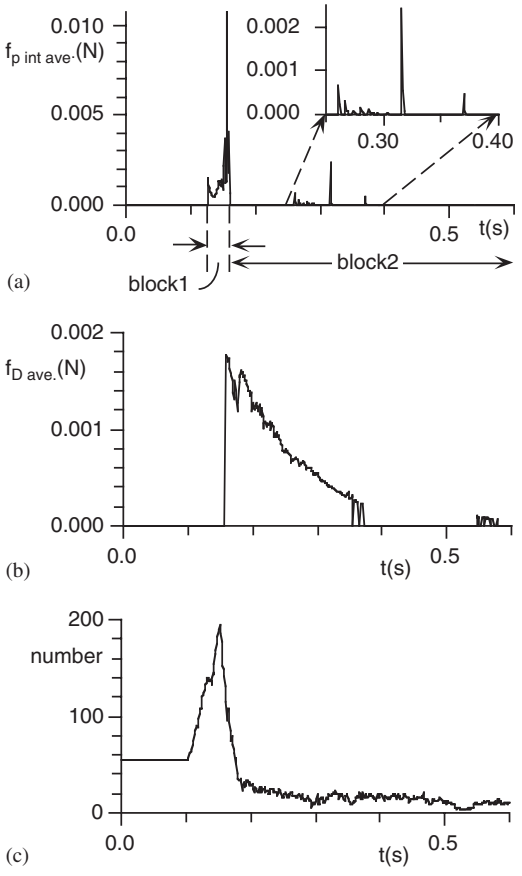


Figure 7. (a) mean inter-paritcle force; (b) middle: mean drag force; (c) total number of contact particles.

at the time $t = 0.04$–0.05 s. So, the equilibrium transport process of the dispersed particles, in which the relative velocity between particles and fluid are small, would be shown.

4 EXPERIMENT

4.1 *Outline of experiment*

A destruction of rubble stones dam is reproduced by acrylic open channel, which is 3.0 m long, with a slit at 0.5 m shown in Figure 8. The cross section of the acrylic open channel is 0.1 m width. The driving force of the destruction of rubble stones dam is broken water power, which is reserved in the left side of the slit, due to pulling up the slit. Motion of the mound particles are recorded by the digital video camera, shatter speed of which is 1/4000 s, from the side of acrylic-resin-wall. The test mound particle is the glass beads, 2.5 in specific density and 0.005 m in diameter. After the

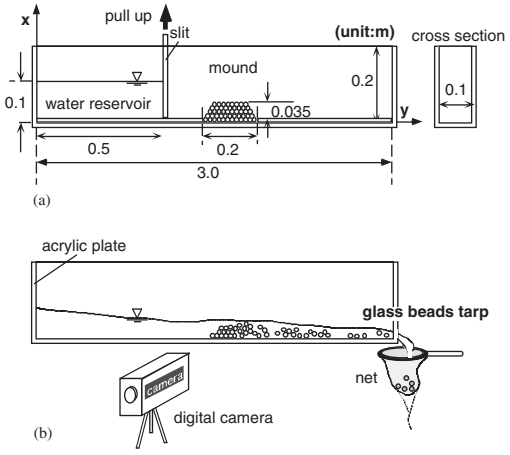


Figure 8. (a) experimental apparatus and setup; (b) schematic of the typical experiment.

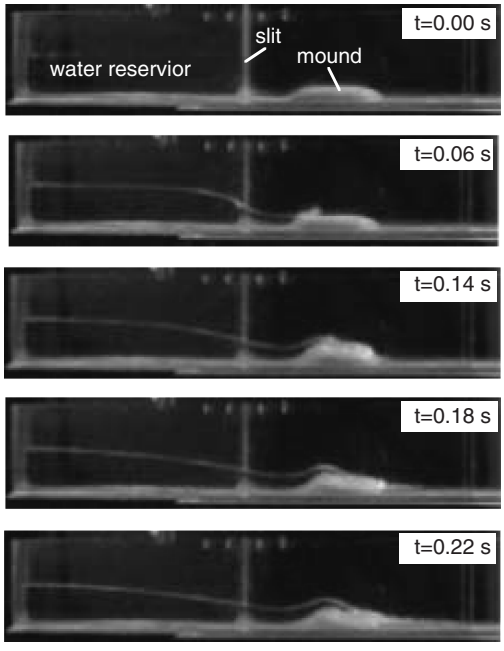


Figure 9. The video frames of destruction process of the rubble stones dam.

destruction of the rubble stones dam due to the broken water, the glass beads are trapped at the right side of the channel by the net.

4.2 *Results*

The video frames of the destruction process of the rubble stones dam are shown in Figure 9. After pulling up

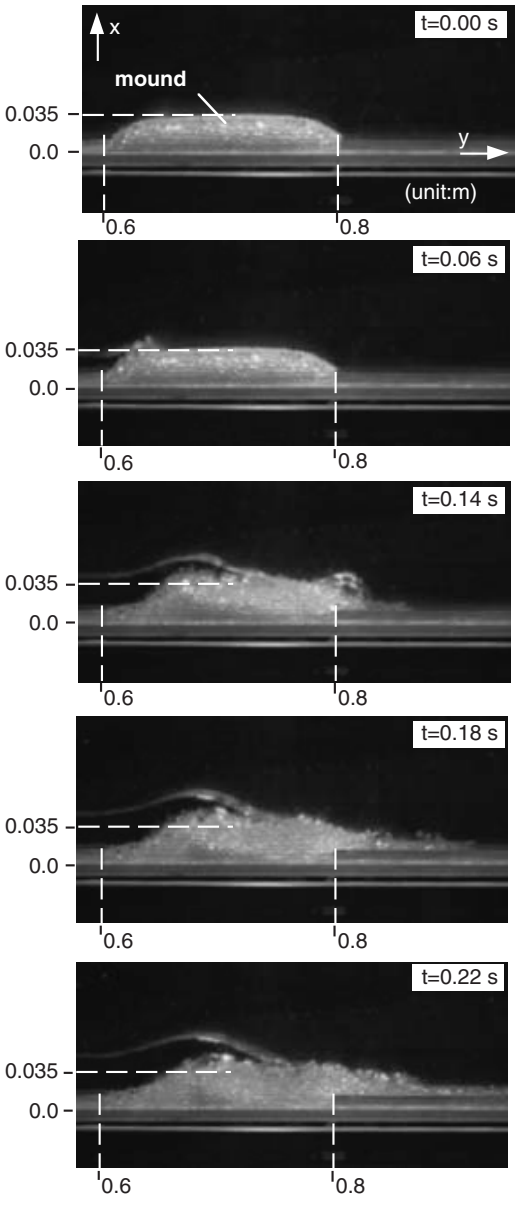


Figure 10. A close-up around the rubble stones dam in experiment.

the slit, the broken water impinges on the left side of the mound edge around the time $t = 0.06$ s. And then, the broken water surmounts the mound with eroding the left side of the mound particles, and the mound is transported.

In particular, to focus the destruction process of the rubble stones dam, the video frames around the mound are shown in Figure 10. The broken water catches

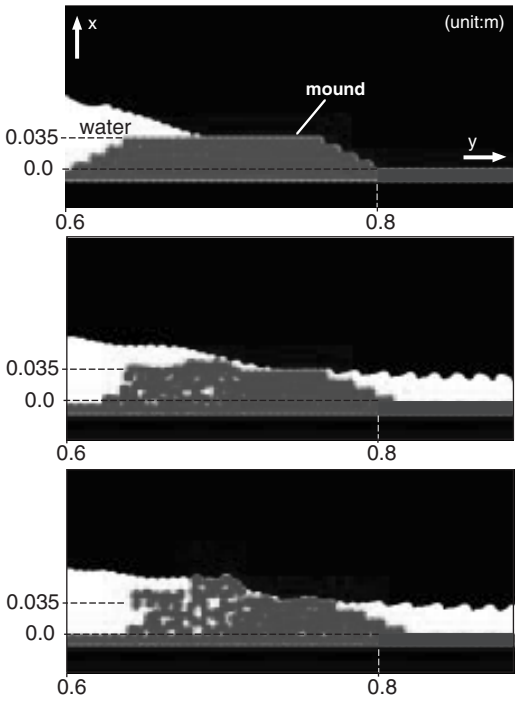


Figure 11. A close-up around the rubble stones dam in simulation.

the glass beads in the left side of the mound, and the glass beads are transported with mixing with the broken water, are observed clearly. Figure 11 shows the destruction process of the rubble stones dam under the same experimental condition. Although the water surface level is different from experiment shown in Figure 10, the eroding process around the left side of the mound due to the force of the broken water is simulated, the same destruction tendency shown in the experiment can be confirmed from the simulation result as well.

5 CONCLUSIONS

The destruction process and mechanism of the rubble stones dam are discussed numerically by using the solid-liquid two phase flow model based on the Euler-Lagrange coupling. The present simulation shows that the static mound particles disperses by the pressure gradient force and inter-particle force in the early stage, and then the equilibrium state is confirmed that the dispersed particles are mainly transported by the drag force. Although the interface between solid and liquid is expressed simply by the only drag force in this paper, the simulation result about the destruction process of the mound shows good agreement with

experiment. So, the validity of the evaluation to the motion of the rubble stones is shown. However, the repeatability of water dynamics are in poor agreement with the experimental data. This might be a reason that the evaluation of the interaction between fluid phase and solid phase is insufficient. In the near feature, unsteady process of the destruction of the rubble stones dam have to be discussed in detail in consideration of the additional force due to the unsteady flow and the modeling of turbulent fluctuation due to the particles laden flow. And also, high accurate numerical simulation about the solid-liquid two phase flow should be developed by comparison with experiments.

ACKNOWLEDGMENTS

Thanks are offered to Mr. S. Senba & Mr. K. Obayashi for help with the experiments.

REFERENCES

Cundall, P.A. & Strack, O.D.L. 1979. Discrete Numerical Model for Granular Assemblies. *Geotechnique*, Vol. 29: 47–65.

Gotoh, H. & Sakai, T. 1997. Numerical Simulation of Sheetflow as Granular Material. *Jour. of Waterway, Port, Coastal and Ocean Engrg., ASCE*, Vol. 123, No. 6: 329–336.

Gotoh, H. et al. 2001. Optimization of Parameters in DEM-Based Numerical Movable Bed Simulator. *Jour. of Hydraulic, Coastal and Environmental Engrg., JSCE*, No. 691/II-57: 159–164.

Hirt, C.W. & Cook, J.L. 1972. Calculating three-dimensional flows around structures and over rough terrain. *Jour. Comp. Phys.*, Vol. 10: 324–340.

Koshizuka, S. et al. 1995. A particle method for incompressible viscous flow with fluid fragmentation. *Comp. Fluid Dynamics Jour.*, Vol. 4, No. 1: 29–46.

Launder, B.E. & Spalding, D.B. 1974. The numerical computation of turbulent flows. *Comp. Meth. Appl. Mech. Engrg.*, Vol. 3: 269–289.

River Flow 2004 – Greco, Carravetta & Della Morte (eds.)
© 2004 Taylor & Francis Group, London, ISBN 90 5809 658 0

Effects of gradient pressure on resistance law in roll waves and effects of tension surface

S. Longo
Department of Civil Engineering, University of Parma, Parma, Italy

ABSTRACT: Free surface flow in sufficiently steep channels is unstable and progressive waves develop as periodic distribution of bores connected by smooth profiles. The amplitude of the breakers is higher than the normal water depth. Roll waves in the initial phase development (before overtaking) develop, dissipating for friction less energy than the equivalent uniform stream. Including the gradient pressure effects, an extra saving of energy is computed, which can partially balance the dissipation in the breaker. Assuming different values of the momentum and energy coefficients on the two sides of the breaker, physically acceptable value of the water stream depths are obtained with a limited dissipation rate in the jump. Including the tension surface effects, a new family of roll waves is depicted.

1 INTRODUCTION

Free surface instabilities of flows down inclined channels have been widely observed in Newtonian and non-Newtonian fluids. If there is enough space for the instabilities to grow, in some condition roll waves develop, with several bores having height, period, length and celerity increasing downstream.

The observations of roll waves in a torrent by Maw in the late 19th century were followed by the first description due to Forchheimer (1903) and to Cornish (1934). Observations of roll waves in mud flows are reported by several Authors in many areas. The first study of the phenomenon was based on linear stability analysis of the basic equations written in the long wave approximation. The development of a finite amplitude wave theory is due to Dressler (1949). Dressler's theory, originally developed for fully turbulent flows, was extended to laminar flows for Newtonian fluids by Ishihara et al. (1954) and to power–law fluids by Ng & Mei (1994), who essentially focussed on pseudoplastic fluids (mud). Recently Prasad et al. (2000) applied Dressler's theory to flowing grains, and Longo (2003) applied Dressler's theory to dilatant fluid.

Roll waves are essentially controlled by Froude number, and can develop in laminar and in turbulent streams. The usual approach is linear stability analysis: the basic flow field (the uniform flow), is perturbed assuming small variations in the water depth and mean velocity. The set of equations in perturbed variables is linearised and solved. If perturbations grow, the basic motion is linear asymptotic unstable, otherwise it is stable. Froude number correspondent to marginal stability (perturbation do not grow nor decay) depends on velocity profile and resistance law. In laminar flow, Yih (1954, 1963) and Benjamin (1957a,b), perturbed Navier-Stokes equations assuming free surface perturbation of sinus shape and recovered Orr-Sommerfeld equation finding a critical Froude number equal to 0.527. Similar result was obtained by Chen (1992), perturbing the shallow water 1-D equation including derivative of Boussinesq coefficient of momentum along the stream motion.

Vedernikov (1945) introduced the so called Vedernikov number to state the necessary condition for roll waves formation. Montuori (1961) state the sufficient condition for roll wave formation.

In turbulent flow in rectangular channels, assuming a Chézy resistance law with a constant coefficient, Jeffreys (1925), Stoker (1957), Liggett (1975) found a critical Froude number equal to 2. Several Researchers as Iwasa (1954); Koloseus & Davidian, (1966); Berlamont & Vanderstappen (1981) put in evidence the strong sensitivity of critical Froude number on velocity profile, Reynolds number, friction law. In particular according to Rouse (1963); Rosso et al. (1990), the Darcy-Weisbach friction factor increases for increasing Froude number in supercritical streams. According to Brock (1966, 1967), no firm conclusion on such a dependence could be drawn because experimental data were not enough accurate, especially the water depth measurements. Moreover an apparent increment of friction factor could better be explained as energy transfer from mean flow to waves.

In addition several laboratory experiments with water streams were conducted by Ishihara et al. (1954), Brock (1967), Julien & Hartley (1985, 1986). Brock (1967, 1969) carried out experiments in a rectangular small channel 40 m long and ∼12 cm wide, and essentially classified two families of roll waves. A first family included natural roll waves, generally non periodic; a second family included artificial periodic roll waves, obtained imposing a controlled disturb at the inlet and characterised by a strong regularity. In both cases there is an initial stage with waves of constant period, and a second stage of growing and with a wave period and length increment. The growth of natural roll waves also happens as coalescence of two or more waves. In the second stage the significant wave characteristics (wave height, celerity and mean wave length) coincide in both natural and artificial roll waves with similar Froude number and channel bottom slope.

Roll waves analysis is a challenging topic from a mathematical point of view and roll waves knowledge has also a practical application. In fact roll waves strongly enhance the maximum water depth (up to 3 times the normal depth) and the maximum fluid velocity, increasing its threatening. Most of the available results refer to the limit condition for roll waves existence, but no one can infer the determination of roll wave parameters (wave length, wave height, celerity) for a given system. There are some experimental indications due to Ponce & Maisner (1993), who using Brock's data (1967) found that the observed periodic roll waves are those corresponding to the maximum growth rate (in linear stability analysis). Ng & Mei (1994) infer that the observed roll wave has the lowest amplitude corresponding to no energy loss across the shock.

In the present study we analyse the energy balance in permanent periodic roll waves. Dissipation in a free surface flow is generally controlled by wall stress and depends on Reynolds and Froude numbers, wall roughness, shape of the transversal section, channel profile, channel plan and non stationarity parameter. Uniform flow in a channel dissipates energy per unit weight and unit length equal to bottom slope. If bores or jumps are present, part of the energy is dissipated in the shock area with a dissipation depending on the conjugate water depth. Lamberti & Longo (2000) demonstrated that assuming a reliable wave form and resistance law for a free surface flow, in some condition the stream dissipates per unit wave length less energy respect to the uniform stream; the energy excess is then dissipated in the shock. In such a situation the conjugate water depths are obtained imposing the energy balance over a single wave length. They also demonstrated that using the same energy balance criterion and integrating the water depth in a moving reference solidal with the wave form (Thomas, 1939; Dressler, 1949; Brock, 1967), it is possible to evaluate all the waves characteristics for a given water discharge and bottom slope and wall roughness.

In the present manuscript the first part of the analysis is devoted to the boundary layer effects on roll waves. Friction is usually evaluated assuming a quasi-steady motion, neglecting the pressure gradient. If the boundary layer has an adverse gradient pressure, friction is reduced and also dissipation in the stream is reduced.

The second part of the analysis is devoted to tension surface effects. In principle, tension surface can lead to a new family of solution obtained using Dressler's approach. These solution can have practical interest in fluid with a strong tension surface.

The next Section is devoted to deriving the basic equations applying Karman's momentum integral method. In Section 3 we describe the structure of the boundary layer in a roll wave and its effects on resistance law. In Section 4 we describe the 'special solution' with a modified resistance law and in Section 5 we obtain the admissibility conditions for roll waves. In Section 6 the effects of tension surface on admissibility criteria for finite amplitude waves is studied. Sections 7, 8 and 9 are devoted to shock conditions and to energy balance in the discontinuity and in the unstable stream.

2 BALANCE EQUATIONS

Let us consider a 2-D laminar flow of a fluid down a plane of inclination θ. The coordinate system has the x-axis along the bed and the y-axis normal to it (Fig. 1). For long waves, applying Karman's momentum integral method to mass balance and linear momentum balance, we obtain the following set of equations:

$$\begin{cases} A_{,t} + (uA)_{,x} = 0 \\ u_{,t} + \beta u u_{,x} - (\beta - 1)\dfrac{u}{A}\dfrac{dA}{dy} y_{,t} + \\ g\cos\theta\, y_{,x} + \dfrac{\sigma}{\rho} y_{,xxx} + u^2 \beta_{,x} = g\sin\theta - \dfrac{\tau_b}{\rho R} \end{cases} \tag{1,2}$$

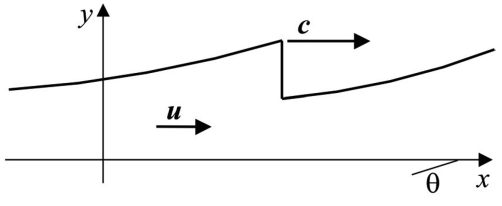


Figure 1. Schematic of periodic waves with sharp front in shallow fluid flows.

where u is the depth average velocity of flow function of the longitudinal coordinate x and time t, A is the cross sectional area of flow, y is the depth of the flow, β is the momentum flux factor, τ_b is the average boundary shear stress and R is the hydraulic radius of the flow, ρ is the mass density of the fluid, g is acceleration of gravity and σ is the surface tension.

Introducing a moving reference having celerity c and assuming that in the moving reference the chosen state variables U and Y are function of $\xi = x - ct$ only (Fig. 2):

$$\begin{aligned} u(x,t) &= U(x-ct) = U(\xi) \\ y(x,t) &= Y(x-ct) = Y(\xi) \end{aligned} \tag{3}$$

The two equations (1, 2) for a wide channel ($R \approx Y$) become:

$$\begin{cases} (UY)_{,\xi} - cY_{,\xi} = 0 \\ -cU_{,\xi} + \beta UU_{,\xi} + c(\beta - 1)\dfrac{U}{Y}Y_{,\xi} + \\ \mathrm{g}\cos\theta Y_{,\xi} + \dfrac{\sigma}{\rho}Y_{,xxx} = \mathrm{g}\sin\theta - \dfrac{\tau_b}{\rho Y} \end{cases} \tag{4,5}$$

where the spatial variation of the momentum flux correction term is neglected.

Eqs (4–5) can be rearranged as:

$$\begin{cases} U_{,\xi} = \dfrac{g\left(\sin\theta - \dfrac{\tau_b}{\gamma Y} - \dfrac{\sigma}{\gamma}Y_{,xxx}\right)(U-c)}{\left[(U-c)(\beta U - c) - c(\beta - 1)U - \mathrm{g}Y\cos\theta\right]} \\ Y_{,\xi} = -\dfrac{gY\left(\sin\theta - \dfrac{\tau_b}{\gamma Y} - \dfrac{\sigma}{\gamma}Y_{,xxx}\right)}{\left[(U-c)(\beta U - c) - c(\beta - 1)U - \mathrm{g}Y\cos\theta\right]} \end{cases} \tag{6,7}$$

with $\gamma = \rho g$ the specific weight of the fluid. Dividing these two equations and integrating results:

$$U = \frac{(cY - K)}{Y} \tag{8}$$

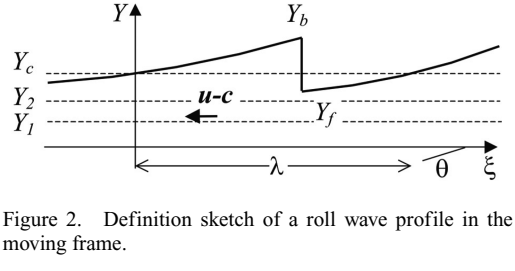


Figure 2. Definition sketch of a roll wave profile in the moving frame.

K is the constant discharge per unit width in the moving frame. It was defined as 'overrun' by Chow (1959) and 'progressive discharge' by Dressler (1949). The discharge in the fixed frame varies with space and time.

3 RESISTANCE AND BOUNDARY LAYER STRUCTURE

Resistance to flow in open channels is function of several independent variables. For a rectangular straight channel of uniform inclination, the force per unit length, intended as that which, when multiplied by the mean velocity of flow yields the rate of energy dissipation, can be expressed as (Rouse, 1965):

$$\frac{\partial F}{\partial x} = f(y, U, k, \varsigma, \rho, g, \mu, \partial y / \partial t) \tag{9}$$

where y is the mean depth, U is the mean velocity, k is a length describing the surface roughness, ζ is a parameter describing the shape of the cross section, ρ is the fluid density, g is the gravity acceleration, μ is fluid viscosity and $\partial y / \partial t$ is the rate of change of depth with time. Using Buckingham's theorem results in a relation among non dimensional group as:

$$\frac{\partial F / \partial x}{\rho U^2 y} = f\left(\frac{\rho U y}{\mu}, \frac{k}{y}, \varsigma, \frac{U}{\sqrt{gy}}, \frac{\partial y / \partial t}{U}\right) \tag{10}$$

The term on the left hand is essentially a friction factor, the terms on the right hand are Reynolds' number, non dimensional roughness, the cross section shape factor, the Froude number and the degree of unsteadiness. The effects of the Froude number have been widely discussed. According to Rouse (1965) there is an apparent increase in channel resistance as the Froude number exceeds the stability limit, with waves formation. The increase in channel resistance can be intended as a transformation from mean-flow energy to wave energy instead of pure dissipation. Beyond the stability limit roll waves develop and the flow cannot be treated as uniform and steady. In a discussion to Rouse's paper by Brock (1966) the concept of apparent increase in channel resistance is better focused, highlighting that if part of energy gained by gravity is transferred to waves and then dissipated by waves, the apparent dissipation due to boundary friction is higher whenever waves effects are not taken into account in the energy balance. This hypothesis has been supported by detailed measurements (e.g. Rosso et al., 1990).

The dependence of friction factor on the degree of unsteadiness is more complicated. Unsteadiness is usually connected with gradient pressure and it can

be verified that self preserving solutions in boundary layers (i.e. solutions invariant respect to horizontal coordinate and function of non-dimensional vertical coordinate and non dimensional velocity) can be obtained only with a careful adjustment of the pressure (Clauser, 1956). As a consequence the dependence of friction factor on unsteadiness parameter is not theoretically available except for specific controlled flow fields. Nevertheless it is interesting to study the effects of the unsteadiness parameter on energy dissipation.

Assuming the wave profile obtained by Dressler as a first approximation, we can demonstrate that the bottom boundary layer has an adverse pressure gradient. Neglecting gravity effects and viscous forces in the outer region, the pressure gradient is simply related to fluid acceleration:

$$\frac{dp_e}{dx} \simeq -\rho\left(\frac{\partial U}{\partial t} + U\frac{\partial U}{\partial x}\right) \tag{11}$$

On using eq.(3) and eq.(8) the pressure gradient in the external flow is expressed as:

$$\frac{dp_e}{d\xi} \simeq \frac{\rho K}{Y}\frac{dU}{d\xi} \tag{12}$$

The right hand term in eq.(12) is always positive because fluid velocity increases from the back to the front of the wave and water depth is always positive. The qualitative plot of the external pressure gradient is shown in Figure 3.

The structure of the boundary layer is clearly quite complicate. In the laboratory reference the wall boundary layer has a periodic structure with wave length equal to the length of the roll waves. The adverse gradient pressure tends to grow up the boundary layer thickness behind the moving roller, with increasing efficiency from the front to the back. We can infer that for periodic roll waves the boundary layer attains also

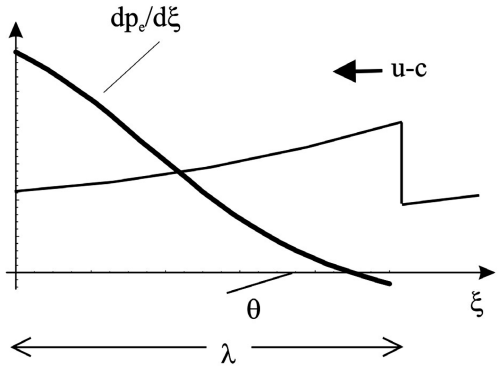


Figure 3. Qualitative plot of the pressure gradient.

a time periodic structure with possible similar solutions. In fact neglecting the time dependent term, the boundary layer can be treated as a stationary boundary layer in adverse pressure gradient subject to growing thickness and growing bottom tangential stress and decreasing pressure gradient. The Rotta-Clauser parameter:

$$\beta_{RC} = \frac{\delta_1}{\tau_b}\frac{dp_e}{d\xi} \tag{13}$$

where δ_1 is the displacement thickness, can be constant or nearly constant. More experimental activity is necessary in order to assess a friction factor formula depending on unsteadiness parameter but it is plausible that friction factor decreases from the back to the front of the roll waves. However in eq.(10) the non-dimensional group $(\partial y/\partial t)/U$ can be written as:

$$\frac{\partial y/\partial t}{U} = \frac{c}{U}\frac{\partial Y}{\partial \xi} \tag{14}$$

and to investigate the structure of roll waves in presence of a decreasing friction factor, we assume a resistance law as:

$$J = \frac{U^2}{g}\frac{r^2}{R}\left(1 - a\frac{\partial Y}{\partial \xi}\right) \tag{15}$$

with a modified friction factor:

$$r^2\left(1 - a\frac{\partial Y}{\partial \xi}\right) \tag{16}$$

where a is a non dimensional parameter. The modified friction factor collapses to the standard friction factor in uniform flow ($\partial Y/\partial \xi = 0$). In presence of roll waves it decreases from the back to the front because $\partial Y/\partial \xi$ is positive and growing. For the sake of simplicity, also considering that this model is not experimentally verified, we assume a constant value for a.

4 THE DISCONTINUOUS SOLUTION WITH THE MODIFIED FRICTION FACTOR AND NEGLECTING THE SURFACE TENSION

On using the modified friction factor in eq.(16), eq.(7) becomes:

$$Y_{,\xi} = -\frac{gY^3 \sin\theta - r^2\left(cY - K\right)^2}{K^2 - gY^3 + ar^2\left(cY - K\right)^2} \tag{17}$$

where the surface tension term has been dropped. The denominator of eq.(17) admits always at least a real

zero named Y_c, which is positive if $a > 0$. The profile would have to be vertical in the neighbour of Y_c if $d^2\xi/dY^2 \neq 0$ in Y_c, otherwise for $d^2\xi/dY^2 \neq 0$ in Y_c a maximum or a minimum is expected. If $a = 0$ Dressler (1949) demonstrated that the function $d^2\xi/dY^2$ cannot be zero in the critical point. It can be demonstrated that:

$$\left.\begin{aligned} \left.\frac{d\xi}{dY}\right|_{Y=Y_c} &= 0 \\ \left.\frac{d^2\xi}{dY^2}\right|_{Y=Y_c} &= 0 \end{aligned}\right\} \text{ if } a = \frac{gY_c^3 + 2K^2}{2r^2K\left(cY_c - K\right)} \tag{18}$$

In the limit of the present analysis, this profile must be disregarded because the basic equations were derived in the hypothesis of small stream curvature, which is not this case. Hence an acceptable profile can be obtained using eq.(17) eliminating the zero of the denominator, imposing that it is also a zero of the numerator. If Y_c is a zero of the denominator, using eq.(8) results:

$$\begin{cases} gY_c^3 \sin\theta - r^2\left(U_cY_c\right)^2 = 0 \\ \left(c - U_c\right)^2 Y_c^2 - gY_c^3 + ar^2\left(U_cY_c\right)^2 = 0 \end{cases} \tag{19,20}$$

that can be reduced to:

$$\begin{cases} gY_c \sin\theta - r^2U_c^2 = 0 \\ \left(c - U_c\right)^2 - gY_c + ar^2U_c^2 = 0 \end{cases} \tag{20,21}$$

The system admits the two couples of solutions, but only the couple:

$$\begin{cases} Y_c = \dfrac{c^2/g}{\left(\dfrac{\sqrt{\sin\theta}}{r} + \sqrt{1 - a\sin\theta}\right)} \\ U_c = \dfrac{c}{1 + r\sqrt{\dfrac{1 - a\sin\theta}{\sin\theta}}} \end{cases} \tag{22,23}$$

satisfies the condition of roll waves existence $c > U_c$ (Whitham, 1973). The solution is real only if $a < 1/\sin\theta$.

Using these quantities, the progressive discharge rate necessary for this special case is:

$$K = \frac{c^3/g}{\left(\dfrac{\sqrt{\sin\theta}}{r} + \sqrt{1 - a\sin\theta}\right)}\sqrt{1 - a\sin\theta} \tag{24}$$

and the following relation holds:

$$Y_c = \frac{K^{2/3}}{g^{1/3}\left(1 - a\sin\theta\right)^{1/3}} \tag{25}$$

Introducing the variable $z = Y/Y_c$ and eliminating the pole $z = 1$, eq.(17) can be written as:

$$Y_{,\xi} = \frac{\sin\theta\left\{\left[z^2 + \left[1 - \dfrac{\left(\sqrt{\sin\theta} + r\sqrt{1 - a\sin\theta}\right)^2}{\sin\theta}\right]z + \dfrac{r^2}{\sin\theta}\left(1 - a\sin\theta\right)\right\}}{\left\{\left[z^2 + \left[1 - a\left(\sqrt{\sin\theta} + r\sqrt{1 - a\sin\theta}\right)^2\right]z + \left(ar^2 - 1\right)\left(1 - a\sin\theta\right)\right\}} \tag{26}$$

5 LIMITING CONDITION FOR A POSITIVE STEEPNESS OF THE PROFILE

In order to construct roll waves from the previous profile, it is necessary that:

$$\left.\frac{dY}{d\xi}\right|_{Y_c} > 0 \tag{27}$$

It can be verified that the numerator in eq.(26) is positive in $z = 1$ if:

$$4r^2 < \frac{\sin\theta}{1 - a\sin\theta} \tag{28}$$

and the numerator is positive in $z = 1$ if:

$$4r^2 < \frac{\left(2a\sin\theta - 3\right)^2}{a^2\sin\theta\left(1 - a\sin\theta\right)} \tag{29}$$

Also results:

$$\frac{\sin\theta}{1 - a\sin\theta} < \frac{\left(2a\sin\theta - 3\right)^2}{a^2\sin\theta\left(1 - a\sin\theta\right)} \text{ if } a < \frac{1}{\sin\theta} \tag{30}$$

As a consequence results:

$$\left.\frac{dY}{d\xi}\right|_{Y_c} > 0 \text{ if } \begin{cases} 4r^2 < \dfrac{\sin\theta}{1 - a\sin\theta} \\ 4r^2 > \dfrac{\left(2a\sin\theta - 3\right)^2}{a^2\sin\theta\left(1 - a\sin\theta\right)} \end{cases} \tag{31}$$

However only the first inequality in eq.(31) is acceptable, because the second inequality results in an unphysical wave profile. The denominator in eq.(26) is always positive for physically acceptable values of the parameters, the numerator has two real roots named Y_1 and Y_2:

$$\frac{Y_{1,2}}{Y_c} = \frac{r}{2\sin\theta}\left[\begin{matrix} r(1-a\sin\theta)+ \\ 2\sqrt{\sin\theta(1-a\sin\theta)} \end{matrix}\right] \mp \frac{r}{2\sin\theta}\sqrt{\left[r(1-a\sin\theta)+2\sqrt{\sin\theta(1-a\sin\theta)}\right]^2 - 4\sin\theta(1-a\sin\theta)} \tag{32}$$

It can be verified that $0 < Y_1 < Y_2 < Y_c$ if the first inequality (31) is satisfied. The eq.(26) can be integrated in analytical form as $\xi = f(Y)$.

6 THE CRITICAL POINT INCLUDING THE SURFACE TENSION

Including the surface tension term, eq.(17) becomes:

$$Y_{,\xi} = -\frac{gY^3 \sin\theta - r^2(cY-K)^2 - \frac{\sigma}{\rho}Y^3 Y_{,\xi\xi\xi}}{K^2 - gY^3 + ar^2(cY-K)^2} \tag{33}$$

or

$$\frac{\sigma}{\rho}Y^3 Y_{,\xi\xi\xi} + \left[K^2 - gY^3 + ar^2(cY-K)^2\right]Y_{,\xi} + gY^3 \sin\theta - r^2(cY-K)^2 = 0 \tag{34}$$

It is a non linear third order equation which can be expressed as a third order non linear autonomous system:

$$\begin{aligned} Y_{,\xi} &= Y_1 \\ Y_{1,\xi} &= Y_2 \\ Y_{2,\xi} &= \frac{\left\{\begin{matrix}\left[K^2 - gY^3 + ar^2(cY-K)^2\right]Y_1 + \\ gY^3 \sin\theta - r^2(cY-K)^2\end{matrix}\right\}}{\frac{\sigma}{\rho}Y^3} \end{aligned} \tag{35}$$

The system has a singular point at $(Y_s, 0, 0)$, where Y_s is the solution of the equation:

$$gY_s^3 \sin\theta - r^2(cY_s - K)^2 = 0 \tag{36}$$

It can be demonstrated that this equation has three real solutions if

$$c > \left(\frac{27gK\sin\theta}{4r^2}\right) \tag{37}$$

and a single real solution if

$$c < \left(\frac{27gK\sin\theta}{4r^2}\right) \tag{38}$$

In both cases there is always a real positive solution. Near the critical point we let $(Y, Y_1, Y_2) = (Y_s + \varepsilon, \varepsilon_1, \varepsilon_2)$ and we approximate the system of equation as:

$$\begin{aligned} \varepsilon_{,\xi} &= \varepsilon_1 \\ \varepsilon_{1,\xi} &= \varepsilon_2 \\ \varepsilon_{2,\xi} &= \underbrace{\left[\frac{3gY_s^2 \sin\theta + 2r^2 c(K - cY_s)}{\frac{\sigma}{\rho}Y_s^3}\right]}_{d}\varepsilon + \underbrace{\left[\frac{K^2 - gY_s^3 + ar^2(cY_s - K)^2}{\frac{\sigma}{\rho}Y_s^3}\right]}_{f}\varepsilon_1 \end{aligned} \tag{39}$$

It is a linear autonomous system of equations in the perturbations of the singular point. In compact form it can be expressed as

$$\begin{Bmatrix}\varepsilon \\ \varepsilon_1 \\ \varepsilon_2\end{Bmatrix}_{,\xi} = \begin{bmatrix}0 & 1 & 0 \\ 0 & 0 & 1 \\ d & f & 0\end{bmatrix}\begin{Bmatrix}\varepsilon \\ \varepsilon_1 \\ \varepsilon_2\end{Bmatrix} \tag{40}$$

and the eigenvalues are the solutions of the characteristic equation:

$$\lambda^3 - f\lambda - d = 0\,. \tag{41}$$

The classification of the singular point is based on the eigenvalues. The eigenvalues are all real if

$$\frac{d^2}{4} - \frac{f^3}{27} > 0 \tag{42}$$

In the present analysis this condition is satisfied for reasonable values of the parameters involved. The singular point is classified as hyperbolic fixed point. A zero eigenvalue is obtained if $d = 0$ or

$$c = \frac{rK + \sqrt{r^2K^2 + 6gY_s^3 \sin\theta}}{2rY_s} \tag{43}$$

and the singular point becomes nonhyperbolic. The analysis on the singular point is in progress but the great variety of singularity suggest different families of solutions if tension surface is non negligible.

7 SHOCK CONDITIONS

The shock condition is obtained from the mass and momentum balance equations for a control volume across the shock:

$$\begin{cases} c\left[Y\right]_f^b = \left[UY\right]_f^b \\ c\left[UY\right]_f^b = \left[\beta U^2 Y + \frac{1}{2} gY^2 \cos\theta\right]_f^b \end{cases} \tag{44,45}$$

where the square brackets are the operator $[<.>]_a^b = <.>|_b - <.>|_a$ and b and f stand for the back and front sections of the shock. The mass balance equation (8) in extended form is:

$$\left(c - U_b\right)Y_b = \left(c - U_f\right)Y_f = K \equiv K_c \tag{46}$$

with K the apparent discharge in the moving frame. The linear momentum balance equation (6) can be written as:

$$\begin{aligned} &\frac{2c^2}{g}\left(Y_b - Y_f\right) - \left(Y_b^2 - Y_f^2\right)\cos\theta = \\ &\frac{2\beta_b}{gY_b}\left(cY_b - K_c\right)^2 - \frac{2\beta_f}{gY_f}\left(cY_f - K_c\right)^2 \end{aligned} \tag{47}$$

where eq.(46) has already been used. The usual trivial solution $Y_f = Y_b$ (no shock) holds if in addition $\beta_f = \beta_b$ is assumed. Equation (47) can be solved obtaining $Y_b = f(Y_s)$ and choosing the solution $Y_b > Y_f > 0$. Note that in general the momentum correction coefficients should depend on the 'age' of the boundary layer and on the jump height $Y_b - Y_f$.

8 ENERGY DISSIPATION IN THE SHOCK

The rate of change of mechanical energy across the jump is equal to:

$$\Delta P = -\left\{ \begin{aligned} &\frac{1}{2g} U_b^2 Y_b \left(\alpha_b U_b - \beta_b c\right) - \\ &\frac{1}{2g} U_f^2 Y_f \left(\alpha_f U_f - \beta_f c\right) + \\ &\cos\theta \left[Y_b^2 \left(U_b - \frac{1}{2}c\right) - Y_f^2 \left(U_f - \frac{1}{2}c\right) \right] \end{aligned} \right\} \tag{48}$$

where α_b and α_f are the energy flux correction factors. Assuming $Y^*_{<.>} = Y_{<.>} g/c^2$, eq.(48) reads:

$$\begin{aligned} &\Delta P^* = -\frac{1}{2}\left(1 - \frac{K_c^*}{Y_b^*}\right)^2 Y_b^* \left(\alpha_b - \alpha_b \frac{K_c^*}{Y_b^*} - \beta_b\right) + \\ &\frac{1}{2}\left(1 - \frac{K_c^*}{Y_f^*}\right)^2 Y_f^* \left(\alpha_f - \alpha_f \frac{K_c^*}{Y_f^*} - \beta_f\right) - \\ &\cos\theta \left[Y_b^{*2} \left(\frac{1}{2} - \frac{K_c^*}{Y_b^*}\right) - Y_f^{*2} \left(\frac{1}{2} - \frac{K_c^*}{Y_f^*}\right) \right] \end{aligned} \tag{49}$$

Substituting the expression for discharge in the moving reference and dividing by the discharge per unit width in the moving reference, it is possible to obtain the energy drop across the jump. The expression is cumbersome and is not reported. For $\alpha_f = \beta_f = \alpha_b = \beta_b = 1$ the energy drop has the classical expression:

$$\Delta E_j^* = -\cos\theta \frac{\left(Y_b^{*3} - Y_f^{*3}\right)}{4Y_b^* Y_f^*} \tag{50}$$

The assumption of a boundary layer with a gradient pressure is not consistent with the common assumption of constant momentum and energy coefficients. Instead, if we assume $\beta_b > \beta_f > 1$ and $\alpha_b > \alpha_f > 1$ a domain of acceptable conditions ($Y_b^* > Y_f^*$) and limited dissipation rate ($\Delta E_j^* \to 0$) is possible (see Fig. 4).

9 DISCUSSION ON ENERGY DISSIPATION IN THE UNSTABLE STREAM

The mean energy dissipated for friction in a wave length is computed as:

$$\Delta E_f = -\int_{Y_f}^{Y_b} \frac{r^2U^2}{gY} \frac{1}{Y_{,\xi}} dY + \int_{Y_f}^{Y_b} \frac{ar^2U^2}{gY} dY \tag{51}$$

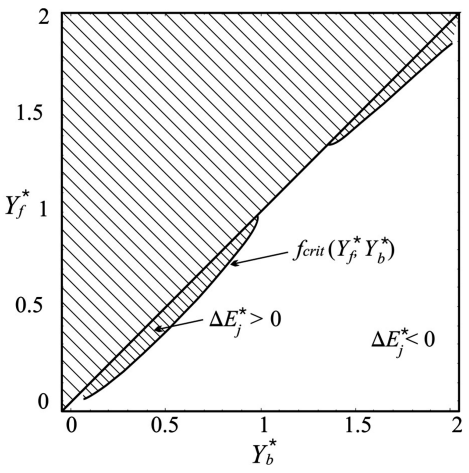


Figure 4. Energy balance in the jump. The hatched area is unacceptable because $Y_f^* > Y_b^*$. The closed hatched area corresponds to energy production in the jump, physically unacceptable. $\beta_b = 1.03$, $\beta_f = 1.02$, $\alpha_b = 1.06$, $\alpha_b = 1.03$, $\theta = 10°$.

A stream in steady uniform motion obviously results in $\Delta E_f + \lambda \sin\theta = 0$ for any value of the wave length λ. In the presence of roll waves, including the energy dissipated in the jump, the energy balance over a wave length results in:

$$\Delta E = \Delta E_f + \Delta E_j + \lambda \sin\theta \tag{52}$$

Assuming the modified resistance, which includes the gradient pressure effects, an energy saving term appears (the last term on the right hand of eq.50), although, on the basis of some numerical experiments, it is still not enough to close the energy budget, i.e. the system dissipates more energy than the energy gained from gravity. The jump enhances dissipation and the stream in unstable motion dissipates more than the equivalent stream in stable steady uniform motion (equivalent means having the same average discharge with identical channel characteristics). All the computations have neglected the finite size of the moving shock, the contribution of the weight of the fluid in the shock, surface tension effects and the trajectories curvature. It has been demonstrated that inclusion of the weight of the fluid in the jump in linear momentum balance across the shock, tends to reduce the ratio Y_b^*/Y_f^* (Brock 1967) and favors smaller wave lengths. Surface tension contrasts instabilities growth and rounds the wave crest (Hwang et al. 1994). In addition, neglecting dissipation due to friction in the shock (assumed of finite length) it is possible to find a zero energy budget (eq.52) corresponding to a situation where the dissipation by friction in the permanent wave profile plus the dissipation in the jump equals the energy gained by gravity (Lamberti & Longo 2000). The balance is very sensitive to small variations in the parameters. Also the assumption of a different friction law gives different results. According to Kapitza (1948) and Ng & Mei (1994) the observed roll wave has the smallest mean energy averaged over the wave length. Assuming that the momentum and the energy correction coefficients are higher on the back than on the front side of the shock, the energy dissipated in the jump can be zero for $Y_f^* < Y_b^*$. The energy balance criterion holds if and only if the roll waves are assumed permanent and periodic. If a small space variation of the waves is expected, the energy balance should be closed on a group of waves and not on a single wave.

10 CONCLUSION

The proposed solution for finite amplitude roll waves using a modified friction factor is similar to the solution proposed by Dressler (1949) for a Newtonian fluid. The solution is expressed as a discontinuous function obtained by connecting two continuous profiles with a shock. The continuous profiles are obtained in the shallow equations approximation. In order to construct the profile between two shocks, it is necessary that the steepness is finite and positive in the section where critical condition is reached. It results in the limiting value for the pressure gradient factor vs. bottom slope and in a limiting value for the roughness.

Including the momentum and energy coefficients variation in the front and in the back side of the hydraulic jump, a reduced dissipation rate in the jump is obtained for physical acceptable condition ($Y_f^* < Y_b^*$).

Including the tension surface effects a new family of possible solution is explored. The results on this approach are preliminary and suggest that a limiting value for celerity is imposed by the behavior of the solution near the singular point. The singular point collapses to the critical point if the surface tension is neglected.

ACKNOWLEDGEMENTS

The author acknowledges support for this work from the University of Parma, FIL 2003.

REFERENCES

Benjamin, T. B., 1957a. Wave formation in laminar flow down an inclined plane. *Journal of Fluid Mechanics*, 2: 554–574.

Benjamin, T. B., 1957b. Corrections to: Wave formation in laminar flow down an inclined plane. *Journal of Fluid Mechanics*, 3: 657.

Berlamont, J. E. & Vanderstappen, N., 1981. Unstable turbulent flow in open channels. *Journal of Hydraulic Divison, ASCE*, Vol. 107, No. HY4: 427–449.

Brock, R. R., 1966. Discussion of Critical analysis of open-channel resistance, by H. Rouse. *Journal of Hydraulic Divison, ASCE*, Vol. 92, No. HY2: 403–409.

Brock, R. R., 1967. *Development of roll waves in open channels*. W. M. Keck Laboratory of Hydraulics and Water Resources, California Institute of Technology, Report No. KH-R-16, pp. 226

Brock, R. R., 1969. Development of roll wave trains in open channels. *Journal of Hydraulic Division, ASCE*, Vol. 95, No. HY4: 1401–1427.

Chen, C. L., 1992. Momentum and energy coefficients based on power-law velocity profile. *Journal of Hydraulic Engineering, ASCE*, Vol. 118, No. 11: 1571–1584.

Chow, V. T., (1959) 1973. *Open Channel Hydraulics*, McGraw Hill, pp.680.

Chun, F., 1982. Stability of flow of a generalized Newtonian fluid down an inclined plane. *Journal of Applied Mathematics and Physics (ZAMP)*, Vol. 33: 181–188.

Clauser, F. H., 1956. The turbulent boundary layer. *Advances in Applied Mechanics* IV, 1–51.

Cornish, V., 1934. *Ocean waves*. Cambridge University Press.

Dressler, R. F., 1949. Mathematical solution of the problem of roll waves in inclined open channels. *Communications on Pure and Applied Mathematics*, Vol. 2: 149–194.

Forchheimer, P., 1903. Wasserbewegung in Wardewellen. *Zeitschrift für Gewässerkunde* 6(6): 321–339.

Hwang, C., Chen, J., Wang, J. & Lin, J., 1994. Linear stability of power-law liquid film flows down an inclined plane. *Journal of Physics D: Applied Physics* 27: 2297–2301.

Ishihara, T., Iwagaki, Y. & Iwasa, Y., 1954. Theory of the roll wave train in laminar water flow on a steep slope surface. *Transactions of Japan Society of Civil Engineers* 19: 46–57 (in Japanese)

Iwasa, Y., 1954. The criterion for instability of steady uniform flows in open channels. *Memoirs of the Faculty of Engineering*, Kyoto University, Japan, Vol. 16, No. 6: 264–275.

Jeffreys, H. J., 1925. The flow of water in an inclined channel of rectangular section. *Philosophical Magazine*, series 6, Vol. 49: 793–807.

Julien, P. Y. & Hartley, D. M., 1985. *Formation of roll waves in laminar sheet flow* – Rep. CER84-85PYJ-DMH18. Department of Civil Engineering, Colorado State University.

Julien, P. Y. & Hartley, D. M., 1986. Formation of roll waves in laminar sheet flow. *Journal of Hydraulic Research* 24: 5–17.

Kapitza, P. L., 1948. *Wave flow of thin layers of a viscous fluid*. Collected Papers of P. L. Kapitza, Vol. II, 1938–1964, Pergamon Press (1965), pp. 662–709.

Koloseus, H. J. & Davidian, J., 1966. Free surface instabilities correlations. *Geological Survey Water-Supply* Paper 1592-C, pp. 72

Lamberti, A. & Longo, S., 2000. *Roll waves e dissipazione in correnti idriche e nei debris flow (Roll waves and dissipation in water streams and in debris flow)*. Proc. XXVII National Conference on Hydraulics, GNDCI, Vol. 1: 85–94 (in italian).

Ligget, J. A., 1975. *Stability. In Unsteady flow in Open Channels,* Chapter 6, pp. 259–282, WRP.

Longo, S., 2003. Roll waves on a shallow layer of debris modeled as a dilatant fluid. D. Rickenmann & Cheng-lung Chen (eds) *Proc. of the Third International DFHM Conference*, Davos, Switzerland, September 10–12, 2003, Millpress Science Publishers, Rotterdam, Vol. 1, pp. 339–350, 2003, ISBN 90 77017 78 X.

Montuori, C., 1961. La formazione spontanea dei treni d'onde su canali a pendenza molto forte. *L'Energia Elettrica*, N. 2: 127–141.

Ng, C. & Mei, C. C., 1994. Roll waves on a shallow layer of mud modelled as a power-law fluid. *Journal of Fluid Mechanics* 263: 151–183.

Ponce, V. M. & Maisner M. B., 1993. Verification of theory of roll wave formation. *Journal of Hydraulic Engineering*, ASCE, 119(6): 768–773.

Prasad, S. N., Pal, D. & Römkens, M. J. M., 2000. Wave formation on a shallow layer of flowing grains. *Journal of Fluid Mechanics* 413: 89–110.

Rosso, M., Schiara M. & Berlamont, J., 1990. Flow stability and friction factor in rough channels. *Journal of Hydraulic Engineering, ASCE*, Vol. 116, No. 9: 1109–1118.

Rouse, H., 1965. Critical analysis of open-channel resistance. *Journal of Hydraulic Engineering, ASCE*, Vol. 91, No. HY4: 1–25.

Stoker, J. J., 1957. *Mathematical hydraulics*, in Water waves, Wiley Interscience, pp. 451–509.

Thomas, H. A., 1939. The propagation of waves in steep prismatic conduits. *Proc. Hydraulic Conference, Univ. of Iowa*, pp. 214–229.

Vedernikov, V. V., 1945. Conditions at the front of a translation wave disturbing a steady motion of a real fluid. *Comptes Rendus de L'Académie des Sciences URSS* 48(4): 239–242.

Whitham, G. B., 1974. *Linear and nonlinear waves*. Wiley-Interscience Publication, John Wiley & Sons, New York.

Yih, C. S., 1954. Stability of parallel laminar flow with a free surface. *Proc. 2nd U.S. Congress in Applied Mechanics*, pp. 623–628.

Yih, C. S., 1963. Stability of liquid flow down an inclined plane. *Physics of Fluids*, Vol. 6: 321–334.

This page intentionally left blank

River Flow 2004 – Greco, Carravetta & Della Morte (eds.)
© 2004 Taylor & Francis Group, London, ISBN 90 5809 658 0

Mathematical simulation of the effects of bridges and structures on flood waves propagation

L. Natale & G. Petaccia
Department of Environmental and Hydraulic Engineering, University of Pavia, Pavia, Italy

F. Savi
University of Roma "La Sapienza", Roma, Italy

ABSTRACT: The movement of flood wave in rivers is greatly influenced by channel transitions and controls such as bridges, sills, weirs, sluices or other types of hydraulic structures. The mathematical simulation of the flow conditions through these obstructions often asks for the reproduction of changes from subcritical to supercritical flow and vice versa. This paper presents a suitable technique for simulation of flow through channel controls that uses internal boundary conditions of 1D shallow water mathematical model. The numerical solver is first order finite volume, and is able to reproduce changes of the flow regime through the hydraulic structure and tailwater control. The model was verified simulating experiments on flume reported in literature. Moreover several experiments were performed in the Hydraulic Laboratory of the Department of Hydraulic and Environmental Engineering of the University of Pavia: calculated water profiles fit acceptably observed ones. The 1D mathematical model can not simulate the weir-nappe profiles immediately downstream the structures which are curvilinear and three-dimensional, but it is a practical tool that usefully reproduces the increasing of the water stages and the slowing down of the wave movement caused by structures.

1 INTRODUCTION

The mathematical simulation of flood routing in rivers has been increasingly studied in the last decades. When a flood wave moves along mountain reaches the flow regime varies from subcritical to supercritical and vice versa in space and time due to the formation of hydraulic surges and control sections. These variations of flow regime are mainly due to abrupt changes in channel geometry and can be simulated only by numerical solvers able to reproduce discontinuities (shocks) of the free surface.

Many numerical solvers have been proposed to integrate the shallow water equations and to schematize the effects of source terms for transcritical flow (Toro, 1997; Hirsch, 1990): their accuracy was verified by simulating experiments on flumes in a wide range of abrupt channel transitions (Morris, 2000; Morris and Galland, 2000; Petaccia and Savi, 2002). Even in natural watercourses, flow regime can be controlled by hydraulic structures such as bridges, weirs or sluice-gates, causing subcritical flow upstream and supercritical flow downstream. The tailwater effects due to these structures must be carefully simulated in order to recognise where levees might be overtopped.

Goutal and Maurel (2002), Rissoan et al. (2002) simulated simple obstacles, such as weirs or constrictions, modifying locally the river geometry (bottom elevation or channel width). Soares Frazao and Zech (2000) simulated flow through bridge with a local constriction of the cross section.

This schematization is not suitable when different hydraulic flow conditions through bridges can occur: free surface flow, pressure flow, pressure and overtopping flow. Moreover minor losses cannot be directly taken into account by shallow water equations. Therefore, as a common practice, internal boundary conditions (rating curves) are adopted. An internal boundary condition relates the flow conditions in the two river reaches, upstream and downstream the structure, where shallow water equations are valid. Usually these rating curves are computed in steady flow conditions taking into account minor losses.

This approach is widely used by models that deal with a single flow regime (subcritical or supercritical): for instance ISIS (Rosu and Ahmed, 1999), NWS FLDWAV (Jin and Fread, 1997; Fread and Lewis, 1998) computer codes. TEVERE (Natale et al., 1999) model, based on Preissmann scheme, simulates in this way flow through a wide range of hydraulic structures.

Some of these models, such as MIKE11 (DHI, 2000), NWS FLDWAV (Fread and Lewis, 1998), RUBAR 3 (Paquier, 1998) simulate flow through structures using numerical solvers able to reproduce subcritical and supercritical flow regimes. However some of these codes simulate in simplified way transcritical flow: for instance in NSW FLDWAV and MIKE11 codes, the convective inertial terms are progressively reduced as Froude number increases, up to neglect them when its value approaches unity. Such models simulate the tailwater effects approximately and do not reproduce changes in time of flow regime, upstream and/or downstream the structure.

Garcia Navarro and Alcrudo (1992) simulated a series of weirs using internal boundary conditions; in their application the flow regime did not change and supercritical flow occurred downstream any weir.

In the following is presented the simulation of the flow across structures taking into account transcritical flow conditions, adopting 1D shallow water equations written in complete form and solved by means of an upwind finite volume scheme. The numerical results are verified on the basis of laboratory tests reported in literature or expressly carried out in the Laboratory of Hydraulic and Environmental Engineering of the University of Pavia.

2 MATHEMATICAL MODEL

Propagation of a dam-break wave can be described by the shallow water equations coming from the mass and momentum balance equations (Cunge et al., 1980):

$$\frac{\partial \boldsymbol{U}}{\partial t}+\frac{\partial \boldsymbol{F}}{\partial x}=\boldsymbol{S} \tag{1}$$

$$\boldsymbol{U}=\begin{pmatrix} A \\ Q \end{pmatrix} \boldsymbol{F}=\begin{pmatrix} Q \\ \dfrac{Q^2}{A}+gI_1 \end{pmatrix} \tag{2a}$$

$$\boldsymbol{S}=\begin{pmatrix} 0 \\ gA\left(S_0-S_f\right)+gI_2 \end{pmatrix} \tag{2b}$$

where x is the spatial co-ordinate measured along the channel, t the time, Q the discharge, A the wetted area, g the gravitational acceleration, S_0 the bottom slope, S_f the friction slope. The terms I_1 and I_2 are related to the hydrostatic pressure force:

$$I_1=\int_0^h (h-\eta)b(x,\eta)d\eta \ , \quad I_2=\int_0^h (h-\eta)\frac{\partial b}{\partial x}d\eta \tag{3}$$

h is the water depth and $b(x,\eta)$ the width of the cross section at the distance x and height η, above the channel bed.

3 NUMERICAL SOLVERS

System (1) is solved by means of a first order finite volume numerical solver based on Roe's approximated Jacobian of the flux schematization (Roe, 1981):

$$\boldsymbol{U}_i^{n+1}=\boldsymbol{U}_i^n-\frac{\Delta t}{\Delta x}\left(\boldsymbol{F}_{i+1/2}^*-\boldsymbol{F}_{i-1/2}^*\right) \tag{4}$$

The numerical fluxes $\boldsymbol{F}$ are computed as

$$\boldsymbol{F}_{i-1/2}^*=\frac{1}{2}\left(\boldsymbol{F}_i^n+\boldsymbol{F}_{i+1}^n\right)- \frac{1}{2}\cdot\sum_{k=1,2}\left|\tilde{a}_{i+1/2}^k\right|\cdot\alpha_{i+1/2}^k\cdot\tilde{\boldsymbol{e}}_{i+1/2}^k \tag{5}$$

with

$$\alpha_{i+1/2}^{1,2}=\frac{1}{2}\left[\left(A_{i+1}^n-A_i^n\right)\pm\frac{\left(Q_{i+1}^n-Q_i^n\right)-\tilde{u}_{i+1/2}^n\left(A_{i+1}^n-A_i^n\right)}{\left(\tilde{c}_{i+1/2}^n\right)}\right] \tag{6}$$

and

$$\boldsymbol{e}_{i+1/2}^{1,2}=\begin{pmatrix} 1 \\ \tilde{a}_{i+1/2}^{1,2} \end{pmatrix} \text{ where } \quad \tilde{a}_{i+1/2}^{1,2}=\tilde{u}_{i+1/2}^n\pm\tilde{c}_{i+1/2}^n \tag{7}$$

The eigenvalues a and the eigenvectors $\boldsymbol{e}$ of the Jacobian matrix depend on the flow velocity u and celerity c:

$$\tilde{u}_{i+1/2}^n=\frac{\sqrt{A_{i+1}^n}u_{i+1}^n+\sqrt{A_i^n}u_i^n}{\sqrt{A_{i+1}^n}+\sqrt{A_i^n}} \tag{8}$$

$$\tilde{c}_{i+1/2}^n=\sqrt{g\frac{I_{1i+1}^n-I_{1i}^n}{A_{i+1}^n-A_i^n}} \tag{9}$$

In order to avoid non-physical discontinuities (zero eigenvalues), that are incompatible with the entropy principle, the absolute value of the eigenvalues of $\boldsymbol{J}$ is modified by defining the quantity:

$$\varepsilon_{i+1/2}^k=\max\left[o,\left(\tilde{a}_{i+1/2}^k-a_i^k\right),\left(a_{i+1}^k-\tilde{a}_{i+1/2}^k\right)\right] \quad k=1,2 \tag{10}$$

The new absolute value of each eigenvalue in equation (5) is defined as:

$$\Psi_{i+1/2}^k=\begin{cases}\left|\tilde{a}_{i+1/2}^k\right| & \text{if } \left|\tilde{a}_{i+1/2}^k\right|\geq\varepsilon_{i+1/2}^k \\ \varepsilon_{i+1/2}^k & \text{if } \left|\tilde{a}_{i+1/2}^k\right|<\varepsilon_{i+1/2}^k\end{cases} (k=1,2) \tag{11}$$

4 SOURCE TERMS

The source terms (2b) are schematized in two different ways:

4.1 *Pointwise (Brufau et al., 2002)*

$$S_{0i} = -\frac{z_{i+1} - z_{i-1}}{2\Delta x} \text{ and } S_{f\,i}{}^{n} = \frac{n^2 Q_i^{n+1}\left|Q_i^{n+1}\right|}{A_i^n R_i^{n\,4/3}} \tag{12}$$

where n is the Manning roughness coefficient.

The I_2 term is schematized as

$$I_2 = \frac{1}{2}\cdot h_i^2 \frac{b_{i+1} - b_{i-1}}{2\Delta x} \tag{13}$$

where b is the flume width.

4.2 *Upwind (Garcia Navarro and Vasquez-Cendon, 2000)*

According to equation (1), the decomposition of the source terms can be expressed as

$$\boldsymbol{S} = \begin{pmatrix} -\beta_{i+1/2} + \beta_{i-1/2} \\ \beta_{i-1/2}\cdot\left(\tilde{u}_{i-1/2} + \tilde{c}_{i-1/2}\right) - \beta_{i+1/2}\cdot\left(\tilde{u}_{i+1/2} + \tilde{c}_{i+1/2}\right) \end{pmatrix} \tag{14}$$

where the values of β coefficients are chosen in order to produce the balance the momentum equation for rectangular cross sections.

5 INTERNAL BOUNDARY CONDITIONS

Internal boundary conditions were introduced in the unsteady flow simulation in order to reproduce minor losses through structures. Let's focus on the generic structure (i.e. sluice-gate, sharp channel contraction) located at the cross section (i) in Fig. 1. Upstream ($i-1$) and downstream ($i+1$) channel cross sections have the same shape of the intermediate section (i). The computational domain is then disconnected in two reaches upstream (from section 1 to $i-2$) and downstream (from section $i+2$ to section N) the structure, where equations (4) are applied and the values of A_i^{n+1} and Q_i^{n+1} are computed.

Considering that no water is stored in the short stretch from ($i-1$) and ($i+1$) since the two sections are very close, the mass balance equation across the structure is considered:

$$Q_{i-1}^{n+1} = Q_{i+1}^{n+1} \tag{15}$$

Further relationships that depend on the flow regime are needed to estimate the three unknowns $A_{i-1}^{n+1}, A_{i+1}^{n+1}$ and Q_{i-1}^{n+1}. The model computes both subcritical and supercritical flow solutions and compares the total momentum fluxes plus the total hydrostatic pressures to assess which solution is correct. In the following this procedure will be explained in details.

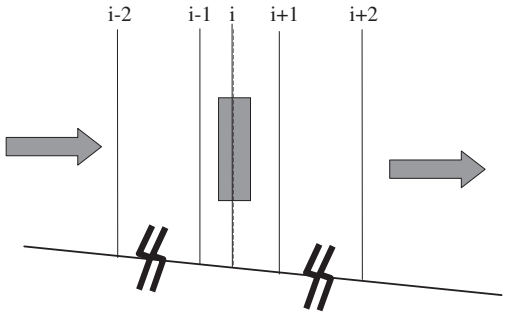


Figure 1. Schematization of an internal boundary condition.

Supercritical flow through the structure may occur if in section $i-2$ the flow is supercritical. In this case the values of $\hat{A}_{i+1}^{n+1}$ and $\hat{Q}_{i+1}^{n+1}$ (the symbol $\hat{}$ means that this a possible supercritical solution) are estimated considering a backward schematization of the fluxes, i.e.

$$\boldsymbol{U}_i^{n+1} = \boldsymbol{U}_i^n - \frac{\Delta t}{\Delta x}\left(\boldsymbol{F}_i^n - \boldsymbol{F}_{i-1}^n\right) \tag{16}$$

The energy or the momentum equation in steady state condition is applied between section $i-1$ and $i+1$ to simulate the contraction and the expansion of the supercritical flow through the structure. This equation relates $\hat{A}_{i+1}^{n+1}$ to the values of $\hat{A}_{i-1}^{n+1}$ and $\hat{Q}_{i+1}^{n+1}$ only.

If the flow in section $i+2$ is supercritical no backwater effects occur, then

$$A_{i-1}^{n+1} = \hat{A}_{i-1}^{n+1},\ A_{i+1}^{n+1} = \hat{A}_{i+1}^{n+1} \text{ and } Q_{i\pm1}^{n+1} = \hat{Q}_{i\pm1}^{n+1} \tag{17}$$

Otherwise, subcritical flow condition may exist.

In this case the flow regime depends on the flow conditions both in sections $i-2$ and $i+2$ simultaneously. The following system of 3 equations can be written:

(a) continuity equation between sections $i+1$ and $i+2$, i.e.

$$\frac{\tilde{A}_{i+1}^{n+1} - A_{i+1}^n}{\Delta t} - \frac{Q_{i+2}^{n+1} - \tilde{Q}_{i+1}^{n+1}}{x_{i+2} - x_{i+1}} = 0 \tag{18}$$

(b) rating curve in subcritical flow conditions between sections $i+1$ and $i-1$, i.e.

$$\tilde{A}_{i-1}^{n+1} = f(\tilde{A}_{i+1}^{n+1}, \tilde{Q}_{i+1}^{n+1}) \tag{19}$$

(c) continuity equation between sections $i-1$ and $i-2$, i.e.

$$\frac{\tilde{A}_{i-1}^{n+1} - A_{i-1}^{n}}{\Delta t} - \frac{\tilde{Q}_{i-1}^{n+1} - Q_{i-2}^{n+1}}{x_{i-1} - x_{i-2}} = 0 \qquad (20)$$

The symbol ~ means that this a possible (subcritical) solution and it can be computed by solving the above system of equations.

In many cases both subcritical and supercritical solutions do not exist. This means that section i controls the flow with subcritical flow upstream and supercritical flow downstream the structure. Continuity equations are applied to evaluate water depths in $i-1$ and $i+1$ which depends on the rate of discharge only.

If more than one solution exists, i.e. both subcritical and supercritical solutions can be obtained, to check which solution is correct, the momentum functions are compared starting from section $i+1$ and moving upstream.

6 SURGE FORMATION

The equations described in section 2 do not represent properly the dynamics of the surge formation since the volume of water in the roll of the hydraulic jump is neglected.

In fact the model represents a shock discontinuity in the mathematical solution and the numerical solver locates the variations of the flow regimes in a few space intervals (Δx); all in all it does not consider the length of the hydraulic jump.

The backward movement of the surge was simulated as follows: when the supercritical flow impact against the gate the lower part of the current remains essentially undisturbed. Therefore in the model the discharge through the gate is maintained constant in time. The difference between the discharge in the upstream section and the discharge through the gate is stored by the model until it becomes equal to the volume in the roll of the hydraulic jump (V_j).

The upper part of the current impacts against the gate and accelerates vertically generating the roll of the hydraulic jump. The surge does not move until the volume of water in the roll, taking into account a constant value of air concentration in water ($C_w = 0.3$), corresponds to the hydraulic jump length evaluated by means of the Peterka formula (1958).

Up to this time the lower part of the current and the flow through the gate remains supercritical. The volume of water in the jump (V_j), assuming a linear roll profile, is estimated.

When the hydraulic jump is formed at the upstream face of the gate (section i − 1 of Fig. 1) subcritical conditions occur. The model simulates the switch between undisturbed current and under gate flow, described adopting the rating curve in Fig. 4. The surge keeps then to move backward.

7 EXPERIMENTAL VERIFICATIONS

7.1 *WES test case*

The proposed approach was firstly tested comparing the results of the model with the observations of a flume experiment (5.1 test case) carried out at the USACE Waterways Experiment Station (Chen, 1980). The experimental setup consists of a 122 m long, 1.22 m wide rectangular flume with a slope $S_0 = 0.005$. A removable dam, 0.305 m high, is located at the midpoint of the flume ($x = 61$ m). It involves a constricted breach width of 0.122 m, or 1/10 channel width.

The Manning coefficient applied is $0.009\ \mathrm{ms}^{-1/3}$. This experiment, which constitute a severe benchmark for numerical solver since is characterized by an abrupt variation of the channel width, was simulated by Sanders (2001), that used a II order scheme and more recently by Bradford and Sanders (2002), a 2D approach.

First of all we simulated WES experiments integrating shallow water equations without imposing any internal boundary conditions. In Fig. 2 the observed water depths hydrographs are compared with those computed adopting both pointwise (continuous line) and upwind (dotted line) schematizations of the source terms.

Pointwise schematization is unacceptable since overestimates the outflow so that in the simulation the reservoir empties much faster than real one and the computed wave front celerity is considerably higher than the experimental one. For this reason in Fig. 2 the pointwise simulation of the reservoir emptying is not shown.

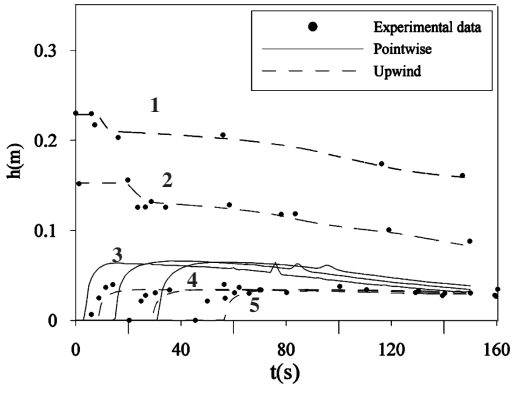


Figure 2. Comparison between upwind and pointwise source term schematizations without internal boundary conditions: (1) at $x = 30.5$ m, (2) at $x = 45.75$, (3) at $x = 68.6$ m, (4) at $x = 85.4$, (5) at $x = 106.75$ m.

The upwind schematization is significantly more accurate.

If internal boundary conditions are introduced, also the pointwise schematization gives acceptable results: the simulations obtained with internal boundary conditions applied to the pointwise treatment are shown in Fig. 3. Similar results are obtained coupling the upwind treatment and internal boundary conditions.

7.2 *Pavia test cases*

In order to investigate more extensively the importance of internal boundary conditions, experimental tests were carried out at Hydraulic Laboratory of the University of Pavia. The flume was 9.30 m long, 0.48 m wide, horizontal, with a bottom friction coefficient of 0.12 $ms^{-1/3}$. The steep wave was generated by the instantaneous opening of a hinged sluice gate placed at $x = 3.36$ m. The still water stored upstream the gate was 0.20 m deep.

The experiments considered a first sluice-gate, 4 cm open, placed at $x = 8.40$ m and a second sluice-gate, 2 cm open, at the end of the flume ($x = 9.3$ m) to produce evolving tailwater condition in the flume. To estimate the rating curve through the first gate, preliminary experiments in steady state conditions were performed supplying constant discharge and measuring water stages immediately upstream and downstream the gate and fitting the experimental observations using discharge coefficient reported by Ven Te Chow (1959)(Fig. 4).

In the following pictures (5, 6, 7, 8, 9, 10 and 11), the computed (grey and black line) and experimental instantaneous surface profiles taken by a standard video camera (25 frame per second) are compared at various time steps.

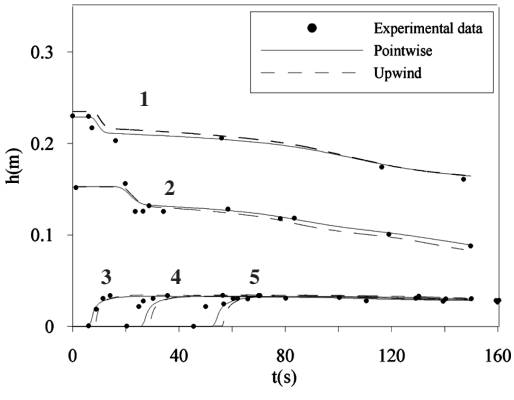


Figure 3. Comparison between upwind and pointwise source term schematizations with internal boundary conditions: (1) at $x = 30.5$ m, (2) at $x = 45.75$, (3) at $x = 68.6$ m, (4) at $x = 85.4$, (5) at $x = 106.75$ m.

The black line represents the simulation I obtained with the surge formation model explained in section 6. The grey line represents the simulation II obtained without the surge formation model.

Both the mathematical models simulate supercritical flow (Fig. 5) when the flow depth is lower than the upstream gate opening.

Figure 6 shows that only a part of the current supplies water to the roll of the hydraulic jump; the computed volume stored by the model at that time is represented by the thinner black line; until the water volume stored by the model I does not equal V_j the model I does not simulate the formation of the surge. The model II (grey line) simulates erroneously the formation of the surge. The stored volume for the

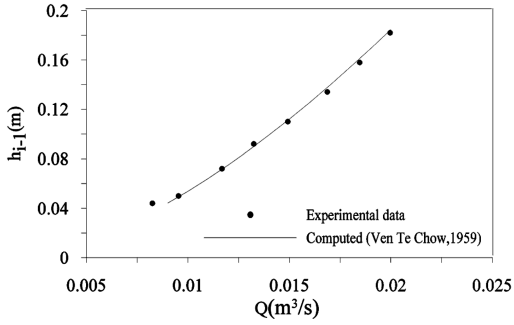


Figure 4. Rating curve for the gate.

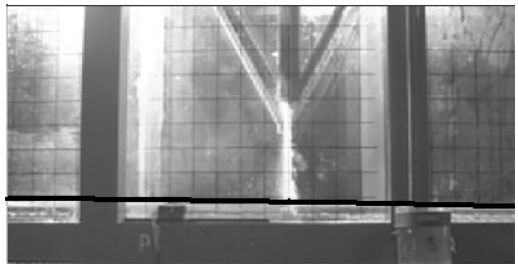


Figure 5. Measured and computed instantaneous profiles at $t = 4$ s.

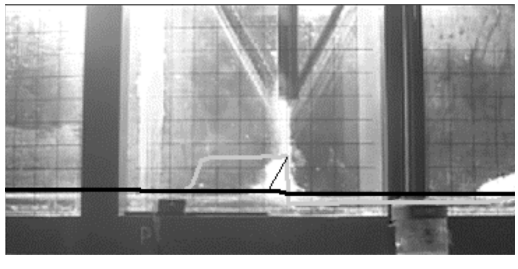


Figure 6. Measured and computed instantaneous profiles at $t = 5$ s.

second gate is not represented since is too far from the experimental window.

Figure 7 depicts the instant where the flow regime upstream of the gate changes from supercritical to subcritical.

Figure 8 shows that the downstream surge reaches and submerges the upstream gate.

In Fig. 9 computed and observed water depth after 7.7 s are compared. Upstream the gate water depth increases immediately after submergence of the gate becomes effective.

The comparison with the experimental images shows that the model II fails in the simulations of the first instants of the flow impact against the gate (Fig. 6). The discrepancies between the results of the simulation II and experiments mainly depend on the simulation of the bore upstream the gate. It is confirmed that the model does not reproduce correctly the changes of the flow regimes immediately after the impact against the gate (Fig. 6): in this short transient the model simulates subcritical flow although the experiments show that the flow is essentially supercritical. The results of the model II (grey line) underestimate the discharge through the gate and overestimate the celerity of surge moving from the upstream gate. As a consequence the celerity of the surge moving from the downstream gate is underestimated.

As time goes on, the model II reproduces maximum water depths upstream the gate but overestimates the celerity of the surge moving upstream from the gate (Fig. 7). Consequently the model II simulates the submersion of the upstream gate with a short delay in comparison with the experiments (Fig. 8).

Comparing the two simulations can be remarked that the celerity of the surge is not affected by the mechanics of the surge formation, since both the simulated celerities are greater than the observed one.

On the basis of these results some more investigation are going to be performed in the Hydraulic Laboratory of the University of Pavia.

The experimental setup includes a sharp contraction that reduces the cross section to one half of the original one and a bridge.

As an example of preliminary results, the computed and observed water depths profiles for the constriction are compared in Figs. 10 and 11.

Figures 10 and 11 show that the downstream water depths are underestimated due to aeration of the flow and strong surface turbulence induced by the falling

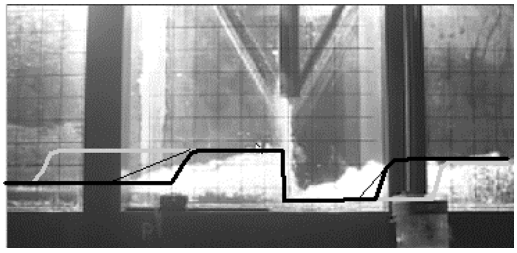


Figure 7. Measured and computed instantaneous profiles at $t = 6.0$ s.

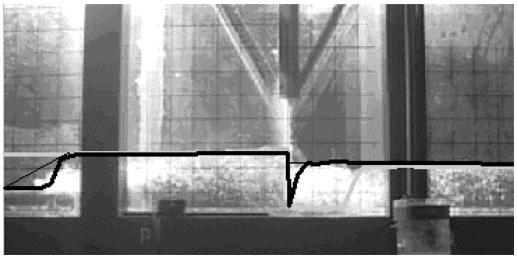


Figure 8. Measured and computed instantaneous profiles at $t = 6.9$ s.

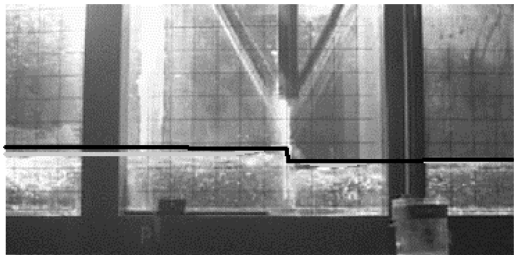


Figure 9. Measured and computed instantaneous profiles at $t = 7.7$ s.

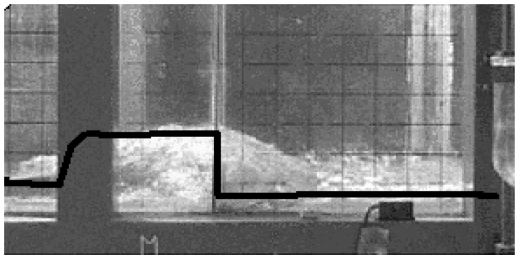


Figure 10. Measured and calculated instantaneous profiles at $t = 3.2$ s

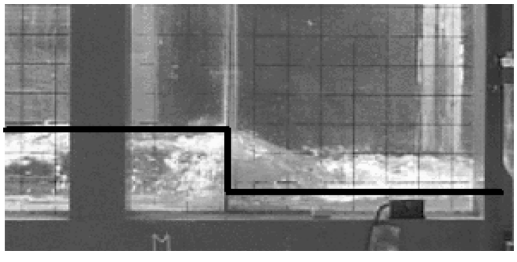


Figure 11. Measured and calculated instantaneous profiles at $t = 4.0$ s.

nappe; instead water depths upstream the constriction are described with sufficient detail.

The two dimensionality of the phenomenon will be studied and the limits of the one dimensional model will be analysed.

8 CONCLUSIONS

The flow conditions through hydraulic structures and channel transitions were investigated very extensively, at first working on the schematization of source terms, then inserting internal boundary conditions and modifying the mathematical model. A first order accurate finite volume numerical solver was used and the results obtained with the internal boundary conditions as well as modifying the mathematical model are compared with experimental investigations on laboratory flumes.

The mathematical model that takes into account the volume of the hydraulic jump reproduces satisfactorily the impact of the wave front against the obstacles when the flow is three dimensional and the shallow water model is inadequate. The model simulates satisfactorily the water depth upstream the gate and the change of the flow regime through the obstacle from supercritical to subcritical due to tailwater. More specifically the position of the surge moving upstream and the consequent submergence of the sluice-gate with the increase of the water stage immediately upstream the gate are simulated correctly.

ACKNOWLEDGEMENTS

This work is funded by CNR-GNDCI, Linee 1 and 3.

REFERENCES

Alcrudo F. 1992: *Esquemas de alta resolucion de variacion total decreciente para el estudio de flujos discontinuos de superficie libre*, Ph.d. Thesis, Universidad de Saragoza

Brufau P., Vasquez-Cendon M.E., Garcia Navarro P. (2002): A numerical model for the flooding and drying of irregular domain, *International Journal for numerical methods in fluids*, 39: 247–275

Bradford S.F., Sanders B.F. 2002: Finite-Volume Model for shallow water flooding of arbitrary topography, *Journal of Hydraulic Engineering*, 128: 289–298

Chen C.I. 1980: Laboratory verification of a dam-Break flood model, ASCE, *Journal of the Hydraulic Division*: 535–556

Chow V.T. 1959: *Open Channel Hydraulics*, McGraw-Hill Publisher

Cunge J.A., Holly F.M., Vervey A. 1980: *Practical Aspects of Computational River Hydraulics*, Pitman Publ. Inc.

DHI, Mike 11 2000: *A modelling system for Rivers and Channels*, Reference Manual

Fread D.L., Lewis J.M. 1998: *NWS FLDWAV Model: theoretical description and user documentation*, Hydrologic Research Laboratory, National Weather Service, Silver Spring

Garcia Navarro P., Alcrudo F. 1992: High resolution 1D schemes for unsteady open channel flow simulation, *Jornadas de encuentro trilateral para el estudio de la hydraulica de las ondas de submersion*, Zaragoza: 1–14

Garcia Navarro P., Brufau P. 1998: One-dimensional dambreak flow modelling: some results, 1st CADAM Meeting, paper 10, Wallingford

Garcia Navarro P., Fras A., Villanueva I. 1999: Dam-break flow simulation: some results for one dimensional models of real cases, *Journal of Hydrology*, 216: 227–247

Garcia Navarro P., Vasquez-Cendon M.E. 2000: "On numerical treatment of the source terms in the shallow water equations", *Computer & Fluids*, 29: 951–979

Goutal N., Maurel F. 2002: A finite volume solver for 1D shallow water equations applied to an actual river, *International Journal for Numerical Methods in Fluids*, 38:1–19

Henderson F.M. 1966: *Open Channel Flow*, MacMillan Publisher

Hirsch, C. 1990: *Numerical Computation of Internal and External Flows*, Vol.2, John Wiley & Son, Chichester

Jin M., Fread D.L. 1997: Dynamic flood routing with explicit and implicit numerical solution schemes, *Journal of Hydraulic Engineering*, ASCE, 123 (3): 166–173

Morris M.W. 2000: *CADAM Concerted Action on Dambreak Modelling, Final Report*, Report SR 571, Wallingford

Morris M.W., Galland J.C. 2000: *CADAM Concerted Action on Dambreak Modelling, Dambreak Modelling Guidelines & Best Practice*, Report SR 571, Wallingford

Natale L., Savi F., Ubertini L. 1999: Probability of inundation of Rome, *IASTED International Conference on Modelling and Simulation*, Philadelphia

Paquier A. 1998: 1-D and 2-D models for simulating dambreak waves and natural floods, *1st CADAM Meeting*, HR Wallingford, march: 127–140

Petaccia G., Savi F. 2002: Numerical modelling of shock waves: simulation of a large number of laboratory experiments, *International Conference Riverflow 2002*, 1: 449–458

Rissoan C., Goutal N., Herledan R. 2002: 1D hydraulic simulation of a dam break wave on the Rhone river, *ICHE 2002*, Warsav

Roe P.L. 1981: Approximate Riemann Solvers, parameter vectors and difference schemes, *Journal of Computational Physics*, 43: 357–372

Rosu C., Ahmed M. 1999: Toce River dam-break test case. A comparison between the ISIS numerical model and the physical model, *4th CADAM Meeting*, Milan

Sanders B.F. 2001: High resolution and non oscillatory solution of the St. Venant equations in non rectangular and non prismatic channels, *Journal of Hydraulic Research*, 39 (3): 321–330

Soarez Frazao S., Zech Y. 2000: Computation of extreme flood through the Toce valley *4th CADAM Meeting*, Milan

Toro E.F. 1997: *Riemann solvers and numerical methods for fluid dynamics: a practical introduction*, Springer Verlag, Berlin

This page intentionally left blank

River Flow 2004 – Greco, Carravetta & Della Morte (eds.)
© 2004 Taylor & Francis Group, London, ISBN 90 5809 658 0

Soil/water interaction during the breaching process of overtopped embankments

Pickert, G. & Jirka, G.H.
Institute for Hydromechanics, University of Karlsruhe, Germany

Bieberstein, A. & Brauns, J.
Division of Embankment Dams and Landfill Technology, Institute of Soil Mechanics and Rock Mechanics, University of Karlsruhe, Germany

ABSTRACT: When a flood exceeds the design level of an embankment dam, the dam will be overtopped and breaching can occur. Consequences are major flooding of the area beyond the dam, which can at least cause high economical damage. Residents, local governmental administrations and environmental agencies are highly interested in knowing the precise description of possible breach development and outflow hydrograph Q(t). Many publications and models are available on this topic and model outputs can vary up to ±50% from the original data. This is due to a limited understanding of the processes involved in the breaching of embankments and the lack of fundamental experimental data. The research presented in this paper has the following aims: First, to generate a reliable data base by carrying out physical experiments (scaled 1:10) and measuring the outflow hydrograph and the erosion of the embankment material per time (erosion curve). Second, to improve the knowledge of the soil/water interactions in partly saturated soils, represented by the water tension in the breach slopes. And third, to provide a 3D elevation picture of a breaching geometry in homogeneous embankments.

1 INTRODUCTION

When a flood exceeds the design level of an embankment dam, the dam will be overtopped and breaching will occur. Consequences are major flooding of the area beyond the dam, which can at least cause high economical damage. Residents, local governmental administrations and environmental agencies are highly interested in knowing the precise description of the breach development and outflow hydrograph Q(t). Appropriate emergency plans and scenarios could be developed based on this information and the loss of life and/or properties could be minimized.

Existing models, for example the NWS-BREACH-model developed by Fread (1991), describe overtopping events by hydrodynamic equations, erosion equations and simple geotechnical considerations. These simplifications of the breaching process, and especially the processes for the breach widening, have negative influence on the modeling results. Breach widening strongly depends on the neglected soil/water interactions in the soil matrix. These interactions, for example the tension in partly saturated soils have a strong influence on the erodibility of the soil and on the stability of the breach slope.

The present research is focusing an overtopped earthen embankment and has the following aims: First, to generate a reliable data base by carrying out physical experiments (scaled 1:10) and measure the outflow hydrograph and the erosion of the embankment material per time (erosion curve). Second, to improve the knowledge of the soil/water interactions in partly saturated soils, represented by the water tension on the breach slopes. And third, to provide a 3D elevation picture of a breaching geometry in homogeneous embankments.

2 BACKGROUND

2.1 *State of the art*

A comparison of different dam breach models by Morris (2000) done within the EU workshop of Concerned Action on Dambreak Modelling (CADAM) showed the wide variability of model results. Figure 1 shows the computed breach discharges over time (Q [l/s]) of six models. Apart from the results of the Broich2D model which was calibrated against their own measured data, the output variation is rather high.

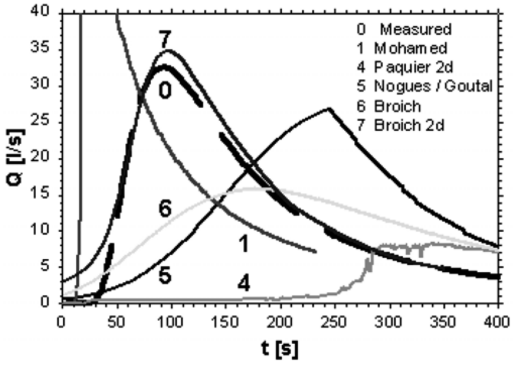


Figure 1. Breach discharges of six models compared to experimetal data (Morris, 2000).

Broich (1998) reports that the accuracy of predicting the peak discharge is perhaps ±50%, and considered the accuracy in predicting the onset of breach formation as even worse.

Morris (2000) published a list of existing dam breach models specifying the implemented breach morphology, flow equations, sediment transport equation and the geomechanics of the breach-side slope. Other summaries and analysis of dam breach models were done by Wahl (1998), Broich (1998), Lecoint (1998) and Mohamed et al. (2000).

During the CADAM workshop Graham (1998) stated that the modeling of breach formation through embankments is done by using process based models. Most breach models are based on steady state sediment equations related to homogeneous banks and adopted breach growth mechanisms. The modelers must therefore make a significant number of assumptions and simplifications in order to model the breach, all of which can greatly affect the modeling results.

The breaching process is dominated by the interaction of these three processes:

– hydraulics of the flow over the embankment and through the breach
– erosion process
– soil properties and geotechnical considerations.

Simplification in one of these processes will certainly affect the overall modelling results. Especially the geotechnical simplification concerning the breach widening processes, affects the modelling results. Breach widening depends mainly on two effects. First the erosion of embankment material due to the transport capacity of the breach flow, and second on the failure of the breach side slopes.

2.2 *Erosion process*

Mohamed et al. (2002) stated that the implemented sediment transport equations are derived for subcritical steady state flow conditions, for a specific type of sediment, and for a certain range of grains sizes. These conditions are likely to be violated during the breaching process since conditions change from subcritical flow to unsteady supercritical flow and back. Soil types do also vary widely in embankment construction. But in the absence of any other method to predict the sediment transport, a careful selection from the existing sediment transport formulas should be done, by considering their applicability to flow on steep slopes and for supercritical flow and additionally their derivation, based on dam breach experimental data.

As stated above, the choice of a sediment transport equation requires professional judgment and knowledge about the breaching mechanisms. In addition to the above stated considerations following verifications of the transport equation can be done:

1. Verify the developed model on very good documented historical dam failures, for example the Teton dam failure 1975 (USA), and compare the results with the actual breach width and depth.
2. Experimental data of the erosion curves for a falling water level in the reservoir. (Bechteler)
3. Explicit breach width and depth for different breaching times. (Coleman, 2000)
4. Carry out experimental models.

2.3 *Key issues for research*

A more accurate failure analysis of the breach side slope, especially the soil/water interactions within the embankment material, would highly improve the understanding of the breaching process.

Experimental data of erosion and transport of embankment material for calibrating numerical models would close the gap between model results and real breaching events.

3 BREACH SLOPE FAILURE

Slope movements are classified in many ways in the geotechnical and geologic sciences, each having some usefulness in emphasizing features pertinent to recognition, avoidance, control, correction or other purpose for the classification.

3.1 *Classification of slope failures*

Among the attributes that are used as criteria for identification and classification of failures, in respect to the subject of breach slope failures, are:

– type of movement
– kind of material
– rate of movement
– geometry of the area of failure.

In geotechnics the following failure characterization (type of movement) is done:

– falls
– topples
– slides
– lateral Spreads
– flows
– complex.

The breaching of an embankment is certainly a complex failure, which has to be simplified based on the experimental research.

3.2 *Causes of slope movements*

The processes involved in slides, movements or failures, comprise a continuous series of events from cause to effect. All slides involve the failure of earth materials under shear stress. The initiation of the process can therefore be reviewed according to (a) the factors that contribute to increased shear stress and (b) the factors that contribute to low or reduced shear strength.

Factors that contribute to increased shear stress can also be classified in different categories:

– the removal of lateral support
– removal of underlying support
– lateral pressure
– surcharge (additional loads)
– transitory earth stresses (e.g. earthquakes)
– regional tilting.

The important factors concerning the breach slope failure are the first and the second.

Factors that contribute to reduced shear strength of rock or soil may be divided in two groups. The first group includes factors based on the initial state or inherent characteristics of the material, such as composition, texture, structure and slope geometry. Organic materials, clays, decomposed rock are inherently weak or become weak upon change in their water content. Additionally, these materials may have a loose structure and/or texture.

The second group includes the variable factors that tend to lower the shear strength of the material. These factors (a) are changes due to weathering and other chemical reactions and (b) changes in inter-granular forces due to water content and pressure in pores and fractures: Water in soils causes an increase in weight of the mass, an increase in pore water pressure, and a decrease in apparent cohesion.

The second factor, changes in intergranular forces (b), has an important influence on the breaching process. Thus, the presented investigations and the current experiments respectively are focused on it.

3.3 *Soil water interactions*

The analysis of the breaches in dams and embankments showed a wide variation of the breach slope, some are very steep others are flat (Bücker, 1998). This is mainly due to the dam material parameters and the effluent water volume.

As stated before the water content of the soil has a great influence on the slope stability. First, as a destabilising factor if the water content is too high, and second, as a stabilising factor in unsaturated soils with a moisture content $w < 1$ [-]. This stabilising force introduced on the soil matrix by the soil/water interactions is based on the soil-moisture tension.

Soil-moisture tension can take values of a compressive stress (positive) or tensile strength (negative), depending on the water content of the soil matrix. The tensile strength also known as suction power, increases the effective stresses and so the apparent cohesion of the soil.

All water movements in the soil depend directly on the soil-moisture tension, since water will tend to flow from areas of high potential to those with lower potential. The soil-moisture tension reflects the sum of the water holding forces of the soil. With tensiometers, this force can be determined directly:

$$\psi = m \times g \times h \tag{1}$$

where ψ = water tension [Nm]; m = mass [kg]; g = gravity [m/s^2]; and h = height [m] above level of saturation.

Compared to all other measuring principles, the capillary binding of water to soil is measured with tensiometers directly.

4 EXPERIMENTAL SETUP AND PROCEDURE

In the research laboratory of the Institute for Hydromechanics of the University of Karlsruhe a 1:10 scaled model of a homogeneous embankment has been realized in a flume of 15 m length, 1 m in width and 0.7 m in depth. The model has a height of 0.3 m, is 1.9 m long and is built over the whole flume width of 1 m (Figure 2).

The homogeneous embankment model is built up with three sands on a fixed bed (see Table 1).

With respect to a flood embankment the upstream as well as the downstream slope is 1:3, which ensures the geometrical similarity of the embankment model. In fact the slopes angles are smaller than the angle of friction of the used soil. Thus the slopes are stable.

The embankment is constructed of several layers of sand. In all experiments the mean moisture content of the embankment material is $w = 0.05$ [-] and the mean material compaction factor is $D = 0.5$ [-].

Within the embankment six tensiometer probes are installed during the construction. The tensiometer probes are located in different heights and in different distances from the breach.

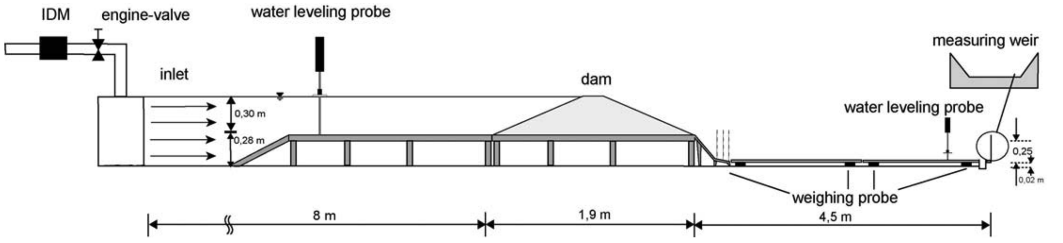


Figure 2. Side view of the experimental setup.

Table 1. Dam materials used in the experimental models.

Label	Type	d_{50} [mm]
Sand 1	Coarse sand	2
Sand 2	Medium sand	0.22
Sand 3	Coarse silt	0.035

A drainage toe ensures that the embankment withstands the hydraulic load and that seepage is discharged safely at the drainage toe. The reservoir level will have no effect on the downstream slope.

Before filling the reservoir, the initial breach plug is located on one of the side walls. This plug is a wooden block with a length of 0.1 m (crest width), width of 0.02 m. With this plug a rectangular initial breach channel of 0.02 m width and 0.02 m depth over the total width of the embankment crest of 0.1 m is initiated. The plug is used for initialising the overtopping at a defined location at the glass wall.

The reservoir is filled up slowly, so that a constant seepage line will arise in the embankment. The experiment is started by withdrawing the plug, when the reservoir is filled up to water level of 0.29 m (0.01 m below the embankment crest) and a constant seepage is reached.

During the breaching process the outflow hydrograph, the erosion rate and the suction pressure are measured. Furthermore, the breaching process is recorded for a detailed analysis.

5 MEASUREMENT TECHNIQUE

5.1 *Erosion and flow measurement*

The experimental setup described in Chapter 4 and in Figure 2 is designed in such a way that it is possible to measure the erosion of the dam material with constant water level in the reservoir and no backwater influences on the breaching process.

Right behind the dam toe a sill leads to a channel within the flume where the flow velocity is reduced by three grids in such a way that the eroded dam materials will deposit. This channel is bedded on weighing sensors so that the instantaneous weight of the eroded material and the outflow is measured as W_{total} [kg]. The outflow from the breach is measured at the end of this channel by a measuring weir. The erosion curve is obtained by subtracting the weight of the water W_{wat} [kg] from the total weight W_{total} [kg] for each time step, see equation 2.

$$W_{sed}(t) = W_{total}(t) - W_{wat}(t)\,[kg] \tag{2}$$

During the calibration phase, a deposition rate of 95% of the eroded material was achieved as well as a measurement error of ±1% of the total weight.

Water leveling probes measure the reservoir water level and the water level in the sedimentation channel. Additional to the reservoir level the inflow to the reservoir is measured with a inductive flow meter (IDM).

5.2 *Fringe projection*

The breaching of an embankment is a highly transient process. Due to that, it is difficult to receive a profile of the breach itself. Coleman (2000) has achieved very good results by stopping the breaching process and mapping the dried breach at certain time steps. But to evaluate or even to model the different stages of collapse of the breach slopes another nonintrusive mapping technique has to be used for continuous measurements.

A technique which is frequently employed in mechanical engineering and in medicine to measure surface distortions or curvations is the Moiré Projection, also named Fringe Projection.

The simplest Fringe Projection for contouring an object is to project interference fringes or a grating onto an object and then view from another direction. Figure 3 shows a definition diagram for Fringe Projection and in Figure 4 the present experimental setup.

From the triangle B-a-b in Figure 3, we find the out-of-plane displacement equation (3) at point B with:

$$W = \frac{g \times N_z}{\tan\alpha} \tag{3}$$

where W = displacement; N_z = the fringe order at point B, g = grading pitch; and α = angle.

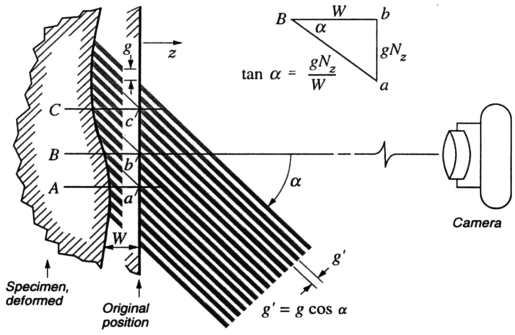


Figure 3. Optical setup for Fringe Projection (Post, 1994).

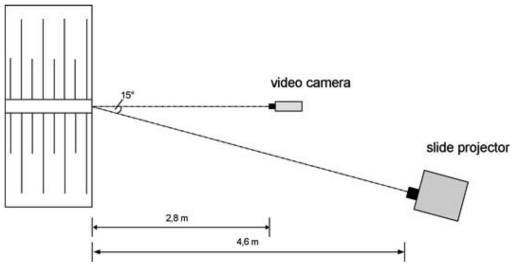


Figure 4. Fringe Projection setup (top view).

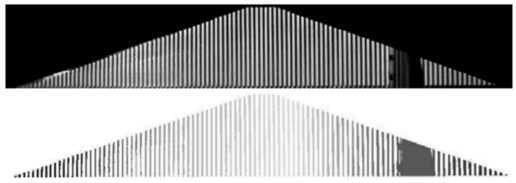


Figure 5. Fringe Projection and extracted fringes.

The easiest way to produce a stripe pattern on the surface is the direct projection using a light source and an alternating black/transparent stripe pattern image and an optical system to project a sharp image of the stripes onto the surface. Most convenient a slide projector is used with a framed stripe image of black and transparent stripes of a distinct stripe width. As these stripes are projected, however, only nearly parallel light sheets are received, depending on the distance of the projector. The planes of equal light intensity or light phase are – more or less parallel to the axis of the light projector.

The camera must have a distinct angle relative to the projection axis. If the camera has the same axis like the projector and the surface is moved away from the projector, it will not be able to detect any change in the stripe pattern except for a slight change of stripe frequency induced by the not completely parallel light sheets.

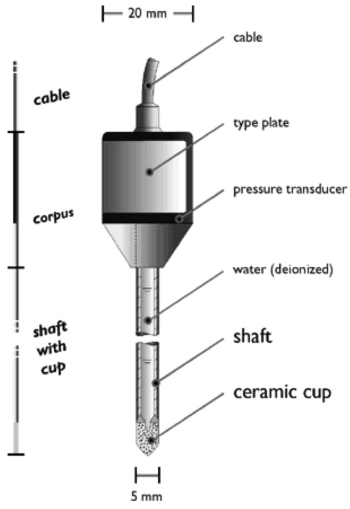


Figure 6. Principle setup of a micro tensiometer probe (UMS, 2003).

As the stripe width is very large compared to the wave length of the light, even very rough surfaces can be inspected. This is the case in the conducted experiments, preliminary experiments showed that the breach slope is rough with overhang. The analysis system consists of a slide projector which produces the pattern of white and black stripes on the dam profile.

The accuracy of all optical methods strongly depends on the knowledge of all geometrical information of the measuring setup. These are projector distance and angle, the optics of the projection system, camera distance and angle relative to the projector and the surface. If all this information is available, the reconstruction of the surface can be done very accurately. Subpixel algorithms, i.e. algorithms that take into account the gradient of gray level changes in the image, provide a much higher resolution than the size of a single pixel. Depending on the pattern and the algorithm used, a resolution of 1/10 of a pixel size can be achieved when looking for edges or the center of gravity of the area of objects.

5.3 *Tensiometer probes*

Tensiometers are inexpensive moisture measurement tools. The accuracy of a well-maintained tensiometer is in the 90–95% range. They use a porous ceramic cup at the end of a long tube which is inserted in the soil, see Figure 6.

The tensiometer is a point sensor because the ceramic cup at the tip of the tube is the contact point with the soil. The measurement is based on a soil tension effect that occurs when the tube is partially filled with water and sealed at the top with a tension measurement device. As the soil drys it absorbs water

through the porous ceramic cup and creates a suction (partial vacuum) inside the tube that is proportionate to the change in soil water content.

As the soil water content increases, the ambient soil water pressure increases and forces water back into the ceramic cup, thereby reducing the suction or applying a positive pressure to the sensor. Tensiometers are not affected by salinity or other soil conductivity factors.

5.4 *Data acquisition*

For the data acquisition and experimental setup control a DAQ-PCI-card is used. The 16 analogue input channels are scanned with 100 Hz and saved directly to the hard drive. Two digital outputs are used to control the motor gate valve.

The National Instruments software Labview 6.0 is used as control and acquisition software.

An IEEE 1394 CCD video camera with a resolution of 1280*980 pixels records the breaching process through the glass wall of the flume. This system has the advantage that video films can be recorded directly on hard disc up to the maximum hard drive space of 80 GBytes, which is very useful for cohesive materials where the breaching process is very long.

6 EXPERIMENTAL RESULTS

The test embankment has a height of 0.3 m, a length of 1.9 m, a crest width of 0.1 m and a total width of 1 m. The embankment was built from medium sand with a compaction of $D = 0.5$ [-] and a moisture content of $w = 0.15$ [-], the total weight of the embankment was approximately 650 kg.

From removal of the initial breach plug to the end of measurements with an unaffected flow 110 sec elapsed. Figure 7 shows a time series of pictures from this test.

At $t = 0$ sec the embankment is intact, the reservoir is filled up to the crest and the initial breach plug is still in place. The second picture ($t = 40$ sec) shows the initial breach phase. This phase is dominated by set of vertical steps which are merging together. This type of erosion is introduced by Hanson (1997) as headcut erosion in cohesive materials. The breaching phase begins in picture 3 ($t = 65$ sec). All steps are merged and an erosion channel parallel to the downstream embankment slope is formed. The breach channel has been cut upstream, across the total width of the embankment crest.

At $t = 80$ sec breach crest is migrating upstream on the embankment slope, whereas the discharge funnel migrates with the breach crest. The breach inclination increases referred to the downstream embankment slope. At $t = 110$ sec the breach crest migrates further upstream and the inclination of the breach increases.

Figure 8 shows the breached embankment viewed from upstream looking downstream after the depletion of the reservoir. The hourglass shape with the bottle neck at the embankment crest of the breach well defined by Coleman (2000) is recognisable. Additionally the streamlines of the breach flow are clearly visible in the embankment material.

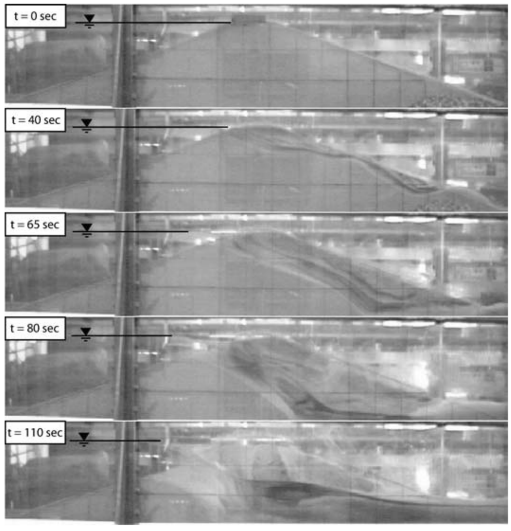


Figure 7. Breaching sequence.

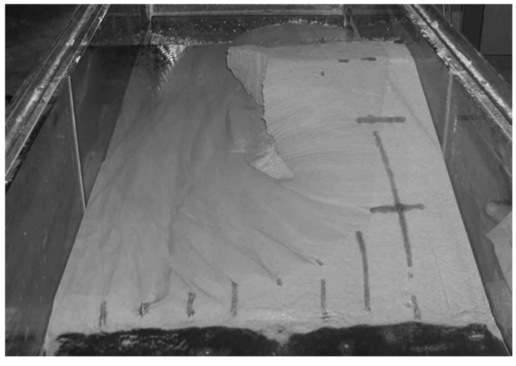


Figure 8. Breached test embankment (view from upstream).

The geotechnical aspect of this research is also evident. Looking at the bottle neck the overhang of the breach slope is stable due to the negative soil-moisture tension.

A dry medium sand ($d_{50} = 0.22$ mm) is cohesionless and has an angle of friction of $\varphi \approx 30°$ with a standard slope stability, which would make an overhang impossible.

But taking the negative soil-moisture tension into account the so-called capillary cohesion stabilizes this overhang. Thus soil mechanical and geotechnical considerations must be included in the understanding of breaching processes.

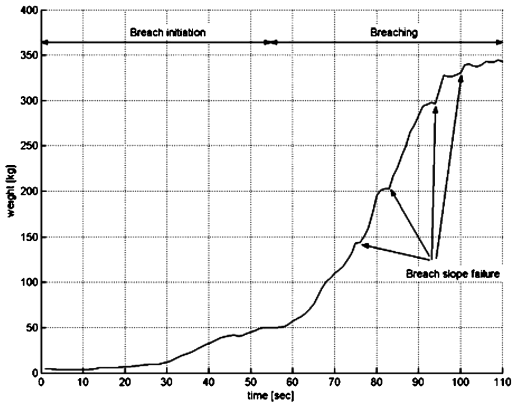


Figure 9. Measured erosion curve of breached embankment.

Figure 9 shows the graph of the correspondent erosion curve. A quantitative comparison of the photograph and the erosion curve indicates that half of the embankment was eroded. The mass of the eroded material was measured in the sedimentation channel.

This graph (Figure 9) with the increasing mean sediment weight per time is in good accordance to the video taped breaching process (Figure 8). The initial breaching phase and the main breaching phase can be identified. Additionally to this, major collapses of the breaching channel due to failure of the breach slope can be correlated in the graph and in the video.

7 CONCLUSION

This paper first results of ongoing work on the understanding of breach development and the aim of developing a fundamental data base for modelers.

The preliminary experimental results show good support for the concept of a breaching process occurring in three phases:

– breach initiation
– breaching
– depletion of the reservoir.

But not only the breaching phases correlate with literature results (Coleman, 2000). The breach development and the breach propagation also show good agreement with results of other experiments (Hanson, 1997; Coleman, 2000).

With respect to the erosion curve it can be stated that the breaching process is measured quite well, but further improvement on the analysis is necessary.

Based on this experiments, the failure mode of the breach side slope can be identified as a fall failure.

The Fringe Projection technique in order to receive a 3D model of a breach and the measurements of negative soil-moisture tension are introduced in this paper, and results will follow.

A drawback of this experimental setup is, that the breaching process herein can only be observed in the initial phase and in the beginning of the breaching phase, which is due to the width of the experimental flume. The further breach development with the possible maximum breach outflow cannot be observed.

REFERENCES

BECHTELER, W. n.a. Bruch eines Deiches durch Erosion, München, Germany

BROICH, K. 1997. Computergestützte Analyse des Dammerosionsbruchs; Universität der Bundeswehr München, Institut für Wasserwesen, München

BROICH, K. 1998. Conclusions from the test case modelling. Proceedings of the 2nd CADAM workshop, Munich, Germany

BÜCKER, M. 1998. Breschenbildung in Erdämmen – Auswertung historischer Dammbrüche und Zusammenstellung wesentlicher Einflussparameter – Literaturstudie, Institut für Bodenmechanik und Felsmechanik, Abteilung Erddammbau und Deponiebau (unpublished), Karlsruhe, Germany

COLEMAN, S. E., ANDREWS, D. P. 2000. Overtopping Breaching of Noncohesive Homogeneous Embankments, Department of Civil and Resource Engineering, Auckland, New Zealand

FÄH, R. 1997. Numerische Simulation der Strömung in Offenen Gerinnen mit beweglicher Sohle, Mitteilungen der VAW Technische Hochschule Zürich, Zürich, Switzerland

FREAD, D. L. 1991. BREACH: An erosion model for earthen dam failures, Silver Spring, USA: National Weather Service

GRAHAM, W. 1998. Dam failure inundation maps – are they accurate? Proceedings of the 2nd CADAM workshop, Munich, Germany

HANSON, G. J., et al. 1997. Headcut migration analysis of a compacted soil, Transaction of the American Society of Agricultural Engineers

JOHNSON, F. A., ILLES, P. 1976. A Classification of Dam Failures, Int. Water Power and Dam Construction. Vol. 28, Nr. 12

KAST, K., BIEBRSTEIN, A. 1997. Detection and assessment of dambreak-scenarios, Dams and Safety Management at Downstream Valleys, Balkema, Rotterdam, Netherland

LECOINT, G. 1998. Breaching mechanisms of embankments – an overview of previous studies and the models produced. Proceedings of the 2nd CADAM workshop, Munich, Germany

MOHAMED, M. A. A., SAMUELS, P. G., GHATAORA, G. S., MORRIS, M. W. 1999. A new methodology to model the breaching of non-cohesive homogeneous embankments, Proceedings of the 4th CADAM Concerted Action Meeting, University of Zaragoza, Spain

MOHAMED, M. A. A., SAMUELS, P. G., MORRIS, M. W. 2002. Improving the Accuracy of Prediction of Breach Formation through Embankment Dams and Flood Embankments HR Wallingford, Wallingford, UK

MORRIS, M. W. 2000. Concerted Action on Dambreak Modeling Final Report – CADAM, http://blakes.hrwalling-ford. co.uk/projects/CADAM/CADAM/index.html

NISHIMURA, T., et al. 1998. Influence of stress history on the strengh paramerters of an unsaturated statistically compacted soil, Canadian Geotechnique Journal No. 36, p. 251–261

POST, D., et al. 1994. High Sensitivity Moiré, Springer Verlag, New York, USA

SINGH, V. P. 1996. Dam Breach Modeling Technology, Kluwer Academic Publisher, Netherlands

UMS GmbH 2003. Datasheet for micro tensiometer T5, Munich, Germany

WAHL, T. L. 1997. Predicting Embankment Dam Breach Parameters – A Needs Assessment, XXVIIth IAHR Congress, San Francisco, California, USA

River Flow 2004 – Greco, Carravetta & Della Morte (eds.)
© 2004 Taylor & Francis Group, London, ISBN 90 5809 658 0

Experiments of dam-break flow in the presence of obstacles

S. Soares Frazão
Fonds National de la Recherche Scientifique and Department of Civil and Environmental Engineering, Université catholique de Louvain, Belgium

B. Noël & Y. Zech
Department of Civil and Environmental Engineering, Université catholique de Louvain, Belgium

ABSTRACT: Dam-break flows are likely to occur in area that are not subject to more common floods. Also, the importance of the wave might be such that the flow route is no more directed by the thalweg of the river. The whole valley is involved, and the roads, bridges and urban buildings become obstacles to the flow. The purpose of the paper is to study the influence of such an obstacle on a dam-break wave, the obstacle being an idealized representation of a single building. The experimental set-up consists in a channel with a rectangular shaped obstacle, representing a building, placed immediately downstream from the dam. The building is not centred in the channel, and is not aligned with the flow direction. Flow observation shows that after the violent impact of the wave on the building, the flow is forced to change its direction to pass the building. This implies the formation of hydraulic jumps with the consequence that the water level is locally more important than without building. Behind the building, a wake zone is observed. Then, further downstream, the flow slowly recovers the structure it would have without the building. Several measurement devices were used to characterize the flow. The water level evolution was measured at five different locations by means of water level gauges. At each gauging point, the velocity was measured by means of acoustic Doppler velocimeter. Then, the surface velocity field was obtained using digital imaging techniques. This study is part of the IMPACT European project which aims at investigating extreme flood processes and uncertainty. The experimental data set presented here was used in the IMPACT benchmarking programme, as a validation means for numerical models.

1 INTRODUCTION

Flows may be considerably affected by the presence of natural or artificial obstacles. In the case of severe floods, for example due to dam- or dike-break, the influence of such obstacles is even amplified. Neglecting this influence in numerical simulations of such flows could lead to heavy misinterpretation.

The presence of obstacles is common in river as well in minor bed (bridge piers) as in floodplains (abutments, dikes, trees and vegetation, debris from former floods, etc.). Moreover, if the river embankments are overtopped or the flood dikes breached, flow will occur in areas that are normally not subject to inundation, not prepared to support such a hazard, and thus presenting a series of obstacles (roads, railways, dwellings, industrial and commercial structures, etc.).

In steady flows, two major effects of obstacles are observed: an obstruction effect and a wave formation due to nonlinear alignment of the obstacle.

The obstruction effect, even in straight reaches, is best illustrated by the bridge-pier case (see for instance Chow, 1959). The flow is schematized as represented in Figure 1, where an additional constriction appears due to the limitation in flow-filament curvature.

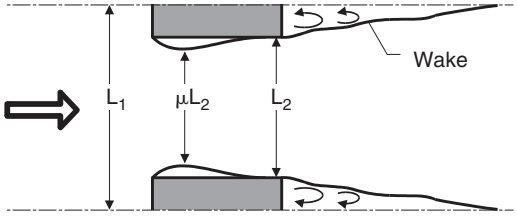


Figure 1. Schematization of bridge-pier constriction.

In uniform-flow channel with mild slope, the flow is mainly subcritical. If the cross-section reduction is limited, the obstruction induces a backwater effect that may extend over a long distance upstream (Fig. 2a).

However, if the relative obstruction is larger, it may happen that the specific-energy curve rises in such a way that its minimum C2, corresponding to the critical

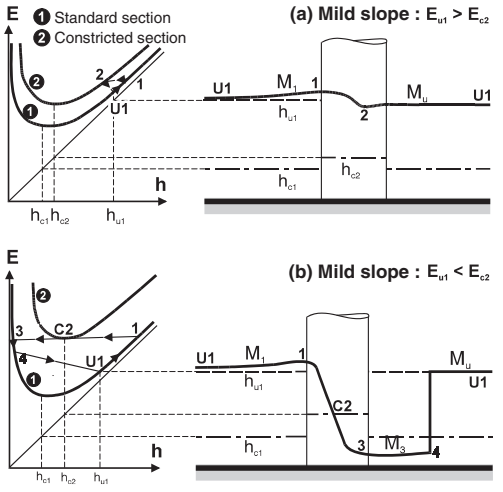


Figure 2. Water profiles along bridge piers in mild-slope cases.

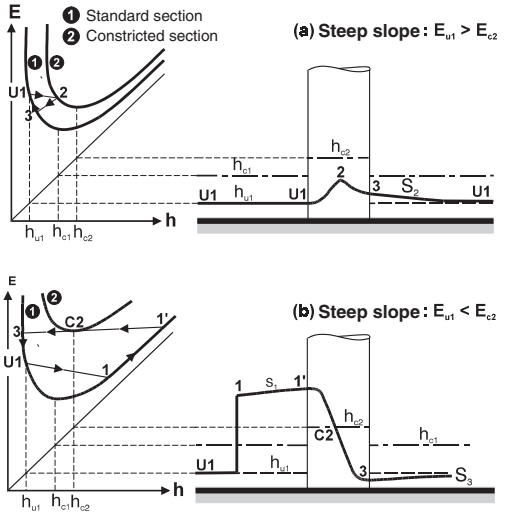


Figure 3. Water profiles along bridge piers in steep-slope cases.

stage, is higher that the uniform condition in the standard section (Fig. 2b). This results in a control section in the constricted section and in the development of a supercritical water profile, which returns to normal conditions through a hydraulic jump.

A similar behavior may be observed in steep-slope conditions, where the flow is generally supercritical. In these situations, the water profile presents the two configurations of Figure 3.

If the constriction is limited, only the water surface close to the constriction is disturbed and the effect

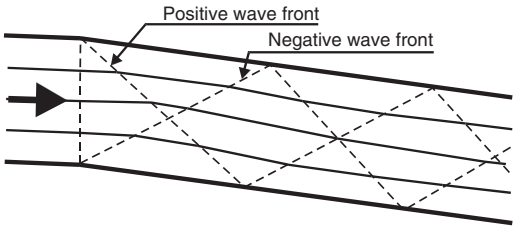


Figure 4. Cross waves in nonlinear alignment (after Chow, 1959).

will not extend farther upstream. If the constriction becomes significant, the minimum possible energy in the constricted section becomes too high to be reached immediately. The specific energy thus needs to increase in the upstream reach, which is only possible in subcritical flow, thus requiring the formation of a hydraulic jump. The resulting upstream water profile extends only over a short distance.

The above description of the obstruction effect caused by the presence of an obstacle is based on a one-dimensional flow modeling. If the resulting constriction is important, two-dimensional aspects may predominate and change significantly the location and shape of discontinuities.

The second observed consequence of an obstacle concerns the effect of nonlinear alignment, which may be rather complex.

In subcritical flows, a transverse superelevation may arise near the outer bank (or along the obstacle). In supercritical case, the outer wall, which turns inward to the flow, will produce an oblique hydraulic jump and a corresponding positive wave front, while the inner wall, which turns away from the flow, will develop a negative wave front, both forming cross waves (Fig. 4).

When the flow is unsteady, and above all in severe transient situations (dam- or dike break for example), this already complex behavior becomes even more complicated. The obstacle now induces reflected waves that in turn may reflect against the banks or other obstacles.

Few descriptions of such transient flow phenomena against obstacles are available. However, they could be of great interest in the modeling of dam-break flow. Above all it is important to evaluate the extension in space and time of the influence of an obstacle to limit accurate and refined computations where they are really needed.

At the large scale of a real flood event, it is not always possible to distinguish between the different features of the flow. Therefore, it was decided to design an idealized experiment that limits the parameters involved in the flow. A single obstacle representing a building is placed in a channel, immediately downstream from the dam. Through appropriate

measurements of the flow, it is possible to identify its specific features.

The experiment presented in this paper was used in the benchmarking program of the IMPACT European project (Soares Frazão et al., 2003). This research project, which addresses the assessment and reduction of risks from extreme flooding caused by natural events or by the failure of dams and flood defense structures (Morris, 2002; Morris and Vaskinn, 2002) has also a special focus on floods in urban areas and in the presence of obstacles.

2 EXPERIMENTAL SET-UP

The experiments were carried out in the laboratory of the Civil Engineering Department of the Université catholique de Louvain (UCL) in Belgium. The channel is sketched in Figures 5–7.

It has a total length of 35.80 m and is 3.60 m wide. The upstream reservoir is 6.90 m long. The cross section is trapezoidal near the bed (Fig. 7a). The dam is represented by a gate located between two solid blocks; its cross-section is rectangular and it is 1.00 m wide (Fig. 7b). To simulate a dam break, the gate is pulled up rapidly. The building, located 3.40 m downstream from the dam, consists in a rectangular block with dimensions 0.80×0.40 m. It makes an angle of 64° with the channel axis (Fig. 6). After measurement in uniform conditions, the Manning bed friction coefficient is $n = 0.01\ \mathrm{s\,m^{-1/3}}$.

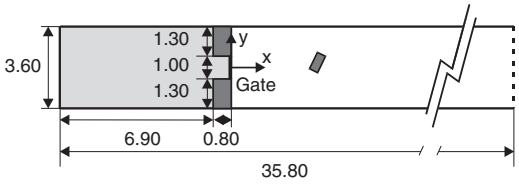


Figure 5. Experimental set-up (dimensions in meters).

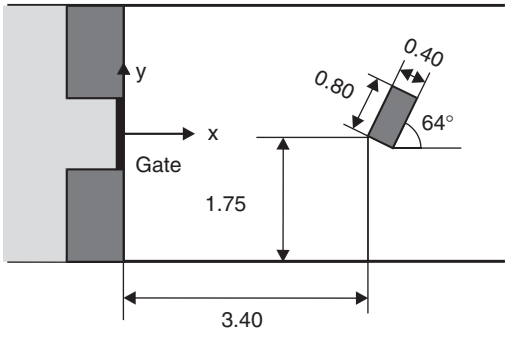


Figure 6. Location and dimensions of the building (in meters).

The channel is closed by a wall at the upstream end. The downstream boundary condition consists in a weir and a chute, but has no influence on the flow during the test duration, which is 30 s. The initial conditions consist in a water level of 0.40 m in the upstream reservoir and a thin layer of 0.01 m of water in the downstream part of the channel.

3 GENERAL FLOW DESCRIPTION

After the rapid opening of the gate, the strong dam-break wave reflects against the building, almost submerging it, and the flow separates, forming a series of shock waves crossing each other. A wake zone can be identified just downstream from the building, surrounded by cross waves. The flow rapidly reaches an almost steady state with a decreasing discharge due to the emptying of the reservoir. Also, re-circulation zones can be identified between the building and the walls.

This description of the flow is illustrated by means of figures obtained from computed results (Noël et al., 2003). Figure 8 shows the free-surface elevation at $t = 1$ s, with the two-dimensional spreading of the flood wave.

At $t = 3$ s, the reflection of the wave against the building has occurred and results in the formation of

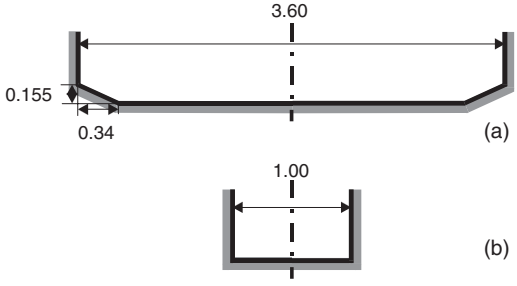


Figure 7. Channel cross section (a) in the reservoir and in the main channel, (b) at the dam location.

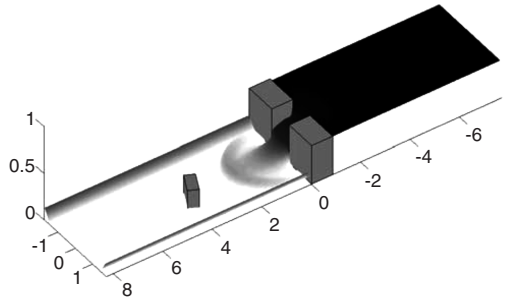


Figure 8. Computed image of the flow at time $t = 1$ s.

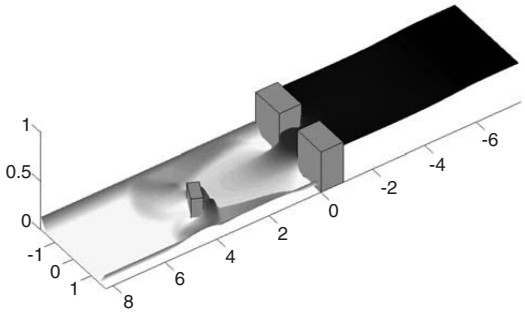


Figure 9. Computed image of the flow at time $t = 3$ s.

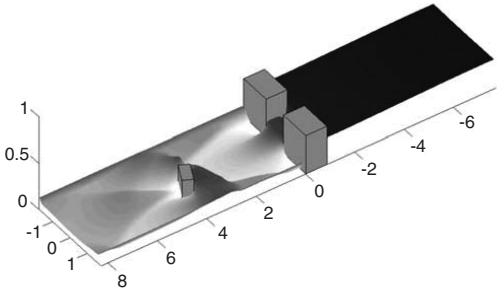


Figure 10. Computed image of the flow at time $t = 10$ s.

an oblique hydraulic jump (Fig. 9). The circular front wave also reflects against the side walls of the channel and lateral jumps are formed. Figure 10 shows the flow after 10 s: the upstream reservoir empties and the hydraulic jump formed by the reflection against the building migrates in the upstream direction. The separation of the flow around the building and the wake zone can also be identified.

4 FLOW MEASUREMENT

4.1 *Point measurements*

The water level is measured by means of 6 water-level gauges located in the channel as indicated on Figure 11: one gauge in the reservoir to monitor its emptying and thus the inflow discharge, and the others around the building. Their exact position is summarized in Table 1.

The experiment was run several times and showed a very good reproducibility. The velocity was also measured at the same locations by means of an Acoustic Doppler Velocimeter (ADV). However, no complete vertical velocity profiles were measured. Only one velocity data was measured at each gauging point, at a height of 3.6 cm above the channel bed to ensure that the transducers were submerged during the whole experiment. As the flow is a rapid transient with

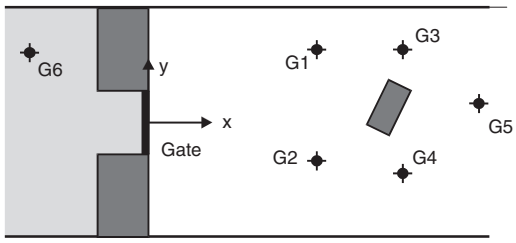


Figure 11. Sketch of the position of the gauging points where the water level and the velocity are measured.

Table 1. Position of the gauges.

Gauge	x (m)	y (m)
G1	2.65	1.15
G2	2.65	−0.60
G3	4.00	1.15
G4	4.00	−0.80
G5	5.20	0.30
G6	−1.87	1.10

hydraulic jumps and re-circulation zones, it is not fully developed i.e. there is no logarithmic velocity profile. The velocity distribution is closer to a uniform distribution and this kind of "mid-depth" measurement yields good results. This will be detailed in a further section.

4.1.1 *Field measurements*

A complete surface-velocity field was measured by a digital imaging technique yielding high-quality results. High-resolution CCD cameras were placed above the channel to film the flow seeded with tracers at a rate of 38 images per second. This results in a series of images where the white tracers can be clearly identified.

Using the Voronoï technique (Capart et al., 2002, Spinewine et al., 2003) to reconstruct the trajectories of the tracers on the free surface, it is possible to measure the velocity field in the filmed zone.

Thanks to the good reproducibility of the experiment, it was possible to run it several times and to combine the resulting images to cover a large area of the channel. Such a combination of filmed images is shown in Figure 12. The white tracers can be also be identified on the figure.

4.1.2 *Validity of velocity measurements*

By means of the ADV probe, the velocities u and v in the x and y directions respectively are obtained at a position 3.6 cm above the channel bed. The digital imaging technique provides the surface velocity. Both are different from the depth-averaged velocity in fully developed flows. However, in this rapidly varying

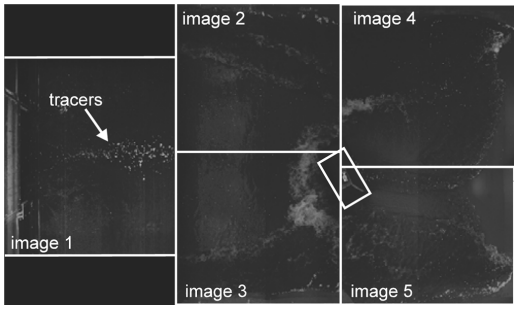


Figure 12. Combination of filmed images from five experiments to cover a whole field around the building ($t = 1.2$ s).

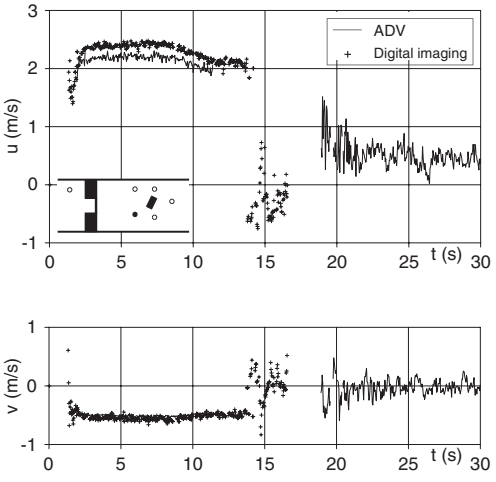


Figure 13. Velocity measurements at gauge G2, (a) u- and (b) v-component of the velocity.

flow, we can observe that both measurements are in a surprisingly good agreement. Figure 13 compares the ADV and digital imaging data at the location of gauge G2, while Figure 14 shows a similar comparison at gauge G4.

Gauge G2 measures the arrival of the reflected front around time $t = 15$ s. Before this time, the flow is supercritical and the u-component of the velocity is high. A difference is observed between ADV and digital imaging measurements, which indicates that the u-velocity distribution is not completely uniform. For the v-component, the correspondence is very good, as well as for the measurements at gauge G4.

5 EXPERIMENTAL RESULTS

5.1 *Digital imaging measurements*

By tracking the tracers on the combined filmed images and applying the Voronoï technique developed by

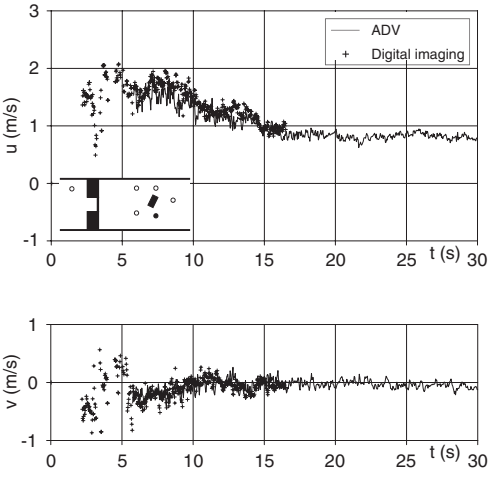


Figure 14. Velocity measurements at gauge G4, (a) u- and (b) v-component of the velocity.

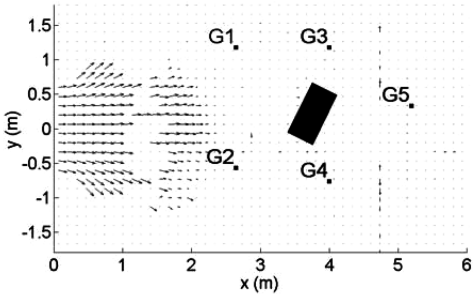


Figure 15. Measured velocity field at $t = 1$ s.

Capart et al. (2002) and Spinewine et al. (2003), surface-velocity fields are obtained as shown in the following figures.

Figure 15 shows the flow at $t = 1$ s. The two-dimensional spreading of the front wave is clearly visible. Then, at $t = 2$ s (Fig. 16), the front reaches the building and also the inclined side walls of the channel where a first reflection occurs. This reflection appears in the figure as a sudden change in direction and in amplitude of the velocity vectors.

At time $t = 5$ s, the hydraulic jumps formed by the reflection of the front wave against the building can be identified in Figure 17 as the limit between high velocities upstream from the building and an area of water almost at rest. The lateral hydraulic jump are still present. The flow separates to pass around the building and a wake is formed behind this.

Those latter features then remain and attenuate while the flow reaches an almost steady state as the reservoir empties. Figure 18 shows the velocity field after 10 s: the hydraulic jump has propagated slowly

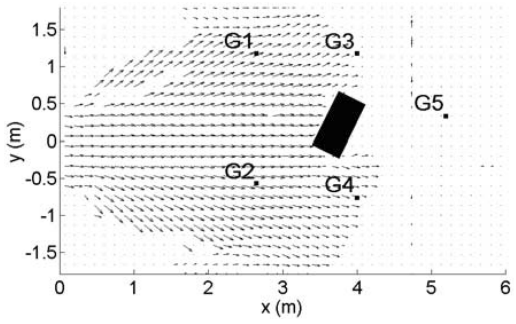


Figure 16. Measured velocity field at $t = 2$ s.

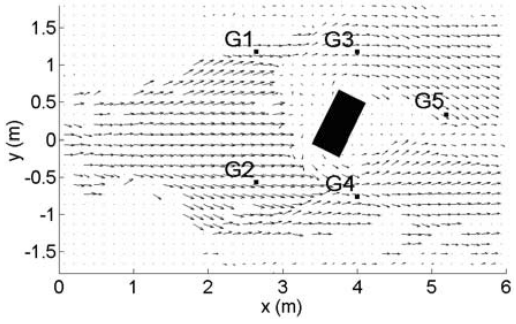


Figure 17. Measured velocity field at $t = 5$ s.

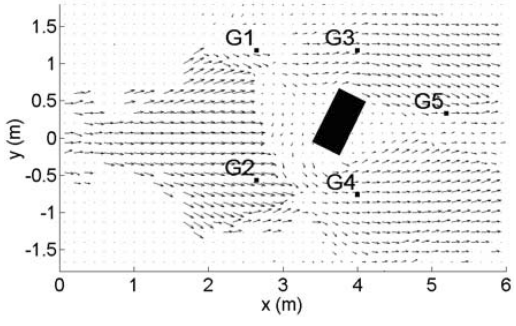


Figure 18. Measured velocity field at $t = 10$ s.

in the upstream direction, the lateral jumps take also more space in the flow, the wake zone is still present but the velocities have a decreasing amplitude.

5.2 *Water-level measurements*

The points where the water level was measured are indicated in Figure 11. Gauge G6, located in the upstream reservoir, shows a steady decrease of the water level as the reservoir empties (Fig. 19). Oscillations of the free surface in the reservoir occur as the back wave reaches the borders of the reservoir at

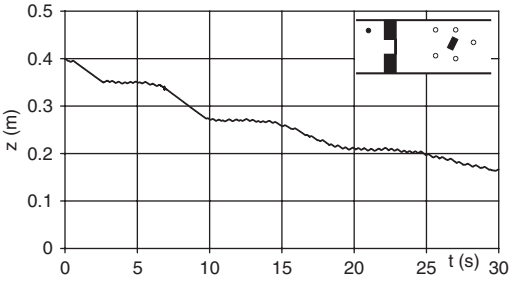


Figure 19. Water level evolution at gauge G6.

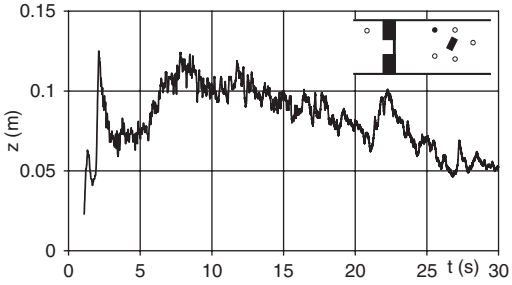


Figure 20. Water level evolution at gauge G1.

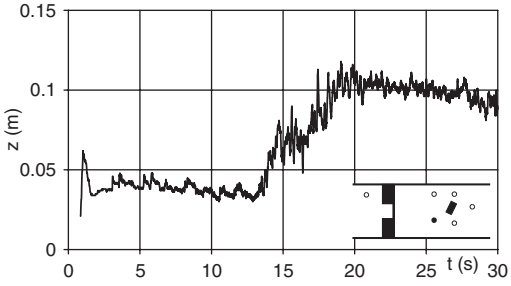


Figure 21. Water level evolution at gauge G2.

different times and reflect, resulting in a superposition of smooth waves.

Gauge G1 (Fig. 20) is located upstream from the building and close to the left bank of the channel. The water level rapidly rises due to reflection of the front wave against the inclined banks of the channel, appearing as a "splash" in the gauge measurements. Then, around $t = 8$ s, the oblique hydraulic jump formed by the reflection against the banks reaches the gauge.

The main hydraulic jump formed by the reflection of the wave against the building is well captured by gauge G2 (Fig. 21) around $t = 15$ s.

Gauge G4 (Fig. 22), located on the right side of the building, records several reflections of the water. First, there is a kind of "splash" at $t = 2.5$ s due to the strong reflection of the water against the building. Then, the

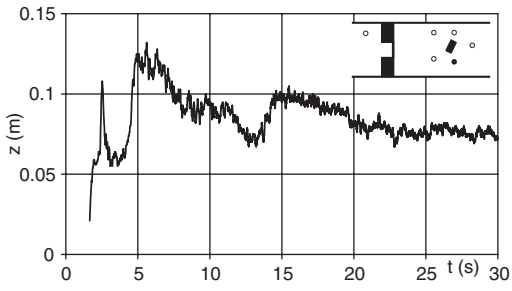


Figure 22. Water level evolution at gauge G4.

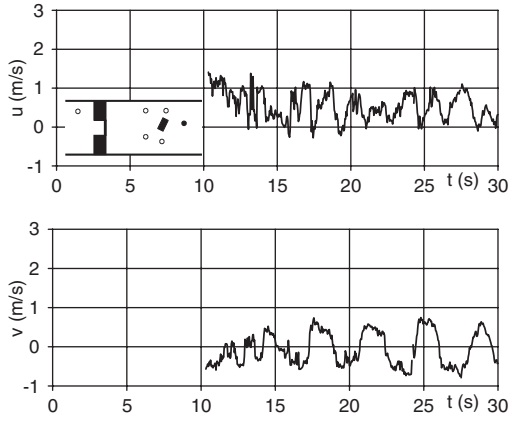


Figure 23. Velocity measurements at gauge G5.

arrival of the oblique hydraulic jump formed by the reflection of the front wave against the side walls of the channel ($t = 5$ s) can be observed. Finally a new rise of the water level is observed (around $t = 15$ s) when the oblique hydraulic jump and the main hydraulic jump come together and start moving in the upstream direction.

5.3 *ADV-velocity measurements*

The good agreement between both measurements techniques has already been outlined in a preceding section.

Interesting results were also obtained at gauge G5, located in the wake of the building. Figure 23 shows the *u*- and *v*-components of the velocity. The oscillations clearly indicate the presence of wake eddies.

6 RESULTS INTERPRETATION

6.1 *Zone of influence of the building*

Dam-break modeling aims at reproducing the water level and the velocity where water rise and/or forces

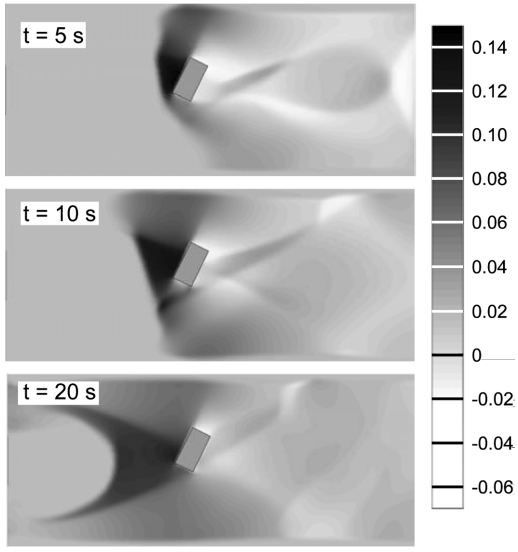


Figure 24. Difference of water depth (in meters) between results computed with and without obstacle.

induced by the current may endanger the population or the properties.

The presence of an obstacle may considerably modify those figures and thus also the associated risks. It is thus beneficial to estimate the changes induced by the obstacle. Figure 24 shows such a result for times $t = 5$, 10 and 20 s, respectively.

The upstream part of the flow, between the dam and the obstacle, is practically not influenced by this, which is not the case just in front of the building where significant increase of the water elevation occurs (0.14 m above the flow without obstacle, for a water depth of 0.40 m in the upstream reservoir). Also along the banks, above all the left bank, the influence of the obstacle is considerable.

Behind the building, the influence is less noticeable. Only a relative depression appears in the wake zones, which is not unexpected.

At $t = 20$ s, the influence downstream is very limited, in such a way that a modeling without obstacle would not affect too much the results in the far field.

6.2 *Comparison with steady flow*

If we now compare the longitudinal water profile at a certain distance (0.75 m) of the canal axis, at a time (20 s) when the first transient effects vanish, it is remarkable to observe that the profile is very comparable to the steep-slope case of Figure 3b, although the flume bed is horizontal. But, in case of dam break, the flow is highly supercritical, which corresponds to the typical steep-slope behavior. For mild

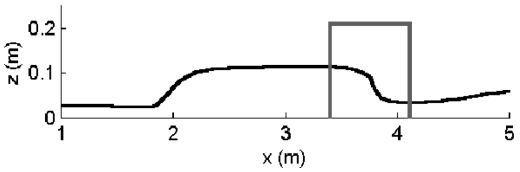


Figure 25. Water profile at $t = 20$ s along the line $y = 0.75$ m.

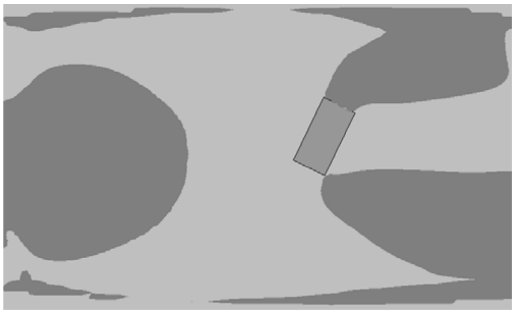


Figure 26. Supercritical (in dark gray) and subcritical-flow (in light gray) regions ($t = 20$ s).

or horizontal slopes the specific energy is decreasing along a supercritical water profile whereas this has to increase to reach the minimum energy required by the constriction. Only a passage to subcritical flow through a hydraulic jump may ensure this rise in energy.

Obviously this region just in front of the building would be poorly modeled by a simplified representation without obstacle.

Figure 26 shows the regions where the flow is super- or subcritical. The succession of regimes clearly appears: supercritical upstream, passing to subcritical flow through a hydraulic jump, then a control section near the constricted section and a second jump to return to normal regime.

7 CONCLUSION

The purpose of the paper was to study the influence of an obstacle on a dam-break wave, the obstacle being an idealized representation of a single building.

The measurement of water depths and velocity field were challenging, taking into account the limited thickness of water at many places and the large velocities in those regions. Digital imaging appeared as the best solution at least for surface velocity field.

The measurement confirmed that the flow pattern is deeply perturbed in the near-zone of the obstacle, above all at the front of this, while the far field downstream is less and less influenced by the presence of the obstacle, which allows to neglect the obstacle influence in the modeling if only the far field is concerned.

ACKNOWLEDGEMENTS

The authors wish to acknowledge the contribution of Benoit Spinewine in the experiments, especially concerning the use of the Voronoï digital-imaging technique.

The authors wish also to acknowledge the financial support offered by the European commission for the IMPACT project under the fifth framework programme (1998–2002), environment and sustainable development thematic programme, for which Karen Fabbri was the EC project officer.

REFERENCES

Capart, H., Young, D.L. & Zech, Y. 2002. Voronoï imaging methods for the measurements of granular flows. *Experiments in Fluids* 32 (1): 121–135.

Chow, V.T. 1959. *Open channel hydraulics*. New York: McGraw-Hill.

Morris, M. (ed) 2002. *EC Contract EVG1-CT-2001-00037 IMPACT Investigation of Extreme Flood Processes and Uncertainty, Proceedings 1st Project Workshop, Wallingford, UK 16–17 May 2002* (CD-ROM). Brussels: European Commission. Also available at www.impact-project.net

Morris, M. & Vaskinn, K.A. (eds) 2002. *EC Contract EVG1-CT-2001-00037 IMPACT Investigation of Extreme Flood Processes and Uncertainty, Proceedings 2nd Project Workshop, Mo-i-Rana, Norway 12–13 September 2002* (CD-ROM). Brussels: European Commission. Also available at www.impact-project.net

Noël, B., Soares Frazão, S. & Zech, Y. 2003. Computation of the "isolated building test case" and the "model city experiment" benchmarks. In *EC Contract EVG1-CT-2001-00037 IMPACT Investigation of Extreme Flood Processes and Uncertainty, Proceedings 3rd Project Workshop, Louvain-la-Neuve, Belgium 6–7 November 2003* (CD-ROM).

Soares Frazão, S., Noël, B., Spinewine, B. & Zech, Y. 2003. Flood propagation – The isolated building test case – Results from the benchmark. In *EC Contract EVG1-CT-2001-00037 IMPACT Investigation of Extreme Flood Processes and Uncertainty, Proceedings 3rd Project Workshop, Louvain-la-Neuve, Belgium 6–7 November 2003* (CD-ROM).

Spinewine, B., Capart, H., Larcher, M. & Zech, Y. 2003. Three-dimensional Voronoï imaging methods for the measurement of near-wall particulate flows. *Experiments in Fluids* 34 (2): 227–241.

River Flow 2004 – Greco, Carravetta & Della Morte (eds.)
© 2004 Taylor & Francis Group, London, ISBN 90 5809 658 0

Sph simulation of dam-break flow in shallow water approximation

M. Gallati & D. Sturla
Hydraulic and Environmental Engineering Dept, University of Pavia, Italy

ABSTRACT: This paper reports on the application of the Smoothed Particle Hydrodynamics technique to model 1D and 2D dam-break flows under the shallow water approximation. Following an introduction of the basic equations and a short description of the numerical technique, one dimensional simulations are presented and compared to analytical solutions or to laboratory experiments taken from technical literature. Finally the results of two dimensional dam-break flows are reported: several cases have been simulated comparing results to the ones obtained by an eulerian code (PFP) and experimental evidence.

1 INTRODUCTION

Smoothed Particle Hydrodynamics (SPH) is a meshless lagrangian method for modeling mass flow that was introduced independently by Gingold & Monaghan (1977) and Lucy (1977) in order to model complicated phenomena in astrophysics. Since then the method has been successfully applied to a vast range of problems, including elastic-plastic flow, heat transfer and incompressible flows, to name but a few.

At the Hydraulic and Environmental Engineering Department of Pavia University in 2001 SPH began to be applied to Hydraulics. Several studies and numerical experiments have been performed (Gallati & Sturla 2000, 2001; Braschi & Gallati 2000, 2001, 2003), showing the capability of the method to model rapidly varied unsteady flows with free surfaces.

The aim of the present work is to report on the studies and the experience gained regarding the application of SPH to solve the shallow water approximation of Navier-Stokes equations: the De Saint Venant equations. SPH has already been applied to solve these equations by Wang and Shen (1999) to simulate the Stoker problem. Here more complex 1D and 2D cases of dam-break simulation are reported.

Several adaptations have been introduced into the original technique (developed to solve Euler equations) in order to adapt SPH to the shallow water context. Another computational skill deals with the treatment of domain boundaries since the original SPH was in an astrophysical context with unbounded domains.

The main part of this paper is devoted to the description of the code, named SW-SPH, developed by the authors. Its performance is shown in 1D cases by comparison to analytical solutions or to laboratory experiments taken from technical literature. In the 2D dam-break simulations results are compared to ones obtained by an eulerian code or laboratory data expressly obtained for this purpose.

2 MATHEMATICAL MODEL

The shallow water equations, also referred to as the De Saint Venant equations, describe two-dimensional unsteady, free-surface flows under the assumption of hydrostatic pressure distribution, small channel bottom slopes and uniform velocity distribution in the vertical direction. These assumptions are usually valid except when the water surface has sharp curvatures.

In lagrangian form these equations are written as:

$$\frac{D\eta}{Dt} + \eta \nabla \cdot \mathbf{v} = 0 \tag{1}$$

$$\frac{D\mathbf{v}}{Dt} = -g\nabla\eta + g(\mathbf{S}_0 - \mathbf{S}_f) \tag{2}$$

where $\eta =$ water depth; $\mathbf{v} =$ flow velocity vector; $g =$ gravity acceleration; $\mathbf{S}_0 =$ channel bottom slope vector; $\mathbf{S}_f =$ slope of energy grade line vector, computed using the steady state friction formula

$$\mathbf{S}_f = n^2 \frac{\mathbf{v}v}{\eta^{1.33}} \tag{3}$$

in which $n =$ Manning's roughness coefficient.

Equation (1) and (2) describe, respectively, the mass and momentum conservation principles. Once specified the boundary conditions their solution allows the

state variables $\eta(\boldsymbol{r}, t)$ and $\boldsymbol{r}(\boldsymbol{v}, t)$ to be defined. It is well known that such variables may be discontinuous along moving boundaries (hydraulic jumps).

3 NUMERICAL MODEL

3.1 *The basic idea of SPH*

Standard finite element or finite difference techniques in hydrodynamics follow an Eulerian approach: the space is discretized with fixed grid of cells across which the inflow and outflow together with the stored mass are computed. A lagrangian approach, as SPH, on the contrary, follows the evolution of selected fluid elements over space and time. We describe in this section the fundamentals of this formalism as it provides sound bases for the SW-SPH code.

The foundation of the SPH is an interpolation theory. The conservation laws of continuum fluid dynamics are transformed into integral equations through the use of an interpolating function that provides the "kernel estimate" of the field variable at a point. The term "kernel" refers to a weighting function and defines how much surrounding field variable values contribute to the value of the field variable at the point $\mathbf{r}$.

For a better understanding let's start with the exact relation for any quantity (scalar or vector) A,

$$A(\mathbf{r}) = \int_{\Omega} A(\mathbf{r}')\delta(\mathbf{r}-\mathbf{r}')d\omega \tag{4}$$

where Ω is the space domain, δ is the delta Dirac function and $d\omega$ is the space element.

If we replace δ-function by an interpolating kernel $W(\mathbf{r}, h)$ we obtain an integral interpolation of the function $A(\mathbf{r})$,

$$A_{\text{int}}(\mathbf{r}) = \int_{\Omega} A(\mathbf{r}')W(\mathbf{r}-\mathbf{r}', h)d\omega \tag{5}$$

In (5) h is the so-called "smoothing length" that defines the width of the kernel.

The kernel, that mimics a δ-function, has the following two properties:

$$\int_{\Omega} W(\mathbf{r}-\mathbf{r}', h)d\omega = 1 \tag{6.1}$$

$$\lim_{h \to 0} W(\mathbf{r}-\mathbf{r}', h) = \delta(\mathbf{r}-\mathbf{r}') \tag{6.2}$$

The integral interpolation A_{int} can be thought as a smoothed version of the original function A. This is the origin of "Smoothed" in SPH.

If $A(\mathbf{r}')$ is known only at a discrete set of N points (particles) $\mathbf{r}_1, \mathbf{r}_2, \ldots, \mathbf{r}_N$, then we can approximate the integral interpolant with a summation interpolant as,

$$A_{sum}(\mathbf{r}) = \sum_j A(\mathbf{r}_j)W(\mathbf{r}-\mathbf{r}_j, h)d\omega_j \tag{7}$$

The final step is to express the differential space element $d\omega$ as $m_j/\rho(\mathbf{r}_j)$ where m_j is the mass associated with particle j and $\rho(\mathbf{r}_j)$ is the density at point $\mathbf{r}_j$. The crucial point to note is that, if W is a differentiable function, we can calculate the derivatives of A by differentiating (8).

For example the gradient of the function A is,

$$\nabla A_{sum}(\mathbf{r}) = \sum_j A(\mathbf{r}_j)\nabla W(\mathbf{r}-\mathbf{r}_j, h)d\omega_j \tag{8}$$

In SPH the continuum is discretized by particles each one has a defined mass and brings its information in terms of velocity, pressure, etc. distributed around the center according to the kernel function. These particles are free to move under their mutual interaction and the action of any external body forces. Then, since we have to follow these particles, we are interested in knowing the value of variable A at the particle position $A_i = A(\mathbf{r}_i)$. Eqs. (7) and (8) become:

$$A_i = \sum_{j=1} A_j W_{ij} d\omega_j \tag{7.1}$$

$$\nabla A_i = \sum_j A_j \nabla W_{ij} d\omega_j \tag{8.1}$$

where

$$W_{ij} = W(\mathbf{r}_i - \mathbf{r}_j, h). \tag{9}$$

Once the value at the particle position is computed, using (8) the properties of fluid can be found at any point of the domain.

3.2 *The kernel function*

Theoretically, the choice of kernel is arbitrary, provided that it satisfies equations (6.1) and (6.2). In this paper the cubic spline (figure 1) has been employed,

$$W(r,h) = \frac{\sigma}{h^{\nu}} \begin{cases} \left(1 - \frac{3}{2}s^2 + \frac{3}{4}s^3\right), & \text{if} \quad 0 \le s \le 1, \\ \frac{1}{4}(2-s)^3, & \text{if} \quad 1 \le s \le 2 \\ 0, & \text{otherwise} \end{cases} \tag{10}$$

where $s = r/h$, ν is the number of dimensions and σ is the normalization constant with values $2/3, 10/7\pi$, or $1/\pi$ in one, two, or three dimensions respectively. The cubic spline kernel is adopted since it belongs to the family of compact support kernels: a potentially small number of neighboring particles are the only contributors in the sums over the particles (particles belonging to the circular region with radius $2h$ centered at the specific point, see figure 2). This is, of course, a great computational advantage.

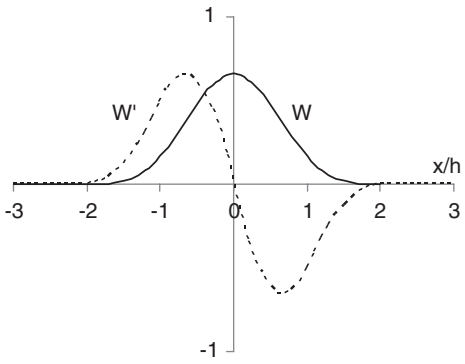


Figure 1. Cubic spline (W) and its derivative (W′) in 1D.

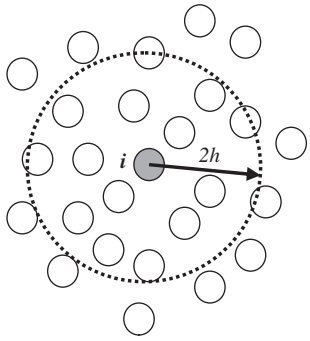


Figure 2. Particle *i* interacts with other particles only out to a distance of 2*h*.

3.3 *Smoothing length*

The smoothing length represents the effective width of the kernel, or the distance at which the particle in question interacts with other particles (figure 2). Changing smoothing length in SPH corresponds to changing the numerical resolution. If the fluid to be modeled does not undergo substantial rarefaction (or compression) constant h is sufficient. If particles become so distant, that they cease to interact (or so close, that a large number are within a smoothing length) h should be changed accordingly. The interpolation precision of SPH depends on having a sufficient number of particles within $2h$ and the speed of the computation depends on this number being relatively small. SPH works best when the number of neighbors is about 5 in one dimension and about 21 in two dimensions. These numbers all correspond to the number of neighbors on a cubic lattice with a smoothing length 1.2 times the particle spacing (using cubic spline).

There are many ways to dynamically change h so that the number of neighbors is kept approximately constant.

In this study the simplest approach is used: each particle has its own smoothing length which varies in space and time according to particle density.

Later, it will be shown that particle density is proportional to water depth, then the following expression is used to calculate smoothing length associated to particle *i*:

$$h_i = h_0 \left(\frac{\eta_0}{\eta_i} \right)^{\frac{1}{\nu}} \tag{11}$$

where h_0 and η_0 are the reference (initial) smoothing length and the reference water depth respectively.

Since each particle has its own smoothing length, each particle pair interaction, must have a smoothing length h_{ij} associated with it. In order to conserve momentum exactly, symmetry of particle interaction is preserved defining:

$$W_{ij} = W\left(\mathbf{r}_i - \mathbf{r}_j, h_{ij}\right) \tag{12}$$

where

$$h_{ij} = \frac{h_i + h_j}{2} \tag{13}$$

3.4 *The SW-SPH model*

With the previous basic rules the shallow water equations in the lagrangian form are converted into equations for particles.

The fluid is sampled by a set of particles. A particle *i* has a fixed volume V_i (that correspond to the particle mass m_i in the original SPH context), a position $\mathbf{r}_i$, a velocity $\mathbf{v}_i$ and a water depth η_i (that correspond to the density ρ_i in the original SPH context). The differential area element $d\omega_i$ is V_i/η_i.

In the Lagrangian approach we move the particles with the velocity of the fluid, thus,

$$\frac{d\mathbf{r}_i}{dt} = \mathbf{v}_i \tag{14}$$

where $\mathbf{v}_i$ is updated using (2). With (8.1) we can calculate the gradient of η and then we obtain the SPH approximation of the motion equation (2),

$$\frac{D\mathbf{v}_i}{Dt} = \sum_j (g + \Pi_{ij}) \nabla W_{ij} V_j + g\left(\mathbf{S}_0 - \mathbf{S}_f\right)_i \tag{15}$$

in which Π_{ij} is the so-called "artificial viscosity". This term is introduced in the computation in order to avoid large unphysical oscillations (particle interpenetration) near to discontinuities (shocks). In this paper the standard artificial equation of Monaghan

and Gingold (1983) has been employed and adapted to shallow water context.

$$\Pi_{ij} = \begin{cases} \dfrac{-\alpha\, c_{ij}\mu_{ij}}{\eta_{ij}} & if \quad (\mathbf{v}_i - \mathbf{v}_j)\cdot(\mathbf{r}_i - \mathbf{r}_j) < 0 \\ 0 & otherwise \end{cases} \tag{16}$$

where

$$\mu_{ij} = \frac{h_{ij}(\mathbf{v}_i - \mathbf{v}_j)\cdot(\mathbf{r}_i - \mathbf{r}_j)}{\left\|(\mathbf{r}_i - \mathbf{r}_j)\right\|^2 + \varepsilon h^2} \tag{17}$$

and

$$c_{ij} = \tfrac{1}{2}(c_i + c_j);\ \ \eta_{ij} = \tfrac{1}{2}(\eta_i + \eta_j);\ \ h_{ij} = \tfrac{1}{2}(h_i + h_j) \tag{18}$$

Here c_i denotes the shallow water wave speed $c_i = (g\eta_i)^{0.5}$; α is an empirical constant commonly $= 2$, $\varepsilon = 0.01$ is introduced to keep the viscosity bounded for particles as they approach.

Finally, the SPH representation of the continuity principle is obtained in integral form by means of (7.1) applied to η:

$$\eta_i = \sum_j W_{ij} V_j \tag{19}$$

Shallow water equations have been discretized in space for each particle and for the time interval Δt to get the flow characteristics (velocity, water depth, etc. for each particle) at the advanced time step starting from an initial distribution. The time integration of the SW-SPH equations is explicit thus the time step is chosen to accommodate CFL condition which, keeping in mind that the natural SPH scale length is h, is:

$$\Delta t \le \min_i \left(\frac{h_i}{c_i + |\mathbf{v}_i|} \right). \tag{20}$$

The time integration strategy from time t^N to time t^{N+1} is the following (excluding first time step):

– calculation of time step Δt^N using $h_i^N, c_i^N, \mathbf{v}_i^N$ in (20);
– calculation of particles acceleration at time t^N using equation (15), separated in two parts:

$$\left(\frac{D\mathbf{v}_i^N}{Dt}\right)_1 = \sum_j (g + \Pi_{ij}^N)\nabla W_{ij}^N V_j + g\mathbf{S}_{0\,i}^N \tag{21.1}$$

$$\left(\frac{D\mathbf{v}_i^N}{Dt}\right)_2 = -gn^2 \frac{|\mathbf{v}_i^N|\mathbf{v}_i^{N+1/2}}{\eta^{1.33^N}} \tag{21.2}$$

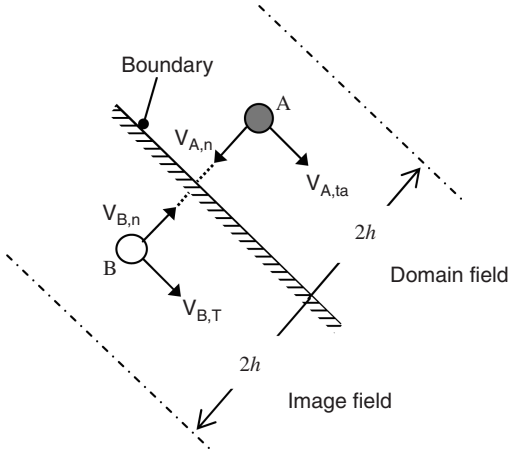


Figure 3. Image (B) of the particle A. Free slip condition: $v_{B,n} = -v_{A,n}$ and $v_{B,t} = -v_{A,t}$.

– velocity updating of each particle at time $t^{N+1/2}$ in a semi-implicit way

$$\mathbf{v}_i^{N+1/2} = \frac{\mathbf{v}_i^{N-1/2} + \left(\dfrac{D\mathbf{v}_i^N}{Dt}\right)_1 \dfrac{\Delta t^{N-1} + \Delta t^N}{2}}{1 + gn^2 \dfrac{|\mathbf{v}_i^N|}{\eta^{1.33^N}} \dfrac{\Delta t^{N-1} + \Delta t^N}{2}} \tag{22}$$

– position updating of each particle

$$\mathbf{r}_i^{N+1} = \mathbf{r}_i^N + \mathbf{v}_i^{N+1/2}\Delta t^N \tag{23.1}$$

– water depth updating using (19)

$$\eta_i^{N+1} = \sum_j W_{ij}^{n+1} V_j \tag{23.2}$$

– smoothing length updating using new water depth in (11).

In this paper only free slip boundary conditions are considered. They are assigned as follows: the field is extended out of its borders by adding a strip of thickness $2h$ where image particles. To each image particle the values of variables of the corresponding field particle are given except for the velocity component normal to the boundary, which is reversed in sign (figure 3).

4 DAM-BREAK SIMULATIONS

In this paragraph the results of several test problems selected for the validation of SW-SPH code are shown. One dimensional and two-dimensional simulations of the catastrophic failure of a dam have been considered.

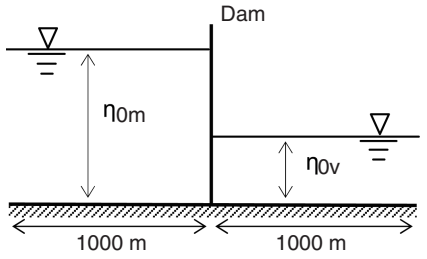


Figure 4. Definition sketch.

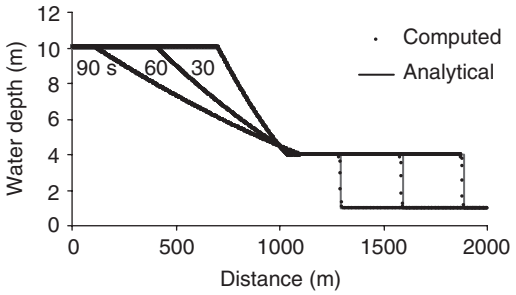


Figure 5. Stoker's problem.

4.1 *One-dimensional simulations*

The first simulations here reported deal with two simple cases for which analytical solutions are available.

At the midpoint of a channel 2000 m long a dam separates two basins with different heights of still water (Figure 4).

At time t = 0 the dam is instantaneously removed, then a negative wave moves upstream and a surge rushes downstream. For the case of a 1 m wide horizontal rectangular channel, with negligible resistance, an exact solution is given by Stoker (1957). This problem, although idealized, is very interesting to test the shock capturing ability of the method.

We consider the case with $\eta_{0m} = 10$ and $\eta_{0v} = 1$. In the simulation here presented the initial water mass upstream of the dam is discretized with 1000 particles having a constant volume of 10 m^3/m, placed on a regular grid with a step of 2 m. Water mass downstream instead is represented by 100 particles having the same volume but placed on a coarser grid with a step of 20 m. The reference water depth, η_0, to be used in (11) is η_{0m}, the reference smoothing length, h_0, has been set 1.5 times the upstream particle distance so that about 7 particles interact. Note that with this initialization eq. (19) gives $\eta_i = \eta_{0m}$ upstream and $\eta_i = \eta_{0v}$ downstream.

The result, as shown in figure 5, is clearly in agreement with the exact solution.

The same problem was run considering the initial tailwater $\eta_{0v} = 0$ (dry bed test case). In this case the analytical solution is given by Ritter.

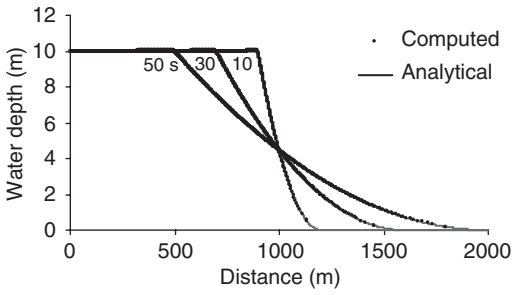


Figure 6. Ritter's problem.

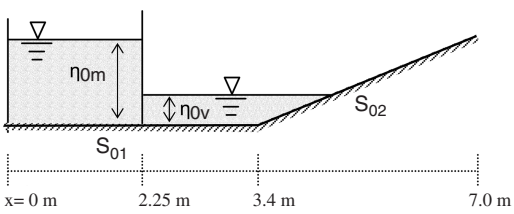


Figure 7. Experimental set-up (from Mignosa et al., 2001).

Table 1. Experimental test conditions.

Test	S_{01} (%)	S_{02} (%)	Manning n	η_{0m} (cm)	η_{0v} (cm)
A	0	−0.1	0.01	25	0.0
B	0	−0.1	0.01	25	4.5

The result, as shown in figure 6, is also clearly in good agreement with the exact solution. Note than no special treatment of dry areas has been employed.

The effect of the "source" term S_0 and S_f have been tested simulating dam-break laboratory experiment. Two sets of experimental data, taken from Mignosa et al. (2001), have been used for comparison. The experimental set up is shown in figure 7. The rectangular flume is 1.0 m wide, 0.5 m high and 7.0 m long.

The instantaneous dam failure is simulated by means of the sudden removal of the gate. The flow field is characterized by shock propagation, reverse flow and wetting and drying conditions.

The experimental conditions of "test A" and "test B" (with and without tailwater depth) are summarized in table 1.

In both the test cases the initial condition is set by placing upstream of the dam 225 particles on a regular grid with step of 1 cm. The volume of each particle is 25 cm^3/cm and the reference smoothing length 1.5 times the grid step.

In the simulation of test B (non-zero tailwater depth) 32 more particles are placed downstream of the gate on a regular grid with a step of 5.5 cm.

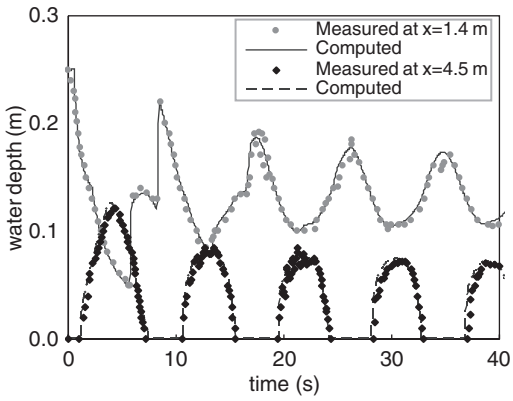


Figure 7.1. Computed and measured stage hydrographs for test case A.

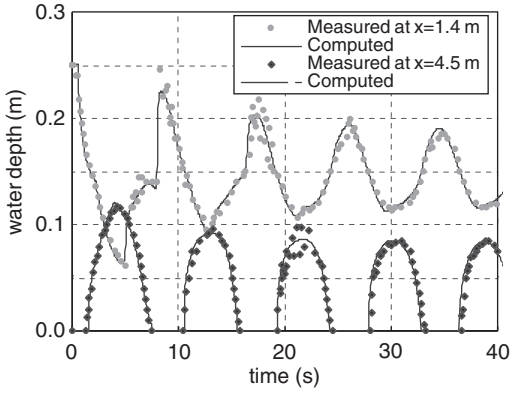


Figure 7.2. Computed and measured stage hydrographs for test case B.

In figures 7.1 and 7.2 the experimental hydrographs are compared to the numerical results. The sections along the flume are set at x = 1.4 m and x = 4.5 m. The water depth in those sections is recovered by eq. (7).

A good agreement between numerical results and experimental evidence can be observed.

4.2 *Two-dimensional simulations*

The first test case of two-dimensional simulations is the idealized partial dam breach reported in Fennema et al. (1990). It deals with a partial failure of a dam in a 200 × 200 m basin of simplified geometry depicted in figure 8. The non-symmetrical breach is 75 m wide and the dam is 10 m thick. The bottom of the basin is horizontal and friction losses are neglected ($n = 0$).

We report the case of initial reservoir depth $\eta_{0m} = 10$ m and tailwater depth $\eta_{0v} = 5$ m.

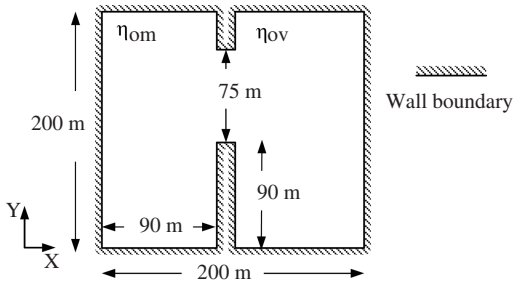


Figure 8. Definition sketch for partial dam-break.

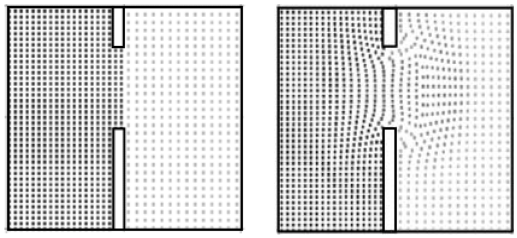


Figure 9.1. Particle position at time $t = 0$ s and time $t = 7.16$ s.

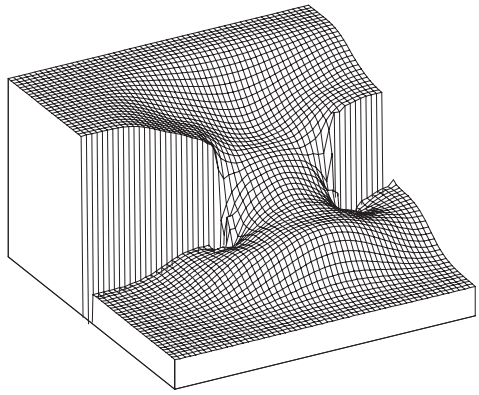


Figure 9.2. Water surface profile computed at time t = 7.16 s.

In the simulation the initial water mass upstream the dam is modeled with 750 particles with constant volume of 250 m^3, placed on a regular grid with step of 5 × 5 m. The downstream water mass is instead represented by 216 particles having the same volume but placed on a coarser grid with step 7.05 × 7.05 m. The reference water depth, η_0, to be used in (11) is η_{0m}, the reference smoothing length, h_0, has been set 1.5 times the upstream particles initialization grid step.

The flow conditions have been computed at time t = 7.16 s and results are shown in figure 9.1 (particle position) and in figure 9.2 (water surface profile).

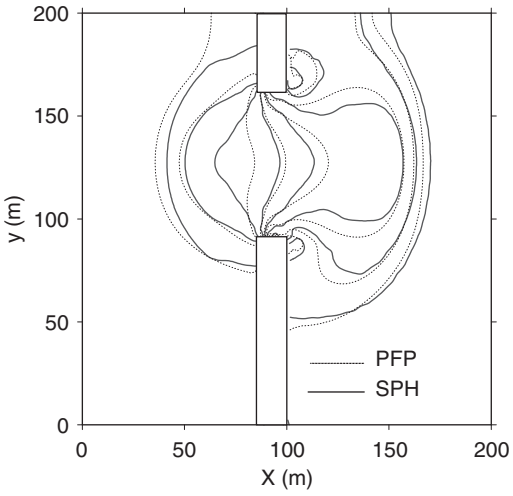


Figure 10. SW-SPH result vs PFP results in terms of water levels (ranging from 5 m to 9 m with step 0.5 m).

In figure 10 the results are compared to the ones obtained by the shock-capturing eulerian code PFP (Braschi & Gallati, 1990). The mesh size of the eulerian simulation is 5 m × 5 m.

After the preliminary tests of the code with simple 1D problems and 2D literature numerical results, a laboratory experiment was decided to get a better understanding of the capabilities of the model.

The scheme and the relevant geometrical data of the experimental setup is reported in figure 11. At the sudden gate opening the reservoir water spreads over the trasparent plane. The boundaries of the plane are plexiglass walls that reflected the flow forming cross shock waves. In order to visualize the characteristics of the flow field the water is colored with methylene blue ink and the plane is lighted from below. By this way it is possible to follow the position of the wave front.

The experiment was shot with a video camera able to record 25 frames per second, fixed 2 m above the plane. Using suitable software it is possible to select from the whole film the frames at given times after the gate opening. Although the evaluation of the water depth can be obtained from the color intensity only a qualitative comparison between experimental evidence and simulation is shown in the following.

Two sets of experiments are reported. For both the initial water level in the reservoir is of 8 cm and the plane is initially dry.

In the second experiment a rectangular obstacle 10 cm high is placed in front of the gate as depicted in figure 12.

The simulation of the flow has been performed modeling the initial reservoir mass water by 333 particles

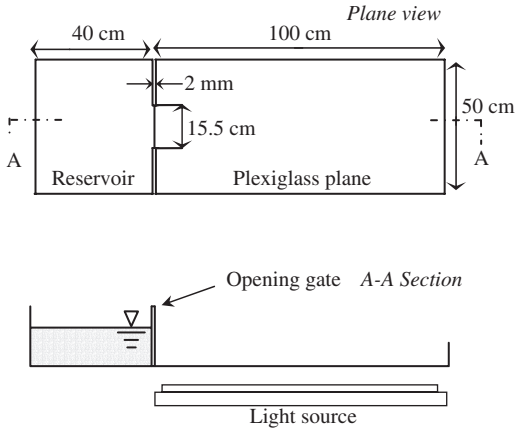


Figure 11. Experimental set-up for experiment 1.

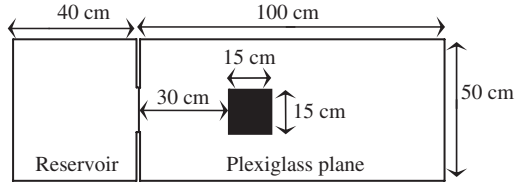


Figure 12. Experimental set-up for experiment 2.

placed on a regular grid with step of 2 × 2 cm; η_{0m} is the initial water depth in the reservoir, h_0, has been set 1.5 times the particles initialization grid step; the Manning coefficient of $n = 0.01$ has been assumed.

In figures 13 and 14 several computed and recorded flow fields are displayed at selected times after the opening. In the first and second column, observed and computed flow fields are reported respectively. The computed results are represented by the particle position in the plane. The particle's color is proportional to water depth associated to it.

In the third column results of the numerical model are displayed in terms of velocity field: in order to obtain these pictures, particle velocities are interpolated on a regular grid using (7).

There is an acceptable agreement between observation and simulation in both the experiments. Qualitatively, the main depth distribution features are retained and the shape and velocity of the two-dimensional hydraulic jumps calculated are in good agreement with the observed ones.

5 CONCLUSION

This paper reports on the application of the Smoothed Particle Hydrodynamics technique to Hydraulics in

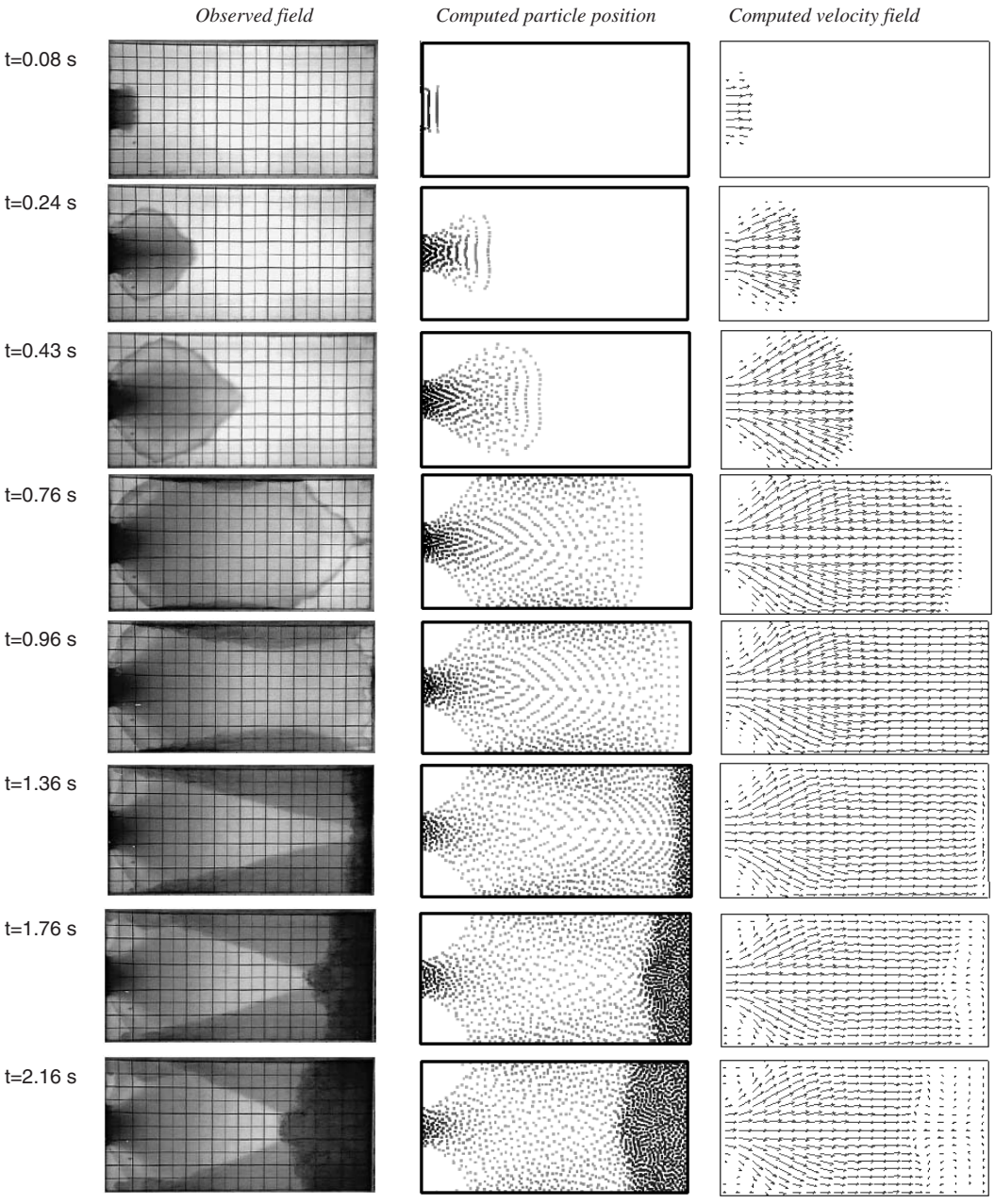


Figure 13. Comparison between computed and observed flow field – Experiment 1.

order to model free surface channel flows under the shallow water approximation. The original technique, born in an astrophysical context, has been adapted to solve the De Saint Venant equations under bounded domains.

Several 1D and 2D simulations of the idealized failure of a dam have been used to validate the code developed by the authors.

The method was shown to be robust and flexible to get realistic results both in 1D simple cases and in

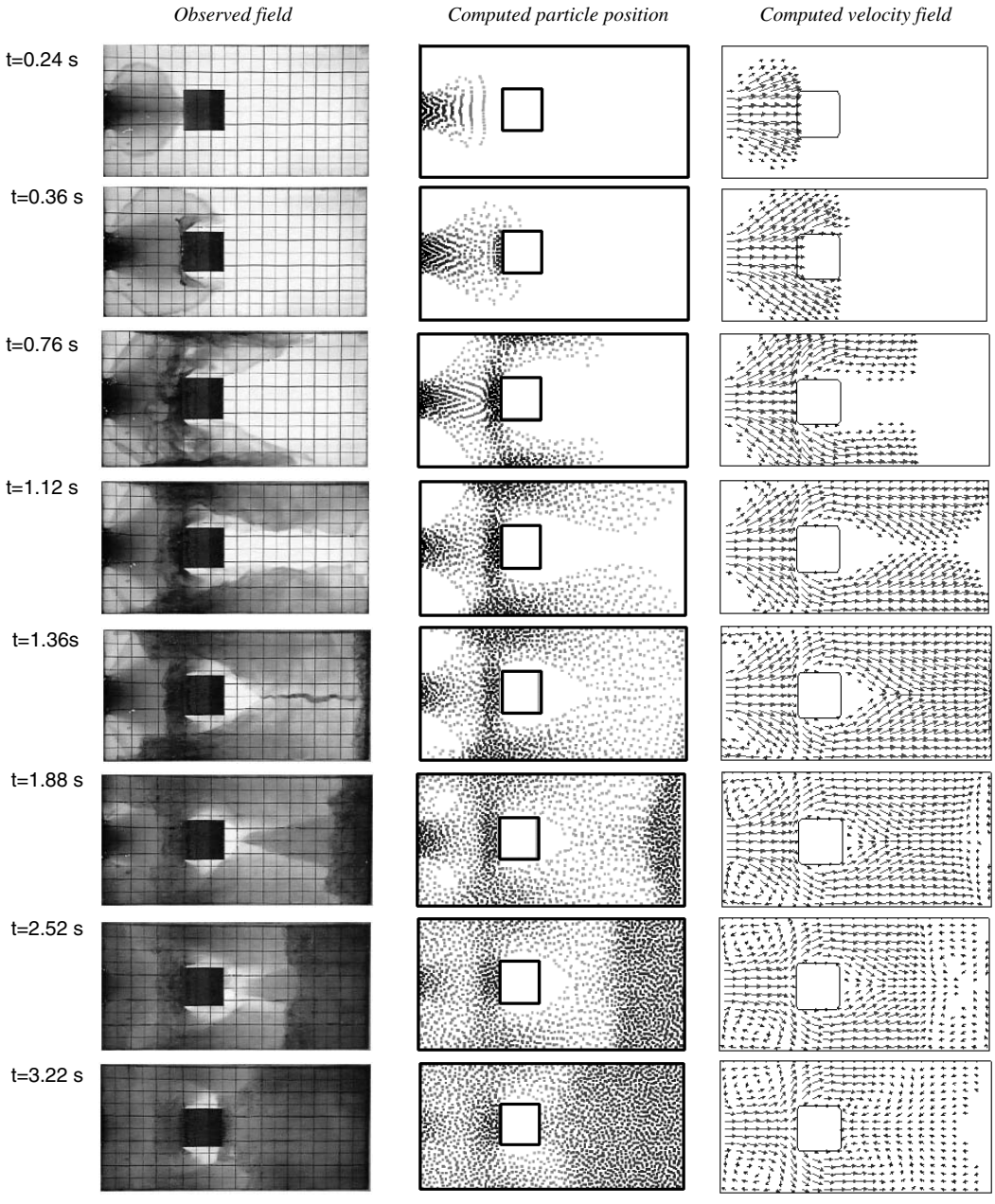


Figure 14. Comparison between computed and observed flow field – Experiment 2.

2D complex problems. It is suited especially to problems with sharp moving fronts since the shock waves can easily be captured and accurately simulated. The method is also able to simulate the propagation of flow over dry areas: no special treatment of dry regions is necessary since field values are computed only where the fluid is.

More complex situations dealing with inflow and outflow boundary conditions and real world dam-break simulations will be the subject of future studies.

REFERENCES

Aureli, F.M., Belicchi, M., Maione, P., Mignosa, P. & Tomirotti, M. 2001. Fenomeni di moto vario conseguenti al crollo di opere di ritenuta II: Indagini sperimentali e modellazione numerica in presenza di onde di shock. *L'acqua* 5: 27–36.

Fennema, R.J. & Chaudhry, M.H. 1990. Explicit methods for 2D transient free surface flows. *Journal of Hydraulic Engineering* 116: 1013–1034.

Gallati, M. & Sturla, D. Impiego della tecnica SPH per simulare la dinamica di flussi liquidi con superficie libera in moto rapidamente variato. 2000. *CAPI Calcolo ad Alte Prestazioni in Italia*, Milano, 25–30 September.

Gallati, M. & Braschi, G. 2000. Simulazione lagrangiana di flussi con superficie libera in problemi di idraulica. *L'acqua* 5: 7–18.

Gallati, M. & Sturla, D. 2001. Simulazione numerica dei flussi con superficie libera in acque poco profonde con metodo lagrangiano. *XV AIMETA Congress*, 25–30 September.

Gallati, M. & Braschi, G. 2002. Numerical description of rapidly varied flows via SPH method. *IASTED Int. Conf. ASM*, Crete, 25–28 June.

Gallati, M. & Braschi, G. 2002. SPH simulation of 2D shock propagation in shallow water. *IASTED Int. Conf. ASM*, Crete, 25–28 June.

Gallati, M. & Braschi, G. 2003. SPH simulation of the wave produced by a block falling into a water tank. *Int. Conf. On Modelling Fluid Flow*, Budapest, 3–6 September.

Gallati, M. & Braschi, G. 2003. Numerical simulation of the jump formation over a sill via SPH method. *Int. Conf. On Modelling Fluid Flow*, Budapest, 3–6 September.

Gingold, R.A. & Monaghan, J.J. 1977. Smoothed particle hydrodynamics: theory and application to nonspherical stars. *Monthly Notices of the Royal Astronomical Society* 181: 275–389.

Gingold, R.A. & Monaghan, J.J. 1983. Shock simulation by the particle method SPH. *Journal of Computational Physics* 52: 374–389.

Lucy, L.B. 1977. A numerical approach to the testing of the fission hypothesis. *Astronomomy Journal* 82: 1013–1020.

Stoker, J.J. 1957. Water Waves. New York: Interscience publisher, Wiley.

Wang, Z. & Shen, H.T. 1999. Lagrangian Simulation of One-Dimensional Dam Break Flow. *Journal of Hydraulic Engineering* 125: 1217–1221.

River Flow 2004 – Greco, Carravetta & Della Morte (eds.)
© 2004 Taylor & Francis Group, London, ISBN 90 5809 658 0

Simulation of flooding caused by an embankment breaking by means of a 2D finite volume numerical model

F. Aureli, A. Maranzoni & P. Mignosa
Dipartimento di Ingegneria Civile, dell'Ambiente, del Territorio & Architettura, Parma, Italy

ABSTRACT: The results of a mathematical simulation of flooding due to the breaking of a railway embankment crossing a river valley are presented. During recent floods, the considered embankment was slightly damaged by piping phenomena. Since two kilometres downstream is located a high risk industrial area the potential flood related with a breaking of the structure would represent an extremely dangerous occurrence. A numerical model was built in order to simulate some catastrophic flooding scenarios. The numerical scheme is based on a finite volume discretization of the 2D shallow water equations. The model was validated performing a simulation of the October 2000 flood event, with good agreement between computed and observed water depths. Then the flooding derived by the failure of the embankment was simulated. The results obtained, together with those derived by the simulation of other possible scenarios, were then utilized in order to design the protection structures for the industrial area.

1 INTRODUCTION

The flood event occurred in October 2000 in northern Italy was a severe test for the embankment system of several rivers, somewhere causing the formation of breaks. Whereas the occurring of catastrophic collapses can be very dangerous for the environment and human lives, the identification of the risk derived by flooding must be evaluated *a-priori* in order to organize civil protection plans. At this aim historical information is essential, but sometimes not enough to understand all the potential hazards, as for dam-breaks or levee-breaks never occurred before. In these cases the risk evaluation can be performed only with the help of numerical simulations or, more rarely, by means of physical scale models. In order to give reliable results, the mathematical models must be capable to describe the main characteristics of the flooding scenarios such as inundated areas, water depths, velocities, arrival times of the wetting fronts and permanence of the water on the ground.

In this paper the results of mathematical simulation of flooding due to the hypothetical break of a railway embankment crossing the river valley of an important tributary of the Po river (northern Italy) are presented. During two severe floods occurred in the recent past (1993 and especially 2000) the backwater effect due to the valley constriction gave rise to the storage of a considerable water volume just upstream the embankment. This in turn caused high stresses on the structure, which was not designed at this aim, and the beginning of piping phenomena. Since just downstream the railway is located a high risk industrial area, the potential additional flood related with the breaking of the embankment would create an extremely dangerous situation. Due to the impossibility to move in the near future the industrial plants, some catastrophic flooding scenarios were then simulated with a mathematical model in order to obtain design criteria for the protection plans.

The mathematical modelling of the flooding scenarios was accomplished by means of a two-dimensional finite volume numerical code, realised by the authors themselves, whose description and main features are explained in another paper presented at this Conference (Aureli et al. 2004a). Thanks to the information acquired during the recent historical event of October 2000, it was also possible to attempt a calibration of the model parameters and to compare to some extent simulated and historical water levels and flooded areas.

2 DESCRIPTION OF THE STUDY AREA

In order to reproduce the complex flow field in the area of interest it was necessary to describe the main morphological characteristics of the river, of the flood plains and of the structures crossing the river valley such as motorways, railways, waterways and irrigation

channels (Fig. 1). It was also essential to obtain a correct representation of the water volume temporarily stored upstream the railway embankment during the floods. At this aim the considered domain was extended far upstream the motorway that determines the upper limit of the backwater effects induced by the railway embankment.

In the meantime the displacement of the upstream boundary from the area of main interest reduces the influence of the approximate representation of the inflow boundary condition. For the same reason the outflow boundary was assumed beyond the waterway that constricts the river valley downstream the industrial site. On the lateral sides the inundation is naturally bounded by the morphological step of the river valley, so that also the considered domain was prolonged up to there.

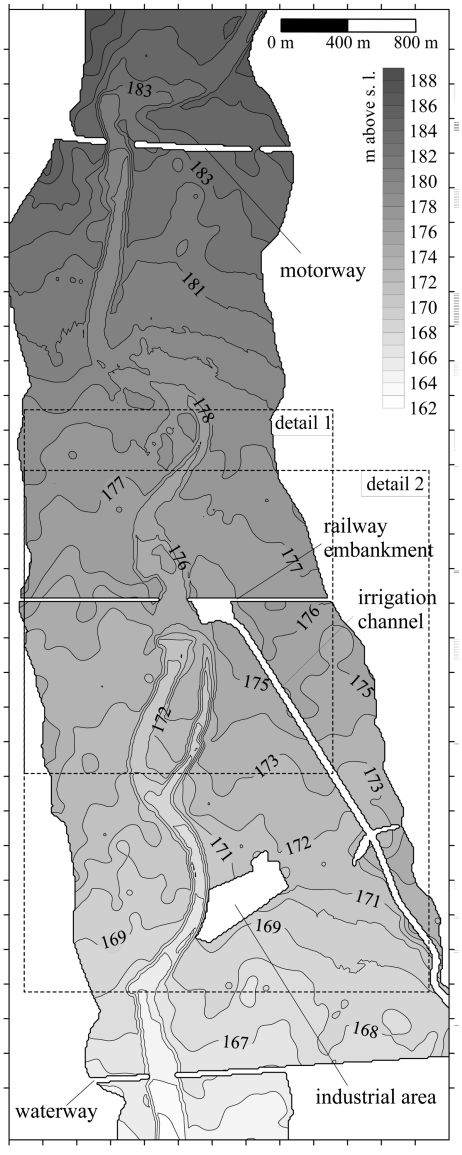


Figure 1. Bathymetry of the domain of interest.

Even if the area under investigation is considerably more extended in the longitudinal rather then in the transversal direction, a one-dimensional shallow water model would not be able to represent the complex behaviour of the flow field in this area. The three consecutive constrictions (from upstream to downstream: the motorway, the railway and the waterway), together with the irrigation channel and its intake structures, influence indeed in a determinant way the flow paths during the floods. Transitions from subcritical to supercritical flows are expected through the constrictions, together with the formation of hydraulic jumps downstream. The hypotesised break of the railway would further complicate the situation, inducing the formation of a steep wave (shock) moving downstream towards the industrial area.

For all these reasons it was considered necessary to perform the simulations by means of a model based on the 2D shallow water equations written in conservation form and solved with a shock-capturing numerical scheme.

The bathymetry of the river and of the floodable region was then described by means of a DEM with a square regular mesh of size 10 m, obtained by an interpolation procedure on the available cartographic maps and river cross sections. The dimension of the grid was chosen as a compromise between the estimated computational time and the satisfactory modeling of the region under study. The main constraints were due to the description of the structures such as river crossings, irrigation channels, bridges and so on. A more flexible mesh, such as a structured non-orthogonal Cartesian or a non-structured one, would be helpful for a refined description of the main structures crossing the valley, reducing in the meantime the overall number on grid nodes. Nevertheless, the necessity to track the moving fronts and shocks would require a refined mesh almost everywhere.

The embankment system of the river and the most important structures located in the domain were described as vertical and insuperable boundaries; a check was carried out at the end of the calculations in order to verify that all the embankments were really never overtopped by the waters during the flood. Since the main object of the simulations was to obtain water depths and velocities on the perimeter of the industrial site for design purposes, the area inside was considered as completely unfloodable. At this aim the interior nodes were excluded from the calculations (blanked in Fig. 1).

3 NUMERICAL MODEL

The adopted numerical code is based on a finite-volumes discretization of the 2D shallow water equations written in integral form:

$$\frac{d}{dt}\int_A \mathbf{U}\, dA + \int_C \mathbf{H}(\mathbf{U})\cdot\mathbf{n}\, dC = \int_A \mathbf{S}(\mathbf{U})\, dA \qquad (1)$$

where A represents the area of the integration cell, C the cell boundary, $\mathbf{n}$ is the outward unit vector normal to C, while $\mathbf{H} = (\mathbf{F}, \mathbf{G})$ represents the tensor of fluxes. The corresponding conservation differential form of (1) is:

$$\frac{\partial \mathbf{U}}{\partial t} + \frac{\partial \mathbf{F}}{\partial x} + \frac{\partial \mathbf{G}}{\partial y} = \mathbf{S}$$

$$\mathbf{U} = \begin{pmatrix} h \\ uh \\ vh \end{pmatrix}, \quad \mathbf{F} = \begin{pmatrix} uh \\ u^2h + \frac{1}{2}gh^2 \\ uvh \end{pmatrix}, \quad \mathbf{G} = \begin{pmatrix} vh \\ uvh \\ v^2h + \frac{1}{2}gh^2 \end{pmatrix}, \quad \mathbf{S} = \begin{pmatrix} 0 \\ gh\left(S_{0x} - S_{fx}\right) \\ gh\left(S_{0y} - S_{fy}\right) \end{pmatrix} \qquad (2)$$

The solution of the homogeneous part of (1) is based on the Weighted Average Flux (WAF) scheme, where second order of accuracy both in time and space is achieved by solving the conventional *piece-wise constant* Riemann problem and averaging it over space and time (Toro 1992). To avoid spurious oscillations in the vicinity of high gradients of the solution a TVD constraint was enforced on the scheme by means of different well-known limiter functions (Toro 1997). The solution of the Riemann problem was based on the approximate HLLC solver (Toro 2001), that is a modification of the basic HLL scheme to account for the influence of intermediate waves. A more detailed description of the numerical scheme and of the treatment of the source terms can be found in a related paper presented at this Conference (Aureli et al. 2004a).

4 CALIBRATION OF THE MODEL

The value of the roughness coefficients must account for the energy losses due to distributed and local resistance caused, for example, by the interaction of the flow with obstacles of lower dimensions with respect to the elements of the computational mesh. Also the energy dissipation due to the modification of the riverbed, to trees uprooting and to sediment transport have to be implicitly combined in this coefficients. Only two homogeneous regions, the riverbed and the floodplains, were identified in the domain, each characterised by a different behaviour with respect to flow resistance phenomena. The two Manning n roughness coefficients were firstly assumed on the basis of literature suggestions and then refined by trials searching for the values that allowed to reproduce at best with the model the maximum water levels observed during the October 2000 flood event. At the inflow boundary a 3000 m^3/s constant discharge, corresponding to the estimated peak discharge of the October 2000 flood event, was considered. The discharge was assumed entering the domain orthogonally the inflow section and was distributed amongst the nodes unevenly, with a higher specific discharge on the riverbed.

Downstream the waterway (Fig. 1), at the outflow section of the considered domain, a far-field (non-reflective) condition was introduced, whereas at solid boundaries a free-slip condition was imposed. The simulations were extended in time until the maximum differences between the values of the three conserved variables at two consecutive time steps were less than specified tolerances. Then steady-state conditions were considered reached. From the described procedure a value of Manning $n = 0.050\ s \cdot m^{-1/3}$ for the floodplains was identified, while to the river channels was assigned $n = 0.033\ s \cdot m^{-1/3}$. Figure 2 shows the comparison between computed and observed maximum water depths at some significant points in the neighbourhood of the railway embankment.

The good agreement between observed and computed water depths confirms the suitability of the

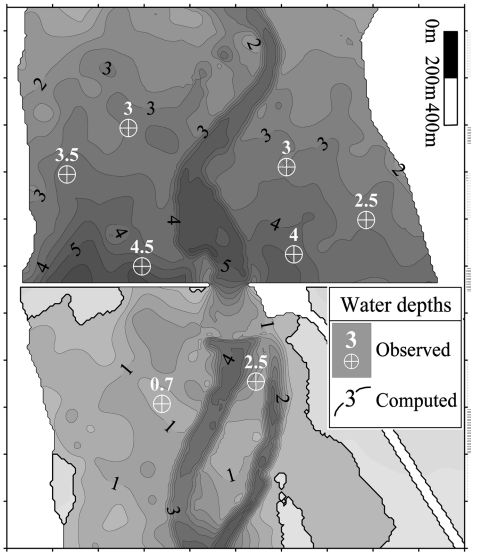


Figure 2. Comparison between observed and computed maximum water depths for October 2000 flood event (detail 1).

overall assumptions of the mathematical model concerning topographical description, grid size, roughness coefficient and representation of the main crossings.

5 FLOOD FREQUENCY ANALYSIS AND SYNTHETIC DESIGN HYDROGRAPHS DERIVATION

A gauged river section is located close upstream the area of interest, recording water levels almost continuously from 1925 and with an up-to-date stage-discharge relationship. A reliable flood frequency analysis can then be performed. From the records a 76 years long annual maximum peak flow (Q_0) series was extracted.

Log-normal, Gumbel (EV1) and General Extreme Value (GEV) probability distributions were considered in order to describe $Q_0(T)$. Parameters estimation was based on the Method of Moments for the first two distributions, whereas for the third the method based on L-moments was adopted. Figure 3 shows, on Gumbel probability chart, the data sample (Gringorten plotting position) together with the fitted probability distributions. The Hosking test (Hosking et al. 1985) on the $k = 0$ hypothesis with a significance level $\alpha = 5\%$, k being the exponent of the GEV distribution, demonstrates that the choice of the GEV distribution is justified.

From the GEV distribution a peak discharge of 3043 m^3/s for $T = 200$ years was derived. This value is close to the estimated peak discharge of the October 2000 flood event, which is also the maximum value of the overall historical series.

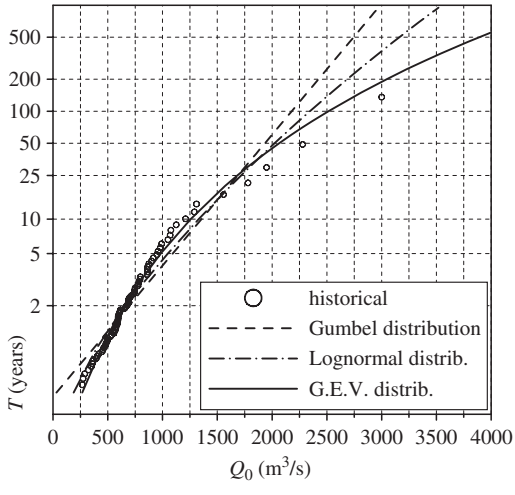


Figure 3. Q_0 data sample together with the fitted probability distributions.

In order to evaluate if a steady state solution would be a reasonable choice as initial condition before the hypothesized railway break occurs, Synthetic Design Hydrographs (SDH) were derived. The methodology (Maione et al. 2000a, b; Aureli et al. 2004b) is based on the statistical analysis of recorded flood waves through the construction of the Flow Duration Frequency (FDF) reduction curves of given return period and the determination of the temporal location of the peak value for each duration. The procedure was applied to a 62 years long historical sub-series, since the older strips have been lost. From the recorded flood waves, the annual maximum average discharges for each duration ranging from 0 to 96 hours were extracted and then processed. The resulting SDHs, for return periods ranging from 5 to 200 years, are shown in Figure 4. From the figure it can be observed that the rising limbs of the SDHs are quite gradual, taking about 22 hours from the starting value to the peak discharge.

The transient induced by the embankment breaking is surely faster than the potential hydrological stress. For this reason it is justified to assume as initial condition the steady state solution obtained by the model with as inflow discharge the peak value of the 200 years SDH. This in turn substantially coincides with the condition assumed for the calibration of the model.

Figure 5 shows the steady state water surface elevations, together with the velocity field (vector map) obtained by the calculations. Figure 6 shows a detail of the Froude values across the railway. The effect induced by the railway constriction is quite evident from the figures: upstream water levels rise up to about one meter below the top of the embankment, whereas downstream a short distance of supercritical flow occurs, abruptly blocked by an impressive

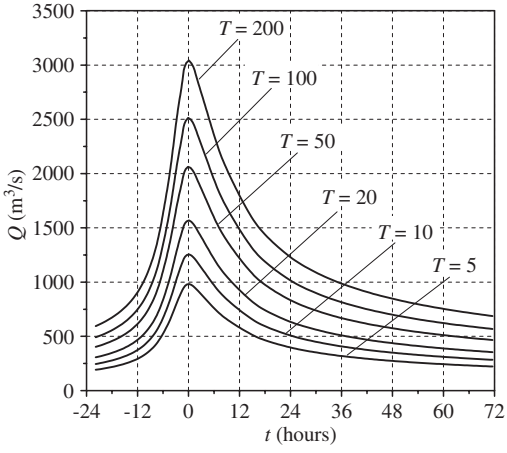


Figure 4. SDHs for the considered gauging station.

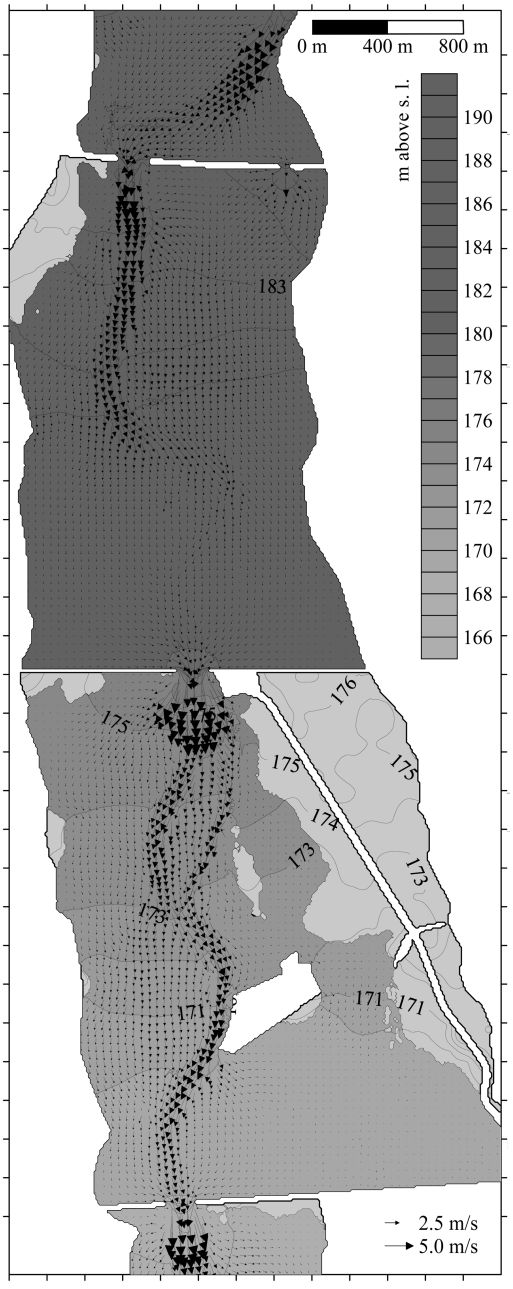


Figure 5. Steady state water surface elevations and velocity field (vector map) before the hypothesized embankment breaking.

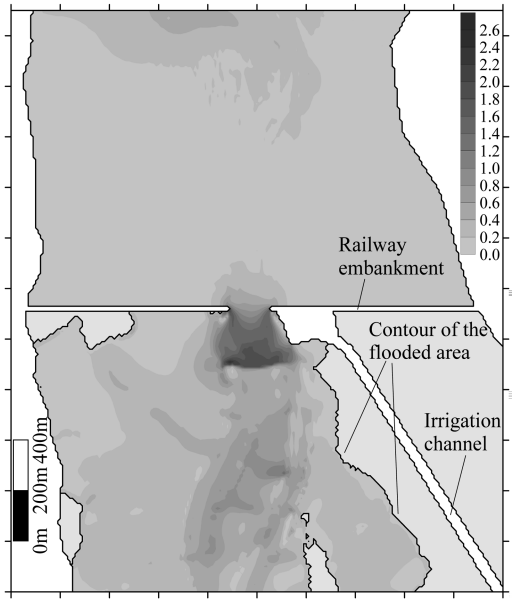


Figure 6. Froude values across the constriction at steady state (detail 1).

hydraulic jump. An analogous, though less marked, effect is caused by the downstream waterway constriction. Close to the industrial area the steady-state results reproduce substantially well what happened during the October 2000 flood event, when the site was slightly flooded, with water depths of about 0.3 ÷ 0.8 meters.

6 FLOODING SCENARIO DUE TO THE RAILWAY EMBANKMENT BREAKING

The results obtained from the steady-state simulation were then used as hot-start initial condition for the railway breaking scenario. The collapse was assumed to involve a considerable portion of the left side of the embankment, where the most alarming symptoms of piping occurred during the recent historical floods. Together with the railway embankment also the intake structures of the irrigation channel and a portion of the channel itself were assumed to suddenly collapse. A reasonable bathymetry was reconstructed where the structures were originally located.

Figures 7 to 10 show details of the computed water surface elevations and flooded areas at different times after the breaking. Due to the considerable water volume stored upstream the railway embankment (about $8.5 \cdot 10^6$ m^3), the sudden collapse of the structure induces the formation of a flood wave that in few minutes reaches the industrial area. Then the flow divides into two branches (Fig. 9): one collides with the top side of the area and then proceeds towards the riverbed; the other follows the right side of the industrial plants and then connects to the flooding due to the

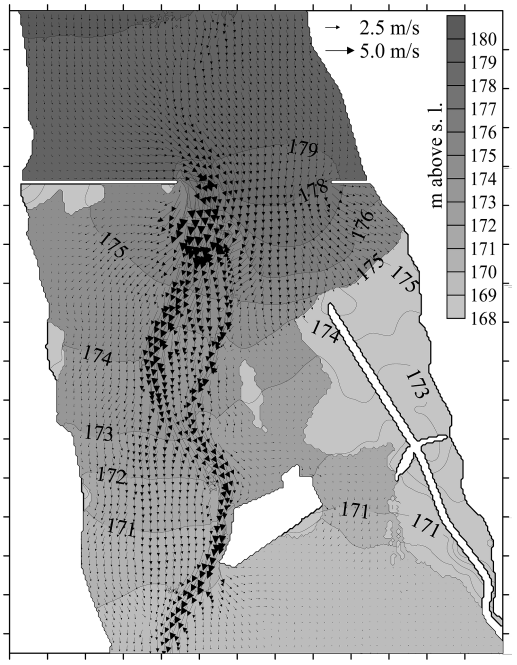


Figure 7. Computed water surface elevations and velocity field (vector map) five minutes after the breaking (detail 2).

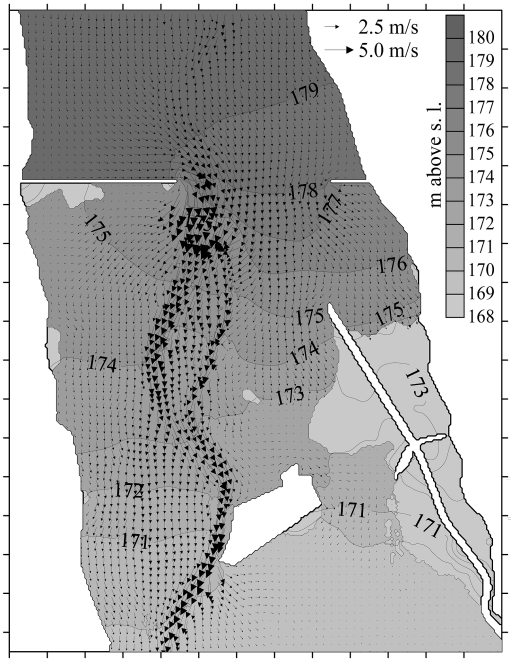


Figure 8. Computed water surface elevations and velocity field (vector map) ten minutes after the breaking (detail 2).

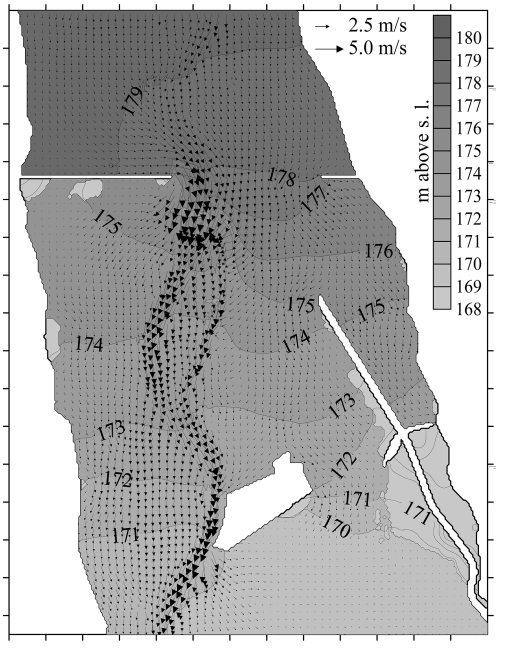


Figure 9. Computed water surface elevations and velocity field (vector map) twenty minutes after the breaking (detail 2).

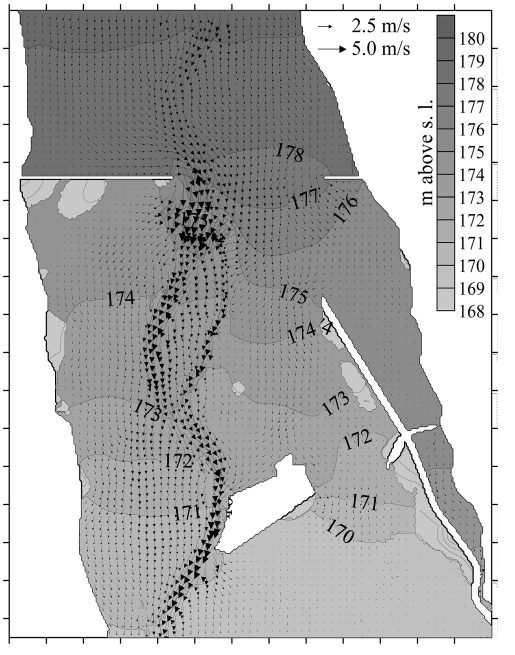


Figure 10. Computed water surface elevations and velocity field (vector map) 60 minutes after the breaking (detail 2).

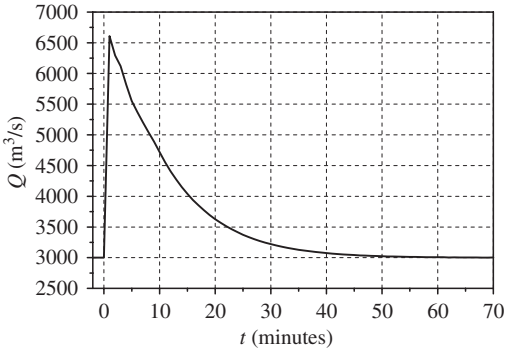


Figure 11. Computed discharge through the original railway line. The break occurs at time zero.

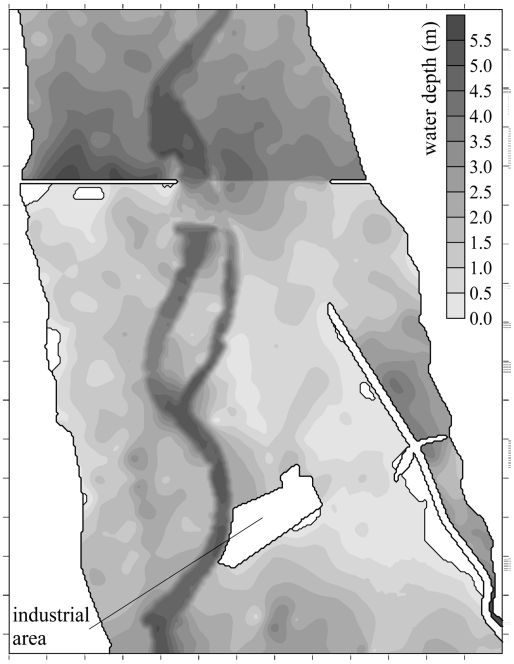


Figure 12. Envelope of computed water depths (detail 2).

backwater effects of the waterways crossing constriction. After one hour (Fig. 10) the flow became again almost steady everywhere. This is also confirmed by the computed discharge flowing through the original railway line, shown in Figure 11.

From the figure it can be easily derived that only a volume of about $2.6 \cdot 10^6$ m^3 (out of $8.5 \cdot 10^6$ m^3) was actually released from the storage upstream the railway, the remaining part being necessary for the maintenance of the base flow discharge.

Figures 12 and 13 show details of the envelopes of computed water depths and velocity norm.

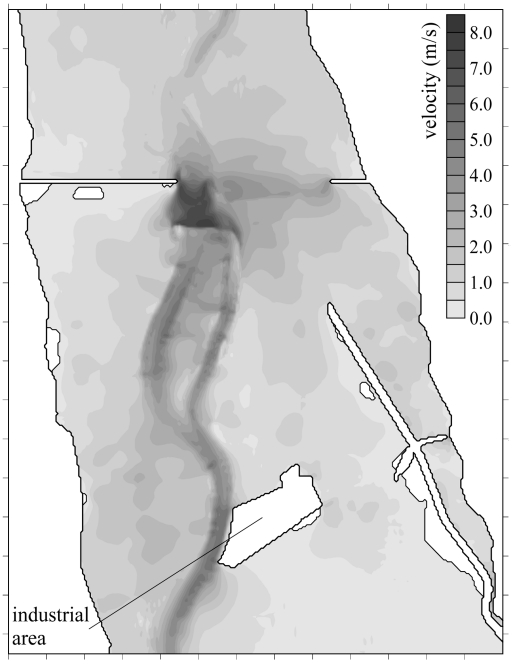


Figure 13. Envelope of computed velocity norm (detail 2).

The maximum of the water depths is reached at the top side of the area, with values of more than two meters. The maximum velocity is attained at the side adjacent to the riverbed with values of about 3 m/s. Considerable velocities of more than 1 m/s are also reached in correspondence of the right side of the industrial area.

7 CONCLUSIONS

A mathematical simulation of flooding due to the hypothetical failure of a railway embankment crossing the river valley of an important tributary of the Po river (northern Italy) was presented.

Thanks to the information acquired during the recent historical event of October 2000, it was possible to attempt a calibration of the model parameters and to some extent to compare simulated and observed water levels and flooded areas. Also the historical hydrological information was rich enough to perform a reliable flood frequency analysis and a Synthetic Design Hydrograph derivation.

The results of the mathematical model, together with those obtained by the simulation of other catastrophic scenarios, were then utilized to design the protection structures for the industrial plant. In the meantime the railway embankment will be strengthened and a deep diaphragm wall will be realized in order to avoid piping and then reduce failure risks.

ACKNOWLEDGMENTS

This work was developed within a research agreement between the Civil Engineering Department of Parma University and the Po River Basin Authority. The Authors wish to thank the a.m. Authority for the consent to publish the main results of the study.

REFERENCES

Aureli, F., Maranzoni, A. & Mignosa, P. 2004a. Two dimensional modeling of rapidly varying flows by finite volume schemes, submitted to River Flow 2004.

Aureli, F., Maranzoni, A., Maione U. & Mignosa, P. 2004b. Synthetic hydrographs as a design tool for flood routing evaluation, submitted to River Flow 2004.

Gumbel, E.J. 1962. Multivariate Extreme Distributions, *Bulletin of the International Statistical Institute* 39(2): 471–475.

Hosking, J.R.M., Wallis, J.R. & Wood, E.F., 1985. Estimation of the Generalized Extreme-Value Distribution by the Method of Probability-Weighted Moments, *Technometrics* 27(3): 251–261.

Maione, U., Mignosa, P. & Tomirotti, M. 2000a. Synthetic design hydrographs for flood-control reservoirs and floodplain management. In U. Maione, B. Majone Lehto, R. Monti (eds.), *New Trends in Water and Environmental Engineering for Safety and Life: Eco-compatible Solutions for Aquatic Environments; Proc. Int. Conf., Capri, 3–7 July 2000*. Rotterdam: Balkema.

Maione, U., Mignosa, P. & Tomirotti, M. 2000b. Synthetic design hydrographs for river flood management. In Toensmann F., Koch M. (eds.), *River Flood Defence Proc. Int. Symp.*, *Kassel, 20–23 September 2000*. Kassel: Herkules Verlag.

Provincia di Vercelli 2000. Analisi degli effetti indotti dalla piena del 13–16 ottobre 2000 nel Comprensorio Nucleare di Saluggia, Vercelli (in Italian).

Toro, E.F. 1992. Riemann problems and the WAF method for solving the two-dimensional shallow water equations. *Phil. Trans. R. Soc. London A* 338: 43–68.

Toro, E.F. 1997. *Riemann Solvers and Numerical Methods for Fluid Dynamics*. Berlin: Springer Verlag.

Toro, E.F. 2001 *Shock–Capturing Methods for Free Surface Shallow Flows*. Chichester: John Wiley & Sons.

River Flow 2004 – Greco, Carravetta & Della Morte (eds.)
© 2004 Taylor & Francis Group, London, ISBN 90 5809 658 0

Dike-break induced flow: validation of numerical simulations and case study

M. Harms, S. Briechle & J. Köngeter
Institute of Hydraulic Engineering and Water Resources Management, Aachen University, Germany

D. Schwanenberg
WL/delft hydraulics, Delft, The Netherlands

ABSTRACT: A TVD Runge Kutta Discontinuous Galerkin finite element method for two-dimensional depth-averaged shallow water equations is used to simulate dike-break induced flows. This paper presents comparisons of experimental data obtained by a physical model to results of the numerical simulation. Furthermore, the numerical method is applied to computations of flood wave propagation initiated by dike-breaks at the River Rhine. The aim of this case study is to evaluate effects of flood protection improvements, which are intended by a partitioning of the area at risk into compartments.

1 INTRODUCTION

Recurring events of extreme rainfall resulting in river hazards have shown the disastrous damages that can be caused by floods. Not only the occurrences of 99 dike-breaks at the River Elbe during the flood in August 2002 indicated that flood protection is vulnerable. A Risk Assessment procedure, subdivided into the three stages Risk Analysis, Risk Assessment and Risk Management, was developed for German dams at the Institute of Hydraulic Engineering and Water Resources Management (IWW), Aachen University, by Rettemeier et al. (2000). The basic principle of the approach can be transferred to rivers and dikes.

To assess the risk provoked by floods and potential dike-breaks within the scope of Risk Analysis the potential damage on people and property has to be determined. Thus, objectives that need to be investigated are the identification of inundated areas as well as flow depth and flow velocities of the initiated wave.

Dike-break induced flood waves are characterized by unsteady, rapidly varying flows over non-trivial bathymetry and by propagation on a dry bed. In contrary to dam-break flows there is a constant discharge in the river and the river will not empty like a reservoir.

A physical model, which takes into account the discharge in the river, the sudden break of the dike as well as wave propagation into an area, has been developed and build at the IWW. Thus, computations can be validated with the measured data of the two-dimensional wave propagation. Similar tests concerning the propagation of the wave into an area were proceeded by Kulisch (2003), Fraccarollo & Toro (1995) and Jovanovic & Djordjevic (1995). All of these authors consider dam-breaks, but not dike-breaks. Aureli & Mignosa (2002) present the single investigation also taking into account the river discharge. They perform computations of the induced wave, while taking measurements in the channel.

A Runge Kutta Discontinuous Galerkin (RKDG) finite element method has been developed and validated for dam-break flow (Schwanenberg & Harms, 2002). Possessing the ability to simulate unsteady, transcritical flow and wave propagation on a dry bed, it will be applied to dike-break flow. As the numerical method has already been presented in detail the following paragraph will merely give a brief outline.

2 RKDG METHOD FOR SHALLOW WATER FLOW

2.1 *Governing equations*

The mathematical description of a depth-averaged incompressible fluid is given by the shallow water equations in the form

$$\partial_t \boldsymbol{U} + \nabla \cdot \boldsymbol{F}(\boldsymbol{U}) = \boldsymbol{S}(\boldsymbol{U}), \tag{1}$$

where

$$\boldsymbol{U} = \begin{pmatrix} h \\ p \\ q \end{pmatrix} = \begin{pmatrix} h \\ uh \\ vh \end{pmatrix}, \tag{2}$$

$$\boldsymbol{F} = \begin{pmatrix} p \\ \beta_{xx}\dfrac{p^2}{h} + \dfrac{1}{2}gh^2 \\ \beta_{yx}\dfrac{pq}{h} \end{pmatrix}, \quad \boldsymbol{G} = \begin{pmatrix} q \\ \beta_{xy}\dfrac{pq}{h} \\ \beta_{yy}\dfrac{q^2}{h} + \dfrac{1}{2}gh^2 \end{pmatrix}, \tag{3}$$

$$\boldsymbol{S} = \begin{pmatrix} 0 \\ gh(-\partial_x z_b - \dfrac{n^2 p\sqrt{p^2+q^2}}{h^{10/3}}) \\ gh(-\partial_y z_b - \dfrac{n^2 q\sqrt{p^2+q^2}}{h^{10/3}}) \end{pmatrix}, \tag{4}$$

in which h = water depth; p, q = unit discharge in x- and y-directions; u, v = horizontal flow velocities in x and y-directions; β_{ij} = correction factor for non-linear momentum flux; $g = 9.81$ m/s^2 = acceleration due to gravity; ρ = fluid density; and z_b = channel bed elevation. Bed roughness is approximated by the empirical Manning formula with Manning's roughness coefficient n.

Mild bed slope, constant density and hydrostatic pressure distribution is assumed deriving these equations from the three-dimensional Navier-Stokes-Equations. As these assumptions limit the applicability of the equations their effects should be considered.

2.2 *Numerical method*

The presented numerical scheme is based on the RKDG method for hyperbolic equation systems. Detailed introductions to these methods can be found in Cockburn (1999) and Cockburn et al. (2000). Schwanenberg & Köngeter (2000) presented the first implementation of the RKDG method for the shallow water equations and its application to practical problems. The method is divided into three main steps:

- The partial differential equations are decoupled by DG space discretization with a polynomial degree k into a set of ordinary differential equations.
- The ordinary differential equations are integrated in time by a $k+1$ order TVD Runge Kutta method.
- A slope limiter is applied on every intermediate time step of the Runge Kutta method introducing a selective amount of dissipation in order to obtain stability at shocks.

Due to its explicit TVD Runge Kutta time integration, the method can be efficiently applied to transient and transcritical flows. The method was shown to have sharp representation of shocks. The implementation of source terms and boundary conditions is straightforward. For a in depth presentation see Schwanenberg (2002, 2003, 2004).

3 VALIDATION

3.1 *Physical model*

To validate the applicability of the method to dike-break flows the flow in a physical model (Fig. 1) is simulated. The model in the Institute's laboratory consists of a 1 m wide channel with a pneumatically driven gate at one bank and an adjacent propagation area (3.5 m × 4.0 m). The water can fall off freely at the three boundaries of this glass area. Discharge in the channel can be varied from 0 to 390 l/s, while the water level ranges between 30 and 50 cm.

The flap gate opens in a minimized time span of less than 0.1 s by rotating upwards. It is intended interfere as little as possible with the flow.

Measurements are performed on the propagation area. The water depth is determined by ultrasonic sensors with a measuring frequency of 50 Hz in a dense raster. Furthermore a CCD-camera takes 50 pictures per second from top view, thus the propagation of the wave front is recorded.

A detailed description of measuring techniques and the flap gate is given by Briechle & Köngeter (2004).

3.2 *Numerical simulations*

Firstly comparisons of measurements and computations concerning the flow depths on the propagation area are considered. Calculations and measurements are performed on dry bed as well as for a small amount of water on the propagation area. Furthermore, different initial conditions are considered.

Secondly the propagation and shape of the computed wave front is compared to evaluations obtained by the CCD-Camera.

Figure 2 shows computed and measured water depths over time for three points at different distance, 1300, 2300 and 3300 mm to the channel on the axis perpendicular to the channel.

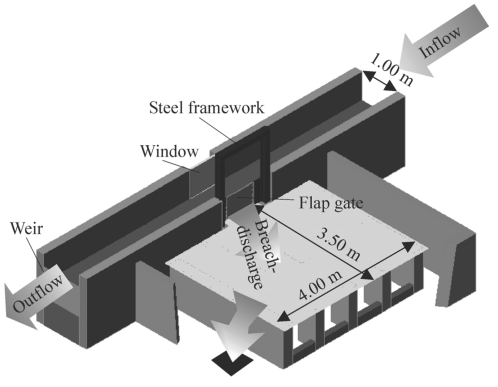


Figure 1. Physical model.

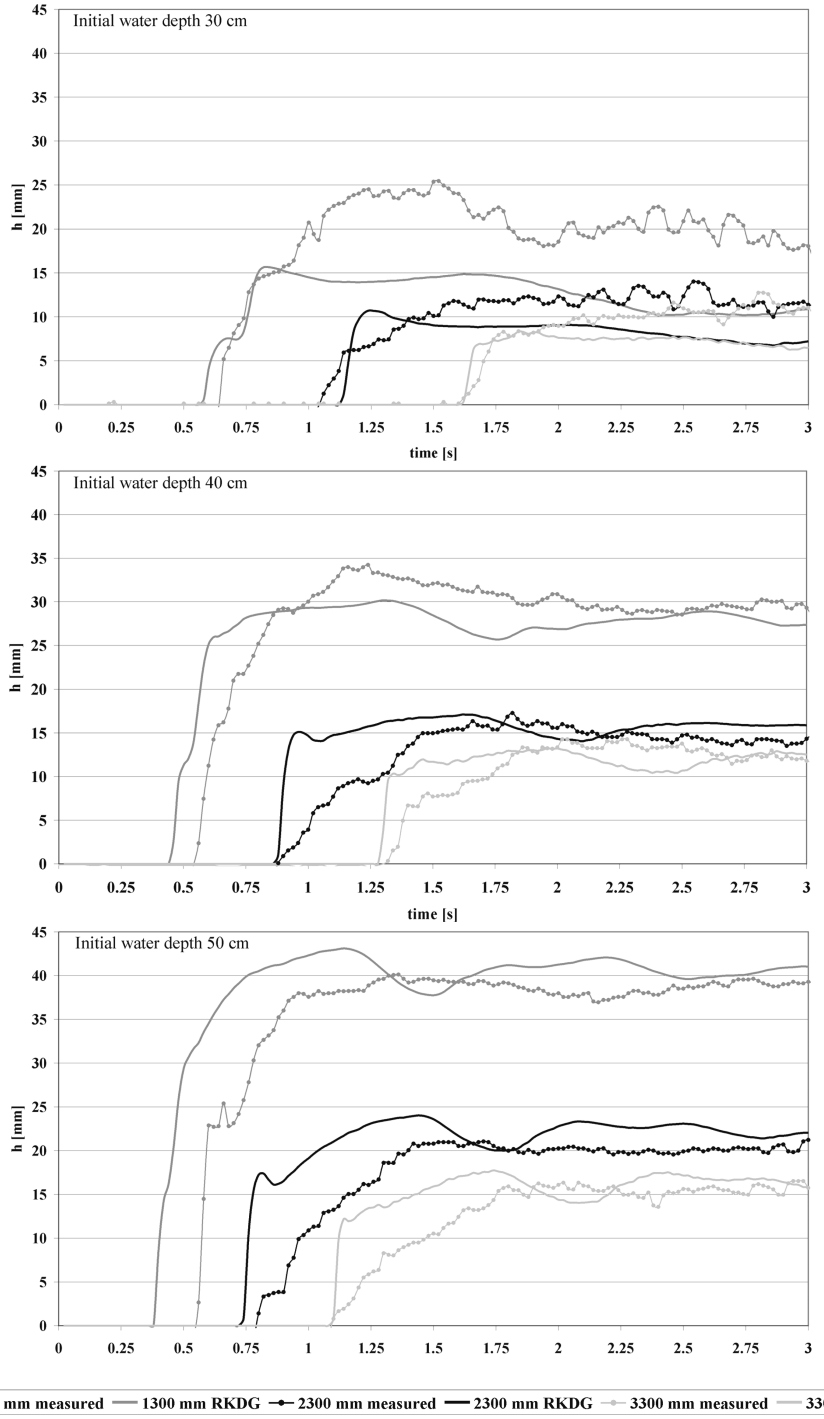


Figure 2. Water depth as function of time for three different initial water depths at three gauges at different distances from the flap gate on the axis perpendicular to the channel. Discharge in channel $Q = 300$ l/s.

A constant discharge of $Q = 300$ l/s is applied. Results are shown for three different initial flow depths, computed on dry ground with a Manning value of $n = 0.0083$ s/m$^{1/3}$.

Computations were performed on an unstructured grid with element sizes of less than 5 cm. The CFL number was set to 0.3.

Flow conditions in the channel in the different initial states are characterized by initial flow depth and discharge and can be expressed by Froude numbers.

For an initial water depth of 30 cm arrival times of the wave differ slightly from the measured values at each gauge, while computed water depths are to low after the wave front passes the gauge. Combining a discharge of 300 l/s with a water depth in the channel of 30 cm, Froude number before the opening of the flap gate is nearly $Fr = 0.6$. In case of this very shallow flow with high velocities in the channel, the influence of the flow in the channel on the propagation is overestimated. Propagation is not reproduced well on the axis perpendicular to the channel, as the main flow direction is diverted strongly into the direction of the flow in the channel in the simulations.

Better results can be achieved for an initial depth of $h = 40$ cm ($Fr = 0.38$) and $h = 50$ cm ($Fr = 0.27$) respectively. Arrival times and flow depth of the propagating wave are displayed very well. It can be observed that the wave front at the gauges in 2300 and 3300 mm distance is represented to steep, while measurements indicate a slower rising of the water.

Results in 1300 mm distance from the flap gate are very good for all initial flow depths as regards the maximum flow depth. However, arrival times of the wave front are predicted to early. Possibly, close to the breach vertical components of the flow slow down the velocity in main flow direction, as indicated by the water surface curvature. The vertical momentum increases with initial water depth, therefore the underestimation of the arrival time increases with flow depth as vertical components are neglected in the computation. Thus, differences can be attributed to the assumption of the shallow water approach.

Additionally, in spite of the rapid opening mechanism it can be presumed that a deceleration of the flow is caused by the flap gate in comparison to the simulations, as the gate is not taken into account. This effect might also be enforced for higher initial flow depths, as a larger part of the water body is in contact to the gate.

Some experiments were undertaken without drying the propagation area before the measurement. It is found that the wave is affected by the water film on the area. Measurements showed that propagation was decelerated by the water on the area and the front of the wave is significantly altered. This effect can be reproduced in the computations by assuming 1 mm of water on the area.

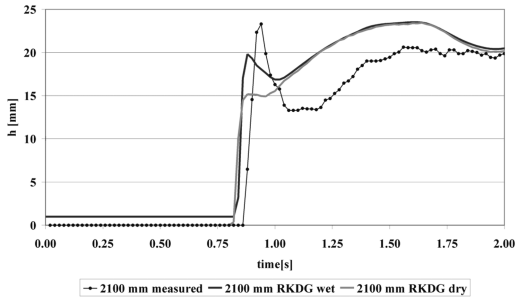


Figure 3. Water depth as function of time for initial water depth of $h = 40$ cm and discharge of $Q = 120$ l/s measured on a wet propagation area.

Figure 3 indicates that the peak at the wave front can only be displayed, if the thin layer of water on the area is taken into account. Observations during the measurements confirm that the front of the wave is strongly influenced by air entrainment. This explains that the computed water depth does not reach the maximum height of the measurement, as constant density is assumed in the computation.

Flow velocities have not jet been determined in the physical model. Computed maximum flow velocities are detected at a distance of 1 m from the flap gate. For an initial water depth of 30 cm the resulting velocity is $v_{max} = 2.75$ m/s, for 40 cm $v_{max} = 3.11$ m/s and for 50 cm $v_{max} = 3.5$ m/s.

Secondly the shape of the wave is considered in plan view to compare it to measurements by the CCD-Camera. The derivation of the wave front from the symmetrical propagation is affected by flow conditions in the channel. Figure 4 shows a comparison of the wave front computed to results obtained by the CCD-Camera for different time steps and a discharge in the channel of 120 l/s ($Fr = 0.15$) and 300 l/s ($Fr = 0.27$).

The figures indicate that the shape of the wave is reproduced quite well. Propagation on the main axis shows good agreement to the measurement. However, the derivation of the flow in the direction of the discharge in the channel is overestimated by the computation for both discharges as mentioned above. Again a reason could be the vertical momentum, which leads the wave to propagate perpendicular to the channel.

Derivation of the wave front increases with discharge in the channel and decreases with an increasing flow depth. Thus is can be found that derivation increases with an increasing Froude number in the channel. The second picture in Figure 4, representing results for higher Froude number in initial state, shows a stronger derivation from the main axis for both computations and measurements. Differences between measurement and computations also increase with an increasing Froude number, as was observed already

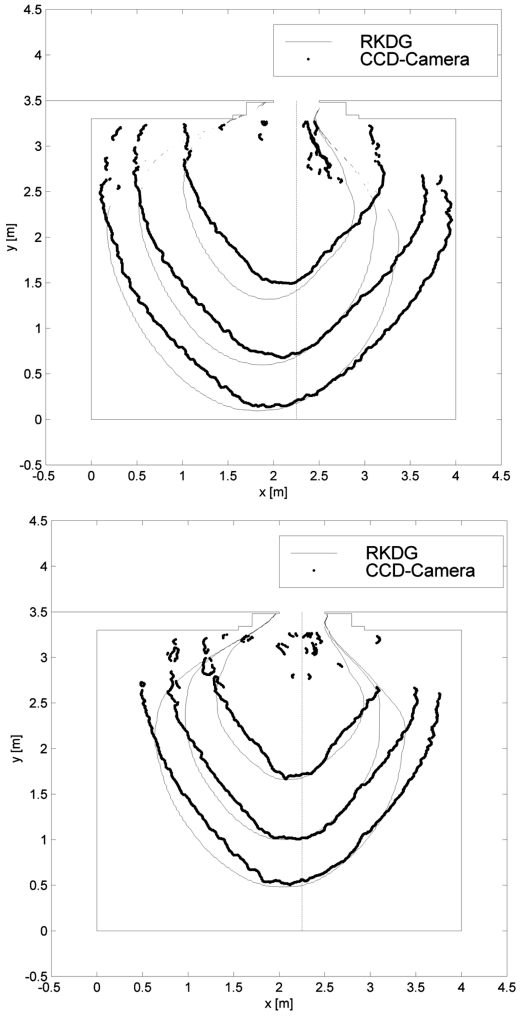


Figure 4. Wave front computed and recorded for $Q = 120$ l/s and $h = 40$ cm ($Fr = 0.15$) and $Q = 300$ l/s and $h = 50$ cm ($Fr = 0.27$).

concerning a discharge of $Q = 300$ l/s and $h = 30$ cm resulting in a Froude number $Fr = 0.58$. Lateral Propagation to the side opposed to the channel's flow direction is not represented very well. The flow in the model is constricted and a steep water surface curvature induces a non-hydrostatic pressure distribution. This effect can not be displayed by computations based on the shallow water approach. Some points of the measurement near the gate indicate a borderline between main outflow and water with very strong surface curvatures.

Furthermore, the computed shape of the wave is chubbier and more onion shaped while the recorded one has a clearer apex in the front. Computational results of Aureli & Mignosa (2002) are comparable with the ones presented here. An explanation might be again the neglection of the vertical momentum in the shallow water equations.

We conclude that the shown results indicate a satisfying agreement with the measurement. Arrival time and height of the wave are displayed very well. As the physical model is focussed on the initial phase of dike-breaks, the neglection of vertical momentum is noticed. Conditions in the channel with a flow of high Froude numbers ($Fr > 0.5$) are not computed well. But it can be presumed that in natural rivers Froude numbers are smaller even during floods. For example Froude numbers in the river Rhine are less than $Fr = 0.4$ during a 500 years flood.

4 APPLICATION

4.1 *Flood protection improvement*

Due to mining activities the left polder area of the Rhine north of Cologne suffers from heavy surface settlements. With a height of up to 15 m the dikes in this region are among the highest in Europe. Though the construction of the dikes is of high standard resulting in a low possibility of failure, the risk provoked by a dike-break is high as the potentially flooded area is large.

To improve flood protection and reduce the risk, a partitioning of the polder area of 400 km^2 into compartments is considered. Thus, it is intended to diminish the risk by decreasing the probability of flooding of the whole region. Furthermore, evacuation times can be extended for areas, which are not directly affected by a dike-break. In this case the risk provoked by a dike-break is lowered because of a reduction of the potential damage.

It is intended to use mainly existing structures like street and railway dam rather than to build a second defense line with the height of the dikes at the river. This case study is a first consideration of the partitioning. The aim is to identify structures, which can be used as borders of the compartments with small effort for construction and at the same time allocate a sufficient volume to detain the water for a certain time. According to information of the German Civil Protection the gained time spans should be more than six hours, to provide sufficient time to evacuate people.

Figure 5 shows a part of the partitioned polder area. The whole area under investigation is separated into 19 compartments utilizing primarily highway and railroad embankments as well as natural given steps in the territory.

4.2 *Assessment of the effects*

To evaluate effects of the partitioning of the polder area into compartments on flood protection and the

risk provoked by dike-breaks, different scenarios were computed for actual and design state. Thus enhancement of premonition time spans and reduction of inundated areas can be determined.

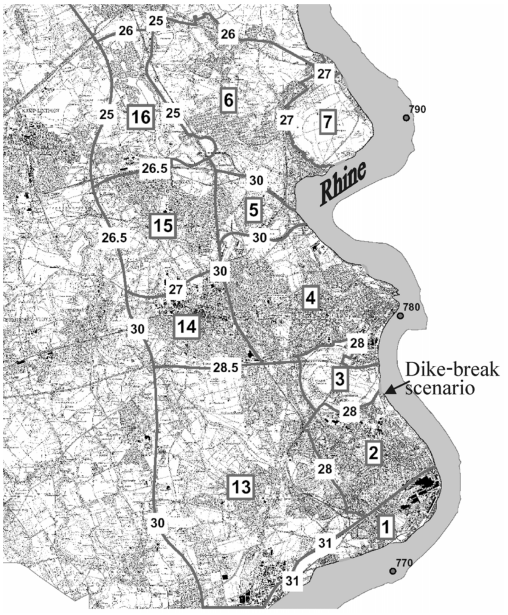


Figure 5. Detail of the polder area partitioned into compartments. Labels on the lines indicate the required heights. Compartments are numbered from 1 to 19.

We will consider one of these scenarios located at Rhine km 777 as indicated in Figure 5. After simulating steady state in the river Rhine, an unsteady, synthetic discharge hydrograph of a flood with recovering period of 500 years is applied. Eight days of the nearly 30 days lasting flood are simulated. At the begin of the unsteady computations, two days before the maximum discharge is reached, the complete failure of the dike at a length of 300 m on the left bank is assumed.

Computation of this case study on a mesh of approximately 25,000 unstructured triangles with minimum length of 15 m are performed setting the CFL number to 0.35. To take into account the flooding of areas of different land use, zones of different Manning values are introduced. For example, flow in urban areas is carried out with Manning values of $n = 0.2\ \mathrm{s/m^{1/3}}$. Values are chosen according to references from CADAM (2000) and DVWK (1990) guidelines.

Comparing the discharge through the assumed breach for actual and design state it is found that the discharge is reduced by about 40–80 $\mathrm{m^3/s}$ due to the retention in the compartments. Thus, the volume of water flooding the area is decreased from 180 Mio. $\mathrm{m^3}$ in present state to 130 Mio. $\mathrm{m^3}$ in design state.

Analysis of the results show that the main effects of the partitioning are enlarged times of premonition and reduced areas of inundation.

Figure 6 compares results of present and design state for the time two days after the dike-break. It becomes obvious that the propagation in present state is advanced much further into the area at risk. Parts of three more compartments are affected. At this time

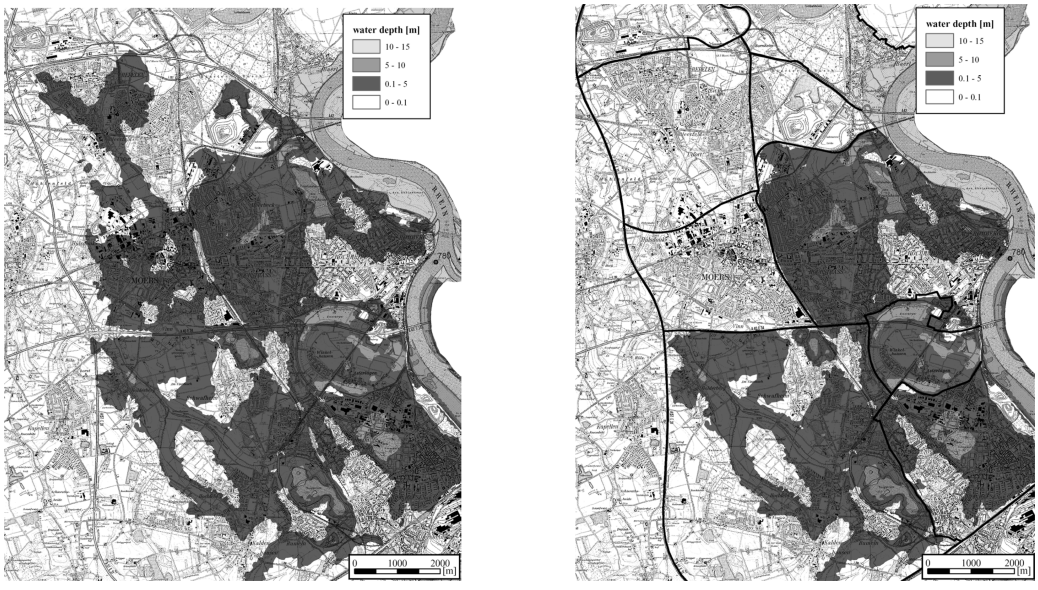


Figure 6. Inundation maps at $t = 48$ h after the dike-break. Present state on the left, design state on the right.

the difference of the inundated areas is 8 km^2. But, it has to be taken into account that due to the reduction of inundation areas in total inside of the compartments the water levels might be higher. Compared to the avoidance of flooding in compartment 5, 14 and 15, this increase of water level can be considered as insignificant.

Analysing the temporal development, it becomes clear that premonition time span for the area inside of compartment 14 is increased from 30 to 50 hours. For the northern area enhancement is even more than 25 hours, while compartment 5 will not be affected by the flood due to partitioning the region.

Another effect is observed considering the arrival time of the flood. In present state the water is spread into the area of three compartments within six hours, while in design state this will take one and a half days.

Considering the maximum water levels that occur during the eight days of propagation, a difference of 23 km^2 concerning inundated areas is determined. Figure 7 indicates that the northern part of the area under investigation is not affected as a result of partitioning into compartments.

Summarizing the investigation yields that the calculation of the scenario proofs the achievement of the required aims. For compartments directly affected by the dike-break induced flood wave or located close to the breach premonition time enhancement is determined to be two to three hours. But for further propagation of the flood wave premonition times are enlarged significantly. Results of a different scenario demonstrate that in that case the water could be kept in the first compartment causing a strong decrease of discharge through the breach and a reduction of inundated areas of 85%.

Thus, based on the performed computations the effect of the partitioning can be assessed as positive. However, it has to be considered that results display conditions of specific scenarios. Computations of dike-breaks at different locations along the river Rhine showed that the outgoing discharge through the breach varies highly in dependence on the territory

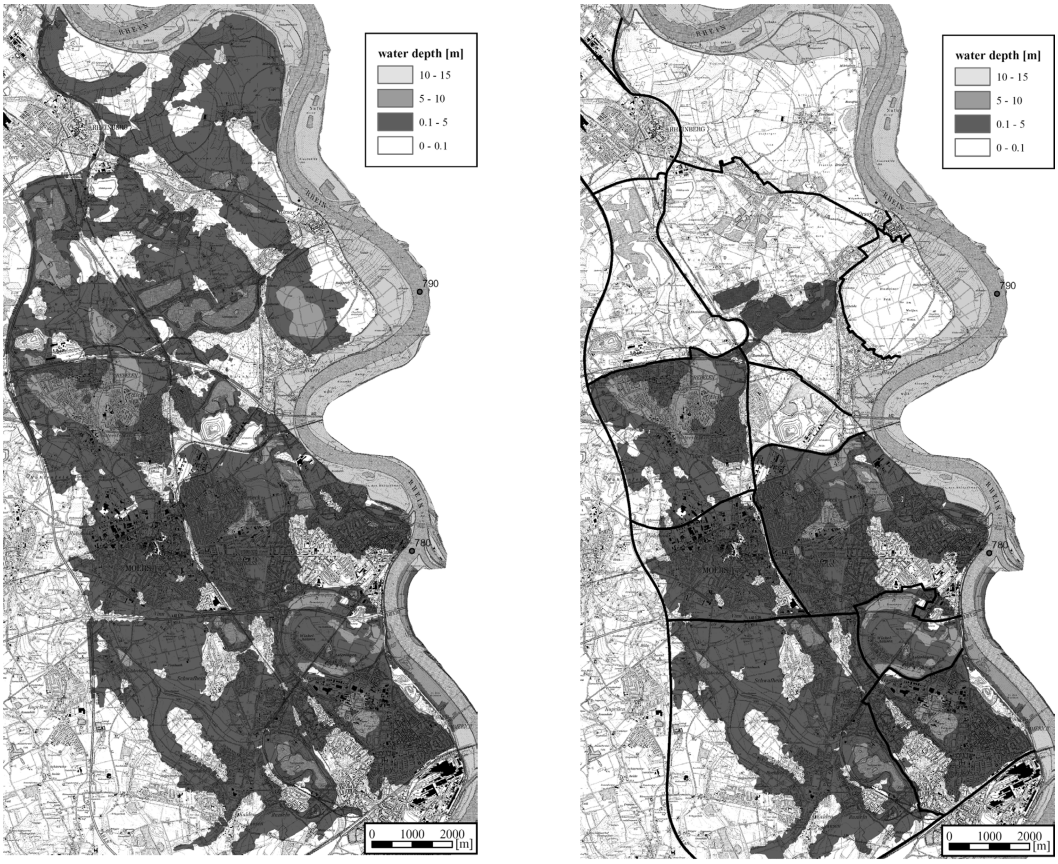


Figure 7. Inundation maps of maximum values during eight days of flooding. Present state on the left, design state on the right.

directly behind the dike, to flow conditions and to characteristics of the river.

Furthermore the detailed investigation of damage potentials caused in present state and in case of partitioning allow for well-founded recommendations.

5 CONCLUSIONS

A TVD RKDG finite element method for 2D depth-averaged shallow water equations has been applied to dike-break flows.

Comparisons of numerical simulations to experimental investigations concerning dike-break induced flood wave propagations in a physical model are presented. The aim of the study was the validation of the numerical method. Computed results show good agreement to the measured data in term of water level time series as well as the shape and propagation of the wave front recorded by a CCD camera. Thus, it could be proved that the model is capable to reproduce the main characteristics of dike-break induced flow. Still computations are limited due to the assumptions of the shallow water approach, especially concerning the hydro-static pressure distribution.

These limitations can be overcome using 3D models. But, especially the presented application of the 2D model to dike-break flow at the River Rhine demonstrate that real-world dike-break flows have to be performed for large scales, to which 3D models are not applicable. Actually, in natural dike-break induced flow propagation in horizontal directions is obviously large compared to 3D effects in the flow. Thus, for investigations concerning the far field effects of dike-breaks the shallow water approach is justifiable.

Performing the case study the model is used to evaluate the increase of premonition time spans and the reduction of flooded areas, which is intended by partitioning the area at risk into compartments. It is confirmed that an improvement of flood protection is achieved. At the same time the model is demonstrated to be a useful tool to deliver input data that is needed within the scope of risk analysis for dikes.

REFERENCES

Aureli, F. & Mignosa, P. 2002. Rapidly varying flows due to levee-breaking. In D. Bousmar & Y. Zech (eds.), River Flow 2002, *Proc. International Conference on Fluvial Hydraulics, Louvain-la-Neuve, Belgium, 4–6 September, 2002*. Rotterdam: Balkema: 459–466.

Briechle, S., Joeppen, A. & Köngeter, J. 2004. Physical model tests for dike-break induced, two-dimensional flood wave propagation. In River Flow 2004, *Proc. International Conference on Fluvial Hydraulics, Neapel, Italy, 23–25 June, 2004*. Rotterdam: Balkema: in print.

Cockburn, B. (1999). Discontinuous Galerkin Methods for Convection-Dominated Problems, in LNCSE Vol. 9: "High-Order Methods for Computational Physics" (Eds.: T. J. Barth & Deconinck), 69–224, Springer, Berlin.

Cockburn, B., Karniadakis, G. E. & Shu, C.-W. (2000). Discontinuous Galerkin Methods, LNCSE Vol. 11, Springer, Berlin.

Fraccarollo, L. & Toro, E.F. 1995. Experimental and numerical assessment of the shallow water model for two-dimensional dam-break type problems. *Journal of Hydraulic Research* 33(6): 843–863.

Jovanovic, M. & Djordjevic, D. 1995. Experimental verification of the MacCormack numerical scheme. *Advances in Engineering Software* 23: 61–67.

Kulisch 2003. Ausbreitung von Dammbruchwellen im physikalischen Modell. *Mitteilungen des Institut für Wasserwesen, Universität der Bundeswehr München*, Heft 79. München: Oldenbourg.

Rettemeier, K., Falkenhagen, B. & Köngeter, J. (2000). Risk Assessment – New Trends in Germany. *Proc. Twentieth Congress on Large Dams Q. 76 - R. 41*: 19–22 September 2000, Beijing, China. Transactions, Vol. I: Question No. 76. Paris: Commission International des Grands Barrages (ICOLD) – ISSN 0254-0703, 625–641.

Schwanenberg, D. & Köngeter, J. (2000). A Discontinuous Galerkin Method for the Shallow Water Equations with Source Terms, in LNCSE Vol. 11: "*Discontinuous Galerkin Methods*" (Eds.: B. Cockburn, G. E. Karniadakis, and C.-W. Shu), 419–424, Springer, Berlin.

Schwanenberg, D. & Harms, M. (2002). Discontinuous Galerkin Method for Dam-break Flow, In D. Bousmar & Y. Zech (eds.), River Flow 2002, *Proc. International Conference on Fluvial Hydraulics, Louvain-la-Neuve, Belgium, 4–6 September, 2002*. Rotterdam: Balkema: 443–448.

Schwanenberg, D. (2003). Runge Kutta Discontinuous Galerkin method for convection-dominated depth-averaged shallow water problems, PhD thesis, Dept. of Civil Engrg., Inst. Of Hydraulic Eng. and Water Resources Management, Aachen Univ., Germany (in German).

Schwanenberg, D. & Harms, M. (2004). Discontinuous Galerkin Finite-Element Method for Transcritical Two-dimensional Shallow Water Flows, *ASCE Journal of Hydraulic Engineering*, Vol. 130, No. 5 ISSN 0733-9429/2004/5-1-10/$18.00 (in print).

Morris, M. (2000). CADAM Concerted Action on Dambreak Modelling; Dambreak Modelling guidelines & Best Practise, EC contract number ENV4-CT97-0555.

DVWK-Schriftenreihe H 92 (1990). Hydraulische Methoden zur Erfassung von Rauheiten, Verlag Paul Parey.

River Flow 2004 – Greco, Carravetta & Della Morte (eds.)
© 2004 Taylor & Francis Group, London, ISBN 90 5809 658 0

Surge wave front in a moving reference system

A. Bornschein
Institute of Hydraulic Engineering and Applied Hydromechanics, Dresden University of Technology, Germany

ABSTRACT: A surge wave is a very unsteady flow. For better observation and measurement an experimental set-up with a standing surge wave front in a moving reference system was developed. Experimental facilities and instrumentation are presented. Preliminary tests were conducted in order to confirm that the test results are similar to measurements of traditional channels.

1 INTRODUCTION

In its simplest form the dam break wave problem was solved 110 years ago by Ritter (1892) considering a smooth channel bed without roughness. As Hager & Lauber (1996) wrote the results of experimental investigations in test channels confirmed this theoretical solution in the main. One exception is the propagation of a surge wave front downstream of a broken dam which is strongly influenced by bed roughness.

Dressler (1952) and Witham (1955) tried to determine the influence of the bed roughness and found the following equation to determine wave front velocity u_F:

$$u_F = 2 \cdot \sqrt{g \cdot h_0} - a \cdot \sqrt[3]{g \cdot h_0} \cdot \sqrt[3]{g \cdot t} \cdot \sqrt[3]{\frac{g}{C^2}} \qquad (1)$$

where h_0 = depth of water at the dam site before failure, g = acceleration due to gravity, C = Chezy roughness parameter and a = coefficient of decreasing of velocity. This equation means that the roughness reduces the propagation of the flood wave, while the start velocity is Ritter's velocity. But obviously this solution by Dressler does not reflect the actual influence of the bed roughness exactly.

Lauber (1997) conducted dam break wave investigations in horizontal and sloping channel with smooth bed using advanced measurement techniques. The measured wave front velocities were compared with calculated values based on Dressler's equation. Lauber had to consider unrealistic low values of Chezy roughness parameter to get satisfactory results.

It seems there is no feasible solution of wave front propagation available. The propagation of the wave front after a certain time due to dam failure is influenced by the bed roughness, bed slope and water surface slope in the front region.

Furthermore the knowledge in the field of surge waves is necessary to predict e.g. the inundation area and destruction potential of a flood wave resulting from dam rupture, to determine the effectiveness of surges which occur when flushing sewers and to design irrigation systems with grooves.

To find out some rules for the propagation of an assumed triangular shaped wave front on a dry bed Martin & Bollrich (1989) treat the wave front in a moving reference system and found out following equation:

$$u_F = h_F^{2/3} \cdot \frac{1}{n} \cdot \sqrt{\frac{1 + b \cdot I}{3b}} \qquad (2)$$

where h_F = height of the wave front at the boundary between turbulent wave-tip and the following flow being approximately as one-dimensional flow, b = shape parameter of the wave-tip, I = bed slope and n = *Manning's* roughness parameter. The formula has still to be verified by experimental results. Other theories consider a stepped wave front (Schoklitsch 1950) or a sine curved wave front (Wackernagel 1962). Experimental investigations of dam break waves often dealt with the dam failure as well as the flood wave propagating downstream of the dam (see Fig. 1). The front created by the flood wave was very small and it was difficult to get detailed measurement results. There is no knowledge available about the velocity distribution in a wave front and about the shear stress caused by a turbulent wave front.

An experimental set-up for investigations at the wave front has to create the turbulent front on its own.

2 EXPERIMENTAL FACILITY

The basic idea of an experimental set-up described by Bornschein (1999) is analogous to theoretical derivation by Martin & Bollrich (1989) to transform the unsteady flow of a surge into be steady from the observers point of view. The experimental set-up with a conveyer belt as the bed depicts the moving reference system.

Up to now experimental facilities with moving-bed were used especially to investigate air flow, debris flow, open channel flow and large eddy flow as for instance described by Tamburrino & Gulliver 1992. The model tests on surge wave front are performed in the Hubert-Engels-Laboratory of the Institute of Hydraulic Engineering and Applied Hydromechanics, Dresden University of Technology, Germany (Fig. 3).

The testing flume has glass sides and is 0.4 m high, 0.3 m wide and 10 m long. It is possible to tilt the flume. The bed slope can be varied from 0 to 0.04.

A frequency-controlled motor drives the moving bed, the conveyer belt. The bed being used currently has a smooth surface. A velocity of the conveyer belt up to 5 m/s can be realized.

It is possible to generate waves with different wave heights and different wave velocities.

Ultrasonic sensors measure the wave shape. Three sensors were mounted on a mobile monitoring car, which can drive on aluminium tracks on the top of the glass flume along the channel. The position of the car was recorded together with ultrasonic signals. In this way a continuous touchless measurement of water surface was possible. Because of the steep slope of the water surface at the wave front there were hard requirements to ultrasonic sensors to get satisfactory results of wave shape.

The flow velocity field of the wave front is measured with a 2D Laser Doppler Anemometer System (Fig. 4). As a light source a 5 W Argon Ion Laser (Innova 70) manufactured by Coherent is used. The light is separated into 2 times 2 colours in the TSI Color Burst. The 4 beams are focused into optical fibres bringing them to a probe containing transmitting/receiving optics. The optical probes are mounted on a 3 dimensional traversing system to reach all measurement points in the flow computer controlled.

The emitted light signal is detected and transformed to electrical signals in the TSI Color Link. These raw

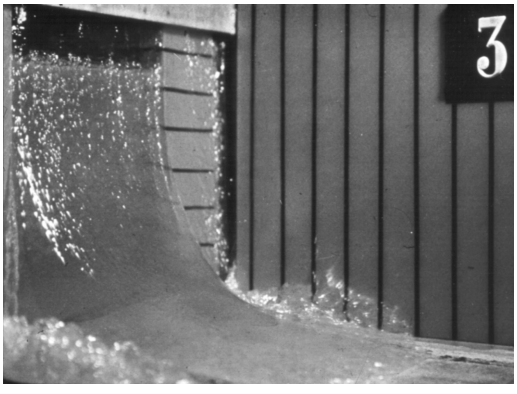


Figure 1. Experimental investigations by Estrade (1967) – dam break wave together with the reservoir outflow.



Figure 3. Laboratory channel with the conveyer belt mechanism.

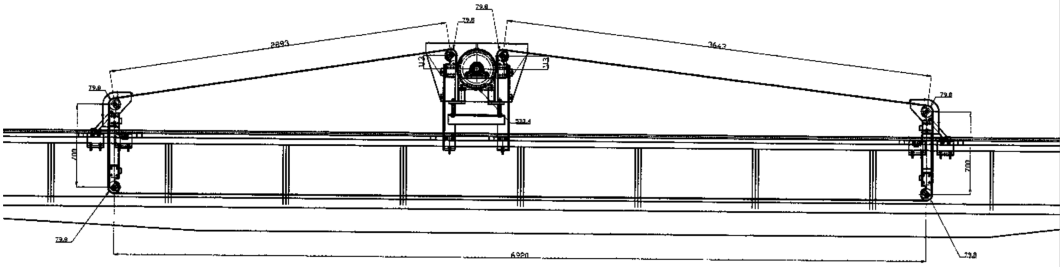


Figure 2. Technical drawing of the experimental set-up.

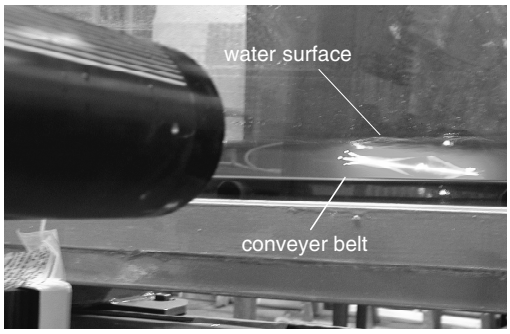


Figure 4. LDA measurement through flume side glass wall (conveyer belt moves to the right side with 2.36 m/s, bed slope = 0.04).

signals are filtered and processed with the TSI Digital Burst Correlator IFA 650. The final processing of the data is done with the TSI Software FIND for Windows.

Hence it was possible to measure the horizontal flow velocity along the channel as well as the vertical flow velocity.

3 TEST CONDITIONS

The wave front tests were conducted as follow: a certain amount of water was filled into the test flume and the conveyer belt was started. Then the velocity of the belt was adjusted in order to get a steady turbulent wave front near one end of the moving bed. The wave shape (water depth as a function of horizontal coordinate x) and the velocity were measured.

In the context of velocity measurement the vertical distance of measurement volume from bed and from water surface was limited by the distance of the two vertical laser beams. In the optical probe the parallel exit beams from the fibres are focused by a lens into the measurement volume where the beams intersect. In the lens the distance between the two beams is 5 cm. Hence good measurement results are only possible when the point in which the two laser beams meet each other located about 0.5 to 1 cm above the bed or under the water level. Obviously the determination of surface velocity by LDA was not possible.

Furthermore the surface velocity was conducted by measurement of the time and the path of tracer particles transported on the water surface. In Figure 5 the surface velocity versus the belt velocity for different bed slopes are shown. In average the surface velocity is about 10 % of the bed velocity in the moving reference system.

That means in the nature the water particles of the water surface travel faster than the wave body. This depends not clearly from the bed slope.

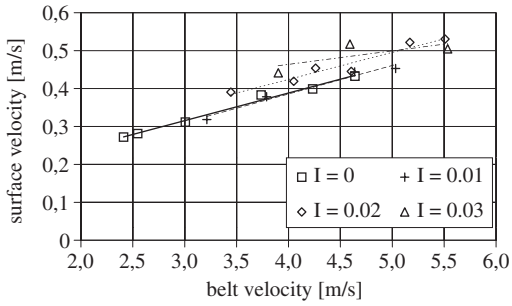


Figure 5. Surface velocity versus belt velocity.

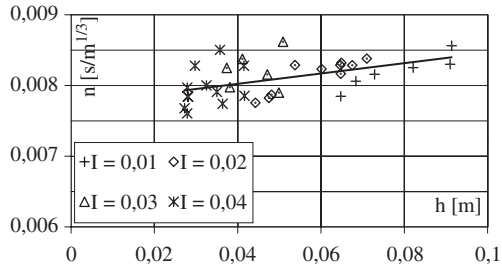


Figure 6. Manning roughness parameter of the smooth conveyer belt.

For further comparison of testing results with different surface roughness, Manning roughness parameter of the smooth belt was determined too. For this test series belt velocity was adjusted that a nearly bed-parallel water surface was resulted.

Since the flow was induced by the moving of the conveyer belt the relevant wetted perimeter was equal to belt wide. Thus the hydraulic radius can be set equal to the water depth. To determine Manning roughness parameter defined by Manning's formula:

$$u_{belt} = \frac{1}{n} \cdot h^{2/3} \cdot \sqrt{I} \qquad (3)$$

water depth h, bed slope I_B, water surface slope I_S and belt velocity as the mean velocity of flow were measured in that test series.

In Figure 6 Manning's roughness parameter versus the water depth is shown. There is no significant correlation. The mean value of all test cases is 0.008 and will be used for calculation and comparison with other test results.

The measured distribution of the horizontal velocity indicates a very turbulent flow. In Figure 9 an example is shown, measured under the condition of bed slope = 0.01, belt velocity = 2.38 m/s and mean water

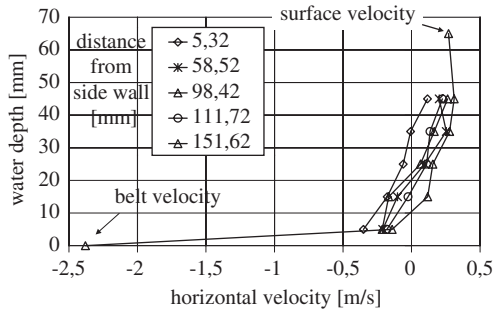


Figure 7. Flow velocity distribution of the horizontal velocity along channel axis due to the moving bed (bed slope = 0.01, belt velocity = −2.38 m/s, water depth = 0.065 m).

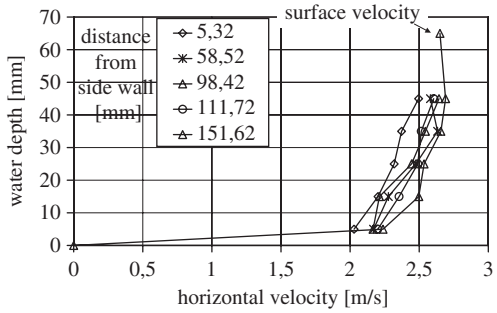


Figure 8. Flow velocity distribution from Figure 8 transformed to the natural reference system.

depth = 0.065 m. The velocity of the surface was estimated due to Figure 5. For better understanding the belt velocity is displayed in the figure.

To transfer experimental results from moving reference system to nature the Galilean transformation must be used:

$$\vec{u}_n = \vec{u}_{mrs} - \vec{u}_b \quad (4)$$

where u_n = horizontal velocity in nature, u_{mrs} = horizontal velocity measured in the moving reference system and u_b = belt velocity. Transformed data from Figure 7 are shown in Figure 8. Generally this flow profile agrees to flow profile of steady flow in a rectangular open channel.

The measured vertical velocity profile for the same test case as in Figure 7 is shown in Figure 9. The vertical velocity has values near zero except for the region near side wall of the flume.

Hence the main velocity in the case of steady flow condition in the moving-bed flume is the horizontal velocity analogous to the steady flow in traditional channels.

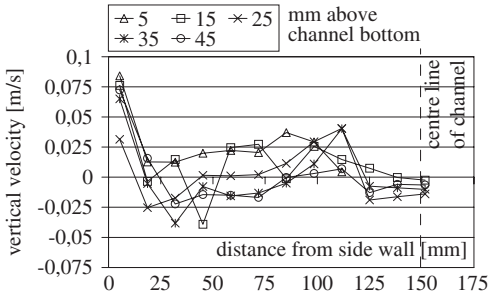


Figure 9. Vertical velocity profile (bed slope = 0.01, belt velocity = −2.38 m/s, water depth = 0.065 m).

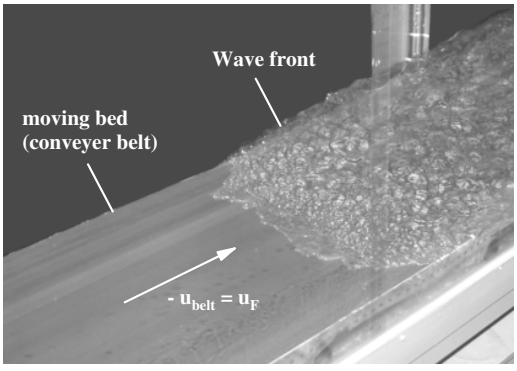


Figure 10. Steady state of wave front in the experimental set-up.

Generally the results from the model tests with an moving-bed flume can be transformed and compared with results from traditional flumes.

4 RESULTS OF WAVE FRONT

The wave front obtained in the experiment is presented in Figure 10. It possesses a very long and flat shape appropriate to the smooth surface of the moving bed. The water surface is very curly. This is similar to waves in standard flumes like at dam break tests by Bell, Elliot & Chaudry 1992.

The slope of the water surface increases until the front where the slope is up to vertical. In traditional dam break experiments with smooth beds the resulting wave front is too small to observe this phenomena. But a steep wave front is observed in channels with a rough bed and in cases of real dam breaks.

Measurement results of the wave head shape shown in Figure 2 and confirms the above description of the shape of the wave front.

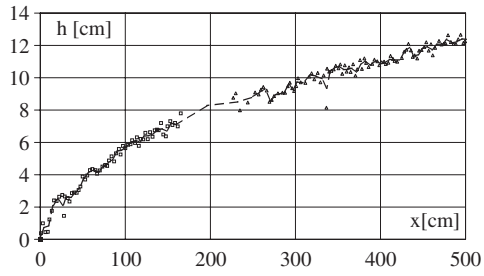


Figure 11. Shape of wave front – dots = measured with ultrasonic sensors, line = mean values (bed slope = 0.01, $v_{bed} = 4.24$ m/s).

5 CONCLUSIONS

The knowledge in the field of surge waves is necessary to predict the inundation area and potential of destruction of a flood wave resulting from dam failure, to determine effectiveness of surges which occur by flushing of sewers and to design irrigation systems with grooves.

Nevertheless the knowledge about the flow at the wave front and about the propagation of the wave front depending on the bed roughness and turbulence is very limited. A better understanding of these relations is of general importance for the calibration of numerical models to simulate flood waves resulting from breaching dams.

There are various theories about shape and velocity of the wave front. Previous experimental investigations consider wave front together with the whole dam break wave and reservoir outflow.

An experimental set-up was developed basing on the consideration of the wave front in a moving reference system. Thus the unsteady flow of a surge wave was converted to a steady flow from the observer's point of view.

For further comparison is it important that in the case that a flow is induced by a moving bed the wetted perimeter is equal to channel width and the hydraulic radius can be set equal to the water depth.

Due to the velocity distribution and the wave shape it is obviously that the moving-bed flume measurements can compared with test results from traditional flumes.

Further tests with a rough surface belt are in process now.

REFERENCES

Bell, S.W., Elliot, R.C. & Chaudry, M.H. 1992. Experimental results of two-dimensional dam-break flows. In Journal of Hydraulic Research, Vol. 30(2): 225–252.

Bornschein, A. 1999. Propagation of surges over initially dry and wet beds. In Proc. Anniversary Scientific Conference 50 Years Faculty of Hydromechanics at the University of Architecture, Civil Engineering and Geodesy, Sofia, Bulgaria, Vol. 1: 105–110.

Dressler, F.R. 1952. Hydraulic resistance effect upon the dam-break-functions. In Journal of Research of the National Bureau of Standards, Vol. 49(3): 217–225.

Estrade, J. 1967. Contribution á l'étude de la suppression d'un barrage. Direction des Etudes et Recherches, Chatou Serie A Bulletin, 1: 3–128.

Hager, W.H. & Lauber, G. 1996. Hydraulische Experimente zum Talsperrenbruchproblem. In Schweizer Ingenieur und Architekt, 114(24): 25–38.

Lauber, G. 1997. Experimente zur Talsperrenbruch-Welle im glatten geneigten Rechteckkanal. Dissertation Nr. 12115, Eidgenössische Technische Hochschule Zürich.

Martin, H. & Bollrich, G. 1989. Berechnungsgrundlagen für Schwall- und Sunkwellen sowie Dammbruchprobleme. In Wiener Mitteilungen Wasser.Abwasser.Gewässer, Symposium: Hydraulik offener Gerinne, TU Wien, Band, 79: 139–164.

Ritter, A. 1892. Die Fortpflanzung der Wasserwellen. In Zeitschrift Verein Deutscher Ingenieure, Band, 36(33): 947–954.

Schoklitsch, A. 1950. Handbuch des Wasserbaus. Springer Verlag. Wien.

Tamburrino, A. & Gulliver, J.S. 1992. Comparative flow characteristics of a moving-bed flume. In Experiments in Fluids No. 13: 289–298.

Wackernagel, A. 1962. Die Berechnung der Flutwellen bei Bruch von Talsperren. In Schwerzerische Bauzeitung, 80. Jg. No. 22: 370–373.

Witham, G. B. 1955. The effects of hydraulic resistance in the dam-break problem. In Proceedings of the Royal Society No. 1170: 399–407.

This page intentionally left blank

River Flow 2004 – Greco, Carravetta & Della Morte (eds.)
© 2004 Taylor & Francis Group, London, ISBN 90 5809 658 0

Roll waves evolution in channels

G.F. Maciel
Department of Civil Engineering, São Paulo State University, Ilha Solteira, São Paulo, Brazil

ABSTRACT: Flows that process under accentuated steep slopes may develop instabilities called roll waves. Roll waves can be developed in laminar and in turbulent streams. The purpose of this article is to analyze the criteria for the occurrence of roll wave phenomenon in the case of supercritical and turbulent Newtonian and non-Newtonian flows from the engineering point of view. Rewriting the shallow water equations and taking into account the Bingham fluid behavior and fluid viscosity, first, the conditions for the development of roll waves using the stability linear technique are presented; second, it is presented a numerical simulation performed by a finite volume technique using Godunov-VanLeer schemes. Imposing a constant discharge at the upstream of the high gradient channel and superposing very small perturbations (with different frequencies and amplitudes), it was observed that roll waves can be developed more easily for small wavenumbers and for high cohesions of material.

1 INTRODUCTION

Flows that process under accentuated steep slopes may develop instabilities. However, the chaotic aspect present in the nature of these instable phenomena, seem to tend, at the end of a finite time, to a stationary flow, more stable, with the appearance of periodic long waves as a hydraulic jump or "bore waves". Such perturbations are called "roll waves". If, on one hand, these waves are rare in natural flows, on the other, they are frequent in artificial canals and in water flowing from dams.

The proposition of this scientific communication is to study, from the theoretical standpoint, with numerical appreciation, instability problems in the fluid flow with rheologic behavior of Bingham fluid type. In particular, it will try to verify the aptitude of the "shallow water" equations, combined to a "Bingham" rheology, to "roll waves" propagation and generation in debris or mudflows. In a first part, the conditions of existence of "roll waves" and formation criteria, either in Newtonian fluids (clean water) or in non-Newtonian fluids ("debris flow" case) will be analytically verified; in a second part, such instabilities would be numerically generated. The equation system used is a modified shallow water type with and without diffusion terms. The numeric modeling proposed is the finite volume type where the schemes Godunov-VanLeer (1981) (compatible to the hyperbolic non-linear systems) are applied.

2 THEORETICAL MODELLING THROUGH "SHALLOW WATER" EQUATIONS – CONSERVATIVE FORM

"Shallow water" equations with shock used here are obtained from the classic equations of fluid mechanics to which a representative behavior law of a Bingham fluid rheology is added, such as $\tau = \tau_c + \mu.\,(\mathrm{d}u/\mathrm{d}y)$ if $\tau > \tau_c$ and $\mathrm{d}u/\mathrm{d}y = 0$ se $\tau < \tau_c$. τ_c represents the critic tension of shearing or initial stress (yield value), μ the dynamic viscosity and $\mathrm{d}u/\mathrm{d}y$ the velocity gradient (shear rate). "Shallow water" system consists of a mass conservation equation (1), a momentum conservation equation (2) and, in this case, two relatives to the hydraulic jump (3 and 4).

$$\frac{\partial h}{\partial t} + \frac{\partial (hu)}{\partial x} = 0 \tag{1}$$

$$\frac{\partial (hu)}{\partial t} + \frac{\partial (\alpha h u^2)}{\partial x} + g.h.\cos(\theta).\frac{\partial h}{\partial x} = g.h.\sin(\theta) - \frac{\tau_c}{\rho} - \frac{g u^2}{C_h^2} \tag{2}$$

$$\rho.h.(w-u) = \rho_0.h_0.w \tag{3}$$

$$\rho_0.h_0.w.u = \frac{1}{2}.\rho.g.h^2.\cos(\theta) - \tau_c.h_0 \tag{4}$$

In these equations "h" is the flow depth; "h_0" is the uniform flow depth; "u" is the vertical average velocity; "w" is the propagation velocity of the front flow (celerity); "C_h" is Chézy coefficient; "θ" the canal declivity; "ρ" the specific mass of the fluid and "α" the velocity profile coefficient ($\alpha = 1$, by simplification). The Bingham Number considered is this article is high, in order that critical stress dominates largely over viscosity effect.

2.1 *Existence conditions of "roll waves" in the new Bingham fluid rheology, without viscous term*

The proposal of this item is to determine the necessary and sufficient conditions to the generation of "roll waves" as the solution of "shallow water" equations in a Bingham fluid rheology without the diffusion term. At first, the interest variables and thus the work scales should be defined:

$$\textbf{length scale:}\quad H = \frac{h}{h_0} \quad \text{and} \quad X = \frac{x \cdot tan(\theta)}{h_0}$$

$$\textbf{velocity scale:}\quad U = \frac{u}{\sqrt{g \cdot h_0 \cdot cos(\theta)}} \quad \text{and}$$

$$W = \frac{w}{\sqrt{g \cdot h_0 \cdot cos(\theta)}}$$

$$\textbf{time scale:}\quad T = \frac{t}{\frac{h_0}{tg(\theta)} \cdot \frac{1}{\sqrt{g \cdot h_0 \cdot cos(\theta)}}}$$

in which $\sqrt{g \cdot h_0 \cdot cos(\theta)}$ is the propagation speed of the gravitational waves. Introducing the dimensionless variables in the equations (1)–(4), and disregarding the specific mass variations, the following equations are obtained:

$$\frac{\partial H}{\partial T} + \frac{\partial (H.U)}{\partial X} = 0 \qquad (5)$$

$$\frac{\partial U}{\partial T} + U\,\frac{\partial U}{\partial X} + \frac{\partial H}{\partial X} = 1 - \frac{C^*}{H} - \beta.\frac{U^2}{H} \qquad (6)$$

$$H.(W-U) = W \quad \text{e} \quad W.U = \frac{1}{2}.H^2 - C^* \qquad (7)$$

$$\text{with} \quad C^* = \frac{\tau_c}{\rho.g.h_0.\sin(\theta)} \quad \text{and} \quad \beta = \frac{g}{C_h^2 \tan(\theta)}$$

The determination of the "roll waves" formation criterion, demands, first of all, a solution to the free surface equation. First, the equations (5) and (6) are rewritten in a moving system of co-ordinates. By hypothesis $\zeta = X - W.T$, where W represents the dimensionless velocity of the front flow propagation (celerity). Starting from these presuppositions, we obtain two linear equations with two incognitos (U′ and H′). This system resolution will provide two differentials equations with U′ and H′:

$$H' = \frac{\partial H}{\partial \zeta} = -\frac{H.\left(1 - \frac{C^*}{H} - \beta.\frac{U^2}{H}\right)}{(U-W)^2 - H} \qquad (8)$$

$$U' = \frac{\partial U}{\partial \zeta} = \frac{(U-W).\left(1 - \frac{C^*}{H} - \beta.\frac{U^2}{H}\right)}{(U-W)^2 - H} \qquad (9)$$

The relation between (8) and (9) allow to verify that the specific discharge is a constant as described below:

$$\frac{H'}{U'} = \frac{H}{W-U} \quad ; H(W-U) = K = \text{constant} \qquad (10a,b)$$

If we apply (10b) in the expression of H′ (equation 8), an equation non-linear of 1st order will be obtained, as shown in equation (11):

$$\frac{\partial H}{\partial \zeta} = -\frac{H.\left(1 - \frac{C^*}{H} - \beta.\frac{(H.W - K)^2}{H^3}\right)}{\left(\frac{K}{H}\right)^2 - H} \qquad (11)$$

The resolution of (11) will provide us the wished profile of the free surface. However, it is verified that there is no solution to this periodic equation. Thus, the proposal would be to try to "build" periodic solutions from continued intercalated solutions by hydraulic jumps.

For this, it is necessary to find continuous solutions presenting the property in which, in a determined section, the flow is supercritical and, in a posterior one, subcritical. By continuity, there should exist an abscissa point ζ_0, a depth point H_0, a speed point U_0, where the Froude number is equal to the unity (critic flow). Thus, $W - U_0 = \sqrt{H_0}$. To this point, especially, the equation denomination (11) is null, which means a discontinuity, except for the case in which the numerator is also null. This critical point is necessarily different of that where the jump occurs, in a way that is only possible to construct the "roll waves" when the numerator and the denominator concomitantly null themselves. Thus:

$$H_0 = \left(\frac{-\beta \cdot W + \sqrt{C^* \cdot (1-\beta) + \beta \cdot W^2}}{1-\beta}\right)^2$$

$$U_0 = \frac{W - \sqrt{C^* \cdot (1-\beta) + \beta \cdot W^2}}{1-\beta}$$

$$K = (W - U_0) \cdot H_0 = (H_0)^{\frac{3}{2}}$$

Substituting (10b) in (11), and after some mathematical developments, the differential equation to the free surface in the continuous interval is obtained:

$$\frac{\partial H}{\partial \varsigma} = \frac{H^2 + H \cdot (H_0 - C^* - W^2 \cdot \beta) + \beta \cdot {H_0}^2}{\left({H_0}^2 + H \cdot H_0 + H^2\right)} \qquad (12)$$

Finally, in order to generate "roll waves", starting from the equation (12), it is necessary that $\partial H / \partial \zeta H = H_0 > 0$, implicates in:

$$2.\beta \frac{1 - \sqrt{\beta + \frac{C^*.(1-\beta)}{W^2}}}{-\beta + \sqrt{\beta + \frac{C^*.(1-\beta)}{W^2}}} < 1 \qquad (13)$$

2.2 *Discussing the theoretical results, without diffusion*

The inequality (13) defines a dominion into which "roll waves" can be formed. Such results are illustrated in the Figure 1. It is observed that for an addition of the Bingham term (cohesion effect or critic tension τ_c), "roll waves" can be developed easily, i.e., the increase of this parameter would favour the development of these disturbances. This conclusion agrees, for example, with the experimental observations of Takahashi (1990), who generates "roll waves" in laboratory to Froude numbers $F < 2$. If the fluid cohesion C^* is null, the inequality (13) is given by $\beta < 1/4 \Leftrightarrow \tan(\theta) > 4 \cdot g / C^2$, which agrees with Dressler (1949) – generation of "roll waves" in "clean water".

2.3 *Criterion for "roll waves" generation based on the analysis of linear stability, in the new Bingham rheology and with the inclusion of the viscous term*

The purpose of this paragraph is to evidence the formation criteria of "roll waves" based in the analysis of linear stability. In order to do that, resource will be made to the "shallow water system" (equations (1) and (2)). Adding the diffusion term $\partial/\partial x(h\upsilon\partial u/\partial x$ to the equation (2), throughout the current, in which "ν" represents the average kinematics viscosity; the quantity of movement equation becomes:

$$\frac{\partial(hu)}{\partial t} + \frac{\partial(\alpha h u^2)}{\partial x} + gh \cos(\theta) \frac{\partial h}{\partial x} = g.h.\sin(\theta) - \frac{\tau_c}{\rho} - \frac{g u^2}{C_h^2} + \frac{\partial}{\partial x}\left(h \upsilon \frac{\partial u}{\partial x}\right) \qquad (14)$$

Thus, the second member of the equation (14) takes into consideration four effects: the weight force, represented by the gravity, the shearing due to the Bingham fluid modeling, turbulent dissipation through Chézy coefficient and, finally, the viscous dissipation represented by the term in "ν", adapted to the "shallow water" system.

The parameters that may at times evidence the probable instabilities in the flow curve pass necessarily by a process of system adimensionalization. Taking the uniform flow as a basis in the adimensionalization process, and applying the characteristic scales, such as $x = L \cdot x'$, $h = h_n \cdot h'$ to lengths, $u = u_n \cdot u'$ to velocities and $C^* = \tau c / \rho \cdot g \cdot h_n \cdot \sin(\theta)$ to tensions.

Where L represents the wave length and n an index that characterizes the normal or uniform regime, it is obtained (omitting the character ($'$)):

$$\frac{\partial h}{\partial t} + \frac{\partial(hu)}{\partial x} = 0 \qquad (15)$$

$$\frac{\partial u}{\partial t} + \alpha.u. \frac{\partial u}{\partial x} - (\alpha - 1).\frac{u}{h} \cdot \frac{\partial h}{\partial t} + \frac{1}{F^2} \cdot \frac{\partial h}{\partial x} = \frac{\tan(\theta)}{\varepsilon.F^2}.\left((1 - C^*).\frac{u^2}{h}\right) + \frac{1}{Re}.\left(\frac{\partial^2 u}{\partial x^2} + \frac{1}{h} \cdot \frac{\partial u}{\partial x} \cdot \frac{\partial h}{\partial x}\right)$$

with:

$$F = \frac{u_n}{\sqrt{g.h_n.\cos(\theta)}} \; ; \; Re = \frac{u_n.L}{\nu} \text{ and } \varepsilon = \frac{h_n}{L} \qquad (16)$$

Concerning the study of linear stability, it is admitted that heights and velocities are submitted to small perturbations, such as: $u = 1 + \hat{u}$ with $\hat{u} \ll 1$ and $h = 1 + \hat{h}$ with $\hat{h} \ll 1$. Introducing the equation (15) in (16) and disregarding the second order terms, the equation system of the perturbed quantities h and u is obtained. Finally, omitting the notation ($\hat{}$):

$$\frac{\partial h}{\partial t} + \frac{\partial h}{\partial x} + \frac{\partial u}{\partial x} = 0 \qquad (17)$$

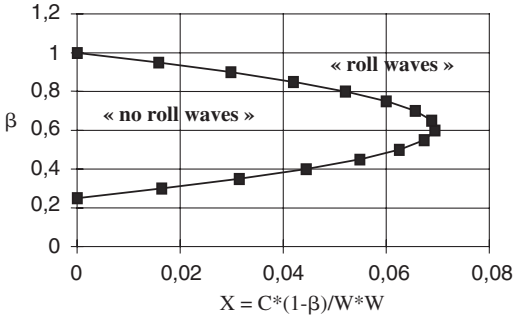


Figure 1. Dominion of existence of "roll waves".

$$\frac{\partial u}{\partial t} + \alpha.(1+u).\frac{\partial u}{\partial x} - (\alpha-1).\frac{(1+u)}{(1+h)}.\frac{\partial h}{\partial t} + \frac{1}{F^2}.\frac{\partial h}{\partial x} = \frac{tg(\theta)}{\varepsilon.F^2}\left(1-\frac{C^*}{(1+h)}\right)(1-C^*)\frac{(1+2u)}{1+h}) + \frac{1}{Re}\left(\frac{\partial^2 u}{\partial x^2} + \frac{1}{(1+h)}\frac{\partial u}{\partial x}\frac{\partial h}{\partial x}\right) \quad (18)$$

The equation (17) can be inserted in (18), allowing the elimination of "u" and obtain an equation that only takes into consideration the variable "h":

$$\frac{\partial^2 h}{\partial t^2} + 2\alpha\nu\frac{\partial^2 h}{\partial x \partial t} + \left(\alpha - \frac{1}{F^2}\right)\frac{\partial^2 h}{\partial x^2} = \frac{1}{Re}\left(\frac{\partial^3 h}{\partial t \partial x^2} + \frac{\partial^3 h}{\partial x^3}\right) - \left(\frac{tg(\theta)}{\varepsilon.F^2}\right)\left(C^*\frac{\partial h}{\partial x} - (1-C^*)\left(-2\frac{\partial u}{\partial x} - 3\frac{\partial h}{\partial x}\right)\right) \quad (19)$$

With the equation (19), the development criteria of instabilities of wave number k and of frequency *w* are researched. The solutions of the form $\mathbf{h(x,t) = H(k)\cdot e^{(ikx-wt)}}$ where $\mathbf{w = w_r + i\cdot w_i}$, are interesting to be obtained, observing that $w_r \geq 0$ in order to assure stability. Introducing h(x, t) in the equation (19), an equation of order 2 with complex coefficients is obtained. From this point, the real and the imaginary parts are separated, thus creating two other equations (one to w_r and another to w_i), which allows the obtaining of polynomial $P(w_r)$, having as only incognito w_r. Here, it is interesting to discuss the existence and the nature of the root signals of $P(w_r)$. It is known that stability will only occur if the roots of $P(w_r)$ are positive or null. After some mathematical developments, it is demonstrated that $P(w_r)$ is a strictly monotonous function, decreasing in the interval $]-\infty; 0]$; thus, it is concluded that the condition needed and enough that the roots of $P(w_r)$ are positive is that P(0) is positive ($P(0) > 0$). After some mathematical developments, the critic Froude number F_c is obtained:

$$F_c = \sqrt{\frac{1}{\left(\frac{1}{2\cdot(1-C^*)+\frac{k^2\cdot\sigma}{Re}} - (\alpha-1)\right)^2 - \alpha\cdot(\alpha-1)}} \quad (20)$$

$$h_p = \frac{\tau_c}{\rho\, g \sin(\theta)} \quad (h_p : \text{depth of the 'plug'})$$

$$\alpha = \frac{9}{15}\frac{\left(8+7.\frac{h_p}{h_n}\right)}{\left(2+\frac{h_p}{h_n}\right)^2} \qquad \sigma = \frac{\varepsilon.F^2}{\tan(\theta)}$$

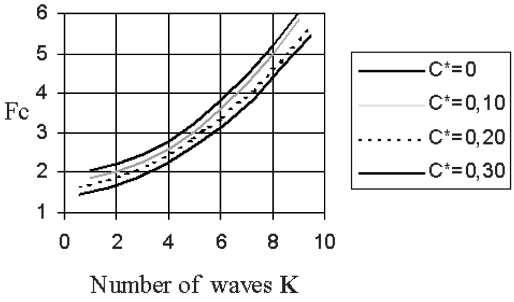


Figure 2. Critic Froude in function of the number k of waves.

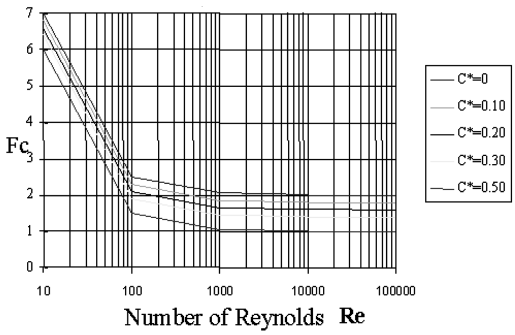


Figure 3. Critic Froude in function of Reynolds' number.

2.4 *Discussing the theoretical results, with diffusion*

From the previous results, some guiding formation criteria and the development of "roll waves" in function of the physic parameters can be illustrated. The following figures show the influence of the Reynolds' number Re and of the wave number k in function of the critic Froude number F_c for various cohesion values C* (Bingham effect). The Figure 2 shows the influence of the number of waves (wavelength) over critic Froude for two fixed parameters, $\zeta = \sigma/R_e = 0.05$ and $\alpha = 1.00$. It can be deduced from the Figure 2 that roll waves tend to develop more easily or more quickly to a scenery of small wave numbers and high values of critic tension of Bingham (cohesion effect C*). On one hand, it could be asserted that an increase in the cohesion value would guide or favor the appearance of instabilities of roll waves; on the other, long waves would be the first to destabilize.

Figure 3 shows the influence of the adimensional rigidity C* over the Froude number as a function of the Reynolds' number. It can be observed that in the same way that in the result illustrated in the Figure 2, an increase in the fluid cohesion would cause the precocious appearance of roll waves, to fixed Froude and Reynolds numbers.

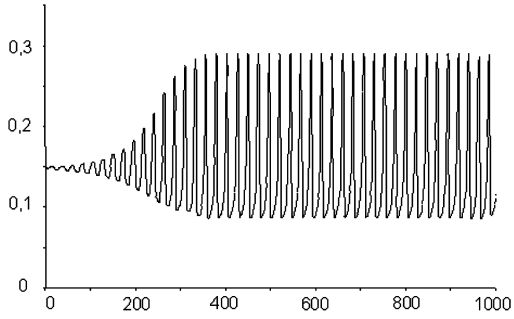


Figure 4. Roll waves amplitudes generated versus longitudinal distances (sinusoidal perturbation of T = 3. 14 s; C* = 0 and 1% of discharge).

3 VALIDATION TESTS – NUMERIC RESULTS AND DISCUSSIONS

The purpose of this paragraph is to present some results of numeric order in generating roll waves in Newtonian and non-Newtonian fluids. The simulation program developed had its theoretical formulation in the hyperbolic non-linear systems and its derivations, notedly the resolution of the Riemman problems (Vila, 1985). The numeric simulations were executed from VanLeer numeric schemes (second order in time and space) and effectuated in rectangular section canal of 1000 m length (with increment of space $\Delta x = 1.00$ m) and significant slope of 30%. Working with flow regimes preferentially turbulent and supercritical, two upstream limit conditions could be fixed: discharge of 800 l/s/m and depth of 0.15 m. On this discharge, small perturbations (of per cent order) were imposed, so as to generate stable roll waves to the canal downstream, as illustrated by the diagrams below.

A first series of tests were carried out, allowing a more global assessment of the phenomenon, mainly concerning the initial conditions of the perturbation imposed, as described below:

(a) an upstream perturbation on the discharge, sinusoidal perturbation type, was capable of generating well defined roll waves (Figure 4);
(b) a random perturbation was not able of generating well defined roll waves, i.e., with a preferential marked frequency; however, it generated a pulsing free surface, with chaotic aspects, as shown in Figure 5.

Concerning the amplitude of the imposed perturbation (sinusoidal perturbation), the results show that:

(a) to a given frequency, the perturbation amplitude should not influence over the amplitude of the generated roll wave;

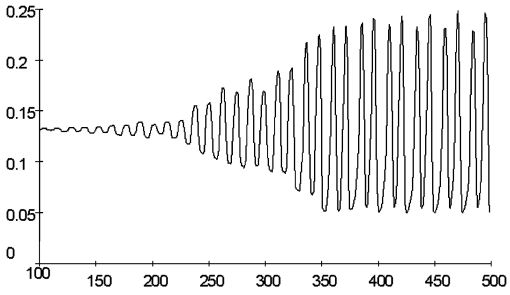


Figure 5. Pulsing surface from random perturbation versus longitudinal distances.

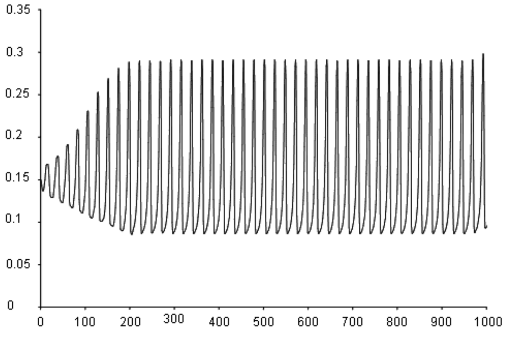


Figure 6. Roll waves amplitude generated versus longitudinal distances (10% discharge perturbation (C* = 0).

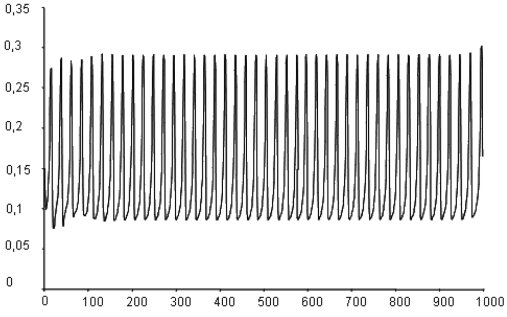


Figure 7. Roll waves amplitude generated versus longitudinal distances (50% discharge perturbation (C* = 0).

(b) however, a higher or a lower perturbation amplitude should anticipate or postpone the appearance of the roll wave, as if perturbing the base flow without altering the amplitude of the generated roll wave.

See Figures 6 and 7.

Concerning the wave length of the imposed perturbation, the numeric tests show that the generated roll wave has the same length. A small perturbation of T = 3.14 s generated a roll wave of the same

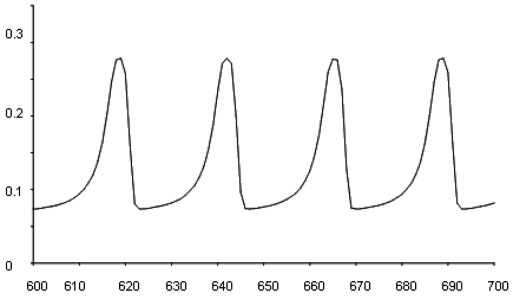


Figure 8. Detail of the roll wave illustrated in Figure 6.

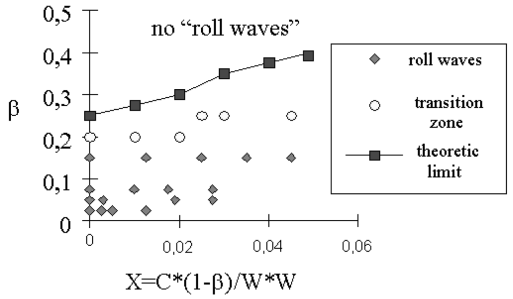


Figure 9. Generation dominions of roll waves in function of the canal declivity and Bingham effects.

period (with respective wave length of 25 m). Figure 8 illustrates this result.

A second series of tests were performed, taking into consideration the new rheology and its implication over the generation and characteristics of the produced waves. Various tests were carried out, allowing the establishment of a border or dominion of roll waves formation in function of the parameters being used: β taking into consideration the canal declivity and its resistance; Bingham tension $X = C^*(1-\beta)/W * W$ (Figure 9).

For this case we could certify that for constant β, the Bingham tension effect seems not to influence, in a significant way, the period or the wave length, thus reconfirming the same conclusions for a newtonian fluid. On the other hand, when taking into consideration the cohesive effect (C*), to a given amplitude of perturbation, the roll waves appear earlier and present higher height values. Figures 10 and 11 illustrate these results.

A third series of tests consisted in verifying the sensibility of our system nonlinear when submitted to simultaneous small perturbations and frequencies and amplitude different of $h(x, t) = H_0 e^{(kx-w(t)t)}$, where k is the number of waves and w(t) are the frequencies. The diagram below illustrates some results for various configurations: Figures 12, 13 (for Newtonian fluids) and Figures 14, 15 (non-Newtonian fluids).

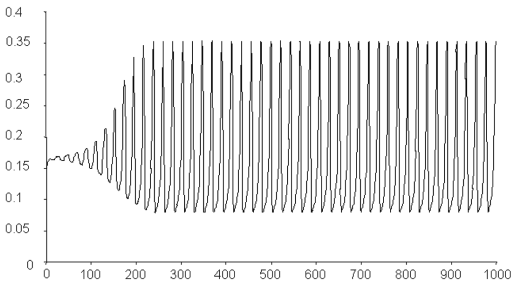


Figure 10. Roll waves with T perturbation of 3.14 s ($C^* = 0.10$).

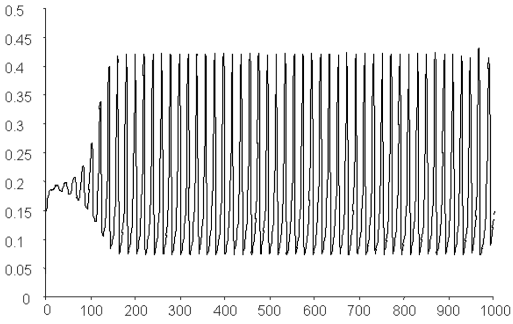


Figure 11. Roll waves with T perturbation of 3.14 s ($C^* = 0.20$).

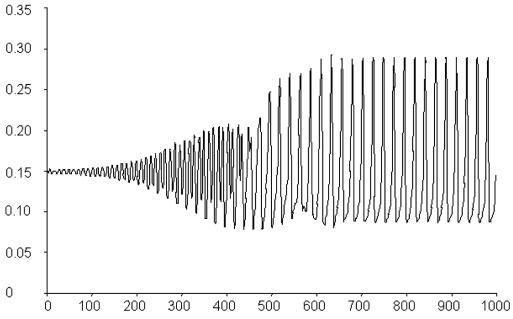


Figure 12. Roll waves with T perturbation = 3.14 s and different amplitudes ($C^* = 0$).

From these results, some comments are in order:

(a) the perturbation amplitude does not intervene in the generated roll wave amplitude;
(b) the generated downstream roll wave presents the wave period or length regarding the bigger wave length of the different perturbations imposed upstream, after passing and capturing other frequencies (lower wavelengths). Another analysis which could be made, confirming such results, is related to the fact that long waves (big wavelengths)

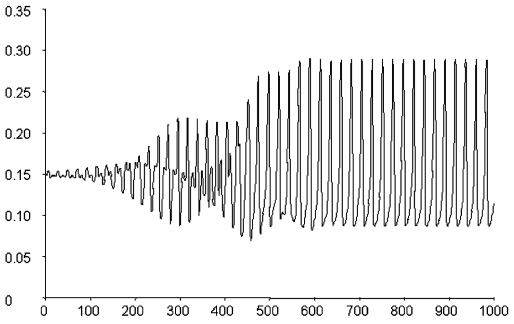


Figure 13. Roll waves with T perturbation = 1.00s, 1.57s and 3.14s and constant amplitudes (C* = 0).

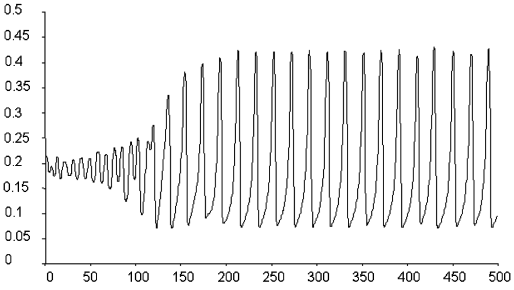


Figure 14. Roll waves with T perturbation = 1.00 s, 1.57 s and 3.14 s and different amplitudes (C* = 0.2).

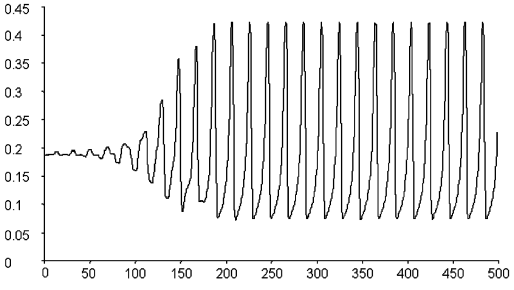


Figure 15. Roll waves with T perturbation = 1.00 s, 1.57 s and 3.14 s and constant amplitudes (C* = 0.2).

are almost always the first to destabilize, as illustrated in Figure 2;

(c) to the new Bingham rheology, based in Figures 10, 11, it is proved that the tendencies are the same shown for the Newtonian fluid, i.e., the roll waves appear earlier and with higher height values.

REFERENCES

Brock, R. R. 1966. Discussion of Critical analysis of open-channel resistance, by H. Rouse. Journal Of Hydraulic Divison, ASCE, Vol. 92, No. HY2: 403–409.

Brock, R. R. 1967. Development of roll waves in open channels – Report No. KH-R-16. W. M. Keck Laboratory of Hydraulics and Water Resources, California Institute of Technology.

Chen, C. L. 1992. Momentum and energy coefficients based on power-law velocity profile. J. Of Hydraulic Engineering, ASCE, Vol. 118, No. 11, pp. 1571–1584.

Dressler, R. F. 1949. Mathematical solution of the problem of roll waves in inclined open channels. Communs Pure Appl. Math., Vol. 2: 149–194.

Godunov, S. K. 1959. A difference method for numerical calculation of discontinuous equations of hydrodynamics. Math. Sb, 47(89): 271–300.

Ishihara, T., Iwagaki, Y. & Iwasa, Y. 1954. Theory of the roll wave train in laminar water flow on a steep slope surface. Transactions of Japan Society of Civil Engineers 19: 46–57 (in Japanese).

Iwasa, Y. 1954. The criterion for instability of steady uniform flows in open channels. Memoirs of the Faculty of Engineering, Kyoto University, Japan, Vol. 16, No. 6: 264–275.

Jeffreys, H. J. 1925. The flow of water in an inclined channel of rectangular section. Philosophical Magazine, Series 6, Vol. 49: 793–807.

Julien, P. Y. & Hartley, D. M. 1985. Formation of roll waves in laminar sheet flow – Rep. Cer84-85pyj-dmh18. Department of civil engineering, Colorado state university.

Julien, P. Y. & Hartley, D. M. 1986. Formation of roll waves in laminar sheet flow. Journal of Hydraulic Research 24: 5–17.

Kranenburg, C. 1992. On the evolution of roll waves. Journal of Hydraulic Research, Vol. 245: 249–261.

Lamberti, A. & Longo, S. 2000. Roll waves e dissipazione in correnti idriche e nei debris flow (Roll waves and dissipation in water streams and in debris flow). Proc. XXVII National Conference on Hydraulics, Gndci, Vol. 1: 85–94.

Mayer, P. G. W. 1957. A study of roll waves and slug flows in inclined open channels. Dissertation cornell univ.

Needham, D. J. & Merkin, J. H. 1984. On roll waves down an open inclined channel. Proc. r. soc. lond a 394: 259–278

Ng, C. & Mei, C. C. 1994. Roll waves on a shallow layer of mud modelled as a power-law Fluid. Journal of Fluid Mechanics, 263: 151–183.

Roe, P. L. Approximate riemann solvers, parameter vectors and difference schemes, J. Comp. Phys. Vol. 43: 357–372.

Saint Venant, B. 1871. Théorie du mouvement non permanent des eaux, Institut de France, Académie des sciences, Comptes Rendus, Paris, Vol. 73: 147–237.

Takahashi, T. 1990. Debris flow, Monograph, Iahr, Balkema, Rotterdam.

Vanleer, B. 1981. Toward the ultimate conservative difference scheme. Journal of Comp. Phys. 32, 101–136.

Vila, J. P. 1986. Simplified godounov schemes for (2,2) systems of conservation laws. Siam J. Numerical Anal. Vol. 23 No. 6: 1173–1192.

This page intentionally left blank

River Flow 2004 – Greco, Carravetta & Della Morte (eds.)
© 2004 Taylor & Francis Group, London, ISBN 90 5809 658 0

Physical model tests for dike-break induced, two-dimensional flood wave propagation

S. Briechle, A. Joeppen & J. Köngeter
Institute of Hydraulic Engineering and Water Resources Management, Aachen University, Germany

ABSTRACT: There is a lack of knowledge about the properties of a flood wave due to dike break and failure of (mobile) flood protection walls, on which a prediction of the implicated risk could be based. Fore this reason a physical model, which takes into account the special boundary conditions of such an incident, was built and measurements were undertaken. The results of a variation of initial water depth and discharge in the river and the effect of a thin water film on the propagation area are presented and discussed.

1 MOTIVATION AND AIMS

Dikes and (mobile) flood protection walls defend areas used by man from flooding. In case of failure however, the resulting flood wave implicates an extra risk to people and goods in the near field of the breach because of the strong dynamic forces. At the moment it is hard to assess this risk. Due to the rareness and dangerousness of such failures, data from real-world incidents are insufficient to base a prediction of the flood wave propagation on these and there are no analytical solutions for this problem. Attempts to predict the wave numerically are made frequently, but produce uncertain results: Assumptions and simplifications to make the problem computable usually do not reproduce all the complex effects of roughness, turbulence, flow inhomogeneities (e.g. air entrainment) and vertical momentum at places of strong surface slope (e.g. in the near field of the breach or at the wave front). Furthermore validation examples are mostly unavailable. The extend of deviation of the calculation results from the reality is therefore not known unerringly and it is not easy to ascertain how to improve numerical models best.

For this reason experiments are conducted in a physical model. Data of the flood wave propagation are gathered, which later can be used for the validation and improvement of numerical models. Furthermore insight into the wave is gained, especially concerning flow processes, effects of systematically varied parameters, scalability of the results to other dimensions and as a basis for a simplified projection of the flood wave propagation without an expensive numerical calculation.

2 PROBLEM DEFINITION

2.1 *Comparison of dam- and dike-break*

For the *dam*-break case there can be found several detailed investigations in literature, Hager & Lauber (1996) give a good review. Most physical investigations took place in flumes and therefore reduced the problem to one dimension – propagation takes place only along the flume, lateral propagation is not considered –, in addition breach and reservoir have the same width. Only few investigations allow for a propagation into an area, combined with a breach width smaller than the width of the reservoir. Most recent example is Kulisch (2003), other model tests were conducted by Jovanović & Djordjević (1995), Fraccarollo & Toro (1995), Naaim & Brugnot (1994), Tingsanchali & Rattanapitikon (1993) and Memos et al. (1983).

However, those findings are not directly transferable to a wave resulting from the failure of a flood protection structure on a river. Figure 1 depicts the

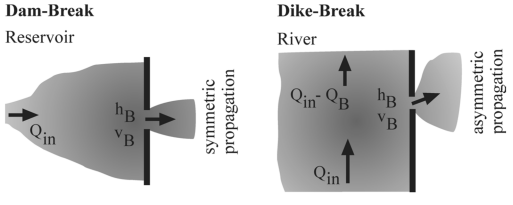


Figure 1. Comparison of flood wave propagation caused by dam- and by dike-break, Q_{in} = discharge into reservoir/river respectively, Q_b = discharge through breach, h_b = water depth in breach, v_b = velocity in breach.

other two mayor differences: Compared to the reservoir of a dam, in which the water depth converges to zero with time, the discharge Q_{in} in a river can not be neglected – the river bed will not empty completely, but after a certain transitional period a steady state condition will be reached with constant water depth h_B in the breach. Additionally in a river the velocity component parallel to the protection structure has to be considered, since it will deform the wave asymmetrically. The only physical model known to the authors, which accounts for the river flow apart from there own can be found in Aureli & Mignosa (2002).

2.2 *Delimitation of this investigation*

A complete, instantaneous failure is assumed with the chosen mechanism (see section 3.1). A real dike or (mobile) flood protection wall will probably not fail in this idealized way. However, this assumption seems justifiable due to the following reasons:

- Analytical solutions for the dam-break problem and most numerical simulations start from a vertical water front at the breach section. To be able to compare our results with those calculations this idealized scenario seems most appropriate.
- At present knowledge on the various failure mechanisms of dikes and (mobile) flood protection walls and their interaction with the flow is poor, resulting in high uncertainties. To reduce these for this investigation, the failure mechanisms were neglected for the time being.
- It is considered a well defined worst case scenario which corresponds to an instantaneous and total failure at starting time giving the highest factor of safety for risk considerations.

The two-dimensional wave propagation is investigated in the near field of the breach, where the dynamic forces are crucial with respect to the later use of the results in risk assessment procedures. Also in this area (i.e. near the breach) the vertical momentum is likely to become important for the flow process.

The unsteady state immediately after the failure is investigated. Additionally and in contrast to past investigations, the steady state case, reached after a certain time span due to the constant discharge in the river as described above, is examined.

There is no fixed scaling factor applied. Considering initial water depth before break it ranges between nearly 1:1, as would be applicable for small mobile flood protection walls in Germany, to up to 1:30 and more, for example for dikes in the Lower Rhine Area in Germany of up to 15 m height. Therefore scalability is of particular interest.

3 EXPERIMENTAL SETUP AND MEASURING TECHNIQUES

3.1 *Physical model*

To satisfy the needs described above a physical model was built at the Institute of Hydraulic Engineering and Water Resources Management (IWW) at Aachen University, which takes into account the special boundary conditions of the dike-break problem.

A channel, 1.0 m wide and representing the river, is joined to an area (3.5 m × 4.0 m), on which the propagation of the flood wave can be measured (see fig. 2). Channel and area are separated by the channel wall, i.e. the dike or flood protection wall, in which a pneumatically driven gate is installed for simulation of the breach (see below). The water is allowed to fall freely off the other three boundaries of the area. The floor of the propagation area is made from glass, not only to minimize roughness, but to observe the wave and take measurements from below as well.

In this physical model the following parameters can be varied to study their effect on the flood wave propagation: The initial water depth can be risen to up to 50 cm by adjusting a weir at the end of the channel, the discharge in the channel can be set from $Q_{in} = 0$ to 390 l/s and the breach width can be chosen to 30, 50 or 70 cm, rectangular in shape. The area is horizontal and can be covered with different materials to study roughness effects.

The flap initializes the flood wave propagation by opening in a minimized time span of less than 0.1 s. The movement of the flap is illustrated in figure 3. The design aimed at the immediate clearance of the entire vertical water front in the breach. This distinguishes the mechanism from the gates used in the past in dam- and dike-break experiments, were the wave propagation was usually initialized by lifting a sliding panel. However, in that case the foot of the wave is

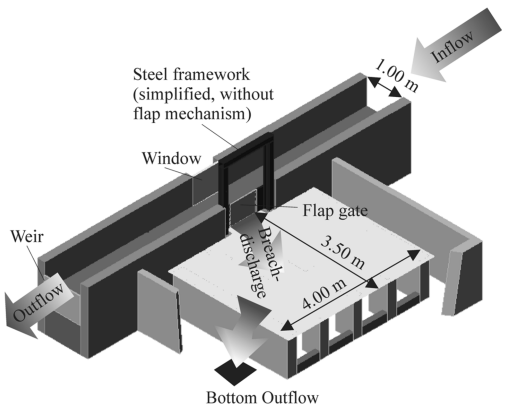


Figure 2. Physical model.

released first, the whole front only after a short delay. This problem is eliminated by the new flap mechanism, but a pull could be exerted on the water body by the horizontal component of its movement. This is however reduced by the hinges on top, which allow the flap to swing. The effect could be shown in comparison to a flap which was fixed to the steel framework.

3.2 *Measuring techniques*

The two-dimensional measuring arrangement is demanding. Strong spatial and temporal changes of the propagating wave, air entrainment and piling up of water (if the measuring technique is intrusive) entail manifold problems. The wave is difficult to access on the propagation area and all data have to be gathered in two dimensions, which results in a great amount of data.

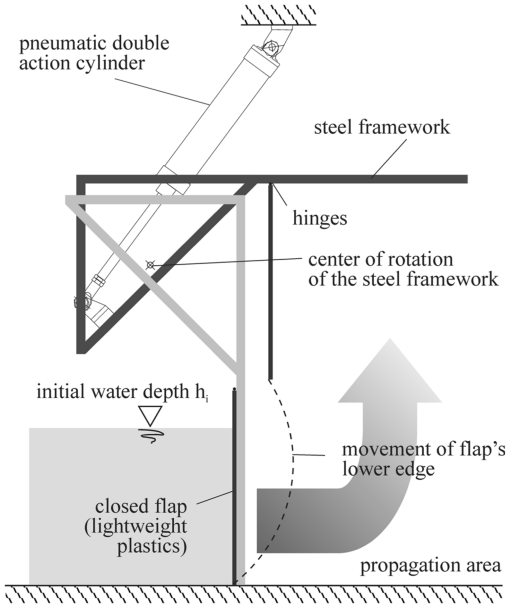


Figure 3. Opening mechanism.

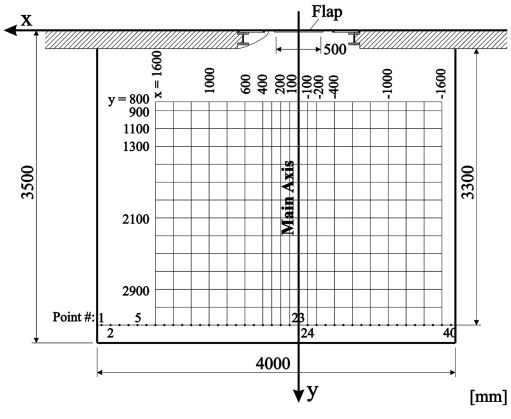


Figure 4. Coordinate system.

The water depth is measured by ultrasonic sensors in a dense raster on the propagation area. The measuring locations are the intersection points of the raster lines in figure 4. The sensors have a measuring frequency of 50 Hz and are optimized for steep wave fronts. They are not influenced by the vertical momentum of the wave, like pressure gauges installed in the floor would be. Our experience on the physical model indicates that the error is usually less than 2 mm. Unfortunately measurement is not possible in the range of flap movement up to approximately 800 mm distance from the breach. However, in the breach itself the water depth can be determined.

Complementary a CCD-camera was installed, recording the whole flood wave from top with a spatial resolution of 756 × 550 pixels (in gray scales), again giving results with a frequency of 50 Hz after de-interlacing of the recorded images. Digital image processing is used to adjust distortion, for automated wave front localization and for post-processing with respect to front velocities, asymmetry etc. When a thin water film remains on the propagation area between the experiments, the entrained air can be used as white contrast for automated digital image processing of the images (see section 4). To detect the wave front in the dried case, the water must be colored to increase contrast, those images can not yet be presented.

Both measuring devices are triggered with the opening mechanism to bear relation to the start of the opening process.

Additionally the wave is recorded by high-speed camera or camcorder to gain an insight into details as the need arises.

3.3 *Measuring program*

The measuring campaign is still under way. Different boundary conditions, namely initial water depth, discharge in the channel, breach width and roughness materials on the propagation area will be systematically tested to be able to quantify their effects. In this paper combinations of $Q_{in} =$ 30 l/s discharge in the river and initial water depth of $h_i = 30$ to 50 cm are presented. The breach width was 0.5 m and the floor of the propagation area was plain glass.

4 RESULTS

4.1 *Effect of initial water depth in the channel*

Figure 5 shows water depth over time on the main axis for a variety of initial water depths at three different distances from the flap. As a first attempt the data

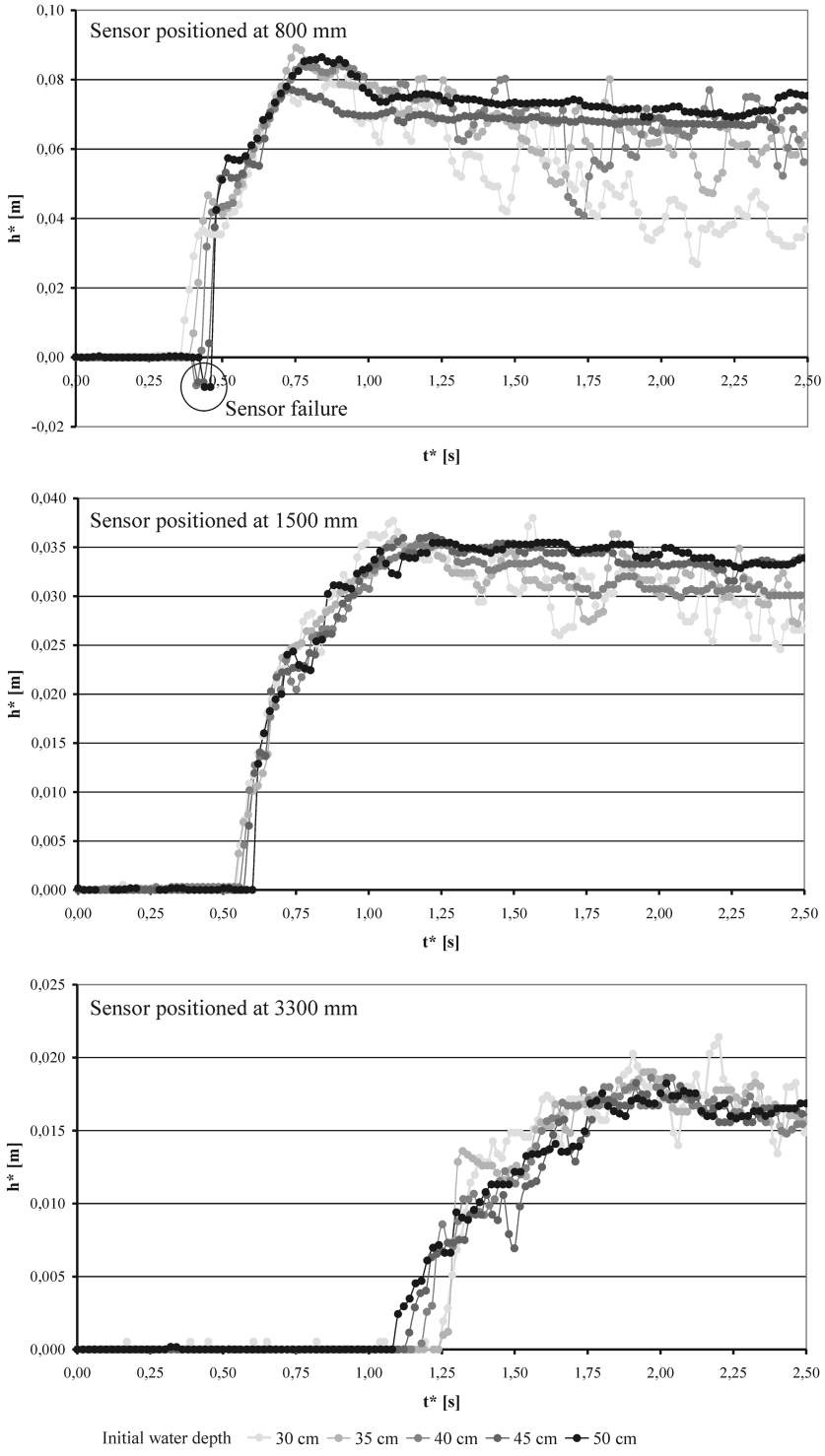


Figure 5. Non-dimensional water depth for five different initial water depths on the main axis at three distances from the flap. Discharge in channel $Q_{in} = 300$ l/s, the propagation area was dried before every experiment.

was scaled by applying Froude's law. For this purpose the model is considered superelevated. In the horizontal directions x and y the scale basis is set to $L_{basis} = 0.50$ m (breach width). This width does not change with the modification of the initial water depth, therefore the horizontal scaling factor L equals 1.0. The same would hold for the distances of the sensors from the breach in y direction. As a scale basis in vertical direction the initial water depth of $H_{basis} = 0.50$ m is chosen, giving different vertical scale factors H for different initial water depths. Based on Kobus (1978) the following equations can be derived for the superelevation in this case:

$$L = \frac{L_{basis}}{L_{variable}} = \frac{0.50\ \text{m}}{0.50\ \text{m}} = 1.0 = const. \quad (1)$$

$$H = \frac{H_{basis}}{H_{variable}} = \frac{0.50\ \text{m}}{h_i} \quad (2)$$

$$n = \frac{L}{H} = \frac{h_i}{0.50\ \text{m}} \quad (3)$$

$$T = \sqrt{L \cdot n} = \sqrt{n} \quad (4)$$

where n = superelevation factor, T = time scaling factor.

Table 1 assembles the results of the equations (1) to (4) for the different initial water depths.

With these values and the following equation (5) the data for figure 5 were obtained:

$$h^* = H \cdot h = 0.50\ \text{m} \cdot \frac{h}{h_i} \quad \text{and} \quad t^* = T \cdot t = \sqrt{\frac{h_i}{0.50\ \text{m}}} \cdot t \quad (5)$$

where h^* and t^* are the scaled values for the measured water depth and time respectively.

At position 800 mm the sensors failed for higher initial water depth, presumably due to the extreme steepness of the front in this place. However, the time the sensor failure occurs can be assumed to be the arrival time.

If the waves were scalable this way, all lines in the graphs should coincide. The water depth h therefore seems to be scalable reasonably well within the proximity of the maximum. Differences can be found in a little "step" in the rise before the maximum – the step is lower for lower initial water depths. After the maximum the water depth reduces stronger and fluctuation increases with reduced initial water depth. The reduction in depth is explicable by the fact that the discharge in the channel was not scaled as well, but stayed at 300 l/s and the weir at the outflow of the channel was adjusted accordingly to obtain the different initial water depths and was fixed during the experiments.

Table 1. Results of the equations (1) to (4) for the different initial water depths.

Initial water depth	Vertical scaling factor	Superelevation factor	Time scaling factor
h_i [m]	H [-]	n [-]	T [-]
0.50	1.0	1.0	1.000
0.45	1.111	0.9	0.949
0.40	1.25	0.8	0.894
0.35	1.429	0.7	0.837
0.30	1.667	0.6	0.775

Regarding the arrival time of the wave, at position 800 mm the wave with the lowest initial water depth arrives first, at position 1500 mm the arrival times are nearly identical and at 3300 mm the relation is conversed and the wave with the highest initial water depth arrives first.

An explanation for the growing deviation of the measured values with decreasing initial water depth could be, that the simple superelevation rules are only applicable in cases in which the effects of vertical velocity components can be neglected. This is not the case especially near the breach, where all the kinetic energy is derived from the potential difference and the water surface is strongly inclined – this could explain the overestimation of acceleration especially for the lower initial water depth. Additionally a discrepancy of roughness effects can develop – this could be an explanation for the underestimation of the wave velocity in the longer run, where the water depths for the lower initial water depth is less and roughness effects are stronger.

4.2 *Effect of a thin water film*

If a thin water film remains between two tests, i.e. the water drains off over the three free boundaries of the propagation area but it is not dried explicitly, the wave front is significantly altered. Figure 6 shows the differences between the two cases "thin water film" and "completely dried" for a discharge of 300 l/s in the channel and an initial water depth of 50 cm. Near the flap the two cases are similar, between 1300 and 1700 mm distance however, a difference starts to appear: in the "water film" case the tip of the wave starts to built up a high peak whereas the "dried" case flattens more and more. The envelope of both cases is adumbrated in the figure for orientation. Parallely the arrival time of the wave front at the sensor is increased in the "water film" case compared to the "dried" case, i.e. the velocity of the wave front slowed down by the water film.

The building up of the peak could be due to piling up of the water in the film in front of the strong growing circumference of the wave. However, this can not be the full explanation, since the peak flattens down again after a maximum at about 2500 mm distance from the flap. In the photographs in figure 7, recorded

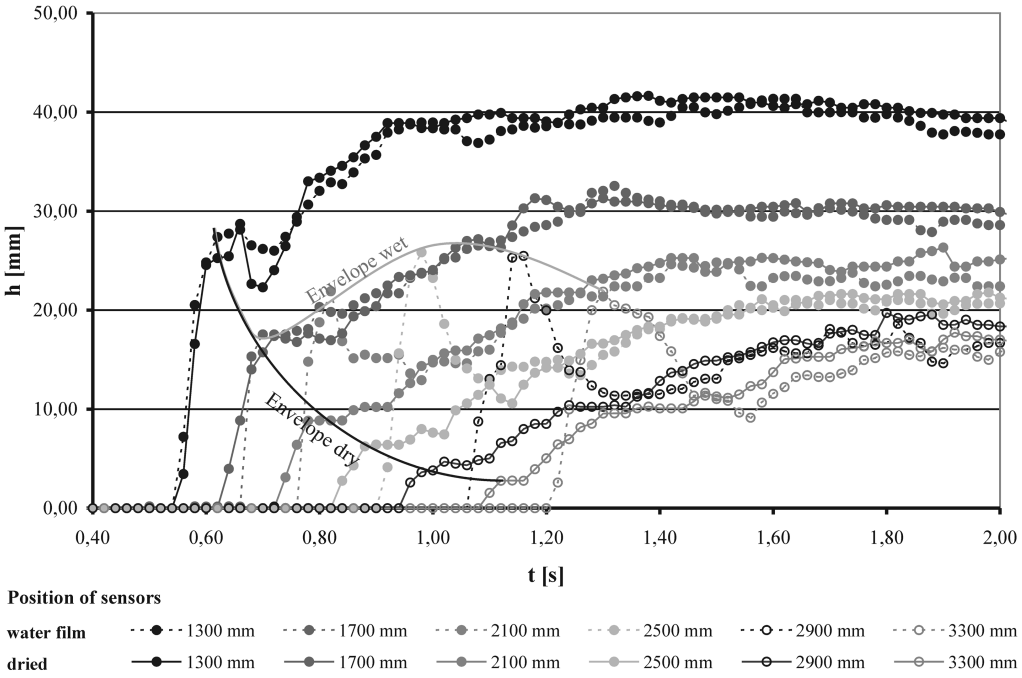


Figure 6. Comparison of the cases "thin water film" and "dried" at six different distances from the flap. Water depth on the main axis over time for intitial water depth $h_i = 50$ cm and discharge in channel $Q_{in} = 300$ l/s.

by the CCD-camera, strong air entrainment can be perceived as a white band at the wave front, which indicates strong turbulence and roughness effects. The white band is completely absent in the case of a dried propagation area.

A similar peak can be found in Stansby et al. (1998) with a ratio of 0.1 between the water depth on the propagation area and in the reservoir before dam-break. Using a camera, recording through the sides of their flume they observed a "mushroom" shaped wave front.

4.3 *Effect of discharge in the channel*

In figure 5 the water depth seems to converge to a constant final value with time. This quasi steady state however lasts only for a short time, since when the negative surge is reflected at the ends of the channel, it causes the water level to drop in progressive stages. In case of higher discharge in the river, the decrease in water level is more even, i.e. the surge reflection is less influential.

Figure 8 shows the position of the wave front with an interval of $\Delta t = 0.02$ s for the cases of no discharge in the channel and, for comparison, with 300 l/s. The sporadic interruptions of the lines at small y-values are caused by the moving flap. The propagation area was not dried, i.e. the thin water film remained between the experiments and air entrainment made the wave visible (see section 3.2).

In the case of no discharge in the top part of the figure, the wave propagation is symmetric and onion shaped. In the bottom part of the figure the trajectory of the wave tips were added. The derivation from the main axis is relatively small. Therefore in the preceding sections the main axis only was considered the water depth discussions.

The deviation of the wave tip is defined by an interaction of initial water depth and the discharge in the channel. The effect of initial water depth and discharge can be combined in the Froude number of the channel before break:

$$Fr = \frac{v}{\sqrt{g \cdot h}} \tag{6}$$

in which the numerator with the velocity v represents the momentum resulting from the discharge parallel to the channel and the denominator with water depth h and gravitational constant g represents the momentum from gravitation. The result is shown in figure 9, in which the data points coincide reasonable well with a trend line. The angle of deviation is greater with greater discharge, i.e. velocity in the channel. Furthermore the deviation is greater for lower initial water depth, i.e. lower velocities of the wave front propagation.

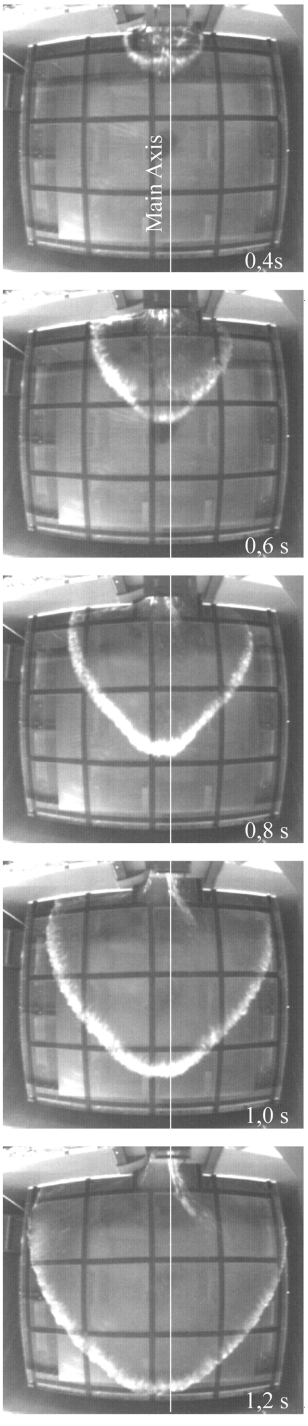


Figure 7. CCD-camera recordings at five different time steps with an interval of $\Delta t = 0.2$ s. Initial water depth $h_i = 50$ cm, discharge in channel $Q_{in} = 300$ l/s.

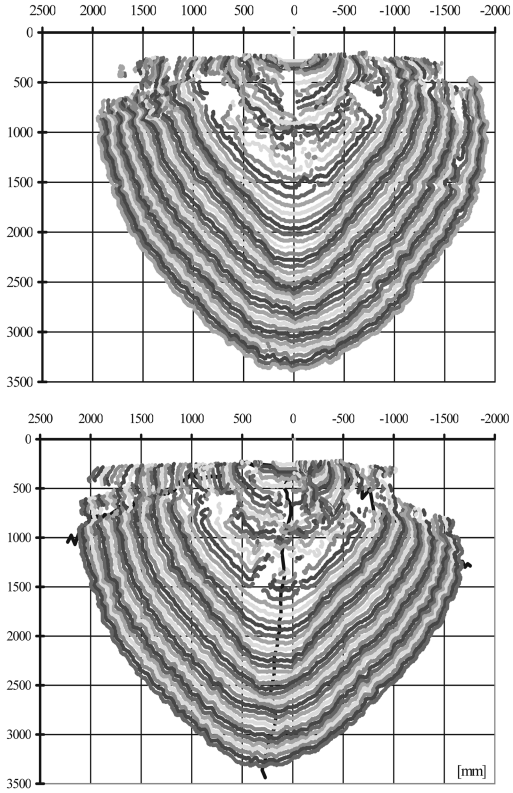


Figure 8. Position of the wave front with an interval of $\Delta t = 0.02$ s. Initial water depth $h_i = 50$ cm, discharge in channel $Q_{in} = 0$ l/s (top) and 300 l/s (bottom). In the bottom part of the figure the trajectory of the wave tips were added. The propagation area was not dried, i.e. covered with a thin water film.

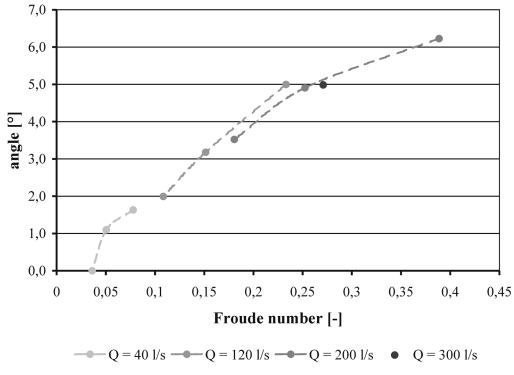


Figure 9. Deviation angle of the wave tip over Froude number before breach. For every discharge (except 300 l/s) the three initial water depths (30, 40 and 50 cm) are plotted, the data points with the smallest angle corresponds to the highest initial water depth.

5 CONCLUSIONS AND FUTURE WORK

There are many open questions concerning the flood wave propagation following a dike-break or the failure of a (mobile) flood protection wall. This paper presents first results of a systematic investigation of the influence factors and thereby starts to answer some of those questions.

The analysis of the data shows, that the water depth of the propagating wave is already scalable with respect to the initial water depth by easy means, but there are still some deviations which have to be investigated further. This holds especially in the case of the arrival time, which implies the velocity of the wave front.

A thin water film, which remains when the propagation area is not dried explicitly between the experiments, alters the shape of the wave front significantly by building up a prominent peak and slowing down the wave front velocity.

The sideways deviation of the wave tip position from the main axis is determined by an interaction of initial water depth and the discharge in the channel and can be estimated reasonably well by using the Froude number of the channel before failure.

In the future the physical model tests will be systematically completed, to gain more insight into the flow processes of the flood wave, to be able to quantify the influence factors and to assure accurate scaling of the results to other dimensions.

REFERENCES

Aureli, F. & Mignosa, P. 2002. Rapidly varying flows due to levee-breaking. In D. Bousmar & Y. Zech (eds.), River Flow 2002, *Proc. International Conference on Fluvial Hydraulics, Louvain-la-Neuve, Belgium, 4–6 September, 2002*. Rotterdam: Balkema: 459–466.

Fraccarollo, L. & Toro, E.F. 1995. Experimental and numerical assessment of the shallow water model for two-dimensional dam-break type problems. *Journal of Hydraulic Research* 33(6): 843–863.

Hager, W.H. & Lauber, G. 1996. Hydraulische Experimente zum Talsperrenbruchproblem. *Schweizer Ingenieur und Architekt* 114(24): 515–524.

Jovanovic, M. & Djordjevic, D. 1995. Experimental verification of the MacCormack numerical scheme. *Advances in Engineering Software* 23: 61–67.

Kobus, H. (ed.) 1978. *Wasserbauliches Versuchswesen*. Arbeitsausschuss Wasserbauliches Versuchs- und Messwesen, Deutscher Verband für Wasserwirtschaft, Mitteilungsheft 4. Berlin: DVWW.

Kulisch 2003. *Ausbreitung von Dammbruchwellen im physikalischen Modell*. Mitteilungen des Institut für Wasserwesen, Universität der Bundeswehr München, Heft 79. München: Oldenbourg.

Memos, C.D., Georgakakos, A. & Vomvoris, S. 1983. Some experimental results of the two-dimensional dam-break problem. *Proc. 20th IAHR Congress for Hydraulic Research, Moscow, September 1983*: 555–563.

Naaim, M. & Brugnot, G. 1994. Free surface flow modelling on a complex topography. In R. Molinaro & L. Natale (eds.), *Modelling of Flood Propagation over Initially Dry Areas, Proc. of the Specialty Conference at Enel-Dsr-Cris, Milan, Italy, 29 June–1 July, 1994*: 298–308. New York: American Society of Civil Engineers.

Stansby, P.K., Chegini, A. & Barnes, T.C.D. 1998. The initial stages of dam-break flow. *Journal of Fluid Mechanics* 374: 407–424.

Tingsanchali, T. & Rattanapitikon, W. 1993. 2-D mathematical modelling for dam break wave propagation in supercritical and subcritical flows. *Proc. 25th IAHR Congress for Hydraulic Research, Tokyo, Japan, 29 August–3 September* 1993: 25–32.

River Flow 2004 – Greco, Carravetta & Della Morte (eds.)
© 2004 Taylor & Francis Group, London, ISBN 90 5809 658 0

Dispersive effects on linear instability of the Saint Venant flow model

C. Di Cristo
Dipartimento di Ingegneria Idraulica ed Ambientale "Girolamo Ippolito", Università degli Studi di Napoli "Federico II", Napoli, Italy

A. Vacca
Dipartimento di Ingegneria Civile, Seconda Università degli Studi di Napoli, Aversa (Ce), Italy

ABSTRACT: A spatial linear stability analysis of the one-dimensional St. Venant flow model, accounting for the dispersive effects, is carried out in the present paper. The theoretical investigation allows to discuss about the influence of channel length on roll-waves occurrence. In order to provide a rigorous justification for selecting the spatial stability theory, a preliminary proof of the convective nature of the flow instability is furthermore performed. The results of the spatial analysis show a non-negligible influence of the disturbance frequency on the perturbation spatial growth rate. As a consequence the semi-empirical criteria commonly employed for predicting roll-waves occurrence, which do not take into account the frequency effects, may lead to overestimate the minimum channel length above which the phenomenon is not perceivable.

1 INTRODUCTION

High velocity flows in steep channels may exhibit surface instabilities, perceivable as a series of water waves. As these waves propagate downstream they increase in amplitude and eventually break forming hydraulic bores. The series of waves just described are the so called "roll waves" and occur usually in man-made channels, such as draining systems and dam spill-ways. Generally, roll-waves presence is undesirable since they may determine a water overflow from the channel sides and excessive intermittency at the outlet. In studying such a phenomenon, two basic issues arise:

- identifying the necessary conditions under which roll-waves appear;
- predicting roll-waves evolution along the channel.

Only the former question will be addressed herein.

From the theoretical point of view, the generation process of roll-waves has been thoroughly and deeply investigated. In what follows we will restrict the discussion on the analyses performed with reference to the linearized one-dimensional flow model (St Venant equations) in which the field variables, mean velocity and flow depth, are assumed to be smooth. Under such assumptions roll-waves generation process has been fruitfully interpreted in terms of instability of the linearized flow model.

Many temporal linear stability analyses have been performed (Brock, 1970; Berlamont, 1976; Ponce & Simon, 1977; Berlamont & Vanderstappen, 1981) in order to individuate the critical values of relevant dimensionless – Reynolds and Froude – numbers corresponding to the appearance of roll-waves. For instance, assuming the channel to be sufficiently wide and expressing the bottom shear stress as a quadratic function of the mean velocity, a critical value of the Froude number, $F_{rc} = 2$, below which roll waves cannot occur, has been found (Brock, 1970). Furthermore all conditions of flow characterized by $F_r > F_{rc}$ are unstable, independently of the perturbation wavelength values. Several experiments (see for instance Brock, 1969) confirmed the absence of roll-waves for $F_r < F_{rc}$, while their presence was not always detected for $F_r > F_{rc}$.

In contrast with the temporal analysis and to take into account the developing character of roll-waves, spatial linear stability analyses have been performed, starting from the hyperbolic character of the St Venant equations (Vedernikov, 1945, 1946; Liggett, 1975; Julien & Hartley, 1986). The point-wise perturbation is assumed to propagate downstream with the celerity of the faster shallow-water wave, according to the hyperbolic wave theory. In terms of stability region

the results of the temporal analysis are essentially confirmed, despite the strong different space-time evolution of the perturbation.

Whether the temporal or the spatial technique is more appropriate to investigate the instability of St Venant flow model depends on the nature, *Convective* or *Absolute*, of the instability (Huerre & Monkewitz, 1990). An instability is defined as Convective if a localized initial small perturbation, growing in time, is swept away from the source only in one direction, whereas the instability is Absolute if it spreads in all directions. Only when the instability is Convective, spatial analysis may describe fruitfully its evolution.

The definition of the instability nature allows to verify the theoretical assumptions embodied in some semi-empirical criteria defining the minimum channel length below which the roll-waves presence is not perceivable, even in linearly unstable conditions of flow. These criteria, tested and calibrated using many available experimental data, start from the space-time evolution of perturbations resulting from the spatial linear hyperbolic analysis.

Montuori (1961, 1963), and later Liggett (1975), proposed to relate the critical Froude number value upon the channel length L; for sufficiently small values of L no roll-waves appear. Considering the process as Reynolds independent, the critical Froude number is expressed as a monotone decreasing function of the channel length whose value, for sufficiently large L, is F_{rc}. Similar conclusions have been drawn by Julien & Hartley (1986) who studied roll waves formation process in highly viscous mud-flows observable in steep mountain channels. It is worth of note that the above semi-empirical criteria share some similarities with the e^n-method, originally proposed by Van Ingen (1956) and by Smith & Gamberoni (1956), commonly used to give an engineering prediction of the boundary layers transition location.

In the present paper the convective nature of the instability is preliminarily proved by examining the linear impulse response of a given uniform base flow. Following the Briggs criterion (Briggs, 1964), an analysis concerning the behaviour of the spatial branches associated with the dispersion equation is carried out in the complex k and ω planes, where ω and k are the complex pulsation and wave-number of the disturbance, respectively.

Furthermore a spatial linear stability analysis in terms of flow response to a point-wise time periodic perturbation is performed. The analysis naturally accounts for dispersive effects. The strict dependence on the source frequency of the perturbation spatial growth rate, whose expression constitutes the theoretical starting point of some criteria commonly employed in hydraulic engineering applications, is finally discussed.

2 GOVERNING EQUATIONS

The system under investigation is an incompressible fluid flowing in a broad rectangular channel without inflow or outflow with a non-erodible plane sloping bed. The one-dimensional equations governing the motion are the well-known St. Venant equations:

$$\frac{\partial u}{\partial t}+u\frac{\partial u}{\partial x}+g\frac{\partial h}{\partial x}+\frac{\tau_b}{\rho h}=gS_0 \tag{1}$$

$$\frac{\partial h}{\partial t}+u\frac{\partial h}{\partial x}+h\frac{\partial u}{\partial x}=0 \tag{2}$$

in which $x=$ streamwise coordinate, $t=$ time variable, $g=$ gravity, $\rho=$ water density, $u=$ depth-averaged velocity, $h=$ depth of the water surface, $S_0=$ bed slope, $\tau_b=$ bed shear stress.

Starting from a steady uniform flow $u=u_0$, $h=h_0$, the base state is perturbed by an infinitesimal fluctuation, so that $u=u_0+u'$, $h=h_0+h'$, $\tau_b=\tau_{b0}+\tau_b'$. The substitution of the perturbed variables in equations (1)–(2) leads, after the linearization, to the following problem:

$$\frac{\partial u'}{\partial \tilde{t}}+u_0\frac{\partial u'}{\partial \tilde{x}}+g\frac{\partial h'}{\partial \tilde{x}}+gS_0\left(\frac{\tau_b'}{\tau_{b0}}-\frac{h'}{h_0}\right)=0 \tag{3}$$

$$\frac{\partial h'}{\partial t}+u_0\frac{\partial h'}{\partial x}+h_0\frac{\partial u'}{\partial x}=0 \tag{4}$$

Expressing the bed shear stress in terms of bulk velocity square as $\tau_b=\rho C_f u^2$ and assuming a constant value of the friction coefficient ($C_f=C_{f0}$) equation (3) becomes:

$$\frac{\partial u'}{\partial t}+u_0\frac{\partial u'}{\partial x}+g\frac{\partial h'}{\partial x}+gS_0\left(2\frac{u'}{u_0}-\frac{h'}{h_0}\right)=0 \tag{5}$$

Considering the following non-dimensional variables:

$$\tilde{x}=\frac{xS_0}{h_0};\tilde{t}=\frac{tS_0u_0}{h_0};\tilde{u}'=\frac{u'}{u_0};\tilde{h}'=\frac{h'}{h_0} \tag{6}$$

equations (5)–(4) can be rewritten in dimensionless form as

$$\frac{\partial \tilde{u}'}{\partial \tilde{t}}+\frac{\partial \tilde{u}'}{\partial \tilde{x}}+\frac{1}{F_r^2}\frac{\partial \tilde{h}'}{\partial \tilde{x}}+\frac{1}{F_r^2}\left(2\tilde{u}'-\tilde{h}'\right)=0 \tag{7}$$

$$\frac{\partial \tilde{h}'}{\partial \tilde{t}}+\frac{\partial \tilde{h}'}{\partial \tilde{x}}+\frac{\partial \tilde{u}'}{\partial \tilde{x}}=0 \tag{8}$$

where $F_r = u_0/(gh_0)^{1/2}$ denotes the unperturbed Froude number.

The first order system (7)–(8) can be easily reformulated only in terms of depth and it reads:

$$\frac{\partial^2 \tilde{h}'}{\partial \tilde{t}^2} + 2\frac{\partial^2 \tilde{h}'}{\partial \tilde{x}\partial \tilde{t}} + \left(1 - \frac{1}{F_r^2}\right)\frac{\partial^2 \tilde{h}'}{\partial \tilde{x}^2} + \frac{1}{F_r^2}\left(3\frac{\partial \tilde{h}'}{\partial \tilde{x}} + 2\frac{\partial \tilde{h}'}{\partial \tilde{t}}\right) = 0 \tag{9}$$

As the classical linear stability theory prescribes, the perturbation $\tilde{h}'$ is decomposed into elementary waves like $exp\, i(k\tilde{x} - \omega\tilde{t})$, with the complex wave number $k = k_r + ik_i$ and the complex frequency $\omega = \omega_r + i\omega_i$. The substitution of such perturbation into equation (9) leads to the quadratic dispersion equation:

$$D(k, \omega, F_r) = F_r^2 i(\omega - k)^2 - k^2 i - 2\omega + 3k = 0 \tag{10}$$

In performing a *spatial* stability analysis the frequency ω has to be considered real and the instability is related to the occurrence of complex wave numbers k, roots of equation (10), characterized by positive imaginary part. On the other hand, in a *temporal* stability analysis, the wave-number k is assumed to be real and the unstable conditions are related to the existence of complex frequencies ω, roots of equation (10), characterized by negative imaginary part. Performed linear temporal stability analyses (Brock, 1970; Ponce & Simons, 1977) have shown that the flow model (9) is unstable when the Froude number exceeds the limit value 2, independently on the of the perturbation wave-length value.

In order to ascertain which of the two techniques is the most appropriate to describe an unstable process, a study about instability nature can be performed. As mentioned before, instabilities have been distinguished between *Convective* and *Absolute* (Huerre & Monkewitz, 1990). In the Convective instability an initial disturbance, localized in space, is swept away from the source leaving the flow domain unperturbed as time tends to infinity. By contrast, the instability is classified as *Absolute*, if a preferential direction of propagation does not exist. In this case the disturbance spreads both in downstream and upstream directions contaminating the whole domain as time tends to infinity.

A spatial analysis leads to a well posed problem only when the instability is of convective type. Contributions to the theoretical foundations underlying these notions have been brought out in studies concerning plasma (Bers, 1975) and hydrodynamic (see the review of Huerre & Monkewitz, 1990) stability. In a morphodynamic context the nature of bar formation process has been investigated recently by Federici & Seminara (2003).

3 STUDY OF INSTABILITY NATURE

The nature of instability of the linearized St. Venant flow model can be ascertained by studying the impulsive response of equation (9). The usual approach leads to investigate the asymptotic time behavior of the solution (Green's function) of the following initial value problem:

$$\frac{\partial^2 G}{\partial \tilde{t}^2} + 2\frac{\partial^2 G}{\partial \tilde{x}\partial \tilde{t}} + \left(1 - \frac{1}{F_r^2}\right)\frac{\partial^2 G}{\partial \tilde{x}^2} + \frac{1}{F_r^2}\left(3\frac{\partial G}{\partial \tilde{x}} + 2\frac{\partial G}{\partial \tilde{t}}\right) = \delta(\tilde{x})\delta(\tilde{t}) \tag{11}$$

where $\delta =$ the Dirac delta function. The spatial domain is assumed to be unbounded and homogeneous initial conditions are prescribed. Following Huerre & Monkewitz (1990), the base flow is classified as linearly unstable if there exists a ray $\tilde{x}/\tilde{t} =$ cost along which

$$\lim_{\tilde{t}\to\infty} G(\tilde{x}, \tilde{t}) = \infty \tag{12}$$

A linear unstable condition of flow is convective if, along

ray $\tilde{x}/\tilde{t} = 0$, it occurs

$$\lim_{\tilde{t}\to\infty} G(\tilde{x}, \tilde{t}) = 0 \tag{13}$$

whereas it is absolutely unstable when, along the ray $\tilde{x}/\tilde{t} = 0$,

$$\lim_{\tilde{t}\to\infty} G(\tilde{x}, \tilde{t}) = \infty \tag{14}$$

The asymptotic behavior of the Green's function (12)–(14) can be analyzed representing $G(\tilde{x}, \tilde{t})$ as double Fourier integral in the complex ω and k planes

$$G(\tilde{x}, \tilde{t}) = \frac{1}{(2\pi)^2}\int\int_{BC} e^{i(k\tilde{x} - \omega\tilde{t})}\frac{dkd\omega}{D(k, \omega, F_r)} \tag{15}$$

in which $D(k, \omega, F_r) =$ the dispersion operator given by equation (10). The contours B and C are placed in the region of absolute convergence of $G(\tilde{x}, \tilde{t})$. The application of the steepest descend method to equation (15) allows to analyze the asymptotic conditions (12)–(14) only through the study of both temporal $\omega(k)$ and spatial $k(\omega)$ branches of the dispersion relation $D(k, \omega, F_r)$ in the complex ω and k planes (Briggs, 1964; Huerre & Monkewitz, 1990).

It can be shown (Huerre & Monkewitz, 1990) that condition (12) is not fulfilled, i.e. linearly stable conditions of flow occur, if, for all $k = k_r$ and for all temporal

branches $\omega(k_r)$, $\omega_i(k_r) < 0$. Therefore, the presence of linearly unstable conditions of flow will be detected if the maximum value ω_i^{max} of $\omega_i(k_r)$ is positive definite.

The simple structure of the dispersion equation (10) allows to deduce in an analytic form the temporal branches $\omega(k)$

$$\omega = k - \frac{i}{F_r^2} \pm \sqrt{\left(k - \frac{i}{F_r^2}\right)^2 - k^2\left(1 - \frac{1}{F_r^2}\right) + 3i\frac{k}{F_r^2}} \tag{16}$$

Setting $k = k_r$ in the right hand side of expression (16), it follows that, according to previous results (Brock, 1970), linearly unstable conditions of flow are permitted only when the Froude number exceeds the limit value $F_{rc} = 2$.

In order to ascertain the nature of unstable conditions of flow, occurring when $F_r > F_{rc}$, a careful study of the spatial branches is required. Briggs (1964) proved that the absolute character of the instability can be defined looking for the complex frequencies ω^0 for which two (or more) spatial branches $k(\omega)$ merge (pinch-type singularities). The positive definiteness of ω_i^0 is the necessary condition for the absolute character of the instability. The sufficient condition comes from the analysis, for large enough ω values, i.e. $\omega_i > \omega_i^{max}$, of the spatial branches $k(\omega)$ that coalesce for $\omega = \omega^0$. The instability will be of absolute type if for $\omega_i > \omega_i^{max}$ at least two of such branches are placed on opposite sides of the real k-axis.

The study of the branches location, in condition of spatial evanescence $\omega_i > \omega_i^{max}$, ensures that the instability, corresponding to the pinch, will appear as two waves, propagating in opposite directions, without any discontinuity at the origin of the spatial coordinates. The time growth of these waves, that behave as only one wave (normal mode), will lead to the contamination of the whole domain as time tends to infinity.

Since the spatial branches merging points correspond to the saddle points of the temporal branches $\omega(k)$ (Huerre & Monkewitz, 1990), the necessary condition of the Briggs criterion can be analyzed alternatively looking for the complex wave number k^0 such that $\partial\omega/\partial k = 0$, i.e. $\omega^0 = \omega(k^0)$.

The last technique is the most useful when many spatial branches are present. The above procedures may be applied only when pinch-type singularities occur at finite values of k^0. If such an instance does not occur the singularities will be defined as essential and the Brigg's criterion cannot be straightforwardly applied. In this case, a direct numerical evaluation of $G(\tilde{x}, \tilde{t})$ is needed (Park & Huerre, 1988).

In the St. Venant flow model (9) only two spatial branches exist

$$k = \frac{2F_r^2\omega + 3i \pm \sqrt{4F_r^2\omega(\omega + i) - 9 + 8i\omega}}{2\left(F_r^2 - 1\right)} \tag{17}$$

whose merging points are given by

$$\omega^0 = \frac{-i\left(F_r^2 - 2\right) \pm i\sqrt{\left(F_r^2 - 4\right)\left(F_r^2 - 1\right)}}{2F_r^2} \tag{18}$$

The inspection of (18) and of (17) with $\omega = \omega^0$ allows to conclude that the instability of the St. Venant flow model has a convective nature, since only finite pinch-type singularities characterized by negative imaginary part exist, for $F_r > 2$.

4 RESPONSE TO A POINT-WISE TIME-PERIODIC DISTURBANCE

The absence of absolute instabilities suggests analysing roll-waves generation process by linear spatial analysis. In this context, considering the dispersive effects, the time-asymptotic response of the flow model to a point-wise external source oscillating with a prescribed frequency is studied.

The dimensionless pulsation of the oscillation is denoted as $\omega_e = 2\pi f_e / S_0$, being $f_e = h_0/(u_0 T_e)$ the source frequency and T_e its dimensional period. The time asymptotic response of the flow model can be studied by investigating the time asymptotic behavior of the solution (Green's function) of the following problem:

$$\frac{\partial^2 R}{\partial \tilde{t}^2} + 2\frac{\partial^2 R}{\partial \tilde{x}\partial \tilde{t}} + \left(1 - \frac{1}{F_r^2}\right)\frac{\partial^2 R}{\partial \tilde{x}^2} + \frac{1}{F_r^2}\left(3\frac{\partial R}{\partial \tilde{x}} + 2\frac{\partial R}{\partial \tilde{t}}\right) = \\ = \delta(\tilde{x})e^{-i\omega_e \tilde{t}} \tag{19}$$

in which the flow domain is assumed to be unbounded and $\delta =$ the Dirac delta function. As in the pulse case, the solution of problem (19) can be described as double Fourier integral in the complex ω and k planes.

$$R(\tilde{x}, \tilde{t}) = \frac{1}{(2\pi)^2}\int\int_{BC} e^{i(k\tilde{x} - \omega\tilde{t})}\frac{dk d\omega}{(\omega - \omega_e)D(k, \omega, F_r)} \tag{20}$$

being $D(k, \omega, F_r) =$ the dispersion operator given by (10).

In unstable condition of flow ($F_r > F_{rc}$), the time asymptotic behavior of relation (20) can be written

as a superposition of two waves traveling both in the downstream direction (Bers, 1975):

$$R(\tilde{x},\tilde{t}) = i\sum_{l=1,2}\frac{u(\tilde{x})}{\left(\frac{\partial D}{\partial k}\right)_{k=k_l}} \quad e^{-i[\omega_e\tilde{t}-k_l(\omega_e)\tilde{x}]} \tag{21}$$

where $u(\tilde{x}) =$ the unit-step function, $k_l(\omega_e)$ with $l = 1, 2$ are the two spatial branches, obtained setting $\omega = \omega_e$ in expression (17)

$$k_l(\omega_e) = \frac{2F_r^2\omega + 3i \pm \sqrt{4F_r^2\omega_e(\omega_e + i) - 9 + 8i\omega_e}}{2\left(F_r^2 - 1\right)} \tag{22}$$

and finally

$$\left(\frac{\partial D}{\partial k}\right)_{k=k_l} = 2iF_r^2(\omega_e - k_l(\omega_e)) + 2k_l(\omega_e)i - 3 \tag{23}$$

4.1 *Spatial grow rate*

Independently of the ω_e value, the inspection of (22) leads to recognize the existence of only one spatially excited wave ($k_i(\omega_e) < 0$); the other one is spatial evanescent. A graphical evidence of such findings is given in Figure 1 in which the imaginary part of the two spatial branches $k(\omega_e)$ for $F_r = 2.5$ is showed.

Let focus the attention on the primary excited wave. Equation (22) indicates that, for a constant Froude number value, the imaginary part of the wave-number, i.e. the spatial grow rate, is a bounded monotone function of ω_e or, equivalently, of the source frequency f_e, for a fixed bed slope. Independently of the Froude number, very small values of the frequency lead to a vanishing spatial growth rate. On the other hand, the limit process for very high frequencies ($f_e \to \infty$), furnishes the minimum asymptotic value of the k_i, i.e. maximum spatial grow rate, that reads

$$k_i^{\min} = \frac{2 - F_r}{2F_r\left(F_r + 1\right)} \tag{24}$$

4.2 *Propagation phase speed*

The analysis of propagation phase speed $c = \omega_e / k_r(\omega_e)$ suggests that the excited waves is the *primary* one (faster) while the evanescent one is the *secondary* one (slower). In Figure 2 the propagation phase speed of both waves versus ω_e is depicted for $F_r = 2.5$. The diagram reveals that the c value of both waves is not constant and strongly depends on the value of the source pulsation. Similar results have been derived by Supino (1960) in studying the evolution of small waves in hydraulic channel, starting from the linearized St. Venant flow model.

For fixed value of the bed channel, the propagation phase speed is a monotone function of the dimensionless source frequency f_e and decreases as the frequency increase, tending to the asymptotic value $1 + 1/F_r$, which represents its minimum value. The maximum celerity value occurs at $f_e = 0$ and it is 1.5, independently of the Froude number.

4.3 *Distance for roll waves formation*

Spatial growth rates, formally equivalent to the asymptotic value (24), have been deduced from previous

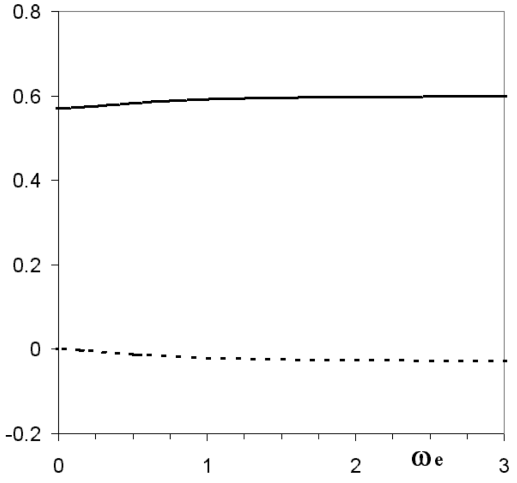


Figure 1. Imaginary part of the wave number: solid line unstable wave, k_1; dashed line evanescent wave, k_2. – $F_r = 2.5$.

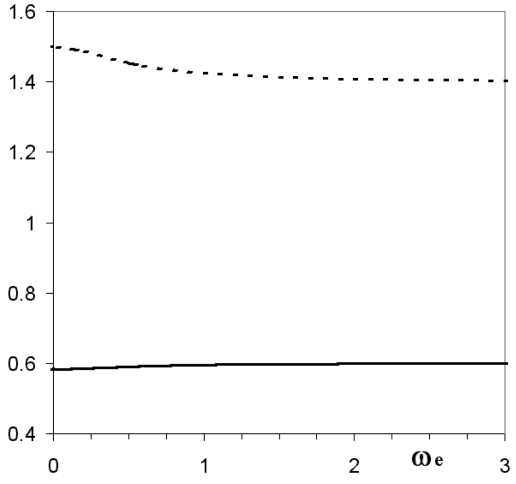


Figure 2. Phase speed: solid line unstable wave, c_1; dashed line evanescent wave, c_2. – $F_r = 2.5$.

linear analyses that do not consider the dispersive effects (Vedernikov, 1945, 1946; Liggett, 1975). Moreover, these growth rate expressions have constituted the theoretical justification to semi-empirical criteria for predicting the presence of the roll-waves (Montuori, 1961; Julien & Hartley, 1986).

In particular, Montuori (1961, 1963) related the formation of the roll-waves not only to the Froude number but also to the channel length L. Starting from the results of the spatial linear analysis of Vedernikov (1945, 1946), the author introduced a functional dependence of the critical Froude number value upon the non-dimensional channel length, LS_0/h_0, that, as far as wide rectangular channels are concerned, may be rewritten as follows:

$$\frac{S_0 L}{h_0} = \frac{\ln(\varepsilon)}{k_i^{\min}(F_r)} \tag{25}$$

The amplification factor $\varepsilon = 10^{-4}$ appearing in (25) has been calibrated starting from numerous field data collected in Europe and in Russia. The curve defined by equation (25) individuates two disjoint regions, in the $LS_0/h_0 - F_r$ plane. Roll-waves formation is inhibited in flow conditions characterized by $LS_0/h_0 - F_r$ pairs laying below the curve.

Figures (3) and (4) depict the deviation of the calculated spatial growth rate from its asymptotic value ($\alpha = k_i/k_i^{min}$) versus the frequency f_e, for two different channel bed slope values ($S_0 = 0.01$ and $S_0 = 0.30$). In each figure three different values of the Froude number ($F_r = 2.5$, $F_r = 5$ and $F_r = 7.5$) have been considered.

In the $S_0 = 0.01$ case (Fig. 3) only for very low frequency values ($T_e > 500\, h_0/u_0$) substantial deviations from the asymptotic value can be detected. In contrast, for higher bed channel slope value (Fig. 4) considerable differences appear in a broader frequency range. Independently of the bed channel slope, the deviations reduce when the Froude number is increased, even though the Froude number effect appears to be less significant.

From the above results it follows that the spatial evolution of the perturbation, according to the dispersion effects in a linear approximation context, is governed by three dimensionless parameters xS_0/h_0, F_r, f_e/S_0. Therefore the conventional approaches employing only two parameters xS_0/h_0, F_r (Zanuttigh & Lamberti, 2003, 2004; and Montuori, 2004) require an additional constrain on the minimum value of the physical disturbance frequency. We whish to stress that such a lower bound may be particularly severe in presence of channels with huge bed slope (Fig. 4). Furthermore, neglecting the frequency effects leads to overestimate the spatial growth of the disturbance. This final remark provides a theoretical justification for the experimentally ascertained underestimation of the minimum channel length above which equation

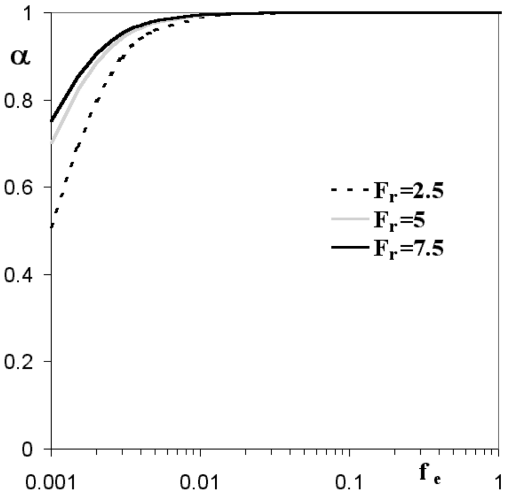


Figure 3. Spatial grow rate $\alpha = k_i/k_i^{min}$ versus the dimensionless frequency f_e, – $S_0 = 0.01$.

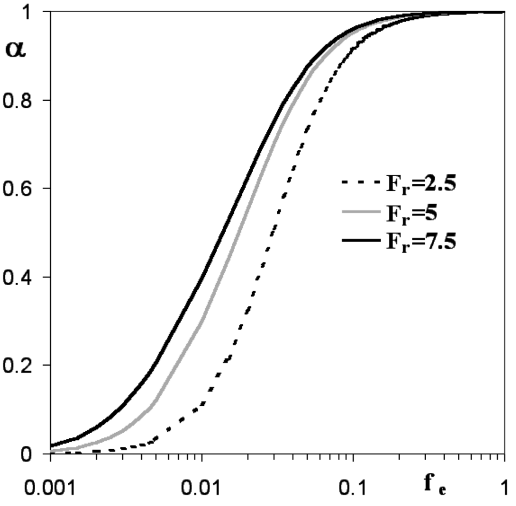


Figure 4. Spatial grow rate $\alpha = k_i/k_i^{min}$ versus the dimensionless frequency f_e, – $S_0 = 0.3$.

(25) predicts the presence of roll-waves (Montuori, 1961).

As a matter of fact Figure 4 clearly shows that for large bed slopes the amplification factor is considerably reduced compared to its asymptotic value, in large range of dimensionless frequencies f_e. Therefore equation (25) would correctly account for the above quoted experimental evidences, provided k_i^{min} is replaced by the correct spatial growth rate of the unstable wave given in (22) and the frequency of the disturbance is not excessively large. Which is the appropriate disturbance

frequency value is still, as far as the authors are aware, an open question and requires properly design experiments or direct numerical simulations.

5 CONCLUSION

In the present paper, the convective instability property of the one-dimensional linearized flow model has been preliminarily demonstrated. The Briggs criterion, concerning the analysis of the branch-point singularities of the dispersion relation, has been applied. Starting from the ascertained convective character of the instability a spatial linear stability analysis, which naturally accounts for the dispersive effects, has been carried out. Results showed that, in unstable condition of flow, a point-wise temporal oscillating perturbation generates two waves, both propagating in the downstream direction. The primary is spatially growing, the secondary is spatially evanescent. The spatial growth rate of the unstable wave strongly depends on the frequency of the disturbance, particularly as far as high bed slope channels are concerned. It follows that the description of the spatial evolution of the perturbation only through the Froude number and the non-dimensional distance, commonly assumed in hydraulic engineering criteria, may lead to overestimate the spatial amplification of the perturbation, depending on the temporal frequency of the disturbance and on the bed slope of the channel.

REFERENCES

Berlamont, J.F. 1976. Roll-waves in inclined rectangular open channels. *Proceedings of International Symposium on Unsteady flow in open channels*, BHRA Fluid Engineering, Newcastle, A2: 13–26.

Berlamont, J.F. & Vanderstappen, N. 1981. Unstable turbulent flow in open channels. *Journal of Hydraulic Division*, ASCE, 107 (HY4): 427–449.

Bers, A. 1975. Linear waves instabilities. In *Physique des Plasmas*, ed. De Witt, C. and Peyraund, J. Gordon & Breach, New York: 117–215.

Briggs, R.J. 1964. *Electon-Steam Interaction with plasmas*. MIT Press, Cambridge.

Brock, R.R. 1969. Development of roll-waves trains in open channels. *Journal of Hydraulic Division*, ASCE, 95(HY4): 1401–1427.

Brock, R.R. 1970. Periodic permanent roll waves. *Journal of Hydraulic Division*, ASCE, 96(HY12): 2565–2580.

Federici, B. & Seminara, G. 2003. On the convective nature of bar instability. *Journal of Fluid Mechanics*, 487: 125–145.

Huerre, P. & Monkewitz, P.A. 1990. Local and global instability in spatially developing flows. *Ann. Rev. Fluid Mech*., 22: 473–537.

Julien, P.Y. & Hartley, D.M. 1986. Formation of roll waves in laminar sheet flow. *Journal of Hydraulic Research*, 24 (1): 5–17.

Liggett, J.A. 1975. Stability in Unsteady flow in open channel. Vol.1, ed. Mahmood, K. and Yevjevich, V., *Water Resources Publications*, Fort Collins.

Montuori, C. 1961. La formazione spontanea dei treni d'onde su canali a pendenza molto forte. L'Energia Elettrica, 2: 127–141 (in Italian).

Montuori, C. 1963. Discussion of Stability aspect of flow in open channels. *Journal of Hydraulic Division*, ASCE, 89(HY4): 264–273.

Montuori, C. 2004. Discussion: Roll waves Simulation using shallow water equations and Weight Flux Metod. *Journal of Hydraulic Research* (in press).

Park, D. & Huerre, P. 1988. On the convective nature of the Goertler instability. *Bulletin of American Physical Society*, 33: 2552.

Ponce, V.M. & Simon, D.B. 1977. Shallow water propagation in open channel flow. *Journal of Hydraulic Division*, ASCE, 103(HY12): 1461–1476.

Smith, A. M. O. & Gamberoni, N. 1956. Transition Pressure Gradient and Stability Theory. *Douglas Aircraft Co*., Rept. ES 26388, California.

Supino, G. 1960. Sopra le onde di traslazione nei canali. *Rendiconti Lincei*, 5–6 (in Italian).

Van Ingen, J. L. 1956. A suggested Semi-empirical Method for the Calculation of the Boundary Layer Transition. *Univ. of Tecn., Dept of Aero. Eng*., Rept. UTH-74, Delft.

Vedernikov, V.V. 1945. Condition at the front of a translation waves disturbing a steady motion of a real fluid. *USSR Academy of Science*, 48: 239–242.

Vedernikov, V.V. 1946. Characteristics feature of a liquid flow in open channel, *USSR Academy of Science*, 52: 207–210.

Zanuttigh, B. & Lamberti, A. 2003. Roll waves simulation using shallow water equations and weighted average flux method. *Journal of Hydraulic Research*, 40(5): 610–622.

Zanuttigh, B. & Lamberti, A. 2004. Discussion: Roll waves Simulation using shallow water equations and Weight Flux Metod. *Journal of Hydraulic Research* (in press).

This page intentionally left blank

B.2. Bank failure

This page intentionally left blank

River Flow 2004 – Greco, Carravetta & Della Morte (eds.)
© 2004 Taylor & Francis Group, London, ISBN 90 5809 658 0

Non-intrusive imaging measurements of the morphological evolution of a channel during a dam-break flow

N. le Grelle[1], B. Spinewine[1,2], S. Soares Frazão[1,3] & Y. Zech[1]
[1] *Department of Civil and Environmental Engineering, Université catholique de Louvain, Belgium*
[2] *Fonds pour la Recherche dans l'Industrie et l'Agriculture, Belgium*
[3] *Fonds National de la Recherche Scientifique, Belgium*

ABSTRACT: Among the damaging consequences of a dam-break flow on the downstream valley, the morphological changes due to the heavy transport of sediments are not the least. The rapid flow has an important erosive power and a high transport capacity. Besides scouring of the river bed, erosion of the banks can drastically increase the river width and hence completely reshape the valley. Simplified dam-break experiments have been undertaken to investigate this problem at the laboratory scale. They were conducted in an asymmetric horizontal channel with a single bank on one side and a glass side-wall on the opposite side, allowing visual observation of the flow features. The bed and the banks are made of uniform sand. By means of those simplified experiments it was possible to reproduce qualitatively the main features of real events such as the important enlargement of the valley due to the failure of the banks and the deposition of the material eroded from the banks. The major difficulty with such experiments is to obtain reliable data of the rapid evolution of the system. This concerns the water profile, the bed profile and the shape of the cross sections. Indeed, using intrusive probes in rapid flows over movable bed and banks heavily disturbs the system and modifies considerably the results (for example: scouring around a level probe). Furthermore, it provides only a one-point measurement, hence making it unfeasible to obtain a wide set of data given the amount of work required for test preparation. As an alternative we resort to imaging techniques for the non-intrusive characterisation of the flow features over the full coverage of the digital images. The present work relies on an original imaging technique based on laser-sheet technology to track the evolution in time of the whole cross-sectional profiles, both above and below water.

1 INTRODUCTION

Erosion of the bed and banks of a river is usually a long-term and never-ending process that slowly induces geomorphic changes to a valley. In some extreme cases, rapid and important geomorphic changes may occur after a catastrophic event such as a dam or dike break. The debris-flow like rheology of the wave in the early stages of the dam-break flow evolves to intense bed- and suspended-load transport with a particularly high concentration. This flow is highly transient and invades parts of the valley that were probably never inundated in the past. The geological equilibrium of the banks is ruined and dramatic morphological changes can be expected.

In July 1996, the heavy rainfall in the Saguenay region of Quebec induced severe floods in many rivers and a dike-break on the lake Ha!Ha! (Brooks & Lawrence, 1999). The flood wave completely reshaped the alluvial valley and the river Ha!Ha! bed (Fig. 1), with successive reaches of intense erosion and deposition, and an overall increase in channel width that reached 700% in some locations.

In the last years, a number of authors have studied the problem of rapid geomorphic changes induced by a dam-break flow. The problem was first tackled from a 1D perspective with laboratory experiments in idealised conditions and with artificial sediment analogues (see e.g. Capart & Young, 1998, Fraccarollo et al., 2003). In order to get closer to natural valleys, an attempt is now made to investigate the impact of dam-break flows on lateral erosion of the valley flanks. Small-scale laboratory experiments proved to be able to reproduce quite well the behavior observed in real events, at least with non-cohesive material. Recently, experiments were carried out in a half-channel (Spinewine et al., 2002) and imaged in such a way to obtain the time evolution of the water and bed level.

The key problem with such flows is to obtain reliable data without perturbing the flow. Intrusive measuring

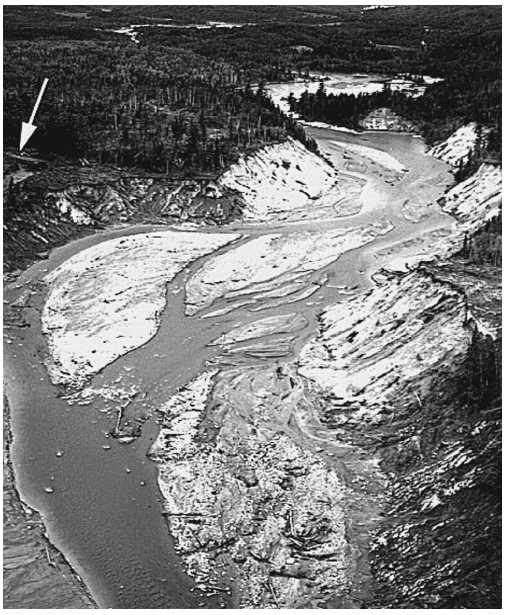


Figure 1. Geomorphic changes induced by the lake Ha!Ha! dam-break in July 1996.

techniques can modify the results significantly. For example, local scouring around a bed level probe may completely alter the bed evolution.

As an alternative to intrusive measurements, this paper presents an original non-intrusive imaging technique based on laser-sheet technology. The rapid evolution of a whole cross-section is tracked during the dam-break experiment, both below and above the water surface.

The experiment presented in this paper is used in the benchmarking program of the IMPACT European project (le Grelle & Zech, 2003). This research project addresses the assessment and reduction of risks from extreme flooding caused by natural events or by the failure of dams and flood defense structures.

2 EXPERIMENT DESCRIPTION

2.1 *Experimental set-up*

Dam-break flow experiments in an erodible channel were carried out at the Civil Engineering Laboratory of the Université catholique de Louvain. The experimental set-up is sketched in Figure 2. It consists in a half-width channel with a single erodible bank. The total length is about 3 m. The initial shape of the section is prepared by profiling compacted sand as defined in Figure 3a, where the banks make an angle of 50° with the bed. In the longitudinal direction, the bed and the bank crest are initially horizontal (Fig. 3b).

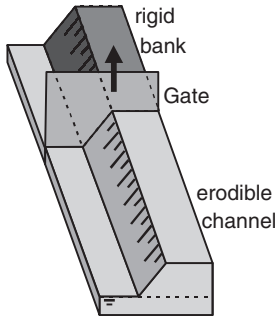


Figure 2. Experimental set-up.

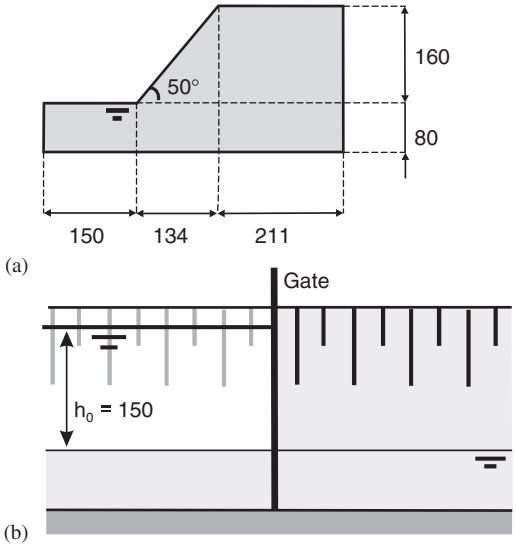


Figure 3. Initial conditions, (a) cross-section and (b) elevation (dimensions in millimeters).

The erodible bed is initially fully saturated while the banks are only partially saturated with water. The important drainage capacity of the sand used in the experiment makes it impossible to maintain the banks in a fully saturated state.

The reservoir upstream from the gate is filled up to 15 cm. In the reservoir, the banks are rigid and no erosion is thus possible. The sediments consist in uniform sand with the following characteristics: a median diameter of 1.8 mm, a unit mass of 2615 kg/m^3, a lose bed porosity of 40.5% and a permeability of 1.5 cm/s.

The experimental set-up used here is similar to the set-up used by Spinewine et al. (2002). These authors performed geostatic bank failure experiments to define a stable initial bank slope for the humid sand and to measure the angles of repose of the sand after a bank failure. Their observation is reproduced in

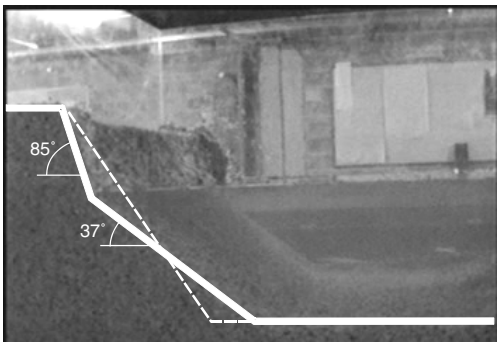


Figure 4. Angles of repose after a bank failure, from the geostatic experiments by Spinewine et al. (2002).



Figure 5. Bank erosion resulting from intermittent block failure.

Figure 4: the angle of the bank is 85° above the water level and 37° under water.

2.2 *General flow description*

The experience is launched by suddenly raising the gate. This releases a dam-break wave which rapidly propagates down the channel and triggers a series of bank failures. The water does not fill the channel up to the top of the embankments and the flow can thus not erode them only by bedload transport. In fact, the rapid erosive flow attacks the toe of the banks with the consequence that they become steeper near the bed and thus destabilized. Bank erosion then occurs in fact as a series of intermittent block failures (Fig. 5) that feed the flow with an important quantity of sediments.

The channel enlargement due to bank failures is the most important in the immediate vicinity of the dam. The water depth there is greater and the flow shows a two-dimensional expansion from the reservoir into the channel.

After about 10 s, most of the geomorphic action has occurred. Only light bedload transport can be observed and the banks are no longer affected.

3 LASER MEASUREMENT TECHNIQUE

The overall principle of the method is to use a laser light sheet to enlighten a given cross-section, to localise the trace of the imprinted laser line onto digital images of a remote camera through the transparent side-wall, and to project the line back in 3D space using distinct projective transforms for the immerged and emerged portions.

The method is detailed somewhat further in the next sections. However, a detailed description of the camera calibration method and specific projective transforms goes beyond the scope of the present paper whose objective is to focus on the results of the method. We refer the interested reader to Spinewine et al. (2003) for more details. The companion paper in this conference (Spinewine et al., 2004) applies a similar technique to dike breaching experiments for tracking the evolution of the breach geometry as a function of time.

3.1 *Set-up*

A laser light sheet is used to enlighten a cross-section through the channel side-wall. The flume, the laser-sheet and the camera are sketched in Figure 6. Illumination from above through the water surface would induce uncontrolled refraction effects at the air/water interface. Orthogonal illumination through the side-wall, on the contrary, avoids such alterations.

The trace of the laser light sheet imprinted on the cross-section (Fig. 7) is imaged with a digital camera located more upstream at the same height as the laser source. An example of a resulting image is shown in Figure 8. Two portions of the line are visible on the figure: one profile for the dry bank above water, and one for the submerged part of the bank. The transition between both curves generally escapes to observation. This explains why the resulting profiles shown in further figures present an interruption around the location of the water surface.

3.2 *Treatment of the images*

After the experiment, a series of images of type of Figure 8 are obtained. On each image, the pixel coordinates corresponding to the trace of the laser are identified using an automated algorithm.

Those pixel coordinates are then projected in 3D space using separate geometrical transformations for the above-water and under-water profiles: indeed, the differing refractive conditions need to be accounted for through separate calibration procedures (Fig. 9). Both profiles are merged together to yield the shape of the full cross-section in a given instant. Details about geometrical transformations can be found in Spinewine et al. (2003).

The results were found to be surprisingly reproducible, even though the bank erosion mechanism

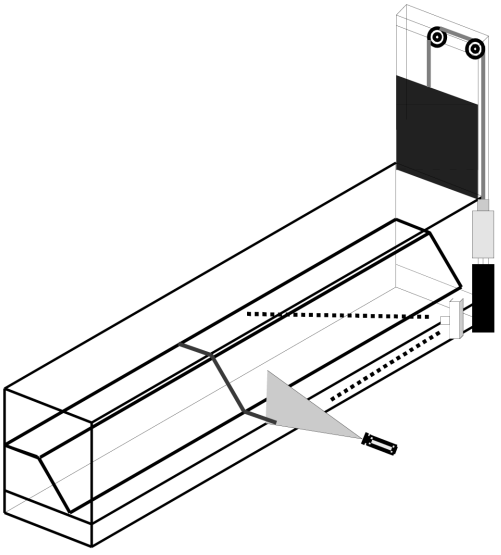


Figure 6. Set-up for the laser-sheet measuring technique.

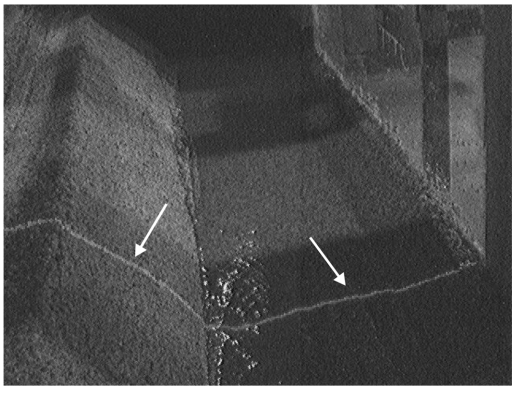


Figure 7. Trace of the laser sheet on the channel.

through intermittent block failures is quite stochastic. Three runs were carried out for each cross-section. An example of the reproducibility (three different runs, same section, same time) is shown in Figure 10.

4 EXPERIMENTAL RESULTS

The experiment was carried out several times to measure the evolution in time of 8 cross-sections located at 0.25 m, 0.50 m, 0.75 m, 0.95 m, 1.25 m, 1.5 m, 1.75 m and 2.25 m from the gate, respectively (Fig. 11). Those measurements allow to investigate in detail the processes of bank failure and subsequent deposition of the failed material over the channel bed.

The evolution of cross-section S2 located 0.50 m downstream from the gate is shown in Figure 12. The

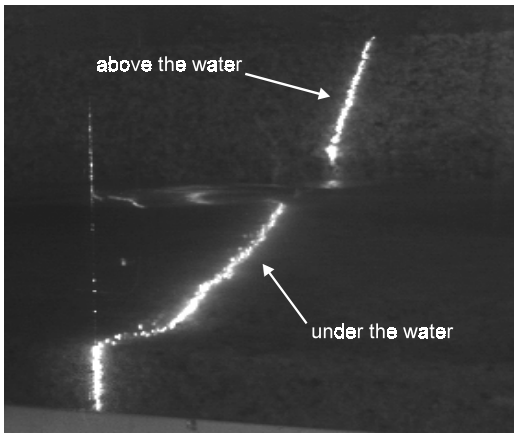


Figure 8. Sample image obtained during the experiment.

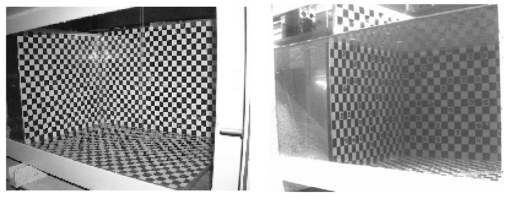


Figure 9. Calibration of above-water and under-water situations.

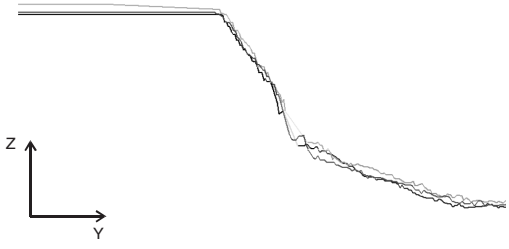


Figure 10. Reproducibility of the experiment – Cross-section at $x = 2.25$ m after 5 s.

rapid rise of the water level following the dam-break induces rapid and important bank failures. After 2 s (Fig. 12b), the water has reached the section and a block failure occurred. The shape of the cross-section indicates deposited sediments at the toe of the bank. After 5 s (Fig. 12c), the cross-section has already evolved towards the final shape, with the bank making an angle of 37° with the bed, corresponding to the angle of repose under water. The portion of the bank with a steep slope could not be measured on this image. The flow at this stage is highly transient and the rapid moving water surface induces perturbing reflection effects on these images.

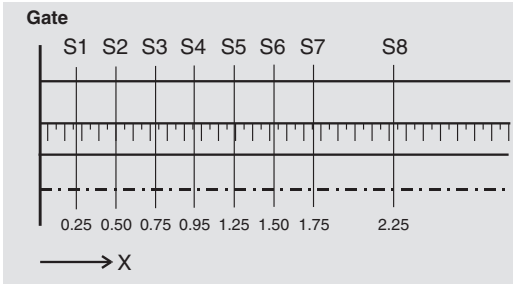


Figure 11. Cross-sections imaged with the laser-sheet technique.

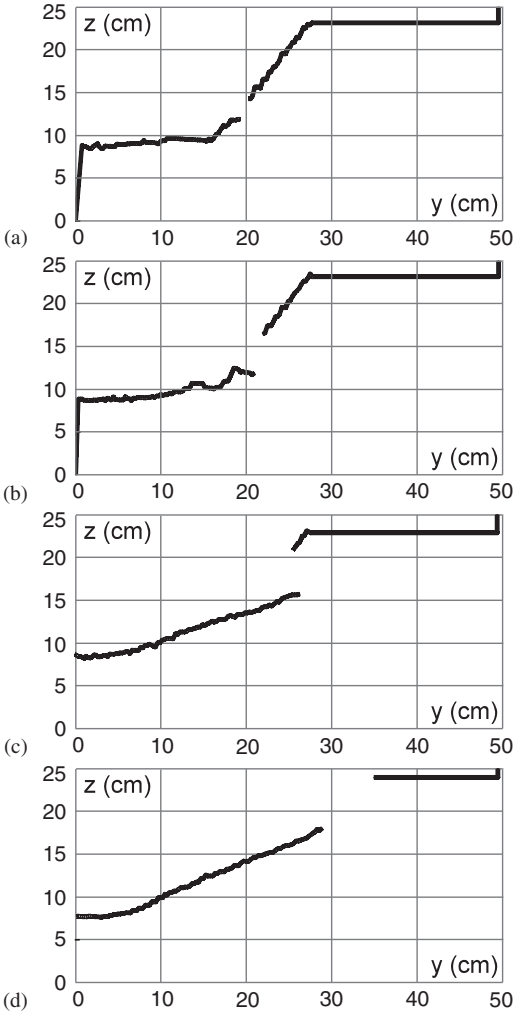


Figure 12. Evolution of section S2 ($x = 0.50$ m) – (a) $t = 1$ s, (b) $t = 2$ s, (c) $t = 5$ s, and (d) $t = 10$ s.

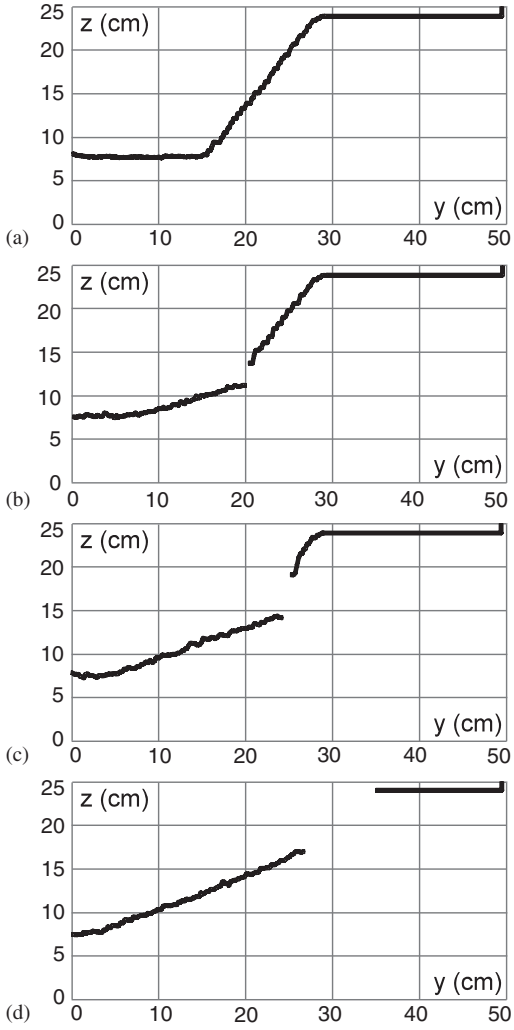


Figure 13. Evolution of section S8 ($x = 2.25$ m) – (a) $t = 1$ s, (b) $t = 5$ s, (c) $t = 10$ s, and (d) $t = 15$ s.

Figure 13 shows the evolution of section S8 located 2.25 m downstream from the dam. The erosion of the bank is more progressive. At $t = 5$ s (Fig. 13b), only the lower part of the bank failed due to the arrival of the dam-break wave. Then, after $t = 10$ s (Fig. 13c), erosion at the toe of the bank has induced a new failure but the crest of the bank is still not reached. After 15 s (Fig. 13d), the width of the valley has increased as a consequence of further failures of the bank.

5 CONCLUSION

For accurately measuring rapid transient flows involving significant geomorphic aspects, it is important to

use non-intrusive techniques. Using a laser sheet to enlighten a cross-section of the channel, it was possible to obtain an accurate description of the evolution of this cross-section, both above and under the water surface. Combining this technique with bed elevation and water surface measurements obtained by imaging the flow through the side wall of the channel (Spinewine et al., 2002) yields a valuable characterization of the experiment. This then allows a refined analysis of the ongoing processes.

The bank erosion is driven by a succession of block failures slumping into the water. This feature, observed in the experiments, also appears on the measured profiles. Despite the discrete character of the bank failure mechanism, the measured profiles show a very good reproducibility of the experiment.

ACKNOWLEDGEMENTS

The authors wish to acknowledge the financial support offered by the European commission for the IMPACT project under the fifth framework programme (1998–2002), environment and sustainable development thematic programme, for which Karen Fabbri was the EC project officer.

REFERENCES

Brooks, G.R. & Lawrence, D.E. 1999. The drainage of lake Ha!Ha! River, Saguenay area, Quebec, Canada. *Geomorphology* 28:141–168.

Fraccarollo, L., Capart, H. & Zech, Y. 2003. A Godunov method for the computation of erosional shallow water transients. *Int. J. Num. Meth. Fluids* 41(9): 951–976.

le Grelle, N. & Zech, Y. 2003. Presentation of the benchmark on dam-break induced geomorphic changes in a valley with uniform sediments. In *EC Contract EVG1-CT-2001-00037 IMPACT Investigation of Extreme Flood Processes and Uncertainty, Proceedings 3rd Project Workshop, Louvain-la-Neuve, Belgium 6–7 November 2003* (CD-ROM).

Spinewine, B., Capart, H., le Grelle, N., Soares Frazão, S. & Zech, Y. 2002. Experiments and computations of bankline retreat due to geomorphic dam-break floods. *Proc. River Flow 2002 Int. Conf. on Fluvial Hydraulics* (1): 651–661.

Spinewine, B., Capart, H., Larcher, M. & Zech, Y. 2003. Three-dimensional Voronoï imaging methods for the measurement of near-wall particulate flows. *Experiments in Fluids* 34(2): 227–241.

Spinewine, B., Delobbe, A., Elslander, L. & Zech, Y. 2004. Experimental investigation of the breach growth process in sand dikes. RiverFlow 2004.

River Flow 2004 – Greco, Carravetta & Della Morte (eds.)
© 2004 Taylor & Francis Group, London, ISBN 90 5809 658 0

Experimental investigation of the breach growth process in sand dikes

B. Spinewine
Dept. Civ. & Env. Engrg., Université catholique de Louvain, Louvain-la-Neuve & Fonds pour la Recherche dans l'Industrie et l'Agriculture, Belgium

A. Delobbe, L. Elslander & Y. Zech
Dept. Civ. & Env. Engrg., Université catholique de Louvain, Louvain-la-Neuve, Belgium

ABSTRACT: We present results from a series of laboratory experiments simulating the breaching of a coarse sand dike by overtopping. The focus is set on a range of measuring systems used to gather as much information as possible on the evolution of flow parameters and breach geometry during the tests. In particular, we present an original non intrusive technique involving a sweeping laser light sheet system combined with digital imaging algorithms, whose objective is to obtain full digital terrain models of the evolving breach topography. Results are emphasized, and some degree of interpretation is performed in light of other observations and breach modelling frameworks found in the literature.

1 INTRODUCTION

Understanding and preventing the occurrence and development of breaches in dams and/or river dikes has recently attracted widespread interest from both the research community and the civil society. The probable increase in the occurrence of extreme hydrological events resulting from climate changes, combined with the increased industrialization of river valleys, has brought the expected human and economic consequences in case of dike breaches to a critical point at many dams and along large portions of embanked low-land rivers.

However, the development of numerical models for the prediction of breach formation and development is still in the early stage (Wahl, 1998; Singh, 1996). Most available models do rely on crude assumptions for the flow (uniform, gradually varied), breach discharge (weir formulas), cross-section (rectangular, triangular, etc.) and erosion rates (lateral, vertical). Breach width and peak outflow, two utmost important parameters for risk analysis studies, are often derived from semi-empirical relations calibrated against a limited number of data sets (Morris and Hassan, 2002). How such relations are linked to dike characteristics and soil properties remains unclear, and estimation of the associated uncertainty in terms of parameter sensitivity is somehow left over to the rule of thumb.

This comes in contrast with an integrated framework of governing equations able to grasp the underlying mechanisms of the coupling between flow dynamics, breach erosion, sediment transport and lateral bank failures in a unified description. Since recently, such physically-based models try to start from scratch, and to build up evolution equations that do not rely on a-priori assumptions on discharge, breach geometry and erosion rates (see e.g. Froehlich, 2002).

Breach models in general, and the latter class of models in particular, are still facing the lack of reliable data sets for validation. Real failures are not scarce in recent history, but are often poorly documented.

At a different scale, laboratory experiments offer the advantage to control more precisely dike characteristics and to force failure mode (Benoist, 1989; Kulisch, 1994). They also allow the continuous observation of the breach growth process during the whole duration of breach formation and development. However, the measurements performed have, to the knowledge of the authors, mostly been restricted to global parameters such as e.g. discharge and crest width.

The focus of the present paper is precisely set on such measuring techniques. We present results of an experimental campaign of breaching tests in a homogeneous coarse sand dike (Delobbe and Elslander, 2002). A range of measuring systems has been used and cross-validated, with the intention to gain as much information as possible on the evolution of discharges, water levels, and breach geometry. In particular, we present in more details a novel digital imaging technique whose objective is to track the evolution of the entire dike topography as a function of time. The method relies on a sweeping laser light sheet

to visualize breach cross-sections, and on 3D projective transforms to merge individual profiles and reconstruct the whole breach topography.

The remainder of the paper is structured as follows: in the next section we present the experimental set-up, including sediment characteristics and initial breach geometry. Section 3 focuses on the various measuring systems, and present in more details the original imaging technique developed for tracking the evolution of breach topography. Results are presented in section 4, preceding some concluding remarks.

2 EXPERIMENTAL SET-UP

2.1 *The flume*

Breaching tests were undertaken in a fixed horizontal flume with a length of 36 m and a width of 3.6 m, as illustrated in Figure 1. The dike was constructed across the flume with a crest length of 2.4 m, the remainder of the flume width being taken over by fixed abutments on both sides. The dike crest is at 15 m from the upstream end of the flume, this length providing sufficient volume for acting as upstream storage reservoir.

The upstream part is separated in two parts (indicated as 1 and 2 in Fig. 1) by a large gate. This has two advantages: at first, it allows to store the volume of water in the upper part, keeping the rest of the flume dry for building the dike. Secondly, the level in this upper reach is chosen in such a way that after gradual opening of the intermediate gate the level attained at the upstream side of the dike is at the desired height. Adequate operation of the gate allows to fill the upstream part of the dike relatively fast, and hence avoid other modes of failure such as piping or seepage through the embankment.

Water in the downstream part of the flume discharges freely in a lower reservoir at the downstream end, and the length of the lower reach is long enough to ensure that the downstream boundary condition does not affect the flow conditions in the breach over the entire duration of the test.

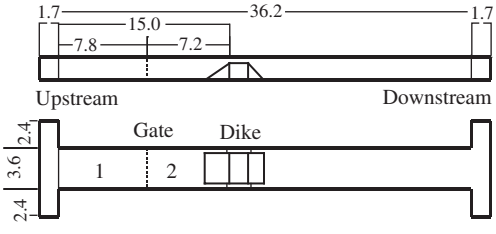


Figure 1. Plane view and elevation of the flume, indicating dike location and upstream gate position.

2.2 *Dike geometry*

The dike itself is built onto the rigid bottom of the flume. It has a length of 2.4 m, a crest width of 35 cm, and upstream and downstream slopes of 1:2 and 1:3 respectively. The height of the dike is 37 cm. In a second series of tests, the whole geometry was raised by 10 cm to provide a uniform layer of the same loose material below and downstream of the dike, in order to investigate the potential effect of the creation of a scour hole on the outflow and breach development.

Failure by overtopping was enforced by digging an initial pilot channel in the middle of the dike. This initial breach has a trapezoidal cross-section, with a crest width of 19 cm, bottom width of 5 cm, height of 7 cm and slope angles of 45°. The overall dike geometry is represented in Figure 2.

2.3 *Dike material*

The type of sediments used as dike material and bottom layer is crushed coarse sand with grain sizes uniformly distributed in the range 1 to 2 mm. A range of standard tests (Vane test, Casagrande, Proctor) were performed to measure soil properties such as density, void ratio, friction angle, residual cohesion, permeability. Results are summarized in Table 1.

Dike stability and seepage flow were simulated with a Finite Element commercial geotechnical package (Geo-Slope). Results, illustrated in Figure 3, were

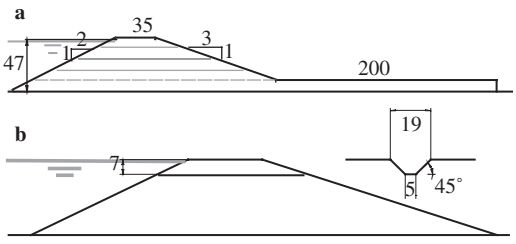


Figure 2. (**a**) Cross-section of the dike for the first and second series of tests, with the presence or not of a loose layer of 10 cm below the dike; (**b**) geometry of the initial pilot channel at the centreline. Dimensions in cm.

Table 1. Summary of soil parameters.

Grain size	Uniform 1–2	mm
Shape	Angular, crushed	[–]
Void ratio when compacted	42	[%]
Permeability	1.5×10^{-2}	[m/s]
Saturated volumetric weight	19.74	[kN/m^3]
Friction angle	34	[°]
Cohesion	0	[kPa]

faced with experimental data of a preliminary seepage test. Measured (1.43 l/s) and simulated (2.39 l/s) seeping discharges were close to each other, giving confidence in the soil properties obtained from the various geotechnical tests.

To ensure dike homogeneity and reproducibility of the test, the dike was built in successive layers of 10 cm. Each layer was compacted with a given number of strokes with a mass of 10 kg falling onto a steel plate of 35 × 25 cm. In-situ soil samples were taken to verify that the same desired degree of compaction was reached. The bottom layer used in the second series of tests was compacted in a similar way.

2.4 *Mode of operation*

Tests were initiated by gradually opening the upstream gate and filling the whole upstream part of the dike up to the desired height, i.e. 2 cm below the dike crest level or 5 cm above the bottom of the initial pilot channel. This smooth filling phase lasts 1.5 minute, in order to avoid water waves reflecting on the upstream slope of the dike and threatening its stability.

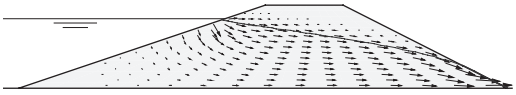


Figure 3. Modelling of the seepage curve and outflow through the dike, using a finite-element geotechnical software.

The breach then develops in time, and its geometry evolves to an equilibrium as the level in the reservoir decreases. Indeed, no inflow is added to the reservoir during the test.

11 tests were performed in total, 5 identical tests with the dike onto the rigid bottom (tests numbered C1 to C5) and 6 identical tests with a loose layer of sand below and downstream of the dike (tests D1 to D6).

Figure 4 illustrates four characteristic stages of breach development, ranging from initiation to equilibrium.

3 MEASURING SYSTEMS

A range of measuring systems were used during the first and second series of tests, in order to gain as much information as possible on the evolution of breach geometry, water levels, discharges and flow velocities. Those include both intrusive and non-intrusive, and point-wise or full coverage measurements. Not all the devices were used simultaneously. However cross-validation between successive tests confirmed an acceptable degree of reproducibility.

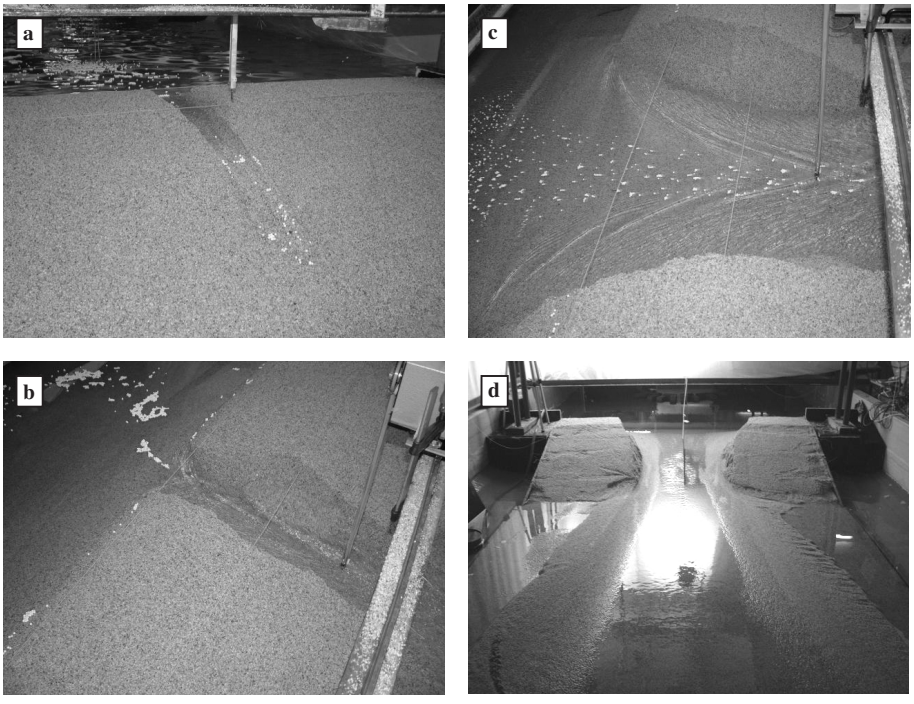


Figure 4. Four stages of breach development: (**a**) initiation; (**b**) erosion along the downstream slope; (**c**) lateral migration; (**d**) equilibrium stage.

The following system of coordinates is used throughout the remainder of the paper: x-, y- and z-axis are respectively taken along the longitudinal, transverse and vertical directions, and the origin is placed in the middle of the flume at the upstream side of the dike crest, and at the bottom level of the flume.

3.1 *Standard measurements*

Rather standard measurements are listed first:

- a series of two-wires resistive probes were placed along the flume axis in the upstream reservoir to measure the evolution of water levels. Discharge through the breach was estimated from those water level measurements;
- surface velocities in the breach were obtained through tracking small floating tracer particles with a fast digital camera placed at the vertical of the dike breach, 2.5 m above the flume (see Fig. 5). Tracers were expanded polystyrene particles with a diameter of approximately 3 mm, and delivered from a vibrated silo in the reservoir. Custom particle identification and tracking algorithms (Capart et al., 2002; Spinewine et al., 2003) delivered the horizontal component of surface velocities;
- the breach width at various locations was manually deduced from the same images of the camera located above the dike crest;
- point measurements of water and bed elevations in the breach were obtained with a level profiler probe, used alternatively for the bed and water levels. The probe was located in the axis of symmetry along the downstream slope at $x = 59$ cm;
- the evolution of bed and water profiles along the thalweg were obtained by imaging a thin calibrated checker-board panel buried in the middle of the breach (see Fig. 6); the perturbation created by this panel was negligibly small, as verified by comparing the results with the point measurements performed independently on a test where this panel was absent.

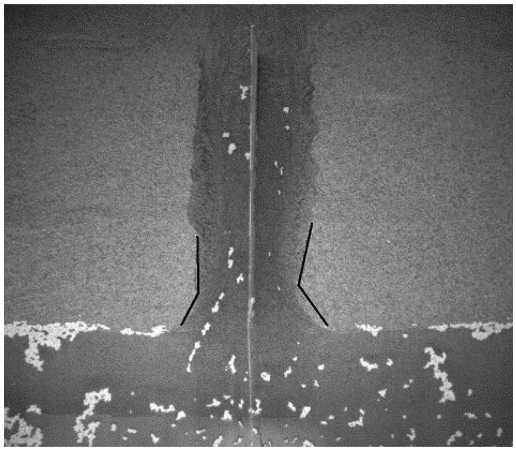


Figure 5. Vertical image and floating tracers used to derive velocity measurements.

3.2 *Sweeping laser topography*

A more original technique was developed with the objective to reconstruct the entire topography of the breach using a non-intrusive imaging technique. The principle is to use a laser light sheet to illuminate a particular cross-section of the breach, capture the line imprinted on the dike onto digital images of a remote camera, and ultimately project it in 3D space with appropriate camera calibration. A similar principle was used in a companion paper (Le Grelle et al., 2004) for tracking bank failure events with a fixed laser line. Here, the ambition is to survey the whole dike by sweeping successive cross-sections with an oscillating laser line. The procedure (see Fig. 7) is described in more details here below.

A laser is placed horizontally at the vertical of the dike crest (approximate position $x = 0.55$ m, $y = 0$, $z = 2.50$ m), and passes through a cylindrical prism to



Figure 6. Thin checkerboard panel buried along the breach centreline to visualise water and bed profiles.

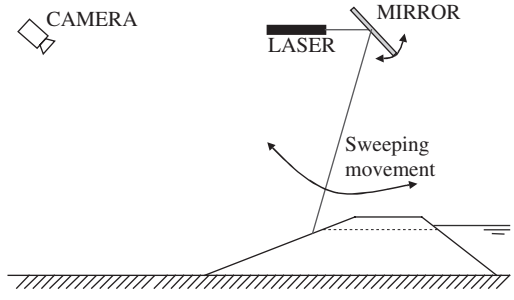


Figure 7. Sketch of the laser surveying technique used for reconstruction of the breach topography.

produce a thin light sheet. The laser used is a red diode laser with 12 mW output power, and the light sheet has an opening angle of 39.3°.

The light sheet is reflected towards the dike using an oscillating mirror, adjusted in order to sweep the dike from the upstream slope to about 1 m below the downstream toe. The sweeping cycle takes about 5 seconds, which is small enough compared to the speed of breach evolution to be assumed as quasi instantaneous.

A remote camera is placed more downstream (approximate position $x = 4.4$ m, $y = 0$, $z = 2.45$ m) and oriented to cover the whole range of sweeping laser lines. The camera is a Dalsa CAD4 operating at 40 frames per second for a resolution of 1024×1024 pixels $\times$ 256 grey scales. Given the covered field of view, one pixel represents less than 2 mm in reality.

The images are recorded and processed offline. The contrasted line is automatically detected on the images using a series of filters, following tightly the procedure described in Capart et al. (2002).

The line, expressed as pixel coordinates, must now be projected in 3D space and world coordinates. This requires to know the position (or equation) of the laser light sheet. The latter is derived from two reference points of the laser line printed on two thin rods fixed above the dike. The procedure also requires a camera calibration transform, from which each pixel may be associated with a 3D ray originating from the camera focal point. Those rays are then intersected with the known plane of the laser light sheet to obtain the 3D position of the line. A detailed description is beyond the scope of the present paper. Nevertheless, we refer the interested reader to Spinewine et al. (2003) where details of camera calibration and projective transforms may be found.

Relying on the above assumption that the sweeping speed of the laser is an order of magnitude faster than the speed of evolution of the breach, the images corresponding to one sweeping cycle are then assembled into a single set of 3D data, from which a digital terrain model of the entire dike may be obtained through standard interpolation techniques.

The advantage of the method is that all the required geometrical information is implicitly encapsulated in the images, and that it is not required to manually measure the respective positions of the mirror, laser lines and camera. The method overall is relatively simple to implement and provides an unprecedented degree of details in the results.

However, it has an advantage that turns out to be a drawback too. Since the laser light passes through the water surface, what is seen from the camera is the line printed onto the sediment bed. On the one hand, this allows to have a detailed perception of the underwater bed geometry and slope angles. On the other hand, the underwater portion of the laser line undergoes alteration at the water surface due to the difference in refractive index of air and water. This is illustrated in Figure 8. Consequently the measured bed level has an error proportional to the water depth and slope of the water profile.

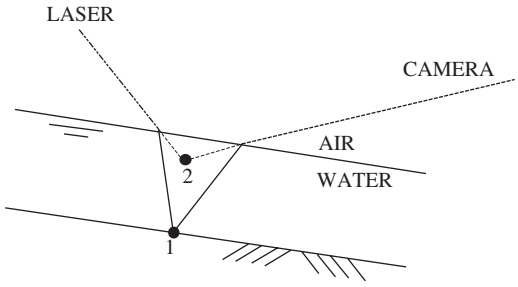


Figure 8. The vertical error due to differing refractive indexes in the air and water regions. Point 2 is actually measured on the image, whereas point 1 is the true position of the bed interface. Note that angles and refractive error is here extremely exaggerated for illustration purposes.

While it may not be impossible to account for those refractive effects, this goes beyond the scope of the paper, and would require a measure of the water depth and longitudinal slope of the water profile. As an alternative, what we performed at least is an estimation of an upper bound for the associated error. In the worse conditions corresponding to maximal water depth and inclination of the water profile, the vertical error has been estimated to be in the order of 30 mm. Provided that it constitutes an extreme case, this is small but may not be considered as negligible. On the contrary, measurements along the emerged flanks of the breach are not altered by this error, and the accuracy in this region is mainly related to pixel size and camera resolution.

4 RESULTS AND INTERPRETATION

Results obtained with the various techniques described in the previous section are now presented. All results are presented using the system of coordinates outlined in section 3, and with reference time $t = 0$ corresponding to the moment when water starts to enter into the breach. The test to which measurements pertain is also indicated (test C1 to C5 and D1 to D6).

4.1 *Discharge*

A typical curve for the evolution of the discharge through the breach is plotted in Figure 9. Peak outflow was typically close to 65 litres per second, and time to peak is about 3 minutes. The curve is surprisingly smooth and nearly symmetrical, a feature that seem to be related to the failure mode and material characteristics. The breaching development in the present experiments is mainly diffusive and progresses smoothly

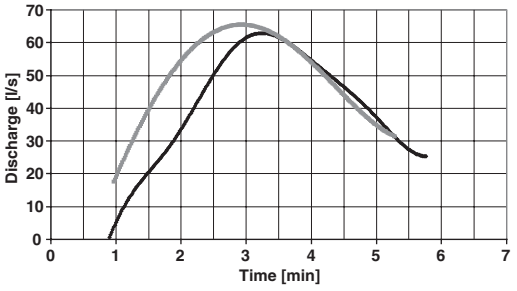


Figure 9. Outflow hydrographs for test C4 (black line) and test D2 (grey line).

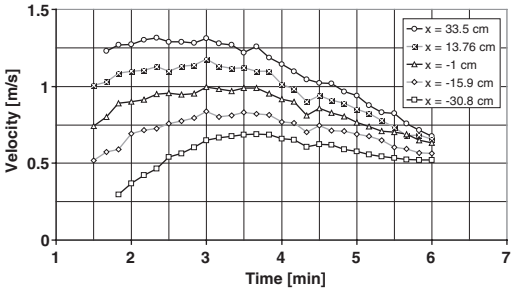


Figure 10. Mean surface velocities, obtained from particle tracking measurements, at selected sections along the dike.

with nearly uniform flow conditions along the downstream slope. This is in accordance with observations by Visser (1998) in largescale breaches of sand dikes, but not with observation of breaches in moraine dams or cohesive dikes (Morris & Hassan, 2002; Temple & Hanson, 1994). In the latter type of breaching, failure is triggered by the upstream migration of a head-cut on the downstream slope, whereby the discharge hydrograph shows a long period of relatively low discharge during the first stage, and then a sudden and drastic increase of discharge as the head-cut reaches the dike crest and the breach fully develops.

4.2 *Surface velocities*

Mean surface velocities were derived from the particle tracking measurements. Selected results for test C3 are presented in Figure 10, showing the time evolution of velocities at selected sections close to the dike crest. The curved profiles reflect somehow the shape of the outflow hydrograph, whereas the intercomparison of the various profiles clearly shows the increase in velocities as one progresses downstream.

We recall that the plotted values are mean surface velocities averaged over the entire width of the breach cross-section. Actual velocities along the centerline are higher than those presented here.

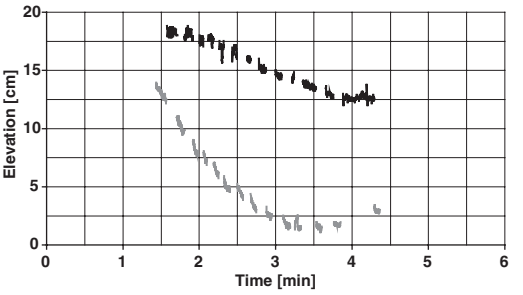


Figure 11. Water level (black line) and bed level (grey line) evolution obtained from the level profiler located at section $x = 59$ cm.

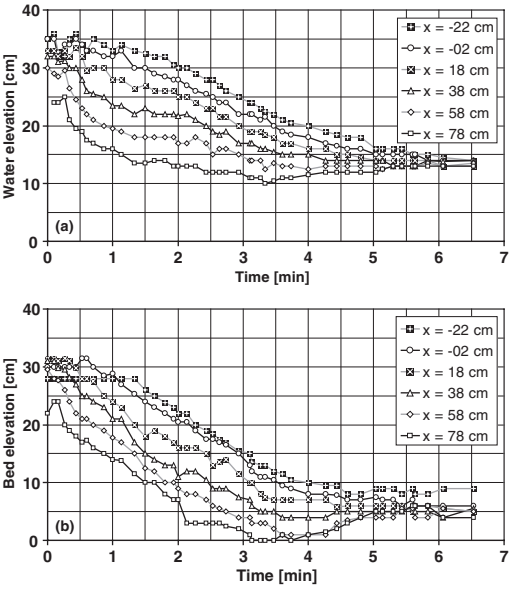


Figure 12. Centreline profiles of (**a**) water and (**b**) bed elevations obtained for test C4 with the method of the thin checkerboard panel, at selected cross-sections along the dike.

4.3 *Water- and bed-level profiles at the centreline*

Water and bed levels obtained for test C4 with the level profiler located at $x = 59$ cm are plotted in Figure 11. Results for the whole series of C-tests ranged within a margin of less than 10% around those values. Note that the lowest attained bed level corresponds to the time of peak outflow. Past this moment it seems that lateral breach erosion continues whereas the flow has no longer enough transport capacity to evacuate all the sediments eroded from the breach side-walls.

Profiles obtained manually from the observation along the thin checker-board panel buried along the centreline are presented in Figures 12a and 12b for test C4.

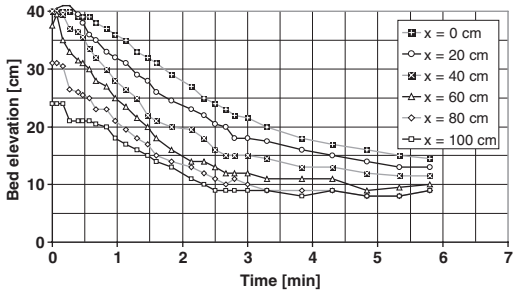


Figure 13. Centreline profiles of bed elevations obtained for test D2 with the same method as for Figure 12.

Figure 13 shows the related bed profiles for test D2, where an additional bottom layer of 10 cm of loose material was provided below and downstream of the dike. Comparison with Figure 12b indicates a slower process towards equilibrium, as the various levels have not converged after 6 minutes. One may also remark a noticeable influence of the presence of the bottom layer on the vertical erosion, the latter allowing a deeper incision of the breach and a scour hole to develop on the downstream side.

4.4 *Breach width*

Breach width was obtained from the vertical images at three different sections: upstream side of the dike crest at $x = 0$ cm, middle at $x = 17.5$ cm, and downstream side at $x = 35$ cm. Results are illustrated in Figure 14 for test C1. In a first stage, the breach is wider along the downstream slope. After some time however, the breach widening develops faster on the upstream side, and the overall breach adopts a converging shape. Stabilization occurs after about 4.5 minutes.

4.5 *Laser topography*

Measurements obtained with the system of sweeping laser light-sheet are now emphasized. Figure 15 shows an example of the set of reconstructed laser line traces corresponding to one full sweeping cycle of the mirror. The instant chosen, at $t = 45$ s, corresponds to the first phase of breach development: erosion occurs along the downstream slope, and the transported sediments are re-deposited in the wider reach downstream as flow velocities decrease. This creates a fan-like deposit, which is then later reincised as breach erosion progresses and outflow approaches its maximum value.

Full digital terrain models of the evolving breach topography are then obtained by interpolating between the sets of laser traces. Figure 16 on the following page, compares the results at selected times. The

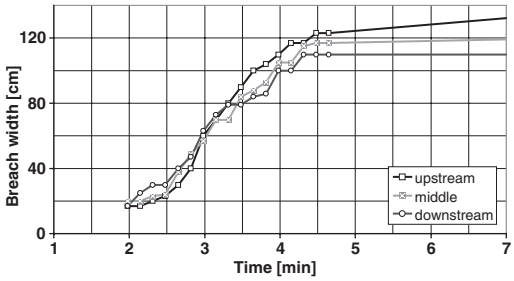


Figure 14. Evolution of the breach width as manually measured on the vertical digital images of run C1. The three profiles respectively refer to the upstream side ($x = 0$ cm), the middle ($x = 17.5$ cm), and the downstream side ($x = 35$ cm) of the dike crest.

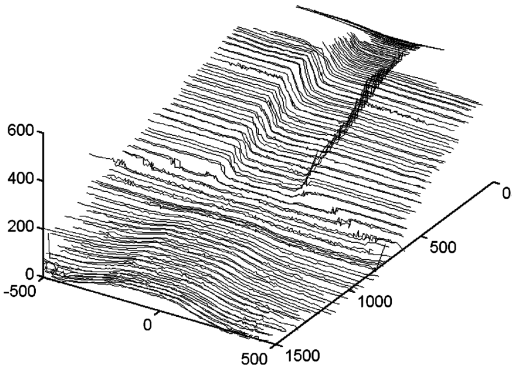


Figure 15. An example of the set of reconstructed laser traces corresponding to one sweeping cycle at time $t = 45$ s. These profiles are then used to obtain interpolated digital terrain models, as illustrated in Figure 16.

initial geometry is plotted in Fig. 16**a**. Figures 16**b** and 16**c** correspond to the first phase, as described above. The fan deposit is re-incised starting from Figure 16**d**, and the deepening of the breach progresses from downstream to upstream. Figure 16**e** corresponds approximately to the time of peak outflow, with an important rate of lateral erosion and deepening. The scour hole that develops at the toe of the downstream slope is particularly visible in Figures 16**f** and 16**g**. The breach then reaches an equilibrium stage when the drainage of the upstream reservoir is nearly completed. As seen in Figure 16**h**, the scour hole then gradually fills up again as transport intensity decreases.

5 CONCLUSIONS

We presented results from a series of laboratory experiments involving the controlled overtopping and breaching of a coarse sand dike. Special care has been

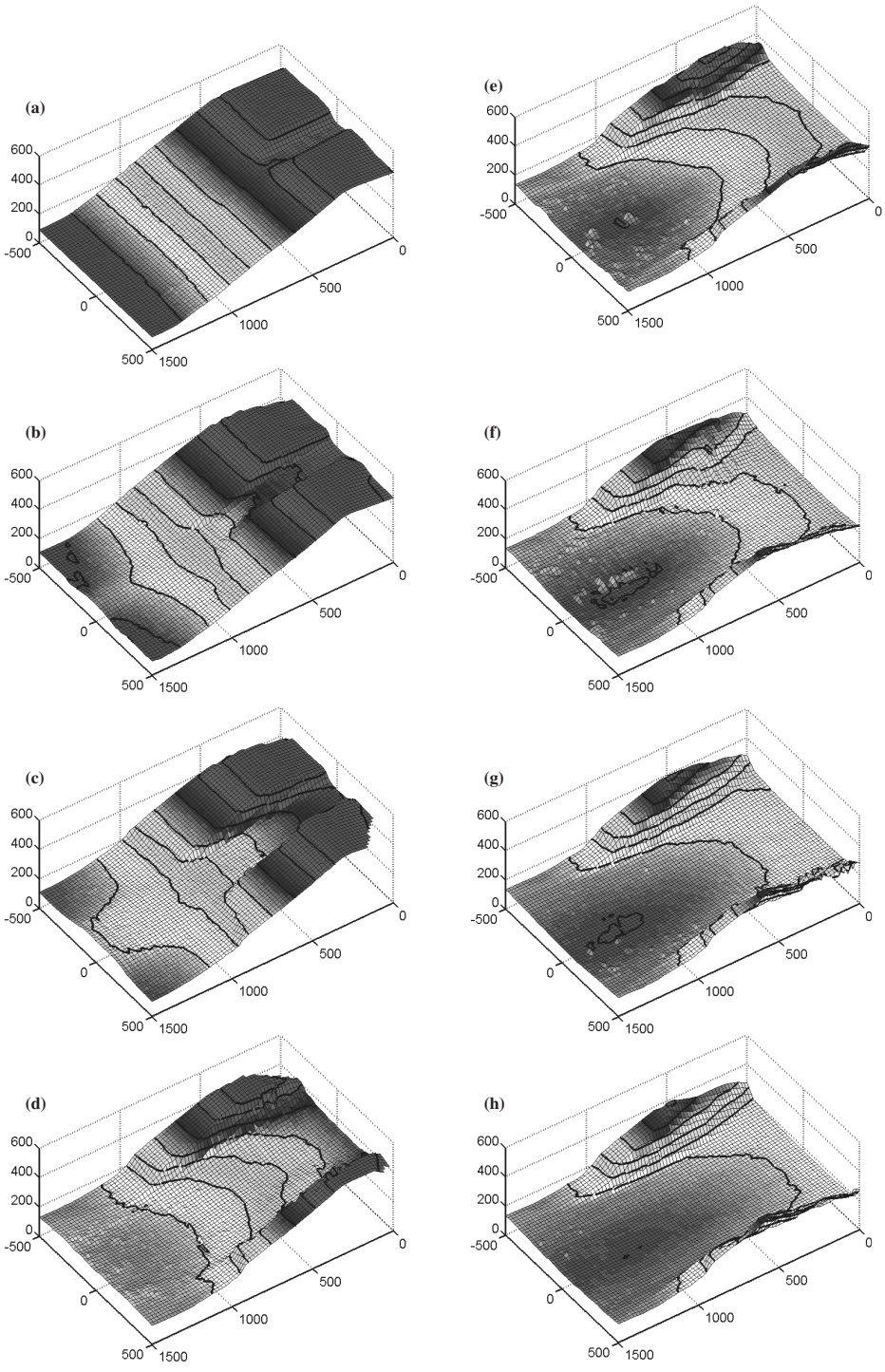


Figure 16. Digital terrain models of the dike at selected times. Respectively from **a** to **h**: $t = 0$ s, 20 s, 45 s, 1.75 min, 2.9 min, 4 min, 5 min, 6.2 min. Dimensions in mm. Black contours are plotted at levels ranging from 100 mm to 450 mm in steps of 50 mm.

paid to insure well-controlled soil parameters and test reproducibility.

A wide range of measuring systems has been tested on the experiments with success. In particular, the non-intrusive laser imaging technique has proven to provide an unprecedented degree of detail in the evolution of the breach geometry. Such measurements are crucial for the validation of physicallybased breach models that do not rely on any assumption for outflow, breach topology and lateral erosion rates. We have shown how refractive effects at the air-water interface affects the underwater laser measurements, and have quantified an upper bound of the associated error.

Many results were presented, and preliminary experimental findings were briefly discussed and compared with the observations of previous authors. However, much of the interpretation work remains to be done. Further research will be carried out along this line in the future in our research team, including the development and validation of a physically-based mathematical framework and numerical model.

REFERENCES

Benoist, G. 1989. Les etudes d'ondes de submersion des grands barrages d'EDF. La Houille Blanche, 1-1989, 43–54.

Capart, H., Young, D.L. & Zech, Y. 2002. *Voronoï imaging methods for the measurement of granular flows*. Experiments in Fluids **32**, 121–135.

Delobbe, A. & Elslander, L. 2002. *Modélisation expérimentale de la rupture progressive d'une digue à partir d'une brèche*. B. Eng. Thesis, Université catholique de Louvain, Louvain-la-Neuve, Belgium (in French).

Froehlich, D.C. 2002. *IMPACT Project field tests 1 and 2: "blind" simulation by DaveF.* Proceedings of the 1st IMPACT project Workshop, Wallingford, United Kingdom, 16–17 May 2002.

Kulisch, H. 1994. *Physical 3D-Simulations of Erosion-caused Dam-breaks*. International Workshop on Floods and Inundations related to Large Earth Movements, Trento, Italy, 4–7 October 1994.

Le Grelle, N., Spinewine, B., Soares Frazão, S. & Zech, Y. 2004. Non-intrusive imaging measurements of the morphological evolution of a channel during a dam-break flow. River Flow 2004. Proc. of the Second Int. Conf. on Fluvial Hydraulics, Napoli, Italy, 23–25 June 2004.

Morris, M.W. & Hassan, M.A.A.M. 2002. *Breach formation through embankment dams & flood defense embankments: a state of the art review*. Proceedings of the 1st IMPACT project Workshop, Wallingford, United Kingdom, 16–17 May 2002.

Singh, V.P. 1996. *Dam-breach modeling technology*. Kluwer Academic Publishers, Dordrecht, The Netherlands, 242 pp.

Spinewine, B., Capart, H., Larcher, M. & Zech, Y. 2003. *Three-dimensional Voronoï imaging methods for the measurement of near-wall particulate flows*. Experiments in Fluids **34**-2, 227–241.

Temple, D.M. & Hanson, G.J. 1994. *Headcut development in vegetated earth spillways*. Applied Engineering in Agriculture, **10**-5, American Society of Agricultural Engineers.

Visser, P.J. 1998. *Breach growth in sand dikes*. PhD thesis and Communications on Hydraulic and Geotechnical Engineering Series, Report 98-1, Delft University of Technology, Delft, The Netherlands.

Wahl, T.L. 1998. *Prediction of embankment dam breach parameters: literature review and needs assessment*. USBR, Water Resources Research Laboratory, PAP-735, Denver, USA.

This page intentionally left blank

River Flow 2004 – Greco, Carravetta & Della Morte (eds.)
© 2004 Taylor & Francis Group, London, ISBN 90 5809 658 0

Monitoring and modelling river bank processes: a new methodological approach

L. Rossi Romanelli & M. Rinaldi
Dipartimento di Ingegneria Civile, Università di Firenze, Florence, Italy

S.E. Darby
Department of Geography, University of Southampton, Highfield, Southampton, UK

L. Luppi & L. Nardi
Dipartimento di Ingegneria Civile, Università di Firenze, Florence, Italy

ABSTRACT: Fluvial erosion and mass failure are the two dominant processes causing river bank retreat. In order to investigate the interaction between these two processes and to establish the relative dominance of them under different conditions, research is being undertaken at two diverse study sites: Cecina River (Central Italy) and the River Asker (Southern UK). The study is divided into two main phases: the first phase consists of monitoring bank erosion processes; the second involves numerical modelling of the observed bank retreat. This paper presents a description of the river sites, including relevant geotechnical and hydrological characteristics of the bank materials, a description of the monitoring implementation including the beginning of the monitoring activity, and the methodological approach for the modelling phase.

1 INTRODUCTION

River bank erosion can contribute significantly to the sediment yielded from river catchments. Accordingly, knowledge of the rates and controls on bank erosion events is fundamental to understanding sediment flux. Bank erosion occurs through a combination of mass failures under gravity and fluvial erosion due to the direct action of the flow. While progress has recently been made in understanding the processes controlling large-scale mass failure of stream banks (e.g. Osman & Thorne, 1988; Rinaldi & Casagli, 1999; Casagli et al., 1999; Darby et al., 2000; Dapporto et al., 2001; Simon & Collison, 2002), much less attention has been paid to the role that direct fluvial erosion plays in bank retreat. This is unfortunate because fluvial bank erosion can be a significant process in its own right, and also is frequently the trigger for a mass failure event.

To address this limitation, the aim of this research is to quantify the controls on fluvial bank erosion, examine the interaction between fluvial erosion and mass failure, and to establish the relative dominance of the two processes under different conditions. One of the key problems that has prevented progress being made on these topics is that it has proved very difficult to obtain reliable empirical data that describe relevant physical controls on the process, particularly during the flood flows that typically generate erosion. Specifically, detailed studies of the erodibility of bank materials, and of near-bank boundary shear stresses, are virtually absent from the literature, primarily due to the problems associated with undertaking accurate fieldwork in the hazardous environment of eroding riverbanks.

In this study we have therefore devised a new methodological approach that involves undertaking a combination of monitoring and hydraulic modelling investigations at two diverse study sites. Our rationale is to employ Computational Fluid Dynamics (CFD) techniques to obtain simulated high-resolution near-bank boundary shear stress data as a substitute for empirical data. The first study site is a reach of the Cecina River (central Italy), a gravel-bed river with large lateral bars and actively migrating outer banks. The second is a reach of the River Asker (southern UK), which is a low-gradient meandering river. These sites were chosen because they represent end-members in a spectrum ranging from very active (Cecina bank erosion rate ~7–17 m/yr) to mildly active (Asker bank erosion rate ~0.2 m/yr) eroding river meanders. This

paper outlines the methodological approach that we are adopting at the Cecina and Asker and includes a description of the monitoring implementation, the monitoring activity since autumn 2003, and the methodological approach for the modelling phase.

2 STUDY AREAS

2.1 *Fiume Cecina*

The Cecina river (900 km^2) is situated in Tuscany (Central Italy). The study site is located near Casino di Terra (Pisa) where the tributary Sterza meets the Cecina on its left bank. The main criteria for selecting this site were the high annual bank erosion rate and the availability of river stage and flow discharge data from a gauging station, situated about 2 km upstream, at Ponte di Monterufoli. The study reach is about 500 m long, though the actively eroding part of the bank (on the left side of the Cecina) extends about 170 m upstream from the Sterza confluence. The average gradient of the reach is about 0.0021.

The eroding bank has an average height of about 5–5.5 m and it can be defined as a layered type. The stratigraphy has been characterised by grain size analyses of samples collected from the exposed part of the bank in six vertical sections, combined with the results of two static penetration tests (CPT). Six main units, not all of which are present in every section, were therefore identified (Figure 2) as being composed of the following materials: (1) gravel; (2) gravel-sand; (3) well sorted sand; (4) silt-sand-clay; (5) massive sandy-silt; (6) sandy-silt.

A preliminary geotechnical characterization of these sediments were performed on the fine-grained materials (units 4, 5, 6). Samples were collected using a range of *in situ* and laboratory tests. Laboratory tests, in addition to grain size analyses, included phase relationship analyses and triaxial consolidated-undrained tests (CU) (units 5 and 6). *In situ* tests included seepage tests (unit 6) to determine the saturated hydraulic conductivity k_s (Amoozemeter test: Amoozegar, 1989), Borehole Shear Tests (BST: Lutenegger & Hallberg, 1981) (unit 6) and matric suction measurements using a tensiometer. Erodibility parameters (critical shear stress, τ_c, and erodibility coefficient, k_d) were also determined (units 4 and 6) by *in situ* jet tests (Hanson & Simon, 2001) using a non-vertical jet test device recently applied specifically to river banks (Dapporto, 2001). A summary of the grain size analyses, geotechnical and erodibility data is provided in Table 1 and 2.

2.2 *River Asker*

The River Asker (49.1 km^2) is situated in Dorset (Southern UK). The study site is located near Bridport.

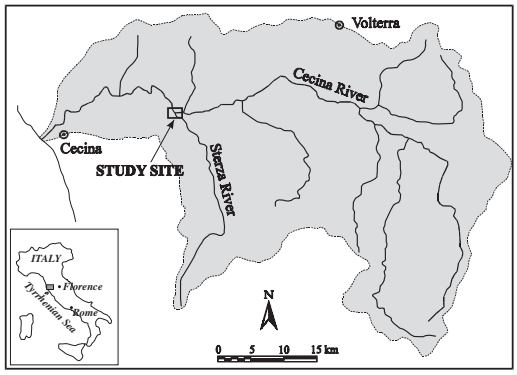


Figure 1. Cecina river basin (Central Italy): location map.

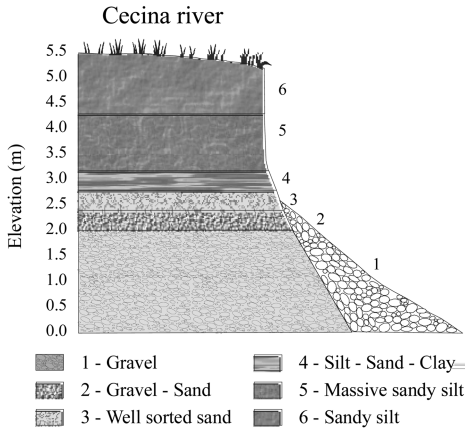


Figure 2. Cecina river: stratigraphy of the bank.

Table 1. Cecina river: grain size analyses.

	1	2	3	4	5	6
Gravel (%)	74.9	44.5	0	0	0	0
Sand (%)	25.1	55.5	100	10.1	18.6	26
Silt (%)	0	0	0	63.9	70.3	65.8
Clay (%)	0	0	0	26	11	8.2
D16 (mm)	11	0.4	0.11	–	0.01	0.02
D50 (mm)	12.6	1.4	0.19	0.011	0.05	0.05
D84 (mm)	41.8	17.9	0.27	0.023	0.07	0.08

This site was selected as river stage and discharge data are readily available from a gauging station, situated about 150 m downstream from the bank monitoring reach. Moreover, the Asker site contrasts with the Cecina in that annual bank erosion rates are relatively low, so that the two sites between them cover a wide range of bank erosion rates. The study reach is about 200 m long, with an average gradient of about 0.007.

Table 2. Cecina river: geotechnical properties and erodibility parameters for the upper layers.

Parameter	Units	4	5	6
Water content	%	–	–	19.7
Bulk unit weight	kN/m^3	–	–	17.50
Dry unit weight	kN/m^3	26.48	26.09	26.62
Saturated perm.	m/s	–	–	$0.87 \cdot 10^{-6}$
Eff. friction ang. (situ)	°	–	–	37.3
Appar. cohesion	kPa	–	–	4.8
Suction frict. ang.	°	–	–	21.5
Eff. frict. ang. (lab.)	°	–	35.9	38.3
Total cohesion	kPa	–	0	0
Erodibility coeff.	m^3/Ns	$6.61 \cdot 10^{-6}$	–	$4.97 \cdot 10^{-6}$
Critic. shear str.	Pa	0.763	–	1.013

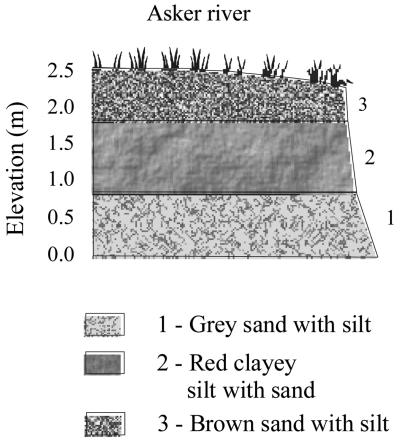


Figure 3. River Asker: stratigraphy of the bank.

The eroding bank has an averaged height of about 2–2.5 m and it can be defined as a layered type. The stratigraphy has been characterised by grain size analyses of samples collected from two vertical sections of the bank. Three main units were identified (Figure 3) as being composed of the following materials: (1) grey sand with silt (about 0.8–1 m thick); (2) red clayey silt with sand (about 1 m thick); (3) brown sand with silt (about 0.4 m thick).

A series of samples were collected for laboratory phase relationship analyses. Shear strength parameters were estimated by *in situ* Borehole Shear Tests. Erodibility parameters (critical shear stress, τ_c, and erodibility coefficient, k_d) were determined by *in situ* jet tests as described previously. A summary of the grain size analyses, geotechnical and erodibility data is provided in Table 3 and 4.

Table 3. River Asker: grain size analyses.

	1	2	3
Gravel (%)	0	0	0
Sand (%)	59.4	41.8	57.9
Silt (%)	37.5	52	38.2
Clay (%)	3.1	6.2	2.7
D16 (mm)	0.017	0.008	0.013
D50 (mm)	0.073	0.050	0.064
D84 (mm)	0.135	0.100	0.158

3 MONITORING ACTIVITY

The principles of the monitoring activity are identical at each study site, though there are differences in the actual implementation of these activities at each study site. Nevertheless, in general the monitoring activity is focused on: (1) characterising bed topography of the study reaches, for subsequent use in CFD modelling; (2) evaluating the peak flow discharge and water surface profile of that peak flow discharge along the study reaches for a range of flows, again for subsequent use in CFD modelling; (3) monitoring the magnitude of fluvial bank erosion generated by each flow event.

The magnitude of bank erosion generated by each flow event is monitored using a combination of low-resolution networks of erosion pins together with high-resolution digital photogrammetry (e.g. Lawler, 1993). At the Cecina study site erosion pins have been installed in 6 sections, spaced at about 6 m intervals along the reach. At each section a set of 3 horizontal erosion pins, spaced at 0.5 m intervals up from the bottom of the bank have been installed. At the River Asker, a total of 19 pin sections are used at approximately 3 m intervals, with 4 pins spaced at about 0.3 m intervals up from the base of the bank. In addition, after each flow event a series of ground-based photographs of the eroding banks in each reach are taken for subsequent use in high-resolution digital photogrammetry. This technique, not discussed herein, allows estimates of bank retreat to be obtained across the entire eroding bank face, at approximately 0.2 m^2 spatial resolution.

The hydrological characteristics of each flow event are recorded at the Cecina site in a semi-automated way using a network of pressure transducers and crest-gauges. In particular two piezometers and a water level sensor have been installed in a section of the reach. These instruments are connected to a data logger that records at 15 minute intervals. In Figure 4 a flow event recorded by the water level sensor and the piezometers is shown. In addition, 11 crest gauges have been installed at different elevations (to cover a large range of flows) along both the Cecina study reach and the tributary Sterza. These sensors and gauges

Table 4. River Asker: geotechnical properties and erodibility parameters.

Parameter	Units	1	2	3
Bulk unit weight	kN/m^3	18.03	17.93	17.99
Dry unit weight	kN/m^3	13.72	13.72	14.74
Vol. moist. cont.	%	44.0	43.0	33.2
Porosity	–	47.2	47.3	43.3
Deg. of saturation	%	93.1	91.2	76.6
Saturated perm.	m/s	$3.50 \cdot 10^{-8}$	$5.63 \cdot 10^{-10}$	$4.23 \cdot 10^{-6}$
Eff. friction ang.	°	28.1	39.4	38.4
Apparent cohesion	KPa	2.4	2.2	1.6
Erodibility coef.	m^3/Ns	$9.55 \cdot 10^{-5}$	$5.86 \cdot 10^{-6}$	–
Critic. shear str.	Pa	0.296	2.351	–

between them are able to characterise the water surface profile along the reach at peak flows, thereby defining the 'lid' for subsequent use in CFD modelling (see below). The peak flow discharge is available at the gauging station located about 2 km upstream at Ponte di Monterufoli. Hydrological monitoring on the Asker is restricted to a network of 10 crest-gauges, spaced at approximately 20 m intervals along the study reach. Similar to the Cecina site, peak flow discharge data is available from the gauging station at Bridport, Dorset, located approximately 150 m downstream of the bank monitoring reach. At both study sites, efforts are made to acquire flow velocity data across the inlet of the study reach using 2D electromagnetic flow velocimeters during the flood events. These data are helpful in specifying the boundary conditions for use in the CFD modelling.

4 MODELLING PHASE

During the modelling phase, a range of specific flow events that occurred during autumn 2003 are selected for further analysis, using hydraulic and geotechnical data collected during the monitoring phase for the modelling implementation. The first phase of the modelling involves the evaluation of near-bank boundary shear stress distributions through the use of CFD modelling. This allows quantification of the bank erosion rate due only to fluvial erosion, using an excess shear stress formula (see §4.1). The second phase comprises bank stability analysis to determine the bank erosion rate due to geotechnical failure. This involves the use of the finite element seepage and slope stability analyses SEEP and SLOPE for dynamic simulation of bank pore pressures and mass failure conditions (see §4.2). The two modelling phases are, however, linked because the bank erosion rate due to fluvial erosion, determined in the first step, is used to provide dynamically adjusting bank profiles during the seepage and stability analyses. The two modelling phases are now described in more detail.

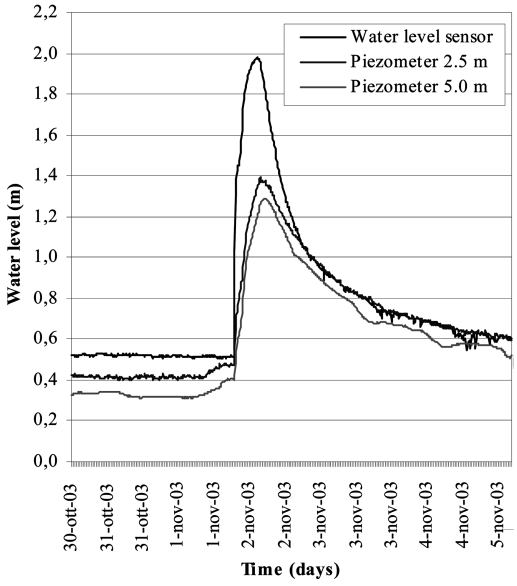


Figure 4. Cecina river: flow event recorded by the water level sensor and the piezometers.

4.1 *Computational Fluid Dynamics simulations*

The shear stress distribution exerted on the bank face by flows of varying magnitude is evaluated by undertaking hydraulic modelling using 3-dimensional Computational Fluid Dynamics (CFD) simulations of monitored flows (e.g. Olsen, 1991; Olsen & Skoglund, 1994; Olsen & Stokseth, 1995; Booker et al., 2001). Models are built using the high resolution topography data sets collected during the monitoring phase, with initial and boundary conditions specified using the flow velocity and water surface profile data obtained during the monitoring.

Preliminary analyses of near-bank boundary shear stress distribution have also been evaluated at low resolution by applying a 1-dimensional HEC-RAS model,

which allows determination of hydraulic parameters (water surface profile, flow velocity and mean boundary shear stress) under a steady state flow simulation (Hydrologic Engineering Center, 1997). The near-bank shear stress distribution is then estimated from the 1D simulation data using the results of research from laboratory channels (Leutheusser, 1963; Kartha & Leutheusser, 1972; Knight et al., 1984).

The modelled shear stress distribution allows the deformation of the bank profile caused by fluvial erosion (recall that this is necessary to assess the influence of fluvial erosion on mass bank failure) to be quantified using a simple excess shear stress formula (Partheniades, 1965)

$$\varepsilon = k_d(\tau_0 - \tau_c)^a \quad (1)$$

where ε (m/s) is the fluvial bank erosion rate per unit time and unit area, τ_0 (Pa) is the modelled shear stress distribution, k_d and τ_c (Pa) are the erodibility parameters (defined previously) and a is an empirically-derived exponent. Since the erodibility parameters k_d and τ_c are determined through the jet-testing undertaken as part of the field monitoring described previously, and because a can be assumed equal to unity (Dapporto, 2001), the modelled shear stress is the only unknown parameter required to estimated the fluvial bank erosion rate.

4.2 *Geotechnical modelling*

Groundwater seepage and slope stability analysis are undertaken using the off-the-shelf software packages SEEP/W and SLOPE/W (GEO-SLOPE International Ltd, 2000). SEEP/W is a finite element code for determining pore water pressure distributions at the scale of a single flow event, and can model both saturated and unsaturated flow under steady state or transient conditions. By assigning initial and boundary conditions, and defining hydraulic and soil material properties in relation to the field data collected in the monitoring phase, the pore water pressure distribution is computed using the flow equation in conjunction with the continuity equation expressed in generalized form for unsaturated soils (Richards, 1931; Fredlund & Rahardjio, 1993) as follows:

$$\frac{\partial}{\partial x}\left(K_x \frac{\partial H}{\partial x}\right) + \frac{\partial}{\partial y}\left(K_y \frac{\partial H}{\partial y}\right) + Q = \frac{\partial \Theta}{\partial t} \quad (2)$$

where H is the unknown total head, K_x and K_y the hydraulic conductivity respectively in x and y directions, Q is the external flux and Θ is the water content.

The bank geometry is discretised using rectangular or triangular finite elements and divided into regions

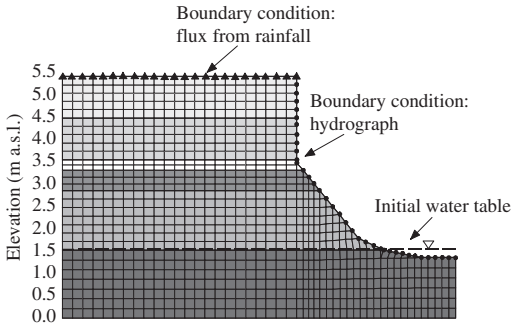


Figure 5. Finite element seepage analyses: geometry of the problem for the Cecina river.

composed of materials with different hydraulic and sedimentary properties. Different volumetric water content and hydraulic conductivity functions, based on the measured grain size distribution, are assigned to each material within the bank. The geometry of the problem in the case of the Cecina River is shown in Figure 5. For the initial point in the simulation, the water table is set to the same level of the river at the start of the selected flow event. Boundary conditions are then defined for transient simulations. These comprise an infiltration intensity versus time function based on rainfall data available from rainfall stations situated close to the sites and assigned to the nodes on the top of the bank, while the flow hydrograph, based on results of hydraulic analyses or on data measured during the monitoring phase for the selected events (Cecina River), is assigned to nodes along the slope of the bank. The hydrograph is divided into discrete time steps, the model output consisting of the computed pore water pressure in each element within each time step. In the case of the Cecina, these results can be calibrated and compared with observed data from the installed pressure transducers.

SLOPE/W is a software package that performs slope stability analyses by applying limit equilibrium methods (including Morgenstern-Price, Bishop, Fellenius, Janbu and more) to compute the factor of safety of the bank. This software is integrated with SEEP/W in such a way that the results (pore pressure distributions) of the seepage analyses are used as input data for the stability analysis. The bank geometry can be irregular so that changes in bank geometry due to fluvial erosion can be modelled. The slip surface geometry can be planar, rotational and composite, with or without tension cracks. Confining pressure is taken into account by specifying the surface water elevation. The Mohr-Coulomb failure criterion in terms of effective stress is used in the case of positive pore water pressure, while the extended Fredlund et al. (1978) failure criterion for unsaturated soils is used in the case

of negative pore water pressure. Geotechnical properties, unit weight and shear strength parameters (c′, ϕ' and ϕ^b), all determined from the field monitoring as described previously, are defined for each different material composing the bank.

In order to address the interaction between mass failure and fluvial erosion, SEEP and SLOPE are used to simulate the evolution of bank stability during and after selected events. Two simulation scenarios are investigated: on the one hand bank deformation by fluvial erosion, previously determined using the CFD modelling and equation (1), is taken into account by updating deformed bank profiles at each time step of the selected flow events; on the other hand control simulations in which the bank has not been deformed are performed. Comparison of the results derived from these two scenarios will enable the effect of bank deformation on bank stability to be isolated.

5 CONCLUSIONS

In this paper we have outlined research being undertaken at two different study sites in order to investigate the interaction and relative dominance between fluvial erosion and mass failure in determining bank retreat.

A description of the study areas and of the main riverbank characteristics sites is provided here. Monitoring activity includes: (a) an initial topographic survey of the study reaches; (b) measurements of water stages and water surface profiles during flow events; (c) measurements of bank retreat generated by each flow event.

A new methodological approach is undertaken for the modelling phase, based on the combination of empirical data collected during the monitoring activity with hydraulic and geotechnical modelling. This approach involves: (a) the evaluation of a near-bank shear stress distribution by applying 3D CFD simulations to quantify the bank erosion rate due to fluvial erosion; (b) finite element seepage and slope stability analyses for dynamic simulations of pore water pressure changes and mass failures.

REFERENCES

Amoozegar, A. 1989. A compact constant-head permeameter for measuring saturated hydraulic conductivity of the vadose zone. *Soil Science Society of American Journal* 53:1356–1361.

Booker, D.J., Sear, D.A. & Payne, A.J. 2001. Modelling 3D flow structures and patterns of boundary shear stress in a natural pool-riffle sequence. *Earth Surf. Proc. & Lndfrms.* 26:553–576.

Casagli, N., Rinaldi, M., Gargini, A. & Curini, A. 1999. Pore water pressure and streambank stability: results from a monitoring site on Sieve River, Italy, *Earth Surf. Proc. & Lndfrms.* 24:1095–1114.

Darby, S.E., Gessler, D. & Thorne, C.R., 2000. Computer program for stability analysis of steep, cohesive riverbanks, *Earth Surf. Proc. & Lndfrms.* 25, 2:175–190.

Dapporto, S. 2001. *Non-vertical jet testing of cohesive streambank toe material*. School of Geography, University of Nottingham, in collaboration with USDA-ARS National Sedimentation Laboratory, Oxford, Mississippi.

Dapporto, S., Rinaldi, M. & Casagli, N. 2001. Failure mechanisms and pore water pressure conditions: analysis of a riverbank along the Arno River (Central Italy). *Engineering Geology* 61:221–242.

Fredlund, D.G., Morgenstern, N.R. & e Widger, R.A. 1978. Shear strength of unsaturated soils. *Can. Geotech. J.* 15:313–321.

Hanson, G. & Simon, A. 2001. Erodibility of cohesive streambeds in the loess area of the midwestern USA. *Hydrol. Proc*. 15:23–38.

Hydrologic Engineering Center, 1997. *HEC-RAS River Analysis System version 2.0 User's Manual*. Davis, California: US Army Corps of Engineers.

Kartha, V.C. & Leutheusser, H.J. 1972. Distributio of Tractive Force in Open Channels. *J. Hydr. Div*. ASCE 96:1469–1483.

Knight, D., Demetriou, J.D. & Hamed, M.E. 1984. Boundary Shear in Smooth Rectangular Channels. *J. Hydr. Eng.* ASCE 110:405–422.

Lawler, D.M. 1993. The measurement of river bank erosion & lateral channel change: A review. *Earth Surf. Proc. & Lndfrms.* 18:777–821.

Leutheusser, H.J. 1963 Turbulent Flow in Rectangular Ducts. *Proc. Am. Soc. Civ. Engrs*. 89, HY3.

Lutenegger, A.J. & Hallberg, G.R. 1981. Borehole Shear Test in geotechnical investigation. *Special Technical Publ. American Society for Testing and Materials* 740:566–578.

Olsen, N.R.B. 1991. *A Numerical Model for Simulation of Sediment Movements in Water Intakes*, PhD Thesis, The Norweigan Institute of Technology, Trondheim.

Olsen, N.R.B. & Skoglund, M. 1994. Three-dimensional modelling of water & sediment in a sand trap. *J. Hydr. Res.* 32:833–844.

Olsen, N.R.B. & Stokseth, S. 1995. Three-dimensional numerical modelling of flow in a river with large bed roughness. *J. Hydr. Res.* 33:571–581.

Osman, A.M. & Thorne, C.R. 1988. Riverbank stability analysis. I: Theory. *J. Hydr. Eng*. 114:134–150.

Partheniades, E. 1965. Erosion and deposition of cohesive soils. *J. Hydr. Div.* ASCE 91:105–139.

Rinaldi, M. & Casagli, N. 1999. Stability of streambanks formed in partially saturated soils and effects of negative pore water pressures: the Sieve River (Italy) *Geomorphology* 26:253–277.

Simon, A. & Collison, A.J.C. 2002. Quantifying the mechanical & hydrologic effects of riparian vegetation on streambank stability. *Earth Surf. Proc. & Lndfrms.* 27:527–546.

River Flow 2004 – Greco, Carravetta & Della Morte (eds.)
© 2004 Taylor & Francis Group, London, ISBN 90 5809 658 0

Two-dimensional fluvial channel model with bank erosion on triangular grid

D. Farshi[1] & H.-E. Minor
Federal Institute of Technology Zurich (ETHZ), The Laboratory of Hydraulics, Hydrology and Glaciology (VAW), Switzerland

ABSTRACT: A 2D numerical model to simulate the bed load transport and bank erosion in alluvial channels is developed based on shallow water equations (SWE) and Exner equation by Finite Volume (FV) spatial discretization. The Roe Riemann Solver has been utilized for the Flux estimation in SWE and the Local Lax-Friedrich solver is used for the bed load transport. A new formulation of bed shear stress has been presented and the bank erosion simulation been achieved through a new approach. Accuracy and stability of the code are tested against an available set of experimental data.

1 INTRODUCTION

In natural rivers and channels the erosion, sedimentation and bank line migration cause land loss, bridge failure, shoaling of waterways and flooding. In order to obtain maximum benefit and reduce the adverse effects, research on the prediction of the mentioned processes and the effective control strategy has always been a key concern of hydraulic, geological and river engineers. Therefore the analysis of flow, bed level variations and bank erosion is a fundamental prerequisite for many hydraulic engineering problems.

The complicated fluvial phenomenon is dominated by the flowing water, sediment transport, bed forms and bank erosion as well. Hence, numerical simulation of movable bed channels requires the accurate prediction of the flow field, sediment transport and bank erosion. The latter is one of the most difficult points in numerical simulation, therefore many existing alluvial channel models assume that the channel banks are rigid, or adjust bank geometry according to theoretical, but non-mechanical, arguments regarding energy or stream power expenditure (Chang 1988), (Yang & Song 1986). Although changes in channel depth caused by aggradation or degradation of river bed can be simulated, changes in width cannot be computed by most of the mathematical models. When attempting to model natural systems this is a significant limitation because channel morphology usually changes with time and adjustment of both width and depth are the rule rather than exception.

[1] Formerly at German Armed Forces University, Hydroscience Institute, Neubiberg, Germany.

Developing two-dimensional models for the fluvial process in channel with bank erosion is indeed a new challenge between researchers in recent years. An example is the model of Mosselman (1992), who has extended the model of Olesen (1987) by adding a mechanism for the erosion of cohesive banks, partly using a time averaged description of Osman and Thorne (1988). The model is formulated in a horizontal, channel-fitted coordinate system (s, n) which can be curvilinear and non-orthogonal. Duan et al. (2001) have developed an equation for bank erosion based on the sediment mass balance within a control volume near the bank. They implemented this equation in the enhanced model CCHE2D and simulated meandering process in channels. These models are applied to structured mesh, in which the implementation of the discussed problems is much easier.

From the overview on recent literature it is obvious that there is still no general model to simulate the fluvial process, in particular the bank erosion, on an unstructured grid. The important advantage of unstructured grid is the ability to handle complex geometries with ease. The purpose of this work is to develop a two-dimensional numerical model which is also capable of simulating these processes.

2 GOVERNING EQUATIONS

2.1 *Hydrodynamics equations*

The two-dimensional unsteady flow of water can be described by Shallow Water Equations (SWE). By assuming hydrostatic pressure distribution and neglecting wind shear, Coriolis acceleration and eddy

viscosity, the following form of shallow water equations (SWE) can be derived:

$$\boldsymbol{U}_t + \nabla.\boldsymbol{Q} + \boldsymbol{S} = 0 \tag{1}$$

where $\boldsymbol{U}$, $\boldsymbol{Q}$ and $\boldsymbol{S}$ are the vectors of primitive variables, fluxes in the x and y directions and source term respectively, given as:

$$\boldsymbol{U} = \begin{pmatrix} \zeta \\ uh \\ vh \end{pmatrix}$$

$$\boldsymbol{Q} = (\boldsymbol{F}, \boldsymbol{G}); \boldsymbol{F} = \begin{pmatrix} uh \\ u^2h + \frac{1}{2}gh^2 \\ uvh \end{pmatrix}; \boldsymbol{G} = \begin{pmatrix} vh \\ uvh \\ v^2h + \frac{1}{2}gh^2 \end{pmatrix}$$

$$\boldsymbol{S} = \begin{pmatrix} 0 \\ \tau_{Bx}/\rho - ghS_{Bx} \\ \tau_{By}/\rho - ghS_{By} \end{pmatrix} \tag{2}$$

Here h represents the water depth, ζ the water elevation, u and v the velocity components in x and y directions and g the acceleration due to gravity. S_{Bx} and S_{By} denote the bed slope in x and y directions. We developed a new formulation of bed stress components in order to consider the bed topography and some of two-dimensional effect of water flow (Farshi 2002):

$$\boldsymbol{\tau_B} = \frac{1}{\sqrt{1+(\partial z/\partial x)^2 + (\partial z/\partial y)^2}} \begin{pmatrix} \begin{pmatrix} \rho g n^2 u\sqrt{u^2+v^2}/h^{1/3}\left(1+(\partial z/\partial y)^2\right) - \\ \rho g n^2 v\sqrt{u^2+v^2}/h^{1/3}(\partial z/\partial x)(\partial z/\partial y) \end{pmatrix} \\ \begin{pmatrix} \rho g n^2 v\sqrt{u^2+v^2}/h^{1/3}\left(1+(\partial z/\partial x)^2\right) - \\ \rho g n^2 u\sqrt{u^2+v^2}/h^{1/3}(\partial z/\partial x)(\partial z/\partial y) \end{pmatrix} \\ \begin{pmatrix} \rho g n^2 u\sqrt{u^2+v^2}/h^{1/3}(\partial z/\partial x) + \\ \rho g n^2 v\sqrt{u^2+v^2}/h^{1/3}(\partial z/\partial y) \end{pmatrix} \end{pmatrix} \tag{3}$$

where $\boldsymbol{\tau_B}$ = Bed stress vector and z = bed elevation

The first and second component of bed stress vector correspond to $\boldsymbol{\tau_{B_x}}$ and $\boldsymbol{\tau_{B_y}}$ respectively.

2.2 *Bed load equation*

The bed load continuity or bottom conservation equation can be written in following form:

$$\nabla[(1-p)\rho_s \boldsymbol{u_s}] = 0 \tag{4}$$

Where
p reperesents porosity, ρ_s bed material density and $\boldsymbol{u_s}$ bed load flow velocity vector.

Introducing the bed load flux vector $\boldsymbol{\Phi} = (1-p)\rho_s \boldsymbol{u_s}$ and after integration, (4) becomes:

$$(1-p)\frac{\partial z}{\partial t} + \nabla.\boldsymbol{q_b} = 0$$

where z denotes bottom level and $\boldsymbol{q_b} = 1/\rho_s \int_{Z_F}^{Z_B} \boldsymbol{\Phi}\, dz$ bed load transport rate vector.

The bed load transport rates (q_{bx}, q_{by}) can be estimated by different equations such as Meyer-Peter and Müller (1948). In order to take the bed slope effects into account, the critical Shields parameter as well as bed load equations have to be modified (van Rijn 1993).

3 NUMERICAL MODEL

3.1 *Hydrodynamic model*

The SWE and sediment flow equation are a nonlinear, coupled partial differential equations system. A unique analytical solution is only possible for idealised and simple conditions. For practical cases, it is required to implement the numerical methods. Keeping this in mind that an unstructured triangular mesh will be used, the Finite Volume (FV) method has been used for the discretization of SWE:

$$\int_\Omega \boldsymbol{U}_t \, d\Omega + \int_\Omega \nabla \cdot \boldsymbol{Q} \, d\Omega + \int_\Omega \boldsymbol{S} \, d\Omega = 0 \tag{5}$$

in which Ω = the area of the calculation cell

Assuming $\boldsymbol{U_t}$ is constant over the domain for first order accuracy, it can be written:

$$\boldsymbol{U}_t + \frac{1}{\Omega}\int_{\partial\Omega} \boldsymbol{Q}\cdot\boldsymbol{n}_s \, dl + \int_\Omega \boldsymbol{S} \, d\Omega = 0 \tag{6}$$

The equation (13) can be discretized as follows:

$$\boldsymbol{U}_i^{n+1} = \boldsymbol{U}_i^n - \frac{\Delta t}{\Omega}\sum_{j=1}^{3} \boldsymbol{Q}_{i,j}^{*n}\cdot\boldsymbol{n}_j \, \boldsymbol{dl}_j - \Delta t \, \boldsymbol{S}_i^n$$

where m is number of cell or element sides, $\boldsymbol{Q}_{i,j}^* = (\boldsymbol{F}_{i,j}^*, \boldsymbol{G}_{i,j}^*)$ numerical flux through the side of the cell and $\boldsymbol{n_j}$ unit vector of the cell side.

In FV method, the key problem is to estimate the normal flux through each side of the domain namely $(\boldsymbol{Q}\cdot\boldsymbol{n_s})$. There are several algorithms to estimate this flux. The set of SWE is hyperbolic and, therefore, it has an inherent directional property of propagation. Algorithms to estimate the flux should appropriately

handle this property. The *Riemann solver*, which is based on characteristic theory, is such an algorithm. In this work we used an approximate Riemann Solver due to Roe (1981):

$$\boldsymbol{Q}^{*} = \frac{1}{2}\left[\boldsymbol{Q}_{R} + \boldsymbol{Q}_{L} - \left|\widetilde{\boldsymbol{J}}^{*}\right|\left(\boldsymbol{U}_{R} - \boldsymbol{U}_{L}\right)\right] \tag{7}$$

where $\left|\widetilde{\boldsymbol{J}}^{*}\right| = \widetilde{\boldsymbol{R}}\left|\widetilde{\boldsymbol{\Lambda}}\right|\widetilde{\boldsymbol{R}}^{-1}$, $\widetilde{\boldsymbol{R}}$ is the eigenvectors matrix of $\widetilde{\boldsymbol{J}}^{*}$, denoted by $\widetilde{\boldsymbol{e}}^{1}, \ldots, \widetilde{\boldsymbol{e}}^{\boldsymbol{m}}$ with corresponding eigenvalues $\widetilde{\boldsymbol{a}}^{1}, \ldots, \widetilde{\boldsymbol{a}}^{\boldsymbol{m}}$, $\left|\widetilde{\boldsymbol{\Lambda}}\right| = \boldsymbol{diag}\left(\left|\widetilde{\boldsymbol{a}}^{1}\right|, \ldots, \left|\widetilde{\boldsymbol{a}}^{\boldsymbol{m}}\right|\right)$, subscripts R and L are referred to the right and the left side of the cell interface respectively.

3.2 *Morphodynamic model*

There are three different formulations for the numerical approximation of the bed-updating or Exner equation:

- The SWE and Exner equation are separately and numerically approximated using the same time step
- The SWE is converged to a steady solution and then the bed will be updated. The overall time step of this formulation is the morphological time step of the Exner equation and the SWE is converged to a steady state solution every time the bed is updated. This approach gives inaccurate results and also takes considerably longer computational run times. (Hudson & Sweby, 2000)
- The whole system of the SWE and Exner equations are numerically approximated. Unfortunately in this case the Jacobean matrix of the equation system is singular, which might be expected to create difficulties when implementing a numerical scheme for this formulation. Moreover, it needs an accurate estimation of the wave speed of Exner equation, which is generally not possible, due to the empirical form of bed-load relations.

In this work, the first approach is used, in which; the bed-updating calculation is decoupled from the flow computation. The flow is assumed to be quasi-steady in hydrodynamic model, which might be reasonable due to the explicit simulation method. The FV method has been also utilized to discretize the Exner equation. The bed-updating equation (4) can be rewritten in the following integral form:

$$(1-p)\int_{\Omega}\frac{\partial z}{\partial t}d\Omega + \int_{\partial\Omega}\boldsymbol{q}_{\boldsymbol{B}}\cdot\boldsymbol{n}_{s}\,dl = 0 \tag{8}$$

The above equation can be discretized as follows:

$$z_{i}^{n+1} = z_{i}^{n} - \frac{\Delta t}{\Omega}\sum_{j=1}^{m}\boldsymbol{q}_{Bi,j}^{*n}\,\boldsymbol{n}_{s\ j}\,dl_{j} \tag{9}$$

where $\boldsymbol{q}_{Bi,j}^{*}$ is numerical bed load flux through the cell side.

A simple flux solver like Local Lax-Friedrich (LLF) solver is used to determine the numerical bed load flux through the computational edge:

$$\boldsymbol{q}_{\boldsymbol{B}}^{*} = 0.5\left(\boldsymbol{q}_{\boldsymbol{BL}} + \boldsymbol{q}_{\boldsymbol{BR}} - \alpha_{s}^{*}\left(z_{R} - z_{L}\right)\right) \tag{10}$$

where $\alpha_{s}^{*} = \max\left(|u_{BL}|, |u_{BR}|\right)$, u_{BL} and u_{BR} are the sediment migrating velocities in left and right side of the calculation edge.

3.3 *Numerical treatment*

The computation of bank erosion can be decoupled from the computation of bed topography if these phenomena occur slowly. Due to the explicit approach and small time steps of computation, this assumption can be reasonable.

The stability of bank strongly depends on the inclination angle. Referring to topography of bed, the maximum slope has to be computed to be compared with critical slope, namely $\tan\gamma_{cr}$. The maximum slope of a computational cell can be computed by magnitude of gradient vector (***SD***) of bed topography at each cell:

$$\tan\gamma_{\max} = \left|\nabla z\right| = \sqrt{\left(\frac{\partial z}{\partial x}\right)^{2} + \left(\frac{\partial z}{\partial y}\right)^{2}} \tag{11}$$

After comparing $\gamma_{\max}$ and γ_{cr}, it can be decided whether or not the bank will be deformed. In the case of deformation, the cell will be rotated by $(\gamma_{\max} - \gamma_{cr})$ about the rotational axis. The main task is to find a method to determine the rotation axes, which is appropriate to unstructured mesh such as in Figure 1.

The rotation axis can be represented by rotation vector (***RA***) as follows:

$$\boldsymbol{RA} = \frac{\partial z}{\partial y}\,\boldsymbol{i} - \frac{\partial z}{\partial x}\,\boldsymbol{j} \tag{12}$$

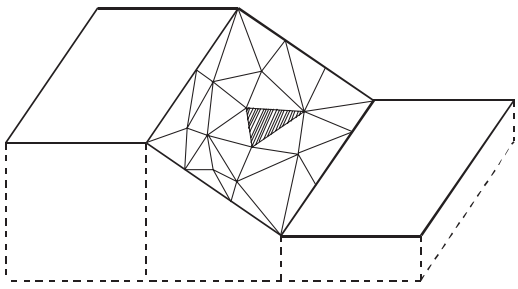


Figure 1. A schematic discretization of a channel bank.

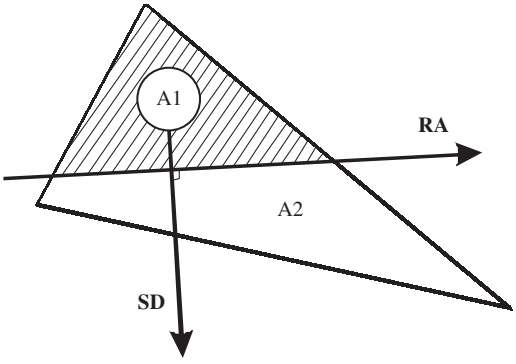


Figure 2. Slope and rotation vectors of a cell A1 = A2.

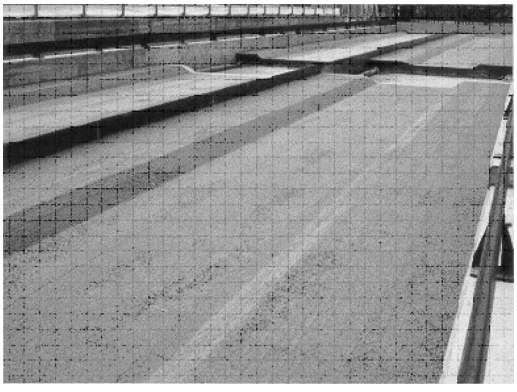


Figure 3. Physical model of TUM.

The rotation axis is located on the cell in such a form that the areas of degradation and aggradation in the cell are equal (Fig. 2).

Each cell is handled individually and rotated to reach the stable angle. Since the individual handling of each cell, it is necessary to implement this method in an iterative approach. Therewith it can be guaranteed that the calculated elevation of common grid nodes of cells has the same elevation.

4 APPLICATION

4.1 *Straight channel with movable bed*

Experiments on a physical model were conducted at the Technical University Munich (TUM) in Germany to understand the fundamental flow behaviour to be used in river restoration activities' planning of two rivers Iller and Isar in Bavaria, Germany (Schmautz, 2003). The experiments took place in different series in a specially established, spread over 100 ms long and 8 ms wide, model channel (Fig. 3).

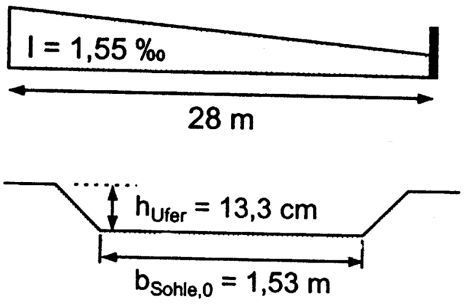


Figure 4. Geometry of the experiment (Q = 115.6 l/sec).

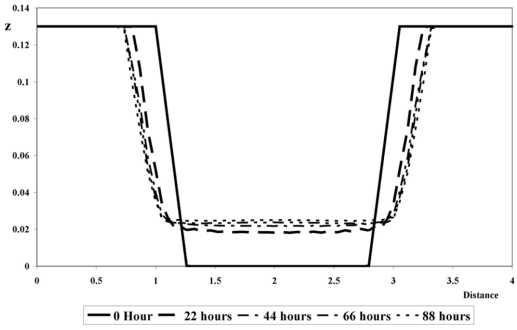


Figure 5. Evolution of bed and bank erosion.

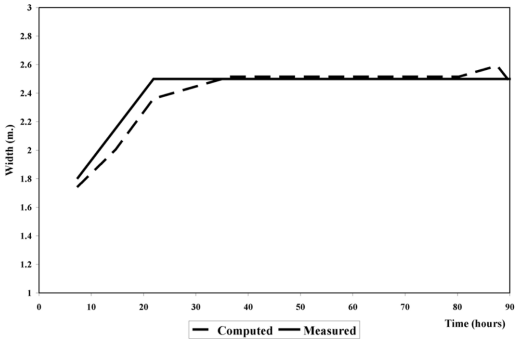


Figure 6. Evolution of width in the half depth.

Between different alternatives we choose the following experiment to validate and test the code (Fig. 4):

The numerical simulation has been made for the above experiment for 87.6 hours. The bank erosion and bed evolution process is computed and compared with the experimental data. Figure 5 shows the simulated bed elevation changes and bank erosion at a cross section. Figure 6 represents the evolution of channel width with the half depth. As it can be seen

there is a good agreement between the experiment and computational results.

5 CONCLUSION

This paper reports the research on the development and verification of a two-dimensional model in simulation of alluvial processes in a channel on a triangular mesh, which enables us to handle and define complex geometry, easily.

The bed stress term has been handled in a new form in order to consider the two-dimensional effects of flow and the bed slope effects in bed stress calculation. The bank erosion evolution has been dealt in a form, which is suitable for unstructured grids, especially the triangular mesh. However, this method needs large computational time due to its iterative process.

ACKNOWLEDGEMENT

The first author would like to express his best thanks to Professor Dr.-Ing. Wihelm Bechteler, ex-director of the Hydroscience Institute of German Armed Forces University in Munich, where the main of this work was done.

REFERENCES

Chang, H. H. 1988 "*Fluvial Process in River Engineering*", Jon Wiley & Sons, Inc., USA.

Duan, J. G.; Wang, S. S. Y. & Jia, Y. 1998 "*The Application of the Enhanced CCHE2D Model to Study the Alluvial Channel Migration Processes*", Journal of Hydraulic Research, Vol. 39, 2001, No. 5, pp 1–12.

Farshi, D. 2002 "*Two-Dimensional Simualtion of Sediment Transport on Unstructured Mesh*", Ph.D. Thesis, German Armed Forces University, Hydroscience Institute, Neubiberg (Munich), Germany.

Hudson, J. & Sweby, P. K. 2000 "*Numerical Formulation for Approximating the Equations Governing Bed-Load Sediment Transport in Channels and Rivers*", Numerical Analysis Report 2/2000, The University of Reading, Dept. of Mathematics, Reading, Berkshire.

Mosselman, E. 1992 "*Mathematical Modelling of Morphological Processes in Rivers with Erodible Cohesive Banks*", Communications on Hydraulic and Geotechnical Engineering, 92, Delft Univrsity of Technology, Delft.

Müller, R. 1943 "*Theoretische Grundlagen der Fluss-und Wildbachverbauungen*", Mitteilungen der Versuchsanstalt für Wasserbau, ETH Zürich, Nr. 4.

Olesen, K. W. 1987 "*Bed Topography in Shallow River Bends*", Communications on Hydraulic and Geotechnical Engineering, 87, Delft Univrsity of Technology, Delft.

Osman, A. M. & Thorne, C. R. 1988 "*Riverbank Stability Analysis, I: Theory*", Journal of Hydraulic Engineering, ASCE, Vol. 114, pp. 134–150.

Roe, P. L. 1981 "*Approximate Riemann Solvers, Parameter Vectors, and Difference Schemes*", Journal of Computational Physics, 40, 263–293.

Schmautuz, M. 2003 "*Eigendynamische Aufweitung in einer geraden Gewässerstrecke*", Ph.D. Thesis, Technical University Munich, Laboratory of Hydraulic and Water Resources Engineering, Munich, Germany (in German).

Van Rijn, L. C. 1993 "*Principles of Sediment Transport in Rivers, Estuaries and Coastal Seas*" AQUA Publication, Amsterdam, The Netherlands.

Wiberg, P. L. & Smith, D. L. 1989 "*Model for Calculating Bed-Load Transport of Sediment*" Journal of Hydraulic Engineering., ASCE, Vol. 115, No. 1.

Yang, C. T. & Song, C. C. S. 1986 "*Theory of Minimum Energy and Energy Dissipation Rate*", Encyclopedia of Fluid Mechanics, Vol. 1, Chapter 11, Gulf Publishing Company, Ed. Cheremisinoff, N. P.

Yen, C. & Lee, K. T. 1995 "*Bed Topography and Sediment Sorting in Channel Bend with Unsteady Flow*", Journal of Hydraulic Engineering, Vol. 121, No. 8, pp. 591–599.

Zhao, D. H.; Shen, H. W.; Lai, J. S. & Tabios, G. Q. 1996 "*Approximate Riemann Solvers in FVM for 2D Hydraulic Shock Wave Modeling*", Journal of Hydraulic Engineering, Vol. 122, No. 12, December, pp. 692–702.

This page intentionally left blank

B.3. Flood propagation

This page intentionally left blank

River Flow 2004 – Greco, Carravetta & Della Morte (eds.)
© 2004 Taylor & Francis Group, London, ISBN 90 5809 658 0

Influencing factors of flow instabilities in steep and stepped channels

T.F. Ganz
Bayerisches Landesamt für Wasserwirtschaft München, Germany

F. Schöberl
Institute of Geography, Natural Hazards Research, Innsbruck University, Austria

ABSTRACT: Grade control structures are effective measures for restricting flow energy and bed erosion and therefore frequently applied in steep creeks and torrents. Unfortunately in some cases they seem to be predisposed for initiating hazardous flow instabilities during flood flows, e.g. instable flow waves at the Ruetz river/Tyrol overtopping the river banks and causing dynamic stresses on new bank revetments could be observed, triggered the launch of a systematic model study at the University of Innsbruck. In a first phase limiting discharges for the occurrence of the instabilities were investigated. In a second step influences on the wave height and the development along the channel reach were analysed. Significant parameters influencing the emergence of flow instabilities proved to be the flow discharge and the mean bed slope. In addition to the quantification of these parameters, the experiments focused on determining further influences like bed roughness, geometry of the control structures and concentration of clay suspension. It could be proved that bed roughness and clay concentration do not influence the onset of the instabilities but have a certain effect on the development of the wave height. Wave frequencies turned out to be independent of slope, discharge, bed roughness and concentration of suspension, but proved to be strongly related to the step height of the control structures.

1 INTRODUCTION

Drop structures are effective measures for the control of flow energy and bed erosion and therefore frequently applied in steep creeks and torrents. Unfortunately in some cases they seem to be predisposed for initiating hazardous flow instabilities during flood flows, e.g. instable flow waves could be observed at the Ruetz river/Tyrol, triggering the launch of a systematic investigation at the University of Innsbruck. When waves develop, channel banks can be overtopped and inundations are the consequence. Furthermore, the dynamic stress of wave-crests on the riverbank may become dangerous for the bank protection. Concerning the design of the river banks it is important to predict the occurrence of waves and the development of wave height along the river reach. To analyse the influence of different boundary conditions on the emergence of flow instabilities, model tests were performed in a stepped laboratory flume. In a first phase, limiting discharges for the occurrence of the instabilities were investigated. In a second step influences on the wave height and the wave development along the channel reach were analysed.

Most of earlier investigations deal with flow instabilities of clear water in smooth channels, e.g. Dressler (1949), Koloseus (1966) and Brock (1969). Whittaker (1982) was one of the first to study the effect of steps and the appearance of unstable tumbling flow conditions when the fully developed submerged hydraulic jump interferes with the physical boundaries of the step-pool system. Recent contributions were for instance provided by De Fessant (2001). Experimental and theoretical evidence for the occurrence of flow instabilities in mudflows goes back to Davies (1988), Savage (1989) and Coussot (1994). Cohesion and increasing viscosity may be seen as factors increasing the possibility of the development of instabilities.

2 EXPERIMENTAL RESEARCH

This study is part of a wider research project analysing and assessing the conditions and dependencies of flow instabilities in stepped channels. In a first stage, limiting discharges for the occurrence of the instabilities were investigated, Ganz & Schöberl (2003). In the recently finished second phase, further factors influencing the wave properties and the development along the channel reach were analysed. Particular focus lay on the effect of bed roughness and the influence of varying water-clay mixtures on the developing wave

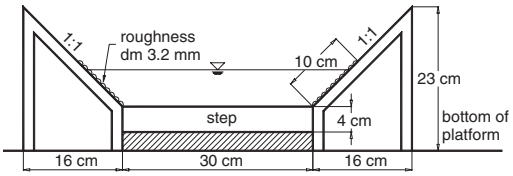


Figure 1. Scale model of the stepped channel, cross-section, example with smooth bed.

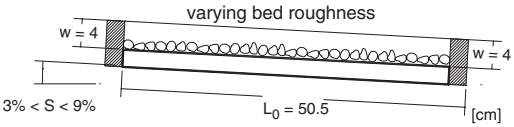


Figure 2. Longitudinal profile of a step-pool sequence, roughness of the bed is produced by pasted grains.

Table 1. Density and viscosity of the used concentrations of water-clay-mixtures.

Concentration C_f (Vol.%)	Densitiy ρ_s (g/l)	Viscosity η_s (mPas)
18	1296	3.89
12	1197	2.33
0	998	1.06

amplitudes. As this research was initiated by a real flood event at the Ruetz river, an alpine river in Austria, the shape of the model channel resembles approximately that of the river reach.

In the experiments, a tilting platform of 12 m length with a slope adjustable up to 10% inclination formed the basis for the channel model. The simulated channel (bed width 0.3 m and height 0.2 m) was straight aligned and had a trapezoidal cross section, (Figure 1). The dimensions of the channel correspond to a model scale of 1:40. At the bottom of the channel cascade-drops with a constant field length L of 0.505 m and step height w of 0.04 m, were installed, (Figure 2).

Fluid discharges up to 70 l/s with varying concentrations of clay were recirculated. The concentration of the water-clay mixture was stepwise varied from clear water to 18 Vol.%. Results of the determined fluid properties according to Ganz (2003) are given in (Table 1).

The roughness of the side walls was formed by pasted grains ($d_m = 3.2$ mm). The flume-bed between the steps was formed by surfaces of varying roughness by different nearly uniform grain mixtures, (Figure 3).

The equivalent bed sand roughness k was evaluated by the concept of Monzavi (1972). In the experiments discharge Q and slope S were systematically varied for a given clay concentration and step-pool geometry.

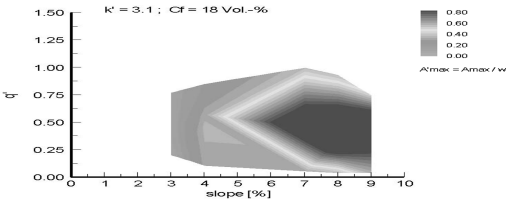


Figure 3. Used roughness categories.

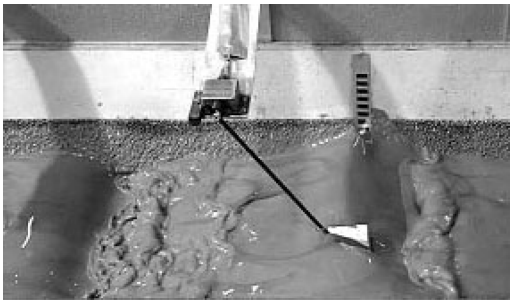


Figure 4. Arrangement of the floating device in the pool field.

The progression of water depths was followed by floating gauges installed in each pool field, (Figure 4).

Based on this equipment, the development of the waves along the channel and the maximum wave amplitudes at the end of the test reach as well as the wave frequency could be recorded for each test run.

3 WAVE FORMATION

The tests demonstrated that beyond a minimum slope instabilities form only between a lower and upper limit of discharge, The step-pool configuration essentially influences the upper flow limit, Ganz & Schöberl (2003), Ganz (2003). Boundary conditions also affect the increment of wave depths along the channel reach. The wave height is strongly related to the flow distance from the inlet section. In Figure 5 the development of the maximum flow depth from gauge to gauge is displayed. As in this example, most of the experiments indicate that the maximum of wave height is reached before the end of the experimental channel. In terms of relative distance from the entrance $x' = x/L$ a maximum is reached for $x' < 22$. When hm is the undisturbed flow depth infront of each step and hmax the peak of the water depth generated by the waves, the local wave amplitude A is given by A = hmax – hm. Figure 5 shows the relative maximum water depth hmax/hm against the distance and the discharge for a given step geometry, mean slope and roughness. The maximum envelop of hmax occurs in the central region between the upper and lower discharge limit.

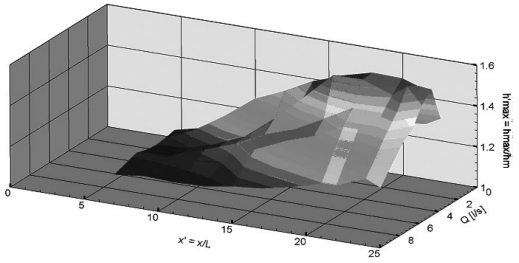


Figure 5. Development of hmax/hm along the channel for a given slope, step geometry and roughness dependent on discharge.

For the generalization of relations and criteria, dimensionless numbers are used. For constant fluid properties, dependencies according to Froude are to be expected, thus discharge is expressed by

$$q' = \frac{q}{\sqrt{g}\, w^{3/2}} \tag{1}$$

with q the specific discharge per width (m^3/s, m), g gravity acceleration (m/s^2) and w the step height of the control structure. Relative bed roughness k∗ is given by k/w. Particularly for the analysis of viscosity effects it seems important to cover the whole range between smooth-bed and rough-bed conditions. In this case a combination with the fluid property number

$$\eta_s' = \frac{\eta_s}{\sqrt{g}\cdot\rho_s\, w^{3/2}} \tag{2}$$

is used, thus the combined term is

$$k' = \frac{k\, g^{1/3}\rho_s^{\,2/3}}{\eta_s^{\,2/3}} \tag{3}$$

with k sand roughness of the bed (m), g gravity acceleration (m/s^2), ρ_s density of suspension (kg/m^3), η_s viscosity of suspension (mPas).

A'_{max} represents the maximum amplitude A_{max} divided by the step height w. Mean bed slope S and the volume concentration C_f of the clay mixture are originally dimensionless numbers.

The main object of the investigation was the evaluation of the role of viscosity and bed roughness. Therefore different scenarios of bed roughness and water-clay mixtures were tested to determine effect on the wave formation.

3.1 *Influence of roughness*

The development of wave amplitudes for smooth bed conditions as well as 3 different rough surfaces ranging from k = 4.0 mm to 13.6 mm were tested against

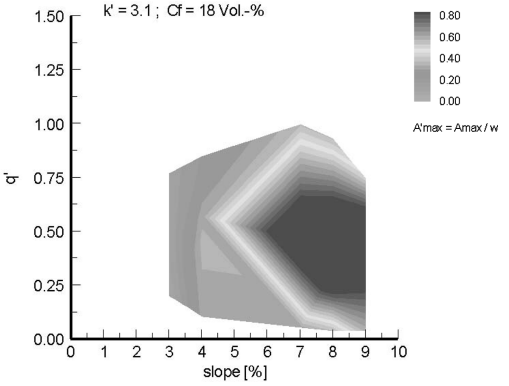


Figure 6. A'_{max} dependent on q′ and slope S for smooth bed conditions; %, k = 0.3 mm; k′ = 3.1; C_f = constant = 18%.

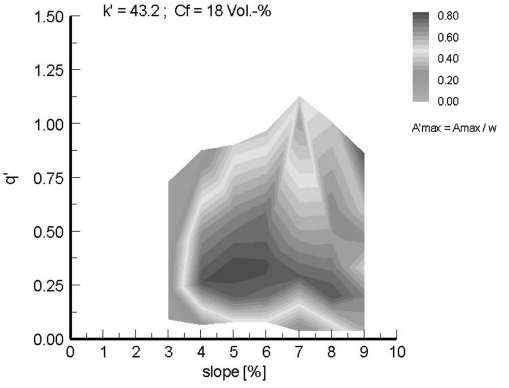


Figure 7. A'_{max} dependent on q′ and slope S, rough bed conditions 1; k = 4 mm; k′ = 43.2; C_f = constant = 18%.

discharge and slope; k′ of the smooth bed equalled 3.1, compared to rough beds with k′ between 43,2 and 139,9. Step-pool geometry and clay mixture were kept constant. Due to the complex dependencies, results were analysed by 2D colour plots (Figures 6–9). Distinct differences in the behaviour between the flow in smooth or rough-bed channels are obvious. According to Figure 6, smooth beds lead to higher amplitudes for rising slopes and a pronounced maximum in the range of 6.5% < S < 9% and 0,25 < q′ < 0, 70.

For rough beds a clear attenuation of the amplitudes with rising roughness as well as a shift of the area of maximum wave height to higher slopes can be observed. While for the smaller roughness k′ = 43, 2 the maximum area is reached for S = 5%, the area broadens for higher k′ and ends up for k′ = 139, 9 at S between 6–9%.

Figure 10 and 11 allow a detailed inspection of A′ dependent on varying roughness k′ and constant slopes of 4% and 8%.

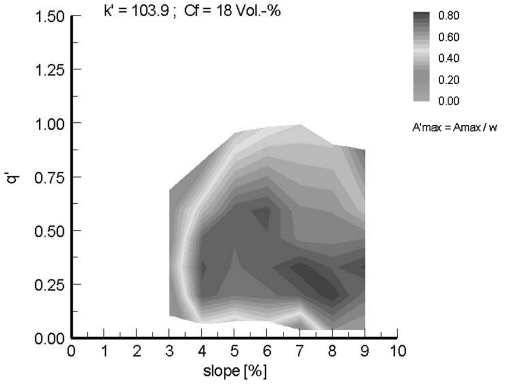


Figure 8. A'_{max} dependent on q′ and slope S, rough bed conditions 2; k = 10.1 mm; k′ = 103.9; C_f = constant = 18%.

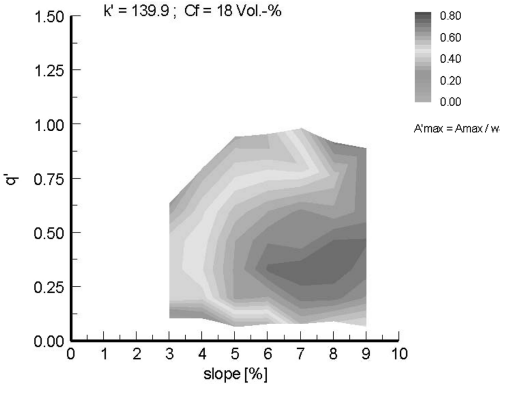


Figure 9. A'_{max} dependent on q′ and slope S, rough bed conditions 3; k = 13.6 mm; k′ = 139.9; C_f = constant = 18%.

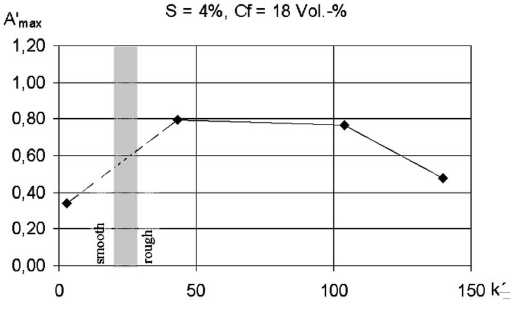


Figure 10. A'_{max} versus varying C_f, S = 4%, rough bed conditions 3; k = 13.6 mm; k′ = 139.9.

Smooth beds behave contrary to rough beds. With the higher slope A′ is amplified, with the smaller slope attenuated. The grey area marks approximately the transition between rough- and smooth-turbulent flow conditions. For rough beds the dampening effect is more pronounced for smaller slopes than for higher slopes.

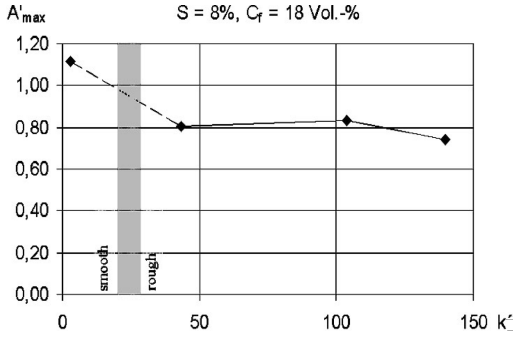


Figure 11. A'_{max} versus varying C_f, S = 8%, rough bed conditions 3; k = 13.6 mm; k′ = 139.9.

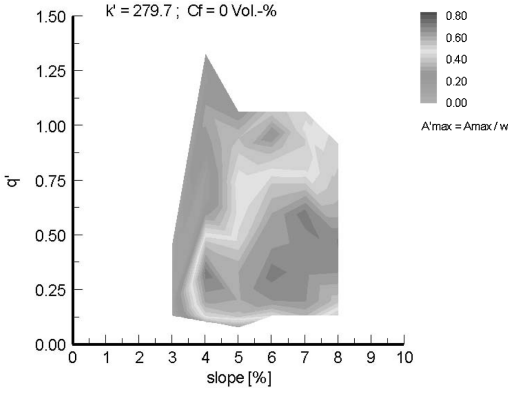


Figure 12. A'_{max} dependent on q′ and slope S, rough bed conditions 3; k = 13.6 mm; k′ = 279.7; C_f = 0%.

3.2 *Influence of viscosity*

The variation of the concentration of water-clay mixture was investigated in the range of C_f = 0% – 18%. Overall, the influence of varying concentrations kept astonishing small and can be neglected for first approximations. A detailed demonstration of the influence of concentration on A_{max} is provided by the 2D colour plots in Figures 12–14. For these test- runs different inflow conditions were applied so that the limits of discharge differs slightly to those given in Figures 6–9.

Figures 15 and 16 allow a detailed inspection of the wave development for constant mean bed slopes. For larger slopes like S = 8%, rising concentrations up to C_f = 12% produce an increase of the wave amplitude in the range of 10% . With higher concentrations, A′ is reduced even below the level of A′ of clear water conditions. This marked behaviour for higher slopes almost completely disappears for smaller slopes as S = 4%.

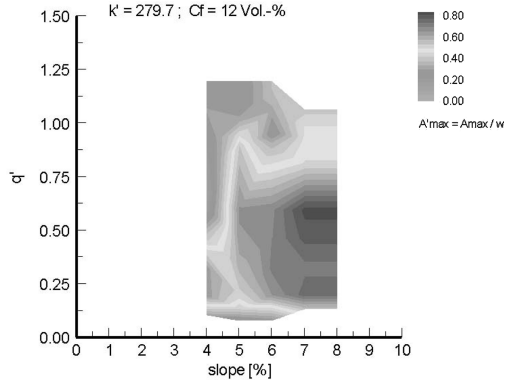


Figure 13. A'_{max} dependent on q′ and slope S, rough bed conditions 3; k = 13.6 mm; k′ = 279.7; C_f = 12 %.

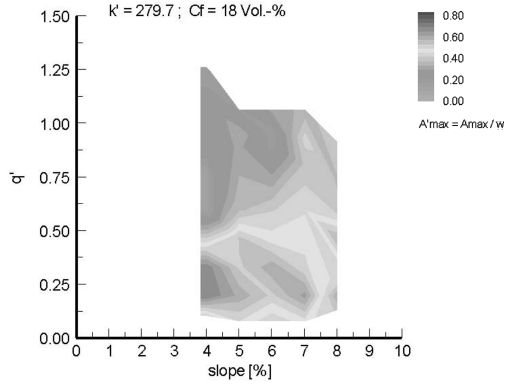


Figure 14. A'_{max} dependent on q′ and slope S, rough bed conditions 3; k = 13.6 mm; k′ = 279.7; C_f = 18%.

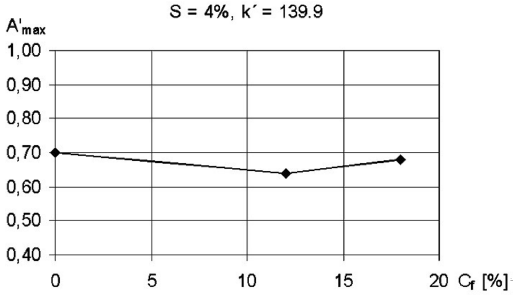


Figure 15. A'_{max} versus variable C_f; constant slope S = 4%, roughness 3; k = 13.6 mm.

3.3 *Wave frequency*

Wave frequencies have been checked downstream from drop to drop in relation to main boundary parameters. Along the channel no change in frequency could

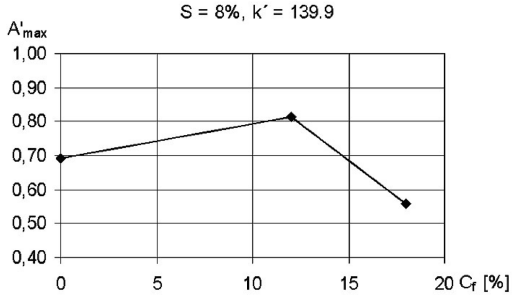


Figure 16. A'_{max} versus variable C_f, constant slope S = 8%, roughness 3; k = 13.6 mm.

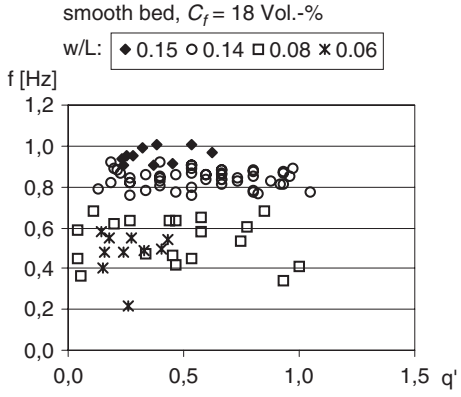


Figure 17. Range of frequencies for different step – pool ratios.

be detected. For the analysis discharge and one further parameter respectively were varied, while all other factors were kept constant. For different discharges, the analysis yielded a certain scatter of data but no definite dependency, (Figure 17).

The same was observed for variations of roughness, slope and clay concentration. However, a clear trend could be determined in relation to the step height of the system. As shown by Figure 18, wave frequency is quasi linearly related to w/L, which further demonstrates the importance of the configuration of the step-pool for the wave formation.

4 CONCLUSIONS AND PERSPECTIVES

The study clearly revealed the high complexity of the formation of instabilities in stepped channels. The wave formation is restricted to a certain range of discharge and slope. Maximum wave heights formed between an upper and lower limit of discharge. For a given step-pool geometry, the investigation

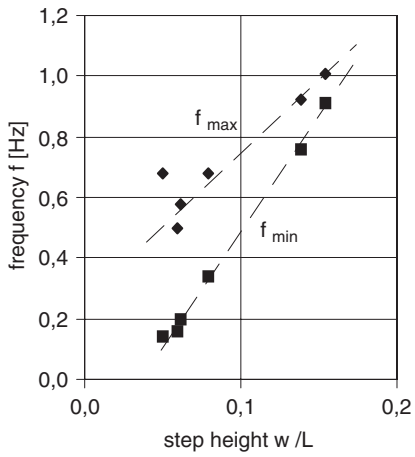


Figure 18. Range of upper and lower envelops of wave frequencies for different step pool aspect ratios.

demonstrated a significant trend of dampening of the maximum wave amplitude with increasing roughness. In addition to this, clear differences in the behaviour between the flow in smooth or rough-bed channels could be observed. Smooth beds lead to higher amplitudes for rising slopes and a distinct maximum in the range of $6.5\% < S < 9\%$ and $0.25 < q' < 0.70$. For the analyses colour plots proved to be valuable tools to illustrate the multidimensional dependencies. The variation of the clay concentration showed only limited effects on the wave formation. The impact of increasing concentration was mainly traceable with steeper slopes. An increase of concentration up to 12% generated a increase of A_{max} while a further increase reduced the amplitudes again. Overall, the effect was not as significant as the change in roughness. Thus in a first approximation, for conditions with concentrations below 18% and rough turbulent beds, a Froude-dependency for the wave formation can be presumed. Wave frequencies turned out to be independent of slope, discharge, bed roughness and the concentration of suspension, but proved to be strongly related to the step height of the control structures.

The determined influences of different parameters are mainly to be seen as a first step for understanding this phenomenon. In order to widen the range of boundary conditions as well as to condense the hydraulic information within the step-pool configuration, numerical simulations have been launched. This additional approach will allow to extend and strengthen the criteria developed in the scale model.

ACKNOWLEDGEMENTS

The Authors wish to thank the “Forsttechnischer Dienst für Wildbach und Lawinenverbauung” for the financial support of the project.

REFERENCES

Brock, R.R. 1969. Development of roll wave trains in open channels. *Journal of the Hydraulics Division*, ASCE, Vol. 95, No. HY 4, Proc. Paper 6704, pp. 1401–1427

Coussot, Ph. 1994. Mud Flow Dynamics. *International Workshop on Floods and Inundations related to Large Earth Movements*, pp. A7.1–A7.12

Davies, T. 1988. Debris Flow Surges – A Laboratory Investigation. Mitteilung der Versuchsanstalt für Wasserbau, Hydrologie und Glaziologie, ETH Zürich

Dressler, R.F. 1949. Mathematical Solution of the Problem of Roll-Waves in Inclined Open Channels. *Communications on pure and applied mathematics*. Vol. 2, pp. 149–194

De Fessant, A.-L. 2001. Étude des instabilités d’un écoulement à surface libre – Sur un fond à géométrie périodique. Ph.D. thesis, Institut National Polytechnique de Toulouse, France

Ganz, T. 2003. Entstehung und Entwicklung von Abflussinstabilitäten bei Absturztreppen, Dissertation, Institut für Wasserbau, Universität Innsbruck

Ganz, T., Schöberl, F. 2003. Limit of Flow Instability in Steep Stepped Channels, XXX IAHR Congress Thessaloniki

Monzavi, M.T. 1972. Widerstandsgesetz auf statistischer Basis für extreme natürliche Rauheiten, Bericht des Institutes für Hydraulik und Hydrologie der Technischen Hochschule Darmstadt, Nr. 8

Koloseus, H.J., Davidian, J. 1966. Free-Surface Instability Correlation. U.S.G.S. Water-Supply Paper 1592-C

Savage, S.B. 1989. Flow of Granular Materials. In: Germain et al (eds.), *Theoretical and Applied Mechanics*, pp. 241–266. Amsterdam: Elsevier

Whittaker, J.G. 1982. Flow and Sediment Movement in Stepped Channels. Ph.D. thesis, Lincoln College, University of Canterbury, Christchurch, New Zealand

River Flow 2004 – Greco, Carravetta & Della Morte (eds.)
© 2004 Taylor & Francis Group, London, ISBN 90 5809 658 0

3D calculation of curved open channel flow using physical curvilinear coordinates

Mu-lan Zhu
Hydro-soft Technology Institute Co., Ltd., Tokyo, Japan

Yasuyuki Shimizu
Hokkaido University, Hokkaido, Japan

Mitsuhiro Nakata & Kazufumi Hayashida
Development and Construction office of Ishikari River, Hokkaido, Japan

Kunio Ezaki
Foundation of Hokkaido River Disaster Prevention Research Center, Hokkaido, Japan

Hideaki Mizutani
Hydro-soft Technology Institute Co., Ltd., Tokyo, Japan

ABSTRACT: Three difficulties exist in numerical simulations of the flowfield at estuary. (a)Water depths are large and it is difficult to apply a 2-dimensional shallow water model to this kind of flowfield; (b) The boundaries are curved and complex, and do not coincide with coordinate lines in the Cartesian system (x^1, x^2, x^3); (c) It is not easy to generate a grid that varies gradually throughout the whole flowfield. The authors solve these three difficulties by adopting the 3D governing equations and the use of physical curvilinear coordinates $(\xi^{(1)}, \xi^{(2)}, \xi^{(3)})$ which is a physical counterpart of the generalized curvilinear coordinates and was originally proposed by Truesdell. The proposed model is applied to an experimental channel, and calculated values are compared to observed values and the agreement between them is generally good. Our next step of study is to apply the model to real rivers and include sediment transportation to the model.

1 INTRODUCTION

It is very important to predict flowfield and river-bed deformation for channel planning work. However, there are three difficulties in numerical simulations of the flowfield at estuary. First, water depths are large and the flowfield shows a strong 3-dimensional property, thus it is difficult to apply a 2-dimensional shallow water model to this kind of flowfield; Secondly, the boundaries are very complex, they include the external curved boundary of the high-water channel and the internal curved boundary of the low-water channel, and do not coincide with coordinate lines in the Cartesian system (x^1, x^2, x^3). Moreover, the water surface, namely the boundary in the vertical direction keeps varying during a flood; Thirdly, it is not easy to generate a grid that varies gradually throughout the whole flowfield. Usually as shown in Figure 1.1, a significant difference of adjacent mesh size can exist near the boundary between the low-water and high-water channel, unless a complex process for grid generation is employed.

Most existing numerical models in river hydraulics are 2-dimensional, and are unable to deal with the first difficulty. Although some existing models are developed in 3D, they use the Cartesian system (x^1, x^2, x^3) and make the imposition of boundary conditions difficult, namely they still retain the disadvantage of the second difficulty. Only a few existing models for rivers can solve both the first and second difficulty by adopting the 3D governing equations and the use of generalized curvilinear coordinates (ξ^1, ξ^2, ξ^3).

The generalized coordinate domain is constructed so that a computational boundary in physical space coincides with a coordinate line in generalized-coordinate space (called computational space also). Figure 1.2 shows a 2-dimensional mapping condition from an irregular physical domain to a square generalized-coordinate domain, where the non-uniform curved segments of Δs, Δn which are

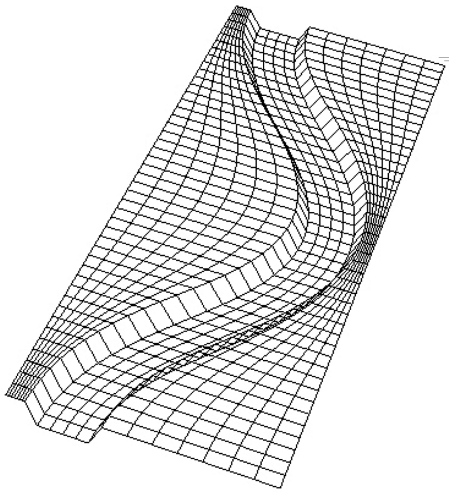


Figure 1.1. An image of generated grid.

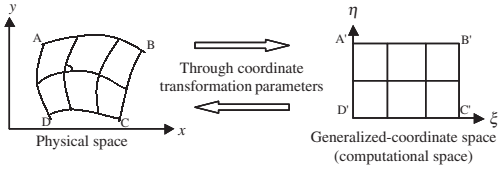


Figure 1.2. A mapping from physical domain to generalized-coordinate domain.

non-orthogonal to each other are mapped to the uniform straight segments of $\Delta\xi^1$, $\Delta\xi^2$ which are orthogonal to each other. The mapping not only deforms the boundaries but also transforms the directions and magnitudes of flow variables, i.e., it also transforms the governing equations. There are many options in formulating the governing equations transformed from Cartesian coordinates (x^1, x^2, x^3) to generalized curvilinear coordinates (ξ^1, ξ^2, ξ^3). The main options can be classified as follows:

(a) The governing equations may be expressed in a semi-contravariant form in terms of generalized curvilinear coordinates (ξ^1, ξ^2, ξ^3), in which the Cartesian velocity of u and the contravariant velocity of U coexist. This is the most extensively used option and most of the numerical models in computational hydraulics are developed in this way. However, this kind of method has two problems. First, the velocity variables should be arranged at the boundary of a control volume in generalized-coordinate space (ξ^1, ξ^2, ξ^3) when using a staggered mesh, but it is impossible to arrange the Cartesian velocity in this way. Secondly, the method suffers from a problem of undesirable mesh sensitivities. According to some theoretical error analyses [1], additional errors associated with the use of generalized curvilinear coordinates (ξ^1, ξ^2, ξ^3) may be significant and consequently, result in a computational stability problem if non-uniformity of the grid in physical space is considerable. Therefore, it is necessary when using this method to have the generated grid in the physical domain grow slowly.

(b) The governing equations may be expressed in a complete-contravariant form in terms of generalized curvilinear coordinates (ξ^1, ξ^2, ξ^3), in which the Cartesian velocity is no longer involved. This method eliminates the first problem stated in (a) which is caused by the coexisting of Cartesian velocity, but still retains the disadvantage of undesirable mesh sensitivities like that in (a). Koshizuka et al. [2] [3] [4] show, theoretically as well as numerically, that stability problems may occur when the mesh size of the adjacent cells differ by more than a factor of 3.

From the above descriptions, it can be seen that the existing 3-dimensional model using generalized curvilinear coordinates can deal with the first and second difficulties, but still suffers from a problem of mesh sensitivities caused by the third difficulty stated above. It is the above weaknesses in the existing models that motivate our studies. Namely, our study objective is to develop a new model applicable to the severe calculation conditions with three difficulties at estuary, and provide the useful prediction results of flowfield for channel planning work. As the first step of our study, the developed model is applied to an experimental channel for the easier program debugging and the model verification. Our next step of study is to apply the model to real rivers and include sediment transportation to the present model of flow calculation.

2 THREE-DIMENSIONAL FLOW CALCULATION MODEL

As stated in the above, there is a problem of mesh sensitivity when using the generalized curvilinear coordinate. To solve this problem, we must first find out the cause of the problem.

When the governing equations are transformed from the Cartesian coordinate system into the generalized curvilinear coordinate system, the Cartesian velocities in physical space of (u^1, u^2, u^3) are transformed to the contra-variant velocity of (U^1, U^2, U^3) (or co-variant velocity) in generalized-coordinate space. It can be derived out that $U^i = u^{(i)}/\Delta\xi^{(i)}$ where $u^{(i)}$ is identical to the velocity along i mesh-line direction in physical space and $\Delta\xi^{(i)}$ is identical to the mesh width in i direction in physical space. Thus, the field of contra-variant velocity in generalized-coordinate space will be very non-uniform once if the generated mesh sizes are rather non-uniform, even if the field of velocity in physical space is uniform. Especially when the field of velocity is also non-uniform, and its

most varying place is the exactly same as that of mesh size, then this kind of variation will be doubled and the calculation stability problem will be aggravated.

To solve this problem, Demirdzic et al. [5], Koshizuka [2–4] and Takizwa et al. [6] introduce the use of physical components to generalized curvilinear coordinates that was originally proposed by Truesdell. The transformed governing equations are expressed in the coordinate system $(\xi^{(1)}, \xi^{(2)}, \xi^{(3)})$ with the velocity of $u^{(i)}$, where coordinate system $(\xi^{(1)}, \xi^{(2)}, \xi^{(3)})$ is the physical counterpart of the generalized curvilinear coordinates (ξ^1, ξ^2, ξ^3), and the velocity $u^{(i)}$, equal to $U^i \times \Delta\xi^{(i)}$, is the physical counterpart of contravariant velocity U^i in the physical curvilinear space. It can be derived out that $u^{(i)}$ in physical curvilinear space $(\xi^{(1)}, \xi^{(2)}, \xi^{(3)})$ is actually identical to the velocity along the mesh-line direction of i in physical space.

It should be noted that the superscript parentheses are used to denote physical components throughout the paper.

To avoid possible confusion, the coordinate systems and the velocity denotations mentioned in the paper are summarized below. (x^1, x^2, x^3) represents the well-known Cartesian coordinate system in physical space. (ξ^1, ξ^2, ξ^3) represents the generalized curvilinear coordinate system in generalized-coordinate space (called computational space also). $(\xi^{(1)}, \xi^{(2)}, \xi^{(3)})$ represents the physical curvilinear coordinate system in physical curvilinear space which is actually identical to physical space. Figure 2.1 shows these analytical spaces and coordinate systems. (u^1, u^2, u^3) are the Cartesian velocities in physical space; (U^1, U^2, U^3) are the contra-variant velocities in generalized-curvilinear space; $(u^{(1)}, u^{(2)}, u^{(3)})$ in physical curvilinear space are identical to the velocities along the mesh-line direction in physical space.

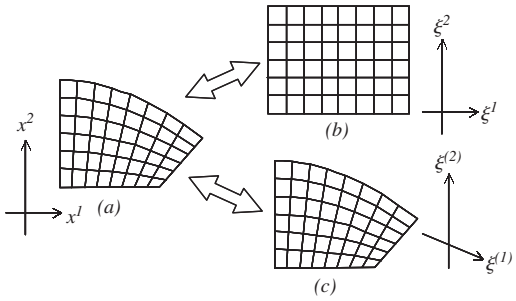


Figure 2.1. Analytical space and coordinate systems (a) physical space, Cartesian coordinate system, (b) generalized-coordinate space, generalized curvilinear coordinate system and (c) physical curvilinear space identical to physical space, physical curvilinear coordinate system.

2.1 *Governing equations in the physical curvilinear coordinate system*

(a) Governing equations in the Cartesian coordinate system

- Continuity equation

$$\frac{\partial u^i}{\partial x^i} = 0 \tag{2.1}$$

- Momentum equation

$$\frac{\partial u^i}{\partial t} + \frac{\partial}{\partial x^j}(u^i u^j - \tau^{ij}) = S^i - \frac{1}{\rho}\delta^{ij}\frac{\partial P}{\partial x^j} \tag{2.2}$$

and,

$$\tau^{ij} = \nu_T\left(\delta^{im}\frac{\partial u^j}{\partial x^m} + \delta^{jm}\frac{\partial u^i}{\partial x^m}\right) \tag{2.3}$$

where, $i, j, k = 1, 2, 3$, u^i is velocity in x^i direction; P is pressure $= \rho GH$, and ρ, H, G is water density, water level and gravitational acceleration $= 9.8\ \mathrm{m^2/s}$ respectively; δ^{ij} is Kronecker's delta defined as $\delta^{ij} = 1$ if $i = j$ and $\delta^{ij} = 0$ if $i \neq j$; S^i is external forces in x^i direction, τ^{ij} is a tensor representing Reynolds stresses; ν_T is the turbulent viscosity and can be evaluated as follows:

$$\nu_T = \kappa u_\star z'\left(1 - \frac{z'}{h_s}\right) \tag{2.4}$$

where κ is the Von Karman constant (≈ 0.4), h_s is the water depth; u_* is the shear velocity at channel bed; and z' is the height from the channel bed.

(b) Basic concepts related to transformation of coordinate system

Chain rule is often used in the transformation of coordinate system. However, when using this method, the contra-variant velocity of U^i and the Cartesian velocity of u^i coexist in the transformed governing equations. In this paper, instead of using chain rule, we transform the governing equations based on the geometric differential calculus. Several fundamental concepts of geometric differential calculus related to the coordinate system transformation are introduced as follows:

(b-1) fundamental co-variant tensor g_{ij}

If the coordinates of two neighbor grid points in computational space are represented by ξ^i and $\xi^i + d\xi^i$ respectively, then their physical distance of ds in physical space has an expression as:

$$ds^2 = g_{ij}\, d\xi^i d\xi^j \tag{2.5}$$

The physical meaning of g_{ij} can be explained as follows:

When the mesh width of $d\xi^i$ in computational space is equal to 1, $\sqrt{g_{ii}}$ represents the mesh width in i direction in physical space, and $\sqrt{g_{ij}}$ represents the area of (i,j) mesh in physical space.

(b-2) Determinant of fundamental co-variant tensor g

$$g = \left|g_{ij}\right| = \begin{vmatrix} g_{11} & g_{12} & g_{13} \\ g_{21} & g_{22} & g_{23} \\ g_{31} & g_{32} & g_{33} \end{vmatrix} = J^2 \tag{2.6}$$

where J is the well-known Jacobian which can be also defined by the determinant of coordinate transformation coefficients. The physical meaning of g is: if the mesh width in computational space is equal to 1, then $\sqrt{g}$ represents the cubic volume of (i,j,k) mesh.

(b-3) Physical fundamental co- and contra-variant tensor $g_{(ij)}$ and $g^{(ij)}$

$$g_{(ij)} = \frac{g_{ij}}{\sqrt{g_{ii}g_{jj}}} \qquad g^{(ij)} = \sqrt{g_{ii}g_{jj}}\,g^{ij} \tag{2.7}$$

(b-4) Christoffel Symbol and Physical Christoffel Symbol

Christoffel symbol can be expressed by coordinate transformation coefficients as follows:

$$\begin{Bmatrix} i \\ j \quad k \end{Bmatrix} = \frac{\partial \xi^i}{\partial x^m}\frac{\partial^2 x^m}{\partial \xi^j \partial \xi^k} \tag{2.8}$$

and physical christoffel symbol has a relationship with christoffel symbol as follows:

$$\begin{pmatrix} i \\ j \quad k \end{pmatrix} = \sqrt{\frac{g_{ii}}{g_{jj}g_{kk}}}\left(\begin{Bmatrix} i \\ j \quad k \end{Bmatrix} - \delta^i_j \frac{g_{jm}}{g_{jj}}\begin{Bmatrix} m \\ j \quad k \end{Bmatrix}\right) \tag{2.9}$$

Christoffel symbol represents how many changes of the vector component in i direction are caused when the unit vector in j direction moves one unit length in k direction.

Figure 2.2 shows the cases of $\left\{{}_2{}^1{}_2\right\}$ *and* $\left\{{}_1{}^2{}_1\right\}$ which actually represent the curvatures of mesh-line in j direction and i direction.

(c) Transformation based on geometric differential calculus

The following transformations from the Cartesian coordinate system to the physical curvilinear coordinate system based on geometric differential calculus are introduced:

- Scalars

$$\phi \to \phi \tag{2.10}$$

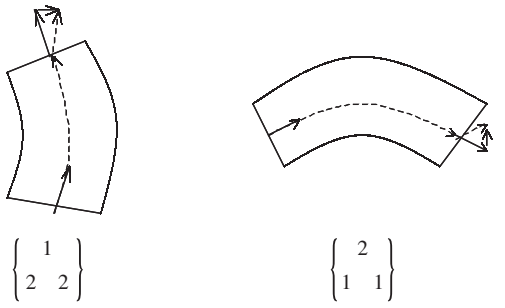


Figure 2.2. Physical meaning of the physical christoffel symbol $\left\{{}_2{}^1{}_2\right\}$ and $\left\{{}_1{}^2{}_1\right\}$.

$$\frac{\partial \phi}{\partial x^j} \to \frac{\partial \phi}{\partial \xi^{(j)}} \tag{2.11}$$

- Vectors

$$a^i \to a^{(i)} \tag{2.12}$$

$$\frac{\partial a^i}{\partial x^j} \to \nabla_{(j)} a^{(i)} = \frac{\partial a^{(i)}}{\partial \xi^{(j)}} + a^{(m)}\begin{pmatrix} i \\ m \quad j \end{pmatrix} \tag{2.13}$$

$$\frac{\partial a^j}{\partial x^j} \to \nabla_{(J)} a^{(J)} = \frac{\Delta a^{(J)}}{\Delta \xi^{(J)}} \tag{2.14}$$

- Tensors

$$A^{ij} \to A \quad (\delta^{ij} \to g^{(ij)} \quad \delta_{ij} \to g_{(ij)}) \tag{2.15}$$

$$\frac{\partial A^{ij}}{\partial x^j} \to \nabla_{(J)} A^{(ij)} = \frac{\Delta A^{(ij)}}{\Delta \xi^{(J)}} + A^{(mj)}\begin{pmatrix} i \\ m \quad j \end{pmatrix} \tag{2.16}$$

where, $a^{(i)}$ and $A^{(i)}$ are physical vector and tensor components in the physical curvilinear coordinate system $\xi^{(i)}$, and $\Delta / \Delta\xi^{(j)}$ is the differential operator defined as:

$$\frac{\Delta}{\Delta \xi^{(J)}} = \sqrt{\frac{g_{jj}}{g}}\frac{\partial}{\partial \xi^{(J)}}\sqrt{\frac{g}{g_{jj}}} \tag{2.17}$$

(d) Governing equations in the physical curvilinear coordinate system

Based on the transformation given in (c), the governing equations can be transformed from the Cartesian coordinate system to the physical curvilinear coordinate system as follows:

- Continuity equation:

$$\frac{\Delta}{\Delta^{(i)}} u^{(i)} = 0 \tag{2.18}$$

- Momentum equation:

$$\frac{\partial u^{(i)}}{\partial t}+\frac{\Delta}{\Delta\xi^{(j)}}(u^{(i)}u^{(j)}-\tau^{(ij)}) +\begin{pmatrix} i \\ m \quad j \end{pmatrix}(u^{(m)}u^{(j)}-\tau^{(mj)})=S^{(i)}-g^{(ij)}\frac{\partial P}{\partial\xi^{(j)}} \tag{2.19}$$

2.2 *Calculation algorithm*

SMAC algorithm is employed in the calculation. The characteristic of SMAC algorithm is that only the velocity derivative term in the continuity equation and the pressure derivative term in the momentum equation are calculated implicitly, while other terms are calculated explicitly, and the time derivative term in the momentum equation is discretized with Euler's method. Besides, a CIP (Cubic-Interpolated Pseudoparticle) originally proposed by Yabe [7–8] is employ to deal with the convective term in the momentum equation. It is well known that a problem of calculation stability is often caused by the convective term when velocity is high, while the CIP method has the advantage of calculation stability in dealing with the convective term with high velocity.

The transformed governing equations shown in Eq.(2.18–2.19) seem very simple, however they are actually complicated when they are unfolded. The momentum equation in the $\xi^{(1)}$ direction unfolded from Eq.(2.19) has an expression as:

$$\frac{u_{n+1}^{(1)}-u_n^{(1)}}{\Delta t}+u^{(1)}\frac{\partial u^{(1)}}{\partial\xi^{(1)}}+u^{(2)}\frac{\partial u^{(1)}}{\partial\xi^{(2)}}+u^{(3)}\frac{\partial u^{(1)}}{\partial\xi^{(3)}}=R_{n+1}^{(1)} \tag{2.20}$$

where n denotes time step and $R_{n+1}^{(1)}$ is expressed as:

$$\begin{aligned}R_{n+1}^{(1)}=&\sqrt{\frac{g_{11}}{g}}\frac{\partial}{\partial\xi^{(1)}}\left(\sqrt{\frac{g}{g_{11}}}\tau^{(11)}\right)+\sqrt{\frac{g_{22}}{g}}\frac{\partial}{\partial\xi^{(2)}}\left(\sqrt{\frac{g}{g_{22}}}\tau^{(12)}\right)\\&+\sqrt{\frac{g_{33}}{g}}\frac{\partial}{\partial\xi^{(3)}}\left(\sqrt{\frac{g}{g_{33}}}\tau^{(13)}\right)\\&+\begin{pmatrix}1\\1\quad1\end{pmatrix}(\tau^{(11)}-u_n^{(1)}u_n^{(1)})+\begin{pmatrix}1\\1\quad2\end{pmatrix}(\tau^{(12)}-u_n^{(1)}u_n^{(2)})\\&+\begin{pmatrix}1\\1\quad3\end{pmatrix}(\tau^{(13)}-u_n^{(1)}u_n^{(3)})\\&+\begin{pmatrix}1\\2\quad1\end{pmatrix}(\tau^{(21)}-u_n^{(2)}u_n^{(1)})+\begin{pmatrix}1\\2\quad2\end{pmatrix}(\tau^{(22)}-u_n^{(2)}u_n^{(2)})\\&+\begin{pmatrix}1\\2\quad3\end{pmatrix}(\tau^{(23)}-u_n^{(2)}u_n^{(3)})\\&+\begin{pmatrix}1\\3\quad1\end{pmatrix}(\tau^{(31)}-u_n^{(3)}u_n^{(1)})+\begin{pmatrix}1\\3\quad2\end{pmatrix}(\tau^{(32)}-u_n^{(3)}u_n^{(2)})\\&+\begin{pmatrix}1\\3\quad3\end{pmatrix}(\tau_n^{(33)}-u_n^{(3)}u_n^{(3)})\\&-g^{(11)}\frac{1}{\rho}\frac{\partial P_{n+1}}{\partial\xi^{(1)}}-g^{(12)}\frac{1}{\rho}\frac{\partial P_{n+1}}{\partial\xi^{(2)}}-g^{(13)}\frac{\partial P_{n+1}}{\partial\xi^{(3)}}+S_n^{(1)}\end{aligned} \tag{2.21}$$

Herein, Eq.(2.21) is expressed in a non-conservation form for using CIP method to calculate the convective terms. To explain the essence of CIP method, considering an one-dimensional momentum equation with free water surface as expressed in Eq.(2.22):

$$\frac{\partial f}{\partial t}+u\frac{\partial f}{\partial x}=g^{*} \tag{2.22}$$

where g^{*} represents pressure derivative term, friction term, viscous stresses as well as Reynolds stresses and etc.; f represents velocity. Eq.(2.22) can be split into the following two phases which are advection phase and non-advection phase.

Advection phase:

$$\frac{f^{*}-f^{n}}{\Delta t}+u\frac{\partial f}{\partial x}=0 \tag{2.23}$$

Non-advection phase:

$$\frac{f^{n+1}-f^{*}}{\Delta t}=g^{*} \tag{2.24}$$

where n denotes time step. It can be seen that Eq (2.23) is actually a wave motion equation. According to the characteristic of wave motion equation, the value of f at future $t+\Delta t$ time at the place of x_i is actually equal to the value of f at present t time at the place of $x_i-u\Delta t$ as shown in Figure 2.3, i.e.,

$$f(x_i,t+\Delta t)=f(x_i-u\Delta t,t) \tag{2.25}$$

When $u>0$ and Δt is small enough so that the point of $x_i-u\Delta t$ is between the two points of x_{i-1} and x_i, the value of $f(x_i-u\Delta t,\ t)$ can be estimated based on the known values of $f(x_{i-1},t)$ and $f(x_i,t)$ by various methods. One of those methods is the CIP method proposed by Yabe [7–8]. The CIP method employs a cubic polynomial function $F(X)$ as expressed in Eq.(2.26) to do interpolation between the two points of x_{i-1} and x_i.

$$f(x_i-u\Delta t,t)=F(X)=a_iX^3+b_iX^2+\frac{\partial f_i}{\partial x}X+f_i \tag{2.26}$$

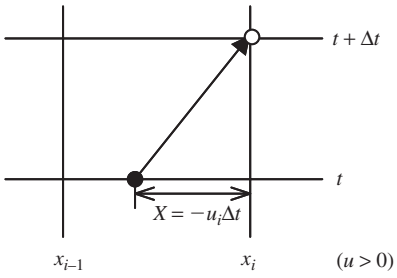


Figure 2.3. Characteristic of wave motion.

where $X=-u_i\Delta t$, and the coefficients of a_i, b_i can be evaluated based on the known values of $f(x_{i-1}, t)$ and $f(x_i, t)$ at present time of t. Therefore, using the central finite difference method to calculate advection phase shown in Eq.(2.23), and then using the CIP method to calculate non-advection phase shown in Eq.(2.24), we can obtain the answer of original governing equation of Eq.(2.22).

By extending the above approach to 3-D system, we have [8]:

$$\frac{\partial f}{\partial t}+u^{(1)}\frac{\partial f}{\partial \xi^{(1)}}+u^{(2)}\frac{\partial f}{\partial \xi^{(2)}}+u^{(3)}\frac{\partial f}{\partial \xi^{(3)}}=g^{*} \qquad (2.27)$$

The interpolation function within a cubic grid cell is:

$$\begin{aligned}
&F_{i,j,k}(X^{(1)},X^{(2)},X^{(3)})=\\
&[(A1_{i,j,k}X^{(1)}+A2_{i,j,k}X^{(2)}+A3_{i,j,k}X^{(3)}+A4_{i,j,k})X^{(1)}+\\
&A5_{i,j,k}X^{(2)}+\partial_{\xi^{(1)}}f_{i,j,k}]X^{(1)}+\\
&[(A6_{i,j,k}X^{(2)}+A7_{i,j,k}X^{(3)}+A8_{i,j,k}X^{(1)}+A9_{i,j,k})X^{(2)}+\\
&A10_{i,j,k}X^{(3)}+\partial_{\xi^{(2)}}f_{i,j,k}]X^{(2)}+\\
&[(A11_{i,j,k}X^{(3)}+A12_{i,j,k}X^{(1)}+A13_{i,j,k}X^{(2)}+A14_{i,j,k})X^{(3)}\\
&+A15_{i,j,k}X^{(1)}+\partial_{\xi^{(3)}}f_{i,j,k}]X^{(3)}+\\
&A16_{i,j,k}X^{(1)}X^{(2)}X^{(3)}+f_{i,j,k} \qquad (2.28)
\end{aligned}$$

where

$$X^{(1)}=-u^{(1)}\Delta t \quad X^{(2)}=-u^{(2)}\Delta t \quad X^{(3)}=-u^{(3)}\Delta t$$

$$\partial_{\xi^{(1)}}f=\partial f/\partial\xi^{(1)} \quad \partial_{\xi^{(2)}}f=\partial f/\partial\xi^{(2)} \quad \partial_{\xi^{(3)}}f=\partial f/\partial\xi^{(3)}$$

and,

$$A1_{i,j,k}=[-2D_i+\partial_{\xi^{(1)}}(f_{im,j,k}+f_{i,j,k})\Delta\xi^{(1)}]/[\Delta\xi^{(1)}]^3$$

$$A2_{i,j,k}=-[A17_{i,j,k}+\partial_{\xi^{(1)}}D_j\Delta\xi^{(1)}]/[\Delta\xi^{(1)}]^2\Delta\xi^{(2)}$$

$$A3_{i,j,k}=-[A18_{i,j,k}+\partial_{\xi^{(1)}}D_k\Delta\xi^{(1)}]/[\Delta\xi^{(1)}]^2\Delta\xi^{(3)}$$

$$A4_{i,j,k}=[3D_i-\partial_{\xi^{(1)}}(f_{im,j,k}+2f_{i,j,k})\Delta\xi^{(1)}]/[\Delta\xi^{(1)}]^2$$

$$A5_{i,j,k}=[A17_{i,j,k}+\partial_{\xi^{(1)}}D_j\Delta\xi^{(1)}+\partial_{\xi^{(2)}}D_i\Delta\xi^{(2)}]/\Delta\xi^{(1)}\Delta\xi^{(2)}$$

$$A6_{i,j,k}=[-2D_j+\partial_{\xi^{(2)}}(f_{i,jm,k}+f_{i,j,k})\Delta\xi^{(2)}]/[\Delta\xi^{(2)}]^3$$

$$A7_{i,j,k}=-[A19_{i,j,k}+\partial_{\xi^{(2)}}D_k\Delta\xi^{(2)}]/[\Delta\xi^{(2)}]^2\Delta\xi^{(3)}$$

$$A8_{i,j,k}=-[A17_{i,j,k}+\partial_{\xi^{(2)}}D_i\Delta\xi^{(2)}]/\Delta\xi^{(1)}[\Delta\xi^{(2)}]^2$$

$$A9_{i,j,k}=[3D_j-\partial_{\xi^{(2)}}(f_{i,jm,k}+2f_{i,j,k})\Delta\xi^{(2)}]/[\Delta\xi^{(2)}]^2$$

$$A10_{i,j,k}=[A19_{i,j,k}+\partial_{\xi^{(2)}}D_k\Delta\xi^{(2)}+\partial_{\xi^{(3)}}D_j\Delta\xi^{(3)}]/\Delta\xi^{(2)}\Delta\xi^{(3)}$$

$$A11_{i,j,k}=[-2D_k+\partial_{\xi^{(3)}}(f_{i,j,km}+f_{i,j,k})\Delta\xi^{(3)}]/[\Delta\xi^{(3)}]^3$$

$$A12_{i,j,k}=-[A18_{i,j,k}+\partial_{\xi^{(3)}}D_i\Delta\xi^{(3)}]/\Delta\xi^{(1)}[\Delta\xi^{(3)}]^2$$

$$A13_{i,j,k}=-[A19_{i,j,k}+\partial_{\xi^{(3)}}D_j\Delta\xi^{(3)}]/\Delta\xi^{(2)}[\Delta\xi^{(3)}]^2$$

$$A14_{i,j,k}=[3D_k-\partial_{\xi^{(3)}}(f_{i,j,km}+2f_{i,j,k})\Delta\xi^{(3)}]/[\Delta\xi^{(3)}]^2$$

$$A15_{i,j,k}=[A18_{i,j,k}+\partial_{\xi^{(3)}}D_i\Delta\xi^{(3)}+\partial_{\xi^{(1)}}D_k\Delta\xi^{(1)}]/\Delta\xi^{(1)}\Delta\xi^{(3)}$$

$$\begin{aligned}
A16_{i,j,k}=&[A17_{i,j,k}+f_{i,j,km}-(f_{i,jm,km}+f_{im,j,km})+\\
&f_{im,jm,km}]/\Delta\xi^{(1)}\Delta\xi^{(2)}\Delta\xi^{(3)} \qquad (2.29)
\end{aligned}$$

where,

$$\begin{aligned}
D_i&=f_{im,j,k}-f_{i,j,k}\\
D_j&=f_{i,jm,k}-f_{i,j,k}\\
D_k&=f_{i,j,km}-f_{i,j,k}\\
A17_{i,j,k}&=-f_{i,j,k}+f_{im,j,k}+f_{i,jm,k}-f_{im,jm,k}\\
A18_{i,j,k}&=-f_{i,j,k}+f_{im,j,k}+f_{i,j,km}-f_{im,j,km}\\
A19_{i,j,k}&=-f_{i,j,k}+f_{i,jm,k}+f_{i,j,km}-f_{i,jm,km} \qquad (2.30)
\end{aligned}$$

and,

$$\begin{cases} im=i-1 & if\ u^{(1)}>0 \\ im=i+1 & if\ u^{(1)}<0 \end{cases}$$

$$\begin{cases} jm=i-1 & if\ u^{(2)}>0 \\ jm=i+1 & if\ u^{(2)}<0 \end{cases} \quad \begin{cases} km=k-1 & if\ u^{(3)}>0 \\ km=k+1 & if\ u^{(3)}<0 \end{cases} \qquad (2.31)$$

where $\Delta\xi^{(1)}, \Delta\xi^{(2)}, \Delta\xi^{(3)}$ are the mesh widths in $\xi^{(1)}, \xi^{(2)}, \xi^{(3)}$direction respectively.

The whole calculation procedure can be summarized as the following four steps:

(1) To calculate the pseudo-velocity $\hat{u}_{n+1}^{(i)}$

Eq.(20) can be modified to Eq.(2.32) by substituting the implicit term of $\partial P_{n+1}/\partial\xi^{(i)}$ for the explicit term of $\partial P_n/\partial\xi^{(i)}$ in Eq.(2,21), then pseudo-velocity $\hat{u}_{n+1}^{(1)}$ can be estimated based on Eq.(2.32) using CIP method.

$$\frac{\hat{u}_{n+1}^{(1)} - u_n^{(1)}}{\Delta t} + u^{(1)}\frac{\partial u^{(1)}}{\partial \xi^{(1)}} + u^{(2)}\frac{\partial u^{(1)}}{\partial \xi^{(2)}} + u^{(3)}\frac{\partial u^{(1)}}{\partial \xi^{(3)}} = R_n^{(1)} \tag{2.32}$$

The same procedure can be applied to estimate the pseudo-velocity of $\hat{u}_{n+1}^{(2)}$, $\hat{u}_{n+1}^{(3)}$

(2) To estimate the pressure correction P'

Let,

$$P_{n+1} = P_n + P' \tag{2.33}$$

Then, the following equation can be obtained by subtracting Eq.(2.32) from Eq.(2.20).

$$u_{n+1}^{(1)} = \hat{u}_{n+1}^{(1)} - \Delta t\left(g^{(11)}\frac{\partial P'}{\partial \xi^{(1)}} + g^{(12)}\frac{\partial P'}{\partial \xi^{(2)}} + g^{(13)}\frac{\partial P'}{\partial \xi^{(3)}}\right) \tag{2.34}$$

Also, the similar relationships between $u_{n+1}^{(2)}$ and P', $u_{n+1}^{(3)}$ and P' can be obtained in the same way. Putting these relationships between $(u_{n+1}^{(1)}, u_{n+1}^{(2)}, u_{n+1}^{(3)})$ and P' into the continuity equations of Eq.(2.18) , an equation related to P' can be obtained. Thus, the pressure correction of P' can be obtained by solving the equation with TDMA algorithm (Tri-Diagonal Matrix Algorithm).

(3) To calculate the pressure P_{n+1} and the velocities $(u_{n+1}^{(1)}, u_{n+1}^{(2)}, u_{n+1}^{(3)})$

The velocity of $u_{n+1}^{(1)}$ can be obtained based on Eq.(2.34), and $u_{n+1}^{(2)}$, $u_{n+1}^{(3)}$ can be evaluated similarly. The pressure of P_{n+1} can be obtained based on Eq.(2.33).

(4) To calculate the water level H

The water level is calculated based on the 2D depth-integrated continuity equation. Concretely, Eq.(2.20) can be split into the following two equations:

$$\frac{\tilde{u}_{n+1}^{(1)} - u_n^{(1)}}{\Delta t} + u^{(1)}\frac{\partial u^{(1)}}{\partial \xi^{(1)}} + u^{(2)}\frac{\partial u^{(1)}}{\partial \xi^{(2)}} + u^{(3)}\frac{\partial u^{(1)}}{\partial \xi^{(3)}} = \tilde{R}_n^{(1)} \tag{2.35}$$

$$\frac{u_{n+1}^{(1)} - \tilde{u}_{n+1}^{(1)}}{\Delta t} = -g^{(11)}\frac{1}{\rho}\frac{\partial P_{n+1}}{\partial \xi^{(1)}} - g^{(12)}\frac{1}{\rho}\frac{\partial P_{n+1}}{\partial \xi^{(2)}} - g^{(13)}\frac{1}{\rho}\frac{\partial P_{n+1}}{\partial \xi^{(3)}} \tag{2.36}$$

where the difference between $\tilde{R}_n^{(1)}$ in Eq.(2.35) and $R_{n+1}^{(1)}$ in Eq.(2.20) is that the former excludes three pressure derivative terms from eq.(2.21).

From Eq.(2.36), the following equation can be obtained:

$$u_{n+1}^{(1)} = \tilde{u}_{n+1}^{(1)} - \Delta t\left(g^{(11)}\frac{1}{\rho}\frac{\partial P_{n+1}}{\partial \xi^{(1)}} - g^{(12)}\frac{1}{\rho}\frac{\partial P_{n+1}}{\partial \xi^{(2)}} - g^{(13)}\frac{1}{\rho}\frac{\partial P_{n+1}}{\partial \xi^{(3)}}\right) \tag{2.37}$$

where $\tilde{u}_{n+1}^{(1)}$ can be calculated based on Eq.(2.35). Similarly, the equations for $u_{n+1}^{(2)}$ and $u_{n+1}^{(3)}$ can be obtained. Putting these equations into the continuity equation, an equation associated with pressure P is obtained. Here, the pressure of P is approximated by the static pressure of P_s which can be expressed by water level of H.

Integrating the equation in depth direction then we can obtain an equation related to the water level of H. The equation is then solved implicitly by TDMA algorithm to obtain the water level of H at the future time $t + \Delta t$.

In the above, we have introduced the 3-dimensional model in the physical curvilinear coordinate system of $\xi^{(1)}\angle\xi^{(2)}\angle\xi^{(3)}$ where the coordinates in three directions can be non-orthogonal to each other. Although many coefficients related to coordinate transformation become 0 once if the coordinates are orthogonal to each other, it is difficult to generate a mesh being orthogonal to each other in all of three directions. Therefore, considering the balance between the difficulty of mesh generation and the complication of calculation, it is more practical to use coordinate system as $(\xi^{(1)}\perp\xi^{(2)})\angle\xi^{(3)}$ in most simulation calculations in river hydraulics.

3 NUMERICAL EXAMPLES

As our first step of study, the developed model is applied to an experimental channel for verifying its correctness. The calculation objective is a meandering channel whose shape is a sine-generated curve expressed as

$$\theta = \theta_{\max}\sin(2\pi s/L) \tag{3.1}$$

Table 3.1. Simulation condition of example-1.

Total width of channel(cm)	20
Length of channel (cm)	220
$\theta_{\max}$	35^0
Discharge Q (l/s)	2.15
Slope i_b	0.009
Manning roughness coefficient	0.015

where θ is the angle between the curved centerline and the down-valley axis at an arch distance of s; $\theta_{\max}$ is the maximum value of θ; and L is the wavelength measured along the curved centerline. Simulation conditions are shown in Table 3.1.

The initial and boundary conditions are adopted as follows:

- Initial condition: The initial values of velocity $u^{(1)}$, water depth h_s and water level H are defined by the uniform flow calculation. The initial values of velocities $u^{(2)}$, $u^{(3)}$ are defined as 0.
- Boundary condition: At upstream $(i=1)$ and downstream $(i=nend)$, the cyclical conditions of $\phi(1,j)=\phi(nend,j)$, $\phi(nend+1,j)=\phi(2,j)$ are employed.
- At side wall: free-slip condition is employed.

In the calculation, we choose to use the coordinate system of $(\xi^{(1)}\perp\xi^{(2)})\angle\xi^{(3)}$ by considering the balance between the difficulty of orthogonal mesh's generation and the complication of calculation. The following sigma function σ is employed to generate the boundary-fitted mesh in vertical direction. The divisions in vertical direction are 5 layers as shown in Figure 3.1 and the divisions on plane are 48*10 meshes as shown in Figure 3.2.

$$\sigma = \frac{z - z_b}{H - z_b} \tag{3.2}$$

where z_b is the elevation of channel bed and H is water level.

Since the water level of H keeps varying during the calculation process toward convergence, the boundary-fitted mesh in vertical direction must be regenerated by Eq.(3.2) with time. The ALE (Arbitrary Lagrangian and Eulerian) [9] method is employed to handle the mesh's moving problem. Concretely, for the momentum equation of $u^{(1)}$ shown in Eq.(2.20), Eq.(2.32) and Eq.(2.35), the convective term of $u^{(3)}\partial u^{(1)}/\partial\xi^{(3)}$ is replaced by the term of $(u^{(3)} - w_0)\partial u^{(1)}/\partial\xi^{(3)}$ where w_0 is the mesh moving speed in vertical direction. The same treatment is applied to the momentum equations of $u^{(2)}$ and $u^{(3)}$.

The contours of pressure P calculated at layer of $k=1,2$ are shown in Figure 3.3 and Figure 3.4 respectively. The contours of the water depth calculated and measured are shown in Figure 3.5 and Figure 3.6 respectively. The vectors as well as the contours of the cross velocity calculated and measured in the cross sections of $i=29$ and $i=33$ are shown in Figure

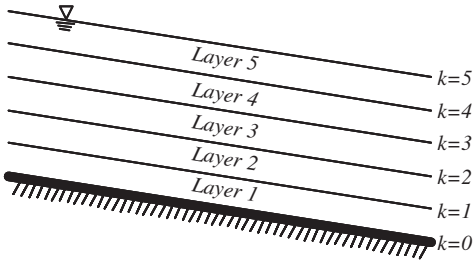


Figure 3.1. The divisions in vertical direction.

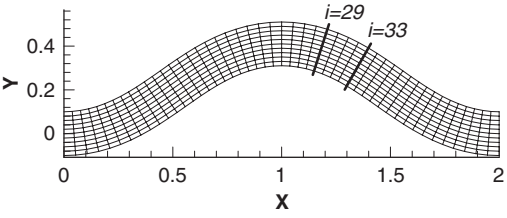


Figure 3.2. The divisions on plane.

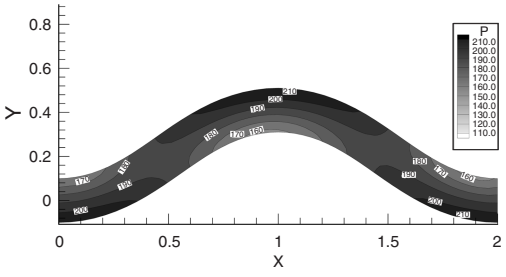


Figure 3.3. The contours of pressure P at the layer of $k=1$ (Calculation) (Unit:Pa).

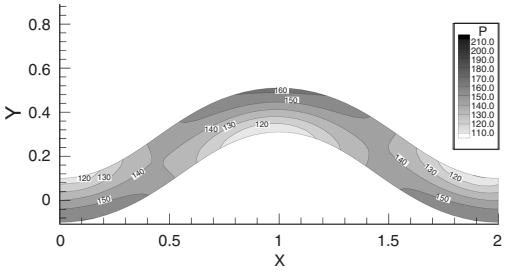


Figure 3.4. The contours of pressure P at the layer of $k=2$ (Calculation) (Unit:Pa).

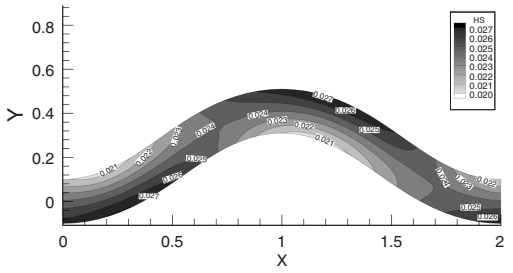


Figure 3.5. The contours of the water depth (Calculation) (Unit:m).

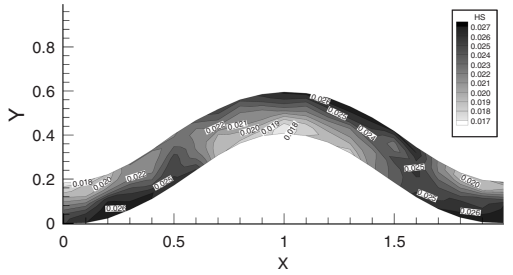


Figure 3.6. The contours of the water depth (Observation) (Unit:m).

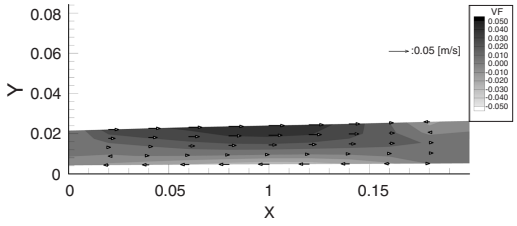


Figure 3.7. The vectors and the contours of the cross velocity in the cross section of $i = 29$ (Calculation) (Unit:m/s).

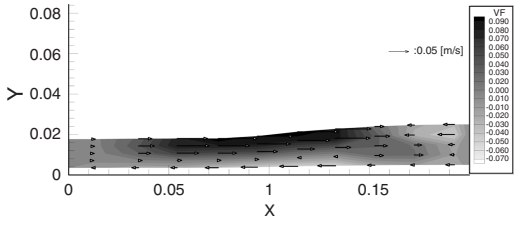


Figure 3.8. The vectors and the contours of the cross velocity in the cross section of $i = 29$(Observation) (Unit:m/s).

3.7–3.8 and Figure 3.9–3.10 respectively, where the positions of the cross sections $i = 29,\ 33$ are shown in Figure 3.2. The vectors of plain velocity calculated and measured at the layer of $k = 1, 5$ are shown in Figure 3.11–3.12 and Figure 3.11–3.12 respectively

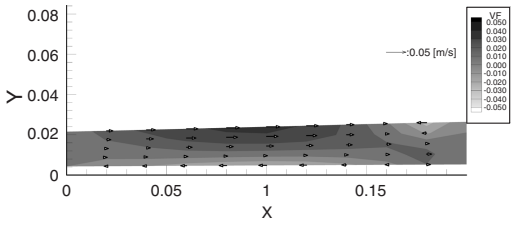


Figure 3.9. The vectors and the contours of the cross velocity in the cross section of $i = 33$ (Observation) (Unit:m/s).

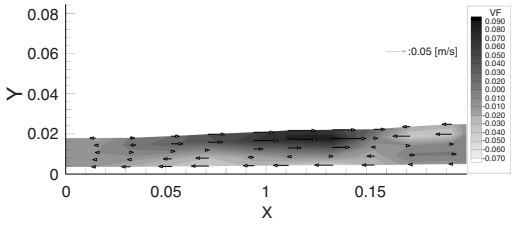


Figure 3.10. The vectors and the contours of the cross velocity in the cross section of $i = 33$ (Observation) (Unit:m/s).

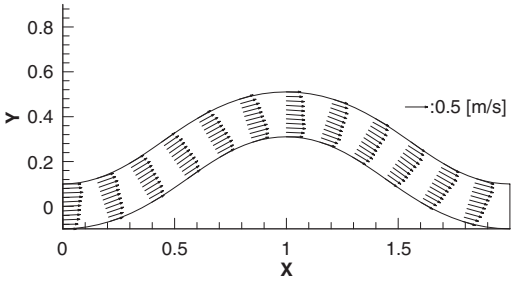


Figure 3.11. The vectors of plain velocity at the layer of $k = 1$ (Calculation).

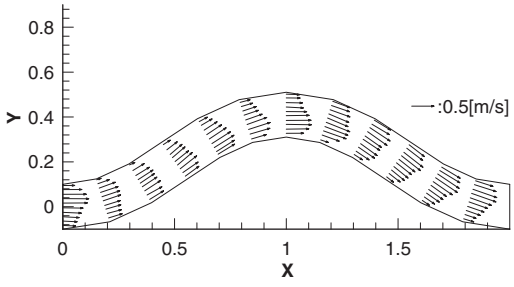


Figure 3.12. The vectors of plain velocity at the layer of $k = 1$ (Observation).

Comparing the results between calculation and observation, the agreements between them from the whole condition are generally good, although the cross- and plain-velocities appear smaller than the observed ones.

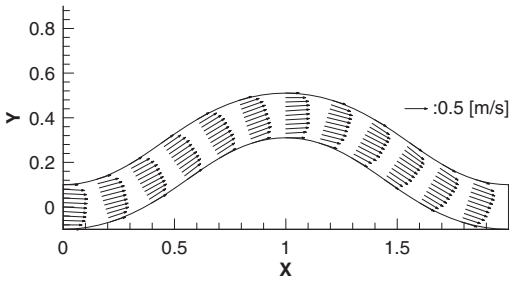


Figure 3.13. The vectors of plain velocity at the layer of $k = 5$ (Calculation).

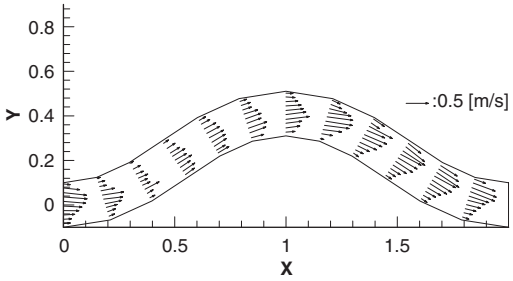


Figure 3.14. The vectors of plain velocity at the layer of $k = 5$ (Observation).

4 CONCLUSION

In this paper, a 3-dimensional flow calculation model is developed. The model introduces the physical curvilinear coordinate system to solve the mesh sensitivity problem, and employs a calculation algorithm having the convective term treated by CIP method to improve the calculation stability for the flowfield with high velocity. The developed model is applied to an experimental channel, and calculation values are compared to observation values, and the agreement between them is generally good. Our next step of study is to apply the model to real rivers and include sediment transportation to the present flow calculation model.

REFERENCES

Fletcher C.A.J. *Computational Techniques for Fluid Dynamics. Volume II, Fundamental and General Techniques*, Second Edition, Springer-Verlag, 1991; pp.47–78.

Koshizuka S., Oka Y. and Kondo S. "A staggered differencing technique on boundary-fitted curvilinear grid for incompressible Navier-Stokes equation written with physical components", *A Collection of Technical Papers, 3rd International Symposium on Computational Fluid Dynamics*, Nagoya, Japan, 1989.

Koshizuka S., Oka Y. and Kondo S. "A boundary-fitted staggered difference method for incompressible flow using Riemann geometry", *Proc. 1st Int. conf. On Supercomputing in Nuclear Applications*, Mito, Japan 1990.

Koshizuka S., Oka Y. and Kondo S. "A staggered differencing technique on boundary-fitted curvilinear grids for incompressible flows along curvilinear or slant walls", *J. Comput. Mech.*, 1990; **7**: pp.123–136.

Demirdzic I., Gosman A.D., Issa R.I. and Peric M. "A calculation procedure for turbulent flow in complex geometries", *Computers & Fluids* 1987; **15**: pp.251–273.

Takizawa A., Koshizuka S. and Kondo S. "Generalization of physical component boundary fitted co-ordinate (PCBFC) method for the analysis of free-surface flow", *Int. j. numer. methods fluids*, Vol. 15, 1992; pp.1213–1237.

Yabe T. "A universal solver for hyperbolic equations by cubic-polynomial interpolation I. One-dimensional solver", *Computer Physics Communications* 66 (1991) 219–232; Elsevier Science Publishers B.V. (North-Holland).

Yabe T., Ishikawa T. and Wang P.Y. "A universal solver for hyperbolic equations by cubic-polynomial interpolation II. Two- and three-dimensional solvers", *Computer Physics Communications* 66 (1991) 233-242; Elsevier Science Publishers B.V. (North-Holland).

Kawahara M, *Analysis of Moving Boundary Flows (Computational Fluid Dynamics Series 4)*, University of Tokyo Press, 1995, ISBN4-13-065104-8, pp.46 (in Japaness).

River Flow 2004 – Greco, Carravetta & Della Morte (eds.)
© 2004 Taylor & Francis Group, London, ISBN 90 5809 658 0

Application of a 2D semi-lagrangian model to unsteady shallow water flow over dry bed

J. Murillo & P. García-Navarro
Fluid Mechanics, CPS, University of Zaragoza, Spain

ABSTRACT: The work is devoted to the study of the applicability of a Semi-lagrangian method to the two-dimensional shallow water equations. The method is based on the characteristic formulation of the system and relies on the use of the bicharacteristic curves and a suitable interpolation technique. The interpolation is based on non-oscillatory bicubic Hermite polynomials. The technique is applied to transient problems involving front advance over dry beds with special emphasis put on the treatment of the advancing front.

1 INTRODUCTION

The hyperbolic character of the shallow water or St. Venant equations implies the existence of their characteristic formulation. The related characteristic based numerical methods gained wide acceptance in one-dimensional applications at the early years of Computational Hydraulics due to their conceptual simplicity and the fact that they are physically based and can lead to highly accurate results. Numerical models based on many alternative approaches appeared since then.

In two-dimensional shallow water models, finite differences, finite elements and more recently finite volumes have filled the scientific journals almost from the beginning. Only a few authors have reported experiences using semi-lagrangian methods as applied to 2D flow models. The simplicity of this approach is less evident in 2D than in 1D applications but the fact that the method is physically based remains the same and renders attractive any attempt of validation.

The shallow water equations represent physical laws defined on a domain filled with water and do not describe properly the advance over a dry boundary. This constitutes a moving boundary problem in which the water column goes to zero. The solution proposed in this work is based on the information coming from the interior wet region along the bicharacteristic curves.

2 MATHEMATICAL MODEL

The one-dimensional approximation of open channel flow problems using the Saint-Venant equations gives excellent results in general when the underlying hypothesis are justified. The main limitations of this approach are the cross sectional uniform velocity and horizontal free surface. In many cases, a two-dimensional approach is required in order to be closer to reality. The mass conservation equation and momentum balance in the x and y directions lead to the following system:

$$\frac{\partial h}{\partial t}+\frac{\partial (uh)}{\partial x}+\frac{\partial (vh)}{\partial y}=0 \tag{1}$$

$$\frac{1}{g}\frac{\partial u}{\partial t}+\frac{u}{g}\frac{\partial u}{\partial x}+\frac{v}{g}\frac{\partial u}{\partial y}+\frac{\partial h}{\partial x}=S_o^x-S_f^x \tag{2}$$

$$\frac{1}{g}\frac{\partial v}{\partial t}+\frac{u}{g}\frac{\partial v}{\partial x}+\frac{v}{g}\frac{\partial v}{\partial y}+\frac{\partial h}{\partial y}=S_o^x-S_f^y \tag{3}$$

where h is the water depth, u is the velocity component in the x direction and v is the component along the y direction, S_o^x and S_o^y are the bottom slopes along directions x and y respectively; S_f^x and S_f^y represent the hydraulic resistance in the two directions and are formulated as [22]:

$$S_f^x=\frac{n^2u\sqrt{u^2+v^2}}{C_u^2h^{4/3}} \tag{4}$$

$$S_f^y=\frac{n^2v\sqrt{u^2+v^2}}{C_u^2h^{4/3}} \tag{5}$$

with n the Manning roughness coefficient and C_u the cubic root of the rate of the acceleration of gravity g in

any unit system and its value in the International Unit System.

The partial differential system defined by (1,2,3) is hyperbolic and therefore admits a characteristic formulation. This is next presented and exploited.

2.1 *The characteristic form*

The characteristic form of the equations in a 1D approach leads to a system of ordinary differential equations and therefore to a simpler mathematical formulation. This formulation is associated to the idea that the information propagates in space and time along characteristic surfaces forming a cone. The practical application of the method based on this formulation relies on curves, called bicharacteristic curves, contained on these surfaces.

The polar formulation of the bicharacteristic curves is:

$$\frac{dx}{dt} = u + c\cos\theta \tag{6}$$

$$\frac{dy}{dt} = v + c\sin\theta \tag{7}$$

Eqs. (6) and (7) suggest the linear combination required to eliminate the partial derivatives from the flow equations. If (1) is added to (2) multiplied by $c\cos\theta$ and to (3) multiplied by $c\sin\theta$, we get:

$$\frac{dh}{dt} + \frac{c}{g}\left(\cos\theta\frac{du}{dt} + \sin\theta\frac{dv}{dt}\right) =$$

$$c\cos\theta(S_o^x - S_f^x) + c\sin\theta(S_o^y - S_f^y) - \frac{c^2}{g}s \tag{8}$$

where

$$s = \sin^2\theta\frac{\partial u}{\partial x} - \sin\theta\cos\theta\left(\frac{\partial u}{\partial y} + \frac{\partial v}{\partial x}\right) + \cos^2\theta\frac{\partial v}{\partial y}$$

A numerical technique can be implemented based on the existence of the bicharacteristic curves. It can be used to supply information at different time levels following an approach similar to the Hartree method. As suggested by Fig. 1, the solution at point (t_o, x_o, y_o), can be found following backward in time the characteristic cone up to its intersection with the plane corresponding to time $t = t_o - \delta t$. Three bicharacteristics are only required to furnish the solution for u_o, v_o, h_o, at (t_o, x_o, y_o). However, if a second order solution is required, the cross derivatives $\partial u/\partial y$ and $\partial v/\partial x$ must also be known at the solution point. One option is to involve four bicharacteristic instead of

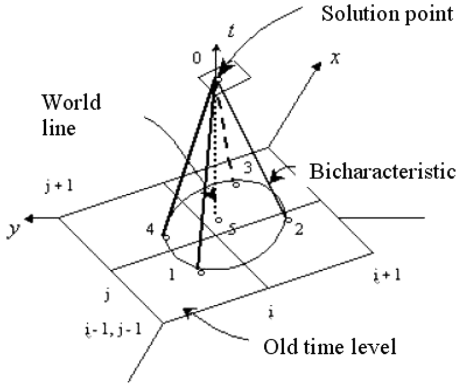


Figure 1. Elements of the bicharacteristic cone.

three and an additional equation called the world line. The four bicharacteristics are chosen at increments of $\pi/2$ in the polar angle φ. The world line is tangent to the vector $(1\ uv)^T$ and corresponds to a streamline in the plane (x, y). The mass continuity equation along the world line can be expressed as:

$$\frac{dh}{dt} + \frac{c^2}{g}\left(\frac{\partial u}{\partial x} + \frac{\partial v}{\partial y}\right) = 0 \tag{9}$$

2.2 *Resolution scheme.*

To solve the system of equations at a time t_o the first step is to know the trajectory of the bicharacteristics, since information propagates along those directions.

The coordinates of the intersections of the bicharacteristics with the plane $t_o - \delta t$ can be found using (6, 7) through a first order approximation in δt for the four bicharacteristics.

The intersection of the world line with the plane $t_o - \delta t$ is also found in first order. The flow conditions at points 1-5 and their partial derivatives along directions x and y are detrmined by the interpolation among grid points in the plane $t_o - \delta t$. The final solution is strongly dependent on the interpolation technique used. The knowledge of the flow variables at points 1–5 allows a second order approximation in δt for equation (8).

2.3 *Grid movement at the front wave*

The solution at the advancing wave front is calculated using information from the wet points at the front itself in a previous time step. Katopodes and Strelkoff (1978) and Katopodes and Schamber (1987) defined an integration domain including both interior points and points at the leading front.

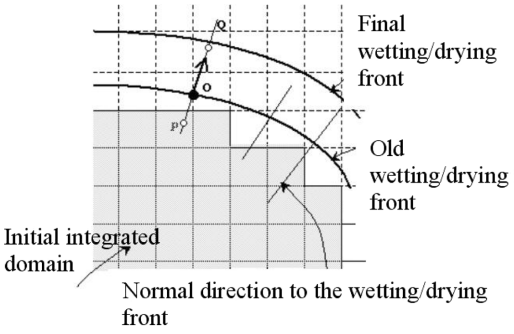


Figure 2. Front wave advance.

A different approach consists of approximating the velocity of the front points using information from the interior points. Taking into account that the front propagation speed must be given by the normal component of the water velocity at the wave frontier (the flow does not cross that boundary), the proposed method is based on the projection onto the direction normal to the front wave, of the flow velocities at the front positions (Fig. 2).

The actual values of the variables at the front position at a new time level are unknown and must be obtained from interpolation based on fictitious values at the outer dry area. The alternative is to neglect all information both from the front itself and from the dry zone and therefore to build interpolation polynomials only over the available information at the wet zone. The calculation is hence simplified.

The stability criterion within the calculation grid is:

$$\delta t \le \frac{\delta x\, \delta y}{\delta x \max\left\{\left|u_{ij}+c_{ij}\right|,\left|u_{ij}-c_{ij}\right|\right\}+\delta y \max\left\{\left|v_{ij}+c_{ij}\right|,\left|v_{ij}-c_{ij}\right|\right\}}$$

for all points *ij* in the plane, where δx, δy are the lengths of the interpolation cells.

2.4 *Wetting-drying condition*

Any numerical model intended to simulate unsteady free surface flows must be able to reproduce moving boundaries separating dry and wet zones. The careless treatment of these boundaries negatively affects the numerical results.

The points chosen for the calculation of the advancing front are not, in general, aligned along a direction normal to it. Being this an essential condition for the correct front simulation, it becomes necessary to introduce some kind of modification in the information relying on them. The projection of the velocity on the direction normal to the front is calculated and the tangential component is elliminated from th predicted

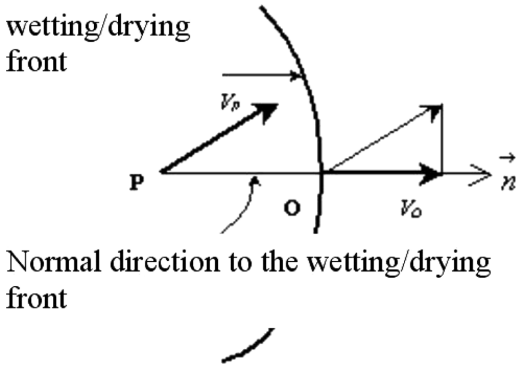


Figure 3. Velocity projection at the wetting front.

solution (Fig. 3). Otherwise, the numerical results are erroneous.

When, on the other hand, the front advances over a positive (adverse) slope, a further point must be taken into account: the local bed slope must be redefined to zero value. If this is not implemented the wave front is not able to advance up the hill as expected leading even to velocity values in the opposite sense to the advancing direction.

3 INTERPOLATION IN TWO DIMENSIONS

The interpolation used in the process of calculation of the variables at the intersection of the bicharacteristics and the plane $t_o - \delta t$ is determinant of the problem evolution and numerical accuracy.

As in one-dimensional problems, the interpolation must be able to supply accurate and smooth results. The accuracy is related to the method used to estimate the derivatives and the smoothness depends on the restrictions imposed on their values. The interpolative polynomial must not present any undesirable minimum or maximum within the computational cell for stability reasons.

In order to achieve the desired properties, the bicubic Hermite interpolation has been used. This procedure requires a refined treatment of the supplied information but produces oscillation free polynomials (Williamson and Rasch 1989). The value of the function as well as an estimation of the derivatives D_{ij} are required at the four cell vertices (Frischt and Carlson, 1980).

4 TEST CASES

Two different problems have been used to assess the suitability of the proposed meted: A flooding wave from a corner and a laboratory dam break problem.

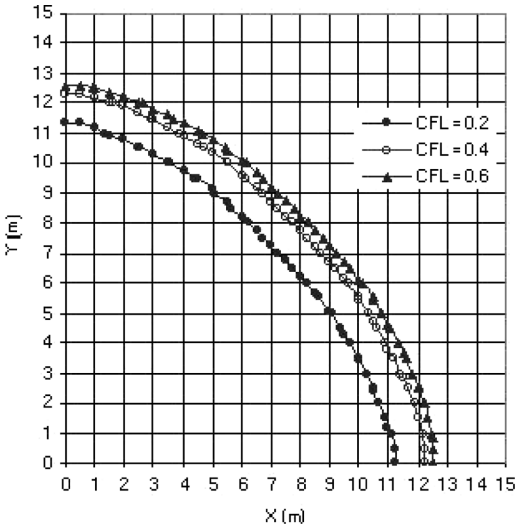


Figure 4. Advancing front position at $t = 9$ min using CFL = 0.2, 0.4 and 0.6.

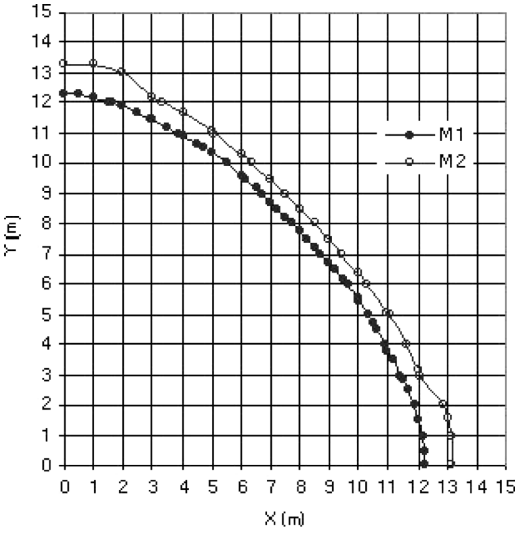


Figure 5. Advancing front position at $t = 9$ min using grids M1 and M2 with CFL = 0.4.

If discharge is applied at one of the corner points of a rectangular domain in which there are uniform slope, and roughness, the problem can be considered one-dimensional in the radial direction of a set of polar coordinates. The proposed method will be used on a rectangular structured mesh in order to verify that the solution is well behaved. The flow problem is a challenge for the interpolation scheme in this kind of grid.

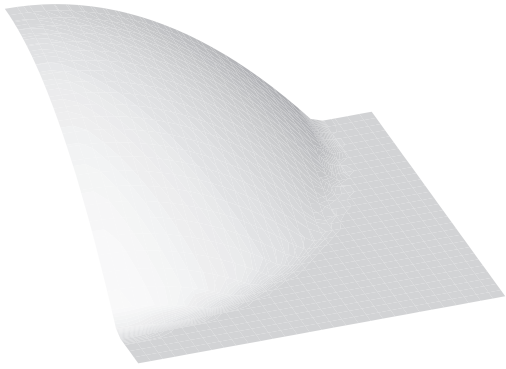


Figure 6. Bottom level for the positive slope radial flow test case.

In a second stage, the advance of the front in presence of sloping beds will be analyzed.

4.1 *Radial front over flat dry bed*

In order to study the performance of the proposed scheme and the sensitivity to the numerical parameters a first test case is envisaged using two different grids made of squared cells. The first, $M1$, with cell side lengths of 0.5 m. The second, $M2$, made of cell side lengths of 1 m.

The test case consists of a radial flooding wave advancing over dry bed from a corner. The inlet discharge is $Q = 0.00648\, m^3 s^{-1}$. The bottom is flat and characterized by a roughness Manning coefficient $n = 0.04$.

The numerical results obtained on grid $M1$ will be compared using different values of the *CFL*. Fig. 4 shows the advancing front position at $t = 9\, min$ with $CFL = 0.2$, 0.4 and 0.6. The figure indicates that the differences in advance using CFL = 0.4 y 0.6 are minimum, and that there is some delay when using CFL = 0.2.

The comparison of the results using different grid and the same CFL = 0.4 is shown in Fig. 5. This figure contains the plot of the advancing fronts at time $t = 9$ min. The radial symmetry is conserved in both grids but the results are of worse quality on the larger grid due to the increment in the size of interpolation cell.

4.2 *Radial flow over dry slope*

The second test case is intended to analyze the behaviour of the numerical solution for the radial flood wave in presence of a slope. The test case is analogous to the previous except for the definition of a slope in both directions x and y following the shape of an inverted paraboloid as represented in Fig. 6. The radial wave starts at a corner situated on the uppermost

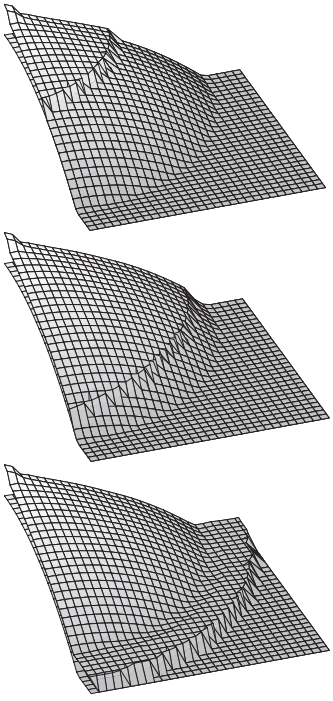


Figure 7. Water and bottom levels at $t = 3$, 6 and 9 min.

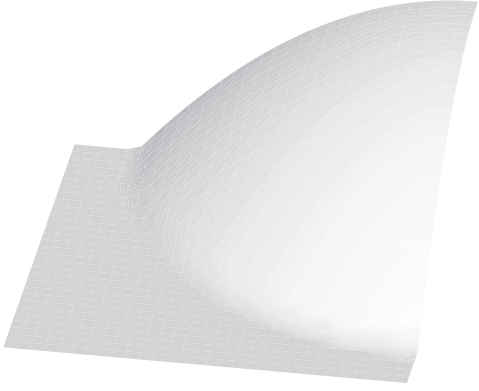


Figure 8. Bottom level for the adverse slope radial wave.

point and the advancing solution progresses without any difficulty and not requiring any special numerical treatment.

Initially, the flow changes very quickly due to the acceleration induced by the slope. Therefore, the water level is reduced as the wave advances. When the front reaches the horizontal part, its advancing speed is reduced and, at the same time, the water level at the front increases. The leading grid cells of the wetting front do not require special treatments.

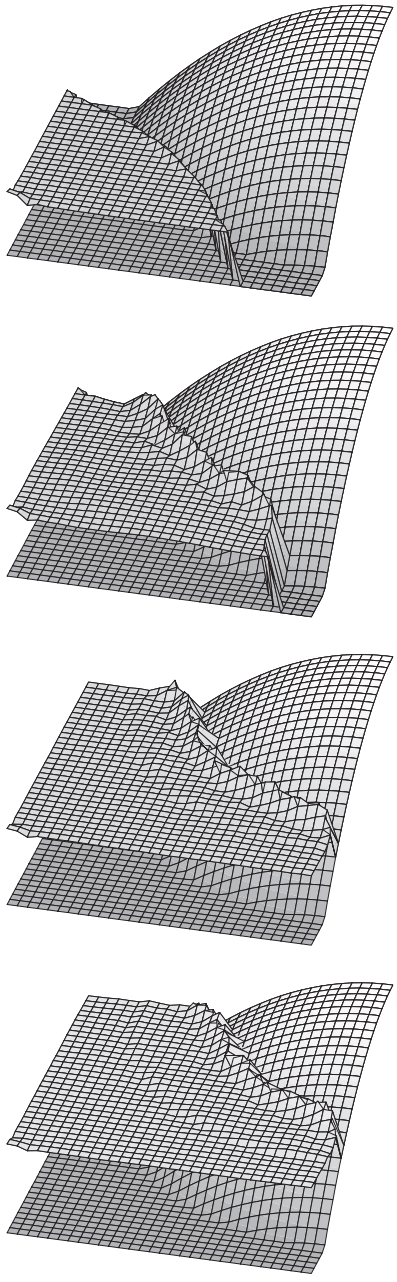


Figure 9. Bottom and water levels at $T = 3$, 6, 9 and 15 min.

4.3 *Radial flow over dry adverse slope*

In this test case, the evolution of the radial flooding wave over a dry adverse slope as the one shown on Fig. 8 is analyzed.

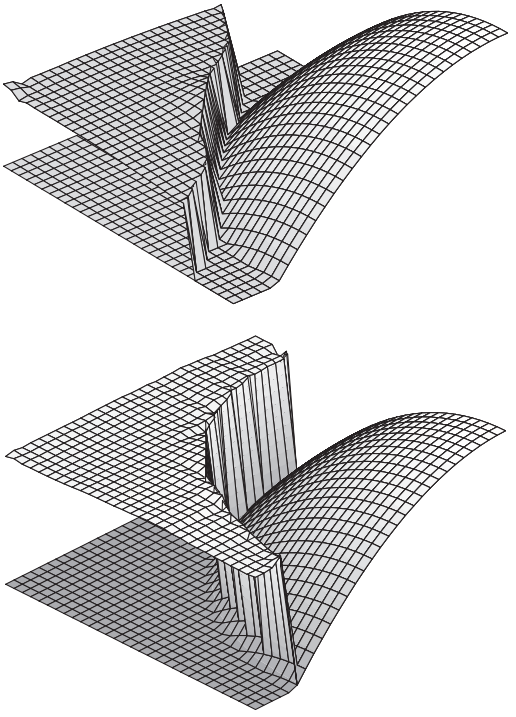


Figure 10. Wrong results due to the incorrect treatment of the wetting/drying front at $t = 6$ min and $t = 7$ min.

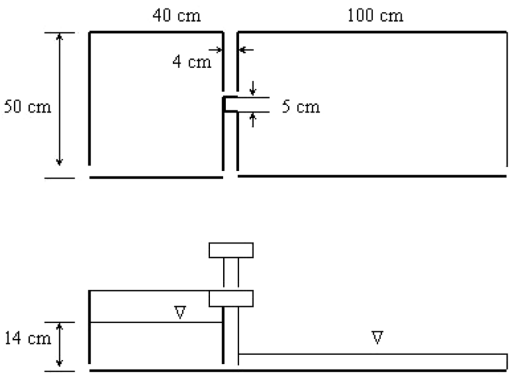


Figure 11. Experimental setup.

The simulation was performed over grid $M1$ using $CFL = 0.4$. The wetting front advances with radial symmetry until the base of the slope is reached The flow field is then adapted to the bump progressively flooding it. The numerical results shown in Fig. 9 indicate that the water level rises and the wetting profile changes due to the presence of the adverse slope.

The previously indicated modifications in bottom level and velocity direction at the wetting cells was



Figure 12. Dam break surface level at $t = 0.08$ and 0.24 s.

crucial in this example. Fig. 10 displays two samples of the solution obtained at different times in a simulation carried out without the mentioned modifications. The front was stuck at the foot of the slope generating a non-physical growing discontinuity in water levels when the bottom level was not adequately modified at the leading edge grid cells. If the velocity corrections had not been implemented, the results would have been totally incoherent.

4.4 *Validation: Dam break wave*

The last test case presented is the validation of the numerical meted against the experimental data obtained in a laboratory scaled dam break setup. The experiment was carried up as described in (Braschi et al. 1994) and the sketch of the experimental facility is presentd in Fig. 11. Two reservoirs are connected by a gate. One is dry and the other is full of water up to a horizontal level 0.14 m. The sudden removal of the gate is used to simulate an instantaneous dam breaking and releases the water leading to a flooding wave that advances over the dry part.

The simulation of the flow generated was performed using a uniform square grid of size 0.5 cm, a *CFL* of 0.45 and a Manning coefficient $n = 0.01$. Variations of this parameter do not influence the results sensibly



Figure 13. Dam break water levels at $t = 0, 32$, and 0.48 s.



Figure 14. Dam break water levels at $t = 0.56$ and 0.64 s.

since the flow is dominated by inertial and pressure effects.

When the gate is opened, a negative wave propagates into the wet reservoir with a celerity depending only on the unperturbed water level.

Fig. 12 shows the flow water levels 0.08s and 0.24s after the gate removal. The positive wave advances over the dry platform, both in a longitudinal and a transversal direction. As the front advances, two zones can be identified, the inner dominated by inertial effects and the outer more affected by the surface roughness.

At $t = 0.24$s The depresión wave is near the solid walls. At time $t = 0.32$ s after the dam breaking, the depression wave has already been affected by reflection at the reservoir lateral walls and progresses towards the interior. This can be seen on Fig. 13.

At $t = 0.40$ s, the depression wave reaches the upstream end of the initially full reservoir. When time reaches $t = 0.48$ s the reflection waves in the reservoir cross each other (Fig. 13). On the other hand, at that time the wetting front has reached the side walls of the dry reservoir with an abrupt reflection leading to a considerable rise in water levels. At time $t = 0.56$ s and later, the wetting front presents a growing tendency of the zone dominated by inertial effects with respect to the roughness dominated zone. Within the reservoir, several surface waves interact.

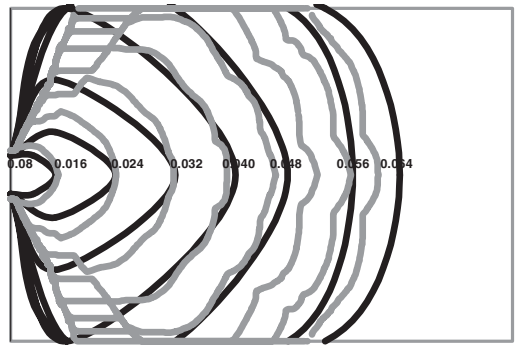


Figure 15. Advancing front positions at times $t = 0.08$, 0.16, 0.24, 0.32, 0.40, 0.48, 0.56 and 0.64 s. Grey lines: simulated results. Black lines: experimental results.

Fig. 15 shows a comparison of the computational and experimental results for different positions of the advancing front. Up to $t = 0.40$ seconds, the flow properties are calculated with an excellent agreement. From this time, the numerical front is slower and

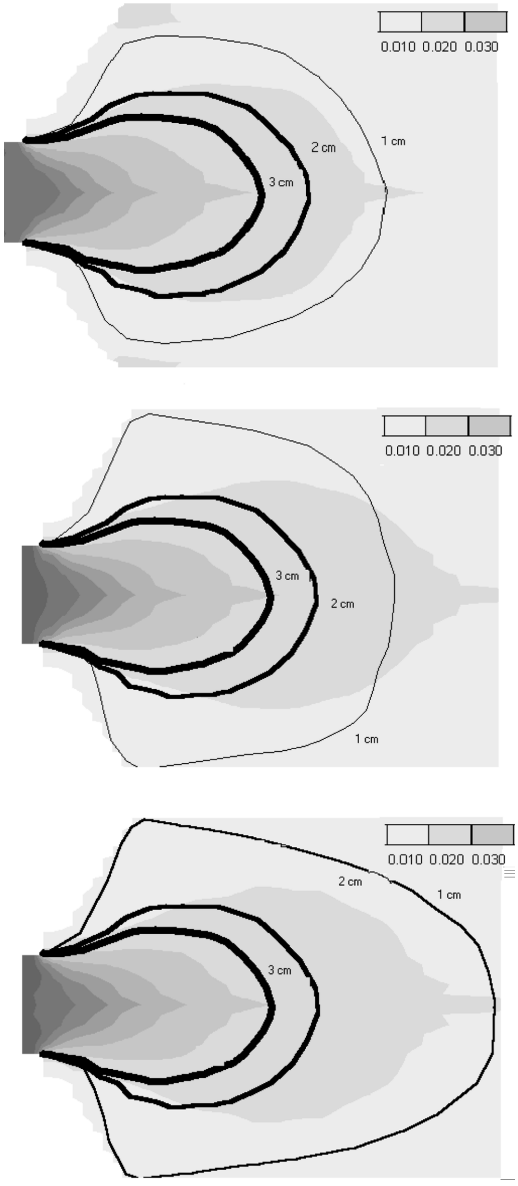


Figure 16. Water level distributions a times $t = 0.24$, 0.40, 0.56 s. Thick lines indicate contour lines from the experimental results.

the agreement is worse. On the other hand, the simulated front presents different parts advancing more irregularly than the experimental front.

Fig. 16 displays water level distributions for different times, both measured and calculated. The calculated distribution reproduces well the distinctive characteristics of the real water levels distribution and the agreement is satisfactory despite the underlying hydrostatic pressure assumption.

The water levels at the reflections with the walls does also match properly the measured evolution.

5 CONCLUSIONS

The proposed numerical technique is suitable for the numerical resolution of complex flow problems involving the advance of front waves over dry irregular beds. The front advances conserving the correct shape and the water distribution levels agrees well with experimental results.

The method is able to capture all the wave phenomena in the flow.

A special numerical treatment at the advancing front position is crucial in order to obtain accurate and sound numerical results specially in presence of adverse dry slopes.

REFERENCES

Rasch P.J. and Williamson D.L. On shape-preserving interpolation and semi-lagrangian transport. *Siam J. Sci. Stat Comput*. Vol 11. No 4, 1990.

Fritsch F.N. and Carlson R.E., Monotone piecewise cubic interpolation. *Siam J. Numer. Anal.* Vol 17 No 2, 1980.

Katopodes N. and Schamber R. Applicability of dam-break flood wave models. *Journal of Hydraulic Engineering.* May 1983, 109 No 5, ASCE.

Katopodes N. and Strelkoff T. Computing two dimensional dam-break flood waves. 1987, 14036 HY9. *Journal of the Hydraulics Division*.

Williamson D.L. and Rash P.J. Two-dimensional semi-lagrangian transport with shape-preserving interpolation. *Monthly Weather Review*, Vol 117, No 1, 1989. American Metereological Society.

Braschi G., Dadone F. and Gallati M. Plain flooding, nearfield and far field simulations, *Modelling of flood over initially dry areas*, ASCE, 1994.

River Flow 2004 – Greco, Carravetta & Della Morte (eds.)
© 2004 Taylor & Francis Group, London, ISBN 90 5809 658 0

How a 2-D code can simulate urban flood situations

E. Mignot & A. Paquier
Cemagref, R. U. Hydrology-Hydraulics, Lyon, France

N. Rivière
LMFA, INSA de Lyon, Lyon, France

ABSTRACT: Numerical codes are being used to simulate flood progress in cities but no real knowledge about the accuracy of these numerical calculations are available. The objective of this study is to check the capabilities of a 2D code to model a flood in an urban area. A simplified city flood was then modelled experimentally and its data were compared with the simulation results. Although results can be considered accurate enough for operational purposes, water depth differences remain, even with a refined mesh. In order to find out which typical urban situations are difficult to simulate by the code, two experimental test cases representing urban details were then modelled and calculated. The first one is the flow around a building where the reflections of the wave on the walls and recirculation behind the building are of major importance. The second one is the distribution of flow discharge in a four branches crossroad with two incoming and two outgoing streets with the same width and same bottom slope of 1%.

1 INTRODUCTION

Various computational fluid dynamics methods have already been used in order to simulate flood scenarios in urban zones (Neary & Sotiropoulos, 1996; Khan et al., 2000; Hervouet et al., 2000; Paquier et al., 2003). The results are encouraging but there is still a lack of knowledge in the accuracy of the risk assessment. In order to check the real capabilities of a 2D numerical code to simulate a urban flood, we use three experimental test cases (two of which are part of the European Project IMPACT (Soares et al., 2004; Soares et al., 2003)) representing a simplified city, the flow around a building and finally the flow within a four branches crossroad. The comparisons between the experimental and numerical records should permit to check the difficulties remaining when simulating a urban flood numerically.

2 PRESENTATION OF THE CODE

The code we used is Rubar20. Here below are provided the equations that are solved and the corresponding numerical scheme. The explicit second-order finite volume scheme solves the 2-D shallow water equations.

$$\frac{\partial h}{\partial t}+\frac{\partial (hu)}{\partial x}+\frac{\partial (hv)}{\partial y}=0 \qquad (1)$$

$$\frac{\partial (hu)}{\partial t}+\frac{\partial \left(hu^2+g\frac{h^2}{2}\right)}{\partial x}+\frac{\partial (huv)}{\partial y}=-gh\frac{\partial Z}{\partial x}-g\frac{u\sqrt{u^2+v^2}}{K_s{}^2h^{1/3}}+K\left(\frac{\partial}{\partial x}\left(h\frac{\partial u}{\partial x}\right)+\frac{\partial}{\partial y}\left(h\frac{\partial u}{\partial y}\right)\right) \qquad (2)$$

$$\frac{\partial (hv)}{\partial t}+\frac{\partial (huv)}{\partial x}+\frac{\partial \left(hv^2+g\frac{h^2}{2}\right)}{\partial y}=-gh\frac{\partial Z}{\partial y}-g\frac{v\sqrt{u^2+v^2}}{K_s{}^2h^{1/3}}+K\left(\frac{\partial}{\partial x}\left(h\frac{\partial v}{\partial x}\right)+\frac{\partial}{\partial y}\left(h\frac{\partial v}{\partial y}\right)\right) \qquad (3)$$

The Godunov-type scheme includes 4 steps (Paquier 1998):

1. computing slope of each one of the 3 variables h (or z water level), hu and hv in every cell on x and y axis by the method of the least squares and applying limitations of slopes following in order to obtain TVD (Total Variation Diminishing) scheme.
2. computing values of $W=(h, hu, hv)$ at intermediate time $t_{n+1/2}$ in the middle of the edge of cell M_i to obtain second-order scheme.
3. solving a 1-D Riemann problem in the direction normal to the edge at $t_{n+1/2}$ in order to estimate the fluxes through edges for the conservative part of the equations. It is possible to use a Roe type linearization that directly provides an estimate of the fluxes.
4. integrating the terms of the second member of the set of equations (1) to (3) on the surface of the cell

in order to add the corresponding contribution and to obtain the final value of the solution.

3 MODEL CITY EXPERIMENT

3.1 *Presentation of the test case*

The aim of this Impact Project (Soares et al., 2004) which took place in Milano (ENEL-CESI) is to simulate the flow within a simplified urban (or semi-urban) area. Cubic impervious blocks (simulating buildings or groups of buildings) are placed within a valley laboratory model upstream, which a flood hydrograph is introduced. Several urban configurations are modelled, based on the same valley topography:

- Two buildings configurations (aligned or staggered blocks)
- Two area widths (a whole valley or use of walls to confine the flow around the buildings area)
- Two discharge hydrographs as upstream conditions.

The case presented here below is the confined valley with 16 aligned buildings. Within the urban area, eight gauges (S3–S10) are used in order to describe the water depth evolution during the experiment.

3.2 *Description of the flow*

During the high upstream discharge period, the flow is rapid in the upstream part of the domain with low water depths. When getting near the building area, the flow slows down and the water depths rise strongly. Then the flow reaccelerates in the streets and the velocity remains low behind the buildings. Downstream from the urban area, the increased passing section leads to high velocities throughout the whole section.

3.3 *Comparison Experimental/Numerical results*

On the one hand, the numerical hydrographs obtained have globally the same shape as the experimental water depth curves and the highest and lowest water levels are located at the same places. On the other hand, important hydrograph differences remain.

3.3.1 *Shock against the buildings*

The first difference that can be outlined between numerical and experimental hydrographs is the front wave reflection on the urban area at S3 and S4. The numerical calculation does not simulate accurately this short increase of water depth because of the size of the cells and due to the equations. In a real case, this could be a problem when comparing natural water marks with calculated higher water depths after a flood.

3.3.2 *Hydrographs comparisons*

In term of typical water depth in the urban area, we present the histogram of the water depth at $t = 30$ s at all the gauges. We notice that the highest water depths appear upstream from the urban area (S3 and S4); and within the urban area, the high water depths are in the streets in the centre of the city (S7 and S8) and the lowest are downstream from this area (S10).

The water depths calculated in the urban area (S5 to S9) are very homogeneous, all between $h = 30.7$ mm and $h = 36.5$ mm, whereas in the experimental conditions, the water depth vary much more between $h = 28.9$ mm and $h = 45$ mm. This homogeneity could be due to the lack of capability of the equations to model accurately the reflections and recirculations or to a diffusion caused by too large cells within the urban area, which cannot provide a convenient representation of the structures of the secondary flows. Furthermore,

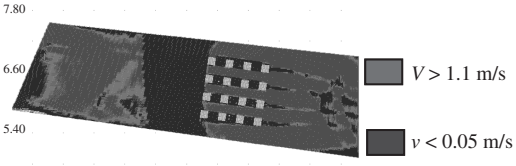


Figure 2. Model city velocity at t = 18 s.

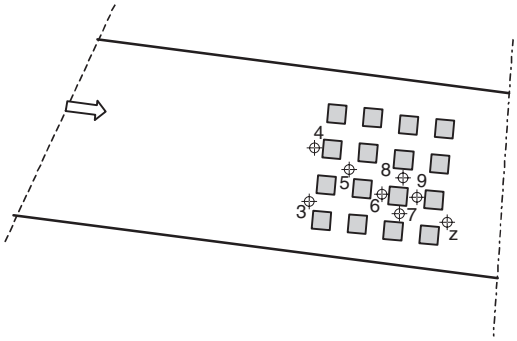


Figure 1. Model city benchmark.

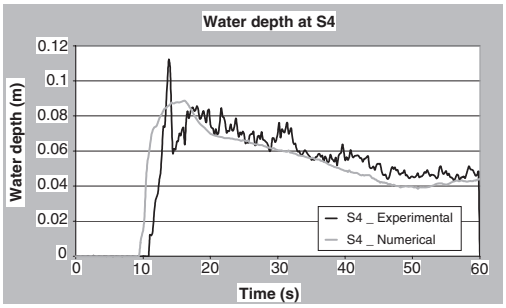


Figure 3. Numerical and experimental water depths at S4.

the water depth is usually higher in the experimental records than in the numerical results except at S5 and S10.

All the numerically calculated water depth curves have a very similar shape and the difference between them is usually only homothetic while the experimental hydrographs have different shapes: for example, the falling curves have different slopes.

3.3.3 *Influence of the friction coefficient*

As the water depths are usually underestimated, we tested an increase of the Manning coefficient from $n = 0.0162$ to $n = 0.025$. Of course, this tends to increase the water depth: thus, when the water depth is underestimated (S7 and S8), the high friction hydrograph fits the experimental curve better but, if the hydrograph is well estimated with the experimental friction coefficient, the water depth becomes overestimated with a higher friction.

Increasing the friction coefficient also reduces the front wave propagation and then the delay between the calculation and experimental hydrographs. However, this timing difference is not only reduced upstream from the urban area (S3 and S4), it is also reduced when travelling within the urban area and the propagation velocity is then not as well described as in the original friction coefficient case. The friction coefficient cannot be the right parameter to improve accuracy of calculation results.

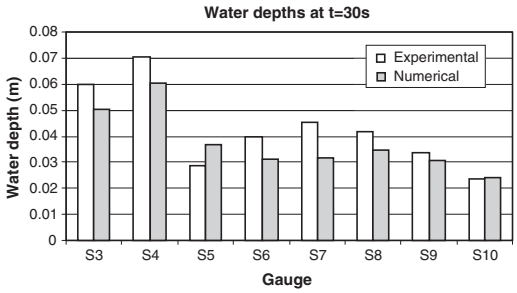


Figure 4. Water depth histogram at $t = 30$ s.

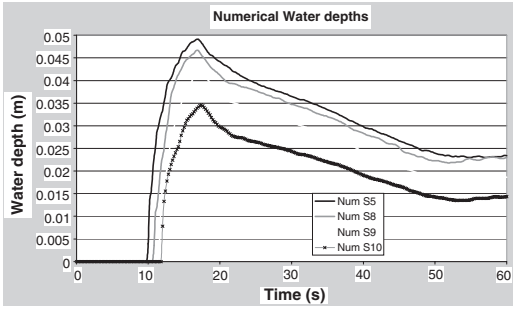


Figure 5. Calculated water depth hydrographs.

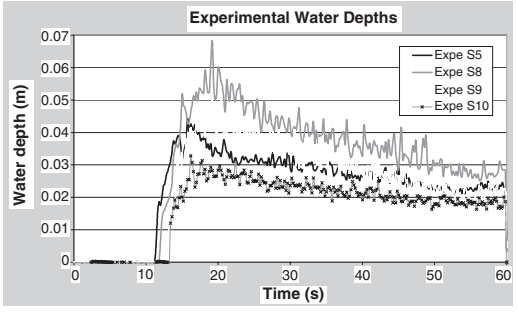


Figure 6. Experimental water depth hydrographs.

3.3.4 *Influence of refining the mesh*

A new mesh with a typical cell size of 1 cm is established. Figure 8 shows that the results in term of water depths comparisons are not improved.

The meshing size does not seem either to be the parameter responsible for the lack of accuracy of the flow simulation.

3.4 *Conclusion*

Here above, we presented one configuration among the seven experimental test cases. However, all of them

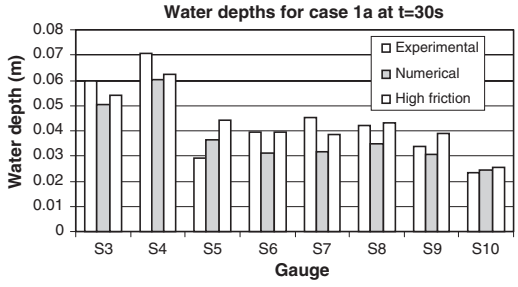


Figure 7. High friction water depth histogram.

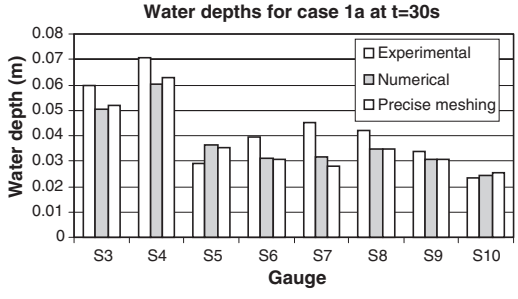


Figure 8. Fine mesh water depth histogram.

lead to the same conclusions: the 2D code can globally simulate the flow within a simplified city, but the errors are locally quite strong:

- The calculated water depths are too homogeneous within the urban area
- The numerical hydrographs are usually underestimated
- The calculated hydrographs do not reproduce exactly the experimental hydrograph shapes.

Thus, it is useful to check the quality of modelling in more detailed situations such as the flow around a building or the flow in a crossroad in order to figure out from what the main errors come.

4 THE ISOLATED BUILDING TEST CASE

4.1 *Presentation of the test case*

The aim of this experiment which took place in Université catholique de Louvian is to investigate the effect induced by a building placed within a sudden dam-break flow. Note that, depending on the working scale, this experiment could also represent the flow around an obstacle such as a parked car within a street during an urban flood. The experimental benchmark (Soares et al., 2003) was carried out within a horizontal open channel with a reservoir where steady water is stored until the beginning of the experiment. At the reservoir downstream boundary, the width of the channel is narrowed to 1 m in order to concentrate the flow and represent a natural dam-break when opening the gate. Further downstream, at around 3.5 m from the reservoir, in front of the gate, a 0.8×0.4 m impervious building is introduced with a specific angle to the flow direction. The following measurements are taken in order to compare the experimental data with the results of the simulations: water depths at the five gauge points and velocity fields at $t = 1$ s, $t = 2$ s, $t = 10$ s.

4.2 *Description of the flow*

The flow is rapid when getting off the reservoir creating two recirculation zones on the sides of the dam gate due to depression; then, it slows down suddenly (and water depth rises) when arriving close to the building. The flow passes around the building and a clockwise re-circulation zone appears downstream. At around one channel width downstream from the building, the flow tends to become one-dimensional (the velocity magnitude tends to be homogeneous on the channel section). Reflections against the channel sides bottom slopes and against the building are strong, and create complex local secondary flows.

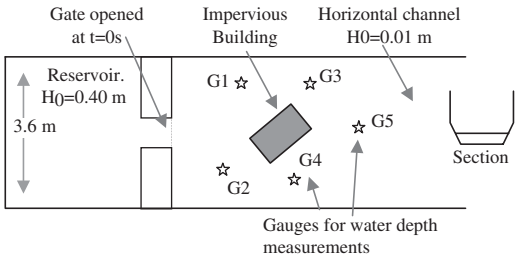


Figure 9. Isolated building benchmark scheme.

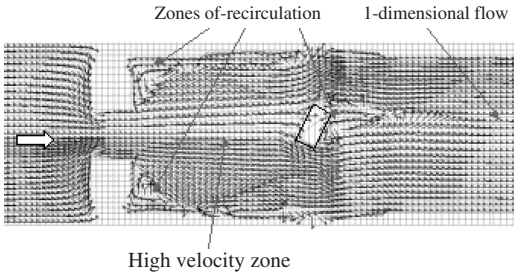


Figure 10. Velocity field at time $t = 15$ s.

4.3 *Numerical calculation of single building*

This experimental test case was simulated using a grid based on the regularity of the mesh upstream and downstream from the building, the cells around the building are then somewhat distorted. The typical size of the cells is 10 cm for a total number of cells around 10 000.

4.3.1 *Influence of the building*

In order to investigate the influence of the introduction of the building (or obstacle to the flow) in the channel, we present gauges G1 and G5 hydrographs with and without the building (plain channel).

Upstream from the building (G1), the water depths are similar in both cases at the beginning of the experiment until the flood wave reflects on the building wall and that backwater effect appears. Then, the original hydrograph rises suddenly, the lager water level being induced by the flow section reduction with the obstacle. Afterwards the hydrographs keep the same shape but the plain channel has lower water depths.

Downstream from the building (G5), Fig. 12 shows a slight wave delay of 0.4 seconds when introducing the building. Furthermore, the wave peak remarkable without the building does not appear with the building, case in which the highest water depth is lower. During the second part of the event ($t > 15$ s), the limnigrams are very similar.

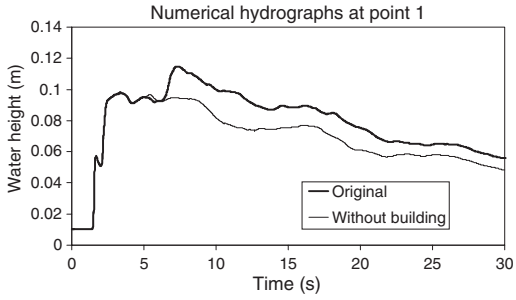


Figure 11. Building influence water depths at G1.

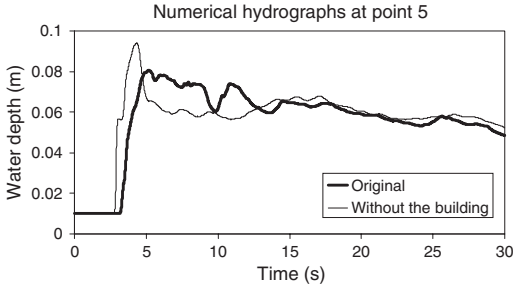


Figure 12. Building influence water depths at G5.

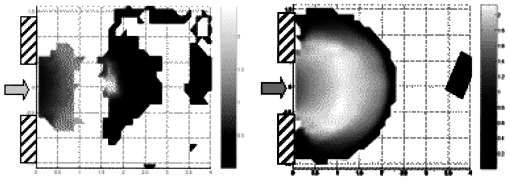


Figure 13. Velocity (m/s) at $t = 1$ s.

4.4 *Experimental/Numerical comparison*

4.4.1 *Global comparison*

The experimental velocity field could not be measured in the whole wetted area because of technical difficulties in the most oscillating water level zones (for instance around the hydraulic jumps). Moreover, at $t = 1$ s, the velocity was measured both in the area reached by the wave and in the zones where some wind disturbance or channel oscillations created a slight water motion.

T = 1 s: flood wave propagation

At $t = 1$ s, the front wave has an ellipsoid aspect and the front wave has reached the distance $x = 2.1$ m. This first wave seems to be well simulated, even if one

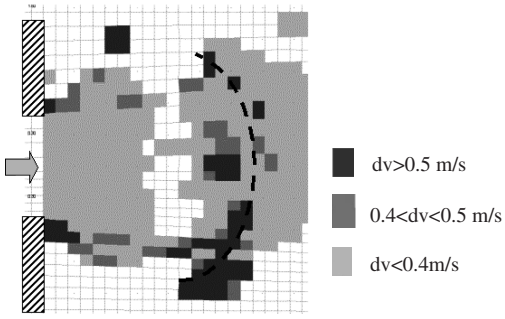


Figure 14. Velocity differences between numerical results and experimental records at $t = 1$ s.

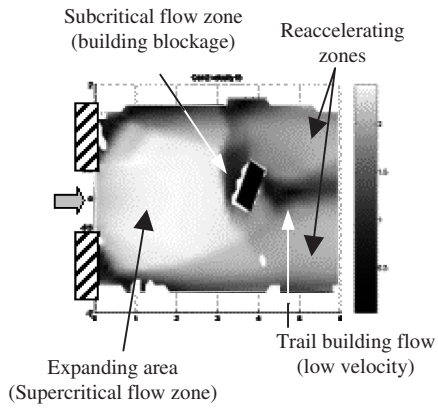


Figure 15a. Numerical velocity (m/s) at $t = 5$ s.

main error seems to be related to the shape of the front.

In the experimental record, the maximum water level (white colour) is very close to the front of the wave whereas this distance is larger in the numerical cases. This is confirmed by the image below where the main differences (dash line) are situated in the highest velocity zone (wave front). There seem to be a slight error in the dimension of the expanding front wave; however, this dimension difference is of the order of magnitude of one cell of calculation.

T = 5 s: developed structures

After 5 s of experiment, the front wave has already passed the building area and the flow structure is established. Figure 15 shows that the flow structures appear on the experimental records and numerical results at the same place and with almost the same size.

Figure 16 shows that the main differences between numerically calculated water depths and the experimental records are located in four specific areas:

Zone B: calculation overestimates the velocity values.

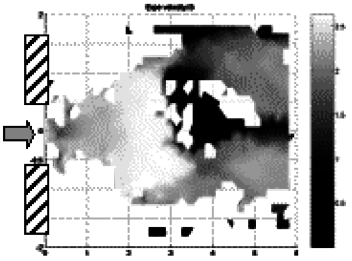


Figure 15b. Experimental velocity records (m/s) at $t = 5$ s.

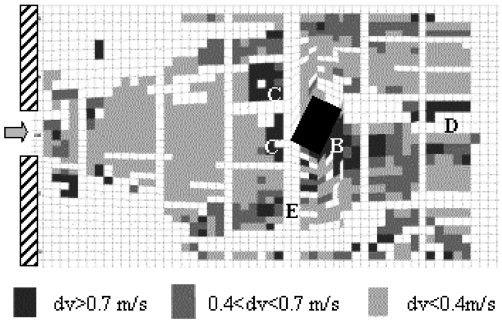


Figure 16. Differences between numerical and experimental velocity results at $t = 5$ s.

Zone C + C': the low velocity zone is shorter in the numerical calculations compared to the experimental case. This result shows the larger impact of the building on the overall flow in the experimental case compared to the numerical one.

Zone D: The low velocity zone protected by the building, is wider in the calculation compared to the experimental case.

Zone E: We see in both the numerical results and experimental records that there is a frontier near point E between a high velocity zone and a lower one. This frontier is not exactly at the same place in both cases.

4.4.2 *Hydrograph comparison at the gauges*

The 5 gauges were placed in very specific locations within the flow: either next to hydraulic regime change zones (supercritical to subcritical and vice versa: G1, G2, G4), in high wall reflection zones (G3) or finally at the border of the trailing zone behind the building (G5).

In a hydraulic jump location zone (example next to G2), the hydrographs are influenced by the motion of the hydraulic jump. In the experimental conditions, the hydraulic jump passes slowly through the gauge location and afterwards, G2 remains on its subcritical side. In the numerical calculation, at $t \sim 19$ s, the gauge 2 enters the subcritical zone after the displacement of the

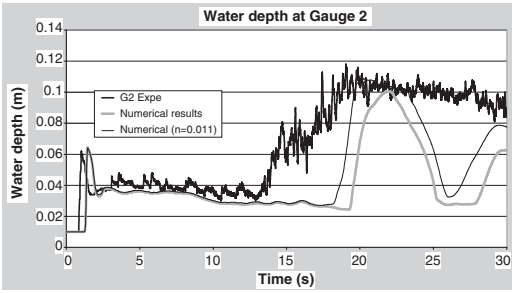


Figure 17. Water depths at G2.



Figure 18. Water depth around G2. In dark: $h < 5$ cm, in light grey $h > 8$ cm. White cross = G2 location.

hydraulic jump so its water depth increases suddenly. However, shortly after, the hydraulic jump travels back, passes G2 and the water depth decreases again. But, a slight change of a numerical parameter (example Manning increasing from 0.1 to 0.11) can modify the hydraulic jump location slightly but with a large influence on the hydrograph shape at G2. Note that the water depth in both regimes is estimated accurately.

Figure 18 shows that the displacement of the regime frontier implies a displacement of G2 from the supercritical to subcritical zone. However, G2 remains close to the hydraulic jump.

Thus, only errors in the location of the hydraulic jump spoiled the simulation of water depth at G2.

Another difficulty to model locally the water depths is in the areas of high reflections like near G3. Indeed, the shallow water equations cannot integrate the large slope (the slopes of the channel side are 45%) and have difficulties to represent these reflections. Then, the results are smoother than the experimental data but the shape of the hydrograph is similar.

4.5 *Conclusions*

When comparing calculation results with experimental data, we noticed that the numerical code could provide a convenient overall representation of the flow: high and low velocity areas, hydraulic jumps and trailing zones. However, concerning the water depths and velocities at the five gauge points situated around the building, we found differences corresponding to the difficulties of the code to simulate local flow characteristics accurately. The major differences seem

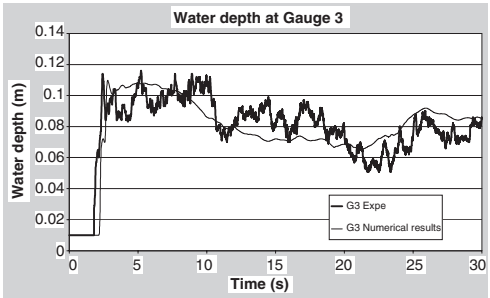


Figure 19. Water depths at G3.

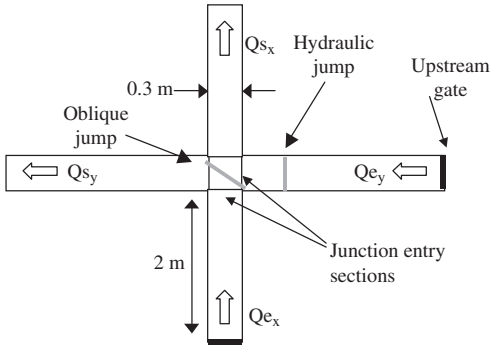


Figure 20. Four channel crossroad.

to come from:

- Slight errors in the locations of the hydraulic jumps (spatial errors).
- The difficulty to represent the reflections on the walls (building or banks).
- The size of the trailing zone downstream from the building.

5 FOUR BRANCHES CROSSROAD TEST CASE

In dense urban areas, the flows take place mainly in the streets and the crossroads. The influence of the crossroads is mostly the distribution of the flow between the different streets joining there. This experiment aims at improving the knowledge of the discharge distribution in a four channels crossroad that is the most popular street junction configuration in a city. In a future study, the capabilities of the numerical code to predict the flow distribution in a crossroad should be tested. Previous studies about open channel junctions mainly focused on three channels junctions either in dividing or combining flows and almost exclusively in subcritical conditions. To the authors' knowledge, the only work with 4 channel junctions was performed by (Nania, 1999); it includes an experimental study of 2 incoming and 2 outgoing flows with equal width concrete channels and for three slope configurations; from the experiments, an empirical relation was built to provide the discharge distribution as a function of the inflow Discharge Weighted Head ($W = \rho g H_s$, with H_s the Specific Head of the flow). Thus, experiments are performed at LMFA to increase the knowledge in such configurations.

5.1 *Experimental set-up*

The set-up is composed of 4 rectangular channels, made of glass, of length $L = 2$ m and of width $b = 0.3$ m) oriented perpendicularly to each other, with the (xy) frame defined Fig. 18. The channels slope is 1.27% and the junction is a horizontal square. The water enters the two incoming channels through honeycombs and a gate used to adjust the normal depth, as the flow is supercritical. Both incoming and outgoing discharges are measures thanks to electromagnetic flowmeters. Upstream water depths are acquired thanks to a moveable point gauge, with a reading accuracy of 0.1 mm and junction entry section water depths are measured by resistive probes to obtain an average water depth over about ten seconds.

5.2 *Description of the flows*

The upstream flows are usually supercritical and meet within the junction creating locally a very complex secondary flow. The crossroad causes an abrupt flow deviation, resulting in hydraulic jumps. As reported by (Nania 1999) and depending on the upstream discharges, the general flow can be of two types. When the two upstream discharges (Qe_x and Qe_y) are not too different one from another, a hydraulic jump occurs in each inflow channel at specific distances from the junction depending on both discharges: this is called "*type 1*" flow. A "*type 2*" flow is obtained when one incoming discharge is much larger than the other. Then an oblique jump appears in the large discharge inflow channel and a hydraulic jump occurs in the low discharge channel. For a specific discharge rate (one inflow discharge much larger than the other), the flow can become entirely subcritical in the low discharge incoming channel but a virtual hydraulic jump can be located upstream from the gate.

Downstream from the junction, two recirculation zones appear along with two contraction zones. Further downstream, the flow regime becomes supercritical again because of the slope.

5.3 *Choice of parameters*

First aim of the study is to find one single equation providing the part of discharge in each direction as a

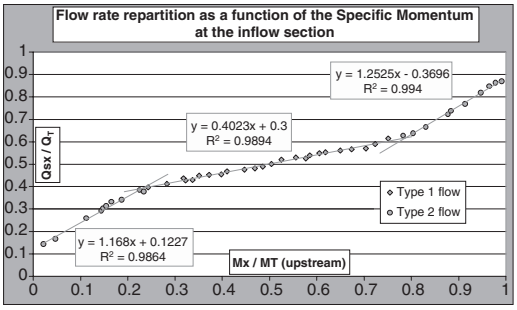


Figure 21. Flow distribution as a function of the upstream Specific Momentum.

function of the inflow conditions. The slope of each channel is constant (1.27%) and should not appear as a parameter. A parameter representing the inflow conditions can be the Specific Momentum:

$$M=\rho\frac{Q^2}{bh}+\frac{\rho g b h^2}{2}$$

where h is the local water depth and Q is the inflow discharge. The Specific Momentum is conserved through the hydraulic jumps, contrarily to the Discharge Weighted Head used by Nania (1999).

In fact, the parameter considered is M_x/M_T (Specific Momentum in the x direction divided by the total Specific Momentum ($M_T = M_x + M_y$)) calculated using the inflow discharge and the normal water depth set upstream from the hydraulic jump, to express the discharge distribution: Qs_x/Q_T ($Qs_x =$ Outflow discharge along x channel and $Q_T = QS_x + QS_y$). So, the final equation may be written as:

$$\frac{Qs_x}{Q_T}=f\left(\frac{Mx}{M_T}\right)$$

5.4 *Experimental results*

The results obtained for 45 different inflow discharge configurations set for the 1.27% slopes are sketched Fig. 21.

It seems that two linear regimes exist, a first one concerning the type 2 flow (on the right side, the oblique hydraulic jump is from the x channel, and on the left side, it is from the y channel) and another one, in the centre of the graph, corresponds to type 1 flows. It should be noticed that the configurations where the flow is completely subcritical in one upstream channel fit perfectly with the curve when considering their virtual normal depths upstream from a virtual hydraulic jump. When using the inflow Discharge Weighted Head ($W = \rho g H_s$ instead of the Specific Momentum, the results are quite similar. Hence, further experimental measurements, with different geometric configurations as for example with different slopes, must be performed to underline all the parameters describing the flow distribution.

5.5 *Conclusions*

This test case is the first step of a global experimental benchmark, which should improve the knowledge about the flow distribution at a crossroad. The results presented here permitted to test several parameters to use in order to establish the flow distribution law but more experiments are necessary to validate the various options (Specific Moment, Discharge Weighted Head. . .).

In addition to this experimental benchmark, simulations using the 2D code presented in paragraph 2 will be performed to check if the flow distribution can be estimated accurately.

6 CONCLUSIONS

We simulated a flood in a simplified urban area with 20 cubic buildings. We noted that the numerical results qualitatively corresponded to the experimental data but that some differences existed and could not be reduced with a finer mesh. Then, we modelled two typical urban flood configurations: the flow around a building and the flow distribution in a four channels crossroad. The numerical simulation of the flow around the building agrees with the experimental data; however, a perfect representation of the flow requires a fine mesh and then the use of many cells. The experimental study of the flow distribution in a crossroad permitted to present a distribution curve for a 1% slope crossroad in which two regimes seem to appear; more experiments are still necessary to validate both this last curve and 2D model in this context.

More generally, the numerical simulations of these test cases permit to improve our knowledge about the capability of a 2D code to model a flood in a dense urban area and the way to define the calculation grid. However, a complementary validation on various field test cases remains necessary.

ACKNOWLEDGMENTS

This research work was partly funded by the European Commission under the fifth framework program as part of the IMPACT project and by the RIO 2 program of the French Ministry of Ecology and Sustainable Development (MEDD) as part of the project “Estimation des écoulements de surface pour une crue extrême en milieu urbanisé”.

REFERENCES

Hervouet, J.-M., Samie, R. & Moreau B. 2000. Modelling urban areas in dam-break flood wave numerical simulations. Proceedings of *RESCDAM* workshop. Seinäjoki, Finland: Finnish Environment Institute.

Khan, A., Cadavid, R. & Wang, S.S.Y. 2000. Simulation of channel confluence and bifurcation using the CCHE2D model. *Water and Maritime Engineering*, 142: 97–102.

Neary, V.S. & Sotiropoulos, F. 1996. Numerical investigation of laminar flows through 90-degree diversions of rectangular cross-section. *Computers and Fluids*, 25(2): 95–118.

Nania, L.S. 1999. PhD thesis: Metodologia numéricoexperimental para el analisis del riesgo asociado a la escorrentia pluvial en una red de calles. *Departamento de Ingéniera Hidraulica, Maritima y Ambiental*. Barcelona, Universitat politècnica de Catalunya.

Paquier, A. 1998. 1-D and 2-D models for simulating dam-break waves and natural floods. *Concerted action on dam-break modelling, proceedings of the CADAM meeting, Wallingford, United Kingdom*. M. Morris, J.-C. Galland and P. Balabanis. L2985, Luxembourg, European Commission, Science Research Development, Hydrological and hydrogeological risks.: 127–140.

Paquier, A., Tanguy, J.M., Haider, S. & Zhang, B. 2003. Estimation des niveaux d'inondation pour une crue éclair en milieu urbain: comparaison de deux modèles hydrodynamiques sur la crue de Nîmes d'octobre 1988. *Revue des Sciences de l'Eau*, 16(1): 79–102.

Soares Frazäo, S., Noël, B. & Zech, Y. 2004. Experiments of dam-break flow in the presence of obstacles. Submitted to *River Flow 2004*.

Soares Frazäo, S., Noël, B., Spinewine, B. & Zech Y. 2003. Dam-break flow through urban areas – The isolated building test case: review of the IMPACT benchmark. To be published in *EC Contract EVG1-CT-2001-00037 IMPACT Investigation of Extreme Flood Processes and Uncertainty*, Proceedings 3rd Project Workshop, Louvain-la-Neuve, Belgium 6–7 November 2003 (CD-ROM).

This page intentionally left blank

River Flow 2004 – Greco, Carravetta & Della Morte (eds.)
© 2004 Taylor & Francis Group, London, ISBN 90 5809 658 0

Detailed validation of CFD for flows in straight channels

N.G. Wright, A.J. Crossley & H.P. Morvan
School of Civil Engineering, The University of Nottingham, UK

T. Stoesser
Institute for Hydromechanics, University of Karlsruhe, Germany

ABSTRACT: An investigation has been made into the flow in open channels using a commercial Computational Fluid Dynamics (CFD) package. The study has focused on the ability of the software to correctly predict the complex flow phenomena that occur in channel flows. Previous work (Morvan et al. 2002) has shown the capability of CFD in predicting the flow in natural rivers. In this project, the predictions are contrasted against high quality flume measurements obtained for a trapezoidal channel, and a comparison is made between the different turbulence models available. The results show that whilst all the models generally give similar predictions for the bulk features of the flow, there is a marked difference between the secondary flow characteristics, and that the accuracy of the predictions increases with the level of complexity of the turbulence model used. Results from a LES model confirm the importance of turbulence modelling.

1 INTRODUCTION

The features inherent in open channel flow result from the complex interaction between the fluid and a number of mechanisms including the channel bed and walls, friction, gravity and turbulence. In the past such flows have been modelled using simplified models (for example the Saint Venant equations), which predict mean characteristics of the flow and often contain a high level of empiricism. With advances in computer power, interest has risen in applying more sophisticated techniques providing more accurate results and more in-depth information. In other fluid flow fields such as aeronautics, the implementation of more complex models has mirrored the advances in computer technology and 3D models are now commonly used. However this transition has not occurred as rapidly in open channel flow modelling, and most hydraulics models are either 1D or 2D with very few applications of 3D models. This is, in part, due to the inherent difficulties found in applying CFD in a natural river channel (Wright 2001): inter alia, irregular geometry, vegetation and roughness representation.

In this work the application of a generic commercial Computational Fluid Dynamics (CFD) package to open channel flows is considered. The software includes various models to solve general fluid flow problems and is widely accepted as a modelling tool in other fields. In this study, the Reynolds Averaged Navier-Stokes equations (RANS) are used to represent the fully developed flow in a prismatic trapezoidal channel. The RANS equations are obtained by applying time averaging to the full Navier-Stokes equations, which results in six new terms known as the Reynolds stresses. A turbulence model is then needed to account for the Reynolds stresses in order to close the system of equations. In industry the accepted standard is the two equation k-ε model which assumes that the turbulence is isotropic. More complex models exist which account for the anisotropic nature of turbulence, but at an increased computational cost to the user often making the choice prohibitively expensive. The technique of Large Eddy Simulation does not rely on Reynolds averaging and directly predicts larger eddies whilst using a model for smaller ones (Smagorinsky 1963). In collaboration with researchers at the University of Karlsruhe, LES has been implemented for the channel under consideration here and preliminary results are reported.

In the present study, the very nature of the flow is driven by the anisotropy of the turbulence and several different turbulence models are evaluated including the k-ε model, various standard Reynolds stress models and the new ω Reynolds stress model.

The research programme is being conducted by the Universities of Birmingham and Nottingham and involves detailed CFD experiments for comparison with experimental data collected at Birmingham (Yuen 1989, Knight et al. 1994). The latter encompasses discharge, velocities and shear stresses. So far the

investigation has focused on a trapezoidal channel which whilst being a simple geometry involves some complex fluid flow patterns. These patterns are similar to those found in a rectangular open channel (Broglia et al. 2003).

The CFD investigations have examined the influence of grid size and structure, discretisation, turbulence model and wall treatment. The research programme has focused on generating the correct qualitative and quantitative flow features from the CFD software. Bulk quantities such discharge (bulk velocity), maximum velocity and mean shear stress have been used to ascertain the quality of the predictions, in respect to the experimental data. In addition, consideration has also been given to the velocity and bed shear stress distributions, with particular emphasis on generating the secondary flow (recirculation) patterns that should be present in a prismatic channel.

Results to date have demonstrated that the CFD is able to correctly predict the mean shear stress and subsequent shear force on the channel bed and banks. However, with standard turbulence models it is not possible to obtain the correct shear stress profiles. The study has also highlighted the complexities involved in obtaining the correct secondary flow pattern. The currents which are known to be induced by turbulence and the wall effects in open channel flow, should lead to the maximum velocity occurring below the free surface. However in all of the results obtained so far in the study, the maximum velocity has occurred at the free surface. Initial results obtained using a Large Eddy Simulations (LES) model have demonstrated that LES can predict open channel flow phenomena more successfully than RANS based models, and this application is being further investigated.

2 MATHEMATICAL MODEL

The CFD software is designed to solve generic fluid flow problems and the model components are derivatives of the full unsteady Navier-Stokes equations which for an incompressible fluid can be written as

$$div\ \boldsymbol{u} = 0 \tag{1}$$

$$\frac{\partial u}{\partial t} + div(u\boldsymbol{u}) = -\frac{1}{\rho}\frac{\partial p}{\partial x} + \nu\, div\ grad\ u + \frac{1}{\rho}S_{M_x} \tag{2}$$

$$\frac{\partial v}{\partial t} + div(v\boldsymbol{u}) = -\frac{1}{\rho}\frac{\partial p}{\partial y} + \nu\, div\ grad\ v + \frac{1}{\rho}S_{M_y} \tag{3}$$

$$\frac{\partial w}{\partial t} + div(w\boldsymbol{u}) = -\frac{1}{\rho}\frac{\partial p}{\partial z} + \nu\, div\ grad\ w + \frac{1}{\rho}S_{M_z} \tag{4}$$

where $\boldsymbol{u}$ is the velocity vector with components u, v and w, p is the pressure, ρ is the density, υ is the kinematic viscosity and the S_M components represent additional momentum source terms such as the effects of gravity. For a complete derivation of the equations see Versteeg & Malalasekera (1995). To fully resolve the Navier-Stokes equations at all length scales would require excessively fine grids and small time steps due to the effects of turbulence. This renders the direct solution of Equations 1 to 4 impractical for all but low Reynolds number flows. However it is possible to model the effects of turbulence on the flow without considering every single eddy, by considering time averaged effects. This is encompassed by defining mean values which when substituted into the full Navier-Stokes equations, give rise to the Reynolds Averaged Navier-Stokes equations which were used in the CFX simulations.

Instead of using these mean values it is possible to use LES to predict the time variation of the larger eddies. The LES code LESOCC developed at the Institute for Hydromechanics (Breuer & Rodi 1996) was used to perform the LES simulations. The code solves the filtered Navier-Stokes equations on a curvilinear, block-structured grid discretised with the finite volume method. A non-staggered grid with Cartesian velocity components was used and both, convective and diffusive fluxes are approximated with central differences of second order accuracy. The SIMPLE algorithm is employed in order to ensure mass conservation and to couple the pressure to the velocity field. Time advancement is achieved by a second order, explicit Runge-Kutta method. LESOCC is highly vectorised and parallelisation is accomplished by domain decomposition and explicit message passing via MPI. The subgrid stress of the filtered Navier-Stokes equations is computed using the dynamic approach of Germano et al. (1991). The linear no-slip ($u^+ = y^+$) boundary condition is used for the bottom and the side walls since the first grid point is placed in the viscous sub-layer ($y^+ \approx 7$).

3 GEOMETRY AND DATA

3.1 *Experimental data*

To evaluate the performance of the CFD software, a comparison has been made against high calibre experimental measurements obtained from the SERC funded FCF programme (Knight et al. 1994) and by Kenneth Yuen as part of his PhD study at the University of Birmingham (Yuen 1989).

The project has not only been concerned with demonstrating that the CFD is providing solutions that are quantitatively correct with respect to the experimental data, but also that the flow properties are qualitatively in line with expectations, for example the presence of re-circulations. The knowledge gained from this study will also be used to provide guidance

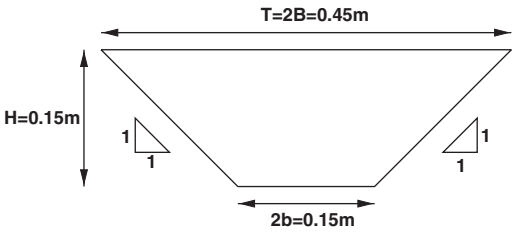


Figure 1. Cross-sectional geometry of experiment 16.

Table 1. Summary of the experimental values.

H	0.15000	2b	0.15000	A	0.04500	P	0.57426
R	0.07836	T	0.45000	D	0.10000	n	0.00990
S_0	0.00100	Q	0.02630	U_{av}	0.58444	F_r	0.59018
Re	0.11564	S_f	0.44130	τ_{av}	0.76846	U*	0.02772

to the hydraulic community on how to apply CFD to open channel flows.

The results presented in this report focus on one particular geometry from Kenneth Yuen's PhD thesis which serves to illustrate the difference in performance between the different turbulence models. In the original experiments various channel geometries were considered including simple and compound channels. Parameters such as the slope and cross-section were altered and the measurements recorded at a given cross-section once a uniform flow had developed. Different flow depths were considered which led to a series of data being collected for different discharges and Froude numbers. In this report Experiment 16 is considered, where the cross-sectional geometry is shown in Figure 1. The channel slope was 0.001 and the discharge was recorded at 0.02630 $m^3\ s^{-1}$ with the water temperature measured at 14°C. The characteristics of the flow are summarised in Table 1.

3.2 *Model data for the RANS simulations*

A model based on the geometry of Experiment 16 was created with the same cross-section as shown in Figure 1. Periodic boundaries were used at the channel inlet and outlet such that the predicted profile would be the same throughout the channel length. This enabled a much shorter length to be utilised than if a mass flow condition was implemented, whereby the flow profile would need a significant length to develop. Choosing to implement periodic boundary conditions thus reduced the number of cells required in the streamwise direction, enabling more cells to be concentrated on the cross-section. A channel length of 0.1 m was chosen and a symmetry plane was imposed along the central plane of the channel (such that only half of the geometry was modelled), as shown in Figure 2 together with

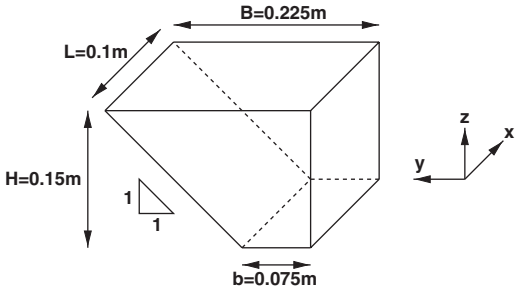


Figure 2. Computational geometry in CFX.

the co-ordinate frame of reference. The channel itself was constructed as half of a flat trapezoidal box with the centreline coinciding with the x axis. The channel bottom was aligned with the y co-ordinate line and z co-ordinate represents changes in the vertical direction. The flow was driven by introducing a momentum source into the equations which accounted for the effects of gravity. This force was resolved into components acting parallel and perpendicular to the channel length to allow for the co-ordinate transformation whereby

$$-\rho \boldsymbol{g} = (\rho g \sin\theta, 0, -\rho g \cos\theta)^T \tag{5}$$

given that $\tan\theta = S_0$. As the water temperature in the original experiment was measured to be 14°C, a value of 999.25 kg m^3 was used for the water density and together with $g = 9.8066502$ (the internal value of g in CFX) this gave

$$-\rho \boldsymbol{g} = (9.7993, 0, -9.7993 \times 10^3)^T. \tag{6}$$

Additionally the dynamic viscosity of the water was set to $\mu = 1.1666 \times 10^{-3}$ N s m^{-2}. Note that in the results presented the z-component of the momentum source was set to zero as it was causing a number of numerical difficulties, whilst having no influence on the flow field. If required, a hydrostatic pressure field can be added as a post-process. The flow was initialised by setting the initial velocity equal to the mean recorded value in all of the cells i.e.

$$U^0 = (0.58444, 0, 0)^T. \tag{7}$$

The free surface was represented as a symmetry plane, and smooth no slip walls were applied at the remaining boundaries.

3.2.1 *Mesh for the RANS simulations*

Two different meshes were constructed based on the requirements of the turbulence models used. Both meshes consisted of structured hexahedral cells. Emphasis was placed upon creating a sufficient use

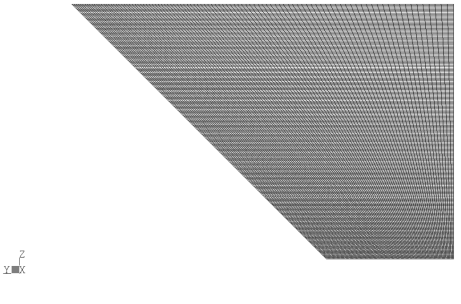


Figure 3. A cross-section of Mesh 1.

of periodic boundary conditions reducing the need for many elements in the streamwise direction. The first mesh consisted of $10 \times 100 \times 200$ (200000) cells. A cross-section of the mesh is shown in Figure 3. Note that a biased seeding was used along the spanwise component of the free surface in order to reduce the y^+ variation at the channel wall. Thus the cell at the centre of the channel was three times the width of the cell at the bank. The second mesh followed the same structure as the first but consisted of $10 \times 200 \times 200$ (800000) cells.

3.2.2 *Mesh for the LES simulations*

The LES simulation used a mesh of $161 \times 100 \times 100$ in the x, y and z directions respectively. It should be noted that in the LES the streamwise length is much greater than for the RANS models. This length is required to allow the eddy structure to develop. This is unnecessary with a RANS simulation as these fluctuations are averaged out. To account for wall effects, van Driest damping functions and the Werner-Wengle wall model were used.

4 RESULTS

Comparative results were obtained using five different turbulence models. The first model considered was the industrial standard k-ε model (Versteeg & Malalasekera 1995) which assumes that the turbulence is isotropic and does not solve the Reynolds stresses explicitly. As the name implies, the model is based upon solving the turbulent kinetic energy, k, and the turbulence eddy dissipation, ε. In contrast to this, the Reynolds stress models solve the six Reynolds stresses directly hence accounting for the anisotropic nature of turbulence and are thus more computationally demanding. Note that ε is still present in the standard formulation. Three different variants of the standard Reynolds Stress approach were tested in which the differences were accounted for by different values for the model constants. These models were the Launder, Reece and Rodi Isotropisation of Production (LRR-IP) (Launder et al. 1975), Launder, Reece and Rodi Quasi-Isotropic (LRR-QI) (Launder et al. 1975) and the model due to Speziale, Sarkar and Gatski (SSG) (Speziale et al. 1991).

Table 2. Summary of results from the turbulence model comparison.

Turbulence model	Wall shear (Pa)	Max. velocity (m/s)	Mass flow (kg/s)	Min. y^+	Max. y^+
k-ε	0.7679	0.7767	14.86	9.73	20.44
LRR IP	0.7679	0.7971	15.17	10.27	20.50
LRR-QI	0.7679	0.7900	15.10	11.37	20.71
SSG	0.7679	0.7767	15.02	11.32	20.68
SMC-ω	0.7679	0.7527	14.66	5.36	10.26
Theory	0.7679	–	13.14	–	–
Experiment	0.7685	–	13.15	–	–

Both the k-ε and standard Reynolds Stress models use wall functions in the near wall region which relate the tangential velocity to the wall shear stress in the log-law region of the flow. This prevents the need to introduce a fine mesh near the wall, which would be required if the viscous sub-layer was to be resolved.

The final RANS model tested was the Reynolds stress-ω or SMC-ω model (CFX Ltd. 2003), in which the flow equations are solved right through to the wall without the use of wall functions. The formulation is based on an equation for ω, the turbulent frequency as opposed to ε in the standard Reynolds stress models. One of the benefits of the approach is that the viscous sub-layer can be resolved with fewer cells than would be required for an ε based model such as k-ε or the standard Reynolds stress approaches.

The bulk property results from the model comparison are summarised in Table 2 and compared with the theoretical and experimental values. Note that the k-ε, LRR-IP, LRR-QI and SSG results were obtained on Mesh 1, and that the SMC-ω results were produced on Mesh 2.

From Table 2 it can be seen that all the turbulence models predict the correct value for the mean shear stress compared with the theoretical value, which is in close agreement with the value recorded in the experiment. However in all of the simulation cases, the mass flow rate is over-predicted by between 12 and 15%. This may be due to the use of a smooth wall in the CFD as it has been assumed that the low Manning's n value from the experiment represented an almost smooth wall.

Contour plots and vector plots of the secondary flow are shown in Figures 4–13 for the CFX results. Note that to improve clarity not all of the vectors are shown and the display magnitudes have been adjusted for each turbulence model. As expected the results from the k-ε model show no indication of the contours bulging towards the bottom corner of the channel, and there

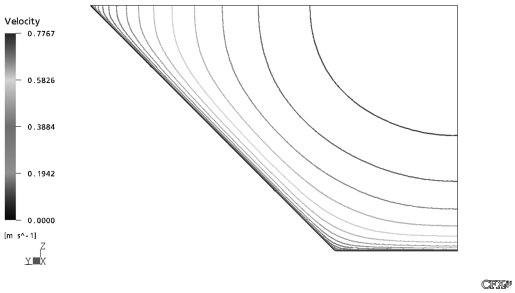


Figure 4. Velocity contours from the *k*-ε model.

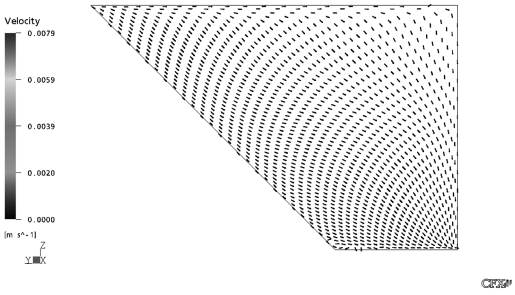


Figure 5. Secondary velocity vectors from the *k*-ε model.

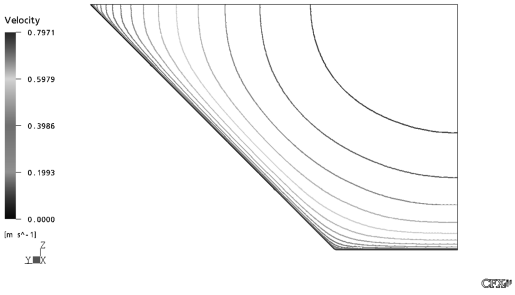


Figure 6. Velocity contours from the LRR-IP model.

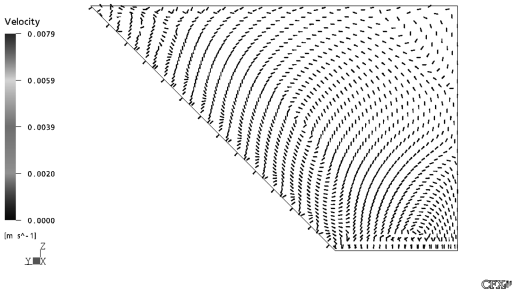


Figure 7. Secondary velocity vectors from the LRR-IP model.

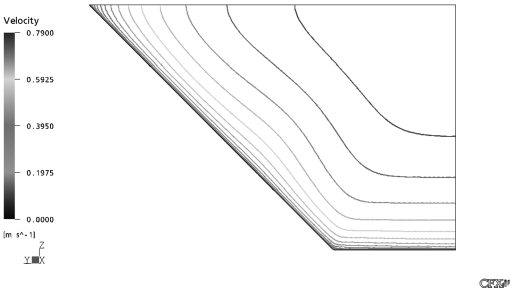


Figure 8. Velocity contours from the LRR-QI model.

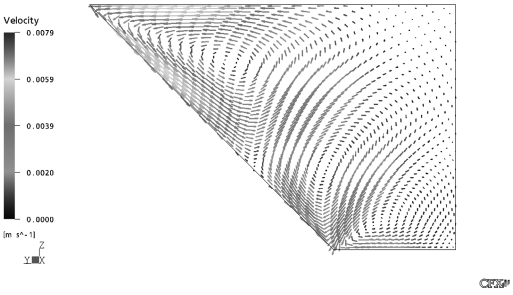


Figure 9. Secondary velocity vectors from the LRR-QI model.

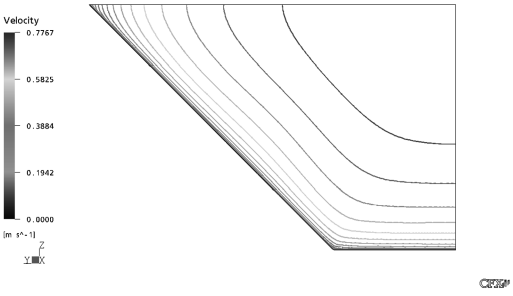


Figure 10. Velocity contours from the SSG model.

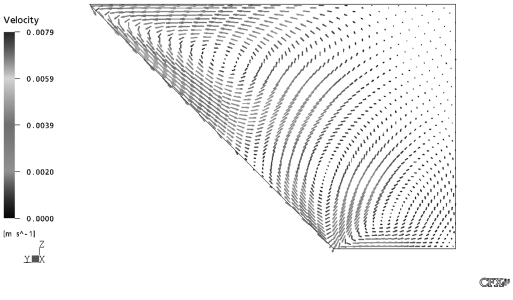


Figure 11. Secondary velocity vectors from the SSG model.

is no evidence of re-circulation currents in the vector plot beyond numerical error. Both features should be evident in the profiles and are thought to be attributed to the turbulence anisotropy and the interaction with the wall. The results from the LRR-IP model are fairly similar to the k-ε profiles. It is noted by CFX that this formulation does not contain any wall reflection terms which may partially account for the results obtained. The LRR-QI and SSG results both show bulging of the contours and evidence of re-circulation although the magnitudes of the phenomena are less that expected. Typically the scale of the secondary velocity should be of the order of 2–3% of the bulk streamwise velocity (Broglia et al. 2003). The results most in line with expectations are those from the SMC-ω turbulence model which show significant bulging of the contours and strong evidence of secondary flow. A feature of all of the predictions is that the maximum velocity occurs at the free surface, which in reality is not the case.

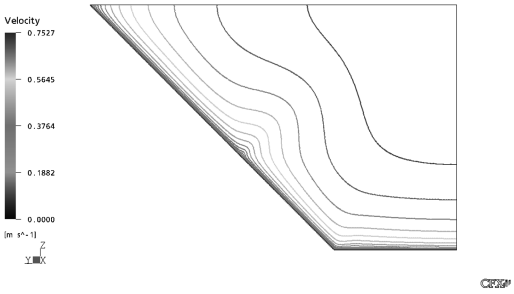


Figure 12. Velocity contours from the SMC-ω model.

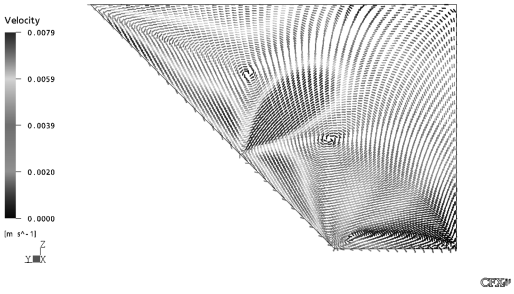


Figure 13. Secondary velocity vectors from the SMC-ω model.

Consideration has also been given to the shear stress distribution occurring on the channel bed and walls. Figure 14 shows a comparison between the results from the various turbulence models and those measured in the original experiment. All of the results show a characteristic local minimum at the corner of the channel and a decrease towards the free surface in line with expectations and the experimental measurements. The predictions all show the shear stress increasing towards the centre of the channel, whereas the experimental value decreases. In addition the LRR-QI, SSG and SMC-ω models all indicate a decrease at a point approximately two thirds below the free surface, with a marked decline present in the SMC-ω results comparable to that at the channel corner. Note that this point coincides with where the maximum distortion of the contours is present and the strongest secondary flows occur.

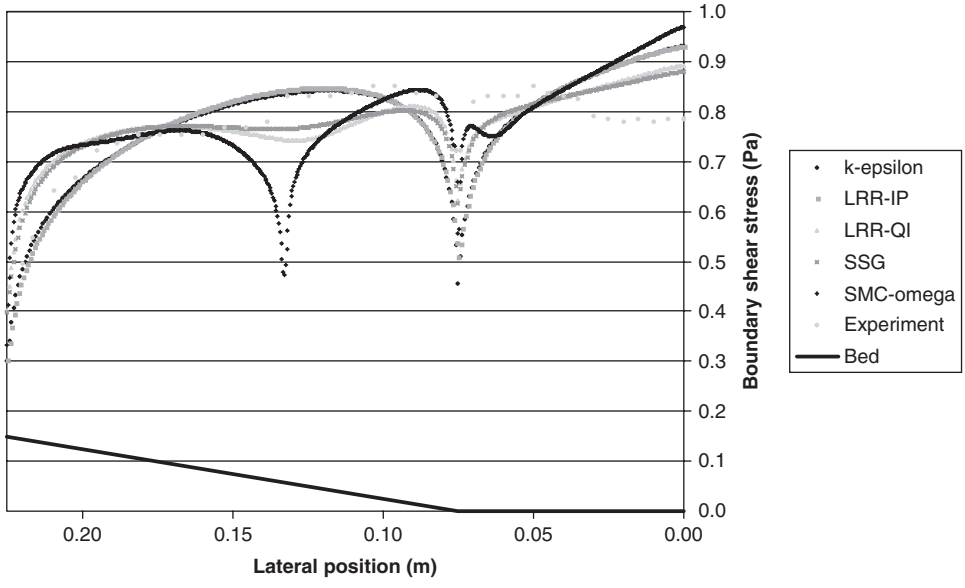


Figure 14. Wall shear stress distribution results from the RANS model comparison.

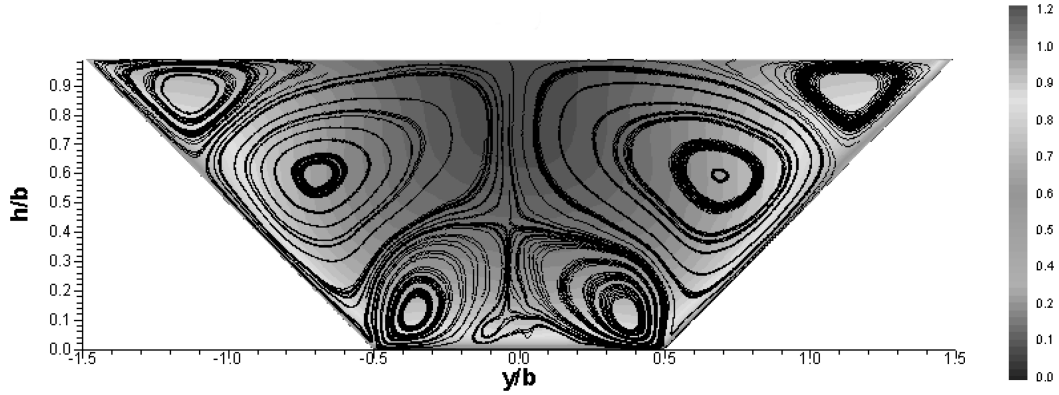


Figure 15. Mean velocity profile from LES simulation.

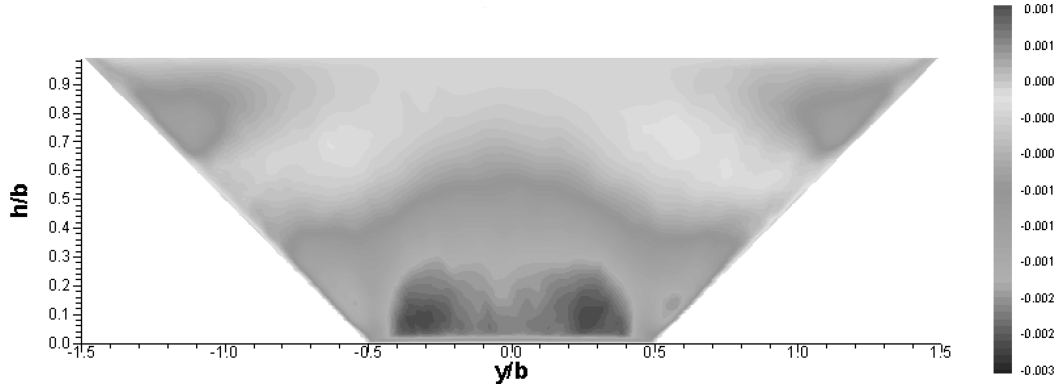


Figure 16. $u'w'$ Reynolds stress distribution from LES simulation.

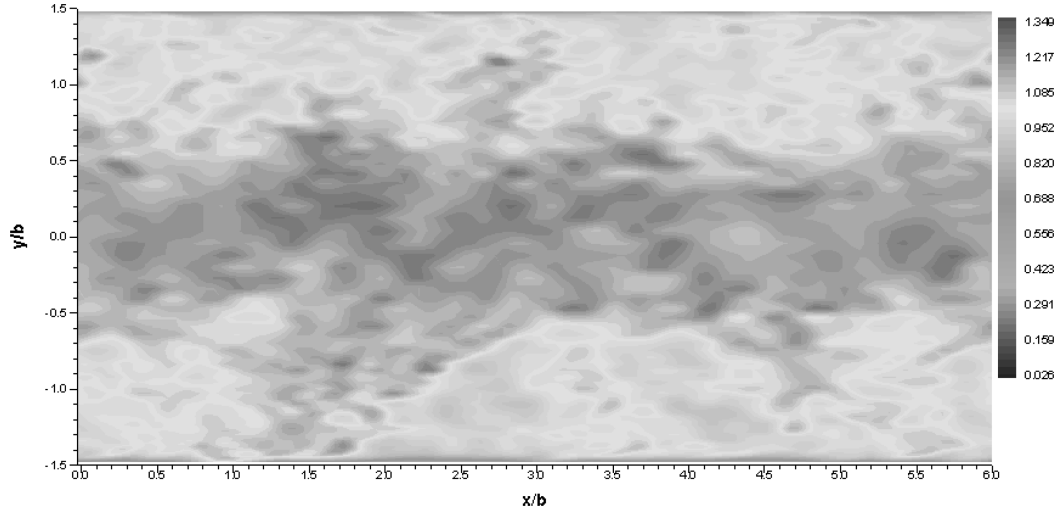


Figure 17. Instantaneous streawise velocity profile from LES simulation.

The LES results in Figure 15 show the bulging of the contours towards the bottom corners in a similar manner to the SMC-ω results. This figure also shows the streamlines which demonstrate a three cell pattern in a similar way to the more complex RANS models. Figure 16 shows the $u'w'$ Reynolds stress. To emphasis the fact that LES can predict time-varying velocities Figure 17 shows an instantaneous velocity field.

5 CONCLUSIONS

The results show that the CFD predictions accurately predict the average shear stress value for all of the turbulence models tested. In all of the cases, the mass flow rate was over predicted, with none of the models appearing significantly better than the others. It was observed that the k-ε model failed to predict any evidence of secondary flow, and that the standard Reynolds stress approaches indicated some re-circulation with varying degrees, but all were below the expected magnitudes. The most realistic results were obtained using a non-standard Reynolds stress model in which the equations were integrated through to the wall without the use of wall functions. A comparison of the bed shear stress distributions showed that whilst all of the models gave the correct average value, none of the models captured the expected profile, which was observed in the experimental measurements. Whilst the LES results need more analysis the results so far indicate that this approach has considerable benefit compare with the standard RANS models and even the more complex SMC-ω model. However, it must be borne in mind that this technique requires considerably longer run times.

A number of choices had to be made within the modelling strategy that can have a significant effect on the results. These have to be carefully considered, just as in experimental work, and novice users may not always be aware of these.

6 FURTHER WORK

This study has focused on the application of a generic CFD package to a smooth prismatic trapezoidal open channel. Further work will extend the geometries to compound and rough channels. In addition more sophisticated numerical methods will be considered and further work using LES modelling will be conducted.

REFERENCES

Breuer, M. & Rodi, W. 1996. Large eddy simulation of complex turbulent flows of practical interest. In (ed.), Hirschel, E.H. *Notes On Numerical Fluid Mech., Flow Simulations With High Performance Computers II*: 258–274. Braunschweig: Vieweg.

Broglia, R., Pascarelli, A. & Piomelli, U. 2003. Large-eddy simulations of ducts with a free surface. *J. Fluid Mech.* 484: 223–253.

CFX Ltd. 2003. CFX user manual.

Germano, M., Piomelli, U., Moin, P., Cabot, W.H. 1991. A dynamic subgrid-scale eddy viscosity model. *Physics of Fluids* 3: 1760–1765.

Knight, D.W., Yuen, K.W.H. & Alhamid, A.A.I. 1994. Boundary shear stress distributions in open channel flow. In Beven K. (ed.), *Physical Mechanisms of Mixing and Transport in the Environment*: 51–87. London: J. Wiley.

Launder, B.E., Reece, G.J. & Rodi, W. 1975. Progress in the developments of a Reynolds-stress turbulence closure *J. Fluid Mech.* 68: 537–566.

Morvan, H., Pender, G., Wright, N.G. & Ervine, D. 2002. Three-dimensional hydrodynamics of meandering compound channels. *J. Hydraul. Eng.* 128(7): 674–682.

Smagorinsky, J. 1963. General circulation experiments with primitive equations Part 1: Basic experiments. *Monthly Weather Review* 91: 99–164.

Speziale, C.G., Sarkar, S. & Gatski, T.B. 1991. Modelling the pressure-strain correlation of turbulence: an invariant dynamical systems approach. *J. Fluid Mech.* 277: 245–272.

Versteeg, H.K. & Malalasekera, W. 1995. *An introduction to computational fluid dynamics – the finite volume method*. Essex: Pearson Education.

Wright, N. 2001. Conveyance implications for 2D and 3D modelling. In *Scoping study for reducing uncertainty in river flood conveyance*. Bristol: Environment Agency.

Yuen, K.W.H. 1989. *A study of boundary shear stress, flow resistance and momentum transfer in open channels with simple and compound trapezoidal cross section*. PhD thesis: The University of Birmingham.

River Flow 2004 – Greco, Carravetta & Della Morte (eds.)
© 2004 Taylor & Francis Group, London, ISBN 90 5809 658 0

Synthetic hydrographs as a design tool for flood routing evaluation

F. Aureli, A. Maranzoni & P. Mignosa
Dipartimento di Ingegneria Civile, dell'Ambiente, del Territorio & Architettura, Parma, Italy

U. Maione
Dipartimento di Ingegneria Idraulica, Ambientale e del Rilevamento, Milano, Italy

ABSTRACT: In this paper the procedure for the determination of Synthetic Design Hydrographs (SDHs), proposed by some of the Authors in previous works, is validated comparing the statistical distribution of peak discharges obtained at the end of a river reach by routing a long series of historical floods and by routing the synthetic floods only. The selected reach is the end branch of the Parma river, a tributary of the Po river (Northern Italy). The mathematical model was calibrated on the basis of three recent historical floods. Then all the historical floods and the SDHs have been routed in the river reach. Historical and synthetic peak discharges at a downstream section were then compared in probability plots. The results show that the distribution obtained by routing the historical floods seems to be correctly described by the results obtained by routing the SDHs.

1 INTRODUCTION

Peak discharges are significantly reduced in mild slopes river reaches by routing effects due to water volumes temporarily stored in the main channel and in the flood plains. Often these effects are masked by the contribution of tributaries or hill slopes encountered downstream. If concentrated or distributed inputs are negligible, as in the lower reaches of many tributaries of the Po river (Northern Italy), peak discharges really decrease. The amount of reduction depends on a combination of hydrological input and geometry of the reach and flood plains. Flood waves with the same peak discharge but different volumes are of course reduced in different ways.

There is then an interest to define Synthetic Design Hydrographs (SDHs) which are capable to model in a statistically correct way the dumping effect due to routing on the historical floods. In this way it would be possible to derive the peak discharge distribution at a downstream section of a river reach by routing only few SDHs instead of a long series of historical floods.

In previous works (Maione et al. 2000a, b) the Authors proposed a procedure to estimate SDH in gauged river sections where a long series of hydrographs is available. The method is based on the statistical analysis of recorded flood waves through the construction of the Flow Duration Frequency (FDF) reduction curves of given return period and the determination of the temporal location of the peak value for each duration.

In this paper the procedure for the determination of SDHs is validated comparing the statistical distribution of peak discharges obtained at the end of a river reach by routing a long series of historical floods and by routing the synthetic floods only.

2 SYNTHETIC DESIGN HYDROGRAPHS (SDHS) DERIVATION PROCEDURE

SDHs can be derived (Maione et al. 2000a, b) from Flow Duration Frequency reduction curves (FDF) that furnish the maximum average discharge $Q_D(T)$ in a given duration D for each value of the return period T, where

$$Q_D = \max\left(\frac{1}{D}\int_{t-D}^{t} Q(\tau)d\tau\right). \quad (1)$$

The FDF reduction curves are analogous to the IDF curves that relate the maximum average intensity, duration and frequency of rainfall. Their construction is obtained through the statistical processing of historical hydrographs. The analysis can be performed on the annual maximum average discharges for each duration ranging from 0 (corresponding to an instantaneous discharge) to a sufficiently large value, say, D_f representing the characteristic duration of flood events for a given river section. Alternatively, the maximum values of the average discharges that exceed a given threshold

value for each duration can be sampled according to the Peaks Over Threshold method (POT).

The estimation of the FDF reduction curve can be conveniently obtained relating the quantiles $Q_D(T)$ to $Q_0(T)$ by means of the reduction ratio $\varepsilon_D(T)$:

$$Q_D(T) = \varepsilon_D(T) Q_0(T), \quad \varepsilon_D(T) = \frac{Q_D(T)}{Q_0(T)}. \tag{2}$$

In the more general case, the reduction ratio is a function of duration D and return period T. The convenience of the position (2) comes from the circumstance that if the $CV(Q_D)$ and the functional form of the probability distribution of Q_D are independent of the duration D, ε_D is independent of return period T and reduces to the ratio of the averages of Q_D and Q_0:

$$\varepsilon_D = \frac{\mu(Q_D)}{\mu(Q_0)}. \tag{3}$$

Under these assumptions the estimation of the FDF curves reduces to the estimation of peak flood discharge quantiles $Q_0(T)$ and of the reduction ratio ε_D.

Some different approaches have been proposed in literature for the identification of the functional form of the reduction ratio ε_D that best fits the experimental data (NERC 1975, Fiorentino 1985, Bacchi et al. 1992)

Bacchi et al. (1992) used a deductive approach for the derivation of the reduction ratio based on a formulation that considers the crossing properties of continuous gaussian stationary stochastic processes. From this formulation the following equation for the reduction ratio has been deduced:

$$\varepsilon_D \approx \sqrt{\Gamma(D)} = \sqrt{\frac{\theta}{2D}\left[2 + e^{-\frac{4D}{\theta}} - \frac{3\theta}{4D}\left(1 - e^{-\frac{4D}{\theta}}\right)\right]}, \tag{4}$$

in which $\Gamma(D)$ is the variance function, i.e. the ratio of the variances of the instantaneous process and integrated one. The parameter θ is the scale of fluctuation, i.e. the integral of the autocorrelation function of the instantaneous process.

Once the FDF reduction curves have been obtained, the construction of the SDH is performed imposing that the maximum average discharge for each duration coincides with the value deduced from the FDF; the shape of the hydrograph is defined by the Peak-Duration values r_D ($0 \le r_D \le 1$), that are the ratios between the time prior to the peak (in the time interval in which the maximum average discharge of given duration falls) and the duration D. For each duration the value of r_D is calculated from all the historical hydrographs; then the average value is computed and adopted for the construction of the SDH. The data sampling modality is illustrated in Figure 1. The procedure

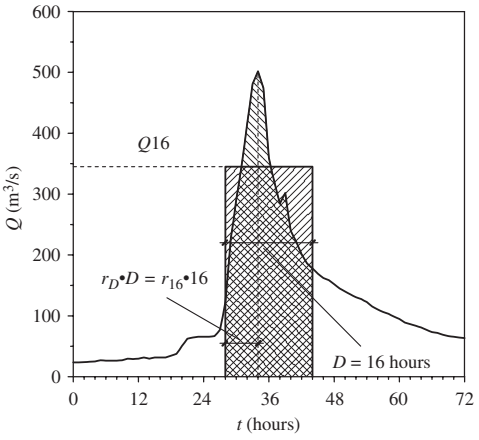


Figure 1. Data sampling of Q_D and r_D from historical hydrographs (in this example $D = 16$ hours).

is similar to that employed for the Chicago Design Storm (Keifer & Chu 1957). However, in the present case the coefficient r_D is a function of D, whereas in the Chicago Design Hyetograph r is defined as the ratio between the time prior to peak intensity and the total rainfall duration and is made a constant for all durations.

Therefore the following conditions determine the SDH:

$$\begin{aligned} &\int_{-r_D D}^{0} Q(\tau)d\tau = r_D D Q_D(T); \\ &\int_{0}^{(1-r_D)D} Q(\tau)d\tau = (1-r_D) D Q_D(T). \end{aligned} \tag{5}$$

The rising and the falling limbs of the SDH are obtained by differentiating Equation 5 with respect to duration D as follows:

$$Q(t) = \frac{\left.\frac{d}{dD}\left(r_D D Q_D(T)\right)\right|_{D=D(t)}}{\left.\frac{d}{dD}\left(r_D D\right)\right|_{D=D(t)}}, \tag{6}$$

$$\text{for} \quad t = -r_D D \qquad -r_{D_f} D_f \le t \le 0$$

$$Q(t) = \frac{\left.\frac{d}{dD}\left((1-r_D) D Q_D(T)\right)\right|_{D=D(t)}}{\left.\frac{d}{dD}\left((1-r_D) D\right)\right|_{D=D(t)}}, \tag{7}$$

$$\text{for} \quad t = (1-r_D) D \qquad 0 \le t \le (1-r_{D_f}) D_f$$

If both FDF and peak duration ratios r_D can be fitted by derivable curves, Equations 6 and 7 can be solved

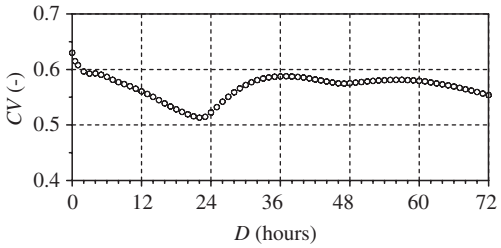


Figure 2. Coefficient of variation $CV(Q_D)$ versus D.

analytically; otherwise numerical methods must be applied.

3 SYNTHETIC DESIGN HYDROGRAPHS FOR PONTE BOTTEGO GAUGING STATION

The mentioned procedure was applied to the 45 years long historical series of floods recorded at the Ponte Bottego gauging station on the Parma river, a tributary of the main italian river Po.

From the 67 recorded flood waves, the 45 annual maximum average discharges for each duration ranging from 0 to 72 hours have been extracted. In some years (10 out of 45) the annual maximum for the selected durations belongs to different flood events.

Figure 2, in which the coefficient of variation $CV(Q_D)$ versus D is reported, shows that the assumption of $CV(Q_D)$ constant with the duration can be reasonably accepted for the considered sample.

Log-normal, Gumbel (EV1) and General Extreme Value (GEV) probability distributions have been considered in order to describe $Q_0(T)$. Parameters estimation was based on the Method of Moments for the first two distributions, whereas for the third the method based on L-moments has been adopted. Figure 3 shows, on Gumbel probability chart, the data sample (Gringorten plotting position) together with the fitted probability distributions.

The Hosking test (Hosking et al. 1985) on the $k = 0$ hypothesis with a significance level $\alpha = 5\%$, k being the exponent of the GEV distribution, demonstrates that the choice of the GEV distribution is justified, so that the peak discharge $Q_0(T)$ have been expressed in the form:

$$Q_0(T) = \xi + \frac{\alpha}{k}\left\{1 - \left[-\ln\left(1 - \frac{1}{T}\right)\right]^k\right\} \quad (k \neq 0) \qquad (8)$$

The estimation of ε_D has been performed by means of Equation 4, which was demonstrated by Ballarin et al. (2001) particularly suitable to fit the empirical reduction ratios of medium-large catchments.

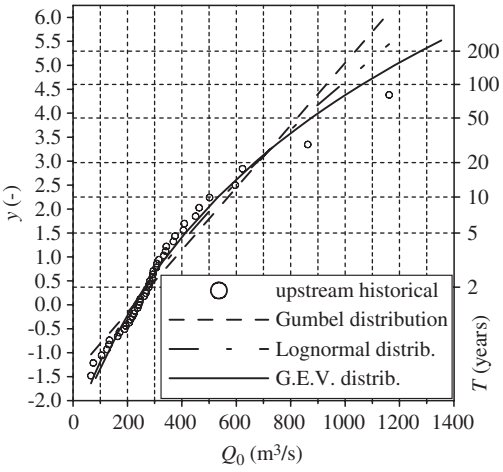


Figure 3. Q_0 data sample together with the fitted probability distributions.

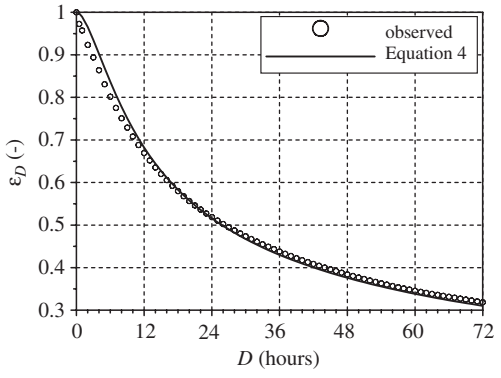


Figure 4. Reduction ratio.

The value of $\theta = 7.2$ hours was obtained by a least squares estimation. The corresponding reduction ratio is plotted in Figure 4 together with the empirical ones. Considering that Equation 4 is a one-parameter curve the agreement is quite good for all the durations.

Figure 5 shows the FDF curves for return periods ranging from 2 to 200 years.

The equation of the Peak-Duration curve has been obtained by interpolation of the empirical patterns available for the gauging station. The interpolating function $r_D(D)$ was chosen of the form indicated below together with the least squares estimates of the four parameters:

$$r_D(D) = a + \frac{b}{c + (D)^d}, \qquad (9)$$

with $a = 0.260$, $b = 3.432$, $c = 18.636$, $d = 1.49$, D being the duration in hours.

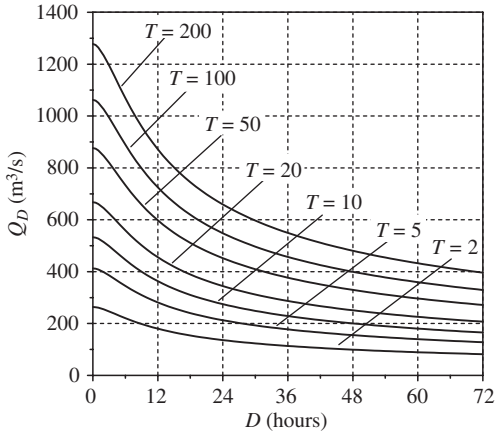


Figure 5. FDF reduction curves at Ponte Bottego gauging station for return periods ranging between 2 and 200 years.

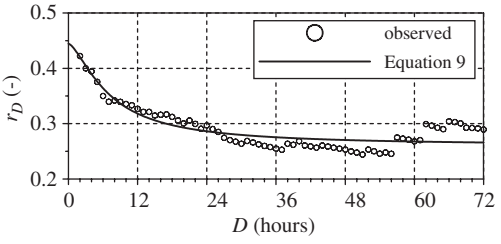


Figure 6. Peak position and interpolating function.

In Figure 6 the interpolating Equation 9 is plotted together with the average values obtained from the historical series. The average absolute difference between the empirical values of r_D and those obtained from Equation 9 is 5%.

Once the estimates of FDF and Peak-Duration curves have been obtained, the SDHs follow immediately by analytical derivation of Equations 6 and 7. Figure 7 shows the SDHs obtained for return periods ranging from 2 to 200 years.

4 TOPOLOGICAL AND MATHEMATICAL DESCRIPTION OF THE RIVER REACH

The selected reach (Fig. 8) is the end branch of the Parma river, starting at Ponte Bottego gauging station and ending at the confluence with the Po river (northern Italy). The total length measured along the thalweg is about 38 km with a very mild average slope of 0.06%.

The river is formed by a deep main channel which meanders within two levels that maintain high levels over the surrounding plains. Once flood waters leave

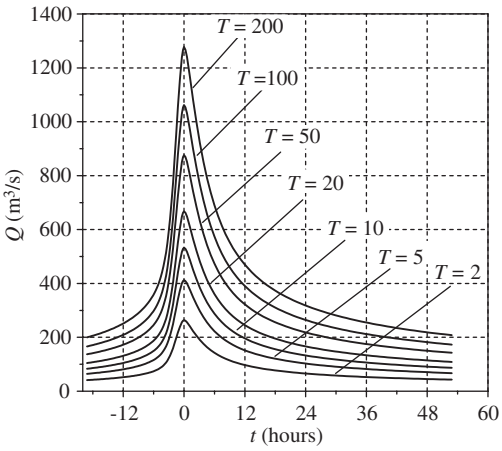


Figure 7. SDHs for Ponte Bottego gauging station.

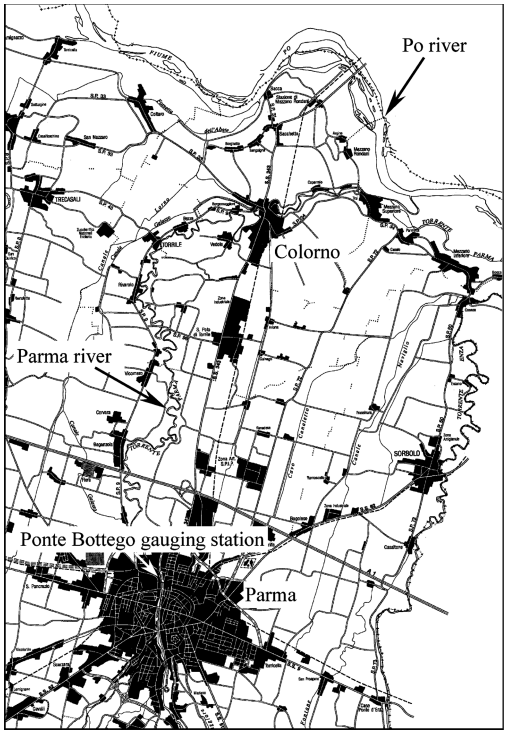


Figure 8. Location of the considered river reach.

the main channel, flood plains of significant width are inundated; in some places flood plains are directly connected with the main channel; elsewhere one or more dikes must be overtopped before the inundation of the flood plain commences; this allows flooding only for high return periods and in the meantime increases the routing efficiency.

The mathematical model adopted for the flood routing is the hydrodynamic module of the software Mike11, produced by the Danish Hydraulic Institute (DHI, 2002). The model solves the vertically integrated equations of conservation of mass and momentum, under the usual St. Venant hypotheses:

$$\frac{\partial Q}{\partial x}+\frac{\partial A}{\partial t}=q$$

$$\frac{\partial Q}{\partial t}+\frac{\partial}{\partial x}\left(\frac{\alpha Q^2}{A}\right)+gA\frac{\partial h}{\partial x}+g\frac{Q|Q|}{C^2AR}=0 \qquad (10)$$

where Q = discharge, A = wetted area, q = lateral inflow, h = stage above datum, R = hydraulic or resistance radius, C = Chezy resistance coefficient, α = momentum distribution coefficient, x = distance along the channel (positive downstream), t = time, g = gravitational acceleration.

The solution of the complete Saint Venant Equations is based on a six-nodes implicit finite difference scheme (Abbott & Ionescu 1967).

Using the cross sections derived from a recent topographical survey a quasi-2D mathematical model of the river reach was implemented.

The topographical description of the area to be modeled is achieved through the introduction of cross sections of the channels and flood plains which lie approximately perpendicular to the direction of flow. The transverse extent l of each cross section depends on whether the flood plain is to be simulated and by what method. In order to describe in a more complete way the characteristics of natural rivers, the presence of flood plains can be represented with several schematizations.

Open flood plains have been directly connected with the main channel and considered to contribute to the total conveyance of the section, even if the roughness is usually higher. Closed flood plains have been described as "pockets" linked to the main channel (and sometimes together) through broad-crested weirs representing length and elevation of the separation dykes. Pocket areas were assumed to contribute only to the storage of the reach.

The existing bridges have been introduced by means of the *culvert structure* available in the model. This was necessary in order to take into account the occurrence that, for high return period flood events, the bridges can result partly full.

5 CALIBRATION OF THE ROUTING MODEL

The November 2000 historical flood was simulated in order to calibrate the roughness coefficients of the main channel and of the open flood plains. The discharge time-series, obtained by converting the recorded hydrograph at Ponte Bottego by means of a stage-discharge relationship, was adopted as upstream boundary condition. As downstream condition the corresponding water level time-series at the confluence with the Po river was considered. Both conditions are shown in Figure 9.

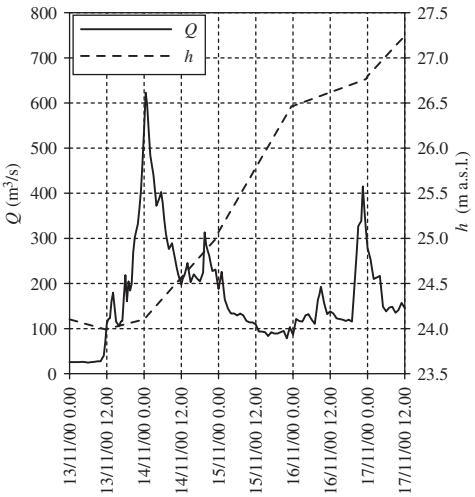


Figure 9. Ponte Bottego discharge and Po water level time-series for November 2000 event.

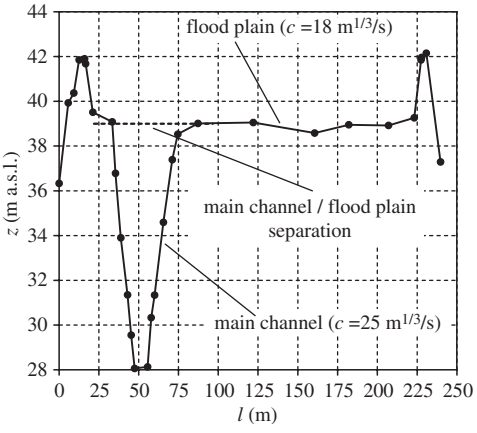


Figure 10. Schematization of a cross section with open flood plains and calibrated roughness coefficients.

The calibration was performed by trials assuming two different roughness coefficients for the main channel and the open flood plains, constant along the reach. The values that allowed to reproduce at best the recorded water levels at the Colorno gauging station, about 30 km downstream the initial section, are shown in Figure 10, together with the schematisation adopted for a generic cross section with open flood plains.

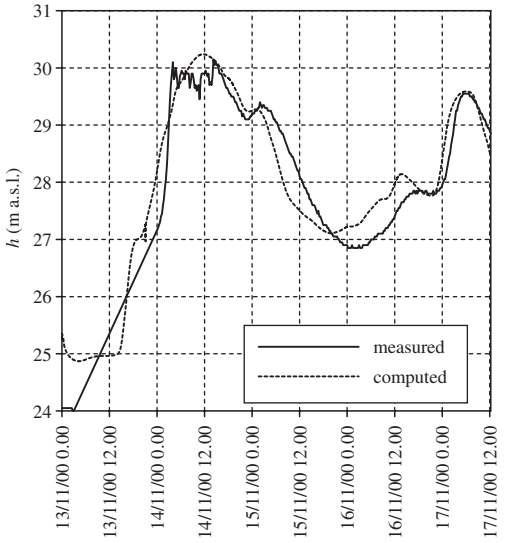


Figure 11. Comparison between recorded and calculated water levels at Colorno gauging station.

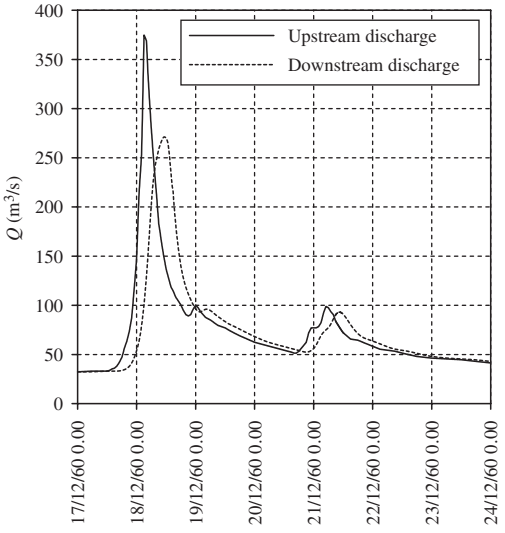


Figure 12. Comparison between upstream (Bottego) and downstream (Colorno) discharges for December 1960 flood event.

Comparison between recorded and calculated water levels at Colorno gauging station is shown in Figure 11. The measured peak water level was probably slightly underestimated since the gage is located on the downstream face of an arc bridge which was partly full. Apart from the first hours, in which the behavior of the computed level differs significantly from the recorded one, the overall characteristics of the recorded water levels at Colorno station are satisfactorily reproduced. As a validation of the chosen roughness coefficients two further recent historical floods were simulated. Also in these cases the overall characteristics of the recorded hydrographs were satisfactorily reproduced with differences of less then 0.20 m in the evaluation of the peak levels.

6 ROUTING OF THE HISTORICAL FLOODS AND OF THE SDHS

The historical series of floods and the SDHs previously derived have then been routed in the river reach.

For each historical flood the discharge time-series obtained by converting the recorded level hydrograph at Ponte Bottego was imposed as upstream boundary condition. The more suitable downstream boundary condition would be represented by the historical water level time-series at the confluence with the Po river. Since these data were not available for all the historical floods, the same constant water level ($\hat{h} = 25$ m a.s.l.) for all was assumed in the computations. The negligible influence of this assumption on the discharges at the reference section of Colorno was verified by routing the few historical floods for which recorded water levels were available at the confluence twice: once adopting the recorded water level hydrographs, then imposing the constant water level $\hat{h}$ as downstream boundary conditions. Consistently the same boundary condition $\hat{h}$ was adopted for routing the SDHs.

In order to obtain the initial conditions (Q and h at $t = 0$ along the river reach) a steady-state profile was computed corresponding to the first value of the discharge time-series and to the $\hat{h}$ water level at the downstream section (subcritical flow).

As an example, in Figure 12 the comparison between upstream (Bottego) and downstream (Colorno) discharge time-series for December 1960 flood event is shown.

Figure 13 shows the SDHs in the same sections while in Table 1 are reported the numerical values of the peak discharges Q_0 for the SDHs, together with the routing coefficient $\eta = Q_{0\,\text{Upstr.}}/Q_{0\,\text{Dwnst.}}$ for all the return periods considered.

The routing coefficient is high (i.e. the dumping effect is small) for $T = 2$ since for this return period neither open nor closed flood plains are involved by the flow. The routing coefficient then decreases for intermediate return periods (between $T = 10$ and $T = 100$ years) when the inundation of the flood plains by the water leaving the main channel is significant. For the higher value of the return period ($T = 200$ years) the routing coefficient again increases due to the high flood volumes involved.

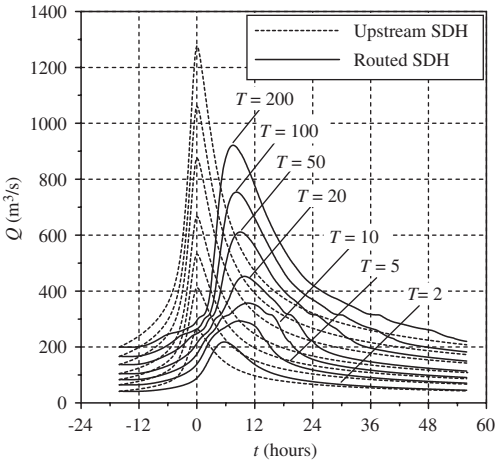


Figure 13. Upstream (Bottego) and downstream (Colorno) SDHs.

Table 1. Upstream and routed peak discharges for the SDHs together with routing coefficients η.

T years	$Q_{0\,\mathrm{Upstr.}}$ m^3/s	$Q_{0\,\mathrm{Dwnstr.}^*}$ m^3/s	$\eta = Q_{0\,\mathrm{Upstr.}}/Q_{0\,\mathrm{Dwnstr.}}$
2	264	218	0.83
5	412	293	0.71
10	533	357	0.67
20	668	453	0.68
50	876	611	0.70
10	1062	754	0.71
20	1277	922	0.72

*Colorno section.

All the 67 historical floods were considered in order to obtain the annual maximum peak discharge series at the Colorno section (Table 2). For comparable events belonging to the same year it could in fact take place the swap between maximum upstream and downstream peak discharge, the latter depending also on the behaviour of the complete inflow hydrograph (see for example years 1987 and 1998 in Table 2). Considering only one flood event per year could then lead to an incorrect evaluation of the sample of annual maximum peak discharges at the downstream section of Colorno.

From the 67 routed historical hydrographs the sample of the 45 annual maximum peak discharges was extracted and placed on a Gumbel chart according to the Gringorten plotting position. On the same graph the peak discharges of the routed SDHs were placed, attaching to each value, at first in a somehow arbitrary way, the return period of the corresponding starting SDH.

Table 2. Upstream and routed peak discharges for the considered historical events (in bold are highlighted the maximum annual values).

Date dd/mm/yy	$Q_{0\,\mathrm{Upstr.}}$ m^3/s	$Q^*_{0\,\mathrm{Dwnstr.}}$ m^3/s	Date dd/mm/yy	$Q_{0\,\mathrm{Upstr.}}$ m^3/s	$Q^*_{0\,\mathrm{Dwnstr.}}$ m^3/s
28/04/56	**105**	**101**	11/04/78	**315**	**261**
08/04/57	**134**	**126**	11/10/79	**224**	**164**
07/11/57	120	111	15/10/80	**1162**	**852**
13/12/58	**206**	**158**	31/01/80	194	155
26/03/59	166	157	28/12/81	**245**	**220**
23/12/59	**309**	**244**	08/11/82	**464**	**255**
15/04/60	291	261	02/10/84	**241**	**185**
14/10/60	**450**	**320**	26/04/86	**66**	**56**
15/12/60	375	271	09/04/87	117	**112**
03/01/61	**291**	**252**	05/10/87	**124**	110
23/04/61	276	251	11/02/88	**74**	**53**
25/11/61	215	177	24/02/89	71	60
04/03/62	**189**	**185**	21/11/89	**132**	**123**
04/03/63	**262**	**231**	15/10/90	154	107
24/03/64	**212**	**200**	22/11/90	**283**	**219**
26/11/64	206	189	02/05/91	**164**	**149**
17/11/65	**295**	**254**	16/10/92	272	238
01/12/66	**502**	**346**	16/11/92	**343**	**253**
03/11/67	**334**	**249**	01/10/93	**218**	**154**
20/02/68	231	215	11/06/94	**293**	**269**
14/11/68	**369**	**272**	08/09/94	268	188
13/01/69	**406**	**288**	22/12/95	**247**	**207**
05/01/70	**194**	**178**	02/10/96	**238**	**221**
18/03/71	**268**	**231**	26/06/97	172	101
08/09/72	**278**	**257**	06/11/97	**280**	**180**
21/01/73	234	222	17/12/97	142	131
21/09/73	**409**	**226**	07/04/98	96	77
27/04/74	**340**	**278**	30/09/98	**226**	133
03/04/75	199	180	04/11/98	208	**156**
14/12/75	**270**	**234**	18/10/99	**863**	**374**
16/12/76	**171**	**139**	01/11/00	**623**	**390**
20/02/77	257	235	12/03/01	**306**	**240**
28/08/77	**375**	**261**	15/10/02	**596**	**339**
24/02/78	234	196			

*Colorno section.

Figure 14 shows the comparison between historical and synthetic peak discharges at the Colorno section. For a more immediate comprehension of the appreciable routing effect of the river reach, the upstream peak discharges (historical and synthetic) are also plotted in the same figure.

The overall behaviour of the routed SDHs peak discharges fits satisfactorily those of the routed historical floods: this confirms that the return periods, at first somehow arbitrarily attached to the routed SDHs, are statistically meaningful. Synthetic results are in better agreement with historical ones especially for return periods ranging from 2 to 10 years. In this range the fit can be evaluated at first sight and is besides more reliable due to the less uncertainty in positioning the historical data on the probability chart. For higher return periods (20–200 years) the comparison is much

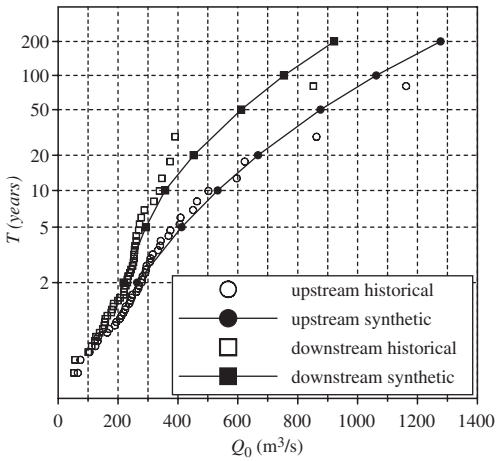


Figure 14. Peak discharges probability plots of historical floods and SDHs for upstream (Bottego) and downstream (Colorno) sections.

more difficult as it would require a deeper statistical interpretation of the historical results. However, the trend of the historical peak discharge distribution seems to be correctly described by the results obtained by means of the SDHs.

7 CONCLUSIONS

A procedure of estimation of Synthetic Design Hydrographs has been proposed in previous works by some of the Authors (Maione et al. 2000a, b). The method is based on the construction of the Flow Duration Frequency reduction curves (FDF), obtained from the statistical analysis of the average flood discharges of given duration and on the determination of the Peak-Duration r_D.

In this paper the SDHs are evaluated and then applied to model the flood routing effect in a mild slope river reach where a long series of historical floods is available.

The statistical significance of the derived SDHs is then evaluated comparing the distribution of peak discharges obtained at a downstream section of a river reach by routing a long series of historical floods and by routing the synthetic floods only.

The satisfactory results obtained suggest that SDHs construction procedure is reliable and the return periods attached, at first in a somehow arbitrary way, to the routed synthetic floods have statistical meaning.

This approach has a twofold advantage. Firstly, whereas a historical series of floods is available, it allows to evaluate the distribution of peak discharges at a downstream section simply routing few synthetic instead of several historical floods. Furthermore, for ungauged sites, regional procedures to determine the SDHs can be applied (Maione et al. 2003) and the derived SDHs consequently used to estimate the routing effect of the considered river reach.

Analogous validations have been performed to confirm the SDHs construction procedure with reference to other river management problems such as flood control reservoirs (Maione et al. 2000a, b) and embankment seepage (Butera & Tanda 2002), with good and satisfactory results, respectively. SDHs seem to be really able to synthesise the main characteristics of the historical floods and can then be applied with confidence to many river flood management problems.

REFERENCES

Abbott, M.B. & Ionescu, F. 1967. On the numerical computation of nearly-horizontal flows. *Journal of Hydraulic research* 5: 97–117.

Bacchi, B., Brath, A. & Kottegoda, N.T. 1992. Analysis of the relationships between flood peaks and flood volumes based on crossing properties of river flow processes. *Water Resources Research* 28(10): 2773–2782.

Ballarin, C., Maione, U., Mignosa, P. & Tomirotti, M. 2001. Una metodologia di stima indiretta degli idrogrammi sintetici per il progetto di opere di difesa idraulica del territorio. *L'Acqua* (3): 9–16.

Butera, I. & Tanda, M.G. 2002. Semi-analytical transient analysis of river embankments with a synthetic design hydrograph. In G. Becciu et al. (eds.), *New Trends in Water and Environmental Engineering for Safety and Life: Eco-compatible Solutions for Aquatic Environments; Proc. Int. Conf., Capri, 24–28 June 2002*. Rotterdam: Balkema.

Danish Hydraulic Institute 2002. *Mike 11 Reference manual*. Hørsholm: DHI.

Fiorentino, M. 1985. La valutazione dei volumi di piena nelle reti di drenaggio urbano. *Idrotecnica* (3): 141–152.

Hosking, J.R.M., Wallis, J.R. & Wood, E.F. 1985. Estimation of the Generalized Extreme-Value Distribution by the Method of Probability-Weighted Moments, *Technometrics* 27(3): 251–261.

Keifer, C.J. & Chu, H.H. 1957. Synthetic storm pattern for drainage design. *Journal of the Hydraulic Division* 83(HY4): 1–25.

Maione, U., Mignosa, P. & Tomirotti, M. 2000a. Synthetic design hydrographs for flood-control reservoirs and floodplain management. In U. Maione, B. Majone Lehto, R. Monti (eds.), *New Trends in Water and Environmental Engineering for Safety and Life: Eco-compatible Solutions for Aquatic Environments; Proc. Int. Conf., Capri, 3–7 July 2000*. Rotterdam: Balkema.

Maione, U., Mignosa, P. & Tomirotti, M. 2000b. Synthetic design hydrographs for river flood management. In Toensmann F., Koch M. (eds.), *River Flood Defence Proc. Int. Symp.*, *Kassel, 20–23 September 2000*. Kassel: Herkules Verlag.

Maione, U., Mignosa, P. & Tomirotti, M. 2003. Regional estimation of synthetic design hydrographs. *Intl. J. River Basin Management* 1(2): 1–13.

NERC (National Environmental Research Council) 1975. *Flood Studies Report.* London.

River Flow 2004 – Greco, Carravetta & Della Morte (eds.)
© 2004 Taylor & Francis Group, London, ISBN 90 5809 658 0

Surface water modeling of the Biebrza River network

R. Verhoeven & R. Banasiak
Hydraulics Laboratory, Ghent University, Belgium

D. Swiątek, J. Chormański & T. Okruszko
SGGW, Warsaw, Poland

ABSTRACT: The Biebrza River, situated in the north-eastern part of Poland, flows through the last extensive, fairly undisturbed river-marginal peatland in Europe. Its valley intensively drains the surrounding plateau and the outwash plain into the river and creates a very complex ground and surface water system. The carried study focuses on the upper and middle basin of the river with a length of about 80 km. It aims at the elaboration of a surface water model as a tool for the water resources management in the catchment. During intensive field measurement campaigns a large amount of information on the topography and on the hydraulic characteristics has been gathered. The data is used to provide an accurate and reliable input for a flood-routing model and to guarantee high quality modeling after ample calibration. Special attention is paid to the simulation problems related to storage and flow in the complex network of inundation fields as an important part of the drainage system and to the impact of dense vegetation on the discharge characteristics. Coping with these difficulties, the simulation results show fairly good agreement with measurement data.

1 INTRODUCTION

The Biebrza River and surrounding wetlands are situated in the northeastern part of Poland, in an ice-marginal valley, some 195 000 hectares in area (Fig. 1). This region forms the last extensive, fairly undisturbed river-marginal peatland in Europe, containing endangered plant and animal species in a large variety of fully developed ecosystems. It is internationally recognised as a reference area for restoration of deteriorated peatlands.

Biebrza Valley, according to the geomorphologic description, is an extensive depression formed during the last glaciation. It is filled with several thick deposits of fluvioglacial sands. The Biebrza Valley was divided [Zurek, 1984] into basins using a relation of higher order morphologic features such as ancient and young morainic plates, glacier outwash plains or river flood terraces. There are 3 major basins, respectively identified as the Upper Basin reaching from the springs of Biebrza to the mouth of the Netta River; the Middle Basin covering the area from Netta to the mouth of Rudzki Channel and the Lower Basin situated in the southern part of the valley up to the alluvial cone of the recipient Narew River.

The *Upper Basin* has a length of some 40 km (62 km along the river) and a width of 2–3 km, with two

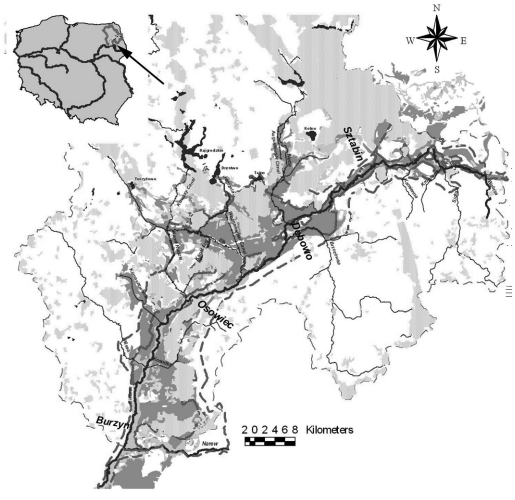


Figure 1. Biebrza Valley – site map.

basin-lake widenings: in its middle part and in the transition zone to the Middle Basin.

The *Middle Basin* is the biggest, 40 km long and up to 20 km wide. It forms a vast, very plat depression paludified by the surface waters of Biebrza and its

tributaries flowing from the Lake District, as well as by the ground waters of two aquifers.

The river in *Lower Basin* has a length of 30 km and a width ranging from 12 to 15 km. The flood plain composes of flat peatlands and a mud zone of 2 km along the river border.

The Biebrza river, as a whole, is a typical lowland river. It has mild slopes (in average about 10 cm per 1 km) and a strongly meandering character. It features varying cross-sections and an irregular longitudinal profile. The variability of the hydrological characteristics along the river is also typical. This is due to the fact that the valley intensively drains the surrounding plateau and the outwash plain into the river. The surface water system is quite complicated consisting of a complex drainage system, network of inundation fields and storage areas. The flow is highly influenced by the dense vegetation.

A comprehensive study has been launched to tackle several water management problems, especially in the Upper and Middle Basin of the river. This happens within a bilateral project joining efforts of Flemish and Polish research teams. The project is aimed at the development of methods to increase the use and the efficiency of wetland area's, the creation of new artificial area's where the same functions could be implemented and at the study of water management measures to be taken to protect the wetlands ecosystem. Special effort is put on the development of a numerical model, allowing the simulation of the impact of different measures on the water balance of the catchment. For this, starting from the existing data, additional measurement campaigns need to be performed in order to define the input parameters and the boundary conditions of the model.

So far, starting from 1999 several intensive field measurement campaigns have been realised over the vast area of the Upper and Middle Basins, delivering a large amount of data, which can be used to provide an accurate and reliable input for flood routing model.

2 DATA COLLECTION

2.1 *Topographical data*

A Digital Elevation Model (DEM) of the research area is being developed. For this the ArcInfo 7.2 TOPOGRID command is used. This method, originally developed to interpolate DEM for hydrologic modelling purposes, was also several times successfully applied to construct a model of floodplain topography (Cera et al., 1996; Townsend & Walsh, 1998; Chormanski, 2003). For the elaboration of DEM, first, the necessary data were collected by field measurements and map analysis. Consequently, the Digital Elevation Model has been created as a raster model by spatial interpolation.

The main data source for the model generation was a set of contour lines elaborated in digital form on the basis of topographic maps with a scale of 1:25 000. The DEM of the research area was created as a raster network with a cell resolution of 25 meters. Because the topographic maps do not accurately show the flat areas at the valley bottom, the construction of a proper elevation model needs additional measurements. Therefore, the database was extended with topographical data from field measurements. The efforts were focussed on the area close to the river channel. Information was collected along the Biebrza River banks every few hundred meters making use of a precise GPS set working in Differential RTK mode (Hoffmann-Wallenhof et al., 1997). Also, a number of valley cross-sections were measured by traditional levelling. As a result, Figure 2 shows the DEM of Biebrza valley for the section between Jastrzêbna and Sztabin.

2.2 *Hydraulic data*

The hydraulic data collection focuses on the determination of the friction coefficients of the different river reaches and on the steady state calibration of the numerical model to be developed.

Until now, several intensive field-measuring campaigns have been developed in different seasons over the period 1999–2003. Figure 3 gives a schematic overview of the measurement locations along the river over a length of about 80 km. The track length of the strongly meandering river between the consecutive cross-sections has been calculated using the digital topographical maps. In all these locations discharges were recorded from a bridge or from a boat using propeller meters or electromagnetic velocity meters. Usually, the measurements were conducted twice in order to increase the measurement accuracy.

The local water surface has been recorded in multiple, discrete cross-sections along the river leading to a fairly accurate recognition of the longitudinal water surface profile (Fig. 4). From these recordings the friction slope of every reach of the river was calculated. Input of these data into the simulation model lead to the determination of the friction characteristics.

3 NUMERICAL SIMULATION

3.1 *Numerical tool*

The HEC-RAS software package is adopted to model the surface water flow. This tool, developed by Hydrologic Engineering Center (HEC) of the US Army Corps of Engineers (USACE), is a software package intended for calculating water surface profiles in a full network of channels, a dendritic system, or single river reach (HEC, 2000). The HEC-RAS software

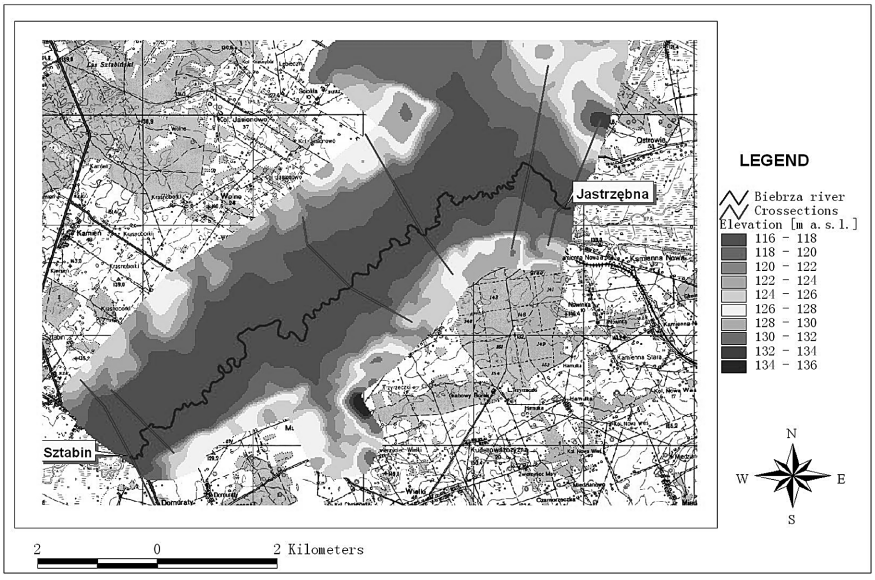


Figure 2. Digital Elevation Model for Biebrza valley – Upper Basin section.

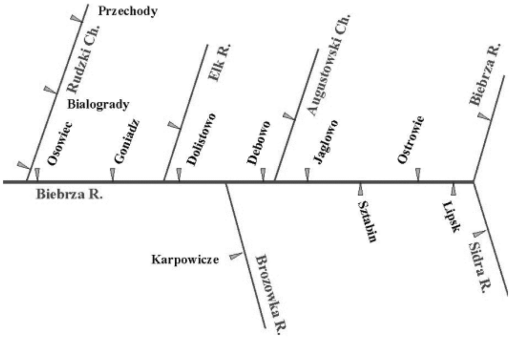


Figure 3. Schematic representation of discharge measurements.



Figure 4. Recorded water surface profile along the section between Sztabin and Ostrowie (14.05.2003).

uses the St. Venant equations to compute water surface profiles given cross-section data, roughness coefficients, and flow rates. In addition, the program has a number of special capabilities related to the analysis of culverts and bridges at roadway crossings and to model weir overflow structures, dam-burst and water storage interactions. It can be considered as quasi-two-dimensional software, as it is capable to include off-channel storage and inundation fields. Depending on the flow conditions, inundation fields are simulated as separate channels or as storage cells. The total flow is distributed according to conveyance between the main river channel and the floodplain. The upstream boundary conditions can be a discharge or a stage hydrograph. The available downstream boundary conditions are: a stage hydrograph, a flow hydrograph, a single-valued rating curve or a looped rating curve (Manning's equation).

Furthermore, the software is supported by the inundation fields mapping system, as described above, by the delivery of supplementary topography information in order to construct full flood plain cross sections that reflect accurate channel and overbank data. Inversely, results exported from HEC-RAS may be processed in the ArcView3D analysis extension for floodplain mapping and analysis. This includes the locations of the cross-section cut lines (Fig. 2) along with water surface profile data and a set of polygons that describe the extend of the modelled floodplain.

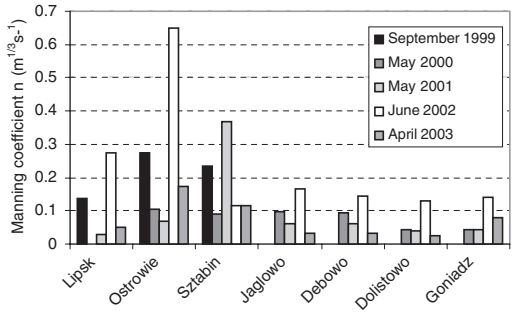


Figure 5. Friction coefficients.

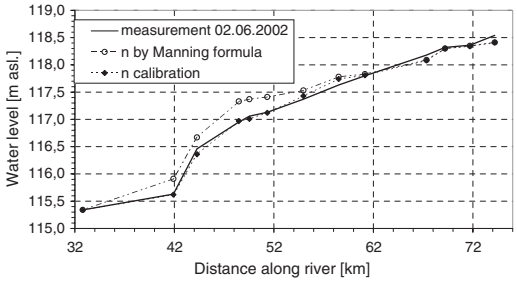


Figure 6. Determination of friction coefficient.

3.2 *Friction coefficients in the steady state model*

Once all discharge data have been processed, the friction coefficient of each part of the river network can be calculated in two different ways: As the field campaigns were performed in periods with stable water conditions, one can suppose the flow regime do be in a steady state with uniform flow and apply the Manning formula in each gauging point to calculate the friction coefficient. The values of the coefficients obtained by this approach are shown in Figure 5.

The strong variation of the friction coefficient as a function of vegetation development is striking. In this region vegetation starts to grow in late April and reaches full growth in early summer. By this it isn't surprising that although the water stages recorded during the campaigns of June 2002 and April 2003 were very similar, the discharges in April were 2 to 3 times higher in April than in June. The alternation of the friction characteristics is particularly strong in the upper section of the river, where the channel is relatively small and where almost the whole cross-section is taken by plants. The growth of the plants not only increases the resistance to flow but also reduces flow velocities and disturbs the velocity distribution. This important effect has also to be accounted for in the unsteady state flow simulation presented in the next section.

The second method uses the theory of hydraulic water surface profiles: Starting from the data on

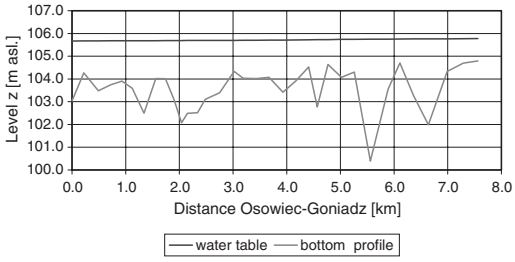


Figure 7. Longitudinal profile.

geometry, water levels and discharge, the Bresse equation allows calculation of the friction coefficient in a river reach between two gauging locations. When looking at Figure 6, it is clear that the second method delivers much better results. The irregularity of profiles, with significant changes in cross-sectional area and longitudinal slope (Fig. 7), that could not be completely recognized, must be compensated by the calibrated friction factor.

3.3 *Extension to floodplains*

The knowledge of the value of the friction coefficients as well as accurate information on the geometry is of primordial importance for the quality of the results of the hydrodynamic models. Up till now only information on the low water level friction characteristics is available. As during flood flow the value of these coefficients might be substantially different, it is also important to focus the field campaigns on high water level situations that normally occur between early and late spring. This is the reason why most field campaigns were planned in this period. Unfortunately, in the last four years springs have been (very) dry in the Biebrza region, leading to a lack of important data concerning the flood routing. Therefore, for a good and reliable reconstruction of the hydraulic flow conditions fluctuations related to different water level and flow regimes in the river catchment, additional field measurement campaigns under high water level conditions need to be elaborated in the (nearby) future.

The actual situation necessitated the use of other data. A flood event recorded in Spring of 1996 has been employed as an auxiliary data set for model development on flood conveyance in the Biebrza valley.

3.4 *Unsteady state simulation*

In the first stage, the modeling of surface water flow is performed for a part of the Upper Basin of the Biebrza River, restricted to the cross-sections between Sztabin (downstream) and Ostrowie (Jastrzebna). The distance between both these section is 15 km. For both cross-sections discharge hydrograms

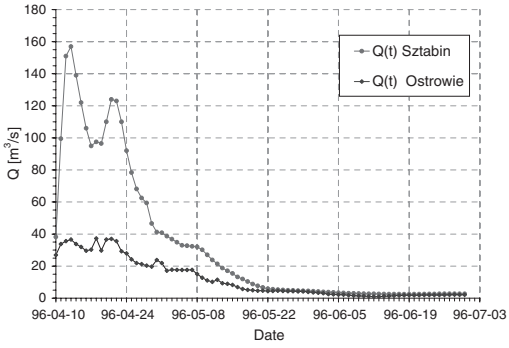


Figure 8. Discharge observed at upstream and downstream gauges.

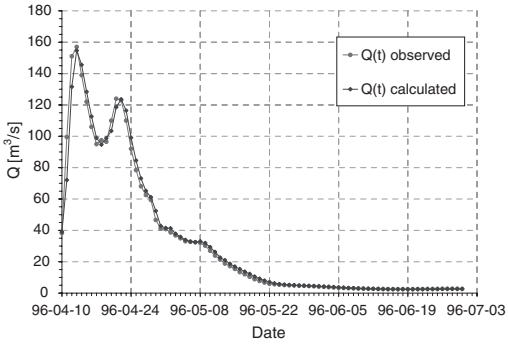


Figure 9. Discharge calculated and observed at Sztabin.

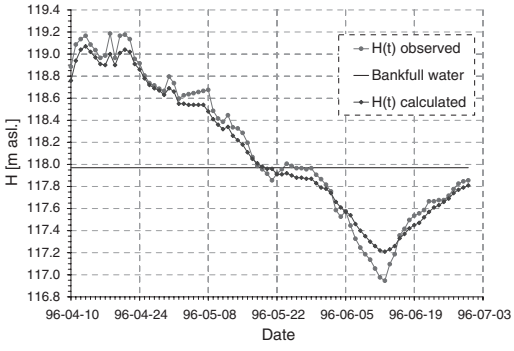


Figure 10. Water stages calculated and observed at Ostrowie.

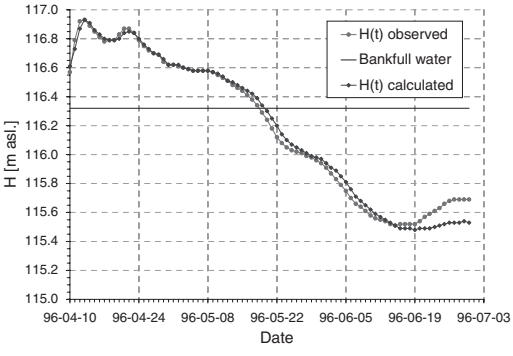


Figure 11. Water stages calculated and observed at Sztabin.

Q(t) for the period 10.04.1996–30.06.1996, (shown in Fig. 8) are used to define the upstream and downstream boundary conditions. There is a significant difference in discharge rates between these two cross-sections. This is mainly due to the lateral inflow of melting snow during the flood event. The lateral discharge inflow, $Q_{leb}(t)$, from the Lebiedzianka brook is added 12.23 km upstream of Sztabin. Next, the uniform lateral inflow is imposed along the river section as $Q_{in}(t) = Q_{Sztabin}(t) - Q\ Q_{Ostrowie}(t) - Q_{leb}(t)$. This solution is obviously a rough approximation of the actual situation, as it does not account for the temporal and spatial variation of the lateral inflow. A more realistic approach on this issue needs to be elaborated in further study.

During flood periods, the river valley consists of parts which mainly act as a storage for flood water and of effective transport areas. The particular areas have been identified according to topography reading and land use. Consequently, the storage areas and friction coefficients for the flow active zones were adapted by calibration for steady and unsteady flow so that the observed and calculated values became congruent.

To obtain a better agreement between observed and calculated water levels in the unsteady flow simulation, the friction coefficient had to be varied in such a way that it takes into account the temporal change of flow resistance due to the growth of vegetation. This appeared of crucial importance for the period under concern. Not only modification of the roughness was incorporated in this step but also the changes in the transport effective area over the cross-section had to be anticipated. The increase of the n-coefficients only to reflect the growth of the plants results in a reduction of the flow velocity and subsequently in a delay of the flood propagation in respects to the recorded event.

Based on all these considerations and on a careful calibration procedure it is possible to develop a reliable numerical model, able to reproduce the natural situation. Figures 9–11 present the calculated and observed discharge hydrographs and water levels at the downstream and upstream cross-sections. The boundary conditions used are those presented in Figure 8 for discharge at the inlet cross-section and in Figure 11 for water level at the downstream cross-section. As a result the variation of the water levels in both limit cross-sections and the flood wave propagation speed are reasonably well simulated.

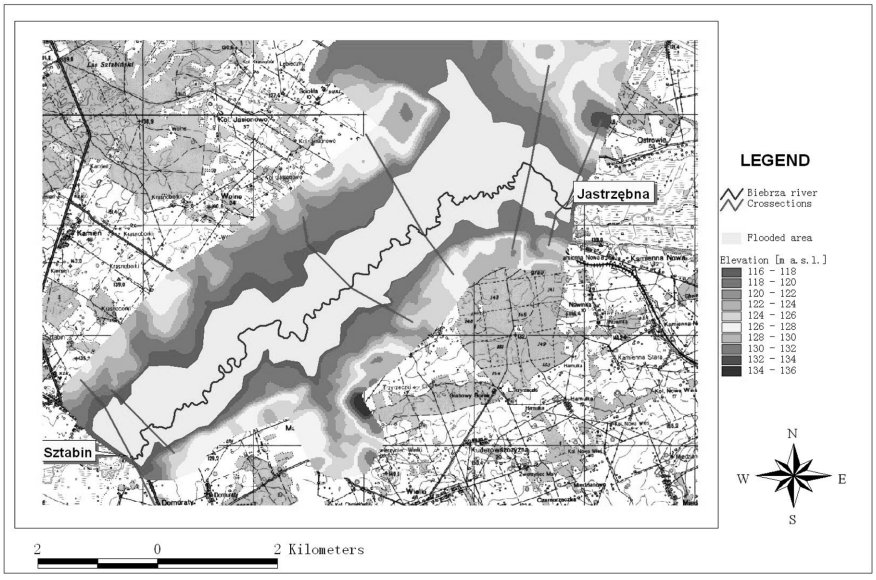


Figure 12. Flood mapping in the Biebrza Valley – Upper Basin (13.04.1996).

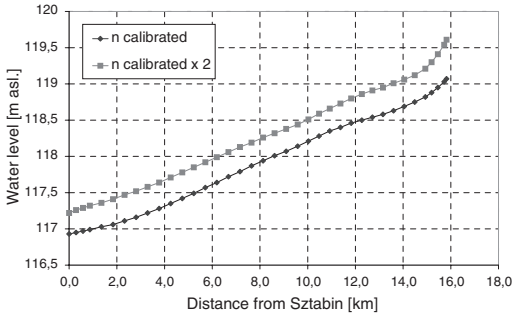


Figure 13. Water stages calculated for 2 different friction situations.

The level of the water surface profile for maximum discharge as generated by the model is used to delineate the flooding boundaries across the valley. The results from this floodplain mapping, as obtained from ArcView are presented in Figure 12.

It is clear that possible flow condition alternations will influence the conveyance of the flow in channel and valley. Therefore, different scenarios need to be tested in terms of impact of individual or groups of parameters, or changes in the water supply configurations. An example will demonstrate the impact of changing the friction on the flood water stages for the same event as considered above but supposed to happen e.g. in late spring. Therefore the friction coefficients for the floodplain and the channel are increased by a factor 2. Figure 13 shows the water levels along the river for both scenarios. The water levels in the second case rise around 30 cm. This results also in an increase of the flooding area from 13.483 km^2 to 15.896 km^2.

Certainly, this example does not fully reflect the potential changes in the flood plain area of the valley due to the growth of vegetation. In analogy to variation of the friction factor in the main channel, as shown in Figure 5, the variation in flood plain area can be even much more considerable.

4 CONCLUSIONS

The surface water management in the Biebrza valley is under extended and well-designed study. The numerical model for surface water flow is being developed using handsome and effective tools. The numerical modelling approach, although based on some primary assumptions, reveals promising results. The first flooding simulations on a restricted part of the network revealed a good reproduction of recorded field data. The model performance will further be improved given a more extended base of hydrometrical data, especially in terms of overbank flow conditions.

It is obvious that due to the large area to be covered by accurate and reliable data sets and the complexity of the river network, the development of a complete simulation model is a long-term business. However, large progress has been made so far, identifying weak spots of the data acquisition, schematic representation and numerical solution. The feasibility of the numerical model has been well recognized. A right approach combining both field recognition and numerical experience should guarantee the successful

realization of the ambitious task to facilitate and encourage the water management and the conservation of the natural beauty of the region, in particular of the Biebrza National Park.

REFERENCES

Byczkowski, A., Kiciński, T. 1984. Surface water in the Biebrza River drainage basin. *Pol. Ecol. l Stud.* Vol. 10 (3–4), pp. 271–299.

Cera, T.B., Tremwel, T.K., Burleson, R.W. 1996. Use Arc/INFO, EPA-SWMM, and UNIX text processing tools to determine flood extend. *AWRA Symposioum on GIS and Water Resources*. Sept. 22–26, 1996FT. Lauderdale, USA, pp. 8. http://www.awra.org/proceedings/gis32/cera/index.html

Chormański, J. 2003. Methodology of flood extent determination in the Biebrza Lower Basin. PhD thesis. Warsaw Agricultural University, pp. 160.

Dodson, R.D., Li, X. 1999. The accuracy and efficiency of GIS-based floodplain determinations. *Proceedings of the 19th Annual ESRI User Conference*. San Diego, California. ESRI, *http://gis.esri.com/library.*

Hoffmann-Wallenhof, B., Lichtenegger, H., Collins, J. 1997. GPS Theory and Practice. Springler, Wien New York.

U.S. Army Corps of Engineers (USACE). 2000. HEC-RAS river analysis system Version 3.0. Users Manual. Hydrologic Engineering Center, Davis, CA.

Verhoeven, R., Van Poucke, L., Huygens, M., Okruszko, T., Ignar, S., Mucka, A., Michalowski, R., Chormanski, J., Swiatek, D., Kardel, I. 2003. Surface water management in Biebrza valley. Annals of Warsaw Agricultural University, Land Reclamation, No. 33.

Verhoeven, R., Banasiak, R., Okruszko, T., Swiatek, D., Chormanski, J., Nowakowski, P. 2003. Numerical Modelling of river flow – data collection and problem solving. Key note lecture. *Proceedings of the Conference on Advances in Fluid Mechanics*, in edition, 22–24 March 2004, Lisbon, Portugal.

Townsend, P.A., Walsh, S.J. 1998: Modelling floodplain inundation using integrated GIS with radar and optical remote sensing. *Geomorphology*, No. 21, pp. 295–312.

Żurek, S. Relief, Geologic structure and hydrography of the Biebrza ice-marginal valley. *Pol. Ecol. l Stud.* Vol. 10 (3–4), pp. 239–251.

This page intentionally left blank

River Flow 2004 – Greco, Carravetta & Della Morte (eds.)
© 2004 Taylor & Francis Group, London, ISBN 90 5809 658 0

An improved, robust implicit solution for the two dimensional shallow water equations on unstructured grids

S. Komaei
Electrowatt-Ekono AG, Zurich, Switzerland & German Armed Forces University Munich, Neubiberg, Germany

W. Bechteler
German Armed Forces University Munich, Neubiberg, Germany

ABSTRACT: In this paper, an implicit unstructured gird algorithm for solving two dimensional Shallow Water Equations (SWE) has been developed. It is based on cell-centred Finite Volume Method (FVM) and can handle cells of triangular and Quadrilateral types. The algorithm includes piecewise linear least-square interpolation and uses Roe's approximate Riemann solver to compute fluxes. In addition, a new technique is introduced to prevent instabilities and oscillations caused from the bed slope terms in the case of problems with arbitrary topography and hydraulic structures. The method results set of nonlinear algebraic equations for the flow variables in each cell. The system of equations can be iteratively solved. Second order accuracy in time and second or higher order accuracy in space can be achieved in this method. The proposed method is validated and verified via solving some examples and comparison of the results obtained from the new method with the other methods.

1 INTRODUCTION

Flows in open channels are often modelled by a set of hyperbolic partial differential equations, i.e. the well known shallow water equations (SWE). Algorithms for solving SWE on structured grids have become widespread in recent years (Delis et al. 2000; Fennema and Chaudhry 1989; Panagiotopoulos and Soulis 2000; Valiani et al. 1999). However, these algorithms have shown difficulties in predicting satisfactory results in complex geometries due to mesh irregularities. As a result, attention has turned to the development of the algorithms on arbitrary unstructured grids. Many current unstructured algorithms utilize explicit time integration (Anastasiou and Chan 1997; Beffa and Connell 2001; Nujic 1995; Zhao et al. 1996) that can be computationally expensive if a long period of time has to be simulated. On the other hand, the explicit approach is computationally efficient when applied to meshes that are coarse. For cases where finer meshes are used, the time of computations significantly increases. For the sediment transport problem, which is not a high gradient phenomenon and often needs a time range of several years or decades, the simulation takes a lot of time therefore, an implicit scheme could be more useful which allows large time steps to obtain solutions in a computationally efficient manner.

The application of the implicit schemes in SWE is often an extension of the schemes used in computational fluid dynamics (CFD). As pioneers, Fennema and Chaudhry (1989) have used implicit finite difference schemes, developed by Beam and Warming (Beam and Warming 1976; 1978) for hyperbolic systems in conservation law form, for the solution of two-dimensional SWE without source terms. In general, good results are reported, even though quite dissipative. However, these schemes are only first order accurate in space and employ the flux splitting in a nonconservative way. Later, Jha et al. (1996) proposed a modification for achieving full conservation, employing the use of the Roe-average approximate Jacobian (Roe 1981). MacCormack (1982) presented an implicit analog of his earlier widely used explicit method (MacCormack and Paullay 1972) for solving the equations of compressible viscous flow. Panagiotopoulos and Soulis (2000) have extended the implicit MacCormack scheme to integrate the flow equations. They developed a numerical method to solve SWE in generalized coordinates describing the depth-averaged, steady, subcritical and supercritical free-surface flows with the presence of hydraulic jumps. In the other paper, Klonidis and Soulis (2001) have developed another finite volume scheme to calculate steady, two-dimensional SWE. The formulation is based on transformation of the flow equations into

a non-orthogonal, boundary-fitted coordinate system. Therefore, the method is suitable for structured grids.

The shortcoming of an implicit finite volume model for two-dimensional SWE on unstructured grids can be seen. This method should have the shock capturing capability and a suitable treatment of bed source terms. In this paper, an implicit robust model for numerical solving of SWE on unstructured grids is introduced. The proposed method has a special treatment of the bed source terms therefore it is able to model flow over an initially dry and irregular bed.

2 SYSTEM OF GOVERNING EQUATIONS, SWE

The system of SWE in the conservative form is given by:

$$\frac{\partial \mathbf{q}}{\partial t}+\frac{\partial \mathbf{f}(\mathbf{q})}{\partial x}+\frac{\partial \mathbf{g}(\mathbf{q})}{\partial y}=\mathbf{S}(\mathbf{q}) \tag{1}$$

with

$$\mathbf{q}=\begin{Bmatrix} h \\ hu \\ hv \end{Bmatrix} \qquad \mathbf{S}(\mathbf{q})=\begin{Bmatrix} 0 \\ gh(S_{0x}-S_{fx}) \\ gh(S_{0y}-S_{fy}) \end{Bmatrix}$$
$$\mathbf{f}(\mathbf{q})=\begin{Bmatrix} hu \\ hu^2+gh^2/2 \\ huv \end{Bmatrix} \qquad \mathbf{g}(\mathbf{q})=\begin{Bmatrix} hv \\ huv \\ hv^2+gh^2/2 \end{Bmatrix} \tag{2}$$

where $\mathbf{F}(\mathbf{q})=[\mathbf{f}(\mathbf{q}),\mathbf{g}(\mathbf{q})]^T$ is the flux vector, h is the water depth, u, v depth averaged velocity in x- and y-direction, respectively, S_{0x}, S_{fx} are bed and friction slope in x-direction and S_{0y}, S_{fy} are bed and friction slope in y-direction. The bed slope is defined in x-direction as:

$$S_{0x}=-\frac{\partial Z_b(x,y)}{\partial x} \tag{3}$$

and the friction slope is estimated using the Manning's formula. For example, in x-direction, it is:

$$S_{fx}=\frac{n^2 u\sqrt{u^2+v^2}}{h^{4/3}} \tag{4}$$

S_{0y}, S_{fy} are defined in a similar way.

3 NUMERICAL ALGORITHM

3.1 *Discretization of the governing equations*

The system of governing equations is discretized using the finite volume method (FVM). Integrating Eq. (1) over an arbitrary triangular cell Ω and using the divergence theorem, the basic equation of the FVM is obtained as:

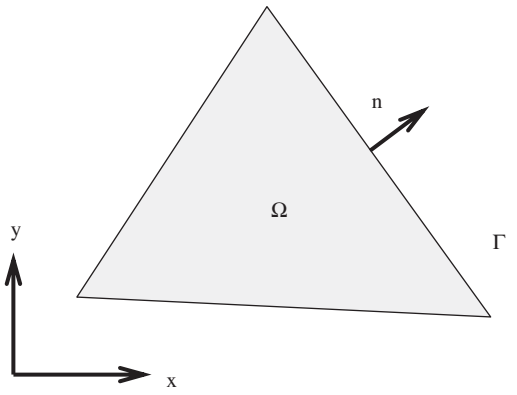


Figure 1. Notation for finite volume method.

$$\iint_{\Omega}\mathbf{q}_t\,dA=-\int_{\Gamma}\mathbf{F}(\mathbf{q}).\mathbf{n}\,dl+\iint_{\Omega}\mathbf{S}(\mathbf{q})\,dA \tag{5}$$

in which $\mathbf{n}$ is unit outward vector normal to the boundary Γ (see Figure 1); *dA, dl* are area and arc element, respectively. After some manipulation, the semi-discrete form of the equation is:

$$A_i\frac{d\,\mathbf{q}_i}{dt}+\sum_{m=1}^{N_i}\mathbf{F}_m\cdot\mathbf{n}_m\,l_m=A_i\,\mathbf{S}(\mathbf{q}_i) \tag{6}$$

where the subscripts i and m denote quantities for the i-th cell and m-th face of the cell, respectively and N is the total number of the faces for that cell.

In an implicit scheme, the flux vector $\mathbf{F}$ is computed at the new time level $k+1$. Using implicit scheme, Eq. (6) can be rewritten in the following form:

$$A_i\frac{\mathbf{q}_i^{k+1}-\mathbf{q}_i^{k}}{\Delta t}+\sum_{m=1}^{N_i}\mathbf{F}_m^{k+1}\cdot\mathbf{n}_m\,l_m=\mathbf{R}_i \tag{7}$$

where $\mathbf{R}_i=A_i\mathbf{S}(\mathbf{q}_i)$ is the right hand side terms evaluated in cell i at the known time level k. Expanding $\mathbf{F}$ about a known time level, we get:

$$\mathbf{F}^{k+1}=\mathbf{F}^{k}+\left(\frac{\partial\mathbf{F}}{\partial\mathbf{q}}\right)^{k}\left(\mathbf{q}^{k+1}-\mathbf{q}^{k}\right)+O\left(\Delta t^2\right)$$
$$\mathbf{F}^{k+1}=\mathbf{F}^{k}+\mathbf{J}\,\Delta\mathbf{q}+O\left(\Delta t^2\right) \tag{8}$$

where $\mathbf{J}=\partial\mathbf{F}/\partial\mathbf{q}$ is the flux Jacobian matrix. Substituting Eq. (8) into (7) leads to:

$$A_i\frac{\mathbf{q}_i^{k+1}-\mathbf{q}_i^{k}}{\Delta t}+\sum_{m=1}^{N_i}(\mathbf{J}\,\Delta\mathbf{q})\cdot\mathbf{n}_m l_m=\mathbf{R}_i-\sum_{m=1}^{N_i}\mathbf{F}_m^{k}\cdot\mathbf{n}_m l_m \tag{9}$$

Following Jameson and Turkel (1981) and Yoon and Kwak (1992), the flux Jacobian matrices are splitted as follows:

$$\mathbf{J}^{\pm} = \frac{\mathbf{J} \pm \mathbf{I}\alpha\lambda_{\max}}{2} \tag{10}$$

with

$$\lambda_{\max} = |\mathbf{V}\cdot\mathbf{n}| + c \tag{11}$$

where $\mathbf{V}$ and $c = \sqrt{gh}$ are the velocity vector and speed of the wave, respectively and α is a relaxation factor of order unity. Eq. (9) now becomes:

$$A_i \frac{\mathbf{q}_i^{k+1} - \mathbf{q}_i^k}{\Delta t} + \sum_{m=1}^{N_i} (\mathbf{J}^+ \Delta\mathbf{q}_i)\cdot\mathbf{n}_m l_m = \mathbf{R}_i - \sum_{m=1}^{N_i} \mathbf{F}_m^k \cdot \mathbf{n}_m l_m - \sum_{m=1}^{N_i} (\mathbf{J}^- \Delta\mathbf{q}_m)\cdot\mathbf{n}_m l_m \tag{12}$$

or written in matrix form:

$$\mathbf{M}\ \Delta\mathbf{q}_i = \mathbf{RHS}^k \tag{13}$$

in which:

$$\Delta\mathbf{q}_i = \mathbf{q}_i^{k+1} - \mathbf{q}_i^k = [\Delta h, \Delta(hu), \Delta(hv)]^T \tag{14}$$

is the unknown vector. The formulation of the matrix **M** and the vector **RHS** are given by Komaie (2003). To numerically solve the discretized Eq. (12), the major steps of the solution procedure are reconstruction, flux computation and evolution. These steps are illustrated below.

3.2 *Reconstruction*

For the first step, reconstruction, a cell-centered scheme is used. The piecewise linear, least-square reconstruction procedure used here is similar to those used by Barth (1993) and Coirier (1994). Each of the three primitive variables h; u and v is assumed to linearly vary within a finite volume as:

$$U(x,y) = \overline{U} + U_x(x - \bar{x}) + U_y(y - \bar{y}) \tag{15}$$

where U can be any of the above variables. The bars in Eq. (15) denote cell-averaged values as defined in the last equations. In high gradient regions, a gradient limiter is normally used in Eq. (15) to ensure that the reconstruction polynomial does not produce new extrema near a flow discontinuity such as a shock wave. Limiters can also control the numerical oscillation that are common with second and higher order numerical schemes. In this paper, the limiter is applied to the gradient terms (Anastasiou and Chan 1997) so that:

$$U = \overline{U} + \Phi\nabla U.\vec{r} \tag{16}$$

where **r** is the vector from cell centroid to the midpoint of the edge and $0 < \Phi < 1$ is a chosen limiter.

When Φ is set to zero, the computation domain is characterized by piecewise constant regions resulting in a first-order scheme. The non-linear limiter is given by:

$$\Phi = \max[\min(\beta D_j, 1), \min(D_j, \beta)] \tag{17}$$

where:

$$D_j = \begin{cases} (U_j^{\max} - U_j)/(U_L - U_j) & if \quad U_L > U_j \\ (U_j^{\min} - U_j)/(U_L - U_j) & if \quad U_L < U_j \\ 1 & if \quad U_L = U_j \end{cases} \tag{18}$$

with:

$$U_j^{\min} = \min(U_j, U_i), \quad U_j^{\max} = \max(U_j, U_i) \tag{19}$$

This procedure is carried out sequentially for the two cells separated by the common edge. These values are then used in the Riemann solver to estimate the flux across the edge in the flux computation phase. When $\beta = 1$, Φ is the *Minmod* limiter and when $\beta = 2$, the limiter is *Roe's Superbee* limiter. The Minmod limiter is used in this paper.

3.3 *Flux computation*

In the next step, the normal component of the flux vector, i.e. $\mathbf{F}_m.\mathbf{n}_m$ in Eq. (12), should be estimated. With the piecewise linear reconstruction, the unknown variables are continuous and assumed to linearly vary within a finite volume. However, no guarantee exists that the variables will be continuous across adjacent finite volumes because a different polynomial is used in each finite volume. As a result, a flux formula is needed to compute a single flux at a finite volume boundary using fluxes from the adjacent volumes. In this paper the Roe's approximate Riemann solver is used (Roe 1981). Roe's method may be the most famous Riemann solver in CFD and SWE (Brufau et al. 2002; Erduran et al. 2002; Roe 1981; Sanders 2001; Toro 2001; Tseng and Chu 2000). Define the normal component of the flux vector as:

$$\mathbf{F}_n = \mathbf{F}\cdot\mathbf{n} \tag{20}$$

Then $\mathbf{F}_n$ can be computed using the Roe FDS method as:

$$\mathbf{F}_{n,i+1/2} = \frac{1}{2}\left[\mathbf{F}_{n,L} + \mathbf{F}_{n,R} + \left|\hat{\mathbf{A}}_{i+1/2}\right|\left(\bar{\mathbf{q}}_L - \bar{\mathbf{q}}_R\right)\right] \tag{21}$$

where the subscripts L and R denote the flow conditions to the left and right sides of the cell face and $\mathbf{A}_{i+1/2}$ is Roe flux difference splitting matrix.

3.4 *Evolution*

Now it is possible to solve the Eq. (12) for each cell. There is a part of RHS in Eq. (12) that relates to the unknowns of the neighbour cells. Therefore, the system of the algebraic equations should be solved iteratively. The nature of the method enables us to implement it on parallel computer systems. In addition, it is efficient because no block or scalar tridiagonal inversions need to be calculated. After achieving convergence, the solution is updated to find the flow variables at the end of a time step. The main question is whether there is any condition to restrict the time step of the computation for the proposed implicit scheme. It is clear that the CFL condition is not applicable here. But from the mathematics it is well known that to achieve a numerically stable method, the Matrix $\mathbf{M} = [m_{ij}]$ should be diagonally dominant. It means:

$$\left|m_{ii}\right| \geq \sum_{j \neq i} \left|m_{ij}\right| \qquad \forall i \tag{22}$$

3.5 *Treatment of the bed source terms*

Here, the new developed method for numerical implementation of the bed source terms is presented. The proposed method is simple and robust and it is independent of the Riemann solver. It also holds the conservation property that is defined by Bermudez et al. (1998). For the description of the method, two options should be considered:

- How the method deals with the terms $0.5\,gh^2$ in the flux terms.
- Which scheme is used to numerically compute $\mathbf{S}_b(\mathbf{q})$.

3.5.1 *Flux modification*

The flux vector on the edge can be computed with a desired Riemann solver but after that, the term $0.5\,gh^2$ should be recomputed for the sloped edge (Komaie 2003):

$$\frac{1}{2}gh^2 = \frac{1}{2}g\bar{\bar{h}}^2 = \frac{1}{2}g\frac{h_i^2 + h_i h_j + h_j^2}{3} \tag{23}$$

which h_i and h_j are the water depth at the two ends of the edge based on the constant water level assumption over the edge.

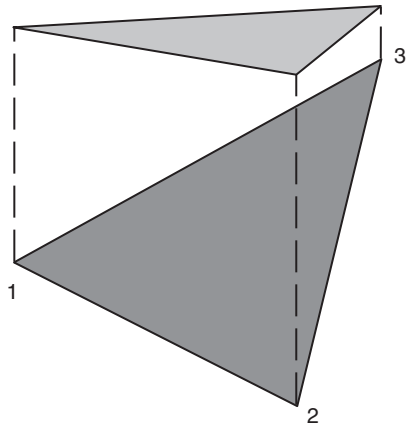


Figure 2. Sloped wet cell and the water surface level, 3D imagination.

3.5.2 *Source terms*

Now it is required to compute the integral of the bed source term vector over a cell Ω:

$$\iint_{\Omega} \mathbf{S}_b(\mathbf{q})\,dA = \iint_{\Omega} \begin{pmatrix} 0 \\ ghS_{0x} \\ ghS_{0y} \end{pmatrix} dA = g \iint_{\Omega} h \begin{pmatrix} 0 \\ -\dfrac{\partial Z_b(x,y)}{\partial x} \\ -\dfrac{\partial Z_b(x,y)}{\partial y} \end{pmatrix} dA \tag{24}$$

If we assume that the bed slope in x- and y-direction in every cell Ω is constant, then we have

$$\iint_{\Omega} \mathbf{S}_b(\mathbf{q})\,dA = g\left(\iint_{\Omega} h dA\right)\begin{pmatrix} 0 \\ S_{0x} \\ S_{0y} \end{pmatrix} = gVol_{water}\begin{pmatrix} 0 \\ S_{0x} \\ S_{0y} \end{pmatrix} \tag{25}$$

It means that the bed term integral is converted to the multiplication of two parameters: cell bed slope and the volume of water in the cell between water surface level and bed level. For the case of wet cell, i.e. all three nodes are under the water surface (Figure 2), the volume of water is:

$$Vol_{water} = \left(\frac{h_1 + h_2 + h_3}{3}\right) \cdot A \tag{26}$$

which A is the cell area and h_i ($i = 1, 2, 3$) is the water depth at ith-node of the cell. For the partially wet cell the above Eq. should be modified so that the real volume of water is obtained.

In the case that only one node is under water surface (Figure 3), the location of points "a" and "b" should be

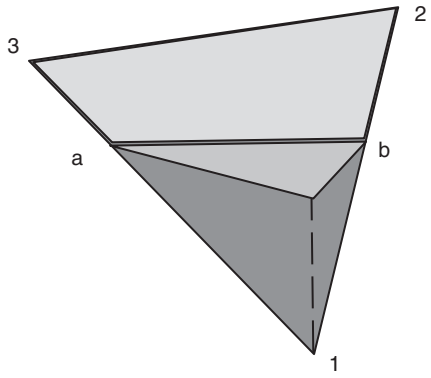


Figure 3. Sloped partially wet cell and the water surface level, 3D imagination.

found at which the water surface plane, i.e. . $\eta = const.$, intersect the edge lines. At these points, the water depth is zero. With the help of similarity of triangles in , one can easily find for the point "a",

$$x_a = x_1 + \frac{\eta - Z_{b,1}}{Z_{b,3} - Z_{b,1}}\left(x_3 - x_1\right)$$
$$y_a = y_1 + \frac{\eta - Z_{b,1}}{Z_{b,3} - Z_{b,1}}\left(y_3 - y_1\right) \tag{27}$$

in above Eqs., x_k and y_k are the coordinates of the point k. For the location of the point "b", similar formulations can be found. Now it is possible to compute the wet horizontal area of the element, i.e. A_{ab1}:

$$2A_{ab1} = \det\begin{vmatrix} 1 & x_1 & y_1 \\ 1 & x_a & y_a \\ 1 & x_b & y_b \end{vmatrix} \tag{28}$$

and finally the volume of the water in the cell can be computed as follows

$$Vol_{water} = \frac{A_{ab1} \cdot h_1}{3} \tag{29}$$

In the case that two nodes are under water surface, the same method can be used.

4 NUMERICAL EXAMPLE

Under a research work mainly supported by the central public funding organization for academic research in Germany (DFG), a physical model has been studied at the Aachen University of Technology (RWTH) to understand the fundamental flow behaviour in meandering channels and rivers with overflow into floodplains (Stein 1990).

In order to perform the experiment, a 15.0 m long, 3.0 m wide and 0.35 m deep channel was built from PVC with a variable longitudinal slope in the range of 0 to 0.2% (Figure 4). The channel was equipped by the Laser Doppler Anemometer (LDA) tools to record the velocities.

Stein (1990) has tested two basic variants whose essential difference was the existence or nonexistence of the vegetation on floodplains. The flow behaviour for the dominant flow in floodplain or in main channel could be systematically analyzed through the variation of the vegetation on floodplains. The analysis of the measured data of both variants showed that the mechanisms of flow in the case of dominated flow in main channel exhibits partly strong three-dimensional character (Stein 1990). This experiment has been already used by different researchers to verify their models (Farshi 2002; MinhDuc 1998; Schröder 1996; Stein 1990; Wenka 1992). In this work, we also simulated this experiment with smooth conditions on the floodplains.

In accordance with the statements of Stein (1990) and Wenka (1992) and based on the objective of the current work, it was not expected that our two-dimensional model can simulate the threedimensional flow processes. However, the quality of measured data makes it possible to determine, how far the numerical results are and whether the numerical model is able to approximate the considered phenomena basically and to describe their influence on the averaged flow parameters.

Here the test case A5 with the constant longitudinal slope of 0.05% is considered. For this variant, the average water depth in the main channel at the inlet section is $h_m = 0.15$ m , where the subscript "m" means the average in main channel. It is tried to keep the above water depth constant along the channel, as long as this is admitted by the flow conditions. Wenka (1992) used different input velocities for the main channel and the floodplains in variant A5, i.e. $V_m = 0.23$ m/sec for the main channel and $V_f = 0.30$ m/sec for the flood plains. The subscript "f" represents the average in the flood plains.

To test the ability of the model, a computational mesh has been generated (depicted in Figure 4). It is an unstructured grid that contains triangular and quadrilateral cells. It includes 4802 nodes and 5219 cells in which 4093 cells are quadrilateral and 1126 cells are triangular. The element size ranges between 0.02 m and 0.20 m. In order to reduce the effect of boundary condition on the results, the simulated channel is longer than physical model (15 m instead of 11.34 m) but the other geometrical parameters are the same.

The above discharge with the described velocity distribution was applied to the proposed model as inlet boundary condition in the form of the inlet hydrograph.

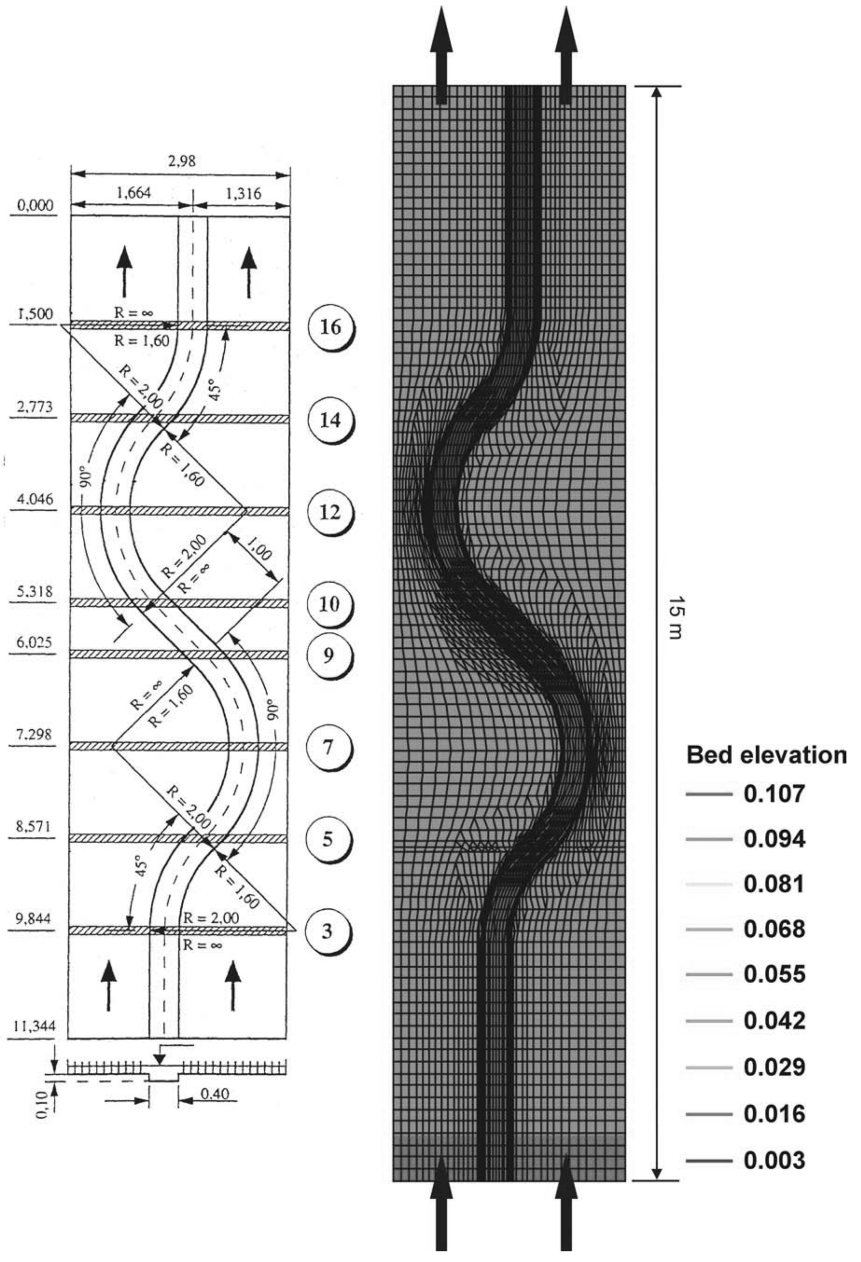


Figure 4. Meandering channel: geometrical dimensions and computational grid.

The outlet boundary condition was selected in the form of critical depth in the wet edges.

After calibration, the constant Manning's coefficient $n = 0.015$ was selected. The time step of 0.015 sec was chosen. After shock capturing the time step and Courant number has been increased. At the end of computation at runtime 850 sec, the time step has reached 1.334 sec that corresponds to average Courant number 32.3.

Figure 5 shows the comparison between the computed and the measured values of the resultant velocity at cross-section 7. A very good agreement between

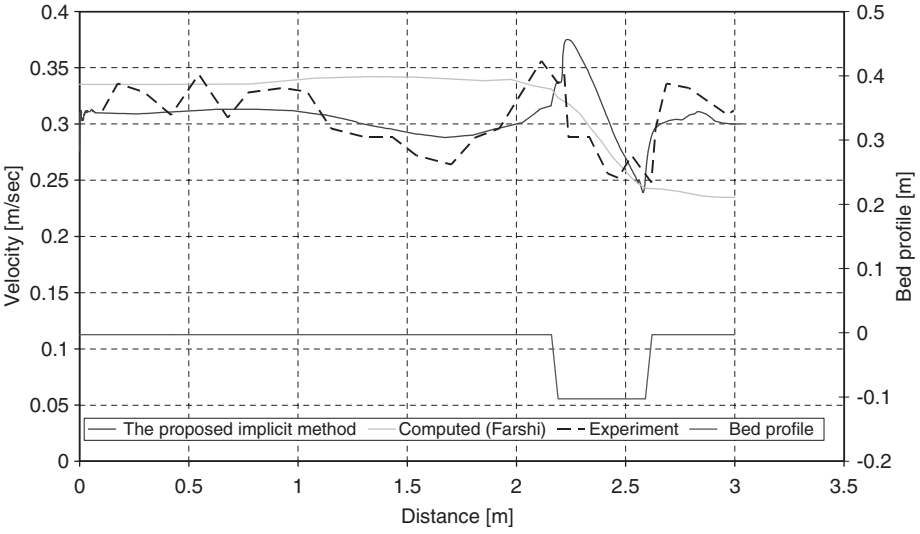


Figure 5. Experiment A5: Velocity distribution in cross-section 7.

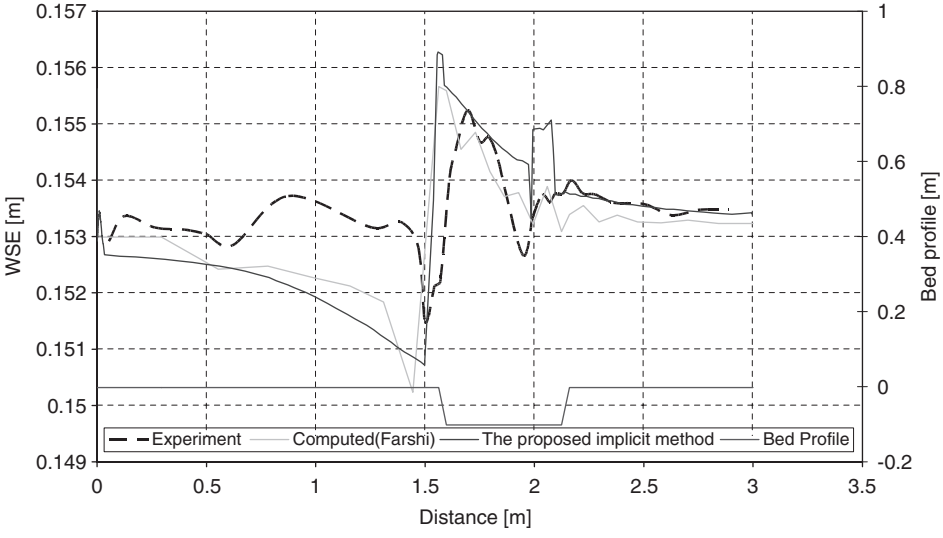


Figure 6. Experiment A5: Water surface elevation in cross-section 5.

the computed and measured results can be seen. Stein (1990) and Wenka (1992) are not successful to simulate the velocity distribution in this region by their turbulence models. Minh Duc (1998) has also simulated this variant and could reproduce the velocity distribution at the right hand side of the main channel well but his model could not achieve good agreement at the left side.

In practical applications, it is most interested to compute the water surface elevation (WSE). In such a complex flow system, correctly computing the WSE is also a difficult task. In Figure 6, the computed values and measured data are compared in cross-section 5 for test case A5.

5 CONCLUSIONS

A new implicit numerical scheme has been introduced and applied for SWE. The method can be applied on unstructured grids with triangular cells. In addition, a new simple treatment of source terms is proposed. The results show a good agreement of the proposed

method with the comparable sources. The new method gives a well-computed velocity distribution that could result quite reasonable bed shear stresses. For the high gradient applications, the new method needs more runtime than explicit methods. The main advantage of this method is for the quasi steady state conditions in which the much higher time steps could be used.

REFERENCES

Anastasiou, K., and Chan, C. T. (1997). "Solution of the 2D shallow water equations using the finite volume method on unstructured triangular meshes." *International Journal for Numerical Methods in Fluids*, 24(11), 1225–1245.

Barth, T. J. "Recent developments in high order K-Exact reconstruction on unstructured meshes." *31st Aerospace Sciences Meeting & Exhibit*, Reno, NV.

Beam, R. M., and Warming, R. F. (1976). "An implicit finite difference algorithm for hyperbolic systems in conservation law form." *Journal of Computational Physics*, 22, 87–110.

Beffa, C., and Connell, R. J. (2001). "Two-Dimensional Flood Plain Flow. I:Model Description." *Journal of Hydrologic Engineering, ASCE*, 6(5), 397–405.

Bermudez, A., Dervieux, A., Desideri, J.-A., and Vazquez, M. E. (1998). "Upwind schemes for the twodimensional shallow water equations with variable depth using unstructured meshes." *Computer methods in applied mechanics and engineering*, 155, 49–72.

Brufau, P., Vazquez-Cendon, M. E., and Garcia-Navarro, P. (2002). "A numerical model for the flooding and drying of irregular domains." *Int. J. Numer. Meth. Fluids*, 39, 247–275.

Coirier, W. J. (1994). "An adaptively-refined, cartesian, cell-based scheme for the Euler and Navier-Stocks equations," The University of Michigan.

Delis, A. I., Skeels, C. P., and Ryrie, S. C. (2000). "Evaluation of some approximate Riemann solvers for transient open channel flows." *Journal of Hydraulic research*, 38(3), 369–382.

Erduran, K. S., Kutija, V., and Hewett, C. J. M. (2002). "Performance of finite volume solutions to the shallow water equations with shock-capturing schemes." *Int. J. Numer. Meth. Fluids*, 40, 1237–1273.

Farshi, D. (2002). "Two-Dimensional Simulation of Sediment Transport on Unstructured Mesh," German Armed Forces University Munich, Munich.

Fennema, R. J., and Chaudhry, M. H. (1989). "Implicit methods for two-dimensional unsteady freesurface flows." *Journal of Hydraulic Research*, 27(3), 321–332.

Jameson, A., and Turkel, E. (1981). "Implicit schemes and LU decompositions." *Mathematics of Computation*, 37(156), 385–397.

Jha, A., Akiyama, J., and Ura, M. (1996). "A fully conservative Beam and Warming scheme for transient open channel flow." *Journal of Hydraulic Research*, 34(5), 605.

Klonidis, A. J., and Soulis, J. (2001). "An implicit scheme for steady two-dimensional free-surface flow calculation." *Journal of Hydraulic Research*, 39(4), 393–402.

Komaie, S. (2003). "A Robust Implicit Shallow Water Equations Solver on Unstructured Grids," German Armed Forces University Munich, Munich.

MacCormack, R. W. (1982). "A numerical method for solving the equations of compressible viscous flow." *AIAA Journal*, 20(9), 1275–1281.

MacCormack, R. W., and Paullay, A. J. (1972). "Computational efficiency achieved by time splitting of finite difference operators." *paper 72–154*, AIAA, San Diego.

MinhDuc, B. (1998). "Berechnung der Stömung und des Sedimenttransports mit einem tiefengemittelten numerischen Verfahren (in German)," Universität Fridericiana zu Karlsruhe (TH), Karlsruhe.

Nujic, M. (1995). "Efficient Implementation of Nonoscillatory Schemes for the Computation of Free-Surface Flows." *Journal of Hydraulic Research*, 33(1), 101–111.

Panagiotopoulos, A. G., and Soulis, J. V. (2000). "Implicit biadiagonal scheme for depth-averaged free-surface flow equations." *ASCE, Journal of Hydraulic Engineering*, 126(6), 425–436.

Roe, P. L. (1981). "Approximate riemann solvers, parameter vectors, and difference schemes." *Journal of Computational Physics*, 43, 357–372.

Sanders, B. F. (2001). "High-resolution and non-oscillatory solution of the St.Venant equations in nonrectangular and non-prismatic channels." *Journal of Hydraulic Research*, 39(3), 321–330.

Schröder, P. M. (1996). "Zur numerischen Simulation turbulenter Freispiegelströmungen mit ausgeprägt dreidimensionaler Charakteristik (in German)," Aachen University, Aachen.

Stein, C. J. (1990). "Mäandrierende Fließgewässer mit überströmten Vorländern- Experimentelle Untersuchung und numerische Simulation (in German)," Aachen University, Aachen.

Toro, E. F. (2001). *Shock-Capturing Methods for Free-Sufrace Shallow Flows*, Wiley and Sons Ltd.

Tseng, M. H., and Chu, C. R. (2000). "Two-dimensional shallow water flows simulation using TVD-MacCormack scheme." *Journal of Hydraulic Research*, 38(2), 123–131.

Valiani, A., Caleffi, V., and Zanni, A. "Finite Volume Scheme for 2D Shallow-Water Equations Application to The Malpasset Dam-Break." *CADAM*, Zaragoza.

Warming, R. F., and Beam, R. M. "On the construction and application of implicit factored schemes for conservation laws." *Proc. Symposium on Computational Fluid Dynamics, SIAM-AMS, Vol 11*, New York, 85–129.

Wenka, T. (1992). "Numerische Berechnung von Strömungsvorgängen in naturnahen Flußläufen mit einem tiefengemittelten Modell (in German)," Universität Fridericiana zu Karlsruhe (TH), Karlsruhe.

Yoon, S., and Kwak, D. (1992). "Implicit Navier-Stokes solver for three-dimensional compressible flows." *AIAA Journal*, 30(11), 2653–2659.

Zhao, D. H., Shen, H. W., Lai, J. S., and Tabios III, G. Q. (1996). "Approximate Riemann solvers in FVM for 2D hydraulic shock wave modeling." *Journal of Hydraulic Engineering, AISC*, 122(12), 692–702.

River Flow 2004 – Greco, Carravetta & Della Morte (eds.)
© 2004 Taylor & Francis Group, London, ISBN 90 5809 658 0

Supercritical flow in channel intersections

N. Rivière & R.J. Perkins
LMFA, Lyon, France

ABSTRACT: Experiments have been conducted in a configuration formed by the intersection of four identical channels. Each channel is made from glass and measures 2 m long and 0.3 m wide; the slope of each channel can be fixed independently, as can the flow rate in the channel. In this configuration the flow enters the intersection through one of the channels, and is evacuated by the other three. The results show that, immediately after entering the intersection, the incoming flow behaves as a free, rectangular supercritical jet. The surface profiles of the jet as it collapses correspond well to the theoretical solution obtained for the classical dam break problem. Close to the exit from the intersection the walls of the side channels have an important influence on the flow in the main channel, and the dam break solution has to be corrected in a way that is still to be precise.

1 INTRODUCTION

During severe flooding of urban areas, the water in the streets can reach a depth of a metre or more, causing severe economic losses, and possible loss of life. We therefore need to be able to predict flood propagation in urban areas, in order to design suitable protection (possibly by directing the flood waters to previously identified sacrificial zones) and to develop reasonable and realistic emergency planning. Because of the complexity of the problem, and the number of different situations that have to be considered, the most suitable approach is by numerical simulation, usually by solution of the St Venant equations. This approach has the additional advantage that as more and more detailed information on street geometry becomes available through GIS databases, this information can be readily – indeed automatically – included in the numerical model. In the simplest possible configuration, the city street can be considered as a rectangular channel with a free surface flow, and there have now been many simulations of flood propagation in urban areas based on this approach. In general, we can conclude from these studies that the St. Venant equations provide a reasonable model for the flow in individual streets, but that they are not well-suited to flow in street intersections, where the flow is necessarily strongly three-dimensional, and the slope of the free surface can be significant. Unfortunately for these numerical simulations, street intersections often play a crucial role in determining how the incoming flow is distributed between the various outlets, and in determining the corresponding depths. The failure to model these intersections correctly can therefore have serious consequences for the overall quality of the modelling.

There have been very few experimental studies of flow in channel junctions, and even fewer for conditions that correspond to those encountered in city streets. Most studies have been related to flow distribution in networks of irrigation channels, where the intersection is usually formed by the junction of three channels (in the form of a T or a Y), and where the flow regime is sub-critical. They can be divided in two groups: the junctions with two upstream reaches and only one downstream, and the bifurcations, with only one upstream reach.

In urban applications the basic configuration is more likely to be a cross, with one or possibly two of the streets feeding the junction. The slope of a city street can easily be of the order of a few percent, so it is quite common for the flow regime to be supercritical in certain areas.

Most of the available literature describes experimental or numerical studies of subcritical flow in simple channel junctions. For example Weber et al. (2001) provide a complete set of experimental data for a 90° junction, including water depth, surface and bulk velocity fields and turbulence characteristics. The available analytical models are mainly based on mass, momentum and energy balances (see, for example, Gurram and Karki (1997) or Shabayek and Hicks (2002)). Usually, this approach requires additional assumptions such as a uniform depth of the flow in the whole intersection, a critical Froude number in the contraction zone or a hydrostatic pressure distribution.

Such assumptions will not usually be valid for flooding in urban areas. Empirical models have also been proposed, in which several physical phenomena are modeled by a single coefficient, such as a contraction coefficient (Hsu et al., 1998). Again, these methods depend strongly on the experimental conditions and are, as far as we are aware, restricted to the subcritical regime. In the supercritical regime, Greated (1966), and Schwalt and Hager (1994), focus on the development of the surface wave, whereas Hager (1989) also measures velocities but in quasi-constant depth flows.

Even fewer studies have been devoted to channel bifurcations, and the introduction of a third outlet channel complicates the problem considerably, especially for analytical studies. Ramamurthy and Satish (1988) derive an expression for the flow division in short open-channel branches, based on momentum and mass conservation. This gives the upstream/branch discharge ratio as a function of the channel widths ratio and the downstream main channel Froude number. The model assumes a hydrostatic pressure distribution, negligible head losses in the vicinity of the intersection and is restricted to branch Froude numbers higher than 0.35 and upstream Froude numbers smaller than 0.7. For rectangular equal width channels, the model was improved to become independent of the branch channel Froude number (Ramamurthy et al., 1990). To avoid the need for such assumptions, other researchers have proposed empirical models. Krishnappa and Seetharamiah (1963) provide an experimental correlation for the discharge ratio as a function of the upstream Froude number and the channel depths ratio, which is restricted to 90° angle separations and to subcritical upstream flows and supercritical branch flows. Nougaro and Boyer (1974) provide a diagram giving the discharge ratio valid on a wide range of Froude numbers (sub- and supercritical) and of junction angles, but they show a strong dependency of the results on the downstream conditions (Nougaro et al., 1975). More recently, there have been several 1D and 2D numerical simulations of flow in channel junctions. Shettar and Murty (1996) used a 2D code with a k-ε closure to study a 90° bifurcation. The widths of the main channel and the branch are identical and the depth to width ratio is approximately 0.15. Their results compare well with experimental measurements available in the literature. Khan et al. (2000) adopt a mixing length model, which is more applicable for large-scale problems. All these studies are restricted to subcritical flows, avoiding the problems arising in the application of suitable boundary conditions for supercritical flows. Finally, Nania et al. (1998) simulate flow in the intersection of 4 channels (2 inlets – 2 outlets), using 1D and 2D codes, for subcritical and supercritical flows.

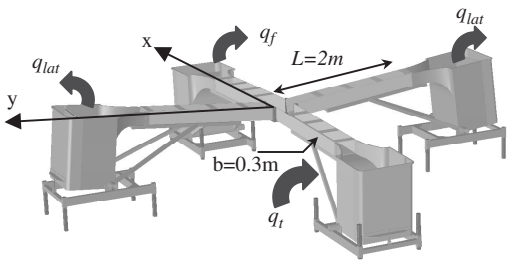


Figure 1. Experimental set-up.

2 EXPERIMENTAL SET-UP

The set-up consists of an intersection of four identical channels (fig. 1). Each channel is made from glass, with a length $L = 2$ m and width $b = 0.3$ m. The slopes of the four channels can be fixed independently, and each channel can function either as an inlet or an outlet for the intersection. In this study, only one channel functions as an inlet, with a discharge q_t that varies from 2 to 20 l/s; the x-axis is therefore aligned with this channel. The flow leaves the intersection via the other three channels – two lateral channels (aligned with the y axis) and one longitudinal channel (x-axis). The flow enters the inlet channel through a honeycomb and then passes under a sluice gate, which serves to impose the upstream water depth and hence the Froude number. The outlet conditions are free. Discharges are measured by electromagnetic flowmeters; the discharge from the longitudinal channel was also calculated by measuring the filling time of the outlet reservoir. Water depths were measured using a moveable point gauge with an accuracy of ± 0.15 mm. This last technique becomes unusable in the strongly perturbed zones close to the intersection.

3 ANALOGY BETWEEN A SUPERCRITICAL JET DEVELOPMENT AND A DAM BREAK

The flow in the inlet channel is supercritical as it enters the intersection, and it traverses the intersection as a free, supercritical, jet. Hager and Yasuda (1997) studied the development of a supercritical jet in a semi-infinite expansion, and showed that the jet profile was similar to the evolution of the water surface during the breaking of a dam on a dry bed. In their study, the upstream Froude number was greater than 3, and the initial section of the jet was square; as a result the depression wave reaches the centerline of the jet rather rapidly, and the theory becomes rather complicated. In this study the ratio of the upstream depth to

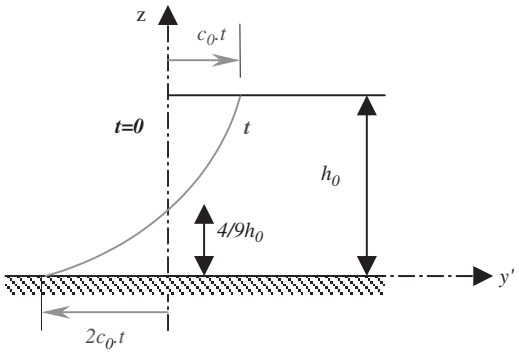


Figure 2-a. The unsteady problem: the dam-break.

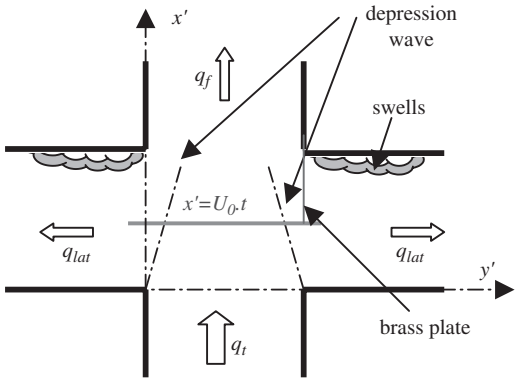


Figure 2-b. The spatial problem: the jet development.

the channel width (h_0/b) is much smaller than 1, and so the dam break model is more applicable.

Consider a dam holding back a semi-infinite reservoir of initial depth h_0 (fig. 2-a); at $t = 0$ the dam fails and the water surface then evolves as (Stoker, 1957):

$$z = \frac{1}{9g}.(\frac{y'}{t} + 2.c_0)^2 \quad (1)$$

where t is the time and c_0 is the velocity of propagation of the depression wave in the reservoir:

$$c_0 = \sqrt{gh_0} \quad (2)$$

The water propagates over the dry bed with a velocity $2c_0$, whilst the depth of the water at the site of the dam ($y' = 0$) remains constant, equal to $z = 4h_0/9$ (fig. 2-a). We can apply this model to compute the evolution of the jet in the intersection (fig. 2-b). Upstream of the intersection ($x' < 0$) the flow is confined by the walls of the rectangular channel; within the intersection the water surface is modified by the propagation of dam break waves into the two lateral channels, which we can model using the solution for unsteady case, by making the transformation $t = x'/U_0$.

To justify the assumption of a semi-infinite body of fluid upstream of the breaking wave we have to ensure that there is no interaction between the two negative waves produced by the flow into each of the lateral channels. This means that $c_0.t < b/2$, or, in other words $x/Fr_0 < b/2$; since the length of the intersection (x_{max}) is equal to b we can write: $Fr_0 > 2$.

Two configurations have been studied, with the characteristics given in table 1.

The surface profile in the side channel is plotted in figure 3, in dimensionless form (z/h_0v $y/(x'/Fr_0)$)

Table 1. Main characteristics of the two jets ($Fr_0 > 2$).

Configuration	5%–0%	1%–1%
q_t (m^3/s)	0.01	0.01
bed slope S_{0x}	0.05	0.012
bed slope S_{0y}	0	0.012
h_0 (cm)	2.06	2.8
Fr_0	3.6	2.16
h_0/b	0.14	0.2

for different values of the dimensionless distance travelled by the jet (x'/Fr_0). The error bars plotted on the first figure are indicative of the errors for the other profiles. The strong axial velocities in the jet create intense eddying motions on the walls of the side channels (fig. 2-b) which increase the water level and limit the applicability of the model to $x'/b <$ 0.7–0.8.

The dimensionless results for the two conditions are in close agreement with each other, and with the theoretical curve based on the dam break model. The increase in z' observed for $y' < 0$ in the 5%–0% configuration can be explained by the difficulty of generating a flow in a horizontal canal; this effect disappears when the canal is inclined (the 1%–1% configuration).

In the following section we will develop a model for the flow distribution in the different channels, based on the surface profiles given by the dam break model.

4 A MODEL FOR THE FLOW DISTRIBUTION

The cross section of the axial flow in the intersection decreases as the jet advances. By continuity, the lateral flow q_{lat} must be given by the flow that has left the jet;

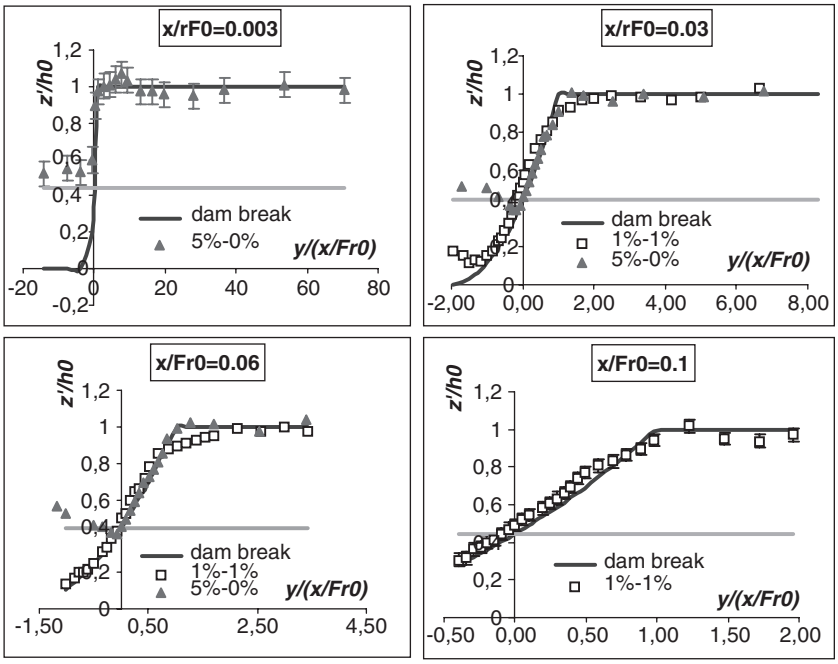


Figure 3. Theoretical and experimental surface profiles at different locations within the intersection ($S_0 = 1$, 2% et 5%).

at any distance x' from the entrance to the intersection we can therefore write:

$$q_{lat}(x') = U_0 \cdot \left[\frac{c_0 x}{U_0} h_0 - \int_0^{c_0 x/U_0} \frac{1}{9g} \left(\frac{y'}{x/U_0} + 2c_0 \right)^2 dy' \right] \quad (3)$$

from which we obtain:

$$\frac{q_{lat}(x')}{q_{tot}} = \frac{8}{27} \frac{x'}{b} \frac{1}{Fr_0} \quad (4)$$

The total flow in the lateral canal is given by evaluating this expression for $x' = b$:

$$\frac{q_{lat}}{q_{tot}} = \frac{8}{27 Fr_0} \quad (5)$$

The strong eddying motions around $x' = b$ modify the structure of the jet significantly, and hence tend to invalidate the theoretical model for the lateral flow. To test the influence of these motions thin brass plates were installed at the downstream end of the intersection, so as to extend the walls of the outlet channel and isolate the flow from the influence of the stagnation regions (fig. 2-b). The lateral flow rates were measured for different plate lengths, and the results are shown in figure 4. These curves confirm that the theoretical

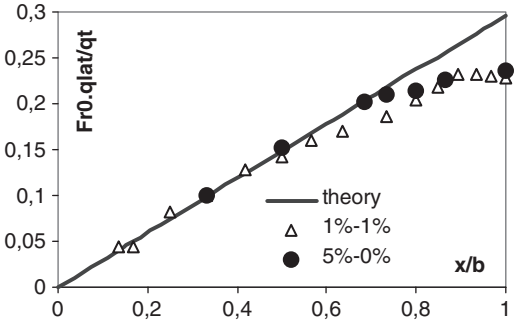


Figure 4. Influence of the stagnation regions on the applicability of the theoretical model.

model provides a good estimate for the lateral flows provided that the stagnation regions do not influence the flow ($x'/b < 0.7$). On the other hand, the greater the zone of influence ($x'/b > 0.7 \rightarrow 1$), the more the side flow is diminished, relative to its theoretical value.

The principle explanation for this reduction in flow rate is that the increased surface levels in the stagnation regions serve to drive flow back out of the side channels into the main channel; as a result, equation (5) overestimates the total lateral flow by about 25% in both configurations.

In order to assess the accuracy of equation (5) over a much wider range of flow rates we have compared the

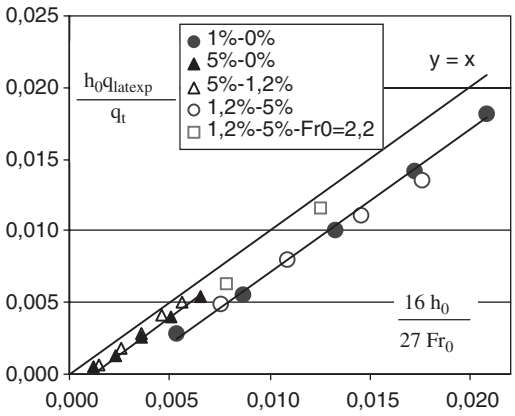


Figure 5. Theoretical (eq. 5) and experimental values of the lateral flow rates for flow conditions in the range 2–20 l/s.

measured $q_{lat-exp}$ and theoretical $q_{lat-theo}$ values for a range of different conditions. The results are shown in figure 5, with the measured flow rates plotted as a function of the theoretical value (eq. 5). This figure shows that the different data sets can be grouped together according to the slope of the inlet channel; since the upstream Froude number depends essentially on this slope, this is equivalent to grouping them according to Froude number.

The first two data sets are for a longitudinal slope of 5% with an average Froude number $F_{r0} \approx 3.5$, and side slopes of either $S_{0y} = 0\%$ or $S_{0y} = 1.2\%$. The experimental points are very close to the theoretical values, and the difference does not seem to depend on S_{0y}. This probably remains true provided that the water level in the exit canal does not impede the development of the jet within the intersection; this was always observed to be the case for $S_{0y} \geq 0$. For any given upstream Froude number the difference between theoretical and measured values varies as α/h_0, where α is a constant. This dependence should be related to the capacity of water in the side channels to flow back into the main channel, above the level $z' = 4/9h_0$.

The other data sets correspond to lower values of the longitudinal slope, with Froude numbers less than 2. For $S_{0x} = 1\%$, we have $F_{r0} \approx 1.6$ and $S_{0y} = 0\%$, and for $S_{0x} = 1.2\%$, $F_{r0} \approx 1.8$ and $S_{0y} = 5\%$. The measured flow rates are rather less than those predicted by the dam break model, principally because of the influence of the stagnation regions on the downstream walls of the lateral channels; this effect depends strongly on the upstream Froude number, and increases as the Froude number decreases. For example, for the configuration $S_{0x} = 1.2\%$, $S_{0y} = 5\%$ the Froude number was increased to $F_{r0} \approx 2.2$ (by lowering the upstream sluice gate) and the measured flow rate becomes closer to the theoretical value.

These observations are based on a rather limited number of data sets, and more results are needed, both to confirm these preliminary conclusions, and to develop an expression for the dimensionless coefficient α as a function of the different parameters that characterise the configuration.

5 CONCLUSIONS

Flow rates and water levels have been measured in the intersection of four independent channels. Supercritical flow enters the intersection from one of the four channels, and is evacuated by the other three. Within the intersection the incoming flow behaves as a supercritical jet. The evolution of the jet can be modelled by the propagation in the side channels of waves similar to those obtained by the solution of the dam break problem. This result has been used to develop an expression for the flow rates in the three channels; the theoretical expression agrees well with the measured flow rates for high inlet Froude numbers, but overestimates the lateral flow rates for lower Froude numbers. The principle reason for this is the development of stagnation regions on the downstream walls of the side channels, which drive fluid back into the main channel. This has been conserved by the installation of vertical plates to isolate the stagnation regions from the flow in the main channel. Further experiments are necessary to determine the exact dependence of this effect on upstream Froude number.

ACKNOWLEDGEMENTS

The experimental installation was designed and assembled by P. Dutheil, and we gratefully acknowledge his contribution to the project. The research was funded by the French CNRS (SPI-ACI jeune chercheur "Hydraulique en milieu urbain", 2002) and by the French Environment Ministry under the RIO2 Program "Estimation des écoulements de surface pour une crue extrême en milieu urbanisé".

REFERENCES

Greated C.A. 1968. Supercritical flow through a junction. *La Houille Blanche* 23(8), 693–695

Gurram S.K., Karki K.S. 1997. Subcritical junction flow. *Journal of Hydraulic Engineering* 123(5): 447–455.

Hager W.H. 1989. Supercritical flow in channel junctions. *Journal of Hydraulic Engineering* 124(1): 595–617.

Hager W.H., Yasuda Y. 1997. Unconfined expansion of supercritical water flow. *Journal of Engineering Mechanics* 123(5): 451–457.

Hsu D.C., Wu F.-S., Lee W.-J. 1998. Flow At 90° Open-Channel Equal-Width Junction. *Journal of Hydraulic Engineering* 124(2): 186–191.

Khan A.A., Cadavid R., Wang S.S.-Y. 2000. Simulation of channel confluence and bifurcation using the CCHE2D model, *Proc. Instn. Civ. Engrs Water and Mar. Eng,* 142: 97–102, June 2000.

Krishnappa G., Seetharamiah J. 1963. A new method of predicting the flow in a 90° branch channel. *La Houille Blanche* 7: 775–778

Nania L., Gomez M., Dolz J. 1998. Modelacion de la escorrentia pluvial en cruces de calles, *Proc. XVIII Congreso LatinoAmericano de Hidraulica:* 233–242, Oxaca, Mexico, October 1998 *(in spanish).*

Nougaro J., Boyer P. 1974. Sur la séparation des eaux dans les dérivations de canaux à section rectangulaire. *La Houille Blanche* 3: 199–203 *(in french)*

Nougaro J., Boyer P., Claria J. 1975. Comportement d'une dérivation de canaux lorsque les biefs aval sont pourvus de retenues. *La Houille Blanche* 4: 267–275 *(in french)*

Ramamurthy A.S., Tran D.M., Carballada L.B. 1990. Dividing flow in open channels. *Journal of Hydraulic Engineering* 116(3): 449–455.

Ramamurthy A.S., Satish M.G. 1988. Division of flow in short open channel branches. *Journal of Hydraulic Engineering* 114(4): 428-438.

Schwalt M., Hager W.H. 1995. Experiments to supercritical junction flow. *Experiments in Fluids* 18: 429–437.

Shabayek, S., Hicks. 2002. Dynamic model for Subcritical Combining flows in channel Junctions. *Journal of Hydraulic Engineering* 128(9): 821–828.

Shettar A.S., Murty K.K. 1996. A numerical study of division of flow in open channels. *Journal of Hydraulic Research* 34(5): 651–675.

Stoker J.J. 1957. *Water Waves: the mathematical theory with applications*, New York: Interscience Publishers, Inc.

Weber L.J., Schumate E.D., Mawer N. 2001. Experiments on flow at a 90° open channel junction, *Journal of Hydraulic Engineering* 127(5), 340–350.

River Flow 2004 – Greco, Carravetta & Della Morte (eds.)
© 2004 Taylor & Francis Group, London, ISBN 90 5809 658 0

Factors on flood problems in Ubon Ratchathani province, Thailand

C. Chinnarasri, U. Israngkura & S. Jarukamol
Water Resources Engineering Research Lab. (WAREE), Department of Civil Engineering, King Mongkut's University of Technology Thonburi, Bangkok, Thailand

ABSTRACT: Lowland areas alongside of Mun River in Ubon Ratchathani Province, Thailand are flooded frequently. The investigation on the significance of the flood causing factors was done by calculating the river water levels at different magnitudes of these factors. The combination of these magnitudes resulted in 108 study cases. Flood hydrographs from river tributaries were constructed by NAM Model using 30 day rainfall over each basin. Mekong River water levels were analyzed from measured data at Kong-Chiam gauging station. The discharges and water levels at different locations along the river reach were computed by MIKE 11 Model covering 30 days period. The results showed that the flood flow at station M7 was the most significant factor as it could produce flooding on the target area when its magnitude was at only 2 year return period or 2,500 m^3/s. and when its magnitude was increased the river water level then increased considerably.

1 INTRODUCTION

Ubon Ratchathani is a province in the northeastern region of Thailand. Mun River which is the largest river in this region flows across this province from west to east approximately and discharges into Mekong River at Khong Jeam district. Lowland areas alongside the river reach from the confluence of Chi River to Mekong River as shown in Figure 1 are flooded very frequently.

The latest flood in August 2002 resulted in a damage of about US$ 47 million. The major causes of flooding, apart from the lowland topography, are the large floods from the upstream watershed and from the river tributaries along the river reach and the backwater effect from Mekong River. In planning a flood mitigation scheme for this area, it is necessary that the boundary of the flooded area and the flood levels under different hydrologic conditions as well as the significance of each hydrologic factor must be identified so that the proper mitigation measure could be established. The objectives of this study are to determine the area which is subjected to severe flooding, the combination of hydrologic events at the commencement of flooding, and the most significant hydrologic factors which causes flooding.

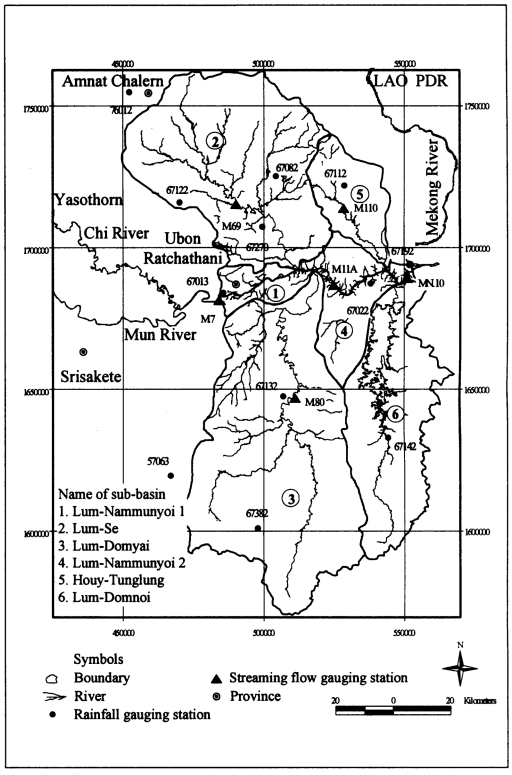


Figure 1. Study area with streamflow and rainfall gauging stations.

2 METHODOLOGY

2.1 *General*

The flood hydrographs from the upstream watershed, the lateral inflow hydrographs from river tributaries

Table 1. Peak flow at M7 and peak water levels at Klong Jeam.

Return periods (yr.)	Peak flow at M7 (m^3/s)	Peak WL Khong Jeam (m.MSL)
2	2500.0	102.65
5	3918.0	104.01
10	4856.7	104.50
20	5757.3	105.76
50	6922.9	106.87
100	7796.4	107.70

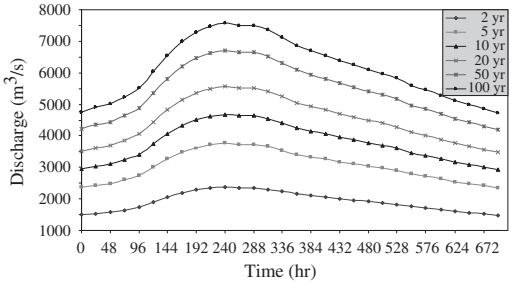


Figure 2. Flood hydrographs from upstream watershed (at M7).

and the stage hydrograph in Mekong River at various return periods were determined then the stage hydrographs along the river reach as caused by several combinations of those three hydrologic factors were derived. The peak stage profiles were then plotted and the areas subjected to frequent floodings were identified. The hydrologic conditions which lead to the commencement of flooding over this area were observed. The hydrologic factor which caused flooding at the lowest return period and which caused the flood stage rising sharply when its magnitude was increased would be considered as the most significant factor.

2.2 *Flood hydrographs from upstream watershed and Mekong River water level*

Flood Hydrographs from the upstream watershed were derived from the recorded flow data at gauging station M7 which is just downstream of Chi River confluence and has a drainage area of about 106,673 sq.km. The derived hydrograph of a return period covered a length of 30 days and had the peak discharge equal to the value at that return period. The position of peak discharge and the shape of the hydrograph were made nearly similar to the 30 days hydrograph of large flood in 2001. The peak discharges at various return periods are as shown in Table 1. Figure 2 shows the derived flood hydrographs from the upstream watershed which were used in the study.

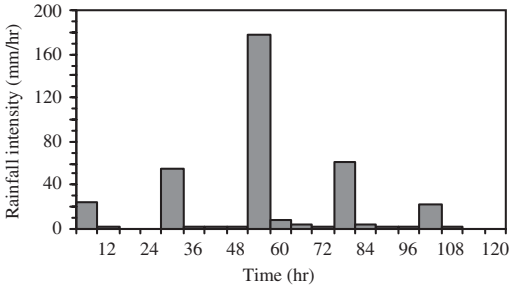


Figure 3. Examples of synthesized rainfall over Lam-Se sub-basin.

The Mekong River water levels at various return periods were derived from the recorded data at Khong Jeam gauging station at the mouth of Mun River. The peak water levels at various return periods are as shown in Table 1. As observed from historical data, during severe flood occurrences the water level varied just slightly so in this study it was assumed to be constant at the value of the specified return period.

2.3 *Flood hydrographs from tributary river basins*

The drainage area of 12,751 sq.km. from M7 to Mekong River consists of 6 sub-basins. Their boundaries together with the rainfall and streamflow gauging stations are as shown in Figure 1. Since there were no streamflow gauging stations at the outlets of these sub-basins, their outflow flood hydrographs which drain into Mun River had to be determined from a rainfall–runoff model. NAM model developed by the Danish Hydraulics Institute (DHI) was used in this study.

This model was calibrated and verified by the data of three watersheds above stations M69, M80, and M110 (see Figure 1). The model parameters of each basin obtained from these processes were correlated with some physical characteristics of the watershed and the best relationships were used to determine the Nam parameters for each subbasins.

The rainfall of a return period which was used to generate runoff from a sub-basin was the areal average maximum 5-day rainfall which contained maximum 1 day and 3 days rainfall of that return period and had a time distribution pattern similar to the average pattern of heavy storms over this region. Figure 3 is the example of the synthesized rainfall.

2.4 *Computation of flood stages along the river*

The flood stages along the river reach as caused by several combinations of those three hydrologic factors were computed by the one-dimensional hydrodynamic flood routing model which is a module of MIKE 11 computer program package developed by the Danish Hydraulics Institute (DHI 1982). The model

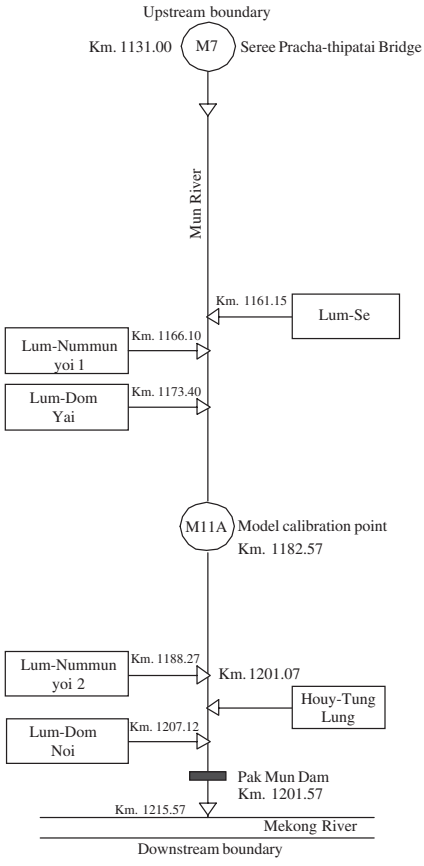


Figure 4. Model configuration.

configuration cover the river reach of about 80 km. is as shown in Figure 4. River cross sections spacing at about 3 km. interval were used in the computation. River section at Sta. 1131 + 00 km. where M7 is located is the upstream boundary.

The model was calibrated and verified by the observed hydrologic data during August 1 to October 31, 1996 and during July 1 to September 31, 1997 respectively. Figure 5 shows the computed water levels at gauging station M 11 A from model calibration and verification against the observed water levels.

The model was then used to compute the flood stage hydrographs under several combinations of the three hydrologic factors.

3 RESULTS

3.1 *Flood prone area*

The peak flood level profiles under each combination of hydrologic factors were plotted as shown in Figure 6 as an example. From these plots, it could be observed

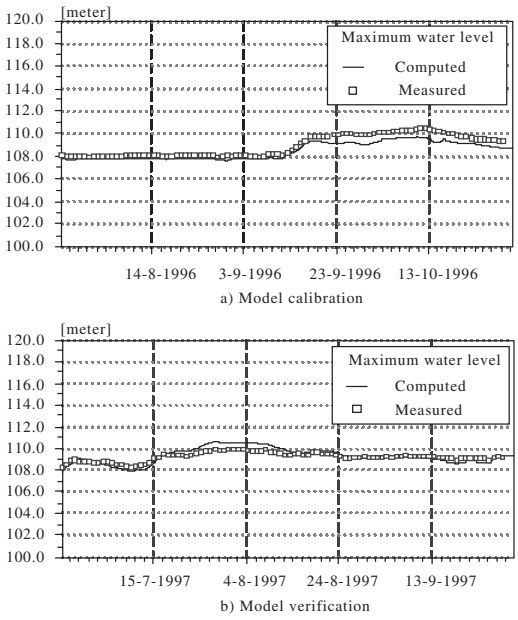


Figure 5. Calibration and verification of MIKE-11 hydrodynamic model.

that the area subjected to severe floodings lies between River Sta. 1133 + 050 km. to Sta. 1161 + 150 km. This flood prone area lies in the urban and semi-urban area in Muang District and Warin Chamrab District.

3.2 *Peak flood stage and flood commencement conditions*

The peak flood stage at River Sta. 1133 + 050 km. which is at the upstream end of the flood prone area was used as the index to indicate the flood harshness over this area. Its values under several study cases are as shown in Table 2. As can be observed from Figure 6, large area on both banks of the river would be flooded when the water level at this station is at +114 m.MSL or higher. When the upstream flood hydrograph at M7 is at 2 year return period this condition will commence when the flood hydrographs from tributary watersheds are at 10-year return period and the Mekong water level is at 100-year return period. But when the upstream flood hydrograph increases to 5-year return period, whatever the Mekong water level may be, the flooding would always occur even when the river tributary flood hydrographs were at the return period lover than 2 year. Combinations of hydrologic events on the right and below the bold line in Table 2 are those which will produce severe floodings.

3.3 *Significant level of each hydrologic factor*

As can be seen from Table 2, when the flood at M7 is at a magnitude lower than or equal to the flood magnitude

Table 2. Peak flood levels at Sta. 1133 + 050 km.

Return Period (yr)		Return Period of Lateral Inflow (yr)					
M7 Flood	Mekong River stage	2	5	10	20	50	100
2	5	113.68*	113.79	113.84	113.92	114.07	114.21
	20	113.71	113.83	113.88	113.96	114.11	114.25
	100	113.82	113.94	113.99	114.07	114.22	114.37
5	5	115.89	115.99	116.03	116.09	116.16	116.22
	20	115.91	116.01	116.05	116.11	116.18	116.25
	100	115.98	116.08	116.12	116.18	116.25	116.32
10	5	117.07	117.16	117.19	117.25	117.30	117.35
	20	117.09	117.18	117.22	117.27	117.32	117.38
	100	117.15	117.23	117.27	117.32	117.38	117.43
20	5	118.09	118.17	118.20	118.25	118.27	118.35
	20	118.10	118.19	118.22	118.27	118.32	118.37
	100	118.15	118.23	118.27	118.32	118.36	118.41
50	5	119.29	119.37	119.41	119.45	119.49	119.53
	20	119.31	119.39	119.42	119.47	119.51	119.54
	100	119.35	119.42	119.46	119.50	119.54	119.35
100	5	120.13	120.20	120.24	120.28	120.32	120.35
	20	120.14	120.22	120.25	120.29	120.33	120.37
	100	120.17	120.25	120.28	120.33	120.36	120.40

Notes. 1)* Water level in m. MSL
2) Flood producing conditions are under the bold line

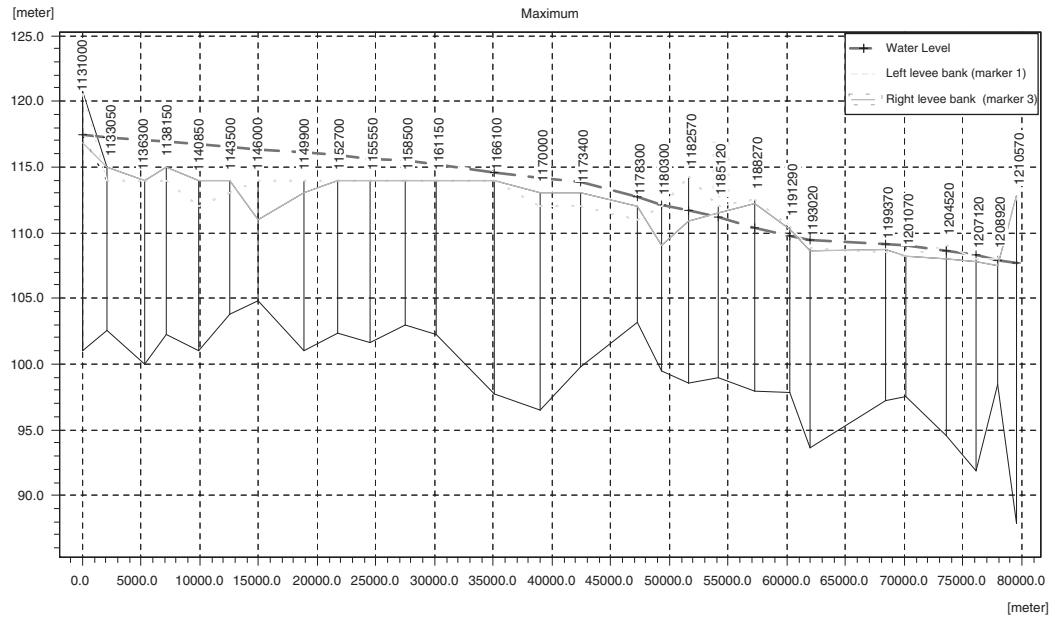


Figure 6. Peak flood level profile: 5-yr flood at M7, 10-yr lateral inflow and 100-yr Mekong River level.

at 2-year return period the chances of the area being flooded is very rare, i.e., it will occur only when the lateral inflow is at the magnitude of up to 10-year return periods and the water level in Mekong reaches the 100-year return periods level but when the upstream flood magnitude increases to 5-year return period flooding could occur even there in very low lateral inflow. This indicated that the upstream flood is more significant than the lateral inflow flood and the Mekong water level.

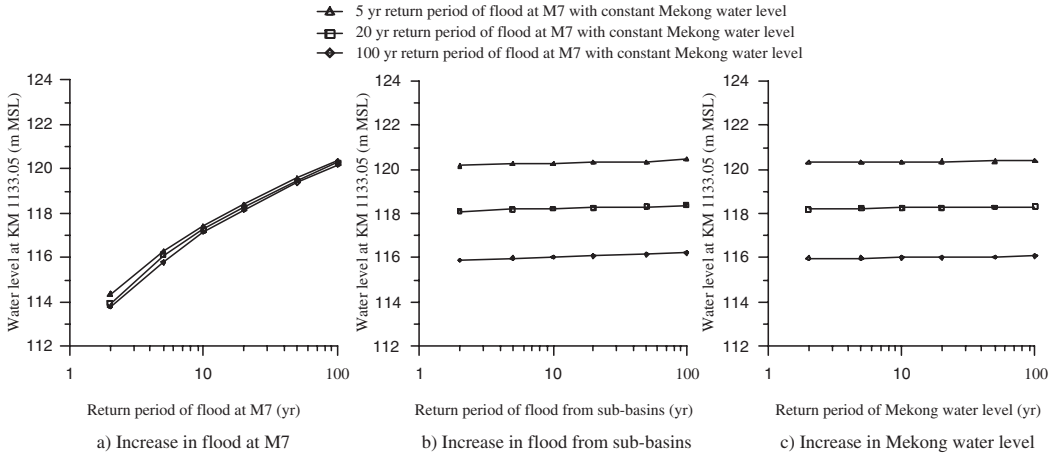


Figure 7. Increase in flood level with increase in return period of a factor.

Figure 7 shows the effects on flood water level as caused by increasing the return period of one factor while holding the other two factors constant at a return period. For the same increase in return period, the increase in upstream flood magnitude resulted in the largest increase in flood level while the increase in Mekong water level yielded the least increment.

From these investigations, it is justified to rank the flood from upstream watershed as the must significant flood causing factors and the Mekong water level as the least significant one.

4 CONCLUSIONS

It could be concluded from this study that:

1) The river flood plain where severe flooding occurred lies between River Sta. 1133 + 050 km. and Sta. 1161 + 150 km. just downstream of gauging station M7. Larger part of this area is the urban or semi-urban area in Muang district and Warin Chamrab district of Ubon Ratchathani Province.
2) Severe floods would rarely occur if the flood magnitude at M7 is lower than or equal to 2-year return period flood but would occur when flood magnitude at M7 is at 5-year return period upward even though there is very small amount of lateral inflow and very low water level in Mekong River.
3) As the flood from watershed area above M7 is the most significant flood causing factors, any flood mitigation plan which can reduce this flood to the magnitude at 2-year return period at the optimum cost would be the most desirable one.

REFERENCE

Danish Hydraulic Institute (DHI). 1992. MIKE 11 reference manual. HØrsholm. Denmark: p.469.

This page intentionally left blank

River Flow 2004 – Greco, Carravetta & Della Morte (eds.)
© 2004 Taylor & Francis Group, London, ISBN 90 5809 658 0

Urban fluvial flood modeling using a two-dimensional diffusion wave treatment

D. Yu & S.N. Lane
School of Geography, University of Leeds, Leeds, UK

ABSTRACT: This paper applies a 2-D raster-based diffusion wave model to determine patterns of fluvial flood inundation in urban areas using high resolution topographic data. As this is a new application area, the aim of this paper is to explore the effects of model spatial resolution upon estimated inundation extent. Model response shows that even relatively small changes in model resolution have considerable effects upon the predicted inundation extent as well as the flood wave travel time. This is associated with two connected effects: (1) poorer representation of both cell blockage and the associated surface routing process resultant from the smoother floodplain as the mesh is coarsened, where the flow routing is especially complex; and (2) the effects of (1) upon both the water velocities and water levels which in turn determine which parts of the floodplain the flow can actually travel to. Thus, coupling of high resolution data, which can capture small scale variation in topography, to more sophisticated representation of the inundation process will be required in order to obtain effective predictions of flood inundation extent in urban areas.

1 INTRODUCTION

Fluvial flood modeling usually requires the prediction of flows over complex topography. Flow routing over floodplains is known to be highly two-dimensional and notably where strong shear layer develops between the main channel and the floodplain, even three-dimensional (Knight & Shiono, 1996). Two-dimensional, depth averaged models have been extensively described in the engineering literature for some time and are increasingly being applied to natural river-floodplain systems (see the review in Lane, 1998). Indeed, developments have seen two-dimensional models of floodplain flows come into widespread use (Beven, 2000), including TELEMAC-2D (e.g. Galland et al., 1991, Bates et al., 1995) and RMA2 (e.g. Bates et al., 1992, 1995). Traditionally, two-dimensional models have been constrained by the scarcity of detailed topographic data (Marks & Bates, 2000, Horritt & Bates, 2001). This constraint is being gradually relieved by the emergence of new data capture techniques, particularly in the field of airborne remote sensing, including interferometric synthetic aperture radar (SAR) (e.g. Brackett et al., 1995, Horritt & Bates, 2001), aerial digital photogrammetry (e.g. Biggin & Blyth, 1996, Lane, 2000, Westaway et al., 2001, 2003) and LiDAR (laser induced direction and ranging) (Krabill et al., 1984, Flood & Gutelius, 1997, Marks & Bates, 2000). These new topographic data sources, which can yield synoptic information at a resolution that in some cases is better than 2.0 m and a precision that is better than 0.15 m, are providing new opportunities for modeling floodplain inundation from both fluvial and pluvial sources.

More recently, raster-based models have gained credence in the modeling of floodplain flow inundation extent (Bates & De Roo, 2000, Horritt & Bates, 2001a, b). This typically uses a one-dimensional representation of channel flow linked to a two-dimensional treatment of flow over the floodplain, commonly involving a diffusion wave treatment. An application of the diffusion wave approach was first reported by Cunge et al. (1976) and similar methods have been used by Estrela & Quanias (1994) and Bechteler et al. (1994). These approaches use an explicit two-dimensional treatment of mass conservation but a highly simplified representation of momentum conservation, commonly based upon determining the magnitude of flow between any two adjacent cells according to the water surface elevation difference and the Manning equation. Bates and De Roo (2000) developed a raster-based model (LISFLOOD-FP) based on this concept and compared it with a relatively coarse resolution (50–250 m) two-dimensional finite element scheme. Unlike other models, this model was specifically designed to predict flood inundation and ignored or minimized the representation of processes that were not considered central to the aim (Bates & De Roo,

2000). Tentatively, these results indicated that topography and a basic process representation was more important than a complete process representation for effective prediction of inundation extent. However, issues such as model calibration, friction parameter representation and the differing resolutions of the two models needed to be addressed before these conclusions are confirmed (Horritt & Bates, 2001b). Horritt and Bates (2001b) compared LISFLOOD-FP with a two-dimensional finite-element model (TELEMAC-2D). Though the raster-based and the two-dimensional finite-element models showed similar performance, insufficiently accurate validation data and the lack of friction parameterization data made it difficult to distinguish between the two kinds of model formulations. More recently, the ability of the LISFLOOD-FP model to predict flood extent and flood wave travel times has been compared with a 1D model (HEC-RAS) and a 2D model (TELEMAC-2D) using independent calibration data from hydrometric and satellite sources (Horritt & Bates, 2002). Results revealed that the LISFLOOD-FP model required independent inundated area data for calibration in order to achieve good predictions of inundation extent. It is also debatable as to whether or not raster-based models can provide an adequate representation of inundation velocities and hence the development of inundation through time. In summary, these results suggest that, compared to fully explicit numerical solutions including finite element (e.g. Bates et al., 1992), finite difference (e.g. Gee et al., 1990) and finite volume (e.g. Lane & Richards, 1998) formulations, raster-based models have major advantages in terms of their ease of formulation, computational efficiency and simplified calibration. However, questions remain over their relatively simple representation of the flow processes, due partially to the poor representation of momentum transfer on the floodplain.

Much existing research into two-dimensional modeling of flood inundation has focused upon relatively rural areas. Wheater (2002) identified the improved representation of urban flooding at both local and catchments scale as one of the key priorities in current fluvial flood modeling practice. Thus, the aim of this paper is to evaluate the extent to which diffusion wave based models can be applied to situations where there is inundation of relatively urbanized areas. This is an interesting application area because potential flood damage is proportionately greater than rural areas and urban flood inundation receives a relatively high political profile. In modeling terms, these areas may also benefit significantly from the availability of high resolution topographic data as urbanization leads to the presence of structural elements on the floodplain which may have significant impacts upon patterns of flood inundation. These may not be well-represented through traditional treatments of roughness involving up-scaling of sinks in the momentum equations. Thus, the focus of this paper is application of a basic 2D raster-based model to understand inundation in an urbanized area.

2 FLUVIAL FLOOD PROCESSES IN URBAN AREAS

The presence of significant structural features (houses, walls etc.) on a river floodplain is important in relation to both the volume of the floodplain that can be occupied by the flow and the direction that the flow takes across the floodplain. Harnessing high resolution topographic data has appeal as it may reduce the uncertainty into how to parameterize the effects of structural 'topography' upon inundation. In both one- and two-dimensional (both diffusion wave and depth-averaged) models, topographic structure is commonly represented through up-scaling of a roughness parameter with calibration where necessary. This is well-established for representing the effects of individual grains and grain organizations in models of flow in gravel-bed rivers where the roughness length is multiplied upwards (e.g. Lane & Richards, 1998, Lane et al., 1999) and for representing the effects of vegetative roughness in floodplain flow models, where Manning's n is scaled upwards (e.g. Mason et al., 2003). In one-dimensional modeling, using the St. Venant equations, the roughness parameter commonly appears through a friction slope relationship that not only represents bed roughness, but also turbulence effects and dispersion processes, the latter resulting from depth- and width-integrating the full three-dimensional form of the Navier-Stokes equations. One-dimensional models tend to have high sensitivity to roughness and this makes roughness a key focus of parameterization in one-dimensional models. Raster-based flood inundation models have commonly used a uniform roughness coefficient for the floodplain but have treated it as the key calibration parameter (Bates & De Roo, 2000, Horritt & Bates, 2001a, b, Horritt & Bates, 2002). In relation to sensitivity, it has been found that LISFLOOD-FP is insensitive to roughness coefficient on the floodplain (Horritt & Bates, 2002) when inundation area was considered.

In relation to flood inundation, roughness parameterization could become more complex if the required roughness value were allowed to vary spatially as a function of local structural complexity. Horritt (2000) used a simple distributed roughness calibration scheme in fluvial flood modeling and got a minor improvement over the uniform parameterization. LiDAR data has been successfully used to upscale n in a distributed way for floodplain vegetation (Mason et al., 2003) although this assumes that: (1) vegetative roughness relationships developed from flume

experiments can be applied to two-dimensional mapping of n from vegetation height; and (2) the prime control on n is vegetative roughness and there is no need to calibrate roughness to take into account the effects of other processes (e.g. turbulence). However, the extent to which this approach can be extended to urban areas is questionable. First, parameterization of n is based upon manipulation of a sink in the momentum equations, either through the bottom stress term that appears in a full solution of the depth-averaged equations, or through n in the simpler momentum representation in a 2D diffusion model. Structural features such as houses, walls etc. also have a blockage effect which reduces the volume of storage that is possible on the floodplain and which can have a major effect upon routing. Research by Lane et al. (in press) shows that traditional parameterization of high resolution topographic variability in 3D hydraulic models using up-scaling of roughness heights does not necessarily represent mass blockage effects properly. The same conclusion may hold for floodplain structural elements in 2D models. Second, many structural elements have topological properties that create complete barriers to flow (e.g. walls) and which can have a very major effect upon the flow routing process. Upscaling of n may reduce flux across linear sets of grid cells, but will not necessarily recognize the full topological features of a structure.

High resolution topographic data has the capability to deliver sufficient information on floodplain structural elements for modeling purposes. However, as yet, there has been no application of this information to urban flood inundation modeling. In this paper, we focus upon diffusion wave treatments of urban flood modeling as these make it possible to use higher spatial resolution topographic data as compared with more computationally intensive methods such as those based on finite elements. As raster-based fluvial flood modeling gives poor representation of the momentum transfer over the floodplain, there is a related need to describe local wetting and drying processes more adequately to compensate the effect. Various algorithms describing the wetting and drying processes in flood modeling have been developed in finite element methods (e.g. Defina et al., 1994, Bates, 2000). LISFLOOD-FP has no explicit treatment of the wetting process and water is allowed to flow out of the cell as long as the outflow energy slope is positive. This is not realistic in reality in that, in most cases, the water front during wetting will lie within the cell and only part of the cell will be wet at a particular time step. It is also more likely to affect inundation extent in urban areas. As the routing process is strongly controlled by elevation differences between cells, if diffusion across the floodplain is too rapid, water will not necessarily reach higher elevation areas as the spread of flow reduces water surface elevations locally, confining spread to lower elevation areas. In urban areas, the complexity of elevation variation makes this particularly important. The importance of this process will be model resolution dependent: with coarser grid cells, representing this process adequately will become more important. Given the above, in addition to explicit representation of structural elements in a diffusion wave model, we also explore the interaction between model resolution and inundation extent and the role of wetting and drying parameters.

3 MODEL APPLICATION: DATA SOURCES

The model used in this paper takes the same structure as that of the JFLOW model developed by Bradbrook et al. (in review), but modified for the purposes of urban flood inundation modeling. The model is applied to a reach of the River Ouse in Yorkshire, U.K (Fig. 1) near Tadcaster. This reach was chosen because of the availability of a one-dimensional hydraulic model for the main river flow, high quality LiDAR data for the floodplain surface, and remotely sensed data on inundation extent and water levels for a large flood inundation event in November 2000, as well as the dense presence of structural features on the floodplain. The latter data have been used to determine inundation patterns and water levels using digital photogrammetry and image analysis (Lane et al., 2003).

The LiDAR had a resolution of 2 meters. The original LiDAR data had been post-processed to standard data quality requirements using methods set by the U.K. Environment Agency's National Centre for Environmental Data Surveillance in Twerton, Bath. This

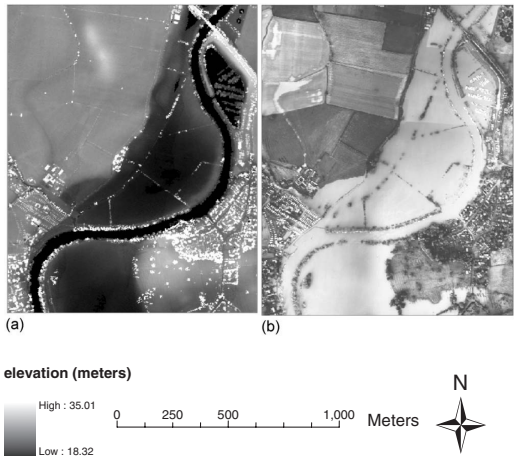


Figure 1. The reach of the River Ouse in Yorkshire, UK, on which the flood event in 2000 was simulated. (a) LiDAR data of 2-meter resolution. (b) Flooding imagery which provides the validation data for the model.

includes standard assessment of data quality to guarantee a precision of ±0.25 m throughout, improving to ±0.15 m in relatively flat areas with solid reflectance surfaces. The data includes returns from building and trees. For the purpose of urban inundation modeling, some additional image processing was undertaken. Whilst buildings needed to be retained, it was necessary to remove elevations within the LiDAR dataset associated with tree canopies under the assumption that only tree trunks would have a significant effect upon inundation. The removal of trees was achieved using the same data source used for model validation. Similarly, different surfaces (e.g. grass, road, garden etc.) might need to be allocated different roughness parameters. Spatial distribution of roughness parameters is not addressed in this study. Instead, a uniform roughness value of 0.06 was used based on the typical values suggested by Chow et al. (1988). Although most previous studies use roughness parameters as key calibration parameters, this has not been attempted in this study.

In order to remove tree canopies and also to provide model validation data, 1:4500 scale aerial imagery was obtained. This had been acquired during the falling limb of a major flood event on the 11th November 2000 (Fig. 1). This flood was estimated to be the highest recorded in York since 1625. The imagery was scanned at 21.2 μm resolution using a standard desktop scanner. Ordnance Survey benchmark data were used to rectify the imagery to a root mean square error of better than ±2.0 m (i.e. commensurate with the resolution of the LiDAR data). Supervised classification was then used to assign the floodplain into functional units: (1) inundated areas, to provide data on flood extent during the falling limb of the hydrograph for model validation; (2) trees, in order to allow correction of the LiDAR data for canopy height effects; and (3) other elevations. Only canopy locations were removed from the LiDAR data.

A one-dimensional hydraulic model of the Ouse from Skelton (upstream of the city) through to Naburn Weir (downstream of the city) is used to provide estimates of flux from the river to the floodplain for a major flood inundation event (estimated to have a return period of greater than 100 years) in November 2000 in the form of a stage hydrograph in 530 hours (Fig. 2). The connectivity between the one-dimensional model and the floodplain is established through a weir equation. This assumes that the floodplain is protected by an embankment that essentially acts as a continuous, broad-crested weir. This may be identified from topographic data (e.g. LiDAR). The flux to the floodplain is then determined from predictions of water stage in the river channel using a weir equation:

$$q = 1.704(H - \Delta z)^{3/2} \quad (1)$$

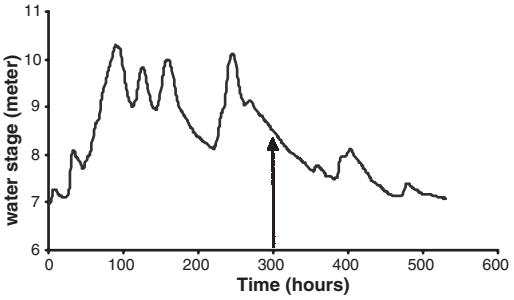


Figure 2. Stage hydrograph in the main river channel. Arrow points to the time when the validation imagery was acquired.

where H is the water surface elevation of the river channel and Δz is the height of the river embankment on the floodplain. Water level hydrographs are interpolated to each river adjacent floodplain cell at each time step and inflow from the river channel occurs once the water surface of the river channel is higher than that of the adjacent floodplain cells. The flow in the river channel at each time step is assumed to be uniform throughout the simulation.

4 MODEL APPLICATION: SIMULATIONS, ACCURACY ANALYSIS AND VALIDATION

The flood event was simulated using three different spatial resolutions: 8-meter, 16-meter and 32-meter and time series of inundation extents for these simulations are shown in Figures 3–5. These show the wetting process for 38 hours. The comparison of the predicted inundation extents obtained using different model resolutions at the time when the validation data was acquired are shown in Figure 6. Comparison of the time series inundation extents obtained using different model resolutions for the first 38 hours shows that model is quite sensitive to spatial resolution with respect to both the inundation extent and the flood wave travel time. Flood inundation is more rapid with a coarser resolution. For example, the model with a 32-meter resolution has roughly the same inundation pattern at around 30.5 hours, as that obtained from the 8-meter resolution model at 38 hours. For the 16-meter case, it took about 32 hours to get the same pattern. This is expected considering the poorly represented inertial processes in a diffusion wave model.

In order to compare the accuracy of the predicted inundation extents statistically, accuracy assessment was undertaken using a method adopted from remote sensing (Congalton & Green, 1999). In this method, an error matrix is set up to express the number of sample units assigned to a particular classification category in one classification relative to the number of sample

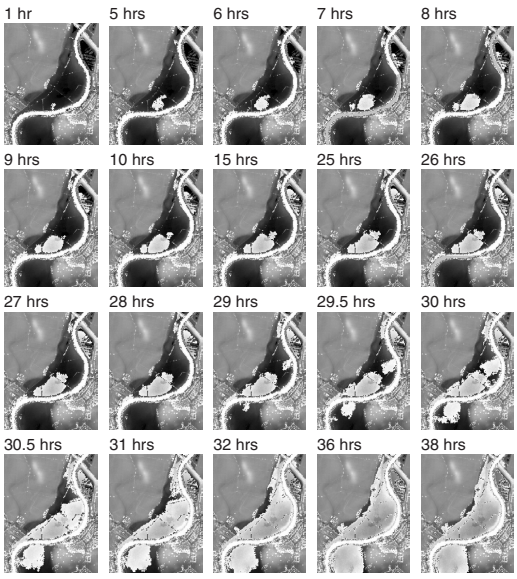


Figure 3. Time series inundation extents (in 38 hours) obtained from model simulation using an 8-meter model resolution.

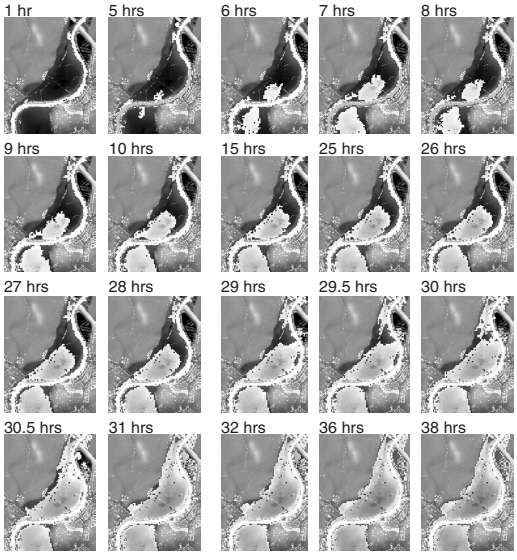


Figure 4. Time series inundation extents (in 38 hours) obtained from model simulation using a 16-meter model resolution.

units in another classification. In most of the cases, one of the classifications is assumed to be correct (reference data). The columns usually represent the reference data and the rows usually represent the classification data. In this application, the validation aerial

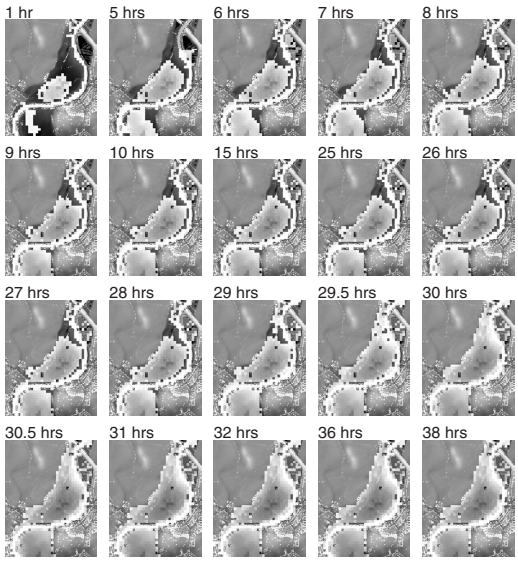


Figure 5. Time series inundation extents (in 38 hours) obtained from model simulation using a 32-meter model resolution.

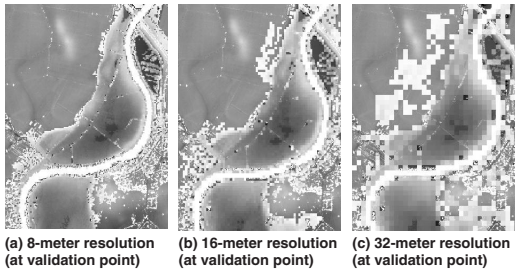


Figure 6. The comparison of the predicted inundation extents obtained using different model resolutions at the time when the validation data was acquired.

imagery on the falling limb of the flood event was classified into three classes: dry areas, wet areas and the wetting front. At each time step, the model divides the whole modeling site into three categories to represent the wetness of the grid cells, namely wet cells, wetting front cells and dry cells. The wetness of a particular cell is decided by the wetting parameter. A wet cell is one with a wetting parameter equal or greater than one, a dry cell is one with a wetting parameter equal to zero and a wetting front cell is one with a wetting parameter greater than zero and smaller than one. If temporal validation data in the form of inundation extent at a regular time interval is available, the accuracy of the model prediction can be assessed at each particular time points where the validation data is available. Thus, more insight into how the model behaves in relation to both the flood wave travel time and inundation extent

can be gained. However, in this application, as only the validation data at one point on the falling limb of the hydrograph is available, the accuracy of the model prediction was only assessed against the validation data for this point. Once the error matrix has been constructed, the overall accuracy can be computed as the sum of the corrected classified cells divided by the total number of cells. Besides the overall accuracy, a discrete multivariate technique called Kappa analysis can be used to statistically determine if one error matrix is significantly different from another (Bishop et al., 1975). The result of performing a Kappa analysis is a KHAT statistic, which is the measure of accuracy or agreement (Cohen, 1960). The KHAT statistic is based on the difference between the actual agreement in the error matrix (i.e., the agreement between the predicted cell status and the reference data as indicated by the major diagonal) and the chance agreement as indicated by the row and column totals (i.e. marginal). A KHAT value can be calculated for each error matrix and is a measure of how well the predicted data agrees with the reference data. Confidence intervals can then be computed using the approximate large sample variance and the fact that the KHAT statistic is asymptotically normally distributed. The significance of the KHAT value for a single error matrix can be tested to determine if the agreement between the predicted data and the reference data is significantly different to no agreement by calculating the Z statistic. In addition to computing the Kappa coefficient for an entire error matrix, it may be useful to look at the agreement for an individual category within the matrix. This can be tested using the conditional Kappa coefficient, resulting in a KHAT statistic which is an estimate of the conditional Kappa coefficient. Similar to the overall KHAT statistic, the variance of the conditional KHAT value and the Z statistic can then be calculated to determine if the classification is significantly better than a random result. The overall accuracy, KHAT value and conditional KHAT value for wet cells at the point when the validation data is acquired for model simulations using 8-meter, 16-meter and 32-meter resolution are compared in Table 1.

Comparison of the inundation extents and the accuracy assessment of the model predictions obtained shows that the model performance is sensitive to spatial resolution when the inundation extent is considered. The overall accuracy of the model prediction decreases as the mesh is coarsened. KHAT statistics give a similar pattern. Landis & Koch (1977) divided the possible ranges for KHAT into three groups: a value greater than 0.80 (i.e., 80%) represents strong agreement; a value between 0.40 and 0.80 (i.e., 40–80%) represents moderate agreement; and a value below 0.40 (i.e., 40%) represents poor agreement. In this application, the simulation with the 8-meter resolution gives a KHAT of 0.76 which represent strong agreement of the model prediction with the validation data. According to KHAT statistics, prediction from simulation with 16-meter resolution also shows strong agreement with the validation data. While the agreement is rather poor for the 32-meter case.

Table 1. Overall accuracy for model simulations.

	8-meter	16-meter	32-meter
Overall accuracy	0.87	0.83	0.71
KHAT	0.76	0.70	0.51
Conditional KHAT for wet cells	0.74	0.63	0.41

The high sensitivity of model prediction to model resolution is thought to be the causes of two connected effects. First, the effect of resampling a dense mesh onto a coarse one will result in a smoother floodplain. It is found that, for the finite-element method, the two-stage filtration effect of raw data into a digital elevation model and then into a numerical mesh coarsens the data used in the model (Bates et al., 1996) and will reduce the detail and accuracy of the resultant land surface (Marks & Bates, 2000). This also holds for the resampling process in raster-based modeling. Three commonly used resample methods: nearest-neighbor interpolation, bilinear interpolation and cubic convolution interpolation have some degree of smoothing effect on the input data. Bilinear interpolation determines the value of a cell based upon the weighed distance average of the four nearest input cell centers. It generally causes some smoothing to the data. Convolution interpolation tends to smooth the data more than the bilinear interpolation due to the smooth curve used and the large number of cells involved. The smoothing effect of the nearest-neighbor interpolation is the least among these three methods and was the resample method used in this model.

Second, the representation of small-scale wetting processes will be simplified when the mesh is coarsened. The effect of the wetting treatment in the model is to slow down the flow transfer. The velocity controls the timing of the wetting process for a grid cell and the evaluation of the velocity will be resolution dependent. As the mesh is coarsened, the variance in velocity decreases and the timing of the wetting front migration tends to have a greater possibility of error due to the simplified description of the timing of the flow routing which will otherwise become much more complex in a denser mesh. This explains the high model sensitivity to model resolution in relation to flood wave travel time. Likewise, the difference between water surface elevations of two grid cells determines the direction of the flow routing and the variance in water surface elevations tends to decrease as the mesh is coarsened. The heterogeneity of water surface elevations in the

cells will decrease and this may result in a significant chance of errors in terms of the direction of flow. This is especially true for the flow routing in urban areas where structural features on the floodplain can have considerable effect on flow direction and timing. The cell blockage effect associated with structural features will have a less control on the timing and direction of the flow with a smoother floodplain resultant from a coarser resolution. It is expected that the higher resolution the data, the more adequately represented small-scale routing processes and thus the more accurate prediction with respect to both flood wave travel time and the inundation extent.

The effect of mesh resolution will also depend on floodplain configuration in relation to the magnitude of flow associated with a given return period. For a floodplain that is fully occupied with a low return period, mesh resolution will have less effect on high flows. For an unconstrained floodplain, where the lateral extent of a flood continues to increase even at low flows, resolution effects are likely to cause significant error.

5 DISCUSSION

This paper demonstrated the effect of model spatial resolution upon the estimated inundation extent in a two-dimensional raster-based diffusion wave model, with application to a reach of the River Ouse in Yorkshire, U.K to simulate a flood event in the year 2000. Model response shows that the model is quite sensitive to spatial resolution in terms of both the flood wave travel time and the inundation extent. This is thought to be caused by two interrelated effects: (1) the smoothing effect of mesh coarsening on the topological data; and (2) the poorer representation of small-scale flow routing processes associated with the reduced topological complexity resultant from (1). The local topological complexity due to the presence of small-scale structural features on the floodplain in urban areas makes this even more complex for urban flood modeling, as many of these features have topological properties that may have a major effect upon both the timing and direction of the flow routing. First, the details of the structural features may be reduced as the mesh is coarsened, resulting in a poorer representation of these features in the model. Second, current methods of representing small-scale flow routing processes associated with structural features in flood models have their limitations. Traditional methods of representing structural features usually involves up-scaling of the roughness parameter which, in previous research, has been used as a key calibration parameter to compensate for the poorly represented momentum transfer process in raster-based modeling. This may has the effect of reducing the flux through these features, but will not necessarily recognize the whole topological features of the structure. In this application, the wetting treatment approach that is used has the effect of reducing model dependence upon the roughness parameter. The combined effects of the wetting and roughness parameters can compensate in part for a coarser mesh resolution. However, the coarser the resolution, the lower the ability to control the inundation process as these parameters only partly control the speed and not the direction of wetting. Thus, coupling of high resolution data, which can capture small scale variation in topography, to more sophisticated representation of the inundation process will be required in order to obtain effective predictions of flood inundation extent for urban fluvial flood modeling.

REFERENCES

Bate, P.D. 2000. Development and testing of a subgrid-scale model for moving-boundary hydrodynamic problems in shallow water. *Hydrological processes* 14: 2073–2088.

Bates, P.D. and Anderson, M.G. 1996. A preliminary investigation into the impact of initial conditions on flood inundation predictions using a time/space distributed sensitivity analysis. *Catena* 26: 115–134.

Bates, P.D., Anderson, M.G., Baird, L., Walling, D.E. and Simm, D. 1992. Modeling floodplain flows using a two-dimensional finite element model. *Earth Surface Processes and Landforms* 17: 575–588.

Bates, P.D., Anderson, M.G. and Hervouet, J.-M. 1995. An initial comparison of two 2-dimensional finite element codes for river flood simulation. *Proceedings of the Institution of Civil Engineers, Water, Maritime and Energy* 112: 238–248.

Bates, P.D. and De Roo, A.P.J. 2000. A simple raster-based model for flood inundation simulation. *Journal of Hydrology* 236: 54–57.

Bechteler, W., Hartmaan, S. and Otto, A.J. 1994. Coupling of 2D and 1D models and integration into Geographic Information Systems (GIS). In White, W.R. and Watts, J. (eds.), *Proceedings of the 2nd International Conference on River Flood Hydraulics.* Chichester: John Wiley and Sons. pp. 155–165.

Beven, K.J. 2000. *Rainfall-Runoff Modeling: the primer*. Chichester: John Wiley and Sons.

Biggin, D.S. and Blyth, K. 1996. A comparison of ERS-1 satellite radar and aerial photography for river flood mapping. *Journal of the Chartered Institute of Water and Environmental Management* 10: 59–64.

Bishop, Y., Fienberg, S. and Holland, P. 1975. *Discrete Multivariate Analysis: Theory and Practice*. Cambridge: MIT Press, MA.

Bradbrook, K.F., Lane, S.N., Waller, S.G. and Bates, P.D., in review. Paper submitted to *Journal of River Basin Management*.

Brackett, R.A., Arvidson, R.E., Izenberg, N.R. and Saatchi, S.S. 1995. Use of polarmetric and interferometric radar data for flood routing models: first results for the Missouri River, Session 36 – Planetary Geology: Radar Remote

Sensing of Flood Plains, Mountain Belts, and Volcanoes. *Annual Meeting of the Geological Society of America*, 5–9 November, New Orleans.

Chow, V.T., Maidment, D.R. and Mays, L.W. 1988. *Applied Hydrology*. New York: McGraw-Hill.

Cohen, J. 1960. A coefficient of agreement for nominal scales. *Educational and Psychological Measurement* 20: 37–40.

Congalton, R.G. and Green, K. 1999. *Assessing the Accuracy of Remotely Sensed Data: Principles and Practice*. Boca Raton: Lewis Publishers.

Cunge, J.A., Holly, Jr.F.M. and Verwey, A. 1976. *Practical aspects of computational river hydraulics.* London: Pitman.

Defina, A., D'Alpaos, L. and Matticchio, B. 1994. A new set of equations for very shallow water and partially dry areas suitable to 2D numerical models. In Molinaro, P. and Natale, L. (eds.), *Modeling Flood Propagation over Initially dry Areas*. New York: American Society of Civil Engineers. pp. 72–81.

Estrela, T. and Quintas, L. 1994. Use of GIS in the modeling of flows on floodplains. In White, W.R. (eds.), *Proceedings of the 2nd International Conference on River Flood Hydraulics*. Chichester: Wiley and Sons. pp. 177–189.

Flood, M. and Gutelius, B. 1997. Commercial implications of topographic terrain mapping using scanning airborne laser radar. *Photogrammetric Engineering and Remote Sensing* 63: 327–366.

Galland, J.C., Goutal, N. and Hervouet, J-m. 1991. TELEMAC-a new numerical model for solving shallow-water equations. *Advances in Water Resources* 14 (3): 138–148.

Gee, D.M., Anderson, M.G. and Baird, L. 1990. Large scale floodplain modeling. *Earth Surface Processes and Landforms* 15: 512–523.

Horritt, M.S. 2000. Calibration of a two-dimensional finite element flood flow model using satellite radar imagery. *Water Resources Research* 36 (11): 3279–3291.

Horritt, M.S. and Bates, P.D. 2001a. Effects of spatial resolution on a raster based model of flood flow. *Journal of Hydrology* 253: 239–249.

Horritt, M.S. and Bates, P.D. 2001b. Predicting floodplain inundation: raster-based modeling versus the finite-element approach. *Hydrological processes* 15: 825–842.

Horritt, M.S. and Bates, P.D. 2002. Evaluation of a 1D and 2D numerical models for predicting river flood inundation. *Journal of Hydrology* 268: 87–99.

Knight, D.W. and Shiono, K. 1996. River channel and floodplain hydraulics. In Anderson M.G. et al. (eds.), *Floodplain Processes*. Chichester: John Wiley and Sons. pp. 139–181.

Krabill, W.B., Collins, J.G., Link, L.E., Swift, R.N. and Butler, M.L. 1984. Airborne laser topographic mapping results. *Photogrammetric Engineering and Remote Sensing* 50: 685–694.

Landis, J. and Koch, G. 1977. The measurement of observer agreement for categorical data. *Biometrics* 33: 159–174.

Lane, S.N. 1998. Hydraulic modeling in hydrology and geomorphology: A review of high resolution approaches. *Hydrological Processes* 12: 1131–1150.

Lane, S.N., Bradbrook, K.F., Richards, K.S., Biron, P.M. and Roy, A.G. 1999. The application of computational fluid dynamics to natural river channels: three-dimensional versus two-dimensional approaches. *Geomorphology* 29: 1–20.

Lane, S.N., Chandler, H.H. and Richards, K.S. 1994. Developments in monitoring and modeling small-scale river bed topography. *Earth Surface Processes and Landforms* 19: 349–368.

Lane, S.N., James, T., Pritchard, H. and Saunders, M. 2003. Photogrammetric and laser altimetric reconstruction of water levels for extreme flood event analysis. Paper forthcoming in the *Photogrammetric Record* 18(104): 293–307.

Lane, S.N., James, T.D. and Crowell, M.D. 2000. The application of digital photogrammetry to complex topography for geomorphological research. *Photogrammetric Record* 32: 793–821.

Lane, S.N., Hardy, R.J., Ingham, D.B. and Elliott, D.B., in press. Numerical modeling of flow processes over gravelly-surfaces using structured grids and a numerical porosity treatment. Paper forthcoming in *Water Resources Research*.

Lane, S.N. and Richards, K.S. 1998. Two-dimensional modeling of flow processes in a multi-thread Channel. *Hydrological Processes* 12: 1279–1298.

Marks, K.J. and Bates, P.D. 2000. Integration of high-resolution topographic data with floodplain flow Models. *Hydrological Processes* 14: 2109–2122.

Mason, D.C., Cobby, D.M., Horritt, M.S. and Bates, P.D. 2003. Floodplain friction parameterization in two-dimensional river flood models using vegetation heights derived from airborne scanning laser altimetry. *Hydrological Processes* 17: 1711–1732.

Westaway, R.M., Lane, S.N. and Hicks, D.M. 2001. Airborne remote sensing of clear water, shallow, gravel-bed rivers using digital photogrammetry and image analysis. *Photogrammetric Engineering and Remote Sensing* 67: 1271–1281.

Westaway, R.M., Lane, S.N. and Hicks, D.M. 2003. Remote survey of large-scale braided rivers using digital photogrammetry and image analysis. *International Journal of Remote Sensing* 24: 795–816.

Wheater, H.S. 2002. Progress in and prospects for fluvial flood modeling. *Philosophical transactions of the Royal Society of London: Mathematical physical and engineering sciences* 360 (1796): 1409–1431.

B.4. Hyper-concentrated flows

This page intentionally left blank

River Flow 2004 – Greco, Carravetta & Della Morte (eds.)
© 2004 Taylor & Francis Group, London, ISBN 90 5809 658 0

Morphology of alluvial fans formed by hyperconcentrated tributaries

S.C. Chen & S.H. Peng
Department of Soil and Water Conservation, National Chung-Hsing University, Taiwan

H. Capart
Department of Civil Engineering, National Taiwan University, Taiwan

ABSTRACT: This study uses digital image processing to survey the confluence behavior of a tributary with hyperconcentrated flow entering the main river. The experiment has two parts: in the first, digital terrain data were computed via coordinate transformation from profiles extracted by laserlines; in the second, velocity fields were obtained by using Voronoï imaging method to analyze the images through low-pass and high-pass filters when trace-particles were added. The measurement approach is described and preliminary results are presented. Through the discussion of alluvial fan morphology, we can better understand the interaction of this mechanism.

1 INTRODUCTION

With both heavy rainfall and mountainous terrain of weak geological structure, the island of Taiwan is subject to frequent debris flows. In upland basins, torrential river valleys and steep gullies are subject to both flooding and landslides. This study examines various ways in which flow slides and river currents interact, including blocking of rivers due to either accumulated debris or to the formation of landslide dams across the channel width. In other situations, local narrowing of a channel can occur due to partial invasion by a debris fan. At the outlets of debris flow gullies, thick deposits may be left for water currents to slowly transport downstream.

The confluence behavior of a tributary with hyperconcentrated flow into the main river is a common phenomenon in mountainous regions. When the hyperconcentrated flow tributary enters a main river, a natural dam would be formed by the enormous sediment carried by the tributary. Chen (1999) collects and analyzes numerous kinds of natural dams from the literature and field survey after the Chichi earthquake of September 21, 1999 in Taiwan. In addition, a preliminary classification is established according to the basic concepts of sediment transport (Chen & Peng 2003a). Parker *et al*. (1998a, b) propose a theory and application for alluvial fans and fan-deltas formed by channelized fluvial and sheet flow. Tsai & Shieh (1997) find the morphological similarity of debris-flow fans by laboratory experiments and numerical simulations.

However, previous studies which research the confluence behavior are very limited because it involves numerous factors concerning the confluence mechanism. To study the morphology of an alluvial fan formed by a tributary entering the main river, we did experiments to measure the alluvial fan terrain and confluence velocity field by applying digital image processing. The methods of measurement used in this paper can increase the precision and convenience over previous methods.

2 EXPERIMENTS

2.1 *Experimental device*

The experimental device includes a main channel which is 3.5 m long, 0.2 m wide and 0.15 m high, and a minor branch which is 0.8 m long, 0.1 m wide and 0.25 m high. There is also a gate which can be opened suddenly at the middle of the branch channel to release the mixture of water and sediment as a dam-break type. Besides, in the main channel there are two tanks, one above the upstream end and the other below the downstream end, to construct the circulatory system. To keep the circulatory system working, we used a pump to draw out the water in the downstream tank into the upstream tank which can overflow by controlling two valves to determine discharge of inflow into the main channel and outflow into the downstream tank.

When the hyperconcentrated flow in the branch enters the main channel, it forms an alluvial fan under the water surface of main channel. We measured the morphology of this alluvial fan and the velocity field of confluence to study this mechanism.

The overall experimental process was separated into pre-test and formal-test. The purpose of the pre-test was to determine the physical parameters of experimental materials. Then formal testing was carried out, including several procedures as follows: (1) determine the discharge of main channel in uniform flow; (2) determine the concentration and volume of the hyperconcentrated tributary; (3) calibrate the branch slope and the confluence angle between main channel and branch, when the main channel slope set to zero; (4) release the mixture into the branch and measure the velocity field of confluence; (5) stop the inflow of main channel and survey the topography of the alluvial fan; (6) repeat these steps for different conditions.

2.2 *Methods of measurement*

The experiment included two parts: the first is that the digital terrain data of the alluvial fan was computed using coordinate transformation from profiles extracted by laserlines; the second is that the velocity fields were obtained using Voronoï imaging method to analyze the images via low-pass and high-pass filters when adding the trace-particles. These two methods are illustrated as follows.

2.2.1 *Survey of topography*

The measurement is illustrated in Figure 1. By using a laserline projection above the measured region of the alluvial fan, the profile image was captured via a digital camera set beside the region with an angle of depression. Then the 2D images of various profiles can be transformed into 3D space coordinates, using the method of transformation proposed by Spinewine *et al*. (2003) and illustrated in Figure 2. A transformation is then required to relate the set of 2D image coordinates of any point P to its world coordinates. Define $\mathbf{r}_P = [x_P \; y_P \; z_P]^{\mathrm{T}}$ as the world coordinates of point P (see Fig. 2), and $\mathbf{R}_P^{(A)} = [X_P^{(A)} \; Y_P^{(A)}]^{\mathrm{T}}$ as the 2D image coordinates of point P associated with the camera viewpoint A. The transition from camera to world coordinates generally requires a translation and a rotation (Jähne 2002). Thus for each viewpoint A, one can specify a matrix $[\mathbf{A}^{(A)}]$ and a vector $\mathbf{b}^{(A)}$ such that

$$\alpha \begin{bmatrix} X^{(A)} \\ Y^{(A)} \\ 1 \end{bmatrix} = \left[\mathbf{A}^{(A)}\right] \begin{bmatrix} x \\ y \\ z \end{bmatrix} + \mathbf{b}^{(A)} \tag{1}$$

where α is a scalar parameter; matrix $[\mathbf{A}^{(A)}]$ and vector $\mathbf{b}^{(A)}$ must be calibrated from a set of points for which both the world coordinates and the image coordinates are known (see Spinewine *et al*. 2003, Ni 2004 for details). The overall procedures are shown in Figure 3, and the digital terrain data were obtained from executing them.

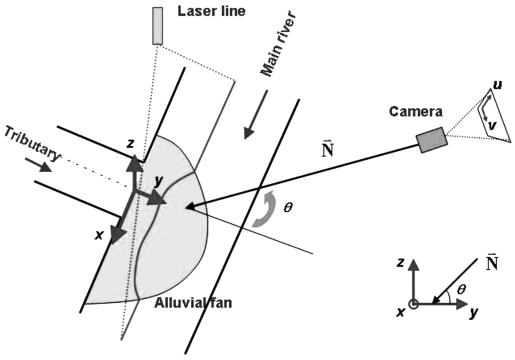


Figure 1. Illustration of the system used to survey topography.

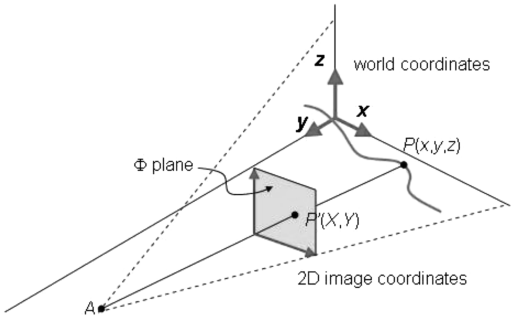


Figure 2. Illustration of coordinate transformation.

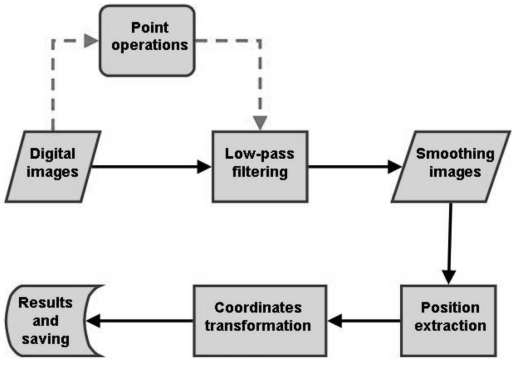


Figure 3. Flow chart of digital image processing.

2.2.2 *Measurement of velocity field*

Consider a 2D velocity field of confluence between the main river and a tributary, which is governed by shallow water equations. If the variation of velocity in vertical direction can be negligible, then the velocity field of water surface will be regarded as the mean velocity field over the flow depth. Therefore the surface velocity field can be measured by

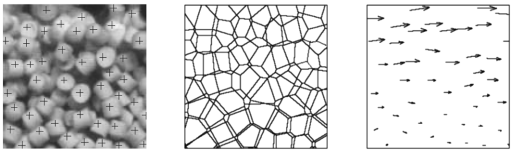


Figure 4. Overview of the Voronoï match algorithm: (left) image of a granular flow abstracted into point-like particles (+); (center) Voronoï diagrams constructed on these points (thin lines) and on the points of the next image of the sequence (thick lines); (right) displacement vectors (true scale) obtained by matching the Voronoï 1-stars (Capart *et al*. 2002).



Figure 5a. Photo of alluvial fan at the sample site.

using the Voronoï imaging method after adding the trace particles. The Voronoï imaging method was basically developed for the measurement of granular flows (Capart *et al*. 2002). Its principle is to first extract the point-like particle positions of discrete digital images, secondly to construct the Voronoï diagrams for these points at two successive time instants, and finally to compute the velocity vectors by matching the local Voronoï patterns (Fig. 4). Generally, the surface velocity fields can be effectively captured by a digital video camera if they do not have especially large velocities (Chen & Peng 2003b).

2.3 *Experimental materials and conditions*

The experimental materials were sampled from the alluvial fan located on the Cho-Shui River close to 24k + 500 of Highway 16 in Taiwan (Fig. 5a) and the particle size distribution diagram of materials is sketched as Figure 5b. Based on these materials, we designed a series of experiments to study the confluence mechanism between a main channel and its tributary. The factors of influencing confluence are generally considered to be the angle of confluence, the ratio of discharge between main channel and tributary, the slopes of main channel and tributary, and

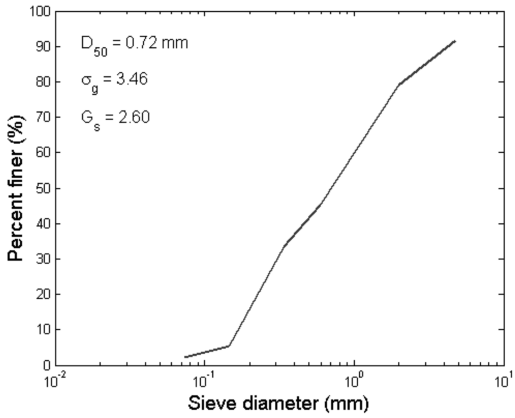


Figure 5b. Distribution of particle size.

Table 1. Experimental conditions.

	Main channel		Branch	
Confluence angle (degree)	Discharge (cms) $\times 10^{-4}$	Flow depth[a] (cm)	Density of mixture[b] (g/cm^3)	Slope[c] (%)
45	0.66 1.99 4.35	3.8 4.1 4.3	1.6 and 1.9	10, 20, and 30
90	0.66 1.99 4.35	3.8 4.1 4.3	1.6 and 1.9	10, 20, and 30
135	0.66 1.99 4.35	3.8 4.1 4.3	1.6 and 1.9	10, 20, and 30

[a] Used sill downstream to raise the water surface to easily make the alluvial fan.
[b] The total volume of mixture was 4200 cm^3 in each case.
[c] The main channel slope was zero.

the sediment concentration of the tributary, etc. (Zhu *et al*. 2000, Chen 2000, Kao 2003). The experimental conditions are shown in Table 1.

3 RESULTS

We carried out numerous tests based on these experimental methods and obtained the following results. The results include 54 sets of digital terrain data for the alluvial fan and 30 sets of velocity field of confluence.

3.1 *Morphology of alluvial fan*

An example of the results is shown as Figure 6. From these results of digital terrain data, we calculated the

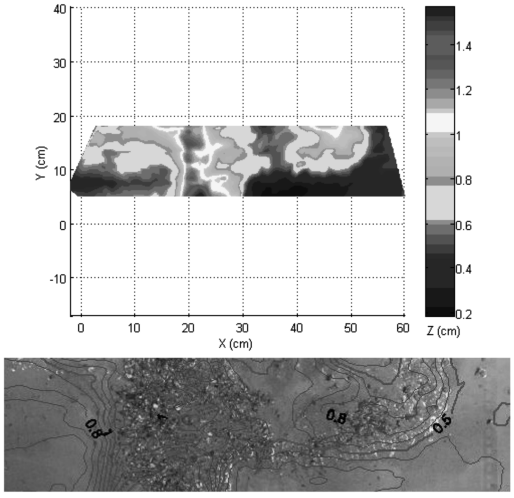


Figure 6. Measurement results in the terrain (where confluence angle is 90 degrees, discharge of main channel is 0.66×10^{-4} cms, density of mixture is 1.9 g/cm^3, and slope of branch is 10%): (top) digital terrain data of survey; (bottom) comparison between measurement and actual terrain.

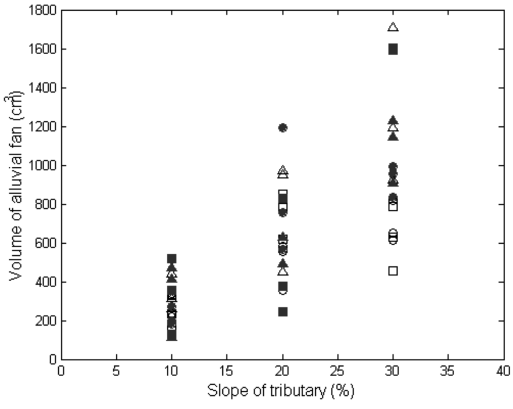


Figure 7. Relation between volume of alluvial fan and slope of tributary (▲: confluence angle = 45 degrees; ■: confluence angle = 90 degrees; ●: confluence angle = 135 degrees; solid and hollow symbols represent density of mixture 1.9 g/cm^3 and 1.6 g/cm^3, respectively).

residual volume of alluvial fan in the main channel and found the relation between volume and slope of tributary (Fig. 7). Figure 7 indicates that the volume of alluvial fan could not be affected apparently by confluence angle and density of mixture; it is predominated by the slope of tributary. Meanwhile, a high density of the mixture in the tributary also increases the residual volume in main channel when the slope of tributary is 30%. We suggest that the amount of alluvial fan carried by tributary could be determined by gravity force

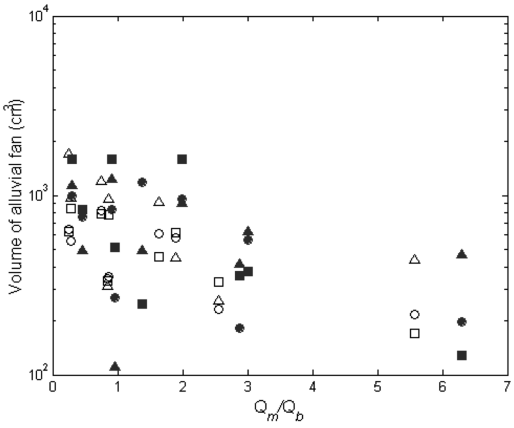


Figure 8. Relation between volume of alluvial fan and ratio of discharge (Q_m: discharge of main channel; Q_b: discharge of tributary; the others are the same as Figure 7).

induced by the branch slope and the tributary density if the flow intensity of the main channel is neglected.

To realize the effect of main channel flow, we compared the volume of alluvial fan with the ratio of discharge between main channel and tributary (Fig. 8). Figure 8 shows that large ratio of discharge between main channel and tributary (Q_m/Q_b) can decrease the volume of alluvial fan because a portion of the alluvial fan sediment may be carried away by the main channel flow. From Figure 7 and Figure 8, it can be seen that the angle of confluence and sediment concentration of tributary do not markedly relate to the volume of alluvial fan. In fact, the concentration of tributary is one of factors which cause the gravity force to drive the tributary ahead, and the angle of confluence may affect the shape of alluvial fan in our experiment (see Sec. 4.1 for details).

3.2 *Results of velocity field*

Figure 9 indicates an example of the results from measuring the velocity field by the Voronoï imaging method. In this case, the velocity field is initially very disordered because the tributary shoots rapidly across the main channel to reach the opposite bank. About 1 sec later, two vortices form on both sides gradually; at $t = 1.2$ sec or so, the vortices fully develop and hold their shapes till about $t = 2.0$ sec; they then start to move downstream after $t = 2.0$ sec; until $t = 2.8$ sec or so, the vortices begin to disperse gradually (Fig. 9). The results of velocity field can be regarded as references for the numerical modeling in the future.

To study the velocity vibration in the x-direction at confluence ($x = 23.5$ cm), we took the x-component of the velocity (u) at different y-positions (y) and divided it by the mean velocity of the main channel (U_0) and

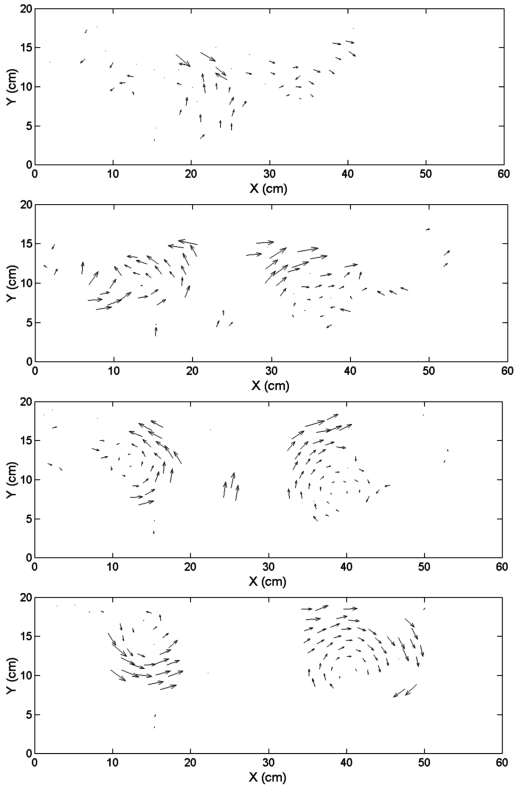


Figure 9. Results of measurement in the velocity field (e.g. confluence angle is 90 degrees, discharge of main channel is 0.66×10^{-4} cms, density of mixture is 1.9 g/cm^3, and slope of branch is 30%): (top) $t = 0.5$ sec; (second from the top) $t = 1.0$ sec; (second from the bottom) $t = 1.2$ sec; (bottom) $t = 2.0$ sec.

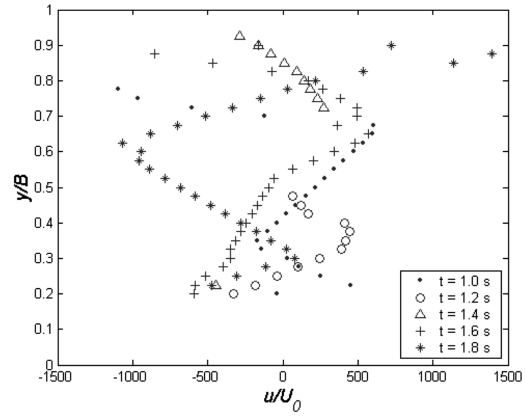


Figure 10a. Relation between u/U_0 and y/B at $x = 23.5$ cm (confluence) when $t = 1.0$, 1.2, 1.4, 1.6 and 1.8 sec (other conditions are the same as Figure 9).

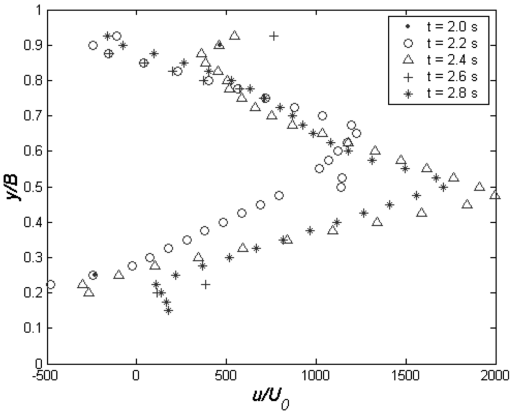


Figure 10b. Relation between u/U_0 and y/B at $x = 23.5$ cm (confluence) when $t = 2.0$, 2.2, 2.4, 2.6 and 2.8 sec (other conditions are the same as Figure 9).

the width of the main channel (B), respectively, for a dimensionless value (Figs. 10a, b). In Figure 10a, the velocity profiles are unstable with different time instants due to the vortices during $t = 1.0 \sim 1.8$ sec intervals. In contrast, the dimensionless profiles of the x-component velocity maintain a similar profile during $t = 2.0 \sim 2.8$ sec intervals because the vortices are affected by main channel flow to move downstream and then to finally disperse. In sum, the velocity field usually determines the motion of sediment, which affects the alluvial fan morphology. In next section, we discuss the morphological details of alluvial fans.

4 DISCUSSION

4.1 *Centroids of alluvial fans*

The volume of alluvial fan is defined by the following integral:

$$V = \iint z(x, y)\,dxdy \tag{2}$$

Thus, the coordinates X_{CG} and Y_{CG} of the centroid of alluvial fan are equal to the first moments divided by the volume:

$$X_{CG} = \frac{\iint xz(x, y)\,dxdy}{V} \tag{3}$$

$$Y_{CG} = \frac{\iint yz(x, y)\,dxdy}{V} \tag{4}$$

Assume that the centroids of alluvial fans can represent their location. To realize the effect of confluence angle,

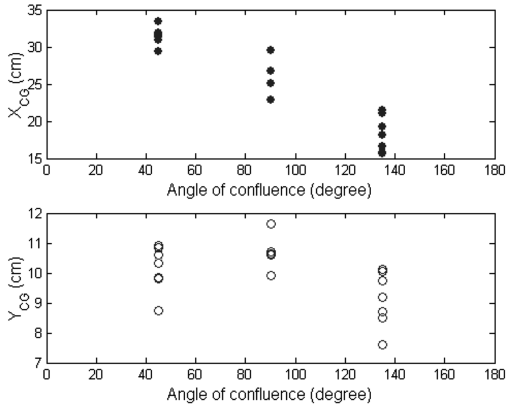


Figure 11. Relation between the centroids of alluvial fans and angles of confluence: (top) when the angle of confluence is larger, the tributary encounters stronger resistance and X_{CG} decreases; (bottom) Y_{CG} is similar to X_{CG}, but Y_{CG} is larger than the others when the angle of confluence is 90 degrees.

we calculated the centroids of 19 alluvial fans which have more complete shapes with different angles of confluence (Fig. 11). Figure 11 shows that the confluence angle could primarily determine the alluvial fan location. In addition, the "erosion angle" can be also defined by the alluvial fan centroid. If the longitudinal center line of the tributary, called the "axis line", is extended to the wall of main channel, the line from the confluence point ($x = 23.5$, $y = 0$) to the centroid and axis line forms the erosion angle. Previous research indicates that a positive relation exists between erosion angle and discharge ratio (Q_m/Q_b) (Chen 2000). Our experiments show the similar results, although their relation is not significant.

4.2 *Shapes of alluvial fan*

We extracted the longitudinal profile and cross-section at the alluvial fan centroid (Fig. 12) to analyze shape characteristics of alluvial fans. In these profiles of alluvial fans, the shapes are markedly affected by confluence angle. For example, the peak of the longitudinal profile deflects downstream when the confluence angle is 45 degrees (Fig. 12a). In contrast, the peak of the longitudinal profile deflects upstream when the confluence angle is 135 degrees (Fig. 12c). Furthermore, when the confluence angle is 90 degrees, the shape of the longitudinal profile is shaped like a hat, and the cross-section (Fig. 12b) seems to have two peaks. The reason that there are two peaks might be that the tributary shoots directly to hit the opposite wall of the main channel and to deposit the sediment on the bed.

The alluvial fan contours in different confluence angles are illustrated in Figure 13 as an example.

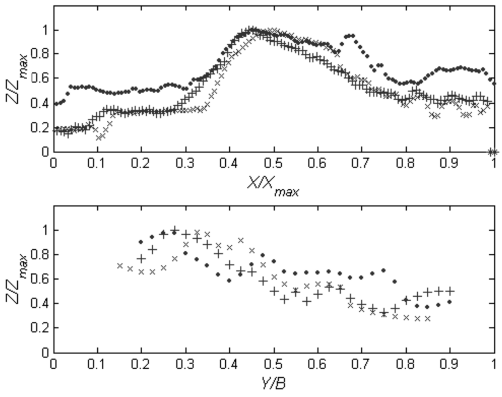


Figure 12a. Extracted profiles at alluvial fan centroid (X_{CG}, Y_{CG}) for confluence angle 45 degrees: (top) longitudinal profile; (bottom) cross-section profile (•: slope of branch = 20%, $Q_m = 0.66 \times 10^{-4}$ cms; +: slope of branch = 20%, $Q_m = 1.99 \times 10^{-4}$ cms; ×: slope of branch = 30%, $Q_m = 4.35 \times 10^{-4}$ cms; density of mixture is 1.9 g/cm^3).

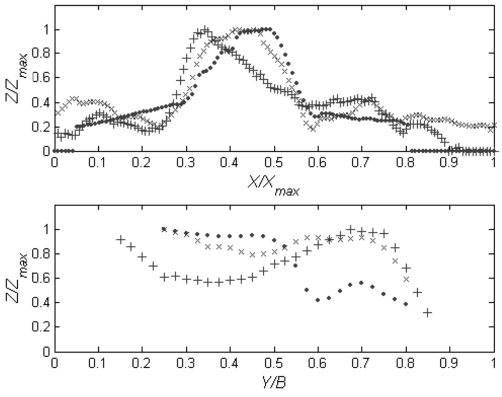


Figure 12b. Extracted profiles at alluvial fan centroid (X_{CG}, Y_{CG}) for confluence angle 90 degrees: (top) longitudinal profile; (bottom) cross-section profile (•: slope of branch = 20%, $Q_m = 1.99 \times 10^{-4}$ cms; +: slope of branch = 30%, $Q_m = 0.66 \times 10^{-4}$ cms; ×: slope of branch = 30%, $Q_m = 1.99 \times 10^{-4}$ cms; density of mixture is 1.6 g/cm^3).

According to these contours, the outlines of alluvial fans in different confluence angles are simplified and summarized as Figure 14. The types of alluvial fan in Figure 14 are similar to the classification, i.e. partial blocks to the main river (Chen & Peng 2003a, Chen 2000). The results of this laboratory experiment can be used for preliminary assistance for numerical simulation. Using either laboratory experiment or numerical simulation, the mechanism of confluence between the tributary and main river can be clarified.

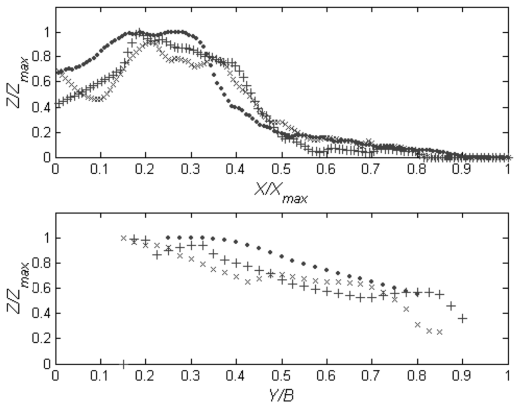


Figure 12c. Extracted profiles at alluvial fan centroid (X_{CG}, Y_{CG}) for confluence angle 135 degrees: (top) longitudinal profile; (bottom) cross-section profile (•: slope of branch = 30%, $Q_m = 0.66 \times 10^{-4}$ cms; +: slope of branch = 30%, $Q_m = 1.99 \times 10^{-4}$ cms; ×: slope of branch = 30%, $Q_m = 4.35 \times 10^{-4}$ cms; density of mixture is 1.9 g/cm^3).

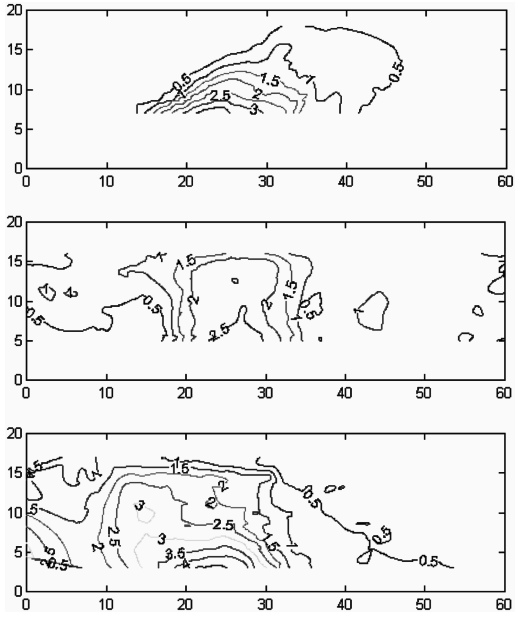


Figure 13. Contour examples of alluvial fans: (top) confluence angle = 45 degrees; (center) confluence angle = 90 degrees; (bottom) confluence angle = 135 degrees.

5 CONCLUSIONS

As stated in the introduction, the major contribution of this study is the measurement of morphological information on the alluvial fan and the velocity field of confluence between tributary and main flow. We used digital image processing, including topography survey and Voronoï imaging method, to obtain the experimental results. The results show that the methods of measurement in this paper can capture the information precisely and conveniently. From our experiment, the measurement approach is effective and worth advanced research. Besides, through the discussion of alluvial fan morphology, the qualitative descriptions are interpreted for alluvial fan shape, alluvial fan volume, and sediment transportation. However quantitative analysis and further study are still needed.

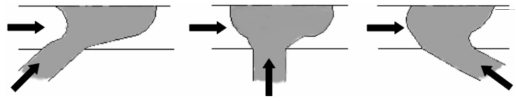


Figure 14. Summary of alluvial fan types: (left) confluence angle of 45 degrees; (center) confluence angle of 90 degrees; (right) confluence angle of 135 degrees.

REFERENCES

Capart, H., Young, D.L. & Zech, Y. 2002. Voronoï imaging methods for the measurement of granular flows. *Experiments in Fluids* 32: 121–135.

Chen, D.M. 2000. *Mechanism of confluence between debris flow and the main river*. Ph.D. thesis, China Inst. of Water Resources and Hydropower Research, China (in Chinese).

Chen, S.C. & Peng, S.H. 2003a. Confluence of debris slides and river flows in Taiwan. In C.F. Lee & L.G. Tham (eds), *Proceedings of the International Conference on Slope Engineering*: 757–762. Hongkong: University of Hong Kong.

Chen, S.C. & Peng, S.H. 2003b. Experiment of confluence between main river and tributary by applying digital image processing. *J. Chin. Soil Water Conserv.* 34(2): 195–205 (in Chinese).

Chen, S.C. 1999. Failure mechanism and disaster mitigation on landslide-dammed lakes. *J. Chin. Soil Water Conserv.* 30(4): 299–311 (in Chinese).

Jähne, B. 2002. *Digital Image Processing*. Berlin: Springer.

Kao, P.S. 2003. *The effects in main river morphology from hyperconcentrated tributary flow*. MSc thesis, National Chung-Hsing University, Taiwan (in Chinese).

Ni, W.J. 2004. MSc thesis, Dept. of Civil Engineering and Hydrotech Research Institute, National Taiwan University, Taiwan (in preparation).

Parker, G. *et al*. 1998a. Alluvial fans formed by channelized fluvial and sheet flow. I: theory. *J. of Hydraulic Engineering* ASCE 124(10): 985–995.

Parker, G. *et al*. 1998b. Alluvial fans formed by channelized fluvial and sheet flow. II: application. *J. of Hydraulic Engineering* ASCE 124(10): 996–1004.

Spinewine, B., Capart, H., Larcher, M. & Zech, Y. 2003. Three-dimensional Voronoï imaging methods for the measurement of near-wall particulate flows. *Experiments in Fluids* 34: 227–241.

Tsai, Y.F. & Shieh, C.L. 1997. Experimental and numerical studies on the morphological similarity of debris-flow fans. *Journal of the Chinese Institute of Engineers* 20(6): 629–642.

Zhu, P.Y., Cheng, Z.L. & You, Y. 2000. Research on causes of river blocking by sediment delivery of Peilonggou Gully debris flow in the Sichuan-Xizang Highway. *Journal of Natural Disasters* 9(1): 80–83 (in Chinese).

River Flow 2004 – Greco, Carravetta & Della Morte (eds.)
© 2004 Taylor & Francis Group, London, ISBN 90 5809 658 0

Transient hyper-concentrated flows: limits of some hypotheses in mathematical modelling

D. Berzi & E. Larcan
Politecnico di Milano, Dept. I.I.A.R., Milan, Italy

ABSTRACT: A one-dimensional mathematical finite-difference model used for simulation of unsteady hyper-concentrated flow is described. This model is based on the Saint Venant equations, integrated via the MacCormack method. Two mass balance equations and one momentum equation are used, thus, the model can be seen as a quasi-two phase model. In the momentum equation the resistance term is derived from a semi-empirical formulation of shear stress in a generalized visco-plastic fluid (Chen 1996). Bed erosion and deposition effects are also included and numerical results are experimentally verified for high concentration flows in mild slope channel. Though the assumed hypothesis largely simplify the mathematical model, the validity of the model is confirmed, with particular attention on the role of the yield stress. A good agreement between numerical and experimental results is found, but, when the solid concentration is high and the densities of the two phases are significantly different, a quasi-two phase model seems to be unable to simulate the phenomenon. Considerations about the limits of the mathematical approach and the opportunity of more complicated models are underlined.

1 INTRODUCTION

The behaviour of a granular debris flow (flow of rigid spheres in an interstitial fluid) can be analysed through either a microscopic or a macroscopic approach. The former involves statistical mechanics, in particular the kinetic theory (Savage 1984, 1989, Jenkins 1987); the latter considers debris flow as a continuum, such as in classical fluid mechanics (McTigue 1982, Chen 1986, 1988). Anyhow, the aim of this paper is to find the constitutive equations of the liquid–solid mixture and define the relation between the resistance terms and the kinematic quantities.

This paper concerns with the mathematical simulation of debris flows due to dam-break. Shear stresses in the mathematical model are approximated following the continuum mechanics approach. The use of formulas of uniform flow for a typical unsteady phenomenon represents another approximation. Nevertheless, a simple model with an empirical approach, such as the mathematical model presented herein, is preferred for practical design purposes. Thus, it seems very important to verify the rightness and the limits of the approximations introduced; hence, numerical results obtained with the model are compared with experimental data. These comparisons are used to define the validity range of the mathematical model, to find the limits imposed by the simplifying hypotheses and to suggest the research guidelines for its improvement.

2 EXPERIMENTAL SET-UP

The parameters of the mathematical model (Section 3) have to be set experimentally; therefore, experimental work has been carried out on a laboratory rig with a 6 m long, square section (0.5×0.5 m) flume of adjustable slope also for the validation of the results obtained with mathematical model. Failure of the dam can be simulated by means of a pneumatic rising sluice-gate (opening time $t = 0.3$ s). Debris flow is modeled by a water–solid mixture, the solid phase is reproduced with either common gravel ($\rho = 2621\ \mathrm{kg/m^3}$, $d_{50} = 0.005$ m) or a plastic homogeneous granular material called "vedril" ($\rho = 1168\ \mathrm{kg/m^3}$, $d_{50} = 0.003$). Tests are performed for several solid concentrations, and different channel characteristics: slope (3.2°, 5°, 10°, 15° and 20°) and bottom roughness (zinc coated plate or fixed homogeneous gravel $d_{50} = 0.005$ m). A complete list of experimental runs is reported by Bertalli et al. (2002).

Sorting phenomenon are not taken into account because of the use of homogeneous solid material in the mixture. This fact appears to be very important in the dynamics of debris flows, yet too complicated to be implemented.

3 MATHEMATICAL MODEL

Usually models of dam-break waves are based on one-dimensional and two-dimensional schemes, while three-dimensional models are extremely rare. Some of these models consider the liquid–solid mixture as a single phase liquid, while others, more complicated, take into account both liquid and solid phases. Some of the later suppose that solid and fluid are characterized by the same average velocity and introduce only changes in solid concentration, caused by the erosion/deposition rate; other models involve also two different momentum equations, one for each of the two phases, defining, in a some way, the missing interaction component that closes the problem.

Herein the one-dimensional approach to the problem, which is the simplest one (Takahashi 1991, Egashira et al. 1997, Ghilardi et al. 1999, Berzi & Mambretti 2003), is used. The mathematical model presented is a quasi-two phase model that simulates the erosion/deposition phenomenon and uses a single momentum equation. Even if the phenomenon is typically impulsive, modeling is performed by numerical integration of the well-known Saint Venant equations through a scheme relying on shock-capturing functions.

The equations can be written in matrix notation:

$$\frac{\partial \mathrm{U}}{\partial t} + \frac{\partial \mathrm{F}}{\partial x} = \mathrm{S} \tag{1a}$$

where:

$$\mathrm{U} = \begin{pmatrix} A \\ \rho_M Q \\ cA \\ A_d \end{pmatrix} \qquad \mathrm{F} = \begin{pmatrix} Q \\ \rho_M \dfrac{Q^2}{A} + \rho_M g I_1 \\ cQ \\ 0 \end{pmatrix}$$

$$\mathrm{S} = \begin{pmatrix} \dfrac{EL}{c^*} \\ \rho_M g A(i - J) + \rho_M g I_2 \\ EL \\ -\dfrac{EL}{c^*} \end{pmatrix} \tag{1b}$$

and x is the coordinate along the bottom of the flume; t is time; g is the gravitational acceleration; i is the channel slope; J is the resistance term; A is the cross-section area of the flow; Q is the flow-rate; ρ_M is the mixture density; c is the solid concentration in the mixture; c^* is the solid concentration at the bed; E is the erosion/deposition rate; L stands for the channel width at the interface between the flow and the movable bed layer; A_d is the cross-section area of the movable bed layer.

Here,

$$I_1 = \int_0^h (h - \eta)\sigma(x, \eta)\, d\eta \qquad I_2 = \int_0^h (h - \eta)\frac{\partial \sigma}{\partial x}\, d\eta \tag{2}$$

where h represents the water depth, while $\sigma(x, \eta)$ represents the channel width at the depth η. Equations 1a, and 1b represent the mass and momentum conservation laws in the solid–liquid mixture, the mass conservation of the solid phase and the mass conservation of the solid–liquid mixture in the movable bed layer. In these equations pressure distribution is considered hydrostatic, even if the presence of solid material should change the normal stress expression (Bagnold 1954, Chen 1996).

Equations 1a and 1b are integrated via a second-order precision finite-difference method (MacCormack & Baldwin 1975).

The numerical scheme can be written as follows:

$$\begin{aligned} \mathrm{U}_i^p &= \mathrm{U}_i^n - \frac{\Delta t}{\Delta x}\left[(1-\theta)\mathrm{F}_{i+1}^n - (1-2\theta)\mathrm{F}_i^n - \theta \mathrm{F}_{i-1}^n\right] + \Delta t \mathrm{S}_i^n \\ \mathrm{U}_i^c &= \mathrm{U}_i^n - \frac{\Delta t}{\Delta x}\left[\theta \mathrm{F}_{i+1}^p + (1-2\theta)\mathrm{F}_i^p + (\theta - 1)\mathrm{F}_{i-1}^p\right] + \Delta t \mathrm{S}_i^p \\ \mathrm{U}_i^{n+1} &= \frac{1}{2}\left(\mathrm{U}_i^p + \mathrm{U}_i^c\right), \\ \theta &= 0,\ 1 \end{aligned} \tag{3}$$

where subscripts p and c are predictor and corrector steps respectively and n and i are the space-time step indices. In order to make computations more stable, $\theta = 1$ as it is verified for hyper-concentrated fluids (Berzi & Mambretti 2003).

Like all finite-difference schemes with second order precision, MacCormack scheme is characterized by large oscillations when the flow becomes supercritical and in presence of singularity points. In order to reduce these effects and remove non-physical shocks due to numerical integration, artificial terms simulating viscosity effects are introduced. These terms become negligible when numerical solution are stable. MacCormack scheme written with the introduction of artificial viscosity terms gives:

$$\begin{aligned} \mathrm{U}_i^p &= \mathrm{U}_i^n - \frac{\Delta t}{\Delta x}\left[(1-\theta)\mathrm{F}_{i+1}^n - (1-2\theta)\mathrm{F}_i^n - \theta \mathrm{F}_{i-1}^n\right] + \Delta t \mathrm{S}_i^n \\ \mathrm{U}_i^c &= \mathrm{U}_i^n - \frac{\Delta t}{\Delta x}\left[\theta \mathrm{F}_{i+1}^p + (1-2\theta)\mathrm{F}_i^p + (\theta - 1)\mathrm{F}_{i-1}^p\right] + \Delta t \mathrm{S}_i^p \\ \mathrm{U}_i^{n+1} &= \frac{1}{2}\left(\mathrm{U}_i^p + \mathrm{U}_i^c\right) + \frac{\Delta t}{\Delta x}\left(\zeta_{i+1/2}^n + \zeta_{i-1/2}^n\right) \\ \theta &= 0,\ 1 \end{aligned} \tag{4}$$

Jameson (1982) expression is used for evaluating parameter ζ:

$$\begin{aligned} \zeta_{i+1/2} &= \varepsilon_{i+1/2}^{(2)}\left(U_{i+1} - U_i\right) + \\ &- \varepsilon_{i+1/2}^{(4)}\left(U_{i+2} - 3U_{i+1} + 3U_i - U_{i-1}\right) \end{aligned} \tag{5}$$

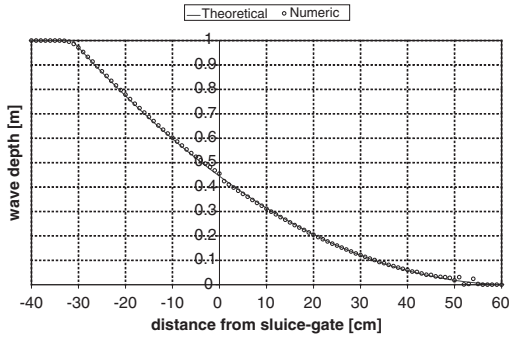


Figure 1. Comparison between Ritter analytical and numerical solution of dam-break wave (10 s after dam-break).

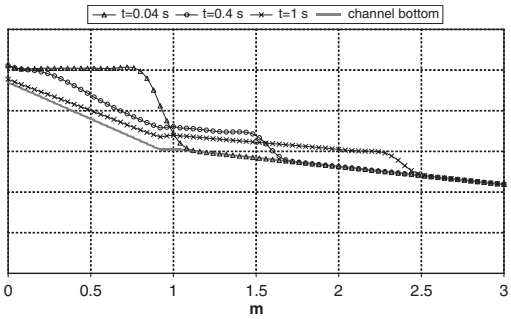


Figure 2. Wave at different times along the channel.

where:

$$\varepsilon_{i+1/2}^{(2)} = \max\left(\varepsilon_i^{(2)}, \varepsilon_{i+1}^{(2)}\right)$$
$$\varepsilon_i^{(2)} = \alpha^{(2)} \frac{\left|h_{i+1} - 2h_i + h_{i-1}\right|}{h_{i+1} + 2h_i + h_{i-1}} \quad (6)$$
$$\varepsilon_{i+1/2}^{(4)} = \max\left(0, \alpha^{(4)} - \varepsilon_{i+1/2}^{(2)}\right)$$

When clear water is considered in dam-break problems, (Aureli et al. 1998 and references therein) one should set $\alpha^{(2)} = 0.5$ and $\alpha^{(4)} = 0.02$. In the case of debris flows the best values are different (see Section 4).

The model has been tested for clear-water dam-break (using $c = 0$, $E = 0$ and the Chézy formula for the resistance term J). Figure 1 shows the good agreement between numerical results and Ritter (1892) analytical solution. The global balance of mass seems to be verified too as it is shown in Figure 2.

When debris flow is considered, terms J and E ought to be described for making possible the integration of the equation system 1a, 1b. If the flow regime is laminar, the resistance term J can be derived from rheology, otherwise some empirical laws have to be considered.

Some expressions based on Bagnold (1954) shear stress and on a Chézy-like formula have been formerly tested (Berzi & Mambretti 2003).

Here, Chen (1996) rheological equation for a simple-shear granular flow is used:

$$\tau = s + \mu_1 \left(\frac{du}{dz}\right)^{\eta_1} \quad (7)$$

where z is the coordinate normal to the flume bottom; u is the local velocity in x-direction; s is the yield stress equal to $p \sin\phi$; ϕ is the static friction angle and p the pressure. Equation 7 is valid for an incompressible Stokesian fluid; thus, the solid phase density and the interstitial liquid density should be the same. This denotes a clear limit of the model. Anyhow, if $\eta_1 = 1$, Equation 7 becomes the expression of a Bingham fluid in a macroviscous regime and if $\eta_1 = 2$ turns into the expression of a dilatant fluid in grain-inertia regime. Hereafter parameters η_1 and μ_1 are defined. For uniform flow in a wide open channel, the relation between the shear stress $\tau(z)$ and the resistance term J is:

$$\tau = \gamma(h - z)J \quad (8)$$

where γ is the specific weight of the mixture. From Equations 7, 8, under the hypothesis of hydrostatic pressure distribution, one can write:

$$\begin{cases} du = \left(\dfrac{\gamma(h-z)(J - \sin\phi)}{\mu_1}\right)^{\frac{1}{\eta_1}} dz & J > \sin\phi \\ du = 0 & J \le \sin\phi \end{cases} \quad (9)$$

The transverse velocity distribution can be obtained by integration of Equations 9:

$$\begin{cases} u(z) = -\dfrac{\mu_1\eta_1}{\gamma(J - \sin\phi)(\eta_1 + 1)}\left(\dfrac{\gamma(h-z)(J-\sin\phi)}{\mu_1}\right)^{\frac{\eta_1+1}{\eta_1}} + C \\ u(z) = 0 \end{cases} \quad (10)$$

where the first of Equations 10 is valid for $J > \sin\phi$, while the second for $J \le \sin\phi$. The constant C can be evaluated with the no slip condition. Thus, when $z = 0$, $u(z) = 0$:

$$C = \frac{\mu_1\eta_1}{\gamma(J - \sin\phi)(\eta_1 + 1)}\left(\frac{\gamma h(J - \sin\phi)}{\mu_1}\right)^{\frac{\eta_1+1}{\eta_1}} \quad (11)$$

Finally:

$$\begin{cases} u(z) = \dfrac{1}{ab}\left((ah)^b - (a(h-z))^b\right) & J > \sin\phi \\ u(z) = 0 & J \le \sin\phi \end{cases} \tag{12}$$

where:

$$\begin{aligned} a &= \frac{\gamma(J - \sin\phi)}{\mu_1} \\ b &= \frac{\eta_1 + 1}{\eta_1} \end{aligned} \tag{13}$$

The flow-rate Q is:

$$Q = VA = \int_A u dA \tag{14}$$

where V is the average velocity. Substituting Equation 12 in Equation 14 and dividing by the channel width L:

$$Vh = \int_0^h \frac{1}{ab}\left((ah)^b - (a(h-z))^b\right)dz$$

$$Vh = \frac{h}{ab}(ah)^b - \frac{1}{ab}\left(-\frac{(a(h-h))^{b+1}}{a(b+1)} + \frac{(ah)^{b+1}}{a(b+1)}\right)$$

$$a^{b-1} = V\frac{(b+1)}{h^b}$$

so that:

$$a = \left((b+1)\frac{V}{h^b}\right)^{\frac{1}{b-1}} \tag{15}$$

Now, introducing Equations 13 in Equation 15, the expression of the resistance term J results:

$$J = \frac{\mu_1}{\gamma}\left(\frac{2\eta_1 + 1}{\eta_1}\right)^{\eta_1}\frac{V^{\eta_1}}{h^{\eta_1+1}} + \sin\phi \tag{16}$$

For a Newtonian fluid ($\mu_1 = \mu, \eta_1 = 1, \phi = 0$), Equation 16 exactly represents the resistance term in laminar flow in an indefinite plain:

$$J = 3\frac{\mu}{\gamma}\frac{V}{h^2} \tag{17}$$

Equation 16 is valid if turbulent stresses in the interstitial fluid are supposed negligible. Otherwise, when the flow regime is grain-inertial, another empirical term has to be added as suggested by Bagnold (1954).

Concerning μ_1, Chen (1986, 1988) provides the following formula:

$$\mu_1 = \alpha_1 \rho_s^{\eta_1 - 1} d^{2(\eta_1 - 1)} \mu^{2-\eta_1} \mu_*(c) \tag{18}$$

where the parameter α_1 is a function of the solid material characteristics; ρ_s is the solid density; d is a characteristic diameter of solid material; μ is the viscosity of the interstitial fluid; μ_* is the relative viscosity of the granular suspension, function of the solid concentration c (Krieger & Dougherty 1959):

$$\mu_*(c) = (1 - Kc)^{-\frac{B}{K}} \tag{19}$$

with $K = 1/c_m$; c_m is the solid maximum concentration and B the intrinsic viscosity, equal to 2.5 for a suspension of very lightly-concentrated rigid uniform spheres but higher for a suspension of heavily-concentrated spheres, in particular if the channel bottom is rough. If turbulent stresses in the interstitial fluid are neglected, only this parameter takes into account the influence on the wave profile of the bottom roughness. This effect is experimentally verified as shown in Figure 3. In this Figure dam-break waves of a hyper-concentrated fluid on smooth and rough bed bottom are depicted. Both tests are performed with a water-gravel mixture ($c = 0.2$) and a channel slope $i = 20°$; wave depth refers to a section placed 1.0 m downstream from the sluice-gate.

Coefficient η_1 (Chen 1996) depends on the shear rate number N, similar to Bagnold number, ratio of the inertial stresses due to the particle collisions and the viscous stresses in the interstitial fluid. N can be expressed as (Chen 1986):

$$N = \frac{\rho_s d^2 D}{\mu} \tag{20}$$

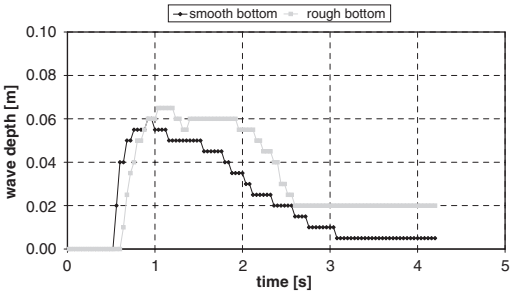


Figure 3. Influence of the bottom roughness on dam-break waves.

where $D = du/dz$. For $N \to 0$ $\eta_1 = 1$ (macroviscous regime), for $N \to \infty$ $\eta_1 = 2$ (grain-inertia regime). Between these two asymptotic regimes, η_1 assumes intermediate values. On the basis of the tests performed by Bagnold (1954) and Savage and McKeown (1983), Chen (1996) obtained the values of η_1 shown in Figure 4.

Figure 4 shows also the interpolating relation between η_1 and N used in this paper.

A similar relation between α_1 and N doesn't exist because α_1 depends on some material constants, such as a coefficient of restitution.

The experimental tests demonstrate an important solid material exchange between the debris flow wave and the movable bed. Hence, it seems essential to introduce the erosion/deposition rate as a function of some relevant quantities.

Erosion/deposition rate E, defined by Honda & Egashira (1997) and modified by Ghilardi et al. (1999), is here used:

$$\frac{E}{V} = K_E \cdot \tan\left(\vartheta_f - \vartheta_e\right) \tag{21}$$

where:

$$\vartheta_f = \tan^{-1}\left(\frac{J}{\cos i_b}\right) \tag{22}$$

where i_b is the bed slope. θ_e is the equilibrium bed slope. In uniform flow condition θ_e is (Takahashi 1991):

$$\tan \vartheta_e = \frac{\left(\frac{\rho_s}{\rho_l} - 1\right) \cdot c}{\left(\frac{\rho_s}{\rho_l} - 1\right) \cdot c + 1} \tan \phi \tag{23}$$

where ρ_l is interstitial fluid density. In Equation 21 the coefficient K_E is introduced in order to obtain the best fitting with experimental results.

4 MODEL SETTING

The mathematical model includes some parameters whose values have to be set. Some of these parameters are introduced in order to reduce the oscillations in the numerical solution due to non-physical shocks. Others are used to calibrate the model and their values can be defined only on the basis of field measurements and best fitting analysis. The latter has been performed by the comparisons between numerical and experimental results of six tests, taken as representative of the whole phenomenon, with different values of channel bed slope, solid concentration, solid material and bottom roughness.

The value of the parameter c^* is chosen by measuring the solid concentration in the deposited material: for the gravel $c^* = 0.49$ and for the vedril $c^* = 0.54$.

The static friction angle ϕ is equal to 0.5233 rad for gravel and to 0.4815 rad for vedril. The mathematical model provides good results when the solid concentration is low-medium ($c = 0.2$–0.4), without considering the yield stress. The yield stress has to be introduced, when the solid concentration is higher ($c = 0.6$). This fact influences the value of the artificial viscosity term parameters $\alpha^{(2)}$ and $\alpha^{(4)}$. Best results are obtained setting $\alpha^{(2)} = 1$ and $\alpha^{(4)} = 4$ when the yield stress is neglected, while $\alpha^{(2)} = 5$ and $\alpha^{(4)} = 2$ are to be considered if the yield stress is introduced. Figure 5 shows several wave profiles for different values of the parameter $\alpha^{(2)}$.

The relation between η_1 and the shear-rate number N is described in the previous Section. Assuming a triangular velocity distribution along the z-direction, Equation 21 becomes:

$$N = \left(\frac{\rho_s}{\rho_l}\right)\left(\frac{d}{h}\right)^2\left(\frac{2Vh\rho_l}{\mu}\right) \tag{24}$$

α_1 is always positive and less than 2 (Chen 1996) but its value depends on the type of the solid material. Since a sensitivity analysis shows that the numerical solution

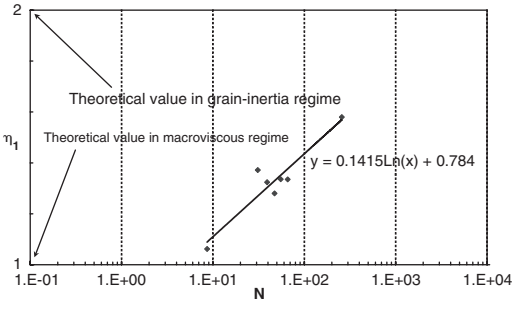


Figure 4. Relation between shear rate number N and coefficient η_1.

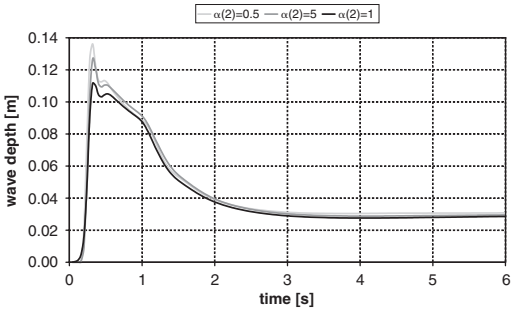


Figure 5. Wave depth versus time in a section at 0.4 m from the sluice-gate with different values of $\alpha^{(2)}$.

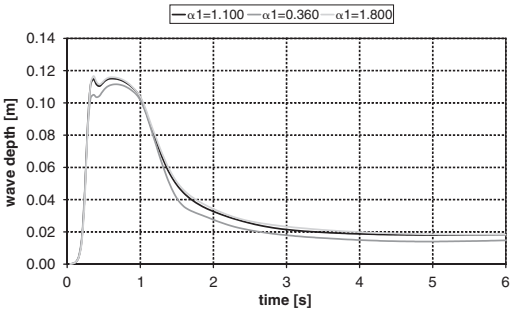


Figure 6. Wave depth versus time in a section at 0.4 m from the sluice-gate with different values of α_1.

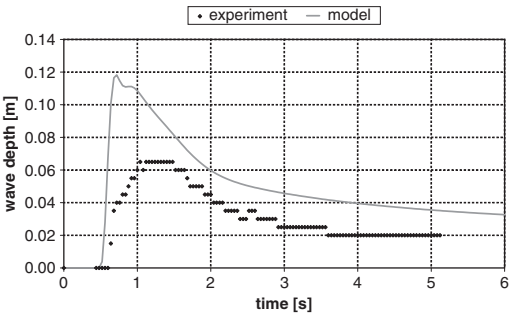


Figure 7. Comparison between numerical and experimental results. Test performed with gravel mixed with water ($c = 0.2$), a rough bottom of slope $i = 5°$, measurement section at 1.0 m from the gate.

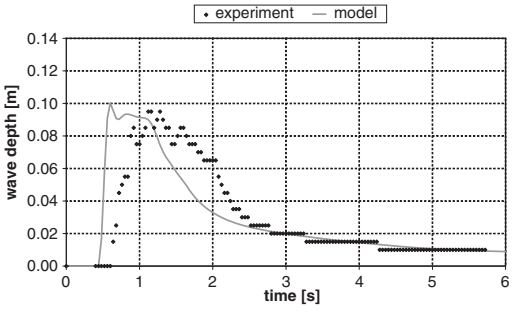


Figure 8. Comparison between numerical and experimental results. Test performed with vedril mixed with water ($c = 0.2$), a rough bottom of slope $i = 5°$, measurement section at 1.0 m from the gate.

is weakly influenced by this parameter (Fig. 6), here α_1 is set 1.1 both for gravel and for vedril material.

The intrinsic viscosity B is important because it takes into account the influence of the bottom roughness on the wave behaviour. A thorough study about the value of this parameter could be performed in the future.

Here, when the flume bottom is a zinc coated plate $B = 3$ and, as suggested by Chen (1996) for the granular flow of neutrally buoyant particles, $B = 4.5$ when the flume bottom is an homogeneous gravel bed.

The K_E parameter, introduced in Equation 21, is set equal to 0.1 as indicated by Ghilardi et al. (1999) for unsteady flow.

5 COMPARISONS WITH EXPERIMENTS

The mathematical model involves large simplifications; first, the solid and the liquid phases are characterised by the same average velocity and the same density: hence a single momentum equation can be employed and the resistance term J can be expressed as described in Section 3. Thus, one can expect that a good agreement between numerical results and experimental data will be obtained only when the solid material is vedril, whose density is similar to water density. Figures 7, 8 show the comparisons between experimental and numerical results: wave depth h versus time t graphs, at a section located 1.0 m downstream from the sluice-gate are shown. Figure 7 regards the test performed with gravel-water mixture while Figure 8 that with vedril-water mixture. The solid concentration in both cases is equal to 0.2 and the flume bottom is set rough with a 5° slope.

Figure 7 shows that numerical results of the maximum wave depth as well as the deposit layer thickness (see for $t \geq 3.5$ s) are definitely overestimated respect to experimental data; on the contrary, the reaching time to the measurement section is well predicted.

In Figure 8 it can be observed that the mathematical model supplies a good estimate of both the maximum wave depth and the deposit thickness. The simulated wave appears to move faster than the experimental wave (around 0.2 s), maybe because of the non-zero opening time of the sluice-gate.

These considerations are valid for all the tests performed and at any section of the flume. For example, Figure 9 shows another comparison between numerical and experimental results at a section located 0.4 m downstream from the sluice-gate. The test is performed with vedril-water mixture (solid concentration equal to 0.2) and on a smooth flume bottom with a 5° slope. In this case perhaps a careful analysis of the intrinsic viscosity value B could improve the agreement between the numerical results and the experimental data.

The Saint Venant equations are based on the hypothesis of mild slope; then, its foreseeable that agreement between the numerical and the experimental results should worsen when the slope increases. Indeed, Figure 10 shows the comparison between numerical and experimental results, at the same section of Figure 9

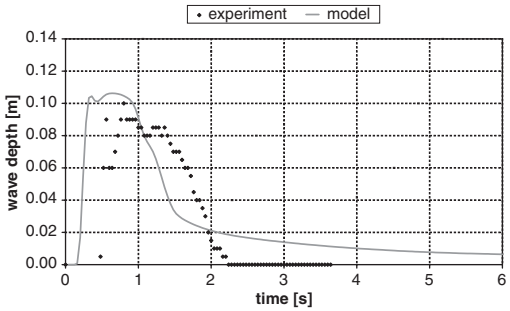


Figure 9. Comparison between numerical and experimental results. Test performed with vedril mixed with water ($c = 0.2$), a smooth bottom of slope $i = 5°$, measurement section at 0.4 m from the gate.

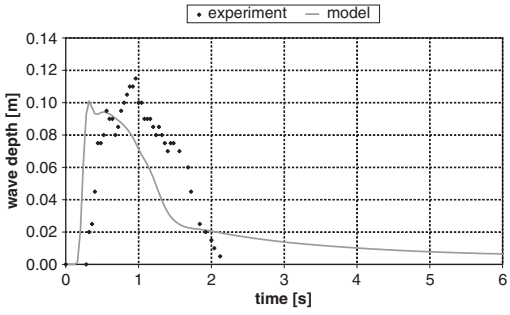


Figure 10. Comparison between numerical and experimental results. Test performed with vedril mixed with water ($c = 0.2$), a smooth bottom of slope $i = 15°$, measurement section at 0.4 m from the gate.

and with the same experimental conditions except that the channel slope. This is set 15° and it can be noticed that the wave depth peak is underestimated (around 20% less than measured one).

The comparisons shown refer to tests performed with mixtures with low solid concentration and neglecting in the mathematical model the yield stress in the resistance term; thus, sin ϕ does not appear in Equation 16. For high solid concentration, the yield stress has to be introduced in order to avoid results that do not reflect the real phenomenon. Yield stress seems to be present only when continuous friction among the grains develops in high concentration flows.

Figures 11, 12 show the comparisons between numerical and experimental results, at a section located 0.4 m downstream from the sluice-gate; whether the yield stress in the model is included or not. Both figures regard tests performed on a rough bottom and a 5° slope with mixtures with a solid concentration equal to 0.6. In Figure 11 the solid material used is gravel, while in Figure 12 it is vedril.

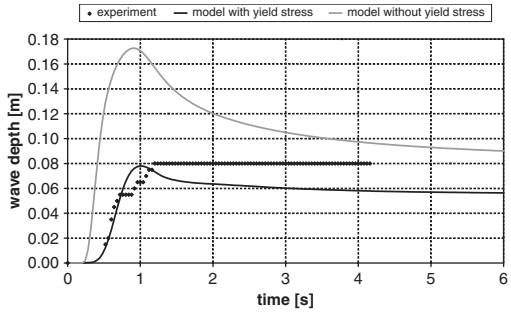


Figure 11. Comparison between numerical and experimental results. Test performed with gravel mixed with water ($c = 0.6$), a rough bottom of slope $i = 5°$, measurement section at 0.4 m from the gate.

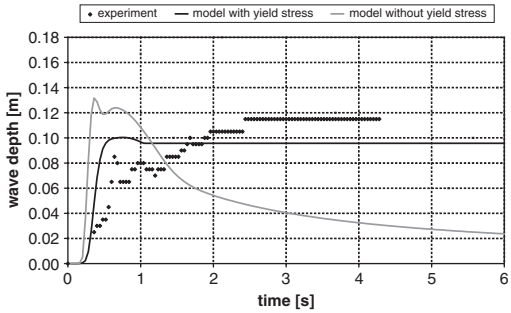


Figure 12. Comparison between numerical and experimental results. Test performed with vedril mixed with water ($c = 0.6$), a rough bottom of slope $i = 5°$, measurement section at 0.4 m from the gate.

It can be seen that the wave behaviour is completely misunderstood if the yield stress is not present in the shear stress expression used for the calculation of the resistance term in the model.

Anyhow, even if the yield stress is taken into account, deposit thickness is largely underestimated (about 20–25%).

6 CONCLUSIONS

The matter of the present paper is the analysis of the hypotheses upon which a one-dimensional mathematical model of granular debris flow consequent to dam-break is based. These hypotheses represent a limitation for the application of the model, although their introduction is necessary in order to simplify the problem. The model equations are integrated via a shock-capturing MacCormack scheme.

The main hypotheses considered are the following:

i. the solid and the liquid phase are characterised by the same average velocity;

ii. the water–solid mixture density is constant, that is the solid material is neutrally buoyant;
iii. pressure distribution along the cross-section of the flow is hydrostatic;
iv. the channel slope is mild;
v. the presence of the solid material does not involve changes in the expression of the normal stresses.

The importance of the hypotheses (i) and (ii) is underlined by the comparisons between numerical and experimental results when the solid material is gravel, whose density is much larger than water density. The hypotheses (iii) and (iv) are used to obtain a one-dimensional version of the mathematical model, while hypothesis (v) allows a further simplification. Moreover, some parameters of the model allow its calibration and avoid oscillations in the numerical solution; the values of the parameters for best fitting with experimental data are indicated.

The comparisons between numerical and experimental data show that the mathematical model can satisfactory predict the wave behaviour consequent to dam-break, if the solid concentration is low-medium and the solid material density is similar to the interstitial fluid density. Concerning higher solid concentrations, the introduction of the yield stress term in the shear stress expression allows a quite satisfactory, yet not excellent, agreement with experimental data. The density of the debris in real granular flows is much larger than the water density, therefore the mathematical model employed seems to oversimplify the problem, though it provides useful indications for a first, often safe, evaluation of the wave depths.

It seems that the correct simulation of the unsteady granular flow consequent to dam-break requires a more complex and complete approach. A first improvement can be reached removing the hypothesis of hydrostatic pressure distributions, that means the use of at least, a two-dimensional mathematical model, which will also solve the problem of modelling the complex geometry that characterizes real debris flows. Finally, it is remarkable that only a two-phase mathematical model, employing two different momentum equations, seems to be able to better reproduce the behaviour of a real debris flow.

REFERENCES

Aureli, F., Maione, U., Mignosa, P. & Tomirotti, M. 1998. Fenomeni di moto vario conseguenti al crollo di opere di ritenuta – Parte II: Indagini sperimentali e modellazione numerica in presenza di onde di shock. (in Italian), *L'Acqua*, 5.

Bertalli, L., Larcan, E. & Mambretti, S. 2002. Leggi di resistenza al moto nelle colate di detriti conseguenti al crollo di dighe. 1: Apparato sperimentale e primi risultati. (in Italian), *Atti del XXVIII Convegno di Idraulica e Costruzioni Idrauliche* 3: 219–226. Potenza.

Berzi, D. & Mambretti, S. 2003. Mathematical modeling and experimental tests of unsteady flow of non-Newtonian fluids. In D. Rickenmann and C. Chen (eds.), *Proc. 3rd ASCE Int. Conf. On Debris flow hazard mitigation: mechanics, prediction ad assessment*: 447–456. Davos Switzerland.

Chen, C. L. 1986. Bingham plastic or Bagnold's dilatant fluid as a rheological model of debris flow? *Proc. 3rd Int. Symp. On River Sedimentation*: 1624–1636, Univ. of Mississipi. United States.

Chen, C. L. 1988. Generalized viscoplastic modeling of debris flow. *J. Hydr. Engrg.*, ASCE, 114(3): 237–258.

Chen, C. L. & Ling, C. H. 1996. Granular-flow rheology: role of shear-rate number in transition regime. *Journal of Engineering Mechanics,* 122(5): 469–480.

Egashira, S., Miyamoto, K. & Itoh, T. 1997. Constitutive equations of debris flow and their applicability. In C. Chen (ed.), *Proc. 1st ASCE Int. Conf. On Debris flow hazard mitigation: mechanics, prediction ad assessment*, August 7–9: 340–349. San Francisco, California.

Ghilardi, P., Natale, L. & Savi, F. 1999. Two mathematical models simulating a real-world debris flow. *Proc. of the IAHR Symposium on "River, Coastal and Estuarine Morphodynamics"*. Genova.

Honda, N. & Egashira, S. 1997. Prediction of debris flow characteristics in mountain torrent. In C. Chen (ed.), *Proc. 1st ASCE Int. Conf. On Debris flow hazard mitigation: mechanics, prediction ad assessment*, August 7–9: 707–716. San Francisco, California.

Jameson, A. 1982. Transonic Airfoil calculations using the Euler equations. In P. L. Roe (ed.), *Numerical Methods in Aeronautical Fluid Dynamics*, Academic Press. New York.

Jenkins, J. T. 1987. Balance laws and constitutive relations for rapid flows of granular materials. In J. Chandra and R. P. Srivastav (eds.), *Constitutive models of Deformation*, Soc. For Industrial and Appl. Math.: 109–119. Philadelphia, Pa.

Krieger, I. M. & Dougherty, T. J. 1959. A mechanism for non-Newtonian flow in suspensions of rigid spheres. *Trans. Soc. of Rheology*, 3: 137–152.

MacCormack, R. W. & Baldwin, B. S. 1975. A numerical method for solving the Navier-Stokes equations with application to shock-boundary layer interaction. *AIAA*, Paper 75-1.

McTigue, D. F. 1982. A nonlinear constitutive model for granular materials: application to gravity flow. *J. Appl. Mech.*, 49(2): 291–296.

Ritter, A. 1892. Die Fortplanzung der Wasserwellen. *Zeitschrift des Vereines Deutscher Ingenieure*, vol. 36, n. 3.

Savage, S. B. 1984. The mechanics of rapid granular flows. *Adv. in Appl. Mech.*, 24: 289–366.

Savage, S. B. 1989. Flow of granular materials. In P. German, M. Piau and D. Caillerie (eds.), *Theoretical and Appl. Mech.*: 241–266. Amsterdam, The Netherlands.

Savage, S. B. & McKeown, S. 1983. Shear stresses developed during rapid shear of concentrated suspensions of large spherical particles between concentric cylinders. *J. Fluid Mech.*, 127: 453–472.

Takahashi, T. 1991. Debris flow. *IAHR Monograph Series*. Balkema.

River Flow 2004 – Greco, Carravetta & Della Morte (eds.)
© 2004 Taylor & Francis Group, London, ISBN 90 5809 658 0

Numerical simulation of hyper-concentrated flows

D. Komatina & D. Đorđević
Faculty of Civil Engineering, University of Belgrade, Belgrade, Serbia & Montenegro

ABSTRACT: Numerical modelling of dam-break or dike-break flows of homogeneous non-Newtonian fluids is presented in the paper. One of the most important tasks when formulating such a model is an estimation of friction losses, so that a constitutive equation must be adopted for the fluid under consideration. The constitutive equation introduced into the presented model is based on a general yield-power law (Herschel-Bulkley's rheological model). Numerical model used herein to solve the governing equations of 1D unsteady free-surface flow is based on the MacCormack explicit finite-difference scheme. The proposed model is verified using results of laboratory dam-break tests of mine tailings mixed with water. The mixtures are considered homogeneous, the material being composed mainly of silt and clay and wave propagation being considered of short duration. A comparison between measured and calculated results is given through a number of diagrams, showing the effect of varied parameters both on the wave propagation speed, and the flow depths.

1 INTRODUCTION

Dam-break flow of mine tailings seems to be one of the most dangerous hazards threatening local people, property and the whole environment. Therefore, a considerable attention has been paid to analysis of unsteady free-surface flows of highly concentrated solid–liquid mixtures, which have a non-Newtonian character, such as liquefied mine tailings (Jeyapalan et al. 1983, Komatina 1998), mud and debris (Han & Wang 1996, Huang & Garcia 1997, Hunt 1994, Jin & Fread 1999, Laigle & Coussot 1997, McArthur & Schamber 1986, O'Brien et al. 1993). Few analytical solutions to the problem have been given (Huang & Garcia 1997, Jeyapalan et al. 1983), applying Bingham plastic rheological model for description of mud and mine tailings flows. Examples of physical modelling of such flows have been presented as well (Coussot 1994, Komatina 1999).

Unsteady dam-break flow of highly viscous solid–liquid mixtures has been numerically studied so far using various constitutive relationships. Newtonian (Aguirre-Pe et al. 1995, Hunt 1994), Bingham (McArthur & Schamber 1986) and Herschel-Bulkley's fluid models (Laigle & Coussot 1997) have been applied to laminar flow modelling, while hybrid models have been employed for turbulent flow modelling – quadratic model (Bingham model, extended to account for turbulent and dispersive stresses) (Liu & Lai 2000, O'Brien et al. 1993), or a model established combining Bingham and Chezy-type relationships (Han & Wang 1996). Explicit numerical schemes of a finite-difference (Aguirre-Pe et al. 1995, Laigle & Coussot 1997) and finite-element type (McArthur & Schamber 1986) have been used in numerical treatments for 1D (Aguirre-Pe et al. 1995, Hunt 1994, McArthur & Schamber 1986) and 2D modelling (Han & Wang 1996, Laigle & Coussot 1997, McArthur & Schamber 1986, O'Brien et al. 1993). Implicit numerical scheme has not been employed to such an extent for modelling unsteady hyper-concentrated flows, due to difficulties when modelling flows having discontinuities (Fraccarollo 1997). It has been accepted as an unconditionally stable, robust and suitable for application to tasks requiring both spatially and temporally huge computational domains (Cunge et al. 1980, Meselhe & Holly 1997), which are likely to occur in nature. Additionally, it has been successfully used in the clear water dam-break subcritical flow modelling (Hicks et al. 1997). However, in a paper of the authors (Komatina & Lalović 2000), where the implicit 4-point finite-difference scheme has been applied, quality of the simulation results decreased due to impossibility of a dry-bed computation – calculated longitudinal profiles of the waves were too smooth and the wave front locations were greater than those measured in laboratory.

In order to improve modelling of discontinuous flows, such as the dam-break hyper-concentrated flow, an application of a shock-capturing scheme, which allows for weak solutions, is analysed in this paper. Therefore, the MacCormack explicit finite-difference

scheme, whose good performance in discontinuous Newtonian flow modelling has been reported in literature (Aguirre-Pe et al. 1995, Bellos & Sakkas 1987, Đorđević 2000, Garcia-Navarro & Saviron 1992, Jovanović & Đorđević 1995), is used for 1D numerical modelling of dam-break flows of liquefied mine tailings, previously performed in laboratory canal (Komatina 1998). Friction losses are calculated in the model using the Herschel-Bulkley's rheological equation.

2 FRICTION FACTOR MODELLING

A case of uniform free-surface flow of a homogeneous time-independent incompressible non-Newtonian fluid in a wide channel is considered. It can be shown from momentum equation that the shear stress distribution over the flow depth is linear, see Figure 1:

$$\tau = \tau_o \cdot (1 - y/h) \tag{1}$$

where τ is the shear stress at a distance y from the bottom, τ_o is the bottom shear stress:

$$\tau_o = \rho g h \cdot \sin\alpha \approx \rho g h S_o \tag{2}$$

ρ is the fluid density, g – gravitational acceleration, h – flow depth, α – bottom slope angle, S_o – bottom slope, ξ – dimensionless distance from the fluid surface:

$$\xi = \tau/\tau_o = 1 - y/h \tag{3}$$

and ξ_c – non-dimensional plug flow width, given by:

$$\xi_c = \tau_c/\tau_o = 1 - y_c/h \tag{4}$$

where y_c is the distance from the bottom where $\tau = \tau_c$.

Evaluation of the friction slope is of a crucial importance in solving the governing equations for a non-Newtonian fluid. For this purpose, a constitutive equation for the material under consideration has to be adopted. The Herschel-Bulkley's model is used in the paper:

$$\begin{aligned} \tau &= \tau_c + \eta \cdot \dot{\gamma}^m, \quad \tau > \tau_c \\ \dot{\gamma} &= 0 \qquad\quad , \quad \tau \le \tau_c \end{aligned} \tag{5}$$

where $\dot{\gamma}$ denotes shear rate; τ_c, η, and m – rheological parameters of the fluid (yield stress, consistency index and flow behaviour index, respectively). The equation comprises yield and viscous stress components and is valid in laminar flow regime only.

By double integration of Equation 5 over the flow depth, the laminar flow equation can be derived in the following form (Coussot 1994):

$$\frac{3U}{h} = \left(\frac{\tau_o}{\eta}\right)^{1/m} \cdot \Phi \tag{6}$$

where U is the mean flow velocity, which is, for a wide channel, equal to the depth-averaged velocity, and the dimensionless function Φ is defined by:

$$\Phi = \frac{3m}{2m+1} \cdot \left[1 + \frac{m}{m+1} \cdot \xi_c\right] \cdot (1 - \xi_c)^{(m+1)/m} \tag{7}$$

It is well known that standard Newtonian relationships for clear water can be applied for calculation of friction factor for a non-Newtonian fluid, if the Reynolds number is expressed in an extended form, so as to include all the rheological parameters of the fluid (Wan & Wang 1994). For the Herschel-Bulkley's model, the extended Reynolds number is defined as (Komatina 1999):

$$\mathrm{Re}_{ext} = \mathrm{Re} \cdot \Phi^m \tag{8}$$

where the Newtonian Reynolds number is equal to:

$$\mathrm{Re} = \frac{4\rho \cdot U^{2-m} \cdot h^m}{\eta \cdot 3^{m-1}} \tag{9}$$

So, the standard Moody relationship, which can be obtained from Equation 6, is applied in the laminar flow regime ($\mathrm{Re}_{ext} < 2100$), (Komatina 1999):

$$f = \frac{24}{\mathrm{Re}_{ext}} \tag{10}$$

and the Blasius formula is applied in the turbulent flow regime (Wan & Wang 1994):

$$f = \frac{0.079}{\mathrm{Re}_{ext}^{1/4}} \tag{11}$$

The bottom shear stress is then determined using the calculated value of the friction factor:

$$\tau_o = f \cdot \frac{\rho U^2}{2} \tag{12}$$

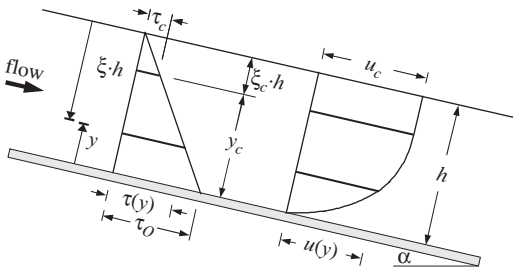


Figure 1. Shear stress (τ) and flow velocity (u) distribution, shown schematically.

3 GOVERNING EQUATIONS

The 1D unsteady free-surface hyper-concentrated flow is described by the De St.-Venant equations in conservative form:

$$\mathbf{U}_t + \mathbf{E}_x = \mathbf{S} \tag{13a}$$

$$\mathbf{U} = \begin{bmatrix} A \\ Q \end{bmatrix}, \qquad \mathbf{E} = \begin{bmatrix} Q \\ \dfrac{Q^2}{A} + g I_1 \end{bmatrix},$$

$$\mathbf{S} = \begin{bmatrix} 0 \\ g A(S_o - S_f) + g I_2 \end{bmatrix} \tag{13b}$$

where x and t are space coordinate and time, respectively; A – the flow area; Q – the discharge; S_o – bottom slope and S_f – friction slope. The terms I_1 and I_2 are related to the hydrostatic pressure force:

$$I_1 = \int_0^h (h - \zeta) b(x, \zeta) \, \mathrm{d}\zeta \;, \quad I_2 = \int_0^h (h - \zeta) \frac{\partial h}{\partial x} \mathrm{d}\zeta \tag{14}$$

in which: the depth integration variable along y-axis is denoted by ζ, the width of the cross-section at the distance ζ from the bottom of the cross-section, which is located at distance x along channel by $b(x, \zeta)$. In prismatic channels $I_2 = 0$.

3.1 *Determination of the friction slope*

It is usually assumed that for unsteady flow, the bottom shear stress at a specific point is equal to the value of the uniform flow with a corresponding flow discharge and depth (Aguirre-Pe et al. 1995, Laigle & Coussot 1997). Consequently, application of simple rheological relationships, such as Equation 5, is possible.

The friction slope in Equation 13 is determined using the relationship:

$$\tau_o = \rho g h S_f \tag{15}$$

on the basis of the bottom shear stress, previously calculated from Equation 12.

4 NUMERICAL MODEL

The system of partial differential hyperbolic-type equations 12 is numerically solved using the MacCormack explicit finite-difference scheme. The scheme is second order accurate in both the space and time. It consists of a two step predictor-corrector sequence:

Predictor:

$$\mathbf{U}_i^p = \mathbf{U}_i^k - \frac{\Delta t}{\Delta x} \nabla_x \mathbf{E}_i^k - \Delta t \, \mathbf{S}_i^k, \; 2 \le i \le N \tag{16}$$

Corrector:

$$\mathbf{U}_i^c = \mathbf{U}_i^p - \frac{\Delta t}{\Delta x} \Delta_x \mathbf{E}_i^p - \Delta t \, \mathbf{S}_i^p, \quad 1 \le i \le N\text{-}1 \tag{17}$$

New value:

$$\mathbf{U}_i^{k+1} = \frac{1}{2}\left(\mathbf{U}_i^k + \mathbf{U}_i^c\right) \tag{18}$$

Here, subscript i defines a position of the cross-section along the x-axis, superscripts k and $k+1$ denote values of the variables at the previous time level (k) and the following time level ($k+1$), whereas superscripts p and c denote values in the predictor and corrector steps, respectively.

The backward and forward difference operators are defined by:

$$\nabla_x \mathbf{E}_i = \mathbf{E}_i - \mathbf{E}_{i-1}, \quad \Delta_x \mathbf{E}_i = \mathbf{E}_{i+1} - \mathbf{E}_i \tag{19}$$

The operator sequence in the predictor and the corrector steps is alternated each time step, which means the operator cycle is concluded in two time steps. In order to provide numerical stability of the scheme, the Courant-Friedrichs-Lewy's criterion is used to determine the time step Δt in Equations 16 and 17.

5 EXPERIMENTS

Mixtures of water and copper tailings taken from the Veliki Krivelj copper mine (Serbia and Montenegro) were used as experimental fluids. The mean diameter of particles is 0.025 mm, with 8% of the material finer than 0.002 mm, and 70% finer than 0.062 mm. The density is 2650 kg/m^3, and its chemical composition: 63% SiO_2, 14% Al_2O_3, 3.5% Fe, 3% K_2O, 3% CaO, 3% MgO and 3% Na_2O. Clayey fractions of the material are of kaolinite-illite type.

Rheological parameters of the mixtures were determined using two types of measurements: in a commercial rotational viscometer and in the laboratory canal, illustrated in Figure 2. Measurement errors were estimated to 13% (viscometer) and 16% (canal), (Komatina 1999). The applied procedures provided data on rheological behaviour of the mixtures in different ranges of shear rate: small shear rates (0.5 to 20 s^{-1}) in the case of steady-state free-surface flow experiments in the canal, and 50 to 250 s^{-1},

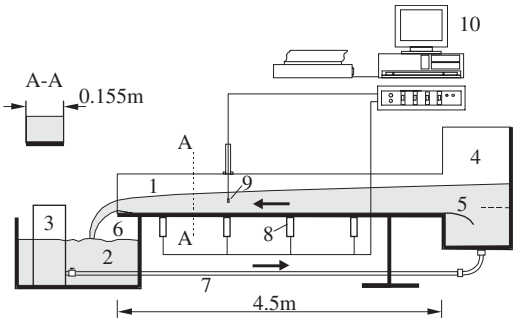


Figure 2. Laboratory flume and measurement equipment: 1 – flume, 2 – lower tank, 3 – pump, 4 – upper tank, 5 – deflector, 6 – control weir, 7 – fluid supply rubber tube, 8 – membrane probes, 9 – electromagnetic probe, 10 – data acquisition and processing system.

Table 1. Rheological properties of mixtures.

Mixture	C_V %	ρ kg/m^3	τ_c Pa	η mPas^m	m
1	13.8	1228	0.7	0.52	0.55
2	18.1	1299	1.0	1.58	0.55
3	32.2	1531	60.0	35.50	0.55
4	36.4	1601	120.0	102.00	0.55

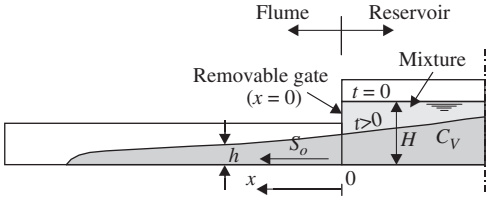


Figure 3. Sketch of a dam-break flow experiment.

using the rotational viscometer. For a mixture, two linear relationships (Bingham model) were defined for each of the shear rate ranges. Finally, a yield power-law (Herschel-Bulkley's model) was defined so as to match the linear relationships. Values of the rheological parameters, obtained in this manner, are listed in Table 1 (where C_V denotes the volumetric concentration of the solid phase).

The dam-break flow experiments were performed in a 4.5 m long, 0.15 m wide glass-walled laboratory flume, with adjustable bottom slope (Fig. 2). The dam-break type of flow was initiated by releasing mixtures from a 2 m long, 0.155 m wide reservoir, situated on the upstream part of the flume. A sketch of the experiment is given in Figure 3 (H – initial reservoir depth). Experimental parameters were varied in the following ranges: $S_o = 0$–1%, $H = 10$–30 cm, $C_V = 0$–45.6%.

6 RESULTS AND DISCUSSION

Results from the laboratory rig, depicted in Figure 2, were used to verify the results of numerical simulation of one-dimensional unsteady hyper-concentrated flow. The flow was caused by a sudden release of the mixture (induced by an abrupt removal of the gate between the reservoir and the canal), stored in the 2.0 m long and 0.155 m wide reservoir that had been formed in the upstream part of the flume. The propagation of a positive wave in an initially dry canal was filmed by a video camera with recording speed of 5 images per second. The glass walls had been covered with a square net ($\Delta x = \Delta z = 1$ cm), thus it was possible to "read" the records – read the flow depths along the canal. Settling of particles during the propagation was neglected, as the propagation time was short relatively to the settling time of the material composed mainly of silt and clay.

The evolution of the measured and the calculated flow depth profiles of four experiments with different mixtures, in which the initial depth in the reservoir was $H = 0.3$ m and the bottom canal slope 1%, are shown in Figures 4–7. The properties of the mixtures are given in Table 1. The initial condition at the opening was defined according to the theoretical Ritter's solution for the one-dimensional dam-break problem: $h = (4/9)H$, $u = (8/17)\sqrt{gH}$, while for numerical reasons, the initial depth downstream from the reservoir was set to 0.001 m. No artificial viscosity was used.

For the sake of easier comparison with the measurements, the time step, used in this simulation, was kept constant $\Delta t = 0.01$ s, which resulted in the maximum Courant's number values of 0.6 for lower concentration mixtures and 0.4 for higher concentration mixtures.

It can be noticed (Figs 4–7), that the wave front propagation speed is generally well reproduced for all the mixtures – the differences between the calculated and the measured wave front locations are less then ±3%. However, discrepancies between the calculated and the measured flow depth profiles expressed in reference to the measured flow depths are somewhat greater for the mixtures with lower concentration of solids (Figs 4–5), than those pertaining to the mixtures with higher concentration of solids (Figs 6–7). The discrepancies for the former mixtures are as high as 45% at the steep front, where it was not possible to read the flow depths from the video tapes accurately. The flow depths were too small to recognize and read easily from the recordings. On the other hand, discrepancies between the calculated and the measured flow depth profiles for the mixtures with higher concentrations of solids (Figs 6–7) are much lesser, since the wave front heights were much greater for these mixtures. Discrepancies for about 90% of the results are within ±15%.

Furthermore, the effect of slowing down the advancing front is readily noticeable for the mixture

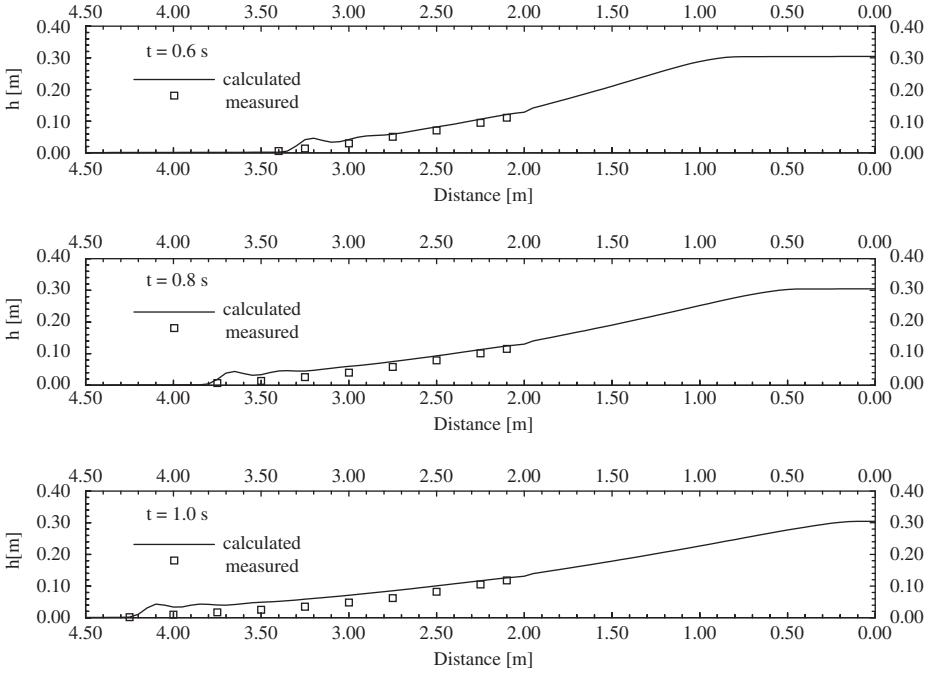


Figure 4. Comparison of the calculated and the measured flow depth profiles for the mixture with $C_V = 13.8\%$.

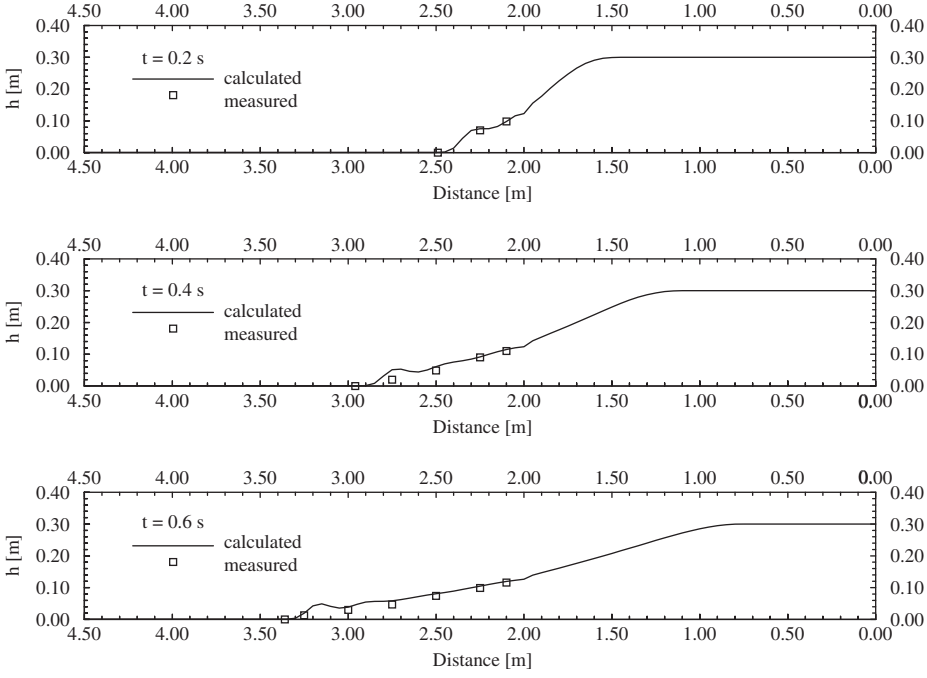


Figure 5. Comparison of the calculated and the measured flow depth profiles for the mixture with $C_V = 18.1\%$.

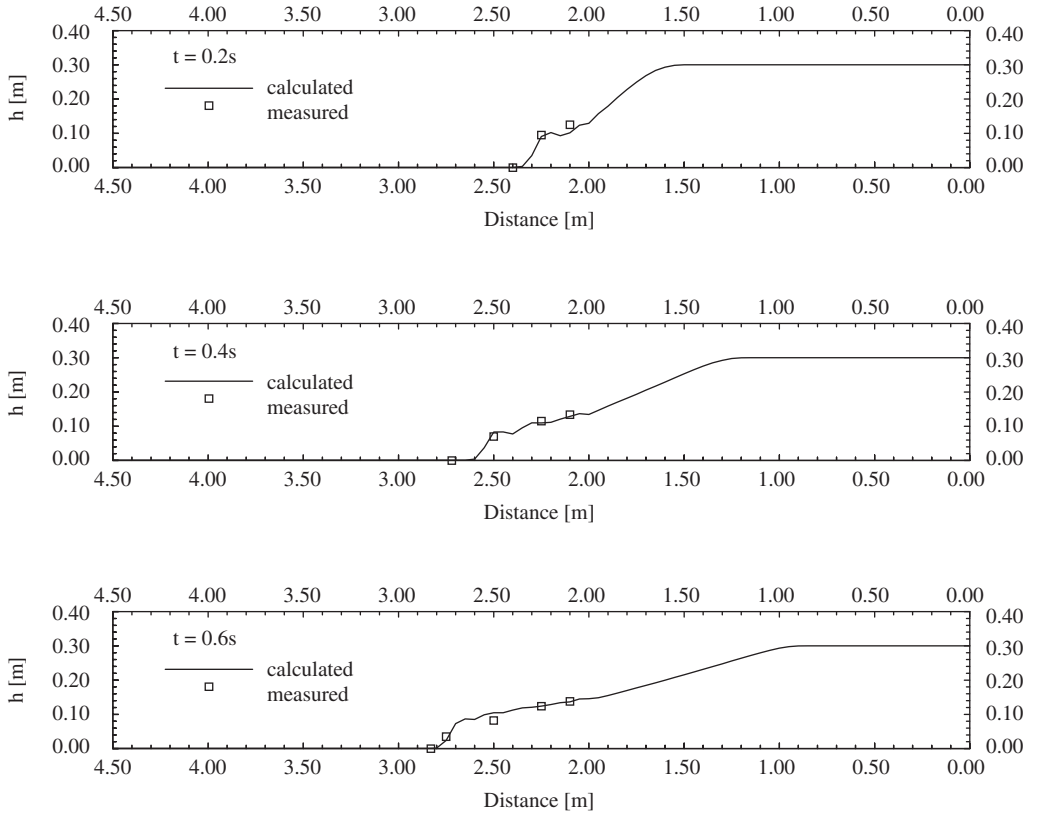


Figure 6. Comparison of the calculated and the measured flow depth profiles for the mixture with $C_V = 32.2\%$.

with the highest concentration of solids ($C_V = 36.4\%$) – Figure 7, which is another very important feature of the proposed model. The influence of the concentration of the solid phase on the wave propagation speed is presented in the Figure 8. The higher the concentration, the lower the propagation speed, which is in agreement with the laboratory observations.

As previously explained, the rheological parameters of the Herschel-Bulkley's model were determined by matching the Bingham linear relationships obtained from two different procedures (viscometer and canal). Although the authors are aware of inconsistency of the procedure, it gave good results in this particular case, as can be seen from the plots of advancing fronts of all the mixtures (Figs 4–7). This justifies the applied procedure for determination of the parameters.

With the rheological parameters obtained in this manner, the calculated flow regime was laminar for all the analysed mixtures released from the reservoir, except the one with the lowest concentration of solids ($C_V = 13.8\%$), see Table 2. For the mixture having $C_V = 13.8\%$, it can be seen that $\mathrm{Re}_{ext} < 10000$. According to the findings of Wan & Wang (1994), this means that the flow conditions have not achieved fully developed turbulence, which justifies application of the Blasius formula in the turbulent flow regime.

7 CONCLUSIONS

Dam-break flow computation is a complex task, affected by a number of factors, such as availability and reliability of boundary and initial conditions, and capability of a numerical scheme to reproduce steep front without introduction of additional algorithms for bore tracking. The computation becomes even more complicated when modelling unsteady flows of highly concentrated solid–liquid mixtures. In such a case, estimation of rheological parameters of the mixture, as well as calculation of the friction slope, appear as new sources of errors.

In this paper, a 1D numerical model for hyperconcentrated dam-break flows is illustrated. The main intention is to reproduce numerically dam-break flows already observed in nature or laboratory. As a further objective, prediction of flows due to dam failure or dike

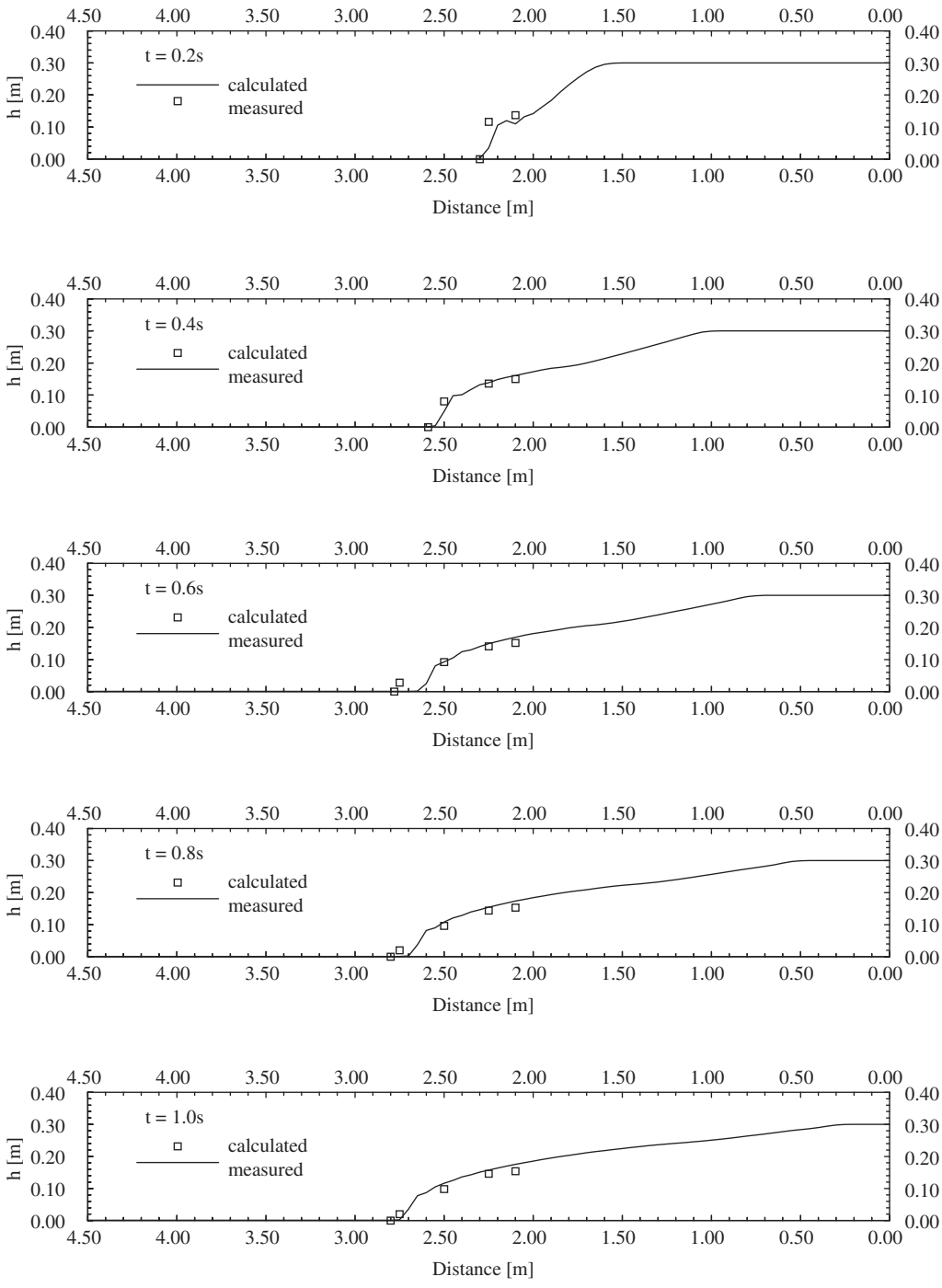


Figure 7. Comparison of the calculated and the measured flow depth profiles for the mixture with $C_V = 36.4\%$.

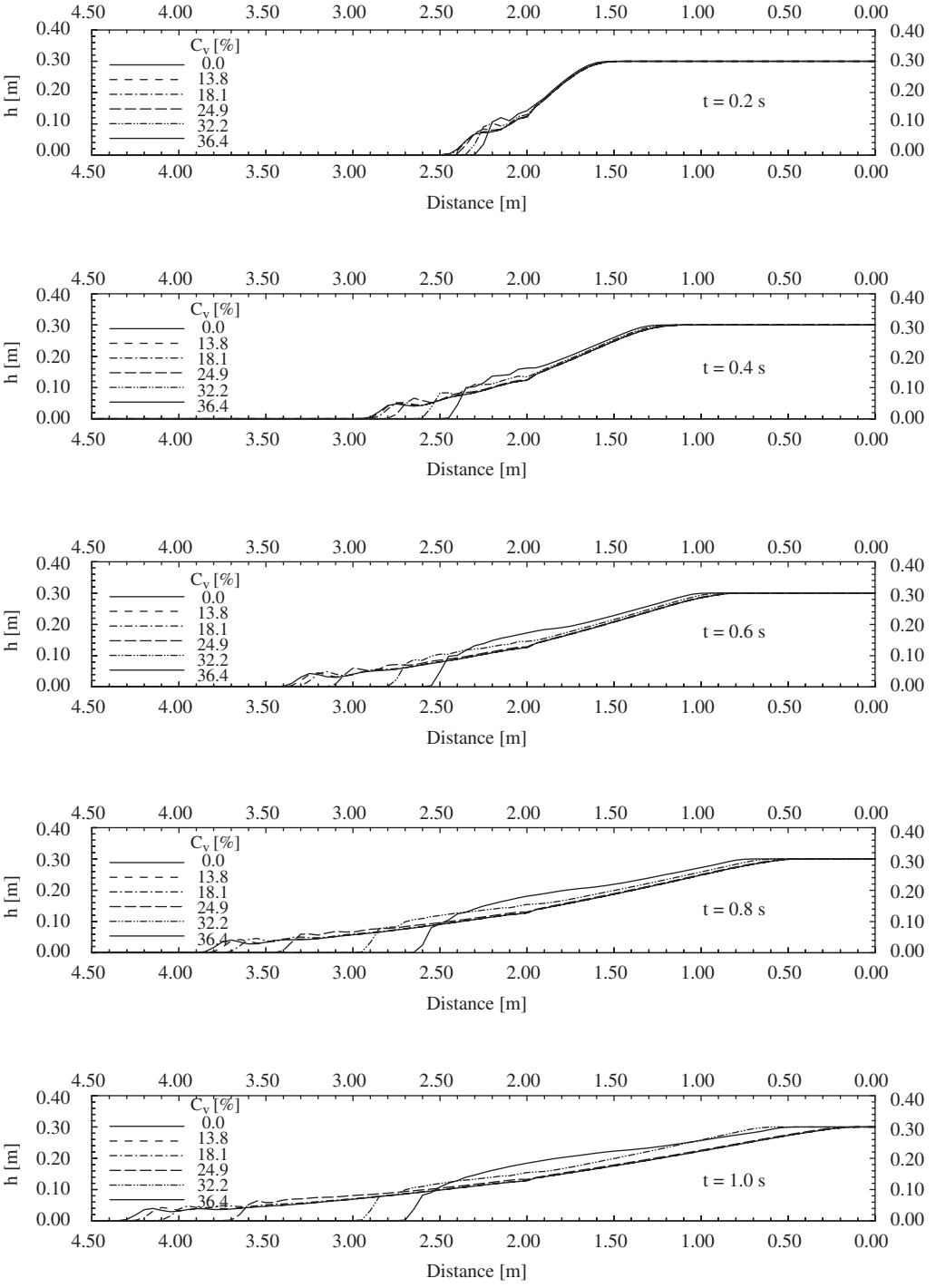


Figure 8. The influence of concentration of solid particles on the wave propagation speed and the flow depths.

Table 2. Values of the Reynolds number and the friction factor.

Mixture	C_V%	Re_{ext}	f
1	13.8	<10000	0.006–0.012
2	18.1	<2000	0.050–0.070
3	32.2	<100	1.20–4.00
4	36.4	<40	5.00–20.0

failure on mine- or ash-tailings deposit sites is planned. The MacCormack explicit finite-difference scheme is used for numerical modelling. As it belongs to the group of shock-capturing methods, it is particularly suitable for solving problems of the main interest to the authors – simulation of flows with a steep front.

Simulation results have shown that the wave front propagation speed is generally well reproduced for all the mixtures. This means that the initial condition at the gate opening, derived for the clear water case, is equally applicable in the case of the hyper-concentrated flow. In addition, the observed effect of slowing down the wave front propagation speed with the increase in the concentration of solid particles is successfully reproduced with the proposed model, which makes it a good predictive tool for solving dam-break or dike-break hyper-concentrated flow problems.

Further, discrepancies between the calculated and the measured flow depth profiles are acceptable. For the mixture with the lowest concentration of solids, the discrepancies at the steep front are high due to the difficulties in reading small depths from the video tapes.

Determination of the rheological parameters of the Hershel-Bulkley's model by matching the Bingham linear relationships obtained from two different procedures (viscometer and canal) is not consistent. However, results from the plots of advancing fronts of all the mixtures justify the applied procedure for determination of the parameters.

With the parameters obtained in this manner, the calculated flow regime was laminar for all the mixtures, except for the one with the lowest concentration of solids ($C_V = 13.8\%$). The values of the extended Reynolds number for this mixture show that fully developed turbulence has not been achieved, which justifies application of the Blasius formula.

The proposed model in its present form gives satisfactory results in simulation of flows of homogeneous, hyper-concentrated mixtures in regular channel geometry. In order to extend its application to real problems occurring in industry and nature, improvement of the model by allowing for computations in irregular geometries is necessary.

REFERENCES

Aguirre-Pe, J. & Quisca, S. & Plachco, F.P. 1995. Tests and numerical one-dimensional modelling of a high-viscosity fluid dam-break wave, *Journal of Hydraulic Research*, 33(1): 17–26.

Akanbi, A.A. & Katopodes, N.D. 1988. Model for Flood Propagation on Initially Dry Land, *Journal of Hydraulic Engineering*, 114(7): 689–706.

Bellos, C.V. & Sakkas, J.G. 1987. 1-D Dam-Break Flood-wave Propagation on Dry Bed, *Journal of Hydraulic Engineering*, 113(12): 1510–1524.

Coussot, P. 1994. Steady, laminar, flow of concentrated mud suspensions in open channel, *Journal of Hydraulic Research*, 32(4): 535–559.

Cunge, J.A. & Holly Jr., F.M. & Verwey, A. 1980. Practical aspects of computational river hydraulics, Pittman Publ., Boston.

Đorđević, D. 2000. *Modelling of free-surface discontinuous flows*, Belgrade, Zadužbina Andrejević (in Serbian).

Fennema, R.J. & Chaudhry, M.H. 1986. Explicit Numerical Schemes for Unsteady Free-Surface Flows with Shocks, *Water Resources Research*, 22(13): 1923–1930.

Fraccarollo, L. 1997. Discussion of paper "Numerical modeling of Anhui debris flow", *Journal of Hydraulic Engineering*, 123(10): 937–938.

Garcia, R. & Kahawita, R.A., 1986. Numerical Solution of the St. Venant Equations with the MacCormack Finite-Difference Scheme, *International Journal for Numerical Methods in Fluids*, 6: 259–274.

Garcia-Navarro, P. & Saviron, J.M. 1992. McCormack's Method for the Numerical Simulation of One-Dimensional Discontinuous Unsteady Open Channel Flow, *Journal of Hydraulic Research*, 30(1): 95–105.

Han, G. & Wang, D. 1996. Numerical modeling of Anhui debris flow, *Journal of Hydraulic Engineering*, 122(5): 262–265.

Hicks, F.E. & Steffler, P.M. & Yasmin, N. 1997. One-dimensional dam-break solutions for variable width channels, *Journal of Hydraulic Engineering*, 123(5): 464–468.

Huang, X. & Garcia, M.H. 1997. A perturbation solution for Bingham-plastic mudflows, *Journal of Hydraulic Engineering*, 123(11): 986–994.

Hunt, B. 1994. Newtonian fluid mechanics treatment of debris flows and avalanches, *Journal of Hydraulic Engineering*, 120(12): 1350–1363.

Jeyapalan, J.K. & Duncan, J.M. & Seed, H.B. 1983. Analyses of flow failures of mine tailings dams, *Journal of Geotechnical Engineering*, 109(2): 150–171.

Jin, M. & Fread, D.L. 1999. 1D modeling of mud/debris unsteady flows, *Journal of Hydraulic Engineering*, 125(8): 827–834.

Jovanović, M. & Đorđević, D. 1995. Experimental Verification of the MacCormack Numerical Scheme, *Advances in Engineering Software*, 23, Elsevier Science Limited: 61–67.

Komatina, D. 1998. An experimental study on the unsteady dam-break flow of mine tailings, *3rd International Conference on Hydrodynamics*: 481–486.

Komatina, D. 1999. Physical processes and modelling of non-Newtonian free-surface flows, Ph.D. thesis, University of Belgrade, Yugoslavia (in Serbian).

Komatina, D. & Lalović, V. 2000. Numerical simulation of unsteady dam-break flow of mine tailings, *4th International Conference on Hydrodynamics*.

Laigle, D. & Coussot, P. 1997. Numerical modeling of mudflows, Journal of Hydraulic Engineering, 123(7): 617–623.

Liu, K.F. & Lai, K.W. 2000. Numerical simulation of two-dimensional debris-flows, *2nd International Conference on Debris-Flow Hazards Mitigation*: 531–535.

McArthur, R.C. & Schamber, D.R. 1986. Numerical methods for simulating mudflows, *3rd International Symposium on River Sedimentation*: 1615–1623.

Meselhe, E.A. & Holly Jr., F.M. 1997. Invalidity of Preissmann scheme for transcritical flow, *Journal of Hydraulic Engineering*, 123(7): 652–655.

O'Brien, J.S. & Julien, P.Y. & Fullerton, W.T. 1993. Two-dimensional water flood and mudflow simulation, *Journal of Hydraulic Engineering*, 119(2): 244–261.

Wan, Z. & Wang, Z. 1994. Hyperconcentrated flow, IAHR monograph series, Balkema, Rotterdam.

River Flow 2004 – Greco, Carravetta & Della Morte (eds.)
© 2004 Taylor & Francis Group, London, ISBN 90 5809 658 0

Probabilistic estimation of debris-flow discharge by Monte Carlo simulation method

J.C. Chen
Disaster Prevention Research Center, National Cheng Kung University, Tainan, Taiwan

C.D. Jan & M.H. Lee
Dept. of Hydraulic and Ocean Engineering, National Cheng Kung University, Tainan, Taiwan

ABSTRACT: Equation of debris-flow discharge contains hydrogeological and topographical parameters. Considering the uncertainty of the parameters and using the Monte Carlo simulation method (MCSM), a debris-flow design discharge versus reliability probability at various return period is developed. The method proposed in this paper is used to estimate the debris-flow design discharge in fushing village, Hualien county, Taiwan. The results also compare with that by First-order second-moment method (FOSM).

1 INTRODUCTION

Reliability modeling and other probabilistic techniques are becoming increasingly important tools in design of debris-flow hazard countermeasures. As an example, a discharge design may be based on reliability to assist the engineering in deciding on the most appropriate design parameters under a variety of uncertainties. Once the design discharge was underestimated, the reliability of debris-flow mitigation plan or structures would be doubtable.

Methods in deterministically calculating debris-flow discharge have been proposed by some investigators, such as Takahashi (1978), Kang (1985), Wang & Chang (1985), Chen et al. (2002), among others. Assume that the debris flow peak discharge can be directly related to the peak discharge of the water stream, a semi-empirical relation of debris-flow discharge for a specified return period is given as (Chen et al. 2002)

$$Q_t = \frac{1}{360}\frac{C A_m (k_1 + k_2 \log T) k_3 I_r}{(1 - C_v)}\left[\left(60\frac{l}{v} + \frac{5}{6}\frac{L^{1.6}}{H^{0.6}}\right) + k_0\right]^{-k_4} \quad (1)$$

in which C = runoff coefficient; A_m = watershed area in hectares (ha); T = rainfall return period in years; L = stream length in km; H = elevation difference of stream length in km. C_v = sediment volumetric concentration. The values of C_v for debris flow are in the range of $0.15 < C_v < 0.9(1-n)$ in which n is porosity of sediment layer; l = the length of overland flow in km; v = the overland flow velocity in km/hr. Generally, the values of v are in the range of $1.08 \sim 2.16$ km/hr (SWCTC 2000) ; I_r = reference of rainfall intensity (mm/hr) that is the rainfall intensity at return period of 25 years and duration of 60 minutes; k_0 is a constant and equals 55. The other coefficients (k_1, k_2, k_3, k_4) and the reference rainfall intensity I_r are directly related to the annual rainfall in the concerned watershed, as indicated in Appendix I. The above equation is a deterministic equation if all parameters involved in the equation are evaluated by their mean values. However, the parameters have some kinds of uncertainties. Considering the uncertainties of the random variables in Eq. (1) and using the first-order second-moment method (FOSM), Chen et al. (2002) have been developed a probabilistic equation of debris-flow discharge. For the FOSM, no distribution is required, but the underlying assumption is that the variables are all normally distributed and the function being analyzed is linear. This assumption can present large errors in some cases where the function or equation is highly nonlinear. Therefore, an exact method, the Monte Carlo simulation method (MCSM), in this paper is used to estimate the debris-flow discharge for different reliability probability, and the result is compared with that by FOSM.

2 UNCERTAINTY OF PARAMETERS

The uncertainty of parameters may result from the facts that (1) the topographical parameters, A_m, l, L and H, measured from a topographic map of watershed have inconsistent values for difference persons (engineers)

Table 1. Statistical properties of seven parameters at Fushing village.

Variables x_i	Samples N	Ranges	Mean values μ_{xi}	Variance CV_{xi} (%)
A_m (ha)	31	310.4 ~ 396.6	355.6	6.81
l (km)	31	1.36~1.73	1.55	5.22
L (km)	31	1.47~1.90	1.69	5.01
H (km)	31	0.21~0.22	0.216	1.64
C_v	–	0.15~0.56	0.355	28.87
C	–	0.5~0.8	0.65	11.54
v (km/hr)	–	1.08~2.16	1.62	16.67

due to their different experiences on drawing the watershed boundary and the initial point of river upstream; (2) the soil properties, the vegetation and topographic properties vary in space and are highly non-homogeneous, and therefore the overland flow velocity v and the runoff coefficient C are random variables; (3) the sediment concentration C_v of debris flow has high uncertainty also, depending on the property of sediment, slope and the amount of sediment and water. The uncertainties of the above mentioned parameters could be quantified by using statistical parameters, such as the mean value, the standard deviation, the coefficient of variation and probability distribution.

Table 1 lists the statistical result of topographical parameters (A_m, l, L and H) at Fushing village in Taiwan (Jan et al. 2003), basing on the measured data individually conducted by 31 graduate students using same kind of map of watershed. One can see that the variances of the parameters A_m, l and L all are larger than 5%, while variance of H is 1.64%. The mean values and the coefficients of variation for other parameters, C_v, C and v, are estimated from the range of possible values owing to the absence of field data. Given the range of possible values of a random variable, the mean value of the variable and the underlying uncertainty may be evaluated by prescribing a suitable distribution within the range (Ang and Tang, 1984). If the given limits are assumed to be ±cover 2 standard deviations in the normal distribution, the mean values and the corresponding coefficient of variation for parameters C_v, C, v, are also summarized in Table 1. All the seven parameters in Eq. (1), A_m, l, L, H, C_v, C, and v, are treated as random variables and assumed following normal distributions while the rest parameters are treated as deterministic parameters in the present paper.

3 MONTE CARLO SIMULATION METHOD

Many methods have been developed for uncertainty assessment (Harr 1987, Ang & Tang 1984, Rubinstein 1981). Generally, these methods can be classified into approximate and exact. The approximate methods are usually of the moment type, e.g. the first-order second-moment method (FOSM) and the advanced-second-moment method (ASM). The exact methods involve a comprehensive analysis using the probability distribution of all component variables, e.g. direct integration method and Monte Carlo simulation method (MCSM). In this study Monte Carlo Simulation (MCSM) is used to generate random samples of parameters in Eq. (1) based on the specified coefficients of variation and distributions. The probabilistic equation of debris-flow discharge based on FOSM (Chen et al. 2002) is also used for comparison in this paper.

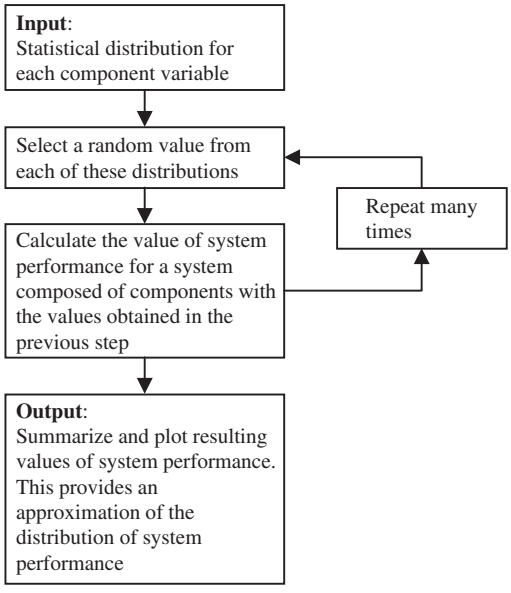


Figure 1. Flow chart of Monte Carlo simulation method.

Monte Carlo simulation is a method for obtaining information about system performance from component data. This method has also been referred to as synthetic sampling or empirical sampling. The procedure of Monte Carlo simulation is shown graphically in Figure 1.

To obtain a probabilistic debris-flow discharge, the following steps were followed:

1. Values for each of random variables in Eq. (1), including (C, C_v, A_m, l, v, L, H), were generated from their respective distributions for each of N = 1000 simulation cycles. All the variables were assumed to be normal with means and standard deviations of Table 1.
2. The debris-flow discharge Q_t was calculated from Eq. (1) based on the generated random variables. This process was repeated for N simulation cycles. Figure 2 shows a frequency histogram of the N = 1,000 simulated debris-flow discharge Q_t.

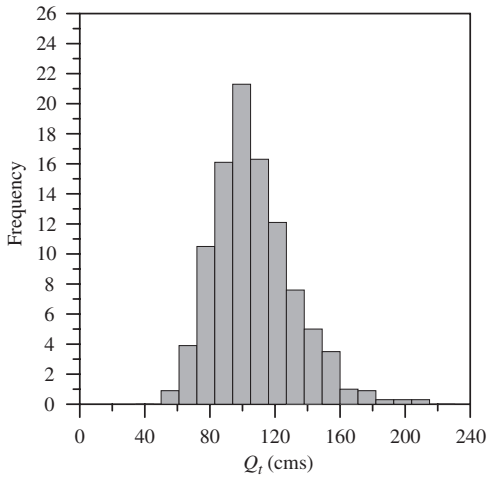


Figure 2. Frequency Histogram for 1,000 simulated debris-flow discharge.

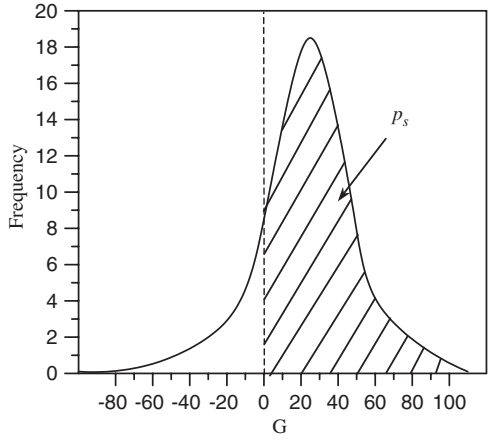


Figure 3. A distribution of sate function G and the reliability probability p_s corresponding for G > 0.

3. Given a certain values of Q_d, i.e., a debris-flow design discharge, a distribution of the state function G ($= Q_d - Q_t$), was calculated based on the N values of Q_t, and the reliability probability p_s corresponding G > 0 was obtained, as indicated in Figure 3.

4 PROBABILISTIC ESTIMATION OF DEBRIS FLOW DISCHARGE IN FUSHIHG VILLAGE

Fushing village is located at Hualien county in eastern Taiwan. There were several severe debris flow events in the village during past five years. Figure 4 shows the debris flow hazard in Fushing village on July 31 2001,

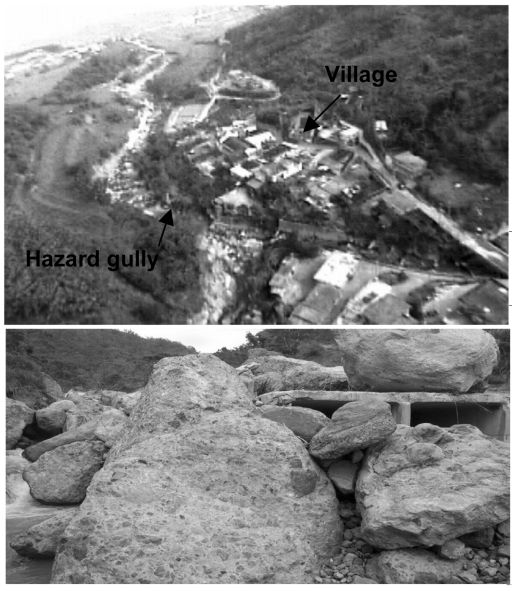


Figure 4. During typhoon Troaji period, a large amount of boulders deposited in the village upstream and damaged the road due to insufficient of bridge crossing section (DPRC 2001).

after typhoon Troaji attacked. A large amount of boulders deposited in the village upstream and damaged the road due to insufficient of bridge crossing section. Hence, how to estimate the debris-flow discharge and determine the design cross section reasonably is an important work in this area.

Given the rainfall coefficients (i.e., $I_r = 92.332$ mm, $k_1 = 0.551$, $k_2 = 0.305$, $k_3 = 18.206$ and $k_4 = 0.594$), a specified return period T and the parameters listed in Table 1, the reliability probability p_s for a certain value of debris-flow design discharge Q_d which exceed Q_t, i.e. $G = Q_d - Q_t > 0$, in Fushing village can be determined by MCSM. Figure 5 shows the relationship of the design debris-flow discharge Q_d against reliability probability p_s for various return period T. The relationship shows that the debris-flow discharge Q_d increases with the increase of T and p_s. This result implies that the larger Q_d is needed if we choose the larger rainfall return period and higher reliability index in design work.

The probabilities of debris-flow design discharge at various return period are also estimated by FOSM (Chen et al. 2002), and indicated in Figure 5 for comparison. Figure 5 shows that Q_d determined by FOSM is trifle greater than that by MCSM in most ranges of reliability probability ($0.2 < p_s < 0.6$). For example, $Q_d = 108$ cms by FOSM and $Q_d = 103$ cms by MCSM if we give $p_s = 0.5$ and $T = 50$ years. That is, the determined debris-flow design discharge from FOSM is

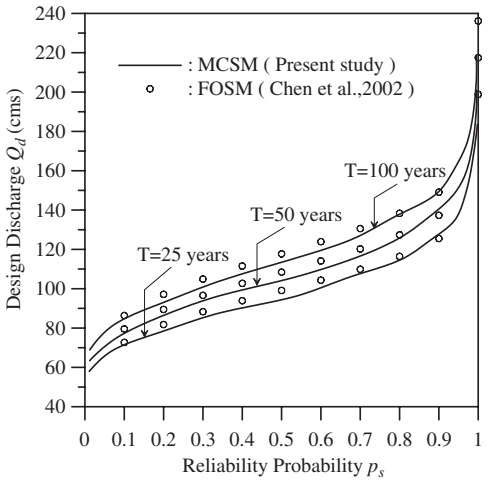


Figure 5. Debris-flow design discharge Q_d versus reliability probability p_s at various return periods T in Fushing village, Taiwan.

more conservative or safety than that from MCSM. Anyway, the debris-flow design discharge determined by FOSM is close to that by MCSM. The relative error is less than 10%. In general, the MCSM may obtain better results than the FOSM, since the MCSM is an exact method. However, the evaluation of p_f by FOSM is much faster than that by MCSM. The comparison in Figure 5 reveals that the debris-flow design discharge obtained by FOSM is indeed a good approximation to that obtained by MCSM.

5 CONCLUSIONS

A debris-flow discharge equation contains three hydrogeological parameters, such as the runoff coefficient, sediment concentration and overland flow velocity, and four topographical parameters, such as the watershed area, the length of overland flow, the horizontal stream length and elevation difference of stream. The uncertainties of the seven parameters in Fushing village in the eastern Taiwan are analyzed and evaluated. Taking into consideration of the parameters uncertainties, we have developed a relationship of debris-flow design discharge versus reliability probability at various return periods by using Monte Carlo simulation method (MCSM). This result obtained by MCSM is also compared with that from previous study by First-order second-moment method (FOSM). These comparisons show that the debris-flow design discharge determined by MCSM is close to that by FOSM.

REFERENCES

Ang, A.H.-S., Tang, W.H. 1984. *Probability Concepts in Engineering Planning and Design*, *Vol. II: Decision, Risk, and Reliability*. New York: John Wiley& Son.

Chen, J.C., Lee, M.H. & Jan, C.D. 2002. Calculation of Debris-Flow Discharge in a View of Probability. In D. Bousmar & Y. Zech (eds), *River Flow 2002; Proceedings of the International Conference on Fluvial Hydraulics, Louvain-la-Neuve, Belgium, 4–6 September 2002*. Rotterdam: Balkema.

DPRC (Disaster Prevent Research Center). 2001. *Investigation of Debris-Flow Disasters in the Typhoon Toraji*. National Cheng Kung University. Taiwan (in Chinese).

Harr, M.E. 1987. *Reliability-based design in civil engineering*. New York: McGraw-Hill.

Jan, C.D., Lee, M.H. & Chen, J.C. 2003. Reliability analysis on design discharge of debris flow. In D. Rickenmann & C.L. Chen (eds). *The third international conference on Debris-Flow Hazards Mitigation: Mechanics, Prediction, and Assessment*. *Davos, Switzerland, 10–12 September 2003*. Rotterdam: Millpress.

SWCTC (Soil and Water Conservation Technique Criteria). 2000. *Soil and Water Conservation Technique Criteria*, Soil and Water Conservation Bureau of Committee of Agriculture, Taiwan. (in Chinese).

Kang, Z.C. 1985. *Analysis of Maximum Discharge of Mud-Flow in Jiangjia Ravine, Dongchuan, Yunnan*. Peking: Science Press. (in Chinese)

Rubinstein, R.Y. 1981. *Simulation and the Monte Carlo method*. New York: John Wiley&Son.

Takahashi, T. 1978. Mechanical Characteristics of Debris Flow. *Journal of the Hydraulics Division*. HY8: 1153–1169.

Wang, M.P. 1995. *Hyperconcentrated flow and Debris Flow*. Peking: Hydraulics and Power press (in Chinese)

Wang, W.J., Chang, S.C. 1985. *Characteristics of Debris Flow in Ice Gully, Xichang*. Peking: Science Press (in Chinese).

APPENDIX I

The coefficients, k_1, k_2, k_3, and k_4, and the reference rainfall intensity I_r in Eq. (1) are related to the averaged annual rainfall P (mm), as following relations,

$$k_1 = \left(\frac{P}{42.89 + 1.33P}\right)^2 \quad \text{(A1)}$$

$$k_2 = \left(\frac{P}{-65.33 + 1.836P}\right)^2 \quad \text{(A2)}$$

$$k_3 = \left(\frac{P}{-189.96 + 0.31P}\right)^2 \quad \text{(A3)}$$

$$k_4 = \left(\frac{P}{-381.71 + 1.45P}\right)^2 \quad \text{(A4)}$$

$$I_r = \left(\frac{P}{25.29 + 0.094P}\right)^2 \quad \text{(A5)}$$

River Flow 2004 – Greco, Carravetta & Della Morte (eds.)
© 2004 Taylor & Francis Group, London, ISBN 90 5809 658 0

Concentrated mud suspensions flowing in open channels

G.F. Maciel & F.L. Santos
Department of Civil Engineering, São Paulo State University, Ilha Solteira, São Paulo, Brazil

ABSTRACT: Mixtures of clay and water exhibit, in general, non-Newtonian property to be up to solid concentration. The purpose of this article is, first, to characterize these mixtures of the physical and rheological point of view. Under controlled conditions, the temperature, pH, and volumetric concentration influence on flow curve of this mixtures, were determined. Second, to carry out dynamic experiments in open channel in order to determine empirical wall stress formula (friction laws) from depths and discharges measured. It can also be obtained, from a global quantity analysis, behavior laws of several rheological parameters due to volumetric concentration. The fitted rheological model was Herschel-Bulkley, $\tau = \tau_c + k(\dot{\gamma})^n$ where τ_c: critical shear stress (yield stress), k: apparent viscosity; n: index of flow; and $\dot{\gamma}$ is shear rate.

Finally, due to rheological properties of material and the dynamic characterization of flow, it was determined the friction law to the hyper-concentrated fluids flowing in wide inclined long channel.

1 INTRODUCTION

Resulting mixtures of Newtonian fluids behavior and solid particle appear with frequency in the nature and industry. Those mixtures exhibit, as a rule, non-Newtonian properties (COUSSOT, 1997). In general, when we approach these mixtures, we identify, first, flows such as wastewater (sewage sludge), slurry coals, mud proceeding of oil explotation, fresh concrete, agroalimentary fluids. Second, we identified phenomena related to sedimentation process in reservoirs, deposition in irrigation channels, transport and finally, the landslides, sand liquefaction, erosive actions and torrential lavas – this real "mud sea" and debris which have banned the life of hundred of people at the world.

From those motivation, came up interests in diagnose, to a better refined way, and with engineering point of view, physic properties of non-Newtonian matrix (water + clay mixture), once characterized, would be insert to flowing studies with laminar behavior (mudflows) or turbulent (mud fronts, urban floods) according to friction laws.



Figure 1a. Mud flowing in a river.

2 WATER + CLAY MIXTURE RHEOLOGICAL CHARACTERIZATION

To the mixtures rheological characterization, R/S rheometer (Figure 2a) was used for controlling shear



Figure 1b. Mud flowing in small channels at FEIS/UNESP laboratory.

stress and shear rate. The chosen geometry is the kind of that uses coaxial cylinder (Figure 2b) equipped with temperature control (circulating water bath). Supported by Rheo2000 software, could be gauged, to a better refined way, the Herschel-Bulkley parameters, as well the flow curves to each material essayed.

The following results aimed to explain some characteristics of essayed mixtures (water + kaolin clay) related to temperature variation, pH, and volume concentration.

2.1 *Temperature changing analysis*

As it was analyzed (Figure 3), the temperature changing at the sample did not seem to influence to a significant on the flow curve, above all if we consider a zone of temperature that comprises the ambient



Figure 2a. R/S Rheometer.



Figure 2b. Coaxial cylinders geometry and spindles.

temperature ($0°C < T < 30°C$). So, we can reassure ourselves when the temperature control at the moment of rheometry tests.

2.2 *Ph variation analysis*

It was noticed, as showed results Figure 4, that the pH influence of the mixture at the rheological curve is small in this study. However, the variation of these

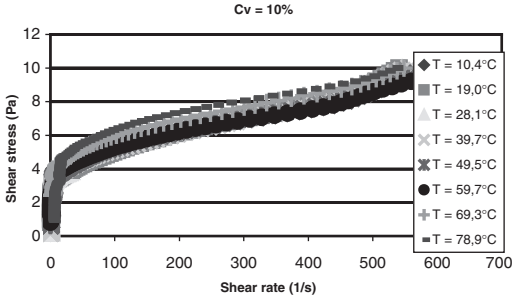


Figure 3. Flow curves in function of temperature.

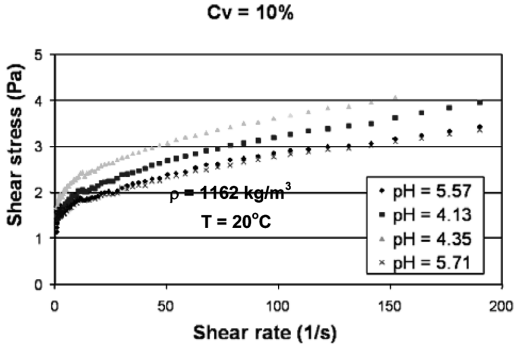


Figure 4. Flow curves in function of pH.

parameters showed itself being more significant than the temperature effect over the shear stress.

2.3 *Concentration variation in volume (Cv) analysis*

It is noticed that hyper-concentrated fluid viscosity goes up due to solid concentration existent to the mixtures. This carry out because as much bigger takes the solid material amount, bigger will be the friction of flowing material, and consequently, it will be larger the stress to produce a certain shear rate.

This way, it also can be noticed that critical stress of fluid increases with the concentration, and, consequently, the minimum stress necessary to produce a deformation is also bigger. Such fact is attested at Figure 5.

2.4 *Comparative global analysis to other rheological models*

Which follows, we show some rheological behavior to some concentrations in volume trying to compare Newtonian, Binghamian and Herschel-Bulkley rheological models to the experimental data. An example of fitting and good adaptability of Herschel-Bulkley is shown at Figure 6, whose data are listed in Table 1.

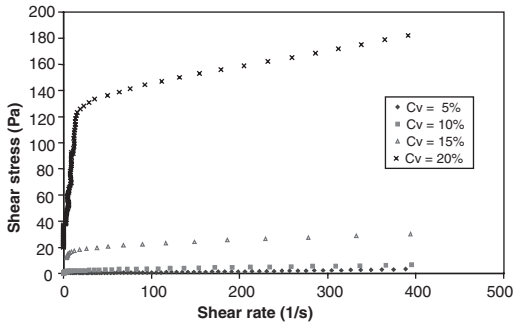


Figure 5. Flow curves in function of Cv variation.

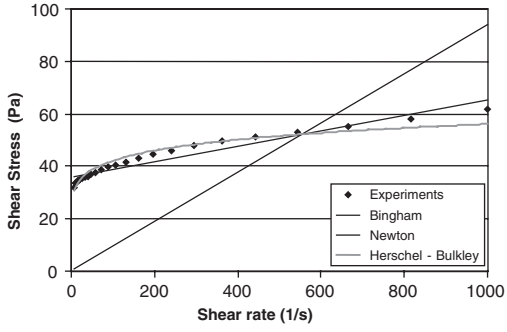


Figure 6. Flow curve of water + kaolin clay – Cv = 15%.

Table 1. Rheological models parameters to water + kaolin clay mixtures.

	Herschel-Bulkley model			
Cv (%)	τ_c (Pa)	k (Pa.s^n)	n	R^2
10	1,26	0,22	0,47	0,99
15	29,45	1,3	0,46	0,98
20	192,27	46,29	0,27	0,98

	Bingham model			Newton model ($\tau_c = 0$en $= 1$)	
Cv (%)	τ_c	μ_B (Pa.s)	R^2	μ (Pa.s)	R^2
10	1,7529	0,01	0,96	0,027	–
15	35,818	0,029	0,929	0,094	–
20	211,66	0,152	0,95	0,515	–

2.5 *Global quantitative analysis of rheological parameters due to Cv variation*

Some scientific works point out that the parameters of rheological model proposed by Herschel-Bulkley follow, to kaoline clays, the following pattern: τ_c values (critical stress) and k (apparent viscosity)

increases exponentially with the solid mixture volume concentration. On the other hand, (flowing index n) value lessens to the concentration, obeying to a power law.

From the data of WAN (1982), HUANG & GARCIA (1998), COUSSOT (1992) and MACIEL et al. (2002), we took the following relation:

$$\tau_c = 0{,}0073e^{0{,}4248C_v}$$

$$k = 0{,}0073e^{0{,}3665 \cdot C_V}$$

$$n = 1{,}529C_v^{-0{,}5039}$$

Those relations above all introduce good coefficients of correlation ($R^2 > 0.90$), comprised a large range of concentration in volume ($5\% < Cv < 20\%$), that includes and explains well the results of other authors.

3 DYNAMIC CHARACTERIZATION OF FLOWING IN CHANNELS

Based on works of COUSSOT (1998) and starting by hypothesis of uniform, steady, laminar and incompressible flow, flowing in an infinitely wide inclined plan, we obtained an expression of specific discharge, that is extremely useful at the dynamic characterization to this kind of flowing.

$$q = \frac{\alpha}{(1+m)} z_0^{(1+m)} \left[h - \frac{z_0}{(2+m)} \right] \quad (1)$$

with:

$$\alpha = \left(\frac{\rho g \sin\theta}{k} \right)^m ; \; z_0 = h - \frac{\tau_c}{\rho g \sin\theta} ; \; m = \frac{1}{n}$$

sin θ: declivity of channel; ρ: volumetric mass; τ_c, k, n: rheological parameters (Herschel-Bulkley); q: specific discharge.

For calculating the friction coefficient, from a dimensional analysis (using convenient scale), we could determine G and H_b dimensionless numbers that show themselves essential to this study as follow:

$$G = \frac{\rho g h \sin\theta}{\tau_c} \quad (2)$$

$$H_b = \frac{\tau_c}{k} \left(\frac{h}{\bar{u}} \right)^n \quad (3)$$

with:
h: normal depth $\bar{u} = \frac{q}{h}$

The friction at the channel bottom is given according SANTOS (2003) by:

$$\tau_p = G\tau_c \quad (4)$$

Equation to be gauged through experimental data, or in addition;

$$\tau_p = \tau_c [1 + H_b^{-1}] \quad (5)$$

Theoretical friction law – it does not depend on the channel geometry, in this stage.

4 EXPERIMENTAL RESULTS IN ORDER TO DETERMINE FRICTION LAW

4.1 *Experimental apparatus description and methodology of essays*

The experimental apparatus (Figure 7) consists to a 10 meter length channel, with variable width (until 0.60 m), and with declivity until 30%. There is a recirculating system where the hyper-concentred flow is warranted by a 7.5 CV motorpump that transport mud to the superior reservoir of constant level. A frequency invertor does the control of discharge. The normal depths were measured with a metallic ruler and ultrasonic sensors in 3 different points of channel. The discharges vary from 1.0 to 10.0 l/s.

From characteristic equation of specific discharge, Equation 1, we prepared a sample with concentration in volume Cv = 13% and we put it to flow on the experimental channel. The essay was done for three declivity of channel, around 6.3°, 12.2° and 17.4°. In



Figure 7. Mud flowing in channel.

each declivity, there was five variation of discharge. At the same time that took place the flowing essay, it was collected a sample to a rheological test.

All the information obtained at related flow, as well the gauged rheological parameters with Brook-field R/S rheometer, are shown at Table 2.

With: n: flowing index; τ_c: critical shear stress, k: apparent viscosity; Cv: Volume concentration; $\rho 0$: Volumetric specific mass mixture; sin θ: Declivity of channel; h: Normal depth; q (theoric): Theoretical specific discharge (semi-experimental, so it depends of h measure and rheological parameters); L: Width channel; q (exp): Experimental specific discharge; error: Relative error among experimental and theoretical specific discharge.

We can notice that the results present, most of the cases, high errors to the discharges. These errors can be explained by great sensibility of some parameters. Even the normal depth (h), showed at Table 2 be an average took out from several measuring done along the channel, such as, any lack of precision at its measuring, produces a considerable error, so this parameter interferes significantly to the calculus of the theoretical specific discharge (Equation 1). Other procedures of essay have being improved for trying to solve this uncertain.

4.2 *Discussing experimental results*

To the analysis of experimental data, the dimensionless numbers $(G - 1) \times H_b$ are illustrated in Figure 8. This way, from comparison among adjusted equation to theoretical points (semi-experimental) obtained through this figure and Equation 5, we can analyze the conformity between the theoretical development and experimental results.

At this analysis, Hb number is obtained by Equation 3, using in the calculus the theoretical specific discharge (semi-experimental). For comparison, it was plotted the data of Hb obtained with experimental values of discharges q (exp), measured by volumetric method.

At this case, we obtained to the following experimental relationship:

$$G = 1 + 1{,}7777\ H_b^{-0{,}8779} \quad (6)$$

$$G = 1 + 1{,}846\ H_b^{-0{,}5393} \quad (7)$$

In order to define the influence of geometry on empirical wall stress formula (friction law), we are undertaking additional experiments, varying width of channel and also the section.

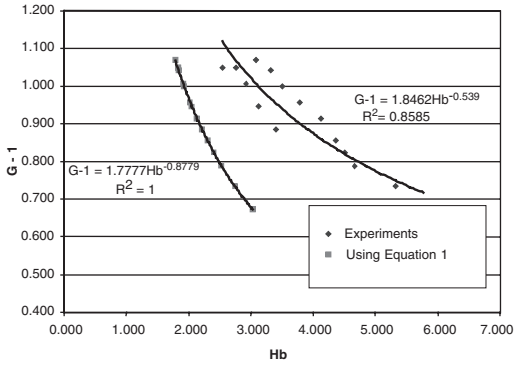


Figure 8. Friction law behavior: G − 1 versus Hb.

Table 2. Rheological, dynamic and geometric parameters obtained to water + kaolin clay mixtures flowing in the big channel.

	n	τ_c (Pa)	k (Pa.s^n)	C_v (%)	ρo (kg/m^3)	sin θ	h (m)	q (theoric) (m^3/s/m)	L (m)	q (exp) (m^3/s/m)	error (%)
decliv1	0.2859	34,545	7,2775	15,4	1249,48	0,0632	0,0746	0,026793	0,6	0,002811	1422,1
	0,2859	34,545	7,2775	15,4	1249,48	0,0632	0,0773	0,040736	0,6	0,004004	1529,0
	0,2859	34,545	7,2775	15,4	1249,48	0,0632	0,0797	0,057555	0,6	0,006765	1251,4
	0,2859	34,545	7,2775	15,4	1249,48	0,0632	0,0813	0,071586	0,6	0,007954	1333,3
	0,2859	34,545	7,2775	15,4	1249,48	0,0632	0,0827	0,086012	0,6	0,009169	1396,8
decliv2	0,2859	34,545	7,2775	15,4	1249,48	0,1207	0,0447	0,032895	0,6	0,003283	1503,4
	0,2859	34,545	7,2775	15,4	1249,48	0,1207	0,0457	0,041225	0,6	0,004651	1310,5
	0,2859	34,545	7,2775	15,4	1249,48	0,1207	0,0467	0,051181	0,6	0,00629	1189,6
	0,2859	34,545	7,2775	15,4	1249,48	0,1207	0,0477	0,062996	0,6	0,008033	1140,4
	0,2859	34,545	7,2775	15,4	1249,48	0,1207	0,0483	0,071082	0,6	0,010548	956,5
decliv3	0,2859	34,545	7,2775	15,4	1249,48	0,1714	0,031	0,013915	0,6	0,003105	580,3
	0,2859	34,545	7,2775	15,4	1249,48	0,1714	0,032	0,019303	0,6	0,004392	565,8
	0,2859	34,545	7,2775	15,4	1249,48	0,1714	0,033	0,026262	0,6	0,005967	566,9
	0,2859	34,545	7,2775	15,4	1249,48	0,1714	0,0337	0,032242	0,6	0,007626	537,9
	0,2859	34,545	7,2775	15,4	1249,48	0,1714	0,0337	0,032242	0,6	0,010203	360,0

Table 3. Values of friction tensions.

(1) Friction (Pa) equation 5	(2) Friction (Pa) equations 6 and 4	(3) Friction (Pa) equations 7 and 4	error (%) (1) and (3)	error (%) (1) and (2)	error (%) (2) and (3)
45,95	57,76	59,33	29,11	25,70	2,72
47,14	59,88	60,43	28,19	27,01	0,93
48,21	61,75	62,35	29,32	28,09	0,97
48,93	63,00	62,88	28,51	28,76	0,19
49,55	64,09	63,35	27,85	29,32	1,16
50,76	66,15	64,27	26,63	30,33	2,93
51,62	67,62	65,70	27,28	31,01	2,93
52,48	69,09	66,96	27,59	31,64	3,18
53,35	70,56	67,99	27,44	32,24	3,77
53,87	71,43	69,29	28,62	32,59	3,09
50,17	65,15	67,54	34,61	29,85	3,67
51,40	67,24	69,01	34,28	30,84	2,63
52,62	69,33	70,34	33,66	31,74	1,45
53,49	70,78	71,48	33,63	32,33	0,98
53,49	70,78	73,17	36,80	32,33	3,38

4.3 *Determination of friction law*

Theoretical (semi-experimental) and experimental friction values estimated to 0.60 m channel of width are presented in Table 3.

5 CONCLUSIONS

The rheological characterization of mixtures and flowing dynamic mud mixture were inferred with success and showed the following conclusions:

- The water + clay essayed showed themselves, such prediction, non-expansible, they did not show thixotropic phenomena (not showed at this article) and changing the basic rheological properties, such as critical shear stress (τ_c), flowing index (n) and apparent viscosity (k) due to volume concentration (Cv);
- The experimental results fitted well to the Herschel-Bulkley rheological model, noticeable at the determining of critical shear stress and to the large shear rates range ($\dot{\gamma} \sim 100\,s^{-1}$: shear rate observed at field to the mudflow phenomena);
- However, it was also verified a good adaptability to Binghamian model to high shear rates.

This way, based on experimental results obtained at FEIS/UNESP, a new database was established. From this, it was obtained evolution laws of several rheological parameters, according to that was presented at item 2.5 of this article.

- The obtained results for friction of wall at the experiments taken at the channel, showed them-selves highlighting. However, the percentual errors over the specific discharge (Table 2) and on Hb calculus are high, we have found errors to friction, final aim, (Table 3) is satisfactory (order of 3%).

Finally, it is really worth point up during the experiments, under some situations of geometry, discharges and declivities, they were noticed roll waves phenomena with wavelength well defined according to reporting by COUSSOT (1997) in his experiments.

The criteria of generation and numerical analyses, from shallow water equations, have been studied by MACIEL et al. (1997, 2002) and others researchers.

REFERENCES

Bingham, E. C. 1992. Fluidity and Plasticity, McGraw-Hill, New York.

Borges, A. L. O., Tarqui, J. L. Z. 1999. Determinação das Propriedades Reológicas de Sedimentos Finos em Suspensão Obtidos de Três Tipos de Solos do Estado do Rio Grande do Sul do Brasil. CD ROM do IV Silusba – Coimbra-Portugal.

Chen, C. L. 1988. Generalized viscoplastic modeling of debris flow. Journ. Hydr. Div., ASCE 114: 237–258.

Chen, C. L. 1998. General solution for viscoplastic debris flow. Journ. Hydr. Div., ASCE 114: 259–282.

Coussot, P. 1988. Rhéologie des boues et laves torrentielles – Etude de dispersions et suspensions concentrées. Tese de doutorado, Institut National Polytechnique de Grenoble.

Coussot, P. 1992. Rhéologie des boues et laves torrentielles – Etude de dispersions et suspensions concentrées, Institut National Polytechnique de Grenoble, 1992.

Coussot, P., Piau, J. M. 1994. On the behavior of mud suspensions. Rheologica Acta, Vol. 33, No. 3, pp. 175–184.

Coussot, P., Proust, S., Ancey, C. 1996. Rheological interpretation of deposits of yield stress fluids. J. Non-Newtonian Fluid Mech., Vol. 66: 55–70.

Coussot, P. 1997. Mudflow rheology and dynamics. IAHR Monograph Series.

Huang, X., Garcia, M. H. 1998. A Herschel-Bulkley model for mud flow down a slope. J. Fluid Mech., Vol. 374: 305–333.

Huang, X., Garcia, M. H. 1998.A Herschel-Bulkley model for mud flow down a slope. J. Fluid Mech., Vol. 374: 305–333.

Li, G., Wei, H., Han, Y., Chen, Y. 1998. Sedimentation in the Yellow River delta, part I: flow and suspended sediment structure in the upper distributary and the estuary. Marine Geology, Vol. 149, Issue: 1–4, pp. 93–111.

Li, J., Yuan, J., BI, C. & LUO, D. 1983. The main features of the mudflow in Jiang-Jia River. Zeit. Geomorph, 3, 27, 325–341.

Liu, K., Mei, C. C. 1989. Slow spreading of a sheet of Bingham fluid on an inclined plane, J. Fluid Mech. 207, 505.

Maciel, G. F., Vila, J. P., Martinet, G. 1997. Roll wave formation in the non Newtonian flows. XIV COBEM. Bauru, São Paulo, Brasil.

Maciel, G. F. et al. 2002. Project technical report of research FAPESP 00/14853–5.

Piau, J. M. 1996. Flow of a yield stress fluid in a long domain, application to flow on an inclined plane. J. Rheology, Vol. 40: 711–723.

Santos, F. L. 2003. Estudo teórico-experimental em via de determinação de uma lei de atrito em escoamentos de fluidos hiperconcentrados, Dissertação de Mestrado, FEIS/Unesp.

Wan, Z. 1982. Bed material movement in hyperconcentrated flow, Ser. Pap. 31 Inst. of Hydrodyn. and Hydraul., Tech. Univ. of Denmark, Lyngby.

This page intentionally left blank

River Flow 2004 – Greco, Carravetta & Della Morte (eds.)
© 2004 Taylor & Francis Group, London, ISBN 90 5809 658 0

Numerical simulation and field observation of debris roll waves in the Illgraben torrent, Switzerland

B. Zanuttigh
University of Bologna, Dipartimento di Ingegneria delle Infrastrutture, Strade, Trasporti, Acque, Rilevamento e Territorio, Bologna, Italy

B.W. McArdell
WSL Swiss Federal Research Institute, Department of Water, Soil, and Rock Movements, Zuerich, Switzerland

ABSTRACT: In natural debris flows, even if the critical Froude number is almost always exceeded, the formation of waves, which eventually develop into surges, is not always observed. This contribution numerically represent a debris flow event occurred in the Illgraben torrent, Swiss Alps, which consisted of a single surge and of about 28 roll waves on the surge tail. Simulations are carried out with two 1-D codes based on Shallow-Water equations and a wide variety of rheological laws (Herschel Bulkley, Bingham, Dilatant Inertial, Generalised Visco-Plastic, Voellmy).

The analysis of flow depth in time, maximum flow depths and velocities along the debris channel shows that a good representation of the main debris features can be obtained with a proper calibration of rheological parameters. More difficult appears to be the representation of flow tail instabilities.

The causes of debris wave development based on literature and interpretation of the model results are examined and an original interpretation is provided.

1 INTRODUCTION

The formation of instabilities in debris or mud flows has been investigated by several authors, among the others Chun (1982), who determined the stability curve for generalised Newtonian flows; Trowbridge (1987), who carried out the same analysis using shallow water equations; Lanzoni and Seminara (1993) experienced that a granular flow becomes unstable for Froude numbers around 1.0; Coussot (1994) showed that for a Herschel-Bulkley fluid the critical Froude number drops to 0.25 or less; Lamberti & Zanuttigh (2003) extended Trowbridge's method to a Generalised Visco-Plastic flow.

In several cases instabilities should be evident according to theory but do not show-up in nature; moreover, the mechanism of formation of multiple surge events is still unclear and the possibility to predict such features is still uncertain.

This contribution aims to examine through numerical simulations and field observations wave development in debris flows. The numerical model is based on Shallow-Water equations, which are able to capture the position and to reproduce the intensity but not the shape of the debris front. An accurate analytical solution for representing the flow profile at the front as well as at the tail, of two-dimensional unsteady non-uniform Bingham and Herschel-Bulkley flows down a steep slope can be found in Huang and Garcia (1997) and (1998) respectively.

This contribution is divided in four main parts. The first part presents the numerical models adopted. The 1D numerical formulation is adopted since reflections, diffractions and refractions, which are clear in water flows, do not seem to substantially affect debris flows, as it is proven by field surveys (Berti et al., 1999; Mortara et al., 1994; Rickenmann et al., 2001) and several video registrations (Arattano & Trebbo, 2000; Lamberti, 1999; Rickenmann, 2000).

The second part presents the catchment under analysis from a hydro-morpho-geological point of view and the debris flow events, a single-peak and a multiple-surge event.

The third part compares numerical results to available flow depth and velocity registrations for different rheological laws and calibrations of the rheological parameters.

Finally, an interpretation for the formation and development of instabilities is provided, based on the analysis of numerical simulations and on hydrographs measured during debris events (Arattano et al., 1997).

2 NUMERICAL MODELS

2.1 *Numerical scheme*

Both numerical models applied in this study are based on one-dimensional solutions to the conservative form of the shallow water equations, where the frictional resistance term typically used for open channel flow (e.g. a Chézy flow resistance law) has been replaced with flow laws which have been proposed to describe debris flow behavior. The primary unknowns are flow depth and specific discharge. Only the main features are summarized here because both models have been described elsewhere.

The DFEM model from WSL is a finite element solution of the shallow water equations in one dimension and is based on the Finite Element Method TOOLbox (FEMTOOL) libraries developed by Rutschmann (1993). Many research problems using the 1-D, 2-D, and 2-D extended shallow water equations have been addressed using the FEMTOOL codes (Näf, 1997, Krüger, 2001) and a 2-D version of the code for debris flows is under development at WSL. The main modifications for application to debris flow routing are the inclusion of debris flow laws and a treatment of the transition from wet-to-dry cells involving simple cut-off velocities and depths. When the predicted velocity or depth is below some small user-specified value (a few cm for the flow depth) the bed is assumed to be dry. To increase the numerical stability, it was necessary to introduce an upwind scheme (e.g. Katopodes, 1984).

The WAF-DF model from the University of Bologna (Zanuttigh & Lamberti, 2002) solves the equations using the weighted average flux (WAF) method of Toro (1997). This method is 'shock-capturing' in the sense that discontinuities are automatically treated correctly without the need for a special tracking algorithm. For this reason, the code has been especially useful in interpreting the propagation of roll waves in debris flow surges using data from the Acquabona torrent in Italy (Zanuttigh & Lamberti, 2003).

2.2 *Rheological laws*

Single-phase flow laws can be divided into three major categories (Iverson, 1997), turbulent flow laws (e.g. the Voellmy flow law, Bartelt et al., 1999), laminar flow laws (e.g. the Herschel-Bulkley formulation, Coussot, 1997), and grain-shearing flow laws (e.g. the dilatant-inertial formulations, Takahashi, 1991).

The DFEM model has been designed to allow for systematic comparisons of the major categories of flow laws and combinations of flow laws when appropriate (O'Brien et al., 1993). For this paper, one example from each of the three categories of resistance relations has been applied, the Voellmy Fluid (VF), Dilatant-Inertial or Grain Shearing (DI), and Simplified Bingham relations (SB). The relations are incorporated into the model in the friction term and are therefore expressed here in terms of the friction slope, S_f.

The Voellmy Fluid (VF) resistance relation (Hungr 1995) consists of a Chézy-type turbulent friction term and a Coulomb-type dry friction term:

$$S_f = \frac{q\sqrt{q^2}}{h^2 C^2 h_r} + \cos\alpha \tan\delta \tag{1}$$

where q is the specific discharge, h is the flow depth, h_r the hydraulic radius, C ($m^{1/2}s^{-1}$) is the Chézy flow resistance coefficient, α is the slope angle of the channel and δ is the angle of internal friction. The Voellmy relation was developed to describe flow-type snow avalanches (Bartelt et al. 1999) and with the Coulomb term allows the flow to stop on inclined surfaces.

The Dilatant-Inertial (DI) law can be stated in a simple form:

$$S_f = \frac{q^2}{h^5 \zeta^2} \tag{2}$$

where ζ is a roughness parameter ($m^{-1/2}s^{-1}$).

The laminar flow relation is the simplified version of the Bingham flow (SB) law (Hungr 1995, Rickenmann 1990). We use the following relation to incorporate the Bingham flow law:

$$S_f = \frac{\tau_0}{\rho g h} \tag{3}$$

where g is the acceleration due to gravity and ρ is the bulk density of the flowing debris, and τ_0, the shear stress, is given by the solution to the cubic equation from the Bingham relation:

$$2\tau_0^3 - 3\left(\tau_C + 2\frac{\mu_B q}{h^2}\right)\tau_0^2 + \tau_C^3 = 0 \tag{4}$$

In the DFEM code, the cubic term may be dropped and leading to:

$$\tau_0 = 1.5\tau_C + 3\frac{\mu_B q}{h^2} \tag{5}$$

where τ_C is the yield stress, μ_B is the viscosity. For the case where the stress ratio τ_C/τ_0 is smaller than 0.5, the error in the mean flow velocity is on the order of 6% (Rickenamm 1990).

The rheological behavior of the WAF-DF model is alternatively supposed to follow:

1) the Herschel-Bulkley (HB) model, which is given by:

$$\tau = \tau_c + K\gamma^{0.33} \tag{6}$$

where τ_c is the cohesion or yield stress parameter, K is the consistency index and γ is the shear rate;

2) the Bingham (B) model

$$\tau = \tau_c + \mu_b \gamma \tag{7}$$

where μ_b is the consistency index;

$$\tau = \tau_c \cos\phi + \sigma \sin\phi + \mu_1 \gamma^{\eta} = \tau_y + \tau' \tag{8}$$

where μ_1 is the consistency index and η is the law's exponent. The sum of the first two terms at the second member of (8) represents the yield stress τ_y whereas the third term is the stress τ' due to shear rate.

B and HB models are trivial special cases of the GVP model: $\phi = 0$ and $\eta = 1.0$ or 1/3 respectively. The GVP model is characterised by two more degrees of freedom than the HB or B models and thus by two more parameters to be calibrated: the exponent of the rheology law η and the friction angle ϕ. Details on the procedure for evaluating flow resistance for this general case can be found in Zanuttigh and Lamberti, 2003.

In both models, the magnitude of the flow resistance term is limited to enhance numerical stability and provide more realistic results. In the DFEM model the magnitude of the friction term (expressed in units of energy) is not allowed to exceed the local kinetic energy of the flow. One implication of this limitation is that the vibrational kinetic energy of a debris flow cannot be converted into translational kinetic energy. In the WAF-DF model the flow resistance for the debris flow is assumed to be not less than turbulent fluid with an appropriate value of the Chézy coefficient, which is assumed equal to 22 $m^{1/2}s^{-1}$ following Rickenmann (1999).

3 ILLGRABEN CATCHMENT

The Illgraben catchment (10.5 km^2 above the fan apex) contains an unusually large proportion of unvegetated, steep, unstable slopes with abundant colluvium derived from weak carbonate and greywacke bedrock. The channel downstream of the fan apex is 2.6 km long, has a mean slope of 10%, and is presently deeply incised.

No information on the geometry of recent debris flow deposits on the alluvial fan is available because all debris flows in the last few years have traveled into the Rhone River where they are immediately reworked by the river flow. In order to stabilize the torrent bed after an avalanche occurred in 1960s, a nearly 50 m high sediment retention dam was installed upstream of the fan apex and many check dams were built up downstream this structure.

Several debris flows per year occur generally following intense rainfall in the catchment (Rickenmann et al., 2001) and some presented (McArdell et al., 2003) multiple peak hydrograph that can be interpreted as the result of instability of uniform debris flow conditions.

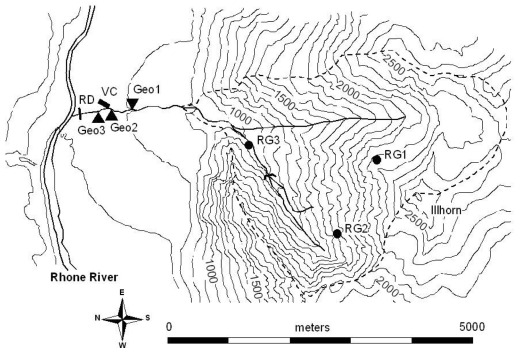


Figure 1. Debris flow observation station at the Illgraben torrent with the location of the geophones (Geo) video camera (VC), radar (RD) and rain gages.

The downstream 850 m of the channel has been instrumented with 3 geophones, a radar flow depth sensor, and a video camera, with data logging triggered automatically by the upstream-most geophone (Figure 1). Observations consist of flow velocities estimated from the travel time between the geophones and a radar sensor and flow depths from the radar. The videos provide additional velocity and depth estimates as well as qualitative observations of the flow behaviour and maximum grain size. An independently-operated network of three rain gages was installed in the upper catchment in 2000.

4 NUMERICAL SIMULATIONS

4.1 *The event of June, 2000*

The event of 28 June 2000 was selected because of the availability of several field data as independent field observations of surface velocity, cross section and mud traces collected after the event to reconstruct maximum flow depths and wetted areas.

From the front travel time between the instruments, the flow depth estimated at the radar and the analysis of video images, the total volume of this event can be evaluated around 35,000 m^3; the maximum discharge was 125 m^3s^{-1}, the front velocity arose 3.9 ms^{-1} and the peak flow depth was close to 3 m. The flow was observed to have a single coarse granular surge moving over an initially dry bed (Figure 2) carrying boulders more than 2 m in diameter. The tail of the debris flow was muddy and low-amplitude roll waves were observed starting about 600 seconds after the passage of the front.

Numerical simulations were carried out on the topography obtained by a field survey performed in



Figure 2. Debris flow front for the 28 June 2000 event from the video tape. The base width of the check dam is about 10 m. Mud traces from an earlier event in summer 2000 are still visible immediately downstream of the front.

2000; the channel cross sections were approximated for simplicity to rectangle with variable-width and the base of the sediment retention dam was used as starting point. As no rainfall data was collected, a simple triangular hydrograph was assumed as upstream boundary condition. Based on the downstream observations of total volume, mean flow velocity and depth, the hydrograph is built up so that after 14 s flow discharge reaches the maximum value of $14\,m^2s^{-1}$ and after 236 s returns to zero. Other hydrographs were tested, but in general the differences from plausible alternatives tend to be damped by the development of near-uniform flow over the more than 3000 m long reach from the base of the retention dam to the observation station, so a detailed parametric analysis of input conditions is not included here.

The models were run with incremental changes of the parameters until a "best fit" was achieved. For comparison with the field data, the results are presented by comparing model results with the front velocity measured between instruments in the field and the flow depth determined from the radar. The results can be difficult to interpret because there may not be a unique combination of parameters that allow one to match both the front velocity and the flow depth. The following 'best' calibrations were adopted in this contribution:

- for the DFEM: SB, $\mu_b = 130$ Pa·s, $\tau_b = 100$ Pa, $\rho = 2200\,kg/m^3$; DI, $\zeta = 14\,m^{-1/2}s^{-1}$; VF, $C = 22\,m^{1/2}/s$, $\delta = 2.5°$;
- for the WAF-DF: HB, $K/\tau_c = 0.1\ s^{1/3}$, $\tau_c/\rho = 0.1\,m^2s^{-2}$; B, $\mu_b/\tau_c = 0.6$ s, $\tau_c/\rho = 0.1\,m^2s^{-2}$; GVP, $\eta = 0.5$, $\mu_b/\tau_c = 1.3$ s, $\tau_c/\rho = 0.2\,m^2s^{-2}$, $\phi = 1°$.

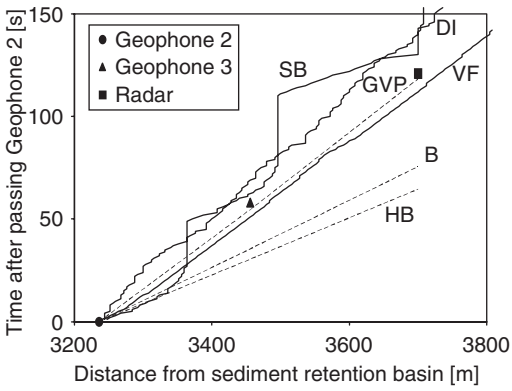


Figure 3. Comparison of front position with field data. Dashed lines indicate WAF-DF results and solid lines indicate DFEM results.

The comparison of front velocity between geophone 2 and the radar (Figure 3) shows a wide variety of flow behaviors for the different flow resistance laws. The curves for the WAF-DF model show a uniform velocity (similar to that observed in the videos), but the flow is too rapid in comparison with the field data for the Bingham and Herschel-Bulkley flow laws. These relatively large velocities are similar to what one would calculate with a Chézy model using $C = 22\,m^{1/2}s^{-1}$, suggesting that the value chosen to limit the magnitude of the friction term may be influencing the results for the flow laws using WAF-DF. However, the slope of the simplified Bingham model during periods of flow, which was run with the exact same set of parameters, is quite similar, so the apparent match with a Chézy model may be a coincidence. The curves for the DFEM model show good agreement for the dilatant and Voellmy resistance laws, but the surge-stop behavior of the simplified Bingham model is probably due to numerical instability and may have no meaningful physical interpretation. An exact match with the dilatant-inertial model was not possible because numerical instabilities. Additional pairs of simplified Bingham viscosities and yield stress values are also capable of matching the front trajectory; in the absence of flow deposits where one can estimate the yield stress, it is difficult to choose one "best fit" set of parameters. The slopes of the simplified Bingham model, when it is flowing, are similar to the Bingham law predicted with the WAF-DF model, suggesting that a different set of yield stress values (in particular a larger yield stress) may provide a better match with the data. The Voellmy fluid law is always numerically stable with this field case.

A comparison of modeled flow depth with the field data (Figure 4) shows that most of the resistance laws predict too shallow depths compared with field observations. In the simplified Bingham model

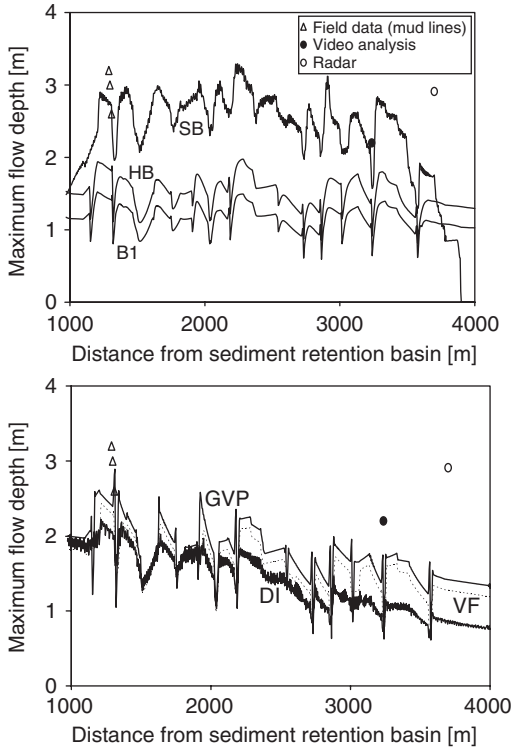


Figure 4. Maximum flow depths (top) obtained from the Simplified Bingham, Bingham, and General Viscoplastic models and the Voellmy Fluid, Dilatant-Inertial and General Viscoplastic model (bottom).

the stop-surge behavior may explain why the simplified Bingham model best reproduces the flow depth near the upstream end of the computational domain (Figure 4). However eyewitnesses did not observe the stop-start behavior and it is not apparent in the video images, suggesting that this is not a reliable numerical result. Perhaps the main difference between the field and model is the downstream diffusion of the wave resulting in lower flow depths downstream. This may be an artifact of simplifying the complex behavior of the debris flow using simple single-phase rheologies with one set of parameters to characterize the entire debris flow wave.

A comparison of the Bingham model results between the two models shows a striking difference in their predicted flow behavior in spite of the fact that the parameters used in the models are identical. Part of the discrepancy can be explained by each model's method of limiting the magnitude of the friction term; another possible explanation is that the Bingham model is inappropriate for such a granular flow. A Bingham Reynolds number, defined as $R_{eB} = 4Vh\rho/\mu_B$, where $V =$ the flow velocity, $h =$ the flow depth, $\rho =$ the bulk

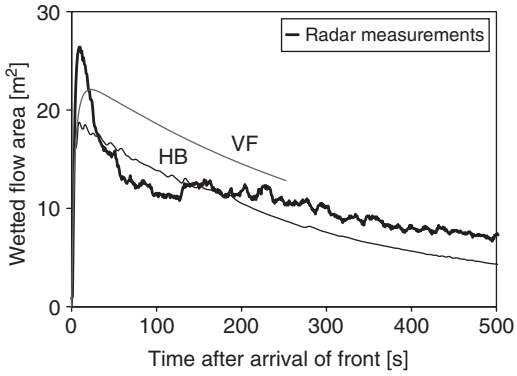


Figure 5. Comparison of field hydrograph for the Voellmy fluid and Herschel-Bulkley flow laws.

density of the debris, and $\mu_B =$ the Bingham viscosity of the flow, calculated for the front at the location of the video camera, is estimated to be on the order of 500, or within the laminar range reported by Rickenmann (1990). This suggests that laminar-type flow law (e.g. the SB, B, HB, and GVP models) does not contradict the simulated flow behavior. An analysis of a boulder motion shows roughly 2/3 of the particles showing periods of both rolling and non-rolling behavior over the 50 m section upstream of the video camera, suggesting that the qualitative description of a laminar fluid is an oversimplification for this granular debris flow.

The comparison of observed and modeled hydrograph shape shows a generally poor agreement between flow depths or areas, with all numerical simulations failing to match the observed flow depths by nearly a factor of 2. The comparison with wetted flow area at the radar location yields a better match with the tail of the debris flow (Figure 5).

All the 'best' calibrations obtained with the WAF-DF model predict an onset of roll wave activity at flow tail that is characterized by different wave periods and heights depending on the rheological law and calibration, as it clearly appears by Figure 6.

Table 1 compares the summary of numerical and measured wave statistics, showing that the calibration with GVP is the only one that reproduce the period of the onset of roll wave activity observed in nature, whereas none of the calibrations adopted is able to accurately represent roll-waves amplitudes.

4.2 *Discussion*

One major problem with the Illgraben data set is a lack of good data on the cessation of motion of the flow – most debris flows that remain in the channel, like this event, continue moving until they reach the Rhone River downstream where they are destroyed.

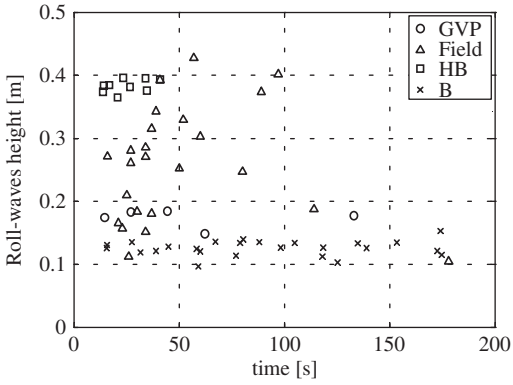


Figure 6. Roll waves height obtained with WAF-DF model.

Table 1. Roll-wave statistics (Results in Figure 6): n is the number of waves, T_m is the mean wave period, H_m is the mean wave height.

	Field	B	HB	GVP
n	24	25	9	8
T_m [s]	8	7	4	19
H_m [m]	0.27	0.13	0.39	0.17

Without information on the stopping angle or location of the debris flows, in many cases it may be impossible to find a unique pair of parameters to match the field results. In the case of the Voellmy model, the practical upper limit on the value of the Coulomb dry friction can be determined by the angle of the channel bed, and the best fit envelope of parameters varies linearly between $C = 14\,\mathrm{m}^{1/2}\mathrm{s}^{-1}$, $\delta = 0.6°$ and $C = 22\,\mathrm{m}^{1/2}\mathrm{s}^{-1}$, $\delta = 2.5°$.

In general the parameters from the model are realistic in that they are similar for values observed in the Acquabona torrent (Zanuttigh & Lamberti, 2003). The Voellmy parameters are also similar to those calculated for a smaller granular debris flow in the Schipfenbach torrent, Switzerland (Hürlimann et al., 2003), using a snow avalanche simulation program was used (with the density adjusted to represent debris instead of snow). The range of Chézy C values is in agreement with empirical values plotted as a function of peak discharge (Rickenmann, 1999).

Regarding the inaccurate representation of roll waves at flow tail for this event and in general the possibility of validated numerical models to accurately reproduce surges and secondary waves in natural events, an important role seems to be played by the upstream input hydrograph. In the case of Acquabona, for which the upstream hydrograph was reconstructed based on available rainfall measurements, it was possible to achieve, by calibrating the rheological parameters, a good match to field data both of wave periods and wave heights (Zanuttigh & Lamberti, 2003).

5 AN INTERPRETATION FOR WAVE DEVELOPMENT IN NATURAL EVENTS

In some cases, debris waves do not develop in nature even if the critical Fr is exceeded, as for the event of June 2000 in the Illgraben.

Among basins in which development of surges in debris events is well documented from measurements and observations, we can consider the Illgraben events already shown and the case of the Moscardo torrent, Northern Italy. The Rio Moscardo generates at least one event per year and has been since ten years object of a continuous and accurate monitoring (Arattano et al., 1997). Hydrographs measured along the channel during some events are reported at the left hand-side in Figure 7. Effects of the channel length cannot be appreciated, because the two hydrographs are measured in correspondence of two stations located at a distance of 300 m.

In all cases, a first surge is present and secondary waves develop during recession and become more evident with increasing effective duration of the event (top-down in Figure 7), independently on peak discharge. The first surge, mainly composed by boulders and coarser fractions, has an almost symmetrical shape and do last for a relevant time; depending on the event duration, instabilities can show-up as small waves in the descending reach of this first surge or as independent muddy secondary waves with asymmetrical shape, similar to water roll waves in the overtaking phase.

On the basis of these field observations and on numerical analysis (Zanuttigh and Lamberti, 2003) performed along Acquabona channel (Northern Italy), the interpretation sketched at the right hand-side in Figure 7 has been developed. Debris flows tend almost always to develop in theoretically unstable conditions, but debris waves are not always observed. In facts, the front of the event moves with the velocity of masses by which is composed ($dx/dt = u_c$), whereas the unstable perturbations are associated to celerities $dx/dt = u + c$, which are higher than front velocity u_c near the peak of the event. The space allowed for waves to develop is therefore larger the later they origin after peak crossing. When instabilities are not evident, space (length of the channel) and time (duration of the event) are insufficient to allow their development.

6 CONCLUSIONS

Debris waves do frequently develop in nature, whenever a critical Froude number Fr_{cr} is exceeded, causing

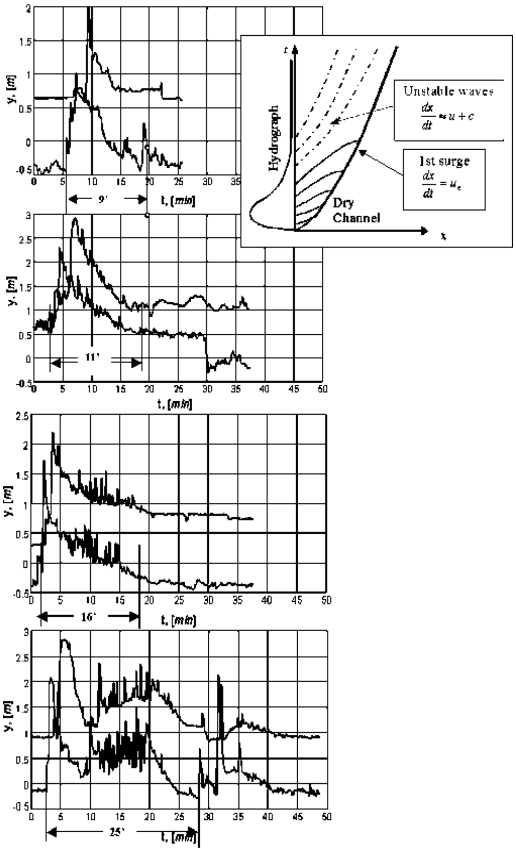


Figure 7. At the left hand side, measured hydrographs at two channel sections (300 m distant) of some events occurred in the Moscardo torrent (original plots in Arattano et al., 1997), on which the real duration of the event is highlighted: with increasing duration, instabilities do develop. At the right hand side, the sketch in the *x*-*t* plane graphically represents the interpretation by the authors for debris wave formation and development in space and time.

a significant increase in peak flow depth and particularly in peak thrust. Debris events are generally composed by a first surge and secondary waves that develop during recession and become more evident with increasing effective duration of the event, independently on peak discharge. When instabilities in nature are not evident, space (length of the channel) and time (duration of the event) may be insufficient to allow their development.

Several flow laws incorporated into two 1D different numerical models, DFEM and WAF-DF, have been compared to field data obtained from a well-documented debris flow event in the Swiss Alps.

The two models, both based on shallow-water equations and on the assumption of a 1-phase flow characterised by a uniform rheology, represent adequately average values of state variables in natural debris flow events.

In general, all flow laws underpredict flow depth in comparison to the field data. By calibrating the rheological flow laws an adequate match of the hydrograph measured at the downstream end of the channel was obtained. The representation of roll wave activity at flow tail is achieved only from a qualitative point of view; further calibrations and in particular an accurate input hydrograph could allow an improvement in numerical results. The travel time of the debris flow front between instruments is 'captured' only by the Generalized Viscoplastic Fluid (for the WAF-DF code) and by the Voellmy Fluid (for the DFEM code) laws.

Discrepancies among computations and field data can be explained with the wide uncertainty on the effective rheology of the flowing material, as the fluid is actually non-homogeneous, the rheological parameters and the concentration vary in space and time, segregation at the front and crushing of stones occur along the stream.

REFERENCES

Arattano, M., Deganutti, A.M. & L. Marchi, 1997: "Debris flow monitoring activities in an instrumented watershed on the Italian Alps", *Proc. 1st ASCE Int. Conf. on Debris-Flow Hazards Mitigation: Mechanics, Prediction and Assessment,* pp. 506–515.

Arattano, M. & P.G. Trebbo, 2000: "Debris flow in ambiente alpino", Video-tape, Consiglio Nazionale delle Ricerche, Istituto per la protezione Idrogeologica del bacino Padano, Turin, Italy.

Bartelt, P., Salm, B. & Gruber, U. 1999: Calculating dense-snow avalanche runout using a Voellmy-fluid model with active/passive longitudinal straining. Journal of Glaciology, 45(150), 242–254.

Berti, M., Genevois, R., Simoni, A. & P. R. Tecca 1969: "Field observations of a debris flow event in the Dolomites", *Geomorphology*, 29, pp. 265–174.

Chen, C. L. 1992: "Momentum and energy coefficients based on power-law velocity profile", *J. of Hydr. Eng., ASCE,* 118(11), 1571–1584.

Chun, F. 1982: "Stability of flow of a generalized Newtonian fluid down an inclined plane", *J. of Appl. Math. & Physics*, 33, 181–188.

Coussot, P. 1994: Mudflow rheology and dynamics, Balkema.

Huang, X. & M.H. García, 1997: "A Perturbation Solution for Bingham Plastic Mud Flows," *J. of Hydr. Eng., ASCE*, 123(11), 984–996.

Huang, X. & M.H. García, 1998: "A Herschel-Bulkley Model for Mud Flows Down a Slope", *J. of Fluid Mech.*, 374, 305–333.

Hungr, O. (1995): A model for the runout analysis of rapid flows slides, debris flows, and avalanches. Canadian Geotechnical Journal, 32(4), 610–623.

Hürlimann, M., Rickenmann, D., & Graf, C. 2003: "Field and monitoring data of debris-flow events in the Swiss Alps", *Can. Geotech. J.*, in press.

Iverson, R.M. (1997): The physics of debris flows. Reviews of Geophysics, 35(3), 245–296.

Katopodes, N.D. 1984: Two-dimensional surges and shocks in open channels. Journal of Hydraulic Engineering, 110(6), 794–812.

Krüger, S. 2001: Computational contribution to highly supercritical flows, Nr. 167, Versuchsanstalt für Wasserbau, Hydrologie und Glaziologie, ETH Zürich.

Lamberti, A. 1999: "Debris flow Risk Project, Final Report, Videos", (CD-ROM), University of Bologna, Bologna, Italy.

Lamberti, A., Zanuttigh, B. 2003: "Impact of debris waves" to be published in *IAHR, J. of Hydr. Res*.

Lanzoni, S. & G. Seminara, 1993: "Debris Waves", *Proc. of XV IAHR Congress, Tech. Sess. B*, pp.79–185.

Mortara, G., M. Cerini & R. Laffi, 1994: "L'evento alluvionale del 22 Luglio 1992 nella conca di Bormio in Alta Valtellina", *Quaderni di studi e di documentazione CNR*, 17, Supplement to GEAM – Geoingegneria Ambientale e Mineraria. Anno XXIX n.4, pp. 25–33, Torino, in italian.

Näf, D.R. 1997: Numerische Simulation von Stosswellen in Freispiegelströmungen, Nr. 148, Versuchsanstalt für Wasserbau, Hydrologie und Glaziologie, ETH Zürich.

O'Brien, J.S., Julien, P.Y., & Fullerton, W.T. (1993): Two-dimensional water flood and mudflow simulation. Journal of Hydraulic Engineering, 119(2), 244–261.

Rickenmann, D. (1990): Bedload transport capacity of slurry flows at steep slopes, Versuchsanstalt für Wasserbau, Hydrologie und Glaziologie der Eidgenoessischen Technischen Hochschule Zuerich, Zurich.

Rickenmann, D. 1999: "Empirical relationship for debris flows", *Natural Hazards,* 19, pp. 47–77.

Rickenmann, D. 2000: "Debris flows events in Switzerland. Video recordings", Video-tape, Swiss-Federal Research Institute, Department of Natural Hazards, Birmensdorf, Switzerland.

Rickenmann, D., Hürlimann M., Graf C., Naef, D. & D. Weber, 2001: "Murgang-Beobachtungsstationen in der Schweiz", *Wasser, Energie, Luft,* 93, Heft 1/2, pp. 1–8.

Rutschmann, P. 1993: FE solver with 4d finite elements in space and time." VIII Int. Conf. on Finite Elements in Fluids, Barcelona, 136–144.

Takahashi, T. 1991: "Debris Flow", IAHR monograph series, Balkema, pp.165.

Toro, E.F. 1997: "Riemann solvers and numerical methods for fluid dynamics", pp. 567, Springer-Verlag.

Trowbridge, J.H. 1987: "Instability of concentrated free surface flow", *J. of Geoph. Res.*, 92, n. c9, 9523–9530.

Zanuttigh, B. & A. Lamberti, 2002: "Exact Riemann solution and Weighted average flux method for power-law channel section", *Int. J. of Comp. Fluid Dynamics,* 16, n.3, 155–170.

Zanuttigh, B. & A. Lamberti, 2003: "Analysis of debris wave development with 1-D Shallow Water equations", *ASCE, J. of Hydr. Eng.,* in press.

This page intentionally left blank

River Flow 2004 – Greco, Carravetta & Della Morte (eds.)
© 2004 Taylor & Francis Group, London, ISBN 90 5809 658 0

Some features of distribution of turbulence parameters of a jet flow in the river mouth

R. Khanbilvardi, B. Shteinman & V. Khazin
International Center for Water Resources and Environmental Research and Department of Civil Engineering, City College of CUNY, USA

O. Ozkurt
The Graduate Center and University Center of CUNY, USA

ABSTRACT: The objective of the study was measurement of the turbulence parameters of a jet flow and establishment of some common patterns of their distribution along the current and in the cross section of the flow. In the river mouth, the jet current is an inertial flow smoothly spreading out in the liquid medium, without a direct contact with the bottom or the banks. The most characteristic feature of such flows is gradual attenuation of the runoff current, accompanied by the corresponding decrease in its kinetic energy. Another remarkable feature is intense turbulent mixing of the two water masses – that of the river and that of the receiving water body. The very retardation of the river jet on its boundaries, along with the diminishing flow gradient, are the main causes of its attenuation.

1 BACKGROUND

River mouth areas are specific natural objects that enclose zones of transition of the river hydrological regime to the hydrological regime of the receiving reservoir (seas and lakes). The most important character of this process is a significant change of hydrodynamic, hydrophysical, chemical and biological parameters of the water masses within a comparatively short distance. An external evidence of these river-mouth processes is the formation of rather stable forms of relief, such as the above-water and underwater deltas, the mouth bar and spits. In the river mouth, the jet current is an inertial flow smoothly spreading out in the liquid medium, without a direct contact with the bottom or the banks. The most characteristic feature of such flows is gradual attenuation of the runoff current, accompanied by the corresponding decrease in its kinetic energy. Another remarkable feature is intense turbulent mixing of the two water masses – that of the river and that of the receiving water body. The very retardation of the river jet on its boundaries, along with the diminishing flow gradient, are the main causes of its attenuation (Mikhailov 1971, Mikhailov 1996, Mikhailov et al. 1986, Shteinman & Kamenir 1998, Shteinman et al. 2000).

A number of empirical, semi-empirical and theoretical methods and models were worked out as an essential part of the assessment of river mouth resources. The publications mentioned deal mainly with the study of mean velocities attenuation along the jet flow in river mouth areas (Mikhailov 1996, Shteinman & Kamenir 1998, Shteinman et al. 2000). Much less studied is the distribution of turbulence characteristics in the jet flows within river mouth areas.

The existing theoretical methods to describe free turbulence observed in jet currents within the river mouths are based on the hypothesis of self-modeling of the respective currents, and on using semi-empirical theories of turbulence. The self-modeling theories are based on some general properties of liquid currents and can also be justified by means of similarity and dimensionality methods. Semi-empirical theories of free turbulence utilize, besides general laws of hydrodynamics, some additional, more specific hypotheses (Monin & Yaglom 1965, 1967, Hintze 1963).

There have been attempts at mathematical simulation when studying turbulence of jet currents (Miligeyev & Sokolov 1986, Svanidze et al. 1984). In these models, in order to choose boundary conditions that would combine turbulence irregularity and statistical orderliness of the averaged motion, boundary conditions from the experiment are introduced (usually the velocities obtained by using quick-response devices).

Although in some cases the theoretical models provide a satisfactory description of the turbulence structure of a river jet flowing into the receiving water body,

they do not take into account a number of important effects occurring on the boundaries of water masses of different density. These effects are caused by thinning out of the flow of fresh river water onto the surface of the receiving water body (sea or lake). In such double-circulation conditions, the flows' turbulence structure has a number of essential features that are not described by theoretical and mathematical models.

Here, taking as a sample the measurements performed in the mouth of the Kura River flowing into the Caspian Sea, some features are established of the turbulence structure of a river jet flowing into a sea.

2 SITE DESCRIPTION

The Kura River mouth area is located on the Western coast of the Caspian Sea (Fig. 1), in the Republic of Azerbaijan. The Kura River, by its length (1,515 km), watershed area (188,000 km^2) and average annual discharge (about 16 km^3) is the largest river in Transcaucasia.

The total area of the Kura's delta amounts now to some 75 sq. km. The river bifurcates, within its delta, into two branches – northern and southern, and the bulk of river runoff (up to 80%) is entering the sea through the southern one.

The average annual discharge of suspended sediments in the mouth of the southern branch is 280 kg per sec. The predominant grain size in the suspended sediments is <0.05 mm, and it is the biggest in the period of high water (April–June), when up to 75% of the annual runoff enters the sea.

The river sediments coming to the mouth coastal waters have formed a crescent-shaped sand bar and mouth spits. The bar crest is at an average distance of about 1 km from the mouth, experiencing insignificant seasonal oscillations corresponding to the sediment balance at different stages of the hydrological regime. At the stage of rising high waters, the bar moves seaward, the water depth at its crest falling down to 0.7−0.5 m. At the low water stage, the bar is being gradually eroded from its seaward slope.

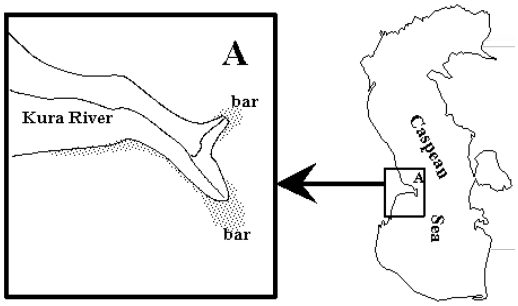


Figure 1. Schematic map of the Kura River Mouth area.

Current velocities at the mouth reach 1.5–2.5 m/s in the high-water periods, while in low-water periods they are 0.5 m/s on the average.

3 FIELD MEASUREMENTS

Because of the complexity of the process of mixture of the river and sea waters, and accordingly – the restructuring of the river turbulence, the goal of field measurements in the first stage was rather simple: to reveal main physical properties of turbulence – its space-time and spectral characteristics. The measuring tool used in this stage was a micropropeller that records the longitudinal component of flow velocity. This measuring tool is described in Nikora et al. (1994) and Nikora & Shteinman (1996).

The first stage of studies resulted in an information base on statistical characteristics of pulsation of the longitudinal component of velocity at different distances from the mouth section, which allowed making a very general conclusion on the process of restructuring of turbulence of the river flow as it was moving into the sea.

In the following stages of experiments, the tasks became more sophisticated. Now the goal was to obtain information on the flow's velocity structure for 3-D plotting. The measurement system used to record the three velocity components included the three-dimensional velocity fluctuation meter consisting of 3 circular piezoelectric slabs (radius 1 m) mounted on a 5 cm × 5 cm × 5 cm cubic frame interfaced with a computer to give real-time readout. Using this system allows obtaining valuable data on the structure of turbulence (Shteinman et al. 1993, Khanbilvardi et al. 2003a, Ozkurt et al. 2003), and substantially expanding the goals of experiments.

It is worth emphasizing that all measurements were done in calm waters, with almost no waves or alongshore movement of sediments, which made it possible to research various models of free spreading of the river jet on the river mouth area in its pure form.

Measurements were conducted under steady hydraulic conditions and embraced the entire cross section of the flow. The duration of measurements in each point was 15 min., so background hydrological and hydraulic conditions were practically unchanged during each experiment.

Measurements were performed at the river mouth cross section and at distances of 25, 50, 75, 100, 150, 200, 300, 400, and 500 m from it along the jet's dynamic axis, at its boundaries, as well as in the area of its free spreading beyond the bar.

4 DATA PROCESSING

Quantization of the continuous records of velocity pulsations was done with the step of 1 s, and in some

cases the quantization step was 0.25 s and 0.1 s. In accordance with this, the upper frequency of analysis, determined by the quantization step, was accepted as 31.4 rad/s.

The main mechanisms used to describe the results were the theory of random processes, the method of structural averaging when studying coherent structures, and the theory of random functions and fields when studying hydrodynamic fields (Grinvald & Nikora 1988, Grinvald 1974, Nikora 1991, Sukhodolov et al. 1998).

When considering jointly the three velocity components, that is the vector fields of velocity, the vector-algebraic method of analysis was used (Rozhkov 1979), which provides important information under conditions of commensurability of the three velocity components. The main element of this analysis is analyzing the correlation tensor of the vector process

$$K_{\vec{v}}(t,\tau) = \begin{pmatrix} K_{v_1v_1} & K_{v_1v_2} \\ K_{v_2v_1} & K_{v_2v_2} \end{pmatrix} \quad (1)$$

which is a dyadic tensor function of the arguments (t, τ). This function characterizes the interrelation of the directional changes of the flow velocity vectors at the moments of time t, $t+\tau$, and provides numerical assessment of the intensity of these changes and of their orientation in the given system of coordinates.

The invariant D of the skew-symmetric part of the tensor K_v, called by Rozhkov (1979) the indicator of spinning (rotational movement of turbulent eddies), can be determined by the relation

$$D_{1,2} = K_{v_1v_2} - K_{v_2v_1} \quad (2)$$

It is composed of the orthogonal components of the vectors $\vec{v}(t)$ and $\vec{v}(t+\tau)$. If $D > 0$, then the vector $\vec{v}(t+\tau)$ is predominantly oriented to the right of the vector $\vec{v}(t)$, and if $D > 0$, then to the left. This means that in the first case the vector's rotation is clockwise, while in the second case it is counterclockwise.

In the equation (2), the basis unit vectors of the tensor $K_{\vec{v}}$ depend on the arguments (t, τ) and are oriented, with respect to the reference system of coordinates, in the direction

$$\alpha^{(K)} = 0.5 arctg\left[\frac{K_{v_1v_2} + K_{v_2v_1}}{K_{v_1v_1} - K_{v_2v_2}}\right] \quad (3)$$

In our experiments, the spatial structure of the correlation characteristics is conducted successively for the vertical (u, v), horizontal (u, w), and transversal (v, w) planes in the left system of coordinates (the X-axis goes with the current, the Y-axis is oriented perpendicular to the gravity vector in the direction of the right edge of the current, and the positive Z-semiaxis goes upward, perpendicular to the bottom plane).

The invariants $D_{i,j}$ characterize the intensity of spinning of the velocity vector in various planes.

For a more complete analysis, the so-called linear invariant J was considered, which can be determined by the equation

$$I = K_{v_1v_2} + K_{v_2v_2} \quad (4)$$

composed of the collinear vector components $\vec{v}(t)$ and $\vec{v}(t+\tau)$. If $J > 0$, the collinear vector components are unidirectional, if $J < 0$, they have opposite directions, and if $J = 0$, the vectors are orthogonal.

A joint analysis of the invariants J and D allows researching, regardless of the chosen system of coordinates, the structure of collinear and orthogonal alterations of the flow velocity vectors, and finally the intensity of spinning of the turbulent eddies in various planes, as well as the spatial orientation of the axes of such spinning.

5 RESULTS

5.1 *Pulsations of the velocity module and the intensity of turbulence*

As a result of multiple theoretical and experimental studies, it has been established that the intensity of turbulence on rectilinear portions of the river channels with a smooth, poorly erodible bottom is evenly increasing from the water surface to the bottom of the flow, where main generation of the turbulence energy takes place.

At the area of inflow of a jet river flow into a receiving water body, the main factor determining the changes in turbulence intensity is the intensity of dissipation of the longitudinal current velocity (Fig. 2).

Turbulence intensity grows the fastest at the river mouth section, where the flow is abruptly getting wider. The farther from the mouth, relative dissipation of velocity being equal, turbulence intensity is growing slower. It should be emphasized that we are talking only about the longitudinal component of velocity. The type of relationship shown in Figure 2 is caused by the fact that, the farther from the mouth and the wider the flow, the greater part of the pulsations energy falls on the transversal (between the mouth and the bar) and vertical (beyond the bar crest) components of velocity.

Pulsations of the longitudinal component of velocity in the jet flow first grow with the distance from the mouth. At a distance equal to the width of the river channel, the intensity of longitudinal turbulence on the jet axis is about the same as in the channel, and then grows in the areas of increased longitudinal gradients of velocity.

Levels of turbulence in the diffusion current are significantly higher than in the steady one because of a higher velocity gradient, and, accordingly, higher

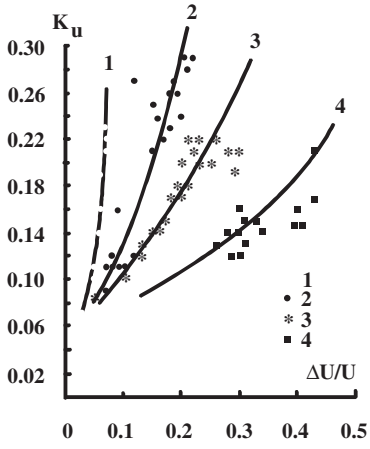


Figure 2. Relationship between turbulence and intensity of attenuation of the longitudinal velocity along the axis of the jet. Flow at various distances from the mouth (1 – 200 m, 2 – 500 m, 3 – 800 m, 4 – 1,400 m)

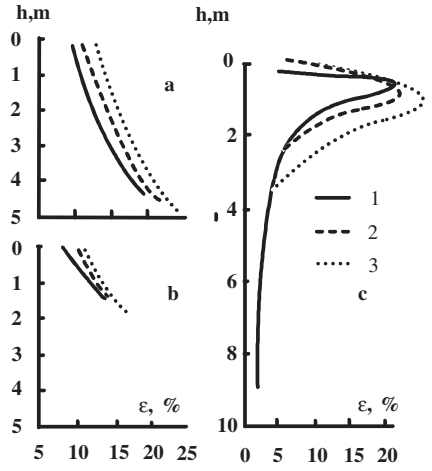


Figure 3. Variability of the intensity of turbulence with the jet flow depth at various distances from the mouth (a – mouth gauge, b – bar crest (500 m from the mouth), c – deeping beyond the bar (800 m from the mouth – zone of detachment of the river jet from the bottom). Curves 1, 2 and 3 correspond to the flow velocities in the mouth equal to 1.58, 2.10, and 2.46 m/s respectively).

generation of turbulence. Within the area, 2–3 widths of the river long, in the river mouth, where abrupt flow deceleration occurs, the level of pulsations is observed to grow considerably.

The greater the river water discharge and, accordingly, the flow velocities, the farther from the river mouth gauge occurs the zone of highest turbulent pulsations.

Multiple studies have established the intensity of turbulence in the river flow is getting higher from the water surface to the bottom. However, in the conditions of free spreading of the jet flow, starting from the bar crest where the jet detaches itself from the bottom (so-called detached flow), the highest intensity of turbulence is observed within the contact zone between the upper layer of fresh river water and the underlying layer of denser sea water mass (Fig. 3). As the velocity of the river jet increases, the layer of maximum turbulence is shifting deeper.

The influence of the bottom topography on the velocity pulsations and on the distribution of turbulence intensity is felt in the jet flow in the same manner as in the river channel. As proven by observations (Ozkurt et al. 2003, Khanbilvardi et al. 2003b), in the area between the river mouth gauge and the bar crest, the linear dimensions of the bottom ridges are rapidly diminishing along the flow.

This leads, first, to the faster decrease in the standard deviation of the longitudinal pulsations of velocity, and second, to a more uniform distribution of turbulence intensity over the depth of the flow.

The mouth bar has also the shape of a large ridge composed of river sediments. According to laboratory studies (Petrosyan 1984), maximum values of the standard deviation of pulsations on the vertical lines beyond the bar crest occur at the crest level, and here we see similarity with the channel flow having a ridged bottom. At the same time, the conclusion that the character of changes in turbulence intensity beyond the bar is similar to that of the area below the bar of a moving sand wave, cannot be extrapolated to the field conditions.

In laboratory conditions, an unstratified flow is observed beyond the bar, while in natural river mouths fresh waters are pinching out to the flow surface as the river jet is moving into the sea. This is why the distribution of velocity pulsations and turbulence intensity on the vertical lines beyond the bar crest has specific features as shown in Figure 3 and the river mouth bar, from the point of view of its influence on turbulence, can be considered not as a bottom ridge characteristic of a river, but as a practically immobile large bottom ridge generating a detached current. Examples of the distribution of turbulence intensity over the cross section of a jet flow at various distances from the river mouth are given in Figure 4.

5.2 *Velocity vector pulsations*

Pulsations of the transversal (w') and vertical (v') velocity differ from the pulsations of the longitudinal component (u'). Within the river area, the ratio $\overline{u'^2}/\overline{v'^2}$ generally displays regular growth from the bottom to the flow surface; the ratio $\overline{u'^2}/\overline{w'^2}$ is also growing, being greater than $\overline{u'^2}/\overline{v'^2}$.

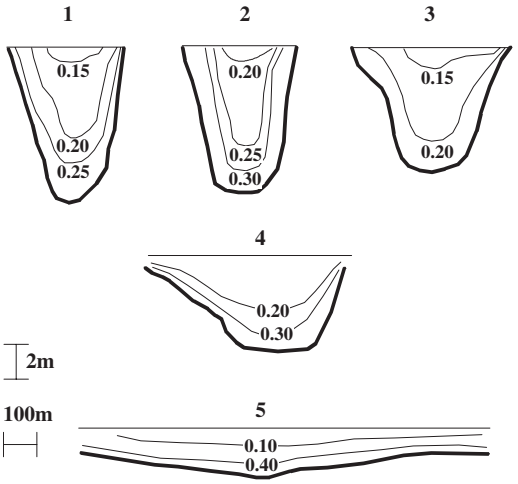


Figure 4. Distribution of Turbulence Intensity over the Cross Section of the Jet Flow at Various Distances from the River Mouth: (1 – mouth gage, 2 – 200 m, 3 – 500 m, 4 – 800 m, 5 – 1,100 m)

In the river mouth jet flow, spatial distribution of the velocity components has some specific features. In the jet flow, at the distance from the mouth equal to the width of the river, $\overline{u'^2}$ starts its regular growth with the distance from the bottom. This is related to the fact that friction at the side boundaries of the jet is 6–9 times higher than friction at the bottom (Mikhailov et al. 1986). For this reason, when the river flow exits the mouth gauge, its surface layer acquires intense additional turbulization as compared to the near-bottom layers experiencing basic friction on the bottom because here the transversal velocity gradient is the smallest. For the same reason, is also growing in the surface layer.

Beyond the bar, where the river jet, possessing insignificant energy, is detaching from the bottom and spreading freely, all three components of velocity have the highest values of pulsation in the surface layer. However, if the jet has significant energy, the $\overline{u'^2}$, $\overline{v'^2}$ and $\overline{w'^2}$ are decreasing from the bottom to the surface, which is due to high vertical gradients of velocity in the near-bottom zone.

Eddy zones on the jet boundaries are the sources of the elevated turbulence, with the velocity of translational motion 5–10 times lower than the velocity in the main body of the jet. Here we observe the highest values of turbulent pulsation and commensurable components u', v' and w'. The intensity of transversal pulsations can be here as high as 60%, while the intensity of longitudinal pulsations is only 25–35%. The transversal pulsations of velocity at a distance equal to 5–6 river widths are 10–20 times higher than those in the jet axis.

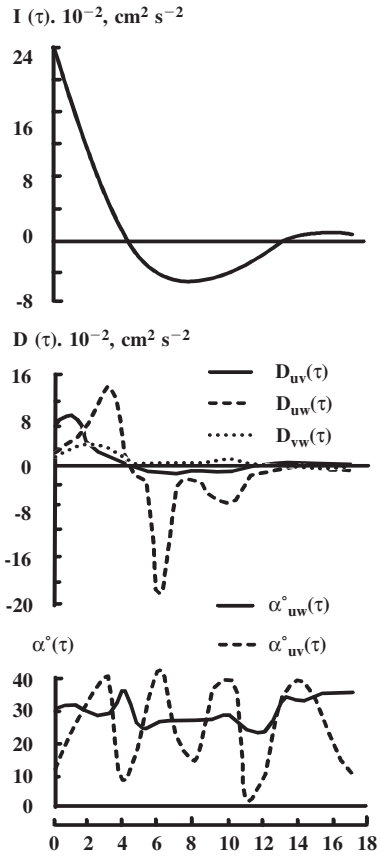


Figure 5. Example of the autocorrelation tensor function invariants.

The above regularities of distribution of the velocity pulsations are the reflection and result of the eddy structure of the flow and of the turbulent eddies spinning in it. Figure 5 presents examples of calculation of the correlation tensor function invariants I and D superposed on various sections of the jet flow.

For functions $D_{uv}(\tau)$, $D_{uw}(\tau)$ and $D_{vw}(\tau)$, corresponding to the channel section, both positive and negative values are present, and lesser than $I(\tau)$ amplitudes of oscillation, the highest ones pertaining to D_{uv} (spinning in a vertical plane), and the smallest to D_{vw}. On the bar, the component D_{uw} dominates other components, testifying to the restructuring of the flow from spinning predominantly in the vertical-longitudinal plane (u, v) to spinning predominantly in the horizontal-transversal plane (u, w).

Beyond the bar, the component D_{uv} is close to zero (spinning in the (u, v) plane is negligible compared to spinning in other planes), powerful spinning occurring in the horizontal plane (u, w).

Analysis of indicators of spinning in different planes has shown that in experiments within the river channel it was in the form of right screw (clockwise), while within the jet part of the flow, as it approaches the bar, toppling and surfacing of eddies occur, with spinning beyond the bar predominantly counterclockwise (in the horizontal plane). Judging by the values of the angle $\alpha^0(\tau)$ given in Figure 5, the direction of the major axis of the tensor curve (direction of the predominant variability of the velocity vector) does not stay constant but is cyclically changing with respect to τ: in the river flow mainly in the plane (u, v), in the jet section up to the bar in the plane (u, w), beyond the bar again in the plane (u, v) because here intense mixing of river and sea water masses occurs.

Comparison of the values of the correlation function $I(\tau)$ of the collinear components of the pulsation velocity vector with the function $D(\tau)$ of the orthogonal components shows that $I(\tau) > D(\tau)$ before the bar, and $I(\tau) < D(\tau)$ on the bar. This means that while at the beginning of the jet the interrelation of the collinear components is predominant, around the bar the interrelation of the orthogonal components is stronger, that is the influence of the changing flow direction is greater than the influence of the changing velocity module.

6 CONCLUSIONS

Analysis of the distribution of the standard deviations of the components of the river jet velocity vector at its inflow into the sea has shown that the structure of channel turbulence is rapidly degenerating. Turbulent eddies change their orientation from the predominantly vertical-longitudinal spinning with a horizontal axis to the predominantly horizontal-transversal spinning with a vertical axis. At the same time, substantial additional turbulent energy is being generated in the zones of contact between the jet flow and the adjacent mass of seawater.

REFERENCES

Grinvald, D.I. 1974. *Turbulence of Channel Flows*. Leningrad, Hydrometeoizdat, (in Russian).

Grinvald, D.I. & Nikora, V.I. 1988. *Turbulence in Rivers*. Leningrad, Hydrometeoizdat, (in Russian).

Hintze, I.O. 1963. *Turbulence, Its Mechanism and Theory*. Fizmatgiz, Moscow, (in Russian).

Khanbilvardi, R., Shteinman, B., Khazin, V. & Ozkurt, O. 2003a. The influence of surface waves on turbulence characteristics of the jet flow in river mouths. *Proc. 3rd IAHR Symposium on River, Coastal and Estuarine Morphodynamics, Barcelona, 1–5 September 2003*.

Khanbilvardi, R., Shteinman, B., Khazin, V. & Ozkurt, O. 2003b. Interaction of flow with mobile bottom in the river mouth. *Proc. 7th International Conf. on Computational Modeling of Free and Moving Boundary Problems, Santa Fe, New Mexico, 4–6 November 2003*.

Mikhailov, V.N. 1971. *Flow and Channel Dynamics in Non-Tidal River Mouths*. Hydrometeoizdat, Moscow, (in Russian).

Mikhailov, V.N. 1996. Methods and models for assessment of hydrological and ecological conditions of river mouth regions. *Proc. Monitoring Tailor-Made II Information Strategies in Water Management, Sept. 1996, Nunspeet, the Netherlands,* 253–262.

Mikhailov, V.N., Rogov, M.M. & Chistyakov, A.A. 1986. *River Deltas. Hydrological/Morphological Processes*. Hydrometeoizdat, Leningrad, (in Russian).

Militeyev, A.N. & Sokolov, B.I. 1986. Mathematical simulation of currents in river mouths of non-tidal seas accounting for real hydrometeorological conditions. *Proc. of the 5th All-Union Hydrological Congress,* 42–43, (in Russian).

Monin, A.S. & Yaglom, A.M. 1965 (Part I), 1967 (Part II). *Statistical Hydromechanics*. USSR Academy of Sciences Publishers, Moscow, (in Russian).

Nikora, V., Rovinski, P., Sukhodolov, A. & Krasuski, D. 1994. Structure of river turbulence behind warm-water discharge. *J. Hydrol. Energy, ASCE*, 120: 191–208.

Nikora, V.I. & Shteinman, B. 1996. Turbulence in the Jordan River: A case study. *In*: *Flow Modeling and Turbulence Measurements*, 1: 581–588. Rotterdam/Brookfield.

Nikora, V.I. 1991. A Physical Model of Fluvial Turbulence. Proc. XXIV Congress IAHR, Madrid, 549–556.

Ozkurt, O., Khanbilvardi, R., Shteinman, B. & Khazin, V. 2003. Some characteristics of the interaction between turbulent flows and movable rippled bottom in the river mouth. *Proc. 2nd International Conf. on Computational Methods in Multiphase Flow, Santa Fe, New Mexico, 3–5 November 2003*.

Shteinman, B. & Kamenir, Y. 1998. Decrease in suspended matter concentration with distance from the Jordan River Mouth, Lake Kinneret: Hydrodynamical Aspects. *Adv. in Hydro-Science and -Engineering,* 3: 122–136.

Shteinman, B. & Gutman, A. 1993. Flow turbulence and dispersion of different matter in the river mouth. *Wat. Sci. Tech.*, 27: 397–404.

Shteinman, B., Gutman, A. & Mechrez, E. 1992. Laboratory study of the turbulent structure of a channel jet flowing into an open basin. *Boundary Layer Meteorology*, 62: 411–416.

Shteinman, B., Mechrez, E. & Gutman, A. 1993. Spatial structure of the jet flow in the river mouth. *Boundary Layer Meteorology*, 62: 379–383.

Shteinman, B., Kamenir, Y., Hochman, A. Itzhak, O. & Ben-Dan, T.B. 2000. Sedimentation process in the jet flow of river-lake contact zones. *Advances in Fluid Mechanics*, 3: 63–72.

Sukhodolov, A., Thiele, M. & Bungartz, H. 1998. Turbulence structure in a river reach with sand bed. *Water Resources Research*, 34 (5): 1317–1334.

Svanidze, G., Shteinman, B. & Bronfenbrener, L. 1984. Calculation of turbulent jets in river mouths by mathematical simulation based on the equivalent problem of the theory of heat conductivity. *Proc. of the Conference "Dynamics and Thermal Conditions of Rivers, Reservoirs and Estuaries"*, 2: 218–210, MGU Publishers, Moscow, (in Russian).

River Flow 2004 – Greco, Carravetta & Della Morte (eds.)
© 2004 Taylor & Francis Group, London, ISBN 90 5809 658 0

An integrated system for prevention of pollution due to sewage and waste waters into rivers

F. Boccia & D. Postiglione
Enel.Hydro B.U. Ismes Engineer, Centro Direzionale, Napoli, Italy

A. Fusco
Enel.Hydro-Ismes Division & Development Department Director, Seriate, Bergamo, Italy

L. Mancusi
Enel.Hydro B.U. Ismes Engineer, Iside Centre, Prignano Cilento, Salerno, Italy

ABSTRACT: In the National Operative Programme (P.O.N.), called AQUATEC "Control, treatment and maintenance innovating technology for water emergency solving", the objective entitled "System for prevention of pollution due to waste waters into rivers" proposes to implement a system for the control and valuation of the effects into the rivers produced by waste waters derived from industrial, human or agricultural activities.

The innovative idea of the project consists in the use, in conjunction with traditional technology of qualitative and quantitative river monitoring and simulation of the pollutants dispersion, of an expert system realized through archives containing both available measurements and simulations of reference scenarios or "classes" of situations. So the system is able to "extrapolate/interpolate" in an intelligent way data in archives to formulate a forecast cause/effect connection of continuous or accidental waste waters.

1 INTRODUCTION

In the last years water ecosystems biotic integrity concept has had a growing importance till to be considered official by Italian regulation 152/99.

This regulation defines general rules for water protection. Its objectives are "to prevent and to reduce water pollution, to recover and to improve water state, to defend special water uses, to assure sustainable uses of the resource and to preserve natural capability of river self-purification, necessary to support wide and well diversified animal and vegetable communities". "Quality objectives" and "protection plans" are the prescribed tools for these aims.

The use of the presented methodology supposes a continuous monitoring, with all benefits short and long term, for territorial planning, for river quality state evolution control, waste waters delivered into river management, for prevision of impacts, as well as for the possibility of quick decision and prompt intervention in situations of emergency.

To reduce the physical complexity of the continuous survey and data transmission net, we use a virtual sensor system implemented with a fuzzy logic.

The present article describes design and implementation phases in a sample basin of decision support system which consents to interpret qualitative and quantitative data from the river monitoring net. In this way it is possible to analyze causes of the present situation and to interprete short and long term effects into river caused by input of waste waters from industrial, human or agricultural activities.

This objective, focusing attention on the river, is in perfect line with the above-mentioned regulation 152/99, in which the imposition logic respect of the single waste waters or area to protect respect of the quality is exceeded. The problem is dealed within a general hydrogeologic context, according to which environmental quality of river is to be reached in a global way, searching balance between natural water flow and the external contribution due to human presence, avoiding causing qualitative and quantitative irreparable damages. The balance is reached when natural capability of river self-purification remains and so the possibility of supporting wide and well diversified animal and vegetable communities, without pollution processes. The system we want to realize needs continuous monitoring with data acquisition in a

S.I.T. from which we get information to execute simulations on different temporal scales. The possibility to get on-line data relative to river state besides assuring real time signalling about critical or warning situations arising, to operate (do) a quick intervention, consents to define initial conditions of the physical environment from which to leave, to get prevision of future scenarios.

2 STATUS OF THE RESEARCH

2.1 *Sensors*

In the last years research in sensors field has had a notable development providing [11] a great number of components suitable for chemical–physical interesting parameters on-line survey. They are founded on potentiometric techniques, for example to measure the oxygen, ph, etc. or colorimetric ones, for example for determination of nitrogen and phosphorus compounds. Parameters considered for the rivers are typically: temperature, dissolved oxygen, conductivity, redox potential, ph, turbidity, suspended and gravity driver-position solids, ammonia. Automatic sampler which consent to evaluate the pollution stress are available. Moreover they are studying both analytical data validation technics and real-time adjournment methods, with communication systems using wireless techniques (GSM), of the data bank of territorial information systems.

To reduce the physical complexity of the continuous survey and in way to make it more similar data transmission net and to evaluate parameters which don't lend oneself to on-line valutation (BOD), we use a virtual sensor system implemented with a fuzzy logic. The fuzzy logic objective is to generalize classic logic to human thinking way. Some intermediate values which can characterize in a more precise way the real situations are added to the two typical values "true" and "false". The logic inference rules used in this case are calibrated on the particular application field. However they operate simulating the typical "good sense" of the field expert. Moreover virtual sensors [2] consent to estimate the trend of simple and complex parameters on the base of only simple parameter measure acquisitions (flow rate, level, dissolved oxygen, ph, etc.). The system is based on analysis of measures historical knowledge and consents to estimate temporal trend of not directly monitored parameters on the base of others monitored ones. Parameters which we want to estimate temporal evolution must be correlated (fuzzy function) to automatically controlled ones. But it is not required correlation between monitored parameters and estimated ones as, on the contrary, it is required for physically founded models. The use of fuzzy logic for the definition of virtual sensors has as objective to explicit the dependence rules among parameters. This individuation process of inferences between input and estimated ones becomes an explicit knowledge patrimony, and consents to value and control by an expert operator (typical characteristic of an expert system).

2.2 *Quality models*

Fluently river quality study is made by formulation of a mathematical model of the real system to employ with a computer. Model must have the ability to describe in quantitative terms space-time real system evolution, and to give system reply to external solicitations considering internal dynamics. Usually in a software implementing a river quality model the whole of elaborations is organized by functional strictly related modules, which we can usually schematise as follows:

- hydraulic model, which describes water flow field and concentration's distribution of dissolved substances;
- chemical model, which describes inorganic substances kinetics degradation in the river;
- biochemical model, which describes organic substances kinetics degradation;
- ecological model, which reproduces photosynthesis mechanics and dynamic of the river ecosystem food chain;
- thermal model, which describes temperature field into river.

As regard to research, hydraulic models have reached a good maturity and three-dimensional software are available giving reliable results. As regard water quality models, since very complex phenomena are described, the research is always in evolution for realizing more complete and reliable models. Now many river quality models are available [10] where we notice the difficulty to realize optimum integration between hydraulic and quality models. Some well-known river quality models are: QUAL2E (EPA, 1995), MIKE11 (Danish Hydraulic Institute), WEST (Wastewater Treatment Plant Engine for Simulation and Training, made in Belgium). River quality models are used to produce single elaborations concerning specific environmental conditions; at present it seems that in Italy, except for specific situations, appliances integrating river quality models with on-line obtained data from a territorial scale monitoring net are not available for describing temporal evolutions of phenomena and then to go up to incidental event causes, or to support choice of reclamation actions.

2.3 *Expert systems*

The project wants to realize a decision support system which gives output of simulation with monitoring net data to consent a result interpretation and a prediction of consequent effects. This system cannot use traditional mathematical models whose elaboration

time are incompatible with a real-time system, but has to use Artificial Intelligence techniques.

Some expert systems applications are known within the limits of very specific sectors of water treatment, in particular:

- research to establish biological efficiency in active sludge depuration plants [5];
- exploitation well safe yeld control, iron and manganese control in potable water, hydraulic net efficiency control [6];
- nitrogen removal from sludge control [7];
- on-line monitoring of waste waters from purification plant [8];
- optimization of chrome fragmentation in industrial water [9].

Research on Artificial Intelligence gave enquiry tools which are over traditional monitoring limits, consenting to use, with monitoring data, also qualitative, dubious or incomplete information as they are used by an expert of the field. Systems operating in this way are called expert systems. They are founded on the use of "Knowledge Base" considered as a whole of highly structured information and association of concepts and rules.

The central element of an expert system is inferential motor which can be synthetized as a whole of rules and strategies of knowledge elaboration to reach a deduction for the problem solution. But data aren't precise, so the operative logic can't be Boolean, but it must consider dubiousnesses and the many shadings of original data; the logic which uses these standards is "Fuzzy Logic".

3 PROJECT PRESENTATION

3.1 *System structure*

The system is essentially composed by two modules based on a common techniques, and precisely [4]:

System for simulation and prevision of short, middle and long term effects due to incidental waste or continuous ones into rivers or sensitive backwater areas. This system wants to estimate, for incidental sources or continuous waste, river areas interested by waste water, to give in short, middle and long terms a prevision of effects in terms of quality and the possible water recycle. It can also give indication about possible recovery intervention which we can suppose, for example an use of solvents, drawn work closing.

Reconstruction and locating of the original scenarios in connection with water quality control systems. This system wants to elaborate, on the base of monitoring indications, (for example on the confluence in the main river) possible scenarios on the origin of measured values, giving indications on the possible risk areas or letting in zones not in norm.

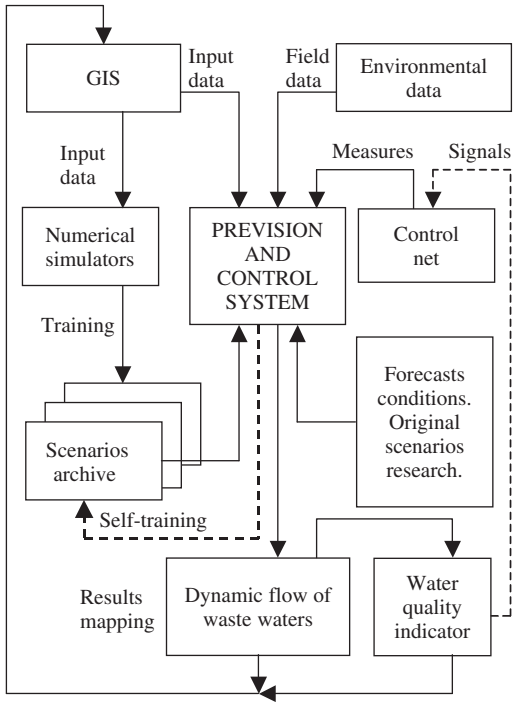


Figure 1. Block scheme of information flux among modules.

Both indicated systems depend on river and territorial characteristics, so we forecast their integration in a GIS from which they will take territorial information, and to which they will give elaboration results for a their mapping in connection with territorial data (waste position, drawn works, effects on bypasses, etc.). Moreover we analyse the possibility to connect the systems with environmental tools (meteo gages flow and/or level meter, current meters, water quality sensors, etc.). All the systems will be "trained" by a series of numerically simulated scenarios able to cover all the possible hydrodynamic situations which depend on environmental and seasonal parameters, and will increase its knowledge in connection with monitoring date.

3.2 *Choice of the experimental site*

Sarno river basin, considered since many years as a social-economic and environmental emergency area, has been chosen as investigation site for this project. This choice is justified by many factors. First of all at present studies and data are available on Sarno basin and we can use them to study pollution evolution, to have knowledge of the present quality status, as well as to the efficacy of renewal interventions [3].

ARPA Campania, an Institutional Organization employed to environmental controls began two years

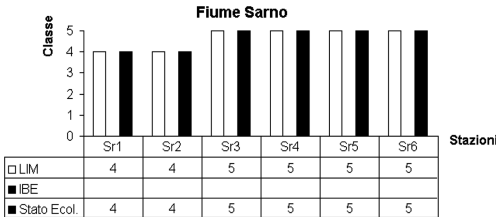


Figure 2. Quality state of Sarno River.

ago sampler and analysis activities for studying quality of rivers in Campania.

Sarno analytical data relative to years 2001 and 2002 have consented operating river first classification according to regulation 152/99. Even if environmental state wasn't defined but pollution level expressed by macro-descripting, it was defined only (LIM). Additional parameters research as organic and inorganic pollutants so far has been limited to metals, measured in all the seven monitoring stations, and to pesticide only in same stations. Since wasn't possible to measure IBE index, the ecological state value (SECA) is strongly conditioned by pollution level expressed by LIM.

From monitoring data analysis and from their elaboration, it is rather clear how strong the Sarno basin decay is, independently from IBE index values and step levels of most important chemical pollutants. The application of mathematical models to study river system behaviour is used whether for the simulation of flow conditions or evaluation of pollutants concentration in the river for convection, dispersive and diffusive transport phenomena. The project forecasts the implementation of mathematical water quality model formed by hydrodynamic, chemical and biochemical modules, open to subsequent integration of ecological and thermal modules. Moreover we forecast to detect, for the realization of a prototype, a part of the river with significant length which is delimited, above and below, by continuous qualitative monitoring station of chemical and physical parameters. The selected zone has a considerable waste inside as pollution load contribution, e.g. the waste of one of the purification of plants of middle Sarno districts. The part which has such characteristics is included between mouth and confluence of Alveo Comune Nocerino, measuring 10 km, where effluent of district n°3 purification plant discharges.

3.3 *Choice of the continuous monitoring parameters and qualitative modeling hypothesis*

By considerations made on results of statistics elaborations realized by ARPA Campania, the pollution which causes high BOD and COD values has an industrial origin prevalently. It is caused by heavy metals as nickel, chrome, plumb and mercury, rather then biochemical origin caused by alimentary industries discharge. The method used for Factor Analysis is the Principal Components one (A.C.P.) followed by varimax rotation; Table 1 reports the factor loadings for each parameter, eigen values and the variance percent explained for the first five factors. First of all the analysis has showed that a large part of informations is contained in the first five factors (56.7% of represented variance). Moreover in the table we can notice that:

- 1st factor (16.3% of explained variance) is strongly related to dissolved oxygen, BOD and COD. It essentially expresses the river organic component. It is thought that the organic load represented by this factor comes from industries owing to unimportant correlation with the classical parameters which indicate civil pollution (ammoniacal nitrogen, total phosphorus, Escherichia coli, etc.).
- 2nd factor (15.8% of explained variance) is related to total chrome, mercury, nickel and lead. We can say that this factor represents industrial pollution parameters.
- 3rd factor (10.3% of explained variance) is characterized by total and ammoniacal nitrogen. We can say that this factor represents nitrogen pollution and it represents reduction state of the system.
- 4th factor (7.5% of explained variance) is related to nitrates and total phosphorus. We can suppose that these correlations are due to photosynthesis and nitrification processes and they are representative of system eutrophication.
- 5th factor (6.8% of explained variance), difficult to interpret, it seems not containing any directly interpretable information.

Besides we will monitor: dissolved oxygen, BOD, COD, organic, ammoniacal, nitroso and nitric nitrogen, organic and dissolved phosphorus, chromium as organic and conservative substance, Escherichia coli, to consider also biological pollution effects. For each of described parameter their correspondent modules operate the integration of convective-dispersive one-dimensional transport equation in which the space-temporal variation of concentration is due to longitudinal dispersion phenomenon, to dilution with other affluents, to the contribution of other outside distributed and concentrated pollutant loads, to the chemical and physical relations that may influence the examined substance concentration in relation to other state variables (temperature, concentration of other present substances, BOD, dissolved oxygen). In a subsequent phase it is made sensitivity analysis and calibration of the model, assignating to parameters in the model equations values obtained by a monitoring activity. Practically from the sensitivity analysis we can detect parameters whose values influence more

Table 1. Factor loadings.

	Factor 1	Factor 2	Factor 3	Factor 4	Factor 5
pH	−0.315149	−0.052836	−0.472621	0.131181	0.120895
Temperature	0.213251	−0.439654	0.124818	0.410357	−0.253403
Conductivity	0.078933	0.291776	0.020146	0.615537	0.542368
Hardness	0.059501	0.168140	0.468067	0.078384	0.587982
Suspended solids	0.467716	−0.145296	−0.061480	0.056930	−0.134976
Dissolved oxygen	**0.574095**	−0.064111	0.025864	−0.009991	**0.624017**
Dissolved oxygen	**−0.602760**	0.148055	−0.027983	0.014675	**−0.617389**
BOD_5	**0.763772**	−0.020290	0.117071	0.000212	0.157066
COD	**0.827853**	−0.069019	0.170124	0.141501	−0.014045
Total nitrogen	0.028777	0.023086	**0.871325**	0.186921	0.141246
Ammoniacal nitrogen	0.001972	−0.086288	**0.905901**	−0.145075	0.091879
Nitric nitrogen	0.168306	0.076075	0.114658	**0.648997**	−0.080729
Total phosphorus	0.366565	0.050539	−0.004764	**0.613464**	−0.019384
Chlorinolog	−0.094359	−0.005959	0.146972	0.074425	**0.631641**
Sulfate	−0.068915	0.367567	−0.066288	**0.571460**	0.444398
Escherichia Coli	−0.165719	−0.084291	−0.065083	0.425861	0.151964
Cadmium	0.005723	0.138419	−0.123534	0.176760	0.177367
Total Chromium	−0.177116	**0.736187**	0.056414	−0.008926	0.254937
Mercury	−0.087544	**0.789699**	−0.017273	0.060177	−0.177228
Nickel	−0.037159	**0.906849**	0.039098	0.084495	−0.084827
Lead	−0.035849	**0.803166**	−0.029546	0.040662	0.021295
Copper	0.148703	0.410809	0.230934	−0.527335	−0.085502
Zinc	0.025382	0.273601	0.222193	−0.063610	−0.393954
Expl.Var	2.604050	3.416202	2.253429	2.287060	2.485226
Prp.Totl	0.113220	0.148531	0.097975	0.099437	0.108053

Table 2. Eigen values and variance percent explained.

Eigen value	% Total	Cumulative	Cumulative
3.741705	16.26828	3.74171	16.26828
3.639613	15.82441	7.38132	32.09269
2.375607	10.32872	9.75693	42.42141
1.736098	7.54825	11.49302	49.96967
1.552945	6.75193	13.04597	56.72160

the answers of the model in particular initial and contour conditions. On the other hand, from planning of data acquisition activities, which characterize the real system behaviour, we go on to the mathematical model calibration of the system. It is possible to forecast making the model calibration using previously obtained data, supposing stationary contour conditions concerning to the temporal contexts in which data acquisition and model calibration were made and completing our data with a special analytical monitoring activity.

3.4 *Assumptions of hydraulic modelling*

Hydraulic model uses one-dimension equations of a slow stream in variable motion resorting to:

- geometry knowledge any 300 meters of water sections, inclination and roughness of Sarno river;
- water level staff measurements in shallow water;
- the knowledge of waste water localization, tipology and diameter;
- the definition of flow time state in upstream or first section of experimental site and water level in downstream or final section of experimental site.

The river quality model used for tests is arranged in 1997 by ISMES (Mancusi, Barbanti) to study quality of river Serio [1].

In hydraulic and biochemical submodel there is one dimension spatial description. Variable values are averaged or integrated on section.

Equation of mass balance of a general quantity, liquid weight or variable is:

$$\frac{\partial(Ac)}{\partial t} + \underbrace{\frac{\partial(Avc)}{\partial l}}_{\text{Convective term}} - \underbrace{\frac{\partial}{\partial l}\left(AD\frac{\partial c}{\partial l}\right)}_{\text{Diffusive term}} = \overbrace{AS}^{\text{Source term}} \qquad (1)$$

with $S = \frac{S_L}{A} + S_c$

where t = time; c = pollutant concentration; l = spatial coordinate; v = average rate of liquid in cross section; A = cross section area; D = longitudinal dispersion

coefficient; S = source term which is addition of two terms: S_L = external contribution or drawing; S_c = contribution by internal dynamics to concentration variations.

Hydraulic submodel
It is made by equations resulting from (1), replacing by respectively water density ρ (mass balance equation and motion quantity density ρv (motion quantity balance equation).

Biochemical submodel
It is made joining conservation equation of water mass and considered compound. In any case there will be a type of equation:

$$\frac{\partial c}{\partial t} + v\frac{\partial c}{\partial l} = \frac{1}{A}\frac{\partial}{\partial l}\left(AD\frac{\partial c}{\partial l}\right) - \frac{S_q}{A}c + \frac{S_L}{A} + S_c \qquad (2)$$

where $S_q c/A$ describes concentration diluition due to water source S_q (dimensionally flow on unit of length).

Model is composed by type (2) equations system, one for any inquired compound. In the S_c term the dynamics of variables are cointained. For any chemical agent can be produced source terms as function of physical and chemical kinetics which control different degradation or concentration addition.

3.4.1 *Nitrogen*
Organic nitrogen N_4

$$S_{N4} = \alpha_1 \cdot \tau \cdot A(t) - \beta_3 \cdot N_4(t) - \sigma_4 \cdot N_4(t) \qquad (3)$$

where α_1 = nitrogen fraction present in algae biomass; τ = algae breathing rate; $A(t)$ = algae biomass concentration; β_3 = organic and ammoniacal nitrogen hydrolisis rate; σ_4 = sedimentation rate.

Ammoniacal nitrogen N_1

$$S_{N1}(t) = -\beta_1 \cdot N_1(t) + \beta_3 \cdot N_4(t) - r_N \cdot \alpha_1 \cdot \mu(t) \cdot A(t) + \frac{\alpha_3}{d(t)} \qquad (4)$$

where β_1 = ammonia oxidation rate; σ_3 = benthic generation ($\sigma_3 > 0$) or consumption ($\sigma_3 < 0$) of ammoniacal nitrogen; $\mu(t)$ = specific growth rate; r_N = ammoniacal nitrogen fraction in $\alpha_1 \cdot \mu(t) \cdot A(t)$ nitrogen used for new algae biomass; α_3 = oxygen photosynthetic production rate; $d(t)$ = stream average depth.

Nitroso nitrogen N_2

$$S_{N2}(t) = -\beta_2 \cdot N_2(t) + \beta_1 \cdot N_1(t) \qquad (5)$$

where β_2 = nitrites oxidization rate.

Nitric nitrogen N_3

$$S_{N3}(t) = \beta_2 \cdot N_2(t) - (1 - r_N) \cdot \alpha_1 \cdot \mu(t) \cdot A(t) \qquad (6)$$

where $\alpha_1 \cdot \mu(t) \cdot A(t)$ = nitrogen used for new algae biomass.

3.4.2 *Phosphorous*
Organic phosphorous P_1

$$S_{P1}(t) = -\beta_4 \cdot P_1(t) - \sigma_5 \cdot P_1(t) + \alpha_2 \cdot \tau \cdot A(t) \qquad (7)$$

where β_4 = organic phosphorous degradation rate; σ_5 = sedimentation rate; α_2 = algae phosphorous fraction.

Dissolved inorganic phosphorous P_2

$$S_{P2}(t) = \beta_4 \cdot P_1(t) - \alpha_2 \cdot \mu(t) \cdot A(t) + \frac{\sigma_2}{d(t)} \qquad (8)$$

where σ_2 = benthic generation ($\sigma_2 > 0$) or consumption ($\sigma_2 < 0$) of dissolved phosphorous.

3.4.3 *Algae*

$$S_A(t) = \mu(t) \cdot A(t) - \tau \cdot A(t) - \frac{\sigma_1}{d(t)} \cdot A(t) \qquad (9)$$

where $A(t)$ = algae biomass concentration; $\mu(t)$ = specific growth rate; τ = breathing rate; σ_1 = sedimentation rate; $d(t)$ = stream average depth.

3.4.4 *BOD*
Carbonic BOD is regulated by degradation and sedimentation processes, described in the following relation:

$$S_B(t) = -k_1 \cdot B(t) - k_3 \cdot B(t) \qquad (10)$$

where k_1 and k_3 are respectively BOD degradation and sedimentation rate; $B(t)$ = BOD concentration.

3.4.5 *Oxygen*
Oxygen is consumed by a lot of processes already presented and is produced by superficial areation and photosynthesis; dynamics can be described by relation:

$$S_C(t) = -k_1 B(t) - \alpha_5 \beta_1 N_1(t) - \alpha_6 \beta_2 N_2(t) + \\ + k_2(C_s - C(t)) + [\alpha_3 \mu(t) - \alpha_4 \tau]A(t) - \frac{k_4}{d(t)} \qquad (11)$$

where α_5, α_6 = oxygen consumption rate on unity of respectively oxidized $NH_4 \cdot NO_2$ concentration; k_2 = aeration rate; C_S = saturation concentration; $C(t)$ = oxygen concentration; α_3 = oxygen photosynthetic production rate; α_4 = algae breathing rate; k_4 = oxygen demand ($k_4 > 0$) or production ($k_4 < 0$) from sediments.

3.4.6 *Fecial coliforms*

$$S_E(t) = -k_5 \cdot E(t) \tag{12}$$

where $k_5 =$ death rate; $E(t) =$ colibatteri fecali concentration.

3.4.7 *Non conservative indicators X_{nc}*
Equation, which is used to describe non conservative general polluting dynamics X_{nc}, is:

$$S_{Xnc}(t) = -k_i \cdot X_{nc}(t) - \sigma_j \cdot X_{nc}(t) - \frac{\sigma_k}{d(t)} \tag{13}$$

where $k_i =$ degration rate; $\sigma_j =$ sedimentation rate; $\sigma_k =$ benthic consumption ($\sigma_k > 0$) or generation ($\sigma_k < 0$) of agent; $X_{nc}(t) =$ non conservative indicators concentration.

Among non conservative indicators phyto-drugs kinetics is modelled by this form equation.

3.4.8 *Conservative indicators X_c*
Equation, which is used to describe conservative general polluting dynamics X_c is:

$$S_{Xc}(t) = -\sigma_j \cdot X_c(t) \tag{14}$$

where $\sigma_j =$ sedimentation rate; $X_c(t) =$ conservative indicators concentration.

Chlorine and boron kinetics is modelled by this form equation.

For all considered pollutants is supposed that they behave like dissolved solids and that their diluition don't change water density. In the case of heavy metals the behaviour inside water matrix was described by conservative kinetics, with concentration distribution varying only because of adsorption on colloidal particles and other suspended solid in stream, sedimentation and probable suspension again of dregs:

$$S_{mc}(t) = -\sigma_j \cdot M_c(t) + \sigma_i(v) \cdot M_c(t) \tag{15}$$

where $\sigma_j =$ parameter sedimentation rate; $\sigma_i =$ suspension again rate, function of cross section average velocity; $M_c(t) =$ heavy metals concentration.

3.5 *Expert system*

Data acquisition of a traditional monitoring system, which works in a stand-alone way, usually gives a lot of measures and alarms, but it doesn't give an explanation to the operator about the cause of signals or a general analysis of the situations to suggest the most suitable actions. To pass these limits, the present project uses an expert system, implemented with neural network, which we will realize by creation of a Knowledge Base containing a series of simulation scenarios of reference. So, it is able to extrapolate/interpolate in a clever way data in archive to formulate a forecast of cause/effect connection of a continuous or accidental waste water, leaving from a series of classes of situations previously detected in the knowledge base, and exhaustive of interesting cases. The building of knowledge base, made of reference scenarios to which the inferential motive will take its elaborations, will be made using the chosen quality model. The system will increase its own knowledge base storing information relative to cases that it is solving. Working way of an expert system is very like the human behaviour, and such is the interactive way with the operator; this important characteristic make its use easy also for not very expert users. Moreover we can see the operative time of an expert system, thanks to the power of elaboration at present available, are perfectly compatible with a real-time use.

3.6 *Input and output of results*

The system is in connecting with field and river characteristics, so we forecast their integration in a GIS from which they will take information about field, and to which they can give elaborations results to realize a mapping in connecting with data of the field (waste waters and sampling works position, effects on bypass channels, etc.). Moreover we forecast the possibility of connecting the systems with environmental tools (meteo gages, flow and/or level meter, current meters, water quality sensors, etc.).

4 CONCLUSIONS

In terms of results, we want to reach the capability of analysing measure and control monitoring data as to be able of previous and in real-time valuing the effect of continuous or accidental waste waters add, and analysing the consequence, on water quality, of regulation intervention or waste waters stop to verify its effectiveness.

ACKNOWLEDGEMENTS

We thank Carelli M., Mainolfi P. and Onorati G. of technical direction of Campania Regional Environment Protection Agency for cluster analysis data of water quality of Sarno river.

REFERENCES

1. Mancusi, L. & Barbanti, A. 1997. Modello della qualità delle acque del fiume Serio. *Rapporto tecnico Prog. STA 9215; Doc. RAT-STA-0053/97 rev.1*. Bergamo, Italy: ISMES S.p.A.

2. Imperiali, P. & Postiglione, D. 2002. Emergenza ambientale nel bacino idrografico del fiume Sarno – Relazione tecnica del Progetto di monitoraggio delle acque sotterranee e superficiali. *Prog. T24200; Doc. RAT-STA-8.1.1*. Bergamo Italy: Enel.Hydro – Business Unit ISMES S.p.A.
3. Postiglione, D., Mancusi, L., Gargiulo, A., Boccia, F., Mainolfi, P., Onorati, G., Carelli, M. & Speranza, P.P. 2003. Progetto di intervento sul fiume Sarno: un sistema integrato per il monitoraggio della qualità delle acque superficiali del bacino idrografico del fiume Sarno. Naples Italy: Enel.Hydro –Business Unit ISMES S.p.A.
4. Mancusi, L. 2003. Sistema di controllo dell'inquinamento dovuto a reflui nei corpi idrici superficiali. *Proceedings of National Conference "Inquinamento del fiume Sarno: il monitoraggio ed i controlli ambientali*. 14 october 2003 Villa Nunziante, Scafati, Italy.
5. Mappa, G. 2000. Microexpert: un sistema esperto per il controllo dei problemi di separazione solido-liquido nei depuratori a fanghi attivi basato sulle metodiche di indagine microscopica. Naples, Italy.
6. Schoorl, J.M. & Mappa, G. 2000. Il monitoraggio consapevole nella gestione delle risorse idriche. *Proceedings of Study Day "La strumentazione per la gestione degli acquedotti"*. Naples, Italy.
7. Tomei, M.C., Di Iaconi, C., Di Pinto, A.C. & Mappa, G. 1996. Development of an export system for nitrogen removal control. *European Water Pollution Control.* Volume 6 number 6, page 45.
8. Bonvicini, V., Mappa, G. & Sabatino, P. 1999. Monitoraggio della qualità delle acque depurate con l'utilizzo di sensori intelligenti low cost. *In workshop AI*IA99 Intelligenza Artificiale per l'Ambiente*. *Proceedings of the Sixth Symposium Italian Association for Artificial Intelligence*. 17 september 1999 Bologna, Italy.
9. Caporusso, R.A., Musella, E., Mappa, G. & Sabatino, P. 1999. Sistema di monitoraggio e gestione del trattamento delle acque cromiche. *In workshop AI*IA99 Intelligenza Artificiale per l'Ambiente*. *Proceedings of the Sixth Symposium Italian Association for Artificial Intelligence.* 17 september 1999 Bologna, Italy.
10. Marsili, S., Giacomelli, V., Cavalieri, S. & Mazzoni, M. 2000. Modellistica fluviale. Florence, Italy: RTI CTN_AIM 2/2000 and ANPA Environment National Protection Agency.
11. A.A. v.v. 2001. Sistema di prevenzione dell'inquinamento dovuto a reflui nei corpi idrici superficiali. *Capitolato tecnico PON AQUATEC.*
12. De Pietro, G. & Graziani, S. 1999. Modelli neurali per la trasformazione afflussi-deflussi in un bacino idrografico. *L'Acqua*. Number 4 page 37. Italy: Associazione Idrotecnica Italiana.
13. Pecora, S. & Veltri, P. 2001. Artificial neural network application for real time forecasting of levels in a natural water course. *L'Acqua*. Number 2 page 11. Italy: Associazione Idrotecnica Italiana.
14. Fiorillo, G. 2002. Stima del trasporto solido nel fiume Po mediante reti neurali artificiali. *Proceedings of 28th Hydraulics and Hydraulic Constructions Symposium*. Volume III, page 129. 16–19 september 2002, Potenza, Italy: BIOS.
15. Cavallo, A., Di Nardo, A. & Di Natale, M. 2002. La gestione di un serbatoio artificiale mediante una strategia di controllo fuzzy. *Proceedings of 28th Hydraulics and Hydraulic Constructions Symposium*. Volume IV page 431. 16–19 september 2002, Potenza, Italy: BIOS.
16. Di Gianmarco P, Longo, S. & Ferraresi, M. 2002. Un modello di qualità e di trasporto solido per aste fluviali. *Proceedings of 28th Hydraulics and Hydraulic Constructions Symposium*. Volume III, page 443. 16–19 september 2002, Potenza, Italy: BIOS.
17. Puca, S., Arena, F. & Tirozzi, B. 2002. Un nuovo approccio per la ricostruzione delle serie temporali dei livelli di altezza significativa con l'impiego di reti neurali. *Proceedings of 28th Hydraulics and Hydraulic Constructions Symposium*. Volume IV, page 3. 16–19 september 2002, Potenza, Italy: BIOS.
18. Cannas, B., Fanni, A. & Di Natale, M. 2002. River flow forecast for reservoir management using neural networks. *Proceedings of 28th Hydraulics and Hydraulic Constructions Symposium*. Volume IV, page 479. 16–19 september 2002, Potenza, Italy: BIOS.
19. Mayr, P., Jugovic, C.J., Koboltsching, G. & Mader, H. 2002. Development of simultaneous measurements of physical parameters in rivers. *Proceedings of 2nd international conference "New Trend and Environmental Engineering for safety and Life: Eco-compatible Solutions for Aquatic Environments*. 24–28 june 2002. Capri, Italy.
20. Chandra Sekhar, M. & Surender Reddy, K. 2002. Modelling stream water chemistry using river basin land use characteristics. *Proceedings of 2nd international conference "New Trend and Environmental Engineering for safety and Life: Eco-compatible Solutions for Aquatic Environments*. 24–28 june 2002. Capri, Italy.
21. Radwan, M., Willems, P., El-Sadek, A. & Berlamont, J. 2002. Modelling of dissolved oxygen and biochemical oxigen demand in river water using a detailed and simplified model. *Proceedings of 2nd international conference "New Trend and Environmental Engineering for safety and Life: Eco-compatible Solutions for Aquatic Environments*. 24–28 june 2002. Capri, Italy.
22. Rauch, W., Henze, M., Koncsos, L., Reichert, P., Shanahan, P., Somlyòdy, L. & Vanrolleghem, P. 1998. River quality modelling: I state of art. *Proceedings of IAWQ Biennal International Conference*. 21–26 june 1998. Vancouver, British Columbia, Canada.
23. Rauch, W., Henze, M., Koncsos, L., Reichert, P., Shanahan, P., Somlyòdy, L. & Vanrolleghem, P. 1998. River quality modelling: III future of art. *Proceedings of IAWQ Biennal International Conference*. 21–26 june 1998. Vancouver, British Columbia, Canada.

River Flow 2004 – Greco, Carravetta & Della Morte (eds.)
© 2004 Taylor & Francis Group, London, ISBN 90 5809 658 0

A random walk approach for investigating near- and far-field transport phenomena in rivers with groin fields

Volker Weitbrecht[1], Wim Uijttewaal[2] & Gerhard H. Jirka[1]
[1]*Institute for Hydromechanics, University of Karlsruhe, Germany*
[2]*Environmental Fluid Mechanics Section, Faculty of Civil Engineering and Geosciences, Delft University of Technology, The Netherlands*

ABSTRACT: Dead-water-zones in rivers formed by groin fields strongly influence the dispersive mass transport of dissolved pollutants. The cause for this influence is the exchange process between groin fields and main stream. With the help of laboratory experiments the most important parameters, such as storage time, velocity distribution and distribution of the diffusivity have been investigated. A transport model using a Lagrangian-Particle-Tracking-Method (*LPTM*) has been developed, to transfer the locally obtained experimental results for a single dead-water-zone into the global parameters of a one-dimensional far field model that comprises the action of many dead water zones. It is shown that in the presence of large dead water zones at the river banks, an equilibrium between longitudinal dispersion and transverse diffusion can be reached if the morphologic conditions do not change. The simulations result in a cross sectional averaged concentration distribution that converges asymptotically to a Gaussian distribution over the longitudinal coordinate. Due to the presence of dead water zones the distribution of tracer material becomes inhomogeneous in transverse direction.

1 INTRODUCTION

Predicting the transport of dissolved pollutants in rivers is difficult, because of the various effects of the morphological conditions. In rivers with strong morphological heterogeneities, like extensive dead-waterzones, the prediction of transport velocities, maximum concentration and skewness contains strong uncertainties that need to be reduced. The River-Rhine-Alarm-Model (Spreafico and van Mazijk 1993) has been developed by the "International Commission for the Hydrology of the River Rhine" (*CHR*) and the "International Commission for the Protection of the Rhine" (*ICPR*). For this kind of predictive models, much effort and money is spent on calibration by means of extensive in-situ tracer measurements (van Mazijk 2002). In the case of the River Rhine Alarm Model, which uses a one-dimensional analytical approximation for the travel time and concentration curve, a dispersion coefficient and a lag coefficient have to be calibrated. The model works well for cases of similar hydrological situations. However, variations in discharge, and thus, changes in water surface levels, lead to increased errors if the same calibrated parameters are used for different hydrological situations. Insufficient knowledge about the relation between river morphology and transport processes are the reason for these uncertainties. Hence, predictive methods that are appropriate for variable flows and changing morphological conditions are needed.

With the present work we focus on the influence of dead water zones, such as groin fields, on the dispersive mass transport in the far field of pollutant releases. Longitudinal dispersion in rivers that can be treated as shallow flows is controlled by two processes. First, the longitudinal stretching due to the horizontal shear, and second, transverse homogenization by turbulent diffusion (Fischer et al. 1979). Detailed velocity and concentration measurements have been performed in the laboratory in order to determine typical flow patterns and local mass transport phenomena. Direct measurements of dispersion coefficients are problematic because the dispersive character of a transport phenomena reaches its final behavior only after a very long travel time (Fischer et al. 1979), which is determined by the width of the flow and the intensity of the transverse turbulent diffusion. In most cases laboratory flumes are far too short, to examine longitudinal dispersion in the far field. To address this problem, laboratory and numerical experiments have been combined in such a way that the effect of local phenomena that have been measured, are translated into the

behavior of tracer clouds in the far field with the help of Lagrangian-Particle-Tracking- Method (*LPTM*).

2 EXPERIMENTS

In the present study the experiments have been performed in a laboratory flume of 20 m length and 1.8 m width, which has an adjustable bottom slope. In all the experiments only half of the channel width has been modelled, which means that only on one side of the flume groins have been placed. The shape of the groins was chosen to be very simple due to the fact that earlier investigations suggest that there is no significant effect of the groin shape on the exchange processes (Lehmann 1999). Using a simple geometry leads to a small number of parameters, which allows clear understanding of the basic relations between geometry and flow or transport phenomena, respectively.

The flume bottom consists of a plastic laminate with small roughness elements <0.2 mm. Level changes in x- and y-direction (Fig. 1) of the flume bottom are smaller than 0.2 mm. The flume is connected to a system of a water storage tank and a constant head tank, which is supplied by three different pumps, enabling discharges up to 100 ℓ/s. The discharge is controlled by an inductive-flow-meter together with an PC controlled gate valve. In the present case, only very small discharges of up to 10 ℓ/s are needed. Therefore, the gate valve is equipped with a pentagonal regulating orifice, which leads to constant discharges (changes smaller than 0.5%), even if the valve is opened only 5%.

In order to simulate flow patterns under the influence of dead-water zones, respectively groin fields, a series of 15 schematized groins made of PVC with a heavy core were built, so that these elements could be placed at variable positions. The outline of a single groin was chosen to be a combination of a rectangular box (0.45 m $\times$ 0.05 m $\times$ 0.05 m) with an attached half cylinder (diameter = 0.05 m). In the present study experiments have been performed with varying groin field aspect ratio W/L (0.17–3.5) and different inclination angles of the groins (Fig. 2).

The velocity measurements were performed using Particle-Image-Velocimetry at the water surface, using the PIV package DaVis from LaVision (Weit-brecht et al. 2002). With the help of a particle dispenser the water surface is seeded with black Polypropylene particles, such that homogeneous particle distribution on the water surface is achieved. The flow field in the main stream and in the groin field is then recorded with a digital camera at a temporal resolution of 7 Hz. The vector fields are obtained by using a cross-correlation technique, leading to spatial resolution of 2 cm $\times$ 2 cm.

In Fig. 3 the measured mean velocity profiles are plotted for the different aspect ratios in the case of the standard groins.

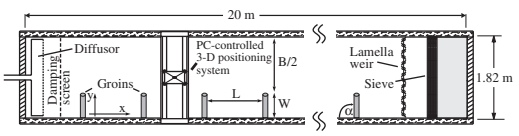


Figure 1. Schematic top view of the laboratory flume showing the groins placed on one side.

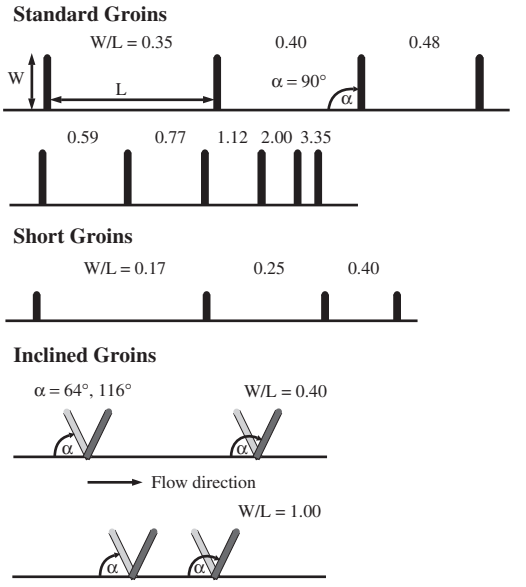


Figure 2. Schematic top view of the different aspect ratios and the different inclination angles that have been analyzed.

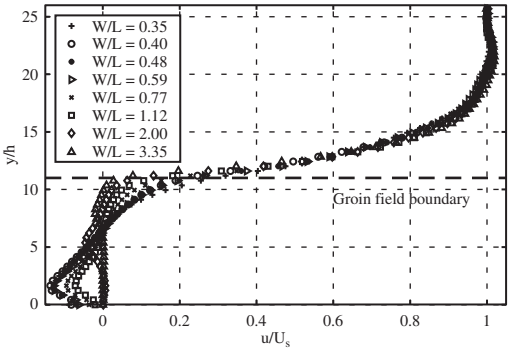


Figure 3. Comparison of the mean velocity profiles for the different W/L aspect ratios. The plotted velocities are averaged in space over the length L of the groin fields, and normalized with the maximum velocity at the water surface U_S.

The comparison in Fig. 3 shows that, the aspect ratio of the groin field has limited influence on the mean flow properties in the main stream. Above the groin field boundary no significant differences between the normalized velocity profiles can be observed. The velocity profile in Fig. 3 in the main stream part of the flow has the typical shape of a mixing layer velocity profile and can be approximated using a hyperbolic tangent function of the form

$$\frac{u(y)}{U_s} = a \tanh\left(\frac{y}{h_S}\, b\right) + c \qquad (1)$$

where a, b and c are constants that have to be adapted. In the present case the profile for the reference case $W/L = 0.4$ leads to the following values: $a = 0.82$, $b = 0.24$ and $c = 0.17$. h_S is the water depth in the main stream. This equation represents the velocity profile that is responsible for the stretching mechanism of a tracer cloud in the main stream.

In Fig. 4 the normalized rms-velocities of the transverse component v'/u_* measured with the PIV system are plotted. These values indicate the strength of the transverse turbulent mixing, which is the second important parameter influencing longitudinal dispersion.

Additional concentration measurements have been performed to measure the mean residence time T_D of tracer material in the dead-water-zones (Kurzke et al. 2002) using a depth averaged adsorptive technique. With the help of a multi-port injection-device tracer has been injected instantaneously into one groin field. The evolution of concentration distribution has been recorded with a CCD-camera. Gray scale analysis, which takes into account inhomogeneous illumination and changing background intensities, finally leads to an exponential decay function for every groin field setup

$$C(t) = C_o\, e^{-\frac{t}{T_D}} \qquad (2)$$

where C is the spatial averaged concentration in the dead zone, C_o the initial concentration. The residence time T_D is used in the LPTM transport model to parameterize the influence of dead-water zones on the mass transport in the river.

T_D can be normalized with the width of the groin field W and the main stream velocity U to give a dimensionless exchange coefficient k

$$k = \frac{W}{T_D U} \qquad (3)$$

The resulting exchange coefficients k for the different groin field setups are shown in Fig. 5.

Figure 5 shows that k reduces with increasing W/L, which means that the residence time T_D is longer in the very narrow cases of groin fields. Another results is the increased mass exchange for backward inclined groins compared to downward inclined or regular groins. For short groins Fig. 5 shows also the tendency towards smaller exchange values with increasing W/L. However, the k-values for short groins are noticeably smaller for the same aspect ratio W/L than in the standard case. This shows, that the groin field volume has to be taken into account for the prediction of k.

A slight modification of the scaling factor W/L into $WL/(W+L)$, which can be interpreted as a kind of hydraulic radius R_D of the dead-water-zone, leads to a better normalization shown in Fig. 6. Why the exchange coefficients should scale with the hydraulic radius R_D can be explained by the following: In the case of very long groin fields with $L \to \infty$ the expression $WL/(W+L)$ tends to W. Therefore, in the case of very long groin fields the recirculating flow is only determined by the width W of the groin field. In the other extreme case for $W \to \infty$ the hydraulic radius R_D tends to L, which means that the mass exchange in this case is only determined by the length of the mixing layer.

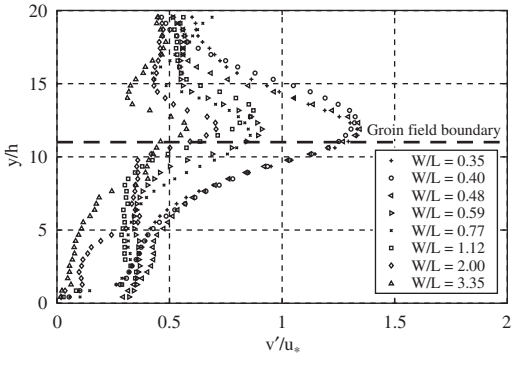


Figure 4. Comparison of the normalized strength of the velocity fluctuations v'/u_* for the different aspect ratios W/L.

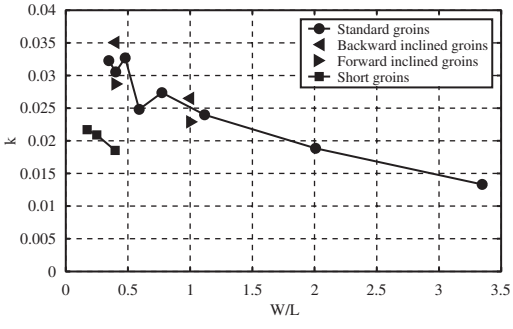


Figure 5. Dimensionless exchange coefficient k against the aspect ratio W/L.

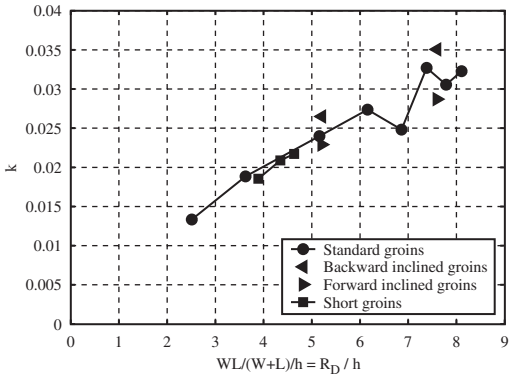


Figure 6. Dimensionless exchange coefficient k versus the normalized hydraulic radius $R_D = h$.

3 LAGRANGIAN PARTICLE TRACKING METHOD

A transport model based on a two-dimensional Lagrangian-Particle-Tracking-Method (*LPTM*) has been developed to transfer the local results of the laboratory experiments for a single dead-water-zone into the global parameters of a one-dimensional far field model that comprises the action of many dead-water- zones. The method represents a random walk approach as has been used, for example, by Sullivan (1971) to model turbulent shear flow based on statistical mechanical transport theories presented by Taylor (1921).

As the present transport problem is basically a problem of longitudinal dispersion, we assume that the dominating processes in this case are longitudinal shear and transverse diffusion. Thus, the behavior of discrete particles under the influence of advection in longitudinal direction and of transverse diffusion is determined in a two-dimensional domain. The idea is to initiate a cloud of particles that is advected within a known mean flow profile. This advective movement is superimposed on a random movement in transverse direction, representing turbulent diffusion.

The characteristic transport parameters, like dispersion coefficient, transport velocity and skewness coefficient, can be determined by analyzing the statistics of such a particle cloud at any position of the simulation. In addition to one-dimensional information this method yields concentration distributions in transverse direction, in order to describe near-field phenomena.

The influences of dead-water zones are included with the help of extra boundary conditions that represent the mean retention time of particles in the area of dead-water zones. Herewith, the influence of different groin field geometries on the mass transport,

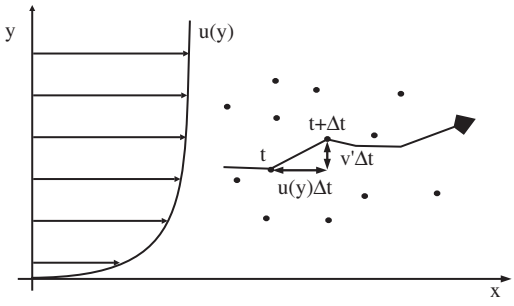


Figure 7. Particle velocity in a two-dimensional flow field with mean velocity in x-direction and turbulent velocities in y-direction.

especially on the mass dispersion, in the far-field of a pollutant spill can be predicted.

The method has been verified with the aid of the analytical solution presented for the Advection-Diffusion-Equation for a Couette-Flow problem (Fischer et al. 1979) and turbulent unbounded vertical shear flow given by Elder (1959). Dispersion coefficients obtained from these solutions are compared with the transport characteristics using the *LPTM* (Weitbrecht et al. 2003).

In the next step the transport model is used to predict the transport parameters for the flow conditions, taken from the experiments. Mean flow quantities and turbulence intensities are determined in pure channel flow and are adapted to the *LPTM*. Finally the influence of dead-zones (groin fields) is implemented.

A random walk simulation can be understood as the tracking of discrete particles, under the influence of the governing flow processes. Typically, the particle displacement dX_i is described by a deterministic and a stochastic part, leading to the so called Langevin equation (Gardiner 1985)

$$dX_i = \underbrace{f(X_i,t)dt}_{deterministic} + \underbrace{Z(t)g(X_i,t)dt}_{stochastic} \qquad (4)$$

where X_i is the position x, y and z. $f(X_i,t)$ represents the advective or drift component, which can be interpreted as the mean flow velocity field. The expression $g(x_i,t)$ describes the diffusive or noise component of the particle movement that describes the strength of the turbulent diffusion in space. The stochastic part is represented by the Langevin force Z, which is a Gaussian distributed variate with a mean value of zero and a variance equal to one.

In the present case the governing processes are advection in x-direction and diffusion in transverse direction (Fig. 7), which implies that we can neglect the drift component in y-direction and the noise component in x-direction in Eq. 4. An important part of such a model is the link between the diffusive step

size and the length of the time step. Here we use the approach given by Taylor (1921) who stated that the spreading of a particle ensemble measured with the standard can be treated as a Fickian type of diffusion, where $\sigma \sim \sqrt{2Dt}$. The diffusive step size for a single particle at a certain time step in y-direction is therefore given with

$$v'\Delta t = \sqrt{2D_y \Delta t} \tag{5}$$

where D_y is the turbulent diffusion coefficient in y-direction. Using these assumptions, the position of the particles in every time step Δt can be described by a simplified two-dimensional version of Eq. 4.

$$x_{new} = x_{old} + \underbrace{(\Delta t \cdot u(y))}_{deterministic} \tag{6}$$

$$y_{new} = y_{old} + \underbrace{Z\sqrt{2D_y \Delta t}}_{stochastic} \tag{7}$$

where x_{old}, y_{old} and x_{new}, y_{new} are the spatial locations at times t and $t + \Delta t$ respectively, and D_y is the transverse component of the turbulent diffusion coefficient. The function $u(y)$ denotes the mean flow velocity in relation to the position in transverse direction. Consequently, in every time step, a particle moves *convectively* in x-direction depending on the velocity profile and does a positive or negative *diffusive* step in transverse y-direction.

The reason why there is no diffusive step in the x-direction needed (Eq. 6), can be explained by the fact, that turbulent diffusion in x-direction and longitudinal dispersion are additive processes (Aris 1959), which means that the final dispersion coefficient can be adjusted by adding the turbulent diffusion coefficient. Fischer et al. (1979) showed that in natural rivers the coefficient of longitudinal dispersion D_L lies in the range of $30 < D_L/(u_* h) < 3000$, while the longitudinal turbulent diffusion coefficient D_x is considerably smaller. A typical approximation of the turbulent diffusion coefficient is given by $D_x \approx (0.6 u_* h)$, which means that in this approach turbulent diffusion in longitudinal direction can be neglected in comparison to longitudinal dispersion. An advantage of this simplification is a shorter computing time.

Flows with inhomogeneous turbulent diffusion coefficients are treated here, which means that D_y is a function of y. A problem in performing LPTM-simulations is given by the fact that particles segregate into regions of low diffusivity (Hunter et al. 1993). In the stochastic model particles move independently from regions with high diffusivity into regions with low diffusivity. As a consequence the probability of a particle to move from a region of high diffusivity into a region of low diffusivity is higher than vice versa. In order to satisfy continuity an extra advection term in y-direction has to be included, to achieve consistency with the governing Advection-Diffusion-Equation. This extra term is called the noise- drift component. By matching the resulting stochastic transport equations with the Advection-Diffusion- Equation Dunsbergen (1994) showed, that in this case, the noise-induced drift component Δy_n can be formulated as follows

$$\Delta y_n = \frac{\partial D_y}{\partial y} \Delta t \tag{8}$$

If Eq. 7 is extended with the given expression for the noise-induced drift component (Eq. 8), the transport problem with varying diffusivity is described consistently with the Advection-Diffusion-Equation.

$$y_{new} = y_{old} + Z\sqrt{2D_y(y)\Delta t} + \frac{\partial D_y}{\partial y} \Delta t \tag{9}$$

Also the boundaries of the calculation domain and their effect on the particles are important. The inflow and outflow boundaries do not affect the particles as in our case the domain has an infinite length. In case of horizontal shear the boundaries representing the channel bank and channel centre line act as reflective walls. Particles which would cross the left or right boundary at a certain time step are reflected into the calculation domain. Consequently, a particle with a calculated y-position outside the calculation domain $y < 0$ is re-introduced as follows

$$y_{new} = -y_{calc} \tag{10}$$

where y_{calc} is the calculated y-position at a certain time step.

With the given equations and boundary conditions transport in open channel flow can be simulated with a depth-averaged velocity profile in transverse direction and a certain distribution of the diffusivity. The next step is to include the influence of dead-water zones (Fig. 8) into the LPTM.

The mean residence time of tracer material in the dead-water zone is the most important parameter to describe the behavior of a dead-water zone. Therefore, it should be possible to model the influence of the mass transport by including this parameter into the LPTM. A possibility is to include the residence time into the boundary condition, such that this boundary simulates the behavior of mass trapping and mass release. Thus, the interface between main channel and dead-water zone has to act as a transient-adhesion boundary, which means that particles that reach such a boundary are fixed to that position until T_D has passed. This mimics to the real dead-zone behavior. A particle that enters a dead-water zone because of turbulent motion in the mixing layer, does not move on average in x-direction, assuming that the longitudinal extension

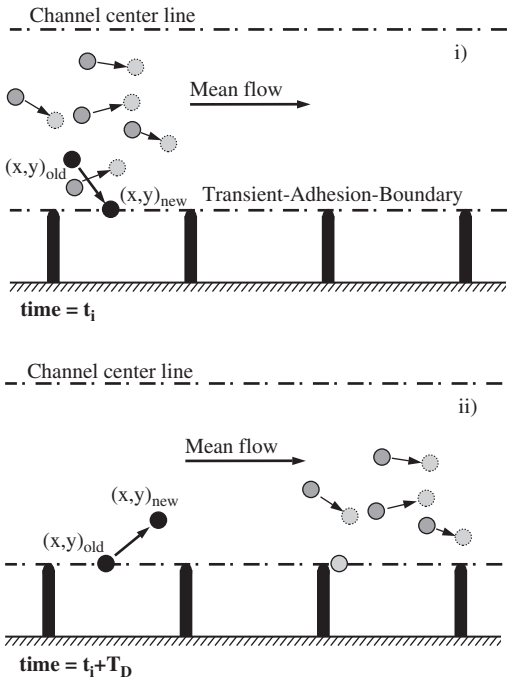


Figure 8. Schematic visualization of a particle approach to a transient adhesion boundary at: (i) time $= t_i$ and (ii) time $= t_i + T_D$, where T_D is the mean residence time.

of the dead-water zone is small compared to the length of the modeled river section. The particle remains in the dead-water zone on average for time period given by the mean residence time T_D, and after that period it gets back into the main stream.

The outcome of a *LPTM* simulation are x and y-positions of every single particle at every time step. By analyzing the statistics of the particle positions, information about the transport characteristics can be determined. The one-dimensional longitudinal dispersion coefficient D_L, as a measure of the spatially averaged spreading rate of a tracer cloud, can be determined by calculating the time change of the longitudinal variance σ_x^2 of the particle distribution (Rutherford 1994) as follows

$$D_L = \frac{1}{2}\frac{\sigma_x^2(t_2) - \sigma_x^2(t_1)}{t_2 - t_1} \tag{11}$$

A second result will be the skewness G_t of the particle cloud. The skewness is defined as the relation between the quotient of the third moment about and the third power of the standard deviation

$$G_t = \frac{\sum_{i=1}^{n}(x_i - \bar{x})^3}{(n-1)\sigma_x^3} \tag{12}$$

where n is the number of particles at the positions x_i with mean position $\bar{x}$ and σ_x is the standard deviation of the particle distribution. The skewness of a certain distribution describes the degree of asymmetry of a distribution. The skewness can be used as an indicator for the length of the advective zone, in order to define when it is acceptable to apply the Taylor solution to a pollutant transport problem.

Another parameter of interest is the transport velocity c of the tracer cloud, defined as the velocity of the center of mass of a particle ensemble. In the case of regular channel flow with ordinary reflective boundary conditions c is equal to the mean velocity if the particles are homogeneously distributed over the river cross section. In case of point sources this can be reached after the tracer has passed the advective zone. The transport velocity can be determined as follows

$$c = \frac{\bar{x}(t_2) - \bar{x}(t_1)}{t_2 - t_1} \tag{13}$$

where $\bar{x}$ represents the center of mass of a particle cloud.

4 APPLICATION AND RESULTS

In this section the *LPTM* is applied to different flow fields, that have been investigated in the laboratory in order to determine the influence of river heterogeneities on the mass transport properties of a river. Three different cases will be analyzed in detail. First the behavior of the dispersive character of pure channel flow without the influence of groin fields is investigated. In a second step groin fields are implemented, and finally the influence of different residence times on the transport characteristics is determined.

4.1 *Straight open channel flow*

A *LPTM*-simulation has been performed, in order to analyze transport phenomena in regular channels without groin fields. Therefore the measured velocity distribution has been approximated with an analytical function, that can be seen in Fig. 9(i). The diffusion coefficient in this case has been chosen to be constant over the whole river cross section, with a value according to Fischer et al. (1979) for regular channels.

$$D_y = 0.15 u_\star h \tag{14}$$

In Table 1 the properties of the flow and the settings of the 2D-*LPTM*-simulation for the case of a straight channel flow are listed.

The equilibrium between longitudinal stretching and transverse diffusion, where the dispersion coefficient does not change any more is reached after about

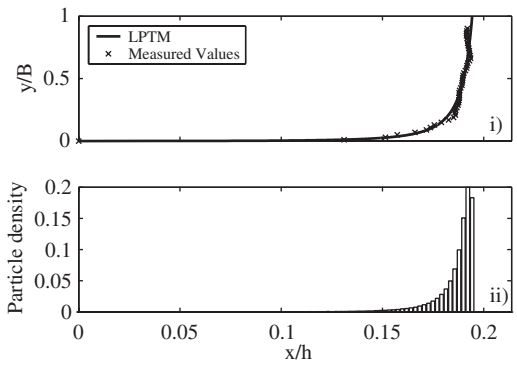


Figure 9. Result of *LPTM*-simulation with pure channel flow, after first time step. (i) Particle position according to the fitted velocity profile and the measured velocities taken from the experiment; (ii) particle density in longitudinal direction.

Table 1. Parameter values for the pure channel flow simulation, taken from the measurements.

Property	Value
Water depth h [m]	0.046
Channel half width B [m]	1
Mean velocity [m/s]	0.19
Horizontal velocity profile	Fig. 9(i)
Channel slope I [%]	0.032
No. of particles	5,000
No. of time steps	40,000
Length of time step Δt [s]	1
Diffusivity D_y [m^2/s]	(Eq. 14)

800 times the channel's half width. The final value of $D_L/(u_* h)$ is 177, and is much larger (30 times) than the dispersion found in a channel with a laterally uniform velocity (Elder 1959).

4.2 *Channel flow with groin fields*

The influence of groin fields is simulated with the transient-adhesion boundary condition (Sec. 3), that represents the mean residence time of a particle in the groin field. These mean residence times have been measured in this study with two different approaches. Concentration measurements have been performed, where concentration decay in a single groin field has been tracked with digital video analysis. Starting with a known homogeneous concentration in the groin field and zero concentration in the main stream an exponential decay could be observed, leading to a typical time scale T_a describing the mean residence time. These experiments are in principle analogous to the measurements that have been performed by Uijttewaal et al. (2001). An improvement could be achieved by the development of a multi-port injection device, that is able to produce reproducible homogeneous concentration fields as initial condition for the concentration measurement (Kurzke et al. 2002). Another possibility to determine the residence times is given by using the velocity fields for the determination of the mass exchange rate between groin field and main stream (Kurzke et al. 2002).

In order to determine the influence of groin fields, a *LPTM*-simulation has been performed with the same flow properties as in the described case above (Table 1). The difference lies in the transient-adhesion boundary condition at the channel wall. This simulation represents groin fields, where the ratio between the width W of a groin field divided by the length L is 0.4 (Fig. 2). These conditions correspond to laboratory measurements with a groin field length 1.25 m and a width of 0.5 m. As the water depth in the groin field and the main stream is the same, the ratio between the cross sectional area of the dead water zone and the main stream is 0.5. The mean residence time T_a of a tracer particle has been set to 90 seconds, which corresponds to the measured dimensionless exchange coefficient

$$k = \frac{W}{T_a U} = 0.028 \tag{15}$$

where W is the width of the groin field and U represents the mean flow velocity in the main channel.

In the case of channel flow with groin fields the velocity profile is slightly changed compared to the pure channel flow, because in the presence of groin fields the velocity profile has to represent the mixing layer between groin field and main stream and can be approximated with a tanh function, where the velocity is still positive at $y = 0$.

The distribution of the diffusivity in that case is not constant over the channel cross section, see Fig. 4. Turbulence measurements showed, that the velocity fluctuations in the region of the mixing layer between groin field and main channel are much stronger than in the undisturbed main channel. Therefore the diffusivity given by Eq. 14 is amplified in the region of the mixing layer, proportional to the increasing transverse velocity fluctuations. This has been done, by fitting a gaussian curve to the transverse *rms*-values of the channel flow, such, that the diffusivity in the mixing layer is three times larger than in the main channel (Weitbrecht et al. 2002).

In Fig. 10 the *LPTM*-simulation with groin fields is visualized after 200 time steps. The main difference with respect to pure channel flow is found in the particle clouds that travel far behind the main tracer cloud, a phenomenon that is also observed in the laboratory flume. These small particle clouds arise by the effect of the dead water zones. Particles that have crossed the

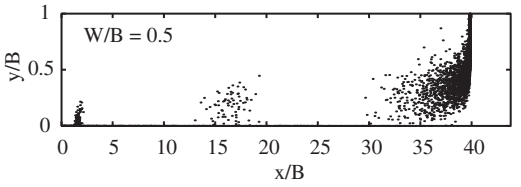


Figure 10. Result of *LPTM*-simulation after 200 time steps with a mean residence time of $T_a = 90$ s, that corresponds to a width to length ratio of a groin field of 0.4.

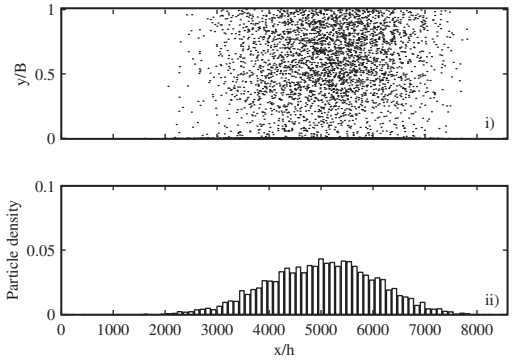


Figure 11. Result of *LPTM*-simulation after 40,000 time steps with a mean residence time of $T_a = 90$ s, that corresponds to a width to length ratio of a groin field of 0.4 and $W/B = 0.5$; (i) particle position; (ii) particle density in longitudinal direction.

lower boundary layer during the simulation, remain at the same x-position for the mean residence time T_a. After T_a has elapsed the particles get back to the flow. The mean distance between those clouds corresponds to the mean residence time T_a.

The final stage of mixing in the case with groins shows again, that after a long period the tracer cloud approximates a Gaussian distribution in longitudinal direction Fig. 11.

The interesting properties of this simulation are the evolution of the dispersion coefficient and of the skewness, as visualized in Fig. 12. The final value of $D_L/(u_* h)$ is in that case approximately 24.800 which is a factor 140 higher than in the case of pure channel flow, and about ten times higher than the values common for natural rivers without groin fields. This can be explained by the exaggerated ratio between the cross sectional area of the dead water zone and the cross sectional area of the main channel, which is 0.5 for this experiment, a value rather high compared to natural rivers.

The equilibrium between longitudinal stretching and transverse diffusion is achieved after approximately 800 times the channel width (Fig. 12), which

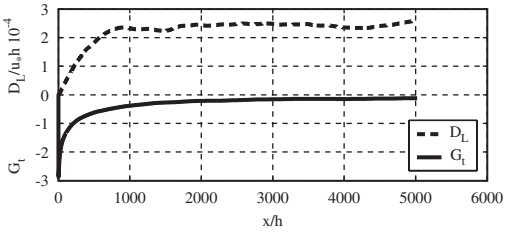


Figure 12. Evolution of Dispersion coefficient $D_L \cdot 10^{-4}$ normalized with the u_* and the water depth h and the evolution of the skewness. D_L is smoothed with a sliding average filter of increasing window size. ($W/B = 0.5$).

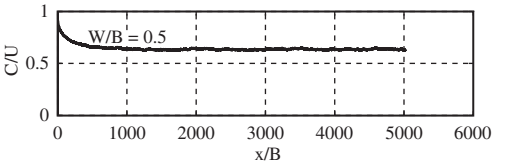


Figure 13. Evolution of transport velocity c of a tracer cloud normalized with mean velocity of the main channel.

indicates that the advective zone has the same length irrespective of the presence of groins.

In the case of a straight channel flow, the transport velocity c, which is defined as the translation velocity of the center of mass of the tracer cloud Eq. 13, always equals the mean flow velocity in the channel. In the case with groin fields the transport velocity of the tracer cloud decreases in time until an equilibrium distribution between the particles in the dead water zones and in the main channel is established, see Fig. 13. In this simulation the transport velocity does not change further after the tracer cloud has travelled approximately 1000 times the channel half width. The final transport velocity is 64% of the mean flow velocity in the main channel.

According to the one-dimensional dead-zone-models by Valentine and Wood (1979, van Mazijk (2002), the transport velocity in the far field can be estimated from the ratio between the cross sectional area of the dead water zone A_d and the cross sectional area of the main stream A_s

$$c = \frac{U}{1 + A_d/A_s} \tag{16}$$

In the presented case this relation would provide a value of 67% of the mean flow velocity, which is close to the result of the *LPTM*-simulation.

Considering the particle distribution in transverse direction of the river cross section, it can be stated that the initial homogeneous distribution (Fig. 14i) remains homogeneous in the case of a pure channel flow. The distribution is affected in the presence of groin fields

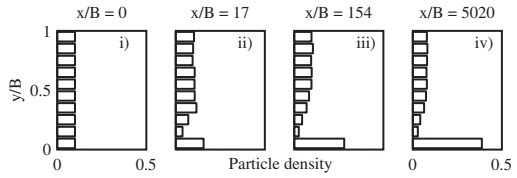


Figure 14. Particle density distribution in river cross-section as a function of the distance x/B.

Table 2. Results of *LPTM*-simulations with different exchange coefficients and $B/W = 0.5$, compared with the case of pure channel flow ($k = \infty$).

	k			
	∞	0.035	0.028	0.02
$D_L/(u_* h)$	177	19,800	24,800	32,400
c/U	1	0.68	0.64	0.56

(Fig. 14ii, iii, iv). A substantial part of the particles accumulate in the dead-zone area during the *LPTM*-simulation. In the final stage of mixing (Fig. 14iv) almost 40% of the tracer material is found in the region of the dead water zones. The remaining 60% of the material is travelling in the main stream.

4.3 *Groin fields with different exchange rates*

The dimensionless exchange coefficient k (Eq. 15), can be found in the literature to be in the order 0.02 ± 0.01 (Valentine and Wood 1979; Uijttewaal et al. 2001), with no clear dependency to the shape of the dead water zone. With our laboratory experiments, we could demonstrate that k varies with the width to length ratio of the groin fields within the range of $0.015-0.035$. Here the longest groin fields ($W/L = 0.3$) are leading to the highest k-values and the shortest groin fields ($W/L = 3.5$) correspond to the lowest k-value (Weitbrecht and Jirka 2001). In all cases the groin field width W was constant. According to Eq. 16 the transport velocity is supposed to be the same in those cases. In order to explore the possible influences of the changing k-values, two extra *LPTM*-simulations have been performed, where the mean residence time has been set to 75, 95 and 130 seconds, respectively. Consequently, the respective k-values used, are 0.035, 0.028 and 0.020.

In Table 2 the results of the simulations with changing k-values are summarized. It can be seen that the dimensionless dispersion coefficient $D_L/(u_* h)$ is proportional to the residence time T_a. The longer the residence time, the higher the stretching rate of the tracer cloud.

It can be seen that the influence of the different k-values on the transport velocities is at maximum 10% for the presented configuration. According to these simulations, the results of the one-dimensional dead-zone-model mentioned above predicts the transport velocity correctly, for a k-value of about 0.035, which corresponds to groin fields with an aspect ratio of about $W/L = 0.33$.

An equilibrium between longitudinal stretching and transverse diffusion is reached in all cases after approximately 800 times the channel's half width B. That again indicates that the dominant time scale is not T_a, but the diffusive time scale $B^2/(2D_y)$ associated with the time needed for a particle to cross B. If we determine the length x/B that corresponds to this time, we get

$$\frac{x}{B} = \frac{cB}{2D} = 750 \quad . \tag{17}$$

which corresponds very well to the observed behavior of the particle clouds in the LPTM-simulations.

5 CONCLUSIONS

Our approach in which laboratory experiments and *LPTM* are combined, creates the possibility to determine transport characteristics in the far field of a pollutant spill in shallow, predominantly two-dimensional river flows. Detailed velocity and concentration measurements are used to determine local flow and transport phenomena in the presence of groin fields. A translation is made via the *LPTM*, to convert these findings into transport velocities, longitudinal dispersion and skewness coefficients of the cross sectional averaged pollutant cloud in the far field. This information can be used to improve the accuracy of one-dimensional alarm-models, and to reduce the need for calibration with tracer experiments.

The finding, that the transverse tracer distribution is influenced by the presence of dead water zones should be taken into account for the planning of future field experiments, and for the interpretation of existing data. In addition to the concentration distribution it is likely that other properties depend also on the lateral coordinate.

The computationally simple two-dimensional approach allows for studying near field effects as well. Point releases of contaminants near one of the banks and not fully mixed states are impossible to predict with a one-dimensional approach. The same holds for strongly varying flow geometries with confluences, weirs, bends etc.

ACKNOWLEDGEMENTS

The numerical part of the project was funded by the "German Research Council" (DFG, Grant No.

Ji18/8-1) and the "Netherlands Organization Scientific Research" (NWO). The laboratory measurements were sponsored by the German "Federal Ministry for Education and Research" (BMBF, Grant No. 02 WT 9934/9).

REFERENCES

Aris, R. (1959). The longitudinal diffusion coefficient in flow through a tube with stagnant pockets. *Chemical Engineering Science 11*, 194–198.

Dunsbergen, D. W. (1994). *Particle Models Transport in Three-Dimensional Shallow Water Flow.* Ph. D. thesis, TU-DELFT, Faculty of Civil Engineering.

Elder, J. W. (1959). The dispersion of marked fluid in turbulent shear flow. *Journal of Fluid Mechanics 5*, 544–560.

Fischer, H. B., E. G. List, R. C. Y. Koh, J. Imberger, and N. H. Brooks. (1979). *Mixing in Inland and Coastal Waters*. New York, NY: Academic Press.

Gardiner, C. W. (1985). *Handbook of Stochastic Methods*. Springer-Verlag.

Hunter, J., P. Craig, and H. Phillips. (1993). On the use of random walk models with spacially variable diffusivity. *Computational Physics 106*, 366–376.

Kurzke, M., V. Weitbrecht, and G. Jirka. (2002). Laboratory concentration measurements for determination of mass exchange between groin fields and main stream. In D. Bousmar and Y. Zech (Eds.), *River Flow 2002*, Volume 1, Louvain-la-Neuve, Belgium, pp. 369–376. IAHR.

Lehmann, D. (1999). Auswirkung von Buhnenfeldern auf den Transport gelöster Stoffe in Flüssen. Master's thesis, University of Karlsruhe, Inst. for Hydromechanics and TU-Delft, Hydromechanics Section.

Rutherford, J. C. (1994). *River Mixing*. Sussex, England: Wiley.

Spreafico, M. and A. van Mazijk. (1993). Alarmmodell Rhein. Ein Modell für die operationelle Vorhersage des Transportes von Schadstoffen im Rhein. Technical Report I-12, Internationale Kommission zur Hydrologie des Rheingebiets, Lelystad.

Sullivan, P. J. (1971). Longitudinal dispersion within a two-dimensional turbulent shear flow. *Journal of Fluid Mechanics 49*, 551–576.

Taylor, G. I. (1921). Diffusion by continuous movements. *Proc. London Math. Soc. 20*, 196–211.

Uijttewaal, W., D. Lehmann, and A. van Mazijk. (2001). Exchange processes between a river and its groyne fields: Model experiments. *Journal of Hydraulic Engineering 127*(11), 928–936.

Valentine, E. M. and I. R. Wood. (1979). Experiments in longitudinal dispersion with dead zones. *Journal of the Hydraulics Division 105*(HY8), 999–1016.

van Mazijk, A. (2002). Modelling the effects of groyne fields on the transport of dissolved matter within the rhine alarmmodel. *Journal of Hydrology 264*, 213–229.

Weitbrecht, V. and G. Jirka. (2001). Flow patterns and exchange processes in dead zones of rivers. In *XXIX IAHR Congress*, Beijing, China.

Weitbrecht, V., G. Kühn, and G. H. Jirka. (2002). Large scale piv-measurements at the surface of shallow water flows. *Flow Measurements and Instrumentation 13*(5–6), 237–245.

Weitbrecht, V., W. Uijttewaal, and G. Jirka. (2003). 2-d particle tracking to determine transport characteristics in rivers with dead zones. In *International Symposium on Shallow Flows*, Delft, The Netherlands.

River Flow 2004 – Greco, Carravetta & Della Morte (eds.)
© 2004 Taylor & Francis Group, London, ISBN 90 5809 658 0

Turbulence of vertical round buoyant jets in a cross flow

M. Ben Meftah & A. Petrillo
Water Engineering and Chemistry Department, Technical University of Bari, Italy

P.A. Davies
Civil Engineering Department, University of Dundee, United Kingdom

D. Malcangio & M. Mossa
Civil and Environmental Engineering Department, Technical University of Bari, Italy

ABSTRACT: The paper looks at a vertical round buoyant jet issued in a cross flow and investigates the effect of turbulence in the cross flow upon the structure of the jet. This general problem of the influence of ambient turbulence has been investigated for the case of cross flow turbulence associated with flow over a rough bottom boundary. The results of laboratory investigations of this problem are described and it is shown that the influence of the roughness of the bottom surface is manifested by significant modifications to the buoyant jet trajectory (as compared to the smooth boundary reference case). Preliminary attempts to quantify and parameterize these modifications are presented.

1 INTRODUCTION

One crucial problem in hydraulic engineering concerns the dilution of turbulent thermal discharges in a cross flow. The effects of cross flow turbulence (generated, as in this case, by the presence of a rough bottom boundary) upon the structure of the discharge flow is an important aspect of this problem. The study of a heated water discharge in the form of a turbulent buoyant jet into a channel with a flat bottom and with a cross current is well established in the literature (*e.g.* Lee, 1984; Il Won Seo *et al*., 2001; Young Do Kim *et al*., 2002). The flow dynamics of the thermal discharge in the near field are governed purely by the momentum source represented by the high velocity injection. In the far field, instead, mixing is governed by ambient currents and stratification. Moreover, processes at the air-water interface, such as heat exchange towards the atmosphere and wind stress, can further affect the heat distribution. As regards the ambient turbulence, the visualization study of Grass *et al*. (1991) revealed that powerful vortical structures with a general horseshoe-type configuration occur over smooth surfaces as well as in the turbulent boundary layer near rough walls and that they are similarly linked to bursting events in both the smooth and rough bed cases. The nature of coherent structures and their processes of development over rough surfaces, therefore, appear to be similar to those originating over smooth walls. Furthermore, Grass *et al*. (1991) and Grass & Mansour-Tehrani (1996) observed that a remarkable feature of the rough wall flow is its apparent ability to order itself very rapidly in a small vertical distance above the tops of the roughness elements. Their measurements indicated that for fully rough wall conditions, the near-wall turbulence structures are directly proportional to the bed roughness size for geometrically similar roughness elements and the packing used in their tests.

In order to clarify the dependence of the buoyant jet upon the background turbulence and to improve knowledge of the physical processes that determine its dilution, an experimental study was conducted. Localized background turbulence was generated within the ambient flow by means of two different corrugated plastic surfaces of known "wavelength" λ and "amplitude" ε, fixed at the bottom of a rectangular channel. During this experimental work, the characteristics of the turbulence field produced in the surrounding flow by particular combinations of λ and ε were analyzed, with the aim of finding a typical characteristic length scale of the turbulent eddies associated with flow over the rough boundary and its effect upon the structure of the buoyant jet. Since the study consisted of a three-dimensional buoyant jet interacting with a three-dimensional "patch" of shear turbulence, measurements of velocity and temperature fields were assessed at different vertical levels to obtain the spatial structure of the temperature and the velocity profile

of the cross flow. Such an approach required a long time for each run, especially because relevant differences were observed at a distance of mms, and accurate and appropriate techniques to collect data, as described below were necessary.

For each configuration, the objectives of the experiments were (i) to compare the mixing of a buoyant jet discharged into a cross flow with a smooth and rough boundary, (ii) to identify a distortion of the jet structure by the presence of the background turbulence generated by the rough bottom and (iii) to quantify this distortion and parameterize it in terms of buoyant jet and corrugated surfaces characteristics.

2 EXPERIMENTAL WORK

2.1 *Experimental set-up*

The laboratory model was constructed in the Coastal Engineering Laboratory of the Technical University, Bari, Italy (Fig. 1). The system consists of a rectangular steel channel 15 m long, 4 m wide and 0.4 m deep, with lateral walls and base made of transparent glass material (Saint Gobain), 15 mm thick. To create a current inside the channel a closed hydraulic circuit was constructed. The fresh water at ambient temperature was supplied from a big metallic tank downstream by a Flygt centrifugal electro-pump, which sucked the water into a steel pipe with diameter 200 mm and then discharged the same water into the upstream steel tank. Into the upstream tank a side-channel spillway with adjustable height was fitted, being made from different plates mounted together. The water that overflowed was directed into a pipe like the one for the water supply and parallel to it, with a 250 mm diameter and finally discharged into the tank downstream of the channel. Two different electromagnetic flow meters were mounted on the two parallel pipes described above in order to measure the flow rate in the channel as the difference of the two discharge measurements. The free surface level of the water into the channel, H_a, was maintained at a constant level with a depth of 26 cm for all of the experiments, to ensure that the discharge into the channel was constant.



Figure 1. A view of the channel.

The second part of the laboratory model consisted of a buoyant jet thermal-hydraulic system. The discharged heated water generating the turbulent buoyant jet was pumped into the channel through a round steel tube mounted at the bottom of the channel and within the central longitudinal section. The tube was mounted vertically and it passed through the glass base. The source diameter $D = 5.0$ mm of the jet was chosen to satisfy different conditions. Firstly, in all cases to ensure that the jet was fully turbulent, *i.e.* to have the Reynolds number *Re,* defined for a round jet as $Re = 4Q_0/\pi D\nu$, with ν the kinematic viscosity of the fluid and Q_0 the source discharge, sufficiently high ($Re > 2000$).

Secondly, the value of D was fixed taking into consideration the length scale l_M, defined in terms of the source momentum (J_0) and buoyancy (B_0) fluxes as

$$l_M = \frac{Jo^{3/4}}{Bo^{1/2}} \tag{1}$$

for a three-dimensional buoyant jet and which represents the distance from the source within which momentum effects are dynamically significant and beyond which the dynamics are dominated by buoyancy. Therefore, when the value of the length scale l_M is high, the momentum flux (J_0) plays a dominant and destabilizing role on the buoyant jet, causing recirculating eddies or mixing over the entire water depth, while when the value of the l_M is low, the buoyancy flux (B_0) is the main and stabilizing element that fosters a stable field in which a buoyant surface layer is formed that does not communicate with the initial buoyant jet zone (Jirka *et al*., 1982). Furthermore, because an ambient cross flow existed in the direction of the channel, its momentum flux, defined as

$$J_a = S\, u_a^2 \tag{2}$$

where S is the transverse surface area of the ambient flow into the channel and u_a is the velocity of the cross flow, was taken into consideration, as destabilizing effect on the buoyant jet development. The values of these three parameters and the relations among them were considered to have a stable flow field; that is, a low value of the length scale l_M was planned so that buoyancy effects were comparable with momentum effects, and a low value of the cross flow momentum flux J_a was chosen so that the position of the free surface level and a cross flow velocity were as low as possible. In particular, for the experiments with

a smooth bottom boundary, and with the source diameter D = 5 mm of the buoyant jet defined, the length scale l_M assumed values between 0.26 m and 0.44 m, whereas the values of the flow ambient momentum flux J_a was $7.5 \cdot 10^{-3}$ m^4/s^2 for all the experimental configurations. For the fresh water supply and its heating, a galvanized iron tank was used, which inside were four resistances of 12,500 W for the heating of the water till the fixed temperature (with maximum value 90°C), each one protected by a thermostat, and a temperature transducer for the water temperature measurement. A pump of 1 Hp, equipped with manometer and interception key, transferred the hot water from this supply reservoir to a second tank, positioned on a lifting platform, whose different levels were able to define the fixed source discharge. A comprehensive view of all of the buoyant jet generation system described is showed in Figure 2.

A Process Computer and a control software (which task was to store the test data and, if decided by the operator, to supervise all the system) was used to control and manage the buoyant jet system. It was able to generate the discharge of a flow with prefixed and constant pressure, flow rate and temperature into the channel described, and all of the facilities connected with the channel and the jet generation system.

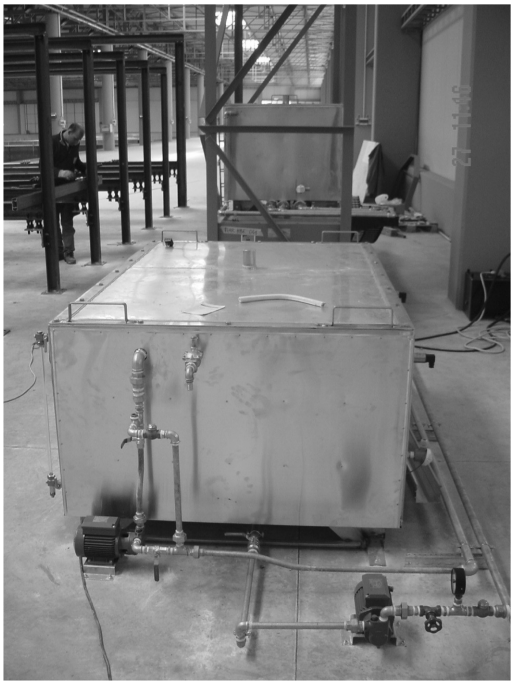


Figure 2. The tanks of the hydraulic circuit of the buoyant jet.

To create a particular turbulence in the ambient cross flow, corrugated plastic elements were positioned on the bottom of the channel, forming a rough bottom boundary (Fig. 3). Three different kinds of roughness elements were used. The first one, was a roll of 10 m length and 3 m width, made of polyester resin strengthened with glass fiber, with a "wavelength" λ of 76 mm and an "amplitude" ε of 18 mm. A hole was made in the center longitudinal section, 6 m from the upstream channel section and 4 m from the downstream section, located in the trough of the bottom boundary "wave" surface. Each of the other kinds of corrugated elements used during the following experimental configurations, was formed by 11 panels of same dimensions, and with same material and technical characteristics of the previous kind, differing only by the values of λ and ε.

Experimental cases and conditions for vertical round buoyant jet issued in a cross flow with rough bottom boundary are listed in Table 1. In order to cover as wide a range of conditions as possible, experiments were conducted using several different values and

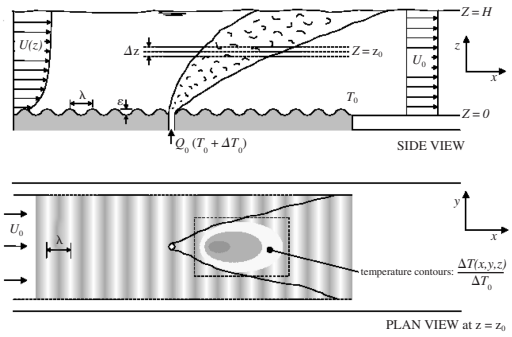


Figure 3. Schematic diagram of the experimental set up with corrugated plastic elements.

Table 1. Summary of experimental conditions.

Test	Q_0 (l/s)	H_a (m)	Q_a (l/s)	T_0 (°C)	T_a (°C)	λ (mm)	ε (mm)
T1	0.3	26	88	52	26	0	0
T2	0.3	26	88	62	27	0	0
T3	0.4	26	88	62	26	0	0
T4	0.4	26	88	52	27	0	0
T5	0.4	26	88	52	27	76	18
T6	0.4	26	88	61	29	76	18
T7	0.3	26	88	53	28	76	18
T8	0.3	26	88	60	25	76	18
T9	0.3	26	88	48	21	146	48
T10	0.3	26	88	54	18	146	48
T11	0.4	26	88	43	17	146	48
T12	0.4	26	88	53	19	146	48

combinations of the buoyant jet and bed-form parameters. Nevertheless, the experiments used the same working fluid (fresh tap water) throughout and the jet source diameter D was kept fixed (5.0 mm) for all runs. Different buoyant jet flow conditions were therefore created by changes in Q_0 and T_0. In particular, the jet temperature was changed for each configuration to have two fixed temperature differences $\Delta T = (T_a - T_0$, with T_a the ambient temperature) of 25°C and 35°C between the ambient and the jet. The first configuration provided a smooth flat bottom boundary, while the following three configurations have adopted the different panels with different values of the parameters λ and ε, described above. Eight different thermocouple sensors were utilised to measure the mixing of the heated water into the cross flow, with and without the rough bottom, whereas for the measurement of the velocity the ADV system was used, together with CollectV software for the data acquisition and ExploreV software for the data analysis, both of them products of Nortek, like the ADV.

2.2 *Laboratory results*

2.2.1 *Velocity field*

In order to study the turbulence effect upon the jet structure, a set of experiments was investigated with different configuration. The purpose of the experiment is to measure the three-velocity components (U, V, W) at different positions around the jet, where, U = mean stream-wise velocity, V = mean transverse velocity and W = mean vertical velocity, the measurement was determined by using an Acoustic Doppler Velocimeter (ADV). Figures 4–6 illustrate some of the experimental tests velocity vector map. It is to be noted that measurements shown in the three figures were made with the same channel discharge, the same source discharge and the same temperature excess at the source, the difference between theme being the nature of the channel bottom, which was a smooth surface bottom for Figure 4, corrugated surface bottom of "wavelength" $\lambda = 76$ mm and "amplitude" $\varepsilon = 18$ mm for Figure 5 and corrugated surface bottom of "wavelength" $\lambda = 146$ mm and "amplitude" $\varepsilon = 48$ mm for Figure 6.

The flow velocity vectors shown in those figures represent the mean velocity modules of the streamwise and the vertical flow velocity components which were measured along the channel axes where $y = 0$.

As shown in Figures 4–6, it can be seen that the flow velocity vector directions and modules around the jet vary spatially. This variation is considered very rapid and more turbulent. Just for 1 or 2 cm in the upstream of the source, the velocity vectors keep the same direction along the vertical axes z and have a uniform distribution for the three bottom configurations.

Over the source nozzle and going toward the downstream end of the channel, the velocity vectors appear to have an upward moving flow area, through which they change their characteristics strongly.

Increasing the spatial coordinates (x, z), the velocity vectors for the three configurations change their

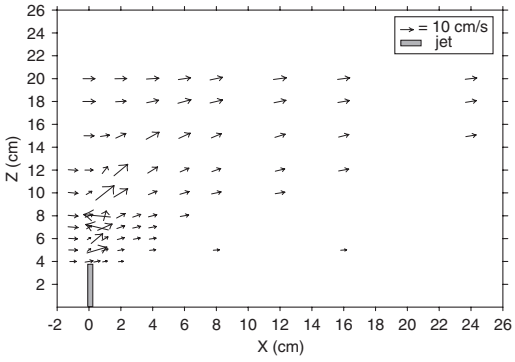


Figure 5. Near field velocity distribution for T7. Side view ($y = 0$).

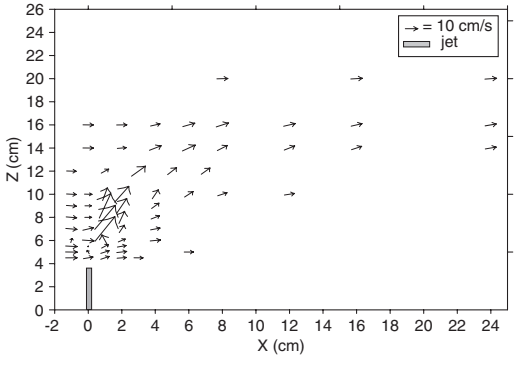


Figure 4. Near field velocity distribution for T1. Side view ($y = 0$).

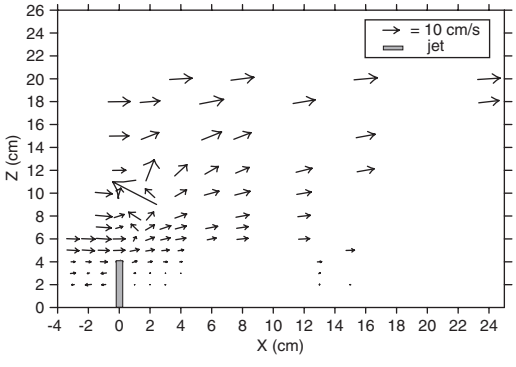


Figure 6. Near field velocity distribution for T9. Side view ($y = 0$).

characteristics step by step, reaching a uniform profile similar to that of the ambient flow.

The other hand, Figures 4–6 show that the ability of the jet to become more vertical depends upon the nature of the channel bottom. In the case when the channel bottom surface was smooth, the jet velocity vectors are deviated more toward the horizontal than the other configurations with the presence of a corrugated channel bottom surface. It can been seen that the velocity vectors direction are influenced by the "wavelength" λ and "amplitude" ε of the corrugated surface. When λ and ε increase the jet velocity vectors become more vertical. This is due to the fact that the jet is confined between the wave crests of the bottom.

2.2.2 *Stress distribution*

As indicated in the previous paragraph, the channel bottom surface nature has a big effect upon the jet structure. In order to study this phenomenon in depth, a Reynolds stress analysis was established. As is well known, the statistical description of a turbulence flow starts by dividing the flow velocity into mean and fluctuating components. So, at each point the three instantaneous velocity components are written as:

$$u = U + u'$$
$$v = V + v'$$
$$w = W + w'$$

where u, v, w are the streamwise, transverse and vertical instantaneous flow velocity components, respectively, and u', v' and w' are the streamwise, transverse and vertical flow velocity fluctuation components, respectively.

The quantities $\overline{u'v'}$, $\overline{u'w'}$ and $\overline{v'w'}$ are the time-averaged streamwise-transverse, streamwise-vertical and transverse-vertical Reynolds shear stresses.

Figures 7–15 show a map of the Reynolds stresses in the x–z plan, with $y = 0$ cm, for Test 1, Test 7 and Test 9.

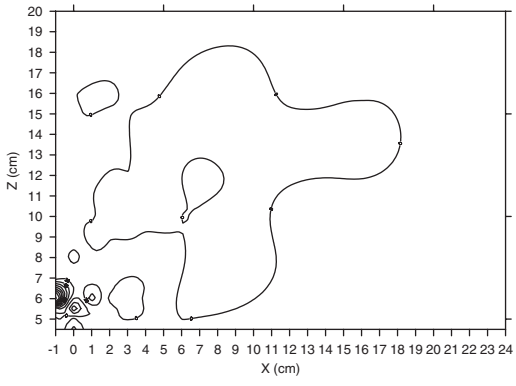


Figure 7. Streamwise-transverse ($u'v'$) stress distribution for T1. Side view ($y = 0$).

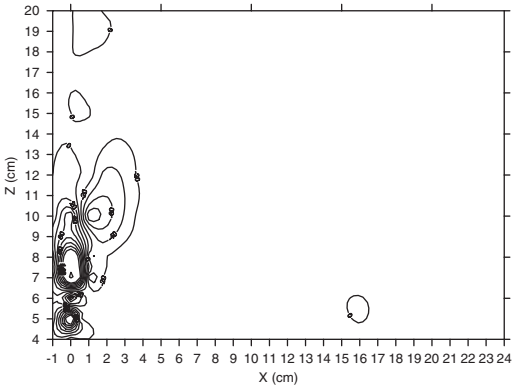


Figure 8. Streamwise-transverse ($u'v'$) stress distribution for T7. Side view ($y = 0$).

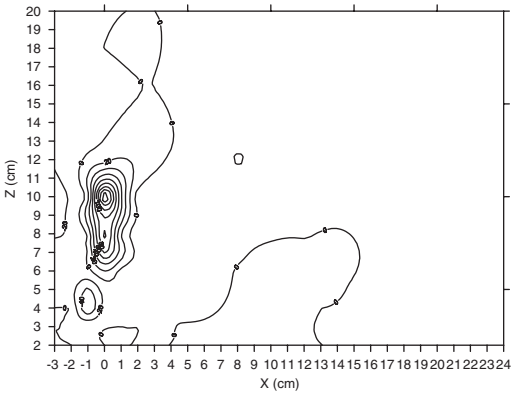


Figure 9. Streamwise-transverse ($u'v'$) stress distribution for T9. Side view ($y = 0$).

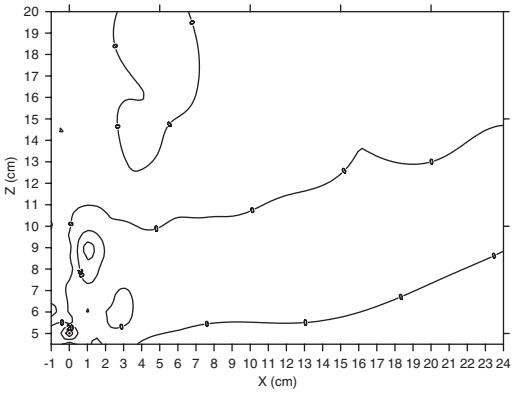


Figure 10. Streamwise-vertical ($u'w'$) stress distribution for T1. Side view ($y = 0$).

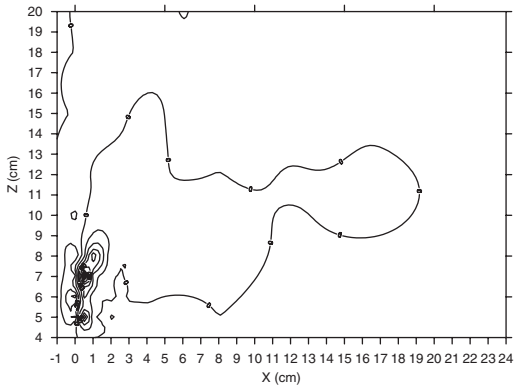


Figure 11. Streamwise-vertical ($u'w'$) stress distribution for T7. Side view ($y = 0$).

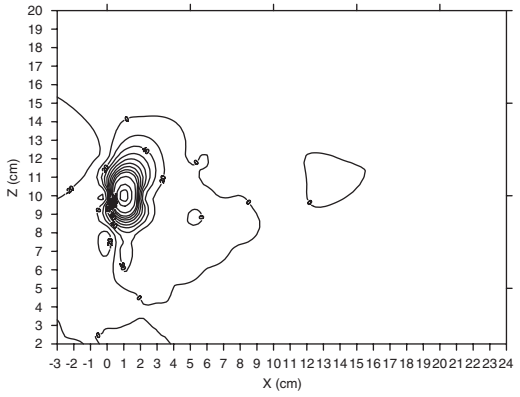


Figure 12. Streamwise-vertical ($u'w'$) stress distribution for T9. Side view ($y = 0$).

Test 1 was a configuration with smooth surface channel bottom, Test 7 was a configuration with corrugated surface channel bottom of "wavelength" $\lambda = 76$ mm and "amplitude" $\varepsilon = 18$ mm, and Test 9 was a configuration of corrugated surface channel bottom of "wavelength" $\lambda = 146$ mm and "amplitude" $\varepsilon = 48$ mm.

From the figures, it is possible to highlight that the strong $\overline{u'v'}$, $\overline{u'w'}$ and $\overline{v'w'}$ Reynolds stresses are present in the area localized near the jet source, where the velocity vectors change their characteristics strongly, as written in the previous paragraph. Furthermore, both positive and negative values of the Reynolds stresses were present in the same plan. In the measurement points far from the jet source, it was highlighted that the Reynolds shear stresses become small for all configurations. This is due to the small velocity fluctuations in these areas and the dominance of the cross flow velocity components with an absence of the jet stream effects.

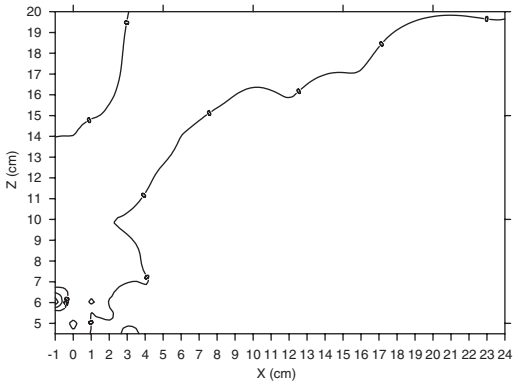


Figure 13. Transverse-vertical ($v'w'$) stress distribution for T1. Side view ($y = 0$).

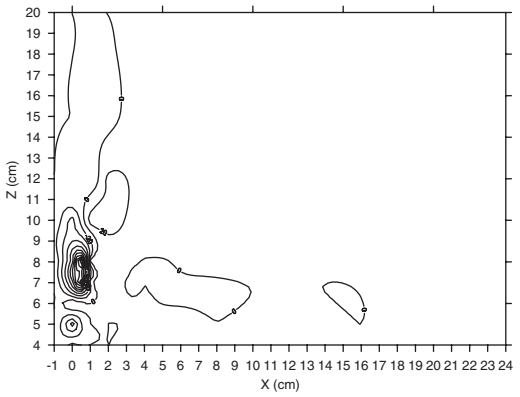


Figure 14. Transverse-vertical ($v'w'$) stress distribution for T7. Side view ($y = 0$).

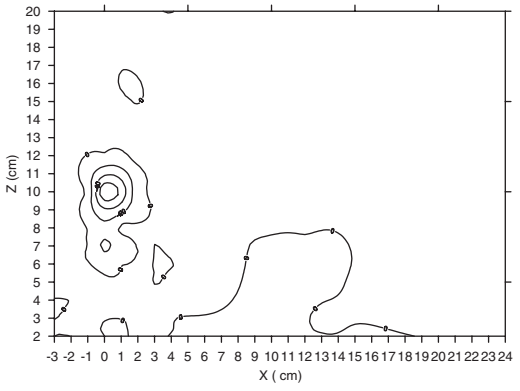


Figure 15. Transverse-vertical ($v'w'$) stress distribution for T9. Side view ($y = 0$).

Table 2. Reynolds stress values for Test 1, Test 7 and Test 9.

	$u'v'$ (m^2/s^2)		$u'w'$ (m^2/s^2)		$v'w'$ (m^2/s^2)	
Test	min.	max.	min.	max.	min.	max.
T1	−60	220	−35	60	−80	0
T7	−120	220	−80	160	−220	20
T9	−60	180	−40	460	−80	20

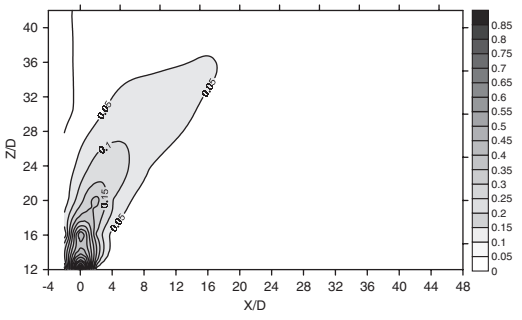


Figure 16. Longitudinal temperature distribution for Test 2.

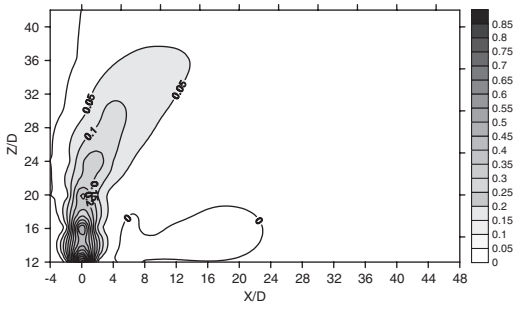


Figure 17. Longitudinal temperature distribution for Test 8.

Furthermore, one can see that there is a difference of the stress distribution between the analysed configurations, depending on the channel bottom surface. The absolute values of $\overline{u'v'}$, $\overline{u'w'}$ and $\overline{v'w'}$ Reynolds shear stresses of the configuration with the smooth channel bottom are generally smaller than those of the other two configurations with corrugated channel bottom, as shown in Table 2. The same table shows also that $\overline{u'w'}$ Reynolds stress component of Test 9 is greater than the ones of Test 1 and Test 7. In addition, it can be seen that Test 9 shows a positive shear stress distribution larger than the negative one, as shown in Figure 12. On the contrary, the $\overline{v'w'}$ Reynolds shear stress component is largely negative.

Examining the different figures, it can be seen clearly that the Reynolds shear stress distributions are more vertical when λ and ε increase.

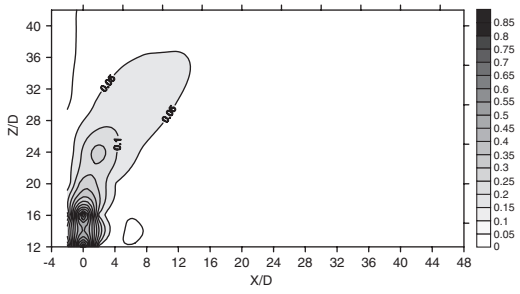


Figure 18. Longitudinal temperature distribution for Test 10.

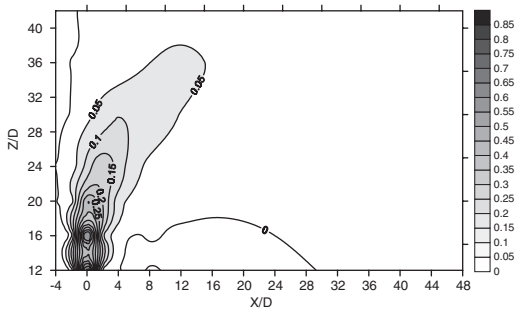


Figure 19. Longitudinal temperature distribution for Test 7.

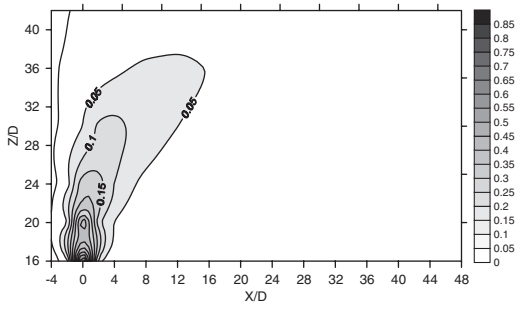


Figure 20. Longitudinal temperature distribution for Test 9.

2.2.3 *Temperature field*

In the present study, another aim was the measurements of the temperature field. The survey was run in a three-dimensional form, taking data at different levels and distances from the source orifice of the heated discharge.

Among the twelve experimental cases, seven typical temperature profiles, at the centre longitudinal section of the channel, are shown in Figures 16–22. In these figures, the ratio $\Delta T / \Delta T_0$ is reported, where ΔT is the difference between the time-averaged temperature in the measurement point and the average ambient temperature, whereas ΔT_0 is the time-averaged excess

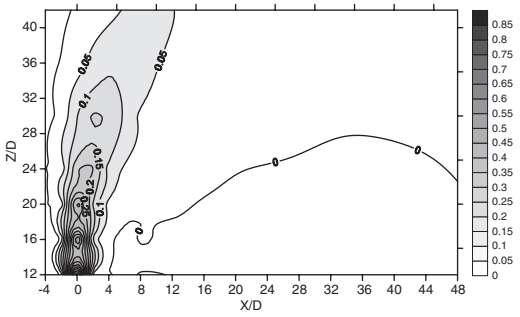


Figure 21. Longitudinal temperature distribution for Test 6.

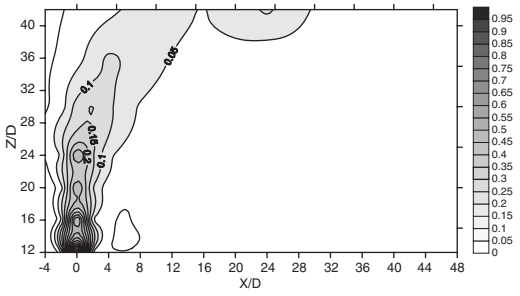


Figure 22. Longitudinal temperature distribution for Test 12.

temperature at the jet nozzle. In other words, this ratio represents the dilution of the buoyant jet into the cross flow. For the sake of brevity, Figures 16–22 were chosen taking into account (i) the three different bottom boundary conditions, which are smooth flat bottom, rough bottom with $\lambda = 76$ mm and $\varepsilon = 18$ mm, and rough bottom with $\lambda = 146$ mm and $\varepsilon = 48$ mm, and (ii) two different buoyant jets with different density, generated by different own temperatures, and different flow rates Q_0. The purpose is to show the different behaviour of the buoyant jet related to parameters such as λ and ε, and to its own characteristics. Attention was paid also to the horizontal distribution of the temperatures into the ambient, so the measurements were assessed also at different vertical layers.

The analysis of the figures show that the jet is more vertical (i.e. is less deviated towards the cross flow direction) in the case of rough bottom. Furthermore, the jet is less deviated in the case of rough bottom with higher values of λ and ε.

3 CONCLUSIONS

Heated water mixing as the result of discharge from a submerged vertical round source located at the bottom of a channel was analysed, and the smooth and rough bottom boundary cases were compared. Several conclusions were attained from the analysis of the experimental data. Firstly, the experimental results reveal that the roughness elements on the bottom boundary affect significantly the trajectory of the buoyant jet. This result is clear from the figures of the longitudinal distributions of the dimensionless excess temperature. The comparison of the results enable us to highlight that the main effect of the roughness is to elevate the trajectory of the buoyant jet, which becomes more vertical. In addition, the kinematic generation by the roughness elements of a vertical component of the cross flow velocity seems to play an important role in this structural modification of the buoyant jet, as evidenced from the turbulence Reynolds stress distributions. Nevertheless, further work is required to establish and parameterise the relative role(s) of the relevant length scales of the flow and the topographic elements upon the structural modifications to the buoyant jet.

REFERENCES

Lee, J.H.W. 1984. Boundary effects on a submerged jet group. *J. of Engineering Mechanics*. ASCE, Vol. 122, No. 1:19–29.

Seo, I.W., Kim, H.S., Yu, D. & Kim, D.S. 2001. Performance of tee diffusers in shallow water with crossflow. *J. of Hydraulic Engineering*, ASCE, Vol. 127, No. 1:53–61.

Kim, Y.D., Seo, I.W., Kang, S.W. & Oh, B.C. 2002. Jet integral-particle tracking hybrid model for single buoyant jets. *J. of Hydraulic Engineering*, ASCE, Vol. 128, No. 8: 753–760.

Grass, A.J., Stuart, R.J. & Mansour-Tehrani, M. 1991. Vortical structures and coherent motion in turbulent flow over smooth and rough boundaries. Phil. Trans. Roy. Soc. London A336: 35–65.

Grass, A.J. & Mansour-Tehrani, M. 1996. Generalized scaling of coherent bursting structures in the near-wall region of turbulent flow over smooth and rough boundaries. Coherent Flow Structures in Open Channels (edit by Phil Ashworth, Sean Bennett, James L. Best, Stuart McLelland): 41–61.

Jirka, G.H., Doneker, R.L. & Hinton, S.W. 1982. User's manual for Cormix: A hydrodynamic mixing zone model and decision support system for pollutant discharges into surface waters. Defrees hydraulics laboratory, School of Civil and Environmental Engineering, Cornell University, Ithaca, New York.

River Flow 2004 – Greco, Carravetta & Della Morte (eds.)
© 2004 Taylor & Francis Group, London, ISBN 90 5809 658 0

Shallowness and longitudinal dispersion in rivers

Robert Booij
Faculty of Civil Engineering and Geosciences, Delft University of Technology, The Netherlands

ABSTRACT: The longitudinal dispersion determines the extent of and the concentration in the cloud of pollutant that descends the river after an accidental spill. It is strongly influenced by the presence of dead water zones along the river. The slow exchange of water and hence of dissolved pollutants between river and dead water zone results in very large values of longitudinal dispersion coefficients. It even leads to the large tails that are often found in the distributions of pollutants. Measurements in a laboratory model of square harbours along a river show that the aspect ratio of dead water zones is important for the residence time of the pollutant in dead water zones. For very shallow dead water zones as common along rivers, with aspect ratios of 20 or more, the flow hardly enters the centre of the zones, leading to very long residence times for the pollutant there. Laboratory models of dead zones along rivers are nearly never deep enough to account for this effect and are hence not useful for the validation of numerical models of longitudinal dispersion.

1 LONGITUDINAL DISPERSION

The spreading of dissolved matter in rivers proceeds in different phases, depending on the distance to the source of the dissolved matter. Because of the shallowness of rivers turbulent mixing over the vertical is the most important process near the source of the dissolved matter. In the next phase turbulent spreading over the width becomes the predominant process. Meanwhile the cloud of dissolved matter undergoes downstream convection by the mean flow and spreading in the longitudinal direction. This longitudinal spreading is more difficult to describe. It hardly depends on direct turbulent diffusion in longitudinal direction, but is mainly due to different convection velocities over the cross-section (e.g. caused by differences in water depth or curvature effects in river bends), and transverse mixing (Fischer et al., 1979).

When the dissolved matter is sufficiently mixed over the width a relatively simple description of the transport in longitudinal direction, based on the method of Taylor (1953), is possible. In this phase, often called the longitudinal mixing phase, the spreading of the cloud of dissolved matter can be described with a longitudinal dispersion coefficient, while the cloud is displaced downstream by convection with the mean flow velocity averaged over the cross-section, u_{av}. Knowledge of the longitudinal dispersion of pollutants in rivers is important, in particular after accidental spills of harmful matter. The longitudinal dispersion determines the extent of and the concentration in the cloud of pollutant that descends the river. The longitudinal dispersion coefficient depends on the transversal exchange of pollutant over the river width and the flow velocity differences over the width.

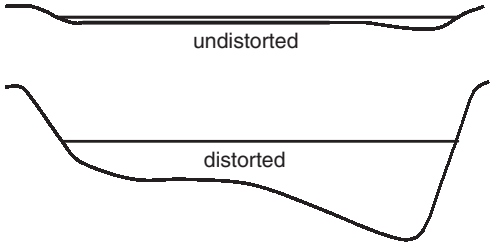


Figure 1. Comparison of a non-distorted plot of the cross-section of a river bend, with a realistic aspect ratio of about 50 (top) and the usual distorted plot of the same bend (bottom).

The flow in a river is a shallow free surface flow. In such a flow the important horizontal length scales of the flow are one or more orders of magnitude larger than the flow depth, h. In rivers aspect ratios W/h, where W is the width of the river, of at least 50 up to a few hundred are observed. This is not always directly obvious from the usual distorted plots of cross-sections of rivers (see Figure 1).

Approximate expressions for the vertical diffusion coefficient, D_v, the transverse mixing coefficient, D_t,

and the longitudinal dispersion coefficient, D_L, in rivers are respectively (Fischer et al., 1979)

$$D_v \approx 0.067\ hu*,$$
$$D_t \approx 0.6\ hu*,$$
$$D_L \approx 0.011\ u_{av}^2 W^2 / hu*,$$

where u^* is the average bed shear velocity. For a river with for example

h = 2 m, W = 100 m, and u_{av} = 15 u^* = 1 m/s

this leads to

$D_v \approx 0.009$ m^2/s, $D_t \approx 0.08$ m^2/s, $D_L \approx 800$ m^2/s.

The times required for a fair mixing of the dissolved matter over the vertical T_v and over the width T_t are respectively (Fischer et al., 1979)

$$T_v \approx 0.4\ h^2 / D_v \quad \text{and} \quad T_t \approx 0.4\ W^2 / D_t$$

and the distances the cloud is displaced downstream by convection in these mixing times are respectively

$$L_v \approx 0.4\ u_{av} h^2 / D_v \quad \text{and} \quad L_t \approx 0.4\ u_{av} W^2 / D_t.$$

For our example river this means

$T_v \approx 180$ s, $L_v \approx 180$ m, $T_t \approx 5*10^4$ s, $L_t \approx 50$ km.

Concluding, the longitudinal dispersion coefficient is very large compared to the vertical and transverse mixing coefficients. The vertical mixing is fast, but the transverse mixing takes much more time, because of the large aspect ratio involved. Important for the discussion here is that the transverse mixing takes place more or less within the distance over which the river changes appreciably, e.g. by confluences with tributaries. This would mean that the longitudinal distribution of the concentration of a cloud of dissolved matter would always be more or less Gaussian.

2 INFLUENCE OF DEAD WATER ZONES

In practice many measured concentration distributions even far downstream of the sources of dissolved matter are found to deviate appreciably from a Gaussian distribution. Often a large tail is observed on the upstream side. As most concentration measurements are executed at a fixed position this leads to a tail for the measurement of the concentration φ over time as

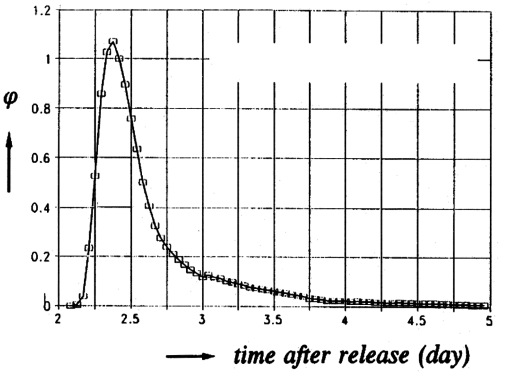


Figure 2. Measured distribution of tracer concentration φ at Maximiliansau at Rhine-kilometer 362 during the tracer experiment 04/89 (from Mazijk, 1996).

seen in Figure 2. Such a tail points to an insufficient transverse mixing and shows that the description of the longitudinal dispersion as Fickian diffusion is not correct.

Such tails are caused by the so-called dead water zones, or stagnant zones, along the river: groyne fields, local broadenings, bordering harbours and lakes, old river branches, etc. These are zones with slow flowing water with low exchange with the main channel of the river. The Taylor method and the resulting approximate expression for the longitudinal dispersion coefficient work well for a river without appreciable stagnant zones. However, when dead water zones are present, then the low exchange with the dead water zones leads to very long transverse mixing times, T_t, and lengths, L_t. When dead zones are present, the mixing length becomes easily much larger than the distance between the important tributaries and the Taylor method is not applicable anymore. A much used approach, the dead zone model, uses in that case a longitudinal dispersion coefficient for the flow in the main channel only and accounts separately for the dead zones (Mazijk, 1996).

To account for the dead zones requires a good knowledge of the exchange flow between dead zones and main channel and of the exchanged concentration. Generally for simplicity well-mixed dead zones are assumed, but more realistic models require knowledge of the flow in the dead zone to compute the concentration of the exchanged water. In principle it is possible to consider the river-dead zones system as a black box. Sufficient measurements of the development of the concentration distributions after earlier spills and tracer experiments may give enough information to predict the concentration development after a new spill. This is however only useful for well-monitored rivers as the Rhine. For other rivers the knowledge will have to be obtained mainly from laboratory experiments where the exchanges between

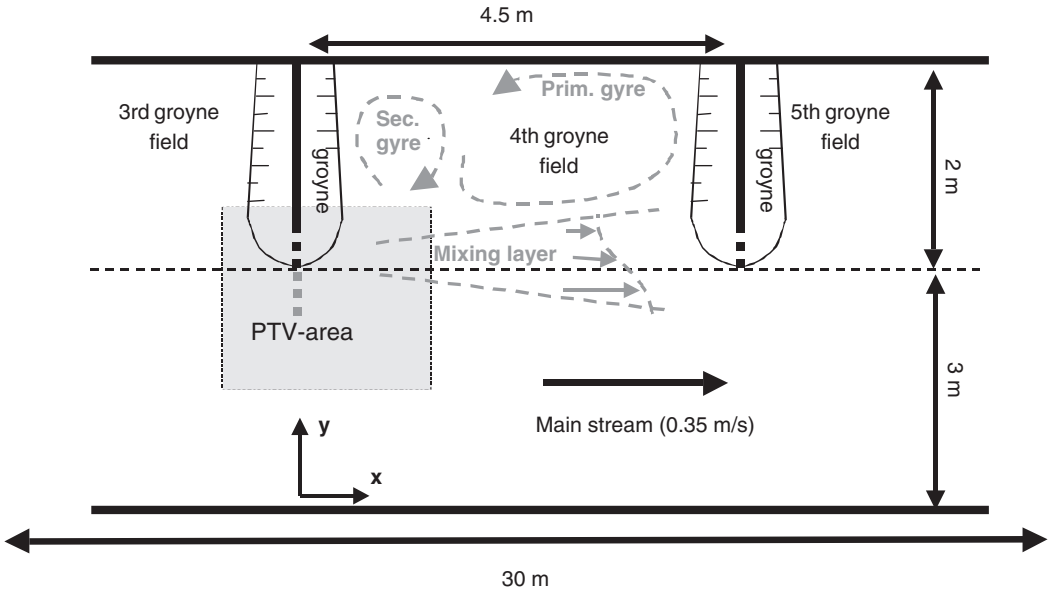


Figure 3. Top view of the experimental setup around the 4th groyne field in the shallow flume of Delft University of Technology used in a experiment of Uijttewaal (2003) for the investigation of the effects of groyne shapes on the flow around the groynes and in the groyne field and on the exchanges with the river.

river and dead zones and the flow in dead zones is investigated, or by computations with numerical models that in their turn have to be validated with data from such experiments.

3 EXPERIMENTS IN SHALLOW FLOWS

Experimental investigations of shallow flows require large flumes because of the contradictory conditions that play a role in such physical models. The flow has to be turbulent, even in the dead water zones, which requires a sufficiently large Reynolds number. Moreover the value of the Froude number has to remain much below 1 to ensure that the flow is not affected by surface disturbances, e.g. around the tip of groynes or at the corners of a harbour entrance. These two conditions lead to a maximum velocity and a minimum depth, depending on the kind of flow to be modelled. The most severe condition is the aspect ratio of the shallow flow that has to be observed. Together with the minimum depth from the Froude and Reynolds conditions this leads to very wide (and long) flumes. An example is the flume used by Uijttewaal (2003) for the investigation of the effects of groyne shapes on the flow around the groynes and in the groyne fields and on the exchanges with the river (see Figure 3). The dimensions of this flume are:

$W = 5$ m, $h = 25$ cm, length $= 30$ m.

The average velocity in the main stream channel is $u_{av} = 0.35$ m/s. An important measure, the ratio of the width of the groyne fields to the mean flow depth between the groynes is between 10 and 15 for the different cases investigated.

Flumes of these dimensions are expensive and hence do not abound. In the chosen compromise between price and performance the aspect ratio is the usual victim. Several experiments in flumes with groyne fields are reported, where the width of the groyne fields is but a few times larger than the flow depth. It is obvious that because of 3-dimensional effects e.g. around the tip of the groynes the flow field will strongly deviate from the shallow flow in a real river. Hence results obtained from those experiments are hardly useful for practical purposes.

In this paper shallow flow experiments in laboratory models of harbours along a river are discussed that suggest that even many experimental flows in wide shallow flumes are not sufficiently shallow. The flow in a shallow harbour along a river resembles in many respects the flow in a groyne field.

4 EXPERIMENTAL SETUP FOR SHALLOW HARBOUR FLOW

Several years ago a series of experiments was executed in a laboratory model of shallow harbours along

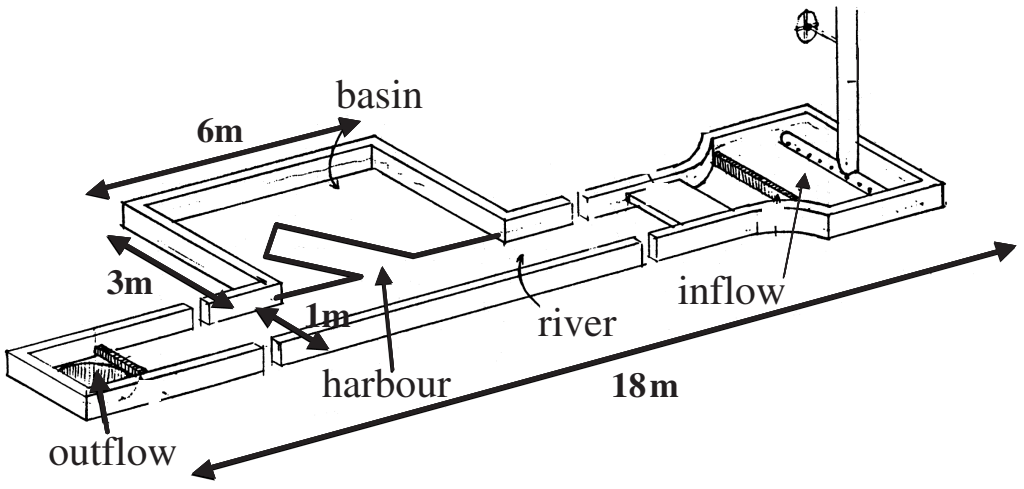


Figure 4. Shallow flume for harbour experiments of Delft University of Technology. The inflow is at the right side, the outflow at the left side. The straight river part has a length of 18 m. Along the river a rectangular basin of 3 m × 6 m allows the construction of different harbours.

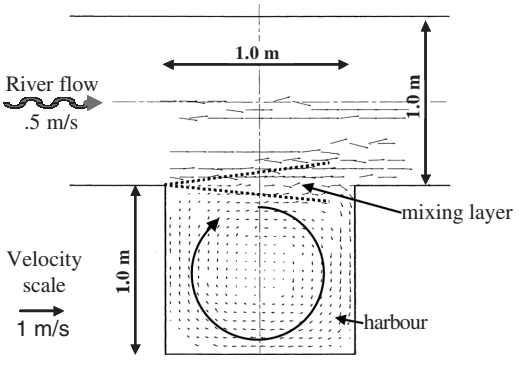


Figure 5. Flow in and around the 1 m × 1 m harbour measured with floats.

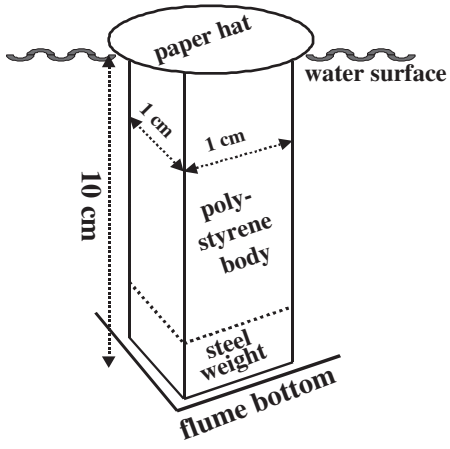


Figure 6. Deep reaching floats, extending to just above the bottom to yield depth-averaged velocities.

a flume to investigate the influence of shallowness and of the layout of harbours and harbour entrances on the flow in the harbours and in the harbour entrance, the exchange through the harbour entrance, etc. (Booij, 1986). A straight flume served as a model for the river. Along this river a basin was made in which several harbours could be constructed (see Figure 4).

The flow in the harbours was driven by momentum transport through the mixing layer in the harbour entrance between river flow and harbour flow. As an example the flow in and around a square harbour with sides of 1 m (the 1 m × 1 m harbour) is shown in Figure 5. In this case the velocities were obtained by measuring the displacements of floats that remained just free from the bottom, in order to yield depth-averaged velocities (see Figure 6). The floats are 10 cm long, while the harbours and the river are kept at a depth of just above 10 cm.

Another velocity measuring method used was by means of micro-impellers. The micro-impellers were placed at half depth where the velocity is not very far from the depth-averaged velocity.

5 EXPERIMENTAL RESULTS

The aspect ratio of rivers W/h is of the order of 50 to several hundreds generally. Most dead water zones are

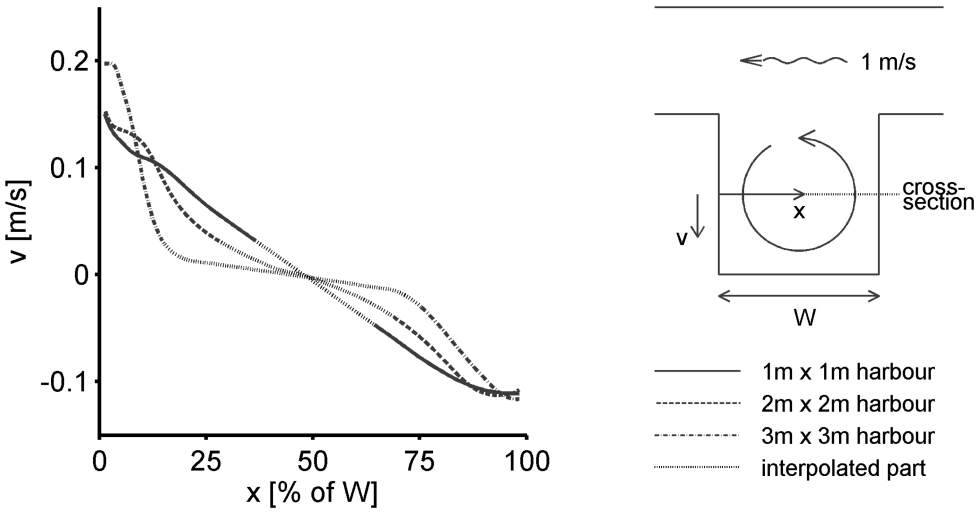


Figure 7. The flow in square harbour models of different shallowness, driven by the river flow. At left the velocity profiles halfway the harbour are plotted. At right the layout and legenda are given.

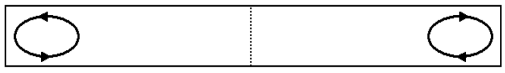


Figure 8. Sketch of the secondary flow vortices restricted to the near wall regions in shallow harbour flow.

equally shallow. Hence we concentrate on the shallowest harbours in the investigation (W/h up to 30, where W is the minimum value of length or width here). The shallowest harbour is a square harbour with $W = 3$ m hence with an aspect ratio $W/h \approx 30$. To investigate the influence of shallowness this harbour is compared with two square harbours with smaller widths, $W = 1$ m and 2 m (or aspects ratios 10 and 20) respectively.

For the investigation of the influence of shallowness the micro-impellers placed at half depth were used. The measurements show that above an aspect ratio of 10 the character of the flow changes considerably (Booij, 2003). From the measured velocities in a cross-section it can be concluded that in the 1 m × 1 m harbour the water rotates as a whole, which is also obvious from the results of the float measurements reproduced in Figure 5. On the contrary in the larger harbours the flow is concentrated along the sides and the centre is hardly affected, see Figure 7. This is due to the suppression of large-scale horizontal coherent structures because of the bottom influence, and to a phenomenon called differential advection (explained in chapter 6), which is connected with the secondary flow in the cross-sections. Both lead to a containment of the wall boundary jet and the secondary flow vortex, see Figure 8.

6 DIFFERENTIAL ADVECTION

Differential advection makes its appearance in curved shallow flow. Its best known effect is in gentle river bends where the largest velocity is found at the outside bend. The same mechanism drives the curved flow in harbours to the near wall regions.

Generally, the largest flow velocities in mildly curved shallow flow are found at the outside of the curved flow, e.g. the outer bend in curved river flow. The mechanism that makes the flow velocity at the outside of the curvature increase at the expense of the velocity at the inside is differential advection, which can be understood as follows. In mildly curved shallow flow the main flow velocity profile over the vertical is almost logarithmic. Hence the centrifugal force due to the curvature of the flow is larger in the upper part of the flow than near the bottom. On the average this centrifugal force is compensated by the pressure gradient due to a surface slope towards the outer bend. The resulting force is directed to the outward side in the upper part of the flow and to the inward side near the bottom and hence leads to a secondary flow to the outside in the upper part and to the inside near the bottom (see Figure 9). The main flow and the secondary flow together form the helical flow observed in curved shallow flow.

In mildly curved shallow flow the amount of water flowing outward is more or less equal to the amount of water flowing inward. However the main flow velocity is larger in the upper part of the flow than in the lower part, hence more main flow momentum is transported outwards in the upper part of the flow than inwards in

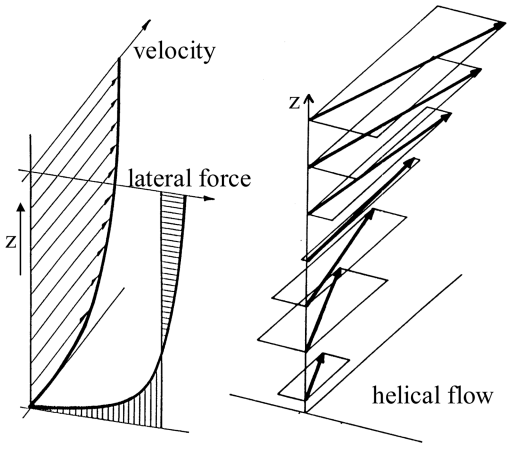


Figure 9. Mechanism of the origin of secondary flow in mildly curved shallow flow and the resulting helical flow.

the lower part. This leads to a net transport of main flow momentum in outward direction and consequently to higher flow velocities at the outer bend.

In the harbour this differential advection leads to a transport of the highest velocities to the outer walls. This counteracts and suppresses the turbulent structures that transport the high velocity from the wall to the centre. This leads to the creation and a containment of a wall boundary jet.

An interesting consequence of differential advection is the poor reproduction of shallow curved flow by 2-dimensional numerical models. In view of the shallowness of rivers and tidal channels the preference for 2-D horizontal models is understandable. However, the momentum transport by differential advection (i.e. from the region of low velocity at the inside bend to the region with high velocity near the outside bend) requires the implementation of a negative eddy viscosity, which will lead to stability problems. In 3-D computations the secondary flow is computed and hence its advection effects are included, without the necessity of a negative eddy viscosity.

7 BEHAVIOUR OF THE HARBOUR CENTRE

In chapter 5 it was observed that the flow velocities in the centre of the shallower harbours are very low. This means that there is hardly an exchange of water and hence dissolved matter between the centre of the harbour and the outer region. This is also evident from a dye experiment in the 3 m × 3 m harbour. This experiment started with a more or less homogeneous dye concentration in the harbour. After some time the outer region had exchanged all its dye with the river,

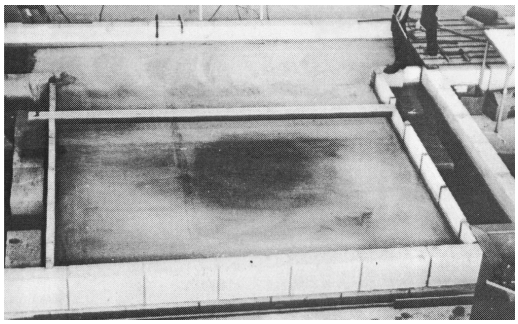


Figure 10. Remaining dye patch in the centre region of the 3 m × 3 m harbour. The river part of the flume is at the top. The river flows from left to right.

whereas the centre region was still strongly coloured see Figure 10.

In less angular harbours the transition from a fully rotating harbour to a harbour with a hardly moving centre appears at slightly lower dimensions, as can be seen in Figure 11. Here a flow in a partly circular harbour is shown, measured with floats. Obvious is the slowly moving centre, although the diameter of the circular part of the harbour is slightly less than the width of a square harbour with corresponding velocity pattern. The angles of the square harbour appear to intensify turbulent disturbances that increase the exchange between centre and outer region.

8 INFLUENCE ON THE LONGITUDINAL DISPERSION

The low exchange of the centre of shallow dead zones with the outer region and hence with the river harbour can have important consequences for the longitudinal dispersion and the tails in the distribution of the dissolved matter. A dead zone influences the convection and the spreading of the dissolved matter by taking in a part of the dissolved matter as the cloud passes and releasing it gradually over the time, depending on the residence time of the water in the dead zone. In this way it decreases the (average) convection velocity of the cloud, increase the longitudinal spreading and may lead to a tail in the distribution.

For a shallow dead zone the intake of dissolved matter from the passing cloud will be less, as the increase of the concentration of the centre lags behind, because of the low exchange. For a shallow dead zone this will lead to a lower increase of the longitudinal spreading by the fast exchanging outer region of the dead zone. As the dissolved matter from the centre is exchanged back more slowly, this exchange will last much longer and lead to a larger longitudinal spreading and a long tail in the distribution. The magnitude of these

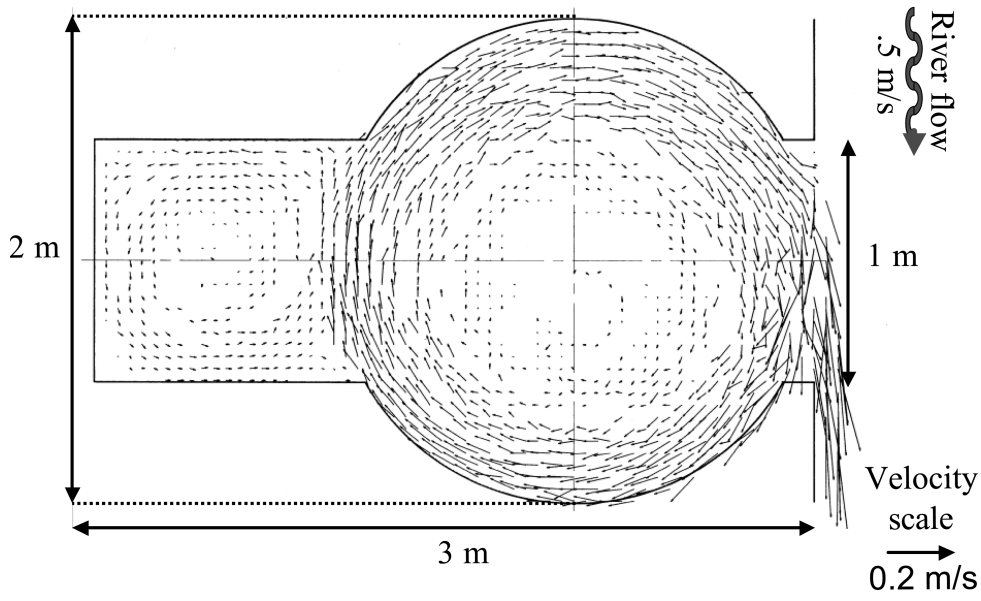


Figure 11. Flow in a partly circular harbour, measured with floats. The river is at right. The flow direction in the river is from top to bottom. Obvious is the slowly moving centre.

different effects depends on the extent of the different parts of the dead zone and of the residence times of those parts in relation to the passing time of the cloud.

Numerical models of the very shallow flow in rivers with dead water zones require ample validation by measurements, for which measurements in laboratory models are used generally. This validation is needed because 2-D models lack a few mechanisms as e.g. differential advection and 3-D models require different momentum exchange coefficients for different directions that are at present not easily predicted. However, the dead water zones in most laboratory models are not sufficiently shallow. Hence the validation is based on too deep flows generally. Consequently most numerical models do not model the flow in the centre of the dead water zones correctly, leading to too short residence times and hence incorrect predictions of the longitudinal dispersion.

9 CONCLUSIONS

- Knowledge of longitudinal dispersion of pollutants in rivers is important, in particular after accidental spills of harmful matter. The longitudinal dispersion determines the extent of and the concentration in the cloud of pollutant that descends the river.
- The longitudinal dispersion is strongly influenced by the presence of slowly moving (so called dead water) zones along the river, as are present between groynes, in old river branches, harbours, lakes or other bodies of water alongside the river.
- The slow exchange of water and hence of dissolved pollutants between river and dead water zone results in very large values of longitudinal dispersion coefficients.
- Dead water zones also lead to the large tails that are often found in the distributions of pollutants, which show that the description of the longitudinal dispersion as Fickian diffusion is not correct.
- Measurements in a laboratory model of square harbours along a river show that above an aspect ratio of 10 the character of the flow changes considerably. For aspect ratios up to 10 the flow in the harbour rotates more or less as a whole. The flow in shallower harbours, or other dead zones, is more concentrated along the sides and the fluid in the centre moves hardly.
- The low velocity in the centre of shallow dead zones leads to very long residence times and hence much higher values of the longitudinal dispersion coefficients and to long tails in the concentration distributions.
- Laboratory models of dead zones along rivers, even those in wide, shallow flumes, are generally not shallow enough to observe this stagnant centre effect, and hence show a behaviour that is quite different from the shallower dead zones found mostly in practice.

- Measurements in flumes with insufficiently shallow dead zones are not useful for the validation of numerical models of longitudinal dispersion.

REFERENCES

Booij, R. 1986. Measurement of exchanges between river and harbour (in Dutch). *Report 9–86.* Hydr. Engrg. Section, Delft Univ. of Techn., The Netherlands.

Booij, R. 2003. Laboratory experiments of shallow free surface flows. *Proc. Int. Symp. on Shallow Flows* I: 101–108. Delft, The Netherlands.

Fischer, H.B. et al. 1979. *Mixing in Inland and Coastal Waters.* New York: Academic Press.

Mazijk, A. van 1996. One-dimensional approach of transport phenomena of dissolved matter in rivers. *Thesis* Fac. Civil Engrg and Geosc., Delft Univ. of Techn., The Netherlands.

Taylor, G.I. 2003. Dispersion of soluble matter in solvent flowing slowly through a tube. *Proc. R. Soc. London Ser. A* 219: 186–203.

Uijttewaal, W.S.J. 2003. Large scale dynamics in groyne field flows: laboratory experiments. Submitted to *J. Hydr. Engrg.*

River Flow 2004 – Greco, Carravetta & Della Morte (eds.)
© 2004 Taylor & Francis Group, London, ISBN 90 5809 658 0

Pollution transport in the lagoon of Grado and Marano: a two dimensional modelling approach

M. Petti & S. Bosa
Dipartimento di Georisorse e Territorio, University of Udine, Italy

ABSTRACT: Pollution and water quality in lagoon areas represent a problem for human health and for the local economy particularly felt by people living nearby. In Italy the lagoon of Grado and Marano, located in the Northeast part of the Adriatic Sea, is subject to mercury pollution. It is held by some that the source of pollution is the river Isonzo that drains polluted sediments from a Slovenian region and partly feeds the lagoon. Others believe that the source of pollutants should be looked for elsewhere, for example in some industrial establishments which, in the past, are believed to have introduced concentrations of polluting material into channels that flow into the lagoon. In this paper a 2D finite volume model is proposed for studying the dispersion of a dissolved pollutant in the lagoon environment and the results obtained in applying the model to the lagoon of Grado and Marano are illustrated.

1 INTRODUCTION

The transport of pollutants is a very complicated environmental problem that involves many disciplines such as ecology, chemistry, toxicology, sedimentology and fluid mechanics. One of the roles of fluid mechanics is to develop hydrodynamic models able to interpret as well as possible the propagation of pollutants in free surface water environments.

A numerical approach to pollutant transport can be based on the classical advection-diffusion equation founded on the passive tracer concept and suitable for a widely dispersed substance. This equation may be integrated by a Lagrangian or Eulerian approach. The first one, known also as particle tracking, is a natural approach in the presence of point sources, but a huge number of particles may be necessary to represent the concentration in each grid box. In the Eulerian approach the concentration equation describes the motion of a substance by numerical advection schemes, but care must be taken over these to control numerical diffusion or oscillations in the presence of sharp gradient (James 2002). The relative importance of advection and diffusion in the dispersion of a tracer is represented by the Péclet number $P_e = U_0 L_0 / D_0$, where U_0 is a horizontal velocity scale, L_0 the length scale and D_0 the horizontal diffusivity scale. As observed by Prandle et al. (1993) in southern North Sea studies, in lagoon basins the Péclet number is very high thus the advective transport prevails on the diffusive.

To simulate an advection problem it is very important to have an efficient hydrodynamic and transport model, and care must be taken in the treatment of the advective terms in non-linear hydrodynamic equations (Dragoslav 2001).

In the present work we propose a numerical model based on the Eulerian approach for the simulation of 2D solute transport with unsteady advection-diffusion. A finite volume method is used to solve non linear equations by a Godunov approach supported by a robust and efficient approximate solver proposed by Harten, Lax and van Leer (HLLC) (Toro 1999). The resulting scheme is second-order accurate in space and time and satisfies the Total Variation Diminishing (TVD) condition.

After a number of tests done to check its validity the model was applied to pollution transport in the lagoon of Grado and Marano, affected by serious forms of mercury pollution. Various scenarios of possible sources of mercury pollution have been studied, also keeping in mind the wind, a meteorological factor which is very important in the lagoon dynamics of Grado and Marano. A discussion is reported on the results obtained simulating those considered to be the principal sources of immission of such a pollutant.

Finally, some conclusions are given, along with a very brief account on ongoing and future work.

2 MODEL EQUATIONS

Two-dimensional unsteady solute transport can be described by the depth-averaged equations in the

vectorial and conservative form:

$$\frac{\partial \mathbf{U}}{\partial t}+\frac{\partial \mathbf{F}_c(\mathbf{U})}{\partial x}+\frac{\partial \mathbf{G}_c(\mathbf{U})}{\partial y}= =\frac{\partial \mathbf{F}_d(\mathbf{U})}{\partial x}+\frac{\partial \mathbf{G}_d(\mathbf{U})}{\partial y}+\mathbf{S}(\mathbf{U}) \quad (1)$$

obtained coupling well-known shallow water equations with the advection-diffusion transport equation (Ligget 1994). Here (x, y) are Cartesian coordinates, $\mathbf{U}(x, y, t)$ is the vector of conserved variables, $\mathbf{F}_c$, $\mathbf{G}_c$, $\mathbf{F}_d$ and $\mathbf{G}_d$ the advective and diffusive fluxes respectively in the x- and y-directions and $\mathbf{S}(\mathbf{U})$ the source term. Thus:

$$\mathbf{U}=\begin{bmatrix} h \\ Uh \\ Vh \\ Ch \end{bmatrix}, \mathbf{F}_c(\mathbf{U})=\begin{bmatrix} Uh \\ U^2h+g\frac{h^2}{2} \\ UVh \\ UCh \end{bmatrix},$$

$$\mathbf{G}_c(\mathbf{U})=\begin{bmatrix} Vh \\ UVh \\ V^2h+g\frac{h^2}{2} \\ VCh \end{bmatrix}, \quad (2)$$

$$\mathbf{F}_d(\mathbf{U})=\begin{bmatrix} 0 \\ 0 \\ 0 \\ D_{xx}\frac{\partial Ch}{\partial x} \end{bmatrix}, \mathbf{G}_d(\mathbf{U})=\begin{bmatrix} 0 \\ 0 \\ 0 \\ D_{yy}\frac{\partial Ch}{\partial x} \end{bmatrix}$$

where U and V are the depth averaged velocities respectively in the x- and y-directions, D_{xx} and D_{yy} the diffusion coefficients of the pollutant, h is the water depth, C the depth averaged pollution concentration, and g the acceleration due to gravity. Source term $\mathbf{S}(\mathbf{U})$ is defined by:

$$\mathbf{S}(\mathbf{U})=\begin{bmatrix} 0 \\ \left(ghS_{0x}-gn^2\frac{U\sqrt{U^2+V^2}}{h^{1/3}}+ \right. \\ \left. +fVh+C_D\frac{\rho_a}{\rho_w}W_x\sqrt{W_x^2+W_y^2} \right) \\ \left(ghS_{0y}-gn^2\frac{V\sqrt{U^2+V^2}}{h^{1/3}}- \right. \\ \left. -fUh+C_D\frac{\rho_a}{\rho_w}W_y\sqrt{W_x^2+W_y^2} \right) \\ Qh \end{bmatrix} \quad (3)$$

where S_{0x} and S_{0y} are the bed slopes, n is the Manning resistance coefficient, f a term that takes the Coriolis's acceleration into account, ρ_a the air density, ρ_w the water density, W_x, W_y the wind velocities in the x and y directions and C_D the wind shear coefficient. Q is the depth averaged pollutant source or sink.

Analyzing the advection-diffusion equation in dimensionless form (starred variables) we obtain:

$$\frac{\partial(C^*h^*)}{\partial t^*}+\left[\frac{\partial\left(C^*h^*\right)}{\partial x^*}+\frac{\partial\left(C^*h^*\right)}{\partial y^*}\right]- -\frac{1}{P_e}\left[\frac{\partial^2(C^*h^*)}{\partial x^{*2}}+\frac{\partial^2(C^*h^*)}{\partial y^{*2}}\right]=Q^*h^* \quad (4)$$

where $P_e = U_0L_0/D_0$ is the Péclet number and U_0, L_0 and D_0 are respectively the velocity, spatial and diffusion scales.

A simple analysis of scales in the lagoon of Grado and Marano gives a Péclet number $P_e \approx 5000$. This means that the advective transport prevails on the diffusive and therefore particular care must be taken over the choice of the numerical scheme to solve the equations in order to avoid an excessive and unrealistic numerical diffusion.

Moreover, observing that a sudden immission of pollutant represents a real shock phenomenon, a scheme of integration which is not very numerically diffusive is necessary as well as a shock-capturing scheme.

3 NUMERICAL METHOD

In accordance with the observation made, which is the necessity for a numerically little diffusive and shock-capturing scheme of integration, a finite volume method (FVM) was chosen.

One way to solve Equation 1 is to keep the time variable t continuous and consider the equation we obtain by integrating Equation 1 over a two-dimensional generic control volume Ω (Fig. 1):

$$\frac{d\left\langle \mathbf{U}(t)\right\rangle}{dt}=-\frac{1}{\Omega}\oint_{\partial\Omega}\mathbf{H}_c\cdot\mathbf{n}\,dl+\frac{1}{\Omega}\oint_{\partial\Omega}\mathbf{H}_d\cdot\mathbf{n}\,dl+\left\langle \mathbf{S}\right\rangle \quad (5)$$

where $\mathbf{H}_c=[\mathbf{F}_c, \mathbf{G}_c]$ is the tensor of advective fluxes, $\mathbf{H}_d=[\mathbf{F}_d, \mathbf{G}_d]$ the tensor of diffusive fluxes, $\mathbf{n}$ the outward unit vector normal to the boundary $\partial\Omega$, dl a length element and $\mathbf{H}\cdot\mathbf{n}\,dl$ the flux components normal to the boundary $\partial\Omega$. $<\mathbf{U}>$ and $<\mathbf{S}>$ represent the values:

$$\left\langle \mathbf{U}\right\rangle=\frac{1}{\Omega_i}\int_{\Omega}\mathbf{U}d\Omega, \qquad \left\langle \mathbf{S}\right\rangle=\frac{1}{\Omega_i}\int_{\Omega}\mathbf{S}d\Omega \quad (6)$$

averaged on the control volume Ω.

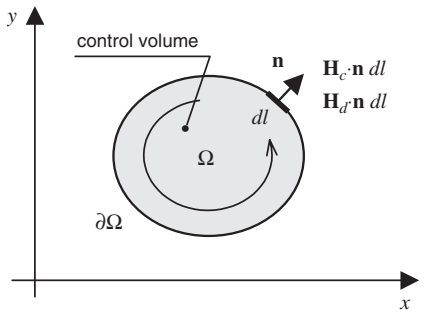


Figure 1. Generic control volume used to integrate Equation 1.

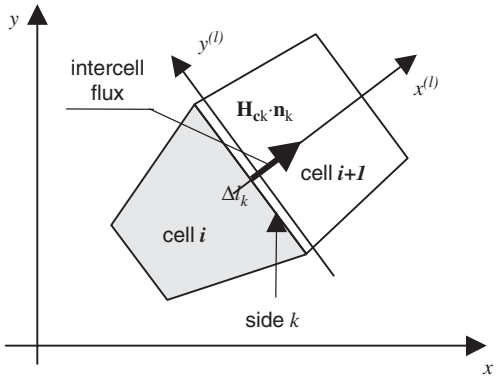


Figure 2. *i*-th control volume and the fluxes associated to its *k*-th side.

In the finite volume approach Equation 5 has to be satisfied on each control volume that results from discretising the physical space into a number of polyhedral control volumes or computing cells; the accuracy of the spatial discretisation depends on the particular scheme with which the fluxes are evaluated.

Assuming quadrilateral finite volume Ω_i, where the subscript *i* identifies a generic cell (Fig. 2), Equation 5 can be discretised as:

$$\frac{d\left\langle \mathbf{U}(t)\right\rangle_i}{dt} = -\frac{1}{\Omega_i}\sum_{k=1}^{4}\left\langle \mathbf{H}_c\right\rangle_k \cdot \mathbf{n}_k\, \Delta l_k + \\ +\frac{1}{\Omega_i}\sum_{k=1}^{4}\left\langle \mathbf{H}_d\right\rangle_k \cdot \mathbf{n}_k\, \Delta l_k + \left\langle \mathbf{S}\right\rangle_i \qquad (7)$$

where k identifies a generic side of the cell, Δl_k its length, and $<\mathbf{H}_c>_k$ and $<\mathbf{H}_d>_k$ are the average fluxes across the intercell boundary Δl_k:

$$\left\langle \mathbf{H}_c\right\rangle_k = \frac{1}{\Delta l_k}\int_{\Delta l_k}\mathbf{H}_c\, dl, \quad \left\langle \mathbf{H}_d\right\rangle_k = \frac{1}{\Delta l_k}\int_{\Delta l_k}\mathbf{H}_d\, dl. \qquad (8)$$

For simplicity in the following we omit the parentheses <>.

To solve the semi-discrete Equation 7 we can use a standard split-operator scheme in which the advective and diffusion-source steps are solved separately. To this purpose we write Equation 7 as:

$$\frac{d\mathbf{U}(t)_i}{dt} = \mathbf{L}_i^{(c)}(\mathbf{U}) + \mathbf{L}_i^{(d)}(\mathbf{U}) \qquad (9)$$

where:

$$\mathbf{L}_i^{(c)} = -\frac{1}{\Omega_i}\sum_{k=1}^{4}\left\langle \mathbf{H}_c\right\rangle_k \cdot \mathbf{n}_k\, \Delta l_k \qquad (10)$$

and:

$$\mathbf{L}_i^{(d)} = \frac{1}{\Omega_i}\sum_{k=1}^{4}\left\langle \mathbf{H}_d\right\rangle_k \cdot \mathbf{n}_k\, \Delta l_k + \left\langle \mathbf{S}\right\rangle_i \qquad (11)$$

are called respectively advection operator and diffusion operator with source term.

Equation 9 can be solved in time by means of standard ODE methods; here we use a splitting scheme that consists in solving (Yanenko 1971, Toro 1999) the two subsequent initial value problems at each time step:

$$\begin{cases} \dfrac{d\mathbf{U}_i(t)}{dt} = \mathbf{L}_\mathbf{i}^{(\mathbf{c})}(\mathbf{U}) \\ \mathbf{U}_i(0) = \mathbf{U}_i^n \qquad \textit{initial condition} \end{cases} \Rightarrow \mathbf{U}_i^{adv} \qquad (12)$$

$$\begin{cases} \dfrac{d\mathbf{U}_i(t)}{dt} = \mathbf{L}_\mathbf{i}^{(d)}(\mathbf{U}) \\ \mathbf{U}_i(0) = \mathbf{U}_i^{adv} \qquad \textit{initial condition} \end{cases} \Rightarrow \mathbf{U}_i^{n+1} \qquad (13)$$

$\mathbf{U}_i^n$ being the solution at time step t and $\mathbf{U}_i^{n+1}$ the target solution at time step $t + \Delta t$. $\mathbf{U}_i^{adv}$ is the solution of the first initial value problem (Eq. 12).

It can be seen immediately that system 12 is hyperbolic while system 13 is diffusive and it has a source term. This means that while for the second system it is possible to choose from a relatively ample range of integration schemes, for the first a more careful evaluation is necessary. One way to solve system 12 is to solve the so-called local 'Riemann problem'.

The most delicate aspect in the solution of this problem is the evaluation of the advective intercell flow $\mathbf{H}_{ck} \cdot \mathbf{n}_k$ (Fig. 2) by an appropriate solver.

In this paper we use the approximate Harten, Lax, van Leer (HLLC) solver modified by Toro (1999).

3.1 *The HLLC solver*

The intercell fluxes $\mathbf{H}_{ck} \cdot \mathbf{n}_k$, as $\mathbf{H}_{dk} \cdot \mathbf{n}_k$, can be estimated by exploiting the rotational invariance (Toro 1999):

$$\mathbf{H}_{ck} \cdot \mathbf{n}_k = \mathbf{T}_k^{-1}\mathbf{F}_c\left(\mathbf{U}_l\right) \qquad (14)$$

where:

$$\mathbf{U}_l = \mathbf{T}_k \mathbf{U} = \begin{bmatrix} h_l & U_l h_l & V_l h_l & C_l h_l \end{bmatrix} \tag{15}$$

is the vector of rotated conserved variables referred to a local $(x^{(l)}, y^{(l)})$ Cartesian system (Fig. 2), $\mathbf{T}_k$ is the rotation matrix:

$$\mathbf{T}_k = \begin{bmatrix} 1 & 0 & 0 & 0 \\ 0 & n_{x_k} & n_{y_k} & 0 \\ 0 & -n_{y_k} & n_{x_k} & 0 \\ 0 & 0 & 0 & 1 \end{bmatrix} \tag{16}$$

and $\mathbf{T}_k^{-1}$ its inverse. Through Equation 14 the evaluation of the intercell fluxes is reduced to that of an augmented one-dimensional problem and the techniques used for the evaluation of the flow in these systems can be applied. The HLLC solver is one of these techniques.

The HLLC method gives an approximate estimation of the fluxes for solving the Riemann problem (Fig. 3):

$$\begin{aligned} &\frac{\partial \mathbf{U}_l}{\partial t} + \frac{\partial \mathbf{F}_c(\mathbf{U}_l)}{\partial x_l} = 0 \\ &\mathbf{U}_l(x^{(l)} = 0, t) = \begin{cases} \mathbf{U}_k^{(1)} & \text{if} \quad x^{(l)} < 0 \\ \mathbf{U}_k^{(4)} & \text{if} \quad x^{(l)} > 0 \end{cases} \end{aligned} \tag{17}$$

across the intercell under consideration (side k of Fig. 2).

Following the 'method of characteristics' proposed by Stoker (1957), and subsequently widely dealt with by Whitham (1974), the Riemann problem is solved by referring to a characteristic diagram $(x^{(l)}, t)$ (Fig. 4). The area $(x^{(l)}, t)$ is divided into four regions delimited by the straight lines representing wave speeds S_m $(m = 1, 4)$ corresponding to eigenvalues of the hyperbolic problem described by Equation (17).

In the regions 1 and 4 conserved variables ($\mathbf{U}_k^{(1)}$ and $\mathbf{U}_k^{(4)}$) and fluxes ($\mathbf{F}_k^{(1)}$ and $\mathbf{F}_k^{(4)}$) are constant and known. In the regions 2 and 3 mean values of the conserved variables ($\mathbf{U}_k^{(2)}$ and $\mathbf{U}_k^{(3)}$) and fluxes ($\mathbf{F}_k^{(2)}$ and $\mathbf{F}_k^{(3)}$) are obtained integrating Equation 17 successively over the control volumes $[x_i^{(l)}, x_{i+1}^{(l)}] \times [0, \Delta t]$, $[S_1 \Delta t,\ S_* \Delta t] \times [0, \Delta t]$ and $[S_* \Delta t,\ S_2 \Delta t] \times [0, \Delta t]$ (Toro, 1999). Results for fluxes are:

$$\mathbf{F}_{c_k} = \begin{cases} \mathbf{F}_k^{(1)} & S_1 \geq 0 \\ \mathbf{F}_k^{(2)} = \mathbf{F}_k^{(1)} + S_1 \left(\mathbf{U}_k^{(2)} - \mathbf{U}_k^{(1)} \right) & S_* \geq 0 > S_1 \\ \mathbf{F}_k^{(3)} = \mathbf{F}_k^{(4)} + S_2 \left(\mathbf{U}_k^{(3)} - \mathbf{U}_k^{(4)} \right) & S_1 \geq 0 > S_* \\ \mathbf{F}_k^{(4)} & 0 > S_1 \end{cases} \tag{18}$$

where $\mathbf{F}_{ck} = \mathbf{H}_{ck} \cdot \mathbf{n}_k$ is the target intercell flux and:

$$\mathbf{U}_k^{(m)} = h_m^{(m)} \left(\frac{S_m - U_k^{(m)}}{S_m - S_*} \right) \begin{bmatrix} 1 \\ S_* \\ V_k^{(m)} \\ C_k^{(m)} \end{bmatrix}, \qquad m = 2, 3 \tag{19}$$

The wave speed estimates S_1 and S_2 are performed according to elementary wave solutions of the Riemann problem (i.e. rarefaction, shear or shock waves). The wave speed $S_* = S_3 = S_4$ is estimated by the equation proposed by Toro (1999):

$$S_* = \frac{S_1 h_k^{(4)} \left(U_k^{(4)} - S_4 \right) - S_4 h_k^{(1)} \left(U_k^{(1)} - S_1 \right)}{h_k^{(4)} \left(U_k^{(4)} - S_4 \right) - h_k^{(1)} \left(U_k^{(1)} - S_1 \right)}. \tag{20}$$

Assuming:

$$\mathbf{U}_k^{(1)} = \mathbf{U}_i^n \qquad \text{and} \qquad \mathbf{U}_k^{(4)} = \mathbf{U}_{i+1}^n \tag{21}$$

the intercell flux $\mathbf{F}_{ck}$ estimated by Equation 18 is first-order accurate in space. To solve the problem

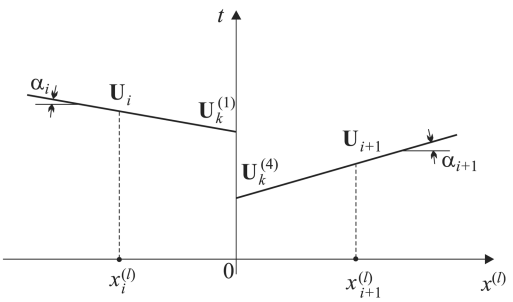


Figure 3. The local Riemann problem solved by the HLLC method and a MUSCL-Hancock TVD scheme.

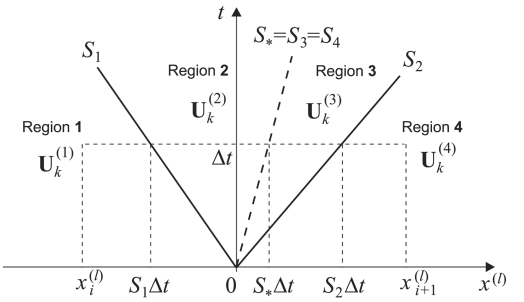


Figure 4. Structure used in the HLLC method to solve the Riemann problem.

at second-order we use a MUSCL-Hancock TDV scheme (Hirsch 1988, Toro 1999) in conjunction with a 'minmod' limiter for slopes α_i and α_{i+1} (Fig. 3).

The solution of system 13 (diffusive with source term) was found by applying a standard finite difference centered scheme which is second-order accurate.

Finally, the second-order time accuracy is obtained using a *split-operator* technique that brings to the scheme:

$$\mathbf{U}_i^{n+1} = \mathbf{L}_\mathbf{i}^{(\mathbf{d})^{(\Delta t/2)}} \mathbf{L}_\mathbf{i}^{(\mathbf{c})^{(\Delta t)}} \mathbf{L}_\mathbf{i}^{(\mathbf{d})^{(\Delta t/2)}} \left[\mathbf{U}_i^n \right]. \tag{22}$$

4 RESULTS OF SOME TESTS

A number of tests were carried out to check the model, here we show the results of a couple of them: one purely advective and one purely diffusive.

4.1 *Advective test*

In this test we analyze the pollutant concentration transport in one-dimensional dam-break problems. The domain, 50 m long (x-axis) and 10 m wide (y-axis), is discretised by cells of dimensions 0.5×0.5 m. The Courant-Friedrichs-Lewy coefficient is $C_{\text{cfl}} = 0.9$. The initial conditions ($t = 0$ s) are given in Table 1.

In Figure 5 is shown the comparison between numerical and analytical solutions of the pollutant concentration transport at time $t = 7$ s.

4.2 *Diffusive test*

In this test we analyze the pollutant concentration transport in a purely diffusive one-dimensional problem.

The domain, 5 m long (x-axis) and 2 m wide (y-axis), is discretised by cells of dimensions 0.1×0.1 m. The Courant-Friedrichs-Lewy coeffcient is $C_{\text{cfl}} = 0.8$. The initial condition is still water, the boundary condition at $x = 0$ is set at a constant immission of pollutant concentration $C = 1$. In this test we assume a constant isotropic diffusion coefficient $D = 0.25\ \text{m}^2/\text{s}$.

In Figure 6 is shown a comparison between numerical and analytical solutions (Fisher et al. 1979) of the pollutant concentration diffusion.

Table 1. Initial conditions for the advective test.

Variable	h (m)	U (m/s)	C –
$x < 10$ m	1.00	2.50	1.00
$x > 10$ m	0.00	0.00	0.00

5 APPLICATION OF THE MODEL TO THE LAGOON OF GRADO AND MARANO

The lagoon of Grado and Marano, situated at the most northern point of the Adriatic Sea, between the mouths of the rivers Tagliamento (to the West) and Isonzo (to the East). The lagoon covers an area of around 16,000 hectares, for a length of around 32 km and a mean width of 5 km. It is connected to the open sea through 6 natural mouths (Fig. 7).

Recent investigations have been carried out for the dredging of the lagoon channels and they have underlined, among the various forms of pollution, a consistent presence of Mercury diffuse more or less throughout the whole Lagoon.

Two hypotheses have been formulated about the origin of this pollution: the former ascribes the polluting

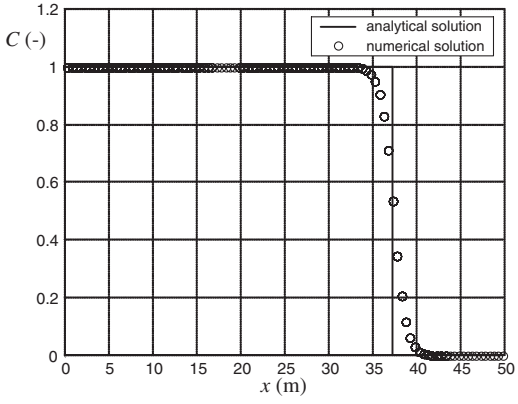


Figure 5. Advective test: comparisons between numerical and analytical solutions of the pollutant concentration transport in one-dimensional dam-break problem ($t = 7$ s).

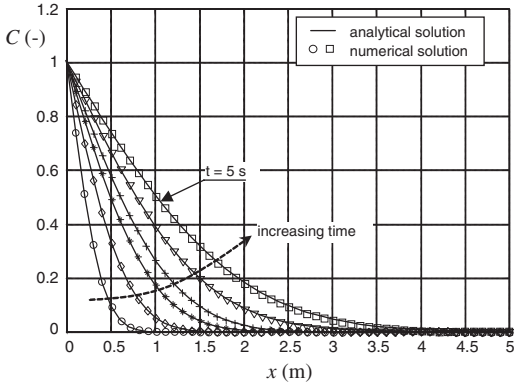


Figure 6. Diffusive test: comparisons between numerical and analytical solutions of the pollutant concentration diffusion in one-dimensional problem.

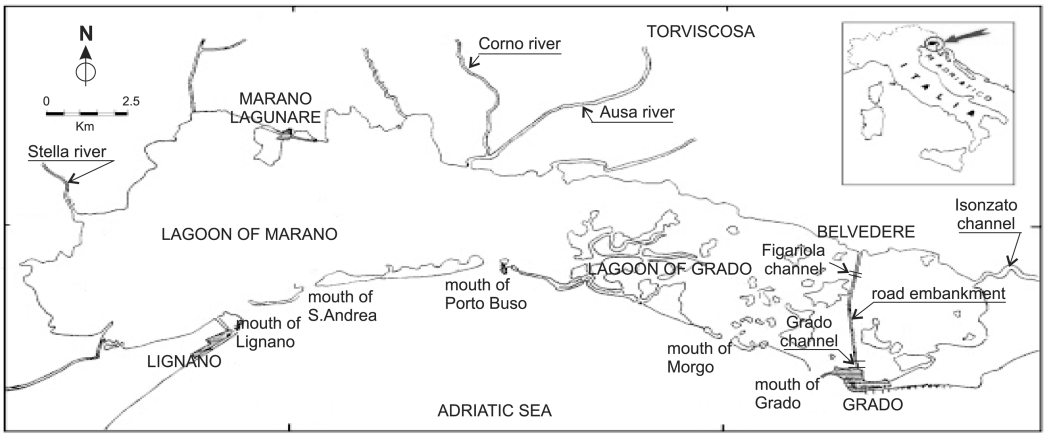


Figure 7. The lagoon of Grado and Marano.

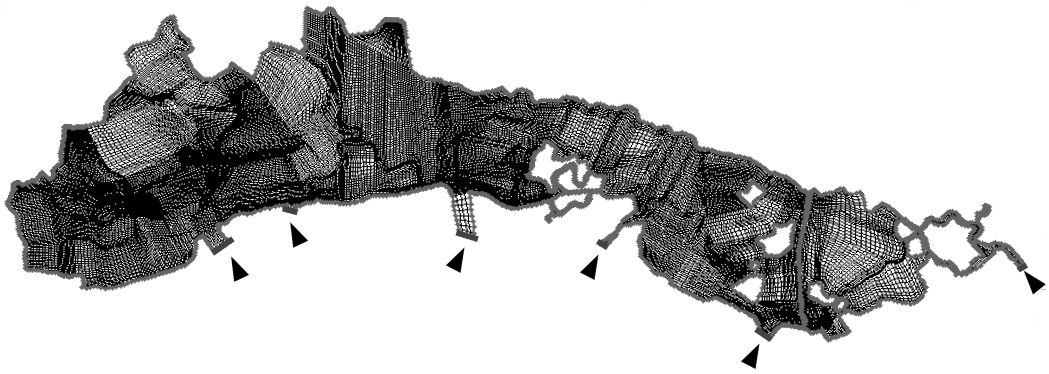


Figure 8. Mesh built for the simulations in the lagoon of Grado and Marano.

source to the mercury area of Idrija in Slovenian territory. This area, close to the Isonzo, nourishes the river that on Italian territory flows into the Lagoon along a channel called Isonzato. The latter hypothesis (Mattassi et al. 1991) ascribes the source to the chemical industries, such as that of chlorine-soda for the production of cellulose in Torviscosa. According to Matassi such chemical industries, located along the river Ausa, have introduced, between 1949 and 1970 around 20 kg/day of pollutant and between 1970 and 1984 around 7 kg/day. Since 1984, the adoption of more efficient systems of recovery of mercury has led to the substantial disappearance of such sources of pollution.

The two hypotheses have been studied using the implemented model.

5.1 *Mesh*

For the simulations a mesh of 31,041 quadrangular elements was built with mean dimensions varying between 6 and 250 m (Fig. 8). The mesh was opportunely thickened in proximity to the lagoon channels.

5.2 *Manning, diffusion and wind coefficients*

A uniform Manning resistance coefficient $n = 0.020$ $m^{-1/3}s$ was assumed on the whole lagoon basin.

This value was obtained by elaborating data from literature and from measurement taken on site, based on the reduction of the wave amplitude and the tidal delay recorded at some measuring points located inside the lagoon (Fig. 9).

As far as concerns the diffusion coefficients D_{xx} and D_{yy}, an isotropic condition was assumed due to the scarce importance of the diffusive process of dispersion in comparison to the advective. The conditions are characterized by a single diffusion coefficient $D = D_{xx} = D_{yy} = 0.25\ m^2/s$ deducted from data from literature (Fisher 1979).

The wind shear coefficient was given the value $C_D = 1.0 \cdot 10^{-3}$, obtained from elaborating data found

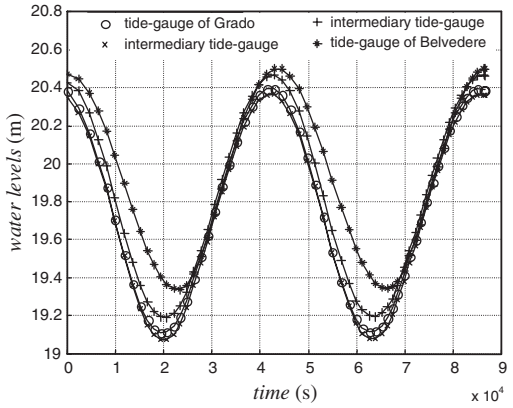


Figure 9. Amplitude reduction and tidal delay between the towns of Grado and Belvedere.

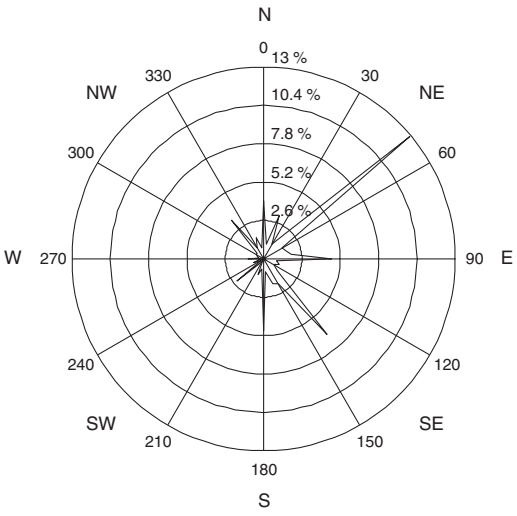


Figure 10. Directional distribution (annual average) of all winds blowing on the lagoon of Grado and Marano.

in literature on the lagoon, which specified changes in the sea water level in correspondence with particular wind event. The value found of C_D agrees with the values proposed by Hicks et al. (1974) in the case of closed basins with reduced water depths.

Finally, to estimate the mean wind velocity W, a statistic analysis was carried out on the data recorded by wind stations considered relevant to the lagoon of Grado and Marano. In Figures 10, 11 are shown the mean directional distribution obtained, this highlight the prevalence of the winds coming from the northeast (Bora) and from the southeast (Scirocco). From this data was drawn out an average occurrence of the Bora

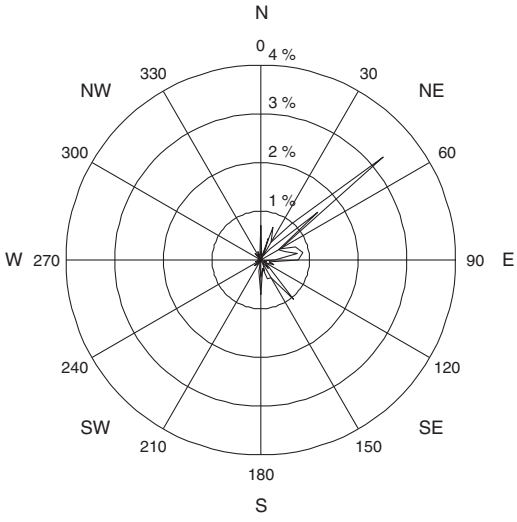


Figure 11. Directional distribution (annual average) of the winds greater than 15 m/s blowing on the lagoon of Grado and Marano.

characterized by a speed $W = 10$ m/s and direction of origin $\theta = 50°$N.

While the Bora blows directly on the free surface of the lagoon water, the Scirocco blowing on the whole Adriatic sea manifests itself with a set-up of the sea due to the wind that increases the tidal level. For this reason the effects of the Scirocco have been included in the amplitude of tidal oscillations.

5.3 *Boundary and initial conditions*

Beach and wall boundary conditions were assumed everywhere except for the six lagoon mouths where tidal oscillations described subsequently were imposed.

As characteristic tides, two oscillations were selected. The first with an amplitude equal to 0.5 m and the second 1 m both with periods of 12 hours. These values were deduced by analyses of the data recorded by the tide-gauges of Trieste and Grado keeping in mind the existing correlation between them. The above mentioned values are held representative of normal oscillations of tides (0.5 m) or of medium to high tides (1.0 m). These tidal values are already inclusive of the set-up induced by the Scirocco.

As initial conditions the values of velocity and level in the basin are those found after some tidal oscillations.

5.4 *Influx of pollutant from the river Ausa*

The study was conducted for two different tidal amplitudes H with the same period T, in the absence and

Table 2. Characteristic conditions used for the simulation of pollutant coming from the mouth of the Ausa-Corno.

	Tide		Wind		Pollutant	
Test	H (m)	T (h)	W (m/s)	θ (°N)	Quantity (Kg)	Time (h)
AUS1	0.5	12	0.0	–	20	3
AUS1A	0.5	12	10.0	50	20	3
AUS2	1.0	12	0.0	–	20	3
AUS2A	1.0	12	10.0	50	20	3

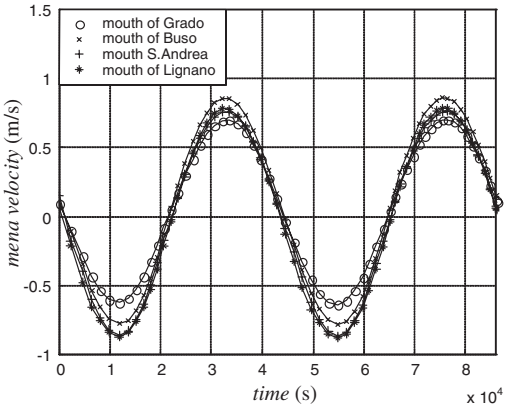


Figure 12. Mean velocities obtained in some lagoon mouths (test AUS1).

in the presence of the Bora. The characteristics of the simulation are shown in Table 2. A value of $C_{cfl} = 0.7$ was used for a duration of the simulation equal to 24 hours.

Figure 12 shows the mean velocities obtained in some lagoon mouths with the simulation AUS1. These values like those of the other simulations, are coherent with the only available measures in literature, even if not very recent (Dorigo, 1965).

Figure 13 shows the results after 18 hours of simulation in absence of wind (test AUS2) and Figure 14 shows those in the presence of the Bora (test AUS2A).

In the absence of wind (Fig. 13) a portion of the total mass of pollutant introduced from the mouth of the Ausa-Corno remains as diluted pollutant inside the basin of Porto Buso and the remainder goes out to sea through the Porto Buso channel. Instead, in the presence of wind (Fig. 14) the level of concentration of pollutant remains rather high because the hydrodynamic regime induced by the wind prevents an immediate exit of the pollutant from the Lagoon. Furthermore, the mass of polluted water is pushed towards the west, involving areas such as Marano and Lignano, apparently immune from a phenomenon of this type.

5.5 *Influx of pollutant from the river Isonzo*

In this simulation we assumed an immission of pollutant into the lagoon from the river Isonzo (along the Isonzato channel) equal to 10 kg for a duration of 2 hours; this amount is considered to be representative of the mercury coming from Slovenia.

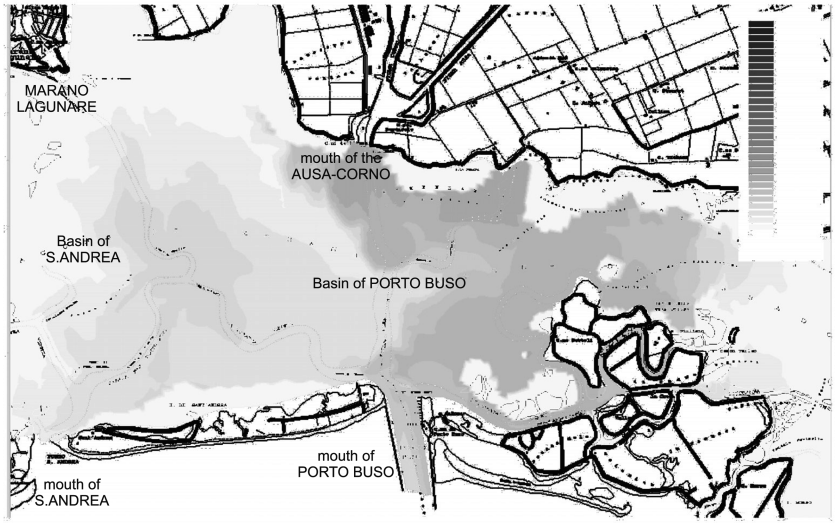


Figure 13. Distribution of the pollutant from the mouth of the Ausa-Corno after 18 h of simulation. Tidal amplitude 1 m, period 12 h, absence of the Bora. Increasing concentration passing from the white tonality to the black.

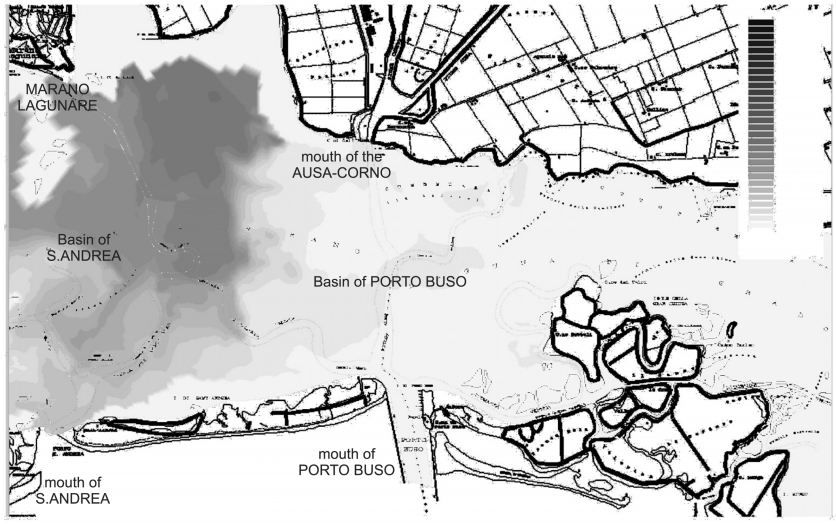


Figure 14. Distribution of the pollutant from the mouth of the Ausa-Corno after 18 h of simulation. Tidal amplitude 1 m, period 12 h, presence of the Bora (10 m/s). Increasing concentration going from the white tonality to the black.

Table 3. Characteristic conditions used for the simulation of pollutant from the River Isonzo (through Isonzato channel).

	Tide		Wind		Pollutant	
Test	H (m)	T (h)	W (m/s)	θ (°N)	Quantity (Kg)	Time (h)
ISO1	0.5	12	0.0	–	10	2
ISO1A	0.5	12	10.0	50	10	2
ISO2	1.0	12	0.0	–	10	2
ISO2A	1.0	12	10.0	50	10	2

Also in this case, after fixing the quantity of introduced pollutant, the study was conducted for two different oscillations of tide (0.5 m and 1 m of amplitude) both in the absence and in the presence of the Bora (Tab. 3). Also in this application a value $C_{cfl} = 0.7$ was used and the duration of the simulation was 24 hours.

In these circumstances, the results both in the presence or the absence of wind are almost the same due to the embankment of the road that connects Grado to Belvedere. In Figure 15 the results after 18 hours of simulation in the presence of the Bora are shown (test ISO2A).

As can be seen (Fig. 15) in this case, even if the total amount of pollutant introduced is equal to that of the previous simulations (20 kg), its concentration remains much higher.

Such a phenomenon can be ascribed to the presence of the Grado-Belvedere road embankment that prevents water exchange between the East (Basin of Primero) and the West (Basin of Grado) part of the lagoon, with the only exception of two small channels (Figariola and Grado). The analysis of the hydrodynamic field also shows the scarce vitality of the basin of Primero, that has low velocity and water level oscillations if compared with the other basins.

Returning to the dispersion of pollutant, this kind of hydrodynamic isolation of the Basin of Primero substantially limits the passage of pollutant from the Isonzato channel over the Grado-Belvedere road embankment. Most of the small amount of pollutant that passes beyond the road remains near the road itself while the rest leaves the lagoon through the mouth of Grado.

6 CONCLUSIONS AND FUTURE WORK

A finite volume numerical model was developed for the study of the dispersion of a pollutant dissolved in shallow water. Many tests of verification showed its reliability and accuracy. Some hydrodynamic tests carried out on the lagoon of Grado and Marano confirmed these characteristics, showing coherence between numerical results and experimental data available in literature.

Subsequently the model was applied to the study of the dispersion of pollutants dissolved in the lagoon of Grado and Marano. The results showed the influence that the Bora and the road embankment that connects the town of Grado and Belvedere have on the dynamics of such a phenomenon.

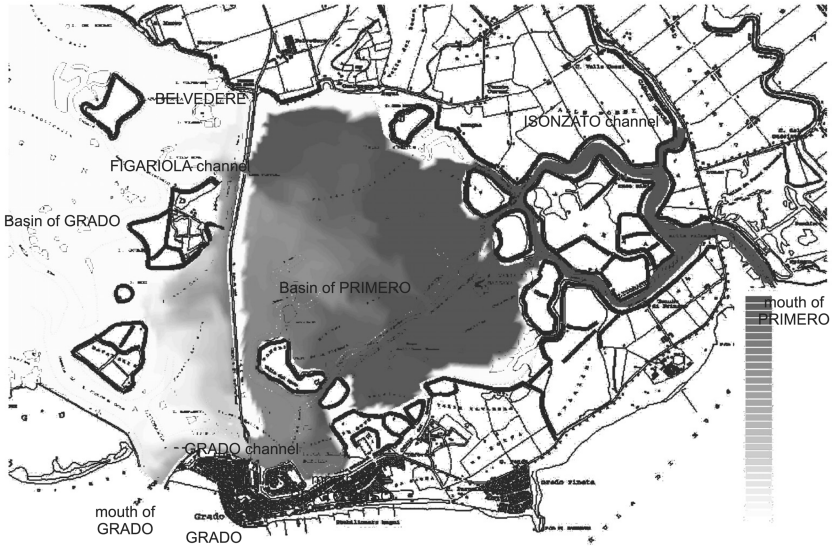


Figure 15. Distribution of the pollutant from the River Isonzo (through Isonzato channel) after 18 h of simulation. Tidal amplitude 1 m, period 12 h, presence of the Bora (10 m/s). Increasing concentration going from the white tonality to the black.

This study showed that a pollutant, for instance mercury, from the river Isonzo, could cross the road embankment only in a small part, and most of it would anyway laeve the lagoon through the mouth of Grado. Thus, it is not very reasonable to ascribe the pollution of the West side of the lagoon (lagoon of Marano) to the Isonzo river. Moreover, a source of pollutant from the river Ausa could easily propagate towards Marano and Lignano, especially in the presence of the Bora. This could justify the presence of mercury in the lagoon of Marano too, with concentrations similar to those present in the basin of Primero.

Improvements of the implemented model, especially for long periods of simulation, can be obtained using techniques of interpolation ENO and WENO (Jiang & Shu, 1996) that allow a more accurate solution of the local 'Riemann problem' (Petti & Bosa 2003).

REFERENCES

Dorigo, L. 1965. *The lagoon of Grado and Marano and its mouths. Researches and hydraulic measures.* Magistrato alle Acque, Ufficio Idrografico. Venezia: Grafiche Gasparoni. (In Italian).

Dragoslav, L.S. & Heinz, G.S. 2001. Accurate Two-Dimensional Simulation of Advective-Diffusive-Reactive Transport. *Journal of Hydraulic Engineering* 127 (9): 728–737.

Fisher, H.B., List, E.J., Koh, R.C.Y., Imberg, J. & Brooks, N.H. 1979. *Mixing in Inland and Coastal Waters*. New York: Academic Press.

Hicks, B.B., Drinklow, R.L. & Grauze, G. 1974. Drag and bulk transfer coefficients associated with a shallow water surface. *Boundary-Layer Meteorol*. 6: 287–297.

Hirsch, C. 1988, *Numerical computation of internal and external flows*. Vol. 1 & 2. New York: John Wiley & Sons.

James, I.D. 2002. Modelling pollution dispersion, the ecosystem and water quality in coastal waters: a review. *Environmental Modelling & Software* 17: 363–385.

Jiang, G. & Shu, C.W. 1996. Efficient implementation of weighted ENO schemes. *Journal of Computational Physics* 126: 202–228.

Ligget, J.A. 1994. *Fluid Mechanics*. Singapore: McGraw-Hill International Editions.

Mattassi, G., Daris, F., Nedoclan, G., Crevatin, E., Modonutti, G.B. & Lach, S. 1991. The water quality of the Lagoon of Grado and Marano. *Regione Autonoma Friuli Venezia Giulia. Trieste: U.S.L. n. 8 "Bassa Friulana"* (In Italian).

Petti, M. & Bosa, S. 2003. Accurate shock-capturing finite volume method for advection-dominated flow and pollution transport. *To be submitted*.

Prandle, D., Jago, C.F., Jones, S.E., Purdie, D.A. & Tappin, A. 1993. The influence of horizontal circulation on the supply and distribution of tracers. *Philosophical Transactions of the Royal Society of London* A 343: 405–421.

Stoker, J.J. 1957. *Water waves*. New York: Interscience.

Toro, E.F. 1999. *Riemann solvers and numerical methods for fluid dynamics, Second Edition*. New York: Springer-Verlag.

Whitham, G.B. 1974. *Linear and Nonlinear Waves*. New York: Wiley.

Yanenko, N.N. 1971. *The Method of Fractional Steps*. Berlin: Springer-Verlag.

River Flow 2004 – Greco, Carravetta & Della Morte (eds.)
© 2004 Taylor & Francis Group, London, ISBN 90 5809 658 0

Numerical simulation of transport processes in not uniform turbulent streams

I. Cotto & R. Revelli
Dipartimento di Idraulica, Trasporti ed Infrastrutture Civili, Politecnico di Torino
Corso Duca degli Abruzzi, Torino, Italy

ABSTRACT: The numerical simulation of the advection dispersion equation with non constant parameters is presented in order to simulate the behaviour of a pollutant in a natural stream with variable geometric and dynamic characteristics, i.e. with a non constant water depth, mean velocity and dispersion coefficient. A collocation-interpolation method based on *sinc* function is used and the results are presented in the form of temporal and spatial moments. Both conservative and non conservative substances are accounted for, this latter with a decay reaction rate both linear and non linear. The results show in particular the behaviour of the centroid, variance and skewness depend on the velocity variation along the river and decay reaction rate. It was also found that the influence of the water depth change is less important than the velocity variation.

1 INTRODUCTION

The presence of pollutants and hazardous substances in a natural stream is a problem of great interest both from the speculative and applicative points of view. It is in fact well known that this problem is important in the environmental economic debate and how a good comprehension and description of the phenomena are necessary to apply correct development and management politics.

Since the early fifties a great deal of work has been devoted to describing the behaviour of the substances in a turbulent stream and natural flow and one of the main theoretical results is the formulation of the advection-dispersion equation (e.g. Taylor 1953, 1954, Aris 1956, Fisher et al. 1979) with the description and formalization of the effect of phenomena such as turbulent diffusion and shear dispersion. This classical advection-dispersion equation however generally considers a uniform stream and if a non conservative substance is taken into consideration the decay reaction is of a linear type.

Under these assumptions the result of the mathematical problem for an instantaneous release is of a Gaussian type form for the concentration (e.g. Fisher et al. 1979); an integral convolution, therefore, makes it possible to find the mathematical form of the concentration distribution for each form of the release. On the contrary, it is not normally possible to find an analytical solution with a non uniform stream or non linear decay reaction.

Starting from these fundamental results, many studies over the last decades have been dedicated to refining the Taylor model in order to better describe some features that are present in natural streams. This has principally been due to the fact that a great number of laboratory and field studies (dedicated to validating the analytical models or to fitting the appropriate parameters), recognised a bias between the theory and the data (for example, the problem known as "skewness persistence", etc. . .).

It is now clear that the presence of transfer mechanisms, of a physical, chemical or biological nature, between the main stream and the boundaries (river bank, bed, free surface), could give rise to discrepancies, in particular due to the occurance of long tails in the concentration distribution (e.g. Hays et al. 1966, Trackston & Schnelle 1970, Day et al. 1975, Valentine & Wood 1977, Benkala et al. 1980, Nordin & Troutman 1980, Kim et al. 1990, Czernuszenko & Rowinski 1995, Hart et al. 1995, Worman 1998, Schmid 2002).

Even sorption-desorption phenomena due to the presence of suspended sediment (e.g. Ng & Yip 2002, Revelli & Ridolfi 2002, 2003) or the kinetics between the river and the neighbouring aquifers (e.g. Kim et al. 1990, Worman 2000) are able to modify the form of the concentration breakthrough.

As in Taylor's model, a quite general characteristic of the models, that are generated according to the previous considerations (i.e. transient storage equation, aggregated dead zone models, stochastic formulation

etc. . .), is to assume a uniform stream, or at least to describe the river as a sum of different reaches with constant characteristics. The possibilities of a variation in the parameters along the river (Zoppou & Knight 1997, Gupta & Cvetkovic 2000) are not often taken in consideration. This is principally due to the fact that in this case it is not generally possible to find an analytical solution to the problem and methods like moments analysis cannot be applied.

The present work intends to join in the debate with a numerical analysis of a non constant coefficient model. In particular, the advection-dispersion equation will be simulated starting from a stream with quantities such as water depth, mean velocity or dispersion coefficient which are variable along the stream. In addition the chemical, physical or biological transfer mechanisms with boundaries or suspended load will be neglected.

The possibilities of simulating the behaviour of a non conservative substance will also be taken into consideration. In particular both the linear and non linear decay rate will be considered in order to model the common chemodynamic nonlinearities (Schwarzenbach et al. 1993, Brezonik 1996, Schnoor 1996).

The paper is organized as follows: in the next section the model is briefly mentioned, and the solution method is presented. The results of several simulations are given in the last sections and some conclusion are drawn.

2 MATHEMATICAL PROBLEM

Let us consider a one dimensional, steady, not uniform turbulent channel flow with a mild slope i_b. A reference system with the x-coordinate along the channel is introduced. The stream has a depth $H(x)$ and a mean velocity $U(x)$.

Without any lack of generality, we assume that the hydraulic geometry of the channel can be expressed as a power law function along the length of the stream (Leopold & Maddock 1953, Gupta & Cvetkovic 2000), so that

$$H(x) = a_H \cdot \left(1 + \frac{x}{L}\right)^{b_H} \tag{1}$$

$$U(x) = a_U \cdot \left(1 + \frac{x}{L}\right)^{b_U} \tag{2}$$

where a_H, and a_U are dimensional constants; b_H and b_U are dimensionless constants; and L is a reference length, which will be assumed to be equal to the length of the channel.

Let us also suppose that a chemical is dispersed in the stream and let us define $C = C(x,t)$ as the averaged concentration of the chemical per volume of water. If we suppose that there is a local balance between the longitudinal advective transport and the cross-sectional turbulent diffusive transport in any point of the stream, and that the chemical is uniformly distributed along the vertical coordinate, we can write

$$\frac{\partial C}{\partial t} + \frac{\partial}{\partial x}[U(x)C] = \frac{\partial}{\partial x}\left[K(x)\frac{\partial C}{\partial x}\right] + R \tag{3}$$

where $K(x)$ is the dispersion coefficient; and R accounts for the decay reaction.

In order to describe the dispersion phenomena we can write (Elder 1959), for sake of simplicity,

$$K(x) = 5.93 \cdot u_* \cdot H = a_K \left(1 + \frac{x}{L}\right)^{b_K} \tag{4}$$

where $u_*(x) = (g i_b H)^{0.5}$ is the friction velocity and g is the gravity acceleration, therefore so that $a_K = 18.57 i_b^{1/2} a_H^{3/2}$ and $b_K = 3/2\, b_H$.

Rearranging 1 gives

$$\frac{\partial C}{\partial t} = [(K' - U)]\frac{\partial C}{\partial x} + K\frac{\partial^2 C}{\partial x^2} - U'C + R \tag{5}$$

where the prime means the derivative with respect to x. By substituting the Equations 2, 3 and 4 in the Equation 5, the mathematical model is recovered.

The mathematical statement of the problem related to Equation 5 can be obtained by linking the previous equations to suitable initial and boundary conditions. The boundary conditions are defined by

$$C(0,t) = C(L,t) = 0 \tag{6}$$

while, as an initial condition, we require

$$C(x,0) = \varphi(x) \tag{7}$$

where $\varphi(x)$ can be any function, e.g. a Dirac delta, in order to simulate an instantaneous release.

3 NUMERICAL METHOD

The mathematical problem of the Equations 5, 6 and 7 is numerically integrated using an interpolation-collocation method based on *sinc* functions (Bellomo & Ridolfi 1995) that is particularly suitable for nonlinear models and to simulate wave phenomena (Revelli & Ridolfi 2004). Although the method has been presented in several papers let us here recall the main steps while reference can be made to the works by Bellomo & Ridolfi (1995) and Revelli & Ridolfi

(2004) for a detailed description and for an extensive bibliographic review.

The method is a modification of the differential quadrature method proposed by Bellman et al. (1972) and Satofuka (1983). It consists of the transformation of the Equation 5 into a system of ordinary differential equation with a spatial discretisation of the variable $C(x,t)$ in a finite number of points and considering the values of the variable itself in the spatial nodes as new unknowns. Let us choose, in the spatial domain, $x \in [0, L]$ a number n of collocation equispaced points

$$x_0 = 0, \ldots, x_i = ih, \ldots, x_{n+1} = L \tag{8}$$

with $i = 0, \ldots, n+1$ and $h = L/(n+1)$. We then collocate an interpolating function $S_i(x)$ in each point so that the solution of the Equation 5 can be approximated with the summation

$$C(x,t) \cong \sum_{i=0}^{n+1} S_i(x) u_i(t) \tag{9}$$

where $u_i(t) = u(t, x_i)$. In this way each term of 9 is given by the product of two functions: the first which depends on space and the second which depends on time. These latter functions $u_i(t)$ are the new unknowns of the problem.

In this work we have choosen a *sinc* as the interpolating function (for alternative possibilities see for example Bonzani 1997)

$$S_i(x) = \frac{\sin z_i}{z_i} \qquad \text{and} \qquad S_i(x_j) = \delta_{ij} \tag{10}$$

with $z_i = \pi(x/h - i)$ and δ Kronecker's delta.

By placing the Equation 10 in the Equation 9 and deriving with respect to x we obtain

$$\frac{\partial u}{\partial x} = \sum_{p=0}^{n+1} a_{pi} u_p \qquad \text{and} \qquad \frac{\partial^2 u}{\partial x^2} = \sum_{p=0}^{n+1} b_{pi} u_p \tag{11}$$

where

$$a_{pi} = \frac{\pi}{h} \frac{z_{pi} \cos z_{pi} - \sin z_{pi}}{z_{pi}^2} \tag{12}$$

$$b_{pi} = \left(\frac{\pi}{h}\right)^2 \frac{(2 - z_{pi}^2) \sin z_{pi} - 2 z_{pi} \cos z_{pi}}{z_{pi}^3} \tag{13}$$

with $a_{ii} = 0$ and $b_{ii} = -1/3(\pi/h)^2$.

The substitution of the Equations 9–13 in the Equation 5 transforms it into a system of ordinary differential equation that can be solved, linked to the proper boundary and initial conditions, with the aid of classical iterative methods such as the Runge-Kutta, multi-step Adams-Multon or Adams-Bashforth methods.

4 TEMPORAL AND SPATIAL MOMENTS

The solution of Equations system 5–7 is analysed through the use of the temporal and spatial moments; some features of the solution of the constant coefficient model can in fact be given in terms of the Laplace transform of the solution itself and with the consideration that the moments can be calculated by expanding in Taylor series the Laplace transform itself (e.g. Aris 1956, Nordin & Troutman 1980, Czernuszenko & Rowinski 1995, Schmid 2002).

Temporal (central) moments of the *p-th* order can be defined as

$$\mu_t^p(x) = \int_0^L (t - m_t^1)^p C(x,t) \cdot dt \tag{14}$$

and similarly the spatial (central) moment of the *p-th* order can be defined as

$$\mu_x^p(t) = \int_0^T (x - m_x^1)^p C(x,t) \cdot dx \tag{15}$$

where m_t^p and m_x^p are temporal and spatial noncentral moments of the *p-th* order respectively.

It is important to note that in 14 and 15 we have replaced the usual superior limit $+\infty$ which T and L which are the time length simulation and the channel length, respectively; this is important for the subsequent discussion of the results.

If we normalize the concentration with respect to m^0 we can find the links between 14 and 15 and the centroid. In this way we are able to find the centroid m, variance σ^2, and skewness coefficient G:

$$m_x = m_x^1 \qquad \text{and} \qquad m_t = m_t^1 \tag{16}$$

$$\sigma_x^2 = \mu_x^2 \qquad \text{and} \qquad \sigma_t^2 = \mu_t^2 \tag{17}$$

$$G_x = \mu_x^3 \sigma_x^{-3/2} \qquad \text{and} \qquad G_t = \mu_t^3 \sigma_t^{-3/2}. \tag{18}$$

In the case of the constant coefficient model and $\varphi(x)$ as a Dirac delta it is possible to find an analytical formulation for 16–18 (e.g. Nordin & Troutman 1980). In this case, for the spatial case, it is easily to obtain

$$\begin{cases} m_{x,0} = a_U t \\ \sigma_{x,0}^2 = 2 a_K t \\ G_{x,0} = 0 \end{cases} \tag{19}$$

while for the temporal case one obtains

$$\begin{cases} m_{t,0} = \dfrac{1}{a_U^{\,2}}\left(x a_U + 2a_K\right) \\ \sigma^2_{t,0} = 2\dfrac{a_K}{a_U^{\,4}}\left(x a_U + 4a_K\right) \\ G_{t,0} = (2a_K)^{1/2}\dfrac{(3x a_U + 16 a_K)}{(x a_U + 4a_K)^{3/2}}. \end{cases} \tag{20}$$

5 SIMULATIONS AND RESULTS

Using the previously described numerical method, the advection-dispersion equation with nonconstant parameters is simulated. The set of parameters that we kept constant for the whole series of simulations are $i_b = 0.001, L = 33.6$ km, $T = 9$ hr, $a_H = 1.27$ m and $a_U = 0.48$ ms^{-1} which means $a_K = 0.84$ m^{2}s^{-1}. These parameters are quite similar to the set proposed by Gupta & Cvektovic (2000) and Revelli et al. (2004) so useful comparison can be made. The parameters that we changed are b_H and b_U which we varied from 0 to 0.6. The analytical solution corresponding to the constant coefficient is given by $b_H = b_U = 0$.

The chosen parameters imply a variation of the velocity from the initial value of 0.48 ms^{-1} ($x = 0$) to 0.73 ms^{-1} for the highest b_U ($x = L$) and a water depth variation in the river from the initial value of 1.27 m ($x = 0$) to 2.22 m for the highest b_H ($x = L$). Correspondingly the variation of dispersion coefficient lies between 0.84 m^{2}s^{-1} to 1.94 m^{2}s^{-1}.

We changed the value of b_H or b_U in every simulation keeping the others identically equal to zero: in this way the influence of each single parameter it easily recognizable.

Regarding the initial condition we always used the same function i.e. a gaussian type form in order to simulate a common source form.

$$C(x,0) \equiv \varphi(x) = 25.6\exp\left[-1.8\cdot 10^{-6}(x-3000)^2\right]. \tag{21}$$

We chose a spatial discretisation grid with n=300 while the system of ordinary differential equations was integrated with the Adam predictor-corrector method with an adaptative time step.

5.1 *Conservative substances ($R = 0$)*

Figure 1 shows the spatial centroid versus time for different values of the parameter b_U.The values were normalized with respect to $m_{x,0}$, i.e. value given by the Equation 19 of the constant parameter model. The centroid increases regularly and at the end of the simulation it can be greater than at the start by about

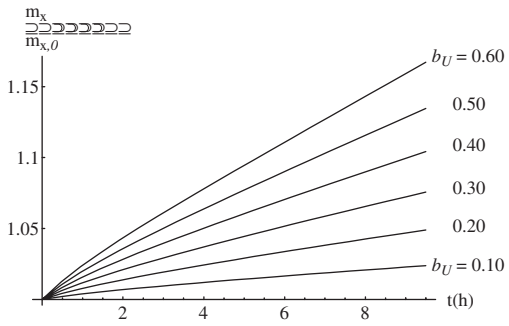


Figure 1. Spatial behaviour of the centroid for different values of b_U ($b_H = 0$). The values are normalized with respect to the constant parameter value $m_{x,0}$.

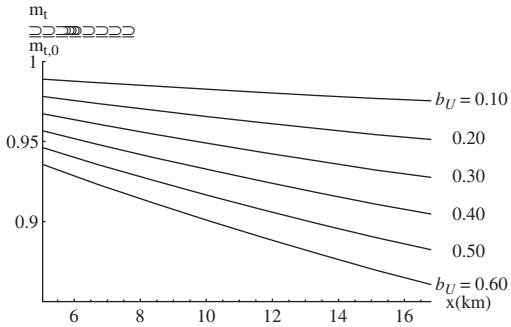


Figure 2. Temporal mean behaviour for different values of b_U ($b_H = 0$). The values are normalized with respect to the constant parameter value $m_{t,0}$.

15–20% for $b_U = 0.60$. The same behaviour occurs if we consider the b_H variation but the change is in the order of 0.1%. This is a characteristic that is almost constant over the whole range of simulations: there is a considerable influence of b_U and a practically nonexisting influence of b_H.

Figure 2 shows the behaviour of the temporal mean for different values of parameter b_U. Even in this case, the influence of b_H is unimportant (a few fractions of unity). The behaviour in this case is different from the previous example, because there is a diminishing value of the rate with respect to time.

The difference, with respect to the constant value model, can be up to 10% and the centroid exhibits a practically linear growth even for non constant coefficient models.

The spatial range in Figure 2 was chosen in order to calculate the temporal moment for the whole cloud; for this reason it results to be lesser than the total spatial considered domain [0, L]. Normally analytical solutions do not suffer from this limitation (see Equation 14) because an indefinite channel length and a simulation time that is greater than the time necessary

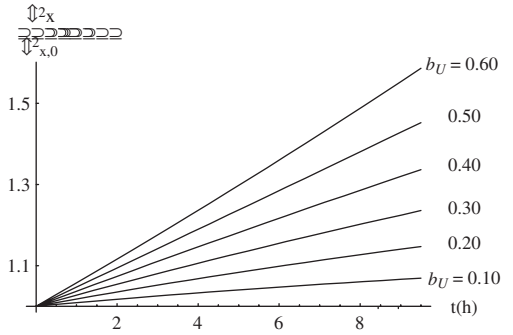


Figure 3. Spatial variance behaviour for different values of b_U ($b_H = 0$). The values are normalized with respect to the constant parameter value $\sigma^2_{x,0}$.

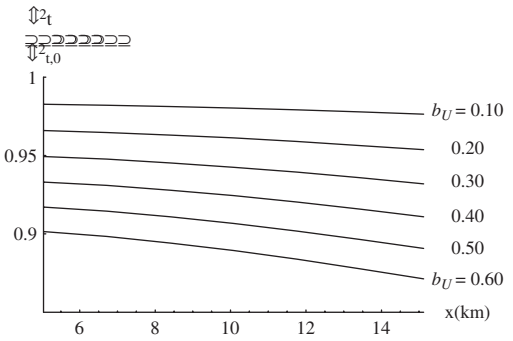


Figure 4. Temporal variance behaviour for different values of b_U ($b_H = 0$). The values are normalized with respect to the constant parameter value $\sigma^2_{t,0}$.

for the whole cloud to reach the prefixed section are often assumed.

The influence on the variance is more marked. Figures 3 and 4 show the spatial and temporal variance respectively, for different values of b_U. The behaviour is similar to that of the corresponding centroids. As expected, there is a general growth in the dimensions of the clouds and this growth is practically linear for the spatial variance while a deviation from linearity is evident when considering the temporal variance. It is important to note that the influence of b_U is up to 60% for spatial case while for the temporal one we find a difference up to 15% with respect to the constant value model. Even for b_H variations, there is a similar influence but it is less marked: about 5–6% for both cases.

As far as the spatial skewness is concerned, the simulation shows that a change in parameters does not change the value of the form of the cloud: i.e. the skewness remains practically equal to zero and the concentration shows evidence of a Gaussian type form during time evolution.

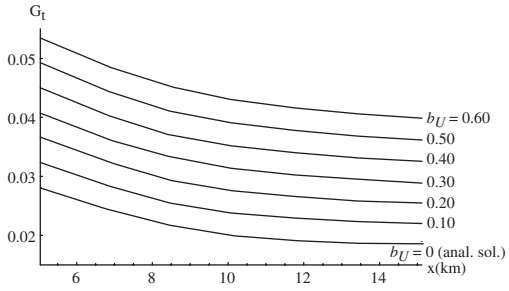


Figure 5. Temporal skewness behaviour for different values of b_U ($b_H = 0$).

However, the temporal skewness, for different values of b_H or b_U exhibits an always decreasing behaviour and tends to $G_{t,0}$ which tends to zero as $x \to \infty$ as $x^{-1/2}$ (Nordin & Troutman 1980) even though the influence of b_H is very low as in previous cases. The skewness now ever always decreases and the difference between the constant parameter model is of the order of +50% at the start of the considered spatial domain (Fig. 5).

5.2 *Non conservative substances ($R \neq 0$)*

The result of the evolution of a non conservative substances is presented as a second series of simulations. In particular, we suppose that a decay rate exists and the most general case is considered in which the decay is nonlinear. The reaction rate, R in the Equation 5 is therefore modelled according to the power law

$$R = -\lambda C^r \tag{22}$$

where λ is the decay rate constants – with units of measure $\mathrm{Kg}^{1-r}\mathrm{m}^{3r-3}\mathrm{s}^{-1}$ – and $r \geq 1$ in order to model the common chemodynamic nonlinearities (Brezonik 1996, Schnoor 1996, Schwarzenbach 1993).

It is possible to find the analytical formulation for the linear case ($r = 1$), for the constant parameter model, corresponding to the Equations 19 and 20. In particular for the temporal case we found (e.g. Schmid 1996)

$$\begin{cases} m_{t,0,r} = \dfrac{1}{\alpha^2}\left(x\alpha + 2a_K\right) \\ \sigma^2_{t,0,r} = 2\dfrac{a_K}{\alpha^4}\left(x\alpha + 4a_K\right) \\ G_{t,0,r} = (2a_K)^{1/2}\dfrac{(3x\alpha + 16a_K)}{(x\alpha + 4a_K)^{3/2}} \end{cases} \tag{23}$$

where $\alpha = (a_U^2 + 4a_K\lambda)^{1/2}$, and $\alpha \to a_U$ as $\lambda \to 0$.

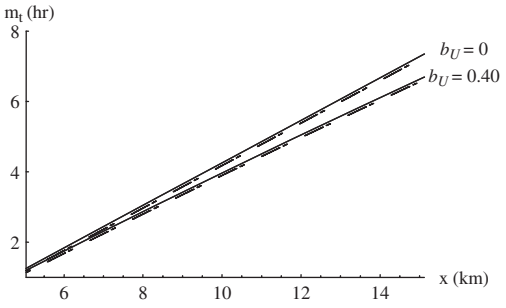


Figure 6. Non conservative substances: temporal centroid behaviour for two different values of b_U. $r = 1$ (dashed line) and $r = 2$ (dotted line). The continuous line represents the conservative substances (no decay).

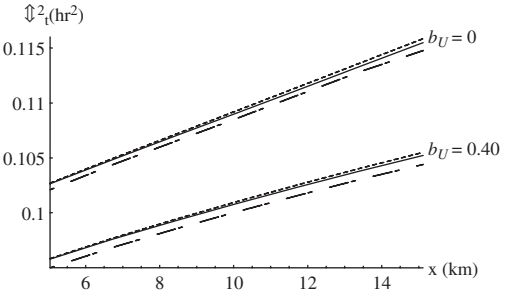


Figure 7. Non conservative substances: temporal variance behaviour for two different values of b_U. $r = 1$ (dashed line) and $r = 2$ (dotted line). The continuous line represents conservative substances (no decay).

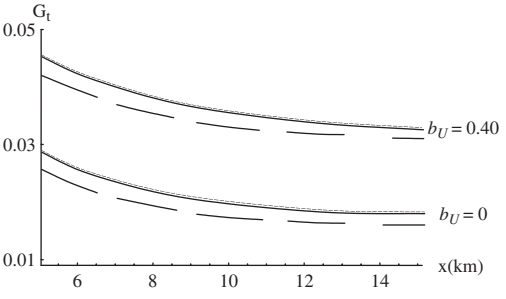


Figure 8. Non conservative substances: temporal skewness behaviour for two different values of b_U. $r = 1$ (dashed line) and $r = 2$ (dotted line). The continuous line represents conservative substances (no decay).

Figures 6–8 show the behaviour of the temporal centroid, variance and skewness respectively for the two cases corresponding to the constant values model ($b_U = 0$) and non uniform stream ($b_U = 0.40$), both for the case with conservative substance, i.e. no decay reaction ($r = 0$), linear reaction ($r = 1$) and not linear reaction ($r = 2$). The decay constant was always kept equal to $2 \cdot 10^{-4}$ $\mathrm{Kg}^{1-r}\mathrm{m}^{3r-3}\mathrm{s}^{-1}$ for each case, which means a half-life time of approximately 1 hr for the linear decay. The dashed line in all the figures represents the case $r = 1$, the dotted line represents the case $r = 2$ and the continuous line represents the conservative substances behaviour.

It can be noted that the trend of the curves is the same as the trend of the centroid, variance and skewness without the decay term. This is consistent, for example, with the results found by Schmid (1995) for the transient storage equation whit decay substances.

In particular it can be seen in Figures 7 and 8 that the simulations with $r = 2$ are very similar to the case $r = 0$ (in Figure 6 the two curves are practically coincident), while $r = 1$ implies the same different value of variance and skewness. This is due to the fact that high r means a low disappearing mass (see Equation 22) so it is reasonable to find the same result as the conservative case due to the short observation time interval; in other words, if the decay order r is much greater than 1, the behaviour is like the conservative case so the results of the previous simulations can be retained. In general the centroid and the variance decrease for an increase in b_U while the corresponding skewness is decreases.

As far as the variance is concerned (Fig. 7) the simulation shows that if $r = 1$ the values are lower (1%) than the conservative case, and the opposite occurs for $r = 2$. The same appears for the skewness behaviour (Fig. 8). A first explanation for this unexpected result could be the complex interaction between the nonlinearities present in the coefficients of the model and in the decay term itself, but this requires further studies. In every case, when it exists, the curves exactly match the analytical solution given by 23.

6 CONCLUSIONS

The numerical simulation of the advection-dispersion equation with non constant parameters is presented in this note. In particular, a collocation-interpolation method based on the use of a *sinc* function is used due to its great ability to deal with nonlinear models. The presented results include the case of conservative substances and non conservative substances with linear and non linear decay reactions.

The results are presented in the form of temporal and spatial moments (i.e. centroid, variance and skewness) and, when possible, the comparison with analytical outcomes is also given. In particular, the results show that the behaviour of the centroid, variance and skewness depend on the velocity variation along the river and the decay reaction rate.

In general, for a conservative substance, an increase in velocity along the river causes a decrease in the

temporal centroid displacement and variance, while the skewness seems to increase. The same specific considerations are valid for non conservative substances with some additional considerations regarding the influence of the non linear decay rate.

REFERENCES

Aris, R. 1956. On the dispersion of a solute in a fluid flowing through a tube . *Proc. R. Soc. Lon. A.* 235: 67–77.

Bellman, R., Kasher, B. & Casti, J. 1972. Differential quadrature: solution of nonlinear partial differential equations. *J. Comp. Phys.* 10: 40–52.

Bellomo, N. & Ridolfi, L. 1995. Solution of linear initial-boundary value problems by sinc collocation-interpolation methods. *Comp. Math. Appl.* 29: 15–28.

Bencala, K.E. & Walters, R.A. 1983. Simulation of solute transport in a mountain pool-and-riffle stream: a transient storage model. *Water Resour. Res.* 19: 718–724.

Bonzani, I. 1997. Solution of nonlinear evolution problems by parallelized collocation-interpolation methods. *Computers Math. Applic* 34: 71–79.

Brezonik, P.L. 1996. *Chemical kinetics and process dynamics in aquatic system*. Boca Raton, FL: Lewis.

Czernuszenko, W. & Rowinski, P.M. 1997. Properties of the dead-zone model of longitudinal dispersion in rivers. *Water Resour. Res.* 35: 491–504.

Day, T. 1975. Longitudinal dispersion in natural channels. *Water Resour. Res.* 11: 909–917.

Elder, J.W. 1959. The dispersion of marked fluid in turbolent shear flow. *J. Fluid Mech.* 5: 544–560.

Fisher, H.B., List, E.J., Koh, R.C.Y., Imberger, J. & Brooks, N. 1979. *Mixing in Inland and Coastal Water*. San Diego: Academic.

Guapta, A. & Cvetkovic, V. 2000. Temporal moment analysis of tracer discharge in streams: combined effect of physico-chemical mass transfer and morphology. *Water Resour. Res*. 36: 2985–2997.

Hays, J.R., Krenkel, P.A. & Schnell, K.B. 1966. Mass transport mechanisms in open-channel flow. *Tech. Rep*. 8. *Vanderbuilt Univ.* Nashville, Tenn.

Hart, D.R. 1995. Parameter estimation and stochastic interpolation of the transient storage model for solute transport in streams. *Water Resour. Res*. 31: 323–328.

Leopold, L.B. & Maddock Jr. 1953. The hydraulic geometry of stream channels and some physiographic implications. *U.S. Geol. Surv. Prof. Pap.* 252.

Kim, B.K., Jackman, A.P. & Triska, F.J. 1990. Modeling transient storage and nitrate uptake kinetics in a flume containing a natural periphyton community. *Water Resour. Res*. 26: 505–515.

Ng, C.O. & Yip, T.L. 2001. Effects of kinetic sorptive exchange on solute transport in open channel flow. *J. Fluid Mech.* 446: 321–345.

Nordin, C.F. & Troutman, B.M. 1980. Longitudinal dispersion in rivers: the persistence of skewness in observed data. *Water Resour. Res.* 14: 123–128.

Revelli, R. & Ridolfi, L. 2002. Influence of suspended sediment on the transport processes of nonlinear reactive substances in turbulent stream . *J. Fluid Mech*. 472: 307–331.

Revelli, R. & Ridolfi, L. 2003. Transport of reactive chemicals in sediment-laden stream. *Advances in Water Resources* 26: 815–831.

Revelli, R. & Ridolfi, L. 2004. Sinc collocation-interpolation method for the simulation of nonlinear waves. *Comp. Math. Appl*. 46(8–9): 1443–1445.

Satofuka, A 1983. *A new explicit method for the solution of parabolic differential equations.* Numerical methodologies and properties in heat transfer. New York: Hemisphere.

Schmid, B.H. 1995. On the transient storage equations for longitudinal solute transport in open channel: temporal moments accounting for the effects of first-order decay. *Journal of Hydraulic Research* 33: 595–608.

Schmid, B.H. 1997. Analytic solution of the transient storage equations accounting for solute decay. *Proc. 27th IAHR Congress, san Francisco, Theme B*1: 15–20. *Journal Hydraul. Res.* 33: 595–610.

Schmid, B.H. 2002. Persistence of Skewness in longitudinal dispersion data: Can the dead zone model explain it after all?. *Journal of Hydraulic Engineering* 128: 848–854.

Schnoor, J.L. 1996. *Environmental modeling*. New York: Wiley.

Schwarzenbach, R.P., Gschwend, P.M. & Imboden, D.M. 1993. *Environmental organic chemistry*. New York: Wiley.

Taylor, G.I. 1953. Dispersion of soluble matter in solvent flowing slowly through a tube. *Proc. R. Soc. Lond. A*. 219: 186–203.

Taylor, G.I. 1954. The dispersion of matter in turbulent flow through a pipe. *Proc. R. Soc. Lond. A*. 223: 446–468.

Thibodeaux, L.J. 1996. *Environmental chemodynamics*. 2nd Ed. New York: Wiley.

Trackston, E.L. & Schnelle, K.B. 1970. Predicting effects of dead zones on stream mixing. *Journal of the Sanitary Engineering Division* 96: 319–331.

Valentine, E.M. & Wood, I.R. 1977. Longitudinal dispersion with dead zones. *Journal Hydraul, Div. Soc. Civ. Eng.* 103: 975–990.

Worman, A. 1998. Analytical solution and timescale for transport of reacting solutes in river and streams. *Water Resour. Res.* 34: 2703–2716.

Worman, A. 2000. Comparison of models for transient storage of solutes in small streams. *Water Resour. Res.* 36: 455–468.

Zoppou, C. & Knight, J.H. 1997. Analytical solutions for advection and advection-diffusion equations with spatially variable coefficients. *Journal of Hydraulic Engineering* 123: 144–148.

This page intentionally left blank

River Flow 2004 – Greco, Carravetta & Della Morte (eds.)
© 2004 Taylor & Francis Group, London, ISBN 90 5809 658 0

Estimation of longitudinal dispersion and storage zone parameters

P.M. Rowiński, T. Dysarz & J.J. Napiórkowski
Institute of Geophysics, Polish Academy of Sciences, Warsaw, Poland

ABSTRACT: Numerical computations are presented for the longitudinal transport of passive, conservative solutes in an actual river channel with the inclusion of its geometrical complexities. Only one-dimensional conditions after a substance has become fully mixed across the depth and width of the river are concerned. In such case a model describing the processes of advection, longitudinal dispersion, and also temporary storage is suitable for the description of the spread of admixture. A special emphasis is put on the method of the identification of model parameters which is based on a specially designed optimisation procedure using random control search algorithm. The algorithm is one of the random global optimisation techniques and particularly its realization by means of the CRS2 method. Two different situations are considered, namely a linear version in which one can assume that the mean velocity does not vary along the channel course and when the model parameters are constant and the nonlinear version implying channel nonuniformity (and variability of model parameters along the channel). The results of tracer tests carried out in the selected reach of the Wkra river in Central Poland have been used in the analyses. A model taking into account the changes of model parameters along river channel proved to provide better results when compared to the experimental data but the parameter identification in such case is computationally much more expensive.

1 INTRODUCTION

Various versions of the storage-zone models have become increasingly popular for the calculation of the longitudinal dispersion of a solute in a river with irregular cross-sections (e.g. Czernuszenko & Rowiński 1997; Czernuszenko et al. 1998; Manson 2000; Thackston & Schnelle 1970, etc.). On top of the mixing processes (advection and dispersion) this model is the reflection of the existence in the rivers of stagnant zones of water that are stationary relative to the faster moving waters near the center of the channel. It constitutes a kind of a compromise between data consuming two-dimensional models and the simpler one-dimensional approach. Mathematically similar approach may pertain to the exchange between the streaming water and the subsurface bed sediment, namely to hyporheic exchange causing the retardation of the solute transfer (e.g. Packman & Bencala 2000; Fernald et al. 2001; Jonsson 2003). As is usually the case in physically based models the main difficulty is the estimate of the proper values of the parameters occurring in the model. All those parameters have relatively clear physical interpretation and as such should assume logical values. It should be noted that even in the much simpler case of the application of the Fickian type advection-dispersion equation, the evaluation of the dispersion coefficient constitutes an important problem since usually the information necessary for its estimate is rather scarce. The methods of its evaluation are disputable (Deng et al. 2002; Sukhodolov et al. 1998; Rowiński et al. 2003). It is then not very surprising that a number of methods, often leading to different results, are proposed in respect to the dead-zone types of models. Recently Seo & Cheong (2001) discussed different methods for the estimates of the parameters of the storage zone model and they concluded that the parameters obtained by the methods of moments are in good agreement with the measured parameters, whereas the fit by the maximum likelihood method as well as the existing literature approaches are not. A number of other estimation methods have been elaborated in literature such as physically based empirical method of Pedersen (1977); fitting of the theoretical slope of the Laplace transformed solution for the concentration of the flow zone to the observed slope (Czernuszenko et al. 1998), moments matching procedure (Lees et al. 2000) or even visual determination of the set of parameters yielding the best fit to the concentration data (Bencala & Walters 1983). An obvious element is the relating the computed solute concentrations to some experimentally obtained curves.

Estimation of the parameters has to obviously be proceeded by a proper formulation of the computational procedure. Computational schemes for the

simulation of the mass transport equations in cross-sectionally averaged form have been widely used for many years. A wide variety of schemes have been produced encompassing much of what is generally available in computational fluid dynamics: finite difference, finite volume and finite element methods for spatial discretization and explicit and implicit time stepping. Discussion of such methods in respect to the advection-dispersion equations but with the inclusion of temporarily storage zone is rather scarce in literature (Runkel & Chapra 1993; Strauber 1995). In this paper we are concerned with the 1D solute transport equations, which are combined with the process of the exchange of mass between the mainstream and the existing in the flow areas that cause temporary storage of the solute.

The overall aim of the paper is to establish a robust and efficient scheme for modelling of solute transport in natural watercourses and to demonstrate its prediction capability. To achieve this goal a relevant procedure for identification of model parameters is proposed. The results of computations will be compared with selected experimental results obtained by means of a dye tracer test in a lowland river. This study is just a first stab and the performance of the model is demonstrated against the measured data from one dye tracer field study in Central Poland. The emphasis is rather put on the elaborated mathematical approach.

2 MATHEMATICAL MODEL OF LONGITUDINAL TRANSPORT OF SOLUTES

We will concern only one-dimensional conditions after a substance has become fully mixed across the depth and width of a river. In such case a model describing the processes of advection, longitudinal dispersion, i.e. the spreading relative to the cross-sectional averaged velocity and also temporary storage is suitable for the description of the spread of conservative, passive pollutants. The transient storage process describes water moving from the flowing stream channel into stagnant areas in which waters are well-mixed but not transported downstream. The detailed description of the transient storage model may be, for example, found in (Czernuszenko and Rowiński 1997; Czernuszenko et al. 1998) and here we will just present the relevant partial differential equations.

Transport of the solutes in the main stream may be described by:

$$\frac{\partial C}{\partial t} + u\frac{\partial C}{\partial x} - \frac{1}{A}\frac{\partial}{\partial x}\left(DA\frac{\partial C}{\partial x}\right) = \frac{\varepsilon}{T}\left(C_D - C\right) \tag{1}$$

where x – longitudinal direction, t-time, $C(x,t)$ – solute concentration, $u(x)$ – cross-sectionally averaged velocity of water, $D(x)$ – dispersion coefficient, A – cross-sectional area of the channel. It has been assumed that the hydraulic conditions in the channel are steady, i.e. parameters u, A, D do not change in time. $C_D(x, t)$ denotes the concentration of solute in the storage zone, parameters $\varepsilon(x)$ and $T(x)$ denote the ratio of the volume of the storage zones to volume of the main stream for unit length and the penetration time of tracer into the storage zones, respectively. In many practical situations we may additionally assume that these parameters do not change along the channel and then the above equation is reduced to the following form:

$$\frac{\partial C}{\partial t} + U\frac{\partial C}{\partial x} - D\frac{\partial^2 C}{\partial x^2} = \frac{\varepsilon}{T}\left(C_D - C\right) \tag{2}$$

where U, D, ε and T are constant parameters.

The balance of mass in the storage zones is represented by:

$$\frac{\partial C_D}{\partial t} = \frac{1}{T}\left(C - C_D\right) \tag{3}$$

Equations 1 or 2 and 3 describe variations of the solute concentrations in both the main channel and the storage zones. The solution domain is the plane Oxt limited by inequalities $0 \le x \le L$ and $t \ge 0$, where L is the length of the modeled channel reach. The model equations are complemented by the following:

– initial conditions:

$$C(x, t = 0) = C_p(x), \quad C_D(x, t = 0) = C_{Dp}(x), \text{ for } x \in [0, L] \tag{4}$$

– and boundary conditions:

$$C(x = 0, t) = C_0(t), \qquad D\frac{\partial C}{\partial x}\bigg|_{x=L} = 0, \quad t \ge 0 \tag{5}$$

where C_p, C_{Dp} are the initial distributions of solute concentration along the channel reach in both the main stream and the storage zones and C_0 describes the inflow of admixture at the initial cross-section.

The effects of simple shift in time and dissipation in traditional Fickian-type advection – dispersion transport are well known. The source term that occurs in Equations 1 and 2 causes additional effects of pollutant decrease and accumulation (Figure 1). The intensity of the exchange of mass between storage zones and the main stream depends on the difference in concentrations. At the beginning the storage zones accumulate the pollutants which causes the decrease of the admixture concentration in the main stream. However, the stored mass is given back to the channel when the concentration in the main stream is lower than in the storage zone. This process may even cause the shift in time of the peak of concentration temporal distribution (Figure 1).

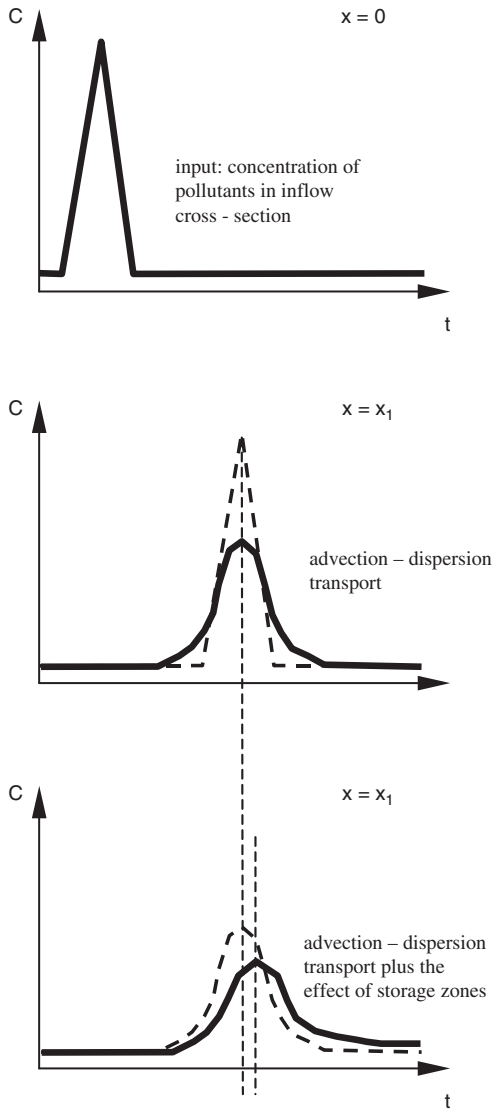


Figure 1. Schematic representation of advection, dispersion and storage zones processes.

3 NUMERICAL SOLUTION

Equations 2 & 3 may be solved analytically only by means of statistical moments (Czernuszenko & Rowiński 1997) and therefore numerical methods are highly demanded. A finite difference method has been applied for the described case. The scheme is set up with a rectangular horizontal mesh. Equally spaced points along both the t- and x-axes are chosen with grid spacing Δt and Δx correspondingly, which makes the channel divided into N computational cross-sections and M temporal levels. A convention is used for which the cross-section denoted by 1 corresponds to $x = 0$, and by N to $x = L$. The Cranck-Nicholson differencing scheme has been used for the representation of Equation 2–3 which reads:

$$-\left(\frac{U\Delta t}{2\Delta x}+\frac{D\Delta t}{2\Delta x^2}\right)C_{j-1}^{i+1}+\left(1+\frac{U\Delta t}{2\Delta x}+\frac{D\Delta t}{\Delta x^2}+\frac{\varepsilon\Delta t}{2T+\Delta t}\right)C_j^{i+1}-\frac{D\Delta t}{2\Delta x^2}C_{j+1}^{i+1}=$$
$$=\left(\frac{U\Delta t}{2\Delta x}+\frac{D\Delta t}{2\Delta x^2}\right)C_{j-1}^{i}+\left(1-\frac{U\Delta t}{2\Delta x}-\frac{D\Delta t}{\Delta x^2}-\frac{\varepsilon\Delta t}{2T+\Delta t}\right)C_j^{i}+\frac{D\Delta t}{2\Delta x^2}C_{j+1}^{i}$$
$$+\frac{2\varepsilon\Delta t}{2T+\Delta t}C_{Dj}^{i} \qquad (6)$$

for cross-sections $j = 2, 3, \ldots, N-1$ and

$$C_{Dj}^{\,i+1}=\frac{\Delta t}{2T+\Delta t}\left(C_j^{i+1}+C_j^{i}\right)+\frac{2T-\Delta t}{2T+\Delta t}C_{Dj}^{\,i} \qquad (7)$$

for $j = 1, 2, \ldots, N$. Approximation of boundary conditions at each temporal level leads to:

$$\text{for } j=1, \quad C_1^{\,i+1}=C_0(t_{i+1}) \qquad (8)$$

for $j = N$

$$-\left(\frac{U\Delta t}{2\Delta x}+\frac{D\Delta t}{\Delta x^2}\right)C_{N-1}^{i+1}+\left(1+\frac{U\Delta t}{2\Delta x}+\frac{D\Delta t}{\Delta x^2}+\frac{\varepsilon\Delta t}{2T+\Delta t}\right)C_N^{i+1}=$$
$$=\left(\frac{U\Delta t}{2\Delta x}+\frac{D\Delta t}{\Delta x^2}\right)C_{N-1}^{i}+\left(1-\frac{U\Delta t}{2\Delta x}-\frac{D\Delta t}{\Delta x^2}-\frac{\varepsilon\Delta t}{2T+\Delta t}\right)C_N^{i}+\frac{2\varepsilon\Delta t}{2T+\Delta t}C_{DN}^{\,i} \qquad (9)$$

Equation 9 has been obtained from 6 with the assumption that

$$C_{N-1}=C_{N+1} \qquad (10)$$

In the case of the model in the form represented by Equations 1 and 3 the situation is much more complex and the application of the Cranck-Nicholson differencing scheme has not led to satisfying results due to the generation of large errors in the process of computations. It has been assumed that the influence of three processes (advection, pure dispersion and transient storage) might best be computed separately as three stages in a three-stage difference scheme. Abbott and Minns (1998) suggest to think about such multi-staging as some processes are being "frozen" or "locked" while the other is implemented. The procedure as described in details below may be schematically presented as in Figure 2.

In the first stage a pure advection process has been considered:

$$\frac{\partial C}{\partial t}+u\frac{\partial C}{\partial x}=0 \qquad (11)$$

In the second stage the results obtained from (11) are corrected by considering the dispersion process:

$$\frac{\partial C}{\partial t}=\frac{1}{A}\frac{\partial}{\partial x}\left(DA\frac{\partial C}{\partial x}\right) \qquad (12)$$

Last stage concerns the existence of the storage zones by means of the following equations:

$$\frac{\partial C}{\partial t} = \frac{\varepsilon}{T}\left(C_D - C\right) \tag{13}$$

$$\frac{\partial C_D}{\partial t} = \frac{1}{T}\left(C - C_D\right) \tag{14}$$

An upwind scheme has been used for approximation of Equation 11

$$\text{for } j = 1 \quad C_1^{i+1} = C_0(t_{i+1}) \tag{15}$$

for $j = 2, 3, \ldots, N$

$$-\theta\frac{u_j \Delta t}{\Delta x} C_{j-1}^{i+1} + \left(1 + \theta\frac{u_j \Delta t}{\Delta x}\right) C_j^{i+1} =$$

$$= \left(1-\theta\right)\frac{u_j \Delta t}{\Delta x} C_{j-1}^{i} + \left[1 - \left(1-\theta\right)\frac{u_j \Delta t}{\Delta x}\right] C_j^{i} \tag{16}$$

The Cranck–Nicholson differencing scheme could be applied for the dispersion equation which resulted in the following:

for $j = 1$

$$C_1^{i+1} = C_1^{i} \tag{17}$$

for $j = 2, 3, \ldots, N-1$

$$-\frac{\Delta t}{4\Delta x^2 A_j}\left(A_{j-1}D_{j-1} + A_j D_j\right) C_{j-1}^{i+1} - \frac{\Delta t}{4\Delta x^2 A_j}\left(A_j D_j + A_{j+1}D_{j+1}\right) C_{j+1}^{i+1}$$
$$+\left[1 + \frac{\Delta t}{4\Delta x^2 A_j}\left(A_{j-1}D_{j-1} + 2A_j D_j + A_{j+1}D_{j+1}\right)\right] C_j^{i+1} +$$
$$= \frac{\Delta t}{4\Delta x^2 A_j}\left(A_j D_j + A_{j+1}D_{j+1}\right) C_{j-1}^{i} + \frac{\Delta t}{4\Delta x^2 A_j}\left(A_j D_j + A_{j+1}D_{j+1}\right) C_{j+1}^{i}$$
$$+\left[1 - \frac{\Delta t}{4\Delta x^2 A_j}\left(A_{j-1}D_{j-1} + 2A_j D_j + A_{j+1}D_{j+1}\right)\right] C_j^{i} \tag{18}$$

and for $j = N$

$$-\frac{\Delta t}{4\Delta x^2 A_j}\left(A_{j-1}D_{j-1} + 2A_j D_j + A_{j+1}D_{j+1}\right) C_{j-1}^{i+1} +$$
$$+\left[1 + \frac{\Delta t}{4\Delta x^2 A_j}\left(A_{j-1}D_{j-1} + 2A_j D_j + A_{j+1}D_{j+1}\right)\right] C_j^{i+1} =$$
$$= \frac{\Delta t}{4\Delta x^2 A_j}\left(A_{j-1}D_{j-1} + 2A_j D_j + A_{j+1}D_{j+1}\right) C_{j-1}^{i} +$$
$$+\left[1 - \frac{\Delta t}{4\Delta x^2 A_j}\left(A_{j-1}D_{j-1} + 2A_j D_j + A_{j+1}D_{j+1}\right)\right] C_j^{i} \tag{19}$$

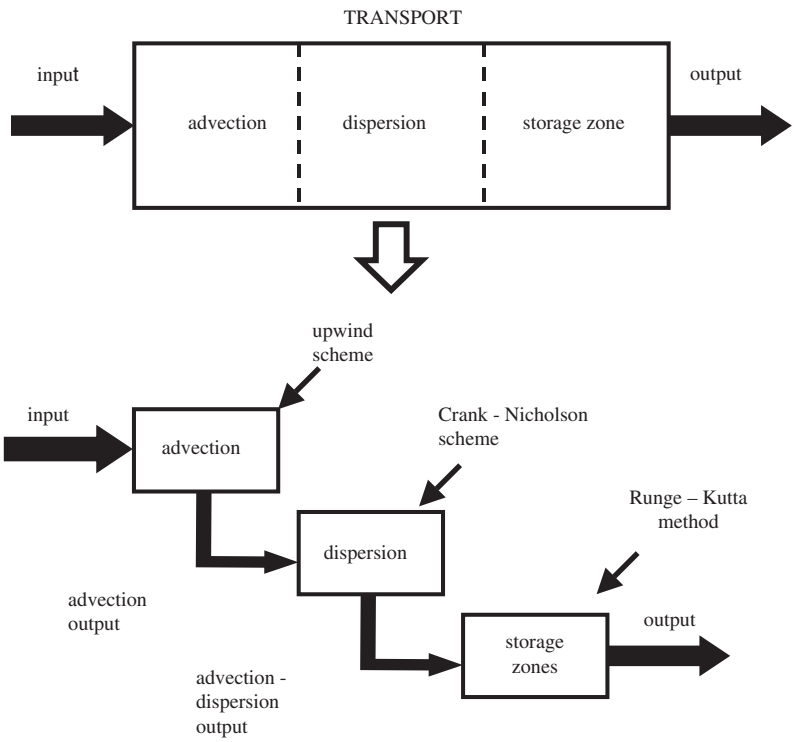


Figure 2. Schematic representation of the applied splitting technique.

It is important to note that in the second stage the input for computations is taken from the first process and not from the actual preceding time level. Equations of the last stage are solved by means of the fourth-order Runge–Kutta method. Let's denote:

$$y_1 = C, \quad y_2 = C_D \tag{20}$$

$$f_1(t,\mathbf{y}) = \frac{\varepsilon}{T}(y_2 - y_1), \; f_2(t,\mathbf{y}) = \frac{1}{T}(y_1 - y_2) \tag{21}$$

which allows us to present the problem 13–14 as ordinary differential equation that reads

$$\frac{d\mathbf{y}}{dt} = \mathbf{f}(t,\mathbf{y}) \tag{22}$$

A single step of this method may be represented as:

$$\mathbf{k}_1 = \Delta t\mathbf{f}\left(t_i,\mathbf{y}^i\right), \; \mathbf{k}_2 = \Delta t\mathbf{f}\left(t_i + \frac{\Delta t}{2}, \mathbf{y}^i + \frac{\mathbf{k}_1}{2}\right) \tag{23}$$

$$\mathbf{k}_3 = \Delta t\mathbf{f}\left(t_i + \frac{\Delta t}{2}, \mathbf{y}^i + \frac{\mathbf{k}_2}{2}\right), \; \mathbf{k}_4 = \Delta t\mathbf{f}\left(t_{i+1}, \mathbf{y}^i + \mathbf{k}_3\right) \tag{24}$$

$$\mathbf{y}^{i+1} = \mathbf{y}^i + \frac{1}{6}\left(\mathbf{k}_1 + 2\mathbf{k}_2 + 2\mathbf{k}_3 + \mathbf{k}_4\right) \tag{25}$$

It is proposed that the described method of taking individual consistencies over to component differential forms and adding these differential component forms to obtain a resultant differential form which brings correct results.

4 FIELD STUDY – DYE TRACER TEST IN THE WKRA RIVER

The presented model has been verified based on the tracer test performed in the lowland river reach in Central Poland, namely the Wkra River. The flow rate as well as other hydraulic and topographic characteristics in respect to all the measuring cross-sections are shown in Tables 1a, 1b, 1c. The measurements were repeated three times in the same river reach. A variety of different irregularities along the river banks were observed. The creation of wakes behind the sand waves as well as the areas on the insides of bends with small radius of curvature most likely causing that the flow "overshoots" the bend could be expected and therefore one may assume the existence of different storage zones in the considered river reach.

The method of instantaneous injection of the tracer was applied and it did not require the complex dosing facilities and allowed to obtain high initial concentrations of the tracer. The dye release consisted of 10 liters of alcoholic solution of a fluorescent red dye (Rhodamine). This dye was released at three points at the cross-section just downstream of the stage of fall which speeded up the cross-sectional mixing of the admixture. Concentrations were measured at five cross-sections as indicated in Table 1. First cross-section was established at a distance at which 1D conditions were supposed to be achieved. During the early stages of a test the dye was visible to the naked eye, which facilitated sample collections. The dye was detected by using the field fluorometer Turner Design with continuous flow cuvette system on the one hand and also water samples were collected at sampling points. Measuring data were stored on graphical

Table 1a. Hydraulic and topographic characteristics – Wkra River (case 1).

Characteristic	Cross-section				
Mean flow [m^3/s]	4.18				
Mean water surface slope [‰]	0.318				
	P-1	P-2	P-3	P-4	P-5
Distance from release point [m]	600	1460	2450	3480	4780
Cross-section area [m^2]	8.07	9.72	9.19	10.15	10.35
Width at the surface level [m]	9.82	10.23	9.69	8.89	11.18
Mean velocity [m/s]	0.518	0.430	0.455	0.412	0.404
Mean depth [m]	0.82	0.95	0.95	1.14	0.93
Wetted perimeter [m]	0.77	0.89	0.81	1.01	0.88
Manning roughness [$m^{-1/3}s$]	0.03	0.0413	0.0370	0.0472	0.0419

Table 1b. Hydraulic and topographic characteristics – Wkra River (case 2).

Characteristic			Cross-section		
Mean flow [m^3/s]			3.97		
Mean water surface slope [‰]			0.318		
	P-1	P-2	P-3	P-4	P-5
Distance from release point [m]	600	1460	2450	3480	4780
Cross-section area [m^2]	7.82	9.36	8.81	9.80	10.02
Width at the surface level [m]	9.73	10.1	9.57	8.77	11.07
Mean velocity [m/s]	0.508	0.424	0.451	0.405	0.396
Mean depth [m]	0.80	0.93	0.92	1.12	0.91
Wetted perimeter [m]	0.75	0.87	0.79	0.99	0.86

Table 1c. Hydraulic and topographic characteristics – Wkra River (case 3).

Characteristic			Cross-section		
Mean flow [m^3/s]			4.32		
Mean water surface slope [‰]			0.323		
	P-1	P-2	P-3	P-4	P-5
Distance from release point [m]	600	1460	2450	3480	4780
Cross-section area [m^2]	8.41	9.87	9.22	10.24	10.49
Width at the surface level [m]	9.93	10.29	9.69	8.92	11.22
Mean velocity [m/s]	0.514	0.438	0.469	0.422	0.412
Mean depth [m]	0.85	0.96	0.95	1.15	0.93
Wetted perimeter [m]	0.79	0.90	0.82	1.01	0.89

registers in the form of concentration distributions and then digitized to obtain relevant concentration time series. Concentration temporal distributions as obtained in the measurements are seen in Figures 3 and 4.

5 IDENTIFICATION OF PARAMETERS – PROBLEM FORMULATION

Model calibration problem is formulated as optimization problem

minimize $F(\mathbf{x})$ with respect to $\mathbf{x} \in D \subset R^n$

where F: $R^n \rightarrow R$ is scalar objective function and D is admissible domain with potential solutions $\mathbf{x}$. Many different methods were used to solve such kind of problems, but no one of them may be recommended if we do not know the features of the objective and constraints in the given problem. The most important features are the convexity of function $F(\mathbf{x})$ as well as the convexity of domain D. The form of constraints guarantees that the set of admissible solutions is compact and convex. However, the described problem is a practical and a very complex task. So, we have expected that the calibration criterion may not be convex. This preliminary assumption was confirmed by further numerical tests.

In such case the global optimization techniques should be preferred. These methods have been developed and investigated for several decades and they have been treated as alternative algorithms for problems with many local optimal points. Originally they have constituted the combination of random global search, i.e. Monte Carlo method, and local accurate procedure. Another kind of methods has become very popular during last 30 years. They are based on natural selection and evolution of wild species such as genetic algorithms, evolutionary strategies or evolutionary programming. One of the first descriptions of genetic algorithms was given by Holland (1975). At the same

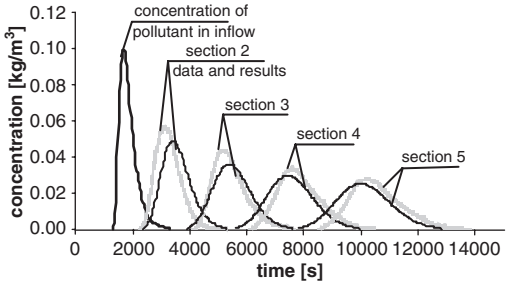


Figure 3. Measured solute concentrations and that obtained by means of linear model.

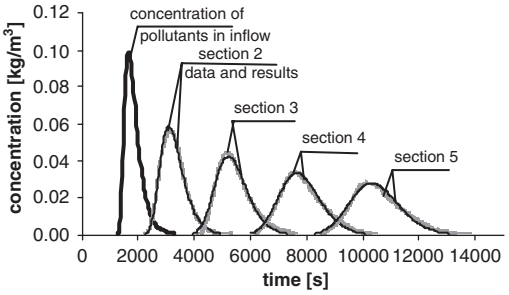


Figure 4. Measured solute concentrations and that obtained by means of nonlinear model.

time non-evolutionary methods of global optimization were developed, and among them the methods based on natural and artificial physical and chemical processes. Simulated annealing (Kirkpatrick et al. 1983; Dekkers & Aarts 1991) and particle trajectory method (Griewank 1981) are well known examples in this area. Current knowledge of optimization and classic methods for convex function was the basis for developing new global techniques, i.e. Price (1983), Ali & Storey (1994).

In the present study the results obtained by means of the dye tracer test in the Wkra River have been used and the time-concentrations distributions $C_m(x_k, t)$ $(k = 1, 2, \ldots,)$ at a few selected cross-sections in the main stream have been used for comparisons. As for the boundary condition at the inflowing cross-section the measurement results from the first cross-section $C_m(x_1, t)$ have been taken. The measurements at the remaining cross-sections have been used for the determination of parameters with the objective function taken as:

$$\min_{u,D,\varepsilon,T}\left\{F[u,D,\varepsilon,T]=\sum_{k=2}^{K}\int_{0}^{T_H}\left[C_m(x_k,t)-C(x_k,t)\right]^2 dt\right\} \quad (26)$$

where F is the criterion function, T_H – the optimization time horizon, K – number of measuring cross-sections.

The wetted cross-section has been determined from the mass balance under steady stated conditions given by:

$$Q = u(x)A(x) \quad (27)$$

where Q is the given discharge.

Special constraints have been put on the sought parameters or functions:

$$X_{\min} \le X(x) \le X_{\max} \quad (28)$$

where $X_{\min}$, $X_{\max}$ are the lower and upper bounds for $X(x)$.

The computations of the values of the objective function for the estimated (by the described method) parameters u, D, ε, T have been realized through the simulations of the transport of solutes and the comparisons of the concentration distributions $C(x_k, t)$.

In case of the identification of parameters of the model 1–3 a linear approximation of the sought parameters has been assumed to lower the dimensionality of the problem. The longitudinal variations of $u(x)$, $D(x)$, $\varepsilon(x)$, $T(x)$ have been determined based on their values at the same cross-sections where the solute concentrations had been measured.

6 CONTROL RANDOM SEARCH METHOD

The optimisation problem 26 was solved by means of the global random search procedure (Price 1987) namely the following version of Controlled Random Search (CRS2) described in details by Dysarz & Napiórkowski (2002). The algorithm is one of the random global optimisation techniques. Its basis is well known simplex method used in non-linear optimisation. The set of points from n-dimensional space is processed in following iterations. In each step, new solution is generated by reflection of a simplex vertex. One of a few well known versions of the method was used, namely CRS2.

The algorithm starts from the creation of the set of points, many more than $n + 1$ points in n-dimensional space, selected randomly from the domain. The optimal quantity of set was taken as suggested by Price (1987), equal to $10(n + 1)$. Let us denote the set as S. After evaluating the objective function for each of the points, the best x_L (i.e. that of the minimal value of the performance index) and the worst x_H (i.e., that of the maximal value of the performance index) points are determined and a simplex in n-space is formed with the best point x_L and n points $(x_2, x_3, \ldots, x_{n+1})$ randomly chosen from S. Afterwards, the centroid x_G of points $x_L, x_2, \ldots, x_n$ is determined. The next trial point x_Q is calculated as the reflection of x_{n+1}, that is $x_Q = 2x_G - x_{n+1}$ (Niewiadomska-Szynkiewicz et al. 1996). Then, if the last derived point x_Q is admissible

and "better" it replaces the worst point x_H in the set S. Otherwise, a new simplex is formed randomly and so on.

If the stop criterion is not satisfied, the next iteration is performed. This part of the algorithm was formed in different way then in the Price original concept. The experiments showed that following condition may be taken as the stop criterion

$$F_{ave} - F(x_L) < \varepsilon \tag{29}$$

where F_{ave} is the mean objective function value in the set, $F(x_L)$ the objective function value at the best point x_L and ε is the expected accuracy determined empirically (Dysarz & Napiórkowski 2002).

Table 2. Constraints for the sought parameters.

	Steady flow			
	Uniform – Equations 2 and 3		Nonuniform – Equations 1 and 3	
Parameter	Min	Max	Min	Max
u [m^3/s]	0.3	0.7	0.4	0.8
D [m^2/s]	0.5	10.0	3.8	9.0
ε [–]	0.0	0.2	0.0	0.2
T [s]	0.001	200.0	0.001	200.0

7 NUMERICAL COMPUTATIONS VISA EXPERIMENTAL RESULTS

The results of a tracer test carried out in the selected reach of the Wkra River have been used in the analyses. Three different experimental tests (the discharge

Table 3. Mean values of criterion function and standard error.

Test	1		2		3	
Flow	Linear model	Non-linear	Linear model	Non-linear	Linear model	Non-linear
Mean value	0.1258	0.0049	0.1724	0.0104	0.1216	0.0052
St. error. %	1.529	4.483	1.671	2.677	2.639	2.830

Table 4. Mean values of the determined parameters and the standard errors – uniform flow conditions.

	u [m/s]					
Parameter	Test 1	Test 2	Test 3	D	ε [–]	T [s]
Mean value	0.5592	0.5546	0.5480	4.76127	0.1186	147.99
Standard deviation %	4.313	3.835	3.105	37.086	31.239	23.480

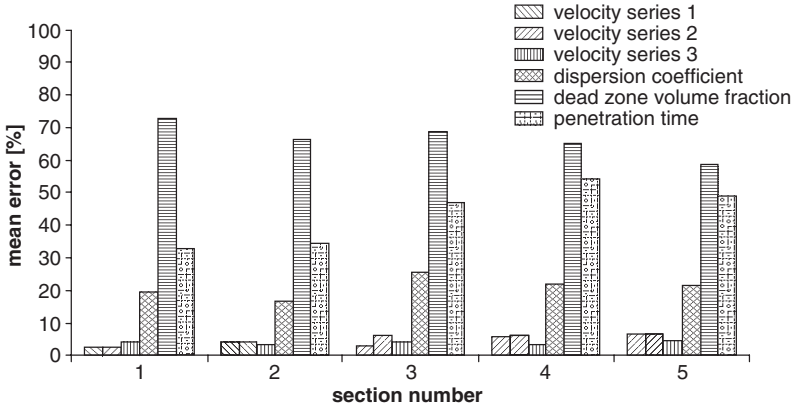


Figure 5. Standard deviations for each determined parameter for nonlinear model.

Q was 4.18, 3.97 and 4.32 m^3/s) performed over a 6 kilometers river reach with 5 measuring cross sections are taken into account. As an initial condition for computations a lack of dissolved solutes in the channel was assumed:

$$C_p(x) = C_{Dp}(x) = 0, \quad \text{dla } x \in [0, L] \tag{30}$$

The time horizon for simulations was taken as 4 h. Time step is taken as $\Delta t = 20$ s and the spatial one $\Delta x = 20$ m.

Admissible range for model parameters is given in Table 2. Since the differences in the values of the sought parameters are large, a normalization was necessary and it was performed by projecting of the admissible set on the unit cube in R^n by means of expression:

$$\alpha = \frac{X - X_{\min}}{X_{\max} - X_{\min}}, \; 0 \le \alpha \le 1 \tag{31}$$

Examples of simulations of the transport of solutes are shown in Figures 3 and 4. These figures show the measured and computed concentration distributions at five cross-sections.

Performance of both linear and nonlinear models is presented. Table 2 provides the mean values of the objective function as well as the values of standard deviation obtained by means of the expression:

$$\sigma_{\%} = \frac{1}{\overline{X}} \sqrt{\frac{\sum_{i=1}^{N} \left(X_i - \overline{X} \right)^2}{N-1}} 100\% \tag{32}$$

where X_i is the single sample from a series of N samples having the mean value $\overline{X}$. It is readily seen that the agreement with the measuring data is much better in case when the variability of model parameters along river channel is taken into account, i.e. in case of Equations 1 and 3. Mean values of the criterion function varied in the range from 0.005 to 0.01 in this case while those values were ten times larger in case of Equations 2 and 3. The values of standard deviation in both cases did not exceed 5% of mean value. However, the increase in the accuracy of results has been obtained at much larger computational cost of parameters' identification. Mean value of the number of runs was 131.4 in case of linear model and it was as large as 4377.6 for the nonlinear model. Table 3 and Figure 5 provide mean values and the standard deviations for each determined parameter for both presented models. The values of the storage zone parameters reflects the relatively simple geometry of the considered channel of Wkra river. Discussion of the performance of these parameters may be, for example, found in (Czernuszenko et al. 1998).

8 CONCLUSIONS

In the study a special procedure was designed for the identification of the parameters of the model of longitudinal transport of pollutants in rivers with the inclusion of the phenomenon of transient storage. A model taking into account the changes of model parameters along river channel proved to provide better results when compared to the experimental data but the parameter identification in such case is computationally much more expensive.

ACKNOWLEDGEMENT

This work was partially supported by The Sendzimir Foundation, USA and by Polish Committee for Scientific Research under grant 6 P04 D 02020.

REFERENCES

Abbott, M.B. & Minns, A.W. 1998. Computational Hydraulics, Ashgate, Aldershot.

Ali, M.M. & Storey, C. 1994. Modified controlled random search algorithms. *Intern. J. Computer Math*., 53: 229–235.

Bencala, K.E. & Walters, R.A. 1983. Simulation of solute transport in a mountain pool-and-riffle stream: a transient storage model. *Water Resources Research*, 19(3): 718–724.

Czernuszenko, W. & Rowiński, P.M. 1997. Properties of the dead-zone model of longitudinal dispersion in rivers, *Journal of Hydraulic Research*, 35(4): 491–504.

Czernuszenko, W., Rowiński, P.M. & Sukhodolov, A.N. 1998. Experimental and numerical validation of the dead-zone model. *Journal of Hydraulic Research,* 36(2): 269–280.

Dekkers, A. & Arts, E. 1991. Global Optimization and Simulation Annealing. *Mathematical Programming*, 50: 367–393.

Deng, Z.Q., Begtsson, F., Singh, V.P. & Adrian, D.D. 2002. Longitudinal dispersion coefficient in single-channel streams. *Journal of Hydraulic Engineering*, ASCE, 128(10): 901–916.

Dysarz, T. & Napiórkowski, J.J. 2002. Determination of reservoir decision rules during flood, *Acta Geophysica Polonica*, 50(1): 135–149.

Fernald, A.G., Wigington, P.J. & Landers, D.H. 2001. Transient storage and hyporheic flow along the Willamette River, Oregon: Field measurements and model estimates. *Water Resources Research*, 37(6): 1681–1694.

Griewank, A.O. 1981. Generalized Descent for Global Optimization. *J. Optimiz. Theory Appl*., 34(1): 11–39.

Holland, J.H. 1975. *Adaptation in Natural and Artificial Systems*. University of Michigan Press, Ann Arbor.

Jonsson, K. 2003. Effects of hyporheic exchange on conservative and reactive solute transport in streams. Model assessments based on tracer tests. *Acta Universitatis Upsaliensis. Comprehensive Summaries of Uppsala Dissertations from the Faculty of Science and Technology 866*, Uppsala.

Kirkpatrick, S., Geatt, C.D. & Vecchi, M.P. 1983. Optimization by Simulated Annealing. *Science*, 220: 671–680.

Lees, M.J., Camacho, L.A. & Chapra, S. 2000. On the relationship of transient storage and aggregated dead zone models of longitudinal solute transport in streams. *Water Resources Research*, 36(1): 213–224.

Manson, J.R. 2000. Predicting stream transient storage zone characteristics from tracer data. *Water Resources Research*, 36(2): 629–631.

Niewiadomska-Szynkiewicz, E., Malinowski, K. & Karbowski, A. 1996. Predictive Methods for Real-Time Control of flood operation of a Multireservoir System: Methodology and Comparative Study, *Water Resources Research*, 32(9): 2885–2895.

Packman, A.I. & Bencala, K.E. 2000. Modeling surface-subsurface hydrological interactions. In J.B. Jones, R.J. Mulholland (Eds.), *Streams and Ground waters*, Academic Press, 45–80.

Pedersen, F.B. 1977. Prediction of longitudinal dispersion in natural streams. *Series Paper 14, Institute of Hydrodynamics and Hydraulic Engineering*, Technical University of Denmark, Lyngby, Denmark.

Price, W.L. 1983. Global optimization by controlled random search. *J. Optimiz. Theory Appl*., 40(3): 333–348.

Price, W.L. 1987. Global optimization algorithms for CAD Workstation, *J. Optimiz. Theory Appl*., 55(1), 133–146.

Rowiński, P.M., Piotrowski, A. & Napiórkowski, J.J. 2003. Are artificial neural networks techniques relevant for the estimates of longitudinal dispersion coefficient in rivers?, submitted for publication.

Runkel, R.L. & Chapra, S.C. 1993. An efficient numerical solution of the transient storage equations for solute transport in small streams, *Water Resources Research*, 29(1): 211–215.

Seo, I.W. & Cheong, T.S. 2001. Moment-based calculation of parameters for the storage zone model for river dispersion, *Journal of Hydraulic Engineering*, ASCE, 127(6): 453–465.

Sukhodolov, A.N., Nikora, V.I., Rowiński, P.M. & Czernuszenko W. 1997. A case study of longitudinal dispersion in small lowland rivers, *Water Environment Research*, 69(7): 1246–1253.

Strauber, G. 1995. Modified box schemes for pollutant transport in rivers with dead zones, *International Journal for Numerical Methods in Fluids*, 21(12): 1123–1135.

Thackstone, E.L. & Schnelle, K.B. 1970. Predicting effects of dead zones on stream mixing. *Journal of Sanitary Engineering Division*, ASCE, 96(2), 319–331.

River Flow 2004 – Greco, Carravetta & Della Morte (eds.)
© 2004 Taylor & Francis Group, London, ISBN 90 5809 658 0

Impact of riverine and CSO inputs on coastal water quality under different environmental conditions

S.M. Kashefipour
Irrigation Department, Shahid Chamran University, Ahwaz, Iran

B. Lin & R.A. Falconer
Civil Engineering Department, Cardiff University, Cardiff, UK

ABSTRACT: Details are given of a hydro-environmental modelling study aimed at investigating the impact of riverine and CSO inputs and several environmental parameters on the bacterial concentration on an EU bathing water (BW) compliance point, located on the Fylde Coast, UK. The several environmental conditions studied including: wind, river discharge, storm flow, and CSO release time in relation to tidal phases, were studied in this project. A series of scenario runs were undertaken to predict BW bacterial concentrations for three continuous riverine inputs, located at the upstream boundaries of the model, and three intermittent CSO inputs, located along the rivers. For each scenario one environmental factor was considered and the inputs were designed to operate separately. To investigate the absolute effect of each factor on the dispersion and distribution of the pollution a zero decay rate was assumed. It was found that increasing river discharges would cause an increase in the bacterial concentration at the BW point. It was also found that the release time of a CSO input would affect considerably bacterial concentration at the considered BW point. Wind direction and storm flows were also found to be important environmental factors that significantly affect pollution distribution in the receiving waters.

1 INTRODUCTION

It is known that many water quality parameters such as the salinity, pH and turbidity levels, solar radiation strength and sediment concentration may affect the bacterial population in coastal waters (Thomann and Muller, 1987; Chapra, 1997). Some other environmental parameters such as tidal conditions, river discharge, wind speed and direction, and flow velocity may also affect the distribution of bacterial concentration (Kashefipour *et al*, 2000). Moreover, the releasing time of bacterial input in relation to the tidal phases and other environmental conditions (e.g. sunlight intensity) can also be a relatively important factor to the bacterial displacements.

This paper presents a hydro-environmental modelling study of the Fylde Coast and Ribble Estuary, aimed at quantifying the impact of various bacterial sources along the river network on the receiving coastal waters under different environmental conditions. The effectiveness of such environmental conditions on the bacterial concentration distribution was illustrated by evaluating the faecal coliform concentration at an EU designated bathing water point.

2 HYDRO-ENVIRONMENTAL MODEL

Kashefipour *et al* (2002) developed an integrated hydro-environmental mathematical model, in which a one-dimensional (1D) model was dynamically linked with a two-dimensional (2D) model enabled the users to apply this single model for modelling the river networks and coastal waters simultaneously. The 1D and 2D shallow water equations were numerically solved and integrated to form the hydrodynamic module of the integrated model. The 1D and 2D advective diffusion equations were solved and integrated to form the water quality module. This model was able to accurately predict the impact of the river inputs on the bathing water quality along the Fylde coast. More information regarding the calibration and validation of this single model for the Ribble Estuary and its tributaries can be found in Lin *et al* (2001) and Kashefipour *et al* (2002). In this study a series of scenario runs were designed to investigate the effect of wind, river discharge, CSO release time in relation to the tidal phases and flood flows on the bacterial concentration at a bathing water location.

3 MATERIALS AND METHODS

Faecal Coliforms (FC) are mostly used as an indicator of the bacterial population. In this study a zero decay rate was assumed for the FC and this was because the main focus of the study was to investigate the effect of the environmental conditions on the FC distribution. The results obtained from this study can also be extended to other bathing water quality indicators.

Ribble Estuary is located along the North West coast of England, UK. Figure 1 shows the Ribble Estuary and its tributaries, including: the Ribble, Darwen and Douglas rivers. Three continuous inputs were located near the upstream boundaries of the rivers, and three CSO inputs, namely the Upper Ribble CSO, Lower Ribble CSO and Douglas Inter (see Figure 1) operate intermittently. The continuous inputs were assumed to operate for the whole simulation time with a discharge of 0.05 m^3/s and FC concentration of 1.0e + 08 cfu/100 ml. A discharge of 1.0 m^3/s and a FC concentration of 3.0e + 07 cfu/100 ml were assumed for all of the CSO inputs and they operated only for three hours. The input sources were set to operate separately for each scenario run, to investigate the effect of each input on the FC concentration at the bathing water location. St Annes Pier, located at the north of the Ribble Estuary, was an EU designed bathing water point (see Figure 1) and was used in this study as a target location for testing different scenarios. Wind direction, river discharge and storm flow and the CSO release time were four variables tested in this study. To drive the model water elevations predicted for a neap tide were used as the downstream open boundary. Discharges at the upstream boundaries of the three rivers including: Ribble, Darwen and Douglas, were used as the upstream boundary conditions. Fresh water with zero bacterial concentration was assumed for the flow entering to the domain from the upstream and downstream boundaries of the model.

The scenarios tested were listed in Table 1. In this table SW means a wind from south towards north with an angle of 225 degrees to the north and NW was a wind from the north to the south with an angle of 315 degrees to the north. Rib, Dar and Dug are abbreviations of the Ribble, Darwen and Douglas rivers, respectively. In Table 1 LW, HW, LS and HS are used for low water, high water, low storm and high storm flows respectively. A constant wind speed of 10 m/s was applied. The hydrographs of the low and high storms are shown in Figure 2.

It can be seen from Table 1 that the results obtained from the scenarios S1 and S2 were used to evaluate the effect of wind direction on the bathing water quality, S1 and S3 for the CSO release time, S1 and S4 for river discharge, and S1 with S5 and S6 for evaluation of the effect of storm on the FC concentration at the bathing water point.

Table 1. Specifications of the scenarios.

	Wind		Discharge (m^3/s)			CSO release time	
Scenarios	SW	NW	Rib	Dar	Dug	HW	LW
S1	+		12	2	2	+	
S2		+	12	2	2	+	
S3	+		12	2	2		+
S4	+		50	10	10	+	
S5	+		LS	LS	LS	+	
S6	+		HS	HS	HS	+	

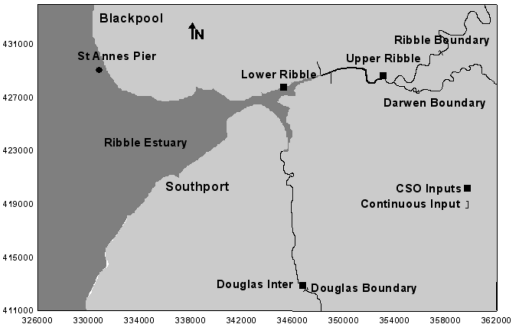


Figure 1. Ribble Estuary and its tributaries.

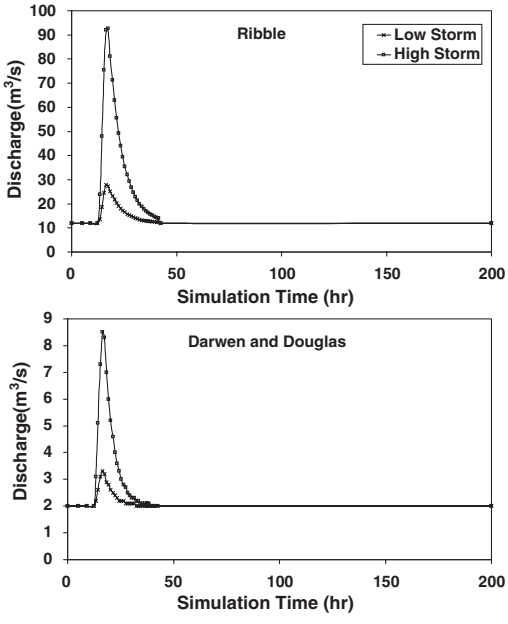


Figure 2. Storm hydrographs for the rivers Ribble, Darwen and Douglas.

It should be noted that the total simulation time for all of the scenario runs was 200 hours, which was about 16 complete tidal cycles.

4 RESULTS AND DISCUSSION

4.1 *The effect of wind direction*

The effect of wind direction on the FC concentrations at St Annes Pier has been shown in Figure 3. As can be seen from this Figure that the south west wind SW225 caused higher FC concentration than that caused by the northwest wind NW315. Since St Annes Pier is located at the northern coastline of the estuary (see Figure 1) these results were expected. The average FC concentrations predicted at the bathing water location due to the continuous and CSO inputs under the above wind directions are summarised in Table 2. This Table shows that for all inputs the FC concentrations for wind direction of SW225 were more than 5 times higher than the corresponding concentrations obtained for NW315 direction.

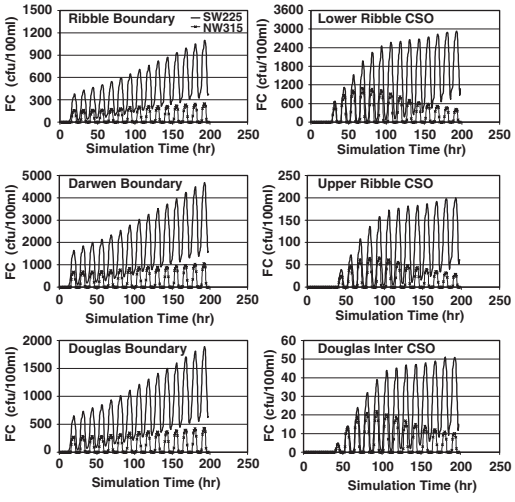


Figure 3. The effect of wind direction on the FC concentration at St Annes Pier.

Table 2. Average FC concentrations at the BW point for different inputs and wind directions.

	FC Concentration (cfu/100 ml)	
Input source	SW225	NW315
Ribble boundary	413	71
Darwen boundary	1804	304
Douglas boundary	701	125
Lower Ribble CSO	1076	254
Upper Ribble CSO	66	15
Douglas inter CSO	16	5

It can also be seen from Figure 3 that for all inputs the minimum FC concentrations at the bathing water point occurred at the high waters and the maximum concentrations at low waters. The sinuous shape of the concentration variations in Figure 3 was due to the tidal conditions.

Since the decay rate was set to zero so for the continuous inputs the maximum FC concentration increases after each tidal cycle. Whereas, for the CSO inputs with only three hours operation it was expected that due to the dispersion process, the FC concentration increases initially, reaches a maximum value and then reduces. This trend occurred for the NW315 wind (see Figure 3). It seems that if the simulation time continues more than 200 hours the same trend may also occur for the SW225 wind. The FC concentrations obtained were generally higher for the inputs closer to the estuary outlet and also for rivers with higher flow velocities (for example Darwen in comparison with Douglas, not shown in this paper).

4.2 *The effect of the CSO release time*

The results obtained for different CSO inputs (see Table 1, scenarios S1 and S3) are compared in Figure 4. In scenario S1 the CSOs discharges were started at the High Water (HW), whereas in scenario S3 the release time was HW plus six hours, or Low Water (LW). As can be seen from this figure different behaviours occurred due to the CSO inputs. For example, for the CSOs located along the Ribble River, including: Upper Ribble and Lower Ribble CSOs (see Figure 1) the FC concentrations at the BW point decreased for scenario S3 in comparison with scenario S1. On the contrary for the Douglas Inter CSO, which is located close to the Douglas boundary, the FC concentrations at the BW point increased when the input was operated at the low water. This phenomenon could be caused by the interaction of river discharge, flow velocity and tide conditions. The travel time for the transport of the pollutants from the Lower Ribble, Upper Ribble and Douglas Inter CSOs to the BW point for scenario S1 were about 14, 27, and 28 hours, respectively. The corresponding values for scenario S3 were 23, 23 and 33 hours respectively. This information shows that for scenario S3 the pollutant reached the BW point for the Lower and Upper Ribble CSOs at the starting of the flood-tide phase and this means that a stronger dispersion effect on the FC plumes.

On the contrary for the Douglas Inter CSO the pollutant reached to the BW point at the middle of ebb-tide phase. It should be noticed that with the neap tide, the tidal limit did not reach to the Ribble and Douglas upstream boundaries and between the tidal limit and river boundaries free flow occurs.

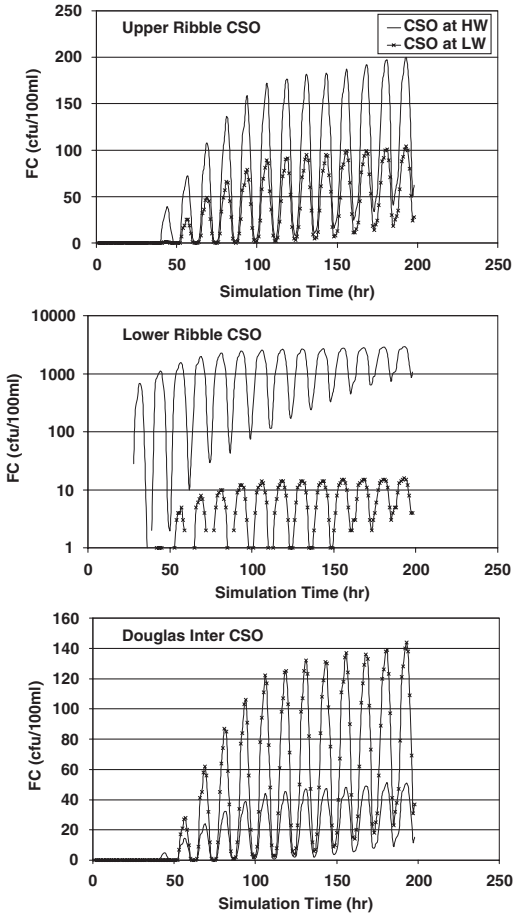


Figure 4. Comparison of the FC concentration for different CSO inputs due to the CSO release time.

These results might be a useful guide to the environmental managers for optimising the release time of the CSOs along the river networks.

4.3 *The effect of river discharge*

Upstream river discharge was another environmental factor considered in this study for investigating the effect of such factor on the FC concentrations at the BW point for different continuous and CSO inputs located along the river networks. In this regard the results obtained for scenarios S1 and S4 were compared and illustrated in Figure 5. As Table 1 shows the upstream river discharges for S4 scenario were about 5 times of the corresponding values for scenario S1. As can be seen from Figure 5 that for all of the continuous and CSO scenario runs the FC concentrations at the BW point will increase significantly when upstream river discharges increase. It seems that the river flow

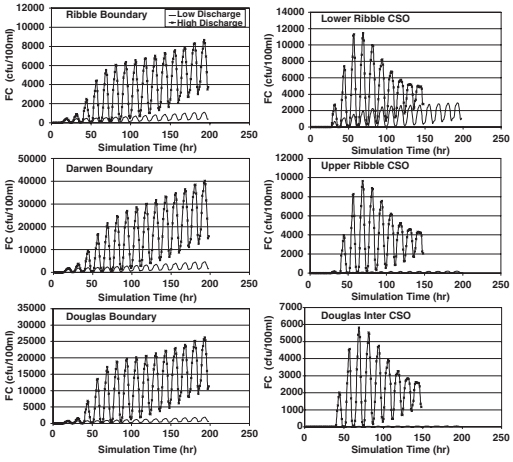


Figure 5. Comparison of the FC concentration for different continuous and CSO inputs due to the river discharge.

velocity, which is generally affected by upstream flow discharge, could be an important factor affecting the pollution distribution. Higher discharge means higher velocity and as a result the dispersion of the pollutants along the river networks would reduce. For this scenario the travel times for the pollutants to reach the bathing water point were 13, 13 and 15 hours for the Lower and Upper Ribble and Douglas Inter CSOs, respectively.

As it has been explained above that the duration of CSO inputs were only three hours and due to dispersion it was expected that the FC concentrations at the BW point take a maximum value and then reduce with time. This phenomenon has happened for the scenario S4 during the simulation time and it could happen for other scenarios if longer duration of the simulation time was conducted.

The average FC concentrations of the different continuous and CSO inputs for the scenarios S1 and S4 were computed and summarised in Table 3. With an increase of about 5 times in the upstream river discharge (from S1 to S4), the FC concentrations at the bathing water point increased by nearly 10 times.

4.4 *The effect of storm*

Two storms, including: low storm with a small hydrograph and high storm with a big hydrograph, as shown in Figure 2, were considered to investigate the behaviour of the distribution of the bacterial population under different storm flows. The results obtained for scenarios S5 and S6 are shown in Figure 6, together with the corresponding results obtained for scenario S1. The FC concentrations at the BW point for all of the inputs were again increased with the increasing of storm flow. No significant difference was found

Table 3. Average FC concentrations at the BW point for different inputs and scenarios-discharge effect.

	FC Concentration (cfu/100 ml)	
Input source	S1	S4
Ribble boundary	413	3133
Darwen boundary	1804	13571
Douglas boundary	701	9430
Lower Ribble CSO	1076	3400
Upper Ribble CSO	66	2663
Douglas inter CSO	16	1585

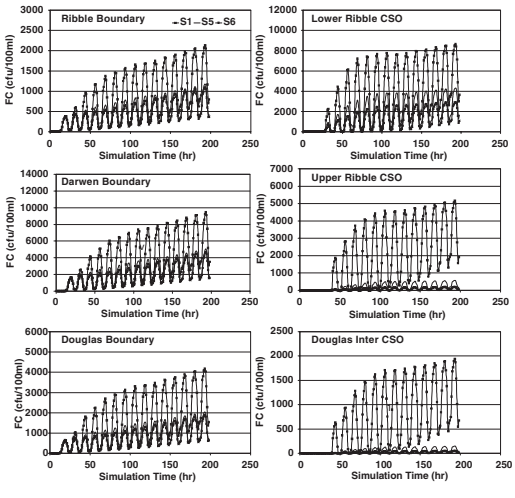


Figure 6. Comparison of the FC concentrations at the BW point for the scenarios S1, S5 and S6.

Table 4. Average FC concentrations at the BW point for different inputs and scenarios-storm effect.

	FC Concentration (cfu/100 ml)		
Input source	S1	S5	S6
Ribble boundary	413	455	815
Darwen boundary	1804	1967	3596
Douglas boundary	701	789	1578
Lower Ribble CSO	1076	1612	3433
Upper Ribble CSO	66	194	1875
Douglas inter CSO	16	48	682

between the low storm (S5) and continuous discharge (S1), and this was due to the small flow and short duration of the storm. The average FC concentrations at St Annes (BW) for all inputs were calculated and summarised in Table 4.

According to Tables 3 and 4 it can be seen that although the peak discharge of the high storm hydrograph was nearly two times of the continuous discharge for scenario S4 the FC concentrations obtained for scenario S6 were less than the corresponding values for S4. This could be due to the short duration of the hydrograph.

5 CONCLUSIONS

In this paper a hydro-environmental model has been used to investigate the effect of several environmental parameters on the bacterial concentration on an EU bathing water compliance point, located on the Fylde Coast, UK. The model was a dynamically integrated 1- and 2-D model, developed by Kashefipour *et al* (2000). Three environmental parameters, including: wind direction, river discharge and storm, and one management factor, namely the CSO release time in relation to the tidal levels, were considered in this study. Three continuous discharges and three intermittent CSO inputs located along the river networks were used as the main sources of pollution. These inputs were assumed to operate separately. The main conclusions drawn from this study may be summarised as follows:

- Wind direction is an important environmental parameter affecting the plume distribution. The bathing water sampling point studied in this project is located at the north of the estuary, thus it is more vulnerable to south-eastern wind.
- The bacterial concentration at the bathing water point decreased considerably when the two Ribble CSO inputs were released at the flood-phase of a tidal cycle including low water. On the contrary, for the same release time the bacterial concentration increased when the Douglas Inter CSO was considered. This phenomenon could be due to the interaction between the flow velocities, pollutant travel time and tidal conditions. This phenomenon could be used utilised by local environmental managers to optimise the release time of the CSOs along the river networks.
- River discharge is another important environmental parameter affecting the bacterial concentrations. Although the concentrations of a continuous input, or a CSO input, was kept the same for all of the scenario runs, the bacterial concentrations at the bathing water point increased significantly with the increase of river discharges.
- The results for the two storm runs showed again that with an increase in the river discharge the bacterial concentrations at the bathing water points also increased.
- Finally it has been concluded that the interaction between river and tidal flows, and interaction between these hydraulic parameters and environmental conditions were the main cause for the fluctuations of bacterial concentration at the bathing water point.

REFERENCES

Chapra, S.C., (1997), "*Surface Water-Quality Modelling*", McGraw-Hill Companies, Inc., USA, 844pp.

Council of the European Communities, (1976), Council Directive of 8th December 1975 Concerning the Quality of Bathing Water. (76/160/EEC) Official Journal of the European Communities NO. L31, 1–7.

Kashefipour, S.M., B. Lin, E. Harris, and R.A. Falconer, (2000), "*Ribble Estuary Water Quality Modelling*", Final Report, Cardiff University, UK, 454pp.

Kashefipour, S.M., B. Lin, E.L. Harris, and R.A. Falconer, "Bathing Water Quality Modelling for Ribble Estuary and Fylde Coast", *Water Research*, IWA, Vol. 36, 2002, pp. 1854–1868.

Lin, B., S.M. Kashefipour, E. Harris, and R.A. Falconer, (2001), Modelling Flow and Water Quality in Estuarine and Riverine Waters: A Dynamically Linked 1-D and 2-D Models Approach, *Proceedings of the XXIX IAHR Congress*, September 17–21, Beijing, China, pp. 469–475.

Thomann, R.V., and J.A. Muller, (1987), "*Principles of Surface Water Quality Modelling Control*", Harper Collins Publishers Inc., New York, 644pp.

River Flow 2004 – Greco, Carravetta & Della Morte (eds.)
© 2004 Taylor & Francis Group, London, ISBN 90 5809 658 0

River model calibration: a genetic algorithm with evolutionary bottlenecking

J. Russell Manson
The Macaulay Institute, Aberdeen, Scotland

Steve G. Wallis
Heriot-Watt University, Edinburgh, Scotland

ABSTRACT: The advection-dispersion equation (ADE) has been used widely to model solute transport in fluvial systems. In this model transport is characterized as having an advective (unidirectional) component represented by the velocity, u, and a dispersion (bi-directional) component represented by the dispersion coefficient, D. A significant body of work has been devoted to enhancing the ADE to include transient storage zones (or dead zones). In these enhanced models two additional parameters (α, A_s) are used to characterize the storage zone. So these enhanced models have four characterizing parameters (u, D, α, A_s). Both the standard and enhanced ADE can be calibrated by fitting the model to experimentally derived solute concentration data. If some objective function is defined, such as the sum of the square residuals between model and observations, then it can be minimized by adjusting the model parameters. There are various algorithms available for doing this. In this research a genetic algorithm (GA) approach was used for this task. This is the first time (to the authors' knowledge) that a GA has been used for this particular application. Clearly, as in any optimization approach, a rapid method of finding the objective function value is required. The objective function was defined in terms of the difference between the "data" and "simulations". The simulations were generated by a numerical method of solution. Since it is well known that numerical solutions to advection-diffusion equations are prone to various deficiencies (e.g. numerical diffusion, grid-scale oscillations), it was important to use a tried and tested numerical method that was known to be free of these problems. Therefore we adopted the semi-Lagrangian method, DISCUS. This method includes an explicit, shape-preserving cubic interpolation update for advection and fully implicit temporal treatments of dispersion and transient storage. Previous work has shown that DISCUS is accurate, robust and computationally efficient over a wide range of Courant and grid Peclet numbers. The semi-Lagrangian approach is also particularly attractive for optimisation problems because it caters well for the use of large time steps. The GA based optimisation of the DISCUS model was applied to a test case of "data" generated with known characterizing parameter values, again using DISCUS. Thus the expectation was that the optimization would correctly identify these known values as the optimum solution. During initial experiments with the GA it was found that it was very good at finding the rough proximity of the global minimum but then it converged very slowly towards the true minimum. To overcome this difficulty, while retaining the GA framework, evolutionary bottlenecking was introduced to the GA. This involved successively and methodologically refining the parameter space and was found to greatly improve convergence.

1 INTRODUCTION

The advection-dispersion equation (ADE) has been used widely to model solute transport in fluvial systems. In this model transport is characterized as having an advective (unidirectional) component represented by the velocity, u, and a dispersion (bi-directional) component represented by the dispersion coefficient, D. Although widely used this model has several deficiencies. One of these is the inability to capture long tails in observed tracer data caused by transient storage zones. Transient storage zones include recirculation areas, streambed irregularities and bed sediment interstices. These zones are thought to be important for nutrient cycling and stream metabolism, [Kim *et al*, 1992; D'Angelo *et al*, 1993; Allan, 1995; DeAngelis *et al*, 1995; Valett *et al*, 1996; Marti *et al*, 1997; Morrice *et al*, 1997] and they have long been recognised as playing an important role in the transport of dissolved or suspended materials in rivers [Thackston

and Schnelle, 1970; Sabol and Nordin, 1978; Valentine and Wood, 1979; Purnama, 1988; Denton, 1990]. The storage zone's size (A_s) and the rate at which solute mass is transferred to and from the zone (α) are thought to be important characterizing parameters. So these enhanced models have four characterizing parameters (u, D, α, A_s).

Both the standard and enhanced ADE can be calibrated by fitting the model to experimentally derived solute concentration data. If some objective function is defined, such as the sum of the square residuals between model and observations, then it can be minimized by adjusting the model parameters. There are various algorithms available for doing this. In this research a genetic algorithm (GA) approach was used for this task. This is the first time (to the authors' knowledge) that a GA has been used for this particular application. Clearly, as in any optimization approach, a rapid method of finding the objective function value is required. Herein the objective function was formulated using a numerical solution to the enhanced ADE model. Indeed, the numerical model was used to create the "data" and the "simulations" on which the parameter optimization was based.

Since it is well known that numerical solutions to advection-diffusion equations are prone to various deficiencies (e.g. numerical diffusion, grid-scale oscillations), it was important to use a tried and tested numerical method that was known to be free of these problems. Therefore we adopted the semi-Lagrangian numerical method DISCUS (Domain of Influence Search for Convective Unconditional Stability). This method has been widely applied to fluvial scenarios, being highly suited to the non-uniformity of flow fields found therein. It is described in several earlier papers that demonstrate the successful application of the method to: pure advection in uniform flow [Manson and Wallis, 1995; Manson and Wallis, 1997]; pure advection in non-uniform flow [Manson and Wallis, 1997]; advection-dispersion in uniform flow [Wallis *et al*, 1998] and advection-dispersion in non-uniform flow [Manson and Wallis, 1999].

This method includes an explicit, shape-preserving cubic interpolation update for advection and fully implicit temporal treatments of dispersion and transient storage. Previous work has shown that DISCUS is accurate, robust and computationally efficient over a wide range of Courant and grid Peclet numbers. The semi-Lagrangian approach is also particularly attractive for optimisation problems because it caters well for the use of large time steps.

During initial experiments with the GA it was found that it was very good at finding the rough proximity of the global minimum but then it converged very slowly towards the true minimum. To overcome this difficulty, while retaining the GA framework, evolutionary bottlenecking was introduced to the GA. This involved successively and methodologically refining the parameter space and was found to improve convergence.

2 MODEL DESCRIPTION

Only the enhanced model will be considered here, in which one-dimensional solute transport in steady, non-uniform flows in rivers with transient storage regions is described by the following mass conservation equations,

$$\frac{\partial m}{\partial t} + \frac{\partial um}{\partial x} = \frac{\partial}{\partial x}\left(DA\frac{\partial c}{\partial x}\right) + \alpha A(s - c) \qquad (1)$$

$$\frac{\partial sA_s}{\partial t} = -\alpha A(s - c) \qquad (2)$$

where m(x,t) is the solute mass per unit length in the main channel (= cA), c(x,t) is the concentration of solute in the main channel, s(x,t) is the concentration of solute in the transient storage zone, Q(x) is the steady main channel river flow, A(x) is the steady main channel cross-sectional area, $A_s(x)$ is the steady transient storage cross-sectional area, D(x) is the longitudinal dispersion coefficient, $\alpha(x)$ is the solute exchange parameter between the main channel and the storage zones, x is the longitudinal spatial co-ordinate and t is time. The following boundary conditions are frequently used with these equations. At the upstream boundary, $c(0,t) = c_i(t)$, which specifies the solute mass entering the computational domain; at the downstream boundary a zero diffusive flux is assumed which implies that solute is advected out of the domain unhindered.

Equations (1) and (2) were solved using a finite volume approach, evaluating the advection term explicitly in time and evaluating the dispersion and transient storage terms (fully) implicitly in time. The DISCUS method was used for equation (1). This employs a conservative semi-Lagrangian algorithm that combines a finite volume discretisation, the method of characteristics and a flux-based interpolation scheme. The method is explained in detail elsewhere [Manson and Wallis, 1995; Wallis and Manson, 1997; Manson and Wallis, 1997; Wallis *et al*, 1998; Manson and Wallis, 1999; Manson and Wallis, 2000; Manson *et al*, 2001]. The backward implicit method used for the dispersion term and the transient storage terms is unconditionally stable and robust. It is deficient in the sense that it assumes that the exchange transport rates at the future time prevail over the entire time step: however, it does not suffer from the grid-scale oscillations of the formally more accurate Crank-Nicolson method. Tests

have indicated that for the range of parameters investigated here the method appears adequate [Manson *et al*, 2001].

When equations (1) and (2) are solved the solution consists of estimates for c and s over some discretised spatial and temporal domain, i.e. (c_i^n, s_i^n) for i = 1 to N and n = 1 to T where N is the number of points in the spatial domain and T is the number of points in the temporal domain. If this model is being fitted to observed data that has been collected at M points in space and time then a fitting parameter may be defined as,

$$R = 1 - \sqrt{\frac{1}{M}\sum_{j=1}^{M}\left(c_j^{obs} - c_j^{model}\right)^2} \qquad (3)$$

so that an R value of 1 indicates a perfect fit. Note that only the in stream concentration has been used for the fitting. Concentrations in the transient storage zone are more difficult to measure and so are rarely documented.

3 PARAMETER ESTIMATION BY GENETIC ALGORITHM

3.1 *Introduction*

As defined in equation (3), R is used as the objective function for the genetic algorithm, which seeks to choose the best combination of parameters in order to maximize R. The genetic algorithm employed is a modified version of secur GA by Carroll [Yang *et al*, 1998] and the reader is referred there for details. Briefly however, a population of individuals is defined. Each individual is characterised by four traits that in the current exercise are simply the fitting parameters (u, D, α, A_s). One can think of this as analogous to say traits in humans such as eye colour, hair colour etc. So, for example, one individual could have large u, large D, low α and low A_s. Another might have low u, high D, low α and high As. Now if such a population is defined and then pairs of individuals from the population are allowed to reproduce, the offspring will have certain traits of both parents. For this next generation Darwinian selection is applied to allow survival of only the fittest individuals in the new population. Fitness is based on the value of R for the individual. After many generations the population is made up of only the fittest individuals.

Now when the algorithm was implemented, rather than using qualitative trait descriptors such as high and low, each trait was allocated a value from a pre-specified range of the corresponding parameter. Clearly by choosing the number of values available from the range, the precision of the final answer is defined, since using a finer resolution (larger number of values) enables a greater number of possible parameter combinations to be explored.

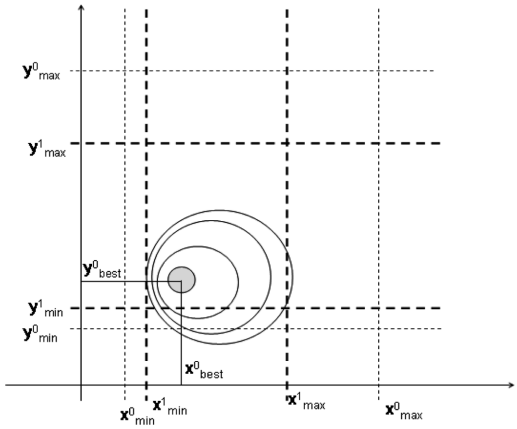


Figure 1. Contours of R over the parameter space (x, y) and important points for the bottlenecking algorithm.

3.2 *Evolutionary bottlenecking*

In evolutionary terminology, "bottlenecking" is defined as a drastic reduction in population size. In the context of the genetic algorithm here we use it to rapidly restrict the parameter search space in a methodological fashion. This has the effect of speeding convergence to the global optimum and is highly effective when convergence is slow, i.e. when the objective function varies very slowly around the optimum point. For ease of explanation let us assume only two parameters (x and y) are involved. If the initial parameter space is defined by the limits: (x^0_{min}, x^0_{max}) and (y^0_{min}, y^0_{max}), see Figure 1, then taking these as the limits of the search space we first use the conventional GA to find the best estimate of the optimum point, let us say this is (x^0_{best}, y^0_{best}). Now we refine our search space to be centred at (x^0_{best}, y^0_{best}) and to extend from x^{i+1}_{min} to x^{i+1}_{max} in the x direction and from y^{i+1}_{min} to y^{i+1}_{max} in the y direction where,

$$x^{i+1}_{max} = x^i_{max} + \zeta_x\left(x^i_{best} - x^i_{max}\right) \qquad (4a)$$

$$y^{i+1}_{max} = y^i_{max} + \zeta_y\left(y^i_{best} - y^i_{max}\right) \qquad (4b)$$

$$x^{i+1}_{min} = x^i_{min} + \zeta_x\left(x^i_{best} - x^i_{min}\right) \qquad (4c)$$

$$y^{i+1}_{min} = y^i_{min} + \zeta_y\left(y^i_{best} - y^i_{min}\right) \qquad (4d)$$

This algorithm can be generalized to n parameters as follows:

$$\left.\begin{aligned} {}_jx^{i+1}_{max} &= {}_jx^i_{max} - \zeta_j\beta \\ {}_jx^{i+1}_{min} &= {}_jx^i_{min} + \zeta_j\beta \end{aligned}\right\} \text{for} \quad j = 1, n \qquad (5)$$

where $\beta = \max_j \left| {}_j x^i_{best} - {}_j x^i_{max} \right|$. The β factor has been introduced to allow a search to move outwith the bottleneck whenever the "best" parameter combination lies at the edge of the bottleneck region.

4 ALGORITHM TESTING

The algorithm was tested by generating some data using the DISCUS model applied to a hypothetical river reach. For this reach the river velocity (u) was set to be $0.05\,ms^{-1}$, the dispersion coefficient (D) was $0.1\,m^2s^{-1}$, the exchange rate parameter (α) was $0.001\,s^{-1}$ and the storage zone size (A_s) was set as $0.05\,m^2$. A tracer distribution was input to the hypothetical river at the upstream end of the reach and allowed to travel for about 2 hours downstream. The simulated concentration versus time curve at the downstream end of the reach was then used as the "data" for the fitting exercise. The genetic algorithm's goal, therefore, was to find the best fit parameters as [0.05, 0.1, 0.001, 0.05].

To achieve this, a total of 64 possible values for each of the traits were specified from the following initial parameter ranges: $(0.0 < u < 0.1)$, $(0.0 < D < 0.02)$, $(0.0 < \alpha < 0.002)$ and $(0.0 < A_s < 0.1)$. The traditional genetic algorithm used a population size of 200 and was allowed to evolve for 50 generations, i.e. a random selection of 200 possible parameter combinations was used to generate 200 simulations of the data, using the DISCUS model. This required 10000 simulations and objective function evaluations. For the new (bottlenecking) genetic algorithm the population size was 100 and only 25 generations were used. Therefore only 2500 simulations and objective function evaluations were required. Five bottlenecks were used. The bottleneck fractions were: $\zeta_u = 0.5$, $\zeta_D = 0.5$, $\zeta_\alpha = 0.5$ and $\zeta_{A_s} = 0.9$.

So for the transient storage area the rate of parameter space reduction was restricted. Initial experiments suggested that this prevented premature and erroneous convergence. The results of both the traditional and the bottlenecking genetic algorithms are presented below in Table 1 and Figures 2 and 3. Table 1 shows the final optimum parameters obtained by both algorithms. Note that the traditional GA used four times as many objective function evaluations as the new GA yet three of the four optimum parameters found were still greatly in error, with the transient storage parameters being the most difficult to correctly identify. By increasing the number of generations better estimates could be obtained but convergence was very slow as a direct result of the shape of the optimization surface. The bottlenecking GA, however, which "zooms in" on the optimum achieves a much greater degree of accuracy in many fewer objective function evaluations.

Table 1. Final result of GA searches and % errors.

	Traditional GA		Bottlenecking GA	
u	0.05%	0.00%	0.049959	0.08%
D	0.0976	2.54%	0.099573	0.43%
α	0.00179	−78.90	0.000924	7.60%
A_s	0.091429	−82.86	0.047494	5.01%

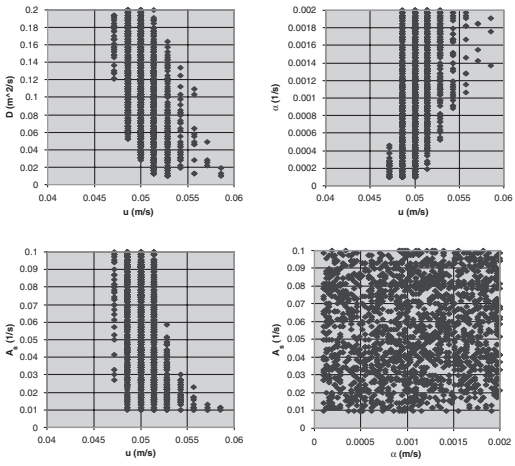


Figure 2. Quasi-confidence regions for traditional genetic algorithm at level R = 0.97.

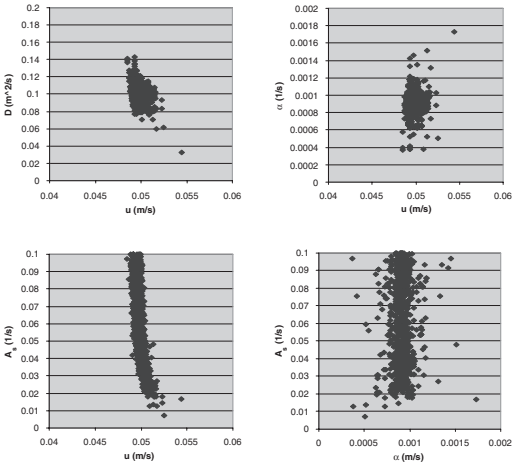


Figure 3. Quasi-confidence regions for bottlenecking genetic algorithm at level R = 0.97.

Figures 2 and 3 show the results of the searches in terms of "quasi-confidence" regions, i.e. a point was plotted in the parameter space wherever R was greater than some pre-defined accuracy level. Large regions

of widespread points then indicate a highly uncertain parameter estimate. The figures show conditions for an accuracy level of $R = 0.97$ and are particularly informative. The traditional GA (Figure 2) shows very large confidence regions for this test case.

Clearly a great degree of uncertainty surrounds the estimates particularly the transient storage parameters (α, A_s). The smallest quasi-confidence region spread is evident in the velocity parameter. The quasi-confidence region for the transient storage parameters (α and A_s) shows that we can only be confident that the parameters lie within the total parameter space, i.e. little information has been gained by the optimisation process. The bottlenecking GA (Figure 3), however, is much more useful. It manages to establish greater confidence in at least u, D and α. However, at this level ($R = 0.97$) it also has trouble establishing any confidence in A_s, although it does manage to find a good estimate of the point of global maximum R.

5 CONCLUSIONS

This paper has presented a new approach for parameter estimation in river models. The approach has been used here to estimate parameters in an advection-dispersion transient storage model but the technique is not limited to this application. It can be applied in other areas of river modeling. For the application presented here the surfaces of the objective function are often very flat and convergence to the optimum can be very slow. The bottlenecking technique that we have introduced seems to have greatly enhanced the convergence. Clearly this is only one application and further testing of the approach is required. In particular it may be necessary to modify the algorithm to preserve genetic diversity so that interesting search regions are not prematurely excluded.

REFERENCES

Allan, J.D. *Stream Ecology*, Chapman and Hall, 1995.

D'Angelo, D.J., Webster, J.R., Gregory, S.V. and Meyer, J.L. Transient storage in Appalachian and Cascade mountain streams as related to hydraulic characteristics, *J. North American Benthological Society*, **12**, 223, 1993.

DeAngelis, D.L., Loreau, M. and Marzolf, E.R. Modelling nutrient – periphyton dynamics in streams: the importance of transient storage zones. *Ecological modelling*, **80**, 149–160, 1995.

Denton, R.A. Analytical asymptotic solutions for longitudinal dispersion with dead zones, *J of Hydraulic Research*, **28**, 309–329, 1990.

Kim, B.K.A., Jackman, A.P. and Triska, F.J. Modeling Biotic Uptake by Periphyton and Transient Hyporrheic Storage of Nitrate in a Natural Stream. *Water Resour. Res.*, **28**, 2743, 1992.

Manson, J.R., Wallis, S.G. and Hope, D.A. Conservative Semi-Lagrangian Transport Model For Rivers with Transient Storage Zones, *Water Resources Research*, **34**(15), 2000.

Manson, J.R. and Wallis, S.G. A conservative, semi-Lagrangian fate and transport model for fluvial systems: Part 1 – Theoretical Development, *Water Research*, **34**(15), 2000.

Manson, J.R. and Wallis, S.G. Conservative Semi-Lagrangian Algorithm for Pollutant Transport in Rivers, *ASCE Journal of Environmental Engineering*, **125**(5), 1999.

Manson, J.R. and Wallis, S.G. An Accurate Numerical Algorithm for Advective Transport, *Communications in Numerical Methods in Engineering*, **11**, pp. 1039–1045, 1995.

Manson, J.R. and Wallis, S.G. Towards an Accurate Fate and Transport Model for Non-uniform Surface Waters, *Advances in Environmental Research*, **1**(1), 1997.

Marti, E., Grimm, N.B. and Fischer, S.G. Pre- and post-flood retention efficiency of nitrogen in a Sonoran Desert stream, *J. North American Benthological Society*, **16**(4), 805, 1997.

Morrice, J.A., Valett, H.M., Dahm, C.N. and Campana, M.E. Alluvial characteristics, groundwater-surface water exchange, and hydrologic retention in headwater streams, *Hydrological Processes*, **11**, 253, 1997.

Purnama, A. The effect of dead zones on longitudinal dispersion in streams, *J of Fluid Mechancis*, **186**, 351–377, 1988.

Sabol, G.V. and Nordin, C.F. Dispersion in rivers as related to storage zones, *J of the Hydraulics Division*, ASCE, **104**, 695–708, 1978.

Thackston, E.L. and Schnelle, K.B. Predicting effects of dead zones on stream mixing, *J of the Sanitary Engineering Division*, ASCE, **96**, 319–31, 1970.

Valentine, E.M. and Wood, I.R. Experiments in longitudinal dispersion with dead zones, *J of the Hydraulics Division*, ASCE, 105, 999–1016, 1979.

Valett, H.M., Morrice, J.A., Dahm, C.N. and Campana, M.E. Parent lithology, surface-groundwater exchange and nitrate retention in headwater streams, *Limnology and Oceanography*, **41**(2), 333, 1996.

Wallis, S.G., Manson, J.R. and Fillippi, L.A. Semi-Lagrangian Algorithm for One-Dimensional Advection-Diffusion, *Communications in Numerical Methods for Engineering*, **14**, pp. 671–679, 1998.

Wallis, S.G. and Manson, J.R. Accurate numerical simulation of advection using large time steps, *International Journal of Numerical Methods in Fluids*, **24**, pp. 127–139, 1997.

Yang, G., Reinstein, L.E., Pai, S., Zhigang, X. and Carroll, D.L. A new genetic algorithm technique in optimization of permanent prostate implants, *Med. Phys*. **25** (12). 1998.

This page intentionally left blank

River Flow 2004 – Greco, Carravetta & Della Morte (eds.)
© 2004 Taylor & Francis Group, London, ISBN 90 5809 658 0

Gas-transfer coefficient in a smooth channel. A preliminary assessment of dimensional analysis-based equation

Carlo Gualtieri & Guelfo Pulci Doria
Hydraulic and Environmental Engineering Department "Girolamo Ippolito", University of Napoli "Federico II", Napoli (Italy)

ABSTRACT: Recent studies have confirmed that literature equations for the estimation of the reaeration rate are not applicable to all stream hydrodynamic conditions. Since recent efforts have been addressed to develop a comprehensive approach to gas-transfer using dimensional analysis to clearly identify the parameters involved in the process, the present paper provides a preliminary quantitative assessment for this approach using 65 literature laboratory data collected in smooth channels.

1 FOREWORD

The exchange of gases across the air–water interface is important in regulating concentrations of various substances of environmental and water quality concern, such as oxygen, nitrogen, and volatile toxics (Thibodeaux 1996; Chapra 1997). Oxygen transfer at free surfaces has been widely studied since dissolved oxygen (DO) is a key water quality parameter and water quality standards and criteria for DO are provided by environmental regulation of many countries, such as USA, UK, Germany and Japan. Also in Italy, D.L. 152/1999 has, recently, established for streams and lakes a classification system which considers DO as a significant parameter (Ciaravino & Gualtieri 1999). The oxygen transferred from the atmosphere by means of natural reaeration replaces the amount consumed due to the oxidation of organic matter discharged into the water body.

The flux of dissolved oxygen Φ at the air–water interface [$ML^{-1}T^{-2}$] has been quantified according to (Chapra 1997):

$$\Phi = K_L \cdot (C_{sat} - C_w) \tag{1}$$

where K_L is the gas-transfer rate [LT^{-1}], C_{sat} is the equilibrium, or saturation, concentration of DO [ML^{-3}] and C_w is the DO concentration in the bulk water [ML^{-3}]. Accordingly, oxygen is lost to the atmosphere when the upper waters are oversaturated ($C_{sat} < C_w$), and reaeration occurs when $C_{sat} > C_w$. The accuracy of estimates of Φ depends on the accuracies of the specifications of the gas-transfer coefficient, K_L, and C_{sat} and C_w. Reaeration process is often parameterised using the volumetric reaeration coefficient K_a [T^{-1}], given, if h [L] is water mean depth, by (Chapra 1997):

$$K_a = \frac{K_L}{h} \tag{2}$$

Since oxygen has low solubility and high vapor pressure, the exchange process is controlled by the liquid side of the air–water interface (Chapra 1997).

Recent studies have confirmed that available equations for the estimation of the reaeration rate are not applicable to all stream hydrodynamic conditions probably since some parameters involved in the process have been neglected in their formulation (Melching & Flores 1999; Gualtieri et al. 2002). Therefore, recent efforts have been addressed to develop a comprehensive approach to gas-transfer using dimensional analysis to clearly identify the parameters involved (Gualtieri et al. 2002; Gualtieri 2003). This approach has provided a relationship between the reaeration coefficient K_L and some classical fluid mechanics index-numbers (Gualtieri et al. 2002). The present paper provides a preliminary quantitative assessment for that relationship using 65 literature laboratory data collected in smooth channels.

2 DIMENSIONAL ANALYSIS OF GAS-TRANSFER PROCESS

In two previous papers a comprehensive approach to the gas transfer process at the air–water interface based

on dimensional analysis was proposed (Gualtieri et al. 2002; Gualtieri 2003).

Gas-transfer is mainly controlled by the turbulence at both side of the air–water interface. Characterizing turbulence influence on gas-transfer across air–water interface has been proved to be difficult since this influence depends on relative phase velocities, roughness of surfaces at the interface, frictional and adhesive forces, surface tensions and several other parameters (Weber & DiGiano 1996). Also, anisotropic turbulent conditions, with significant correlation between the velocity fluctuations and the presence of a velocity gradient and a shearing stress, further complicate modeling effort (Moog & Jirka 1999). However, if the gas-transfer is controlled by the liquid side, the nature of turbulent eddies in the water can affect the parameters influencing the gas-transfer. Therefore, gas-transfer modeling approaches are different in shallow and rapidly flowing waters and in deep and standing waters because the nature of the forcing mechanism is different. In shallow streams, the surface turbulence is mainly due to the water velocity or, more precisely, to the interaction of the water flow with the bottom rugosity and depth variations. At the contrary, the surface of deeper environments is not affected by bottom features, and the shear stress exerted by the wind at the air–water interface is the main physical factor of turbulence (Chu & Jirka 1995). Also, in deep channels isotropic turbulent conditions, where the intensity of the velocity fluctuations in all three directions is very nearly the same, are more likely to exist (Thibodeaux 1997). The proposed analysis was addressed to turbulence generated by bottom shear stress, where the gas-transfer process is affected by the fluid and gas properties and by the hydrodynamics of the flow. A characteristic feature of turbulent flow is the presence of a wide range of eddy sizes, ranging to the flow domain to smaller sizes. If large eddies break down into multiple smaller eddies, they conserve their kinetic energy, which is efficiently transferred through a cascade of eddy sizes (Pope 2000; Socolofsky & Jirka 2002).

When the eddies become small enough, in the order of Kolmogorov scale in size, viscosity takes over and the energy is finally dissipated into heat. This conversion of energy can be quantified using the kinetic turbulent energy dissipation rate ε [$L^2 T^{-3}$]. In a homogeneous turbulent flow, production and dissipation of kinetic energy are balanced and ε must equal the total turbulent kinetic energy of the flow, k. The rate ε is proportional to the energy line slope J_e as:

$$\varepsilon = g\, v\, J_e \tag{3}$$

Therefore, J_e should be included as key parameter in the dimensional analysis of gas-transfer process. Notably, in steady uniform flow, the energy line slope J_e is equal to the water surface slope J_w and to the bed slope J_b, whereas for steady non-uniform flow, they are generally different (Graf 1998). Consider now that it holds that $R_h \approx h$, where R_h is the hydraulic radius. Also, assume that the gas-transfer process is controlled by the water side concentration boundary layer (CBL). Thus, the dimensional analysis could consider the following parameters:

- natural constants and fluid properties such as the gravitational acceleration constant g [LT^{-2}], the water kinematic viscosity ν [$L^2 T^{-1}$], and the water surface tension T_s [MT^{-2}];
- gas exchanged properties, such as the molecular diffusion coefficient D_m[$L^2 T^{-1}$];
- flow properties, such as the mean depth h [L], the mean streamflow velocity v [LT^{-1}], the energy line slope J_e, the channel bed slope J_b and the Manning's roughness coefficient n.

First, the water surface tension, T_s, was transformed into a kinematic parameter as $\tau_s = T_s/\rho$ [$L^3 T^{-2}$], where ρ is the water density [ML^{-3}]. Also, the coefficient n can be expressed as:

$$n = n(\varepsilon_{cw}) \tag{4}$$

where ε_{cw} is the roughness coefficient of Colebrook-White equation, that could be applied with good approximation also for streams and rivers. Thus, it holds:

$$K_L = f_1[g, v, \tau_s, D_m, h, v, J_e, J_b, \varepsilon_{cw}] \tag{5}$$

Assuming as fundamental quantities the water mean depth h, [L] and the molecular diffusivity D_m, [$L^2 T^{-1}$], the dimensional analysis leads to

$$Sh = f_2[Sc, We, Re, Fr, J_e, J_b, S] \tag{6}$$

where Sh, Sc, We, Re, and Fr are the classical Sherwood number, Schmidt number, Weber number, Reynolds number, and Froude number, respectively. Sh, Sc, and We are defined as:

$$Sh = \frac{K_L \cdot h}{D_m} \tag{7}$$

$$Sc = \frac{\nu}{D_m} \tag{8}$$

$$We = \frac{U \cdot h}{(T_s/\rho)^{0.5}} \tag{9}$$

where U is water depth-averaged flow velocity [LT^{-1}]. Finally, the relative roughness S is:

$$S = \frac{\varepsilon_{cw}}{4h} \tag{10}$$

Equation (6) is the final form of the dimensionless gas-transfer rate in an open channel for liquid-controlled chemicals. This equation holds whatever is the gas involved in the gas-transfer. Notably, classical Darcy-Weisbach equation provides a relation between Fr, Re, J_e and S; thus, one of these parameters could be expressed as a function of the remaining three of them (Gualtieri et al. 2002). Also, in eq. (6) the temperature influence is directly accounted for through the temperature dependent parameters, such as Sc and We. This represents an advantage respect to the common application of a temperature corrective coefficient, such as the classical θ of Van't Hoff-Arrhenius equation (Chapra 1997).

2.1 *Comparison with large-eddy and small-eddy models*

Classical literature large-eddies and small-eddies models could be compared with the findings of the outlined dimensional analysis. These models start from surface renewal model, which states that rate of gas-transfer through the air–water interface depends on the length of time that a certain water parcel coming from the bulk water due to turbulent eddies is exposed to the atmosphere. This time could range from zero to infinity. If r is the rate of surface renewal [T^{-1}], the application of Fick's law leads to:

$$K_L = \sqrt{D_m\, r} \tag{11}$$

Therefore, r, which is a characteristic of the turbulence, should be estimated. Two different approaches could be used depending on the considered size of turbulent motions renewing the CBL. If renewal process is mainly affected by the largest, integral-scale eddies, the r is proportional to the intensity and to the scale of turbulence. Thus, vertical fluctuation velocity u′ [LT^{-1}] and Prandtl mixing length l [L] are used to define r (O'Connor & Dobbins 1958; Thibodeaux 1997). Also, they are usually related to the shear velocity u* [LT^{-1}] and to the mean depth h, respectively, to consider that the renewal rate is $r \propto u^*/h$. This is the *large-eddy* model which states that (Moog & Jirka 1999):

$$K_{L\text{-}ND} = \frac{K_L}{u'} \approx \frac{K_L}{u^*} \propto Sc^{-0.5}\, Re^{*-0.5} \tag{12}$$

where $K_{L\text{-}ND}$ is the dimensionless gas-transfer rate and Re* is the shear Reynolds number $Re^* = (u^* 4\,h)/\nu$. At the contrary, since the air–water interface tends to damp the eddies as they approach to it closer than their length scale, the contribution of small eddies, at the Kolmogorov scale, in renewing the CBL could be considered. Following this approach, that is called the *small-eddy* model, the renewal rate is $r \propto (\varepsilon\nu)^{0.5}$ and the dimensionless gas-transfer rate is (Moog & Jirka 1999; Socolofsky & Jirka 2002):

$$K_{L\text{-}ND} \approx \frac{K_L}{u^*} \propto Sc^{-0.5}\, Re^{*-0.25} \tag{13}$$

Therefore, these two models could be generally represented as:

$$K_{L\text{-}ND} = c_1\, Sc^{-0.5}\, Re^{*n} \tag{14}$$

where c_1 is a constant and $n = -0.50$ holds for the *large-eddy* model and $n = -0.25$ holds for the *small-eddy* model. Despite to their expressions, these models could be reduced to the proposed dimensional analysis. In fact, both equations (12) and (13) could be transformed into a form similar to (6). In particular, equations (12) and (13), after some arrangements, become:

$$Sh \propto Sc^{0.5}\, Re^{0.5}\, Fr^{-0.5}\, J_e^{0.25} \tag{15a}$$

$$Sh \propto Sc^{0.5}\, Re^{0.75}\, Fr^{-0.75}\, J_e^{3/8} \tag{15b}$$

where, differently than in eq. (6), there are not the Weber number We, the channel bed slope J_b and the relative roughness S. Thus, *large-eddy* and *small-eddy* models should be considered as a particular form of eq. (6) where the effect of the water surface tension, of the bed slope and of the roughness is not accounted for.

3 DATA ANALYSIS AND DISCUSSION

The present paper provides a preliminary quantitative assessment of the eq. (6) using 65 laboratory data collected in smooth channels, i.e. $S = 0$. The considered data refer to different environmental and hydrodynamic conditions, though uniform flow conditions hold, i.e. $J_e = J_b$. First of all, the Froude number was discarded since it can be expressed using S, Re and J_e. In fact, classical Darcy-Weisbach equation states;

$$J_e = \frac{\lambda}{4\,h}\frac{v^2}{2\,g} = \frac{\lambda}{8}Fr^2 \tag{16}$$

where λ is the friction factor, that in a turbulent flow is $\lambda = \lambda(Re, S)$. Thus, eq. (17) yields:

$$J_e = \frac{\lambda\,(Re, S)}{8}Fr^2 = J_e\,(Fr, Re, S) \tag{17}$$

where Fr, S, Re and $J_e = J_b$ are correlated. Equation (17) could be modified depending on certain;

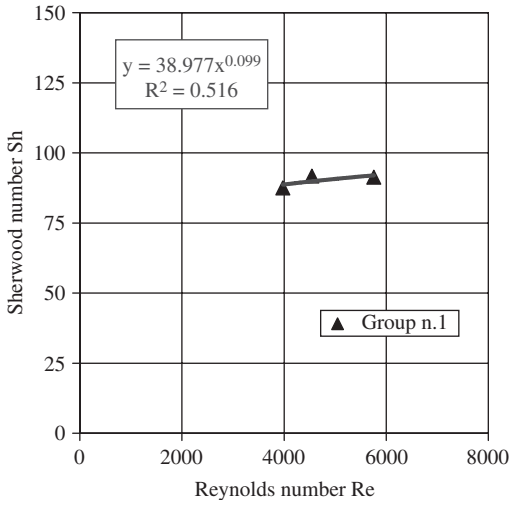


Figure 1. Group n.1.

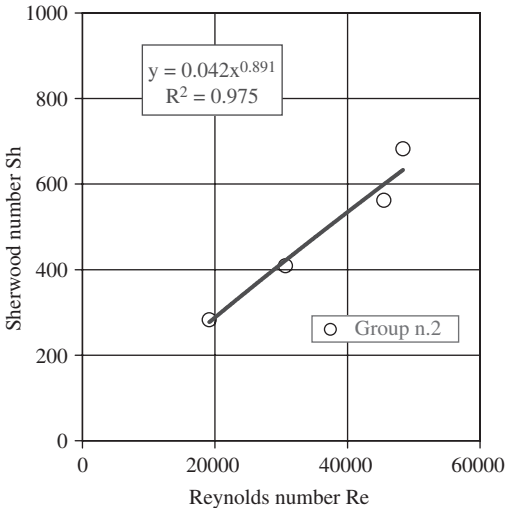


Figure 2. Group n.2.

particularly, each one of the considered parameters could be, in turn, expressed as a function of the others. For example the Froude number could be always expressed as:

$$Fr = \sqrt{\frac{8\,J_b}{\lambda\,(Re, S)}} = Fr\,(J_b, Re, S) \tag{18}$$

Also, as a first approximation, since for the considered data the variation range of the Weber number is narrow, the influence of We was discarded. Thus, equation (1) yields:

$$Sh = f_3\,[Sc, Re, J_b] \tag{19}$$

where Sherwood number is affected by only Sc, Re and J_b. Usually, correlations between Sh and Re are in the form (Incropera & DeWitt 1990):

$$Sh = a \cdot Re^b \cdot Sc^c \tag{20}$$

where a, b, and c are constants which are derived from regression on experimental data. Often, c parameter is set $c = 0.33$, whereas the values of b exponent is reported on literature to be 0.87 (Probstein et al. 1972), 0.91 (Harriott & Hamilton 1965), 0.80 (Incropera & De Witt 1990) and 0.89 ± 0.05 (Steinberger & Hondzo 1999).

The data used in the present study are all taken from literature. Particularly, the considered data are those collected in laboratory flumes by Moog and Jirka (Moog & Jirka 1999), by Ran (Ran et al. 2002; Ran 2003), by Lau (Lau 1975), and by Thackston and Krenkel (Thackston & Krenkel 1969), where well-controlled conditions hold.

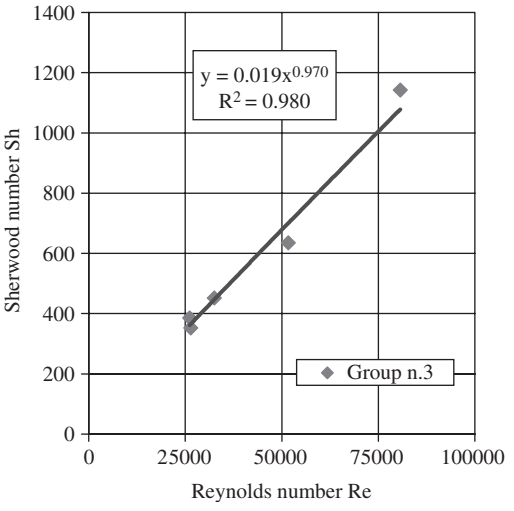


Figure 3. Group n.3.

These four data sets refer to rectangular smooth-channels where the width ranged from 0.4 to 1.00 m. Notably, there is a significant separation in magnitude between the data by Moog-Jirka and the other three flume data sets since the first ones are generally higher (Moog & Jirka 1999).

In the considered experiments the flow velocity ranged from 0.036 to 1.040 m/s, while water depth was from 0.011 to 0.145 m. The aspect ratio W/h_{avg}, which has a significant influence on gas-transfer process (Gualtieri & Gualtieri, in press), ranged from 5.15

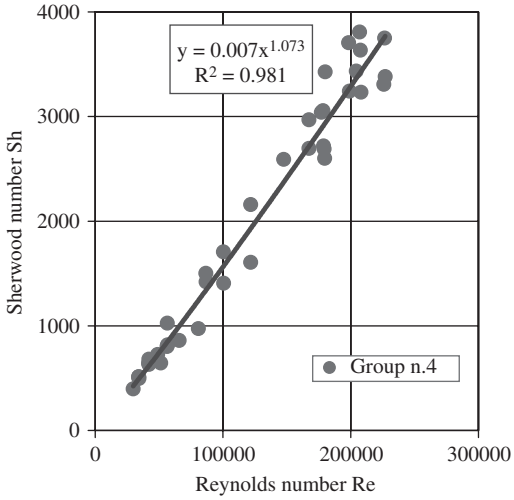


Figure 4. Group n.4.

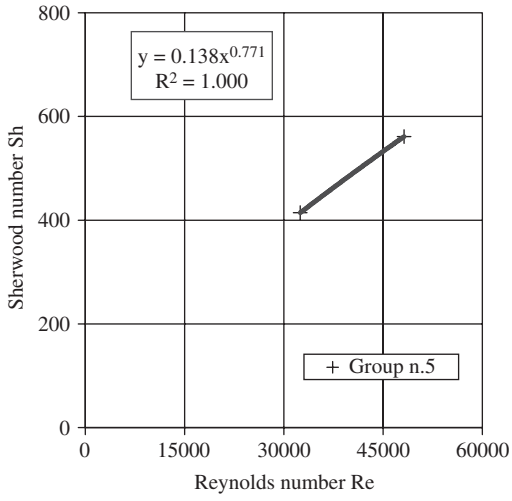


Figure 5. Group n.5.

to 54.15. Interestingly W/h = 5 is the threshold value for a "wide" open channel, where the effect of secondary currents or "corner flows" could be neglected (Nezu & Nakagawa 1993).

Finally, water temperature ranged from 11.3 to 25.7°C. Accordingly, Schmidt number was in the range from 419.6 to 890.6, with an remarkable number of data with Sc = 548, i.e. Lau data.

The analysis of the raw data has shown that they could be divided in 8 groups according the value of the channel bed slope J_b and the Schmidt number Sc.

The main characteristics of each Groups are listed in Table 1, where the number of data, the average bed

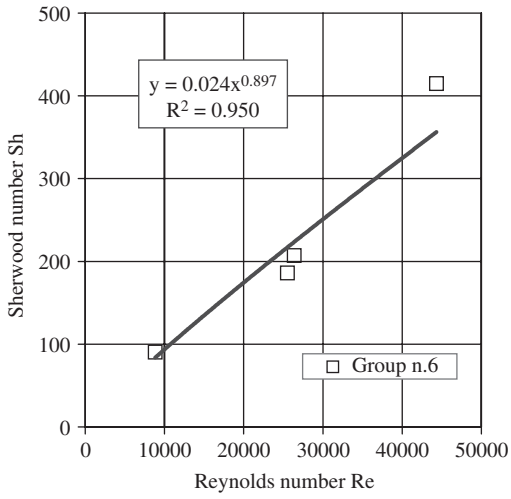


Figure 6. Group n.6.

slope J_b value, the average Sc value, and the average Re value are presented.

Bed slope $J_{b\text{-}avg}$ ranged from 0.00003 to 0.00350. Groups 4 refers to data with the same J_b, which is equal to 0.01. Also, Groups 5 and 6 have similar value of slope $J_{b\text{-}avg}$. while their Sc_{avg} is different. Since the range of water temperature is quite narrow, the average Schmidt number Sc_{avg} of the Groups ranged from 433 to 752. Moreover, Groups 1–5 have the same or very similar values of Sc_{avg} and their overall average Schmidt number is $Sc_{avg} = 526$. Finally, the values of Re_{avg} exhibits an higher range, from 3977 to 227048. Groups 1–3 data belong to Lau set, whereas Group 4 is formed by Ran data. Groups 5 and 6 collect data collected by Lau and by Thackston and Krenkel, respectively. Finally, the higher data by Moog and Jirka are in Groups 7–8. These Groups present the highest Sc_{avg} values, i.e. 704 and 752, respectively.

In the present study a power relation between Sh and Re was proposed as:

$$Sh = \mu_1 \, Re^{\alpha} \tag{21}$$

where μ_1 parameter depends from Sc and from the channel bed slope J_b as:

$$\mu_1 = \mu_1(Sc, J_b) \tag{22}$$

In the proposed model the dimensionless gas-transfer in quiescent water conditions is assumed to be zero. However, in stagnant water, i.e. Re = 0, gas-transfer process occurs due to molecular diffusion (Thibodeaux 1997; Li Ran et al. 2002). Thus, a gas-transfer rate for these conditions should be considered, but the available data does not allow to estimate this

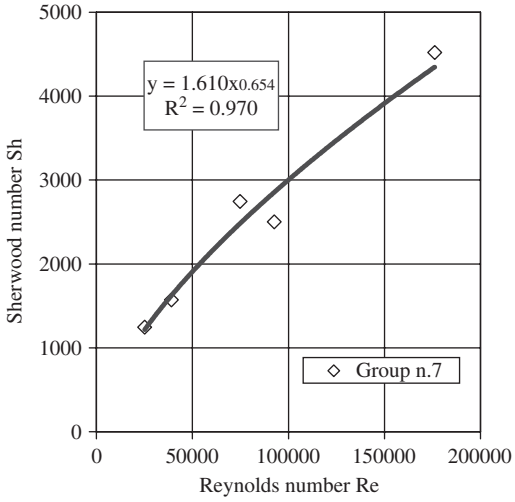


Figure 7. Group n.7.

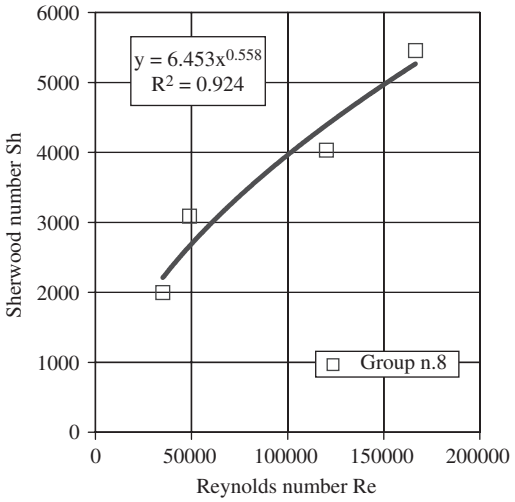


Figure 8. Group n.8.

Table 1. Considered Groups of data.

Group	Data	$J_{b\text{-}avg}$	Sc_{avg}	Re_{avg}	α
1	3	0.00003	548	4759	0.099
2	4	0.00039	548	35909	0.891
3	5	0.00077	548	43491	0.970
4	38	0.00100	518	125004	1.073
5	2	0.00174	548	40322	0.771
6	4	0.00175	433	26260	0.897
7	5	0.00070	752	81550	0.654
8	4	0.00350	704	92659	0.558

Table 2. Corrected values for μ_1 and α parameters.

Group	Data	α	μ_1
1	3	0.78	0.119
2	4	0.78	0.138
3	5	0.78	0.153
4	38	0.78	0.233
5	2	0.78	0.124
6	4	0.78	0.087
7	5	0.78	0.368
8	4	0.78	0.466

rate. Moreover, since gas-transfer process in stagnant water is driven by molecular diffusion, this rate should be a temperature-dependent parameter.

The power relationship, i.e. eq. (21), between Sh and Re is presented for each Group in plots from Fig. 1 to Fig. 8, where R^2 parameter is also indicated.

Moreover, α parameter values are listed in Table 1. These values are mostly close to literature values.

First of all, results demonstrate that eq. (21) provides a general good agreement with laboratory data and the proposed model is supported by the experimental data. Second, since it was assumed that α parameter is independent from Sc, a common value for α should be adopted. Thus, α values obtained from all Groups were corrected using a weight criterion which considers 3 parameters.

The first one is the number of data belonging to each Group, the second one is ratio $\Delta Re/Re_{avg}$, i.e. the ratio of the difference ΔRe between maximum and minimum Reynolds number to Re_{avg} value in each Group, while the third one is $1/Re_{avg}$. As a result, a value of $\alpha = 0.78$ was estimated. This value was adopted as α in eq. (21) for all the Groups. Notably, this value is consistent with those previously reported from literature.

As a result, corrected value for μ_1 values were obtained. They are listed in Table 2. The analysis of μ_1 data supports an interesting trend between μ_1 parameter, on one hand, and the bed slope J_b and Schmidt number, on the other hand (Fig. 9).

In fact, Fig. 9 shows that for $Sc_{avg} = 526$ (the open circles) μ_1 parameter significantly increases with increasing slopes J_b. Also, the data for $Sc = 432$ (the diamonds) presents for the same J_b lower μ_1 than those for $Sc_{avg} = 526$. Moreover, the same trend could be observed in the data with higher Schmidt number (the triangle and the cross), i.e. $Sc = 704$ and $Sc = 752$, where μ_1 parameter increases with increasing J_b.

This results demonstrate that gas-transfer process is enhanced by higher channel bed slope J_b for the same value of the Reynolds number. Thus, they confirmed that the bed slope J_b parameter should be included in gas-transfer modeling framework.

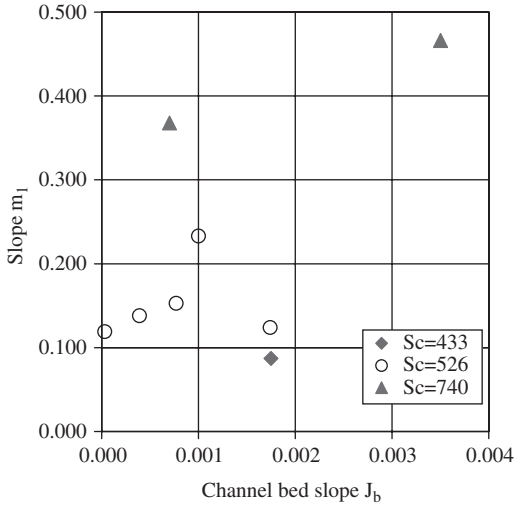


Figure 9. μ_1 parameter vs channel bed slope J_b.

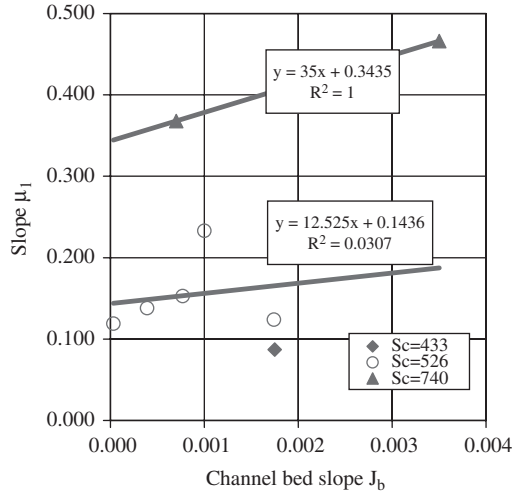


Figure 10. μ_1 parameter vs channel bed slope J_b.

The two data with higher Sc were then regrouped adopting an average Schmidt number, i.e. $Sc_{avg} = 740$. Linear regression of μ_1 parameter on bed slope J_b for both $Sc_{avg} = 526$ and $Sc_{avg} = 740$ is presented in Fig. 10. The Group with $Sc_{avg} = 526$ has 52 data, whereas the Group with and $Sc_{avg} = 740$ has 9 data. Finally, only one data was available for $Sc_{avg} = 433$. Data with lower Sc_{avg} exhibit an higher increase with J_b. Thus, the influence of Sc on μ_1 is supported and it holds:

$$\mu_1 = \mu_2 J_b + \mu_3 \tag{23}$$

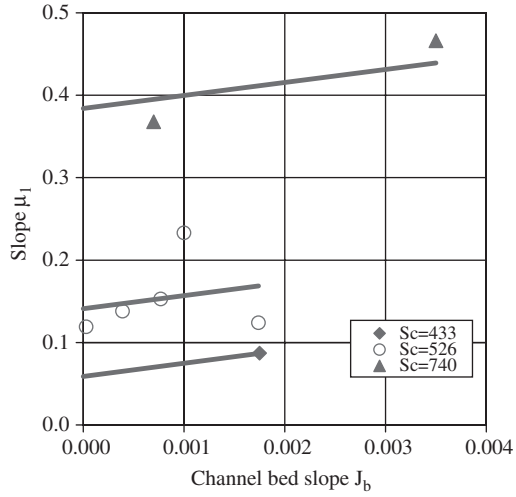


Figure 11. Corrected μ_1 parameter vs channel bed slope J_b.

where μ_2 and μ_3 appear to be both affected by Sc. Fig. 10 shows that μ_3 is 12.52 and 35 for $Sc_{avg} = 526$ and $Sc_{avg} = 740$, respectively. These μ_2 values have been averaged using the number of data with $Sc_{avg} = 526$ and $Sc_{avg} = 740$, i.e. 52 and 9, respectively. A weighted averaged value of $\mu_2 = 15.75$ has been obtained. Results are presented in Fig. 11. Notably, μ_3 parameter data support Sc influence. Therefore, eq. (21) yields:

$$Sh = \left[15.75\, J_b + \mu_3(Sc)\right] Re^{0.78} \tag{24}$$

4 CONCLUDING REMARKS

Recent efforts have been addressed to develop a comprehensive approach to gas-transfer modeling. The present paper has provided a preliminary quantitative assessment for an approach based on dimensional analysis using 65 laboratory data collected in smooth channels.

The present paper proposed a power relationship between the dimensionless gas-transfer rate and Reynolds number. The slope μ_1 of that relationship was found to be affected both by the channel bed slope J_b and by the Schmidt number. A linear relationship between μ_1 and J_b was derived for different Schmidt numbers. Its slope was finally averaged for all the data, providing a predictive equation which relates dimensionless gas-transfer rate with J_b, Sc and Re. Further research should be focused to explore the influence on K_L of surface tension and channel roughness developing a predictive equation including also We and S.

ACKNOWLEDGMENT

The paper was prepared as a part of MURST PRIN 2002 research project. *Influence of vorticity and turbulence in interactions of water bodies with their boundary elements and effects on hydraulic design*.

REFERENCES

Chapra S.C. (1997). *Surface water quality modeling.* McGraw-Hill, New-York, USA

Ciaravino G. & Gualtieri C. (1999). *Dissolved oxygen balance in a stream* (in italian). *Water resources utilization and management* Conference, Roma, Italy, March 29, 1999

Graf W.H. (1998). *Fluvial hydraulics.* John Wiley&Sons, Chichester, UK

Gualtieri C. & Gualtieri P. (1997). Hydrodynamic model for reaeration estimation in surface waters (in italian). *AIMETA '97*, Siena, Italy, 29 September/3 October 1997 vol.1, pp.155–164

Gualtieri C. & Gualtieri P. (1999). Statistical analysis of reaeration rate in streams. *International Agricultural Engineering Conference (ICAE) '99*, Pechino, China, December 14/17, 1999

Gualtieri C. & Gualtieri P. (2000). Field verification for a reaeration model in streams. 4*th International Conference on HydroScience & Engineering (ICHE 2000)*, Seoul (Korea), September 26/29, 2000

Gualtieri C. & Gualtieri P. (in press). Turbulence-based models for gas transfer analysis with channel shape factor. *Environmental Fluid Mechanics*

Gualtieri C., Gualtieri P. & Pulci Doria G. (2002). Dimensional analysis of reaeration rate in streams. *Journal of Environmental Engineering*, *ASCE*, vol.128, n.1, January 2002, pp.12–18

Gualtieri C. (2002). Modeling mass-transfer of VOCs in open channels. *5th International Conference on HydroScience & Engineering (ICHE 2002)*, Warsaw, Poland, September 18/21, 2002

Gualtieri C. (2003). Dimensional analysis of gas-transfer process in a turbulent flow. *XXX IAHR Congress*, Thessaloniki, Greece, August 24/29, 2003

Gulliver J.S. & Halverson M.J. (1989). Air–water gas transfer in open channels. *Water Resources Research*, vol.35, n.8, pp.1783–1793

Incropera F.P & DeWitt D.P. (1990). *Fundamentals of Heat and Mass Transfer*. John Wiley and Sons, New York

Lau Y.L (1975). An experimental investigation of reaeration in open-channel flow. *Progress in Water Technology*, vol.7, n.3/4, pp.519–530

Melching C.S. (1998). *U.S. Geological Survey reaeration rate database*. Personal communication to the first author, April 1998

Melching C.S. & Flores H.E. (1999). Reaeration equations derived from U.S. Geological Survey database. *J.Environmental Engineering Division*, *ASCE*, 125, 5, May 1999, pp.407–414

Moog D.B. & Jirka G.H. (1999). Air–water gas transfer in uniform channel flow. *J.Hydraulic Engineering*, *ASCE*, 125, 1, January 1999, pp.3–10

Nezu I. & Nakagawa H. (1993). *Turbulence in open-channel flows*. IAHR Monograph Series, Balkema, Rotterdam, The Netherlands

Pope S.B. (2000). *Turbulent flows*. Cambridge University Press, Cambridge, U.K.

Probstein R.F, Sonin A.A. and Gur-Arie E. (1972). A turbulent flow theory of electrodialysis. *Desalination*, 11, 165–187

Ran L., Lin L., Xiao-Ying F. & Wendian H. (2002). Study on the effect of hydrodynamic characteristic on reaeration process. *Journal of Environmental Sciences*, 14, n.3, pp.393–398

Ran L. (2003). *Reaeration data*. Personal communication to the first author, May 2003

Socolofsky S.A. and Jirka G.H. (2002). *Environmental Fluid Mechanics. Part I: Mixing, Transport and Transformation*. Engineering. Lectures. Institut für Hydromechanik, University of Kalsruhe, Germany

Steinberger N. & Hondzo M. (1999). Diffusional mass transfer at sediment-water interface. *J. Env. Eng. Div. ASCE*, vol.125, n.2, pp.192–200

Thackston E.L. & Krenkel P.A. (1969). Reaeration prediction in natural streams. *J.Sanitary Engineering Division*, *ASCE*, 95, 1, January–February 1969, pp.65–93

Thibodeaux L.J. (1996). *Environmental chemodynamics*. John Wiley&Sons, Chichester, U.K.

Weber W.J. & DiGiano F.A. (1996). *Process dynamics in environmental systems*. John Wiley&Sons, Chichester, U.K.

River Flow 2004 – Greco, Carravetta & Della Morte (eds.)
© 2004 Taylor & Francis Group, London, ISBN 90 5809 658 0

A methodological approach for surface water vulnerability assessment

M. Giugni
Dip. di Ing. Idraulica ed Ambientale "G. Ippolito", Università degli Studi di Napoli Federico II, Napoli, Italy

G. Pappalardo & G. Lombardi
Autorità di Bacino Regionale Destra Sele, Napoli, Italy

N. Fontana
Dipartimento di Ingegneria, Università degli Studi del Sannio, Benevento, Italy

ABSTRACT: The recently introduced Italian laws (D.L. 152/99 and D.L. 258/00) have drawn attention to the issues of conservation and recovery of the natural environment by defining general guidelines for the protection of surface, ground and coastal waters. A methodological approach has been developed in order to assess the vulnerability of surface waters and to define their environmental quality on the basis of an integrated analysis of the river's ecosystem, which makes it possible for each river (or reach of river) to be attributed with an overall index reflecting its environmental quality (*river's environmental quality map*). This procedure had been applied to the pilot watershed of the Tusciano river (Southern Italy), by means of a monitoring network comprised of 8 experimental sections. The activities carried out have stressed the substantial validity of the methodology and have made it possible to draw up a preliminary draft of the environmental quality map.

1 INTRODUCTION

The Italian law D.L. 152/99 defines the general framework for safeguarding surface, ground and coastal waters by pursuing the objectives of preventing or controlling pollution, restoring water quality, protecting waters used for special purposes, ensuring the sustainable use of available resources and preserving the waters' natural ability to cleanse itself of impurities.

These objectives will be met through the use of a variety of instruments, including the targets of environmental quality and Protection Plans. However, before Protection Plans can be defined, the qualitative and quantitative status of water bodies needs to be determined and information has to be acquired regarding the physical, natural, social and economic characteristics of the basins in order to assess anthropic pressure and impact.

This varied set of investigative and planning activities constitutes a totally new approach to environmental policies regarding water resources in Italy.

2 METHODOLOGICAL APPROACH FOR SURFACE WATER ENVIRONMENTAL QUALITY ASSESSMENT

The first step in implementing Protection Plan calls for an environmental quality status to be attributed to the surface waters. Following the investigative surveys previously carried out in the area under the control of the Destra Sele Water Authority (Giugni et al. 2002), a methodological procedure was defined on the basis of assessments made regarding some indicators of the water quality and the Minimum Instream Flow. This allows a preliminary judgement to be made on the river's environmental quality so that suitable safeguards can be adopted and hence contribute to the planning activity regarding water usage.

More specifically the procedure calls for:

a) Physical, chemical and microbiological investigations aiming to assess the Level of Pollution from Macrodescriptors (LPM), which can be obtained by measuring the *macrodescriptor parameters for the classification of surface waters* (dissolved oxygen, BOD_5, COD, ammonium–nitrogen NH_4, nitrate–nitrogen NO_3, total phosphorous, Escherichia coli). This will enable a preliminary quality assessment to be attributed to the river in question. The subsequent measurement of additional parameters regarding organic and inorganic micropollutants (pesticides, organic solvents, aromatic polycyclical hydrocarbons, cadmium, chromium, mercury, nickel, lead, copper, etc.) will provide further information on the system's quality and vulnerability and on the extent of the transported load;

b) Biological Mapping of the river, aiming to assess the Extended Byothic Index (E.B.I.). Biological mapping allows a further assessment to be made, which is complementary to the physical, chemical and microbiological investigation, by assessing the overall effect of pollutants and various other external influences, even if only present sporadically or in very small quantities (Ghetti 1995, 1997, Ruffo 1995, European Environment Agency 1999). Furthermore, the E.B.I. score corresponds to a preliminary quality class;
c) Classification of the River Ecological Status (RECS) achieved by comparing the quality class supplied by the macrodescriptors (LPM) with the result of the EBI, and attributing the reach in question with the worse of the two values. Table 1 reports the quality classes envisaged by Italian law D.L. 152/99;
d) Determination of the definitive River Environmental Quality Status (REQS), by cross-referencing the ecological data with those regarding the presence of organic and inorganic chemical pollutants according to the diagram reported in Table 2;
e) Definition of the River Functionality Index (RFI): the RFI is derived from the RCE-I (*Riparian Channel Environmental Inventory*). This method was defined by R. C. Petersen (1992) who based it on a 16-question checklist with 4 possible predetermined answers for each one. The main purpose of the proposed model was to collect information regarding the river's main ecological characteristics in order to set up an inventory on the conditions of Swedish rivers and riverbank vegetation. In this framework, although the environmental assessment can be inferred from the scores attributed to the individual characteristics, in actual fact, it was more of a by-product than an explicit goal of the investigation. Its many applications in Italy increasingly brought to light the importance that this methodology could assume not only in helping draw up an inventory of environmental characteristics, but above all as a model for assessing environmental quality. Consequently, the RCE-2 was proposed with a new assessment checklist (Siligardi e Maiolini 1993). When the new index was applied to cases all over Italy, it was seen to be inadequately calibrated with respect to the large number of possible river types, thus fuelling the fear that the RCE was beginning to encompass a heterogeneous family of indices having different contents and goals. Hence the need to update the method so as to make it more general and to allow it to define the goals more rigorously by drawing up guidelines and precise instructions for its users. The modifications made by a working group coordinated by the Italian National Environmental Protection Agency (A.N.P.A.) were so far-reaching that the index was attributed with a new name, the River Functionality Index (ANPA 2000, Siligardi et al. 2000). The RFI checklist comprises 14 questions (with 4 predetermined answers) organised in functional groups:

- questions 1–4 concern the *conditions of plant life along the riverbanks and in the surrounding area*;
- questions 5 and 6 refer to the *relative size of the riverbed* and the *physical and morphological structure of the riverbanks*;
- questions 7–11 consider the *structure of the riverbed*;
- questions 12–14 determine *biological characteristics* through structural analysis of the macrobenthonic and macrophytic community and the conformation of the substrate.

The answers are specified for each bank of the river and are assigned numerical values in 4 ranges (minimum weight 1, maximum weight 30) which express the functional differences between the individual answers. The total score can assume a value between 14 and 300 and this is associated to a Functionality Level and a Functionality Assessment, as shown in Table 3 which also reports the conventional colours used in the mapping activity.

Therefore, the proposed procedure includes not only the indicators specifically envisaged in the national legislation (LPM, EBI, RECS, REQS) but also the River Functionality Index which, in the authors' opinion, constitutes a further important element for the characterisation of a

Table 1. River quality classes.

Quality class	Judgement	Colour
I	Not polluted (or not considerably alterated) environment	Blue
II	Environment that shows some pollution's consequences	Green
III	Polluted environment	Yellow
IV	Very polluted environment	Orange
V	Greatly polluted environment	Red

Table 2. River Environment Quality Status (REQS).

Concentration of organic and inorganic chemical pollutants	REQS Class				
	1	2	3	4	5
≤Threshold value	Very good	Good	Suffic.	Poor	Very bad
>Threshold value	Poor	Poor	Poor	Poor	Very bad

Table 3. RFI score.

RFI	Funct. level	Funct. assessment	Colour
261–300	I	very good	blue
251–260	I–II	very good–good	blue–green
201–250	II	good	green
181–200	II–III	good–medium	green–yellow
121–180	III	medium	yellow
101–120	III–IV	medium–poor	yellow–orange
61–100	IV	poor	orange
51–60	IV–V	poor–very bad	orange–red
14–50	V	very bad	red

river's environmental quality as it considers the river ecosystem overall, including its connections with the surrounding area.

Finally, the above described investigations are integrated with the assessment of the Minimum Instream Flow (MIF), which aims to safeguard the physical characteristics of the river, the physical and chemical characteristics of the water and the typical biocenotic communities in natural environmental conditions, as pointed out in the recent Guidelines (a draft copy of which has been published by the Ministry for the Environment) in order to prepare for the basin's hydrological balance (article 22, paragraph 4, of the law D.L. 152/99).

In order to assess the MIF, reference has been made to the *hydro-biological approach* based on the search for environmental conditions suitable for the development of one or more representative species of the river's wildlife (*biological indicator*) using *in situ* measurement techniques, such as water depth and velocity and characteristics of the bottom substrate, to determine the above mentioned environmental conditions and hence define a habitat quality index as a function of the flow.

In particular, reference is made to the *Microhabitat Method* (Bovee 1978, 1982, Marchetti et al. 1991, Manciola et al. 1994, Santoro 1994, Bovee et al. 1998, Manciola & Neri 2000), using the PHABSIM (Physical HABitat SIMulation system) software (Waddle 2001).

3 SURVEY ON THE ENVIRONMENTAL QUALITY OF THE TUSCIANO RIVER

The methodological procedure briefly illustrated above was applied to the Tusciano river (Campania, Southern Italy), which is under the control of the Destra Sele Water Authority. The waterway's main axis is about 37 km long and has a catchment area measuring approximately 260 km^2. The main tributaries are the Vallone Isca della Serra, the Cornea, the Vallimonio, the Lama, the Rialto. For greater clarity, Figure 1 reports the catchment area and the hydrographic network of the Tusciano river.



Figure 1. Catchment basin and hydrographic network of Tusciano river.

In order to enable a reliable assessment of the environmental quality, the informations obtained in the previous surveys were used to set up a monitoring network comprising 8 sampling stations (indicated in Figure 2) located along the Tusciano (station n. 1, 2, 3, 5, 6 and 8), the Cornea (n. 4) and the Lama (n. 7).

As far as the fish population of the Tusciano river is concerned, the lack of time available meant that it was not possible conduct a field campaign to determine the experimental curves for the fish life in the river and so reference has had to be made to suitability curves taken from the scientific literature. In particular, the knowledge of the river's main characteristic features suggested that, for the survey to be complete, reference should be made to both *Salmonidae* (Salmo Trutta Fario) and *Cyprinidae* (Chub), taking into account two developmental stages (adult and fry) for both species.

The field surveys so far conducted have covered a time scale of six months. The results obtained – which should therefore be regarded as preliminary – are summarised in Table 4, which reports, for each sampled reach:

- the order number;
- the waterway in question;

- the watershed area;
- the results supplied by the physical, chemical and microbiological macrodescriptor parameters in terms of the overall score and the classification level (LPM);

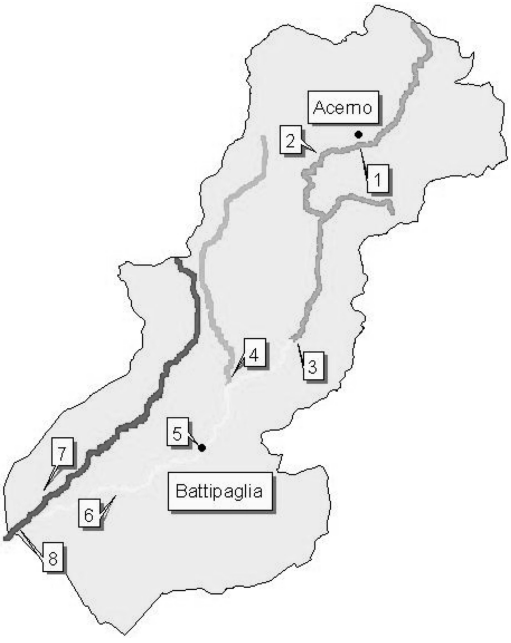


Figure 2. Tusciano river environmental quality map (preliminary draft).

- the results inferred from biological mapping, in terms of the Extended Byothic Index (EBI) and water quality class;
- the Ecological Status (RECS) – which always coincides with the Environmental Status (REQS) – to be attributed to the reach, with the corresponding assessment and the reference colour in the environmental quality map;
- the results supplied by the RFI in terms of the Functionality Assessment and the relative colour;
- the results obtained by applying the Microhabitats method, i.e. the range of the optimal flow (Q_{opt}) for the biological indicators considered (salmo trutta fario and chub).

The survey and study showed that the River Environmental Quality Status (REQS) was:

- satisfactory in the mountain reach of the Tusciano river (sampling sections 1 and 2), attributed with a *good* assessment (green);
- acceptable for the foothill and valley sections of the Tusciano river (sections 3, 5 and 6), attributed with a *sufficient* assessment (yellow);
- *very bad* (red) for the final reach of the Tusciano river (section 8);
- unsatisfactory for the tributaries, with *poor* assessment (orange) for the Cornea and *very bad* assessment (red) for the Lama.

In conclusion, the environmental quality status was insufficient for the final reach of the Tusciano river and for the tributaries Cornea and Lama. It was then possible to draw up the Tusciano river environmental quality map, reported in Figure 2, with the hydrographic

Table 4. Results of the field surveys.

Sect. (n.)	River	Area (km^2)	LPM		EBI		RECS	Judgment	Colour	RFI		Q_{opt} (m^3/s)
			Score	Level	Score	Class				Judg.	Colour	
1	Tusciano	38	390	2	10	I	2	good	green	very good–good	blue–green	0.2–1.2
2	Tusciano	81	390	2	9.5	II	2	good	green	very good–good	blue–green	0.4–1.8
										Left bank		
3	Tusciano	96	350	2	7	III	3	sufficient	yellow	good–medium	green-yellow	0.2–2.0
										Right bank		
										medium–poor	yellow–orange	
4	Cornea	31.4	145	3	4	IV	4	poor	orange	good–medium	green–yellow	0.2–1.8
5	Tusciano	148	250	2	6	III	3	sufficient	yellow	medium	yellow	0.2–2.8
6	Tusciano	154	250	2	7.4	III	3	sufficient	yellow	medium	yellow	0.2–1.4
7	Lama	22.7	70	4	2	V	5	very bad	red	medium	yellow	0.1–2.0
8	Tusciano	215	100	4	3.5	V	5	very bad	red	poor	orange	0.2–3.8

network marked in the colours corresponding to the environmental quality assessment. However, it should not be forgotten that the conclusions achieved on the basis of the data collected so far should be integrated by other *in situ* surveys so as to extend the field measurements to cover a time scale of at least one year.

Moreover, it must be pointed out that:

- with reference to the Level of Pollution from Macrodescriptors (LPM), in the surveys carried out there was an albeit small reduction in the macrodescriptor values as the flow increased. Measurements taken in periods characterised by low flow values – and hence by a lower dilution of pollutants – could therefore yield higher pollution levels;
- with reference to the Extended Byothic Index (EBI), the results are based on one or two measurements and not on a seasonal cycle (four measurements);
- the surveys carried out with reference to the River Functionality Index (RFI) reveal a slightly better situation for the Tusciano river (sections 1, 2 and 8) and a much better one for the tributaries (in particular for the Lama). The "river ecosystem" overall, thus, appears to be characterised by better environmental status compared to that of the surface waters, in particular for the reaches with a worrying Environmental Status (section 8, Tusciano, section 4, Cornea and section 7, Lama).

As far as the assessment of the Minimum Instream Flow is concerned, it must first of all be stressed that application of the Microhabitat method yielded unsatisfactory results for the fry of the biological indicators considered, and so the data reported in Table 4 refer to the adult species. The data obtained also made it possible to assess the unit optimal flow rate values $q = Q_{opt}/S$ (where Q_{opt} and S indicate, respectively, the optimal flow and the watershed area), summarised in Table 5 for the Tusciano river.

Moreover, the unit optimal flow assumes extremely high values for the tributaries, approximately 45–88 $l/s \cdot km^2$ for the Cornea and 53–57 $l/s \cdot km^2$ for the Lama. In this connection it should be pointed out that the Q_{ott} values taken for the tributaries are higher than the flows measured during the *in situ* surveys and hence fall in the area of the simulation performed by the PHABSIM software. There are, therefore, still question marks concerning the advisability of determining the optimal flow of waterways with small-sized basins.

The minimum instream flow, which is obviously much lower than the optimal flow, should on the other hand be determined by assessing the consequences on the biological indicators of a gradual reduction in the Weighted Usable Area (WUA) corresponding to the optimal flow WUA (Q_{opt}). Calculations carried out to this end, although tentative, have yielded the q values reported in Table 6, which were assessed with reference to values of 50% and 25% of the WUA (Q_{opt}).

Table 5. Unit optimal flow rates (Tusciano river).

	Q ($l/s \cdot km^2$)	
Section (n.)	Chub (adult)	Salmo Trutta Fario (adult)
1	31.5	31.5
2, 3, 5	16–17	17–21
6, 8	8, 17.5	9–11

Table 6. Unit optimal flow rates $q_{50\%}$ and $q_{25\%}$ (Tusciano river).

	Chub (adult)		Salmo Trutta Fario (adult)	
Section (n.)	$q_{50\%}$ ($l/s \cdot km^2$)	$q_{25\%}$ ($l/s \cdot km^2$)	$q_{50\%}$ ($l/s \cdot km^2$)	$q_{25\%}$ ($l/s \cdot km^2$)
1	21.3	17.1	21.3	17.1
2, 3, 5	7.5–9.5	4.3–7.1	7.4–10.1	5.1–7.1
6, 8	5.5–7	3.6–4.5	5.3–5.6	2.9–4.4

In conclusion, the application of the proposed integrated approach (physical, chemical, microbiological, toxicological, biological, hydraulic and ecological) has made it possible to provide an albeit preliminary definition of the environmental quality status for the watershed of the Tusciano river.

The results obtained, combined with a soil–land use (climate, soil, crop condition) study of the catchment area and with the availability of an updated map indicating water usage and industrial and urban discharge sources, could suggest a preliminary definition of the areas to be safeguarded and the publication of *practical guidelines for environmental restoration* by means of an integrated strategy of non-structural and structural measures.

REFERENCES

Agenzia Nazionale per la Protezione dell'Ambiente. 2000. *Il monitoraggio dello stato dell'ambiente in Italia*, Roma, ANPA.

Bovee, K.D. 1978. *Probability-of-Use Criteria for the Family Salmonidae*. Instream Flow Information Paper n. 4, Cooperative Instream Flow Group, U.S. Fish and Wildlife Service.

Bovee, K.D. 1982. *A guide to stream habitat analysis using incremental methodology*. Instream Flow Information Paper, U.S.D.I. Fish and Wildlife Service, Office of Biological Services.

Bovee, K.D., Lamb, B.L., Bartholow, J.M., Stalnaker, C.B., Taylor, J. & Henriksen, J. 1998. *Stream Habitat Analysis Using the Instream Flow Incremental Methodology*. U.S.

Geological Survey, Biological Resources Division, Information and Technology Report USGS/BRD-1998-0004.

D.L. 11.05.1999, n. 152. 1999. *Disposizione sulla tutela delle acque dall'inquinamento e recepimento della Direttiva 91/271/CEE concernente il trattamento delle acque reflue urbane e della Direttiva 91/676/CEE relativa alla protezione delle acque dall'inquinamento provocato dai nitrati provenienti da fonti agricole*. Suppl. Ord. n. 101/L to G.U. 29.05.1999, n. 124.

D.L. 18.08.2000, n. 258. 2000. *Disposizioni correttive ed integrative del D.L. 11.05.1999, n. 152, in materia di tutela delle acque dall'inquinamento, a norma dell'art. 1, comma 4, della L. 24.04.1998, n. 128*. Suppl. Ord. n. 153 to G.U. 18.09.2000, n. 218.

European Environment Agency. 1999. *Environmental Indicators: Typology and Overview*. Copenhagen, EEA.

Ghetti, P.F. 1995. *Indice Biotico Esteso (I.B.E.)*. Notiziario dei metodi analitici, IRSA, CNR.

Ghetti, P.F. 1997. *Manuale di applicazione: Indice Biotico Esteso (I.B.E.). I macroinvertebrati nel controllo della qualità degli ambienti di acque correnti*. Ed. Provincia autonoma di Trento – Agenzia provinciale per la protezione dell'ambiente, Trento.

Giugni, M., Celico, P.B., Fontana, N. & Lombardi, G. 2002. A proposed methodology for drawing up water protection plans, In *2nd International Conference New Trends in Water and Environmental Engineering for Safety and Life: Eco-Compatible Solutions for Aquatic Environments, Capri, 24–28 June*.

Manciola, P., Martini, P. & Umbertini, L. 1994. Significato del deflusso minimo vitale e sua determinazione per un corso d'acqua dell'Italia Centrale. *Idrotecnica* (2).

Manciola, P. & Neri, N. 2000. Armouring influence on the estimate of instream flow. In *Proceedings of the IASTED International Conference Modelling and Simulation (MS 2000), May 15–17, Pittsburgh, Pennsylvania-USA*.

Marchetti, R., Crosa, G. & Cotta Ramusino, M. 1991. Applicazione del metodo sperimentale PHABSIM per la valutazione della portata minima: caso del fiume Toce. *Inquinamento* (11).

Petersen, R.C. jr. 1992. The RCE: a Riparian, Channel and Environmental Inventory for small streams in agricultural landscape. *Freshwater Biology*, 27(2).

Ruffo, S. 1995.*Gli ecosistemi fluviali con particolare riguardo alla fauna*. Accademia Nazionale dei Lincei, 90.

Santoro, M. 1994. *Il minimo deflusso vitale*. Idrotecnica (6).

Siligardi, M., Bernabei, S., Cappelletti, C., Chierici, E., Ciutti, F., Egaddi, F., Franceschini, A., Maialini, B., Mancini, L., Minciardi, M.R., Monauni, C., Rossi, G., Sansoni, G., Spaggiari, R. & Zanetti, M. 2000. *Indice di funzionalità fluviale (IFF)*. Roma, ANPA.

Siligardi, M. & Maiolini, B. 1993. L'inventario delle caratteristiche ambientali dei corsi d'acqua alpini. Guida all'uso della scheda RCE-2. *Biologia Ambientale*. CISBA, VII, 30.

Waddle, T.J. 2001. *PHABSIM for Windows: User's Manual and Exercises*. On line publication.

River Flow 2004 – Greco, Carravetta & Della Morte (eds.)
© 2004 Taylor & Francis Group, London, ISBN 90 5809 658 0

Longitudinal dispersion in an extreme meander channel, with changes in shape

J.B. Boxall
Lecturer, Department of Civil and Structural Engineering, University of Sheffield, Sheffield, S1 3JD, UK

I. Guymer
Reader, Department of Civil and Structural Engineering, University of Sheffield, Sheffield, S1 3JD, UK

ABSTRACT: Results are presented from a series of experiments conducted on a large-scale laboratory channel with extreme meander planform geometry. The channel had an idealised 'natural' form, with longitudinally variable cross-sectional shape, but constant cross-sectional area. Tracer studies were conducted to investigate the effects of the channel configuration and different discharges on mixing and transport processes. From this new data set, dispersion coefficients are calculated and compared to results for less extreme geometries. The effects of non-dimensionalising are also explored.

1 INTRODUCTION

Understanding and predictive modelling of the fate of soluble pollutants is essential for the efficient management of river environments. Pollutants may originate from either slowly varying inputs, such as sewerage treatment works, or more rapidly varying inputs, such as accidental spills or intermittent discharges from combined sewer overflows during storm conditions. It is desirable to make predictions of both the travel or retention times and the spreading or dispersion of such pollutants, for applications such as environmental impact assessment, protection of abstraction points or aquifer recharge sites. Application of the European Water Frame Water Directive requires quantification of travel times and mixing processes for the estimation of water quality processes at a catchment scale. It is desirable to understand, quantify and to be able to predict the impact of channel form and discharge on mixing processes.

2 BACKGROUND

Solute mixing has been an area of active research since the work of Taylor (1953, 1954), who showed that for pipe full flow, after an initial period, there exists a balance between the effects of shear dispersion (differential velocities) and turbulent diffusion.

Reviews of fundamental theory, and application to open channel flows through laboratory and field studies can be found in Fischer *et al* (1979) and Rutherford (1994).

Vertical mixing is often neglected in open channel flows because of the relatively short length scale. Transverse mixing is of particular interest below continuous sources, and has an inverse relationship to the processes of longitudinal mixing (Fischer 1969). Longitudinal mixing is associated with the temporal and spatial development of a slug of pollutant or tracer once it has become cross-sectionally well mixed, and is the focus of the study reported here.

Previous studies have investigated the influence of many channel properties on longitudinal mixing. Jobson (1997) presented a compilation and regression analysis of field tracer studies in the USA. In particular looking at the relationship of empirical predictors for various channel properties, such as slope, dimensionless drainage area, relative discharge and local discharge.

Rutherford (1994) prefaces his compilation of longitudinal mixing field study data performed on sinusoidal and meandering channels by noting the difficulties of accurately reporting values for hydraulic parameters for field studies. A similar compilation is presented by Fukuoka and Sayre (1973). The conclusion from these compilations is that a wide range of mixing coefficients are obtained from natural

channels, and that the non-dimensionalising undertaken was not sufficient to account for all the processes present.

Two parameters, which might be expected to have a major influence on mixing processes, are planform curvature and changes in cross-sectional shape. These two parameters will have a dramatic impact on shear dispersion, which Smith (1992) defines as the dominant longitudinal mixing process by at least two orders of magnitude.

Rozovskii (1957) performed fundamental research into the hydraulics of flow in curved channels, deriving simple predictive expressions and providing field and laboratory validation and verification. Based on this, Fischer (1969) derived an expression to predict longitudinal dispersion coefficients under fully developed secondary flow conditions. The expression was proved for an infinitely long bend in the laboratory, but was shown to have limited validity for natural channel data. The expression includes an inverse relationship between transverse and longitudinal mixing. Hence, increased transverse shear effects, due to secondary currents induced by planform curvature (Boxall and Guymer 2003) reduce the rate of longitudinal mixing.

Fukuoka and Sayre (1973) and Guymer (1998) present results for laboratory studies into longitudinal mixing undertaken in sinusoidal and meandering channels. These studies again show a range of standard and non-dimensionalised longitudinal mixing coefficients. Guymer (1998) also studied the effects of various discharges, suggesting that the observed change in non-dimensionalised mixing coefficient with discharge was due to changes in degree of longitudinal variability of cross-sectional shape (trapping or dead zone effects) of the idealised natural channel form studied. The influence of dead or trapping zones in straight channels with boundary dead zones was explored by Valentine and Wood (1977).

The data reported in this paper was collected on the same experimental facility utilised by Guymer (1998), using a similar idealised 'natural', variable cross-sectional profile with a more extreme meander geometry.

3 ANALYSIS METHODS

Expressions based on Fick's law of diffusion can be theoretically derived to explain the mixing processes occurring in natural channels, provided several assumptions are met: sufficient time has elapsed since injection for equilibrium to establish between diffusion and dispersion, turbulence is statistically independent of time, and the flow cross-section is independent of time and distance. These assumptions are not met in most natural channel situations, however application of mathematical solutions has been shown to provide good representation of measured data, Fischer (1979) and Rutherford (1994).

The one dimensional analytical solution to a Fickian dispersion model may be written as:

$$c_A(x,t) = \frac{M}{A\sqrt{4\pi Dt}} \exp\left(-\frac{(x-u_A t)^2}{4Dt}\right) \quad (1)$$

where c_A is area mean concentration, M mass of pollutant or tracer, A area of flow, u_A area mean longitudinal velocity, x longitudinal distance, t time and D the longitudinal dispersion coefficient. Prior knowledge or prediction of D and t are required to make use of such expressions in a predictive manner.

Taylor (1954) showed that in specific situations the variance of a tracer cloud increases linearly with time, hence D can be defined from the change in spatial variance. Fischer (1966) used a frozen cloud approximation to determine the longitudinal dispersion coefficient through the change in temporal variance:

$$D = \frac{u_A^2}{2}\left[\frac{\sigma_t^2(x_2) - \sigma_t^2(x_1)}{\bar{t}_2 - \bar{t}_1}\right] \quad (2)$$

where σ_t^2 is the temporal variance in the longitudinal direction, and 1 and 2 upstream and downstream sites.

Velocity, u_A maybe evaluated from:

$$u_A = \frac{x_2 - x_1}{\bar{t}_2 - \bar{t}_1} \quad (3)$$

where $\bar{t}_i$ is the time of passage of the centroid of the tracer cloud, given by:

$$\bar{t}_i = \frac{\int_{t=-\infty}^{\infty} t c(x_i,t)\,dt}{\int_{t=-\infty}^{\infty} c(x_i,t)\,dt} \quad (4)$$

and the temporal variance from:

$$\sigma_t^2(x_i) = \frac{\int_{t=-\infty}^{\infty} (t-\bar{t}_i)^2 c(x_i,t)\,dt}{\int_{t=-\infty}^{\infty} c(x_i,t)\,dt} \quad (5)$$

This is often referred to as the method of moments. In most experiments concentrations are monitored using Eulerian measurement techniques, hence temporal variances are most readily obtained.

Expression 2 maybe evaluated by calculating the gradient of change in variance with distance along a study reach, from a sequential of measurement sites. This assumes that the mixing processes are constant over the reach. This assumption can be validated by the quality of the straight line fit obtained, this approach was employed by Guymer (1998). Alternatively the

dispersion coefficient can be evaluated between each pairing of tracer measurement sites, and the consistency of mixing processes over a reach evaluated by calculating the mean and standard deviation of the values obtained. This method will be employed in this paper.

Identifying the start and end of the tracer plumes is essential for the above calculations. Variance in particular is highly sensitive to this, since although the concentration maybe low at the plume extremes, the distance from the centroid will be relatively large and this term is squared in the calculation of variance. In the work reported here the plume edges are defined as a sequence of 30 data points with a concentration of less than 0.1% of the peak.

3.1 *Guymer 1998*

Guymer (1998) reports data obtained from the Flood Channel Facility at HR Wallingford in the UK. Two channel were studied one with trapezoidal cross-section and the other an idealised natural channels form. Both channels were based on 60° meander planform geometry and were cast in concrete. The idealised natural channel form had a variable cross-sectional shape with longitudinal distance, but a constant cross-sectional area. This data set was available in its raw data format and has been reanalyzed using the method outlined above. The original and recalculated dispersion coefficients for this data set are presented in table 1.

From table 1 it can be seen that the different methods of identifying the start and end of the data and of averaging the dispersion coefficient for each discharge has resulted in a slight decrease in the values obtained. The variation within the repeat injections at each discharge are indicated by the error bars in figure 1. Figure 1 also shows the variation of dispersion coefficient with discharge, showing a possible trend to increase with discharge, although this is small relative to the scatter in the data.

For predictive purposes it is desirable to attempt to normalise the longitudinal mixing coefficient, such that a single dimensionless predictive value, trend or relationship may be obtained. Previous attempts have utilised bed shear velocity (u*) as a measure of flow resistance generating turbulence. The depth of flow has been adopted as a measure of the maximum length scale of turbulence, or perhaps more applicably to natural or varying channels the hydraulic radius should be used, as a measure of the maximum length scale of turbulence structures and/or as a measure of channel shape. Non-dimensionalising was reported in a tabular form by Guymer (1998), and can also be seen plotted as a function of discharge in figure 2.

Table 1. Dispersion coefficient values for 60° meander channel from Guymer (1998) and from re-analysis.

Channel	Discharge (l/s)	D (1998) (m^2/s)	D (new) (m^2/s)
Trapezoidal	46.1	0.0814	0.0889
Natural	28.6	0.0892	0.0838
Natural	21.4	0.1242	0.0902
Natural	19.1	0.1198	0.1028
Natural	17.7	0.1133	0.1032
Natural	13.7	0.0847	0.0759
Natural	10.5	0.0755	0.0663

Guymer (1998) provides single averaged non-dimensionalised values of longitudinal dispersion coefficient for the 'natural' and trapezoidal channel shapes studied. However from figure 2 it appears that there maybe a more complex relationship with discharge for the natural channel.

Dispersion, or differential shear, is thought to dominate mixing. As discharge increases in a straight uniform channel the transverse variation of longitudinal velocity will become more developed, increasing shear effects. Therefore longitudinal mixing might be expected to increase with increasing discharge.

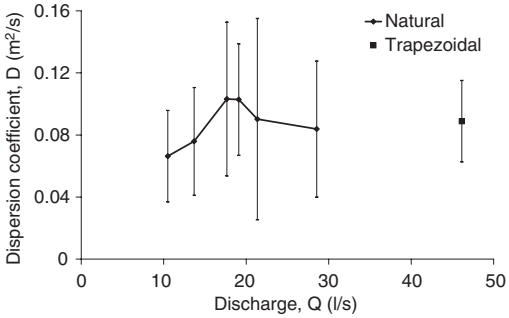


Figure 1. Variation of longitudinal dispersion coefficient for 60° natural and trapezoidal channel data, reanalyzed from Guymer (1998). Error bars represent mean plus and minus standard deviation.

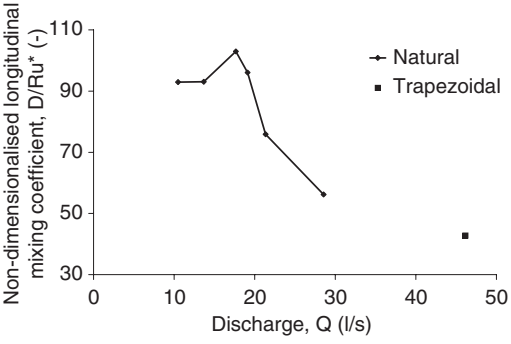


Figure 2. Variation of non-dimensionalised longitudinal dispersion coefficient for 60° natural and trapezoidal channel data, reanalyzed from Guymer (1998).

Guymer (1998) suggests that as discharge and depth decreases the 'tapping' effects of the 'plateaus' on the inside of the bends increases, which could explain the overall increase in non-dimensionalised mixing coefficient with decreasing discharge seen in figure 2.

4 EXPERIMENTAL SETUP

Data is reported from studies undertaken at the Flood Channel Facility at HR Wallingford in the UK. The channel was of the same type of idealised 'natural', longitudinally variable cross-sectional shape as used for study reported by Guymer (1998). This configuration was based on a 110° meander planform. The channel was cast in concrete. The planform geometry can be seen in figure 3 and a representation of 'natural' cross-sectional shape in figure 4. More details of these planforms and cross-sectional forms can be found in Sellin and Greenhill (1992) and Knight *et al* (1992).

Tracer studies were undertaken at a variety of discharges, from bank full (∼25 l/s) down to a minimum cover on the plateau around the inside of each bed of 10 mm (∼12 l/s). Uniform flow conditions were set and monitored using a series of depth gauges. Short duration pulses of Rhodamine WT dye were introduced as a line source across the bed at the channel inlet through a small diameter pipe with 0.5 mm holes at 5 mm centres. This was done to promote cross-sectional mixing, reducing the distance to well-mixed conditions. Five Turner Design Series 10 Fluorometers in continuous pump though mode were employed to obtain simultaneous measurements of the temporal variation of the solute cloud at different longitudinal locations, as indicated in figure 3. A further instrument was located upstream of the injection point to monitor the background buildup associated with re-circulating facilities. These instruments where all logged directly to a PC. 6 repeat injections were made at each flow rate.

5 DATA

5.1 *Raw data*

An example plot of the background corrected, calibration applied, concentration time data obtain is shown in figure 5. This highlights the reduction in peak concentration and increasing spread with time/distance.

Figure 6 shows example data from the furthest downstream measurement site for the highest and the lowest flow rates. The traces have been presented relative to the first arrival of tracer at the site and normalised by the peak concentration of each trace. The trace from the lower flow rate shows greater spreading, although it should be remembered that this pulse of tracer has been in the flow for a relatively longer period, and therefore subject to the mixing processes for longer.

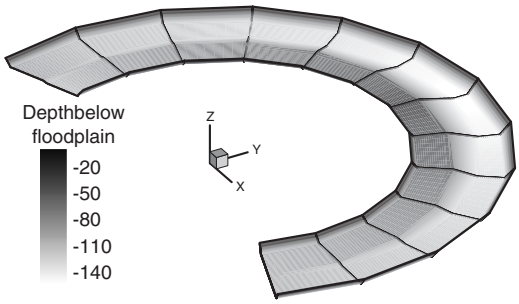


Figure 4. Contour plot of 110° geometry.

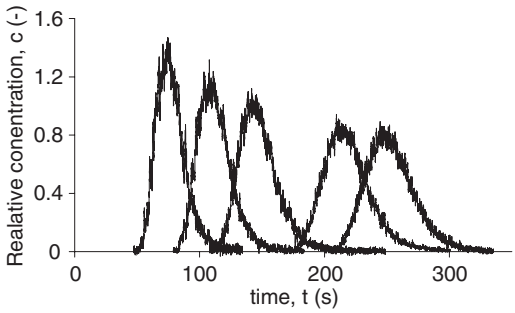


Figure 5. Example concentration time plot from 110° channel at bank full flow conditions.

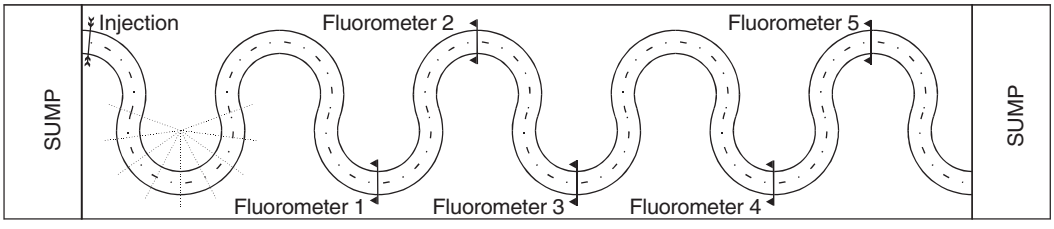


Figure 3. Planform channel layout, injection and monitoring locations.

5.2 *Analysed data*

Figure 7 shows the trend for the mean travel times and velocities calculated from the centroid of the tracer clouds at each flow rate. The plot also includes error bars indicating mean plus and minus the standard deviation for the repeat injections. As expected mean travel time decreases and velocity increases with increasing discharge.

Figure 8 shows the results of calculation for longitudinal dispersion coefficient from the measured tracer data. Again the plot shows mean values, and error bars for mean plus and minus standard deviation of the repeat injections at each flow rate.

Comparing figure 8 with figure 1 suggests that the longitudinal mixing coefficient for the 110° 'natural' channel is of a comparable magnitude to that found for the 60° 'natural' channel, although slightly lower. The longitudinal dispersion coefficients found for the 60° 'natural' channel data set showed a tentative trend, increasing with discharge. Figure 8 suggests that the trend for the 110° is a constant value, or slight reduction with discharge. However, the error bars for each data set indicate that the spread in the data is greater than any of these trends. This spread is associated with the sensitivity of the variance calculation to the definition of the start and end of the measured traces.

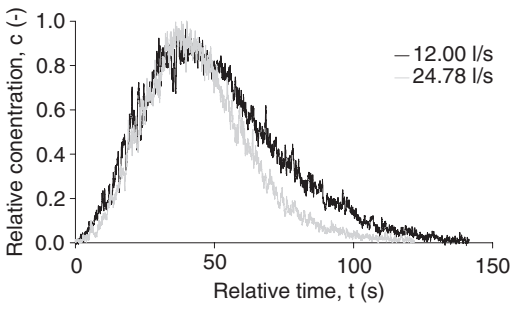


Figure 6. Example concentration time plot from farthest downstream measurement site (plot relative to first arrival times and peak concentration of each trace).

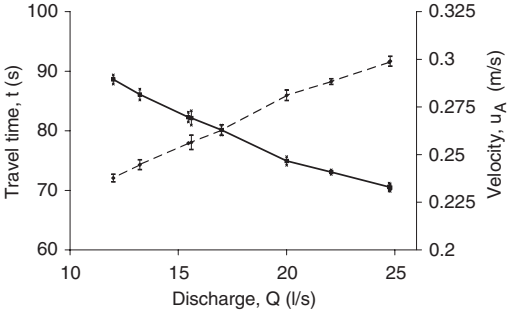


Figure 7. Travel time and velocity for 110° meander channel.

The longitudinal dispersion coefficients found for the 110° degree channel have been non-dimensionalised by the hydraulic radius and the bed shear velocity evaluated from $u^* = (gRS_0)^{0.5}$. The value obtained compares well with the reach average value of the sectional average shear stress presented by Knight *et al* (1992), and recreated in figure 9. This detailed data is only available for bank full flow conditions. Figure 9 highlights the low longitudinal variation in boundary shear stress, with only a slight peak partway into each bend.

Table 2 presents channel properties and average non-dimensionalised longitudinal mixing coefficients as reported by Guymer (1998) with the addition of values for the 110° natural channel form results presented here. As reported by Guymer (1998) the values for the sinuous channels of constant cross-sectional shape are in good agreement, with a slightly greater value obtained for the trapezoidal channel, due to the greater shear dispersion effects associated with such a cross-section. Both the 'natural' channels with constant cross-sectional area, but longitudinally variable cross-sectional shape, show an increase in the value of

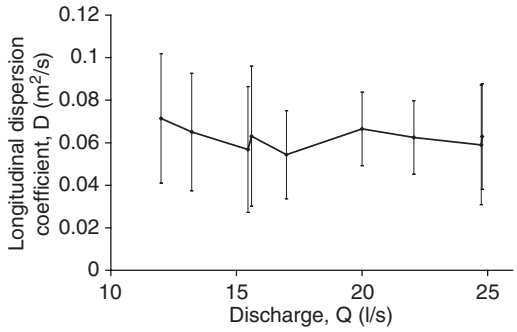


Figure 8. Dispersion coefficient for 110° meander channel.

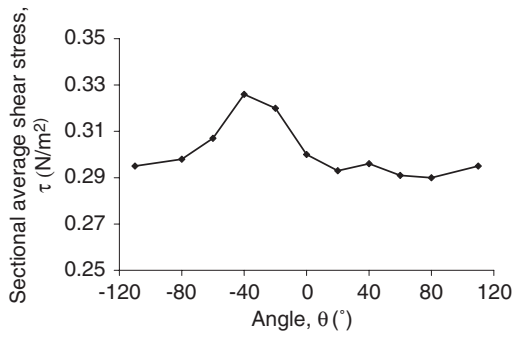


Figure 9. Longitudinal variation in sectional average boundary shear stress for bank full flow in the 110° 'natural' channel, from Knight *et al* (1992). 0° is the apex of the bend.

Table 2. Comparison between Fukuoka and Sayre (1973), Guymer (1998) and present study results.

Study	Channel shape	Sinuosity	Coefficient, D/Ru*
Fukuoka & Sayre (1973)	Rectangular	1.180	28.1 ± 11.4
Guymer (1998)	60°, trapezoidal	1.374	39.2
Guymer (1998)	60°, idealised natural	1.374	99.8 ± 19.99
Present	110°, idealised natural	2.043	63.6 ± 17.94

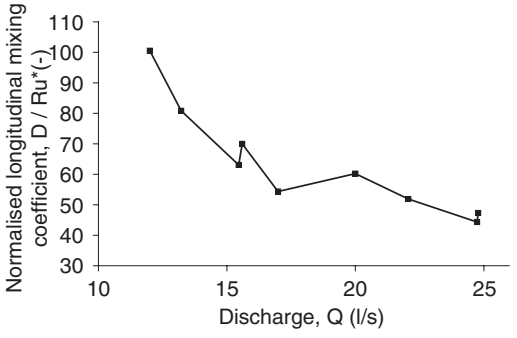


Figure 10. Non-dimensionalised dispersion coefficients for 110° meander channel.

non-dimensionalised longitudinal mixing coefficient, with a greater increase associated with the 60° less extreme meander geometry.

The variation of the non-dimensionalised longitudinal mixing coefficient with discharge for the 110° meander geometry is shown in figure 10. As with the 60° channel it can be seen that the non-dimensionalised longitudinal dispersion coefficient is not constant with discharge. Unlike the 60° data the trend for the 110° data appears to be inversely proportional to discharge.

The trends with discharge of the non-dimensionalised longitudinal dispersion coefficients resulting from both the 60° and 110° idealised natural channel forms are shown in figure 11. From this it can be seen that for both channel planforms the non-dimensionalised longitudinal mixing coefficient shows a similar decrease.

6 DISCUSSION

For both the 60° and the 110° channel planform data sets reviewed and reported respectively in this paper, it has been shown that as discharge increases the longitudinal dispersion coefficient non-dimensionalised

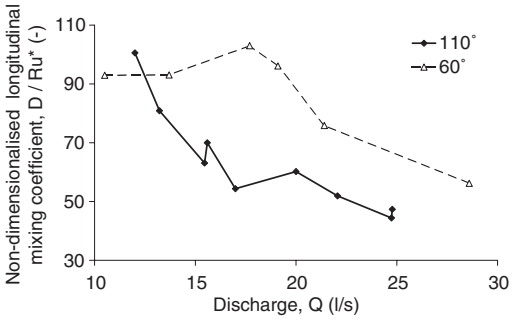


Figure 11. Non-dimensionalised dispersion coefficients for 60° and 110° meander channels.

by hydraulic radius and bed shear velocity, tends to decrease. This suggests that processes other than those accounted for by the non-dimensionalising factors are at work.

Differential shear is thought to dominate longitudinal mixing. Hence as discharge increases in a straight uniform channel, and the velocity profile becomes more developed, the effects of shear dispersion should increase. Therefore longitudinal mixing might be expected to increase with increasing discharge.

According to Rozovskii (1957), the strength of full developed secondary circulation is directly proportional to the mean longitudinal velocity. This taken with the inverse relationship between longitudinal and transverse mixing, highlighted by the expression of Fischer (1969) suggests that as discharge increases in a channel with planform curvature the effects of increasing longitudinal velocity shear will be counteracted by increasing secondary flows. However this trend will be further complicated by the buildup, decay and reversals of secondary circulations associated with meandering channels.

It is suggested that as discharge increases the idealised natural channel shape used for these studies becomes more uniform, hence the trapping effects of the plateau around the bend apexes becomes less, decreasing longitudinal mixing. It is suggested that it is this last trend that dominates the data presented here.

7 CONCLUSIONS

New longitudinal dispersion coefficient values are presented from experiments conducted on a channel with extreme meander geometry and an idealised 'natural' cross-sectional shape. Comparisons of these values with ones from a channel with less extreme geometry, but the same idealised natural cross-sectional form, show close agreement.

Non-dimensionalised longitudinal mixing coefficients from two meandering channels with idealised natural channel forms are shown to be greater than

values resulting from straight rectangular and trapezoidal channels. However it has been found that increasing sinuosity does not correlate with increased longitudinal mixing.

Attempts to normalise longitudinal mixing coefficients resulting from the meandering natural channels at different discharges, using bed shear velocity and hydraulic radius, have been shown to be insufficient to produce a single predictive value. However, a trend with discharge is elucidated for these channels.

REFERENCES

Boxall, J.B. and Guymer, I. (2003) 'On the analysis and Prediction of transverse mixing coefficients in natural channels' Journal of Hydraulic Engineering, ASCE. Vol. 129, No. 2 February 2003, pp 129–139.

Fischer, H.B. (1966) "Longitudinal dispersion in Laboratory and Natural Streams", Technical Report KH-R-12, W.M. Keck Laboratory of Hyd. and Wat. Resources.

Fischer, H.B. (1969) 'The Effects of Bends on Dispersion in Streams' Water Resources Research, April, Vol. 5, No. 2, pp 496–506.

Fischer, H.B., List, E.J., Koh, R.C.Y., Imberger, J. and Brooks, N.H. (1979) "Mixing in Inland and Coastal Waters", Academic Press, New York.

Fukouka, S. and Sayre, W.W. (1973) "Longitudinal Dispersion in Sinuous Channels", A.S.C.E., HY1, 99, pp 195–217.

Greenhill, R.K. and Sellin, R.H.J. (1993) "Development of a Simple Method to Predict Discharges in Compound Meandering Channels", Proc. Instn. Civ. Engrs. Wat., Marit. & Energy, 101, Mar., 37–44.

Guymer, I. (1998) 'Longitudinal Dispersion in a Sinuous Channel with Changes in Shape' Journal of Hydraulic Engineering, ASCE, Vol. 124, No. 1, pp 33–40.

Jobson, H.E. (1997) 'Predicting Travel Time and Dispersion in Rivers and Streams' Journal of Hydraulic Engineering, ASCE, November, pp 971–978.

Knight, D.W., Yuan, Y.M. and Fares, Y.R. "Boundary shear stress in meandering channels" International Symmposium on Hydraulics Research in Nature and Laboratory, Nov 17–20, 1992, Wuhan, China, pp 102–107.

Rosovskii, I.L. (1957) "Flow of Water in Bends of Open Channels", Academy of Sciences of Ukranian SSR, (translated by Isreal Prog. for Scientific Translations, Jerusalem, Isreal, 1961).

Rutherford, J.C. (1994) "River Mixing", J. Wiley & Sons, Chichester, England.

Smith, R. (1992) 'Physics of Dispersion' Coastal and Estuarine Pollution – Methods and Solutions' Technical sessions, Scottish hydraulics study group, One day seminar 3rd April, Glasgow.

Taylor, G.I. (1953) "Dispersion of Soluble Matter in Solvent Flowing Slowly Through a Tube", Proc. R. Soc. London Ser. A, 219, 186–203.

Taylor, G.I. (1954) "The Dispersion of Matter in Turbulent Flow Through a Pipe", Proc. R. Soc. London Ser. A, 223, 446–468.

Valentine, E.M. and Wood, I.R. (1977) "Longitudinal Dispersion with Dead Zones", A.S.C.E., HY9, 103, 975–990.

This page intentionally left blank

River Flow 2004 – Greco, Carravetta & Della Morte (eds.)
© 2004 Taylor & Francis Group, London, ISBN 90 5809 658 0

Evaluation of longitudinal dispersion coefficients for over-bank flow

Steve G. Wallis
Heriot-Watt University, Edinburgh, Scotland

J. Russell Manson
The Macaulay Institute, Aberdeen, Scotland

ABSTRACT: The majority of approaches for predicting pollutant transport in rivers rely on being able to estimate dispersion coefficients. This paper makes predictions of dispersion coefficients for in-bank and over-bank conditions in a two-stage channel, the latter predictions being a new contribution to the field. The work combines a simplified method for predicting the transverse structure of open channel flows with an established technique for evaluating longitudinal dispersion coefficients. The method was applied to an existing hypothetical benchmark channel. For the in-bank case, the dispersion coefficient was very small (less than 3 m^2/s) and increased approximately linearly with flow rate. For the over-bank case, the dispersion coefficient was several orders of magnitude larger and decreased non-linearly with flow rate. The predictions for both flow conditions are consistent with experimentally derived trends reported in the literature, and they provide the first theoretical support for the observations in the over-bank case. The cause of the very large dispersion coefficients in the over-bank case is a strong transverse velocity shear created by areas of low velocity water on the flood plains. The over-bank results have significant implications for users of mathematical models of pollutant transport.

1 INTRODUCTION

Mathematical models are routinely used to predict the fate and transport of pollutants that are accidentally released into rivers. Although several models have been developed for simulating such pollution incidents (Beltaos, 1982, Bencala & Walters, 1983, Wallis et al, 1989, Jobson, 1997, Worman, 2000), the majority are based on the one-dimensional advection-dispersion equation (Fischer, 1967).

The use of this approach requires modellers to estimate dispersion coefficients in rivers. Whereas there is a large body of work devoted to predicting dispersion coefficients in natural and man-made channels for in-bank flows, e.g. McQuiver & Keefer (1974), Jain (1976), Liu (1977), Fischer et al (1979), Rutherford (1994), Seo & Cheong (1998), Deng et al (2002), Wallis & Manson (in prep.), no corresponding work has been undertaken for over-bank flows. The primary aim of this paper is to address this gap in knowledge by making predictions about longitudinal mixing under these conditions that occur when rivers are in flood, with flow taking place in both the main channel and also in the adjacent flood plains. The hydraulics of such flows has been studied extensively in recent years (Keller & Rodi, 1988, Shiono & Knight, 1991, Ackers, 1993, Naot et al, 1993, Lambert & Sellin, 1996, Sofialids & Prionos, 1999, Ervine et al, 2000) primarily because so-called two-stage channels have increasingly been incorporated in the design of flood relief schemes as a means of providing sufficient flow conveyance and/or storage. However, the transport of pollutants that enter these channels during flood conditions has not been extensively studied.

The specific objectives of the paper are to describe a method for predicting dispersion coefficients in channels, to apply the method to in-bank and over-bank flows in a two-stage channel and to discuss the implications of some of the predictions that are made for over-bank flows.

2 THEORETICAL BACKGROUND

The advection-dispersion equation (ADE) for a conservative solute is given below:

$$\frac{\partial C}{\partial t} + \frac{U\partial C}{\partial x} = \frac{D\partial^2 C}{\partial x^2} \qquad (1)$$

where C is the cross-sectional average solute concentration, U is the cross-sectional average longitudinal

flow velocity, D is the longitudinal dispersion coefficient, x is the longitudinal space co-ordinate and t is time.

In this, longitudinal dispersion is modelled using a diffusion term in which the rate of streamwise spreading of a solute cloud is governed by the magnitude of the dispersion coefficient. As a result of the one-dimensional formulation of the ADE the nature of the dispersion coefficient is rather complex because it arises from the interaction of two physical processes, namely differential longitudinal advection and cross-sectional mixing. The former encapsulates the transverse and vertical gradients of the longitudinal velocity that drive the streamwise spreading while the latter continually re-distributes solute within the plane of the cross-section and tempers the streamwise spreading. Both turbulent diffusion and secondary currents contribute to the cross-sectional mixing.

The way in which the dispersion coefficient depends on differential longitudinal advection and cross-sectional mixing is described by the following equation:

$$D = -\frac{1}{A}\int_A U'(y,z)\,f(y,z)\,dA \qquad (2)$$

where A is the cross-sectional area of flow, U′ is the local deviation of the longitudinal velocity from the cross-sectional average longitudinal velocity, f is a function that describes the cross-sectional distribution of the transverse and vertical mixing coefficients, y is the transverse space co-ordinate and z is the vertical space co-ordinate. Given information on the magnitudes and the distributions of the longitudinal velocity and the mixing coefficients in a cross-section, Equation 2 can be used to evaluate D.

Since the work of Fischer (1967), which was based on the earlier work of Taylor (1954), it has generally been accepted that transverse differential longitudinal advection and transverse mixing dominate the generation of longitudinal dispersion in rivers because they are usually much wider than they are deep. The evaluation of D from Equation 2 is then simplified because only the transverse distributions of depth-averaged longitudinal velocity and depth-averaged transverse mixing coefficient are required. Nevertheless, the practical application of this method is far from simple, requiring the evaluation of the following triple integral (Fischer, 1967, Fischer et al, 1979, French, 1986):

$$D = -\frac{1}{A}\int_0^W hu'\int_0^y \frac{1}{\varepsilon_y h}\int_0^y hu'\,dydydy \qquad (3)$$

where W = channel top width (i.e. width at the water surface), h = h(y) is the local flow depth, u′ = u′(y) is the local deviation of the depth-averaged longitudinal velocity from the cross-sectional average longitudinal velocity, $\varepsilon_y = \varepsilon_y(y)$ is the local depth-averaged transverse mixing coefficient and the other symbols are as previously defined.

Alternative approaches for evaluating dispersion coefficients include the method of moments, Fischer's routing method and the use of empirical equations (Fischer et al, 1979, Rutherford, 1994, Wallis & Manson, in prep.). In the context of the current paper, however, the use of Equation 3 is the most appropriate method because much of the information that would be required to use the other methods is not available for over-bank flows.

To use Equation 3 for any given channel cross-sectional shape, we require information on the transverse velocity profile and the transverse distribution of the transverse mixing. A theoretical method for achieving this is described below.

3 THEORETICAL ANALYSIS OF FLOW STRUCTURE

The two-dimensional depth-averaged shallow water equations may be simplified for the case of fully developed steady flow in a river of general cross-section. In the simplest case, the steady depth-averaged longitudinal momentum conservation equation can be written as (Shiono & Knight, 1991):

$$\rho g S_o h = \tau_b \cos\theta - \frac{\partial}{\partial y}\left(h\tau_{yx}\right) \qquad (4)$$

in which ρ is the fluid density, g is the gravitational acceleration, S_o is the channel bed slope, h = h(y) is the local depth, $\tau_b = \tau_b(y)$ is the local longitudinal bed shear stress, θ is the transverse slope of the bed and $\tau_{yx} = \tau_{yx}(y)$ is the local depth-averaged shear stress in the x-direction on the plane perpendicular to the y-direction. Equation 4 applies at all transverse locations and describes a local balance between the component of fluid weight down the channel slope and the resisting longitudinal shear stresses on horizontal and vertical planes (caused by bed roughness and transverse turbulent momentum exchange, respectively). Here, the effect of transverse secondary flows has been ignored. Also note that for a transversely horizontal domain, in which h is constant, $\theta = 0$.

Using a quadratic friction law the local longitudinal bed shear stress can be re-written in terms of Manning's resistance coefficient, n, giving:

$$\tau_b = \frac{\rho g u^2 n^2}{h^{1/3}} \qquad (5)$$

where u = u(y) is the local depth-averaged longitudinal velocity and the hydraulic radius has been replaced with the local depth.

Using the Boussinesq eddy-viscosity concept, the longitudinal shear stress caused by transverse turbulent momentum exchange can be represented in terms of the transverse gradient of local depth-averaged velocity, as follows:

$$\tau_{yx} = \rho\varepsilon_{yx}\frac{\partial u}{\partial y} \tag{6}$$

where ε_{yx} is an eddy-viscosity, which in the simplest case can be written as:

$$\varepsilon_{yx} = \lambda h u_* \tag{7}$$

in which λ is a dimensionless eddy viscosity and $u* = u_*(y)$ is the local shear velocity. In the absence of secondary flows it is often assumed that the turbulent mixing of momentum is similar to the turbulent mixing of solutes, i.e. the eddy viscosity, ε_{yx}, is equal to the transverse mixing coefficient, ε_y. Combining Equations 4–7 gives:

$$S_o h = \frac{u^2 n^2 \cos\theta}{h^{1/3}} - \frac{\alpha}{g}\frac{\partial}{\partial y}\left(\lambda h^2 u_* \frac{\partial u}{\partial y}\right) \tag{8}$$

in which α is a binary constant. If α is set to 0 then a laterally varying velocity profile based only on the local application of Manning's equation results. However, when α is set to 1, the role of the transverse momentum exchange is included. In this paper we simplify the problem by considering the case when $\alpha = 0$, since this is sufficient for our purposes here. The more complex case is considered in Manson & Wallis (in prep.).

Having established equations for predicting u' (Equation 8 with α set to zero) and ε_y (Equation 7), Equation 3 can be solved for D using numerical integration, following the method described in French (1986).

4 APPLICATION TO CASE STUDY

The two-stage channel used here for investigation was based on the hypothetical benchmark channel introduced by Ackers (1993). The channel is shown in Figure 1 and the channel parameters took the following values: $B_1 = 15$ m; $B_2 = 1.5$ m; $B_3 = 20$ m; $B_4 = 1.5$ m; $D_1 = 1.5$ m; $D_2 = 1.5$ m. Manning's n was taken to be 0.03 for both main channel and floodplains. The bed slope, S_o, was set to 0.003 and the non-dimensional eddy viscosity, λ was assigned the value 0.16 – a typical value for straight channels (Rutherford, 1994). The local shear velocity was evaluated by applying Equation 5 locally, assuming that locally $\tau_b = \rho u_*^2$.

Calculations were carried out for main channel flow depths between 0 and 3 m in 0.15 m increments, thus covering both in-bank and over-bank scenarios.

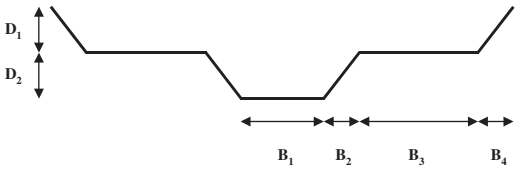


Figure 1. Cross-section of benchmark channel.

Since D was derived from numerical integration, it was essential to study the influence of the transverse discretisation, Δy, on the calculated values. Hence, for each flow depth several evaluations were undertaken with Δy being successively refined until the results became independent of Δy. Only when the results had converged were they deemed to be acceptable. In this application, it was important to capture the shear layers at a sufficiently fine resolution.

5 RESULTS AND DISCUSSION

The results are shown in the form of dispersion coefficient plotted against flow rate in Figures 2 and 3 for in-bank and over-bank flows, respectively. For in-bank flows, the dispersion coefficient increases with increasing flow rate and is very small, being in the range 0–3 m^2/s for flows between 0 and 50 m^3/s. The trend is weakly non-linear, but is well approximated by a linear relationship. The magnitude of the dispersion coefficients is supported by the predicted transverse velocity profiles that consist of a wide uniform velocity region with very narrow shear zones at the channel sides. Since dispersion is promoted by gradients in transverse velocity, the very narrow shear zones are only capable of inducing minimal dispersion. As the flow depth increases, the shear zones become wider resulting in a larger dispersion coefficient.

For over-bank flows the results are significantly different. Not only is the size of the dispersion coefficient different, but so is the variation with flow rate. The dispersion coefficients are now in the range 38000–500 m^2/s for flows between 70 and 330 m^3/s, respectively – several orders of magnitude larger than for the in-bank case. The coefficients decrease rapidly in the flow range 70–100 m^3/s and then more slowly at higher flows.

Clearly, the dispersion is being dominated by the role of the strong shear that develops as the flow begins to occupy the flood plains. This shear is easily recognised in the example transverse velocity profile shown in Figure 4, which shows that for this case the velocity in the main channel is about three times larger than the velocity on the floodplains.

Although the influence of the velocity shear decreases as the flood plain flow depth increases, because the velocity becomes more uniform across

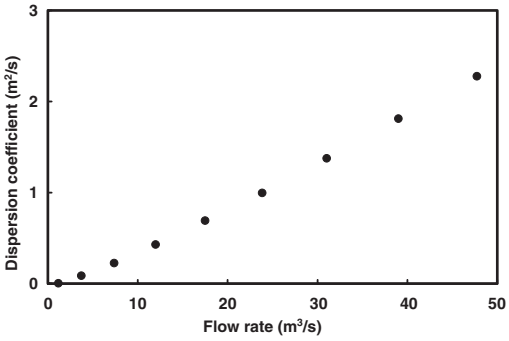


Figure 2. Variation of dispersion coefficient with flow rate for in-bank flows.

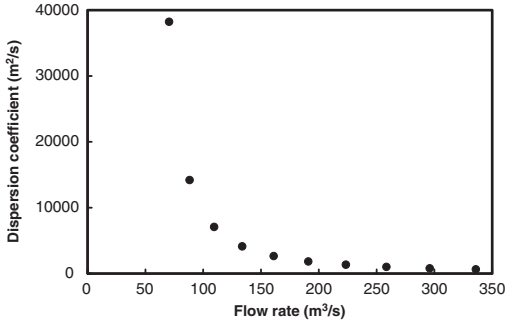


Figure 3. Variation of dispersion coefficient with flow rate for over-bank flows.

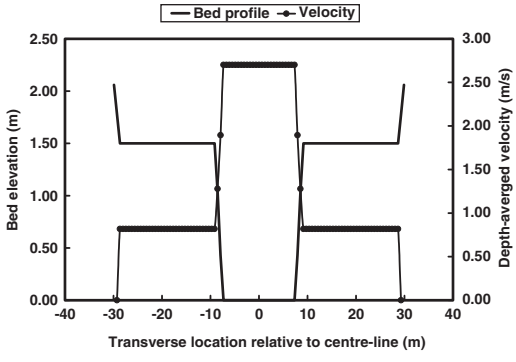


Figure 4. Transverse velocity profile for flow rate of 88 m^3/s.

the channel, it retains its dominant role throughout the flow range considered.

Observation of the convergence of the result of the numerical integration as the transverse step size was decreased showed that very small steps were required, particularly when the shear layer was very narrow. Typically, $W/\Delta y$ needed to be of the order of 1000 to achieve satisfactory convergence using a uniform discretisation. Clearly, this very small step size was dictated by the requirement of accurately resolving the shear layer.

The different behaviour of the dispersion coefficient between in-bank and over-bank flows is an important result. Interestingly, these theoretical results are supported by experimental evidence in Rutherford (1994). Firstly, for the in-bank case Rutherford's Figures 4.7 & 4.6 indicate that dispersion coefficients increase with increasing flow rate. The former is directly comparable to the case studied here because it considers conditions at different flow rates in the same reach, for four rivers. In contrast, the latter shows conditions from a very wide range of reaches from about sixty rivers worldwide. For the over-bank case Rutherford's Figure 5.14 shows dispersion coefficients decreasing with increasing flow rates in four reaches of a single river. Rutherford's explanation is resonant of the conditions in the case studied here, namely that bank side areas of shallow flow create strong transverse velocity shear at low flows, but as the flow increases the velocity in the shallows increases causing a reduction in the transverse shear and a concomitant reduction in the dispersion coefficient.

Finally, workers using the ADE to simulate solute transport in open channels should take note that existing methods for predicting dispersion coefficients cannot be used for the over-bank case. For example, many of the published empirical equations and the relationships available within software packages such as MIKE11 (Anon, 1992) and ISIS (Anon, 1998) do not necessarily cater for either, or both, of the magnitude of the coefficients or the nature of its flow dependence, predicted here.

6 CONCLUSIONS

A method has been proposed for predicting dispersion coefficients in a two-stage channel based on a theoretical approach that requires a prediction of the transverse distribution of the longitudinal velocity field. This was achieved using a local application of the Manning resistance equation, although reference was made to an improved method that includes the effect of transverse turbulent momentum exchange (Manson & Wallis, in prep.). Numerical integration of Fischer's flow structure equation then yielded the dispersion coefficient. Results were obtained for the two-stage channel studied by Ackers (1993) under both in-bank and over-bank conditions. The latter results are believed to be the first predictions of dispersion coefficients in such flows. By their very nature, the results are limited to straight channels with negligible secondary flows. The transverse mixing was modelled using a constant dimensionless mixing coefficient of 0.16 and a truly local representation of depth and shear velocity.

For the in-bank case, the dispersion coefficient was very small (being in the range 0–3 m^2/s for flows between 0 and 50 m^3/s) and increased approximately linearly with flow rate. For the over-bank case, the dispersion coefficient was very large (being in the range 38000–500 m^2/s for flows between 70 and 330 m^3/s) and decreased non-linearly with flow rate. The predictions for both flow conditions are consistent with trends reported in Rutherford (1994).

REFERENCES

Ackers, P. 1993. Flow formulae for straight two-stage channels. *Journal of Hydraulic Research*, 31(4): 509–531.

Anon, 1992. *Reference Manual for MIKE 11*. Horsholm: Danish Hydraulics Institute.

Anon, 1998. *ISIS Quality User Manual*. Wallingford: Halcrow/HR Wallingford.

Beltaos, S. 1982. Dispersion in tumbling flow. *Journal of the Hydraulics Division, American Society of Civil Engineers*, 108(4): 591–612.

Bencala, K. E. & Walters, R. A. 1983. Simulation of solute transport in a mountain pool-riffle stream: a transient storage model. *Water Resources Research*, 19: 718–724.

Deng, Z.-Q., Bengtsson, L., , V. P. & Adrian, D. D. 2002. Longitudinal dispersion coefficient in single-channel streams. *Journal of Hydraulic Engineering, American Society of Civil Engineers*, 128(10): 901–916.

Ervine, D. A., Babaeyan-Koopaei, K. & Sellin, R. H. J. 2000. Two-dimensional solution for straight and meandering overbank flows. *Journal of Hydraulic Engineering, American Society of Civil Engineers*, 126(9): 653–669.

French, R. H. 1986. *Open-channel Hydraulics*. New York: McGraw-Hill.

Fischer, H. B. 1967. The mechanics of dispersion in natural streams. *Journal of the Hydraulics Division, American Society of Civil Engineers*, 93(6): 187–215.

Fischer, H. B., List, E. J., Koh, R. C. Y., Imberger, J. & Brooks, N. H. 1979. *Mixing in Inland and Coastal Waters.* New York: Academic Press.

Jain, S. C. 1976. Longitudinal dispersion coefficients for streams. *Journal of the Environmental Engineering Division, American Society of Civil Engineers*, 102(2): 465–474.

Jobson, H. E. 1997. Predicting traveltime and dispersion in rivers and streams. *Journal of Hydraulic Engineering, American Society of Civil Engineers*, 123(17): 971–978.

Keller, R. J. & Rodi, W. 1988. Predictions of flow characteristics in main channel/flood plain flows. *Journal of Hydraulic Research*, 26(4): 425–441.

Lambert, M. F. & Sellin, R. H. J. 1996. Discharge prediction in straight compound channels using the mixing length concept. *Journal of Hydraulic Research*, 34(3): 381–394.

Liu, H. 1977. Predicting dispersion coefficient of streams. *Journal of the Environmental Engineering Division, American Society of Civil Engineers*, 103(1): 59–69.

Manson, J. R. & Wallis, S. G. in prep. On the theoretical prediction of longitudinal dispersion coefficients in two-stage channels. *Water Resources Research*.

Mcquiver, R. S. & Keffer, T. N. 1974. Simple method for predicting dispersion in streams. *Journal of the Environmental Engineering Division, American Society of Civil Engineers*, 100(4): 997–110.

Naot, D., Nezu, I. & Nakagawa, H. 1993. Hydrodynamic behaviour of compound rectangular open channel flow. *Journal of Hydraulic Engineering, American Society of Civil Engineers*, 119(3): 390–408.

Rutherford, J. C. 1994. *River Mixing.* Chichester: Wiley.

Seo, I. W. & Cheong, T. S. 1998. Predicting longitudinal dispersion coefficient in natural streams. *Journal of Hydraulic Engineering, American Society of Civil Engineers*, 124(1): 25–32.

Shiono, K. & Knight, D. W. 1991. Turbulent open-channel flows with variable depth across the channel. *Journal of Fluid Mechanics*, 222: 617–646.

Sofialids, D. & Prionos, P. 1999. Turbulent flows in open channels with smooth and rough flood plains. *Journal of Hydraulic Research*, 37(5): 615–640.

Taylor, G. I. 1954. The dispersion of matter in turbulent flow through a pipe. *Proceedings of the Royal Society of London*, A223: 446–468.

Wallis, S. G., Young, P. C. & Beven, K. J. 1989. Experimental investigation of the aggregated dead zone model for longitudinal solute transport in stream channels. *Proceedings of the Institution of Civil Engineers*, Part 2, 87: 1–22.

Wallis, S. G. & Manson, J. R. in prep. A review of methods for predicting dispersion coefficients in rivers. *Water & Maritime Engineering, Proceedings of the Institution of Civil Engineers.*

Worman, A. 2000. Comparison of models for transient storage of solutes in small streams. *Water Resources Research*, 36: 455–468.

This page intentionally left blank

River Flow 2004 – Greco, Carravetta & Della Morte (eds.)
© 2004 Taylor & Francis Group, London, ISBN 90 5809 658 0

Evaluation of transverse dispersion coefficient under transient concentration condition

I.W. Seo
Prof., Dept. of Civil Eng., Seoul National Univ., Seoul, Korea

K.O. Baek & S.J. Jeong
Grad. Student, Dept. of Civil Eng., Seoul National Univ., Seoul, Korea

ABSTRACT: Laboratory experiments were conducted to investigate characteristics of both the velocity field and the concentration field in the meandering channel having a rectangular cross-section. The S-curved channel has been built considering river morphology and previous experimental studies. The micro-ADV was used to measure the three-dimensional velocity field. The electrode conductivity meter was used to obtain the tracer concentration. The tracer was instantaneously injected into a flow as a vertical line source. Result of the flow experiments shows that the maximum velocity of the primary flow occurs near the inner bank in a bend taking the shortest course along the channel. For the secondary flow, complex flow pattern appears compared to experimental results in a single-bend channel. Throughout the two-dimensional tracer tests, the meaningful concentration versus time versus lateral distance data could be obtained. Using the tracer data, the transverse dispersion coefficient was evaluated by the change of moment method. In addition, the 2-D routing procedure was developed in order to obtain more accurate transverse dispersion coefficient.

1 INTRODUCTION

Dispersion is the spreading out of particles along a stream or channel due to velocity differences. In a mathematical model, the dispersion term occurs as transforming the three-dimensional advection-diffusion equation into the two-dimensional advection-dispersion equation by integration with respect to a depth. Knowledge of the dispersion characteristics of streams and rivers is essential to the understanding and managing of water pollution problems. Furthermore, the transverse dispersion is more important in water quality management than either vertical or longitudinal mixing, especially, when dealing with the discharge of wastes from point sources or the mixing of tributary inflows. Because of importance to understanding of the pollutant transport in natural streams, many researches including laboratory and field works, and analytical and numerical calculations have been performed on the transverse dispersion. Up to date, many of those researches have concentrated on the mixing in straight, prismatic channels. However, natural streams are rarely straight and prismatic for any considerable distance. The effects induced by non-uniformity and meandering should not be negligible.

When a two-dimensional analysis of the tracer mixing is performed in meandering streams, it is the essential task to determine the transverse dispersion coefficient. There are several methods to determine the transverse dispersion coefficient in case of knowing the concentration versus time data. The change of moment method proposed by Sayre and Chang (1968) has been frequently used. This approach can be obtained by taking the integration with respect to the transverse direction of the steady state conservation equation for two-dimensional flow in a rectangular channel with uniform velocity distribution and no longitudinal dispersion. Holley et al. (1972) suggested the generalized change of moment to overcome disadvantages of the change of moment method. This method can consider transverse velocities, irregular depth, and so on. However, those methods can only be applied to the steady concentration condition, and errors may occur according to inaccurate variance of the concentration curves. In many cases, it would be preferable to perform an instantaneous injection rather than a continuous test. Some of the advantages of the instantaneous injection test are that the amount of tracer needed to perform an instantaneous test is much less than that is required for a continuous test, and an

instantaneous test can provide the information on the longitudinal and time spread characteristics as well as the information on the transverse mixing.

In this study, in order to evaluate the transverse dispersion coefficient under the transient concentration condition, the two-dimensional routing procedure was developed. The laboratory tracer tests were conducted in the meandering channel having a rectangular cross-section to observe behavior of the tracer cloud and to obtain the concentration-time data.

2 THEORETICAL BACKGROUND

In most rivers, the aspect ratio is large and the tracer becomes well mixed vertically before well mixed transversely. The vertical mixing is only important close to the tracer source. In the mid-field, the vertical concentration gradients can be neglected, and our attention can be focused on transverse and longitudinal changes of the depth-averaged concentration. The full three-dimensional advection-diffusion equation can be averaged over the depth to yield the two-dimensional equation. Assuming a non-buoyant tracer being transported in an unsaturated incompressible flow, the two-dimensional advection-diffusion equation in the Cartesian coordinates is

$$\frac{\partial C}{\partial t}+u\frac{\partial C}{\partial x}+v\frac{\partial C}{\partial y}=\frac{1}{h}\frac{\partial}{\partial x}\left[hD_L\frac{\partial C}{\partial x}\right]+\frac{1}{h}\frac{\partial}{\partial y}\left[hD_T\frac{\partial C}{\partial y}\right] \tag{1}$$

where C = depth-averaged concentration; t = time; x, y = Cartesian coordinates systems; u, v = depth-averaged longitudinal and transverse velocities; h = depth; and D_L, D_T = longitudinal and transverse dispersion coefficients respectively.

2.1 *Transformation transient condition into steady condition*

Evaluation of the transverse dispersion coefficient has been associated with continuous injection tests, i.e. tracer is injected into a stream at a constant rate so that a steady-state distribution of concentration is established some time after the commencement of injection. A literature review revealed that the most existing methods are only applicable to steady-state experiments. Extensions to unsteady situations are theoretically possible but they would introduce enormous complexities in the calculation. However, Beltaos (1975) presented a procedure for applying the existing methods to the results of instantaneous tests without increasing the computational efforts or decreasing the accuracy of computations. He introduced the concept of a dosage as

$$\theta\equiv\int_0^\infty C\,dt \tag{2}$$

Integrating Equation (1) with respect to time, Equation (1) becomes

$$u\frac{\partial\theta}{\partial x}+v\frac{\partial\theta}{\partial y}=\frac{\partial}{\partial x}(D_L\frac{\partial\theta}{\partial x})+\frac{\partial}{\partial y}(D_T\frac{\partial\theta}{\partial y}) \tag{3}$$

Equation (3) shows that the quantity θ of a slug test behaves exactly in the same manner as the concentration C of a corresponding continuous test. According to the suggestion of Beltaos (1975), the transient test can be converted into continuous test so that the moment method can be applied to the transient test.

2.2 *Routing procedure*

In this study, the new method for evaluating the transverse dispersion coefficient is developed without any conversion procedure. The new method was based on the routing procedure proposed by Fischer (1968). He proposed the one-dimensional routing procedure to calculate the longitudinal dispersion coefficient. In the routing procedure, the dispersion coefficient is calculated by matching a downstream observation of passage of a tracer cloud to the prediction based on an upstream observation. The equation of the one-dimensional routing procedure can be derived from the solution of the one-dimensional dispersion equation which is

$$\frac{\partial C}{\partial t}=K\frac{\partial^2 C}{\partial x^2} \tag{4}$$

where K = longitudinal dispersion coefficient which accounts for the effects on the cross-sectional averaged tracer concentration of variations of velocity across the channel cross-section. When it is considered that the solution corresponding to a mass M instantaneously released at time $t=0$ at the point $x=\xi$, the solution is

$$C(x,t)=\frac{M}{\sqrt{4\pi Kt}}\exp\left(\frac{-(x-\xi)^2}{4Kt}\right) \tag{5}$$

Suppose that the initial conditions were $C(x,0)=f(x)$, then the concentration at point x and time t resulting from the slug centered at ξ and of width dξ and height $f(\xi)$ is

$$\frac{f(\xi)d\xi}{\sqrt{4\pi Kt}}\exp\left(\frac{-(x-\xi)^2}{4Kt}\right) \tag{6}$$

Therefore, the total contribution is the superposition integral as follows

$$C(x,t)=\int_{-\infty}^{\infty}\frac{f(\xi)}{\sqrt{4\pi Kt}}\exp\left(\frac{-(x-\xi)^2}{4Kt}\right)d\xi \tag{7}$$

In order to route a distribution of the downstream concentration from an upstream concentration, Equation (7) can be rewritten as

$$C(x,t_2)=\int_{-\infty}^{\infty}\frac{C(\xi,t_1)}{\sqrt{4\pi K(t_2-t_1)}}\exp\left(-\frac{(x-\xi)^2}{4K(t_2-t_1)}\right)d\xi \tag{8}$$

where $C(\xi,t_1)=$ observed concentration as a function of distance at time t_1; and $C(x,t_2)=$ predicted concentration as a function of distance at time t_2. Equation (8) requires knowledge of the instantaneous tracer concentration versus distance profile (spatial concentration profile), such as might be determined by an aerial photography. However, it is common to know the tracer concentration as a function of time (temporal concentration profile) at a fixed sampling site downstream. Under the frozen cloud assumption (Fischer, 1968; Rutherford, 1994) which is that no dispersion takes place during passage of tracer cloud past the measuring station, the routing equation of a spatial concentration can be converted into those of a temporal concentration.

$$C(x_2,t)=\int_{-\infty}^{\infty}\frac{C(x_1,\tau)U}{\sqrt{4\pi K(\bar{t}_2-\bar{t}_1)}}\cdot\exp\left(-\frac{U^2(\bar{t}_2-\bar{t}_1-t+\tau)^2}{4K(\bar{t}_2-\bar{t}_1)}\right)d\tau \tag{9}$$

where $C(x_1,\tau)=$ observed concentration as a function of time at an upstream site; $C(x_2,t)=$ predicted concentration as a function of time at a downstream site; $\bar{t}_1$, $\bar{t}_2=$ mean times of passage at upstream and downstream sites respectively; and $\tau=$ a dummy time variable of integration. Through the Equation (9), the concentration profile at a downstream can be calculated, and then by fitting between the calculated concentration and the observed concentration, the longitudinal dispersion coefficient can be obtained.

Based on the one-dimensional routing procedure, the two-dimensional routing procedure is developed in this study. The conceptual diagram of an application of the two dimensional routing procedure at a stream is shown in Figure 1.

The equation of the two-dimensional routing procedure can be derived from the solution of the two-dimensional dispersion equation which is

$$\frac{\partial C}{\partial t}=D_L\frac{\partial^2 C}{\partial x^2}+D_T\frac{\partial^2 C}{\partial y^2} \tag{10}$$

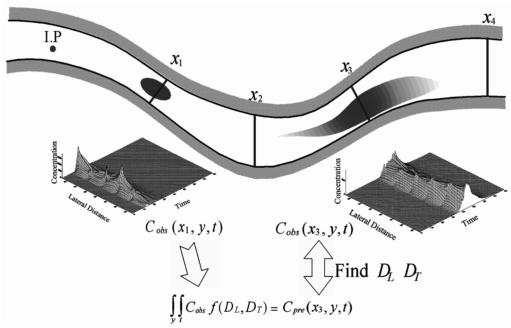


Figure 1. Conceptual diagram of the 2-D routing procedure.

When it is considered that the solution corresponding to a mass M instantaneously released at time $t=0$ at the points $x=\xi$ and $y=\psi$, the solution is

$$C(x,y,t)=\frac{M}{4\pi t\sqrt{D_L D_T}}\exp\left(\frac{-(x-\xi)^2}{4D_L t}+\frac{-(y-\psi)^2}{4D_T t}\right) \tag{11}$$

Through Equation (11), the spatial two-dimensional routing equation can be expressed as

$$C(x,y,t_2)=\int_0^W\int_{-\infty}^{\infty}\frac{C(\xi,\psi,t_1)}{4\pi(t_2-t_1)\sqrt{D_L D_T}}\cdot\exp\left(-\frac{(x-\xi)^2}{4D_L(t_2-t_1)}\right)\exp\left(-\frac{(y-\psi)^2}{4D_T(t_2-t_1)}\right)d\xi d\psi \tag{12}$$

where $C(\xi,\psi,t_1)=$ observed concentration as a function of longitudinal distance and transverse distance at time t_1; and $C(x,y,t_2)=$ predicted concentration as a function of longitudinal distance and transverse distance at time t_2. Under the frozen cloud assumption, Equation (12) can be converted into the temporal two-dimensional routing equation which is

$$C(x_2,y,t)=\int_0^W\int_{-\infty}^{\infty}\frac{C(x_1,\psi,\tau)U}{4\pi(\bar{t}_2-\bar{t}_1)\sqrt{D_L D_T}}\cdot\exp\left(-\frac{U^2(\bar{t}_2-\bar{t}_1-t+\tau)^2}{4D_L(\bar{t}_2-\bar{t}_1)}\right)\exp\left(-\frac{(y-\psi)^2}{4D_T(\bar{t}_2-\bar{t}_1)}\right)d\tau d\psi \tag{13}$$

where $C(x_1,\psi,\tau)=$ observed concentration as a function of time and lateral distance at an upstream site; and $C(x_2,y,t)=$ predicted concentration as a function of time and lateral distance at a downstream site. Using the Equation (13), the concentration profile at a downstream can be calculated, and then by matching between the calculated concentration and the observed

Table 1. Meander properties of the experiemtal channels.

Researcher	R_C/W	θ	λ/W	λ/R_C	Sinuo.
Leopold & Wolman (1960)	2.3	–	10.9	4.7	–
Chang (1971)	3.6	90	–	–	1.11
Krishnappan & Lau (1977)	0.6 ∼ 2.2	–	6.3	2.8 ∼ 10.8	–
Almquist & Holley (1985)	3	125	12	4	1.30
Guymer (1998)	3.5	120	13.7	3.9	1.21
South Han River (Korea)	13.7	86.8	19.7	1.6	1.10
This study	2.4	120	9.7	4	1.32

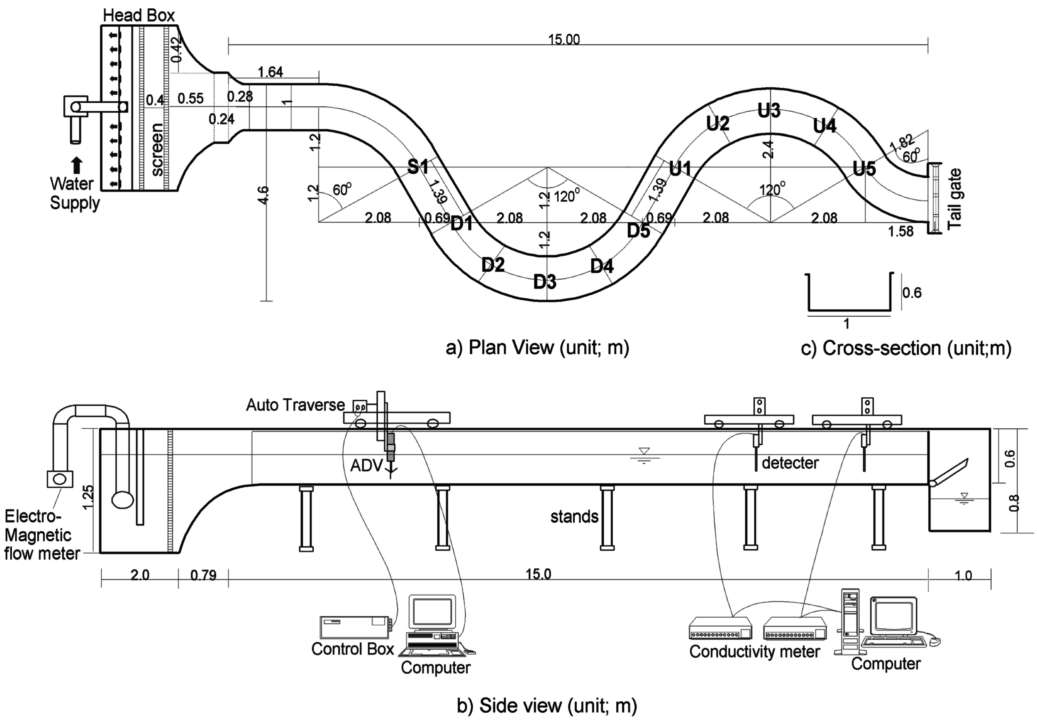


Figure 2. Sketch of the S-curved laboratory channel.

concentration, not only the transverse dispersion coefficient but also the longitudinal dispersion coefficient can be obtained.

The merits of the two-dimensional routing procedure are: (1) dispersion coefficients can be obtained under the transient concentration condition without any conversion procedure; (2) not only the transverse dispersion coefficient but also the longitudinal dispersion coefficient can be obtained simultaneously, whereas only the transverse dispersion coefficient can be obtained through the moment method; and (3) the transverse dispersion coefficient can be obtained in more detail according to the longitudinal positions.

3 EXPERIMENTS

3.1 *Experimental setup*

The S-curved laboratory channel was constructed to investigate meander pattern of natural streams. Among the various hydraulic factors of the meandering channel, channel width (W), radius of curvature (R_C), arc angle (θ), wavelength (λ), and sinuosity were considered. The properties of meander pattern of the S-curved channel used in this study are shown in Table 1. The S-curved laboratory channel which has a rectangular cross-section is 15 m long, 1 m wide, and

0.6 m deep. It consists of circular arcs connected by straight sections as shown in Figure 2. The radius of curvature is 2.4 m, the wavelength is 9.7 m, and the arc angle is 120°. The channel was equipped with instrument carriages, which rested on rails mounted on the flume. One carriage is equipped with an auto-traversing system for the velocity measuring sensor throughout the depth and breadth of the flow field.

An electromagnetic flowmeter was installed to continuously measure the discharge of the flow passing through the channel. A point gauge was used to measure the flow depth. A side-looking micro-ADV, developed by SonTek, was used to measure the three-dimensional distributions of velocity and turbulence. The micro-ADV operates on a pulse-to-pulse coherent Doppler shift to provide a three-component velocity at a rate of 50 Hz. The concentration measurements were made with the electrode conductivity meter, which was developed by KENEK. The probe of electrode conductivity meter is very small like ϕ4 mm, and there is little influence to the flow. The electrode conductivity meter can obtain concentration data at a rate of 10 Hz, the measuring range is 0 ~ 30,000 ppm, and the linearity is ±1.5%.

Six electrode conductivity probes were arranged at each transection by the hand-operated traversing system, and the concentration distributions are measured simultaneously at three transactions. The probe calibration for a response to a concentration was performed by a series of standard salt solutions whose range were from 0 ppm to 10,000 ppm. The concentration signals were fed into the data acquisition system, which converted the sampled signals to digital voltages. The amplifier unit was adjusted to give zero output in the flume water. A calibration curve of output voltage versus concentration was constructed by immersing the probe in each of the standards and recording the voltage output. The tracer was a salt solution, and a red dye ($KMnO_4$) was added to aid in visualizing the diffusing cloud. The density of the tracer solution was adjusted to that of the flume water by addition of the methanol. The tracer was instantaneously injected into the flow as a full-depth vertical line source using the instantaneous injector. The injector consisted of the fixing plate and ϕ9.0 cm cylinder. By lifting the cylinder from the fixing plate, the tracer can be introduced into the water.

3.2 *Experimental conditions*

In the S-curved channel, seven cases of tests on measurements of velocity field were conducted according to flow conditions. The flow experimental conditions are tabulated in Table 2. Measurements of velocity field were conducted at eleven transections whose location was marked at Figure 2. The interval of measuring points at each transection is transversely 7 cm, and vertically 3~5 cm. Thus, the number of measuring points at each section varies from 30 to 90, depending on the water depth.

Table 2. Flow conditions.

Case	H (cm)	V (cm/s)	Q (l/s)	W/H	Fr
070	7	28.6	20	14.3	0.34
101	10	30.0	30	10.0	0.30
151	15	20.0	30	6.7	0.16
152	15	40.0	60	6.7	0.33
211	21	14.3	30	4.8	0.10
212	21	28.6	60	4.8	0.20
213	21	42.9	90	4.8	0.30

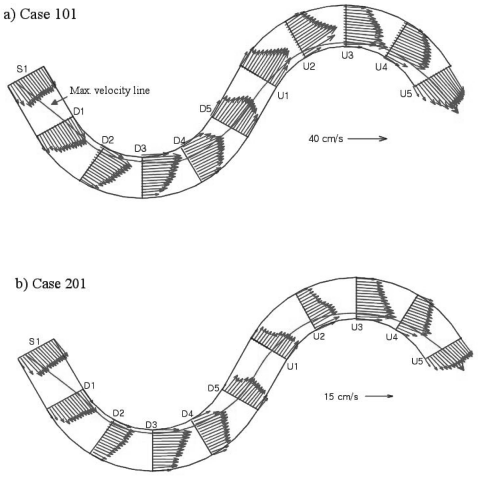


Figure 3. Depth-averaged primary velocity vectors (Case 101).

The concentration experiments were conducted in the all flow conditions. The tracer was instantaneously injected into the flow as a full-depth vertical line source at the centerline, left bank, and right bank of the channels. The injection point was marked at Figure 2. The initial concentration of the tracer was 100,000 mg/l (ppm). The interval of concentration measuring points at each transection is 14 cm transversely.

4 EXPERIMENTAL RESULTS

4.1 *Velocity field*

One of the purposes of laboratory experiments is to investigate flow patterns in the S-curved channel. In order to observe a primary flow pattern, depth-averaged primary velocity vectors are plotted in Figure 3 for the representative cases. The transverse distribution of the primary velocity skews toward

the inner bank at bends and is almost symmetric at the crossovers. The noticeable phenomenon is that the maximum velocity occurs taking the shortest course along the channel, irrespective of flow conditions. In natural streams, however, it has been known that the maximum velocity occurred along the thalweg line which appeared near the outer bank. The reason of this discrepancy in the flow pattern is that experiments were conducted on the rectangular cross-section channel, whereas, the cross-sectional shape of the natural stream is usually triangular, and skewed to the outer bank.

4.2 *Concentration field*

Throughout the tracer test in the S-curved channel, the concentration versus time data could be obtained at six transverse positions in nine transections. The three-dimensional concentration fields, which consisted of concentration, time, and transverse distance from a left bank to a right bank, are drawn for centerline injection of Case 101 in Figure 4.

In order to visualize the behavior of the tracer cloud, the spatial contours of the concentration are plotted through the concentration-time curve using the interpolation technique in Figure 5∼7. As shown in Figure 5 (centerline injection), the tracer cloud was somewhat symmetrical shape entering the first bend zone. At the apex, the tracer cloud separated into two parts and the main part skewed toward the left bank which was the inner bank in the first bend. The sub part remained near the outer bank. Passing the crossover, the tracer

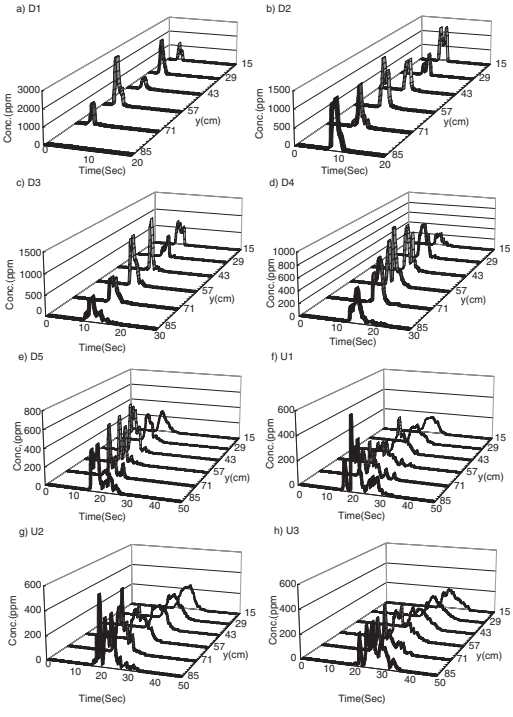


Figure 4. Plots of concentration, time, and transverse distance (Case 101, Centerline injection).

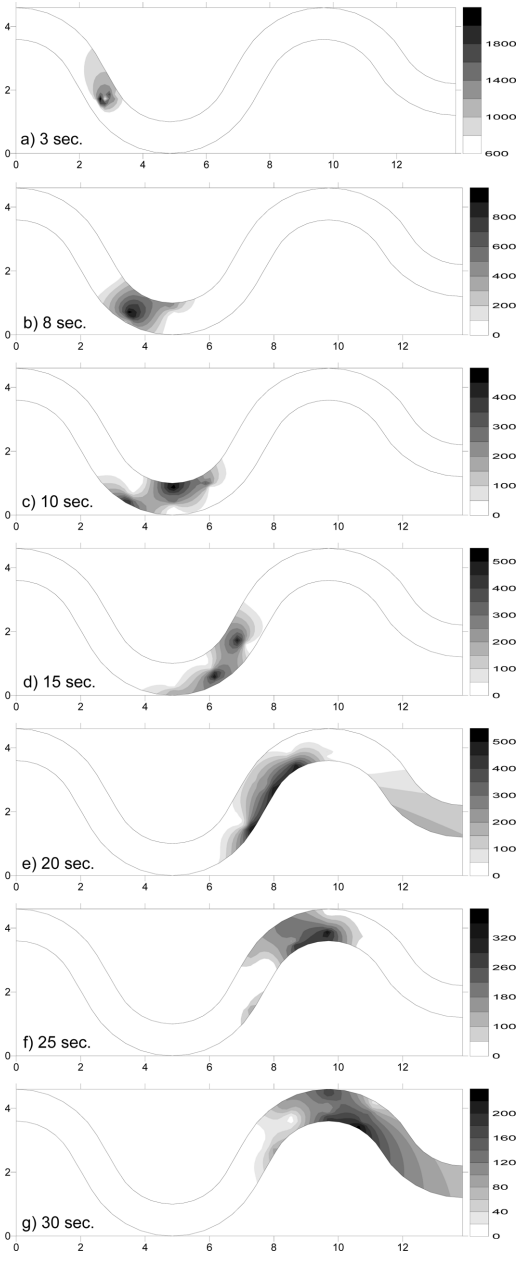


Figure 5. Spatial contour of the tracer cloud (Case 101, centerline injection).

cloud is skewed toward the right bank, and then high concentration was observed near the right bank through the second bend. It is considered that even though tracer cloud travels following the maximum primary velocity, it separates both in longitudinal and transverse directions due to alternating secondary currents. As shown Figure 6, this mechanism is prominent, for the case of the left bank injection. The core of the tracer cloud was taking the shortest course along the channel following the maximum velocity. However, in the case of the right bank injection (Figure 7), the tracer cloud didn't follow the maximum velocity

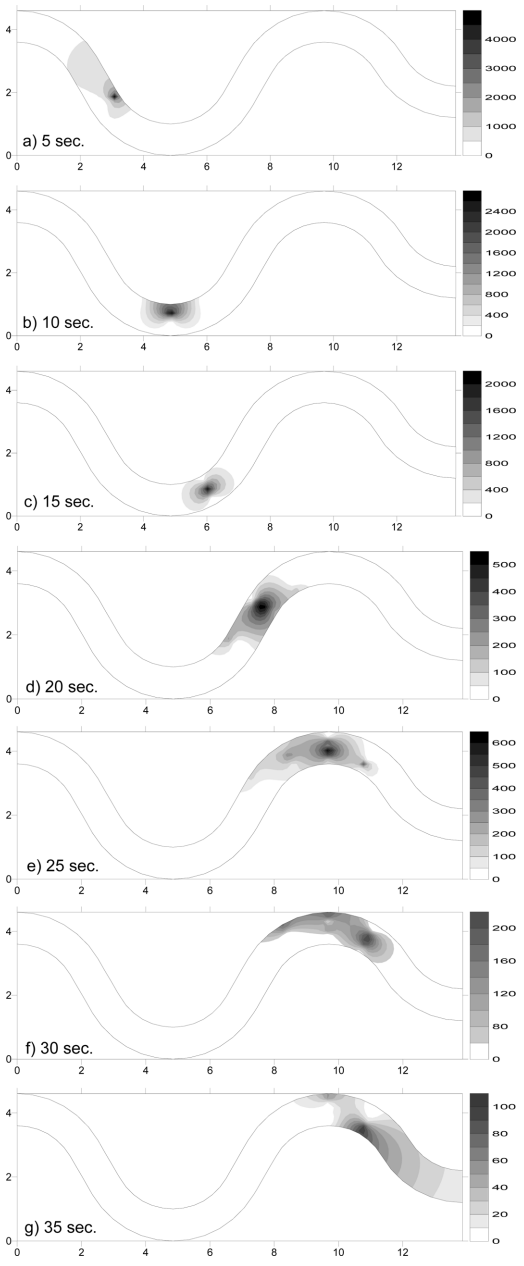


Figure 6. Spatial contour of the tracer cloud (Case 101, left bank injection).

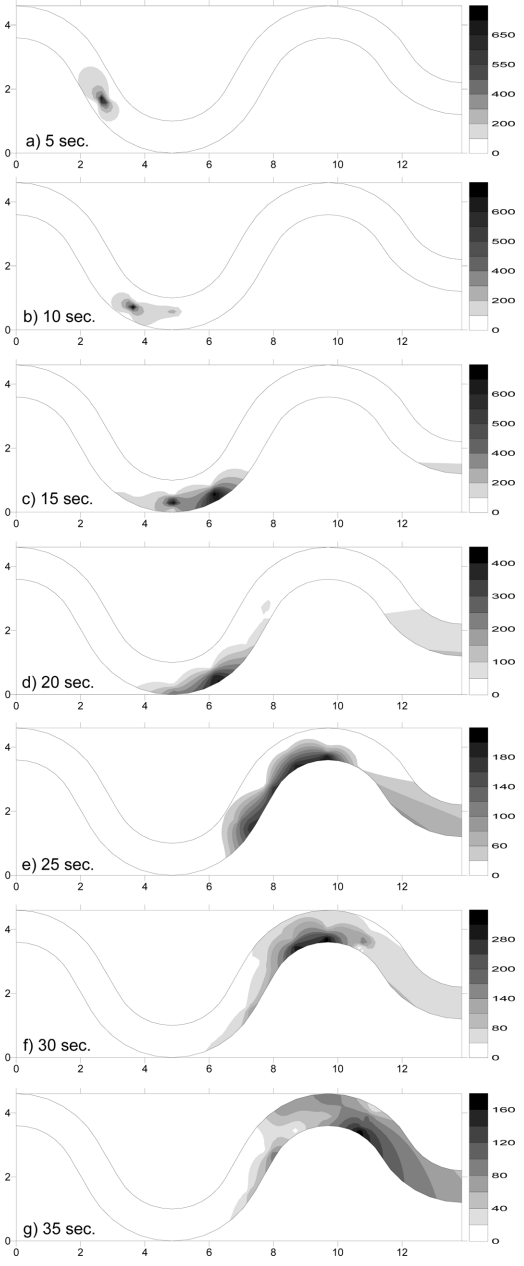


Figure 7. Spatial contour of the tracer cloud (Case 101, right bank injection).

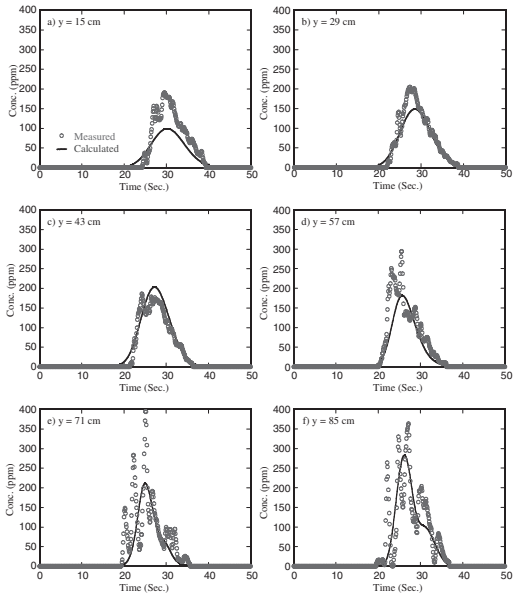


Figure 8. Application of the 2-D routing procedure (Case 101, center injection, Sec. U3).

through the first bend so that high concentration was detected near the right bank along the whole channel. Also, the length of the tracer cloud is longer than others. Not only the transverse mixing but also the longitudinal mixing may increase by the effects of the meander in the case of the right bank injection.

5 ANALYSIS

In this study, the routing procedure and the moment method were applied to evaluate the dispersion coefficients in the S-curved channel. Using the two-dimensional routing equation (Equation 13), both the longitudinal dispersion coefficient and the transverse dispersion coefficient can be evaluated simultaneously. In order to fit the predicted concentration to the measured concentration, the Gauss–Newton method, which is one of the nonlinear multiple regression techniques, was used. The representative case of applying the two-dimensional routing procedure is depicted in Figure 8. As shown in this figure, the calculated concentration distributions are generally in good agreement with the measured concentration distributions though peak points are somewhat underestimated.

Observed dispersion coefficients calculated by both the moment method and the two-dimensional routing procedure for all cases are tabulated in Table 3. The representative transverse dispersion coefficient was chosen among the several values of the dispersion

Table 3. Comparison of the observed dispersion coefficients.

Inject. cond.	Flow cond.	M-M	2-D routing procedure		
		D_T/HU_*	D_T/HU_*	D_L/HU_*	Up-down
Center	070	0.51	0.29	15.1	D2-U4
	101	0.45	0.70	15.6	D1-U4
	151	0.33	0.46	10.9	D2-U3
	211	0.18	0.19	5.9	D1-U3
Left	070	0.69	0.34	5.2	D1-U3
	101	0.58	0.63	5.7	D2-U2
	151	0.46	0.43	3.4	D1-U2
	211	0.19	0.34	3.1	D2-U4
Right	070	0.43	0.70	32.5	D4-U1
	101	0.45	0.56	37.6	D1-U4
	151	0.42	0.35	21.0	D1-U3
	211	0.17	0.10	38.8	D3-U3

coefficients obtained by the routing procedure for each case. The dispersion coefficient had less RMS error and was computed through long distance between upstream and downstream. For the dimensionless transverse dispersion coefficient (D_y/HU_*), results by the moment method and the routing procedure show little differences. Also, it is found that the dimensionless transverse dispersion coefficient is independent of the injection conditions. However, the dimensionless longitudinal dispersion coefficient varies according to the injection conditions. Especially, results on the right bank injection are larger than others. This is due to the separation of the tracer cloud as shown in Figure 7.

6 CONCLUSIONS

The two-dimensional routing procedure which was based on Fischer (1968) was developed to evaluate the transverse dispersion coefficient under the transient concentration condition. Also, the laboratory tracer tests were conducted in the meandering channel having a rectangular cross-section in order to obtain the concentration-time data.

Result of the flow experiments shows that the maximum velocity of the primary flow occurs near the inner bank in a bend taking the shortest course along the channel. Throughout the two-dimensional tracer tests, it reveals that behavior of the tracer cloud was quite different according to the injection conditions. Using the acquired concentration data, the transverse dispersion coefficients were evaluated via the new developed routing procedure. The evaluated transverse dispersion coefficients by the routing method were in good agreement with those by the moment method.

ACKNOWLEDGEMENTS

This research work was supported by the 21C Frontier project of the Ministry of Science and Technology. This research has been conducted in the Research Institute of Engineering Science of Seoul National University, Seoul, Korea.

REFERENCES

Almquist, C.W. & Holley, E.R. 1985. Transverse mixing in meandering laboratory channels with rectangular and naturally varying cross sections. *Technical Report CRWR-205*, Univ. of Texas, Austin, Texas.

Beltaos, S. 1975. Evaluation of transverse mixing coefficients from slug tests. *J. of Hydr. Res*., IAHR, 13(4): 351–360.

Chang, Y. 1971. Lateral mixing in meandering channels. PhD thesis, Univ. of Iowa, Iowa City, Iowa.

Fischer, H.B. 1968. Dispersion predictions in natural streams. *J. of Sanit. Engrg. Div.*, ASCE, 94(SA5): 927–943.

Guymer, I. 1998. Longitudinal dispersion in sinuous channel with changes in shape. *J. Hydr. Engrg.*, ASCE, 124(1): 33–40.

Holley, E.R., Siemons, J. & Abraham, G. 1972. Some aspects of analyzing transverse diffusion in rivers. *J. of Hydr. Res*., IAHR, 10(1): 27–57.

Krishnappan, B.G. & Lau, Y.L. 1977. Transverse mixing in meandering channels with varying bottom topography. *J. of Hydr. Res*., IAHR, 15(4): 351–371.

Leopold, L.B. & Wolman, M. G. 1960. River meanders. *Bulletin of the Geological Society of America*, 71: 769–794.

Rutherford, J.C. 1994. *River mixing*, New York: John Wiley and Sons Ltd.

This page intentionally left blank

C. Hydraulics for river management
C.1. River training and restoration

This page intentionally left blank

River Flow 2004 – Greco, Carravetta & Della Morte (eds.)
© 2004 Taylor & Francis Group, London, ISBN 90 5809 658 0

Numerical simulation of bed change under compound channels flow in two-way main channel

H. Yokoyama, Y. Watanabe & Y. Suzuki
Civil Engineering Research Institute of Hokkaido, Sapporo, Japan

ABSTRACT: In a river with a two-way main channel the flow bifurcates from the straight channel into a meander channel and then reconverges into the straight channel. A numerical simulation model was developed for estimating flow and bed topography change in such a river using 2-D shallow-water equations. Simulation was applied to an actual river with a two-way main channel, and it was generally able to represent the bed topography. Factors of riverbank erosion were then considered by using the simulation results. Velocity and its distribution near the bank were found to affect localized bank erosion. The model was applied to compound flow in a two-way main channel, which was compared to flow in a single meandering main channel. The effects of a two-way channel on flow and bed topography were investigated.

1 INTRODUCTION

River improvement works have been done on many alluvial rivers to lower the water surface level for flood safety and to lower the groundwater surface level for development of agricultural land. Meandering rivers were straightened with cutoffs, which changed the river environment in some cases. Requests for river environmental conservation have been increasing in recent years.

A project to restore the Shibetsu River to its meandering state has been going on since 2000. The river is in the eastern part of Hokkaido, Japan's northernmost prefecture. This project is the first meander restoration in Japan. An oxbow lake was reconnected to the straightened channel in 2002. Currently, flow bifurcates from the straight channel, flows through the restored meander and reconverges with the flow in the straight channel. (We describe such a channel as a "two-way main channel.") In the two years that has passed since the restoration produced the two-way channel, riverbank erosion and change in bed topography have occurred. It is very important to predict the flow and change of riverbed for planning and maintenance of a two-way main channel.

Many studies have addressed flow and bed topography in a meander channel. Development of meander was investigated by linear stability analysis (Ikeda et al., 1981) and nonlinear model (Parker et al., 1982). Struiksma et al. (1985) discussed bed deformation in curved channels by comparing experimental results and mathematical analysis. Odgaard (1989a, b) applied mathematical model to bank scouring and migration in actual rivers. A 2-D simulation model was developed to estimate change of bed topography (Shimizu et al., 1991). Flow in a compound meander channel was investigated experimentally (Fukuoka et al., 1997) and by 3-D simulation (Fukuoka et al., 1999). Channel shift and bank erosion was estimated by using numerical models (Nagata et al., 2000). However, in most of the research on meandering rivers, the main channel was single, and flow in a two-way main channel was not considered.

Sato & Watanabe (2002) conducted experiments on flow in a two-way channel and investigated bed change and the behavior of sandbars. Fujita et al., (2003) developed theoretical analysis and investigated the discharge rate of two-way channel from model experiment and field survey. However, the number of conditions and the number of repetitions is limited in experiments. The development of a computational model that can simulate the flow and change of bed topography would greatly contribute to analysis of phenomena under a complicated river configuration and various hydraulic conditions.

This study aims to develop a numerical model that can solve for flow and bed change in a two-way channel. The simulation model is outlined first. The model is applied to an actual two-way channel on the Shibetsu River. The simulation results are compared to observation data. Factors in erosion in a meander channel are investigated by using the simulation results. After that, simulation is conducted on compound flow in a two-way main channel.

2 NUMERICAL MODEL

2.1 *Equations of flow and sediment transportation*

The flow, which bifurcated and reconverged, had a mixture of horizontal and vertical flow components. In a compound-channel, the difference in flow velocity between the main channel and the flood plain and the complicated boundary shape of the channels causes complex flow. 3-D simulation is desirable for solving flow and bed change because it can consider the effects of vertical flow. However, 3-D simulation takes a very long time, making it difficult to apply. In an actual river, we consider that general hydraulic phenomena can be predicted sufficiently by simulating horizontal flow and bed change. The 2-D shallow-water equations (1)–(3) are transformed to a boundary-fitted coordinate system and used in the model. The upwind differencing scheme is used in the advection term:

$$\frac{\partial u}{\partial t}+u\frac{\partial u}{\partial x}+v\frac{\partial u}{\partial y}=-g\frac{\partial H}{\partial x}-\frac{gn^2u\sqrt{u^2+v^2}}{h^{4/3}} \quad (1)$$

$$+\frac{\partial}{\partial x}\left(2\nu_t\frac{\partial u}{\partial x}\right)+\frac{\partial}{\partial y}\left\{\nu_t\left(\frac{\partial u}{\partial y}+\frac{\partial v}{\partial x}\right)\right\}$$

$$\frac{\partial v}{\partial t}+u\frac{\partial v}{\partial x}+v\frac{\partial v}{\partial y}=-g\frac{\partial H}{\partial y}-\frac{gn^2v\sqrt{u^2+v^2}}{h^{4/3}} \quad (2)$$

$$+\frac{\partial}{\partial x}\left\{\nu_t\left(\frac{\partial u}{\partial y}+\frac{\partial v}{\partial x}\right)\right\}+\frac{\partial}{\partial y}\left(2\nu_t\frac{\partial v}{\partial y}\right)$$

$$\frac{\partial h}{\partial t}+\frac{\partial (uh)}{\partial x}+\frac{\partial (vh)}{\partial y}=0 \quad (3)$$

where t is time, x and y are Cartesian coordinates, u and v are velocity in the x and y directions, H is water surface level, h is water depth, g is gravitational acceleration (9.8 m/s^2), and n is Manning's roughness coefficient. ν_t is kinematic eddy viscosity expressed as follows:

$$\nu_t=\frac{\kappa}{6}U_*h \quad (4)$$

where κ is Karman's constant, and U_* is friction velocity.

The continuity equation of sediment is expressed as follows:

$$\frac{\partial z_b}{\partial t}+\frac{1}{1-\lambda}\left(\frac{\partial q_B{}^x}{\partial x}+\frac{\partial q_B{}^y}{\partial y}\right)=0 \quad (5)$$

where z_b is the elevation of riverbed ($z_b = H - h$), λ is the void ratio of sand ($\lambda = 0.4$), q_B^x and q_B^y are sediment discharge in x and y direction.

Mass of sediment transportation is shown in Equation (6), proposed by Ashida & Michiue (1972). In this study, we assume all sediment transportation to be of bed material.

$$q_B=17.0\tau_*^{1.5}\left(1-\frac{\tau_{*c}}{\tau_*}\right)\left(1-\sqrt{\frac{\tau_{*c}}{\tau_*}}\right)\sqrt{sgd^3} \quad (6)$$

where q_B is total sediment discharge per unit time and unit width, τ^* is dimensionless shear stress, τ_c^* is dimensionless critical shear stress (Iwagaki, 1956), s is specific gravity of sediment (1.58), and d is averaged diameter of sediment.

Near-bed velocity vector is needed to distribute total sediment discharge to two directions. Near-bed velocity in the streamline direction u_b^s and normal direction u_b^n is calculated as follows:

$$u_b{}^s=\left(u^2+v^2\right)^{1/2} \quad (7)$$

$$u_b{}^n=-\frac{\left(u^2+v^2\right)^{1/2}N^*h}{r_s} \quad (8)$$

where N* is Engelund's constant (Engelund, 1974), r_s is the radius of curvature of streamline. The effect of secondary flow is considered in Equation (8). r_s is expressed in Equation (9) (Shimizu & Itakura, 1991):

$$\frac{1}{r_s}=\frac{1}{\left(\sqrt{u^2+v^2}\right)^3}\left[u\left(u\frac{\partial v}{\partial x}-v\frac{\partial u}{\partial x}\right)+v\left(u\frac{\partial v}{\partial y}+v\frac{\partial u}{\partial y}\right)\right] \quad (9)$$

Transformation of sediment discharge from Cartesian system to boundary-fitted coordinate system, ξ and η direction, are expressed as follows:

$$q_B{}^\xi=\xi_r q_B\frac{u_b{}^\xi}{\sqrt{u^2+v^2}}\sqrt{\frac{\tau_*}{\mu_s\mu_k\tau_*}}\left(\xi_r\frac{\partial z_b}{\partial \xi}+\eta_r\frac{\partial z_b}{\partial \eta}\cos\theta\right) \quad (10)$$

$$_B{}^\eta=\eta_r q_B\frac{u_b{}^\eta}{\sqrt{u^2+v^2}}\sqrt{\frac{\tau_*}{\mu_s\mu_k\tau_*}}\left(\xi_r\frac{\partial z_b}{\partial \xi}\cos\theta+\eta_r\frac{\partial z_b}{\partial \eta}\right) \quad (11)$$

where q_B^ξ and q_B^η are sediment discharge in the ξ and η direction, u_b^ξ and u_b^η are near-bed velocity in the ξ and η direction, $\xi_r = \Delta\xi/\Delta s$, $\eta_r = \Delta\eta/\Delta n$, μ_s is a coefficient of static friction, μ_k is a kinematic friction coefficient.

2.2 *Conditions of simulation*

The simulation model is applied for calculation of riverbed change in the area of meandering restoration works in the Shibetsu River. Figure 1 shows grids for the calculation. The gray area in Figure 1 is a "dummy" area, where flow and riverbed evolution are not calculated. S is the distance from the convergence point. A low-head dam is set in the straight channel

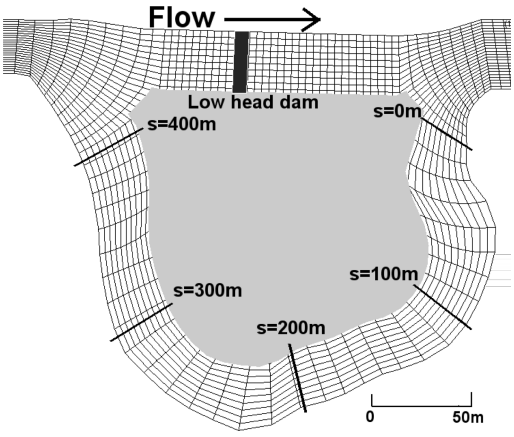


Figure 1. Calculation grid of Shibetu River two-way channel.

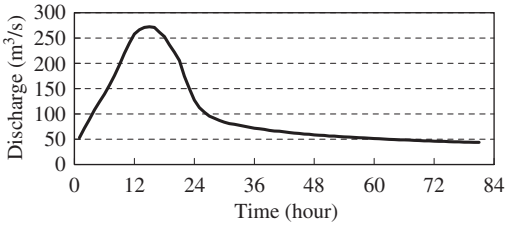


Figure 2. Hydrograph of summer flood on Shibetsu River.

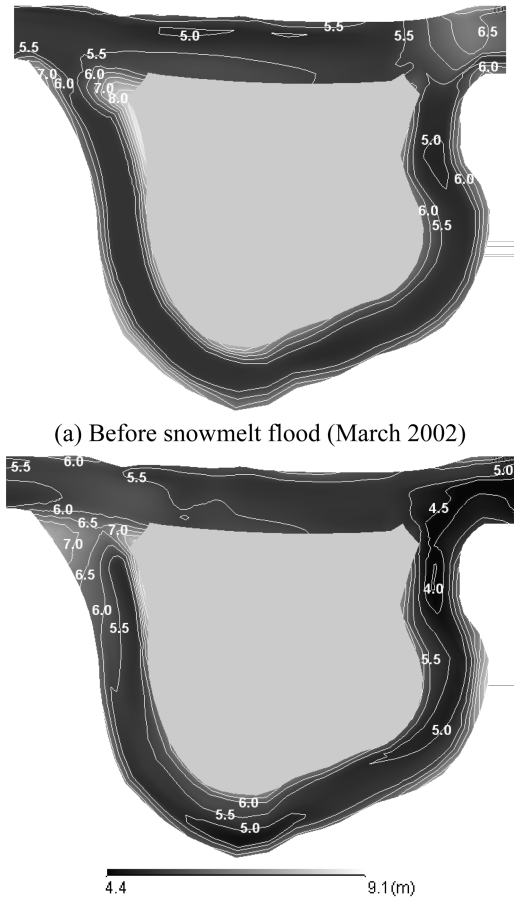
30 m downstream from the bifurcation. The dam head elevation is 6.35 m.

As a boundary condition, discharge is given at the upstream end. Two typical cases of floods are examined. One case is "snowmelt flood." Constant discharge of 47 m^3/s, which was averaged from values observed in April 2002, is assumed to continue for one week. The other case is "summer flood" (Figure 2): discharge observed from October 2 to 4, 2002. Water depth is given by Equation (12) at the downstream end.

$$h = \left(\frac{nQ}{B\sqrt{i}} \right)^{0.6} \tag{12}$$

where Q is discharge at the upstream end, B is channel width (30 m), n is Manning's roughness coefficient of bed, and i is averaged longitudinal bed slope (1/800).

The diameter of bed material is set as 11 mm, the diameter averaged from field measurements. Manning's roughness coefficient is set as 0.017. The initial riverbed configurations in the main channels are from the field measurements obtained in March 2002 for the snowmelt flood and in September 2002 for summer flood. The straight channel upstream and downstream of the bifurcation is assumed to have a rectangular



(a) Before snowmelt flood (March 2002)

(b) After snowmelt flood (July 2002)

Figure 3. Observed bed topography on snowmelt flood.

cross-section, and the channel profile is assumed to gradually change. The longitudinal bed slope of the channel is 1/800, which is the design bed slope of the Shibetsu River. Upstream and downstream length of model is set as 1.6 km each for stabilizing the simulation results.

Bed erosion at the low-head dam is not allowed in calculation of the bed. If bed elevation z_b is lower than the initial value z_{b0} there, then z_b is corrected to z_{b0} automatically.

3 SIMULATION RESULTS FOR THE SHIBETSU RIVER

3.1 *Snowmelt flood*

Figure 3 shows the observed bed topography measured in March 2002 (before the start of snowmelt flood) and in July 2002 (after the flood had ended). Bed form in

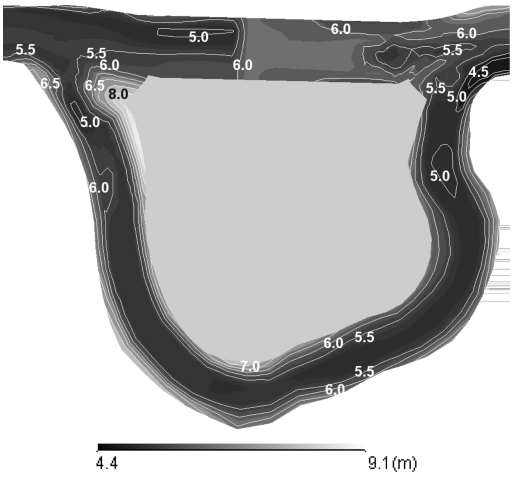


Figure 4. Simulated bed topography after snowmelt flood.

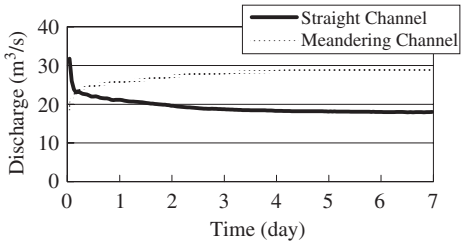
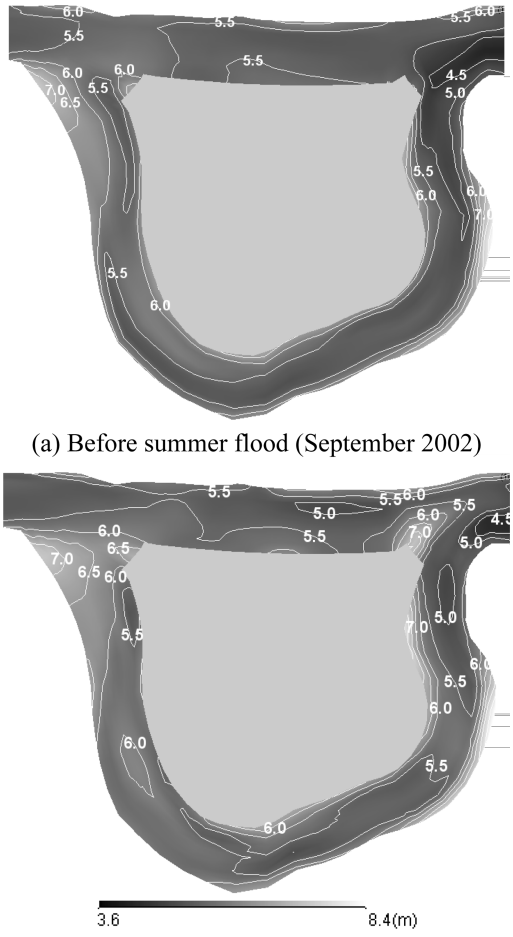


Figure 5. Discharge of two-way channel under snowmelt flood based on simulation results.

March is given as an initial condition in the simulation. Figure 4 shows the simulated bed topography after one week of snowmelt. We compare the calculation results and the observed values.

In the straight channel, deposition on the left bank immediately downstream of the convergence point is washed away after the snowmelt flood in the observation. The simulation also shows a decrease in bed elevation downstream of the convergence point on the left bank. Deposition also appears immediately downstream of the low-head dam in the simulation. In the meander channel, the riverbed elevation rises around the entrance and scouring occurs in the center of the channel immediately upstream of the convergence point in the actual river. But in the simulation, the bed topography hardly changes in the meander channel except around the bifurcation and the convergence.

Discharge in both channels calculated on the basis of simulation results is shown in Figure 5. Discharge in the meander channel increases over the course of 5 days to become almost constant. Discharge into the meander channel in snowmelt flood is about 60% of



(a) Before summer flood (September 2002)

(b) After summer flood (October 2002)

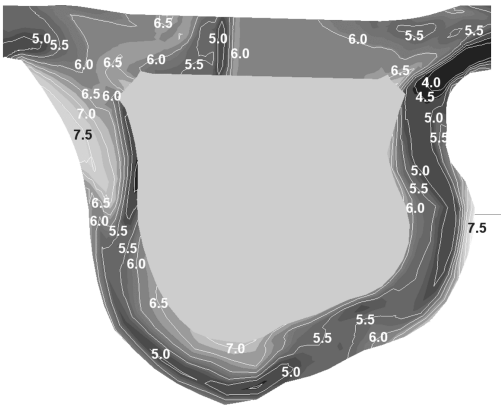
Figure 6. Observed bed topography on summer flood.

the total discharge by field observation. Simulated discharge in the meander channel is 62% of the total discharge at the end of the simulation. The simulation accurately reproduces the observed value.

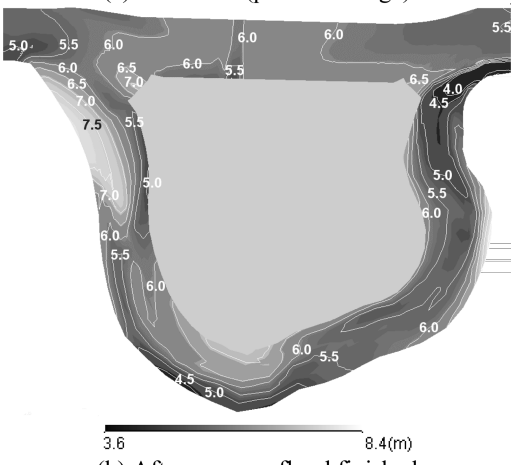
3.2 *Summer flood*

Figure 6 shows bed topography observed in September 2002 (before summer flood) and in October. Observed bed topography is used as the initial riverbed shape in summer flood simulation. Figure 7(a) shows the calculation results of bed topography at t = 15 h, when the hydrograph shows peak discharge. Figure 7(b) shows simulated bed topography after the summer flood has finished.

At peak flood discharge, deposition develops at the right bank between the bifurcation and a point 1/4 of the way downstream of that point in the meander



(a) t=15hours (peak discharge)



(b) After summer flood finished

Figure 7. Bed topography of summer flood (simulated).

channel in the simulation. After the summer flood has finished, this deposition remains in roughly the same place. The simulated deposition is larger in scale than the observed deposition. There is bed erosion on the left bank near the bifurcation in actual river. Bed erosion also occurs at roughly the same place as on the simulated riverbed.

In the straight channel, simulated deposition appears immediately upstream of the convergence on the right bank in observation after the flood has finished. Simulated deposition is at the same area, but it is smaller than actual deposition. Bed elevation downstream of the low-head dam rises in the simulation. However, these trends do not appear in the actual river. In front of the dam, scouring appears at peak discharge. This scouring becomes smaller at the end of the simulation.

Figure 8 shows discharge of a two-way channel under summer flood calculated on the basis of

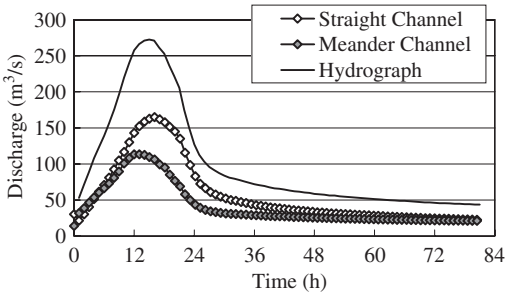


Figure 8. Discharge of two-way channel under summer flood, based on simulation result.

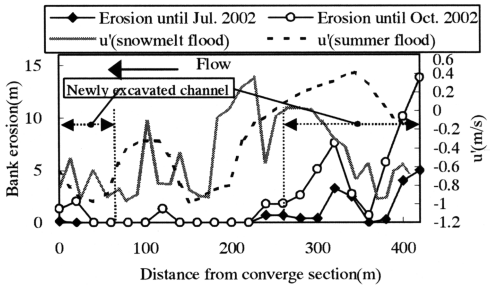
simulation results. The rate of discharge in the meander channel to total discharge is 60% at the start of the flood. It decreases while the total discharge rises. It is about 1/3 at peak discharge and is rising while total discharge is decreasing. It is 45% at the end of the flood. Deposition at the right bank near the bifurcation seems to cause a decrease of discharge in the meander channel.

Through the simulation of bed topography under two floods, simulated results especially differ from the operated value around the bifurcation and low-head dam. Around these areas, the effect of vertical flow is remarkable. 2-D simulation model cannot reproduce near-bed velocity well because vertical distribution of velocity isn't considered well in the model. Accurate estimation of near-bed velocity is one of important factors for appropriate results of simulation.

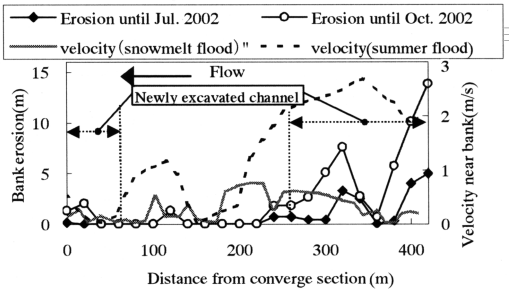
3.3 *Relationship between velocity and riverbank erosion in meander channel*

Since flow was restored in the meander of the Shibetsu River, bank erosion has been occurring on both banks, mainly near the entrance to the meander channel. We analyze the relationship between hydraulic parameters and bank erosion. The near-bank flow velocity and perturbation velocity, which is defined as the difference between near-bank velocities and cross-sectional averaged velocity, correlates closely with riverbank erosion (Suzuki et al., 2003). We examine the correlation between simulated velocity near the riverbank and observed riverbank erosion quantity.

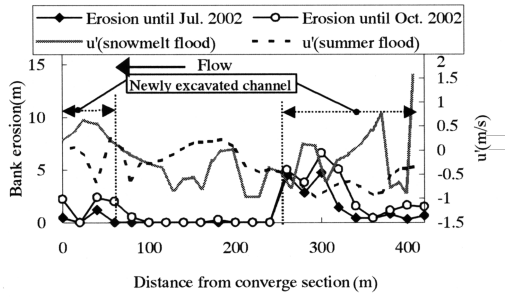
Figure 9 shows the relationship between longitudinal distribution of observed bank erosion, simulated velocity near both banks and perturbation of simulated velocity near the banks under snowmelt flood and under the maximum discharge of summer flood. The horizontal axis of graphs in Figure 9 is the distance upstream from the convergence point in the meander channel, which is indicated as "s" (unit; meters) and shown in Figure 1. Section $s = 0$ m is



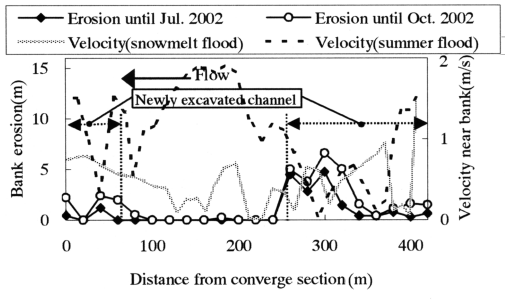
(1) Erosion and perturbation of velocity at the left bank



(2) Erosion and velocity at the left bank



(3) Erosion and perturbation of velocity at the right bank



(4) Erosion and velocity at the right bank

Figure 9. Longitudinal distribution of perturbation of velocity, velocity near both banks and erosion.

the convergence point and s = 420 m is the bifurcation point. The perturbation of velocity near the bank, u', is defined by Equation (13):

$$u' = u_{wall} - u_m \tag{13}$$

where u_{wall} is near-bank flow velocity, and u_m is cross-section averaged velocity. Bank erosion is defined as the change from the riverbank measured in March 2002. Erosion until July is the change caused by snowmelt flood, and erosion until October is the summation of change caused by snowmelt flood and summer flood. This meander channel can be regarded as having two kinds of sections: (1) a section from s = 60 m to s = 260 m (the previous oxbow lake), and (2) a section from s = 0 m to s = 60 m and another from s = 260 m to s = 420 m (the newly excavated parts of the meander channel).

In the meander section between s = 100 m and 240 m, the riverbank erosion is generally less than in the other sections. This section is in the previous oxbow lake and the erosion-resistance of the riverbank seems stronger in this section than in the sections excavated upstream and downstream of the oxbow. The right riverbank from s = 60 m to s = 260 m occurs particularly little change during the two floods.

First, we examine erosion caused by snowmelt flood. Riverbank erosion appears around the convergence point and on the meander section between the bifurcation and s = 250 m. The erosion is remarkable between s = 240 m and s = 300 m on the right bank and between the bifurcation and s = 350 m on the left bank. There isn't clear correlation between riverbank erosion quantity and near-bank velocity. Erosion is particularly remarkable from s = 350 m to the bifurcation on the left bank actually, although simulated near-bank velocity is small. Around this area, flow in the vertical direction is supposed to be strong and bank erosion there may have advanced from causes other than shear stress induced by the near-bank flow. The perturbation velocity is generally small in the meander channel and does not correlate with riverbank erosion quantity in snowmelt flood.

Second, bank erosion after the summer flood is examined. Erosion make progress on the area where the bank had been eroded until July and is noticeable on the left bank of section between the bifurcation and s = 350 m. In this section near-bank flow velocity is large, suggesting that the flow velocity near the riverbank affects the erosion. Also on the right bank, near-bank velocities seem to relate closely to the bank erosion. There isn't clear relation between perturbation velocity and bank erosion quantity around the bifurcation. But around the convergence, there seems to be a little relation between two factors. Simulation doesn't seems to be reproduce the velocity well around the bifurcation and it may be one of the factor that there is

little relation between near-bank velocity, perturbation velocity and bank erosion quantity.

In summary, the calculation results of summer flood suggest that river erosion tends to occur in sections with greater near-bank flow. The near-bank flow velocity or perturbation velocity is somewhat related to riverbank erosion in summer flood. However, little correlation is found between near-bank flow velocity or perturbation velocity and erosion in snowmelt flood or the area where effects of vertical flow cannot be ignored.

4 EFFECTS OF LOW-HEAD DAM ON THE RATIO OF DISCHARGE IN THE MEANDER CHANNEL

The longitudinal slope of the meander channel bed is milder in the two-way channel than in the straight channel bed. The entrance of meander channel may become obstructed by sediment deposition if its discharge is insufficient. Therefore a low-head dam was set in the straight channel to secure proper flow in the meander. In a two-way channel, it is important to establish the proper dam height. We investigate the ratio of discharge in the channels using a simulation to examine the effect of the low-head dam on flow in a two-way channel.

Simulation is carried out on a fixed-bed. Each section of channels is set as rectangular. Longitudinal slope is 1/800 in straight channel. Plane geometry of the channel is same to Figure 1. Three cases of discharge are set: $Q = 20\ m^3/s$, $40\ m^3/s$ and $270\ m^3/s$. Froude number immediately upstream of the bifurcation is 0.47 ($Q = 20\ m^3/s$) and 0.51 ($Q = 40\ m^3/s$).

Figure 10 shows the relationship between height of low-head dam and simulated discharge rate in the meander channel. (Observed value in Figure 10 is quoted from the research by Fujita et al. (2003).) δ/h is the ratio of height of low-head dam to water depth upstream of the bifurcation. "r" is the ratio of discharge in meander channel to total discharge. That ratio determined by theoretical analysis depending on the momentum conservation law (Fujita et al., 2003) is also shown in Figure 10, which can express actual phenomena under the condition of complete overflow and submerged overflow on the dam. Observed value is good agreement with theoretical analysis and simulated value. Under the complete overflow condition (δ/h > 0.6), simulated discharge is in good agreement with theoretical value. Under submerged overflow conditions, there is a difference between theoretical value and simulated value. In theoretical analysis separation streamline is set to divide bifurcation area so cross-sectional velocity distribution is assumed to be uniform around bifurcation. This is one of the factors of the difference between both values. According to the simulation, at least 30% of the total discharge goes into the meander channel. Ratio of discharge in meander channel becomes large slowly with increase of height of low-head dam. Ratio seems to be determined by δ/h and little affected by discharge.

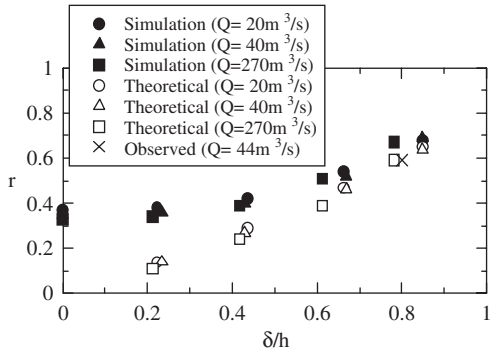


Figure 10. Comparison of ratio of discharge in meander channel to total discharge among simulation, theoretical analysis and observed value.

5 EXTENSION TO COMPOUND FLOW WITH TWO-WAY MAIN CHANNEL

5.1 *Introduction of the calculation*

The discussions in the previous section are limited to hydraulic phenomena in a main channel and do not consider flow on the floodplain. However, in a large-scale flood, inundation of the floodplain will occur and a more complicated flow regime and riverbed evolution can arise. For river planning and management of rivers with compound channel flow, it is very important to include the effects of floodplain flow in calculations of flow and bed topography.

We discuss characteristics of compound flow in a two-way main channel by using a simulation. To examine how flow characteristics in a two-way main channel influence flow and bed topography, simulation is done for main channels of two different shapes: (1) meander channel, and (2) meander channel plus straight channel (i.e., two-way main channel). Simulation results of these two cases are compared. There are neither experimental nor field measurement data for comparison and examination, so we discuss the flow only from the simulation data.

5.2 *Conditions for the calculation*

Figure 11 shows calculation grids of compound flow with two-way main channel. We set the dimensions

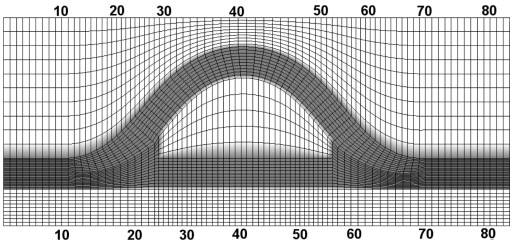


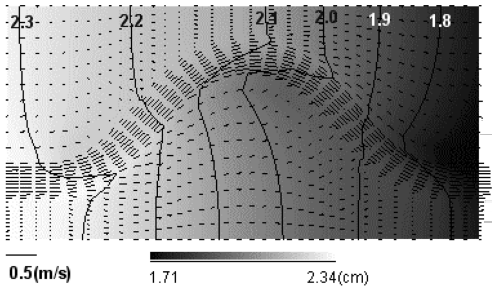
Figure 11. Calculation grid of compound channel with two-way main channel.

of simulation area considering a reduced scale to the Shibetsu River (1:167): The width of the main channel is 0.3 m. The depth of the main channel below the floodplain elevation is 0.03 m. The whole channel width is 2 m. The maximum meandering angle of the meander channel is 50 degrees. Wavelength of the meander channel is 4.2 m. Bed slope in the longitudinal direction is 1/800. For bed friction, Manning's roughness coefficient is set as 0.013 in the main channels and 0.02 in the floodplain. Riverbed evolution is assumed to occur only in the main channels. The diameter of the bed material is 0.75 mm. Total discharge is 0.00167 m^3/s, which is based on planning discharge of the Shibetsu River. Constant discharge is set at the upstream and uniform flow water depth (Equation (12)) is set at downstream ends. To increase calculation stability, the effects of secondary flow are not considered in the simulation of compound flow. We investigate the calculated values three hours after the beginning of water passage.

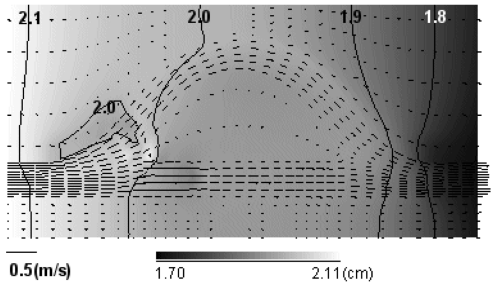
5.3 *Calculation results*

The distributions of water level and velocity in a two-way main channel under compound flow are shown in Figure 12(1). The results for a compound channel with a single-meandering main channel are shown in Figure 12(2). We see that resistance is smaller for a straight main channel. In a two-way main channel, the maximum flow velocity occurs longitudinally in the straight main channel, where flow is concentrated. In a one-way main meander channel, flow is also concentrated in main channel. But discharge in main channel is smaller than one in two-way channel. The straight main channel reduces the water level and discharge on the floodplain. It is expected to improve the safety of flood control.

Figure 13 shows riverbed changes. Bed change is generally more active in straight main channel than in meander channel. In the straight channel, bed elevation rises from the bifurcation to the convergence and decreases in other section. Around the entrance of meander channel, deposition can be seen.



(1) Two-way main channel



(2) Single meandering main channel

Figure 12. Water surface contour and velocity.

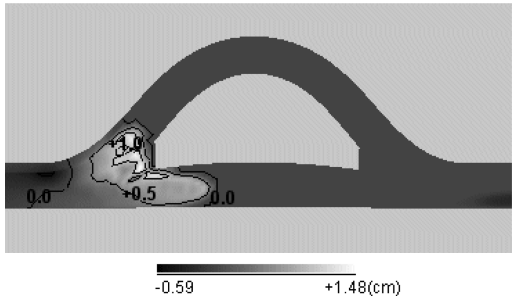


Figure 13. Bed change of compound flow with two-way main channel.

6 CONCLUSION

Simulation was performed for snowmelt and summer floods on the Shibetsu River. The calculation results partly reproduced the changes in bed topography. However, the calculation results did not accurately reproduce the bed topography in some cases, especially around the bifurcation, where near-bed velocity should be affected by vertical flow.

Velocity and perturbation velocity near the riverbanks somewhat correlated with riverbank erosion in the summer flood. The method of predicting erosion using the calculated velocity seems to be effective in

some cases. However, it needs more improvement for estimating near-bank velocity with satisfied accuracy.

The compound flow with two-way main channel was experimentally simulated. Straight channel would be expected to improve safety for flood control.

ACKNOWLEDGEMENTS

The Hokkaido Development Bureau, Ministry of Land, Infrastructure and Transport of Japan, provided a grant for this research. Field measurement data of the Shibetsu River were provided by the Kushiro Development and Construction Department of the Hokkaido Development Bureau. We would like to express our appreciation for this assistance.

REFERENCES

Ashida, K. and Michiue, M. 1972. Study on Hydraulic resistance and bedload transport rate in alluvial streams. *Proceedings of JSCE*, No. 206: 59–64 (in Japanese).

Engelund, F. 1974. Flow and bed topography in channel bends. *Journal of Hydraulic Engineering, ASCE*, Vol. 100, No. HY11.

Fujita, M., Hasegawa, K., Watanabe, Y. and Kuwamura, T. 2003. Bifurcated discharge rate to the oxbow meandering channel regulated by a small dam with overflow condition in the Shibetsu River, *Proceedings of 3rd IAHR Symposium on River, Coastal and Estuarine Morphodynamics, Balcelona, 2003*, 831–844.

Fukuoka, S., Ohgushi, H., Kamura, D. and Hirao, S. 1997. Hydraulic characteristics of the flood flow in a compound meandering channel. *Journal of Hydraulic, Coastal, and Environmental Engineering, JSCE*, No. 579. 83–92 (in Japanese).

Fukuoka, S., Watanabe, A. and Okada, S. 1999. Analysis of bed topography in a compound meandering channel using a 3-D numerical model with assumption of hydrostatic pressure. *Journal of Hydroscience and Hydraulic Engineering, JSCE*, Vol. 17, No. 2, 99–105.

Nagata, N., Hosoda, T. and Muramoto, Y. 2000. Numerical analysis of river channel processes with bank erosion. *Journal of Hydraulic Engineering, ASCE*, Vol. 126, 243–262.

Ikeda, S., Parker, G. and Sawai. K. 1981. Bend theory of river menaders. Part 1. Linear development, *Journal of Fluid Mechanics*, Vol. 112, 363–377.

Iwagaki, Y. 1956. Hydraulic study of critical tractive force: *Proceedings of JSCE*, No. 41: 1–21 (in Japanese).

Odgaard, J. 1989a. River meander model 1: Development, *Journal of Hydraulic Engineering, ASCE*, Vol. 115, No. 11, 1433–1450.

Odgaard, J. 1989b. River meander model 2: Application, *Journal of Hydraulic Engineering, ASCE*, Vol. 115, No. 11, 1451–1464.

Parker, G., Sawai, K. and Ikeda, S. 1982. Bend theory of river menaders. Part 2. Nonlinear deformation of finite amplitude bends, *Journal of Fluid Mechanics*, Vol. 115, 303–314.

Sato, K. and Watanabe, Y. 2002. Influence of bars in river channels with bifurcation and convergence, *Proceedings of River Flow 2002*, *IAHR*, *Louvain-la-Neuve, Belgium*, Vol. 2: 741–750.

Shimizu, Y. and Itakura, T. 1991. Calculation of flow and bed deformation with a general non-orthogonal coordinate system, *Proceedings of XXIV IAHR Congress*, *Madrid, Spain*, C-2: 41–48.

Struiksma, N., Olesen, W. K., Flokstra, C. and De Vriend, J. H. 1985. Bed formation in curved alluvial channels, *Journal of Hydraulic Research*, Vol. 23, No. 1, 57–79.

Suzuki, Y., Watanabe, Y., Hasegawa, K., Mori, A. and Kuga, T. 2003. Changing of two-way river course in restoration project at the Shibetsu River, *Annual Journal of Hydraulic Engineering, JSCE*, Vol. 47, 703–708 (in Japanese).

This page intentionally left blank

River Flow 2004 – Greco, Carravetta & Della Morte (eds.)
© 2004 Taylor & Francis Group, London, ISBN 90 5809 658 0

River meandering restoration – case study and laboratory experiments

R. Banasiak, R. Verhoeven, L. De Vos & S. Verfaille
Hydraulics Laboratory, Ghent University, Belgium

ABSTRACT: In the frame of a pilot project a multidisciplinary study concerning the evaluation of the feasibility and sustainability of river re-naturalisation has been conducted. Special emphasis was put on the hydraulic aspects of the restoration of a natural meandering river course degraded by engineering works in the past. Firstly, an outline is given of several predictions for the river meander pattern. Most formulas however, are of empirical nature, which makes them less suitable for case studies with specific local conditions. Secondly, a case study, performed in order of the environmental department of the Flemish government, is highlighted. Thirdly, a laboratory investigation, performed in a flume set-up, is described. During several tests the development of the meander patterns was recorded using discharge, slope of the river bed and initial channel bed configuration as variable parameters. The influence of artificial interventions, such as deflectors, to promote meander development, has been tested as well.

1 INTRODUCTION

Meandering is a basic feature of natural rivers. In the past many natural watercourses have been trained to meet different economical needs. These training works often neglected ecological aspects in such a way that the transformed rivers were straightened and thus lost their ecological value. Moreover, even the original aim of anti-flood protection has failed since the river straightening and flood plain cutoffs led to a decrease in river storage capacity and faster propagation of flood waters and higher flood peaks. In Flanders this has caused frequent flooding in both rural and urban areas, in particular in the downstream parts of watercourses. The results became clear: wet or water filled cellars, more frequent agriculture losses and streets under water.

To meet these problems the Flemish Administration for Environmental, Nature and Landplanning (AMINAL) has recently conducted a pilot project aiming at the evaluation of the feasibility and sustainability of river restoration. In particular the restoration of meandering river courses is considered. A preliminary study indicated several sites, which are suitable for meandering, taking into account a variety of different aspects. This article mainly investigates several aspects of the hydraulic changes that occur in rivers subjected to meander restoration.

The overall idea behind any restoration is to create a stable channel. In order to avoid potential problems, it is important to understand the changes that a river will experience when different control or regulation schemes are applied. The prediction of these changes is an important aspect of every restoration project.

A brief description of a physical model study, performed in the Hydraulics Laboratory, Ghent University, is included. This model study was performed to gain more information on the mechanism of meander development. The influence of obstacles on the meander development is a specific part of this study.

2 PREDICTORS ON RIVER MEANDERING

The meandering forms that are created even across a range of spatial scales and environmental boundary conditions display often startling regularities. The sinuous shape of the meandering planform has led scientists to look after the factors responsible for shaping river meanders. So far, several theories have been proposed and many, in majority, empirical formulas based on some sets of data have been derived.

In many empirical formulas the discharge is regarded as the dominant independent variable to which the dependent variables, such as width, depth, velocity and meander wave length, adjust. Dependant variables are usually expressed as power functions of bankfull discharge,

$$B=C_B Q^{\alpha} \quad (1)$$

and the meander parameters are related to the channel width, e.g. (Leopold & Wolman, 1964):

$$\lambda=11B^{1.01} \quad (2)$$

$$a=3B^{1.1} \quad (3)$$

$$r_c=2.4B \quad (4)$$

where B = bankfull channel width (m); λ = meander wave length (m), a = meander amplitude (m), r_c = maximum meander radius (m), and C_B and α = constants.

The physical explanation for the selection of the bankfull discharge as bed forming parameter is that with smaller discharges less sediment transport occurs, which hardly affects the river bed transformation. For discharges larger than bankfull the water masses are conveyed over the flood plains with as a consequence presumable lower bed forming activity. The empirical relations obviously do not include many other important factors such as bed and bank material, sediment load, slope, etc. Therefore, the empirical coefficients are usually specific site dependent.

Chitale (1970) investigated meandering patterns of more than 40 rivers in India. Using field data consisting of depths and widths for bankfull discharge, slope and bed material size, single and multiple correlations were performed resulting in the following equations for shape and relative size of meanders:

$$\frac{L_{thalweg}}{L_{vallei}}=\frac{M}{\lambda}=1.429\left(\frac{d_{50}}{D}\right)^{-0.077} S_*^{-0.052}\left(\frac{B}{D}\right)^{-0.065} \quad (5)$$

$$\frac{a}{B}=48.299\left(\frac{B}{D}\right)^{-0.471} S_*^{-0.453}\left(\frac{d_{50}}{D}\right)^{-0.050} \quad (6)$$

in which S_* = slope in feet per 10,000 ft length of the channel, d_{50} = mean bed material diameter, D = average depth of channel, B = surface width of channel, M = meander length. The percentage errors of estimation using this equations were 18.69 and 58.05 respectively. Accuracy did not improve much by increasing the number of variables in Eq. 5 against other single correlation. Significant scatter between the observed and estimated values for the equations were supposed due to omission of the definition of the nature of bank material, sediment concentration, sediment gradation and the inevitable limitation of data. In addition, as both depth and width vary along a meandering channel from bend sections to transition sections, the ratios of d_{50}/D and B/D vary along the channel. Furthermore, the bankfull discharges often had to be estimated, resulting in significant uncertainties.

Stability theories have been applied to delineate the origin of meanders. Analysis by Ikeda et al. (1981) and Parker et al. (1983) using a dynamic equation for longitudinal velocity and a kinematic equation for bank erosion have provided the mechanistic founding of the meander path. An expression for the wavelength was

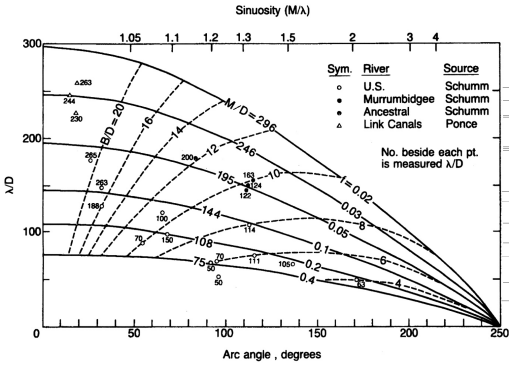


Figure 1. Plan geometry of river meanders (Chang, 1984b).

derived as:

$$\frac{\lambda}{D}=8\left(\frac{\pi B}{fD}\right)^{1/2} \quad (7)$$

where D = flow depth, f = friction coefficient from Darcy-Weisbach formula.

The meander curvature and other geometric features for rivers were analysed by Chang (Chang, 1984a, Chang, 1984b). Chang uses an energy approach combined with relations for flow continuity, sediment load, resistance to flow, bank stability and transverse circulation in channel bends to obtain a mathematical formulation for the equilibrium river state. The analysis establishes the maximum equilibrium curvature, stated as the radius-of-curvature to channel-width ratio, which has an average value of 3; it shows only minor variation within the meandering range:

$$\frac{r_c}{B}=2.2+0.15\left(\frac{B}{D}-4\right) \quad (8)$$

From the regular meander path model Chang obtained a graphical relationship for the plan geometry of river meanders as shown in Figure 1.

3 MEANDERING RIVERS – CASE STUDY

3.1 *Historic and present river courses*

In this section five selected rivers in Flanders showing a typical lowland character, are considered. These rivers are the Kleine Nete, Grote Nete, Marke, Warmbeek and Kemmelbeek. The first data of implemented modifications date from the 19th century. The rivers were subjected to training works, over which the first data found are dated from 19th century. In that time attempts to control frequent flooding and to meet the rising demands for agriculture led to significant changes in the structural quality of most watercourses and reservoirs in the region. Later on,

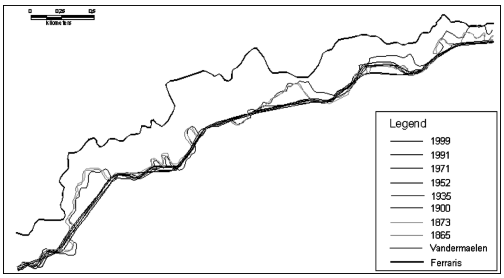


Figure 2. The Kleine Nete river course changes in time (van Wallons, 2002).

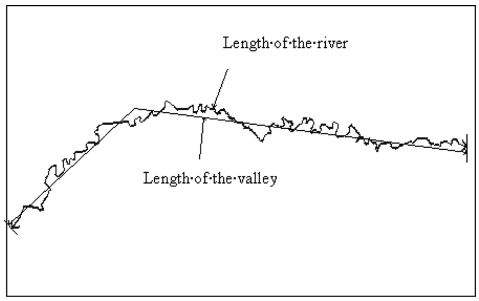


Figure 3. The Grote Nete river – determination of the sinuosity.

the training works were continued, in particular in the 60- and 70-ties of last century. Most of these rivers were channelised and straightlined to their the present far-to-nature state.

As an example, Figure 2 shows the river course changes throughout the time for the river Kleine Nete. For this evaluation more recent and old maps, dating from the eighteenth century, were used.

From this Figure, it is clear that the Kleine Nete indeed was a meandering river. Comparable results were obtained for the 4 other rivers. A large amount of wave lengths has been calculated for each river, in order to determine the predominant wave length, together with other meander characteristics. The old maps show the natural state of the river and thus are valuable sources for determining an equilibrium river pattern. They can serve as a reference for the restoration project. However, some problems were encountered while trying to assess the meander patterns.

It is assumed that the oldest maps by Ferraris (1771–1778) aren't reliable for the determination of the meander characteristics, as significant deviations in the river trajectory were found compared to the later elaborations. Presumably, the topographical methods of that time were not accurate enough. Therefore the first evaluation goes back to the years 1846–1854, to the military maps by Vandermaelen.

Furthermore, due to the irregularity of the river course, instead of immediately determining the meander wavelength, it was mostly calculated as twice the distance between two inflection points, as this was easier to determine.

Finally, the sinuosity of the rivers was determined as the ratio between the actual length of the river over a section to the distance between the begin and the end of the sections (Fig. 3). This was done in a careful way, as it appeared that the section length differs from map to map depending upon the map scale and the number of details included.

3.2 *Geometry and hydraulic parameters*

Parallel with morphologic studies a large amount of geometrical and hydraulic data has been gathered during field measurements. Representative parameters for the selected sections of the rivers were derived from a large set of cross sections. Friction coefficients were established based on discharge and water surface measurements. The river bed material was collected in several points along the rivers and analysed to determine the grain size distribution. The formation of the banks consists mostly of fine graded sand, locally with significant silt-clay content. The main hydraulic parameters of the studied rivers are collated in Table 1.

3.3 *Predicted meander size*

The set of morphologic and hydraulic data is used to determine the meander patterns according to the above presented formulas. Then they are compared with the meander patterns read from historic sources.

The results of these calculations and the average values from map reading are summarised in Table 2.

One can see that significant differences for meander parameters are obtained by different methods, which needs some comments.

The results derived by the Chitale formula are realistic concerning the prediction of the sinuosity of the rivers. On the other hand, the sizes of meanders are significantly overestimated; the predicted amplitudes are 3–4 times larger than those found in the maps.

The determination of the meanders using Chang's graphical method was somewhat problematic. The studied rivers feature relatively small width–depth ratios, as a result of which the values B/D fall in the right-bottom part of the graph were accurate reading is difficult. This results further in very high values for the sinuosity, especially for the Warmbeek and the Grote Nete river, where M/λ is higher than 5. Chang believes that smaller width–depth ratios associated with cohesive properties of channel forming material promote the development of very sinuous channels. The corresponding values for meander wave length are relatively good. However, when using the sinuosity from the maps, the λ/D ratio from the graph would be around 100–120, which is much more than the actual values for the studied rivers.

Table 1. Hydraulic parameters of studied rivers.

		Warmbeek	Grote Nete	Kleine Nete	Marke	Kemmelbeek
Bankfull discharge (m^3/s)	Q_b	4.6	11.1	29.2	18.1	18.6
Depth (m)	D	1.3	2.4	2.5	2.0	2.2
Width (m)	B	4.5	8	14	13	10
Hydraulic radius (m)	R	0.94	1.44	2.26	1.38	1.34
Slope (−)	S	0.00067	0.0005	0.0003	0.00075	0.00145
Friction coeff. (−)	f	0.073	0.09	0.078	0.078	0.091
Sediment size (mm)	d_{50}	0.35	0.18	0.18	0.14	0.25

Table 2. Comparison of different methods for meander shape determination.

			Warm-beek	Grote Nete	Kleine Nete	Marke	Kemmel-beek
Sinuosity (−)	M/λ	Maps	1.24	1.58	1.48	1.37	1.51
		Leopold & Wolman	1.22	1.25	1.27	1.27	1.26
		Chang	5.8	5.8	2	1.7	2.9
		Chitale	1.43	1.63	1.62	1.5	1.49
Length (m)	λ	Maps	50	43	146	150	100
		Leopold & Wolman	50	90	159	147	113
		Chang	30	60	175	170	110
Amplitude (m)	a	Maps	16	33	43	31	32
		Leopold & Wolman	16	30	55	51	38
		Chitale	56	128	221	140	99
Curvature radius (m)	r_c	Leopold & Wolman	11	19	34	31	24
		Chang	10	17	34	33	23

Similarly, overestimated values for meander length are obtained with the relationship suggested by Ikeda & Parker.

The 'best' results are obtained using formulas by Leopold & Wolman. These simple formulas, based on bankfull channel width only, produce the meander amplitude, length, curvature radius that comes reasonable close to the natural development of the studied rivers.

The differences in results are not surprising, as in the reported studies the scatter of the measured meander patterns, to which the formulas were fitted, was also significant. An explanation for the geometrical variations, despite those already mentioned in previous paragraph, is the heterogeneity that exists in natural rivers. The heterogeneity, which includes factors such as vegetation, cohesive sediment content, variation of sediment size, fallen trees, rocks, etc., may inhibit the development of a self-formed meander geometry. That is why more sophisticated formulas, that use some selected factors can produce misleading results.

From this one can conclude that the choice and use of any formula must be done carefully and at best proceeded by verification to the local conditions using reference meander patterns. It is evident that the understanding of the meander development is still far from satisfactory.

4 LABORATORY STUDY

Because of the incompetence of the existing formulas, a physical model study was launched to gain more information on the mechanism of meander development. Hereafter, several laboratory tests are discussed. Considering the complexity of the simulated process, the test should be regarded as a preliminary stage of the ongoing study.

4.1 *Test conditions*

The laboratory experiments were conducted in a test flume that is 15 m long and 2.6 m wide and is enclosed in a circulating water system. The flume was filled with a mixture of sand and caolinite clay. The characteristic diameters of the sand are $d_{10} = 0.17$ mm $d_{50} = 0.23$ mm $d_{90} = 0.315$ mm. The cohesive fraction was added in order to increase the stability of the channel banks. Its content in the sediment mixture was 3%. The sediment was leveled to obtain a flat plain with an average thickness of 15 cm. The longitudinal slope was situated between 0.7 mm/m and 7 mm/m. In the centre of the flume a straight trapezoidal channel was formed. The channel has a depth of 6 or 8 cm, a 15 cm bottom width and a bank slope of 1:1. The initial geometric parameters were chosen in respect to the Warmbeek river, one of the studied meandering rivers.



Figure 4. Testing set-up.



Figure 5. Channel after the end of Test 2.

The morphologic changes that occurred during the tests were recorded on a video camera. The horizontal and vertical geometry was measured with a laser interferometer. The interferometer was mounted on a carriage that could shift over the flume. No sediment was added in the current test.

4.2 *Test performances*

Test 1
In the first test a slope $S = 0.00067$ was applied. The straight channel had a depth of 8 cm and a width of 31 cm. The bankfull discharge was initially 5.7 l/s but was during the test reduced to 2.75 l/s (1 cm below the banks) because water started to flow over the banks in the downstream section. Since after 30 hours no meander patterns were observed to develop, the discharge was increased again to about 3.7 l/s. After another 50 hours of test run no meander patterns were developed.

Test 2
The slope was the same as in Test 1. The channel depth was smaller, 6 cm and had an initiating bend (with $\lambda/2$ 2.6 m and $a = 0.35$ m). Also in this test no meander formation was obtained, see Figure 5.

From these initial conditions, it could be concluded that the flow had not enough potential to transport the sand along the bed and to erode the banks.

Test 3
In this configuration the slope was significantly increased to $S = 0.007$. The channel had a depth of 8 cm and an initiating bend with $\lambda/2 = 2.6$ m and $a = 0.3$ m. The discharge was set to 3.33 l/s. At 17 hours, the bed topography was measured for the first time. The total duration of the test was 86 hours. During this test, significant sediment transport and bank erosion was observed. The obtained transformation is shown in Figures 6 and 7 respectively representing an intermediate and the final meander pattern.



Figure 6. Test 3: Channel development after 20 hours.

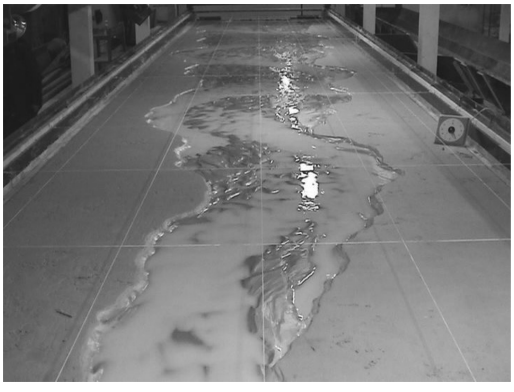


Figure 7. Test 3: Channel development after 86 hours.

Although the channel becomes wide and shallow, a deeper sinuous talweg and an extended downstream wave migration can be easily recognized. In Figure 8, the recorded cross-sections through the top of

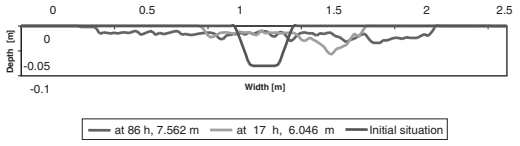


Figure 8. Test 3: Channel cross-section.

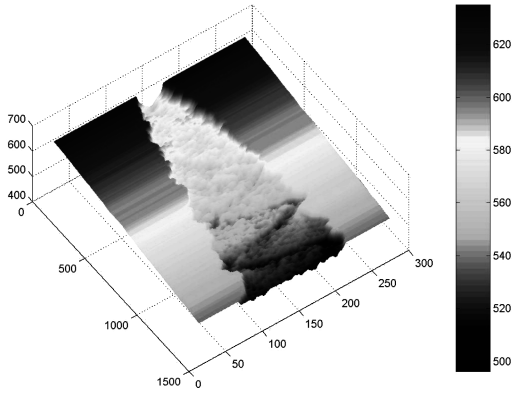


Figure 9. Test 4: 3D-channel development after 29 hours (length and width in cm, depth in mm).

a sinuous wave are shown. The asymmetrical character of this section is remarkable.

At 17 h, the meanders had a wavelength of 2.63, 2.63 and 2.81 m, and an amplitude of about 0.6 m, which was nearly constant along the channel. After 86 h the meanders evolved to 3.41, 4.0 and 4.09 m in length and the amplitude varied from 0.6 to 1.5 m, increasing along the channel. Smaller meanders in the upstream channel section were due to the lack of sediment supply at the entrance, which caused erosion of the bed, consequent flatter slope and loss of capacity to erode the banks.

Test 4

In Test 4 the initial conditions were the same as in Test 3 except for the initiating bend; the channel was straight over the entire length. The discharge of 3.33 l/s was maintained constant throughout 29 hours of testing. The resulting channel configuration is shown in Figure 9. The talweg extends in the downstream direction with a sinuous shape and increasing depth. The width of the meandering channel belt increases linearly from 0.31 m to 1.45 m. The meander length varied from 1.2 to 4.03 m, and the sinuosity reached a value of 1.27.

Test 5

In this and in the following test it was intended to check the influence of an obstacle in the straight channel on the initiation of meander formation. The use of such obstacles, known as deflectors, is a recommended measure to recreate meandering patterns in degraded

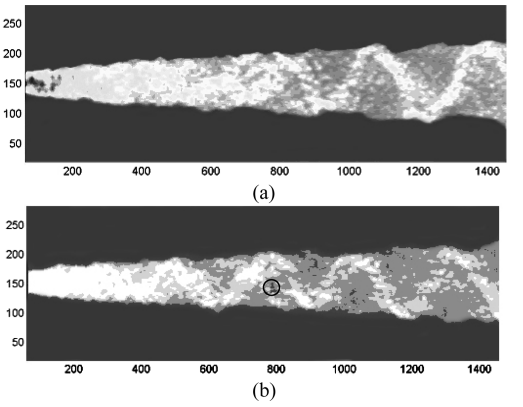


Figure 10. Final channel development in (a) Test 4, (b) Test 5 (units in cm; circle indicates the position of the obstacle).

straight rivers, FISRWG (1998). In this test a single permeable obstacle was placed in the right bank of the channel, at 7.2 m from its beginning. The other channel characteristics remained the same as in Test 4.

During the test it appeared that the deflector had little impact on the development of the meander pattern. Only at the very beginning of the test the deflector influenced the erosion of the opposite bank. Later on, local turbulence caused erosion of the bank around the obstacle, which led to a deflector cut off from the bank it was built in. The deflector lost its significance quite soon and in the end it was just an unnecessary obstacle in the channel.

After 23 hours, the meandering talweg reached a length varying from 2 to 3.2 m and an amplitude up to 1.1 m. The sinuosity reached a value of 1.2 in the most downstream section.

Figure 10 represents the final channel state for the last two tests, which had the same initial configuration except for the deflector, used in Test 5. The larger size of the meandering talweg in Test 4, in comparison with Test 5, is due to the longer duration of the test. Remarkable in Test 4 is the deviation of the sinuous meander pattern. The meander transverses appear to be convex, facing downstream. This is comparable with natural rivers, which usually develop intrinsically asymmetric meanders too (Sun & Parker, 2000).

Test 6

This time, the impact of three thin wall defectors built in the right bank and oriented in different ways towards the channel axis, as shown in Figure 11, were examined.

The deflectors, in particular the two upstream ones, reflect the stream towards the opposite bank causing its almost immediate erosion. Thereby, the speed and magnitude of meander growth was considerably higher than in previous tests. The perpendicular orientation

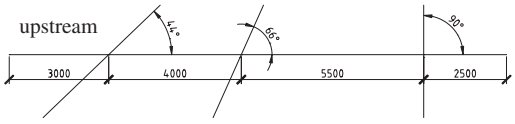


Figure 11. Deflectors orientation.

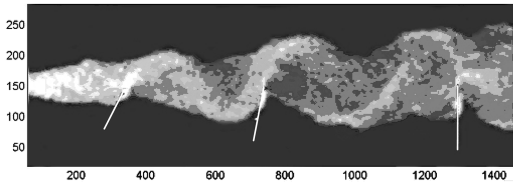


Figure 12. Channel development in Test 6 (units in cm).

of the deflector resulted mainly in local scoring and had a smaller effect on the formation of a meander. In the course of test, it appeared again that the remaining deflectors form an undesired obstacle to further meander development. While the amplitude and length of the meanders increased, the meander also shifted downstream. The deflectors were the cause of the resulting meander pattern, which consists of 1 meander between two successive deflectors, see Figure 12. The discontinuity in the talweg between deflector 2 and 3, was also caused by the presence of the deflectors. This is because the deflectors maintained the position of the first top, that was formed behind each deflector.

4.3 *Discussion*

In the performed tests, the caving banks are the source of the transported material within the meandering channel. The rate of bank erosion appears to be important, not only for determining the meandering state, but also for the determination of depth and width of the cross-sections. Easily eroding banks result in wide and shallow sections. The increased slope or discharge causes rising velocities, through which the bank erosion grows and the channel widens and shoals.

In these experiments, the resulting channel pattern appears to be more like a sinuous talweg than a truly meandering channel. Although a curved channel did develop from an initially straight channel, the sinuosity was rather low. The shoaling of the channel is due to the easily erodible banks, whereas the stream is 'overloaded', having a to steep slope. A next step in the testing should include the use of another type of bed material and the variation of the slope. Slowly eroding banks are supposed to result in deeper and narrower channel cross-sections. As it was already noted, rivers with a small width/depth ratio promote the development of very sinuous channels. Various combinations

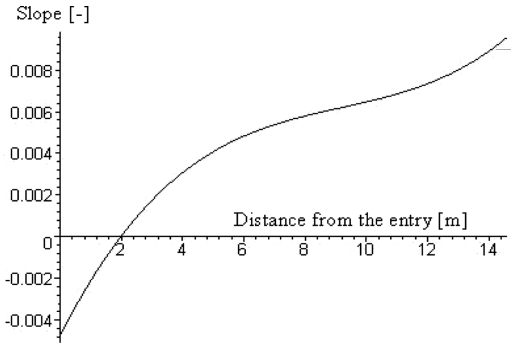


Figure 13. Bottom slope of the channel after Test 4.

of fluvial materials have been recently tested with the aim of reproducing meandering rivers in the lab. The preliminary results show that e.g. a mix of diatomaceous earth and kaolinite clay is able to produce a meandering channel with a sinuosity of almost 2.0 (Smith, 1998).

The initial cross-section of the channel had no significant influence on the meander development. The tests confirm that when an erodible material is used, a river will shape its cross-sections in accordance with its flow, slope and bank materials, irrespective to its initial cross-sections. A river deepens or shoals until it reaches an equilibrium configuration, for which the rate of sediment supplied to the cross-section from the adjacent banks is balanced by the rate of transport towards the downstream sections. The tendency to attain this equilibrium can be illustrated by the elevation of the channel, recorded in Test 4 (Fig. 13). In the upper section, the channel deepens and the slope flattens until the flow no longer has the power to erode the banks. When erodible material is used, the channel shoals, and the slope steepens until the transport capacity of the channel equals the rate of bank erosion. The development of a meandering talweg is also a result of the dissipation of excessive energy. The higher the valley slope is, the higher the rate of meandering will be. The prerequisite is to have stable, not easily erodible banks.

The most remarkable result is that the use of deflectors as an artificial measure to initiate meandering is not a suitable solution for recovery of meandering watercourses. The deflectors need to be removed after the meander has started to develop, otherwise it will disturb the ongoing development of river course. Instead of constructing and removing such deflectors, a deflector which is eliminated by the meander process itself, is a simple and recommendable solution for restoration projects. Test 3 and Test 5 demonstrate that an initiating bend or a permeable deflector does not influence the meander pattern but only the speed of its development.

5 CONCLUSIONS

A comparison between calculated meander geometry and the geometry deducted from old maps of naturally meandering rivers has been performed. This comparison shows that it is hard to find reliable formulas that approach the meander characteristics. The quality of the prediction seems to depend rather on the set of data to which the formulas were fitted, then on the amount of variables in the formulas. Simple relations obtained by Leopold & Wolman (1964) reveal meander patterns close to those found in the considered sites.

The physical experiments provide a better insight in some practical aspects concerning the performance of laboratory tests. They give an idea of the feasibility of artificial interventions to promote the meander restoration in degraded straight rivers. The next testing program will include the change of the sediment strength configuration to reach a higher sinuosity in the small laboratory flume.

REFERENCES

Chang, H.H. 1984a. Analysis of river Meanders. *Journal of Hydraulics Engineering*, Vol. 110, No. 1, pp. 37–50.

Chang, H.H. 1984b. Regular meander path model. *Journal of Hydraulics Engineering*, Vol. 110, No. 10, pp. 1398–1411.

Chitale, S.V. 1970. River Channel Patterns. *Journal of Hydraulics Division*, ASCE, Vol. 96, No. HY1, pp. 201–221.

De Vos, L., Verfaille, S. 2003. Remeandering of small rivers – theoretical and physical model study (in Dutch). Thesis UGent, 187 p.

FISRWG 1998. Stream Corridor Restoration: Principles, Processes and Practices. By the Federal Interagency Stream Restoration Working Group (FISRWG). ISBN-0-934213-59-3.

Friedkin, J.F. 1945. A laboratory study of the meandering in alluvial rivers. In: Schumm, S.A. 1972. *River morphology*. Stroudsburg (Pa), Downden, Hutchinson and Ross, pp. 238–281.

Hansen, H.O. (Ed.) (1996). River Restoration – Danish experience and examples. National Environmental Research Institute, Denmark. 99 p.

Ikeda, S., Parker, G., Sawai, K. 1981. Bend theory of river meanders 1. Linear development, *Journal of Fluid Mechanics*, Vol. 112, pp. 363–377.

Leopold, L.B., Wolman, M.G., Miller, J.P. 1964. *Fluvial Processes in river engineering*. John Wiley & Sons, 432p.

Nielsen, M.B. 1996. Lowland stream Restoration in Denmark. In: Brookes, A. & Shields Jr., F.D. (Eds.): *River Channel Restoration – Guiding Principles for sustainable projects*. John Wiley & Sons, pp. 269–289.

Parker, G., Diplas, P., Akiyama, J. 1983. Meander bends of high amplitude. *Journal of Hydraulics Engineering*, Vol. 109, No. 10, pp. 1323–1337.

Van Liefferinge, C., De Weerdt, B., De Smedt, D. 2002. Investigation of the feasibility, needs and relevance for remeandering of different river courses. *Intern. Report*, (in Dutch) Ghent University.

Vallons, A. 2002. Study on the historic and current topology of Flemish rivers: case studies (in Dutch). Thesis KUL Leuven, 121 p.

Schumm, S.A., Khan, H.R. 1971. Experimental study of channel patterns. *Nature*, 233: 407–409.

Smith, C.A. 1998. Modelling high sinuosity meanders in a small flume. *Geomorphology*, 25: pp. 19–25.

Sun, Y., Parker, G. 2000. Meandering rivers. St. Anthony Falls Laboratory, University of Minnesota: 126 p.

Yang, C.T., Song, C.S. 1979. Theory of minimum rate of energy dissipation. *Journal of Hydraulics Division, ASCE*, Vol. 105, No. HY7, pp. 769–784.

River Flow 2004 – Greco, Carravetta & Della Morte (eds.)
© 2004 Taylor & Francis Group, London, ISBN 90 5809 658 0

Small river re-naturalization and cultural heritage

G. Müller
Department of Civil Engineering, The Queen's University of Belfast, Belfast, UK

G. Himmelsbach
Spessartprojekt, Aschaffenburg, Germany

C. von Carmer
IFMW Karlsruhe, Germany

P. Fröhle
University of Rostock, Civil Engineering Dept.

ABSTRACT: Until the advent of modern power sources such as steam and combustion engines, the small rivers in Middle Europe played a central part in the economy as suppliers of mechanical power, water and means of transport. As a result, virtually all small rivers host a variety of remains of previous industrial activities such as weirs, mill races, ponds etc. which were built in the era ranging from the Middle Ages to the beginning of the 20th Century. Today, these remains are often not even recognized as such any more by hydraulic engineers, planners and the general public. The canalization of many rivers during the 1960s and 70s destroyed many remnants of the pre-steam age industries along the small rivers. As a result of the increasing ecological awareness, the concept of re-naturalization was developed in the 1980s. The current 'ideal' aim of re-naturalization, of re-creating a 'natural' river, does not take the historical context of our rivers into account, so that re-naturalization as well as the 'hard' engineering solutions can both result in the irretrievable loss of the cultural heritage. A current research project conducted by the authors tries to raise awareness of the historical context and to develop concepts of how to integrate the remains of the industrial past into the changing demands on our small rivers whilst contributing to the overall quality of the environment.

1 INTRODUCTION

Before the advent of steam power, the small rivers played a vital part in the economy of the Central European countries as well as in North-America. Rivers supplied mechanical power for industry, irrigation water for agriculture, drinking water for the population, water for defense systems and they were used as transport ways for bulk goods. In order for the rivers to fulfill all these duties, and to ensure that the course of the river remains stable, man made very significant changes to the small rivers ever since the Middle Ages. These changes include the construction of weirs, fortification of banks, change of river course, addition of diversion or transport canals, creation of lakes for water storage, and many other items. With the development of first steam power and then electricity and the internal combustion engine, the use of the small rivers by man declined until it reached a point where they are hardly used at all.

Following the decline of usage, and the increasing demand for rural and urban space, many small rivers were forced into straight beds, concrete channels or even underground, changing the river from an ecosystem into a lifeless drain. This happened in particular during the 1960s and 70s. With the development of an increasing consciousness for our environment, other ecologically acceptable solutions for the small rivers were sought for. The solutions principally include the *re-naturalization* or return of the river to its natural state, using traditional construction methods and natural materials. The river would therefore be allowed to develop its own dynamics and ecosystem. Re-naturalization is today seen by many scientists, engineers and landscape architects and subsequently the public as the most desirable development strategy for rivers.

Many hydraulic engineers are not fully aware of the extent of the former use of the small rivers, or of the purposes they were used for. Quite often the

redevelopment of a river – be it a 'hard' engineering solution or a 'soft' re-naturalization – therefore destroys the remnants of forgotten industrial activities not by intention but by lack of knowledge and awareness. These remnants however constitute a significant part of our cultural heritage and indeed of the development of engineering, which are subsequently and irretrievably lost.

The authors of this article, engineers and an archaeologist, are currently conducting a research project where the character and the importance of this heritage is investigated with the aim to raise awareness of the situation and to develop integrated solutions.

2 CULTURAL HERITAGE AND CULTIVIZED LANDSCAPE

2.1 *Introduction*

When engineers in Germany talk about '*Kulturlandschaft*' (cultivated landscape), they invariably mean the landscape shaped by man's current activity like agriculture, construction, infrastructure and so on. Archaeologists however have a rather different definition of this term. For them, '*Kulturlandschaft*' means the landscape which was shaped by man for hundreds and thousands of years, and which – for today's inhabitants often invisibly – contains significant parts of our cultural heritage. Very often the remains of this field of agricultural and industrial activities are overlooked simply for lack of knowledge about our pre-steam era industrial past both on the side of engineers and the general public. In addition, the question arises as to how far an ecosystem which developed within a man-made environment for up to eight centuries can not be considered as natural. Modern textbooks on river hydraulics and river re-naturalization often completely omit the historical context, e.g. Patt et al. (1998). Only very recently has the term '*Kulturlandschaft*' been introduced into the engineering field, Hintermeier (2003). Today, the extent to which the small rivers were formerly used, and the importance this usage had to society, is hardly known even to specialists working in this field such as hydraulic engineers. Therefore the remains of the former usage are often not even recognized as such.

A small comparison may illustrate the importance of rivers as power source and means of transport in times before steam or combustion engines existed: a typical water wheel of 10 kW provided more, cheaper and more reliable power than 30 to 40 horses or one hundred men; a horse drawing a boat on a canal could shift 40–50 times the weight it could move on a road. Water courses were therefore of prime importance. In the following, some of the principle uses of small rivers and their features will be presented in order to illustrate the way and the extent to which rivers were changed.

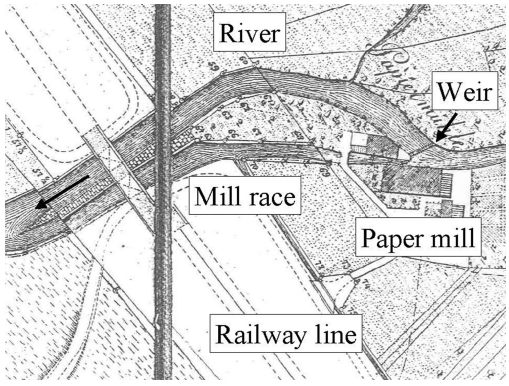


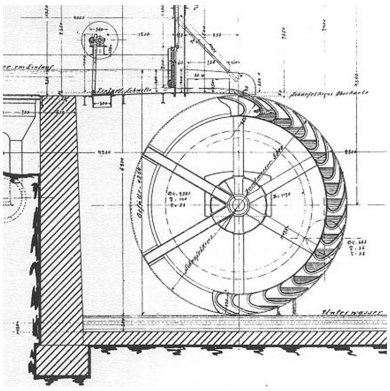
Figure 1. Typical mill installation (WWA Aschaffenburg, 1889).

2.2 *Cultural heritage 1: power production*

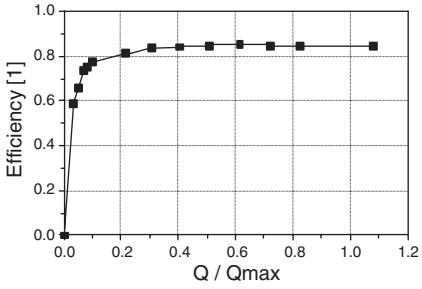
The water wheel is one of man's oldest hydraulic machines; water wheels were already described by the Roman architect Vitruvius (in '*De Re Libri Architecturi X*'). A water wheel installation required a head difference in the river, which was usually provided for by a weir. The wheel installation itself was located at a mill race (today it would be called a 'diversion canal'). Apart from wind mills, water wheels were the only mechanical prime movers before the advent of steam engines and drove flour mills, textile and mechanical machinery, powder and mineral mills, water pumps for drinking water supplies etc., Reynolds (1983). It is estimated that in 1850 there were 25–30,000 water wheels in operation in England, 6,400 in Ireland and around 40,000 in Germany. Even as late as 1925, there were still 33,500 water wheels in operation in Germany with individual capacities of 1–75 kW and an overall capacity of approximately 200 MW. This technology eventually disappeared in the 1950s and is today already virtually forgotten. Figure 1 shows a typical mill installation (River Aschaff/Bavaria 1889) with a weir, inflow detail, mill race, mill building with water wheel and outflow. Water wheels are today regarded as an outdated technology belonging to the romantic ages. Some recent research has however shown that water wheels had been developed into very efficient energy converters. Figure 2 shows some typical water wheels and the measured efficiency curves which indicate the surprisingly high efficiencies of 75–85%. More technical information about water wheels can be found in Müller & Kauppert (2002, 2003).

2.3 *Cultural heritage 2: 17th century fortifications*

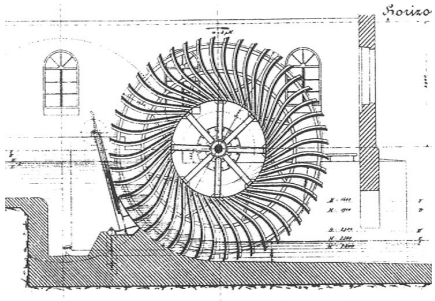
Traditionally, city fortifications are envisaged by most people as walls with towers, possibly with a water filled ditch in front of the wall. This type of fortification was in use until, at the end of the 15th



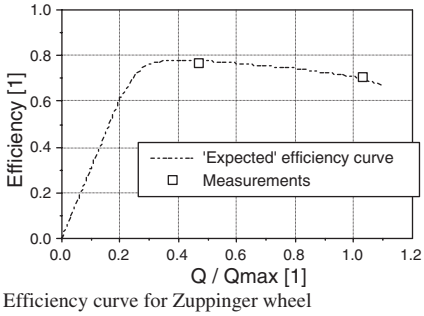
a. Overshot water wheel



b. Efficiency curve for a 3.60 m diameter overshot wheel



c. Undershot (Zuppinger) wheel for textile mill



d. Efficiency curve for Zuppinger wheel

Figure 2. Typical water wheels for head differences of 1.0–5.0 m, Müller & Kauppert (2003).

century, modern cannons were introduced which simply shot stone walls apart in a very short time. As a result, fortification design changed dramatically during the 16th century and a system of earthen ramparts, bastions, outworks and major hydraulic elements, some of which are still visible today, evolved. The City of Braunschweig in Northern Germany is one of the few German cities where even the river course was changed in order to create a wet ditch for the artillery fortification, and where this altered course is still in existence. Today, not even the name of the river branches ('*Umflutgraben*', flood diversion canal) recalls their original purpose. Figure 3 shows two maps of the City from 1650 and from today. In Figure 3a the original course of the River Oker through the city centre is still visible. The river channel running through the city center was maintained, probably for transport purposes, and weirs and mill races were built in order to power mills inside of the city in case of a siege. These canals are also visible, as is the very narrow wet ditch of the mediaeval fortifications (thick dark line). In Figure 3b, most of these items have disappeared and only small sections of the medieval ditch and the wet trench of the 17th Century fortification still exist.

2.4 *Cultural heritage 3: transport and irrigation*

The use of rivers for transport did not only mean navigation, but also e.g. the floating of timber. Often, special float canals were built alongside the river to provide sufficient depth and width of water for floats; as can be seen in Figure 4 for the River Aschaff. Apart from transport, in particular very small water courses were often used for irrigation purposes. The run of such small water courses was therefore frequently changed from its typical location at the lowest point of a valley to a zig-zag course running from the low point to the edge of the valley further downstream. This new and higher course enabled parts of the valley to be irrigated from above, and reduced the river's gradient and dynamics.

In addition, ponds were created for purposes such as storage of logs, provision of water to float logs downstream, fish farming, provision of additional water for mills during daytime etc. In many instances rivers were made navigable by building weirs and possibly side canals; this aspect is also very interesting both from the point of view of cultural heritage and the re-use today for leisure boating. This topic is however beyond the scope of this article.

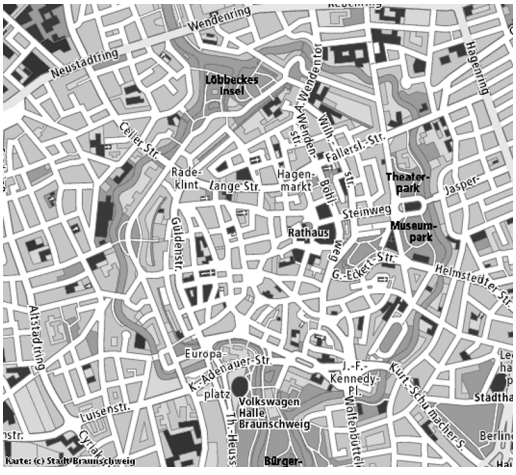
3 RENATURALIZATION AND EXISTING WATER COURSES

3.1 *Re-naturalization*

One characteristic of historic (i.e. before the 1900s) alterations of river courses was that usually only those



a. Plan view 1650, with fortification and mill races (City Archives Braunschweig)



b. Plan view 2003, with remains of the old wet ditch

Figure 3. The City of Braunschweig, Northern Germany, in 1650 and today.

small sections were changed where a change was absolutely required, such as the addition of a mill race. The development of hydraulics as an engineering discipline led to a situation where small rivers were perceived by engineers purely as channels for

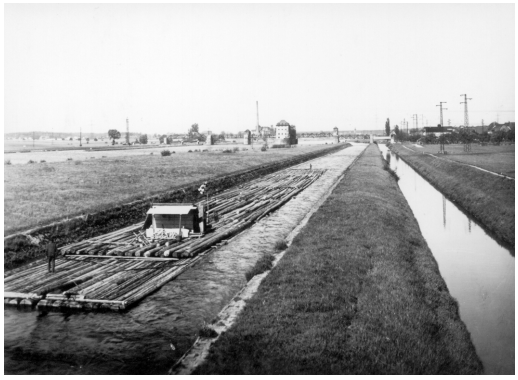


Figure 4. Floating logs (Aschaff, ca. 1920, Spessartprojekt).

rain- and groundwater. During the 1960s and 70s many small rivers were subsequently straightened over long stretches, often using concrete linings, in order to minimize the land required by the river (e.g. to maximize farmland or inner city land usage) or to protect roads and railway lines. This straightening generated a number of very undesirable side effects, such as a deepening of the river bed and the unfavorable superposition of flood waves caused by their accelerated propagation. The rivers running in concrete channels could not support eco-systems or even trees any more, and degenerated into lifeless drains. Following the increasing ecological awareness of the public, engineers tried to develop a concept for an ecologically and hydraulically acceptable alteration of water courses.

The re-naturalization of rivers is a concept which is today regarded by biologists, ecologists, landscape planers, by the public and by many engineers as the most desirable development. The main goal of re-naturalization is to bring the river as close to its original or 'natural' state as possible by removing artificial obstacles such as weirs, by changing of canalized sections, by provision of fish passes, of space for flood plains etc., e.g. Patt et al. (1998). In addition, re-naturalization tries to create a water-land interface to create a living space for aquatic and an access area for land based animals and to increase flood retention areas, although the latter aim is difficult to achieve due to the high demands for space. For these purposes, 'soft' construction techniques using natural material like willow branches, wood and rock were developed.

'One of the primary aims of the national and international effort for the protection of rivers is the creation or re-creation of a free passage; …therefore weirs and barrages can be regarded as a significant anthropogen disturbance of the ecosystem', Schrenk (2003). The German recommendations for the management of small rivers which are currently being developed give a 'potentially natural state of the water course' as the development aim. The 'potentially natural state' is

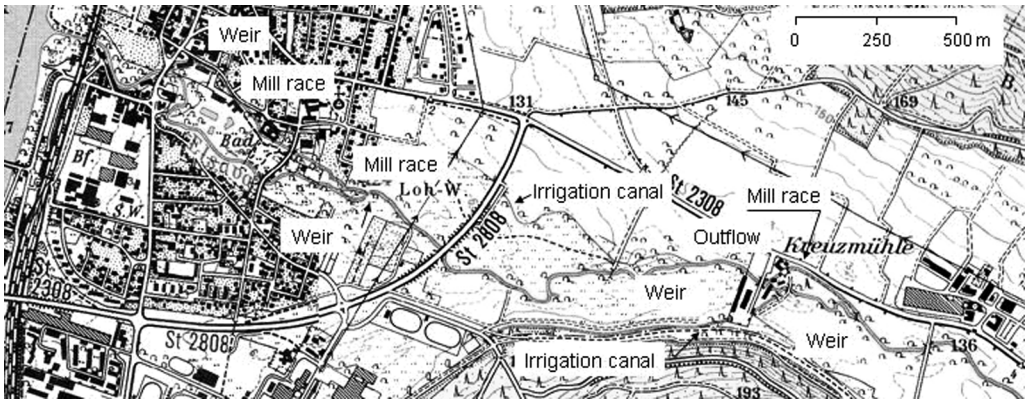


Figure 5. River Elsava.

defined as an ideal conceptual state of future development of the water course which is undisturbed by man. Although this ideal is defined, current practice is to bring water courses 'close to a natural state' rather than creating a truly natural state. The latter concept is very difficult to achieve due to a variety of reasons such as land interests, the proximity of infrastructure installations such as roads, railways, gas, water, sewage and electricity lines etc. which must not be interfered with, recreational use and other reasons.

A review of the interference of man with the rivers since the 1960s however shows that 'hard' engineering solutions and current re-naturalization concepts have one peculiar aspect in common: the historical context is completely omitted, and the implementation of either concept implies the destruction of all historical artefacts along the river.

In the following, three examples will be given in order to illustrate the complexity of the problem of defining what constitutes the natural state of a small river, and which effects the various man-made alterations had or have and to define what constitutes a desirable development.

3.2 *Existing water courses 1: River Elsava*

The River Elsava (NW Bavaria) is a typical small European river with a length of approximately 15 km, a drained area of 142 km^2 and an average flow rate of 1.23 m^3/s. This river has been used by man since the middle ages for power production and irrigation and a large number of man-made features still exist along the river. A water mill at the old monastery of Himmelthal (Elsava) was first mentioned in 1232, water rights for the extraction of water for irrigation purposes were recorded in 1435 (Elsava). It can therefore safely be assumed that weirs and side channels have existed for 600–750 years. Figure 5 shows a stretch of around 3000 m of the river Elsava in North-West Bavaria (flowing into the River Main). On this figure alone, 3 mill races and two irrigation canals are visible. In all, the Elsava once had 12 mills of which one, a saw mill (*Kreuzmühle*), is still in operation. Both irrigation channels are also still in use, one of them to supply cooling water to a chemical factory. The Elsava today constitutes a small river reasonably unaffected by dramatic changes, which has preserved the main features it has had for many centuries. The *Archeological Project Spessart* (see internet references) is trying to raise the consciousness within the population about this heritage of the age of small hydropower and early industry in order to prevent the disappearance of mill races by accident or re-naturalization and possibly to discover new usages for the existing hydraulic systems.

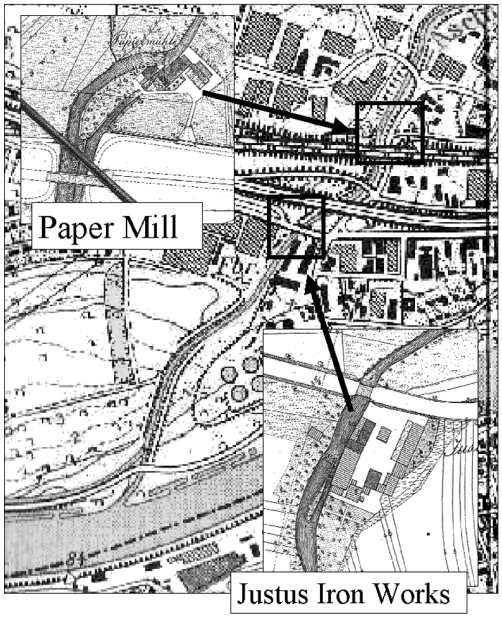
3.3 *Existing water courses 2: River Aschaff*

This river, a tributary of the River Main (NW Bavaria) with length of 8.4 km, a drained area of 144 km^2 and an average flow rate of 1.34 m^3/s once powered nine water mills and was also used as a way to transport logs by floating them down river. For these purposes, weirs were built and artificial lakes created to store wood under water or to provide a mass of water to float the stored wood downstream over shallows and obstacles. When a weir and power station was constructed in the river Main in 1920, the estuary of the Aschaff had to be relocated downstream of the weir in order to maintain the gradient and the water rights connected with the Aschaff, see Figure 6 (Aschaff 1917–1970).

The old estuary was subsequently replaced ('*Mündung bis 1920*') and the lower course of the Aschaff was straightened in 1970, whereby all the old mills, weirs, diversion canals, mill ponds and mill races were destroyed and disappeared, see Figure 7a. Figure 7b shows the canal-cross section then built. The *Archeological Project Spessart* has documented the changes of the river and established a 'Heritage Walking Course' with display boards to familiarize people with the ongoing changes, the previous



Figure 6. Aerial photography of the confluence of the River Aschaff with the River Main, with alterations from 1917 to 2001.



a. Lower course of the Aschaff(2002) with former mills (WWA Aschaffenburg, 1889)



b. Straightened cross section, 1970 (*Spessartprojekt*)

Figure 7. River Aschaff, changes of the estuary section.

importance of the river and thus the reasons for today's situation (including the loss of many aspects of the heritage).

From 2001 to 2002, an upstream section of the River Aschaff was re-naturalized, giving it a meandering plan view with ragged banks and shallow water zones which provide an suitable environment for aquatic animals. The course of the River had to be fixed in order to avoid interference with a newly built motorway and a variety of other infrastructure installations. Figure 8 shows today's course of the river with plan views of the two mills which existed before the re-naturalization with mill races, side channels and weirs. Again it can be seen that all remnants of the previous use of the river have disappeared in favor of a naturally-looking river. The River Aschaff demonstrates visibly the effect of the alterations of the last 40 years which were implemented following the prevailing river development philosophy but disregarding the historical context.

3.4 *Existing water courses 3: the Wallensteingraben*

The *Wallensteingraben* in North-Eastern Germany today looks like a natural water course, draining Lake Schwerin towards Wismar and the Baltic Sea. In reality, it constitutes the remains of a small canal

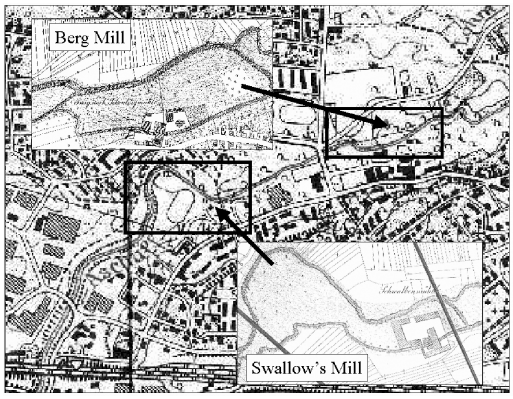


Figure 8. Re-naturalized section of the Aschaff with former mills (WWA Aschaffenburg, 1889).

built at the end of the 16th century to further Wismar's salt trade. The canal was finished in 1580, with a total length of 15.5 km and a height difference of 37.60 m which was overcome with 12 locks. Due to political developments, mainly caused by the 30 Years War (1618–1638) and the fact that Wismar became Swedish, depriving the city of its hinterland, the trade and with it the requirement for the canal practically disappeared. Subsequently the canal fell into disrepair. It still acted as a drainage for the lake, and powered water mills. In Figure 9, the course of the *Wallensteingraben* between Lake Schwerin (bottom) and the City of Wismar is shown. Today's remains of the artificial waterway (Goldammer, 1997) are indicated by circles, the locations of old mill races along the natural river (Hohensee, 1989) by water wheel symbols. Some remnants of the channel are still visible, though much of the canal was destroyed during railroad construction. Figure 10a shows a part of the summit reach excavated up to 10 m deep. In parts, the earthworks of the locks can still be identified, as well as stones and bricks originally used for the sluices can be found which were re-used later in other buildings, Goldammer (1997). A small natural stream which drains the hinterland of Wismar and provided fresh water, fish and water power for the local population and eventually became part of the canal.

Along this small river and the *Wallensteingraben*, 14 water mills were situated which produced mechanical energy from hydro power. Some of the mills can be traced back to the 1250s. At the beginning of the 20th century, the operation of the mills ended at all mill races.

Turbines were installed at some of the historic mill sites to produce electric energy, but only two turbines still utilize this renewable energy resource. Over the centuries a, new biological and morphodynamic equilibrium has established itself in such man-used

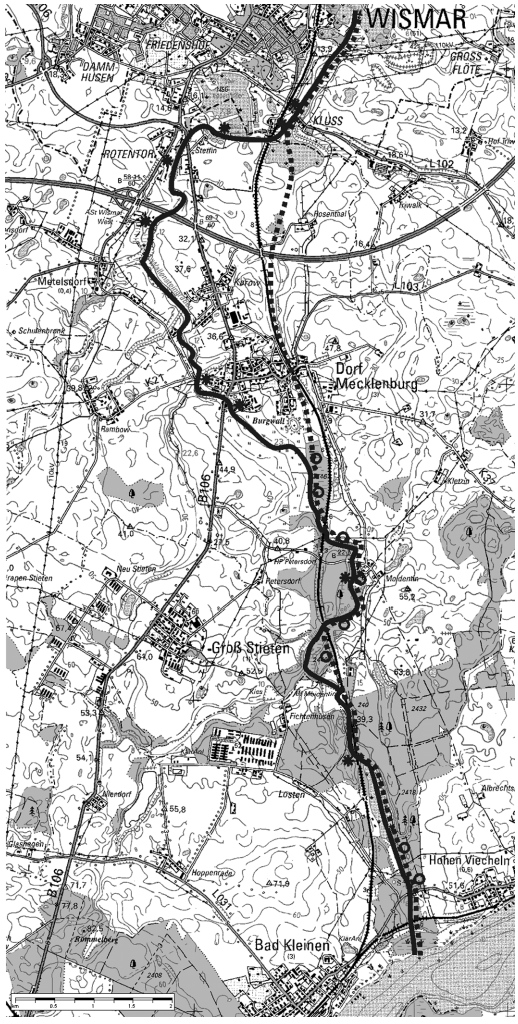


Figure 9. The *Wallensteingraben:* Map, (BUGA, 2000).

and -made 'river' reaches. The development strategies, where weirs and mill races are removed, often mean that the historical remains of early hydraulic and cultural engineering activities are destroyed. Figure 10 illustrates the state of the old canal as it can be seen today.

Currently the *Wallensteingraben* is used for flood control and to stabilize the water level in Lake Schwerin. The average discharge at the northern outflow of the lake is about 0.8 m^3/s. Dating back to the times of the former GDR, parts of the river are designated Nature Preservation Areas. Concerning the channel, plans are currently emerging to again connect Lake Schwerin to the Baltic Sea, thus, to reactivate or rather rebuild the canal along a new, slightly changed course not for the transport of salt, but for



a. The 10 m deep cut of the *Wallensteingraben* through a hill



b. Typical view of the *Wallensteingraben*

Figure 10. *Wallensteingraben*(IFMW).

leisure boating and recreation to further the economic development of the region once more (Buga, 2000).

4 DISCUSSION

4.1 *General*

A study of some small rivers in Central Europe indicated that these water courses have been altered by man for many centuries for varying purposes ranging from power production over transport to fortification. One additional aspect of the changes often was the reduction of the gradient and therefore the dynamics of the river. The geometry and functionality of our small rivers can therefore not be understood without their historical context. The ecosystems which evolved around the rivers are subsequently adjusted to an 'artificial' situation, but have sometimes been established for a very long time. Although the ideal aim of a 'natural river' is under discussion, it appears that in today's world the constraints imposed by infrastructure and settlement are too severe to allow for a river to develop its own natural state again.

4.2 *The Canadian River Heritage System*

The removal of all historical artefacts which usually is a consequence of re-naturalization deprives our society of a part of its cultural heritage and therefore of a part of its identity. In Canada, this has been realized some time ago and the Canadian Government has designated a number of river sections as 'Heritage Rivers', which are protected river sections of (amongst others) special ecological, geological, archeological, historical or recreational interest. The aim is to systematically create and maintain a Canadian River Heritage so that Canada's nature, history and society is reflected in the river system without which the development of the country had been impossible. Within the Canadian River Heritage System (CHRS) these sections are administrated and managed, Nagel & Goldhammer (1997). This system by now comprises nearly 6000 km of rivers, amongst them a long stretch of the Grand River. CHRS incorporates a large variety of nearly 100 organizations ranging from Universities to representatives of the indigeneous people (Six Nations Council), cities, government authorities, newspapers etc. which all have an interest in their river. It appears that the idea of the 'cultivized landscape', as a system not just with hydraulic and environmental aspects but also with a historical context which is worth preserving has been taken to a practical conclusion by CRHS and may serve as a model for further developments in other countries.

4.3 *Re-naturalization and cultural heritage*

Re-naturalization is today considered to provide a natural environment for the development of an ecosystem as well as an area for recreation. The inclusion of the cultural heritage in the management of small rivers today would imply that the river would have to retain some usage apart from recreation. The development of rational strategies of usage of the available power and water which are compatible with the historical usage could present a new area of activity. Some progress in the field of power production has been made recently, where it could be shown that water wheels are not the out-of-date inefficient machines they are usually considered to be. A detailed literature review revealed that water wheels can be regarded as very efficient and ecologically acceptable energy converters for low head hydro power conversion, Müller & Kauppert (2003). This means that even our small rivers can – as renewable energy sources – contribute to the overall aim of carbon-dioxide reduction.

4.4 *Outlook*

The authors are convinced that the re-naturalization in particular of canalized sections of small rivers is of great benefit to our environment. The re-naturalization of rivers which are still in a state where the old usage is recognizable (see section 3.2) would however destroy the cultural heritage. With the inclusion of the historical context, and the preservation and purposeful re-use of the resource river as e.g. a renewable energy source,

it becomes possible to preserve our cultural heritage as well as to develop a functioning eco-system (influenced by man of course to some degree) around our small rivers. In a re-naturalization (or river restoration) project therefore the '*added value for nature*' of the restored river and the '*historical value*' of the river (and a possible further use by man within the context given by history) should be weighed against each other in order to obtain an acceptable solution. An existing water mill e.g. could be protected and, preferably, be operated again and integrated into an overall solution. A very small old canal which can never be used again however, may currently only provide a poor natural environment and should therefore be 'restored' or rather upgraded to create a functioning and ecologically diverse solution with the emphasis on the ecosystem rather than the historical value. In conclusion it can be said that the 'cultivized landscape' as perceived by engineers should be expanded to include another dimension, namely time.

5 CONCLUSIONS

From the Middle Ages onwards the small rivers in Central Europe were re-built and used by man for a variety of purposes. Before the 20th Century, the small rivers formed a vital part of the economy. The remains of these activities are still in existence, but often not even recognized as such for lack of knowledge and awareness. Examples for such remains are:

a. Weirs and mill races belonging to old mills which constituted the nuclei of modern industrial developments.
b. Wet ditches which formed parts of the cities' defensive system.
c. Irrigation canals, storage ponds, canals for floating logs.

In addition, some old artificial waterways built for transport are today considered as being natural. Past and current re-development strategies for small rivers (canalization and re-naturalization) very often neglect the historical context and therefore result in the loss of historical artifacts and a diminution of our cultural heritage. An integrated solution for the development of small rivers which includes and weighs ecological as well as cultural aspects, and possibly incorporates a re-use of the historical installations such as micro hydropower, should therefore be sought. The scope of an engineering evaluation of our environment or, *Kulturlandschaft'* should be expanded to include another dimension, namely time.

ACKNOWLEDGEMENTS

The authors would like to acknowledge the help from Mr. Pfeiffer (*Wasserwirtschaftsamt Aschaffenburg*), the City Archive of Braunschweig, Mr. Höhn (*Pro Schwerin)*, and the critical comments from Dr.-Ing. K. Koll (Technical University of Braunschweig) and thank them for their support.

REFERENCES

BUGA Planungsgruppe. 2000. *Wallensteingraben Schwerin Wismar*, Schwerin/Germany.

Goldammer, G. 1997. *Der Schaale-Kanal. Relikterforschung historischer Binnenkanäle zwischen Elbe und Ostsee.* Mitteilungen der Geographischen Gesellschaft in Hamburg (87) (in German).

Hintermeier, K. 2003. Zeitgemäße Gewässerentwicklungsplanung erfordert auch kultur-historische Landschaftsanalyse – Kommentar (Timely river development planning requires the analysis of cultural and historical aspects – commentary, in German), *Wasserwirtschaft*. No. 9: 3.

Hohensee, F. 1989. *Der Wallensteingraben. Geschichte, Gegenwart und Zukunft eines mecklenburgischen Gewässers*. Ostseedruck Rostock (in German).

Müller G. & Kauppert K. 2002. Old water mills – Britain's new source of energy?. *Proc. ICE Civ. Eng.* Vol. 150. No. 4: 178–186.

Müller, G. & Kauppert, K. 2003. Die Wasserräder als hydraulische Kraftmaschinen (The water wheels as hydraulic energy converters, in German), *Bautechnik*. Vol. 80. No. 3: 181–189.

Nagel, F.N. & Goldammer G. 2001. Wasserwege als Gegenstand der Kulturlandschaftspflege (Waterways as part of the preservation of the cultural heritage, in German), in: Schenk, Fehn & Denecke. 1997. *Kulturlandschaftspflege*. Gebr. Borntraeger, Berlin & Stuttgart: 275–285.

Patt, H., Jürging, P. & Kraus W. 1998. *Naturnaher Wasserbau. Entwicklung und Gestaltung von Fließgewässern* (Natural hydraulic engineering, development and design of water courses, in German). Springer-Verlag. Berlin.

Reynolds, T.S. 1983. *Stronger than a hundred men*, J. Hopkins University Press. Baltimore & London.

Schrenk, G. 2003. Wehre und Staue an kleinen und mittelgroßen Fließgewässern (Weirs and barrages at small and medium rivers, in German), *Wasserwirtschaft*. No. 7–8: 71–79.

INTERNET REFERENCES

www.ifmw-ka.de
www.spessartprojekt.de

This page intentionally left blank

River Flow 2004 – Greco, Carravetta & Della Morte (eds.)
© 2004 Taylor & Francis Group, London, ISBN 90 5809 658 0

Stability of reinforced block ramp

S. Pagliara & P. Chiavaccini
Department of Civil Engineering, University of Pisa, Italy

ABSTRACT: Block ramps are structures able to produce high dissipation energy, ensuring a stable stream bed and are usually used in naturalistic stream restoration projects as alternative method for grade control. A way to increase ramp stability consists in covering the base ramp blocks with boulders. In this work the results of tests performed in a flume located in the Hydraulic Laboratory of the Civil Engineering Department of the University of Pisa are presented. The ramp was founded on a geotextile where two or three layers of the base material were placed. The rocks were angular and crashed with an almost uniform granulometric curve. The stability tests were conducted evaluating the failure discharge as a function of base diameter, boulders concentration and their planimetric arrangment.

1 INTRODUCTION

Block ramps are structures able to produce high dissipation energy, ensuring a stable stream bed and are usually used in naturalistic stream restoration projects as alternative method for grade control because they succeed in putting together hydraulics and ecological exigencies. In fact, they modify the longitudinal profile of the river and, at the same time, guarantee correct biological exchanges between the downstream and upstream reaches. From the hydraulic point of view experimental researches (Pagliara et al., 2000, 2002) have pointed out that block ramps act as an excellent energy dissipator, giving place to strong energy losses. From the environmental point of view block ramps do not act as barriers, as the hydrodynamic conditions on the ramp can be generally compatible with the characteristics of dynamism of the stream fauna. The functionality of the ramp can be ensured only if the structure for the design discharge is stable that means that the shear stresses are not able to move the bed material. Some relations express the link among the diameter of the base rock, the unit discharge and the slope of the ramp to ensure the stability (Whittaker & Jaeggi, 1996, Robinson et al., 1998). Armanini & Scotton (1995) evaluated the stability in term of Shields parameter. The critical part for the ramp stability is the downstream one, in which the shear stresses are greater and the ramp failure is generally sudden; in this part the movement of few elements brings to the total failure of the structure (Pagliara & Chiavaccini, 2003). The present study better investigates the hydraulic conditions which characterize the different failure types of the ramp and the effects on the stability of boulders placed over the ramp. The use of boulders gives different advantages: they can increase the energy dissipation caused by the ramp acting as macroroughness elements and can facilitate stream fishes passage across the ramp, as their presence create on the ramp an alternance of swifter and slower flow zones more favorable to the biologic exchanges (Pagliara & Pozzolini, 2003).

2 MATERIALS AND METHOD

The experimental flume was 0.5 m wide by 9 m long. Ramp height was 0.25 m. The ramp was based on a geotextile where two or three layers of the base material were placed. A sill at the downstream end of the ramp prevented the skidding of the ramp ensuring a stable toe during tests. The rocks were angular and crashed with an almost uniform granulometric curve. The tests were conducted on ramps of different slopes s (1:4, 1:8 and 1:12) covered with rocks having medium diameter of 0.011, 0.022 and 0.032 mm (Figure 1), where boulders in different concentration (up to 40%) were placed. Boulders projected from the base ramp for half diameter.

A schematic drawing describing the experimental apparatus is presented in Figure 2.

The concentration R of the boulders was measured by the following relation (Armanini & Scotton, 1995):

$$R = 100\frac{S_b}{S_{tot}} \tag{1}$$

where S_b is the surface of the boulders and S_{tot} is the total surface of the ramp. The diameter of the boulders

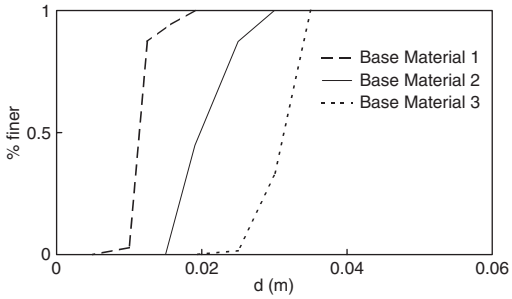


Figure 1. Granulometric curves of the base materials.

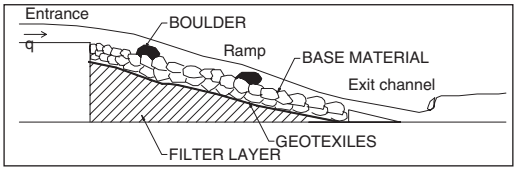


Figure 2. Definition sketch of the studied ramp.

were three times bigger than the base material. Boulders projected from the base material of about half diameter.

The tests were conducted increasing the flow until the reaching of the discharge that provokes the ramp instability. Flow rates were measured with an hydrometer placed upstream of the ramp.



Figure 3. Ramp before and after global failure.

3 FAILURE MECHANISMS

Tests pointed out that the failure of the ramp is characterized by 4 steps:

- the initial movement of the base material, in which the rocks begin to vibrate;
- the entrainment of some isolated elements.
- the local failure in which a group of elements leave their position simultaneously, producing a circular or semicircular scour hole; in some case (for the highest boulder concentrations) the initial movement can happen for the boulders instead of the base material;
- the global failure of the ramp (Figure 3) in which different local failures happens: the ramp presents longitudinal holes and the layers of the base material are completed removed, especially in the downstream part of the ramp.

In this paper the third step has been considered the significant step in order to define the ramp failure. This choice is due to the fact that the condition of local failure modifies the geometry of the ramp, its hydraulic behavior and its functionality. For prototypes this situation means that is necessary to repair the structure itself with burden of costs.

In the base condition, without the use of stabilizing systems the local failure happens in the downstream part of the ramp.

In order to verify the validity of the experimental model, the values of failure discharge measured for the base condition were compared with the values calculated using the block ramp stability formula of Whittaker and Jaeggi (1996):

$$q = 0.257\sqrt{\frac{\rho_s - \rho_w}{\rho_w} g}\,\alpha^{-7/6} d_{65}^{3/2} \qquad (2)$$

where q is the unit critical discharge (m^2/s), ρ_s is rock density (N/m^3), ρ_w is water density (N/m^3), α is the slope of the ramp and d_{65} is the nominal diameter of the material for which 65% of the sample is finer by weight (m).

The results (Figure 4) point out that there is a good correspondence between calculated and measured values with differences generally minor than 20%.

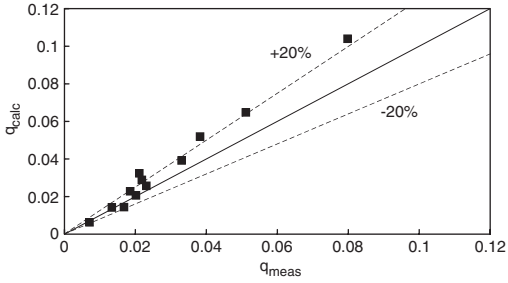


Figure 4. Calculated and measured failure discharge (q) in the base condition.



Figure 5. Boulders placed over the ramp (upstream view).

4 THE USE OF BOULDERS TO INCREASE STABILITY

Tests conducted on the base material have shown that the failure of the ramp is sudden and the weakest part of the ramp is the downstream half. To increase the stability of the ramp, the use of boulders disposed with different concentration has been investigated (Figure 5).

The stability tests were conducted evaluating the failure discharge as a function of boulders concentration and of their position. Boulders placed in rows, random and in arch forms were examined (Figure 6) in order to evaluate what is the best choice for the design of these structures. For each condition at least 3 failure tests (for a total of 108 tests) were performed, increasing incrementally the flow until the identified failure mechanism was reached.

The presence of the boulders improves the stability conditions. The effect depends not only on the concentration but also on the planimetric arrangment used.

In particular arc forms appear less stable than other forms (Figure 7 and Figure 8) because water flow is concentrated to the center of the flume, while there

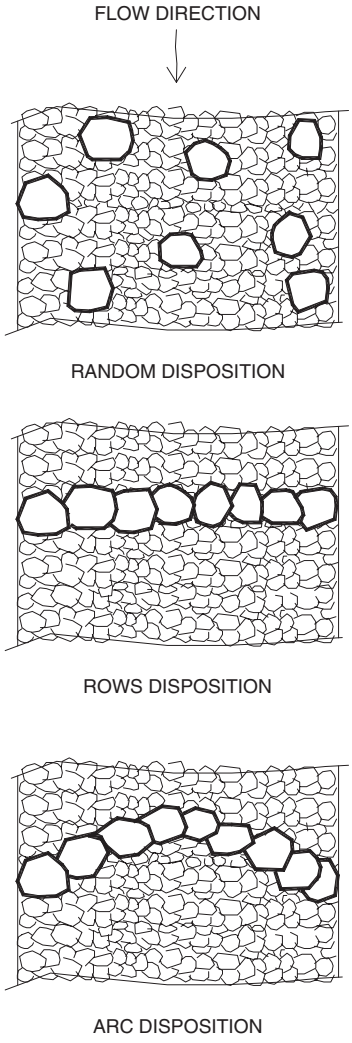


Figure 6. Disposition of the boulders (plan view).

are no evident differences between the random and the rows disposition (Figure 9 and Figure 10).

Besides in the arc form, the weakest part of the ramp are the boulders themselves, because the scour hole formed downstream provokes their instability. Rows and random disposition are different only for the way in which failure is reached. The rows of boulders create a series of little hydraulic jumps downstream each row where the initial movements verify, while for random disposition the flow is uniformly disturbed and the initial movement happens randomly. In Figure 11 the effect of local failure for random arrangement is shown. As evident a little scour hole is formed and consequently boulders has moved downstream.

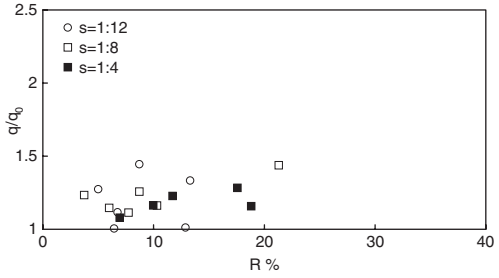


Figure 7. Increase of failure discharge with boulder placed in arc disposition.





Figure 8. Local failure for boulders in arc arrangement.

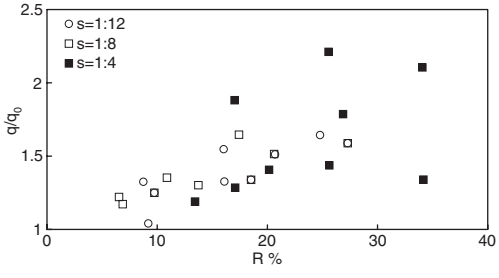


Figure 9. Increase of failure discharge with boulder placed in rows disposition.

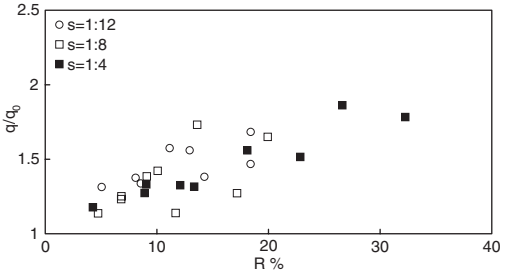


Figure 10. Increase of failure discharge with boulder placed in random disposition.



Figure 11. Local failure for boulders in random disposition.

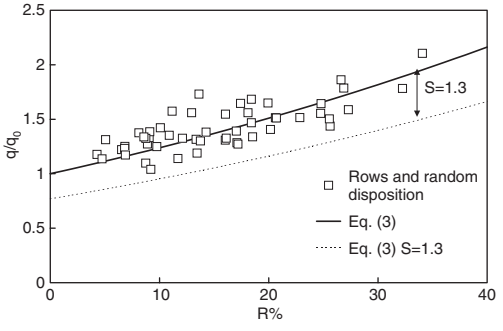


Figure 12. Increase of stability as a function of boulder concentration and fitting curve.

However, the effect of the disposition (rows or random), referring to the values of failure discharges, appears negligible in according with the results obtained for other kinds of stability system such as micropiles (Pagliara & Chiavaccini, 2003).

The increase of stability for random and rows disposition reach values up to 180–190% for concentration of 30–35%. Results show that the slope of the ramp and the dimension of the base material has a little influence on stability (Figure 12).

A new relationship for block ramp stability covered with boulders can be derived. This equation links the increase of stability (the ratio of failure discharge of the ramp with boulders q and the failure discharge of the ramp with only the base material q_0) to the boulders concentration, expressed by means of the parameter R.

The best fitting is obtained with the following equation:

$$\frac{q}{q_0} = (1 + aR)^{1/b} \tag{3}$$

where:

$a = 0.008$

$b = 0.36$

This curve presents a correlation coefficient $r = 0.76$.

The parameters a and b are defined for a ratio of the boulder diameter and the diameter of the base material equal to 3. Therefore Eq. (3) cannot be used for other ratios.

A safety coefficient $S = 1.3$ is recommended for practical uses.

When $R = 100\%$ the ramp is all covered with boulders and its behavior is the same of a ramp where the base material is bigger. In this case stability can be determined using expression (2) in which d_{65} for the ramp all covered with boulders is expressed by d_{65B} while for the ramp in base condition it is expressed by d_{65f}. The test were conducted for $d_{65B} = 3d_{65f}$, thus for $R = 100\%$

$$\frac{q}{q_0} = \frac{0.257\sqrt{\frac{\rho_s - \rho_w}{\rho_w} g}\alpha^{-7/6} d_{65B}^{3/2}}{0.257\sqrt{\frac{\rho_s - \rho_w}{\rho_w} g}\alpha^{-7/6} d_{65f}^{3/2}} \approx 5.11 \tag{4}$$

The Eq. (3) for a value of $R = 100\%$ gives $q/q_0 = 5.11$

5 CONCLUSIONS

The present study analyses the mechanisms of failure of different block ramps. The effect on stability of boulders placed over the ramp is accounted. Failure of the ramp happens in four different steps: *initial movement, initial leaving, local failure and global failure.* Local failure can be considered as the effective instability condition, because ramp changes geometry and looses the original configuration. The disturbance on the flow provoked by the boulders tends to diminish the shear stresses acting on the base material, increasing its stability. This condition happens when boulders are placed in a manner that flow passing over them does not converge. In fact the boulders placed in an arc form don't guarantee an increasing of stability. This is because flow is concentrated downstream of the arc and the shear stresses can be greater than in the base configuration. Besides in this case the weakest part of the ramp are the boulders themselves, while for rows and random disposition the base material moves before boulders, except at higher boulder concentrations.

With the boulders the increase on stability reaches values up to 180–190% in respect to the base condition, and the relation (3) can be used to express analytically this amount.

ACKNOWLEDGEMENTS

The present research was founded by grant PRIN 2001 "Sistemazioni idrauliche non convenzionali a basso impatto ambientale" U.O. Università di Pisa. The authors are grateful to A. Chines for assistance with measurements and for the support in the realization of experimental apparatus.

REFERENCES

Armanini A. & Scotton P. 1995. Criteri di dimensionamento e di verifica delle stabilizzazioni di alveo e di sponda con massi sciolti e massi legati, *Quaderni del dipartimento di Ingegneria Civile ed Ambientale, Università di Trento*, IDR 1/1995.

Pagliara S. & Dazzini D. 2002. Hydraulic of block ramp for river restoration, In *2nd International Conference New Trends in Water and Environmental Engineering for Safety and Life: Eco-compatible Solutions for Aquatic Environments*, Capri, Italy.

Whittaker W. & Jaeggi M. 1996. Blockshwellen, *Mitteilungen der Versuchsanstalt fur Wasserbau, Hydrologie und Glaziologie*, Zurich.

Pagliara S. & Chiavaccini P. 2003. The use of piles to increase block ramp stability. In *XXX IAHR International Conference*, Thessaloniki, Greece, ISBN 960-243-597-6: 449–456.

Pagliara S. & Pozzolini S. 2003. The effects of large boulders on the hydraulic of unsubmerged block ramps. In *XXX IAHR International Conference*, Thessaloniki, Greece, ISBN 960-243-597-6: 199–206.

Pagliara S. & Peruginelli A. 2000. Energy dissipation comparison among stepped channel, drop and ramp structures. In *Workshop on Hydraulics of Stepped Spillways, Zurigo*, Rotterdam, Balkema.

Robinson K.M., Rice C.E. & Kadavy K.C. 1998. Design of rock chutes, *Transactions of the ASAE*, Vol. 41(3): 621–626.

This page intentionally left blank

River Flow 2004 – Greco, Carravetta & Della Morte (eds.)
© 2004 Taylor & Francis Group, London, ISBN 90 5809 658 0

Three dimensional hydrodynamics of pool-riffle sequences for urban stream restoration

J.F. Rodríguez
School of Engineering, University of Newcastle, Australia

M.H. García, F.M. López & C.M. García
V.T. Chow Hydrosystems Laboratory, University of Illinois at Urbana-Champaign, USA

ABSTRACT: A set of laboratory experiments was carried out to investigate the 3D flow structure of pools and riffles in constricted streams. The experiments included four different bed configurations: flat bed (FB), centered pool-riffles (CPR), alternate pool-riffles (APR) and alternate pool-riffles with vegetation (APRV). The CPR configuration was included since centered pools minimize the possibility of scour near the banks, and are thus particularly suitable for urban settings where bank erosion is unacceptable.

1 INTRODUCTION

The present research was motivated by a concrete problem: the restoration of a channelized, low-gradient, urban stream using in-channel structures of the pool-riffle type (Rodríguez et al., 2000). In-channel solutions are preferred in restoration projects on urban settings due to the limitations in planform alignment imposed by the existing infrastructure. If carefully designed, pools and riffles can enhance the aquatic habitat and achieve the restoration goals. Designing artificial pools and riffles is not easy, since knowledge of their 3D hydrodynamic behavior is limited. Most of the analysis to date has been 1 or 2D, and mostly qualitative, despite the fact that 3D flow patterns are fundamental in the development and maintenance of pools and riffles. Past restoration practices have tried to reproduce features of natural pool-riffles based on observations, with limited success.

A set of laboratory experiments was carried out to investigate the 3D flow structure of pools and riffles. The experiments included four different bed configurations: flat bed (FB), centered pool-riffles (CPR), alternate pool-riffles (APR) and alternate pool-riffles with vegetation (APRV). The CPR configuration was included since centered pools minimize the possibility of scour near the banks, and are thus particularly suitable for cases in which bank erosion is unacceptable. The sequence FB-CPR-APR-APRV not only represents an increase in hydrodynamic complexity; it can also be seen as different steps in the restoration process of a degraded stream. The FB series represents the behavior of the channelized stream with no geomorphological diversity, the CPR experiment describes a naturalization alternative with man-made in channel structures, the APR set gives insight into the hydrodynamics of in channel structures that are more likely to be found in a natural stream, and finally the APRV configuration includes the effect of vegetation. Each series included low (run 1) and high (run 2) flow conditions.

2 METHODS

3D velocity measurements were collected using an Acoustic Doppler Velocimeter in a laboratory flume (0.0025 slope) where the four bed configurations were successively set up (Figures 1 and 2). The flume was 12.5 m long, 0.9 m wide and 0.6 m high, with 1-cm diameter crushed stone on the bed to provide a fixed, hydraulically rough surface. The simulated vegetation of the VAPR test was flexible (plastic aquarium plants) and was placed in a hypothetical seasonal flooding zone (Figure 2). The data was collected at five

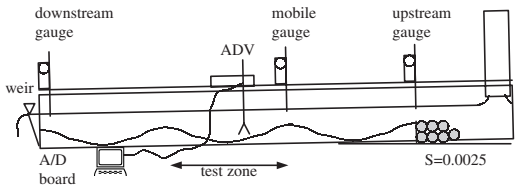


Figure 1. Experimental setup.

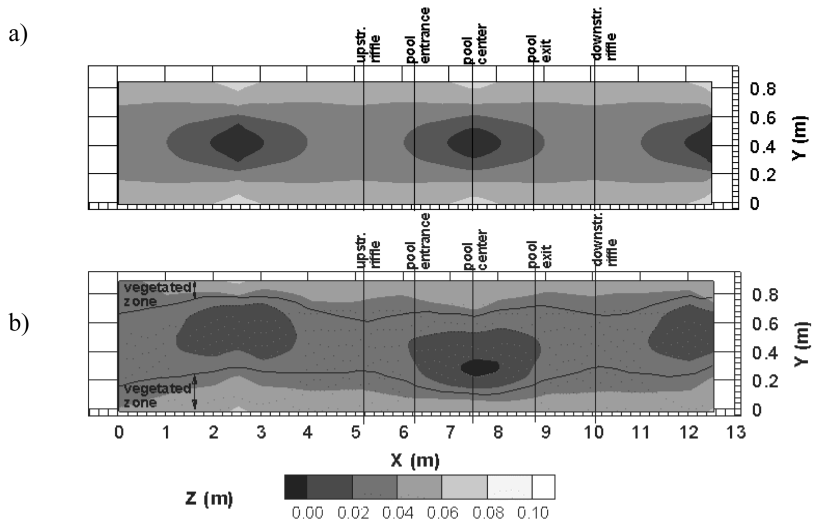


Figure 2. Bed topography and measurement sections for pool-riffle experiments: a) CPR and b) APR and APRV.

Table 1. Summary of experimental conditions. Q, h, U, U_*, Re and Fr respectively denote reach-averaged values of discharge, hydraulic depth, velocity, shear velocity, Reynolds number and Froude number.

Run	Q (m^3/s)	h (m)	U (m/s)	U_* (m/s)	Re $\times 10^{-3}$	Fr
FB1	0.05	0.11	0.48	0.047	44	0.45
FB2	0.10	0.15	0.72	0.053	82	0.60
CPR1	0.03	0.09	0.37	0.045	30	0.38
CPR2	0.11	0.19	0.64	0.068	90	0.47
APR1	0.05	0.09	0.66	0.044	53	0.64
APR2	0.11	0.15	0.80	0.055	97	0.71
APRV1	0.05	0.16	0.35	0.055	55	0.28
APRV2	0.11	0.25	0.49	0.064	121	0.31

cross sections: upstream and downstream riffles and pool entrance, center and exit. At each cross section, measurements were spaced 5 cm and 1 cm in the transverse and vertical directions, respectively. Wall shear stresses were computed using a bed-normal law of the wall. Experimental conditions are shown in Table 1.

3 RESULTS

3.1 *Low flow*

The FB1 test (Figure 3) shows three cores of high streamwise velocity that are evenly spaced. These high velocity zones are about 10% faster than the surrounding flow and are associated with regions of downwelling and high wall shear stress. Secondary circulation is characterized by the presence of six circular cells. All these features are typical of secondary currents produced by turbulence anisotropy at the flow boundaries (Nezu and Nakagawa, 1993).

In the CPR1 experiment, convergence and divergence patterns affect the streamwise as well as the transverse velocity distributions. The streamwise velocity presents two cores of high velocity at the riffles (Figure 4) as a result of transverse flow divergence. Transverse flow convergence consolidates the cores towards the center of the channel at the pool center. The high velocity cores are associated with flow downwelling, and the resulting recirculation pattern is surface divergent on the riffles and surface convergent on the pools, as usually observed in natural pool-riffle sequences.

The wall shear stress distribution shows a concentration towards the centerline of the pool center with a maximum at the pool entrance.

The APR1 test (Figure 5) shows the effect of thalweg curvature generating centrifugal forces. Transverse velocity components are now clearly superimposed to convergence at the pool entrance. This effect is felt only moderately by the streamwise velocity, which has two high velocity cores that remain throughout the pool. The cores are associated with four major cells. At the riffle centerline the cells are surface divergent and at the deepest part of the pool they are surface convergent, as occurs in natural pool-riffle sequences. Shear stresses are higher at the pool entrance. At the pool center cross section shear stresses are higher in the shallower side.

The effect of vegetation in slowing down the flow and raising water levels is observed in the APRV1 test (Figure 6). The streamwise velocity is always concentrated on the vegetation-free central zone, with little

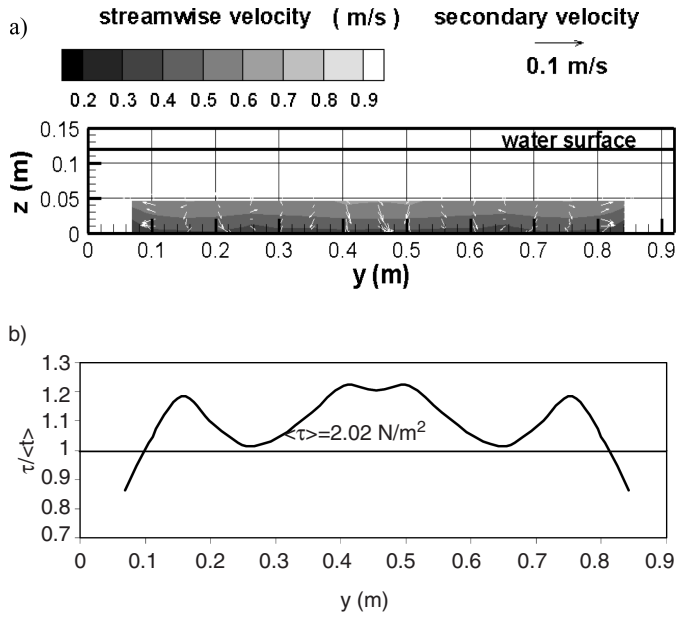


Figure 3. FB1 test: a) velocities, b) dimensionless wall shear stresses.

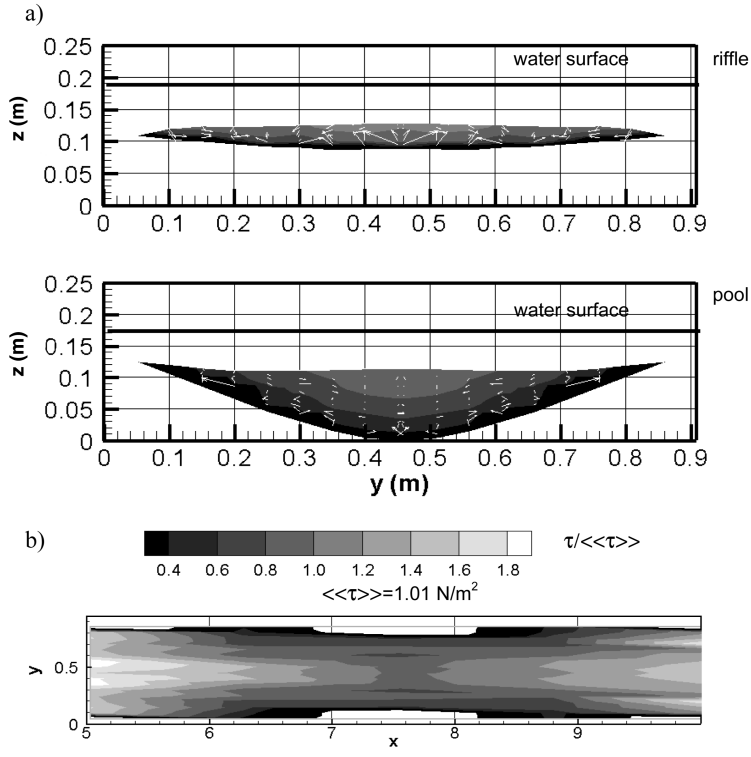


Figure 4. APR1 test: a) velocities (color as in 3a), b) dimensionless wall shear stresses.

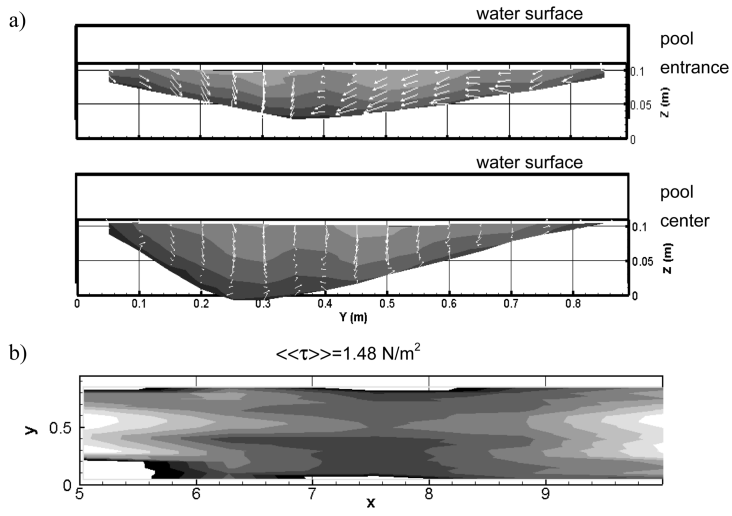


Figure 5. APR1 test: a) velocities (color as in 3a), b) dimensionless wall shear stresses (color as in 4b).

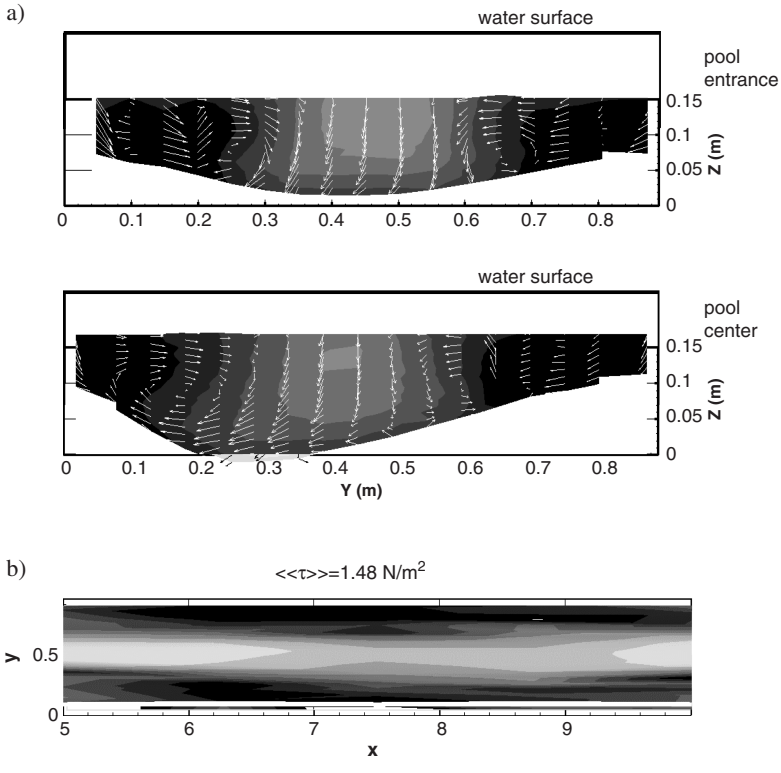


Figure 6. APRV1 test: a) velocities (color as in 3a), b) dimensionless wall shear stresses (color as in 4b).

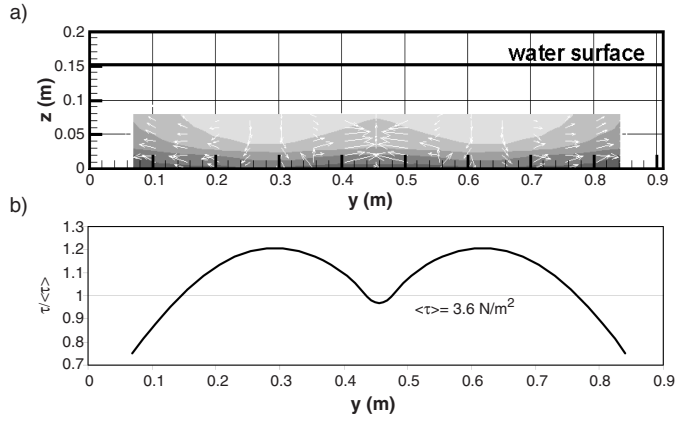


Figure 7. FB2 test: a) velocities (color as in 3a), b) dimensionless wall shear stresses.

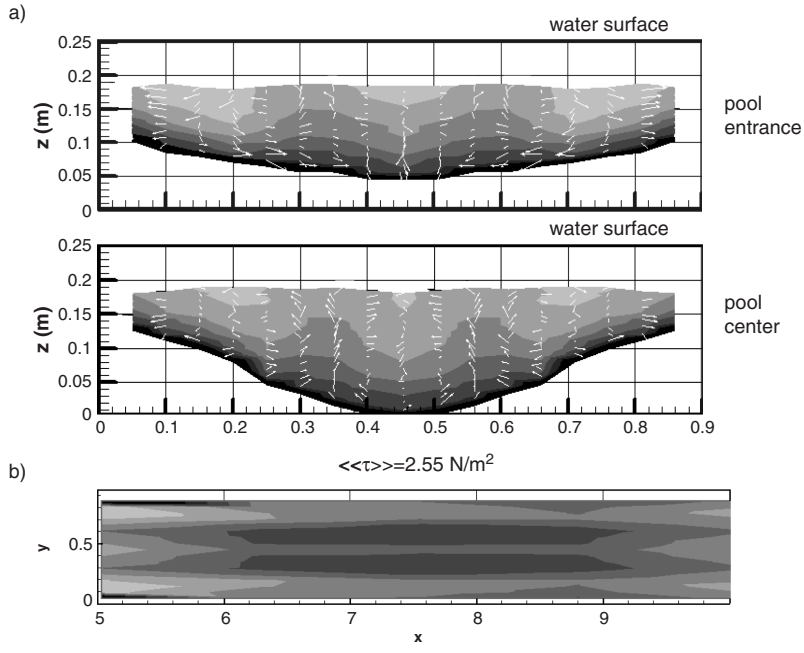


Figure 8. CPR2 test: a) velocities (color as in 3a), b) dimensionless wall shear stresses (color as in 4b).

effect of thalweg curvature. Two central circulation cells are defined by downwelling on the centerline (associated with the high-velocity core) and upwelling at the borders of the vegetation zone. Shear stresses are concentrated along the centerline.

3.2 *High flow*

The FB2 test (Figure 7) shows a structure similar to that of FB1, but with two cores of high velocity only. This is because the secondary circulation cells scale with flow depth, and only four cells can fit in the whole channel width. Wall shear stresses are greater under the high velocity cores. As with the FB1 test, the pattern is characteristic of secondary circulation due to turbulence anisotropy at the flow boundaries.

The similarity between the CPR2 (Figure 8) and the APR2 (Figure 9) tests is remarkable. Velocities are slightly higher in the APR2 experiment, which also has a shallower depth. Three high velocity cores are present throughout the structure, corresponding to six cells. The agreement with the wall shear stress is also very

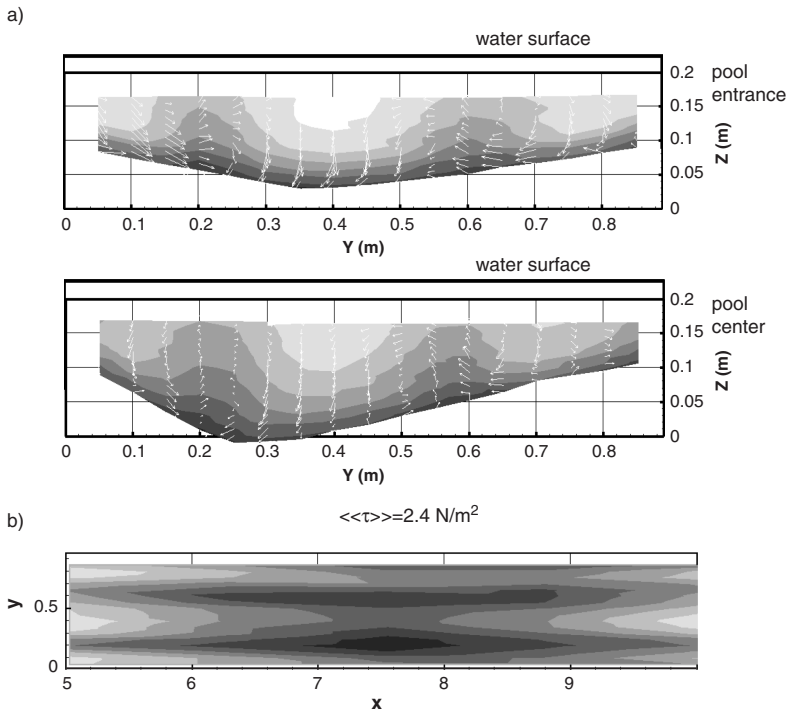


Figure 9. APR2 test: a) velocities (color as in 3a), b) dimensionless wall shear stresses (color as in 4b).

good. The cells scale approximately with the depth of the riffles and stretch down to occupy the whole cross section at the pool. Besides this stretching, the shape of the geometry does not seem to affect the secondary circulation patterns. Compared to the FB2 test, the CPR2 and APR2 tests present two more circulation cells. This difference is due to the fact that cells scale with the flow depth at the riffles, which are considerably shallower than the depth of the FB2 test. In fact, the flow patterns of the pool-riffle experiments correspond better with the FB1 test, which has a depth of the order of the riffle depth.

The APRV2 experiment (Figure 10) has a different pattern, which is similar to the APRV1 test. The vegetation directs the flow towards the center, with only one velocity core and two well defined cells. However, there is some indication of the presence of two incipient high velocity cores at the sides. Wall shear stresses are concentrated on the centerline, with a slight increase towards the shallower side of the pool.

4 ANALYSIS AND DISCUSSION

4.1 *Topographic effects*

The previous section has shown important differences between the high and low flow behavior of the pool-riffle configurations without vegetation (series CPR and APR). For low flow, the geometry of the bed plays an important role in determining the three dimensional hydrodynamics. This is more obvious in the CPR1 case than in the APR1 case, probably due to differences in discharge. The CPR1 case has the lower discharge, and geometric effects are expected to be more effective under this condition.

The bed geometry produces lateral divergence and acceleration on the riffles and lateral convergence and deceleration on the pool. In the APR1 case it also produces lateral shoaling at the pool entrance and exit. The combination of lateral divergence and acceleration generates the splitting of the maximum velocities into two cores at the riffles. These cores induce an undulating pattern on the bed shear stresses, which results in secondary circulation.

As the flow enters the pool, lateral convergence displaces the velocity cores towards the deepest part of the pool, generating a different secondary flow pattern (this effect is less evident in the APR1 case). The velocity cores are associated with surface convergent secondary circulation and downwelling, so they produce surface convergence/near bed divergence in the pool deepest part and surface divergence/near bed convergence at the riffle centerline. The pattern described is in total agreement with the ideas of Thompson

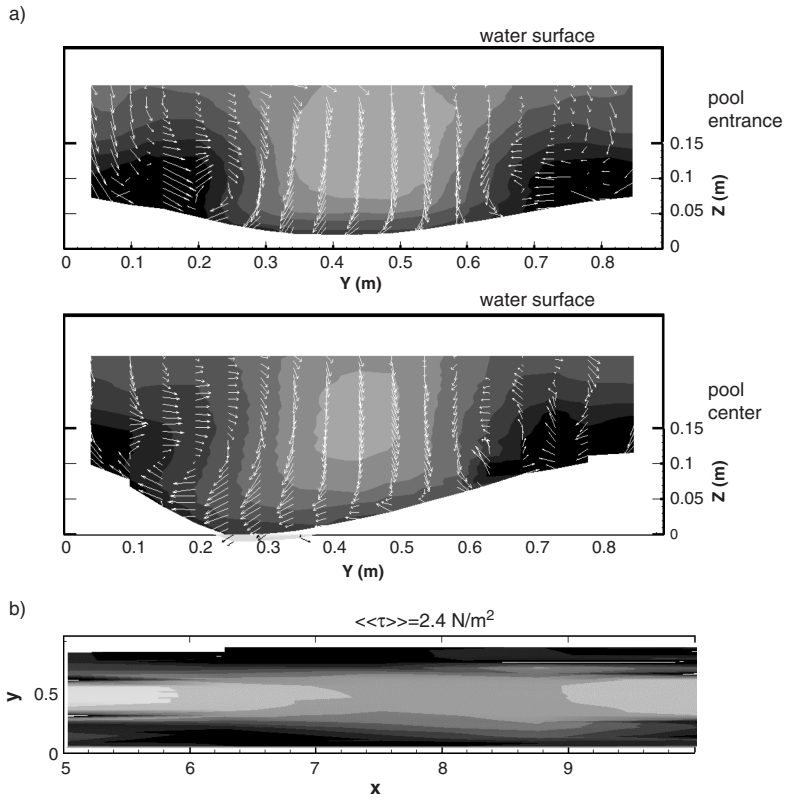


Figure 10.

(1986) based on field observations and is related to Prandtl's first kind secondary currents.

The high flow situation shows no apparent effects of the pool-riffle geometry. The flow behaves essentially like in a uniform flow situation, with turbulence anisotropy in the bed and channel walls generating secondary circulation and associated high-velocity cores. The walls are important in constricting the flow, producing a narrow channel effect. The riffle controls the secondary circulation patterns and the position of the high velocity cores, since the cells scale with the riffle depth. At the pool, the cells stretch vertically to cover the whole cross section. Downwelling or upwelling can occur in the pool and riffle centerlines depending on the width/depth relation. The description resembles a uniform flow situation and is associated with secondary currents of Prandtl's second kind (Nezu and Nakagawa, 1993).

The difference in low and high flow behavior is reflected in the relative magnitudes of the shear velocities at the pool and at the riffle. The high flow situation (CPR2 and APR2) is more uniform, and so the difference between the riffle and the pool shear velocities is smaller than in the low flow case (CPR1 and APR1).

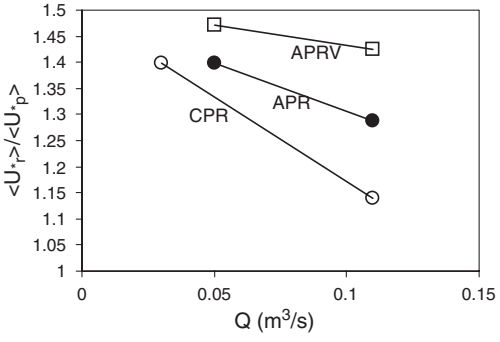


Figure 11. Ratio of riffle to pool wall shear stresses.

This is evident from Figure 11, in which $<U_{*r}>$ and $<U_{*p}>$ are the riffle and pool cross sectional shear velocities, respectively. The convergence with discharge shown by the figure is often observed in natural pool-riffle sequences and has important implications for the self-maintenance of the structures. According to the figures, the CPR case has a higher convergence rate than the APR configuration.

Consequences of this difference in behavior for high and low flow conditions may have other implications for the design and maintenance of pools and riffles in urban streams. The constriction of the walls starts playing an important role when the flow depth raises to more than 1/5 the width, which is not uncommon. Under this condition, higher shear stress zones are located approximately at 1, 3, and 5 times the depth from the walls and may or may not coincide with the position of an artificially placed pool. If the bankfull discharge is regarded as the one responsible for the pool maintenance, the placement of the pool can be done in order to match one of the high shear stress zones for bankfull flow.

4.2 *Vegetation effects*

Vegetation inhibits to some extent the topographic effects. Increased roughness raises the water levels and slows down the flow velocities. The plant zones force the flow towards the centerline both for low (APRV1) and high (APRV2) flow, generating only one high velocity core. Two strong circulation cells are located in the central zone but secondary flow patterns over the plants are less defined. For the APRV2 case, two incipient high velocity cores at the channel sides suggest that the effect of the plants may decreases for higher flow.

The similitude between the APRV1 and APRV2 experiments can be seen in Figure 11. The figure shows that the ratio $<U_{*r}>/<U_{*p}>$ changes considerably less than in the CPR and APR cases.

5 SUMMARY AND CONCLUSIONS

Detailed 3D velocity measurements on a laboratory model have provided important information regarding the effects of topography and vegetation on the flow dynamics of pool-riffle sequences in constricted waterways. After analyzing flat bed (FB), centered pool-riffles (CPR), alternate pool-riffles (APR) and vegetated alternate pool-riffles (VAPR) bed configurations, the following conclusions can be drawn:

- The pool-riffle configurations without vegetation showed low flow patterns qualitatively different than high flow patterns. Low flow characteristics were affected by the bottom geometry while high flow patterns were independent of the shape of the bed.
- The configuration with vegetation showed similar low and high flow patterns, obviously dominated by the vegetation distribution.
- All configurations tested showed a convergence of the pool and riffle shear stresses towards a common value, as observed in natural pool-riffle sequences.
- The location of high velocity cores (and thus high shear stresses) tends to be independent of the bed geometry as the flow increases. This position may not coincide with the position of an artificially placed pool and may not promote self maintenance.
- Vegetation can be used to direct the flow, diverting it from the banks and concentrating it on the central part of the channel.

ACKNOWLEDGEMENTS

Partial financial support came from the project "Development of an Integrated Scientific and Technological Framework for Stream Naturalization," Grant 98–NCERQA-M1, U.S. EPA.

REFERENCES

Nezu, I. and Nakagawa, H. (1993). Turbulence in open-channel flow. IAHR Monogr.

Rodríguez, J.F., García, M.H., Bombardelli, F.A., Guzmán, J.M., Rhoads, B.L. and Herricks, E. (2000). "Naturalization of urban streams using in-channel structures." Proc. Joint Conf. on Water Res. Engrng and Water Res. Plan. and Man., ASCE, Minneapolis, MN.

Thompson, A. (1986). "Secondary flows and the pool-riffle unit: a case study of the process of meander development". Earth Surf. Process. Landforms, 11, 631–641.

River Flow 2004 – Greco, Carravetta & Della Morte (eds.)
© 2004 Taylor & Francis Group, London, ISBN 90 5809 658 0

Morphological rehabilitation and flood protection by controlled river dynamics – a physical model

U. Stephan & M. Hengl
Institute for Hydraulic Engineering and Calibration of Hydrometrical Current-Meters, Vienna, Austria

ABSTRACT: According to the results of a physical model it is shown, how to change the state of a gravel bed river from erosion to a morphological dynamic river system connecting again river and wetlands. The basic idea is to raise the bed level with help of a ramp and to initiate a self-acting bank erosion process increasing the river width. In addition, the currently straight river morphology is converted into a meandering one. The physical model provided valuable experiences regarding self-acting bank erosion and meander development. These measures might be used for river restoration, but must be analyzed in each specific case regarding their suitability for improving a river-wetland-system.

1 INTRODUCTION

Many rivers in Central Europe such as the Salzach, Isar, Inn, Danube or Drau, show a heavy degradation process which has evolved from various human activities in the past such as straightening and constricting the river or bed load entrapment in the catchment. As a typical consequence the river system adjusts in a long-term geomorphologic manner to these human influences with various awkward effects. Bed erosion of many rivers has progressed to such an extent that bank structures as well as bridge piers have become endangered. The groundwater table has decreased remarkably. The river wetlands have been cut off from the river itself, which is closely connected to a loss of habitats and of population diversity in the wetland ecosystems. In addition, the flood run-off occurs chiefly on the main channel. Thus, wetlands are flooded less and tributaries are detached from the main river. Loss of retention areas deteriorates the downstream flood protection as well as the wetland ecosystems.

Even more unfavorable, if not dangerous, is a phenomenon called "*Sohldurchschlag*" or sudden riverbed break-down, which could be observed in many alpine rivers such as the Inn or the Salzach, e.g. Hengl (2000), WRS (2000). The term describes a change in the erosion process due to the presence of fine sediment layers below the gravel bed of a river. If the mean river bed intersects the gravel bed because of the progressive erosion process and reaches these fine sediment layers below the gravel bed, the geomorphologic consequences can no longer be predicted. The erosion process is increased tremendously because of the greatly increased erosion potential of these fine materials. The extent of damage from the above mentioned effects, i.e. endangering of buildings near the river bank and in the river, decreasing groundwater table, destruction of bank protection works, among others, is intensified.

Therefore, the river restoration planning stage of the river Salzach downstream of Salzburg is presented as an example of how to change a state of a river from erosion to a morphological dynamic river system connecting again river, tributaries and wetlands. The main goals of the river restoration measures are to sustainably stabilize the river bed regarding bed load input from the catchment, to guarantee flood risk protection, to raise the river bed, to provide a dynamic river morphology and, finally, to connect again river and wetlands.

2 BASIC CONCEPT

Within the Water management frame study Salzach, a concept for a solution was developed meeting morphological, hydraulic as well as ecological demands (WRS 2001a).

The main idea is to raise the bed level with help of a ramp. The ramp axis is directed towards the river bank and, thus, initiates self-acting bank erosion which, finally, leads to a dynamically curved river morphology. This construction combines a few important solutions: On the one hand, the river bed is raised while bed load transport fills the deposition wedge upstream

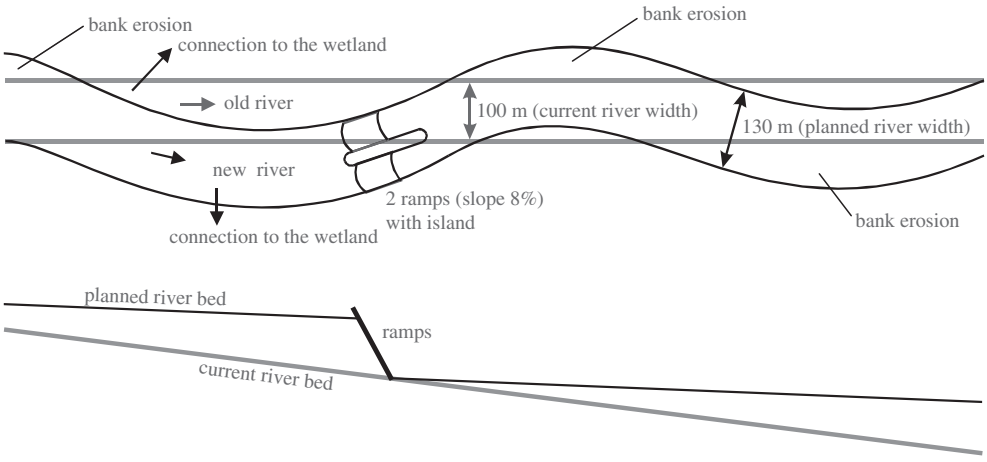


Figure 1. Principles of the solution concept for raising the river bed and improving the morphological state of the river.

of the ramp. Hence, the mean water level is also raised as well as the groundwater table. The former leads to a more frequently flooding of the wetland system and, thus, to an improved connection between river and wetland. In addition, the river width is increased due to the self-acting bank erosion process. This, first, compensates the raised water level due to the raised river bed in case of floods and, secondly, causes an improved morphological as well as ecological diversity of the river bed. During the filling process of the deposition wedge upstream of the ramp, the bank erosion temporarily enables continuous bed load transport downstream of the ramp and, thus, prevents further bed erosion. On the other hand, raising the river bed reduces the risk of "*Sohldurchschlag*" due to a thicker gravel layer covering the fine sediment layers below the gravel bed. The principles of the concept are shown in Figure 1.

For each measure, which is thought to be a solution for a problem, it has to be considered that the guidelines for the future morphological situation of the river-wetland-system are reasonable and realistic (Stephan et al. 2003). On the one hand, the selection of suitable solutions must be based on both the past and the current morphological situation of a river. On the other hand, any contemplated measures must take natural morphological processes into account. Thus, natural bed load input, river geometry as well as discharge of the current river must be suitable for a meander morphology in the future.

To analyse the current morphological situation of a river, the approach developed by da Silva (Yalin & da Silva 2001) may be used (Fig. 2). This method suggests that the morphology (macro bed forms) of a river depends on two factors: the ratio of bed width to flow depth (B/h) and the ratio of flow depth to mean grain size (h/d_m). When the bed width changes, flow depth changes also, as do the ratios B/h and h/d_m. Figure 2 with B as the river width, h the flow depth, J the bed slope and d_m as the mean grain size of the bed material shows that the current possible morphological situation of the river ranges between alternate bars and meanders for the whole extent of discharges, that is the discharge for beginning sediment transport up to the design discharge with a return period of 100 years. Due to the recommended river width of $B = 130$ m, a fundamental morphological change of the river is not to be expected. For the proposed solution, the morphology will not change essentially. But the planned measures would be doomed to fail, if these geomorphologic boundary condition were not considered.

3 DESCRIPTION OF THE MODEL

The main components of the planned river training works were tested in a physical model scaled 1:50. The physical model mainly focused on

- a proper ramp geometry to initiate the self-acting bank erosion process and to ensure a proper hydraulic function for energy dissipation and scour protection;
- needed measures to control the bank erosion process;
- analyses of time variability of the sediment input downstream of the ramp due to the bank erosion process;
- analyses on the development of the meanders in longitudinal direction and the needed bank protection measures;
- bed load transport capacity of a meandering river reach in equilibrium.

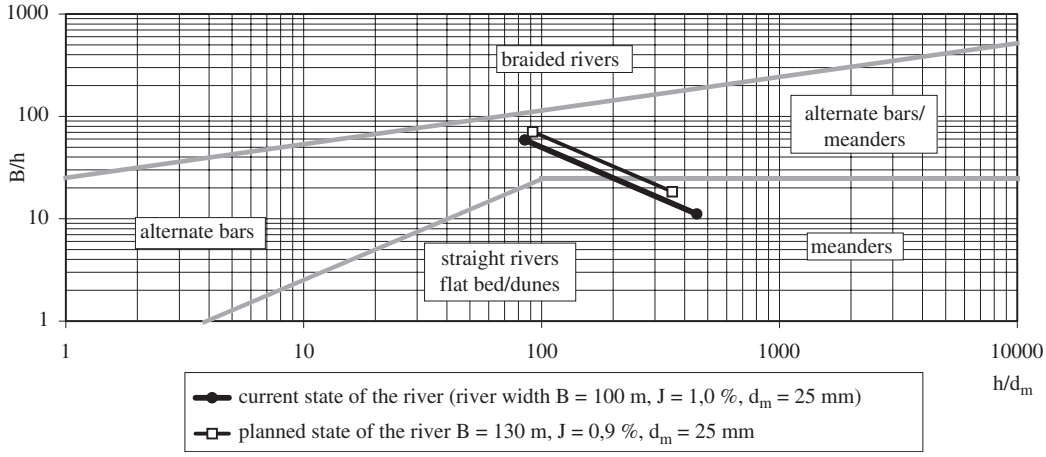


Figure 2. Macro bed forms of the river Salzach – current and planned state of the river (adapted from Yalin & da Silva 2001).

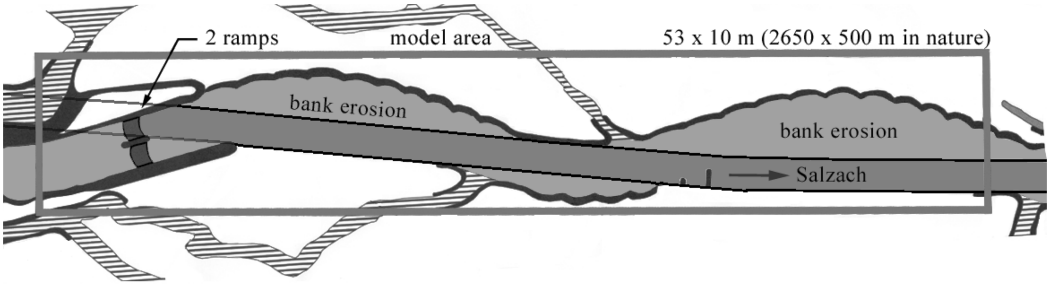


Figure 3. Plan view of the physical model.

A numerical sediment transport model simulating the long term bed level changes of the whole, 60 km long river reach was based on the latter. The design discharge with a return period of 100 years amounts to some 3100 m^3/s. An important part of the concept is the contribution of wetland areas and tributaries as flood retention areas to the flood run-off. Thus, only 2000 m^3/s of the design discharge remain in the main channel, 1100 m^3/s flow in the wetland areas as it resulted from a 2d-flow model. Therefore, the model area was limited to the river itself and the river-adjacent areas and the flood run-off in the wetlands was neglected.

Due to limited space, the physical model was 53 m long and 10 m wide reproducing 1.5 meander wave lengths downstream of the ramp. Figure 3 shows the model section including both the final state of the river and the straight river how it appears today. Meander wave length and width were planned to 1500 m and 130 m, respectively. Thus, the meander angle resulted in 18.6° and the meander amplitude for the inner and outer curve in 80 m. To limit the self-acting bank erosion in advance, a bank protection was built according to this meander geometry.

The ramp building consisted of two parallel ramps sloped 1:12 separated by an island. Each of the ramps was 60 m wide. Ramp curvature and ramp size were defined according to Platzer (2000). Due to fine sediment layers below the gravel bed of the river, the need for an extensive scour protection right behind the ramps arose.

The initial state of the model shows a 100 m wide straight river with a trapezoidal cross section, two parallel ramps and a control groyne to initiate the bank erosion process (Fig. 4). The downstream boundary condition for the physical model regarding the stage-discharge-relationship resulted from the 2d-flow model.

The sand used in the physical model was quartz sand with a mean grain size of $d_m = 33.4$ mm, calculated according to Meyer-Peter & Mueller (1948). 18 sample at different locations of the model were analyzed regarding the sieve curve. The results are shown in Figure 5a. The remarkable scattering of the samples



Figure 4. Initial state of the physical model.

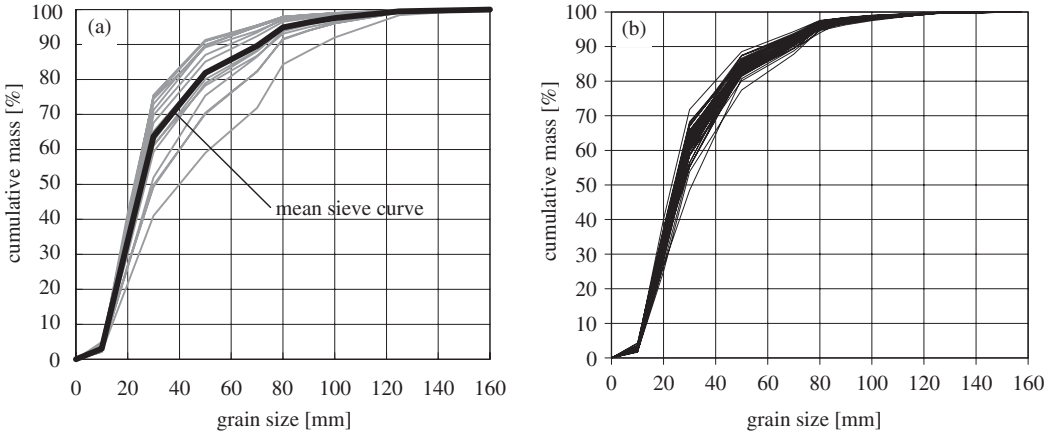


Figure 5. Sieve curves of the model sand (a) and the bed load input (b) (nature size).

might be explained by the method of how the sand was brought into the model area, since the sand was blown into the model. Figure 5b shows the sieve curves of the sand used for bed load input being almost the same as the bed material.

The bed load was added continuously using a conveyer belt (Fig. 6), but was not distributed equally over the river width, since the ramps were situated in a curve. The input ratio between left and right part of the river width was 3:2. The input rates were calculated according to Jäggi (1992) for a 130 m wide river with a bed slope of 0.9%.

The measurement program comprised measurements of water and bed levels as well as bed load measurements. The former were conducted within 54 cross sections covering a channel reach of 2.35 km in nature using ultrasonic probes. The bed load was collected in a sedimentation trap mounted on four pressure gauges at the model outlet and weighed continuously considering buoyancy effects.

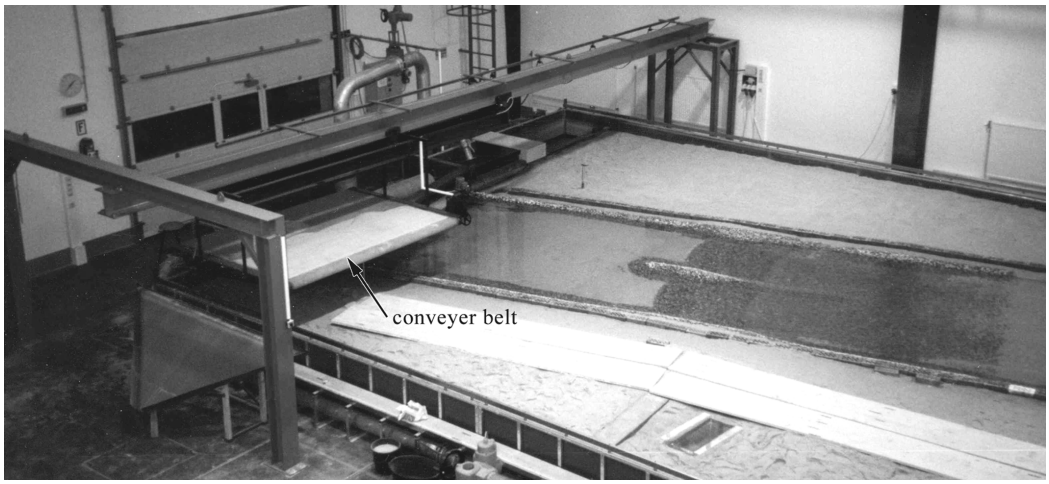


Figure 6. Conveyer belt for bed load input upstream of the ramps.

The experimental program was divided into two main parts: The first part contained the self-acting bank erosion and development of the meanders without bed load input at the model inlet simulating the situation after putting up the ramps. This part took 700 hours. During the second part, the longitudinal changes of the river bed depending on bed load input into the river reach as well as the bed load transport capacity of a curved river morphology were investigated. The total experimental duration amounted to 3608 hours. A detailed description of the physical model is given in WRS (2001b).

4 RESULTS

4.1 *Changes of the ramp building and scour protection*

The right part of the double ramp had to be turned to the left by 8° to improve the flow downstream of the ramp for better initiating the self-acting bank erosion. In addition, the height of the ramp head was reduced by 30 cm.

The hollow shaped scour protection right behind the ramp was 1.1 m deep and 1.5 times the length of the ramp. The hollow itself was lined with two rip-rap layers. Following the hollow, a river reach of, again, 1.5 times the ramp length was covered with stones sized 300 to 500 kg with a stone density of one stone per 2 m^2. Despite of the solid scour protection, scour depths up to 5 m are to be expected.

4.2 *Bank protection and controlling of flow*

The morphological development of the river reach downstream of the ramp is mainly influenced by groynes. Depending on the extent of bank erosion of the outer bank the length of the flow directing control groynes at the inner bank is increased to regulate the bank erosion process. Thus, the formerly straight river develops into a meandering one. Figure 7 shows the final state of the first meander curve behind the ramp building.

At the inner bank of the meander, generally no bank protection measures are needed. From the ford to the vertex of the meander curve, the groyne distance at the outer bank was 100 m and the length of the groynes was 25 m. From the meander vertex to the following ford, the flow direction must be turned. Thus, the flow attack at the outer bank was increased and the groyne distance reduced to 75 m as well as the groyne length increased to 30 m. The groyne heads should be protected separately due to occurring deep local scours. The groynes at the outer bank of the meander stabilize the curved morphology of the river and prevent further bank erosion as well as a fundamental shift of the main channel. Consequently, there is no need to set up the groynes at the outer bank unless the maximum extent of bank erosion is reached.

4.3 *Morphological development (bank shift, volume of bank erosion, depth variation)*

The development of the curved river morphology in the physical model resulted from experimental runs with varying discharges. The return period of the discharges ranged from 1 to 100 years with intermediate low discharge phases and, consequently, little sediment transport. 700 experimental hours, which correspond to 19 years in nature, almost finished the meander development and bank erosion process. The meander geometry, derived from the Farguesch laws



Figure 7. Control groynes at the inner bank to direct the flow to the outer bank and bank protection of the outer bank (final state of the measures).

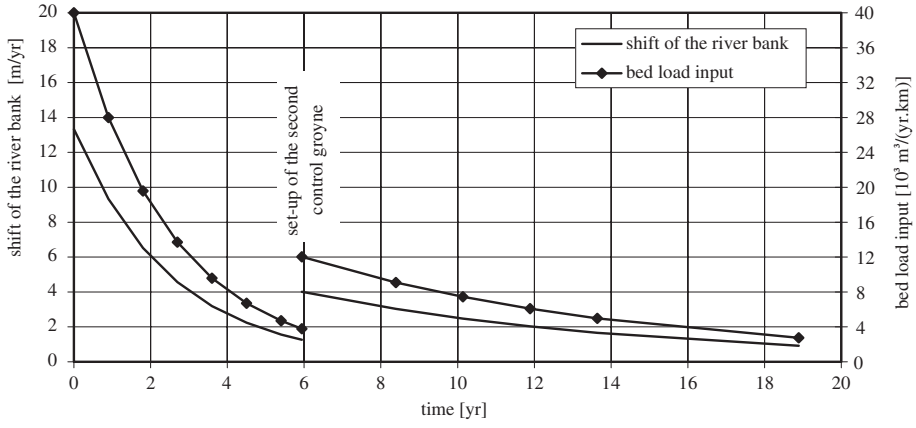


Figure 8. Mean shift of the river bank and volume of bank erosion in a meander assuming a 3 m gravel layer height in the river-adjacent areas.

(Schaffernak 1950), emerged to be too small regarding both the meander wave length and the meander amplitude and had to be increased by 10% and reduced by 20%, respectively. The groynes in the outer bank may be used for adapting the meander geometry.

Bank shift due to the bank erosion process mainly depends on the flow shear forces acting on the banks as well as on the bank material. In the physical model, the same material was used for both the river bed and the river banks. The shift velocity (Fig. 8) was calculated

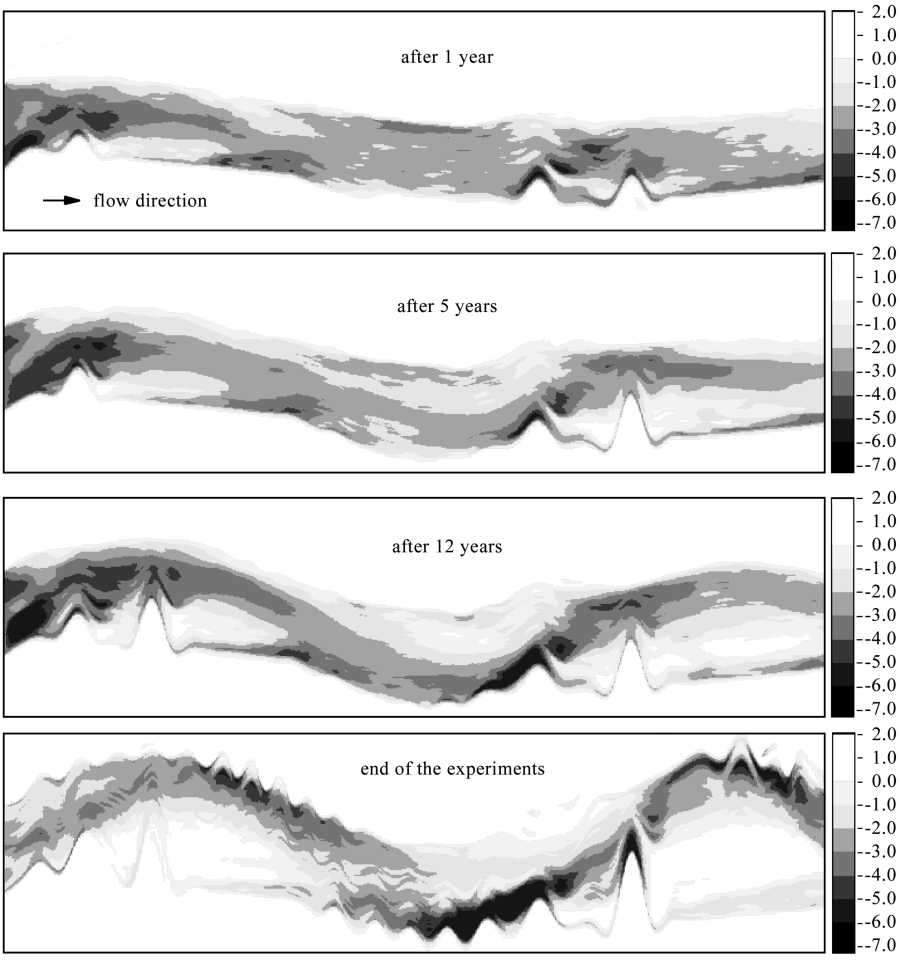


Figure 9. Flow depths [m] for a discharge of $Q = 500\ m^3/s$.

assuming the height of the gravel layer in the river-adjacent areas being not larger than 3 m considering fine sand deposition in the wetlands. The bank shift caused an increase of the river width from formerly 100 m to 130 m.

Figure 8 also shows the volume of bank erosion resulting from the bank shift. Putting up a ramp leads to a temporary deficit in bed load transport downstream of the ramp due to the filling of the deposition wedge upstream of the ramp. Unless the bed load material from the catchment passes the ramp, the self-acting bank erosion process needs to balance the downstream bed load deficit. Therefore, it is important to know grain size, type and layer height of the material of the river-adjacent areas, since the bed load input downstream of the ramp mainly depends on the geological characteristics of the river banks. To meet this demand in the frame study of the Salzach, extensive soil investigations in the river-adjacent areas were performed.

During the experiments as mentioned above, the bed levels were measured regularly within 54 cross sections. Analyses on meander development and bed level variations were based on these measurements. In particular, the latter are an important morphological pattern, since the ecological diversity is strongly enhanced by a morphological diversity of the river bed. Figure 9 shows the meander development with groynes being at the outer banks in four steps from the beginning until the end of the experiments. The dark areas mark the flow concentration at the outer banks. With progressive meander development, bed level variations and, hence, the morphologic diversity is increased.

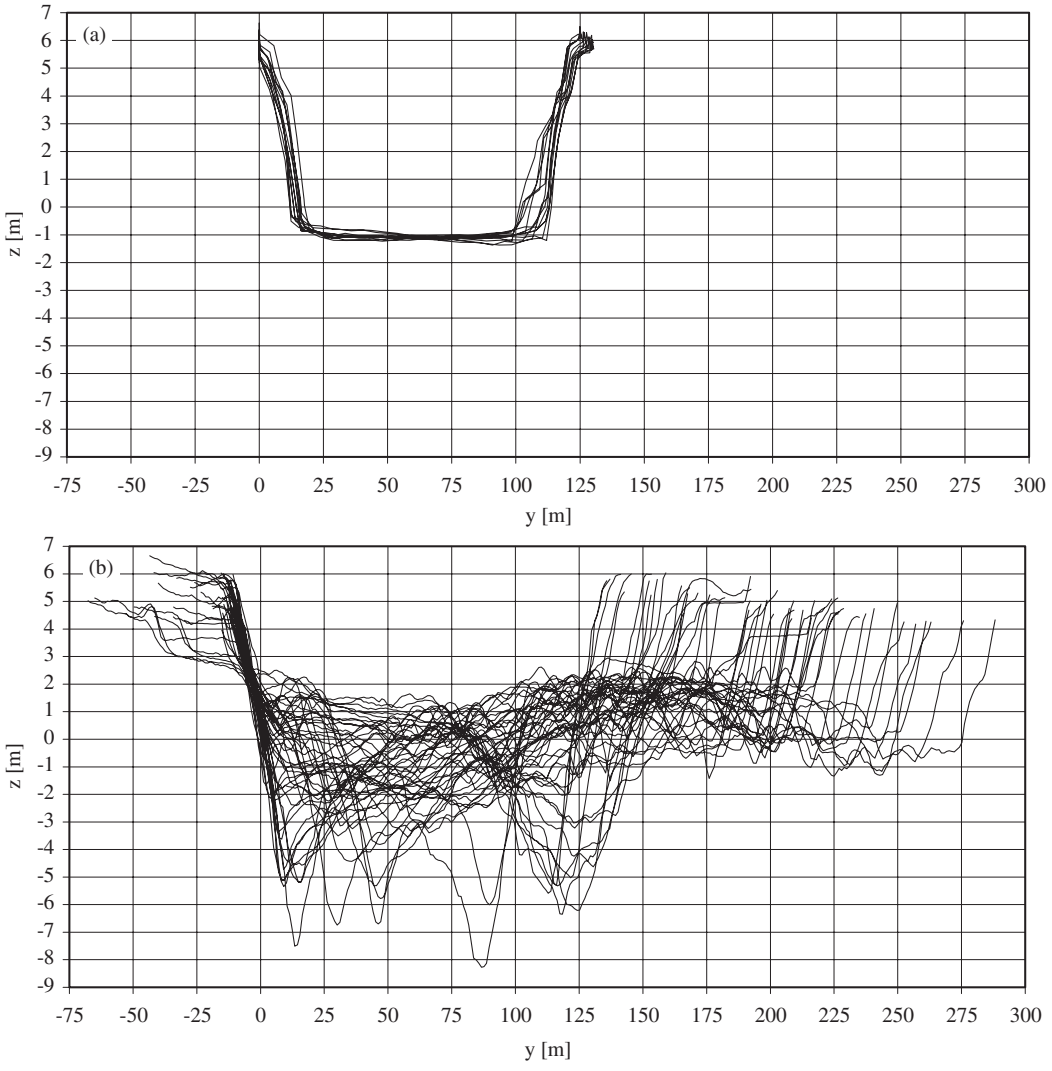


Figure 10. Bed level variations of a river reach of 2.2 km for the current (2001) (a) and the planned (physical model) (b) state of the river Salzach.

In addition, Figures 10a and b show various cross sections of a 2.2 km long river reach of the Salzach comparing the current and the future state of the river. The current state of the river (a) with a straight river morphology in a 100 m wide channel bed does not show any bed level variations for the river reach at all. An ecological diversity is not supported by this obvious monotonous situation. Unlike the current state, the planned meandering state (b) exhibits a wide variety of different channel widths as well as different channel depths caused by longitudinal changes of bends and fords. Both, shallow, low flowing cross sectional parts and deep parts with high flow velocities occur in this channel reach. Depending on discharge and bed load transport, the local morphological pattern of the river changes with space and time.

4.4 *Bed load transport capacity*

The final series of experimental runs focused on investigating the bed load transport capacity of a meandering river reach, which was expected to differ from a straight one. To calculate the bed load transport capacity, the channel reach has to be in equilibrium,

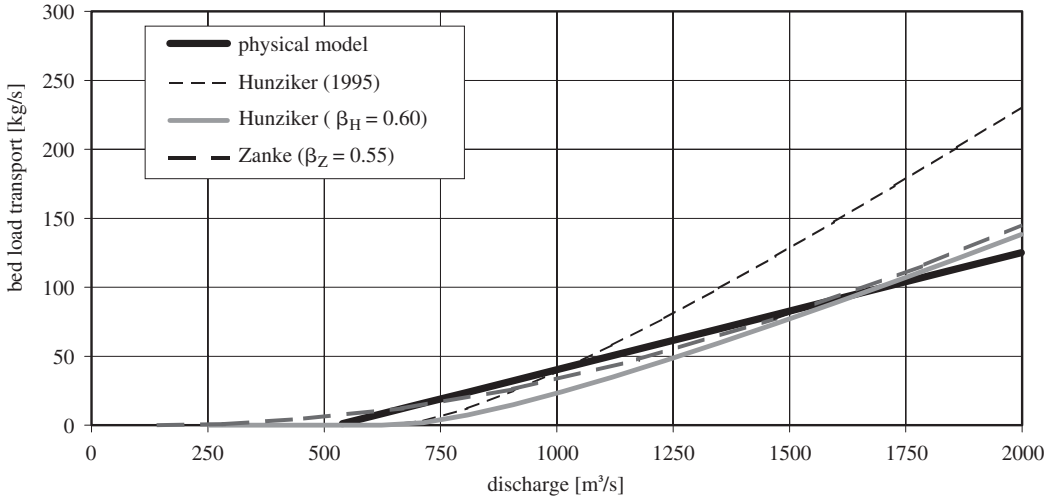


Figure 11. Transport equation of the physical model compared to transport equations of Hunziker (1995) and Zanke (1999).

i.e. the quantity of bed load input and output is to be the same within a certain period. The difference between input and output should not exceed 2%.

The results of the physical model were compared to the transport equation of Hunziker (1995), which also was used in the numerical sediment transport model, as well as of Zanke (1999) (Figure 11). Both transport equations were derived for a straight channel. To achieve the same bed load transport for both the physical model and the theory, the calculated bed load transport had to be reduced by a constant β. The slightly different values of β result from different methods of analysis of Hunziker (1995) and Zanke (1999).

However, the transport capacity of a meandering channel turned out to be less than the transport capacity of the straight one with the same channel width. This might be explained by the increased sinuosity of the meandering channel causing longer flow paths for the bed load, a reduced channel slope and, hence, a reduced shear force at the channel bed.

5 CONCLUSIONS

According to the results of the physical model, the planned river restoration measures turned out to be suitable for sustainably stabilizing the degrading river bed and, thus, ameliorating both the morphological and the ecological state of the river-wetland- system. The river can adjust to changing boundary conditions such as discharge and modify its bed. The ramps stand up to the design discharge and raise the river bed in front of the ramps to better connect river and wetlands. In addition, raising the river bed reduces the risk of "*Sohldurchschlag*" due to a thicker gravel layer covering the fine sediment layers below the gravel bed. Due to energy dissipation on the ramp, the downstream river reach is strained less. The self-acting bank erosion is initiated and directed mainly by control groynes. It leads to an increased river width and, thus, to a reduced bed load transport capacity as well as water levels in case of floods. Compared to mechanical river widening, self-acting bank erosion is a cost-saving method providing varying bed load input as required, i.e. high bed load input due to high bank erosion rates in case of floods and less bed load input in case of low flow periods.

The concept is based on the idea that the meander morphology corresponds to the current as well as future boundary conditions and does not change the current morphological state of the river fundamentally.

REFERENCES

Hengl, M. 2000. An Ecological and Hydraulic Redevelopment – Case Study Untere Salzach. *Kongress Wasser Berlin 2000*. Berlin.

Hunziker, R. 1995. Fraktionsweiser Geschiebetransport. *Mitteilung der Versuchsanstalt fuer Wasserbau, Hydrologie und Glaziologie*. ETH Zuerich. Nr. 138.

Jäggi, M. 1992. Sedimenthaushalt und Stabilitaet von Flussbauten. *Mitteilung der Versuchsanstalt fuer Wasserbau, Hydrologie und Glaziologie*. ETH Zuerich. Nr. 119.

Meyer-Peter, E. & Mueller, R. 1948. Formulae for Bedload Transport. *Proceedings of the 2nd Congress IAHSR. Stockholm*.

Platzer, G. 2000. Dimensionierung muldenfoermiger Blocksteinrampen. *Schriftenreihe des Bundesamtes fuer Wasserwirtschaft*. Wien. Band 9.

Schaffernak, F. 1950. *Grundriss der Flussmorphologie und des Flussbaues*. Wien: Verlag Springer.

Stephan, U., Hengl, M. & Schaipp, B. 2003. River restoration considering geomorphological boundary conditions. *Proceedings of the XXXth IAHR Congress*. Thessaloniki. C(II). 457–464.

WRS 2000. *Wasserwirtschaftliche Rahmenuntersuchung Salzach. Untersuchungen zur Flussmorphologie der Unteren Salzach*. Muenchen: Bayerisches Landesamt fuer Wasserwirtschaft.

WRS 2001a. *Wasserwirtschaftliche Rahmenuntersuchung Salzach – Zusammenfassende Darstellung und Bewertung der Loesungsvarianten*. Salzburg: Amt der Salzburger Landesregierung.

WRS 2001b. *Wasserwirtschaftliche Rahmenuntersuchung Salzach – Physikalisches Modell Sohlrampe mit Maeanderstrecke*. Salzburg: Amt der Salzburger Landesregierung.

Yalin, M.S. & da Silva, A.M.F. 2001. *Fluvial Processes*. Delft: IAHR Monograph.

Zanke, U. 1999. Zur Physik von stroemungsgetriebenem Sediment (Geschiebetrieb). *Mitteilungen des Instituts fuer Wasserbau und Wasserwirtschaft*. TU Darmstadt. Heft 106.

River Flow 2004 – Greco, Carravetta & Della Morte (eds.)
© 2004 Taylor & Francis Group, London, ISBN 90 5809 658 0

Destruction of herbaceous vegetation by flood flow on a floodplain in a recovery process

S. Sugio
University of Miyazaki, Miyazaki, Japan

K. Watanabe
Saga University, Saga, Japan

ABSTRACT: This research focuses on examining the destruction of the herbaceous vegetation on an excavated floodplain in the recovery process. The methods of examination were (i) drawing the distribution chart of the vegetation on the floodplain, (ii) surveying the physical condition of the floodplain, (iii) testing the tensile load to cut off the caulis and the pullout load to extract the roots of the vegetation, (iv) simulating the two dimensional steady flow at the peak of the flood and (v) estimating the maximum size of the transported bed material on the floodplain and the drag force acting on the canopy of vegetation. From these investigations we found that some parts of the vegetation clusters on the floodplain may be destroyed by transport of the bed material. However, almost all of the other parts can be destroyed by the tensile load due to the drag force on the canopy.

1 INTRODUCTION

The vegetation in a river channel plays an important role in the ecosystem. However it becomes an obstacle to flood flow and affects the transport of riverbed material. Therefore, the growing situation of the vegetation becomes an important aspect in river management. Up to the present, although the destruction of woody vegetation due to floods has been examined in various ways, the examination of herbaceous vegetation has been minimal.

The Kita River is a first class river, which flows in the northern part of Miyazaki Prefecture in Japan. In this river, the heavy rainfall of Typhoon No.19 in 1997 caused a severe river disaster and severe damage in the basin. A special emergency project to protect from further severe flood disasters was executed for the channel of the Kita River. In this project, it was requested that the excellent natural environment of this river be conserved, and a fixed degree of safety against flooding secured. Lowering the flood levels in a river reach by increasing the discharge capacity of the river channel is possible by enlarging the conveying cross section and by reducing the roughness of the river. In the Kawasaka district of the Kita River, the cross section was enlarged by excavating the floodplain and the trees in the channel were removed. In excavating, the water zone and the river banks were to be disturbed as little as possible in order to conserve the natural environment.

The revegetation has been monitored to clarify the recovery process of the vegetation after excavation. In monitoring, the destruction of the herbaceous vegetation was observed on the floodplain in the Kawasaka district. This paper describes the monitored results of the revegetation and examines the mechanism of the observed destruction of vegetation.

2 RESEARCH FIELD

A point bar formed on the left convex side of the bend of the Kawasaka district in the Kita River, has developed and become a floodplain. This floodplain between the 14 km and 13 km sections was selected as the research field. This floodplain was excavated on average by a thickness of two meters and flattened in March 2000 according to the execution plan for the river improvement of the special emergency project for the Kita River. A check field of this research is the floodplain between the 12.2 km and 11.4 km sections in the Honmura district which was not excavated. These locations are shown in Figure 1.

2.1 *Vegetation in Kawasaka*

In the Kawasaka district, woods of *Quercus acutissima* and *Rosa mulfiflora Thunb.* thrived before the excavation of the high ground on the floodplain, and the river

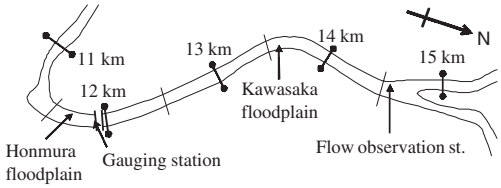


Figure 1. Location of the research field.

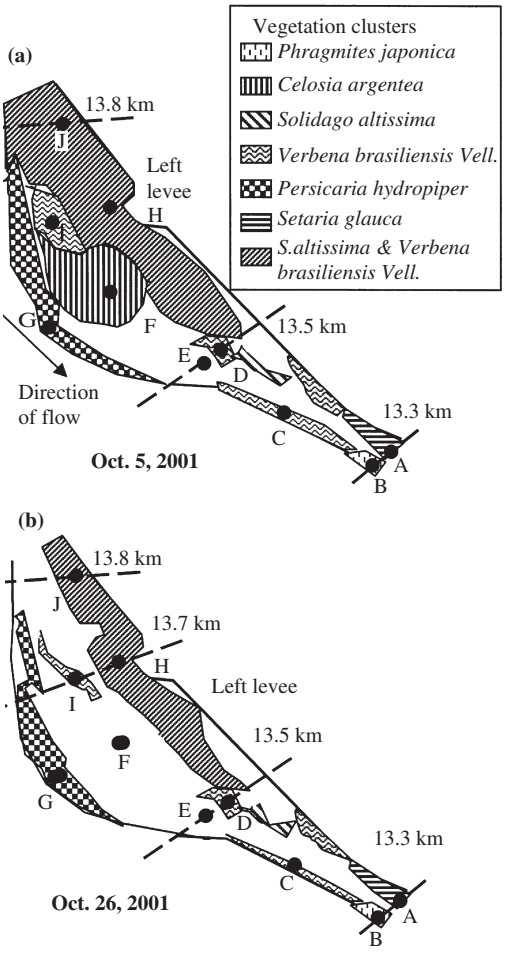


Figure 2. Vegetation distribution chart on the floodplain in Kawasaka.

banks had clusters of *Phragmites australis* or barren ground. Though the floodplain became barren ground overall in March 2000 due to the excavation, herbaceous vegetation germinated in the spring of 2001, and grew up smoothly to the state where the vegetation cover was 20–45% in the summer. Exotic vegetation such as *Verbena brasiliensis Vell*. and *Solidago*

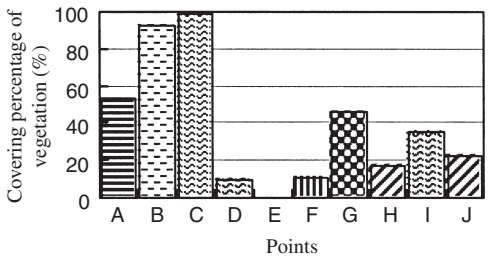


Figure 3. Percentage vegetation cover on the floodplain in Kawasaka.



Photo 1. *Verbena brasiliensis Vell.*



Photo 2. *Solidago altissima Linn.*

altissima Linn. grew about 0.5–2 m high in clusters in the whole area of the floodplain. Figures 2a and 2b show the vegetation distribution chart surveyed on October 5, 2001 and October 26, 2001, respectively. Figure 3 shows the percentage vegetation cover on the floodplain on October 5, 2001. Photos 1–6 show the photographs of the vegetation.

2.2 *Vegetation in Honmura*

It was observed from the monitoring, that most of the vegetation on the floodplain in the Honmura district



Photo 3. *Persicaria hydropiper.*



Photo 4. *Phragmites japonica Steud.*

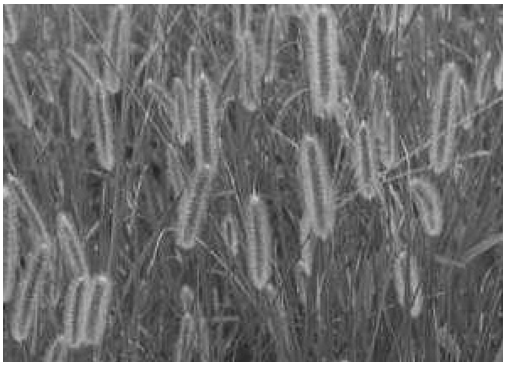


Photo 5. *Setaria glauca.*

was destroyed by the severe floods in 1997, however several woods remained. Subsequently, vegetation recovered gradually, and the floodplain was mostly covered with vegetation by the autumn of 2001. Clusters such as *Rosa mulfiflora Thunb*., *Celtis sinensis var*. *japonica*, and *Salix eriocarpa Fr.Et Sav*. were distributed as woody vegetation, and clusters such as *Phragmites japonica Steud, Reynoutria japonica*



Photo 6. *Celosia argentea Linn.*

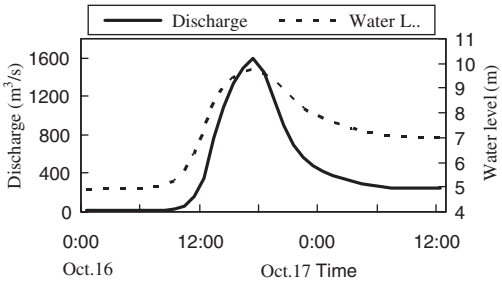


Figure 4. Flood discharge and flood water levels on October 16, 2001.

Houtt, and *Artemisia capillaries Thunb*. as herbaceous vegetation.

3 FLOODING

Floods caused by Typhoon No.21 greatly damaged the basin of the Kita River on October 16, 2001. The flow discharge was observed at the flow observation station at the 14.5 km section, and the water level was observed at the gauging station at the 12 km section. These observed results are shown in Figure 4. The maximum discharge of this flood was 1,600 m^3/s. Figure 5 shows the elevations on the floodplain at a typical cross section before and after the flood. A clear change of bed elevation due to the flood did not take place in

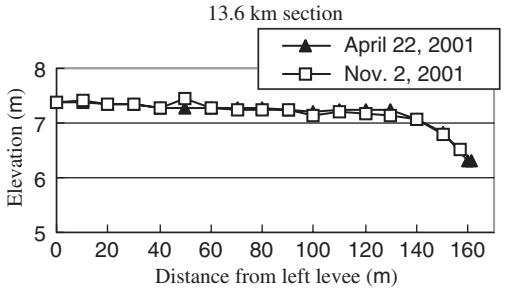


Figure 5. Observed elevation on the floodplain.



Photo 7. Floodplain in Kawasaka district after the flood.

the Kawasaka district. However, the vegetation was destroyed in half of the floodplain due to the flood as shown in Photo 7.

4 VEGETATION DESTRUCTION AND VEGETATION DISTRIBUTION AFTER FLOOD

Figure 2b shows the vegetation distribution chart surveyed after the flood. Comparing this chart with that for before the flood shown in Figure 2a, it can be seen that vegetation disappeared in half of the floodplain, though some parts remained on the low water channel side of the floodplain.

As for the vegetation destruction situation, the following four types were found.

(i) Vegetation disappeared by the roots
(ii) Only the roots remained
(iii) The canopy disappeared, but caulis and roots remained
(iv) Vegetation was buried in river bank area.

In the drawing of Figure 2b, the areas of vegetation where only the roots remained are included in the barren ground assuming that the vegetation was destroyed. Though the composite cluster of *Solidago altissima Linn.* and *Verbena brasiliensis Vell.* remained on the levee side of the floodplain, many canopies of

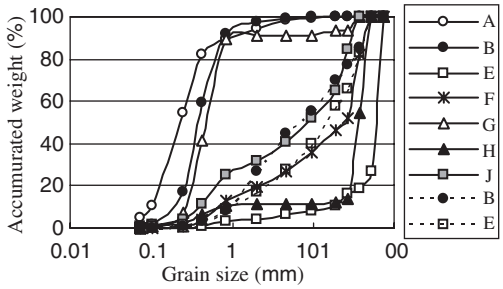


Figure 6. Grain size distribution curves.

Verbena brasiliensis Vell. were cut off. On the other hand, no significant vegetation destruction occurred on the floodplain in the Honmura district.

The grain size distribution curves are shown in Figure 6 by the solid line for the bed material on the floodplain after the flood and by the dotted line for one before the flood. Though the grain sizes are almost the same at the various points on the floodplain before the flood, a significant difference in the grain size distribution was caused in these points after the flood. Gravels larger than 26.5 mm in size occupy the major portion of the grain size distribution at Points E and H. Soils smaller than 0.5 mm in size are the major component at Points A, B and G where the percentages vegetation cover are high.

5 NUMERICAL ANALYSIS

5.1 *Basic equations*

The flow at the peak of the flood was numerically investigated. Two-dimensional St. Venant shallow water equations in a generalized curvilinear coordinate system used were;

$$\frac{\partial(uh)}{\partial\xi}+\frac{1}{r}\frac{\partial(rvh)}{\partial\eta}=0 \tag{1}$$

$$u\frac{\partial u}{\partial\xi}+v\frac{\partial u}{\partial\eta}+\frac{uv}{r}=-\frac{1}{\rho}\frac{\partial p}{\partial\xi}+2\frac{\partial}{\partial\xi}\left(\varepsilon\frac{\partial u}{\partial\xi}\right)+\frac{\partial}{\partial\eta}\left(\varepsilon\frac{\partial u}{\partial\eta}\right)-\frac{\tau_\xi}{\rho h}-\frac{NF_\xi}{\rho h} \tag{2}$$

$$u\frac{\partial v}{\partial\xi}+v\frac{\partial v}{\partial\eta}-\frac{u^2}{r}=-\frac{1}{\rho}\frac{\partial p}{\partial\xi}+\frac{\partial}{\partial\xi}\left(\varepsilon\frac{\partial v}{\partial\xi}\right)+2\frac{\partial}{\partial\eta}\left(\varepsilon\frac{\partial v}{\partial\eta}\right)-\frac{\tau_\eta}{\rho h}-\frac{NF_\eta}{\rho h} \tag{3}$$

where ξ, η = axes in curvilinear coordinates; r = radius of curvature; u, v = velocities in the ξ, η

directions; $p = \rho g(h + z)$; ρ = water density; g = gravitational acceleration; h = flow depth; z = bed elevation; ε = coefficient of eddy viscosity; τ_ξ, τ_η = bed shear stresses in ξ, η directions; F_ξ, F_η = drag forces acting on a dead grass lump in the ξ, η directions; and N = number of grass clumps per unit area. The bed shear stresses were expressed by using the coefficient of Manning's roughness n, as

$$\frac{\tau_\xi}{\rho h} = \frac{gn^2}{h^{4/3}} u\sqrt{u^2 + v^2} \tag{4}$$

$$\frac{\tau_\eta}{\rho h} = \frac{gn^2}{h^{4/3}} v\sqrt{u^2 + v^2} \tag{5}$$

The coefficient of eddy viscosity was expressed as

$$\varepsilon = \frac{\kappa}{6} u_* h \quad , \quad u_* = \sqrt{(\tau_\xi + \tau_\eta)/\rho} \tag{6}$$

where κ = Karman constant = 0.4; and u_* = shear velocity.

5.2 *Drag force*

Many clumps of dead grass twined around canopies of *Verbena brasiliensis Vell.* were observed after the flood in October 2001 and also after a small flood in July 2002. Therefore, the force acting on each canopy is regarded as the drag force acting on the dead grass clump. Regarding a circular plate with diameter of D as a grass clump, the drag force can be expressed as

$$F = \frac{1}{2} \rho C u_\delta^2 \frac{\pi}{4} D^2 \tag{7}$$

where u_δ = velocity at the height δ of the clump from the bed; and C = drag coefficient = 1.0. The velocity u_δ can be given from the Manning-Strickler equation as

$$u_\delta / q = 1.17(\delta/h)^{1/6}, \quad q = \sqrt{u^2 + v^2} \tag{8}$$

The scale of the grass clumps in the flood frow is uncertain. The diameters of clumps ranged from 6 cm to 12 cm in the survey after the floods. In this study, each clump is considered to be a circular plate with diameter of 10 cm. Since the water depth on the floodplain was over 4.0 m and the length of the vegetation was 45 cm to 190 cm, roughly 70 cm on average, all of the vegetation must have been submerged and the height of each clump δ is assumed to be half of the vegetation length, δ = 45 cm herein. By using this value of δ, F_ξ and F_η are expressed finally as, respectively,

$$\frac{F_\xi}{\rho h} = \frac{0.00376}{h^{4/3}} u\sqrt{u^2 + v^2} \tag{9}$$

Table 1. The number of dead grass clumps.

Cluster	Value of N (1/m^2)
Phragmites japonica Steud	0
Celosia argentea Linn.	2
Solidago altissima	0
Verbena brasiliensis Vell.	10
Persicaria hydropiper	0
Setaria glauca	0
Verbena brasiliensis Vell. and Solidago altissima	2

$$\frac{F_\eta}{\rho h} = \frac{0.00376}{h^{4/3}} v\sqrt{u^2 + v^2} \tag{10}$$

The numbers of dead grass clumps are different from each other due to the kind of vegetation and thier density. For example, the grass clumps in the cluster of *Verbena brasiliensis Vell.* numbered about ten per 1 m^2 from the survey after the flood. Based on this value, the number N at each analytical point was estimated from the distribution and density of vegetation before the flood in 2001 as shown in Table 1.

5.3 *Analytical conditions and velocity distributions*

The analytical domain including the floodplain at the Kawasaka district was selected between the 13.0 km and 14.4 km sections. The domain was divided by 50 m in the ξ direction and each cross section was divided into 24 meshes with intervals of 7.5 m to 10.5 m. Values of the coefficient of Manning's roughness were taken as 0.031 for the main channel and 0.035 for the floodplain according to the results of a 1-D simulation of the flood in 1997.

Taking the flood on October 16, 2001 as the flow to simulate, the peak discharge of 1,600 m^3/s was taken as the boundary condition at the upstream end. The water level of 10.63 m at the 13.0 km section was taken as the downstream boundary condition. This value was obtained from a 1-D simulation of the flood by using the measured peak water level of 9.74 m at the 12.0 km section.

Figure 7 demonstrates a numerical result of the flow velocity vector. It can be seen that the low water channel deviates to the right levee between the 14.0 km and 13.4 km sections and velocities are increased there due to the floodplain formed on the convex side of bend. Velocities were 2.2 m/s to 2.8 m/s in the low water channel and 0.8 m/s to 1.8 m/s on the floodplain. In particular, velocities near the center part of the floodplain were significantly decreased due to the cluster of *Verbena brasiliensis Vell.*

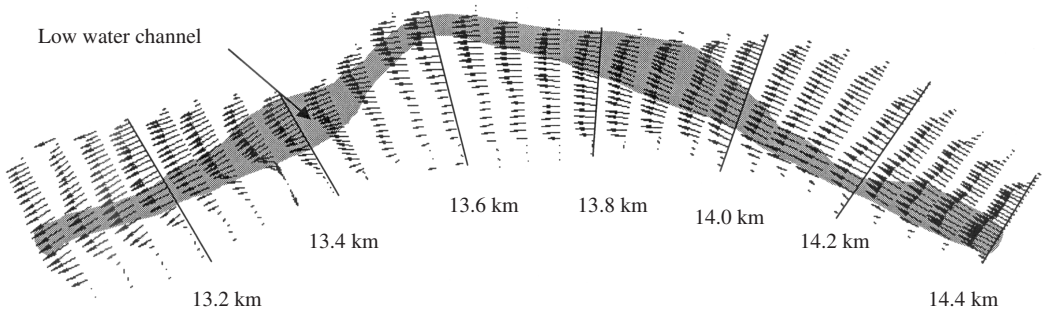


Figure 7. Velocity vector distributions.

6 DESTRUCTION OF VEGETATION

6.1 *Mechanism of destruction*

The effects of flooding on the vegetation have been classified by Ishikawa (1996) into the following four kinds: (1) destruction by the transported bed material, (2) destruction of the physical condition by the flow, (3) burying by the transported bed material, and (4) adverse effect to the physiological activity caused by submergence. The vegetation in the Honmura district was destroyed due to the flood in 1997. Main cause was burying by the bed material. This type of destruction should be considered by the estimation of tractive shear stress related to bed material transport under flood.

Many clumps of dead grass twined around canopies were observed after the flood due to Typhoon No.9 in July 2002. A photograph of a dead grass clump is shown in Photo 8. It is considered that these dead grasses were washed away in the upper reaches and twined around canopies of vegetation on the floodplain during the rising of the water level. When the drag force acts on each grass clump, vegetation is constrained to the flow direction. A comparison between the drag force and tensile load should be considered.



Photo 8. Dead grass clump twined around canopies of *Verbena brasiliensis Vell.*

6.2 *Movement of bed materials on the floodplain*

From the simulated results, the values of shear velocity u_* on the floodplain were 11.0 cm/s to 12.6 cm/s. This means that the maximum size of gravel moved by the shear stress can be estimated to be 1.5 cm to 2.0 cm. Therefore, it is considered that gravels smaller than this size moved during the flood. According to the grain size distribution curves shown in Figure 6, the percentage of gravels with diameters greater than 2 cm at Point E was almost 50% before the flood. This is the reason why the bed elevation was not significantly deformed by the flood as shown in Figure 5.

6.3 *Distribution of drag force acted on grass lump*

Figure 8 shows the distribution of the simulated combined drag force F acting on a grass clump twined around a canopy of vegetation on the floodplain. The horizontal axis denotes the distance from the top of left levee. The value of F is roughly 1 N to 10 N. In the figure, the vegetated areas before and after the flood are also shown.

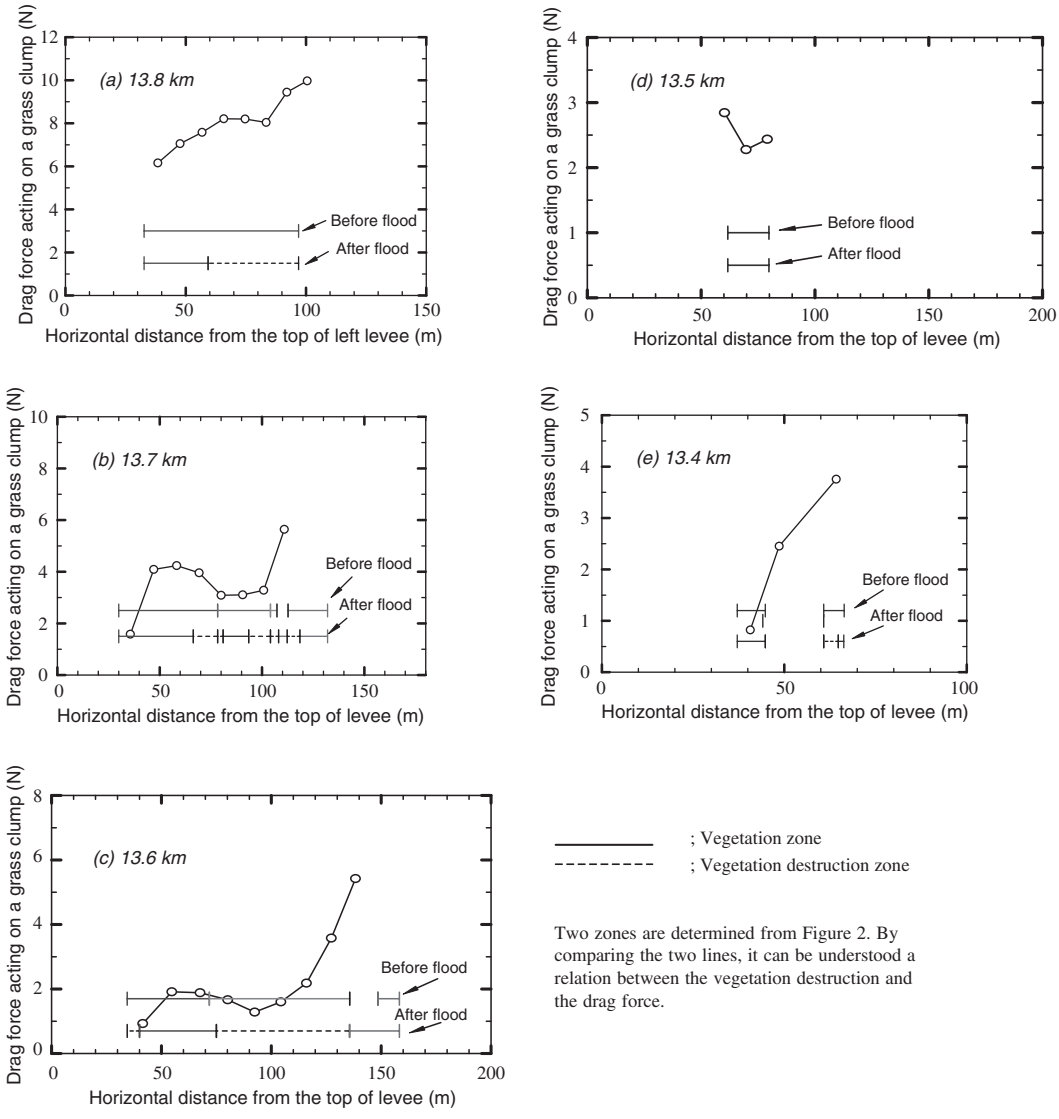


Figure 8. Distributions of combined drag force acting on a dead grass clump at each cross section of the floodplain in the Kawasaka district.

7 TENSILE LOAD OF HERBACEOUS VEGETATION

A tension test for various kinds of vegetation was carried out to clarify the tensile load to cut off the caulis and the pullout load to extract the root. A schematic diagram of the testing method is shown in Figure 9. The caulis of the vegetation was bound with a string, and a load was attached to the other end of the string. The load when the caulis was cut or the root was extracted was measured. Strings were bound at the joint of the

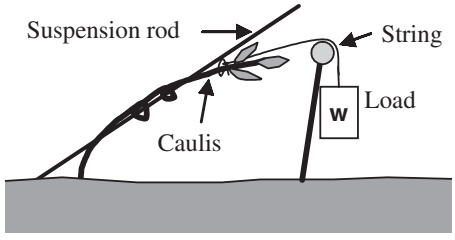


Figure 9. Schematic diagram for tension test method.

Table 2. Results of tension test.

Plants	Loaded position	Tensil load (N)	Height of plant (cm)
Verbena brasiliensis Vell.	Canopy Root	9.8 ~ 4.3 over186.2	95 ~ 164 95
Phragmites japonica Steud	Root	58.8 ~ 156.8	45 ~ 56
Persicaria hydropiper	Canopy Root	14.7 ~ 29.4 over137.2	43 ~ 56 56
Celosia argentea Linn.	Canopy Root	24.5 24.5 ~ 58.8	61 56 ~ 61
Solidago altissima	Canopy Root	49 68.6	80 57
Setaria glauca	Root	49 ~ 63.7	51 ~ 53

canopy for the tension test of the caulis and at the lowest part of the caulis for the root pullout test. In addition, in the test of tensile load, the lower part of the caulis was rolled in a suspension rod to prevent the load from acting on the root part.

The measured results are shown in Table 2. The results show the tensile load of the joint of the canopy is smaller than the pullout load of the root for many kinds of vegetation. From this result, it is understood that cutting the caulis is easier than extracting the root.

8 DISCUSSIONS OF VEGETATION DESTRUCTION

In the composite cluster of *Solidago altissima Linn*. and *Verbena brasiliensis Vell*. between the 13.7 km and 13.8 km sections, many canopies of *Verbena brasiliensis Vell*. were lost in the flood. Since the drag force acting on a dead grass clump is greater than the tensile load as shown in Figure 8a, it is considered that the drag force caused the destruction of *Verbena brasiliensis Vell*. by cutting canopies in this area. At the 13.7 km section (Figure 8b), the drag force decreased because of the decreased velocity due to the resistance of the cluster of *Verbena brasiliensis Vell*. Then, the destruction of this cluster was only partial.

The cluster of *Celosia argentea Linn*. between the 13.6 km and 13.7 km sections almost disappeared by the roots as shown in Figure 2b. According to the simulated results for the tractive force, it is considered that gravels with diameters smaller than 2 cm were transported in the barren ground and in the low density vegetated area. Since the percentage vegetation cover was small in the cluster of *Celosia argentea Linn*. as shown in Figure 3, it can be presumed that gravel movement destroyed the physical condition in this cluster and the root pullout load of *Celosia argentea Linn*. must have decreased. On the other hand, the tensile load of the caulis is larger than the drag force. Therefore, it is reasonable to consider that the caulis of *Celosia argentea Linn*. was not cut and its cluster was washed out by the roots.

At the 13.6 km section, the composite cluster of *Solidago altissima Linn*. and *Verbena brasiliensis Vell*. was not destroyed, because the drag forces were smaller than the tensile load as shown in Figure 8c. The cluster of *Verbena brasiliensis Vell*. at the 13.5 km section was also not destroyed for the same reason, as shown in Figure 8d.

The cluster of *Persicaria hydropiper* along the edge of the floodplain almost survived as shown in Figures 2b. It can be considered that the large drag force near the low water channel could not destroy *Persicaria hydropiper* because of the flexibility of the caulis. Values of root pullout load for *Phragmites japonica Steud* and *Setaria glauca* are larger than the drag forces as shown in Figure 8d. Therefore, both clusters at the 13.3 km section were not destroyed and survived as shown in Figure 8e.

9 SUMMARY

As mentioned above, various field investigations were carried out on the herbaceous vegetation of the floodplain of the Kita River. The destruction of the herbaceous vegetation due to the flood flow was then examined. The results obtained are as follows:

(1) Part of the herbaceous vegetation on the floodplain in the recovery process was destroyed due to a flood flow with a maximum discharge of 1,600 m^3/s caused by Typhoon No. 21 on October 16, 2001.
(2) The destruction situation can be classified roughly into the following four types: (i) vegetation disappeared by the roots, (ii) only the root remained, (iii) the canopy disappeared, but the caulis and roots remained, and (iv) vegetation was buried in the river banks.
(3) Many clumps of dead grass twined around canopies of *Verbena brasiliensis Vell*. were observed after a small flood in July 2002.
(4) Through a numerical analysis of the flood flow on the floodplain, it is recognized that the reason why a clear change of riverbed elevation did not take place on the floodplain in the Kawasaka district was due to lack of movement of gravel larger than 2 cm in size in floods.
(5) It was found from simulated results that a drag force of 2–10 N acted on canopies of the vegetation in large parts of the floodplain.
(6) Through tension tests for various kinds of vegetation, it became clear that cutting the caulis is easier than pulling out the root.
(7) It is confirmed that the disappearance of the canopy of *Verbena brasiliensis Vell*. was caused

by cutting the caulis due to the drag force acting on a dead grass clump.

(8) It is inferred that disappearance of vegetation by the root is due to both movement of gravels with small diameters and the action of the drag force.

(9) It can be presumed that the vegetation on the low water channel side of the floodplain was prostrated by the flow-induced force and survived the flood because of the flexibility of the caulis.

ACKNOWLEDGEMENT

The investigation in this paper was partially supported by research funds from the River Ecology Research Group of Japan. The authors would like to thank the Nobeoka Construction Office of the Ministry of Land, Infrastructure and Transport and the Nobeoka Engineering Works Office of Miyazaki Prefecture for supplying the hydrological data.

REFERENCES

Ishikawa, S. 1996. Characteristics of Riparian Vegetation. In Okuda, S. & Sasaki, Y. (eds). *River Environment and Riparian Vegetation*: 116–139. Tokyo: Soft Science.

Kyushu Regional Development Bureau, Ministry of Land, Infrastructure and Transport & Miyazaki Prefecture (ed.) 1999. *Report on the examination of river improvement in the Kita River*. Tokyo: Riverfront Improvement and Restoration.

River Bureau, Ministry of Land, Infrastructure and Transport (ed.) 2002. *Rivers in Japan*. Tokyo: Infrastructure Development Institute-Japan, Japan River Association.

River Ecology Research Group of Japan (ed.) 2002. *Understanding the Natural Environment of Rivers – Perspectives of River Ecology Research.* Tokyo: Riverfront Improvement and Restoration.

River Environment Division, River Bureau, Ministry of Land, Infrastructure and Transport (ed.) 2002. *Renaturalization of rivers – Restoring natural rivers*. Tokyo: River Environment Division, River bureau, Ministry of Construction.

Sezaki, T., Hattori, A., Kondo, K., Tokuda, M., Fujita, K., Yoshida, M. 2000. Field Study on the Destruction Processes of Herbaceous Vegetation on Gravel Bars due to Flood Flows. *Annual Journal of Hydraulic Eng., JSCE*., 44, 825–830.

Shimizu, Y., 1991. A study on Prediction of Flows and Bed Deformations in Alluvial Streams. *Report of Studies, Civil Engineering Research Institute, Hokkaido Development Bureau*, 93, 1–109.

Shimizu, Y. & Osada, K. 2002. Study on the Destruction Mechanism of Riparian Trees in a Gravel-bed River caused by Flood Disturbance. *Advances in River Eng., JSCE*., 8, 301–306.

Sugio, S., Watanabe, K., Tanoue, A. 2003. Research on the Destruction of Herbaceous Vegetation by Flood Flow on Sand Bar in Recovering Process. *Annual Journal of Hydraulic Eng., JSCE*., 47, 1003–1008.

This page intentionally left blank

River Flow 2004 – Greco, Carravetta & Della Morte (eds.)
© 2004 Taylor & Francis Group, London, ISBN 90 5809 658 0

A new bed for the river Inde: a case study with special view on the risk of depth erosion

P. Kamrath, C. Schweim, S. Briechle & J. Köngeter
Institute of Hydraulic Engineering and Water Resources Management Aachen University, Aachen, Germany

ABSTRACT: This paper presents the results of research about a river relocation in a German coal mining area. The river Inde resides in the lignite dismantling area called the "Rhineland", which is enclosed by the three towns Aachen, Cologne and Mönchengladbach. In the year 2005 the contemporary riverbed will be intersected as a result of the brown coal mines forward movement to the east and the continued use of lignite as energy source for the neighbouring power plants. Long time enduring critical shear stresses throughout flood events could cause depth erosion, which would damage or eventually destroy the sealing layer and therefore flood the pit mine as a worst-case scenario. Hence, the aim is to give the new river as much freedom as possible and to eliminate any uncertainties regarding the flood protection of the coalmine at the same time.

1 INTRODUCTION

The planned riverbed consists of a variable geometry and cross sectional shapes separated in one main channel and two flood plains. According to modern aspects of river-design a partly meandering river was chosen where diverse flow patterns are beneficial to the river ecology.

The new part of the river will cover a reach of 12.0 [km] (Fig. 1). The river Inde has a mean discharge of 4.3 [m^3/s]. Its new riverbed shows a bed slope of 1.2 [‰] and a mean width of the channel of 13.70 [m]. The riverbed of the new Inde is denoted by a wide bandwidth of different roughness regions. For numerical simulations a one-dimensional view is not sufficient, because the lateral resolution of the results would not be detailed enough for erosion forecasting purposes.

The transport of the bed material was tested in the institute's laboratory. Hence, the main influencing parameters regarding the bed load are the materials critical shear stress τ_c and the mass erosion capacity respectively. In addition to the bare materials critical shear stress the influences of sparse vegetation and ripples caused by the construction method are important aspects to consider in the model (Fig. 2, top). For this purpose a vegetation–erosion algorithm is applied to the numerical model.

As a consequence to the sparse and slow growing vegetation the shear stresses are computed for varying scenarios. At first a scenario for the time immediately after flooding the new part of the river is predicted when settlement processes are not finished yet and plants are sparse. Secondly at another point of time in the far future when settlement is finished and vegetation is dense. Except of erosion stability forecasting during annual repeating floods, the initial bed load during an only every one hundred years occurring event is interesting, too.

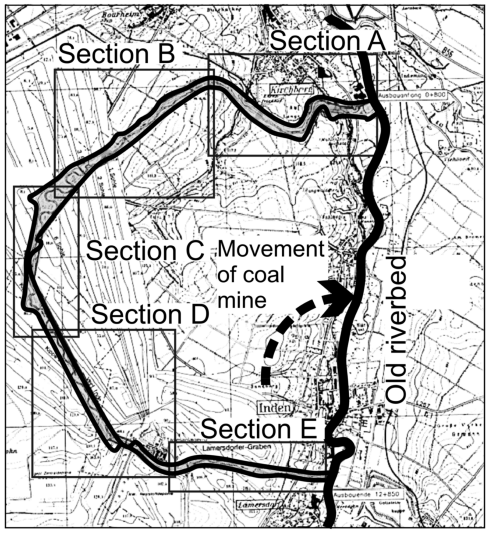


Figure 1. The relocation of the river Inde.

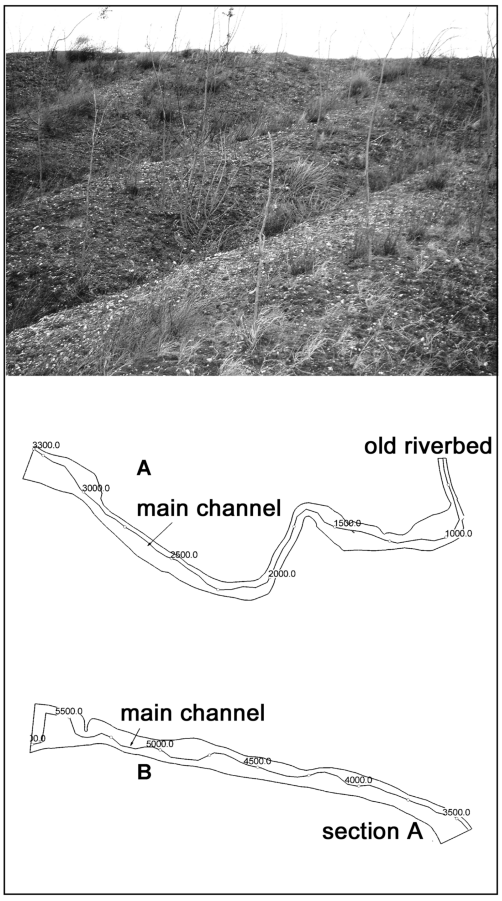


Figure 2. Sparse vegetation and ripples on flood plains (top) and overview of sections A and B (river km $5^{+800} - 0^{+600}$).

2 THE MODEL

2.1 *Simulation of flow characteristics*

The flow processes in the river are dominated by a very heterogeneous river geometry and roughness distribution. To assure the hydromechanical efficiency as well as to get information about the occurring shear stresses at different flood events the two-dimensional depth averaged model RISMO is used. RISMO has been developed at the Institute of Hydraulic Engineering and Water Resources Management and has been applied for several two-dimensional simulations (Rouvé & Schröder 1993).

The numerical model solves the shallow water equations with the finite element method. The shallow water equations are obtained by vertical integration of the Navier–Stokes equations and the continuity equation (Kuipers & Vreugdenhill 1973):

$$H\left(\frac{\partial U_i}{\partial t}+\frac{\partial U_i U_j}{\partial x_j}\right)=H\left(-g\frac{1\partial S}{\rho\partial x_i}+\frac{1\partial}{\rho\partial x_j}\left(V_{ij}+T_{ij}+D_{ij}\right)+F_i\right) \quad (1)$$

$$\frac{\partial H}{\partial t}+\frac{\partial\left(HU_i\right)}{\partial x_i}=0 \qquad \text{continuity equation (2)}$$

with

$$V_{ij}=\rho\nu\frac{\partial U_i}{\partial x_j} \qquad \text{viscous stress tensor (3)}$$

$$T_{ij}=-\rho\overline{u_i u_j} \qquad \text{turbulent stress tensor (4)}$$

where H is the flow depth, U_i are time-averaged horizontal velocities, x_i are the Cartesian coordinates, S is the water surface elevation, F the outer force, ρ the density of water and ν the cinematic viscosity.

A wet–dry algorithm considers bank overflow and partly submerged regions. The flow calculation yields the velocity and the depth of flow for each node for a given discharge and for a set of boundary conditions like the bottom roughness and outflow water level. The simulation is carried out from downstream to upstream to use the results from one section as the outflow boundary condition to the next one. When the flow calculations are completed a decoupled sediment transport module is used to calculate transport rates. The influences of the ripples and the sparse vegetation are all covered into Manning's roughness parameter n. The whole reach of the new riverbed is divided into sections with about 8000 elements each.

2.2 *Applied roughness*

The open pit mine offers a material as a side product which is used for the new riverbed. It consists of a mixture of gravel, sand and loess with a characteristic diameter d_{ch} of 15 [mm]. Resistance to flow is typically characterized by a roughness coefficient. The most commonly used equation for flow resistance is the Manning equation. All other forms of resistance parameters as the Chezy C parameter or the Darcy–Weisbach friction factor f can be converted into Manning's coefficient n.

The roughness of the bare material was tested in an earlier physical experiment in order to transfer the results into the numerical model (Baur et al. 1997). From a series of tests the roughness was determined to be $n = 0.019$ [s/m$^{1/3}$]. The estimation of roughness is very precise, as long as no heterogeneous influences are considered. Unfortunately, the flood plains of the new river Inde consist of ripples and a very sparse vegetation layer (Fig. 2, top). The ripples width is approximately 2.0 [m] and their height about 0.6 [m].

To take these structures into account, an approach recommended by van Rijn (1993) is chosen:

$$\frac{1}{n^R} \approx \frac{26}{k_s^{1/6}} = 26 \cdot \left(20 \cdot \gamma_R \Delta_R \cdot \left(\frac{\Delta_R}{\gamma_R} \right) \right)^{-1/6} \quad (5)$$

In Equation 5 above n^R [s/m$^{1/3}$] is the added Manning roughness resulted by ripples or dunes, k_s [mm] is the equivalent sand roughness parameter, γ_r [–] is called a presence factor ($\gamma_r = 1.0$ for ripples and $\gamma_r = 0.7$ for dunes) and Δ_r [m] is the height of the structures.

2.3 *Influence of sparse vegetation*

The influence of the sparse vegetation on the ground is neglected. Only larger plants e.g. willows and shrubs are simulated. Plants on the floodplain and along banks can increase or even decrease the effective flow resistance. The Manning's resistance coefficient for vegetation is calculated in conformity with the Cowan (1956) method for additive resistance and based on the work of Copeland (2000). According to his research, the modulus of plant stiffness E_s is critical to the calculation of resistance because of the flexibility of the plants and the deformation of leaf masses due to the flow forces. The modulus of plant stiffness is calculated by:

$$E_s = \frac{F_{45} \cdot h^2}{3 \cdot I} = 6,791 \cdot \left(\frac{F_{45} \cdot h^2}{D_s^4} \right) \quad (6)$$

where F_{45} is the force to bend the plant to an angle of 45°, D_s is the thickness of the stem and h the plants heights as to see in Figure 3. With the typical stiffness of willows the roughness for submerged vegetation can be computed by following equation:

$$n = 0,183 \cdot \left(\frac{E_s \cdot A_s}{\rho \cdot A_i \cdot u_\tau^2} \right)^{0,183} \cdot \left(\frac{h}{Y_O} \right)^{0,243} \cdot (M \cdot A_i)^{0,273} \cdot \left(\frac{\nu}{u_\tau \cdot R_h} \right)^{0,115} \cdot \left(\frac{1}{u_\tau} \right) \cdot R_h^{2/3} S^{1/2} \quad (7)$$

with:

A_s	Total cross sectional area of a plant	[m^2]
A_i	Frontal area of a plant blocking flow	[m^2]
u_τ	Shear velocity	[m/s]
Y_O	Flow depth	[m]
M	Plant density	[1/m^2]
R_h	Hydraulic radius	[m]

Equation 7 is applicable only for submerged flow defined by depth $Y_0 > 0.8\,h$. At present time, approximately one willow or shrub for each 50 [m^2] with $E_s = 1.5 \cdot 10^8$ [N/m^2] can be found on the flood plains. Hence, the resulting Manning's roughness coefficient for the river Inde is chosen to be $n = 0.05$ [s/m$^{1/3}$]. The ripples are obviously the parameter with the highest influence. For the moment when the new part of the river is flooded, the influence of sparse vegetation is insignificant.

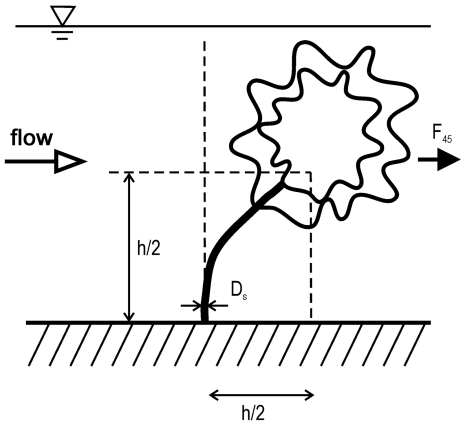


Figure 3. Methodology for measuring the force F_{45} to calculate plant stiffness E_s.

2.4 *Critical shear stress value*

The value of the critical shear stress relies on the degree of fractional ground cover V, which ranges from zero to one. $V_{max} = 1$ is the maximum percent cover that can be supported in a given environment. Unfortunately, only few data sets exist to constrain the relationship between the critical shear stress τ_c and V. In the absence of better information, a linear relationship is a good approximation (Tucker 1999).

$$\tau_c(V) = \tau_{cs} + V \tau_{cv} \quad (8)$$

where τ_{cs} is the critical shear stress for an unvegetated surface and therefore primarily a function of the grain size and τ_{cv} is the added critical shear stress under 100% vegetation cover. The transport capacity then depends mainly on vegetation cover and is commonly written like:

$$q_s = k(\tau - \tau_{krit})^p \quad (9)$$

The transport capacity q_s depends on the difference of the fluid shear stress τ and the critical shear stress τ_c. At present time, the coverage V is about 10%. With $\tau_{cs} = 6$ [N/m^2] as resulted by experiments in a flume and $\tau_{cv} = 50$ [N/m^2] as the maximum value under full coverage the critical shear stress immediately after flooding the Inde is assumed to be approximately 11 [N/m^2].

2.5 *Erosion processes*

The rate of erosion is calculated with one of the common sediment transport formula. It is the method

of Meyer-Peter & Müller (1949) which derives the sediment transport capacity:

$$q_S = 8 \cdot \rho_F \cdot u_\tau \cdot d_{ch} \cdot Fr^* \cdot \left[\frac{Q_S}{Q} \left(\frac{k_{St}}{k_r} \right)^{3/2} - \frac{Fr_c^*}{Fr^*} \right]^{3/2} \quad (10)$$

with:

q_s	transport capacity	[kg/m · s]
ρ_F	bulk density of material	[2650 kg/m^3]
u_τ	shear velocity	[m/s]
d_{ch_*}	characteristic particle size	[15 mm]
Fr	Froude number due to particle = f(τ, d_{ch})	[–]
Fr_c^*	critical Froude number due to particle	[–]
Q_s	flow rate with effect on transport	[m^3/s]
k_{St}	roughness coefficient due to flow	[m$^{1/3}$/s]
k_r	roughness coefficient due to particle	[m$^{1/3}$/s]

By comparing the rates at two following cross sections the model predicts erosion or deposition within the element. By dividing the difference of one sections inflow and outflow with their distance one gets the change in bottom elevation for each time step:

$$\frac{\partial z_B}{\partial t} = \frac{q_s^{in} - q_s^{out}}{\rho_F \cdot d} \quad (11)$$

In Equation 11, d is the distance between the cross sections. Therefore, the derivative of the bottom elevation in time is equal to the derivative of the transport capacity in x-direction. There are no long-term changes in river morphology predicted by the numerical model, because there is more demand on the local accuracy of the estimated initial shear stresses than on long-term prediction.

3 APPLICATION

3.1 *General*

The main intend is to predict depth erosion and the total area with shear stresses above the critical value with the help of a numerical model. Therefore different vegetation coverage levels and specific times are investigated.

In 2005 the old riverbed will be finally intersected and the new one will be flooded. Thus, another aspect is to study the influence of the ripples to the computed shear stress values and to suggest, whether a removal is needed for flood protecting reasons or not. Hence, one main thought is central: minimization of the total area with shear stresses above a critical value. This chapter presents the results and compares the different scenarios. The focus is set on sections A and B which are built in the next year (Fig. 2, bottom).

3.2 *Influence of settlement*

Especially in the first years after cutting the old river and flooding the new part in the year 2005 any flood events could produce great damage, because there is no protection by any vegetation. Because the new riverbed is being built close-by the open pit mine which was refilled with material just a few years ago, the bottom elevation will change over the next 20 years between 0.1 [m] and 0.6 [m]. Thus, as a first step, the influence of the unfinished settlement on the shear stresses should be examined.

Figure 4 shows the computed shear stresses at river km 5^{+400} for two different moments at a discharge of 111.0 [m^3/s]. On the left the computed values for the year 2005 are shown as predicted and on the right the results for the year 2020 are plotted.

It is obvious for this section, that values of shear stresses are minor in the year 2005, when vegetation coverage is little. Table 1 compares the total critical area. For the summation a critical shear stress value of $\tau_c = 11$ [N/m^2] is assumed for both cases. Growing of vegetation between the year 2005 and 2020 is therefore neglected. During an every one hundred years occurring flood the size of the area where erosion is possible increases due to the settlements about 50%. It is important that the risk is not higher in the beginning compared to a later specific time.

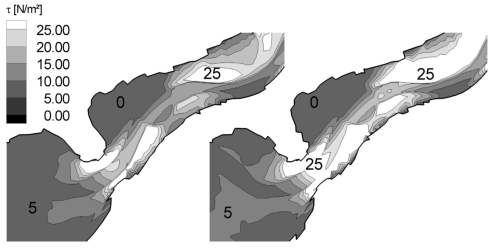


Figure 4. Influence of the unfinished settlement: Computed shear stresses for 2005 (left) and 2020 (right) at km 5^{+400}.

Table 1. Summation of critical area for section "B" at two different specific times.

Section B [km $3^{+300} - 5^{+800}$]		2005 [m^2]	2020 [m^2]
Scenario	SHQ*	7961.4	13,534.2
	HQ_{100}^{**}	53,751.3	76,157.1

* Q = 22.35 m^3/s, summer flood (approximately 5 times a year).
** Q = 111.00 m^3/s.

3.3 *Influence of ripples and dunes*

The ripples on the flood plains are caused by the construction method of the new riverbed. The ripples result from the construction equipment which consists of the typical machines in open pit mines, normally used to remove the enormous quantities of earth. A comparison of calculated shear stresses with and without ripples should help to decide, whether the ripples should better be removed or not. Figure 4 shows the shear stresses at the same Inde km 1^{+750} for both cases.

Figure 5 and Table 2 clearly illustrate the great influence of the ripples at the flood plains. Although water depth becomes smaller and velocities are computed bigger for the case without ripples, the calculated shear stresses are in general of higher values. The influence of the strong roughness dominates. After virtually removing any ripples, the summated critical area is diminished to 29.8% for the HQ_{100} (111.00 m^3/s) case and 70.9% for the SHQ (22.35 m^3/s) case.

3.4 *Influence of vegetation*

The vegetation coverage on the flood plains is central to avoid depth erosion. Thus, when the relocation of the Inde was planned in the early 1990s and first experiments were carried out, it was assumed that the flood plains are covered with a dense layer of vegetation by 100% after a very short period of time. This prediction was wrong. The used material is a side product and was located at a depth of approximately 200 m below the surface. Therefore the percentage of nutrient substances is very little and flora needs more time to grow than usual.

That's why it is of great interest to predict the degree of fractional ground cover which is needed to bisect the total area with supercritical shear stresses. In Figure 6 the critical area A_{Ero} is plotted against the degree of fractional ground cover V and the critical shear stress τ_c respectively. The vertical line at $V = 10\%$ ($\tau_c = 11\ N/m^2$) denotes the present state. When the plants grow, the figure yields clearly that the critical area becomes smaller. The point when the area is bisected differs for every case. But in general a critical shear stress about 20.0 [N/m^2] and a degree of ground cover about $V = 28\%$ is sufficient to reduce the endangered area by 50%. Anyway, this is the total critical area which is endangered that depth erosion can occur. But because erosion and sedimentation are conditional to the derivative in x of the transport capacity and the shear stress (see Equation 11) respectively, both only occurs when the shear stress values change rapidly.

3.5 *Depth erosion*

Figure 7 shows, that the initial depth erosion velocities are varying between 0 and 2.0 [cm/min]. Typical floods at the river Inde last between one and four days, but the duration of discharges above 25 [m^3/s] is less than half a day. Extrapolating an initial velocity of 0.1 [cm/min] results to depth erosion about 0.77 [m] in 12 hours. The alteration of the riverbeds bottom due to erosion has effects on the hydromechanics and therefore on depth erosion velocity, too. But nevertheless for flood protection reasons higher velocities should not be permitted during a flood event. Thus, even when the growth of vegetation helps keeping the

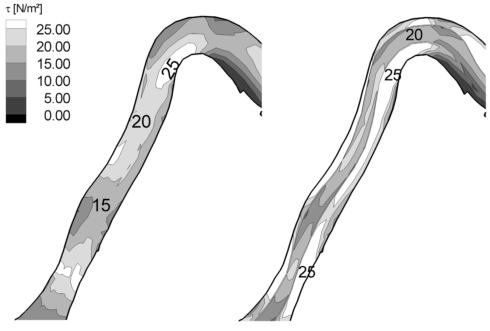


Figure 5. Influence of the ripples: computed shear stresses for removed ripple roughness (left) and with ripples at the flood plains (right) at km 1^{+750}.

Table 2. Summation of critical area for section "A" for the scenarios with and without ripples.

Section B [km $3^{+300} - 5^{+800}$]		With ripples [m^2]	Without ripples [m^2]
Scenario	SHQ	30,639.2	8924.5
	HQ_{100}	99,258.3	69,705.4

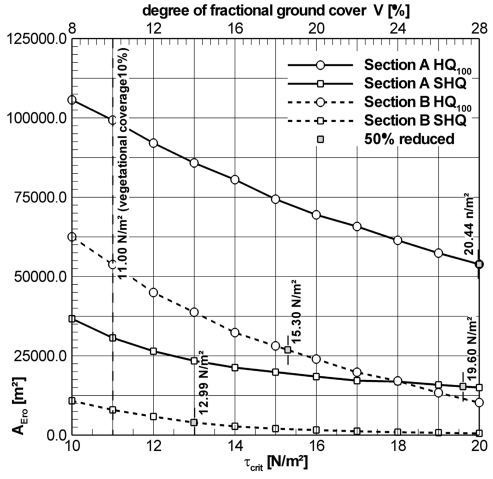


Figure 6. Influence of the degree of fractional ground cover to the total area with supercritical shear stresses.

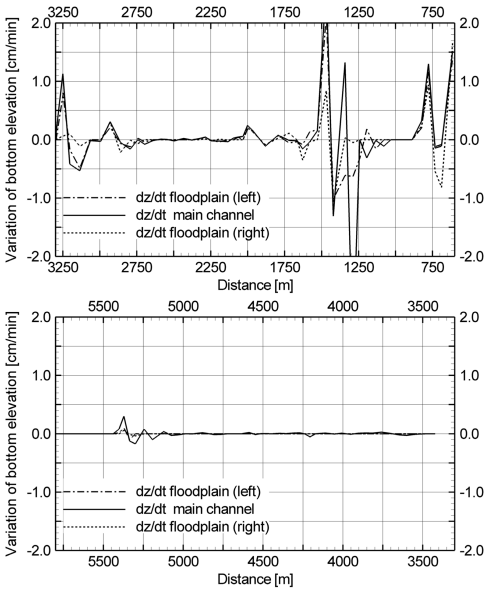


Figure 7. Variation of initial bottom elevation due HQ_{100} for section A (top) and section B (bottom).

Table 3. Sections to stabilize by widening or covering.

	Distance [m]	Left flood plain	Main channel	Right flood plain
1	5500–5100	×	×	×
2	2950–2850	×	×	×
3	2000–1875	×	×	×
4	1725–1650			×
5	1580–1525	×		
6	1525–1420	×	×	×
7	1340–1280		×	

total endangered area small, some cross sections need to be stabilized to increase τ_c.

Conventional stabilization methods (e.g. bed covering layers) as well as local widening of the riverbed geometry as an alternative are suggested operations to eliminate the risk at the identified points. For all sections with velocities higher than 0.1 [cm/min] an enhancement of vegetation is not sufficient, but is suggested as well, because it improves stability for the whole reach of the new Inde. Thus, the new part of the river still keeps its natural character, except for those sections listed in Table 3.

4 CONCLUSIONS

This paper presents the results of numerical modeling the relocation of the river Inde. The aim is to predict influences of ripples, vegetation coverage and the unfinished settlement process.

The results yield, that combining erosion safety and conservation of a natural character is a challenge. A detailed investigation of critical areas and sections endangered by depth erosion is important to estimate the risk of an uncontrolled flooding of the coalmine.

The effects of ripples and slowly growing vegetation during different flood scenarios and specific times between today and the far future were analyzed taking into account the settlement of the river-beds bottom. It is evident, that the best protection against depth erosion is a dense vegetation. Supporting the flora to grow leads to an increase of the critical shear stress and diminishes the total endangered area.

Ripples reduce mean velocities on the one hand but increase shear stresses and prevent a homogenous vegetation layer to grow on the other. The flood plains should be leveled by removing the ripples before the final relocation.

The simulations reveal, that local operations are needed to stabilize regions with initial mass transport rates above 0.1 [cm/min].

Finally, it will be interesting to compare the predicted numerical results with measurements made after the flooding in the beginning of the year 2005.

REFERENCES

Baur, T., Lukowicz, J. von & Köngeter, J. 1997. Numerical Optimization of a Riverbed-Geometry with Special Regard to Erosion. In J. Watts (ed.), *Proc. 3rd int. Conf. on River Flood Hydraulics, November 5–7*, Stellenbosch, South Africa: pp. 285–290.

Copeland, R. R. 2000. *Determination of Flow Resistance Coefficients due to Shrubs and Woody Vegetation.* USACE, ERDC/CHL HETN-II-3.

Cowan, W. 1956. Estimating hydraulic roughness coefficients. *Agricultural Engineering* 37(7): 473–475.

Kuipers, J. & Vreugdenhil, C. B. 1973. *Calculations of Two-dimensional Horizontal Flow*, Delft Hydraulics Laboratories, Report no. S163-1.

Meyer-Peter, E. & Müller, R. 1949. Eine Formel zur Berechnung des Geschiebetriebes. *Schweizerische Bauzeitung* 67(3), Zürich, Switzerland.

Rijn, L. C. van 1993: *Principles of Sediment Transports in Rivers, Estuaries and Coastal Seas*. Amsterdam: Aqua Publications: 13.

Rouvé, G. & Schröder, M. 1993. One-dimensional vs. two-dimensional prediction of compound open channel flow. *Advances in Hydro-Science and Engineering; Proc. of the ICHE-'93, June 7–11, Vol. 1* Washington DC, USA.

Tucker, G. E. & Bras, R. L. 1999. *Dynamics of Vegetation and Runoff Erosion*. Final Technical Report USACERL, Massachusetts Institute of Technology, Cambridge, MA 02139.

River Flow 2004 – Greco, Carravetta & Della Morte (eds.)
© 2004 Taylor & Francis Group, London, ISBN 90 5809 658 0

The complex flow in groyne fields: numerical modelling compared with experiments

W.S.J. Uijttewaal
Environmental Fluid Mechanics Section, Faculty of Civil Engineering and Geosciences, Delft University of Technology, Delft, The Netherlands

S.A.H. van Schijndel
WL | Delft Hydraulics, Delft, The Netherlands

ABSTRACT: Groynes are effective as river training structures. At low water levels the main stream is confined, keeping the navigation channel at a proper depth. The relatively high flow velocities at the tip of a groyne cause strong separation effects with possible consequences for the stability of the bed. At higher water levels groynes are submerged, providing more space for the river in lateral direction up to the river banks. In those circumstances groynes also act as an extra flow resistance. In order to explore possible optimization of the effectiveness of groynes at various stages the flow around different groyne types is investigated. Experiments are performed concurrently with numerical simulations. It turns out that the dynamics of the flow structures which are generated downstream of the groyne have a big influence on the circulation dynamics in the groyne field. This paper focuses on the large-scale flow structures in relation to flow separation. The large scale motion causes the instantaneous flow fields to deviate strongly from the mean flow fields emphasizing their role in the momentum and mass transfer from the main stream to the groyne fields. The importance of the large scale dynamics suggests that these should be included in order to model the flow properly. To that end horizontal large eddy simulation (HLES) is applied to the experimental cases. When compared with standard turbulence models like k-ε, HLES performs much better in predicting the overall flow pattern including separation as well as the areas of high turbulence intensities. However, the submerged cases with flow separation in the horizontal and in the vertical plane caused bigger problems to be modeled accurately. Apparently, the stronger three-dimensionality requires a more detailed analysis with a high vertical resolution. Apart from the conclusions regarding the numerical simulations of such complex flows also conclusions regarding the optimal groyne shape could be drawn. The shape of the groyne tip can be adapted such that the horizontal shear is minimized causing a weaker vortex shedding. This can be done by decreasing the slope of the groyne tip in cross-stream direction or by making the groyne permeable.

1 INTRODUCTION

The large variability in river discharge and the expected problems associated with climate changes, increases the demand for a proper regulation of the water level especially with respect to flooding at high stages and navigation in periods of drought. An effective way to fix and confine the flow in a narrow and deep part is by applying groynes. Groynes are usually constructed in the form of impermeable dikes perpendicular to the river bank. At normal discharges the flow is deflected from the erodible bank and confined by a relatively narrow cross section resulting in high flow velocities. Such an arrangement allows for the formation of a channel with the proper navigable depth even at low discharges. At high discharges the groynes are submerged and the lateral confinement is governed by the dikes which are generally located on the flood plane, sufficiently far away from the river axis. The shape and the arrangement of groynes as they are frequently found in North-Western Europe is the result of decades of what could be called evolutionary design. Given the available construction materials the design has been adapted to the predominant flow conditions United Nations (1953). With the changing climate and the changing viewpoints with respect to the environment and the increasing importance of the ecology a reconsideration of the current river environment appears appropriate. Considerations in this respect are:

- Increasing the discharge at high stages.
- Keeping the navigation channel at proper depth.
- Increasing the biodiversity.

In order to explore the possible improvements that can be made to the river, it is necessary to have the disposal of a realistic and accurate way of modeling the flow. Naturally the flow is not the only important property, but a proper insight in the flow is a prerequisite for the forecasting of e.g. sediment transport and ecological developments, Przedwojski (1995), van Mazijk (2002), Arlinghaus et al. (2002).

Unfortunately it is not always possible to perform a full scale analysis in comparing field measurements with numerical simulations. The intermediate step of a physical scale model is therefore an approved way to validate the proper representation of the physical processes as implemented in the numerical model.

For the purpose of investigating new groyne designs as well as determining the suitability of numerical simulation techniques, a number of experiments has been performed and compared with numerical simulations Uijttewaal (2004). The complexity of the flow in a groyne field provides a test case with respect to many properties. For the groyne designs used in this study the relevant properties are:

- Flow separation in the horizontal and vertical plane, at a sharp edge as well as a straight smooth wall.
- Large vortex structures and gyres.
- Flow through a permeable obstacle.
- Inhomogeneous distribution of turbulent kinetic energy and shear stresses.

A satisfactory representation of these properties will be a hard requirement for a numerical model. Once the reliability of the numerical simulation is established, it can straightforwardly be used for a number of other applications.

2 PROBLEM DESCRIPTION

Accurately modeling the complex flow in groyne fields requires a proper representation of the relevant physical processes in both the physical and the numerical model. Especially in a flow dominated by separation and vortex shedding, the turbulence and its dynamics are considered as very important.

Until now little systematic research has been performed on the effects of the groyne shape on the flow field and its dynamics. The possible advantages of a new groyne design should be known in advance in order to justify modifications to be made on the prototype scale. With the present knowledge and means it is hardly possible to make reliable predictions and to explore new groyne designs.

3 AIMS

In this study we would like to find out what modifications in the groyne design can lead to a more smooth and quiet flow field. This to provide the means to manipulate the flow and to prevent scour.

With respect to the numerical modeling it is important to know how well the present models perform. In view of new developments with respect to Horizontal Large Eddy Simulation (HLES) it is especially important to explore the possibilities of this promising technique in civil engineering applications. An important aspect in this respect is the implementation of the relevant geometrical details determining the properties of the groyne. Given the large scale applications and high Reynolds numbers encountered in practice, performing a full three dimensional LES with sufficient resolution to justify a standard sub-grid model appears unlikely for the coming decades. We therefore have to deal with numerical models with a limited resolution and some remaining degrees of freedom, like the implementation of sub-grid phenomena and boundary conditions and the grid dimension in the vertical direction.

4 APPROACH

Four different groyne designs were tested in laboratory experiments on a schematized and scaled physical model. For a few cases the observed mean flow field and turbulence properties were compared with the results obtained from a numerical model.

4.1 *Experiments*

In order to test the groynes and validate the numerical model, a number of flow conditions and geometries were implemented. These cases were also used in an earlier study on groyne optimization (Uijttewaal et al. 2002, Uijttewaal 2004).

In a physical model scaled 1:40 with respect to a prototype river reach, a schematized bathymetry was realized consisting of an array of groynes situated on a shallow part near the bank. Since the simulated river width was much larger than the range influenced by the groynes it appeared sufficient to mimic only one half of the river. A top view of the flow facility is sketched in figure 1.

Five groyne fields were built in a flume 30 m long and 5 m wide. The bed of the main channel was 8 cm lower than at the transition to the groyne fields. The level rises towards the bank to an elevation of 15 cm. With a water level of 25 cm in the main channel, the most shallow part in the groyne field was 10 cm deep and the groynes are just emerged. For the submerged cases presented here a water level of 30 cm was used, providing a 5 cm thick water layer flowing over the groyne crest. With a mean velocity of 0.35 m/s in the main channel and an estimated velocity of approximately 0.1 m/s in the groyne fields, the

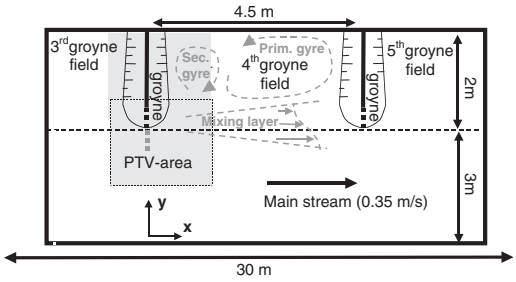


Figure 1. Sketch of the flow facility (top view) including the main flow features.

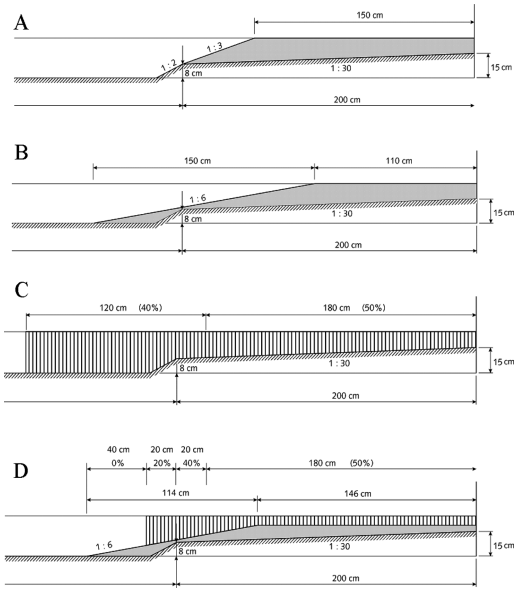


Figure 2. Cross-sectional views of the four groyne types as used in the experiments.

flow can be considered as fully turbulent everywhere in the domain.

The various types of groynes that were tested were designed with respect to minimization of the shear induced vortex formation downstream of the groyne tip. Four different groynes are depicted in figure 2. Type A is considered to be the reference case and represents the design as it is found in many rivers with a slope of the groyne tip of 1:3. With type B the slope at the groyne tip has been adjusted to make it more gentle (1:6) in order to broaden and weaken the mixing layer thereby reducing the formation of large vortex structures. Another way to achieve this is by making the groyne permeable. Type C consists of a pile sheet made of square rods with sides of 1 cm spaced such that in the near bank area the blocking fraction is 50% and 40% near the main channel. Combining the possible advantages of type B and C results in a hybrid groyne D which is partly permeable. An extensive measurement programme has been performed in order to test the design with respect to the required flow properties (Uijttewaal et al. 2002). Measurement techniques used to comprise particle tracking velocimetry (PTV) and laser Doppler anemometry (LDA). The focus is on the area around and downstream of the groyne tip, the location containing the largest shear and highest turbulence intensity. This area is indicated by gray squares in figure 1 and covers 1.5 m by 1.5 m. Floating particles of 3 mm diameter were distributed homogeneously over the domain and recorded with a 1kx1k digital camera at 30 Hz during 5 minutes. Adjacent areas were recorded in separate experiments. The small differences in camera calibration and orientation, in experimental conditions and lens distortion, impeded a seamless connection between the different areas. The observed errors are however sufficiently small to allow conclusions in the comparison with the numerical model.

4.2 *Numerical model*

Given the complexity and the dimensions of the domains that have to be dealt with when used for full-scale applications, a two-dimensional depth averaged description of the flow is the starting point. The results of the simulations should therefore be seen as a test as to what extent the efficient depth average modeling is suitable for our applications. It will be clear in advance that strongly three-dimensional features as occurring with submerged groynes are not likely to be fully covered by the model.

The numerical hydrodynamic modelling system Delft3D-FLOW approximates the non-linear shallow water equations in two or three dimensions. These equations are derived from the fully three dimensional Navier Stokes equations for incompressible free surface flow, assuming hydrostatic pressure. The contribution of 3D turbulent eddies to the vertical exchange of horizontal momentum and mass is usually modelled through a vertical eddy viscosity computed by means of a k-ε turbulence model.

Present questions in river engineering, however, require a more detailed description that resolves the dynamics of the flow, covering a range of turbulence scales, that reaches from the small scale 3D turbulence, through quasi-2D turbulence up to the largest geometry scale. A proper description of quasi-2D turbulence is especially important when dealing with flow dynamics in groyne fields. The classical approach would be to follow the concepts of unsteady Reynolds-averaged Navier-Stokes as mentioned above and accordingly design a closure for quasi-2D turbulence. Previous work however has shown the disadvantages of such

an approach (Nassiri et al. 1999, Bijvelds et al. 1999). We therefore prefer to simulate the quasi-2D turbulence and still model the 3D turbulence with the well known closures. To this end we have applied the depth-averaged option of Delft3D-FLOW in combination with horizontal large eddy simulation, further referred to as HLES. This concept will be used to describe the important dynamical variations of the flow which are necessary to obtain a better understanding of complex processes such as erosion and sedimentation in a groyne field and around a groyne tip.

A particular type of turbulence closure is required for representing the action of the unresolved part of quasi-2D turbulence. The latter turbulence closure is called subgrid-scale (SGS) model as it depends on low-pass filtering of the spatially varying flow field by the choice of the mesh size. The sub-grid scale model as applied in this study has been described extensively in Uittenbogaard & vanVossen (2003). In brief the SGS eddy viscosity accounts for the direct energy loss by bed friction. Rather than spatial filtering, a simple temporal recursive high-pass filter is applied on the resolved velocity field. This filter removes the slow or steady large-scale contributions to the strain rates that enter the sub-grid model. It has been successfully tested in shallow and stratified flows.

To be able to compare the measurements in the physical model directly with the simulations, the numerical model was applied to the same geometry. The mesh size Δx of the model sets limits to the scales that can be resolved, typically of the order of $6\Delta x$. The important energy containing horizontal eddies should typically be larger than this size. Further restrictions are imposed by the geometry of the groynes that can be represented and the details of the flow pattern around them. It is important in this respect to avoid influences of the grid implementation on the separation of the flow at the head of the groyne. An advantage of the geometries as used here is that flow separation occurs at the relatively sharp groyne tip. Because of the combination of a straight flume with groynes perpendicular to the flow a curvilinear grid does not have an added value. A choice is made for a very fine rectangular grid with a typical mesh size of 5–10 cm, being of the order of the water depth, and yielding about 68,000 active horizontal grid points. In the depth averaged case we have obviously used only one layer.

At the upstream boundary we defined a Riemann boundary with the velocity of the main channel (0.35 m/s) and the downstream boundary condition is formed by a constant water level corresponding to the water level in the scale model. The roughness of the main channel and the groynes is characterised by a Nikuradse roughness $k_{nikuradse} = 0.6$ mm, and is based on measurements in the main channel in the scale model. Friction caused by the side walls in the groyne field was accounted for.

Because of the fine grid it was possible to include the shape of the groynes of type A and B in the bathymetry. In the emerged situation we placed so-called 'thin dams' at the crest to prevent numerical disturbances caused by overtopping of the groynes. To be able to simulate the dynamics in the case of permeable groynes of type C and D we prefer to model them as dry points in the numerical grid, but this is only possible if the groynes are not submerged. In case of submerged permeable groynes an additional roughness value needs to be defined to account for the effect of the groynes.

5 RESULTS

In this section the velocities as measured at the free-surface with the PTV-method are compared with the depth-averaged results of the numerical simulations. Although the flows can be considered as shallow different results are expected due to this method of comparison. It will however be clear that the gross features of the flow should be similar.

As a starting point the standard groyne, type A, is considered in non-submerged conditions. For that case the groyne field can be considered as a shallow cavity where the flow separates at the upstream groyne tip as sketched in figure 1. The mixing layer that develops between the main stream and the groyne field plays a role in the momentum transfer to the groyne field circulation. For the chosen width to length ratio of the groyne field a circulation pattern is expected consisting of two counter-rotating gyres which causes a second separation point along the straight side wall. These characteristics are well reflected in the results shown in figure 3, which shows the magnitude of the flow velocities in an area that ranges in streamwise direction from 0.5 m upstream of the groyne to 4 m downstream and in y direction from the bank ($y = 5$ m) into the main stream. In the lower part of the graph the main stream direction is from left to right as indicated by the arrow. The agreement between the numerical and experimental data is good. The same holds for the characteristic enhanced turbulence intensity as found in the mixing layer downstream of the separation point and around the stagnation point at the upstream side of the groyne. In the numerical simulation the mixing layer turbulence is more pronounced while the fluctuations in the upstream part of the groyne are underestimated. Despite this mismatch, the large scale motion appears sufficiently two-dimensional to be represented by a depth averaged model.

As soon as three-dimensional effects start to play a significant role the discrepancies between the experiments and the depth averaged model increase. For groyne B the wake of the submerged groyne tip (with

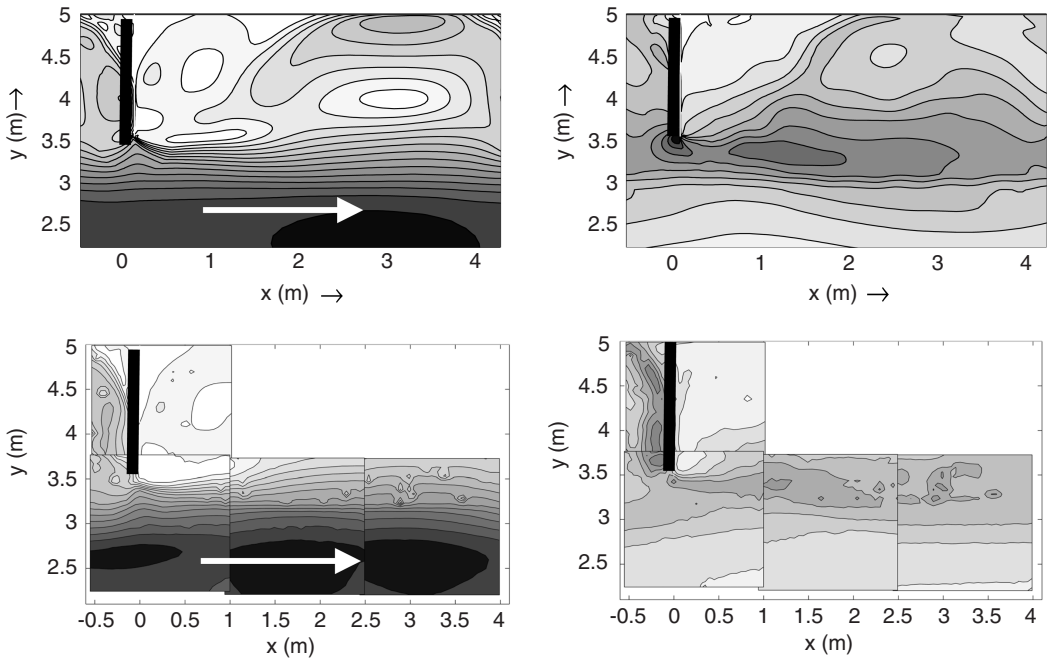


Figure 3. Magnitude (left column) and standard deviation (right column) of time-averaged flow velocity in fourth groyne field of type A in emerged situation, magnitude ranging from 0 m/s (white) to 0.35 m/s (black) in intervals of 0.025 m/s and standard deviation ranging from 0 m/s (white) to 0.1 m/s (black) in intervals of 0.01 m/s. Numerical simulations (upper row) experiments (lower row). Thick line indicates groyne crest.

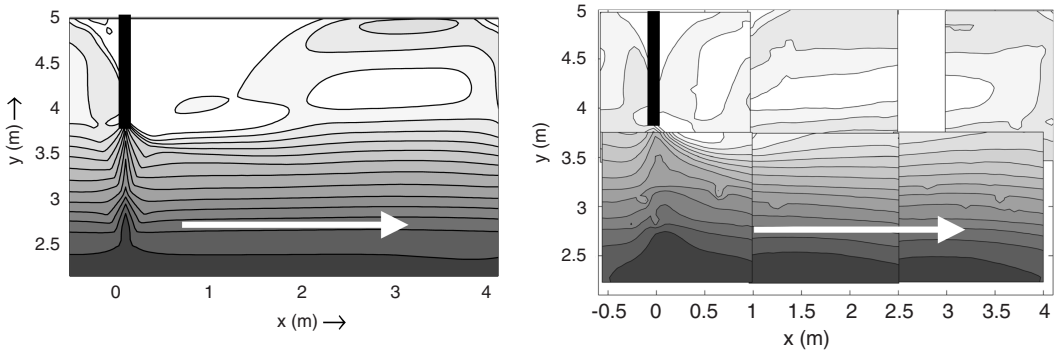


Figure 4. Magnitude of time-averaged flow velocity groyne B in emerged situation, magnitude ranging from 0 m/s (white) to 0.35 m/s (black), a comparison between numerical simulations (left) and experiments (right).

slope 1:6) typically contains strong vertical velocity components. In both the mean flow pattern and the turbulence intensities clear differences are found. Comparing figure 4-left with 4-right, the flow pattern around $x = 0$ m is symmetric. The flow over the groyne tip is asymmetrical in the experiment because of the flow separation in the vertical plane. The separation downstream of the groyne tip gives also rise to an enhanced production of turbulent kinetic energy in this area which can obviously not be reproduced by the numerical model (not shown).

Similar effects are found with the submerged case of groyne A, figure 5. The flow over the groyne crest gives rise to separation in the vertical plane with clear consequences for the effective resistance of the obstacle. Important differences between the experiment and the

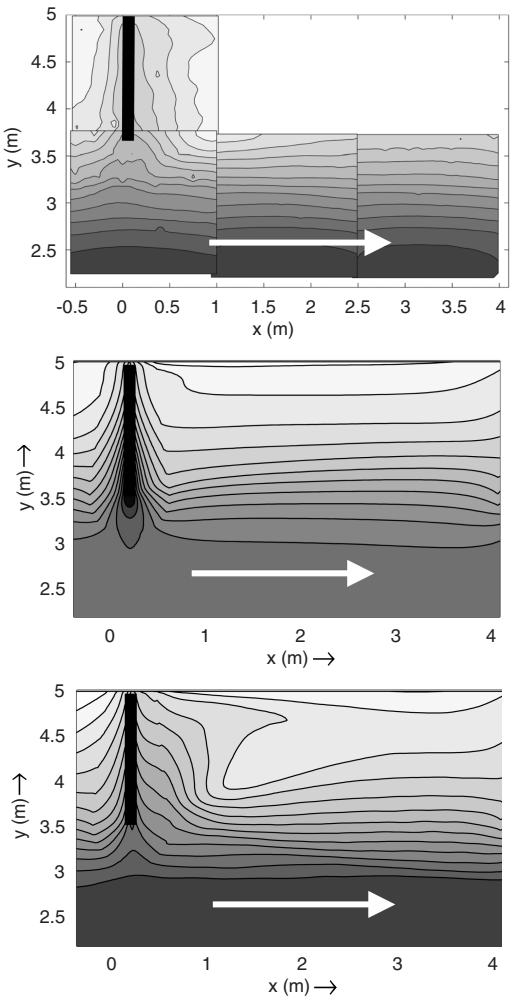


Figure 5. Magnitude to time-averaged flow velocity for the sumberged groyne A. A comparison between experimental data (top) a depth-averaged numerical approach (bottom-left) and a 3D-approach with 20 layers (right).

simulations are therefore found in the mean velocities over the groyne which are generally overestimated by the numerical model (see figure 5-top and 5-bottom-left), in the asymmetry in the flow pattern upstream and downstream of the groyne and in the production of turbulent kinetic energy which is clearly underestimated. A clear improvement is obtained with a 3D-approach of 20 layers (figure 5-right). The asymmetry in the flow over the groyne is clearly reproduced and the maximum velocity is significantly reduced. Such computation are rather expensive and not feasible for general applications. An even more realistic solution is expected from the use of a non-hydrostatic model.

Further complications appear when the groyne is made permeable as in the cases of types C and D. The amount of water that flows through the groyne field is determined by the effective resistance of the pile sheet. It is however far from trivial to implement the effective properties in a realistic manner, since the resolution does not allow the simulation of all flow details around the piles.

A few tests have been made on the configuration of the partially permeable groyne D, for which the experimental results are depicted in figure 7-left. The gradual increase of the area blocked by the groyne going from the channel towards the bank, combined with the permeable part on top gives also rise to a smooth velocity profile. The mixing layer extends over more than 1 m, resulting in a horizontal velocity gradient half of that with groyne A. Still the velocity near the bank ($y > 3.5$ m) is small with a small recirculation zone in the downstream part of the groyne field. The obstruction by impermeable part and the turbulence production by the flow through the groyne give rise to these low velocities, in combination with a relatively high turbulence level downstream of the groyne. The simplest implementation of this flow impediment, is an additional surface roughness on top of the non-permeable part of the groyne. In figure 6-left it is clearly seen that this leads to an unrealistic solution. The roughness hardly affects the flow and the major effects are caused by the bathymetry around the impermeable base of groyne D. The alternative implementation of the permeable part of the groyne in the form of dry points is an improvement but there still is a significant discrepancy with the experiments. Blocking the flow through the groyne has a clear effect on the flow through the groyne field and the formation of a mixing layer at the interface with the main stream. A combination of both the increased roughness and the dry points leads to a more satisfactory solution, figure 7-right. Clearly the resistance of the groyne and the disturbances generated by the piles are both necessary ingredients that govern the flow field. The comparisons with the experiments of figure 7-left show that not only the pattern of the mean velocity is similar in shape and amplitude, but also the distribution of the turbulence intensities. The most important difference is found just downstream of the grid. The extra turbulence produced by the flow through the goynes is not well represented by the model, partly due to insufficient resolution.

6 CONCLUSION

This study shows that the different groyne designs used, give rise to a variety of flow phenomena where flow separation and turbulence production are important. The lateral transport of momentum from the

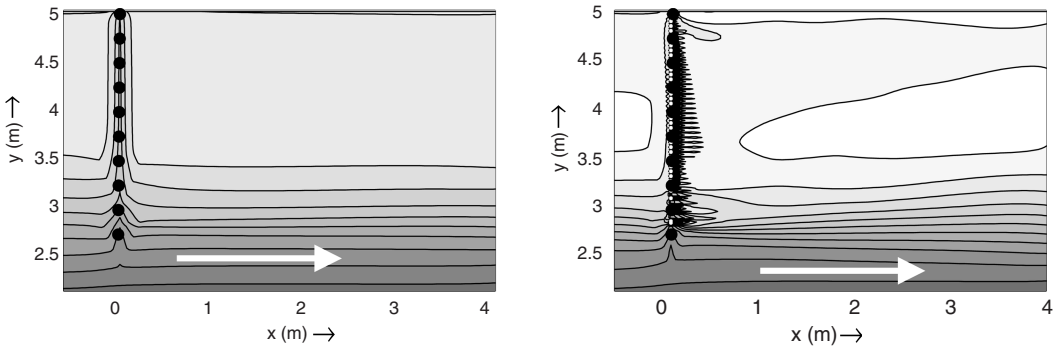


Figure 6. Mean velocity magnitude for hybrid groyne D emerged. Results for hybrid groyne defined as additional roughness in the left graph and results for hybrid groyne defined as dry points in the right graph.

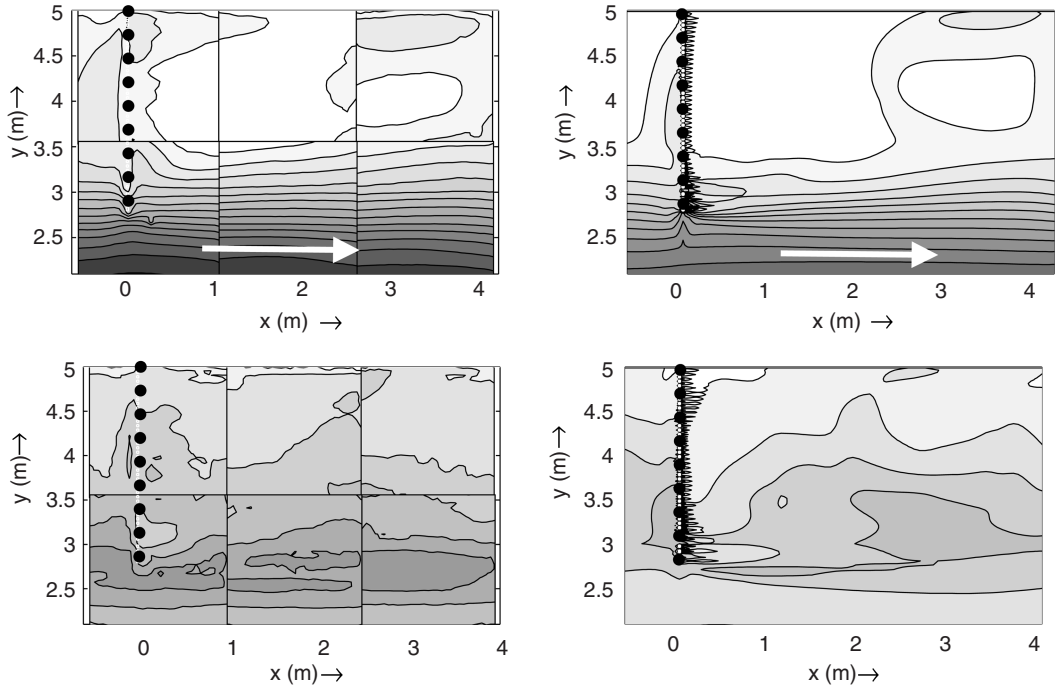


Figure 7. Mean velocity magnitude for hybrid groyne D emerged (upper row) and standard deviation (lower row). Scale model results in left column and computations in right column, where the hybrid groyne is represented as dry points with additional roughness between piles.

main stream drives a circulation in the groyne field. The horizontal velocity gradient in this area gives rise to the enhanced production of turbulent kinetic energy. The strength of the velocity gradient depends on the velocity inside the groyne field and the shape of the groyne tip. By adapting the shape of the groyne, the turbulence properties in the mixing layer can be manipulated. Making the groyne permeable suppresses the recirculation and weakens the shear in the mixing layer. At high water stages the flow over the submerged groynes separates downstream of the groyne crest resulting in an increased flow resistance and small velocities in the groyne field. Knowledge with respect to the relationship between the geometrical properties of the groyne and the hydrodynamical consequences provides us with clues for e.g. optimising the conditions for a certain envisaged habitat for biological species; high versus low exchange rates

with the main stream, high versus low velocities and turbulence intensities etc. The different turbulence production mechanisms associated with the horizontal and vertical flow separation as well as the wall and bottom boundary makes a numerical simulation of such flows troublesome. It is clear that we have tested the numerical model against a number of cases, which are known beforehand to cause difficulties. Especially the submerged case containing typical three-dimensional effects is not very likely to be properly represented by a depth averaged model. Also the permeable and hybrid groynes are problematic when the resolution does not allow for resolving the flow in the wake of the rods and in between the rods. Nevertheless, the important phenomena of the complex flow in groyne fields could be reasonably well simulated after sufficient adaptation of the simulation configuration and boundary conditions. Obviously, it is preferred to have a model that does not need tuning of certain boundary conditions or an unrealistic implementation of an obstacle in the form of roughness elements.

This study has however helped us in finding the important aspects that have to be taken into account when modelling complex flows as found in groyne fields. It is expected that with this knowledge further improvements to our modelling approach can be made, leading to a simulation tool that is of help for a detailed optimisation of the hydrodynamics in groyne fields and its consequences for morphology and ecology. Important properties in this respect are: exchange between main stream an groyne field, velocity magnitude, turbulence intensities, local bed shear stresses, etc.

ACKNOWLEDGEMENTS

The Road and Hydraulic Engineering Division of the Ministry of Transport, Public Works and Water Management is gratefully acknowledged for supporting this research financially. The authors are indebted to M. Berg for her contribution to the experimental work.

REFERENCES

Arlinghaus, R., Engelhardt, C., Sukhodolov, A. & Wolter, C. 2002. Fish recruitment in a canal with intensive navigation: implications for ecosystem management. *J. Fish Biology* 61, pp. 1386–1402.

Bijvelds, M.D.J.P., Kranenburg, C. & Stelling, G.S. 1999. 3D numerical simulation of turbulent shallow-water flow in square harbor. *J. Hydr. Eng.*, 125(1), pp. 26–31.

Mazijk, A. van, 2002. Modelling the effects of groyne fields on the transport of dissolved matter within the Rhine Alarm Model. *J. of Hydrology* 264, pp. 213–229.

Nassiri, M., Babarutsi, S. & Chu, V.H. 1999. Wall Boundary Conditions on Recirculating Flows Dominated by Bottom Friction. *Proceedings XXVIII.* Proceedings XXVIII, IAHR congress, Graz, Austria. 1–6.

Przedwojski, B. 1995. Bed topography and local scour in rivers with banks protected by groynes. *J. Hydr. Res.* 33(2), pp. 257–273.

Uijttewaal, W.S.J., Berg, M.H. & van der Wal, M. 2002. Experiments on physical scale models for submerged and non-submerged groynes of various types. Int. Conf on fluvial Hydraulics, Louvain-la-Neuve, Belgium. pp. 377–383.

Uijttewaal, W.S.J. 2004. Large scale dynamics in groyne field flows: laboratory experiments. *submitted.*

Uittenbogaard, R.E. & Vossen, B. van 2001. 2D DNS of quasi-2D turbulence in shallow water, *DNS/LES Progress and Challenges. Third AFOSR International Conference, Arlington, Texas* (Greyden Press, Columbus, Ohio, USA), pp. 577–588.

Uittenbogaard, R.E. & Vossen, B. van 2003. Subgrid-scale model for Quasi-2D turbulence in shallow water. *Proc. Int. Symposium on Shallow Flows*, Balkema (to appear).

United Nations 1953. Economic commission for Asia and the far east “River training and bank protection”, *Flood control series* 4, Bangkok.

River Flow 2004 – Greco, Carravetta & Della Morte (eds.)
© 2004 Taylor & Francis Group, London, ISBN 90 5809 658 0

Groyne optimisation and river hydrodynamics

G.J. Akkerman & M.A. van Heereveld
Royal Haskoning Consultants, Architects and Engineers, Nijmegen, Netherlands

M. van der Wal & J.M.T. Stam
Ministry of Transport, Public Works and Water Management, Directorate-General of Public Works and Water Management, Road and Hydraulic Engineering Institute, Delft, Netherlands

ABSTRACT: Groynes are widely used in the Netherlands, mainly to promote or maintain nautical depth and a stable main channel. Most of them have been designed and constructed more than a century ago. Since then damage to the groyne head, settlement of the crest or outflanking of some groynes has occurred. A mathematical model study, with a 1-dimensional morphodynamic model, has been carried out to examine the average sedimentation that may be caused by damaged groynes. Based on the work presented in this paper, our understanding of the rate of sedimentation, the effects on the flood water levels and the effects of groyne repair has increased. A challenging outcome is that, although repair should be carried out for river stretches where nautical depth is critical, in other stretches we may consider delaying repair to reduce flood levels. The paper ends with suggestions for further research.

1 BACKGROUND

During the last 150 years, approximately 3600 groynes have been constructed in the main Dutch rivers and channels. Groynes in Dutch rivers have four functions:

- reducing the risk on the formation of ice dams;
- maintaining nautical depth for inland navigation;
- riverbed fixation;
- bank protection and land reclamation between groynes.

The present design method of groynes is mainly done using 'rules of thumb', some of them dating from the 19th century and mainly based on trial and error. Up to now groynes have fulfilled their functions fairly well. However in recent years, extreme river floods have raised the priority for flood protection measures including optimisation of groynes. These extreme floods caused us to regard groynes as obstructions which increase the extreme flood levels. Long term trends such as climate change, increase in size and engine power of inland navigation, as well as the increasing need for maintenance efficiency, compel us to reassess groyne design and groyne maintenance.

2 RESEARCH OBJECTIVES

In this research we seek to develop practical rules for the optimisation of groyne design and groyne maintenance. The most important function groynes have at present is to maintain nautical depth in the fairway. Therefore any changes in groynes might have effect on sedimentation, and as a consequence may bring about costly dredging. A second important aspect is that flood waves should pass the river smoothly with a minimum of resistance so as to avoid flooding. This means that the flow channel should preferably have as few obstacles as possible. Obviously these are two conflicting aspects. From the point of view of flood management, there is a tendency to lower existing groynes. However, this leads to sedimentation of the navigation channel which is undesirable from nautical point of view.

By experimenting with different groyne designs we seek to provide the best design for these two main functions. Another approach is to focus on groyne maintenance. Groynes may sometimes have deteriorated in height, the groyne head may have steepened or the attachment of the groyne with the floodplain may be lost (outflanking by which a bypass channel may develop). An example of the ouflanking is shown in Photograph 1.

The attendant reduction of flow obstruction is favourable for flood wave passage. However, as a secondary effect the reduced obstruction will cause sedimentation of the main channel, which in turn affects the nautical depth. The question rises which of the two effects is most dominant. The present paper

will address this question and will deal with the prediction of the potential sedimentation for the damage types mentioned before.

3 RESEARCH METHOD

3.1 *Typical sedimentation and erosion pattern*

The bed pattern near groynes is strongly 3-dimensional, as illustrated in Figure 1 in which multibeam measurements are depicted for a characteristic section of the Waal river in the Netherlands. The complex bed pattern is due to the complicated flow pattern near the groynes and in between the groyne fields.

A precise method for prediction of these patterns of erosion and sedimentation is not available up to now. However, damaged groynes will cause an overall sedimentation in the main channel in between the groynes on both sides of the fairway. With a 1-dimensional morphodynamic model such an overall sedimentation can be computed rather well. In such a model the sedimentation width can be specified, as well as the pattern of sedimentation, i.e. evenly distributed over the width or linearly with the depth, the latter being the default situation.



Photograph 1. Outflanked groyne in the Waal river.

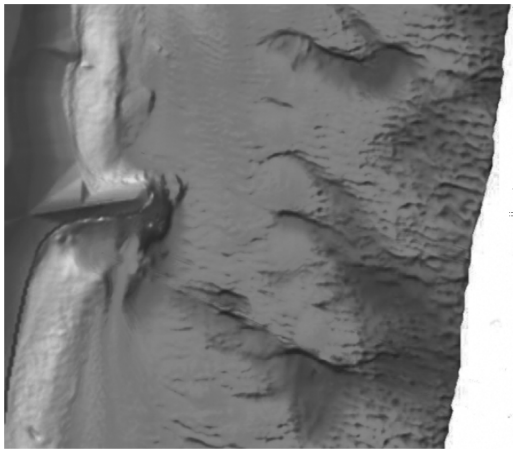


Figure 1. Multibeam measurements of bathymetry near groynes.

3.2 *Mathematical model*

A 1-dimensional morphodynamic model, based on the SOBEK program package, was used in the present study. To this, a 90 km stretch of the Waal river was schematised, taking one characteristic cross-section, including a main channel section, a groyne section and a floodplain section, see Figure 2.

The hydraulic performance of the model was calibrated and validated against measurements at different flow rates. A morphologic validation was beyond the scope of the present investigation. Rather, tests have been performed to check the effect of grid spacing, the required time to arrive at a morphological stable bed, the influence of the time-step and the influence of numerical parameters. The sediment influx to give a stable bed condition in the reference situation (with no damaged groynes) was determined by trial and error. The sediment influx was set at values of 0.021 m^3/s and 0.0312 m^3/s for Q_{50} (50% exceedence discharge = 1467 m^3/s) and Q_{90} (10% exceedence discharge = 2400 m^3/s) respectively. These were the two steady-state discharges with which the model was operated. Furthermore a schematised flood wave was applied, starting with a steady-state flow rate of 2000 m^3/s (corresponding to Q_{60}) and a subsequent flood wave with a peak discharge of 3000 m^3/s (corresponding to Q_{95}); after the flood wave the Q_{60} was maintained for 10 years.

3.3 *Damage situations applied to the model*

In this model three types of groyne damage have been modelled with two damage intensities:

– groyne head steepening: the standard slope is 1:3.5 (vertical to horizontal). Damaged slopes were 1:2 and 1:1;

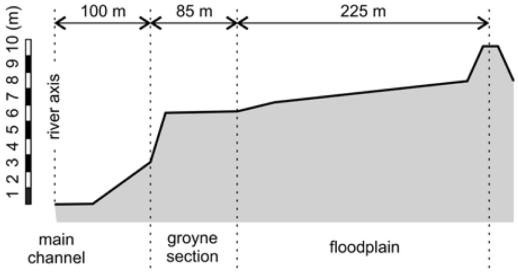


Figure 2. Characteristic cross-section (vertical scale strongly exaggerated).

– groyne height decrease: a decrease of 0.1 m and of 0.2 m was applied;
– groyne outflanking: a shortening of the groyne of some 15 m and 30 m has been applied.

Each damage pattern was introduced in the model as a corresponding increase in flow area of the main channel at the cost of the flow blocking area of the groyne section.

The simulations have been done with one, four and eight successively damaged groynes. It was assumed that the groynes opposite the main channel were damaged as well in the same manner. In total 48 model runs have been made, combining the aforementioned flow rates, types of damage and number of groynes. In each of these cases groyne damage resulted in sedimentation in the cross-sections with the damaged groynes. Just downstream of it, a scour hole develops which gradually extends downstream in time.

Another effect of groyne damage is the water level reduction near the damaged groynes. This reduction extends upstream as a backwater curve. This effect is favourable for extreme flood levels. However, as a secondary effect sedimentation will occur which will decrease river depth and will negatively affect flood level reduction. Simulations are required to indicate the net effect.

3.4 *Repaired damage*

Once damaged groynes are being repaired, related sedimentation migrates as a shoal downstream. At downstream locations the temporary sedimentation will be accompanied by a slight increase in water level. For the repaired groynes, the water levels will increase substantially and will attain the original equilibrium levels.

4 RESULTS

4.1 *Sedimentation rates*

The simulations yielded equilibrium sedimentation rates as shown in Table 1.

These results have been obtained for a permanent discharge of Q_{90} and are independent of the number of subsequently affected groynes. The sedimentation area, obviously, is directly related to the damaged groyne fields and extends from the downstream affected groyne to the upstream one.

Table 1. Review of equilibrium sedimentation rates.

Damage type	Intensity	Sedimentation ($m \times 10^{-2}$)
Head slope steeepening	1:2	6
	1:1	10
Crest height	−0.1 m	4
	−0.2 m	7
Outflanking	≈15 m	14
	≈30 m	27

The results show that for the damage types under consideration considerable sedimentation may occur. Especially outflanking causes serious sedimentation, but the consequences of the other damage types cannot be ignored either. In case of an unfavourable combination of damages and discharges, sedimentation might reach up to about 0.5 m.

It should be remarked that the flow rate influences the sedimentation. The equilibrium sedimentation for Q_{90} is 2 to 4 times as large as for Q_{50}. Sedimentation for the schematized flood wave was in between the results for the permanent Q_{90} and Q_{50} discharges. We consider the outcome for the Q_{90} discharge as most realistic, albeit possibly somewhat conservative.

Further analysis showed that the sedimentation rates can be expressed very well in terms of an increase in cross-sectional flow profile. The computed sedimentation show a nearly linear increase with the increase in flow profile (see Figure 3). In Figure 3 the dependency on the flow rate is also clearly visible. It should be remarked that groyne height reduction is not relevant for the Q_{50} flow condition, as the water level does not exceed the crest of the groynes in that situation. The results show that for damage intensities other than have been considered here, a good prediction can be made based on linear interpolation.

4.2 *Development of sedimentation*

The development of the sedimentation pattern, upon the occurrence of damage, is important as it may take a considerable time to reach equilibrium. The simulations, basically carried out for steady-state conditions (with Q_{50} and Q_{90}) give no definite answer to this. Reaching equilibrium for the Q_{90} discharge took less

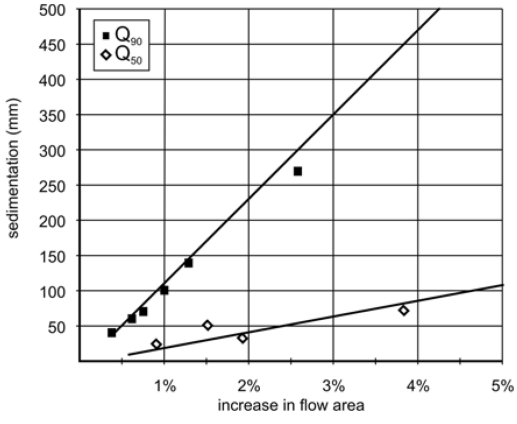


Figure 3. Sedimentation against flow area increase.

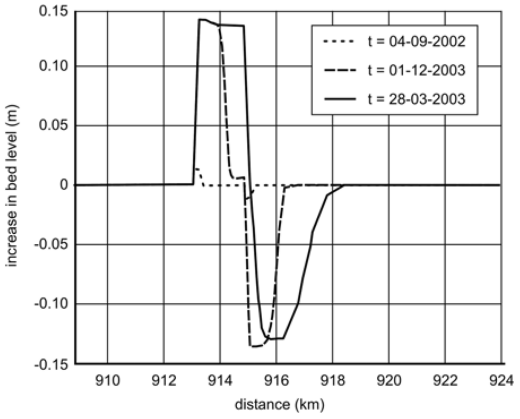


Figure 4. Illustrative example of sedimentation development.

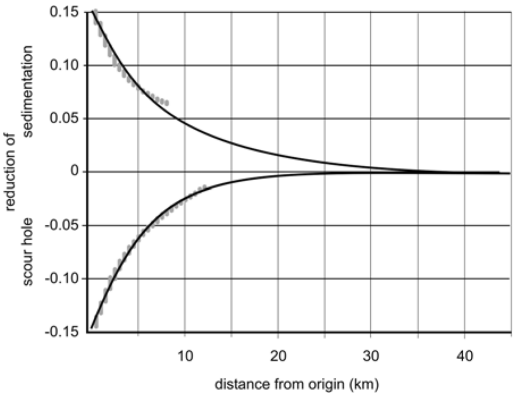


Figure 5. Typical decrease of sedimentation and scouring during downstream migration, after groyne repair.

than 1.3 years in the model. Taking into account the relatively high discharge of Q_{90}, the true time for reaching equilibrium in the Waal river will be in the order of magnitude of maximum 10 years. Consequently, sedimentation is likely to occur within a relatively short time. An illustration of the timely development of the sedimentation and the temporary scour hole downstream is shown in Figure 4.

4.3 *Sediment migration after repair*

The sand wave that migrates downstream after repair of the groyne(s) has been simulated in the model for the permanent Q_{90} discharge. Together with the migration of the sand wave, the scour hole migrates farther downstream, starting from the downstream end of the damaged groyne field. The travel time of the sediment wave was found to be about 3.5 years over a distance of 5 km. Measurements of sand wave propagation in the Waal river show travel speeds which are in the same order of magnitude.

Both types of waves show a clear decrease of intensity during downstream migration, as can be seen in Figure 5. After migration over 5 km, the height of the sand wave reduces to half the original value.

4.4 *Consequences for flood levels*

The increased flow area after groyne damage, as well as the incidental sedimentation pattern, affects the flood levels.

Groyne damage results in an increase of flow area which causes the flood level to decrease. The sedimentation however, increases the flood levels. This effect is however smaller than the flood level decrease. The implications on the flood levels have been checked for the most serious damage, i.e. for the case of outflanking by some 30 m. In the equilibrium situation the net effect on the flood levels is some −5 mm for the arrangement with 4 damaged groynes. This flood level reduction tends to increase for a larger number of damaged groynes. For the Waal river this reduction is of significance, as regards the costs involved to arrive at such a reduction by measures in the floodplain.

5 CONCLUSIONS

The sensitivity analysis with a 1-dimensional morphodynamic model yielded practical results as regards the effects on sedimentation and flood water levels after the occurrence of groyne damage. Three types of groyne damage have been considered: steepening of the groyne head, reduction of groyne height and outflanking of the groyne.

Major conclusions are summarized as follows.

1. Groyne damage results in significant local sedimentation and lower flood water levels. The sedimentation ranges from some centimeters to some decimeters, depending on the type of damage. Hence, a combination of damages may potentially cause up to 0.5 m sedimentation as an average in the stretch with damaged groynes.
2. The sedimentation may require additional dredging to maintain nautical depth.
3. After repair, the sediment that accumulated during the period that the damage exists, migrates downstream as a shoal over some 10 tot 20 km and gradually reduces in height.
4. The flood level reduction may increase to about 1 centimeter for an arrangement of more than 4 groynes (in the case of major outflanking). For less intensive damage it may be in the order of magnitude of millimeters.
5. The findings lead to a challenging concept for groyne maintenance: take action for repair at river

stretches where the nautical depth is critical and consider delay of repair at the remaining river stretches. The objective of the latter is to reduce flood levels. This can be a realistic option when the damage is not progressive, as can be expected for head slope damage and groyne settlement with the protective layers still intact.

6. The dependency of sedimentation and flow rate stresses the need to apply realistic discharge scenarios to the model for proper predictions to be used in a strategy for optimized maintenance of groynes.

6 FUTURE WORK

Study on groyne design for the Dutch rivers will continue. The following studies are foreseen:

- A case study on a characteristic groyne damage event in the Waal river, to analyse the effects of the maintenance strategy applied in the past and to verify the bed level changes with the predictions from the present model. When positive, this case can be extended to a major part of the Waal river and a longer maintenance period.
- Verification of the present 1-dimensional morphodynamic model with a 2-dimensional (depth-averaged) morphodynamic model.
- Identification of potential hazardous sedimentation events, i.e. by combining unfavourable flow events and accumulated groyne damage.
- Development of an optimised maintenance strategy for the Waal river based on actual groyne conditions and realistic discharge scenarios. Herein also the effect of vegetation growth on the groynes has to be considered, as well as the present maintenance strategy of cutting willow trees at the groynes after some 5 years. At river stretches with critical navigation depths, the repair costs of the groynes can be balanced against the costs of maintenance dredging. Alternatively, the latter may possibly be skipped at the cost of reduced ship freight.
- Implementation of field tests of innovative concepts of groynes, e.g. with an adjustable crest, in a pilot stretch of the Waal river.
- Extension of the above for other major rivers in the Netherlands.

This page intentionally left blank

C.2. Habitat management and maintenance flows

This page intentionally left blank

River Flow 2004 – Greco, Carravetta & Della Morte (eds.)
© 2004 Taylor & Francis Group, London, ISBN 90 5809 658 0

The environmental impact of dams and weirs: technical issues related to the minimum vital flow release

C. Comoglio
Dipartimento di Georisorse e Territorio, Politecnico di Torino, Torino, Italy

ABSTRACT: The awareness about impacts on fluvial ecosystems caused by dams and weirs has recently increased in the Italian regulatory framework and the release of the minimum vital flow is now going to be introduced as compulsory for all the new projects and existing sites.

In this paper are identified and discussed the main technical issues that this new legal requirement will determine (technical adjustments in old structures, discharges monitoring and modulated release, flow availability in downstream reaches, release through fish passes, environmental monitoring programme, etc.) and that should be managed through appropriate institutional guidelines and adequately analysed and solved for each site in order to effectively pursue the quantitative and qualitative safeguard of water resources.

1 INTRODUCTION

The use of river water for electricity production, irrigation and other purposes can influence the rivers hydrological balance and cause significant environmental impacts involving directly and indirectly many components of the fluvial ecosystems. Generally the more relevant impacts take place in the downstream reaches because of the alterations of the river hydraulics due to the withdrawal of significant discharges. In particular the reduction (or in many cases the absence) of the discharge in the downstream river sections and, consequently, the alteration of the hydraulic parameters (water level, stream velocity, flow area and wetted perimeter), can alter the water quality and cause significant impacts upon the river biocoenoses.

The release of a limited water discharge from dams and weirs in the downstream river reaches, the so-called minimum vital flow (or instream flow or environmental flow) is the main and essential mitigation measure that can be adopted in order to reduce the environmental impacts and safeguard the involved ecosystems.

The concept of minimum vital flow (*MVF*) appeared for the first time in the Italian regulatory framework in 1989 with the article 3 of the National Law 183/1989: it stated that a rational use of water resources at watershed level must guarantee a minimum constant vital flow in downstream reaches despite the existing system of water abstraction.

Afterwards, the article 5 of the Decree 275/1993 stated that the release of the minimum constant vital flow must be considered in the water abstraction licences, taking into account the requirements of river water quality and seasonal balance safeguard and the opportunities of saving, reusing and recycling this natural resource.

The Law 36/1994 introduced new elements which developed the definition of the concept of *MVF* towards ecological criteria: sites with significant withdrawals must be regulated in order to guarantee the flow required for the life in the downstream reaches and to safeguard the involved ecosystems balance.

This regulatory scenario and the absence of explicit criteria for the minimum vital flow calculation led different authorities (mainly the Regions of Northern Italy) to the definition of own local technical rules aimed at quantifying the discharge to be released downstream the abstraction sites, mainly based on hydrological criteria. An interesting definition of the minimum vital flow was given by Regione Piemonte in 1995: it is the flow which, inside a watercourse, has to be released in order to keep vital at any time the efficiency and quality conditions of the concerned ecosystems. The new legal requirement became compulsory for new projects and on the occasion of the renewal of the water abstraction licence of existing sites.

Afterwards, in 1999, two regulations introduced new elements for a uniform and systematic application of this release requirement, realigning the wide variety of local initiatives. With the article 12 of the Decree 79/1999 the release of the minimum constant vital flow in downstream reaches for new water abstraction sites (only for hydroelectric use with a mean annual

nominal power higher than 3.000 kW) became compulsory and a necessary element to be specified in the water abstraction licences.

The Decree 152/1999 introduced a new approach in the water resources safeguard, previously associated only to pollution problems, stating that the qualitative and quantitative aspects must be managed in an integrated way at hydrographic basin level, fixing specific targets of environmental quality for each significant watercourse. The minimum vital flow must be a fundamental element of the future Plans of watershed safeguard and must be taken into account while defining the measures aimed at ensuring the water balance of each basin. Furthermore all the existing sites must be regulated in order to release a discharge calculated using national guidelines.

While the above mentioned guidelines have not been yet defined (making formally inapplicable the legal requirement) and the local technical rules are still in force, recent initiatives are being developed by the Watershed Authorities (institutions composed of State and Regions to manage the watersheds of national importance). In particular the River Po Watershed Authority (widest italian hydrographical basin with a surface of 71.057 km^2) defined, with the Decision 7/2002, new criteria that will have to be applied to the whole territory. The minimum vital flow is made up of an hydrological component and an environmental component:

$$MVF = MVF_{hyd} \cdot MVF_{env} = k \cdot q_{MEDA} \cdot S \cdot MVF_{env} \quad (1)$$

where $k =$ experimental hydrological parameter defined for each watershed; $q_{MEDA} =$ average annual specific natural discharge [$l/s \cdot km^2$]; and $S =$ basin surface [km^2]. The criteria for the calculation of the environmental component MVF_{env} and its range of application shall be defined by each Region inside every Plan of watershed safeguard taking into account the watercourse morphology, the interaction with groundwater, the anthropic pressures upon water quality, the presence of naturalistic, touristic or social interests. All the new projects shall comply with the previous release requirements, while for the existing sites two relevant deadlines have been fixed: all sites must respect the release of the hydrological component by the end of year 2008 and the release of the environmental component, where defined, by the end of 2016.

While the regulatory framework is developing towards the gradual application of the minimum vital flow release to the whole territory, the number of existing dams and weirs currently subject to this requirement is still not relevant: in Regione Piemonte, which has been one of the first local authorities to face the problem and to define specific rules, less than 13% of the total number of existing sites is releasing a compulsory flow.

2 TECHNICAL ISSUES RELATED TO THE MINIMUM VITAL FLOW RELEASE

Especially in the environmental field the attempt to fix univocal criteria and rules often conflicts to the wide variety of different situations and problems which can occurr in reality. This remark applies also to the definition of the criteria for the minimum vital flow calculation, where, even despite accurate hydrological and environmental models, the real availability of natural discharges and the sensitivity of the involved fluvial ecosystems can significantly vary along the same watercourse. Therefore, the hydrological and environmental criteria for the *MVF* calculation should be adequately adapted and calibrated on every site. In this way, through a detailed analysis of the natural peculiarities of the site and the definition of an adequate monitoring system, the value obtained applying the criteria fixed by law can be assessed in terms of efficiency in guaranteeing and safeguarding the fluvial ecosystems. Despite its usefulness in terms of environmental safeguard, this approach is costly and would be unlikely accepted by the owners of the sites unless imposed by law, especially considering that it can lead to an increase of the discharges that should be released and, consequently, to a further reduction of productivity and proceeds.

A preliminary analysis of the environmental scenario and an assessment of the environmental impacts of a dam or a weir is required as compulsory only during the authorization phase for new projects, according to national and regional laws concerning the environmental impact assessment (EIA) procedures, and, in some cases, for the renewal of expired concessions. The environmental impact study (EIS) targets are the evaluation of the most probable environmental impacts caused by the project and the definition of appropriate mitigation measures and monitoring systems to be implemented after the site construction. Within the authorisation phase some efforts should be usefully made by the competent authorities in order to address the scope of the EIS also towards the prediction of the real environmental effectiveness of the value of *MVF* obtained through the mere application of the criteria defined by the current regulations: in this way regional or national guidelines could better define the contents of the EIS and the analysis to be developed for new projects of dams and weirs.

Finally, when the criteria for *MVF* calculation will be defined by law and applied to the whole territory, two main key-issues will have to be faced: the technical adjustments to be implemented in existing sites (especially in old structures) and, in every site, the evaluation of the calculated *MVF* capability to guarantee the efficiency and the quality of the involved ecosystems. For the second issue specific technical aspects

to be considered and solved for each site will be:

- discharge monitoring;
- flow availability in downstream reaches;
- modulation of the releases;
- release through fish passes;
- environmental monitoring programme.

While the provision for releasing the minimum vital flow can be quite easily managed during the project phase, before the infrastructure construction, the technical problems which have to be faced in adapting existing sites to the new legal requirement can be relevant and are mainly related to the typology of the considered structure (concrete dam, earth dam, movable weir with sluice-gates, fixed weir, temporary weir, etc.), to the local geomorphology, to the amount of water to be released and to the possible need to release the discharge through a fish pass. It has to be outlined that if the "natural" discharge coming from upstream is lower than the fixed value of *MVF* adequate devices and settings will have to be implemented in order to guarantee the downstream release of the whole flow. In fact, in the regulatory framework the release of the minimum vital flow is considered a requirement to be respected at local level (in the section immediately downstream the dam/weir) and in every instant (if the "natural" discharge coming from upstream is lower than the fixed value of minimum vital flow nothing will have to be withdrawn and all the flow will have to be released downstream).

All the previous elements contribute to the technical and economic feasibility of the structure adjustment and, together with the loss of productivity due to the *MVF* release, can determine a relevant economic effort by the sites managers. In order to achieve an homogeneous and efficient implementation on the whole territory appropriate technical guidelines should be defined by the competent authorities adressing the sites managers towards the best available technologies and the most suitable and economically viable solutions to be applied depending on the different typologies of water abstraction sites. In this way Regione Piemonte is now operating, with a specific research developed by Politecnico di Torino, through a preliminary review of the main characteristics of all the existing sites and inspections on representative cases and interviews and discussions with their managers: the results will be a technical guideline which will help the sites managers in complying with the new legal requirement.

While the obligation to measure the abstracted discharges and the consequent periodical data transmission to the competent Authorities has recently become compulsory for all sites, there is not a similar precise legal requirement to assess the compliance to the *MVF* release, which, nevertheless, can be controlled by the competent Authorities through direct inspections in every moment, especially if anomalous flow conditions inside the watercourse are observed. In this scenario the site manager could usefully install adequate devices for the measurement and the recording of both the discharges (abstracted and *MVF*) and the consequent transmission of the recorded data, even in real time. In this case the previous continuous measures could adequately integrate the existing institutional monitoring network, providing new elements for the knowledge of the watershed hydraulic balance. The choice and installation of such devices should be discussed with the competent authorities (or addressed through specific guidelines) and their periodical calibration should be carried out with the supervision of institutional personnel in order to guarantee the reliability of the measures. Furthermore the constant respect of the *MVF* release should be easily verifiable on site by anybody through proper devices showing in real time the value of the flowing discharge.

The measurement of the *MVF* released at the dam/weir section proves the compliance to the legal requirement but not the discharge availability in the downstream river reaches. In fact, depending on the geomorphological and hydrogeological characteristics of the watercourse, the flow could split in many canals or be drained by a river-bed substratum of high permeability, becoming unavailable for the ecosystems needs. The river aptitude to keep in every downstream section the flow distribution of the released discharge in conditions compatible with the environmental safeguard targets is strictly linked to the river slope and width, the sequence of riffles and pools, the granulometry and permeability of the substratum and to the interactions with the surrounding aquifers. All the previous elements should be assessed during the project and operational phases in order to evaluate the adequacy of the calculated *MVF*, implementing, if necessary, adequate mitigation measures such as the increase of the value of released discharge or the setting of a channel inside the watercourse aimed at guaranteeing the constant presence of flow and hydraulic conditions sufficient for the biocoenoses needs. The Plans of watershed safeguard will contain useful elements regarding the basin water balance which could be helpful in outlining the relationships between surface and groundwater and in defining the river reaches more critical in terms of flow availability due to local geomorphologic characteristics.

Since fluvial ecosystems are dynamic, in order to maintain viability and resilience, a range of natural variation in the hydraulic regimen is required and consequently the release of a constant discharge, even if complying with the law, can lead to significant impacts upon the river biocoenoses (fishes and aquatic macroinvertebrates, aquatic and riparian vegetation, etc.). For this reason, especially in reaches of particular naturalistic interest, a preliminary analysis of the

watercourse peculiarities could address to a release modulation depending on the more critical period for the involved species, particularly taking into account the ichthyofauna critical/sensitive periods (migrations, spawning and juvenile phases). In this sense the knowledge of the main peculiarities of the fluvial ecosystems is essential and should be seeked not only during the project phase but also for the adjustment of existing sites. Specific analyses should be addresed to identify the most sensitive species and the period where proper caution should be taken in managing the site in order to avoid negative influences upon the biocoenoses. The previous information can be used both for the management of the releases and for the scheduling of the maintenance operations which can cause an increase of water turbidity and solid transport that usually can affect the survival of eggs, larvae and juveniles.

In some cases, particular needs for increasing the released discharge in limited periods of time can be related to a punctual anthropic presence, such as, for example, when the influx of tourists increases the pressures on water quality and consequently a proper dilution of the pollutants is required, or when the touristic use of the river (canoeing, kayaking, etc.) needs an additional flow.

Then, because of the afore mentioned reasons, the installed hydraulic devices will have to be capable to adequately modulate the downstream release for every circumstance with a consequent increase of the related costs. However, in case of modulated releases, the annual schedule of the additional flows should be included in the water abstraction licence and controlled through the installed monitoring system of the abstracted and released discharges.

The impact of dams and weirs on the river biocoenoses is also relevant because the interruption of the fluvial ecosystem continuity due to the infrastructure can affect fishes migrations and drift phenomena with consequent loss of biodiversity and alterations of the population structure of the involved species. Since the most of the Italian ichthyc species, especially in Alpine streams (Northern Italy), are potamodromous and do not have a significant economical value, except for some interested by sportfishing (mainly Salmonids), fish passes are uncommon (in Regione Piemonte the previous devices are adopted by about 8% of the total number of existing sites) and, where applied, compensatory (e.g. periodical restocking) rather than mitigatory measures were prescribed. A recent local initiative has to be outlined: in 2000 Provincia di Torino defined a regulation which imposed as compulsory the installation of fish passes for the new projects of water abstraction and also for the existing sites on the occasion of licence renewals or extraordinary maintenance works; the requirement applies also to hydraulic works which can interrupt the fluvial continuity.

Nevertheless, due to the fact that existing dams and weirs shall soon face adaptation works in order to comply with the *MVF* release, the competent authorities should seize the opportunity to reorganize the whole sector evaluating if the previous discharge, or part of it, must be released through a fish pass in order to restore the river longitudinal connectivity. This approach should be related to an appropriate knowledge of the watercourse fishes populations and of the characteristics of each species in terms of migratory behaviour during their life cycle. The analyses should consider the whole watershed identifying the potential contribution of each river reach upstream every dam/weir in terms of biological significance for the involved species (availability of spawning grounds, trophic availabilities, etc.) in order to evaluate the real usefulness of such devices and to plan priorities in restoring the ecosystems continuity. A specific section of the Plans of watershed safeguard could usefully deal with the previous aspects. Appropriate technical guidelines could provide the main criteria for the fish passes design, specifying the preliminary hydrobiological and hydrological analyses to be carried out in the project phase, the elements on which the choice of the fish pass typology (artificial by-pass channel, rock-ramp, vertical slot, denil, weir fishways, etc.) should be based (with particular regard to the infrastructure characteristics and local peculiarities), including its location in the infrastructure (on or near the riverbank, in the most upstream point reachable by migrating fishes, etc.), the attractivity of the facility (hydraulic conditions at the downstream entrance, etc.) and the devices available for its protection (screens, deflectors, etc.), its efficiency monitoring (direct inspections during migration periods, installation of counting devices, etc.) and its maintenance.

If the design discharge of the fish pass, defined through hydrobiological and technical considerations, is lower than the *MVF* value, an additional flow shall be released in order to comply with the legal requirement: in this case the site owner should manage two different hydraulic devices, and provide for an adequate measurement system of the two discharges. Although the total or partial release of the *MVF* through a fish pass will certainly increase the costs (construction, maintenance, monitoring) that the sites owners shall face, the restoration of both the flow availability in downstream reaches and the fluvial ecosystem continuity can be considered a necessary measure which shall be no more ignored.

Finally, the efficiency of all the previous measures should be periodically checked and verifed through an appropriate environmental monitoring programme. While the implementation of a specific monitoring system is compulsory for projects subject to the environmental impact assessment procedure, for existing sites it could be essentially addressed to evaluate the

fulfilment of the environmental targets for which the *MVF* has been set and a fish pass has been required; then it could be included as a specific requirement in the water abstraction licence. This approach should not release the competent authorities from their institutional duties charging the sites owner of excessive costs. The definition of adequate indicators, parameters, methods and frequencies should take into account the local peculiarities and be consistent and integrable with the institutional monitoring network of the watershed qualitative and quantitative characteristics. In this way, virtuous initiatives adopted by the sites managers, such as the voluntary adhesion to environmental management systems (ISO 14001 and EMAS), could be appropriately stimulated by the competent institutions since now through the introduction of specific incentives and facilitations.

3 CONCLUSIONS

The release of the minimum vital flow can be considered the main measure for the mitigation of the environmental impact of dams and weirs and the Italian legislation is going to introduce it as compulsory for all the sites. For a useful implementation of this requirement the discharge values obtained applying the normative criteria should be assessed for every site in order to check their efficiency in terms of guaranteeing and safeguarding the fluvial ecosystems. Specific technical issues to be considered and solved for each site are the monitoring of the released discharges, the evaluation of the flow availability in downstream reaches, the modulation of the releases to support ecological and anthropic needs, the release through fish passes and the definition of an environmental monitoring programme. A detailed preliminary analysis of the watercourse natural peculiarities and the subsequent implementation of an adequate monitoring system are fundamental and useful tools to achieve the previous targets.

Since a reorganization of the whole system of water abstractions is necessary for pursuing the quantitative and qualitative safeguard of the water resources it is absolutely desirable that the competent authorities will define appropriate technical guidelines addressing the sites managers towards the best available and economically viable technologies trying to achieve a sustainable use of this precious natural resource.

REFERENCES

Baron, J.S. et al. 2003. Sustaining healthy freshwater ecosystems. In ESA (ed.), *Issues in ecology*, 10/2003.

Comoglio, C. 2002. EMAS implementation in hydropower plants. In Becciu et al. (ed.), *New trends in water and environmental engineering for safety and life: eco-compatible solutions for acquatic environments. Proc. 2nd International Conference, Capri, Italy, 24–28 June 2002.*

Comoglio, C. & Mattalia, W. 2002. River water abstraction environmental compatibility assessment: the Regione Piemonte (Italy) approach. *Environmental Flows for River Systems. Proc. Fourth International Ecohydraulics Symposium, Cape Town, South Africa, 3–8 March 2002.*

Larinier, M., Travade, F. & Porcher, J.P. 2002. Fishways: biological basis, design criteria and monitoring. In FAO, CSP, Cemagref (co-ed.), *Bull. Fr. Peche Piscic., 364 suppl., 208 p.*

This page intentionally left blank

River Flow 2004 – Greco, Carravetta & Della Morte (eds.)
© 2004 Taylor & Francis Group, London, ISBN 90 5809 658 0

Calculation and visualization of fish movement in the flow with artificial structures

Hiromichi Ohashi & Yasuyuki Shimizu
Hokkaido University, Hokkaido, Japan

ABSTRACT: From the engineering and biological view point, it is important to understand the movement of fish in the flow with artificial structures (e.g. fishway) or natural bed topography (e.g. bar and pool). There have been a large number of works on river flow with structures or fishway including numerical computational studies, however, the interaction between real river flow and fish movement have not been clarified. In this paper, an attempt is made to understand the fish movement in the flow by numerical experiment and flow visualization technique. Flow field is calculated by 2-dimensional unsteady, non-compression continuity equation and momentum equations. Momentum equations are separated into the advection phase and non-advection phase. CIP numerical scheme, known as high accuracy numerical calculation, is used in advection phase and central difference method is used in the non-advection phase and diffusion phase. The fish movement is calculated based on the momentum equation of fish derived by the characteristics of fish (e.g. drag and thrust of fish, relation between body length and swimming speed, and relation between swimming speed and sustained time). According to these calculations, the movement for fish in the flow is indicated and visualization of result is shown.

1 INTRODUCTION

In Japan, river improvement works are often made to increace flow capacity, especially in urban area. After river improvement, the ascent of fish is interrupted because bed slope becomes steep or by the influence of artificial structures. Therefore in order to make ascent easy, fishways are installed in rivers where the channel is difficult for fish to ascend. There are a large number of and many kinds of fishways in Japan including Makomanai river, Hokkaido, Japan. Figure 1 is the example of fishway in Makomanai river, Hokkaido, Japan. There are a large number of researches and studies about fishway, fish habitat and fish characteristics. A study of hydraulic characteristics in fishway was made by Izumi et al (1999), an analysis of fish habitat model in relation to the factor that our humanbeings cause was made by Franzin et al (2003) and an experiment to investigate biological evaluation of fish in fishway was made by Wada et al (1999). Characteristics of fish movement was, however, never indicated by the numerical calculation considering the realation with unsteady flow in the fishway.

In this study, the fish movement when the artificial structures, especially fishways, are set in the flumes is indicated by the numerical calculation. Specifically, each fish is calculated in the flow using the momentum equations of fish after flow calculation is made.

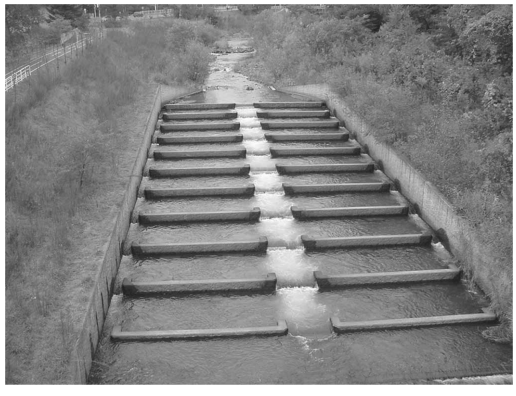


Figure 1. Fishway in the Makomani River.

Furthermore verification of fish movement by the difference of conditions in the fishway (e.g. exist or not the non-submerged obstacles) was made.

2 NUMERICAL CALCULATION OF FLOW

2.1 *Calculation model*

Flow field is calculated by two-dimensional, unsteady, incompressible flow. The continuty equation and

momentum equations are showed as follows.

$$\frac{\partial h}{\partial t}+\frac{\partial (hu)}{\partial x}+\frac{\partial (hv)}{\partial y}=0 \tag{1}$$

$$\frac{\partial (uh)}{\partial t}+\frac{\partial (hu^2)}{\partial x}+\frac{\partial (huv)}{\partial y}=-hg\frac{\partial H}{\partial x}-\frac{\tau_x}{\rho}+D^x \tag{2}$$

$$\frac{\partial (vh)}{\partial t}+\frac{\partial (huv)}{\partial x}+\frac{\partial (hv^2)}{\partial y}=-hg\frac{\partial H}{\partial y}-\frac{\tau_y}{\rho}+D^y \tag{3}$$

where, t is time, x and y are co-orthogonal coordinates, u and v are depth averaged velocity components in x and y directions, respectively. h is flow depth, H is water surface elevation ($=h+\eta$). τ_x and τ_y are bed shear stress in x and y directions, respectively. ρ is water density and g is acceleration due to gravity. τ_x and τ_y can be written using Manning's Equation as follow.

$$\tau_x=\frac{\rho g {n_m}^2 u\sqrt{u^2+v^2}}{h^{1/3}} \tag{4}$$

$$\tau_y=\frac{\rho g {n_m}^2 y\sqrt{u^2+v^2}}{h^{1/3}} \tag{5}$$

where, n_m is Manning's roughness coefficient. D^x, D^y are given by the following equations.

$$D^x=\frac{\partial}{\partial x}\left[\nu_t\frac{\partial (uh)}{\partial x}\right]+\frac{\partial}{\partial y}\left[\nu_t\frac{\partial (uh)}{\partial y}\right] \tag{6}$$

$$D^y=\frac{\partial}{\partial x}\left[\nu_t\frac{\partial (vh)}{\partial x}\right]+\frac{\partial}{\partial y}\left[\nu_t\frac{\partial (vh)}{\partial y}\right] \tag{7}$$

where, ν_t, kinetic eddy viscosity is written as follow.

$$\nu_t=\frac{\kappa}{6}u_* h \tag{8}$$

where, κ is Karman constant, u_* is shear velocity and calculated by

$$u_*=\frac{g{n_m}^2(u^2+v^2)}{h^{1/3}} \tag{9}$$

Flow equations of (1)–(3) are calculated numerically using finite difference method with computational grids in co-orthogonal coordinate system. From Eq. (1) and (2), momentum equation in x direction can be expressed as follow:

$$\frac{\partial u}{\partial t}+u\frac{\partial u}{\partial x}+v\frac{\partial u}{\partial y}=-g\frac{\partial H}{\partial x}-\frac{\tau_x}{\rho h}+\frac{D^x}{h} \tag{10}$$

To solve momentum equations, these equations are separated into two phases of adveciton and non-advection. A high-order Godunov scheme known as the CIP(Cubic-Inrepolated Pseudo-Particle) method, proposed by Yabe & Ishikawa (1990) and modified for the calculation of open channel flow by Nakayama et al (1998), is adopted for advection phase. An assumption is made that at very small time increasements, the change in time of the velocity components at a point in space can be broken down into the time evolution of the inhomogeneous terms and the time evolution at a point due to the advection of the field. Eq. (10) is separated into three phases of advection, nonadvection and viscous term as follows.

$$\frac{\partial u}{\partial t}+u\frac{\partial u}{\partial x}+v\frac{\partial u}{\partial y}=0 \tag{11}$$

$$\frac{\partial u}{\partial t}=-g\frac{\partial H}{\partial x}-\frac{\tau_x}{\rho h} \tag{12}$$

$$\frac{\partial u}{\partial t}=\frac{\partial}{\partial x}\left[\nu_t\frac{\partial u}{\partial x}\right]+\frac{\partial}{\partial y}\left[\nu_t\frac{\partial u}{\partial y}\right] \tag{13}$$

The solution of Adveciton phase for small Δt is simply approximated as:

$$u(x,y,t+\Delta t)\approx u(x-u\Delta t, y-v\Delta t, t) \tag{14}$$

The trick then is to find the value of u at points in space which generally do not lie on the numerical grid points, as specified by the right hand side of Eq. (14). If liner interpolation is used to fine u at points not on the grid, the first order Godunov method is attained. A more accurate solution requires higher order interpolation, and thus high order Godunov schemes. In the CIP method, a cubic interpolation of u is proposed, and when the interpolation is combined with Eq. (14) the resultant equation for u at grid point i, j and time $t+\Delta t$ is given by:

$$\begin{aligned} &u(i,j,t+\Delta t)\\ &=\{(a_1X+c_1Y+e_1)X+g_1Y+u_x(i,j)\}X\\ &+\{(b_1Y+d_1+f_1)Y+u_y(i,j)\}Y+u(i,j) \end{aligned} \tag{15}$$

in which,

$$\begin{aligned} X&=-u\Delta t \quad , \quad Y=-v\Delta t\\ u_x&=\frac{\partial u}{\partial x} \quad , \quad u_y=\frac{\partial u}{\partial y} \end{aligned} \tag{16}$$

And coefficients a_1–g_1 are expressed as follows:

$$\begin{aligned} a_1=\frac{1}{i_s\Delta x^3}\Big[&i_s\left\{u_x(i_m,j)+u_x(i,j)\right\}\Delta x\\ &-2\Delta\left\{u(i,j)-u(i_m,j)\right\}\Big] \end{aligned} \tag{17}$$

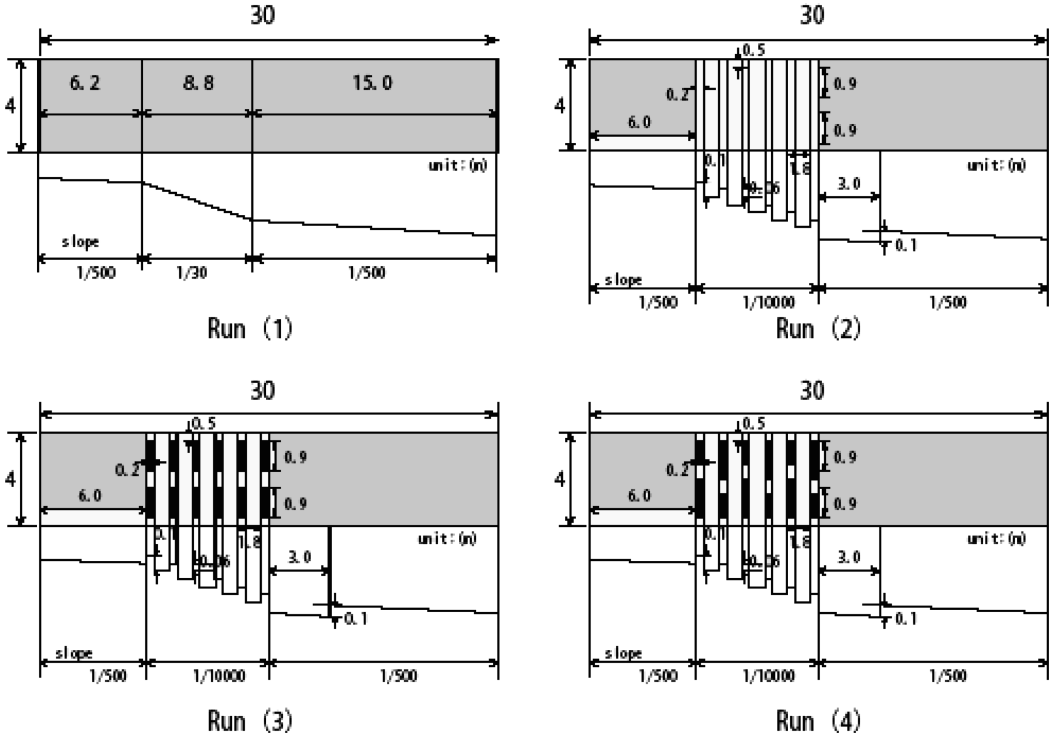


Figure 2. Calculation flume.

$$b_1 = \frac{1}{j_s \Delta y^3}\Big[j_s \left\{u_y(i,j_m) + u_y(i,j)\right\}\Delta y - 2\Delta \left\{u(i,j) - u(i,j_m)\right\}\Big] \quad (18)$$

$$c_1 = \frac{1}{j_s \Delta x^2 \Delta y}\Big[u(i,j) - u(i,j_m) - u(i_m,j) + u(i_m,j_m) - i_s\{u_x(i,j_m) - u_x(i,j)\}\Delta x\Big] \quad (19)$$

$$d_1 = \frac{1}{i_s \Delta x \Delta y^2}\Big[u(i,j) - u(i,j_m) - u(i_m,j) + u(i_m,j_m) - j_s \left\{u_y(i_m,j) - u_y(i,j)\right\}\Delta x\Big] \quad (20)$$

$$e_1 = \frac{1}{i_s \Delta x^2}\Big[i_s \left\{u_x(i_m,j) + 2u_x(i,j)\right\}\Delta x + 3\left\{u(i_m,j) - u(i,j)\right\}\Big] \quad (21)$$

$$f_1 = \frac{1}{j_s \Delta y^2}\Big[j_s \left\{u_y(i,j_m) + 2u_y(i,j)\right\} + 3\left\{u(i_m,j) - u(i,j)\right\}\Big] \quad (22)$$

$$g_1 - \frac{1}{i_s \Delta x}\left\{u_y(i_m,j) - u_y(i,j) + c_1 \Delta x^2\right\} \quad (23)$$

in which,

$$\begin{aligned} i_s &= sign(u), \quad j_s = sign(v) \\ i_m &= i - i_s, \quad j_m = j - j_s \end{aligned} \quad (24)$$

In Eq. (24), Sigmoid function is employed. Eq. (12) is calculated from the continuity equation by taking the divergence of the momentum equations and solving for depth as a Poisson equation. And Eq. (13), the viscous term, is approximated using central finite differences.

In the same way, velocity component of transverve direction can be computed. Each velocity component is defined in the center of two faces of the computational cells, and depth is at the center of the cell. This method has been explained in detail by Shimizu et al.

2.2 *Flume for calculation*

In this study, flow field in 4 flumes are calculated. Figure 2 shows the detail of the flumes for each case. These flumes are decided based on the real condition

of Makomanai River in Hokkaido, Japan. In all flumes, the length and the width are set as 30 *m* and 4 *m*, respectively. In Run (1) it is assumed that the middle part of the flume became steep after river improvement. In Run (2), (3) and (4), fishways are set in the steep part in Run (1), respectively. Flume in Run (2) corresponds to the weir and pool fishway. In Run (3) and Run (4), addition to Run (2), non-submerged obstacles are set regularly and irregularly, respectively.

The slope in Run (1) is set as 1/30, and 1/500 in the middle part which became steep and in the flume except for the middle part. In Run (2), (3) and (4) the slopes in upstream and downstream are, as well as Run (1), set as 1/500 and in the middle part the vertical drops are made. The total of drops is equal to the difference of middle part in Run (1).

2.3 *Boundry conditions*

As boundry conditions, the discharge and depth are given in the upstream and downstream, respectively. The velocities are set as 0 in and around obstacles which are not submerged.

2.4 *Hydraulic conditions*

The discharge is given as $0.15\,m^3/s$ based on usually condition in the Makomanai river. The Manning's roughness coefficient is set as 0.014.

2.5 *Numerical conditions*

Computational grids in the downstream and transverse directions are 100 and 30, respectively. The time steps for computations are set to be 0.01 seconds. Calculations are continued for 200 seconds from the beginning.

The calculation is made by these calculation model, calculation method and conditions. The computational flows are created by repeating the later half (from 50 sec to 100 sec) of the flow for 6 times in the 4 flumes, respectively, after calculation because calculation time, 100 *s*, is not enough to grasp the fish movement completely and initial flow is unstable.

Figure 3 shows the result of calculation in Run (4) by neutually tracer. It is shown that the complicated flow occured around non-submerged obstacles.

3 CALCULATION OF FISH MOVEMENT

In this study, the calculation of fish movement is carried out by the characteristics and calculation method of fish movement shown as follow.

The following characteristics are proposed by Itazawa et al (1991) and Hirose et al (1994).

3.1 *The characteristics of fish swimming*

It was assumed that the fish always tries to keep its body parallell to the flow direction, as it cannot swim perpendicular to the flow. Therefore the fish always ascends the river along with the flow but in the opposite direction.

3.2 *The characteristics of muscles*

In general, fish has 2 kinds of muscles known as the "ordinary muscle" and the "red muscle", respectively. The red muscle can keep being used for a long time as long as the oxygen is supplied without becoming tired. The ordinary muscle can put out to burst up the speed momentarily, but cannot be maintained for a long time because of generating the lactic acid. Fish usually swims in the river using only the red muscle without using ordinary muscle. Ordinary muscle is used only, for example, to avoid danger or to ascend rapid stream. Consequently, the speed of the fish can be characterized as crusing speed (U_{cur}) when only red muscle is used, and Maximum swimming speed (U_{max}) when both muscles are used. Furthermore, these speeds depend on the size of the fish. The value of cruising speed and the maximum swimming speed are usually considered to be about 2–5 BL/s and 10 BL/s, respectively, where BL is the length of the fish. Moreover, the maximum swimming speed is assumed to be maintained only for a few seconds, since fish can use the ordinary muscle only momentarily. In this study, the maximum swimming speed is able to be adapted for fish swimming even after swimming completely at

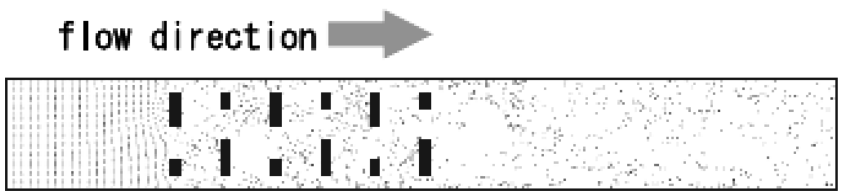


Figure 3. The result of flow calculation.

U_{max} for maximum maitained time based on the above mentioned characteristics in the case that fish swims at cruisig speed or stops moving for constant time.

3.3 *Calculation method*

The method to estimate the fish swimming speed by the momentum equation for fish movement based on the Newton's Second Law was adapted for calculation of fish movement in this study. Because in the case that fish swimming speed are estimated from flow velocity directly, fish turns for many times by the influence of flow rapidly changing at the place where flow is highly fluctuated (e.g. behind obstacles) as the result that direction of fish movement only depends on the flow direction on its moments. Hovever, the swimming direction depends not only on the present flow direciton but also previous direction of fish movement as a result of using the momentum equation for fish. The momentum equation for fish movement is shown as follows.

$$m\frac{\partial \vec{u}}{\partial t} = \vec{T} - \vec{D} \tag{25}$$

where, T and D are the trust and drag of fish, respectively. The acceralation of fish is computed by difference of the trust and drag. The drag of fish D is written as follow.

$$D = \frac{1}{2}\rho C_d U^2 \tag{26}$$

where, ρ is water density, C_d and U are the drag coefficient and relative velocity of fish, respectively. In general, the drag is the sum of the skin friction and pressure drag. In this study the pressure drag, however, is ignored because the pressure drag of streamlined body is small relative to the skin friction. The drag coefficient is decided based on the shape of fish, it is set to be 0.008 in this study. For the trust of fish, T, is separated into 2 kinds by the difference of muscles fish using as previously mentioned. In the case of using both muscles, the red muscle and ordinary muscle, the output is maximum and the trust is written as follow with assumption that the trust is equal to the drag if fish swims at constant speed.

$$T_{max} = \frac{1}{2}\rho C_d {U_{max}}^2 \tag{27}$$

where, U_{max} is the maximum swimming speed. In the case of using only the red muscle, the trust is written as follow because the trust is equal to the drag if fish swims at constant speed.

$$T_{cru} = \frac{1}{2}\rho C_d {U_{cru}}^2 \tag{28}$$

where, U_{cru} is the cruising speed. Seleciton of equation depends on the strength of the flow. In the case that the flow velocity is larger than $0.8U_{cru}$, then the ordinary muscle is used, T_{max} is used and T_{cru} is used in the other case (flow velocity is less than $0.8U_{cru}$).

3.4 *Initial condition of fish movement*

Initial conditions of fish movement for calculation are set as follow. In this study the calculating fish is assumed to be the Sweetfish that inhabits in Makomanai River. The length of fish is 20 cm. The maximum swimming speed (U_{max}) and crusing speed (U_{cru}) of fish are 12 *BL/sec* and 4*BL/sec*, respectively. The maximum swimming speed can be used for 8 *sec*, after that it can be used for 1 *sec* every 10 *sec*. Five fishes are assigned in calculation and they are placed at downstream location when calculation begins.

4 RESULT OF CALCULATION

Figure 4 shows the result of calculation in each four flumes. Solid lines and dotted lines in each rectangles represent the paths of fish movement in the flume. In Run (1) the paths are stopped at the middle way.

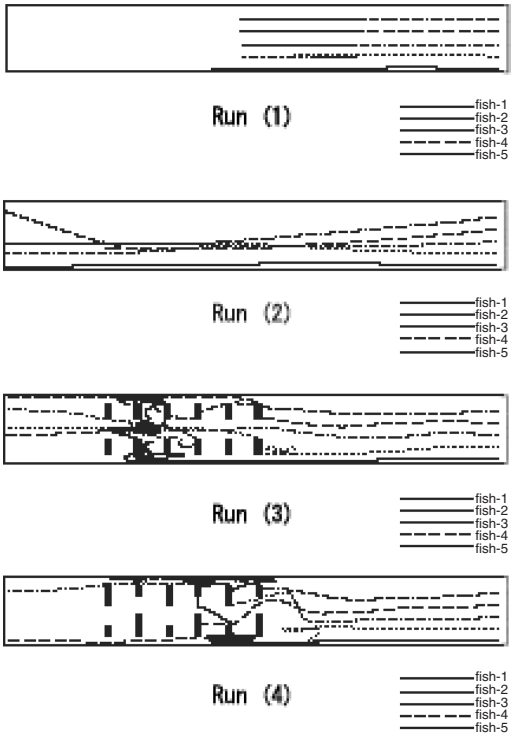


Figure 4. The result of calculation.

It means that fishes could not travel to upstream. In Run (1), compared between the leftside and rightside in the flumes, it is found that the paths in the leftside became thicker. It means that repetition of ascent and descent of fish by the flow in the steep part. In Run (2) all five fishes can ascend because all paths reached upstream oppositely. It is shown in Run (3) that four fishes out of five can reach upstream and each fishes meandered around the non-submerged obstacles different from Run (2). In Run (4), two fishes out of five can go to upstream and meandered around the non-submerged obstacles as well as Run (3).

5 CONCLUSION

It is indicated that not only the ability of fish to ascend, but also the difference of flume configurations. At first the effect of fishway is clarified because no fish which could ascend at all in Run (1). However, fishes are able to ascend in Run (2), (3) and (4) which structures (e.g. vertical drops, pool, non-submerged obstacles) are set.

Next there are two big differences in Run (2), Run (3) and (4). Firstly, one is that fishes meandered for many times in Run (3) and (4) because the flow is constantly changing in transverse direction by the influence of non-submerged obstacles. Secondly, some fishes can reach upstream, while others could not in Run (3), (4). There are several reasons. Fish could not ascend by the influence of turbulence around non-submerged obstacles, and fish cannot go beyond non-submerged obstacles, because flow velocity becomes fast here. It is not clealy indicated that the ascent of fish is difficult in the narrow place from the Figure 4, but we could verify it from the animation from calculation.

There are no outstanding difference compared to Run (3) and Run (4), but it is found that flow which non-submerged obstacles are set irreguraly make fish difficult to ascend because of the number of fishes which can reach upstream.

Characteristics of parallel ascent and two kinds of muscles are not shown from the paths of result, but they are shown at animation from calculation and numerical analysis of fish movement is made based on the characteristics of fish movement.

REFERENCES

Izumi, M., Kudo, A. and Azuma, N. 1999. Flow characteristics and ascending of fishes in Ice Harbor type fishway of Mitumenai-headworks. *Proceedings of Hydraulic Engineerings*, *JSCE*, 989–994 (in Japanese)

Wada, K., Koizumi, N., Ishikawa, M. and Nakamura, S. 1999. Upstream migrating route of juvenile Ayu in a modified larinier pass fishway. *Proceedings of Hydraulic Engineerings*, *JSCE*, 983–988

Franzin, W.G., Nelson, P.A. and Cooley, P.M. 2002. Erosion, transport and deposition; a hydraulics-based approach to fish habitat. *Proc: River Flow* 2002, Louvain-la-Neuve, Belfium

Yabe, T. and Ishikawa, T. 1990. A numerical cubic-interpolated pseudoparticle (CIP) method without time splitting technique for hyperbolic equation, *Journal of the Physical Society of Japan*, Vol. 59, No. 7, 2301–2304

Nakayama, K., Sato, T. and Horikawa, Y. 1998. A numerical study on a shallow water flow using CIP method, *Proceedings of Hydraulic Engineering*, *JSCE*, Vol. 42, pp.1159–1164 (in Japanese)

Shimizu, Y., Fujita, M. and Hirano, M. 1999. Calculation of flow and bed deformation in compound channel with a series of vertical drop spillways. *Proceedings of Hydraulic Engineering, JSCE*, 683–688

Hirose, T. and Nakamura, T. 1994. The design of the fishway (in Japanese)

Nakamura, S. 1994. The story of the fish way (in Japanese)

Itazawa, T. and Habu, I. 1991. Fish physiology (in Japanese)

Blake, R.W. 1983. Fish locomotion

River Flow 2004 – Greco, Carravetta & Della Morte (eds.)
© 2004 Taylor & Francis Group, London, ISBN 90 5809 658 0

An experimental study of velocity fields and flow patterns in aligned deep slot fishways

L. Pena & L. Cea
CITEEC, A Coruña University, A Coruña, Spain

J. Puertas
Civil Engineering School, A Coruña University, A Coruña, Spain

T. Teijeiro
Environmental Engineering School, Santiago de Compostela University, Lugo, Spain

ABSTRACT: This paper is a study of the flow pattern taking place in a specific design of aligned deep slot fishways. The analysis is based on an experimental study in which the flow velocities and the water depths were measured in a laboratory model of the fishway. A spatial 3 dimensional mesh was used to measure the 3 velocity components. To measure the water depth a bidimensional mesh was used. Sills of different heights were placed in the slot in order to analyze its influence in the flow pattern. For each different sill, several discharges were used. As a result of the study, the relationship between the discharge and the different characteristic water depths (medium, maximum and minimum depths in the pool) as well as the discharge equations were obtained for each different sill. Three different flow patterns were observed in function of the height above the bottom of the pool. Finally, the slot velocity and the maximum velocity in the pool were analyzed.

1 INTRODUCTION

One of the most important direct effects of the hydraulic constructions in rivers is the perturbation of fish circulation, which, in some cases, can lead to the disappearance of some migratory specimens (Larinier, 1998, Zhong & Power, 1996).

The most common solution to this problem is the construction of fishways to allow the upstream migration of the fish. The aligned deep slot fishways, which are studied in this paper, are a new design which is still not used at the present time in practice. This new design is an hybrid between the aligned vertical slot design and the deep slot design. The difference with the vertical slot design, in which the slot goes down straight to the bottom, is that a sill is placed in the bottom of the slot. In this way a strong vertical velocity component appears in the slot, destroying the quasi bidimensional behaviour of the vertical slot fishways. The object of this study is to analyze the modifications introduced in the flow pattern by the sill and to characterize the hydraulic behaviour of this new kind of fishways.

A basic design which will be referred to as configuration T1 (Fig. 1) was chosen to perform the study (Teijeiro, 2001; Pena, 2003; Puertas, 2004). In Table 1 are shown the real and the parametric dimensions of the pool. The bottom slope is 10%.

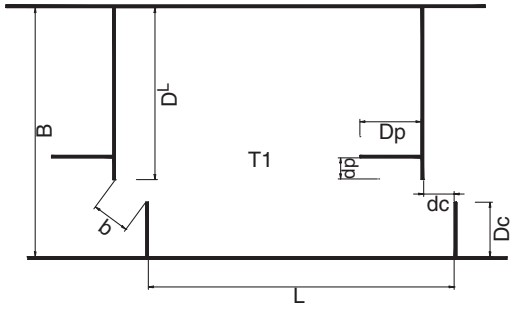


Figure 1. Basic design and dimensions of a configuration T1 pool.

The height of the different sills placed in the bottom of the slot are 100, 200, 300, 400 and 500 mm.

2 EXPERIMENTAL PROCEDURE

The experimental work was carried out at the CITEEC (Centro de Innovación Tecnolóxica en Edificación e

Table 1. Real and parametric dimensions.

	Real (mm)	Parametric (function of the slot width b)
b	160	1.00 b
L	1213	7.58 b
B	1000	6.25 b
D_L	680	4.25 b
D_c	217	1.36 b
d_c	121	0.76 b
D_p	243	1.52 b
d_p	86	0.54 b

Table 2. Height of the different sills which were placed in the bottom of the vertical slot.

Sill (mm)	Parametric dimension (function of width b)
100	0.625 b
200	1.250 b
300	1.875 b
400	2.500 b
500	3.125 b

Enxeñería Civil) at the University of A Coruña (Spain). The fishway model consisted on a metallic structure of 12 m long with a $1 \times 1\ m^2$ rectangular section. The fishway was divided into eleven pools: a head tank receiving the water from an upstream reservoir, nine active pools and a tail tank. The experimental measurements were recorded in pool number 7.

A conceptual state of uniform flow (Rajaratnam et al., 1986, 1992) was used, so that the mean depth measured at the middle transversal section was the same in all the pools. At the lower end of the flume a tailgate causing overflow was used in order to impose the necessary boundary condition to obtain a uniform flow for each different discharge.

A cartesian positioner was placed over the experimental pool in order to automate the positioning of the measurement instruments. Two measurement devices were placed on the cartesian positioner, but not simultaneously: a depth probe and ADV velocimeter.

Velocities were measured by means of a Doppler effect velocimeter (MicroAcoustic Doppler Velocimeter SonTek).

Velocity measurements were carried out in planes parallel to the flume bed with 10 cm in between, starting at 5 cm from the channel bed up to as close as possible to the water surface. In each plane, data points were distributed forming a 10×10 cm mesh, reduced to 5×5 cm in critical zones. Therefore a three-dimensional mesh of $10 \times 10 \times 10$ cm for the measurement of velocity was maintained.

Table 3. Sills and discharges used.

	Water depth		Velocity	
Sill (cm)	Q (m^3/s)	Number of points	Number of levels	Points per level
10	0.025	111	2	140
	0.035	111	3	140
	0.045	111	3	140
	0.055	111	4	140
	0.065	111	4	140
	0.075	111	5	140
	0.084	111	6	140
	0.094	111	7	140
20	0.024	111	3	140
	0.035	111	4	140
	0.045	111	4	140
	0.055	111	5	140
	0.065	111	5	140
	0.075	111	7	140
30	0.026	111	3	140
	0.035	111	4	140
	0.045	111	5	140
	0.055	111	5	140
	0.065	111	6	140
	0.075	111	7	140
40	0.025	111	4	140
	0.034	111	5	140
	0.044	111	6	140
	0.055	111	6	140
	0.065	111	7	140
50	0.025	111	5	140
	0.035	111	6	140
	0.045	111	6	140
	0.055	111	7	140

Water surface height in the pools was measured by means of a conductivity-based depth probe, DHI Wave Gauge Type 202. Depth measurements in the pools were evaluated following a bidimensional mesh with data points at a 10×10 cm maximum separation in between. Calibration tests were performed prior to each working day.

After a previous experimental test, a measurement frequency of 15 Hz was chosen.

2.1 *Sills and discharges studied*

In Table 3 are summarized the different cases which were tested. In all cases the bottom slope of the fishway was 10.054%.

2.2 *Discharge equations*

The discharge equations, which relate the adimensional water depth and discharge, were evaluated. The

Table 4. Discharge equations for the different sill heights. The adimensional discharge is related to the adimensional water depth. r^2 is the correlation coefficient.

$Q^A_{z10} = 0.7939 y_0/b - 0.583$	$r^2 = 0.9956$
$Q^A_{z20} = 0.8185 y_0/b - 1.040$	$r^2 = 0.9862$
$Q^A_{z30} = 0.8571 y_0/b - 1.666$	$r^2 = 0.9746$
$Q^A_{z40} = 0.8174 y_0/b - 1.981$	$r^2 = 0.9968$
$Q^A_{z50} = 0.7741 y_0/b - 2.264$	$r^2 = 0.9978$

water depth is adimensionalized by the width of the slot, while the discharge is adimensionalized as:

$$Q^A = Q / \sqrt{g\, b^5} \tag{1}$$

where Q^A is the adimensional discharge, Q is the experimental discharge, g is the gravitational constant and b is the real width of the slot. The discharge equation can be expressed as:

$$Q^A = \alpha\, (y_0/b)^{\beta} + \mu \tag{2}$$

where y_0 is the mean water depth in the transversal section of the middle of the pool and α, μ and β are proportionality coefficients.

The discharge equations obtained from the experimental data are shown in Table 4, where Q^A_{z10}, Q^A_{z20}, Q^A_{z30}, Q^A_{z40}, Q^A_{z50}, account for the adimensional discharge corresponding to each different sill height: 10, 20, 30, 40 and 50 cm.

It was verified that the discharge and the water depth are linearly correlated (β coefficient is equal to 1) and that the proportionality constant α, as well as the coefficient μ depend on the basic design of the pool and on the height of the sill.

All the discharge relations are almost parallel to each other, which shows that, independently of the sill used, the sensitivity of the design to variations in the discharge remains invariable.

2.3 *Characteristic water depths*

The characteristic water depths are those by which the free water surface can be represented. As it was done in the analysis of the vertical slot fishways (Puertas, 2004), the following characteristic water depths are defined: maximum water depth in the pool, y_{max}, water depth in the vertical slot, y_b, mean water depth, y_m, minimum water depth, y_{min}. The water depth in the vertical slot is defined as the difference between the free water surface and the upper part of the sill. Therefore, the depth at both sides of the sill is bigger than the depth in the slot, being the difference of the same order of magnitude than the height of the sill. For the calculation of the minimum water depth it is not considered the slot depth.

Table 5. Relation between the characteristic water depths and the adimensional depth y_0/b. In all cases a good correlation was found, being the minimum correlation coefficient equal to 0.98.

Sill (mm)	y_{max}/b	y_b/b
100	1.0156 y_o/b + 0.458	0.9984 y_o/b – 0.538
200	1.0432 y_o/b + 0.324	0.9788 y_o/b – 1.027
300	1.0673 y_o/b + 0.221	0.9032 y_o/b – 1.268
400	1.0962 y_o/b + 0.063	0.8233 y_o/b – 1.565
500	1.1072 y_o/b – 0.042	0.9464 y_o/b – 2.656
	y_m/b	y_{min}/b
100	0.9844 y_o/b + 0.070	0.9618 y_o/b – 0.356
200	0.9849 y_o/b + 0.086	0.9499 y_o/b – 0.303
300	0.9903 y_o/b + 0.064	0.9914 y_o/b – 0.454
400	0.9893 y_o/b + 0.074	1.0206 y_o/b – 0.565
500	0.9848 y_o/b + 0.103	0.9096 y_o/b – 0.080

A general relation between the mean water depth in the central transversal section and any of the characteristic depths was used:

$$\frac{Y}{b} = \alpha' \left(\frac{y_o}{b} \right) + \beta' \tag{3}$$

where Y is any of the characteristic water depths defined above ($y_{max}, y_b, y_m, y_{min}$), b is the width of the vertical slot, y_0 is the mean water depth in the central transversal section and α' and β' are proportionality coefficients.

The computed equations are shown in Table 5.

The values of the characteristic water depths are proportional to the flow discharge, as well as to the height of the sill. The water height over the sill depends on the discharge but it is independent of the height of the sill.

2.4 *Free water surface*

In general it can be found a certain similitude between the patterns found for the free water surface and those to the vertical slot fishways (Puertas, 2004):

- There is an area of high water depths upstream the slot.
- There is a strong diminution of the water depth in the slot.
- The minimum water depth occurs downstream the slot, where a circular depth depression exists.
- After this minimum, in the downstream direction, another area of high depths exists next to the transversal vertical wall which separates the pools.

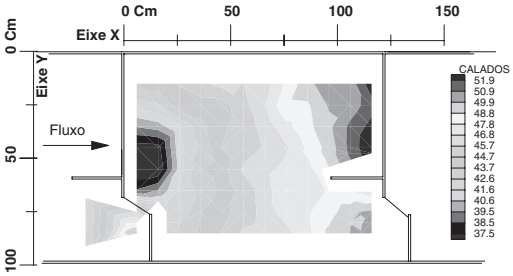


Figure 2. Isodepth lines in the aligned deep slot fishway. The plot corresponds to a discharge of $Q = 0.055\ m^3/s$ and a sill of 0.10 m height.

Apart from these general similitude between the vertical slot and the deep slot designs, there are two mainly differentiating characteristics:

- The position of the circular water depth depression which occurs downstream the slot.
- The distribution of the isodepth lines.

For the vertical slot design, the position of the water depth circular depression is downstream the slot in the direction of the opposite corner of the pool. In the aligned deep slot design, the depression moves upstream towards the transversal pool separation wall.

The second difference is the distribution of the isodepth lines. In the vertical slot design the isodepth lines are approximately perpendicular to the diagonal which goes from the slot to the opposite pool corner, while in the deep slot design they are almost perpendicular to the fishway longitudinal axis (Fig. 2).

Another important property observed is that the free water surface pattern remains invariable to the height of the sill. Each design has a characteristic pattern which depends only on the configuration of the vertical walls that define the pool and which does not depend on the sill placed in the slot.

Finally it was verified that the pattern of the free water surface is also independent of the flow discharge. This behaviour was observed for all the experimental discharges used.

3 VELOCITY FIELDS

3.1 *Horizontal velocity fields*

The introduction of the sill in the vertical slot has a great importance in the velocity field. In the vertical slot design, the flow is quasi bidimensional, the vertical velocities are almost zero and there are not important differences in the velocity fields which occur at different vertical levels. This allows to characterize the flow pattern independently of the level over the bottom of the fishway (Puertas, 2004). When the

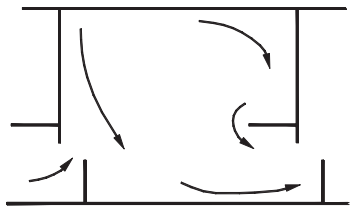


Figure 3. Flow pattern of the horizontal velocity field in a plane situated at 5 cm above the bottom of the pool.

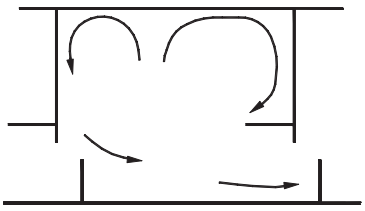


Figure 4. Flow pattern of the horizontal velocity field in planes located between 5 cm above the bottom of the pool and the upper border of the sill.

sill is introduced, this behaviour is no longer true. The horizontal velocity field varies with the height over the bottom and the vertical velocity cannot be neglected, specially near the slot.

One of the aims of this study was to find several flow patterns which allow to describe the flow independently of the discharge and the sill used. Different flow patterns must be defined in order to be able to represent the velocity field in horizontal levels below the sill as well as in horizontal levels above the sill.

Three different flow patterns at three different levels were found after analyzing the experimental data.

The first one (Fig. 3) occurs at 5 cm above the bottom of the pool, no matter which discharge neither which sill is used.

A second pattern was found (Fig. 4) which represents the velocity field in levels higher than 5 cm but lower than the upper border of the sill.

The horizontal velocity field pattern occurring in levels situated over the sill up to the free water surface varies with height. The strongest difference takes place near the sill. Nevertheless, it can be defined a general flow pattern which represents quite accurately the flow field. This third pattern is shown in Figure 5. It is in the slot section where the velocity direction varies most strongly with height. In Figure 5 two directions are defined in the slot. At the deepest levels, the velocity direction turns left, being almost parallel to the transversal wall, while in the most superficial levels the velocity remains perpendicular to the slot.

As it has been said, in the deep slot design, the vertical velocities are not negligible. Near the slot the flow

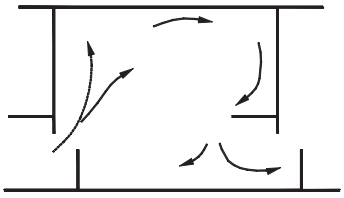


Figure 5. Flow pattern of the horizontal velocity field in levels situated over sill.

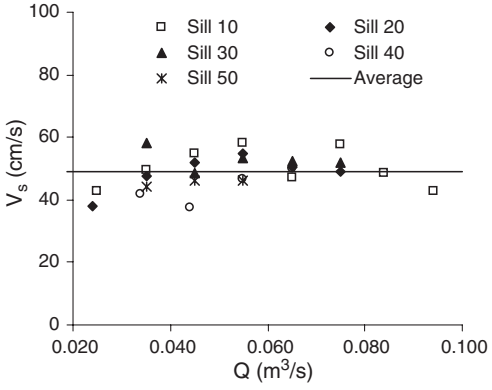


Figure 6. Experimental values of the mean velocity in the slot for different discharges and different sills.

moves up, it is then propelled away from the slot, and when it reaches the opposite vertical wall it moves down. The absolute value of the vertical velocity is usually smaller than the horizontal components, being usually smaller than 20 cm/s. However, as it is shown by the experimental results presented, it is of great importance in the global behaviour of the flow in the fishway.

3.2 *Slot velocity*

The velocity in the slot (V_s) was calculated at different heights. For each height three different experimental points were used to compute the mean value of the velocity.

In Figure 6 it is represented the mean velocity in the slot for each different discharge and each different sill. As it can be seen, all values are quite similar independently of the discharge and the sill used. A mean velocity of 48.82 cm/s can be considered as representative of all situations.

3.3 *Maximum velocity*

The maximum velocity (V_{max}) is another characteristic velocity that can be used to define the hydraulic behaviour of a fishway.

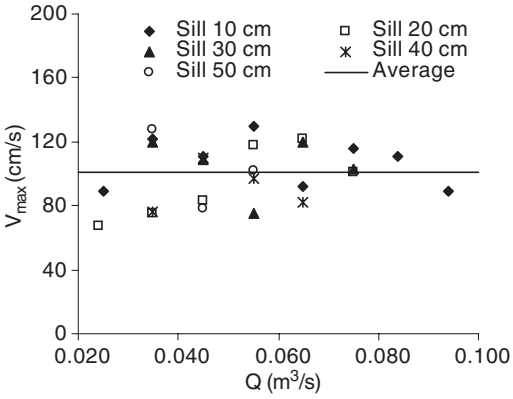


Figure 7. First maximum velocities. Maximum velocities for each different discharge and sill, computed as the mean value of the maxima at the different measurement planes situated above the sill.

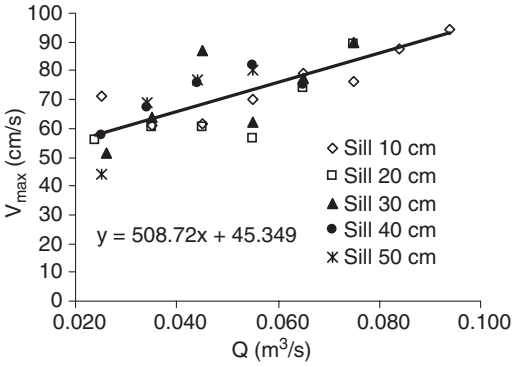


Figure 8. Second maximum velocities. Maximum velocities for each different discharge and sill, computed as the mean value of the maxima at different measurement planes situated below the sill.

As it was expected, it was necessary to define two different maximum velocities. The first maximum corresponds to the points situated above the sill and the second maximum to points situated below the sill. The maximum velocity is defined as the mean of the different maxima occurring at different measurement planes. For the first maximum, only the planes situated above the sill are considered while for the second maximum the planes considered are those ones situated below the sill.

The first maximum velocity is shown in Figure 7. Different discharges and sills are represented. As the maximum velocity is almost independent of the discharge, a mean value was calculated, obtaining a velocity of 101 cm/s.

The second maximum velocities (planes situated below the sill) are plotted in Figure 8. As it can be

seen, the maxima increase with the discharge up to a highest value which is very near to the first maximum (planes situated above the sill) represented in Figure 7. For all discharges, the second maximum is smaller than the first maximum. It should be expected that for bigger discharges both maxima agree.

The velocities measured oscillate in a very wide range. The biggest value measured was 174.7 cm/s. The location of the biggest velocities is always near the slot.

4 CONCLUSIONS

The aligned deep slot fishways are an hybrid design between the so called deep slot fishways and the aligned vertical slot fishways. Therefore, its hydraulic behaviour has common points with the two original designs.

The discharge equations which relate the discharge and the water depth are linear, as it happens in the vertical slot design. However, the equation depends on the height of the sill placed in the slot. The bigger the sill, the bigger the water depth in the pool.

The configuration of the free water surface is independent of the discharge and of the sill used.

It has been found three different flow patterns which allow to represent the horizontal velocity field. Depending on the level over the bottom of the pool, one pattern or another appears. The three patterns found can be summarized as follows:

(1) Independently of the sill used, at a level of 5 cm over the bottom of the pool, the streamlines follow the pattern shown in Figure 3.
(2) For planes situated at a higher level than 5 cm but below the upper border of the sill, the flow pattern is represented in Figure 4.
(3) The planes situated at a higher level than the upper level of the sill follow the pattern shown in Figure 5. The velocity direction is perpendicular to the slot for planes near the free water surface. At lower levels, the velocity direction turns left.

Although the vertical velocity component is much smaller than the horizontal components, it has a great importance in the development of the flow pattern in the pool.

The mean velocity in the slot can be considered almost constant and independent of the discharge and of the sill used.

Regarding the maximum velocities, two different behaviours were observed. In planes located above the sill, the maximum velocity is constant and it does not depend on the discharge neither on the sill used. In planes situated below the upper border of the sill, the maximum velocity is independent of the sill height but it increases with the discharge.

ACKNOWLEDGEMENTS

The authors would like to thank the CITEEC staff (Centro de Innovación Tecnolóxica en Edificación e Enxeñería Civil) at the University of A Coruña (Spain), without whose help the development of experimental work essential to this research would not have been possible, as well as the Spanish Ministry of Science and Technology, which funded this research project (CICYT-HID-1999-0297).

REFERENCES

Larinier, M., Porcher, J.P., Travade, F., Gosset, C. 1998. *Passes à poissons. Expertise conception des ouvrages de franchissement*. Collection Mise au Point, Conseil Superieur de la Pêche, Paris. 336 p.

Pena, L., Teijeiro, T., Puertas, J. 2003. *Experimental study of depth discharge equations and velocity patterns on vertical slot fishways*. Proceedings XXX IAHR Congress, August, 2003. Theme C. p. 433–440. Thessaloniki. Greece.

Puertas, J., Pena, L., Teijeiro, T. 2004. *An experimental approach to the hydraulics of vertical slot fishways*. Journal of Hydraulic Engineering, Vol. 130, No 1.

Rajaratnam, N., Van de Vinne, G., Katopodis, C. 1986. Hydraulics of vertical slot fishways. *Journal of Hydraulic Engineering*, vol. 112, No 10, p. 909–927.

Rajaratnam, N., Katopodis, C., Solanki, S. 1992. New designs for vertical slot fishways. *Journal of Hydraulic Engineering* 19, p. 402–414.

Teijeiro, T. 2001. *Citerios de diseño de escalas de peces de hendidura vertical*. Tesis doctoral. Dpto. de Ingeniería Agroforestal, Universidad de Santiago de Compostela. Lugo.

Zhong, Y., Power, G. 1996. Environmental impacts of hydroelectric projects on fish resources in China. *Regulated rivers: research and management.* Vol 12:81–98.

River Flow 2004 – Greco, Carravetta & Della Morte (eds.)
© 2004 Taylor & Francis Group, London, ISBN 90 5809 658 0

Estimating effect of navigation on fish habitats in inland waterways

C. Engelhardt, A. Sukhodolov & C. Wolter
Institute of Freshwater Ecology and Inland Fisheries, Berlin, Germany

ABSTRACT: The swimming performance of juvenile fishes can be insufficient to overcome return current velocities induced by navigation in inland waterways. A method to assess habitats of fish on the basis of return velocity computations is introduced using general physical principles. A simple analytical model is presented to determine the return velocities in a canal of known dimensions and for a vessel of certain draught and speed. Field measurements were performed in the Oder-Havel canal to evaluate the mathematical model. Comparing predicted values of return velocity for the investigated waterway with thresholds of maximum swimming speed for juvenile fishes a habitat bottleneck could be shown. Suggestions are given as to how the navigation impact on fish can be minimized by canal shoreline design.

1 INTRODUCTION

Navigable inland waterways were always important for the economic development of society; nowadays their total length exceeds half a million kilometers worldwide (Kubec & Podzimek 1996). Aside from their primary functioning as navigation routes, inland waterways provide habitats for sundry species of aquatic animals and plants. Although the necessity of limiting the cruising speed of vessels because of channel protection considerations became an exploitation policy long ago, the ecological aspect of the problem was not considered rigorously either in design of channel or in navigation rules hitherto. In part this situation accounts for the lack of knowledge about the effects of navigation on dynamics of populations for species inhabiting inland waterways.

A vessel propelling in a canal expends energy to overcome the resistance of fluid. That energy is mainly transformed into a complex pattern of currents and waves trailing astern. Helmholz fan, propeller wash (U_p), slope supply flow (U_s), and return currents (U_r) moving in opposition to the direction of the vessel's motion (Figure 1) are the principal constituents of the pattern. In width-restricted canals, when commercial tugs towing loaded barges cruise with the speeds close to navigation limits, the return currents maintain extremely large velocity values (Simons et al. 1981; Mazumder et al. 1993). The magnitude of these currents may greatly exceed the swimming abilities of larval and juvenile fishes and thereby cause high larvae mortality (Wolter & Vicinskas 1997; Arlinghaus et al. 2002). As the young-of-the-year fishes are important

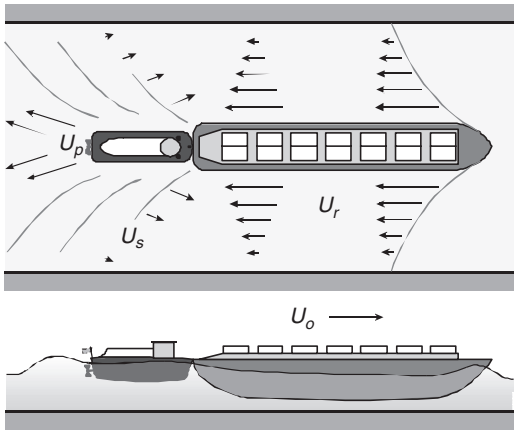


Figure 1. Schematic representation of currents generated by a vessel cruising in a canal (after Blaauw et al. 1984).

indicators of habitat quality (Schiemer et al. 2001), it seems possible to establish quantitative relationships between side effects of navigation and habitat quality by means of comparison of return current velocity and swimming abilities of juvenile fishes. To develop this relationship to the level of a practical computational scheme therefore requires predicting the return velocity for the given characteristics of the canal as well as for typical vessels in addition to predicting swimming abilities of juvenile fishes as a function of the body length.

Although vessel-induced waves and currents have been intensively studied in the shipbuilding

applications (Jiang 2001), available computation schemes are either complex (Stockstill & Berger 1999) or rely heavily on purely empirical approaches (Maynord & Siemsen 1991; Maynord 1996). Moreover, both advanced numerical models and empirical methods require that significant amount of data be collected prior to computations. Numerical models need detailed data sets pertaining to the geometry of the channel and a vessel, characteristics of hydraulic resistance and eddy viscosity (Stockstill & Berger 1999), while development of empirical relationships requires numerous observations. Therefore, there is a need to develop a simplified computational scheme based on fundamental physical laws which can be operated upon a few parameters.

Fish swimming performance depends on a variety of biological and physical factors. Observations undoubtedly indicate that the principal factor is the body length (Wardle 1975; Videler 1993; Haefner & Bowen 2002). Correspondingly, swimming performance was assessed by a model for maximum swimming speed on the basis of the white lateral muscle's contraction time and the relation between tailbeat frequency and forward motion (Wardle 1975).

Present study is focused on the development of a simplified model of return velocity in a straight prismatic canal with still water and its applications to describe effect of navigation on fish habitats. The model was derived from advection-diffusion equation and tested on the original data set of field observations.

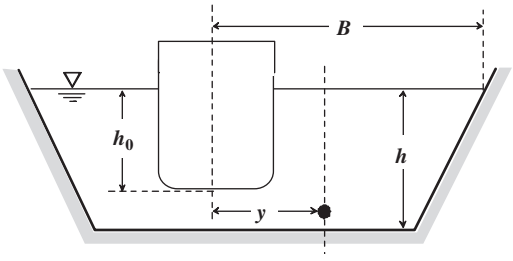


Figure 2. Schematic representation of canal's crosssection with a vessel.

2 RETURN CURRENT MODELING

A moving vessel expends energy to overcome resistance of water while propelling in a waterway. The kinetic energy gained by water from the interaction with the vessel has to be transported away and dissipated during the transport. This energy transfer can be described by the advection-diffusion equation

$$\frac{\partial k}{\partial t} + \mathbf{u}\frac{\partial k}{\partial \mathbf{x}} - \frac{\partial}{\partial \mathbf{x}} D \frac{\partial k}{\partial \mathbf{x}} = 0 \tag{1}$$

where t = time, $\mathbf{x}$ = vector of coordinates, $\mathbf{u}$ = vector of characteristic velocity of the kinetic energy transfer, D = coefficient of kinetic energy diffusion, and k = dimensionless kinetic energy = $U^2h/U_0^2h_0$, U_0 and U = velocities of the vessel and water, h_0 and h = draught and the canal depth respectively (Figure 2).

In inland waterways the canal widths are usually comparable or smaller than the length of commercial vessels (Figure 3) while their draughts at load are slightly smaller then the canal depth. Therefore, accounting for significant cruising speeds of vessels, the ship-induced disturbances occupies the whole water column and reach the banks so quickly that the maximum of return velocities is observed in a cross-section while a ship still passing by. These circumstances allow significant simplification for equation (1). Thus, it is reasonable to consider only depth averaged, steady state energy transfer with constant coefficient of diffusion which for the transverse direction writes to as

$$\frac{\partial^2 k}{\partial y^2} - a\frac{\partial k}{\partial y} = 0, \quad a = \frac{u}{D}, \tag{2}$$

where y = cross-canal distance counted from the centerline of the ship's hull. The condition of steadiness is

$$T >> \frac{y}{u}, \tag{3}$$

here T = period of drawdown wave.

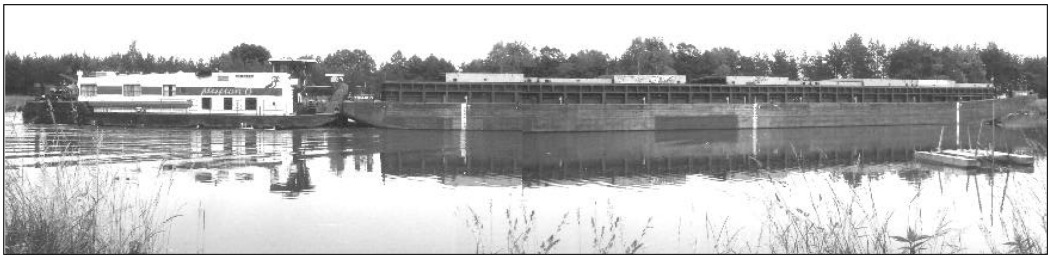


Figure 3. Commercial navigation in the Oder-Havel canal in Germany.

Substituting the variable $\zeta = \partial k/\partial y$ yields

$$\frac{\partial \zeta}{\partial y} - a\zeta = 0, \quad \frac{d\zeta}{\zeta} - a\,dy = 0, \tag{4}$$

and after integration converts to

$$\ln\zeta - a\,y + C = 0, \tag{5}$$

where C = constant of integration. Applying an inverse transformation to (5), one obtains

$$\zeta + C_1 e^{-a\,y} = 0, \; or \; dk + C_1 e^{-ay}\,dy = 0, \; C_1 = e^{C}, \tag{6}$$

that with a substitute for the distance $\eta = y/B$ writes as

$$dk + C_1 e^{-aB\eta}\,d\eta = 0, \tag{7}$$

where B is waterway-width. Integration of equation (7) yields

$$k = \frac{C_1}{aB} e^{-aB\eta} + C_2, \tag{8}$$

where C_2 = constant of integration. C_2 is a small and can be neglected at long distances in still water $k \approx 0$. Now substituting expressions for kinetic energy into (8), one obtains

$$\frac{U^2}{U_0^2}\frac{h}{h_0} = \frac{C_1}{aB} e^{-aB\eta}, \; \frac{U}{U_0} = \sqrt{\frac{C_1}{aB}}\sqrt{\frac{h_0}{h}}\, e^{\frac{aB}{2}\eta}. \tag{9}$$

Finally, one can rewrite equation (9) to as

$$\frac{U}{U_0} = \alpha\sqrt{\frac{h_0}{h}}\, e^{-\beta\frac{y}{B}}, \tag{10}$$

where $\alpha = \sqrt{\frac{C_1}{aB}} = \sqrt{\frac{C_1 D}{uB}}$, and $\beta = \frac{aB}{2} = \frac{uB}{2D}$.

Despite that general relationship of the coefficients α and β to the parameters of the flow are known, their values have to be determined experimentally because of lack of a suitable mathematical description for diffusion coefficient D, and the unknown value of C_1.

Equation (3) can be rewritten to account for a specific case $u = \sqrt{gh}$

$$T = \gamma\frac{L}{U_0} >> \frac{y}{\sqrt{gh}} \tag{11}$$

which is a well recognized group velocity limit in the shallow water canals. The value of coefficient γ is expected to equal 1, and the practical threshold to satisfy condition (11) is an order of magnitude, that means that the period of ship passage should be at least 10 times longer then the time of disturbance wave travel from the ship to the bank.

Equations (10) and (11) comprise a simple model allowing predictions of return velocities in a canal of known dimensions for a vessel with the certain draught and speed. The model requires, however, some parameters that can be obtained experimentally for the certain geometry of the canal (for example trapezoidal shape) and similar types of vessels.

3 FIELD MEASUREMENTS

3.1 *Study reach*

The artificially constructed Oder-Havel canal is a 150 km long inland waterway connecting watersheds of the Oder and the Havel rivers in the northeastern lowlands of Germany. It was opened for navigation in 1620, last modified in 1914; its channel is 34 m wide and 3 m deep, with a steep bank (slopes of 33%) protected by rip-rap embankment. The field measurements were performed in a reach of the canal located at 63.5 km (52°85′N; 13°73′E).

3.2 *Measuring system and equipment*

During the passage of vessels in the study reach the records of instantaneous velocity vectors were collected using acoustic doppler velocimeter (ADV) manufactured by Sontek, Inc. This instrument consists of an ADV probe mounted to submersible field electronics. The sampling volume of the probe is located 10 cm from the sensors and is $<0.25\,cm^3$ in size. The resolution of the ADV is 0.1 mm/s with a noise level of 1% of the velocity range at a sampling frequency of 25 Hz. A special moveable platform was constructed to enable accurate and stable positioning of the measuring systems (Figure 4).

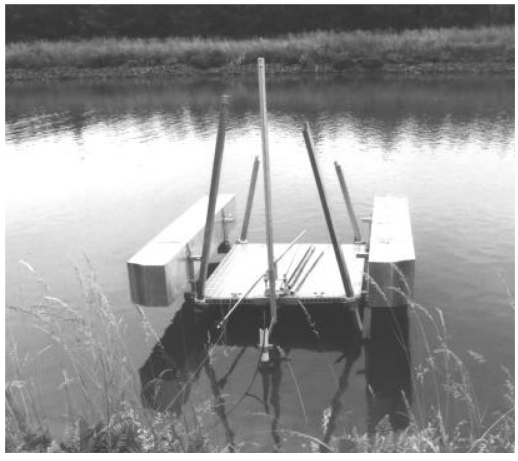


Figure 4. Moveable platform for ADV sensors mounting installed in the cross-section of the Oder-Havel canal, 63.5 km.

Hydrographic survey of the waterway reach, positioning of ADV sensors and the determination of coordinates for vessels were performed with a total station Elta® R55 (Carl Zeiss Geodetic Systems, Germany, distance 5 mm, range 1300 m). The draught was recorded from the draught scale of the vessels, and the length, width and capacity were obtained from the official calibration registers. Speed of vessels was calculated from time consumed by each vessel to pass a defined reference reach. Water levels were recorded using pressure loggers (DL/N, STS Co., Sirnach, Switzerland) mounted into perforated steel pipes and placed close to the locations of ADV probes.

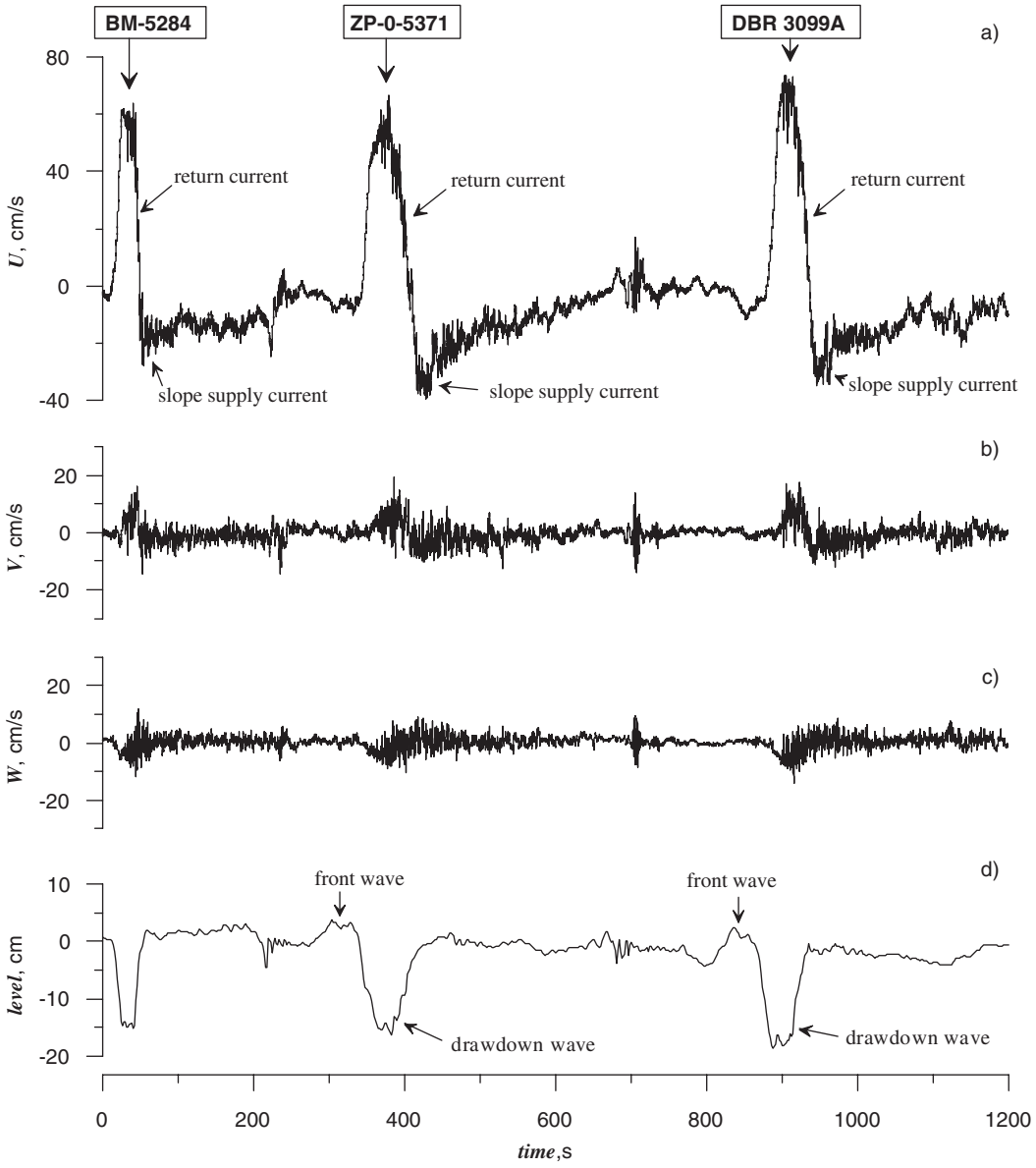


Figure 5. Example of velocity records sampled with ADV in the Oder-Havel canal during the passage of three commercial tows (the registration numbers of tows are displayed in textbox).

3.3 *Measurements and data processing*

For altogether 17 commercial tows the flow velocities were measured close to the bottom (0.15 m) at three locations across a transect of the Oder-Havel canal simultaneously at sampling rate of 25 Hz. The recording started as soon as a vessel became visible from the site and continued until the water surface became practically calm.

The software package ExploreV 1.5 (NortekUSA) was used to process the results of ADV measurements. Prior to computations of the statistical characteristics of turbulence, each record was inspected visually to identify possible problems such as spikes, trends, or abrupt discontinuities in the time series. Post-processing of the data involved removal of the defective portions of the time series using the data clipping capabilities of the software, spikes detection with a set of criteria implemented in the ExploreV and the recovering of bad samples with linearly interpolated values. Editing of time series thus allowed to exclude errors associated with spurious signals emerging from interaction of acoustic signal with large floating particle in the stream such as woody debris.

4 RESULTS

A coordinate system with a streamwise x direction aligned with the direction of vessels motion, a transversal y direction, and a vertical direction z, originating at the canal bed and directed toward the free surface is adopted herein.

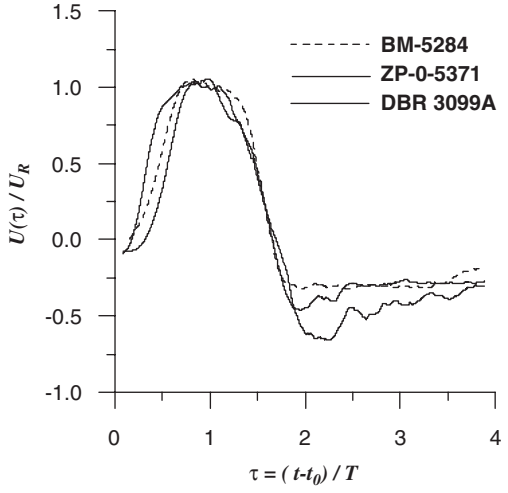


Figure 6. Dimensionless velocity records.

An example of measured velocities and water levels is shown in Figure 5. Analysis of velocity fluctuations and changes of water level allows to unambiguously determine different elements of the vessel's wake pattern. It can be also seen that velocity patterns display apparent similarity, though there are definite differences in length, load and speed of vessels.

Records of velocity and water level were processed to obtain the periods of drawdown waves and mean values for return currents U_R (calculated as an averaged value for the time interval corresponding to the period of drawdown wave). The measured velocity patterns can be scaled with those two parameters (Figure 6).

The data plotted in Figure 6 were smoothed using boxcar procedure to eliminate fluctuations of higher order. Close correspondence between return velocity and small scatter in the data thus confirm that vessel length and speed are the most valuable parameters controlling the formation of return currents. At the same time records exhibited larger scatter for slope supply currents that most probably included the effect of a tug hull and peculiarities of propeller-generated currents individual for different types of tugs.

Close examination of individual patterns of return velocity as the result of zooming and resizing (Figure 7) supports the acceptance for the condition of steadiness (3). Comparison of measured pattern and accepted in the model (10) is presented in Figure 7b.

Periods of drawdown waves and their approximates calculated from length and speed of vessels are shown in Figure 8. A line corresponding to the linear regression between these parameters outlines the area of perfect agreement. These plots reveal that the period of drawdown wave can be simply estimated for a vessel with a certain size.

Transverse distributions of dimensionless return velocities and their comparison with model (10) are presented in Figure 9. Standard least squares procedure yielded values for parameters $\alpha = 2.24$ and $\beta = 2.52$ ($R^2 = 0.92$). The data indicate close agreement with the solution by model (10) indicated as the solid line in Figure 9.

5 DISCUSSION AND CONCLUSIONS

A simplified analytical model for predicting return currents developing in the area of drawdown wave accompanying the passage of large commercial vessels in the canals is presented. The comparison of the model's prediction with the results of field observations indicated a good performance of the model. This allows recommending the model for use in ecological studies as a tool of estimating the effect of navigation on different species of the aquatic life. Below we present an example of the model application for characterization of fish habitats.

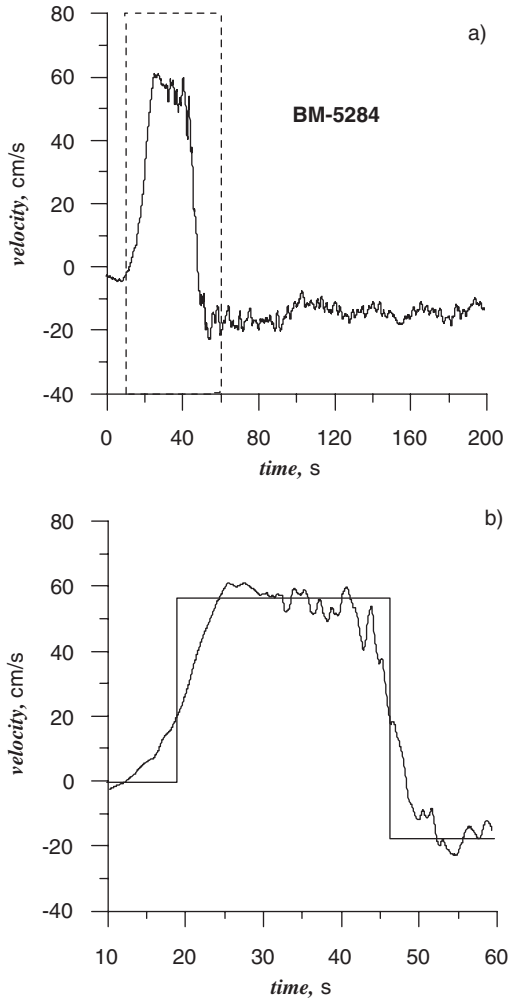


Figure 7. Zoomed velocity record and its approximation in the model (thick line).

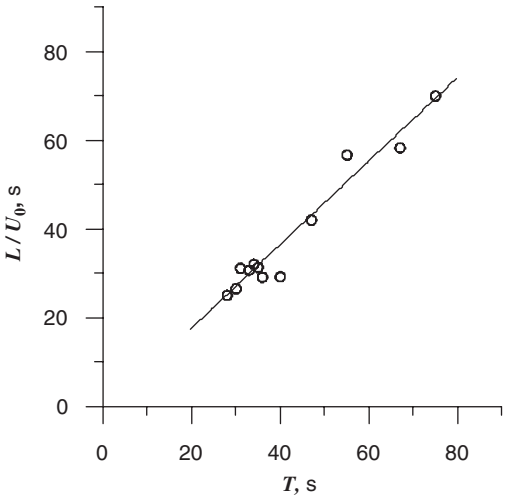


Figure 8. Comparison of measured (T) and computed periods for drawdown waves.

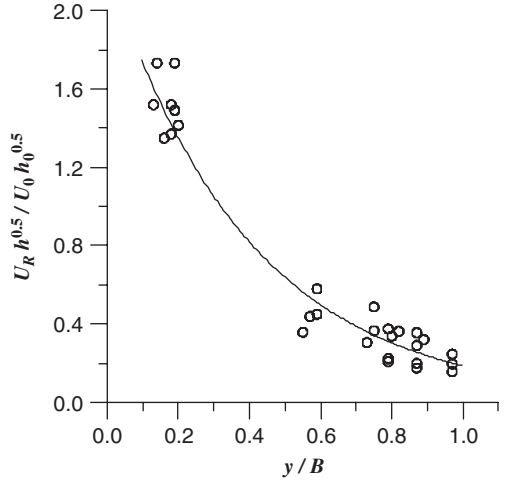


Figure 9. Measured (circles) and predicted (line) values of return velocities.

Fish swimming performance was assessed according to a general model of maximum swimming speed on the basis of white lateral muscle's contraction time and the relation between tailbeat frequency and forward motion (Wardle 1975). According to this estimation, a 15 mm long fish larvae swims with a maximum speed of 0.22 m/s, that is considerably below the navigation-induced return current velocity. The lower level of return current for the Oder-Havel canal of 0.7 m/s would be performed by a 47 mm long fish for less than 20 s (Wardle 1975). However, when larvae of common freshwater fish species hatch at total length of less than 10 mm and swim free between 6–15 mm (Koblickaya 1981; Pinder 2001), their maximum swimming performance covers only a split of the physical threshold conditions (Figure 10).

To conclude, sustainable management of inland waterways requires minimizing the navigation impact by enhancing ecotone diversity and shoreline structures. This can be achieved by (1) preserving existing and creating additional embayments; (2) revitalizing submerged and emerged macrophytes or similar microhabitat structures; and (3) establishing temporal lowered speed limits for commercial tows for the periods especially dangerous for juvenile fishes.

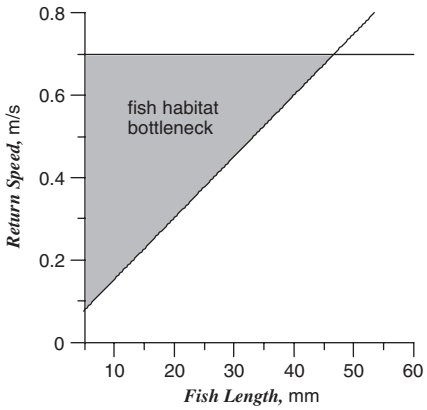


Figure 10. Maximum swimming speed of fish (according to Wardle 1975) in relation to the return velocities.

ACKNOWLEDGEMENTS

The authors wish to express their appreciation to R. Arlinghaus, H. Bungartz and W. Sauer for their participation in field studies. H. Zwadlo is thanked for his help with preparation of the submersible mount for ADV probes.

REFERENCES

Arlinghaus, R., Engelhardt, C., Sukhodolov, A., & Wolter, C. 2002. Fish recruitment in a canal with intensive navigation: implications for ecosystem management. *J. of Fish Biology* 61: 1386–1402.

Blaauw, H.G, van der Knaap, F.M.C., de Groot, M.T., & Pilarchyk, K.W. 1984. Design of bank protection of inland navigation fairways. *Transactions of Delft Hydraulic Lab.* 320.

Haefner, J.W., & Bowen, M.D. 2002. Physical-based model of fish movement in fish extraction facilities. *Ecological Modelling* 152: 227–245.

Koblickaya, A.F. 1981. *A key for identifying young freshwater fishes.* Moscow: Light- and Food Industry Publishing.

Kubec, J., & Podzimek, J. 1996. *Wasserwege.* Hanau: Verlag Werner Dausien.

Maynord, S.T. 1996. Return velocity and drawdown in navigable waterways. *Technical Report of US Army Eng. Waterways Experimental Station*, HL-96-7, Vicksburg.

Maynord, S.T., & Siemsen, T.S. 1991. Return velocities induced by shallow-draft navigation. In: *Hydraulics Engineering*, ASCE, New York: 894–899.

Mazumder, B.S., Bhowmik, N.G., & Soong, T.W. Turbulence in rivers due to navigation traffic. *J. of Hydraulic Eng.* 119(5): 581–597.

Pinder, A.C. 2001. *Keys to larval and juvenile stages of coarse fishes from fresh waters in the British Isles*. Cumbria: Freshwater Biological Association.

Simons, D.B., Li, R.M., Chen, Y.H., Ellis, S.S., & Chang, T.P. 1981. Investigation of effects of navigation trafic activities on hydrologic, hydraulic, and geomorphic characteristics. *Report of Environmental Work Team*, Minneapolis.

Stockstill, R.L., & Berger, R.C. 1994. *HIVEL2D: a two-dimensional flow model for high-velocity channels*. *Technical Report of US Army Eng. Waterways Experimental Station*, REMR-HY-12, Vicksburg.

Vardle, C.S. 1975. Limit of fish swimming speed. *Nature* 255: 725–727.

Wolter, C., & Vilcinskas, A. 1997. Perch (*Perca fluviatilis*) as an indicator species for structural degradation in regulated rivers and canals in the lowlands of Germany. *Ecology of Freshwater Fish* 6: 174–181.

This page intentionally left blank

C.3. Flood management and control

This page intentionally left blank

River Flow 2004 – Greco, Carravetta & Della Morte (eds.)
© 2004 Taylor & Francis Group, London, ISBN 90 5809 658 0

River flow forecast by means of selected black box models

A. Piotrowski, P.M. Rowiński & J.J. Napiórkowski
Institute of Geophysics, Polish Academy of Sciences, Warsaw, Poland

ABSTRACT: Performance of two different types of approaches were investigated with respect to the daily river flow predictions. The first approach is Multi-Layer Perceptron Artificial Neural Network, the second one, based on the deterministic chaos concept, is so called Phase-Space Reconstruction (PSR) model. Both models were applied to daily river flow data collected from several gauges, located in river reaches in western Canada. Each data set consists of more than 10000 consecutive daily measurements. The method based on the phase-space reconstruction theory has been applied despite the fact that the authors doubt in the existence of deterministic chaos in the river system. Classical phase-space method may be applied only to single time series data. In the present study an extension was proposed, in which time series from additional gauge stations added to the system. Comparison of models' performance was made for this extended and classical approaches for both phase-space reconstruction and Artificial Neural Networks models.

1 INTRODUCTION

An accurate forecasting of river flow is a fundamental problem in hydrological sciences. In recent years application of black box type models to runoff prediction has been gaining more popularity due to their easiness of employment and relatively low number of variables involved. Multi-Layer Perceptron Artificial Neural Networks (ANN) are probably most broadly used for forecasting (Hsu et al. 1995, Campolo et al. 1999, Campolo et al. 2003, Dolling & Varas 2002, Chibanga et al. 2003 and many others). They are the simplest among the non-linear neural network models, nevertheless they are capable of making very accurate forecast, when proper set of input variables is taken into account. On top of that they are easy to be trained, contrary to, for example, radial basis functions networks. ANN approach is sometimes called global approximation approach as it deals with all set of historical data values to optimise network weights, which means that all known information about the system is used to make a relevant forecast.

A methodologically different approach, though still quite popular, pertains to phase-space reconstruction (Jayawardena & Lai 1994, Porporato & Ridolfi 1997, Sivakumar et al. 2002). It is a local approximation approach and it has been developed in the framework of the deterministic chaos theory. The presence of low-dimensional chaotic behaviour in the rainfall-runoff process is a matter of an ongoing debate (see e.g. Schertzer et al. 2002) and it will not be discussed in detail herein. Let us only note that the main idea of this approach corresponds to the possibility of the reconstruction of the phase-space from a discrete set of values for a given observable scalar such as water stages at a given gauge station. The authors of the present study will benefit from the phase-space reconstruction method which in fact is a way of finding the most similar situations in historical data and applying only these selected parts of data set for forecasting. It seems that this method may stand alone as a reliable tool without linking it to the existence or nonexistence of a hypothetical deterministic dynamical system leading to disordered solutions. According to Sivakumar et al. (2002), the phase-space reconstruction method is better than ANN approach when dealing with autoregressive forecast problem. Further in the paper it will be shown that such conclusion is premature and in case of the selected Canadian river reaches both ANN and phase-space reconstruction methods boast similar performance of forecasting daily runoffs. Additionally an extension, further called as quasi-phase-space reconstruction method, will be proposed and this method will allow for the use of the data from more than one gauge station. As expected this method will improve the results considerably.

The comparison of the results of two black box models will be presented according to the following scheme:

– version A: as inputs only historical runoff data from the same gauge are applied for both ANN and phase-space reconstruction approaches;

– version B: forecast is made for the same gauge as in version A, but input data set consists of data from 2 or 3 gauges. Additional gauge for version B is selected at the same river where the forecasting gauge or its main tributary is placed.

For each case 3 consecutive measurements from particular gauge were treated as input variables which means that we have 3 input variables in version A, and 6 or 9 in version B.

2 FLOW DATA

Long enough data sets collected in 5 western Canadian rivers (Figure 1) are applied in the analyses (Environment Canada 2003). Table 1 presents the duration of daily data sets, location of the main gauge (used for the forecasts, denoted by number 1) and the additional gauges (applied in version B only, denoted by number 2 or 3). Each data set contains more than 10000 daily measurements, and 5 river reaches are considered in the study. It seems to provide sufficient information to compare the performance of all the considered models. In each case the daily river flow forecast was made for last 5000 measurements. Those 5000 measurements were not taken into account during ANN training process, but they were only used to compare performance of both models at each river reach. The ANNs were trained with the use of the earlier records (larger than 5000 elements in each case).



Figure 1. Location of gauge stations.

Table 1. Description of data sets.

River	Gauge sites	Length
Athabasca*	1. Hinton 2. Jasper	71.01.01– 02.12.31
Fraser* (upper part)	1. Above Texas Creek 2. Shelley	55.01.01– 02.12.31
Fraser* (lower part)	1. Mission 2 Above Texas Creek	65.05.01– 92.12.31
South Saskatchewan**	1. Medicine Hat 2. Bow river 3. Oldman river	65.01.01– 02.12.31
North Saskatchewan**	1. Prince Albert 2. near Deer Creek	70.01.01– 01.12.31

* mountainous terrain, ** steppe.

3 MODELS APPLIED

In this section attention is focused on the implementation of some anticipatory nonlinear methods based on Deterministic Chaos and Artificial Neural Networks for prediction of the inflows.

3.1 *Artificial Neural Network approach*

Multi-Layer Perceptron Artificial Neural Networks have become widespread in recent years and the researchers often claim that they provide a useful tool for the predictions of river flow. Three layer networks with sufficient number of hidden nodes are usually applied due to the continuity of the relevant function. Every network contains an appropriate number of input and output nodes which is equal to the number of input and output variables, and the assumed number of hidden nodes. There is no effective rule for the estimate of the number of hidden nodes. In this study it usually turns out to be close to the number of input nodes, but in each case it is experimentally verified.

The ANN nodes in neighbouring layers are linked via weighted connections. The values of those weights can be adaptively modified during the process of training the network. In this study, due to the relatively simple architecture of all the networks, Levenberg–Marquardt nonlinear optimisation algorithm was adopted (Press et al. 1989).

Shortly the Multi-Layer Perceptron network (see Figure 2) operates in the following way: signals s_i ($i = 1, \ldots, N$) from the input nodes (e.g. values of input variables normalized to 0–1 interval) are multiplied by

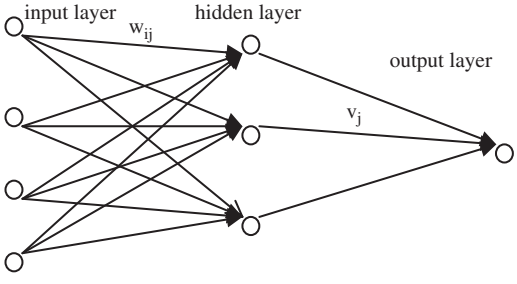


Figure 2. Multi-Layer Perceptron Artificial Neural Network scheme.

proper weights w_{ji} (j = 1, … K), connecting the neuron from which signal has been dispatched and a suitable neuron in the second layer.

In the second layer the weighted sum of all the inputs are computed and then transformed by logistic function

$$f(x) = \frac{1}{1 + e^{-ax}} \tag{1}$$

giving the output value of a neuron in the second layer:

$$z_j = f\left(\sum_{i=1}^{N} s_i w_{ji}\right) \tag{2}$$

Afterwards the weighted signals z_j (multiplied by proper weights v_j), are transferred to the neuron of the third layer. In the neuron of the third layer the new weighted sum is computed

$$y = \sum_{j=1}^{K} v_j f\left(\sum_{i=1}^{N} s_i w_{ji}\right) \tag{3}$$

and after de-normalization of the output, the sought (forecasted) value may be determined. This is a feed-forward network, which means that there is only one direction of the flow of information, from the input to the output layer.

3.2 *"Phase-space reconstruction" approach*

Another method used in runoff forecasting studies is motivated and based on the theory of dynamical systems (Kantz & Schreiber 1997), i.e. the time evolution is defined in some phase-space. For a purely deterministic system, once its present state is fixed, the states at all future times are determined as well. So it is essential to establish a phase-space for the system such that specifying a point in this space specifies the state of the system and vice versa. Then one can study the dynamics of the system by studying the dynamics of the corresponding phase-space points.

Characteristic for chaotic systems is that in many cases the corresponding attractors turn out to be strange attractors of the fractal structure with a non-integer dimension (Kudrewicz 1993, Ott 1993).

Since it is natural to describe a deterministic dynamical system as an object in phase-space, it is also most natural to use a phase-space description for approximation of the dynamic of the system. Such approximate dynamics can be useful for prediction.

The reconstruction of a vector space which is equivalent to the original state space of a system from a scalar time series is the basis of almost all nonlinear methods. Scalar measurements is a projection of unobserved internal variables of a system onto an interval on real axis. It is obvious that even with a precise knowledge of the measurements it may be impossible to reconstruct the state space of the original system from the data. Fortunately, we are rarely keen of obtaining a whole, precise description of the process. It is usually enough to determine its good approximation. Hence a reconstruction of the original space is not really necessary for the data analysis. It is sufficient to construct a new space such that the attractor in this space is "equivalent" to the original one (Kantz & Schreiber 1997).

The classical situation, as treated in hydrological sciences, though being a matter of serious debate (e.g. Schertzer et al. 2002) is the following. A sequence $\{x_i\}$, $x_i \in R^1$, i = 1, . . ., N, of measured values is given. In order to find an approximation of the deterministic system one considers the function F defined by the following relationship

$$y_m^{i+\Delta} = F(y_m^i) = F(x_i, x_{i-1}, ..., x_{i-(m-1)}) \tag{4}$$

with a properly adjusted number m, called *embedding dimension* and a given time delay Δ. Hence, the so-called quasi phase-space composed of m-element subsequences y_m^i is considered

$$y_m^i = (x_i, x_{i-1}, ..., x_{i-(m-1)}) \tag{5}$$

The function F in Equation (4) is a dynamical process in the space R^m, which according to the embedding approach (Takens 1981) forms an attractor in R^m, if the original process is a deterministic chaos. To determine proper embedding dimension from a finite sample of points one determines, for example, correlation integral $C_N(m, r)$ for several embedding dimensions (Grassberger & Procaccia 1983). Then correlation dimension D is determined as the slope of function $\ln C_N(m, r)$ with respect to ln(r), in a respective range of sufficiently small r, such that the function behaves as a linear one (one expects C to scale like power law, $C(r) \propto r^D$). Now using Takens theorem, one can put $m = 2D + 1$ as the searched embedding dimension.

One can proceed then to the stage of determining the prediction model for the relationship F in Equation 4. It is possible for deterministic chaos case: as the process is really deterministic and due to existence of an attractor. The considered prediction model has the form of a function such that it approximates the function F, or even less – a "acomponent" of F, being prediction of a future value of state.

$$x_{i+\mathbf{T}} = f_{\mathbf{T}}(x_i, x_{i-1}, ..., x_{i-(m-1)}) \tag{6}$$

where T is a prediction horizon. Such a function depends on the time instant i of making prediction,

and on the horizon T of this prediction. Thus, one can seek for a function

$$f_{\mathrm{T}}^{i}(y_{m}^{i}) = f_{\mathrm{T}}^{i}(x_{i}, x_{i-1}, \ldots, x_{i-(m-1)}) \tag{7}$$

that would determine a good approximation of the value $x_{\mathrm{i+T}}$ of the given sequence $\{x_{\mathrm{i}}\}$.

Our computations do not confirm the straightforwardness of the application of the described approach and we become skeptical about its correctness. Correlation integral for data described in Section 2 revealed no obvious scaling region as the indicator of self-similar geometry. The saturation value of D (which is just the lower bound of box dimension) with increasing m was not clear at all. We are also aware of the occurrence of noise in the applied data, so the question arises whether those data can be analyzed within the deterministic system.

As a consequence of the above we applied a part of the method derived within the deterministic chaos theory, but as mentioned in Introduction there is no need to decide whether the chaos exists in the system under consideration. We keep the name of the method as the "phase-space reconstruction" approach (Jayawardena & Lai 1994, Sivakumar et al. 2000) to show its origin but we do not claim we have applied the embedding theorem. A method of delays as a realization of the "phase-space reconstruction" approach has been selected for the purpose of the present study. In order to make a forecast one constructs m-dimensional data vectors from measurements spaced equidistant in time (temporal sequence of measured values at the selected gauge) which creates an analogy to the phase-space.

Further the principle of the applied method lies in the search of K-points from the d-dimensional point set that are placed at the smallest distance (according to some assumed measure) from the points representing the current situation. In other words we are interested in finding K vectors of the length m from the past, most of all resembling the current situation. We do assume one day time delay which allows us to use the consecutive recordings from the gauge station. Thus we obtain an autoregressive forecast for each day (version A). In the present study it was assumed that m = 3 which proved to produce reasonable results.

3.3 *Quasi "phase-space reconstruction" approach*

We proceed similarly as in Section 3.2 but this time we test whether the similar forecast is possible using data collected from more than one gauge. Intuitively more information should lead to a better forecast. Being remote from the rigorous treatment of the deterministic chaos we may "extrapolate" the previous considerations from scalar observables (water stages) to vectors. This time we build 2m-dimensional quasi "phase-space" where the first d-vector is made of the consecutive measurements from the first gauge and the second d-vector is made of the consecutive measurements in the second gauge station (time delay is again assumed as one day).

One should note that the measurements from different gauges may have different standard deviations, so the scale related to the first three components and the last three components may be heterogeneous, that can impact the search for N closest neighbours in this space. Fortunately in our case the performance of forecast made using data sets divided by standard deviation is almost the same as for raw data and therefore no normalization was necessary. The above describes the technique for daily runoff forecast in version B.

4 COMPARISON OF APPLIED METHODS

The comparison will be made for both versions A and B by means of correlation coefficient applied to measured and predicted daily or (in one case) 4-daily runoff volume increments (see Table 2). Such approach shows the performance of the model much better than the correlation applied to just actual runoff volumes where almost all results are close to unity independently of the quality of results.

As it was expected inclusion of additional gauge station (version B) improves the results quite significantly for both "phase-space reconstruction" as well as ANN (Figures 3–8). The only exception is the lower Fraser river. The addition of data from the gauge station at Texas Creek did not help the "phase-space reconstruction" technique. The exemplification of this fact is seen in Figure 4. Note that all the Figures 3–8 are prepared for a selected period of about one month only, out of 13 years time series. For clarity the relevant period was chosen to reveal especially large changes in the daily river runoff.

This is worth mentioning that in version A all ANN and phase-space models show similar performance.

Table 2. Correlation coefficients of forecasted and measured (daily, except noted case) runoff changes.

	Version A		Version B		
River	ANN	PSR	ANN	Quasi PSR	No. of gauges
Athabasca	0.674	0.667	0.904	0.899	2
Fraser (upper part)	0.738	0.735	0.928	0.922	2
Fraser (lower part)	0.478	0.512	0.660	0.507	2
South Saskatchewan	0.518	0.507	0.979	0.796	3
North Saskatchewan (1 day forecast)	0.601	0.603	0.736	0.760	2
North Saskatchewan (4 day forecast)	0.364	0.317	0.856	0.847	2

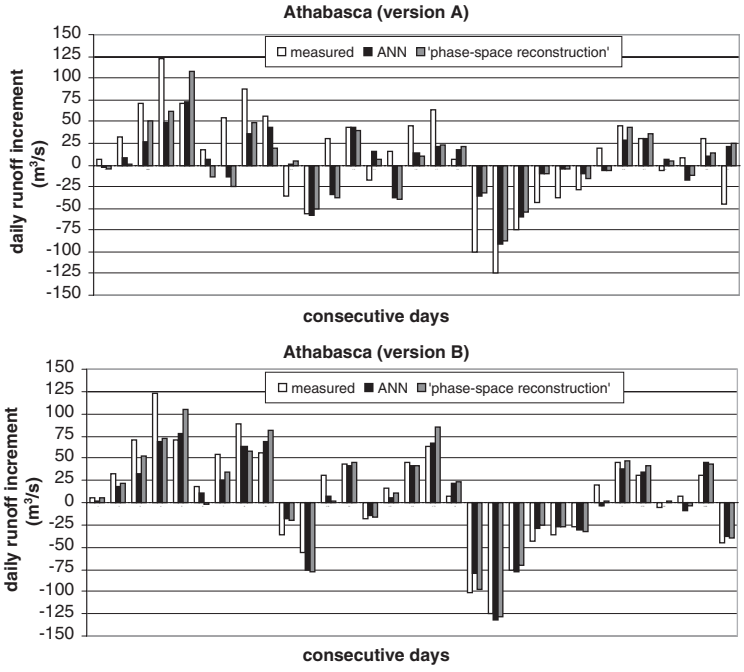


Figure 3. Comparison of one lead day runoff forecast for Hinton gauge station, on Athabasca river, obtained from ANN and quasi "phase-space reconstruction" models in versions A and B.

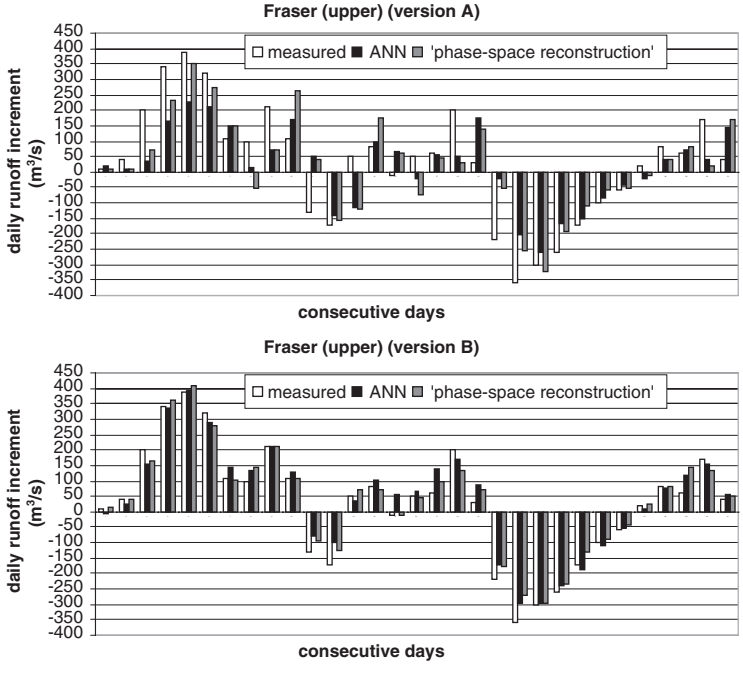


Figure 4. Comparison of one lead day runoff forecast for gauge station near Texas Creek (BC), on upper part of Fraser river, obtained from ANN and quasi "phase-space reconstruction" models in versions A and B.

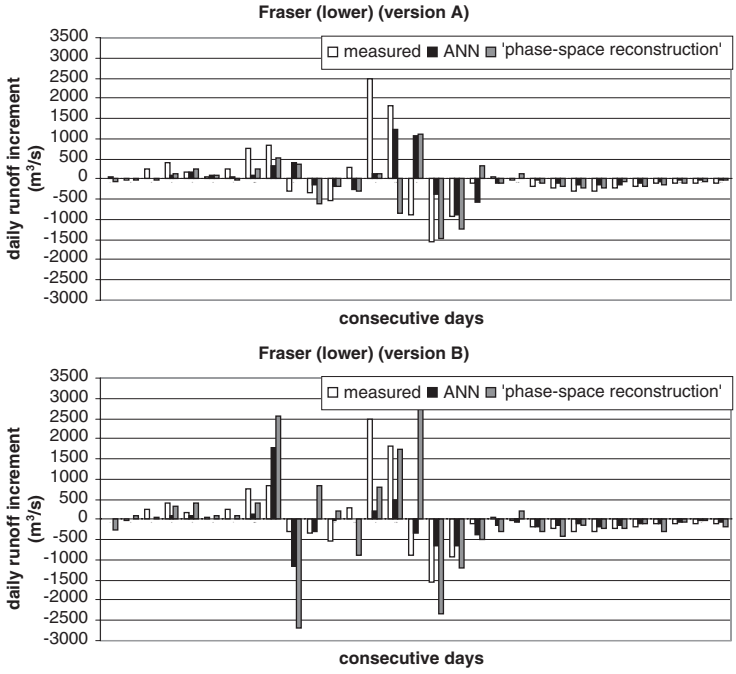


Figure 5. Comparison of one lead day runoff forecast for gauge station near Mission (BC), on lower part of Fraser river, obtained from ANN and quasi "phase-space reconstruction" models in versions A and B.

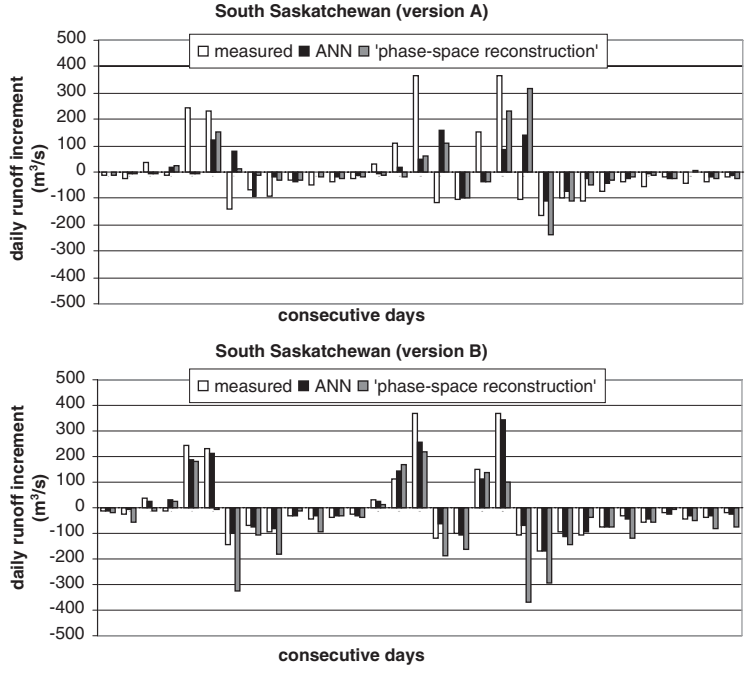


Figure 6. Comparison of one lead day runoff forecast for Medicine Hat gauge station, on South Saskatchewan river, obtained from ANN and quasi "phase-space reconstruction" models in versions A and B.

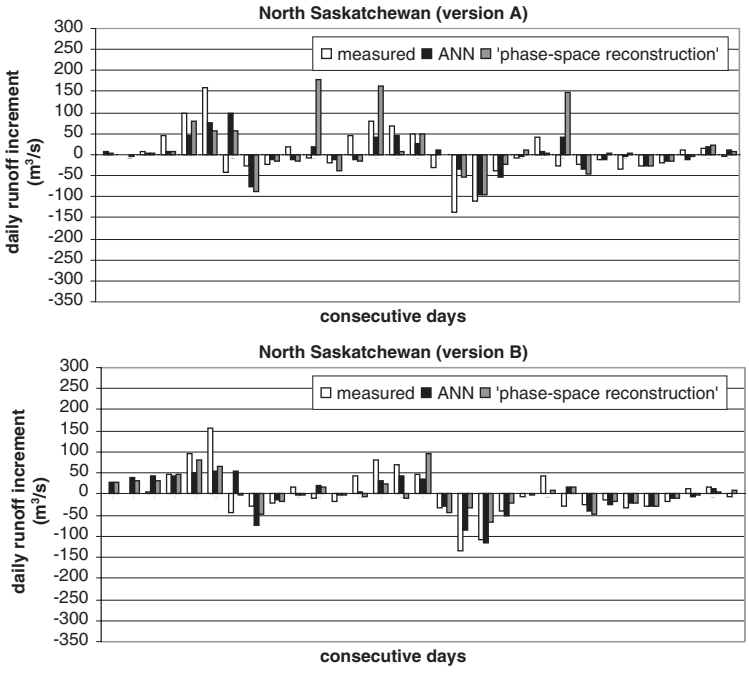


Figure 7. Comparison of one lead day runoff forecast for Prince Albert gauge station, on North Saskatchewan river, obtained from ANN and quasi "phase-space reconstruction" models in versions A and B.

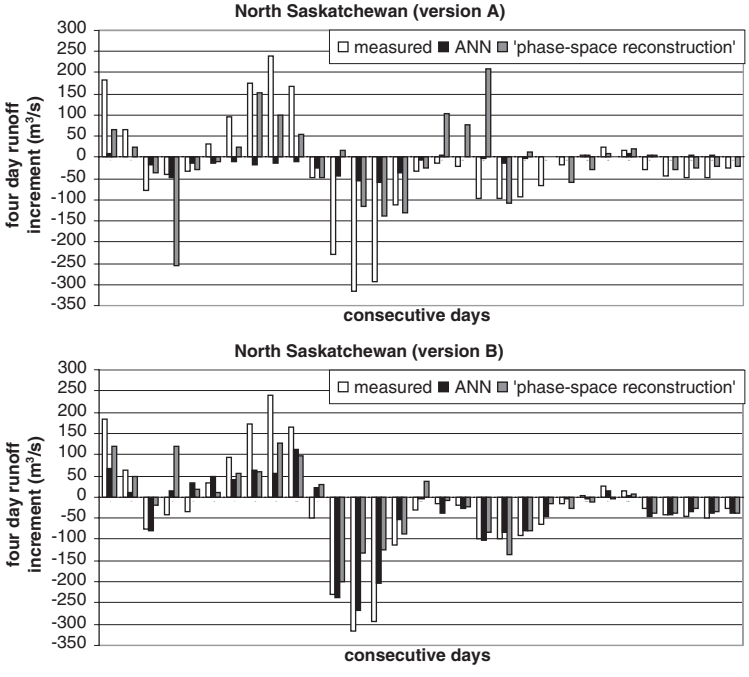


Figure 8. Comparison of four lead day runoff forecast for Prince Albert gauge station, on North Saskatchewan river, obtained from ANN and quasi "phase-space reconstruction" models in versions A and B.

This result is different from the one of Sivakumar et al. 2002 who considered daily river flow data set from only one gauge station in Thailand. A very short time series was analysed in that study, and the authors removed half of the data set because large differences were observed in those two parts of time series. In that study the phase-space model performance was much better than ANN.

Note that in version B in case of South Saskatchewan river prediction made by ANN is very good indeed and better than that by quasi "phase-space reconstruction" (see Figure 6). In case of quasi "phase-space reconstruction" the difficulty lies in the fact that it is quite hard to find enough vectors (3 delayed data from three gauges) in 9-dimensional space similar to the current data allowing for the evaluation of relevant linear regression coefficients.

An astonishing fact is that in version B in respect to North Saskatchewan River, 4-daily runoff forecast (Figure 8) proves to be better than the daily predictions (Figure 7, Table 2). It is the result of the selection of additional gauge at the distance corresponding to flow routing during the time period of 4 days.

5 CONCLUSIONS

The present study that was based on long enough time series from five river reaches shows that the method analogical to the phase-space reconstruction derived in the framework of deterministic chaos theory is useful for runoff predictions even if we have no evidence about the existence or non-existence of chaos in the considered river systems. It has also been shown that contrary to what is suggested in some hydrological articles, Artificial Neural Networks may provide accurate enough forecasts, in many cases even better than those based on "phase-space reconstruction". On top of that it has been shown that the use of additional information from other gauges improves significantly the forecasts based on both ANNs and "phase-space reconstruction". Such proposal has not been considered in respect to "phase-space reconstruction" in literature so far.

REFERENCES

Campolo, M., Andreussi, P. & Soldati, A. 1999. River flood forecasting with a neural network model. *Water Resources Research*, 35(4): 1191–1197.

Campolo, M., Soldati, A. & Andreussi, P. 2003. Artificial neural network approach to flood forecasting in the River Arno. *Hydrological Sciences Journal*, 48(3): 381–398.

Chibanga, R., Berlamont, J. & Vandewalle, J. 2003. Modelling and forecasting of hydrological variables using artificial neural networks: the Kafue River sub-basin. *Hydrological Sciences Journa*, 48(3): 363–379.

Dolling, O.R. & Varas, E.A. 2002. Artificial neural networks for streamflow prediction. *Journal of Hydraulic Research*, 40(5): 547–554.

Environment Canada web page: http://citech.pyr.ec.gc.ca/aterweb/

Grassberger, P. & Procaccia, I. 1983. Measuring the strangeness of strange attractors. Physica 9(D): 189–208.

Hsu, K-L., Gupta, H.V. & Sorooshian, S. 1995. Artificial neural network modeling of the rainfall-runoff process. *Water Resources Research*, 31(10): 2517–2530.

Jayawardena, A.W. & Lai, F. 1994. Analysis and prediction of chaos in rainfall and stream flow time series. *Journal of Hydrology*, 153: 23–52.

Kantz, H. & Schreiber, T. 1997. Nonlinear Time Series Analysis. Cambridge University Press, Cambridge.

Kudrewicz, J. 1993. Fractals and Chaos, *WNT*, Warsaw.

Ott, E. 1993. Chaos in Dynamical Systems. Cambridge University Press.

Porporato, A. & Ridolfi, L. 1997. Nonlinear analysis of river flow time sequences. *Water Resources Research*, 33: 1353–1367.

Press, W.H., Flannery, B.P., Teukolsky, S.A. & Vetterling, W.T. 1988. Numerical recipes: The art of scientific computing (Fortran Version). Cambridge University Press.

Schertzer, D., Tchiguirinskaia, I., Lovejoy, S., Hubert, P., Bendjoudi, H. & Larcheveque, M. 2002. Discussion of "Evidence of chaos in the rainfall-runoff process". *Hydrological Sciences Journal*, 47(1): 139–148.

Sivakumar, B., 2000. Chaos in hydrology: important issues and interpretations. *Journal of Hydrology*, 227: 1–20.

Sivakumar, B., Jayawardena, A.W. & Fernando, T.M.K.G. 2002. River flow forecasting: use of phase-space reconstruction and artificial neural networks approaches. *Journal of Hydrology*, 265: 225–245.

Takens, F. 1981. Detecting strange attractors in turbulence. In: Rand, D., A. & Young, L.S. (Eds.), *Dynamical Systems and Turbulence*, Lecture Notes in Mathematics, 898: 366–381. Springer, Berlin.

River Flow 2004 – Greco, Carravetta & Della Morte (eds.)
© 2004 Taylor & Francis Group, London, ISBN 90 5809 658 0

Merging of river training and restoration in river basin management

N. Tamai
Kanazawa University, Kanazawa, Japan

ABSTRACT: River training works have been executed for flood control or flood damage mitigation and water resources development. Human impacts, for instance, reservoirs, flood levees, straightening of channels, intake structures and so on, have altered natural rivers to great extent. Now river engineers are requested to cope with ever increasing flood peaks and to work for restoration of altered rivers. In some cases river training works and restoration are understood as a choice between two things. But the author points out that this is a fault of dualism.

When our target is to make basin-wide utility maximum, we cannot resort to conventional flood control schemes. We need to pay much attention to non-structural means including floodplain management and river restoration. Floodplain management is one of tools for demand control in land use. River restoration is one of ways for human demand control. In river restoration it is essentially important to give more space or freedom to rivers. This will be accomplished by human demand control. River restoration is a symbolic slogan to accomplish a multiple purpose project considering flood damage mitigation and conservation of ecosystems for river basin management.

1 INTRODUCTION

River training works have been executed for flood control or flood mitigation and water resources development. Human impacts, for instance, reservoirs, flood levees, straightening of channels, intake structures and so on, have altered natural rivers to great extent. Now river engineers are requested to work for restoration of altered rivers. In some cases river training works and restoration are understood as a choice between two things. But the author points out that this is a fault of dualism.

Human impacts on natural environment becomes bigger and bigger since industrial revolution. One clear example is global warming. Human activities developed to exceed capacity of natural environment. Human impacts have reached to an extent to exceed a righting moment of environment in the latter half of the 20th century. Then nature cannot recover its original state and entered into an irreversible process of deterioration. Under such conditions we need asset management to conserve nature as finite resources.

When we understand the essential features of natural asset of a river basin, we will obtain a unified view of entity of a river basin including natural disturbances, human impacts and responses of a basin system, and succession of ecosystems in a basin. We need to change paradigm from selection by dualism to coexistence by consensus among all stakeholders.

2 FLOOD CONTROL AND A NEW CONCEPT OF BASIN MANAGEMENT

At first interaction between human activities and their consequences in river basins is summarized in the area of flood control. The goal of this chapter is to establish a new concept for amalgamation of flood control/ flood mitigation and river restoration.

2.1 *Does flood control investment bring about safer society?*

Design flood discharge increases as flood control works develop. In Figure 1 the historical increase of the fundamental design discharge in case of the Tone River that has the largest basin area in Japan is shown. In the present Master Plan authorized in 1980 the fundamental design discharge is 22,000 m^3/s in which peak cut 6000 m^3/s is planned by reservoirs and a diversion channel.

The river channel and flood levees are designed to cope with the allotted discharge of 16,000m^3/s to the river channel. In this master plan a probabilistic approach was adopted for the first time in determination of the fundamental design flood. Starting from the basin-wide river improvement work planned in 1901, observed maximum discharge was adopted as the design flood until the master plan of 1949. It is clear that the design discharge increased as we

make efforts for flood control works and total investment to flood control increases. In other words flood control works brought about larger amount of peak discharge.

The design flood of the Yodo River that plays a major role for water resources in Osaka area experienced a similar increase. Why does this anomaly happen? The key factor of this anomaly is feedback from human activities in a river basin to a river channel. When flood control works succeed into a certain level, human settlement to a river basin increases and economic activities develop under safer situation from threatening of flooding. Higher rate of urbanization and economic activities tend to develop with positive feedback with each other.

Comparison of the variation of the design discharge with societal items, population and gross domestic product, is shown in Figures 2 & 3. We can recognize good correlation of an increasing rate between the design flood and GDP. But we had sharp reduction in GDP just after the World War II. Therefore, tendency in GDP curve shows unusual disturbance around 1945. Flood control works creates safer living conditions in a river basin. Goals of investment for flood control are to protect floodplain from flood for more safe space for human beings and higher economic products. In this sense Figure 2 shows that goals of flood control projects are accomplished in Japan because GDP showed good growth in the 20th century.

But urbanization and higher economic activities generate negative side effects on a river channel. Urbanization means decrease of forest areas and agricultural land, and increase of non-permeable areas. These changes cause larger amount of runoff and faster convergence of water into river channels. In parallel with higher economic activities human society needs much wider space and in consequence, rivers are confined into a narrow space between flood levees. Infiltration in forest and agricultural land reduces and temporary storage capacity in river basins is lost by housing projects and industrial activities. Consequently, the fundamental design flood from a river basin increases and arrival time of floods becomes short as we develop river improvement works.
Ironically river channels receive bigger flood and water stage becomes higher as a consequence of river improvement works. Therefore, advanced level of flood control projects and larger return period do not necessarily mean that our life becomes safer.

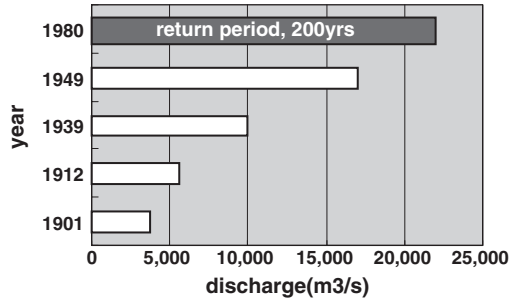


Figure 1. Historical variation of the fundamental design discharge of the Tone River in the Master Plan.

2.2 *How can we create comprehensively safe society?*

As we see in the section 2.1 series of flood control works generate larger design flood. This means that a flood control project needs another flood control works of a larger scale in the future. A typical chain to show the consequences is as follows. In this expression an arrow shows resulted changes of social and hydrological factors in a river basin. A flood

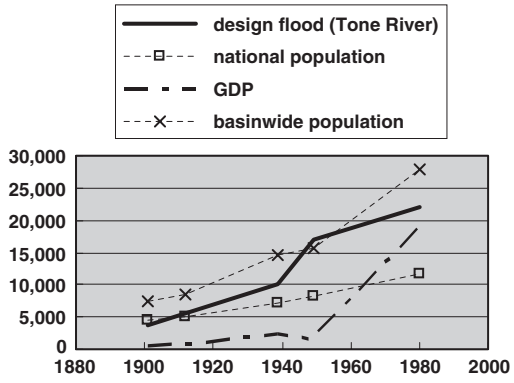


Figure 2. Comparison of the variation of the design discharge of the Tone River with societal items (Unit is as follows: design discharge, m^3/s; national population, 10 thousand persons; GDP, 10 billion yen, adjusted as of 1980; basin-wide population, thousand persons).

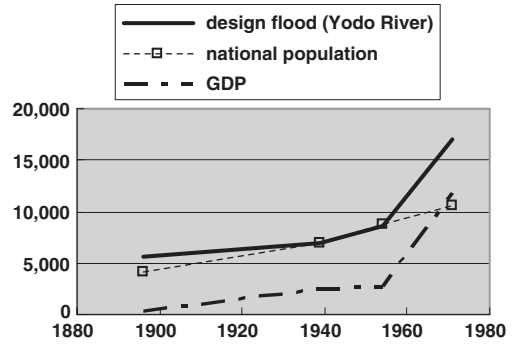


Figure 3. Comparison of the variation of the design discharge of the Yodo River with societal items (Unit is as follows: design discharge, m^3/s; national population, 10 thousand persons; GDP, 10 billion yen, adjusted as of 1980).

control project is executed. → The river channel has larger conveyance of flow and becomes safer against flooding. →Increase of population in river basins occur. → Urbanization develops. → Higher industrial activities develop. → Land use in riparian zones develops. → Increase of peak discharge is generated by the change of hydrological processes in a river basin. →Riparian zones become vulnerable to flooding again. → A new project for higher level of flood control becomes necessary.

We need to remind that flood is a consequence of human settlement. There is no damage even if the water stage becomes extremely high in a river basin under purely wild conditions. Under wild situation a high flow is only a scene of natural disturbances and we recognize no flood damage. This fundamental characteristic is shown in Table 1.

The development of projects and recent tendency related with flood control are summarized in Table 2. Traditionally river engineers were engaged in flood control projects or flood protection projects. Engineers hoped that they were able to control peak discharge and water stage by constructing regulating structures of a flood in a river basin. Engineers tended to consider that when the objectives of the master plan were accomplished, safety level for residents in a river basin was satisfied according to their calculation. But most of engineers considered only behavior of flood in river channels that they constructed. They did not pay much attention to human reactions in a river basin. Human behavior in a river basin is more dynamic than that engineers considered in a planning stage. Once society is given a safe condition in a river basin, land use is altered to satisfy people's desire that never stops expanding.

Developments of human activities in a river basin continuously require additional flood protection works as described in a previous section. Through experiences we gradually understand the following facts in river basins. Firstly, even if a mater plan is completed, a larger flood that exceeds a project level is possible as natural phenomena. Secondly, development of river basin makes damage potential in flood-affected area higher and higher. Thirdly, judgment of safety level by that of each facility, for instance, levee height, reservoir capacity, conveyance of river channels and diversion channels, is insufficient. Safety level of facilities is calculated for a single purpose of the facility and it does not explain safety level for residents.

Voices to require real safety of residents not the safety of facilities became strong during recent decades and importance of "non-structural means" is recognized in society. We understand that we cannot control flood that occurs as a natural event but we can only mitigate flood damage by "structural means" combined with "non-structural means". The target of non-structural means of flood control is to decrease damage potential. For example, in 1997 executive order by the President of the US already requested to avoid further development activities in floodplains below the water stage of a flood the return period of which is 100 years.

Table 1. Difference in high flow and a flood by human factor.

	Natural condition	With human settlement
High flow	High flow	Flood, damage

3 AMALGAMATION OF RIVER RESTORATION WITH FLOODPLAIN MANAGEMENT

3.1 *Dilemma caused by human impacts*

The discussion stated above is summarized schematically in Figure 4. The figure shows that development of river improvement works, which is shown by a thin solid line in Figure 4, steadily increases safety. A safer river basin is quite attractive for land developers and industrialists. They start turning forests and agricultural fields into residential and industrial areas. Land use change is accelerated by population increase in urban areas. Due to increase of non-permeable land surfaces in a river basin, peak discharge increases and arrival time of flood decreases. According to our experience urbanization occurs explosively as shown in

Table 2. Classification of projects related with floods.

Project	Objectives	Basic strategy	Typical facilities or systems
Flood control	• Reduction of the peak discharge • Reduction of the water stage	Structural means	• Reservoir • Retarding basin • Diversion channel
Damage mitigation	• Flood plain management • Evacuation from flood plain	Non-structural means	• Insurance • Hazard map • Rescue systems

Figure 4 where solid squares stand for human impacts and their consequences, such as, population, urbanization, peak discharge, etc. When urbanization rate exceeds certain level, say 50%, river improvement works become very difficult because available land is quite limited and land price becomes too expensive although we suffer from frequent floods with higher damage potential. Reducing factors shown by triangles in Figure 4 show reduction of redundancy with hazards, such as, arrival time of flood, resilience for evacuation, etc. Reduction of these factors corresponds to the increase of vulnerability of urban areas against flood.

In Figure 4 a bold solid line shows basin-wide utility or safety. The basin-wide utility is not a simple increasing function like safety by river improvement works. Safety of river improvement works indicates safety of a river channel. Once better condition is achieved, "increasing factors" and "decreasing factors" in a river basin emerge as human or social responses as are discussed in this section. Therefore, a manager of a river basin needs to consider not only conditions of a river channel (a thin solid line in Figure 4) but also nonlinear social responses (triangle and square symbols in Figure 4) at the same time. If adverse effects by other factors on flooding in a river basin as a whole become very large, basin-wide utility or safety begins to reduce with normal river improvement works as shown by a solid bold line in Figure 4. We are facing with such situations in many countries, regardless of developed and developing countries. I want to show that similar discussion can be applied to discussion in water resources and river environment later. Therefore, let me suggest you to pay attention to the point that general terms are used in Figure 4 to explain essential factors in the problem instead of specific terms in flood control.

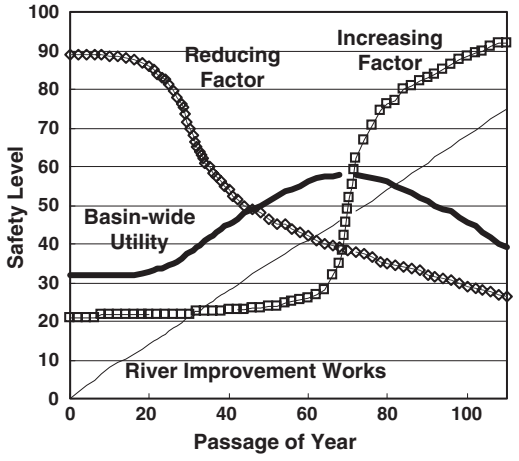


Figure 4. River improvement works and basin-wide utility (Modified from a figure in the final report of the Forum for Public Involvement and Basic Plan of Yoshino River (2001).).

Feedback loops in basin development projects in river engineering and their social influences are summarized in Table 3. Impact and response by projects for flood control, water resources development, and natural environment in a river basin are listed up in the table and the similar discussion and categorization can be applied to all of them.

Figure 4 shows a dilemma that the optimum condition for a part of a system is not the optimum for the whole system. We understand that flood control projects are not the optimum solution to secure comprehensive utility or safety of a whole basin and the mechanism of interaction of major components in a river basin is described in Figure 4.

When we recognize that pressure of urbanization is difficult to suppress and in urbanized area it is very difficult to raise safety level only by conventional means. We need to resort to non-structural means for flood mitigation in parallel with structural means. This phase corresponds to the peak in basin-wide utility in Figure 4. Through structural means for flood control we constructed many structures in a river basin and consequently altered natural conditions of a river basin. Therefore, structural means of flood control stands for alteration of a river channel and a basin.

Table 3. Summary of a feedback loop in basin development projects and their social influences.

Project	Objectives of a single project under conventional institutional structure	Associated changes in a river basin	
		Reducing or deteriorating factor	Increasing factor
Flood control	Lower probability of flooding	Forest, agricultural field, arrival time	Urbanization, non-permeable land, peak discharge
Water resources	Larger reservoir capacity	Water quality	Eutrophication (retarding time), affected area
Safe and prosperous life in river basins	Larger gross domestic product	Natural resources, Biological diversity	Impacts on environment

3.2 *Toward basin-wide consensus – farewell to dualism*

Non-structural means include floodplain management. For floodplain management we need a council that is composed of all stakeholders, typically, managers of governments, water users, residents, and audits or experts. In floodplain management final conclusion may require conservation of hydrological mechanism, conservation of wetlands, conservation of agricultural fields, etc. Conservation can be said a core part of river restoration. Therefore, river restoration is re-presented by conservation of natural conditions. Conservation principles introduce certain constraints to land developers, farmers, recreational activities and so on. In other words floodplain management is demand control in land use. In this sense river restoration is a synonym of floodplain management.

Demand control in water resources and human activities are easily understood using Table 3. Demand control is not to maximize objectives of each single project in the first column of Table 3. In other words demand control is required to derive balance between increasing factor (human needs) and reducing factor (natural assets).

There is delicate difference in terminology. "Floodplain management" was conventionally used in the area of non-structural means of flood mitigation. In this paper the conventional concept is called as "floodplain management conventional". "Floodplain management conventional" was introduced only for flood damage mitigation and considered quantity of water only. But floodplain management in this paper includes wider aspects. This is called as "floodplain management new". "Floodplain management new" includes management of all water related systems in a river basin, for instance, quantity, quality, riparian ecosystems, aquatic recreation, water ethics, local traditions of water related events and so on. River restoration in a broader sense means restoration of all aspects in water related systems. Frequently river restoration is used for enhancement of natural components for ecosystems in a river basin. But natural components are used symbolically for easy understanding of new aspects. It is emphasized that "river restoration" is a synonym of "floodplain management new".

Flood mitigation and river restoration are not conflicting two factors in "floodplain management new". Let me give two examples to explain one project can contribute both to river restoration and flood mitigation. Example 1 is re-meandering of a straightened channel. Re-meandering is a symbolic project in restoration works. A meandering river channel provides less water surface gradient and reduces flow velocity. At downstream of re-meandering reach concentration of river water is avoided and consequently we can deduce flood peak. Example 2 is conservation and restoration of wetlands. Wetlands serve as retarding basins for flood mitigation, provide various habitats to ecosystems, and can contribute to natural conservation in a river basin. We need to deepen the concept of "floodplain management new" and basic principles to guide actual projects in a river basin under "floodplain management new". In order to reach to consensus among all stakeholders we need to apart from dualism. Furthermore, we need to develop a decision support system that is able to evaluate ecosystems and value of environmental assets quantitatively.

4 A NEW HORIZON FOR ECO-COMPATIBLE BASIN MANAGEMENT

4.1 *What is eco-compatibility?*

It is difficult to give a rigorous definition to eco-compatibility in one sentence like "turbulence". Therefore, examples are introduced in the following paragraphs, in which eco-compatibility is satisfied.

In this paper we saw several cases that a single purpose project tends to confront with conservation of natural environment. Then we consider that a multiple stakeholder approach is necessary. In this multiple stakeholder approach ecosystems or nature restoration takes part in the discussion as one of players. A multiple stakeholder approach is one of examples of eco-compatible way in river basin management.

We already discussed tensions between flood control or flood mitigation and nature restoration, and water resources development and nature restoration in previous chapters. It is shown that merging of flood mitigation with nature restoration is possible and balance between water resources and nature restoration brings about comprehensive optimum condition in a river basin. These are examples of eco-compatible basin management.

4.2 *Economic aspects in eco-compatible basin management*

From Figure 4 we can obtain an important result on a basic economic aspect in "river basin management new". The peak in utility curve in Figure 4 appears in a middle level of investment for flood control project (The abscissa corresponds to investment to a flood control project.). This means that a single-purpose flood control project cannot attain a bigger utility even though we increase the amount of investment after the investment level reaches to this optimum point. This means safety level of a conventional flood control project need not to be very high. It should be reasonably high by a plan, say, FC. Let us denote the safety level of this FC is FC-year flood. In order to obtain higher safety level than FC-year flood we need to adopt combination with flood mitigation by non-structural

means. The additional cost for higher safety than FC-year flood should be used not for structural means but for non-structural means. Usually a cost curve for flood control facilities increases nonlinearly with increase of safety level. Adoption of eco-compatible techniques has ample room to seek for less costly flood mitigation.

4.3 *Examples of eco-compatible basin management*

How can we cope with or live with floods? In order to accomplish this goal we need to change the principle of our activities from "flood control" to "eco-compatible basin management". Examples are recent projects in the Mississippi and the Yangtze. After the great floods in 1993 and 1998, respectively, we understood that human beings could not control big floods with man-made facilities and we need to give more space for rivers. Under natural conditions whole alluvial plain is space for rivers and swollen water during floods can move into floodplain freely. But recently rivers are confined into very narrow space between flood levees. Consequently, water stage during flood becomes higher and higher in a river channel as we want rain water to disappear around us as fast as possible.

In the Mississippi basin after the great flood of 1993 major emphasis is laid on flood mitigation or floodplain management. In this new plan buy out, restoration of wetlands, set back of flood levees, and others are core programs for flood mitigation. "Buy out" means a program to stimulate residents in floodplain in danger of inundation to buy alternate land in a higher location out of floodplain for movement. In the Yangtze basin similar principles were introduced after the great flood of 1998. Major projects are re-forestation in mountains, removal of farmers' dikes in reclaimed land along Dong Ting Lake, move of people in floodplain or islands in the river course to higher location and so on.

In these two biggest class river basins in the world amalgamation of nature restoration and flood mitigation takes real form in many actual projects. They are examples and proofs of effectiveness of the concept of "floodplain management new" or "eco-compatible basin management".

5 CONCLUDING REMARKS

It is shown on actual proof that design flood discharge increased with the increase of gross national product. Consequently, we learned that more investment to flood control projects does not guarantee safer condition for residents when the flood control proceeds to certain level due to social response in a river basin. Non-structural means are necessary to secure very high level of safety for flood mitigation. Amalgamation of flood control with restoration or nature conservation provides better solution from basin-wide aspects.

The analysis developed for flood control applies to water resources development, similarly. Based on experiences in flood control and water resources development the concept of eco-compatible basin management is clarified and is shown practical even from economical point of view. Consequently, eco-compatible basin management provides one solution for sustainable basin management.

REFERENCES

Editorial Committee of 100-Year Modern History of Training Works of the Tone River 1987. 100-year modern history of training works of the Tone River, 114–115.

Editorial Committee of 100-Year Modern History of Training Works of the Tone River 1987. 100-year modern history of training works of the Tone River, 166–168.

Forum for Public Involvement and Basic Plan of Yoshino River 2001. For Better Solution of the Renovation of the Weir No.10, Tokushima Work Office (http://www.toku-mlit.go.jp/) / Library of Yoshino River/ Weir No.10/ 24pp. (in Japanese).

Interagency Floodplain Management Review Committee: Sharing the Challenge: Floodplain Management into the 21st Century 1994, 189pp.

Yodo River Work Office, Kinki regional Office, Ministry of Construction, Japan 1998. Brochure of projects in the fiscal year 1998.

River Flow 2004 – Greco, Carravetta & Della Morte (eds.)
© 2004 Taylor & Francis Group, London, ISBN 90 5809 658 0

Floods management in Uruguay. The case study of Tacuarembó city

A. Capeluto, L. Teixeira & G. López
Instituto de Mecánica de los Fluidos e Ingeniería Ambiental (IMFIA). Facultad de Ingeniería. Universidad de la República, Montevideo, Uruguay

ABSTRACT: Tacuarembó city may serve as a paradigm for several province capital cities of Uruguay with respect to floods. As a consequence of this, the presented method of analysis as well as the developed solutions can be used for many other cases. This paper summarizes the results of the work developed at the IMFIA in order to diagnose and evaluate alternatives of flood management in the city of Tacuarembó. The problem approach is based on an integrated watershed management scope, considering different dimensions of present problems. Hydrologic and hydrodynamic models of the river basin were implemented, which allowed the analysis of different alternatives of flood management. A multi-objective decision-making analysis was used as a complementary tool for the determination of the most suitable solution. Particularly the possibility of combining structural and nonstructural measures was analyzed. The reliability of proposed flood control structures was analyzed by techniques of probabilistic methods.

1 INTRODUCTION

For Uruguay, floods mean not only a very important economical problem (about two million dollars per year of losses as a direct consequence) but also a socio-environmental one that hits mainly on lower socio-economical layers and have several repercussions on cities' activities.

Almost every important city in our country has suffered floods and assume them as one of their main structural problem.

Since its origins Uruguay has shown a typical urban population distribution, living nowadays in the cities about 90% of the total population in the country.

The rising number of people settling on risky areas is a consequence of a complex process mainly influenced by the migratory country-city process as well as the expulsion of poorest people from consolidated areas of the cities. These people settle down in a very precarious way, consolidating areas of great vulnerability when occupying floodplains.

Additionally, in recent years, particularly since 1990 this problem has become even more relevant as a result of the detected increase of floods frequency and intensity, reaching even consolidated areas, what can be related to the notorious increase of rainfall frequency and intensity. The last could be probably connected with climate changes or climatic variability cycles longer than a year.

Given the explained situation, as well as the lack of specific studies for this kind of problem, and the scarcity of specific management and protection initiatives, it has become evident the need of developing a local analysis methodology that should fit local tools and resources in order to control or reduce impacts produced by this kind of events.

This article summarizes the obtained experience in the case study of Tacuarembó city floods. As a river-side city, and because of its topographic and population characteristics, Tacuarembó turns to be a paradigmatic case of many other important cities in our country.

In this way, a methodological approach is presented here, to analyze floods problem in Uruguay. The results point out the importance several tools like hydrodynamic models, multi-objective decision-making analyses and probabilistic reliability analyses. The applied approach provides a better understanding of the problem, what gives the chance to find the most suitable solution.

2 METHODOLOGY

The basic analysis tool used in the present study were the hydrologic and hydrodynamic models of the case study system. In this way, a diagnosis of the present situation as well as the analysis of several flood protection and control alternatives were possible, considering both structural and non-structural measures.

By implementing a multi-objective decision-making analysis, a systemic approach was intended in order to select an optimal alternative, considering not

only the classic technical and economical dimensions of the problem, but also its environmental dimension.

Finally, reliability of the selected flood control measures was estimated by probabilistic analysis techniques, using level II methods. These methods make it possible to analyze the failure of a work as a system by considering the uncertainties of every involved variable, as well as compare their respective incidence on reliability results.

2.1 *Diagnosis tools*

First, a diagnosis of the present situation was done, considering on one side the territorial occupation reality, and on the other a statistical analysis of rainfall data in order to detect a possible raising tendency of extreme events parameters related to climate changes or hyper-annual climatic cycles. This analysis was performed over existing data series of Tacuarembó city.

As it is well known, annual accumulated rainfall records have been increasing in recent years in Uruguay. This accumulated rainfall increase does not necessarily implies an increase of potential flood cases, because these ones depend on maximum rainfall records whose durations are similar to the basin's concentration time. Consequently, it becomes particularly interesting to observe what happens to annual maximum daily rainfall, discharge, and stages records (behavior and evolution), what results to be representative information of extreme events in this case.

Statistical information of rainfall data of Tacuarembó city was also compared with similar statistical information of Artigas city, being able in this way to determine if the observed phenomena at Tacuarembó was just a particular case or we could find a larger area with similar behavior.

2.2 *Hydrologic and hydrodynamic modeling*

For this case study, hydrologic and hydrodynamic models were implemented for the analyzed basin, whose scheme is presented in figure 1.

The topographic information employed in this study was based, on one hand, on existing information (basically 1/50 000 topographic maps with level curves each 10 m), and on the other hand on a specially carried out survey. The last involved a special flight, and several field measurements including 21 flood plain cross sections, 9 of the riverbed, and the bridges geometry, gathering enough information so as to generate a digital terrain model.

Daily rainfall data was available for the period 1940–2001 at Tacuarembó, having also available statistical rainfall information of Artigas city, Genta (2003).

Hydrometric and gauge information as well as the estimated discharge – stage curves were supplied by the national office of river management (DNH). From available information (previous inspection), only the 1986–2001 period stage data and its corresponding gauged discharge were taken into account.

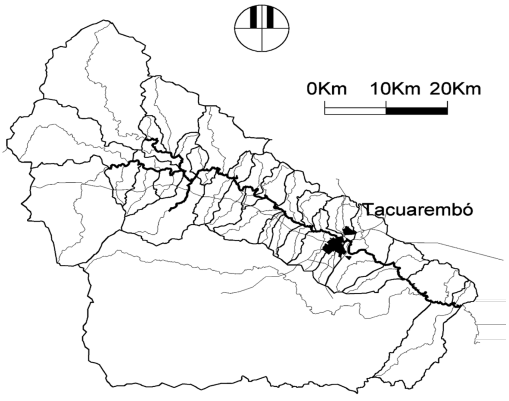


Figure 1. Sub-basins of the modeled stretch.

The hydrological model of the upstream border sub-basin as well as those of tributary sub-basins allowed to define the border conditions of the hydrodynamic model except for the downstream border. Hydrological modeling would finally supply the corresponding hydrographs at each border point.

Hydrographs were obtained by applying the Triangular Unit Hydrograph method on the synthetically generated storm. The storm was configured by following the Alternate Block method which uses the IDF curves information.

With respect to the hydrodynamic model, it can be outlined that a 49 km stretch was represented, taking also into account the hydrologic modeling of 36 tributaries. The involved catchment area is 1378 km^2, being 663 km^2 of them situated downstream Tacuarembó city. The downstream border condition that best fitted the gauged data turned out to be a Q-h relationship given by Manning's equation, considering the last cross section geometry and a hydraulic slope equal to the riverbed slope ($So = 0.0003$). It was demonstrated by this model that flow conditions in this border section does not affect flow characteristics in the area of interest, what leads to conclude that the model was large enough to study this area.

Part of model results, obtained after calibration and validation are presented in figure 2.

Looking at model outputs of maximum river stages at those cross sections associated to the city's stretch, encroached areas of the city were identified for several return period floods. Superimposing the identified areas over the streets and estates plans of the city, damaged families and blocks were quantified for each return period event.

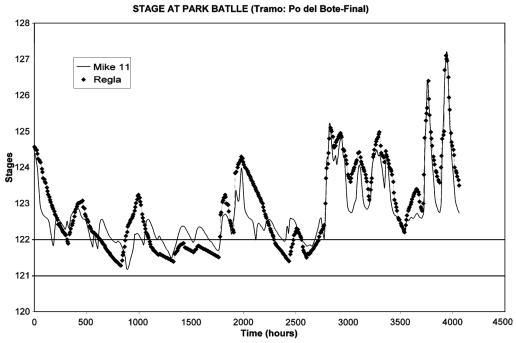


Figure 2. Comparison between modeled and measured stages at Parque Batlle station.

Based on this information and the statistical study results, present situation was described and evaluated.

2.3 *The alternatives*

Several flood control alternatives were also studied by representing different structural measures in the model. Effects of each alternative on floods was determined by noticing the stage decreasing at "Paso del Bote" cross section with respect to the present situation. Damages were quantified in the same way it was done for the present case, counting affected estates and blocks and finally identifying the relieved cases.

The evaluated structural alternatives arise not only from the working group, but also from interaction of this group with local people, turning it necessary to evaluate some alternatives that even being technically unsuitable, they were present in the collective thought. In this way, it was possible to quantify the negligible relevance of these structural solutions and show them to local people so that they could finally approve the resulting alternative. This interaction experience can be outlined itself as a relevant aspect.

The evaluated alternatives were the following:

- Dredging of the riverbed along a 6.5 km stretch downstream the city.
- Removal of two existing bridges at the city.
- Construction of riverside levees
- Construction of regulating dam upstream Tacuarembó city.

2.4 *Multi-objective decision-making analysis*

Aiming to select an optimal solution among the studied group of alternatives, a special approach would be necessary in order to methodically evaluate each alternative from different points of view in accordance to several dimensions, and mark them to allow a comparison.

Technical, economical and environmental aspects where considered as the relevant criteria or analysis dimensions in order to value the different alternatives.

To compare every alternative, valuation scales were established for each dimension, depending on the fulfillment of certain requisites inherent to the considered dimension, the mark assigned to the alternative. Taking an example, from the technical point of view a solution would be valued depending on the offered protection (temporally and spatially), if it tends to a definitive solution (as it could be land use regulation), or if it protects in a transitory way, etc. In a similar way, certain requirements were established for the economical (costs and financial feasibility) and the environmental (different kinds of impacts and degrees of incidence).

Every alternative was marked in a range from 1 to 10 according to each criteria. Weighting coefficients were assigned to each dimension in order to outline their relative importance. A calibration process was required to establish the weight coefficients in order to properly reflect the assumed relevance order.

This methodology allowed to order the alternatives in a systematic way, taking simultaneously into account several analysis dimensions and their relative importance.

2.5 *Reliability calculations methodology*

Goodness of design as well as suitability of the proposed flood control measures will depend on how well predicted the behavior of these structures is in occasion of flood events along their service period.

In a traditional analysis uncertainty is just attributed to rainfall. This information is represented in the way of IDF curves or probability density functions for each rainfall duration. By considering this information, service life and admissible risk criteria, the control structure is traditionally designed. It must be outlined that in this approach, reliability is just estimated as the probability of rainfall records of exceeding certain value.

However, random character can also be attributed to many other design variables. Probabilistic methods of reliability calculation, particularly level II methods, Nowak (2000), Thoft-Christensen (1982), consider these other uncertainties. They work with the probability density functions associated to the respective variables and a mathematical expression of the studied failure mechanism, the so called failure function.

Level II methods operate assuming every variable as normally distributed and doing some approximations when estimating their associated probability. Among their advantages, it must be outlined that they allow to evaluate the relevance of each variable on reliability results. In this way it is possible to obtain a more balanced design by pointing out which are the critical variables with reference to reliability.

Table 1. Considered cases in reliability analysis.

	$P_{3,Tr}$	N_r	N_A	T_c
Case A	X	X	X	
Case B	X	X	X	
Case C	X			X
Case D	X			X
Case E	X	X		X
Case 0	X			

Table 2. Results for 10, 25, 50, and 100 years return period.

Event	Stage (m)	Affected blocks	Affected properties
$T_r = 10$ yrs	128.63	55	326
$T_r = 25$ yrs	128.96	86	613
$T_r = 50$ yrs	129.30	107	871
$T_r = 100$ yrs	129.62	123	1133

In the case study a regulating earth dam was selected as a flood control measure. Its reliability with respect to the overtopping failure mechanism was calculated by means of level II methods, considering several design variables as probabilistic and comparing results to those calculated by the traditional analysis.

Overtopping failure mechanism can be represented by the following reliability function:

$$g = H_C - H_{máx} \quad (1)$$

where failure domain is defined as that which leads to negative values of g, being H_C the height of the dam embankment and $H_{máx}$ the maximum height of the reservoir water raised by an occurrence of a flood.

The variables considered with an associated random character were: rainfall intensity (3 hours, T_r years) $\mathbf{P_{3,Tr}}$, roughness coefficient of the riverbed **Nr**, roughness coefficient of the culverts $\mathbf{N_A}$, and one of the dam's upstream sub-basin's concentration time **Tc**. These variables were not all simultaneously considered as probabilistic, proposing different case studies depending on which variable was considered in a probabilistic way. In Table 1 the studied cases are defined, marking with a cross when the variable was considered in a probabilistic manner.

3 RESULTS

3.1 *Diagnosis*

This case study may serve as a paradigm for many of most important cities in Uruguay, that similarly to Tacuarembó, have historically developed beside rivers.

Land use pattern and its evolution have been related to the migratory and urban expansion processes, which have given as a notorious result the occupation of Tacuarembó Chico's and some of its tributaries' flood plains all over the city. This people settle down in a very precarious way converting the riversides in really vulnerable areas to recurrent floods.

In conclusion, flood plains occupation turn to be one of the obvious causes of flood related damages that Tacuarembó city has historically endured.

On the other hand, as a result of the statistical study, a notorious increase of the maximum rainfall intensities as well as of the accumulated rainfall depth in the last 30 years must be pointed out. A concomitant variation was also observed when analyzing maximum river stages.

Concentration time of Tacuarembó Chico river's basin at Tacuarembó city is about 24 hours.

On the other hand the used accumulated rainfall depth data are daily. Consequently the detected increasing tendency of the daily maximum registries is coherent with the increasing tendency of the annual maximum discharges.

3.2 *Hydrodynamic model. Present situation and analyzed measures*

Present situation is described in a precise manner by analyzing the following results of the hydrodynamic model.

Table 3 summarizes relevant information and behavior of present situation and the analyzed alternatives for a 10 year return period event. The alternatives are compared in terms of the maximum stage at Paso del Bote, quantity of affected properties, consequences, quantity of alleviated properties, economical cost, environmental cost and how the measure protects for larger return period events.

The multi-objective decision-making analysis is summarized in Table 4. Punctuation assigned to each alternative according to different analysis dimensions, weight coefficients (first column) as well as total punctuation per alternative, all of them are presented in this table.

In spite of the fact that weight coefficients, scales and marks are established in a quite subjective way, this method helps to set up the implicit designer's criteria in a clear manner by quantifying them, and so making it possible to compare different alternatives. Furthermore, it also helps to re-evaluate the relative relevance attributed to each dimension.

This method does not bring new results that were no implicit in designer's or decider's mind, but will help to present and see them in a clear way.

From multi-objective decision-making analysis it was clearly set that a regulating earth dam would be the most adequate alternative as a flood control measure for Tacuarembó. Dam's location is shown in figure 3. In addition to this measure, non-structural

Table 3. Summary of results for present situation and different flood control alternatives.

	Present situation	Dredging	Bridge opening	Riverside levee	Regulating dam
Stage (m)	128.63	128.58	128.28	127.18	127.22
Affected properties	326	326	248	89	89
Consequences	–	–	–	Urban drainage	Bridge affection
Relieved properties	–	0	78	237	237
Cost (million dollars)	–	4.5	12	3	1.75
Environmental cost	–	Very high	Medium	High	Medium
Degree of protection	–	Low	Medium	Medium	High

Table 4. Multi-objective decision-making analysis.

		Alternatives			
Dimensions	Weight coefficients	Dredging	Bridge opening	Levee	Dam
Technical	1	2	2	5	6
Economical	0.8	3	1	6	8
Environmental	0.9	3	10	3	6
Total marks		7.1	11.8	12.5	17.8

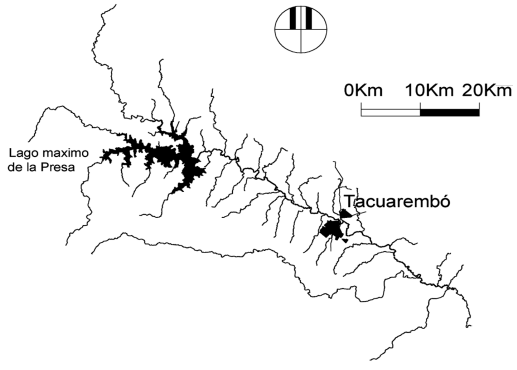


Figure 3. Location of the regulating dam.

measures should also be implemented, being of prior consideration land use policies and regulations. Other non-structural measures were also evaluated, being worth pointing out that of people transfer away from risk areas.

The recommended measure consists on a regulating earth filled dam 15 meters high, with an estimated retaining capacity of 85 000 000 m^3, and a maximum pool area of about 1800 hectares. The discharge is automatic, by means of rectangular culverts.

The proposed structural measure must necessarily be complemented and coordinated with land use regulations that would gradually tend to remove the established housings from the flood plain.

Particular emphasis is required to control indiscriminate land occupation on protected areas. The accomplished damage reduction that results from floods frequency reduction can eventually be equaled or reversed as a result of an increased investment on protected areas. Structures are designed to endure up to specific return period events. Being these surpassed, works will not cope with them, leaving then protected areas again exposed to damage. The larger is the allowed investment, the larger is the potential damage. Civil works inspire false confidence feelings, and planners must be aware of this.

3.3 *Reliability of the proposed dam*

Reliability results can be summarized by the following tables.

Table 5. Reliability of dam for different cases and different service periods.

Service period (years)	Case 0	Case A	Case B	Case C	Case D	Case E
1	0,9999305	0,9999302	0,9999082	0,9999254	0,9999028	0,9998728
10	0,9993052	0,9993022	0,9990824	0,9992543	0,9990284	0,9987287
30	0,9979171	0,9979081	0,9972497	0,9977644	0,9970881	0,9961910
50	0,9965309	0,9965160	0,9954203	0,9962768	0,9951516	0,9936598

Table 6. Return period of the event that leads to failure (annual reliability).

	Return Period (years)
Case 0	14 388
Case A	13 693
Case B	8715
Case C	12 256
Case D	7736
Case E	5000

On Table 5, variation on reliability results can be noticed for annual values as well as for different service periods when considering different combinations of variables with probabilistic behavior.

On Table 6 annual reliability results are shown in a more familiar way by showing the return period associated to that event that will induce to failure of the dam for each case. Special attention must be paid to the fact that, while according to the traditional analysis failure could be expected for a 14 000 years return period event, probabilistic methods would demonstrate that the dam will fail just for a 5000 years return period event when considering the larger number of probabilistic variables.

In order to apply these methods, it becomes a basic requirement to gather statistical information of design variables. In this way, a better representation of the corresponding uncertainties can be achieved by fitting probability density functions to finally obtain more certain reliability results.

4 CONCLUSIONS

A diagnosis of urban floods problem in Uruguay is presented, concluding that the notorious raise in frequency as well as in intensity of these kind of events in the last decades, is clearly associated with two reasons. On one hand, changes in land use occupation pattern have been happening, particularly flood plains encroachment, and on the other hand a notorious raise of rainfall parameters was detected, particularly on its intensity, giving as a result a decrease of the associated return periods for extreme events.

The particular case of a city that may serve as a paradigm for several important cities in Uruguay was analyzed. In this case, based on a multi-objective decision-making analysis and aided by modern risk evaluations, structural flood control measures were defined (regulation dam), complemented also with non-structural ones (land use regulations and policies).

Probabilistic analysis methods, which incorporate consideration of other variables than rainfall in a probabilistic manner, show that the associated values to flood control structures' safety are notoriously inferior than those calculated according to the traditional method. The last leads to conclude about the necessity of reviewing design norms by incorporating the methodology used in this case.

The applied methodology as well as the obtained results, situate this study as one of the pioneers of this kind of analyses in Uruguay, showing the way that modern and internationally applied concepts and methodologies can be adapted to third world's local tools and resources.

A relevant experience to point out is the interaction with local people along the whole study, who participated in different stages of the project, particularly when setting the diagnosis of present problem and finally when identifying and selecting the optimal alternative.

REFERENCES

Genta & Teixeira (2003). *Inundaçoes Urbanas na América do Sul*. Chapter: Inundaciones y Drenaje Urbano en Uruguay. WMO, WGWP, ABRH, 2003. ISBN: 85-88686-07-04.

Nowak & Collins (2000). *Reliability of Structures*. McGraw Hill Company.

Thoft-Christensen & Baker (1982). *Structural Reliability Theory and its Applications*. Springer Verlag, Berlin.

River Flow 2004 – Greco, Carravetta & Della Morte (eds.)
© 2004 Taylor & Francis Group, London, ISBN 90 5809 658 0

New trends in flood risk analysis: working with 2D flow models, laser DEM and a GIS environment

P. Archambeau, B. Dewals, S. Erpicum, S. Detrembleur & M. Pirotton
Laboratory of Applied Hydrodynamics and Hydraulic Constructions, University of Liege, Belgium Second author: Research Fellow of the National Fund for Scientific Research (Belgium)

ABSTRACT: This paper outlines the integration of new and accurate laser DEM into the determination of floodplains. Global and robust GIS environment is absolutely necessary to manage this very large amounts of topographic data. The development and interaction of 2D flow models, simplified or not, ensures to offer more accurate and flexible physically based tools to the decision-makers.

1 INTRODUCTION

Floods control, risk mapping and more generally river management are topics on which a wide range of decision-makers focus a permanently increasing attention. The first step in flood hazard analysis and management, prior to any mitigation policy, is a thorough understanding and assessing of the level of risk. Though lots of work has been carried out for decades in the field, a genuinely reliable and efficient modelling of the corresponding flows remains a challenge. In spite of improved computation capacities, collecting, handling and validating large sets of topographic data as well as simulation results are still challenging tasks for hydro-modellers and practitioners.

The present paper covers a description and a detailed comparison of two state-of-the-art numerical models to be used as strategic tools in the process of flood risk assessment and mitigation. The first one is a 2D model for hydrodynamics, simplified according to the diffusive assumption (DM), quickly generating initial flow fields for the second one, a complete model based on the shallow water equations (SWE).

Those two models are integrated in the software package WOLF, which has been developed for almost ten years at the University of Liege. WOLF includes a complete set of numerical models for simulating free surface flows (process-oriented and spatially distributed hydrology [1], 1D and 2D hydrodynamics [2, 3], sediment transport [4, 5], air entrainment [6] …) as well as optimisation algorithms. This optimisation tool, based on the innovative Genetic Algorithms, allows an objective calibration of friction coefficients [7].

A user-friendly GIS interface, entirely designed and implemented by the authors, makes the pre- and post-processing operations very convenient. Import and export operations are easily feasible from and to various classical GIS tools. Different layers of maps can be handled to analyse information related to topography, ground characteristics, vegetation density and hydrodynamic fields.

The validation of the model has been performed continuously for many years and is still running. Two cases studies on Belgian rivers are presented to illustrate inundation applications in a urban area.

2 MATHEMATICAL MODEL DESCRIPTION

The SWE model simulates any steady or unsteady situation, possibly taking into consideration air transport or sediment-laden flows, in Cartesian or curvilinear coordinates. It is in addition coupled to a turbulence model based on the Prandtl mixing length concept. The DM model is restricted to a specific range of Froude and kinematic numbers, but requires significantly less CPU resources.

In the shallow-water approach (SWE) the only assumption states that velocities normal to a main flow direction are smaller than those in the main flow direction. As a consequence the pressure field is found to be almost hydrostatic everywhere. In the diffusive model (DM) a similar depth-averaging operation is combined to the following hypothesis: the purely advective terms can be neglected. As a consequence the free surface slope is simply balanced by the friction term.

The divergence form of the SWE include the mass balance:

$$\frac{\partial H}{\partial t} + \frac{\partial q_i}{\partial x_i} = 0 \qquad (1)$$

and the momentum balance:

$$\underbrace{\left[\frac{\partial q_i}{\partial t}+\frac{\partial}{\partial x_i}\left(\frac{q_i q_j}{h}\right)\right]}_{\text{inertia terms}}+gh\left(S_{fi}+\frac{\partial H}{\partial x_i}\right)=0;\quad j=1,2 \quad (2)$$

where Einstein's convention of summation over repeated subscripts has been used. H represents the free surface elevation, h is the water height, q_i designates the specific discharge in direction i and S_{fi} is the friction slope.

The *diffusive assumption* leads to a considerable simplification of the momentum equations:

$$S_{fi}=-\frac{\partial H}{\partial x_i}. \quad (3)$$

A friction law is needed for closure of both the SWE and the DM models. Its general formulation can be stated as a relation between the discharge, the water height and the slope:

$$q=\alpha h^{\chi} S_f^{\gamma}=\alpha h^{\chi}\left(\frac{\partial H}{\partial s}\right)^{\gamma}, \quad (4)$$

where α, γ and χ are coefficients suitable for the description of floodplain flows.

A more detailed description of the mathematical formulation can be found in the recent paper by Archambeau et al [3].

3 NUMERICAL IMPLEMENTATION

A finite volume scheme is used in all models to ensure exact mass conservativity. An upwind scheme is exploited for space discretization of the SWE model and extended to the DM.

An implicit pseudo-time integration scheme, suitable for solving non-transient problems, is implemented in the SWE model. In the DM model the GMRES or Conjugate Gradients (CG) algorithms are used for evaluating iteratively the solution of the symmetric linearized system.

3.1 *Space discretization and boundary conditions*

An original upwind scheme is applied for space discretization of the complete set of equations. The stability of this second order upwind scheme has been demonstrated through a theoretical study of the mathematical system as well as a von Neumann stability analysis. Much care has been taken to handle correctly the source terms representing topography gradients. A fitted spatial upwinded scheme is developed similarly to the previously described DM.

The models allow the user to specify any inflow discharge as an upstream boundary condition (BC). The downstream boundary condition can be a free surface elevation, a water height, a Froude number or even no specified condition if the outflow regime is supercritical (SWE only).

3.2 *Resolution of the DM model*

The primary goal of the diffusive formulation is the quick computation of steady-state approximate solutions. Those first estimations of the final solution are intended to serve as fairly good initial condition for the complete SWE model.

A first approach for solving the DM might be a pseudo-time evolution, starting from a user-defined initial condition. In order to prevail the possibility of using large time steps, this pseudo-time integration would need to be performed in an implicit way.

A second approach is to disregard the time derivative term and to solve a non-linear system of time independent equations. Both methods are obviously very similar if the time step becomes very large. Various iterative techniques are available for solving such very large linear systems. Among them are the methods "by point", such as Jacobi, Gaus-Seidel,…[8, 9] or full implicit such as ADI [10–14], GMRES [15], CG [16–19].

3.3 *Time integration for the SWE model*

An implicit pseudo-time integration scheme, suitable for solving steady-state problems, is implemented in the SWE model. This technique allows much larger time steps than those acceptable for an explicit time integration. On the other hand the resolution procedure is more intricate. A Newton method is exploited to solve the large non-linear system. The successive linearized systems are solved with the powerful GMRES algorithm, which is advantageously coupled to a preconditioner. For this purpose an incomplete LU decomposition is applied. The Switched Evolution-Relaxation technique by Van Leer has been used to continuously optimise the time step.

In the DM model the GMRES or CG algorithms are also used for evaluating iteratively the solution of the symmetric linearized system. In both cases the resolution procedure represents a very challenging step because of the complexity of a cost-effective evaluation of the Jaobian matrix. WOLF performs this job effectively, by storing only non-zero elements and their location in the large sparse matrix.

3.4 *Friction modelling*

River and floodplain flows are mainly driven by topography gradients and by friction effects. The total friction includes three components: bottom friction (drag and roughness), wall friction and internal friction.

The bottom friction is classically modelled thanks to an empirical law, such as the Manning formula. The DM and SWE models allow the definition of a spatially non uniform roughness coefficient. This parameter can thus easily be distributed as a function of soil properties, vegetation and sub-grid bed forms.

The friction along vertical boundaries, such as bank walls, is introduced thanks to a physically based model developed by the authors. This modification of the classical friction law presents the advantage of leading to a correct hydraulic radius of the 2D cross-section in case of sufficiently shallow flows.

The internal friction is properly reproduced by the turbulence model.

3.5 *More features of the numerical codes*

In addition an automatic mesh refinement is used to enhance the convergence rate towards accurate steady-state solutions [3]. The computations are performed on several successive grids, first very coarse and then gradually refined. The hydrodynamic fields are almost stabilized when the computer code automatically jumps onto the next grid. This fully automatic method considerably reduces the number of cells in the first grids. Then, the successive so-called initial solutions are interpolated from the coarser towards the finer grid in terms of both water heights and discharges.

In case of an explicit pseudo-time evolution: the stable time step is significantly larger since it depends linearly on the size of the mesh. For an implicit evolution, the benefits of the quadratic convergence are reached since the initial solution is sufficiently close to the steady state solution. In spite of extra computation time to re-mesh and linearly interpolate the initial solution the overall CPU time saving is clearly appealing.

4 LASER DEM

Very recently, the Belgian Ministry of Facilities and Transport (MET) and most particularly the Service of Hydrology Studies (SETHY) acquired a very accurate DEM on the floodplains in the whole Walloon Region.

A method of airborne laser was used for the proximity inundation zones of the entire rivers network. An echo-sonar was applied for measuring the bathymetry of the main channel, exclusively on navigable rivers (Fig. 1).

Consequently, the poor and inaccurate 3D information that has been available for many years, 30 m square and an error of several meters in altitude, is replaced by an exceptional DEM since the precision in altitude is 15 cm and, on top of that, the information density is one point per square meter.

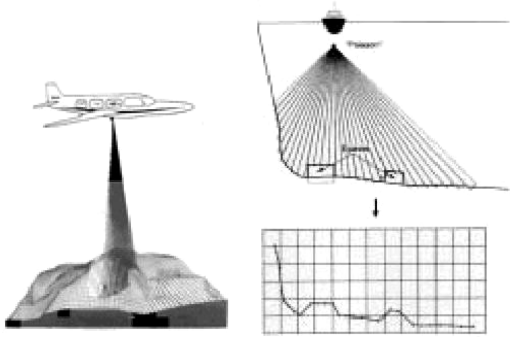


Figure 1. Principle of the DEM acquisition by airborne laser and echo-sonar ship.

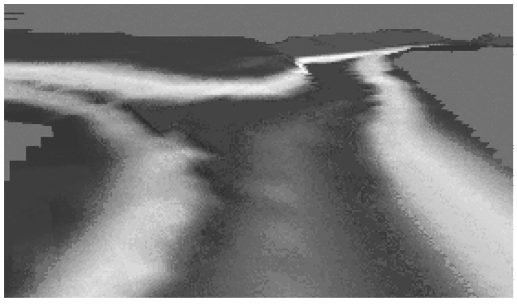


Figure 2a. Béthane: IGN topography (digitalized contour line map).

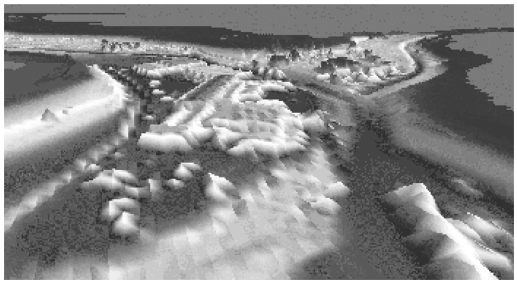


Figure 2b. Béthane: laser data including buildings.

To illustrate the accuracy of the DEM, (Figs. 2 and 3) two comparisons of data on the same regions are presented, the towns of Bethane and Eupen (Belgium).

Generally, specific features of flows in urban area (such as blockage by buildings, slowing down of the wave front propagation, etc) were taken into account by a local modification of the roughness coefficient. While, with this new set of topographic data, irregularities of the topography influence directly the inundation flows. This permits to refocus the roughness coefficient to more proper physical values.

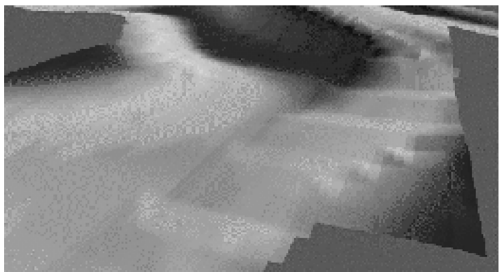


Figure 3a. Eupen: IGN topography (digitalized contour line map).

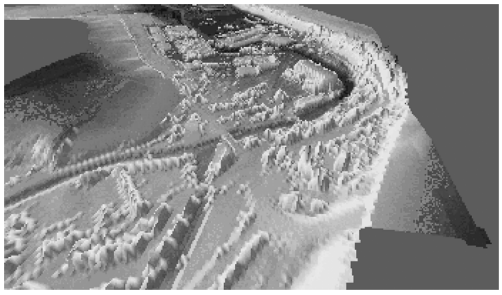


Figure 3b. Eupen: laser data including buildings.

5 GIS ENVIRONMENT

Management and operations on such a large set of data requires a robust and efficient pre- and postprocessing. A GIS environment, entirely designed and implemented by the authors, performs this tools. Several databases containing topographic data, pictures of historic floods, characteristics of structures along the rivers (dams, bridges, weirs, …) are stored on a single data server with their geographic coordinates to be easily downloaded by any modeller.

A difficult task for the preprocessing is the interpolation of the minor river bed when no distributed data are available. It's the case on the non-navigable rivers where the airborne laser is the only source of the DEM. In fact, the laser beam doesn't cross the water surface. Therefore, the only available information are based on cross-sections and thus must be interpolated in 3D to recompose a global DEM. Original methods were developed by Detrembleur [20] to fulfil this job and are implemented in the WOLF package.

6 CASES STUDIES

6.1 *Flood induced inundation on the river Ourthe*

The first case proposed is a flood event on the river Ourthe that occurs 14 February 2002 (study commissioned by the MET-SETHY).

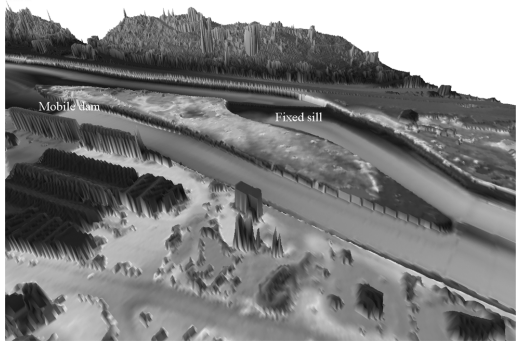


Figure 4. Example of DEM interpolation of the river bed and aggregation with the airborne laser data (river Ourthe, Tilff; Belgium).

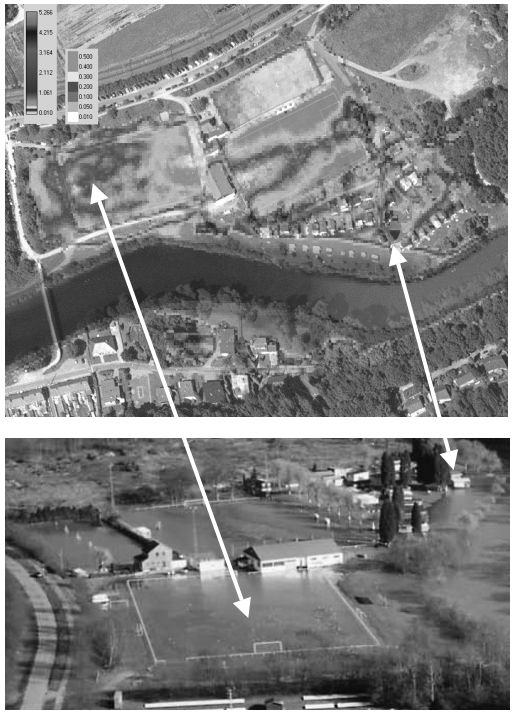


Figure 5. Comparison between water heights and aerial picture of the flood event (football field).

Characteristics of the simulation are:

- Discharge: 570 m^3/s
- Length of the real computed river: 7.35 km
- Total number of computations cells: 300.000
- Uniform size of the cells: 2×2 m
- Two hydraulic structures: a mobile dam and a fixed sill.

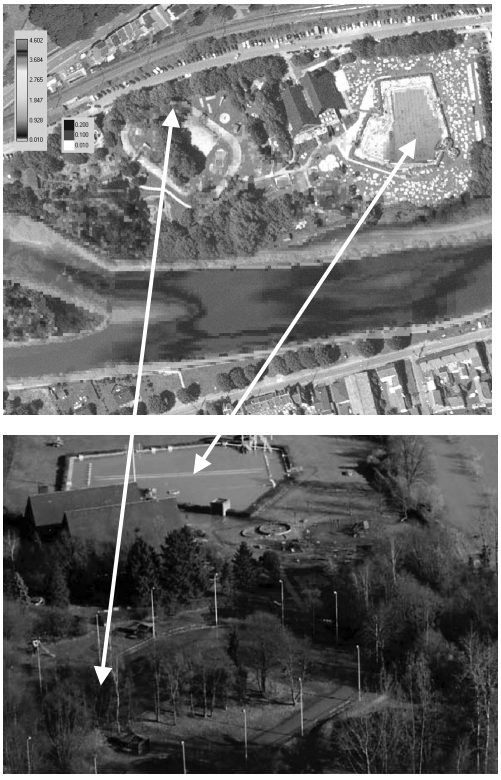


Figure 6. Comparison between water heights and aerial picture of the flood event (water-pool of the "Prés de Tilff").

In this case, there were discrepancies between the first simulation and the real observations. Actually, the interpolation of the main river bed was computed based on cross sections taken in '70 years. Actually, major modifications of this bed were realized to mitigate floods in the town of Tilff. The right bank was newly designed to a vertical wall when it was computed with a slope of 4 : 4. A complete dredging was performed too.

After the introduction of the different modifications in the topography, the results improved significantly as demonstrate the comparisons between numerical water heights and aerial pictures of the floods (Figs. 5–6).

6.2 *Flood inundation on the river Lesse*

The second case presented in this paper consists in the verification of the works protecting from floods in Han-sur-Lesse on the river Lesse, Belgium (study commissioned by DGRNE, Walloon Region).

This town, which attracts tourists, is located at the downstream of geological caves that divert the free surface flow of the Lesse trough underground flow. A maximum discharge of about 25 m^3/s can

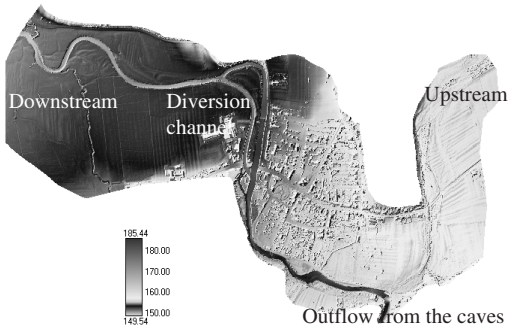


Figure 7. General topography of Han-sur-Lesse.



Figure 8. Enlargement of the downstream topography.

pass by this way. The rest is forced to return to the historical bed.

A first stage was the building of a diversion channel to increase the natural discharge capacity of the river. A side-weir creates a separation between the two channels. Thus, the normal discharge only flows in the natural river. In addition, a second stage consists in the building of walls and small dyke to prohibit the overflow in the urban zone.

Figures 8 and 9 illustrate the precision of the laser DEM. The drainage channels of farm fields, residual erosion of historical floodings, current small dyke and the interpolated topography of the main river bed can be observed.

Characteristics of the simulations are:

- Discharge: 150 m^3/s
- Length of the real computed river: 4 km
- Total number of computations cells: 450.000
- Variable size of cells (Fig. 10)
- Hydraulic structures: a mobile dam and several fixed sills.

A multibloc discretization is used in this problem to limit the total computation time. The finest information is conserved along the river trough the town but a progressive increase in the cells size is performed towards the extremities of the computation domain to ensure evanescent boundary conditions.

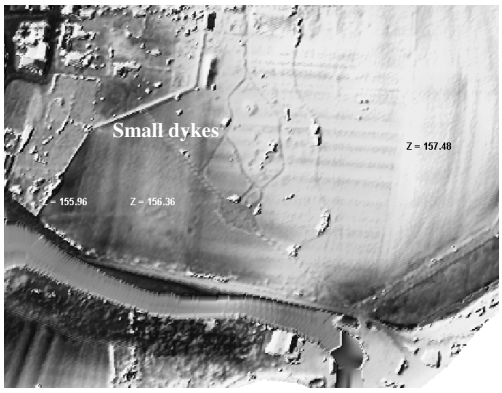


Figure 9. Enlargement of the topography around the exit of the caves.

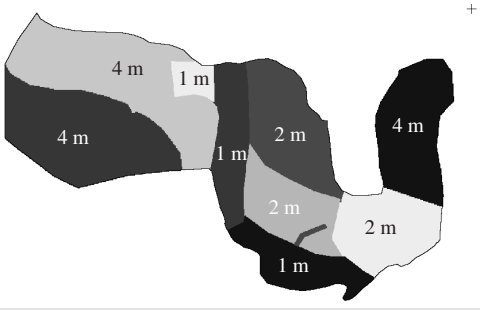


Figure 10. Multiblocs discretization.

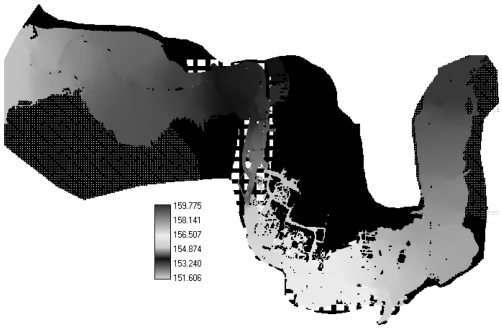


Figure 11. Free surface elevation for the flood of January 2003.

The reference event dates from Jannuary 2003 because it's the only flood after the building of the diversion channel. Figures 11 and 12 illustrate the results in terms of free surface elevation and water heights. A good concordance is obtained between computed results and field observations, and thus both in extension of the flood and in water heights.

An observation of the results in terms of Froude numbers (Fig. 13) permits to indentify a critical

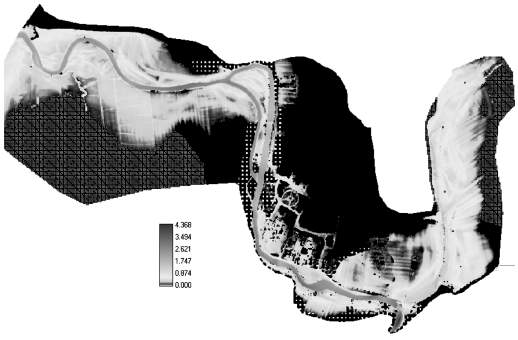


Figure 12. Water heights for the flood of January 2003.

Table 1. Comparison of water height for the flood of January 2003.

Observation (cm)	Computed (cm)
82	86
5	15–30 center of street
25	5 along the houses
20	30
94	95
113	117
100	100

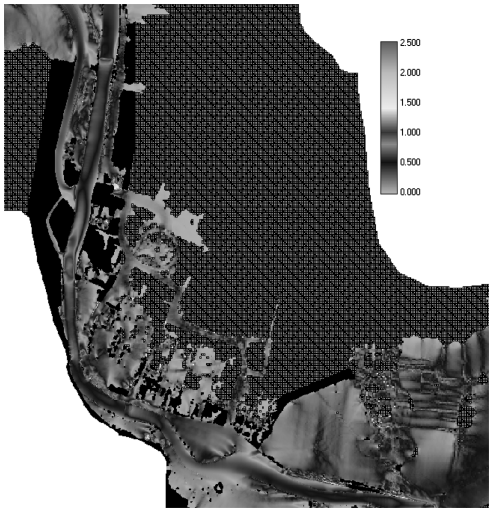


Figure 13. Froude number for the flood of January 2003.

section, just before the side-weir, in an obvious place. The real nature of the problem consists in a rise of the bottom topography due to an outcrop. This critical section reduces significantly the favourable effect of the stage 1 on the upstream. Furthermore, stage 2 doesn't modify this place bacause the buildings just stop at the upstream. Thus, recommendations were made to

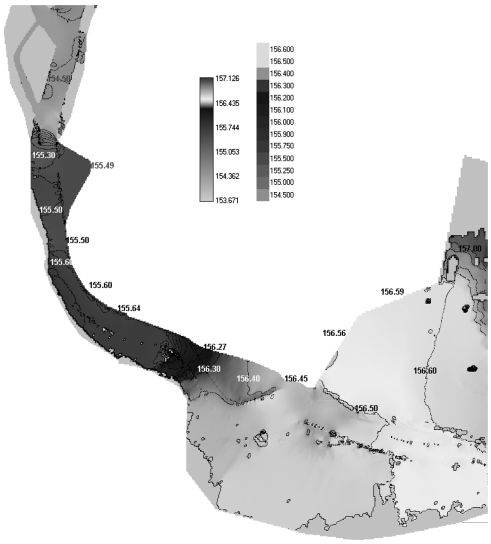


Figure 14. Free surface elevation after the building of stage 2 (m).

the manager to extent the works to redraw this portion of river.

The check of the stage 2 consists in a simulation where the town is untouchable by the floods. Thus, impermeable boundary conditions are applied on the outline of the town. A comparison of the final water heights with the heights of walls and dykes concludes to a good design of the works.

7 CONCLUSION

The present paper offers a comprehensive comparison between both numerical models (DM and SWE) for very practical applications such as floodplains modelling and inundation maps plotting. The key advantages brought by the GIS environment are also illustrated, focusing on the major contemporary requirements of decision-makers in the field of flood control.

Further research is currently undertaken for investigating sediment transport effects and their simulation.

REFERENCES

1. Archambeau, P., et al. Impact studies and water management with WOLFHYDRO: a new physically based hydrological solver. in International Symposium on Environmental Hydraulics. 2001. Arizona State University, USA.
2. Mouzelard, T., et al. Water management of large dams. in International Symposium on Environmental Hydraulics. 2001. Arizona State University, USA.
3. Archambeau, P., et al. A set of efficient numerical tools for floodplain modeling, in Shallow Flows, G.H. Jirka and W.S.J. Uijttewaal, Editors. 2003. IfH & TU Delft: Delft. p. 141–158.
4. Dewals, B., et al. Coupled computations of highly erosive flows with WOLF software. in 5th International Conference on Hydro-Science & -Engineering. 2002. Warsaw University of Technology.
5. Dewals, B., et al. Dam-break hazard mitigation with geomorphic flow computation, using WOLF 2D hydrodynamic software, in Risk Analysis III, C.A. Brebbia, Editor. 2002. WIT Press.
6. André, S., et al. Quasi 2D-numerical model of aerated flow over stepped chutes. in XXX IAHR Congress. 2003. Thessaloniki, Greece: IAHR.
7. Erpicum, S., et al. Optimising a cascade of hydroelectric power stations with the WOLF package, in Water Resources Management, C.A. Brebbia, Editor. 2003. WIT Press. p. 65–74.
8. Hirsch, C., Numerical Computation of Internal and External Flows, Computational Methods for Inviscid and Viscous Flows. Vol. Volume 2. 1990. Wiley. 691.
9. Young, D.M., Iterative solution of large linear system. Englewood Cliffs. 1971, New York: Academic Press.
10. Kim, S. and J. Douglas, Fractional time-stepping methods for unsteady flow problems, http://citeseer.nj.nec.com/382490.html
11. Malhotra, S., Douglas, C. and Schultz, M. Parameter choices for ADI-like methods on parallel computers, 2000, http://citeseer.nj.nec.com/11073.html
12. Douglas, J. and S. Kim, On accuracy of alternating direction implicit methods for parabolic equations, 1999, http://citeseer.nj.nec.com/douglas99accuracy.html
13. Molls, T. and G. Zhao, Depth-averaged simulations of supercritical flow in channel with wavy sidewall. Journal of Hydraulic Engeneering. 2000. 126(6): p. 437–445.
14. Panagiotopoulos, A. and J. Soulis, Implicit bidiagonal scheme for depth-averaged free-surface flow equations. Journal of Hydraulic Engeneering. 2000. 126(6): p. 425–436.
15. Saad, Y. and M. Schultz, GMRES: A generalized minimal residual algorithm for solving non-symmetric linear system. SIAM Journal of Scientific and Statistical Computing. 1986. p. 7.
16. Jones, M. and P. Plassman, An improved incomplete Cholesky factorization. 1991. Mathematics and Computer Science Division, Argonne National Laboratory: Illinois. p. 12,
17. White, D., Solution of capacitance systems using incomplete Cholesky fixed point iteration. Journal for Numerical Methods in Engineering, 1998.
18. Lin, C.-J. and M. J, Incomplete Cholesky factorizations with limited memory. 1997.
19. CACR, C.f.a.c.r., NAG Libraries. 2000, http://www.cacr.caltech.edu.
20. Detrembleur, S., Elaboration d'outils intégrés de gestion des données topographiques et morphologiques pour la modélisation des crues et inondations, in Applied Hydrodynamics and Hydraulic Constructions. 2003. University of Liège: Liège. p. 110.

This page intentionally left blank

River Flow 2004 – Greco, Carravetta & Della Morte (eds.)
© 2004 Taylor & Francis Group, London, ISBN 90 5809 658 0

Floods control in Argentina: learning from the experience

R.A. Lopardo & R. Seoane
INA (National Water Institute), Ezeiza, Argentina

ABSTRACT: This paper deals with flood control and mitigation in large flatland valleys in Argentina and describes the advances, mistakes and omissions over the last twenty years. The authors analyse the advances made and the problems encountered when developing a hydrological measurement network for planning and designing hydraulic structures and a hydrological early warning system. The paper focuses on flood problems along the Paraná River, which affected urban areas, the Southern Salado River, which inundated rich lands in the flatland region of the Province of Buenos Aires, and the Northern Salado River, that caused a severe flood event in 2003. Historically, Argentina has sought to tame floods through the construction of infrastructure works to protect the people of the floodplains. Recent disasters and the need to protect the environment call for non-structural measures, such as floodplain zoning, development control, flood warning and disaster mitigation planning.

1 INTRODUCTION

Flood disasters are a major issue in the life of societies. The objective of this paper is to describe different aspects of flood-related problems, to stress the importance of warning systems, to assess the impact of climate change in Argentina, and to perform a hydrological analysis of the significant rise in the Salado River basin that affected the city of Santa Fe.

Integrated water resources planning, through a basin level Master Plan for flood protection that links and binds structures and protection works with non-structural solutions to control and mitigate emergencies, is a critical and urgent task not only in Argentina and other Latin American countries but also in other parts of the world. Such a plan must be designed when waters are still. Even if the population "forgets about the water problem" because there are no floods, local authorities must take basic needs into account and implement a flood control and disaster prevention policy.

Located in the southern region of the Americas, Argentina has a population of 37 million and a total area of 2,500,000 km^2. Because of their uneven distribution, water resources in Argentina cause both floods and droughts.

Humid regions represent 24% of the country's total area and account for 68% of the total population. On the other hand, arid regions represent 61% of the country's total area but account for only 6% of the population. Mean discharge in Argentina is 25,836 m^3/s (22,000 m^3 per inhabitant per year), i.e., 22 times higher than the "water stress level" adopted by the United Nations.

The Plata River Basin, including the lowland "Pampas" region, accounts for 86% of the total discharge in Argentina. This basin is the most important in terms of human concentration, urban development and economic activity in the country. The waters of the Bermejo, Paraná, Paraguay and Uruguay rivers, which are part of the Plata system, are shared with Bolivia, Brazil, Paraguay and Uruguay.

The Northern Salado River rises in the northwestern region of Argentina and is a tributary of the Paraná River. The Southern Salado River Basin, in the heart of the agricultural and cattle region of the "Pampas" region, forms the southern border of the Plata River Basin.

Heavy convective rains in the "Pampas" Central Region are expected to aggravate actual physical conditions (reservoirs that are already full and groundwater levels that are already high). Floods are likely to cause damages, particularly in areas with vertical drainage processes, as is the case of the sandy soils in the NW region of the Province of Buenos Aires. This situation may seriously affect sowing and harvesting activities that are intensively carried out in the region.

2 THE LOWLAND "SOUTHERN" SALADO RIVER REGION

The Central "Pampas" (Area Pampeana Central) comprises part of the provinces of San Luis, La Pampa,

Buenos Aires, Santa Fe and Córdoba. The Salado River Basin extends over an area of 168,100 km^2 comprising 58 districts of the Province of Buenos Aires with a population of 1.3 million. The area's main economic activity is agriculture, accounting for 25% of the country's total farm crops, 30% of total beef production, and 18% of dairy produce.

Irregular rains and summer rainfall deficit are some of the climate conditions prevailing in the basin. In the last 25 years there have been periods of very heavy rainfall resulting in extensive floods, such as those which affected the north-eastern sub-region in 1986, 1987, 1993, and the recent floods in Lake La Picasa's command area, among others.

There is neither natural drainage nor important waterways. The region's average slope is 3.5 cm/km; it lacks a systematized drainage network; and floods are caused by excessive rainfall. Unplanned construction of canals has transferred the problem from upstream to downstream areas.

In the last few years the area has been subject to an intensive agricultural development process whereby it shifted from cattle raising to grain and crop farming activities.

Water management is crucial for the region's development. Lack of a sustained policy to manage flood problems is one of the main obstacles to their solution. It should be noted that each province in the basin has embarked upon solving their own flood problems. Only two studies (1985, 1999) have attempted a comprehensive diagnosis of the region as a whole.

In order to provide a general view of the case under analysis, we may break down the system into three layers: the natural system, the socio-economic system, both of them interacting and generating mutual actions and reactions, and an institutional subsystem or layer which is closely linked to the other two.

Physically, the NW region of the Province of Buenos Aires is not a standard river basin. Since 1900, when records began to be kept, annual evaporation exceeded rainfall. Downstream from the Salado River, tributaries and other rivers flowing into the sea were channelized (1920) to flush water out and render the land suitable for human occupation.

The natural system is described using the conceptual hydrological model for flatland areas which refers to a landscape with low energy to drain water flows and to the lack of defined basin limits and of major drainage structures or waterways. Consequently, there is a strong predominance of vertical variables, such as infiltration and evaporation, over horizontal variables, which relate to drainage. Surplus rainfall water is stored in shallow surface areas and drainage is generated by accumulation of water and the creation of a hydraulic gradient.

Environmentally, the rainfall regime has great space and time variability and an uneven seasonal distribution though the amount of rain has increased since 1971.

The socio-economic subsystem is characterized by low population density, extensive grain and crop farming and cattle raising activities – depending on the suitability of the soils – little infrastructure – both in terms of road and canal networks – and unplanned land use. Flood problems have increased due to inadequate agricultural practices and poorly designed canals and embankments which sometimes affect downstream areas.

As regards the political-institutional subsystem, Argentina has adopted a federal system for administering its natural resources. According to the National Constitution, natural resources are owned by the provinces and it is them who manage and supervise their water resources without the participation of the national government.

Lack of a long-term active policy for flood management is another issue affecting the region. In the absence of a policy for the entire hydrological system, each province in the basin seeks to find its own solutions to their water problems.

3 THE SALADO RIVER MASTER PLAN

To mitigate the damages caused by torrential floods and severe droughts, the Integrated Master Plan for the Salado River Basin seeks to promote sustainable use of water resources, improve economic conditions, and preserve environmental parameters in the Salado River.

Local roads as well as provincial and national highways have been flooded causing serious economic restrictions that had a strong impact on the transportation of agricultural and dairy products. Not only fields that were not flooded but also important urban and rural areas experienced production losses for they were isolated from the rest.

Estimates show that the value of agricultural production will rise by 10% as a result of drainage works and reservoir construction. The area protected by the Plan represents almost 35% of the basin's total area (6 million hectares).

Maximum annual benefits to be derived directly from the construction of works for the whole basin are estimated to be in the order of U$55 million for grain and crop farming; U$93 million for cattle raising; U$19 million for dairy products; U$10 million for land-holding infrastructure; U$60 million from changes in land use; and U$9 million for public rural infrastructure. This makes up an annual total of mean direct benefits of almost U$250 million once the whole hydraulic infrastructure included in the Plan has been executed.

The total cost of investments in hydraulic drainage and storage works, rural roads and environmental mitigation measures is in the order of U$1.5 to U$1.8 billion. Investment in the said works is planned to take place over a fifteen to eighteen year period, i.e., an annual investment of around U$100 million per year. The Net Present Value of the investment at a 10% rate is U$193 million and the Economic Internal Rate of Return for the whole project is 14.3%.

Finally, it is important to note that the Province of Buenos Aires has enacted Law No. 11257 fostering the creation of Basin Committees and Management Consortia to manage resources and monitor infrastructure construction. The Provincial Government, together with the respective districts, has started outreach and consultation tasks in the belief that dissemination and consultation of the Plan among farmers and potential beneficiaries is a key factor for its success.

From a technical point of view, the Integrated Master Plan is based on analytical tools that facilitate the understanding of the basin's operation and make it possible to predict how it will react to planned interventions. The plan will provide a well-balanced social and environmental development framework by implementing a range of different measures that supplement one another and are coordinated by a flexible execution scheme. Non-structural measures in the Master Plan are:

(a) An Institutional Program that includes institutional restructuring, legal and fiscal measures, capacity building, transparent management tools, and public education and awareness.
(b) An Environmental Program that includes management of wet and inundated areas, environmental analysis and monitoring, regulation of fishing, integrated natural resources management, and wildlife and habitat management.
(c) A Sustainable Economic Development Program that includes soil conservation, improvement of natural pastures, intensive cattle breeding activities, promotion and development of small- and medium-sized tourism businesses, and rural employment opportunities.

4 FLOODS IN THE DOWNSTREAM AREA OF THE PLATA RIVER BASIN

The Plata River Basin comprises an area of some 3,150,000 km^2 over the territories of Bolivia, Paraguay, Brazil, Uruguay and Argentina. It is made up of the following river basins: Alto Paraná, Paraná, Paraguay, Uruguay, Iguazú, Pilcomayo and Bermejo (Figure 1).

The total population in the basin is over 80 million that contribute 70% of the gross domestic product of these five countries. More than forty hydroelectric dams, that produce 60% of the region's total energy, have been built on the rivers flowing in the basin (the well-known Itaipú Dam among them). Some rivers are navigable, and implementation of the "Paraná-Paraguay Hidrovía" navigation scheme is under way. The Paraná River Basin, between 16° and 34° of southern latitude, covers an important part of Brazil, the entire territory of Paraguay, part of Bolivia, and an important part of Argentina. The catchment area in the Delta upstream from the Plata River is 2,600,000 km^2.

The Paraná River Basin comprises four distinct rivers: the Paraguay River, the Iguazú River, the Upper Paraná River and the Paraná River (downstream from the confluence with the Paraguay River). The present analysis focuses on that final stretch of the Paraná River. The town of Paso de la Patria (Argentina) is on the confluence of the Upper Paraná and Paraguay rivers, 687 km downstream from the left bank of the Iguazú River. The Paraná River section at Paso de la Patria is 3,500 m wide, with plenty of islands and sandy banks. This section is 1,240 km from the city of Buenos Aires, where the river rises (Soldano, 1947). Downstream from the confluence with the Paraguay River, the Paraná River turns into a typical "flatland river with movable bed": permanent discharges and low slopes, dune translation on a fine sand bed, and a big floodplain that is inundated only during copious discharges, with the exception of some islands. Downstream from the city of Corrientes, the river slope decreases gradually reaching some 0.01 m/km.

Systematic water level measurements in the Paraná River started in 1901. As noted by Aisiks (1984), if the Paraná River does not reach the 5.5 m level mark in the city of Corrientes (discharging some 25,000 m^3/s), there will be no flood damages in the valley upstream and downstream from that section. An analysis of historical data shows that the Paraná River floods every three or four years and although floods can occur in any season, they are more likely to take place in February and March with a secondary rise in June. The most severe floods occurred in 1905, 1966, 1982–1983, 1992 and 1998. A discharge was gauged in June 1905 ($Q = 43{,}000$ m^3/s); in March 1966 the discharge was 41,000 m^3/s. The 1983 flood had special characteristics because it had started in 1982 after heavy rainfall saturated the soil in the basin. A high discharge was recorded at the Corrientes section ($Q = 51{,}300$ m^3/s) on May 30th, there was a second peak on July 12th ($Q = 45{,}000$ m^3/s), and the maximum discharge took place on July 18th ($Q = 61{,}000$ m^3/s).

A large-scale coupled ocean-atmosphere oscillation in the Pacific Ocean, known as the El Niño-Southern Oscillation (ENSO), is related to interannual variations in precipitation and streamflow in several region of the world. Sea Surface Temperature index (SST) and the Southern Oscillation Index (SOI) are used to

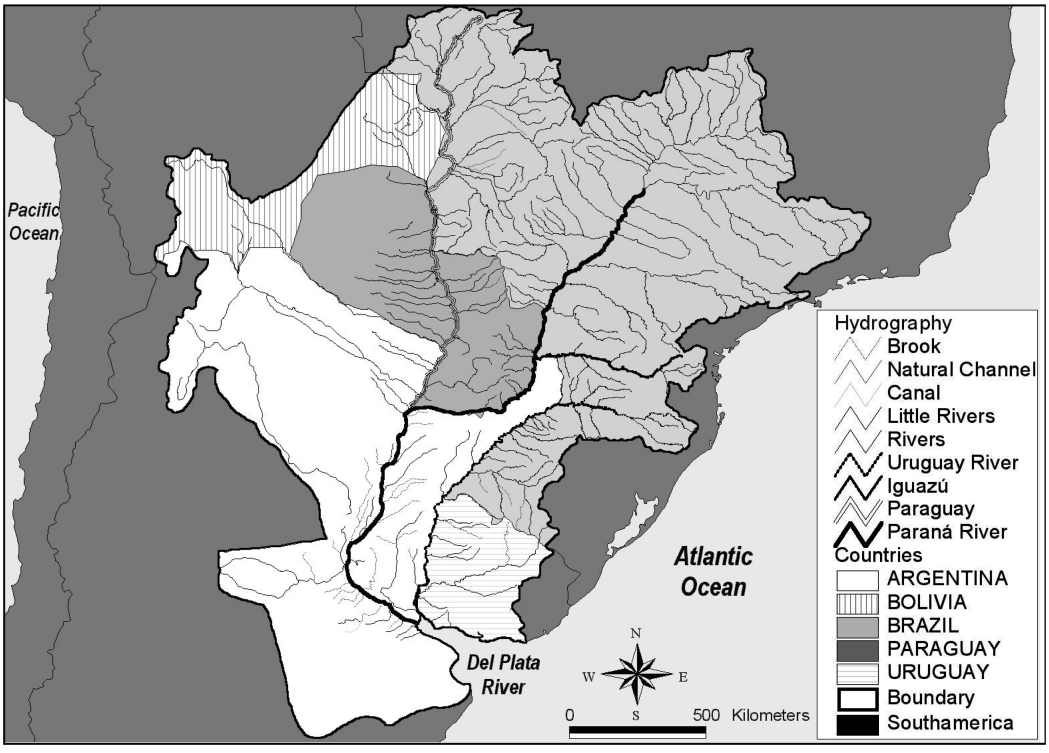


Figure 1. La Plata river basin.

quantify ENSO. SST anomaly is the sea surface temperature departure from the long term mean, averaged over a eastern and central equatorial Pacific Ocean. The warm El Niño phase is associated with high SST anomalies and the higher annual discharge in River Paraná at Corrientes and Posadas (Amarasekera et al., 1997). Floods related with warm phase of El Niño observed during 1982/83, 1992/93 and 1997/98 and the median of daily discharges are shown at the figure 2 for the period 1884/2002.

In 1992 a devastating flood in the city of Santa Fe reached a discharge of $Q = 54{,}000\ m^3/s$. The water level was higher than the one measured during the large flood of 1982–1983 due to excessive anthropic pressure on the floodplains (Paoli, 1997).

The increase in mean discharges and water levels since 1970 shows that the volume of water over the last three decades has increased with respect to similar periods in the past. Even if this condition is not permanent, it can be associated to the global climate change.

Statistical data on monthly minimum mean levels (month of September) and on the usual monthly maximum mean level (month of April) for the period 1970–1992 show a seasonal variation amplitude that decreases through time because flows have been regulated by many Brazilian hydroelectric dams in the upstream basin. The said amplitude reduction exerts a greater impact on low water levels than on high water levels. During severe floods the system's regulation capacity is negligible.

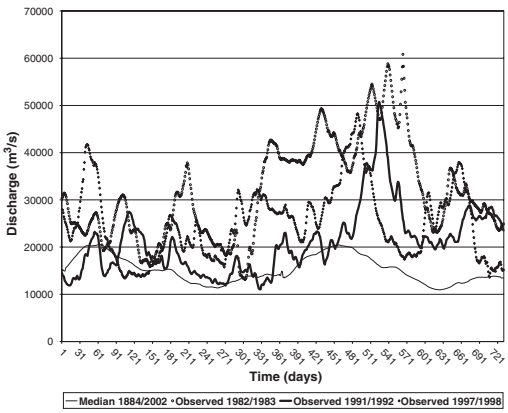


Figure 2. Discharges at Corrientes. Median and discharges associates with ENSO events.

In the case of large rivers flowing in flatland valleys with low slopes, extreme floods can be predicted and forecasted by means of rainfall data in the basin's upstream and middle regions. It must be pointed that even if storm characteristics and conditions are critical, the magnitude of the flood will strongly depend on the previous humidity content in the basin. If the basin's soil is saturated, if the floodplains are waterlogged, and if the reservoirs are full, a storm with heavy rainfall will trigger a flooding disaster.

5 THE HYDROLOGICAL EARLY WARNING SYSTEM

A hydrological warning system provides the Civil Defence and Disaster Control authorities with anticipated information on exceptional hydrological events. Forecasts must be precise. If floods are not accurately predicted credibility is lost and the cost of emergency measures increases. If the flooding event is not predicted, disaster occurs. Precision and regularity of the forecasting system is of the utmost importance for the preservation of life and minimisation of material losses in affected areas.

As a result of the 1982/83 floods, the National Secretariat of Water Resources created a Hydrological Warning System for Plata River Basin, which is operated by the National Water Institute (Goniadzki, 1997). The severe flood of 1992 caused serious damages in the northeastern provinces of Argentina. The Inter American Bank for Reconstruction and Promotion (BIRF) has granted a loan for the flooding restoration program that is administered by the Ministry of the Interior. This agency has signed an agreement with the National Water Institute to improve the technological capacity of the Hydrological Warning System for the Plata River Basin.

The Hydrological Warning System must operate on a continuous basis because it forecasts not only floods but also low water levels strongly required for navigation purposes. In the cities of Rosario and Santa Fe the Paraná River's water level can be predicted more than twenty days in advance while in other cities (Formosa, Corrientes, Goya) prediction levels are different.

The flood of 1992, when INA's early warning system was already in operation, caused physical damages that amounted to approximately U$500 million. Water levels were considerably higher than in 1966; however, in spite of the fact that there was a remarkable increase in investments and in population density, there were less physical damages.

The Plata River Basin System comprises simulation and forecasting models for different real-time hydrological variables. A probabilistic focus is represented by multiple lineal regression models using a recursive estimation algorithm for the parameters with the Kalman filter. Deterministic hydrological models are represented by the Sacramento Model of the National Weather Service, calibrated for the downstream basin of the Iguazú River (24,000 km^2), Chavasse and Seoane (1997).

The HEC-HMS precipitation-discharge transformation model developed by the U.S. Corps of Engineers has been calibrated and is used for the Uruguay River Basin. For floods along the Paraná River, a hydrodynamic translation model (Ezeiza V) has been developed by the National Water Institute (Menéndez, 1998).

The early warning system includes a series of tasks which range from rainfall monitoring (in different time scales) to short-and long-term rainfall forecasting in selected catchments. Main field tasks are: (a) estimation of rainfall areal distribution by means of satellite images combined with field data (real precipitation in the catchment); (b) areal distribution calculation with the "Hydroestimator" model; (c) assessment of different rainfall estimation techniques for use in several hydrological and neuronal models; (d) convective systems monitoring through satellite images (use of the FORTACC algorithm-FORecasting and Tracking for Active Cloud Clusters); and e) mean areal precipitation forecasting (72 hours) at catchment level.

The catchment areas of the Southern Salado River (2001) and of the Salado River (2003) are examples of rainfall estimated with satellite images in cooperation with the National Environmental Data and Information Service (NESDIS/NOAA) from USA.

6 RECENT FLOODING OF THE CITY OF SANTA FE

During the last days of April and early in May 2003 the city of Santa Fe, subject to periodic flooding of the Paraná River, experienced a most devastating flood induced by a tributary of the Paraná River, called Salado River (which is not the Salado River that flows in the "Pampas" region of Buenos Aires, some 1,000 km south).

The loss of more than twenty human lives, the large number of people evacuated, and the huge economic damages characterize this event as a disaster of catastrophic proportions. More than one third of the city's area, including strategic buildings such as schools, hospitals and an electric power plant, was suddenly inundated.

The downstream basin of the Salado River a typical flatland river is in the Province of Santa Fe. The upstream basin flow has little influence on maximum downstream flow discharges. The Salado River flows into the Paraná River between the cities of Santa Fe and Santo Tome.

The Salado River mean discharge in the downstream region is 145,6 m^3/s. Mean annual precipitation in the area ranged from 1,100 mm in the east to 800 mm

in the west during the 1941/1970 period, and from 1,200 mm to 900 mm during the 1971/2000 period. The natural flatland landscape has been modified by anthropogenic activities (construction of roads, canals and land works). In the 1990s the Province of Santa Fe implemented diverse structural and non-structural measures such as Argentina's flood program, which was launched with World Bank financing after the big flood of 1992.

The 2003 flood was caused by heavy rains that fell within the southern basin and which lasted from April 22 to April 24 (saturation of the basin had been detected in January 2003). Most of the rainfall turned into surface flow.

The discharge measured at the railway bridge near the city of Santa Fe was $Q = 3{,}100\ m^3/s$. Previous hydrological analyses (INA, 1998) estimated a discharge of $3{,}010\ m^3/s$ (some kilometres upstream from that section) for a recurrence period $T = 100$ years. Fortunately, the mighty Salado River flood did not occur simultaneously with the Paraná River flood since the backwater effect would have further raised the Salado River water levels.

Some of the anthropogenic activities that contributed to the disaster were:

- A small part of the western protection, erected between 1994 and 1998, was not finished. It seems that this disaster could have been prevented if construction of the structure had been completed.
- The Santa Fe-Rosario highway bridge is narrow (155 m) representing only 8% of the total valley's width (2,000 m) in this section. During the flood the backwater effect raised the water level more than 80 cm and overflowed the western protection 1,800 m upstream from the bridge.
- Since March 2003 the Hydrological Warning System of the Plata River Basin had been reporting that the basin was saturated and that the region was being affected by severe storms. The flood wave translation was already known to the authorities because of the floods that affected small villages and caused bridge damages in the upstream region.
- Land use in the floodplains is not adequately regulated. Construction of permanent strategic buildings in floodplains should not be authorized.
- The city lacked a flood contingency plan for evacuation and social assistance during and after the event.

In conclusion, the vulnerability (from a physical point of view) of the city of Santa Fe is the result of the following major factors:

- Its geographical location: it is located between two big uncontrolled rivers and its large floodplains have been occupied due to urban expansion.
- Its flat topography: inadequate rainfall runoff, lowlands close to the rivers, and high groundwater table levels.
- It lacks comprehensive and consistent urban planning.
- Its roads and protection works: inadequate for the increasing severe water scenarios and poor operation and maintenance plans.
- People should be made aware of the fact that a protected area is still a risk area. The province failed to implement non-structural measures to supplement infra-structure works and to devise an explicit contingency plan.

The damages caused by the extraordinary rise of the Salado River are the result of both natural and anthropogenic vulnerability.

7 RESEARCH PRIORITIES

There are no infallible flood protection structures. A flood protection structure may overflow during its life cycle or have construction problems or be poorly maintained. Therefore, non-structural measures are a must.

It is worth pointing out that flood risk assessment and formulation of emergency plans are tasks involving many disciplines in which professionals in water sciences must participate using a holistic approach.

It should be borne in mind that integrated water resources management related to floods and rising water levels calls for the need to investigate the means to improve administrative and economic management. Some lines of research and development to be considered in the near future, always aiming at diminishing risks and economic losses during critical water events, are:

- Research to improve hydrological modelling in order to gain a better understanding of the selection criteria and of statistic function parameters required to define the flow-return period relationship. This must be supplemented with enhanced knowledge of mathematical modelling of rain-flow transformation processes in order to safely predict possible rated flows for protection works.
- Research to improve hydrodynamic flood modelling in watercourses. It is particularly important to obtain accurate basic data on floodplain topography in areas of low slope, bathymetries, gauging and water quality monitoring.
- Research to use at – a local scale – the results derived from climate prediction models (such as those used for the El Niño-Southern Oscillation phenomenon).
- Comprehensive water resources management studies related to rising water levels and to jurisdictional, economic and legal problems derived from flood protection structural and non-structural measures.
- Research to optimise hydraulic design of infrastructure waterworks.

- Specific research to solve water-related problems in urban areas (floods, waterlogging, and pollution).
- Research on sustainable water resources use to prevent future water disasters.
- Development of techniques that combine satellite information with forecasting and monitoring activities.

"Science and Technology must be useful to society". This means that there must be an interaction between knowledge expansion and the society that will benefit from it, that boundary conditions must be taken into account so that society can profit from scientific production. The services rendered by a hydrological warning system is only one part of an overall process which should be fully operational to be meaningful.

8 CONCLUSIONS

The academic community, specialized agencies and decision-making bodies must interact in order to optimise human and material resources and generate greater benefits to society.

It is then crucial to develop, adapt and promote the use of modern hydro-meteorological technologies and to establish hydrological measurement networks. This can be achieved through the joint action of specialized state agencies that have shown an interest in working together. Cooperation links should be cemented, both formally and informally, across the institutions engaged in emergency response and mitigation activities. This is the only way to promote adequate and timely actions to withstand adversity.

One major problem specialists in this field currently face relates to dissemination of technological advances. Engineers, in particular, have always been and are still considered by the media as some sort of mercenaries reporting to a powerful client who puts the rest of the population at risk. Their voice and opinions are always questioned by professionals from other disciplines, by the journalists themselves, and by people that lack technological knowledge.

Moreover, decision-making bodies usually get conflicting messages about the benefits of some measures or projects from different actors. Such actors, who lack adequate scientific training, exert an influence and cause confusion about the priorities and critical activities that are required for an organized management of water resources.

Therefore, it will not be possible to integrate scientific and technological advances with social growth unless profound changes in management aspects are achieved. To this end, qualified specialists and professionals should have an active participation in the decision-making process and should not be involved with political bodies responsible for deciding on certain programs and processes.

These conclusions are supported by the chapter on "What is needed" in Kundzewicz, Szamalek & Kowalczak (1999). The catastrophic flood that hit Poland in 1997 has shown that local conclusions can help build up general concepts.

REFERENCES

Aisiks, E. G. 1984. La gran crecida del río Paraná de 1983, Organización Techint, Boletín Informativo, 232, Buenos Aires.

Amarasekera, K. N., Lee, R. F., Williams, E. R. & Eltahir, E. A. B. 1997. ENSO and natural variability in the flow of tropical rivers. J. Hydrol. 200, 24–39.

Chavasse, D. & Seoane, R. 1997. Asociación determinístico-estocástica para la predicción de caudales. Ingeniería del Agua. Vol. 4 N° 2, 55–64, España.

Goniadzki, D. 1997. Sistemas de información y alerta hidrológico. La prestación de un servicio esencial, Revista INA, Año 1, N° 1, 21–23.

Kundzewicz, Z. W. & Takeuchi K. 1999. Flood protection and managements: quo vadimus?, Hydrological Sciences Journal, 44(3) 417–432.

Kundzewicz, Z. W. 1999. Flood protection – sustainability issues, Hydrological Sciences Journal, 44(4) 559–572.

Kundzewicz, Z. W., Szamalek, K. & Kowalczak, P. 1999. The great flood of 1997 in Poland, Hydrological Sciences Journal, 44(6) 855–870.

Menéndez, A. 1998. La comprensión de la fenomenología de las inundaciones como requisito para su control, Revista INA, Año II, diciembre, 25–28.

Paoli, C. 1997. Inundaciones en ríos con creciente ocupación, Revista INA, N°1, 78–81.

Soldano, F. A. 1947. Régimen y aprovechamiento de la red fluvial argentina, Editorial Cimera, Buenos Aires.

This page intentionally left blank

River Flow 2004 – Greco, Carravetta & Della Morte (eds.)
© 2004 Taylor & Francis Group, London, ISBN 90 5809 658 0

Flood management and control in an urban environment – Diakoniaris case study

E.I. Daniil, S. Michas, G. Bouklis, P.L. Lazaridou & L.S. Lazarides
HYDROEXIGIANTIKI, L. S. Lazarides & Co. Consulting Engineers, Marousi, Greece

ABSTRACT: In this paper the implementation of general design considerations for flood management and control in an urban environment and their application to Diakoniaris project is presented. Diakoniaris river is located near Patra city, Peloponnese, Greece. It has ephemeral flow, flows from south to north and for the last 5 km before its outlet to the sea flows through the west suburbs of the city of Patra. Presently only 1 km, just before the outlet, is trained with a closed section, running under the main avenue of the area. According to city planning this avenue is proposed to be extended to the north to meet the highway circumventing Patra city, currently under construction. The design was based on an integrated watershed management approach, including works in the upstream mountainous area and consideration of the impact of proposed diversions on adjacent basins. Sediment control dams upstream and a sedimentation basin downstream of the new highway are proposed. Parallel to the closed concrete section, which will have to be extended upstream under the new part of the road, additional culverts running parallel to the existing one will be constructed.

1 INTRODUCTION

Integrated decision making for watershed management is not a simple task. Currently, different tools and approaches are proposed by researchers, and a trend for public involvement is evident in many countries. As the state of the art is far from complete understanding of the processes involved, many times, custom solutions, taking into consideration cultural and other local features, should be preferred.

Diplas (2002) notes that although significant attention has been paid recently on the impact that man-induced changes have on the environment, this has been a well known fact for a very long time, dating back to Plato. While the concept of land use change is not new, the rate, scale, and kind of changes that have been taking place over the last hundred years or so have been unprecedented. Real progress in predicting the modifications caused by human activities within a watershed will require further disciplinary work, research at the interface between disciplines, and improved dynamic interaction of the processes occurring in the abiotic and biotic systems.

General design considerations and principles for flood protection and related stormwater drainage system design, based on an integrated environmental approach, involving less technical works and preservation of the physical condition of streams and creeks in urbanized areas have been presented (Daniil et al. 2000, Lazaridou et al. 2002). Special topics to be taken into consideration include sediment control through check dams and selection of design return period. The design period should be selected depending on the specific location, the associated design of the receiving stream or water body, and considering the consequences of a bigger flood than the one used for the design. It should always be kept in mind that the selected design should be implemented starting from the downstream end and special care should be used in main road crossings.

1.1 *General design principles*

For flood protection design, regulation and management of streams passing through urban areas, an integrated environmental approach should be implemented and many factors taken into account (Daniil et al. 2000). Design considerations to be used as guidelines for practical use are mentioned below.

- Streams should remain in their physical condition, wherever possible. Channelization gains effectiveness by increasing channel slope and reducing bed resistance. This augments the velocity of flow and enables a channel to capacitate greater discharges without overbank flow and consequent flooding. However, rivers are not passive and their morphological structure responds to channelisation by

changing configuration, with undesirable and even detrimental effects (Parker & Andres 1976).

- Technical works should be designed with environment friendly materials and adapted to the natural architecture.
- The design return period should be selected depending on the specific location, the associated design of the receiving stream or water body, and considering the consequences of a bigger flood than the one used for the design. Designing upstream reaches for higher return periods than the downstream reaches may have disastrous effects due to intense flooding.
- Special effort should be made to locate possible sites for the construction of dams or reservoirs for upstream flood control in order to avoid designing a more costly stormwater drainage system.
- Alternative solutions should be evaluated to examine if existing insufficient storm sewers can be used as part of the new design system in their whole or even partly instead of being destroyed and rebuilt.
- Sediment transport calculations and measures for its control in populated areas are necessary.
- Geological mapping and assessment of possible hydrological flushing is also indispensable.

2 HYDROLOGY CONSIDERATIONS

Singh & Woolhiser (2002) in the 150 year anniversary hydrology paper discuss many aspects of mathematical modeling in watershed hydrology, illustrating the complexity of the problems involved.

In the case of complex basins and drainage systems, the use of hydrographs should be preferred over the rational method, that is widely used, but cannot easily give the spatial distribution of discharges over time.

Design for a given return period is not uniquely defined and may vary considerably depending on the selection of the parameters and methodologies involved: choice of appropriate intensity-duration-frequency (idf) curve, rainfall distribution, rainfall height and duration, unit hydrograph type. Implementing the worst profile distribution may result in twice the design discharge, compared to the one resulting from rainfall heights computed by the idf curve without redistribution (Daniil & Lazaridis 2003). Yen (2000) notes that part of the misunderstanding comes from inadequate appreciation of probability and that the more serious problem is that the X-year return period of what is not clearly specified.

2.1 *Rainfall duration*

A common recommendation is that the storm duration should be sufficiently long so that the entire drainage area is contributing to runoff, as a result it should exceed the time of concentration and it is suggested that it should be 3 to 4 times the concentration time. Concentration time can be severely shortened due to urbanization and river training works.

In the USA the National Weather Service reports that the most frequent duration of runoff-producing rainfall is about 12 hours. Levy & McCuen (1999), based on observed data in Maryland, show that 24 hr is a good hypothetical storm. Storm types provided by the Soil Conservation Service (SCS) for different areas in the US have a 24 hr duration. The choice of rainfall duration, as a result, depends largely on the designer's interpretation of the data and the significance of the project.

2.2 *Rainfall distribution*

Alternating block method distribution and Worst profile distribution tend to become popular in recent years. The alternating block method distribution produces a center-loaded storm, while the worst profile distribution produces the highest peak discharge for a given total rainfall height and unit hydrograph.

Levy & McCuen (1999) report that actual data from six Maryland watersheds ($5 < A < 135\,km^2$) suggest that center-loaded design storms are appropriate. Packman & Kidd (1980) also reported that center-loaded hyetograph was most appropriate based on the analysis of data from the United Kingdom.

The concern on the effect of rainfall distribution is also reflected in recent editions of commercially available software packages. HEC-HMS (USACE 2000) for example provides the user in the case of the frequency storm with the choice of placing the hydrograph peak at 25–33–50–67–75% of the storm duration. In every case the user has to give rainfall heights at predetermined times according to the idf curve and the program performs the redistribution. No option for the worst profile scenario is given and the 50% is usually considered the standard. Although the above choices do not give exactly the worst profile scenario, the user can determine the one that gives the highest peak.

Eventually, a frequency or return period should be associated with rainfall distribution patterns, or alternatively certain patterns should be adopted for given return periods of rainfall.

2.3 *Unit hydrograph selection*

Determining an appropriate design hydrograph in ungaged basins becomes almost an art and depends largely on the experience of the design engineer. It involves choices of many parameters including rainfall distribution, once a type of unit hydrograph is selected.

In the third edition of Design of Small Dams (US Dept. of the Interior, Bureau of Reclamation 1987) six types of dimensionless hydrographs are presented based on 162 reconstructed flood hydrographs. The Sierra Nevada type and the Rocky Mountain Thunderstorms seem applicable to some Greek mountainous

basins and have been used by the authors in recent studies.

In order to apply these dimensionless hydrographs, lag time has to be determined, based on the geometric characteristics of the basin and a parameter, Kn. Kn is an average Manning's n value representing the hydraulic characteristics of the drainage network. For Kn higher values are considered appropriate for developing flood hydrographs of more common frequency than, say the 100 yr event.

Lag time was originally defined by Horner & Flynt as the ". . . time difference between . . . center of mass of rainfall and center of mass of runoff. . .". Bureau of Reclamation uses the following definition in conjunction with the dimensionless hydrograph technique: Lag time is the time from the midpoint of the unit rainfall excess to the time that 50% of the volume of unit runoff from the drainage basin has passed the concentration point.

$$L_g = C\left(\frac{L\,L_{ca}}{S^{0,5}}\right)^N \quad (1)$$

Lg is the unit hydrograph time in hours, C, N are constants N = 0.33, C = 26 Kn, L is the longest watercourse from the point of concentration to the boundary of the drainage basin in miles. The point of concentration is the location on the watercourse where a hydrograph is desired, Lca is the length along the longest watercourse from the point of concentration to a point opposite the centroid of the drainage basin in miles, and S is the overall slope of the longest watercourse (along L) in feet per mile.

Unit hydrographs by the Soil Conservation Service (SCS) can also be used and they are offered as an option in mathematical modeling programs (e.g. HEC-HMS), contrary to the aforementioned hydrographs given in the Design of Small Dams. A critical parameter again is the time to peak.

2.4 *Design discharge – return period*

Design for a given return period is not uniquely defined and may vary considerably depending on the selection of the parameters and methodologies involved: choice of appropriate idf curve, rainfall distribution, rainfall height and duration and unit hydrograph type.

Idf curves derived from a limited time series cannot usually be extrapolated to predict rainfall depth at very high return periods. Koutsoyiannis & Baloutsos (2000) have demonstrated that the General Extreme Value (GEV) distribution appears to be suitable for the analysis of annual maximum rainfall, its predictions for large return periods agree with the probable maximum precipitation estimated by the statistical method (Hershfield 1961, 1965) and an idf curve with a wide range of applicability can be derived.

Koutsoyiannis' (1999) methodology provides at the same time a rainfall distribution even at those high return periods and no additional assumptions are needed. Equations of this type should be used wherever possible.

The scale of the catchment area is also important in determining peak discharge, which is not directly proportional to the catchment area. Odgen & Dawdy (2003) based on data from an experimental watershed, 21.2 km^2, report that on the average, individual runoff event peak discharges are described by a power law function of a catchment area. They also found that flood quantiles in nearly all subbasin are self-similar as described by a simple scaling theory.

Finally, another consideration is the impact of stormwater on the water quality of the receiving water body. In some countries, environmental regulations exist that impose strict standards for water quality and measures preventing pollution due to stormwater inflow have to be taken. Calabro (2004) presents an interesting study and shows that design storms with triangular or Chicago shape and duration similar to the time of concentration of the catchment are in most case the worst regarding the water quality impact and can be used in the design.

For complex drainage systems, computational platforms, such as HEC-HMS should be used, as they facilitate determination of time and spatial distribution of discharges.

3 DIAKONIARIS PROJECT

Diakoniaris river is located near Patra city, Peloponnese, Greece (Fig. 1). It has ephemeral flow and flows from south to north. For the last 5 km before its outlet in the sea flows through the west suburbs of the city of Patra. Presently only 1 km, just before the outlet to the sea is trained with a closed section, running under the main avenue of the area. According to city planning this avenue is proposed to be extended to the north to meet the highway circumventing Patra city (PCH), currently under construction.

3.1 *Background*

Diakoniaris river (Fig. 2) and its tributaries, Malamamoutis, Panagitsa, Romanos etc, used to have a total drainage area upstream of the new highway of ∼19.5 km^2 in the 70's, when part of Elekystra's (∼9.6 km^2) basin was diverted through an open diversion channel to Glaykos river. The remaining basin ∼9.8 km^2 develops on the west side of Panachaikos mountain from elevation +150 to +1150 m along a 5.2 km.

In December 2001 a flood resulted in human losses, drawing public awareness to the problem and a new



Figure 1. Location of the project.

study of the project. The project in its introductory and preliminary stage was assigned to Hydroexigiantiki by the Ministry of the Environment, Planning and Public Works. Hydrology of the area, including idf relations and design discharges, was reevaluated.

In the mountainous area geological instabilities and erosion are observed in the area of neogenic formations. This is considered the main source for sediment production. Main sediment producing areas are located within Diakoniaris and Panagitsa catchment areas. Sediment transport rate has not been determined from systematic measurements. However, based on field reconnaissance and on site observations after the December 2001 flood, it can be concluded that sediment yield is high, possibly more than 1000 $m^3/km^2/yr$. This value may be more than doubled for certain years. The river bed upstream of the city limits is wide and flows through a forested area. Within the city limits urban development has limited the width of the river bed and the floodplain has been inhabited.

Sediment control upstream from PCH (Patra Circumventing Highway) is crucial for the design of Diakoniaris training works. Based on this realization a final design study was performed for Diakoniaris and downstream drainage network covering ~11 km^2 drainage area, under the assumption that the area upstream of PCH will be diverted to Glaykos river. Implementing this design the existing close section was constructed with a $2 \times 6 \times 2$ closed conduit section running for 400 m from the outlet to the sea and upstream simple box culvert 6.0×2.6 and 7.5×2.6 up to station $1 + 100$.

Assuming that no significant sediment depositions reducing the conveyance of the system will take place, the existing structure can convey ~90 m^3/s.

The proposed Diakoniaris diversion to Glaykos was never constructed, with the exception of small area ~1 km^2 between Elekystra diversion and PCH. The rest of the watercourses continued to follow their natural course.

3.2 *Intensity – duration – frequency curves*

The following idf curve determined in the old study (1984) and adopted with a fit for return period term in the hydraulic design of the new highway (PCH)

$$i=20.31\ T^{0.25}\ t^{-0.59}=\alpha\ t^{-0.59} \tag{2}$$

where i intensity in mm/hr, t rainfall duration in hrs, T return period in years.

The idf curve was compared to the one used in Xerias River Corinth, also in northern Peloponnese (Lazaridou et al., 2003).

The idf curve adopted for Xerias river, constructed based on Koutsoyiannis methodology, was:

$$i(d,T)=\frac{50.44\left(T^{0.16}-0.636\right)}{\left(d+0.0679\right)^{0.732}} \tag{3}$$

where d is the rainfall duration in hours, i the rainfall intensity in mm/h and T the return period in years.

The comparison of the two curves is given in graphical form in figure 3.

Comparison of hydrographs for the return periods considered gave no significant difference in peak discharge between the two idf curves and consequently eq. (2), used for the design of other works in the area was used in modeling of Diakoniaris basin.

The rainfall distribution resulting from the idf curve was also compared to the SCS synthetic storm hyetographs proposed for use in the USA for storms of 6 and 24 hours duration (Chow et al. 1988). Types I, IA are for the Pacific maritime climate with wet winters and dry summers. Type I is quite close to the alternating block method distribution applied to eq. (2) as shown in figure 4.

3.3 *Design discharge – return period*

A return period of 50 years was specified as the lower acceptable return period in the environmental permit relating to the extension of Diakoniaris Avenue. Due to the complexity of the system it was deemed appropriate to model it in a HEC-HMS environment. Diakoniaris basin was modeled in great detail. Elekystra basin and part of Glaykos basin were also included

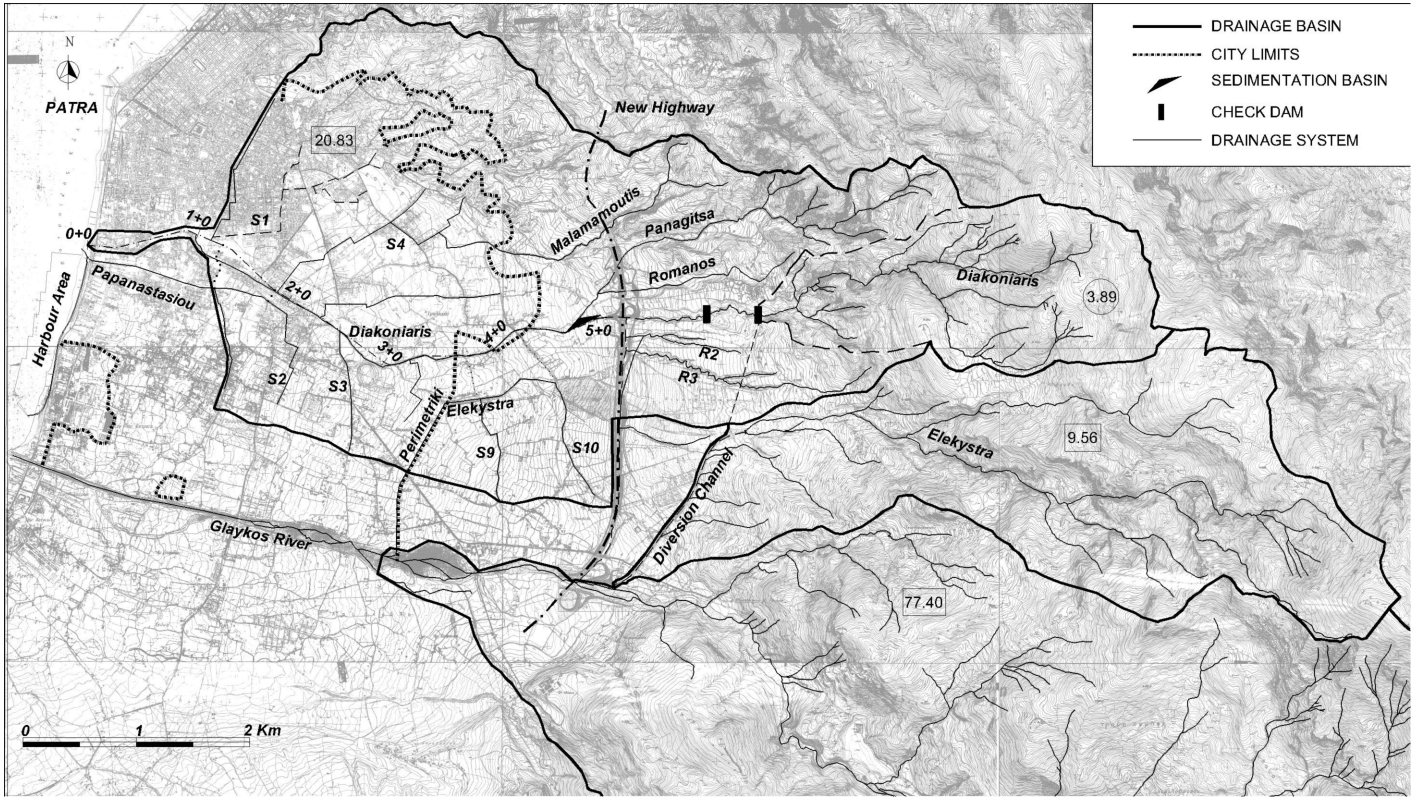


Figure 2. General layout of Diakoniaris basin and drainage system.

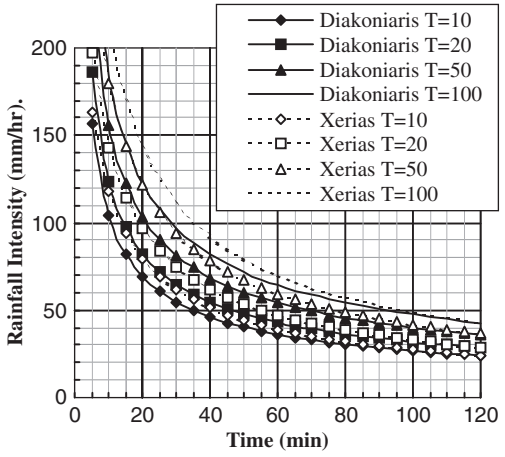


Figure 3. Comparison of idf curves.

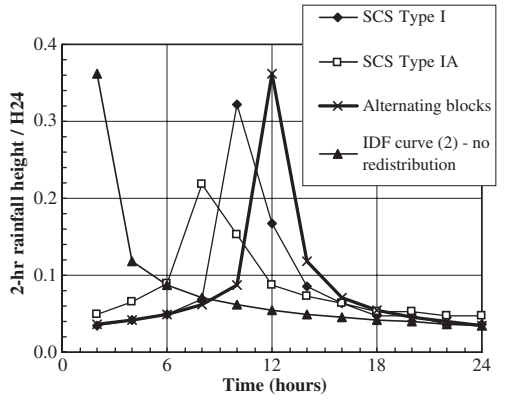


Figure 4. Variation of peak discharge along Diakoniaris river for T = 10, 20, 50, 100 years.

in the model, but not with the same detail, in order to determine the impact of the proposed diversions.

Information from geologic and land resource maps was used for the determination of CN to appropriately include infiltration losses. In the upstream area there is a small part of pseudoalpine zone and fir zone. The largest part of the area just upstream of the city limits is covered by the broadleaved evergreen zone and cultivated land and near the city limits there is a deciduous oak zone. Near the sea we encounter alluvium and tertiary deposits.

In their majority the soils can be considered to be in category C with the exception of the area downstream of Elekystra diversion channel that falls in category B.

Finally, for the modeling three CN curve numbers were implemented: CN = 80 for the upstream Diakoniaris basin, CN = 75 for the areas outside the city limits and CN = 85 for the areas within the city limits.

3.4 *Hydrologic modeling*

For the Diakoniaris project the drainage area (~20 km^2) was modeled with HEC-HMS software. For the mountain area of the basin, hydrographs were also developed according to the design of Small Dams and compared to the SCS hydrographs obtained within the HEC-HMS environment. Many scenarios were run with different idf relations, return periods of 10, 20, 50 and 100 years and different rainfall distributions. Using the developed model many alternatives were examined: diversions both in the mountainous area, involving tunnels and open channels, and closed conduits in the urbanized area.

The whole drainage system was modeled using HEC-HMS (Hydrologic Engineering Center – Hydrologic Modeling System). Modeling in the HEC-HMS environment includes three components.

The basin model where the watersheds or basins are represented and hydrologic elements connected in a dendritic network to simulate runoff process. In this part losses, runoff transformations and open channel routing are selected.

The meteorological model where precipitation to be used is given and the method for its distribution selected.

The control specifications, where the duration and time step of the modeling is defined.

3.5 *Hydrologic modeling parameters*

The whole drainage system was modeled using HEC-HMS with the following parameter selection:

- Hydrographs according to SCS
- SCS curve number loss model
- Lag time was determined using data from hydrographs given in Design of Small Dams and estimated flow velocities in concrete culverts in the order of 6 m/s
- Flood routing through trained sections with the Muskingam – Cunge standard method.

The final design discharges were determined for a 12-hour – center-loaded storm.

For the Sierra Nevada type hydrograph, that is considered applicable to Diakoniaris area,

$$t_p = 0.75\left(L_g + \tfrac{1}{2}D\right) = 0.75L_g + 0.375D \quad (4)$$

where tp is the time to peak, D is the unit rainfall duration and Lg is the lag time.

For a small unit duration, as assumed in HEC-HMS simulations

$$t_p \approx 0.75\,L_g \quad (5)$$

This value was used as time to peak for the SCS hydrographs.

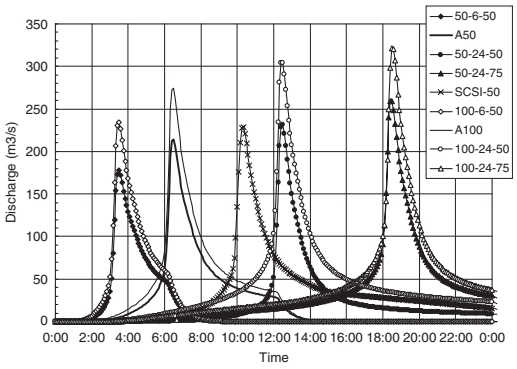


Figure 5. Hydrographs at Diakoniaris outlet for various rainfall duration and distribution for T = 50, 100 years.

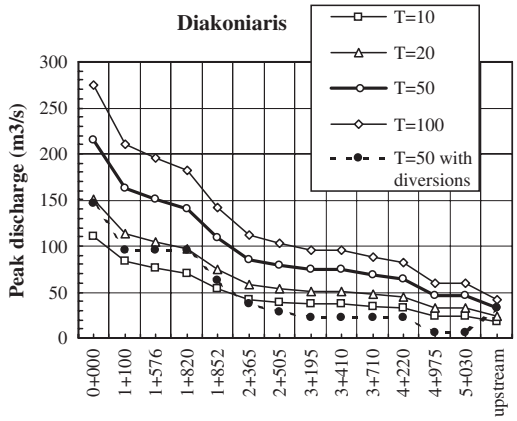


Figure 6. Variation of peak discharge along Diakoniaris river for T = 10, 20, 50, 100 years.

In figure 5 hydrographs at Diakoniaris outlet, without any diversions, for T = 50, 100 yrs, durations of 6, 12, 24 hrs and peak located at 50% (center-loaded) or 75% (closer to the worst profile), along with SCS Storm Profile I are given.

In figure 6 the variation of peak discharge for Diakoniaris watercourse for T = 10, 20, 50, 100 yrs without any diversions and for T = 50 yrs with the proposed diversions is presented.

4 SEDIMENT TRANSPORT

Geological and land resource maps along with new geological studies performed for the study area and especially the upstream sediment producing area, were used for estimating sediment transport conditions in the area.

Sediment production is high in the area causing depositions in the closed sections and the outlet.



Figure 7. Existing sediment control drop structures in the mountainous area filled with sediment.



Figure 8. Existing sediment control structure upstream of the highway crossing.

Average sediment transport in the area is estimated at 2200 $m^3/km^2/yr$ while there is an very active area upstream where 23,000 $m^3/km^2/yr$ sediment production rate is reported in the literature. Therefore, sediment control structures are absolutely necessary.

Sediment control drop structures have been constructed in the past in the mountainous area, but the have been filled with sediment (Fig. 7). A newer sediment control structure exists upstream of the highway crossing (Fig. 8). This structure was filled with sediment during the December 2001 flood and subsequently cleared out.

A sedimentation basin in the natural confluence of Diakoniaris and Panagitsa tributary was designed. This involved a special design. In the main conduit under the road, a spillway was placed so that for discharges up to the design discharge is routed through the sedimentation basin, while for higher discharges it acts as emergency spillway. This special structure will be studied in a model before construction. Check dams to



Figure 9. Existing Diakoniaris outlet structure to the sea.

be used for sediment control, combined with upstream diversions were also proposed.

Additionally two sediment control dams were proposed. The upstream one can be combined with the diversion of the upstream Diakoniaris basin to Elekystra Diversion Channel.

5 DIAKONIARIS TRAINING WORKS

The training works and diversion were designed for the 50-year flood according to the environmental permit. The existing closed section can only convey about 90 m^3/s and possible additional culverts running parallel to the existing one, due to space limitations, can handle only a maximum additional 60 m^3/s.

The downstream closed sections were checked for higher discharges in order to locate critical points. The estimated discharge without any diversions is 215 m^3/s, while with a combination of diversions upstream and in the city area, the discharge at the outlet can be limited to 150 m^3/s.

Higher discharges were assumed to be combined with unfavorable conditions at the outlet, thus creating pressurized flow towards the outlet and the pressure gradient was determined. It was desired that the pressure grade line remains below the ground, so that manhole covers are not affected.

The following possibilities were examined:

- Diversion of the upstream Diakoniaris basin, $A = 3.89\,km^2$.
- Diversion of sewer basins S9 and S10 to "Perimetriki", i.e. a sewer running under the new road running around Patra suburbs.
- Diversion of sewer basins S2 and S3 to Papanastasiou, a road running parallel to Diakoniaris axis and reaching the harbor area. In the harbor area (under construction) a channel running parallel to the sea front and receiving all sewers flowing towards that area will be constructed. The proposed Papanastasiou diversion will also flow in this channel, close to the outlet, with appropriate outlet modification.
- Diversions of local creeks R2 and R3 to Glaykos through the storm sewer system of the new highway.



Figure 10. View of the river bed and pedestrian crossings within the city limits, to be trained.

Various combinations of all the above were simulated with the HEC-HMS model and results for the discharge at the outlet are presented in Table 1.

It should be noted that in modeling the future conditions, with full development of the city and the drainage system, were represented. With the existing conditions, with minimal development of the drainage system, concentration times are expected to be longer and consequently peak discharges lower. This was taken into account in scheduling the construction of the proposed works. As a result construction of the closed conduit upstream of the existing closed section can start before the addition of parallel conduits to the existing structure.

Provision is made in the design for big surface openings (~2–3 × 6–8 m), appropriately fenced, that would facilitate aeration and cleaning by mechanical means of the closed section. Additionally, holes in the bottom of the conduit are provided for water table recharge.

Proposed training works for Diakoniaris main course are summarized in Table 2.

Table 1. Peak discharge at Diakoniaris outlet for T = 10, 20, 50, 100 years (12 hr, center-loaded storm).

Scenario	Scenario name	Diakoniaris upstream diversion	R2 & R3 diversion	Perimetriki diversion (S9 & S10)	Papanastasiou diversion (S2 & S3)	Panagitsa, Romanos upstream diversion	Q10 (m^3/s)	Q20 (m^3/s)	Q50 (m^3/s)	Q100 (m^3/s)
1	(A)	–	–	–	–	–	111	151	214	274
2	(D)	X	–	–	–	–	105	142	200	256
3	(DPAP)	X	–	–	X	–	92	125	178	228
4	(DTX)	X	X	–	–	–	101	136	193	246
5	(DPP)	X	–	X	X	–	81	109	155	198
6	(DPPT)	X	X	X	X	–	77	104	147	187
7	(PP)	–	–	X	X	–	87	119	169	217
8	(DTPAP)	X	X	–	X	–	88	120	170	217
9	(DPER)	X	–	X	–	–	94	126	177	226
10	(TX)	–	X	–	–	–	107	145	206	263
11	(PPT)	–	X	X	X	–	83	109	161	206
12	(PAP)	–	–	–	X	–	98	135	193	248
13	(PER)	–	–	X	–	–	100	135	191	244
14	(PED)		–	X	X*	–	84	111	**154**	195
15	(OREI)	X	X	–	–	X	102	137	194	248
16	**PPN**	**–**	**X****	**X****	**X****	**–**	**79**	**107**	**152**	**195**

*Part of Diakoniaris discharge (26.4 out of 63.7 m^3/s) is assumed to be diverted to S10, while the 37.3 m^3/s continue to flow through the main course.
**In this scenario drainage areas have been revised so that Perimetriki is the divide.

Table 2. Diakoniaris training works.

Reach	Description – cross section
0+000/0+050	open cross section/outlet modification
0+050/0+400	existing section 2 × (6.0 × 2.0) – slope 5.2‰ addition of two conduits 4 × 2
0+400/0+908	existing section (6.0 × 2.6) – slope 11.0‰ addition of two conduits 4 × 2.6
0+908/1+110	existing section (7.5 × 2.6) – slope 11.5‰ addition of two conduits 3.25 × 2.6
1+110/1+852	8.50 × 3.0
1+852/2+365	6.0 × 3.0
2+365/3+412	5.0 × 3.0
3+412/5+028	4.0 × 3.0
5+028/5+084	4.0 × 3.0 (C30/35 concrete)

Special structures are designed at stations 0 + 400 and 1 + 100, where the number of opening changes. A cascade structure is designed at the entrance of the upstream basin in the downstream trained reach, where there is a significant elevation difference due to the construction of the highway.

5.1 *Time planning of training works*

Training works are planned in two stages, taking advantage of the existing situation, i.e. not fully developed urbanization and stormwater drainage system in the area, that results in lower discharges than the ones estimated under the assumption of fully developed drainage system and city layout.

6 CONCLUSIONS

Flood management and control in an urban environment should follow an integrated watershed management plan, but is restricted from existing city planning and development.

In the examined case of Diakoniaris river in Patra, Peloponnese, Greece, a combination of diversions upstream and within the city limits and sediment control measures was used in order to achieve sufficient flood protection in the catchment.

ACKNOWLEDGEMENT

Special thanks to Stella Michailidou for preparing the general layout figure and maps.

REFERENCES

Calabro, P.S. 2004. Design storms and water quality control. *J. Hydrologic Eng*. 9(1): 28–34.

Chow, V.T., Maidment, D.R. & Mays, L.W. 1988. *Applied Hydrology*, McGraw-Hill.

Daniil, E.I., Bouklis, G.D., Lazaridou, P.L. & Lazaridis, L.S. 2000. Integrated Approach for Environmental Flood Protection for northern suburbs of Athens, Greece. *Building Partnerships*, ASCE, Proc. of the 2000 Joint Conf. on Water Resources on CD, Minneapolis, MN, USA, 2000.

Daniil, E.I. & Lazaridis, L.S. 2003. Designer's concerns on the effect of rainfall distribution on dam and

diversion works sizing, *IAHR XXX Congress*, Thessaloniki, GREECE, 24–29 August 2003, Theme B: 95–102.
Diplas, P. 2002. Integrated Decision Making for Watershed Management: Introduction. *Journal of the American Water Resources Association*. 38(2): 337–340.
Hershfield, D.M. 1961. Estimating the probable maximum precipitation, ASCE, *J. Hydraul. Div*. 87(HY5): 99–106.
Hershfield, D.M. 1965. Method for estimating probable maximum precipitation, *Journal of American Waterworks Association*. 57: 965–972.
Koutsoyiannis, D. 1999. A probabilistic view of Hershfield's method for estimating probable maximum precipitation, *Water Resources Research*. 35(4): 1313–1322.
Koutsoyiannis, D. & Baloutsos, G. 2000. Analysis of a long record of annual maximum rainfall in Athens, Greece and design rainfall inferences, *Natural Hazards*. 29: 29–48.
Lazaridou, P.L., Daniil, E.I., Michas, S.N., Papanicolaou, P.N. & Lazarides, L.S. 2002. Integrated Environmental and Hydraulic Design of Training Works for major Watercourses, *Proceedings of the Int. Conf. Protection and Restoration of the Environment VI*, Skiathos, Greece, July 2002, A.G. Kungolos et al (eds), Vol. I: 175–182.
Lazaridou, P.L., Daniil, E.I., Michas, S.N., Papanicolaou, P.N. & Lazarides, L.S. 2003. Integrated environmental and hydraulic design of Xerias river, Corinthos, Greece, training works, *Water, Air, Pollution: Focus/Protection and restoration of the environment, Kluwer Academic* (in press).
Levy, B. & McCuen, R. 1999. Assessment of Storm Duration for Hydrologic Design, *J. Hydrologic Eng*. 4(3): 209–213.
National Environmental Research Council (NERC), Flood Studies Report, Institute of Hydrology, Wallingford, 1975.
Odgen, F.L. & Dawdy, D.R. 2003. Peak discharge scaling in small Hortonian watershed. *J. Hydrologic Eng*. 8(2): 64–73.
Packman, J.C. & Kidd, C.H.R. 1980. A logical approach to the design storm concept. *Water Resour. Res.* 16(6): 994–1000.
Parker, G. & Andres, D. 1976. Detrimental Effects of River Channelization, *ASCE Proceedings of the Symposium on Inland Waters for Navigation, Flood Control & Water Diversions*, Colorado State University, August 10–12: 1248–1266.
Singh, V.J. & Woolhiser, W. 2002. Mathematical Modeling of Watershed Hydrology, *J. Hydrologic Eng*., 7(3): 270–292.
Stedinger, J.R., Heath, D.C. & Thompson, K. Risk Analysis for Dam Safety Evaluation: Hydrologic Risk, U.S. Army Corps of Engineers, Institute for Water Resources, IWR REPORT 96-R-13, March 1996.
US Army Corps of Engineers, Hydrologic Engineering Center. 2000. *Hydrologic Modeling System, HEC-HMS, Technical Reference*.
US Department of the Interior, Bureau of Reclamation 1987. *Design of Small Dams*, 3rd edition, US Government Printing Office, Denver, CO.
Yen, B.C. 2000. 100-Year Return Period of what?, *Building Partnerships*, ASCE, Proceedings, Minneapolis, MN, USA.

River Flow 2004 – Greco, Carravetta & Della Morte (eds.)
© 2004 Taylor & Francis Group, London, ISBN 90 5809 658 0

Flood mitigation planning related to land use

Y. Takeuchi
Kawasaki Geological Engineering Co., Ltd, Tokyo, Japan

M. Takezawa
Nihon University, Tokyo, Japan

ABSTRACT: The present study proposes a new comprehensive flood mitigation system that considers the current stage of land development. The proposal includes the distribution of a flood mitigation guidebook to affected residents, followed by a medium-scale implementation of measures involving the construction of readily achievable structures such as one-sided dikes or unenclosed ring dikes. The project would then extend to a large-scale consultation and the implementation of comprehensive flood mitigation measures.

The present study also presents a unique economic analysis method to increase the relative economic value of a flood migration project by combining previously independent structures like river, highway and railroad dikes and eliminating unnecessary construction. The concept of "time and regional extended effects" is also introduced as an assessment technique for determining the economic value of flood mitigation projects.

1 INTRODUCTION

Many flood mitigation plans for alluvial basins around the world have not been implemented because of problems associated with the economic analyses or the measures themselves. In many cases, failure to implement the flood mitigation measures has lead to an area being under-utilized. In some instances, mitigation projects are not followed through due to plan implementation difficulties, which have often been drawn up without consideration of current levels of development and land usage or the financial capacity of the concerned countries or regions. In other cases, the projects have not been started because the estimated economic value of flood mitigation is insufficient, when implementation of the measures may in fact increase the economic efficiency significantly.

Flood mitigation projects should be designed so as to correspond with target area conditions. The present study proposes a new comprehensive flood mitigation system that considers the current stage of land development. The proposal includes the distribution of a flood mitigation guidebook to the residents concerned, followed by medium-scale implementation involving the construction of readily achievable structures, such as one-side dikes or unenclosed ring dikes. The project would subsequently extend to large-scale consultation and the implementation of comprehensive flood mitigation measures.

The present study also presents a unique economic analysis method that increases the relative economic value of a flood migration project by combining structures, such as previously independent structures like rivers, highways and railroad dikes and eliminating unnecessary construction. The concept of "time and regional extended effects" is also introduced as an economic value assessment of flood mitigation projects, which also ensures that the scope and efficiency of the project is optimized. This measure is calculated based on an existing standard method employed in feasibility studies. The "time extended effect" concept identifies how flood mitigation infrastructures allow the development of property and capital, with accumulated benefits over long periods. Thus, when properties are protected against floods, new properties and capital will accumulate without destruction and confidence will increase. The "regional extended effect" of flood mitigation projects refers to the influence on increased economic activity of a region, locally, nationally and throughout the world.

2 COMPREHENSIVE FLOOD DAMAGE MITIGATION SYSTEM

A comprehensive flood damage mitigation system consists of three main sub-systems that simultaneously

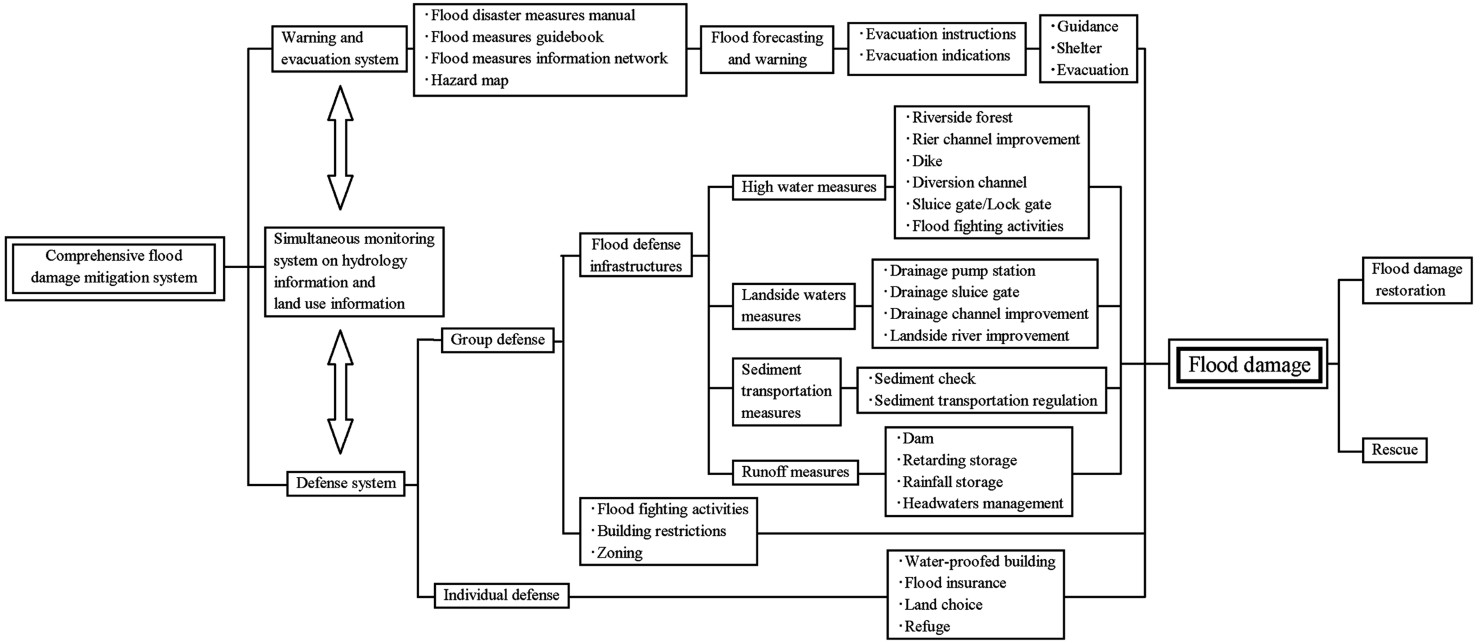


Figure 1. Comprehensive flood damage mitigation system.

monitor hydrology and land use information, warning and evacuation systems and defense systems, as shown in Figure 1. The warning and evacuation sub-system consists of a flood disaster measures manual, a flood measures guidebook, a flood measures information network and hazard map. The defense sub-system consists of individual defense and group defense. Individual defense consists of waterproofed buildings, flood insurance, land choice and refuge availability. Group defense consists of flood mitigation infrastructures, flood fighting activities, building restrictions and zoning.

A comprehensive flood damage mitigation system is based on the assumption that flood damage inevitably happens, regardless of the strength of flood mitigation measures. To minimize flood damage, which includes restoration costs, flood mitigation measures should always be systematically combined with the development stage of engineering, economics and regional land use.

A comprehensive flood damage mitigation system should give priority to the development of linked soft wares of flood mitigation related to land use as a first step in land development. These soft wares include flood disaster measures manuals, flood measures guidebooks, flood measures information networks, hazard maps and flood forecasting and warning systems, which give the highest priority to saving human life with evacuation instructions and evacuation indicators as guidance.

The flood mitigation measures of individual defense include waterproofed buildings, flood insurance, land development choices and refuge availability. In an intensive stage of land development, hard wares of flood measures, such as high water measures, landside water measures, sediment transportation measures and runoff measures become necessary.

3 ECONOMIC ESTIMATION OF DIKE CONSTRUCTION WORKS JOINTED PROJECTS

Some projects were judged infeasible due to low economic effect. If the construction costs of dike combined with flood mitigation and highway infrastructure costs are distributed across each project, higher accuracy economic estimations become feasible. In this case study, the Apure River Flood Mitigation Project is presented.

The flood mitigation project in the Apure River Basin, Venezuela, was subdivided into the following three projects, shown in Figure 2.

Project A: construction of a 187 km-long dike on the right bank of the Portuguese River

Project B: construction of a 145 km-long dike on the right bank of the Guanare River

Project C: construction of a 155 km-long dike on the left bank of the Apure River.

Table 1 shows the dike length, project costs and benefit–cost ratio of these projects. The design life of each dike is 50 years.

The benefit–cost ratio of Project A, Project B, Project C and total projects are 1.39, 1.45, 0.82,

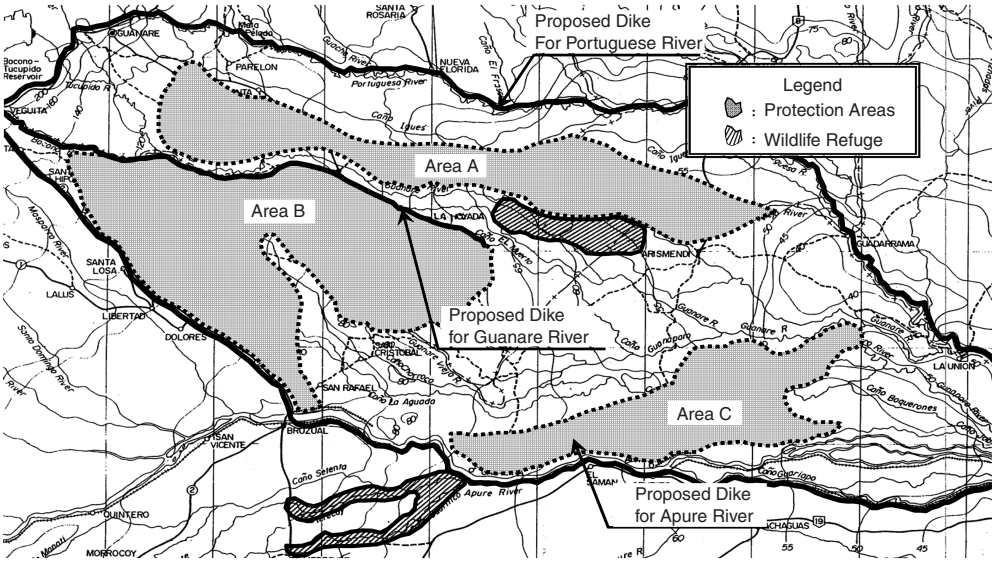


Figure 2. Flood mitigation plan of the Apure River Basin.

1.15, respectively. The total project was economically judged feasible because its benefit–cost ratio was above 1. The tops of the project dikes were designed for use as gravel-paved roads, however, the benefit–cost ratios did not include the road construction benefits. If these were counted in the benefit–cost ratios, the benefits of dike construction would have increased.

4 SEPARATION OF INESTIMABLE CONSTRUCTION WORKS FROM A FLOOD MITIGATION PROJECT

The Action Plan of the Chama River Basin Conservation Project in Venezuela was economically estimated as a large-category disaster prevention project in a basin that includes sub-projects in different areas and with different objectives. The Action Plan consists of the Lower Basin Project to protect the alluvial fan region from El Vijia to the Lake Maracaibo and the Upper Basin Project from El Vijia to the mountain regions. The Lower Basin Project was subdivided into river improvement works on the lower reaches from El Vijia and sediment control works on the upper reaches from El Vijia to the mountain regions. The main sediment control works in the Lower Basin Project, which aim to control sediment load, consisted of 3 high dams, 18 low dams and 340 retaining walls.

Table 1. Comparison of economic efficiency.

Project	Dike length (km)	Project cost US $ (millions)	Benefit/ cost
Project A	187	34.19	1.38
Project B	145	25.55	1.45
Project C	155	34.11	0.82
Total	487	93.85	1.15

The river improvement works of the action plan from El Vijia to Lake Maracaibo are the same as those of Master Plan, which consist of the construction of a 24.7 km-long one-sided dike, a 10.4 km-long dike on the right side bank and a 10.3 km-long dike on the left side bank, and the strengthening of a 12 km long of existing one-side dikes on the left bank, as shown in Figure 3. Consequently, if the Action Plan were implemented, 36.7 km of one-sided dikes would be installed in the 53.4 km between El Vijia to the Lake of Maracaibo.

The costs of the Action Plan are shown in Table 2. The project costs and the benefit–cost ratio of the Action Plan were estimated in 2000 to be US $27.58 million and 1.58, respectively. The economic benefits of executing the Action Plan Project were considerable.

If only 24.7 km of one-sided dikes and 12 km of strengthening works were executed, the project would

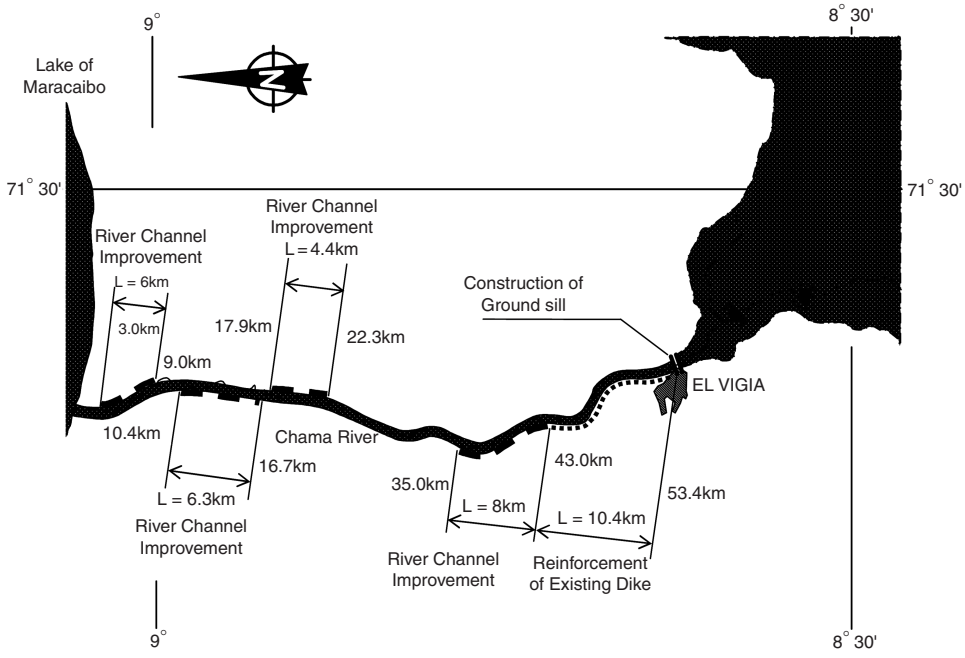


Figure 3. River improvement works from El Vijia to Lake Maracaibo.

Table 2. Project cost of action plan.

No.	Project name	B/C	Project cost (US $ millions)
1	River improvement works on the lower reaches from El Vijia	2.65	12.93
2	Sediment control works on the upper reaches from El Vijia		13.45
3	Lower basin = (1) + (2)		26.38
4	Upper basin		1.20
5	Total = (3) + (4)	1.58	27.58

be more profitable with US $12.93 million in project costs and a 2.65 benefit–cost ratio.

5 "TIME EXTENDED EFFECT"

The "time extended effect" is the effect of flood mitigation infrastructures that allow the development of properties and capital with benefits accumulated over long periods. Thus, economic development, in the form of property and capital accumulation, is impossible in an area submerged by flood every year and the "effect" is the benefits accrued from the enabled development.

Conventional economic assessments of flood mitigation projects have counted direct and indirect damage to inhabited properties. The deprived potential for new property development due to flooding was not counted with the losses of old properties and capital in the flooded areas. In other words, if properties are protected from flooding, new properties are produced and capital is accumulated without potential for destruction. The effect of producing new properties and capital is defined here as the "time extended effect" of flood mitigation infrastructures over long periods.

It is currently difficult to quantitatively calculate the "time extended effect". However, the "time extended effect" of constructing the Okakoi Dike, Japan, in the early 17th century was studied as follows. A 50 km-long of dike was constructed on the left bank of the Kiso River from Inuyama to Yatomi in 1610 as shown in Figure 4. As a result, the height of the left bank was 0.9 m higher than that of the right for approximately 280 years, until 1887. In the 400 years since 1610, there has not been a flood on the left-side plain of the Kiso River, while many floods have occurred on the right-side plain.

Before 1610, both plains were closely connected with the river and their natural, social and economic conditions were almost identical. Economic capital formation in the side plains has been different since the construction of the left-side dike. In the Bisai District of Aichi Prefecture on the left-side plain, from the early

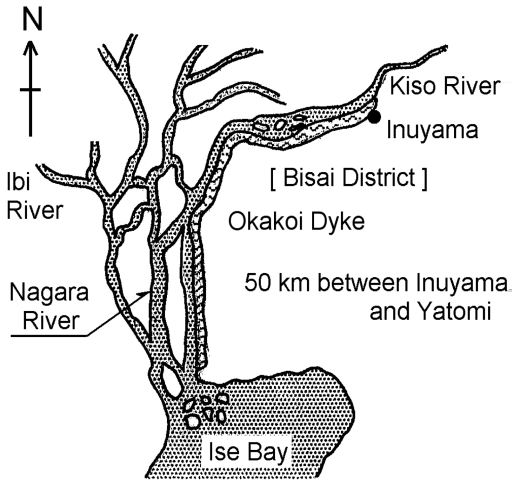


Figure 4. Location of Okakoi Dike.

17th to the early 19th, cotton textiles were produced, in addition to the existing silk textiles. Textile industries developed, which encouraged engineering and capital accumulation, and enabled the production of high quality wool textiles, creating the industrial infrastructure to produce weapons, cars and aircrafts in the whole of Aichi Prefecture until the 1920s. In 1999, industrial production per person in Aichi Prefecture, on the left-side plain, was 1,960 thousand yen and that in Gifu Prefecture, on the right-side plain, was 96 thousand yen. This difference in industrial production per person between the two prefectures is thought to be influenced by the difference in bank height between both sides due to the dike construction.

The difference in flood damage between Aichi Prefecture on the left-side plain and Gifu Prefecture on the right-side plain in the probable flood area of the Kiso River was analyzed in 1953, as shown in Table 1. The inhabitants of Aichi Prefecture were richer in domestic property than those in Giju Prefecture. If the indicators included the industrial and agricultural properties and products, the difference in economic power between the two prefectures would be even more evident. The "time extended effect" from the flood mitigation project was qualitatively proven through the case study of the Okakoi Dike on the left bank of the Kiso River, in which the capital accumulated properties were protected against floods and produced new capital, as listed in Table 3. If this case study were surveyed in detail over several historical stages, a qualitative study of the "time extended effect" would be possible.

6 "REGIONAL EXTENDED EFFECT"

The "regional extended effect" of flood mitigation projects is the influence on economic activities not

Table 3. Difference of flood damage between Aichi Prefecture and Gifu Prefecture in the probable flood area of the Kiso River.

	Aichi prefecture	Gifu prefecture
A: Building (million yen)	159,818	16,374
B: Property except building (million yen)	103,500	11,731
C = A + B	263,313	38,105
D: Family	151,828	16,592
E: Population (person)	725,261	90,304
F: Inundated area (ha.)	48,859	79,999
C/D (10 thousand yen/family)	173.4	169.4
C/D (10 thousand yen/person)	36.3	31.1
C/D (10 thousand yen/ha.)	538.9	351.4
E/F (person/ha.)	14.8	11.3

(price in 1951).

only in the region adjacent to the flooded area, but also in the country and in the world. For example, if the center of Manila is flooded, indirect damage is caused not only in Manila City, but also on the whole Luzon Island, in all of the Philippines and in the world.

On September 12, 2000 the Shinkawa River, Japan, was flooded because of a dike failure. Several car factories in Toyota City, 30 km south-east of the river, stopped working due to the resulting insufficient supply of parts. However, the determination of the "regional extended effect" and the "time extended effect" has not been an objective of the economic evaluations for flood mitigation projects.

We propose to measure the decreases in land prices due to floods, instead of measuring indirect damage from the "regional extended effect" of floods, because the indirect damage is very difficult to measure. If the "regional extended effect" was assessed in the Flood Control and Drainage Project in metropolitan Manila, the Philippines, as an example, the priority between the following two subprojects would be reversed. The Japan International Cooperation Agency (JICA) study selected the Mangahan Drainage Improvement Project as more feasible than the Pasig River Improvement Project, with a higher economic efficiency, as summarized in Table 4.

The SM-2 district of the Pasig River Improvement Project is the center core area in metropolitan Manila, as in shown Figure 5. Land use in the SM-2 district was developed in 1986 and if the Pasig River Improvement Project were executed, a high dense commercial and residential area would be developed in 4.4 km^2 by 2020, as in shown Table 5.

The WM-1 district was planned as the development of 2.86 km^2 of the largest high-density commercial and residential area in the Mangahan Drainage area (as shown in Figure 5 and Table 5).

Each district in the Flood Control and Drainage Project in metropolitan Manila was at a different land-development stage. The capacity for land development in the underdeveloped areas of the Mangahan Drainage Project area was larger than that in the developed area of the Pasig River Improvement Project.

As a consequence of these capacities, the Pasig River Improvement Project, in the center of metropolitan Manila, was determined to have less economic efficiency than the Mangahan Drainage Project in the

Table 4. Economic efficiency.

	High dense commercial and house areas	
A.D.	1986	2020
SM-2 District in the Pasig River Improvement Project	3.97 km^2	4.41 km^2
WM-1 District in the Mangahan Drainage Project	0.00 km^2	2.86 km^2

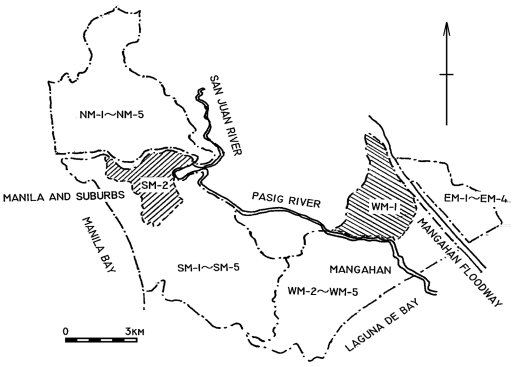


Figure 5. Location of SM-2 district and WM-1 district.

Table 5. Land use conditions.

	Mangahan drainage improvement project	Pasig river improvement project
Total project cost	132.0 million US$	65.8 million US$
Mean annual decreased damage	20.2 million US$	9.3 million US$
B/C: benefit–cost ratio	1.11	1.07
Internal rate of return	16.80%	16.10%

marshland suburbs of Manila. The "regional extended effect" was taken into account when planning the economic evaluation, and the economic efficiencies of developing the projects were reversed.

Through the metropolitan Manila Flood Control and Drainage Project case study, issues such as the "regional extended effect" were studied qualitatively. If land prices decreased by actual flood damage were measured over time and in several districts, it would be possible to quantitatively study the regional extended effects.

The integrated efficiency of the total project was increased by making the area with the higher regional extended effect safer from floods than the lower effect area. The area with a high regional extended effect is the district that would sustain greater indirect flood damage per unit squared than the other area, the highly developed land use area, with high land prices, and the central core cites in the basin with the collective transportation areas such as highways, railways, ports and airports.

The success of a flood mitigation project in regional development depends on the cooperation of social, economic and cultural infrastructures, which are essential in attracting able inhabitants.

7 CONCLUSIONS

The process of executing a flood mitigation project should be related to the stage of land development in the study area. The new basic concept explained in the present paper clarified problems with existing plans. Flood mitigation projects should be designed so as to relate to the land use conditions of the target area.

A comprehensive flood damage mitigation system that considers the current stages of land development should initiate the distribution of flood mitigation guidebooks to the residents concerned, followed by the medium-scale implementation of mitigation measures, involving the construction of readily achievable structures, such as one-sided dikes or unenclosed ring dikes. Subsequently, a large-scale consultation and implementation of comprehensive flood mitigation measures would be implemented.

Depending on the potential for flood and the need for flood mitigation in the area, some flood mitigation projects could not be easily executed without investment, approval of residents and their government. In these areas, the economic effects were often assessed lower than the actual costs. Consequently, it is very important to show the true economic effects. If a river dike is constructed as part of a highway or railway infrastructure, and the inestimable construction works are separated from the flood mitigation project, the economic effects increase and the project would be smoothly implemented.

The "time and regional extended effects" of a flood mitigation project were assessed, in addition to the existing economic evaluation of the direct and indirect damage by flood, to give a project more economic feasibility. These effects were defined as the benefits of capital accumulation due to the construction of flood mitigation infrastructure in the long term, enabling investment in new industrial projects, as shown in the Kiso River Improvement Project case study from the early 17th century.

The "regional extended effect" is the accumulated indirect benefit from flood mitigation infrastructure in a wide area that would be directly impacted by flooding.

To increase the economic benefits of a flood mitigation project, it is important to give the total project a more integrated efficiency by making the higher regional extended effect area safer from floods than the lower effect area. The area that has a high regional extended effect is the district that causes more indirect flood damage per unit squared in another area, with highly developed land use, high-priced land, central core cites in the basin or collective transportation facilities, such as highways, railways, ports and airports.

REFERENCES

Japan International Cooperation Agency. 1990. *Study of Chama River Basin Conservation Project*. 1–16. Final Report: JICA.

Japan International Cooperation Agency. 1990. *The Study of Flood Contol and Drainage Project in Metropolitan Manila Philippines*: S1–13. Main Report: JICA.

Japan International Cooperation Agency. 1993. *Study on Comprehensive Improvement of the Apure River Basin*. 1–4. Figure 25. Final Report, Volume II Main Report: JICA.

Oriental Economic Weekly Review. 1999. *General View of Regional Economy in Japan*: 169: Oriental Economic Weekly Review.

The Asahi Newspaper 1961. *The Kiso River*. 86: The Asahi Newspaper.

Yoichi, T. 1964. *Difference of Flood Damage Between Aichi Prefecture and Gifu Prefecture in the Probable Flood Area of the Kiso River.*

Yoichi, T. 1976. *The Kisosansen*: 5–11, Proceedings of The Seminar on Escape and Typhoon Commitee in Tokyo.

Yoichi, T. & Kyozo, S. 1999. *Study of the Economic Effects on Chama River Basin Conservation Project in Venezuela*: Proceedings of E11 on CD-ROM, XXVIII IAHR CONGRESS: IAHR.

Yoichi, T., Kyozo, S. & Mitsuo, T. 2002. *Time and Regional Extended Effects by Flood Mitigation Project*: 13th APD-IAHR Vol. 1, 520–523: APD-IAHR.

Yoichi, T., Kyozo, S. & Mitsuo, T. 2002. *One-sided Dikes*, CD-ROM of Global Solutions for Urban Drainage: 9ICUD: ASCE.

This page intentionally left blank

River Flow 2004 – Greco, Carravetta & Della Morte (eds.)
© 2004 Taylor & Francis Group, London, ISBN 90 5809 658 0

Modeling floodplain flow on lower Deer Creek, CA

M.L. MacWilliams, Jr., R.L. Street & P.K. Kitanidis
Environmental Fluid Mechanics Laboratory, Department of Civil and Environmental Engineering, Stanford University, Stanford, CA

ABSTRACT: Three-dimensional hydrodynamic modeling of flow in complex river-floodplain systems offers the potential to increase the current understanding of stream stability, channel morphology, and flood conveyance in natural channels. A three-dimensional hydrodynamic model is applied to lower Deer Creek, CA to simulate a large flood event that resulted in levee failure. A description of the numerical model and the development of the model grid and boundary conditions are presented. Simulation results show good agreement with high water surveys and demonstrate the important features influencing flow on the lower Deer Creek floodplain. Simulation results provide detailed information about the capacity of floodplain pathways and demonstrate the value of detailed hydrodynamic modeling as a tool to understand and quantify flow on complex floodplain systems. These results will be used to help guide the planning and implementation of future flood management strategies on lower Deer Creek.

1 INTRODUCTION

Deer Creek is one of the last drainages in the Sacramento River system that supports spring-run Chinook salmon, which have recently been added to the federal list of endangered species. As a result, Deer Creek has been recognized as a priority for habitat restoration by the CALFED Bay-Delta Program (CALFED 2000). A geomorphic study (DCWC 1998) concluded that habitat in Deer Creek is limited mostly because of effects of the existing flood control project. These effects include a lack of habitat diversity and riparian vegetation due to channel maintenance and clearing, and a lack of suitable spawning material due to the high shear stresses which occur in the channel when high flows are constrained within the existing levees.

Various proposals have been put forth to enhance salmon habitat and passage on Deer Creek, including maintaining minimum base flows, artificial addition of smaller gravel for spawning, and planting of riparian trees to address the relative lack of vegetation on the banks of most of lower Deer Creek (CALFED 2000). The CALFED Strategic Plan for Ecosystem Restoration (2000) notes that many of the restoration efforts planned for Deer Creek are treatments of the symptoms of the current flood management strategy and do not address the underlying problems. Their proposed management alternative suggests that if the style of flood management were changed to set levees back, permit overbank flooding, and eliminate channel clearing, Deer Creek would, in the course of one or more floods, reestablish a more natural channel form with better habitat.

The California Department of Water Resources (DWR) is currently considering flood management alternatives for lower Deer Creek which would incorporate the proposed CALFED management strategies. As noted in the Lower Deer Creek Flood Management Study Draft Scope of Work (Cepello 2000): "The opportunity exists through a combination of redesigning existing flood control features and encouraging appropriate land use to restore the reliability of the flood control project, reclaim a large portion of the historic floodplain, and incorporate natural distributary channels into an overflow bypass system for lower Deer Creek. These actions would also help natural stream processes occur and would be the most effective ecological strategy to restoring the terrestrial and aquatic habitats of lower Deer Creek."

A detailed understanding of river stage, flow velocities, bed shear stresses, inundation areas, levy capacity and floodplain storage will be essential to understand the response of the system to various flood discharges and provide information necessary for developing further project objectives. Commonly used one-dimensional hydraulic models are not suitable for assessing complex flow systems that will result

from the proposed flood management strategy, which includes reclamation of the historic floodplain and the incorporation of historic distributary channels. This study utilizes a robust and efficient three-dimensional hydrodynamic model, UnTRIM, to simulate a large flood event which occurred on lower Deer Creek in January, 1997. This modeling effort provides much more detailed information about channel conveyance, flow variability within the river channel, floodplain storage, the capacity of the natural distributary channels and existing culverts for overflow bypass, and the effects of potential levee modifications on the flow system than could be obtained from existing one-dimensional models. Through collaboration with California DWR and the Deer Creek Watershed Conservancy, this information will be used to help guide the implementation of the proposed flood management strategy on lower Deer Creek.

1.1 *Site description*

Deer Creek originates on the west slope of Mount Lassen and ultimately flows into the Sacramento River near Vina, CA. The watershed encompasses approximately 590 km^2 and ranges in elevation from 2400 m to less than 100 m above mean sea level. Historical aerial photographs taken in 1939 show that the lower portion of Deer Creek was highly sinuous, with small-scale bends, point bars, and alternating pools and riffles (CALFED 2000). During floods, Deer Creek would regularly overflow its banks and inundate adjacent floodplains, providing water and nutrients to adjacent riparian zones. Under natural conditions, lower Deer Creek exhibited the multiple channels characteristic of alluvial fans. During floods, water flowed across the floodplain and into some of the multiple distributary channels on the alluvial fan.

The Deer Creek Flood Control Project, authorized by the 1944 Flood Control Act, was completed by the U.S. Army Corps of Engineers in 1953 and transferred to the jurisdiction of the State Reclamation Board in 1956 (Cepello 2000). About 16 km of levees were built along lower Deer Creek by the U.S. Army Corps of Engineers to control flooding, and the channel was straightened and cleared (CALFED 2000). As a result of this work, the role of the natural distributary channels was disrupted and the riparian zone was limited to a small band within the constructed levees.

Although the average flow rate on Deer Creek is only about 9 m^3/s, Deer Creek experiences a high snowmelt flow virtually every year, and large floods often result from warm winter rains on snow. Large floods have occurred in January 1997 (680 m^3/s), 1970 (530 m^3/s), December 1964 (570 m^3/s), 1940 (610 m^3/s), and 1937 (675 m^3/s) (CALFED 2000). Although the 1997 flood experienced flows greater than 7500% of the average flow rate, frequency analysis indicates that this is only considered a 25-year recurrence interval flow event (CALFED 2000). Under the pressure of such floods, maintenance of the stream channel and levee system has been an expensive undertaking. Major levee repair work was undertaken by the Corps of Engineers following the flood of February 1986 and by the National Resources Conservation Service and Tehama County after the January 1997 flood (Cepello 2000).

During the January 1997 flood, Deer Creek breached its levee and flowed across the floodplain for several kilometers. The areas which were flooded during the 1997 flood were predominantly agricultural land, including orchards, grazing land, and farms. Based on field observations following the flood and eyewitness accounts, a conceptual model of the January 1997 flood on lower Deer Creek has been developed by the California DWR. This conceptual model, shown in Figure 1, demonstrates the importance of the role of the floodplain for providing flood storage and the importance of the natural distributary channels in influencing the flow of water on the floodplain. In particular, Delaney Slough (top right) and China Slough (bottom center) play an important role in the natural hydrology of Deer Creek and served as conduits for water on the floodplain during the 1997 flood.

The conceptual model of the 1997 flood on lower Deer Creek provides a valuable resource for identifying the features on the floodplain which had a significant effect on floodplain hydrodynamics; however the conceptual model does not provide any quantifiable information about flow on the lower Deer Creek floodplain. The collection of data during large flood events is not practical, and thus limited quantifiable information is available to help guide efforts to redesign the flood management strategy. The application of a three-dimensional hydrodynamic model to lower Deer Creek provides an opportunity to quantify floodplain storage and the capacity of specific pathways on the floodplain to convey bypass flow.

2 METHODS

2.1 *Model description*

This study applies the three-dimensional non-hydrostatic hydrodynamic model for free-surface flows on unstructured grids, UnTRIM, described in Casulli and Zanolli (2002). The model solves the three-dimensional Navier-Stokes equations on an unstructured grid in the horizontal plane. A structured grid is used in the vertical direction, such that the domain is divided into vertical layers of uniform, but not necessarily equal, thickness. Volume conservation is expressed by the incompressible continuity equation, and the free-surface is calculated by integrating the continuity equation over the depth and using a

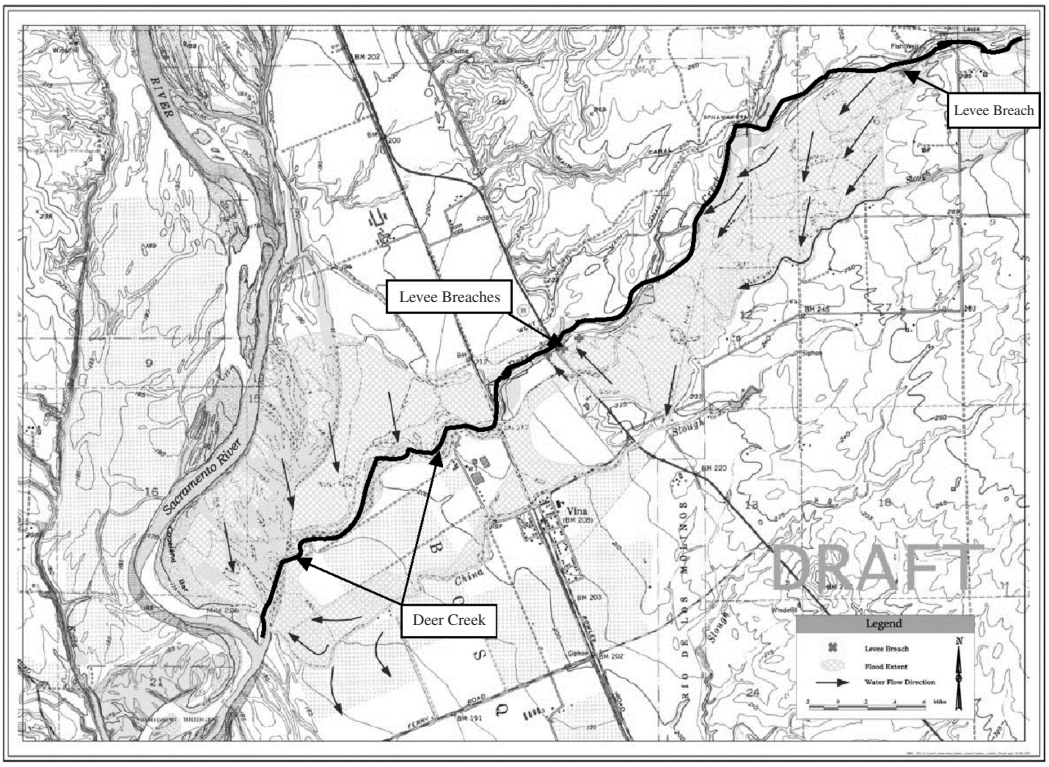


Figure 1. DWR conceptual model of the January 1997 flood. The Sacramento River flows from top left to bottom left, and Deer Creek flows from top right to lower left. The levee breach occurred on the upper right portion of the figure. The breaches shown in the center served to allow water back into the main channel. Note the influence of Delaney Slough and China Slough in influencing the flow of water on the floodplain (*Source*: California DWR).

kinematic condition at the free-surface as described in Casulli and Cheng (1992). The governing equations are discretized using a finite difference – finite volume algorithm. The numerical model accounts for bottom friction, wind stress, convective and viscous acceleration, gravitational acceleration, and vertical eddy viscosity. For the work presented in this study, several additional enhancements were added to the model presented by Casulli and Zanolli (2002). An inflow boundary condition for volume and momentum, a radiation outflow boundary condition, a modified formulation of bed drag and vertical eddy viscosity, and a method for modeling hydraulic structures were added, as described in MacWilliams (2004). The modified UnTRIM code was applied to simulate flow on lower Deer Creek.

2.2 *Grid development*

One of the limitations of using three-dimensional models is the capacity to accurately specify complex topography (Lane *et al*. 1999). At the Deer Creek site, high resolution photogrammetric data had already been collected, and this photogrammetric topography was available in digital form. Photogrammetry was completed as part of the Lower Deer Creek Flood Management Study and includes detailed (0.6 m contours) topography for the lower Deer Creek study area (approximately 75 km^2) based on photography and ground control data provided by the Department of Water Resources. Processing of aerial photography and terrestrial and bathymetric surveys into detailed topography was completed by the U.S. Army Corps of Engineers and the California DWR under the Sacramento and San Joaquin River Basins Comprehensive Study. This terrain and bathymetric data was obtained from California DWR and used in the development of the grids used in UnTRIM. Using this detailed topography it was possible to minimize the difficulties associated with specifying channel geometry and generate a high resolution grid consistent with the actual topography at the site.

An orthogonal unstructured grid was generated over the horizontal domain for use with the UnTRIM

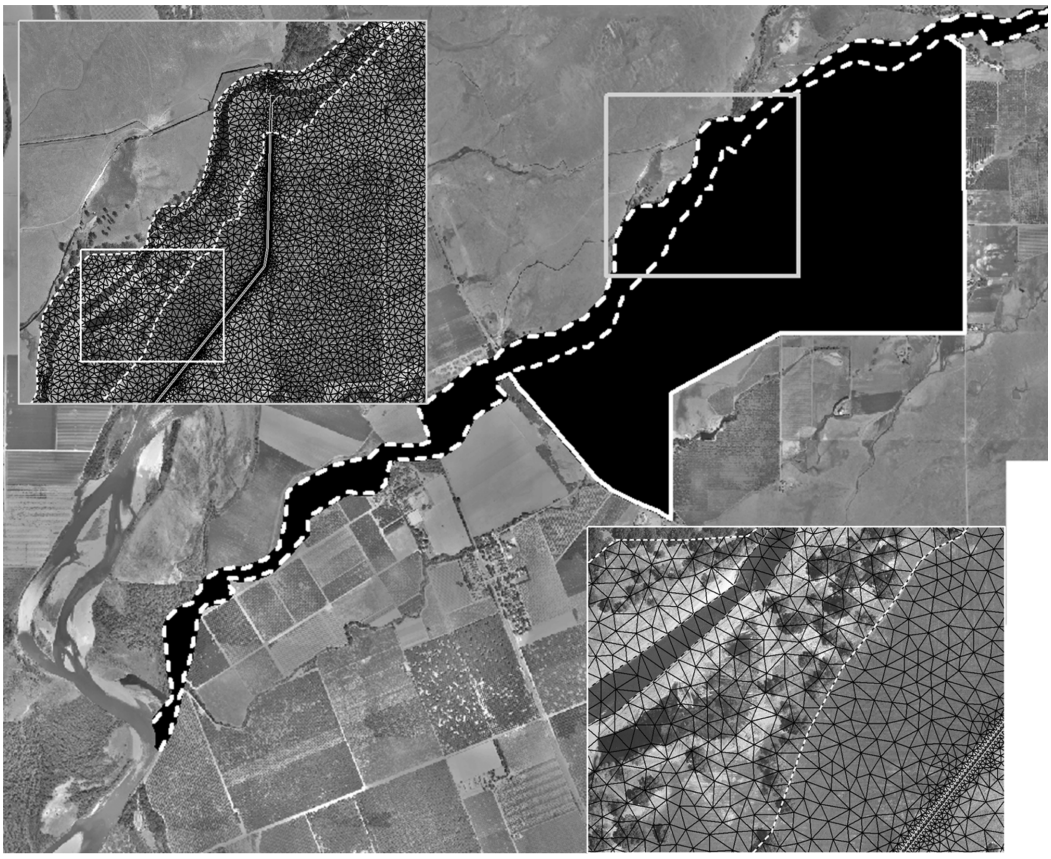


Figure 2. Model grid for lower Deer Creek (black). The grid for the channel of lower Deer Creek is bounded by the levees or high topography (shown as two "parallel" white dotted lines from top right to bottom left). The floodplain grid is bounded predominantly by bordering roads (solid white). The top inset shows a portion of the grid with the low flow channel and the South-Main Canal highlighted. The lower inset shows a close-up view of the area identified in the top inset, again showing a portion of the low flow channel and the South-Main Canal (bottom right). The model grid extends approximately 5 km upstream of the area shown.

model. The grid was generated in two sections using the mesh generation program TRIANGLE (Shewchuck 1996). The first section of the grid was generated for the portion of lower Deer Creek which is bounded by the levees on each side of the channel, shown in Figure 2. In this portion of the grid, the grid was constrained such that the levees and the low water waterlines were aligned with cell edges in the grid mesh. Where no distinct levees were present, the grid is bounded by the local topographic break along the edge of the floodplain. This was done to ensure that the topographic high associated with the levees was captured in the grid, and to delineate the area within the low flow channel as a distinct portion within the grid. Because the topography for lower Deer Creek was obtained through photogrammetric mapping, the topographic data extend only to the edge of the wetted channel on the date which the photogrammetry was collected. No bathymetric data were available for the low water channel.

The bathymetry of the low water channel was estimated through a series of model calibrations. The aerial photogrammetry for lower Deer Creek was completed on May 11, 1999. On this day, the average daily flow in Deer Creek was measured to be 11 m^3/s. A series of UnTRIM simulations was made by assuming an initial bathymetry where the bed was set to be 1 m below the observed water surface in the low flow channel. A constant flow rate of 11 m^3/s was applied and the downstream water surface elevation was set to be 51.5 m, which is the water surface elevation observed in the photogrammetric data at the mouth of Deer Creek on May 11, 1999. By comparing the predicted water surface throughout the low flow channel

to the water surface observed in the photogrammetric survey, the low flow channel bathymetry was adjusted and the procedure was iteratively repeated. Although this method is not expected to provide a highly accurate estimate of low flow bathymetry, visual comparison of calibration results and channel morphology visible on the aerial photographs suggests that this calibration procedure produced a reasonable bathymetric profile for the low flow channel. Because the flow capacity of the low flow channel is only 11 m^3/s, it is not expected that errors associated with this bathymetric calibration will introduce significant effects on modeling flood flows on the order of 500 m^3/s. Additionally, it is believed that this approach is more consistent with the other available topographic data than conducting a present-day bathymetric survey on the low flow channel, which has been altered since 1999 and since the pre-flood 1997 bathymetry.

A grid of the upper portion of the lower Deer Creek floodplain was also developed using TRIANGLE. The western boundary of the floodplain grid was constrained so that the grid sides aligned with the edge of the levee-bounded grid. Additionally, the edges of the South-Main Canal, which flows across the floodplain, were identified and preserved in the floodplain grid. The floodplain grid is bounded by a series of roads which are topographic highs and serve as hydraulic barriers. Highway CA-99 runs along the southwestern edge of the floodplain grid. The merged grid consisting of the levee-bounded grid and the upper floodplain grid, shown in Figure 2, contains 45,668 triangular elements in the horizontal grid and over two and a half million computational cells. As seen in Figure 2, the model grid follows the topography such that the levees, low flow channel, and South-Main Canal are all aligned with grid cell faces. This ensures that the elevations associated with these features are captured in the model grid, because grid elevations are located on the center of each cell side. The resolution of the model grid surrounding the South-Main canal, as seen in the lower offset is on the order of 5 m. The grid spacing on the majority of the floodplain is typically on the order of 25 m, and a slightly finer resolution of approximately 20 m is typically used between the levees and in the low flow channel. A uniform vertical grid spacing of 1 m was used.

2.3 *Boundary conditions*

The simulation of the 1997 flood on lower Deer Creek requires the specification of an inflow hydrograph and a downstream water surface elevation. Additional boundary conditions are applied to model hydraulic structures on the floodplain.

A USGS gauging station is located on Deer Creek, approximately 14.5 km upstream of its confluence with the Sacramento River, and approximately 2.5 km upstream of the upstream end of the model domain. This gauge reports river stage, and a stage-discharge relationship exists for this station. Using the USGS stage-discharge relationship with the measured stage data predicts two flood peaks of 564 and 680 m^3/s. It is known that the second peak resulted in levy failure on Deer Creek and that the first peak did not exceed the capacity of the levees.

Preliminary simulations, an analysis of previous levee failures, and a one-dimensional model indicate that the magnitude of both of these flood peaks exceeds the capacity of the levee system. Annual peak discharge data are available for lower Dear Creek from 1912 through 1997. Comparing the yearly peak discharge with the years in which levee failure occurred indicates that flows greater than 450 m^3/s consistently resulted in levee failure. This suggests that the two peaks predicted by the USGS rating curve are not accurate because if the first flood peak was actually more than 560 m^3/s, as predicted by the measured stage data and the USGS rating curve, levee failure almost certainly would have occurred.

The measured stage for the second flood peak is only 0.33 m greater than the stage measured for the first peak. This small difference in measured stage is inconsistent with eyewitness accounts of river stage near the breach location. Additionally, the measured stage for the second flood peak varies by less than 0.06 m during the seven hours surrounding the peak. This flat stage measurement at the flood peak suggests that the stage for the flood peak has exceeded the height which can be measured at the gauge and that the actual stage at the gauge was greater during the peak than was reported at the station.

By assuming that the actual stage for the second flood peak exhibited a similar shape to the stage measured for the first peak, the flat stage data for the second peak were augmented by an appropriate filter. Using this filter, the difference in stage between the first and second flood peaks was increased from 0.33 to 0.91 m. A new stage-discharge relationship was developed, as shown in Figure 3, which maintained the discharge at the augmented peak stage to be identical to the discharge at the original peak stage for the second flood peak. However, the discharge associated with the first peak in flood stage is reduced relative to the original rating curve. Using the modified stage data and the new stage-discharge relationship, the discharge associated with the second flood peak remained at 680 m^3/s, while the first flood peak was calculated to be 450 m^3/s, which is within the capacity of the levee system. This hydrograph is shown in Figure 4 and was used as the inflow boundary condition. Based on observational information about stage and breach timing, an analysis of past levee failures, one-dimensional simulations and preliminary simulations using the three-dimensional model, this hydrograph

is a more appropriate estimate of the hydrograph for the January 1997 flood than the hydrograph calculated from the raw stage data using the USGS stage-discharge relationship (MacWilliams 2004).

The downstream boundary is specified using the river stage on the Sacramento River measured at DWR Woodson-Vina gauging station at Woodson Bridge, shown in Figure 4. The Woodson Bridge gauge is approximately 1.7 km downstream of the mouth of Deer Creek. Based on the photogrammetric data and the DWR stage data at Woodson Bridge, the stage at the mouth of Deer Creek is estimated to be 0.3 m above the stage observed at the Woodson-Vina Bridge gauge. This estimate is used to calculate the downstream boundary stage and is based on the assumption that the water surface slope on this reach of the Sacramento River does not change significantly during higher flows.

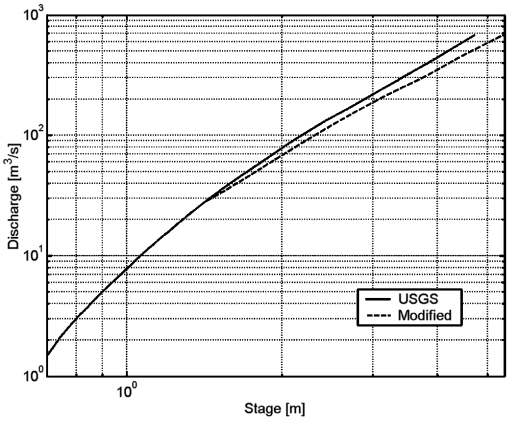


Figure 3. Original USGS stage-discharge relationship and modified stage-discharge relationship.

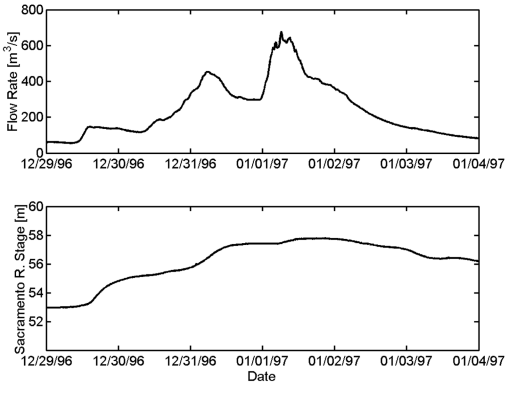


Figure 4. Hydrograph for lower Deer Creek (top) used for inflow boundary condition and Sacramento River stage elevation (bottom) used as downstream boundary condition.

In addition to the upstream and downstream boundary conditions, culvert rating curves were developed for three hydraulic structures that are important conduits for flow on the lower Deer Creek floodplain. The rating curves were developed using HEC-RAS based on field measurements of the culvert dimensions for each of the three culverts. The rating curves used assume free-flow conditions at the outlet, which provides the largest possible flow through the culvert based on the set of rating curves developed.

Using these boundary conditions and rating curves, UnTRIM was used to simulate the 1997 flood on lower Deer Creek. A period of six days was simulated using a time step of 1 second. The bottom roughness was specified over the domain using a roughness height of 1×10^{-3} m in the channel and on the floodplain values of 1×10^{-2} and 1×10^{-1} m were specified for areas delineated as grazing lands and orchards, respectively. The roughness parameters on the floodplain were calculated from the tables of Chow (1959) by converting the appropriate roughness coefficient to a roughness height using the approach described in MacWilliams (2004).

The levee failure resulted in a significant change in local geometry at the location of the levee breach and a section of levee was washed out. To capture this effect in the flood simulations, a similar adjustment is made to the model grid by removing a section of levee at the breach location at the time in the simulation when significant levee topping occurs.

3 RESULTS

Because no data were collected during the 1997 flood, there is only a limited capacity to quantitatively validate the model results. However, efforts have been made to gather as much quantitative or qualitative information as possible about the 1997 flood to perform an assessment of model performance.

Following the 1997 flood, high water mark surveys were conducted on January 13–16, 1997. The data from these surveys were obtained through the California Department of Water Resources Northern District Office. Eighteen high water marks were surveyed on the east levee of Deer Creek and twenty high water marks were surveyed on the west levee of Deer Creek. At each survey point, the high water mark (HWM) was photographed, sketched relative to surrounding features, and surveyed. Using the information available in the survey notes, each of the HWM survey stations within the study area was identified and located on the model grid. The predicted HWM was calculated to be the maximum water surface at the survey location during the flood simulation. The differences between predicted and

measured HWM along the Deer Creek levees for the January 1997 flood are shown in Figure 5. All of the predicted HWM elevations are higher than the observed HWM elevations, which suggests that the modeled peak discharge may exceed the actual peak flood discharge. The average difference between the predicted and observed HWM is 0.36 m. This difference can also be attributed to error associated with the field HWM survey elevations, error in the photogrammetric topography, error in the simulated hydrograph, and model accuracy. The error associated with the topographic data are on the order of 0.15 m; a slightly higher error is associated with the HWM surveys. Based on this, the model results show good agreement with the surveyed HWM elevations within the accuracy of the available data.

In addition to the high water mark surveys, the other primary sources for model validation come from the DWR conceptual model of lower Deer Creek flood actions, shown in Figure 1, and from post-flood aerial photographs. The post-flood aerial photographs give a good indication of flooded areas and flow direction based on disruption of floodplain vegetation and deposition sediment on the floodplain. A comparison between the inundation area predicted by UnTRIM at the time of maximum floodplain inundation and the inundation area incorporated in the DWR conceptual model is shown in Figure 6. As seen in this figure, the results from the UnTRIM simulation show good agreement with the conceptual model both in terms of inundation areas and flow direction on the floodplain.

Figure 7 shows a comparison between post-flood aerial photographs, the DWR conceptual model and the UnTRIM predictions in the section of the floodplain containing the South-Main Canal. The orientation of the conceptual model and the UnTRIM results have been rotated to match the boundaries of the aerial photographs. As seen in this figure, there is good agreement between the inundation areas predicted by UnTRIM and the flooded areas shown by the conceptual model. The grey areas in the UnTRIM model (top left of the right panel) which designate portions of the model grid which remain dry agree well with the areas in the aerial photograph which show no evidence of sediment deposition and thus are assumed to have been above the elevation of the flood waters. One of the major flow pathways back into the main channel is shown crossing the irrigation canal in the top center of each panel on Figure 7 and then entering the main

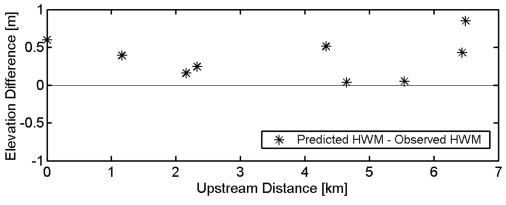


Figure 5. Difference between predicted and observed high water marks at stations surveyed by DWR following the January 1997 flood.

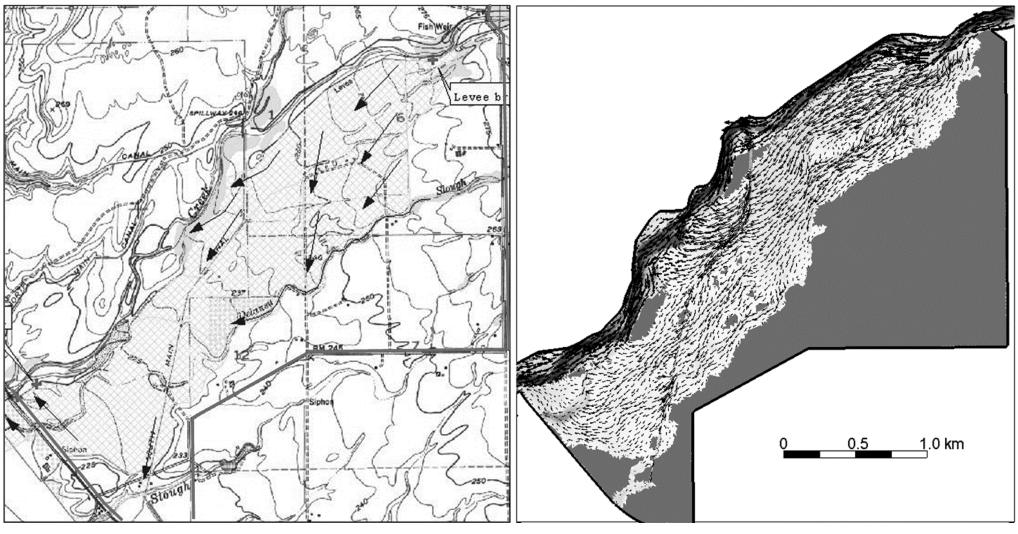


Figure 6. DWR conceptual model of January 1997 flood (left) shown with UnTRIM model predictions during maximum floodplain inundation (right). Lightly hatched area on conceptual model indicates flooded areas; flooded area on the model results shown as light-colored area overlaid by velocity vectors. Arrows on the conceptual model show flow pathways but are not scaled to flow magnitude or velocity. Arrows on the model predictions show surface velocity vectors for a subset of the computational cells.

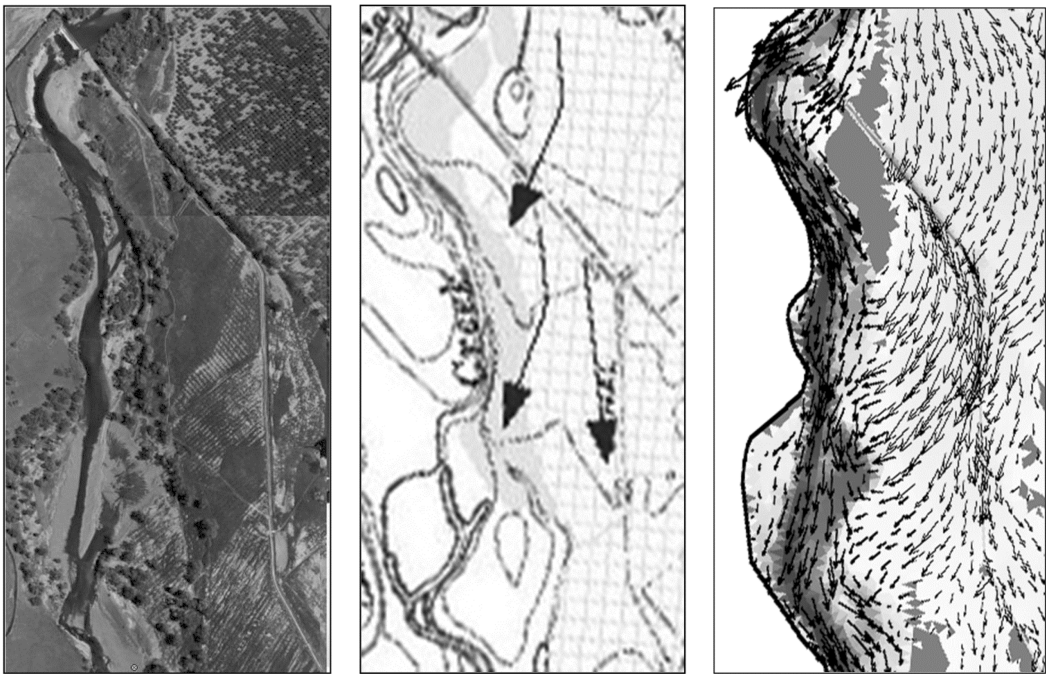


Figure 7. Post-flood aerial photograph showing sediment deposited along flow pathways (left) shown with conceptual model of January 1997 (center) and UnTRIM model predictions during maximum floodplain inundation (right). Arrows on the conceptual model show flow pathways. Arrows on the model predictions show surface velocity vectors for a subset of the computational cells.

channel in the bottom half of each panel. On the aerial photograph, the sediment deposition pattern between the South-Main Canal and the main channel of Deer Creek indicate the significance of this flow pathway. A similar pathway is observed in the UnTRIM results and is shown in the conceptual model. In the aerial photograph, a significant amount of headcut erosion into the floodplain is visible at the location where flow re-enters the main channel. This is consistent with model results which indicate a large fraction of the flow on the floodplain re-enters the main channel in this reach. Overall these comparisons suggest the UnTRIM model is providing a reasonable estimate of flow on the floodplain for the January 1997 flood.

A schematic of the primary flow pathways on the Deer Creek floodplain for the January 1997 flood is shown in Figure 8. The primary levee breach on lower Deer Creek occurred approximately 0.5 km downstream of Leininger Bridge. The majority of the water traveling across the floodplain re-entered the main channel at two locations, downstream of the Stanford-Vina diversion dam, and immediately upstream of highway CA-99. Figure 9 shows the hydrographs for the flow contained between the levees at Leininger Bridge, the Stanford-Vina diversion dam, and at the highway CA-99 Bridge. These hydrographs are

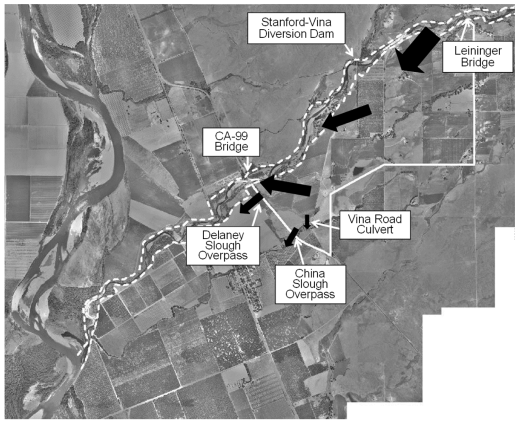


Figure 8. Schematic of primary flood pathways on lower Deer Creek during January 1997 flood. The boundaries of the main channel (white dashed lines) and the boundaries of the floodplain grid (white solid line) are indicated for reference. The dark arrows show primary flow pathways. Text boxes and white arrows identify the locations corresponding to the channel and hydraulic structure hydrographs shown in Figures 9–10.

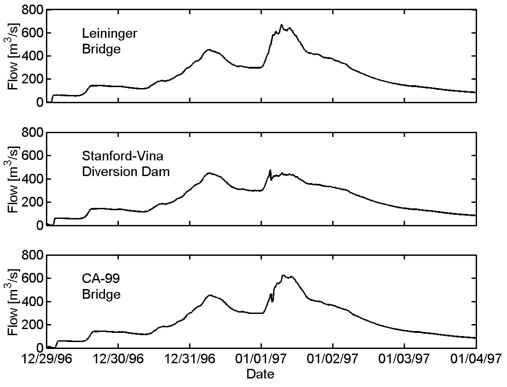


Figure 9. Predicted hydrographs in the main channel of lower Deer Creek at three locations identified on figure 8.

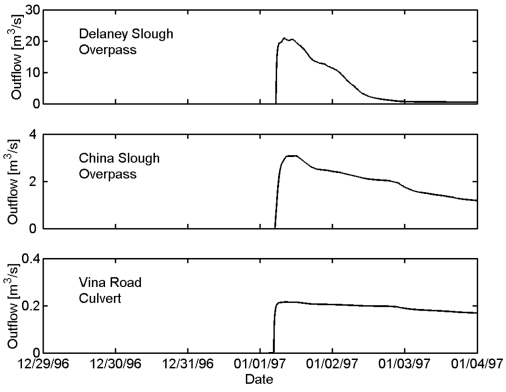


Figure 10. Predicted hydrographs through the hydraulic structures at the locations identified on figure 8.

obtained by calculating the total flow through each of these channel cross-sections during each time step during the simulation. As seen in Figure 9, the levee breach truncates the second flood peak at the Stanford-Vina diversion dam due to the flow across the floodplain. The peak discharge predicted at the Stanford-Vina diversion during the first flood peak was 450 m^3/s. The discharge predicted at the Stanford-Vina diversion at the time of the levee breach was approximately 475 m^3/s and following the levee breach the maximum discharge predicted was 450 m^3/s. This reduction in maximum discharge results because, following the breach, a larger amount of water is diverted onto the floodplain and the effective downstream conveyance capacity of the main channel at the breach is truncated. Downstream of Stanford-Vina diversion dam, the floodplain elevation is sufficiently above the main channel that no significant levees were constructed. As a result, water from the floodplain can freely flow back into the main channel of lower Deer Creek. A significant fraction of the flow on the floodplain during the 1997 flood re-entered the main channel at this location (as seen in Figure 7). The remaining water flowed down the floodplain until it reached highway CA-99. At the highway, which is elevated significantly above the surrounding floodplain, the water backed up until the levees were breached to allow the water to flow back into the main channel immediately above the CA-99 highway bridge. As seen in Figure 9, the hydrograph at the CA-99 Bridge shows a flood peak similar to the hydrograph at Leininger Bridge, which indicates that the majority of water has re-entered the main channel by the time Deer Creek flows under CA-99. The simulation results predict a peak discharge of 670 m^3/s at Leininger Bridge and a peak discharge of 620 m^3/s at CA-99.

The balance of water which does not re-enter the main channel upstream of CA-99 flows under the highway at overpasses located on Delaney Slough and China Slough. The flow hydrographs for these two structures, and the hydrograph for the culvert under Vina Road which connects the main area of the floodplain with China Slough, are shown in Figure 10. The culvert under Vina Road is quite small and based on the large discharge predicted through the end of the simulation it is evident that this culvert is limiting flow into China Slough. The culvert on China Slough under CA-99 provides a larger conveyance capacity but also shows a significant flow rate following the initial flood pulses. If a substantial flow is to be routed through China Slough as is suggested in the Lower Deer Creek Flood Management Study, this culvert would also need to be resized to increase its capacity.

4 DISCUSSION

The three-dimensional simulation of the January 1997 flood on lower Deer Creek provides valuable quantifiable information about water levels, flow velocities, inundation areas, flow pathways on the floodplain, and the performance of existing floodplain hydraulic structures. Coupled with the knowledge provided by the DWR conceptual model of the 1997 flood on lower Deer Creek, this information can serve as a valuable tool in planning future restoration strategies on lower Deer Creek.

The implementation of flood management alternatives that will change the style of flood management to set levees back, permit overbank flooding, and incorporate natural distributary channels back into the floodplain system depends on an adequate understanding of hydrodynamics on the floodplain during large flood events. This understanding is necessary in order to help improve the reliability of the existing flood management system and to help foster the restoration of the terrestrial and aquatic habitats of lower Deer Creek by allowing natural stream processes to occur.

Kondolf (2000) argues that "aquatic and riparian habitat for salmon and other organisms is, in effect, a by-product of the channel geomorphology, which, in alluvial reaches, largely reflects the prevailing flow and sediment regimes, as well as effects of riparian vegetation and human modifications." As a result, a detailed understanding of the flow regime on lower Deer Creek during floods is necessary for the proper evaluation of future restoration efforts on Deer Creek.

Restoration projects, such as that on the Cosumnes River, CA, have demonstrated the benefit of breaching and setting back levees. Based on the result of a levee breach on the Cosumnes River it was concluded that "if the natural process of flooding is allowed to take place, the river can reforest its old flood plain and restore fish and wildlife habitat quickly and effectively. When natural processes are allowed to shape the landscape on a large scale, the habitat becomes very diverse, enabling many species to live together in a balanced ecosystem" (Cosumnes 2003). A similar opportunity exists on lower Deer Creek to setback levees and reclaim a large portion of the historic floodplain. Deer Creek remains one of the least altered streams in the Central Valley and still supports all four runs of Chinook salmon, as well as runs of steelhead. As a result, the preservation of this resource is a high priority.

Using the model developed in this study as a starting point, it is possible to simulate the potential effects of various structural modifications to the floodplain using UnTRIM. Information about flood inundation and frequency under the proposed management plan can be used to recommend sensitive areas that should be obtained through purchase or land-easements to ensure the reliability of the proposed flood management strategy. An analysis of the hydraulic effects of levee setbacks, allowing inundation of the natural floodplain, and the incorporation of natural distributary channels into the flood management strategy, can be used to recommend appropriate modifications to the levee system that will allow natural channel and floodplain processes to occur while still providing adequate protection to existing structures. As a result, the extension of this modeling study can be used to provide information that will help to maximize the effectiveness of the proposed management strategy. Funds spent on this type of planning study can help prevent much larger expenditures on projects that would prove to be ineffective or unnecessary (Kondolf 2000).

5 CONCLUSIONS

These results demonstrate the ability of detailed hydrodynamic modeling to simulate flooding on a large-scale complex river floodplain. Through the application of a newly-developed three-dimensional hydrodynamic model, this study made use of available topographic, and hydrologic data to quantify the major flow pathways on the lower Deer Creek floodplain. In the absence of detailed field measurements during the flood, model results were validated against post-flood high water mark surveys, a conceptual model of the flood developed by California DWR, and post-flood aerial photographs. The UnTRIM simulations provide good overall agreement with these available data sources.

The simulation of the January 1997 flood on lower Deer Creek provides a state-of-the-art analysis of the capacity of the levee system on lower Deer Creek and the important flow pathways on the floodplain. If used in guiding future management decisions, this work has the potential to have a lasting impact on the management and conservation practices in the Deer Creek watershed. The implementation of these management practices through the collaboration of the California DWR and CALFED will provide a unique opportunity within the Central Valley to preserve one of the regions most important salmon habitats, and demonstrate the capacity of innovative flood management strategies to preserve the watershed's ecological and agricultural resources.

ACKNOWLEDGEMENTS

The authors would like to acknowledge the collaboration of Stacy Cepello from the California Department of Water Resources and G. Mathias Kondolf from the University of California, Berkeley. The UnTRIM code was provided by Prof. V. Casulli of the University of Trento, Italy. This work was funded in part through a Conserving California Landscapes Initiative Grant by the David and Lucile Packard Foundation (CCLI Grant # 00-14780) and by a grant from the National Science Foundation (Grant EAR-0087842, Program Manager: Dr. L. Douglas James). Additional funding was provided to MLM by a Stanford Graduate Fellowship and a NSF Graduate Research Fellowship.

REFERENCES

CALFED Bay-Delta Program 2000. *Ecosystem Restoration Program Plan. Volume 3: Strategic Plan for Ecosystem Restoration*. July. Sacramento, CA.

Casulli, V. & Cheng, R.T. 1992. Semi-implicit finite difference methods for three-dimensional shallow water flow. *International Journal for Numerical Methods in Fluids* 15: 629–648.

Casulli, V. & Zanolli, P. 2002. Semi-implicit numerical modeling of non-hydrostatic free-surface flows for environmental problems. *Mathematical and Computer Modeling* 36: 1131–1149.

Cepello, S. 2000. Lower Deer Creek Flood Management Study Preliminary Hydrology and Engineering Draft

Scope of Work. Red Bluff, CA: California Department of Water Resources.
Chow, V.T. 1959. *Open-channel Hydraulics*. New York: McGraw-Hill.
Cosumnes 2003. http://www.cosumnes.org/project.htm
DCWC, 1998. (Deer Creek Watershed Conservancy). Deer Creek Watershed Management Plan. Vina, CA.
Kondolf, G.M. 2000. Some suggested guidelines for geomorphic aspects of anadromous salmonid habitat restoration proposals. *Restoration Ecology* 8(1): 48–56.
Lane, S.N., Bradbrook, K.F., Richards, K.S., Biron, P.A. & Roy, A.G. 1999. The application of computational fluid dynamics to natural river channels: three-dimensional versus two-dimensional approaches. *Geomorphology* 29: 1–20.
MacWilliams, M.L. 2004. Three-dimensional hydrodynamic simulation of river channels and floodplains. Ph.D. Dissertation, Stanford University.
Shewchuck, J.R. 1996. Triangle: Engineering a 2D Quality Mesh Generator and Delaunay Triangulator. In Lin, M.C. & Manocha, M. (eds.). *Applied Computational Geometry: Towards Geometric Engineering*, Lecture Notes in Computer Science Vol. 1148: 203–222. Berlin: Springer-Verlag.

This page intentionally left blank

C.4. Integration of telemetry and GIS

This page intentionally left blank

River Flow 2004 – Greco, Carravetta & Della Morte (eds.)
© 2004 Taylor & Francis Group, London, ISBN 90 5809 658 0

Estimating hydraulic parameters and geometric characteristics of a river from remote sensing data using optimization methods

H. Roux & D. Dartus
Institut de Mécanique des Fluides, Toulouse, France

ABSTRACT: The necessity of an improvement of flood risk management has been emphasized by the importance of the damages caused by several disastrous floods in recent years. An obligatory way to better understand and forecast these events is to be able to accurately simulate the water transport in the river. Application of numerical models requires parameter calibration, even when in situ measurements are available. Here is presented an exploration of the possibility of estimating these parameters from observations provided by telemetry implementing optimization techniques. The originality of this study is to reconstitute information about the geometry of the river and the hydraulic characteristics of the considered event from top sights. Application examples on two different rivers are presented.

1 INTRODUCTION

Recent floods in Europe have had catastrophic consequences from a human but also economic and historic point of view. The total damages have emphasized the need of an accurate prevision of these floods to improve the risk management (Plate, 2002). Huge progresses have been recently realized in the modelling of the hydrodynamic of the flow in the river but also on the floodplain areas (Bates & de Roo, 2000), (Stewart et al., 1999), (Marks & Bates, 2000). However, hydrological modelling requires a thorough knowledge of the river to be able to map flood extents for risk analysis purpose. Some models contain conceptual parameters that usually cannot be assessed by measurements in the field; on the contrary, distributed, physically based models use only parameters that can be assessed from in-situ data. But it is often a long and expensive procedure, sometimes difficult to implement and in practice, it is not possible to determine the parameters at each computational point grid (Madsen, 2003). Therefore, both type of models need calibration and the problem is even more pronounced in the case of ungauged rivers.

New generations of satellite are equipped with sensors of metric resolution, 1m in panchromatic for IKONOS-2, launched by the USA in 1999 and 2.5 m in panchromatic for SPOT-5, launched by France in 2002. Air photo techniques have also developed quickly and compared to the satellite telemetry, they offer a better reactivity in front of the events. Indeed, satellite images taken during a flood remain rare as it needs the concomitancy of the event with the satellite track.

This study starts from these two facts: the need of a thorough knowledge of the river for both model calibration and running and the increasing potential of telemetry as a source of information. Data assimilation methods allow to combine data provided by the model with data provided by space observation to identify information about the river. The formulation of flow-state equations to ascertain the value of the parameters embedded in the simulation process is referred to as an inverse problem (Khatibi et al., 2001). There is no exact solution but it is possible to estimate the best one in a mathematical sense using optimization techniques.

This paper focuses on the identification of parameters necessary to simulate open-channel flows by resolution of the one-dimensional Saint-Venant equations. That is to say discharge, Manning roughness coefficient or geometric characteristics of the channel. A preliminary study (Roux et al., 2004) has shown that the minimization of an error criterion gives satisfactory results for this purpose. This method has then been implemented using two different approaches. Both estimate parameters such as discharge, Manning roughness coefficients and a downstream condition, but they differ in their way of identifying the geometry of the cross-section. The first approach consists in identifying an equivalent river: a hypothesis is made on the geometry of the cross-section and the characteristics of this geometry are then estimated. It has been implemented on the river Lèze (South-West of France). The second approach consists in taking into account the topography of the overbanks in the assimilation process. This topography may also be provided by telemetry. In the cross-section, only the geometry

of the main channel is then identified. This method has been implemented on the river Aisne (North of France).

2 METHODOLOGY

2.1 *Optimization techniques*

The scope of data assimilation is to make the best estimate of the model state using observations and a numerical model.

If $\mathbf{X^t}$ is the true state of the system at a given time (Ide et al., 1997), an observation $\mathbf{y^o}$ of $\mathbf{X^t}$ can be written as (Hoteit, 2001):

$$\mathbf{y^o} = F(\mathbf{X^t}) + \boldsymbol{\varepsilon} \tag{1}$$

where F is an operator linking state space with observation space, called observation operator. It allows to calculate the model equivalent $F(\mathbf{X^t})$ of the observations. $\boldsymbol{\varepsilon}$ is a random vector with zero mean and covariance matrix $\mathbf{R}$, modelling an observation noise.

The best estimate $\mathbf{X^a}$ of the model state $\mathbf{X^t}$ can be obtained by minimization of the sum of a distance to an a priori estimate (often a prevision) of the model state $\mathbf{X^f}$ and a distance to the observations $\mathbf{y^o}$.

$$\Phi=(\mathbf{X}-\mathbf{X^f})^T\mathbf{P}^{-1}(\mathbf{X}-\mathbf{X^f})+(\mathbf{y^o}-F(\mathbf{X}))^T\mathbf{R}^{-1}(\mathbf{y^o}-F(\mathbf{X})) \tag{2}$$

$\mathbf{P}$ is the covariance matrix of the error made in estimating $\mathbf{X^t}$ by $\mathbf{X^f}$.

The numerical calculus of the analysis state $\mathbf{X^a}$ can be very expensive, in terms of computation time, if the size of the vector is big. Several methods have been developed, using simplification hypothesis. They can be divided into two categories: statistical methods calculate $\mathbf{X^a}$ directly using its analytic expression and formulating statistical hypothesis on the form of the matrix $\mathbf{P}$ (Kalman, 1960). Variational methods minimize the cost function Φ in an iterative way, using minimization algorithms (PALM Team, 1998).

These techniques have very different numerical properties. Their equivalence stops as soon as some underlying hypotheses are not verified, like the linearization of the observation operator for instance (Carlier, 1982). A preliminary study (Roux et al., 2004) has shown that the minimization of an error criterion gives satisfactory results for the purpose of this study.

In the case of hydraulic parameter identification, there is no prevision of the model state and therefore no a priori estimate $\mathbf{X^f}$. That's why the cost function only takes into account the distance to gauged data.

2.2 *Model description*

The model that has been developed solves the steady-state one-dimensional Saint-Venant equations (Horritt & Bates, 2002):

$$\begin{cases} \dfrac{dQ}{dx} = q_L \\ \dfrac{dH}{dx} = \dfrac{S_0 - S_f - 2Fr^2\dfrac{Sq_L}{BQ}}{1-Fr^2} \end{cases} \tag{3}$$

where Q is the discharge, q_L the lateral inflow, H the water depth, S_0 the bed slope, S_f the friction slope: $S_f = n^2Q^2/R_H^{4/3}S^2$ (Graf, 1996), n the Manning coefficient, R_H the hydraulic radius, S the cross-sectional area, Fr the Froude number: $Fr = (Q^2B/gS^3)^{1/2}$, B the flow top width and x the distance along the channel. This study will only deal with subcritical flows ($Fr < 1$). Therefore only one downstream boundary condition on the water depth and one on the discharge are necessary to solve (3).

The chosen compound channel modelling supposes the equality of the friction slopes as well as the equality of the velocities in all the cross-sectional subdivisions (Carlier, 1982), (U.S.A.C.E., 1997). It allows to calculate a composite coefficient of roughness n_{comp}, function of the water depth (4).

$$n_{comp}(H) = \left(\frac{\sum_i (P_{w,i} n_i^{3/2})}{P_w} \right)^{2/3} \tag{4}$$

where P_w is the wetted perimeter of the entire channel, $P_{w,i}$ is the wetted perimeter of subdivision i and n_i is the friction coefficient of subdivision i (Figure 1).

Equations (3) are integrated by means of order four Runge-Kutta's method. The resolution requires:

- The definition of the geometry of the cross-section
- The determination of the Manning roughness coefficient for each subdivision of the cross-section
- The determination of the boundary conditions.

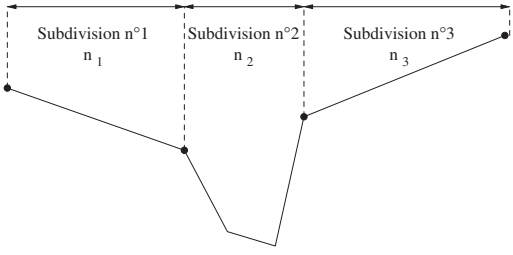


Figure 1. Compound channel.

The purpose of this study is to explore the possibility to determine these data using optimization techniques and the information provided by telemetry. Such a method would be useful for the determination of all the parameters for ungauged or poorly gauged rivers but also for the determination of non-directly measurable parameters, such as the Manning coefficient for instance.

3 IDENTIFICATION OF AN EQUIVALENT RIVER

A 4 km reach of the river Lèze, in the South of France, between the cities of Lagardelle-sur-Lèze and Labarthe-sur-Lèze was considered (Figure 2).

Data concerning this site have been provided by the DIREN Midi-Pyrénées (DIREN Midi-Pyrénées, 2001). They consist in two synthetic flood events, one 15-year event and one exceptional event determined by geomorphology (Figure 3), and two real floods, one occurred in 1977 and the other one in June 2000. Figure 4 shows the extent of the flooded area for each event. The two real floods can be considered as exceptional events, indeed their extents are larger than the one of the exceptional event in some places.

3.1 *Identification from one flood event*

Figure 5 represents the hypothesis made on the geometry of the cross-section. The identified parameters are: the discharge at the downstream boundary, a local inflow as there is a local stream draining into the river, the stage at the downstream boundary, two Manning roughness coefficients, one for the main channel and one for the overbanks, and the characteristics of the geometry of the cross-section (Figure 5), that is to say main channel depths, cross bank and overbank slopes. These geometric parameters are estimated for each side of the river and for each cross-section. Cross-sections are distant of about 70 m.

In addition to the width of the flooded area for each event, the main channel width, that is to say the river bed, was also available as it can be seen in Figure 4.

The most known error criterion in hydrology is the sum of square of errors (Nash & Sutcliffe, 1970), the objective function Φ to be minimized in the assimilation process is then chosen as the sum of square of

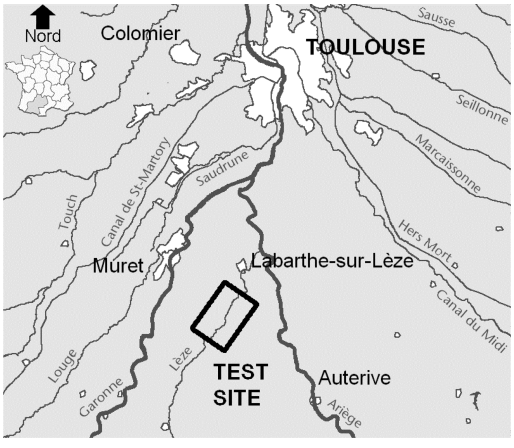


Figure 2. Location map of the test site (from Agence de l'eau Adour-Garonne, 1998/1999).

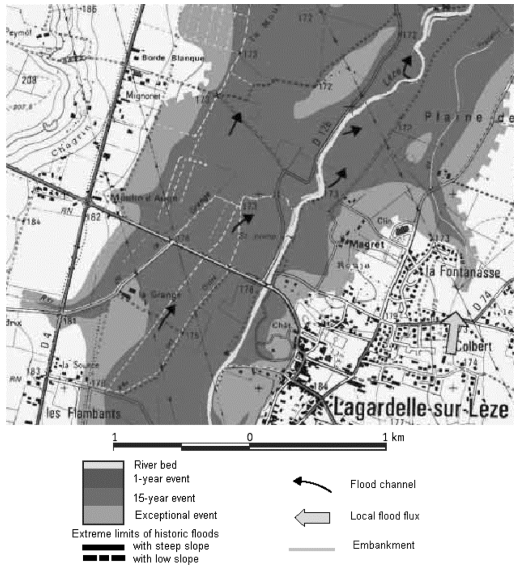


Figure 3. Cartography of the possible floodplains of the river Lèze provided by the DIREN Midi-Pyrénées (from DIREN Midi-Pyrénées, 2001).

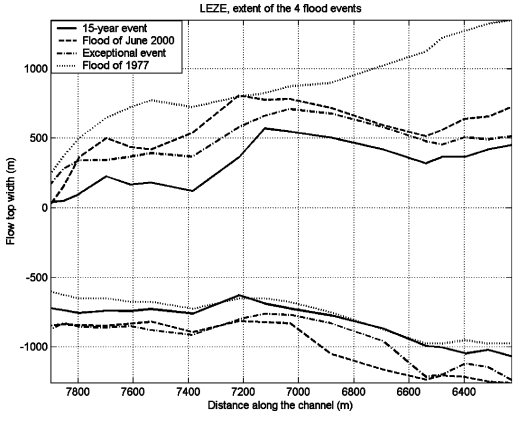


Figure 4. Extent of the 4 studied flood events.

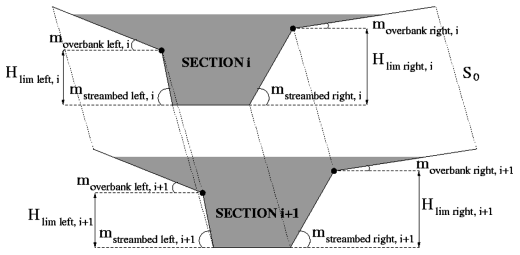


Figure 5. Geometric characteristics of the cross-section.

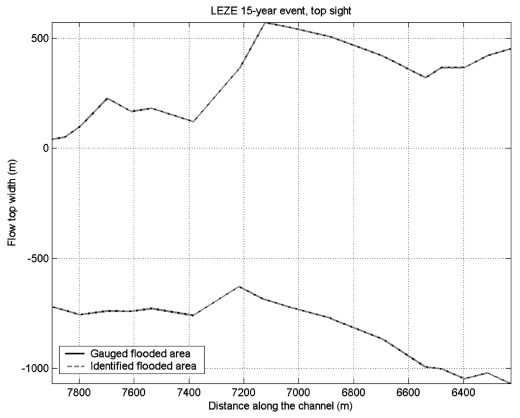


Figure 6. Comparison between gauged and identified flow top widths, 15-year event.

errors between the observed flow top width B_{Obs} and the simulated one B_{Sim}. In order to take into account the asymmetry of the flooded area, the minimised cost function (5) represents the distance between gauged flow top widths and simulated flow top widths for each bank (Roux et al., 2003b).

$$\Phi = \sum_{\text{cross-sections}} \left((B_{Obs} - B_{Sim})^2_{\text{left bank}} + (B_{Obs} - B_{Sim})^2_{\text{right bank}} \right) \quad (5)$$

The minimization is carried out using traditional algorithms based on the non-linear least square technique (Madsen, 2003).

Figure 6 shows the flow top width simulated with the parameters identified from the 15-year event. The result is satisfactory, nevertheless this approach needs a validation: the equivalent geometry (Figure 7) has been identified with only one event, it is necessary to ascertain that it also suits for others events.

The parameters listed above have been identified for each available flood event. Table 1 gives the values found for the hydraulic parameters by minimization of the cost function (5) for each event.

Knowing these values and the geometry, it is then possible to simulate the flow top width for each event. Figure 8 compares the flooded area of the event of

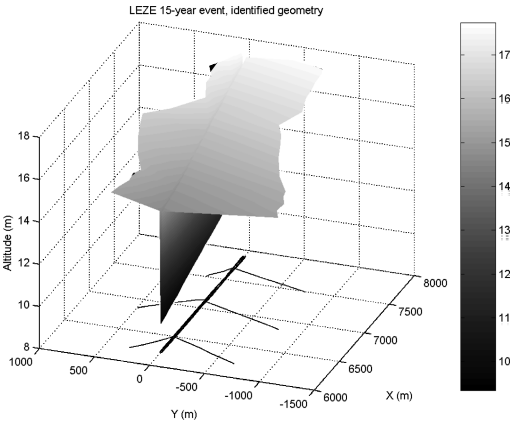


Figure 7. Geometry identified from the 15-year event.

Table 1. Identified value of the hydraulic parameters.

	15-year event	Exceptional event	Flood of June 2000
Discharge at the downstream boundary	122.5 m^3/s	259.0 m^3/s	285.8 m^3/s
Lateral inflow	9.43 m^3/s	12.8 m^3/s	17.3 m^3/s
Stage at the downstream boundary	5.86 m	6.39 m	6.64 m

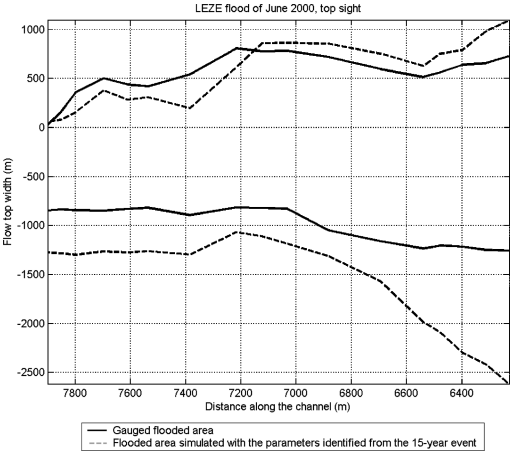


Figure 8. Comparison between gauged and simulated flow top widths for the flood of June 2000.

June 2000 with the flooded area simulated using the geometry identified from the 15-year event.

As these events have very different hydraulic characteristics, the flooded area of the exceptional event

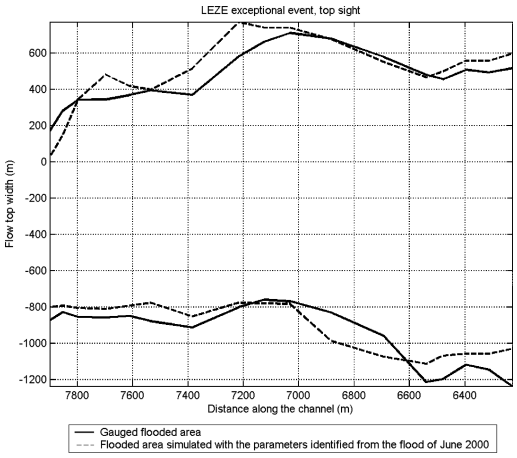


Figure 9. Comparison between gauged and simulated flow top widths for the exceptional event.

obtained by resolution of the Saint-Venant equations with the geometry identified from the 15-year event doesn't correspond to the observed one: the average error on the flow top width is of ±170 m for the right bank and ±580 m for the left bank which corresponds to a average relative error of 37%. But if the two events have closer hydraulic characteristics, like the exceptional event and the flood of June 2000 for instance, the result is better as it can be seen in Figure 9. Indeed, the average error on the flow top width is of ±70 m for the right bank and ±200 m for the left bank, that is to say a relative error of 19%.

Moreover, it is reasonable to say that the relevance of the identification can be improved by introducing more sets of gauged data into the assimilation process (Werner, 2001).

3.2 *Identification from several flood events*

3.2.1 *Simultaneous minimization*

The methodology is the same as in the previous paragraph 3.1 but the cost function (6) represents the distance to several flood events:

$$\Phi = \Phi_{15-year} + \Phi_{2000} + \Phi_{1977} \qquad (6)$$

with

$$\Phi_{\text{each event}} = \sum_{\text{cross section}} \left((B_{Obs} - B_{Sim})^2_{\text{left bank}} + (B_{Obs} - B_{Sim})^2_{\text{right bank}} \right)$$

Discharge, lateral inflow and stage at the downstream boundary are supposed to be known (Table 1) and only the geometric characteristics of the transversal bed profile (Figure 5) are estimated by minimization of the cost function (6). A comparison between the

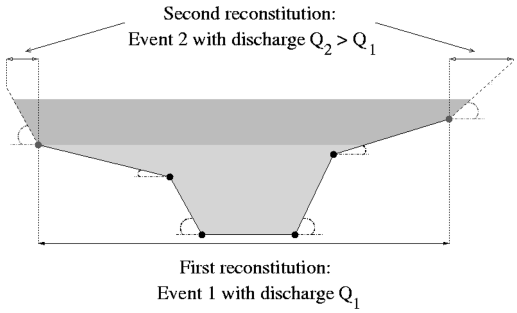


Figure 10. Gradual building of the cross-section bed profile.

gauged flooded areas for the three events and the simulated ones shows that the average relative error on the flow top width is of 14% for the 15-year event, 9.7% for the flood of June 2000 and 7.4% for the exceptional event. Consequently, the use of several flood events to identify an equivalent river actually leads to an improvement of the results. Indeed, the identified geometry allows to simulate the flooded area of the three events with an average error of less than 14%, compare to up to 37% with a reconstitution using only one event. Moreover, it is also possible to add points in the cross-section in order to better adapt the shape to the magnitude of the considered event.

3.2.2 *Gradual building of the cross-section*

The implemented method consists in a gradual building of the transversal bed profile (Figure 10). A first minimization considering an event of discharge Q_1 will estimate the characteristics of a transversal bed profile with four cross-sectional slopes (Figure 5). These points will then be considered as known. The introduction of another event of discharge Q_2, greater than Q_1 will allow to determine a change in the slope of the overbanks.

In the case of the river Lèze, the first minimization considers the 15-year event. The flood of June 2000 and the exceptional event are then introduced into the assimilation process in order to estimate the location of the change of slope and the second slope of the overbank, for each side of the river. Consequently, in this second step, there are 4 new parameters to estimate for each cross-section.

Figure 11 compares the extent of the 1977 flood with the flooded area obtained by simulation of the Saint-Venant equations with the geometry identified using the method of gradual building. The average error on the flow top width is now of ±50 m for the right bank and ±30 m for the left bank, that is to say a relative error of about 4.9% against 19% using only one event as for Figure 9, or 7.4% using several events simultaneously. Hence, there is an important improvement of the portability of the identified geometry.

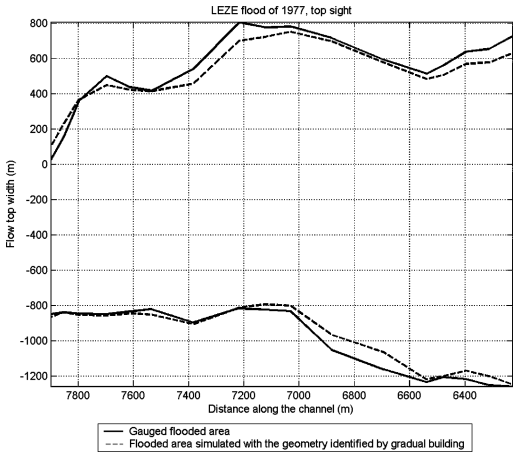


Figure 11. Comparison between gauged and simulated flow top widths, flood of 1977.

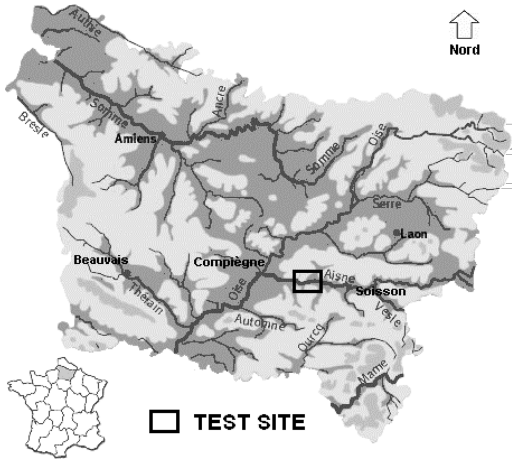


Figure 12. Location map of the river Aisne reach (from Conseil Régional de Picardie, 2003).

Next step will be to compare the flooded area simulated using the equivalent geometry with the one simulated using transversal bed profiles from in situ measurements.

4 UTILISATION OF THE OVERBANK TOPOGRAPHY

A 5 km reach of the river Aisne, located in the north of France, between the cities of Soisson and Compiègne, was considered (Figure 12). Data concerning this event have been provided by the Cemagref of Montpellier. Flow top widths have been extracted from several air photos taken during the flood of December 1993 (Raclot, 2003). Another set of air photos, taken in low water period, provides the main channel width and the flow axe. This additional information can be integrated with profit into the assimilation process. Except the bridges and the locks, the studied flood plain presents few structures that can influence the flow, therefore it suits well the one-dimensional choice for the resolution of the Saint-Venant equations. However, only one set of gauged data is available.

Overbanks topography information (Figure 13) has been obtained by photogrammetry. The precision of this information is supposed to be sufficient for hydraulic simulation purpose (Raclot et al., 2000). However, measurement points are distant of fifty meters approximately in both horizontal directions.

The objective function Φ to be minimized is the same as in the previous case (5). The identified parameters are: the discharge, which is taken constant along the channel reach, the stage at the downstream boundary, two Manning roughness coefficients, one for the main channel and one for the overbanks, and

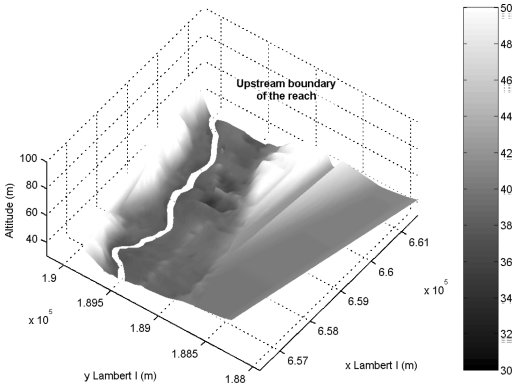


Figure 13. Topography of the overbanks provided by photogrammetry.

the characteristics of the geometry of the main channel (Figure 14), that is to say altitudes of the bottom of the main channel and cross bank slopes. The geometric parameters are estimated for each side of the river and for each cross-section. Cross-sections are distant of 100 m.

Figure 15 compares the gauged flooded area and the simulated one. The result is satisfactory for the right bank, the lower one on the figure. The simulated flow top width of the other bank does not correspond to the gauged flooded area.

This is probably due to the fact that, as it can be easily seen on Figure 15, the left overbank is uneven. As the hydraulic simulation of Saint-Venant equations used to obtain the flow top width is strictly one-dimensional, there is no way for the flow to bypass the obstacles. The incapacity of the model to simulate flows around an elevated part of the floodplain and

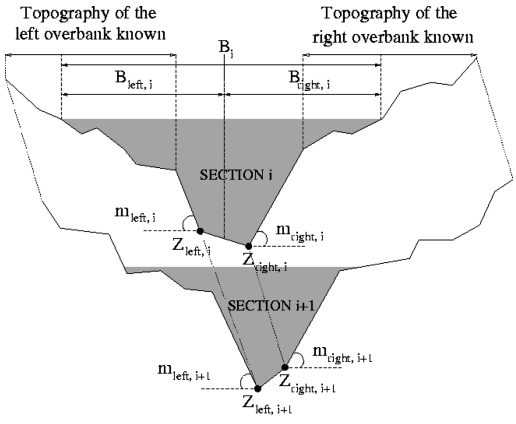


Figure 14. Cross-section geometry.

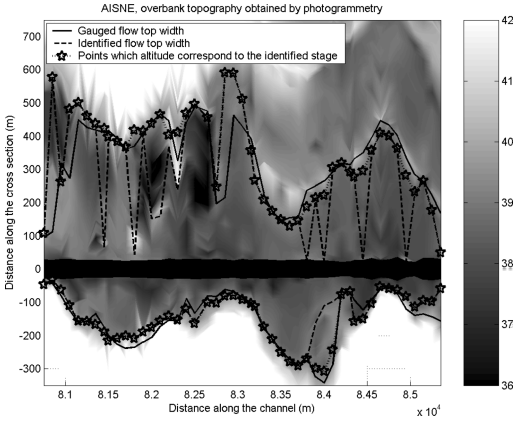


Figure 15. Top sight of the overbanks topography with the limits of both gauged and identified flooded areas and the points which altitude corresponds to the identified stage.

therefore separated from the main channel, explains the peaks of the identified flooded area: the water is stuck behind the topography obstacles (Roux et al., 2003a). Indeed, a bidimensional simulation implemented with Telemac2D (developed by Electricité de France, (Galland et al., 1991)) using the identified parameters calculates a flooded area that doesn't present these peaks. Furthermore, this flooded area better corresponds to the observed one (Figure 16).

Searching for the points beyond the topography obstacles, which altitude corresponds to the identified stage, gives a better approximation of the gauged flooded area (Figure 15), as the 2D simulation already did. This result obviously does not take into account flows around the obstacles of the floodplain. Nevertheless, it shows that the identified altitude is satisfactory (Figure 17). Even if the flow discharge in the areas separated from the main channel is low, this test has

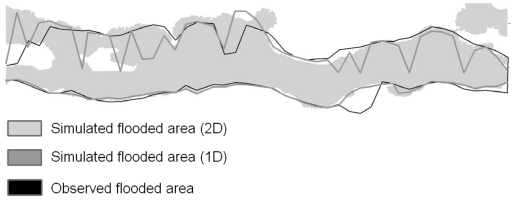


Figure 16. Flooded area simulated with Telemac2D (Chorda & Maubourguet, 2000).

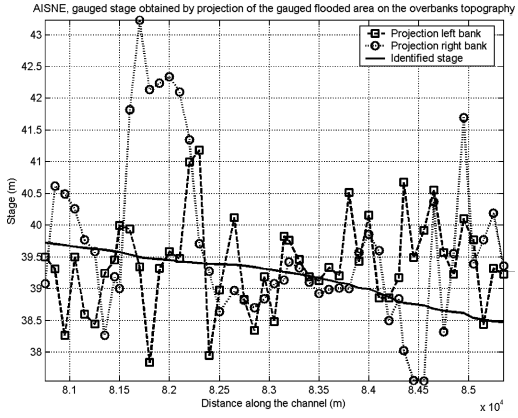


Figure 17. Comparison between the identified stage and the stages obtained by projection of the limits of the flooded area on the overbank topography.

emphasizes the importance of introducing the possibility of bypassing the topography obstacles in the resolution of the Saint-Venant equations, which is now being implemented.

Another observation that can be made from Figure 17 is that the difference of water surface elevation between the two banks can rise up to 5 m, which is obviously incompatible with hydraulic requirements. Therefore a more accurate topography is needed to proceed the study in this direction.

5 CONCLUSIONS

The first approach of hydraulic parameter identification using an equivalent river has given satisfactory results for one set of observation. Adding information by introducing more events in the assimilation process allows to build gradually the transversal bed profile which increases the relevance of the estimated parameters. Indeed, geometric parameters identified from two or three events allow to simulate the flooded area of a third event with a satisfactory precision.

Concerning the introduction of the overbank topography in the assimilation process, it has been shown that the results can be satisfactory provided that

the topography is known with a sufficient precision. According to (Alquier et al., 2000), an horizontal accuracy of 2 m and a vertical accuracy of 0.5 m are needed to simulate correctly the hydrodynamics of the flow on the overbanks and to determine the stage with a precision sufficient for flood risk management. Concerning the determination of the flooded areas, a very good knowledge of the topography is necessary, as local bumps or holes can radically modify the flood inundation conditions. Indeed, (Bates & Anderson, 1996) has demonstrated that a small change in topography ($\pm$10 cm) may have complex and non negligible influence on the model prediction. The case of the river Aisne has emphasised the necessity of the introduction of the modelling of flows separated from the main channel in the resolution of the Saint-Venant equations (Roux et al., 2003a), even if in these areas, the discharge is relatively low because of their high roughness and their low depth.

Moreover, the methodology of this study is easily adaptable to the new sorts of data that the progresses in telemetry are going to make available in a few years (Smith, 1997). Indeed, satellite altimetry (TOPEX/POSEIDON launched in August 1992, or ENVISAT launched in March 2002) has been able to measure time series of water levels on very large rivers, such as the Amazon (Koblinsky et al., 1993), (Birkett, 1998), the Paraná or the Gange. If water levels were also available, the assimilation problem could be formulated in a multi-objective context in which different cost functions those measure different distances, one related to the water level and one related to the flow top width for instance, can be optimised simultaneously. In this framework, the calibration will be tailored to the specific model application being considered (Madsen, 2003).

REFERENCES

Agence de l'eau Adour-Garonne 1998/1999. Qualité des eaux superficielles en Haute-Garonne. http://www.eau-adour-garonne.fr/telechargement/dpt31/31.pdf.

Alquier, M., Chorda, J., Dartus, D., Estupina, V., Guennec, B. L. & Maubourguet, M.-M. 2000. Contribution des données d'observation de la terre à la cartographie de l'aléa. Rapport d'étude ADEMA, Institut de Mécanique des Fluides de Toulouse.

Bates, P. D. & Anderson, M. G. 1996. A preliminary investigation into the impact of initial conditions on flood inundation predictions using a time/space distributed sensitivity analysis. *Catena* 26: 115–134.

Bates, P. D. & de Roo, A. P. J. 2000. A simple raster-based model for flood inundation simulation. *J. of Hydrology* 236: 54–77.

Birkett, C. M. 1998. Contribution of the TOPEX NASA radar altimeter to the global monitoring of large rivers and wetlands. *Water Resources Research* 34 (5): 1223–1239.

Carlier, M. 1982. Hydraulique générale et appliquée.

Chorda, J. & Maubourguet, M.-M. 2000. Flood propagation. EDF-SOGREAH, *7th TELEMAC user club workshop, Grenoble, France*.

Conseil régional de Picardie 2003. La Picardie, le relief et l'hydrographie. http://www.cr-picadie.fr/fr/page.cfm?pageref = environnement ~ picardie ~ hydro.

DIREN Midi-Pyrénées 2001. Cartographie informative des zones inondables de Midi-Pyrénées. http://www.environnement.gouv.fr/midi-pyrenees/.

Galland, J. C., Goutal, N. & Hervouet, J.-M. 1991. TELEMAC-a new numerical-model for solving shallow-water equations. *Advances in Water Resources* 14 (3): 138–148.

Graf, W. H. 1996. Hydraulique fluviale.

Horritt, M. S. & Bates, P. D. 2002. Evaluation of 1D and 2D numerical models for predicting river flood inundation. *J. of Hydrology* 268: 87–99.

Hoteit, I. 2001. Filtres de Kalman réduits et efficaces pour l'assimilation de données en océanographie. PhD Thesis, Université de Grenoble I, Grenoble, France.

Ide, K., Courtier, P., Ghil, M. & Lorenc, A. C. 1997. Unified Notation for Data Assimilation: Operational, Sequential and Variational. *J. Meteo. Soc. Japan* 75 1 (B): 181–189.

Kalman, R. E. 1960. A new approach to linear filtering and prediction problems. *J. Phys. Oceanogr.* 23: 2541–2566.

Khatibi, R. H., Wormleaton, P. R. & Williams, J. J. R. 2001. Parameter quality conditions in open-channel inverse problems. *J. Hydr. Res.* 38 (6): 447–458.

Koblinsky, C. J., Clarke, R. T., Brenne, A. C. & Frey, H. 1993. Measurement of river level variations with satellite altimetry. *Water Resources Research* 29 (6): 1839–1848.

Madsen, H. 2003. Parameter estimation in distributed hydrological catchment modelling using automatic calibration with multiple objectives. *Advances in Water Resources* 26: 205–216.

Marks, K. & Bates, P. D. 2000. Integration of high resolution topographic data with floodplain models. *Hydrological Processes* 14: 2109–2122.

Nash, J. E. & Sutcliffe, J. V. 1970. River flow forecasting through conceptual models. Part I – A discussion of principles. *J. of Hydrology* 10: 282–290.

Palm Team 1998. Etude de faisabilité du projet PALM. Rapport interne, CERFACS.

Plate, E. J. 2002. Flood risk and flood management. *J. of Hydrology* 267: 2–11.

Raclot, D. 2003. Méthodologie d'exploitation quantitative des photographies aériennes d'inondation de plaine. PhD Thesis, Université Montpellier II, Sciences et Techniques du Languedoc, Montpellier, France.

Raclot, D., Puech, C., Blin, C. & Cornet, J.-M. 2000. Guide méthodologique: intégration des photos aériennes d'inondation dans les modèles hydrauliques. Rapport d'étude, Cemagref/Engref, CETMEF.

Roux, H., Raclot, D. & Dartus, D. 2004. Méthodes d'assimilation de données appliquées à la reconstitution de paramètres hydrauliques. *Société Française de Photogrammétrie et Télédétection*: in press.

Roux, H., Raclot, D., Dartus, D. & Puech, C. 2003a. Hydraulic Parameter Identification using Aerial Photographs. IEEE, *International Geoscience and Remote Sensing Symposium, Toulouse, France*.

Roux, H., Raclot, D., Dartus, D. & Puech, C. 2003b. Hydraulic Parameter Identification using Satellite Earth Imagery. European Geophysical Society, *EGS-AGU-EUG Joint Assembly, Nice, France*.

Smith, L. C. 1997. Satellite remote sensing of river inundation area, stage, and discharge: a review. *Hydrol. Process.* 11: 1427–1439.

Stewart, M. D., Bates, P. D., Anderson, M. G., Price, D. A. & Burt, T. P. 1999. Modelling floods in hydrologically complex lowland river reaches. *J. of Hydrology* 223: 85–106.

U.S.A.C.E. 1997. HEC-RAS River Analysis System. U.S. Army Corps of Engineers, Hydrologic Engineering Center.

Werner, M. 2001. Uncertainty in flood extent estimation due to uncertain parameters. *XXIX IAHR Congress Proceedings, Beijing, China*.

This page intentionally left blank

RiverFlow 2004 is the second International Conference on fluvial hydraulics and has established the periodicity of the series. Organized as specialty conferences under the auspices of the International Association of Hydraulics Engineering and Research (IAHR) with its Fluvial Hydraulics and Eco Hydraulics Sections, RiverFlow Conferences appear to be an important moment of aggregation for many researchers involved in river modelling and observation.

The intense land use of the last century and the lack of adequate sustainable development policies are probably the most important reasons of river hazards. As water is of vital importance as a resource in the human well-being we need a better comprehension of river processes and an adequate management of fluvial areas.

Scientists are aware of this necessity and largely conbribute with their researches toward this aim. This clearly appears in the number of papers presented at RiverFlow 2004 (174) and from the number of country represented (43). Papers in this volume are related to the following topics:

Fluvial processes (morphology and morphodynamics; bed forms and flow resistance; overbank flow and vegetation; interaction with structures; sediment supply, entrainment and transport);

River hazards (dam break and fast transients; bank failure; flood propagation; hyperconcentrated flows; water pollution and contaminant transport);

Hydraulics for river management (river training and restoration; habitat management and maintenance flows; flood management and control; integration of telemetry and GIS).